REPORT DOCUMENTATION PAGE	Form Approved OMB NO. 0704-0188

Public Reporting burden for this collection of information is estimated to average 1 hour per response, including the time for reviewing instructions, searching existing data sources, gathering and maintaining the data needed, and completing and reviewing the collection of information. Send comment regarding this burden estimates or any other aspect of this collection of information, including suggestions for reducing this burden, to Washington Headquarters Services, Directorate for information Operations and Reports, 1215 Jefferson Davis Highway, Suite 1204, Arlington, VA 22202-4302, and to the Office of Management and Budget, Paperwork Reduction Project (0704-0188,) Washington, DC 20503.

1. AGENCY USE ONLY (Leave Blank)	2. REPORT DATE May 31, 2006	3. REPORT TYPE AND DATES COVERED Final Progress Report June 1, 2000 – February 28, 2006

4. TITLE AND SUBTITLE A Caltech MURI Center for Quantum Networks	5. FUNDING NUMBERS G DAAD19-00-1-0374 Amendment P00010
6. AUTHOR(S) Hideo Mabuchi	
7. PERFORMING ORGANIZATION NAME(S) AND ADDRESS(ES) California Institute of Technology Office of Sponsored Research MC 1-15, 1200 E. California Blvd. Pasadena, CA 91125	8. PERFORMING ORGANIZATION REPORT NUMBER Awards ARO.000010 and ARO.000014
9. SPONSORING / MONITORING AGENCY NAME(S) AND ADDRESS(ES) U. S. Army Research Office Attn: AMSRD-ARL-RO-SG-SI P.O. Box 12211 Research Triangle Park, NC 27709-2211	10. SPONSORING / MONITORING AGENCY REPORT NUMBER 41048.15-PH-MUR

11. SUPPLEMENTARY NOTES

The views, opinions and/or findings contained in this report are those of the author(s) and should not be construed as an official Department of the Army position, policy or decision, unless so designated by other documentation.

12 a. DISTRIBUTION / AVAILABILITY STATEMENT Approved for public release; distribution unlimited.	12 b. DISTRIBUTION CODE

13. ABSTRACT (Maximum 200 words)

During the MURI performance period we completed a diverse portfolio of world-class research projects. We made remarkable progress in all major topics encompassed by the defining vision of our “Quantum Networks” MURI Center: demonstration of elementary quantum network protocols via cavity QED, development of integrated quantum nodes based on atom chips and photonic bandgap structures, and advancing quantum information theory. Feature accomplishments include the first demonstration of a complete cavity-QED quantum information protocol using a single intracavity atom, the development of chip-scale microtraps and microcavities suitable for cavity QED with strong coupling, and security proofs for quantum key distribution with imperfect devices.

14. SUBJECT TERMS Quantum Networks, Quantum Information Theory, Quantum Information Protocol	15. NUMBER OF PAGES ~~26~~
	16. PRICE CODE

17. SECURITY CLASSIFICATION OR REPORT **UNCLASSIFIED**	18. SECURITY CLASSIFICATION ON THIS PAGE **UNCLASSIFIED**	19. SECURITY CLASSIFICATION OF ABSTRACT **UNCLASSIFIED**	20. LIMITATION OF ABSTRACT ~~UL~~

NSN 7540-01-280-5500

Standard Form 298 (Rev.2-89)
Prescribed by ANSI Std. 239-18
298-102

REPORT DOCUMENTATION PAGE (SF298)
(Continuation Sheet)

(1) (a) List of Manuscripts

Papers published in peer-reviewed journals:

1. JM Geremia, John K. Stockton and Hideo Mabuchi, “Tensor polarizability and dispersive quantum measurement of multilevel atoms,” Phys. Rev. A **73** 042112 (2006).
2. L.-M. Duan, B. Wang and H. J. Kimble, “Robust quantum gates on neutral atoms with cavity-assisted photon scattering,” Phys. Rev. A **72**, 032333 (2005).
3. C. W. Chou, H. de Riedmatten, D. Felinto, S. V. Polyakov, S. J. van Enk and H. J. Kimble, “Measurement-induced entanglement for excitation stored in remote atomic ensembles,” Nature **438**, 828 (2005).
4. D. Felinto, C. W. Chou, H. de Reidmatten, S. V. Polyakov and H. J. Kimble, “Control of decoherence in the generation of photon pairs from atomic ensembles,” Phys. Rev. A **72**, 053809 (2005).
5. S. M. Spillane, T. J. Kippenberg, K. J. Vahala, K. W. Goh, E. Wilcut and H. J. Kimble, “Ultrahigh-Q toroidal microresonators for cavity quantum electrodynamics,” Phys. Rev. A **71**, 013817 (2005).
6. K. M. Birnbaum, A. Boca, R. Miller, A. D. Boozer, T. E. Northup and H. J. Kimble, “Photon blockade in an optical cavity with one trapped atom,” Nature 436, **87** (2005).
7. R. Miller, T. E. Northup, K. M. Birnbaum, A. Boca, A. D. Boozer and H. J. Kimble, “Trapped atoms in cavity QED: coupling quantized light and matter,” J. Phys. B: At. Mol. Opt. Phys. **38**, S551 (2005).
8. R. van Handel, J. K. Stockton and H. Mabuchi, “Feedback control of quantum state reduction,” IEEE T. Automat. Contr. **50**, 768 (2005).
9. JM Geremia, J. K. Stockton and H. Mabuchi, “Suppression of spin projection noise in broadband atomic magnetometry,” Phys. Rev. Lett. **94**, 203002 (2005).
10. R. van Handel, J. K. Stockton and H. Mabuchi, “Modeling and feedback control design for quantum state preparation,” J. Opt. B: Quantum Semiclass. Opt. **7**, S179 (2005).
11. R. Raussendorf, S. Bravyi and J. Harrington, “Long-range quantum entanglement in noisy cluster states,” Phys. Rev. A **71**, 062313 (2005).
12. R. Raussendorf, “Quantum computation via translation-invariant operations on a chain of qubits,” Phys. Rev. A **72**, 052301 (2005).
13. S. V. Polyakov, C. W. Chou, D. Felinto and H. J. Kimble, “Temporal dynamics of photon pairs generated by an atomic ensemble,” Phys. Rev. Lett. **93**, 263601 (2004).
14. J. M. Geremia, J. K. Stockton, and H. Mabuchi, “Deterministic Preparation of Spin-Squeezed States via Real-Time Quantum Feedback,” Science, **304**, 270 (4/9/04).

15. C. W. Chou, S. V. Polyakov, A. Kuzmich, and H. J. Kimble, “Single-photon generation from stored excitation in an atomic ensemble,” Phys. Rev. Lett. **92**, 213601 (5/28/04); available at quant-ph/0401147.

16. A. Boca, R. Miller, K. M. Birnbaum, A. D. Boozer, J. McKeever and H. J. Kimble, “Observation of the vacuum Rabi spectrum for one trapped atom,” Phys. Rev. Lett. **93**, 23363 (2004).

17. J. McKeever, J. R. Buck, A. D. Boozer and H. J. Kimble, “Determination of the Number of Atoms Trapped in an Optical Cavity,” Phys. Rev. Lett. **93**, 143601 (2004); available at quant-ph/0403121.

18. JM Geremia, “Distinguishing between optical coherent states with imperfect detection,” Phys. Rev. A **70**, 062303 (2004).

19. A. Hopkins, B. Lev and H. Mabuchi, “Proposed magnetoelectrostatic ring trap for neutral atoms,” Phys. Rev. A **70**, 053616 (2004).

20. J. K. Stockton, R. van Handel, H. Mabuchi, “Deterministic Dicke state preparation with continuous measurement and control,” Phys. Rev. A, **70**, 022106, (8/26/04).

21. J. M. Geremia, J. K. Stockton, H. Mabuchi, “Real-Time Quantum Feedback Control of Atomic Spin-Squeezing,” Science, **304**, 270 (4/9/04).

22. B. Lev, K. Srinivasan, P. Barclay, O. Painter, H. Mabuchi, “Feasibility of detecting single atoms using photonic bandgap cavities,” Nanotechnology, **15**, S556 (7/23/04); available at quant-ph/0402093.

23. D. Gottesman, H.-K. Lo, N. Lutkenhaus, and J. Preskill, “Security of quantum key distribution with imperfect devices,” Quantum Information and Computation **4**, 325 (2004).

24. A. D. Boozer, A. Boca, J. R. Buck, J. McKeever, and H. J. Kimble, “Comparison of theory and experiment for a one-atom laser in a regime of strong coupling,” Phys. Rev. A **70**, 023814 (2004); available at quant-ph/0309133.

25. L. –M. Duan and H. J. Kimble, “Scalable photonic quantum computation through cavity-assisted interaction,” Phys. Rev. Lett. **92**, 127902 (2004); available at quant-ph/0309187.

26. J. McKeever, A. Boca, A. D. Boozer, R. Miller, J. R. Buck, A. Kuzmich and H. J. Kimble, “Deterministic generation of single photons from one atom trapped in a cavity,” Science **303**, 1992 (2004); published online in Science Express, February 26, 2004, 10.1126/science.1095232.

27. A. Hopkins, K. A. Jacobs, S. Habib, and K. Schwab, “Cooling a nanomechanical resonator using feedback: toward quantum behavior,” Proc. SPIE **5276**, 173 (2004).

28. J. K. Stockton, J. M. Geremia, A. C. Doherty, and H. Mabuchi, “Robust quantum parameter estimation: coherent magnetometry with feedback,” Phys. Rev. A **69**, 032109 (2004).

29. A. Kitaev, D. Mayers and J. Preskill, “Superselection rules and quantum protocols,” Phys. Rev. A **69**, 052326 (2004).

30. B. Lev, “Fabrication of Micro-Magnetic Traps for Cold Neutral Atoms,” Quantum Information and Computation **3**, 450 (2003).

31. JM Geremia, J. K. Stockton, A. C. Doherty and H. Mabuchi, “Quantum Kalman filtering and the Heisenberg Limit in atomic magnetometry,” Phys. Rev. Lett. **91**, 250801 (2003).
32. B. Lev, Y. Lassailly, C. Lee, A. Scherer and H. Mabuchi, “Atom mirror etched from a hard drive,” App. Phys. Lett. **83**, 395 (2003).
33. B. M. Terhal, M. M. Wolf and A. C. Doherty, “Quantum Entanglement: A Modern Perspective,” Physics Today, **56** 46 (2003).
34. B. M. Terhal, A. C. Doherty, and D. Schwab, “Symmetric Extensions of Quantum States and Local Hidden Variable Theories,” Phys. Rev. Lett. **90**, 157903 (2003).
35. J. McKeever, J. R. Buck, A. D. Boozer, A. Kuzmich, H.-C.Nagerl, D. M. Stamper-Kurn and H. J. Kimble, “State-Insensitive Trapping of Single Atoms in an Optical Cavity,” Phys. Rev. Lett. **90**, 133602 (2003).
36. B. Lev, “Fabrication of Micro-Magnetic Traps for Cold Neutral Atoms,” Quantum Information and Computation **3**, 450 (2003).
37. J. McKeever, A. Boca, A. D. Boozer, J. R. Buck and H. J. Kimble, “Experimental Realization of a One-Atom Laser in the Regime of Strong Coupling,” Nature **425**, 268 (2003).
38. L.-M. Duan, A. Kuzmich and H. J. Kimble, “Cavity QED and quantum information processing with “hot” trapped atoms,” Phys. Rev. A **67** 032305 (2003).
39. T. C. Zhang, K. W. Goh, C. W. Chou, P. Lodahl and H. J. Kimble, “Quantum teleportation of light beams,” Phys. Rev. A **67**, 033802 (2003).
40. L.-M. Duan and H. J. Kimble, “Efficient engineering of multiatom entanglement through single-photon detections,” Phys. Rev. Lett. 90, 253601 (2003).
41. A. Kuzmich, W. P. Bowen, A. D. Boozer, A. Boca, C. W. Chou, L.-M. Duan and H. J. Kimble, “Generation of nonclassical photon pairs for scalable quantum communication with atomic ensembles, Nature **423**, 731 (2003).
42. J. R .Buck and H. J. Kimble, “Optimal sizes of dielectric microspheres for cavity QED with strong coupling,” Phys. Rev. A **67**, 033806 (2003).
43. M. Koashi and J. Preskill, “Secure quantum key distribution with an uncharacterized source,” Phys. Rev. Lett. **90**, 057902 (2003).
44. C.-Y. Wang, J. Harrington and J. Preskill, “Confinement-Higgs transition in a disordered gauge theory and the accuracy threshold for quantum memory,” Annals of Physics **303**, 31 (2003).
45. K. Okamoto, M. Loncar, T. Yoshie, A. Scherer, Y. Qiu and P. Gogna, “Near-field scanning optical microscopy of photonic crystal nanocavities,” Appl. Phys. Lett. **82**, 1676 (2003).
46. L.-M. Duan, E. Demler and M. D. Lukin, “Controlling spin exchange interactions of ultracold atoms in optical lattices,” Phys. Rev. Lett. **91**, 090402 (2003).
47. B. M. Terhal, A. C. Doherty and D. Schwab, “Symmetric Extensions of Quantum States and Local Hidden Variable Theories,” Phys. Rev. Lett. **90**, 157903 (2003).

48. J. K. Stockton, J. M. Geremia, A. C. Doherty and H. Mabuchi, "Characterizing the entanglement of symmetric many-particle spin-1/2 systems," Phys. Rev. A **67**, 022112 (2003).
49. E. Dennis, A. Kitaev, A. Landahl and J. Preskill, "Topological quantum memory," J. Math. Phys. **43**, 4452 (2002).
50. D. Beckman, D. Gottesman, A. Kitaev and J. Preskill, "Measurability of Wilson loop operators," Phys. Rev. D **65**, 065022 (2002).
51. A. M. Childs, E. Farhi and J. Preskill, "Robustness of adiabatic quantum computation," Phys. Rev. A **65**, 012322 (2002).
52. A. Scherer, O. Painter, J. Vuckovic, M. Loncar and T. Yoshie, "Photonic crystals for confining, guiding and emitting light," IEEE Transactions on Nanotechnology **1**, 4 (2002).
53. L.-M. Duan, "Entangling many atomic ensembles through laser manipulation," Phys. Rev. Lett. **88**, 170402 (2002).
54. S. J. van Enk and H. J. Kimble, "On the classical character of control fields in quantum information processing," Quantum Information and Computation **2**, 1 (2002).
55. L.-M. Duan, J. I. Cirac and P. Zoller, "Three-dimensional theory for interaction between atomic ensembles and free-space light," Phys. Rev. A **66**, 023818 (2002).
56. J. M. Geremia, J. Williams, and H. Mabuchi, "Inverse-problem approach to designing photonic crystals for cavity QED experiments," Phys. Rev. E **66**, 066606 (2002).
57. B. Rahn, A. C. Doherty, and H. Mabuchi, "Exact performance of concatenated quantum codes," Phys. Rev. A **66**, 032304 (2002).
58. A. C. Doherty, P. Parrilo and F. Spedalieri, "Distinguishing Separable and Entangled States," Phys. Rev. Lett. **88**, 187904 (2002).
59. J. Vuckovic, M. Loncar, H. Mabuchi and A. Scherer, "Optimization of Q-factors in microcavities based on free-standing membranes," IEEE J. Quantum Electron. **38**, 850 (2002).
60. J. Vuckovic, M. Loncar, H. Mabuchi and A. Scherer, "Design of photonic crystal microcavities for cavity QED," Phys. Rev. E **65**, 016608 (2002).
61. M. Loncar, T. Yoshie, A. Scherer, P. Gogna and YM Qiu, "Low-threshold photonic crystal laser," APL, 81, 2680 (2002).
62. T. Yoshie, O. B. Shchekin, H. Chen, D. G. Deppe, A. Scherer, "Quantum dot photonic crystal lasers," Electronic Letters, 38, 967 (2002).
63. C. J. Hood, H. J. Kimble and J. Ye, "Characterization of high-finesse mirrors: Loss, phase shifts, and mode structure in an optical cavity," Phys. Rev. A **64**, 033804 (2001).
64. S. L. Braunstein, C. A. Fuchs, H. J. Kimble and P. van Loock, "Quantum versus classical domains for teleportation with continuous variables," Phys. Rev. A **64**, 022321 (2001).
65. S. J. van Enk, J. McKeever, H. J. Kimble and J. Ye, "Cooling of a single atom in an optical trap inside a resonator," Phys. Rev. A **64**, 013407 (2001).

66. H. J. Kimble, Y. Levin, A. B. Matsko, K. S. Thorne, and S. P. Vyatchanin, "Conversion of conventional gravitational-wave interferometers into quantum nondemolition interferometers by modifying their input and / or output optics," Phys. Rev. D **65**, 022002 (2001).
67. T. Yoshie, J. Vuckovic, A. Scherer, H. Chen and D. Deppe, "High quality two-dimensional photonic crystal slab cavities," Appl. Phys. Lett. **79**, 4289 (2001).
68. D. Gottesman, A. Kitaev and J. Preskill, "Encoding a qubit in an oscillator," Phys. Rev. A **64**, 012310 (2001).
69. J. Harrington and J. Preskill, "Achievable rates for the Gaussian quantum channel," Phys. Rev. A **64**, 062301 (2001).
70. H. Mabuchi, M. Armen, B. Lev, M. Loncar, J. Vuckovic, H. J. Kimble, J. Preskill, M. L. Roukes, and A. Scherer, "Quantum networks based on Cavity QED," Quantum Information and Computation **1**, 7 (2001).

Conference Proceedings:

1. A. Hopkins, K. A. Jacobs, S. Habib, and K. Schwab, "Cooling a nanomechanical resonator using feedback: toward quantum behavior," *Device and Process Technologies for MEMS, Microelectronics, and Photonics III*, eds. Jung-Chih Chiao et al., Proc. SPIE **5276**, 173 (Apr 2004).
2. H. J. Kimble and J. McKeever, "Cavity QED with Cold Atoms," in Proceedings of the XV International Conference on Laser Spectroscopy, Snowbird, Utah USA, 10-15 June 2001, eds. Steven Chu et al. (World Scientific, 2002).
3. H. J. Kimble, "Quantum Networks for Distributed Computation and Communication," Quantum Computers and Computing Special Issue on the XXII Solvay Conference Proceedings (accepted 2002).
4. H. J. Kimble and T. W. Lynn, "Cavity QED with Strong Coupling – Toward the Deterministic Control of Quantum Dynamics," *Proceedings of the 8th Rochester Conference on Coherence and Quantum Optics (CQO8)*, Rochester, New York, June 2001.

Manuscripts submitted, but not published:

1. R. Raussendorf, J. Harrington and K. Goyal, "A fault-tolerant one-way quantum computer," quant-ph/0510135.

(b) Presentations

1. "Physical Measurement and Control: from quantum metrology to tracking FCS," H. Mabuchi, University of California at Los Angeles, Los Angeles, CA (2/21/06).
2. "Quantum measurement/metrology with cold atoms," H. Mabuchi, University of Wisconsin, Madison, WI (2/1/06).
3. "Magnetoelectrostatic Ring Traps for Neutral Atoms," (poster) A. Hopkins, Eighth Annual SQuInT Workshop, Albuquerque, NM (2/06).
4. "A fault-tolerant one-way quantum computer," R. Raussendorf, Albuquerque, NM (2/06).
5. "A fault-tolerant one-way quantum computer," R. Raussendorf, QIP 2006, Paris, France (1/06).
6. "A fault-tolerant one-way quantum computer," R. Raussendorf, University of Munich, Munich, Germany (1/06).

7. “A fault-tolerant one-way quantum computer,” R. Raussendorf, Max Planck Institute for Quantum Optics, Garching, Germany (1/06).
8. “Applications of Quantum Filtering and Feedback,” H. Mabuchi, Workshop on Optimal Control of Quantum Dynamics, Ringberg, Germany (12/6/05).
9. “Magnetic Microtraps for Cavity QED, BECs, and Atom Optics,” B. Lev, Physics Colloquium, Williams College, Williamstown, Massachusetts (11/05).
10. “Magnetic Microtraps for Cavity QED, BECs, and Atom Optics,” B. Lev, Physics Seminar, Yale University, New Haven, Connecticut (11/05).
11. “Feedback Stabilization of Asymmetric States Under Symmetric Measurement,” (poster) A. E. Miller, Hertz Foundation Retreat, Pt. Reyes, CA (10/30/05).
12. “Real-time quantum measurement and feedback control” (series of two lectures), H. Mabuchi, Summer School on Quantum Information Science, Kochi, Japan (9/1-10/2005).
13. “Magnetoelectrostatic Ring Traps for Neutral Atoms,” (poster) A. Hopkins, Summer School on Quantum Information Science, Kochi, Japan (9/1-10/2005).
14. “Feedback Stabilization of Asymmetric States Under Symmetric Measurement,” (poster) A. E. Miller, Summer School on Quantum Information Science, Kochi, Japan (9/1-10/2005).
15. “Real-time quantum measurement and feedback control” (series of two lectures), H. Mabuchi, Quantum Control Summer School, Pasadena, CA (8/8-14/2005).
16. “Progress in Cavity QED with Single Trapped Atoms,” R. Miller, CLEO-PR/IQEC 2005, Tokyo, Japan (7/15/05).
17. “Real-time quantum measurement and feedback control” (series of three lectures), H. Mabuchi, Enrico Fermi Summer School on Quantum Computers, Algorithms and Chaos Varenna, Italy (7/5-15/2005).
18. “Magnetic Microtraps for Cavity QED, BECs, and Atom Optics,” (poster) B. Lev, Atomic Physics Gordon Research Conference, Tilton, New Hampshire (6/05).
19. “Quantum filtering and nonlinear dynamics,” H. Mabuchi, Perimeter Institute, Waterloo, Canada (5/11/05).
20. “Magnetic Microtraps for Cavity QED, BECs, and Atom Optics,” Ben Lev, Caltech Seminar Day, Pasadena, CA (5/05).
21. “Long-range entanglement in 3D noisy cluster states,” R. Raussendorf, Murray Hill (Bell Labs), NJ (5/05).
22. “Cavity QED with single atoms and photons,” T. Northup, JILA, Boulder, CO (4/22/05).
23. “Quantum Dynamics with Single Atoms and Photons,” H. J. Kimble, Colloquium, Welsh Lecture, University of Toronto, Toronto, Canada (4/21/05).
24. “The New Science of Quantum Information: From Quantum Computers to Teleportation of Quantum States,” H. J. Kimble, Public Lecture, Welsh Lecture, University of Toronto, Toronto, Canada (4/21/05).
25. “Cavity QED with Single Atoms and Photons,” H. J. Kimble, Seminar, Universitat Autonoma de Barcelona, Barcelona, Spain (4/8/05).
26. “The Quantum Optics Circus -- Flying Photons, Acrobatic Atoms, and Teleported Tuataras,” H. J. Kimble, Year of Physics Series, CosmoCaixa Science Museum, Barcelona, Spain (4/7/05).
27. “The Atom Chip,” B. Lev, Everheart Lecture, Caltech, Pasadena, CA (4/05).
28. “Exploring the Jaynes-Cummings ladder: experiments in cavity QED,” T. Northup, Physics Colloquium, U.S. Air Force Academy, Colorado Springs, Colorado (3/31/05).

29. “Measurement and control in quantum information science,” H. Mabuchi, APS March Meeting, Los Angeles, CA (3/23/05).
30. “Cavity QED with Single Atoms and Photons,” H. J. Kimble, 2005 APS March Meeting (invited), Los Angeles, California (3/21/05).
31. “Quantum control and nano-photonics in quantum information science,” H. Mabuchi, Cornell University, Ithaca, NY (3/17/05).
32. “Measurement and control in quantum information science,” H. Mabuchi, Quantum Information Science Gordon Research Conference, Ventura, CA (3/3/05).
33. “Progress Toward a Physical Implementation of the Dolinar Receiver,” JM Geremia, NASA Jet Propulsion Laboratory DRDF Seminar, Pasadena, CA (3/05).
34. “Long-range entanglement in 3D noisy cluster states,” R. Raussendorf, Obergurgl, Austria (3/05).
35. “Quantum cellular Automata using boundary,” R. Raussendorf, APS March Meeting, Los Angeles, CA (3/05).
36. “Measurement and control in quantum information science,” H. Mabuchi, Institute for Systems Research Distinguished Lecture Series, College Park, MD (2/23/05).
37. “Storage time of a quantum memory in an ensemble of cold atoms,” C. W. Chou, 5th Annual Southwest Quantum Information and Technology (SQuInT) Workshop, Tucson, Arizona (2/20/05).
38. “Magnetic Microtraps for Cavity QED, BECs, and Atom Optics,” Ben Lev, Southwest Quantum Information and Technology (SQuInT’05) Annual Meeting, Tucson, AZ (2/17-20/2005).
39. “Optimal Discrimination Between Two Optical Coherent States,” JM Geremia, Southwest Quantum Information and Technology (SQuInT’05) Annual Meeting, Tucson, AZ (2/17-20/2005).
40. “Real-time feedback control of quantum state reduction,” H. Mabuchi, AAAS Annual Meeting, Washington, D.C. (2/20/05).
41. “Cavity QED -- from Purcell and Casimir to the Era of Strong Coupling for Single Atoms and Photons,” H. J. Kimble, Physics Colloquium, University of British Columbia, Vancouver, Canada (2/10/05).
42. “Quantum Feedback Control and Precision Measurement with Cold Atoms,” JM Geremia, University of New Mexico Physics Seminar (invited), Albuquerque, NM (2/05).
43. “Nonlinear Dynamics in Single-Atom Cavity QED,” B. Lev, Photonics West 2005, San Jose, CA (1/25/05).
44. “Quantum Information Science Enabled by Quantum Optics,” H. J. Kimble, Complexity, Entropy and the Physics of Information (CEPI) Seminar Series, Santa Fe Institute, Santa Fe, New Mexico (1/19/05).
45. “Magnetic Microtraps for Cavity QED, BECs, and Atom Optics,” B. Lev, Physics Colloquium, California State University of Long Beach, CA (1/05).
46. “Using Continuous Measurement and Real-Time Feedback to Manipulate the Quantum State of Cold Atoms,” JM Geremia, University of Wisconsin Physics Department Seminar (invited), Madison, WI (1/05).
47. “Caltech MURI Center for Quantum Networks,” H. Mabuchi and H. J. Kimble, DARPA Quantum Information Science and Technology (QuIST) Program Review, Scottsdale, AZ (11/16-17/2004).

48. “Measurement and control in quantum information science,” H. Mabuchi, Photonics Asia/APOC Beijing 2004, Beijing, China (11/5-13/2004).
49. “Cavity QED -- from Purcell and Casimir to the Era of Strong Coupling for Single Atoms and Photons,” H. J. Kimble, Quantum Information & Coherence (QUIC) Seminar Series (invited), Naval Research Lab, Washington DC (11/5/04).
50. “Real-Time Quantum Feedback Control,” JM Geremia, Optical Science of America: Frontiers in Optics and Laser Science Meeting (invited) Rochester, NY (11/04).
51. “Magnetic Microtraps for Cavity QED, BECs, and Atom Optics,” B. Lev, Ion Trapping Group Seminar, NIST, Boulder, CO (10/04).
52. “Magnetic Microtraps for Cavity QED, BECs, and Atom Optics,” B. Lev, JILA Seminar, University of Colorado and NIST, Boulder, CO (10/04).
53. “Continuous Quantum Measurement and Control with Atomic Spin Ensembles,” J. Stockton, Hertz Foundation Retreat, Point Reyes, CA (9/24-26/2004).
54. “Cavity QED with Single Atoms and Photons,” H. J. Kimble, Workshop on Microcavities in Quantum Optics (invited), Lake Tegernsee, Bavaria, Germany (9/23/04).
55. “Quantum control, information and metrology,” Princeton University, Princeton, NJ (9/16/04).
56. “Magnetic Microtraps for Cavity QED, BECs, and Atom Optics,” B. Lev, Atomic, Molecular, and Optical Sciences Seminar, University of California, Berkeley, CA (9/04).
57. “Long-range entanglement in 3D noisy cluster states,” R. Raussendorf, Ann Arbor, MI (9/04).
58. “Control and Dynamics Approach to Robust Quantum Computing,” H. Mabuchi, 2004 Quantum Computing Program Review (QCPR), Orlando, FL (8/15-17/2004).
59. “Converting Photons to Decibels -- Travels with John Hall in Quantum Optics Land,” H. J. Kimble, John Hall Symposium (invited), JILA, University of Colorado, Boulder (8/14/04).
60. “Quantum Aspects of Precision Measurement,” JM Geremia, Los Alamos QUEST Annual Meeting, Santa Fe, NM (8/04).
61. “Optimal Classical Communication at the Quantum Noise Limit,” JM Geremia, Caltech Principles and Applications of Control in Quantum Systems (PRACQSYS’04) Meeting, Pasadena, CA (8/04).
62. “Real-time feedback control of quantum state reduction,” Hideo Mabuchi, XIX International Conference on Atomic Physics (ICAP 2004), Rio de Janeiro, Brazil (7/27/04).
63. “Cavity QED with single atoms and photons,” H. J. Kimble, XIX International Conference on Atomic Physics (ICAP 2004) (invited), Rio de Janeiro, Brazil (7/26/04).
64. “Feedback stabilization of quantum entangled-state preparation,” Hideo Mabuchi, Fields Institute Meeting on Quantum Information and Quantum Control, Toronto, Canada (7/22/04).
65. “Quantum Computation,” John Preskill, 17th International Conference on General Relativity and Gravitation, Dublin, Ireland (7/21/04).
66. “Feedback Control of Continuous Projective Measurement,” (poster) J. Stockton, Quantum Information and Quantum Control, University of Toronto, Toronto, Canada (7/19-23/2004).
67. “Feedback control for quantum and classical uncertainty management,” Hideo Mabuchi, Connections: 50th Birthday Celebration for John Doyle, Pasadena, CA (7/15/04).
68. “Long-range entanglement in 3D noisy cluster states,” R. Raussendorf, Toronto, Canada (7/04).

69. “Cavity QED with single atoms and photons,” H. J. Kimble, 2004 IEEE/LEOS Summer Topical Meetings (invited), San Diego, CA (6/28/04).
70. “Continuous Measurement and Control of Atomic Spin Ensembles,” J. Stockton, Caltech Candidacy Talk, Pasadena, CA (6/17/04).
71. “Cavity QED with single atoms and photons,” H. J. Kimble, FOCUS -- Building Computational Devices Using Coherent Control (invited), University of Michigan, Ann Arbor, MI (6/9/04).
72. “Feedback Control of Continuous Projective Measurement,” (poster) J. Stockton, FOCUS -- Building Computational Devices Using Coherent Control (invited), University of Michigan, Ann Arbor, MI (6/7-9/2004).
73. “Feedback control of quantum state reduction,” H. Mabuchi, FOCUS -- Building Computational Devices Using Coherent Control (invited), University of Michigan, Ann Arbor, MI (6/9/04).
74. “Topological quantum computing for beginners,” John Preskill, KITP Conference on Exotic Order, Santa Barbara, CA (6/7/04).
75. “Quantum Measurement, Entanglement and Feedback,” J. M. Geremia, Physics Department Seminar (invited), California State University Long Beach, Long Beach, CA (6/04).
76. “Quantum measurement and feedback with atomic spins,” Hideo Mabuchi, APS Division of Atomic, Molecular, Optical, and Plasma Physics, Tucson, AZ (5/26/04).
77. “Cavity QED with Trapped Atoms for Quantum Optics and Quantum Information,” J. McKeever, Ph.D. Defense, Caltech, Pasadena, CA (5/24/04).
78. “Cavity QED with multiple atomic excited states,” K. Birnbaum, CLEO/IQEC 2004, San Francisco, CA (5/18/04).
79. “Single photon generation ‘on demand’ from a single trapped atom strongly coupled to an optical cavity,” J. McKeever, A. Boca, A. D. Boozer, R. Miller, J. R. Buck, A. Kuzmich and H. J. Kimble, New Focus/Bookham Student Award Session, CLEO/IQEC 2004, San Francisco, CA (5/16-21/2004).
80. “Single photon generation ‘on demand’ from a single trapped atom strongly coupled to an optical cavity,” J. McKeever, A. Boca, A. D. Boozer, R. Miller, J. R. Buck, A. Kuzmich and H. J. Kimble, Single Photon Symposium I, CLEO/IQEC 2004, San Francisco, CA (5/16-21/2004).
81. “Nonclassical Photon Pairs from a Cold Atomic Ensemble for Scalable Quantum Communication,” S. Polyakov, CLEO/IQEC 2004 (invited), San Francisco, CA (5/16-21/2004).
82. “Recent Progress in Quantum Information Science,” John Preskill, Seven Pines Conference, Stillwater, MN (5/8/04).
83. “Feedback Control of Quantum Star Reduction,” R. van Handel, 8th Southern California Nonlinear Control Workshop, UCSB, Santa Barbara, CA (5/8/04).
84. “Cavity QED -- From Purcell and Casimir to the Era of Strong Coupling for Single Atoms and Photons,” H. J. Kimble, Lilienfeld Prize Talk, APS April Meeting 2004, Denver, CO (5/2/04).
85. “Collective Spin State Preparation with Quantum Measurement and Control,” J. K. Stockton, Workshop on Control of Quantum Mechanical Systems (CONQUEST), UC Berkeley, Berkeley, CA (4/30/04).

86. “Cavity Quantum Electrodynamics,” H. J. Kimble, Workshop on Quantum Information Science and Emerging Technologies (invited), NIST, Boulder, CO (4/30/04).
87. “Fault-tolerant quantum computation using graph states,” Robert Raussendorf, University of Innsbruck, Austria (4/28/04).
88. “Recent Progress toward the Realization of Quantum Networks,” H. J. Kimble (invited), Harvard University, Cambridge, MA (4/19/04).
89. “Extending and Generalizing the Kochen-Specker theorem,” Ben Toner, Université de Montreal, Parts I and II, Montreal, Canada (4/15-16/2004).
90. “Quantum Teleportation -- Fact and Fantasy,” H. J. Kimble, Biedenharn Lecture IV, University of Texas at Austin, Austin, TX (4/6/04).
91. “Quantum Teleportation -- Fact and Fantasy,” H. J. Kimble, Dean’s Scholars Lecture, University of Texas at Austin, Austin, TX (4/2/04).
92. “Scalable Quantum Communication Networks with Photon Pairs from Atomic Ensembles,” H. J. Kimble, Biedenharn Lecture III, University of Texas at Austin, Austin, TX (4/1/04).
93. “Deterministic Generation of Single Photons from One Atom Trapped in a Cavity,” J. McKeever, A. Boca, A. D. Boozer, R. Miller, J. R. Buck A. Kuzmich and H. J. Kimble, Seminar, NIST Ion Storage Group (invited), Boulder, CO (4/04).
94. “Deterministic Generation of Single Photons from One Atom Trapped in a Cavity,” J. McKeever, A. Boca, A. D. Boozer, R. Miller, J. R. Buck A. Kuzmich and H. J. Kimble, JILA Seminar (invited), Boulder, CO (4/04).
95. “The New Science of Quantum Information,” H. J. Kimble, Dean’s Scholars Lecture, University of Texas at Austin, Austin, TX (3/26/04).
96. “More Cavity Quantum Electrodynamics,” H. J. Kimble, Biedenharn Lecture II, University of Texas at Austin, Austin, TX (3/26/04).
97. “Measurement-based quantum computation with cluster states,” Robert Raussendorf, University of New Mexico, Albuquerque, NM (3/26/04).
98. “Cavity Quantum Electrodynamics -- from Purcell and Casimir to the Era of Strong Coupling with Single Atoms and Photons,” H. J. Kimble, Department of Physics Colloquium, Biedenharn Lecture I, University of Texas at Austin, Austin, TX (3/24/04).
99. “Real-Time Quantum Feedback Control and Precision Measurement,” JM Geremia, University of Oregon Physics Department Seminar (invited) (3/04).
100. “Quantum error correction for continuously detected errors,” Charlene Ahn, IBM, Yorktown, NY (3/04).
101. “Robust quantum memory with local controls,” Jim Harrington, LANL Quantum Institute, Los Alamos, NM (3/04).
102. “Robust quantum memory with local controls,” Jim Harrington, University of New Mexico, Albuquerque, NM (3/04).
103. “Quantum measurement and feedback control with cold atoms,” Hideo Mabuchi, Harvard/MIT Center for Ultracold Atoms Seminar, Cambridge, MA (3/2/04).
104. “Knowing what you know: estimation and control in nanoscale systems,” Hideo Mabuchi, MIT Center for Bits and Atoms Colloquium, Cambridge, MA (3/1/04).
105. “Superselection Rules and Quantum Protocols,” John Preskill, Gordon Research Conference on Quantum Information Science, Ventura, CA (2/25/04).
106. “Nonlocal games,” Ben Toner, SQuInT 2004 (invited), UC San Diego, San Diego, CA (2/20–22/2004).

107. “Feedback Control of Continuous Projective Measurement,” (poster) J. Stockton, SQuInT 2004 (invited), UC San Diego, San Diego, CA (2/20-22/2004).
108. “Conditional anti-bunching of photons generated in a cold atomic ensemble,” S. Polyakov, SQuInT 2004 (invited), UC San Diego, San Diego, CA (2/20-22/2004).
109. “Real-Time Quantum Feedback Control: Deterministic State Reduction in Cold Atoms,” J. M. Geremia, SQuInT 2004 (invited), UC San Diego, San Diego, CA (2/20/04).
110. “Deterministic Generation of Single Photons from One Atom Trapped in a Cavity,” J. McKeever, A. Boca, A. D. Boozer, R. Miller, J. R. Buck A. Kuzmich and H. J. Kimble, Sixth Annual Southwest Quantum Information and Technology (SQuInT) 2004 Workshop (invited), San Diego, CA (2/19/04).
111. “Magnetic Microtraps for Cavity QED, BECs, and Atom Optics,” B. Lev, IEEE Nanoscale Devices and System Integration Conference, Miami, FL (2/15/04).
112. “Putting Weirdness to Work,” John Preskill, AAAS Annual Meeting, Seattle, WA (2/14/04).
113. “Teleportation of Quantum States -- Fact and Fantasy,” H. J. Kimble, Quantum Weirdness -- In Nature, In the Lab Symposium, AAAS Annual Meeting (invited), Seattle, WA (2/14/04).
114. “Real-Time Quantum Feedback Control of Atomic Spin Squeezing,” JM Geremia, SQuInT Annual Meeting, San Diego, (2/04).
115. “Encoding a qubit into many oscillators,” Jim Harrington, SQuInT 2004 (invited), UC San Diego, San Diego, CA (2/04).
116. “Magnetic Microtraps for Cavity QED, BECs, and Atom Optics,” (poster) B. Lev, Southwest Quantum Information and Technology Network 6th Annual Meeting, UCSD, San Diego, California (2/04).
117. “Continuous Quantum Nondemolition Measurement and Feedback with Cold Atoms,” JM Geremia, University of California Berkeley AMO Physics Seminar (invited) (2/04).
118. “Photonic Quantum Computation through Cavity Assisted Interaction,” H. J. Kimble, Focused Quantum Systems (FoQuS) Workshop, Falls Church, VA (1/28/04).
119. “Generation of Nonclassical Photon Pairs for Scalable Quantum Communication with Atomic Ensembles,” Chin-wen Chou, 34th Winter Colloquium on the Physics of Quantum Electronics (PQE) (invited), Snowbird, UT (1/8/04).
120. “A One-Atom Laser in the Regime of Strong Coupling,” H. J. Kimble, 34th Winter Colloquium on the Physics of Quantum Electronics (PQE) (invited), Snowbird, UT (1/5/04).
121. “Real-Time Quantum Feedback Control of Atomic Spin Squeezing,” JM Geremia, Deutsche Forschungsgemeinschaft (DFG) Focused Meeting (invited) Bad Honef, Germany (1/04).
122. “Protecting quantum states through feedback control,” Charlene Ahn, 34th Winter Colloquium on The Physics of Quantum Electronics (PQE), Snowbird, UT (1/04).
123. “Quantum error correction for continuously detected errors,” Charlene Ahn, Perimeter Institute, Waterloo, Ontario, Canada (1/04).
124. “Real-time quantum feedback control,” Hideo Mabuchi, SAMSI Workshop on Multiscale Modeling and Control Design, Research Triangle Park, NC (1/04).
125. “Deterministic preparation of spin-squeezed states via real-time quantum feedback,” H. Mabuchi, Stanford-ENS Quantum Entanglement Symposium, Stanford (12/16/03).

126. "The New Science of Quantum Information," H. J. Kimble, Northwestern University (invited), Evanston, IL (11/7/03).
127. "An Introduction to Control Theory from Classical to Quantum," JM Geremia, Physics Winter School, University of Heidelberg, Germany (invited lecturer), (11/03).
128. "Identification, modeling, and control of quantum and bio-molecular systems," H. Mabuchi, Workshop on New Horizons in Molecular Sciences and Systems: An Integrated Approach, Okinawa, Japan (10/17/03).
129. "Experimental Realization of a One-Atom Laser in a Regime of Strong Coupling," J. McKeever, Quantum Optics Seminar, University of Toronto (invited), Toronto, Canada (10/14/03).
130. "A One-Atom Laser in a Regime of Strong Coupling," J. McKeever, A. Boca, A. D. Boozer, J. R. Buck and H. J. Kimble, 87th OSA Annual Meeting/Laser Science XIX (invited), Tucson, AZ (10/8/03).
131. "Magnetic Microtraps for Cavity QED, BECs, and Atom Optics," B. Lev, Seminar, Max Plank Institute for Quantum Optics, Garching, Germany (10/03).
132. "Overview of Caltech MURI Center for Quantum Networks," B. Lev, MURI Kick-Off Meeting, Stanford, Palo Alto (10/03).
133. "Quantum filtering and broadband atomic magnetometry," H. Mabuchi, EURESCO Conference on Quantum Optics, Granada, Spain (9/28/03).
134. "Continuous observation of open quantum systems," H. Mabuchi, US-Japan Joint Workshop on Coherence in Quantum Systems, Yatsugatake, Japan (9/17/03).
135. "Coherence in broadband atomic magnetometry," H. Mabuchi, Tokyo University, Tokyo, Japan (9/15/03).
136. "Continuous observation of open quantum systems: conditional spin-squeezing and broadband atomic magnetometry," H. Mabuchi, U.S.-Japan Conference on Coherence and Quantum Systems, Hokkaido, Japan (9/12-18/2003).
137. "Teleportation of continuous quantum variables using squeezed-state entanglement," K. W. Goh, The International Symposium on Optical Science and Technology, SPIE's 48th Annual Meeting (invited), San Diego, CA (8/6/03).
138. "Spin Squeezing in Cold Atoms with Continuous Measurement," JM Geremia, Los Alamos QUEST Annual Meeting, Santa Fe, (8/03).
139. "Cavity QED by the Numbers," H. J. Kimble, 16th International Conference on Laser Spectroscopy (ICOLS03) (invited), Palm Cove, Australia. (7/16/03).
140. "Microcavities: strong coupling of atoms and photons," H. Mabuchi, Photonics Technologies Advancement Program Workshop on Optical microcavities, San Diego. CA (7/15/03).
141. "Quantum optics and quantum information science," H. Mabuchi, OSA Topical Meeting on Optics in Computing, Washington D.C. (6/20/03).
142. "Quantum Control Lecture 2," A. C. Doherty, SQuInT Student Summer Retreat, Monterey, CA (6/19/03).
143. "Quantum Control Lecture 1," A. C. Doherty, SQuInT Student Summer Retreat, Monterey, CA (6/18/03).
144. "Quantum Optics with Cold Atoms -- Cavity QED & Atomic Ensembles," H. J. Kimble, Gordon Research Conference - Atomic Physics (invited), Tilton, NH (6/17/03).
145. "Applications for Continuous Quantum Measurement of Spin Ensembles", (poster) J. K. Stockton, Gordon Research Conference on Atomic Physics, Tilton, NH, (6/15-20/2003).

146. “The New Science of Quantum Information,” H. J. Kimble, QELS Plenary Session (invited), CLEO/QELS Conference 2003, Baltimore, MD (6/4/03).
147. “Experiments in quantum feedback,” H. Mabuchi, SPIE Conference on Fluctuations and Noise, Santa Fe, NM (6/2/03).
148. “Magnetic Microtraps for Cavity QED,” B. Lev, Niels Bohr Institute, Copenhagen, Denmark (5/30/03).
149. “Quantum Optics Enabling Information Science,” H. J. Kimble, Hertz Memorial Lecture (invited), UC Davis, Davis, CA (5/28/03).
150. “Quantum Optics with Single Atoms and Photons,” H. J. Kimble, AMO Student Symposium, DAMOP 2003 Meeting (invited), Boulder, CO (5/20/03).
151. “Cavity QED – From Purcell and Casimir to the Era of Strong Coupling,” H. J. Kimble, University of Washington Colloquium (invited), Seattle, WA (5/12/03).
152. “Symmetric extensions, local hidden variables and modified de Finetti theorems,” A. C. Doherty, Information Physics Group Seminar, Department of Physics, University of New Mexico, Albuquerque, NM (4/30/03).
153. “Linear matrix inequalities for quantum entanglement and control,” A. C. Doherty, Department of Mechanical and Environmental Engineering, UC Santa Barbara, Santa Barbara, CA (4/21/03).
154. “Physics with photons, from quantum to bio,” H. Mabuchi, Physics colloquium, Temple University, Philadelphia, PA (4/19-22/2003).
155. “Cavity QED -- The Plumbing,” H. J. Kimble, Loeb Lecture Series (invited), Harvard University, Boston, MA (4/15/03).
156. “Physics with photons: from quantum to bio,” H. Mabuchi, Physics colloquium, University of Arizona, Tucson, AZ (4/11/03).
157. “Quantum Teleportation -- Fact and Fantasy,” H. J. Kimble, Loeb Lecture Series (invited), Harvard University, Boston, MA (4/10/03).
158. “An Overview of Cavity Quantum Electrodynamics -- from Purcell and Casimir to the Era of Strong Coupling,” H. J. Kimble, Loeb Lecture Series (invited), Harvard University, Boston, MA (4/8/03).
159. “The New Science of Quantum Information,” H. J. Kimble, Colloquium (invited), Loeb Lecture Series, Harvard University, Boston, MA (4/7/03).
160. “Physics with photons: from quantum to bio,” H. Mabuchi, Optics and electronics seminar, University of Stanford, CA (4/6-8/2003).
161. “The Symmetric Group can be as Entangled as Possible, Almost,” JM Geremia, Caltech Institute for Quantum Information Science seminar (invited) April 2003.
162. “Quantum Information and Quantum Control,” H. Mabuchi, Gordon Research Conference on Quantum Information Science, Ventura, CA (3/24-28/2003).
163. “Experiments in Quantum Information Science -- What's the Point?” H. J. Kimble, Gordon Research Conference, Quantum Information Science (invited), Ventura, CA (3/23/03).
164. “Quantum Entanglement and Non-locality: Semidefinite relaxations for problems in Quantum Information Processing,” A. C. Doherty, Workshop on Robustness Analysis Tools with Applications to the Biological and Physical Sciences, Kavli Institute of Theoretical Physics, UC Santa Barbara, Santa Barbara, CA (3/21/03).
165. “Magnetic Microtraps for Cavity QED,” B. Lev, Research Seminar, NIST Gaithersburg, Maryland (3/18/03).

166. “Putting Quantum Mechanics to Work,” A. C. Doherty, Department of Physics, University of Oregon, Eugene, OR (3/6/03).
167. “Quantum Information Science with Single Atoms and Photons,” H. J. Kimble, APS Annual Meeting (invited), Austin, TX (3/5/03).
168. “Experiments in Quantum Feedback,” H. Mabuchi, Quantum information sciences seminar, MIT, Cambridge, MA (3/3/03).
169. “Quantum Physics in Light of Quantum Engineering,” A. C. Doherty, Department of Physics, University of Michigan, Ann Arbor, MI (2/13/03).
170. “Cavity QED in the Present and Future,” J. Buck, Communications Research Laboratory, Japan (2/13/03).
171. “State-Insensitive Trapping of Single Atoms in Cavity QED,” J. McKeever, SQuInT Annual Meeting, Santa Fe, NM (2/7/03).
172. “Quantum Entanglement in the Symmetric Subspace,” JM Geremia, SQuInT Annual Meeting, Santa Fe, NM, February 2003.
173. “Cavity QED in the Present and Future,” J. Buck, University of Tokyo, Japan (2/5/03).
174. “Magnetic Microtraps for Cavity QED,” B. Lev, Weekly Research Seminar, Ludwig-Maximilians University, Munich, Germany (1/30/03).
175. “Magnetic Microtraps for Cavity QED,” B. Lev, Weekly Research Seminar, University of Heidelberg, Germany (1/20/03).
176. “Physics with photons: from quantum to bio,” H. Mabuchi, Solid State Sciences Seminar Series, Caltech, Pasadena, CA (1/15/03).
177. “State-Insensitive Trapping of Single Atoms in Cavity QED,” J. McKeever, Institute for Applied Physics, University of Bonn, Germany (1/10/03).
178. “Quantum and classical control: theory & experiment,” H. Mabuchi, University of Heidelberg Physics of Information symposium, Heidelberg, Germany (1/10/03).
179. “State-Insensitive Trapping of Single Atoms in Cavity QED,” J. McKeever, Institute for Experimental Physics, University of Innsbruck, Austria (1/9/03).
180. “Tracking and trapping single atoms for quantum logic in cavity QED,” T. W. Lynn, 5th Workshop on Laser Cooling, Awaji Yumebutai, Japan (1/8/03).
181. “Quantum Feedback and Measurement: Arranging for Theory to Visit the Laboratory,” A. C. Doherty, US-Australia Workshop on Solid State and Optical Approaches to Quantum Information Science (invited), Newport, Australia (1/7/03).
182. “Experiments in quantum feedback,” H. Mabuchi, Winter Colloquium on The Physics of Quantum Electronics, Snowbird, UT (1/6/03).
183. “A New Physics/A New Control,” Invited presentation, A. C. Doherty, IEEE 2002 Conference on Decision and Control, Las Vegas, NV (12/13/02).
184. “Physics with photons: from quantum to bio,” H. Mabuchi, Joint Atomic Physics Colloquium, Harvard University, Boston, MA (12/11/02).
185. “Control and Systems Theoretic Approaches to Quantum Physics,” A. C. Doherty, IEEE 2002 Conference on Decision and Control, Las Vegas, NV (12/10-13/2002).
186. “Experiments in real-time quantum feedback,” H. Mabuchi, IEEE 2002 Conference on Decision and Control, Las Vegas, NV (12/10/02).
187. “Measurement and feedback in quantum systems,” H. Mabuchi, tutorial workshop on control of quantum systems, IEEE 2002 Conference On Decision and Control, Las Vegas, NV (12/9/02).

188. “Quantum Information Science -- The Promise, the Problems, and the Plumbing,” Invited presentation, H. J. Kimble, Frontiers of Science and Technology: Quantum Computation and Information, Lawrence Livermore National Laboratory, Livermore, CA (12/9/02).
189. “Quantum Control and Quantum Information Processing,” A. C. Doherty, Institute for Quantum Information (IQI) Review, Caltech, Pasadena, CA (12/5/02).
190. “Quantum Measurement: Arranging for Theory to Visit the Laboratory,” Invited presentation, A. C. Doherty, Atomic Physics Seminar, University of California, Berkeley, CA (11/20/02).
191. “Complexity and robustness in quantum networks,” Invited presentation, H. Mabuchi, Vanguard NextGens Conference, San Diego, CA (11/18/02).
192. “Local Hidden Variable Theories for Quantum States,” Invited presentation, A. C. Doherty, Quantum Information and Cryptography Workshop, MSRI, Berkeley, CA (11/8/02).
193. “Quantum Dynamics with Single Atoms and Photons,” Invited presentation, H. J. Kimble, 5th Workshop on Nonlinear Dynamics and Chaos, Courant Institute of Mathematical Sciences, NYU, New York, NY (10/25/02).
194. “Quantum Physics in Light of Quantum Engineering,” Invited presentation, A. C. Doherty, Department of Physics, University of Oxford, Oxford, United Kingdom (10/21/02).
195. “Magnetic Microtraps for Cavity QE,” B. Lev, MURI Center for Quantum Networks Review, Caltech, Pasadena, CA (10/16/02).
196. “Experiments in quantum feedback,” H. Mabuchi, Mechanical Engineering Seminar, Caltech, Pasadena, CA (10/15/02).
197. “Quantum Information Theory for Quantum Networks,” A. C. Doherty, MURI Center for Quantum Networks Review, Caltech, Pasadena, CA (10/15/02).
198. “The secret life of photons and atoms,” H. Mabuchi, MacArthur Fellows Reunion, St. Louis, MO (10/10-13/2002).
199. “Strong coupling of motion and light in cavity QED,” Invited presentation, H. J. Kimble, OSA Annual Meeting, Orlando, FL (10/2/02).
200. “Tracking, trapping, and training atomic motion in cavity QED,” Invited presentation, T. W. Lynn, OSA Annual Meeting, Orlando, FL (10/1/02).
201. “Magnetic Microtraps for Cavity QED,” B. Lev, Physics Graduate Student Seminar, Caltech, Pasadena, CA (10/1/02).
202. “Experimental and theoretical foundations of quantum and biochemical networks,” H. Mabuchi, IPAM Workshop on Alternative Computing, UCLA, Los Angeles, CA (9/30/02).
203. “Physics with photons: from quantum to bio,” H. Mabuchi, Physics Colloquium, Yale, New Haven, CT (9/27/02).
204. “Mathematics in nanoscale science and engineering,” H. Mabuchi, UCLA IPAM mini-retreat, Malibu, CA (9/16/02).
205. “Quantum networks based on cavity QED,” H. Mabuchi, DARPA QuIST PI’s meeting, Boston, MA (9/10-13/02).
206. “Experiments on quantum feedback,” H. Mabuchi, Decoherence Workshop, Ann Arbor, MI (8/20-28/02).
207. “Adaptive Quantum Metrology and Control,” J. Stockton, Quantum Enabled Science and Technology (QUEST) 2002 Summer Workshop, Santa Fe, NM (8/5-9/2002).
208. “Exact and Approximated Performance of Concatenated Quantum Codes,” B. Rahn, 6th International Conference on Quantum Communication, Measurement and Computing (QCMC’02), Cambridge, MA (7/22/2002).

209. “Quantum Dynamics with Single Atoms and Photons,” Invited presentation, H. J. Kimble, 6th International Conference on Quantum Communication, Measurement and Computing (QCMC '02), MIT, Boston, MA (7/22-26/2002).
210. “Adaptive quantum measurement and quantum feedback control,” Invited presentation, H. Mabuchi, 6th International Conference on Quantum Communication, Measurements, and Computing (QCMC’02), Boston, MA (7/18-23/2002).
211. “Quantum Measurements: Setting Up a Meeting Between Experiments and Theory,” Invited presentation, A. C. Doherty, Physics Department Seminar, Yale University, New Haven, CT (7/9/02).
212. “Distinguishing Separable and Entangled States,” Invited presentation, A. C. Doherty, Department of Applied Mathematics and Theoretical Physics, Cambridge University, Cambridge, United Kingdom (6/24/02).
213. “Quantum Measurement Theory Visits the Laboratory,” Invited presentation, A. C. Doherty, BEC Group Seminar, Department of Physics, University of Otago, Dunedin, New Zealand (6/4/02).
214. “Cavity QED with neutral atoms,” H. Mabuchi, NIST Workshop on Neutral Atom Quantum Computing, Gaithersburg, MD (6/3-4/2002).
215. “Cavity QED with Strong Coupling -- Toward the Deterministic Control of Quantum Dynamics,” Invited presentation, H. J. Kimble, Innsbruck, Austria (5/29/02).
216. “Magnetic Microtraps for Cavity QED,” B. Lev, Laser Seminar at the Max-Plank Institute for Quantum Optics, Garching, Germany (4/18/02).
217. “Magnetic Microtraps for Cavity QED,” B. Lev, Seminar at the University of Innsbruck, Innsbruck, Austria (4/12/02).
218. “Magnetic Microtraps for Cavity QED,” B. Lev, Seminar at the University of Trento, Trento, Italy (4/11/02).
219. “Quantum information processing with atoms and photons,” Alex Kuzmich, Physics Department Colloquium, Georgia Institute of Technology, Atlanta, GA (3/29/02).
220. “A Model Reduction Analysis of Concatenated Quantum Codes,” B. Rahn, CIMMS Workshop, California Institute of Technology, Pasadena, CA (3/22/02).
221. “Measurement, feedback, and the quantum-classical transition,” H. Mabuchi, John Wheeler Symposium, Princeton, NJ (3/16/02).
222. “Quantum Dynamics with Single Atoms and Photons,” Invited presentation, H. J. Kimble, 10th JST International Symposium on Quantum Computing, Nano-Science & Technology for Implementation of Quantum Computers, Tokyo, Japan (3/12-14/2002).
223. “Distinguishing Separable and Entangled States,” A. C. Doherty, SQuInT ’02 Annual Meeting, Boulder, CO (3/9/02).
224. “Quantum Teleportation of Light Beams,” Tiancai Zhang, Kok Win Goh, Chin-wen Chou, Peter Lodahl, and H. J. Kimble, poster presentation at SQuInT ’02 Annual Meeting, Boulder, CO (3/7-10/2002).
225. “Designing and Characterizing Photonic Band Gap Materials for Cavity QED,” J. M. Geremia and J. Williams, SQuInT ’02 Annual Meeting, Boulder, CO (3/8/02).
226. “Exact and Approximate Performance of Concatenated Quantum Codes,” B. Rahn, poster presentation at SQuInT ’02 Annual Meeting, Boulder, CO (3/7-10/2002).
227. “Single Atom Trapping in Cavity QED,” J. McKeever, poster presentation at SQuInT ’02 Annual Meeting, Boulder, CO (3/7-10/2002).

228. “Multiscale science: from quantum to bio,” H. Mabuchi, Physics Colloquium, JILA, Boulder, CO (2/21/02).
229. “Control theory and foundations of quantum mechanics,” H. Mabuchi, Mohammed Dahleh Memorial Symposium at University of California at Santa Barbara (2/8/02).
230. “Distinguishing Separable and Entangled States,” A. C. Doherty, IQI Seminar, Caltech, Pasadena, CA (1/15/02).
231. “Multiscale science: from quantum to bio,” H. Mabuchi, Physics Research Conference at the California Institute of Technology, Pasadena, CA (1/10/02).
232. “Distributed Compression of a Quantum Source,” A. C. Doherty, Australasian Conference on Optics, Lasers and Spectroscopy (invited), Brisbane, Australia (12/3-6/01).
233. “Progress toward the Realization of Quantum Networks,” H. J. Kimble, the Quantum Information conference at UCSB Institute for Theoretical Physics, Santa Barbara, CA (12/3-7/2001).
234. “The quantum-classical transition on trial: is the whole more than the sum of the parts?” H. Mabuchi, Caltech’s Watson Lecture Series (public lecture), Pasadena, CA (11/14/01).
235. “Quantum Measurements: arranging a meeting between theory and experiment,” A. C. Doherty, Atomic Molecular and Optical Physics Group Seminar, University of Texas, Austin, Austin, TX (11/9/01).
236. “Control Methods for Analysis of Concatenated Quantum Codes,” B. Rahn, Lloyd Group Meeting, Massachusetts Institute of Technology (invited), Cambridge, MA (11/2/01).
237. “Cooling of a single atom in an optical trap inside a resonator,” J. McKeever, poster presentation of the Optical Society of America Annual Meeting/ Interdisciplinary Laser Science XVII (ILS-XVII) Conference, Long Beach, CA (10/18/01).
238. “Sensitivities of atom-cavity microscopes,” K. Birnbaum, poster presentation at the Optical Society of America Annual Meeting/ Interdisciplinary Laser Science XVII (ILS-XVII) Conference, Long Beach, CA (10/18/01).
239. “Dynamics of Single-Atom, Single-Photon Trapping in Cavity QED,” T. Lynn, poster presentation at the Optical Society of America Annual Meeting/ Interdisciplinary Laser Science XVII (ILS-XVII) Conference, Long Beach, CA (10/18/01).
240. “Quantum teleportation of quadrature amplitudes,” T. Zhang, Optical Society of America Annual Meeting/ Interdisciplinary Laser Science XVII (ILS-XVII) Conference, Long Beach, CA (10/17/01).
241. “Determining optimal microsphere sizes for cavity QED,” J. R. Buck, Optical Society of America Annual Meeting/ Interdisciplinary Laser Science XVII (ILS-XVII) Conference. Long Beach, CA (10/17/01).
242. “Entangled atoms and photons,” A. Kuzmich, New Laser Scientists Conference (NLSC – 2001)/ Optical Society of America Annual Meeting 2001(invited), Long Beach, CA (10/12/01).
243. “Quantum Information Science – The Promise, the Problems, and the Plumbing,” H. J. Kimble, invited presentation at Shanxi University, Taiyuan, China (10/9/01).
244. “Cavity QED with Strong Coupling,” H. J. Kimble, invited presentation at Shanxi University, Taiyuan, China (10/9/01).
245. “Experiments in quantum feedback,” H. Mabuchi, Physics Colloquium at University of California, Berkeley, Berkeley, CA (10/8/01).
246. “Micromagnetic Traps for Cavity QED,” B. Lev, The Quantum Technology Seminar at Los Alamos National Laboratory (invited), Los Alamos, New Mexico (9/19/01).

247. “Quantum measurement and real-time feedback,” H. Mabuchi, Nonlinear Optics and Lasers Gordon Research Conference, New London, NH (7/29/01).
248. “Quantum measurement and feedback,” H. Mabuchi, SIAM Meeting on Control and its Applications (plenary), San Diego, CA (7/12/01).
249. “Closed-Loop Quantum System Identification,” JM Geremia, Caltech Institute for Quantum Information Science Seminar (7/01).
250. “Real-time feedback for quantum measurement and control,” H. Mabuchi, Atomic Physics Gordon Research Conference, Williamstown, MA (6/19/01).
251. “Dynamics of Single-Atom, Single-Photon Trapping in Cavity QED,” T. Lynn, poster presentation at the Eighth Rochester Conference on Coherence and Quantum Optics (CQO8), Rochester, NY (6/14/01).
252. “Cavity QED with Strong Coupling,” H. J. Kimble, Eighth Rochester Conference on Coherence and Quantum Optics (CQO8) (invited), Rochester, NY (6/12-17/2001).
253. “Cavity QED with Cold Atoms,” H. J. Kimble, ICOLS-XV Conference(invited), Snowbird, UT (6/10-12/2001).
254. “Real-time feedback for quantum measurement and control,” H. Mabuchi, Canadian Institute for Advanced Research (CIAR) Workshop on Quantum Computation, Toronto, Canada (5/19-20/2001).
255. “Real-time feedback for quantum measurement and control,” H. Mabuchi, 1st Summer School and Conference on Spintronics and Quantum Information (invited), Maui, HI (5/16/01).
256. “Cavity QED and quantum measurement,” H. Mabuchi, 1st Summer School and Conference on Spintronics and Quantum Information (invited tutorial), Maui, HI (5/15/01).
257. “Quantum feedback and adaptive measurement,” H. Mabuchi, Conference on Lasers and Electro-Optics/Quantum Electronics and Laser Science (CLEO/QELS), Baltimore, MD (5/10/01).
258. “Science and Technology at the quantum-classical interface,” H. Mabuchi, Simon Fraser University (Physics Colloquium), Vancouver, Canada (3/16/01).
259. “Science and Technology at the quantum-classical interface,” H. Mabuchi, University of British Columbia (Physics Colloquium), Vancouver, Canada (3/15/01).
260. “Quantum networks based on cavity QED,” H. Mabuchi, NEDO Workshop on Quantum Functional Devices (invited guest lecture), Tokyo, Japan (3/8/01).
261. “Adaptive measurement of quantum phase,” H. Mabuchi, Fourth Annual Meeting of the Southwest Quantum Information and Technology Network (invited), Pasadena, CA (3/4/01).
262. “Science and Technology at the quantum-classical interface,” H. Mabuchi, UCSB (Physics Colloquium), Santa Barbara, CA (1/23/01).
263. “Quantum networks based on cavity QED,” H. Mabuchi, First International Conference on Experimental Implementation of Quantum Computation (invited), Sydney, Australia (1/19/01).
264. “Robust Control in the Quantum Domain,” A. C. Doherty, 39th IEEE Conference on Decision and Control, Sydney, Australia (12/12-15/2000).
265. “Atoms in Optical Cavities,” H. J. Kimble, The Quantum Theory Centenary, Berlin, Germany (12/11/00).
266. “Real-time measurement and feedback in quantum systems,” H. Mabuchi, Laboratory for Information and Decision Systems Colloquium, MIT (11/28/00).

267. “What is an observable?” John Preskill, IQI Workshop on quantum computation and information (11/15/00).
268. “Cavity QED with Single Atoms and Photons – Toward Deterministic Control of Quantum Dynamics,” H. J. Kimble, JILA/NIST Colloquium, Boulder, CO (11/8/00).
269. “Quantum Measurement, feedback, and nonlinear dynamics in cavity QED,” H. Mabuchi, Northern New Mexico Complexity, Entropy and Physics of Information (CEPI) Seminar, Albuquerque, NM (11/1/00).
270. “Photonic crystal microcavities for strong coupling between an atom and the cavity field”, J. Vuckovic, M. Loncar, H. Mabuchi and A. Scherer, Proceedings of the LEOS 2000, pp. 840-841, Rio Grande, Puerto Rico (11/00).
271. “Modal analysis of waveguides based on a triangular photonic crystal lattice,” M. Loncar, J. Vuckovic and A. Scherer, Proceedings of the LEOS 2000, Rio Grande, Puerto Rico (11/00).
272. “Quantum Teleportation” and “Cavity QED,” H. J. Kimble, Chaos, Decoherence and Quantum Entanglement (Pan-American Advanced Study Institute), Ushuaia, Argentina (10/9-20/2000).
273. “Quantum clock synchronization and quantum error correction,” John Preskill, NASA-D.O.D. Workshop on Quantum Information and Clock Synchronization (9/25/00).
274. “Cavity QED with Cold Atoms,” H. J. Kimble, Mysteries, Puzzles, and Paradoxes in Quantum Mechanics, Garda Lake, Italy (9/19/00).
275. “Trapping and Tracking Single Atoms and Single Photons,” A. C. Doherty, U.S./Japan Joint Seminar “Coherent Quantum Systems”, Newport, Rhode Island (9/17-21/2000).
276. “Real-time measurement and feedback in quantum systems,” H. Mabuchi, Optical sciences colloquium, University of Arizona, Tucson, AZ (9/14/00).
277. “Cavity QED with Trapped Atoms,” H. J. Kimble, European Conference on Lasers and Electro-optics/International Quantum Electronics Conference 2000 (CLEO-Europe/IQEC 2000), Nice Acropolis, France (9/14/00).
278. “Information and the quantum—classical transition,” H. Mabuchi, Physics colloquium, Harvey Mudd College, Pomona, CA (9/12/00).
279. “Quantum networks based on cavity QED,” H. Mabuchi, Canadian Institute for Advanced Research Workshop on Quantum Computation, Calgary, Canada (9/1-5/2000).
280. “Quantum error correction and fault tolerance,” John Preskill, Quantum Computing Symposium sponsored by ARO, Baltimore, MD (8/28/00).
281. “The Quantum Internet – Distributed Quantum Networks for Computation & Communication,” H. J. Kimble, Quantum Computing Symposium sponsored by ARO, Baltimore, MD (8/28/00).
282. “Information dynamics in cavity QED,” H. Mabuchi, American Chemical Society National Meeting, Washington D.C. (8/20-24/2000).
283. “Real-time Tracking and Trapping of Single Atoms in Cavity QED,” H. J. Kimble, XVII International Conference on Atomic Physics (ICAP), Florence, Italy (6/00).
284. “Quantum Communication and Memory MURI Kickoff Meeting,” H. Mabuchi, Program review at the D.O.D. in Ft. Monmouth, NJ (6/13-14/2000).
285. “Encoding a qubit in an oscillator,” John Preskill, MURI Kickoff, Fort Monmouth, NJ (6/13-14/2000).
286. “Real-Time Tracking and Trapping of Single Atoms in Cavity QED,” H. J. Kimble, Institute of Physics and Astronomy, Aarhus University, Aarhus, Denmark (6/10/00).

287. "Codes for continuous quantum variables," John Preskill, Aspen 2000 Workshop -- Quantum Information and Computation (6/6/00).
288. "Real-time measurement and feedback in cavity QED," H. Mabuchi, Quantum information sciences colloquium, UCSB, Santa Barbara, CA (6/2/00).

(2) Scientific Personnel

Faculty, supported by this grant, who are members of the National Academy: H. J. Kimble
Number of Graduate Students Supported: 33
Mark L. Adams, Charlene Ahn, Michael Armen, John Au, Paul Barclay, David N. Barsic, Andreea Boca, A. David Boozer, Joseph R. Buck, Chin-wen Chou, Kok Win Goh, Kovid Goyal, Laurence C. Gunn, Jim Harrington, Asa Hopkins, Ali Husain, Shwetank Kumar, Andrew Landahl, Benjamin Lev, Marko Loncar, Jason McKeever, Russell Miller, Terrell D. Neal, Tracy Northup, Benjamin Rahn, Federico Spedalieri, Kartik Srinivasan, John Stockton, Ben Toner, Ramon van Handel, Jelena Vuckovic, Elizabeth Wilcut and Tomoyuki Yoshie
Number of Post Doctorates Supported: 15
Takao Aoki, Warwick Bowen, Eyal M. Buks, Andrew C. Doherty, Luming Duan, J. M. Geremia, Alex Kuzmich, Chungsok Lee, Debbie Leung, Hanns-Christoph Naegerl, Robert Raussendorf, Dan Stamper-Kurn, Steven van Enk, Jon Williams and Tiancai Zhang
Number of Faculty Supported: 6
Hideo Mabuchi, H. J. Kimble, John Preskill, Axel Scherer, Oskar Painter, Mladen Barbic
Number of PhDs Awarded: 16
Names of personnel receiving PhDs: Mark L. Adams, Charlene Ahn, David N. Barsic, Andreea Boca, A. David Boozer, Joseph R. Buck, Jim Harrington, Ali Husain, Andrew Landahl, Benjamin Lev, Marko Loncar, Jason McKeever, Federico Spedalieri, Kartik Srinivasan, Jelena Vuckovic and Tomoyuki Yoshie.
Number of Undergraduate Students Supported: 6
Wei Lien Dang, Nathan E. Flowers-Jacobs, Arjun Menon, Nicolay M. Tanushev, Chenyang Wang, Ernest C. Yeung

Prizes, Fellowships and Awards –

H. J. Kimble was awarded the Julius Edgar Lilienfeld Prize by the American Physical Society.
Hideo Mabuchi, Office of Naval Research Young Investigator Award, 2000 – 2003
John D. and Catherine T. MacArthur Foundation Fellowship, awarded June 2000
Discover magazine's "20 Scientists to Watch in the Next 20 Years", October 2000
Office of Naval Research Young Investigator Award, 2000 - 2003
Classroom Teaching Award (Graduate Student Council, Caltech) 2000

(3) Report of Inventions

Number of Patents Disclosed: One
Number of Patents Awarded: One

"Photonic crystal microcavities for strong coupling between an atom and the cavity field and method of fabricating the same," A. Scherer, J. Vuckovic, M. Loncar, and H. Mabuchi (US Patent #6,466,709 B1, issued 15 October 2002)

(4) Scientific Progress and Accomplishments

During the MURI performance period we completed a diverse portfolio of world-class research projects. We made remarkable progress in all major topics encompassed by the defining vision of our “Quantum Networks” MURI Center: demonstration of elementary quantum network protocols via cavity QED, development of integrated quantum nodes based on atom chips and photonic bandgap structures, and advancing quantum information theory. What follows is an executive summary of our main accomplishments in core areas of MURI research.

Quantum network protocols via cavity QED

The results described in this section are mainly attributed to the group of Jeff Kimble and to Luming Duan; see our cumulative publication list for details.

A long-standing ambition in the field of cavity quantum electrodynamics (QED) has been to trap single atoms inside high-Q cavities in a regime of strong coupling. Diverse avenues have been pursued for creating the trapping potential for atom confinement, including additional far off-resonant trapping beams, near-resonant light with mean intracavity photon number ~1, and single trapped ions in high-finesse optical cavities. A critical aspect of this research is the development of techniques for atom localization that are compatible with strong coupling in cavity QED, as required for the realization of various quantum network protocols.

Early in the MURI performance period we reached a significant milestone in our quest to trap and cool single atoms in cavity QED: we achieved extended trapping times for single atoms in a cavity while still maintaining strong coupling, with a trapping potential for the center-of-mass motion that is largely independent of the internal atomic state, and demonstrated a scheme that allows continuous observation of trapped atoms by way of the atom-field coupling. More specifically, we recorded trapping times up to 3s for single Cs atoms stored in an intracavity far-off resonance trap (FORT), which represented a 100-fold improvement beyond the sole previous realization of trapping in cavity QED (also by Kimble’s group, in 1999). We also continuously monitored trapped atoms by way of strong coupling to a probe beam, including observations of trap loss atom by atom over intervals ~1s. These measurements incorporated auxiliary cooling beams, and provided the first realization of cooling for trapped atoms strongly coupled to a cavity. Our protocols are enabled by the choice of a “magic” wavelength for the FORT, for which the relevant atomic levels are shifted almost equally, thereby providing significant advantages for coherent state manipulation of the atom-cavity system.

Also early in the MURI period, we proposed a method to implement quantum information processing in high-Q cavities with a single trapped but non-localized atom. Our method is based on adiabatic passage, which makes the relevant dynamics insensitive to the randomness of the atom position with an appropriate interaction configuration. We validated our protocol with both approximate analytical calculations and exact numerical simulations.

In the middle years of the MURI we exploited the new technical tools described above in a series of important demonstrations of the practical utility of strong coupling. We realized a one-atom laser in the regime of strong coupling, generated single photons “on-demand” from one atom trapped in a cavity, and developed a protocol for real-time determination of the number of trapped atoms in our cavity. We then directed our attention to the development of a new set of technical tools for cavity-QED-based Quantum Information Science. In particular we developed non-invasive methods for characterizing and tuning the local environment of a trapped intracavity atom, such as background magnetic fields, trapping potential fluctuations, and polarization fluctuations of the FORT beam. We also developed “in situ" Doppler and blue-detuned Sisyphus cooling methods for reducing the radial motion of a trapped intracavity atom, as well as a laser system for driving Raman transitions between hyperfine ground states of the atom. This latter capability is central to many proposed schemes for quantum information processing in cavity QED.

In the final years of our MURI effort we achieved two more major advances including the first demonstration of a complete protocol based on an individual intracavity trapped atom and a demonstration of cavity-mediate strong coupling between flying qubits. The Kimble research group reported observations of the vacuum Rabi spectrum for one trapped atom, which marks a major milestone for cavity QED. Previous experiments on the vacuum Rabi spectrum have required integration of signals collected from large numbers of atoms in order to accumulate sufficient signal-to-noise ratio, but the new work by Kimble et al. exploits their unique capability for non-invasive atom trapping. Their experiment involved a sequence of trapping, cooling, probing, and re-cooling stages. It is highly significant that individual trapped atoms could be reset into a "data-ready" state multiple times to combat decoherence. The Kimble group has also recently reported the observation of photon blockade in the transmission of light through a cavity containing one strongly-coupled atom. This effect, which is analogous to the Coulomb blockade effect in microelectronics, is a consequence of single-photon optical nonlinearity, and provides a basis for devices such as deterministic single-photon generators and possibly quantum logic gates for flying qubits.

Development of integrated quantum nodes

The results described in this section are main attributable to the groups of Axel Scherer, Oskar Painter and Hideo Mabuchi.

During the early years of our MURI effort, our efforts in the area of integrated quantum nodes proceeded separately along two main fronts. The first was the development of magnetic microtraps suitable for confining atoms in close proximity to a dielectric microcavity; the second was work on developing dielectric microcavities with sufficiently high Q-factor for cavity QED with resonance frequencies near the D2 line of atomic Cs. Much of our early work on magnetic microtraps focused on improving loading protocols for transferring Cs atoms from macroscopic "mirror MOT" traps into lithographically defined microtraps. This necessitated some detailed work on the characterization of light-induced collisions that limit the transfer efficiency. We found excellent agreement between our measurements and an atomic physics model based on values for scattering cross-sections that were previously measured by researchers interested in Bose-Einstein Condensation. These experimental results give us confidence that we could design optimal loading protocols to maximize the efficiency and phase-space density of atom transfer into magnetic microtraps. Early on we also investigated the possibility of using lithographically-patterned permanent magnets for atom trapping, which has great appeal because such traps would not need to dissipate significant heat while operating. We specifically used electron beam lithography to pattern the surface of a commercial hard disk platter, and demonstrated (utilizing a mirror MOT) that cold atoms bounce off of its magnetic field pattern without detectable perturbations. We later went on to propose a concrete scheme for combining such an atom mirror with metallic pads to create stable magnetoelectrostatic microtraps for chip-scale cavity QED. We are currently working to fabricate and demonstrate such microtraps.

Our early work on dielectric microcavities focused on defect resonators within InGaAs photonic crystals, even though this material was known to be unsuitable for work with Cs atoms, mainly because it was a known material system in which to tackle the primary question of whether the Q-factors of photonic crystal cavities could ever be made sufficiently high to be of interest for cavity QED with strong coupling. There were some promising advances at the time, but we ultimately had to switch to a different material (SiN_x) in order to achieve compatibility with atomic Cs. In addition to working to raise the Q-factors of fabricated microcavities, we explored the inclusion of quantum wells and quantum dots and created low-threshold power photonic crystal lasers. This work was eventually "spun off" from the MURI program and continues to provide the basis for work on photonic-crystal based optical information processing and for ultra-sensitive liquid phase sensor devices.

In the middle years of our MURI effort, we turned our attention to formulating a proof-of-principle demonstration of strong coupling between magnetically confined neutral atoms and a photonic bandgap defect resonator. This has proven to be a highly challenging undertaking which has only now come close to fruition. Initially we continued to pursue two main lines of work: construction of an appropriate "atom chip" for loading and guiding of cold atoms to the photonic bandgap (PBG) structure, and adaptation of the PBG-resonator designs from InGaAs to GaAs to make them compatible (or so we thought) with the resonant optical wavelengths for atomic Cs.

We successfully fabricated an atom chip design that incorporates all the features necessary for an initial experiment on coupling magnetically-guided atoms to a PBG cavity. Small-scale wires, used in the final stages of compression and guiding, were produced by lithographic patterning of gold on sapphire. Intermediate loading and compression was accomplished using medium-scale wires that we cut into a copper clad Teflon circuit board using a computer-controlled mill. Initial loading from a background Cs vapor required the transient use of a large copper wire underneath the circuit board. We used this atom chip to optimize our laser cooling protocols for transferring Cs atoms from a room-temperature background vapor to magnetostatic guiding elements on the chip, which we planned to use to deliver cold atoms to the vicinity of an on-chip PBG cavity.

On the PBG side of our effort we developed a novel configuration for coupling an optical fiber-taper to a PBG defect cavity, via a PBG waveguide. Using such a setup, we successfully demonstrated laser coupling to and spectroscopic characterization of a PBG defect cavity fabricated in InGaAs. We found an excellent quality factor Q~48,000 and achieved an input-output coupling efficiency of nearly fifty percent, which would be more than sufficient for demonstration experiments with magnetically guided atoms.

In order to transfer these results to a material system suitable for cavity QED with Cs atoms, we first spent over a year attempting to achieve comparably high Q-factors with AlGaAs photonic bandgap structures. We ultimately realized that there were oxidation and impurity issues endemic to AlGaAs, such that it would never be a good material to use. Fortunately, we finally found the right material system in SiN_x (Silicon Nitride), although we had to take a bit of a step backward to using microdisk resonators rather than PBG defect resonators because the complex etching protocols required for fabricating the latter geometry had not yet been optimized in SiN_x. Our focus then turned to task of functionally integrating our atom chip with the microcavity and optical-fiber coupling structures. Doing this has been far more challenging than we at first could appreciate, largely because our previous work on the photonic bandgap tapered-fiber couplers had not been done under vacuum. We first successfully debugged several major problems involving thermal management in the fiber tapers and mechanical stability of the couplers, developing along the way a novel "micro-joint" technique for rigidly and permanently attaching the fiber taper in an optimally coupled position. We are now using this technique to achieve simultaneous coupling to arrays of ~10 microdisk resonators on a single chip, which we believe will in the long run facilitate the creation of multi-cavity quantum nodes, and in the short run help to alleviate an unfortunate Cs-exposure issue that we recently discovered. During our first attempt to run a complete experiment on coupling chip-guided atoms to a semiconductor microcavity, we found that exposure of the cavity to background Cs vapor resulted in gradual but strong shift of its resonance frequency. This shift seems to saturate at a magnitude of about 0.2 nm and is not accompanied by any degradation of the microcavity Q-factor. This is highly inconvenient because it takes the microcavity out of our achievable tuning window for coupling to the Cs D2 line, and prevented our first attempt at the experiment from succeeding. At this point in time we are in the final stages of preparing a second attempt, in which we will anticipate this Cs-exposure shift when we trim the initial resonance frequencies of our SiN_x microdisks, and in which we will employ an array of ten microdisks (as described above) with a range of resonance frequencies just in case the saturation shift is different this time around. We hope to be able to report a successful demonstration of chip-scale cavity QED within the next few months.

Advancing quantum information theory

The results presented in this section are mainly attributable to John Preskill and his group, MURI visitors, Rob Raussendorf, and Andrew Doherty.

Our early theoretical activities focused on the accuracy threshold for fault-tolerant quantum computing using topological codes and the security of quantum key distribution with imperfect sources and detectors. Topological codes are well suited for robust storage and processing of quantum information because the code's check operators can be efficiently measured with local quantum gates. We studied the order-disorder transition for these codes, which corresponds to the accuracy threshold. It was shown that encoded quantum states are arbitrarily well protected in the limit of a large code block provided that the probability of error in each syndrome bit measurement is below three percent.

If implemented with perfect equipment, quantum key distribution is provably secure against arbitrary eavesdropping attacks. But how do flaws in the source or detector affect security? We proved that security is robust against arbitrary flaws in the source as long as the detector is perfect and the source does not leak to the eavesdropper any information about what basis is used in the protocol. The proof, which uses a new and remarkably simple method, also applies to the case where the source is perfect and the detector has arbitrary flaws (a case treated earlier by Mayers). We showed that security is robust against flaws (such as the emission of weak coherent states instead of single-photon states) that reveal a little bit of information about the basis.

We subsequently developed a new method for analyzing security, in which the classical coin flips that determine the basis in which the signals are sent and detected are treated quantumly. The advantage of this new viewpoint is that the basis dependence of flaws in the equipment can be characterized according to how much the adversary's attack disturbs the coins. Using the new method, unconditional security can be proven for *generic* small flaws in the source and detector. In related work, we also studied the impact of local conservation laws (superselection rules) on quantum games. We say that a game is *secure* if a cheater who breaks the rules is unable to alter the outcome of the game. Naively, it seems that in an *invariant* world subject to a superselection rule, a cheater would have less power than in the *unrestricted* world, not subject to a superselection rule. But on the contrary, we showed that any cheating strategy in the unrestricted world can be accurately simulated in the invariant world. By explaining how the physics of the invariant world (subject to the conservation law) can be simulated in the unrestricted world and vice versa, we clarified the physical implications of superselection rules, which have a central role in modern quantum field theory. We also analyzed how quantum protocols can be composed without compromising security. We showed in particular that classical authentication can be securely composed with quantum key distribution. This result means that a key generated in a round of key distribution can be used safely to authenticate further rounds. Continuing work now focuses on formulating more flexible definitions of security that will allow composability theory to be applied to a broader family of quantum protocols.

More recently, we have shown that any strong quantum coin flipping protocol is susceptible to same-sided bias – by cheating, one player or the other can force the coin to come up heads with probability ~0.707. Student Carlos Mochon found a weak coin tossing protocol in which the cheater cannot force a win with probability above 0.692; he also found improved bounds on the cheat sensitivity of quantum bit commitment protocols. In work currently in progress, the methods used to prove these results are being extended to a general theory of two-player quantum games. It is hoped that this theory will resolve the long-standing question whether there is a weak quantum coin tossing protocol with arbitrarily small bias. Student Ben Toner, together with visiting scholars Hoyer, Cleve, and Watrous, studied the power of entanglement in two-party cooperative games. They showed that shared entanglement profoundly alters the soundness of two-prover interactive proof systems, and formulated generalizations of Tsirelson's inequality, which provide upper bounds on quantum nonlocality.

Robert Raussendorf, Sergey Bravyi, and student Jim Harringon studied a quantum phase transition that occurs in a three-dimensional cluster state subject to noise. Using topological encoding methods, they estimated the (nonzero) critical “temperature” at which the entanglement length changes from infinite to finite. In related work, Raussendorf has developed protocols for purification of cluster states that can be used to achieve fault tolerance in the one-way quantum computer. Student Charlene Ahn studied the blowup in circuit depth that occurs when an ideal quantum circuit is simulated using noisy quantum gates. By combining topological coding with methods for studying the robustness of classical cellular automata, she showed that if the ideal circuit has size L, the blowup in depth can be a factor of order $\log(\log(L))$; this is a big improvement over the best previously known result (a factor polynomial in $\log(L)$). Student Jim Harringon developed fault-tolerant schemes for the case in which all gates (both quantum and classical) are local in space. He obtained analytic and numerical estimates of the accuracy threshold for this case, which had never been carefully analyzed before. The analytic result established a critical noise rate order 10^{-9}, but the numerical results indicate that the actual error threshold is better by many orders of magnitude.

Andrew Doherty, in joint work with Pablo Parrilo and student Federico Spedalieri, developed a new approach to characterizing entanglement using the theory of semi-definite programming realizations. This ties the quantum information-theoretic topic of separability testing to a host of other NP-hard problems such as minimization, number partitioning and set non-inclusion.

(5) Technology Transfer -- None.

Suppression of Spin Projection Noise in Broadband Atomic Magnetometry

JM Geremia,* John K. Stockton, and Hideo Mabuchi
Physics and Control & Dynamical Systems, California Institute of Technology, Pasadena CA 91125

(Dated: February 15, 2005)

We demonstrate that quantum nondemolition (QND) measurement, combined with a suitable parameter estimation procedure, can improve the sensitivity of a broadband atomic magnetometer by reducing uncertainty due to spin projection noise. Furthermore, we provide evidence that real-time quantum feedback control offers robustness to classical uncertainties, including shot-to-shot atom number fluctuations, that would otherwise prevent quantum-limited performance.

PACS numbers: 07.55.Ge, 03.65.Ta, 42.50.Lc, 02.30.Yy

Atomic magnetometers estimate the magnitude of an external magnetic field by observing Larmor precession in a spin-polarized atomic sample [1]. A canonical procedure for "detecting" a magnetic field oriented along the y-axis (in a laboratory-fixed coordinate system) operates by aligning the magnetic moments of N spin-f atoms along the x-axis. The resulting polarized atomic state is characterized by its net magnetization, $\mathbf{F} \equiv \langle \hat{\mathbf{F}} \rangle$, where the quantum operator, $\hat{\mathbf{F}}$, corresponds to the total angular momentum of the collective atomic system.

Under the influence of the field, $\mathbf{b} = B\hat{\mathbf{y}}$, the atomic magnetization precesses from its initial value,

$$d\,\mathbf{F}(t) = -\gamma\,(\mathbf{F}(t) \times \mathbf{b})\,dt, \quad \mathbf{F}(0) = \hbar F \hat{\mathbf{x}}, \tag{1}$$

where $F = Nf$ for N spin-f atoms and the Larmor frequency, $\omega_\mathrm{L} = \gamma B$, is determined by the gyromagnetic ratio, γ. These dynamics confine the mean spin vector to the xz-plane such that, in the small-time (and small-decoherence) limit appropriate for discussing detection thresholds, the z-component of the atomic magnetization is given by $F_\mathrm{z}(t) = \gamma B F t$, $t \ll \omega_L^{-1}$.

The magnetic field can thus be inferred from the slope of F_z during its small-angle Larmor precession,

$$\tilde{B} = \frac{1}{\gamma F}\left(\frac{F_\mathrm{z}(t)}{t}\right) = \frac{1}{\gamma F} F_\mathrm{z}', \quad 0 \le t < \tau. \tag{2}$$

Uncertainty in the field estimation, $\Delta\tilde{B}$, results from various sources of error that can be divided into three classes: (1) spin projection noise [2], or quantum uncertainty in the initial orientation of $\mathbf{F}$ due to non-commutativity of the quantum operators, F_x, F_y and F_z, (2) finite signal to noise in the physical measurement used to determine F_z, and (3) classical parameter uncertainties in Eq. (2), namely fluctuations in F that arise from shot-to-shot variance in the atom number, N.

Here we demonstrate that, given a quantum nondemolition (QND) measurement of F_z with a finite signal to noise ratio, degradation of the field sensitivity due to projection noise can be minimized by an estimation procedure [3, 4] that exploits the spin-squeezing produced by the QND measurement [5–7]. However, we find that the simplest procedure for suppressing spin projection noise is susceptible to classical parameter uncertainty. Incorporating real-time quantum feedback control into the estimation procedure alleviates this source of error.

We consider a QND measurement of F_z performed by quantum-limited detection of an optical field scattered by the atomic system [7, 8]. Such a measurement is described by the continuous photocurrent,

$$y(t) = \sqrt{M} F_\mathrm{z}(t) + \zeta(t), \tag{3}$$

where the $\zeta(t)$ are Gaussian stochastic increments that reflect detection (optical) noise. The *measurement strength*, M, relates the mean value of the photocurrent to the z-component of the collective atomic spin [7].

Our procedure [3] based on quantum Kalman filtering [9, 10] estimates the magnetic field from the average slope, $\bar{y}'(\tau)$, obtained by regressing the QND photocurrent over the interval $0 \le t \le \tau$. Fig. 1 schematically illustrates this procedure. Beginning from the spin-polarized state at $t = 0$, the measurement reveals both the slope due to (small angle) Larmor precession and an offset due to the initial uncertainty in the orientation of $\mathbf{F}$. This spin projection noise offset is randomly distributed with variance $\Delta\hat{F}_\mathrm{z}^2(0) \approx F/2$ in an ensemble of measurement trajectories, according to the Heisenberg-Robertson relation, $\Delta\hat{F}_\mathrm{y}^2\Delta\hat{F}_\mathrm{z}^2 \ge \frac{1}{4}\hbar^2|\langle\hat{F}_\mathrm{x}\rangle|$. Freedom to absorb the non-zero value of $F_\mathrm{z}(0)$ into the regression intercept rather than the slope minimizes the impact of the quantum projection noise on the estimated field, $\tilde{B}$.

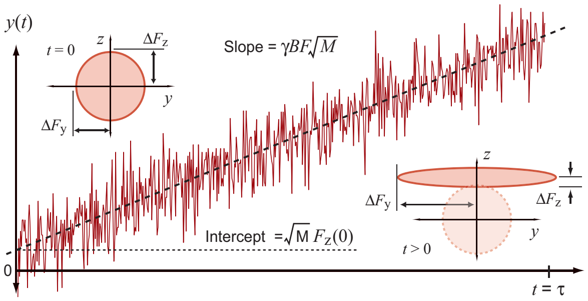

FIG. 1: Atomic magnetometry based on continuous QND measurement and quantum filtering enables field estimation procedures that suppress projection noise of the initial atomic state (simulated data).

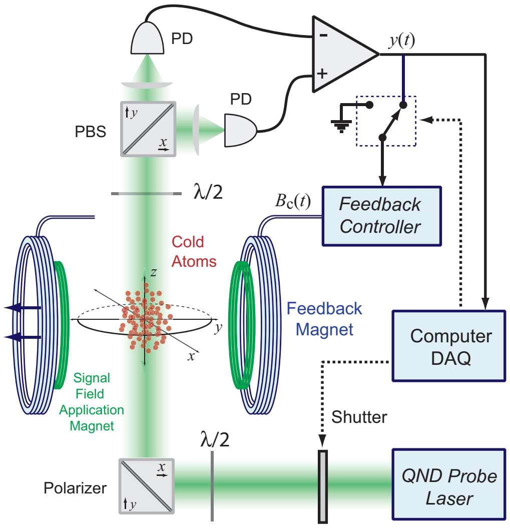

FIG. 2: Schematic of our apparatus for broadband atomic magnetometry based on continuous QND measurement and real time quantum feedback control.

Our single-shot magnetic field estimate is given by

$$\tilde{B}(\tau) = \frac{\bar{y}'_\tau}{\gamma F\sqrt{M}}, \quad \tau \ll \omega_L^{-1}, \tag{4}$$

where $\bar{y}'_\tau$ is the photocurrent slope obtained by linear regression of $y(t)$ over the time interval, $0 \le t < \tau$. In principle, field uncertainty is limited only by statistical regression error [3],

$$\Delta\tilde{B}(\tau) = \frac{1}{\gamma F\tau}\sqrt{\frac{3\Delta\zeta_\tau^2}{M}}, \tag{5}$$

where $\Delta\zeta_\tau^2 \equiv \mathbb{E}[\frac{1}{\tau}\int_0^\tau \zeta(t)dt]^2$ is the integrated noise variance in a $1/\tau$ bandwidth. The unitless QND signal to noise ratio, SNR $= \sqrt{M}/\Delta\zeta_\tau$, (both M and $\Delta\zeta_\tau^2$ have units proportional to frequency) is determined by experimental parameters, such as the optical probe power and detuning, and the scattering interaction strength [7].

The uncertainty of our optimal estimator, Eq. (5), should be compared to that of a procedure which cannot distinguish between Larmor precession and the initial spin projection noise. Such is the case for steady-state atomic magnetometers [11, 12] where the uncertainty,

$$\Delta\tilde{B}(\tau) = \frac{2}{\gamma F\tau}\sqrt{\Delta F_z^2(0) + \frac{\Delta\zeta_\tau^2}{M}}, \tag{6}$$

retains a contribution from both $\Delta\hat{F}_z^2(0) \approx F/2$ and the optical shotnoise. In the limit of infinite signal to noise this expression saturates to the so-called *shotnoise magnetometry limit* [11]. Eq. (6) corresponds to an estimation procedure that averages the photocurrent,

$$\tilde{B}(\tau) = \frac{2}{\gamma F\tau^2\sqrt{M}}\int_0^\tau y(t)\,dt, \tag{7}$$

rather than determining its slope. It is readily shown that steady-state atomic magnetometers operate in a manner logically equivalent to this type of direct averaging.

Our estimation procedure, which suppresses projection noise, requires precise knowledge of the QND measurement sensitivity $F\sqrt{M}$. Shot-to-shot variation in N produces fluctuations, ΔF, in the length of $\mathbf{F}$ that directly propagate into the field estimation as a proportional error, $\Delta\tilde{B}_\mathrm{F} = \bar{y}'\Delta F/(\gamma F\sqrt{M}) \approx B(\Delta F/F)$. A similar argument applies to M. While relative parameter uncertainties introduce essentially no error when $B = 0$, they can completely mask the improved resolution provided by spin-squeezing when $B \neq 0$.

To reduce the effects of classical parameter uncertainty, our magnetometer is implemented according to the closed-loop methodology [4] illustrated in Fig. 2. The QND photocurrent, $y(t)$, drives a precision y-axis magnet in negative feedback configuration to stabilize F_z to zero [8, 13]. In the presence of an external magnetic field, the controller imposes a compensating field, $\mathbf{b}_\mathrm{c}(t) \simeq -B(t)\hat{\mathbf{y}}$ to prevent the atomic magnetization from precessing out of the xy-plane. The magnetic field is estimated from the time-averaged feedback signal,

$$\tilde{B}(\tau) = -\frac{1}{\tau}\int_0^\tau B_\mathrm{c}(t)\,dt, \tag{8}$$

rather than the photocurrent. Since the magnetometer always operates with $F_\mathrm{z} \sim 0$, the closed-loop estimation is reasonably immune to atom number fluctuations.

We have recently demonstrated QND detection and real-time quantum-limited feedback control with an apparatus similar to that in Fig. 2 [7, 13]. Our spin system is provided by the $6^2\mathrm{S}_{1/2}$(F=4) ground state hyperfine manifold in ^{133}Cs. We obtain samples with $N \sim 10^{10} - 10^{11}$ atoms at a temperature of $T = 10$ μK via dark spontaneous-force optical trapping. Shot-to-shot fluctuations in N are <20%. Spin polarization along the x-axis is achieved by optical pumping on the $6^2\mathrm{S}_{1/2}(\mathrm{F}{=}4) \rightarrow 6^2\mathrm{P}_{3/2}(\mathrm{F}'{=}4)$ hyperfine transition and continuous QND measurement of F_z is implemented by balanced polarimetric detection of a laser detuned from the 4→5 transition by $\Delta = 550$ MHz.

Background magnetic fields are continually nulled using a combination of large (1 m) external three-axis Helmholtz coils and smaller computer controlled trim-coils. The experiment is synchronized with respect to the 60 Hz line cycle, and we estimate the resulting shot-to-shot field fluctuations in a 100 μs measurement window to be ∼850 nG. Atomic decoherence is <6% over the $t = 100$ μs measurement trajectories we consider [7]. Further characterization of our state preparation, atom number, transverse spin relaxation, spin-squeezing, and quantum noise limited feedback performance can be found in Ref. [13]. A detailed procedure for determining the degree of atomic polarization and the QND signal to noise ratio can be found in Ref. [7].

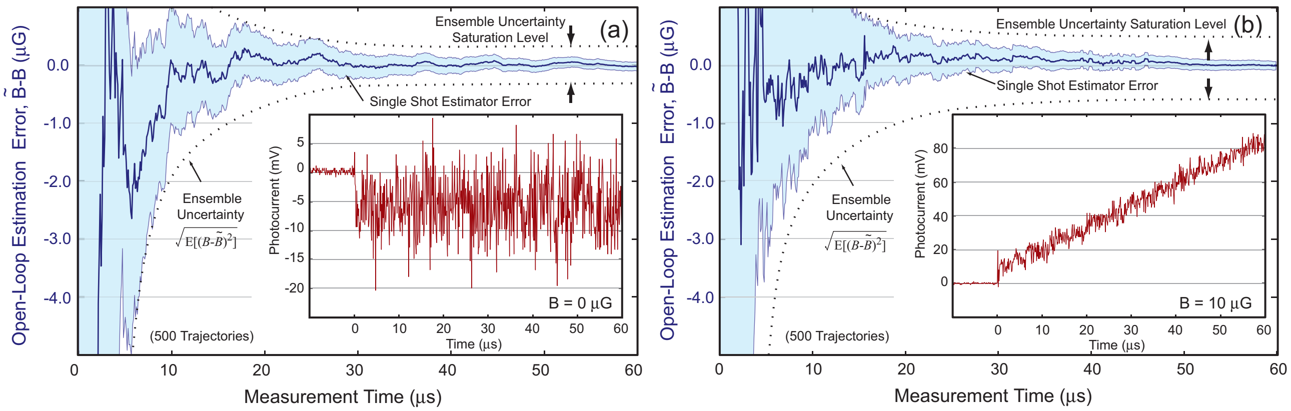

FIG. 3: Open-loop magnetic field estimation error, $\tilde{B} - B$, as a function of measurement time for (a) $B = 0$ and (b) $B = 10$ μG. Inset plots show the Faraday polarimeter photocurrent for each QND measurement trajectory. The shaded regions indicate the single-shot regression uncertainty while the dotted curves reflect the ensemble error measured from 500 trajectories.

We began by operating our magnetometer with feedback disabled in order to characterize the adverse effects of classical parameter uncertainty. Fig. 3 shows example open-loop field estimations performed using the procedure in Eq. (4) for two different magnetic fields, $B = 0$ and $B = 10$ μG. When the QND measurement is initiated at $t = 0$ by opening the probe laser shutter [refer to Fig. 2] the photocurrent establishes an average offset [inset of Fig. 3(a)] that is randomly distributed in an ensemble of similar trajectories. Our ability to observe this random offset reflects sufficient signal to noise in our QND measurement to produce squeezing [3, 7, 13].

Since $B = 0$ in Fig. 3(a), the atoms do not undergo Larmor precession and the slope of $y(t)$ is, as expected, $\bar{y}' \sim 0$. As described above, statistical fluctuations due to optical noise require that this slope be obtained by regression, as filtering the photocurrent reduces the stationary noise by time-averaging. The single-shot estimation trajectory for $B = 0$ computed according to Eq. (4) is depicted by the dark solid line in Fig. 3(a) while the light shaded region denotes the single-shot field uncertainty, $\Delta\tilde{B}$, due to statistical error in the linear regression. Values for F and M needed to evaluate Eq. (4) were obtained from full-scale atomic Larmor precession according to the procedure detailed in Ref. [7].

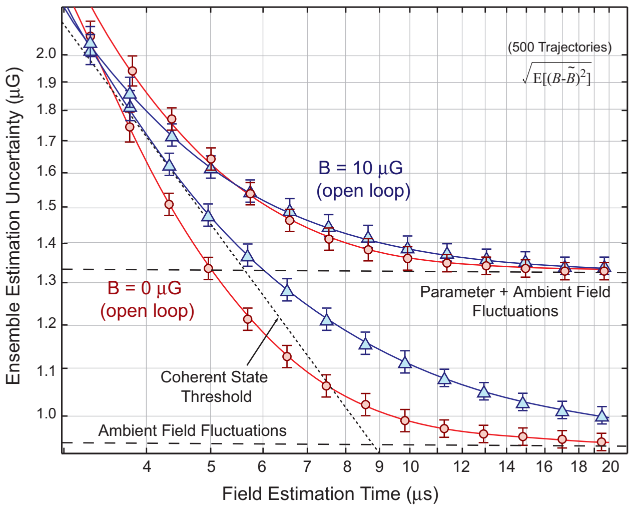

FIG. 4: Comparison of the two field estimation procedures, Eqs. (4) and (7) (circles and triangles, respectively) with $B = 0$ and $B = 10$ μG. The dotted line reflects the theoretical sensitivity limit, Eq. (6), of a magnetometer with the same signal to noise ratio that does not exploit spin-squeezing.

The dotted lines in Fig. 3(a) indicate the ensemble field variance, computed as $\mathbb{E}[(\tilde{B}-B)^2]^{1/2}$ from 500 QND trajectories, for the $B = 0$ field estimate. At long times, this measure of the magnetometer performance saturates to the level of shot-to-shot background magnetic field fluctuations in our experimental apparatus, approximately 850 nG. However, prior to saturation, as depicted by the $B = 0$ curves in Fig. 4, the regression estimation procedure (circles) outperforms the direct averaging estimator (triangles) given by Eq. (7). Unlike direct averaging, the regression estimator suppresses the uncertainty due to initial spin projection noise— the ensemble uncertainty drops below the field uncertainty threshold given by Eq. (6) [dotted line in Fig. 4].

It is important to note that the coherent state projection uncertainty (dotted line in Fig. 4) was computed using an absolute calibration [7] of M, and the average value of F inferred from full-amplitude Larmor precession measurements. Even though our optically pumped atomic system did not likely begin from a true minimum-uncertainty state due to imperfect pumping, sufficient QND spin noise reduction was achieved to allow the magnetometer to outperform the projection noise uncertainty corresponding to that of an actual coherent state.

In contrast, the $B = 10$ μG open loop estimation uncertainty fails to surpass the coherent state threshold despite a clearly visible photocurrent offset [inset in Fig. 3(b)] suggesting the presence of spin-squeezing. Evidently, the non-zero slope renders the open loop estimation susceptible to classical parameter uncertainty in F and M. As such, the long time estimation uncertainty

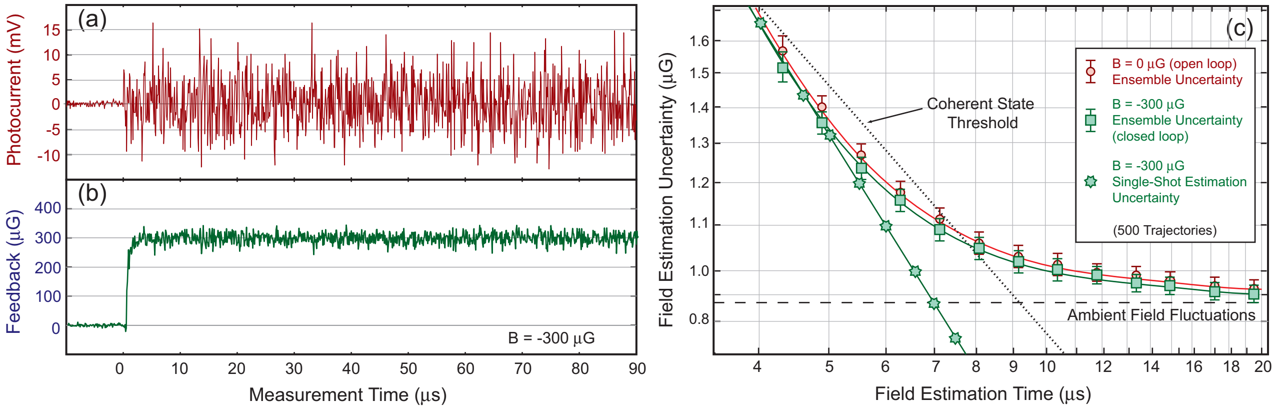

FIG. 5: (a) Closed-loop photocurrent for a $B = -300$ μG field, (b) real-time feedback field and (c) the resulting closed-loop field estimation error, $\tilde{B} - B$, as a function of measurement time.

for $B = 10$ μG saturates to a level much higher than that of the ambient magnetic field fluctuations, as in Fig. 4.

To alleviate the effects of classical parameter uncertainty, we next performed our closed-loop estimation procedure by enabling the feedback loop for the entire duration of each QND trajectory. The photocurrent in Fig. 5(a) displays no discernable slope despite the presence of a $B = -300$ μG field as the feedback loop drives a cancellation field [Fig. 5(b)], B_c, to maintain $F_z \sim 0$. The closed-loop field estimate, computed according to Eq. (8) for $0 \leq t \leq \tau$, is seen to be robust to shot-to-shot parameter fluctuations— it is evident from Fig. 5(c) that the ensemble uncertainty of the closed-loop estimator for $B = -300$ μG (squares) achieves similar performance to the $B = 0$ open loop estimation (circles). Despite the large magnitude of the estimated field, the closed-loop procedure is able to outperform the coherent state projection noise theshold [dotted line in Fig. 5(c)].

It should also be pointed out that in closed loop configuration, where the estimation uncertainty is due almost entirely to QND detection noise, the ensemble variance is an overly conservative measure of the magnetometer performance. After all, ambient fluctuations that produce the 850 nG sensitivity floor in Figs. 4 and 5(c) are real magnetic fields sensed by the atoms. Where other contributions to the detection threshold are well-controlled, the single-shot estimation error [Fig. 5(c) stars] more accurately reflects the magnetometer's performance. This single-shot closed-loop uncertainty surpasses the coherent spin state threshold at even long times in this case prior to the onset of significant atomic decoherence.

These results highlight what we anticipate will become a central theme in quantum-limited metrology. Feedback enables a precision measurement to achieve optimal insensitivity to classical uncertainty without sacrificing resolution [4, 14]. Furthermore, our closed loop methodology can be immediately extended to detection of non-stationary fields. Such an approach is likely to be essential for obtaining acceptable performance in various precision metrological applications including spin resonance measurements, atomic frequency standards, and matter-wave gravimetry.

This work was supported by the NSF (PHY-9987541, EIA-0086038), the ONR (N00014-00-1-0479), and the Caltech MURI Center for Quantum Networks (DAAD19-00-1-0374). JKS acknowledges a Hertz fellowship. We thank Ramon van Handel, Andrew Berglund, Michael Armen, Andrew Doherty, Dima Budker and especially Dan Kleppner and Vladan Vuletic for helpful discussions.

---

[*] Electronic address: `jgeremia@Caltech.EDU`

[1] J. Dupont-Roc, S. Haroche, and C. Cohen-Tannoudji, Phys. Lett. A **28**, 638 (1969).
[2] W. Itano, J. Berquist, J. Bollinger, J. Gilligan, D. Heinzen, F. Moore, M. Raizen, and D.J.Wineland, Phys. Rev. A **47**, 3554 (1993).
[3] JM Geremia, J. K. Stockton, A. C. Doherty, and H. Mabuchi, Phys. Rev. Lett. **91**, 250801 (2003).
[4] J. K. Stockton, JM Geremia, A. Doherty, and H. Mabuchi, Phys. Rev. A. **69**, 32109 (2004).
[5] A. Kuzmich, L. Mandel, and N. P. Bigelow, Phys. Rev. Lett. **85**, 1594 (2000).
[6] B. Julsgaard, A. Kozhekin, and E. S. Polzik, Nature **413**, 400 (2001).
[7] JM Geremia, J. K. Stockton, and H. Mabuchi (2005), quant-ph/0501033 (note that the data presented in Ref. [7] was acquired after an overhaul of the apparatus utilized here and in Ref. [13]).
[8] L. K. Thomsen, S. Mancini, and H. M. Wiseman, Phys. Rev. A **65**, 061801 (2002).
[9] V. P. Belavkin, Rep. on Math. Phys. **43**, 405 (1999).
[10] H. Mabuchi, Quantum Semiclass. Opt. **8**, 1103 (1996).
[11] D. Budker, W. Gawlik, D. Kimball, S. Rochester, V. Yashchuk, and A. Weiss, Rev. Mod. Phys. **74**, 1153 (2002).
[12] I. K. Kominis, T. W. Kornack, J. C. Allred, and M. Romalis, Nature **422**, 596 (2003).
[13] JM Geremia, J. K. Stockton, and H. Mabuchi, Science **304**, 270 (2004).
[14] D. W. Berry and H. M. Wiseman, Phys. Rev. A **65**, 043803 (2002).

Feedback Control of Quantum State Reduction

Ramon van Handel, John K. Stockton, and Hideo Mabuchi

***Abstract*—Feedback control of quantum mechanical systems must take into account the probabilistic nature of quantum measurement. We formulate quantum feedback control as a problem of stochastic nonlinear control by considering separately a quantum filtering problem and a state feedback control problem for the filter. We explore the use of stochastic Lyapunov techniques for the design of feedback controllers for quantum spin systems and demonstrate the possibility of stabilizing one outcome of a quantum measurement with unit probability.**

***Index Terms*—Lyapunov functions, quantum filtering, quantum mechanics, quantum probability, stochastic nonlinear control.**

I. INTRODUCTION

IT IS A basic fact of nature that at small scales—at the level of atoms and photons—observations are inherently probabilistic, as described by the theory of quantum mechanics. The traditional formulation of quantum mechanics is very different, however, from the way stochastic processes are modeled. The theory of quantum measurement is notoriously strange in that it does not allow all quantum observables to be measured simultaneously. As such there is yet much progress to be made in the extension of control theory, particularly feedback control, to the quantum domain.

One approach to quantum feedback control is to circumvent measurement entirely by directly feeding back the physical output from the system [1], [2]. In quantum optics, where the system is observed by coupling it to a mode of the electromagnetic field, this corresponds to all-optical feedback. Though this is in many ways an attractive option it is clear that performing a measurement allows greater flexibility in the control design, enabling the use of sophisticated in-loop signal processing and nonoptical feedback actuators. Moreover, it is known that some quantum states obtained by measurement are not easily prepared in other ways [3]–[5].

We take a different route to quantum feedback control, where measurements play a central role. The key to this approach is that quantum theory, despite its entirely different appearance, is in fact very closely related to Kolmogorov's classical theory of probability. The essential departure from classical probability is the fact that in quantum theory observables need not commute, which precludes their simultaneous measurement. Kolmogorov's theory is not equipped to deal with such objects: One can always obtain a joint probability distribution for random variables on a probability space, implying that they can be measured simultaneously. Formalizing these ideas leads naturally to the rich field of *noncommutative* or *quantum probability* [6]–[8]. Classical probability is obtained as a special case if we consider only commuting observables.

Let us briefly recall the setting of stochastic control theory. The system dynamics and the observation process are usually described by stochastic differential equations of the Itô type. A generic approach to stochastic control [9], [10] separates the problem into two parts. First one constructs a filter which propagates our knowledge of the system state given all observations up to the current time. Then one finds a state feedback law to control the filtering equation. Stochastic control theory has traditionally focused on linear systems, where the optimal [linear quadratic Gaussian (LQG)] control problem can be solved explicitly.

A theory of quantum feedback control with measurement can now be developed simply by replacing each ingredient of stochastic control theory by its noncommutative counterpart. In this framework, the system and observations are described by quantum stochastic differential equations. The next step is to obtain quantum filtering equations [11]–[14]. Remarkably, the filter is a classical Itô equation due to the fact that the output signal of a laboratory measuring device is a classical stochastic process. The remaining control problem now reduces to a problem of classical stochastic nonlinear control. As in the classical case, the optimal control problem can be solved explicitly for quantum systems with linear dynamics.

The field of quantum stochastic control was pioneered by V. P. Belavkin in a remarkable series of papers [11]–[13], [15] in which the quantum counterparts of nonlinear filtering and LQG control were developed. The advantage of the quantum stochastic approach is that the details of quantum probability and measurement are hidden in a quantum filtering equation and we can concentrate our efforts on the classical control problem associated with this equation. Recently the quantum filtering problem was reconsidered by Bouten *et al.* [14] and quantum optimal control has received some attention in the physics literature [16], [17].

The goal of this paper is twofold. We review the basic ingredients of quantum stochastic control: Quantum probability, filtering, and the associated geometric structures. We then demonstrate the use of this framework in a *nonlinear* control problem. To this end, we study in detail an example directly related to our experimental apparatus [4]. As this is not a linear system, the optimal control problem is intractable and we must resort to methods of stochastic nonlinear control. We use stochastic Lyapunov techniques to design stabilizing controllers, demonstrating the feasibility of such an approach.

Manuscript received February 20, 2004; revised December 15, 2004. Recommended by Associate Editor A. Garulli. This work was supported by the Army Research Office under Grant DAAD19-03-1-0073 and by the Caltech MURI Center for Quantum Networks under Grant DAAD19-00-1-0374. J. K. Stockton acknowledges a Hertz fellowship.

The authors are with the Departments of Physics and Control and Dynamical Systems, California Institute of Technology 266–33, Pasadena, CA 91125 USA (e-mail: ramon@its.caltech.edu).

Digital Object Identifier 10.1109/TAC.2005.849193

0018-9286/$20.00 © 2005 IEEE

We are motivated in studying the quantum control problem by recent developments in experimental quantum optics [4], [18]–[20]. Technology has now matured to the point that state-of-the-art experiments can monitor and manipulate atomic and optical systems in real time *at the quantum limit*, i.e., the sources of extraneous noise are sufficiently suppressed that essentially all the noise is fundamental in nature. The experimental implementation of quantum control systems is thus within reach of current experiments, with important applications in, e.g., precision metrology [20]–[23] and quantum computing [24], [25]. Further development of quantum control theory is an essential step in this direction.

This paper is organized as follows. In Section II, we give an introduction to quantum probability and sketch a simple derivation of quantum filtering equations. We also introduce the particular physical system that we study in the remainder of this paper. In Section III, we study the dynamical behavior of the filtering equation and the underlying geometric structures. Finally, Section IV is devoted to the design of stabilizing controllers using stochastic Lyapunov methods.

II. QUANTUM PROBABILITY AND FILTERING

The purpose of this section is to clarify the connections between quantum mechanics and classical probability theory. The emphasis is not on rigor as we aim for a brief but broad overview; we refer to the references for a complete treatment.

A. *Finite-Dimensional Quantum Probability*

We begin by reviewing some of the traditional elements of quantum mechanics (e.g., [26]) with a probabilistic flavor.

An *observable* of a finite-dimensional quantum system is represented by a self-adjoint linear operator $X = X^*$ on some underlying finite-dimensional complex Hilbert space $\mathcal{H}$ ($*$ denotes Hermitian conjugation). Every self-adjoint operator has a spectral decomposition

$$X = \sum_i \lambda_i P_i, \qquad \lambda_i \in \mathbb{R}, \quad P_i = P_i^2 = P_i^* \tag{1}$$

where λ_i are the eigenvalues of X and P_i are projectors onto orthogonal eigenspaces in $\mathcal{H}$ such that $\sum_i P_i = \mathrm{Id}_{\mathcal{H}}$.

If we were to measure X we would obtain one of the values λ_i as the measurement outcome. The P_i represent the events that can be measured. To complete the picture we still need a probability measure. This is provided by the *density operator* ρ, which is a linear operator on $\mathcal{H}$ satisfying

$$\rho = \rho^*, \quad \operatorname{Tr}\rho = 1, \qquad \rho \geq 0. \tag{2}$$

The probability of an event P_i is given by

$$p_i = \operatorname{Tr}[\rho P_i]. \tag{3}$$

We can now easily find the expectation of X

$$\langle X\rangle = \sum_i \lambda_i \operatorname{Tr}[\rho P_i] = \operatorname{Tr}[\rho X]. \tag{4}$$

In quantum mechanics ρ is also called the system state.

As in classical probability, it will be useful to formalize these ideas into a mathematical theory of quantum probability [6]–[8]. The main ingredient of the theory is the quantum probability space $(\mathcal{A}, \rho)$. Here, $\mathcal{A}$ is a $*$-algebra, i.e., an algebra with involution $*$ of linear operators on $\mathcal{H}$, and ρ is the associated state. An observable on $(\mathcal{A}, \rho)$ is a sum of the form (1) with $P_i \in \mathcal{A}$. In the finite-dimensional case this implies that every observable is a member of $\mathcal{A}$, but we will see that this need not be the case in infinite dimensions.

$\mathcal{A}$ does not necessarily contain all self-adjoint operators on $\mathcal{H}$. Of special importance is the case in which $\mathcal{A}$ is a commutative algebra, i.e., all the elements of $\mathcal{A}$ commute ($[X, Y] = XY - YX = 0\,\forall X, Y \in \mathcal{A}$). It is easily verified that there is a one-to-one correspondence (up to isomorphism) between commutative quantum probability spaces $(\mathcal{A}, \rho)$ and classical probability spaces $(\Omega, \mathcal{F}, \mathbb{P})$ with $\operatorname{card}\Omega = \dim\mathcal{H}$. As $\mathcal{A}$ is commutative we may represent all its elements by diagonal matrices; the diagonals are then interpreted as functions $f : \Omega \to \mathbb{R}$. The projectors $P_i \in \mathcal{A}$ now correspond to indicator functions χ_{A_i} on Ω and hence define the σ-algebra $\mathcal{F} = \{A_i\}$. Finally, $\mathbb{P}$ is defined by $\mathbb{P}[A_i] = \operatorname{Tr}[P_i\rho]$.

Clearly, classical probability is a special case of quantum probability. However, noncommutative $\mathcal{A}$ are inherent to quantum mechanical models. Suppose A, B are two events (projectors) that do not commute. Then, A and B cannot be diagonalized simultaneously, and hence they cannot be represented as events on a single classical probability space. Suppose we wish to measure A and B simultaneously, i.e., we ask what is the probability of the event (A and B)? In the classical case this would be given by the joint probability $\mathbb{P}[A, B] = \mathbb{P}[A \cap B] = \mathbb{E}[\chi_A \chi_B]$. However, in the noncommutative case this expression is ambiguous as $\operatorname{Tr}[\rho AB] \neq \operatorname{Tr}[\rho BA]$. We conclude that ($A$ and B) is an invalid question and its probability is undefined. In this case, the events A and B are said to be *incompatible*. Similarly, two observables on $\mathcal{A}$ can be measured simultaneously only if they commute.

We conclude this section with the important topic of conditional expectation. A traditional element of the theory of quantum measurement is the projection postulate, which can be stated as follows. Suppose we measure an observable X and obtain the outcome λ_i. Then, the measurement causes the state to collapse

$$\rho|_i = \frac{P_i \rho P_i}{\operatorname{Tr}[\rho P_i]}. \tag{5}$$

Suppose that we measure another observable X' after measuring X. Using (5), we write

$$P[X' = \lambda'_j \mid X = \lambda_i] = \operatorname{Tr}[P'_j \rho|_i] = \frac{\operatorname{Tr}[\rho P_i P'_j P_i]}{\operatorname{Tr}[\rho P_i]}. \tag{6}$$

Now, compare to the definition of conditional probability in classical probability theory

$$\mathbb{P}[B \mid A] = \frac{\mathbb{P}[B \cap A]}{\mathbb{P}[A]}, \qquad A, B \in \mathcal{F}. \tag{7}$$

Clearly, (6) and (7) are completely equivalent if X, X' commute. It is now straightforward to define the quantum analog of conditional expectation

$$\mathcal{E}[X' \,|\, \mathcal{B}] = \sum_i \frac{\mathrm{Tr}[\rho P_i X' P_i]}{\mathrm{Tr}[\rho P_i]} P_i. \tag{8}$$

Here, $\mathcal{B}$ is the $*$-algebra generated by X, i.e., it is the algebra whose smallest projectors are P_i. This definition also coincides with the classical conditional expectation if X, X' commute.

We obtain ambiguous results, however, when X, X' do not commute, as then the fundamental property $\langle \mathcal{E}[X' \,|\, \mathcal{B}] \rangle = \langle X' \rangle$ is generally lost. This implies that if we measure an observable, but "throw away" the measurement outcome, the expectation of the observable may change. Clearly this is inconsistent with the concept of conditional expectation which only changes the observer's state of knowledge about the system, but this is not surprising: noncommuting X, X' cannot be measured simultaneously, so any attempt of statistical inference of X' based on a measurement of X is likely to be ambiguous. To avoid this problem we define the conditional expectation only for the case that X' commutes with every element of $\mathcal{B}$. The measurement $\mathcal{B}$ is then said to be *nondemolition* [11] with respect to X'.

The essence of the formalism we have outlined is that the foundation of quantum theory is an extension of classical probability theory. This point of view lies at the heart of quantum stochastic control. The traditional formulation of quantum mechanics can be directly recovered from this formalism. Even the nondemolition requirement is not a restriction: We will show that the collapse rule (5) emerges in a quantum filtering theory that is based entirely on nondemolition measurements.

B. Infinite-Dimensional Quantum Probability

The theory of the previous section exhibits the main features of quantum probability, but only allows for finite-state random variables. A general theory which allows for continuous random variables is developed along essentially the same lines where linear algebra, the foundation of finite-dimensional quantum mechanics, is replaced by functional analysis. We will only briefly sketch the constructions here; a lucid introduction to the general theory can be found in [6].

A quantum probability space $(\mathcal{A}, \rho)$ consists of a Von Neumann algebra $\mathcal{A}$ and a state ρ. A Von Neumann algebra is a $*$-algebra of bounded linear operators on a complex Hilbert space $\mathcal{H}$ and $\rho : \mathcal{A} \to \mathbb{C}$ is a linear map such that $\rho(\mathrm{Id}_{\mathcal{H}}) = 1, \rho(A^*A) \geq 0 \;\forall A \in \mathcal{A}$, and $\rho(A^*A) = 0$ iff $A = 0$. We gloss over additional requirements related to limits of sequences of operators. It is easily verified that the definition reduces in the finite-dimensional case to the theory in the previous section, where the density operator ρ is identified with the map $X \mapsto \mathrm{Tr}[\rho X]$. We always assume $\mathrm{Id}_{\mathcal{H}} \in \mathcal{A}$.

As in the finite-dimensional case there is a correspondence between classical probability spaces and commutative algebras. Given the classical space $(\Omega, \mathcal{F}, \mathbb{P})$ the associated quantum probability space is constructed as follows:

$$\mathcal{H} = L^2(\Omega; \mathbb{C}) \quad \mathcal{A} = L^\infty(\Omega; \mathbb{C}) \quad \rho : f \mapsto \int_\Omega f \, d\mathbb{P} \tag{9}$$

where $\mathcal{A}$ acts on $\mathcal{H}$ by pointwise multiplication. Conversely, every commutative quantum probability space corresponds to a classical probability space. This fundamental result in the theory of operator algebras is known as Gel'fand's theorem.

Observables are represented by linear operators that are self-adjoint with respect to some dense domain of $\mathcal{H}$. The spectral decomposition (1) is now replaced by the spectral theorem of functional analysis, which states that every self-adjoint operator X can be represented as

$$X = \int_{\mathbb{R}} \lambda E(d\lambda) \quad E : \mathcal{B}_{\mathbb{R}} \to \mathcal{P}(\mathcal{H}). \tag{10}$$

Here, E is the spectral or projection-valued measure associated to $X, \mathcal{P}(\mathcal{H})$ is the set of all projection operators on $\mathcal{H}$, and $\mathcal{B}_{\mathbb{R}}$ is the Borel σ-algebra on $\mathbb{R}$. X is *affiliated* to $\mathcal{A}$ if $E(\Lambda) \in \mathcal{A} \;\forall \Lambda \in \mathcal{B}_{\mathbb{R}}$, replacing the concept of measurability in classical probability theory. For X affiliated to $\mathcal{A}$, the probability law and expectation are given by

$$P[X \in \Lambda] = \rho(E(\Lambda)) \quad \langle X \rangle = \int_{\mathbb{R}} \lambda \rho(E(d\lambda)). \tag{11}$$

Note that unlike in finite dimensions not all observables affiliated to $\mathcal{A}$ are elements of $\mathcal{A}$; observables may be unbounded operators, while $\mathcal{A}$ only contains bounded operators.

It remains to generalize conditional expectations to the infinite-dimensional setting, a task that is not entirely straightforward even in the classical case. Let $\mathcal{B} \subset \mathcal{A}$ be a commutative Von Neumann subalgebra. As before, we will only define conditional expectations for observables that are not demolished by $\mathcal{B}$, i.e., for observables affiliated to the commutant $\mathcal{B}' = \{A \in \mathcal{A} : [A, B] = 0 \;\forall B \in \mathcal{B}\}$.

Definition 1: The conditional expectation onto $\mathcal{B}$ is the linear surjective map $\mathcal{E}[\cdot \,|\, \mathcal{B}] : \mathcal{B}' \to \mathcal{B}$ with the following properties, for all $A \in \mathcal{B}'$:

1) $\mathcal{E}[\mathrm{Id}_{\mathcal{H}} \,|\, \mathcal{B}] = \mathrm{Id}_{\mathcal{H}}$;
2) $\mathcal{E}[A \,|\, \mathcal{B}] \geq 0$ if $A \geq 0$;
3) $\mathcal{E}[B_1 A B_2 \,|\, \mathcal{B}] = B_1 \mathcal{E}[A \,|\, \mathcal{B}] B_2 \;\forall B_1, B_2 \in \mathcal{B}$;
4) $\rho(\mathcal{E}[A \,|\, \mathcal{B}]) = \rho(A)$.

The definition extends to any observable X affiliated to $\mathcal{B}'$ by operating $\mathcal{E}[\cdot \,|\, \mathcal{B}]$ on the associated spectral measure.

It is possible to prove (e.g., [14]) that the conditional expectation exists and is unique.

C. Quantum Stochastic Calculus

Having extended probability theory to the quantum setting, we now sketch the development of a quantum Itô calculus.

We must first find a quantum analog of the Wiener process. Denote by $(\Omega, \mathcal{F}, \mathbb{P})$ the canonical Wiener space of a classical Brownian motion. The analysis in the previous section suggests that quantum Brownian motion will be represented by a set of observables on the Hilbert space $\Gamma = L^2(\Omega; \mathbb{C})$. Define the symmetric Fock space over $L^2(U)$ as

$$\Gamma_s(L^2(U)) = \mathbb{C} \oplus \bigoplus_{n=1}^{\infty} L^2(U; \mathbb{C})^{\odot n} \quad U \subset \mathbb{R}_+ \tag{12}$$

where $\odot$ denotes the symmetrized tensor product. It is well known in stochastic analysis (e.g., [8]) that Γ and $\Gamma_s(L^2(\mathbb{R}_+))$

are isomorphic, as every L^2-functional on Ω is associated to its Wiener chaos expansion. Now define the operators

$$\begin{aligned} A_g\mathbf{k} &= \sum_{i=1}^{n} k_1 \odot \cdots \odot \hat{k}_i \odot \cdots \odot k_n \int_{\mathbb{R}_+} g^* k_i \, dt \\ A_g^*\mathbf{k} &= g \odot k_1 \odot \cdots \odot k_n \end{aligned} \tag{13}$$

where $\mathbf{k} = k_1 \odot \cdots \odot k_n, g, k_i \in L^2(\mathbb{R}_+)$ and $\hat{k}_i$ means that the term i is omitted. It is sufficient to define the operators for such vectors as their linear span Γ_0 is dense in Γ. We get

$$[A_g, A_h] = [A_g^*, A_h^*] = 0 \quad [A_g, A_h^*] = \int_{\mathbb{R}_+} g^* h \, dt \tag{14}$$

and indeed $(v, A_g w) = (A_g^* v, w)$ for $v, w \in \Gamma_0$.

We will construct Wiener processes from A and A^*, but first we must set up the quantum probability space. We take $\mathcal{A}$ to contain all bounded linear operators on Γ. To construct ρ consider the vector $\Delta = 1 \oplus 0 \in \Gamma_s(L^2(\mathbb{R}_+))$. Then

$$\rho : \mathcal{A} \to \mathbb{C} \quad \rho(X) = (\Delta, X\Delta). \tag{15}$$

Now, consider the operator $A_g^* + A_g$. Using (14) and the Baker–Campbell–Hausdorff lemma, we obtain

$$\left\langle e^{i(A_g^* + A_g)} \right\rangle = \left(\Delta, e^{iA_g^*} e^{-\frac{1}{2}\|g\|^2} e^{iA_g} \Delta\right) = e^{-\frac{1}{2}\|g\|^2} \tag{16}$$

where $\|g\|^2$ is the integral of $|g|^2$ over $\mathbb{R}_+$. However, the characteristic functional of a classical Wiener process is

$$\mathbb{E}\left[e^{i\int_0^\infty \tilde{g}(t)\, dW_t}\right] = e^{-\frac{1}{2}\|\tilde{g}\|^2} \tag{17}$$

where $\tilde{g}$ is a real function. Clearly, $A_g^* + A_g$ is equivalent in law to a classical Wiener integral, and any $Q_t = A_{g_t}^* + A_{g_t}$ with $g_t(s) = \chi_{[0,t]}(s) e^{i\varphi(s)}$ is a quantum Wiener process.

It is easy to verify that $[Q_t, Q_s] = 0 \ \forall t, s$. This important property allows us to represent all $Q_t, t \in \mathbb{R}_+$ on a single classical probability space and, hence, Q_t is entirely equivalent to a classical Wiener process. Two such processes with different φ do not commute, however, and are thus incompatible.

The Fock space (12) has the following factorization property: for any sequence of times $t_1 < t_2 < \cdots < t_n \in \mathbb{R}_+$

$$\Gamma = \Gamma_{t_1]} \otimes \Gamma_{t_1,t_2} \otimes \Gamma_{t_2,t_3} \otimes \cdots \otimes \Gamma_{t_{n-1},t_n} \otimes \Gamma_{[t_n} \tag{18}$$

with $\Gamma_{s,t} = \Gamma_s(L^2([s,t])), \Gamma_{t]} = \Gamma_{0,t}$, and $\Gamma_{[t} = \Gamma_{t,\infty}$. Thus, Γ can be formally considered as a continuous tensor product over $\Gamma_s(L^2(\{t\}))$, a construction often used implicitly in physics literature. A process S_t is called *adapted* if $S_t = S_{t]} \otimes \mathrm{Id}$ in $\Gamma_{t]} \otimes \Gamma_{[t}$ for every $t \in \mathbb{R}_+$. Q_t is adapted for any φ.

It is customary to define the standard noises

$$A_t = A_{\chi_{[0,t]}} \quad A_t^* = A_{\chi_{[0,t]}}^*, \qquad t \in \mathbb{R}_+. \tag{19}$$

One can now define Itô integrals and calculus with respect to A_t, A_t^* in complete analogy to the classical case. We will only describe the main results, due to Hudson and Parthasarathy [27], and refer to [7], [8], and [27] for the full theory.

Let $\mathcal{H}$ be the Hilbert space of the system of interest; we will assume that $\dim \mathcal{H} < \infty$. Now, let $\mathcal{A}$ be the set of all bounded operators on $\mathcal{H} \otimes \Gamma$. The state $\rho = \rho_{\mathcal{H}} \otimes \rho_\Gamma$ is given in terms some state $\rho_{\mathcal{H}}$ on $\mathcal{H}$ and ρ_Γ as defined in (15). The Hudson–Parthasarathy equation

$$U_{s,t} = \mathrm{Id} + \int_s^t \left(L dA_t^* - L^* dA_t - \left(iH + \frac{1}{2} L^* L \right) dt \right) U_{s,t} \tag{20}$$

defines the flow $U_{s,t}$ of the noisy dynamics. Here, L and H are operators of the form $L \otimes \mathrm{Id}$ on $\mathcal{H} \otimes \Gamma$ and H is self-adjoint. It can be shown that $U_{s,t}$ is a unitary transformation of $\mathcal{H} \otimes \Gamma_{s,t}$ and $U_{s,t} = U_{k,t} U_{s,k}$. Given an observable S at time 0, the flow defines the associated process $S_t = U_{0,t}^* S U_{0,t}$.

Quantum stochastic differential equations are easily manipulated using the following rules. The expectation of any integral over dA_t or dA_t^* vanishes. The differentials dA_t, dA_t^* commute with any adapted process. Finally, the quantum Itô rules are $dA_t \, dA_t^* = dt, dA_t^2 = (dA_t^*)^2 = dA_t^* \, dA_t = 0$.

Let $X \in \mathcal{H}$ be any system observable; its time evolution is given by $j_t(X) = U_{0,t}^* (X \otimes \mathrm{Id}) U_{0,t}$. We easily obtain

$$dj_t(X) = j_t(\mathcal{L}X)\, dt + j_t([L^*, X])\, dA_t + j_t([X, L])\, dA_t^* \tag{21}$$

where $\mathcal{L}X = i[H, X] + L^* X L - (1/2)(L^* L X + X L^* L)$. This expression is the quantum analog of the classical Itô formula

$$dj_t(f) = j_t(\boldsymbol{L} f)\, dt + j_t(\Sigma f)\, dW_t \tag{22}$$

where $j_t(f) = f(x_t)$ with $dx_t = b(x_t)\, dt + \sigma(x_t)\, dW_t, \boldsymbol{L}$ is the infinitesimal generator of x_t and $\Sigma f = \sigma^i \partial_i f$. Similarly, $\mathcal{L}$ is called the generator of the quantum diffusion $U_{s,t}$.

In fact, the quantum theory is very similar to the classical theory of stochastic flows [28], [29] with one notable exception: the existence of incompatible observables does not allow for a unique sample path interpretation (x_t in the classical case) of the underlying system. Hence the dynamics is necessarily expressed in terms of observables, as in (21).

D. Measurements and Filtering

We now complete the picture by introducing observations and conditioning the system observables on the observed process. The following treatment is inspired by [12] and [13].

1) Classical Filtering: To set the stage for the quantum filtering problem we first treat its classical counterpart. Suppose the system dynamics (22) is observed as y_t with

$$dy_t = j_t(h)\, dt + \kappa\, dV_t \tag{23}$$

for uncorrelated noise V_t with strength $\kappa > 0$. We wish to calculate the conditional expectation $\pi_t(f) = \mathbb{E}[j_t(f) \mid \mathcal{F}_t^y]$.

Recall the classical definition: $\mathbb{E}[X \mid \mathcal{F}]$ is the $\mathcal{F}$-measurable random variable such that $\mathbb{E}[\mathbb{E}[X \mid \mathcal{F}] Y] = \mathbb{E}[XY]$ for all $\mathcal{F}$-measurable Y. Suppose $\mathcal{F}$ is generated by some random variable F. The definition suggests that to prove $\hat{X} = \mathbb{E}[X \mid \mathcal{F}]$ for some $\mathcal{F}$-measurable $\hat{X}$, it should be sufficient to show that

$$\mathbb{E}[\hat{X}e^{F\xi}] = \mathbb{E}[Xe^{F\xi}] \qquad \forall \xi \in \mathbb{R} \tag{24}$$

i.e., the conditional generating functions coincide.

We will apply this strategy in the continuous case. As $\pi_t(f)$ is an $\mathcal{F}_t^y$-semimartingale we introduce the ansatz

$$d\pi_t(f) = C_t\,dt + D_t\,dy_t \tag{25}$$

with C_t, D_t $\mathcal{F}_t^y$-adapted. We will choose C_t, D_t such that $\mathbb{E}[e_t^g \pi_t(f)] = \mathbb{E}[e_t^g j_t(f)]$ for all functions g, where

$$e_t^g = e^{\int_0^t g(s)\,dy_s - \frac{1}{2}\kappa^2 \int_0^t g(s)^2\,ds}, \qquad de_t^g = g(t)e_t^g\,dy_t. \tag{26}$$

The Itô correction term in the exponent was chosen for convenience and does not otherwise affect the procedure.

Using Itô's rule and the usual properties of conditional expectations, we easily obtain

$$\frac{d\mathbb{E}\left[e_t^g j_t(f)\right]}{dt} = \mathbb{E}\left[e_t^g \pi_t(\boldsymbol{L}f) + g(t)e_t^g \pi_t(hf)\right] \tag{27}$$

$$\begin{aligned}\frac{d\mathbb{E}\left[e_t^g \pi_t(f)\right]}{dt} &= \mathbb{E}\left[e_t^g(C_t + \pi_t(h)D_t)\right.\\ &\quad \left. + \, g(t)e_t^g(\kappa^2 D_t + \pi_t(h)\pi_t(f))\right].\end{aligned} \tag{28}$$

Requiring these expressions to be identical for any g gives

$$d\pi_t(f) = \pi_t(\boldsymbol{L}f)\,dt + \kappa^{-1}(\pi_t(hf) - \pi_t(h)\pi_t(f))\,d\bar{W}_t \tag{29}$$

where the innovations process $d\bar{W}_t = \kappa^{-1}(dy_t - \pi_t(h)\,dt)$ is a Wiener process. Equation (29) is the well-known Kushner–Stratonovich equation of nonlinear filtering [30], [31].

2) Quantum Filtering: The classical approach generalizes directly to the quantum case. The main difficulty here is how to define in a sensible way the observation (23)?

We approach the problem from a physical perspective [32]. The quantum noise represents an electromagnetic field coupled to the system (e.g., an atom.) Unlike classically, where any observation is in principle admissible, a physical measurement is performed by placing a detector in the field. Hence, the same noise that drives the system is used for detection, placing a physical restriction on the form of the observation.

We will consider the observation $Y'_t = U^*_{0,t}(A^*_t + A_t)U_{0,t} + \kappa(B^*_t + B_t)$. Here, B_t is a noise uncorrelated from A_t that does not interact with the system (the Hilbert space is $\mathcal{H}\otimes\Gamma\otimes\Gamma$, etc.) Physically, we are measuring the field observable $A^*_t + A_t$ after interaction with the system, corrupted by uncorrelated noise of strength $\kappa > 0$. Using the Itô rule and (20) we get

$$dY'_t = j_t(L^* + L)\,dt + dA^*_t + dA_t + \kappa(dB^*_t + dB_t). \tag{30}$$

It is customary in physics to use a normalized observation Y_t such that $dY_t^2 = dt$. We will use the standard notation

$$dY_t = \sqrt{\eta}(j_t(L^* + L)\,dt + dA^*_t + dA_t) + \sqrt{1-\eta}\,dV_t \tag{31}$$

where $V_t = B^*_t + B_t$ and $\eta = (1 + \kappa^2)^{-1} \in (0, 1]$.

Y'_t and Y_t satisfy the following two crucial properties.

1) Y'_t is *self-nondemolition*, i.e., $[Y'_t, Y'_s] = 0\ \forall s < t$. To see this, note that $[Y'_t, Y'_s] = [U^*_{0,t}Q_tU_{0,t}, U^*_{0,s}Q_sU_{0,s}]$ with $Q_t = A^*_t + A_t$. But $U_{s,t}$ is a unitary transformation of $\mathcal{H} \otimes \Gamma_{s,t}$ and $Q_s = \mathrm{Id} \otimes Q_{s]} \otimes \mathrm{Id}$ on $\mathcal{H}\otimes\Gamma_{s]}\otimes\Gamma_{[s}$; thus we get $U^*_{s,t}Q_sU_{s,t} = Q_sU^*_{s,t}U_{s,t} = Q_s$, so $U^*_{0,s}Q_sU_{0,s} = U^*_{0,t}Q_sU_{0,t}$. But then $[Y'_t, Y'_s] = U^*_{0,t}[Q_t, Q_s]U_{0,t} = 0$ as we have already seen that Q_t is self-nondemolition.

2) Y'_t is *nondemolition*, i.e., $[j_t(X), Y'_s] = 0\ \forall s < t$ for all system observables X on $\mathcal{H}$. The proof is identical to the proof of the self-nondemolition property.

These properties are essential in any sensible quantum filtering theory: Self-nondemolition implies that the observation is a classical stochastic process, whereas nondemolition is required for the conditional expectations to exist. A general filtering theory can be developed that allows any such observation [11], [12]; we will restrict ourselves to our physically motivated Y_t.

We wish to calculate $\pi_t(X) = \mathcal{E}[j_t(X) \mid \mathcal{B}_t]$ where $\mathcal{B}_t$ is the algebra generated by $Y_{s\le t}$. Introduce the ansatz

$$d\pi_t(X) = C_t\,dt + D_t\,dY_t \tag{32}$$

where C_t, D_t are affiliated to $\mathcal{B}_t$. Define

$$e_t^g = e^{\int_0^t g(s)\,dY_s - \frac{1}{2}\int_0^t g(s)^2\,ds}, \qquad de_t^g = g(t)e_t^g\,dY_t. \tag{33}$$

Using the quantum Itô rule and Definition 1, we get

$$\frac{d\left\langle e_t^g j_t(X)\right\rangle}{dt} = \left\langle e_t^g \pi_t(\mathcal{L}X) + g(t)e_t^g \pi_t(XL + L^*X)\sqrt{\eta}\right\rangle \tag{34}$$

$$\begin{aligned}\frac{d\left\langle e_t^g \pi_t(X)\right\rangle}{dt} &= \left\langle e_t^g(C_t + \pi_t(L^* + L)D_t\sqrt{\eta})\right.\\ &\quad \left. + \, g(t)e_t^g(D_t + \pi_t(L^* + L)\pi_t(X)\sqrt{\eta})\right\rangle.\end{aligned} \tag{35}$$

Requiring these expressions to be identical for any g gives

$$\begin{aligned}d\pi_t(X) &= \pi_t(\mathcal{L}X)\,dt + \sqrt{\eta}(\pi_t(XL + L^*X)\\ &\quad -\pi_t(L^* + L)\pi_t(X))(dY_t - \sqrt{\eta}\,\pi_t(L^* + L)\,dt)\end{aligned} \tag{36}$$

which is the quantum analog of (29). It can be shown that the innovations process $dW_t = dY_t - \sqrt{\eta}\pi_t(L^* + L)\,dt$ is a martingale (e.g., [14]) and, hence, it is a Wiener process by Lévy's classical theorem.

E. The Physical Model

Quantum (or classical) probability does not by itself describe any particular physical system; it only provides the mathematical framework in which physical systems can be modeled. The modeling of particular systems is largely the physicist's task and a detailed discussion of the issues involved is beyond the scope of this article; we limit ourselves to a few general remarks. The main goal of this section is to introduce a prototypical quantum system which we will use in the remainder of this article.

The emergence of quantum models can be justified in different ways. The traditional approach involves "quantization" of classical mechanical theories using an empirical quantization rule. A more fundamental theory builds quantum models as "statistical" representations of mechanical symmetry groups [33], [34]. Both approaches generally lead to the same theory.

The model considered in this paper (Fig. 1) is prototypical for experiments in quantum optics; in fact, it is very similar to our laboratory apparatus [4]. The system consists of a cloud of atoms, collectively labeled "spin", interacting with an optical field (along $\hat{z}$) produced by a laser. After interacting with the system the optical field is detected using a photodetector configuration known as a homodyne detector. A pair of magnetic coils (along $\hat{y}$) are used as feedback actuators.

The optical and magnetic fields are configured so they only interact, to good approximation, with the collective angular momentum degrees of freedom of all the atoms [35]. Rotational symmetry implies that observables of angular momentum must form the rotation Lie algebra $\mathfrak{so}(3)$. If we impose additionally that the total angular momentum is conserved, then it is a standard result in quantum mechanics [26] that the angular momentum observables form an irreducible representation of $\mathfrak{so}(3)$. Such a system is called a spin.

We take $\mathcal{H}$ to be the spin Hilbert space. Any finite dimension $2 \leq \dim \mathcal{H} < \infty$ supports an irrep of $\mathfrak{so}(3)$; the choice of $\dim \mathcal{H} = 2j + 1$ depends on the number of atoms and their properties. We can choose an orthonormal basis $\{\psi_m \in \mathcal{H}, m = -j, -j+1, \ldots, j\}$ such that the observables $J_{x,y,z}$ of angular momentum around the x, y, z-axis are defined by[1]

$$\begin{aligned} J_x \psi_m &= c_m \psi_{m+1} + c_{-m} \psi_{m-1} \\ J_y \psi_m &= i c_m \psi_{m+1} - i c_{-m} \psi_{m-1} \\ J_z \psi_m &= m \psi_m \end{aligned} \tag{37}$$

with $c_m = (1/2)\sqrt{(j-m)(j+m+1)}$. It is easily verified that $J_{x,y,z}$ indeed generate $\mathfrak{so}(3)$, e.g., $[J_x, J_y] = iJ_z$.

Note that $J_{x,y,z}$ are discrete random variables; the fact that angular momentum is "quantized," unlike in classical mechanics, is one of the remarkable predictions of quantum mechanics that give the theory its name. Another remarkable nonclassical effect is that $J_{x,y,z}$ are incompatible observables.

The noise in our model and its interaction with the atoms emerges naturally from quantum electrodynamics, the quantum theory of light [36]. Physical noise is not white; however, as the correlation time of the optical noise is much shorter than the time scale of the spin dynamics, a quantum analog of the classical Wong–Zakai procedure [37], [38] can be employed to approximate the dynamics by an equation of the form (20). In fact, the term $-(1/2)L^*L$ in (20) is precisely the Wong–Zakai correction term that emerges in the white noise limit.

We now state the details of our model without further physical justification. The system is described by (20) with $L = \sqrt{M}J_z$ and $H = B(t)J_y$. Here $M > 0$ is the strength of the interaction between the light and the atoms; it is regulated experimentally by the optical cavity. $B(t)$ is the applied magnetic field and serves as the control input. Finally, homodyne detection [32] provides exactly the measurement[2] (31), where η is determined by the efficiency of the photodetectors.

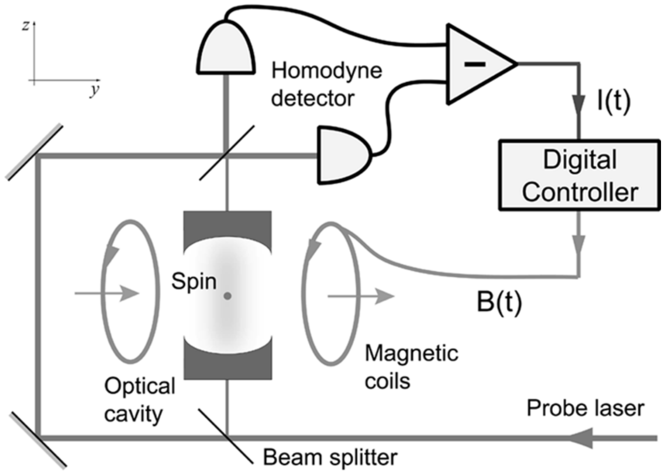

Fig. 1. Schematic of an experiment for continuous quantum measurement and control. The spin interacts with an optical mode, which is measured continuously by homodyne detection. A magnetic field is used for feedback.

In the remainder of this paper, we will study the spin system of Fig. 1. Before we devote ourselves entirely to this situation, however, we mention a couple of other common scenarios.

Often L is not self-adjoint; in this case, the system can emit or absorb energy through interaction with the field. This situation occurs when the optical frequency of the cavity field is resonant with an atomic transition. In our case the frequency is chosen to be far off-resonant; this leads to self-adjoint L after adiabatic elimination of the cavity dynamics (e.g., [16]). The filter dynamics in this scenario, to be described later, is known as state reduction. The sequence of approximations that is used for our particular model is described in [39].

Finally, a different detector configuration may be chosen. For example, a drastically different observation, known as photon counting, gives rise to a Poisson (jump) process. We refer to [32] for a full account of the quantum stochastic approach to observations in quantum optics.

III. GEOMETRY AND DYNAMICS OF THE FILTER

In the previous section, we introduced our physical model. A detailed analysis resulted in the filtering equation (36), where $\pi_t(X)$ is the best estimate of the observable X given the observations $Y_{s \leq t}$. We will now study this equation in detail.

Note that (36) is driven by the observation Y_t, which is a classical stochastic process. Hence, (36) is entirely equivalent to a classical Itô equation. This is an important point, as it means that in the remainder of this article we only need classical stochastic calculus.

---

[1] Angular momentum is given in units of $\hbar \simeq 1.055 \times 10^{-34}$ kg m^{2}s^{-1}. To simplify the notation we always work in units such that $\hbar = 1$.

[2] In practice one measures not Y_t but its formal derivative $I(t) = dY_t/dt$. As in classical stochastics we prefer to deal mathematically with the integrated observation Y_t rather than the singular "white noise" photocurrent $I(t)$.

A. The State–Space

We begin by investigating the state space on which the filter evolves. Clearly (36) defines the time evolution of a map π_t; we will show how this map can be represented efficiently.

The map π_t associates to every observable X on $\mathcal{H}$ a classical stochastic process which represents the expectation of X conditioned on the observations up to time t. It is easily verified that π_t is linear, identity preserving, and maps positive observables to positive numbers: In fact, it acts exactly like the expectation of X with respect to some finite-dimensional state on $\mathcal{H}$. We will denote this state by ρ_t, the conditional density at time t, where by definition $\pi_t(X) = \mathrm{Tr}[\rho_t X]$.

It is straightforward to find an expression for ρ_t. We get

$$d\rho_t = \mathcal{L}^*\rho_t\,dt + \sqrt{\eta}(L\rho_t + \rho_t L^* - \mathrm{Tr}[\rho_t(L+L^*)]\rho_t)\,dW_t \quad (38)$$

with the innovations $dW_t = dY_t - \sqrt{\eta}\mathrm{Tr}[\rho_t(L+L^*)]\,dt$ and the adjoint generator $\mathcal{L}^*\rho = -i[H,\rho] + L\rho L^* - (1/2)(L^*L\rho + \rho L^*L)$. In physics, this equation is also known as a quantum trajectory equation or stochastic master equation.

Let $\dim\mathcal{H} = n$; as n is finite, we can represent linear operators on $\mathcal{H}$ by complex matrices. Thus, (38) is an ordinary, finite-dimensional Itô equation. We saw in Section II-A that ρ_t is a density matrix, i.e., it belongs to the space

$$\mathcal{P} = \{\rho \in \mathbb{C}^{n\times n} : \rho = \rho^*, \mathrm{Tr}\,\rho = 1, \rho \geq 0\}. \quad (39)$$

By construction $\mathcal{P}$ is an invariant set of (38), and forms the natural state space of the filter.

B. Geometry of $\mathcal{P}$

The geometry of $\mathcal{P}$ is rather complicated [40]. To make the space more manageable we will reparametrize $\mathcal{P}$ so it can be expressed as a semialgebraic set.

Let us choose the matrix elements ρ_{ij} of ρ as follows. For $i > j$ set $\rho_{ij} = \lambda_{ij} + i\mu_{ij}$ with $\lambda_{ij}, \mu_{ij} \in \mathbb{R}$. For $i < j$ set $\rho_{ij} = \rho_{ji}^*$. Finally, choose an integer k between 1 and n. For $i \neq k$ set $\rho_{ii} = \nu_i, \nu_i \in \mathbb{R}$, and $\rho_{kk} = 1 - \sum_{i\neq k}\nu_i$. Collect all $n^2 - 1$ numbers $\lambda_{ij}, \mu_{ij}, \nu_i$ into a vector Λ. Then, clearly, the map $h : \Lambda \mapsto \rho$ is an isomorphism between $\mathbb{R}^{n^2-1}$ and $\{\rho \in \mathbb{C}^{n\times n} : \rho = \rho^*, \mathrm{Tr}\,\rho = 1\}$.

It remains to find the subset $K \subset \mathbb{R}^{n^2-1}$ that corresponds to positive–definite matrices. This is nontrivial, however, as it requires us to express nonnegativity of the eigenvalues of ρ as constraints on ρ_{ij}. The problem was solved by Kimura [40] using Descartes' sign rule and the Newton–Girard identities for symmetric polynomials; we quote the following result.

Proposition 1: Define $k_p(\rho), p = 2\ldots n$ recursively by

$$pk_p(\rho) = \sum_{q=1}^{p}(-1)^{q-1}\,\mathrm{Tr}[\rho^q]k_{p-q}(\rho) \quad (40)$$

with $k_0 = k_1 = 1$. Define the semialgebraic set

$$K = \{\Lambda \in \mathbb{R}^{n^2-1} : k_p(h(\Lambda)) \geq 0, p = 2\ldots n\}. \quad (41)$$

Then, h is an isomorphism between K and $\mathcal{P}$.

Note that $2k_2 = 1 - \mathrm{Tr}[\rho^2] \geq 0$ implies $\|\Lambda\|^2 = \sum_i \nu_i^2 + \sum_{i>j}(\lambda_{ij}^2 + \mu_{ij}^2) \leq \mathrm{Tr}[h(\Lambda)^2] \leq 1$. Hence, K is compact.

We work out explicitly the simplest case $n = 2$ (spin $j = (1/2)$). Set $\rho_{11} = \nu, \rho_{22} = 1 - \nu, \rho_{21} = \lambda + i\mu = \rho_{12}^*$. Then

$$K_2 = \{\Lambda = (\lambda, \mu, \nu) \in \mathbb{R}^3 : \lambda^2 + \mu^2 + \nu(\nu - 1) \leq 0\}. \quad (42)$$

This is just a solid sphere with radius $(1/2)$, centered at $(0, 0, (1/2))$. The case $n = 2$ is deceptively simple, however: it is the only case with a simple topology [41], [40].

We can also express (38) in terms of Λ. Specifically, we will consider the spin system $L = \sqrt{M}J_z, H = B(t)J_y$ in the basis $\psi_{1/2} = (1, 0), \psi_{-1/2} = (0, 1)$ on $\mathbb{C}^{2\times 2}$. We obtain

$$\begin{aligned} d\lambda_t &= \left(B(t)\left(\nu_t - \frac{1}{2}\right) - \frac{1}{2}M\lambda_t\right)dt \\ &\quad + \sqrt{M\eta}\lambda_t(1 - 2\nu_t)\,dW_t \\ d\mu_t &= -\frac{1}{2}M\mu_t\,dt + \sqrt{M\eta}\mu_t(1 - 2\nu_t)\,dW_t \\ d\nu_t &= -B(t)\lambda_t dt - 2\sqrt{M\eta}\nu_t(\nu_t - 1)\,dW_t. \end{aligned} \quad (43)$$

By construction, K_2 is an invariant set for this system.

C. Convexity and Pure States

Just like its classical counterpart, the set of densities $\mathcal{P}$ is convex. We have the following fundamental result.

Proposition 2: The set $\mathcal{P}$ is the convex hull of the set of pure states $\mathcal{Q} = \{vv^* \in \mathbb{C}^{n\times n} : v \in \mathbb{C}^n, \|v\| = 1\} \subset \mathcal{P}$.

Proof: As any $\rho \in \mathcal{P}$ is self-adjoint it can be written as $\rho = \sum_i \lambda_i v_i v_i^*$, where v_i are orthonormal eigenvectors of ρ and λ_i are the corresponding eigenvalues. However, $\mathrm{Tr}\rho = 1, \rho \geq 0$ imply that $\sum_i \lambda_i = 1$ and $\lambda_i \in [0, 1]$. Hence $\mathcal{P} \subset \mathrm{conv}\,\mathcal{Q}$. Conversely, it is easily verified that $\mathrm{conv}\,\mathcal{Q} \subset \mathcal{P}$. ■

Pure states are the extremal elements of $\mathcal{P}$; they represent quantum states of maximal information. Note that classically extremal measures are deterministic, i.e., $\mathbb{P}[A]$ is either 0 or 1 for any event A. This is not the case for pure states $\rho = vv^*$, however: any event $A = ww^*$ with $0 < \|w^*v\| < 1, \|w\| = 1$ will have $0 < \mathrm{Tr}[\rho A] < 1$. Thus, no quantum state is deterministic, unless we restrict to a commutative algebra $\mathcal{A}$.

Intuitively one would expect that if the output Y_t is not corrupted by independent noise, i.e., $\eta = 1$, then there is no loss of information and, hence, an initially pure ρ_0 would remain pure under (38). This is indeed the case. Define

$$dv_t = \left[\left(h_t L - \frac{1}{2}L^*L - \frac{1}{2}h_t^2 - iH\right)dt + (L - h_t)\,dW_t\right]v_t \quad (44)$$

where $h_t = (1/2)v_t^*(L^* + L)v_t$. Then, it is easily verified that $\rho_t = v_t v_t^*$ obeys (38) with $\eta = 1$. It follows that if $\eta = 1, \mathcal{Q}$ is an invariant set of (38). In the concrete example (43) it is not difficult to verify this property directly: when $\eta = 1$, the sphere $\lambda^2 + \mu^2 + \nu(\nu - 1) = 0$ is invariant under (43).

D. Quantum State Reduction

We now study the dynamics of the spin filtering equation without feedback $B(t) = 0$. We follow the approach of [42].

Consider the quantity $V_t = \pi_t(J_z^2) - \pi_t(J_z)^2$. We obtain

$$\frac{d\mathbb{E}[V_t]}{dt} = -4M\eta\mathbb{E}\left[V_t^2\right]. \quad (45)$$

Clearly, $\mathbb{E}[V_t^2] \geq 0$, so $\mathbb{E}[V_t]$ decreases monotonically. But $V_t \geq 0$ and $\mathbb{E}[V_t^2] = 0$ iff $V_t = 0$ a.s. We conclude that

$$\lim_{t\to\infty} \mathbb{E}[V_t] = 0 \tag{46}$$

and, hence, $V_t \to 0$ a.s. as $t \to \infty$. However, the only states $\rho \in \mathcal{P}$ with $V_t = \mathrm{Tr}[J_z^2\rho] - \mathrm{Tr}[J_z\rho]^2 = 0$ are the eigenstates $\psi_m\psi_m^*$ of J_z. Hence, in the long-time limit the conditional state *collapses* onto one of the eigenstates of J_z, as predicted by (5) for a "direct" measurement of J_z.

With what probability does the state collapse onto eigenstate m? To study this, let us calculate $\pi_t(\psi_m\psi_m^*)$. We get

$$d\pi_t(\psi_m\psi_m^*) = 2\sqrt{M\eta}\,\pi_t(\psi_m\psi_m^*)(m - \pi_t(J_z))\,dW_t. \tag{47}$$

Clearly, $\pi_t(\psi_m\psi_m^*)$ is a martingale, so

$$p_m = \mathbb{E}[\pi_\infty(\psi_m\psi_m^*)] = \pi_0(\psi_m\psi_m^*). \tag{48}$$

We have already shown that ρ_∞ is one of $\psi_n\psi_n^*$, and as the ψ_m are orthonormal this implies that $\pi_\infty(\psi_m\psi_m^*) = \mathrm{Tr}[\rho_\infty\psi_m\psi_m^*]$ is 1 if $n = m$ and 0, otherwise. Thus, p_m is just the probability of collapsing onto the eigenstate m. However, note that $\pi_0(\psi_m\psi_m^*) = \mathrm{Tr}[\rho_0\psi_m\psi_m^*]$, so (48) gives exactly the same collapse probability as the "direct" measurement (3).

We conclude that the predictions of quantum filtering theory are entirely consistent with the traditional quantum mechanics. A continuous reduction process replaces, but is asymptotically equivalent to, the instantaneous state collapse of Section II-A. This phenomenon is known as *quantum state reduction*.[3] We emphasize that quantum filtering is purely a statistical inference process and is obtained entirely through nondemolition measurements. Note also that state reduction occurs because $L = J_z$ is self-adjoint; other cases are of equal physical interest, but we will not consider them in this paper.

Physically, the filtering approach shows that realistic measurements are not instantaneous but take some finite time. The time scale of state reduction is of order M^{-1}, an experimentally controlled parameter. A carefully designed experiment can thus have a reduction time scale of an order attainable by modern digital electronics [43], which opens the door to both measuring and manipulating the process in real time.

IV. STABILIZATION OF SPIN STATE REDUCTION

A. The Control Problem

It is a standard idea in stochastic control that an output feedback control problem can be converted into a state feedback problem for the filter [9], [10]. This is shown schematically in Fig. 2. The filtering equations (36) or (38) are driven by Y_t; hence, at least in principle, the conditional state ρ_t can be calculated recursively in real time by a digital processor.

The filter describes optimally our knowledge of the system; clearly, the extent of our knowledge of the system state limits the precision with which it can be controlled. The best we can hope to do is to control the system to the best of our knowledge, i.e., to control the filter. The latter is a well-posed problem, despite that we cannot predict the observations Y_t, because we know the statistics of the innovations process W_t.

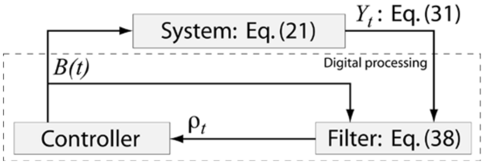

Fig. 2. Schematic of the feedback control strategy. The output from the system is used to propagate the conditional state of the filter. The feedback signal is of state feedback form with respect to the conditional state.

For such a scheme to be successful the system dynamics (21) must be known, as the optimal filter is matched to the system dynamics. Designing controllers that perform well even when the system dynamics is not known precisely is the subject of robust control theory. Also, efficient signal processing algorithms and hardware are necessary to propagate (38) in real time, which is particularly problematic when $\dim\mathcal{H}$ is large. Neither of these issues will be considered in this paper.

The state reduction dynamics discussed in the previous section immediately suggests the following control problem: We wish to find state feedback $B(t) = \Phi(\rho_t)$ so that one of the eigenstates $\rho = \psi_m\psi_m^*$ is globally stabilized. The idea that a quantum measurement can be engineered to collapse deterministically onto an eigenstate of our choice is somewhat remarkable from a traditional physics perspective, but clearly the measurement scenario we have described provides us with this opportunity. For additional motivation and numerical simulations relating to this control problem, see [3].

B. Stochastic Stability

In nonlinear control theory [44] stabilization of nonlinear systems is usually performed using the powerful tools of Lyapunov stability theory. In this section we will describe the stochastic counterpart of deterministic Lyapunov theory, developed in the 1960s by Has'minskiĭ and others. We will not give proofs, for which we refer to [45]–[48].

Let W_t be a Wiener process on the canonical Wiener space $(\Omega, \mathcal{F}, \mathbb{P})$. Consider an Itô equation on $\mathbb{R}^n$ of the form

$$dx_t = b(x_t)\,dt + \sigma(x_t)\,dW_t \tag{49}$$

where $b, \sigma : \mathbb{R}^n \to \mathbb{R}^n$ satisfy the usual linear growth and local Lipschitz conditions for existence and uniqueness of solutions [49]. Let x^* be a fixed point of (49), i.e., $b(x^*) = \sigma(x^*) = 0$.

Definition 2: The equilibrium solution $x_t = x^*$ of (49) is

1) *stable in probability* if

$$\lim_{x_0\to x^*} \mathbb{P}[\sup_{t\geq 0} |x_t - x^*| > \epsilon] = 0 \qquad \forall\epsilon > 0;$$

2) *asymptotically stable* if it is stable in probability and

$$\lim_{x_0\to x^*} \mathbb{P}[\lim_{t\to\infty} |x_t - x^*| = 0] = 1;$$

3) *globally stable* if it is stable in probability and

$$\mathbb{P}[\lim_{t\to\infty} |x_t - x^*| = 0] = 1.$$

---

[3] The term state reduction is sometimes associated with quantum state diffusion, an attempt to empirically modify the laws of quantum mechanics so that state collapse becomes a dynamical property. The state diffusion equation, which is postulated rather than derived, is exactly (44) with $L = L^*$. We use the term state reduction as describing the reduction dynamics without any relation to its interpretation. The analysis of [42] is presented in the context of quantum state diffusion, but applies equally well to our case.

Note that 1) and 2) are local properties, whereas 3) is a global property of the system.

Recall that the infinitesimal generator of x_t is given by

$$\boldsymbol{L} = \sum_i b^i(x)\frac{\partial}{\partial x^i} + \frac{1}{2}\sum_{ij}\sigma^i(x)\sigma^j(x)\frac{\partial^2}{\partial x^i \partial x^j} \tag{50}$$

so $d\mathbb{E}[f(x_t)]/dt = \mathbb{E}[\boldsymbol{L}f(x_t)]$. We can now state the stochastic equivalent of Lyapunov's direct method [45]–[47].

Theorem 1: Define $U_h = \{x : |x - x^*| < h\}$. Suppose there exists some $h > 0$ and a function $V : U_h \to \mathbb{R}_+$ that is continuous and twice differentiable on $U_h\backslash\{x^*\}$, such that $V(x^*) = 0$ and $V(x) > 0$, otherwise, and $\boldsymbol{L}V(x) \le 0$ on U_h. Then the equilibrium solution $x_t = x^*$ is stable in probability. If $\boldsymbol{L}V(x) < 0$ on $U_h\backslash\{x^*\}$, then x^* is asymptotically stable.

Theorem 1 is a local theorem; to prove global stability we need additional methods. When dealing with quantum filtering equations a useful global result is the following stochastic LaSalle-type theorem of Mao [48]. In the theorem we will assume that the dynamics of (49) are confined to a *bounded invariant set* G.

Theorem 2: Let G be a bounded invariant set with respect to the solutions of (49) and $x_0 \in G$. Suppose there exists a continuous, twice differentiable function $V : G \to \mathbb{R}_+$ such that $\boldsymbol{L}V(x) \le 0 \; \forall x \in G$. Then $\lim_{t\to\infty} \boldsymbol{L}V(x_t) = 0$ a.s.

Finally, we will find it useful to prove that a particular fixed point *repels* trajectories that do not originate on it. To this end, we use the following theorem of Has'minskiĭ [45].

Theorem 3: Suppose there exists some $h > 0$ and a function $V : U_h \to \mathbb{R}$ that is continuous and twice differentiable on $U_h\backslash\{x^*\}$, such that

$$\lim_{x\to x^*} V(x) = +\infty$$

and $\boldsymbol{L}V(x) < 0$ on $U_h\backslash\{x^*\}$. Then, the equilibrium solution $x_t = x^*$ is not stable in probability and, moreover

$$\mathbb{P}[\sup_{t>0} |x_t - x^*| < h] = 0 \qquad \forall x_0 \in U_h\backslash\{x^*\}. \tag{51}$$

C. A Toy Problem: The Disc and the Circle

We treat in detail an important toy problem: spin $j = (1/2)$. The low dimension and the simple topology make this problem easy to visualize. Nonetheless we will see that the stabilization problem is not easy to solve even in this simple case.

We have already obtained the filter (43) on K_2 for this case. Conveniently, the origin in K_2 is mapped to the lower eigenstate $\psi_{-1/2}\psi^*_{-1/2}$; we will attempt to stabilize this state.

Note that the equations for λ_t, ν_t are decoupled from μ_t. Moreover, the only point in K_2 with $(\lambda, \nu) = (0,0)$ has $\mu = 0$. Hence, we can equivalently consider the control problem

$$\begin{aligned} d\lambda_t &= \left(B(t)\left(\nu_t - \frac{1}{2}\right) - \frac{1}{2}M\lambda_t\right)dt \\ &\quad + \sqrt{M\eta}\lambda_t(1 - 2\nu_t)\,dW_t \\ d\nu_t &= -B(t)\lambda_t\,dt - 2\sqrt{M\eta}\nu_t(\nu_t - 1)\,dW_t \end{aligned} \tag{52}$$

on the disc $B^2 = \{(\lambda, \nu) \in \mathbb{R}^2 : \lambda^2 + \nu(\nu - 1) \le 0\}$. Controlling (52) is entirely equivalent to controlling (43), as globally stabilizing $(\lambda, \nu) = (0,0)$ guarantees that μ is attracted to zero due to the geometry of K_2.

An even simpler toy problem is obtained as follows. Suppose $\eta = 1$; we have seen that then the sphere $\lambda^2 + \mu^2 + \nu(\nu - 1) = 0$ is invariant under (43). Now, suppose that additionally $\mu_0 = 0$. Then, clearly the circle $S^1 = \{(\lambda, \nu) \in \mathbb{R}^2 : \lambda^2 + \nu(\nu - 1) = 0\}$ is an invariant set. We find

$$d\theta_t = \left(B(t) - \frac{1}{2}M\sin\theta_t\cos\theta_t\right)dt - \sqrt{M}\sin\theta_t\,dW_t \tag{53}$$

after a change of variables $(2\lambda_t, 2\nu_t) = (\sin\theta_t, 1 + \cos\theta_t)$.

System (52) could in principle be realized by performing the experiment of Fig. 1 with a single atom. The reduced system (53) is unrealistic, however; it would require perfect photodetectors and perfect preparation of the initial state. Nonetheless, it is instructive to study this case, as it provides intuition which can be applied in more complicated scenarios. Note that (53) is a special case of (52) where $\eta = 1$ and the dynamics is restricted to the boundary of B^2.

D. Almost Global Control on S^1

We wish to stabilize $(\lambda, \nu) = (0,0)$, which corresponds to $\theta = \pi$. Note that by (53) a positive magnetic field $B > 0$ causes an increasing drift in θ, i.e., a clockwise rotation on the circle. Hence, a natural choice of controller is one which causes the state to rotate in the direction nearest to $\theta = \pi$ from the current position. This situation is sketched in Fig. 3(a).

A drawback of any such controller is that by symmetry, the feedback must vanish not only on $\theta = \pi$ but also on $\theta = 0$; hence, $\theta = 0$ remains a fixed point of the controlled system and the system is not *globally* stable. We will show, however, that under certain conditions such feedback renders the system *almost globally* stable, in the sense that all paths that do not start on $\theta = 0$ are attracted to $\theta = \pi$ a.s.

For simplicity, we choose a controller that is linear in (λ, ν)

$$B(t) = 2G\lambda_t = G\sin\theta_t, \qquad G > 0. \tag{54}$$

Here, G is the feedback gain. The generator of (53) is then

$$\boldsymbol{L} = \left(G\sin\theta - \frac{1}{2}M\sin\theta\cos\theta\right)\frac{\partial}{\partial\theta} + \frac{1}{2}M\sin^2\theta\frac{\partial^2}{\partial\theta^2}. \tag{55}$$

As a first step we will show that the fixed point $\theta = \pi$ is asymptotically stable and that the system is always attracted to one of the fixed points (there are no limit cycles, etc.). To this end, consider the Lyapunov function

$$V(\theta) = 1 + \cos\theta, \quad V(\pi) = 0, \qquad V(\theta \ne \pi) > 0. \tag{56}$$

We obtain

$$\boldsymbol{L}V(\theta) = -G\sin^2\theta. \tag{57}$$

It follows from Theorem 1 that $\theta = \pi$ is asymptotically stable, and from Theorem 2 that $\lim_{t\to\infty}\theta_t \in \{0, \pi\}$ a.s.

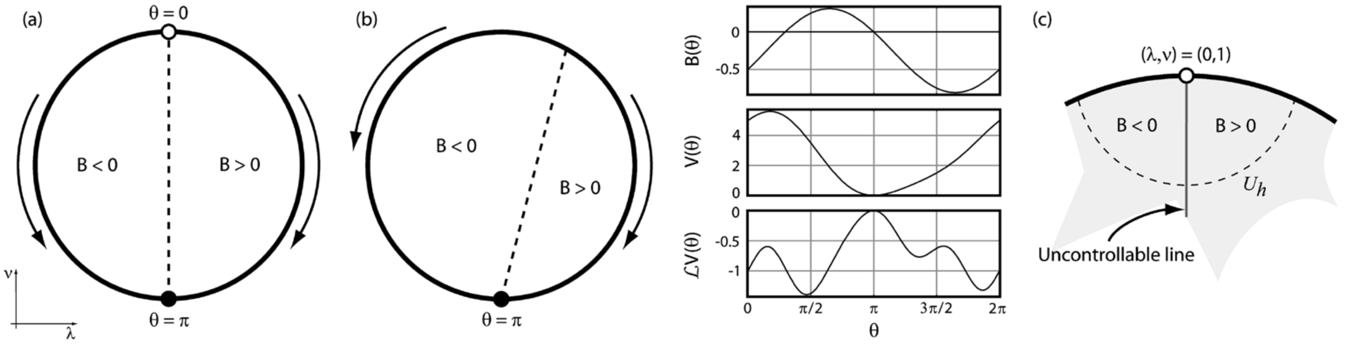

Fig. 3. Cartoons of the various control schemes; the arrows denote the rotation direction of the magnetic field. (a) Almost global control on the circle: The magnetic field always rotates in the direction of least distance to $\theta = \pi$, but $\theta = 0$ remains a fixed point. (b) Global control on the circle: We intentionally break the symmetry of the controller to remove the undesired fixed point. The graphs show a typical feedback law and Lyapunov design with $M = 1, B(\theta) = (1/2)\sin\theta - (1/4)(1+\cos\theta), V(\theta) = ((5/2)+\sin\theta)(1+\cos\theta)$. (c) A neighborhood of $(\lambda, \nu) = (0,1)$ showing why the almost global control law fails on the disc. The control vanishes on the line $\lambda = 0$; hence, points on this line are never repelled with unit probability, in violation of (51).

What remains to be shown is that any trajectory which does not start on $\theta = 0$ ends up at $\theta = \pi$ a.s. To prove this, consider

$$\tilde{V}(\theta) = -\log(1-\cos\theta) \quad \lim_{\theta\to 0}\tilde{V}(\theta) = +\infty. \tag{58}$$

We easily find

$$\boldsymbol{L}\tilde{V}(\theta) = \cos^2(\theta/2)(M + M\cos\theta - 2G). \tag{59}$$

Now, note that

$$\boldsymbol{L}\tilde{V}(\theta) < 0 \quad \forall\theta \in (-\pi,\pi)\backslash\{0\} \quad \text{iff} \quad G \ge M. \tag{60}$$

Thus, by Theorem 3 we have

$$\mathbb{P}[\sup_{t>0}|\theta_t| < \pi] = 0 \quad \text{if } \theta_0 \in (-\pi,\pi)\backslash\{0\}. \tag{61}$$

However, as $\theta \in S^1$ this implies $\theta_t \to \pi$ a.s. if $\theta_0 \in (-\pi,\pi)\backslash\{0\}$. We conclude that the control law (54) almost globally stabilizes the system if we have sufficient gain $G \ge M$.

E. Global Control on S^1

Any deterministic system on the circle is topologically obstructed[4] from having a globally stabilizing controller: A continuous vector field on S^1 with a stable fixed point necessarily has an unstable fixed point as well. In the stochastic case, however, this is not the case. Though the drift and diffusion terms must each have two fixed points, we may design the system in such a way that only the stable fixed points coincide.

To apply such a trick in our system we must break the natural symmetry of the control law. This situation is shown in Fig. 3(b). There is a region of the circle where the control rotates in the direction with a longer distance to $\theta = \pi$; the advantage is that $\theta = 0$ is no longer a fixed point.

The linear control law that has this property has the form

$$B(t) = 2G\lambda_t + 2H\nu_t = G\sin\theta_t + H(1+\cos\theta_t) \tag{62}$$

with $G > 0$. We can prove global stability by applying Theorems 1 and 2 with a Lyapunov function of the form

$$V(\theta) = (\alpha + \sin\theta)(1+\cos\theta), \qquad \alpha > 1. \tag{63}$$

Unfortunately, it is not obvious from the analytic form of $\boldsymbol{L}V$ how α must be chosen to satisfy the Lyapunov condition. It is however straightforward to plot $\boldsymbol{L}V$, so that in this simple case it is not difficult to search for α by hand.

A typical design for a particular choice of parameters is shown in Fig. 3(b). The conditions of Theorems 1 and 2 are clearly satisfied, proving that the system is globally stable. Note that when the symmetry is broken we no longer need to fight the attraction of the undesired fixed point; hence, there is no lower bound on G. In fact, in Fig. 3(b) we have $G < M$.

F. Almost Global Control on B^2

Unfortunately, the simple almost global control design on S^1 does not generalize to B^2. The problem is illustrated in Fig. 3(c). The controller (54) vanishes at $\theta = 0$ and π, but we can prove that $\theta = 0$ is repelling. On B^2, however, the control vanishes on the entire line $\lambda = 0$ which becomes an invariant set of (52). However, then it follows from (48) that any trajectory with $\lambda_0 = 0, \nu_0 \notin \{0,1\}$ has a nonzero probability of being attracted to either fixed point.

Consider a neighborhood U_h of the point $(\lambda,\nu) = (0,1)$ that we wish to destabilize. For any $h > 0$, however small, U_h contains points on the line $\lambda = 0$ for which $\nu < 1$, and we have seen that trajectories starting at such points have a nonzero probability of being attracted to $(0,1)$. However, this violates (51), so clearly we cannot prove Theorem 3 on B^2.

One could attempt to prove that all points except those with $\lambda = 0$ are attracted to the origin with unit probability. The Lyapunov theory of Section IV-B is not equipped to handle such a case, however, and new methods must be developed [50]. Instead, we will focus on the global control problem.

G. Global Control on B^2 and Semialgebraic Geometry

Once again we consider the asymmetric control law

$$B(t) = 2G\lambda_t + 2H\nu_t, \qquad G > 0 \tag{64}$$

and try to show that it globally stabilizes the system. Before we can solve this problem, however, we must find a systematic method for proving global stability. Searching "by hand" for Lyapunov functions is clearly impractical in two dimensions, and is essentially impossible in higher dimensions where the state–space cannot be visualized.

---

[4] This is only the case for systems with continuous vector fields and continuous, pure state feedback. The obstruction can be lifted if one considers feedback laws that are discontinuous or that have explicit time dependence.

In fact, even if we are given a Lyapunov function V, testing whether $\boldsymbol{L}V \leq 0$ on K is highly nontrivial. The problem can be reduced to the following question: Is the set $\{\Lambda \in \mathbb{R}^{n^2-1} : \boldsymbol{L}V > 0, k_p(h(\Lambda)) \geq 0, p = 2 \dots n\}$ empty? Such problems are notoriously difficult to solve and their solution is known to be NP-hard in general [51].

The following result, due to Putinar [52], suggests one way to proceed. Let S be a semialgebraic set, i.e., $S = \{x \in \mathbb{R}^m : s_i(x) \geq 0, i = 1 \dots n\}$ with polynomial s_i. Suppose that for some i the set $\{x \in \mathbb{R}^m : s_i(x) \geq 0\}$ is compact. Then, any polynomial p that is strictly positive on S is of the form

$$p(x) = p_0(x) + \sum_{i=1}^{n} p_i(x) s_i(x) \quad p_k(x) = \sum_j p_{kj}(x)^2 \quad (65)$$

where p_{kj} are polynomials, i.e., p is an affine combination of the constraints s_i and *sum-of-squares* polynomials p_k.

Conversely, it is easy to check that any polynomial of the form (65) is nonnegative on S. We may thus consider the following relaxation: Instead of testing nonnegativity of a polynomial on S, we may test whether the polynomial can be represented in the form (65). Though it is not true that any nonnegative polynomial on S can be represented in this form, Putinar's result suggests that the relaxation is not overly restrictive. The principal advantage of this approach is that the relaxed problem can be solved in polynomial time using semidefinite programming techniques [53], [54].

The approach is easily adapted to our situation as K is a semialgebraic set, and we solve the relaxed problem of testing whether $-\boldsymbol{L}V$ can be expressed in the form (65). In fact, the semidefinite programming approach of [53] and [54] even allows us to search for polynomial V such that (65) is satisfied; hence we can search numerically for a global stability proof using a computer program. Such searches are easily implemented using the Matlab toolbox SOSTOOLS [55].

A typical design for a particular choice of parameters is shown in Fig. 4. After fixing the parameters $M = 2, \eta = (1/2)$, and the control law $B(t) = 4\lambda_t - \nu_t$, an SOSTOOLS search found the Lyapunov function

$$V(\lambda, \nu) = 21.8\,\nu - 5.73\lambda^2 + 10.4\lambda\nu - 5.63\nu^2 \qquad (66)$$

where $-\boldsymbol{L}V$ is of the form (65). Hence, Theorems 1 and 2 are satisfied, proving that the system is globally stable.

A couple of technical points should be made at this point. Note that formally the filtering equation (38) and its parametrizations do not satisfy the linear growth condition. However, as the filter evolves on a compact invariant set K, we could modify the equations smoothly outside K to be of linear growth without affecting the dynamics in K. Hence, the results of Section IV-B can still be used. Moreover, it is also not strictly necessary that V be nonnegative, as adding a constant to V does not affect $\boldsymbol{L}V$. Hence, it is sufficient to search for polynomial V using SOSTOOLS.

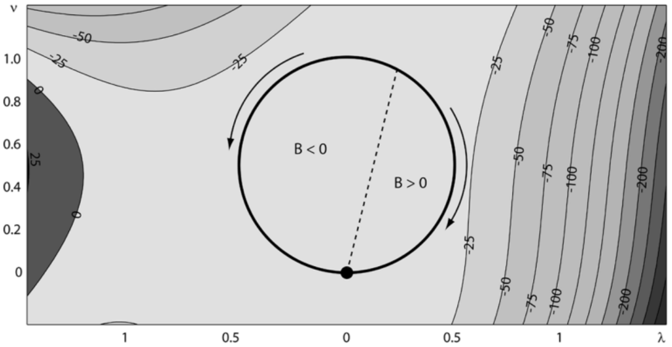

Fig. 4. Contour plot of $\boldsymbol{L}V$ for the control law $B(t) = 4\lambda_t - \nu_t$, with $M = 2$ and $\eta = (1/2)$. The function V was found by semidefinite programming.

H. Global Control for Higher Spin

The approach for proving global stability described in the previous section works for arbitrary spin j. To generalize our control scheme we need to convert to the parametrization of Section III-B, as we did for spin $j = (1/2)$ in (52). We must also propose a control law that works for general spin systems.

We do not explicitly convert to the parametrized form or generate the constraints k_p, as this procedure is easily automated using Matlab's symbolic toolbox. Note that the parameter k determines which eigenstate is mapped to the origin. This is convenient for SOSTOOLS searches, as polynomials can be fixed to vanish at the origin simply by removing the constant term. We always wish to stabilize the origin in the parametrized coordinate system.

To speed up computations we can eliminate all the parameters μ_{ij} as was done in going from (43) to (52). The fact that the remaining equations are decoupled from μ_{ij} is easily seen from (38), as both iJ_y and J_z are real matrices. Moreover, it is easily verified that, by convexity of K, the orthogonal projection of any $\rho \in K$ onto $\{\mathbb{R}^{n^2-1} : \mu_{ij} = 0\ \forall i > j\}$ lies inside K. Hence, we only need to consider the reduced control problem with $\mu_{ij} = 0$.

In [3], we numerically studied two control laws for general spin systems. The first law, $B_1(t) = \pi_t(J_x J_z + J_z J_x - 2m_d J_x)$ (m_d is the eigenstate we wish to stabilize), reduces to our almost global control law when $j = (1/2)$. However, numerical simulations suggest that for $j > (1/2)$ this control law gives a finite collapse probability onto $m \neq m_d$. The second law, $B_2(t) = \pi_t(J_z) - m_d$, reduces to $B_2(t) = \nu_t$ in the case $j = (1/2)$, which is not locally stable. Our experience with $j = (1/2)$ suggests that a control law of the form

$$B(t) = G\,\pi_t(J_x J_z + J_z J_x - 2m_d J_x) + H(\pi_t(J_z) - m_d) \quad (67)$$

should globally stabilize the eigenstate m_d of a spin j system.

We have verified global stability for a typical design with $j = 1, M = 2, \eta = (1/2)$, and $B(t) = 2\pi_t(J_x J_z + J_z J_x) + \pi_t(J_z)$ using SOSTOOLS. A Lyapunov function was indeed found that guarantees global stability of the eigenstate $\psi_0 \psi_0^*$.

Physically the case $j > (1/2)$ is much more interesting than $j = (1/2)$. An experiment with $j > (1/2)$ can be performed with multiple atoms, in which case the control produces statistical correlations between the atoms. Such correlations, known as entanglement, are important in quantum computing.

The structure of the control problem is, however, essentially the same for any j. We refer to [3] and [56] for details on entanglement generation in spin systems.

V. CONCLUSION

In this paper, we have argued that quantum mechanical systems that are subjected to measurement are naturally treated within the framework of (albeit noncommutative) stochastic filtering theory. The quantum control problem is then reduced to a classical stochastic control problem for the filter. We have demonstrated the viability of this approach by stabilizing state reduction in simple quantum spin systems using techniques of stochastic nonlinear control theory.

Unfortunately, the stabilization techniques of Section IV have many drawbacks. We do not have a systematic procedure for finding control laws: we postulate linear controllers and search for corresponding Lyapunov functions. Even when the control law is known, verifying global stability is nontrivial even in the simplest case. Our numerical approach, though very successful in the examples we have shown, rapidly becomes intractable as the dimension of the Hilbert space grows. Finally, our methods do not allow us to make general statements; for example, though it seems plausible that the control law (67) is globally stabilizing for any $j, m_d, M, \eta, H \neq 0$, and $G > 0$, we have not yet succeeded in proving such a statement.

Nonetheless, we believe that the general approach outlined in this paper provides a useful framework for the control of quantum systems. It is important in this context to develop methods for the control of classical stochastic nonlinear systems [57]–[60], as well as methods that exploit the specific structure of quantum control problems. The design of realistic control systems will also require efficient signal processing algorithms for high-dimensional quantum filtering and methods for robust quantum control [61].

ACKNOWLEDGMENT

The would like to thank L. Bouten, A. Doherty, R. Murray, and S. Prajna for enlightening discussions.

REFERENCES

[1] H. M. Wiseman and G. J. Milburn, "All-optical versus electro-optical quantum-limited feedback," *Phys. Rev. A*, vol. 49, pp. 4110–4125, 1994.

[2] M. Yanagisawa and H. Kimura, "Transfer function approach to quantum control—Part II: Control concepts and applications," *IEEE Trans. Autom. Control*, vol. 48, no. 12, pp. 2121–2132, Dec. 2003.

[3] J. K. Stockton, R. Van Handel, and H. Mabuchi, "Deterministic Dicke state preparation with continuous measurement and control," *Phys. Rev. A*, vol. 70, p. 022 106, 2004.

[4] J. M. Geremia, J. K. Stockton, and H. Mabuchi, "Real-time quantum feedback control of atomic spin-squeezing," *Science*, vol. 304, pp. 270–273, 2004.

[5] E. Knill, R. Laflamme, and G. J. Milburn, "A scheme for efficient quantum computation with linear optics," *Nature*, vol. 409, pp. 46–52, 2001.

[6] H. Maassen, "Quantum probability applied to the damped harmonic oscillator," in *Quantum Probability Communications XII*, S. Attal and J. M. Lindsay, Eds. Singapore: World Scientific, 2003, pp. 23–58.

[7] P. Biane, "Calcul stochastique noncommutatif," in *Lectures on Probability Theory*. ser. Lecture Notes in Mathematics 1608, P. Bernard, Ed. New York: Springer-Verlag, 1995.

[8] P. A. Meyer, *Quantum Probability for Probabilists*, ser. Lecture Notes in Mathematics 1538. New York: Springer-Verlag, 1995.

[9] R. E. Mortensen, "Stochastic optimal control with noisy observations," *Int. J. Control*, vol. 4, pp. 455–464, 1966.

[10] K. J. Åström, "Optimal control of a Markov process with incomplete state information," *J. Math. Anal. Appl.*, vol. 10, pp. 174–205, 1965.

[11] V. P. Belavkin, "Quantum stochastic calculus and quantum nonlinear filtering," *J. Multivariate Anal.*, vol. 42, pp. 171–201, 1992.

[12] ——, "Quantum diffusion, measurement, and filtering I," *Theory Probab. Appl.*, vol. 38, pp. 573–585, 1994.

[13] ——, "Quantum continual measurements and a posteriori collapse on CCR," *Commun. Math. Phys.*, vol. 146, pp. 611–635, 1992.

[14] L. Bouten, M. Guţă, and H. Maassen, "Stochastic Schrödinger equations," *J. Phys. A*, vol. 37, pp. 3189–3209, 2004.

[15] V. P. Belavkin, "Nondemolition measurements, nonlinear filtering, and dynamic programming of quantum stochastic processes," in *Proceedings, Bellman Continuum, Sophia-Antipolis 1988*, ser. Lecture Notes in Control and Information Sciences 121. New York: Springer-Verlag, 1988, pp. 245–265.

[16] A. C. Doherty and K. Jacobs, "Feedback control of quantum systems using continuous state estimation," *Phys. Rev. A*, vol. 60, pp. 2700–2711, 1999.

[17] A. C. Doherty, S. Habib, K. Jacobs, H. Mabuchi, and S. M. Tan, "Quantum feedback control and classical control theory," *Phys. Rev. A*, vol. 62, p. 012 105, 2000.

[18] H. Mabuchi, J. Ye, and H. J. Kimble, "Full observation of single-atom dynamics in cavity QED," *Appl. Phys. B*, vol. 68, pp. 1095–1108, 1999.

[19] J. M. Geremia, J. K. Stockton, and H. Mabuchi, "Sub-shotnoise atomic magnetometry," *Phys. Rev. Lett.*, 2005, to be published.

[20] M. A. Armen, J. K. Au, J. K. Stockton, A. C. Doherty, and H. Mabuchi, "Adaptive homodyne measurement of optical phase," *Phys. Rev. Lett.*, vol. 89, p. 133 602, 2002.

[21] J. M. Geremia, J. K. Stockton, A. C. Doherty, and H. Mabuchi, "Quantum Kalman filtering and the Heisenberg limit in atomic magnetometry," *Phys. Rev. Lett.*, vol. 91, p. 250 801, 2003.

[22] J. K. Stockton, J. M. Geremia, A. C. Doherty, and H. Mabuchi, "Robust quantum parameter estimation: Coherent magnetometry with feedback," *Phys. Rev. A*, vol. 69, p. 032 109, 2004.

[23] A. André, A. S. Sørensen, and M. D. Lukin, "Stability of atomic clocks based on entangled atoms," *Phys. Rev. Lett.*, vol. 92, p. 230 801, 2004.

[24] C. Ahn, A. C. Doherty, and A. J. Landahl, "Continuous quantum error correction via quantum feedback control," *Phys. Rev. A*, vol. 65, p. 042 301, 2002.

[25] C. Ahn, H. M. Wiseman, and G. J. Milburn, "Quantum error correction for continuously detected errors," *Phys. Rev. A*, vol. 67, p. 052 310, 2003.

[26] E. Merzbacher, *Quantum Mechanics*, 3rd ed. New York: Wiley, 1998.

[27] R. L. Hudson and K. R. Parthasarathy, "Quantum Itô's formula and stochastic evolutions," *Commun. Math. Phys.*, vol. 93, pp. 301–323, 1984.

[28] J.-M. Bismut, *Mécanique Aléatoire*, ser. Lecture Notes in Mathematics 866. New York: Springer-Verlag, 1981.

[29] L. Arnold, "The unfolding of dynamics in stochastic analysis," *Comput. Appl. Math.*, vol. 16, pp. 3–25, 1997.

[30] M. H. A. Davis and S. I. Marcus, "An introduction to nonlinear filtering," in *Stochastic Systems: The Mathematics of Filtering and Identification and Applications*, M. Hazewinkel and J. C. Willems, Eds. Amsterdam, The Netherlands: Reidel, 1981, pp. 53–75.

[31] R. S. Liptser and A. N. Shiryaev, *Statistics of Random Processes I: General Theory*. New York: Springer-Verlag, 2001.

[32] A. Barchielli, *Continual Measurements in Quantum Mechanics*, ser. Lecture Notes of the Summer School on Quantum Open Systems. Grenoble, France: Institut Fourier, 2003.

[33] A. S. Holevo, *Probabilistic and Statistical Aspects of Quantum Theory*. Amsterdam, The Netherlands: North-Holland, 1982.

[34] R. Haag, *Local Quantum Physics*, 2nd ed. New York: Springer-Verlag, 1996.

[35] R. H. Dicke, "Coherence in spontaneous radiation processes," *Phys. Rev.*, vol. 93, pp. 99–110, 1954.

[36] L. Mandel and E. Wolf, *Optical Coherence and Quantum Optics*. Cambridge, U.K.: Cambridge Univ. Press, 1995.

[37] J. Gough, "Quantum flows as Markovian limit of emission, absorption, and scattering interactions," *Commun. Math. Phys.*, vol. 254, pp. 489–512, 2005.

[38] L. Accardi, A. Frigerio, and Y. G. Lu, "Weak coupling limit as a quantum functional central limit theorem," *Commun. Math. Phys.*, vol. 131, pp. 537–570, 1990.

[39] L. K. Thomsen, S. Mancini, and H. M. Wiseman, “Continuous quantum nondemolition feedback and unconditional atomic spin squeezing,” *J. Phys. B*, vol. 35, pp. 4937–4952, 2002.
[40] G. Kimura, “The Bloch vector for N-level systems,” *Phys. Lett. A*, vol. 314, pp. 339–349, 2003.
[41] K. Życzkowski and W. Słomczyński, “The Monge metric on the sphere and geometry of quantum states,” *J. Phys. A*, vol. 34, pp. 6689–6722, 2001.
[42] S. L. Adler, D. C. Brody, T. A. Brun, and L. P. Hughston, “Martingale models for quantum state reduction,” *J. Phys. A*, vol. 34, pp. 8795–8820, 2001.
[43] J. K. Stockton, M. A. Armen, and H. Mabuchi, “Programmable logic devices in experimental quantum optics,” *J. Opt. Soc. Amer. B*, vol. 19, pp. 3019–3027, 2002.
[44] H. Nijmeijer and A. Van Der Schaft, *Nonlinear Dynamical Control Systems*. New York: Springer-Verlag, 1990.
[45] R. Z. Has’minskiĭ, *Stochastic Stability of Differential Equations*. Amsterdam, The Netherlands: Sijthoff Noordhoff, 1980.
[46] H. J. Kushner, *Stochastic Stability and Control*. New York: Academic, 1967.
[47] L. Arnold, *Stochastic Differential Equations: Theory and Applications*. New York: Wiley, 1974.
[48] X. Mao, “Stochastic versions of the LaSalle theorem,” *J. Diff. Equat.*, vol. 153, pp. 175–195, 1999.
[49] L. C. G. Rogers and D. Williams, *Diffusions, Markov Processes and Martingales, Volume 2: Itô Calculus*, 2nd ed. Cambridge, U.K.: Cambridge Univ. Press, 2000.
[50] R. Van Handel, “Almost global stochastic stability,” preprint, 2004.
[51] P. A. Parrilo, “Semidefinite programming relaxations for semialgebraic problems,” *Math. Prog. B*, vol. 96, pp. 293–320, 2003.
[52] M. Putinar, “Positive polynomials on compact semi-algebraic sets,” *Indiana Univ. Math. J.*, vol. 42, pp. 969–984, 1993.
[53] P. A. Parrilo, “Structured semidefinite programs and semialgebraic geometry methods in robustness and optimization,” Ph.D. dissertation, California Inst. Technol., Pasadena, CA, 2000.
[54] A. Papachristodoulou and S. Prajna, “On the construction of Lyapunov functions using the sum of squares decomposition,” in *Proc. 41st IEEE Conf. Decision and Control*, vol. 3, 2002, pp. 3482–3487.
[55] S. Prajna, A. Papachristodoulou, P. Seiler, and P. A. Parrilo. SOSTOOLS: Sum of squares optimization toolbox for Matlab. California Inst. Technol., Pasadena, CA. [Online]. Available: http://www.cds.caltech.edu/sostools
[56] J. K. Stockton, J. M. Geremia, A. C. Doherty, and H. Mabuchi, “Characterizing the entanglement of symmetric multi-particle spin-$1/2$ systems,” *Phys. Rev. A*, vol. 67, p. 022 112, 2003.
[57] P. Florchinger, “A universal formula for the stabilization of control stochastic differential equations,” *Stoch. Anal. Appl.*, vol. 11, pp. 155–162, 1993.
[58] ——, “Lyapunov-like techniques for stochastic stability,” *SIAM J. Control Optim.*, vol. 33, pp. 1151–1169, 1995.
[59] ——, “Feedback stabilization of affine in the control stochastic differential systems by the control Lyapunov function method,” *SIAM J. Control Optim.*, vol. 35, pp. 500–511, 1997.
[60] ——, “A stochastic Jurdjevic–Quinn theorem,” *SIAM J. Control Optim.*, vol. 41, pp. 83–88, 2002.
[61] M. R. James, “Risk-sensitive optimal control of quantum systems,” *Phys. Rev. A*, vol. 69, p. 032 108, 2004.

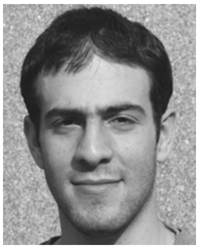

Ramon van Handel received the M.Sc. degree in theoretical and physical chemistry from the Vrije Universiteit, Amsterdam, The Netherlands, in 2002. He is currently working toward the Ph.D. degree in the Department of Physics, the California Institute of Technology, Pasadena.

His research interests include dynamics, filtering, and control of classical and quantum mechanical stochastic systems.

John K. Stockton received the B.S. degree in physics from Stanford University, Stanford, CA, in 1999. He is currently working toward the Ph.D. degree in the Department of Physics, the California Institute of Technology, Pasadena, and is supported by a Hertz Foundation Fellowship.

His research interests include quantum measurement and the use of feedback control with quantum noise limited devices for metrology applications.

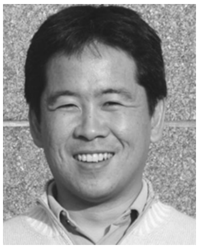

Hideo Mabuchi received the A.B. degree from Princeton University, Princeton, NJ, and the Ph.D. degree from the California Institute of Technology, Pasadena, in 1992 and 1998, respectively.

He has worked in optical and atomic physics, using a combination of experimental and theoretical approaches to study the behavior of quantum-mechanical systems under continuous observation. His continuing research focuses on the use of real-time feedback for active control of quantum systems, and on clarifying the transition from quantum to classical behavior. Developing new interests include the application of mathematical methods from control theory to analyze and design complex physical systems, quantum optics with nanostructures, molecular biophysics, translating quantum mechanics, and the role of information technology in higher education. He is currently an Associate Professor of Physics and Control and Dynamical Systems at the California Institute of Technology.

Dr. Mabuchi received the Office of Naval Research Young Investigator Award, an A.P. Sloan Research Fellowship, and a John D. and Catherine T. MacArthur Foundation Fellowship.

INSTITUTE OF PHYSICS PUBLISHING JOURNAL OF PHYSICS B: ATOMIC, MOLECULAR AND OPTICAL PHYSICS

J. Phys. B: At. Mol. Opt. Phys. **38** (2005) S551–S565 doi:10.1088/0953-4075/38/9/007

Trapped atoms in cavity QED: coupling quantized light and matter

R Miller, T E Northup, K M Birnbaum, A Boca, A D Boozer and H J Kimble

Norman Bridge Laboratory of Physics 12-33, California Institute of Technology, Pasadena, CA 91125, USA

E-mail: hjkimble@caltech.edu

Received 2 November 2004
Published 25 April 2005
Online at stacks.iop.org/JPhysB/38/S551

Abstract

On the occasion of the hundredth anniversary of Albert Einstein's *annus mirabilis*, we reflect on the development and current state of research in cavity quantum electrodynamics in the optical domain. Cavity QED is a field which undeniably traces its origins to Einstein's seminal work on the statistical theory of light and the nature of its quantized interaction with matter. In this paper, we emphasize the development of techniques for the confinement of atoms strongly coupled to high-finesse resonators and the experiments which these techniques enable.

(Some figures in this article are in colour only in the electronic version)

1. From Einstein to cavity QED

In the years prior to his seminal 1905 papers, Albert Einstein had given much thought to the statistical properties of electromagnetic fields [1], especially with regard to the theory of black-body radiation developed by Max Planck [2]. Einstein realized that the quantization of light—particularly the creation and annihilation of 'light quanta'—is something more fundamental than a tacit consequence of the assumption that the total energy of a black-body is discretely distributed between a set of microstates. Beginning in 1905 with *On a heuristic point of view about the creation and conversion of light* [3] and in four subsequent papers on quantization [4–7], he laid the foundations of the 'old quantum theory' [8], summarized in what is commonly referred to as the 'light quantization hypothesis':

> … the energy of a light ray emitted from a point [is] not continuously distributed over an ever increasing space, but consists of a finite number of energy quanta which are localized at points in space, which move without dividing, and which can only be produced and absorbed as complete units [3].

0953-4075/05/090551+15$30.00 © 2005 IOP Publishing Ltd Printed in the UK

He argued that the existence of light quanta was essential to Planck's hypothesis. In his treatment of the problem, he developed a formalism based upon the inversion of Boltzmann's law to describe the statistical variances in the energy of a black body. Using this technique, he was able to separate these energy fluctuations into the sum of two quantities, one representing the fluctuation of a number of particles and the other corresponding to the variances of a classical wave [6, 9]. The wave–particle duality to which Einstein alluded is, of course, now one of the tenets of modern quantum mechanics. These early papers also began, for the first time, to broach phenomenological problems in terms of quantized light. In a very literal sense, Einstein's descriptions of the photoelectric effect and the ultraviolet photoionization of gases [3] constitute the first applications of *quantum* electrodynamics as well as the first microscopic (rather than statistical) descriptions of quantized electromagnetic phenomena.

While the same could be said of vast expanses of modern physics, much of the intellectual underpinnings of cavity quantum electrodynamics are certainly due to this early work by Einstein. Einstein wrote

> The wave theory of light which operates with continuous functions in space has been excellently justified for the representation of a purely optical phenomena and it is unlikely ever to be replaced by another theory. One should, however, bear in mind that optical observations refer to time averages and not to instantaneous values and notwithstanding the complete experimental verification of the theory of diffraction, reflection, refraction, dispersion and so on, it is quite conceivable that a theory of light involving the use of continuous functions in space will lead to contradictions of experience, if it is applied to the phenomena of the creation and conversion of light [3].

As will be described in the following sections, an atom strongly coupled to the mode of a resonant cavity is precisely one such situation. In fact the atom–cavity system is uniquely well-suited to the efficient generation of single photons, a phenomenon wherein Einstein's 'contradictions of experience' certainly dominate. The quantized description of light is manifestly that which is needed to describe cavity QED.

In what follows, we introduce cavity quantum electrodynamics in the regime of strong coupling. With an emphasis on the current state-of-the-art experiments, particularly those carried out by our group at Caltech, involving atoms trapped within a optical cavity, we also review the evolution of experiments in cavity QED and discuss future research directions.

2. Fundamentals of the cavity QED system

2.1. Introduction

Cavity quantum electrodynamics explores the measurement and control of quantized electromagnetic fields and atomic systems coherently coupled inside an electromagnetic resonator. A simple, representative model of the cavity QED system, as illustrated in figure 1, consists of exactly one two-state atomic system at rest within the mode of a resonator formed by two spherical mirrors. The dynamics of this system are described by the well-known Jaynes–Cummings Hamiltonian [10, 11] which is composed of the sum of separate terms for both the atom and field as well as a third term which arises from the total atom–field dipole interaction:

$$\hat{H} = \tfrac{1}{2}\hbar\omega_A\hat{\sigma}_z + \hbar\omega_C\left(\hat{a}^\dagger\hat{a} + \tfrac{1}{2}\right) + \hbar g(\mathbf{r})(\hat{a}^\dagger\hat{\sigma} + \hat{a}\hat{\sigma}^\dagger). \tag{1}$$

The operators $(\hat{\sigma}_z, \hat{\sigma}^\dagger, \hat{\sigma})$ are the Pauli operators corresponding to inversion, raising and lowering of the atomic state, while $(\hat{a}^\dagger, \hat{a})$ are the creation and annihilation operators for

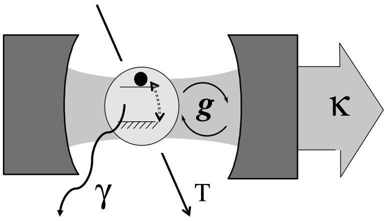

Figure 1. Characteristic parameters of atom, cavity, and environment: κ, the rate of decay of the cavity field; γ, the rate at which the atomic dipole radiates into modes other than the cavity field mode; T, the transit time of an atom through the cavity mode; and g, the rate of coherent atom–field coupling. Strong coupling requires that $g/(\gamma, \kappa, \frac{1}{T}) \gg 1$.

photons in the coupled mode of the resonator. (ω_A, ω_C) are the resonant frequencies of the atom and cavity, respectively.

The magnitude of the coupling is a function of the atom's position, $\mathbf{r}$, within the standing wave structure of the mode and is given by

$$g(\mathbf{r}) = \left(\frac{\mu^2\omega_C}{2\hbar\epsilon_0 V_M}\right)^{\frac{1}{2}} U(\mathbf{r}) \equiv g_0 U(\mathbf{r}). \tag{2}$$

Here, μ is the atomic dipole matrix element, V_M is the resonant mode volume, a geometric parameter of cavity, and $U(\mathbf{r})$ is the cavity mode function, defined such that $V_M = \int |U(\mathbf{r})|^2\,\mathrm{d}^3x$. The coupling coefficient $2g_0$ is known as the single-photon Rabi frequency and represents the maximum rate at which one quantum of excitation is exchanged between atom and field [12].

This idealized model captures the essential dynamics of the interaction but makes no accounting of the dissipative processes which naturally accompany real cavities and atoms. The dominant loss associated with the cavity results from the leakage of photons through the mirrors at a rate 2κ, where κ, the frequency half-width of the resonant mode, is specified by the quality factor of the cavity,

$$Q = \frac{\omega_C}{2\kappa}. \tag{3}$$

A second dissipative channel is the result of spontaneous emission from the atom into field modes other than that which is preferentially coupled to the resonator. In general, there are two distinct atomic decay rates along the transverse and longitudinal directions of the cavity $(\gamma_\perp, \gamma_\parallel)$, both of which are functions of the position of the atom, $\mathbf{r}$ [13]. In practice, with current state-of-the-art optical Fabry–Perot cavities this position dependence is largely negligible. In this case, the angle subtended by the mode of the cavity is small, and the transverse decay rate is very closely approximated by the atomic free space decay rate, $\gamma_\perp = \gamma = \gamma_\parallel/2$ (this is not generally true, however, for cavities of different geometries [14–16]). A third consideration is the length of time, T, during which the atom resides within the cavity mode, after which no coherent evolution is possible. While each of these three dissipative channels damp the desired quantum evolution of the system, it should be noted that they do not necessarily stand on equal footing. In particular, the rate κ is characterized by emission of the cavity field into one, well-defined spatial mode which facilitates efficient readout of the state of the coupled system. The other two rates, (γ, T^{-1}), represent, in general, irreversible loss of information to the environment. As photons are coupled into a continuum of experimentally inaccessible spatial modes, and as atoms leave the cavity volume (though not necessarily so in the microwave domain), it is difficult to extract useful information from the system.

The description, above, is generally applicable to cavities with resonant frequencies ranging from the microwave [11] to optical regimes and which may be coupled to appropriate two-level systems as diverse as Cooper pair boxes [17, 18] and Rydberg atoms [19, 20]. Whereas high-finesse Fabry–Perot cavities coupled to alkali atoms in the optical regime will be the focus of this discussion, broad reviews of cavity QED in this and other regimes are available [12, 21].

2.2. *Strong coupling*

As we have seen, cavity QED is parametrized by four rates $(g_0, \kappa, \gamma, T^{-1})$. In order to emphasize the coherent evolution of the system, it is useful to require that the coupling coefficient dominate dissipation:

$$g_0/(\gamma, \kappa, T^{-1}) \gg 1. \tag{4}$$

This condition is commonly known as the strong coupling criterion [12].

It is instructive to explore strong coupling in terms of two dimensionless parameters known as the critical photon and atom numbers. The critical (or saturation) photon number describes the number of photons such that for a cavity of a given geometry the intracavity optical intensity is sufficient to saturate the atomic response (I_{sat}):

$$n_0 = \frac{\gamma^2}{2g_0^2}. \tag{5}$$

Similarly, the critical atom number describes the number of strongly coupled atoms necessary to affect appreciably the intracavity field:

$$N_0 = \frac{2\kappa\gamma}{g_0^2}. \tag{6}$$

Many quantum optical systems—lasers for instance, with $\sqrt{n_0} \sim 10^3$–10^4—have large critical parameters and therefore adding or removing one photon or atom does not significantly alter the dynamics as a whole. In these systems, the coherent coupling parameter g_0 is scaled away as processes approach the semi-classical regime. By contrast, the necessary (though not sufficient) criteria for strong coupling are that $(n_0, N_0) \ll 1$. This means that in the regime of strong coupling, single quanta dominate the dynamics of the system such that the interaction between atom and photon can be manifestly nonclassical and nonlinear for single atoms and photons. Strong coupling thereby provides a powerful tool for the study of quantum optics as well as the interaction of the quantized electromagnetic field with matter.

2.3. *The Jaynes–Cummings ladder*

In the strong coupling regime, coherent interaction dominates dissipation and so the Jaynes–Cummings Hamiltonian (1) provides a foundation for the description of the evolution of the system. Allowing the cavity mode to be resonant with the atomic transition frequency $(\omega_C = \omega_A)$ and diagonalizing (1) yields a set of eigenstates for the system,

$$|\pm\rangle_n = \tfrac{1}{\sqrt{2}}(|g, n\rangle \pm |e, n-1\rangle), \tag{7}$$

where (g, e) denote the ground and excited states of the atom and there are n quanta of excitation in the system. These are the dressed states of the Jaynes–Cummings model and represent the equal distribution of excitation between atom and field with corresponding energy eigenvalues $E_\pm = n\hbar\omega \pm \sqrt{n}\hbar g(\mathbf{r})$.

Experimentally, as an atom enters the mode of the cavity the transmission and absorption spectra in the weak-field limit will no longer exhibit a single, empty-cavity resonance at $\omega = \omega_C$ but instead a two-peaked structure with maxima at $\omega = \omega_C \pm \sqrt{n}g(\mathbf{r})$, corresponding to the energy eigenvalues of $|\pm\rangle_1$ for one quantum of excitation. This characteristic spectral feature is known as the vacuum-Rabi splitting and serves as a hallmark of strong coupling.

2.4. Cavities in the laboratory

While defining the criteria for strong coupling is a relatively simple matter ($g_0 \gg (\gamma, \kappa, T^{-1})$), realizing cavities which in practice meet these criteria is a decidedly more complicated task. Over the past 25 years, experiments in optical cavity QED have pushed progressively farther into the regime of strong coupling such that typical values for state-of-the-art optical cavities today are $n_0 \approx 10^{-3}$–10^{-4} photons and $N_0 \approx 10^{-2}$–10^{-3} atoms. These cavities are of Fabry–Perot geometry and consist of two superpolished spherical mirror substrates which have been coated with a highly reflective stack of dielectric layers ($R = 0.999\,9984$ is a representative value for the reflectivity of one such state-of-the-art mirror) [22]. The reflectivity of these mirrors is sufficiently large that the inter-mirror spacing (and therefore the mode volume, V_m) can be made relatively small without κ growing larger than $g_0 \propto V_M^{-1/2}$. Current experiments underway in our group at Caltech involve atomic caesium coupled to a cavity of length $L = 42.2\ \mu$m and with mirrors of radius of curvature $R = 20$ cm such that

$$(g_0, \kappa, \gamma) = (34, 4.1, 2.5)\ \text{MHz}, \tag{8}$$

well into the regime of strong coupling. The finesse of this cavity at the D2 line in atomic caesium ($\lambda = 852.4$ nm, made resonant with the TEM$_{00}$ mode of the cavity) is $\mathcal{F} = 4.2 \times 10^5$, and the critical parameters are $n_0 = 0.0029$ and $N_0 = 0.018$. In future experiments, it may be possible to achieve even higher finesse by coupling to the whispering gallery modes of quartz microspheres [14–16] or microtoroidal resonators [23, 24] or to photonic bandgap resonators [25, 26].

3. Experiments in the regime of strong coupling

In the following sections, we briefly review the experimental evolution of optical cavity QED in the regime of strong coupling, particularly with regard to those techniques developed by our group at Caltech. The goal is to set the stage for a description of the new set of tools made available by the recent marriage of atom–cavity systems and laser cooling and trapping. A common theme throughout the discussion will be the quest to localize and isolate a single atom which is strongly coupled to the cavity mode, as required by, for instance, a variety of schemes for implementing quantum computation and communication protocols [27–30, 25].

3.1. Early work

The first observations of atoms strongly coupled to optical resonators came in the early 1990s with experiments involving atomic beam transits through the mode of a high-finesse cavity [31, 32]. The average duration of each single atom transit was $T = 0.4\ \mu$s and the flux of the beam was adjustable such that the average intracavity atom number $\bar{N} \sim 1$. By measuring the transmission of a weak probe of variable detuning about the caesium ($6S_{1/2}, F = 4 \to 6P_{3/2}, F' = 5'$) transition, the vacuum-Rabi splitting for one atom (on average) was observed for the first time, albeit weighted over a range of values for

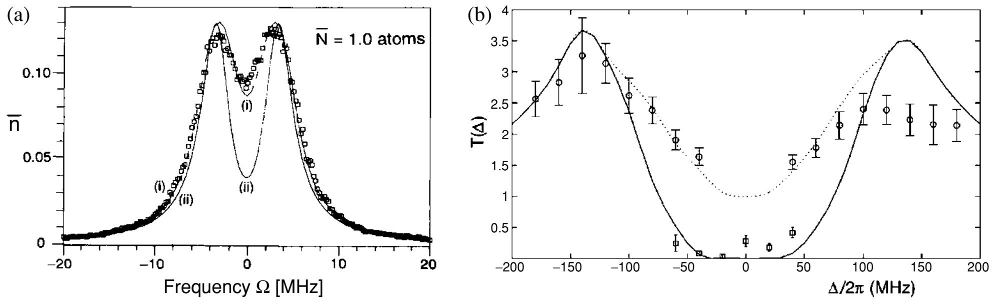

Figure 2. Early one-atom vacuum-Rabi splitting measurements. (a) The vacuum-Rabi splitting for $\bar{N} = 1$ as measured with an atomic beam by Thompson *et al* [32]. Curve (i) represents the theoretical transmission averaged over the relevant range of values for $g(\mathbf{r})$ and N, while (ii) describes precisely one atom with maximal coupling g_0. (b) Vacuum-Rabi spectrum measured using individual atomic transits from a MOT, as described by Hood *et al* [37]. The solid line is the predicted spectrum based upon evolution of the master equation for maximally coupled atoms while the dashed line represents couplings $g(\mathbf{r}) < g_0$.

$g(\mathbf{r})$ and an ensemble of atoms (figure 2(a)) [32, 33]. Similar optical normal-mode spectra have been obtained by the group of Feld using a beam of barium atoms [34], while direct observation of atom–field Rabi nutation in the microwave domain was made by the group of Haroche using a beam of rubidium atoms in Rydberg excited states [35].

The brief duration of each transit and uncertainty in the instantaneous rate of atom–field coupling presented a significant limitation on the amount of information made available per atom in these atomic beam experiments [32–35]. Subsequent experiments instead made use of a cloud of cold atoms cooled to sub-Doppler temperatures in a magneto-optic trap (MOT) located a few millimetres above the cavity. When the MOT is released, some fraction of the cold atoms fall between the mirrors, and it is possible to observe in real time their individual trajectories and the durations of their transits [36]. Using this technique, the vacuum-Rabi spectrum (figure 2(b)) was extracted from the transmission of a weak probe interacting with many individual transits (each of duration $T \approx 100\ \mu$s) on an atom-by-atom basis [37]. Likewise, this technique has also enabled measurements of the nonlinear optical response of individual atoms to drive fields corresponding to $\bar{n} \ll 1$ intracavity photon [37]. It should be noted that while each individual atom contributes significantly more information to the spectrum in this experiment than in those with atomic beams, the data in figure 2(b) is still the result of an ensemble average over many atoms.

3.2. The atom–cavity microscope

By way of the marriage of laser cooled atomic sources and cavity QED, as discussed above, has come an exciting new regime in which the kinetic energy K of atoms in transit through the cavity is comparable to the energy $\hbar g(\mathbf{r})$ associated with the atom–field coupling. In this domain, the presence of just one photon is sufficient to alter profoundly the atom's centre-of-mass motion. Indeed if $\hbar g_0 > K$ and the cavity is slightly detuned from the bare atomic resonance, then the dressed state $|-\rangle_1$, as discussed above, is confined by an attractive pseudopotential due to the intracavity field [38–40]. The pseudopotential wells are of depth determined as a function of the probe intensity and the atom–cavity detuning, and have facilitated atomic trapping times $T \sim 0.5$ ms.

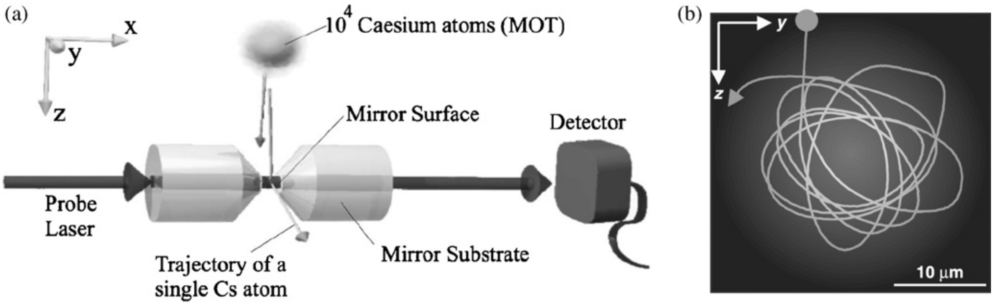

Figure 3. Diagram of the atom–cavity microscope. (a) Cold atoms are delivered to the cavity mode by releasing the contents of a magneto-optic trap (MOT) a few millimetres above the cavity. The transmission of weak probe beam is recorded using balanced heterodyne detection [38]. (b) A reconstruction of the trajectory of a single atom bound to the quantized intracavity field with $\bar{n} = 1$ photon. Animations of transits reconstructed using this technique are available at http://www.its.caltech.edu/~qoptics/atomorbits/.

This technique for intracavity confinement enabled the so-called atom–cavity microscope, a protocol for reconstructing the trajectories of single atoms based upon the variations in transmission of a weak probe beam (which also generates the trapping pseudopotential). Experimentally, as a caesium atom enters the mode of the cavity its presence is detected in real time. The resulting signal is used to switch rapidly the intensity of the probe, which is detuned to the red vacuum-Rabi sideband at $(\omega_A - \hbar g_0)$, in order to form the trap, pushing atoms towards larger values of $g(\mathbf{r})$. The transmitted probe field is then monitored and recorded via heterodyne detection. For each individual atomic transmission profile, which is indicative of the instantaneous rate of coherent coupling to field, it is then possible to extract information about the orbit in which the confined atoms move (such as that shown in figure 3(b)). This work represents a first step towards addressing the motion of an atom strongly coupled to a cavity, but is limited in the sense that the QED interaction and the trapping potential are intertwined, precluding the ability to address and control the state of the atom while confined by the trap.

3.3. State-insensitive cooling and trapping

While atomic confinement using the quantized cavity QED field offers an important advance towards the realization of well-localized, trapped atoms, it remains preferable to decouple the trap from the QED interaction. Towards this goal, a number of groups [41–44] have successfully implemented optical dipole force traps (also known as far off-resonant traps or FORTs) consisting of a far-detuned optical beam able to induce a dissipative, attractive force on an atom and yet only weakly drive atomic transitions.

The principle of operation for a FORT, as applied to a simple two-level atomic model, is rather straightforward [45]. The FORT beam, detuned by δ from the resonant frequency of the transition, ω_A, induces an ac-Stark shift,

$$\Delta E_{g,e} = \pm \frac{3\pi c^2 \gamma}{\omega_A^3} \frac{I(\mathbf{r})}{\delta}, \tag{9}$$

of equal magnitude but opposite sign for each of the excited and ground states. For a red-detuned field ($\delta < 0$), an atom in its ground state with kinetic energy $K < U_{\mathrm{dip}} = \Delta E_g(\mathbf{r})$ is confined in a potential which varies spatially as the intensity of the FORT beam (likewise, an atom in its excited state will, rather undesirably, see a repulsive potential). This process is readily extrapolated to more complicated, multilevel systems such as the alkali atoms commonly used in cavity QED, though the overall functional form of (9) remains similar [46].

The earliest implementations of intracavity FORT fields for cavity QED used lasers at frequencies an integer number of cavity free spectral ranges away from the probe field [44]. In so doing, a cavity which is length-stabilized to be resonant with the TEM_{00} mode of the probe will simultaneously support the TEM_{00} mode of the FORT as well. The resultant intracavity standing wave provides a series of potential wells into which sufficiently cold atoms can be loaded. The first experiment of this sort involved trapping caesium in a FORT with $\lambda_{\mathrm{FORT}} = 869$ nm, characterized by a trap lifetime $T = 28$ ms, which was evidently limited by parametric heating and FM-to-AM noise conversion due to the relatively high finesse of the cavity at the FORT wavelength.

These early difficulties were remedied by choosing a value λ_{FORT} for which the differential ac-Stark shift between excited and ground states was very nearly zero and at which the cavity mirrors were less reflective. Certain atomic lines, including the caesium D2 transition, have the property that for a narrow range of wavelengths the ac-Stark shifts of the excited and ground state manifolds are in the same (trapping) direction [47–49]. By considering couplings to the full manifold of caesium excited states it is possible to recognize a nearly state-insensitive trapping potential (i.e., with only small differential ac-Stark shifts) at $\lambda_{\mathrm{FORT}} = 935.6$ nm, colloquially referred to as the ‘magic’ wavelength of caesium [50, 41]. Indeed, it has been shown that an intracavity FORT at this wavelength with a depth corresponding to $U_0 \approx 3$ mK allows for trap lifetimes $T \approx 3$ s ‘in the dark’ (i.e., in the absence of QED fields), likely limited by the rate of collision with background gas, and $T \approx 1$ s even in the presence of a probe field [41]. This technique constitutes a milestone in optical cavity QED, opening the door to a myriad of experiments involving one-and-the-same atom. These exciting new experiments are to be discussed in the next section.

The use of optical dipole traps for localization of atoms within the mode of a high-finesse cavity has developed rapidly in the past two years. In addition to the work described above, the group of Rempe at the Max Planck Institute in Garching has also implemented the co-resonant FORT technique at $\lambda_{\mathrm{FORT}} = 785$ nm for trapping rubidium [43]. The group of Chapman at Georgia Tech has developed a novel scheme whereby an optical dipole lattice *transverse* to the cavity axis acts as a ‘conveyor belt’ [51], transporting rubidium atoms into and out of a region of interaction with a weak probe field which is used to monitor the state of the system in real-time [42]. Beyond the use of optical traps, the groups of Walther and Blatt have made tremendous progress towards coupling single, trapped atomic ions to high-finesse cavities [52, 53]. While these experiments have yet to enter the regime of strong coupling, practically limitless trap lifetimes and the powerful tools for coherent control which have already been developed within the ion trap community [54–57] hold great promise for future integration with optical cavities.

4. Experiments with trapped atoms

The development of a state-insensitive trap for strongly coupled atoms has not only extended the duration of individual transits far beyond the characteristic time scales for coherent atom–field coupling (i.e., $T \approx 3$ s whereas $g_0^{-1} \approx 30$ ns), but also into a domain wherein complex experimental protocols can be performed using one-and-the-same atom. The cavity QED group at Caltech, working with atomic caesium, has begun exploring this domain with schemes for the generation of single photons, with measurements of the full vacuum-Rabi spectrum for just one atom, and with a new technique for *in situ* control of the system.

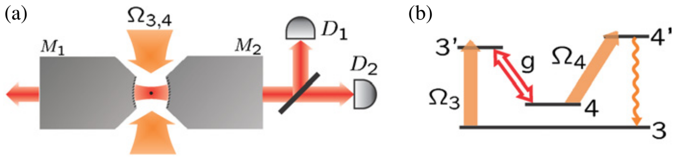

Figure 4. The one-atom laser. (a) Schematic diagram of the one-atom laser. Fields $\Omega_{3,4}$ are applied to a single caesium atom confined by an intracavity FORT, producing excitation in the TEM_{00} mode of the cavity. Photons which escape mirror M_2 are detected by single photon-counting avalanche photodiodes $D_{1,2}$. (b) Energy level diagram for the one-atom laser, as discussed in the text.

4.1. The one-atom laser

An optically driven single atom bound to a resonant cavity is, in some sense, a laser extrapolated to its fundamental, conceptual limit (theoretical descriptions of such devices have existed for a number of years [58–67]). In this analogy, the single atom serves as a gain medium which, as it ‘lases’, couples photons into the resonant mode of the cavity. However, the emission from such a device (like the device, itself) is qualitatively very *unlike* a conventional (semi-classical) laser, exhibiting a variety of manifestly quantum properties.

In a recent experiment to explore these phenomena [68, 69], a field Ω_3 is applied from the side of the cavity (i.e., transverse to the cavity axis) which pumps the caesium atom from the $(6S_{1/2}, F = 3)$ ground state to the $(6P_{3/2}, F' = 3')$ excited state (see figure 4). The atomic population is rapidly transferred to $(6S_{1/2}, F = 4)$ via strong coupling to the cavity (which is tuned to be resonant with the $(6P_{3/2}, F' = 3' \rightarrow 6S_{1/2}, F = 4)$ transition), leaving a single excitation in the ‘laser’ mode. A second field Ω_4, continuously applied to the atom, pumps to $(6P_{3/2}, F' = 4')$ from which spontaneous emission returns the system to its (initial) ground state. As the resulting photons exit the cavity at a rate 2κ, their arrival times are recorded using a pair of single photon-counting avalanche photodiodes. Experimentally, we observe ‘thresholdless lasing’ and a maximum intracavity photon number which is rate-limited due to the (irreversible) recycling of the one atom through its energy levels by $\Omega_{3,4}$. Moreover, the one-atom laser exhibits photon antibunching and sub-Poissonian photon statistics, evidence that it is a manifestly quantum light source. For comparison with our experimental results, we have extensively analysed the theory of ‘lasing’ in the strong-coupling regime, as discussed in [69].

4.2. Deterministic generation of single photons

While the one-atom laser produces a nonclassical stream of photons, it is also possible to add an extra layer of control to the system in order to reliably and deterministically produce one photon on demand. We have shown that by iteratively pulsing the $\Omega_{3,4}$ beams, a single photon can be generated in the cavity mode with near unit efficiency [70]. Operationally, the $\Omega_3(t)$ pulse, in concert with an atom strongly coupled to a cavity on resonance with $(6P_{3/2}, F' = 3' \rightarrow 6P_{1/2}, F = 4)$, drives coherent, adiabatic transfer of atomic population between hyperfine ground states [71]. Simultaneously, this process introduces a single photon into the intracavity field, which subsequently escapes with a spatial profile fixed by the TEM_{00} mode of the cavity and with a temporal profile determined by that of the $\Omega_3(t)$ pulse. A short pulse of Ω_4 light incoherently repumps the atom to the $F = 3$ manifold and resets the system to generate subsequent photons.

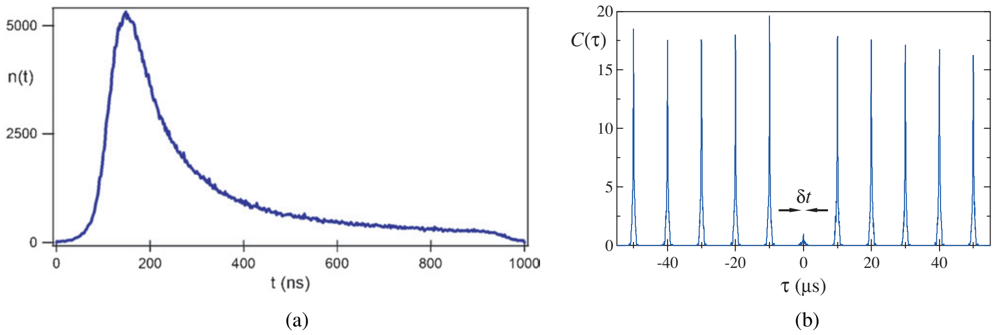

(a) (b)

Figure 5. Single photon generation on demand. (a) The temporal profile of single photons generated from one caesium atom strongly coupled to a cavity [70]. The full-width at half-maximum is $\tau_{\mathrm{FWHM}} = 120$ ns and the long tail is the result of inhomogeneous preparation of initial Zeeman states. (b) The correlation function $C(\tau)$ as a function of time delay τ for counts from two single photon-counting photodiodes. The significant suppression of the peak at $\tau = 0$ indicates that spurious two-photon events are rare.

In the regime of strong coupling, the rate $g(\mathbf{r})$ is sufficiently large that single photons are generated within the cavity with inferred efficiency $\phi_G = 1.15 \pm 0.18$, where the uncertainty is determined from measurements of systematic losses and rare occurrences of two-photon events. Unpolarized photons escape the cavity with efficiency $(69 \pm 10)\%$ and are detected by two photoelectric detectors at the ports of a 50/50 beam splitter, leading to an overall detection efficiency of $\sim$2.4% (intracavity photon to photoelectric event). The temporal full-width at half-maximum of the photons is $\tau_{\mathrm{FHWM}} = 120$ ns for an $\Omega_3(t)$ pulse of uniform intensity over a duration of 1 μs (see figure 5(a)). The mean trap lifetime for a single atom during this process was 140 ms, limited by heating from $\Omega_{3,4}$, allowing 1.4×10^4 single photons to be generated from each individual atom. The small probability of a two-photon event taking place is clearly evident from the suppression of a peak at $\tau = 0$ in the correlation function between the two detectors, figure 5(b). As a metric for how closely this system approximates an *ideal* single-photon source we consider the quantity R, which quantifies the probability of two-photon events relative to a coherent state ($R \approx 1$ for a weak coherent state and approaches infinity for an ideal single-photon source). Averaged over all generation attempts, we measure $R = 15.9 \pm 1.0$ which approaches $R \approx 150$ when considering only attempts occurring late in the trapping interval. We thereby demonstrate the predominantly single-photon character of our source and hypothesize that rare two-photon events are principally the result of 'contamination' from rare occurrences in which two atoms are simultaneously loaded into the trap, both generating photons [70].

The non-negligible likelihood of two or more atoms being loaded into the FORT is an unavoidable consequence of our Poissonian technique for introducing cold atoms to the cavity. As in earlier work, a cloud of $\sim 10^5$ sub-Doppler cooled caesium atoms is released from a MOT and allowed to fall freely through the narrow space between the two cavity mirrors which, due to its prohibitive geometry, admits only a few atoms per attempt. We can control the mean number by adjusting the efficiency of the cooling beams which prepare the MOT, but not without detriment to the frequency with which we load single atoms. As a solution to this problem, the Caltech group has developed a technique whereby we can observe in real time discrete, 'step-like' increases in the transmission of probe beam as, one-by-one, multiple atoms are heated out of the FORT [72]. In future work, this protocol will provide an efficient means for ensuring that precisely $N = 1$ atom is always loaded, or that a certain number

$N > 1$ is always loaded as required by some schemes for processing quantum information [27, 73].

4.3. Intracavity Raman transitions and sideband cooling

Beyond these advances enabled by the state-insensitive FORT [41, 70, 72], there exist a number of experimental parameters which remain inaccessible without more precise control over the atom and its motion. Among these are the location of the atom $\mathbf{r}$ relative to the QED field (and, implicitly, the range of coupling rates $g(\mathbf{r})$ that atom experiences as it moves within the mode of the cavity) and the characteristics of the ambient magnetic field at $\mathbf{r}$. In order to resolve these concerns and gain some *a priori* knowledge about atoms trapped in our FORT, we have developed a novel technique for driving stimulated Raman transitions between the hyperfine ground states of an atom in the FORT.

The presence of the cavity places certain geometric constraints on the beams which drive these transitions, so we have chosen to use the intracavity FORT field not only as a trap but also as one arm of the characteristic Raman Λ configuration. The second arm is an auxiliary 'Raman' laser, phase-locked and orthogonally polarized relative to the FORT and offset by a frequency $\Delta_{\text{Raman}} = \Delta_{\text{HF}} + \delta$ where $\Delta_{\text{HF}} = 9.192\,632$ GHz, the caesium $6S_{1/2}(F = 3, F = 4)$ splitting. δ is a variable frequency detuning. Both lasers drive the same cavity mode, with the Raman beam off cavity resonance by Δ_{Raman}, and generate intracavity fields with individual Rabi frequencies $(\Omega_{\text{FORT}}, \Omega_{\text{Raman}})$. In the limit that $\Delta' = (\nu_A - \nu_{\text{FORT}}) \gg \{\Omega_F, \Omega_R, \Delta_{\text{Raman}}, \delta, \gamma\}$, (where ν_A, ν_{FORT} are the frequencies of the caesium D2 line and the FORT laser, respectively) the net effective Rabi frequency is given by

$$\Omega_E(t) = \frac{\Omega_{\text{FORT}}\Omega_{\text{Raman}}}{2\Delta'}. \tag{10}$$

As the detuning δ is varied, it is possible to map out a spectrum of resonances between the various Zeeman and motional substates of the two hyperfine ground manifolds. After an atom is cooled into the FORT, a small magnetic field is applied along the cavity axis to break any degeneracy of Zeeman states so the atoms may be optically pumped into the $(F = 3, m_F = 0)$ ground state. The Raman laser at a fixed detuning δ is then pulsed ON for a duration τ_{Raman} in order to drive a $\theta_{\text{Raman}} = \tau_{\text{Raman}}\Omega_E$ rotation in the $(F = 3, 4)$ basis. Next, a probe pulse resonant with the $(F = 4 \rightarrow F' = 5')$ transition detects whether the atom is in the $F = 4$ ground state (using the type of cavity QED interaction discussed in the first section; large (small) transmission of the probe means the atom is decoupled from (coupled to) the cavity, namely in the $F = 3$ $(F = 4)$ ground state). Many iterations of this procedure yield the probability $P(\delta)$ to drive a Raman transition at that specific detuning. As δ is varied, the result is a spectrum such as that in figure 6(a), showing a clearly resolved peak corresponding to the carrier $(F = 3, m_F = 0) \leftrightarrow (F = 4, m_F = 0)$ transition (with linewidth Ω_E) as well as sidebands corresponding to $\Delta n = \pm 2$ vibrational transitions, which will be discussed in detail, below. By scanning over a broader range, it is possible to map out the full spectrum of $\Delta m_F = 0$ transitions (or $\Delta m_F = \pm 1$, in a transverse bias field) from which information about the magnitude and direction of the local magnetic field can be extracted. Similarly, when the Raman pulse duration τ_{Raman} at $\delta \approx 0$ MHz is scanned in steps much smaller than Ω_E^{-1}, it is possible to map out the so-called 'Rabi flopping,' the coherent transfer of atomic population between ground states (figure 6(b)).

Within the context of atomic systems bound to harmonic potentials, Raman transitions between quantized vibrational levels have become a standard tool. Raman sideband cooling is an essential component of experiments involving trapped ions [54] and has also been demonstrated for alkali atoms in free space [74, 75]. In the Fock basis we denote the

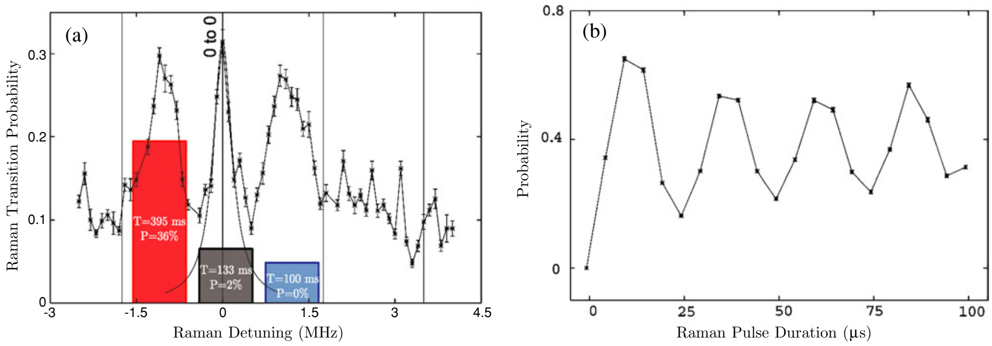

Figure 6. A Raman spectrum. (a) The 'carrier' transition ($m_F = 0 \leftrightarrow m_F = 0$) and $\Delta n = 2$ motional sidebands measured by driving stimulated Raman transitions between the hyperfine ground states of a single caesium atom confined in an intracavity FORT. Imposed over the trace are the results of cooling measurements undertaken on each of the resonances. The extended trap lifetime observed by driving the red transition constitutes empirical evidence of Raman sideband cooling. (b) 'Rabi flopping' on the $\Delta m_F = 0$ 'carrier' transition as discussed in the text.

vibrational state of an atom in our FORT as n. By tuning our Raman beam (blue, red) of the carrier transition by twice the harmonic frequency of our FORT, it is possible to excite the atom from n to $(n+2, n-2)$, the two sidebands observed in figure 6(a). Note that because the fields associated with the Raman and FORT beams are symmetric with respect to the boundary conditions set by the cavity, only even numbered Δn transitions are allowed. The positions of the sidebands in the figure correspond reasonably well to the expectation $\pm 2\nu_0 \simeq \pm 1.1$ MHz, where ν_0 is the vibrational frequency for harmonic motion at the antinode of the FORT, which is independently determined from the FORT and caesium parameters. However, we do not yet understand the observed lineshapes nor the loss of contrast evidenced in figure 6, which may be due to the considerable anharmonicity of the FORT for weakly bound atoms. Preliminary attempts at cooling centre-of-mass motion by driving Raman vibrational sidebands empirically suggest that we can extend the lifetime of trapped atoms within our cavity, as indicated in the bar plots superimposed over the Raman scan. In a series of trials, atoms loaded into the FORT were driven on either of the blue, red or carrier transitions while being probed at regular intervals. For each, the corresponding trapping durations T, represented by the relative sizes of the bars, and probabilities P that an atom loaded at the beginning of a 1 s long trial would survive until the end of the trial were recorded. On average, atoms driven on the red (cooling) sideband remained in the cavity substantially longer than those driven on the other motional transitions.

4.4. The vacuum-Rabi spectrum of one-and-the-same atom

Assisted by the capability to perform axial cooling using Raman transitions, our group was recently able to undertake measurements of the vacuum-Rabi spectrum for one-and-the-same atom. This is in contrast to the measurements discussed above [32, 37] and other recent observations made with atoms trapped in a FORT [76], all of which require averaging over a large ensemble of atoms (e.g., 10^3–10^4 atoms in [76]). After a single atom is loaded into the FORT, a probe beam of frequency ω_p, varied over a range near the atom–cavity resonance ($\omega_A = \omega_{C_1}$), is mode-matched into the cavity, and the transmission of the probe $T(\omega_p)$ is recorded. After each probe interval, a cycle of Raman sideband cooling is interspersed before the probe frequency is iterated forwards and the process repeated. By choosing only those

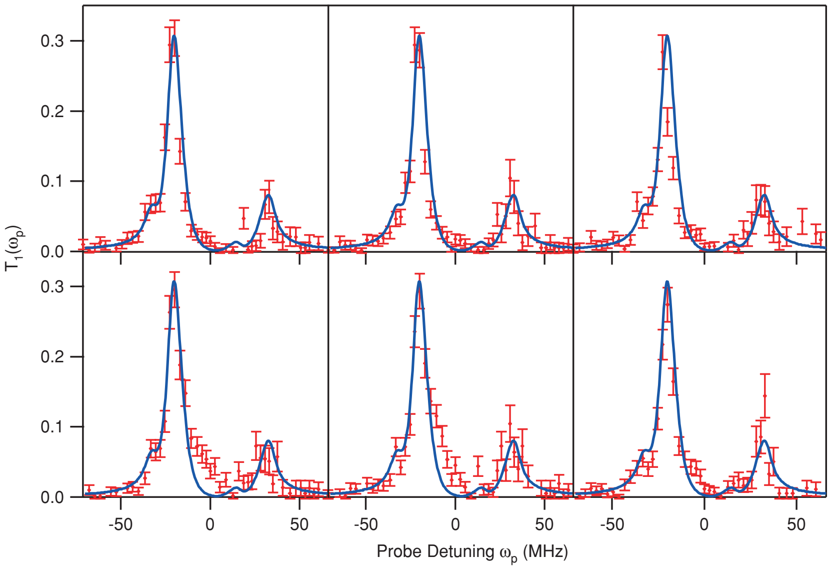

Figure 7. Vacuum-Rabi splitting of one-and-the-same atom. The complete vacuum-Rabi transmission spectra, $T(\omega_p)$ for six atoms, selected at random from a pool of 28 such spectra. The error bars represent statistical uncertainties. The blue trace is the solution of the master equation for the system [77].

trials for which the empty cavity resonance at $\omega_p = \omega_{C_1}$ is suppressed (i.e., those with strong resonant absorption indicating that an atom is coupled to the cavity), we are able to obtain the vacuum-Rabi spectrum for precisely one atom (six of which, for six separate atoms, were randomly selected and are shown in figure 7) [77].

For comparison, also included in figure 7 is the solution to the steady-state master equation for this system, incorporating only known experimental parameters and averaged over the top 1/3 of FORT wells for which $g(\mathbf{r})$ is closest to its maximum value, g_0 (i.e., $g(\mathbf{r}) \gtrsim 0.87g_0$). The results are in quite good agreement with the data, and the characteristic two peaked vacuum-Rabi structure is clearly present for each atom. The asymmetric features of the spectrum (i.e., peak heights, centroid locations) are principally the result of the small Zeeman state-dependent ac-Stark shifts induced by the FORT in conjunction with optical pumping effects due to the probe. In summation, these spectra contain detailed quantitative information about $g(\mathbf{r})$, indicating that atoms trapped and cooled within the FORT exist in a narrow range of near maximal values. This result is emblematic of the type of measurement which we expect the Raman technique to enable in the future.

5. Conclusion

We have discussed the evolution of experiments in optical cavity quantum electrodynamics, emphasizing those recent experiments enabled by intracavity state-insensitive optical dipole trapping. This work includes a demonstration of a one-atom laser, deterministic generation of single photons, the capacity for driving stimulated Raman transitions between hyperfine ground states of a trapped atom, and the observation of the vacuum-Rabi spectrum, the hallmark of strong coupling, for one-and-the-same atom.

In recent years, many advances in cavity QED have been driven by an interplay with quantum information science [78]. In the near future, the tools discussed above will begin to play an important role as it becomes possible to perform complex quantum information protocols [27–30]. In particular it may even be possible, via Raman sideband cooling, to enter a regime requiring a quantized treatment for all degrees of freedom in QED, namely the state of the atom, its centre-of-mass motion, and the field to which it is coupled. This hearkens back to Einstein and his introduction of the quantum hypothesis, which, one hundred years ago, set the stage for the remarkable experimental advances of today.

Acknowledgments

This work was supported by the National Science Foundation (NSF), by the Caltech MURI Center for Quantum Networks, by the Advanced Research and Development Activity (ARDA), and by the Office of Naval Research (ONR). RM acknowledges support from the Army Research Office (ARO) QuaCGR programme.

References

[1] Stachel J (ed) 1989 *The Collected Papers of Albert Einstein* (Princeton, NJ: Princeton University Press) p 135
[2] Planck M 1901 *Ann. Phys., Lpz.* **4** 561
[3] Einstein A 1905 *Ann. Phys., Lpz.* **17** 132
[4] Einstein A 1906 *Ann. Phys., Lpz.* **20** 199
[5] Einstein A 1907 *Ann. Phys., Lpz.* **22** 180
[6] Einstein A 1909 *Phys. Z.* **10** 185
[7] Einstein A 1909 *Phys. Z.* **10** 817
[8] ter Haar D 1967 *The Old Quantum Theory* (Oxford: Pergamon)
[9] Mandel L and Wolf E 1995 *Optical Coherence and Quantum Optics* (Cambridge: Cambridge University Press)
[10] Jaynes E T and Cummings F W 1963 *Proc. IEEE* **51** 89
[11] Meystre P 1982 *Progress in Optics* vol 30 ed E Wolf (Amsterdam: Elsevier) p 261
[12] Kimble H J 1998 *Phys. Scr.* T **76** 127
[13] Carmichael H J 1993 *An Open Systems Approach to Quantum Optics (Lecture Notes in Physics* vol 18*)* (Berlin: Springer)
[14] Vernooy D and Kimble H J 1997 *Phys. Rev.* A **55** 1239
[15] Vernooy D, Ilchenko V S, Mabuchi H, Streed E and Kimble H J 1998 *Opt. Lett.* **23** 247
[16] Buck J R and Kimble H J 2003 *Phys. Rev.* A **67** 033806
[17] Chiorescu I, Bertet P, Semba K, Nakamura Y, Harmas C J P M and Mooij J E 2004 *Nature* **431** 159
[18] Wallraff A, Schuster D I, Blais A, Frunzio L, Huang R-S, Majer J, Kumar S, Girvin S M and Schoelkopf R J 2004 *Nature* **431** 162
[19] Raimond J M, Brune M and Haroche S 2001 *Rev. Mod. Phys.* **73** 565
[20] Walther H 1998 *Proc. R. Soc. L.* A **454** 431
[21] Berman P (ed) 1994 *Cavity Quantum Electrodynamics* (San Diego: Academic)
[22] Rempe G, Thompson R J, Kimble H J and Lalezari R 1992 *Opt. Lett.* **17** 363
[23] Vahala K 2003 *Nature* **404** 6950
[24] Spillane S M, Kippenberg T J, Vahala K H, Goh K W, Wilcut E and Kimble H J 2005 *Phys. Rev.* A **71** 013817
[25] Mabuchi H and Doherty A C 2002 *Science* **298** 1372
[26] Lev B, Srinivasan K, Barclay P, Painter O and Mabuchi H 2004 *Nanotechnology* **15** S556
[27] Pellizzari T, Gardiner S A, Cirac J I and Zoller P 1995 *Phys. Rev. Lett.* **75** 3788
[28] Duan L-M and Kimble H J 2004 *Phys. Rev. Lett.* **92** 127902
[29] Cirac J I, Zoller P, Kimble H J and Mabuchi H 1997 *Phys. Rev. Lett.* **78** 3221
[30] Briegel H J *et al The Physics of Quantum Information* ed D Bouwmeester, A Ekert and A Zeilinger (Berlin: Springer) p 192
[31] Rempe G, Thompson R J, Brecha R J, Lee W D and Kimble H J 1991 *Phys. Rev. Lett.* **67** 1727
[32] Thompson R J, Rempe G and Kimble H J 1992 *Phys. Rev. Lett.* **68** 1132
[33] Thompson R J, Turchette Q A, Carnal O and Kimble H J 1998 *Phys. Rev.* A **57** 3084
[34] Childs J J, An K, Otteson M S, Dasari R R and Feld M S 1996 *Phys. Rev. Lett.* **77** 2901

[35] Brune M, Schmidt-Kaler F, Maali A, Dreyer J, Hagley E, Raimond J M and Haroche S 1996 *Phys. Rev. Lett.* **76** 1800

[36] Mabuchi H, Turchette Q A, Chapman M S and Kimble H J 1996 *Opt. Lett.* **21** 1393

[37] Hood C J, Lynn T, Chapman M and Kimble H J 1998 *Phys. Rev. Lett.* **80** 4157

[38] Hood C J, Lynn T W, Doherty A C, Parkins A S and Kimble H J 2000 *Science* **287** 1457

[39] Pinkse P W H, Fischer T, Maunz P and Rempe G 2000 *Nature* **404** 365

[40] Doherty A C, Lynn T W, Hood C J and Kimble H J 2001 *Phys. Rev.* A **63** 013401

[41] McKeever J, Buck J R, Boozer A D, Kuzmich A, Nägerl H-C, Stamper-Kurn D M and Kimble H J 2003 *Phys. Rev. Lett.* **90** 133602

[42] Sauer J A, Fortier K M, Chang M S, Hamley C D and Chapman M S 2004 *Phys. Rev.* A **69** 051804

[43] Maunz P, Puppe T, Schuster I, Syassen N, Pinkse P W H and Rempe G 2004 *Nature* **428** 50

[44] Ye J, Vernooy D W and Kimble H J 1999 *Phys. Rev. Lett.* **83** 4987

[45] Metcalf H and van der Straten P 1999 *Laser Cooling and Trapping* (Berlin: Springer)

[46] Grimm R, Weidemüller M and Ovchinnikov Y B 2000 *Adv. At. Mol. Opt. Phys.* **42** 95

[47] Kimble H J 1999 *ICOLS 99: Proc. 14 Int. Conf. on Laser Spectroscopy* ed R Blatt, J Eschner, D Leibfried and F Schmidt-Kaler (Innsbruck: ICOLS)

[48] Hood C J 2000 *Doctoral Dissertation* California Institute of Technology

[49] Ido T, Isoya Y and Katori H 1999 *J. Phys. Soc. Japan* **68** 2479

[50] McKeever J 2004 *Doctoral Dissertation* California Institute of Technology

[51] Kuhr S, Alt W, Schrader D, Müller M, Gomer V and Meschede D 2001 *Science* **293** 278

[52] Keller M, Lange B, Hayasaka K, Lange W and Walther H 2004 *Nature* **431** 1075

[53] Mundt A B, Kreuter A, Becher C, Leibfried D, Eschner J, Schmidt-Kaler F and Blatt R 2002 *Phys. Rev. Lett.* **89** 103001

[54] Monroe C, Meekhof D, King B, Jefferts S, Itano W, Wineland D and Gould P 1995 *Phys. Rev. Lett.* **75** 4011

[55] Barrett M D *et al* 2004 *Nature* **429** 737

[56] Riebe M *et al* 2004 *Nature* **429** 734

[57] Blinov B B, Moehring D L, Duan L-M and Monroe C 2004 *Nature* **428** 153

[58] Mu Y and Savage C 1992 *Phys. Rev.* A **46** 5944

[59] Ginzel C, Briegel H-J, Martini U, Englert B-G and Schenzle A 1993 *Phys. Rev.* A **48** 732

[60] Pellizzarri T and Ritsch H 1994 *Phys. Rev. Lett.* **72** 3973

[61] Horak P, Gheri K M and Ritsch H 1995 *Phys. Rev.* A **51** 3257

[62] Meyer G M, Briegel H-J and Walther H 1997 *Europhys. Lett.* **37** 317

[63] Löffler M, Meyer G M and Walther H 1997 *Phys. Rev.* A **55** 3923

[64] Meyer G M, Löffler M and Walther H 1997 *Phys. Rev.* A **56** R1099

[65] Meyer G M and Briegel H-J 1998 *Phys. Rev.* A **58** 3210

[66] Jones B, Ghose S, Clemens J P, Rice P R and Pedrotti L M 1999 *Phys. Rev.* A **60** 3267

[67] Kilin S Ya and Karlovich T B 2002 *JETP* **95** 805

[68] McKeever J, Boca A, Boozer A D, Buck J R and Kimble H J 2003 *Nature* **425** 268

[69] Boozer A D, Boca A, Buck J R, McKeever J and Kimble H J 2004 *Phys. Rev.* A **70** 023814

[70] McKeever J, Boca A, Boozer A D, Miller R, Buck J R, Kuzmich A and Kimble H J 2004 *Science* **303** 1992

[71] Parkins A S, Marte P, Zoller P and Kimble H J 1993 *Phys. Rev. Lett.* **71** 3095

[72] McKeever J, Buck J R, Boozer A D and Kimble H J 2004 *Phys. Rev. Lett.* **93** 143601

[73] Duan L-M and Kimble H J 2003 *Phys. Rev. Lett.* **90** 253601

[74] Hamann S E, Haycock D L, Klose G, Pax P H, Deutsch I H and Jessen P S 1998 *Phys. Rev. Lett.* **80** 4149

[75] Vuletić V, Chin C, Kerman A J and Chu S 1998 *Phys. Rev. Lett.* **81** 5768

[76] Maunz P, Puppe T, Schuster I, Syassen N, Pinkse P W H and Rempe G 2004 *Preprint* quant-ph/045136

[77] Boca A, Miller R, Birnbaum K M, Boozer A D, McKeever J and Kimble H J 2004 *Phys. Rev. Lett.* **93** 233603

[78] Nielsen M A and Chuang I L 2000 *Quantum Computation and Quantum Information* (Cambridge: Cambridge University Press)

Vol 436|7 July 2005|doi:10.1038/nature03804

nature

LETTERS

Photon blockade in an optical cavity with one trapped atom

K. M. Birnbaum[1], A. Boca[1], R. Miller[1], A. D. Boozer[1], T. E. Northup[1] & H. J. Kimble[1]

At low temperatures, sufficiently small metallic[1] and semiconductor[2] devices exhibit the 'Coulomb blockade' effect, in which charge transport through the device occurs on an electron-by-electron basis[3]. For example, a single electron on a metallic island can block the flow of another electron if the charging energy of the island greatly exceeds the thermal energy. The analogous effect of 'photon blockade' has been proposed for the transport of light through an optical system; this involves photon–photon interactions in a nonlinear optical cavity[4–13]. Here we report observations of photon blockade for the light transmitted by an optical cavity containing one trapped atom, in the regime of strong atom–cavity coupling[14]. Excitation of the atom–cavity system by a first photon blocks the transmission of a second photon, thereby converting an incident poissonian stream of photons into a sub-poissonian, anti-bunched stream. This is confirmed by measurements of the photon statistics of the transmitted field. Our observations of photon blockade represent an advance over traditional nonlinear optics and laser physics, into a regime with dynamical processes involving atoms and photons taken one-by-one.

An analogy between electron transport in mesoscopic electronic devices and photon transport through strongly coupled optical systems was originally suggested in ref. 5. These authors proposed that an effect similar to Coulomb blockade for electrons[1–3] might be possible for photons by using photon–photon interactions in a nonlinear optical cavity[5]. In this scheme, strong dispersive interactions enabled by electromagnetically induced transparency (EIT) cause the presence of a 'first' photon within the cavity to block the transmission of a 'second' photon, leading to an ordered flow of photons in the transmitted field.

After resolution of an initial difficulty[6], subsequent work has confirmed that such photon blockade is indeed feasible for a single intracavity atom by way of a multi-state EIT scheme[7–9]. Photon blockade is possible in other settings, including in concert with Coulomb blockade[10] and via tunnelling with localized surface plasmons[11]. Photon blockade has also been predicted for a two-state atom coupled to a cavity mode[4,9,12,13]. As illustrated in Fig. 1a, the underlying mechanism is the anharmonicity of the Jaynes–Cummings ladder of eigenstates[4,15]. Resonant absorption of a photon of frequency ω_- to reach the state $|1,-\rangle$ (where $|n,+(-)\rangle$ denotes the higher- (lower-) energy eigenstate with n excitations) 'blocks' the absorption of a second photon at ω_- because transitions to $|2,\pm\rangle$ are detuned from resonance.

Whereas electrons interact directly via Coulomb repulsion, photon–photon interactions must be mediated by matter. Furthermore, verification of this effect requires measurements of the quantum statistics of the field; in contrast, Coulomb blockade can be inferred directly from mean transport. Scattering from a single atom in free space, for example, provides a fundamental example of photon blockade[16], albeit with the fluorescent field distributed over 4π and the flux limited by the rate of spontaneous decay γ. In contrast, cavity-mediated schemes offer the possibility of photon emission into a collimated spatial mode with high efficiency and at a rate set by the cavity decay rate κ, which can be much larger than γ. Achieving photon blockade for a single atom in a cavity requires us to operate in the regime of strong coupling, for which the frequency scale g_0 associated with reversible evolution of the atom–cavity system exceeds the dissipative rates (γ, κ) (ref. 14).

Here we report observations of photon blockade in the light transmitted by an optical cavity containing one atom strongly coupled to the cavity field. For coherent excitation at the cavity

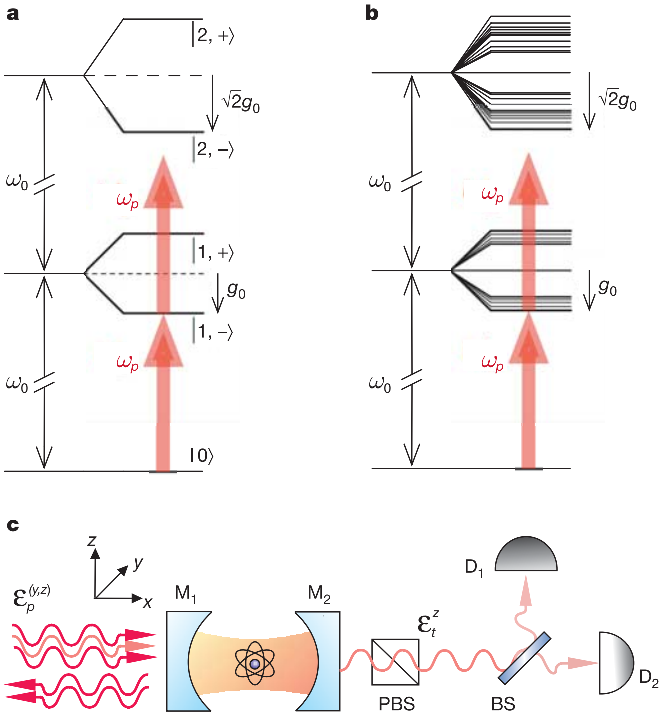

Figure 1 | The atomic level structure used for implementation of the photon blockade effect, and a simple diagram of the experiment. a, Atomic level diagram showing the lowest-energy states for a two-state atom of transition frequency ω_A coupled (with single-photon Rabi frequency g_0) to a mode of the electromagnetic field of frequency ω_C, with $\omega_A = \omega_C \equiv \omega_0$ (ref. 15). Two-photon absorption is suppressed for a probe field ω_p (arrows) tuned to excite the transition $|0\rangle \rightarrow |1,-\rangle$, $\omega_p = \omega_0 - g_0$, leading to $g^{(2)}(0) < 1$ (ref. 13). **b**, Eigenvalue structure for the $(F=4, m_F) \leftrightarrow (F'=5', m_F')$ transition coupled to two degenerate cavity modes $l_{y,z}$, as discussed in the Supplementary Information. Two-photon absorption is likewise blocked for excitation tuned to the lowest eigenstate (arrows). **c**, Simple diagram of the experiment. BS, beam splitter.

---

[1]Norman Bridge Laboratory of Physics 12-33, California Institute of Technology, Pasadena, California 91125, USA.

© 2005 Nature Publishing Group

input, the photon statistics for the cavity output are investigated by measurement of the intensity correlation function $g^{(2)}(\tau)$, which demonstrates the manifestly nonclassical character of the transmitted field. Explicitly, we find $g^{(2)}(0) = (0.13 \pm 0.11) < 1$ with $g^{(2)}(0) < g^{(2)}(\tau)$, so that the output light is both subpoissonian and antibunched[17]. We find that $g^{(2)}(\tau)$ rises to unity at a time $\tau \simeq 45\,\mathrm{ns}$, which is consistent with the lifetime $\tau_- = 2/(\gamma+\kappa) = 48\,\mathrm{ns}$ for the state $|1,-\rangle$ associated with the blockade. Over longer timescales, cavity transmission exhibits modulation arising from the oscillatory motion of the atom trapped within the cavity mode. We use this modulation to make an estimate of the energy distribution for the atomic centre-of-mass motion and infer a maximum energy $E/k_B \approx 250\,\mu K$, where k_B is the Boltzmann constant

The schematic of our experiment in Fig. 1c illustrates the Fabry–Perot cavity formed by mirrors (M_1, M_2) into which single optically cooled caesium atoms are loaded. Atoms are trapped within the cavity by a far-off-resonance trap (FORT), which is created by exciting a TEM_{00} cavity mode at $\lambda_F = 935.6\,\mathrm{nm}$ (ref. 18). To achieve strong coupling, we use the $6S_{1/2}, F=4 \rightarrow 6P_{3/2}, F'=5'$ transition of the D2 line in caesium at $\lambda_A = 852.4\,\mathrm{nm}$ (subscript A refers to 'atom'), for which the maximum rate of coherent coupling is $g_0/2\pi = 34\,\mathrm{MHz}$ for $(F=4, m_F=\pm4) \rightarrow (F'=5', m'_F=\pm5)$. The transverse decay rate for the $6P_{3/2}$ atomic states is $\gamma/2\pi = 2.6\,\mathrm{MHz}$, while the cavity field decays at rate $\kappa/2\pi = 4.1\,\mathrm{MHz}$. The parameters of the cavity are further discussed in the Methods.

A variety of factors make our atom–cavity system more complex than the simple situation described by the Jaynes–Cummings eigenstates, including most significantly that (1) the cavity supports two modes $l_{y,z}$ with orthogonal linear polarizations $(\hat{y}, \hat{z})$ near $\lambda_A = 852.4\,\mathrm{nm}$ as described in the Methods section, and (2) a multiplicity of Zeeman states are individually coupled to these modes for transitions between the manifolds $(F=4, m_F) \leftrightarrow (F'=5', m'_F)$. An indication of the potential for this system to achieve photon blockade is provided in Fig. 1b, which displays the actual eigenvalue structure for the first two excited manifolds obtained by direct diagonalization of the interaction hamiltonian, as discussed in the Supplementary Information. As for the basic two-state system, excitation to the lowest-energy state in the one-excitation manifold 'blocks' subsequent excitation because the transitions to the two-excitation manifold are out of resonance.

To substantiate this picture quantitatively, we present in Fig. 2 theoretical results from the steady-state solution to the master equation in various situations, all for the case of coincident atomic and cavity resonances $\omega_A = \omega_{C_1} \equiv \omega_0$. (Subscripts C_1 and C_2 refer to the cavity resonances near λ_A and λ_F, respectively). Beginning with the ideal setting of a two-state atom coupled to a single cavity mode, we display in Fig. 2a results for the probe transmission spectrum $T(\omega_p)$ and the intensity correlation function $g^{(2)}(0)$ of the field ε_t transmitted by mirror M_2 for excitation by a coherent-state probe ε_p of variable frequency ω_p incident upon the cavity mirror M_1. Clearly evident in $T(\omega_p)$ are two peaks at $\omega_p = \omega_\pm \equiv \omega_0 \pm g_0$ associated with the vacuum-Rabi splitting for the states $|1,\pm\rangle$. At these peaks, ε_p is detuned for excitation $|1,\pm\rangle \rightarrow |2,\pm\rangle$, resulting in $g^{(2)}(0) < 1$ for ε_t. The poissonian photon statistics of the incident probe are thereby converted to subpoissonian statistics for the transmitted field by way of the photon blockade effect illustrated in Fig. 1a. For strong coupling in the weak-field limit, $g^{(2)}(0) \propto (\kappa+\gamma)^2/g_0^2$ for $\omega_p = \omega_\pm$ (ref. 12), hence the premium on achieving $g_0 \gg (\kappa, \gamma)$. By contrast, for $\omega_p = \omega_0 \pm g_0/\sqrt{2}, \varepsilon_p$ is resonant with the two-photon transition $|0\rangle \rightarrow |2,\pm\rangle$, resulting in superpoissonian statistics with $g^{(2)}(0) \gg 1$. For $\omega_p = \omega_0$, there is extremely large bunching due to quantum interference between ε_p and the atomic polarization[12,19].

In Fig. 2b we examine the more complex situation relevant to our actual experiment, namely a multi-state atom coupled to two cavity modes with orthogonal polarizations $\hat{y}, \hat{z}$. Most directly related to the simple case of Fig. 2a is to excite one polarization eigenmode with the incident probe, taken here to be ε_p^z, and to detect the transmitted field ε_t^z for this same polarization, with the transmission spectrum and intensity correlation function denoted by $T_{zz}(\omega_p)$, $g_{zz}^{(2)}(0)$, respectively. Even for the full multiplicity of states for the $F=4 \rightarrow F'=5'$ transition coupled to the two cavity modes $l_{y,z}$, $T_{zz}(\omega_p)$ displays a rather simple structure, now with a multiplet structure in place of the single vacuum-Rabi peak around $\omega_p \simeq \omega_0 \pm g_0$. For a probe frequency tuned to the eigenvalues $\omega_p = \omega_0 \pm g_0$, $g_{zz}^{(2)}(0) \simeq 0.7$, once again dropping below unity as in Fig. 2a.

An alternative scheme is to detect along $\hat{z}$, but excite along orthogonal polarization $\hat{y}$, with the respective transmission and correlation functions $T_{yz}(\omega_p)$, $g_{yz}^{(2)}(0)$ also shown in Fig. 2b. Similar to $T_{zz}(\omega_p)$, $T_{yz}(\omega_p)$ exhibits a multiplet structure in the vicinity of $\omega_p \simeq \omega_0 \pm g_0$ owing to the nature of the first excited states of the atom–cavity system. At the extremal $\omega_p = \omega_0 \pm g_0$, $g_{yz}^{(2)}(0)$ reaches a value $g_{yz}^{(2)}(0) \simeq 0.03$ much smaller than for either $g^{(2)}(0)$ in Fig. 2a, or $g_{zz}^{(2)}(0)$ in Fig. 2b, for the same values of (g_0, κ, γ). Our preliminary hypothesis is that this reduction relates to the absence of the superposed driving field ε_p^y with the transmitted field ε_t^z of orthogonal polarization $\hat{z}$ (ref. 20); photons in the mode l_z derive from emissions associated with the atomic components of atom-field eigenstates.

Tuning the probe to $\omega_p = \omega_0 \pm g_0$ has the additional benefit of reducing sensitivity to atomic position, which varies experimentally owing to atomic motion and the multiplicity of trapping sites within the cavity[21]. The atomic position affects the transmission via the position dependence of the coupling $g = g_0\psi(\mathbf{r})$, where ψ is the TEM_{00} spatial mode at λ_{C_1} with maximum $|\psi| = 1$, and $\mathbf{r}$ is the position of the atom. $T_{yz}(\omega_p)$ is small when $|\omega_p - \omega_0| \gtrsim g$, so atoms which have a lower-than-expected value of g will have a reduced contribution to the photon statistics.

An important step in the implementation of this strategy is our recent measurement of the vacuum-Rabi spectrum $T_{zz}(\omega_p)$ for one trapped atom[21]. In that work we obtained quantitative agreement on an atom-by-atom basis between our observations and an extension of the theoretical model used to generate the various plots in Fig. 2b. The extended model incorporates a.c.-Stark shifts from the FORT as well as cavity birefringence. This model predicts that corrections to

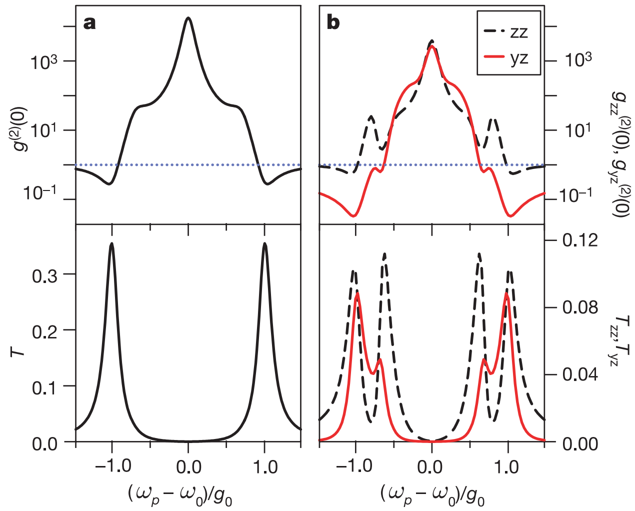

Figure 2 | Theoretical results for the transmission spectra and intensity correlation functions. **a**, $T(\omega_p)$, $g^{(2)}(0)$; **b**, $T_{zz}(\omega_p)$, $g_{zz}^{(2)}(0)$ (dashed) and $T_{yz}(\omega_p)$, $g_{yz}^{(2)}(0)$ (red) from the steady-state solution to the master equation. Included are all transitions $(F=4, m_F) \leftrightarrow (F'=5', m'_F)$ with their respective coupling coefficients $g_0^{(m_F, m'_F)}$, as well as the two cavity modes $l_{y,z}$ here assumed to be degenerate in frequency (see Supplementary Information for further discussion). The blue dotted lines indicate poissonian statistics. Parameters are $(g_0, \kappa, \gamma)/2\pi = (33.9, 4.1, 2.6)$ MHz, and the probe strength is such that the intracavity photon number on resonance without an atom is 0.05.

© 2005 Nature Publishing Group

$g_{yz}^{(2)}(0)$ due to these effects are small for our parameters, as discussed in the Supplementary Information.

With these capabilities, we now report measurements of $g_{yz}^{(2)}(\tau)$ for the light transmitted by a cavity containing a single trapped atom. We tune the probe $\varepsilon_{\rm p}^{y}$ to $(\omega_{\rm p} - \omega_0)/2\pi = -34\,{\rm MHz}$, near $-g_0$, and acquire photoelectric counting statistics of the field $\varepsilon_{\rm t}^{z}$ by way of two avalanche photodiodes (D_1, D_2), as illustrated in Fig. 1c. From the record of these counts, we are able to determine $g_{yz}^{(2)}(\tau)$ by using the procedures discussed in ref. 22. Data are acquired for each trapped atom by cycling through probing, testing, and cooling intervals (of durations $\Delta t_{\rm probe} = 500\,\mu{\rm s}$, $\Delta t_{\rm test} = 100\,\mu{\rm s}$ and $\Delta t_{\rm cool} = 1.4\,{\rm ms}$, respectively) using a procedure similar to that of ref. 21. The test beam is polarized along $\hat{z}$ and resonant with the cavity. A repumping beam transverse to the cavity axis and resonant with $6S_{1/2},\ F=3 \rightarrow 6P_{3/2},\ F'=4'$ also illuminates the atom during the probe and test intervals. This beam prevents accumulation of population in the $F=3$ ground state caused by the probe off-resonantly exciting the $F=4 \rightarrow F'=4'$ transition. All probing/cooling cycles end after an interval $\Delta t_{\rm tot} = 0.3\,{\rm s}$, at which point a new loading cycle is initiated. We select for the presence of an atom by requiring that $T_{zz}(\omega_{\rm p} \simeq \omega_{\rm C_1}) \lesssim 0.35$ for the test beam. We use only those data records associated with probing intervals after which the presence of an atom was detected and for which the presence of an atom was detected in all preceding intervals. If there is no atom and the probe is tuned to be resonant with the cavity ($\omega_{\rm p} = \omega_{\rm C_1}$), then the photon number in mode l_y due to $\varepsilon_{\rm p}^{y}$ is 0.21 and the polarizing beam splitter at the output of the cavity (PBS in Fig. 1c) suppresses detection of this light by a factor of ~94.

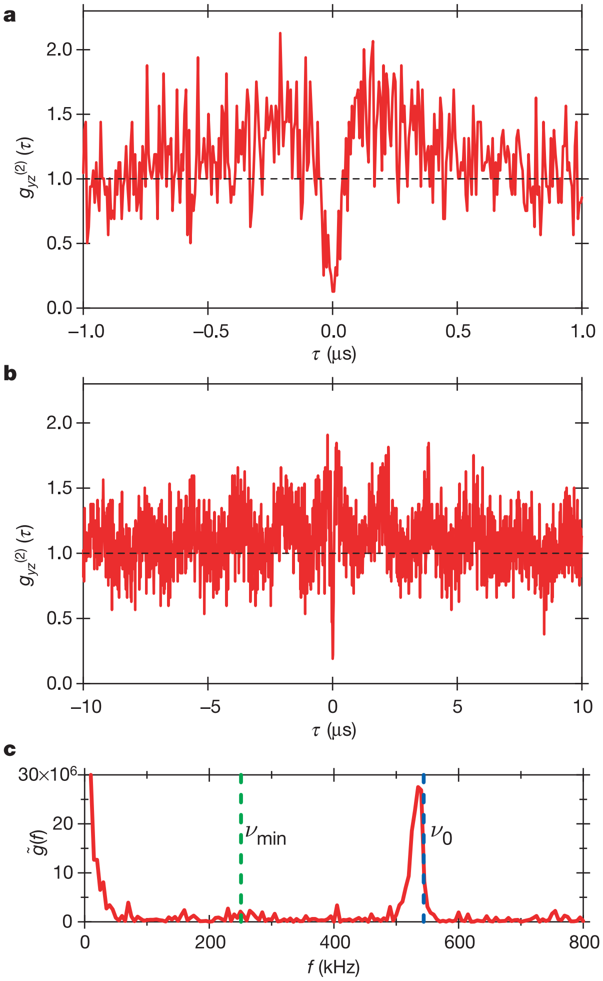

Figure 3 | Experimental measurements of the intensity correlation function $g_{yz}^{(2)}(\tau)$ for incident excitation with polarization along $\hat{y}$ and detection with orthogonal polarization $\hat{z}$. **a**, $g_{yz}^{(2)}(\tau)$ over the interval $|\tau| \leq 1.0\,\mu{\rm s}$ demonstrates that the transmitted field exhibits both subpoissonian photon statistics $g_{yz}^{(2)}(0) = (0.13 \pm 0.11) < 1$ and photon antibunching $g_{yz}^{(2)}(0) < g_{yz}^{(2)}(\tau)$ (ref. 17). **b**, $g_{yz}^{(2)}(\tau)$ over longer intervals $|\tau| \leq 10\,\mu{\rm s}$ displays a pronounced modulation due to axial motion of the trapped atom. **c**, The Fourier transform $\tilde{g}(f)$ of $g_{yz}^{(2)}(\tau)$ with the independently determined minimum and maximum frequencies $\nu_{\rm min}$ and ν_0 for axial motion in a FORT well indicated by the dotted lines. $g_{yz}^{(2)}(\tau)$ is plotted with 6-ns resolution in **a** and with 12-ns resolution in **b**.

Figure 3 presents an example of $g_{yz}^{(2)}(\tau)$ determined from the recorded time-resolved coincidences at (D_1, D_2). In Fig. 3a, the manifestly nonclassical character of the transmitted field is clearly observed with a large reduction in $g_{yz}^{(2)}(0)$ below unity, $g_{yz}^{(2)}(0) = (0.13 \pm 0.11) < 1$, corresponding to the subpoissonian character of the transmitted field, and with $g_{yz}^{(2)}(0) < g_{yz}^{(2)}(\tau)$ as a manifestation of photon antibunching. We find that $g^{(2)}(\tau)$ rises to unity at a time $\tau \simeq 45\,{\rm ns}$, which is consistent with a simple estimate of $\tau_- = 2/(\gamma + \kappa) = 48\,{\rm ns}$ based upon the lifetime for the state $|1,-\rangle$.

Although for small $|\tau|$ our observations of $g_{yz}^{(2)}(\tau)$ are in reasonable agreement with the predictions from our theoretical model, there are significant deviations on longer timescales. Modulation that is not present in the model is evident in Fig. 3b, which arises from the centre-of-mass motion of the trapped atom. In support of this assertion, Fig. 3c displays the Fourier transform $\tilde{g}(f)$ of $g_{yz}^{(2)}(\tau)$, which exhibits a narrow peak at frequency $f_0 \simeq 535\,{\rm kHz}$ just below the independently determined frequency $\nu_0 \simeq 544\,{\rm kHz}$ for harmonic motion of a trapped atom about an antinode of the FORT in the axial direction x. This modulation is analogous to that observed in ref. 23 for $g^{(2)}(\tau)$ for the light from a single ion, which arose from micro-motion of the ion in the radio-frequency trap.

Here, $U(\mathbf{r}) = U_0 \sin^2(2\pi x/\lambda_{\rm C_2})\exp(-2\rho^2/w_{\rm C_2}^2)$ is the FORT potential, which gives rise to an anharmonic ladder of vibrational states with energies $\{E_m\}$. Here $m = 0$ to $m_{\rm max} = 99$ correspond to the bound states in the axial dimension for radial coordinate $\rho \equiv \sqrt{y^2 + z^2} = 0$. The anharmonicity leads to the observed offset $f_0 < \nu_0$ due to the distribution of energies for axial motion in the FORT well. Indeed, the frequency $\nu_{\rm min} = (E_{m_{\rm max}} - E_{m_{\rm max}-1})/h$ at the top of the well is approximately half that at the bottom of the well, $\nu_0 = (E_1 - E_0)/h$. By comparing the measured distribution of frequencies exhibited by $\tilde{g}(f)$ with the calculated axial frequencies $\{\nu_m\}$, we estimate that those atoms from which data was obtained are trapped in the lowest-lying axial states $m \lesssim 10$, which corresponds to a maximum energy $E/k_{\rm B} \approx 250\,\mu{\rm K}$. This energy estimate is consistent with other measurements of $g_{yz}^{(2)}(\tau)$ that we have made, as well as the Fourier transform of the record of the transmitted intensity and the transmission spectra of ref. 21.

We have demonstrated photon blockade for the transmission of an optical cavity strongly coupled to a single trapped atom[4–9,12,13]. The observed nonclassical photon statistics for the transmitted field result from strong nonlinear interactions at the single-photon level, in analogy with the phenomena of Coulomb blockade for electron transport[1–3]. Extensions of our work include operation in a pulsed mode, as was analysed in ref. 5, thereby realizing a source for single photons 'on demand'[22]. As we improve the effectiveness of our cooling procedure, we should be able to explore the dependence of $g_{yz}^{(2)}(\tau)$ on probe detuning, $\omega_{\rm p} - \omega_0$, as well as to move to higher levels of excitation to increase the intracavity photon number towards unity and the output flux towards the maximum value $\lesssim \kappa$ for subpoissonian photons.

METHODS

Cavity and detection parameters. The physical length of the cavity used in this work is 42.2 μm and the finesse is 4.3×10^5. The cavity length is independently stabilized such that a $\rm TEM_{00}$ longitudinal mode at $\lambda_{\rm C_1}$ is resonant with the free-space atomic transition at $\lambda_{\rm A}$ and another $\rm TEM_{00}$ mode at $\lambda_{\rm C_2}$ is resonant at λ_F. At the cavity centre $x = 0$, the mode waists $w_{\rm C_{1,2}} = \{23.4, 24.5\}\ \mu{\rm m}$ at $\lambda_{\rm C_{1,2}} = \{852.4, 935.6\}\ {\rm nm}$.

© 2005 Nature Publishing Group

The TEM_{00} longitudinal mode for the FORT is driven by a linearly polarized input field $\varepsilon_{\mathrm{FORT}}$, resulting in nearly equal a.c. Stark shifts for Zeeman states in the $6S_{1/2},\ F = 3, 4$ manifold. At an antinode of the field, the peak value of the trapping potential for these states is $U_0/h = -43\,\mathrm{MHz}$ for all our measurements. Zeeman states of the $6P_{3/2},\ F' = 5'$ manifold experience a similar trapping potential, but with a weak dependence on m'_F (ref. 18).

Stress-induced birefringence in the cavity mirrors leads to a mode splitting $\Delta\omega_{\mathrm{C}_1}/2\pi = 4.4 \pm 0.2\,\mathrm{MHz}$ of the two cavity modes $l_{y,z}$ with orthogonal linear polarizations $(\hat{y}, \hat{z})$. $\varepsilon_{\mathrm{FORT}}$ is linearly polarized and aligned along $\hat{z}$, the higher-frequency mode.

The efficiency for photon escape from the cavity, limited by losses inherent to the mirror substrates, is $\alpha_{\mathrm{e2}} = 0.6 \pm 0.1$. The propagation efficiency from M_2 to detectors $(\mathrm{D}_1, \mathrm{D}_2)$ is $\alpha_{\mathrm{P}} = 0.41 \pm 0.03$, with each detector then receiving half of the photons. The avalanche photodiodes $(\mathrm{D}_1, \mathrm{D}_2)$ have quantum efficiencies $\alpha_{\mathrm{D}} = 0.49 \pm 0.05$.

Photon statistics. The transmission spectrum $T(\omega_{\mathrm{p}})$ is proportional to the ratio of photon flux $\langle \varepsilon_t^{\dagger} \varepsilon_t \rangle$ transmitted by M_2 to the flux $|\varepsilon_{\mathrm{p}}|^2$ incident upon M_1, and normalized such that a cavity without an atom has a resonant transmission of unity, i.e. $T(\omega_{\mathrm{p}} = \omega_{\mathrm{C}_1}) = 1$. For a field with intensity operator $\hat{I}(t), g^{(2)}(\tau) \equiv \langle : \hat{I}(t)\hat{I}(t+\tau) : \rangle / \langle : \hat{I}(t) : \rangle \langle : \hat{I}(t+\tau) : \rangle$, where the colons denote time and normal ordering (ref. 17). $g_{yz}^{(2)}(\tau)$, displayed in Fig. 3a and shown with a 6-ns resolution, has been corrected for background counts due to detector dark counts and scattered light from the repumping beam. Without this correction, $g_{yz}^{(2)}(0) \simeq (0.18 \pm 0.10)$ is directly derived from the recorded counts.

Received 26 March; accepted 5 May 2005.

1. Fulton, T. A. & Dolan, G. J. Observation of single-electron charging effects in small tunnel junctions. *Phys. Rev. Lett.* **59,** 109–112 (1987).
2. Kastner, M. A. The single-electron transistor. *Rev. Mod. Phys.* **64,** 849–858 (1992).
3. Likharev, K. K. Single-electron devices and their applications. *Proc. IEEE* **87,** 606–632 (1999).
4. Tian, L. & Carmichael, H. J. Quantum trajectory simulations of two-state behavior in an optical cavity containing one atom. *Phys. Rev. A* **46,** R6801 (1992).
5. Imamoğlu, A., Schmidt, H., Woods, G. & Deutsch, M. Strongly interacting photons in a nonlinear cavity. *Phys. Rev. Lett.* **79,** 1467–1470 (1997).
6. Grangier, P., Walls, D. F. & Gheri, K. M. Comment on "Strongly interacting photons in a nonlinear cavity". *Phys. Rev. Lett.* **81,** 2833 (1998).
7. Werner, M. J. & Imamoğlu, A. Photon-photon interactions in cavity electromagnetically induced transparency. *Phys. Rev. A* **61,** 011801 (1999).
8. Rebić, S., Tan, S. M., Parkins, A. S. & Walls, D. F. Large Kerr nonlinearity with a single atom. *J. Opt. B* **1,** 490–495 (1999).
9. Rebić, S., Parkins, A. S. & Tan, S. M. Polariton analysis of a four-level atom strongly coupled to a cavity mode. *Phys. Rev. A* **65,** 043806 (2002); Photon statistics of a single-atom intracavity system involving electromagnetically induced transparency. *Phys. Rev. A* **65,** 063804 (2002).
10. Kim, J., Bensen, O., Kan, H. & Yamamoto, Y. A single-photon turnstile device. *Nature* **397,** 500–503 (1999).
11. Smolyaninov, I. I., Zayats, A. V., Gungor, A. & Davis, C. C. Single-photon tunneling via localized surface plasmons. *Phys. Rev. Lett.* **88,** 187402 (2002).
12. Brecha, R. J., Rice, P. R. & Xiao, M. N two-level atoms in a driven optical cavity: quantum dynamics of forward photon scattering for weak incident fields. *Phys. Rev. A* **59,** 2392–2417 (1999).
13. Hood, C. J. *Real-time Measurement and Trapping of Single Atoms by Single Photons*. Section 6.2. PhD dissertation, California Institute of Technology (2000).
14. Kimble, H. J. Strong interactions of single atoms and photons in cavity QED. *Phys. Scr.* **T76,** 127–138 (1998).
15. Jaynes, E. T. & Cummings, F. W. Comparison of quantum and semiclassical radiation theories with application to the beam maser. *Proc. IEEE* **51,** 89–109 (1963).
16. Kimble, H. J., Dagenais, M. & Mandel, L. Photon antibunching in resonance fluorescence. *Phys. Rev. Lett.* **39,** 691–695 (1977).
17. Mandel, L. & Wolf, E. *Optical Coherence and Quantum Optics* (Cambridge Univ. Press, Cambridge, 1995).
18. McKeever, J. *et al.* State-insensitive cooling and trapping of single atoms in an optical cavity. *Phys. Rev. Lett.* **90,** 133602 (2003).
19. Carmichael, H. J., Brecha, R. J. & Rice, P. R. Quantum interference and collapse of the wavefunction in cavity QED. *Opt. Commun.* **82,** 73–79 (1991).
20. Carmichael, H. J. Photon antibunching and squeezing for a single atom in a resonant cavity. *Phys. Rev. Lett.* **55,** 2790–2793 (1985).
21. Boca, A. *et al.* Observation of the vacuum Rabi spectrum for one trapped atom. *Phys. Rev. Lett.* **93,** 233603 (2004).
22. McKeever, J. *et al.* Deterministic generation of single photons from one atom trapped in a cavity. *Science* **303,** 1992–1994 (2004).
23. Diedrich, F. & Walther, H. Nonclassical radiation of a single stored ion. *Phys. Rev. Lett.* **58,** 203–260 (1987).

Supplementary Information is linked to the online version of the paper at www.nature.com/nature.

Acknowledgements We gratefully acknowledge the contributions of J. McKeever and C. J. Hood. This research is supported by the National Science Foundation, by the Caltech MURI Center for Quantum Networks, and by the Advanced Research and Development Activity (ARDA).

Author Information Reprints and permissions information is available at npg.nature.com/reprintsandpermissions. The authors declare no competing financial interests. Correspondence and requests for materials should be addressed to H.J.K. (hjkimble@caltech.edu).

© 2005 Nature Publishing Group

PHYSICAL REVIEW A **71**, 013817 (2005)

Ultrahigh-*Q* toroidal microresonators for cavity quantum electrodynamics

S. M. Spillane, T. J. Kippenberg, and K. J. Vahala
Thomas J. Watson Laboratory of Applied Physics, California Institute of Technology, Pasadena, California 91125, USA

K. W. Goh, E. Wilcut, and H. J. Kimble
Norman Bridge Laboratory of Physics, California Institute of Technology, Pasadena, California 91125, USA

(Received 27 August 2004; published 26 January 2005)

We investigate the suitability of toroidal microcavities for strong-coupling cavity quantum electrodynamics (QED). Numerical modeling of the optical modes demonstrate a significant reduction of the modal volume with respect to the whispering gallery modes of dielectric spheres, while retaining the high-quality factors representative of spherical cavities. The extra degree of freedom of toroid microcavities can be used to achieve improved cavity QED characteristics. Numerical results for atom-cavity coupling strength g, critical atom number N_0, and critical photon number n_0 for cesium are calculated and shown to exceed values currently possible using Fabry-Perot cavities. Modeling predicts coupling rates $g/2\pi$ exceeding 700 MHz and critical atom numbers approaching 10^{-7} in optimized structures. Furthermore, preliminary experimental measurements of toroidal cavities at a wavelength of 852 nm indicate that quality factors in excess of 10^8 can be obtained in a 50-μm principal diameter cavity, which would result in strong-coupling values of $(g/(2\pi), n_0, N_0) = (86\text{ MHz}, 4.6\times10^{-4}, 1.0\times10^{-3})$.

DOI: 10.1103/PhysRevA.71.013817 PACS number(s): 42.50.Pq, 32.80.−t, 42.50.Ct, 42.60.Da

I. INTRODUCTION

The use of an optical microcavity can greatly enhance the interaction of an atom with the electromagnetic field such that even a single atom or photon can significantly change the dynamical evolution of the atom-cavity system [1]. Achieving the regime of "strong coupling" [2,3] is critically dependent on the characteristics of the optical cavity and generally requires the optical modes to be confined in a small mode volume for extended periods of time (or equivalently high Q factor).

Recent experimental realizations of strong coupling have employed high-finesse Fabry-Perot (FP) optical microcavities [4–9]. Our experiments at Caltech include the realization of an "atom-cavity microscope" with a single atom bound in orbit by single photons [4] and the development of a laser that operates with "one and the same" atom [10]. Fabry-Perot cavities, while possessing ultrahigh-quality factors and finesse, are difficult to manufacture and control, requiring sophisticated dielectric mirror coatings as well as accurate feedback for resonant wavelength control. Due in part to these reasons, there has been increased interest in other microcavity systems which not only can address some or all of the limitations of Fabry-Perot cavities, but which in principle can have improved optical properties.

Based upon the pioneering work of Braginsky and colleagues [11], whispering-gallery-mode cavities have also been investigated for cavity QED (CQED) experiments for many years [12]. Experimental studies have demonstrated Q factors approaching 10^{10} in a silica microsphere whispering gallery cavity [13,14], with values exceeding 10^8 readily achievable over a broad range of cavity diameters and wavelengths. The combination of their very low cavity losses, small mode volumes, and their relative ease of fabrication makes them promising candidates for experiments in CQED [15,16]. Furthermore, the ability to couple these cavities with record coupling efficiencies to an optical fiber [17] (the medium of choice for low-loss transport of classical and nonclassical states [18]) is fundamentally important in CQED and bears promise for realizing quantum networks.

Recently, a new type of whispering-gallery-mode optical microcavity was demonstrated, which not only retains the high-quality factors of spherical cavities, but also has significant advantages in fabrication reproducibility, control, and mode structure. These cavities consist of a toroidally shaped silica cavity supported by a silicon pillar on a microelectronic chip [19]. The toroidal cavity shape allows an extra level of geometric control over that provided by a spherical cavity and thus begs the question as to how these structures compare with silica microspheres and other microcavity designs for strong-coupling cavity QED. In this paper we numerically investigate the suitability of toroidal microcavities for strong-coupling cavity QED experiments, and for purposes of comparison, we focus on the interaction with atomic cesium [4,20]. We show that toroid microcavities can achieve ultrahigh-quality factors exceeding 10^8 while simultaneously obtaining very large coupling rates between the cavity and a cesium atom. It is found that these cavities not only surpass the projected limits of FP technology [20], but also either exceed or compare favorably to other cavity designs such as photonic band-gap devices [21,22]. Last, we present preliminary experimental measurements of quality factors for toroidal cavities at a wavelength of 852 nm, suitable for strong-coupling CQED with atomic cesium. These results show that currently attainable Q values are already quite promising.

II. STRONG COUPLING IN AN ATOM-CAVITY SYSTEM

The coupling rate g between an atomic system and an electromagnetic field is related to the single-photon Rabi fre-

©2005 The American Physical Society

quency $\Omega = 2g$ and can be expressed in terms of the atomic and cavity parameters by [1]

$$g(\mathbf{r}) = \gamma_{\perp} |\vec{E}(\mathbf{r}) / \vec{E}_{\max}| \sqrt{V_a / V_m}, \tag{1}$$

$$V_a = 3c\lambda^2 / (4\pi\gamma_{\perp}), \tag{2}$$

where $\gamma_{\perp}$ is the transverse atomic dipole transition rate, $|\vec{E}(\mathbf{r}) / \vec{E}_{max}|$ denotes the normalized electric field strength at the atom's location $\mathbf{r}$, V_a is a characteristic atomic interaction volume (which depends on the atomic dipole transition rate, the transition wavelength λ, and the speed of light c), and V_m is the cavity-electromagnetic-mode volume. Assuming the atom interacts with the electromagnetic field for a time T, strong atom-field coupling occurs if the rate of coupling exceeds all dissipative mechanisms—i.e., $g \gg (\kappa, \gamma_{\perp}, T^{-1})$. In this expression κ denotes the cavity field decay rate, given in terms of the cavity quality factor Q by $\kappa \equiv \pi c / (\lambda Q)$. The degree of strong coupling can also be related to a set of normalized parameters [1],

$$n_0 \equiv \gamma_{\perp}^2 / (2g^2), \tag{3}$$

$$N_0 \equiv 2\gamma_{\perp}\kappa / (g^2), \tag{4}$$

where n_0 is the critical photon number, which is the number of photons required to saturate an intracavity atom, and N_0 is the critical atom number, which gives the number of atoms required to have an appreciable effect on the cavity transmission. Note that $(N_0, n_0) \ll 1$ provides a necessary but not sufficient condition for strong coupling.

Examining these parameters, we see that only the critical atom number $N_0 \propto V_m / Q$ is dependent on the cavity-loss rate (or equivalently Q factor). It is the possibility of realizing extremely low critical atom numbers with ultrahigh-Q microcavities that has fostered the investigation of silica microspheres for strong-coupling CQED experiments. However, the geometry of a spherical dielectric dictates a definite relationship between cavity-mode volume V_m and the associated quality factor Q and, hence, of the value of the coupling parameter $g \propto V_m^{-1/2}$ while still maintaining ultrahigh-quality factors [23]. This is a result of the fact that to achieve large atom-cavity coupling rates (comparable to or exceeding those of FP cavities) the cavity diameter must be made small [8-μm-diameter sphere gives $g/(2\pi) \approx 740$ MHz] in order to both lower the modal volume and to increase the electric field strength at the atomic position (assumed to be the cavity surface at the point of maximum electric field strength). However, at the optimum radius for atom-coupling strength, the tunneling loss of the microcavity results in a low achievable Q factor ($Q \approx 4 \times 10^4$), thereby raising the critical atom number. While the relatively large mode volumes of silica microsphere cavities preclude them from competing with ultrasmall mode volume cavities (such as photonic band-gap cavities) on the basis of coupling strength alone, there is the possibility to access simultaneously both ultrahigh-Q and small mode volume, using toroidal microresonators.

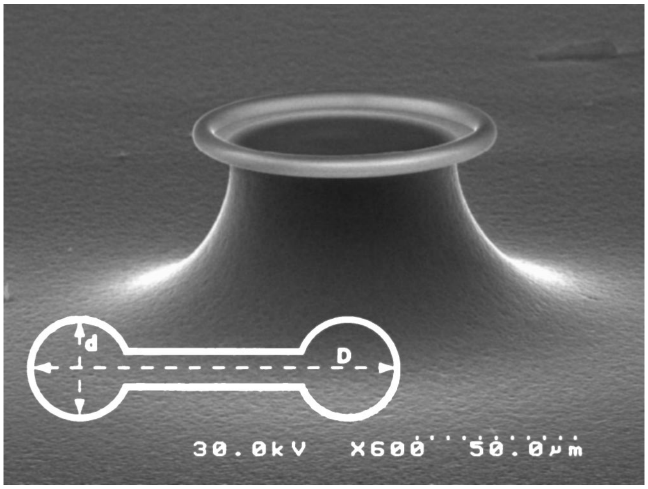

FIG. 1. Scanning electron micrograph of a toroidal microcavity. The principal and minor diameters are denoted by D and d, respectively.

III. TOROIDAL MICRORESONATORS

Toroidal microresonators are chip-based microcavities that possess ultrahigh-Q ($>10^8$) whispering-gallery type modes [19]. The realization of ultrahigh-Q chip-based resonators allows improvements in fabrication and control, while additionally allowing integration with complementary optical, mechanical, or electrical components. In brief, these resonators are fabricated by standard lithographic and etching techniques, followed by a laser-reflow process, as outlined in Ref. [19]. The combination of thermal isolation of the initial preform periphery and thermal heat sinking of the preform interior through the strong heat conduction of the silicon support pillar results in a preferential melting of the preform along the disk periphery under CO_2 laser irradiation. Surface tension then induces a collapse of the silica disk preform, resulting in a toroidally shaped boundary, with the final geometry controlled by a combination of irradiation flux and exposure time. Importantly, as the optical mode resides in the extremely uniform and smooth (reflowed) periphery of the structure, the quality factors of optical whispering-gallery modes can achieve ultrahigh-Q performance, exceeding 10^8. Figure 1 shows a scanning electron micrograph of the side view of a typical toroidal microcavity. Quality factors as high as 4×10^8 at a wavelength of 1550 nm (corresponding to a photon lifetime of ~300 ns) have been measured [24].

IV. MICROTOROID NUMERICAL MODELING

In order to investigate the properties of microtoroids for CQED, this paper will focus on the D_2 transition of cesium which occurs at a wavelength of 852.359 nm ($\gamma_{\perp}/2\pi \approx 2.6$ MHz) [20], with scaling to other systems accomplished in the fashion of Ref. [23]. Fundamentally, the coupling between an atom and a cavity field can be specified by four parameters: the atomic transition moment, the cavity field strength at the atom's location, the cavity mode volume V_m, and the cavity quality factor Q. Since the optical modes

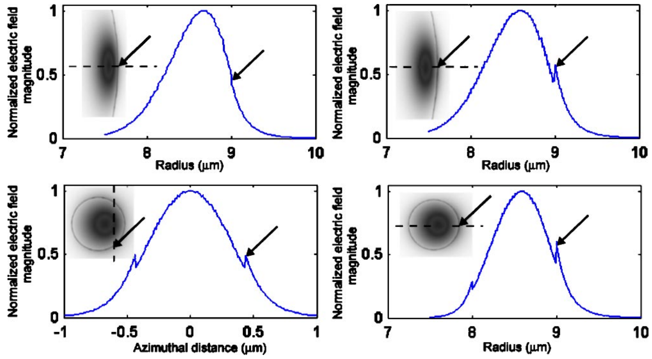

FIG. 2. Electric field magnitude for the whispering-gallery modes of a spherical (top row) cavity of diameter 18 μm and a toroidal cavity (bottom row) with principal diameter of 18 μm and a minor diameter of 1 μm. The left (right) column shows the TE- (TM-) polarized mode near 850 nm. The arrows indicate the location of the maximum external electric field strength, where we assume the atom is located. The dotted lines in the two-dimensional field distribution indicate the cross section where the electric field is displayed.

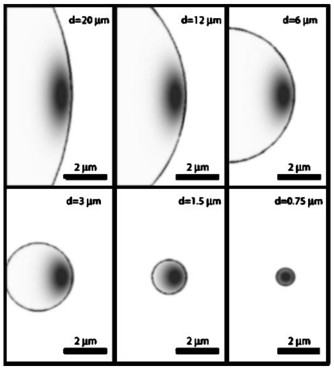

FIG. 3. Electric field profiles for a toroidal cavity with a principal diameter $D=20$ μm and minor diameters $d=20$, 12, 6, 3, 1.5, and 0.75 μm. The calculations correspond to a TM-polarized mode near 850 nm. The optical mode behaves as a whispering-gallery-type mode until the minor diameter is below approximately 1.5 μm, at which point the mode approaches that of a step-index optical fiber [28].

are confined to the interior dielectric in whispering-gallery-type resonators, the atom can interact only with the evanescent field of the cavity mode. In the following discussion, the atom is assumed to be located near the resonator surface at the location where the electric field strength is largest, as illustrated in Fig. 2. For TM-polarized modes (defined such that the dominant electric field component is in the radial direction) this occurs at the outer cavity boundary in the equatorial plane, while for TE-polarized modes (dominant electric field component in the azimuthal-vertical direction) the location of the maximum external field strength is more complicated. As the toroidal geometry is compressed with respect to a sphere (i.e., reducing the ratio of minor-to-principal toroid diameter), the maximum field strength for a TE-polarized mode changes from the equatorial outer cavity boundary to approaching the azimuthal axis (see Fig. 2). While the precise localization of the atom at the cavity evanescent field maximum has been analyzed in detail [25,26], such localization has not yet been achieved experimentally. Nonetheless, this assumption allows a simple way to characterize the relative merit of this cavity geometry with respect to other cavity designs. Also, in what follows we will only consider the fundamental radial and azimuthal modes for both polarizations (TE and TM), as they possess the smallest modal volumes and thus the highest coupling strengths.

The microtoroid geometry, which exhibits a dumbbell-shaped cross section, can in most cases be considered a torus, as the presence of the supporting disk structure only affects the optical mode when the torus diameter becomes comparable to the radial extent of the optical mode. As shown in Fig. 3, this point occurs when the toroid minor diameter (i.e., the cross-sectional diameter of the torus) is below approximately 1.5 μm for a principal diameter of 16 μm. Furthermore, through improvements in fabrication the influence of the toroid support can in principle be minimized. In contrast to FP and microsphere cavities, the optical modes of a toroid do not possess analytic solutions. While one can derive approximate expressions for the optical behavior of these structures for both the low transverse compression (spherelike) and high transverse compression (step-index, fiberlike) regimes, we are mostly interested in the intermediate geometrical regimes, as these are both experimentally accessible and retain the most desirable properties of whispering-gallery-type microcavities. To accomplish this task, a two-dimensional finite-element eigenmode-eigenvalue solver was used to characterize the optical modes of the cavity over the complete geometrical range, after explicitly accounting for the rotational symmetry. The optical modes were calculated in a full-vectorial model, which provides the complete electric field dependence. The accuracy of the numerical technique was carefully verified by comparison with results using the analytical solution for a microsphere cavity [27]. The results for the mode volumes, resonance wavelengths, and field profiles were in good agreement (fractional error was less than 10^{-4} and 10^{-2} for the resonance wavelength and modal volume, respectively). Furthermore, the error in the radiation quality factor was less than 10% over a wide value of radiation *Q*'s (10^{3}–10^{14}), demonstrating that this method can give the accuracy required to investigate the fundamental radiation-loss limits in the cavity geometries of interest in this work. Due to the fact that for smaller cavity geometries the resonance wavelengths do not necessarily coincide with the cesium transition of interest, the data in this work were evaluated by using values calculated at the closest resonance wavelengths, both blueshifted and redshifted with respect to the desired resonance, to extrapolate values at the desired wavelength (the mode volumes were linearly extrapolated and the radiation quality factors exponentially extrapolated as a function of wavelength).

A. Mode volume

The optical-mode volume is determined by

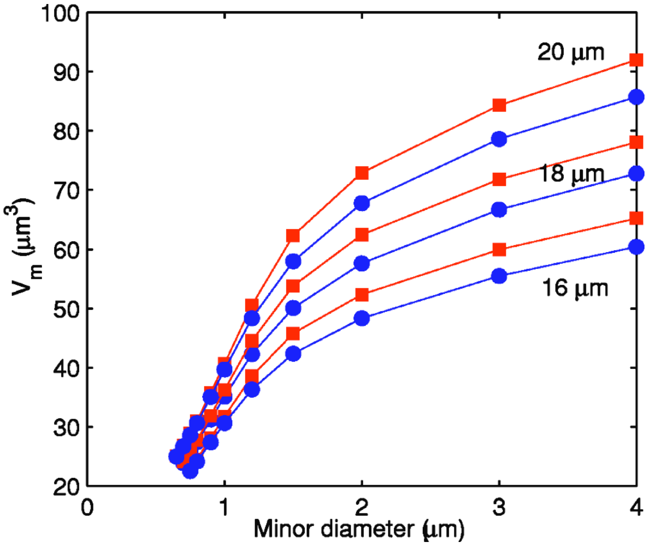

FIG. 4. Calculated mode volumes for a silica toroidal microresonator versus minor diameter for principal diameters of 20, 18, and 16 μm. The plot shows both TM (squares) and TE (circles) polarizations. As the minor diameter is reduced a slow reduction of modal volume due to confinement in the azimuthal direction occurs, followed by a fast reduction for large confinement when the optical mode is strongly compressed in both the radial and azimuthal directions.

$$V_m \equiv \frac{\int_{V_Q} \epsilon(\vec{r})|\vec{E}(\vec{r})|^2 d^3\vec{r}}{|\vec{E}_{\max}|^2}, \tag{5}$$

where V_Q represents a quantization volume of the electromagnetic field and $|\vec{E}|$ is the electric field strength [26]. In these calculations, we have chosen the quantization volume cross section to consist of a square region of approximately 10 μm width and height centered about the radial cavity boundary. This choice allows the mode volume to be determined to a good accuracy while minimizing computational requirements. As a further confirmation of the validity of this approach, we note that the radiation loss is weak for the range of geometries modeled in this work, resulting in only a marginal difference in the numerically calculated mode volume for different choices of quantization volume.

Figure 4 shows the calculated modal volume for the fundamental mode of a toroidal cavity as a function of minor diameter and for principal diameters ranging from 16 to 20 μm. For clarity, only data for minor diameters below 4 μm are shown. Both TM (squares) and TE (circles) polarizations are shown. The calculations show a reduction of modal volume for both polarizations as the toroid minor diameter is decreased. This is expected when considering the additional confinement provided by the toroid geometry beyond the spherical geometry, as illustrated in the electric field plots of Fig. 3. As the minor diameter is decreased, there is initially a slow reduction of modal volume, which agrees very well with a simple model that accounts for transverse guiding (azimuthal direction) using an approximate one-dimensional harmonic oscillator model. This approach results in a reduction of modal volume which scales as $(d/D)^{1/4}$ with respect to that of a spherical cavity. This formula holds for minor diameters greater than approximately 2 μm for the principal diameters considered in this work. For smaller diameters, the spatial confinement becomes strong enough that the optical mode is additionally compressed in the radial direction. This results in a faster reduction of modal volume, with the optical modes approaching those of a step-index optical fiber (this occurs for a minor diameter below approximately 1 μm) [28]. The mode volume reduces until the point where the optical mode becomes delocalized due to the weak geometrical confinement, causing a finite minimum value. Determination of the exact point of the minimum modal volume upon reduction of minor diameter (for a fixed principal diameter) can be uncertain, as the choice of quantization volume now plays a critical role (as discussed above). For this reason the results in Fig. 4 show the modal volume only for inner diameters down to 0.65 μm, where mode volume determination was unambiguous.

Calculation of the modal volume and the maximum electric field amplitude at the exterior cavity equatorial boundary is straightforward, giving a simple way to calculate both the coupling strength and the critical photon number. In order to obtain the cavity decay rate κ and the critical atom number N_0, however, the cavity Q factor must be determined.

B. Quality factor

The radiation loss of the optical modes of a spherical cavity is easily found by consideration of the analytic characteristic equation [29]

$$n^{1-2b}\frac{[nkRj_\ell(nkR)]'}{nkRj_\ell(nkR)} = \frac{[kRh_\ell^{(1)}(kR)]'}{kRh_\ell^{(1)}(kR)}, \tag{6}$$

where n is the refractive index of the spherical cavity (the external index is assumed to be unity), R is the cavity radius, b represents the polarization of the optical mode (1 for TM and 0 for TE), and j_ℓ ($h_\ell^{(1)}$) represents the spherical Bessel (Hankel) function. The prime denotes differentiation with respect to the argument of the Bessel (Hankel) function. This equation accounts for radiation loss through the use of an outgoing wave outside the cavity, as given by the complex Hankel function of the first kind. Solution of this equation results in a complex wave number $k=k_{Re}+ik_{Im}$, which determines both the resonance wavelength $(\lambda=2\pi/k_{Re})$ and the radiation quality factor $[Q_{rad}=k_{Re}/(2k_{Im})]$.

However, while the spherical solution can provide some insight into the scaling of the radiation quality factor for toroidal cavities where the minor diameter is large (sphere like), the radiation loss when the optical mode is strongly confined (as represented by small minor diameters) is expected to decrease much more rapidly. Figure 5 shows numerical calculations of the radiative quality factor as the minor diameter is decreased for various principal diameters of 16, 18, and 20 μm. We observe an initially slow reduction of the radiative quality factor in the geometrical regime where the minor diameter exceeds the radial extent of the optical

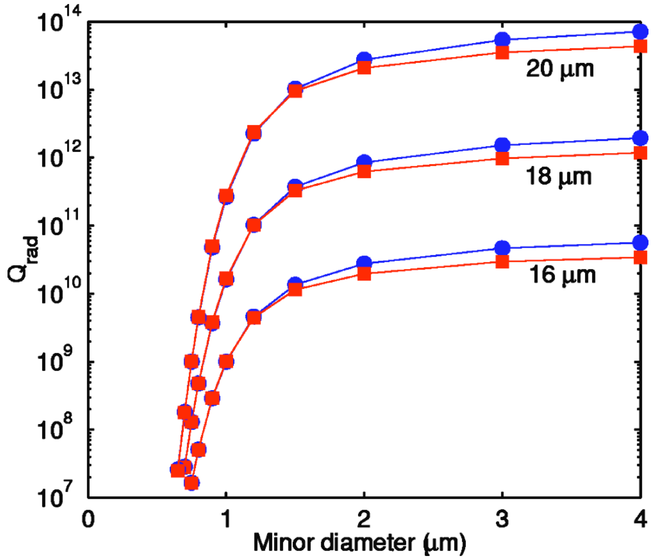

FIG. 5. Calculated radiation loss for a toroidal microcavity as a function of minor diameter, for principal diameters of 20, 18, and 16 μm. Both TM (squares) and TE (circles) polarizations are shown. The data show a slow reduction of Q as the minor diameter is reduced while the mode behaves primarily as a whispering-gallery-type mode. However, as the geometrical confinement increases to such a point as the optical mode approaches that of a step-index fiber, there is a significant reduction of the quality factor.

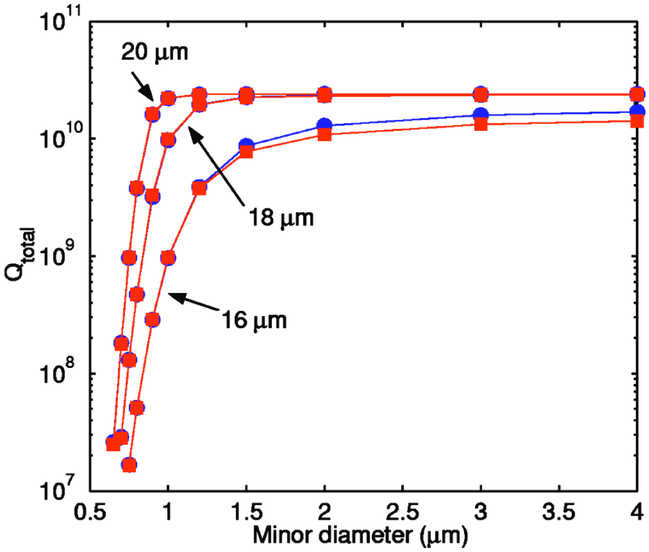

FIG. 6. Total quality factor for a toroidal microcavity versus minor diameter for principal diameters of 16, 18, and 20 μm. Both TE (circles) and TM (squares) polarizations are shown. The total quality factor is composed of the radiative quality factor from Fig. 5 along with the silica-absorption-limited $Q_{mat}=2.4\times10^{10}$ at a wavelength of 852 nm. The plots indicate that the total quality factor is limited by silica absorption when the principal diameter is larger than 16 μm and the minor diameter is larger than approximately 1 μm. Furthermore, both polarizations have similar quality factors over the range of geometries studied.

mode (i.e., where the optical mode exhibits whispering-gallery behavior). As the minor diameter is reduced to a level comparable to or smaller than the radial extent of the optical mode (step-index fiber like regime), the drop-off of the radiative Q is much more dramatic, with a decrease of over an order of magnitude for a reduction of inner diameter of just 50 nm.

The total optical loss of a cavity has contributions not only from radiation loss, but also includes other dissipative mechanisms, such as intrinsic material absorption, losses resulting from both surface and bulk scattering, and losses stemming from contaminates on the resonator surface [30]. One of the dominant contaminates which adversely affects the cavity Q is OH and water adsorbed onto the cavity surface. While prior investigations of these loss mechanisms have resulted in approximate expressions for water absorption and surface scattering [14,31], only very large resonators were studied, as opposed to the much smaller diameter cavities studied in this work. To obtain an improved estimate of the effect of water on the small diameter cavities in this paper, a simple model was used which determines the fraction of optical energy absorbed by a monolayer of water located at the cavity surface. This method gives an estimated quality factor for a monolayer of water to be greater than 10^{10} for the case of a spherical resonator with a principal diameter of 50 μm. While the water-limited quality factor will be slightly lower for the smaller principal diameter cavities in this work and also slightly lower due to the increased overlap between the optical mode and the cavity surface in a toroidal geometry, these values are comparable to the quality factor due solely to the intrinsic absorption of silica in the 800-nm wavelength band. As in principle with proper fabrication the presence of water and OH can be prevented, with surface scattering minimized, we will focus only on the contributions from intrinsic silica absorption and radiation loss. These two mechanisms put a fundamental limit on the Q possible in these structures.

Figure 6 shows the calculated total quality factor for various principal toroid diameters in the range of 16–20 μm, as a function of the minor diameter. The total quality factor is calculated through the relation $1/Q_{total}=1/Q_{rad}+1/Q_{mat}$, where only radiation loss and silica absorption are included. For principal diameters less than 18 μm, there is a monotonic decrease in quality factor as the minor diameter is decreased. This is a result of the whispering-gallery-loss increase due to the additional confinement. For larger principal diameters, the overall quality factor is clamped near the limiting value resulting from silica absorption for most minor diameters (with only a slight decrease as minor diameter is reduced), until the minor diameter is small enough that the radiative quality factor decreases below the quality factor due to silica absorption. For the principal diameters studied in this work, this point occurs as a minor diameter of around 1 μm.

C. Cavity QED parameters

The determination of the coupling strength from the modal volume follows from Eq. (1). Figure 7 shows the

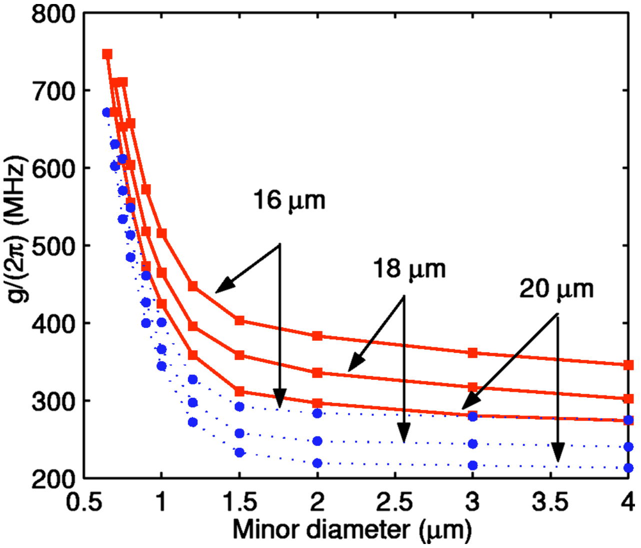

FIG. 7. Atom-cavity coupling parameter g vs minor diameter for toroidal cavities having a principal diameter of 16, 18, and 20 μm, with g increasing for smaller principal diameters. Both TE (circles) and TM (squares) polarizations are shown. The plots indicate that the coupling strength increases dramatically as the minor diameter decreases below 1.5 μm, which is a result of the rapid reduction of mode volume and the increased electric field strength at the cavity surface.

atom-cavity coupling rate $g/(2\pi)$ for various toroid principal diameters as the toroid minor diameter is decreased. It can be seen that there is a monotonic rise in g for higher-aspect-ratio toroids (i.e., D/d), as a direct result of the compression of modal volume. The rate of increase of g as the minor diameter is reduced increases dramatically as the toroid geometry transitions from a whispering-gallery-type mode to a strongly confined step-index fiber-type mode. This is due not only to the faster rate of reduction of mode volume in the step-index fiber like regime as the minor diameter is decreased, but also due to the increase in electric field strength at the cavity surface [as $g \propto |E|(V_m)^{-1/2}$]. Note that the coupling strengths shown do not correspond to the absolute maximum for these structures, as this work has focused on the simultaneous realization of high-quality factors and small modal volume. Therefore, mode volumes were calculated only down to where the radiation quality factor is equal to or slightly exceeds 10^7. Also, as mentioned previously, by making this restriction we prevent any uncertainty in the calculated mode volumes (and hence g) through the definition of the modal quantization volume. Under these assumptions, the calculations indicate that coupling parameters exceeding 700 MHz are possible.

Figure 8 shows the corresponding critical photon numbers (n_0). The results reveal that values as low as 6×10^{-6} are possible, with the associated quality factors exceeding 10^7. As will be discussed in more detail in the next section, this value is not only comparable to the fundamental limit of FP technology, but also vastly exceeds that possible for fused silica microspheres with a comparable quality factor.

One of the primary reasons high-Q whispering-gallery-mode cavities are promising for CQED is their very low

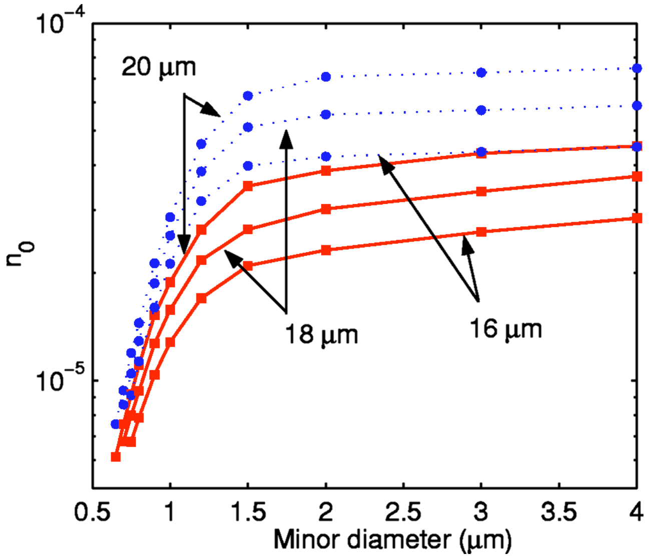

FIG. 8. Critical photon number n_0 vs minor toroid diameter for a cavity with principal diameters of 16, 18, and 20 μm. Both TE (circles) and TM (squares) polarizations are shown. The plots show that as both toroid principal diameter and minor diameter are reduced, the critical photon number decreases. This follows directly from the behavior of the atom-cavity coupling parameter g, as indicated in Fig. 7. The calculations show that critical photon numbers of 6×10^{-6} are possible (with quality factors exceeding 10^7).

critical atom number. Figure 9 shows the calculated critical atom number versus minor diameter for toroid principal diameters of 16, 18, and 20 μm. The plot shows that for the larger principal diameters of 18 and 20 μm there is a minimum in the critical atom number as the toroidal minor diam-

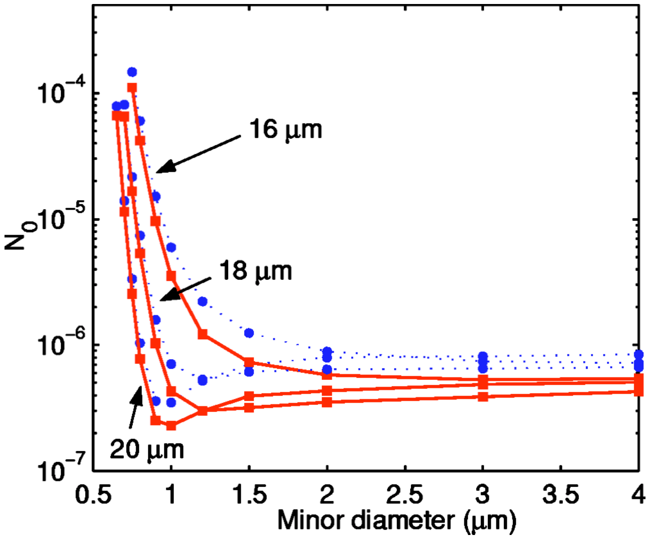

FIG. 9. Critical atom number N_0 vs minor diameter for a toroidal microcavity with principal diameters of 16, 18, and 20 μm. For small minor diameters the critical atom number decreases as the principal diameter increases. Both TE (circles) and TM (squares) polarizations are shown. The plots indicate that there is a minimum value of the critical atom number near 2×10^{-7} for a toroidal cavity with a principal diameter of 20 μm and an inner diameter of 1 μm (TM mode).

eter is reduced. The minimum occurs near a minor diameter of 1 μm. This minimum arises from the clamping of the total quality factor (to the quality factor resulting from silica absorption) for larger minor diameters when the principal diameter is greater than approximately 18 μm. Thus, by reducing the minor diameter for a fixed principal diameter, the quality factor is nearly unchanged while the coupling strength is monotonically increasing. The critical atom number decreases until the region where the minor diameter is such that the overall Q is determined by whispering-gallery loss. At this point the critical atom number increases approximately exponentially. The plot for the 20 μm principal diameter shows that in a toroidal geometry slightly larger principal diameters can offer some benefit, as the minor diameter can be compressed more strongly while maintaining high radiative quality factors and, thereby, lowering the critical atom number. A critical atom number of approximately 2×10^{-7} is possible using a toroid principal diameter of 20 μm and a minor diameter of 1 μm.

V. EXPERIMENTAL MEASUREMENT OF MICROTOROIDS FOR STRONG-COUPLING CAVITY QED AT 852 nm

The presented numerical results indicate that toroidal cavities can theoretically obtain high values of atom-cavity coupling while simultaneously retaining an extremely low critical photon number and in particular an exceedingly small critical atom number. While in principle the critical atom number can be more than 100 times smaller than any currently demonstrated cavity, the necessity of realizing material-limited quality factors exceeding 2×10^{10} is experimentally challenging. The current record for any cavity is 9×10^{9} [14], in a large-diameter microsphere cavity, whereas for toroidal cavities quality factors as high as 4×10^{8} at a resonance wavelength of 1550 nm have been realized [24]. However, for cavity quality factors much larger than 10^{8}, the dominant dissipative mechanism in the atom-cavity system is the radiative decay rate of the atomic medium, which is 2.61 MHz for the D_2 transition of cesium. For this reason more "modest" quality factors, in the range of current experimentally achievable values (e.g., a few hundred million) are attractive. As these values are currently realizable for toroidal cavities at a wavelength of 1550 nm, we have investigated experimentally the quality factors and fabrication limits for structures designed for strong coupling to the cesium transition at a wavelength of 852 nm.

As toroidal cavities are fabricated using a combination of lithography and a silica reflow process, the advantages of lithographic control and parallelism are obtained and, in fact, are a significant step forward over spherical cavities. As the shape of the initial silica preform dictates the maximum possible principal and minor diameter and is lithographically formed, precise control of the geometry dimensions is possible. Reproducible principal diameters ranging from >100 to 12μm have been fabricated. This lower value, while currently dictated by the available laser power in our setup, is sufficient to obtain the range of principal diameters optimally suited for CQED, as indicated above. While the capability to obtain reproducible principal diameters is a significant improvement over spherical cavities, the ability to accurately control the minor diameter is particularly important to CQED. As noted previously [19], the final minor diameter of the fabricated structures is a result of a combination of factors, which are the initial silica preform thickness, the supporting pillar size, and the laser irradiation intensity and duration. Minor diameters as small as 3 μm at principal diameters as low as 12 μm have been realized experimentally.

We have measured the quality factor of a series of fiber-taper-coupled toroidal microcavities at a wavelength of 852 nm, using an experimental apparatus similar to previous work [19,32]. The excitation laser was a New Focus Vortex laser with a tunability of 40 GHz with a center wavelength of 852.359 nm. The laser output was double passed through an acousto-optic modulator for the purpose of performing a cavity ringdown measurement. The resulting beam was able to be extinguished by a TTL electrical control signal, with a corresponding optical decay time of 15 ns. This beam was then coupled into a single-mode 850 nm fiber and subsequently interacted with the toroidal resonators through the tapered portion of the fiber. Due to the limited tuning range of the excitation laser (which is less than the free-spectral range between fundamental modes in the cavity principal diameters of interest), overlap of a fundamental resonance with the laser wavelength range was difficult. Obtaining an optical fundamental mode at 852.359 nm was achieved by thermally shifting the optical resonance through the use of a Peltier heating element, which allowed tuning of the cavity resonance by up to approximately 50 GHz. Upon realization of a fundamental cavity resonance at the proper wavelength, the intrinsic quality factor was inferred two ways (Fig. 10): through cavity ringdown [19] and through the threshold for stimulated Raman scattering [32]. The results of both measurements were in agreement and resulted in a measured quality factor as high as $Q_{total}=1.2\times10^{8}$ in a cavity with a principal diameter of 50 μm and a minor diameter of 6 μm. For this cavity geometry, the whispering-gallery loss is negligible ($Q_{rad}\approx10^{36}$) compared to the intrinsic silica absorption loss, such that the overall theoretical quality factor can be as high as $Q_{total}\approx2\times10^{10}$. We expect upon further measurements that this quality factor can be increased to levels comparable to measurements performed at a wavelength of 1550 nm (4×10^{8}).

While this cavity geometry is far from the optimal geometry suggested in this paper, this structure was chosen in order to increase the likelihood of finding a fundamental resonance at 852 nm. Even for this relatively large structure, cavity QED parameters of $(g/(2\pi),n_0,N_0)=(86\text{ MHz},4.6\times10^{-4},1.0\times10^{-3})$ are calculated. Comparison of these values to current FP cavities [4,10,20] indicates that even without additional improvements in fabrication these results are close in coupling strength and improved with respect to the critical atom number. Additionally, if we restrict the geometry and overall quality factor to values which are currently realizable (i.e., a quality factor of 10^{8} at a wavelength of 852 nm with a minor diameter of 3.5 μm, which represents a reasonably comfortable margin from the actual current limits), the optimal principal diameter is 13 μm (this geometry

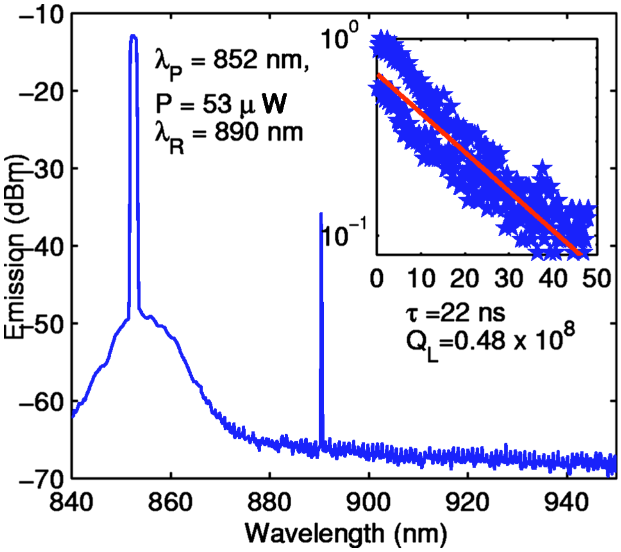

FIG. 10. Experimental measurement of the intrinsic quality factor for a toroidal microresonator at a resonance wavelength of 852 nm. The main figure shows the generation of stimulated Raman scattering, illustrated by the secondary peak located at a wavelength of 890 nm. The threshold pump power for stimulated Raman scattering (53 μW) can be used to infer the intrinsic quality factor of 1×10^8 for this cavity. The inset shows the temporal cavity decay resulting from a series of ringdown measurements for a different toroidal microcavity. The measured photon lifetime of τ=22 ns corresponds to a loaded quality factor of $Q_L=0.48\times10^8$. After correcting for fiber-taper loading and the presence of backscattering, an intrinsic quality factor of 1.2×10^8 is obtained.

has a radiative quality factor of 1.8×10^8). For these values the TM-polarized optical mode would have CQED parameters of $(g/(2\pi),n_0,N_0)=(450\text{ MHz},1.7\times10^{-5},4.5\times10^{-5})$, which are far superior to current FP cavities.

VI. COMPARISON OF MICROTOROIDS WITH OTHER RESONATORS FOR CAVITY QED

Table I presents a comparison of CQED parameters for various cavity types including toroidal, FP, and photonic crystal. To date, most experimental work has involved the use of Fabry-Perot cavities, with current state-of-the-art fabrication technology allowing the attainment of coupling strengths of 110 MHz, with corresponding critical atom numbers of 6×10^{-3} [4]. Estimates on the theoretical performance limits of FP cavities have also been investigated [20], predicting coupling rates as large as 770 MHz, with a corresponding critical atom number of 2×10^{-4}. While this level of performance may be theoretically possible, the current necessity of expensive and sophisticated high-reflection dielectric mirror coatings does not bode well for easy improvements with respect to current technology. This is one of the reasons silica microspheres are of such high interest. Calculation of the limits possible with silica microspheres [23] shows that not only is it possible to obtain high values of atom-cavity coupling solely by changing the cavity diameter, which is easily in the realm of current fabrication capability, but their ultra high-quality factors result in significant improvement in the critical atom number (with values approaching 3×10^{-6} possible provided that silica absorption-limited quality factors can be obtained). Even using quality factors in the range of a few hundred million, which is already experimentally demonstrated, critical atom numbers around 10^{-4} are possible, which is comparable to the FP limit. From the analysis of the previous section, we see that toroidal cavities can attain coupling strengths comparable to or exceeding the best values possible for either FP or microsphere cavities, while at the same time providing much lower critical atom numbers. As discussed previously, this arises from the extra level of geometrical control possible in a toroidally shaped cavity, which allows one to retain both the high-coupling strength representative of small-mode volume cavities while preserving high-quality factors. Clearly this fact, along with other advantages in control and reproducibility over spherical cavities, suggests that these structures are promising for CQED experiments.

Last, a comparison with photonic band-gap (PBG) cavities is also provided in the table. Due to the realization of optical mode volumes near the fundamental limit in a dielectric cavity [21], combined with recent results demonstrating reasonably high-quality factors (∼45 000) [33], these cavities are strong candidates for chip-based strong-coupling CQED [22]. While these structures can potentially achieve atom-cavity coupling strengths $g\gtrsim17$ GHz [22], far greater than those possible in a silica dielectric cavity, their much lower quality factors result in greater critical atom numbers than possible in toroidal microcavities. For example, the work of Ref. [22] projects $N_0=6.4\times10^{-5}$. We also note that the correspondingly lower quality factors also result in modest ratios of coupling to dissipation $g/\max(\gamma_\perp,\kappa)$ (a figure of merit indicative of the number of Rabi oscillations which occur) of ∼4 [22], much lower than predicted for toroidal structures (∼165). Furthermore, we can consider an additional figure of merit: namely, the "rate of optical information per atom" [1], given by $R\equiv g^2/\kappa$. The table indicates that toroidal cavities compare favorably with PBG cavities in this figure of merit as well.

VII. CONCLUSION

Our work has demonstrated that toroidal resonators are promising cavities for investigation of the coupling of an atomic system to the electromagnetic field in the regime of strong coupling. Not only are these structures arguably simpler to manufacture and control than other structures such as microspheres and FP cavities, but also allow integration on a silicon chip, paving the way for the addition of atom traps [34] and waveguides which can enhance the capability and possibly reduce the experimental complexity of CQED studies. Furthermore, we note that in addition to the enhanced

TABLE I. Summary of the relevant parameters for cavity QED for a variety of resonator systems. The table shows both the experimental state of the art [23] and the projected limits for a Fabry-Perot cavity [20], plus current experimental results with silica microspheres [16]. Furthermore, a theoretical comparison between silica microspheres [23], photonic band-gap cavities [22], and toroidal microresonators (this work) is also given. The results indicate that toroidal cavities can uniformly exceed the performance on these parameters for both FP cavities and silica microspheres. Comparison with PBG cavities indicates that toroids possess much lower atom-cavity coupling strengths (as a result of their much larger mode volumes), but still result in greatly improved critical atom numbers due to their very large quality factors.

Resonator system	Coupling coefficient $g/(2\pi)$ (MHz)	Critical photon number n_0	Critical atom number N_0	Coupling to dissipation ratio $g/\max(\gamma_\perp,\kappa)$	Rate of optical information $R\equiv g^2/\kappa$ (Mbits/sec)
Fabry-Perot experimental state of the art	110	2.8×10^{-4}	6.1×10^{-3}	7.8	5.4×10^{3}
Fabry-Perot projected limits	770	5.7×10^{-6}	1.9×10^{-4}	36	1.7×10^{5}
Microsphere experimental ($D=120$ μm)	24	5.5×10^{-3}	3.0×10^{-2}	7.2	1.1×10^{3}
Microsphere theory					
Maximum g ($D=7.25$ μm)	750	6.1×10^{-6}	7.3×10^{-1}	0.01	4.5×10^{1}
Minimum N_0 ($D=18$ μm)	280	4.3×10^{-5}	3.1×10^{-6}	107	1.1×10^{7}
Photonic band-gap cavity	17000	7.6×10^{-9}	6.4×10^{-5}	3.9	5.1×10^{5}
Toroidal microcavity theory					
Maximum g	>700	6.0×10^{-6}	2.0×10^{-4}	40	1.6×10^{5}
Minimum N_0	430	2.0×10^{-5}	2.0×10^{-7}	165	1.6×10^{8}

performance benefit of having a toroidal geometry, the capability to retain a relatively large resonator diameter over other structures results in a smaller free-spectral range (FSR). This allows not only easier tuning of the cavity resonance location to correspond precisely to the atomic transition wavelength, but also may allow integration of a supplemental far-off-resonance trap by exciting the cavity at a multiple of the free-spectral range. The realization of a cavity with a smaller FSR may allow a closer matching of a secondary resonance location to the pump wavelength which corresponds to state-insensitive trapping of atomic cesium [7], which can simplify the atom-cavity dynamics. The use of a silica dielectric whispering-gallery cavity also allows operation over a broad range of wavelengths, with very-high-quality factors possible for nearly all resonances. This is in strong contrast to the mirror reflectivity limits of coated FP cavities.

The ability to connect distant quantum nodes with high efficiency, preferably over optical fiber, is very desirable for quantum networks. Using FP cavities, optical fiber coupling is possible; however, the overall coupling efficiency is modest (∼70%). Fiber-taper-coupled microtoroids allow coupling efficiencies in excess of 99% [17], above both FP and PBG cavities (97%) [35]. This capability to obtain near-complete input and output coupling efficiencies strongly suggests the use of fiber-coupled silica whispering-gallery cavities, such as microtoroids, as building blocks to enable high-performance quantum networks.

As a further note, the use of higher-index contrast dielectric material can allow additional improvements in the performance of these structures. The use of silica as the dielectric of choice in both the spherical geometry and in the toroidal microcavities studied in this work was convenient, as these structures not only possess record high-quality factors but are currently producible. However, as the radiative quality factor of a whispering-gallery-type cavity is strongly dependent on the refractive index difference between the structure and external environment, much smaller modal volumes are possible for a given quality factor with the use of a higher-index resonator material. In fact, this is one of the reasons PBG cavities fabricated from silicon or other high-index dielectrics can obtain ultrasmall mode volumes. A simple comparison of the mode volume possible in a silicon toroid shows that a mode volume on the order of only about 10 times larger than PBG cavities is possible, with much higher-quality factors. While this work has focused on silica microcavities, the reflow process is a relatively flexible method, thus suggesting that it may be possible to also create high-index ultrahigh-*Q* quality factor cavities which come closer to the large coupling strengths of PBG cavities while further improving the critical atom number.

Last, the current experimental ability to obtain large coupling strengths with quality factors exceeding 10^8 is promising for the immediate use of these structures in strong-coupling studies. We are currently pressing forward on improving the fabrication capabilities and losses of these structures. Coupled with the intrinsic fiber-optic compatibility of these structures and the demonstration of near lossless excitation and extraction of optical energy from these structures using tapered optical fibers [17], toroidal microcavities can provide a highly advantageous experimental system for the investigation of strong-coupling cavity QED.

ACKNOWLEDGMENTS

The work of K.J.V. was supported by DARPA, the Caltech Lee Center, and the National Science Foundation. The work of H.J.K. was supported by the National Science Foundation, by the Caltech MURI Center for Quantum Networks, by the Advanced Research and Development Activity, and by the California Institute of Technology.

---

[1] H. J. Kimble, Phys. Scr. **T76**, 127 (1998).
[2] *Cavity Quantum Electrodynamics*, edited by P. R. Berman (Academic Press, San Diego, 1994).
[3] H. Mabuchi and A. C. Doherty, Science **298**, 1372 (2002).
[4] C. J. Hood, T. W. Lynn, A. C. Doherty, A. S. Parkins, and H. J. Kimble, Science **287**, 1447 (2000).
[5] P. W. H. Pinkse, T. Fischer, P. Maunz, and G. Rempe, Nature (London) **404**, 365 (2000).
[6] Y. Shimizu, N. Shiokawa, N. Yamamoto, M. Kozuma, T. Kuga, L. Deng, and E. W. Hagley, Phys. Rev. Lett. **89**, 233001 (2002).
[7] J. McKeever, J. R. Buck, A. D. Boozer, A. Kuzmich, H.-C. Naegerl, D. M. Stamper-Kurn, and H. J. Kimble, Phys. Rev. Lett. **90**, 133602 (2003).
[8] P. Maunz, T. Puppe, I. Schuster, N. Syassen, P. W. H. Pinkse, and G. Rempe, Nature (London) **428**, 50 (2004).
[9] J. A. Sauer, K. M. Fortier, M. S. Chang, C. D. Hamley, and M. S. Chapman, Phys. Rev. A **69**, 051804(R) (2004).
[10] J. McKeever, A. Boca, A. D. Boozer, J. R. Buck, and H. J. Kimble, Nature (London) **425**, 268 (2003).
[11] V. B. Braginsky, M. L. Gorodetsky, and V. S. Ilchenko, Phys. Lett. A **137**, 393 (1989).
[12] For a recent review of microcavities, see K. J. Vahala, Nature (London) **424**, 839 (2003) and references therein.
[13] M. L. Gorodetsky, A. A. Savchenkov, and V. S. Ilchenko, Opt. Lett. **21**, 453 (1996).
[14] D. W. Vernooy, V. S. Ilchenko, H. Mabuchi, E. W. Streed, and H. J. Kimble, Opt. Lett. **23**, 247 (1998).
[15] V. Lefevre-Seguin and S. Haroche, Mater. Sci. Eng., B **48**, 53 (1997).
[16] D. W. Vernooy, A. Furusawa, N. P. Georgiades, V. S. Ilchenko, and H. J. Kimble, Phys. Rev. A **57**, R2293 (1998).
[17] S. M. Spillane, T. J. Kippenberg, O. J. Painter, and K. J. Vahala, Phys. Rev. Lett. **91**, 043902 (2003).
[18] J. I. Cirac, P. Zoller, H. J. Kimble, and H. Mabuchi, Phys. Rev. Lett. **78**, 3221 (1997).
[19] D. K. Armani, T. J. Kippenberg, S. M. Spillane, and K. J. Vahala, Nature (London) **421**, 925 (2003).
[20] C. J. Hood, H. J. Kimble, and J. Ye, Phys. Rev. A **64**, 033804 (2001).
[21] J. Vuckovic, M. Loncar, H. Mabuchi, and A. Scherer, Phys. Rev. E **65**, 016608 (2001).
[22] B. Lev, K. Srinivasan, P. Barclay, O. Painter, and H. Mabuchi, Nanotechnology **15**, S556 (2004).
[23] J. R. Buck and H. J. Kimble, Phys. Rev. A **67**, 033806 (2003).
[24] T. J. Kippenberg, S. M. Spillane, and K. J. Vahala, Appl. Phys. Lett. **85**, 6113 (2004).
[25] H. Mabuchi and H. J. Kimble, Opt. Lett. **19**, 749 (1994).
[26] D. W. Vernooy and H. J. Kimble, Phys. Rev. A **55**, 1239 (1997).
[27] J. A. Stratton, *Electromagnetic Theory* (McGraw Hill, New York, 1997).
[28] A. W. Snyder and J. D. Love, *Optical Waveguide Theory* (Chapman and Hall, London, 1983).
[29] L. A. Weinstein, *Open Resonators and Open Waveguides* (Golem, Boulder, CO, 1969).
[30] M. L. Gorodetsky, A. A. Savchenkov, and V. S. Ilchenko, Opt. Lett. **21**, 453 (1996).
[31] M. L. Gorodetsky, A. D. Pryamikov, and V. S. Ilchenko, J. Opt. Soc. Am. B **17**, 1051 (2000).
[32] S. M. Spillane, T. J. Kippenberg, and K. J. Vahala, Nature (London) **415**, 621 (2002).
[33] Y. Akahane, T. Asano, B.-S. Song, and S. Noda, Nature (London) **425**, 944 (2003).
[34] W. Hansel, P. Hommelhoff, T. W. Hansch, and J. Reichel, Nature (London) **413**, 498 (2001).
[35] A coupling efficiency of 97% between a fiber-taper and a photonic crystal waveguide has been demonstrated [P. E. Barclay, K. Srinivasan, M. Borselli, and O. J. Painter, Opt. Lett. **29**, 697 (2004)]. For a photonic crystal defect cavity the currently demonstrated efficiency is 44% (P. E. Barclay, K. Srinivasan, and O. J. Painter, http://arxiv.org/abs/physics/0405064).

arXiv:quant-ph/0507127 v1 13 Jul 2005

Control of decoherence in the generation of photon pairs from atomic ensembles

D. Felinto, C. W. Chou, H. de Riedmatten, S. V. Polyakov, and H. J. Kimble
Norman Bridge Laboratory of Physics 12-33, California Institute of Technology, Pasadena, California 91125, USA

(Dated: May 26, 2006)

We report an investigation to establish the physical mechanisms responsible for decoherence in the generation of photon pairs from atomic ensembles, via the protocol of Duan *et. al.* for long distance quantum communication [Nature (London) **414**, 413 (2001)] and present the experimental techniques necessary to properly control the process. We develop a theory to model in detail the decoherence process in experiments with magneto-optical traps. The inhomogeneous broadening of the ground state by the trap magnetic field is identified as the principal mechanism for decoherence. The theory includes the Zeeman structure of the atomic hyperfine levels used in the experiment, and the polarization of both excitation fields and detected photons. In conjunction with our theoretical analysis, we report a series of measurements to characterize and control the coherence time in our experimental setup. We use copropagating stimulated Raman spectroscopy to access directly the ground state energy distribution of the ensemble. These spectroscopic measurements allow us to switch off the trap magnetic field in a controlled way, optimizing the repetition rate for single-photon measurements. With the magnetic field off, we then measure nonclassical correlations for pairs of photons generated by the ensemble as a function of the storage time of the single collective atomic excitation. We report coherence times longer than 10 μs, corresponding to an increase of two orders of magnitude compared to previous results in cold ensembles. The coherence time is now two orders of magnitude longer than the duration of the excitation pulses. The comparison between these experimental results and the theory shows good agreement. Finally, we employ our theory to devise ways to improve the experiment by optical pumping to specific initial states.

I. INTRODUCTION

Quantum memory is a key resource for many quantum-information protocols. Usually it is associated with the basic requirements for quantum computation [1, 2], but in recent years also quantum communication protocols started to rely on it. The requirement of memory was introduced in quantum communication as part of the idea for quantum repeaters [3, 4], a possible solution for the problem of quantum communication over long distances. In this case, memory is essential to increase the probability of success of the chain of conditional steps that underlies the protocol, and makes feasible scalable quantum networks.

A significant step toward the realization of the quantum repeater idea was a proposal by Duan, Lukin, Cirac, and Zoller (DLCZ) for its implementation using linear optics and atomic ensembles [5]. The DLCZ protocol is based on the generation of single photons by spontaneous Raman scattering in atomic ensembles [6]. The detection of a single photon in the forward propagating mode heralds the presence of a single collective atomic excitation in the sample, due to a collective enhancement effect. This excitation can be stored for a time up to the coherence time of the ground states of the atoms and then converted back into a light field. Entanglement of distant ensembles in the excitation number basis is generated by interference [7], and extended to longer distances by entanglement swapping [8, 9]. The final pairs of ensembles, far apart, can then be used for entanglement-based quantum cryptography [5, 10], probabilistic quantum teleportation and violation of Bell inequality. This proposal has received much attention in the past two years and several groups are presently pursuing its experimental implementation [11, 12, 13, 14, 15, 16, 17, 18].

In this article, we analyze the decoherence processes present in the DLCZ protocol, and describe experiments to mitigate the problem. We construct a theory for the decoherence process in the photon-pair generation. Particularly, our analysis concentrates in its implementation with cold atomic ensembles, but many results should also apply to studies with room-temperature ensembles in vapor cells. We propose various strategies to increase the system's coherence time, and introduce experimental techniques necessary for its characterization and control. We also report the first experimental steps in this direction, with an increase of more than two order of magnitude in the coherence time with respect to the previously reported works with cold atoms [11, 14, 16, 17, 18].

The coherence times reported up to now by the several groups working on the implementation of the protocol are all shorter or of the order of a couple of microseconds. Furthermore, for all experiments to date, the reported coherence times are of the order of the excitation pulses duration. However, for using this system as a quantum memory, it is important to obtain storage time much longer than the excitation pulses. Moreover, for the DLCZ protocol to become a viable alternative for long distance quantum communication, long coherence time is crucial and major efforts are required to increase it. The main goal of the present article is then to provide the initial steps in this direction, and to establish several techniques and ideas for the next steps.

Only two types of systems have been employed in the experiments up to now: vapor cells [12, 13, 15] and cold atoms in magneto-optical traps [11, 14, 16, 17, 18]. In both systems, however, the experiments have not achieved yet their respective state-of-the-art coherence times. The vapor-cell studies, for example, did not employ paraffin coated cells [19, 20]; the coherence times were effectively limited to the time the atoms take to diffuse out of the excitation region, which is of the order of microseconds. Recently, high fidelity atomic quantum memory of the state of a light pulse was achieved with such paraffin coated cells [21] with memory times of up to 4 ms. Coherence times of tens of milliseconds, however, are commonly achieved in this system [22], and there are reports of coherence times as high as one second [19]. The difference in these values is largely due to measurements of decay of different coherent processes [19]. How the coherence required for the generation of photon pairs from atomic vapors will decay as the atoms collide with the walls of paraffin coated cells is still to be determined.

The use of atomic traps to generate photon pairs for the DLCZ protocol has the advantage of providing a high density of atoms distributed in a small spectral region, due to the suppression of Doppler broadening by the cooling process. This allows the use of excitation laser pulses tuned closer to resonance, which requires much less power and makes it easier to filter the excitation pulses from the Ramam-scattered photons. However, atomic traps also introduce a different set of complications. In the case of the magneto-optical traps (MOT) used up to now, the magnetic field of the trap induces decoherence on a timescale of the order or smaller than a few hundreds nanoseconds [16, 17, 18]. The first results with the MOT magnetic field off are reported in the present article, with coherence times on the order of 10 μs. As will be discussed below in detail, a better nulling of the magnetic field combined with optical pumping to specific Zeeman levels might increase the coherence time, in a straightforward way, to hundreds of microseconds.

Further improvements with MOTs would face the problem of diffusion of atoms from the excitation region and, most troublesome, from the MOT itself. This problem can in principle be mitigated by improved cooling techniques. However, along these lines, it would be difficult to increase the coherence time above a couple of milliseconds. A possible solution then is to use an optical dipole trap to hold the atoms during the write-and-read process. Hyperfine coherence times of hundreds of milliseconds have already been observed in such traps [23, 24].

In the following, Secs. II and IV are devoted to theoretical results and Sec. III to associated experiments. In Sec. II A we give a general introduction to the photon-pair generation process behind the DLCZ protocol. In Sec. II B, we derive a theory for the probability of joint detection of these photons pairs generated from an atomic ensemble in a magneto-optical trap. This theory is a direct extension of a previous theoretical treatment reported in Ref. 6, to which we added explicitly the reading process and the Zeeman structure of the levels. In this way, we are able to model the action of the magnetic field over the atoms, and to study the dependence of the correlations with the light polarization.

Section III describes an experimental investigation leading to the nulling of the magnetic field in the photon-pair correlation measurements, with the subsequent increase in the system coherence time and degree of correlation. In Sec. III A, we describe a series of Raman-spectroscopy experiments to characterize the system and optimize the process of zeroing the magnetic field. We determine the set of experimental conditions that result in a good compromise between atomic density and magnetic field cancellation, which we used in the correlation measurements. Section III B describes then measurements of nonclassical correlations for the photon pairs generated by the MOT. We compare results with magnetic field on and with magnetic field off. The magnetic field off measurements present a higher degree of correlation, and a hundred times larger coherence time. We compare the shape of the experimental curves with magnetic field on and off to our theory, obtaining good agreement. We also show how the two-photon wavepacket that describes the detailed temporal structure of the photon pair generation is modified by the magnetic field.

Finally, based on the procedure for comparison between theory and experiment described in Sec. III B, we formulate in Sec. IV a proposal to improve our experimental signal. We suggest using a combination of optical pumping to a specific initial state and polarization of the light fields to increase both our detection efficiency and coherence time. Section V is dedicated to our conclusions.

II. THEORY

The basic theory for the DLCZ protocol is described in Refs. [5] and [6]. The general idea of the protocol is treated in Ref. [5], while Ref. [6] gives a detailed analysis of the collective emission of photons through spontaneous Raman scattering following excitation by free-space light. Section II B provides an extension of the theoretical treatment of Ref. [6] to better account for our experimental conditions. The emphasis here is the modeling of the decoherence process due to external magnetic fields, and in particular for experiments using magneto-optical traps. To model this decoherence, the essential elements to be introduced in the previous theory of Ref. [6] are the Zeeman structure of all levels and an explicit treatment of the reading process. On the other hand, the theory in Sec. II B is a simplification of the treatment of Ref. [6] concerning the spatial mode of the photons. We consider only the forward, collectively enhanced emission. The reading process is also treated in a simplified, perturbative way, while the experiments are done with stronger read pulses on resonance. This later difference between theory and experiment will result in some noticeable discrepancy in Sec. III B 2, where we discuss measurements of the two-photon wavepacket of the pair-generation process. In general, however, the comparison between theory and experiment performed in Sec. III B results in very good agreement, which indicates that the theory in Sec. II B takes into account the essential physical elements behind the decoherence process.

A. Photon pair generation

The building block of the DLCZ protocol is an ensemble of N identical atoms with lambda-type energy level configuration as shown in Fig. 1, which we briefly discuss here in an ideal setting. In the experiments discussed in this article, the lower states $|g\rangle$ and $|s\rangle$ are hyperfine sublevels of the electronic ground state of Cesium atoms. First, all atoms are prepared in the state $|g\rangle$. By sending in a weak, off-resonant laser pulse, one atom of the ensemble might be transfered from $|g\rangle$ to $|s\rangle$, thus emitting a photon (field 1) at a frequency or polarization different from the original exciting field. A key element of the protocol is the collective enhancement of this spontaneous Raman scattering in a forward direction, which is determined by the spatial mode of the laser pulse and the geometry of the excitation region [6]. If the laser intensity is low enough so that two excitations are very unlikely, the detection of the photon generated in this process is a signature that the ensemble was excited to a symmetrical collective state [5, 6], which in the ideal case can be explicitly written as

$$|1_a\rangle = \frac{1}{\sqrt{N}} \sum_{i=1}^{N} |g\rangle_1 \cdots |s\rangle_i \cdots |g\rangle_N, \tag{1}$$

where the sum goes over all atoms addressed by the laser pulse, and $|1_a\rangle$ indicates the state of the atomic ensemble with just one excitation. This is the "writing" step of the protocol (Fig. 1a).

Since the excitation probability χ is very small, the whole state of the system consisting of atoms and forward-scattered mode of light is in the following form:

$$|\phi\rangle = |0_a\rangle|0_1\rangle + e^{i\beta}\sqrt{\chi}\,|1_a\rangle|1_1\rangle + O(\chi), \tag{2}$$

where $\chi << 1$, $|n_1\rangle$ stands for the state of the forward-propagating light field 1 with n photons, β is a phase set by propagation to and from the ensemble, and $|0_a\rangle \equiv \bigotimes_i^{N_a} |g\rangle_i$. $O(\chi)$ represents all the other possible excitation processes, which in the ideal case occur with probabilities of order χ^2. The system remains in this state for a time on the order of the lifetime of the ground states. By sending in a second ("read") pulse resonant with the $|s\rangle \rightarrow |b\rangle$ transition, the state of the atomic ensemble can be transferred deterministically (read out) to another forward-propagating light field 2 at the $|b\rangle \rightarrow |g\rangle$ transition (see Fig. 1b). In this way, it is possible to access the quantum state of the atoms. This reading process is then closely related to low-light-level Electromagnetically Induced Transparency [25, 26]. After the read out, the state of the system becomes:

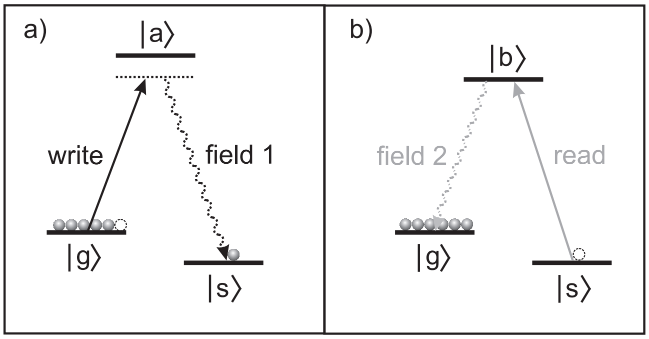

FIG. 1: Relevant level structure of the atoms in the ensemble for (a) writing and (b) reading processes, with $|g\rangle$ the initial ground state and $|s\rangle$ the ground state for storing an excitation. $|a\rangle$ and $|b\rangle$ are excited states. The transition $|g\rangle \rightarrow |a\rangle$ is initially coupled by a classical laser pulse (write beam) detuned from resonance, and the forward-scattered Stokes light (field 1) comes from the transition $|a\rangle \rightarrow |s\rangle$, which has different polarization or frequency to the write light. A classical read pulse then couples the transition $|s\rangle \rightarrow |b\rangle$, leading to the emission of forward-scattered anti-Stokes light (field 2) from the transition $|b\rangle \rightarrow |g\rangle$.

$$|\phi\rangle = |0_1\rangle|0_2\rangle + e^{i\gamma}\sqrt{\chi}\,|1_1\rangle|1_2\rangle + O(\chi), \tag{3}$$

where γ is a phase that includes β and the propagation phases to and from the ensemble related to the reading process. Fields 1 and 2 exhibit now strong correlations in the photon number basis, and can be described as photon pairs. These non-classical correlations can be measured by photoelectric detection. Since the field 2 maps the state of the atoms, the correlations between field 1 and field 2 can then be used to infer correlations between field 1 and the collective atomic excitations in the sample.

B. Decoherence

In order to analyze the decoherence process in the generation of pairs from an atomic ensemble as described in Sec. II A, we need to expand the theoretical treatment of Ref. [6] to include other experimentally relevant features. For our experiments in particular, it is essential to include the splitting of the Zeeman structure of the atomic ground states due to the magnetic field. The MOT quadrupole field generates an inhomogeneous distribution of splittings throughout the ensemble. As the system evolves in time, this results in dephasing between different regions of the atomic cloud, and in a respective decay of the coherence of the collective state. It is also important to include explicitly the reading process in the theory. For simplicity, this is done by considering a read process similar to the write process, i.e., with small probability of excitation and detuned from the excited state. Note that in the actual experiment, the read beam is stronger than the write beam and is on resonance. This will lead to small discrepancies when comparing the experimental results to the theory, that will be discussed in section III B 2.

The inclusion of Zeeman structure in the theory allows a detailed discussion of the effect of light polarization in the experiment. This is important to evaluate different excitation and detection schemes. It also gives a better description of the initial state, and of its role on the subsequent coherent pair generation. Together, the analysis of different polarization schemes and of different initial states led to specific proposals of ways to improve the whole process. These features of the theory are not specifically related to the MOT magnetic field, and should apply to pair generation in other systems, like vapor cells or dipole traps.

Our treatment starts by considering a sample of N four-level atoms, such as in Fig. 2. The four levels represent manifolds of Zeeman sublevels and are indicated by their respective F quantum numbers. A specific state of the F_j manifold of the i-th atom is represented by its ket $|m_j\rangle_i$, where m_j is the azimuthal quantum number. Two pumping fields act on the system, namely a write field $\vec{\mathcal{E}}_{ga}$ and a read field $\vec{\mathcal{E}}_{sb}$, where

$$\vec{\mathcal{E}}_{ga}(\vec{r},t) \;=\; u_w(\vec{r},t)e^{i(k_w z-\omega_w t)}\vec{e}_{p_w}\,, \tag{4a}$$

$$\vec{\mathcal{E}}_{sb}(\vec{r},t) \;=\; u_r(\vec{r},t)e^{i(k_r z-\omega_r t)}\vec{e}_{p_r}\,, \tag{4b}$$

which couple the transitions $F_g \rightarrow F_a$ and $F_s \rightarrow F_b$, respectively. The functions u_w and u_r give the slowly-varying envelopes of the *write* and *read* pulses, respectively, and $\vec{e}_{p_w}$ and $\vec{e}_{p_r}$ are their polarization vectors. As a result of their action, two Raman fields are spontaneously generated in the sample:

$$\hat{\vec{\mathcal{E}}}_{sa}(\vec{r},t) \;\propto\; \sum_{p_1}\int d\vec{k}_1\hat{a}_{\vec{k}_1p_1}e^{i(\vec{k}_1\cdot\vec{r}-\omega_{\vec{k}_1}t)}\vec{e}_{p_1}\,, \tag{5a}$$

$$\hat{\vec{\mathcal{E}}}_{gb}(\vec{r},t) \;\propto\; \sum_{p_2}\int d\vec{k}_2\hat{b}_{\vec{k}_2p_2}e^{i(\vec{k}_2\cdot\vec{r}-\omega_{\vec{k}_2}t)}\vec{e}_{p_2}\,, \tag{5b}$$

where $\omega_{\vec{k}_i} = |\vec{k}_i|c$ and p_i is a label for the field polarization. $\hat{a}_{\vec{k}_1p_1}$ and $\hat{b}_{\vec{k}_2p_2}$ are the annihilation operators for the Raman fields 1 and 2, respectively, which couple the transitions $F_s \rightarrow F_a$ and $F_g \rightarrow F_b$. The state of field 1 with just one photon excited in mode $\vec{k}_1p_1$ will be designated by $|1_{\vec{k}_1p_1}\rangle$. A similar notation will be used for field 2.

The Hamiltonian for the system of N atoms can be written as

$$\hat{H}(t) = \hat{H}_0 + \hat{V}(t)\,, \tag{6}$$

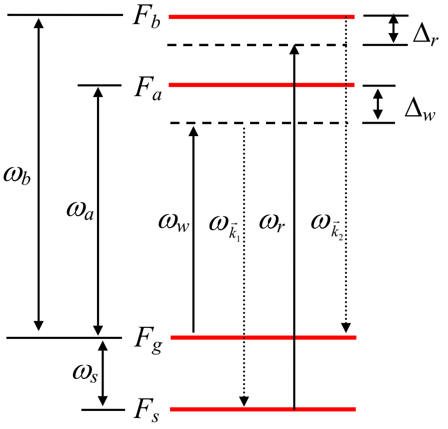

FIG. 2: Energy level scheme considered for the atomic ensembles

where

$$\begin{aligned}\hat{H}_0 = \sum_{i=1}^{N}\Bigg\{ &\sum_{m_s=-F_s}^{F_s}(-\hbar\omega_s + \mu_B g_s m_s B_{z_i})\,|m_s\rangle_i\langle m_s| \\ &+ \sum_{m_g=-F_g}^{F_g}\mu_B g_g m_g B_{z_i}|m_g\rangle_i\langle m_g| \\ &+ \sum_{m_a=-F_a}^{F_a}\hbar\omega_a|m_a\rangle_i\langle m_a| + \sum_{m_b=-F_b}^{F_b}\hbar\omega_b|m_b\rangle_i\langle m_b|\Bigg\}\end{aligned} \tag{7}$$

is the free-atom Hamiltonian, and

$$\begin{aligned}\hat{V}(t) = \sum_{i=1}^{N}\Bigg\{ &\sum_{m_a=-F_a}^{F_a}\sum_{m_g=-F_g}^{F_g}\left(-\vec{d}_{m_am_g}\cdot\vec{\mathcal{E}}_{ga}\right)|m_a\rangle_i\langle m_g| \\ &+ \sum_{m_s=-F_s}^{F_s}\sum_{m_a=-F_a}^{F_a}\left(-\vec{d}_{m_sm_a}\cdot\hat{\vec{\mathcal{E}}}^{\dagger}_{sa}\right)|m_s\rangle_i\langle m_a| \\ &+ \sum_{m_b=-F_b}^{F_b}\sum_{m_s=-F_s}^{F_s}\left(-\vec{d}_{m_bm_s}\cdot\vec{\mathcal{E}}_{sb}\right)|m_b\rangle_i\langle m_s| \\ &+ \sum_{m_g=-F_g}^{F_g}\sum_{m_b=-F_b}^{F_b}\left(-\vec{d}_{m_gm_b}\cdot\hat{\vec{\mathcal{E}}}^{\dagger}_{gb}\right)|m_g\rangle_i\langle m_b|\Bigg\}\end{aligned} \tag{8}$$

gives the time-dependent interaction Hamiltonian. $\vec{d}_{jk}$ is the dipole moment for the $j \rightarrow k$ transition, μ_B the Bohr magneton, g_j the hyperfine Landé factor for level F_j, and B_{z_i} is the magnetic field in the position of the i-th atom. The magnetic field direction is taken as the quantization z axis. We neglect the Zeeman splitting of the excited states since we want to investigate a situation where it is always smaller than the excited-states natural linewidths. The factors $-\vec{d}_{jk}\cdot\vec{\mathcal{E}}_{kj}$ can also be written as

$$-\vec{d}_{m_am_g}\cdot\vec{\mathcal{E}}_{ga} = K_{m_am_g}u_w(\vec{r}_i,t)e^{i(k_wz_i-\omega_wt)}\,, \tag{9a}$$

$$-\vec{d}_{m_sm_a}\cdot\hat{\vec{\mathcal{E}}}^{\dagger}_{sa} = \sum_{p_1}\int d\vec{k}_1K^{\vec{k}_1p_1}_{m_sm_a}\hat{a}^{\dagger}_{\vec{k}_1p_1}e^{-i(\vec{k}_1\cdot\vec{r}-\omega_{\vec{k}_1}t)}\,, \tag{9b}$$

$$-\vec{d}_{m_bm_s}\cdot\vec{\mathcal{E}}_{sb} = K_{m_bm_s}u_r(\vec{r}_i,t)e^{i(k_rz_i-\omega_rt)}\,, \tag{9c}$$

$$-\vec{d}_{m_gm_b}\cdot\hat{\vec{\mathcal{E}}}^{\dagger}_{gb} = \sum_{p_2}\int d\vec{k}_2K^{\vec{k}_2p_2}_{m_gm_b}\hat{b}^{\dagger}_{\vec{k}_2p_2}e^{-i(\vec{k}_2\cdot\vec{r}-\omega_{\vec{k}_2}t)}\,, \tag{9d}$$

where $K_{m_am_g}$, $K^{\vec{k}_1p_1}_{m_sm_a}$, $K_{m_bm_s}$, and $K^{\vec{k}_2p_2}_{m_gm_b}$ are coupling constants for the corresponding transition.

The temporal evolution of the coupled system consisting of ensemble + Raman fields is described by the evolution of its density matrix $\hat{\rho}(t)$. In the interaction picture, the corresponding operator $\hat{\rho}_I(t)$ is given by

$$\hat{\rho}_I(t) = \hat{U}_I(t)\hat{\rho}(0)\hat{U}_I^{\dagger}(t)\,, \tag{10}$$

where $\hat{U}_I(t)$ is the temporal evolution operator, and the initial state $\hat{\rho}(0)$ can be written as

$$\hat{\rho}(0) = \hat{\rho}_{F_1}(0)\otimes\hat{\rho}_{F_2}(0)\otimes\hat{\rho}_1(0)\otimes\hat{\rho}_2(0)\otimes\cdots\otimes\hat{\rho}_N(0)\,, \tag{11}$$

with $\hat{\rho}_{F_1}(0)$ the initial state of field 1, $\hat{\rho}_{F_2}(0)$ the initial state of field 2, and $\hat{\rho}_i(0)$ the initial state of the i-th atom. For most of what follows, we will be interested in the case where the fields 1 and 2 are initially vacuum states, $\hat{\rho}_{F_1}(0) = |vac_{F_1}\rangle\langle vac_{F_1}|$ and $\hat{\rho}_{F_2}(0) = |vac_{F_2}\rangle\langle vac_{F_2}|$, and all atoms are initially in the same incoherent distribution over the Zeeman sublevels of the F_g state:

$$\hat{\rho}_i(0) = \sum_{m_g=-F_g}^{F_g} D_{m_g}|m_g\rangle_i\langle m_g|\,, \tag{12}$$

with D_{m_g} giving the probability of finding an atom in the m_g state at $t=0$. In section IV however, we will consider the case where all the atoms are optically pumped in one of the Zeeman sublevel ($m_F=0$).

The operator $\hat{U}(t)$ can be written as a Dyson series in the form

$$\hat{U}_I(t) = 1+\sum_{i=1}^{N}\hat{\mathcal{U}}_i^{(1)}(t)+\sum_{i=1}^{N}\hat{\mathcal{U}}_i^{(2)}(t)+\cdots\,, \tag{13}$$

where

$$\begin{aligned}\hat{\mathcal{U}}_i^{(1)}(t) &= \left(-\frac{i}{\hbar}\right)\int_0^t dt'\hat{\mathcal{V}}_i(t')\,,\\ \hat{\mathcal{U}}_i^{(2)}(t) &= \left(-\frac{i}{\hbar}\right)^2\int_0^t dt'\int_0^{t'} dt''\hat{\mathcal{V}}_i(t')\hat{\mathcal{V}}_i(t'')\,,\end{aligned} \tag{14}$$

and so on. The single-atom interaction operator $\hat{\mathcal{V}}_i(t)$ is defined from the expression for the general interaction Hamiltonian $\hat{V}_I(t)$ in the interaction picture as

$$\hat{V}_I(t) = e^{i\hat{H}_0t/\hbar}\hat{V}(t)e^{-i\hat{H}_0t/\hbar} = \sum_{i=1}^{N}\hat{\mathcal{V}}_i(t)\,. \tag{15}$$

1. *Probability for joint detections*

We want to calculate in the lowest order of perturbation the probability of detecting a single photon in field 1 followed by another photon in field 2. The first step is then to calculate the restriction of the coupled state $\hat{\rho}(t)$ to the space of states of fields 1 and 2:

$$\hat{\rho}_{F_1F_2}(t) = \mathrm{Tr}_A\left[\hat{\rho}(t)\right]\,. \tag{16}$$

The symbol Tr_A indicates a partial trace over all atomic states. The probability for detecting two photons, one in mode $\vec{k}_1p_1$ and the other in mode $\vec{k}_2p_2$, up to time t is then given by

$$\begin{aligned}p_{12}^{th}(t,\vec{k}_1p_1,\vec{k}_2p_2) &= \langle 1_{\vec{k}_1p_1}|\langle 1_{\vec{k}_2p_2}|\hat{\rho}_{F_1F_2}(t)|1_{\vec{k}_2p_2}\rangle|1_{\vec{k}_1p_1}\rangle\\ &= \langle 1_{\vec{k}_1p_1}|\langle 1_{\vec{k}_2p_2}|\mathrm{Tr}_A\left[\hat{\rho}(t)\right]|1_{\vec{k}_2p_2}\rangle|1_{\vec{k}_1p_1}\rangle.\end{aligned} \tag{17}$$

Since all atoms are initially in the ground state F_g, the lowest order term of series (13) that results in a single photon in field 1 and another photon in field 2 is the fifth term, which accounts for the four transitions carried successively by the write field, photon 1, read field, and photon 2, respectively. Substituting Eqs. (10) and (13) into Eq. (17) and keeping only the lowest order term, we arrive then at

$$\begin{aligned}&p_{12}^{th}(t,\vec{k}_1p_1,\vec{k}_2p_2) =\\ &\sum_{i,j=1}^{N}\langle 1_{\vec{k}_1p_1}|\langle 1_{\vec{k}_2p_2}|\mathrm{Tr}_A\Big[\hat{\mathcal{U}}_i^{(4)}(t)\hat{\rho}(0)\hat{\mathcal{U}}_j^{(4)\dagger}(t)\Big]|1_{\vec{k}_2p_2}\rangle|1_{\vec{k}_1p_1}\rangle.\end{aligned} \tag{18}$$

Note that $\hat{\mathcal{U}}_k^{(4)}$ acts only over the k-th atom. Thus, the trace Tr_A on each term of the double sum can be written as a trace Tr_k over the states of the atoms at which the $\hat{\mathcal{U}}_k^{(4)}$ operator is acting, since all other atoms remain in their initial state. Two different cases are present in Eq. (18). If $i\neq j$, the two operators act over two different atoms and the initial state $\hat{\rho}(0)$ simplifies to $\hat{\rho}_{F_1}(0)\otimes\hat{\rho}_{F_2}(0)\otimes\hat{\rho}_i(0)\otimes\hat{\rho}_j(0)$. If $i=j$, then $\hat{\rho}(0)\to\hat{\rho}_{F_1}(0)\otimes\hat{\rho}_{F_2}(0)\otimes\hat{\rho}_i(0)$. With these observations in mind, we see that Eq. (18) can then be written as

$$
\begin{aligned}
&p_{12}^{th}(t,\vec{k}_1p_1,\vec{k}_2p_2) = \\
&\sum_{\substack{i,j=1\\ i\neq j}}^{N} \langle 1_{\vec{k}_1p_1}|\langle 1_{\vec{k}_2p_2}|\mathrm{Tr}_i\left[\hat{\mathcal{U}}_i^{(4)}(t)\hat{\rho}_i(0)\right]|vac_{F_2}\rangle|vac_{F_1}\rangle \\
&\qquad \times \langle vac_{F_1}|\langle vac_{F_2}|\mathrm{Tr}_j\left[\hat{\rho}_j(0)\hat{\mathcal{U}}_j^{(4)\dagger}(t)\right]|1_{\vec{k}_2p_2}\rangle|1_{\vec{k}_1p_1}\rangle \\
&+\sum_{i=1}^{N}\langle 1_{\vec{k}_1p_1}|\langle 1_{\vec{k}_2p_2}|\mathrm{Tr}_i\Big[\hat{\mathcal{U}}_i^{(4)}(t)\hat{\rho}_{F_1}(0)\otimes\hat{\rho}_{F_2}(0)\otimes\hat{\rho}_i(0) \\
&\qquad \times \hat{\mathcal{U}}_i^{(4)\dagger}(t)\Big]|1_{\vec{k}_2p_2}\rangle|1_{\vec{k}_1p_1}\rangle .
\end{aligned}
\tag{19}
$$

Substituting Eq. (12), we have

$$
\begin{aligned}
p_{12}^{th}(t,\vec{k}_1p_1,\vec{k}_2p_2) = &\left|\sum_{i=1}^{N}\sum_{m_g=-F_g}^{F_g} D_{mg}A_i(m_g,m_g)\right|^2 \\
&+\sum_{i=1}^{N}\sum_{m'_g=-F_g}^{F_g}\sum_{m_g=-F_g}^{F_g} D_{mg}|A_i(m'_g,m_g)|^2 \\
&-\sum_{i=1}^{N}\left|\sum_{m_g=-F_g}^{F_g} D_{mg}A_i(m_g,m_g)\right|^2 ,
\end{aligned}
\tag{20}
$$

where

$$
\begin{aligned}
&A_i(m'_g,m_g) = \\
&\quad\langle 1_{\vec{k}_1p_1}|\langle 1_{\vec{k}_2p_2}|\langle m'_g|_i\hat{\mathcal{U}}_i^{(4)}(t)|m_g\rangle_i|vac_{F_2}\rangle|vac_{F_1}\rangle .
\end{aligned}
\tag{21}
$$

Note that the first term on the right side of Eq. (20) scales as N^2, while the two remaining terms scale with N only. Since we are interested in the limit of large N, we can then approximate

$$
p_{12}^{th}(t,\vec{k}_1p_1,\vec{k}_2p_2) = \left|\sum_{i=1}^{N}\sum_{m_g=-F_g}^{F_g} D_{mg}A_i(m_g,m_g)\right|^2 .
\tag{22}
$$

Thus, for large N, only transitions that start and end in the same state contribute to the pair generation. This result can be understood as a constructive interference between all pathways that connect the ensemble back to its initial state, after which it is not possible to distinguish which atom made the transition [27]. Pathways connecting different initial and final states leave a trace in the ensemble, which in principle can give information on which specific atom made the transition. In this last case, the number of possible pathways generating the pair of photons is then linearly proportional to the number of atoms N. Eq (22) expresses the collective enhancement that is essential to the scheme of ref. [5].

Finally, substituting the specific expressions for $\hat{\mathcal{U}}_i^{(4)}(t)$ and $\hat{\mathcal{V}}_i(t)$, we find that $A_i(m_g,m_g)$ can be written as

$$
\begin{aligned}
A_i(m_g,m_g) = &\sum_{m_s=-F_s}^{F_s}\frac{d(m_g,ms)}{\hbar^4}\,e^{i(k_rz_i+k_wz_i-\vec{k}_1\cdot\vec{r}_i-\vec{k}_2\cdot\vec{r}_i)} \\
&\times\int_0^t dt' e^{i(\Delta\omega_{\vec{k}_2}-\Delta_r+a_{ig})t'} \\
&\times\int_0^{t'} dt'' u_r(\vec{r}_i,t'')e^{i(\Delta_r-a_{is})t''} \\
&\times\int_0^{t''} dt''' e^{i(\Delta\omega_{\vec{k}_1}-\Delta_w+a_{is})t'''} \\
&\times\int_0^{t'''} dt'^{\nu} u_w(\vec{r}_i,t'^{\nu})e^{i(\Delta_w-a_{ig})t'^{\nu}} ,
\end{aligned}
\tag{23}
$$

where $\Delta_w = \omega_a-\omega_w$, $\Delta_r = \omega_b+\omega_s-\omega_r$, $\Delta\omega_{\vec{k}_1} = \omega_{\vec{k}_1}-\omega_w-\omega_s$, $\Delta\omega_{\vec{k}_2} = \omega_{\vec{k}_2}-\omega_r+\omega_s$, and

$$
d(m_g,m_s) = \sum_{m_b=-F_b}^{F_b}\sum_{m_a=-F_a}^{F_a} K_{m_gm_b}^{\vec{k}_2p_2}K_{m_bm_s}^{r}K_{m_sm_a}^{\vec{k}_1p_1}K_{m_am_g}^{w}
\tag{24}
$$

gives the strength of an specific excitation pathway in which the atom starts at m_g, then goes to m_s, and ends at m_g again. The Zeeman splittings are written in terms of the parameters $a_{ig} = \mu_B g_g m_g B_{z_i}/\hbar$ and $a_{is} = \mu_B g_s m_s B_{z_i}/\hbar$.

2. *Forward emission*

In order to simplify the following analysis while keeping the essential trends of the temporal dynamics, we will focus now on the treatment of the forward, resonant emission from the atomic ensemble. In the forward direction, the light emitted by the sample satisfies the phase-matching condition

$$
k_rz_i+k_wz_i-\vec{k}_1\cdot\vec{r}_i-\vec{k}_2\cdot\vec{r}_i = 0 .
\tag{25}
$$

The resonant conditions for the Raman fields are $\Delta\omega_{\vec{k}_1} = 0$ and $\Delta\omega_{\vec{k}_2} = 0$. A discussion about deviations from these conditions can be found at Ref. [6].

Under these assumptions, and with the slow envelope functions written as

$$
u_r(\vec{r}_i,t) = q_r(\vec{r}_i)f_r(t)\,, \tag{26a}
$$

$$
u_w(\vec{r}_i,t) = q_w(\vec{r}_i)f_w(t)\,, \tag{26b}
$$

Equation (23) becomes

$$
A_i(m_g,m_g) = q_r(\vec{r}_i)q_w(\vec{r}_i)\sum_{m_s=-F_s}^{F_s}\frac{d(m_g,ms)}{\hbar^4}\,F(t,z_i)\,,
\tag{27}
$$

with

$$F(t,z_i) = \int_0^t dt' e^{i(-\Delta_r + a_{ig})t'} \int_0^{t'} dt'' f_r(t'') e^{i(\Delta_r - a_{is})t''} \times \int_0^{t''} dt''' e^{i(-\Delta_w + a_{is})t'''} \int_0^{t'''} dt'^{\nu} f_w(t'^{\nu}) e^{i(\Delta_w - a_{ig})t'^{\nu}} . \tag{28}$$

Note that the F function depends on the parameters for a specific atom only through z_i that specifies its position along the quantization axis. In this way, after a certain time, atoms in different parts of the ensemble contribute to the probability amplitude of the process with different phases.

If we consider a uniform distribution of atoms throughout the beam path, and neglecting the z dependence on the q functions, the sum over all atoms may be transformed in the following integral

$$\begin{aligned} \sum_{i=1}^{N} q_r(\vec{r}_i) q_w(\vec{r}_i) \rightarrow \frac{N}{V} \int\int\int dx\, dy\, dz\, q_r(x,y) q_w(x,y) = \\ = \int\int dx\, dy\, \frac{q_r(x,y) q_w(x,y)}{A} \frac{N}{L} \int dz \\ = \langle q_r(x,y) q_w(x,y) \rangle \; N \int_{-L/2}^{L/2} \frac{dz}{L} \,, \end{aligned} \tag{29}$$

where $V = AL$ gives the volume of the excitation region, A its transverse area, and L its length.

Substituting Eqs. (27) and (29) in Eq. (22), we finally obtain

$$p_{12}^{th}(t) = C \left| \sum_{m_g=-F_g}^{F_g} \sum_{m_s=-F_s}^{F_g} D_{m_g} d(m_g, m_s) \int_{-L/2}^{L/2} \frac{dz}{L} F(t,z) \right|^2 , \tag{30}$$

where

$$C = N^2 \left| \langle q_r(x,y) q_w(x,y) \rangle \right|^2 , \tag{31}$$

is a constant. After the read pulse has left the sample (i.e., when $t \rightarrow \infty$), Expression (30) is then proportional to the total probability of detecting the pair of photons in one trial. Details on how to compare this expression to the experimental results will be discussed in Sec. III B 1. In the experimentally important case of square pulses, it is straightforward to obtain analytical expressions for both $F(t,z)$ and $p_{12}(t)$ in the limit of large Δ_w and Δ_r.

3. *Probability density*

Equation (30) gives the total probability of detecting one photon in field 2 after detecting a photon in field 1. Now we want to obtain the probability of finding photon 2 between times t_2 and $t_2 + \Delta t_2$ and photon 1 between times t_1 and $t_1 + \Delta t_1$, for small Δt_2 and Δt_1.

The first step in this calculation is to note that Eq. (30) can be written as,

$$p_{12}^{th}(t) = |\phi(t)|^2 . \tag{32}$$

The function $\phi(t)$ gives then a probability amplitude for the process where the two photons are found up to time t. It consists of an integral over all possible pairs of detection times (t_2, t_1), representing different excitation pathways, and can in principle also be written as

$$\phi(t) = \int_0^t dt_1 \int_{t_1}^t dt_2 P(t_2, t_1), \tag{33}$$

where we considered explicitly $t_2 > t_1$. $P(t_2, t_1)$ represents then a density of probability amplitude.

The probability amplitude for finding photon 2 between times t_2 and $t_2 + \Delta t_2$, and photon 1 between times t_1 and $t_1 + \Delta t_1$, can be obtained then by restriction over the temporal integral in Eq. (30). Since all the temporal dynamics in Eq. (30) is in the function $F(t,z)$, we need to calculate first the restriction of $F(t,z)$ for these specific processes. In order to do so, note that, in the fourth order integral of $F(t,z)$, the emission of photon 2 is described by the last integral (over t'), while photon 1 emission is described by the third integral (over t'''). The restriction of $F(t,z)$ for the emission of photon 2 between times t_2 and $t_2 + \Delta t_2$, and photon 1 between times t_1 and $t_1 + \Delta t_1$, is then given by [28]

$$G(t_2, \Delta t_2, t_1, \Delta t_1) = \int_{t_2}^{t_2 + \Delta t_2} dt' e^{i(-\Delta_r + a_{ig})t'} \times \int_0^{t'} dt'' f_r(t'') e^{i(\Delta_r - a_{is})t''} \int_{t_1}^{t_1 + \Delta t_1} dt''' e^{i(-\Delta_w + a_{is})t'''} \times \int_0^{t'''} dt'^{\nu} f_w(t'^{\nu}) e^{i(\Delta_w - a_{ig})t'^{\nu}} . \tag{34}$$

Equation (34) can be directly evaluated for the case of square pulses and large detunings, such that $\Delta_r, \Delta_w >> \Delta t_2^{-1}, \Delta t_1^{-1}$. If the time intervals are also small when compared to the timescale of oscillations determined by the Zeeman shifts (i.e., $\Delta t_2, \Delta t_1 << a_g^{-1}, a_s^{-1}$), then Eq. (34) can be written as

$$G(t_2, \Delta t_2, t_1, \Delta t_1) = g(t_2, t_1) \Delta t_1 \Delta t_2 \,, \tag{35}$$

with

$$g(t_2, t_1) = -\frac{f_r(t_2) f_w(t_1)}{\Delta_r \Delta_w} e^{i(a_g - a_s)(t_2 - t_1)} . \tag{36}$$

In this case, $F(t,z)$ can be derived by:

$$F(t,z) = \int_0^t dt_1 \int_{t1}^t dt_2\, g(t_2, t_1) \,. \tag{37}$$

An important remark is that, since any pulse envelope can be approximated by a sum of square pulses of different intensities and small duration, Eq. (36) is indeed valid for arbitrary pulse shapes, as long as the envelope temporal variation occurs in a much longer timescale than Δt_1 or Δt_2.

The connection between $g(t_2, t_1)$ and the density of probability amplitude $P(t_2, t_1)$ is then made through the relation

$$P(t_2, t_1) = \sqrt{C} \sum_{m_g=-F_g}^{F_g} \sum_{m_s=-F_s}^{F_g} D_{m_g} d(m_g, m_s) \times \int_{-L/2}^{L/2} \frac{dz}{L} g(t_2, t_1). \tag{38}$$

Finally, the probability density for detecting one photon from field 1 at time t_1 and another from field 2 at t_2 is associated to

$$\mathcal{P}(t_2, t_1) = |P(t_2, t_1)|^2. \tag{39}$$

This is the quantity to be compared with the experimental results of Sec. III B 2, for the two-photon wavepacket of the photon pair.

III. EXPERIMENTS

Up to now, the experimental implementation of the DLCZ protocol in MOTs have been plagued by extremely short coherence times [11, 14, 16, 17]. As discussed above, this short coherence time is a result of the action of the MOT quadrupole field over the Zeeman structure of the hyperfine ground states. In the following, we are going to describe a series of experiments that allowed us to obtain photon pairs from the trapped atomic cloud in a situation of very small magnetic field. In this way, we were able to measure coherence times of more than 10 μs (more than two orders of magnitude longer than the duration of the excitation pulses), and two-photon wavepackets for the photon pairs that do not exhibit distortion by decoherence even when write and read pulses cease overlapping in time [17].

The crucial point is to turn off the MOT magnetic field and determine the experimental conditions with a best tradeoff between high repetition rate and high optical density. Note that the atoms fly away from the trap and the density starts to decrease when the magnetic field is turned off. Hence, the MOT field has to be turned off as fast as possible, to decrease the transient time and maximize the region with low magnetic field and high density. A fast turning off of the magnetic field in our metallic vacuum chambers, however, is not straightforward and requires specific techniques, as will be discussed in Sec. III A.

Inside each MOT-off period, it is possible to conduct many trials of the photon pair experiments. These are photon counting measurements that require many events in order to acquire good statistics. Hence, we would like to have as many MOT-off periods as possible to accumulate a large number of trials. However, the MOT needs some time to recover its original density after each off period, and this time limits how often it can be turned off while still keeping a high enough atomic density.

During the process of turning off the magnetic field and determining the proper conditions for the photon counting experiments, it was essential to be able to perform simpler experiments giving direct access to the ground state broadening by the magnetic field. We chose then to setup a copropagating stimulated Raman spectroscopy apparatus to help us in this process. The results for the Raman spectroscopy measurements and the investigation to determine the best experimental conditions for the photon pair generation are described also in Sec. III A.

The nonclassical correlation experiments are discussed in Sec. III B. There we show that the coherence time increases by more than two orders of magnitude once the magnetic field is switched off, and describe measurements of the shape of the two-photon wavepacket in both situations. In this section, we also compare the experimental results with the theory of Sec. II B.

A. Characterization and magnetic field nulling

As anticipated above, we use copropagating stimulated Raman spectroscopy [29] to probe directly the broadening of the hyperfine ground states. Our choice for this specific technique is based on the fact that it is insensitive to Doppler broadening, but very sensitive to any broadening caused by magnetic fields, exactly like the spontaneous Raman emission process underlying the photon pair generation in our experiment. Raman stimulated transitions (see Fig. 3a) are two-photon transitions connecting one ground-state hyperfine level to the other one, in which a single photon is absorbed from one Raman beam and another photon is emitted in the other beam by stimulated emission through a virtual level, which is located 3 GHz below the Cesium D_2 line in our setup.

The Raman process is resonant if the frequency difference of the two Raman beams equals the ground-state hyperfine interval, around 9.192631770 GHz for Cesium. In the absence of collisions and transit broadening, this two-photon resonance is very sharp, with a linewidth limited only by the power and duration of the Raman beams [29]. In this way, since the specific value of the hyperfine interval for transitions between $|m_g\rangle$ and $|m_s\rangle$ states changes with the magnetic field, scanning the frequency of one Raman beam with respect to the other gives direct information on the frequency distribution of possible two-photon resonances dislocated by the magnetic field, i.e., on the broadening of the ground state.

Our setup for Raman spectroscopy is shown in Fig. 3a. The two Raman beams and a probe beam are coupled to the same polarization maintaining fiber, which takes the beams close to the MOT and provides good mode-matching between them. The probe beam is coupled with the same polarization as the Raman field connecting the $F = 3$ ground state to the virtual level, the other Raman field is coupled with the orthogonal polarization. The lens at the fiber output focus the beam to a diameter of 150 μm in the MOT region. After the fiber, the beams pass through a 50/50 beam splitter cube. The transmitted parts of the beams are used as a reference to compensate for power fluctuations. The reflected part is directed to the MOT, forming an angle of about $\theta \approx 3°$ with the quadrupole-field z axis. The shaded area around the z axis in Fig. 3a indicates the path of one of our trapping beams. The absorption of the probe beam by the atoms in the MOT is then measured with a second detector, by comparing the probe pulse height with MOT on and off.

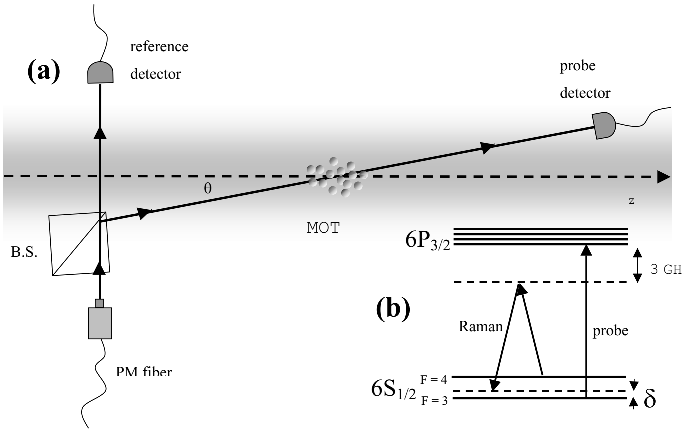

FIG. 3: (a) Experimental Raman spectroscopy setup. The Raman beams and the probe beam are coupled into a polarization maintaining (PM) fiber and sent trough a beam spitter cube (BS). The reflected part is focused into the sample with an angle of 3 degrees with respect to the quadrupole field z axis, while the transmitted part is used as a reference. (b) Relevant level structures and laser frequencies for Raman spectroscopy.

Before the Raman pulses reach the MOT, an optical pumping cycle moves the whole atomic population to just one of the hyperfine ground states. Note that for the following experiments, we make no attempt to optically pump the atoms onto a specific Zeeman state. Hence, the atomic ensemble is unpolarized and all Zeeman substates are populated. The action of the Raman pulses, of about 150 μs duration and 10 μW power, then transfers some population to the initially empty level if their relative detuning matches one of the two-photon transitions of the sample. The probe pulse has a duration of 5 μs and comes 50 μs after the Raman pulses. It is resonant with the cycling transition connecting the initially empty ground state to the $6P_{3/2}$ level [$F = 4 \rightarrow F' = 5$ if the empty ground state is $F = 4$, $F = 3 \rightarrow F' = 2$ for empty $F = 3$ state]. The probe power is about 50 nW, to guarantee a low saturation of the transition. It is then very sensitive to any change in the initial population, and its absorption indicates that the Raman pulses succeeded in transferring some population from one ground state to the other.

In this way, a plot of the medium optical depth for the probe pulse as a function of the detuning between the two Raman fields gives a direct measure of the ensemble distribution of energies in the ground states. Examples of such plots with the MOT magnetic field on and off are shown in Figs. 4a and 4b, respectively. In Fig. 4b the Raman pulses are delayed 4 ms from the moment the magnetic field was turned off, and the nulling of the field was performed using additional bias coils located around the MOT and looking for a reduced width of the Raman trace. From Fig. 4a to 4b, the width of the signal is then reduced by more than two orders of magnitude, from 5 MHz to about 20 kHz. The 20 kHz linewidth of Fig. 4b, however, also includes about 10 kHz that comes from power broadening by the Raman beams. To measure this power broadening, we applied an extra DC field in the z direction in order to split the central peak between the various $m_F \rightarrow m'_F$ transitions, and then measured the width of the magnetic-field-insensitive transition $m_F = 0 \rightarrow m'_F = 0$. As mentioned above, the quadrupole field of the MOT should be switched off as fast as possible, in order to maintain the high optical density needed for the DLCZ-type experiments. However, switching off the magnetic field generated by the MOT coils is usually retarded for two reasons. First, the current in the coils decays exponentially, with a time constant proportional to the inductance of the coils. Second, the field decay time is increased by eddy currents in the metallic part of our vacuum chamber. Depending on the metallic configuration of chamber and coils, the transient period can last for tens of ms. In order to obtain a faster transient, we use a fast-switching electronic circuit [30, 31]. This circuit allows a quick reversal of the current in the quadrupole coils in order to compensate for the eddy currents, and resulted in a substantial reduction of the transient time in our system.

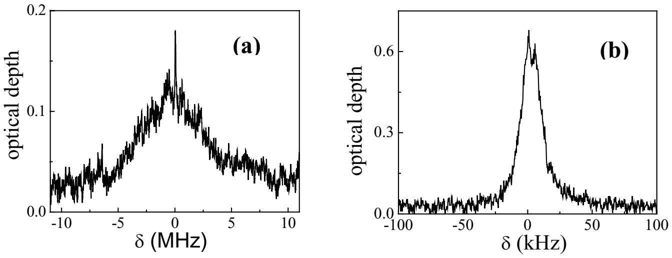

FIG. 4: (a) Raman trace with the quadrupole MOT magnetic field on. The trace represents the absorbtion of the probe pulse following the Raman beams, as a function of the Raman detuning δ. The line width FWHM is around 5 MHz. (b) Raman trace 4 ms after the quadrupole field has been switched off. The fitted linewidth is 20 kHz, including 10 kHz of power broadening due to the Raman beams

A detailed description of the magnetic field transient is given in Fig. 5a, which plots the Raman scan linewidth as a function of the delay from the moment the field was switched off. Figure 5a then shows the timescale over which the ground state has its energy-distribution profile changed from Fig. 4a to Fig. 4b. We can see that after a few miliseconds, the linewidth asymptotically reaches a plateau, given by the residual DC field in the chamber, that we estimate in this case to be on the order of 10 mG. The dashed line in Fig. 5a indicates the measured power broadening. Shorter transients can be obtained with a different metallic chamber configuration (like in Ref. 30) or using non-metallic vacuum chambers.

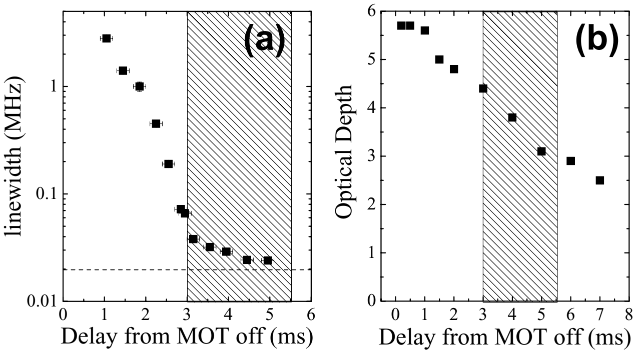

FIG. 5: (a) Evolution of the ground state linewidth and (b) of the optical depth of the sample as a function of the delay from the time when the current is switched off in the MOT coils. The linewidth is measured with Raman spectroscopy. The dashed line represents the measured power broadening due to the Raman beams. The OD is determined by measuring the absorbtion of a probe pulse in the sample. In both graphs, the dashed area represents the window used for measuring correlations at the single photon level.

In order to estimate the optimal region for photon counting measurements, it is important to independently measure the decay of the optical depth after the magnetic field is switched off. In our setup this is done in a straightforward way by turning off the Raman beams and using a probe pulse close to resonance with the ground state that concentrates all the atomic population. The results of such measurement are shown in Fig. 5b, for which the population was initially pumped to $F = 4$ and the probe tuned 10 MHz below the $F = 4 \rightarrow F' = 5$ transition. The optical depth measurements in Fig. 5b were obtained from the absorption at 10 MHz detuning and assuming a Lorentzian lineshape for the atomic transition with a natural linewidth corrected for power broadening by the probe beam.

Together, the results in Figs. 5a and 5b allow us to determine an optimal window for the experiments of Sec. III B, i.e., between 3 and 5.5 ms (dashed region in both figures). The lower limit of this region is determined by the moment when the residual magnetic field reaches a reasonably small value corresponding to an acceptable decoherence time, and the higher limit by the restriction that the density should not vary too much throughout the region. We accepted a variation of about 30% in the density. The linewidth varies by about 30 kHz in the same interval.

A better cancellation of the magnetic field can in principle lead to even smaller linewidths and, consequently, longer coherence times. However, improvements along this line will eventually be limited by a different problem: the diffusion of atoms out of the excitation region. This effect of course depends on the temperature of the sample and on the diameter of the excitation beams. In order to directly measure this diffusion time, we use again Raman spectroscopy. In this case, Raman traces are recorded as a function of the delay between the Raman pulses and probe. The measurement is done when the magnetic field is off, such that there is only one narrow peak in the Raman trace, like in Fig. 3d. In this case, the area of the peak profile is proportional to the number of atoms in the excitation region. Figure 6 shows a plot of this area as a function of delay. We see that the population decays with a time constant of 900 μs, as given by an exponential fit to the data (solid line). Note that this measurement was done with beams that have 150 μm diameter, while in the correlation measurements described later we use beams with 60 μm diameter, leading to a diffusion time of the order of 360 μs.

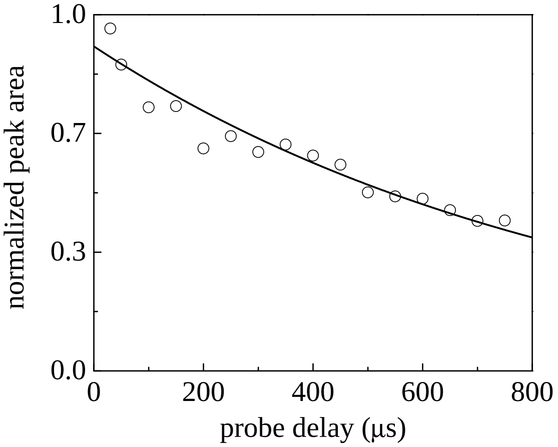

FIG. 6: Diffusion of atoms out of the excitation region. The solid line is an exponential fit with a time constant of 900 μs. The Raman beam diameter is 150 μm.

B. Nonclassical correlations

In order to characterize the coherence time of the system for various quantum information applications, e.g. for the DLCZ protocol or for generation of conditional single photons, the measurements must be performed at the single-photon level. In particular, one must know how long a single excitation can be stored in the quantum memory. For this purpose, we perform correlation measurements between fields 1 and 2 as a function of the time delay Δt between write and read pulses, thereby probing how the nonclassical character of these correlations (and hence of the correlations between field 1 and the collective atomic excitations) is preserved during the storage process.

In order to investigate the quantum nature of the correlations, we use the fact that there exists a well-defined border between the classical and quantum domains for fields 1 and 2 that can be operationally accessed via coincidence detection, as was first demonstrated in the pioneering work by Clauser [32]. In this way, we measure the joint detection probability p_{12} for detecting a photon in both fields 1 and 2 in the same trial, and the probabilities p_1 and p_2 to register a single detection event in field 1 and field 2, respectively. By splitting field i with a 50-50 beamsplitter and directing the output to the two detectors, the joint probabilities p_{ii} are also measured, where $i = 1$ or 2. Fields for which the Glauber-Sudarshan phase-space function is well-behaved (i.e., classical fields) are constrained by a Cauchy-Schwarz inequality for the various probabilities [32, 33], namely:

$$R = \frac{[g_{12}(t)]^2}{g_{11}\, g_{22}} \leq 1\,, \tag{40}$$

where $g_{11} \equiv p_{11}/p_1^2$, $g_{22} \equiv p_{22}/p_2^2$, $g_{12}(t) \equiv p_{12}/(p_1 p_2)$, and t denotes the time separation between the detection of photons 1 and 2. In our system, $g_{11} = g_{22} = 2$ in the ideal case. However, in practice, g_{11} and g_{22} are measured to be smaller than 2, due to various experimental imperfections. Hence in our case measuring $g_{12} > 2$ heralds nonclassical correlations, and in the following we will use this quantity as another figure of merit to quantify the loss of coherence in the quantum memory.

The experimental setup used to measure nonclassical correlations between fields 1 and 2 is shown in Fig. 7. As already mentioned the sample consists in a cold atomic ensemble of Cesium atoms in a magneto-optical trap. Each trial consists of a period of cooling and trapping, and of a period of measurement during which all the beams responsible for cooling and trapping the atoms are switched off. During the measurement period, the atoms are initially prepared in level $|g\rangle$ (F=4) by optical pumping with a laser beam resonant with the transition $6S_{1/2}(F = 3) \rightarrow 6P_{3/2}(F' = 4)$.

A laser pulse with 150 ns duration from the write beam then illuminates the sample. The write beam is tuned near the $|g\rangle \rightarrow |a\rangle$ (corresponding to $F = 4 \rightarrow F' = 4$ of the D_2 line, at 852 nm) and induces spontaneous Raman scattering to the initially empty level $|s\rangle$ ($F = 3$). The intensity of the pulse is made sufficiently weak, such that the probability of creating more than one excitation in the symmetric collective mode is very low. After a variable delay Δt, the stored excitation is converted into a photon in field 2, by sending a read pulse tuned to the transition $|s\rangle \rightarrow |b\rangle$ (corresponding to $F = 3 \rightarrow F' = 4$ transition of the D_1 line, at 894 nm). The write and read beams are orthogonally polarized and combined at the polarizing beam splitter PBS 1 (see Fig. 7). At PBS 1, the write and read beams are spatially mode-matched with a measured overlap of about 93%. The beams are focussed to a waist of about $30\mu m$ in the sample region.

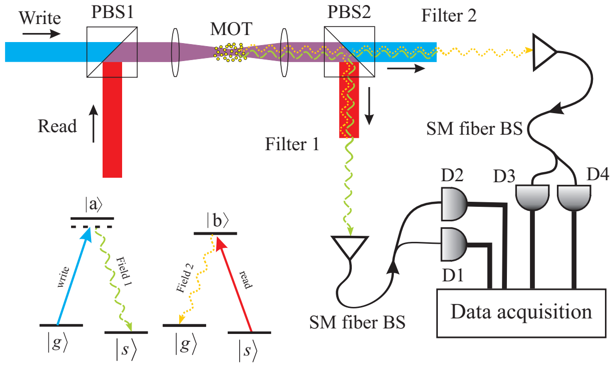

FIG. 7: Experimental setup. Write and read pulses propagate sequentially into a cloud of cold Cs atoms (MOT), generating pairs of correlated output photons 1 and 2. The write and read pulses have orthogonal polarizations, are combined at polarizing beam splitter PBS1, and then focused in the Cs MOT with a waist of approximately 30 μm. The output fields are split by PBS2, which also serves as a first stage of filtering the (write, read) beams from the (1,2) fields. For example, field 2 is transmitted by PBS2 to be subsequently registered by detector D3 or D4 while the read pulse itself is reflected at PBS2. Further filtering is achieved by passing each of the outputs from PBS2 through separate frequency filters. SM stands for single mode.

After the MOT, fields 1 and 2 are detected at the two different outputs of PBS 2. A challenging aspect of the experiment is to separate the classical pulses from the weak nonclassical fields, since they are temporally and spatially overlapped, and their frequencies are only 9 GHz apart. This is done in several steps, which are explained in detail in Refs. [11], [14], and [17]. After the filters, fields 1 and 2 are coupled into optical fibers, split by 50/50 fiber beam splitters, and detected by four single-photon Silicon avalanche photodiodes (APD). Finally, the electronic signals of the APDs are sent to a data acquisition card, in order to record the detection events and analyze the correlations.

1. *Coherence time measurements*

In order to characterize the system's coherence time, we measure g_{12} and R as a function of the delay Δt between write and read pulses. We then compare the theoretical quantity $\tilde{p}_{12}(\Delta t) = \xi p_{12}^{th}(\Delta t)$ to the measured $g_{12}(\Delta t)$ by way of a single overall scaling parameter ξ for all Δt, as the rate of single counts in fields 1 and 2 (p_1 and p_2) is measured not to depend on Δt, to within 20%. In Fig. 8a we show our results for g_{12} with the

MOT magnetic field on together with the corresponding theoretical fitting. This figure was presented already in a previous article [17] and shows a fast decay of the coherence between fields 1 and 2, taking place in a time scale of less than 200 ns. Note, however, that the coherence time is actually smaller than 100 ns, since the write pulse itself has a duration of 150 ns. The repetition rate of the trials in this case is 250 kHz. The rate of coincidence events (detection of photon 1 and photon 2 within the same trial) is between 2 and 3 counts per second.

The theoretical joint probability p_{12}^{th} is calculated from Eq. (30), assuming $C = 1$. In this way, we need to perform integrals of the F function over the z coordinate. This function depends on z only through the parameters a_g and a_s. The atomic ensemble is assumed to be initially unpolarized, i.e., with the atoms evenly distributed among all Zeeman states of the $|g\rangle$ level. For the ground states of Cesium, we have that the hyperfine Landé factors g_g and g_s of levels $|g\rangle$ and $|s\rangle$, respectively, are given by $\mu_B g_g/h = -\mu_B g_s/h = 0.35\,\text{MHz/G}$, so that we can write

$$a_g = 2\pi K m_g \left(\frac{z}{L}\right) , \tag{41a}$$

$$a_s = -2\pi K m_s \left(\frac{z}{L}\right) , \tag{41b}$$

where we considered the magnetic field for the MOT in the form $B_z = bz$, with b the field gradient in the center of the MOT, and the constant K given by

$$K = \frac{\mu_B g_g b L}{h} . \tag{42}$$

The value of Km_F gives an estimate for the inhomogeneous broadening associated with level $|F, m_F\rangle$ due to the magnetic-field gradient b. Note that writing a_g and a_s as in Eqs. (41) allows us to perform all spatial integrations over the dimensionless coordinate $s = z/L$, and to combine many of the relevant experimental parameters in a single parameter (K). For our experiment, $L = 3.6$ mm and $b = 8.7$ G/cm, so that $K = 1.1$ MHz. This K value is consistent with the measurement of the ground-state broadening shown in Fig. 4a.

The solid curve in Fig. 8a shows the theoretical fitting of $\tilde{p}_{12}(\Delta t)$ to the experimental data. We considered $K = 1.1$ MHz in the theory, as estimated above for our experimental conditions. The only fitting parameter used was ξ, which was found to be $\xi = 1.05 \times 10^8$. Note that the theoretical quantity p_{12}^{th} gives the probability for joint detection of the two photons, while g_{12} is a measure of this joint probability normalized by the probability of uncorrelated coincidence detections. Thus the scaling factor ξ should be given roughly by the inverse of the probability for these uncorrelated coincidences. A theoretical estimation for this value is given by $\xi^{th} = [p_{12}^{th}(\Delta t \to \infty)]^{-1}$, i.e., the inverse of the theoretical joint probability after the coherence has completely decayed. For the solid curve in Fig. 8a, we find $\xi^{th} = 1.96 \times 10^8$. The difference between ξ and ξ^{th} can be attributed to other sources of uncorrelated coincidences (such as dark counts in the detectors, or leakage from the filters) that are not accounted by the theory, which leads to $\xi < \xi^{th}$. It is also important to have in mind that the noise floor is higher when the pulses are overlapping, since there is more leakage from the filters in this condition. This results in some extra discrepancy when comparing theory to experiment by means of one single scaling parameter to all regions of Fig. 8a.

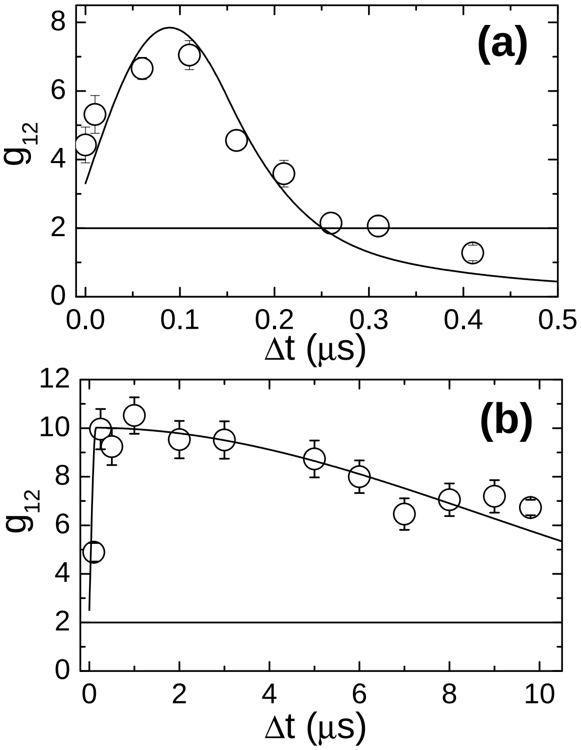

FIG. 8: Measurement of g_{12} as a function of the storage time, (a) with the quadrupole field on (taken from [17]) and (b) with the quadrupole field off. The observed decay in (b) is consistent with the residual magnetic field in the chamber, as measured by Raman spectroscopy.

The $g_{12}(\Delta t)$ measurements with magnetic field off are presented in Fig. 8b. In this case, we use the information acquired from the investigation of Sec. III A and turn off the field for a duration of 5.5 ms, at 40 Hz repetition rate. From the magnetic-field-off period, we use for correlation measurements only the 2.5 ms window shown in Fig. 5. This 2.5 ms window is then divided in 208 trial periods of 12 μs, which results in an overall repetition rate of 8.3 kHz. In the beginning of each trial, the trap light of the MOT (tuned in the $F = 4$ to $F' = 5$ transition of the D_2 line) is turned on for 0.6 μs, and its repumper laser (tuned from $F = 3$ to $F' = 4$) for 1 μs. This procedure prepares the system in the proper initial state, with all atoms at the $F = 4$ hyperfine level of the ground state. In this case, the rate of coincidence counts drops to about 0.33 coincidences/s.

Figure 8b shows then an increase of more than two orders of magnitude on the coherence time of the system, when the magnetic field is turned off. The coherence time is now limited mainly by the rate at which we can turn off the magnetic field, and also to some extent by our ability to magnetically isolate the system. Note that in Fig. 5a the Raman-trace linewidth indicates that the magnetic field in the measurement window is still decaying. The solid curve in Fig. 8b gives the decay theoretically expected for a magnetic-field gradient such that $K = 12$ kHz, corresponding to magnetic fields of the order or smaller than 30 mG acting on the ensemble. This gives a reasonable approximation to the behavior of g_{12} under the action of the residual magnetic field, even though the spatial dependence of this field can be more complicated than a simple linear gradient. The change in K from 1.1 MHz to 12 kHz is consistent with the reduction of the ground state linewidth between the two cases, as measured directly by the Raman spectroscopy setup. Finally, for Fig. 8b $\xi = 0.67 \times 10^8$ and $\xi^{th} = 2.2 \times 10^8$.

From Fig. 8.b, we see that the correlations are still highly nonclassical after a storage time of 10 μs. However, from the theoretical fitting we can infer that g_{12} should became smaller than 2 at about 25 μs, which gives an estimation for our quantum memory time.

As discussed above, the measurements with $g_{12} > 2$ give a strong indication of the nonclassical correlations observed in our system, based on reasonable assumptions for g_{11} and g_{22}. The most appropriate verification of the nonclassical nature of fields 1 and 2, however, is given by the measurement of R as defined in Eq. (40). Such measurements with the magnetic field off are shown in Fig. 9. More specifically, in Fig. 9a we show the measurements of g_{11} and g_{22} for the same data points of Fig. 8b. Substituting the results of Figs. 8b and 9a in (40), we then obtain the values of R shown in Fig. 9b, which confirm the strong nonclassical correlation present in our system for more than 10 μs.

The R measurement presents considerably larger error bars than for g_{12}. This comes from the large statistical uncertainties involved in the determination of g_{22}, which requires measurement of the two-photon component of field 2 [14]. For this reason, we decided to carry out a much longer run of the experiment for the longest coherence time we were able to probe, 10 μs, which resulted in the considerably smaller statistical error of this point.

2. *Two-photon wavepackets*

Central to the DLCZ protocol is the ability to write and read collective spin excitations into and out of an atomic ensemble, with efficient conversion of discrete spin excitations to single-photon wavepackets. A critical aspect of such wave packets is that they are emitted into well defined spatiotemporal modes to enable quantum interference between emissions from separate ensembles (e.g., for entanglement based quantum cryptography [5]).

The high efficiencies achieved in the work of Ref. 14 enabled us to investigate in detail the temporal properties of the nonclassical correlations between emitted photon pairs [17], providing a direct look at various important features of the two-photon wavepacket (field 1 + field 2) generated by the system. In the following analysis, our main quantity of interest is $p_\tau(t_1, t_2)$, the joint probability for photoelectric detection of photon 1 at time t_1 and photon 2 at time t_2 within a time window of duration τ. The times for this quantity are counted starting from the beginning of the write pulse. This quantities is determined from the record of time-stamped detections on all four photodetectors. The detectors have a time resolution of 2 ns (minimum bin size), but usually we need to consider larger bins to acquire enough events for the statistics.

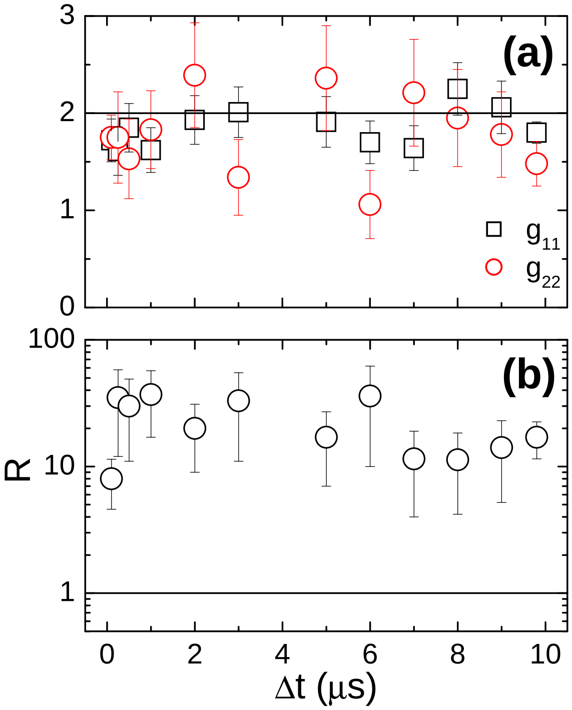

FIG. 9: (a) Measurement of g_{11} (open squares) and g_{22} (open circles) as a function of the storage time. (b) Measurement of the coefficient R as a function of the storage time. The big statistical errors are mainly due to statistical uncertainties in the measurement of g_{11} and g_{22}. The points at 10μs have been measured for a much longer time and exhibit smaller statistical error.

In our earlier experiments [17], we focused on two cases: (I) nearly simultaneous application of write and read pulses with offset $\Delta t = 50$ ns shorter than the duration of either pulse, and (II) consecutive (non overlapping) application of write and read pulses with $\Delta t = 200$ ns. Results for $p_\tau(t_1, t_2)$ are presented in Fig. 10. In case (I), Fig. 10a shows that $p_\tau(t_1, t_2)$ peaks along the line $t_2 - t_1 = \delta t_{12} \simeq 50$ ns with a width $\Delta t_{12} \simeq 60$ ns, in correspondence to the delay δt_{12} and duration Δt_{12} for read-out associated with the transition $|s\rangle \rightarrow |b\rangle \rightarrow |g\rangle$ given an initial transition $|g\rangle \rightarrow |a\rangle \rightarrow |s\rangle$ [12]. In case (II) with the read pulse launched 200 ns after the write pulse, the excitation is "stored" in the atomic ensemble until the readout. The production of correlated photon pairs should now be distributed along $t_2 \simeq \Delta t + \delta t_{12}$ with width $\simeq \Delta t_{12}$. Instead, as shown in Fig. 10c, $p_\tau(t_1, t_2)$ peaks towards the end of the write pulse (i.e., $t_1 \gtrsim 100$ ns), and near the beginning of the read pulse (i.e., $200 \lesssim t_2 \lesssim 300$ ns). Early events for field 1 lead to fewer correlated events for field 2, as $p_\tau(t_1, t_2)$ decays rapidly beyond the line $t_2 - t_1 = \tau_d \simeq 175$ ns. The marked contrast between $p_\tau(t_1, t_2)$ for $\Delta t = 50$ and 200 ns results in a diminished ability for the conditional generation of single photons from excitation stored within the atomic ensemble [14] and, more generally, for the implementation of the DLCZ protocol for increasing Δt. The underlying mechanism is again decoherence within the ensemble.

By contrast, when the magnetic field is turned off, this distortion in the two-photon wavepacket is eliminated due to the extended coherence time. We now observe the shape shown in Fig. 10e. The delay in Fig. 10e is $\Delta t = 1\ \mu$s.

The theoretical results corresponding to these three situations are shown in frames (b), (d), and (f) of Fig. 10. These are plots of Eq. (39) averaged over 4 ns time windows for both t_2 and t_1, the same time window used for the experimental data. We also considered pulses of trapezoidal shape, with 20 ns rising time, and FWHM of 150 ns for the write pulse and 120 ns for the read pulse. These values correspond to the experimental parameters. The only effect of both the time window and pulse rising time is to smooth the edges of the distribution. Differently from the case of integrated probabilities, it is necessary here to introduce more details in the description of the pulse shapes, since the theoretical description for this signal predicts that it is directly related to the pulse profiles [see Eq. (36)].

The main point that calls our attention in these figures is the fact that the theory offers a reasonable explanation for the data from consecutive pulses ($\Delta t = 200$ ns) with magnetic field on, but not for overlapping pulses or $\Delta t = 1\ \mu$s with magnetic field off. This discrepancy can be simply understood, however, if we remember that one of the main approximations of our theory is to consider low intensities for both write and read pulses. At low intensities and zero magnetic field, the theory gives a small and constant probability for the photon 2 emission after photon 1. From Eq. (36), we see that the magnetic field introduces different phases for different groups of atoms. These different phases are proportional to the time difference between the emission of photons 2 and 1, and result in an overall decay of the probability of emission of the second photon over time. In Figs. 10b and 10f, however, we see that the predicted decay time is much longer than the one inferred from the experimental data.

On the other hand, for the actual experiment, the high intensity of the read pulse should lead to a fast emission of photon 2 once the atom is transferred to level F_s. This is consistent with the short duration of correlation $\Delta t_{1,2}$ in Figs. 10a and 10e, which can be understood as coming from the fast depletion of the F_s state. However, this reasoning cannot explain the shape of Fig. 10c, since the strong excitation alone should result in a similar fast depletion in the beginning of the read pulse for any detection time of photon 1 (as seen in Fig. 10e). The good comparison between Figs. 10c and 10d comes from the fact that the decay due to the magnetic field takes place before the delayed readout process occurs. The shape in Fig. 10c is then a convolution of a uniform excitation probability over t_1 (like in Fig. 10e) with the excitation-probability distribution of 10d.

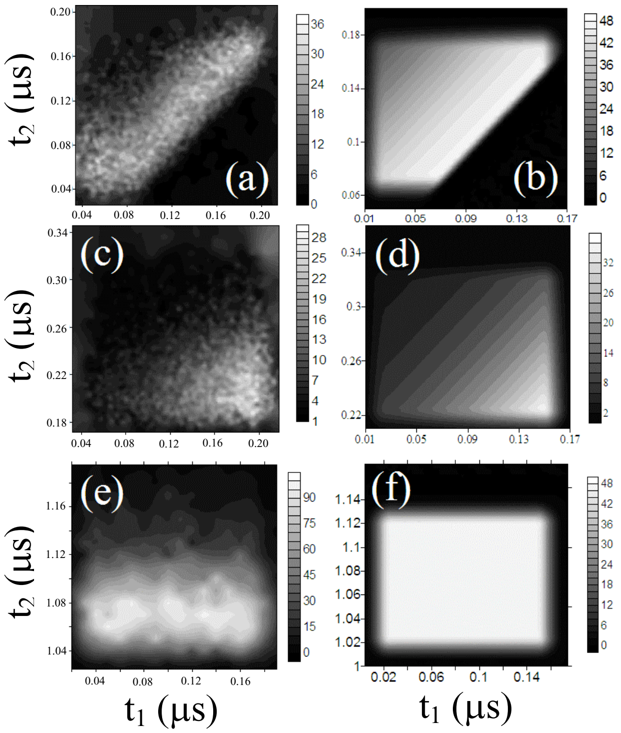

FIG. 10: Theory and experiment for two-photon wavepackets $P_\tau(t_1, t_2)$. (a) Measured two-photon wavepackets for the case where write and read pulses are overlaped with a delay of 50 ns, with the quadrupole magnetic field on. (b) Theoretical predictions for the same conditions as in (a). (c) Measured two-photon wavepackets for the case of consecutive (non overlapping) write and read puses with a delay of 200 ns, with quadrupole field on. (d) Theoretical predictions for the same conditions as in (c). (e) Measured two-photon wavepackets for nonoverlapping write and read pulses, with quadrupole field off. The delay between write and read pulses is 1 μs. (f) Theoretical predictions for the same conditions as in (e). The vertical scales are given in arbitrary units proportional to the joint probability of detecting photons 1 and 2. See text for further details.

IV. OPTICAL PUMPING

The theory developed to explain the data in Fig. 8 can also be used to devise new ways to improve the system. The inclusion of the Zeeman structure in the theory, for example, allows the study of different polarization schemes for both classical excitation and photon detection. It also allows the investigation of the role of the atomic initial state on the measured correlations. In Fig. 11 we give two examples of possible ways to improve the system. The solid and dashed lines in the figure represent the two experimental conditions of Fig. 8 (initially unpolarized samples with $K = 1.1$ MHz and $K = 12$ kHz), but now with the same scaling factor. The dash-dotted curve shows how the $K = 12$ kHz curve changes if the system is initially spin polarized, with all atoms in the $|F = 4, m_F = 0\rangle$ state. Note that in this case the value of $\tilde{p}_{1,2}$ considerably increases, and the system develops a plateau coming from the predominant transition $|F = 4, m_F = 0\rangle \to |F = 3, m_F = 0\rangle \to |F = 4, m_F = 0\rangle$, which is magnetic-field insensitive. Furthermore, it is possible to devise a polarization scheme of excitation that allows only this specific transition for any Δt, e.g. as when the write pulse and field-1 detection are σ^+ polarized, and the read pulse and field-2 detection are σ^-. This is the case for the dotted curve in Fig. 11.

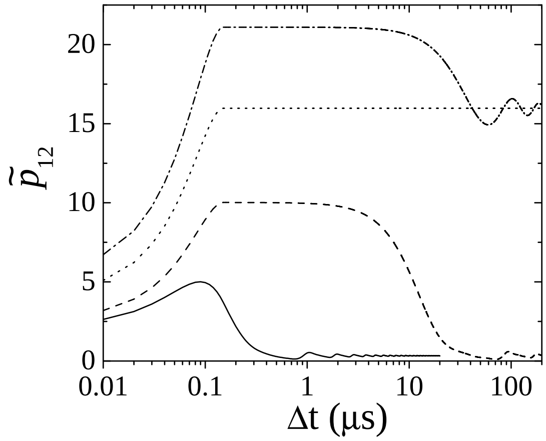

FIG. 11: Variation of $\tilde{p}_{1,2}$ with the delay Δt between write and read pulses for (solid curve) $K = 1.1$ MHz and an unpolarized sample, (dashed curve) $K = 12$ kHz and an unpolarized sample, and (dash-dotted curve) $K = 12$ kHz and an initially spin polarized sample with all atoms in $|F = 4, m_F = 0\rangle$. The dotted curve corresponds to an initially spin polarized sample classically excited by fields with polarizations such that only a magnetic insensitive transition is allowed, see text for details. The same arbitrary scaling factor was used for all curves.

The idealized improvements described by the dotted and dash-dotted curves of Fig. 11, however, will probably be limited by two effects which are not taken into account by the theory. First, in our experimental setup we should see a decay with a timescale on the order of 360 μs due to the average time the cold atoms take to cross the 60 μm beam diameter of the classical write and read pulses. Second, the theory assumes the presence of a magnetic field predominantly in the z direction, which defines the quantization axis. This can be obtained by applying an extra DC magnetic field along that direction,[34, 35] but any residual transverse field should lead to some decay of the plateau. In spite of these restrictions, however, we believe that such improvements could lead to an increase of more than an order of magnitude over the largest experimental decoherence time of Fig. 8. It is also clear that there is a benefit in the careful preparation of the initial state for the magnitude of the measured correlations. This is an important point that should also be taken into account when considering the implementation of the DLCZ protocol in vapor cells.

V. CONCLUSION

We have presented a detailed study of the decoherence processes in the generation of photon pairs from atomic ensembles, via the DLCZ protocol of ref. [5]. We have identified the main cause of decoherence for cold atoms in magneto-optical traps as being the inhomogeneous broadening of the hyperfine ground states due to the quadrupole magnetic field used to trap the atoms. A detailed theory has been developed to model this effect. We also reported a series of measurement to characterize and control the decoherence using copropagating stimulated Raman scattering. These measurement allowed us to switch off the quadrupole magnetic field in a controlled way. With the magnetic field off, we observed highly nonclassical correlations between the two emitted photons, for a storage time of up to 10 μs, an improvement of more than two orders of magnitude compared to previous results with cold atoms. Furthermore, contrary to all related experiments reported up to now, the coherence time is now two orders of magnitude larger than the excitation pulses duration. This is a crucial step in order to use atomic ensembles as a quantum memory to store conditional single photon states or entanglement between two distant ensembles.

Acknowledgments

This work is supported by ARDA, by the Caltech MURI Center for Quantum Networks, and by the NSF. D.F. acknowledges financial support by CNPq (Brazilian agency). H.d.R. aknowledges financial support by the Swiss National Science Foundation.

[1] *The Physics of Quantum Information*, D. Bouwmeester, A. Ekert, and A. Zeilinger (Springer-Verlag, Berlin, Germany, 2001).

[2] *Quantum Computation and Quantum Information*, M. A. Nielsen and I. L. Chuang (Cambridge University Press, Cambridge, United Kingdon, 2003).

[3] H.-J. Briegel, W. Dür, J.I. Cirac, and P. Zoller, Phys. Rev. Lett. **81**, 5932 (1998).

[4] W. Dür, H.-J. Briegel, J.I. Cirac, and P. Zoller, Phys. Rev. A **59**, 169 (1999).

[5] L.-M. Duan, M.D. Lukin, J.I. Cirac, and P. Zoller, Nature **414**, 413 (2001).

[6] L.-M. Duan, J.I. Cirac, and P. Zoller, Phys. Rev. A **66**, 023818 (2002).

[7] C. Cabrillo, J. I. Cirac, P. Garcı́a-Fernández, and P. Zoller, Phys. Rev. A **59**, 1025 (1999).

[8] C.H. Bennett, G. Brassard, C. Crépeau, R. Jozsa, A. Peres, and W.K. Wootters, Phys. Rev. Lett. **70**, 1895 (1993).

[9] M. Zukowski, A. Zeilinger, M.A. Horne, and A.K. Ekert, Phys. Rev. Lett. **71**, 4287 (1993).

[10] A. Ekert, Phys. Rev. Lett. **67**, 661 (1991).

[11] A. Kuzmich, W.P. Bowen, A.D. Boozer, A. Boca, C.W. Chou, L.-M. Duan, and H.J. Kimble, Nature **423**, 731 (2003).

[12] C.H. van der Wal, M.D. Eisaman, A. André, R.L. Walsworth, D.F. Phillips, A.S. Zibrov, and M.D. Lukin, Science **301**, 196 (2003).

[13] W. Jiang, C. Han, P. Xue, L.-M. Duan, and G.-C. Guo, Phys. Rev. A **69**, 043819 (2004).

[14] C.W. Chou, S.V. Polyakov, A. Kuzmich, and H.J. Kimble, Phys. Rev. Lett. **92**, 213601 (2004).

[15] M.D. Eisaman, L. Childress, A. André, F. Massou, A.S. Zibrov, and M.D. Lukin, Phys. Rev. Lett. **93**, 233602 (2004).

[16] D. N. Matsukevich and A. Kuzmich, Science **306**, 663 (2004).

[17] S.V. Polyakov, C.W. Chou, D. Felinto, and H.J. Kimble, Phys. Rev. Lett. **93**, 263601 (2004).

[18] V. Balic, D.A. Braje, P. Kolchin, G.Y. Yin, and S.E. Harris, Phys. Rev. Lett. **94**, 183601 (2005).

[19] M. A. Bouchiat and J. Brossel, Phys. Rev. **147**, 41 (1966).

[20] E. B. Alexandrov, M. V. Balabas, D. Budker, D. English, D. F. Kimball, C.-H. Li, and V. V. Yashchuk, Phys. Rev. A **66**, 042903 (2002).

[21] B. Julsgaard, J. Sherson, J. I. Cirac, J. Fiurášek, and E. S. Polzik, Nature 432, 482 (2004).

[22] B. Julsgaard, J. Sherson, J. L. Sorensen, and E. S. Polzik, J. Opt. B: Quantum Semiclass. Opt. **6**, 5 (2004).

[23] S. Kuhr, W. Alt, D. Schrader, I. Dotsenko, Y. Miroshnychenko, W. Rosenfeld, M. Khudaverdyan, V. Gomer, A. Rauschenbeutel, and D. Meschede, Phys. Rev. Lett. **91**, 213002 (2003).

[24] M. F. Andersen, A. Kaplan, T. Grünzweig, and N. Davidson, Phys. Rev. A **70**, 013405 (2004).

[25] M.D. Lukin, Rev. Mod. Phys. **75**, 457 (2003).

[26] D.A. Braje, V. Balić, S. Goda, G.Y. Yin, and S.E. Harris, Phys. Rev. Lett. **93**, 183601 (2004).

[27] S. van Enk, private communication.

[28] Equation (34) can also be deduced in a more formal way, beginning by considering that the probability amplitude for detecting photon 2 between t_2 and $t_2 + \Delta t_2$ is given by $\phi(t_2 + \Delta t_2) - \phi(t_2)$, then following all the way down by similar restrictions, and finally making the approximation of small time intervals.

[29] J. Ringot, P. Szriftgiser, and J.C. Garreau, Phys. Rev. A **65**, 013403 (2001).

[30] C. J. Dedman, K. G. H. Baldwin, and M. Colla, Rev. Sci. Instr. **72**, 4055 (2001).

[31] C. L. Garrido Alzar, P. G. Petrov, D. Oblak, J. H. Müller, and E. S. Polzik, submitted to publication.

[32] J.F. Clauser, Phys. Rev. D **9**, 853 (1974).

[33] *Optical Coherence and Quantum Optics*, L. Mandel and E. Wolf (Cambridge Univ. Press, Cambridge, UK, 1995).

[34] G. Avila, V. Giordano, V. Candelier, E. de Clercq, G. Theobald, and P. Cerez, Phys. Rev. A **36**, 3719 (1987).

[35] S.-I. Ohshima, Y. Nakadan, and Y. Koga, IEEE Trans. Instrum. Meas. **37**, 409 (1988).

nature

Vol 438|8 December 2005|doi:10.1038/nature04353

LETTERS

Measurement-induced entanglement for excitation stored in remote atomic ensembles

C. W. Chou[1], H. de Riedmatten[1], D. Felinto[1], S. V. Polyakov[1], S. J. van Enk[2] & H. J. Kimble[1]

A critical requirement for diverse applications in quantum information science is the capability to disseminate quantum resources over complex quantum networks[1,2]. For example, the coherent distribution of entangled quantum states together with quantum memory (for storing the states) can enable scalable architectures for quantum computation[3], communication[4] and metrology[5]. Here we report observations of entanglement between two atomic ensembles located in distinct, spatially separated set-ups. Quantum interference in the detection of a photon emitted by one of the samples projects the otherwise independent ensembles into an entangled state with one joint excitation stored remotely in 10^5 atoms at each site[6]. After a programmable delay, we confirm entanglement by mapping the state of the atoms to optical fields and measuring mutual coherences and photon statistics for these fields. We thereby determine a quantitative lower bound for the entanglement of the joint state of the ensembles. Our observations represent significant progress in the ability to distribute and store entangled quantum states.

Entanglement is a uniquely quantum mechanical property of the correlations among various components of a physical system. Initial demonstrations of entanglement were made for photon pairs from the fluorescence in atomic cascades[7,8] and from parametric down-conversion[9]. More recently, entanglement has been recognized as a critical resource for accomplishing tasks that are otherwise impossible in the classical domain[1]. Spectacular advances have been made in the generation of quantum entanglement for diverse physical systems[1,2], including entanglement stored for many seconds in trapped ions for distances on the millimetre scale[10,11], long-lived entanglement of macroscopic quantum spins persisting for milliseconds on the centimetre scale[12], and remote entanglement carried by photon pairs over distances of tens of kilometres of optical fibres[13].

For applications in quantum information science, entanglement can be created deterministically by precisely controlling quantum dynamics for a physical system, or probabilistically by quantum interference in a suitable measurement with random instances of success. In the latter case, it is essential that success be heralded unambiguously so that the resulting entangled state is available for subsequent use. In either case, quantum memory is required to store the entangled states until they are required for the protocol at hand.

There are by now several examples of entanglement generated 'on demand'[1], beginning with the realization of the Einstein–Podolsky–Rosen (EPR) paradox for continuous quantum variables[14] and the deterministic entanglement of the discrete internal states of two trapped ions[15]. Important progress has been made towards measurement-induced entanglement on various fronts, including the observation of entanglement between a trapped ion and a photon (ref. 16 and references therein).

Here, we report the initial observation of entanglement created probabilistically from quantum interference in the measurement process, with the resulting entangled state heralded unambiguously and stored in quantum memory for subsequent use. As illustrated in Fig. 1, the detection of a photon from either of two atomic ensembles (L, R) in an indistinguishable fashion results in an entangled state with one 'spin' excitation shared at a distance of 2.8 m between the ensembles and distributed symmetrically among $\sim 10^5$ atoms at each site[6]. Confirmation of entanglement is achieved by mapping this stored excitation onto light fields after 1-μs delay[6,17] and by suitable measurements of the quantum statistics of the resulting optical fields. Our results provide the first realization of the capability to transfer a stored entangled state of matter to an entangled state of light.

Our experiment is motivated by the protocol of Duan, Lukin, Cirac and Zoller (DLCZ)[6] for the realization of scalable quantum communication networks with atomic ensembles. The DLCZ protocol introduced a number of ideas for quantum information processing and is the subject of active investigation. In this direction, nonclassical correlations[17–24] and entanglement[25] have been observed between pairs of photons emitted by a single atomic ensemble. Observations of coherence between two cylindrical volumes of cold rubidium atoms within a single magneto-optical trap have also been reported[26], although entanglement was not demonstrated between the two regions[27,28].

A simple schematic of our experiment is given in Fig. 1, with further details provided in refs 17, 21 and 23. For the writing stage of the protocol, two classical pulses traverse the L and R ensembles in parallel and generate fields 1_L, 1_R by spontaneous Raman scattering (see Fig. 1a). The intensity of the pulses is made sufficiently weak that the probability of creating more than one excitation in the symmetric collective mode[6] of the ensemble is very low[21].

Entanglement between the L and R ensembles is created by combining the output fields 1_L, 1_R on the beamsplitter BS_1, with outputs directed to two photodetectors D_{1a}, D_{1b} (see Fig. 1a). For small excitation probability and with unit overlap of the fields at BS_1, a detection event at D_{1a} or D_{1b} arises indistinguishably from either field 1_L or 1_R, so that the L and R ensembles are projected into an entangled state, which in the ideal case can be written as[6,29]:

$$|\Psi_{L,R}\rangle = \epsilon_L |1\rangle_L |0\rangle_R \pm e^{i\eta_1} \epsilon_R |0\rangle_L |1\rangle_R \quad (1)$$

where $|0\rangle_{L,R}$, $|1\rangle_{L,R}$ refers to the two ensembles L and R with 0 and 1 collective excitations respectively, ϵ_L (or ϵ_R) is the normalized amplitude of photon generation from ensemble L (or R), and the sign (+ or −) is set by whichever detector records the event. The phase $\eta_1 = \Delta\beta_w + \Delta\gamma_1$, where $\Delta\beta_w$ is the phase difference of the write beams at the L and R ensembles, and $\Delta\gamma_1$ is the phase

---

[1]Norman Bridge Laboratory of Physics 12-33, California Institute of Technology, Pasadena, California 91125, USA. [2]Bell Labs, Lucent Technologies, Room 1D-428, 600-700 Mountain Avenue, Murray Hill, New Jersey 07974, USA.

© 2005 Nature Publishing Group

difference acquired by the 1_L and 1_R fields in propagation from the ensembles to the beamsplitter BS_1. We note that to achieve entanglement as in equation (1), η_1 has to be kept constant from trial to trial.

To verify the entanglement, we map the delocalized atomic excitation into a field state by applying simultaneously strong read beams at the two ensembles (see Fig. 1b). If the state transfer were to succeed with unit probability, the conditional state $|\Psi_{L,R}\rangle$ of the ensembles would be mapped to an entangled state of two modes for the Stokes fields 2_L and 2_R given in the ideal case by[6,29]:

$$|\Phi_{LR}\rangle = \epsilon_L|1\rangle_{2_L}|0\rangle_{2_R} \pm e^{i(\eta_1+\eta_2)}\epsilon_R|0\rangle_{2_L}|1\rangle_{2_R} \qquad (2)$$

where $|0\rangle_{2_L,2_R}, |1\rangle_{2_L,2_R}$ refer to the Raman fields 2_L, 2_R with 0, 1 photons, respectively. Here, $\eta_2 = \Delta\beta_r + \Delta\gamma_2$, where $\Delta\beta_r$ is the phase difference of the read beams at the L and R ensembles, and $\Delta\gamma_2$ is the phase difference acquired by the 2_L and 2_R fields in propagation from the ensembles to the beamsplitter BS_2 in Fig. 1b. In our experiment, the phases η_1 and η_2 can be independently controlled and are actively stabilized by utilizing auxiliary fields at 1.06 μm that co-propagate along the paths of the write and read beams and of the 1_L, 1_R and 2_L, 2_R fields.

Of course, the states in equations (1) and (2) are idealizations that must be generalized to describe our actual experiment[6,27,29]. Specifically, the presence of various sources of noise necessarily transforms these pure states into mixed states. Equations (1) and (2) also neglect the vacuum contribution as well as higher-order terms, which are intrinsic to DLCZ protocol and which otherwise arise from diverse experimental imperfections. Moreover, the above analysis assumes that all excitations are in the correct 'modes' (both for optical fields and for the collective atomic 'spin flips'), that excitations of the ensembles map one-to-one to photons in fields 1 and 2, and that diverse sources of background light are absent.

The procedure that we have devised to provide a robust, model-independent determination of entanglement is based upon quantum tomography of the 2_L and 2_R fields (see Supplementary Information for details). Because entanglement cannot be increased by local operations on either of the two ensembles, the entanglement for the state of the ensembles will be always greater than or equal to that

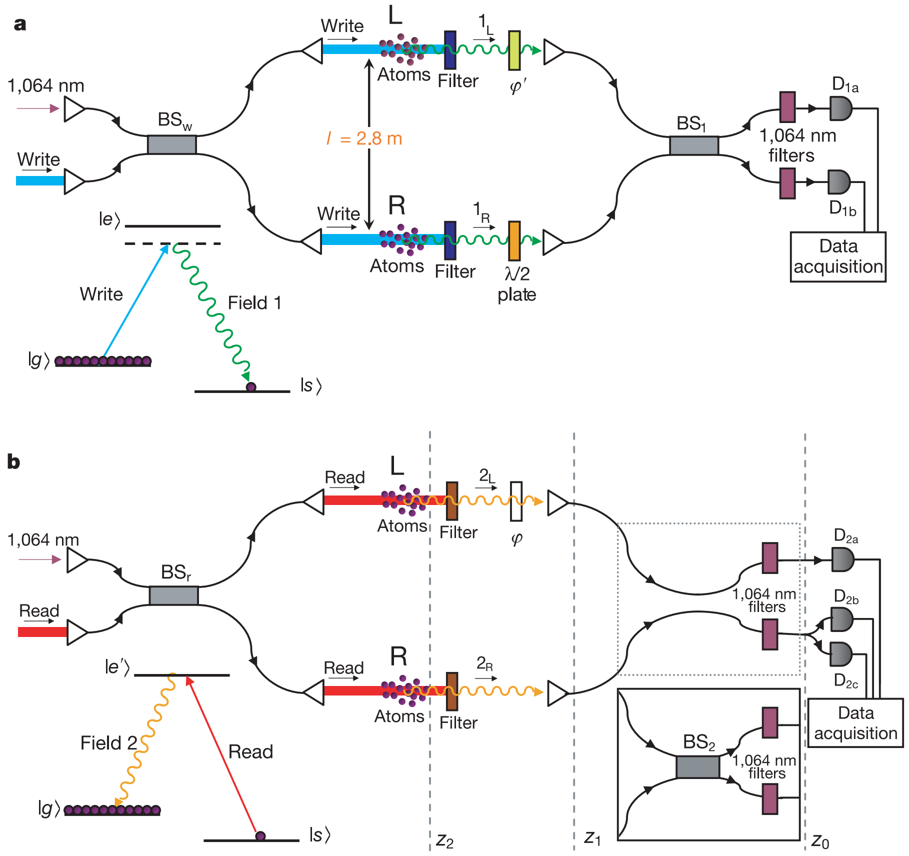

Figure 1 | An overview of our experiment to entangle two atomic ensembles is shown. **a**, Set-up for generating entanglement between two pencil-shaped ensembles L and R located within spherical clouds of cold caesium atoms. The atomic level structure for the writing process consists of the initial ground state $|g\rangle$ ($6S_{1/2}$, $F = 4$ level of atomic caesium), the ground state $|s\rangle$ for storing a collective spin flip ($6S_{1/2}$, $F = 3$ level), and the excited level $|e\rangle$ ($6P_{3/2}$, $F' = 4$). The transition $|g\rangle \rightarrow |e\rangle$ in each ensemble is initially coupled by a write pulse detuned from resonance to generate the forward-scattered anti-Stokes field 1 from the transition $|e\rangle \rightarrow |s\rangle$. The L and R ensembles are excited by synchronized writing pulses obtained from beamsplitter BS_w. After filtering, the anti-Stokes fields 1_L and 1_R are collected, coupled to fibre-optic channels, and interfere at beamsplitter BS_1, with outputs directed towards two single-photon detectors D_{1a} and D_{1b}. **b**, Schematic for verification of entanglement between the L and R ensembles by conversion of atomic to field excitation by way of simultaneous read pulses obtained from BS_r. The read pulses reach the samples after a programmable delay from the write pulses, and couple the transition $|s\rangle \rightarrow |e'\rangle$ ($|e'\rangle$ being the $6P_{1/2}$, $F' = 4$ level), leading to the emission of the forward-scattered Stokes fields 2_L and 2_R from the transition $|e'\rangle \rightarrow |g\rangle$. The upper inset shows the configuration used to measure the diagonal elements p_{ij} of $\tilde{\rho}_{2_L,2_R}$ in equation (3) from the photo-detection events at D_{2a}, D_{2b} and D_{2c}. Reconfiguring the fibre connections, we can easily pass from the configuration of the upper inset to the one of the lower inset, which is used to generate interference of the 2_L and 2_R fields at beamsplitter BS_2 to measure the off-diagonal coherence d in $\tilde{\rho}_{2_L,2_R}$. In **a** and **b**, the incident write and read beams are orthogonally polarized and combined at a polarizing beamsplitter (not shown), and are focused to a waist of about 30 μm in the sample region. All beamsplitters BS are polarization-maintaining fibre beamsplitters. The ~12 m arms of both write and read interferometers are actively stabilized using an auxiliary Nd:YAG laser at 1.06 μm.

© 2005 Nature Publishing Group

measured for the state of the light fields. Specifically, conditioned upon a detection at D_{1a} or D_{1b}, we consider the density matrix:

$$\tilde{\rho}_{2_L,2_R} = \frac{1}{\tilde{P}} \begin{pmatrix} p_{00} & 0 & 0 & 0 \\ 0 & p_{01} & d & 0 \\ 0 & d^{\star} & p_{10} & 0 \\ 0 & 0 & 0 & p_{11} \end{pmatrix} \tag{3}$$

which is written in the basis $|n\rangle_{2_L}|m\rangle_{2_R}$, with the number of photons $\{n, m\} = \{0, 1\}$. p_{ij} is then the probability to find i photons in mode 2_L and j photons in mode 2_R, and d gives the coherence between the $|1\rangle_{2_L}|0\rangle_{2_R}$ and $|0\rangle_{2_L}|1\rangle_{2_R}$ states. $\tilde{\rho}_{2_L,2_R}$ is obtained from the full density matrix $\rho_{2_L,2_R}$ by restricting it to the subspace where there is at most one photon in each mode, with then $\tilde{P} = p_{00} + p_{01} + p_{10} + p_{11}$. The concurrence $C(\tilde{\rho}_{2_L,2_R})$ for $\tilde{\rho}_{2_L,2_R}$ provides a lower bound for the concurrence $C(\rho_{2_L,2_R})$ for $\rho_{2_L,2_R}$ $[C(\rho_{2_L,2_R}) \geq \tilde{P}C(\tilde{\rho}_{2_L,2_R})]$, so we devise measurements to deduce the various components of $\tilde{\rho}_{2_L,2_R}$. The concurrence $C(\tilde{\rho}_{2_L,2_R})$ can then be calculated from equation (3) by way of ref. 30:

$$\tilde{P}C = \max(2|d| - 2\sqrt{(p_{00}p_{11})}, 0) \tag{4}$$

The entanglement of formation E follows directly from C, where E and C both range from 0 to 1 for our system and E is a monotonically increasing function of C (ref. 30).

As a first step in the determination of C we measure the diagonal elements p_{ij}. As shown in Fig. 1b, the field-2 output of each ensemble is directed to different sets of detectors in order to record photon-counting probabilities for the fields 2_L, 2_R separately. From the record of photoelectric counting events, we then deduce the diagonal elements of $\tilde{\rho}_{2_L,2_R}$, which are listed in Table 1. From equation (4) and noting that $|d|^2 \leq p_{10}p_{01}$, a necessary requirement for $C > 0$ is that there be a suppression of two-photon events relative to the square of the probability for single-photon events for the fields 2_L, 2_R, that is: $h_c^{(2)} \equiv p_{11}/(p_{10}p_{01}) < 1$. For our measurements, we find $h_c^{(2)} = 0.30 \pm 0.04$ for events conditioned on detection at D_{1a}, and $h_c^{(2)} = 0.35 \pm 0.04$ for events conditioned on D_{1b} (ref. 21). In contrast, for non-conditioned events, we find $h_{nc}^{(2)} = 0.99 \pm 0.04$.

The second step in our tomography protocol is to determine the coherence term d in equation (3), which we accomplish by adding a relative phase shift φ for the fields 2_L, 2_R, and by combining them at the beamsplitter BS_2 shown in Fig. 1b. By recording the conditional count rate after the beam splitter as function of φ, we can measure an interference fringe with a visibility V, with $|d|$ then following from V and the p_{ij}. Roughly, for 50/50 beamsplitters and neglecting higher-order terms (that are employed in our actual analysis), we would have $|d| \cong V(p_{10} + p_{01})/2$.

Figure 2 shows conditional counts N_{2a}, $N_{2b} + N_{2c}$ as functions of φ. These data demonstrate that the indistinguishable character of measurement events at detectors D_{1a} (Fig. 2a) and D_{1b} (Fig. 2b) induces a high degree of coherence between the otherwise independent ensembles L, R (refs 6 and 26). Indeed, we deduce visibilities $V_{1a} = (70 \pm 2)\%$ and $V_{1b} = (71 \pm 2)\%$ for the associated conditional states.

Table 1 | Diagonal elements of the density matrix $\tilde{\rho}_{2_L,2_R}$, deduced from the records of photo-electric counts

Probability	D_{1a}	D_{1b}
p_{00}	0.98510 ± 0.00007	0.98501 ± 0.00007
p_{10}	$(7.38 \pm 0.05) \times 10^{-3}$	$(6.19 \pm 0.04) \times 10^{-3}$
p_{01}	$(7.51 \pm 0.05) \times 10^{-3}$	$(8.78 \pm 0.05) \times 10^{-3}$
p_{11}	$(1.7 \pm 0.2) \times 10^{-5}$	$(1.9 \pm 0.2) \times 10^{-5}$

The values of p_{ij} are referenced to the location of detectors $D_{2a,2b,2c}$, and were obtained by considering unit detection efficiency, which gives a more conservative (smaller) lower bound for the concurrence than the actual (larger) field concurrence for finite efficiency <1. See the Supplementary Information for further details, and equation (3).

A notable feature of these results is that the interference fringes have relative phase π for the cases of detection at D_{1a}, D_{1b}, in agreement with equations (1) and (2). We observe similar fringes if the phase η_1 between the write beams is varied instead of φ. Moreover, if the fields 1_L, 1_R are combined at the beamsplitter BS_1 with orthogonal polarizations (by way of the half-wave plate in Fig. 1a), we find that the visibility from interference of fields 2_L, 2_R drops to near zero, because in this case there is no longer measurement-induced entanglement associated with quantum interference for detection of fields 1_L, 1_R (see Supplementary Information).

With equation (4), the measured values for the visibility V and for the various p_{ij} are sufficient to deduce a lower bound for the concurrence C for the field state $\tilde{\rho}_{2_L,2_R}$ at the location of detectors $D_{2a,2b,2c}$. With no correction for detection efficiencies or propagation losses, and without subtraction of any background, we find:

$$\begin{aligned} C_{1a}(\tilde{\rho}_{2_L,2_R}) &= (2.4 \pm 0.6) \times 10^{-3} > 0, \\ C_{1b}(\tilde{\rho}_{2_L,2_R}) &= (1.9 \pm 0.6) \times 10^{-3} > 0 \end{aligned} \tag{5}$$

conditioned upon detection at either D_{1a} or D_{1b}. This conclusively demonstrates a non-zero degree of entanglement between the ensembles, albeit with the concurrence $C_{L,R}$ small. The small difference between the concurrence for the states conditioned on D_{1a} or D_{1b} can be explained by an asymmetry in BS_1 (see Supplementary Information).

Beyond the firm lower bound given by equation (5), we can make a better estimate of the degree of entanglement $C_{L,R}$ between the L and R ensembles by using detailed measurements of the propagation

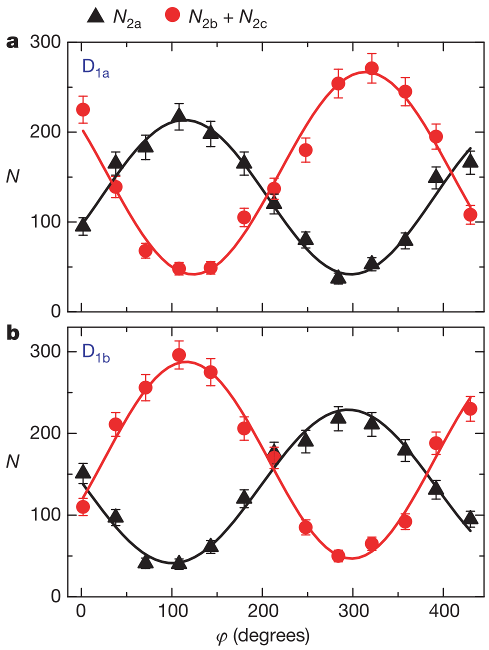

Figure 2 | Coherence between the atomic ensembles *L*, *R* induced by a measurement event of the fields 1_L and 1_R at detector D_{1a} or D_{1b}. Shown is the number of coincidences N_{2a} (triangles) and $N_{2b} + N_{2c}$ (circles) recorded by the respective detectors $D_{2a,2b,2c}$ for the fields 2_L and 2_R with the interferometer arrangement of Fig. 1b as a function of the relative phase φ. In **a**, $N_{2a,2b,2c}$ are conditioned upon a detection event at D_{1a} with no count at D_{1b}, while in **b**, $N_{2a,2b,2c}$ are conditioned upon an event at D_{1b} with no count at D_{1a}. At each setting of φ, data are acquired for 150 s with a detection window of width 190 ns. Although the interference fringes have comparable visibility, the different sizes arise from unequal quantum efficiencies for detectors D_{2a} and $D_{2b,2c}$ (see Supplementary Information). The visibility values are obtained from an average of the visibilities of the red and black curves, respectively. Error bars reflect ± one standard deviation due to the finite number of counts.

© 2005 Nature Publishing Group

efficiencies from the atomic ensembles to the plane z_0 of the detectors shown in Fig. 1b (see Supplementary Information). Figure 3 gives an inference of the density matrix $\tilde\rho^{z_i}_{2_L,2_R}$ and thereby of the concurrence $C^{z_i}(\tilde\rho^{z_i}_{2_L,2_R})$ at z_0 and at two other locations $z_{i=1,2}$ along the path from the ensembles to the detectors (see Fig. 1b), assuming a constant visibility. In general, C increases in direct correspondence to the reduced level of losses for the 2_L and 2_R fields at locations closer to the ensembles. At location z_2 corresponding to the output edges of the atomic ensembles, we find the result:

$$C^{1a}_{L,R} \geq C^{z_2}_{1a}\left(\tilde\rho^{z_2}_{2_L,2_R}\right) \simeq 0.021 \pm 0.006 > 0,$$
$$C^{1b}_{L,R} \geq C^{z_2}_{1b}\left(\tilde\rho^{z_2}_{2_L,2_R}\right) \simeq 0.016 \pm 0.006 > 0 \qquad (6)$$

To move beyond this result, we need more detailed information about the efficiencies $\xi_{L,R}$ with which stored excitation in the atomic ensembles is converted to the propagating light fields 2_L and 2_R. Our earlier measurements included comparisons to a simple model[21] and allowed an inference $\xi_{L,R} \approx 0.10 \pm 0.05$. The measurement of the losses together with the values of p_{ij} at the detectors yields $p_{10} + p_{01} \approx 11\%$ at the output of the ensembles (z_2 plane) for our current experiment. This value together with the estimated $\xi_{L,R}$ then indicates that $p_{00} \rightarrow 0$ for the conditional state $\rho_{L,R}$ of the ensembles, so that $C_{L,R} \approx V \approx 0.7$, suggesting that $\rho_{L,R}$ is close to the ideal entangled state of equation (1). The low measured values for the entanglement between fields 2_L and 2_R are apparently principally a consequence of the low readout efficiency $\xi_{L,R}$ of the atomic excitation. We stress that this inference of C for the state inside the ensembles must be confirmed by subsequent experiments and is offered here to provide some insight into future prospects for quantum protocols with entangled ensembles. This also emphasizes that a central point in subsequent work should be the improvement of $\xi_{L,R}$.

In conclusion, we have achieved entanglement between a pair of atomic ensembles separated by 2.8 m, with the entangled state involving one spin excitation within a collective system of roughly 10^5 atoms at each site L and R. The entangled state is generated by and conditioned upon an initial detection event, and is thus produced in a probabilistic fashion. However, this initial event heralds unambiguously the creation of an entangled state between L and R ensembles, which is physically available for subsequent use, as, for example, by mapping to propagating optical fields, which can in principle be accomplished with high efficiency. We emphasize that our measurements relate to an actual physical state of the L and R ensembles and of the 2_L and 2_R fields, and are not an inference of a state based upon post-selection. Our work provides the first example of a stored atomic entangled state that can be transfered to entangled light fields, and significantly extends laboratory capabilities for entanglement generation, with now-entangled states of matter stored with separation a thousand-fold larger than was heretofore possible for qubits. With our current set-up, we have demonstrated $\Delta t_s \simeq 1\,\mu$s for storing entanglement. However, this should readily be extended to $\Delta t_s \simeq 10\,\mu$s, and new trapping schemes have the potential to lead to $\Delta t_s \simeq 1$ s (ref. 17). The distance scale for separating the L and R ensembles is limited by the length $l_0 \simeq 2$ km for fibre optic attenuation at our write wavelength of 852 nm. Extensions to scalable quantum networks over larger distances will require the realization of a quantum repeater[6], for which we have now laid the essential foundation.

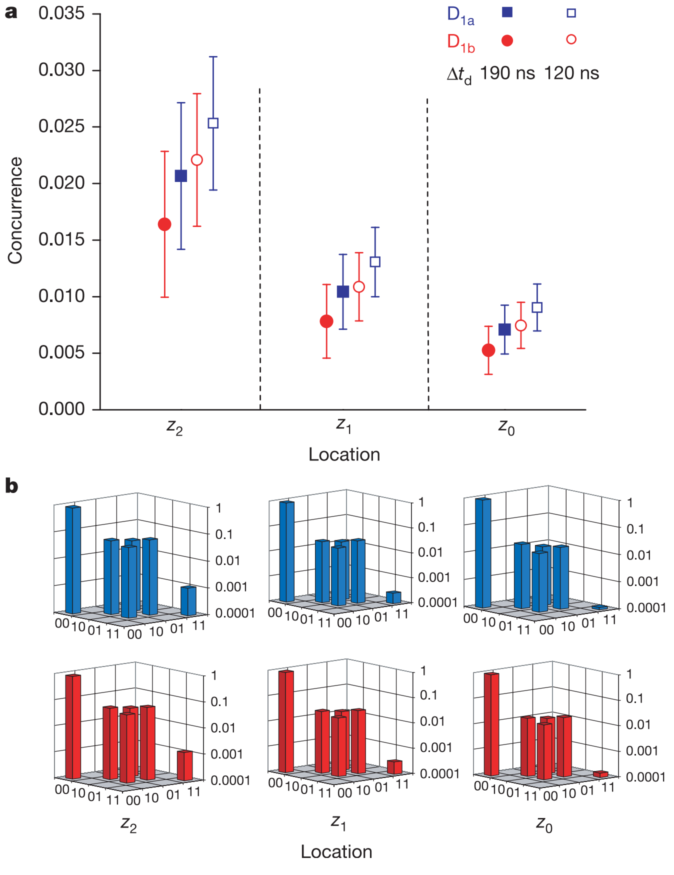

Figure 3 | Inference of the concurrence C^{z_i} (a) and density matrix $\tilde\rho^{z_i}_{2_L,2_R}$ (b) at the three locations z_i indicated in Fig. 1b. At each location, two pairs of results are given corresponding to the measurement-induced state created from detection at D_{1a} and D_{1b}, taking into account the efficiency of the detectors and propagation losses. **a**, Concurrence C, for two different detection windows Δt_d at $D_{2a,2b,2c}$. Filled symbols are for $\Delta t_d = 190$ ns, enough to acquire the whole temporal wavepacket of field 2. Open symbols are for $\Delta t_d = 120$ ns. We see then that the degree of entanglement can be further enhanced, similar to the increase of nonclassical correlations between fields 1 and 2 reported in ref. 23 for specific detection windows for these fields. All values shown in this figure, including the ones for z_0, are already corrected for the efficiencies of the detectors. Error bars reflect ± 1 standard deviation, taking into account the finite number of counts and the uncertainties in the efficiency and propagation loss. **b**, Density matrix $\tilde\rho^{z_i}_{2_L,2_R}$ given in the basis $|n\rangle_{2_L}|m\rangle_{2_R}$ corresponding to equation (3) with $\{n, m\} = \{0, 1\}$ for $\Delta t_d = 190$ ns.

METHODS

Atomic ensembles and optical pulses. Each of the L and R atomic ensembles is obtained from caesium atoms in a magneto-optical trap (MOT)[17,21]. Measurements are carried out in a cyclic fashion consisting first of a period of cooling and trapping to form the MOT, followed by an interval during which the magnetic fields for the MOT are switched off. After waiting 3 ms for the magnetic field to decay[17], we initiate a sequence of measurement trials, where for each trial the atoms are initially prepared in level $|g\rangle$. The write pulse is at 852 nm, with a duration of 150 ns and is detuned 10 MHz below the $|g\rangle \rightarrow |e\rangle$ transition. The read pulse is at 894 nm, with a duration of 130 ns and is resonant with the $|s\rangle \rightarrow |e'\rangle$ transition. At the end of each trial, the sample is pumped back to level $|g\rangle$ by illuminating the atomic cloud with trapping and repumping light for 0.7 μs and 1 μs respectively, and then a new trial is initiated with period of 3 μs. The total duration for a sequence of measurement trials is 5 ms, after which the measurement interval is terminated and a new MOT is formed in preparation for the next sequence of trials at a rate of 40 Hz.

Received 31 August; accepted 19 October 2005.

1. Nielsen, M. A. & Chuang, I. L. *Quantum Computation and Quantum Information* (Cambridge Univ. Press, Cambridge, UK, 2000).
2. *Quantum Information and Computation Roadmap* ⟨http://qist.lanl.gov/qcomp_map.shtml⟩ (2004).
3. Copsey, D. *et al.* Toward a scalable, silicon-based quantum computing architecture. *IEEE J. Selected Topics Quant. Electron.* 9, 1552–1569 (2003).
4. Briegel, H.-J., Dür, W., Cirac, J. I. & Zoller, P. Quantum repeaters: the role of imperfect local operations in quantum communication. *Phys. Rev. Lett.* 81, 5932–5935 (1998).

© 2005 Nature Publishing Group

5. Giovannetti, G., Lloyd, S. & Maccone, L. Quantum-enhanced measurements: beating the standard quantum limit. *Science* **306,** 1330–1336 (2004).
6. Duan, L.-M., Lukin, M., Cirac, J. I. & Zoller, P. Long-distance quantum communication with atomic ensembles and linear optics. *Nature* **414,** 413–418 (2001).
7. Clauser, J. F. & Shimony, A. Bell's theorem: experimental tests and implications. *Rep. Prog. Phys.* **41,** 1881–1927 (1978).
8. Aspect, A., Dalibard, J. & Roger, G. Experimental test of Bell's inequalities using time-varying analyzers. *Phys. Rev. Lett.* **49,** 1804–1807 (1982).
9. Mandel, L. & Wolf, E. *Optical Coherence and Quantum Optics* Ch. 12 (Cambridge Univ. Press, New York, 1995).
10. Haffner, H. *et al.* Robust entanglement. *Appl. Phys. B* **81,** 151–153 (2005).
11. Langer, C. *et al.* Long-lived qubit memory using atomic ions. *Phys. Rev. Lett.* **95,** 060502 (2005).
12. Julsgaard, B., Kozhekin, A. & Polzik, E. S. Experimental long-lived entanglement of two macroscopic objects. *Nature* **413,** 400–403 (2001).
13. Marcikic, I. *et al.* Distribution of time-bin entangled qubits over 50 km of optical fiber. *Phys. Rev. Lett.* **93,** 180502 (2004).
14. Ou, Z. Y., Pereira, S. F., Kimble, H. J. & Peng, K.-C. Realization of the Einstein–Podolsky–Rosen paradox for continuous variables. *Phys. Rev. Lett.* **68,** 3663–3666 (1992).
15. Turchette, Q. A. *et al.* Deterministic entanglement of two trapped ions. *Phys. Rev. Lett.* **81,** 3631–3634 (1998).
16. Blinov, B. B., Moehring, D. L., Duan, L.-M. & Monroe, C. Observation of entanglement between a single-trapped atom and a single photon. *Nature* **428,** 153–157 (2004).
17. Felinto, D., Chou, C. W., de Riedmatten, H., Polyakov, S. V. & Kimble, H. J. Control of decoherence in the generation of photon pairs from atomic ensembles. *Phys. Rev. A* **72,** 053809 (2005).
18. Kuzmich, A. *et al.* Generation of nonclassical photon pairs for scalable quantum communication with atomic ensembles. *Nature* **423,** 731–734 (2003).
19. van der Wal, C. H. *et al.* Atomic memory for correlated photon states. *Science* **301,** 196–200 (2003).
20. Jiang, W., Han, C., Xue, P., Duan, L.-M. & Guo, G.-C. Nonclassical photon pairs generated from a room-temperature atomic ensemble. *Phys. Rev. A* **69,** 043819 (2004).
21. Chou, C. W., Polyakov, S. V., Kuzmich, A. & Kimble, H. J. Single-photon generation from stored excitation in an atomic ensemble. *Phys. Rev. Lett.* **92,** 213601 (2004).
22. Eisaman, M. D. *et al.* Shaping quantum pulses of light via coherent atomic memory. *Phys. Rev. Lett.* **93,** 233602 (2004).
23. Polyakov, S. V., Chou, C. W., Felinto, D. & Kimble, H. J. Temporal dynamics of photon pairs generated by an atomic ensemble. *Phys. Rev. Lett.* **93,** 263601 (2004).
24. Balic, V., Braje, D. A., Kolchin, P., Yin, G. Y. & Harris, S. E. Generation of paired photons with controllable waveforms. *Phys. Rev. Lett.* **94,** 183601 (2005).
25. Matsukevich, D. N. *et al.* Entanglement of a photon and a collective atomic excitation. *Phys. Rev. Lett.* **95,** 040405 (2005).
26. Matsukevich, D. N. & Kuzmich, A. Quantum state transfer between matter and light. *Science* **306,** 663–666 (2004).
27. van Enk, S. & Kimble, H. J. Comment on 'Quantum state transfer between matter and light'. *Science* **309,** 1187b (2005).
28. Matsukevich, D. N. & Kuzmich, A. Response to comment on 'Quantum state transfer between matter and light'. *Science* **309,** 1187c (2005).
29. Duan, L.-M., Cirac, J. I. & Zoller, P. Three-dimensional theory for interaction between atomic ensembles and free-space light. *Phys. Rev. A* **66,** 023818 (2002).
30. Wootters, W. K. Entanglement of formation of an arbitrary state of two qubits. *Phys. Rev. Lett.* **80,** 2245–2248 (1998).

Supplementary Information is linked to the online version of the paper at www.nature.com/nature.

Acknowledgements We gratefully acknowledge J. Hall and J. Ye for discussions about phase stabilization. This research is supported by the Advanced Research and Development Activity (ARDA), by the National Science Foundation, and by the Caltech MURI Center for Quantum Networks. D.F. acknowledges financial support by CNPq (Brazilian agency). H.d.R. acknowledges financial support by the Swiss National Science Foundation. S.J.v.E. thanks L. Huelsbergen for assistance in computer matters.

Author Information Reprints and permissions information is available at npg.nature.com/reprintsandpermissions. The authors declare no competing financial interests. Correspondence and requests for materials should be addressed to H.J.K. (hjkimble@caltech.edu).

© 2005 Nature Publishing Group

PHYSICAL REVIEW A **72**, 032333 (2005)

Robust quantum gates on neutral atoms with cavity-assisted photon scattering

L.-M. Duan,[1] B. Wang,[1] and H. J. Kimble[2]

[1]*FOCUS Center and MCTP, Department of Physics, University of Michigan, Ann Arbor, Michigan 48109-1120, USA*

[2]*Norman Bridge Laboratory of Physics 12-33, California Institute of Technology, Pasadena, California 91125, USA*

(Received 6 July 2005; published 28 September 2005)

We propose a scheme to achieve quantum computation with neutral atoms whose interactions are catalyzed by single photons. Conditional quantum gates, including an N-atom Toffoli gate and nonlocal gates on remote atoms, are obtained through cavity-assisted photon scattering in a manner that is robust to random variation in the atom-photon coupling rate and which does not require localization in the Lamb-Dicke regime. The dominant noise in our scheme is automatically detected for each gate operation, leading to signalled errors which do not preclude efficient quantum computation even if the error probability is close to the unity.

DOI: 10.1103/PhysRevA.72.032333 PACS number(s): 03.67.Lx, 03.67.Hk, 42.50.Pq

Neutral atoms in optical cavities have been one of the pioneering avenues for the implementation of quantum computation and networking [1–4]. Nevertheless, the experimental requirements associated with these approaches turn out to be very challenging. In particular, although significant experimental advances have been reported recently in transmitting and trapping single atoms in high finesse cavities [4–12], no experiment has yet achieved a well defined number of atoms $N \geqslant 2$ each of which is strongly coupled to the cavity mode, individually addressable, and localized to the Lamb-Dicke limit, as is required for the protocol of Ref. [1]. To realize a more scalable system, Chapman *et al.* proposed an architecture in which a transverse optical lattice is employed to translate atoms into and out of a high-finesse cavity for entangling gate operations [6]. Transport that preserves internal state coherence has been demonstrated for both ions [13] and atoms [14]. However, although the approach of Ref. [6] does solve the problem of separate addressing of many atoms in a tiny cavity, there remain significant obstacles to achieving Lamb-Dicke confinement [15] and strong coupling for any scheme that has yet been proposed.

To overcome these difficulties and to provide several capabilities for quantum logic, in this paper we propose a scheme for atomic quantum gates whereby atom-atom interactions are catalyzed by single photons in a fashion that is robust to various sources of practical noise. More specifically, a controlled phase-flip gate between two atoms is achieved by cavity-assisted scattering of a single-photon pulse from the cavity in which the atoms are localized [16]. This gate is insensitive to uncertainties in the atom-photon coupling rate, thereby obviating the requirement for Lamb-Dicke localization. It is also robust to all sources of photon loss, including, for instance, atomic spontaneous emission, photon collection and detection inefficiency, and any vacuum component in the scattering pulse. Such noise is automatically detected for each gate, leading to a finite failure probability of the gate operation. As shown in Refs. [17,18], efficient quantum computation can nevertheless be achieved even if the associated failure probability is close to unity. Moreover, our scheme can be readily extended to achieve a Toffoli gate for N atoms in a single step and to realize nonlocal gates on remote atoms trapped in different cavities. The direct N-bit gate could lead to more efficient construction of quantum circuits, and the nonlocal gates on remote atoms naturally integrates local computation with quantum networking.

To explain the idea of the gate operation, we first consider two atoms in a single-sided cavity. To have a scalable architecture, one can follow Ref. [6] to assume there are transverse optical lattice potentials to move the target atoms into and outside the cavity [19,20]. Each atom has three relevant levels as shown in Fig. 1. The qubit is represented by different hyperfine levels $|0\rangle$ and $|1\rangle$ in the ground-state manifold. The atomic transition from $|1\rangle$ to an excited level $|e\rangle$ is resonantly coupled to a cavity mode a_c. The state $|0\rangle$ is decoupled due to the large hyperfine splitting.

To perform a collective quantum gate on the two atoms, we reflect a single-photon pulse from the cavity. This single-photon pulse, with its state denoted as $|p\rangle$, is resonant with the bare cavity mode a_c. If the photon pulse is sufficiently long (with its bandwidth $\Delta\Omega$ much smaller than the cavity decay rate κ), reflection of the pulse from a resonant cavity absent an atom will leave the pulse shape almost unchanged but will flip its global phase, as we later characterize in detail. For the case that both of the atoms are in the $|0\rangle$ state, this is precisely the nature of the resonant reflection since

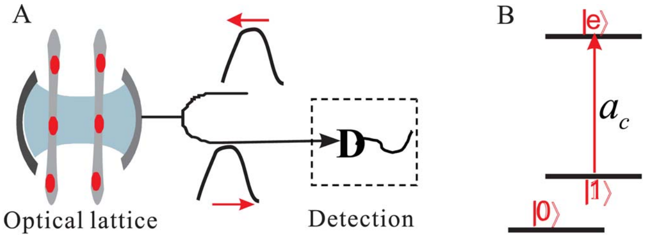

FIG. 1. (Color online) (A) Schematic setup for implementation of the controlled phase flip (CPF) gate on two atoms inside the cavity through the photon-scattering interaction. Any pair of atoms can be transmitted into the cavity for a collective gate operation through a transverse optical lattice potential as suggested in Refs. [6,21]. For a more robust implementation of the gate, we add a single-photon detector to detect the output photon pulse as illustrated inside the dashed box. (B) The relevant level structure of the atoms and the coupling configuration.

©2005 The American Physical Society

there is negligible atom-cavity coupling and hence no shift of the resonant frequency of the cavity mode. After reflection, the atom-photon state $|0\rangle_1|0\rangle_2|p\rangle$ evolves into $-|0\rangle_1|0\rangle_2|p\rangle$, where the subscripts 1, 2 denote the two intracavity atoms. However, if either or both of the atoms are in the state $|1\rangle$, the effective frequency of the dressed cavity mode will be shifted due to the atom-cavity coupling, which is described by the Hamiltonian

$$H=\hbar\sum_{i=1,2} g_i(|e\rangle_i\langle 1|a_c+|1\rangle_i\langle e|a_c^{\dagger}). \qquad (1)$$

If the coupling rates $g_i \gg (\Delta\Omega,\kappa,\gamma_s)$, where γ_s is the rate of spontaneous decay of $|e\rangle$, then the frequency shift will have a magnitude comparable with g_i, so that the incident single-photon pulse will be reflected by an off-resonant cavity. Hence, both the shape and global phase will remain unchanged for the reflected pulse. Due to this property, the component states $|0\rangle_1|1\rangle_2|p\rangle$, $|1\rangle_1|0\rangle_2|p\rangle$, and $|1\rangle_1|1\rangle_2|p\rangle$ are likewise unaffected by reflection process. The net effect of these two subprocesses is that the reflection of a single-photon pulse from the cavity actually performs a controlled phase-flip gate (CPF) $U_{12}=\exp(i\pi|00\rangle_{12}\langle 00|)$ on the two atoms while leaving the photon state unchanged (unentangled). Hence, in the ideal case the reflected photon can be utilized to catalyze subsequent gate operations.

However, in a realistic setting our scheme can be performed in a more robust fashion by detecting the output pulse with a single-photon detector. By this means, gate errors due to all sources of photon loss, including atomic spontaneous emission, cavity mirror absorption and scattering, imperfection in the photon source, and photon collection and detection inefficiencies, are always signaled by the absence of a photon count. As a result, these dominant sources of noise only lead to probabilistic signaled errors, which yield a finite failure probability of the gate but which have no contribution to the gate infidelity if the operation succeeds (i.e., if a photon count is registered). For this class of errors, efficient quantum computation is possible with an arbitrarily small gate success probability p [17]. Compared with deterministic gates, the required extra computational overhead due to the small gate success probability p scales efficiently (polynomially) both with $1/p$ and the computational scale characterized by the number of qubits n [17]. Because of this robustness, the input single-photon pulse can also be replaced by a simple weak coherent pulse $|\alpha\rangle$ with the mean photon number $|\alpha|^2 \ll 1$. This replacement does not give any essential problem in terms of scaling, although the individual gate efficiency (the success probability) is indeed significantly reduced by a factor of $|\alpha|^2$.

Before going to the detailed theoretical characterization of the gate fidelity and efficiency, we next present some extensions of the above scheme. First, our scheme can be readily extended to perform a Toffoli gate on N atoms in a single time step. If one reflects a single-photon pulse from a cavity with N atoms trapped inside, the pulse will have a flip of its global phase if and only if all the atoms are in the $|0\rangle$ state. So, this reflection performs a Toffoli gate $U_{12\cdots N}=\exp(i\pi|00\cdots 0\rangle_{12\cdots N}\langle 00\cdots 0|)$ on all the atoms while leaving the photon state unentangled. This direct N-bit gate could lead to more efficient construction of circuits for quantum computation. For instance, the reflection operation in the Grover's search algorithm can be realized in a single step with the N-bit Toffoli gate [21].

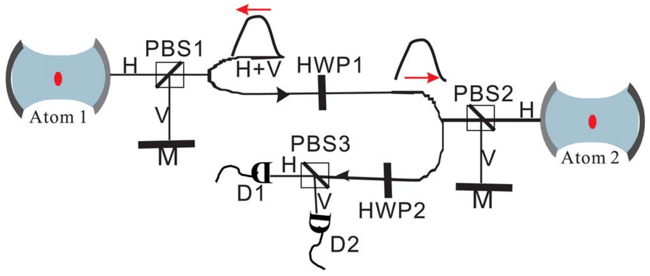

FIG. 2. (Color online) Schematic of the setup for implementation of nonlocal gates on two atoms 1 and 2 trapped in distant cavities. Not shown are circulators (e.g., Faraday devices) to redirect the output beams along paths distinct from the inputs. See the text for further explanation.

Second, the above scheme can also be extended to perform nonlocal gates on two remote atoms trapped in different cavities, as illustrated in Fig. 2. A similar nonlocal gate was also proposed recently in a different system with rare-earth atoms [22]. For this purpose, one uses a single-photon (or weak-coherent) pulse which is in an equal superposition state $(|H\rangle+|V\rangle)/\sqrt{2}$ of the H and V polarization components. With a polarization beam splitter (PBS1), the H and V components of the pulse are "bounced" back from the atom-cavity system and a mirror M, respectively, with the reflection from M leaving the incident pulse unchanged. The overall reflection from the cavity and the mirror M actually performs the gate operation $U_{1p}=\exp(i\pi|0H\rangle_{1p}\langle 0H|)$ on atom 1 and the photon pulse p, so that there is a phase flip only when the atom is in the state $|0\rangle$ and the photon is in the polarization $|H\rangle$ [16]. The pulse is reflected successively from the two cavity setups, with a half-wave plate (HWP1) inserted into the optical path between the two reflections which performs a Hardmard rotation on the photon's polarization $|H\rangle \to (|H\rangle+|V\rangle)/\sqrt{2}, |V\rangle \to (|V\rangle-|H\rangle)/\sqrt{2}$. The photon is detected by two single-photon detectors D1 and D2 after the reflections, corresponding to a measurement of its polarization in the basis $(|V\rangle \pm |H\rangle)/\sqrt{2}$ (after the HWP2 and the PBS3; see Fig. 2). For a detection event in D2, a phase flip operation σ_1^z is performed on the atom 1, while no operation is applied if D1 clicks. The net effect of these operations is the desired CPF gate $U_{12}=\exp(i\pi|00\rangle_{12}\langle 00|)$ on the two remote atoms 1, 2. Among other applications, this nonlocal gate and its extension to multiple atom-cavity systems provide a convenient avenue for quantum networking. As before for the case of a single cavity, in this distributed setting any noise leading to photon loss is always signaled by the absence of a photon count from either D1 or D2.

We now present a more detailed theoretical model of our scheme and characterize the influence of some practical sources of noise. The input single-photon pulse with a normalized shape function $f_{\text{in}}(t)$ and a duration T can be described by the state $|p\rangle=\int_0^T f_{\text{in}}(t)a_{\text{in}}^{\dagger}(t)dt|\text{vac}\rangle$, where $|\text{vac}\rangle$ denotes the vacuum state and $a_{\text{in}}^{\dagger}(t)$ is the one-dimensional optical field operator with the commutation relation $[a_{\text{in}}(t), a_{\text{in}}^{\dagger}(t')] = \delta(t-t')$ [23]. The cavity mode a_c is driven by the input field $a_{\text{in}}(t)$ through the Langevin equation [23]

$$\dot{a}_c = -i[a_c, H] - (\kappa/2)a_c - \sqrt{\kappa}a_{\text{in}}(t), \tag{2}$$

where κ is the cavity decay rate and the Hamiltonian H is given in Eq. (1) for the case of two atoms; generalization to multiple atoms is straightforward. To account for atomic spontaneous emission with a rate γ_s, we add an effective term $(-i\gamma_s)|e\rangle\langle e|$ to the Hamiltonian H. The output field $a_{\text{out}}(t)$ of the cavity is connected with the input through the input-output relation $a_{\text{out}}(t) = a_{\text{in}}(t) + \sqrt{\kappa}a_c$.

The final atom-photon state can be numerically solved from the above set of equations through discretization of the continuum optical fields (for details on the numerical method, see Refs. [16,24]). We use the following two quantities to characterize the imperfections in our scheme. (1) Due to various sources of photon loss, photons in the cavity may be lost with then no photon count at the detectors. Hence, we calculate the success probability of a photon count at the detector to characterize the efficiency of the scheme. (2) Even if a photon emerges, there may still be imperfections of the atomic gate mainly due to the shape distortion of the photon pulse after reflection from the cavity, which can be characterized through the gate fidelity. Without loss of the photon, the final atom-photon state can be written as $|\Psi_{\text{out}}\rangle = \Sigma_{i_1 i_2} c_{i_1 i_2} |i_1 i_2\rangle_a |p\rangle_{i_1 i_2}$, where $\Sigma_{i_1 i_2} c_{i_1 i_2} |i_1 i_2\rangle_a (i_1, i_2 = 0, 1)$ is the general form for the input state of the two atoms. The output photon state $|p\rangle_{i_1 i_2}$ corresponds to the atomic component $|i_1 i_2\rangle_a$, and is given by $|p\rangle_{i_1 i_2} = \int_0^T f_{i_1 i_2}^{\text{out}}(t) a_{\text{out}}^{\dagger}(t) dt |\text{vac}\rangle$ with a shape $f_{i_1 i_2}^{\text{out}}(t)$. Ideally, the output state $|\Psi_{\text{out}}^{id}\rangle$ would have the shape functions $f_{00}^{\text{out}}(t) = -f_{\text{in}}(t)$ and $f_{i_1 i_2}^{\text{out}}(t) = f_{\text{in}}(t)$ (for $i_1, i_2 \neq 0$), which realizes a perfect CPF gate U_{12} on the atoms. Hence to characterize the gate imperfection, we calculate the fidelity $F \equiv |\langle \Psi_{\text{out}}^{id} | \Psi_{\text{out}} \rangle|^2$, which is directly extendable to any number of atoms. In the following calculation of the fidelity F, we choose the input state $[(|0\rangle + |1\rangle)/\sqrt{2}]^{\otimes N}$ for the case of N atoms.

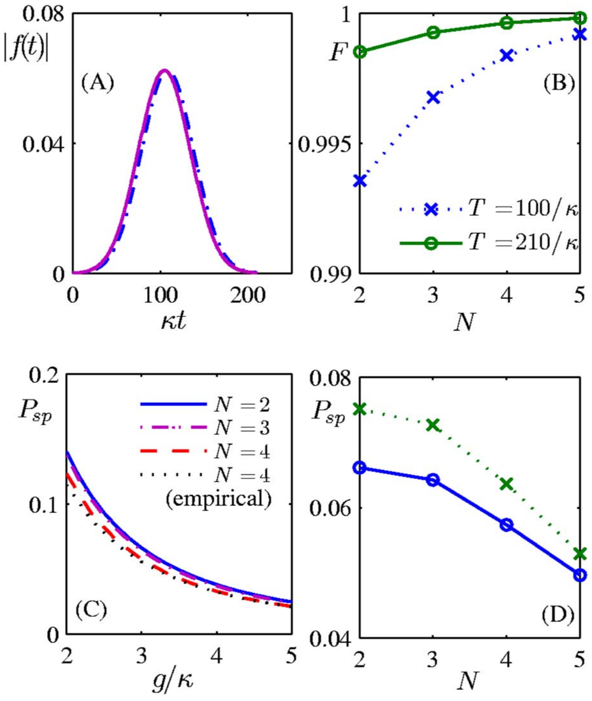

FIG. 3. (Color online) (A) The shape functions $|f(t)|$ for the input pulse (solid curve) and the reflected pulses with the atoms in different component states $|i_1 i_2\rangle_a$. The shape function for the atom in the state $|00\rangle_a$ is shown by the dash-dot curve. With the coupling rate g in a typical range from 2κ to 6κ, the shape functions for the atoms in all the other component states are indistinguishable from that of the input pulse (the solid curve). We have assumed a Gaussian shape for the input pulse with $f_{\text{in}}(t) \propto \exp[-(t-T/2)^2/(T/5)^2]$, where t ranges from 0 to T and $T = 210/\kappa$ for this example. (B) The gate fidelity versus the number of atoms with the pulse duration $T = 100/\kappa$ (the dotted curve) and $T = 210/\kappa$ (the solid curve), respectively. (C) The photon loss probability P_{sp} due to atomic spontaneous emission shown as a function of the coupling rate g in units of κ with the atom number $N = 2, 3, 4$. The dotted curves shows P_{sp} calculated from the empirical formula given in the text for $N = 4$. (D) Comparison of the photon loss P_{sp} for a constant coupling rate $g = 3\kappa$ (the solid curve) and for a time varying rate $g_i(t) = 3\kappa[1 + \sin(\nu t + \phi_i)/3]$ (the dotted curve) for the ith atom, where $\nu = \kappa/6$ corresponds to a typical atom's axial oscillation frequency in the trap, and ϕ_i are taken as random numbers accounting for the atoms' random initial positions. $g_i(t)$ is chosen so that its maximum and minimum differ by a factor of 2, which exceeds that in current experiments [9]. Other parameters for (A) and (B) are $\gamma_s = \kappa$ and $g = 3\kappa$, and for (C) and (D), $\gamma_s = \kappa$ and $T = 210\kappa$.

The results from our calculations are summarized in Fig. 3. First, Fig. 3(a) shows the component pulse shape $f_{i_1 i_2}^{\text{out}}(t)$ corresponding to a Gaussian input $f_{\text{in}}(t)$ for the case of two atoms. Only the component $f_{00}^{\text{out}}(t)$ has a notable shape distortion; all others are basically indistinguishable from the input. To account for random variation in the coupling rates g_i, we have also calculated $f_{i_1 i_2}^{\text{out}}(t)$ for g_i varying from 2κ to 6κ. The output pulse shapes are nearly identical for g_i varying in this range, which is typical of current experiments [4–10]. Figure 3(b) shows the corresponding fidelity F of the CPF (or Toffoli) gate from the shape distortion noise with the atom number $N = 2, 3, 4, 5$. The fidelity F improves with increase of the pulse duration T since the shape distortion is reduced for longer pulses. F also increases with the atom number N, which is a bit surprising but actually reasonable: for the N-atom state $[(|0\rangle + |1\rangle)/\sqrt{2}]^{\otimes N}$, the fraction of the component $|0\rangle^{\otimes N}$ goes down as $1/2^N$, and the pulse shape distortion noise comes dominantly from this component. Because the component $|0\rangle^{\otimes N}$ dominates the contribution to the gate infidelity, F is also very insensitive to variation of the coupling rates g_i. We have verified that there is no notable change of F ($\delta F < 10^{-4}$) in Fig. 3(b) for g_i varying from 2κ to 6κ.

Any source of photon loss has no contribution to the gate fidelity but instead influences gate efficiency (success probability). A fundamental source of photon loss is atomic spontaneous emission. Figure 3(c) shows the failure probability P_{sp} of the gate due to this source of noise, with the noise rate $\gamma_s = \kappa$. For N atoms with equal $g_i = g$, the probability P_{sp} can be well fit by an empirical formula $P_{\text{sp}} \approx P_{\text{emp}}$

$\equiv \Sigma_{n=1}^{N}[N!/n!(N-n)!2^N][1+ng^2/\kappa\gamma_s]^{-1}$. The empirical P_{emp} can be understood as a probability averaged over all the Dicke-state components in the input state $[(|0\rangle+|1\rangle)/\sqrt{2}]^{\otimes N}$, with the nth Dicke-component having an effective coupling rate $\sqrt{n}g$ to the cavity mode. We have also simulated the loss probability P_{sp} when the coupling rates g_i are different and vary during the gate operation, for instance, as would be caused by the atoms' thermal motion. With some typical choice of the relevant experimental parameters, the result is shown in Figure 3 D, which is qualitatively similar to the constant coupling rate case with an effective average over $|g_i|$. Other sources of photon loss can be similarly characterized. For instance, with a finite photon collection and detection efficiency η, the success probability of each gate will be simply reduced by a factor of η.

In summary, we have proposed a new scheme for robust atomic gates by way of interactions mediated by cavity-assisted photon scattering. These gates are robust to all sources of photon loss that are typically the dominant source of noise in experimental implementations, and are furthermore insensitive to randomness in the coupling rates caused by fluctuations in atomic position. Beyond two-atom gates illustrated in Fig. 1, our scheme can also be employed for realization of an N-atom Toffoli gate in a single step and for the implementation of nonlocal gates on distant atoms as in Fig. 2. We have characterized the efficacy of our scheme through exact numerical simulations that incorporate various sources of experimental noise. These results demonstrate the practicality of our scheme by way of current experimental technology.

Note added. After submission of this work, we were informed that a similar idea was also investigated by the authors X.-M. Lin *et al.* (unpublished).

We gratefully acknowledge the contributions of W. D. Phillips, whose question stimulated these investigations. We thank also S. Lloyd for helpful discussions. This work was supported by the National Science Foundation (Grant Nos. 0431476, EIA-0086038, and PHY-0140355), the Advanced Research and Development Activity under ARO contracts, the A. P. Sloan foundation (L.M.D.), and the Caltech MURI Center for Quantum Networks (H.J.K.).

---

[1] T. Pellizzari, S. A. Gardiner, J. I. Cirac, and P. Zoller, Phys. Rev. Lett. **75**, 3788 (1995).

[2] Q. A. Turchette *et al.*, Phys. Rev. Lett. **75**, 4710 (1995).

[3] J. I. Cirac, P. Zoller, H. J. Kimble, and H. Mabuchi, Phys. Rev. Lett. **78**, 3221 (1997).

[4] For a review, see C. Monroe, Nature (London) **416**, 238 (2002).

[5] J. McKeever *et al.*, Phys. Rev. Lett. **90**, 133602 (2003).

[6] M. Chapmann, unpublished; J. A. Sauer *et al.*, Phys. Rev. A **69**, 051804(R) (2004).

[7] P. Maunz *et al.*, Nature (London) **428**, 50 (2004).

[8] J. McKeever, J. R. Buck, A. D. Boozer, and H. J. Kimble, Phys. Rev. Lett. **93**, 143601 (2004).

[9] A. Boca *et al.*, Phys. Rev. Lett. **93**, 233603 (2004).

[10] P. Maunz *et al.*, Phys. Rev. Lett. **94**, 033002 (2005).

[11] M. Keller *et al.*, Nature (London) **431**, 1075 (2004).

[12] A. Kreuter *et al.*, Phys. Rev. Lett. **92**, 203002 (2004).

[13] M. A. Rowe *et al.*, Quantum Inf. Comput. **2**, 257 (2002).

[14] S. Kuhr *et al.*, Phys. Rev. Lett. **91**, 213002 (2003).

[15] For example, if a far-off resonance dipole-force trap (FORT) is utilized for conveying an atom along a direction transverse to the cavity axis [6,14] and if an atom is cooled to the motional ground state of the FORT, the spread of the atomic wave packet along the direction of the cavity axis is typically still comparable to the optical wavelength for the cavity QED field due to focusing the FORT beams within the constraints of the cavity geometry. This causes significant uncertainty in the atom-photon coupling rate.

[16] L.-M. Duan and H. J. Kimble, Phys. Rev. Lett. **92**, 127902 (2004); B. Wang and L.-M. Duan, Phys. Rev. A **72**, 022320 (2005).

[17] L.-M. Duan and R. Raussendorf, Phys. Rev. Lett. **95**, 080503 (2005).

[18] S. D. Barrett, and P. Kok, Phys. Rev. A **71**, 060310(R) (2005).

[19] The scheme also applies to the more traditional cavity quantum computation architecture with an array of atoms in the cavity. Separate addressing of different atoms could be achieved through frequency selection either with Stark shifts from focused laser beams or with gradients from effective magnetic fields [20].

[20] D. Schrader *et al.*, Phys. Rev. Lett. **93**, 150501 (2004).

[21] M. A. Nielsen, I. L. Chuang, *Quantum Computation and Quantum Information* (Cambridge University Press, Cambridge, 2000).

[22] Yun-Feng Xiao *et al.*, Phys. Rev. A **70**, 042314 (2004).

[23] D. F. Walls and G. J. Milburn, *Quantum Optics* (Springer-Verlag, Berlin, 1994).

[24] L.-M. Duan, A. Kuzmich, and H. J. Kimble, Phys. Rev. A **67**, 032305 (2003).

Tensor polarizability and dispersive quantum measurement of multilevel atoms

JM Geremia, John K. Stockton,* and Hideo Mabuchi
Physical Measurement and Control 266-33, California Institute of Technology, Pasadena, CA 91125
(Dated: November 11, 2005)

Optimally extracting information from measurements performed on a physical system requires an accurate model of the measurement interaction. Continuously probing the collective spin of an Alkali atom cloud via its interaction with an off-resonant optical probe is an important example of such a measurement where realistic modeling at the quantum level is possible using standard techniques from atomic physics. Typically, however, tutorial descriptions of this technique have neglected the multilevel structure of realistic atoms for the sake of simplification. In this paper we account for the full multilevel structure of Alkali atoms and derive the irreducible form of the polarizability Hamiltonian describing a typical dispersive quantum measurement. For a specific set of parameters, we then show that semiclassical predictions of the theory are consistent with our experimental observations of polarization scattering by a polarized cloud of laser-cooled Cesium atoms. We also derive the signal-to-noise ratio under a single measurement trial and use this to predict the rate of spin-squeezing with multilevel Alkali atoms for arbitrary detuning of the probe beam.

PACS numbers: 03.65.Ta, 42.50.Lc, 02.30.Yy

I. INTRODUCTION

Information gained by performing measurements on a quantum system can reduce uncertainty about one or more of its physical observables. It is, however, a basic property of quantum mechanics that measurements are invasive in the sense that they necessarily degrade one's ability to make subsequent predictions about the values of complementary observables [1]. This type of disturbance is often called measurement backaction, and it is a natural consequence of the Hamiltonian coupling between a probe (such as an electromagnetic field mode) and the system of interest. In a special class of "back-action evading" experimental scenarios, it is possible to channel the disturbance into observables that are not dynamically coupled to the main quantities of interest. When such measurements are performed with minimal technical imperfection on systems whose initial preparations are sufficiently pure, which qualifies them as what is referred to in the quantum optics literature as quantum non-demolition (QND) measurement [2, 3], it is possible to create conditionally squeezed states of the measured observable.

While measurement-induced squeezing can easily be understood in an abstract sense, predicting the precise degree of squeezing that can be achieved in a realistic experiment requires detailed physical modeling of the system-probe interaction (in addition to any operative decoherence mechanisms). Squeezed states of atomic spins have recently emerged [4–7] as a versatile and robust resource for quantum information science [8, 9] and quantum metrology [10–14]. In these contexts, the degree of spin squeezing is directly linked to entanglement measures, to achievable reductions in averaging times for precision measurement, and to achievable improvements over communication protocols that utilize only classical information resources.

Theoretical analyses of measurement-induced spin squeezing typically consider a system of $N \gg 1$ atoms whose collective spin is described by an observable

$$\hat{\mathbf{F}} = \sum_{i=1}^{N} {}^{(i)}\hat{\mathbf{f}}, \tag{1}$$

where ${}^{(i)}\hat{\mathbf{f}} = \cdots \otimes \mathbb{1}_{i-1} \otimes \hat{\mathbf{f}} \otimes \mathbb{1}_{i+1} \otimes \cdots$ is the angular momentum (vector) operator for the ith atom. Cartesian components $\hat{F}_x$, $\hat{F}_y$ and $\hat{F}_z$ follow from this in an obvious way. Under physical conditions that preserve permutation symmetry of the label i, the collective spin of an initially polarized atomic sample can be restricted [15] to its maximum angular momentum shell. The associated Hilbert sub-space is spanned by eigenstates $|F, M\rangle$ of the collective spin observable $\hat{\mathbf{F}}$ that satisfy $\hat{\mathbf{F}}^2|F, M\rangle = \hbar^2 F(F+1)|F, M\rangle$, where $F = Nf$ for atoms with individual spin f.

It is natural to conceptualize the quantum state of such a system as a Bloch-like magnetization vector $\mathbf{F} \equiv$

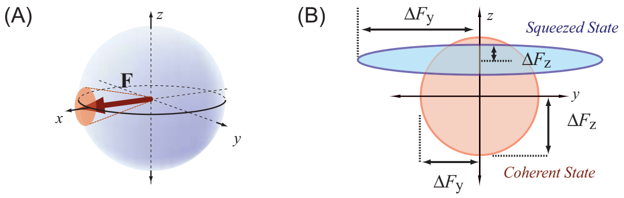

FIG. 1: (A) Graphical representation of the spin-polarized atomic sample as a classical magnetization vector with transverse quantum uncertainty. (B) Schematic of the transverse quantum uncertainties for coherent and squeezed spin states.

---

*Electronic address: `jks@caltech.edu`

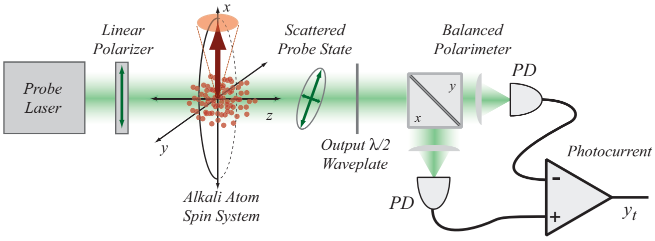

FIG. 2: Schematic of an experimental apparatus for continuous measurement of collective spin in an Alkali atom sample based on polarimetric detection of a forward scattered probe laser. Information gained from the measurement can be used to achieve conditional spin squeezing.

$[\langle\hat{F}_x\rangle, \langle\hat{F}_y\rangle, \langle\hat{F}_z\rangle]$ plus a transverse uncertainty $\mathbf{\Delta F}_\perp$ associated with the variances of $\hat{F}_x$, $\hat{F}_y$ and $\hat{F}_z$ (see Fig. 1). The transverse uncertainty $\mathbf{\Delta F}_\perp$ can never vanish since $\hat{F}_x$, $\hat{F}_y$ and $\hat{F}_z$ do not commute; this constraint can be interpreted to mean that we can never have perfect knowledge of the orientation of the collective magnetization.

Conditional spin-squeezing experiments operate on the principle that weakly measuring F_z gradually reduces its uncertainty below that of the initially-prepared spin state. A typical apparatus for such procedures is depicted in Fig. 2. Continuous measurement of F_z is implemented by passing a linearly polarized probe laser through an atomic sample prepared in an initial (approximate) coherent state [16] by optical pumping [17]. Qualitatively speaking, the atoms rotate (via state-dependent optical activity) the probe polarization by an amount proportional to F_z [18]. In a quantum analysis the atoms and optical probe field evolve into an entangled state [19] as the result of this scattering interaction. Detection of the scattered probe field then yields information about F_z via these correlations [20–24].

The interpretation of existing squeezing experiments has (at least implicitly) assumed that polarimetric detection of the forward scattered probe laser yields a detector photocurrent,

$$y_t dt = \sqrt{M} F_z dt + dW_t. \tag{2}$$

Here M is a constant (known as the *measurement strength*) that describes the rate at which photodetection provides information about F_z. The dW_t are noise increments which exhibit Gaussian white noise statistics $\mathbb{E}[dW_t] = 0$ and $dW_t^2 = dt$ [25].

The measurement strength, M, is the key parameter for predicting the degree of squeezing that can be achieved as a result of the measurement. It is thus important to determine M in terms of physical properties of the atomic sample and optical probe. While the form of Eq. (2) has been derived in previous analyses [20–25], this has generally been done relative to a simplifying assumption that the atoms behave qualitatively as spin-$\frac{1}{2}$ particles. But measurement-induced spin squeezing experiments have utilized Alkali atoms with higher spin [5, 7, 26], and recent data show that the deviation from spin-$\frac{1}{2}$ behavior can be significant [27]. While nonlinearities in the atom-probe scattering process are not always bad (proposals for capitalizing on these effects for quantum state tomography are being explored [28]), they do raise complications for spin-squeezing experiments by invalidating the form of Eq. (2).

We find that the photocurrent in Eq. (2) can be recovered even for higher-spin atoms by suppressing tensor scattering interactions via a properly chosen experimental geometry. Using standard techniques [29, 30] to address the atom-probe scattering physics, combined with a semiclassical treatment of the atomic magnetization vector, we derive an expression for the measurement strength, M, in terms of characteristic experimental parameters. This allows us to obtain an expression for the photocurrent in terms of the duration of the measurement and the properties of the atomic system and the probe laser. We observe close agreement between our scattering model and data obtained using an apparatus of the type in Fig. 2.

Finally, we derive an expression for the signal-to-noise ratio of the measurement photocurrent which can be used to calculate the rate of spin-squeezing in experiments of the form shown in Fig. 2. The results we obtain are valid in the short-measurement limit in which atomic decoherence due to scattering probe light in unobserved (non-paraxial) electromagnetic field modes [31] can be safely ignored. Current spin-squeezing experiments all fall into this regime where the degree of quantum uncertainty reduction is small compared to the Heisenberg spin-squeezing limit [4].

II. CONTINUOUS MEASUREMENT AND THE MULTILEVEL ATOM-PROBE HAMILTONIAN

We begin by considering the experiment depicted in the schematic of Fig. 2. An off-resonant linearly polarized probe beam is sent through a cloud of cold spin-polarized atoms. The forward scattered polarization state of the light is then detected using a polarimeter, consisting of polarization shifting waveplates, a polarizing beam splitter, and two detectors..

In general, it is a rather complicated problem to predict the output polarization state of the probe beam after it has passed through the spatially extended atom cloud. We can simplify the problem to one dimension by assuming that the beam is predominantly forward scattered due to the coherent re-radiation from a large number of atoms. This approximation can be extracted from a full three-dimensional model of the diffraction as considered in references [32–34]. Under this assumption, we only consider paraxial modes of the beam. Neglecting non-paraxial modes prevents us from computing the decoherence rate of the atomic magnetization, but it does not limit our ability to analyze the dynamics in the small-decoherence (short measurement time) limit.

Even in the one-dimensional problem, the depth of the atomic cloud along the probe direction introduces further complications. To simplify further, we assume that the overall optical density of the cloud is small enough that the total rotation of the optical polarization state due to the atoms is small. This allows us to neglect *propagation effects* by which the atoms in the front edge of the cloud would see a substantially different input state than the back edge of the cloud. These effects lead to complicated multi-mode dynamics which are considered (along with the tensor polarizability) in [26].

Under these approximations, we approach the simplified scattering problem as follows. The probe beam consists of two orthogonal polarizations and, for each polarization component, the continuous beam is divided into a series of distinct spatial traveling-wave modes, each with a length equal to the depth of the atomic cloud, L. Thus each atom interacts with a pair of orthogonal polarization modes with the same spatial profile for a length of time $\delta t = L/c$. This approach clearly avoids propagation effects by allowing all of the atoms to interact with the same modes simultaneously. After the two polarization modes corresponding to one time-slice have interacted with the cloud for the discrete time δt , those two modes are detected with the polarimeter, a new time-slice begins to interact with the cloud, and the process is repeated, leading to a continuous measurement. More detailed approaches to continuous measurement with discrete modes can be found in references [24, 35].

Now we define the electric-field and polarization operators associated with each of these optical modes before considering the Hamiltonian interaction of probe beam with a single multilevel atom. This procedure is discussed with more detail in Appendix A.

A. Probe Field Polarization States

For each traveling-wave spatial mode, we consider the field operators

$$\hat{\mathbf{E}}^{(-)} = \sqrt{\hbar g}\left[\hat{a}_-^\dagger \vec{\mathbf{e}}_-^* + \hat{a}_+^\dagger \vec{\mathbf{e}}_+^*\right] \tag{3}$$

and

$$\hat{\mathbf{E}}^{(+)} = \sqrt{\hbar g}\left[\hat{a}_- \vec{\mathbf{e}}_- + \hat{a}_+ \vec{\mathbf{e}}_+\right], \tag{4}$$

where $\hat{a}_-^\dagger$ and $\hat{a}_-$ are Heisenberg-picture creation and annihilation operators for the z-axis propagating mode with left circular polarization and $\hat{a}_+^\dagger$ and $\hat{a}_+$ are the creation and annihilation operators for right circular polarization. Each field operator implicitly refers to a single traveling mode as discussed above, and we neglect to provide indices for the modes unless they are required for clarity. The coefficient $g = \omega_0/(2\epsilon_0 V)$ is a form factor, V will be taken to be the volume of the atomic cloud, and $\vec{\mathbf{e}}_-$ and $\vec{\mathbf{e}}_+$ are the (complex) spherical basis vectors for left and right helicity.

In the expansion of the polarizability Hamiltonian we get terms which can be recast as Schwinger boson operators

$$\begin{aligned}
\hat{S}_0 &= \frac{1}{2}\left(\hat{a}_+^\dagger \hat{a}_+ + \hat{a}_-^\dagger \hat{a}_-\right) \\
\hat{S}_\mathrm{x} &= \frac{1}{2}\left(\hat{a}_+^\dagger \hat{a}_- + \hat{a}_-^\dagger \hat{a}_+\right) \\
&= \frac{1}{2}\left(\hat{a}_\mathrm{y}^\dagger \hat{a}_\mathrm{y} - \hat{a}_\mathrm{x}^\dagger \hat{a}_\mathrm{x}\right) \\
\hat{S}_\mathrm{y} &= \frac{i}{2}\left(\hat{a}_-^\dagger \hat{a}_+ - \hat{a}_+^\dagger \hat{a}_-\right) \\
&= \frac{1}{2}\left(\hat{a}_{\mathrm{y}'}^\dagger \hat{a}_{\mathrm{y}'} - \hat{a}_{\mathrm{x}'}^\dagger \hat{a}_{\mathrm{x}'}\right) \\
\hat{S}_\mathrm{z} &= \frac{1}{2}\left(\hat{a}_+^\dagger \hat{a}_+ - \hat{a}_-^\dagger \hat{a}_-\right)
\end{aligned} \tag{5}$$

These operators obey the usual angular momentum commutation relations and the components form a basis for the Stokes vector which is used to represent the polarization state of the light. The quantity $\hat{S}_0$ is proportional to the number of photons interacting with the atomic system in one time increment. On any given measurement, the quantity $\hat{S}_0$ and a single component of the Stokes vector representing the polarization state (e.g., $\hat{S}_\mathrm{x}$) can be measured with an appropriate selection of polarization rotating waveplates situated after the atoms and prior to the polarizing beam-splitter. In the usual configuration (of Fig. (2)), $\hat{S}_\mathrm{x}$ is measured without any waveplates, $\hat{S}_\mathrm{y}$ is measured with a half-waveplate that rotates the linear polarization by 45-degrees, and $\hat{S}_\mathrm{z}$ is measured by adding a quarter-waveplate that completely circularizes linear polarized light.

In the case where a full quantum mechanical description is used, this choice of basis will change the nature of the information gained from the measurement which is then used to update the conditional collective quantum state describing the atoms. In other words, the choice of basis will lead to a different *unravelling* of the conditional dynamics.

B. Scattering Hamiltonian

We now introduce the polarizability Hamiltonian that determines the joint evolution of the single-atom spin and the polarization of the traveling-wave optical mode. Subsequently, we summarize the results from Appendix A where we derive a more convenient and intuitive way of representing the irreducible components of the Hamiltonian in terms of atomic spin operators instead of dipole operators.

For a field which is off-resonant to the transition of interest, the usual dipole Hamiltonian can be approximated and recast into a polarizability form. This can be derived, for example, by using adiabatic elimination under the assumption that the off-resonant field only weakly populates the excited states. The polarizability Hamiltonian [17, 30, 36] is then expressed as

$$\hat{H} = \sum_{f,f'} \hat{\mathbf{E}}^{(-)} \cdot \frac{\hat{P}_f \hat{\mathbf{d}} \hat{P}_{f'} \hat{\mathbf{d}}^\dagger \hat{P}_f}{\hbar \Delta_{f,f'}} \cdot \hat{\mathbf{E}}^{(+)}. \tag{6}$$

where we omit indices identifying the particular atom and spatial optical mode being considered. This definition consists of several terms which are also defined in Appendix A. The negative and positive frequency probe field operators, $\hat{\mathbf{E}}^{(-)}$ and $\hat{\mathbf{E}}^{(+)}$, describe the creation and annihilation of photons in the contributing probe modes. The atomic operators $\hat{\mathbf{d}}^\dagger$ and $\hat{\mathbf{d}}$ are the vector dipole raising and lowering operators. The ground and excited state angular momentum numbers are give by f and f' respectively. The probe detuning, $\Delta_{f,f'} = \omega - \omega_{f,f'}$, is defined as the difference between the probe frequency ω and a particular atomic resonance frequency. For the purposes of this paper we consider all of the population to remain in one ground state manifold ($f = 4$ for Cesium, ignoring $f = 3$) and sum only over the excited states ($f' = 2, 3, 4, 5$). The operators $\hat{P}_f$ and $\hat{P}_{f'}$ are projectors onto the ground and excited states respectively.

This Hamiltonian has a satisfying physical interpretation as a scattering interaction: the atom is first brought from its ground state to a virtual excited state via the raising operator, $\hat{\mathbf{d}}^\dagger$, by annihilating a photon from the probe field through $\hat{\mathbf{E}}^{(+)}$. Then, the temporarily excited atom returns to a (potentially different) ground state by emitting a photon into a (potentially different) scattered probe mode via $\hat{\mathbf{d}}$ and $\hat{\mathbf{E}}^{(-)}$.

The central operator in the scattering Hamiltonian,

$$\hat{\boldsymbol{\alpha}}_{f,f'} = \hat{P}_f \hat{\mathbf{d}} \hat{P}_{f'} \hat{\mathbf{d}}^\dagger \hat{P}_f, \tag{7}$$

commonly called the *atomic polarizability tensor*, is a dyad involving vector operators [29]. Thus $\hat{\boldsymbol{\alpha}}_{f,f'}$ is a rank-2 spherical tensor that can be decomposed into irreducible components,

$$\hat{\boldsymbol{\alpha}}_{f,f'} = \hat{\boldsymbol{\alpha}}^{(0)}_{f,f'} + \hat{\boldsymbol{\alpha}}^{(1)}_{f,f'} + \hat{\boldsymbol{\alpha}}^{(2)}_{f,f'}. \tag{8}$$

The scattering Hamiltonian similarly decomposes into irreducible spherical tensor operators,

$$\hat{H} = \hat{H}^{(0)} + \hat{H}^{(1)} + \hat{H}^{(2)} \tag{9}$$

where

$$\hat{H}^{(j)} = \sum_{f,f'} \hat{\mathbf{E}}^{(-)} \cdot \frac{\hat{\boldsymbol{\alpha}}^{(j)}_{f,f'}}{\hbar \Delta_{f,f'}} \cdot \hat{\mathbf{E}}^{(+)}. \tag{10}$$

The $\hat{H}^{(0)}$ is a scalar contribution, $\hat{H}^{(1)}$ transforms as a vector, and $\hat{H}^{(2)}$ transforms as a rank-2 symmetric tensor in the group representation theory of $SO(3)$. Were the atomic system composed of spin-$\frac{1}{2}$ particles, it would be possible to neglect the rank-2 Hamiltonian [30] (as will become explicit), however, we can not do so for higher-spin Alkali atoms [26, 27, 37].

The full Hamiltonian for the collective atomic spin resulting from N atoms is obtained by taking the symmetric sum of these single particle operators.

C. Hamiltonian Decomposition

Now we recast the single atom Hamiltonian of Eqs. (9, 10) into irreducible terms involving only atomic spin operators $\hat{f}_i$ and probe polarization operators $\hat{S}_i$ then discuss each component in physical terms. The derivation of these expressions is sketched in Appendix A.

1. *The Scalar Hamiltonian*

The scalar scattering Hamiltonian, $\hat{H}^{(0)}$, can be represented as a product of operators on the separate atomic and probe field Hilbert spaces. This is accomplished by combining the expressions for the field mode operators, Eqs. (3) and (4), with the rank-0 irreducible component of the atomic polarizability tensor. Evaluating this Hamiltonian using the form of the rank-0 atomic polarizability derived in Appendix A leads to the scalar scattering Hamiltonian,

$$\hat{H}^{(0)} \;=\; g \sum_{f'} \frac{\alpha^{(0)}_{f,f'}}{\Delta_{f,f'}} \frac{2}{3} \hat{S}_0 \hat{\mathbb{1}}_f. \tag{11}$$

where the constants $\alpha^{(0)}_{f,f'}$, defined in equation (A28) of the appendix, are related to the transition dipole matrix elements for the atomic hyperfine transitions.

This rank-0 Hamiltonian couples the atomic identity operator $\hat{\mathbb{1}}_f$ to the field mode number operator and can be interpreted as an atomic state-independent light shift. It therefore affects both polarization modes of the probe field in an equivalent manner and will not influence the measurement process since it does not provide any state-dependent information. However, this Hamiltonian would be important if the measurement was meant to distinguish between populations across hyperfine states (e.g. $f = 3$ and $f = 4$ using homodyne detection) instead of across the sub-level populations within one hyperfine state (using polarimetry, as discussed here). This term is also of importance if the Hamiltonian is being considered as a spatially dependent potential for the atoms (e.g., in an optical lattice).

2. *The Vector Hamiltonian*

The vector contribution to the atom-probe scattering Hamiltonian, can be evaluated in a similar manner using expressions for the rank-1 polarizability derived in the appendix,

$$\hat{H}^{(1)} \;=\; g \sum_{f'} \frac{\alpha^{(1)}_{f,f'}}{\Delta_{f,f'}} \hat{S}_{\mathrm{z}} \hat{f}_{\mathrm{z}}. \tag{12}$$

Here, the vector polarizability constant, $\alpha^{(1)}_{f,f'}$, is given by Eq. (A29), $\hat{f}_{\mathrm{z}}$ is the z-component of the (single-particle) atomic spin angular momentum.

The rank-1 Hamiltonian can be interpreted as causing a differential phase shift on the two circular polarization modes by an amount that is proportional to the z-component of the atomic angular momentum. Thus the vector Hamiltonian leads to optical activity in the atomic sample and produces the familiar Faraday rotation effect often used to address continuous measurement of collective spin [18, 20, 22–24].

3. *The Tensor Hamiltonian*

Finally the tensor Hamiltonian, can be evaluated using expressions for the rank-2 polarizability derived in the appendix to give,

$$\begin{aligned}\hat{H}^{(2)} &= g\sum_{f'}\frac{\alpha^{(2)}_{f,f'}}{\Delta_{f,f'}}\left(\hat{S}_{\mathrm{x}}\left(\hat{f}^2_{\mathrm{x}}-\hat{f}^2_{\mathrm{y}}\right)\right. \\ &\quad +\hat{S}_{\mathrm{y}}\left(\hat{f}_{\mathrm{x}}\hat{f}_{\mathrm{y}}+\hat{f}_{\mathrm{y}}\hat{f}_{\mathrm{x}}\right) \\ &\quad \left.+\,\hat{S}_0\left(3\hat{f}^2_{\mathrm{z}}-f(f+1)\hat{\mathbb{1}}_f\right)/3\right). \end{aligned} \tag{13}$$

Here, the tensor polarizability constant, $\alpha^{(2)}_{f,f'}$, is given by Eq. (A30).

The rank-2 Hamiltonian couples spin coordinates to the elliptical components of the probe laser field and produces a second-order light shift proportional to the atomic quadrupole moment. These terms vanish for $f = 1/2$ (as can be seen by evaluating the operators within the parentheses above) but are non-zero for any higher spin number. For a linearly polarized input beam, the tensor term leads to an elliptically polarized scattered probe field [26, 29]. The rank-2 interaction potentially limits the validity of any analysis of a continuous measurement of collective atomic spin in Alkali atoms based on the qualitative behavior of spin-$\frac{1}{2}$ particles.

D. Semiclassical Evolution of Probe State

We can greatly simplify the dynamics by eliminating atomic evolution due to the probe beam and only considering the evolution of the probe beam due to the atomic state. Under this semiclassical approximation, we replace all atomic operators with their expectation values with respect to an assumed fixed spin state. (This is the opposite of the semiclassical situation often considered in atom-light interactions where the atomic system is considered quantum mechanically while the optical beam is made classical.) For a large ensemble of atoms and small interaction times, fixing the atomic state will accurately reproduce the mean behavior of the measured photocurrent corresponding to one of the Stokes vector components. This is confirmed experimentally in the next section, where the atomic state is fixed and adiabatically positioned with a magnetic holding field. The holding field serves to both position the atomic state and protect it from the influence of the probe light, such that the analysis of this section remains valid even for long interaction times or large optical depth clouds. Ultimately, however, probe induced decoherence will dominate all interactions. In the final section, we then reconsider the full analysis including the atomic quantum noise (related to spin squeezing) for a particular alignment of the collective spin state.

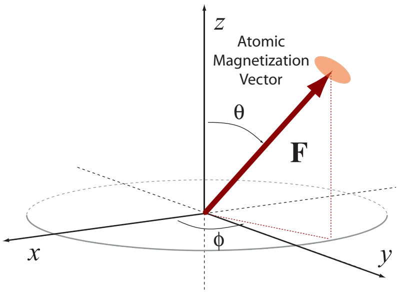

FIG. 3: Definition of the spherical coordinate angles used to describe the orientation of the collective atomic magnetization vector, **F**, relative to the fixed laboratory cartesian coordinate system. The polarization vector of the input probe light resides in the xy-plane and forms an angle, ϕ_p, with respect to the laboratory x-axis.

We approximate the N-atom Hamiltonian, $\hat{H}_N$, by replacing the single-atom operators with their expectation value taken with respect to an optically pumped spin pointing with direction θ and φ given in spherical coordinates (Fig. 3). In other words, for an individual atom operator $\hat{O}_f$, we take

$$\hat{O}_f \rightarrow \langle\hat{O}_f\rangle = \langle\Psi(\theta,\varphi)|\hat{O}_f|\Psi(\theta,\varphi)\rangle \tag{14}$$

where $|\Psi(\theta,\varphi)\rangle = \exp[-i\hat{f}_z\varphi]\exp[-i\hat{f}_y\theta]|f,f\rangle_z$.

The relevant operators from the Hamiltonian decomposition are given by

$$\begin{aligned}\langle\hat{f}_{\mathrm{z}}\rangle &= f\cos\theta && (15)\\ \langle\hat{f}^2_{\mathrm{x}}-\hat{f}^2_{\mathrm{y}}\rangle &= f(f-1/2)\sin^2\theta\cos 2\varphi && (16)\\ \langle\hat{f}_{\mathrm{x}}\hat{f}_{\mathrm{y}}-\hat{f}_{\mathrm{y}}\hat{f}_{\mathrm{x}}\rangle &= f(f-1/2)\sin^2\theta\sin 2\varphi && (17)\end{aligned}$$

Within the semiclassical approximation, we obtain an effective scattering interaction Hamiltonian that only involves operators on the probe field Hilbert space. Ignoring all terms proportional to $\hat{S}_0$ (because it commutes with each term of the semiclassical Hamiltonian) we have

$$\begin{aligned}\tilde{H} &= \tilde{H}^{(1)}_N + \tilde{H}^{(2)}_N \\ &= (\gamma_x\hat{S}_{\mathrm{x}}+\gamma_y\hat{S}_{\mathrm{y}}+\gamma_z\hat{S}_{\mathrm{z}})\frac{\hbar}{\delta t}\end{aligned} \tag{18}$$

which leads to a rotation of the Stokes vector $\hat{\mathbf{S}}$ about a vector $\vec{\gamma} = [\gamma_x, \gamma_y, \gamma_z]$ according to the evolution operator

$$\begin{aligned}\tilde{U}_{\delta t} &= \exp\left[-i\tilde{H}\frac{\delta t}{\hbar}\right] \\ &= \exp\left[-i(\gamma_{\rm x}\hat{S}_{\rm x}+\gamma_{\rm y}\hat{S}_{\rm y}+\gamma_{\rm z}\hat{S}_{\rm z})\right] \qquad (19)\end{aligned}$$

where $\delta t = L/c$ is the interaction (transit) time of the discrete spatial modes of the probe beam across the atomic cloud of length L. The rotation vector $\vec{\gamma}$ is defined by

$$\gamma_x = \gamma_0 f(f-1/2)\sin^2\theta\cos 2\varphi\sum_{f'}\frac{\alpha^{(2)}_{f,f'}}{\alpha_0\Delta_{f,f'}} \qquad (20)$$

$$\gamma_y = \gamma_0 f(f-1/2)\sin^2\theta\sin 2\varphi\sum_{f'}\frac{\alpha^{(2)}_{f,f'}}{\alpha_0\Delta_{f,f'}} \qquad (21)$$

$$\gamma_z = \gamma_0 f\cos\theta\sum_{f'}\frac{\alpha^{(1)}_{f,f'}}{\alpha_0\Delta_{f,f'}} \qquad (22)$$

Here we have normalized by the state-independent polarizability constant (see Appendix A)

$$\begin{aligned}\alpha_0 &= \frac{3\epsilon_0\hbar\Gamma\lambda_0^3}{8\pi^2} \qquad (23)\\ &= \left|\langle j||\hat{\mathbf{d}}||j'\rangle\right|^2\frac{(2j+1)}{(2j'+1)}\end{aligned}$$

such that $\alpha^{(j)}_{f,f'}/\alpha_0$ is dimensionless. The rotation strength is represented by

$$\gamma_0 = \frac{Ng\delta t\alpha_0}{\hbar}$$

where we have used the field coefficient $g = \omega_0/(2\epsilon_0 V)$, the atomic resonance frequency ω_0, and the interaction volume (the volume of the atomic sample) $V = AL$.

From an experimental standpoint, it is useful to note that γ_0 is directly related to the on-resonance optical depth OD of the atomic sample and the decay rate Γ via,

$$\gamma_0 = \left(\frac{\Gamma}{4}\right)\mathrm{OD} \qquad (24)$$

where

$$\mathrm{OD} = N\frac{\sigma_0}{A}, \quad \sigma_0 = \frac{3\lambda_0^2}{2\pi}. \qquad (25)$$

The quantity, σ_0, is the resonant atomic scattering cross section and $A = \pi r^2$ is the cross-sectional area of the atomic sample.

In Appendix B , the equations for a general rotation of $\mathbf{\hat{S}}$ about $\vec{\gamma}$ are given. Here we specialize to the case where the input beam is linearly polarized in the x-direction such that $\langle\hat{S}_y\rangle = \langle\hat{S}_z\rangle = 0$. The output expectation values are then given by

$$\begin{aligned}\langle\hat{S}'_x\rangle &= \langle\hat{S}_x\rangle\left(\cos\gamma+\frac{\gamma_x^2}{\gamma^2}(1-\cos\gamma)\right) \qquad (26)\\ \langle\hat{S}'_y\rangle &= \langle\hat{S}_x\rangle\left(-\frac{\gamma_z}{\gamma}\sin\gamma+\frac{\gamma_y\gamma_x}{\gamma^2}(1-\cos\gamma)\right)\\ \langle\hat{S}'_z\rangle &= \langle\hat{S}_x\rangle\left(\frac{\gamma_y}{\gamma}\sin\gamma+\frac{\gamma_z\gamma_x}{\gamma^2}(1-\cos\gamma)\right)\end{aligned}$$

Taking the total rotation angle small ($\gamma \ll 1$) this becomes (to second order in γ)

$$\langle\hat{S}'_x\rangle \approx \langle\hat{S}_x\rangle\left(1-\gamma_z^2/2-\gamma_y^2/2\right) \qquad (27)$$

$$\langle\hat{S}'_y\rangle \approx \langle\hat{S}_x\rangle\left(-\gamma_z+\frac{\gamma_y\gamma_x}{2}\right) \qquad (28)$$

$$\langle\hat{S}'_z\rangle \approx \langle\hat{S}_x\rangle\left(\gamma_y+\frac{\gamma_z\gamma_x}{2}\right) \qquad (29)$$

In this semiclassical approximation, we have completely neglected any evolution of the atomic state due to the probe beam. We demonstrate in the next section that the above model agrees well with experimental data when the spin state is fixed with a magnetic holding field.

III. EXPERIMENTAL RESULTS

In this section, we show that the model described above is consistent with representative data collected from our experiment with laser cooled Cs atoms and balanced polarimetric detection of a forward-scattered, off-resonant probe laser field.

A. Experimental Apparatus

Figure 4 provides a schematic of the major components of the experimental apparatus. Our single-particle Alkali atom spin system is the $6^2\mathrm{S}_{1/2}$(f=4) ground state hyperfine manifold in ^{133}Cs with $4\hbar$ of intrinsic angular momentum due to a combination of the $i = 7/2$ nuclear spin and the $s = 1/2$ spin of an unpaired 6s valence electron. We obtain cold atom samples from a 10^{-9} Torr background Cs vapor using standard laser cooling and trapping techniques by collecting more than 10^9 atoms in a magneto-optic trap (MOT). Trapping beams are derived from a 150 mW injection-locked diode laser tuned (11-15) MHz red of the Cs $6^2\mathrm{S}_{1/2}$(f=4)→$6^2\mathrm{P}_{3/2}$(f′=5) cycling transition. Each 35 mW trapping beam has an approximately constant intensity profile and a 2.5 cm diameter. A 10 mW repump laser tuned to the $6^2\mathrm{S}_{1/2}$(f=3)→$6^2\mathrm{P}_{3/2}$(f′=4) transition is used to prevent atomic population from decaying out of the trapping cycling transition.

Following the atom collection phase, the sample is sub-Doppler cooled [38] to a temperature of $T \sim 10\ \mu$K and the initial x-polarized spin state is prepared with a circularly polarized 100 μW optical pumping beam (pulsed

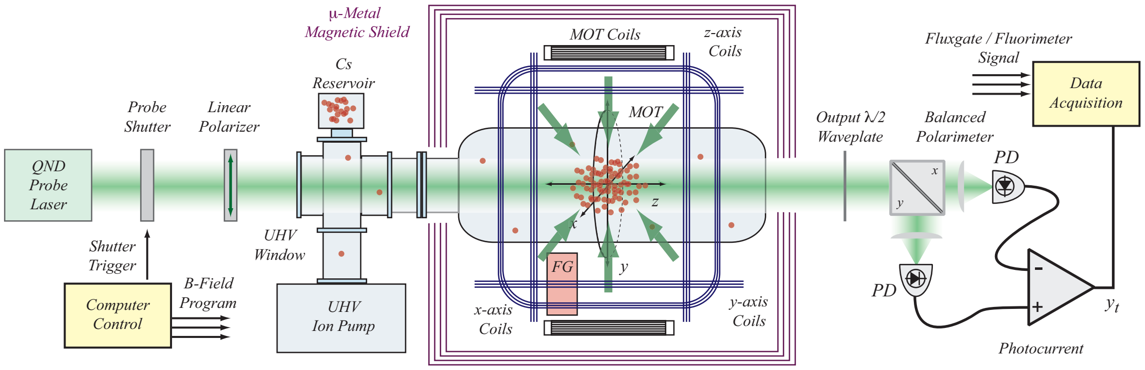

FIG. 4: Schematic of our experimental apparatus in which collective spin angular momentum of a cloud of laser cooled Cs atoms is measured by polarimetric detection of a scattered off-resonant probe laser. Ambient magnetic field fluctuations are supressed by magnetic shielding and can be monitored with a fluxgate magnetometer (FG) situated nearby the atomic sample. Components not shown include the optical pumping laser (aligned along the laboratory x-axis) and external trim coils used to zero ambient magnetic fields and their first order gradients.

for 2-4 ms) propagating along the x-axis and tuned to the (f=4)→(f′=4) hyperfine transition. A 100 mG magnetic holding field is applied along the laboratory x-axis to define the optical pumping direction.

Continuous measurement of the polarized atomic ensemble is implemented with a nearly quantum shotnoise-limited probe laser that can be detuned from the $6^2\mathrm{S}_{1/2}$(f=4)→$6^2\mathrm{P}_{3/2}$(f′=5) Cs transition over a range $\Delta = \pm 1.4$ GHz. The probe beam is linearly polarized by a high extinction Glan-Thompson prism prior to passing through the cold atom cloud, and the orientation of the linear polarization vector with respect to the laboratory coordinate system may be rotated via an input half-waveplate. The scattered probe field is detected with a polarimeter constructed from a Glan-Thompson polarizing beam splitter and a DC-balanced photodetector with >1 MHz measurement bandwidth.

A computer controls the experiment timing and records the polarimeter output as well as diagnostic information including background magnetic field fluctuations (measured with a flux-gate magnetometer) and atom number (measured by fluorescence imaging). The computer enables/disables the measurement by controlling a shutter on the probe laser, constructed from a switched acousto-optic modulator, with 100 ns resolution. Magnetic fields with magnitudes up to ~ 0.5 G can be applied in arbitrary (time-dependent) directions by driving 3 pairs of computer-controlled Helmholtz coils, oriented along the laboratory x-, y-, and z-axes, with a bandwidth of ~ 1 MHz.

Background magnetic field fluctuations are suppressed through a combination of passive μ-metal shielding and field cancellation via external trim coils. Each atom preparation (trapping, cooling and optical pumping) and measurement cycle is synchronized with respect to the 60-Hz building power lines to suppress the effects of induced magnetic fields. Slow magnetic drift due to natural and anthropogenic sources are cancelled by adjusting the external trim coils based on the output of the fluxgate magnetometer.

B. Verification of the Probe Scattering Model

Our model of the scattered probe polarization as a function of the orientation of the atomic magnetization vector was compared against experiment by observing the polarimeter photocurrent as the orientation of the atomic polarization was varied according to different specified paths in the laboratory coordinate system. This was accomplished as follows. An x-polarized cold atom sample was prepared according to the description above and an x-axis magnetic holding field of 100 mG was applied. At this point, the probe shutter was opened and the balanced polarimeter photocurrent was monitored while the orientation of the magnetic holding field was varied according to the specified path. The rate of change of the holding field orientation was chosen to be slow (ms) compared to the atomic Larmor precession frequency (hundreds of kHz) such that the atomic magnetization vector adiabatically followed the path traced by the holding field. Furthermore the holding field was large enough to dominate the probe light induced dynamics at short times, but not so strong as to shift the levels significantly compared to the detuning.

With a strong enough holding field, the spin state (and hence the semiclassical rotation vector $\vec{\gamma}$) will be fixed across the spatially extended cloud. Because rotations of the Stokes vector about the same vector will commute, the semiclassical analysis of the previous section will be valid for even large optical depth samples where the total optical polarization rotation is significant.

This process was performed for two different adiabatic paths on the atomic Bloch sphere:

- ***xz*-Plane Rotation**: the atomic magnetization follows a path beginning along the x-axis and rotates around the y-axis: $\theta = \pi/2 \rightarrow -\pi/2$ with

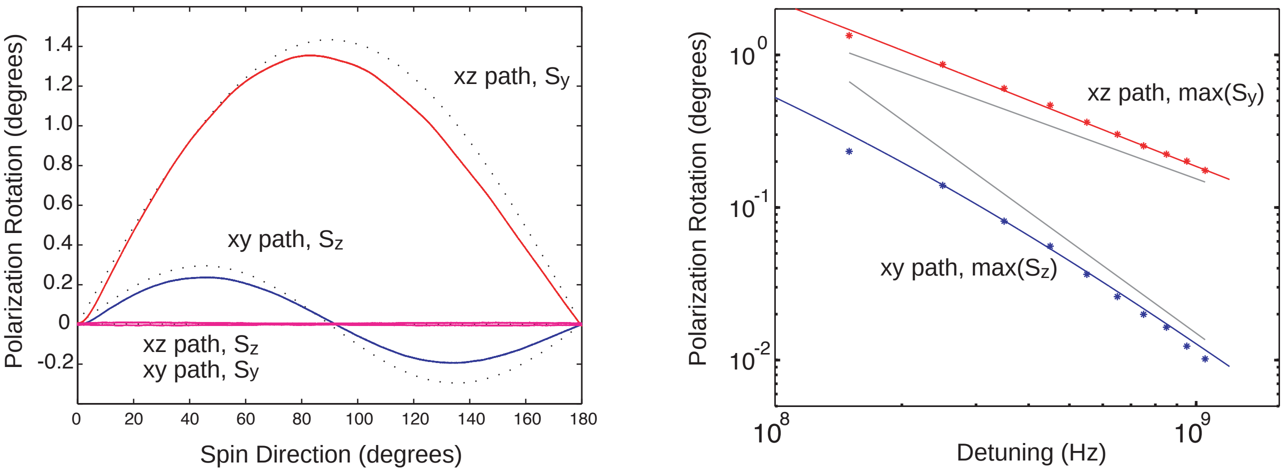

FIG. 5: Comparison of our model of continuous measurement with photocurrents obtained from from the experiment with $N = 1 \times 10^9$ Cs atoms in an $r = 4$ mm spherical trap and a $P = 10$ μW probe field blue-detuned from the (f=4)→(f′=5) D_2 hyperfine transition ($\lambda_0 = 852$ nm). Each trajectory is averaged 10 times. (A) For an input probe beam with x-polarization and a detuning of 150 MHz, $\hat{S}_\mathrm{y}$ and $\hat{S}_\mathrm{z}$ were measured for both the xz and xy trajectories (described in the text) resulting in the solid curves. All trajectory times are $\tau = 2$ ms, during which we observe some atomic decoherence which causes the prediction (dotted curves) to stray from the data. (B) As a function of probe detuning, we plot the peak of the $\hat{S}_\mathrm{y}$ measurement (for the xz trajectory) which depends only on rank-1 terms and the peak of the $\hat{S}_\mathrm{z}$ measurement (for the xy trajectory) which depends only on rank-2 terms. The predicted behavior (solid curves) shows good agreement with the data out to large detunings where the curves asymptote to the $1/\Delta$ and $1/\Delta^2$ lines provided to guide the eye.

fixed $\varphi = 0$.

- ***xy*-Plane Rotation**: the atomic magnetization follows a path beginning along the x-axis and rotates around the z-axis: $\varphi = 0 \to \pi$ with fixed $\theta = \pi/2$.

We chose these two trajectories because they highlight the different contributions from the rank-1 and rank-2 scattering interactions, as seen from Eqs. (20, 21, 22). The xz-plane trajectory, where $\varphi = 0$, virtually eliminates the rank-2 tensor contribution to the photocurrent leaving nearly ideal Faraday rotation. Conversely, the xy-plane rotation eliminates rank-1 contributions and produces elliptical scattered probe polarizations.

1. *Measuring the Scattering Probe Stokes Vector*

Fig. 5A compares the measured polarimeter photocurrents (solid curves) for these two adiabatic trajectories with those predicted by our atom-field scattering model (dotted curves). The input state was polarized in the x direction and because the total polarization rotation angle induced by the atoms γ was small, we measured only the other two components $\hat{S}_\mathrm{y}$ and $\hat{S}_\mathrm{z}$ with the appropriate arrangement of waveplates prior to the polarimeter. For measuring $\hat{S}_\mathrm{y}$ a single half-waveplate is placed prior to the polarizing beamsplitter (PBS) to rotate the polarization by 45 degrees, and for $\hat{S}_\mathrm{z}$ a quarter-waveplate is used to circularize the initial linearly polarized light.

We now refer to Eq. (28) and Eq. (29) to explain the observed trajectories. For the xz trajectory, we have $\gamma_y = 0$ such that $\hat{S}_\mathrm{y}$ contains a large linear term in γ_z but $\hat{S}_\mathrm{z}$ only contains terms quadratic in γ. Thus, for this path, the measurement of $\hat{S}_\mathrm{y}$ leads to the top curve in Fig. 5A which is proportional to the rank-1 polarizability, while the measurement of $\hat{S}_\mathrm{z}$ is much smaller and effectively zero. For the xy trajectory, we have $\gamma_z = 0$ such that $\hat{S}_\mathrm{z}$ contains a large linear term in γ_y but $\hat{S}_\mathrm{y}$ only contains terms quadratic in γ. Thus, for this path, the measurement of $\hat{S}_\mathrm{z}$ leads to the middle curve in Fig. 5A which is proportional to the rank-2 polarizability, while the measurement of $\hat{S}_\mathrm{y}$ is much smaller and effectively zero. The doubling of frequency between the two dominant curves is a direct consequence of the tensor nature of the rank-2 term.

Note that there is some structure expected in the two curves (quadratic in γ) which are approximately zero, but these are more polluted by technical noise and do not reveal any essentially new information about the interaction. For the larger curves (linear in γ), deviations of the measured photocurrents relative to the predicted values seen in Fig. 5A result mainly from the fact that the model does not consider the probe-induced damping.

The predicted curves use values for the atom number, trap volume, probe power and detuning consistent with independent characterizations of those parameters. The atom number and trap volume were obtained from fluorescence detection of the MOT and a CCD image of the atom cloud, and the resulting values, $N = 1 \times 10^9$ and

$r = 4$ mm, correspond to an optical depth, OD ~ 7, which is consistent with absorption measurements that we performed. Given our uncertainty in measuring the number of atoms, it can be inferred that our optical pumping efficiency in these (relatively) optically thin atomic samples is no less than 85% (but is more likely >90%) [16].

2. *Relative Scaling of the Scattering Terms with Probe Detuning*

As further verification of our scattering model, we investigated the scaling of the rank-1 and rank-2 contributions to the polarimeter photocurrent as a function of the probe detuning. With reference to Fig. (5A), the magnitude of the vector and tensor scattering interactions were measured from the peak amplitude of the $\hat{S}_\mathrm{y}$ measurement (for the xz plane rotation) and the amplitude of the $\hat{S}_\mathrm{z}$ measurement (for the xy-plane rotation) respectively. This plot compares these measured signal amplitudes (stars) with those predicted by our scattering model (solid curves) for detunings (with respect to the (f=4)→(f′=5) hyperfine transition) ranging from 150 MHz to 1.05 GHz.

The fact that multiple excited state hyperfine levels participate in the scattering interaction is evident from scalings which are not constant in Δ^{-1} or Δ^{-2}. As supported by our full model of the scattering interaction, we observe no qualitative difference in the continuous measurement for probe detunings smaller than the hyperfine splittings. This suggests that conditional spin-squeezing experiments can be performed with small detunings provided that the probe intensity is weak enough that the small decoherence requirement is satisfied.

IV. SPIN-SQUEEZING WITH MULTILEVEL ATOMS

Until this point we have considered only the semiclassical evolution of the optical probe beam due to an ensemble of atoms with a fixed atomic spin state. Now we consider a different experimental scenario appropriate for preparing conditional spin-squeezed states of the atomic ensemble. As opposed to the previous situation, we remove the adiabatic holding field which makes spin-squeezing impossible as it will cause undesired mixing of the squeezed and anti-squeezed components perpendicular to the mean spin. Although the holding field may serve to validate the previous semiclassical analysis for longer times by eliminating the probe-induced evolution of the atomic state, this analysis is still valid for small times and weak interactions without a holding field. Thus our goal is to derive the small time signal-to-noise ratio by deriving the signal strength from the previous section and comparing this to the optical shotnoise. We then use the signal-to-noise ratio to predict the rate of squeezing in a typical experimental configuration where the tensor terms can be ignored.

Considering only the relatively low optical density limit, the measurement of $\hat{S}_\mathrm{y}$ will result in Eq. (28). Now we wish to re-write this equation in the form of Eq. (2) including measurement noise. It is readily shown that all terms not linear in F_z vanish in Eq. (28) provided that $\theta = \pi/2$ and $\phi = 0$. That is, a pure Faraday rotation Hamiltonian is recovered when the atomic magnetization vector is oriented along the x-axis. However, rotating $\mathbf{F}$ in the xy-plane results in elliptically polarized scattered probe light, and moving out of this plane results in nonlinear atomic dephasing due to scattering terms which are quadratic in the single-particle spin operators, $\hat{f}_\mathrm{z}$. These adverse effects are avoided for the experimental geometry where $\mathbf{F}$ is collinear with the x-axis. Fortunately, spin-squeezing experiments are easily operated under such conditions [7].

Taking the input probe field to be in an x-polarized optical coherent state, and considering the small γ limit, Equation (28) leads to a semiclassical photocurrent (with units of optical power) of the form,

$$y_t = \eta\sqrt{S}F_\mathrm{z} + \sqrt{\eta}\,\zeta_t, \tag{30}$$

where we have made the substitution, $\hbar N f \cos\theta \rightarrow F_\mathrm{z}$ (refer to Eq. (15)), and included the photodetector quantum efficiency, η. Note that we have introduced ζ_t which represents optical shotnoise. We have also introduced a constant, S, the *scattering strength*,

$$S = \frac{1}{\hbar^2}\left[I_p\sigma_0\left(\frac{\Gamma}{4}\right)\sum_{f'}\frac{\alpha^{(1)}_{f,f'}}{\alpha_0\Delta_{f,f'}}\right]^2, \tag{31}$$

that depends up the probe intensity, $I_p = P/A$, determined by the coherent state amplitude, $P = 2\hbar\omega|\beta|^2$ and cross-sectional area, $A = \pi r^2$ (for a mode-matched probe laser). It is useful to note that the scattering strength has units of $\mathrm{W}^2/\hbar^2$ (power squared per $\hbar^2$) and characterizes the degree of coupling between the atoms and the probe field; $\sqrt{S}$ quantifies the polarimeter optical power imbalance per unit spin (as F_z has units of $\hbar$).

Our expressions are similar to previous results [21, 24, 39] in that it appears as a Faraday rotation signal. However, our specific expressions for γ_x, γ_y and γ_z account for the detailed hyperfine structure of the atomic excited states, including the fact that the oscillator strengths and signs of the contributions from different participating excited states are not equal, and doing so is required for quantitative agreement between theory and experiment.

To arrive at an expression for the *measurement strength*, M, as defined in Eq. (2), we must consider the variance, $\Delta\zeta^2$, of the white noise increments ζ_t. For an optical coherent state [40, 41], this noise variance is given by the familiar optical shotnoise expression,

$$\Delta\zeta^2 = \mathbb{E}[\zeta_t^2] = 2\hbar\omega P, \tag{32}$$

which has units of W^2/Hz (power squared per frequency). Comparing the semiclassical photocurrent of Eq. (30) to the photocurrent of Eq. (2), the measurement strength is seen to be given by the ratio

$$M = \frac{S}{\Delta\zeta^2} = \frac{1}{2\hbar^2}\tau_{\mathrm{s}}^{-1}\left(\frac{\sigma_0}{A}\right), \tag{33}$$

where we have defined the reciprocal scattering time as

$$\tau_{\mathrm{s}}^{-1} = \frac{I\sigma_0}{\hbar\omega}\left(\frac{\Gamma}{4}\sum_{f'}\frac{\alpha^{(1)}_{f,f'}}{\alpha_0\Delta_{f,f'}}\right)^2, \tag{34}$$

which is essentially the rate that probe photons are scattered by the atomic system. This expression is similar to that derived in Ref. [18].

Now consider a measurement of F_{z} by Eq. (2). In the small time limit where probe induced decoherence can be neglected, the full quantum filter describing this measurement is equivalent a classical model in which F_{z} is simply a random constant on every trial drawn from a distribution with variance equal to the quantum variance of $\langle\Delta F_{\mathrm{z}}^2\rangle_0$ [42]. Then the generally complicated full quantum filter [25] is equivalent to linear regression, or fitting a constant to the noisy measurement record in real time. In essence, the optimal filter serves to average away the optical shotnoise to reveal the underlying value of F_{z}. Under these statistical assumptions, at small times the quantum uncertainty is given by

$$\langle\Delta F_{\mathrm{z}}^2\rangle_\tau = \frac{\langle\Delta F_{\mathrm{z}}^2\rangle_0}{1+\eta\langle\Delta F_{\mathrm{z}}^2\rangle_0 M\tau}. \tag{35}$$

This can be shown either with the full quantum filter or by using the equivalent classical model combined with Bayesian estimation (from which a Kalman filter or linear regression can be derived).

These concepts are illustrated by the simulated measurement trajectory in Fig. 6. The plot begins with the probe laser turned off, during which all necessary state preparation of the atomic system such as atom trapping, cooling and optical pumping into an x-polarized coherent spin state is performed. Once the probe light is enabled at $t = 0$, the photocurrent acquires a mean offset, $\eta\sqrt{S}F_{\mathrm{z}}$, proportional to the spin measurement outcome, F_{z}, but this mean value is masked by photocurrent noise. At short times, the signal is overwhelmed by local statistical fluctuations; however, averaging the photocurrent suppresses the uncertainty in the mean signal by integrating away the white noise, illustrated by the dotted lines in Fig. 6.

If we define the signal to noise ratio as

$$\mathrm{SNR}^2 \equiv \eta\langle\Delta F_{\mathrm{z}}^2\rangle_0 M\tau \tag{36}$$

we can then express the degree of squeezing (ignoring decay of the F_{x}) as

$$\begin{aligned} W &\equiv \frac{\langle\Delta F_{\mathrm{z}}^2\rangle_t}{\langle\Delta F_{\mathrm{z}}^2\rangle_0} \\ &= \frac{1}{1+\mathrm{SNR}^2} \end{aligned} \tag{37}$$

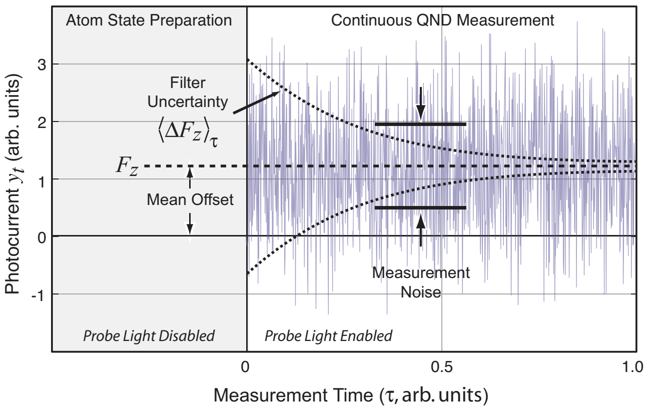

FIG. 6: Simulated photocurrent ($\eta = 1$) for a continuous measurement of atomic spin angular momentum via balanced polarimetry. At the onset of the measurement, $t = 0$, the photocurrent assumes a mean offset proportional to the z-component of the spin, but this offset is masked by white noise due, in part, to optical shotnoise on the probe laser. Filtering the photocurrent gradually reduces the uncertainty in the photocurrent offset and produces spin-squeezing.

Using $\langle\Delta F_{\mathrm{z}}^2\rangle_0 = \hbar^2 Nf/2$, we can express the signal to noise ratio as

$$\mathrm{SNR}^2 = \eta\mathrm{OD}\frac{f}{4}\frac{\tau}{\tau_s} \tag{38}$$

To keep this expression valid we must have $\tau \ll \tau_s$, so our only recourse to creating large amounts of squeezing in free space is to increase both the quantum efficiency η and the optical depth OD as much as possible.

V. CONCLUSION

In this work, we have derived the most useful form of the polarizability Hamiltonian describing the realistic measurement of an ensemble of multilevel alkali atoms with an off-resonant probe beam. We then showed that this model was consistent with experimental observations in the semiclassical limit where the atomic state was adiabatically directed with a strong magnetic field. We found that an adequate comparison was only possible after including all relevant hyperfine transitions including their relative (non-unit) oscillator strengths in our model of the atomic physics.

We then developed a model for describing conditional spin-squeezing in Alkali atoms. Detailed investigation of the atom probe scattering physics indicates that it is possible to eliminate unwanted tensor components of the atomic polarizability by adopting a suitable atomic and optical polarization geometry. This includes the elimination of dephasing due to the quadratic light shift [27] without sacrificing a fixed laboratory coordinate system for the measurement. Moreover, we found that conditional spin-squeezing experiments could be performed at small optical detunings without a substantial change in the form of the photocurrent or filtering approach.

Acknowledgments

The authors would like to thank Poul Jessen, Ivan Deutsch, Andrew Silberfarb, Dima Budker and especially Ramon van Handel and Andrew Doherty for numerous insightful discussions. We would also like to thank Sebastian de Echaniz, Jacob Sherson, and Eugene Polzik for pointing out important corrections. This work was supported by the Caltech MURI Center for Quantum Networks (DAAD19-00-1-0374). JMG acknowledges support from the Caltech Center for Physics of Information and JKS acknowledges support from a Hertz Fellowship.

---

[1] V. Braginski and F. Khalili, *Quantum Measurements* (Cambridge University Press, 1992).

[2] M. Brune, S. Haroche, V. Lefevre, J. Raimond, and N. Zagury, Phys. Rev. Lett. **65**, 976 (1990).

[3] G. Nogues, A. Rauschenbeutel, S. Osnaghi, M. Brune, J. Raimond, and S. Haroche, Nature **400**, 239 (1999).

[4] M. Kitagawa and M. Ueda, Phys. Rev. A **47**, 5138 (1993).

[5] A. Kuzmich, L. Mandel, and N. P. Bigelow, Phys. Rev. Lett. **85**, 1594 (2000).

[6] B. Julsgaard, A. Kozhekin, and E. S. Polzik, Nature **413**, 400 (2001).

[7] J. Geremia, J. K. Stockton, and H. Mabuchi, Science **304**, 270 (2004).

[8] A. Sørensen, L.-M. Duan, J. Cirac, and P. Zoller, Nature **63**, 409 (2001).

[9] A. Sørensen and K. Mølmer, Phys. Rev. Lett. **86**, 4431 (2001).

[10] D. J. Wineland, J. J. Bollinger, W. M. Itano, and D. J. Heinzen, Phys. Rev. A **50**, 67ñ88 (1994).

[11] J. Geremia, J. K. Stockton, A. C. Doherty, and H. Mabuchi, Phys. Rev. Lett. **91**, 250801 (2003).

[12] J. Geremia, J. K. Stockton, and H. Mabuchi, Phys. Rev. Lett. **94**, 203002 (2005).

[13] A. Andre, A. Sørensen, and M. Lukin, Phys. Rev. Lett. **92**, 230801 (2004).

[14] V. Peterson, L. B. Madsen, and K. Mølmer, Phys. Rev. A **71**, 012312 (2005).

[15] J. K. Stockton, J. Geremia, A. C. Doherty, and H. Mabuchi, Phys. Rev. A **67**, 022122 (2003).

[16] B. Julsgaard, J. Sherson, J. Sorensen, and E. Polzik, J. Opt. B: Quantum Semiclass. Opt. **6**, 5 (2004).

[17] W. Happer, Rev. Mod. Phys **44**, 169 (1972).

[18] G. A. Smith, S. Chaudhury, and P. S. Jessen, J. Opt. B: Quant. Semiclass. Opt. **5**, 323 (2003).

[19] Y. Takahashi, K. Honda, N. Tanaka, K. Toyoda, K. Ishikawa, and T. Yabuzaki, Phys. Rev. A **60**, 4974 (1999).

[20] A. Kuzmich, N. Bigelow, and L. Mandel, Europhys. Lett. **42**, 481 (1998).

[21] L. K. Thomsen, S. Mancini, and H. M. Wiseman, Phys. Rev. A **65**, 061801 (2002).

[22] L. K. Thomsen and H. Wiseman, Phys. Rev. A **65** (2002).

[23] L. K. Thomsen, S. Mancini, and H. Wiseman, J. Phys. B: At. Mol. Opt. Phys. **35**, 4937 (2002).

[24] A. Silberfarb and I. Deutsch, Phys. Rev. A **68**, 013817 (2003).

[25] R. van Handel, J. K. Stockton, and H. Mabuchi, J. Opt. B: Quantum Semiclass. Opt. **7**, S179 (2005).

[26] D. Kupriyanov, O. Mishina, I. Sokolov, B. Julsgaard, and E. Polzik, Phys. Rev. A **71**, 032348 (2005).

[27] G. A. Smith, S. Chaudhury, A. Silberfarb, I. H. Deutsch, and P. S. Jessen, Phys. Rev. Lett. **93**, 163602 (2004).

[28] A. Silberfarb, P. S. Jessen, and I. H. Deutsch (2005), quant-ph/0412032.

[29] W. Happer and B. Mathur, Phys. Rev. Lett. **163**, 12 (1967).

[30] I. H. Deutsch and P. Jessen, Phys. Rev. A **57**, 1972 (1998).

[31] H. Nha and H. Carmichael, Phys. Rev. A **71**, 013805 (2005).

[32] J. Mueller, P. Petrov, D. Oblak, C. G. Alzar, S. de Echaniz, and E. Polzik, Phys. Rev. A **71**, 033803 (2005).

[33] L. M. Duan, J. I. Cirac, and P. Zoller, Phys. Rev. A **66**, 023818 (2002).

[34] I. Bouchoule and K. Mølmer, Phys. Rev. A **66**, 043811 (2002).

[35] C. M. Caves, Phys. Rev. D **35**, 1815 (1987).

[36] C. Cohen-Tannoudji, J. Dupont-Roc, and G. Grynberg, *Atom Photon Interactions* (Wiley-Interscience, New York, 1992).

[37] I. Carusotto and E. J. Mueller, J. Phys. B **37**, S115 (2004).

[38] P. L. Gould and H. J. Metcalf, Phys. Rev. Lett. **61**, 169 (1988).

[39] D. Oblak, J. K. Mikkelsen, W. Tittel, A. K. Vershovski, J. L. Sorensen, P. G. Petrov, C. L. G. Alzar, and E. S. Polzik, Phys. Rev. A **71**, 043807 (2005).

[40] R. Glauber, Phys. Rev. Lett. **131**, 2766 (1963).

[41] L. Mandel and E. Wolf, *Optical Coherence and Quantum Optics* (Cambridge University Press, 1995).

[42] J. K. Stockton, J. Geremia, A. C. Doherty, and H. Mabuchi, Phys. Rev. A **69**, 032109 (2004).

[43] G. Baym, *Lectures on Quantum Mechanics* (W. A. Benjamin, Inc., 1969).

[44] J. J. Sakurai, *Modern Quantum Mechanics* (Addison-Wesley Publishing Company, 1994).

[45] D. A. Varshalovich, A. N. Moskalev, and V. K. Khersonskii, *Quantum Theory of Angular Momentum* (World Scientific, 1988).

APPENDIX A: THE IRREDUCIBLE REPRESENTATION OF THE POLARIZABILITY HAMILTONIAN

In this appendix, we derive the irreducible components of the polarizability Hamiltonian, Eqs. (11, 12, 13), from the less useful form of Eq. (6). We begin by clarifying notation used for the spherical basis and the spin states of the Alkali atoms. Then we discuss properties of the polarizability Hamiltonian and the dipole operator before detailing the decomposition and re-formatting of the Hamiltonian into its irreducible form.

1. Spherical basis

The spherical basis is the preferred basis when dealing with atomic transitions due to its symmetry properties. The basis is defined by the transformation from Cartesian coordinates

$$\begin{aligned} \vec{\mathbf{e}}_{+} &= -(\vec{\mathbf{e}}_x + i\vec{\mathbf{e}}_y)/\sqrt{2} \\ \vec{\mathbf{e}}_{-} &= (\vec{\mathbf{e}}_x - i\vec{\mathbf{e}}_y)/\sqrt{2} \\ \vec{\mathbf{e}}_0 &= \vec{\mathbf{e}}_z \end{aligned} \tag{A1}$$

Thus elements in the spherical basis have the properties

$$\begin{gathered} \vec{\mathbf{e}}_q^{*} = \vec{\mathbf{e}}_{-q}(-1)^q \\ \vec{\mathbf{e}}_q \cdot \vec{\mathbf{e}}_{q'}^{*} = \delta_{q,q'} \end{gathered} \tag{A2}$$

and for an arbitrary vector $\mathbf{A}$ we have $A_q = \vec{\mathbf{e}}_q \cdot \mathbf{A}$ so that $\mathbf{A} = \sum_q A_q \vec{\mathbf{e}}_q^{*} = \sum_q (-1)^q A_q \vec{\mathbf{e}}_{-q}$.

2. Alkali spin states

We represent the internal state of the atom in terms of the (Zeeman degenerate) atomic hyperfine states, $|f, m\rangle$. Here f and f' are the total spin quantum numbers for the ground and excited hyperfine levels respectively while m and m' are their projections on the z-axis. That is to say, $|f, m\rangle$ are eigenstates of the total atomic angular momentum,

$$\hat{\mathbf{f}} = \hat{\mathbf{s}} \otimes \mathbb{1}_{l\otimes i} + \mathbb{1}_s \otimes \hat{\mathbf{l}} \otimes \mathbb{1}_i + \mathbb{1}_{s\otimes l}\hat{\mathbf{i}} \tag{A3}$$

where $\hat{\mathbf{s}}$, $\hat{\mathbf{l}}$, and $\hat{\mathbf{i}}$ are respectively the electron spin, orbital angular momentum, and the nuclear spin. The quantum numbers, f, and m, are defined in the usual manner,

$$\begin{aligned} \hat{\mathbf{f}}^2|f, m\rangle &= \hbar^2 f(f+1)|f, m\rangle \\ \hat{f}_z|f, m\rangle &= \hbar m|f, m\rangle \end{aligned} \tag{A4}$$

We use the notation that $\hat{f}_{\pm}$ are in the spherical basis

$$\hat{f}_{\pm} = \mp(\hat{f}_{\mathrm{x}} \pm i\hat{f}_{\mathrm{y}})/\sqrt{2}. \tag{A5}$$

It will also be useful to define a projector onto the ground state f

$$\hat{P}_f = \sum_m |f, m\rangle\langle f, m| \tag{A6}$$

and a projector onto the excited state f'

$$\hat{P}_{f'} = \sum_{m'} |f', m'\rangle\langle f', m'|. \tag{A7}$$

3. Hamiltonian approximation

We begin with the single-particle dipole Hamiltonian $H = -\hat{\mathbf{d}} \cdot \hat{\mathbf{E}}$. The dipole operator $\hat{\mathbf{d}} = e\hat{\mathbf{r}}_e$ can be split into its raising and lowering components

$$\begin{aligned} \hat{\mathbf{d}} &= \hat{\mathbf{d}}^{(-)} + \hat{\mathbf{d}}^{(+)} \\ \hat{\mathbf{d}}^{(-)} &= \sum_{f,f'} \hat{P}_f \hat{\mathbf{d}} \hat{P}_{f'} \\ \hat{\mathbf{d}}^{(+)} &= \sum_{f,f'} \hat{P}_{f'} \hat{\mathbf{d}} \hat{P}_f \end{aligned} \tag{A8}$$

and the electric field operator can be split into rotating and counter-rotating terms

$$\begin{aligned} \hat{\mathbf{E}} &= \hat{\mathbf{E}}^{(-)} + \hat{\mathbf{E}}^{(+)} \\ \hat{\mathbf{E}}^{(-)} &= \sqrt{\hbar g}\left[\hat{a}_{-}^{\dagger}\vec{\mathbf{e}}_{-}^{*} + \hat{a}_{+}^{\dagger}\vec{\mathbf{e}}_{+}^{*}\right] \\ \hat{\mathbf{E}}^{(+)} &= \sqrt{\hbar g}\left[\hat{a}_{-}\vec{\mathbf{e}}_{-} + \hat{a}_{+}\vec{\mathbf{e}}_{+}\right] \end{aligned} \tag{A9}$$

After using the rotating wave approximation and one of many available perturbation expansion techniques (e.g., adiabatic elimination) we arrive at the familiar polarizability Hamiltonian [17, 30, 36],

$$\hat{H} = \sum_{f,f'} \hat{\mathbf{E}}^{(-)} \cdot \frac{\hat{\boldsymbol{\alpha}}_{f,f'}}{\hbar\Delta_{f,f'}} \cdot \hat{\mathbf{E}}^{(+)} \tag{A10}$$

where the atomic polarizability between a particular ground state (f) and excited state (f') is defined as

$$\hat{\boldsymbol{\alpha}}_{f,f'} = \hat{P}_f \hat{\mathbf{d}} \hat{P}_{f'} \hat{\mathbf{d}}^{\dagger} \hat{P}_f \tag{A11}$$

$$= \sum_m \sum_{m'} \sum_{m''} |f, m''\rangle\langle f, m''|\hat{\mathbf{d}}|f', m'\rangle \times\langle f', m'|\hat{\mathbf{d}}^{\dagger}|f, m\rangle\langle f, m|. \tag{A12}$$

This expanded expression involves dipole operator matrix elements of the form, $\langle f', m'|\hat{d}_q|f, m\rangle$ where $|f, m\rangle$ is a Zeeman sub-level in the ground-state hyperfine manifold, $|f', m'\rangle$ is a virtual state in the excited hyperfine manifold, and $q = 0, \pm1$ labels the helicity of the electromagnetic field.

The above notation is complete, but for the rest of this appendix we work with only one particular f, f' combination and remove the subscripts with the simplifying notation change

$$\begin{gathered} \hat{P}_f \hat{\mathbf{d}}^{(-)} \hat{P}_{f'} \to \hat{\mathbf{d}} \\ \hat{P}_{f'} \hat{\mathbf{d}}^{(+)} \hat{P}_f \to \hat{\mathbf{d}}^{\dagger} \\ \hat{\boldsymbol{\alpha}}_{f,f'} \to \hat{\boldsymbol{\alpha}} \end{gathered} \tag{A13}$$

However, when the complete Hamiltonian is considered, the summation over all possible f, f' combinations is reestablished.

4. Matrix element decomposition

In order to work with the above expressions, it is advantageous to simplify the dipole matrix elements as far as possible. By employing the Wigner-Eckart theorem, the angular dependence of the matrix element, $\langle f', m'|\hat{\mathbf{d}}|f, m\rangle$ can be factored into the product of a Clebsch-Gordan coefficient and a reduced matrix element,

$$\langle f, m|\hat{d}_q|f', m'\rangle = \langle f, m|1, q; f', m-q\rangle\langle f||\hat{\mathbf{d}}||f'\rangle. \tag{A14}$$

Since the dipole operator acts only on electronic degrees of freedom, it is further possible to factor out the nuclear spin degrees of freedom via the explicit coupling,

$$\begin{aligned}\langle f||\hat{\mathbf{d}}||f'\rangle \;&=\; (-1)^{f'+j+i+1}\sqrt{(2f'+1)(2j+1)} \\ &\quad\times\left\{\begin{matrix} 1 & j & j' \\ i & f' & f\end{matrix}\right\}\langle j||\hat{\mathbf{d}}_{\mathrm{e}}||j'\rangle \end{aligned}\tag{A15}$$

where i is the nuclear spin quantum number, j and j' are the ground and excited state fine structure quantum numbers, and $\hat{\mathbf{d}}_{\mathrm{e}}$ is the dipole operator with respect to the electronic degrees of freedom.

5. Tensor decomposition

From Eq. (17-89) of reference [43] we see that we can form an irreducible tensor, $\hat{Z}^{(j)}_m$, from a linear combination of tensor operators $\hat{U}^{(\kappa)}_q$ and $\hat{V}^{(\kappa')}_{q'}$ via the definition

$$\hat{Z}^{(j)}_m = \sum_{q,q'}\hat{U}^{(\kappa)}_q\hat{V}^{(\kappa')}_{q'}\langle\kappa, q; \kappa', q'|j, m\rangle \tag{A16}$$

where $\langle\kappa, q; \kappa', q'|j, m\rangle$ are Clebsch-Gordan coefficients. This expression can then be inverted using

$$\hat{U}^{(\kappa)}_q\hat{V}^{(\kappa')}_{q'} = \sum_{j,m}\hat{Z}^{(j)}_m\langle\kappa, q; \kappa', q'|j, m\rangle. \tag{A17}$$

We now specialize to the case where $\hat{Z}^{(j)}_m = \hat{T}^{(j)}_m$, $\hat{\mathbf{U}} = \hat{\mathbf{d}}$, and $\hat{\mathbf{V}} = \hat{\mathbf{d}}^\dagger$. Because we are creating a dyad (with two vectors), we have $\kappa = \kappa' = 1$. Inserting these above gives the definition

$$\hat{T}^{(j)}_m = \sum_{q,q'}\hat{d}_q\hat{d}^\dagger_{q'}\langle 1, q; 1, q'|j, m\rangle \tag{A18}$$

and the inverse

$$\hat{d}_q\hat{d}^\dagger_{q'} = \sum_{j,m}\hat{T}^{(j)}_m\langle 1, q; 1, q'|j, m\rangle. \tag{A19}$$

We can use this latter expression to write the polarizability as

$$\begin{aligned}
\hat{\boldsymbol{\alpha}} \;&=\; \hat{\mathbf{d}}\hat{\mathbf{d}}^\dagger && \text{(A20)}\\
&=\; \sum_{q,q'}\vec{\mathbf{e}}^*_q\vec{\mathbf{e}}^*_{q'}\hat{d}_q\hat{d}^\dagger_{q'} && \text{(A21)}\\
&=\; \sum_{j,m}\sum_{q,q'}\vec{\mathbf{e}}^*_q\vec{\mathbf{e}}^*_{q'}\hat{T}^{(j)}_m\langle 1, q; 1, q'|j, m\rangle && \text{(A22)}\\
&=\; \hat{\boldsymbol{\alpha}}^{(0)}\oplus\hat{\boldsymbol{\alpha}}^{(1)}\oplus\hat{\boldsymbol{\alpha}}^{(2)} && \text{(A23)}
\end{aligned}$$

where

$$\hat{\boldsymbol{\alpha}}^{(j)} = \sum_{m=-j}^{j}\hat{T}^{(j)}_m\sum_{q,q'}\vec{\mathbf{e}}^*_q\vec{\mathbf{e}}^*_{q'}\langle 1, q; 1, q'|j, m\rangle \tag{A24}$$

Filling in these Clebsch-Gordan coefficients explicitly, we get

$$\begin{aligned}
\hat{\boldsymbol{\alpha}}^{(0)} \;&=\; \hat{T}^{(0)}_0\left[-\frac{1}{\sqrt{3}}\vec{\mathbf{e}}^*_0\vec{\mathbf{e}}^*_0 + \frac{1}{\sqrt{3}}\vec{\mathbf{e}}^*_+\vec{\mathbf{e}}^*_- + \frac{1}{\sqrt{3}}\vec{\mathbf{e}}^*_-\vec{\mathbf{e}}^*_+\right]\\
\hat{\boldsymbol{\alpha}}^{(1)} \;&=\; \hat{T}^{(1)}_0\left[\frac{1}{\sqrt{2}}\vec{\mathbf{e}}^*_+\vec{\mathbf{e}}^*_- - \frac{1}{\sqrt{2}}\vec{\mathbf{e}}^*_-\vec{\mathbf{e}}^*_+\right]\\
&\quad+\hat{T}^{(1)}_{+1}\left[-\frac{1}{\sqrt{2}}\vec{\mathbf{e}}^*_0\vec{\mathbf{e}}^*_+ + \frac{1}{\sqrt{2}}\vec{\mathbf{e}}^*_+\vec{\mathbf{e}}^*_0\right]\\
&\quad+\hat{T}^{(1)}_{-1}\left[\frac{1}{\sqrt{2}}\vec{\mathbf{e}}^*_0\vec{\mathbf{e}}^*_- - \frac{1}{\sqrt{2}}\vec{\mathbf{e}}^*_-\vec{\mathbf{e}}^*_0\right]\\
\hat{\boldsymbol{\alpha}}^{(2)} \;&=\; \hat{T}^{(2)}_0\left[\frac{2}{\sqrt{6}}\vec{\mathbf{e}}^*_0\vec{\mathbf{e}}^*_0 + \frac{1}{\sqrt{6}}\vec{\mathbf{e}}^*_+\vec{\mathbf{e}}^*_- + \frac{1}{\sqrt{6}}\vec{\mathbf{e}}^*_-\vec{\mathbf{e}}^*_+\right]\\
&\quad+\hat{T}^{(2)}_{+1}\left[\frac{1}{\sqrt{2}}\vec{\mathbf{e}}^*_0\vec{\mathbf{e}}^*_+ + \frac{1}{\sqrt{2}}\vec{\mathbf{e}}^*_+\vec{\mathbf{e}}^*_0\right]\\
&\quad+\hat{T}^{(2)}_{-1}\left[\frac{1}{\sqrt{2}}\vec{\mathbf{e}}^*_0\vec{\mathbf{e}}^*_- + \frac{1}{\sqrt{2}}\vec{\mathbf{e}}^*_-\vec{\mathbf{e}}^*_0\right]\\
&\quad+\hat{T}^{(2)}_{+2}\left[\vec{\mathbf{e}}^*_+\vec{\mathbf{e}}^*_+\right]\\
&\quad+\hat{T}^{(2)}_{-2}\left[\vec{\mathbf{e}}^*_-\vec{\mathbf{e}}^*_-\right]
\end{aligned}\tag{A25}$$

Furthermore, using the definition of $\hat{T}^{(j)}_m$ and filling in the Clebsch-Gordan coefficients explicitly, we get

$$\begin{aligned}
\hat{T}^{(0)}_0 \;&=\; -\frac{1}{\sqrt{3}}\left(\hat{d}_0\hat{d}^\dagger_0 - \hat{d}_+\hat{d}^\dagger_- - \hat{d}_-\hat{d}^\dagger_+\right) && \text{(A26)}\\
\hat{T}^{(1)}_0 \;&=\; \frac{1}{\sqrt{2}}\left(\hat{d}_+\hat{d}^\dagger_- - \hat{d}_-\hat{d}^\dagger_+\right)\\
\hat{T}^{(1)}_{+1} \;&=\; \frac{1}{\sqrt{2}}\left(-\hat{d}_0\hat{d}^\dagger_+ + \hat{d}_+\hat{d}^\dagger_0\right)\\
\hat{T}^{(1)}_{-1} \;&=\; \frac{1}{\sqrt{2}}\left(\hat{d}_0\hat{d}^\dagger_- - \hat{d}_-\hat{d}^\dagger_0\right)\\
\hat{T}^{(2)}_0 \;&=\; \frac{1}{\sqrt{6}}\left(\hat{d}_+\hat{d}^\dagger_- + 2\hat{d}_0\hat{d}^\dagger_0 + \hat{d}_-\hat{d}^\dagger_+\right)\\
\hat{T}^{(2)}_{+1} \;&=\; \frac{1}{\sqrt{2}}\left(\hat{d}_0\hat{d}^\dagger_+ + \hat{d}_+\hat{d}^\dagger_0\right)\\
\hat{T}^{(2)}_{-1} \;&=\; \frac{1}{\sqrt{2}}\left(\hat{d}_0\hat{d}^\dagger_- + \hat{d}_-\hat{d}^\dagger_0\right)\\
\hat{T}^{(2)}_{+2} \;&=\; \hat{d}_+\hat{d}^\dagger_+\\
\hat{T}^{(2)}_{-2} \;&=\; \hat{d}_-\hat{d}^\dagger_-
\end{aligned}$$

Note that several standard references (including references [43, 44]) contain an error in the prefactor of the $j = 0$ term and in the sign of the $j = 1$ terms. However, the fundamental definitions of $\hat{T}^{(j)}_m$ and its inverse above are valid.

Using recursion relations for the Clebsch-Gordan coefficients we can recast the tensor operators in terms of more intuitive $\hat{f}$ operators [26, 45]

$$\begin{aligned}
\hat{T}^{(0)}_0 &= -\alpha^{(0)}_{f,f'}\hat{\mathbb{1}}_f/\sqrt{3} && \text{(A27)}\\
\hat{T}^{(1)}_0 &= +\alpha^{(1)}_{f,f'}\hat{f}_z/\sqrt{2} \\
\hat{T}^{(1)}_{+1} &= +\alpha^{(1)}_{f,f'}\hat{f}_+/\sqrt{2} \\
\hat{T}^{(1)}_{-1} &= +\alpha^{(1)}_{f,f'}\hat{f}_-/\sqrt{2} \\
\hat{T}^{(2)}_0 &= -\alpha^{(2)}_{f,f'}\left(3\hat{f}^2_z - f(f+1)\hat{\mathbb{1}}_f\right)/\sqrt{6} \\
\hat{T}^{(2)}_{+1} &= -\alpha^{(2)}_{f,f'}\sqrt{2}\hat{f}_+\left(\hat{f}_z + \hat{\mathbb{1}}_f/2\right) \\
\hat{T}^{(2)}_{-1} &= -\alpha^{(2)}_{f,f'}\sqrt{2}\hat{f}_-\left(\hat{f}_z - \hat{\mathbb{1}}_f/2\right) \\
\hat{T}^{(2)}_{+2} &= -\alpha^{(2)}_{f,f'}\hat{f}^2_+ \\
\hat{T}^{(2)}_{-2} &= -\alpha^{(2)}_{f,f'}\hat{f}^2_-
\end{aligned}$$

Here we have defined

$$\begin{aligned}
\alpha^{(0)}_{f,f'} &= \alpha^{f'}_f\Big((2f-1)\delta^{f'}_{f-1} + (2f+1)\delta^{f'}_f \\
&\quad +(2f+3)\delta^{f'}_{f+1}\Big) && \text{(A28)}\\
\alpha^{(1)}_{f,f'} &= \alpha^{f'}_f\Big(-\frac{2f-1}{f}\delta^{f'}_{f-1} - \frac{2f+1}{f(f+1)}\delta^{f'}_f \\
&\quad +\frac{2f+3}{f+1}\delta^{f'}_{f+1}\Big) && \text{(A29)}\\
\alpha^{(2)}_{f,f'} &= \alpha^{f'}_f\Big(\frac{1}{f}\delta^{f'}_{f-1} - \frac{2f+1}{f(f+1)}\delta^{f'}_f \\
&\quad +\frac{1}{f+1}\delta^{f'}_{f+1}\Big) && \text{(A30)}
\end{aligned}$$

These definitions have been chosen to make the each of the quantities

$$\sum_{f'}\frac{\alpha^{(j)}_{f,f'}}{\alpha_0\Delta_{f,f'}} > 0 \qquad \text{(A31)}$$

for $\Delta_{f,f'} \gg 0$ for each term j. We have defined the polarizability constants

$$\alpha^{f'}_f = \alpha_0\frac{(2j'+1)^2}{(2j+1)^2}\left|\begin{Bmatrix} 1 & j & j' \\ i & f' & f\end{Bmatrix}\right|^2 \qquad \text{(A32)}$$

and

$$\begin{aligned}
\alpha_0 &= \frac{3\epsilon_0\hbar\Gamma\lambda_0^3}{8\pi^2} && \text{(A33)}\\
&= \left|\langle j||\hat{\mathbf{d}}||j'\rangle\right|^2\frac{(2j+1)}{(2j'+1)}
\end{aligned}$$

which involves the atomic the spontaneous emission rate, Γ, and transition wavelength, λ_0.

Now, to complete the derivation, insert Eqs. (A27) into the polarizability components of Eqs. (A25), then insert this and the definition of the electric field, Eq. (A9), into the Hamiltonian, Eqs. (9-10). Expanding, using the properties of the spherical dot product, and the Stokes component definitions (Eqs. 5), and summing over the f', we get the final expressions used in the text (Eqs. 11, 12, 13).

APPENDIX B: ARBITRARY VECTOR OPERATOR ROTATIONS

Here we are interested in evaluating the general operation of rotating a vector about an arbitrary direction by an arbitrary amount in order to determine the semiclassical evolution of the probe light as used in Eqs. (26).

Consider the rotation of the vector spin operator

$$\vec{S} = \left[\hat{S}_x, \hat{S}_y, \hat{S}_z\right] \qquad \text{(B1)}$$

in Cartesian coordinates about an arbitrary direction $\vec{n} = [\gamma_x, \gamma_y, \gamma_z]/\gamma$ by the angle $\gamma = \sqrt{\gamma_x^2 + \gamma_y^2 + \gamma_z^2}$. This rotation can be represented in the Heisenberg picture as

$$\hat{S}'_i = \hat{U}\hat{S}_i\hat{U}^\dagger \qquad \text{(B2)}$$

where

$$\hat{U} = \exp[-i\gamma\vec{S}\cdot\vec{n}] = \exp[-i(\gamma_x\hat{S}_x + \gamma_z\hat{S}_z + \gamma_z\hat{S}_z)] \qquad \text{(B3)}$$

The $\hat{S}'_i$ can be derived explicitly using the following equation for the arbitrary rotation of any vector

$$\begin{aligned}
\hat{S}'_i &= (\vec{S}\cdot\vec{i})\cos\gamma + (\vec{n}\cdot\vec{i})(\vec{n}\cdot\vec{S})(1-\cos\gamma) \\
&\quad +\left((\vec{n}\times\vec{i})\cdot\vec{S}\right)\sin\gamma && \text{(B4)}
\end{aligned}$$

Expanding and rearranging terms we get

$$\begin{aligned}
\hat{S}'_x &= \hat{S}_x\left(\frac{\gamma_x^2}{\gamma^2}(1-\cos\gamma) + \cos\gamma\right) \\
&\quad +\hat{S}_y\left(\frac{\gamma_x\gamma_y}{\gamma^2}(1-\cos\gamma) + \frac{\gamma_z}{\gamma}\sin\gamma\right) \\
&\quad +\hat{S}_z\left(\frac{\gamma_x\gamma_z}{\gamma^2}(1-\cos\gamma) - \frac{\gamma_y}{\gamma}\sin\gamma\right) && \text{(B5)}\\
\hat{S}'_y &= \hat{S}_x\left(\frac{\gamma_y\gamma_x}{\gamma^2}(1-\cos\gamma) - \frac{\gamma_z}{\gamma}\sin\gamma\right) \\
&\quad +\hat{S}_y\left(\frac{\gamma_y^2}{\gamma^2}(1-\cos\gamma) + \cos\gamma\right) \\
&\quad +\hat{S}_z\left(\frac{\gamma_y\gamma_z}{\gamma^2}(1-\cos\gamma) + \frac{\gamma_x}{\gamma}\sin\gamma\right) && \text{(B6)}\\
\hat{S}'_z &= \hat{S}_x\left(\frac{\gamma_z\gamma_x}{\gamma^2}(1-\cos\gamma) + \frac{\gamma_y}{\gamma}\sin\gamma\right)
\end{aligned}$$

$$+\hat{S}_y\left(\frac{\gamma_z\gamma_y}{\gamma^2}(1-\cos\gamma)-\frac{\gamma_x}{\gamma}\sin\gamma\right)$$
$$+\hat{S}_z\left(\frac{\gamma_z^2}{\gamma^2}(1-\cos\gamma)+\cos\gamma\right) \tag{B7}$$

These equations can be specialized to Eqs. (26) which describes the experimental situation considered in this work.

Modeling and feedback control design for quantum state preparation

Ramon van Handel, John K. Stockton, Hideo Mabuchi

Physical Measurement and Control 266-33, California Institute of Technology, Pasadena, CA 91125, USA

E-mail: `ramon@caltech.edu`, `jks@caltech.edu`, `hmabuchi@caltech.edu`

Abstract. The goal of this article is to provide a largely self-contained introduction to the modeling of controlled quantum systems under continuous observation, and to the design of feedback controls that prepare particular quantum states. We describe a bottom-up approach, where a field-theoretic model is subjected to statistical inference and is ultimately controlled. As an example, the formalism is applied to a highly idealized interaction of an atomic ensemble with an optical field. Our aim is to provide a unified outline for the modeling, from first principles, of realistic experiments in quantum control.

PACS numbers: 0.0

1. Introduction

In recent years, advances in technology have enabled a proliferation of experiments where objects can be probed and manipulated near the fundamental quantum limits of performance. The manipulation and readout of single qubits with unprecedented coherence times both in condensed matter and in atomic setups, the reliable trapping, cooling and shot-noise limited continuous observation of single atoms in high-finesse optical cavities, and the production of various nonclassical states of light and of atomic ensembles is only a subset of recent achievements. The large degree of control that can be exerted at the quantum level suggests that classical engineering methodology can be fruitfully adapted to this new setting. In particular, it seems that the concept of feedback control should be of central importance in the engineering of reliable quantum technologies, as in the classical case.

This article is intended as an introduction to the theoretical description of quantum feedback control systems. We concentrate on a scenario that is common in quantum optical experiments, where the system to be controlled is brought in weak interaction with an external probe field which is subsequently detected. The detected signal can then be processed and fed back to the system through some actuator. There are various theoretical challenges in describing such a system:

- How does one model the system-probe interaction?
- How does one model a continuous measurement of the probe?
- How does one infer information on the system from the probe measurements?
- How does one design a feedback law that utilizes this information to achieve a particular control goal?

In the following we will address each of these questions in turn. Needless to say, it would be impossible to cover every aspect and intricacy of each of these questions within the scope of this article; rather, we aim to give a sufficiently detailed discussion to keep the article (mostly) self-contained, and refer to the bibliography for complete treatments.

As an example throughout the article, we discuss the preparation of entangled states of an atomic ensemble using feedback control. The model consists of an ensemble of atomic spins interacting dispersively with an optical probe, which is subjected to homodyne detection. Several recent experiments have exploited a similar setup to produce spin-squeezed states (SSS) [28, 30, 47] which have applications in a variety of metrology tasks, including magnetometers [29, 65] and atomic clocks [50, 59, 76].

We consider this model because it is illustrative in several respects. First, the model spans two quite different and interesting regimes. At short times the dynamics are approximately linear [65] and the model describes the production of spin squeezing. However, at long times the linear description is no longer valid, and we will show that then an eigenstate of the collective angular momentum of the ensemble (a Dicke state) is obtained. Although the long time limit described by this model is difficult to realize experimentally at this time, the consideration of the substantial differences between the regimes clearly demonstrates the challenges of quantum control. Second, the model is a convenient example to demonstrate the modeling of a quantum control system from first principles. Ultimately, by approaching the entire problem—from physical modeling to inference to control—in a systematic manner, we hope to provide a unified outline for future modeling efforts.

The article is roughly divided into two parts. The first part, consisting of sections 2, 3 and 4, is somewhat technical in nature. Its goal is to obtain from first principles, using a simplified field-theoretical model of the interaction of an atomic ensemble with a probe field, the quantum filtering equation (52). To this end, we begin by reviewing in section 2 the statistical inference of quantum states. In section 3 we introduce a field-theoretical model of an atomic ensemble coupled to an electromagnetic probe field, and we discuss how it can be reduced to a stochastic equation. In section 4 we detail how to properly condition the ensemble state upon the results from continuous optical measurements in the field.

The second part, section 5, presents general principles of feedback control and demonstrates how they can be applied to enable quantum state preparation. This procedure is discussed in both the short time limit, where a linear approximation is valid, and in the long time limit, where a more complete description is required [66]. Section 5 is fairly independent from the first part of the article, and a reader who has some familiarity with the filtering equation, Eq. (52), could skip directly ahead to this section. We have attempted, however, to give in sections 2–5 a unified picture of quantum feedback control design, from the elementary physical interactions through feedback-enabled state preparation.

As we proceed, we attempt to review the literature concerning measurement and feedback control of atomic ensembles, while also putting into context related, but more mathematical, works concerning estimation and control. In the end, we hope to inspire further development in this field by highlighting the numerous connections between the problems of quantum control and problems considered in the culturally distinct context of the mathematics and control communities [4, 18, 71].

2. What is a quantum state?

Quantum mechanics describes the statistics of observable quantities, very much like classical probability theory. In fact, the foundation of quantum mechanics is just an extension of probability theory, as we will discuss in this section. Such a point of view allows us to apply classical constructions of probability theory directly to quantum models. Though this section contains no surprises, we aim to clarify the concepts and terminology used in the remainder of the article. We will pay particular attention to what is meant by a "quantum state", an issue that must be resolved before we can discuss state preparation.

2.1. Classical probability

To set the stage for quantum probability we first discuss some of the elements of classical probability theory [75]. As an illustration, consider throwing two dice. The first ingredient we need in our theory is the *sample space*, usually denoted by Ω. This is just a set which describes all the "microstates" of the system; in our case, it is the set of $6^2 = 36$ possible outcomes of a throw 11, 12, ..., 21, 22, ..., 65, 66. A *random variable* f is now a map $f : \Omega \to \mathbb{R}$. For example, we could define a random variable X that describes the sum of the two outcomes, i.e. $X(11) = 2$, $X(53) = 8$, etc.

To complete the picture we need to introduce an object that can provide answers to questions such as *what is the probability of having thrown 66?*, or *what is the probability of having thrown at least one three?* This is exactly provided by the notion of a *probability measure*. Note that we can represent any question as a subset of Ω; e.g., our first question is represented by the set $\{66\}$, while the second is represented by $\{31, 32, \ldots, 36, 13, 23, \ldots, 63\}$. These sets (and the questions they represent) are called *events*. The probability measure $\mathbb{P}$ is a map that associates to every event a probability.

We can compose new events as follows. Given two events $A, B \subset \Omega$, the question *A or B?* is represented by $A \cup B$, whereas *A and B?* corresponds to $A \cap B$. In particular, the latter operation defines the *joint probability* $\mathbb{P}(A \cap B)$ of A and B. The probability measure needs to be consistently defined with respect to these operations in the sense that $\mathbb{P}(A \cup B) = \mathbb{P}(A) + \mathbb{P}(B)$ if $A \cap B = \varnothing$, i.e. if A and B are mutually exclusive. Furthermore $\mathbb{P}(\varnothing) = 0$ and $\mathbb{P}(\Omega) = 1$. In our example there is an equal probability of having thrown any combination; hence $\mathbb{P}(A) = \frac{1}{36}$ for any event A with a single element. Any other event can be constructed as a union of these "elementary" events and its probability can be found using the formula for $\mathbb{P}(A \cup B)$.

Now suppose we wish to perform a particular observation on the system; we have already defined such observations (random variables) as maps on Ω. To obtain the probability of a particular observation, we simply invert the corresponding map. For example, the probability that we throw a combination that sums to 4 is $\mathbb{P}(X = 4) = \mathbb{P}(X^{-1}(4)) = \mathbb{P}(\{13, 22, 31\}) = \frac{1}{12}$. Hence the probability measure contains all the information available on the outcome of any observation, i.e., $\mathbb{P}$ represents the *state* of the system. The philosophy behind this choice of terminology is that physical theories exist to model the outcomes of observations; the "state" is the object of the theory that gives rise to the statistics of any such observation.

Let us now consider classical state preparation. The physical mechanism that prepares the state of the dice, i.e. that causes every combination to have equal probability, is the throwing process. Suppose we want to prepare a different state, for example a state that has a high probability of obtaining two sixes. We could obtain such a state by modifying the physical process that creates it. For example, we could engineer dice with an nonuniform mass distribution, so the sixth face is lighter than the other faces; then the rolling of the dice is more likely to terminate with the sixth face facing up.

There is a different way in which we can change the state. The *conditional probability* of event A given that we have measured event B is

$$\mathbb{P}(A|B) = \frac{\mathbb{P}(A \cap B)}{\mathbb{P}(B)} \tag{1}$$

Suppose we observe $X = 12$. Then the conditional probability of having thrown 66 is $\mathbb{P}(\{66\}|X = 12) = 1$, whereas without conditioning $\mathbb{P}(\{66\}) = \frac{1}{36}$. However, if we happened to measure $X \neq 12$ then $\mathbb{P}(\{66\}|X \neq 12) = 0$. This corresponds to the intuitive notion that if we *see* that we have thrown 66, then the probability that we have thrown 66 is one, no matter what its probability was before we had gained that information. However the probability that we would see 66 in the first place is only $\frac{1}{36}$. Hence we can create states by conditioning a "prior" state on a measurement, but only very inefficiently: to prepare a state with high probability of obtaining 66, we have to keep throwing the dice until we happen to observe $X = 12$.

There is a final possibility which combines the two methods of state preparation. Suppose that we perform an observation not after the throw has completed, but while it is still in progress. Moreover, we allow ourselves to interfere with the dice: if the rolling dice threaten to terminate with a low value of X, we give them a shove so they keep rolling. This way the probability of throwing high numbers is elevated. In other words, we prepare the state of our choice by performing observation and applying *feedback* to the system dynamics. This crude example represents the type of state preparation that we consider in this article for quantum systems.

We conclude this section by introducing expectations and conditional expectations. If Ω is a finite countable set (which we have implicitly assumed in this section) then we may always decompose a random variable $f : \Omega \to \mathbb{R}$ as follows. The map f takes the values $f_i \in \mathbb{R}$ on disjoint subsets $S_i = f^{-1}(f_i) \subset \Omega$ such that $\bigcup_i S_i = \Omega$. Hence we can write

$$f(\omega) = \sum_i f_i \chi_{S_i}(\omega) \tag{2}$$

where χ_{S_i} is the indicator function of S_i, i.e. $\chi_{S_i}(\omega) = 1$ if $\omega \in S_i$, 0 otherwise. The *expectation* of f is given by

$$\mathbb{E}f = \sum_i f_i \mathbb{P}(S_i) \tag{3}$$

and represents the value that f takes on "on average". Note that the state $\mathbb{P}$ uniquely determines $\mathbb{E}$, but the converse is also true as by construction $\mathbb{E}\chi_S = \mathbb{P}(S)$ for any event $S \subset \Omega$. Hence we can equivalently define the state of the system by specifying the expectation of every system observable.

Similarly, we can define the *conditional expectation* of $f = \sum_i f_i \chi_{S_i}$ given that we have measured $g = \sum_i g_i \chi_{T_i}$:

$$\mathbb{E}(f|g)(\omega) = \sum_i \sum_j f_j \mathbb{P}(S_j|T_i) \chi_{T_i}(\omega) \tag{4}$$

Now $\mathbb{E}(\chi_S|g)(\omega) = \mathbb{P}(S|g = g(\omega))$. Hence we can equivalently define the state of the system, conditioned on a measurement of g, by specifying the conditional expectation of every system observable with respect to g.

Though entirely natural from a probabilist's point of view, it is not customary in physics to think of the conditional expectation as a random variable. One way to interpret Eq. (4) is that the random variable $\mathbb{E}(f|g)$ is the *best estimate* of f given g [60, 75]. To see this, first note that $\mathbb{E}(f|g)$ is by construction a function of g: $\mathbb{E}(f|g)(\omega) = \mathcal{X}(g(\omega))$ where we define $\mathcal{X} : g_i \mapsto \sum_j f_j \mathbb{P}(S_j|T_i)$. It is not difficult to show that of all functions $\mathcal{X}'$, the one that minimizes the least-squares criterion $\mathbb{E}[(f - \mathcal{X}'(g))^2]$ is exactly $\mathcal{X}' = \mathcal{X}$. This is precisely what we mean by $\mathbb{E}(f|g)$ being the *best* estimate of f *given* g. Evidently this idea is equivalent, or in some sense dual, to the notion of a conditional state that we introduced earlier.

2.2. Quantum probability

We will now formulate quantum mechanics in the same language as the classical case [53, 68]. An observable (random variable) in quantum theory is given by a self-adjoint operator F on some complex Hilbert space $\mathcal{H}$. Assuming $\mathcal{H}$ is finite-dimensional, we always have the spectral decomposition

$$F = \sum_i f_i P_i \tag{5}$$

where $f_i \in \mathbb{R}$ are the eigenvalues of F and $P_i = P_i^2 = P_i^\dagger$ are projection operators onto the corresponding eigenspaces. The picture is completed by introducing a map $\mathbb{E} : \cdot \mapsto \mathrm{Tr}[\cdot\rho]$ with some $\rho = \rho^\dagger \geq 0$, $\mathrm{Tr}\rho = 1$. Then $\mathbb{E}F$ is the expectation of the observable F. In terms of the spectral decomposition

$$\mathbb{E}F = \sum_i f_i \, \mathbb{E}P_i \tag{6}$$

Clearly the projectors P_i play the role of events χ_{S_i} in the classical theory. Indeed, a measurement of F yields the outcome f_i with probability $\mathbb{E}P_i$. Thus any quantum observable is identical to a classical random variable.

We can make the correspondence explicit in the following way. As we are free to choose any basis in the Hilbert space, we may always choose a basis in which F is diagonal. We can then interpret the diagonal elements of F as the values of the random variable f, where Ω is just the set of diagonal entries: $f : i \mapsto F_{ii}$. The P_i now correspond exactly to indicator functions on Ω and $\mathbb{P}(S) = \sum_i \chi_S(i)\rho_{ii}$. Note that the underlying Hilbert space plays a passive role in the theory, just like the sample space Ω in classical probability—the central element of the theory is the set of observables we are interested in. As long as we are interested in a set of observables that all commute with each other, then quantum and classical probability are identical theories: commuting observables can be simultaneously diagonalized, so we can follow the above "recipe" to transform between the classical and quantum descriptions. In other words, classical probability theory is a special case of quantum probability theory.

The embedding of classical in quantum probability allows us to carry over directly concepts from classical probability to sets of commuting quantum observables. For example, in the classical case we defined the *joint probability* of two events A and B as $\mathbb{P}(A \cap B) = \mathbb{E}(\chi_A \chi_B)$. This carries over directly to the quantum case for two quantum events P, Q as long as they commute: i.e. the joint probability of P and Q

is $\mathbb{E}(PQ) = \mathrm{Tr}[PQ\rho]$. Similarly, we obtain an expression for conditional expectation for two commuting quantum observables $F = \sum_i f_i P_i$ and $G = \sum_i g_i Q_i$,

$$\mathbb{E}(F|G) = \sum_i \sum_j f_j \frac{\mathbb{E}(P_j Q_i)}{\mathbb{E}(Q_i)} Q_i \tag{7}$$

which is itself an observable as in the classical case, interpreted as the best estimate (in the least mean square sense) of F given G. Note that these are not even "quantum analogs" of classical concepts—these are entirely *classical* operations. We can obtain these expressions by writing the commuting set of events in the diagonal basis, transforming to the classical picture, applying the classical operation, and transforming back to the quantum picture in the original basis.

What makes quantum probability different from classical probability is the existence of noncommuting observables. For events or observables that do not commute the classical probabilistic concepts do not make any sense: for example, the joint probability of P, Q with $[P, Q] \neq 0$ cannot be unambiguously defined as $\mathbb{E}(PQ) \neq \mathbb{E}(QP)$. Similarly $\mathbb{E}(F|G)$ cannot be defined for $[F, G] \neq 0$. Hence we *do not allow* simultaneous measurement or statistical inference of noncommuting observables. The fact that noncommuting observables are inherent to quantum models restricts the amount of information that can be obtained from the system by measurement.

Once we have fixed a commuting family of observables to measure, however, the measurement process is reduced to straightforward application of classical probability theory. In particular, even if we are interested in modeling a pair of observables F and G that do not commute, we can still perform statistical inference as long as both observables commute with the observation H. After all, by Eq. (7), $\mathbb{E}(F|H)$ and $\mathbb{E}(G|H)$ commute and can hence be measured simultaneously, despite that F and G do not commute. We will repeatedly exploit this fact throughout this article.

To illustrate these ideas, consider the example of a single spin-$\frac{1}{2}$ atom, and suppose we are interested in controlling the spin observables (Pauli matrices) $\sigma_x, \sigma_y, \sigma_z$. We run into problems if we try to directly measure σ_z, as this does not commute with σ_x and σ_y. Because the best estimate of σ_x or σ_y with respect to σ_z is undefined, it is unclear in what sense one could control σ_x and σ_y if we keep observing σ_z.

We have already hinted at the solution to this problem: we must observe a fourth observable X that commutes with $\sigma_x, \sigma_y, \sigma_z$. Then all three conditional expectations are well defined. A famous example of this procedure is the Stern-Gerlach apparatus: in this case the atom passes through a strong magnetic gradient which correlates the spin observables $\sigma_{x,y,z}$ with the spatial position X of the atom. By measuring X, which commutes with $\sigma_{x,y,z}$, we can form best estimates of the latter three observables, and thus at least conceptually these can be controlled.

In practice the Stern-Gerlach device is not a good system for controlling the spin, as the observable X is a different degree of freedom of the same atom that carries the spin. When the atom hits the screen, enacting a measurement of X, the atom is effectively destroyed and there is no point in updating the spin state for further control. The approach we take in this article is a realistic, though conceptually identical, version of this example. Instead of coupling the atomic spin to the atomic position, the spin interacts with an external electromagnetic field. Even though photodetection of the field is destructive this will not affect the atom itself.

The *quantum state* is an object that associates an expectation to the relevant set of observables. We refrain from defining the quantum state as the *density matrix* ρ.

The properties that any expectation map must obey imply that we can always find a density matrix ρ such that the expectation can be expressed as $\mathbb{E}F = \mathrm{Tr}[\rho F]$ for the relevant set of observables F. What this relevant set is, however, depends on the context.

To illustrate this subtle distinction let us consider again the Stern-Gerlach example. Before conditioning we consider the four observables $\sigma_{x,y,z}$ and X. Hence we naturally express the state as a density matrix on $\mathcal{H}_s \otimes \mathcal{H}_q$, the tensor product of the atomic spin and position Hilbert spaces. However, we can only condition observables on X that commute with X. Hence after conditioning a spin-position density matrix is no longer meaningful, as many observables on the position Hilbert space (e.g. momentum) will have an undefined conditional expectation‡.

To find the natural state after conditioning, recall that $\mathbb{E}(\sigma_{x,y,z}|X)$ all commute. Hence we can describe them as classical random variables $s_{x,y,z}(\omega)$ on some probability space Ω. To express the state as a density matrix, then, we must also make it random: we define $\rho(\omega)$ on $\mathcal{H}_s$ through $s_{x,y,z}(\omega) = \mathrm{Tr}[\rho(\omega)\sigma_{x,y,z}]$. This conforms to the intuitive idea that after measurement, the conditional state is itself a classical random variable, where Ω is simply the set of possible outcomes of X. It also highlights, however, that in order to talk sensibly about state preparation we must carefully select which observables we wish to specify. Though the "dual" description in terms of a density matrix is often more economical, we will often find it both conceptually and technically simpler to obtain results by considering conditional expectations to be observables on $\mathcal{H}_s \otimes \mathcal{H}_q$.

The three methods of state preparation discussed in the previous section carry over directly to the quantum case. All these methods have been discussed to various extent in the literature; references to their various experimental implementations will be given in section 5. The first method corresponds to designing a Hamiltonian whose time evolution generates the desired state. The drawback of this method is that such a Hamiltonian may be highly nonlinear and difficult to engineer in practice.

The second method corresponds to conditioning. As we saw in the example above, to do this we must "open" the system by introducing another observable. We emphasize, however, that there is no physical "collapse" associated to the actual measurement: we just use *classical* conditioning to update our state of knowledge. The drawback of this method is that the outcome of the measurement is random and will not always result in the desired state; particularly in cases where the state is prepared with low probability, this may not be a desirable option.

The third method, which is the main topic of this article, is that of conditioning with feedback. The advantage of such a method is that it can be implemented with simple Hamiltonians, while it does not suffer from the indeterminism of pure conditioning. The method can also be more robust than simple Hamiltonian evolution, as it is not as sensitive to e.g. timing errors or precise knowledge of experimental parameters [65, 70]. However, succesful implementation of such a method requires sensitive, continuous-time quantum-limited measurements and fast in-line signal processing, techniques that have only recently become available.

We separate the development of quantum feedback control into three parts. In order to interpret the measurement current and feedback we must develop a physical model of the system and its interaction with the environment. This first step, the *physical modeling* step, embodies the "physical content" of the problem. In the second step we condition the system dynamics based on an observation of the environment. This *statistical inference* step is, as we have discussed, entirely classical in nature. The third step is the *control problem*, finding a control law that will prepare the desired state. In the following sections we consider each of these problems separately.

---

‡ Of course if we were interested in both position and momentum, we could couple to yet another observable that commutes with $\sigma_{x,y,z}$ as well as position and momentum. This way we move further and further down the "Heisenberg chain". Ultimately, however, we have to make an observation, which will rule out some incompatible observables.

Note that all the constructions in this section can be generalized to infinite-dimensional Hilbert spaces in the quantum case, and to infinite or continuous Ω in the classical case. However, a rigorous discussion of the associated mathematics is beyond the scope of this article. Though conceptually the finite and infinite cases are very similar, we will need to extend the finite techniques somewhat in section 4.2 in order to deal with continuous systems. For lucid introductions to the general theories of classical and quantum probability we refer to [75] and [53], respectively.

3. The physical model: from QED to stochastic equations

In this section we will describe a microscopic model for the class of systems we consider. The model consists of an atomic ensemble coupled weakly to an external electromagnetic field which is ultimately detected.

3.1. System model from quantum electrodynamics

It is well known from quantum electrodynamics [13, 54] that the observable for the free electric field is given by

$$\mathbf{E}(\mathbf{r},t) = \sqrt{\frac{\hbar}{(2\pi)^3\varepsilon_0}} \sum_s \int \sqrt{\frac{\omega}{2}} \left(i a_{\mathbf{k},s} \boldsymbol{\varepsilon}_{\mathbf{k},s} e^{i(\mathbf{k}\cdot\mathbf{r}-\omega t)} + \text{h.c.} \right) d^3k \tag{8}$$

where $\omega = c|\mathbf{k}|$, $\boldsymbol{\varepsilon}_{\mathbf{k},s}$ are polarization vectors and $a_{\mathbf{k},s}$ are plane wave (Fourier) mode annihilation operators that satisfy the commutation relations $[a_{\mathbf{k},s}, a^\dagger_{\mathbf{k}',s'}] = \delta^3(\mathbf{k}-\mathbf{k}')\delta_{ss'}$. We assume that the atomic ensemble (centered at the origin) interacts with the field predominantly through its collective dipole moment; i.e., the interaction Hamiltonian will be of the form $H_I(t) = -\mathbf{d}(t)\cdot\mathbf{E}(0,t)$ where $\mathbf{d}(t)$ is the ensemble dipole operator. In practice there will be some ultraviolet cutoff, which we can obtain e.g. by averaging the electric field over the volume of the cloud of atoms instead of evaluating it at the origin. We will write

$$\mathbf{E}^{(+)}(\mathbf{r},t) = [\mathbf{E}^{(-)}(\mathbf{r},t)]^\dagger = \sum_s \int g(\mathbf{k})\, a_{\mathbf{k},s} \boldsymbol{\varepsilon}_{\mathbf{k},s} e^{i(\mathbf{k}\cdot\mathbf{r}-\omega t)}\, d^3k \tag{9}$$

where $\mathbf{E} = i(\mathbf{E}^{(+)} - \mathbf{E}^{(-)})$ and $g(\mathbf{k})$ is the mode function, e.g. $g(\mathbf{k}) \propto \sqrt{\omega}\, e^{-d\omega^2}$ if we average $\mathbf{E}$ over a spatial Gaussian distribution.

The full interaction is sketched in cartoon form in Fig. 1a. The atomic ensemble interacts through its dipole moment with all plane wave modes in three dimensions. A strong, focused laser beam at frequency ω_0 is modeled by bringing the corresponding modes into a large-amplitude coherent state. The drive is scattered predominantly in the forward direction, and is ultimately detected. The remaining modes are in the vacuum state and drive spontaneous emission of the ensemble in all directions. This essentially complete description of the interaction embodies all the physics of the problem, and thus allows one to predict quantities such as the spontaneous

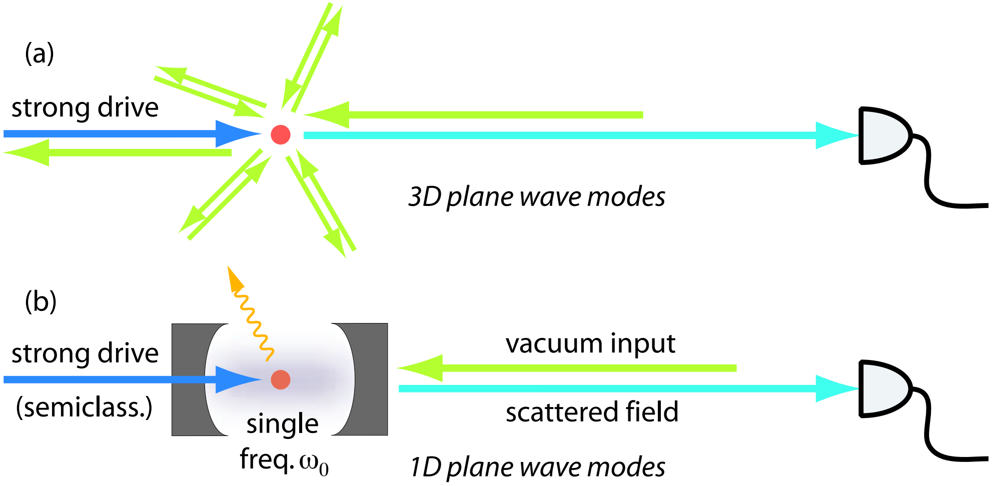

Figure 1. (a) Schematic of the full interaction Hamiltonian, where all plane wave modes in three dimensions interact with an atomic ensemble. One of the incoming modes is coherently excited with frequency ω_0 and large amplitude; the coherent excitation scatters mainly in the forward direction. The remaining incoming modes are in the vacuum state and drive spontaneous emission. (b) Simplified one-dimensional model, where plane waves are scattered off a single-mode cavity in one direction only. The strong driving field is treated semiclassically and coherently excites the cavity mode, which has frequency ω_0. Spontaneous emission can be added to the model in a phenomenological manner.

emission rate. The full picture is also very complicated, however, as it requires a detailed analysis of the atomic structure, a partitioning of the field into observed and unobserved modes, etc. Such an analysis is beyond the scope of this article.

Instead, we will investigate a highly simplified model (Fig. 1b) that is widely used in quantum optics [27, 78, 83]. To justify such a model, we claim that most of the interesting physics occurs in the direction of the driving laser, as most of the light is scattered forward and observed in this direction. Hence we can approximate the system by a one-dimensional model where only the forward modes are treated exactly and the strong drive is treated semiclassically. Spontaneous emission into the eliminated modes is unobserved, and hence we could include it phenomenologically by adding decoherence. Finally, to simplify the interaction with the ensemble, we place the ensemble into a leaky single mode cavity. This allows us to treat the interaction between the ensemble and the field for a single frequency only, that of the cavity mode, which is chosen to be at the laser driving frequency ω_0. The cavity dynamics is then adiabatically eliminated to give an effective interaction between the ensemble and the external field.

Let us systematically work out this simplified model. We begin by treating the one-dimensional external field that is ultimately detected. We can obtain an expression for the field by integrating Eq. (8) over a transverse area [27], or alternatively by directly quantizing the wave equation in one dimension [78]. We obtain

$$E(z,t) = \sqrt{\frac{\hbar}{2\pi\varepsilon_0 c}} \int_0^\infty \sqrt{\frac{\omega}{2}} \, (i a_\omega e^{-i\omega(t - z/c)} + \text{h.c.}) \, d\omega \tag{10}$$

for the electric field intensity in a single polarization state (we will assume polarized light), where $[a_\omega, a^\dagger_{\omega'}] = \delta(\omega - \omega')$. The annihilators a_ω correspond to plane wave modes in the z-direction, $\mathbf{k} = (\omega/c)\hat{\mathbf{z}}$, where positive z is defined to be on the left in Fig. 1. Thus the field for $z < 0$ is propagating towards the cavity mirror in time, whereas $z > 0$ propagates away from the mirror. In practice the cavity mirror will reverse the propagation direction, so we can reinterpret $z > 0$ as the component of the field propagating toward the detector, whereas $z < 0$ is the incident part of the field§.

We now introduce the cavity mode with annihilation operator $b(t) = be^{-i\omega_0 t}$. The interaction Hamiltonian between the cavity mode and the external field is given by

$$\begin{aligned} H_{CF} &= \hbar \int_0^\infty \kappa(\omega)(ia_\omega^\dagger b e^{i(\omega-\omega_0)t} + ia_\omega^\dagger b^\dagger e^{i(\omega+\omega_0)t} + \text{h.c.})d\omega \\ &= i\hbar(b(t) + b(t)^\dagger)(E^{(-)}(0,t) - E^{(+)}(0,t)) \end{aligned} \tag{11}$$

where we have used

$$E^{(+)}(z,t) = [E^{(-)}(z,t)]^\dagger = \int_0^\infty \kappa(\omega) a_\omega e^{-i\omega(t-z/c)} d\omega \tag{12}$$

Here $\kappa(\omega)$ does not only depend on the external field but also on the frequency-dependent transmission of the cavity mirror, and is unitless. An interaction Hamiltonian of this form can be obtained from the QED Hamiltoian by expanding it into "quasi-modes" corresponding to either inside or outside the cavity; see [15].

We will briefly describe the remaining Hamiltonians. The interaction Hamiltonian of the cavity mode with a resonant classical drive is given by

$$H_D = \hbar\mathcal{E}(b + b^\dagger) \tag{13}$$

where $\mathcal{E}$ is the drive amplitude. Spontaneous emission is treated by introducing another field $\tilde{E}$ with annihilation operators c_ω, called the side channel, and adding another Hamiltonian $H_\perp = -d(t)\tilde{E}(0,t)$ where $d(t)$ is an atomic dipole operator. Unlike the forward channel E, which we will ultimately observe, the side channel is left unobserved. This is a simple but effective way to model the partitioning of the full three-dimensional field $\mathbf{E}(\mathbf{r},t)$ into observed and unobserved modes.

The atomic Hamiltonian H_A and the ensemble-cavity mode interaction H_{AC} are more variable, as they depend on the structure of the atoms in the ensemble. In particular, we get drastically different behavior when the atoms have a transition that is resonant with the cavity mode than in the far detuned case. We will consider a specific example in section 3.3.

3.2. Quantum noise and the Markov limit

The discussion in the previous section was based entirely on "mechanical" arguments; i.e., the electric field emerged naturally by quantization of Maxwell's equations and the dipole coupling to matter. Any physical model ultimately has its roots in this level of description. However, we have already discussed that the foundations of quantum theory are essentially a glorified probability theory, where any observable is equivalent to a random variable on some probability space. As we will be interested in observations of the field, it is essential to make the connection between the physical model and its manifestation as a (quantum) probabilistic dynamical system.

§ In a full three-dimensional description the cavity mirror would be modeled by an interaction Hamiltonian that scatters into the backward propagating modes with terms such as $a_{-\mathbf{k}}^\dagger a_{\mathbf{k}}$. In the one-dimensional case, however, we can simply absorb this reflection into the definition of the field.

We can consider Eq. (12) as the Fourier transform of the operator distribution $\kappa(\omega)\theta(\omega)a_\omega$, where θ is the step function. We will always take the incoming field to be in the vacuum state as in Fig. 1. Each a_ω can be thought of as an independent quantum "complex Gaussian" random variable, in the sense that its "real" and "imaginary" parts $a_\omega + a_\omega^\dagger$ and $ia_\omega^\dagger - ia_\omega$ are precisely Gaussian random variables. Hence $E^{(+)}(0,t)$ will be some sort of quantum complex Gaussian noise. Note that the two quadratures $E^{(+)} + E^{(-)}$ and $iE^{(-)} - iE^{(+)}$ do not commute, so we cannot interpret $E^{(+)}(0,t)$ as a classical complex noise. We would now like to consider the Heisenberg equation (in the interaction picture with respect to the field dynamics)

$$\dot{X}_t = \frac{i}{\hbar}[H_\perp + H_A + H_{AC} + H_D + H_{CF}(t), X_t] \tag{14}$$

as being driven by the noise $iE^{(-)} - iE^{(+)}$, together with an observation of the field which need not commute with the driving noise. Then the statistical inference step can be formulated as finding the best estimate of the noisy time evolution of atomic observables given noisy observations of the field.

Similar problems have been studied in classical probability for about a century, and the main lessons learned there appear to carry over to the quantum case. In particular:

(i) Statistical inference of continuous-time processes is essentially intractable unless we approximate the noise process by a *white noise*. In this case, the time evolution of the system is Markovian [60] (i.e. the distribution of future system states depends only on the present state and not on past history) and statistical inference is described by the elegant theory of Markov nonlinear filtering [16, 51].

(ii) Dealing with white noise directly is possible, but the resulting theory is very technical due to the fact that white noise is an extremely singular object [35, 43, 45]. It is much easier to build a theory from a Wiener process, the integral of white noise, which is at least continuous [60].

We fill follow a similar program below for quantum systems; i.e., we will first find a Markov approximation of the full field-theoretic model described previously, then develop a theory of quantum Markov filtering.

Before we embark on this path, it should be mentioned that the problem with colored noise takes on an even more severe form in the quantum case. In the classical case the problem is mainly technical; there is no conceptual problem associated to statistical inference with colored noise, but it is not possible to obtain filtering equations in a recursive form [14]. In the quantum case, however, it is not even clear what we mean by an observation of colored noise, let alone the associated statistical inference problem, as the field operators may not commute with themselves at different times or with the system [25]. There is as of yet no satisfactory solution to this problem; in particular, a satisfactory theory of quantum non-Markovian continuous measurement has yet to be developed. As we will see, however, these problems do not appear in the Markov case.

3.2.1. Classical and quantum stochastic differential equations Let us briefly review the classical concept of a stochastic differential equation (SDE) [60]. We denote by W_t a one-dimensional Wiener process. It is defined on a probability space Ω where each $\omega \in \Omega$ corresponds to a single sample path $\{W_t(\omega)\}$ of the Wiener process.

Heuristically the time derivative $\dot{W}_t$ would be white noise, so we wish to give meaning to a differential equation of the form

$$\frac{d}{dt}X_t(\omega) = f(X_t(\omega)) + \sigma(X_t(\omega))\frac{dW_t(\omega)}{dt} \tag{15}$$

However, this equation makes no mathematical sense as W_t is differentiable with probability zero. The solution is to rewrite it as an integral equation

$$X_t = X_0 + \int_0^t f(X_s)\,ds + \int_0^t \sigma(X_s)\cdot dW_s \tag{16}$$

and then to define the stochastic integral. As a notational analogy with ordinary differential equations we will also write

$$dX_t = f(X_t)\,dt + \sigma(X_t)\cdot dW_t \tag{17}$$

which is equivalent to (16) by definition.

Itô defined a stochastic integral in the following way:

$$\int_{t_0}^{t_n} f_s\,dW_s = \lim_{|t_{i+1}-t_i|\to 0}\sum_{k=0}^{n-1} f_{t_k}(W_{t_{k+1}} - W_{t_k}) \tag{18}$$

Precisely in which sense the limit is taken is a central construction in Itô's theory which we gloss over. A different definition, due to Stratonovich, is

$$\int_{t_0}^{t_n} f_s\circ dW_s = \lim_{|t_{i+1}-t_i|\to 0}\sum_{k=0}^{n-1} \frac{1}{2}(f_{t_{k+1}} + f_{t_k})(W_{t_{k+1}} - W_{t_k}) \tag{19}$$

It is a signature of the singularity of the problem that these two integrals do not give the same answer; such integrals would necessarily be the same if we could interpret them in the Riemann-Stieltjes sense. It is now ambiguous, however, how we should interpret Eq. (16).

A major difference between the two integrals is their transformation property. Ordinary Riemann-Stieltjes integrals obey the Leibnitz rule $d(X_tY_t) = Y_tdX_t + X_tdY_t$ (we use the shorthand notation of Eq. (17)). It turns out that this property is also obeyed by the Stratonovich integral (19). The Itô integral, on the other hand, obeys the modified transformation property $d(X_tY_t) = Y_tdX_t + X_tdY_t + dX_t\,dY_t$, where we use the Itô rules $dW_t^2 = dt$, $dt^2 = dW_t\,dt = 0$ to evaluate the rightmost term. Similarly, the Itô transformation rule for arbitrary functions becomes

$$dg(X_t) = g'(X_t)dX_t + \tfrac{1}{2}g''(X_t)dX_t^2 \tag{20}$$

Note how the shorthand notation of Eq. (17) allows us to express these deep results in a compact way. The power of the Itô calculus lies in the fact that complicated transformations can be perfomed using only simple symbolic manipulations.

The fact that the Stratonovich integral obeys the Leibnitz rule suggests that physical systems should be described by a Stratonovich SDE; after all, if we take a physical system with a smooth driving force, and add some noise to this force, we do not expect the transformation properties of the system to change. We will investigate this further in the next section. On the other hand, the Itô integral has the nice property that its expectation vanishes‖, which suggests that Itô SDE are natural from the point of view of statistical inference. Fortunately we can have it both ways, as there is a conversion formula between Itô and Stratonovich SDE: the solution of $dX_t = f(X_t)dt + \sigma(X_t) \circ dW_t$ is equivalent to the solution of

---

‖ The Itô integral is only defined for *nonanticipative* integrands, i.e. f_t must be independent from any increment $W_{t_2} - W_{t_1}$ with $t_2 > t_1 \geq t$. It follows immediately from (18) that the integral has vanishing expectation.

$$dX_t = f(X_t)dt + \tfrac{1}{2}\sigma(X_t) \cdot \nabla\sigma(X_t)dt + \sigma(X_t)\, dW_t \tag{21}$$

We see that in the mean, the Stratonovich noise results in an effective drift. This additional term is known as the Itô correction.

Let us return to the quantum case. Define

$$a_t = \frac{1}{\sqrt{2\pi}} \int_{-\infty}^{\infty} a_\omega e^{-i\omega t} d\omega \tag{22}$$

where we have extended a_ω to negative frequencies. In the vacuum state, the two quadratures $x_t = a_t + a_t^\dagger$ and $y_t = ia_t - ia_t^\dagger$ have zero mean and delta-correlated covariance, e.g. $\mathbb{E}x_t = 0$ and $\mathbb{E}[x_t x_s] = \mathbb{E}[a_t a_s^\dagger] = \delta(t-s)$. Moreover, it is easily verified that $[x_t, x_s] = 0$ for $t \neq s$ (and similarly for y_t); this is important, as it means that we can interpret x_t as a classical random process. Indeed, following the procedure of section 2.2, we can simultaneously diagonalize the operators x_t at all times and transform to a classical probability space. We find that both x_t and y_t are entirely identical to classical white noise. We will thus call the field a_t *quantum white noise.*

Note that the noise $E^{(+)}(0,t)$ that drives Eq. (14) is not white. However, if the system response has a sufficiently narrow bandwidth we would expect the noise to "look" white on the slow timescale of the system, as $\kappa(\omega)$ is locally flat. Equation (22), and the associated introduction of negative frequencies, should be seen purely as a mathematical construction that corresponds to noncommutative white noise. In the next section we will make these ideas more precise by showing in what sense the physical model (14) can be approximated using noises of this form.

We now proceed as in the classical case. Define the quantum Wiener process

$$A_t = \int_0^t a_t\, dt \tag{23}$$

We can now introduce the quantum Itô integral [10, 26, 37, 55]

$$\int_{t_0}^{t_n} X_s\, dA_s = \lim_{|t_{i+1}-t_i| \to 0} \sum_{k=0}^{n-1} X_{t_k}(A_{t_{k+1}} - A_{t_k}) \tag{24}$$

for nonanticipative X_t (i.e., X_t is independent of any increment $A_u - A_v$, $u > v \geq t$.) It immediately follows that the integral has vanishing expectation in the vacuum state. Moreover, as X_{t_k} is independent from $A_{t_{k+1}} - A_{t_k}$, the process and increment commute: hence $X_t\, dA_t = dA_t\, X_t$. The quantum Itô rules are $dA_t\, dA_t^\dagger = dt$, $dA_t\, dt = dA_t^\dagger\, dA_t = dA_t^2 = 0$.

Similarly, we can define a quantum Stratonovich integral [26, 31, 32]

$$\int_{t_0}^{t_n} X_s \circ dA_s = \lim_{|t_{i+1}-t_i| \to 0} \sum_{k=0}^{n-1} \frac{1}{2}(X_{t_{k+1}} + X_{t_k})(A_{t_{k+1}} - A_{t_k}) \tag{25}$$

which obeys the Leibnitz rule but does not have vanishing expectation. Additionally, in this case X_t does not commute with the noise increment, so $X_t \circ dA_t$ and $dA_t \circ X_t$ are two distinct forms of the Stratonovich integral.

Note that the above discussion is entirely heuristic; the mathematical objects we are using are extremely singular and require careful definition. The quantum Itô theory was introduced in a rigorous way by Hudson and Parthasarathy [37]; a more heuristic treatment can be found in Gardiner and Collett [26]. More recently the relations between the quantum Itô, Stratonovich and white noise formalisms were investigated by Gough [31, 32]. We refer to these references for a detailed treatment.

3.2.2. The Wong-Zakai theorem and the Markov limit Mathematically, (quantum) stochastic differential equations are rather peculiar objects—strictly speaking they are not even differential equations, but integral equations. Nonetheless SDE are widely used to model physical phenomena. The reason that this is so succesful stems from an important result, originally due to Wong and Zakai [82], which can be stated as follows. Suppose we have an ordinary differential equation of the form

$$\frac{dx^\lambda(t)}{dt} = f(x^\lambda(t)) + \sigma(x^\lambda(t))\xi^\lambda(t) \tag{26}$$

where $\xi^\lambda(t)$ is some piecewise smooth random process that converges to white noise in some appropriate sense as $\lambda \to 0$. Then the solution $x^\lambda(t)$ of Eq. (26) converges as $\lambda \to 0$ to the solution of

$$dX_t = f(X_t)\,dt + \sigma(X_t) \circ dW_t \tag{27}$$

This result tells us that the behavior of a "real" physical system is well approximated by the solution of an SDE as long as the noise is sufficiently wideband. Additionally our notion that physical systems are well described by Stratonovich equations is now rigorously justified. In the remainder of this section we will give a simple introduction to the quantum analog of the Wong-Zakai procedure. For a rigorous treatment, we refer to [1, 33].

As a first step we partition our system into fast and slow timescales. The electromagnetic noise and the high-frequency oscillation of the cavity mode operate on the fast timescale, whereas the driving field and the coupling to the atoms operate on a much slower timescale. In order to study the Wong-Zakai limit we completely ignore the slow interactions by turning them off—a very good approximation if the correlation time of the noise is short. This is equivalent to the assumptions mentioned in the previous section: a short correlation time implies that $\kappa(\omega)$ is slowly varying, whereas ignoring the slow interactions assumes that these do not significantly shift the resonance frequency of the cavity.

What remains is the fast dynamics, which we write in propagator form

$$\frac{dU_t}{dt} = -\frac{i}{\hbar}H_{CF}U_t = (b(t) + b(t)^\dagger)(E^{(-)}(0,t) - E^{(+)}(0,t))U_t \tag{28}$$

The key physical assumption we must make to obtain the white noise limit is that the cavity is weakly coupled to the external field. Naively one would expect that we could implement this limit by solving the equation $dU_t/dt = -i\lambda H_{CF}U_t/\hbar$ and then taking the limit $\lambda \to 0$. This clearly doesn't work, however, as this would just turn off the interaction between the cavity and the field. The problem is that λ not only changes the coupling strength, but also the timescale of the interaction dynamics.

The effect that we are trying to capture in the weak coupling limit is not a precise description of fast dynamics, but the effective contribution of the noise to the slow dynamics. We saw in the classical case, Eq. (21), that the noise causes an effective drift in the system dynamics. If we replace $\sigma(x) \mapsto \lambda\sigma(x)$, we infer from (21) that this drift occurs on a timescale t/λ^2. This suggests what we can make the substitution $H_{CF} \mapsto \lambda H_{CF}$ and let $\lambda \to 0$, but we will only obtain the weak coupling limit if we simultaneously rescale time as $t \mapsto t/\lambda^2$. This idea was originally suggested in the context of classical stochastic approximations by Stratonovich [67] and was introduced independently in the physics literature by Van Hove [72].

After performing these rescalings we obtain

$$\begin{aligned}\frac{dU_t^\lambda}{dt} &= \frac{1}{\lambda}\left[b\left(\frac{t}{\lambda^2}\right) + b^\dagger\left(\frac{t}{\lambda^2}\right)\right]\left[E^{(-)}\left(0,\frac{t}{\lambda^2}\right) - E^{(+)}\left(0,\frac{t}{\lambda^2}\right)\right]U_t^\lambda \\ &= \left[a_\lambda^\dagger(t)b + \tilde{a}_\lambda^\dagger(t)b^\dagger - a_\lambda(t)b^\dagger - \tilde{a}_\lambda(t)b\right]U_t^\lambda\end{aligned} \tag{29}$$

Let us investigate the behavior of the rescaled noise

$$a_\lambda(t) = \frac{1}{\lambda}\int_0^\infty \kappa(\omega)\, a_\omega e^{-i(\omega-\omega_0)t/\lambda^2} d\omega \tag{30}$$

as $\lambda \to 0$. In particular, we obtain for the correlation function

$$\mathbb{E}[a_\lambda(t)a_\lambda^\dagger(s)] = \frac{1}{\lambda^2}\int_0^\infty \kappa(\omega)^2 e^{-i(\omega-\omega_0)(t-s)/\lambda^2} d\omega \xrightarrow{\lambda\to 0} \gamma'\,\delta(t-s) \tag{31}$$

with $\gamma' = 2\pi\kappa(\omega_0)^2$, where we have used $\lim_{\lambda\to 0} e^{-i\omega t/\lambda^2}/\lambda^2 = 2\pi\delta(\omega)\delta(t)$ (in the sense of Schwartz distributions). Hence in the weak coupling limit the resonant terms converge to white noise driving terms. However, for the rescaled noise

$$\tilde{a}_\lambda(t) = \frac{1}{\lambda}\int_0^\infty \kappa(\omega)\, a_\omega e^{-i(\omega+\omega_0)t/\lambda^2} d\omega \tag{32}$$

we obtain

$$\mathbb{E}[\tilde{a}_\lambda(t)\tilde{a}_\lambda^\dagger(s)] = \frac{1}{\lambda^2}\int_0^\infty \kappa(\omega)^2 e^{-i(\omega+\omega_0)(t-s)/\lambda^2} d\omega \xrightarrow{\lambda\to 0} 0 \tag{33}$$

Hence the nonresonant terms vanish in the weak coupling limit. We see that the weak coupling limit gives us the commonly used rotating wave approximation for free.

Studying the convergence of U_t^λ is more complicated, but can be performed by investigating the convergence of each term in the associated Dyson series [1, 33]. The result is, however, not surprising: Eq. (29) converges to the Stratonovich equation [31, 32]

$$dU_t = \sqrt{\gamma'}\left[dA_t^\dagger \circ bU_t - dA_t \circ b^\dagger U_t\right] \tag{34}$$

which is essentially the quantum version of the Wong-Zakai theorem [33]. We can equivalently express the result in the Itô form as

$$dU_t = \left[\sqrt{\gamma'}\, b\, dA_t^\dagger - \sqrt{\gamma'}\, b^\dagger\, dA_t - \tfrac{1}{2}\gamma' b^\dagger b\, dt\right]U_t \tag{35}$$

where an Itô correction term emerges as in the classical case.

In addition to the emerging quantum stochastic equation, a detailed treatment of the quantum Wong-Zakai limit usually results in an additional small energy shift to the system Hamiltonian [1, 33]. This energy shift can be normalized away by a proper choice of the system Hamiltonian.

3.3. Example: spins with dispersive coupling

Now that we have made a Markovian approximation to the interaction, it remains to add the slow dynamics back in. We do this simply by adding the corresponding Hamiltonians. As discussed before, spontanous emission is modeled by coupling the atoms directly to an unobserved field $\tilde{E}$ through their dipole moment $d(t) = \sigma e^{-i\omega_d t} + \sigma^\dagger e^{i\omega_d t}$ (here σ is an atomic decay operator and ω_d is the dipole rotation frequency.) Through a similar analysis as the one performed above, we obtain our complete physical model:

$$dU_t = \Big[\sqrt{\gamma'}\, b\, dA_t^\dagger - \sqrt{\gamma'}\, b^\dagger\, dA_t + \sqrt{\gamma_\perp}\, \sigma\, d\tilde{A}_t^\dagger - \sqrt{\gamma_\perp}\, \sigma^\dagger\, d\tilde{A}_t \\ - \tfrac{1}{2}\gamma' b^\dagger b\, dt - \tfrac{1}{2}\gamma_\perp \sigma^\dagger \sigma\, dt - \tfrac{i}{\hbar}(H_A + H_{AC} + H_D)\, dt\Big]\, U_t \tag{36}$$

Before we specialize to the particular model that will be used in the remainder of the paper, let us digress for a moment and calculate the Heisenberg evolution $X_t = U_t^\dagger X U_t$ of an arbitrary observable X of the atom or cavity mode, as expressed symbolically in Eq. (14). Using the quantum Itô rules we easily obtain

$$dX_t = \frac{i}{\hbar}[H_A + H_{AC} + H_D, X_t]\, dt + \gamma' \mathcal{L}_{b_t} X_t\, dt + \gamma_\perp \mathcal{L}_{\sigma_t} X_t\, dt + \sqrt{\gamma'}[b_t^\dagger, X_t]\, dA_t \\ + \sqrt{\gamma'}[X_t, b_t]\, dA_t^\dagger + \sqrt{\gamma_\perp}[\sigma_t^\dagger, X_t]\, d\tilde{A}_t + \sqrt{\gamma_\perp}[X_t, \sigma_t]\, d\tilde{A}_t^\dagger \tag{37}$$

where $\mathcal{L}_c X = c^\dagger X c - \frac{1}{2}(c^\dagger c X + X c^\dagger c)$ is the well-known Lindblad term. As the expectations of Itô integrals vanish, clearly averaging away the noise terms ("tracing over the bath") results in a Lindblad-type master equation in the Heisenberg picture, which is ubiquitous in the description of quantum open systems (see e.g. [26]). In the language of quantum probability, the unitary solution U_t of the quantum Itô equation provides a *unitary dilation* of the associated Lindblad equation [36].

We now introduce a highly simplified model of an atomic ensemble interacting with an electromagnetic field [69, 70]. Consider an atomic ensemble consisting of a set of N atoms with a degenerate two-level ground state. We will assume that all atomic transitions are far detuned from the cavity resonance, so the interaction between the atoms and the cavity is well described by the dispersive Hamiltonian $H_{AC} = \hbar\chi F_z b^\dagger b$ where F_z is the collective dipole moment of the ensemble, i.e. it is a spin-$N/2$ angular momentum operator, and χ determines the coupling strength. Such a Hamiltonian can be obtained, for example, by considering the full dipole coupling and then adiabatically eliminating all the excited states. We furthermore consider the atomic Hamiltonian $H_A = \hbar\Delta F_z + \hbar\, h(t) F_y$, where Δ is the atomic detuning and $h(t)$ is the strength of a magnetic field in the y-direction. The latter will allow us to apply feedback to the system by varying the external magnetic field. We obtain

$$dU_t = \Big[\sqrt{\gamma'}\, b\, dA_t^\dagger - \sqrt{\gamma'}\, b^\dagger\, dA_t + \sqrt{\gamma_\perp}\, \sigma\, d\tilde{A}_t^\dagger - \sqrt{\gamma_\perp}\, \sigma^\dagger\, d\tilde{A}_t - \tfrac{1}{2}\gamma_\perp \sigma^\dagger \sigma\, dt \\ - \tfrac{1}{2}\gamma' b^\dagger b\, dt - i(\Delta F_z + h(t) F_y + \chi F_z b^\dagger b + \mathcal{E}(b + b^\dagger))\, dt\Big]\, U_t \tag{38}$$

Adiabatically eliminating the cavity [19, 24, 74], assuming that γ' and $\mathcal{E}$ are sufficiently large so this is a good approximation, yields

$$dU_t = \Big[\sqrt{\gamma_\perp}\, \sigma\, d\tilde{A}_t^\dagger - \sqrt{\gamma_\perp}\, \sigma^\dagger\, d\tilde{A}_t + \sqrt{M}\, F_z(dA_t^\dagger - dA_t) \\ - \tfrac{1}{2}\gamma_\perp \sigma^\dagger \sigma\, dt - \tfrac{1}{2} M F_z^2\, dt - i(\tfrac{4\chi\mathcal{E}^2}{(\gamma')^2} + \Delta) F_z\, dt - i h(t) F_y\, dt\Big]\, U_t \tag{39}$$

where $M = 16\chi^2\mathcal{E}^2/(\gamma')^3$ is the effective interaction strength. It is convenient to choose the atomic detuning $\Delta = -4\chi\mathcal{E}^2/(\gamma')^2$, and we will henceforth assume that this is the case (experimentally we can always fix the detuning by applying a magnetic field in the z-direction.)

Finally, we will for simplicity neglect spontaneous emission by setting $\gamma_\perp = 0$, a good approximation if $\gamma_\perp \ll M$ (in this case the interesting system dynamics takes place long before spontaneous emission sets in.) This gives

$$dU_t = \left[\sqrt{M}\, F_z(dA_t^\dagger - dA_t) - \tfrac{1}{2}MF_z^2\, dt - ih(t)F_y\, dt\right] U_t \tag{40}$$

We will use this highly simplified model as an example throughout the remainder of the article.

4. Conditioning: classical probability and quantum filtering

In the previous section we considered in detail the physical interactions between an atomic ensemble and the electromagnetic field, which, after many simplifications, were condensed into Eq. (40). This expression contains all the physical dynamics of our model. We now start the second step in our program, in which we perform statistical inference of the atomic dynamics based on an observation of the field. Our approach [71] is inspired by [5, 7].

4.1. Optical detection

Before we can derive a filtering equation we must specify what measurement is performed. We will consider the case of (balanced) homodyne detection, which measures a quadrature of the outgoing field. The principles of this method are discussed in many textbooks [62, 73] and a continuous time description in terms of quantum stochastic calculus can be found in [3]. Homodyne detection has the advantage that it gives rise to a continuous, Wiener process-type integrated photocurrent, which is particularly convenient for continuous time feedback control.

Other types of detection may be convenient in different situations depending on the experimental setup. For example, the spin squeezing experiment [30] makes use of polarimetry, which can be modeled in a very similar way as homodyne detection. Though photon counting detection also has a continuous time description in terms of quantum stochastic calculus, it gives rise to a discrete jump process which is much less convenient for the purpose of feedback control.

Heuristically, consider Eq. (40) as being driven by the white noise a_t, the "derivative" of A_t. An ideal wide-band homodyne detector will measure the field observable $a_t + a_t^\dagger$ after the field has interacted with the ensemble; i.e., we observe the photocurrent $I(t) = U_t^\dagger(a_t + a_t^\dagger)U_t$. As usual mathematically rigorous results are much more easily obtained in integrated form; hence we define as our observation the *integrated photocurrent*

$$Y_t = U_t^\dagger(A_t + A_t^\dagger)U_t \tag{41}$$

where $I(t)$ can be considered the "derivative" of Y_t. For a rigorous treatment directly from the quantum stochastic description we refer to [3].

Finding an explicit expression for Y_t is a straightforward exercise in the use of the quantum Itô rules. From Eqs. (40) and (41) we directly obtain

$$dY_t = 2\sqrt{M}\, U_t^\dagger F_z U_t\, dt + dA_t + dA_t^\dagger \tag{42}$$

Thus clearly homodyne detection of the field provides a measurement of the system observable $F_z(t)$ corrupted by the incident field noise.

We will extend our observation model a little further. We assumed in the above analysis that the detection efficiency is perfect. In practice there will always be some technical noise added to the signal, either due to the intrinsic loss mechanisms in the photodetectors or due to noise in the detection electronics (e.g. amplifier noise). We will model these effects by the addition of an uncorrelated white noise term dW'_t to the observation current; i.e.

$$dY_t = 2\sqrt{M\eta}\,U_t^\dagger F_z U_t\,dt + \sqrt{\eta}\,(dA_t + dA_t^\dagger) + \sqrt{1-\eta}\,dW'_t \tag{43}$$

where $\eta \in (0,1]$ determines the relative strength of the technical noise ($\eta = 1$ is perfect detection.) We can interpret the white noise dW'_t as an operator process by embedding it in a quantum probability space, e.g. $dW'_t = dB_t + dB_t^\dagger$ for some uncorrelated field B_t that does not interact with the system. Note that we have rescaled the current Y_t so that the total corrupting noise has unit variance, i.e. $dY_t^2 = dt$; this gives a convenient normalization of the photocurrent. Experimentally the observed current will have some arbitrary amplification.

In order to make sense as an observed current Y_t must be a classical stochastic process, i.e. $[Y_t, Y_s] = 0\ \forall s \neq t$; clearly any sample path recorded in the laboratory is classical. From Eq. (43), however, it is not at all obvious that this is the case. Once again we resort to a heuristic argument which can be made rigorous in a detailed treatment of quantum stochastic calculus. Eq. (40) implies that the observable a_t only interacts with the system at time t. As a_t is independent from a_s when $t \neq s$, it follows that $U_t^\dagger a_s U_t = U_s^\dagger a_s U_s\ \forall t \geq s$. But then $[I(t), I(s)] = U_t^\dagger [a_t + a_t^\dagger, a_s + a_s^\dagger] U_t = 0$, as we have already established that $a_t + a_t^\dagger$ is entirely classical white noise. Hence Y_t, the integral of $I(t)$ plus technical noise, is also a classical stochastic process.

There is another property of the observation, called the *nondemolition property* by Belavkin [6], that is essential in what follows. Let X be some observable of the atomic ensemble. Then it is easy to show, in exactly the same way we showed that Y_t is a classical process, that $[U_t^\dagger X U_t, Y_s] = 0\ \forall s \leq t$; i.e., any system observable at time t commutes with all prior observations. This means, as we saw in section 2.2, that finding the best estimate of a system observable given all prior observations is an entirely *classical* statistical inference problem. We will find the explicit solution to this problem, the quantum filtering equation, in the next section.

4.2. The quantum filter

Let us begin by establishing some notation. If X is an atomic ensemble observable, denote by $j_t(X) = U_t^\dagger X U_t$ its Heisenberg evolution at time t. Using Eq. (40) and the quantum Itô rules we easily obtain

$$dj_t(X) = j_t(\mathcal{L}[X])\,dt + \sqrt{M}\,j_t([X, F_z])\,(dA_t^\dagger - dA_t) \tag{44}$$

where $\mathcal{L}[X] = ih(t)[F_y, X] + MF_zXF_z - \frac{1}{2}M(F_z^2X + XF_z^2)$. We have already established the observation equation

$$dY_t = 2\sqrt{M\eta}\,j_t(F_z)\,dt + \sqrt{\eta}\,(dA_t + dA_t^\dagger) + \sqrt{1-\eta}\,dW'_t \tag{45}$$

Together, Eqs. (44) and (45) form the system-observation pair of our model. Eq. (44) describes the time evolution of any system observable, whereas Eq. (45) describes the observed current. The goal of the filtering problem is to find an expression for $\pi_t(X) = \mathbb{E}[j_t(X)|Y_{s\leq t}]$, the (least mean square) best estimate of the observable

X given the prior observations $Y_{s\le t}$. An essential point is that the conditional expectations $\pi_t(X)$ are guaranteed to be well-defined by the nondemolition property.

Due to the nondemolition property we could in principle simultaneously diagonalize $j_t(X)$ and Y_s, $s \le t$ for every X, drop down to the associated classical probability space, and calculate the classical conditional expectation $\pi_t(X)$. This is not a very practical course of action, however, so we will need a shortcut. Moreover, our description of the conditional expectation in section 2.1 was rather limited: we only defined the conditional expectation with respect to one discrete random variable, whereas $Y_{s\le t}$ is a continuous family of continuous random variables. To manipulate such continuous quantities one needs the mathematical machinery of real analysis.

We take the following approach. From the definition of conditional expectation is section 2.1 we can extract the following properties:

(i) $\mathbb{E}[X|Y]$ is a function on Y.

(ii) For any random variable Z that is a function of Y, we must have $\mathbb{E}[\mathbb{E}[X|Y]Z] = \mathbb{E}[XZ]$.

It is easy to see that the definition of section 2.1 implies these properties, and it is not hard to show that the converse is also true. In the continuous case we just take these properties as the definition of conditional expectation. This is precisely the real analytic definition, where the intuitive idea of being "a function of Y" is replaced by the notion of measurability [75].

We are now ready to take our shortcut. By property (1), $\pi_t(X)$ must be a function of $Y_{s\le t}$. Introduce the ansatz

$$d\pi_t(X) = C_t(X)\,dt + D_t(X)\,dY_t \tag{46}$$

where $C_t(X)$, $D_t(X)$ are functions of $Y_{s\le t}$ to be determined. If we can determine C_t and D_t, the filtering problem has been solved.

To implement property (2) we use the following trick. We require that

$$\mathbb{E}\left[\pi_t(X)\,e^{\int_0^t g(s)dY_s}\right] = \mathbb{E}\left[j_t(X)\,e^{\int_0^t g(s)dY_s}\right] \tag{47}$$

for any function $g(t)$. The idea behind this is the same as that of a moment generating function: we can generate any (analytic) function of $Y_{s\le t}$ by using an appropriate $g(t)$ and taking derivatives. Hence, if we have proved the relation (47) then we have essentially satisfied property (2).

What remains is mostly a direct application of the Itô rules. For convenience we multiply both sides of (47) by $\exp(-\frac{1}{2}\int_0^t g(s)^2 ds)$. Define

$$e_t^g = e^{\int_0^t g(s)dY_s - \frac{1}{2}\int_0^t g(s)^2 ds} \qquad de_t^g = g(t)e_t^g\,dY_t \tag{48}$$

It is now straightforward to evaluate

$$\begin{aligned}\frac{d\mathbb{E}[e_t^g\pi_t(X)]}{dt} &= \mathbb{E}[e_t^g(C_t(X) + 2\sqrt{M\eta}\,j_t(F_z)D_t(X)) \\ &\quad + g(t)e_t^g(D_t(X) + 2\sqrt{M\eta}\,j_t(F_z)\pi_t(X))]\end{aligned} \tag{49}$$

$$\frac{d\mathbb{E}[e_t^g j_t(X)]}{dt} = \mathbb{E}[e_t^g j_t(\mathcal{L}[X]) + \sqrt{M\eta}\,g(t)e_t^g\,j_t(F_zX + XF_z)] \tag{50}$$

We now invoke Eq. (47) and attempt to find $C_t(X)$, $D_t(X)$ by comparing (49) and (50) term by term. We run into a snag, however, as a naive comparison would yield C_t and D_t in terms of $j_t(F_z)$, etc., which are not functions of $Y_{s\le t}$. Fortunately we can use property (2) of conditional expectations to change all the j_t terms in (49) and (50) to the corresponding π_t terms ($\mathbb{E}[j_t(\cdot)] = \mathbb{E}[\pi_t(\cdot)]$, etc.) This gives immediately

$$\begin{aligned} d\pi_t(X) = \pi_t(\mathcal{L}[X])\,dt + \sqrt{M\eta}\,(\pi_t(F_z X + X F_z) \\ -2\pi_t(F_z)\pi_t(X))(dY_t - 2\sqrt{M\eta}\,\pi_t(F_z)\,dt) \end{aligned} \tag{51}$$

which is the quantum filtering equation for our model.

It is instructive to recall the example of section 2.2. There a simple filtering scenario was constructed by coupling a spin to a commuting observable, then conditioning the spin observables on the commuting observable. This gave rise to a set of classical random variables, representing the conditioned spin observables. Similarly, we have coupled an atomic ensemble to an optical mode and conditioned the atomic observables on a homodyne measurement in the field. This gave rise to a classical Itô equation (51) for the conditioned atomic observables, driven by the observations Y_t.

As in section 2.2 we will find it useful to represent the filter in its adjoint (density) form. To this end, we define the conditional atomic density matrix ρ_t as the random matrix that satisfies $\pi_t(X) = \mathrm{Tr}[\rho_t X]$. Eq. (51) gives

$$d\rho_t = -ih(t)[F_y, \rho_t]\,dt + M\,\mathcal{D}[F_z]\rho_t\,dt + \sqrt{M\eta}\,\mathcal{H}[F_z]\rho_t\,dW_t \tag{52}$$

where we have used the notation

$$\mathcal{D}[c]\rho \equiv c\rho c^\dagger - (c^\dagger c\rho + \rho c^\dagger c)/2 \tag{53}$$

$$\mathcal{H}[c]\rho \equiv c\rho + \rho c^\dagger - \mathrm{Tr}[(c + c^\dagger)\rho]\rho \tag{54}$$

and we have defined the *innovations process*

$$dW_t = dY_t - 2\sqrt{M\eta}\,\mathrm{Tr}[\rho_t F_z]\,dt \tag{55}$$

An important result in filtering theory is that the innovations process W_t is in fact a Wiener process [6, 12]. Though we have not introduced sufficient technical machinery to prove this fact, we can can give a simple interpretation. We can write W_t in the form

$$dW_t = 2\sqrt{M\eta}\,(j_t(F_z) - \pi_t(F_z))\,dt + \sqrt{\eta}\,(dA_t + dA_t^\dagger) + \sqrt{1-\eta}\,dW_t' \tag{56}$$

This expression consists of two parts: the last two terms are white noise terms, whereas the first term is the difference between an atomic observable and our best estimate of that observable, i.e. it represents the new information (the "innovation") contained in the measurement.

4.3. Conditional spin dynamics

Before we add control to the picture it is interesting to take a look at the open-loop properties of the filtering equation (52), i.e. without feedback, by setting $h(t) = 0$. The equation propagates a density matrix, defined as the adjoint of a set of classical conditional expectations, which carries the interpretation of the "statistically inferred" density matrix of the ensemble given the observations in the probe field. One might wonder how such a picture is related to the traditional picture of quantum measurements.

To illustrate the filtering process we have simulated Eq. (52) for a spin $F = 5$ ensemble (e.g., 10 two-level atoms) [66]. Such simulations are highly simplified by the fact that the innovations process is a Wiener process. This means that we do not have to simulate the full quantum-mechanical model, Eqs. (44) and (45), to obtain

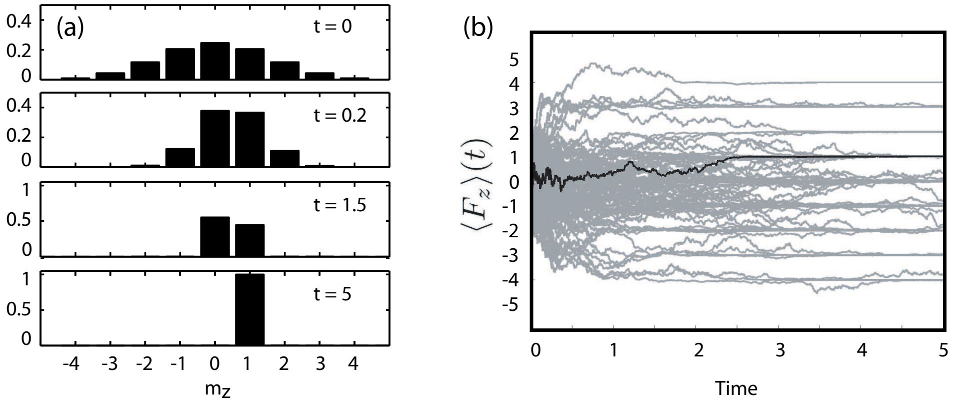

Figure 2. (a) Time evolution of the conditional state from a coherent spin state at $t = 0$ to an eigenstate at long times. The graph shows the population of each F_z eigenstate. (b) 100 sample paths of $\pi_t(F_z)$, with $M = \eta = 1$. The dark line is the sample path shown in (a), resulting in $m_z = 1$. Von Neumann projection is clearly visible at long times.

a photocurrent Y_t to drive (52). Instead, we just plug in a Wiener process for the innovations, for which straightforward numerical methods are available. The results are shown in Fig. 2.

At long times the conditional state is clearly driven to one of the eigenstates of F_z, i.e. Dicke states [17], just as predicted by the Von Neumann projection postulate. In fact, it can be rigorously proved that the $t \to \infty$ limit of Eq. (52) is *exactly* identical to the projection postulate, i.e. the probability of collapse onto each eigenstate is predicted correctly by the filtering equation [2, 66, 71].

Note that we have not previously mentioned the projection postulate in this article. As this result follows from our theory we do not need to postulate it: instead, we have "derived" it using quantum dynamics and classical statistics¶. In some sense the filtering process exposes the anatomy of a quantum measurement. We have explicitly modeled the coupling between the probe field and the system under measurement, Eq. (44), and we considered separately a step that involved purely the gain of information. Both processes conspire to bring about the traditional projection of the system state in the long-time limit.

At intermediate times, $t < \infty$, the conditional state gradually collapses onto the F_z eigenstates. This process, for a single sample path, is shown in Fig. 2a. Whereas a Von Neumann measurement would take the state discontinuously from the initial state to the final collapsed state, the filtering process continuously narrows the distribution over the eigenstates until only one remains. Aside from giving a more realistic description of continuous optical measurements, this description creates an opportunity that has no analog with projective measurements: we can interfere with the collapse process while it is occuring by applying real-time feedback.

¶ The reader should not get the impression, however, that we have now reduced all the peculiarities of quantum measurement to pure classical probability. In particular, we cannot derive why the measurement of an observable rules out the measurement of noncommuting observables, which has no counterpart in classical probability. Only the conditioning, which takes place after a measurement has been performed and the measurement result has been obtained, can be given a purely classical interpretation in this way as a statistical inference procedure. On the other hand, the "back action" on the system is caused by the quantum dynamics of the interaction between the system and the probe, which we have explicitly modeled by a quantum stochastic differential equation.

Finally, we should remark that not all filtering equations give rise to Von-Neumann type collapse. For example, homodyne detection of spontaneously emitted photons, or an atomic ensemble resonantly interacting with the probe field, will result in continuous decay of the conditional state into the ground state. Projective dynamics is obtained in our case because of the dispersive (off-resonant) interaction of the ensemble with the probe and the neglect of spontaneous emission. The latter can be justified, however, if there is a large separation of time scales between the time of collapse and the time at which the spontaneous emission sets in. In this case, the intermediate regime will be very similar to the long-time limit of our model.

The range of dynamics emerging from filtering equations highlights the need for the separate modeling of the system-probe interation. Though we have only presented a very simple model, we have outlined a bottom-up approach in which the system-probe interaction is modeled from first principles using quantum electrodynamics. The detailed modeling of realistic experimental configurations will be invaluable for quantitative comparison of theoretical predictions and experimental data [28].

5. Feedback control and quantum state preparation

The intrinsic randomness of quantum measurement should not dissuade the capable observer from trying to control the dynamics of a system. In fact, it should do just the opposite. The inherent uncertainty in observation is the inspiration for the use of feedback control, and promotes it to the status of fundamental.

Although the physical constraints imposed by quantum mechanics are performance limiting, quantum feedback control problems are well defined and worth pursuing for all of the same reasons engineers use control on classical systems. Furthermore, quantum feedback control, while technically difficult, is simply a branch of traditional control and amenable to the techniques developed therein [4, 18, 71]. Far from introducing an entirely new kind of problem, the challenges presented here highlight and motivate the extension of mathematical methods already in development elsewhere.

In this section we begin by discussing the types of problems and structure encountered in a typical quantum feedback control scenario, building upon the formalism developed above. Here we use language from classical control theory, and discuss the possible application of optimal and robust control theories to the quantum setting. We also emphasize experimental constraints which motivate simplifications of desired controls through model reduction. Next we demonstrate the utility of feedback in a review of applications to atomic ensemble experiments. We finish by focusing on the particular theoretical example of deterministically preparing a state with continuous measurement and control.

5.1. Defining feedback control

The term "quantum feedback control" as used in this article refers to a particular class of problems that should be distinguished from other types of control with quantum systems. The class we consider involves the measurement of a quantum system by interaction with a quantum field. The field is destructively measured resulting in a classical measurement record. That measurement record is then processed and fed back to Hamiltonian parameters affecting the same system.

The rest of this article is concerned with problems of this kind. However, it should be noted that there exist further types of control with this arrangement that we will not discuss. Aside from actuating Hamiltonian parameters of the system with feedback, the observer may possess the ability to adaptively change the measurement itself according to the measurement record. This leads to different “unravellings” of the dynamics [79]. By the nature of the measurement, the ensemble average behavior of the system will be the same for any chosen unravelling or adaptive measurement scheme. Of course, the same will not be true for the average trajectory behavior of the system under different Hamiltonian control laws.

Additionally, there exist completely different types of control with quantum systems bearing little resemblance to the measurement techniques discussed here. For instance, one can imagine doing a type of feedback experiment where, instead of destructively measuring the ancilla system, it is returned to interact with the system of interest again, and possibly repeatedly. For the case of the usual optical ancilla system, this has been referred to as “all-optical feedback” to distinguish it from the electrical measurement signal alternatively produced [81]. In certain cases this kind of “coherent control” [52] can achieve state preparation goals with minimal processing overhead and delay. In the formalism presented here, one could describe such a process completely at the quantum stochastic level of section 3.

Finally, the term “quantum control” is also used in the literature to refer to yet another scenario, with not one system, but an ensemble of identically prepared systems. Here a system is driven with a pulse, then the result is measured. Subsequently, another system is prepared, another pulse is used to drive it, the result is again measured, and so on. In between trials, the pulse shape is changed based on the previous measurements in some algorithmic way to optimize the effect of the pulse [61]. This procedure is a type of “learning control” and, unlike in the examples we study, no feedback occurs during the lifetime of an individual system.

5.2. Separation structure

Generally speaking, the control problem consists of finding a mapping of the measurement record onto the actuation variables such that some pre-defined task is achieved. When stated in this way the problem is very difficult to solve; after all, when we allow any functional from the photocurrent history to the control variables, it is hard to know where to start.

Fortunately we can simplify the problem description considerably using what is sometimes referred to as the *separation principle* or the *information state approach*, originally introduced in classical control theory by Mortensen [57]. The basic idea behind this approach is that we can never control the system more precisely than the precision with which the system state can be inferred from the observations. In many ways this is a statement of the obvious: for example if we know that the system is controlled to within some bound, then clearly we can infer that the system state is within that bound. As a consequence, the best we can do is to control the best estimate of the system state, i.e. the conditional state.

The advantage of this approach is that we have converted the *output feedback* control problem into a *state feedback* control problem for the filter. Operationally, we then consider the filtering equation (52) as our new “effective” dynamical equation to be controlled, where the feedback $h(t)$ can now be taken to be a function of the conditional state ρ_t as opposed to the measurement record. This is a less constrained

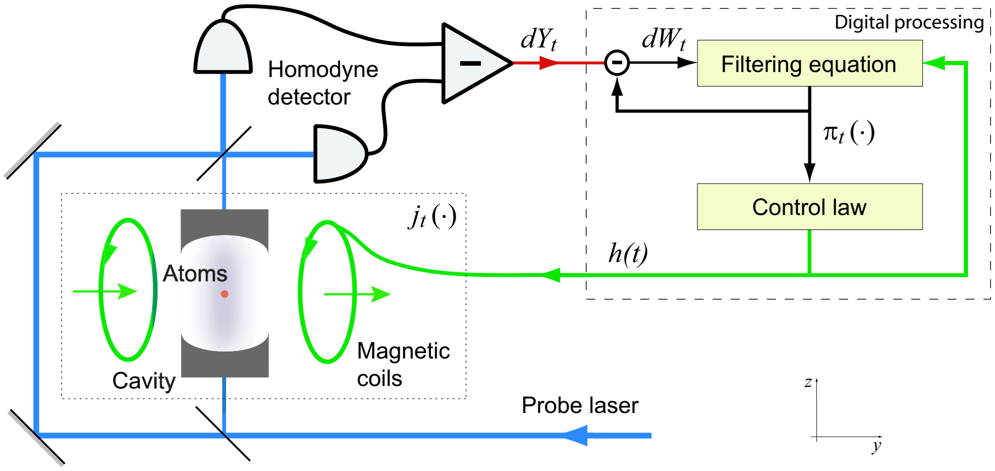

Figure 3. Schematic of the entire feedback control problem for an atomic ensemble. On the experimental level an ensemble interacts with a probe field, as described by Eq. (44). Homodyne detection gives rise to the photocurrent (45), which is processed by a digital controller. A magnetic field is used for feedback. On the controller level, the photocurrent drives the quantum filter (51) which updates recursively the best estimate of the atomic state. The control law is a functional of the current conditional state. The innovations structure (55) allows the control design to be based directly on the filtering dynamics.

problem than the output feedback problem and hence often easier to solve. Control design is further simplified by the fact that the innovation, Eq. (55), is white. This means we can consider Eq. (52) as an ordinary Itô equation to be controlled, without separately modeling the statistics of the photocurrent driving noise.

The structure of the entire control setup, in the context of the model discussed in the previous sections, is shown in Fig. 3. The atomic ensemble and its interaction with the optical probe field and the magnetic control field was modeled in section 3. Homodyne detection was the subject of section 4.1. The photocurrent is processed by a digital control circuit which produces the feedback signal. Inside the controller, the "whitened" photocurrent drives the quantum filter, as described in section 4.2. The control law is a function of the best estimate of the system state. To design the control law, however, we only need to consider the "internal" feedback loop inside the digital circuit. From the controller's effective perspective, the only role of the physical experiment is to provide the innovation dW_t, which is white by construction.

5.3. Defining an objective

We have separated the control design into an estimation problem, which was the subject of section 4.2, and a control problem. The control problem is undefined, however, until we state a goal that our controller should achieve.

As an example, an experimentalist may want to minimize some functional of the system and control variables, e.g.,

$$C[h(t)] = \mathbb{E}\int_0^T \left(j_t(F_z^2) + \mu h(t)^2\right) dt \tag{57}$$

where μ is a parameter that limits the degree that the control input is applied. To apply the separation principle to this case we must first convert the cost function

C into a form which is only a function of the filter state. This is straightforward, however, due to the property $\mathbb{E}j_t(\cdot) = \mathbb{E}\pi_t(\cdot)$ of conditional expectations: we obtain

$$C[h(t)] = \mathbb{E}\int_0^T \left(\pi_t(F_z^2) + \mu h(t)^2\right) dt \tag{58}$$

As expected, the control goal depends only on the conditional state, i.e., the filter state is a *sufficient statistic* for this control problem.

In principle, the minimization of (58) using the dynamics of the filtering equation would produce a control law which is the optimal time-dependent mapping of the conditional state onto the control parameters. This type of problem is known as "optimal control", and is one of the primary modes of thought in classical control theory [8, 20, 38]. As is apparent from Eq. (52), the general form of the filtering equation is non-linear in the state and, as an unfortunate result, the optimal control solution is extremely difficult to find. Although both non-linear and stochastic control theories are well developed fields classically, there is still much work to be done in their intersection.

Fortunately, there are alternative methods for gaining ground on the quantum feedback control problem. First, in some instances, it is possible to linearize the dynamics of the filtering equation via moment expansions. In this case, one can readily adopt "LQG" techniques from classical control [8, 38] for linear systems (L), a cost function quadratic in linear observables and control variables as above (Q), and Gaussian dynamics (G), to solve the problem completely [4, 18, 19, 65]. In any given example, the needed linearization may only work for particular initial states and limited periods of time, but the LQG results can still be remarkably far reaching.

Second, we can choose to be less demanding of our controller, and instead formulate a non-optimal goal. For instance, suppose we are interested in preparing the quantum state ρ_c at long times. The control goal can then be formulated as *find a control law* $h(t)$ *so that* $\mathbb{E}[j_t(X)] \to \mathrm{Tr}[X\rho_c]$ *as* $t \to \infty$ *for any system observable* X. As above, it is easy to see that the filter state is a sufficient statistic and hence we can directly apply the separation principle. In particular, if we can find a controller that makes ρ_c a global (stochastically) stable state for the filter dynamics, the eventual preparation of ρ_c is ensured. Although the state might not be prepared as fast as is physically possible, it is an accomplishment to know that it will eventually be prepared with unit probability. Here there is much work to be done on constructively generating controllers and methods for proving the stability, but progress has been made for some simple problems [71].

5.4. Robustness and model reduction

If given the choice between a controller that works optimally under one set of ideal circumstances and a controller that works sub-optimally, but adequately, over a wide set of possible conditions, the wise experimentalist would always choose the latter. Due to unexpected modeling uncertainties and exogenous noise sources, the optimal control approach has the potential to fail catastrophically in realistic environments, a possibility that has motivated the development of "robust control" for many years [84]. One could say the reason experiments are performed at all is to test the robustness of our model and control design.

The concept of robust control has been extensively studied in the classical deterministic setting, but the same logic holds true for quantum applications. Even as quantum technology reaches its limits, there will always be some degree of non-intrinsic system uncertainty to which the system should be robust. Not surprisingly, quantum feedback techniques have been shown to enable robustness to model uncertainty in metrology applications [65]. Of course one need not draw the line too sharply between optimal and robust control, as there exist types of risk-sensitive optimal quantum control that inherently consider certain kinds of robustness [39, 40].

Another practical reason why optimal control may not be ultimately relevant is that real-time information processing takes time. Even if the modeling is perfect and there are no excess noise sources, an optimal controller may not work due to processing constraints. If the processing delay of the actual controller is large compared to the relevant time-scale of the filtering dynamics, then another approach will be needed. Despite the improving performance of programmable logic devices that might best implement the optimal control, there are few experiments with slow enough time-scales that modern electronics can be optimally effective at real-time estimation and control [64].

Clearly it is of significant interest to be able to derive a controller that works without having to evolve the full filtering equation in real time. Recognizing this, physicists have proposed and used controllers for quantum feedback applications that use a simplified control law which bypasses the full state estimation. Even more easily, one can sometimes feed the measurement record directly back to the system with a gain tailored intelligently in time [69, 77, 80]. However, with any of these approaches, one must be cognizant of realistic gain and bandwidth constraints. For example, one cannot realistically feed pure white noise back into a system, as this would imply infinite sensor and detection bandwidths. Although most of the simplified quantum controllers suggested in the literature have been constructed through more or less heuristic means, we expect the continuing development of these techniques to resort to more mathematical notions of model reduction, where the degree of approximation and its effect on the feedback performance can be more explicitly quantified.

5.5. Measurement and Feedback in Atomic Ensembles

When considering systems with the potential for interesting applications related to quantum information processing, there exists a natural tendency within many physicists to consider conceptually simplified systems, e.g., a single atom or ion. While much progress has been made in trapping, measuring, and controlling single particles, it has also been realized for some time that the use of atomic ensembles does not preclude the observation of uniquely quantum effects nor a simple description. As compared to alternative systems, ensembles are experimentally convenient and, by the sheer number of participants, sufficient signal can be generated to make them powerful in quantum applications, with atomic clocks being just one prominent example.

Here we consider those experiments where continuous measurement and feedback have been used to generate entanglement either within or between atomic ensembles. We begin by discussing the use of dispersive measurement to produce a spin-squeezed state in a single ensemble in the short-time limit, and how feedback can be used to make this process deterministic. We then focus on a particular theoretical limit where the linear approximation fails, but still highly entangled eigenstates of the measured F_z can be prepared by using the more complete filtering equation and an intuitive feedback law. Finally, we briefly discuss experiments and proposals involving the creation of entanglement between two ensembles with and without feedback.

5.5.1. One Ensemble For state preparation with atomic ensembles, spin-squeezed states (SSS) [44] are natural target states. These collective spin states are internally entangled, simply characterized by measured moments of the spin-operators, and useful in metrology tasks [29, 65, 76]. For an ensemble with N spin-f particles and collective angular momentum operators F_i, a state is defined as spin-squeezed, and entangled, if[+]

$$\frac{2fN\langle \Delta F_z^2\rangle}{\langle F_x\rangle^2} < 1 \tag{59}$$

where the spin-state is pointing along x so that $\langle F_x\rangle = F = Nf$ and $\langle F_y\rangle = \langle F_z\rangle = 0$ [63]. Methods to produce these states typically begin with an unentangled coherent spin state (CSS) with all spins exactly polarized along the x direction and realizing the equality of the uncertainty relation

$$\langle \Delta F_y^2\rangle\langle \Delta F_z^2\rangle \geq \frac{\hbar^2\langle F_x\rangle^2}{4}. \tag{60}$$

For the SSS, the equality is roughly maintained with one component $\langle \Delta F_z^2\rangle$ squeezed smaller than the CSS value and the other $\langle \Delta F_y^2\rangle$ anti-squeezed.

There are many ways one can imagine producing the spin-correlations within the ensemble needed for the collective state to be squeezed. Examples include using direct Hamiltonian interactions [63] and also transferring correlations from an auxiliary system, e.g. squeezed states of light [34, 49, 56]. We shall focus on the production of spin squeezed states via dispersive measurement, the effects of which were originally discussed and demonstrated in references [47, 48]. Subsequently, Thomsen, *et al.* [69] proposed a feedback procedure, discussed below, that used a measurement based field rotation to remove the randomness of the measurement while retaining the desired squeezing effect. Others have proposed using feedback to an optical pumping beam to achieve a similar result [56]. It has since been experimentally demonstrated that using a procedure similar to [69] feedback can enable the deterministic production of spin-squeezed states in cold atomic samples [28, 30]. Much work continues in this direction, in particular towards creating squeezed states with the Cesium clock transition, which would considerably improve current atomic clock performance [59].

To understand the conditional preparation of spin-squeezed states by dispersive measurement, consider the apparatus in Figure 3. As shown above, the filtering equation is given by Eq. (52). This equation is only applicable at long times $t \gg 1/M$ if a sufficiently strong cavity is used to suppress the spontaneous emission to an insignificant level. Given existing experimental technology this is currently unrealistic; nevertheless we consider the long time dynamics for purposes of demonstration.

The filtering equation was derived using a simplified one-dimensional model of the interaction. Although this model is often an adequate description of free-space experiments where a distribution of atoms interacts with a spatially extended probe beam, there is much interest in making the model more accurate by extending it to three dimensions. A complete model would consider the scattering process where all free-space field modes interact with the atomic distribution. Some of those channels would then be measured, and the results used to condition the atomic state. In this picture, the conditional entanglement results from the indistinguishability of the atoms in the measurement and "spontaneous emission" is a term used to describe the effect

---

[+] We will denote by $\langle\cdot\rangle$ the expectation of an observable in a general sense. The associated state can be prepared either unconditionally or conditionally.

of the remaining unobserved channels. A considerable amount of work remains to be done in describing collective scattering in terms of measurement theory, but much progress has been made [11, 21, 46, 58].

Returning to the one-dimensional model, we can extract the conditional evolution equations for the moments of any operator from the filtering equation. Under the approximation that there are many atoms and the initial collective state is nearly polarized along the x-direction, we can derive the closed set of equations

$$d\pi_t(F_z) \quad \approx F\exp[-Mt/2]\,h(t)\,dt + 2\sqrt{M\eta}\,\pi_t(\Delta F_z^2)\,dW_t \tag{61}$$

$$d\pi_t(\Delta F_z^2) \approx -4M\eta\,\pi_t(\Delta F_z^2)^2\,dt \tag{62}$$

These equations are obtained by truncating the exact coupled expressions for $\pi_t(F_z^n)$, calculated from Eq. (51), at $n = 2$ [29, 65]. This reduced description is equivalent to a classical Kalman filter [8, 38] and corresponds to a local linearization of the spin dynamics.

Eqs. (61) and (62) are valid only in the short time limit $t \ll 1/M$, past which the full filtering equation is needed. At longer times terms neglected in the approximation grow to the point that the variance becomes stochastic [65], and the moment truncation is no longer a good description. This process can be seen in Fig. 4a, where at small times the variance is deterministic, but then becomes random at longer times.

The deterministically shrinking variance of Eq. (62) at short times signifies that a spin squeezed state is prepared with a random offset given by Eq. (61). The idea of [69] was to choose $h(t) \propto \dot{Y}_t$ with an intelligently chosen gain such that the first term effectively cancels the second term in Eq. (61), preparing the same SSS on every trial. Although this exact procedure cannot be implemented in practice due to the infinite detector and actuator bandwidths implied by the control law, it was essentially a similar, but filtered, current feedback law used in the experiment [30]. Because of the linearity of the dynamics in the short-time limit, the simple current-based feedback law does not perform significantly worse than a law that changes $h(t)$ more optimally according to the state $\pi_t(F_z)$ [65].

Given these dynamics, another control strategy would be to separate the measurement and control in time: simply measuring for a finite amount of time, turning off the probe, and using the measurement result to rotate the spin-squeezed state to the desired location. However, as pointed out in [69], the continuous feedback approach is more robust than this procedure to e.g. uncertainty in the total atom number which is necessary to compute the size of the correcting rotation.

To further demonstrate the utility of continuous measurement and feedback, we now consider the long time behavior of the filtering equation, past the point in time $t > 1/M$ when the linearized description fails. As discussed in section 4.3, the filtering equation stochastically prepares a random eigenstate of F_z asymptotically in time*. In [66] we investigated numerically the performance of particular controllers at producing one F_z eigenstate deterministically on every trial.

Here it is critical to point out that, unlike with the Gaussian spin-squeezed states, a post-measurement rotation strategy will not work in this regime. If the wrong eigenstate is randomly prepared in one measurement, it cannot be transformed into the correct eigenstate by a rotation alone. Furthermore, despite the adequacy of the direct current feedback law at short times, such a controller is less useful at longer

---

* There are other schemes that produce superpositions of F_z eigenstates conditionally but without control, based on single photon detection of an ensemble in a cavity [22].

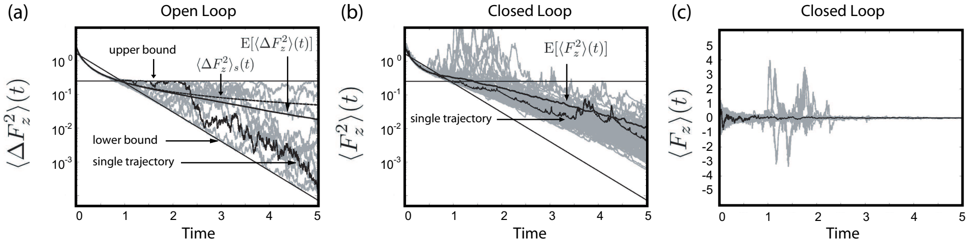

Figure 4. (a) $\langle \Delta F_z^2 \rangle(t) = \pi_t(\Delta F_z^2)$ in open loop $h(t) = 0$. $\langle \Delta F_z^2 \rangle_s$ is the approximate variance of Eq. (62). (b) $\langle F_z^2 \rangle(t) = \pi_t(F_z^2)$ and (c) $\langle F_z \rangle(t) = \pi_t(F_z)$ with the control law (63) and $\lambda = 10$. Note that $\mathbb{E}\pi_t(F_z^2)$, the cost for preparation of the $m_z = 0$ eigenstate, decreases monotonically. All plots show 100 sample paths and $M = \eta = 1$.

times. As opposed to state-based control, this type of control will feed noise into the system even if the target state is reached, unless the gain is turned to zero. Although certain gain-tailored schemes can be made to optimize the feedback at small times [69], it is not at all obvious how such a procedure could be generalized to the long time case.

In contrast, if the control variable $h(t)$ is made a function of the conditional state, then it will naturally know when the goal has been achieved and no longer disturb the state unnecessarily. Numerically we were able to demonstrate [65] that with an initial x-polarized state, the control law

$$h(t) = -\lambda\, \pi_t(F_z) \tag{63}$$

appeared to deterministically prepare the highly entangled state $m_z = 0$ on every trial, as seen in figure 4. Thus, continuous feedback, in addition to being robust, is also capable of preparing states on every trial that would be impossible to generate deterministically with measurement and control pulses separated in time.

Numerical evidence is encouraging, but more analytic statements about the performance of particular control laws are still desirable. Unfortunately, the more atoms the ensemble contains, the larger the Hilbert space becomes, and the more difficult it is to analytically prove that certain states are global attractors under particular feedback laws. However, as we have shown in [71], there exist methods adapted from non-linear and stochastic control theory that can prove the global stability of F_z eigenstates for this problem. Although this has only been demonstrated for few atom systems, there is hope that the techniques can be extended to consider dynamics on larger Hilbert spaces. Much of the control design process remains guesswork, but ultimately we desire methodology that allows us to systematically construct both controllers and proofs that validate those controllers.

5.5.2. Two Ensembles The creation of a collective entanglement within a single atomic ensemble can be motivated with, for example, the need for noise reduction in metrology tasks, where the system is used as a relatively localized probe of some parameter of interest. In other practical applications, like quantum communication, it is desirable to have an entangled quantum state, but with constituents separated substantially in space [23]. Indeed it has been experimentally demonstrated that by detecting a single probe beam after it passes through two spatially separate atomic ensembles, the two ensembles can be made conditionally entangled [41].

Just as single-mode spin squeezing can be quantified with the collective variables for the one ensemble, here the "two-mode" squeezing can be quantified with the joint collective operators describing both ensembles. Furthermore, in analogy to the work of [69], the random offset observed in the measurement process can in principle be eliminated with a suitable feedback law to deterministically produce the same two-mode spin squeezed state on every trial [9].

In a related context, it has recently been experimentally demonstrated that the two-ensemble system may serve as an effective quantum memory for states of light [42]. This procedure differs from the deterministic state preparation discussed previously in that the state of light to be mapped onto the ensembles is not known beforehand. However, the procedure described in [42] is similar in that it does use feedback to rotate the Gaussian ensemble state in a way that maps one measured quadrature of the optical state onto the atoms, while the other unmeasured quadrature is mapped unconditionally by the interaction alone. Clearly, this process shares many of the same properties as the applications discussed previously and can similarly benefit from analyses with technical notions of robustness and optimality. Finally, this procedure becomes even more efficient if the input atomic state is a two-mode squeezed state, which highlights yet another practical application of deterministic entangled quantum state preparation.

6. Conclusion

In this article we have attempted to give a unified picture of a quantum feedback control setup. Starting from elementary physical interactions, as described by a field-theoretic model, we first performed statistical inference on this model, and then used this framework to develop feedback control strategies for state preparation in atomic ensembles. The latter is directly related to recent experimental work which we briefly summarized. It is our hope that such a unified picture will help linking the basic physics and experimental reality to a high-level, control-theoretic point of view.

Many open problems remain on both ends of the spectrum. On the physics side much work remains to be done on the realistic modeling of laboratory experiments. Ultimately a full three-dimensional field-theoretic model will be invaluable for quantitative comparison of theory and experiments. On the control-theoretic side many of the techniques that have been used are still heuristic in nature. Systematic, constructive design methods for nonlinear stochastic controllers, the incorporation of realistic robustness criteria, and efficient model reduction techniques with controllable approximation errors are some of the major outstanding issues. We believe that a fruitful interaction between the physics and mathematical control theory communities will open the road to significant advances in these directions.

Acknowledgments

The authors would like to thank Luc Bouten, JM Geremia and Howard Wiseman for many fruitful discussions. This work was supported by ARO and the Caltech MURI Center for Quantum Networks. JKS acknowledges a Hertz fellowship.

References

[1] L. Accardi, A. Frigerio, and Y. G. Lu. Weak coupling limit as a quantum functional central limit theorem. *Commun. Math. Phys.*, 131:537–570, 1990.

[2] S. L. Adler, D. C. Brody, T. A. Brun, and L. P. Hughston. Martingale models for quantum state reduction. *J. Phys. A*, 34:8795–8820, 2001.

[3] A. Barchielli. Continual measurements in quantum mechanics. Lecture notes of the Summer School on Quantum Open Systems, Institut Fourier, Grenoble, 2003.

[4] V. P. Belavkin. Nondemolition measurements, nonlinear filtering and dynamic programming of quantum stochastic processes. In *Proceedings, Bellman Continuum, Sophia-Antipolis 1988*, Lecture Notes in Control and Information Sciences 121, pages 245–265. Springer-Verlag, 1988.

[5] V. P. Belavkin. Quantum continual measurements and a posteriori collapse on CCR. *Commun. Math. Phys.*, 146:611–635, 1992.

[6] V. P. Belavkin. Quantum stochastic calculus and quantum nonlinear filtering. *J. Multivariate Anal.*, 42:171–201, 1992.

[7] V. P. Belavkin. Quantum diffusion, measurement and filtering I. *Theory Probab. Appl.*, 38:573–585, 1994.

[8] A. Bensoussan. *Stochastic Control of Partially Observable Systems.* Cambridge University Press, 1992.

[9] D. W. Berry and B. C. Sanders. Near-optimal two-mode spin squeezing via feedback. *Phys. Rev. A*, 66:012313, 2002.

[10] P. Biane. Calcul stochastique non-commutatif. In P. Bernard, editor, *Lectures on Probability Theory*, Lecture Notes in Mathematics 1608. Springer, 1995.

[11] I. Bouchoule and K. Mølmer. Preparation of spin-squeezed atomic states by optical-phase-shift measurement. *Phys. Rev. A*, 66:043811, 2002.

[12] L. Bouten, M. Guţă, and H. Maassen. Stochastic Schrödinger equations. *J. Phys. A*, 37:3189–3209, 2004.

[13] C. Cohen-Tannoudji, J. Dupont-Roc, and G. Grynberg. *Photons and Atoms: introduction to quantum electrodynamics.* Wiley, 1989.

[14] L. Coutin and L. Decreusefond. Abstract non-linear filtering theory in presence of fractional Brownian motion. *Ann. Appl. Prob.*, 9:1058–1090, 2000.

[15] B. J. Dalton, S. M. Barnett, and P. L. Knight. Quasi mode theory of macroscopic canonical quantization in quantum optics and cavity quantum electrodynamics. *J. Mod. Opt.*, 46:1315–1341, 1999.

[16] M. H. A. Davis and S. I. Marcus. An introduction to nonlinear filtering. In M. Hazewinkel and J. C. Willems, editors, *Stochastic Systems: The Mathematics of Filtering and Identification and Applications*, pages 53–75. D. Reidel, 1981.

[17] R. H. Dicke. Coherence in spontaneous radiation processes. *Phys. Rev.*, 93:99, 1954.

[18] A. C. Doherty, S. Habib, K. Jacobs, H. Mabuchi, and S. M. Tan. Quantum feedback control and classical control theory. *Phys. Rev. A*, 62:012105, 2000.

[19] A. C. Doherty and K. Jacobs. Feedback control of quantum systems using continuous state estimation. *Phys. Rev. A*, 60:2700, 1999.

[20] J. Doyle, B. Francis, and A. Tannenbaum. *Feedback Control Theory.* Macmillan Publishing Co., 1990.

[21] L. M. Duan, J. I. Cirac, and P. Zoller. Three-dimensional theory for interaction between atomic ensembles and free-space light. *Phys. Rev. A*, 66:023818, 2002.

[22] L. M. Duan and H. J. Kimble. Efficient engineering of multiatom entanglement through single-photon detections. *Phys. Rev. Lett.*, 90:253601, 2003.

[23] L. M. Duan, M. D. Lukin, J. I. Cirac, and P. Zoller. Long-distance quantum communication with atomic ensembles and linear optics. *Nature*, 414:413–418, 2001.

[24] J. A. Dunningham, H. M. Wiseman, and D. F. Walls. Manipulating the motion of a single atom in a standing wave via feedback. *Phys. Rev. A*, 55:1398, 1997.

[25] J. Gambetta and H. M. Wiseman. Non-Markovian stochastic Schrödinger equations: Generalization to real-valued noise using quantum-measurement theory. *Phys. Rev. A*, 66:012108, 2002.

[26] C. W. Gardiner and M. J. Collett. Input and output in damped quantum systems: Quantum stochastic differential equations and the master equation. *Phys. Rev. A*, 31:3761–3774, 1985.

[27] C. W. Gardiner and P. Zoller. *Quantum Noise.* Springer, 3d edition, 2004.

[28] J. Geremia, J. K. Stockton, and H. Mabuchi. Continuous quantum measurement and conditional spin-squeezing in Alkali atoms. *quant-ph/0501033*, 2005.

[29] J. M. Geremia, J. K. Stockton, A. C. Doherty, and H. Mabuchi. Quantum Kalman filtering and

the Heisenberg limit in atomic magnetometry. *Phys. Rev. Lett.*, 91:250801, 2003.

[30] J. M. Geremia, J. K. Stockton, and H. Mabuchi. Real-time quantum feedback control of atomic spin-squeezing. *Science*, 304:270, 2004.

[31] J. Gough. Asymptotic stochastic transformations for nonlinear quantum dynamical systems. *Rep. Math. Phys.*, 44:313–338, 1999.

[32] J. Gough. The Stratonovich interpretation of quantum stochastic approximations. *Potential Anal.*, 11:213–233, 1999.

[33] J. Gough. Quantum flows as Markovian limit of emission, absorption and scattering interactions. *Commun. Math. Phys.*, 254:489–512, 2005.

[34] J. Hald, J. L. Sørensen, C. Schori, and E. S. Polzik. Spin squeezed atoms: A macroscopic entangled ensemble created by light. *Phys. Rev. Lett*, 83:1319–1322, 1999.

[35] H. Holden, B. Øksendal, J. Ubøe, and T. Zhang. *Stochastic Partial Differential Equations: A Modeling, White Noise Functional Approach.* Birkhäuser, 1996.

[36] A. S. Holevo. *Statistical Structure of Quantum Theory.* Springer-Verlag, 2001.

[37] R. L. Hudson and K. R. Parthasarathy. Quantum Itô's formula and stochastic evolutions. *Commun. Math. Phys.*, 93:301–323, 1984.

[38] O. L. R. Jacobs. *Introduction to Control Theory.* Oxford University Press, New York, 2nd edition, 1996.

[39] M. R. James. Risk-sensitive optimal control of quantum systems. *Phys. Rev. A*, 69:032108, 2004.

[40] M. R. James. A quantum Langevin formulation of risk-sensitive optimal control. *J. Opt. B, this issue*, 2005.

[41] B. Julsgaard, A. Kozhekin, and E. S. Polzik. Experimental long-lived entanglement of two macroscopic objects. *Nature*, 413:400, 2001.

[42] B. Julsgaard, J. Sherson, J. I. Cirac, J. Fiurasek, and E. S. Polzik. Experimental demonstration of quantum memory for light. *Nature*, 432:482, 2004.

[43] G. Kallianpur and R. L. Karandikar. White noise calculus and nonlinear filtering theory. *Ann. Prob.*, 13:1033–1107, 1985.

[44] M. Kitagawa and M. Ueda. Squeezed spin states. *Phys. Rev. A*, 47:5138, 1993.

[45] H. H. Kuo. *White Noise Distribution Theory.* CRC Press, 1996.

[46] D. Kupriyanov, O. Mishina, I. Sokolov, B. Julsgaard, and E.S.Polzik. Multimode entanglement of light and atomic ensembles via off-resonant coherent forward scattering. *Phys. Rev. A*, 71:032348, 2005.

[47] A. Kuzmich, L. Mandel, and N. P. Bigelow. Generation of spin squeezing via continuous quantum nondemolition measurement. *Phys. Rev. Lett.*, 85:1594–1597, 2000.

[48] A. Kuzmich, L. Mandel, J. Janis, Y. E. Young, R. Ejnisman, and N. P. Bigelow. Quantum nondemolition measurements of collective atomic spin. *Phys. Rev. A*, 60:2346, 1999.

[49] A. Kuzmich, K. Mølmer, and E. Polzik. Spin squeezing in an ensemble of atoms illuminated with squeezed light. *Phys. Rev. Lett.*, 79:4782, 1997.

[50] D. Leibfried, M. D. Barrett, T. Schaetz, J. Britton, J. Chiaverini, W. M. Itano, J. D. Jost, C. Langer, and D. J. Wineland. Toward Heisenberg-limited spectroscopy with multiparticle entangled states. *Science*, 304:1476, 2004.

[51] R. S. Liptser and A. N. Shiryaev. *Statistics of Random Processes I: General Theory.* Springer, 2001.

[52] S. Lloyd. Coherent quantum feedback. *Phys. Rev. A*, 62:022108, 2000.

[53] H. Maassen. Quantum probability applied to the damped harmonic oscillator. In S. Attal and J. M. Lindsay, editors, *Quantum Probability Communications XII*, pages 23–58. World Scientific, 2003.

[54] L. Mandel and E. Wolf. *Optical Coherence and Quantum Optics.* Cambridge University Press, Cambridge, United Kingdom, 1997.

[55] P. A. Meyer. *Quantum Probability for Probabilists.* Lecture Notes in Mathematics 1538. Springer, 1995.

[56] K. Mølmer. Twin-correlations in atoms. *Eur. Phys. J. D*, 5:301–305, 1999.

[57] R. E. Mortensen. Stochastic optimal control with noisy observations. *Int. J. Control*, 4:455–464, 1966.

[58] J. H. Mueller, P. Petrov, D. Oblak, C. L. G. Alzar, S. R. de Echaniz, and E. S. Polzik. Diffraction effects on light-atomic ensemble quantum interface. *Phys. Rev. A*, 71:033803, 2005.

[59] D. Oblak, J. K. Mikkelsen, W. Tittel, A. K. Vershovski, J. L. Sorensen, P. G. Petrov, C. L. G. Alzar, and E. S. Polzik. Quantum noise limited interferometric measurement of atomic noise: towards spin squeezing on the Cs clock transition. *Phys. Rev. A*, 71:043807, 2005.

[60] B. Øksendal. *Stochastic Differential Equations.* Springer, 5th edition, 1998.

[61] H. Rabitz, R. de Vivie-Riedle, M. Motzkus, and K. Kompa. Whither the future of controlling quantum phenomena? *Science*, 288:824, 2000.

[62] M. O. Scully and M. S. Zubairy. *Quantum Optics*. Cambridge University Press, 1997.

[63] A. Sorensen, L. M. Duan, J. I. Cirac, and P. Zoller. Many-particle entanglement with Bose-Einstein condensates. *Nature*, 409:63, 2001.

[64] J. Stockton, M. Armen, and H. Mabuchi. Programmable logic devices in experimental quantum optics. *J. Opt. Soc. Am. B*, 19:3019, 2002.

[65] J. K. Stockton, J. Geremia, A. C. Doherty, and H. Mabuchi. Robust quantum parameter estimation: coherent magnetometry with feedback. *Phys. Rev. A*, 69:032109, 2004.

[66] J. K. Stockton, R. Van Handel, and H. Mabuchi. Deterministic Dicke-state preparation with continuous measurement and control. *Phys. Rev. A*, 70:022106, 2004.

[67] R. L. Stratonovich. *Topics in the theory of random noise*. Gordon and Breach, 1963.

[68] R. F. Streater. *Statistical Dynamics*. Imperial College Press, 1995.

[69] L. K. Thomsen, S. Mancini, and H. M. Wiseman. Continuous quantum nondemolition feedback and unconditional atomic spin squeezing. *J. Phys. B: At. Mol. Opt. Phys.*, 35:4937, 2002.

[70] L. K. Thomsen, S. Mancini, and H. M. Wiseman. Spin squeezing via quantum feedback. *Phys. Rev. A*, 65:061801(R), 2002.

[71] R. Van Handel, J. K. Stockton, and H. Mabuchi. Feedback control of quantum state reduction. *IEEE Trans. Automat. Control*, 50:768–780, 2005.

[72] L. Van Hove. Quantum mechanical perturbations giving rise to a statistical transport equation. *Physica*, 21:617–640, 1955.

[73] D. F. Walls and G. J. Milburn. *Quantum Optics*. Springer, 1994.

[74] P. Warszawski and H. M. Wiseman. Adiabatic elimination in compound quantum systems with feedback. *Phys. Rev. A*, 63:013803, 2000.

[75] D. Williams. *Probability with Martingales*. Cambridge University Press, 1991.

[76] D. J. Wineland, J. J. Bollinger, W. M. Itano, and D. J. Heinzen. Squeezed atomic states and projection noise in spectroscopy. *Phys. Rev. A*, 50:67–88, 1994.

[77] H. M. Wiseman. Quantum theory of continuous feedback. *Phys. Rev. A*, 49:2133, 1994.

[78] H. M. Wiseman. Quantum trajectories and feedback, 1994. Ph.D. thesis, Univ. of Queensland.

[79] H. M. Wiseman and A. C. Doherty. Optimal unravellings for feedback control in linear quantum systems. *quant-ph/0408099, accepted by Phys. Rev. Lett.*, 2004.

[80] H. M. Wiseman, S. Mancini, and J. Wang. Bayesian feedback versus Markovian feedback in a two-level atom. *Phys. Rev. A*, 66:013807, 2002.

[81] H. M. Wiseman and G. J. Milburn. All-optical versus electro-optical quantum-limited feedback. *Phys. Rev. A*, 49:4110, 1994.

[82] E. Wong and M. Zakai. On the relationship between ordinary and stochastic differential equations. *Int. J. Engin. Sci.*, 3:213–229, 1965.

[83] H. P. Yuen and J. H. Shapiro. Optical communication with two-photon coherent states. I—Quantum-state propagation and quantum-noise reduction. *IEEE Trans. Inf. Th.*, 24:657–668, 1978.

[84] K. Zhou and J. C. Doyle. *Essentials of Robust Control*. Prentice-Hall, Inc., New Jersey, 1st edition, 1997.

PHYSICAL REVIEW A **69**, 052326 (2004)

Superselection rules and quantum protocols

Alexei Kitaev,[1] Dominic Mayers,[1,2] and John Preskill[1]
[1]*Institute for Quantum Information, California Institute of Technology, Pasadena, California 91125, USA*
[2]*Département de Mathématiques et d'Informatique, Université de Sherbrooke, Québec, Canada*

(Received 19 October 2003; published 21 May 2004)

We show that superselection rules do not enhance the information-theoretic security of quantum cryptographic protocols. Our analysis employs two quite different methods. The first method uses the concept of a *reference system*—in a world subject to a superselection rule, unrestricted operations can be simulated by parties who share access to a reference system with suitable properties. By this method, we prove that if an n-party protocol is secure in a world subject to a superselection rule, then the security is maintained even if the superselection rule is relaxed. However, the proof applies only to a limited class of superselection rules, those in which the superselection sectors are labeled by unitary irreducible representations of a compact symmetry group. The second method uses the concept of the *format* of a message sent between parties—by verifying the format, the recipient of a message can check whether the message could have been sent by a party who performed charge-conserving operations. By this method, we prove that protocols subject to general superselection rules (including those pertaining to non-Abelian anyons in two dimensions) are no more secure than protocols in the unrestricted world. However, the proof applies only to two-party protocols. Our results show in particular that, if no assumptions are made about the computational power of the cheater, then secure quantum bit commitment and strong quantum coin flipping with arbitrarily small bias are impossible in a world subject to superselection rules.

DOI: 10.1103/PhysRevA.69.052326 PACS number(s): 03.67.Dd

I. INTRODUCTION

The central aim of modern cryptography is to formulate protocols that achieve cryptographic tasks with *computational security*, meaning that a dishonest party would need to perform a prohibitively difficult computation to break the protocol. A major goal of quantum cryptography is to formulate protocols, involving the exchange of quantum states, that achieve *information-theoretic security*, meaning that even an adversary with unlimited computational power would be unable to defeat the protocol [1]. Information-theoretic security (sometimes called "unconditional security") has been established for quantum key distribution protocols [2–7] but it has also been shown that, even in the quantum world, information-theoretic security is not attainable for certain tasks. For example, unconditionally secure quantum bit commitment is impossible [8,9], as is (strong) quantum coin flipping with arbitrarily small bias [10,11].

Superselection rules are limitations on the physically realizable quantum operations that can be carried out by a local agent. For example, it is impossible to create or destroy an isolated particle that carries locally conserved charges, such as an electrically charged particle, a fermion, or (in a two-dimensional medium) an anyon. Recently, Popescu [12] has suggested that superselection rules might have interesting implications for the security of quantum cryptographic protocols. The intuitive idea behind this suggestion is that superselection rules could place inviolable limits on the cheating strategies available to the dishonest parties, thus enhancing security. Might, say, unconditionally secure bit commitment be possible in worlds (perhaps including the physical world that we inhabit) governed by suitable superselection rules? An affirmative answer could shake the foundations of cryptography.

The purpose of this paper is to answer Popescu's intriguing question. Sadly, our conclusion is that superselection rules can never foil a cheater who has unlimited quantum-computational power.

In the case of quantum bit commitment, and other two-party protocols, our argument hinges on a quite simple observation. In a two-party protocol, one participant (Alice) has control of a local system A, and the other participant (Bob) has control of another local system B. In addition, there is a message system M that they pass back and forth. In each step of the protocol, one party performs a joint quantum operation on her/his local system and the message system, and then sends the message system to the other party. Suppose that in each step, any part of the full system ABM that is beyond Alice's control is under Bob's control and vice versa—no part of the full system is inaccessible or in the possession of a third party. Suppose further that the full system ABM has trivial total charge (belongs to the trivial superselection sector). Then at any stage of the protocol, the algebra of operations that Alice can perform is the *commutant* of the algebra of operations that Bob can perform; that is, Alice's algebra contains *all* operations that commute with Bob's algebra. Likewise, Bob's algebra is the commutant of Alice's. By a minor extension of the standard argument, it then follows that unconditionally secure quantum bit commitment is impossible *if* the total charge shared by the parties is trivial.

Now, if the total charge in *nontrivial*, then Alice's algebra is surely a subalgebra of the commutant of Bob's, but it may be a *proper* subalgebra; similarly, Bob's algebra may be a proper subalgebra of Alice's. This unusual property of the local operations seems to open new possibilities for the design of quantum protocols. Regrettably, though, there is no way for an honest party to ensure that the total charge is really nontrivial when the other party is dishonest. Though

©2004 The American Physical Society

the honest protocol may call for the parties to start out with nontrivial charges, we may always imagine that there are actually compensating charges beyond the grasp of Alice and Bob, so that the total charge of the world is really trivial. Furthermore, a cheater might seize control of the compensating charge, while for an honest party it makes no difference whether the compensating charge is present or not. It follows that a protocol that calls for the total charge to be nontrivial can be no more secure than one in which the total charge is actually trivial; we conclude again that unconditionally secure quantum bit commitment is impossible, irrespective of the value of the total charge shared by the parties in the honest protocol.

Aside from quantum bit commitment, we will also study the impact of superselection rules on the information-theoretic security of a broad class of other quantum protocols, using two different methods. We analyze in detail the important special case in which the superselection sectors can be identified with the unitary irreducible representations of a compact symmetry group. In that case, we argue that it is possible in principle to prepare a *reference state* that establishes a preferred orientation in the symmetry group. A party with access to the reference state can use it to perform operations that are ostensibly forbidden by the superselection rule. In particular, consider an n-party quantum protocol where up to $k<n$ of the parties are dishonest, and suppose that in a world with no superselection rules the dishonest parties have a cheating strategy that breaks the protocol. Then, even in a world with superselection rules, the dishonest parties, by sharing a suitable reference state, can simulate this cheating strategy faithfully. We conclude that if a quantum protocol is information-theoretically secure in a world with a superselection rule, the security will be maintained even if the superselection rule is relaxed, at least in the case where the superselection rule arises from a compact symmetry group.

Superselection rules arising from compact symmetry groups are not the most general possible ones. In particular, an especially rich variety of superselection rules are potentially realizable in two-dimensional systems such as those that admit non-Abelian anyons. However, even superselection rules of this more general kind cannot foil a cheater. We find that for any two-party protocol that is secure in a world subject to a superselection rule, the security is maintained when the superselection rule is relaxed.

Our analysis of these more general superselection rules does not rely on the concept of a reference system; rather it is founded on a completely different idea, the concept of the *format* of a message. A superselection rule can always be characterized by saying that there are charges that must be conserved by all local operations, and when we relax the superselection rule, in effect we are permitting a cheater to violate these conservation laws. For the purpose of assessing the security of a two-party protocol, we are interested in how the actions of the cheating party (Alice) affect the outcomes of measurements performed by the honest party (Bob). Potentially, if Alice is granted the power to violate conservation of "charge," her ability to influence Bob's measurements will be strengthened.

However, if the total charge shared by Alice and Bob is trivial (as we are entitled to assume in an analysis of security), then if charge is conserved, Alice and Bob hold conjugate charges at each stage of the protocol. Therefore, Bob always knows what charge Alice is supposed to have, which constrains the type of message that Alice can send to Bob if she is honest. When Bob receives a message he can verify its format, checking whether the message could have been sent by a party who performed a charge-conserving operation, and he can abort the protocol if the verification fails. Therefore, if the protocol ends normally, Alice has been forced to respect charge conservation—her power to flout the superselection rule does not enhance her ability to fool Bob. This reasoning shows that superselection rules cannot thwart cheating, but because the argument relies on the property that Alice and Bob hold perfectly correlated charges, it works only for two-party protocols.

For cryptographic protocols with more than two parties, and for general superselection rules, new subtleties arise. In two spatial dimensions, general charges are not merely locally conserved, they may also have nontrivial *braiding* properties—the exchange of two charges may induce a nontrivial transformation on their joint Hilbert space. This means that the effect of sending a message from one party to another can depend on the path along which the message travels. It is an interesting problem to specify appropriate definitions of security for protocols in this setting, but we will not attempt to address this issue here. For the special case of charges labeled by unitary representations of compact groups, the braiding properties are trivial; therefore in that case we can analyze multiparty protocols without confronting such questions.

Verstraete and Cirac [13] recently discussed a data-hiding protocol whose security is premised on a superselection rule. However, as the authors recognized, the protocol is not unconditionally secure; it can be broken if the parties establish a suitable shared reference state via quantum communication. The notion that the naive implications of a superselection rule can be evaded through the use of a suitable reference system was emphasized long ago by Aharonov and Susskind [14]; see [15] for a recent discussion. A special case of our main result was reported earlier in [16].

The rest of this paper is organized as follows: We develop the concept of a reference system in Sec. II, first for Abelian, then for non-Abelian symmetries, and we explain how a reference system can be used to simulate unrestricted operations in a world subject to superselection rules arising from a symmetry group; this observation is applied in Sec. III to the analysis of the security of quantum protocols. In Sec. IV we explore the distinction between an *itinerant* reference system that is passed from party to party as needed during a protocol, and a *distributed* reference system that can be prepared and passed out to the parties before the protocol begins. Superselection rules arising from non-Abelian symmetries are further characterized in Sec. V, and we comment in Sec. VI on the data-hiding protocol of Verstraete and Cirac. Our analysis of the impact of superselection rules on the security of quantum bit commitment is in Sec. VII; we also show there that for the analysis of security of an n-party protocol, it suffices to consider the case in which the total charge held by the parties is trivial. Two-party protocols subject to general superselection rules are investigated in Sec. VIII, and Sec. IX contains some concluding comments.

II. SUPERSELECTION RULES AND REFERENCE SYSTEMS

A superselection rule is a decomposition of Hilbert space into sectors that are preserved by local operations. The different sectors can be distinguished by attaching to each sector a label, which we refer to as the sector's "charge." Therefore, an equivalent way to characterize a superselection rule is to say that the charge is locally conserved. In the context of a cryptographic protocol, this means that when one of the parties (Alice, say) performs an operation, the charge in Alice's laboratory is preserved.

An important special case arises if the Hilbert space $\mathcal{H}$ transforms as a unitary representation of a compact group G, and the sectors are labeled by the irreducible representations of G. An equivalent way to describe the superselection rule in that case is to say that the allowed operations must commute with the action of G on $\mathcal{H}$. In fact, it has been shown by Doplicher and Roberts [17] that such superselection rules are almost the most general ones allowed under rather weak conditions that apply in particular to quantum field theories (without gravity) in three or more spatial dimensions. We say "almost" because there is an additional freedom to assign to a localized state an even or odd fermion number. This fermion number is more than just a conserved charge, because of the property that the wave function changes sign when two fermions are exchanged.

In two spatial dimensions, there is a richer classification of superselection rules, reflecting the exotic quantum numbers carried by pointlike non-Abelian anyons that occur in topological quantum field theories [18–20]. We will postpone further discussion of non-Abelian anyons until Sec. VIII, concentrating for now on the superselection rules associated with compact symmetry groups (and ignoring fermions).

An important example is the group U(1) associated with conservation of the electric charge Q. An agent acting locally can create or annihilate pairs of particles that carry equal and opposite charges, but cannot change the total charge in her vicinity. In particular, this agent is unable to transform any eigenstate of Q into a coherent superposition of states with different charges, as emphasized by Wick, Wightman, and Wigner [21,22].

While we might readily accept that local creation of electric charge is physically impossible, other conservation laws impose superselection rules that do more violence to our intuition. Suppose, for example (in nonrelativistic quantum mechanics), that our agent's actions are required to conserve the angular momentum $\vec{J}$ locally. Are we to conclude that if the agent is presented with a spin-$\frac{1}{2}$ object polarized spin-up along the z axis, it is impossible for him to transform it to a coherent superposition of the spin-up and spin-down states? How are we to describe what happens when a magnetic field is turned on pointing in the x direction and the spin begins to precess? A partial resolution of this puzzle is attained by noting that the angular momentum of a classical magnet has an uncertainty large compared to $\hbar$, so that conservation of angular momentum need not prevent the magnet from coherently exchanging $J_z = \hbar$ with the spin. But this explanation does not fully address how the existence of the classical magnet is itself compatible with the superselection rule.

Such issues were cogently discussed many years ago by Aharonov and Susskind [14]. They emphasized that even if the total angular momentum has a definite value (like zero), we can still speak sensibly of the *relative* orientation of two subsystems. Whenever an experimentalist observes the precession of a spin, it is implicit that a reference state has been established that in effect breaks the rotational symmetry, and that the precession is measured relative to this reference standard. Furthermore, Aharonov and Susskind [14] emphasized that just as conservation of angular momentum need not prevent us from measuring the relative angular orientation of two objects, so the charge superselection rule need not prevent us from measuring relative phases in superpositions of states of different charge.

A. Abelian case

Before we discuss the more general case in which the symmetry may be non-Abelian, it will be useful to consider the symmetry group $G = \mathrm{U}(1)$. Then the charge operator Q (the generator of G) has eigenvalues $q \in Z$, and we denote the corresponding orthonormal eigenstates by $|q\rangle$. Formal states of definite phase (with continuum normalization) can be constructed as

$$|\theta\rangle = \frac{1}{\sqrt{2\pi}} \sum_{q=-\infty}^{\infty} e^{-iq\theta} |q\rangle \quad (0 \leq \theta < 2\pi), \tag{1}$$

where

$$\langle \theta' | \theta \rangle = \frac{1}{2\pi} \sum_{q=-\infty}^{\infty} e^{-iq(\theta-\theta')} = \delta(\theta' - \theta) \tag{2}$$

and

$$|q\rangle = \frac{1}{\sqrt{2\pi}} \int_0^{2\pi} d\theta \, e^{iq\theta} |\theta\rangle . \tag{3}$$

The phase state $|\theta\rangle$ is the improper eigenstate with eigenvalue $e^{i\theta}$ of the unitary operator

$$U_+ = \sum_{q=-\infty}^{\infty} |q+1\rangle\langle q| \tag{4}$$

that increments the value of the charge by one unit. While the phase θ is physically unobservable due to the charge superselection rule, the relative phase of $\theta' - \theta$ of the two states $|\theta'\rangle$ and $|\theta\rangle$ commutes with the charge operator Q and so is measurable in principle. Indeed, the state

$$\int_0^{2\pi} d\theta'' |\theta' + \theta''\rangle \otimes |\theta + \theta''\rangle = \sum_{q=-\infty}^{\infty} e^{-iq(\theta-\theta')} |-q\rangle \otimes |q\rangle \tag{5}$$

has a definite value of the relative phase $\theta' - \theta$ and total charge zero. That is, it is an (unnormalizable) eigenstate with eigenvalue $e^{i(\theta-\theta')}$ of the charge-conserving operator $U_- \otimes U_+$, where $U_- = U_+^\dagger$.

Similarly, the phases ϕ_q appearing in the expansion of the state $|\psi\rangle_A$ of a system A,

$$|\psi\rangle_A = \sum_q \psi_q e^{-iq\phi_q}|q\rangle_A \tag{6}$$

(where the ψ_q's are real and positive), are themselves unobservable, but they can be meaningfully compared to the phases appearing in the state $|\theta\rangle_R$ of a charge reservoir R. For example, by projecting $|\theta\rangle_R \otimes |\psi\rangle_A$ onto the sector with total charge zero, we obtain the state

$$\begin{aligned}|\psi\rangle_{RA} &= \frac{1}{\sqrt{2\pi}}\int d\theta' |\theta+\theta'\rangle_R \otimes e^{-iQ\theta'}|\psi\rangle_A \\ &= \sum_q \psi_q e^{-iq(\phi_q-\theta)}|-q\rangle_R \otimes |q\rangle_A \end{aligned}\tag{7}$$

which has measurable relative phases. A state like $|\theta\rangle_R$ of a charge reservoir R that provides a phase standard with which other states can be compared will be called a "reference state" or a "condensate."

In the state $|\psi\rangle_{RA}$, the charge of the system A is compensated ("screened") by the charge of the reservoir R. Therefore, the system and reservoir are entangled, and tracing out the reservoir destroys the coherence of the superposition of charge states for the system. While formally correct, this statement can be misleading if the reservoir remains accessible and is allowed to interact with the system during subsequent operations. For example, the operator $(U_+)_A$ that increases the charge of the system by one unit is disallowed by the superselection rule, but it can be accurately simulated by the allowed charge-conserving operator $(U_-)_R \otimes (U_+)_A$ acting on $|\psi\rangle_{RA}$—this operator increases the charge of A by borrowing a unit of charge from R. If the reservoir remains accessible at all times, then an arbitrary (not necessarily charge-conserving) operation acting on A can be perfectly simulated by a charge-conserving operation acting on RA. Thus, at least as a matter of principle, the charge superselection rule places no inescapable restrictions on the allowed operations. This is the main point stressed by Aharonov and Susskind [14].

The phase reference state can be interpreted physically as a static piece of superconducting material with a definite value of the superconducting phase. While the phase itself is not gauge-invariant, the relative phase of the system and reservoir has observable consequences (like the Josephson effect) when the two are brought into contact. Similar issues, discussed in [23–27], arise when considering the physical content of relative phases in optical systems.

B. Non-Abelian case

Our discussion of the Abelian case has suggested that superselection rules are nullified if suitable reference systems are available. Now we consider the more general case, where the symmetry group is G, which may be either a finite group or a compact Lie group. The superselection rule dictates that allowed local operations must commute with G. But we may anticipate that if a condensate is accessible that completely breaks the G symmetry, then in effect there is no operative symmetry at all, and the superselection rules place no restrictions on the allowed operations.

Formally, if the symmetry is completely broken, then the possible orientations of the condensate are in one-to-one correspondence with the elements of the symmetry group G. In a particular "fixed gauge," the states of the condensate are denoted $|\phi\rangle$, where $\phi \in G$, and these states transform as the left regular representation of G. That is, a symmetry transformation $g \in G$ acting on the condensate is represented by the unitary $U(g)$ where

$$U(g)|\phi\rangle \to |g\phi\rangle. \tag{8}$$

These states can be expanded in the basis of irreducible representations of G as

$$|\phi\rangle = \sum_{q,i,a}\sqrt{\frac{n_q}{n_G}}D^q_{ia}(\phi)|q,i,a\rangle, \tag{9}$$

where n_q denotes the dimension of the irreducible representation $D^q(\phi)$ and n_G is the order of G. Inverting the Fourier transform we obtain

$$|q,i,a\rangle = \sum_{\phi\in G}\sqrt{\frac{n_q}{n_G}}\quad D^{q*}_{ia}(\phi)|\phi\rangle. \tag{10}$$

Note that in Eqs. (9) and (10) we have used notation appropriate for a finite group; in the case of a compact Lie group, the sum over $\phi \in G$ would be replaced by an integral with respect to an invariant measure on the group. The states $|q,i,a\rangle$ transform under G as

$$U(g)|q,i,a\rangle = \sum_j |q,j,a\rangle D^q_{ji}(g). \tag{11}$$

In keeping with standard physics terminology, we will refer to the index $i=1,2,\ldots,n_q$ in $|q,i,a\rangle$ as the "color index," and to the action Eq. (11) of $U(g)$ on this index as a "gauge transformation." The index $a=1,2,\ldots,n_q$, distinguishing the n_q copies of the representation D^q that occur in the decomposition of the regular representation, will be called the "flavor" index. The physical "G-invariant" operations are those that commute with all gauge transformations—these preserve q and act nontrivially only on the flavor, not the color. Therefore, by including the color we have chosen a redundant description of the physical Hilbert space. This redundancy, while not absolutely necessary, is quite convenient, and in particular will be useful for our discussion in Sec. III of the security of quantum protocols.

In addition to the G gauge symmetry, there is also a group G of "global" transformations that commute with $U(g)$, under which the states $|\phi\rangle$ transform as the right regular representation of G; the element h of the global group is represented by $V(h)$, where

$$V(h)|\phi\rangle = |\phi h^{-1}\rangle \tag{12}$$

and

$$V(h)|q,i,a\rangle = \sum_b |q,i,b\rangle D^{q*}_{ba}(h). \tag{13}$$

Thus the global transformations act on the flavor index a of the states in the $\{|q,i,a\rangle\}$ basis—unlike the gauge transformations, they act nontrivially on the physical states.

In more geometric terms, a condensate may be interpreted as an asymmetric classical rigid body that can be rotated either "actively" or "passively." What we have called the color (gauge) rotation is a passive rotation that acts on the space-fixed axes—it does not change the actual orientation of the body but only changes our mathematical description of the orientation. In contrast, what we have called the flavor (global) rotation is an active rotation that acts on the body-fixed axes and alters the physical orientation. A flavor rotation is G-invariant in the sense that it commutes with color rotations, and so is a physical operation, allowed by the superselection rule.

In contrast to the flavor orientation, the color orientation of an isolated system A has no invariant meaning, as it is modified by a color rotation. However, the orientation of A *relative to the condensate* R does have meaning, and an operator that rotates the relative orientation admits an invariant description. Suppose, for example, that system A is itself a condensate in the state ϕ_A, while the state of R is ϕ_R. The relative orientation

$$\phi_{\overline{RA}} \equiv \phi_R^{-1}\phi_A \tag{14}$$

is invariant if a common color rotation

$$U(h)_{RA}{:}\phi_A \to h\phi_A, \quad \phi_R \to h\phi_R \tag{15}$$

is applied to both objects. The transformation $U(g)^{\mathrm{inv}}_{RA}$ that changes the relative orientation according to

$$U(g)^{\mathrm{inv}}_{RA}{:}\phi_{\overline{RA}} \to g\phi_{\overline{RA}} \tag{16}$$

has an invariant meaning and commutes with the color rotation $U(h)_{RA}$. We may interpret the invariant rotation as one that rotates A while R is "held fixed," acting as

$$U(g)^{\mathrm{inv}}_{RA}(|\phi_R\rangle \otimes |\phi_A\rangle) = |\phi_R\rangle \otimes |\phi_R g \phi_R^{-1}\phi_A\rangle, \tag{17}$$

or equivalently

$$U(g)^{\mathrm{inv}}_{RA} = \sum_{\phi\in G} (|\phi\rangle\langle\phi|)_R \otimes \mathrm{U}(\phi g \phi^{-1})_A. \tag{18}$$

If system A is not a reference system but rather an object transforming as the irreducible representation q of G, then $U(\phi g \phi^{-1})$ can be expanded as

$$U(g)^{\mathrm{inv}}_{RA} = \sum_{\phi\in G} (|\phi\rangle\langle\phi|)_R \otimes \left(\sum_{i,j,a,b} |q,i\rangle D^q_{ia}(\phi) D^q_{ab}(g) D^q_{bj}(\phi^{-1}) \langle q,j|\right)_A. \tag{19}$$

More generally, any transformation

$$M_A{:}|q,i\rangle_A \to \sum_j |q,j\rangle_A M_{ji} \tag{20}$$

acting on the color degree of freedom can be simulated by the invariant operation

$$M^{\mathrm{inv}}_{RA} = \sum_{\phi\in G} (|\phi\rangle\langle\phi|)_R \otimes \left(\sum_{i,j,a,b} |q,i\rangle D^q_{ia}(\phi) M_{ab} D^q_{bj}(\phi^{-1}) \langle q,j|\right)_A. \tag{21}$$

M^{inv}_{RA} has an invariant meaning because it transforms the color of A relative to the color of the reference system R; in effect, the color rotation is simulated by converting the color index into a flavor index (depending on ϕ), on which M may act with impunity. For fixed ϕ, the simulation is achieved via the isomorphism

$$|q,a\rangle_A \to |q,\phi,a\rangle_{RA} \equiv |\phi\rangle_R \otimes \sum_j |q,j\rangle_A D^q_{ja}(\phi), \tag{22}$$

such that

$$M^{\mathrm{inv}}_{RA}|q,\phi,a\rangle_{RA} = \sum_b |q,\phi,b\rangle_{RA} M_{ba}. \tag{23}$$

Furthermore, this isomorphism can be extended to operators M that change the value of q as well as rotating the color for fixed q; the operator

$$M_A{:}|q,i\rangle_A \to \sum_{q',j} |q',j\rangle_A M^{q'q}_{ji} \tag{24}$$

is simulated by

$$M^{\mathrm{inv}}_{RA}|q,\phi,a\rangle_{RA} = \sum_{q',b} |q',\phi,b\rangle_{RA} M^{q'q}_{ba}, \tag{25}$$

which generalizes the result

$$M^{\mathrm{inv}}_{RA}(|\theta\rangle_R \otimes e^{-iq\theta}|q\rangle_A) = |\theta\rangle_R \otimes \sum_{q'} e^{-iq'\theta}|q'\rangle M^{q'q} \tag{26}$$

that we found in the case of $G=\mathrm{U}(1)$.

C. Properties of the simulation

We will refer to the world in which all operations are required to commute with the action of the symmetry group G as the "invariant world" or "I world," and we refer to the world in which arbitrary operations are allowed as the "unrestricted world" or "U world." What we have observed in Eqs. (22) and (25) is that the physics of the U world can be faithfully reproduced in the I world, as long as a suitable reference system is at our disposal.

Let us restate the main conclusion in a more succinct notation: Suppose A is an arbitrary system that transforms as some representation of the group G, and let R be a "reference system" that transforms as the left regular representation of G. Let M be an arbitrary transformation acting on A. Then there is a corresponding transformation M^{inv} acting on R and A defined as

$$M^{\mathrm{inv}} = \sum_{\phi\in G} (|\phi\rangle\langle\phi|)_R \otimes [U(\phi) M U(\phi)^{-1}]_A. \tag{27}$$

M^{inv} is an invariant operator whose action on *RA simulates* the action of M on A.

That is, the operators M^{inv} have the following easily verified properties:

(i) M^{inv} is *G-invariant*. Proof: From the transformation properties of R and A we have

$$\begin{aligned}&[U(g)\otimes U(g)]M^{\mathrm{inv}}[U(g)^{-1}\otimes U(g)^{-1}]\\ &\quad=\sum_{\phi\in G}(|g\phi\rangle\langle g\phi|)\otimes[U(g\phi)MU(g\phi)^{-1}]=M^{\mathrm{inv}},\end{aligned}\tag{28}$$

where in the last step we have reparametrized the sum by replacing $\phi\to g^{-1}\phi$.

(ii) *Invariant operators on RA provide a representation of operators on A*. Proof: We have

$$\begin{aligned}M_1^{\mathrm{inv}}M_2^{\mathrm{inv}}&=\sum_{\phi_1,\phi_2\in G}(|\phi_1\rangle\langle\phi_1|\phi_2\rangle\langle\phi_2|)\\ &\quad\otimes[U(\phi_1)M_1U(\phi_1^{-1})U(\phi_2)M_2U(\phi_2^{-1})]\\ &=\sum_{\phi\in G}(|\phi\rangle\langle\phi|)\otimes[U(\phi)M_1M_2U(\phi)^{-1}]\\ &=(M_1M_2)^{\mathrm{inv}}.\end{aligned}\tag{29}$$

(iii) *If M is G-invariant, then* $M^{\mathrm{inv}}=I_R\otimes M_A$. Proof: If $U(\phi)$ commutes with M for each ϕ, then

$$M^{\mathrm{inv}}=\sum_{\phi\in G}(|\phi\rangle\langle\phi|)\otimes M=I\otimes M.\tag{30}$$

(iv) *If ρ is invariant and* $\mathrm{tr}(\rho_R)=1$, *then*

$$\mathrm{tr}\ M^{\mathrm{inv}}(\rho_R\otimes\rho)=\mathrm{tr}\ M\rho.\tag{31}$$

Proof: If $U(\phi)$ commutes with ρ for each ϕ, then

$$\begin{aligned}\mathrm{tr}\ M^{\mathrm{inv}}(\rho_R\otimes\rho)&=\sum_{\phi\in G}\langle\phi|\rho_R|\phi\rangle\mathrm{tr}[M\ U(\phi)^{-1}\rho U(\phi)]\\ &=\mathrm{tr}(\rho_R)\mathrm{tr}(M\rho)=\mathrm{tr}(M\rho).\end{aligned}\tag{32}$$

The properties (i) and (iv) mean that as long as the state ρ of A is G-invariant, then by making use of a reference system, measurements in the U world can be faithfully simulated by measurements in the I world. That is, given an arbitrary measurement performed on A (with operation elements that are not necessarily G-invariant), there is an invariant measurement performed on *RA* (with G-invariant operation elements) that has the same probability distribution of outcomes. Furthermore, it follows from property (ii) that the physics of the U world can be faithfully reproduced in the I world even if the measurement is preceded by a series of unitary transformations—applying V^{inv} in the I world has the same effect as applying V in the U world. Property (iii) tells us that, as expected, the reference system R is superfluous if the U-world transformation acting on A is already G-invariant.

To derive these properties, we require that the reference system transform as the regular representation of G, but no condition is needed on the *state* ρ_R of the reference system. Loosely speaking, the reference system is needed so that when a noninvariant operation acts on A, the change in the charge of A can be balanced by a compensating change in the charge of R. But if the state ρ of A is invariant, then only the charge-conserving part of M contributes to the expectation value $\mathrm{tr}(M\rho)$ anyway. In the simulation of this charge-conserving part of M, the reference system is superfluous and its state irrelevant.

Note that if G is a Lie group rather than a finite group, then the regular representation is infinite-dimensional, and our formal arguments require R to be an infinite-dimensional system. How is the fidelity of the simulation affected if R is truncated to a finite-dimensional system? In fact, the fidelity will still be perfect if the charge remains bounded in the process to be simulated. Consider, for example, the case $G=\mathrm{U}(1)$, for which Eq. (27) becomes, e.g.,

$$(|q-r\rangle\langle q|)^{\mathrm{inv}}=\sum_{q'}(|q'+r\rangle\langle q'|)_R\otimes(|q-r\rangle\langle q|)_A;\tag{33}$$

in the I world, a process in which r units of charge are removed from A is simulated by adding the r units to R. Suppose we are assured that the total charge added to or removed from A will never exceed r units. Then we may choose the initial state of R to carry charge zero, and we can limit R to the $(2r+1)$-dimensional space spanned by the states $|q_R\rangle$, $q_R=-r,-r+1,\ldots,r-1,r$. This truncated reference system suffices because states with $|q_R|>r$ will never be accessed in the simulation anyway. A similar remark applies if G is an arbitrary compact Lie group.

III. REFERENCE SYSTEMS AND QUANTUM PROTOCOLS

We have concluded that in the presence of a suitable reference system, superselection rules place no inescapable restrictions on the allowed operations. We may anticipate, therefore, that a cryptographic protocol is secure in the invariant "*I* world" (governed by the superselection rule) if and only if it is secure in the unrestricted "*U* world." If we faithfully adhere to the usual stringent principles of quantum cryptology and place no restrictions on the resources available to our adversaries, then we must admit the possibility that the dishonest parties could share access to a reference system during the execution of the protocol. For the case of superselection rules arising from compact symmetry groups, this observation suffices to answer Popescu's question about the impact of superselection rules on the security of quantum protocols.

Let us now discuss this point in greater detail. To be explicit, consider at first a protocol involving two parties, Alice and Bob. Alice holds a private local system A that is beyond Bob's control, and Bob holds a private local system B that is beyond Alice's control. In addition, there is a message system M that they can pass back and forth. At the beginning of the protocol, they share a product state $\rho_A\otimes\rho_B\otimes\rho_M$. In each round of the protocol, one of the parties performs a joint quantum operation on her/his local system and the message, and then sends the message system to the other party. Finally, after all quantum communication is completed, both parties perform local measurements. (See Fig. 1.)

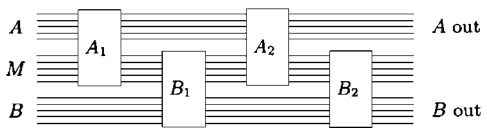

FIG. 1. A two-player quantum game. Alice and Bob have private systems, and a message system that they pass back and forth. At the end of the game, Alice and Bob measure their private systems.

For example, the goal of the protocol might be to flip an unbiased coin. In that case, the final measurement performed by each party has two possible outcomes, 0 or 1. If both parties follow the protocol, then both obtain the same outcome. Furthermore, the two outcomes are equiprobable. A coin-flipping protocol is *secure* if neither party, by departing from the protocol, can bias significantly the outcome of the other party's measurement.

We say that a *strong* coin-flipping protocol has bias ε if neither party by cheating can force *either* outcome to occur with probability greater than $\frac{1}{2}+\epsilon$. In a *weak* coin-flipping protocol, Alice wins if the outcome is 0 and Bob wins if the outcome is 1, and we say that the bias is ε if neither can force a *win* with probability greater than $\frac{1}{2}+\epsilon$. (Thus, in a weak protocol with bias ε, a cheater might be able to *lose* on purpose with a probability exceeding $\frac{1}{2}+\epsilon$.) Note that the protocol might abort if cheating is detected; by "the probability of outcome 0" we mean the joint probability that the protocol does not abort and the outcome is 0. Kitaev [10,11] has shown that, if no superselection rules are imposed, then strong quantum coin flipping is impossible with bias $\epsilon < (1/\sqrt{2}) - \frac{1}{2} = 0.207$. Ambainis [28] has shown that a weak coin-flipping protocol with bias ε requires at least $\Omega[\log \log(1/\varepsilon)]$ rounds of communication.

We are interested in whether these conclusions about coin-flipping in the *U* world remain valid in the *I* world. For a coin-flipping protocol in the *I* world, we may assume that the initial state shared by Alice and Bob is a tensor product of invariant states $\rho_A \otimes \rho_B \otimes \rho_M$. In the honest protocol, Alice and Bob take turns applying *G*-invariant operations to the system that they share, then measure invariant observables. In fact, without loss of generality, we may assume [8] that each operation applied by Alice or Bob is an invariant unitary transformation, and that the final measurement is an invariant projective measurement.

If Alice and Bob play the game honestly, then the probability $P_B(b)$ that Bob's measurement yields the particular outcome b can be expressed as

$$P_B(b) = \mathrm{tr}[E_{B,b}\; V(\rho_A \otimes \rho_B \otimes \rho_M)V^\dagger], \tag{34}$$

where

$$V = V_{B_n} V_{A_n} \cdots V_{B_2} V_{A_2} V_{B_1} V_{A_1}. \tag{35}$$

Here the V_{A_j} are unitary transformations applied to *AM* (we have assumed that Alice makes the first move in the game), the V_{B_j} are unitary transformations applied to *BM*, and the $E_{B,b}$ are the projectors defining Bob's final measurement. Furthermore, in the *I*-world protocol, V_{A_j}, V_{B_j}, and $E_{B,b}$ are *G*-invariant. In effect, then, Bob measures the invariant operator

$$F_{B,b} = V^\dagger E_{B,b} V \tag{36}$$

in the invariant state $\rho_A \otimes \rho_B \otimes \rho_M$.

Of course, a protocol in the *I* world can be regarded as a special case of a protocol in the *U* world, where the initial state is a product state, and Kitaev's result applies to this *U*-world protocol. Therefore, one of the parties (Alice, say) can force one of the outcomes (0, say) with probability at least $1/\sqrt{2}$. However, Alice's cheating strategy that achieves this result might employ operations that are not *G*-invariant. To show that Kitaev's result also applies to the original *I*-world protocol, we must show that Alice's cheating strategy in the *U* world can be faithfully simulated in the *I* world by making use of a suitable reference system. For this purpose, we apply the properties of the invariant operator M^{inv} that were discussed in Sec. II C.

When Alice cheats in the *U* world, she replaces the operator V_{A_j} called for in the honest protocol with an arbitrary operator V'_{A_j} applied to *AM*, where V'_{A_j} is not necessarily *G*-invariant. Then Bob's measurement yields the outcome b with probability

$$P'_B(b) = \mathrm{tr}[F'_{B,b}(\rho_A \otimes \rho_B \otimes \rho_M)], \tag{37}$$

where

$$F'_{B,b} = V'^\dagger E_{B,b} V' \tag{38}$$

and

$$V' = V_{B_n} V'_{A_n} \cdots V_{B_2} V'_{A_2} V_{B_1} V'_{A_1}. \tag{39}$$

This cheating strategy in the *U* world can be simulated in the *I* world if Alice has a reference system *R*—instead of applying the noninvariant operator V'_{A_j} to the system *AM*, she applies the invariant operator $V'^{\mathrm{inv}}_{A_j}$ to *RAM*. Note that since Bob follows the honest protocol, which requires V_{B_j} to be *G*-invariant, applying V_{B_j} to *BM* is equivalent to applying $V^{\mathrm{inv}}_{B_j}$ to *RBM*, by property (iii) in Sec. II C. Therefore, when Alice adopts the *I*-world strategy, Bob obtains outcome b with probability

$$\tilde{P}'_B(b) = \mathrm{tr}[\tilde{F}'_{B,b}(\rho_R \otimes \rho_A \otimes \rho_B \otimes \rho_M)], \tag{40}$$

where

$$\tilde{F}'_{B,b} = \tilde{V}'^\dagger E_{B,b} \tilde{V}' \tag{41}$$

and

$$\tilde{V}' = V^{\mathrm{inv}}_{B_n} V'^{\mathrm{inv}}_{A_n} \cdots V^{\mathrm{inv}}_{B_2} V'^{\mathrm{inv}}_{A_2} V^{\mathrm{inv}}_{B_1} V'^{\mathrm{inv}}_{A_1}. \tag{42}$$

But since the invariant operators provide a representation [property (ii)], we may write $\tilde{V}' = V'^{\mathrm{inv}}$, and since $E_{B,b} = E^{\mathrm{inv}}_{B,b}$ as well, we have

$$\tilde{F}'_{B,b} = F'^{\,\mathrm{inv}}_{B,b}. \tag{43}$$

Finally, the initial state $\rho_A \otimes \rho_B \otimes \rho_M$ shared by Alice and Bob is G-invariant; therefore, by property (iv),

$$\tilde{P}'_B(b) = P'_B(b); \tag{44}$$

the measurement outcome b in the I-world protocol occurs with the same probability as the outcome b in the U-world protocol.

Therefore, Alice's simulated cheating strategy in the I world perfectly reproduces the probability distribution for Bob's measurement outcome that is achieved by her cheating strategy in the U world. The same is true if Bob makes the first move in the game instead of Alice. Similarly, if Bob is the cheater, Bob has a strategy in the I world that simulates his U world cheating strategy. We conclude that if Alice (or Bob) can cheat in the U world, then she (he) can cheat just as successfully in the I world. Thus, Kitaev's proof of the impossibility of strong coin flipping with bias $\epsilon < (1/\sqrt{2}) - \frac{1}{2}$, originally formulated in the U world, also applies to the I world. Similarly, Ambainis's lower bound on the number of rounds of communication needed for weak coin flipping also applies to the I world.

This conclusion that cheating in the U world can be successfully simulated in the I world applies not just to coin flipping protocols, but to any two-party protocol in which the goal of a cheating Alice is to bias the outcome of a measurement performed by an honest Bob. Furthermore, it is straightforward to generalize the argument to an n-party protocol, in which k cheating parties wish to bias the outcomes of measurements performed by the $n-k$ honest parties. For such a protocol in the I world, where the initial state is a product of invariant states, any cheating strategy that can be executed in the U world can be simulated perfectly in the I world if the k cheating parties share access to a reference system. Therefore, the protocol can be no more secure in the I world than in the U world.

To summarize, let us refer to an n-party quantum game as an I-world game if the initial state is a product of invariant states, and if in the honest protocol all operations performed by the parties are invariant operations. If $k<n$ parties are cheaters, we say that their cheating strategy is an I-world cheating strategy if the cheaters are required to perform invariant operations, and we say that their cheating strategy is a U-world cheating strategy if the operations performed by the cheaters are unrestricted. Let us say that an I-world cheating strategy is *equivalent* to a U-world cheating strategy if both strategies produce the same probability distributions for the outcomes of the measurements performed by the $n-k$ honest parties. We have proved the following.

Theorem 1. Suppose that in the I world all quantum operations are required to be G-invariant, where G is a compact Lie group, and that in the U world quantum operations are unrestricted. Consider an n-party I-world quantum game, and a U-world cheating strategy A' in which $k<n$ parties cheat. Then there is an I-world cheating strategy $\tilde{A}'$ that is equivalent to A'.

As we observed in Sec. II C, the reference system required by the cheaters in the I world can be finite-dimensional, as long as the cheaters in the U world apply operations that change the "charge" by a bounded amount.

IV. DISTRIBUTED REFERENCE SYSTEMS

The key ingredient in our discussion of I-world quantum protocols is the observation that G-noninvariant operations can be faithfully simulated through the use of a reference system. Suppose, for example, that Alice and Bob take turns acting on a system C that they pass back and forth. Then Alice and Bob in the I-world can simulate an arbitrary U-world protocol in which the initial state of C is G-invariant. They carry out the simulation by passing the reference system R back and forth along with C, each taking turns applying invariant operations to RC. Similarly, in our analysis of cheating in Sec. III, we allowed the k cheaters to pass the reference system R among themselves as needed during the execution of the protocol. A reference system that travels from place to place might be called *itinerant*.

Here we will briefly discuss an alternative scenario, in which the parties share a *distributed* reference system—each party holds a fixed portion of this system throughout the execution of the protocol. This discussion is not actually needed for our analysis of security, but it is helpful nonetheless for understanding the physics of superselection rules. Indeed, in many physical situations in which reference systems are used (e.g., in optical physics), the system is distributed rather than itinerant.

Let A denote Alice's part of the reference system, B denote Bob's part, and suppose that at the start of the protocol AB is prepared in the state

$$|0\rangle_{AB} = \frac{1}{\sqrt{n_G}} \sum_{\phi\in G} |\phi\rangle_A \otimes |\phi\rangle_B. \tag{45}$$

This state has trivial total charge; indeed, when expressed in the Fourier-transformed charge-eigenstate basis, it is

$$|0\rangle_{AB} = \frac{1}{\sqrt{n_G}} \sum_{q,i,a} |\bar{q},i,a\rangle_A \otimes |q,i,a\rangle_B. \tag{46}$$

Thus, in principle Alice (say) could prepare $|0\rangle_{AB}$ in her lab and then ship half of it to Bob. (The state $|0\rangle_{AB}$ is unnormalizable and unphysical if G is a Lie group. For now we will suppose that G is a finite group, but we will comment on the case of a Lie group below.)

In the state $|0\rangle_{AB}$, Alice's condensate and Bob's, have values that are distributed uniformly over the group G, but these values are locked together. Therefore, if $|\psi\rangle_C$ is any pure state of C, then M^{inv}_{AC} and M^{inv}_{BC} act on $|0\rangle_{AB}\otimes|\psi\rangle_C$ in the same way,

$$\begin{aligned} M^{\mathrm{inv}}_{AC}(|0\rangle_{AB} \otimes |\psi\rangle_C) &= M^{\mathrm{inv}}_{BC}(|0\rangle_{AB} \otimes |\psi\rangle_C) \\ &= \frac{1}{\sqrt{n_G}} \sum_{\phi\in G} |\phi\rangle_A \otimes |\phi\rangle_B \\ &\quad \otimes [U(\phi) M U(\phi)^{-1}] |\psi\rangle_C. \end{aligned} \tag{47}$$

Furthermore M_{AC}^{inv} and M_{BC}^{inv} act identically on any state of the form

$$|\Psi\rangle_{ABC} = \frac{1}{\sqrt{n_G}} \sum_{\phi \in G} |\phi\rangle_A \otimes |\phi\rangle_B \otimes |\psi_\phi\rangle_C, \tag{48}$$

where $|\psi_\phi\rangle_C$ might depend on ϕ, a form that is maintained as successive invariant operations are applied to AC and to BC. Therefore, the outcome of the protocol would be the same if each invariant operation M_{BC}^{inv} applied to BC were replaced by the corresponding invariant operation M_{AC}^{inv} applied to AC. We conclude that the simulation in which the distributed reference system AB is prepared in the initial state $|0\rangle_{AB}$ is equivalent to a simulation that uses an itinerant reference system A. Since this latter simulation has all of the properties listed in Sec. II C, we find that a bipartite I-world protocol using the distributed reference system can faithfully simulate an arbitrary U-world protocol.

Note that the distributed state can serve the same purpose if there is a fixed offset of Bob's condensate relative to Alice's, as long as the offset is known. That is, if Alice and Bob share the state

$$\begin{aligned} |0,\tilde{\phi}\rangle_{AB} &= \frac{1}{\sqrt{n_G}} \sum_{\phi \in G} |\phi\rangle_A \otimes |\phi\tilde{\phi}\rangle_B \\ &= \frac{1}{\sqrt{n_G}} \sum_{q,a,b} D_{ab}^{q}(\tilde{\phi}) \\ &\quad \times \left(\sum_i |\overline{q},i,a\rangle_A \otimes |q,i,b\rangle_B \right), \end{aligned} \tag{49}$$

then the invariant operations M_{BC}^{inv} and $[U(\tilde{\phi})MU(\tilde{\phi})^{-1}]_{AC}^{\text{inv}}$ act in the same way. If Bob knows $\tilde{\phi}$, then he can participate successfully in the simulation by "twisting" his operations appropriately.

Similarly, in a protocol with k parties, the distributed reference state

$$|0\rangle_{k \text{ parties}} = \frac{1}{\sqrt{n_G}} \sum_{\phi \in G} |\phi\rangle_{R_1} \otimes |\phi\rangle_{R_2} \cdots \otimes |\phi\rangle_{R_k} \tag{50}$$

provides a common "phase standard" for all the participants, allowing them to simulate a U-world protocol in the I world—the ℓth party simulates the noninvariant operation M by applying M^{inv} to the target system and her part R_ℓ of the reference system. Again, the parties can twist their local operations to compensate for known relative offsets of their condensates, if necessary.

In the state $|0\rangle_{AB}$, there is a quantum correlation between Alice's condensate and Bob's. A common reference standard can be provided instead by a classically correlated state such as

$$\rho_{AB} = \frac{1}{n_G} \sum_{\phi \in G} (|\phi\rangle\langle\phi|)_A \otimes (|\phi\rangle\langle\phi|)_B. \tag{51}$$

If Alice and Bob are equipped with the state ρ_{AB}, then again M_{AC}^{inv} and M_{BC}^{inv} act in the same way, hence they can use this distributed reference state to simulate a U-world protocol in the I world. The state is G-invariant, but unlike $|0\rangle_{AB}$ it is not a charge eigenstate; rather it is a mixture of (invariant) states with various charges. For example, in the case $G = U(1)$, $|0\rangle_{AB}$ is the (unnormalizable) state

$$|0\rangle_{AB} = \int_0^{2\pi} |\theta\rangle_A \otimes |\theta\rangle_B = \sum_{q=-\infty}^{\infty} |-q\rangle_A \otimes |q\rangle_B; \tag{52}$$

Alice's charge and Bob's charge are perfectly anticorrelated. In contrast, ρ_{AB} is

$$\begin{aligned} \rho_{AB} &\propto \int d\theta\, (|\theta\rangle\langle\theta|)_A \otimes (|\theta\rangle\langle\theta|)_B \\ &\propto \sum_{q_A,q_B,q} |q_A,q_B\rangle\langle q_A - q, q_B + q|. \end{aligned} \tag{53}$$

Formally, this state appears to be separable, as it is a mixture of the product states $|\theta\rangle \otimes |\theta\rangle$, but this is deceptive, because $|\theta\rangle \otimes |\theta\rangle$ is not G-invariant and is therefore incompatible with the superselection rule. On the other hand, in the charge-eigenstate basis, ρ_{AB} can be expressed as a mixture of G-invariant pure states, each with a definite total charge; however, these pure states are highly entangled, with an indefinite value of Alice's (and Bob's) local charge. The state ρ_{AB} is not a mixture of invariant product states, and therefore cannot be prepared without quantum communication between Alice and Bob. Classical communication alone is insufficient for Alice and Bob to establish their common phase standard.

Now let us return to the question we postponed earlier: what if G is a Lie group, so that the states $|0\rangle_{AB}$ and ρ_{AB} are unnormalizable? To be specific, consider again the case $G = U(1)$, and suppose that Alice and Bob are instructed to perform this protocol: Alice is presented with a charge-zero state $|0\rangle$. She is instructed to rotate this state to the superposition of charge eigenstates $(|0\rangle + |1\rangle)/\sqrt{2}$ and to send the resulting state to Bob. Bob is to perform an orthogonal measurement in the basis $(|0\rangle \pm |1\rangle)/\sqrt{2}$ and so verify that Alice prepared the correct state. To make sense of this procedure, Alice and Bob must share a common reference state that serves to lock together their phase conventions; for example, this state could be a shared pure state $|\psi\rangle_{AB}$ with definite total charge. Alice's coherent operation on system C acts as

$$|\psi\rangle_{AB} \otimes |0\rangle_C \to \frac{1}{\sqrt{2}} [|\psi\rangle_{AB} \otimes |0\rangle_C + (U_-)_A |\psi\rangle_{AB} \otimes |1\rangle_C]; \tag{54}$$

that is, Alice simulates the charge-nonconserving operator $(U_+)_C$ by applying the invariant operator $(U_-)_A \otimes (U_+)_C$ to AC. When Bob receives system C, he performs his measurement by first simulating the transformation

$$|0\rangle_C \to \frac{1}{\sqrt{2}} (|0\rangle_C + |1\rangle_C), \tag{55}$$

$$|1\rangle_C \to \frac{1}{\sqrt{2}}(|0\rangle_C - |1\rangle_C),$$

and then measuring the charge of C. After Bob's first step, the state of ABC has become

$$\frac{1}{2}[I_A \otimes I_B + (U_-)_A \otimes (U_+)_B]|\psi\rangle_{AB} \otimes |0\rangle_C + \frac{1}{2}[I_A \otimes (U_-)_B - (U_-)_A \otimes I_B]|\psi\rangle_{AB} \otimes |1\rangle_C. \qquad (56)$$

When Bob measures the charge, the probability that he obtains the outcome $|1\rangle_C$ and fails to verify Alice's state is

$$P_1 = \frac{1}{2}[1 - \mathrm{Re}\ {}_{AB}\langle\psi|(U_-)_A \otimes (U_+)_B|\psi\rangle_{AB}]. \qquad (57)$$

If, for example, the shared reference state is

$$|\psi\rangle_{AB} = \frac{1}{\sqrt{N}}\left(\sum_{q=0}^{N-1} |-q\rangle_A \otimes |q\rangle_B\right), \qquad (58)$$

a normalizable approximation to the state $|0\rangle_{AB}$, our expression for P_1 becomes

$$P_1 = \frac{1}{2N}. \qquad (59)$$

Thus, for finite N, the state received by Bob does not match perfectly with the state prepared by Alice—the superposition of charge eigenstates decoheres slightly. But this decoherence becomes negligible in the limit $N \to \infty$, where the "charge fluctuations" of the shared condensate are large.

The lesson we learn from this example generalizes to non-Abelian compact Lie groups. We can replace the unnormalizable state

$$|0\rangle_{AB} = \frac{1}{\sqrt{n_G}} \sum_{q,i,a} |\overline{q},i,a\rangle_A \otimes |q,i,a\rangle_B \qquad (60)$$

by a normalizable state with a truncated sum over the charge q. If Alice and Bob use this truncated distributed reference state to simulate a U-world protocol, their simulation will not have perfect fidelity. But as long as all operations applied by Alice and Bob change the charge by a bounded amount, the fidelity can be arbitrarily close to 1 if the reference state is chosen appropriately. If Alice and Bob are permitted to use a truncated *itinerant* reference system rather than a distributed one, then perfect fidelity can be achieved, as observed in Sec. II C.

V. INVARIANT OPERATIONS AND COMMUTANTS

Our observations in Sec. II B emphasized the similarities between Abelian and non-Abelian superselection rules, enabling us to formulate a security analysis in Sec. III that applies to both Abelian and non-Abelian symmetry groups. But in several respects the arguments in Sec. III are still not adequate. For one thing, so far we have treated only the special case of superselection sectors labeled by unitary irreducible representations of compact groups. For another, while it is possible to formulate a security analysis of quantum bit commitment within the framework of our argument in Sec. III, it is more natural to structure the argument differently, following more closely the standard analysis of quantum bit commitment.

In this section, we will emphasize the essential differences between superselection rules arising from non-Abelian symmetry groups and those arising from Abelian groups. The discussion will pave the way for our analysis of quantum bit commitment in Sec. VII and of general two-party protocols in Sec. VIII.

A crucial difference between Abelian and non-Abelian charges is that non-Abelian charges are nonadditive: the charges of two subsystems A and B do not necessarily determine the charge of the composite system AB. This feature can be restated as a property of the algebra of observables of the bipartite system. Let $\mathcal{A}$ denote the algebra of local operators (an associative algebra, closed under Hermitian conjugation, that commutes with all locally conserved charges) acting on subsystem A, and let $\mathcal{B}$ denote the algebra of local operators acting on B. The commutant of $\mathcal{A}$, denoted $\mathcal{A}'$, is the algebra of operators acting on the composite system AB that commute with everything in $\mathcal{A}$, and similarly for $\mathcal{B}'$. Now, if all superselection rules are Abelian, then $\mathcal{A}'=\mathcal{B}$ and $\mathcal{B}'=\mathcal{A}$. But if the superselection rules are non-Abelian, the theory has sectors with nontrivial total charge in which this relation does not hold. This unusual structure of the local observables has potential implications for the security of quantum protocols.

To be more explicit, suppose that the superselection rules arise from a non-Abelian symmetry group G, and the operations that Alice (or Bob) can perform must commute with G. A state $|\psi\rangle$ in Alice's (or Bob's) Hilbert space can be decomposed into irreducible representations of G, as

$$|\psi\rangle = \sum_{q,i,a} \psi^q_{i,a}|q,i,a\rangle; \qquad (61)$$

here q labels the irreducible representation (or "charge"), i is the "color" index acted upon by the representation of G, and a is the "flavor" index that distinguishes among the various copies of the irreducible representation q appearing in the decomposition. Note that since we are no longer assuming that Alice's system transforms as the regular representation of G, there need be no connection between the number of flavors and the number of colors associated with q. The action of a color gauge rotation representing $g \in G$ on $|\psi\rangle$ is

$$U(g)|\psi\rangle = \sum_{q,i,j,a} \psi^q_{i,a}|q,j,a\rangle D^q_{ji}(g). \qquad (62)$$

An operator M allowed by the superselection rule, which must commute with each $D^q(g)$, preserves the charge q and acts only on the flavor index according to

$$M|\psi\rangle = \sum_{q,i,a,b} \psi^q_{i,a}|q,i,b\rangle M^q_{ba}. \qquad (63)$$

Since allowed operations act nontrivially only on the flavor index, it is convenient to use a notation that suppresses the color index i. We denote by $\mathcal{H}_q$ the *invariant* Hilbert space in the charge-q sector, spanned by states $|q,a\rangle$ that are labeled only by the flavor a within the sector. The corresponding operator algebra respecting the superselection rule is $\mathcal{L}(\mathcal{H}_q)$, spanned by linear operators acting on this invariant space. Thus Alice's invariant Hilbert space is

$$\mathcal{H}_A = \oplus_q \mathcal{H}_{A,q} \tag{64}$$

and Alice's local operator algebra is

$$\mathcal{A} = \oplus_q \mathcal{L}(\mathcal{H}_{A,q}). \tag{65}$$

Similarly, Bob's operator algebra is

$$\mathcal{B} = \oplus_q \mathcal{L}(\mathcal{H}_{B,q}). \tag{66}$$

Now consider the composite system AB. Its invariant Hilbert space too can be expressed as a direct sum over charge sectors

$$\mathcal{H} = \oplus_q \mathcal{H}_q, \tag{67}$$

while the full operator algebra is $\oplus_q \mathcal{L}(\mathcal{H}_q)$. But we should consider how $\mathcal{H}_q$ is related to the invariant Hilbert spaces of the subsystems. The charge-q Hilbert space of the joint system can be expressed as

$$\mathcal{H}_q = \oplus_{q_A,q_B} \mathcal{H}_{A,q_A} \otimes \mathcal{H}_{B,q_B} \otimes V_q^{q_A,q_B}, \tag{68}$$

where $V_q^{q_A,q_B}$ denotes the space of invariant linear maps from the irreducible representation q to the tensor product of irreducible representations $q_A \otimes q_B$. This space can be nontrivial (of dimension greater than 1) if the tensor product contains the representation q more than once.

When expressed in terms of a particular color basis for the irreducible representations q, q_A, and q_B, the components of $V_q^{q_A,q_B}$ are the Clebsch-Gordon coefficients ($3j$ symbols), of the group G. Let $\{|q_A,i\rangle\}$ denote an orthonormal basis for the representation q_A, $\{|q_B,j\rangle\}$ a basis for q_B, and $\{|q(\alpha),k\rangle\}$ a basis for $q(\alpha)$, where the index α labels the various copies of the representation q that may be contained in $q_A \otimes q_B$. Then the components of $V_q^{q_A,q_B}$ are

$$[V_q^{q_A,q_B}(\alpha)]_k^{ij} = (\langle q_A,i| \otimes \langle q_B,j|)|q(\alpha),k\rangle. \tag{69}$$

These components comprise a G-invariant tensor with the property

$$[V_q^{q_A,q_B}(\alpha)]_k^{ij} = \sum_{i',j',k'} D^{q_A}_{ii'}(g) D^{q_B}_{jj'}(g) [V_q^{q_A,q_B}(\alpha)]_{k'}^{i'j'} D^{q}_{k'k}(g). \tag{70}$$

Invariant operations act not on the color indices of $[V_q^{q_A,q_B}(\alpha)]_k^{ij}$, but rather on the index α that distinguishes the flavors of q contained in $q_A \otimes q_B$. Furthermore, the invariant operations can also alter the charges q_A and q_B appearing in Eq. (68), while preserving the total charge q.

The notation of Eq. (68) and its implications may be clarified by discussing specific examples. The trivial representation ($q=1$) is contained only in the tensor product of q_A with its conjugate representation $\overline{q_A}$, and it occurs only once in this product. Therefore, in the case where the total charge is $q=1$, Eq. (68) reduces to

$$\mathcal{H}_1 = \oplus_q \mathcal{H}_{A,q} \otimes \mathcal{H}_{B,\bar{q}}; \tag{71}$$

in this case, the factor $V_q^{q_A,q_B}$ is superfluous. Now, the joint operator algebra contains operations that cannot be executed by Alice and Bob locally—these operations change Alice's charge and Bob's while preserving the total charge (of course, this can happen even if G is Abelian). But any operation that commutes with Alice's algebra $\mathcal{A}$ must preserve Alice's charge q, and act trivially in each of Alice's charge sectors; such operations preserve Bob's charge $\bar{q}$ as well, and thus are in Bob's algebra $\mathcal{B}$. Therefore, $\mathcal{A}$ and $\mathcal{B}$ are commutants of one another.

However, if the total charge is nontrivial, then $\mathcal{B}$ need not be the commutant of $\mathcal{A}$. To illustrate this phenomenon, consider the case $G=\mathrm{SU}(2)$, where the irreducible representation is labeled by the spin j. For SU(2), $V_j^{j_A,j_B}$ is always one- (or zero-) dimensional, and Eq. (68) reduces to

$$\mathcal{H}_j = \oplus_{j_A,j_B} \mathcal{H}_{A,j_A} \otimes \mathcal{H}_{B,j_B}, \tag{72}$$

where it is implicit that each product of representations appearing on the right-hand side transforms as spin j. To be concrete, suppose that Alice's system has spin $\frac{1}{2}$, Bob's contains both a spin-0 and a spin-1 component, and the total spin is $\frac{1}{2}$; then

$$\mathcal{H}_{1/2} = \mathcal{H}_{A,1/2} \otimes (\mathcal{H}_{B,0} \oplus \mathcal{H}_{B,1}). \tag{73}$$

Note that in this case, contrary to the case in which the total charge is trivial, a single value of j_A can be combined with either of two different values of j_B to obtain the same total charge j. Therefore, there are invariant operations acting on the joint system that preserve Alice's charge and the total charge, but change Bob's charge. These operations are in the commutant of $\mathcal{A}$ but not in $\mathcal{B}$; hence $\mathcal{A}' \neq \mathcal{B}$.

We arrive at another way of looking at this property of $\mathcal{H}_{1/2}$ if we imagine that there is a third party Charlie who holds a compensating charge, so that the total charge is trivial. Now

$$\mathcal{H}_0 = \mathcal{H}_{A,1/2} \otimes (\mathcal{H}_{B,0} \otimes \mathcal{H}_{C,1/2} \oplus \mathcal{H}_{B,1} \otimes \mathcal{H}_{C,1/2}); \tag{74}$$

an operation in $\mathcal{A}'$ can be performed by Bob and Charlie acting together, but not by Bob alone.

In order that $\mathcal{A}' \neq \mathcal{B}$, it is not necessary for one of the parties to possess a state with indefinite charge. For example, in the case $G=\mathrm{SU}(3)$, the tensor product of the irreducible octet representation 8 with itself contains two copies of 8, one symmetric and one antisymmetric under interchange of the factors,

$$8_A \otimes 8_B \supseteq 8_{\mathrm{sym}} \oplus 8_{\mathrm{anti}}. \tag{75}$$

Thus, in the decomposition

$$\mathcal{H}_8 = \mathcal{H}_{A,8} \otimes \mathcal{H}_{B,8} \otimes V_8^{8,8}, \tag{76}$$

the joint invariant Hilbert space is two-dimensional, while Alice and Bob both have one-dimensional Hilbert spaces and trivial invariant operator algebras. Then $\mathcal{A}'$ is the full operator algebra, clearly different from $\mathcal{B}$, and similarly $\mathcal{B}'$ is different from $\mathcal{A}$. Again, an alternative description of the invariant space is to note that Charlie could hold a compensating 8 charge, in which case the total charge is trivial and

$$\mathcal{H}_1 = (\mathcal{H}_{A,8} \otimes \mathcal{H}_{B,8} \otimes \mathcal{H}_{C,8}) \otimes V_1^{8,8,8} \tag{77}$$

is two-dimensional.

For the purpose of describing G-invariant operations, it is always legitimate to introduce a compensating charge without incurring any loss of generality. To see this, first note that if $\mathcal{E}$ is a G-invariant quantum operation, then

$$\mathcal{E}[U(g)\rho U(g)^{-1}] = U(g)\mathcal{E}(\rho)U(g)^{-1} \tag{78}$$

for any $g \in G$ and any state ρ. In particular, then,

$$\mathcal{E}[\mathcal{G}(\rho)] = \mathcal{G}[\mathcal{E}(\rho)], \tag{79}$$

where $\mathcal{G}$ is the map

$$\mathcal{G}(\rho) = \frac{1}{n_G} \sum_{g \in G} U(g)\rho U(g)^{-1}, \tag{80}$$

which induces decoherence of a superposition of distinct irreducible representations of G,

$$\mathcal{G}(|q,i,a\rangle\langle q',j,b|) = \delta^{qq'}\delta_{ij}\left(\frac{1}{n_q}\sum_l |q,l,a\rangle\langle q,l,b|\right). \tag{81}$$

Equation (79) means [26] that the state

$$|\psi\rangle = \sum_{i,a} \psi^q_{i,a}|q,i,a\rangle \tag{82}$$

cannot be distinguished by any G-invariant operation from the state

$$\mathcal{G}(|\psi\rangle\langle\psi|) = \sum_{q,a,b,i} \psi^q_{i,a}\psi^{q*}_{i,b}\left(\frac{1}{n_q}\sum_j |q,j,a\rangle\langle q,j,b|\right). \tag{83}$$

Now, consider a system A whose charge is screened by a system C, so that the state of the joint system has trivial total charge,

$$|\psi\rangle_{AC} = \sum_{q,a,i} \psi^q_a\, |q,i,a\rangle_A \otimes |\overline{q},i\rangle_C. \tag{84}$$

Tracing over system C produces the state

$$\mathrm{tr}_C(|\psi\rangle\langle\psi|)_{AC} = \sum_{q,a,b} \psi^q_a\psi^{q*}_b\left(\frac{1}{n_q}\sum_j |q,j,a\rangle\langle q,j,b|\right). \tag{85}$$

But the state Eq. (83) is just a convex combination of states of the form Eq. (85). Therefore, if only G-invariant operations are to be considered, it is always harmless to replace system A by half of a bipartite state that carries trivial total charge.

Up until now, we have explicitly discussed only the case of superselection sectors arising from a compact symmetry group, but much of the formalism we have outlined in this section can be extended to a more general setting. Whatever the origin of the superselection rule, the allowed operations act on a suitable invariant space. Sectors can still be classified by conserved charges, but in the general case, the space $V_q^{q_A,q_B}$ is defined more abstractly, rather than in terms of group representations. One important property that continues to hold in the general setting (which will play a central role in our analysis of quantum bit commitment in Sec. VII and of general two-party games in Sec. VIII) is that for each value q of the charge, there is a unique conjugate charge $\overline{q}$ such that the fusion of the charges contains the trivial charge sector.

VI. DATA HIDING

Verstraete and Cirac [13] described a data-hiding protocol whose security is founded on the charge superselection rule for $G=\mathrm{U}(1)$. Suppose that a trusted third party Charlie prepares one of the two orthogonal states,

$$|\pm\rangle = \frac{1}{\sqrt{2}}(|01\rangle \pm |10\rangle), \tag{86}$$

where $|0\rangle$ and $|1\rangle$ denote states of charge 0 and 1, respectively, and distributes half to Alice and half to Bob. If Alice and Bob could each measure the Pauli operator X that interchanges $|0\rangle$ and $|1\rangle$, they could distinguishthe states $|+\rangle$ and $|-\rangle$ by performing these measurements and comparing their outcomes. However, X does not commute with the electric charge Q; if Alice and Bob are permitted only to perform local charge-conserving operations and to communicate classically, then they will be powerless to distinguish the two possible states.

On the other hand, if Alice and Bob share access to a common phase reference state, their activities will be unrestricted and nothing will prevent them from performing the X measurements that unlock the classical bit stored in the state prepared by Charlie [aside from the small loss of fidelity that arises if the reference state has large but finite charge fluctuations, as in Eq. (58)]. In Bloch sphere language, Alice and Bob have no *a priori* means of orienting their measurement axes in the x-y plane, but a shared phase standard enables them to lock their axes together and compare their measurements. Since the state prepared by Charlie is invariant under rotations about the z axis, the overall orientation in the x-y plane is irrelevant; only the relative orientation needs to be fixed to identify Charlie's state.

To be more explicit, while X does not commute with the charge,

$$X^{\mathrm{inv}}_{AA'} = (U_-)_A \otimes \sigma^+_{A'} + (U_+)_A \otimes \sigma^-_{A'}, \tag{87}$$

commutes with Q, as does $X^{\mathrm{inv}}_{BB'}$. If Alice and Bob share a distributed reference state $|\psi\rangle_{AB}$ that is an eigenstate of $(U_-)_A \otimes (U_+)_B$ with eigenvalue 1, then

$$|\psi\rangle_{AB}\otimes|\pm\rangle_{A'B'} \tag{88}$$

is an eigenstate of

$$X^{\mathrm{inv}}_{AA'}\otimes X^{\mathrm{inv}}_{BB'} \tag{89}$$

with eigenvalue ± 1. Therefore, Alice and Bob can unlock the hidden bit by each measuring X^{inv} and comparing their results. The same holds, of course, if the shared reference state ρ_{AB} is a mixture of eigenstates of $(U_-)_A\otimes(U_+)_B$, each with eigenvalue 1, as in Eq. (53). As Verstraete and Cirac observed [13], quantum communication is needed to establish this shared phase standard.

In the absence of a shared phase standard, neither Alice nor Bob can detect the bit encoded in the state $|\pm\rangle$ of Eq. (86); however, either Alice or Bob can manipulate the bit. Each can measure the charge q, and either can apply a phase to the state conditioned on the charge, flipping $|+\rangle\leftrightarrow|-\rangle$. But the property that $\mathcal{B}'\neq\mathcal{A}$ indicates that the situation can be more subtle in the non-Abelian case (with nontrivial total charge). Suppose, for example, that $G=\mathrm{SU}(2)$ with total charge $j=\frac{1}{2}$ as in Eq. (73). Two states with the same value of the total charge and of Alice's charge, but different values of Bob's charge, are $|j=\frac{1}{2},j_A=\frac{1}{2},j_B=0\rangle$ and $|j=\frac{1}{2},j_A=\frac{1}{2},j_B=1\rangle$. Charlie might prepare either of the linear combinations

$$|\pm\rangle=\frac{1}{\sqrt{2}}\left(\left|j=\frac{1}{2},j_A=\frac{1}{2},j_B=0\right\rangle\pm\left|j=\frac{1}{2},j_A=\frac{1}{2},j_B=1\right\rangle\right), \tag{90}$$

and then distribute the AB system to Alice and Bob. Again, neither Alice nor Bob can detect the hidden bit, but now there is a notable asymmetry between Alice's power and Bob's. Since Bob has a superposition of two different charge states, he can tamper with the hidden bit by applying a phase controlled by the charge. Alice, on the other hand, has a trivial invariant operator algebra, and has no control over the shared state.

We may take this observation a step further. Suppose, for example, that $G=\mathrm{SU}(3)$ with total charge $q=8$ as in Eq. (76). Charlie might prepare either of the linear combinations

$$|\pm\rangle=\frac{1}{\sqrt{2}}(|q=8_{\mathrm{sym}},q_A=8,q_B=8\rangle\pm|q=8_{\mathrm{anti}},q_A=8,q_B=8\rangle), \tag{91}$$

and then distribute the AB system to Alice and Bob. Again, neither Alice nor Bob can detect the hidden bit, but furthermore, neither one can tamper with the bit's value.

However, in the non-Abelian case as in the Abelian case, the hidden bit can be opened via local operations and classical communication between Alice and Bob if they are provided with correlated reference systems that effectively remove the restrictions imposed by the superselection rule.

VII. QUANTUM BIT COMMITMENT AND SUPERSELECTION RULES

During the commitment stage of quantum bit commitment, Alice encodes a classical bit by preparing one of two distinguishable quantum states with density operators ρ_0 or ρ_1, and then she sends half of the state to Bob. In the unveiling stage, Alice sends the other half of the state to Bob, so that he can verify whether the state is ρ_0 or ρ_1. The protocol is binding if, after commitment, Alice is unable to change the value of the bit. The protocol is concealing if, after commitment and before unveiling, Bob is unable to discern the value of the bit. The protocol is secure if it is both binding and concealing.

In the absence of superselection rules, unconditionally secure quantum bit commitment is impossible [8,9]. If we imagine that the states ρ_0 and ρ_1 are pure states shared by Alice and Bob, then if the protocol is concealing, Bob's density operator (obtained by tracing over Alice's system) must be the same in both cases: $\rho_{0,B}=\rho_{1,B}$. But then by the HJW theorem [29] Alice can apply a unitary transformation to her half of the state that transforms ρ_0 to ρ_1, so that the protocol is not binding.

A. Bit commitment with mixed states

We reached this conclusion under the assumption that ρ_0 and ρ_1 are pure states, but we can extend the argument to the case were the states are mixed by appealing to the concept of a *purification* of a mixed state. We will describe this extension in detail, as we will follow very similar reasoning in our discussion in Sec. VII C of bit commitment with nontrivial total charge.

Suppose that at the start of the bit commitment protocol, Alice and Bob share a product state $\rho_A\otimes\rho_B$, where the states ρ_A and ρ_B are mixed. An equivalent way to describe Alice's initial state is to introduce the ancilla system C and a pure state $|\psi\rangle_{AC}$ (a purification of ρ_A), such that the density operator ρ_A is obtained from $|\psi\rangle_{AC}$ by tracing over system C:

$$\rho_A=\mathrm{tr}_C(|\psi\rangle\langle\psi|)_{AC}. \tag{92}$$

Similarly, to describe ρ_B we can introduce the ancilla D and a state $|\varphi\rangle_{BD}$ that purifies ρ_B. Without loss of generality, we may assume that in each step of the protocol, Alice or Bob applies a unitary transformation, so that the state of the full system $ABCD$ remains pure. (A general quantum operation performed by Alice, say, can be realized as a unitary transformation applied jointly to Alice's system and to an appropriate ancilla; therefore, the operation is unitary provided that we include this ancilla as part of the system.) In particular, after the bit is committed, the state of the full system is one of the two pure states $|\psi_0\rangle_{ABCD}$ or $|\psi_1\rangle_{ABCD}$.

If both parties are honest, the ancillas C and D are off limits—Alice can manipulate only A and Bob can manipulate only B—and in that case the mixed state protocol and its purification are completely equivalent. Furthermore, if one party cheats, whether the other party starts out with a mixed state or its purification has no impact on the effectiveness of the cheating strategy, because the honest party never touches the purifying ancilla anyway.

Now let us see that in any quantum bit commitment protocol, one of the players can cheat successfully. First suppose that Bob cheats. Though the honest protocol calls for Bob to start our with the mixed state ρ_B, a cheating Bob can throw this state away, and replace it with the purification $|\varphi\rangle_{BD}$, where D is now *an ancilla system that Bob controls*. Therefore, if the protocol is perfectly concealing (even when Bob cheats), then

$$\rho_{0,BD} \equiv \mathrm{tr}_{AC}(|\psi_0\rangle\langle\psi_0|)_{ABCD} = \rho_{1,BD} \equiv \mathrm{tr}_{AC}(|\psi_1\rangle\langle\psi_1|)_{ABCD}; \tag{93}$$

Bob is unable to collect any information about the committed bit through any joint measurement on BD.

Similarly, a cheating Alice could throw away her initial state and replace it by its purification; then Alice could control both A and the ancilla C. Applying the HJW theorem as before, we conclude that if $\rho_{0,BD}=\rho_{1,BD}$, then Alice can apply a unitary transformation to AC that transforms $|\psi_0\rangle_{ABCD}$ to $|\psi_1\rangle_{ABCD}$. We conclude that if the protocol is concealing, then it is not binding. Unconditionally secure quantum bit commitment is impossible, even with mixed states. That quantum bit commitment is impossible even when mixed strategies are used was proved in [8] using a slightly different approach.

B. Trivial total charge

The argument in Sec. VII A shows that for an analysis of the security of quantum bit commitment, we may assume that Alice and Bob share a pure state. But how is the security affected if superselection rules constrain Alice's and Bob's operations? We will first consider the special case in which the total charge that Alice and Bob share is trivial. After commitment, then, Alice and Bob share one of the two pure states $|\psi_0\rangle$ or $|\psi_1\rangle$, each with trivial total charge. Choosing the Schmidt basis in each charge sector, the state $|\psi_0\rangle$ can be expanded as

$$|\psi_0\rangle_{AB} = \sum_q \sqrt{p_q} \sum_b \sqrt{\lambda_{q,b}}\ |\overline{q},b\rangle_A \otimes |q,b\rangle_B, \tag{94}$$

where Bob's density operator is

$$\rho_{0,B} = \mathrm{tr}_A(|\psi_0\rangle\langle\psi_0|) = \sum_q p_q \rho_{0,B,q} \tag{95}$$

and

$$\rho_{0,B,q} = \sum_b \lambda_{q,b}\ |q,b\rangle\langle q,b|. \tag{96}$$

Bob can measure the probability p_q that his charge is q; therefore if the protocol is concealing, then the distribution $\{p_q\}$ must be the same for $|\psi_1\rangle$ as for $|\psi_0\rangle$. Furthermore, Bob's density operator in the charge-q sector must not depend on whether the state is $|\psi_0\rangle$ or $|\psi_1\rangle$; therefore $|\psi_1\rangle$ can be expanded as

$$|\psi_1\rangle_{AB} = \sum_q \sqrt{p_q} \sum_b \sqrt{\lambda_{q,b}}\ |\overline{q},\widetilde{b}\rangle_A \otimes |q,b\rangle_B, \tag{97}$$

where $\{|\overline{q},\widetilde{b}\rangle_A\}$ is another basis for Alice's charge-$\overline{q}$ sector. But now Alice can apply a unitary transformation conditioned on the charge that rotates one basis to the other:

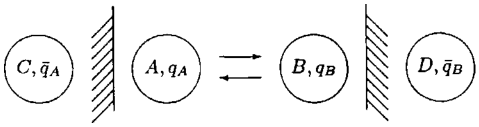

FIG. 2. "Purification" of a two-party game with nontrivial total charge. At the beginning of the game, the charge of C (hidden behind a brick wall) compensates for Alice's charge q_A, and the charge of D (also hidden) compensates for Bob's charge q_B. Honest players never touch the compensating charges, but a cheating Alice might manipulate C and a cheating Bob might manipulate D.

$$U_{\bar{q}}:|\overline{q},b\rangle \to |\overline{q},\widetilde{b}\rangle, \tag{98}$$

which transforms $|\psi_0\rangle$ to $|\psi_1\rangle$. Therefore, the protocol is not binding.

Obviously, the same argument applies, in the Abelian case, even if the total charge is nontrivial [16]. The key property of the states that is used in the argument is that Alice's charge is perfectly correlated with Bob's, so that $\mathcal{B}'=\mathcal{A}$.

C. Nontrivial total charge

The property that $\mathcal{B}' \neq \mathcal{A}$ in the non-Abelian case (with nontrivial total charge) encourages one to hope that a bit commitment protocol can be formulated whose security is founded on a non-Abelian superselection rule. Indeed, consider again the case $G=\mathrm{SU}(2)$ with total charge $j=\frac{1}{2}$ as in Eq. (73). When Alice has control of the full AB system, she can prepare either of the states $|\pm\rangle_{AB}$ shown in Eq. (90), and then she can send the B system to Bob. Now Bob is unable to distinguish the two states, because he cannot measure the relative phase in a superposition of two states of different charge. Furthermore there is no invariant operation Alice can apply that changes $|+\rangle$ to $|-\rangle$ or vice versa. It seems, then, that the protocol is both concealing and binding. At any rate, quantum bit commitment in a world with non-Abelian superselection rules seems fundamentally different from quantum bit commitment in a world in which all superselection rules are Abelian.

But, as always in a discussion of information-theoretic security, we must be sure to consider the most general possible cheating strategies. And in fact, we can argue that for the security analysis, there is no loss of generality if we assume that the charge shared by the parties is trivial, the case we have already dealt with in Sec. VII B. This reduction to the case of trivial total charge follows closely our discussion in Sec. VII A, where we showed that it suffices to assume that the parties share a pure state.

Consider a general two-party quantum bit commitment protocol in which the initial state shared by Alice and Bob is a tensor product $\rho_A \otimes \rho_B$ of invariant states. The state ρ_A can be purified if we introduce an ancilla C; furthermore, the pure state of AC can be chosen to have trivial total charge. Similar, we can purify ρ_B using the ancilla D, in such a way that the pure state of BD has trivial total charge. (See Fig. 2.) Each operation performed by Alice or Bob can be taken to be a charge-conserving unitary transformation; therefore, at each stage of the protocol, the state of the full system $ABCD$ is a pure state with trivial total charge.

In the honest protocol, the ancillas C and D are inaccessible. But if Bob cheats, he can throw away the initial invariant state ρ_A called for in the protocol, and replace it by a trivially charged pure state of BD, where D is now an ancilla that Bob controls. Therefore, if the bit commitment protocol is concealing, then $\rho_{0,BD}=\rho_{1,BD}$—Bob cannot learn anything about the committed bit from any invariant joint measurement on BD. Since the state of the full system $ABCD$ is a pure state with trivial charge, the argument of Sec. VII B suffices to show that Alice can transform $|\psi_0\rangle$ to $|\psi_1\rangle$ with an invariant local operation applied to AC. Hence, the protocol is not binding. We have proved, then, that, even when the protocol calls for a nontrivial total charge, if Bob is unable to cheat then Alice can cheat—unconditionally secure quantum bit commitment is impossible. We have the following.

Theorem 2. Consider a quantum bit commitment protocol in the I world, where at the beginning of the protocol Alice and Bob share a product of invariant states. Then if the protocol is concealing, it is not binding.

Our proof, which reduces the case of nontrivial total charge to the case of trivial total charge, is really just a minor variant of the argument in Sec. VII A that reduces the case of a protocol where Alice and Bob share a mixed state to the case where they share a pure state.

In the case of our bit commitment protocol in which the total charge of AB is $j=\frac{1}{2}$, if Alice is unable to access the compensating charge in C, then she cannot cheat successfully. But if Alice controls the whole AC system, then Alice's charge $j_{AC}=0,1$ is perfectly correlated with Bob's, and she can rotate the relative phase of the $j_{AC}=0$ and $j_{AC}=1$ components of her state, transforming $|+\rangle$ to $|-\rangle$.

This reduction of a protocol with nontrivial total charge to a protocol with trivial total charge can be generalized. In the I world, consider an n-party protocol in which up to $k<n$ of the parties might cheat, where the initial state is the product of invariant states $\otimes_{i=1}^{n}\rho_i$, and where all operations performed by the parties are required to conserve the local charge. Then we may imagine that each party is issued a compensating charge at the beginning of the protocol, so that each party actually starts out with trivial charge. The honest parties will never touch their compensating charges, but a cheating party cannot be prevented from performing arbitrary joint operations on her system and her compensating charge. This strategy is realizable because the cheater might throw away the invariant state she holds at the beginning of the protocol, and replace it by a charge-zero state that she controls fully. Furthermore, if an attack by the cheaters is successful in the protocol where the honest players start out with trivial charge, then it will also be successful if the honest players start out with a product of charged invariant states; since honest players never make use of the compensating charges, their presence can have no impact on the effectiveness of the attack. Therefore, we have the following.

Theorem 3. Let P be an n-party quantum protocol in the I world that securely realizes a task Π, where the initial state in P is a product of n invariant states. Then there is an I-world protocol P' that also securely realizes Π, where the initial state in P' is a product of n pure states, each with trivial charge.

In other words, in a security analysis, we may assume without any loss of generality that each party holds a pure state with trivial charge at the start of the protocol.

Note that for the proofs of Theorems 2 and 3, our observations from Secs. II and III on the use of reference systems are not needed. Rather, to prove Theorems 2 and 3, we use only two properties of the I-world superselection sectors: first, that for each charge sector $\mathcal{H}_q$ there is a unique conjugate charge sector $\mathcal{H}_{\overline{q}}$ such that the trivial sector $\mathcal{H}_1$ is contained in $\mathcal{H}_q\otimes\mathcal{H}_{\overline{q}}$, and second, that any invariant state has a purification with trivial total charge. These properties hold not just for the case of superselection rules arising from a symmetry group G, but also for the more general superselection rules considered in Sec. VIII. Therefore, Theorems 2 and 3 apply in this more general setting.

VIII. TWO-PARTY PROTOCOLS IN GENERAL

A. Overview

We will now analyze the impact of superselection rules on the security of general two-party protocols. We will show that for any protocol P in the invariant world (I world) subject to the superselection rule, there is a corresponding protocol $\widetilde{P}$ in the unrestricted world (U world), where $\widetilde{P}$ *simulates* P in the following sense: First, when performed honestly, $\widetilde{P}$ and P accomplish the same task. And second, for any cheating strategy that can be adopted by a dishonest party in $\widetilde{P}$, there is a corresponding cheating strategy in P that is just as effective. In particular then, if $\widetilde{P}$ is insecure, then so is P. We conclude, therefore, that superselection rules cannot enhance the (information-theoretic) security of two-party protocols. The methods we will use to establish this result are quite different from those used in Sec. III to treat the case of superselection rules arising from a symmetry group.

Before going into detail, we will briefly describe the main ideas used in our argument. First of all, we will restrict out attention to a protocol in which the total charge shared by the two parties is trivial (belongs to the trivial superselection sector). We know from Theorem 3 in Sec. VII C that it suffices to treat this special case in an analysis of security. A protocol with trivial total charge has this useful property: if Alice knows that she holds charge q after sending a message to Bob, then Alice also knows that Bob will hold the conjugate charge $\overline{q}$ upon receiving the message. Similarly, Bob knows what Alice's charge will be after she receives a message sent by Bob. Our analysis of security relies on the property that Bob has a definite charge if Alice does, and therefore it applies only to two-party protocols.

In the I world, charge is conserved, so that the total charge shared by Alice and Bob is trivial at each stage of the protocol; furthermore, local operations performed by Alice or Bob must preserve the conserved charge. In the U world, charge need not be conserved, but the protocol $\widetilde{P}$ that simulates the I-world protocol P can be chosen to respect conservation of a fictitious "charge" that behaves like the actual conserved charge of the I world. However, a dishonest party who is not bound to follow the protocol $\widetilde{P}$ can perform operations that violate "charge" conservation. Our task is to ensure that the greater freedom enjoyed by a dishonest party in the U world does not enhance her ability to cheat successfully.

For this purpose, our argument relies on the concept of the *format* of a message exchanged between the parties. In the U world, the format is simply the Hilbert space containing the message. In the protocol $\tilde{P}$, the recipient of a message always checks that the format of the message is valid, and aborts the protocol if the message is invalid. A valid message corresponds to one that could have been sent in the I world, while a message is invalid only if the sender violated the local conservation of "charge" before sending it. Thus, a message that upon receipt is found to be in the proper format could have been sent by a party who performed a charge-conserving local operation—in effect the sender is unable to play a charge-nonconserving strategy without being detected. Since effective charge conservation is enforced by halting the protocol when a charge nonconservation is detected, it will be essential for our argument to consider games that can be aborted at any stage by either party. A cheating strategy for the I-world protocol P and the corresponding cheating strategy for its U-world counterpart $\tilde{P}$ will cause the game to halt prematurely with the same probability, as well as produce the same probability distribution of outcomes in the event that the game ends normally, without being aborted.

B. Superselection rules and charges

Before proceeding to our proof, we should recall the properties of superselection rules and charges that will be invoked in the argument. These properties have been explored already in Sec. V, for the special case of super-selection sectors labeled by irreducible unitary representations of compact groups. Here we wish to emphasize that some of the same ideas can be extended to a more general setting, and we will indicate how a two-party protocol in which conserved charges are exchanged can be simulated using ordinary qubits.

In general, a superselection rule is a decomposition of Hilbert space into a direct sum of sectors such that each sector is preserved by the allowed operations. The charge q is a label that distinguishes the distinct sectors, and we may say that the operations allowed by the superselection rule conserve the charge. Thus, the Hilbert space is expressed as

$$\mathcal{H} = \bigoplus_{q} \mathcal{H}_q, \tag{99}$$

and the allowed operations belong to the algebra

$$\bigoplus_{q} \mathcal{L}(\mathcal{H}_q), \tag{100}$$

where $\mathcal{L}(\mathcal{H}_q)$ denotes linear operators acting on $\mathcal{H}_q$.

Depending on the particular form of the superselection rule, there are specific rules governing how the charge behaves when a system splits into two subsystems, or when two systems fuse to become a single system. These rules can be encoded in vector spaces $V_c^{a,b}$ defined by

$$\mathcal{H}_c = \bigoplus_{a,b} \mathcal{H}_a \otimes \mathcal{H}_b \otimes V_c^{a,b}. \tag{101}$$

The space $V_c^{a,b}$ is n-dimensional if there are n distinguishable ways that a charge c object can arise when objects with charges a and b fuse. Consistency of Eq. (101) with associativity of the tensor product requires the $V_c^{a,b}$'s to obey certain identities, but we will not discuss these further as they will not be needed for our proof.

There is a trivial-charge sector, denoted $\mathcal{H}_1$, that behaves as the identity under fusion,

$$\mathcal{H}_c \otimes \mathcal{H}_1 = \mathcal{H}_c. \tag{102}$$

Furthermore, there is a unique charge $\overline{q}$, the conjugate of q, that can fuse with q to yield the identity

$$\mathcal{H}_1 = \bigoplus_{q} \mathcal{H}_q \otimes \mathcal{H}_{\overline{q}}. \tag{103}$$

Now, in the I world, consider a bipartite system shared by Alice and Bob. The Hilbert space decomposes as

$$\mathcal{H} = \bigoplus_{q} \mathcal{H}_q,$$

$$\mathcal{H}_q = \bigoplus_{q_A,q_B} \mathcal{H}_{A,q_A} \otimes \mathcal{H}_{B,q_B} \otimes V_q^{q_A,q_B}, \tag{104}$$

where q is the total charge, q_A is the charge of Alice's system, and q_B is the charge of Bob's system. The physical operations, allowed by the superselection rule, conserve the total charge, and hence belong to the algebra

$$\mathcal{O} = \bigoplus_{q} \mathcal{L}(\mathcal{H}_q). \tag{105}$$

The operations Alice can perform, which conserve Alice's charge and act trivially on Bob's system, belong to

$$\mathcal{A} = \bigoplus_{q,q_A,q_B} \mathcal{L}(\mathcal{H}_{A,q_A}) \otimes I_{B,q}^{q_A,q_B}, \tag{106}$$

where $I_{B,q}^{q_A,q_B}$ denotes the identity acting on $\mathcal{H}_{B,q_B} \otimes V_q^{q_A,q_B}$. Similarly, the algebra of operations that Bob can perform is

$$\mathcal{B} = \bigoplus_{q,q_A,q_B} I_{A,q}^{q_A,q_B} \otimes \mathcal{L}(\mathcal{H}_{B,q_B}), \tag{107}$$

where $I_{A,q}^{q_A,q_B}$ denotes the identity acting on $\mathcal{H}_{A,q_A} \otimes V_q^{q_A,q_B}$. In contrast, the commutant $\mathcal{B}'$ of $\mathcal{B}$, which conserves the total charge and Bob's charge but need not conserve Alice's, is

$$\mathcal{B}' = \bigoplus_{q,q_B} \mathcal{L}\left(\bigoplus_{q_A} \mathcal{H}_{A,q_A} \otimes V_q^{q_A,q_B}\right) \otimes I_{B,q_B}, \tag{108}$$

where I_{B,q_B} is the identity on $\mathcal{H}_{B,q_B}$, and similarly

$$\mathcal{A}' = \bigoplus_{q,q_A} I_{A,q_A} \otimes \mathcal{L}\left(\bigoplus_{q_B} \mathcal{H}_{B,q_B} \otimes V_q^{q_A,q_B}\right). \tag{109}$$

Thus $\mathcal{A}' = \mathcal{B}$ and $\mathcal{B}' = \mathcal{A}$ if and only if the charges q_A and q_B are perfectly correlated (there is a unique q_B corresponding to each q_A and vice versa). This condition holds, in particular, if the total charge is trivial, in which case our formulas simplify to

$$\mathcal{H} = \mathcal{H}_1 = \bigoplus_q \mathcal{H}_{A,q} \otimes \mathcal{H}_{B,\overline{q}},$$

$$\mathcal{A} = \mathcal{B}' = \bigoplus_q \mathcal{L}(\mathcal{H}_{A,q}) \otimes I_{B,\overline{q}},$$

$$\mathcal{B} = \mathcal{A}' = \bigoplus_q I_{A,q} \otimes \mathcal{L}(\mathcal{H}_{B,\overline{q}}). \qquad (110)$$

C. Simulating charge exchange

A novelty of a two-party protocol in the *I* world is that when Alice (for example) sends a message to Bob, she may choose to split the charge she possesses into two parts—the charge she retains and the charge of the message that she sends. If the total charge is trivial, then the full Hilbert space comprising Alice's system *A*, Bob's system *B*, and the message system *M* can be expressed as

$$\mathcal{H}_1 = \bigoplus_{q_A,q_B,q_M} \mathcal{H}_{A,q_A} \otimes \mathcal{H}_{B,q_B} \otimes \mathcal{H}_{M,q_M} \otimes V_1^{q_A,q_B,q_M}. \qquad (111)$$

The isomorphisms

$$V_1^{q_A,q_B,q_M} \cong V_{\overline{q_B}}^{q_A,q_M} \cong V_{\overline{q_A}}^{q_B,q_M} \qquad (112)$$

invite us to interpret Eq. (111) in complementary ways—namely, the charge $\overline{q_B}$ of *AM* is conjugate to the charge q_B of *B*, and the charge $\overline{q_A}$ of *BM* is conjugate to the charge q_A of *A*. Thus, Eq. (111) describes the splitting of Alice's initial charge $\overline{q_B}$ into the charge q_A that she retains and the charge q_M of the message, as well as the fusion of the charge q_M of the message with Bob's initial charge q_B to yield Bob's final charge $\overline{q_A}$. Furthermore, if $V_1^{q_A,q_B,q_M}$ is of dimension greater than 1, then a vector in $V_1^{q_A,q_B,q_M}$ describes the particular manner in which Alice performs the splitting, which in turn determines the result of Bob's fusion.

While the information encoded in $V_1^{q_A,q_B,q_M}$ is an intrinsic property in the *I* world, if we are to simulate the process of charge exchange in the *U* world, then this information must be carried by ordinary qubits. In such a simulation, the Hilbert space of Alice's system, Bob's system, and the message is expanded to

$$\tilde{\mathcal{H}} = \bigoplus_{q_1,q_2,q_A,q_B,q_M} \mathcal{H}_{A,q_1} \otimes \mathcal{H}_{B,q_2} \otimes \mathcal{H}_{M,q_M} \otimes V_1^{q_A,q_B,q_M}, \qquad (113)$$

but where now $V_1^{q_A,q_B,q_M}$ is to be regarded as an explicit part of the message. If the conditions $q_1 = q_A$ and $q_2 = q_B$ were imposed, then the "format" of this message would coincide perfectly with the information content of a message sent in the *I* world. But while in the *I* world these conditions arise from the intrinsic physics of the superselection rule, in the *U* world they must be imposed by hand through proper design of the protocol.

Thus, in the *U*-world protocol $\tilde{P}$ that simulates the *I*-world protocol *P*, we will require the recipient of a message to verify its format—Alice checks that $q_1 = q_A$ and Bob checks that $q_2 = q_B$. Of course, at a given stage of the protocol *P*, Alice or Bob might hold a coherent superposition of different charges, even though the total charge is always guaranteed to be trivial. Therefore, the verification step in $\tilde{P}$ must be performed coherently; Alice, for example, checks that q_1 and q_A match without learning the value of q_1 or q_A. If verification fails, then the message recipient has detected cheating by the other party and aborts the protocol. If verification succeeds, then the message has been projected onto the valid format, and as far as the recipient is concerned, it is just as though the message had been sent in the right format to begin with.

Whenever Alice cheats in the *U*-world protocol $\tilde{P}$ by modifying her charge, she risks detection, and if her cheating is undetected, then her operation is equivalent to a charge-conserving one. Therefore, Alice has an equivalent strategy in the *I*-world protocol *P*, in which she either halts the game herself with some probability before sending her message, or if the game does not halt, performs an operation allowed by the superselection rule. This observation suffices to establish that $\tilde{P}$ simulates *P*, and thus that the superselection rule cannot thwart cheating.

To summarize, for the purpose of characterizing Alice's ability to cheat, we are only interested in how Alice's activities will affect Bob's measurements. Although in the *U* world Alice has the power to violate conservation of "charge," she is unable to fool Bob into accepting a message that is not isomorphic to one that could have been created in the *I* world. Therefore, Alice's elevated power in the *U* world gives her no advantage.

D. Definitions

Having explained the main ideas, we will now present a more formal proof of our result. To begin, we must define the general notions of "protocol" and "simulation" in accord with our goals. The definitions are quite natural, but there are some technicalities that are necessary for the proof to work.

We consider quantum games between two parties, Alice and Bob. We assume that Alice sends the first message and the players alternate. The *protocol* of a game specifies the total number of messages, their format, the strategies for honest players, and a way to determine the game outcome. By "format" in the *U* world we mean the Hilbert space $\mathcal{H}_M$ of a given message. In the *I* world, we specify the space $\mathcal{H}_{M,q_M}$ for each value of the message charge q_M.

To define an honest strategy in the *I* world, we specify for each value of Alice's charge q_A her corresponding space $\mathcal{H}_{A,q_A}$; likewise, we specify Bob's space $\mathcal{H}_{B,q_B}$ for each q_B. The game starts with a pure state

$$|\xi_A\rangle \otimes |\xi_B\rangle \in \mathcal{H}_{A,1} \otimes \mathcal{H}_{B,1}, \qquad (114)$$

where 1 stands for the trivial charge. If one of the players (say, Alice) cheats, she may use a different set of private spaces H'_{A,q_A}, but the initial state still must be of the form $|\xi'_A\rangle \otimes |\xi_B\rangle$, where $|\xi'_A\rangle \in \mathcal{H}'_{A,1}$.

Alice's and Bob's actions in the *k*th step are described by operators W_{A_k}, W_{B_k}. The final outcome is determined by a pair of measurements that are performed independently on Al-

	I-world	U-world
Protocol	P ⟶	$\tilde{P}$
Alice strategy	A'	⟵ $\tilde{A}'$
Bob strategy	B'	⟵ $\tilde{B}'$

FIG. 3. The U-world protocol $\tilde{P}$ *simulates* the I-world protocol P if the honest protocols realize the same task, and if for any cheating strategy in $\tilde{P}$ there is an equivalent cheating strategy in P.

ice's and Bob's subsystems at the end of the game. We are interested in the joint probability distribution of the measurement results. However, if one of the players cheats, only the honest player's subsystem is measured.

For the reasons explained in Sec. VIII A, we will assume that the game can be aborted by either player. If the game is aborted, we will not need to keep track of who ends the game or when it ends—we will only be interested in whether the game ends normally and if so what is the outcome. For this purpose, the quantum state can be characterized by a vector $|\psi\rangle$ such that $\langle\psi|\psi\rangle$ is the probability that the game has not been aborted. Operations performed by each player may then be described by contracting maps, i.e., operators W such that $W^\dagger W \leq I$. We assume that the game is never aborted if both players are honest, so that the probabilities of different outcomes add up to 1 in the honest game. If one of the players cheats, the total probability of all outcomes is generally less than 1.

Now we define what it means for one protocol to *simulate* another (see Fig. 3).

Definition. A protocol $\tilde{P}$ *simulates* the protocol P if the following conditions are fulfilled:

(i) The honest strategies in P and $\tilde{P}$ give rise to the same probability distribution of the outcomes.

(ii) For any cheating strategy $\tilde{A}'$ by Alice compatible with the protocol $\tilde{P}$, there exists an equivalent strategy A' for the protocol P. ("Equivalent" means that Bob's measurement result has the same probability distribution in both cases.)

(iii) For any cheating strategy $\tilde{B}'$ by Bob compatible with the protocol $\tilde{P}$ there is an equivalent strategy B' for the protocol P.

Note that when we say that the two cheating strategies are equivalent, we mean in particular that the probability that the game ends normally is the same for both strategies.

To better understand our concept of simulation, it is very helpful to consider this simple example: Suppose that the message space $\mathcal{H}_M$ of P is embedded in a larger space $\tilde{\mathcal{H}}_M$ of $\tilde{P}$. Honest players follow the same strategies in $\tilde{P}$ as in P, so that condition (i) is obviously satisfied. However, the players in $\tilde{P}$ must be prepared to receive messages that do not obey the format of P, i.e., do not fit into the subspace $\mathcal{H}_M$. In $\tilde{P}$ such messages are rejected, and the game is aborted. This rule prevents a dishonest player from gaining any advantage (relative to simply quitting the game) by sending an invalid message. More formally, suppose that Alice cheats using some strategy $\tilde{A}'$. In the corresponding strategy A', Alice projects her message system $\tilde{\mathcal{H}}_M$ onto the subspace $\mathcal{H}_M$, before sending each message. Thus if the strategy $\tilde{A}'$ calls for Alice to apply the operator $\tilde{W}'_{A_k}$ in the kth round, then in the strategy A' Alice applies the contracting map $W'_{A_k} = \Pi \tilde{W}'_{A_k}$, where Π is the orthogonal projector onto $\mathcal{H}_M$. The strategies $\tilde{A}'$ and A' are equivalent: whenever a message sent according to $\tilde{A}'$ causes Bob to abort the game, the strategy A' requires Alice to abort the game herself. Similarly, given any cheating strategy $\tilde{B}'$ for Bob in the game $\tilde{P}$, there is an equivalent cheating strategy B' in P. Thus, conditions (ii) and (iii) are satisfied, and $\tilde{P}$ simulates P.

Our analysis of superselection rules in Sec. VIII E will be based on a closely related method of simulation.

We also remark that Theorem 1 proved in Sec. III can be restated: for a multiparty protocol P in the G-invariant world, there is a U-world protocol $\tilde{P}$ that simulates P. In that case, we implicitly adopt a redundant description of the physical states appearing in P, admitting fictitious color degrees of freedom. Then $\tilde{P}$ is exactly the same protocol as P, but with the color now reinterpreted as a physical variable. Similarly, Theorem 3 in Sec. VII C can be stated: any n-party I-world protocol in which the initial state is a product of n invariant states can be simulated by an I-world protocol in which the initial state is a product of n pure states, each with trivial charge.

E. Proof

Our goal is to prove the following.

Theorem 4. Let P be a two-party game in the I world, such that both parties hold trivial charges at the beginning of the game. Then there is a U-world game $\tilde{P}$ that simulates P.

In the proof, we construct the U-world protocol $\tilde{P}$ that simulates the I-world protocol P, and explain how the cheating strategy A' that is equivalent to $\tilde{A}'$ is formulated. We achieve this by applying the procedure for simulating charge exchange in the U world that was described in Sec. VIII C.

Consider the I-world protocol P. If the total charge is trivial, then the full Hilbert space including Alice's system A, Bob's system B, and the message M is

$$\mathcal{H} = \bigoplus_{q_A, q_B, q_M} \mathcal{H}_{A,q_A} \otimes \mathcal{H}_{B,q_B} \otimes \mathcal{H}_{M,q_M} \otimes V_1^{q_A,q_B,q_M}. \tag{115}$$

Without loss of generality, we assume that the spaces $\mathcal{H}_{A,q_A}$, $\mathcal{H}_{B,q_B}$, $\mathcal{H}_{M,q_M}$ are the same in each step of the protocol. We may also assume that the message is present at the beginning and at the end of the game and that the initial state has the form $|\xi_A\rangle \otimes |\xi_B\rangle \otimes |0\rangle$, where $|0\rangle \in \mathcal{H}_{M,1}$.

Each time Alice receives one message and sends another, she applies an operator to AM that preserves Bob's charge q_B; this is a contracting map belonging to the algebra

$$\bigoplus_{q_B}\mathcal{L}\Bigg(\bigoplus_{q_A,q_M}\mathcal{H}_{A,q_A}\otimes\mathcal{H}_{M,q_M}\otimes V_1^{q_A,q_B,q_M}\Bigg). \tag{116}$$

Alice's honest strategy consists of a sequence of such operators—in the kth step she applies an operator W_{A_k}. Similarly, Bob's honest strategy is defined by operators W_{B_k}.

Now consider the U-world protocol $\widetilde{P}$ that simulates P. The Hilbert space of $\widetilde{P}$ is

$$\widetilde{\mathcal{H}}=\widetilde{\mathcal{H}}_A\otimes\widetilde{\mathcal{H}}_B\otimes\widetilde{\mathcal{H}}_M, \tag{117}$$

where

$$\widetilde{\mathcal{H}}_A=\bigoplus_{q_1}\mathcal{H}_{A,q_1},\quad \widetilde{\mathcal{H}}_B=\bigoplus_{q_2}\mathcal{H}_{B,q_2},$$

$$\widetilde{\mathcal{H}}_M=\bigoplus_{q_A,q_B,q_M}\mathcal{H}_{M,q_M}\otimes V_1^{q_A,q_B,q_M}. \tag{118}$$

Thus the space $\mathcal{H}$ of the protocol P can be embedded in $\widetilde{\mathcal{H}}$ by requiring $q_1=q_A$ and $q_2=q_B$. In $\widetilde{P}$, these constraints are enforced by checks performed by both parties. A dishonest player's attempt to break the constraints will be detected immediately by the other party, in which case the game will halt.

Let us describe Alice's honest strategy in $\widetilde{P}$. When Alice receives a message, she gains control of the space $\widetilde{\mathcal{H}}_A\otimes\widetilde{\mathcal{H}}_M$. First she verifies that $q_1=q_A$ (without determining the value of q_1 or q_A); if verification fails, she aborts the game. Thus Alice effectively projects her input state onto the subspace

$$\mathcal{H}_{AM}=\bigoplus_{q_A,q_B,q_M}\mathcal{H}_{A,q_A}\otimes\mathcal{H}_{M,q_M}\otimes V_1^{q_A,q_B,q_M}\subseteq\widetilde{\mathcal{H}}_A\otimes\widetilde{\mathcal{H}}_M. \tag{119}$$

Then she applies the operator W_{A_k} (from the protocol P), which acts on $\mathcal{H}_{AM}$ and preserves q_B. Thus Alice's strategy is defined by the contracting maps

$$\widetilde{W}_{A_k}=FW_{A_k}F^{\dagger}, \tag{120}$$

where F denotes the embedding $\mathcal{H}_{AM}\to\widetilde{\mathcal{H}}_A\otimes\widetilde{\mathcal{H}}_M$. Bob's honest strategy is defined similarly.

If both players play the game $\widetilde{P}$ honestly, then the verification always succeeds and the conditions $q_1=q_A$ and $q_2=q_B$ are maintained throughout the game. Thus the honest strategies for $\widetilde{P}$ and P are clearly equivalent. Note that in $\widetilde{P}$ some information is encoded redundantly—for example, Alice can access the value of q_A by examining either the charge label of $\mathcal{H}_{A,q_A}$ or one of the slots of the tensor $V_1^{q_A,q_B,q_M}$; similarly q_M is encoded both in $\mathcal{H}_{M,q_M}$ and in $V_1^{q_A,q_B,q_M}$. However, this redundancy has no deleterious effect on the fidelity of the simulation.

Now suppose that Alice cheats in the game $\widetilde{P}$. Then she may use an arbitrary Hilbert space $\widetilde{\mathcal{H}}'_A$ and operators $\widetilde{W}'_{A_k}$ acting on

$$\widetilde{\mathcal{H}}'_{AM}=\widetilde{\mathcal{H}}'_A\otimes\widetilde{\mathcal{H}}_M=\widetilde{\mathcal{H}}'_A\otimes\Big(\bigoplus_{q_A,q_B,q_M}\mathcal{H}_{M,q_M}\otimes V_1^{q_A,q_B,q_M}\Big). \tag{121}$$

In particular, when Alice cheats, her action on the message need not respect the condition $q_B=q_2$. To prove the theorem, we are to define an equivalent cheating strategy for the game P.

When Alice cheats in P, she uses an arbitrary Hilbert space $\mathcal{H}'_{A,q_A}$ for each value of her charge q_A, and she applies operators W'_{A_k} that conserve Bob's charge q_B to the space

$$\mathcal{H}'_{AM}=\bigoplus_{q_A,q_B,q_M}\mathcal{H}'_{A,q_A}\otimes\mathcal{H}_{M,q_M}\otimes V_1^{q_A,q_B,q_M}. \tag{122}$$

The spaces $\widetilde{\mathcal{H}}'_{AM}$ and $\mathcal{H}'_{AM}$ seem to be distinct—in $\mathcal{H}'_{AM}$ the charge label carried by $\mathcal{H}'_{A,q_A}$ matches the label in one of the slots of $V_1^{q_A,q_B,q_M}$, while in $\widetilde{\mathcal{H}}'_{AM}$ there is no such correlation. However, in the U world the variable q_A would be encoded redundantly if it appeared in both $\mathcal{H}'_{A,q_A}$ and $V_1^{q_A,q_B,q_M}$, and it is not necessary to adopt this redundant encoding in order to emulate the physics of the I world. Instead, let us specify $\mathcal{H}'_{A,q_A}=\widetilde{\mathcal{H}}'_A$ for each q_A—then $\mathcal{H}'_{AM}$ and $\widetilde{\mathcal{H}}'_{AM}$ are of the same form, but where it is understood in Eq. (121) that the information about the charge q_A is carried only by $V_1^{q_A,q_B,q_M}$. With this choice Alice's operator $\widetilde{W}'_{A_k}$ in $\widetilde{P}$ and her operator W'_{A_k} in P act on isomorphic spaces; however, W'_{A_k} must conserve Bob's charge q_B, while $\widetilde{W}'_{A_k}$ need not conserve charge.

Therefore, we define the corresponding cheating strategy in P by specifying

$$W'_{A_k}=\sum_{q_B}\Pi_{q_B}\widetilde{W}'_{A_k}\Pi_{q_B}, \tag{123}$$

where Π_{q_B} is the projector onto the subspace with the given value of q_B. That is, Π_{q_B} projects $\widetilde{\mathcal{H}}_M$ onto the space in which $V_1^{q_A,q_B,q_M}$ has the value q_B in the appropriate slot. The contracting map W'_{A_k} preserves q_B and therefore is admissible in the protocol P. Applying this W'_{A_k} causes *Alice* to abort the game P in the case where q_B would change in the game $\widetilde{P}$. But in that case the new value of q_B would not match Bob's variable q_2; therefore, *Bob* would reject Alice's message and abort the game $\widetilde{P}$. Hence the two games P and $\widetilde{P}$ are aborted with the same probability; furthermore, the final state that Bob measures in $\widetilde{P}$, if $\widetilde{P}$ does not abort, is identical to the final state that Bob measures in P, if P does not abort. Therefore, when Alice cheats, Bob's measurement outcome has the same probability distribution in $\widetilde{P}$ as in P. The same is true for Alice's measurement when Bob cheats. Therefore, $\widetilde{P}$ simulates P, which completes the proof of Theorem 4.

IX. CONCLUSIONS

Recent progress in the theory of quantum computation and quantum cryptography highlights the importance of adopting a computational model compatible with fundamental physics—tasks that would be impossible in a classical world may be physically realizable because Nature is quantum-mechanical. Further refinements of the model could lead to further insights regarding what information-processing tasks are achievable. Therefore, as Popescu [12] emphasized, the impact of superselection rules on the security of quantum protocols is of considerable potential interest. However, our disappointing conclusion is that superselection rules cannot foil a cheater who has unlimited quantum-computational power.

Contemplating this issue has led us to consider how physics in the invariant world can simulate physics in the unrestricted world, and vice versa. We feel that the simulation schemes we have devised offer fruitful insights into the physical meaning of superselection rules.

Our results do not address whether the security of protocols with more than two parties can be enhanced by superselection rules that do not arise from compact symmetry groups. New issues arise in this setting, because of the nontrivial braiding properties of non-Abelian anyons. For example, in the case of three parties (Alice, Bob, and Charlie), Alice can split her charge into two parts, and send one part on a voyage that circles Bob's lab and then returns to Alice's lab. This action can induce a change in the charge held by Alice, accompanied by a compensating change in the total charge held by Bob and Charlie, even though the local charge in Bob's lab, and in Charlie's, is unaltered. Though strictly speaking Alice's operation is not "local," she can carry it out surreptitiously, without any cooperation from Bob and Charlie. Such new possibilities enhance the potential power of cheaters, but may also provide the honest parties with new methods for detecting cheating. Addressing the security of multiparty quantum protocols subject to general superselection rules will require different methods from those we have used in this paper, and might provide further enlightenment concerning the physics of non-Abelian anyons.

ACKNOWLEDGMENTS

We thank Stephen Bartlett, Michael Ben-Or, and Sandu Popescu for discussions. This work has been supported in part by the Department of Energy under Grant No. DE-FG03-92-ER40701, by the National Science Foundation under Grant No. EIA-0086038, and by the Caltech MURI Center for Quantum Networks under ARO Grant No. DAAD19-00-1-0374.

[1] C. H. Bennett and G. Brassard, *Quantum Cryptography: Public Key Distribution and Coin Tossing*, in Proceedings of IEEE International Conference on Computers, Systems and Signal Processing, Bangalore, India (IEEE, New York, 1984), pp. 175–179.
[2] D. Mayers, *Quantum Key Distribution and String Oblivious Transfer in Noisy Channels*, in Advances in Cryptography—Proceedings of Crypto'96 (Springer-Verlag, New York, 1996), pp. 343–357; J. ACM **48**, 351 (2001).
[3] H.-K. Lo and H. F. Chau, Science **283**, 2050 (1999).
[4] E. Biham, M. Boyer, P. O. Boykin, T. Mor, and V. Roychowdhury, *A Proof of the Security of Quantum Key Distribution*, in Proceedings of the 32nd Annual ACM Symposium on Theory of Computing (ACM Press, New York, 2000), pp. 715–724.
[5] P. W. Shor and J. Preskill, Phys. Rev. Lett. **85**, 441 (2000).
[6] M. Koashi and J. Preskill, Phys. Rev. Lett. **90**, 057902 (2003).
[7] K. Tamaki, M. Koashi, and N. Imoto, Phys. Rev. Lett. **90**, 167904 (2003).
[8] D. Mayers, Phys. Rev. Lett. **78**, 3414 (1997).
[9] H.-K. Lo and H. F. Chau, Phys. Rev. Lett. **78**, 3410 (1997).
[10] A. Kitaev, http://www.msri.org/publications/ln/msri/2002/qip/kitaev/1/
[11] A. Ambainis, H. Buhrman, Y. Dodis, and H. Roehrig, e-print quant-ph/0304112.
[12] S. Popescu (unpublished).
[13] F. Verstraete and J. I. Cirac, e-print quant-ph/0302039.
[14] Y. Aharonov and L. Susskind, Phys. Rev. **155**, 1428 (1967).
[15] S. D. Bartlett and H. M. Wiseman, e-print quant-ph/0303140.
[16] D. Mayers, e-print quant-ph/0212159.
[17] S. Doplicher and J. E. Roberts, Commun. Math. Phys. **131**, 51 (1990).
[18] K.-H. Rehren, *Braid Group Statistics and their Superselection Rules*, in The Algebraic Theory of Superselection Sectors, edited by D. Kastler (World Scientific, Singapore, 1990), pp. 333–355.
[19] A. Yu Kitaev, Ann. Phys. **303**, 2 (2003).
[20] M. H. Freedman, A. Kitaev, and Z. Wang, Commun. Math. Phys. **227**, 587 (2002).
[21] G.-C. Wick, A. S. Wightman, and E. P. Wigner, Phys. Rev. **88**, 101 (1952).
[22] G.-C. Wick, A. S. Wightman, and E. P. Wigner, Phys. Rev. D **1**, 3267 (1970).
[23] K. Mølmer, Phys. Rev. A **55**, 3195 (1997).
[24] T. Rudolf and B. C. Sanders, Phys. Rev. Lett. **87**, 077903 (2001).
[25] S. J. van Enk and C. A. Fuchs, Quantum Inf. Comput. **2**, 151 (2002).
[26] S. D. Bartlett, T. Rudolf, and R. W. Spekkens, e-print quant-ph/0302111.
[27] S. J. van Enk and T. Rudolf, e-print quant-ph/0303096.
[28] A. Ambainis, e-print quant-ph/0204022.
[29] L. P. Hughston, R. Jozsa, and W. K. Wootters, Phys. Lett. A **183**, 14 (1993).

PHYSICAL REVIEW A **69**, 032109 (2004)

Robust quantum parameter estimation: Coherent magnetometry with feedback

John K. Stockton,[*] J. M. Geremia, Andrew C. Doherty, and Hideo Mabuchi
Norman Bridge Laboratory of Physics, Mail Code 12-33, California Institute of Technology, Pasadena, California 91125, USA

(Received 11 September 2003; published 23 March 2004)

We describe the formalism for optimally estimating and controlling both the state of a spin ensemble and a scalar magnetic field with information obtained from a continuous quantum limited measurement of the spin precession due to the field. The full quantum parameter estimation model is reduced to a simplified equivalent representation to which classical estimation and control theory is applied. We consider both the tracking of static and fluctuating fields in the transient and steady-state regimes. By using feedback control, the field estimation can be made robust to uncertainty about the total spin number.

DOI: 10.1103/PhysRevA.69.032109 PACS number(s): 03.65.Ta, 07.55.Ge, 42.50.Lc, 02.30.Yy

I. INTRODUCTION

As experimental methods for manipulating physical systems near their fundamental quantum limits improve [1–5], the need for quantum state and parameter estimation methods becomes critical. Integrating a modern perspective on quantum measurement theory with the extensive methodologies of classical estimation and control theory provides insight into how the limits imposed by quantum mechanics affect our ability to measure and control physical systems [6–9].

In this paper, we illustrate the processes of state estimation and control for a continuously observed, coherent spin ensemble (such as an optically pumped cloud of atoms) interacting with an external magnetic field. In the situation where the magnetic field is either zero or well characterized, continuous measurement (e.g., via the dispersive phase shift or Faraday rotation of a far off-resonant probe beam) can produce a spin-squeezed state [10] conditioned on the measurement record [11]. Spin-squeezing indicates internal entanglement between the different particles in the ensemble [12] and promises to improve precision measurements [13]. When, however, the ambient magnetic environment is either unknown or changing in time, the external field can be estimated by observing Larmor precession in the measurement signal [2,14–16], see Fig. 1. Recently, we have shown that uncertainty in both the magnetic field and the spin ensemble can be simultaneously reduced through continuous measurement and adequate quantum filtering [17].

Here, we expand on our recent results [17] involving Heisenberg-limited magnetometry by demonstrating the advantages of including feedback control in the estimation process. Feedback is a ubiquitous concept in classical applications because it enables precision performance despite the presence of potentially large system uncertainty. Quantum optical experiments are evolving to the point where feedback can been used, for example, to stabilize atomic motion within optical lattices [4] and high finesse cavities [5]. Recently, we demonstrated the use of feedback on a polarized ensemble of laser-cooled cesium atoms to robustly estimate an applied magnetic field [2]. In this work, we investigate the theoretical limits of such an approach and demonstrate that an external magnetic field can be measured with high precision despite substantial ignorance of the size of the spin ensemble.

The paper is organized as follows. In Sec. II, we provide a general introduction to quantum parameter estimation followed by a specialization to the case of a continuously measured spin ensemble in a magnetic field. By capitalizing on the Gaussian properties of both coherent and spin-squeezed states, we formulate the parameter estimation problem in such a way that techniques from classical estimation theory apply to the quantum system. Sec. III presents basic filtering and control theory in a pedagogical manner with the simplified spin model as an example. This theory is applied in Sec. IV, where we simultaneously derive mutually dependent magnetometry and spin-squeezing limits in the ideal case where the observer is certain of the spin number. We consider the optimal measurement of both constant and fluctuating fields in the transient and steady-state regimes. Finally, we show in Sec. V that the estimation can be made robust to uncertainty about the total spin number by using precision feedback control.

II. QUANTUM PARAMETER ESTIMATION

First, we present a generic description of quantum parameter estimation [6–9]. This involves describing the quantum system with a density matrix and our knowledge of the unknown parameter with a classical probability distribution. The objective of parameter estimation is then to utilize information gained about the system through measurement to conditionally update both the density matrix and the parameter distribution. After framing the general case, our particular example of a continuously measured spin ensemble is introduced.

A. General problem

The following outline of the parameter estimation process could be generalized to treat a wide class of problems (discrete measurement, multiple parameters), but for simplicity,

---

[*] Electronic address: jks@caltech.edu

©2004 The American Physical Society

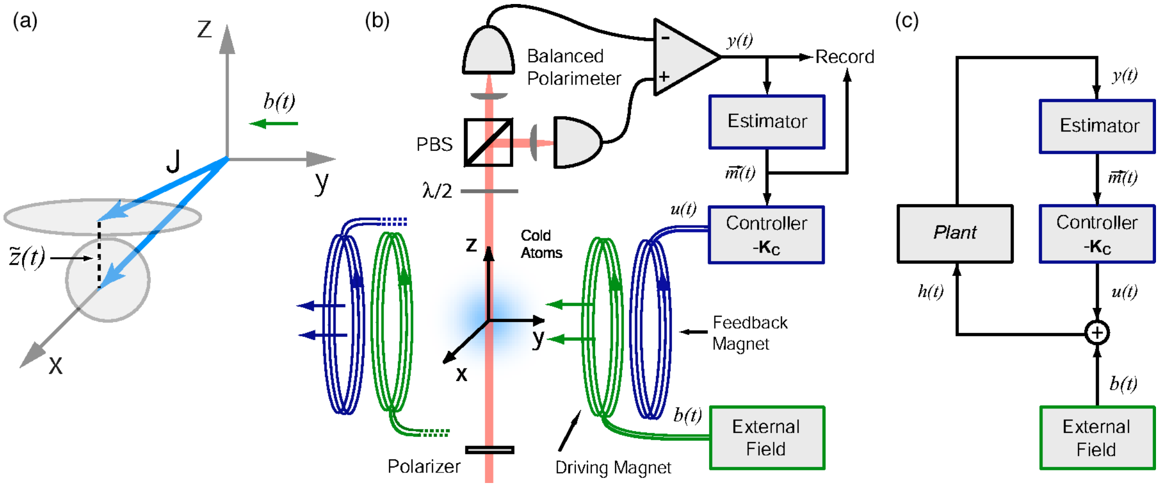

FIG. 1. (a) A spin ensemble is initially prepared in a coherent-state polarized along x, with symmetric variance in the y and z directions. Subsequently, a field along y causes the spin to rotate as the z component is continuously measured. (b) Experimental schematic for the measurement process. A far-off-resonant probe beam traverses the sample and measures the z component of spin via Faraday rotation. The measurement strength could be improved by surrounding the ensemble with a cavity. (c) Experimental apparatus subsumed by the *Plant* block, which serves to map the total field to the photocurrent, $h(t) \rightarrow y(t)$.

we will consider a continuously measured quantum system with scalar Hamiltonian parameter θ and measurement record $y(t)$.

Suppose first that the observer has full knowledge of the parameter θ. The proper description of the system would then be a density matrix $\rho_\theta(t)$ conditioned on the measurement record $y(t)$. The first problem is to find a rule to update this density matrix with the knowledge obtained from the measurement. As in the problem of this paper, this mapping may take the form of a stochastic master equation (SME). The SME is by definition a filter that maps the measurement record to an optimal estimate of the system state.

Now if we allow for uncertainty in θ, then a particularly intuitive choice for our new description of the system is

$$\rho(t) \equiv \int_\theta \rho_\theta(t) p(\theta,t) d\theta, \tag{1}$$

where $p(\theta,t)$ is a probability distribution representing our knowledge of the system parameter. In addition to the rule for updating each $\rho_\theta(t)$, we also need to find a rule for updating $p(\theta,t)$ according to the measurement record. By requiring internal consistency, it is possible to find a Bayes rule for updating $p(\theta,t)$ [6]. These two update rules in principle solve the estimation problem completely.

Because evolving $\rho(t)$ involves performing calculations with the full Hilbert space in question, which is often computationally expensive, it is desirable to find a reduced description of the system. Fortunately, it is often possible to find a closed set of dynamical equations for a small set of moments of $\rho(t)$. For example, if c is an operator, then we can define the estimate moments

$$\langle c\rangle(t) \equiv \mathrm{Tr}[\rho(t)c],$$

$$\langle \Delta c^2\rangle(t) \equiv \mathrm{Tr}[\rho(t)(c-\langle c\rangle)^2],$$

$$\langle \theta\rangle(t) \equiv \int p(\theta,t)\theta d\theta,$$

$$\langle \Delta\theta^2\rangle(t) \equiv \int p(\theta,t)(\theta-\langle\theta\rangle)^2 d\theta,$$

and derive their update rules from the full update rules, resulting in a set of $y(t)$-dependent differential equations. If those differential equations are closed, then this reduced description is adequate for the parameter estimation task at hand. This situation (with closure and Gaussian distributions) is to be expected when the system is approximately linear.

B. Continuously measured spin system

This approach can be applied directly to the problem of magnetometry considered in this paper. The problem can be summarized by the situation illustrated in Fig. 1: a spin ensemble of possibly unknown number is initially polarized along the x axis (e.g., via optical pumping), an unknown possibly fluctuating scalar magnetic field b directed along the y-axis causes the spins to then rotate within the x-z plane, and the z-component of the collective spin is measured continuously. The measurement can, for example, be implemented as shown, where we observe the difference photocurrent, $y(t)$, in a polarimeter which measures the Faraday rotation of a linearly polarized far-off-resonant probe beam traveling along z [2,14,18]. The goal is to optimally estimate $b(t)$ via the measurement record and unbiased prior information. If a control field $u(t)$ is included, as it will be eventually, the total field is represented by $h(t)=b(t)+u(t)$.

In terms of our previous discussion, we have here the observable $c=\sqrt{M}J_z$, where M is the measurement rate (defined in terms of probe beam parameters), and the parameter $\theta = b$. When b is known, our state estimate evolves by the stochastic master equation [19]

$$d\rho_b(t) = -i[H(b),\rho_b(t)]dt + \mathcal{D}[\sqrt{M}J_z]\rho_b(t)dt + \sqrt{\eta}\mathcal{H}[\sqrt{M}J_z] \times (2\sqrt{M\eta}[y(t)dt - \langle J_z\rangle_b dt])\rho_b(t), \qquad (2)$$

where $H(b) = \gamma J_y b$, γ is the gyromagnetic ratio, and

$$\mathcal{D}[c]\rho \equiv c\rho c^\dagger - (c^\dagger c\rho + \rho c^\dagger c)/2,$$

$$\mathcal{H}[c]\rho \equiv c\rho + \rho c^\dagger - \mathrm{Tr}[(c + c^\dagger)\rho]\rho.$$

The stochastic quantity $2\sqrt{M\eta}[y(t)dt - \langle J_z\rangle_b(t)dt] \equiv d\overline{W}(t)$ is a Wiener increment (Gaussian white noise with variance dt) by the optimality of the filter. The definition of the photocurrent may be scaled by any constant gain factor, as in Ref. [17], as long as the statistics of the SME remains invariant. The sensitivity of the photodetection per $\sqrt{\mathrm{Hz}}$ is represented by $1/2\sqrt{M\eta}$, where the quantity η represents the quantum efficiency of the detection. If $\eta = 0$, we are essentially ignoring the measurement result and the conditional SME becomes a deterministic unconditional master equation. If $\eta = 1$, the detectors are maximally efficient. Note that our initial state $\rho(0) = \rho_b(0)$ is made equal to a coherent state (polarized in x) and is representative of our prior information.

The stochastic master equation, Eq. (2), has previously been derived for homodyne detection of the output of a cavity with a single mode dispersively coupled to the collective atomic spin within the cavity [19]. The resulting form of the equation is, however, the most generic form of a continuous stochastic QND measurement and also applies under similar approximations to the free space Faraday rotation measurement [18] diagrammed in Fig. 1.

It can be shown that the unnormalized probability $\overline{p(b,t)}$ evolves according to [6]

$$d\overline{p(b,t)} = 4M\eta\langle J_z\rangle_b(t)\overline{p(b,t)}y(t)dt. \qquad (3)$$

The evolution Eqs. (2) and (3) together with Eq. (1) solve the problem completely, albeit in a computationally expensive way. Clearly, for large ensembles it would be advantageous to reduce the problem to a simpler description.

If we consider only the estimate moments $\langle J_z\rangle(t)$, $\langle \Delta J_z^2\rangle(t)$, $\langle b\rangle(t)$, and $\langle \Delta b^2\rangle(t)$ and derive their evolution with the above rules, it can be shown that the filtering equations for those variables are closed under certain approximations. First, the spin number J must be large enough that the distributions for J_y and J_z are approximately Gaussian for an x-polarized coherent state. Second, we only consider times $t \ll 1/M$ because the total spin becomes damped by the measurement at times comparable to the inverse of the measurement rate.

Although this approach is rigorous and fail-safe, the resulting filtering equations for the moments can be arrived at in a more direct manner as discussed in Appendix A. Essentially, the full quantum-mechanical mapping from $h(t)$ to $y(t)$ is equivalent to the mapping derived from a model which appears classical, and assumes an actual, but random, value for the z component of spin. This correspondence generally holds for a stochastic master equation corresponding to an arbitrary linear quantum-mechanical system with continuous measurement of observables that are linear combinations of the canonical variables [20].

From this point on we will only consider the simplified Gaussian representation (used in the following section) since it allows us to apply established techniques from estimation and control theory. The replacement of the quantum mechanical model with a classical noise model is discussed more fully in the Appendix. Throughout this treatment, we keep in mind the constraints that the original model imposed. Again, we assume J is large enough to maintain the Gaussian approximation and that time is small compared to the measurement induced damping rate, $t \ll 1/M$. Also, the description of our original problem demands that $\langle \Delta J_z^2\rangle(0) = J/2$ for a coherent state [32]. Hence our prior information for the initial value of the spin component will always be dictated by the structure of Hilbert space.

III. OPTIMAL ESTIMATION AND CONTROL

We now describe the dynamics of the simplified representation. Given a linear state-space model (L), a quadratic performance criterion (Q), and Gaussian noise (G), we show how to apply standard LQG analysis to optimize the estimation and control performance [21].

The system state we are trying to estimate is represented by

State.

$$\vec{x}(t) \equiv \begin{bmatrix} z(t) \\ b(t) \end{bmatrix}, \qquad (4)$$

where $z(t)$ represents the small z component of the collective angular momentum and $b(t)$ is a scalar field along the y axis.

Our best guess of $\vec{x}(t)$, as we filter the measurement record, will be denoted as

Estimate.

$$\vec{m}(t) \equiv \begin{bmatrix} \tilde{z}(t) \\ \tilde{b}(t) \end{bmatrix}. \qquad (5)$$

As stated in the Appendix, we implicitly make the associations: $\tilde{z}(t) = \langle J_z\rangle(t) = \mathrm{Tr}[\rho(t)J_z]$ and $\tilde{b}(t) = \int p(b,t)b\, db$, although no further mention of $\rho(t)$ or $p(b,t)$ will be made.

We assume the measurement induced damping of J to be negligible for short times ($J\exp[-Mt/2] \approx J$ if $t \ll 1/M$) and approximate the dynamics as

Dynamics.

$$d\vec{x}(t) = \mathbf{A}\vec{x}(t)dt + \mathbf{B}u(t)dt + \begin{bmatrix} 0 \\ \sqrt{\sigma_{bF}} \end{bmatrix} dW_1, \qquad (6)$$

$$\mathbf{A} \equiv \begin{bmatrix} 0 & \gamma J \\ 0 & -\gamma_b \end{bmatrix},$$

$$\mathbf{B} \equiv \begin{bmatrix} \gamma J \\ 0 \end{bmatrix},$$

$$\mathbf{\Sigma}_0 \equiv \begin{bmatrix} \sigma_{z0} & 0 \\ 0 & \sigma_{b0} \end{bmatrix},$$

$$\mathbf{\Sigma}_1 \equiv \begin{bmatrix} 0 & 0 \\ 0 & \sigma_{bF} \end{bmatrix},$$

where the initial value $\vec{x}(0)$ for each trial is drawn randomly from a Gaussian distribution of mean zero and covariance matrix $\mathbf{\Sigma}_0$. The initial field variance σ_{b0} is considered to be due to classical uncertainty, whereas the initial spin variance σ_{z0} is inherently nonzero due to the original quantum state description. Specifically, we impose $\sigma_{z0}=\langle\Delta J_z^2\rangle(0)$. The Wiener increment $dW_1(t)$ has a Gaussian distribution with mean zero and variance dt. $\mathbf{\Sigma}_1$ represents the covariance matrix of the last vector in Eq. (6).

We have given ourselves a magnetic-field control input, $u(t)$, along the same axis, y, of the field to be measured, $b(t)$. We have allowed $b(t)$ to fluctuate via a damped diffusion (Ornstein-Uhlenbeck) process [22]

$$db(t) = -\gamma_b b(t)dt + \sqrt{\sigma_{bF}}dW_1. \tag{7}$$

The $b(t)$ fluctuations are represented in this particular way because Gaussian noise processes are amenable to LQG analysis. The variance of the field at any particular time is given by the expectation $\sigma_{bFree}\equiv E[b(t)^2]=\sigma_{bF}/2\gamma_b$. (Throughout the paper we use the notation $E[x(t)]$ to represent the average of the generally stochastic variable $x(t)$ at the same point in time, over many trajectories.) The bandwidth of the field is determined by the frequency γ_b alone. When considering the measurement of fluctuating fields, a valid choice of prior might be $\sigma_{b0}=\sigma_{bFree}$, but we choose to let σ_{b0} remain independent. For constant fields, we set $\sigma_{bFree}=0$, but $\sigma_{b0}\neq 0$.

Note that only the small angle limit of the spin motion is considered. Otherwise we would have to consider different components of the spin vector rotating into each other. The small angle approximation would be invalid if a field caused the spins to rotate excessively, but using adequate control ensures this will not happen. Hence, we use control for essentially two reasons in this paper: first to keep our small angle approximation valid and second to make our estimation process robust to our ignorance of J. The latter point will be discussed in Sec. V.

Our measurement of z is described by the process

Measurement.

$$y(t)dt = \mathbf{C}\vec{x}(t)dt + \sqrt{\sigma_M}dW_2(t),$$

$$\mathbf{C} \equiv [1 \quad 0], \tag{8}$$

$$\mathbf{\Sigma}_2 \equiv \sigma_M \equiv 1/4M\eta,$$

where the measurement shot noise is represented by the Wiener increment $dW_2(t)$ of variance dt. Again, $\sqrt{\sigma_M}$ represents the sensitivity of the measurement, M is the measurement rate (with unspecified physical definition in terms of probe parameters), and η is the quantum efficiency of the measurement. The increments dW_1 and dW_2 are uncorrelated.

Following Ref. [21], the optimal estimator for mapping $y(t)$ to $\vec{m}(t)$ takes the form

Estimator.

$$d\vec{m}(t) = \mathbf{A}\vec{m}(t)dt + \mathbf{B}u(t)dt + \mathbf{K}_O(t)[y(t) - \mathbf{C}\vec{m}(t)]dt, \tag{9}$$

$$\vec{m}(0) = \begin{bmatrix} 0 \\ 0 \end{bmatrix},$$

$$\mathbf{K}_O(t) \equiv \mathbf{\Sigma}(t)\mathbf{C}^T\mathbf{\Sigma}_2^{-1}, \tag{10}$$

$$\frac{d\mathbf{\Sigma}(t)}{dt} = \mathbf{\Sigma}_1 + \mathbf{A}\mathbf{\Sigma}(t) + \mathbf{\Sigma}(t)\mathbf{A}^T - \mathbf{\Sigma}(t)\mathbf{C}^T\mathbf{\Sigma}_2^{-1}\mathbf{C}\mathbf{\Sigma}(t),$$

$$\mathbf{\Sigma}(t) \equiv \begin{bmatrix} \sigma_{zR}(t) & \sigma_{cR}(t) \\ \sigma_{cR}(t) & \sigma_{bR}(t) \end{bmatrix}, \tag{11}$$

$$\mathbf{\Sigma}(0) = \mathbf{\Sigma}_0 \equiv \begin{bmatrix} \sigma_{z0} & 0 \\ 0 & \sigma_{b0} \end{bmatrix}. \tag{12}$$

Equation (9) is the Kalman filter which depends on the solution of the matrix Riccati equation (10). The Riccati equation gives the optimal observation gain $\mathbf{K}_O(t)$ for the filter. The estimator is designed to minimize the average quadratic estimation error for each variable: $E[(z(t)-\tilde{z}(t))^2]$ and $E[(b(t)-\tilde{b}(t))^2]$. If the model is correct, and we assume the observer chooses his prior information $\mathbf{\Sigma}(0)$ to match the actual variance of the initial data $\mathbf{\Sigma}_0$, then we have the self-consistent result

$$\sigma_{zE}(t) \equiv E[(z(t) - \tilde{z}(t))^2] = \sigma_{zR}(t),$$

$$\sigma_{bE}(t) \equiv E[(b(t) - \tilde{b}(t))^2] = \sigma_{bR}(t).$$

Hence, the Riccati equation solution represents both the observer gain and the expected performance of an optimal filter using that same gain.

Now consider the control problem, which is in many respects dual to the estimation problem. We would like to design a controller to map $y(t)$ to $u(t)$ in a manner that minimizes the quadratic cost function

Minimized cost.

$$H = \int_0^T [\vec{x}^T(t)\mathbf{P}\vec{x}(t) + u(t)\mathbf{Q}u(t)]dt + \vec{x}^T(T)\mathbf{P}_1\vec{x}(T), \tag{13}$$

$$\mathbf{P} \equiv \begin{bmatrix} p & 0 \\ 0 & 0 \end{bmatrix},$$

$$\mathbf{Q} \equiv q,$$

where $\mathbf{P}_1$ is the end-point cost. Only the ratio p/q ever appears, of course, so we define the parameter $\lambda \equiv \sqrt{p/q}$ and use it to represent the cost of control. By setting $\lambda \to \infty$, as we often choose to do in the subsequent analysis to simplify results, we are putting no cost on our control output. This is unrealistic because, for example, making λ arbitrarily large implies that we can apply transfer functions with finite gain at arbitrarily high frequencies, which is not experimentally possible. Despite this, we will often consider the limit $\lambda \to \infty$ to set bounds on achievable estimation and control performance. The optimal controller for minimizing Eq. (13) is

Controller.

$$u(t) = -\mathbf{K}_C(t)\vec{m}(t), \tag{14}$$

$$\mathbf{K}_C(t) \equiv \mathbf{Q}^{-1}\mathbf{B}^T\mathbf{V}(T-t),$$

$$\frac{d\mathbf{V}(T)}{dT} = \mathbf{P} + \mathbf{A}^T\mathbf{V}(T) + \mathbf{V}(T)\mathbf{A} - \mathbf{V}(T)\mathbf{B}\mathbf{Q}^{-1}\mathbf{B}^T\mathbf{V}(T),$$

$$\mathbf{V}(T=0) \equiv \mathbf{P}_1. \tag{15}$$

Here $\mathbf{V}(T)$ is solved in reverse time T, which can be interpreted as the time left to go until the stopping point. Thus if $T \to \infty$, then we only need to use the steady state of the $\mathbf{V}$ Riccati equation (15) to give the steady-state controller gain $\mathbf{K}_C$ for all times. In this case, we can ignore the (reverse) initial condition P_1 because the controller is not designed to stop. Henceforth, we will make $\mathbf{K}_C$ equal to this constant steady-state value, such that the only time varying coefficients will come from $\mathbf{K}_O(t)$.

In principle, the above results give the entire solution to the ideal estimation and control problem. However, in the nonideal case where our knowledge of the system is incomplete, e.g., J is unknown, our estimation performance will suffer. Notation is now introduced which produces trivial results in the ideal case, but is helpful otherwise. Our goal is to collect the above equations into a single structure which can be used to solve the nonideal problem. We define the *total* state of the system and estimator as

Total state.

$$\vec{\theta}(t) \equiv \begin{bmatrix} \vec{x}(t) \\ \vec{m}(t) \end{bmatrix} = \begin{bmatrix} z(t) \\ b(t) \\ \tilde{z}(t) \\ \tilde{b}(t) \end{bmatrix}. \tag{16}$$

Consider the general case where the observer assumes the plant contains spin J', which may or may not be equal to the actual J. All design elements depending on J' instead of J are now labeled with a prime. Then it can be shown that the total state dynamics from the above estimator-controller architecture are a time-dependent Ornstein-Uhlenbeck process,

Total state dynamics.

$$d\vec{\theta}(t) = \alpha(t)\vec{\theta}(t)dt + \beta(t)d\vec{W}(t),$$

$$\alpha(t) \equiv \begin{bmatrix} \mathbf{A} & -\mathbf{B}\mathbf{K}_C' \\ \mathbf{K}_O'(t)\mathbf{C} & \mathbf{A}' - \mathbf{B}'\mathbf{K}_C' - \mathbf{K}_O'(t)\mathbf{C} \end{bmatrix}, \tag{17}$$

$$\beta(t) \equiv \begin{bmatrix} 0 & 0 & 0 & 0 \\ 0 & \sqrt{\sigma_{bF}} & 0 & 0 \\ 0 & 0 & \sqrt{\sigma_M}K_{O1}'(t) & 0 \\ 0 & 0 & \sqrt{\sigma_M}K_{O2}'(t) & 0 \end{bmatrix},$$

where the covariance matrix of $d\vec{W}$ is dt times the identity. Now the quantity of interest is the following covariance matrix:

Total state covariance.

$$\mathbf{\Theta}(t) \equiv \mathrm{E}[\vec{\theta}(t)\vec{\theta}^T(t)] \equiv \begin{bmatrix} \sigma_{zz} & \sigma_{zb} & \sigma_{z\tilde{z}} & \sigma_{z\tilde{b}} \\ \sigma_{zb} & \sigma_{bb} & \sigma_{b\tilde{z}} & \sigma_{b\tilde{b}} \\ \sigma_{z\tilde{z}} & \sigma_{b\tilde{z}} & \sigma_{\tilde{z}\tilde{z}} & \sigma_{\tilde{z}\tilde{b}} \\ \sigma_{z\tilde{b}} & \sigma_{b\tilde{b}} & \sigma_{\tilde{z}\tilde{b}} & \sigma_{\tilde{b}\tilde{b}} \end{bmatrix}, \tag{18}$$

$$\sigma_{zz} \equiv E[z(t)^2],$$

$$\sigma_{zb} \equiv E[z(t)b(t)],$$

$$\vdots \equiv \vdots\,.$$

It can be shown that this total covariance matrix obeys the deterministic equations of motion.

Total state covariance dynamics.

$$\frac{d\mathbf{\Theta}(t)}{dt} = \alpha(t)\mathbf{\Theta}(t) + \mathbf{\Theta}(t)\alpha^T(t) + \beta(t)\beta^T(t), \tag{19}$$

$$\begin{aligned}\mathbf{\Theta}(t) = {} & \exp\left[-\int_0^t \alpha(t')dt'\right]\mathbf{\Theta}_0\exp\left[-\int_0^t \alpha^T(t')dt'\right] \\ & + \int_0^t dt'\exp\left[-\int_{t'}^t \alpha(s)ds\right]\beta(t')\beta^T(t') \\ & \times\exp\left[-\int_{t'}^t \alpha^T(s)ds\right],\end{aligned} \tag{20}$$

$$\mathbf{\Theta}_0 = \begin{bmatrix} \sigma_{z0} & 0 & 0 & 0 \\ 0 & \sigma_{b0} & 0 & 0 \\ 0 & 0 & 0 & 0 \\ 0 & 0 & 0 & 0 \end{bmatrix}.$$

Equation (20) is the matrix form of the standard integrating factor solution for time-dependent scalar ordinary differential equations [22]. Whether we solve this problem numerically or analytically, the solution provides the quantity that we ultimately care about.

Average magnetometry error.

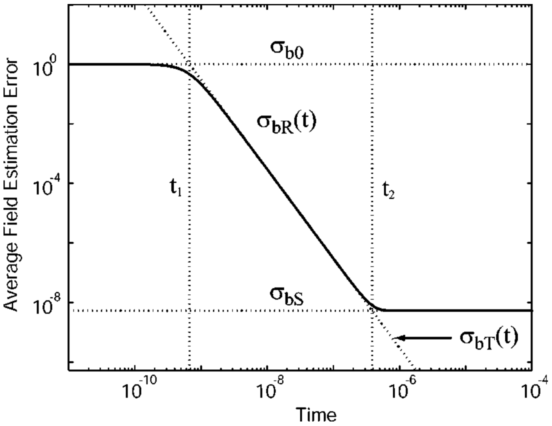

FIG. 2. The Riccati equation solution gives the ideal field estimation performance. The parameters used here are $J=10^6$, $\sigma_{z0}=J/2$ (for ensemble of spin-1/2's), $\gamma=10^6$, $M=10^4$, $\sigma_{b0}=\sigma_{bFree}=1$. (All quantities within the figures are kept dimensionless, although expressions within the text may be interpreted as having dimension.) The solution starts at the free field fluctuation variance and saturates at σ_{bS}. The plot is not valid at times $t>1/M$.

$$\begin{aligned}\sigma_{bE}(t) &\equiv \mathrm{E}[(\tilde{b}(t)-b(t))^2]\\ &= \mathrm{E}[b^2(t)]+\mathrm{E}[\tilde{b}^2(t)]-2\mathrm{E}[b(t)\tilde{b}(t)]\\ &= \sigma_{bb}(t)+\sigma_{\tilde{b}\tilde{b}}(t)-2\sigma_{b\tilde{b}}(t).\end{aligned} \tag{21}$$

When all parameters are known (and $J'=J$), this total state description is unnecessary because $\sigma_{bE}(t)=\sigma_{bR}(t)$. This equality is by *design*. However, when the wrong parameters are assumed (e.g., $J'\neq J$) the equality does not hold $\sigma_{bE}(t)\neq\sigma_{bR}(t)$ and either Eqs. (19) and (20) must be used to find $\sigma_{bE}(t)$. Before addressing this problem, we consider in detail the performance in the ideal case, where all system parameters are known by the observer, including J.

At this point, we have defined several variables. For clarity, let us review the meaning of several before continuing. Inputs to the problem include the field fluctuation strength σ_{bF}, Eq. (7), and the measurement sensitivity σ_M, Eq. (8). The prior information for the field is labeled σ_{b0}, Eq. (12). The solution to the Riccati equation is $\sigma_{bR}(t)$, Eq. (11), and is equal to the estimation variance $\sigma_{bE}(t)$, Eq. (21), when the estimator model is correct. In the following section, we additionally use σ_{bS}, Eq. (24), and $\sigma_{bT}(t)$, Eq. (25), to represent the steady state and transient values of $\sigma_{bE}(t)$, respectively.

IV. OPTIMAL PERFORMANCE: *J* KNOWN

We start by observing qualitative characteristics of the b-estimation dynamics. Figure 2 shows the average estimation performance, $\sigma_{bR}(t)$, as a function of time for a realistic set of parameters. Note that σ_{bR} is constant for small and large times, below t_1 and above t_2. If σ_{b0} is noninfinite then the curve is constant for small times, as it takes some time to begin improving the estimate from the prior. If σ_{b0} is infinite, then $t_1=0$ and the sloped transient portion extends towards infinity as $t\rightarrow 0$. At long times, σ_{bR} will become constant again, but only if the field is fluctuating ($\sigma_{bF}\neq 0$ and $\gamma_b\neq 0$). The performance saturates because one can track a field only so well if the field is changing and the signal-to-noise ratio is finite. If the field to be tracked is constant, then $t_2=\infty$ and the sloped portion of the curve extends to zero as $t\rightarrow\infty$ (given the approximations discussed in Sec. II B). After the point where the performance saturates ($t\gg t_2$), all of the observer and control gains have become time independent and the filter can be described by a transfer function.

However, as will be shown, applying only this steady-state transfer function is nonoptimal in the transient regime ($t_1\ll t\ll t_2$), because the time dependence of the gains is clearly crucial for optimal transient performance.

A. Steady-state performance

We start by examining the steady-state performance of the filter. At large enough times (where we have yet to define large enough), $\mathbf{K}_O$ becomes constant and if we set $T\rightarrow\infty$ (ignoring the end-point cost), then $\mathbf{K}_C$ is always constant. Setting $d\mathbf{\Sigma}/dt=0$ and $d\mathbf{V}/dt=0$ we find

$$\mathbf{K}_O(t)\rightarrow\left[\begin{array}{c}\sqrt{2\gamma J\sqrt{\dfrac{\sigma_{bF}}{\sigma_M}}+\gamma_b^2}-\gamma_b\\ \sqrt{\dfrac{\sigma_{bF}}{\sigma_M}-\dfrac{\gamma_b}{\gamma J}\left(\sqrt{2\gamma J\sqrt{\dfrac{\sigma_{bF}}{\sigma_M}}+\gamma_b^2}-\gamma_b\right)}\end{array}\right],$$

$$\mathbf{K}_C(t)\rightarrow\left[\lambda\quad 1\bigg/\left(1+\frac{\gamma_b}{\gamma J\lambda}\right)\right],$$

where $\lambda=\sqrt{p/q}$.

Now assuming the gains to be constant, we can derive the three relevant transfer functions from $y(t)$ to $\vec{m}(t)$ ($\tilde{z}$ and $\tilde{b}$) and u. We proceed as follows. First, we express the estimates in terms of only themselves and the photocurrent

$$\begin{aligned}\frac{d\vec{m}(t)}{dt} &= \mathbf{A}\vec{m}(t)+\mathbf{B}u(t)+\mathbf{K}_O[y(t)-\mathbf{C}\vec{m}(t)]\\ &= \mathbf{A}\vec{m}(t)+\mathbf{B}[-\mathbf{K}_C\vec{m}(t)]+\mathbf{K}_O[y(t)-\mathbf{C}\vec{m}(t)]\\ &= (\mathbf{A}-\mathbf{B}\mathbf{K}_C-\mathbf{K}_O\mathbf{C})\vec{m}(t)+\mathbf{K}_O y(t).\end{aligned}$$

To get the transfer functions, we take the Laplace transform of the entire equation, use differential transform rules to give s factors (where $s=j\omega$, $j=\sqrt{-1}$), ignore initial condition factors, and rearrange terms. However, this process only gives meaningful transfer functions if the coefficients $\mathbf{K}_O$ and $\mathbf{K}_C$ are constant. Following this procedure, we have

$$\vec{m}(s)=(s\mathbf{I}-\mathbf{A}+\mathbf{B}\mathbf{K}_C+\mathbf{K}_O\mathbf{C})^{-1}\mathbf{K}_O y(s)=\vec{G}_m(s)y(s),$$

$$\begin{aligned}u(s) &= -\mathbf{K}_C\vec{m}(s)=-\mathbf{K}_C(s-\mathbf{A}+\mathbf{B}\mathbf{K}_C+\mathbf{K}_O\mathbf{C})^{-1}\mathbf{K}_O y(s)\\ &= G_u(s)y(s),\end{aligned}$$

where

$$\vec{G}_m(s)=\left[\begin{array}{c}G_z(s)\\ G_b(s)\end{array}\right].$$

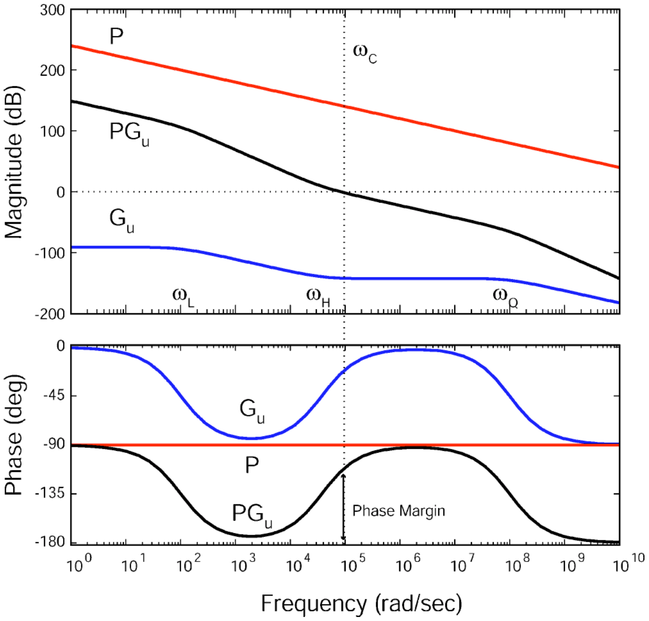

FIG. 3. The Bode plot of $G_u(s)$, the transfer function of the filter in steady state, for a typical parameter regime. Notice that the controller closes the plant with adequate phase margin to avoid closed-loop instability. At high frequencies the controller rolls off at ω_Q if $\lambda \neq \infty$.

The three transfer functions [$G_z(s)$, $G_b(s)$, and $G_u(s)$] serve three different tasks. If estimation is the concern, then $G_b(s)$ will perform optimally in steady state. Note that, while the Riccati solution is the same with and without control ($\mathbf{K}_C$ nonzero or zero), this transfer function is not the same in the two cases. So, even though the transfer functions are different, they give the same steady-state performance.

Let us now consider the controller transfer function $G_u(s)$ in more detail. We find the controller to be of the form

$$G_u(s) = G_{u,DC}\frac{1 + s/\omega_H}{1 + (1 + s/\omega_Q)s/\omega_L}. \tag{22}$$

Here each frequency ω represents a transition in the Bode plot of Fig. 3. A similar controller transfer function is derived via a different method in Appendix C.

If we are not constrained experimentally, we can make the approximations $\lambda^2 \gg \sqrt{\sqrt{\sigma_{bF}/\sigma_M}/2\gamma J}$ and $\gamma J \gg \gamma_b^2\sqrt{\sigma_M/\sigma_{bF}}$ giving

$$G_u(s) \rightarrow G_{u,DC}\frac{1 + s/\omega_H}{1 + s/\omega_L},$$

$$\omega_L \rightarrow \gamma_b,$$

$$\omega_H \rightarrow \sqrt{\frac{\gamma J}{2}\sqrt{\frac{\sigma_{bF}}{\sigma_M}}},$$

$$\omega_C \rightarrow \sqrt{2\gamma J\sqrt{\frac{\sigma_{bF}}{\sigma_M}}} = 2\omega_H,$$

$$\omega_Q \rightarrow \lambda\gamma J,$$

$$G_{u,DC} \rightarrow -\frac{1}{\gamma_b}\sqrt{\frac{\sigma_{bF}}{\sigma_M}},$$

$$G_{u,AC} \rightarrow G_{u,DC}\frac{\omega_L}{\omega_H} = -\sqrt{\frac{2}{\gamma J}\sqrt{\frac{\sigma_{bF}}{\sigma_M}}},$$

where $G_{u,AC}$ is the gain at high frequencies ($\omega > \omega_H$) and we find the closing frequency ω_C from the condition $|P_z(j\omega_C)G_u(j\omega_C)| = 1$, with the plant transfer function being the normal integrator $P_z(s) = \gamma J/s$. Notice that the controller closes in the very beginning of the flat high-frequency region (hence with adequate phase margin) because $\omega_C = 2\omega_H$.

Finally, consider the steady-state estimation performance. These are the same with and without control (hence λ independent) and, under the simplifying assumption $\gamma J \gg \gamma_b^2\sqrt{\sigma_M/\sigma_{bF}}$, are given by

$$\sigma_{zR}(t) \rightarrow \sqrt{2\gamma J}\sigma_M^{3/4}\sigma_{bF}^{1/4} \equiv \sigma_{zS}, \tag{23}$$

$$\sigma_{bR}(t) \rightarrow \sqrt{\frac{2}{\gamma J}}\sigma_{bF}^{3/4}\sigma_M^{1/4} \equiv \sigma_{bS}. \tag{24}$$

If the estimator reaches steady state at $t \ll 1/M$, then the above variance σ_{zR} represents a limit to the amount of spin squeezing possible in the presence of fluctuating fields.

Also the J scaling of the saturated field sensitivity $\sigma_{bR} \propto J^{-1/2}$ is not nearly as strong as the J scaling in the transient period $\sigma_{bR} \propto J^{-2}$. Next, we demonstrate this latter result as we move from the steady-state analysis to calculating the estimation performance during the transient period.

B. Transient performance

We now consider the transient performance of the ideal filter: how quickly and how well the estimator-controller will *lock* onto the signal and achieve steady-state performance. In many control applications, the transient response is not of interest because the time it takes to acquire the lock is negligible compared to the long steady-state period of the system. However, in systems where the measurement induces continuous decay, this transient period can be a significant portion of the total lifetime of the experiment.

We will evaluate the transient performance of two different filters. First, we look at the ideal dynamic version, with time-dependent observer gains derived from the Riccati equation. This limits to a transfer function at long times when the gains have become constant. Second, we numerically look at the case where the same steady-state transfer functions are used for the *entire* duration of the measurement. Because the gains are not adjusted smoothly, the small time performance of this estimator suffers. Of course, for long times the estimators are equivalent.

1. Dynamic estimation and control

Now consider the transient response of $\mathbf{\Sigma}(t)$ [giving $\mathbf{K}_O(t)$]. We will continue to impose that $\mathbf{V}$ (thus $\mathbf{K}_C$) is constant because we are not interested in any particular stopping time.

TABLE I. Field tracking error, $\sigma_{bR}(t)$, for different initial variences of b and z.

	$\sigma_{b0}=0$	σ_{b0}	$\sigma_{b0}\rightarrow\infty$
$\sigma_{z0}=0$	0	$3\sigma_{b0}\sigma_M(3\sigma_M+\gamma^2J^2\sigma_{b0}t^3)^{-1}$	$3\sigma_M(\gamma^2J^2t^3)^{-1}$
σ_{z0}	0	$12\sigma_{b0}\sigma_M(\sigma_M+\sigma_{z0}t)12\sigma_M^2+\gamma^2J^2\sigma_{b0}\sigma_{z0}t^4$ $+4\sigma_M(3\sigma_{z0}t+\gamma^2J^2t^3\sigma_{b0})$	$12\sigma_M(\sigma_M+\sigma_{z0}t)(\gamma^2J^2t^3(4\sigma_M+\sigma_{z0}t))^{-1}$
$\sigma_{z0}\rightarrow\infty$	0	$12\sigma_{b0}\sigma_M(12\sigma_M+\gamma^2J^2t^3\sigma_{b0})^{-1}$	$12\sigma_M(\gamma^2J^2t^3)^{-1}$

The Riccati equation for $\mathbf{\Sigma}(t)$ [Eq. (10)] appears difficult to solve because it is nonlinear. Fortunately, it can be reduced to a much simpler linear problem. See Appendix B for an outline of this method.

The solution to the fluctuating field problem ($\sigma_{bF}\neq 0$ and $\gamma_b\neq 0$) is represented in Fig. 2. This solution is simply the constant field solution ($\sigma_{bF}=0$ and $\gamma_b=0$) smoothly saturating at the steady-state value of Eq. (24) at time t_2. Thus, considering the long-time behavior of the constant field solution will tell us about the transient behavior when measuring fluctuating fields. Because the analytic form for the constant field solution is simple, we consider only it and disregard the full analytic form of the fluctuating field solution.

The analytic form of $\mathbf{\Sigma}(t)$ is highly instructive. The general solutions to $\sigma_{bR}(t)$ and $\sigma_{zR}(t)$, with arbitrary prior information σ_{b0} and σ_{z0}, are presented in the central entries of Tables I and II, respectively. The other entries of the tables represent the limits of these somewhat complicated expressions as the prior information assumes extremely large or small values. Here, we notice several interesting tradeoffs.

First, the left-hand column of Table I is zero because if a constant field is being measured, and we start with complete knowledge of the field ($\sigma_{b0}=0$), then our job is completed trivially. Now notice that if σ_{b0} and σ_{z0} are both nonzero, then at long times we have the lower right entry of Table I,

$$\sigma_{bR}(t)=\frac{12\sigma_M}{\gamma^2J^2t^3}\equiv\sigma_{bT}(t). \tag{25}$$

This is the same result one gets when the estimation procedure is simply to perform a least-squares line fit to the noisy measurement curve for constant fields. (Note that all of these results are equivalent to the solutions of Ref. [17], but without J damping.) If it were physically possible to ensure $\sigma_{z0}=0$, then our estimation would improve by a factor of 4 to the upper right result. However, quantum mechanics imposes that this initial variance is nonzero (e.g., $\sigma_{z0}=J/2$ for a coherent state and less, but still nonzero, for a squeezed state), and the upper right solution is unattainable.

Now consider the dual problem of spin estimation performance $\sigma_{zR}(t)$ as represented in Table II, where we can make analogous tradeoff observations. If there is no field present, we set $\sigma_{b0}=0$ and

$$\sigma_{zR}(t)=\frac{\sigma_{z0}\sigma_M}{\sigma_M+t\sigma_{z0}}. \tag{26}$$

When $\sigma_{zR}(t)$ is interpreted as the quantum variance $\langle\Delta J_z^2\rangle(t)$, this is the ideal (nondamped) conditional spin-squeezing result which is valid at $t\ll 1/M$, before damping in J begins to take effect [19]. If we consider the solution for $t\gg 1/JM$, we have the lower left entry of Table II, $\sigma_{zR}(t)=\sigma_M/t$. However, if we must include constant field uncertainty in our estimation, then our estimate becomes the lower right entry $\sigma_{zR}(t)=4\sigma_M/t$ which is, again, a factor of 4 worse.

If our task is field estimation, intrinsic quantum mechanical uncertainty in z limits our performance just as, if our task is spin-squeezed state preparation, field uncertainty limits our performance.

2. Transfer function estimation and control

Suppose that the controller did not have the capability to adjust the gains in time as it tracked a fluctuating field. One approach would then be to apply the steady-state transfer functions derived above for the *entire* measurement. While this approach performs optimally in steady state, it approaches the steady state in a nonoptimal manner compared to the dynamic controller. Figure 4 demonstrates this poor transient performance for tracking fluctuating fields of differing bandwidth. Notice that the performance only begins to improve around the time that the dynamic controller saturates.

Also notice that the transfer function $G_b(s)$ is dependent on whether or not the state is being controlled, i.e., whether or not λ is zero. The performance shown in Fig. 4 is for one particular value of λ, but others will give different estimation performances for short times. Still, all of the transfer functions generated from any value of λ will limit to the same

TABLE II. Spin tracking error, $\sigma_{zR}(t)$, for different initial variances of b and z.

	$\sigma_{b0}=0$	σ_{b0}	$\sigma_{b0}\rightarrow\infty$
$\sigma_{z0}=0$	0	$3\gamma^2J^2\sigma_{b0}\sigma_Mt^2(3\sigma_M+\gamma^2J^2\sigma_{b0}t^3)^{-1}$	$3\sigma_Mt^{-1}$
σ_{z0}	$\sigma_M\sigma_{z0}(\sigma_M+\sigma_{z0}t)^{-1}$	$4\sigma_M(\gamma^2J^2\sigma_{b0}\sigma_{z0}t^3+3\sigma_M(\sigma_{z0}+\gamma^2J^2t^2\sigma_{b0}))/$ $12\sigma_M^2+\gamma^2J^2\sigma_{b0}\sigma_{z0}t^4+4\sigma_M(3\sigma_{z0}t+\gamma^2J^2t^3\sigma_{b0})$	$4\sigma_M(3\sigma_M+\sigma_{z0}t)(t(4\sigma_M+\sigma_{z0}t))^{-1}$
$\sigma_{z0}\rightarrow\infty$	σ_Mt^{-1}	$4\sigma_M(3\sigma_M+\gamma^2J^2t^3\sigma_{b0})(12\sigma_Mt+\gamma^2J^2t^4\sigma_{b0})^{-1}$	$4\sigma_Mt^{-1}$

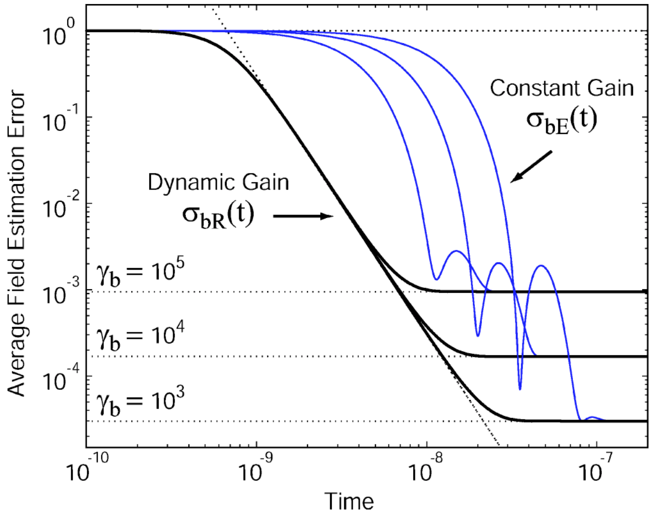

FIG. 4. Estimation performance for estimators based on the dynamic gain solution of the Riccati equation, compared against estimators with constant estimation gain. The latter are the transfer function limits of the former; hence they have the same long-term performance. Three different bandwidth b processes are considered.

performance at long times. Also, all of them will perform poorly compared to the dynamic approach during the transient time.

V. ROBUST PERFORMANCE: J UNKNOWN

Until this point, we have assumed the observer has complete knowledge of the system parameters, in particular, the spin number J. We will now relax this assumption and consider the possibility that, for each measurement, the collective spin J is drawn randomly from a particular distribution. Although we will be ignorant of a given J, we may still possess knowledge about the distribution from which it is derived. For example, we may be certain that J never assumes a value below a minimal value J_{min} or above a maximal value J_{max}. This is a realistic experimental situation, as it is unusual to have particularly long tails on, for example, trapped atom number distributions. We do not explicitly consider the problem of J fluctuating during an individual measurement, although the subsequent analysis can clearly be extended to this problem.

Given a J distribution, one might imagine completely reoptimizing the estimator-controller with the full distribution information in mind. Our initial approach is more basic and in line with robust control theory: we design our filter as before, assuming a particular J', then analyze how well this filter performs on an ensemble with $J \neq J'$. With this information in mind, we can decide if estimator-controllers built with J' are robust, with and without control, given the bounds on J. We will find that, under certain conditions, using control makes our estimates robust to uncertainty about the total spin number.

The essential reason for this robustness is that when a control field is applied to zero the measured signal, that control field must be approximately equal to the field to be tracked. Because J is basically an effective gain, variations in J will affect the performance, but not critically, so the error signal will still be approximately zero. If the applied signal is set to be the estimate, then the tracking error must also be approximately zero. (See Appendix C for a robustness analysis along these lines in frequency space.)

Of course, this analysis assumes that we can apply fields with the same precision that we measure them. While the precision with which we can apply a field is experimentally limited, we here consider the ideal case of infinite precision. In this admittedly idealized problem, our estimation is limited by only the measurement noise and our knowledge of J.

First, to motivate this problem, we describe how poorly our estimator performs given ignorance about J without control.

A. Uncontrolled ignorance

Let us consider the performance of our estimation procedure at estimating constant fields when $J' \neq J$. In general, this involves solving the complicated total covariance matrix Eq. (20). However, in the long-time limit $(t \gg 1/JM)$ of estimating constant fields, the procedure amounts to simply fitting a line to the noisy measurement with a least-squares estimate. Suppose we record an open-loop measurement which appears as a noisy sloped line for small angles of rotation due to the Larmor precession. Regardless of whether or not we know J, we can measure the slope of that line and estimate it to be $\tilde{m}$. If we knew J, we would know how to extract the field from the slope correctly: $\tilde{b} = \tilde{m}/\gamma J$. If we assumed the wrong spin number, $J' \neq J$, we would get the nonoptimal estimate: $\tilde{b}' = \tilde{m}/\gamma J' = \tilde{b} J/J'$.

First assume that this is a *systematic* error and J is unknown, but the same, on every trial. We assume that the constant field is drawn randomly from the σ_{b0} distribution for every trial. In this case, if we are wrong, then we are always wrong by the same factor. It can be shown that the error always saturates

$$\sigma_{bE} \to (1-f)^2 \sigma_{b0},$$

where $f = J/J'$. Of course, because this error is systematic, the variance of the estimate does not saturate, only the error. This problem is analogous to ignorance of the constant electronic gains in the measurement and can also be calibrated away.

However, a significant problem arises when, on every trial, a constant b is drawn at random and J is drawn at random from a distribution, so the error is no longer systematic. In this case, we would not know whether to attribute the size of the measured slope to the size of J or to the size of b. Given the same b every trial, all possible measurement curves fan out over some angle due to the variation in J. After measuring the slope of an individual line to beyond this fan-out precision, it makes no sense to continue measuring.

We should also point out procedures for estimating fields in open-loop configuration, but *without* the small-angle approximation. For constant large fields, we could observe many cycles before the spin damped significantly. By fitting the amplitude and frequency independently, or computing the Fourier transform, we could estimate the field somewhat independently of J, which only determines the amplitude. However, the point here is that b might not be large enough to give many cycles before the damping time or any other desired stopping time. In this case, we could not independently fit the amplitude and frequency because they appear as a product in the initial slope. Similar considerations apply for the case of fluctuating b and fluctuating J. See Ref. [23], for a complete analysis of Bayesian spectrum analysis with free induction decay examples.

Fortunately, using precise control can make the estimation process relatively robust to such spin number fluctuations.

B. Controlled ignorance: Steady-state performance

We first analyze how the estimator designed with J' performs on a plant with J at tracking fluctuating fields with and without control. To determine this we calculate the steady state of Eq. (19).

For the case of no control ($\lambda=0$), we simplify the resulting expression by taking the same large J' approximation as before. This gives the steady-state uncontrolled error

$$\sigma_{bE} \rightarrow (1-f)^2 \frac{\sigma_{bF}}{2\gamma_b} = (1-f)^2 \sigma_{bFree},$$

where $f=J/J'$. Because the variance of the fluctuating b is σ_{bFree}, the uncontrolled estimation performs worse than no estimation at all if $f>2$.

On the other hand, when we use precise control the performance improves dramatically. We again simplify the steady-state solution with the large J' and λ assumptions from before, giving

$$\sigma_{bS}(J,J') \rightarrow \left(\frac{1+f}{2f}\right)\sqrt{\frac{2}{\gamma J'}}\sigma_{bF}^{3/4}\sigma_M^{1/4} = \left(\frac{1+f}{2f}\right)\sigma_{bS}(J'),$$

where $\sigma_{bS}(J,J')$ is the steady-state controlled error when a plant with J is controlled with a J' controller and $\sigma_{bS}(J')$ is the error when $J=J'$. One simple interpretation of this result is that if we set J' to be the minimum of the J distribution ($f>1$) then we never do worse than $\sigma_{bS}(J')$ and we never do better than twice as well ($f\rightarrow\infty$). See Fig. 5 for a demonstration of this performance.

C. Controlled ignorance: Transient performance

Now consider measuring constant fields with the wrong assumed J'. Again, when control is not used, the error saturates at

$$\sigma_{bE} \rightarrow (1-f)^2 \sigma_{b0}.$$

When control is used, the transient performance again improves under certain conditions. The long-time transient solution of Eq. (19) is difficult to manage analytically, yet the behavior under certain limits is again simple. For large λ and J' and for $f>1/2$, we numerically find the transient performance to be approximately

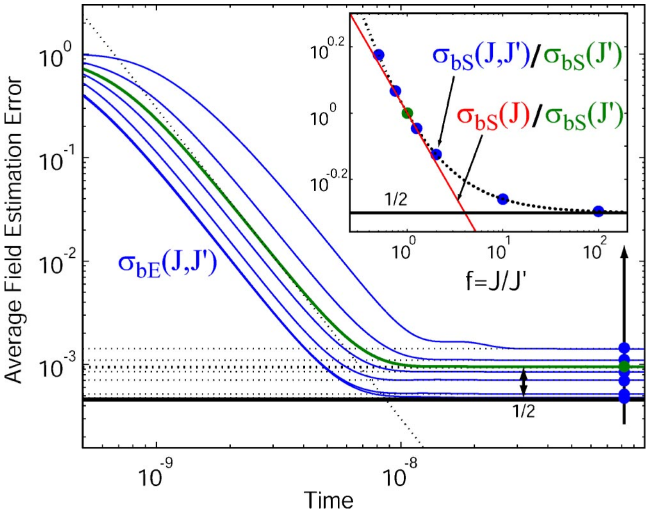

FIG. 5. Steady-state estimation performance for estimator designed with $J'=10^6$, and actual spin numbers: $J=J'\times[0.5,0.75,1,1.25,2,10,100]$. Other parameters: $\gamma=10^6$, $M=10^4$, $\gamma_b=10^5$, $\sigma_{bFree}=1$ (fluctuating field), $\lambda=0.1$ (this is large enough to satisfy large-λ limits discussed in text). The inset compares the normalized robust estimation performance (curve) at a particular time, to the ideal performance (line) when J is known.

$$\sigma_{bT}(J,J') \rightarrow \left(\frac{f^2+2}{4f^2-1}\right)\frac{12\sigma_M}{\gamma^2 J'^2 t^3} = \left(\frac{f^2+2}{4f^2-1}\right)\sigma_{bT}(J'), \tag{27}$$

where $\sigma_{bT}(J,J')$ is the transient controlled error when a plant with J is controlled with a J' controller and $\sigma_{bT}(J')$ is the error when $J=J'$. See Fig. 6 for a demonstration of this performance for realistic parameters. As $f\rightarrow\infty$ the f-dependent

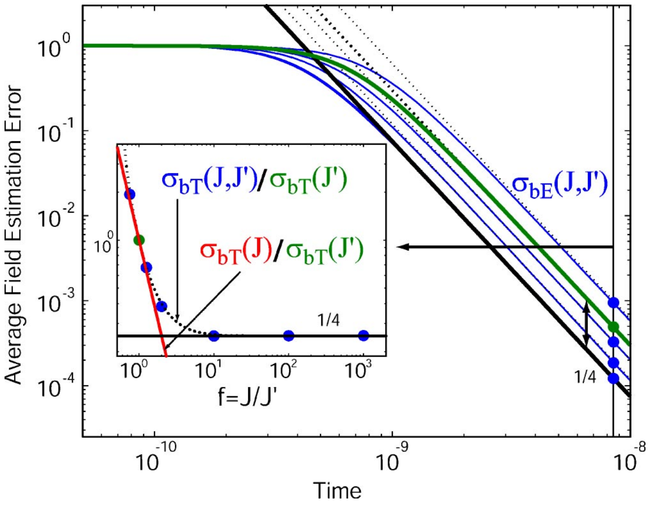

FIG. 6. Transient estimation performance for controller designed with $J'=10^6$, and actual spin numbers: $J=J'\times[0.75,1,1.25,2,10,100,1000]$. Other parameters: $\gamma=10^6$, $M=10^4$, $\gamma_b=0$, $\sigma_{bFree}=0$ (constant field), $\lambda=1$. Note that this behavior is valid for $t<1/M=10^{-4}$. The inset compares the normalized robust estimation performance (curve) at a particular time, to the ideal performance (line) when J is known.

prefactor saturates at a value of $1/4$. However, as $f \rightarrow 1/2$ then the system takes longer to reach such a simple asymptotic form, and the solution of Eq. (27) becomes invalid.

Accordingly, one robust strategy would be the following. Suppose that the lower bound of the J-distribution was known and equal to $J_{\min}$. Also assume that $\sigma_{bT}(J_{\min})$ represents an acceptable level of performance. In this case, we could simply design our estimator based on $J' = J_{\min}$ and we would be guaranteed at least the performance $\sigma_{bT}(J_{\min})$ and at best the performance $\sigma_{bT}(J_{\min})/4$.

This approach would be suitable for experimental situations because typical J distributions are narrow: the difference between $J_{\min}$ and $J_{\max}$ is rarely greater than an order of magnitude. Thus, the overall sacrifice in performance between the ideal case and the robust case would be small. The estimation performance still suffers because of our ignorance of J, but not nearly as much as in the uncontrolled case.

VI. CONCLUSION

The analysis of this paper contained several key steps which should be emphasized. Our first goal was to outline the proper approach to quantum parameter estimation. The second was to demonstrate that reduced representations of the full filtering problem are relevant and convenient because, if a simple representation can be found, then existing classical estimation and control methods can be readily applied. The characteristic that led to this simple description was the approximately Gaussian nature of the problem. Next, we attempted to present basic classical filtering and control methodology in a self-contained, pedagogical format. The results emphasized the inherent tradeoffs in simultaneous estimation of distinct, but dynamically coupled, system parameters. Because these methods are potentially critical in any field involving optimal estimation, we consider the full exposition of this elementary example to be a useful resource for future analogous work.

We have also demonstrated the general principle that precision feedback control can make estimation robust to the uncertainty of system parameters. Despite the need to assume that the controller produced a precise cancellation field, this approach deserves further investigation because of its inherent ability to precisely track broadband field signals [2]. It is anticipated that these techniques will become more pervasive in the experimental community as quantum systems are refined to levels approaching their fundamental limits of performance.

ACKNOWLEDGMENTS

This work was supported by the NSF Grant Nos. (PHY-9987541, EIA-0086038), the ONR Grant No. (N00014-00-1-0479), and the Caltech MURI Center for Quantum Networks Grant No. (DAAD19-00-1-0374). J.K.S. acknowledges financial support from the Hertz Foundation. The authors thank Ramon van Handel for useful discussions. Additional information is available at http://minty.caltech.edu/Ensemble.

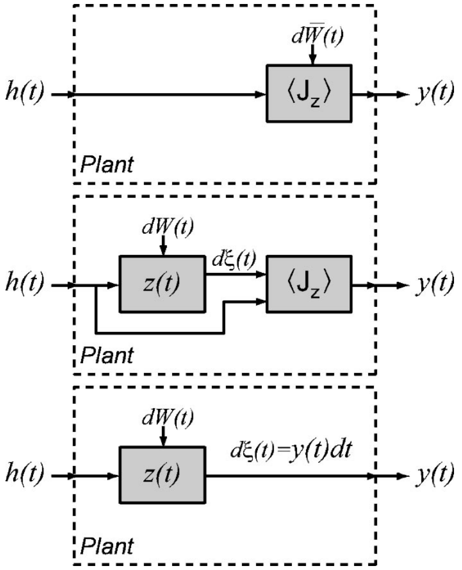

FIG. 7. Equivalent models for the filtering problem (see discussion at the beginning of Appendix A). Each version can be inserted into the plant block of Fig. 1(c). The filters all presume complete knowledge of $h(t) = b(t) + u(t)$.

APPENDIX A: SIMPLIFIED REPRESENTATION OF THE PLAN

In Sec. II we outlined a general approach to quantum parameter estimation based on the stochastic master equation (SME), but subsequently we derived optimal observer and controller gains from an explicit representation of the plant dynamics [Eq. (6)]. This representation appears classical in that the plant state is given by a scalar variable z rather than a density operator. In this section we present a derivation of this simplified representation and discuss the equivalence of our approach to the original quantum estimation problem.

From the perspective of quantum filtering theory we will simply show that a Gaussian approximation to the relevant SME can be viewed as a Kalman filter, which in turn induces a simplified representation of the dynamics of the spin state. In this simplified representation the quantum state of the spin system is replaced by a scalar variable z and $\langle J_z \rangle(t)$ is viewed as the optimal estimate of the random process $z(t)$. Equations for $dz(t)$ and its relation to the observed photocurrent $y(t)dt$ are given in Eqs. (A3) and (A6), which have the convenient property of being formally time invariant. The technical approach in the main body of the text is then to replace Eq. (A1), which is derived from the SME, by a state-space observer derived directly from the simplified model of Eq. (A3). By doing so we achieve transparent correspondence with classical estimation and control theory. We should note that the diagrams in Fig. 7 indicate signal flows and dependencies in a way that is quite at odds with the quantum filtering perspective. This figure is meant solely to motivate the simplified model [Eq. (A3)] for readers who prefer a more traditional quantum optics perspective, in which the Ito increment in the SME corresponds to optical shot-noise (as opposed to an innovation process derived from the photocurrent) and the SME itself plays the role of a "physical" evolution equation mapping $h(t)$ to $y(t)dt$.

Adopting the latter perspective, let us briefly discuss (with reference to the top diagram in Fig. 7) the overall structure of our estimation problem. The physical system that exists in the laboratory (the spins and optical probe beam) acts as a transducer, whose key role in the magnetometry scheme is to imprint a statistical signature of the magnetic field $h(t)$ onto the observable photocurrent, $y(t)dt$. Hence whatever theoretical model we adopt for describing the spin and probe dynamics must provide an accurate description of the mapping from $h(t)$ to $y(t)dt$, as represented by the plant in Fig. 1(c). An open-loop estimator, designed on the basis of this plant model, would construct a conditional probability distribution for $h(t)$ based on passive observation of $y(t)dt$. In a closed-loop estimation procedure we would allow the controller to apply compensation fields to the system in order to gain accuracy and/or robustness. In either case, the essential role of the spin-probe (plant) model in the design process is to provide an accurate description of the influence of an arbitrary time-dependent field $h(t)$ on the photocurrent $y(t)dt$. Note that the consideration of arbitrary $h(t)$ subsumes all possible effects of real-time feedback.

Thomsen and co-workers [19] have derived an accurate plant model for our magnetometry problem, in the form of an SME [Eq. (2)]. Following a common convention in quantum optics, let us here write this SME and the corresponding photocurrent equation in the form

$$d\rho(t) = -idt[H(h),\rho(t)] + \mathcal{D}[\sqrt{M}J_z]\rho(t)dt + \sqrt{\eta}\mathcal{H}[\sqrt{M}J_z]\rho(t)d\overline{W}(t),$$

$$y(t)dt = \langle J_z\rangle(t)dt + \sqrt{\sigma_M}d\overline{W}(t),$$

where $H(h)=\gamma h J_y$ and $\rho(t)$ is the state of the spin system conditioned on the measurement record $y(t)dt$. The quantity $d\overline{W}(t)$ is a Wiener increment that heuristically represents shot noise in the photodetection process [24], and these are to be interpreted as Ito stochastic differential equations. If $h(t)$ and $y(t)dt$ are considered as input and output signals, respectively, this pair of equations jointly implement a plant transfer function as depicted in Fig. 7, with $\rho(t)$ taking on the role of the plant state.

For a large spin ensemble, however, $\rho(t)$ will have very high dimension and it would be impractical to utilize the full SME for design purposes. It is straightforward to derive a reduced model by employing a moment expansion for the observable of interest. Extracting the conditional expectation values of the first two moments of J_z from SME gives the following scalar stochastic differential equations:

$$d\langle J_z\rangle(t) = \gamma\langle J_x\rangle(t)h(t)dt + \frac{\langle\Delta J_z^2\rangle(t)}{\sqrt{\sigma_M}}d\overline{W}(t),$$

$$d\langle\Delta J_z^2\rangle(t) = -\frac{\langle\Delta J_z^2\rangle^2(t)}{\sigma_M}dt - i\gamma\langle[\Delta J_z^2,J_y]\rangle(t)h(t)dt + \frac{\langle\Delta J_z^3\rangle(t)}{\sqrt{\sigma_M}}d\overline{W}(t).$$

If the spins are initially fully polarized along x and the spin angle $\sim\langle J_z\rangle/\langle J_x\rangle$ is kept small (e.g., by active control), then, by using the evolution equation for the x component, we can show $\langle J_x\rangle(t)\approx J\exp[-Mt/2]\approx J$ for times $t<1/M$. Making the Gaussian approximation at small times, the third-order terms $\langle\Delta J_z^3\rangle$ and $-i\gamma\langle[\Delta J_z^2,J_y]\rangle(t)h(t)$ can be neglected. The Holstein-Primakoff transformation [25], commonly used in the condensed matter physics literature, makes it possible to derive this Gaussian approximation as an expansion in $1/J$. Both of the removed terms can be shown to be $\approx 1/J\sqrt{J}$ smaller than the retained nonlinear term. Additionally, the second removed term will be reduced if $h(t)\approx 0$ by active control.

These approximations give

$$d\langle J_z\rangle(t) = \gamma J h(t)dt + \frac{\langle\Delta J_z^2\rangle(t)}{\sqrt{\sigma_M}}d\overline{W}(t), \tag{A1}$$

$$d\langle\Delta J_z^2\rangle(t) = -\frac{\langle\Delta J_z^2\rangle^2(t)}{\sigma_M}dt, \tag{A2}$$

which constitute a Gaussian, small-time approximation to the full SME that represents the essential dynamics for magnetometry. Note that we can analytically solve

$$\langle\Delta J_z^2\rangle(t) = \frac{\langle\Delta J_z^2\rangle(0)\sigma_M}{\sigma_M + \langle\Delta J_z^2\rangle(0)t},$$

where $\langle\Delta J_z^2\rangle(0)=J/2$ for an initial coherent spin state.

At this point we may note that Eqs. (A1) and (A2) have the algebraic form of a Kalman filter. [This is not at all surprising since the SME, as written in Eq. (2), represents an optimal nonlinear filter for the reduced spin state [6,9] and our subsequent approximations have enforced both linearity and sufficiency of second-order moments.] Viewed as such, the quantity $\langle J_z\rangle(t)$ would represent an optimal (least square) estimate of some underlying variable $z(t)$ based on observation of a signal $d\xi(t)$, and $\langle\Delta J_z^2\rangle(t)$ would represent the uncertainty (variance) of this estimate. It thus stands to reason that we might be able to simplify our magnetometry model even further if we could find an "underlying" model for the evolution of $z(t)$ and $d\xi(t)$, for which our equations derived from the SME would be the Kalman filter.

It is not difficult to do so, and indeed a very simple model suffices,

$$dz(t) = \gamma J h(t)dt,$$

$$d\xi(t) = z(t)dt + \sqrt{\sigma_M}dW(t), \tag{A3}$$

where $dW(t)$ is an Wiener increment that is distinct from (though related to) $d\overline{W}(t)$. In order to match initial conditions with the equations derived from the SME, we should assume that the expected value of $z(t=0)$ is zero and that the variance of our prior distribution for $z(0)$ is $J/2$. Written in canonical form, the Kalman filter for this hypothetical system is then

$$d\tilde{z}(t) = \gamma J h(t)dt + \frac{\sigma_{zR}(t)}{\sqrt{\sigma_M}}\frac{[d\xi(t)-\tilde{z}(t)dt]}{\sqrt{\sigma_M}},$$

$$d\sigma_{zR}(t) = -\frac{\sigma_{zR}^2(t)}{\sigma_M}dt.$$

Here $\tilde{z}(t)$ is the optimal estimate of $z(t)$ and $\sigma_{zR}(t)$ is the variance. We exactly recover the SME model, Eqs. (A1) and (A2), by the identifications

$$\tilde{z}(t) \leftrightarrow \langle J_z\rangle(t),$$

$$\sigma_{zR}(t) \leftrightarrow \langle \Delta J_z^2\rangle(t), \tag{A4}$$

$$\frac{[d\xi(t) - \tilde{z}(t)dt]}{\sqrt{\sigma_M}} \leftrightarrow d\overline{W}(t).$$

It is important to note that the quantity $[d\xi(t)-\tilde{z}dt]/\sqrt{\sigma_M}$ represents the so-called *innovation process* of this Kalman filter, and it is thus guaranteed (by least-squares optimality of the filter [26]) to have Gaussian white-noise statistics. Hence we have solid grounds for identifying it with the Ito increment appearing in the SME.

Given this insight, we see that our original magnetometry problem can equivalently be viewed in a way that corresponds to the middle diagram of Fig. 7. In this version, we posit the existence of a hidden transducer that imprints statistical information about the magnetic field $h(t)$ onto a signal $d\xi(t)$. A Kalman filter receives this signal, and from it computes an estimate $\tilde{z}(t)$ as well as an innovation process $d\overline{W}(t)$. [Note that as indicated in the diagram, the Kalman filter will only function correctly if it "has knowledge of" the true magnetic field $h(t)$ in the way that a physical system would, but this is not an important point for what follows.] According to the model equations, the Kalman filter then emits the following signal to be received by our photodetector,

$$y(t)dt = \tilde{z}(t)dt + \sqrt{\sigma_M}d\overline{W}(t). \tag{A5}$$

Note that $d\overline{W}(t)$ now appears as an internal variable to the Kalman filter, computed from the input signal $d\xi(t)$ and the recursive estimate $\tilde{z}(t)$, while the inherent randomness is referred back to $dW(t)$. Although this may seem like an unnecessarily complicated story, it should be noted that the compound model with $z(t)$ and the Kalman filter predicts an identical transfer function from $h(t)$ to the experimentally observed signal $y(t)dt$ to that of the equations originally derived from the SME (top diagram in Fig. 7). Hence, for the purposes of analyzing and designing magnetometry schemes, these are equivalent models.

Combining several definitions above we find

$$y(t)dt = \tilde{z}(t)dt + \sqrt{\sigma_M}\frac{[d\xi(t) - \tilde{z}(t)dt]}{\sqrt{\sigma_M}} = d\xi(t). \tag{A6}$$

It thus follows that in the compound model, the Kalman filter actually implements a trivial transfer function and can in fact be eliminated from the diagram. Doing this, we obtain the simplified representation in the bottom diagram of Fig. 7. Here the perspective is to pretend that the internal dynamics of the transducing physical system corresponds to the simplified model [Eq. (A3)], since we can do so without making any error in our description of the effect of $h(t)$ on the recorded signal. We thus conclude that for the purposes of open- or closed-loop estimations of $h(t)$, filters and controllers can in fact be designed—without loss of performance—using the simplified model [Eq. (A3)].

It is interesting to note that $z(t)$ can loosely be interpreted as a "classical value" of the spin projection J_z. Since the operator J_z is a backaction evading observable, the continuous measurement we consider is quantum nondemolition and its backaction on the system state is minimal (conditioning without disturbance). Hence if $h(t)=0$, we may think of the measurement process as gradually "collapsing" the quantum state of the spin system from an initial coherent state towards an eigenstate of J_z; the hidden variable $z(t)$ in the simplified model Eq. (A3) would then represent the eigenvalue corresponding to the ultimate eigenstate, and $\tilde{z}(t)=\langle J_z\rangle(t)$ in the Kalman filter would be our converging estimate of it. (Again, this is as expected from the abstract perspective of quantum filtering theory for open quantum systems.) Conditional spin squeezing in this case can then be understood as nothing more than the reduction of our uncertainty as to the underlying value of z—as we acquire information about z through observation of $d\xi(t)=y(t)dt$, our uncertainty $\sigma_{zR}(t)\leftrightarrow\langle\Delta J_z^2\rangle \times (t)$ naturally decreases below its initial coherent-state value of $J/2$. Still, the quantum-mechanical nature of the spin system is not without consequence, as it is known that continuous QND measurement produces entanglement among the spins in the ensemble [12].

It seems worth commenting on the fact that Eq. (A3) clearly predicts stationary statistics for the photocurrent $y(t)dt$, whereas Eq. (A1) contains a time-dependent diffusion coefficient that might color the statistics of $y(t)dt=\langle J_z\rangle(t)dt + \sqrt{\sigma_M}d\overline{W}(t)$. In fact there is no discrepancy. It is possible [24] to derive the second-order time-correlation function of the observed signal $y(t)dt$ directly from the stochastic master Eq. (2),

$$\langle y(t)y(t+\tau)\rangle = [\langle J_z(t)J_z(t+\tau)\rangle + \langle J_z(t+\tau)J_z(t)\rangle]/2 + \frac{1}{4\eta M}\delta(\tau).$$

(This result could also be obtained from the standard input-output theory of quantum optics.) Since the master equation results in linear equations for the mean values $\langle J_x(t)\rangle$ and $\langle J_z(t)\rangle$ the quantum regression theorem [27] allows the correlation functions $\langle J_z(t)J_z(t+\tau)\rangle$ and $\langle J_z(t+\tau)J_z(t)\rangle$ to be calculated explicitly. In this paper we are most interested in the early time evolution for which we obtain the expressions

$$\langle y(t)\rangle = \langle J_z(t)\rangle = \gamma bJt + O(t^2),$$

$$\langle y(0)y(t)\rangle - \langle y(0)\rangle\langle y(t)\rangle = \frac{1}{4\eta M}\delta(t) + \langle\Delta J_z^2\rangle(0) + O(t^2).$$

These correlation functions correspond to a white-noise signal which is a linear ramp with gradient γbJ with a random offset of variance $\langle\Delta J_z^2\rangle(0)$, in perfect agreement with our simplified model Eq. (A3). If the statistics of $y(t)$ were Gaussian these first and second-order moments would be enough to characterize the signal completely, and indeed for sufficiently large J the problem does become effectively Gaussian.

As a final comment we note that the essential step in the above discussion is to observe that the equations for the first-and second-order moments of the quantum state derived from the stochastic master equation correspond to a Kalman filter for some classical model of a noisy measurement. This correspondence holds for the stochastic master equation corresponding to an arbitrary linear quantum mechanical systems with continuous measurement of observables that are linear combinations of the canonical variables [20]. In the general case of measurements that are not QND the equivalent classical model will have noise-driven dynamical equations as well as noise on the measured signal. The noise processes driving the dynamics and the measured signal may also be correlated. The case of position measurement of a harmonic oscillator shows all of these features [28].

APPENDIX B: RICCATI EQUATION SOLUTION METHOD

The matrix Riccati equation is ubiquitous in optimal control. Here, following Ref. [29], we show how to reduce the nonlinear problem to a set of linear differential equations. Consider the generic Riccati equation

$$\frac{d\mathbf{V}(t)}{dt} = \mathbf{C} - \mathbf{D}\mathbf{V}(t) - \mathbf{V}(t)\mathbf{A} - \mathbf{V}(t)\mathbf{B}\mathbf{V}(t).$$

We propose the decomposition

$$\mathbf{V}(t) = \mathbf{W}(t)\mathbf{U}^{-1}(t)$$

with the linear dynamics

$$\begin{bmatrix} \dfrac{d\mathbf{W}(t)}{dt} \\ \dfrac{d\mathbf{U}(t)}{dt} \end{bmatrix} = \begin{bmatrix} -\mathbf{D} & \mathbf{C} \\ \mathbf{B} & \mathbf{A} \end{bmatrix} \begin{bmatrix} \mathbf{W}(t) \\ \mathbf{U}(t) \end{bmatrix}.$$

It is straightforward to then show that this linearized solution is equivalent to the Riccati equation

$$\begin{aligned} \frac{d\mathbf{V}(t)}{dt} &= \frac{d\mathbf{W}(t)}{dt}\mathbf{U}^{-1} + \mathbf{W}(t)\frac{d\mathbf{U}^{-1}(t)}{dt} \\ &= \frac{d\mathbf{W}(t)}{dt}\mathbf{U}^{-1}(t) + \mathbf{W}(t)\left(-\mathbf{U}^{-1}(t)\frac{d\mathbf{U}(t)}{dt}\mathbf{U}^{-1}(t)\right) \\ &= [-\mathbf{D}\mathbf{W}(t) + \mathbf{C}\mathbf{U}(t)]\mathbf{U}^{-1}(t) - \mathbf{W}(t)\mathbf{U}^{-1}(t)(\mathbf{B}\mathbf{W}(t) \\ &\quad + \mathbf{A}\mathbf{U}(t))\mathbf{U}^{-1}(t) = \mathbf{C} - \mathbf{D}\mathbf{V}(t) - \mathbf{V}(t)\mathbf{A} - \mathbf{V}(t)\mathbf{B}\mathbf{V}(t), \end{aligned}$$

where we have used the identity

$$\frac{d\mathbf{U}^{-1}(t)}{dt} = -\mathbf{U}^{-1}(t)\frac{d\mathbf{U}(t)}{dt}\mathbf{U}^{-1}(t).$$

Thus the proposed solution works and the problem can be solved with a linear set of differential equations.

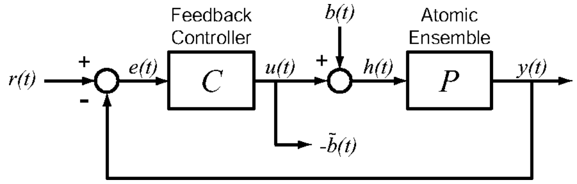

FIG. 8. Spin control system with plant transfer function $P(s) = \gamma J/s$. $r(t)$ is the reference signal, which is usually zero. $e(t)$ is the error signal. $u(t)$ is the controller output. $b(t)$ is the external field to be tracked. $h(t)=b(t)+u(t)$ is the total field. $\tilde{b}(t)$ is the field estimate.

APPENDIX C: ROBUST CONTROL IN FREQUENCY SPACE

Here we apply traditional frequency-space robust control methods [30,31] to the classical version of our system. This analysis is different from the treatment in the body of the paper in several respects. First, we assume nothing about the noise sources (bandwidth, strength, etc.). Also, this approach is meant for steady-state situations, with the resulting estimator-controller being a constant gain transfer function. The performance criterion we present here is only loosely related to the more complete estimation description above. Despite these differences, this analysis gives a very similar design procedure for the steady-state situation.

We proceed as follows with the control system shown in Fig. 8, where we label $h(t)=u(t)+b(t)$ as the total field. Consider the usual spin system but ignore noise sources and assume we can measure $z(t)$ directly, so that $z(t)=y(t)$. For small angles of rotation, the transfer function from $h(t)$ to $y(t)$ is an integrator

$$\frac{dy(t)}{dt} = \frac{dz(t)}{dt} = \gamma J h(t),$$

$$s y(s) = \gamma J h(s),$$

$$y(s) = P(s)h(s),$$

$$P(s) = \gamma J/s.$$

Now we define the performance criterion. First notice that the transfer function from the field to be measured $b(t)$ to the total field $h(t)$ is $S(s)$ where

$$h(s) = S(s)b(s),$$

$$S(s) = \frac{1}{1 + P(s)C(s)}.$$

[Also notice that this represents the transfer function from the reference to the error signal $e(s)=S(s)r(s)$.] Because our field estimate will be $\tilde{b}(t)=-u(t)$, we desire $h(t)$ to be significantly suppressed. Thus we would like $S(s)$ to be small in magnitude [controller gain $|C(s)|$ large] in the frequency range of interest. However, because the gain $|C(s)|$ must physically decrease to zero at high frequencies we must close the feedback loop with adequate phase margin to keep the closed-loop system stable. This is what makes the design of $C(s)$ nontrivial.

Proceeding, we now define a function $W_1(s)$ which represents the degree of suppression we desire at the frequency $s=j\omega$. So our controller $C(s)$ should satisfy the following performance criterion:

$$\|W_1(s)S(s)\|_\infty < 1.$$

Thus the larger $W_1(s)$ becomes, the more precision we desire at the frequency s. We choose the following performance function:

$$W_1(s) = \frac{W_{10}}{1 + s/\omega_1},$$

such that ω_1 is the frequency below which we desire suppression $1/W_{10}$.

Because our knowledge of J is imperfect, we need to consider all plant transfer functions in the range

$$P = \frac{\gamma}{s}\{J_{\min} \to J_{\max}\}.$$

Our goal is now to find a $C(s)$ that can satisfy the performance condition for any plant in this family. We choose our nominal controller as

$$C_0(s) = \frac{\omega_C}{\gamma J'}.$$

So if $J=J'$ then the system closes at ω_C (i.e., $|P(i\omega_C)C_0(i\omega_C)|=1$, whereas in general the system will close at $\omega_{CR}=\omega_C(J/J')$. We choose this controller because $P(s)C(s)$ should be an integrator ($\propto 1/s$) near the closing frequency for optimal phase margin and closed-loop stability.

Next we insert this solution into the performance condition. We make the simplifying assumption $\omega_1 \ll \omega_C(J/J')$ (we will check this later to be self-consistent). Then the optimum of the function is obvious and the condition of Eq. (C1) becomes

$$\omega_1 W_{10} < \omega_{CR} = \omega_C \frac{J}{J'}.$$

We want this condition to be satisfied for all possible spin numbers, so we must have

$$\omega_1 W_{10} = \min[\omega_{CR}] = \omega_C \frac{J_{\min}}{J'}. \tag{C1}$$

Experimentally, we are forced to rolloff the controller at some high frequency that we shall call ω_Q. Electronics can only be so fast. Of course, we never want to close above this frequency because the phase margin would become too small, so this determines the maximum J that the controller can reliably handle

$$\omega_Q = \max[\omega_{CR}] = \omega_C \frac{J_{\max}}{J'}. \tag{C2}$$

Combining Eqs. (C1) and (C2) we find our fundamental tradeoff

$$\omega_1 W_{10} = \omega_Q \frac{J_{\min}}{J_{\max}} \tag{C3}$$

which is the basic result of this section. Given experimental constraints (such as $J_{\min}$, $J_{\max}$, and ω_Q), it tells us what performance to expect ($1/W_{10}$ suppression) below a chosen frequency ω_1.

From Eq. (C3), we recognize that the controller gain at the closing frequency needs to be

$$|C|_C = \frac{\omega_C}{\gamma J'} = \frac{\omega_1 W_{10}}{\gamma J_{\min}} = \frac{\omega_Q}{\gamma J_{\max}}.$$

In the final analysis, we do not need to use J' and ω_C to parametrize the controller, only the tradeoff and the gain. Also, notice that now we can express $\min[\omega_{CR}]=\omega_1 W_{10}$.

To check our previous assumption

$$\omega_1 \ll \omega_C \frac{J}{J'}$$

$$= \omega_1 W_{10} \frac{J}{J_{\min}},$$

which is true if $W_{10} \gg 1$.

Finally, the system will never close below the frequency $\min[\omega_{CR}]$ so we should increase the gain below a frequency ω_H which we might as well set equal to $\min[\omega_{CR}]$. This improves the performance above and beyond the criterion above. Of course we will be forced to level off the gain at some even lower frequency ω_L because infinite dc gain (a real integrator) is unreasonable. So the final controller can be expressed as

$$C(s) = |C|_C \frac{1}{1 + s/\omega_Q} \frac{\omega_H(1 + s/\omega_H)}{\omega_L(1 + s/\omega_L)}$$

with the frequencies obeying the order

$$\omega_L <$$

$$\omega_H = \min[\omega_{CR}] = \omega_1 W_{10} <$$

$$\omega_{CR} = \frac{J}{J_{min}} \omega_1 W_{10} <$$

$$\omega_Q = \max[\omega_{CR}] = \frac{J_{max}}{J_{min}} \omega_1 W_{10}.$$

Notice that the controller now looks like the steady-state transfer function in Fig. 3 derived from the steady state of the full dynamic filter. (The notation is the same to make this correspondence clear). Here ω_Q was simply stated, whereas there it was a function of λ that went to infinity as $\lambda \to \infty$. Here the high gain due to ω_L and ω_H was added manually, whereas before it came from the design procedure directly.

[1] M. A. Armen, J. K. Au, J. K. Stockton, A . C. Doherty, and H. Mabuchi, Phys. Rev. Lett. **89**, 133602 (2002).

[2] J. M. Geremia, J. K. Stockton, and H. Mabuchi, e-print quant-ph/0401107.

[3] W. P. Smith, J. E. Reiner, L. A. Orozco, S. Kuhr, and H. M. Wiseman, Phys. Rev. Lett. **89**, 133601 (2002).

[4] N. V. Morrow, S. K. Dutta, and G. Raithel, Phys. Rev. Lett. **88**, 093003 (2002).

[5] T. Fischer, P. Maunz, P. W. H. Pinkse, T. Puppe, and G. Rempe, Phys. Rev. Lett. **88**, 163002 (2002).

[6] F. Verstraete, A. C. Doherty, and H. Mabuchi, Phys. Rev. A **64**, 032111 (2001).

[7] J. Gambetta and H. M. Wiseman, Phys. Rev. A **64**, 042105 (2001).

[8] H. Mabuchi, Quantum Semiclassic. Opt. **8**, 1103 (1996).

[9] V. Belavkin, Rep. Math. Phys. **43**, 405 (1999).

[10] M. Kitagawa and M. Ueda, Phys. Rev. A **47**, 5138 (1993).

[11] A. Kuzmich, L. Mandel, and N. P. Bigelow, Phys. Rev. Lett. **85**, 1594 (2000).

[12] J. K. Stockton, J. Geremia, A. C. Doherty, and H. Mabuchi, Phys. Rev. A **67**, 022112 (2003).

[13] D. J. Wineland, J. J. Bollinger, W. M. Itano, and D. J. Heinzen, Phys. Rev. A **50**, 67 (1994).

[14] G. A. Smith, S. Chaudhury, and P. S. Jessen, J. Opt. B: Quantum Semiclassical Opt. **5**, 323 (2003).

[15] I. K. Kominis, T. W. Kornack, J. C. Allred, and M. Romalis, Nature (London) **422**, 596 (2003).

[16] D. Budker, W. Gawlik, D. Kimball, S. Rochester, V. Yashchuk, and A. Weiss, Rev. Mod. Phys. **74**, 1153 (2002).

[17] J. M. Geremia, J. K. Stockton, A. C. Doherty, and H. Mabuchi, Phys. Rev. Lett. **91**, 250801 (2003).

[18] A. Silberfarb and I. Deutsch, Phys. Rev. A **68**, 013817 (2003).

[19] L. K. Thomsen, S. Mancini, and H. M. Wiseman, Phys. Rev. A **65**, 061801 (2002).

[20] A. C. Doherty and H. M. Wiseman (in preparation).

[21] O. L. R. Jacobs, *Introduction to Control Theory*, 2nd ed. (Oxford University Press, New York, 1996).

[22] C. W. Gardiner, *Handbook of Stochastic Methods*, 2nd ed. (Springer, New York, 1985).

[23] G. L. Bretthorst, *Bayesian Spectrum Analysis and Parameter Estimation* (Springer-Verlag, Berlin, 1988).

[24] H. M. Wiseman and G. J. Milburn, Phys. Rev. A **47**, 642 (1993).

[25] T. Holstein and H. Primakoff, Phys. Rev. **58**, 1098 (1940).

[26] B. Oksendal, *Stochastic Differential Equations*, 5th ed. (Springer-Verlag, Berlin, 1998).

[27] D. F. Walls and G. J. Milburn, *Quantum Optics* (Springer-Verlag, Berlin, 1994).

[28] A. C. Doherty, S. M. Tan, A. S. Parkins, and D. F. Walls, Phys. Rev. A **60**, 2380 (1999).

[29] W. T. Reid, *Riccati Differential Equations* (Academic, New York, 1972).

[30] J. Doyle, B. Francis, and A. Tannenbaum, *Feedback Control Theory* (Macmillan Co., New York, 1990).

[31] K. Zhou and J. C. Doyle, *Essentials of Robust Control*, 1st ed. (Prentice-Hall, Englewood Cliffs, NJ, 1997).

[32] We assume throughout the paper that we have a system of N spin-$1/2$ particles, so for a polarized state along $x,\langle J_x\rangle = J = N/2$ and $\sigma_{z0} = \langle \Delta J_z^2\rangle(0) = J/2 = N/4$. This is an arbitary choice and our results are indepent of any constituent spin value, apart from defining these moments. In Ref. [2], for example, we work with an ensemble of Cs atoms, each atom in a gorond state of spin 4.

PHYSICAL REVIEW B **68**, 235328 (2003)

Feedback cooling of a nanomechanical resonator

Asa Hopkins,[1,2] Kurt Jacobs,[1] Salman Habib,[1] and Keith Schwab[3]
[1]*T-8, Theoretical Division, Los Alamos National Laboratory, Los Alamos, New Mexico 87545, USA*
[2]*Norman Bridge Laboratory of Physics 12-33, California Institute of Technology, Pasadena, California 91125, USA*
[3]*Laboratory for Physical Sciences, College Park, Maryland 20740, USA*

(Received 25 February 2003; revised manuscript received 2 July 2003; published 24 December 2003)

Cooled, low-loss nanomechanical resonators offer the prospect of directly observing the quantum dynamics of mesoscopic systems. However, the present state of the art requires cooling down to the milliKelvin regime in order to observe quantum effects. Here we present an active feedback strategy based on continuous observation of the resonator position for the purpose of obtaining these low temperatures. In addition, we apply this to an experimentally realizable configuration, where the position monitoring is carried out by a single-electron transistor. Our estimates indicate that with current technology this technique is likely to bring the required low temperatures within reach.

DOI: 10.1103/PhysRevB.68.235328 PACS number(s): 85.85.+j, 85.35.Gv, 03.65.Ta, 45.80.+r

I. INTRODUCTION

Nanomechanical resonators are now being built with quality factors in the range, $Q \approx 10^4$, and resonance frequencies of up to several hundred MHz.[1] The ground state energy of these devices can correspond to temperatures in the milliKelvin range. As a result, the observation of quantum behavior in these devices is becoming a real possibility.[2] To detect such behavior, the resonator must be sufficiently cold; since a quantum harmonic oscillator driven by thermal noise behaves as a classical oscillator driven by thermal noise, one must ensure that the signatures of quantum effects are not swamped by the thermal behavior. The approach taken so far to achieve low temperatures is to place the resonator in a refrigerator. However, cooling very small devices in this way is inherently inefficient in that the system becomes weakly coupled to the thermal bath. Here we explore the possibility of using feedback control to effect an ‘‘active’’ cooling of the resonator, in order to cool below the possible limits set by the ‘‘passive’’ refrigeration technique.

To perform such feedback cooling the resonator must be monitored, and the result fed back in real time to affect the dynamics. A practical method of performing a continuous measurement of the position of the resonator is to use a single-electron transistor (SET).[3–5] To measure the position of the resonator one locates the central island of the SET next to the resonator. When the resonator is charged, and the SET is biased so that current flows through it, changes in the resonator's position alter the potential on the central island, which in turn changes the current. The current therefore provides a continuous measurement of the position of the resonator, and this is just what is required for implementing a linear feedback cooling algorithm.[6,7] A feedback force can be applied by applying a voltage to a gate capacitively coupled to the resonator, and adjusting the voltage so as to damp the resonator (see Fig. 1), or by passing a variable current through the oscillator in the presence of a fixed external magnetic field. We will analyze the first system, although the results should apply to the second as well. In our analysis we will use the theory of the dc-SET. While an experiment would most likely use a radio-frequency SET,[8,20] the characteristic frequency of a SET is typically of the order of 10 GHz, so that the rf drive looks constant to the SET, and the dc-SET equations can be used.

We will use a quantum mechanical model of the measurement and feedback process, but discuss how, in this case, such a description is equivalent to a classical measurement of a noisy classical system. Thus, this paper is intended for both experimentalists familiar with classical descriptions of noise in systems as well as quantum measurement theorists.

Rather than performing a microscopic analysis of the measurement process in terms of the interaction of the SET and the resonator, we start by introducing equations which describe the continuous observation of a quantum observable, and show how this includes the shot noise and back-action, these being the key sources of noise in a continuous quantum measurement. This description can then be tailored to the case of a measurement with a SET by choosing the parameters so that the noise sources match those calculated in microscopic noise analyses which have been performed for the SET.[3,8]

A treatment of the continuous quantum measurement of a two-state system using a SET has been carried out by Korotkov,[9] using what might be referred to as a partially

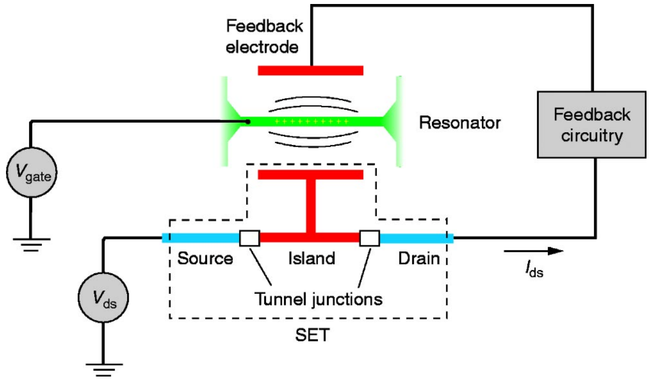

FIG. 1. A schematic of the resonator, measuring, and feedback apparatus. As the resonator moves closer to the SET, the current flowing through the SET changes, and that information is then used to generate a feedback voltage applied to an actuating gate.

©2003 The American Physical Society

microscopic approach. The equations we use here may be derived by replacing the two-state observable in those equations by the resonator position.[10] A full analysis, along the lines of those performed for quantum optical systems,[11,12] can also be expected to produce the same equations under reasonable approximations. The form of these equations is determined by how information is obtained, and not by the specific implementation, which explains why the form of the equations is similar in optical position measurements and position measurement using SETs. If the measurement is of a physical observable, and the resulting error about the expectation value of that observable in a short time interval Δt is Gaussian, then the most straightforward implementation of that measurement process has the form used here.

In Sec. II we introduce the equations that describe a continuous measurement process, derive the form of the resulting noise, and give the equivalent classical model. We then discuss how this model can be applied to position measurement using a SET, and compare our formulas to those derived using a semiclassical treatment of the SET (Refs. 3 and 8) in order to express our results in terms of experimental parameters. In Sec. III we discuss the implementation of a feedback algorithm and calculate the minimum achievable temperature in terms of physical parameters. We then calculate estimates of realistic achievable temperatures for an an experimentally realizable sample system in Sec. IV, and finally conclude with a summary of the results obtained.

II. CONTINUOUS QUANTUM MEASUREMENT OF POSITION

Given a quantum system whose state is specified by the density matrix ρ, and whose evolution is determined by the Hamiltonian H, then a continuous measurement of the observable O of that system, which provides the continuous output results (measurement record),

$$dr=\langle O\rangle dt+\frac{1}{\sqrt{8k}}dW, \tag{1}$$

induces the following evolution of the system:[6,13,14]

$$\begin{aligned} d\rho=&-(i/\hbar)[H,\rho]dt-k[O,[O,\rho]]dt\\ &+\sqrt{2k}(O\rho+\rho O-2\langle O\rangle\rho)dW. \end{aligned} \tag{2}$$

Here k is proportional to the measurement strength, and dW is a Weiner process. The noise contained in the measurement record is a necessary result of the fact that only a finite amount of information is obtained regarding the observable O in a finite time. This direct noise on the record is called the *shot noise*. However, this is not the only noise resulting from the measurement process. As a result of Heisenberg's uncertainty relation, information about one observable makes other observables less certain. Due to the dynamics, the uncertainty (noise) in these observables can feed into the observable being measured. This source of noise is referred to as *back-action*. If the Hamiltonian is such that the increased uncertainty is not fed back into the observable being measured, then the measurement is referred to as "back-action evading."

Now let us examine the case of a position measurement on a harmonic oscillator. To do this, we set $O=x$, and the Hamiltonian becomes

$$H=\frac{p^2}{2m}+\frac{1}{2}m\omega_0^2x^2, \tag{3}$$

where m is the mass of the particle, ω_0 is the (angular) frequency of the oscillation, and x and p are the position and momentum operators, respectively. To make our model sufficiently realistic, we need to include two more sources of noise: the first is the intrinsic thermal noise of the harmonic oscillator, and the second is the possibility that the oscillator may be driven by white noise over and above that required by Heisenberg's uncertainty principle (excess "technical noise").

The second of these is easily included by adding a term $-\beta[x,[x,\rho]]$ to the equation of motion of ρ; this describes a noise term identical to the one caused by the back-action, but without the corresponding dynamics of ρ associated with obtaining a measurement result which causes the back-action. It is equivalent to adding a term linear in x to Hamiltonian (3) multiplied by white noise.

The inclusion of thermal fluctuations is only a little more involved, and can be achieved by coupling the oscillator to a thermal bath. In our case the effect of the thermal bath may be included by adding the "standard Brownian motion master equation" (SBMME) (Ref. 15) to our equation of motion for ρ:

$$\begin{aligned} d\rho=&-\frac{i}{\hbar}[H,\rho]dt-\frac{i\Gamma}{2\hbar}[x,\{p,\rho\}_+]dt\\ &-\left(k+\beta+\frac{m\omega_0\Gamma}{2\hbar}\coth\frac{\hbar\omega_0}{2k_BT}\right)[x,[x,\rho]]dt\\ &+\sqrt{2k}(x\rho+\rho x-2\langle x\rangle\rho)dW, \end{aligned} \tag{4}$$

where $\Gamma=\omega/Q$, Q being the quality factor of the resonator. The two terms proportional to Γ are due to the inclusion of the SBMME, the first representing dissipation due to the reservoir while the second is a diffusion term due to environmental fluctuations. Here we are using an approximate form of the SBMME appropriate for the weak coupling regime (small Γ, large Q) but covering all ranges of temperatures.[16] Since the nanomechanical resonators we consider all have large values of Q, the weak coupling requirement is easily satisfied. The temperature dependence of the diffusion coefficient is given by $\coth(\hbar\omega_0/2k_BT)$ so that the diffusion does not vanish as $k_BT\rightarrow 0$: this correctly accounts for the existence of quantum vacuum fluctuations which exist even at zero temperature. In the absence of a rigorous characterization of the dissipation channels of nanomechanical systems there is as yet no need to include a more sophisticated description of SBMME environmental effects.[17] Phenomenological corrections to the SBMME such as the temperature dependence of Γ can be added if needed, but these are not significant effects in the high-Q regime.

We also need to include in our model the possibility that there is noise driving the oscillator which is correlated with the noise on the measurement record (the shot noise). This can happen if the noisy behavior of the oscillator explicitly causes some of the noise in the measurement apparatus, or vice versa. In this situation, the measurement record contains more information about the oscillator position, so when it comes to adding feedback, we are able to cool the oscillator further than would otherwise be expected. In Eq. (2) the noise driving the oscillator is purely the quantum back-action. It may appear from Eqs. (1) and (2) that the quantum back-action is correlated with the shot noise due to the fact that the same noise term (dW) appears in both equations. However, this is not the case. The term proportional to dW which appears in the equation for ρ describes the random way in which the measurement changes the observers state of knowledge about the system. Thus, on average, this noise term *decreases* the entropy of ρ. The back-action noise, which is driving the oscillator and consequently *increasing* the entropy of ρ, is described by the term proportional to k. The quantum back-action is, in fact, completely uncorrelated with the shot noise.

To drive the oscillator with a random force, one applies the Hamiltonian $\hbar\xi(t)x$, where $\xi(t)$ is the magnitude of the random force. We can choose $\xi(t)$ to be correlated with the shot noise, with the correlation coefficient κ, by setting

$$d\xi=\sqrt{2\alpha}(\sqrt{\kappa}dW+\sqrt{1-\kappa}dV), \tag{5}$$

where dV is a Wiener noise uncorrelated with dW. The resulting spectral density of $\xi(t)$ is α, so that $\langle\xi(t)\xi(t')\rangle=\alpha\delta(t-t')$. The Stratonovich equation which describes the driving by $\xi(t)$ is

$$|\dot{\psi}\rangle=-i\xi(t)x|\psi\rangle, \tag{6}$$

and converting this to an Ito equation gives

$$d|\psi\rangle=-i\sqrt{2\alpha}x|\psi\rangle d\xi-\alpha x^2|\psi\rangle dt. \tag{7}$$

Converting the Ito equation further to an equation for ρ one obtains

$$d\rho=-\alpha[x,[x,\rho]]dt-i\sqrt{2\alpha}[x,\rho]d\xi. \tag{8}$$

Since the observer has access to dW, but not to dV, she must average over dV, and this gives

$$d\rho=-\alpha[x,[x,\rho]]dt-i\sqrt{2\kappa\alpha}[x,\rho]dW. \tag{9}$$

If we allow part of the excess noise given by β in our model to be due to driving by the shot noise dW (that is, this noise is correlated with the shot noise dW with correlation coefficient κ) then the equation of motion for the system becomes

$$\begin{aligned} d\rho=&-\frac{i}{\hbar}[H,\rho]dt-\frac{i\Gamma}{2\hbar}[x,\{p,\rho\}_+]dt \\ &-\left(k+\beta+\frac{m\omega_0\Gamma}{2\hbar}\coth\frac{\hbar\omega_0}{2k_BT}\right)[x,[x,\rho]]dt \\ &-i\sqrt{2\kappa\beta}[x,\rho]dW+\sqrt{2k}(x\rho+\rho x-2\langle x\rangle\rho)dW. \end{aligned} \tag{10}$$

This completes our quantum mechanical description of a resonator under continuous observation.

Now that we have an equation that includes all the relevant noise terms, the noise spectrum of the measurement record can be obtained:

$$\begin{aligned} S(\omega)=&\frac{1}{8k}+\left(k+\beta+\frac{m\omega_0\Gamma}{2\hbar}\coth\frac{\hbar\omega_0}{2k_BT}\right) \\ &\times\ \frac{2(\hbar/m)^2}{\Gamma^2\omega^2+(\omega^2-\omega_0^2)^2}. \end{aligned} \tag{11}$$

The first term is the shot noise, which is white, the term proportional to k is the quantum back-action, the term proportional to Γ is the effect of the noise from the resonator's thermal environment, and the term proportional to β gives any excess noise over and above the necessary quantum back-action. Note that the last three terms all have the same form as a function of ω. This is because they are all white noises filtered through the harmonic oscillator spectral response function.

While our treatment so far has been fully quantum mechanical, it is worth noting that a purely classical model of a measured, damped oscillator will completely reproduce the dynamics of this measured quantum system, no matter how cold the resonator, so long as the initial density matrix is Gaussian in x and p.[6] Thus, one can understand the behavior of the oscillator in terms of classical noise and a classical measurement process. The equations of motion for the position x_{c} and momentum p_{c} of this equivalent classical oscillator are

$$dx_{\mathrm{c}}=\frac{1}{m}p_{\mathrm{c}}dt, \tag{12}$$

$$\begin{aligned} dp_{\mathrm{c}}=&-m\omega_0^2x_{\mathrm{c}}dt-\Gamma p_{\mathrm{c}}dt+\hbar\sqrt{2k}dY_{\mathrm{c}}+\hbar\sqrt{2\beta}dV_{\mathrm{c}} \\ &+\sqrt{m\hbar\omega_0\Gamma\coth\frac{\hbar\omega_0}{2k_BT}}dU_{\mathrm{c}}, \end{aligned} \tag{13}$$

where dY_{c}, dV_{c}, and dU_{c} are each zero-mean Gaussian white noise, and mutually uncorrelated. The position of the oscillator is then observed by a continuous classical measurement, which generates the output record

$$dr_{\mathrm{c}}=x_{\mathrm{c}}dt+\frac{1}{\sqrt{8k}}dZ_{\mathrm{c}}, \tag{14}$$

and where dZ_{c} is zero-mean Gaussian white noise, uncorrelated with dY_{c}. The noise term dY_{c} is what is required in the classical model to correctly include the back-action of the quantum measurement process. It is now explicit that this noise is uncorrelated with the shot noise on the measurement, $dZ_{\rm c}$.

In the classical case, the observer's state of knowledge about the oscillator is given by a joint probability density over $x_{\rm c}$ and $p_{\rm c}$. This probability density is the classical equivalent of the density matrix ρ. So long as the initial probability density is Gaussian, it remains Gaussian as time passes, and as a result the observer's full state of knowledge may be represented by merely five variables: the mean position and momentum, $\langle x_{\rm c}\rangle$ and $\langle p_{\rm c}\rangle$, and the variances and covariance, given by

$$\sigma_x^2=\langle x_{\rm c}^2\rangle-\langle x_{\rm c}\rangle^2, \tag{15}$$

$$\sigma_p^2=\langle p_{\rm c}^2\rangle-\langle p_{\rm c}\rangle^2, \tag{16}$$

$$\sigma_{xp}^2=\langle x_{\rm c}p_{\rm c}\rangle-\langle x_{\rm c}\rangle\langle p_{\rm c}\rangle. \tag{17}$$

It is the means $\langle x_{\rm c}\rangle$ and $\langle p_{\rm c}\rangle$ (being the observer's best estimates of the value of $x_{\rm c}$ and $p_{\rm c}$)which are the classical equivalents of the quantum expectation values $\langle x\rangle$ and $\langle p\rangle$. It turns out that if one writes the classical measurement record as

$$dr_{\rm c}=\langle x_{\rm c}\rangle dt+\frac{1}{\sqrt{8k}}dW_{\rm c}, \tag{18}$$

then $dW_{\rm c}$ is zero-mean Gaussian white noise,[7] uncorrelated with $dZ_{\rm c}$. The classical model is then equivalent to the quantum model if we equate $dW_{\rm c}$ with the quantum measurement noise, dW, and correlate $dV_{\rm c}$ with $dW_{\rm c}$, so that $\langle V_{\rm c}(t)W_{\rm c}(t')\rangle=\kappa\delta(t-t')$.

III. CONTINUOUS MEASUREMENT WITH A SINGLE-ELECTRON TRANSISTOR

Having obtained a model which is sufficiently general to encompass the dynamics of a resonator monitored by a SET, we need to express the theoretical parameters k, β, and κ in terms of the actual experimental parameters of the SET. Since it is by measuring current through the SET that we measure the resonator position, it is the spectral density of this current which determines the shot noise of the measurement. The back-action from the measurement is due to the action of the SET on the resonator, which is the force that the resonator feels from the charge on the SET island. As a result the back-action noise β can be calculated from the spectral density of the charge fluctuations on the SET island, and hence κ is determined by the correlation between the current and the island charge fluctuations.

However, the dynamics of the SET are sufficiently complex that analytic results for these spectra have as yet only been obtained for certain parameter regimes. These calculations have been performed by Zhang and Blencowe,[8] using previous results of Korotkov.[3] The technique used is to approximate the dynamics of the electron tunneling on and off the SET island by a classical master equation. That is, the electrons are assumed to tunnel independently across each of the junctions, with certain rates (the rates being obtained using a perturbative quantum calculation). This ignores the possibility that electrons will tunnel coherently across both junctions simultaneously, a quantum effect referred to as *cotunneling*. This method may be referred to as a "semiclassical" model for the dynamics of the SET, and it is the model that we will use here.

It is important to note that the above semiclassical method for calculating the charge fluctuations, does not include the quantum back-action noise. This can be seen from the following argument.[18] In the classical treatment, since the fluctuating force on the resonator is due to the electrons jumping on and off the island, in principle the time history of this force can be known by detecting the electrons flowing in the circuit. In principle, then, the effect of the noise can be known, and if desired, undone. As a result it cannot include the quantum back-action, since this cannot, even in principle, be undone. Thus, the charge fluctuations calculated using the semiclassical SET model gives the excess noise β and the current shot noise gives k.

The quantum mechanical measurement model, [Eqs. (1) and (2)], describe a valid quantum measurement for any value of k and β, However, the classical model of the SET will only give an accurate description of the dynamics of the SET, and thus of the true values of k and β, in certain parameter regimes. In fact, it is useful to note that the ratio k/β provides a diagnostic tool for determining when the classical calculation breaks down; if $k/\beta\ll 1$ is not satisfied, then the classical calculation no longer provides a good estimate of the total force noise on the resonator. Thus it should be noted that if $k/\beta\gtrsim 1$, then the classical calculation cannot be relied upon. That is, it is possible in this case that the total noise on the resonator is significantly larger than our estimate $k+\beta$, due to quantum contributions not taken into account in the classical calculation.

We find that in the regions of best cooling, which we explore in the following, k is not necessarily much smaller than β (although near-optimal cooling can be obtained with $k\ll\beta$, and in particular we will give as an example results for $k=\beta/10$). Hence our calculations should be regarded as estimates of the performance of the feedback algorithm, rather than exact results. We note, however, that a more sophisticated analysis using the diagrammatic techniques developed by Schoeller and Schön[19] might provide analytic, or semianalytic results for the parameter regime of most interest for quantum measurement and control, and therefore may provide a method for more accurate calculations.

The spectral densities given by the classical calculation are derived in the Appendix. Approximations which are used in the derivation are detailed there, and come primarily from Zhang and Blencowe.[8] The noise spectrum of the displacement of the resonator due to the shot noise of the SET current is

$$S_X^I=\frac{S_{\rm I}(\omega)}{(dI_{\rm ds}/dx)^2}, \tag{19}$$

where $S_I(\omega)$ is the spectral density of the shot noise, given in Eq. (A10), and I is the current through the SET, given in Eq. (A8). The dependence of the current on the displacement of the resonator comes from its dependence on the gate capacitance, which can be approximated by

$$C_{\mathrm{g}} \approx C_{g0}\left(1-\frac{x}{d}\right). \tag{20}$$

The shot noise $S_I(\omega)$ is, to a very good approximation, frequency independent, as required by our quantum measurement model. Thus

$$\frac{1}{8k} = S_X^I\bigg|_{\omega=0} = \frac{S_I(\omega)}{(dI_{\mathrm{ds}}/dx)^2}\bigg|_{\omega=0}. \tag{21}$$

The spectral density of the classical part of the displacement noise due to the fluctuating force on the resonator is

$$S_X^{\mathrm{F}}(\omega) = \frac{S_{\mathrm{F}}(\omega)/m^2}{\Gamma^2\omega^2 + (\omega^2-\omega_0^2)^2}, \tag{22}$$

where $S_{\mathrm{F}}(\omega)$ is the spectral density of the fluctuating force given in Eq. (A13). Since, once again, $S_{\mathrm{F}}(\omega)$ is effectively frequency independent, we have

$$\beta = \frac{S_{\mathrm{F}}}{2\hbar^2}\bigg|_{\omega=0}. \tag{23}$$

The correlation coefficient, κ, between the shot noise and the excess back-action is therefore simply the correlation C between S_I and S_{F}, which is given in Eq. (A11).

IV. FEEDBACK CONTROL

We wish to cool the dynamics of the resonator by using the information obtained continuously about the state of the resonator to direct a time-dependent external force. Such a force may be applied, for example, by passing current through the resonator and immersing it in a magnetic field. It can also be applied by placing an actuating gate near the resonator, and varying the potential difference between the charged resonator and the actuating gate.

In this case the results of modern optimal control theory apply, since the dynamics of the resonator are equivalent to that of a classical oscillator driven by Gaussian noise, so long as we restrict ourselves to a linear external force.[6,21] This allows us to obtain the optimal feedback algorithm in a straightforward manner. Choosing the minimization of the energy of the resonator as the feedback objective it turns out that as long as the force we apply is sufficiently large, this force should be chosen to be[6]

$$F = -\gamma(m\omega_0\langle x\rangle + \langle p\rangle), \tag{24}$$

where γ is a rate constant which determines the overall strength of the force. This equation gives an optimal performance so long as $\gamma \gg \omega_0$, which is within reach of current experiments, as detailed below.

To calculate the average energy of the controlled resonator, we first need the equations of motion for the means and covariances of x and p in the continually observed and controlled case. To derive these equations, we note that the equation of motion for ρ, under feedback, is given by Eq. (10), where one sets

$$H = \frac{p^2}{2m} + \frac{1}{2}m\omega_0^2x^2 - \gamma(m\omega_0\langle x\rangle + \langle p\rangle)x \tag{25}$$

to include the feedback force. Using the fact that $d\langle O\rangle = \mathrm{Tr}[O\,d\rho]$, and $dW^2 = dt$, one obtains, for the means,

$$d\langle x\rangle = \frac{\langle p\rangle}{m}dt + 2\sqrt{2k}\sigma_x^2 dW, \tag{26}$$

$$\begin{aligned} d\langle p\rangle = {} & -m\omega^2\langle x\rangle dt - \Gamma\langle p\rangle dt - \gamma(m\omega\langle x\rangle + \langle p\rangle)dt \\ & + \sqrt{2\kappa\beta}\hbar\, dW + 2\sqrt{2k}\sigma_{xp}^2 dW, \end{aligned} \tag{27}$$

and, for the covariances,

$$\dot{\sigma}_x^2 = \frac{2}{m}\sigma_{xp}^2 - 8k(\sigma_x^2)^2, \tag{28}$$

$$\begin{aligned} \dot{\sigma}_p^2 = {} & -2m\omega^2\sigma_{xp}^2 - 8k(\sigma_{xp}^2)^2 - 2\Gamma\sigma_p^2 + 2\hbar^2k \\ & + 2\hbar^2\left[(1-\kappa)\beta + \frac{m\omega_0\Gamma}{2\hbar}\coth\frac{\hbar\omega_0}{2k_BT}\right], \end{aligned} \tag{29}$$

$$\dot{\sigma}_{xp}^2 = \frac{\sigma_p^2}{m} - m\omega^2\sigma_x^2 - \frac{\Gamma}{2}\sigma_{xp}^2 - 8k\sigma_x^2\sigma_{xp}^2 - 4\sqrt{\kappa\beta k}\hbar\sigma_x^2. \tag{30}$$

In these equations, σ_x^2 and σ_p^2 are the variances in position and momentum, respectively, and

$$\sigma_{xp}^2 = \frac{1}{2}\langle xp + px\rangle - \langle x\rangle\langle p\rangle \tag{31}$$

is the symmetrized covariance. This system of equations is exactly equivalent to Eq. (10) as long as the initial state is Gaussian. In order to solve this set of equations most easily, we make what we call the truncated Gaussian approximation. We assume that the feedback rate γ is much larger than the system's small intrinsic damping Γ, and we therefore drop all damping terms proportional to Γ from the above equations. This approximation is easily justified for current experiments.

The steady-state solutions to these equations are

$$\sigma_x^2 = \frac{\sqrt{2}\omega}{8k}\sqrt{\Lambda}, \tag{32}$$

$$\sigma_p^2 = \frac{\sqrt{2}m^2\omega^3}{8k}[\sqrt{\Lambda} + \Lambda^{3/2}] + \frac{\hbar m\omega}{\sqrt{2k}}\sqrt{\kappa\beta}\sqrt{\Lambda}, \tag{33}$$

$$\sigma_{xp}^2 = \frac{m\omega^2}{8k}\Lambda, \tag{34}$$

where

$$\Lambda+1 = \left[1+16\frac{k\hbar^2\left\{k+(1-\kappa)\beta+\frac{m\omega_0\Gamma}{2\hbar}\coth\frac{\hbar\omega_0}{2k_BT}\Bigr)\Bigr)\right\}}{m^2\omega^4}\right]^{1/2}. \tag{35}$$

In the limit of both large and small values of k, $\Lambda \sim k$.

The average energy of the resonator under feedback control, being the expectation value of the Hamiltonian [Eq. (25)] averaged over all trajectories, is a linear combination of the variances of x and p, since the expectation values of both x and p are zero. These variances are the sum of the intrinsic variances of the Gaussian steady state for each trajectory, and the variances of the means of x and p for each trajectory (usually referred to as the *conditional* means) across all trajectories. We can calculate these latter variances, which we will denote by $\sigma^2_{\langle x\rangle}$ and $\sigma^2_{\langle p\rangle}$, by substituting into Eqs. (26) and (27) the solutions for the steady-state values of the variances σ_x^2 and σ_{xp}^2, and solving for the first and second moments of the conditional means.[22] One obtains

$$\sigma^2_{\langle x\rangle} = \frac{\omega(\gamma^2+\gamma\omega+\omega^2)}{8k\gamma(\omega+\gamma)}\Lambda + \frac{\sqrt{2}\omega^2}{8k(\omega+\gamma)}\Lambda^{3/2} + \frac{\omega^3}{16k\gamma(\omega+\gamma)}\Lambda^2 + \frac{\kappa\beta\hbar^2}{m^2\omega\gamma(\omega+\gamma)} + \frac{\hbar\sqrt{\kappa\beta k}}{2km(\omega+\gamma)}\left[\sqrt{2\Lambda}+\frac{\omega\Lambda}{2\gamma}\right] \tag{36}$$

$$\sigma^2_{\langle p\rangle} = \frac{m^2\omega^3(\omega+\gamma)}{8k\gamma}\Lambda + \frac{m^2\omega^4}{16k\gamma}\Lambda^2 + \frac{\kappa\beta\hbar^2}{\gamma} + \frac{m\omega^2\hbar\sqrt{\kappa\beta k}}{4k\gamma}\Lambda. \tag{37}$$

Thus the average energy of the oscillator, under feedback, is

$$E = \frac{1}{2}m\omega^2(\sigma_x^2+\sigma^2_{\langle x\rangle}) + \frac{\sigma_p^2+\sigma^2_{\langle p\rangle}}{2m} \tag{38}$$

$$= \frac{m\omega^3}{8k}\left[\sqrt{2\Lambda}+\Lambda+\frac{\sqrt{2}}{2}\Lambda^{3/2}+\frac{\omega}{4\gamma}\Lambda^2\right] + \frac{\kappa\beta\hbar^2}{2m\gamma} + \frac{\hbar\omega\sqrt{\kappa\beta k}}{4k}\left[\sqrt{2\Lambda}+\frac{\omega}{2\gamma}\Lambda\right]. \tag{39}$$

Here we have used the simplifying assumption $\gamma \gg \omega$, since this is inherent in the optimal control condition.

It is clear from Eqs. (35) and (39) that reducing the background temperature allows for lower final temperatures. Extremely low values of k lead to heating, as can be seen from the fact that $\Lambda \sim k$. For large k (corresponding to large gate voltage), the increased sensitivity of the measurement cancels the increased disturbance due to the measurement, with the result that the minimal temperature levels off as k is increased.

V. ESTIMATES FOR ACHIEVABLE TEMPERATURES

Current refrigeration technology allows experiments on nanomechanical resonators to be performed at temperatures of about 100 mK. It is therefore sensible to assume that the feedback algorithm will be applied to a device which is initially at this temperature. In such experiments the resonators typically have fundamental frequencies in the range $f_0 = 1$–100 MHz. As our example system we take a realistic resonator with $f_0 = 12$ MHz, which is 6 μm in length, 50 nm wide, and 150 nm thick. We restrict ourselves to relatively low frequencies because of the limits of feedback circuitry, which we estimate can easily operate at 50 MHz. The effective mass of such a resonator is roughly 10^{-16} kg. An achievable quality factor Q is on the order of 10^4.

Realistic values for the resistances and capacitances of the junctions of a SET which would be used to monitor the resonator are $R_1 = R_2 = 50$ kΩ and $C_1 = C_2 = 100$ aF, and we place it $d \sim 100$ nm from the resonator. We estimate that the capacitance between the gate of the SET and the resonator will be roughly $C_{\mathrm{d}} = 50$ aF, so that $C_\Sigma = 250$ aF ($C_\Sigma = 2C_j + C_{\mathrm{g}}$). It is important to note that the analysis we use in the appendix to obtain the noise spectra is only a good approximation in certain parameter regimes. In particular, we require that V_{g}, being the drain-source voltage across the SET, satisfies $V_{\mathrm{ds}} \ll e/C_\Sigma$, and that $k/\beta \ll 1$, as discussed in Sec. III.

To apply the feedback force, we place the resonator 100 nm from the actuating gate, and allow the controller to vary the voltage difference between the gate and the resonator from -4 to 4 V. The capacitance of this arrangement is about 50 aF, so the maximum force that can be applied to the resonator is of the order of 10^{-8} N. This corresponds to $\gamma \approx 1.08 \times 10^{13}$ s^{-1}, which is much larger than ω and Γ, as required by the optimal control condition and truncated Gaussian approximation used in Sec. IV.

In evaluating the effectiveness of the feedback loop at cooling the resonator, it should be noted that the concept of temperature is only well defined for a system at equilibrium with a thermal reservoir. While the resonator starts at thermal equilibrium, the action of the feedback loop is to reduce the energy of the resonator so that it is far from equilibrium. Thus, when we quote results for the achievable steady-state effective "temperature," we will mean the temperature which the resonator would have if it were in thermal equilibrium and had the average energy achieved by the feedback loop.

Before giving theoretical estimates of the achievable steady-state effective temperature (or equivalently, the steady-state average occupation number of the oscillator, $\langle N\rangle = \langle a^\dagger a\rangle$), we need to explain two subtleties which affect the presentation of our results. When one examines the dependence of the steady state $\langle N\rangle$ on the gate voltage, one finds that it oscillates very rapidly, with minima occurring in closely spaced pairs. Since V_{g} is experimentally easy to tune, all else being equal it would make sense simply to plot these minima and ignore the complex structure. However, as discussed in Sec. III, our results are more trustworthy the smaller k/β, but this quantity is not necessarily small at the minima. The situation is shown in detail in Fig. 2, in which

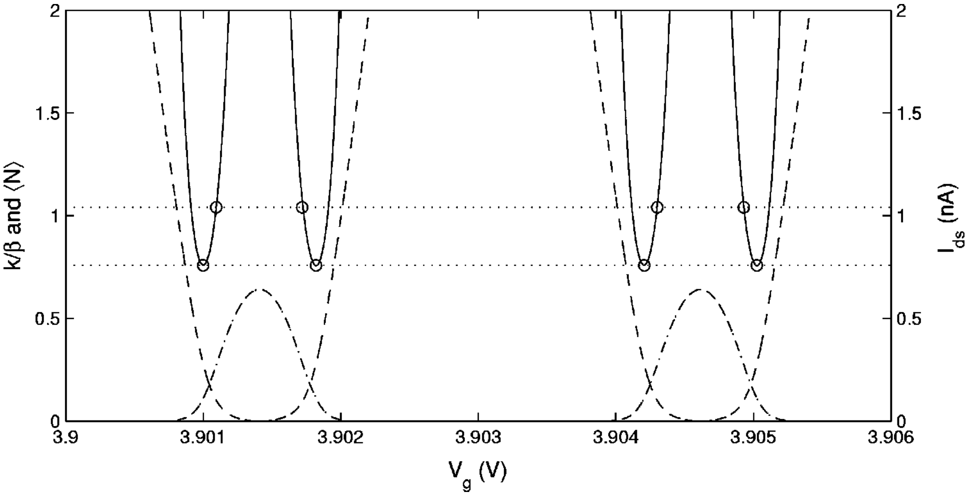

FIG. 2. The steady-state average occupation number, $\langle N\rangle$, as a function of the gate voltage (solid line), plotted along with the ratio k/β (dashed line), and the drain-source current, I_{ds} (dot-dashed line). The lower dotted line gives the minima of $\langle N\rangle$, and the upper dotted line gives the values of $\langle N\rangle$ when $k/\beta = 0.1$.

we display, as a function of V_g, two pairs of the $\langle N\rangle$ minima, as well as k/β and the current I_{ds}. In view of this, when plotting results in what follows, we will show both the minima of the effective temperature with respect to V_g, and the (somewhat higher) effective temperature which results if we demand that $k/\beta \leqslant 0.1$. For clarity the points at which $k/\beta = 0.1$ are also displayed in Fig. 2. As will be clear from Figs. 3 and 4, for $T = 100$ mK and $Q = 10^4$, the effect of the restriction $k/\beta \leqslant 0.1$ on the achievable temperature is small. In addition, k/β remains fairly small at the minima. Since this is the case, when we quote values in the following, we will give the values obtained at the minima, along with the corresponding values for k/β.

As an example of the relative magnitudes of the various noise sources at the minima displayed in Fig. 2, if we set the drain-source voltage at $V_{ds} = e/(4C_\Sigma) = 0.16$ mV and the gate voltage at $V_g \sim 1$ V, then the noise sources are

$$\beta = 1.01\times 10^{31}\ \mathrm{m}^{-2}\mathrm{s}^{-1}, \tag{40}$$

$$k = 0.184\ \ \beta, \tag{41}$$

$$\frac{m\omega_0\Gamma}{2\hbar}\coth\frac{\hbar\omega_0}{2k_BT} = 9.25\ \ \beta, \tag{42}$$

and the correlation coefficient is $\kappa = 0.638$.

Using the above parameter values to calculate the effective temperature, T_{eff}, at the minima, we find that $\Lambda = 5.1\times 10^{-5}$, and $T_{\mathrm{eff}} = 2.11$ mK. This corresponds to an energy of about $E_{ss} = 2.91\times 10^{-26}$ J, and an average occupation number $\langle N\rangle = 3.17$. While this is very encouraging, ideally

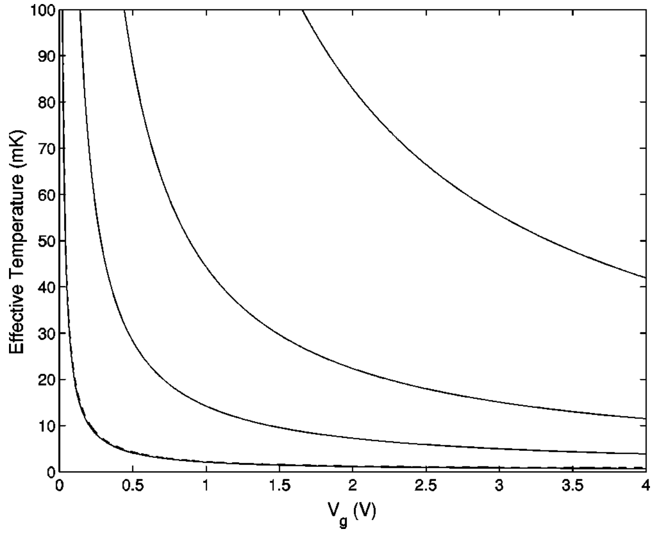

FIG. 3. Estimates for the minimum achievable effective temperatures as a function of gate voltage for a range of initial temperatures, *T*. On this plot, the increase in achievable temperature which results from the restriction $k/\beta \leqslant 0.1$ is virtually imperceptible for *T* above 100 mK. For $T = 100$ mK the dotted line shows the result under this restriction. From top to bottom, the initial temperatures are 2 K, 1 K, 500 mK, and 100 mK.

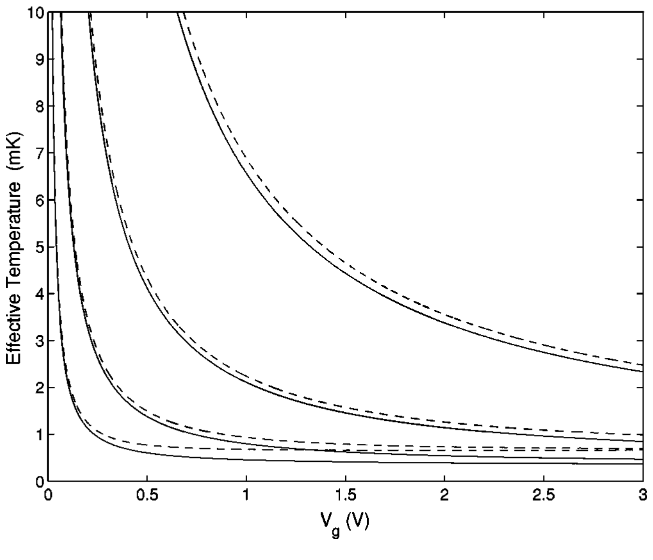

FIG. 4. Estimates for the minimum achievable effective temperatures as a function of gate voltage for a range of resonator quality factors and an initial temperature of 100 mK. The dotted lines give the minimum temperature under the additional restriction that $k/\beta \leqslant 0.1$. From top to bottom, the quality factors are 10^3, 10^4, 10^5, and 10^6. A quality factor of 10^4 is achievable with current technology.

one wants to cool below the energy of the first excited state, and we now examine what is required to do this.

While classically an increase in measurement strength would automatically lead to an improved tracking of the resonator, and therefore a more efficient cooling, quantum mechanically the situation is more complex due to the fact that a more precise measurement also leads to increased heating due to back-action. Nevertheless, in the present case one finds that the increased sensitivity of the measurement with increasing measurement strength effectively cancels this heating, and as a result a larger value of V_g corresponds to better cooling. However, after a sharp increase in cooling with increasing V_g, the minimal temperature levels off, so a greater V_g no longer provides much benefit. In addition, at some value of V_g snap-in is likely to occur as the force between the SET gate and the resonator becomes too strong. This voltage, in our example system, is estimated to be roughly 4 V. As a result, we limit ourselves to $V_g \leqslant 4$ V. At $V_g = 4$ V the steady-state minimum energy $E = 9.83 \times 10^{-27}$ J, which is below the energy of the first excited state. This corresponds to $T_{\mathrm{eff}} = 0.71$ mK and $\langle N \rangle = 0.74$, with $k/\beta = 0.28$. Thus, if the energy were to be measured directly, immediately after turning off the feedback, energy jumps as a signature of quantum behavior may well be observable. As an indication of the return from increasing the gate voltage, the minimum steady-state energy is $E = 1.58 \times 10^{-26}$ J for $V_g \approx 2$ V, which corresponds to $\langle N \rangle \approx 1.5$, with $k/\beta = 0.21$.

In Fig. 3 we plot the theoretical estimates for the achievable steady-state effective temperature as a function of V_g for a range of starting temperatures. The solid lines correspond to the absolute minima, and the dotted lines to the minimum values under the restriction that $k/\beta \leqslant 0.1$. Of particular interest is the fact that for a starting temperature of 2 K (i.e., with pumped liquid He), we obtain minimum temperatures in the range of 50 mK. Thus, even for an initial temperature of 2 K, feedback cooling might well be able to compete with dilution refrigerators. If the resonator is first cooled in a dilution refrigerator, and then feedback cooled, the semiclassical theory predicts achievable temperatures below 1 mK, as discussed above. In Fig. 4 we plot the dependence of the minimum temperature on V_g for a range of quality factors, which shows that somewhat lower final temperatures could be achieved by increasing Q.

VI. DISCUSSION AND CONCLUSION

The results obtained above are consistent with heuristic arguments. The response of cooling to the measurement strength is as expected: for very weak continuous measurements, we do not learn enough about the state of the system to cool it effectively, and can in fact heat the system due to acting on our poor information. For very strong continuous measurements, we gain sensitivity, but inject more quantum back-action, and approach a minimum only asymptotically. The range of improvement is limited, however, and beyond a few volts, the benefits may not warrant the additional effort.

Higher drain-source voltages provide a larger signal-to-noise ratio, and therefore improve cooling. However, since we do not know exactly how our approximations will fail as V_{ds} approaches e/C_Σ, and we lack a complete theory of the SET once more than two island states play a significant role in the dynamics, we have chosen to stay below that limit.

We have made a few additional simplifying assumptions, as a way to indicate a goal, rather than an immediately achievable experimental realization. First, we have assumed a perfectly efficient (and infinite bandwidth) measurement — that is, that no electron passes the detector without being detected. While detection efficiency is not as much of a problem here as in optical experiments, detectors will necessarily be inefficient to some extent. Second, we have assumed a perfect, noiseless feedback. In reality, the actuating gate applying the feedback will not provide a perfect noiseless voltage. Also, we have assumed that the actuating gate does not affect the SET. This last assumption is realistic, however, for two reasons. First, the resonator itself acts as a shield between the gate and the SET. Second, since the observer knows the voltage on the feedback gate, she can subtract that effect off the SET signal, albeit with the addition of some noise.

As mentioned previously, the dynamics of a quantum mechanical harmonic oscillator and a classical one are indistinguishable as long as the wave function is Gaussian, which is the case in the present analysis. Therefore, although the oscillator is near the quantum mechanical ground state, the SET measurement of position will not show any quantum behavior. In the face of these limitations, it is a pleasant result that experimentally obtainable situations today allow for the feedback cooling of a resonator to the point that quantum behavior could become distinguishable from classical behavior with an appropriate measurement scheme.

ACKNOWLEDGMENTS

The authors would like to thank Miles Blencowe, Alexander Korotkov, Daniel Steck, Howard Wiseman, Bernard Yerke, and Yong Zhang for helpful conversations and suggestions. Figure 1 is reprinted courtesy of Los Alamos Science. This research was supported in part by the Department of Energy, under Contract No. W-7405-ENG-36.

APPENDIX: SPECTRA OF THE SET SHOT NOISE AND BACK-ACTION

Here we discuss briefly how the expressions for the shot noise and back-action of the position measurement via a SET are obtained. For more details the reader is referred to Zhang and Blencowe[8] (from which we obtain most of the following expressions) and Korotkov.[3]

The SET consists of a central island, which electrons tunnel in and out of via junctions on either side. If one requires that the spacing between the energy levels of the electron states on the island are sufficiently large compared to the voltage drop across the SET, then only two island states will be appreciably populated, these being the states in which there are n and $n+1$ electrons on the island, for some n. This is because the transition rates which connect these states to the other states are suppressed. The value of n can be set by biasing the central island. In particular, n is determined by the condition

$$n < \left(\frac{C_{\mathrm{g}}}{e}\right)(V_g - V_{\mathrm{ds}}/2) < n+1. \tag{A1}$$

As a result, we can write a master equation for the probability density for the occupation of the two states. Denoting this density by $\tilde{\sigma} = [\sigma(n), \sigma(n+1)]^T$, we have

$$\frac{d\tilde{\sigma}}{dt} = \begin{pmatrix} -a(n) & b(n+1) \\ a(n) & -b(n+1) \end{pmatrix} \tilde{\sigma}, \tag{A2}$$

where $a(n)$ is the transition rate from n to $n+1$, and $b(n+1)$ is the transition rate from $n+1$ to n.

If we denote the tunneling rates into the island across the source junction and the drain junction (see Fig. 1) as $a_-(n)$ and $a_+(n)$, respectively (the plus and minus subscripts record whether the tunneling event has a positive or negative contribution to the SET current), and out of the island as b_+ and b_-, respectively, then

$$a(n) = a_+(n) + a_-(n), \tag{A3}$$

$$b(n+1) = b_+(n+1) + b_-(n+1). \tag{A4}$$

It is also useful to define

$$f(n) = a_+(n) - a_-(n), \tag{A5}$$

$$g(n+1) = b_+(n+1) - b_-(n+1). \tag{A6}$$

In what follows we will repress the arguments of these functions, so that $a \equiv a(n)$, $b \equiv b(n+1)$ etc. The solution to the master equation is

$$\tilde{\sigma}(t) = \left[\begin{pmatrix} b & b \\ a & a \end{pmatrix} + \begin{pmatrix} a & -b \\ -a & b \end{pmatrix} e^{-(a+b)t}\right] \frac{\tilde{\sigma}(0)}{(a+b)}. \tag{A7}$$

From this it is straightforward to calculate the average steady-state current flowing through the SET, the noise spectra of the current, $S_I(\omega)$, along with that of an arbitrary function, $\phi(n)$, of the island electron number $S_\phi(\omega)$, and their mutual correlation spectrum, $C(\omega)$. The average current is

$$I = e\left(\frac{C}{C_\Sigma}\right)\frac{(ag+bf)}{(a+b)}, \tag{A8}$$

and the spectra are

$$S_\phi(\omega) = \frac{2ab}{(a+b)} \frac{[\phi(n) - \phi(n+1)]^2}{(a+b)^2 + \omega^2} \tag{A9}$$

$$S_I(\omega) = \frac{2e^2 C^2}{(a+b)C_\Sigma^2}\left[ab + \frac{(f-g)(a^2 g - b^2 f)}{(a+b)^2 + \omega^2}\right] \tag{A10}$$

$$C^2(\omega) = \frac{(ag+bf)^2(a-b)^2 + \omega^2(ag-bf)^2}{4ab[ab[(a+b)^2+\omega^2] + (f-g)(a^2 g - b^2 f)]}. \tag{A11}$$

The force from the island on the resonator is given by[8]

$$F = (A/d)[C(V_{\mathrm{ds}} - 2V_{\mathrm{g}}) - ne]^2, \tag{A12}$$

with $A = C_{\mathrm{g}}(2C - C_{\mathrm{g}})/(2C_\Sigma^3)$. Thus, using Eq. (A9) we have

$$S_{\mathrm{F}}(\omega) = \frac{2abe^2A^2}{(a+b)d^2} \frac{[2C(V_{\mathrm{ds}} - 2V_{\mathrm{g}}) - e(2n+1)]^2}{(a+b)^2 + \omega^2}. \tag{A13}$$

Recall that in deriving these expressions we require that the two-level approximation is valid, and this demands that

$$V_{\mathrm{ds}} \ll e/C_\Sigma, \tag{A14}$$

$$k_B T \ll e V_{\mathrm{ds}}. \tag{A15}$$

The tunneling rates are given by

$$\begin{aligned} a_\pm(n) &= \frac{(\Delta n \pm \tilde{V}_{\mathrm{ds}})/(R_j C_\Sigma)}{1 - \exp[-(\Delta n \pm \tilde{V}_{\mathrm{ds}})/\tilde{T}]}, \\ b_\pm(n+1) &= \frac{(-\Delta n \pm \tilde{V}_{\mathrm{ds}})/(R_j C_\Sigma)}{1 - \exp[-(-\Delta n \pm \tilde{V}_{\mathrm{ds}})/\tilde{T}]}, \end{aligned} \tag{A16}$$

where

$$\begin{aligned} \Delta n &= \frac{C_g V_g}{e} - \frac{C_g V_{\mathrm{ds}}}{2e} - n - \frac{1}{2}, \\ \tilde{V}_{\mathrm{ds}} &= \frac{C_\Sigma V_{\mathrm{ds}}}{2e}, \\ \tilde{T} &= \frac{C_\Sigma k_B T}{e^2}. \end{aligned} \tag{A17}$$

Note that the condition which determines n [Eq. (A1)] is equivalent to $-0.5 < \Delta n < 0.5$.

From the expressions for the noise spectra we see that both sources of noise are effectively white (independent of ω) so long as ω^2 is much less than $[a(n) + b(n+1)]^2$. If this is the case then the simple quantum theory of continuous position measurement presented in the main body of the paper provides a good model for the SET measurement. Note that the actual back-action noise on the position of the resonator is the force noise filtered through the resonator spectral function. This is therefore

$$S_X^{\mathrm{F}}(\omega) = \frac{S_{\mathrm{F}}(\omega)/m_{\mathrm{eff}}^2}{(\omega^2 - \omega_0^2)^2 + \omega^2\omega_0^2/Q^2}, \tag{A18}$$

and has the same form as that predicted using the quantum mechanical model [Eq. (11)], so long as the force noise is white.

We must therefore evaluate $[a(n) + b(n+1)]^2$ for the range of parameters of interest, and verify that it is much larger than ω^2 over the relevant frequency range. First we note that the form of the spectral equations is such that they are periodic in the gate voltage. That is, the values of $a(n)$ and $b(n+1)$ depend only on Δn, not on the particular value of n in question. As a result we merely need evaluate $[a(n)+b(n+1)]^2$ for a single value of n, and check all values of Δn between -0.5 and 0.5.

Substituting in realistic parameter values (those that we use in our examples in the body of paper) in Eqs. (A16) and (A17), we find that, regardless of the value of Δn,

$$[a(n)+b(n+1)] \geqslant 2\times 10^{10} \tag{A18}$$

for the range of initial temperatures that we consider, and this is much greater than the range of ω relevant for the dynamics of the resonator, as required. Thus, we can drop ω from the expressions for the spectra, [Eqs. (A10), (A13), and (A11)], and use these to determine the parameters k, β, and κ in the model of the quantum position measurement.

---

[1] A.N. Clelandand M.L. Roukes, Appl. Phys. Lett. **69**, 2653 (1996).

[2] See, e.g., A.D. Armour, M.P. Blencowe, and K.C. Schwab, Phys. Rev. Lett. **88**, 148301 (2002).

[3] A.N. Korotkov, Phys. Rev. B **49**, 10 381 (1994).

[4] U. Hanke *et al.*, Appl. Phys. Lett. **65**, 1847 (1994).

[5] A. Shnirman and G. Schön, Phys. Rev. B **57**, 15 400 (1998).

[6] A.C. Doherty and K. Jacobs, Phys. Rev. A **60**, 2700 (1999).

[7] O.L.R. Jacobs, *Introduction to Control Theory* (Oxford University Press, Oxford, 1993).

[8] Y. Zhang and M.P. Blencowe, J. Appl. Phys. **91**, 4249 (2002), cond-mat/0109412 (unpublished)

[9] A.N. Korotkov, Phys. Rev. B **63**, 115403 (2001). In this paper Korotkov also considers the application of feedback control to a single qubit. See also R. Ruskov and A.N. Korotkov, *ibid.* **66**, 041401 (2002).

[10] Note that there is a qualitative difference between the system we consider and the system Korotkov considers in Ref. 9, since the latter is a measurement of a QND observable. However, the formalism employed there is quite general in that it can be used to describe a measurement of any observable, which is why our equations have the same form as those derived by Korotkov.

[11] H.M. Wiseman and G.J. Milburn, Phys. Rev. A **47**, 642 (1993).

[12] G.J. Milburn, K. Jacobs, and D.F. Walls, Phys. Rev. A **50**, 5256 (1994).

[13] C.M. Caves and G.J. Milburn, Phys. Rev. A **36**, 5543 (1987).

[14] K. Jacobs and P.L. Knight, Phys. Rev. A **57**, 2301 (1998).

[15] C.W. Gardiner, *Quantum Noise* (Springer, Berlin, 2000).

[16] A.O. Caldeira, H.A. Cerdeira, and R. Ramaswamy, Phys. Rev. A **40**, 3438 (1989).

[17] See, e.g., B.L. Hu, J.P. Paz and Y. Zhang, Phys. Rev. D **45**, 2843 (1992); **47**, 1576 (1993); V. Giovannetti and D. Vitali, Phys. Rev. A **63**, 023812 (2001).

[18] H.M. Wiseman (private communication).

[19] H. Schoeller and G. Schön, Phys. Rev. B **50**, 18 436 (1994).

[20] M.P. Blencowe and M.N. Wybourne, Appl. Phys. Lett. **77**, 3845 (2000).

[21] A.C. Doherty, S. Habib, K. Jacobs, H. Mabuchi, and S.M. Tan, Phys. Rev. A **62**, 012105 (2000).

[22] This uses standard techniques for solving stochastic differential equations. See, for example, C.W. Gardiner, *Stochastic Methods* (Springer, Berlin, 1995).

in our optical scattered light image may consist of primordial solid material.

Within ~50 AU of the star, the time scales for grain removal by collisions and PR drag become significantly shorter than the stellar age. Primordial dust at the inner limit of our images (Figs. 1 and 2) has mostly vanished, and the grains observed here, as well as those discovered as close as 17 AU from the star (*14*), must be continually replenished by the collisional erosion of much larger objects such as comets and asteroids. The existence of planetesimals in this region lends plausibility to the argument that the same objects will form planets by accretion. Given that AU Mic is only ~10 My old, we may be able to observe planets that are still in the process of accreting mass, or at least discern disk structure that is sculpted by planet-mass bodies. Because AU Mic is closer to the Sun than β Pic, the 2 to 30 AU zone where terrestrial and gas giant planets might form can be resolved by current and future instrumentation (fig. S5). Planets around AU Mic may also be detected by indirect methods. The low stellar mass means that the star will display a significant astrometric reflex motion (2 milli–arc sec for a Jupiter analog). The near edge-on orientation favors planet detection by transits of the stellar photosphere. Finally, if a planet is detected by radial velocity techniques, then the near edge-on orientation gives the planet mass by constraining the sin(*i*) ambiguity intrinsic to these measurements.

References and Notes

1. D. E. Backman, F. Paresce, in *Protostars and Protoplanets III*, E. H. Levy, J. I. Lunine, Eds. (University of Arizona Press, Tucson, 1993), pp. 1253–1304.
2. F. Roques, H. Scholl, B. Sicardy, B. A. Smith, *Icarus* **108**, 37 (1994).
3. J.-C. Liou, H. A. Zook, *Astron. J.* **118**, 580 (1999).
4. L. M. Ozernoy, N. N. Gorkavyi, J. C. Mather, T. A. Taidakova, *Astrophys. J.* **537**, L147 (2000).
5. B. A. Smith, R. J. Terrile, *Science* **226**, 1421 (1984).
6. G. Schneider *et al.*, *Astrophys. J.* **513**, L127 (1999).
7. M. D. Silverstone *et al.*, *Bull. Am. Astron. Soc.* **30**, 1363 (1998).
8. W. S. Holland *et al.*, *Nature* **392**, 788 (1998).
9. J. S. Greaves *et al.*, *Astrophys. J.* **506**, L133 (1998).
10. D. Barrado y Navascues, J. R. Stauffer, I. Song, J.-P. Caillault, *Astrophys. J.* **520**, L123 (1999).
11. B. Zuckerman, I. Song, M. S. Bessell, R. A. Webb, *Astrophys. J.* **562**, L87 (2001).
12. V. Tsikoudi, *Astron. J.* **95**, 1797 (1988).
13. I. Song, A. J. Weinberger, E. E. Becklin, B. Zuckerman, C. Chen, *Astron. J.* **124**, 514 (2002).
14. M. C. Liu, B. C. Matthews, J. P. Williams, P. G. Kalas, *Astrophys. J.*, in press.
15. Materials and methods are available as supporting material on *Science* Online.
16. P. Kalas, D. Jewitt, *Astron. J.* **110**, 794 (1995).
17. To increase the signal-to-noise of the data shown in Fig. 1, we binned the data 3 × 3 pixels and then smoothed by a Gaussian function with $\sigma = 0.5$ pixel. This smoothed image was used to find the maximum outer extent of the disk. All other measurements were made using the unbinned and unsmoothed image shown in Fig. 1.
18. P. Kalas, D. Jewitt, *Astron. J.* **111**, 1347 (1996).
19. R. Saija *et al.*, *Mon. Not. R. Astron. Soc.* **341**, 1239 (2003).
20. P. Artymowicz, *Astrophys. J.* **335**, L79 (1988).
21. M. S. Bessel, F. Castelli, B. Plez, *Astron. Astrophys.* **333**, 231 (1998).
22. F. Crifo, A. Vidal-Madjar, R. Lallement, R. Ferlet, M. Gerbaldi, *Astron. Astrophys.* **320**, L29 (1997).
23. J. D. Larwood, P. G. Kalas, *Mon. Not. R. Astron. Soc.* **323**, 402 (2001).
24. W. R. F. Dent, H. J. Walker, W. S. Holland, J. S. Greaves, *Mon. Not. R. Astron. Soc.* **314**, 702 (2000).

25. Supported by the NASA Origins Programme under grant NAG5-11769, and the NSF Center for Adaptive Optics, managed by the University of California at Santa Cruz under cooperative agreement no. AST-9876783. B.C.M. acknowledges support from NSF grant AST-0228963. M.C.L. acknowledges support from a Hubble Postdoctoral Fellowship (NASA Grant HST-HF-01152.01). The authors acknowledge the insightful contributions of two anonymous referees.

Supporting Online Material
www.sciencemag.org/cgi/content/full/1093420/DC1
Materials and Methods
Figs. S1 to S5
Table S1
References

7 November 2003; accepted 9 February 2004

Published online 26 February 2004;

10.1126/science.1093420
Include this information when citing this paper.

Deterministic Generation of Single Photons from One Atom Trapped in a Cavity

J. McKeever, A. Boca, A. D. Boozer, R. Miller, J. R. Buck, A. Kuzmich, H. J. Kimble*

A single cesium atom trapped within the mode of an optical cavity is used to generate single photons on demand. The photon wave packets are emitted as a Gaussian beam with temporal profile and repetition rate controlled by external driving fields. Each generation attempt is inferred to succeed with a probability near unity, whereas the efficiency for creating an unpolarized photon in the total cavity output is 0.69 ± 0.10, as limited by passive cavity losses. An average of 1.4×10^4 photons are produced by each trapped atom. These results constitute an important step in quantum information science, for example, toward the realization of distributed quantum networking.

A crucial building-block for quantum information science is a deterministic source of single photons that generates one-quantum wave packets in a well-controlled spatiotemporal mode of the electromagnetic field. For example, protocols for the implementation of quantum cryptography (*1*) and of distributed quantum networks rely on this capability (*2*), as do models for scalable quantum computation with single-photon pulses as flying qubits (*3–6*).

The earliest observations of single-photon emission used the fluorescent light from single atoms in two- and three-level configurations (*7–9*), and thereby produced light with manifestly quantum or nonclassical character. Fluctuations in the number of atoms provided inherent limitations to these original schemes, and have since been mitigated by isolating single ions (*10*) and molecules (*11*, *12*) and by using individual quantum dots (*13*, *14*) and color centers (*15*, *16*).

With a single dipole, pulsed excitation allows for "triggered" emission of a single photon within a prescribed interval, albeit into 4π steradians. To achieve emission as a directed output with high efficiency, the dipole emitter can be placed inside an optical resonator, as by coupling single quantum dots to microcavities (*17–19*). These experiments make use of the Purcell effect to enhance radiative decay into a cavity mode of interest and thereby achieve a deterministic bit stream of single-photon pulses (*20*) in a regime of weak coupling in cavity quantum electrodynamics (cQED).

By contrast, the generation of single photons within the domain of strong coupling in cQED (*21*, *22*) enables diverse new capabilities, including the reversible transfer of quantum states between atoms and photons as a fundamental primitive for the realization of quantum networks (*2*). A single photon source consisting of a trapped atom strongly coupled to an optical cavity represents an ideal node for such a network, in which long-lived internal atomic states can be mapped to quantum states of the electromagnetic field by way of "dark" eigenstates of the atom-cavity system (*23*). By way of a quantum repeater architecture, converting stationary qubits to flying qubits in this way enables distributed quantum entanglement over long distances (*2*).

We report on the deterministic generation of single-photon pulses by a single atom strongly coupled to an optical cavity in a configuration suitable for quantum network protocols. Single cesium atoms are cooled and loaded into an optical trap (Fig. 1A), which localizes them within the mode of a high-finesse optical cavity (*24–26*). The atom

---

Norman Bridge Laboratory of Physics 12-33, California Institute of Technology, Pasadena, CA 91125, USA.

*To whom correspondence should be addressed. E-mail: hjkimble@caltech.edu

is then illuminated by a sequence of laser pulses $\{\Omega_3^j(t),\Omega_4^j(t)\}$, the first of which, $\Omega_3(t)$, drives a "dark-state" transfer between hyperfine ground states, $F = 3 \rightarrow 4$ (Fig. 1, B and C). In this process, one photon is created in the cavity mode because the atomic transition $F' = 3' \rightarrow F = 4$ is strongly coupled to the cavity field with rate g (*2*, *23*). The emitted photon leaves the cavity as a freely propagating, spatially Gaussian wave packet whose temporal profile is determined by the external field $\Omega_3(t)$ (*2*, *20*, *23*). The atom is then recycled back to the original ground state by a second laser pulse, $\Omega_4(t)$, and the protocol is repeated for subsequent single-photon generations.

The lifetime for a trapped atom in the presence of the driving $\Omega_{3,4}$ fields is $\tau_{\text{trap}} \cong 0.14$ s, which should be compared to the repetition period $\Delta t = 10$ μs for single-photon generation and to the lifetime of 3 s recorded in the absence of the $\Omega_{3,4}$ fields (*25*). Given our measured overall efficiency $\alpha = (2.4 \pm 0.4)\%$ for escape from the cavity, for propagation, and for photodetection (*26*), this means that on average, we generate (detect) about 1.4×10^4 (350) single-photon pulses from each trapped atom.

The Gaussian beam emerging from the cavity mirror M_2 is directed to a beam splitter and then to two photon-counting detectors (D_A,D_B). For each atom k, photoelectric pulses from $D_{A,B}$ that occur during the trapping interval are stamped with their time of detection (with $\delta =$ 2 ns time resolution) and recorded for later analysis. An example of the pulse shape for single-photon generation is shown (Fig. 2A) over the detection window $[t_0^j,t_0^j+\delta t]$ within which the control field $\Omega_3^j(t)$ is ON, where $\delta t =$ 1 μs and t_0^j is the onset of $\Omega_3^j(t)$. The histogram of the total counts $n(t)$ from both detectors $D_{A,B}$, binned according to their delay with respect to t_0^j, is a sum over all repeated trials $\{j\}$ of the generation process from all atomic trapping events $\{k\}$. For the particular choice of $\Omega_3(t)$ used here, single-photon pulses have duration $\tau \cong 120$ ns (full width at half maximum). The extended tail for $n(t)$ likely arises from generation attempts for which the atom resides in Zeeman sublevels that are weakly coupled to the control field at the beginning of the $\Omega_3(t)$ pulse (*27*, *28*), as well as from roughly twofold variations in the coupling coefficient $g(\vec{r})$ (*29*). Qualitative agreement of this measured pulse shape has been obtained with multilevel quantum Monte Carlo simulations (*28*).

To investigate the quantum character of the emitted field, we calculate the function $C(\tau)$ obtained by cross-correlating the photoelectric counting events from the detectors $D_{A,B}$ as a function of time separation τ (Fig. 3) (*26*). The large suppression of $C(\tau)$ around $\tau = 0$ strongly supports the nonclassical character of the light pulses emitted by the atom-cavity system. The likelihood of two photons being detected within the same trial is greatly reduced relative to that for detection events in different trials.

Suppression of two-photon events is also quantified by the time dependence of the photon statistics over the course of the pulse (Fig. 2, B and C). Figure 2B displays the integrated probabilities for single $P_1(t)$ and joint $P_2(t)$ detection events for times t after the onset t_0^j of the control pulse $\Omega_3^j(t)$, with $P_2(t)$ normalized to $P_1(t)/2$. We calculate $P_1(t)$ and $P_2(t)$ for an effective single detector without dead time or after-pulsing, and define $P_{1,2} \equiv P_{1,2}(\delta t)$. Over the duration of the control pulse $0 \leq t \leq \delta t$, $P_1(t)$ rises to a final value $P_1 = 0.0284$; that is, the probability of registering a single photoelectric event in a trial is 2.84%. The lower trace in Fig. 2B quantifies the suppression of joint detection events relative to that expected for a weak coherent state, which would have $2P_2(t)/P_1(t) \approx P_1(t)$ (as we have confirmed in separate measurements). By the end of the control pulse, $2P_2/P_1$ has reached the value 1.8×10^{-3}, which represents a 16-fold suppression of joint detection events relative to a Poisson process.

Figure 2C examines the ratio $R(t) \equiv [(P_1^2(t))/(2P_2(t))]$, where $R \approx 1$ for a weak coherent state and increases with suppression of two-photon events. Significantly, R is independent of propagation and detection losses for $P_1 \gg P_2$. The trace in Fig. 2C restates the result that two-photon events are greatly suppressed relative to a coherent state, namely $R \equiv R(\delta t) = 15.9 \pm 1.0$. Also, in Fig. 3, the average area of the large peaks in $C(\tau)$ around $\tau = j\Delta t$ should exceed that of the central peak around $\tau = 0$ by a factor of about R, which we have confirmed.

The background rate during the Ω_3 drive pulses is time independent, and can be obtained from the record of photoelectric detections when no atom is trapped. The measured background count probability is $P_B = 2.7 \times 10^{-4}$ for the entire window, of which $P_D = 0.82P_B$ comes from detector dark counts, and the rest come from various sources of scattered light. For an ideal single-photon source, coincidence events

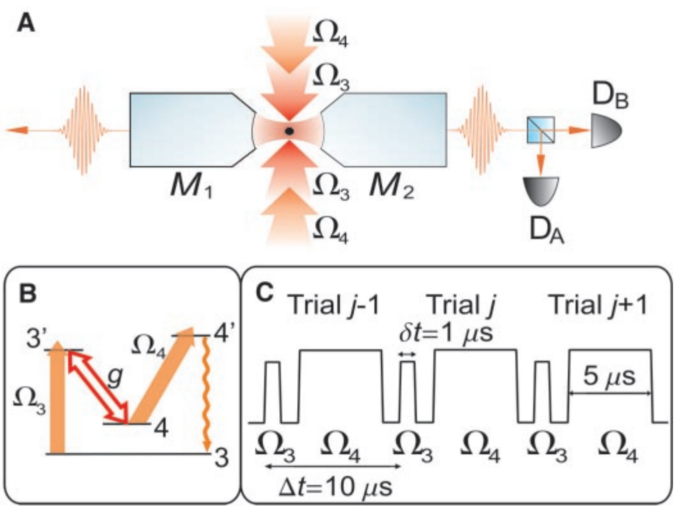

Fig. 1. Illustration of the generation of single photons by one atom trapped in an optical cavity. (**A**) A single Cs atom is trapped in a cavity formed by the reflective surfaces of mirrors (M_1, M_2) and is pumped by the external fields (Ω_3, Ω_4) (*25*). (**B**) The relevant atomic levels of the Cs D_2 line at 852.4 nm. Strong coupling at rate g is achieved for the transition $F' = 3' \rightarrow F = 4$ near a cavity resonance, where $g = 2\pi \times 16$ MHz. Atom and cavity decay rates $(\gamma,\kappa)/2\pi = (2.6$ MHz, 4.2 MHz$)$. (**C**) The timing sequence for the generation of successive single photons by way of the $\Omega_{3,4}$ fields.

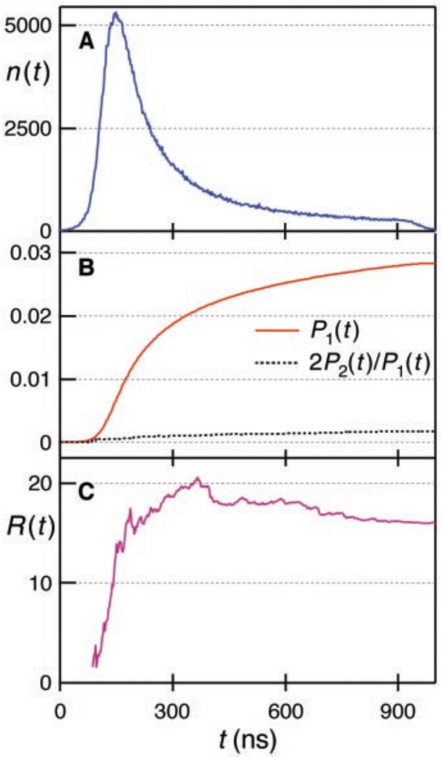

Fig. 2. (**A**) Total histogram of photoelectric detection events $n(t)$ from both detectors $D_{A,B}$. In all cases, the control field $\Omega_3(t)$ is initiated at time $t = 0$ with rise time 100 ns. (**B**) The integrated probability $P_1(t)$ for a single photoelectric event and ratio $2P_2(t)/P_1(t)$, where $P_2(t)$ is proportional to the integrated coincidence probability for joint detections from $D_{A,B}$. For a weak coherent state, the two traces would nearly overlap. (**C**) The ratio $R(t) = [(P_1^2(t))/(2P_2(t))]$ versus time, which indicates as high as 20-fold suppression of coincidences relative to a Poisson process.

at $D_{A,B}$ in the same trial would arise only because of background counts, because the source never emits two photons in one trial. Using the known values of $P_1(t)$ and P_B, the background-limited value $R_B(t)$ for this idealized scenario can be predicted. Our measured values are actually lower than this prediction [$R_B \equiv R_B(\delta t) = 52.5$], indicating a substantial rate of excess coincidences.

These excess coincidences most likely arise from rare events with two atoms trapped within the cavity (*26*). We test this hypothesis in Fig. 4 by noting that the two-atom population should decay at roughly twice the rate of the single-atom population [as we have confirmed in other measurements related to figure 4 in (*25*)]. The probability P_2 for joint detection should therefore diminish as a function of duration of the trapping interval, with a corresponding increase in the ratio R, which is precisely the behavior evidenced in Fig. 4.

Operationally, we bin all our detection timestamps according to their delay with respect to the trap-loading time ($t_T = 0$), and then compute photon statistics separately for each bin. Only four intervals in t_T are used owing to poor statistics for the coincidence counts, especially for large t_T. The analysis is the same as for Fig. 2, but we concentrate on the value $R \equiv R(\delta t)$, at the end of the $\Omega_3(t)$ pulse window. Furthermore, the ratio R_0 plotted in Fig. 4 is obtained from R with the contribution from the measured dark-count probability P_D removed, thereby providing a characterization of the atom-cavity source that is independent of the dark counts for our particular detectors. The results clearly support the hypothesis that rare two-atom events are responsible for our excess of coincidences.

Also shown in Fig. 4 as the full curve is the result for R_0 from a model calculation that assumes that a fraction η_I of our data are acquired with a single trapped atom, and that a fraction $\eta_{II} = 1 - \eta_I$ has two atoms trapped, with η_I,η_{II} functions of the time t_T within the trapping interval (*26*). The correspondence between the model and our measurements supports the conclusion that excess coincidences arise from rare events with two atoms loaded into the trap. From this model, we infer that (i) ~3% of the trials are taken with two trapped atoms; and (ii) the generation of single photons succeeds with probability consistent with unity, $\phi_G = 1.15 \pm 0.18$ as constrained by our absolute knowledge of the various efficiencies (*26*).

Given our ability to distinguish multiatom trap-loading events in real time [as demonstrated in figure 4 of (*25*)], events with $N \geq 2$ atoms trapped in the cavity could be actively discarded; alternatively, the extra atoms could be heated out of the trap, before even attempting single-photon generation. Moreover, in its current implementation, our atom-cavity system generates unpolarized single photons, and a well-defined polarization is subsequently selected with 50% efficiency. This efficiency could be greatly improved by separating the functions of cooling and of single-photon generation for the Ω_3 control field, so that the atom is optically pumped into a known Zeeman sublevel before excitation. This separation of function would allow the interaction configuration of (*29*) to be implemented, making the pulse shape and phase for the photon wave packets insensitive to randomness of the atomic position.

We have used a single atom trapped within a high-finesse optical cavity as an efficient source for the generation of single photons on demand. The photons are emitted as a Gaussian beam with user-controlled pulse shapes. As shown in Fig. 4, the average ratio of single- to two-photon event probabilities is $R_0 = 20.8 \pm 1.8$, whereas $R_0 \geq 150$ for single-photon generation at long trapping times $t_T \cong 0.4$ s. With this large suppression of two-photon probability, the Mandel-Q parameter is determined almost exclusively by propagation efficiency. For example, for polarized (unpolarized) photon wave packets, $Q = -0.34 \pm 0.05$ ($Q = -0.68 \pm 0.10$) referenced to the total cavity output from (M_1,M_2). Absent passive losses from the cavity boundaries, the generation of single photons succeeds with probability close to unity, where this high success probability derives from the near-ideal nature of the atom-cavity interaction in a regime of strong coupling.

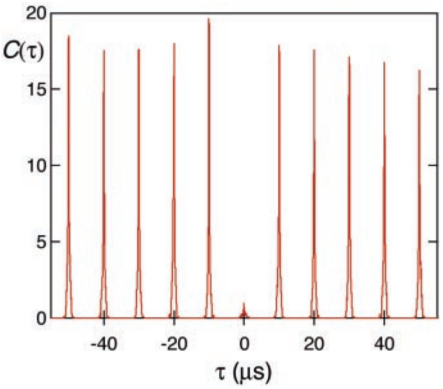

Fig. 3. Time-resolved coincidences $C(\tau)$ as a function of delay τ between detections at $D_{A,B}$. Around $\tau = 0$, $C(\tau)$ is suppressed for two events from the same trial relative to its values for $\tau = j\Delta t$ for two events from different trials, where $j = \pm 1, 2, \ldots$. As indicated in Fig. 1C, $\Delta t = 10$ μs is the repetition interval for the generation of single photons and $\delta t = 1$ μs is the duration of our control pulse $\Omega_3(t)$.

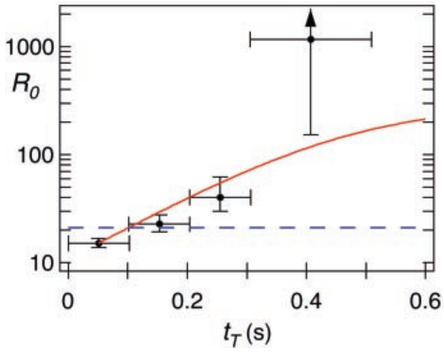

Fig. 4. Evolution of the ratio $R_0 \equiv [(P_1{}^2)/(2P_2)]$ versus trapping time t_T, here corrected for detector dark counts. The data points are experimentally determined as discussed in the text, with vertical error bars based on counting statistics of coincidence events, and horizontal bars indicating the bin widths in t_T. The full curve is the prediction from our model calculation that includes (rare) two-atom events. The dashed line represents the measured overall average of R_0 for all t_T.

References and Notes

1. N. Lutkenhaus, *Phys. Rev. A*. **61**, 52304 (2000).
2. H.-J. Briegel, S. J. van Enk, J. I. Cirac, P. Zoller, in *The Physics of Quantum Information*, D. Bouwmeester, A. Ekert, A. Zeilinger, Eds. (Springer, Berlin, 2000), pp. 192–197.
3. I. L. Chuang, Y. Yamamoto, *Phys. Rev. A*. **52**, 3489 (1995).
4. Q. A. Turchette, C. J. Hood, W. Lange, H. Mabuchi, H. J. Kimble, *Phys. Rev. Lett*. **75**, 4710 (1995).
5. E. Knill, R. Laflamme, G. Milburn, *Nature* **409**, 46 (2001).
6. L.-M. Duan, H. J. Kimble, in press; preprint available at http://arXiv.org/abs/quant-ph/0309187.
7. J. F. Clauser, *Phys. Rev. D* **9**, 853 (1974).
8. H. J. Kimble, M. Dagenais, L. Mandel, *Phys. Rev. Lett*. **39**, 691 (1977).
9. P. Grangier, G. Roger, A. Aspect, *Europhys. Lett*. **1**, 173 (1986).
10. F. Diedrich, H. Walther, *Phys. Rev. Lett*. **58**, 203 (1987).
11. T. Basche, W. E. Moerner, M. Orrit, H. Talon, *Phys. Rev. Lett*. **69**, 1516 (1992).
12. B. Lounis, W. E. Moerner, *Nature* **407**, 491 (2000).
13. P. Michler *et al*., *Nature* **406**, 968 (2000).
14. C. Santori, M. Pelton, G. Solomon, Y. Dale, Y. Yamamoto, *Phys. Rev. Lett*. **86**, 1502 (2001).
15. R. Brouri, A. Beveratos, J.-P. Poizat, P. Grangier, *Opt. Lett*. **25**, 1294 (2000).
16. C. Kurtsiefer, S. Mayer, P. Zarda, H. Weinfurter, *Phys. Rev. Lett*. **85**, 290 (2000).
17. P. Michler *et al*., *Science* **290**, 2282 (2000).
18. E. Moreau *et al*., *Appl. Phys. Lett*. **79**, 2865 (2001).
19. M. Pelton *et al*., *Phys. Rev. Lett*. **89**, 233602 (2002).
20. C. K. Law, H. J. Kimble, *J. Mod. Opt*. **44**, 2067 (1997).
21. A. Kuhn, M. Hennrich, G. Rempe, *Phys. Rev. Lett*. **89**, 67901 (2002).
22. H. J. Kimble, *Phys. Rev. Lett*. **90**, 249801 (2003).
23. A. S. Parkins, P. Marte, P. Zoller, H. J. Kimble, *Phys. Rev. Lett*. **71**, 3095 (1993).
24. J. Ye, D. W. Vernooy, H. J. Kimble, *Phys. Rev. Lett*. **83**, 4987 (1999).
25. J. McKeever *et al*., *Phys. Rev. Lett*. **90**, 133602 (2003).
26. Materials and methods are available as supporting material on *Science* Online.
27. J. McKeever, A. Boca, A. D. Boozer, J. R. Buck, H. J. Kimble, *Nature* **425**, 268 (2003).
28. A. D. Boozer, A. Boca, J. R. Buck, J. McKeever, H. J. Kimble, in press; preprint available at http://arXiv.org/abs/quant-ph/0309133.
29. L.-M. Duan, A. Kuzmich, H. J. Kimble, *Phys. Rev. A*. **67**, 032305 (2003).
30. We gratefully acknowledge the contributions of K. M. Birnbaum, S. J. van Enk, H.-C. Nägerl, D. M. Stamper-Kurn, D. W. Vernooy, and J. Ye. This work was supported by the Caltech MURI Center for Quantum Networks under U.S. Army Research Office grant DAAD19-00-1-0374, by the NSF, and by the Office of Naval Research.

Supporting Online Material

www.sciencemag.org/cgi/content/full/1095232/DC1
Materials and Methods
Table S1
References

31 December 2003; accepted 18 February 2004
Published online 26 February 2004;
10.1126/science.1095232
Include this information when citing this paper.

arXiv:quant-ph/0309187 v1 25 Sep 2003

Scalable photonic quantum computation through cavity-assisted interaction

L.-M. Duan[1] and H. J. Kimble[2]
[1]*Department of Physics and FOCUS Center, University of Michigan, Ann Arbor, MI 48109-1120*
[2]*Norman Bridge Laboratory of Physics 12-33, California Institute of Technology, Pasadena, CA 91125*

We propose a scheme for scalable photonic quantum computation based on cavity assisted interaction between single-photon pulses. The prototypical quantum controlled phase-flip gate between the single-photon pulses is achieved by successively reflecting them from an optical cavity with a single-trapped atom. Our proposed protocol is shown to be robust to practical nose and experimental imperfections in current cavity-QED setups.

Realization of quantum computation requires accurate coherent control of a set of qubits. A small volume optical cavity provides a platform to achieve strong coherent interactions between atoms and photons, and has been exploited as the critical component in several schemes for implementation of quantum computation and communication [1–3]. In a prototypical cavity-based quantum computation scheme of Ref. [1], the atoms are adopted as qubits while photons mediate the interaction between them. Scaling to large-scale quantum computation via this paradigm then requires that many atoms be localized and separately addressed within a tiny optical cavity [1], or alternatively be coherently transported into and out of the cavity mode [4]. However, in spite of recent significant laboratory advances [5,6,4,7,8], these tasks remain daunting experimental challenges.

Here, we propose a scalable quantum computation scheme where qubits are encoded as polarizations of single-photon pulses. An optical cavity with a single trapped atom is employed as the critical resource to achieve controlled gate operations between photonic qubits and to act as a high efficiency single-photon detector. The proposed computation architecture is based on the state-of-the-art in cavity quantum electrodynamics [5], can be readily scaled up to many qubits, and could be integrated with protocols for the realization of quantum networks [2].

Quantum computation with single-photon polarizations as qubits [9,10] has the obvious advantage that the number of qubits can readily be scaled up by generating many single-photon pulses. The main obstacle to this approach is that it is exceedingly difficult to achieve quantum gate operations between single-photon pulses. The typical photon-photon coupling rate in available materials is orders of magnitude too small to allow for any meaningful gate operation at the single-quantum level. An interesting idea, as has been put forward recently in the so-called linear optics quantum computation scheme [11], is to achieve effective nonlinear interaction between photons through feed-forward from high efficiency single-photon detectors. Though this approach is a very important advance, a significant obstacle is that the required efficiency α of the single-photon detectors for scalable quantum computing is extremely high (e.g., for gate success with probability $p \simeq 0.99$, $\alpha \gtrsim 0.999987$ [12]).

In our proposed scheme, we combine the advantage of scalability from the photonic qubits and the power of strong atom-photon coupling in a high-finesse optical resonator. Such a cavity with one or few atoms in a configuration of far-off-resonant interactions provides an effective Kerr nonlinearity for the input light [10,13,14], as was first observed in Ref. [10]. However, this nonlinear phase shift is typically too small for realization of the operation of the prototypical quantum Controlled-NOT gate (C-NOT). Compared with the approach of Ref. [10], our new protocol has the following significant advances: *(i)* A different interaction mechanism between photon pulses leads to a much larger effective interaction rate sufficient for the realization of a quantum C-NOT gate with current experimental capabilities. *(ii)* The conditional phase flip in our scheme is very insensitive to variation of the atom-photon coupling rate, so that high-fidelity gate operations can be realized even if the atom is not localized in the Lamb-Dicke regime. *(iii)* The pulse shapes for pairs of interacting single photons suffer very small changes due to interactions with the atom-cavity system, which is otherwise quite difficult to achieve [14]. *(iv)* Finally, the noise properties of our scheme are quite favorable, and should allow significant improvement in the error threshold for large-scale, fault-tolerant quantum computation.

The basis states for our qubit consist of two orthogonal polarization states of a single-photon pulse, denoted by $|h\rangle$ and $|v\rangle$. A series of single-photon pulses is generated by emission from a single atom in a cavity [15,2]; single-qubit operations on these photonic qubits are accurately performed through polarization rotations. The critical problem for quantum computation with these qubits is to achieve a nontrivial two-qubit interaction. Here, we choose the quantum controlled phase flip (CPF), where the CPF gate for qubits j and k flips the phase of the input state if both qubits are in $|h\rangle$ polarizations, and has no effect otherwise. The CPF gates, together with simple single-qubit operations, realize universal quantum computation [16].

As illustrated in Fig. 1a, the CPF gate for two arbitrary pulses j and k is implemented by simply reflecting them successively from a high-Q cavity which contains a single-trapped atom. The atom has three relevant levels as shown in Fig. 1b, and is initially prepared in an equal superposition of the two ground states, i.e., $|\Phi_{ai}\rangle = (|0\rangle + |1\rangle)/\sqrt{2}$. The atomic transition $|1\rangle \longrightarrow |e\rangle$

is resonantly coupled to a cavity mode a_h, which has h polarization and is resonantly driven by the h polarization component of the input single-photon pulse. The v polarization component of the input pulse is reflected by the mirror M.

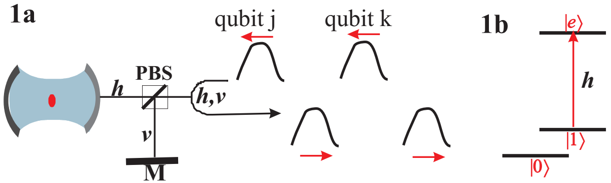

FIG. 1. (a) Schematic setup to implement the controlled phase flip (CPF) gate between two single-photon pulses j and k. With a polarization beam splitter (PBS), the h-polarized component of the single-photon pulse is reflected by the cavity, while the v-polarized component is reflected via the mirror M. The optical paths from the polarization beam splitter (PBS) to the cavity and to the mirror M are assumed to be equal. (b) The relevant level structure of the atom trapped in the cavity (e.g., the states $|0\rangle$ and $|1\rangle$ could denote hyperfine states of an alkali atom in the ground-state manifold while $|e\rangle$ is an excited state).

Before describing the detailed model and supporting calculations, first we summarize the basic ideas of our scheme, which consists of two critical steps. *(A)* By reflecting one single-photon pulse, say j, from the cavity and the mirror, a CPF gate between the atom and the pulse j is achieved as described by the unitary operator $U_{aj}^{CPF} = e^{i\pi|0\rangle_a\langle 0|\otimes|h\rangle_j\langle h|}$. *(B)* A composition of the CPF gates between the atom and the pulses j,k generates a CPF gate between the pulses j and k described by the unitary operator $U_{jk}^{CPF} = e^{i\pi|h\rangle_j\langle h|\otimes|h\rangle_k\langle h|}$, while restoring the atom into its initial state $|\Phi_{ai}\rangle$. Experimentally the composition is performed by successively "bouncing" the pulses from the cavity (see Fig. 1a).

Step (A) – When the incoming photon is v polarized, it will be reflected by the mirror M without any phase and shape change. When the incoming photon is in h polarization, it is resonant with the bare cavity mode if the atom is in the $|0\rangle$ state and thus acquires a phase of $e^{i\pi}$ after its reflection; however, if the atom is in the $|1\rangle$ state, the frequency of the dressed cavity mode from the resonant atom-cavity coupling is significantly detuned from the frequency of the incoming pulse. In this case, the cavity functions in the same fashion as the mirror M and the photon pulse is reflected without a phase change. A composition of the above sub-processes realizes the desired CPF gate U_{aj}^{CPF} between the atom and the photon.

Step (B) – Critical to the second step of our protocol is the following operator identity:

$$U_{jk}^{CPF}|\Psi_{jk}\rangle\otimes|\Phi_{ai}\rangle = U_{aj}^{CPF}R_a(-\pi/2)\,U_{ak}^{CPF}R_a(\pi/2) \times U_{aj}^{CPF}|\Psi_{jk}\rangle\otimes|\Phi_{ai}\rangle\ , \tag{1}$$

where $|\Psi_{jk}\rangle$ denotes an arbitrary state of the photonic qubits j and k, and $R_a(\theta)$ is a single-bit rotation on the atom which transforms according to $R_a(\theta)|0\rangle = \cos\theta/2\,|0\rangle + \sin\theta/2\,|1\rangle$ and $R_a(\theta)|1\rangle = -\sin\theta/2\,|0\rangle + \cos\theta/2\,|1\rangle$. The identity (1) demonstrates that the CPF gate between two arbitrary single-photon pulses j and k can be implemented by first reflecting the pulse j from the cavity as shown in Fig. 1a, then applying a $(\pi/2)$-pulse laser on the atom, then reflecting the pulse k from the cavity, then applying a $(-\pi/2)$-pulse laser on the atom, and finally reflecting the pulse j again from the cavity.

The CPF gate U_{aj}^{CPF} between the atom and the photon pulse can also be used to achieve quantum nondemolition (QND) measurement of the photon number in the pulse. For this purpose, we simply prepare the atom in the state $|\Phi_{ai}\rangle$, reflect the to-be-measured photon pulse from the cavity, apply a $R_a(\pi/2)$ rotation on the atom, and finally perform a measurement of the atomic state in the basis $\{|0\rangle,|1\rangle\}$. The measurement outcome is "0" if and only if the h component of the pulse has a photon. By the same avenue, we can also measure the parity of several photonic qubits ("parity" concerns whether a series of pulses has a total even or odd photon number in their h components) by successively reflecting them from the cavity, and can as well measure the total photon number of both h and v components of a single pulse by reflecting it twice from the cavity with a polarization flip between the two reflections. Such QND measurements have wide applications for quantum information processing [17,18]. Note that the measurement of atomic internal states can be done with near 100% efficiency through the quantum jump technique [3]. So, the efficiency of our QND measurement is principally only limited by the inefficiency of the CPF gate between the atom and the photon pulse caused by atomic spontaneous emission loss, which as we will see later, is significantly less than the inefficiency of conventional destructive single-photon detectors.

Now we present a detailed theoretical model to demonstrate that the CPF gate U_{aj}^{CPF} between the atom and the single-photon pulse j can be obtained simply by reflecting the latter from the cavity. The initial state of the pulse j can be expressed as $|\Psi_p\rangle_j = c_{hj}|h\rangle_j + c_{vj}|v\rangle_j$, where c_{hj} and c_{vj} are arbitrary superposition coefficients. The polarization component states $|\mu\rangle_j$ ($\mu = h, v$) have the form $|\mu\rangle_j = \int_0^T f_j(t)\,a_\mu^{in\dagger}(t)\,dt\,|\mathrm{vac}\rangle$, where $f_j(t)$ is the normalized pulse shape as a function of time t, T is the pulse duration, $a_\mu^{in}(t)$ are one-dimensional field operators (cavity input operators) with the standard commutation relations $\left[a_\mu^{in}(t), a_{\mu'}^{in\dagger}(t')\right] = \delta_{\mu\mu'}\delta(t-t')$ [19], and $|\mathrm{vac}\rangle$ denotes the vacuum of all the optical modes. The cavity mode a_h is driven by the corresponding cavity input operator $a_h^{in}(t)$ through [19]

$$\dot{a}_h = -i[a_h, H] - (i\Delta + \kappa/2)\,a_h - \sqrt{\kappa}a_h^{in}(t)\ , \tag{2}$$

where κ is the cavity (energy) decay rate and the Hamiltonian

$$H = \hbar g\left(|e\rangle\langle 1|\,a_h + |1\rangle\langle e|\,a_h^\dagger\right) \tag{3}$$

describes the coherent interaction between the atom and the cavity mode a_h. The detuning Δ in Eq. (2) is meant to be 0 for our scheme, but we retain it here for subsequent pedagogical purposes. The cavity output $a_h^{out}(t)$ is connected with the input by the standard input-output relation

$$a_h^{out}(t) = a_h^{in}(t) + \sqrt{\kappa} a_h \ . \tag{4}$$

As the v component of the pulse is reflected by the mirror M, we simply have $a_v^{out}(t) = a_v^{in}(t)$.

Equations (2)-(4) determine the evolution of the joint state of atom and photon pulse, and can be solved without further approximation through numerical simulation. However, before presenting the simulation results, first we attack this problem analytically with some rough approximations to reveal the underlying physics. If the atom is in the state $|0\rangle$, the Hamiltonian H does not play a role in Eq. (2). In this case, from Eqs. (2) and (4) we find

$$a_h^{out}(t) \approx \frac{i\Delta - \kappa/2}{i\Delta + \kappa/2} a_h^{in}(t) \ , \tag{5}$$

where the high-frequency components of the field operators $a_\mu^{in}(t)$ and $a_\mu^{out}(t)$ have been discarded, which is a valid approximation if the input pulse shape $f_j(t)$ changes slowly with time t compared with the cavity decay rate, i.e., $|\partial_t f_j(t)/f_j(t)| \ll \kappa$. Under this approximation, we have $a_h^{out}(t) \approx -a_h^{in}(t)$ for resonant interaction $\Delta = 0$, so the h component acquires the phase π after reflection from the cavity. However, if the atom is in the state $|1\rangle$, the response function of the cavity is modified by the coupling (3), where for the case of strong coupling [20], the two dressed cavity modes have frequencies that are effectively detuned from that of the input pulse by $\Delta = \pm g$, respectively. In the case that $g \gg \kappa$, we have $a_h^{out}(t) \approx a_h^{in}(t)$ from Eq. (5), thereby confirming the preceding analysis to give the desired CPF gate U_{aj}^{CPF}.

Armed with this understanding, we finally present exact numerical simulations for the theoretical model described by Eqs. (2)-(4). In the simulation, we discretize the continuum field operators $a_h^{in}(t)$ and $a_h^{out}(t)$, and change the dynamics into the Schrodinger picture to avoid operator ordering. The details of the simulation method can be found in Ref. [21]. Atomic spontaneous emission noise is effectively described by an imaginary part $(-i\gamma_s/2)(|e\rangle\langle e| - |1\rangle\langle 1|)$ in the Hamiltonian H [21], where γ_s is the spontaneous emission rate from the state $|e\rangle$. The input pulse is taken to be Gaussian with $f_j(t) \propto \exp\left[-(t-T/2)^2/(T/5)^2\right]$, where t ranges from 0 to T.

The numerical simulations show that the CPF gate U_{aj}^{CPF} works remarkably well. First of all, the conditional phase factor is either $e^{i\pi}$ or e^{i0} depending on the atomic state $|0\rangle$ or $|1\rangle$, and this phase factor is very insensitive to the variation of the coupling rate g in the typical parameter region. For instance, its variation is smaller than 10^{-6} for g varying from 6κ to κ. This result cannot be understood naively from Eq. (5), from which one gets a phase of e^{i0} only when $g \gg \kappa$. The reason for this discrepancy is that we have two addressed cavity modes with symmetric effective detunings $\Delta = \pm g$, and their joint effect makes the phase factor e^{i0} very stable even if g is reduced to a value comparable with κ. The stability of the conditional phase against variations of g in the typical parameter region is an important advantage of our scheme, as g in current experiments suffers significant random variation (roughly by a factor of 2) due to residual atomic motion [5].

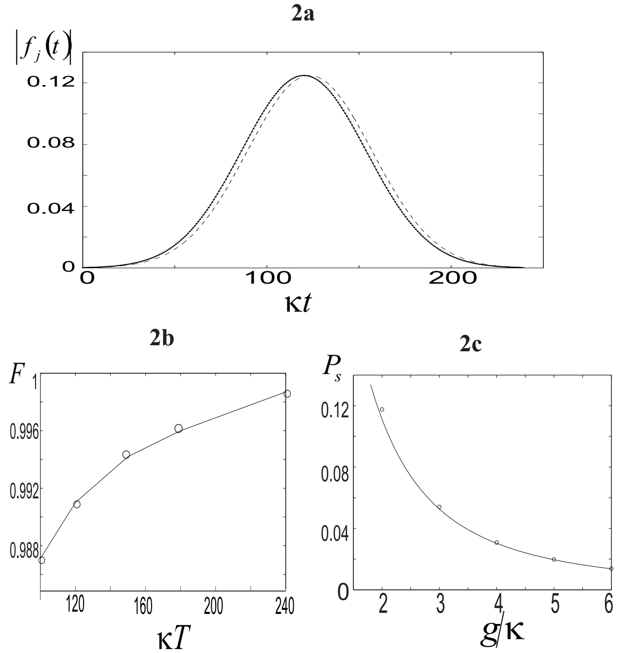

FIG. 2. (a) The shape functions $|f_j(t)|$ for the input pulse (solid curve) and the reflected pulse with the atom in the state $|0\rangle$ (dashed curve) and $|1\rangle$ (dotted curve), respectively. The dotted and solid curves closely match and are hardly distinguishable in the figure. (b) Fidelity F due to shape mismatch for the quantum CPF gate as a function of the input pulse duration T in units of κ^{-1}. The gate fidelity quickly approaches 1 for $\kappa T \gg 1$. (c) The probability P_s of spontaneous emission loss versus the normalized cavity coupling rate g/κ, assuming $\gamma_s = \kappa$ (circles). The solid curve shows the fit by the empirical formula $P_s \approx 1/\left(1 + 2g^2/\kappa\gamma_s\right)$. Other parameters for (a), (b), $g = 3\kappa$, $\gamma_s = \kappa$, $\Delta = 0$, and for (c), $T/5 = 24/\kappa$, $\Delta = 0$.

The simulation also shows that the output pulse basically has the same shape as the input pulse if the pulse duration $T \gg 1/\kappa$. Fig. 2a shows the output pulse shapes $|f_i(t)|$ for the cases of the atomic states $|1\rangle$ and $|0\rangle$, respectively, and demonstrates very good overlap with the input pulse shape shown in the same figure. In more quantitative terms, we consider the fidelity F of the CPF gate U_{aj}^{CPF} for the input atom-photon state $|\Phi_{ai}\rangle \otimes [|\Psi_{pi}\rangle = (|h\rangle + |v\rangle)/\sqrt{2}]$. Reductions in F below unity are caused by shape mismatching between the input and the output pulses and can be numerically calculated. Fig. 2b shows the gate fidelity F calculated in this way for different pulse durations T. For $T = 240/\kappa$ (corresponding to a pulse width $T/5 \sim 1\mu$s for the parameters of Ref. [5]), the gate fidelity is about 99.9%. The shape of the output pulse is also very insensitive to variation of the coupling rate g in the typical parameter region. For instance, the relative shape change is smaller than 10^{-4} for g varying from 6κ to κ.

The dominant noise in our CPF gate arises from photon loss due to atomic spontaneous emission, leading to a vacuum-state output when the input is a single-photon pulse. This noise yields a leakage error (also called an erasure error) which means that the final state is outside of the qubit Hilbert space $\{|h\rangle, |v\rangle\}$ [16]. Fig. 2c shows the probability P_s of spontaneous emission loss as a function of g/κ for the input state $|1\rangle \otimes |h\rangle$, assuming $\gamma_s = \kappa$. The curve is well simulated by the empirical formula $P_s \approx 1/\left(1 + 2g^2/\kappa\gamma_s\right)$. If the initial state of the system is $|\Phi_{ai}\rangle \otimes |\Psi_{pi}\rangle$, the average probability of the leakage error per U_{aj}^{CPF} gate is given by $P_e = P_s/4$. In current experiments [5], typically $(\kappa, \gamma_s)/2\pi \approx (8, 5.2)$ MHz, and $g/2\pi \approx 25$ MHz, which yields $P_e \approx 0.8\%$. With these parameters, a typical pulse width $T/5 \approx 24/\kappa \approx 0.5$ μs. As the pulses j and k are injected successively for the CPF gate U_{jk}^{CPF}, we need to introduce a time delay of few μs between them. For demonstration-of-principle experiments, this time delay can be routinely achieved through simple fiber loops. To obtain longer time delay, atomic ensembles could be employed to store photon pulses for several seconds [22–24].

Because the principal noise in our scheme is photon loss during gate operations which is modeled as a leakage error, very efficient quantum error correcting codes can be incorporated into this computation scheme to achieve fault-tolerance [16]. For instance, a rough estimate in Ref. [26] shows that through concatenated coding, quantum computation can tolerate leakage error at a percent level per gate, as compared to the error threshold of about 10^{-5} for general quantum errors [16]. The leakage error only affects the probability to register a photon from each pulse and has no influence on the fidelity of its polarization state if a photon is registered for each qubit (e.g., through QND or destructive measurements). So, leakage error induces small inefficiency for each gate (at a level of a few percents), which is not debilitating for experimental quantum computing up to dozens of CPF gates even without quantum error correction.

In summary, we have shown that a cavity with a single-trapped atom, conventionally used as a single-photon source, can be exploited to realize scalable, fully-functional quantum computation. The proposed scheme is well based on the state-of-the-art in cavity quantum electrodynamics, is robust to various experimental sources of noise, and offers a promising approach to the realization of large-scale fault-tolerant quantum computation.

This work was supported by the Michigan start-up fund, by the FOCUS center, by the MURI Center for Quantum Networks (No. DAAD19-00-1-0374), by the NSF (Nos. EIA-0086038 and PHY-0140355), and by the Office of Naval Research (No. N00014-02-1-0828).

[1] T. Pellizzari, S. A. Gardiner, J. I. Cirac, and P. Zoller, *Phys. Rev. Lett.* **75**, 3788 (1995).

[2] J. I. Cirac, P. Zoller, H. J. Kimble, and H. Mabuchi, *Phys. Rev. Lett.* **78**, 3221 (1997).

[3] For a review , see C. Monroe, *Nature* **416**, 238 (2002).

[4] J. A. Sauer *et al.,* quant-ph/0309052.

[5] J. McKeever *et al.*, *Phys. Rev. Lett.* **90**, 133602 (2003); J. McKeever *et al., Nature* **425**, 268 (2003).

[6] M. Keller *et al.*, Appl. Phys. B **76**, 125 (03).

[7] M. A. Rowe *et al.*, Q. Inf. & Comp. **2**, 257 (2002).

[8] A. Kuhn, M. Hennrich, G. Rempe, *Phys. Rev. Lett.* **89**, 067901 (2002).

[9] I. L. Chuang and Y. Yamamoto, *Phys. Rev. A* **52**, 3489 (1995).

[10] Q. A. Turchette *et al.*, *Phys. Rev. Lett.* **75**, 4710 (1995).

[11] E. Knill, R. Laflamme, and G. Milburn, *Nature* **409**, 46 (2001).

[12] S. Glancy, J. M. LoSecco, H. M. Vasconcelos, and C. E. Tanner, *Phys. Rev. A* **65**, 062317 (2002).

[13] A. Imamoglu, H. Schmidt, G. Woods, and M. Deutsch, *Phys. Rev. Lett.* **79**, 1467 (1997).

[14] K. M. Gheri, K. Ellinger, T. Pellizzari, and P. Zoller, *Fortsch. Phys.* **46**, 401 (1998).

[15] C. K. Law, H. J. Kimble, *J. Mod. Opt.* **44**, 2067 (1997).

[16] J. Preskill, Lecture Notes on Quantum Computation, see http://www.theory.caltech.edu/people/preskill/ph229.

[17] K. Banaszek and K. Wodkiewicz, Phys. Rev. Lett. **82**, 2009 (1999).

[18] L.-M. Duan, G. Giedke, J. I. Cirac, and P. Zoller, *Phys. Rev. Lett.* **84**, 4002 (2000).

[19] D. F. Walls, and G. J. Milburn, *Quantum Optics*, Springer-Verlag (1994).

[20] H. J. Kimble, *Phys. Scr.* **T76**, 127 (1998).

[21] L.-M. Duan, A. Kuzmich, H. J. Kimble, *Phys. Rev. A* **67**, 032305 (2003).

[22] M. Fleischhauer and M. D. Lukin, *Phys. Rev. Lett.* **84**, 5094 (2000).

[23] L. M. Duan, M. D. Lukin, J. I. Cirac, and P. Zoller, *Nature* **414**, 413 (2001).

[24] A. Kuzmich *et al.*, *Nature* **423**, 731 (2003).

[25] C. H. van der Wal *et al.*, *Science* **301**, 196 (2003).

[26] E. Knill, R. Laflamme, and G. J. Milburn, quant-ph/0006120.

arXiv:quant-ph/0309133 v2 26 May 2004

Comparison of Theory and Experiment
for a One-Atom Laser in a Regime of Strong Coupling

A. D. Boozer, A. Boca, J. R. Buck, J. McKeever, and H. J. Kimble
Norman Bridge Laboratory of Physics 12-33, California Institute of Technology, Pasadena, CA 91125

(Dated: May 25, 2006)

Our recent paper reports the experimental realization of a one-atom laser in a regime of strong coupling [1]. Here we provide the supporting theoretical analysis relevant to the operating regime of our experiment. By way of a simplified four-state model, we investigate the passage from the domain of conventional laser theory into the regime of strong coupling for a single intracavity atom pumped by coherent external fields. The four-state model is also employed to exhibit the vacuum-Rabi splitting and to calculate the optical spectrum. We next extend this model to incorporate the relevant Zeeman hyperfine states as well as a simple description of the pumping processes in the presence of polarization gradients and atomic motion. This extended model is employed to make quantitative comparisons with the measurements of Ref. [1] for the intracavity photon number versus pump strength and for the photon statistics as expressed by the intensity correlation function $g^{(2)}(\tau)$.

I. INTRODUCTION

Although a number of theoretical analyses related to a one-atom laser have appeared in the literature [2, 3, 4, 5, 6, 7, 8, 9, 10, 11, 12, 13, 14, 15, 16, 17], these prior treatments have not been specific to the parameter range of our recent experiment as reported in Ref. [1]. Because of this circumstance, we have carried out theoretical investigations in support of our experimental program, and present comparisons of these model calculations with our measurements in this paper. In Section II we introduce a simplified four-state model that captures the essential features of the operation of our one-atom laser in a domain of strong coupling but which avoids the complexity of the full Zeeman substructure of the hyperfine levels in atomic Cesium. Sections III and IV then present in turn semiclassical and quantum solutions for this four-state model system. By way of a physically motivated transformation for which the length of a Fabry-Perot cavity is made progressively shorter, we utilize these results to investigate the continuous passage from a domain in which conventional laser theory is applicable into a regime of strong coupling for which the full quantum theory is required. We thereby gain some insight into the relationship of our system to prior theoretical treatments related to the definition of the laser threshold and to "thresholdless" lasing [18, 19, 20, 21, 22]. The four-state model is further employed to calculate the intracavity photon number versus pump detuning, thereby exhibiting the "vacuum-Rabi" splitting for the atom-cavity system [23, 24, 25] and to compute the optical spectrum of the intracavity field.

In Section V we describe the procedures followed to obtain solutions for an expanded model that incorporates the relevant Zeeman substructure for the Cesium atom (32 atomic states), two modes of the cavity with orthogonal polarizations, and a simple model to account for the polarization gradients of the optical fields. Comparisons of the results from quantum jumps simulations based upon this expanded model with our measurements of the mean intracavity photon number $\bar{n}$ versus normalized pump intensity x (Figure 3 of Ref. [1]) and with our experimental determination of the intensity correlation function $g^{(2)}(\tau)$ (Figure 4 of Ref. [1]) are given in Sections V(a) and V(b), respectively.

Our intent here is not to belabor the comparison of our experiment with prior work on micro-masers and lasers, for which extensive reviews are available [26, 27, 28, 29, 30]. Instead, our principal goal is to establish quantitative correspondence between our measurements and fundamental theoretical models. Having thereby validated the suitability of the theoretical treatments, we can then use these models to inform further experimental investigations of the atom-cavity system.

II. FOUR-STATE MODEL

We begin with a four-state model to describe our experiment in which a single Cesium atom is trapped inside an optical cavity as illustrated in Figure 1. Although the actual level structure of the Cesium $6S_{1/2} \leftrightarrow 6P_{3/2}$ transition is more complex due to the Zeeman substructure, this simpler model offers considerable insight into the nature of the steady states and dynamics. Following the labelling convention in Fig. 1, we introduce the following set of

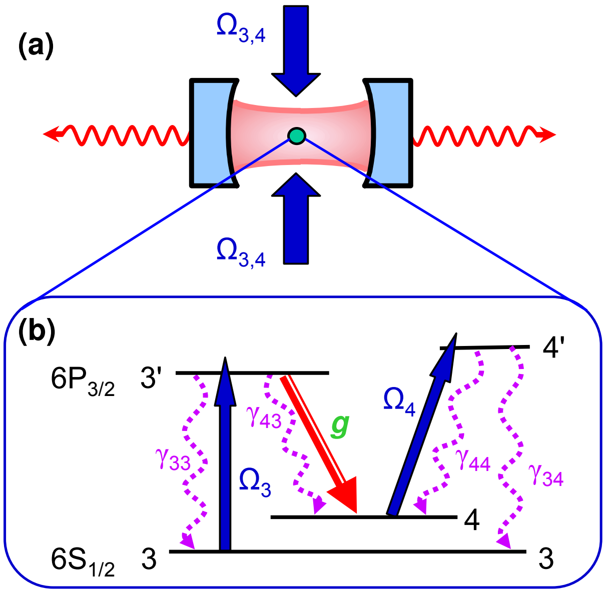

FIG. 1: Illustration of a one-atom laser. (a) The atom is located in a high-Q optical cavity of decay rate κ, and is driven by the fields $\Omega_{3,4}$. (b) Inset of the atomic level scheme relevant to our experiment with the $6S_{1/2} \leftrightarrow 6P_{3/2}$ transition in atomic Cesium. The "lasing" transition is from the excited level $F = 3'$ to the ground level $F = 4$. Pumping of the excited $3'$ level is by way of coherent excitation from a laser with Rabi frequency Ω_3. Effective decay from the ground 4 level is provided by the combination of a second field with Rabi frequency Ω_4 and spontaneous decay $4' \rightarrow 3$. Various radiative decay rates γ_{ij} appropriate to the D_2 line in Cs are given in the text.

Hamiltonians H_i in a suitably defined interaction picture ($\hbar = 1$):

$$\begin{aligned}
\hat{H}_1 &= g_{43}(\hat{a}^\dagger \hat{\sigma}_{g4,e3} + \hat{\sigma}_{e3,g4}\hat{a}), \\
\hat{H}_2 &= \frac{1}{2}\Omega_3(\hat{\sigma}_{g3,e3} + \hat{\sigma}_{e3,g3}), \\
\hat{H}_3 &= \frac{1}{2}\Omega_4(\hat{\sigma}_{g3,e3} + \hat{\sigma}_{e3,g3}), \\
\hat{H}_4 &= (\Delta_{AC} + \Delta_4)\hat{a}^\dagger \hat{a}, \\
\hat{H}_5 &= \Delta_3 \hat{\sigma}_{e3,e3} + \Delta_4 \hat{\sigma}_{e4,e4}, \\
\hat{H}_{tot} &= \hat{H}_1 + \hat{H}_2 + \hat{H}_3 + \hat{H}_4 + \hat{H}_5 \ .
\end{aligned} \tag{1}$$

In a standard convention, the atomic operators are $\hat{\sigma}_{i,j} \equiv |i\rangle\langle j|$ for states (i, j), with the association of the $F = 3, 4$ ground and the $F' = 3', 4'$ levels with $g3, g4, e3, e4$, respectively. The Hamiltonian $\hat{H}_1$ accounts for the coherent coupling of the atomic transition $e3 \leftrightarrow g4$ to the field of a single mode of the cavity with creation and annihilation operators $(\hat{a}^\dagger, \hat{a})$. The upper state $e3$ of the lasing transition is pumped by the (coherent-state) field Ω_3, while the lower state $g4$ is depleted by the field Ω_4 as described by $(\hat{H}_2, \hat{H}_3)$, respectively. $(\hat{H}_4, \hat{H}_5)$ account for various detunings, including Δ_{AC} for the offset between the cavity resonance and the $e3 \leftrightarrow g4$ atomic transition, Δ_3 for the offset between the field Ω_3 and the $g3 \leftrightarrow e3$ transition, and Δ_4 for the offset between the field Ω_4 and the $g4 \leftrightarrow e4$ transition. Beyond these interactions, we also account for irreversible processes by assuming that the atom is coupled to a continuum of modes other than the privileged cavity mode, and likewise for the coupling of the cavity mode to an independent continuum of external modes.

With these preliminaries, it is then straightforward to derive a master equation for the density operator $\hat{\rho}$ for the atom-cavity system [31, 32] in the Born-Markov approximation. For our model system, this equation is

$$\frac{d\hat{\rho}}{dt} = -i[\hat{H}_{tot}, \hat{\rho}] + \sum_{i=1}^{5} \hat{L}_i, \tag{2}$$

Here, the terms $\hat{L}_i$ account for each of the various decay channels, and are given explicitly by

$$\begin{aligned}
\hat{L}_1 &= \kappa(2\hat{a}\hat{\rho}\hat{a}^\dagger - \hat{a}^\dagger\hat{a}\hat{\rho} - \hat{\rho}\hat{a}^\dagger\hat{a}), \\
\hat{L}_2 &= \gamma_{33}(2\hat{\sigma}_{g3,e3}\hat{\rho}\hat{\sigma}_{e3,g3} - \hat{\sigma}_{e3,e3}\hat{\rho} - \hat{\rho}\hat{\sigma}_{e3,e3}), \\
\hat{L}_3 &= \gamma_{43}(2\hat{\sigma}_{g4,e3}\hat{\rho}\hat{\sigma}_{e3,g4} - \hat{\sigma}_{e3,e3}\hat{\rho} - \hat{\rho}\hat{\sigma}_{e3,e3}), \\
\hat{L}_4 &= \gamma_{34}(2\hat{\sigma}_{g3,e4}\hat{\rho}\hat{\sigma}_{e4,g3} - \hat{\sigma}_{e4,e4}\hat{\rho} - \hat{\rho}\hat{\sigma}_{e4,e4}), \\
\hat{L}_5 &= \gamma_{44}(2\hat{\sigma}_{g4,e4}\hat{\rho}\hat{\sigma}_{e4,g4} - \hat{\sigma}_{e4,e4}\hat{\rho} - \hat{\rho}\hat{\sigma}_{e4,e4}) \ ,
\end{aligned} \tag{3}$$

where the association of each term $\hat{L}_i$ with the decay processes in Fig. 1 should be obvious. Spontaneous decay of the various atomic transitions to modes other than the cavity mode proceeds at (amplitude) rate γ_{ij} as indicated in Fig. 1, while the cavity (field) decay rate is given by κ.

The master equation allows us to derive a set of equations for expectation values of atom $\langle\hat{\sigma}_{i,j}\rangle$ and field $\langle\hat{a}\rangle$ operators. One example is for the atomic polarization $\langle\hat{\sigma}_{g4,e3}\rangle$ on the $e3 \leftrightarrow g4$ transition, namely

$$\begin{aligned}
\frac{d\langle\hat{\sigma}_{g4,e3}\rangle}{dt} &= -\left[(\gamma_{33}+\gamma_{43}) + i\Delta_3\right]\langle\hat{\sigma}_{g4,e3}\rangle \\
&\quad -i\left(\Omega_3\langle\hat{\sigma}_{g4,g3}\rangle - \Omega_4\langle\hat{\sigma}_{e4,e3}\rangle\right) \\
&\quad +ig_{43}\left(\langle\hat{\sigma}_{e3,e3}\hat{a}\rangle - \langle\hat{\sigma}_{g4,g4}\hat{a}\rangle\right) \ .
\end{aligned} \tag{4}$$

A solution to this equation requires not only knowledge of single-operator expectation values $\langle\hat{\sigma}_{i,j}\rangle$ and $\langle\hat{a}\rangle$, but also of operator products such as $\langle\hat{\sigma}_{e3,e3}\hat{a}\rangle$. We can develop coupled equations for such products $\langle\hat{\sigma}_{i,j}\hat{a}\rangle$ but would find that their solution requires in turn yet higher order correlations, ultimately leading to an unbounded set of equations.

Conventional theories of the laser proceed beyond this impasse by one of several ultimately equivalent avenues. Within the setting of our current approach, a standard way forward is to factorize operator products in the fashion

$$\langle\hat{\sigma}_{i,j}\hat{a}\rangle = \langle\hat{\sigma}_{i,j}\rangle\langle\hat{a}\rangle + \left(\langle\hat{\sigma}_{i,j}\hat{a}\rangle - \langle\hat{\sigma}_{i,j}\rangle\langle\hat{a}\rangle\right) \tag{5}$$

with then the additional terms of the form $(\langle\hat{\sigma}_{i,j}\hat{a}\rangle - \langle\hat{\sigma}_{i,j}\rangle\langle\hat{a}\rangle)$ treated as Langevin noise. Such approaches rely on system-size expansions in terms of the small parameters $(1/n_0, 1/N_0)$, where (n_0, N_0) are the critical photon and atom number introduced in Ref. [1] for our one-atom laser. Within the context of conventional laser theory, these parameters are described more fully in Ref. [31, 32], while their significance in cavity QED is discussed more extensively in Ref. [33]. In qualitative terms, conventional theories of the laser in regimes for which $(n_0, N_0) \gg 1$ result in dynamics described by evolution of mean values $\langle\hat{\sigma}_{i,j}\rangle$ and $\langle\hat{a}\rangle$ (that are of order unity when suitably scaled), with then small amounts of quantum noise (that arise from higher order correlations of order $(1/n_0, 1/N_0) \ll 1$).

In the following section, we discuss the so-called semiclassical solutions obtained from the factorization $\langle\hat{\sigma}_{i,j}\hat{a}\rangle = \langle\hat{\sigma}_{i,j}\rangle\langle\hat{a}\rangle$ neglecting quantum noise. In Section IV, we then describe the full quantum solution obtained directly from the master equation.

III. SEMICLASSICAL THEORY FOR A FOUR-STATE ATOM

We will not present the full set of semiclassical equations here since they are derived in a standard fashion from the master equation Eq. 2 [32, 34]. One example is for the atomic polarization $\langle\hat{\sigma}_{g4,e3}\rangle$ on the $e3 \leftrightarrow g4$ transition, for which Eq. 4 becomes

$$\begin{aligned}
\frac{d\langle\hat{\sigma}_{g4,e3}\rangle}{dt} &= -\left[(\gamma_{33}+\gamma_{43}) + i\Delta_3\right]\langle\hat{\sigma}_{g4,e3}\rangle \\
&\quad -i\left(\Omega_3\langle\hat{\sigma}_{g4,g3}\rangle - \Omega_4\langle\hat{\sigma}_{e4,e3}\rangle\right) \\
&\quad +ig_{43}\left(\langle\hat{\sigma}_{e3,e3}\rangle - \langle\hat{\sigma}_{g4,g4}\rangle\right)\alpha \ ,
\end{aligned} \tag{6}$$

where $\alpha \equiv \langle\hat{a}\rangle$. There is a set of 18 such equations for the real and imaginary components of the various field and atomic operators, together with the constraint that the sum of populations over the four atomic states be unity. We obtain the steady state solutions to these equations, where for the present purposes, we restrict attention to the case of zero detunings $\Delta_{AC} = \Delta_3 = \Delta_4 = 0$. Allowing for nonzero detunings of atom and cavity would add to the complexity of the semiclassical analysis because of the requirement for the self-consistent solution for the frequency of emission [see, for example, Ref. [35] for the case of a (multi-atom) Raman laser].

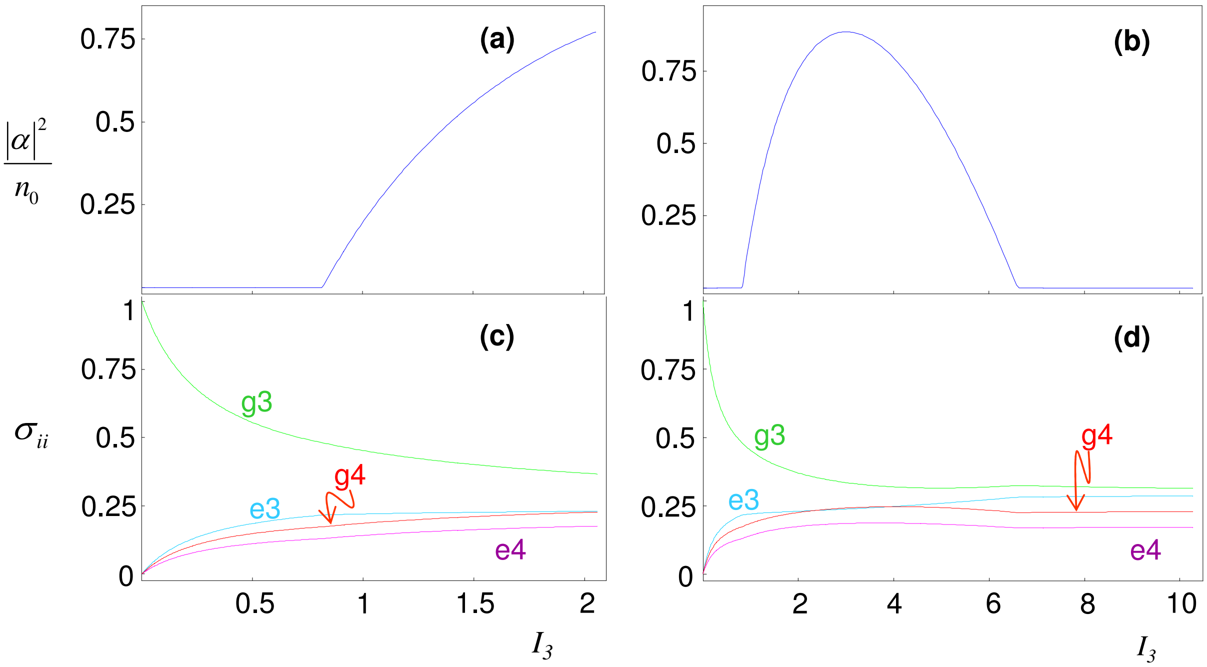

FIG. 2: Results from the semiclassical theory as applied to the atom-cavity system in Fig. 1. (a,b) Intracavity intensity $|\alpha|^2$ in units of the critical photon number n_0 is plotted as a function of the pump intensity $I_3 = (\frac{\Omega_3}{2\gamma})^2$. A threshold for $|\alpha|^2$ is evident for $I_3 \simeq 0.8$. (c,d) Populations $\sigma_{ii} = \langle \hat{\sigma}_{ii} \rangle$ versus I_3. In (c), population inversion $\sigma_{e3,e3} > \sigma_{g4,g4}$ occurs over a wide range as the pump intensity I_3 is increased from 0, including in the threshold region $I_3 \simeq 0.8$, with then "population clamping" for $\sigma_{e3,e3}$ as I_3 increases beyond threshold. In all cases, the recycling intensity $I_4 = (\frac{\Omega_4}{2\gamma})^2 = 3$ and the detunings $\Delta_{AC} = \Delta_3 = \Delta_4 = 0$.

The semiclassical solutions are obtained for the parameters relevant to our experiment with atomic Cs, namely

$$(\gamma_{33}, \gamma_{43}, \gamma_{44}, \gamma_{34}) = (\frac{3}{4}, \frac{1}{4}, \frac{7}{12}, \frac{5}{12})\gamma \ , \tag{7}$$

where these rates are appropriate to the (amplitude) decay of the levels $6P_{3/2}, F' = 3', 4' \rightarrow 6S_{1/2}, F = 3, 4$ with $\gamma = 2\pi \times 2.6$ MHz (i.e., a radiative lifetime $\tau = 1/2\gamma = 30.6$ ns). The cavity (field) decay rate κ is measured to be $\kappa = 2\pi \times 4.2$ MHz. The rate of coherent coupling g_{43} for the $e3 \leftrightarrow g4$ transition (i.e., $6P_{3/2}, F' = 3' \leftrightarrow 6S_{1/2}, F = 4$) is calculated from the known cavity geometry (waist and length) and the decay rate γ, and is found to be $g_{43} = 2\pi \times 16$ MHz based upon the effective dipole moment of the transition.

Examples of the resulting steady-state solutions for the intracavity intensity $|\alpha|^2$ together with the populations σ_{ii} of the four atomic states are displayed in Figure 2. Parts (a) and (c) of the figure illustrate the behavior of $|\alpha|^2$ and σ_{ii} around the semiclassical threshold as functions of the pump intensity I_3. Parts (b) and (d) explore these dependencies over a wider range in I_3. For fixed ratios among the various decay rates as in Eq. 7, the semiclassical solutions for $|\alpha|^2/n_0$ as well as the various populations σ_{ii} plotted in Fig. 2 depend only on the critical atom number N_0 (or equivalently, the cooperativity parameter $C_1 = 1/N_0$ for a single atom in the cavity). Hence, as emphasized in the *Supplementary Information* published with our paper Ref. [1], these steady state solutions from the semiclassical theory are independent of the cavity length l, and provide a point of reference for understanding "lasing" for a single atom in a cavity. This is because $N_0 = \frac{2\kappa\gamma}{g^2}$ is independent of cavity length l for a cavity with constant mirror reflectivity and cavity waist w_0.

Importantly, the semiclassical theory predicts threshold behavior for parameters relevant to our experiment, including inversion $\sigma_{e3,e3} > \sigma_{g4,g4}$ in the threshold region, although this is not essential for Raman gain for $g3 \rightarrow g4$ via $e3$. One atom in a cavity can exhibit such a "laser" transition for the steady state solutions in the semiclassical theory because the cooperativity parameter $C_1 \gg 1$. Indeed, in these calculations we used our experimental value for the cooperativity parameter $C_1 = 1/N_0 \simeq 12$. Among other relevant features illustrated in Fig. 2 is the quenching of the laser emission around $I_3 \simeq 6.5$, presumably due to an Autler-Townes splitting of the excited state $e3$ at high pump intensity [8].

A. Relationship to a Raman laser

In many respects our system is quite similar to a three-level Raman scheme, for which there is an extended literature (e.g., Ref. [35] and references therein). In fact we have carried out an extensive analysis of a Raman scheme analogous to our system in Fig. 1. Pumping is still done by the field Ω_3 on the $3 \rightarrow 3'$ transition. However, recycling $4 \rightarrow 4' \rightarrow 3$ by the field Ω_4 and decay γ_{34} is replaced by direct decay $4 \rightarrow 3$ at a fictitious incoherent rate of decay β_{34} with level $4'$ absent. In all essential details, the results from this analysis are in correspondence with those presented from our four-level analysis in this section. In particular, the threshold onsets in precisely the same fashion as in Fig. 2(a), and the output is "extinguished" at high pump levels for Ω_3. This turn-off appears to be associated with an AC-Stark splitting of the excited $3'$ level by the Ω_3 field that drives the $3' \rightarrow 4$ level out of resonance with the cavity due to the splitting of the upper level $3'$. Over the range of intensities explored in this section, the "quenching" behavior seems to be unrelated to any coherence effect associated with the combination of the field Ω_4 and decay γ_{34}.

IV. QUANTUM THEORY FOR A FOUR-STATE ATOM

A one-atom laser operated in a regime of strong coupling has characteristics that are profoundly altered from the familiar case (described e.g. in Refs. [31, 32]), for which the semiclassical equations are supplemented with (small) quantum noise terms. The question then arises as how to recognize a laser in this new regime of strong coupling, where we recall the difficulty that this issue engenders even for systems with critical photon number much greater than unity [19, 20, 21, 22]. The perspective that we adopt here is to investigate the continuous transformation of a one-atom laser from a domain of weak coupling for which the conventional theory should be approximately valid into a regime of strong coupling for which the full quantum theory is required.

Towards this end, we consider a scenario in which the cavity length (and hence its volume) is gradually reduced from a "large" value for which the conventional theory is valid to a "small" value for which the system is well into a regime of strong coupling. As illustrated in Figure 3 , this transformation is assumed to be under conditions of constant cavity waist w_0 and mirror reflectivity R, in which case scaling the length by a factor f causes the other parameters to scale as follows:

$$\begin{aligned} l &\rightarrow l_f = fl, \\ g &\rightarrow g_f = g/f^{1/2}, \\ \kappa &\rightarrow \kappa_f = \kappa/f, \\ \gamma &\rightarrow \gamma, \\ N_0 &\rightarrow N_0, \\ n_0 &\rightarrow n_{0f} = fn_0 \ . \end{aligned} \tag{8}$$

Recall that in the semiclassical theory illustrated in Fig. 2, the quantity $|\alpha|^2/n_{0f}$ is invariant under this transformation. By contrast, the role of single photons becomes increasingly important as the cavity length is reduced (i.e., n_{0f} becomes ever smaller), so that deviations from the familiar semiclassical characteristics should become more important, and eventually dominant.

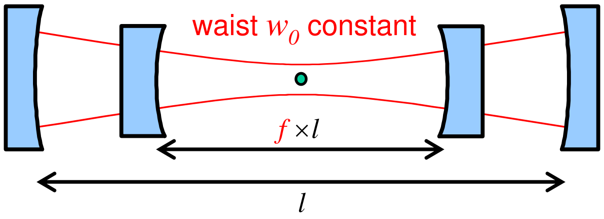

FIG. 3: Illustration of the scaling transformation considered in Eqn. 8 whereby the length of a spherical mirror Fabry-Perot cavity is transformed $l \rightarrow fl$ while the cavity waist w_0 and the atomic position are held constant. The atom is indicated by the "dot" in the center of the cavity mode.

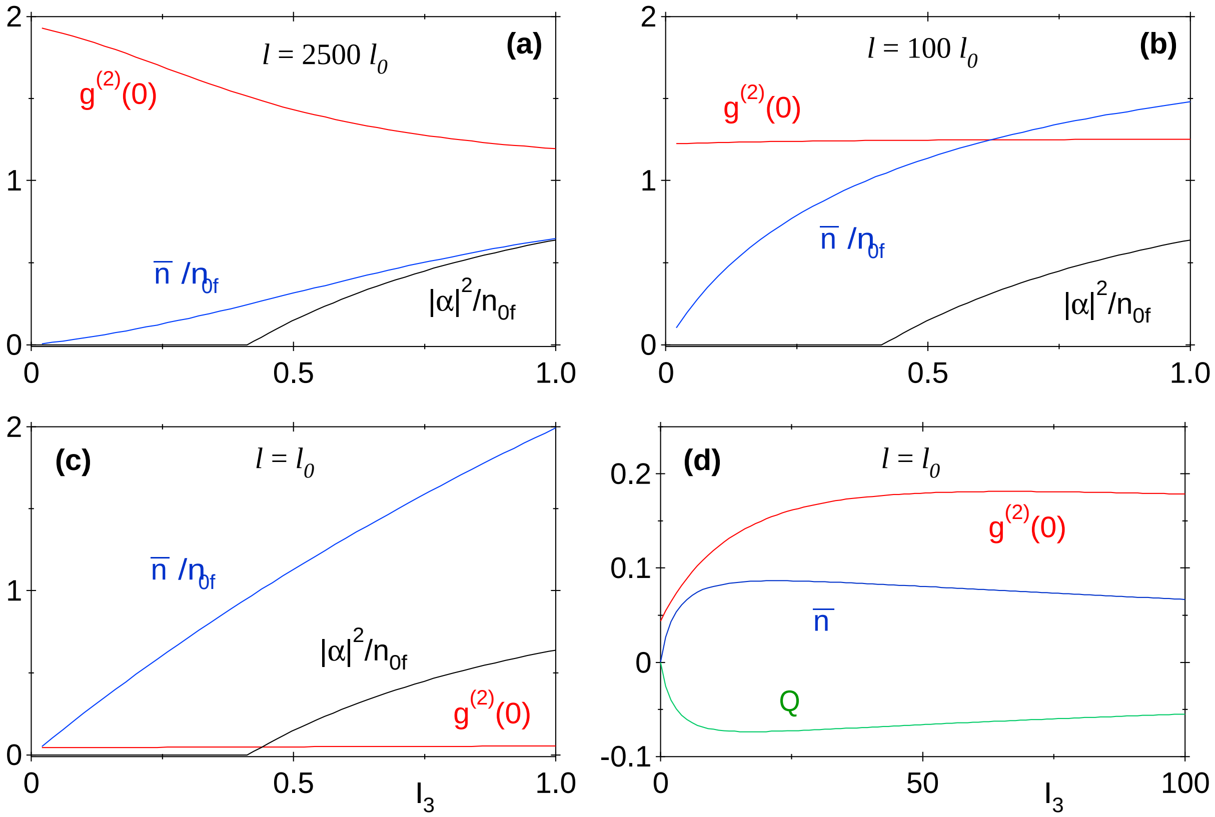

FIG. 4: The mean intracavity photon number $\bar{n}/n_{0f}$ (blue) and normalized intensity correlation function $g^{(2)}(0)$ (red) are plotted as functions of pump intensity $I_3 = (\Omega_3/2\gamma)^2$ in (a)-(d). In (a)-(c), the cavity length is made progressively shorter ($2500 l_0$, $100 l_0$, l_0), where $l_0 = 42.2\ \mu$m is the length of our actual cavity. The corresponding saturation photon numbers are n_{0f} =(33.0, 1.32, 0.013). $\bar{n}/n_{0f}$ and $g^{(2)}(0)$ are calculated from the quantum theory for the four-state system in Fig. 1, while $|\alpha|^2/n_{0f}$ given by the black curve is from the semiclassical theory. (d) $\bar{n}$ (blue), $g^{(2)}(0)$ (red), and the Mandel Q parameter (green) shown over an extended range of pump intensity I_3 for $l = l_0$. In all cases, $I_4 = (\Omega_4/2\gamma)^2 = 2$, the $3 \rightarrow 4'$ and $4 \rightarrow 4'$ transitions are driven on resonance, and the cavity detuning $\omega_{CA} = 0$. Other parameters are as given in the text.

A. Field and atom variables for various cavity lengths

Framed by this perspective, we now present results from the quantum treatment for a four-state model for the atom. Our approach is to obtain steady state results for various operator expectation values directly from numerical solutions of the master equation given in Eq. 2 by way of the *Quantum Optics Toolbox* written by S. Tan [36]. Since such numerical methods are by now familiar tools, we turn directly to results from this investigation presented in Figs. 4-9.

These figures display the behavior of various characteristics of the atom-cavity system as the cavity length is reduced from $l = 2500 l_0$ to $l = 100 l_0$ to $l = l_0$ to $l = l_0/99$, where $l_0 = 42.2 \mu$m is the actual length of our cavity. Figure 4 provides an overview of the evolution and is reproduced from the *Supplementary Information* in Ref. [1], while Figures 5-9 provide more detailed information about the intracavity field and atomic populations.

Figure 4(a-c) and part (a) in Figs. 5, 6, and 7 display the mean intracavity photon number $\bar{n}/n_{0f}$ (where n_{0f} is calculated for the particular length), and compare this result to $|\alpha|^2/n_{0f}$ from the semiclassical theory. The correspondence is close in Figs. 4(a) and 5(a) since $n_{0f} = 33$ in this case, but becomes increasingly divergent in Figs. 4(b) and 6(a) for which $n_{0f} = 1.3$, and in Figs. 4(c) and 7(a) for which $n_{0f}(f = 1) = n_0 = 0.013$ (as in our experiment).

In qualitative terms, the peak in each of the curves for $\bar{n}/n_{0f}$ in Figs. 5, 6, and 7 arises because of a "bottleneck" in the cycle $g3 \rightarrow e3 \rightarrow g4 \rightarrow e4 \rightarrow g3$. For our scheme with one atom in a cavity, this cycle can proceed at a rate no faster than that set by the decay rate γ_{34}. For higher pump intensities I_3, the quenching of the emission displayed by the semiclassical theory becomes less and less evident with decreasing l as the coherent coupling rate g becomes larger in a regime of strong coupling.

Part (b) in Figs. 5, 6, and 7 shows the populations σ_{ii} of the four states. A noteworthy trend here is the rapid

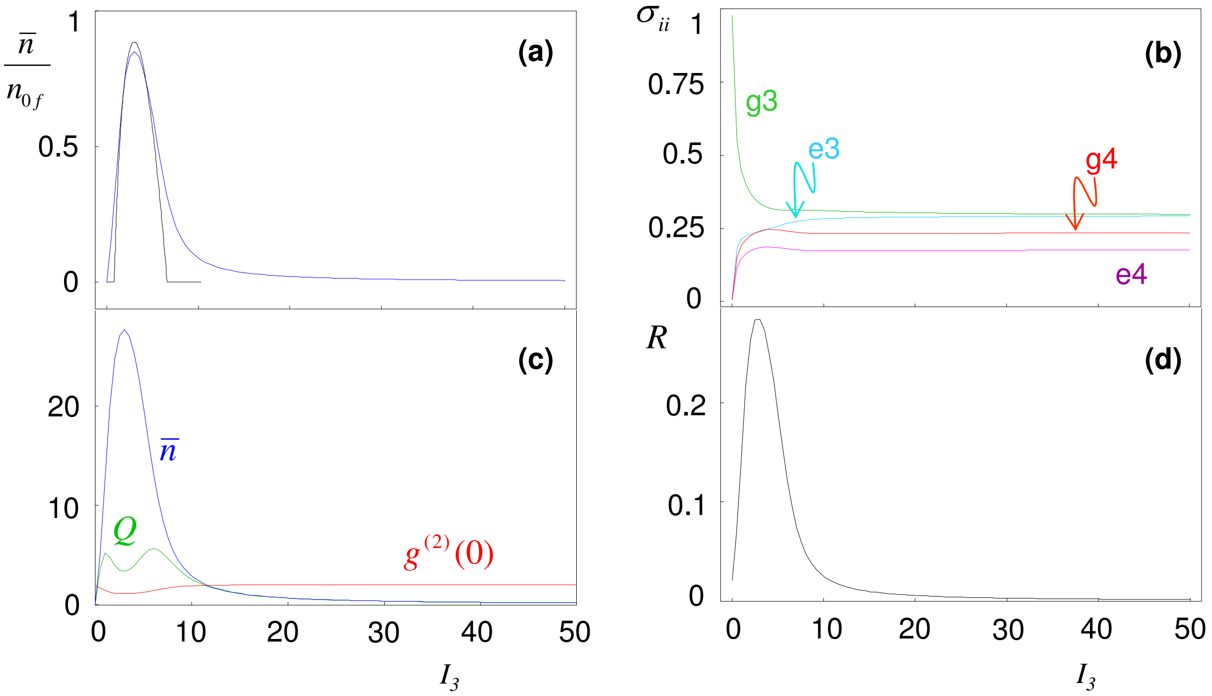

FIG. 5: Steady state solutions as functions of pump intensity I_3 obtained from the numerical solution of the master equation 2 for the four-state atom in a cavity illustrated in Fig. 1. Here, the cavity length $l = 2500 l_0$, where $l_0 = 42.2\mu$m is the cavity length in our experiment. (a) Mean intracavity photon number $\bar{n}$ normalized to the saturation photon number $n_{0f} = 33$ (in blue). The corresponding result for $|\alpha|^2/n_{0f}$ from the semiclassical theory is given by the black curve. (b) Populations σ_{ii} of the four states as labelled. (c) Mean intracavity photon number $\bar{n}$ (blue), Mandel Q parameter (green), and intensity correlation function $g^{(2)}(0)$ (red). (d) Ratio R of photon flux from the cavity mode $\kappa_f\ \bar{n}$ as compared to the rate of atomic fluorescence $\gamma_{43}\sigma_{e3,e3}$ for the excited state $e3$. In all cases, the depleting intensity $I_4 = (\frac{\Omega_4}{2\gamma})^2 = 3$ and the detunings $\Delta_{AC} = \Delta_3 = \Delta_4 = 0$. Field and atom decay rates are as specified in the text.

reduction of the population $\sigma_{e3,e3}$ with decreasing cavity length. Again, the rate g becomes larger as l is reduced, and eventually overwhelms all other rates, so that population promoted to this state is suppressed.

Figure 4 and part (c) in Figs. 5, 6, and 7 address the question of the photon statistics by plotting the Mandel Q parameter (or equivalently the Fano factor $F = Q + 1$) as well as the normalized second-order intensity correlation function $g^{(2)}(0)$ [37]. As shown in Fig. 4(a), for large $l = 2500 l_0$, the region around the semiclassical threshold displays the familiar behavior associated with a conventional laser [32, 34, 37, 38, 39], namely that $g^{(2)}(0)$ evolves smoothly from $g^{(2)}(0) \approx 2$ below the semiclassical threshold to $g^{(2)}(0) \approx 1$ above this threshold. Furthermore, Fig. 5(c) shows that the Mandel Q parameter has a maximum in the region of the threshold [19]. Beyond this conventional (first) threshold, the Mandel Q parameter in Fig. 5 (c) also exhibits a second maximum, that has been described as a "second" threshold for one-atom lasers [8], and $g^{(2)}(0)$ rises back from 1 to 2. With decreasing cavity length, these features are lost as we move into a regime of strong coupling. For example, the two peaks in Q merge into one broad minimum with $Q < 0$ indicating the onset of manifestly quantum or nonclassical character for the emission from the atom-cavity system.

Finally, part (d) in Figs. 5, 6, and 7 presents results for the ratio R, where

$$R \equiv \frac{\kappa_f \bar{n}}{\gamma_{43}\sigma_{e3,e3}} \tag{9}$$

gives the ratio of photon flux $\kappa_f \bar{n}$ from the cavity mode to the photon flux $\gamma_{43}\sigma_{e3,e3}$ appearing as fluorescence into modes other than the cavity mode from the spontaneous decay $e3 \rightarrow g4$. For a conventional laser, $\kappa_f \bar{n} \ll \gamma_{43}\sigma_{e3,e3}$ below threshold, and $\kappa_f \bar{n} \gg \gamma_{43}\sigma_{e3,e3}$ above threshold, with the laser threshold serving as the abrupt transition between these cases in the manner of a nonequilibrium phase transition [34, 39]. As illustrated in Fig. 7, no such transition is required in the regime of strong coupling; $R \gg 1$ from the onset as the pump I_3 is increased. This behavior is analogous to the "thresholdless" lasing discussed in Refs. [18, 20, 21, 22] and reviewed by Rice and Carmichael [19].

For the system illustrated in Figure 3, the progression in length reduction has a limit at $l = \lambda_0/2$ corresponding

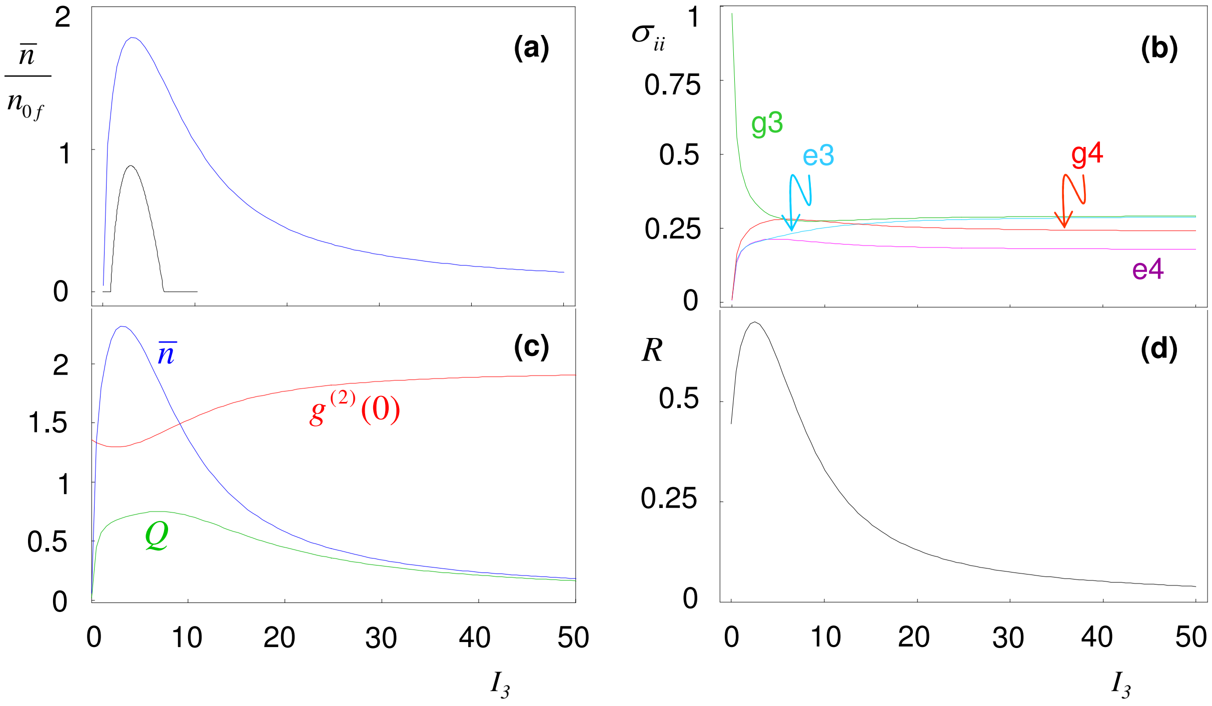

FIG. 6: Steady state solutions as functions of pump intensity I_3 obtained from the numerical solution of the master equation 2 for the four-state atom in a cavity illustrated in Fig. 1. Here, the cavity length $l = 100 l_0$, where $l_0 = 42.2 \mu$m is the cavity length in our experiment. (a) Mean intracavity photon number $\bar{n}$ normalized to the saturation photon number $n_{0f} = 1.3$ (in blue). The corresponding result for $|\alpha|^2/n_{0f}$ from the semiclassical theory is given by the black curve. (b) Populations σ_{ii} of the four states as labelled. (c) Mean intracavity photon number $\bar{n}$ (blue), Mandel Q parameter (green), and intensity correlation function $g^{(2)}(0)$ (red). (d) Ratio R of photon flux from the cavity mode $\kappa_f \ \bar{n}$ as compared to the rate of atomic fluorescence $\gamma_{43}\sigma_{e3,e3}$ for the excited state $e3$. In all cases, the depleting intensity $I_4 = (\frac{\Omega_4}{2\gamma})^2 = 3$ and the detunings $\Delta_{AC} = \Delta_3 = \Delta_4 = 0$. Field and atom decay rates are as specified in the text.

to a Fabry-Perot cavity with length equal to the lowest order longitudinal mode $\lambda_0/2$, where $\lambda_0 = 852.3$ nm is the wavelength of the cavity QED transition. To reach this limit from the length l_0 appropriate to our actual cavity, we must scale $l_0 \rightarrow f l_0$ with $f = 1/99$. In a continuation of the sequence shown in Figs. 5 , 6, and 7, we display in Fig. 8 results for such a cavity with $l = \lambda_0/2$. Note that although $C_1 = 1/N_0 \simeq 12$ is invariant with respect to this scaling and the saturation photon number is reduced to $n_{0f} = 1.31 \times 10^{-4}$, nevertheless the atom-cavity system has passed out of the domain of strong coupling, even though $(n_{0f}, N_0) \ll 1$. This is because strong coupling requires that $g_0 \gg (\gamma, \kappa)$, so that $(n_0, N_0) \ll 1$ is a necessary but not sufficient condition for achieving strong coupling. For the progression that we are considering with diminishing length (but otherwise with the parameters of our system), $l = \lambda_0/2$ does not lie within the regime of strong coupling ($g_{43}/\gamma = 61, g_{43}/\kappa = 0.40$), but rather more toward the domain of a "one-dimensional atom", for which $\kappa \gg g^2/\kappa \gg \gamma$ (see, for example, Refs. [40, 41] for theoretical discussions and a previous experimental investigation). In this domain of the Purcell effect [26, 28, 29, 30], the fractional emission into the cavity mode as compared to fluorescent emission into free space for the $3' \rightarrow 4$ transition is characterized by the parameter

$$\beta_{43} \equiv \frac{2C_1^{(43)}}{1 + 2C_1^{(43)}} \simeq 0.99, \tag{10}$$

where $C_1^{(43)} = C_1 \times (\gamma/\gamma_{43}) \simeq 48$.

As compared to Figs. 5, 6, and 7, a noteworthy feature of the regime depicted in Fig. 8 is the absence of a dependence of $g^{(2)}(0)$ on the pump level I_3. In fact, $g^{(2)}(0) \simeq 0$ over the entire range shown, so that the cavity field is effectively occupied only by photon numbers 0 and 1. In correspondence to this situation, the Mandel Q parameter in Fig. 8(c) is essentially given by the mean of the intracavity photon number, $Q \simeq -\bar{n}$, with $\bar{n} \ll 1$. Furthermore, the dominance of emission into the cavity mode over fluorescence decay becomes even more pronounced than in Fig. 7(d), as documented by the ratio R in Fig. 8(d). In agreement with expectation set by Eq. 10, note that $R \simeq \beta_{43}/(1-\beta_{43})$. All in all, the "bad-cavity" limit specified by $\kappa \gg g^2/\kappa \gg \gamma$ [40, 41] (toward which Fig. 8 is pressing) is a domain of

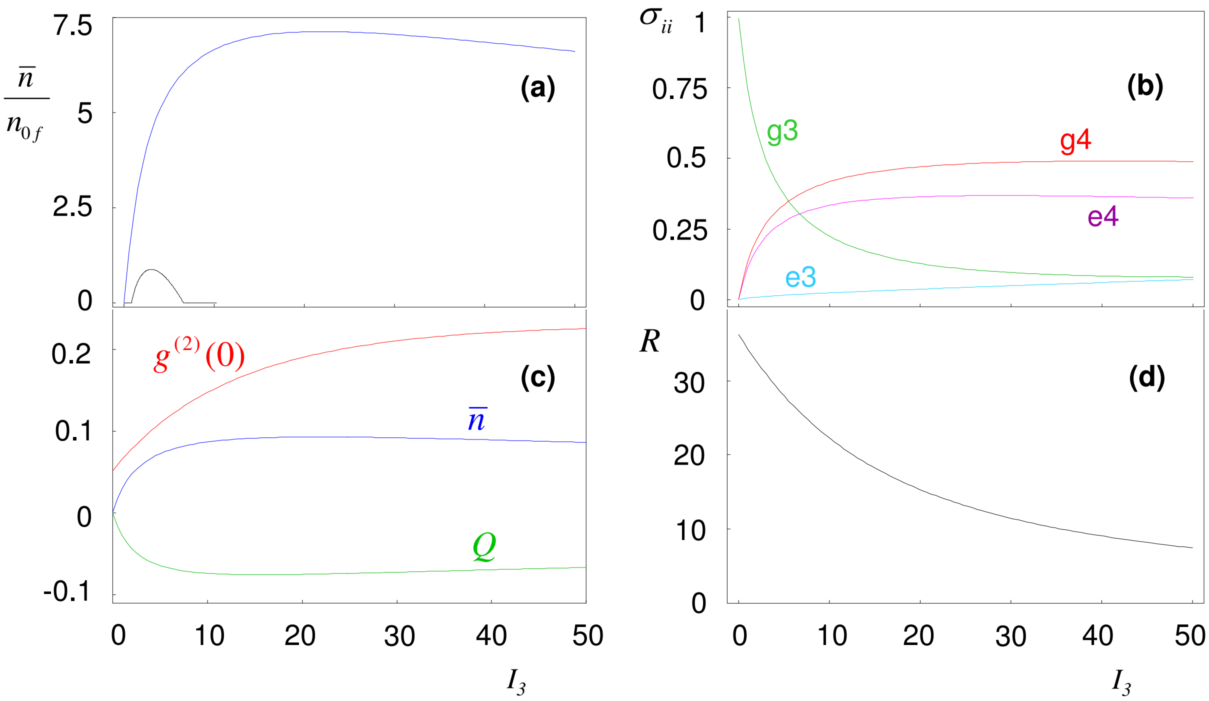

FIG. 7: Steady state solutions as functions of pump intensity I_3 obtained from the numerical solution of the master equation 2 for the four-state atom in a cavity illustrated in Fig. 1. Here, the cavity length $l = l_0$, where $l_0 = 42.2\mu$m is the cavity length in our experiment. (a) Mean intracavity photon number $\bar{n}$ normalized to the saturation photon number $n_0 = 0.013$ (in blue). The corresponding result for $|\alpha|^2/n_0$ from the semiclassical theory is given by the black curve. (b) Populations σ_{ii} of the four states as labelled. (c) Mean intracavity photon number $\bar{n}$ (blue), Mandel Q parameter (green), and intensity correlation function $g^{(2)}(0)$ (red). (d) Ratio R of photon flux from the cavity mode $\kappa\ \bar{n}$ as compared to the rate of atomic fluorescence $\gamma_{43}\sigma_{e3,e3}$ for the excited state $e3$. In all cases, the depleting intensity $I_4 = (\frac{\Omega_4}{2\gamma})^2 = 3$ and the detunings $\Delta_{AC} = \Delta_3 = \Delta_4 = 0$. Field and atom decay rates are as specified in the text.

single-photon generation for the atom-cavity system, which for $f \ll 1$ has passed out of the regime of strong coupling.

Figures 5, 6, 7, and 8 provide a step-by-step description of the evolution of the atom-cavity system from the domain of conventional laser theory ($l \gg l_0$ as in Fig. 5 with $f = 2500$), into the regime of strong coupling ($l = l_0$ as in Fig. 7 with $f = 1$), and then out of the strong-coupling regime into the Purcell domain ($l = l_0/99 \simeq \lambda_0/2$ as approached in Fig. 8 with $f = 0.01$) [26, 28, 29, 30]. We now attempt to give a more global perspective of the scaling behavior of the atom-cavity system by examining various field and atomic variables directly as functions of the scale parameter $f = l/l_0$. A particular set of such results is displayed in Figure 9, where the pump intensity $I_3 = 3$ is fixed near the peak in the output from the semiclassical theory in Fig. 2, and the recycling intensity I_4 is held constant at $I_4 = 3$.

In Fig. 9(a) the mean intracavity photon number $\bar{n}$ is seen to undergo a precipitous drop as the cavity length is made progressively shorter (i.e., increasing $f^{-1/2}$, since $l \propto f$). However, when $\bar{n}$ is normalized to the critical photon number n_{0f} , the quantity $\bar{n}/n_{0f}$ is seen to approach unity for small $f^{-1/2}$ (i.e., long cavities with $l \gg l_0$) as appropriate to the conventional theory in Fig. 5). With increases in $f^{-1/2}$ (i.e., shorter cavity lengths), $\bar{n}/n_{0f}$ rises to a maximum around $f \sim 3$ for strong coupling with $l \sim l_0$ as in Fig. 7, before then decreasing to approach a constant value for yet larger values of $f^{-1/2}$ as the system exits from the domain of strong coupling.

Also shown in Fig. 9(a) are the quantities $g^{(2)}(0)$ and $Q+1$ that characterize the photon statistics of the intracavity field. As previously noted, $g^{(2)}(0)$ lies in the range $1 \leq g^{(2)}(0) \leq 2$ for conventional laser theory, but drops below unity in the regime of strong coupling and approaches zero for $f \ll 1$. In this same limit of very small cavities in the Purcell regime, $Q \simeq -\bar{n}$.

Fig. 9(b) displays the populations for the four-state system as functions of $f^{-1/2}$. For the conventional regime with $f^{-1/2} \ll 1$, there is population inversion, $\sigma_{e3,e3} > \sigma_{g4,g4}$ (which was shown in Fig. 2 for small values of I_3), but this possibility is lost for increasing $f^{-1/2}$ (i.e., decreasing cavity length). Strong coupling dictates that the rate g dominates all others, so that appreciable population cannot be maintained in the state $e3$. Finally, Fig. 9(d) displays the dependence of the ratio $R = (\kappa_f \bar{n})/(\gamma_{43}\sigma_{e3,e3})$ on $f^{-1/2}$. From values $R < 1$ in the conventional domain, R rises monotonically with decreasing cavity length reaching the plateau $R \gg 1$ specified by Eq. 10.

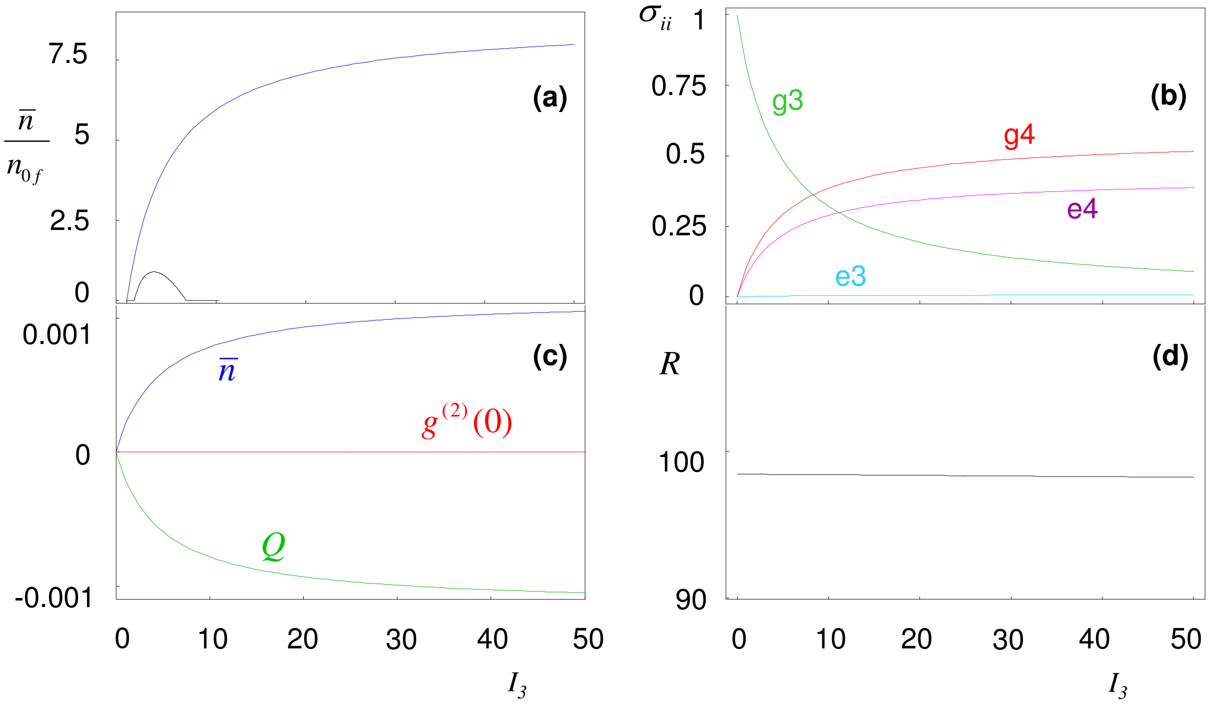

FIG. 8: Steady state solutions as functions of pump intensity I_3 obtained from the numerical solution of the master equation 2 for the four-state atom in a cavity illustrated in Fig. 1. Here, the cavity length $l = l_0/99 \simeq \lambda_0/2$ (i.e., $f = 1/99$), where $l_0 = 42.2\mu$m is the cavity length in our experiment and $\lambda_0 = 852.3$ nm is the wavelength of the cavity QED transition. (a) Mean intracavity photon number $\bar{n}$ normalized to the saturation photon number $n_{0f} = 1.31 \times 10^{-4}$ (in blue). The corresponding result for $|\alpha|^2/n_{0f}$ from the semiclassical theory is given by the black curve. (b) Populations σ_{ii} of the four states as labelled. (c) Mean intracavity photon number $\bar{n}$ (blue), Mandel Q parameter (green), and intensity correlation function $g^{(2)}(0)$ (red). (d) Ratio R of photon flux from the cavity mode $\kappa_f\ \bar{n}$ as compared to the rate of atomic fluorescence $\gamma_{43}\sigma_{e3,e3}$ for the excited state $e3$. In all cases, the depleting intensity $I_4 = (\frac{\Omega_4}{2\gamma})^2 = 3$ and the detunings $\Delta_{AC} = \Delta_3 = \Delta_4 = 0$. Field and atom decay rates are as specified in the text.

B. Vacuum-Rabi splitting

In the preceding discussion, we have compared various aspects of our one-atom system with conventional lasers and have restricted the analysis to the case of resonant excitation with $\Delta_3 = 0$. Our actual system operates in a regime of strong coupling, so that there should be an explicit manifestation of the "vacuum-Rabi" splitting associated with one quantum of excitation in the $4 \leftrightarrow 3'$ manifold [23, 24, 25].

To investigate this question, we consider the dependence of the average intracavity photon number $\bar{n}$ on the detuning Δ_3 of the pump field Ω_3, with the result of this analysis illustrated in Fig. 10. For weak excitation $I_3 \lesssim 1$ (well below the peak in Fig. 7(a)), the intracavity photon $\bar{n}$ is maximized around $\Delta_3 = \pm g_{43}$ (and not at $\Delta_3 = 0$) in correspondence to the eigenvalue structure for the $g4 \leftrightarrow e3$ manifold in presence of strong coupling. The excited state $e3$ is now represented by a superposition of the nondegenerate states $|\psi_\pm\rangle$ whose energies are split by the coupling energy $\pm\hbar g_{43}$. However, for large pump intensities $I_3 \sim 10$, this splitting is lost as the Autler-Townes effect associated with the pump field on the $g3 \leftrightarrow e3$ transition grows to exceed g_{43}.

C. Optical spectrum of the cavity emission

A central feature of a conventional laser is the optical spectrum of the emitted field, defined by

$$\Phi(\Omega) \equiv \int_{-\infty}^{+\infty} d\tau \{ \lim_{t\to\infty} \langle \hat{a}^\dagger(t)\hat{a}(t+\tau)\rangle \} \exp(-i\Omega\tau) \ , \tag{11}$$

where as in Eq. 1, $(\hat{a}^\dagger, \hat{a})$ are the creation and annihilation operators for the single-mode field of the cavity coupled to the atomic transition $e3 \leftrightarrow g4$. The results for the Schawlow-Townes linewidth are well-known and will not be

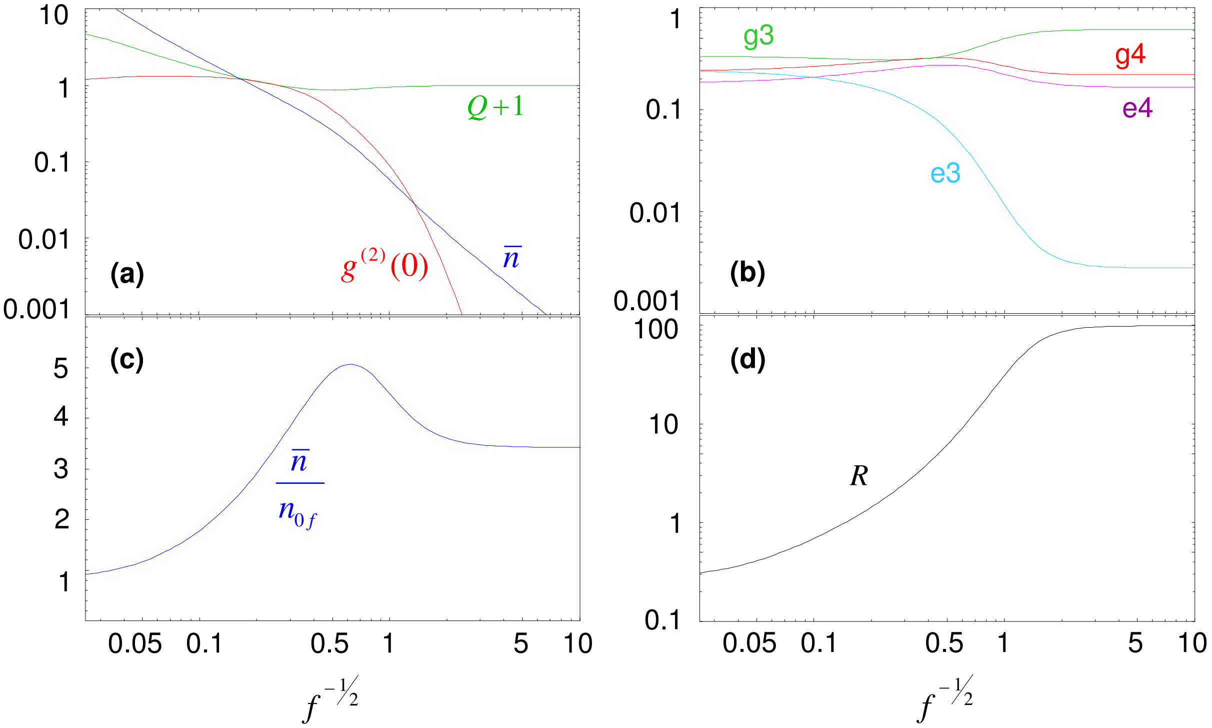

FIG. 9: Scaling behavior of various quantities as the cavity length l is varied, where $f = l/l_0$, and $l_0 = 42.2$ μm for our actual cavity. Note that $g \propto f^{-1/2}$ and $\kappa \propto f^{-1}$ and that the range in f corresponds to that spanned by Figs. 5 to 8, namely $0.01 \lesssim f \lesssim 2500$. (a) Mean intracavity photon number $\bar{n}$ (blue), the Mandel Q parameter ($Q+1$ in green), and the intensity correlation function $g^{(2)}(0)$ (red). (b) Populations σ_{ii} of the four states as labelled. (c) Mean intracavity photon number $\bar{n}$ normalized to the saturation photon number $n_{0f} = n_0 f = 0.013 \times f$. (d) Ratio R of photon flux from the cavity mode $\kappa_f \bar{n}$ as compared to the rate of atomic fluorescence $\gamma_{43}\sigma_{e3,e3}$ for the excited state $e3$, where $\kappa_f = \kappa/f$. In all cases, the pumping and recycling intensities $I_{3,4} = 3$ and the detunings $\Delta_{AC} = \Delta_3 = \Delta_4 = 0$. Field and atom decay rates are as specified in the text.

discussed here [31, 32, 34, 38, 39]. Instead, in Fig. 11 we present results specific to the domain of operation of our system.

For the choice of parameters corresponding to Fig. 7, $\Phi(\Omega)$ in Fig. 11(a) exhibits a pronounced two-peak structure, with the positions of the peaks corresponding to the Autler-Townes splitting of the ground state by the recycling field Ω_4. Contrary to what might have been expected from the analysis of the previous section, $\Phi(\Omega)$ shows no distinctive features associated with the vacuum-Rabi splitting of the excited state. For reduced values of pumping and recycling intensities $I_{3,4} = 0.5$, there are small features in the optical spectrum at $\Omega \approx \pm g_{43}$, as is illustrated in Fig. 11 when $\Phi(\Omega)$ is plotted on logarithmic scale. With respect to the complex degree of coherence [37], the coherence properties of the light from the one-atom laser in the regime of strong coupling are set simply by the inverse of the spectral width of $\Phi(\Omega)$, which can be determined from the plots in Fig. 11.

The curves shown in Fig. 11 are calculated by way of the quantum regression theorem applied to the four-state system of Fig. 1. From the quantum regression theorem, we have that the two time correlation function in Eq. 11 is given by

$$\langle a^\dagger(0)a(\tau)\rangle = Tr[\rho_{ss}a^\dagger(0)a(\tau)] = Tr[\rho(\tau)a(0)]$$

where $\rho(\tau)$ is obtained by numerically evolving

$$\rho_0 = \rho_{ss}a^\dagger(0)$$

under the master equation, and ρ_{ss} is the steady state density matrix. By Fourier transforming the correlation function according to Eq. 11, we obtain the optical spectrum.

The optical spectrum of the emitted light from our cavity could in principle be measured by way of heterodyne detection. The cavity output would be combined on a highly transmissive beam splitter with a local oscillator beam that is frequency shifted by an interval $\Delta\omega$ that is large compared to the range of frequencies in the output field. The optical spectrum is then obtained by taking the Fourier transform of autocorrelation function of the resulting

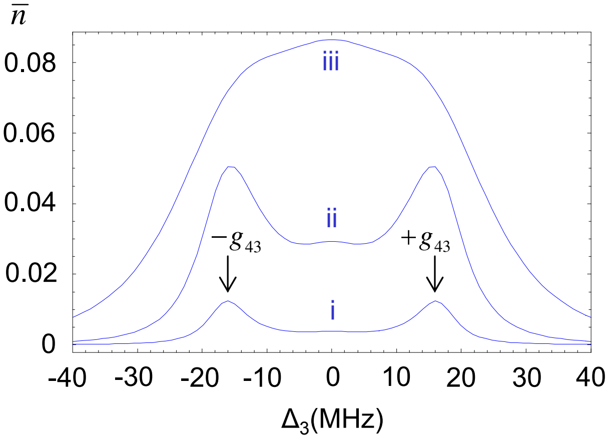

FIG. 10: The mean intracavity photon number $\bar{n}$ versus the detuning Δ_3 (in cycles/sec) of the pump field Ω_3, where $\Delta_3 = 0$ corresponds to the transition frequency ω_{33}. The three curves are for increasing pump intensity *(i)* $I_3 = 0.1$, *(ii)* $I_3 = 1.0$, *(iii)* $I_3 = 10.0$. The arrows indicate the positions of the expected "vacuum-Rabi" peaks at $\pm g_{43}$, where $g_{43}/2\pi = 16$ MHz. In all cases, the recycling field Ω_4 is on resonance $\Delta_4 = 0$ and has intensity $I_4 = 3$.

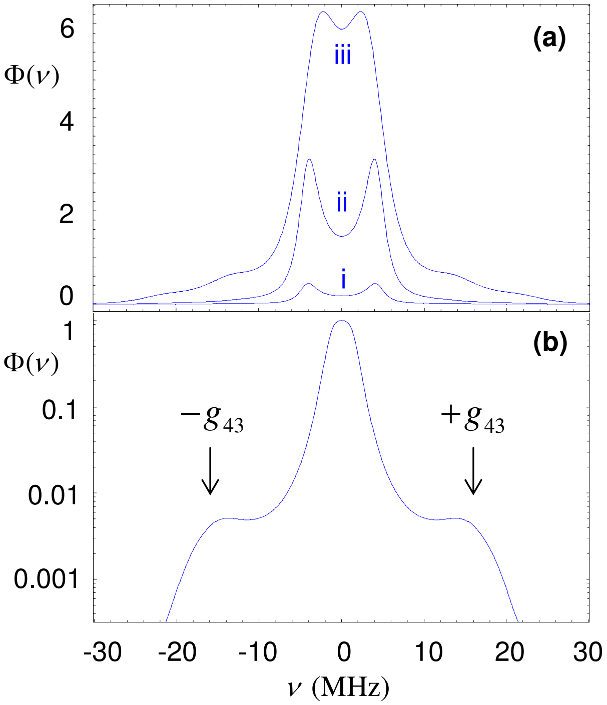

FIG. 11: The optical spectrum $\Phi(\nu)$ as a function of frequency offset ν (in cycles/sec, $\Omega = 2\pi\nu$), where $\nu = 0$ corresponds to the transition frequency ω_{43}. (a) Three spectra $\Phi(\nu)$ for increasing pump intensity *(i)* $I_3 = 0.1$, *(ii)* $I_3 = 1.0$, *(iii)* $I_3 = 10.0$, with the recycling intensity $I_4 = 3$ in all cases. The overall normalization of $\Phi(\nu)$ is arbitrary, but is common for the three cases. (b) $\Phi(\nu)$ on a logarithmic scale for decreased intensities $I_3 = I_4 = 0.5$, with the peak value of Φ scaled to unity. The arrows indicate the position of the expected "vacuum-Rabi" peaks at $\pm g_{43}$, where $g_{43}/2\pi = 16$ MHz. In all cases in (a) and (b), the pumping field Ω_3 and the recycling field Ω_4 are on resonance with their respective transitions ($\Delta_3 = 0 = \Delta_4$).

heterodyne current. Although we have not carried out this procedure experimentally, it is straightforward to model using a quantum jumps simulation of the four state model. We have computed such spectra for several values of I_3, using a local oscillator flux equal to κ. This is an experimentally reasonable value, since it is small enough so as to not saturate the detectors, yet large enough that, as our further simulations indicate, increasing the flux does not significantly change the resulting spectrum. The results for the spectrum obtained from this quantum jumps simulation agree reasonably well with results from the quantum regression theorem presented in Fig. 11.

V. QUANTUM THEORY INCLUDING ZEEMAN STATES AND TWO CAVITY MODES

In an attempt to provide a more detailed quantitative treatment of our experiment, we have developed a model that includes all of the Zeeman states (F, m_F) for the $F = 3, 4$ ground levels and the $F' = 3', 4'$ excited levels of the $6S_{1/2} \leftrightarrow 6P_{3/2}$ transition in atomic Cesium, of which there are 32 in total. We also include two cavity modes with orthogonal linear polarizations to describe the two nearly degenerate TEM_{00} modes of our cavity [43], with three Fock states for each mode $\{|0\rangle, |1\rangle, |2\rangle\}$. The total dimension of the Hilbert space for this set of atomic and field states is then $d = 32 \times 3 \times 3 = 288$, making it impractical to obtain steady state solutions from the master equation directly. Instead, we employ the *Quantum Optics Toolbox* [36] to implement a quantum jumps simulation, with various expectation values computed from the stochastic trials.

In broad outline, our expanded model includes Hamiltonian terms of the form of Eq. 1, with now the terms $\hat{\sigma}_{ij}$ generalized to incorporate each of the various Zeeman states. Likewise, the coherent coupling of the atom to the cavity takes into account two orthogonally polarized modes $(\hat{a}, \hat{b})$. The operators $\hat{L}_i$ are similarly modified to obtain a new master equation that includes the full set of decay paths among the various states (i.e., $\sigma_\pm, \pi$ transitions), as well as the associated quantum collapse terms in the simulation.

We attempt to describe the dynamics arising from the complex state of spatially varying polarization associated with the $\Omega_{3,4}$ beams by way of the following simple model. In a coordinate system with the x, z directions perpendicular to the cavity axis along y, the $\Omega_{3,4}$ beams propagate along x, z with orthogonal $\sigma_\pm$ configurations. The helical patterns of linear polarization from pairs of counter-propagating beams then give rise to terms in the interaction Hamiltonians $\hat{H}_{2,3}$ of the form

$$\begin{aligned} \hat{H}_2 \;=\; & \frac{1}{2\sqrt{2}}\Omega_3[(\hat{\Sigma}^z_{g3,e3} + \hat{\Sigma}^z_{e3,g3})\sin(\theta_{3x}) \\ & +(\hat{\Sigma}^x_{g3,e3} + \hat{\Sigma}^x_{e3,g3})\sin(\theta_{3z})] \\ & +\frac{1}{2}\Omega_3[(\hat{\Sigma}^y_{g3,e3} + \hat{\Sigma}^y_{e3,g3})(\cos(\theta_{3x}) + \cos(\theta_{3z}))] \end{aligned} \tag{12}$$

and similarly for $\hat{H}_3$ to describe the Ω_4 beams with independent phases $(\theta_{4x}, \theta_{4z})$. Here Ω_3 and Ω_4 are Rabi frequencies corresponding to the incoherent sum of the intensities of the four individual beams. In Eq. 12, the operators $\hat{\Sigma}^{x,y,z}_{g3,e3}$ are linear combinations of various atomic projection operators for the diverse Zeeman-specific transitions for linear polarization along x, y, z, and are given explicitly by

$$\hat{\Sigma}^x_{g3,e3} \;=\; -\frac{1}{\sqrt{2}}(\hat{\Sigma}^{+1}_{g3,e3} - \hat{\Sigma}^{-1}_{g3,e3}) \tag{13}$$

$$\hat{\Sigma}^y_{g3,e3} \;=\; \frac{i}{\sqrt{2}}(\hat{\Sigma}^{+1}_{g3,e3} + \hat{\Sigma}^{-1}_{g3,e3}) \tag{14}$$

$$\hat{\Sigma}^x_{g3,e3} \;=\; \hat{\Sigma}^0_{g3,e3} \tag{15}$$

where

$$\hat{\Sigma}^q_{g3,e3} = \sum_m \sum_{m'} |g3, m\rangle\langle 3, m; 1, q|4, m'\rangle\langle g4, m'| \tag{16}$$

The phases θ_i arise from the spatial variations of the polarization state of the $\Omega_{3,4}$ beams, and are given, for example, by $\theta_{3x} = k_{3x}x$ with k_{3x} as the wave vector of the pair of Ω_3 beams propagating along x.

The $\Omega_{3,4}$ beams tend to optically pump the atom into dark states, with this pumping counterbalanced by atomic motion leading to cooling [44] and by any residual magnetic field. In our case, imperfections in the FORT polarization [42, 43] result in a small pseudo-magnetic field along the cavity axis y [45] with peak magnitude $B^F_y \simeq 0.75$ G. This pseudo-field B^F_y is included in our simulations and tends to counteract optical pumping by the $\Omega_{3,4}$ beams into dark states for linear polarization in the $x - z$ plane, $\theta_{3x} = \theta_{3z} = \theta_{4x} = \theta_{4z} = \pi/2$, but has no effect for polarization along the cavity axis y, $\theta_{3x} = \theta_{3z} = \theta_{4x} = \theta_{4z} = 0$.

Overall, the operation of our driven atom-cavity system involves an interplay of cycling through the levels $g3 \rightarrow e3 \rightarrow g4 \rightarrow e4 \rightarrow g3$ to achieve output light on the $e3 \rightarrow g4$ transition, and of polarization gradient cooling for extended trapping times. This latter process involves atomic motion through the polarization gradients of the $\Omega_{3,4}$ beams and is greatly complicated by the presence of B^F_y. The detunings and intensities of the $\Omega_{3,4}$ beams are chosen operationally such as to optimize the output from our one-atom laser in a regime of strong coupling, while at the same time maintaining acceptable trapping times, as shown in Fig. 2 of Ref. [1].

A. Mean intracavity photon number as a function of pump intensity

In this section, we present simulation results for the mean intracavity photon number versus pump intensity. In qualitative terms, we should expect that the output flux $\kappa\bar{n}$ predicted from the full multi-state model is significantly below that calculated from the four-state model presented in Section IV. This is because the atom necessarily spends increased time in manifolds of dark states associated with the pumping by the $\Omega_{3,4}$ beams.

We can modify the four level model to account for these effects by reducing the decay rate $\gamma_{34} \rightarrow \gamma'_{34}$. The slower cycling of the atom due to the reduction of γ'_{34} approximates, in a phenomenological way, the slowing effect on the recycling of the atom due to optical pumping into dark states. We find that a value $\gamma'_{34} = 0.07 \times \gamma_{34}$ gives a good fit to the data (Fig. 12(a,b)). We plot the intracavity photon number versus $x \equiv (7/9)(I_3/I_4)$, since we estimate that either measured intensity alone is uncertain by a factor of about 2, but the ratio is known much more accurately.

For the multi-level simulation, we use two different models to generate mean intracavity photon number versus pump intensity curves. In the first model, we neglect the motion of the atom and attempt to capture the essential features of the optical pumping processes via a single constant phase $\theta = \theta_{3x} = \theta_{3z} = \theta_{4x} = \theta_{4z}$. The choice $\theta = 0$ gives no output light, since the $\Omega_{3,4}$ beams pump the atom into dark states. The value $\theta = \pi/2$ chosen for the comparison in Fig. 12(c,d) gives good correspondence between the simulations and our measurements with the adjustment of no other parameters. For this curve, we plot the average $(\bar{n}_a + \bar{n}_b)/2$ of the intracavity field for the two cavity modes a and b.

As a second, more sophisticated model, we assume that the atom moves at a constant velocity in the radial direction. This gives time dependent phases; for example, if we assume that the x coordinate of the atom is

$$x(t) = x_0 + v_x t$$

then

$$\theta_{3x}(t) = k_{3x}x = \theta_{3x,0} + \omega_{3x}t$$

where $\theta_{3x,0} = k_{3x}x_0$, $\omega_{3x} = k_{3x}v_x$. For a single simulation run we randomly choose the velocity of the atom and initial phases of the $\Omega_{3,4}$ pumping beams; the intensities from 20 such runs are averaged for each value of x. The velocities are chosen uniformly in the range $10 - 20cm/s$, which gives angular frequencies in the range $2\pi 100 - 200kHz$. The resulting input/output curve is plotted in Fig 12(e,f). As before, we plot the average of the intracavity field for the two cavity modes.

We make no claim for detailed quantitative agreement between theory and experiment, as the simulations are sensitive to the parameters which are known only approximately, such as the intensity of the $\Omega_{3,4}$ pumping beams and the magnitude of the pseudo and real magnetic fields. Also, the simulations neglect a number of features of the real system, such as atomic motion in the axial direction, the dependence of the cavity coupling g on the position of the atom, and a possible intensity imbalance in the $\Omega_{3,4}$ pumping beams. However, the simulations do support the conclusion that the range of coupling values g that contribute to our results is restricted roughly to $0.5g_0 \lesssim g \lesssim g_0$. Furthermore, the simulations yield information about the atomic populations, from which we deduce that the rate of emission from the cavity $\kappa\bar{n}$ exceeds that by way of fluorescent decay $3' \rightarrow 4$, $\gamma_{43'}\langle\sigma_{3'3'}\rangle$, by roughly tenfold over the range of pump intensity I_3 shown in Fig. 12a.

B. Photon statistics as expressed by the intensity correlation function $g^{(2)}(\tau)$

In addition to measurements of $\bar{n}$ versus pumping rate, we have also investigated the photon statistics of the light emitted by the TEM$_{00}$ mode of the cavity by way of the two single-photon detectors $D_{1,2}$ illustrated in Fig. 1 of Ref. [1]. From the cross-correlation of the resulting binned photon arrival times and the mean counting rates of the signals and the background, we construct the normalized intensity correlation function (see the *Supplementary Information* accompanying Ref. [1])

$$g^{(2)}(\tau) = \frac{\langle : \hat{I}(t)\hat{I}(t+\tau) : \rangle}{\langle : \hat{I}(t) : \rangle^2} \ , \tag{17}$$

where the colons denote normal and time ordering for the intensity operators $\hat{I}$ [37].

Two measurements for $g^{(2)}(\tau)$ from Figure 4 of Ref. [1] are reproduced in (a,b) of Figs. 13 and 14, together with results from our quantum jumps simulation from the constant phase model with $\theta = \pi/2$, in (c,d). In Fig. 13, we again have $I_4 \simeq 13$ and the pump intensity I_3 is set for operation with $x \simeq 0.17$ near the "knee" in $\bar{n}$ versus x, while in Fig. 14, the pump level is increased to $x \simeq 0.83$. These measurements demonstrate that the light from the

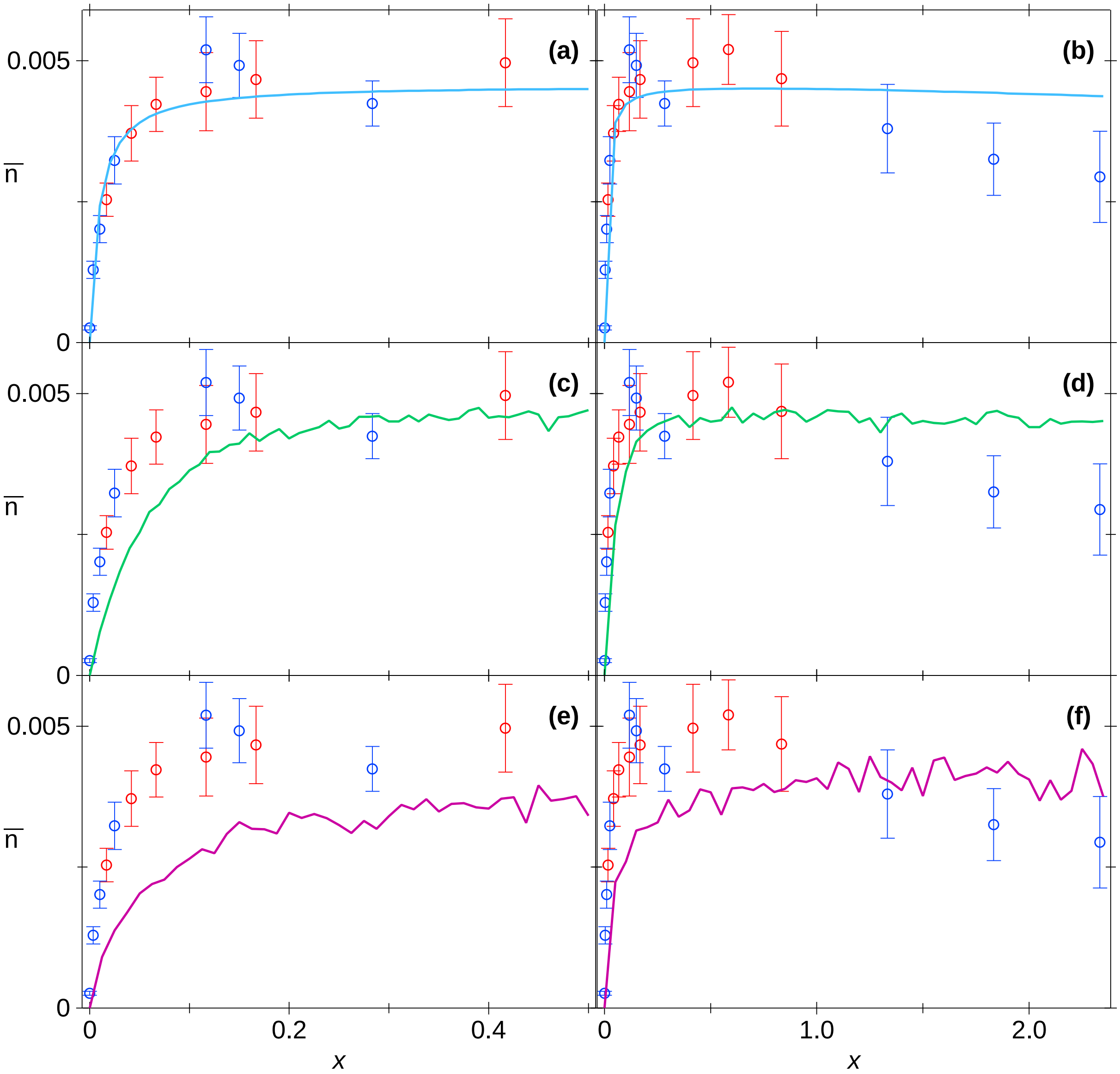

FIG. 12: Comparison of theory and experiment for the intracavity photon number $\bar{n}$ as a function of pump intensity $x \equiv (7/9)(I_3/I_4)$ for fixed $I_4 = 13$ (corresponding to a measured intensity of $50mW/cm^2$). The measurements (points with error bars) are from Figure 3 of Ref. [1]. (a,b) $\bar{n}$ versus pump strength x for the four level model with $\gamma'_{43} = 0.07 \times \gamma_{43}$. (c,d) $\bar{n}$ versus pump strength x for the constant phase model with $\theta = \pi/2$. (e,f) $\bar{n}$ versus pump strength x for the constant velocity model described in the text. The immediate onset of emission supports the conclusion of “thresholdless” lasing. Two independent sets of measurements are shown as the red and blue points, and agree reasonably well with each other. Details of the measurements can be found in Ref. [1], while the parameters for the simulation are given in the text.

atom-cavity system is manifestly quantum (i.e., nonclassical) and exhibits photon antibunching $g^{(2)}(0) < g^{(2)}(\tau)$ and sub-Poissonian photon statistics $g^{(2)}(0) < 1$ [37]. In agreement with the trend predicted by the four-state model in Fig. 7(c) (as well as by the full quantum jumps simulation), $g^{(2)}(0)$ increases with increasing pump intensity, with a concomitant decrease in these nonclassical effects. The bottleneck associated with the recycling process leads to this nonclassical character, since detection of a second photon given the first detection event requires that the atom be recycled from the $F = 4$ ground state back to the $F = 3$ ground. In this regard, we point to the prior work on pump-noise suppressed lasers in multi-level atomic systems, as for example, in Ref. [47].

In more quantitative terms, theoretical results for $g^{(2)}(\tau)$ from the full quantum jumps simulation are given in parts (c,d) of Figs. 13 and 14 for $x = 0.17$ and $x = 0.83$. The excess fluctuations $g^{(2)}(\tau) \gtrsim 1$ extending over $\tau \simeq \pm 1$ μs appear to be related to the interplay of atomic motion and optical pumping into dark states [44], as well as Larmor precession that arises from residual ellipticity in polarization of the intracavity FORT [43, 45].

These results for $g^{(2)}(\tau)$ provide a perspective on the issue of whether the cavity is effectively "empty" since $\bar{n}$ is quite small. Based upon the mean photon flux from the cavity, this is a reasonably inference, but it is also misleading. The nonzero values for $g^{(2)}(\tau=0) \simeq 0.3, 0.6 \gg 0.01$ in Figs. 13 and 14 are in fact due to the presence of more than one photon in the cavity. Although the mean intracavity photon number is only $\bar{n} \sim 0.005$, this number is comparable to the saturation photon number $n_0 \simeq 0.013$. Indeed, the quantum statistical character of the intracavity field is determined from the self-consistent interplay of atom and cavity field as in standard laser theories, even though it might appear as this interplay is not relevant to the determination of a dynamic steady state. Figure 9 attempts to illustrate this point by investigating the passage from the domain of conventional laser theory through the regime of strong coupling and thence into a domain of single photon generation with $g^{(2)}(\tau=0) \simeq 0$ over the entire range of pumping conditions.

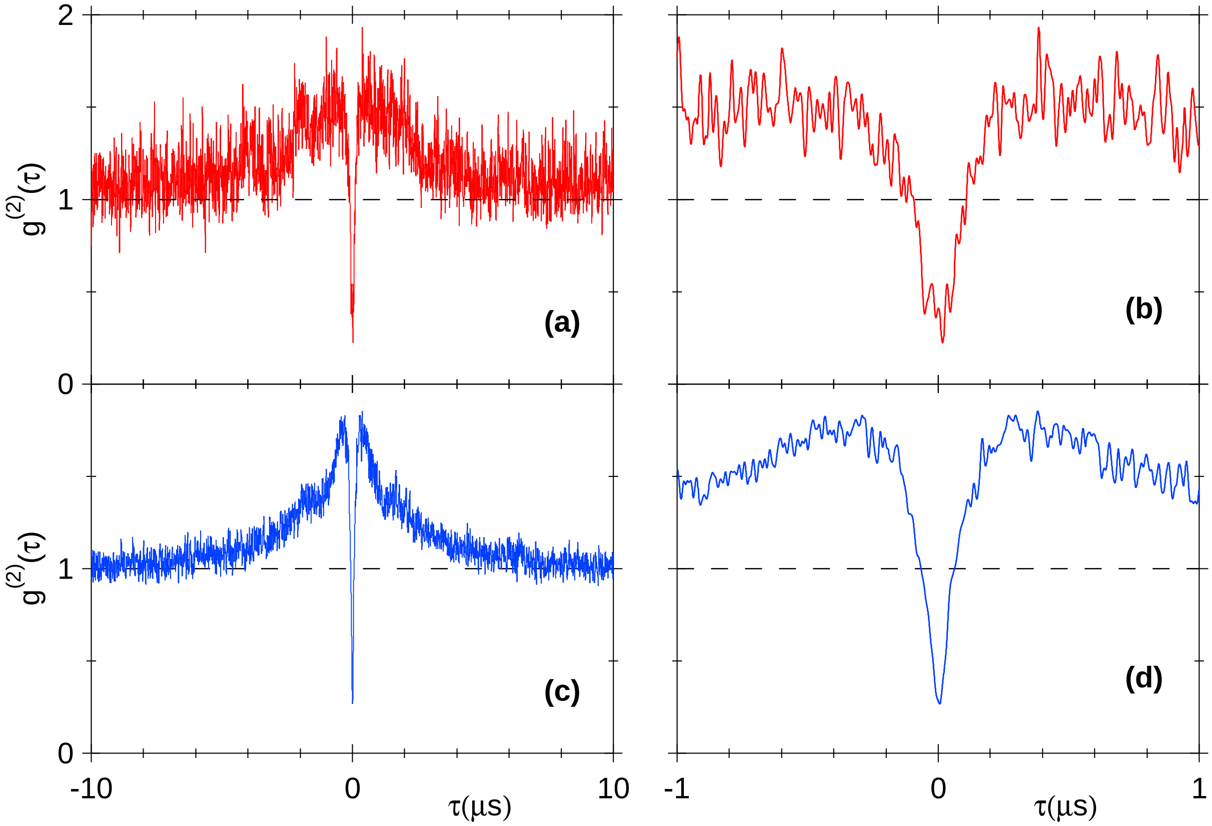

FIG. 13: The intensity correlation function $g^{(2)}(\tau)$ of the one-atom laser. (a,b) $g^{(2)}(\tau)$ for $x \simeq 0.17$ as experimentally determined in Ref. [1]. (c,d) Theoretical result for $g^{(2)}(\tau)$ for $x = 0.17$ from a quantum jumps simulation with $\theta = \pi/2$. All traces have been "smoothed" by convolution with a Gaussian function of width $\sigma = 5$ ns.

C. Discussion of possible coherence effects

In Section IIIA we briefly described our analysis of an equivalent Raman scheme to address the question of possible coherence effects associated with the Ω_4 recycling beam. Beyond this analysis, we have also considered the possibility that various other coherent processes associated with the pump fields might be important. One concern relates to the possibility that 4-wave mixing processes could be important, as for example, in a wave-mixing process that cycles the atom $3 \rightarrow 3' \rightarrow 4 \rightarrow 4' \rightarrow 3$ [46]. From an operational perspective, if there were to be a correlated process involved in the cycling of the atom $3 \rightarrow 3' \rightarrow 4 \rightarrow 4' \rightarrow 3$, then two photons would be emitted into the cavity mode (the "signal" on the $3' \rightarrow 4$ transition and the "idler" on the $4' \rightarrow 3$ transition). In this case since we employ no filter to block the "idler" field separated by 9.2GHz, the measured intensity correlation function $g^{(2)}(\tau)$ for the emitted light from the cavity would exhibit bunching around $\tau = 0$, instead of the observed antibunching and sub-Poissonian character. The measured character of $g^{(2)}(\tau)$ therefore argues against a coherent process that cycles the atom from an initial quantum state and back to that state by way of coherent processes involving coupling to the cavity field.

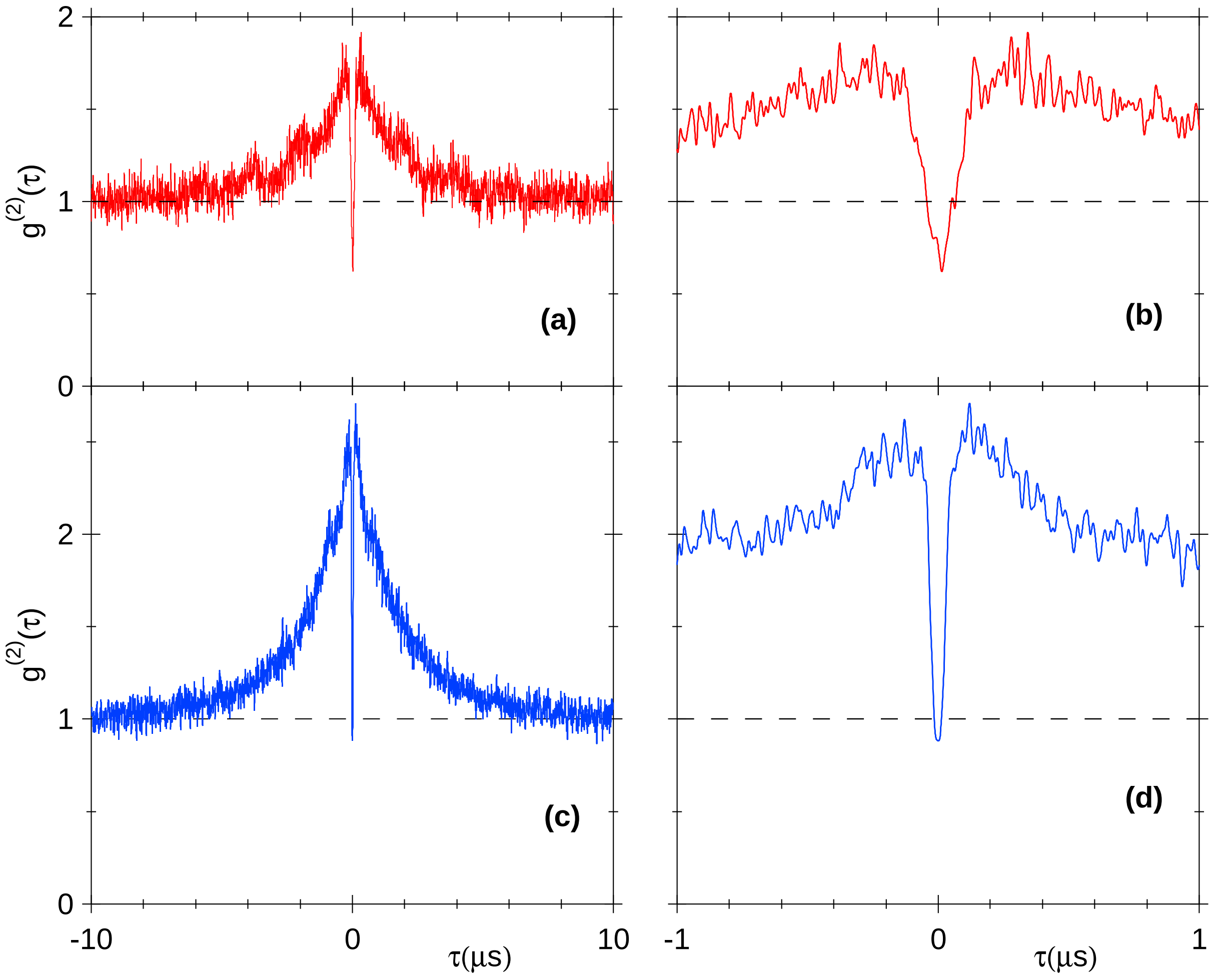

FIG. 14: The intensity correlation function $g^{(2)}(\tau)$ of the one-atom laser. (a,b) $g^{(2)}(\tau)$ for $x \simeq 0.83$ as experimentally determined in Ref. [1]. (c,d) Theoretical result for $g^{(2)}(\tau)$ for $x = 0.83$ from a quantum jumps simulation with $\theta = \pi/2$. All traces have been "smoothed" by convolution with a Gaussian function of width $\sigma = 5$ ns.

We also note that the coherent coupling of the cavity field and atom for the $4' \rightarrow 3$ transition is greatly suppressed due to the large detuning $\simeq 9.2$GHz, leading to an effective coupling coefficient $(g_{eff}/2\pi \sim 30$ kHz$) \ll (\gamma_{||}/2\pi \simeq 5.2$ MHz). Therefore, for whatever mixing processes, the coupling to the external vacuum modes characterized by the rate $\gamma_{||}$ should dominate that due to g_{eff}. In this regard, note that we have included the effect of off-resonant coupling of the $4'$ excited state in our simulations (which is only $\simeq 200$ MHz detuned). The relevant process is then excitation $4 \rightarrow 4'$ via the Ω_4 pump field, followed by emission into the cavity mode due to the coherent coupling of the transition $4' \rightarrow 4$. This coupling increases the intracavity photon number by only about 10%, suggesting that coupling for the $4' \rightarrow 3$ transition 9.2 GHz away is negligible.

In support of these comments, our detailed numerical simulations agree sensibly well with the observed behavior of $g^{(2)}(\tau)$ (as in Figures 13 and 14), and do not include any "wave-mixing" effects. This statement is likewise valid for the dependence of photon number versus pump level Ω_3^2. Furthermore, as previously discussed, the model calculation for a four-state system agrees well in its essential characteristics with a three-state system where the decay of the ground state $4 \rightarrow 3$ is via an ad hoc spontaneous process (as in a Raman laser) rather than by pumping $4 \rightarrow 4'$ and decay $4' \rightarrow 3$.

A final general comment relates to the nature of phase-matching (e.g., as applied to 4-wave mixing and parametric down conversion) for a single atom in a cavity. For a sample of atoms (or a crystal), there is a geometry that defines directions for which fields from successive atoms might add constructively for various waves (e.g., pump, signal, idler). Cavities can then be placed around these directions to enhance the processes (e.g., the threshold for an optical parametric oscillator is reduced by a factor of the square of the cavity finesse for resonant enhancement of both signal and idler fields). Clearly a cavity would be ineffective if its geometry did not match the preferred geometry defined by the sample and pump beams. However, for a single atom as in our experiment, these considerations do not apply in nearly the same fashion. The relevant issues are the coherent coupling coefficients g_{ij} of the various atomic transitions to the cavity field.

VI. SUMMARY

We have presented a simplified four-level model which describes the qualitative features of our experiment. We have shown how decreasing the cavity length causes the model system to move from a regime of weak coupling, where the semiclassical laser theory applies, into a regime of strong coupling, where quantum deviations become important. The four-state model predicts many of the observed features of our experimental system, including the qualitative shape of the intracavity photon number versus pumping intensity curve, and photon antibunching.

In addition, to predict quantitative values for comparison with our experimental results, we have developed a full multi-level model which correctly describes optical pumping and Larmor precession effects within the Zeeman substructure. We have shown that these effects play an important role in describing the observed input/ output characteristics of the system, and that by including a simple model for the motion of the atom we can obtain reasonable agreement with the experimentally observed curve. We have also used the simulation to calculate intensity correlation functions, and have compared these results to measurements of $g^{(2)}(\tau)$ from our experiment.

We gratefully acknowledge interactions with K. Birnbaum, L.-M. Duan, D. J. Gauthier, T. Lynn, T. Northup, A. S. Parkins, and D. M. Stamper-Kurn. This work was supported by the National Science Foundation, by the Caltech MURI Center for Quantum Networks under ARO Grant No. DAAD19-00-1-0374, and by the Office of Naval Research.

---

[1] J. McKeever, A. Boca, A. D. Boozer, J. R. Buck, and H. J. Kimble, Nature (London) **425**, 268 (2003).
[2] Y. Mu and C. M. Savage, Phys. Rev. A **46**, 5944 (1992).
[3] C. Ginzel, H.-J. Briegel, U. Martini, B.-G. Englert, and A. Schenzle, Phys. Rev. A **48**, 732 (1993).
[4] T. Pellizzari and H. Ritsch, Phys. Rev. Lett. **72**, 3973 (1994).
[5] T. Pellizzari and H. Ritsch, J. Mod. Opt. **41** , 609 (1994).
[6] P. Horak, K. M. Gheri, and H. Ritsch, Phys. Rev. A **51**, 3257 (1995).
[7] H.-J. Briegel, G. M. Meyer, and B.-G. Englert, Phys. Rev. A **53**, 1143 (1996).
[8] G. M. Meyer, H.-J. Briegel, and H. Walther, Europhys. Lett. **37**, 317 (1997).
[9] M. Löffler, G. M. Meyer, and H. Walther, Phys. Rev. A **55**, 3923 (1997).
[10] G. M. Meyer, M. Löffler, and H. Walther, Phys. Rev. A **56**, R1099 (1997).
[11] G. M. Meyer and H.-J. Briegel, Phys. Rev. A **58**, 3210 (1998).
[12] B. Jones, S. Ghose, J. P. Clemens, P. R. Rice, and L. M. Pedrotti, Phys. Rev. A **60**, 3267 (1999).
[13] Y.-T. Chough, H.-J. Moon, H. Nha, and K. An, Phys. Rev. A **63**, 013804 (1996).
[14] C. Di Fidio, W. Vogel, R. L. de Matos Filho, and L. Davidovich, Phys. Rev. A **65**, 013811 (2001).
[15] S. Ya. Kilin and T. B. Karlovich, JETP **95**, 805 (2002).
[16] J. P. Clemens, P. R. Rice, and L. M. Pedrotti (2003).
[17] T. Salzburger and H. Ritsch, quant-ph/0312181.
[18] F. De Martini and G. R. Jacobivitz, Phys. Rev. Lett. **60**, 1711 (1988).
[19] P. R. Rice and H. J. Carmichael, Phys. Rev. A **50**, 4318 (1994).
[20] R. Jin, D. Boggavarapu, M. Sargent III, P. Meystre, H. M. Gibbs, and G. Khitrova, Phys. Rev. A **49**, 4038 (1994).
[21] G. Björk, A. Karlsson, and Y. Yamamoto, Phys. Rev. A **50**, 1675 (1994).
[22] I. Protsenko, P. Domokos, V. Lefevre-Seguin, J. Hare, J. M. Raimond, and L. Davidovich, Phys. Rev. A **59**, 1667 (2001).
[23] J. J. Sanchez-Mondragon, N. B. Narozhny, and J. H. Eberly, Phys. Rev. Lett. **51**, 550 (1983).
[24] G. S. Agarwal, Phys. Rev. Lett. **53**, 1732 (1984).
[25] R. J. Thompson, G. Rempe, and H. J. Kimble, Phys. Rev. Lett. **68**, 1132 (1992).
[26] *Cavity Quantum Electrodynamics*, edited by P. Berman (Academic Press, San Diego, 1994).
[27] *Cavity Quantum Optics and the Quantum Measurement* , P. Meystre, in *Progress in Optics, Vol. XXX* edited by E. Wolf (Elsevier Science Publishers B.V., Amsterdam, 1992), pp. 261-355.
[28] Y. Yamamoto and R. E. Slusher, Phys. Today **46**(6), 66 (1993).
[29] *Optical Processes in Microcavities*, edited by R. K. Chang and A. J. Campillo, (World Scientific, Singapore, 1996).
[30] K. J. Vahala, Nature (London) **424**, 839 (2003).
[31] H. J. Carmichael, *Statistical Methods in Quantum Optics 1* (Springer-Verlag, Berlin, 1999).
[32] C. W. Gardiner and P. Zoller, *Quantum Noise* (Springer-Verlag, Berlin, 2000).
[33] H. J. Kimble, Physica Scripta **T76**, 127 (1998).
[34] M. Sargent III, M. O. Scully, and W. E. Lamb Jr., *Laser Physics* (Addison-Wesley, Reading Mass., 1974).
[35] A. Eschmann and R. J. Ballagh, Phys. Rev. A **60** , 559 (1999).

[36] S. M. Tan, J. Opt. B: Quantum Semiclass. Opt. **1**, 424 (1999).
[37] L. Mandel and E. Wolf, *Optical Coherence and Quantum Optics* (Cambridge University Press, New York, 1995).
[38] H. Haken, *Laser Theory* (Springer Verlag, Berlin, 1984).
[39] M. O. Scully and M. S. Zubairy, *Quantum Optics* (Cambridge University Press, Cambridge, 1997).
[40] *Theory of Optical Bistability*, L. A. Lugiato, in *Progress in Optics, Vol. XXI* edited by E. Wolf (Elsevier Science Publishers B.V., Amsterdam, 1984), pp. 69-216.
[41] Q. A. Turchette, R. J. Thompson, and H. J. Kimble, Appl. Phys. B **60**, S1 (1995).
[42] C. J. Hood, H. J. Kimble, and J. Ye, Phys. Rev. A **64** , 033804 (2001).
[43] J. McKeever, J. R. Buck, A. D. Boozer, A. Kuzmich, H.-C. Nägerl, D. M. Stamper-Kurn, H. J. Kimble, Phys. Rev. Lett. **90**, 133602 (2003).
[44] D. Boiron, A. Michaud, P. Lemonde, Y. Castin, and C. Salomon, Phys. Rev. A **53**, R3734 (1996) and references therein.
[45] K. L. Corwin, S. J. M. Kuppens, D. Cho, and C. E. Wieman, Phys. Rev. Lett. **83**, 1311 (1999).
[46] The discussion about possible coherent wave-mixing effects was initiated by D. J. Gauthier, to whom we are most grateful.
[47] H. Ritsch, P. Zoller, C. W. Gardiner, and D. F. Walls, Phys. Rev. A **44**, 3361 (1991), and references therein.

Quantum Information and Computation, Vol. 4, No. 5 (2004) 325–360
© Rinton Press

SECURITY OF QUANTUM KEY DISTRIBUTION WITH IMPERFECT DEVICES

DANIEL GOTTESMAN
Perimeter Institute
Waterloo ON N2V 1Z3, Canada

HOI-KWONG LO
Department of Electrical and Computer Engineering and Department of Physics
University of Toronto, Toronto, Canada M5G 3G4

NORBERT LÜTKENHAUS
Institute of Theoretical Physics and Max Planck Research Group, Institute of Optics, Information, and Photonics
University of Erlangen–Nuremberg, 91058 Erlangen, Germany

JOHN PRESKILL
Institute for Quantum Information, California Institute of Technology
Pasadena, CA 91125, USA

Received December 20, 2002
Revised September 2, 2004

We prove the security of the Bennett-Brassard (BB84) quantum key distribution protocol in the case where the source and detector are under the limited control of an adversary. Our proof applies when both the source and the detector have small basis-dependent flaws, as is typical in practical implementations of the protocol. We derive a general lower bound on the asymptotic key generation rate for weakly basis-dependent eavesdropping attacks, and also estimate the rate in some special cases: sources that emit weak coherent states with random phases, detectors with basis-dependent efficiency, and misaligned sources and detectors.

Keywords: Quantum cryptography, quantum key distribution

Communicated by: B Kane & M Mosca

1 Introduction

The security of quantum cryptography is founded on principles of fundamental physics, rather than assumptions about the resources available to a potential adversary. In the BB84 quantum key distribution protocol [1], two parties (Alice and Bob) establish a secret key about which the eavesdropper (Eve) cannot obtain a significant amount of information. Alice sends a key bit to Bob by preparing a qubit in one of two conjugate bases and Bob measures the qubit in one of the two bases; Eve, who does not know the basis chosen by Alice or by Bob, cannot collect information about the key without producing a detectable disturbance. This protocol, when suitably augmented by classical error correction and privacy amplification, is provably secure against any attack by Eve allowed by quantum mechanics [2, 3, 4, 5, 6].

Though security can be proven without imposing any restriction on Eve's attack (other than the requirement that she has no *a priori* information about the basis used), it is necessary to place conditions on the performance of the source and detector employed in the protocol. In the Shor-Preskill proof [5], it is assumed that any flaws in the source and detector can be absorbed into Eve's basis-independent attack. In the proof by Mayers [2], the source is assumed to be perfect, but the detector is completely uncharacterized. In the Koashi-Preskill proof [6], the detector is perfect, but the source is uncharacterized, aside from the proviso that it leaks no information about the basis choice to Eve. In all of these cases, serious faults in the apparatus can be detected in the protocol, so that Alice and Bob will reject the key if the equipment performs badly.

But none of these proofs apply when both the source and detector have small imperfections that depend on the basis used in the protocol, the case relevant to typical real-world implementations of quantum key distribution. Since the BB84 protocol with perfect sources and detectors is secure, it is intuitively clear that BB84 should remain secure if the imperfections are "sufficiently small." We will sharpen this intuition into a quantitative statement, by calculating how the rate of generation of private key depends on the tolerance to which the equipment is characterized.

The simplest way to analyze the consequences of characterized imperfections is to absorb the defective performance of the equipment into the eavesdropper's attack. Primarily for this reason, we are led to consider the security of the BB84 protocol in a different framework than in previous security proofs: the flaws in the source and detector may depend on the bases chosen, and furthermore Eve may know these bases, but her power to exploit this knowledge is limited. We will prove security under an *assumption* that limits the basis dependence of Eve's attack.

It is natural to ask whether this assumption can be verified by conducting suitable tests on the source and detector (perhaps with testing equipment that is also not fully trustworthy, as in [7]). For now we put aside the issue of testing the equipment, and we will trust that our equipment performs *approximately* as expected. However, as cautious cryptologists we will assume that, within the prescribed limits, the performance of the equipment is controlled by Eve and maximally exploited by her to gain information about the shared key.

Our analysis follows the method of Shor and Preskill [5], who proved the security of BB84 by relating it to an entanglement distillation protocol. Their argument exploited a symmetry between the two bases used in the protocol, whose consequence is that the entangled pairs to be distilled have equal rates of bit errors and phase errors. Our task in this paper is to extend the analysis to the case where the symmetry between the bases is broken because the adversary has information about the basis used. We will give a general argument showing that if the basis-dependence of the attack is sufficiently weak, then the gap between the bit error rate and the phase error rate is small; this argument allows us to establish security against arbitrary attacks that satisfy a particular criterion for weak basis dependence, and to derive a lower bound on the asymptotic key generation rate.

To formulate our criterion for the attack to be weakly basis dependent, we focus on the coin that is flipped to determine the basis — the basis dependence is weak if the adversary interacts only weakly with the coin. The Shor-Preskill argument shows that, for the purpose of analyzing the security of BB84, it is convenient to imagine that Alice chooses each of her key bits by measuring half of an entangled state, and that she delays these measurements until after Eve has attacked the signals. Likewise, for analyzing weakly basis-dependent attacks, we find it convenient to imagine that the coin flip that determines the basis is realized by measuring a qubit, and that this measurement is delayed until after the adversary's attack. Then we can quantify the extent of the adversary's interactions with the coin according to how much the state of the coin is *disturbed.* Our general argument shows that if the disturbance of the coin is slight, then a secure key can be generated at a calculable nonzero rate.

Aside from presenting this general argument, we will also apply our methods to a few specific scenarios in which quantum key distribution is executed with imperfect devices. In some of these special cases, we can derive tighter lower bounds on the key generation rate than are obtained by the general argument. The examples we discuss include:

Tagging. A faulty source may "tag" some of the qubits with information, readable by the eavesdropper, that reveals the basis used in the preparation. An important special case, also recently analyzed by Inamori, Lütkenhaus and Mayers [8], is a source emitting weak coherent states which with nonnegligible probability contain multiple photons prepared in the same polarization state. An adversary might intercept the extra photons and collect information about the basis used without causing any disturbance, compromising security.

Basis-dependent detector efficiency. If the detector sometimes misfires, the probability that a qubit is successfully detected might depend on the basis used. An adversary that can control whether the detector fires can use this power to disguise eavesdropping.

Basis-dependent misalignment in the source or detector. The source or detector might not be properly aligned to emit or detect a qubit in the desired basis. The adversary can exploit her freedom to rotate these devices to reduce the disturbance caused by her eavesdropping.

Our results do not subsume, nor are they subsumed by, the results of [2, 6, 8]. Mayers and Koashi-Preskill assume that the detector or source is uncharacterized, but that the adversary is unable to influence the behavior of the devices to suit her purposes. We assume that the flaws in the devices are limited, but that the adversary controls the apparatus within these limits; furthermore, our security proof (unlike the Koashi-Preskill proof) applies to a source that leaks a small amount of information about the choice of basis. And more important, while Mayers assumes that the source is perfect, and Koashi and Preskill assume that the detector is perfect, our new techniques apply when both the source and the detector have small basis-dependent imperfections, the generic case in practical settings. In addition, while Koashi and Preskill assume that the signals emitted by Alice's source are uncorrelated with one another (the state describing the emission of n signals is a tensor product of n individual signals), and while Mayers likewise assumes that the signals are detected individually rather than collectively by Bob, our results are not inherently subject to such limitations. (However, we *do* assume that the signals are emitted and detected individually in many of the examples that we analyze.)

Aspects of the security of quantum key distribution in realistic settings have been analyzed previously [9, 10, 11, 12, 13, 14]. However, our proof of security holds for arbitrary collective attacks by the eavesdropper, while individual attacks were considered in most previous work. (An important exception is the recent study by Inamori, Lütkenhaus and Mayers [8] of sources that emit weak coherent states.) Although our results do not yet constitute a definitive analysis of the security of realistic quantum cryptography, we expect that the tools we have developed will prove useful in further studies.

Beyond any of our particular results, we have broadened notably the domain of applicability of the Shor-Preskill method for proving security. This method has many further applications, and in particular allows one to easily analyze the effectiveness of various enhancements of the protocol such as two-way postprocessing [15].

Our findings are of both practical and conceptual interest. It is important to address whether practical implementations of quantum key distribution are truly secure, and in real-world implementations the apparatus is never flawless. And apart from practical concerns, quantum key distribution provides a fascinating theoretical laboratory for quantitatively exploring the unavoidable tradeoff between collecting information about a quantum system and disturbing the system.

We note that the security against arbitrary eavesdropping attacks of quantum key distribution performed with imperfect devices has also been analyzed by Ben-Or [16].

The rest of this paper is organized as follows. In Sec. 2, we clarify the setting of our analysis by introducing Eve's collaborator Fred, who controls the flaws in the source and detector. We review the connection between the BB84 protocol and entanglement-based quantum key distribution in Sec. 3, and reprise the Shor-Preskill argument which is the foundation for all that follows. We carefully formulate our models for sources and detectors in Sec. 4, and point out in Sec. 5 some ways in which these models fail to capture fully the properties of real devices. In Sec. 6 we introduce the concept of a quantum coin, which is a useful tool for analyzing the power of Fred's basis-dependent attack on the equipment, and in Sec. 7 we present our security proof for a general class of attacks that depend sufficiently weakly on the basis. We then proceed to explore various applications of this result: In Sec. 8, we prove security for the case where the detector is perfect but the source has small generic flaws, and in Sec. 9, we treat the case where the detector has small flaws and the source is flawed but *oblivious*; that is, it leaks no information about the basis used. Sec. 10 analyzes the case where the source and detector are both slightly misaligned, and in Sec. 11 we state without proof a result for the case where the both the source and detector have small generic flaws (where the source is not necessarily oblivious). The case in which a fraction of the signals emitted by the source are tagged with basis information is dealt with in Sec. 12; this analysis is relevant to sources that emit weak coherent states with random phases, sources that are close to single photon sources, and a scenario where some of the basis and key bits are selected by flipping biased coins. Finally, in Sec. 13 we discuss the case of a detector with imperfect efficiency that is controlled by the adversary, and Sec. 14 contains some concluding comments.

2 Alice and Bob and Eve and Fred

To clarify our assumptions about the source and detector imperfections, it is helpful to imagine that two collaborating adversaries are trying to foil the key distribution protocol: Eve and Fred. The goal of Alice and Bob is to generate a shared key not known to the Eve/Fred alliance.

Fred knows the basis chosen by Alice and/or Bob, and he can tamper with the source and/or detector, but only within certain prescribed limits. Because the basis dependence of his attack is limited, Fred can acquire only limited knowledge of what signal was emitted by the source and what outcome was recorded by the detector.

Eve on the other hand has no *a priori* knowledge of the basis chosen by Alice or by Bob, and she has no direct control over the source or the detector. But Eve is permitted to attack all of the signals sent by Alice to Bob collectively in any manner allowed by quantum mechanics. For example, Eve may entangle an ancilla that she controls with each signal after the signal is emitted by the source and before it is absorbed by the detector. Then Eve may delay the measurement of her ancilla until after all public discussion by Alice and Bob is concluded, choosing her measurement to optimize her information about the key.

While Eve can send to Fred any quantum or classical message of her choice, communication from Fred to Eve is restricted. Before Eve interacts with the signals, Fred may wish to notify her about Alice's basis choice, but his only means of conveying this information is through his limited ability to control the source. After Bob confirms receipt of the signals, Fred is permitted to share further information with Eve by sending it via a classical or quantum side channel. Apart from this restriction on their communication, Eve and Fred are free to choose a common strategy that optimally exploits Fred's limited power to manipulate the source and detector.

Various security proofs apply to settings that can be distinguished by describing Fred's role. In the setting considered by Mayers and by Koashi and Preskill, Fred does not share information with Eve, and the goal of Alice and Bob is to generate a shared key that Eve does not know. Mayers assumes that the source is perfect, but Fred is free to choose the measurement performed by the detector, which can depend at Fred's discretion on Bob's declared basis, and to report to Bob a portion of the information collected in the measurement. Koashi and Preskill assume that the detector is perfect, but Fred is free to choose the states emitted by the source except for one proviso: the emitted state, averaged over Alice's key bit, is independent of Alice's basis. In the setting considered in this paper, Eve again applies an arbitrary basis-independent quantum operation to her probe and the transmitted signals. And again, Fred, who has information about the declared bases, can influence how the equipment operates. But now, the basis dependence of Fred's attack is limited, and Fred and Eve can pool their knowledge *after* the signals are detected.

All of these settings are interesting. In the Mayers model, the detector can be arbitrarily flaky, and in the Koashi-Preskill model, the source leaks no basis information but is otherwise arbitrary. In the model we consider, both the source and detector are "pretty good" but controlled (within limits) by the adversary. Our models of the source and the detector will be described in more detail in Sec. 4.

3 Distillation and privacy

Our analysis follows the method of proof used by Shor and Preskill [5], which we will now briefly review. In this method, security is first established, following [3], for a protocol based on an entanglement distillation protocol (EDP). Then the security of a "prepare-and-measure" protocol, namely BB84, is established through a reduction to the EDP protocol.

We remark that entanglement distillation was first discussed in [17], that its relevance to the security of quantum key distribution was emphasized in [18], and that this connection was established rigorously in [3]. Entanglement distillation protocols have also been called "entanglement purification protocols," abbreviated EPP. We prefer to say "distillation" rather than "purification" as "purification" now has another widely accepted meaning in quantum information theory.

In the EDP protocol, Alice creates $n+m$ pairs of qubits, each in the state

$$|\phi^+\rangle = \frac{1}{\sqrt{2}}\left(|00\rangle + |11\rangle\right) \ , \tag{1}$$

the simultaneous eigenstate with eigenvalue one of the two commuting operators $X \otimes X$ and $Z \otimes Z$, where

$$X = \begin{pmatrix} 0 & 1 \\ 1 & 0 \end{pmatrix} \ , \quad Z = \begin{pmatrix} 1 & 0 \\ 0 & -1 \end{pmatrix} \tag{2}$$

are the Pauli operators. Then she sends half of each pair to Bob. Alice and Bob sacrifice m randomly selected pairs to test the "error rates" in the X and Z bases by measuring $X \otimes X$ and $Z \otimes Z$. If the error rate is too high, they abort the protocol. Otherwise, they conduct the EDP, extracting k high-fidelity pairs from the n noisy pairs. Finally, Alice and Bob both measure Z on each of these pairs, producing a k-bit shared random key about which Eve has negligible information. The protocol is secure because the EDP removes Eve's entanglement with the pairs, leaving her powerless to discern the outcome of the measurements by Alice and Bob.

If the EDP protocol has special properties, then proving the security of BB84 can be reduced to proving security of the EDP. Shor and Preskill considered EDP's with one-way communication [19], which are equivalent to quantum error-correcting codes, and furthermore, considered the specific class of codes known as Calderbank-Shor-Steane (CSS) codes [20, 21]. (Gottesman and Lo [15] have described how a similar reduction can be applied to certain EDP's with two-way communication.) Like any quantum error-correcting code, a CSS code can correct both bit errors (pairs with $Z \otimes Z = -1$) and phase errors (pairs with $X \otimes X = -1$). But the crucial property of a CSS code is that the bit and phase error correction procedures can be decoupled — Z errors can be corrected without knowing anything about the X errors and vice-versa.

In the EDP protocol, the key is affected by the bit error correction but not by the phase error correction. The phase error correction is important to expunge entanglement with Eve and so ensure the privacy of the key. But Eve's information about the final key is unaffected if Alice and Bob dispense with the phase error correction. What is essential is not that the phase error correction is actually done, but rather that it would have been successful if it had been done.

With the phase error correction removed, the extraction of the final key from the n noisy pairs is much simplified. Rather than first carrying out the EDP and then measuring Z for each of the k distilled pairs, Alice and Bob can instead measure Z for each of the n noisy pairs, and then do classical postprocessing of their measurement results to extract the final key. In this form, the entanglement-based protocol becomes equivalent to BB84.

We can see the equivalence more clearly by adding one further wrinkle to the entanglement-based protocol. In the BB84 protocol, Alice and Bob choose their bases at random, so that about half of the sifted key bits are transmitted in the X basis and about half in the Z basis. But in the entanglement-based protocol as we have described it, all of the final key bits are generated by measuring in the Z basis. To relate the two protocols, suppose that in the entanglement-based protocol a subset of the pairs is selected at random, and that for each pair in this subset, Alice and Bob apply the Hadamard transformation $H : X \leftrightarrow Z$ to their qubits before measuring Z. Equivalently, we can instruct Alice and Bob to measure X rather than Z for these selected qubits. Each measurement by Alice in the entanglement-based protocol prepares a qubit to be sent to Bob in one of the four BB84 states: $X = \pm 1, Z = \pm 1$, chosen at random. In BB84, Bob measures either X or Z, and through public discussion Alice and Bob reject the key bits where they used different bases; the remaining key, for which their bases agree, is called the "sifted key." As far as an eavesdropper is concerned, there is no difference between generating a bit of sifted key in BB84, where a qubit is prepared by Alice in a randomly chosen eigenstate of either X or Z and measured by Bob in the same basis, and generating a bit of key in the entanglement-based protocol, where Alice and Bob both measure their halves of an entangled pair of qubits.

A vestige of the CSS code of the EDP survives as a scheme for error correction and privacy amplification in this prepare-and-measure protocol. In a CSS code, classical linear codes C_1 and $C_2^\perp$ are used for bit and phase error correction respectively, where $C_2 \subset C_1$. The entanglement-based protocol is secure (whether or not the phase error correction is done) if, with "high probability" (probability of success exponentially close to unity), C_1 can correct the bit errors and $C_2^\perp$ can correct the phase errors. In the BB84 protocol, C_1 is used to correct bit errors in the key, and C_2 to amplify privacy. Specifically, Alice transmits the random string w through the quantum channel, randomly selects a codeword u of C_1, and announces $u + w$. Bob receives the corrupted string $w + e$, computes $u + e$, and corrects to u. The final key is the coset $u + C_2$ of C_2 in C_1.

If this method is used to compute the final key in the BB84 protocol, and if the key being distributed is very long, at what asymptotic rate can secure final key be extracted from the sifted key? The answer is the rate k/n at which high-fidelity pairs can be distilled from noisy pairs in the EDP, which depends on how noisy the pairs are. The purpose of the verification test included in the protocol is to obtain a reliable estimate of the noise. In the EDP, a useful way to characterize the noise is to imagine that, after the final Hadamard transformations are applied to the pairs, all n pairs are measured in the Bell basis — that is, both $Z \otimes Z$ and $X \otimes X$ are measured. If there were no noise at all, we would find $Z \otimes Z = X \otimes X = 1$ for every pair. Denote by $n\tilde{\delta}$ the number of pairs for which we have $Z \otimes Z = -1$ instead; we say that $\tilde{\delta}$ is the bit error rate of the noisy pairs. Denote by $n\tilde{\delta}_p$ the number of pairs for which we have $X \otimes X = -1$; we say that $\tilde{\delta}_p$ is the phase error rate of the pairs.

For a given state of the n pairs, the rates $\tilde{\delta}$ and $\tilde{\delta}_p$ are actually random variables, because the quantum measurement of the pairs is nondeterministic. But suppose that from the verification test, we can infer that for sufficiently large n and any $\varepsilon > 0$, the inequalities $\tilde{\delta} < \delta + \varepsilon$ and $\tilde{\delta}_p < \delta_p + \varepsilon$ are satisfied with high probability. Furthermore, we may imagine that the key bits are subjected in the protocol to a publicly announced random permutation (or equivalently that the CSS code is correspondingly randomized), so that the bit and phase errors are randomly distributed among the qubits. It can then be shown [22, 23] that, for sufficiently large n and any $\varepsilon' > 0$, there exists a CSS code such that the EDP distills k high-fidelity pairs from the n noisy pairs, where

$$k/n > 1 - H_2(\delta + \varepsilon + \varepsilon') - H_2(\delta_p + \varepsilon + \varepsilon') \ , \tag{3}$$

and $H_2(\delta) = -\delta \log_2 \delta - (1-\delta)\log_2(1-\delta)$ is the binary entropy function. Therefore, in BB84, we establish an asymptotically achievable rate of extraction of secure final key from sifted key ("key generation rate"):

$$R = 1 - H_2(\delta) - H_2(\delta_p) \ , \tag{4}$$

That is, in the BB84 protocol, a fraction $H_2(\delta)$ of the sifted key bits are sacrificed asymptotically to perform error correction and a fraction $H_2(\delta_p)$ of the sifted key bits are sacrificed to perform privacy amplification.

We note that, although the permutation randomizes the positions of both the bit errors and the phase errors, correlations between bit errors and phase errors may remain. However, these correlations do not affect the achievable rate, because with CSS codes the bit error correction and phase error correction are performed separately. We also remark that the code C_1 used to correct bit errors can be chosen to be efficiently decodable [24]. It may not be possible to simultaneously choose the code $C_2^{\perp}$ to be efficiently decodable, but this is not important, since the phase error correction using $C_2^{\perp}$ is not actually carried out in the BB84 protocol — it need only be possible in principle.

Our arguments so far have reduced the problem of demonstrating the security of BB84 to inferring sufficiently stringent upper bounds on both the bit error rate and the phase error rate of the pairs used to generate the key in the corresponding entanglement-based protocol, based on the results of the verification test. Inferring the upper bound on the bit error rate is straightforward. Let us consider the version of the entanglement-based protocol in which Alice and Bob measure both the test pairs and the key generating pairs in the Z basis, but a Hadamard transformation is applied to randomly selected pairs just prior to the measurement. When Eve interacts with the qubits traveling from Alice to Bob, she has no *a priori* knowledge concerning which pairs will be used for the test and which will be used for key generation. Therefore, the test pairs are a fair sample; it follows from classical sampling theory that the joint probability of observing $n\delta$ errors in the test set and more than $n(\delta+\varepsilon)$ errors in the key set is exponentially small for any $\varepsilon > 0$ and n sufficiently large. Note that this argument works even if Eve's attack induces strong correlations among the pairs; all that is required is that the sample selected for the test is chosen randomly.

Inferring an upper bound on the phase error rate requires an extra step. In the Shor-Preskill argument, it is assumed that the adversary has no *a priori* knowledge about the basis that Alice uses to send her signals and Bob uses to detect them. In the entanglement-based protocol, this becomes the statement that the adversary does not know to which pairs the Hadamard transformation is applied. But since the Hadamard interchanges the bit errors and the phase errors, it enforces a symmetry between the two types of errors. Therefore, the error rate measured in the test serves as an estimate of the phase error rate as well as the bit error rate: with high probability the phase error rate of the key generating pairs is also less than $\delta+\varepsilon$. We conclude that final key can be extracted from sifted key at the rate $R = 1 - 2H_2(\delta)$.

Now we have sketched the complete proof of security of BB84, except for one technicality. The sampling theory argument actually shows that the *joint* probability of a error rate δ in the test pairs and an error greater than $\delta + \varepsilon$ for the key generating pairs is exponentially small. For a security analysis, we should show that the *conditional* probability of an error rate for the key generating pairs greater than $\delta + \varepsilon$ is exponentially small, given the error rate δ found in the test. The desired result follows from Bayes's theorem as long as we assume that

Eve's attack "passes" the verification test with a probability that is not itself exponentially small. That is, we exclude strategies by Eve such that extraordinary luck is required to induce the (small) error rate δ found in the test. With this caveat in mind, we propose this definition of security:

Definition. Security of quantum key distribution. *A quantum key distribution protocol is secure if for any attack by Eve that passes the verification test with a probability that is not exponentially small, with high probability Alice and Bob agree on a final key that is nearly uniformly distributed and Eve's information about the final key is exponentially small. Here "exponentially small" means bounded above by* e^{-CN} *where* N *is the number of signals transmitted in the protocol and* C *is a positive constant, "high probability" means exponentially close to 1, and "nearly uniformly distributed" means with a probability distribution exponentially close to the uniform distribution.*

And we conclude:

Theorem 1. Security of BB84 against basis-independent attacks. *The BB84 protocol is secure if Eve launches a basis-independent attack. Secure final key can be extracted from sifted key at the asymptotic rate*

$$R = \mathrm{Max}\big(1 - 2H_2(\delta), 0\big) \tag{5}$$

where δ *is the bit error rate found in the verification test (assuming* $\delta < 1/2$*).*

To reiterate, two error rates are relevant to whether quantum key distribution is successful. The bit error rate is "measured" by conducting a verification test on a randomly sampled subset of the sifted key bits; that is, the observed bit error rate δ found in the test provides an estimate of the error rate $\tilde{\delta}$ in the key generating bits that is accurate with high probability. If δ is low enough, we can be confident that error correction will succeed, so that Alice and Bob share a common key. The phase error rate $\tilde{\delta}_p$ is not measured by direct sampling — rather an upper bound $\tilde{\delta}_p < \delta_p + \varepsilon$ is inferred from the bit error rate. If the inferred phase error rate δ_p is low enough, we can be confident that phase error correction (if done) will succeed, so that Eve will have a negligible amount of information about the key.

If the adversary has no knowledge of the basis, then with high probability the gap $|\tilde{\delta}_p - \tilde{\delta}|$ between the bit and phase error rates is asymptotically negligible, and the inference is straightforward. For example, if the effect of Eve's attack is to apply X to Bob's qubit, this action will induce a bit error if Alice and Bob both measure Z to generate a key bit in the entanglement-based protocol, and it will induce a phase error if Alice and Bob both measure X. Since Eve doesn't know the basis, her action generates bit errors and phase errors with the same probability. But in this paper, going beyond Shor's and Preskill's original argument, we will allow Fred to know the basis, enabling him to enhance $\tilde{\delta}_p$ relative to $\tilde{\delta}$. In many cases of interest, the basis dependence of Fred's attack is limited; we can infer an upper bound $\tilde{\delta}_p < \delta_p + \varepsilon$ and so through Eq. (4) establish an achievable key length.

In the BB84 protocol, Alice and Bob can measure both the error rate δ_X when they use the X basis and the error rate δ_Z when they use the Z basis. These rates need not be equal even if Eve does not know the bases that Alice and Bob use. For example, Eve might measure in the Z basis each qubit she receives from Alice, and resend to Bob the Z eigenstate found by her measurement, resulting in expected values $\delta_Z = 0$ and $\delta_X = 1/2$. We emphasize that δ and δ_p should not be confused with δ_Z and δ_X. The bit error rate $\delta \approx (\delta_X + \delta_Z)/2$ is observed in the verification test, but the phase error rate δ_p is not directly "measured" in the protocol.[a]

4 Model devices

Because the Shor-Preskill argument, both in its original incarnation and in its extension to basis-dependent attacks, makes use of an EDP, there are limitations on the sources and detectors to which it applies. In the entanglement-based protocol, Alice and Bob both measure qubits, in either the X basis or the Z basis — what we will call *standard measurements*. In the corresponding prepare and measure protocol, Alice's source need not emit a qubit, but whatever it emits can be simulated by a standard measurement performed on half of a bipartite state [22]. The state that arrives at Bob's detector also might not be a qubit, but the measurement can be realized as a standard measurement preceded by an operation that "squashes" the incoming state to a two-dimensional Hilbert space.

To be more specific, the source model that we adopt is as follows: Alice's source emits a state in a Hilbert space A, where A can be arbitrary, and she launches a state by acting on an auxiliary *qubit* A'. Alice's basis choice $a \in \{0,1\}$ is determined by flipping a coin. Then a state ρ_a of $\mathcal{H}_A \otimes \mathcal{H}_{A'}$, which can depend on the basis a, is prepared by Fred. Alice proceeds to perform a standard measurement on her qubit A' in the basis indicated by a; that is, a Hadamard transformation is performed on A' if and only if $a = 1$, and then Alice measures the qubit in the Z basis. Her measurement determines her key bit: $g = 0$ for outcome $+1$, $g = 1$ for outcome -1. (Note that, depending on the state ρ_a, the key bits $g = 0, 1$ need not be equiprobable.) If Fred's states ρ_0 and ρ_1 are close to one another, then the states emitted by the source, averaged over the key bit, depend only weakly on the basis.

Actually we can generalize this source model to allow successive emissions to be correlated with one another. Now let A' denote a system of n qubits, A the system in which Alice's n signals reside, and ρ_a a state of $\mathcal{H}_A \otimes \mathcal{H}_{A'}$; the state ρ_a may depend on the n-bit string a that specifies Alice's basis choice for each of the n signals. Alice applies a Hadamard transformation to the ith qubit if and only if $a_i = 1$, then measures the qubits in the Z basis. The measurement outcomes determine her n-bit key g. Some of the results we report in this paper (Theorem 2, for example) apply to this more general source model.

The n signals emitted by the source are attacked by Eve, who sends to the detector a state that lives in a Hilbert space $\mathcal{H}_B$. We model the detector as follows: Bob's basis choice $b \in \{0,1\}^{\otimes n}$ for the n signals is determined by flipping n coins. Then Fred applies to the state received by the detector a quantum channel $\mathcal{E}_b$ that "squashes" $\mathcal{H}_B$ to the n-qubit space $\mathcal{H}_{B'}$; this squash operation may depend on the basis b. Bob proceeds to perform standard measurements on the qubits; a Hadamard is performed on the ith qubit if and only if $b_i = 1$, then Bob measures the qubits in the Z basis. The measurements determine his n-bit key h : $h_i = 0$ if the outcome of the measurement of the ith qubit is $+1$ and $h_i = 1$ for outcome -1. Since the channel taking $\mathcal{H}_B$ to $\mathcal{H}_{B'}$ can act collectively on the incoming signals, our model allows the detector to perform a collective measurement on the n signals it receives.

---

[a] If Alice and Bob perform a *refined error analysis* [25] (measuring separate error rates for the two bases), they can improve the key generation rate to $R = 1 - H_2(\delta_Z) - H_2(\delta_X)$ [23].

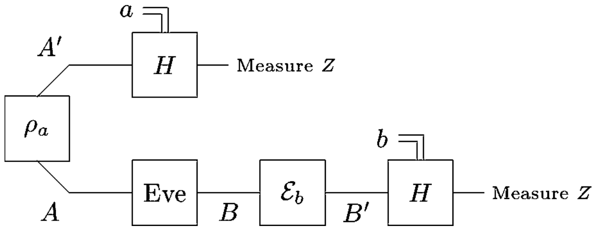

Fig. 1. Roles of Alice, Bob, Eve, and Fred in the key distribution protocol. Fred prepares an entangled state ρ_a (which may depend slightly on Alice's basis choice a) of Alice's n-qubit Hilbert space A' and the signal space A; then Alice triggers the source by performing a standard measurement on A'. Eve applies an arbitrary basis-independent attack, and then Fred applies a channel $\mathcal{E}_b$ (which may depend slightly on Bob's basis choice b) that "squashes" the signals from the Hilbert space B to the n-qubit space B'. Finally, the qubits in B' are subjected to a standard measurement by Bob. The goal of the protocol is to generate a key that is not known by Eve and Fred, who may communicate freely after Bob measures.

The basis-dependence in the detector's performance is encoded in Fred's channel $\mathcal{E}_b$.

The prepare-and-measure BB84 protocol, for the source and detector models we have described, is depicted in Fig. 1. It can be related to a protocol in which entangled pairs of qubits are prepared by Eve (with help from Fred). Half of each pair is delivered to Alice, half to Bob, and they then proceed to perform standard measurements. The security of this latter protocol follows from the security of the corresponding EDP. Therefore, for this model of source and detector, we can use the Shor-Preskill method to analyze the security of BB84.

It may be instructive to contrast our models of the source and detector with those considered in the proofs of Mayers [2] and Koashi and Preskill [6]. Mayers allows the detector to perform an arbitrary two-outcome POVM on each signal it receives, while in our model the POVM must be one that can be realized by a squash followed by a standard measurement. In principle, our model entails no loss of generality, since the Mayers POVM could be followed by the preparation of a qubit in a state chosen so that the standard measurement will reproduce the outcome of the POVM. However, our security proof works only if the channel $\mathcal{E}_b$ applied by Fred depends sufficiently weakly on the basis b, while Mayers requires no such condition. Koashi and Preskill consider a source that can be realized by the preparation of a *basis-independent* state of an bipartite system, followed by an arbitrary two-outcome POVM on half of the system, while in our model the POVM must be a standard measurement of a qubit. For the signals emitted by a general Koashi-Preskill source, though it would be possible to launch the same signals by performing a standard measurement on a qubit, this can be done only by choosing bipartite states that depend strongly on the basis, and our security proof works only when the dependence of the states on the basis is sufficiently weak. Therefore, our analysis of security does not apply to the general Mayers detector or the general Koashi-Preskill source. On the other hand, Mayers does not allow Fred to attack the source, Koashi and Preskill do not allow Fred to attack the detector, and the signals emitted by the Koashi-Preskill source reveal no information about the basis used. In contrast, our model allows the performance of both the source and the detector to depend on the basis, and allows the source to leak some information about the basis.

Another noteworthy difference between our model and those of Mayers and Koashi-Preskill is that our model allows Alice's source to emit successive signals that are entangled with one another, and allows the detector to measure the signals collectively. In contrast, Koashi and Preskill assume that the signals emitted by Alice's source are unentangled with one another, and Mayers likewise assumes that the signals are detected by Bob individually rather than collectively. This assumption is used because a crucial step in the Mayers proof is to show that Eve's information about Alice's key would be unchanged if Bob were to flip the basis in which he measures the key bits, but not the basis in which he measures the test bits. A general collective measurement of the signals by Bob would generate correlations between key bit measurements and test bit measurements; therefore, when Bob announces the outcome of his measurements of the test bits he might reveal to Eve some information about his choice of basis for the measurement of the key bits. For this reason, we do not know how to justify the invariance of Eve's information under the basis flip in the case of a collective measurement (though it is not inconceivable that the argument can be extended to cover that case). Similarly, the Koashi–Preskill proof uses the property that Eve's information about Bob's key would be unchanged if Alice were to flip the basis in which she sends the key bits but not the basis in which she sends the test bits, which cannot be justified unless Alice's signals are unentangled.

Our model of the detector can easily be generalized by endowing the detector with imperfect efficiency, so that it sometimes misfires and fails to record an outcome. One simple modification attaches an additional flag bit d_i to each of Bob's qubits. If $d_i = 0$, then the ith qubit is measured as above, but if $d_i = 1$ then the ith qubit is discarded and no outcome is recorded.

Detector inefficiencies and other types of losses can be incorporated into the Shor-Preskill security analysis easily enough. Through public discussion, Alice and Bob can eliminate from their sifted key all signals for which Bob failed to record a measurement result. In the entanglement-based protocol, then, we consider an EDP applied to all the pairs from which sifted key bits will be successfully extracted when the measurements are performed. That is, before the EDP is applied we discard all pairs for which Alice and Bob chose different bases or for which the detector misfired, as well as the pairs consumed by the verification test. Security is then proven if we can infer from the test that, with high probability, the remaining pairs have sufficiently low rates of bit errors and phase errors. However, this inference must take into account any basis dependence in the detector efficiency that might contribute to the gap between $\tilde{\delta}$ and $\tilde{\delta}_p$, as we will discuss further in Sec. 13. Basis-dependent detector inefficiencies are more problematic for the Mayers argument, since the basis dependence may spoil the invariance of Eve's information about Alice's key when Bob flips his basis for the key bits (but not the test bits).

5 Real devices

We are interested in analyzing the security of quantum key distribution with imperfect equipment because we seek assurance that our protocols are secure not just in an ideal world but also in the real world. Therefore, the inherent limitations of our source and detector models should be soberly contemplated.

For example, real sources typically emit not qubits but bosonic modes of the electromagnetic field, and if the likelihood that a mode is multiply occupied is too high, security may be compromised. To evaluate this security threat in our limited framework, we will need to adjust our source model (as we will discuss in Sec. 12) to incorporate the relevant features, even if not all the detailed physics, of the real source.

A similar comment applies to detectors. In a typical detector setup for BB84, the incoming photonic mode encounters a polarizing beam splitter that routes the $Z = 1$ and $Z = -1$ polarization states (or the $X = \pm 1$ states) to two different photon detectors — *threshold* detectors that do not distinguish one photon from many. If one or the other detector fires, the polarization state is identified. But if more than one photon is present, both detectors might fire, an ambiguous result. If Bob is equipped with such a detector, Eve can trigger the ambiguous result at will by flooding the detector with photons. Even more troubling, Eve can arrange that Bob receive the ambiguous result if he chooses one basis but not the other. For example, Eve can intercept and measure in the Z basis the signal emitted by Alice, and then send on to Bob many Z-polarized photons in the state she detects. Then Bob will reproduce Eve's result if he measures in the Z basis, but will obtain the ambiguous result if he measures in the X basis [27]. Thus, by exploiting the flaw in the design of the detector, Eve can launch a "Trojan horse" attack, in effect switching Bob's detector off when it is poised to detect eavesdropping [28]. Although our detector model may not fully incorporate all the physics of the polarization beam splitter, we will nonetheless be able to investigate in Sec. 13 the power of a Trojan horse attack within an EDP framework.

6 Choosing the basis quantumly

For a security analysis that is applicable to BB84 performed with imperfect equipment, we wish to bound the adversary's information in the case of an attack that depends weakly on the basis used to send and detect the signals. For this purpose, we should find a precise formulation of what it means for the basis dependence to be "weak." Therefore, let us focus attention on the coins that Alice and Bob flip to determine their random choices of basis. An attack that depends weakly on the basis is one that depends only slightly on the outcomes of the coin flips.

In the entanglement-based protocol as we have described it up to now, the coin flip is treated classically, and the outcome of the flip determines whether a Hadamard transformation is applied to a qubit before it is measured in the Z basis. Denote by $a_i \in \{0,1\}$ the outcome of the flip of the ith coin and by the length n string a the outcome of the flip of n coins. (In the BB84 protocol, Alice and Bob flip separate coins. But for our security analysis we may confine our attention to the sifted key, for which their coin flips agree; therefore in effect there is only one basis choice a_i for each signal.) Denote by $H(a)$ the operation which applies a Hadamard to the ith qubit if $a_i = 1$ and the identity to the ith qubit if $a_i = 0$. Then in the setting where Eve knows nothing about the basis choice, the effect of the randomly applied Hadamards by Alice and Bob (after the attack by Eve) is to transform the state of the n pairs according to

$$\rho \to \rho' = \frac{1}{2^n} \sum_{a=0}^{2^n-1} \left(H(a) \otimes H(a)\right) \rho \left(H(a) \otimes H(a)\right) \ . \tag{6}$$

Then since $H(b)H(a) = H(a \oplus b)$, ρ' has the property of Hadamard invariance: for any bit string b,

$$\left(H(b) \otimes H(b)\right) \rho' \left(H(b) \otimes H(b)\right) = \rho' \ . \tag{7}$$

In the Shor-Preskill argument, this symmetry of ρ' is used to infer that the bit error rate and phase error rate of the key generating pairs are, with high probability, nearly the same.

In order to analyze (weakly) basis-dependent attacks, it is convenient to treat the coin flip quantumly rather than classically — we can imagine that each coin is in a coherent superposition of heads and tails, and that the Hadamard transform is conditioned on the state of the coins. In the ideal protocol, the n coins are prepared in the state

$$\left(\frac{1}{\sqrt{2}}(|0\rangle + |1\rangle)\right)^{\otimes n} = \frac{1}{\sqrt{2^n}} \sum_{a=0}^{2^n-1} |a\rangle \ , \tag{8}$$

and the Hadamard is applied to the ith pair if $a_i = 1$ — therefore, if $|\Psi\rangle$ is the state of the pairs, then the effect of the random basis choice can be expressed as

$$|\Psi\rangle \otimes |a\rangle \rightarrow (H(a) \otimes H(a))\, |\Psi\rangle \otimes |a\rangle \ . \tag{9}$$

When we trace over the state of the coin, the effect on the quantum state of the pairs is just as in eq. (6).

Now, in this formulation, it is easy to describe the distinction between Eve's basis-independent attack and Fred's basis-dependent attack. Eve interacts only with the pairs, but Fred is permitted to tamper with both the pairs *and* the coins, as in Fig. 2. In the actual protocol, the coin is classical, but it will not make Fred any less powerful if we allow him to attack a quantum coin instead. (When we say that the coin is "classical," we mean Fred's attack is a quantum operation applied to the pairs that is conditioned on the state of the coin in a preferred basis. We will prove security for general attacks by Fred with weak dependence on the state of the coin, so our results will apply in particular to the case of a classical coin.) Furthermore, it is easy to state precisely what it means for the attack to depend only weakly on the basis: the basis dependence is weak if Fred's attack disturbs the coin only slightly. This notion of weak basis dependence applies even if we allow Fred to attack the signals twice, at the source (before Eve's attack) and at the detector (after Eve's attack). Actually, once we introduce the quantum coin in this way, it is not so important to keep Fred in the picture at all — we can go back to the usual picture in which there is only one adversary, but limit Eve's attack on the coin.

Definition. Δ-balanced attack. *Suppose that after n pairs and the n corresponding coins are attacked by the adversary (but before the final Hadamard transformations, conditioned on the coins, that precede the measurement of the pairs in the Z basis), the n coins are all measured in the X basis. The attack is Δ-balanced if, with high probability, the number of coins for which the measurement outcome is $X = -1$ is less than $n\Delta$.*

If $\Delta \approx 0$, the attack is *balanced* — that is, basis-independent. We will prove in Sec. 7 that if the attack is Δ-balanced and Δ is sufficiently small, then secure quantum key distribution is possible, and we will obtain a lower bound on the achievable key generation rate. Later we will discuss some more specific examples of Δ-balanced attacks, and for some of those attacks we will obtain stronger lower bounds on the rate.

We emphasize again that for a security analysis it suffices to imagine that Alice and Bob share a *single* quantum coin that determines the choice of basis for each signal. Of course, in the BB84 protocol, Alice and Bob use separate classical coins to determine whether to use

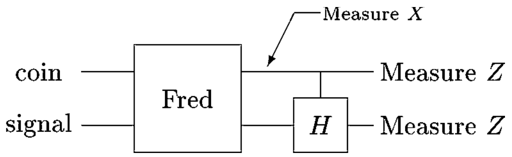

Fig. 2. The quantum coin. The basis choice for the detector (and the source) is determined by measuring a qubit (the coin) in the Z basis. To generate each bit of sifted key, a conditional Hadamard transformation, controlled by the coin, is applied to the signal qubit, and then the signal qubit is measured in the Z basis. Fred's basis-dependent attack on the signal can be described as a joint attack on the coin and the signal. To quantify how the coin is disturbed by Fred's attack, we consider measuring the coin in the X basis after the attack and before the conditional Hadamard.

the Z basis or the X basis. But the quantum coin is not intended to provide an accurate portrayal of the actual protocol; it is a mathematical device for analyzing the impact of the basis dependence of the attack. For the purpose of this analysis, we replace the two classical coins by a single quantum coin only after discarding the cases in which Alice's classical coin flip and Bob's classical coin flip yield different outcomes.

We have seen that for the analysis of the BB84 protocol, it is convenient to imagine that Alice delays the measurement that launches her signals until after Eve's attack. That way, we can relate the classical privacy amplification in BB84 to an EDP, and so establish security. Here we are taking this idea a step further. It is convenient to imagine that the measurement of the coin that determines the basis is also delayed until after the attack by Eve and Fred. That way, we can infer a bound on the asymmetry between the bit error rate and the phase error rate for pairs subjected to the EDP, and so establish that the EDP will be effective.

7 Security proof for small basis-dependent flaws

To analyze security, we'd like to relate the asymmetry of the coin (as parametrized by Δ) to the gap between the bit error rate $\tilde{\delta}$ and the phase error rate $\tilde{\delta}_p$ when the pairs are measured in the Bell basis. First we need to write down a convenient expression for this gap.

In the entanglement-based protocol, the random variables $n\tilde{\delta}$ and $n\tilde{\delta}_p$ are defined as the number of bit errors and phase errors that would be found if the n key generating pairs were all measured in the Bell basis. For a particular pair, consider the observable

$$\frac{1}{2}\left(Z\otimes Z - X\otimes X\right) = |\phi^-\rangle\langle\phi^-| - |\psi^+\rangle\langle\psi^+| \ , \tag{10}$$

where $|\phi^-\rangle$ and $|\psi^+\rangle$ are the Bell states

$$\begin{aligned} |\phi^-\rangle &= \frac{1}{\sqrt{2}}\left(|00\rangle - |11\rangle\right) \ , \\ |\psi^+\rangle &= \frac{1}{\sqrt{2}}\left(|01\rangle + |10\rangle\right) \ . \end{aligned} \tag{11}$$

This observable has eigenvalues $\{+1, 0, -1\}$. If the pair is to be measured in the Z basis, we say that there is a bit error if $Z\otimes Z = -1$ and that there is a phase error if $X\otimes X = -1$. Therefore, the eigenvalue of $\frac{1}{2}(Z\otimes Z - X\otimes X)$ is -1 if there is a bit error but no phase error, $+1$ if there is a phase error but no bit error, and 0 if either there are no errors or both a bit error and a phase error. Similarly, if the pair is to be measured in the X basis, we say that there is a phase error if $Z \otimes Z = -1$ and that there is a bit error if $X \otimes X = -1$. Therefore, the eigenvalue of $\frac{1}{2}(Z \otimes Z - X \otimes X)$ is $+1$ if there is a bit error but no phase error, -1 if there is a phase error but no bit error, and 0 if either there are no errors or both a bit error and a phase error.

Suppose that the basis choice is decided by flipping a coin, where the pairs are to be measured in the Z basis if the outcome of the coin flip is $|0\rangle$ ($Z_{\text{coin}} = 1$), and the pairs are to be measured in the X basis if the outcome of the coin flip is $|1\rangle$ ($Z_{\text{coin}} = -1$). Then the observable

$$\frac{1}{2}\left(Z \otimes Z - X \otimes X\right)_{\text{pair}} \otimes Z_{\text{coin}} \tag{12}$$

has the eigenvalue -1 if the pair has a bit error but no phase error, the eigenvalue $+1$ if the pair has a phase error but no bit error, and the eigenvalue 0 otherwise. We see, then, that for the n key generating pairs, the gap between the number of phase errors and the number of bit errors can be expressed as

$$\begin{aligned} n_{\text{gap}} &\equiv n\left(\tilde{\delta}_p - \tilde{\delta}\right) \\ &= \sum_{i=1}^{n} \frac{1}{2}\left(Z \otimes Z - X \otimes X\right)_{\text{pair},i} \otimes Z_{\text{coin},i} \ . \end{aligned} \tag{13}$$

Eq. (13) means that n_{gap} is a random variable whose probability distribution is the distribution of outcomes if the observable on the right-hand side of eq. (13) is measured. We might imagine that $Z \otimes Z$ and $X \otimes X$ are measured for every pair (this is a complete Bell measurement) and that Z_{coin} is measured for every coin; then n_{gap} is found by summing up all the results of these measurements. But since the Bell measurements and the coin measurements all commute with our expression for n_{gap} in eq. (13), we could just as well imagine that n_{gap} is measured first, and that the other measurements are completed later — the probability distribution for n_{gap} will be the same either way. In any case, our expression for n_{gap} is valid even if there are strong correlations among the pairs and the coins.

If we imagine that all of the coins are measured in the X basis (as in the definition of a Δ-balanced attack), then the random variable that represents the number of coins for which the outcome is $X = -1$ can be expressed as

$$n_{\text{coin}}^{(X)} = \sum_{i=1}^{n} \left(I \otimes I\right)_{\text{pair},i} \otimes \frac{1}{2}(I - X)_{\text{coin},i} \ . \tag{14}$$

We wish to obtain a bound on n_{gap} that will hold with high probability for any possible state of the pairs and the coins such that $n_{\text{coin}}^{(X)}$ is less than $n\Delta$ with high probability. It is convenient to express the gap as a sum of two terms, $n_{\text{gap}} = n_{\text{gap}}^{(Z)} + n_{\text{gap}}^{(X)}$, and to bound each term separately. First, consider

$$n_{\text{gap}}^{(Z)} = \frac{1}{2}\sum_{i=1}^{n} \left(Z \otimes Z\right)_{\text{pair},i} \otimes Z_{\text{coin},i} \ . \tag{15}$$

For each value of i, imagine that we perform two successive controlled-NOT gates, one with Alice's qubit as the control and the coin as the target, and the other with Bob's qubit as the control and the coin as the target. Acting by conjugation, the effect of these gates is

$$\begin{aligned}(Z\otimes Z)_{\text{pair}}\otimes Z_{\text{coin}} &\to (I\otimes I)_{\text{pair}}\otimes Z_{\text{coin}} \ , \\ (I\otimes I)_{\text{pair}}\otimes X_{\text{coin}} &\to (I\otimes I)_{\text{pair}}\otimes X_{\text{coin}} \ . \end{aligned} \tag{16}$$

Therefore, this change of basis has no effect on the statistics of the observable $n^{(X)}_{\text{coin}}$, while transforming the observable $n^{(Z)}_{\text{gap}}$ according to

$$n^{(Z)}_{\text{gap}} \to \frac{n}{2} - n^{(Z)}_{\text{coin}} \ , \tag{17}$$

where

$$n^{(Z)}_{\text{coin}} = \sum_{i=1}^{n} (I\otimes I)_{\text{pair},i}\otimes \frac{1}{2}(I-Z)_{\text{coin},i} \tag{18}$$

(the number of coins for which $Z=-1$, if all n are measured in the Z basis).

We are interested in analyzing how the statistics of $n^{(Z)}_{\text{gap}}$ is related to the statistics of $n^{(X)}_{\text{coin}}$. Let ρ denote the state of the n coins and the n pairs, and suppose that the controlled-NOT gates described above transform this state to a new state ρ'. We see that the statistics of $n^{(X)}_{\text{coin}}$ and $n^{(Z)}_{\text{gap}}$ in the state ρ is identical to the statistics of $n^{(X)}_{\text{coin}}$ and $\frac{n}{2}-n^{(Z)}_{\text{coin}}$ in the state ρ'. Therefore, to derive a relation between $n^{(X)}_{\text{coin}}$ and $n^{(Z)}_{\text{gap}}$ that holds with high probability for an arbitrary state ρ, it suffices to analyze how $n^{(Z)}_{\text{coin}}$ and $n^{(X)}_{\text{coin}}$ are related for an arbitrary state ρ'. For this we appeal to the following lemma, which asserts that if $n^{(X)}_{\text{coin}}$ is small, then $n^{(Z)}_{\text{coin}}$ is close to $n/2$:

Lemma 1 *For a quantum state of n coins, suppose that with high probability $n^{(X)}_{\text{coin}} < n\Delta$. Then, for any positive ε, with high probability*

$$|n/2 - n^{(Z)}_{\text{coin}}| < n(f(\Delta)+\varepsilon) \ , \tag{19}$$

where Δ and $f(\Delta)$ are related by

$$H_2(1/2-f(\Delta)) + H_2(\Delta) = 1 \ . \tag{20}$$

Proof: The proof for the case of a pure quantum state $|\psi\rangle$ of n coins, where $n^{(X)} < n\Delta$ with probability 1, is in Appendix A of [26]. But if instead $n^{(X)} < n\Delta$ with high probability, we can write $|\psi\rangle = |\psi\rangle_{\text{good}} + |\psi\rangle_{\text{bad}}$, where the (unnormalized) state $|\psi\rangle_{\text{good}}$ has $n^{(X)} < n\Delta$ with probability 1, and $\| \psi_{\text{bad}} \|$ is exponentially small. Hence $|\psi\rangle_{\text{good}}$, and therefore also $|\psi\rangle$, has the property eq. (19) with high probability. Therefore, Lemma 1 holds for pure states. Now, a mixed state can be realized as an ensemble of pure states. By the hypothesis of Lemma 1, all of the pure states in this ensemble, except for those occuring with exponentially small probability, satisfy $n^{(X)} < n\Delta$ with high probability, and therefore also satisfy eq. (19) with high probability. This proves Lemma 1.

We note that by expanding $H_2(1/2-f)$ as a power series in f, and using the convexity of H_2, we can derive from eq. (20) a useful inequality satisfied by $f(\Delta)$:

$$\left(f(\Delta)\right)^2 \le \frac{1}{2}(\ln 2)H_2(\Delta) \ . \tag{21}$$

Expanding this expression for small Δ and using convexity again, we obtain

$$f(\Delta) \leq \sqrt{\frac{\Delta}{2} \ln\left(\frac{e}{\Delta}\right)} \ . \tag{22}$$

From Lemma 1 and eq. (17), we infer that, for a Δ-balanced attack, $|n_{\text{gap}}^{(Z)}| < n(f(\Delta) + \varepsilon)$ with high probability. A similar argument shows that also $|n_{\text{gap}}^{(X)}| < n(f(\Delta) + \varepsilon)$ with high probability, where

$$n_{\text{gap}}^{(X)} = -\frac{1}{2} \sum_{i=1}^{n} (X \otimes X)_{\text{pairs},i} \otimes Z_{\text{coin},i} \ . \tag{23}$$

(For this argument, we apply Hadamard transformations to all pairs before applying the CNOT gates.) Since $n_{\text{gap}} = n_{\text{gap}}^{(Z)} + n_{\text{gap}}^{(X)}$, we have proved:

Lemma 2 *For a Δ-balanced attack on n pairs and n coins, the state of the pairs has the property*

$$|\tilde{\delta}_p - \tilde{\delta}| < 2(f(\Delta) + \varepsilon) \tag{24}$$

with high probability, for any positive ε.

With Lemma 2 in hand, we can now complete the proof of security following the steps outlined in Sec. 3. If the error rate found in the test is δ, then the number of bit errors in the key-generating pairs is less than $n(\delta + \varepsilon)$ with high probability (assuming that Eve's attack passes the test with a probability that is not exponentially small). For a Δ-balanced attack, we infer that the number of phase errors in the key-generating pairs is less than $n(\delta + 2f(\Delta) + \varepsilon)$ with high probability. By introducing a random permutation (not known by Eve or Fred) we can ensure that the errors are randomly distributed among the pairs. Therefore, for a suitable CSS code, high fidelity pairs (and hence secure key) can be extracted at a rate $1 - H_2(\delta + \varepsilon) - H_2(\delta + 2f(\Delta) + \varepsilon)$, for any positive ε. We have proved:

Theorem 2. Security of BB84 against weakly basis-dependent attacks. *The BB84 protocol is secure if Eve and Fred launch a Δ-balanced attack. Secure final key can be extracted from sifted key at the asymptotic rate*

$$R = \text{Max}\big(1 - H_2(\delta) - H_2(\delta + 2f(\Delta)), 0\big) \tag{25}$$

where δ is the bit error rate found in the verification test and $f(\Delta)$ is defined as in eq. (20). (We assume $\delta + 2f(\Delta) < 1/2$.)

We note that the key generation rate found in Theorem 2 is nonzero only for $2f(\Delta) < 1/2$, or $\Delta < .0289$.

Theorem 2 is our central result concerning security for equipment with generic flaws. In the remainder of this paper, we will analyze some specific examples. As we will see, for some special cases we can establish a key generation rate exceeding the rate eq. (25) found for the general case.

8 Individual source flaws and a perfect detector

As our first application of Theorem 2, we consider the case where the detector is perfect, but the source is subject to individual flaws that may leak some information to Eve about Alice's basis choice. We will prove security by showing that the attack is Δ-balanced.

Suppose that Alice's source emits one of four possible states of a single qubit. In the ideal protocol, these states are the four BB84 states, chosen equiprobably. Suppose, though, that the source is imperfect, so that the four states differ from the corresponding BB84 states, but only slightly.

Let $a \in \{0,1\}$ denote Alice's declared basis choice (ideally, the Z basis for $a=0$ and the X basis for $a=1$) and let $g \in \{0,1\}$ denote Alice's key bit. Suppose that a and g are chosen with the joint probability $p_{a,g}$, and that once the values of a and g are chosen, Alice's source emits a state $\rho_{a,g}$. The Koashi-Preskill analysis applies if $p_{0,0}\rho_{0,0}+p_{0,1}\rho_{0,1} = p_{1,0}\rho_{1,0}+p_{1,1}\rho_{1,1}$, the case in which the source does not reveal any information about a. We will say that the source is *oblivious* when it has this property. Now we are interested in the case were the source is nonoblivious — it leaks a small amount of information about the basis choice.

We can characterize the flawed source by imagining that Alice prepares her states by performing an ideal measurement on half of an entangled pair. The state of the pair (prior to Alice's measurement) is ρ_0 for $a=0$ and ρ_1 for $a=1$. The basis-dependence of the source is weak in the sense that the states ρ_0 and ρ_1 differ only slightly — their fidelity is close to one:

$$\sqrt{F(\rho_0,\rho_1)} \equiv \quad \| \sqrt{\rho_0}\sqrt{\rho_1} \|_{\rm tr} \quad > 1-2\varepsilon_s \ . \tag{26}$$

If n signals are sent, the state that Fred prepares is a product state: $\bigotimes_{i=1}^{n} \rho_{a_i}^{(i)}$, where a_i denotes the basis choice for the ith signal, and $\sqrt{F(\rho_0^{(i)},\rho_1^{(i)})} > 1-2\varepsilon_s$ for each i. Thus we say that Fred's attack on the source is *individual*, and that the basis-dependence is characterized by ε_s. We will suppose for now that any flaws in the detector are basis independent, so that Fred attacks only the source.

The states ρ_0 and ρ_1 may be mixed in general, but they can be "purified" by introducing a suitable "environment" E; that is, there are pure states $|\Psi_0\rangle$ and $|\Psi_1\rangle$ such that

$$\mathrm{tr}_E\big(|\Psi_0\rangle\langle\Psi_0|\big) = \rho_0 \ , \quad \mathrm{tr}_E\big(|\Psi_1\rangle\langle\Psi_1|\big) = \rho_1 \ . \tag{27}$$

Furthermore, it follows from eq. (26) that the purifications can be chosen to have a large overlap [29, 30]:

$$\mathrm{Re}\ \langle\Psi_1|\Psi_0\rangle > 1-2\varepsilon_s \ . \tag{28}$$

Now suppose that, as in Sec. 6, we imagine that the basis choice is determined by a "quantum coin." Then, the state of the coin, the pair, and the environment can be described as a pure state

$$\frac{1}{\sqrt{2}}\big(|\Psi_0\rangle\otimes|0\rangle + |\Psi_1\rangle\otimes|1\rangle\big) \ . \tag{29}$$

If the state of the pair used by Alice to prepare her signal depends on the choice of basis, then the coin will be entangled with the pair and environment, and the strength of this entanglement will depend on how much $|\Psi_0\rangle$ and $|\Psi_1\rangle$ differ. Of course, the quantum coin is merely a mathematical fiction that we invoke for the purpose of analyzing the basis dependence of the pairs that are used to generate the key in the entanglement-based key distribution protocol. Furthermore, the state of the pairs does not depend on how we choose the purifications of ρ_0 and ρ_1. But the state of the coins *does* depend on this choice, and we may exploit our freedom in choosing the purifications to obtain the strongest possible bound on the basis dependence of the pairs.

Since we are assuming that any flaws in the detector are basis independent, these may be absorbed into Eve's basis-independent attack. Then since Eve's attack has no effect on the coins, the state of any coin can be completely characterized by tracing out the pair and environment from eq. (29). If the state of the coin is now measured in the X basis, the outcome $X = -1$ occurs with probability

$$\begin{aligned} p &= \frac{1}{4} \parallel |\Psi_0\rangle - |\Psi_1\rangle \parallel^2 \\ &= \frac{1}{2}\Big(1 - \mathrm{Re}\ \langle\Psi_1|\Psi_0\rangle\Big) < \varepsilon_s \ . \end{aligned} \tag{30}$$

Because the attack is individual, the coins are independent and this bound on p applies to each one of the n coins; therefore we conclude that the attack is $(\varepsilon_s + \varepsilon)$-balanced, for any positive ε. Hence from Theorem 2 we obtain

Theorem 3. Security of BB84 for a source with individual weakly basis-dependent flaws. *Suppose that the flaws in the detector are basis-independent, and that the flaws in the source are individual. The ith signal sent by Alice is prepared by performing a standard qubit measurement on half of an entangled state — this state is* $\rho_0^{(i)}$ *when the Z basis is declared and* $\rho_1^{(i)}$ *when the X basis is declared, where* $\sqrt{F(\rho_0^{(i)},\rho_1^{(i)})} > 1-2\varepsilon_s$ *for all i. Then the BB84 protocol is secure, and secure final key can be extracted from sifted key at the asymptotic rate*

$$R = \mathrm{Max}\,(1 - H_2(\delta) - H_2(\delta + 2f(\varepsilon_s)), 0) \tag{31}$$

where δ *is the bit error rate found in the verification test and* $f(\varepsilon_s)$ *is defined as in eq. (20). (We assume* $\delta + 2f(\varepsilon_s) < 1/2$*.)*

Note that in the formulation of Theorem 3 we have assumed that all signals are detected — we have not considered the effects of loss in the channel or imperfect detector efficiency. In principle, Eve can amplify the basis-dependence of Fred's attack by eliminating some of the signals. In the worst case, the coin is an $X = 1$ eigenstate for each of the signals that Eve removes. Then, if a fraction f of all the signals are lost, Δ is enhanced according to

$$\Delta \rightarrow \Delta' \leq \Delta/(1-f)\ . \tag{32}$$

The effects of loss will be discussed further in Sec. 12 and Sec. 13.

9 Imperfect oblivious source and imperfect detector

We recall that Koashi and Preskill [6] proved the security of BB84 in the case where the detector is perfect and the signals emitted by the source, when averaged over the key bits, are basis independent (an *oblivious* source). The situation they considered can be depicted as in Fig. 3. In effect, Eve prepares an entangled state of n qubits, which are delivered to Bob, and n general signals, which are delivered to Alice. To generate the sifted key, Alice performs

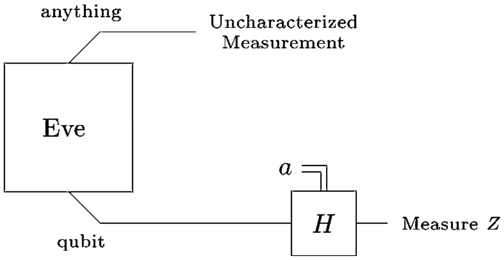

Fig. 3. An uncharacterized oblivious source and a perfect detector. Eve prepares an entangled state of n signals and n qubits. Alice prepares an uncharacterized measurement on the n signals and Bob performs standard measurements on the n qubits. Interchanging the roles of Alice and Bob, we obtain the case of a perfect source and an uncharacterized detector.

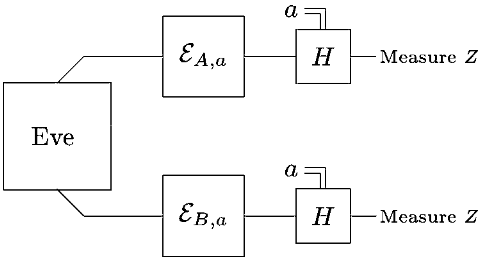

Fig. 4. An oblivious source and an imperfect detector.

an uncharacterized measurement on each of her n signals, and Bob performs a standard measurement on each of his n qubits. By simply reversing the roles of Alice and Bob, we obtain the situation considered by Mayers, in which the source is perfect and the detector is uncharacterized [2].

We will now consider a special case of the Koashi-Preskill source: the source is oblivious, but we further assume that the source can be realized by the preparation of a basis-independent entangled state of the signal space and a *qubit*, followed by a basis-dependent channel applied to the qubit, and finally a standard measurement of the qubit. However, we will go beyond Koashi and Preskill by allowing the detector to have basis-dependent flaws, as shown in Fig. 4. Actually, it will be no harder to analyze the more general case shown in Fig. 5: Eve prepares an arbitrary state of n entangled signals, which is mapped by Fred to a state of n pairs of qubits; then the pairs are distributed to Alice and Bob, who perform standard measurements. An important feature of this setting is that, although Fred's channel can depend on the basis in which Alice and Bob measure, there is no way for Fred to convey any information about the basis to Eve. In this sense the source is oblivious.

We will further assume that the channel applied by Fred is a product of n individual channels, and that each of these n channels depends only weakly on the basis. For analyzing the impact on the quantum coin, it will be convenient to characterize the basis dependence of Fred's attack as follows: A channel $\mathcal{E}$ that takes Eve's arbitrary pair to a pair of qubits can be realized by its *dilation*, an isometric embedding U of Eve's space into the space of the qubit pair and a suitable ancilla. Thus Fred's basis-dependent individual attack can be expressed as the tensor product $U_a \equiv \bigotimes_{i=1}^{n} U_{a_i}^{(i)}$, where i labels the pairs, and a_i denotes the

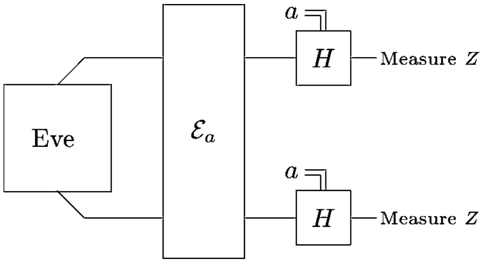

Fig. 5. Stronger version of the attack in Fig. 4.

basis choice for the ith signal. Furthermore the attack depends only weakly on the basis, in the sense that $\frac{1}{4}\|U_0^{(i)} - U_1^{(i)}\|_{\sup}^2 < \varepsilon$ for each i.

Using this characterization, we can analyze how Fred's attack affects the coins that determine the basis. The basis choice is determined by n quantum coins, each a qubit initially prepared in the $X = 1$ eigenstate, and suppose that the initial state of the n pairs and their environment (before Fred's attack) is the pure state $|\varphi\rangle$. Then after Fred's attack, the state of the coins, the pairs, and the environment can be written as

$$\frac{1}{2^{n/2}} \sum_a U_a|\varphi\rangle \otimes |Z;a\rangle \ , \tag{33}$$

where a is the n bit string indicating the basis choice, and the states $\{|Z;a\rangle\}$ are the basis states of the coins in the Z basis. After Fred's attack, suppose that all of the n coins are measured in the X basis. Let x be an n-bit string, and let $|X;x\rangle$ denote a product of n X eigenstates, such that $X_i = 1$ for $x_i = 0$ and $X_i = -1$ for $x_i = 1$. Then the probability that the measurement of the coins yields the outcome x is

$$\begin{aligned} P(x) &= \left\| \frac{1}{2^{n/2}} \sum_a U_a|\varphi\rangle \otimes \langle X;x|Z;a\rangle \right\|^2 , \\ &= \left\| \frac{1}{2^n} \left(\sum_a (-1)^{a.x}\, U_a \right) |\varphi\rangle \right\|^2 \\ &\le \left\| \frac{1}{2^n} \left(\sum_a (-1)^{a.x}\, U_a \right) \right\|_{\sup}^2 \ . \end{aligned} \tag{34}$$

The sum in this expression can be factorized:

$$\frac{1}{2^n} \sum_a (-1)^{a.x}\, U_a = \bigotimes_{i=1}^n \frac{1}{2} \left(U_0^{(i)} + (-1)^{x_i} U_1^{(i)} \right) \ . \tag{35}$$

Furthermore, the sup norm of a tensor product is a product of sup norms. Since for each i

$$\begin{aligned} \left\| \frac{1}{2} \left(U_0^{(i)} - U_1^{(i)} \right) \right\|_{\sup}^2 &< \varepsilon \ , \\ \left\| \frac{1}{2} \left(U_0^{(i)} + U_1^{(i)} \right) \right\|_{\sup}^2 &\le 1 \ , \end{aligned} \tag{36}$$

we have

$$\left\| \frac{1}{2^n} \left(\sum_a (-1)^{a.x}\, U_a \right) \right\|_{\sup}^2 < (\varepsilon)^{|x|} , \tag{37}$$

where $|x|$ denotes the Hamming weight of x, and therefore

$$P(x) < (\varepsilon)^{|x|} . \tag{38}$$

From this bound on $P(x)$, it is elementary to show that the probability that $|x| > (e\varepsilon + \varepsilon')n$ is exponentially small for any positive ε' and $e = 2.71828\cdots$. Therefore we have

Lemma 3. A weakly basis-dependent individual oblivious attack by Fred is Δ-balanced. *Consider an individual attack by Fred, in which Fred applies $U_0^{(i)}$ to the ith pair if the basis choice is $a_i = 0$ and applies $U_1^{(i)}$ if the basis choice is $a_i = 1$, where $\frac{1}{4}\|U_0^{(i)} - U_1^{(i)}\|_{\sup}^2 < \varepsilon$ for each i. This attack is $\Delta -$ balanced for any $\Delta > e\varepsilon$.*

And from Theorem 2 we obtain:

Theorem 4. Security of entanglement-based key distribution against weakly basis-dependent individual oblivious attacks.. *Consider an individual attack by Fred, in which Fred applies $U_0^{(i)}$ to the ith pair if the basis choice is $a_i = 0$ and applies $U_1^{(i)}$ if the basis choice is $a_i = 1$, where $\frac{1}{4}\|U_0^{(i)} - U_1^{(i)}\|_{\sup}^2 < \varepsilon$ for each i. Then the entanglement-based key distribution protocol is secure, and secure final key can be extracted from sifted key at the asymptotic rate*

$$R = \mathrm{Max}\,(1 - H_2(\delta) - H_2(\delta + 2f(e\varepsilon), 0) \tag{39}$$

where δ is the bit error rate found in the verification test and $f(e\varepsilon)$ is defined as in eq. (20). (We assume $\delta + 2f(e\varepsilon) < 1/2$.)

In our formulation of Theorem 4, we have chosen to characterize the basis-dependence of the attack in terms of the sup norm distance between the two isometric embeddings U_0 and U_1 that realize Fred's channels $\mathcal{E}_0$ and $\mathcal{E}_1$. It would be more natural to use the intrinsic distance $\|\mathcal{E}_0 - \mathcal{E}_1\|_\diamond$ defined by the "diamond norm"[31]. But the proof of Lemma 3 uses the property that U_0 and U_1 are close in the sup norm; therefore if we want to reformulate Theorem 4 using the characterization that the channels are close in the diamond norm, we need to show that if two channels are close to one another in the diamond norm, then the dilations of the channels can be chosen to be close in the sup norm. The following lemma, proved in Appendix A, partially solves this problem:

Lemma 4. Similar channels have similar dilations. *Suppose that $\mathcal{E}_0$ and $\mathcal{E}_1$ are quantum channels mapping a d-dimensional system S to a d'-dimensional system T, such that $\| \mathcal{E}_0 - \mathcal{E}_1 \|_\diamond < \varepsilon$. Then there are dilations U_0 and U_1 of the channels (isometric embeddings of S in TE, where E is dd'-dimensional) such that $\| U_0 - U_1 \|_{\sup}^2 < d\varepsilon$.*

However, Lemma 4 has the unpleasant property that the dimension d appears in the upper bound on $\| U_0 - U_1 \|_{\sup}^2$. In principle, the state that Eve delivers to the detector could have arbitrarily high dimension, and Theorem 4 no longer applies if we fix ε while allowing the dimension to grow without bound. For that reason, we prefer to formulate the statement of Theorem 4 in terms of the sup norm, rather than inferring a bound on the distance between dilations in the sup norm from a bound on the distance between channels in the diamond norm.

10 Misalignment

Suppose that Bob is unable to control the orientation of his detector perfectly. When he tries to measure the polarization of his qubit along the z-axis, he actually measures along an axis that lies somewhere in a cone around the z-axis with opening half-angle θ; similarly when he tries to measure along the x-axis, he can only guarantee that his axis is within angle θ of the desired axis. This scenario is equivalent to one in which Bob's measurement is perfect, but Fred rotates the polarization of the qubit by an angle up to θ right before the measurement. Furthermore the rotation Fred applies may depend on whether Bob is trying to measure Z or X, possibly enhancing the phase error rate relative to the bit error rate.

Suppose, in addition, that Alice is unable to control the orientation of her source perfectly — it too might be rotated by an angle up to θ from the ideal orientation. Equivalently, we may suppose that Alice's source is perfect, but that Fred rotates the qubit slightly (exploiting his knowledge of the basis) immediately after it is emitted by the source. One way to realize such a source is for Alice to prepare a perfect Bell pair $|\phi^+\rangle$ and give half to Fred (who rotates his half); then Alice performs a standard measurement on her half. But a unitary transformation U applied by Fred to his qubit is equivalent to U^T applied to Alice's (where U^T denotes the transpose of U); therefore it would make no difference if Alice's qubit were rotated instead of Fred's. Looked at another way, the reason we can replace Fred's rotation by a rotation acting on Alice's qubit is that the source is oblivious — the emitted state, averaged over the key bits, is maximally mixed, and Fred's attack does not change this property.

In the entanglement-based protocol, then, the attack in which Fred rotates the orientation of the source and detector is equivalent to an attack in which pairs of qubits are prepared by Eve however she pleases and distributed to Alice and Bob, and then Fred rotates both Alice's and Bob's qubits slightly (by no more than θ) just before standard measurements are performed. Furthermore, we are assuming that Fred's attack is *individual* — the rotation he applies to the ith pair is controlled by only the outcome of the flip of the ith coin. Therefore, Theorem 4 applies. We can estimate the rate of generation of secure key by calculating the maximum value of

$$\frac{1}{4}||U_0 - U_1||^2_{\text{sup}} = \sup_{|\psi\rangle} \frac{\frac{1}{2}\left(1 - \text{Re}\langle\psi|U_1^{-1}U_0|\psi\rangle\right)}{\langle\psi|\psi\rangle} , \tag{40}$$

where U_0 and U_1 are unitary transformations applied to the pairs that are consistent with our characterization of the source and detector.

It is not hard to see that the supremum occurs for $|\psi\rangle$ a maximally entangled state, which, after a suitable choice of basis and phase conventions we may choose to be $|\phi^+\rangle$. Fred applies separate single-qubit rotations to Alice's qubit and to Bob's; acting on $|\phi^+\rangle$, the combined effect of the two is equivalent to a rotation applied to Bob's qubit alone, by an angle no larger than 2θ. The overlap $\langle\phi^+|U_1^{-1}U_0|\phi^+\rangle$ is minimized (for $|\theta| \le \pi/4$) if $U_1^{-1} = U_0$; we may choose U_0 to be the transformation $I \otimes \tilde{U}_0$, where $\tilde{U}_0$ is the single-qubit rotation

$$\tilde{U}_0 = \begin{pmatrix} e^{i\theta} & 0 \\ 0 & e^{-i\theta} \end{pmatrix} . \tag{41}$$

We find that

$$\langle\phi^+|I \otimes \tilde{U}_0^2|\phi^+\rangle = \cos 2\theta , \tag{42}$$

which implies

$$\frac{1}{4}\|U_0 - U_1\|^2_{\mathrm{sup}} = \sin^2\theta \ . \tag{43}$$

From Lemma 3, then, we find that Fred's attack is $(e \cdot \sin^2\theta + \varepsilon)$-balanced for any positive ε, and we therefore obtain

Theorem 5. Security of BB84 against individual misalignment of the source and detector. *Suppose that, for each signal, Fred can perform a basis-dependent adjustment of the polarization axes of the source and detector by any angle up to θ. Then the BB84 protocol is secure, and secure final key can be extracted from sifted key at the asymptotic rate*

$$R = \mathrm{Max}\left(1 - H_2(\delta) - H_2(\delta + 2f(e \cdot \sin^2\theta), 0\right) \tag{44}$$

where δ is the bit error rate found in the verification test and $f(e \cdot \sin^2\theta)$ is defined as in eq. (20). (We assume $\delta + 2f(e \cdot \sin^2\theta) < 1/2$ and $\theta \leq \pi/4$).)

Thus for $\delta = 0$ we obtain a nonzero rate of key generation for $\theta < 5.92°$.

We remark again that in the formulation of Theorem 5 the misalignment of the detector or source is assumed to be adversarial, within the angular tolerance specified in our characterization of the device — Alice and Bob wish to conceal the key from the Eve/Fred alliance. The arguments of Mayers [2] (for detectors) and Koashi-Preskill [6] (for sources) apply to an uncharacterized misalignment that is not adversarial — Alice and Bob wish to conceal the key from Eve and don't care what Fred knows. In that case, the large potential misalignments do not reduce the key generation rate below that achievable with perfect devices, given a specified bit error rate δ observed in the test. However, the conclusion of [2] about security in the case of an uncharacterized detector applies only if the source is perfect, and likewise the conclusion [6] about the case of an uncharacterized source applies only if the detector is perfect. In contrast, our analysis applies to the case where both the detector and the source are subject to a characterized misalignment.

11 Generic individual flaws in source and detector

Suppose that the source and detector are both subject to individual flaws that depend weakly on the basis. The source can be modeled as in Sec. 8: For each signal to be sent, Fred first prepares a joint state of a qubit A' and a general system A. The state that Fred prepares can depend on the basis. Alice then launches the signal by performing a standard measurement on the qubit. If n signals are to be sent, Fred prepares a product state $\bigotimes_{i=1}^n \rho^{(i)}_{a_i}$, where a_i denotes the basis choice for the ith signal. Thus we say that Fred's attack on the source is individual. The basis dependence of the source is weak in the sense that $\sqrt{F(\rho^{(i)}_0, \rho^{(i)}_1)} > 1 - 2\varepsilon_s$ for each i.

We model the detector as follows: Each signal, after Eve's basis-independent attack, is a state of a general system B. The signal is received by Fred, who applies a channel that "squashes" the signal to a qubit B'; Fred's channel may depend on the basis in which Bob will conduct his measurement. Then Bob performs a standard single-qubit measurement on the qubit. Fred's basis-dependent squash can be realized as a basis-dependent isometric embedding of B in $B'E$ where E is a suitable ancilla. If n signals are received by the detector, this transformation can be expressed as the tensor product $\bigotimes_{i=1}^n U^{(i)}_{a_i}$. Thus we say that Fred's attack on the detector is individual. Furthermore the attack depends only weakly on the basis, in the sense that $\frac{1}{4}\|U_0^{(i)} - U_1^{(i)}\|_{\text{sup}}^2 < \varepsilon_d$ for each i.

By simultaneously allowing basis-dependent flaws in the source and in the detector, we are going beyond the analysis in Sec. 8 and Sec. 9. But we may anticipate that, as in those cases considered previously, we can show that the attack is Δ-balanced for small Δ, if ε_s and ε_d are small. Indeed, this is the case; for example, if $\varepsilon_s = \varepsilon_d \equiv \varepsilon$ we can show

Lemma 5. *Suppose that the source and detector are subject to basis-dependent flaws. The ith signal sent by Alice is prepared by performing a standard qubit measurement on half of an entangled state — this state is $\rho_0^{(i)}$ when the Z basis is declared and $\rho_1^{(i)}$ when the X basis is declared, where $\sqrt{F(\rho_0^{(i)}, \rho_1^{(i)})} > 1 - 2\varepsilon$ for all i. The ith signal received by the detector is first squashed to a qubit and then a standard measurement is performed. The squash is described by a channel that can be realized by the isometric embedding $U_0^{(i)}$ when the Z basis is declared and by $U_1^{(i)}$ when the X channel is declared, where $\frac{1}{4}\|U_0^{(i)} - U_1^{(i)}\|_{\text{sup}}^2 < \varepsilon$ for each i. This attack is Δ – balanced for any $\Delta > 8\sqrt{\varepsilon} + 4\varepsilon$.*

Lemma 5, together with Theorem 2, provides a proof of security for generic individual flaws in the source and detector that depend sufficiently weakly on the basis. We omit the proof of Lemma 5, which is rather long and unenlightening.

A surprising feature of Lemma 5 is the term scaling like $\sqrt{\varepsilon}$ in our bound on Δ — one might reasonably have expected a stronger result, that the attack is Δ-balanced for some Δ linear in ε. However, we have not succeeded in proving a linear bound.

12 Tagged signals

Suppose that a fraction Δ of the qubits emitted by the source are *tagged* by Fred. The tag informs Eve which basis was used, so that she can measure the qubit without disturbing it. Eve has no information about the basis used for the untagged qubits (a fraction $1 - \Delta$ of the total).

Note that tagged qubits arise in QKD with weak coherent states. The phase of a signal emitted by a coherent light source may be regarded as random if Eve has no information about the phase [11, 32], so that the signal state is a mixture of photon number eigenstates. If the source emits more than one photon, we pessimistically assume that Eve stores the extra photons until after the bases are broadcast, and then measures in the proper basis to learn the key bit without introducing any disturbance. Then the tagging probability is $\Delta = p_M/p_D$, where p_M is the probability of emitting a multiphoton, and p_D is the probability that an emitted photon is detected (we pessimistically assume that all of the photons that fail to arrive were emitted as single photons). Arguably we know p_M if we understand our source well, and p_D can be measured. Hence Δ is a known (or at least knowable) parameter characterizing a practical implementation of quantum key distribution.

We can incorporate tagging into our source model by allowing Fred to append to each qubit emitted by Alice's source an auxiliary qutrit that conveys information about the basis to Eve. For a fraction Δ of the signals (Fred gets to decide which ones), he sets the value of the qutrit to $|a\rangle$, where $a = 0$ indicates the Z basis and $a = 1$ indicates the X basis. For the remaining fraction $1 - \Delta$ of the qubits sent by Alice, Fred sets the qutrit to $|2\rangle$, passing no basis information to Eve. Eve can read the auxiliary qutrit to learn the basis for each tagged qubit, and so measure the key bit without introducing any disturbance. If each coin that determines the basis choice is a qubit initially prepared in the $X = 1$ eigenstate $(|0\rangle + |1\rangle)/\sqrt{2}$, then Fred's attack causes the coin to decohere in the $\{|0\rangle, |1\rangle\}$ basis if the corresponding signal is tagged, but leaves the coin undisturbed if the signal is untagged.

It follows that the attack is $(\Delta/2 + \varepsilon)$-balanced for any positive ε, and we could prove security by applying Theorem 2. But in this case it is possible to prove a stronger result, because we know more about the quantum state of the coins. Suppose that, as in Sec. 7, we apply controlled-NOT gates from the pairs to the coins, transforming $n_{\rm gap}^{(Z)}$ to $\frac{1}{2}\sum_{i=1}^{n} Z_{{\rm coin},i}$. The action on the coin of a controlled-NOT gate preserves an X-eigenstate. Therefore, the probability distribution governing the value of $n_{\rm gap}^{(Z)}$ is the same as the probability distribution governing $\frac{1}{2}\sum_{i=1}^{n} Z_{{\rm coin},i}$ in a state of the n coins with the property that $n(1-\Delta)$ of the coins are in eigenstates of X with eigenvalue $+1$. Hence with high probability $|n_{\rm gap}^{(Z)}| < n\Delta/2+\varepsilon$ for any positive ε. A similar argument applies to $|n_{\rm gap}^{(X)}|$, and we find that $|n_{\rm gap}| = |n_{\rm gap}^{(Z)} + n_{\rm gap}^{(X)}| < n\Delta + \varepsilon$ for any positive ε. We conclude that secure key can be extracted from sifted key at the asymptotic rate

$$R = 1 - H_2(\delta) - H_2(\delta + \Delta) \ , \tag{45}$$

where we have assumed that $\delta + \Delta \leq 1/2$.

Note that to obtain the upper bound on $n_{\rm gap}$, all that we needed was the property that Fred interacts with no more than $n\Delta$ of the coins. Therefore, the argument can be applied more broadly than to the particular tagging model that we have defined above. For example, it applies to a setting where there are flaws in the random number generators used by Alice and Bob to select the basis and the key bits. Suppose that for a fraction $n(1 - \Delta)$ of the signals, the basis choice and the key bit are chosen by flipping fair coins, but for a fraction $n\Delta$ of the signals, Fred is free to choose the basis and the key bit however he chooses. In this model, if the source and the detector are perfect otherwise, Fred need not touch $n(1 - \Delta)$ of the coins, and secure key can be generated at the rate eq. (45). (In this estimate of the rate, however, we have continued to assume that the qubits selected for the verification test are a fair sample, and so provide an accurate estimate of the error rate for the key generating pairs. The argument can be extended further to cover the case where Fred is permitted to select a small portion of the test set, by adjusting the estimate of the error rate to take into account the bias in the test.)

With a more sophisticated argument we can obtain a higher rate of secure key generation than eq. (45). After correcting errors in the sifted key (sacrificing a fraction $H_2(\delta)$ of the key, asymptotically) we imagine executing privacy amplification on two different strings, the sifted key bits arising from the tagged qubits and the sifted key bits arising from the untagged qubits. Since the privacy amplification scheme described in Sec. 3 is linear (the private key can be computed by applying the C_2 parity check matrix to the sifted key after error correction), the key obtained is the bitwise XOR

$$s_{\rm untagged} \oplus s_{\rm tagged} \tag{46}$$

of keys that could be obtained from the tagged and untagged bits separately. If $s_{\rm untagged}$ is private and random, then it doesn't matter if Eve knows everything about $s_{\rm tagged}$ – the sum is still private and random.

Therefore we ask if privacy amplification is successful applied to the untagged bits alone. Under the worst case assumption that the bit error rate is zero for tagged qubits, the overall bit error rate $\tilde{\delta}$ is related to the bit error rate $\tilde{\delta}_{\text{untagged}}$ for the untagged qubits by

$$\tilde{\delta} = (1-\Delta)\tilde{\delta}_{\text{untagged}} \ . \tag{47}$$

Since the bit errors and phase errors are related by symmetry for the untagged qubits, the phase error rate $\tilde{\delta}_{p,\text{untagged}}$ for the untagged qubits satisfies

$$\tilde{\delta}_{p,\text{untagged}} < \tilde{\delta}_{\text{untagged}} + \varepsilon = \frac{\tilde{\delta}}{1-\Delta} + \varepsilon \tag{48}$$

with high probability. Since the error rate δ observed in the test provides a good estimate of $\tilde{\delta}$ for the key generating pairs, we conclude that

$$\tilde{\delta}_{p,\text{untagged}} < \frac{\delta}{1-\Delta} + \varepsilon' \ . \tag{49}$$

with high probability, for any positive ε' and sufficiently large n. If there are n bits of sifted key, then $(1-\Delta)n$ of these bits come from untagged qubits, and (since bit errors are already corrected) we can extract a private key by sacrificing a fraction $H_2(\tilde{\delta}_{p,\text{untagged}} + \varepsilon'')$ of these for privacy amplification. Thus we have proved:

Theorem 6. Security of BB84 against tagging. *Suppose that Fred interacts with only $n\Delta$ of the n coins that determine the basis used by Alice and Bob. Then the BB84 protocol is secure, and secure final key can be extracted from sifted key at the asymptotic rate*

$$R = \text{Max}\left((1-\Delta) - H_2(\delta) - (1-\Delta)H_2\left(\frac{\delta}{1-\Delta}\right), 0\right) \tag{50}$$

where δ is the bit error rate found in the verification test (assuming $\delta/(1-\Delta) < 1/2$). In particular, this rate of key generation is achievable, assuming that the source and the detector are perfect otherwise, if Fred reveals the basis to Eve for $n\Delta$ of the signals, or if Fred chooses the basis and key bits for $n\Delta$ of the signals.

In the case where the source emits weak coherent states with random phases, a rate of key generation similar to eq. (50) was established by Inamori, Lütkenhaus, and Mayers (ILM) [8]. Actually, the rate quoted by ILM is below R in Eq. (50) — in their Eq. (18) the argument of H_2 in the last term is $2\delta/(1-\Delta)$ rather than $\delta/(1-\Delta)$. However, we believe that their argument can be refined to match the rate Eq. (50). With that refinement the ILM result is stronger in a sense than what we have derived here, as it applies to the case of a general uncharacterized detector.

Theorem 6 can be applied if there is loss in the quantum channel connecting Alice and Bob and/or if Bob's detector has imperfect efficiency, provided that the loss is basis-independent. For example, suppose that each signal emitted by Alice's source is a phase-randomized weak coherent state with mean photon number $\mu \ll 1$, so that the signal is a single photon with probability $p_1 = \mu + O\left(\mu^2\right)$, and more than one photon with probability $p_M = \frac{1}{2}\mu^2 + O\left(\mu^3\right)$. We can describe these signals by imagining a source that never emits multiple photons, followed by a basis-dependent attack by Fred in which Fred interacts with a fraction p_M of all the coins. Now suppose that Eve's attack can be modeled by a basis-independent lossy channel, such that a fraction η of all the nonvacuum signals are detected. (Here by "basis-independent" we mean that Eve's attack has no *a priori* dependence on the basis, though of course Eve can exploit the multiphotons to acquire some information about the basis; the important thing is that Eve can launch her attack without interacting with the coins.) Then a fraction $p_D = \eta\left(\mu + O(\mu^2)\right)$ of all the signals are detected, and of the coins associated with detected signals, Fred interacts with at most a fraction

$$\Delta = p_M/p_D = \frac{1}{2\eta}\left(\mu + O\left(\mu^2\right)\right) . \tag{51}$$

Sifted key is generated at the rate

$$\frac{1}{2}\nu p_D \approx \frac{1}{2}\nu\eta\mu \approx \nu\eta^2\Delta , \tag{52}$$

where ν is the repetition frequency of the source. Therefore, if Δ (and hence also the rate R of generation of final key from sifted key) is held fixed as η gets small, then the overall key generation rate $\frac{1}{2}\nu p_D R$ is $O(\eta^2)$, as ILM observed [8]. This scaling of the rate with η holds approximately as long as dark counts in the detector are not too important, so that the bit error rate δ is roughly independent of η. In some current implementations of quantum key distribution using weak coherent states transmitted through optical fibers, dark counts are relatively unimportant, and our analysis of security is applicable, up to a range of approximately 20 km.

Theorem 6 applies if Fred tags any $n\Delta$ of the signals. But it does not apply to a *coherent superposition* of such attacks. Suppose, for example, that in the entanglement-based protocol, Fred's attack on the pairs and the coins produces a state

$$|\Psi\rangle = \sum_{S:|S|\leq n\Delta} a_S|\Psi_S\rangle ; \tag{53}$$

here the sum is over subsets S that contain no more than $n\Delta$ of the n pairs, and $|\Psi_S\rangle$ is the state resulting from tagging the pairs in the set S. Although Theorem 6 does not apply to a general superposition of tagged states as in eq. (53), Theorem 2 *does* apply to this case. After we trace out Fred's labeling qutrits, the state of the coin can be realized as an ensemble of states, where for each state in the ensemble at least $n(1-\Delta)$ of the coins are $X = 1$ eigenstates and the rest are mixtures of Z eigenstates. Therefore, if the coins are all measured in the X basis, with high probability the number of coins for which the outcome $X = -1$ is found will be less than $n(\Delta/2 + \varepsilon)$. Thus the attack is $(\Delta/2 + \varepsilon)$-balanced for any positive ε and sufficiently large n, and it follows from Theorem 2 that secure key can be generated at the corresponding rate (a lower rate than found in Theorem 6).

In particular, then, Theorem 2 can be applied to a general source that emits signals that are sufficiently close to perfect single photon pulses, even if the multiphotons occur with nonrandom phases. Unfortunately, though, our arguments do not allow us to address the case where the source emits weak coherent states with nonrandom phases — in that case the states are dominated by the amplitude to emit the vacuum state, and the tagging model we have analyzed here does not apply. This difficulty seems to be more than a mere shortcoming of our model; the deeper problem is that weak coherent states with nonrandom phases leak a significant amount of basis information, which may compromise security.

As for all of the cases that we consider in this paper, the crux of our analysis of tagging is a bound on the phase error rate $\tilde{\delta}_p$ of the key generating pairs that holds *with high probability* — it does not suffice for $\tilde{\delta}_p$ to be bounded after *averaging* over Fred's strategy. Therefore, our security proof need not apply for a highly correlated basis-dependent attack on the signals, even if the bit error rate $\tilde{\delta}$ and phase error rate $\tilde{\delta}_p$ resulting from the attack have mean values that are nearly equal.[b]

For example, suppose that with a small probability r, Fred tells Eve the basis for *every* signal, while with probability $1 - r$, Fred tells Eve nothing. Then on average the disparity between the bit error rate and the phase error rate is small. However, with a fixed probability r that does not depend on the key length, Eve can learn the whole key. Therefore, the quantum key distribution protocol is insecure for a source of this type.

13 Trojan pony

Suppose that the detector is not perfectly efficient. A fraction Δ of the signals that enter the detector fail to trigger it, resulting in no recorded outcome. Suppose further that Fred, who knows Bob's basis, controls whether the detector fires or not, subject to the constraint that only a fraction Δ of the detection events can be eliminated. Note that the parameter Δ can be measured in the protocol.

Fred can use his power to disguise Eve's attack, enhancing the detection rate when Bob measures in the same basis as Eve did and suppressing the detection rate when Bob measures in a different basis than Eve's. This is a limited version of the "Trojan horse" attack [28] — we call it the "Trojan pony." As we remarked in Sec. 5, one version of the Trojan pony attack can be launched if Bob's detector is configured as a polarization beam splitter that directs the signals to a pair of threshold detectors; Eve can ensure that the detector fails to register a conclusive result by flooding it with many photons. We will analyze this attack in a different setting, in which Bob's detector receives qubits rather than bosonic modes.

In the EDP setting, we allow Fred to eliminate a fraction Δ of the pairs (corresponding to the qubits for which he "turns off" Bob's detector). In the worst case, every pair that he eliminates has a bit error and no phase error. Before any pairs were eliminated, the error rate was essentially the same in both bases — call this rate p. After eliminating the undetected pairs, the error rates are

$$\tilde{\delta} \approx \frac{p-\Delta}{1-\Delta} , \quad \tilde{\delta}_p \approx \frac{p}{1-\Delta} \tag{54}$$

(assuming $\Delta \leq p \leq 1 - \Delta$). Note that, for ease of presentation, we have not included the ε's in eq. (54); instead we have used the symbol $\approx$ to indicate relations that are satisfied to arbitrarily good accuracy with high probability asymptotically. Eliminating p we find

$$\tilde{\delta}_p \approx \tilde{\delta} + \frac{\Delta}{1-\Delta} , \tag{55}$$

and, since the error rate δ measured in the test provides a reliable estimate of $\tilde{\delta}$, we infer that final key can be generated from sifted key at the achievable rate

---

[b] We thank Dominic Mayers for a helpful discussion of this point.

$$R = 1 - H_2(\delta) - H_2\left(\delta + \frac{\Delta}{1-\Delta}\right) , \tag{56}$$

where we have assumed that

$$\delta + \frac{\Delta}{1-\Delta} \leq 1/2 . \tag{57}$$

We can use similar reasoning if the detector efficiency is low, but we trust that most of the instances where the detector fails to fire are chosen at random, and only a small percentage of all the detector failures are due to Fred's intervention. In the absence of other imperfections, random misfires merely reduce the number of sifted key bits, but without breaking the symmetry between the bases. Eq. (56) still applies if a fraction f of detection events are removed by random errors, and a fraction Δ of the remaining events are removed adversarially, resulting in an overall efficiency $\eta = (1-f)(1-\Delta)$. Thus we have proved

Theorem 7. Security of BB84 against basis-dependent detector efficiency. *Suppose that of the signals that arrive at Bob's detector, a fraction f chosen at random are removed, and of those that remain a fraction Δ chosen adversarially by Fred are also removed, so that the overall efficiency of the detector is $\eta = (1-f)(1-\Delta)$. Then the BB84 protocol is secure, and secure final key can be extracted from the (detected) sifted key at the asymptotic rate*

$$R = \mathrm{Max}\left(1 - H_2(\delta) - H_2\left(\delta + \frac{\Delta}{1-\Delta}\right), 0\right) \tag{58}$$

where δ is the bit error rate found in the verification test (assuming $\delta + \Delta/(1-\Delta) < 1/2$).

Note that we can measure the efficiency η in the protocol, but can determine Δ only by acquiring a good understanding of the vulnerability of the detector to tampering. In fact, in current implementations the typical efficiency for detection of single photons at telecommunication wavelengths is about 15% [33]. Theorem 7 can also be applied to the case where basis-dependent losses occur in the quantum channel connecting Alice and Bob, with Δ parametrizing the basis dependence.

ILM [8, 27] discussed the specific type of Trojan pony attack in which Eve floods Bob's polarization beam splitter with many photons of the same polarization, generating a "double click" in Bob's two photon detectors when he tries to measure the polarization in the conjugate basis. For this case they proposed that Bob choose his key bit randomly each time he encounters a double click event. Security of this scheme is ensured by the result of Mayers [2]: the POVM that assigns a random outcome to the "double-click" subspace is a possible measurement that Fred could arrange, and Mayers proved security for an arbitrary detector POVM. If double clicks occur a fraction Δ of the time, and the bit error rate is δ when single clicks occur, then the overall error rate under the ILM prescription will be $(1-\Delta)\delta + \Delta/2$, resulting in a key generation rate

$$R = 1 - 2H_2\Big((1-\Delta)\delta + \Delta/2\Big) . \tag{59}$$

The rate is further enhanced by the factor $(1-\Delta)^{-1}$ relative to Eq. (56), since all detection events, including the double clicks, contribute to the sifted key. Thus the achievable rate established by ILM exceeds the rate we have derived, except for relatively large Δ and relatively small δ. However, the two results cannot be compared directly, because they apply to two different models of the adversary. The ILM result Eq. (59) applies to a particular Trojan pony attack that can be launched by Eve if the Bob/Fred POVM has suitable properties; it provides a condition for Eve (but not Fred) to have negligible information about the key. Eq. (56) is the rate at which key can be extracted under a Trojan pony attack in which Fred receives qubits, and can prevent some of the qubits from registering in Bob's detector. But in this case the key is kept secret not just from Eve but from the Eve/Fred alliance.

A different type of issue relating to detector efficiency arises if the detector failures occur at different rates when measuring in the X and Z bases, but are otherwise randomly distributed. The bias in the detector efficiency breaks the symmetry between the bases, but a simple variant of the Shor-Preskill argument still applies. In the entanglement distillation picture, we may imagine that Alice and Bob at first share many noisy pairs; furthermore, after a random permutation unknown to the adversary is applied, the pairs are symmetrized so that all have the same marginal density operator. Then some of the pairs are removed from the sample by a random process. Though the probability of removal may depend on the basis used to generate the key bit, Alice and Bob can still infer the phase error rate from the bit error rate if they conduct a refined data analysis [25], measuring separate error rates δ_X and δ_Z for the X and Z bases respectively. If a fraction p_X of the sifted key bits are generated in the X basis and a fraction p_Z in the Z basis (where $p_X + p_Z = 1$), so that the bit error rate is $\delta = p_X\delta_X + p_Z\delta_Z$, then the phase error rate to insert in Eq. (4) becomes $\delta_p = p_X\delta_Z + p_Z\delta_X$.

14 Conclusions

We have shown that the BB84 quantum key distribution protocol is secure when the source and/or detector are subject to small errors that are controlled by an adversary who knows the basis used by Alice and Bob. We have formulated a method for estimating the key generation rate in the presence of such errors, and we have applied the method to various model sources and detectors. Our results are complementary to earlier proofs of security [2, 6] that apply to flaws in the apparatus that may be large but are nonadversarial; furthermore, our results unlike those of [2, 6] apply when both the source and the detector have small basis-dependent flaws, as will be the case in typical real-world implementations of quantum key distribution. We have argued that the security holes of real sources and detectors can be usefully investigated within our framework, and we expect that the methods we have developed will find further applications.

However, the model sources and detectors to which our analysis applies are not completely general. In our model of the source, each signal is launched by preparing an entangled state of a *qubit* and a general system, followed by an ideal measurement of the qubit. To establish security, we require that the entangled state depend only weakly on the basis used in the protocol. With this model, we are unable to treat, for example, the case where the source emits weak coherent states with *nonrandom* phases. Likewise, we model the detector as a quantum channel followed by an ideal measurement of a qubit, and to establish security we require that the quantum channel depend only weakly on the basis. In particular, we are unable to treat the case where the signals received by the detector reside in a Hilbert space of arbitrarily high dimension.

Various other issues regarding the security of BB84 and other quantum key distribution protocols have not been addressed here. We have not considered how to characterize devices reliably using testing equipment that is itself untrustworthy (as in [7]). We have not discussed how to improve the rate of key generation beyond the rate in Eq. (4) through privacy amplification schemes that use two-way communication between Alice and Bob [15]. Finally, our security analysis applies to the asymptotic limit of an infinite key — we have not analyzed the practical aspects of error correction and privacy amplification in the case of finite key length.

Acknowledgements

We thank Michael Ben-Or, Jim Harrington, Masato Koashi, Dominic Mayers, and Peter Shor for helpful discussions. This work has been supported in part by: the Department of Energy under Grant No. DE-FG03-92-ER40701, the National Science Foundation under Grant No. EIA-0086038, the Caltech MURI Center for Quantum Networks under ARO Grant No. DAAD19-00-1-0374, the Clay Mathematics Institute, Canadian NSERC, Canada Research Chairs Program, Canadian Foundation for Innovation, Ontario Innovation Trust, Premier's Research Excellence Award, Canadian Institute for Photonics Innovation, MagiQ Technologies, Inc., and the German Research Council (DFG) under the Emmy-Noether Programme.

References

1. C. H. Bennett and G. Brassard, "Quantum cryptography: Public key distribution and coin tossing," in *Proceedings of IEEE International Conference on Computers, Systems and Signal Processing, Bangalore, India* (IEEE, New York, 1984), pp. 175–179.
2. D. Mayers, "Quantum key distribution and string oblivious transfer in noisy channels," in *Advances in Cryptography—Proceedings of Crypto'96* (Springer-Verlag, New York, 1996), pp. 343-357; "Unconditional security in quantum cryptography," J. Assoc. Comp. Mach. **48**, 351 (2001), arXiv:quant-ph/9802025.
3. H.-K. Lo and H. F. Chau, "Unconditional security of quantum key distribution over arbitrarily long distances," Science **283**, 2050–2056 (1999), arXiv:quant-ph/9803006.
4. E. Biham, M. Boyer, P. O. Boykin, T. Mor, and V. Roychowdhury, "A proof of the security of quantum key distribution," in *Proceedings of the 32nd Annual ACM Symposium on Theory of Computing* (ACM Press, New York, 2000), pp. 715–724, arXiv:quant-ph/9912053.
5. P. W. Shor and J. Preskill, "Simple proof of security of the BB84 quantum key distribution protocol," Phys. Rev. Lett. **85**, 441–444 (2000), arXiv:quant-ph/0003004.
6. M. Koashi and J. Preskill, "Secure quantum key distribution with an uncharacterized source," Phys. Rev. Lett. **90**, 057902 (2003), arXiv:quant-ph/0208155 (2002).
7. D. Mayers and A. Yao, "Quantum cryptography with imperfect apparatus," arXiv:quant-ph/9809039 (1998); D. Mayers and A. Yao, "Self testing quantum apparatus," arXiv:quant-ph/0307205.
8. H. Inamori, N. Lütkenhaus and D. Mayers, "Unconditional security of practical quantum key distribution," arXiv:quant-ph/0107017 (2001).
9. B. A. Slutsky, R. Rao, P.-C. Sun, and Y. Fainman, "Security of quantum cryptography against individual attacks," Phys. Rev. A **57**, 2383–2398 (1998).
10. N. Lütkenhaus, "Security against individual attacks for realistic quantum key distribution," Phys. Rev. A **61**, 052304 (2000), arXiv:quant-ph/9910093.
11. G. Brassard, N. Lütkenhaus, T. Mor, and B. C. Sanders, "Security aspects of practical quantum cryptography," Phys. Rev. Lett. **85**, 1330–1333 (2000), arXiv:quant-ph/9911054.
12. S. Felix, N. Gisin, A. Stefanov, H. Zbinden, "Faint laser quantum key distribution: Eavesdropping

exploiting multiphoton pulses," J. Mod. Opt. **48**, 2009 (2001), arXiv:quant-ph/0102062.

13. G. Gilbert and M. Hamrick, "Practical quantum cryptography: a comprehensive analysis (part one)," arXiv:quant-ph/0009027 (2000).
14. G. Gilbert and M. Hamrick, "Secrecy, computational loads and rates in practical quantum cryptography," Algorithmica **34**, 314-339 (2002), arXiv:quant-ph/0106043 (2001).
15. D. Gottesman and H.-K. Lo, "Proof of security of quantum key distribution with two-way classical communications," IEEE Trans. Information Theory **49**, 457 (2003), arXiv:quant-ph/0105121 (2001).
16. M. Ben-Or,"Simple security proof for quantum key distribution," online presentation available at http://www.msri.org/publications/ln/msri/2002/qip/ben-or/1/index.html (2002).
17. C. H. Bennett, G. Brassard, S. Popescu, B. Schumacher, J. A. Smolin, and W. K. Wootters, "Purification of noisy entanglement and faithful teleportation via noisy channels," Phys. Rev. Lett. **76**, 722-725 (1996), arXiv:quant-ph/9511027. Erratum: Phys. Rev. Lett. **78**, 2031 (1997).
18. D. Deutsch, A. Ekert, R. Jozsa, C. Macchiavello, S. Popescu, and A. Sanpera, "Quantum privacy amplification and the security of quantum cryptography over noisy channels," Phys. Rev. Lett. **77**, 2818-2821 (1996), arXiv.org:quant-ph/9604039. Erratum: Phys. Rev. Lett. **80**, 2022 (1998).
19. C. H. Bennett, D. P. DiVincenzo, J. A. Smolin and W. K. Wootters, "Mixed state entanglement and quantum error correction," Phys. Rev. A **54**, 3824–3851 (1996), arXiv:quant-ph/9604024.
20. A. R. Calderbank and P. W. Shor, "Good quantum error correcting codes exist," Phys. Rev. A **54**, 1098–1105 (1996), arXiv:quant-ph/9512032.
21. A. M. Steane, "Multiple particle interference and quantum error correction," Proc. Roy. Soc. Lond. A **452**, 2551–2577 (1996), arXiv:quant-ph/9601029.
22. D. Gottesman and J. Preskill, "Secure quantum key distribution using squeezed states," Phys. Rev. A **63**, 022309 (2001), arXiv:quant-ph/0008046.
23. M. Hamada, "Reliability of Calderbank-Shor-Steane codes and the security of quantum key distribution," arXiv:quant-ph/0311003 (2003).
24. D. A. Spielman, "Linear-time encodable and decodable error-correcting codes, IEEE Trans. Information Theory **42**, 1723–1731 (1996).
25. H.-K. Lo, H. F. Chau, and M. Ardehali, "Efficient quantum key distribution scheme and proof of its unconditional security," arXiv:quant-ph/0011056 (2000).
26. D. Gottesman and I. L. Chuang, "Quantum digital signatures," arXiv:quant-ph/0205032 (2001).
27. N. Lütkenhaus, "Estimates for practical quantum cryptography," Phys. Rev. A **59** 3301–3319 (1999), arXiv:quant-ph/9806008.
28. H.-K. Lo, "Proof of unconditional security of six-state quantum key distribution scheme," Quant. Info. Comp. **1**, 81–94 (2001), arXiv:quant-ph/0102138.
29. A. Uhlmann, "The 'transition probability' in the state space of a *-algebra," Reports on Mathematical Physics **9**, 273–279 (1976).
30. R. Jozsa, "Fidelity for mixed quantum states," J. Mod. Opt. **41**, 2315-2323 (1994).
31. D. Aharonov, A, Kitaev, and N. Nisan, "Quantum circuits with mixed states," in *Proceedings of the Thirtieth Annual ACM Symposium on Theory of Computing (STOC)* (ACM Press, New York, 1998), pp. 20-30, arXiv:quant-ph/9806029.
32. S. J. van Enk and C. A. Fuchs, "The quantum state of a laser field," Quant. Info. Comp. **2**, 151–165 (2002), arXiv:quant-ph/0111157.
33. N. Gisin, G. Ribordy, W. Tittel, and H. Zbinden, "Quantum cryptography," Rev. Mod. Phys. **74**, 145-195 (2002) arXiv:quant-ph/0101098

Appendix A

Here we will prove:

Lemma 4. Similar channels have similar dilations. *Suppose that $\mathcal{E}_0$ and $\mathcal{E}_1$ are quantum channels mapping a d-dimensional system S to a d'-dimensional system T, such that* $\| \mathcal{E}_0 -$

$\mathcal{E}_1 \|_\diamond < \varepsilon$. *Then there are dilations* U_0 *and* U_1 *of the channels (isometric embeddings of* S *in* TE*, where* E *is* dd'*-dimensional) such that* $\| U_0 - U_1 \|_{\sup}^2 < d\varepsilon$.

It is convenient to characterize a quantum channel $\mathcal{E}$ mapping system S to system T by considering the action of $I \otimes \mathcal{E}$ on a reference system R and the system S, where dim $R =$ dim $S \equiv d$. Let

$$|\tilde{\Phi}\rangle = \sum_i |i\rangle_R \otimes |i\rangle_S \tag{A.1}$$

denote an unconventionally normalized maximally entangled pure state on RS, satisfying $\langle\tilde{\Phi}|\tilde{\Phi}\rangle = d$. We may define

$$\tilde{\rho} = I \otimes \mathcal{E}\big(|\tilde{\Phi}\rangle\langle\tilde{\Phi}|\big) \ , \tag{A.2}$$

where $\tilde{\rho}$ is an unconventionally normalized density operator on RT, satisfying tr $\tilde{\rho} = d$. The action of $\mathcal{E}$ on a pure state $|\varphi\rangle = \sum_i a_i|i\rangle$ on S can then be expressed as

$$\mathcal{E}\big(|\varphi\rangle\langle\varphi|\big) = \langle\varphi^*|\tilde{\rho}|\varphi^*\rangle \tag{A.3}$$

where $|\varphi^*\rangle = \sum_i a_i^*|i\rangle$ is the "index state" on R corresponding to $|\varphi\rangle$. If we introduce an additional system E (the "environment," of dimension dd'), we can construct a purification $|\tilde{\Phi}'\rangle$ of $\tilde{\rho}$ on RTE such that $\langle\tilde{\Phi}'|\tilde{\Phi}'\rangle = d$. This purification defines a "dilation" U of the channel $\mathcal{E}$ that realizes $\mathcal{E}$ as an isometric embedding of S in TE. The action of the dilation on the pure state $|\varphi\rangle$ is

$$|\varphi\rangle \to U|\varphi\rangle = \langle\varphi^*|\tilde{\Phi}'\rangle \ . \tag{A.4}$$

Now suppose that $\mathcal{E}_0$ and $\mathcal{E}_1$ are two channels acting on S, satisfying the inequality

$$\|\mathcal{E}_0 - \mathcal{E}_1\|_\diamond < \varepsilon \ , \tag{A.5}$$

and that $\tilde{\rho}_0$ and $\tilde{\rho}_1$ are the corresponding states obtained from the action of $I \otimes \mathcal{E}_0$ and $I \otimes \mathcal{E}_1$ on $|\tilde{\Phi}\rangle$. The diamond norm [31] is defined by

$$\|\mathcal{E}\|_\diamond \equiv \sup_{X \neq 0} \frac{\|I \otimes \mathcal{E}(X)\|_{\rm tr}}{\|X\|_{\rm tr}} \ ; \tag{A.6}$$

since $\langle\tilde{\Phi}|\tilde{\Phi}\rangle = d$, it follows that the trace distance between $\tilde{\rho}_0$ and $\tilde{\rho}_1$ satisfies

$$\| \tilde{\rho}_0 - \tilde{\rho}_1 \|_{\rm tr} \ < d\varepsilon \ . \tag{A.7}$$

Since, for conventionally normalized density operators, the fidelity and trace distance are related by

$$\sqrt{F(\rho_0,\rho_1)} \geq 1 - \frac{1}{2} \parallel \rho_0 - \rho_1 \parallel_{\rm tr} \ , \tag{A.8}$$

it follows [29, 30] that $\tilde{\rho}_0$ and $\tilde{\rho}_1$ have purifications $|\tilde{\Phi}_0'\rangle$ and $|\tilde{\Phi}_1'\rangle$ on RSE with norm $\sqrt{d}$ and overlap satisfying

$$\text{Re } \langle\tilde{\Phi}_1'|\tilde{\Phi}_0'\rangle > d\left(1 - \frac{\varepsilon}{2}\right) \ . \tag{A.9}$$

This large overlap of the purifications $|\tilde{\Phi}_0'\rangle$ and $|\tilde{\Phi}_1'\rangle$ implies that the corresponding dilations U_0 and U_1 of the channels are close to one another in the sup norm. Given any $|\varphi\rangle$ on

S, we may regard it as one element of a basis $\{|\varphi_i\rangle\}$ for S. Then eq. (A.9) may be rewritten as

$$\begin{aligned}&\mathrm{Re}\ \sum_{i=1}^{d}\langle\varphi_i|U_1^\dagger U_0|\varphi_i\rangle\\&= \mathrm{Re}\ \sum_{i=1}^{d}\langle\tilde{\Phi}_1'|\varphi_i^*\rangle\langle\varphi_i^*|\tilde{\Phi}_0'\rangle > d\left(1-\frac{\varepsilon}{2}\right)\ .\end{aligned} \tag{A.10}$$

But each of the d terms in the sum is no larger than 1, and since the sum is greater than $d - d\varepsilon/2$, each term must be greater than $d - d\varepsilon/2 - (d-1) = 1 - d\varepsilon/2$. We conclude, then, that for any pure state $|\varphi\rangle$ on S,

$$\mathrm{Re}\ \langle\varphi|U_1^\dagger U_0|\varphi\rangle > 1 - \frac{d\varepsilon}{2}\ . \tag{A.11}$$

Therefore, for any $|\varphi\rangle$

$$\|\ (U_0 - U_1)|\varphi\rangle\ \|^2 < d\varepsilon\ , \tag{A.12}$$

and hence

$$\|\ U_0 - U_1\ \|_{\mathrm{sup}}^2 < d\varepsilon\ . \tag{A.13}$$

This proves Lemma 4.

INSTITUTE OF PHYSICS PUBLISHING NANOTECHNOLOGY
Nanotechnology **15** (2004) S556–S561 PII: S0957-4484(04)76731-8

Feasibility of detecting single atoms using photonic bandgap cavities

Benjamin Lev[1]**, Kartik Srinivasan**[2]**, Paul Barclay**[2]**, Oskar Painter**[2]
and Hideo Mabuchi[1]

[1] Norman Bridge Laboratory of Physics, California Institute of Technology, Pasadena, CA 91125, USA
[2] Department of Applied Physics, California Institute of Technology, Pasadena, CA 91125, USA

E-mail: benlev@caltech.edu

Received 23 February 2004
Published 23 July 2004
Online at stacks.iop.org/Nano/15/S556
doi:10.1088/0957-4484/15/10/010

Abstract
We propose an atom–cavity chip that combines laser cooling and trapping of neutral atoms with magnetic microtraps and waveguides to deliver a cold atom to the mode of a fibre taper coupled photonic bandgap (PBG) cavity. The feasibility of this device for detecting single atoms is analysed using both a semiclassical treatment and an unconditional master equation approach. Single-atom detection seems achievable in an initial experiment involving the non-deterministic delivery of weakly trapped atoms into the mode of the PBG cavity.

(Some figures in this article are in colour only in the electronic version)

1. Introduction

The development of techniques necessary to manipulate single atoms and photons and to control their interactions is an important addition to the toolbox of nanotechnology. An important advance would be the development of a compact and integrable device to serve as a single-atom detector [1, 2]. The system comprised of a strongly interacting atom and photon—cavity quantum electrodynamics (QED) [3–5]—provides the basis for realizing such a device. These single-atom detectors could play as important a role in the burgeoning field of atom optics [6] as single-photon detectors do in conventional optics. The advent of Bose–Einstein condensates (BECs) of neutral atoms and the production of degenerate fermionic condensates [7] further highlights the importance of developing single-atom read-out devices.

To achieve these goals in cavity QED, a neutral atom must be inside the mode of a high finesse cavity with small mode volume: the atom–cavity system must be in the strong coupling regime. Strong coupling requires the atom–cavity coupling, g_0, to be much larger than both the atomic dipole decay rate, $\gamma_\perp$, and the decay rate of the cavity field, κ. Specifically, the saturation photon number, $m_0 = \gamma_\perp^2/2g_0^2$, and the critical atom number, $N_0 = 2\gamma_\perp\kappa/g_0^2$, must both be much less than unity.

State-of-the-art cavity QED experiments have achieved strong coupling parameters as small as $[m_0, N_0] \approx [10^{-4}, 10^{-3}]$ by either dropping [8] or vertically tossing [9] a cold neutral atom between the mirrors of a high finesse, low mode volume Fabry–Perot cavity. Recently, intracavity atom trapping for durations up to 3 s has been demonstrated by coupling a secondary optical beam into the Fabry–Perot cavity to form a far off resonance trap (FORT) [10].

The intent of this paper is to introduce a cavity QED system based on magnetostatic delivery of atoms to a photonic bandgap cavity, and to discuss the ability of this system to detect single atoms. This experimental system—magnetostatic confinement of atoms inside the field modes of photonic bandgap cavities—raises the possibility of achieving an experimentally robust, integrated, and scalable system. Mastering the integration of a single atom and photons—quintessentially quantum components—presents an entirely new prospect for technology: quantum computation and communication. Cavity QED provides a rich experimental setting for quantum information processing (QIP), both in the implementation of quantum logic gates and in the development of quantum networks [11, 12]. While not necessary for single-atom detection, confining the atom in the Lamb–Dicke regime inside the cavity for long periods of time is an important step towards accomplishing QIP using cavity QED. An atom is trapped in the Lamb–Dicke regime when its recoil energy is less than the trap's vibrational level spacing, $\eta = (E_{\text{recoil}}/E_{\text{vib}})^{1/2} < 1$. This regime has been achieved using a FORT [10], and magnetic microwire traps—such as those discussed in this paper—may also be capable of trapping atoms three-dimensionally inside a cavity in the Lamb–Dicke regime [13, 12].

2. Magnetic microtraps and photonic bandgap cavities

Patterns of micron-sized wires can create magnetic field gradients and curvatures sufficiently large to accurately guide and trap atoms above the surface of the substrate [13]. These magnetic microtrap devices—commonly known as atom chips [14, 15]—can be fabricated using standard photolithography techniques [16, 17] and have been successfully used not only to trap and waveguide neutral atoms, but also to create and manipulate Bose–Einstein condensates [18, 19].

Atom chips exploit the interaction potential, $V = -\vec{\mu} \cdot \vec{B}$, between an atom's magnetic moment, $\vec{\mu}$, and a wire's magnetic field, $\vec{B}$, to trap or guide weak field seeking states of a neutral atom. The simplest example of a magnetic microtrap involves the combination of the field from a U-shaped wire with a homogeneous bias field, B_{bias} [20]. The bias field, parallel to the wire substrate and perpendicular to the base of the U-wire, serves to cancel the curling field of the wire to form a two-dimensional quadrupole trap for the weak field seeking atoms. The atoms are confined in the third dimension by the fields from the side wires of the U-trap, forming a cigar-shaped trap above the wire surface. The position of the trap minimum above the wire surface, r, and the gradient of the trap are completely determined by the magnitude of B_{bias} and the current, I, in the U-wire,

$$r = \frac{\mu_0}{2\pi}\frac{I}{B_{\text{bias}}}, \qquad \nabla B = \frac{2\pi}{\mu_0}\frac{B_{\text{bias}}^2}{I}. \tag{1}$$

For example, with a wire current of 1 A and a bias field of 10 G, the atoms are trapped 200 μm above the surface in a field gradient—perpendicular to the base of the U-wire—of 500 G cm^{-1}. Ioffe traps—which are not susceptible to trap losses due to Majorana spin flips—may be formed either by a similar Z-trap [20] or by using wires forming patterns of nested arcs [13]. Although this latter Ioffe trap is more complicated, it does allow the possibility of trapping atoms three-dimensionally in the Lamb–Dicke regime inside a photonic bandgap cavity coplanar with the wires [12]. Simple waveguides for the atoms can be formed from the Z-trap by extending the base of the Z-wire, allowing the atoms to ballistically expand along the field minimum above the elongated wire. Beam splitters and conveyor belts have been demonstrated using similar techniques [14, 15].

Standard laser cooling and trapping techniques [21] are used to load cold atoms into the magnetic microtraps and waveguides. Typically, atoms are collected in a variant of the magneto-optical trap (MOT) that uses the atom chip surface as a mirror to form four of the six required laser cooling beams [20]. This mirror MOT and subsequent sub-Doppler cooling allows the collection of approximately 10^6 atoms of temperature 10 μK a few millimetres above the chip's surface. Conveniently, the quadrupole field from the U-trap is in the same orientation as the magnetic field required to form a mirror MOT. In the simplest case, the atoms can be transferred to the U-trap by replacing the mirror MOT's quadrupole field with that of the U-trap while maintaining the cooling lasers in the same configuration: this creates a U-MOT using the microwire magnetic field. An alternative and more experimentally compact and robust method—and the one employed in our lab—traps the atoms directly from vapour using a large copper U-shaped block carrying 30 A and located underneath the atom chip [22]. The atoms in this macro-U-MOT are subsequently transferred to smaller, magnetostatic U-traps on the atom chip surface.

The proximity of the atoms to the chip's surface naturally facilitates the integration of magnetically trapped atoms with on-chip cavities such as microdiscs or photonic crystals. Two-dimensional photonic bandgap (PBG) cavities—perforated semiconductor structures that confine light through the dual action of distributed Bragg reflection and internal reflection—are in many respects ideal for cavity QED [23]. Their small mode volume and modest quality factors open the possibility of achieving extremely small strong coupling parameters: $[m_0, N_0] = \left[10^{-8}, 10^{-4}\right]$. With regard to atom–cavity coupling, these cavities have the advantage over microdiscs and microspheres in that the mode's field maximum can be located in the holes rather than inside the dielectric material. As an inherently stable, monolithic structure, PBG cavities will not need the support structure for active stabilization that Fabry–Perot cavities require. Moreover, their compactness and compatibility with fibre optics-based input and output couplers [24, 25] allow one to envision an array of PBG cavities, atom microtraps, input/output couplers, and other processing devices all on the same integrated chip.

We plan to use PBG cavities of the graded defect design discussed in [26], which consist of a rectangular lattice of airholes in an optically thin, high refractive index slab waveguide. The holes gradually decrease in diameter towards the cavity centre, and experimental measurements of such cavities fabricated in silicon membranes (see figure 1(a)) and operating at $\lambda \sim 1.6$ μm possess Qs as high as 40 000 with modal volumes of $V_{\text{eff}} \sim 0.9$ cubic wavelengths $(\lambda/n)^3$ [27]. In future experiments with single atoms, cavities will be etched in a thin AlGaAs membrane, chosen for its transparency at the wavelength of caesium's D2 transition, 852 nm. For the Q and V_{eff} values mentioned above, the atom–cavity coupling can be a high as $g_0 = 2\pi \times 17$ GHz while the decoherence rates are $[\kappa, \gamma_\perp]/2\pi = [4.4\ \text{GHz}, 2.6\ \text{MHz}]$. This gives strong coupling parameters of $[m_0, N_0] = \left[1.2 \times 10^{-8}, 8.4 \times 10^{-5}\right]$, which are much smaller than those achieved in recent experiments using Fabry–Perot cavities, $[m_0, N_0] = \left[2.8 \times 10^{-4}, 6.1 \times 10^{-3}\right]$ [8]. The central hole diameter is ~100 nm and the membrane thickness is ~170 nm. An atom in this small hole will be affected by the Casimir–Polder potential [29], and cavity QED dynamics in the presence of this force will need to be investigated.

The cavity is coupled to a photonic crystal waveguide, which in turn is evanescently coupled to an optical fibre taper. By positioning the fibre taper—whose minimum diameter is of

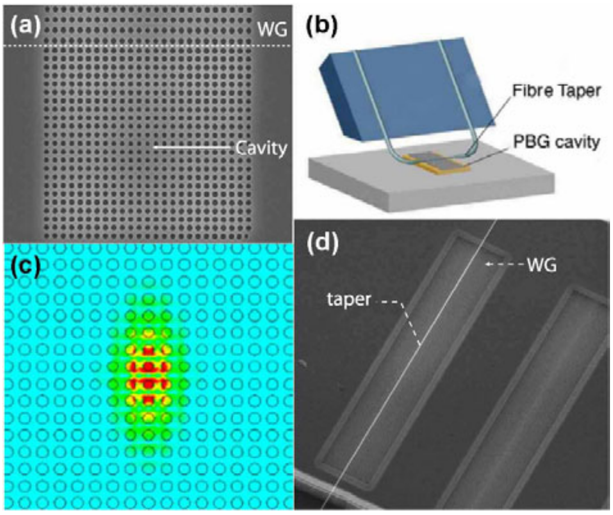

Figure 1. (a) A scanning electron microscope (SEM) image of a photonic bandgap cavity and waveguide (WG) fabricated in silicon. (b) A schematic diagram of the fibre taper coupler. (c) The finite difference time-domain calculated electric field amplitude of the cavity mode taken in the centre of the membrane. (d) An SEM image of an optical fibre taper aligned above a photonic crystal waveguide.

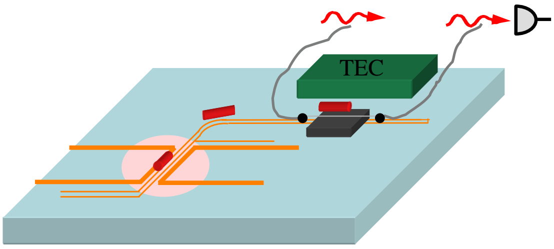

Figure 2. A schematic diagram of the atom–cavity chip experiment. The microwire U-traps and atomic waveguides are shown as yellow wires (light grey), and the light red area (lightest grey) centred about the U-traps represents the footprint of the reflected trapping lasers. The atoms are the red (dark grey) cylinders, pictured as they are transported towards the PBG cavity which is shown as the black chip glued to the substrate's surface. The grey line is the optical fibre and fibre taper.

the order of a micron—in the near field of the photonic crystal waveguide and aligned along its axis (see figures 1(b) and (d)), highly efficient (greater than 98%) fibre coupling into and out of the photonic crystal waveguide can be achieved [25]. Light coupled into the photonic crystal waveguide is reflected by the PBG cavity and recollected in the backward propagating fibre taper mode [28]. Figure 1(a) shows the boundary between the waveguide and the cavity: the top four rows of holes are the end of the waveguide, which is formed in a similar fashion to the cavity, except that the holes are graded in only the lateral dimension. This design maximizes the mode matching between the waveguide and the cavity modes [24]. The waveguide may be bent to allow access to the cavity unencumbered by the fibre.

3. Experimental proposal

As a first-generation experiment, we would like to bring a trapped cloud of cold neutral atoms—caesium in our case—into contact with a PBG cavity, simultaneously demonstrating the integration of a cavity with an atom chip and the strong coupling of a neutral atom to a PBG cavity. Figure 2 shows a rough schematic diagram of the atom–cavity chip experiment. The chip is divided into two regions, one for laser trapping and cooling of the atoms in a U-MOT and U-traps, and the other for the PBG cavity and its tapered fibre and photonic crystal waveguide couplers. The two regions are connected by a microwire waveguide to transport the atoms from the laser cooling region to the PBG cavity. These regions must be separated by 1–2 cm in order for the bulk of the cavity to not obstruct the 1 cm^2 U-MOT beams. Furthermore, to position the cavity outside of the horizontal U-MOT beam that grazes the substrate surface, the waveguide must convey the atoms around a 90° turn. This will be accomplished either by using a two-wire guide (chosen for depiction in figure 2 for simplicity of illustration) [30] or by rotating the atoms in a P-trap—similar to a U-trap but with the base wire bent allowing a rotating bias field to change the orientation of the atoms [31]—before transferring the atoms into a Z-trap waveguide aligned perpendicular to the initial U-trap. This latter design has the advantage that the simple addition of a few coplanar wires can serve to loosely confine the atoms once they reach the PBG cavity.

In the PBG region, the atoms are suspended a few hundred microns above the surface of the waveguide's microwires, and this allows enough room for the $\sim$200 μm thin PBG substrate to be placed in the gap between the atoms and the microwires. Once the atoms are transported to a position above the PBG cavity, the current and bias field of the guide are adjusted to lower the cold atom cloud into the surface of the PBG cavity. A thermoelectric cooler (TEC) is located near the PBG cavity to counteract heating due to the microwire waveguide, maintaining a specific cavity detuning from the frequency driving laser and the atomic resonance. We estimate a cavity tunability of 20 GHz $^\circ$C^{-1}, and with TEC control of 10^{-2} $^\circ$C, we should be able to achieve a 200 MHz tuning resolution. This resolution is sufficient, as we expect to operate with detunings of the order of 1–10 GHz.

The delivery scheme described above provides a non-deterministic source of weakly trapped atoms to the cavity mode. The field of the cavity mode is concentrated in the central $\sim$10 holes (see figure 1(c)). The field maximum is offset by 45 nm from the axis of each of the two centre holes. We expect to transport 10^5 atoms in a cigar-shaped cloud of density 10^{11} cm^{-3}. The cross-sectional area of this cloud parallel to the chip is larger than the 0.4 μm^2 area of the PBG cavity that is occupied by the field, and we estimate that there is a $\sim$10% probability of an atom encountering one of the central 10 holes per cloud interaction. With an experimental repetition once every $\sim$5 s—limited by the U-MOT replenishing time—we foresee the accumulation of a significant number of events in a reasonable amount of time, and as discussed in section 4 below, we expect to detect strong signals during single-atom transits through the PBG cavity's central holes. If we assume a caesium cloud temperature of 10 μK, then a caesium atom whose velocity is parallel to the axis, $\hat{z}$, of a central hole will interact with the mode for a time duration of $\sim$10 μs.

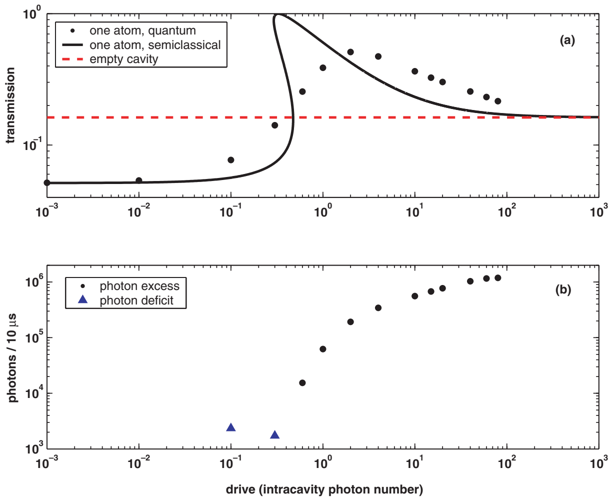

Figure 3. (a) The transmission of the cavity as a function of drive strength—measured in intracavity photon numbers for a resonant and empty cavity—calculated from equation (2) (black line) and from equation (3) (points). The empty cavity transmission is shown as a dashed red line. (b) The difference in output—during the expected 10 μs of atom–cavity interaction—between a cavity with one atom and an empty cavity. The detunings are $[\Delta, \theta]/2\pi = [10, 10]$ GHz.

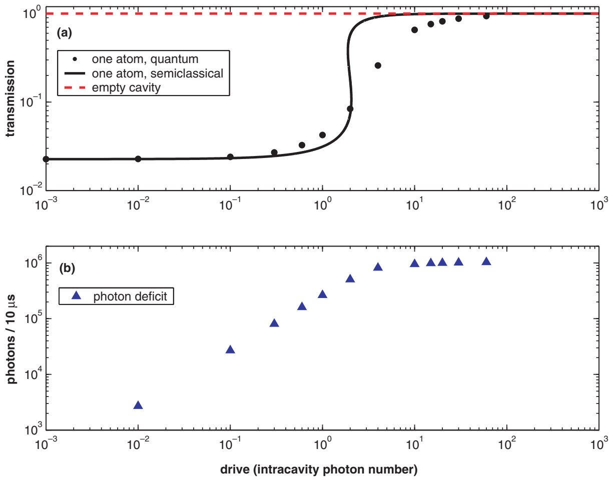

Figure 4. (a) and (b) are the same as figures 3(a) and (b) except with detunings of $[\Delta, \theta]/2\pi = [10, 0]$ GHz.

4. Single-atom detectability

To investigate the PBG cavity's response to a strongly coupled atom falling through a central hole, we solve—using a two-level atom—the semiclassical optical bistability equation for a qualitative understanding of the interaction and the quantum master equation to obtain a more quantitative description. Although neither of these treatments fully encompasses the complexity of the system, we presume that they are sufficient for demonstrating the feasibility of the device for single-atom detection. These calculations ignore the fact that g_0 and the detunings are of the same order or much larger than both the hyperfine ground-state and excited-state splittings, which for caesium are 9.2 GHz and 151–251 MHz, respectively. In other words, the atom–photon coupling is much stronger than the coupling between the electron and nuclear spins. This is an unusual situation and requires a full quantum calculation of the atom–PBG cavity interaction that includes the full caesium D2 manifold of states. We are in the process of performing this computation.

The optical bistability equation is a semiclassical description of the transmission of a cavity containing atoms [32],

$$y = \frac{x}{\left[\left(1+\frac{2}{N_0(1+(\Delta/\gamma_\perp)^2+y^2)}\right)^2 + \mathrm{i}\left(\frac{\theta}{\kappa} - \frac{2\Delta}{\gamma_\perp N_0(1+(\Delta/\gamma_\perp)^2+y^2)}\right)^2\right]^{\frac{1}{2}}}. \tag{2}$$

In the above equation, x is the input field, $E/\sqrt{m_0}$, where E is the amplitude of the driving field; y is the output field, $\alpha/\sqrt{m_0}$, where α is the intracavity coherent state amplitude; Δ is the atom–laser detuning; and θ is the cavity–laser detuning. The black curves in figures 3(a) and 4(a) show the solution to equation (2) for $[\Delta, \theta]/2\pi = [10, 10]$ GHz and $[\Delta, \theta]/2\pi = [10, 0]$ GHz, respectively. These two sets of detunings are chosen to highlight different atom–cavity response regimes where we expect to be able to detect single atoms. In both plots, $[g_0, \kappa, \gamma_\perp]/2\pi = [17\text{ GHz}, 4.4\text{ GHz}, 2.6\text{ MHz}]$. The horizontal dashed lines are the empty cavity transmissions. Both semiclassical solutions show signs of bistability in the region around one intracavity photon. Within the context of the approximation of equation (2), figure 3(a) shows that for 10 GHz detunings of the atom and cavity from the probe laser, an excess of photons transmitted through the cavity—an 'up-transit'—can be detected for a drive of a few intracavity photons. Figure 4(a) shows that with the cavity on resonance with the laser and the atom 10 GHz detuned, a deficit of photons—a 'down-transit'—can be detected for similar drive strengths of a few intracavity photons.

The solutions to the unconditional master equation paint a more accurate picture of the atom–cavity system. Under the two-level atom, electric dipole, and rotating-wave approximations, the equation for the density matrix, ρ, of the joint state of the atom and cavity is as follows:

$$\begin{aligned}\dot{\rho} &= \frac{-\mathrm{i}}{\hbar}[\hat{H}_0, \rho] + \gamma_\perp(2\hat{\sigma}\rho\hat{\sigma}^\dagger - \hat{\sigma}^\dagger\hat{\sigma}\rho - \rho\hat{\sigma}^\dagger\hat{\sigma}) \\ &\quad + \kappa(2\hat{a}\rho\hat{a}^\dagger - \hat{a}^\dagger\hat{a}\rho - \rho\hat{a}^\dagger\hat{a}), \qquad (3)\\ \hat{H}_0 &= \hbar\Delta\hat{\sigma}^\dagger\hat{\sigma} + \hbar\theta\hat{a}^\dagger\hat{a} + \mathrm{i}\hbar E(\hat{a}^\dagger - \hat{a}) + \hat{H}_{\mathrm{int}}, \qquad (4)\\ \hat{H}_{\mathrm{int}} &= \mathrm{i}\hbar g_0\psi(\hat{r})\left[\hat{a}^\dagger\hat{\sigma} - \hat{\sigma}^\dagger\hat{a}\right]. \qquad (5)\end{aligned}$$

In this equation, $\hat{\sigma}$ is the atomic lowering operator and $\hat{a}$ is the cavity field annihilation operator. Along the axis of the central cavity hole, the mode function, $\psi(z)$, closely approximates a Gaussian of width ~225 nm, centred about the mid-point of the ~170 nm thick cavity membrane. The steady-state density operator, ρ_{ss}, as a function of various drive strengths, coupling strengths, and detunings, is found by solving equation (3) with $\dot{\rho}_{\mathrm{ss}} = 0$. Operator expectations are $\langle\hat{O}\rangle = \mathrm{Tr}[\rho_{\mathrm{ss}}\hat{O}]$. The expected cavity output in photons per detector integration time, Δt, is

$$N = \kappa\Delta t\langle\hat{a}^\dagger\hat{a}\rangle, \tag{6}$$

with noise fluctuations of variance

$$(\Delta N)^2 = \kappa\Delta t(\langle\hat{a}^\dagger\hat{a}\hat{a}^\dagger\hat{a}\rangle - \langle\hat{a}^\dagger\hat{a}\rangle^2). \tag{7}$$

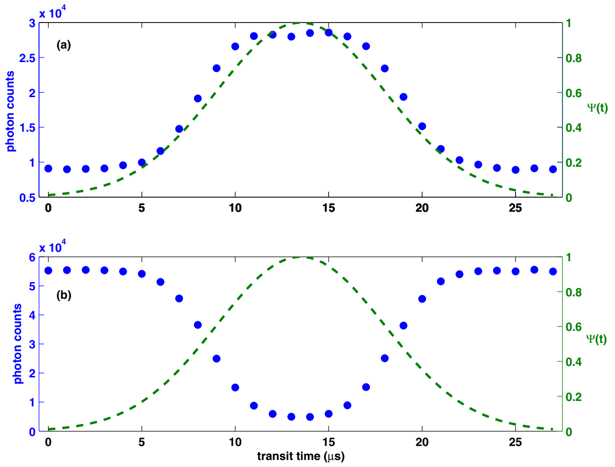

Figure 5. Simulated photon counts due to atoms transits through the axis of the cavity's central hole. Blue dots (left axis) are the photon counts, and the green, dashed curve (right axis) is the Gaussian variation of $g(t)/g_0 = \psi(z(t))$ experienced by the atom during its transit. Calculations are for detunings of (a) $[\Delta, \theta]/2\pi = [10, 10]$ GHz and (b) $[\Delta, \theta]/2\pi = [10, 0]$ GHz.

Note that instead of photon counting, heterodyne detection may be used, in which case expectations of $\hat{a}$ rather than $\hat{a}^\dagger\hat{a}$ are the relevant quantities. The results presented in figures 3–5 are qualitatively similar for the two cases.

The points in figures 3(a) and 4(a) represent N calculated from solutions to equation (3) for various drive strengths and for the same g_0, κ, and detunings as used in the semiclassical calculation. These points do not extend past a drive strength of 80 intracavity photons because our limited computational resources necessitate the use of a truncated Fock basis. The cavity transmission as a function of drive qualitatively follows the semiclassical solutions; however, there is no longer a sign of bistability, which is to be expected since the unconditional master equation is linear in the state variables, ρ, and we plot only $\langle N\rangle$. We also see that for a drive of 1–10 photons, up-transits occur for a probe laser detuned 10 GHz from both the atom and the cavity (figure 3(a)), and down-transits for a probe laser and cavity 10 GHz detuned from the atom (figure 4(a)). Figures 3(b) and 4(b) show the change in the output of the cavity—using the master equation solutions—during the 10 μs in which we expect the atom to interact with the cavity mode. The black dots show the up-transits and blue triangles the down-transits. For drive powers of $\sim$1 nW (1–10 intracavity photons), photon excesses of 10^5–10^6 can be seen in the up-transits of the $[\Delta, \theta]/2\pi = [10, 10]$ GHz case (figure 3(b)), and photon deficits of 10^5–10^6 in the down-transits of the $[\Delta, \theta]/2\pi = [10, 0]$ GHz case (figure 4(b)). For both sets of detunings, we see that for drive strengths less (greater) than one intracavity photon, there are super- (sub-) Poissonian noise fluctuations of the photon number. Plots of the Q-function [33] in the sub-Poissonian regions show excess spread—and even a bifurcation in the $[\Delta, \theta]/2\pi = [10, 0]$ GHz case—of the phase quadrature corresponding to photon number squeezing.

Simulated photon counts during atom transits are shown in figures 5(a) and (b). We assume that the atom moves with constant velocity, $v = 2.5$ cm s^{-1}, through the axis of the cavity mode $\psi(z)$, making a full transit of the Gaussian waist in 10 μs. In both plots the drive strength is two intracavity photons. As the atom transverses the cavity, the coupling $g(t) = g_0\psi(vt)$ also varies as a Gaussian, which modulates the output photon flux. The mean photon count, N, and variance, $(\Delta N)^2$, are found by solving for ρ_{ss} for each $g(t)$ in time steps of $\Delta t = 1$ μs, chosen to simulate a finite bandwidth photodetector. Each point includes additional shot noise selected randomly from a normal distribution of standard deviation ΔN. Figures 5(a) and (b) show that even with shot noise, up- and down-transits of single atoms through the axis of the central PGB cavity hole are clearly detectable. Moreover, it seems possible to detect atom transits that only experience 20%–30% of g_0. During an experiment, we expect to detect a low background of signals from marginally coupled atoms—such as those grazing the field extending from the surface of the PBG membrane or slipping into holes away from the central region—punctuated by sharp pikes representing atoms fully coupled to the field inside the central holes. It should be noted that the mean photon numbers and noise in figures 5(a) and (b) are not derived from a quantum trajectory calculated from the conditional master equation [34], but are simply calculated using ρ_{ss} from the unconditional equation (3). This is acceptable given the inherent limitations of the model as mentioned at the beginning of this section.

The atom will experience a force,

$$\langle\vec{f}\rangle = -\mathrm{i}\hbar\nabla g(\vec{r})\langle\hat{a}^\dagger\hat{\sigma} - \hat{a}\hat{\sigma}^\dagger\rangle, \tag{8}$$

as it encounters the cavity mode. The maximum acceleration on an atom dragged though the cavity mode at velocity 2.5 cm s^{-1}—for either of the sets of detunings used above—is $|\langle f_{\max}\rangle|/M_{\mathrm{Cs}} = 2.4 \times 10^8$ m s^{-2}, corresponding to a change in velocity of

$$\Delta v = \sqrt{\frac{|\langle f_{\max}\rangle|\Delta z}{M_{\mathrm{Cs}}}} \approx 5 \text{ m s}^{-1} \tag{9}$$

over half the length of the cavity mode, $\Delta z = 100$ nm. In the above equations, M_{Cs} is the mass of a caesium atom. This agrees with a simple estimate using

$$\hbar g_0 = 0.5 M_{\mathrm{Cs}}(\Delta v)^2, \tag{10}$$

which yields $\Delta v = 10$ m s^{-1}. Fabry–Perot experiments have detected effects of the cavity interaction on the atomic motion [35]. The simple estimate using equation (10) gives a smaller value of $\Delta v \approx 0.7$ m s^{-1} for the Fabry–Perot experiments, implying that the motion of the atom traversing the mode of the PBG cavity will also be significantly affected. A more detailed calculation [36] of the force and momentum diffusion using a master equation beyond the two-level atom approximation is necessary to make predictions about the behaviour of an atom in an attractive, red-detuned cavity mode or in a repulsive, blue-detuned mode. The close proximity of the atom to the sides of the PGB cavity's holes will surely affect the system's dynamics due to the Casimir–Polder potential [29], and this will need to be addressed in more detailed simulations.

5. Conclusion

The integration of atom trapping and cooling with photonic bandgap cavities on a chip introduces a robust and scalable cavity QED system to the toolbox of nanotechnology. A device allowing cooled neutral atoms to be delivered via a magnetic microtrap and waveguide to the mode of a graded lattice PBG cavity is feasible given present technology. Calculations using the semiclassical optical bistability equation and the unconditional master equation indicate that it will be possible to detect single strongly coupled atoms with this atom–cavity chip.

Acknowledgments

This work was supported by the Multidisciplinary University Research Initiative programme under Grant No DAAD19-00-1-0374 and the Charles Lee Powell Foundation. KS thanks the Hertz Foundation for financial support.

References

[1] Horak P, Klappauf B G, Haase A, Folman R, Schmiedmayer J, Domokos P and Hinds E A 2003 *Phys. Rev.* A **67** 043806

[2] Long R, Steinmetz T, Hommelhoff P, Hänsel W, Hänsch T W and Reichel J 2003 *Phil. Trans. R. Soc.* A **361** 1

[3] Kimble H J 1994 *Cavity Quantum Electrodynamics* ed P Berman (San Diego, CA: Academic) p 203

[4] Kimble H J 1998 *Phys. Scr.* T **76** 127

[5] Mabuchi H and Doherty A C 2002 *Science* **298** 1372

[6] 1996 *Quantum Semiclass. Opt.* **8** (3) (special issue on Atom Optics)

[7] Regal C A, Greiner M and Jin D S 2004 *Phys. Rev. Lett.* **92** 040403

[8] Hood C J, Lynn T W, Doherty A C, Parkins A S and Kimble H J 2000 *Science* **287** 1447

[9] Pinkse P W H, Fisher T, Maunz P and Rempe G 2000 *Nature* **404** 365

[10] McKeever J, Buck J R, Boozer A D, Kuzmich A, Nägerl H C, Stamper-Kurn D M and Kimble H J 2003 *Phys. Rev. Lett.* **90** 133602

[11] Pellizzari T, Gardiner S A, Cirac J I and Zoller P 1995 *Phys. Rev. Lett.* **75** 3788

[12] Mabuchi H, Armen M, Lev B, Loncar M, Vuckovic J, Kimble H J, Preskill J, Roukes M and Scherer A 2001 *Quantum Inf. Comput.* **1** 7

[13] Weinstein J D and Libbrecht K G 1995 *Phys. Rev.* A **52** 4004

[14] Folman R, Krüger P, Schmiedmayer J, Denschlag J and Henkel C 2002 *Adv. At. Mol. Opt. Phys.* **48** 263

[15] Reichel J, Hänsel W, Hommelhoff P and Hänsch T W 2001 *Appl. Phys.* B **72** 81

[16] Johnson K S, Drndic M, Thywissen J H, Zabow G, Westervelt R M and Prentiss M 1998 *Phys. Rev. Lett.* **81** 1137

[17] Lev B 2003 *Quantum Inf. Comput.* **3** 450

[18] Hansel W, Hommelhoff P, Hänsch T W and Reichel J 2001 *Nature* **413** 498

[19] Ott H, Fortagh J, Schlotterbeck G, Grossmann A and Zimmermann C 2001 *Phys. Rev. Lett.* **87** 230401

[20] Reichel J, Hänsel W and Hänsch T W 1999 *Phys. Rev. Lett.* **83** 3398

[21] Metcalf H and van der Straten P 1999 *Laser Cooling and Trapping* (New York: Springer)

[22] Wildermuth S, Krüger P, Becker C, Brajdic M, Haupt S, Kasper A, Folman R and Schmiedmayer J 2003 *Preprint* cond-mat/0311475

[23] Vuĉković J, Lonĉar M, Mabuchi H and Scherer A 2001 *Phys. Rev.* E **65** 016608

[24] Barclay P E, Srinivasan K and Painter O 2003 *J. Opt. Soc. Am.* B **20** 2274

[25] Barclay P E, Srinivasan K, Borselli M and Painter O 2003 *Preprint* quant-ph/0308070

[26] Srinivasan K and Painter O 2003 *Opt. Express* **10** 670

[27] Srinivasan K, Barclay P E, Borselli M and Painter O 2003 *Preprint* quant-ph/0309190

[28] Barclay P E, Srinivasan K, Borselli M and Painter O 2003 *Preprint* physics/0311006

[29] Lin Y, Teper I, Chin C and Vuletić V 2003 *Phys. Rev. Lett.* **92** 050404

[30] Luo X, Krüger P, Brugger K, Wildermuth S, Gimpel H, Klein M W, Groth S, Folman R, Bar-Joseph I and Schmiedmayer J 2003 *Preprint* quant-ph/0311174

[31] Long R and Reichel J 2002 private communication

[32] Lugiato L A 1984 *Progress in Optics* (Amsterdam: Elsevier Science) p 71

[33] Mandel L and Wolf E 1997 *Optical Coherence and Quantum Optics* (Cambridge: Cambridge University Press)

[34] Carmichael H 1993 *An Open Systems Approach to Quantum Optics* (Berlin: Springer)

[35] Mabuchi H, Ye J and Kimble H J 1999 *Appl. Phys.* B **68** 1095

[36] Doherty A C, Parkins A S, Tan S M and Walls D F 1996 *Phys. Rev.* A **56** 833

PHYSICAL REVIEW A **70**, 022106 (2004)

Deterministic Dicke-state preparation with continuous measurement and control

John K. Stockton,* Ramon van Handel, and Hideo Mabuchi
Norman Bridge Laboratory of Physics, M.C. 12-33, California Institute of Technology, Pasadena, California 91125, USA

(Received 19 February 2004; published 26 August 2004)

We characterize the long-time projective behavior of the stochastic master equation describing a continuous, collective spin measurement of an atomic ensemble both analytically and numerically. By adding state-based feedback, we show that it is possible to prepare highly entangled Dicke states deterministically.

DOI: 10.1103/PhysRevA.70.022106 PACS number(s): 03.65.Ta, 42.50.Lc, 02.30.Yy

I. INTRODUCTION

It has long been recognized that measurement can be used as a *nondeterministic* means of preparing quantum states that are otherwise difficult to obtain. With projective measurements that are truly discrete in time, the only way an experimentalist can direct the outcome of the measurement is by preparing the initial state to make the desired result most probable. Generally, it is impossible to make this probability equal to 1, as the measurement will, with some nonzero probability, result in other undesirable states. If the experimentalist can afford to be patient, then accepting a low efficiency is not a problem, but this is not always the case. In recent years, a theory of continuous quantum measurement has been developed that fundamentally changes the nature of state preparation via measurement [1]. When a measurement and the corresponding acquisition of information are sufficiently gradual, there exists a window of opportunity for the experimentalist to affect the outcome of the measurement by using feedback control [2]. In this paper, we demonstrate that it is possible to deterministically prepare highly entangled Dicke states [3,4] of an atomic spin ensemble by adding state-based feedback to a continuous projective measurement.

It has been shown that models of quantum state reduction exist that exhibit the usual rules of projective measurement except the state reduction occurs in a continuous, stochastic manner [5]. These models are not without physical relevance as they are the same as those derived to describe the conditional evolution of atomic spin states under continuous quantum nondemolition (QND) measurement [6–11]. By measuring the collective angular momentum operator J_z of an initially polarized coherent spin state via the phase shift of an off-resonant probe beam, conditional spin-squeezed states have been experimentally produced [12,13]. These states are of considerable interest for applications in quantum information processing and precision metrology [14,15].

In these models, the reduction in variance that initially leads to conditional spin squeezing is the precursor of the projection onto a random eigenstate of J_z at longer times. Figure 1 demonstrates the projection process for a single numerically simulated measurement trajectory.[1] Like spin-squeezed states, these Dicke states offer potential for quantum information applications because of their unique entanglement properties [16]. Although the experimental difficulties in obtaining these states via QND measurement or other experimental methods [17–19] are considerable, the details of the continuous projective process that leads to them are of fundamental interest.

Whenever the measurement is sufficiently slow, an experimentalist may steer the result by feeding back the measurement results in real time to a Hamiltonian parameter. Indeed, the measurement process, as a state preparation process, can be made deterministic with the use of feedback control. Recently, we have experimentally demonstrated this concept by modulating a compensation magnetic field with the measurement record to deterministically prepare spin-squeezed states [12] as proposed in [6,7]. This is just one example of the growing confluence of quantum measurement with classical estimation and control theory [20,21]. Other applications of quantum feedback include parameter estimation, metrology, and quantum error correction [22–26].

In this paper, we focus on the long-time limit of the QND measurement and feedback process. Just as spin-squeezed states can be deterministically prepared at short times, we numerically demonstrate that individual Dicke states can be deterministically prepared at long times with the use of state-based feedback [27]. While our proposed feedback laws are nonoptimal, they demonstrate the adequacy of intuitive controllers with finite gain for directing the diffusion of the quantum state towards desirable regions of Hilbert space with unity efficiency. This is in contrast to other proposed schemes using measurements to prepare Dicke states probabilistically [17,18]. A more systematic approach utilizing stochastic notions of stability and convergence in the continuous measurement and control of a single spin is presented in Ref. [28].

This paper is organized as follows. In Sec. II, we introduce the stochastic master equation which represents the rule for updating the system state in real time via the incoming measurement record. Here we discuss the various represen-

---

*URL: http://minty.caltech.edu/Ensemble. Electronic address: jks@caltech.edu

[1] All numerical simulations shown were performed using the parameters $\{N=10,\ M=1,\ T=5,\ dt=0.001\}$. The stochastic integrator used the norm-preserving, nonlinear SSE of Eq. (5) and a weak second-order derivative-free predictor-corrector structure as can be found in [39].

©2004 The American Physical Society

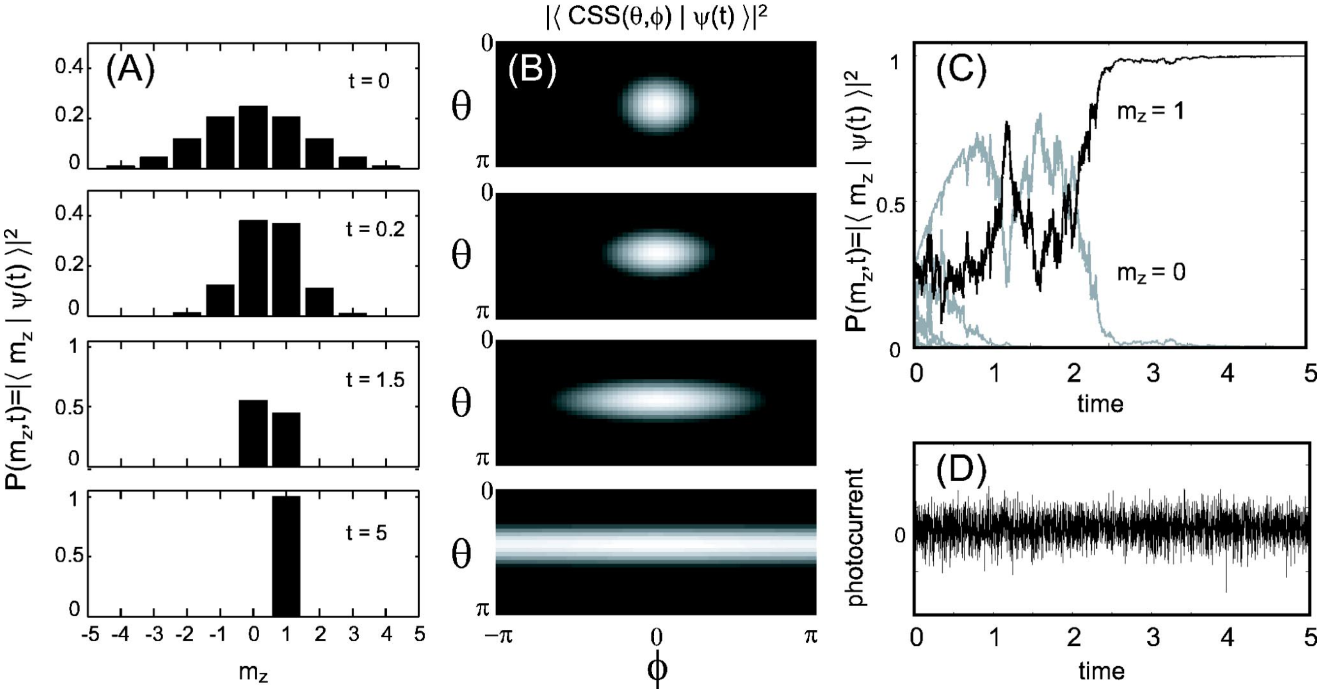

FIG. 1. The results of a single numerical simulation[1] of the stochastic Schrödinger equation (SSE), Eq. (5), with $M=1$, $\eta=1$, and $N=10$ spins initially aligned along the x axis. (A) In a quantization axis perpendicular to the polarization, the level distribution of a coherent spin state (CSS) is Gaussian for large N. Under conditional measurements the state evolves at short times into a spin-squeezed state and, eventually, into a random eigenstate of J_z. (B) A map of the state's angular distribution on the Bloch sphere in spherical coordinates. The uncertainty in the transverse direction to the measurement axis grows until there is no information about the perpendicular component direction. (C) At long times, the population is at most divided among two levels that compete to be the final winner, which in this case appears to be $m=1$. (D) All of the state information is obtained by properly filtering the noisy photocurrent.

tations of the dynamics in both the short- and long-time limits. Section III describes the probabilistic preparation of Dicke states via observation alone. The numerical demonstration of the open-loop projection process reveals statistical features that clarify the details of the projection. Feedback is added to the procedure in Sec. IV, where we show that state-based control allows one to prepare the same Dicke state deterministically on every measurement. Finally, in Sec. V, we discuss future directions and imminent challenges regarding quantum-state preparation via measurement and control.

II. REPRESENTATIONS OF THE CONDITIONAL EVOLUTION

The physical system we will consider is an ensemble of N spin-1/2 particles contained within a cavity and interacting with a far off-resonant single-mode field. We will denote the conditional state of the spin ensemble as $\rho(t)$ and the homodyne measurement record of the output as $y(t)$. The stochastic master equation (SME) describing the conditional evolution is [6,7]

$$d\rho(t) = -i[H(t),\rho(t)]dt + \mathcal{D}[\sqrt{M}J_z]\rho(t)dt + \sqrt{\eta}\mathcal{H}[\sqrt{M}J_z]\rho(t) \times\{2\sqrt{M\eta}[y(t)dt - \langle J_z\rangle dt]\}, \tag{1}$$

where $H(t)=\gamma J_y b(t)$ is the control Hamiltonian that we will allow ourselves [without feedback $b(t)=0$], γ is the gyromagnetic ratio, M is the probe-parameter-dependent measurement rate, and

$$\mathcal{D}[c]\rho \equiv c\rho c^\dagger - (c^\dagger c\rho + \rho c^\dagger c)/2, \tag{2}$$

$$\mathcal{H}[c]\rho \equiv c\rho + \rho c^\dagger - \mathrm{Tr}[(c + c^\dagger)\rho]\rho. \tag{3}$$

The (scaled) difference photocurrent is represented as

$$y(t)dt = \langle J_z\rangle(t)dt + dW(t)/2\sqrt{M\eta}. \tag{4}$$

The stochastic quantity $dW(t)\equiv 2\sqrt{M\eta}[y(t)dt - \langle J_z\rangle(t)dt]$ is a Wiener increment and $dW(t)/dt$ is a Gaussian white noise that can be identified with the shot noise of the homodyne local oscillator. [See [29,30] for an introduction to stochastic differential equations (SDE's).] The sensitivity of the photodetection per $\sqrt{\mathrm{Hz}}$ is represented by $1/2\sqrt{M\eta}$, where the quantity $\eta\in[0,1]$ represents the quantum efficiency of the detection. If $\eta=0$, we are essentially ignoring the measurement result and the conditional SME becomes a deterministic unconditional master equation. If $\eta=1$, the detectors are maximally efficient. In this latter case, the conditioned state will remain pure for the entire measurement, thus we can use a state vector description, and the SME can be replaced with a SSE

$$d|\psi(t)\rangle = \{-iH(t) - M[J_z - \langle J_z\rangle(t)]^2/2\}|\psi(t)\rangle dt + \sqrt{M}[J_z - \langle J_z\rangle(t)]|\psi(t)\rangle dW(t). \qquad (5)$$

This SSE was considered in [5] where the motivation was more abstract and less concerned with the experimental filtering perspective presented here. We emphasize that the SME or SSE is physically derived and is an explicit function of a measured photocurrent variable $y(t)$, through which the randomness enters. The states are considered as states of knowledge and, in practice, an experimentalist updates the description of the system, $\rho(t)$ [Figs. 1(A)—1(C)], as the measurement results, $y(t)$ [Fig. 1(D)], arrive in time.

The stochastic master equation (1) describes only the dispersive part of the atom-field interaction. Physically, however, any dispersive phase shift must be accompanied by some degree of decohering absorption and spontaneous emission from the auxiliary excited-state level(s). Generally, the dispersive SME will be valid until some time, at which point spontaneous emission catches up to destroy the validity of the above description. The resulting cutoff time will impose a limit on the amount of observable squeezing or projection.

In free space measurements, e.g., free space Faraday rotation [12,13,31,32], the effects of spontaneous emission make this cutoff time relatively short. By surrounding the atomic cloud with a cavity, however, spontaneous emission can be suppressed and the validity of the SME correspondingly extended.

For a cavity with decay rate κ, N atoms with a decay rate γ, and an atom-cavity coupling constant g, the requirement to see any spin squeezing is only $g^2/\kappa\gamma > 1/N$. On the edge of the strong-coupling regime, with $g^2/\kappa\gamma \approx 1$, spin variances can be further decreased from initial values $\langle \Delta J_z^2\rangle \propto N$ to levels $\propto \sqrt{N}$ [7,9,10]. (In free space, it is in principle possible to achieve this degree of squeezing with a maximally focused probe beam, but one can do no better because of the diffraction limit.) To further reduce the uncertainty to the point where $\langle \Delta J_z^2\rangle \propto 1$ (i.e., the Heisenberg limit of spin squeezing) the cavity needs to be in the *very* strong-coupling regime with $g^2/\kappa\gamma > N$. If one requires that a single J_z eigenstate becomes resolvable ($\langle \Delta J_z^2\rangle \ll 1$), the cavity coupling requirements become even more stringent depending on the degree of projection desired.

While there are currently few experimental systems even in the strong-coupling regime, we expect this very-strong-coupling regime to eventually be reached for moderate numbers of atoms. With this attitude we continue to focus on the long-time limit of the pure dispersive SME in the interest of understanding the idealized limits of continuous projective measurement. For a more complete discussion of the realistic physical limits of this type of QND measurement, see Refs. [6–11].

A. Hilbert space, coherent spin states, and Dicke states

Under certain idealizations, we can considerably reduce the size of the Hilbert space needed to describe the conditionally measured ensemble. Throughout this paper, the initial state $\rho(0)$ will be made equal to a coherent spin state (CSS) polarized along an arbitrary direction [4]. For example, a CSS pointing along the z axis is denoted $|\uparrow_1\uparrow_2\cdots\uparrow_N\rangle_z$ and all others can be prepared by rotating this state with the angular momentum operators J_i, with $i \in \{x,y,z\}$. A CSS, typically obtained via a dissipative optical pumping process, is an eigenstate of $\mathbf{J}^2$ with maximal eigenvalue $J(J+1)$, where $J=N/2$. Because the SME works under the QND approximation of negligible absorption (i.e., the large detuning dispersive limit), no angular momentum will be exchanged between the probe beam and the ensemble. The only other allowed dynamics possible are rotations of the angular momentum induced by applied magnetic fields; thus, the state will maintain maximal $\langle \mathbf{J}^2\rangle$ over the course of the measurement.

The Dicke states are defined [4] as the states $|l,m\rangle$ that are simultaneous eigenstates of both $\mathbf{J}^2$ and J_z:

$$J_z|l,m\rangle = m|l,m\rangle, \qquad (6)$$

$$\mathbf{J}^2|l,m\rangle = l(l+1)|l,m\rangle, \qquad (7)$$

where

$$|m| \leqslant l \leqslant J = N/2. \qquad (8)$$

Under the above approximations, we can neglect any state with $l \neq J$. We then shorten the labelling of our complete basis from $|J,m\rangle$ to $|m\rangle$ so that

$$J_z|m\rangle = m|m\rangle, \qquad (9)$$

$$\mathbf{J}^2|m\rangle = J(J+1)|m\rangle, \qquad (10)$$

where $m \in \{-N/2, -N/2+1, \ldots, N/2-1, N/2\}$.

When the physical evolution is such that the $|m\rangle$ states remain complete, we can limit ourselves to a density matrix of size $(N+1)\times(N+1)$ rather than the full size $2^N \times 2^N$. This reduced space is referred to as the symmetric subspace, as its states are invariant to particle exchange [33,34]. For the case of two spins, the symmetric subspace contains the triplet states, but not the singlet. States contained within the symmetric subspace can be described as a pseudospin of size $J = N/2$.

In the z basis, the extremal values of m, $\pm N/2$, are simply the coherent spin states pointing along the z axis:

$$|m = +N/2\rangle = |\uparrow_1\uparrow_2\cdots\uparrow_N\rangle, \qquad (11)$$

$$|m = -N/2\rangle = |\downarrow_1\downarrow_2\cdots\downarrow_N\rangle. \qquad (12)$$

In terms of the constituent spins, these states are obviously unentangled. In contrast, consider the state with $m=0$ (for N even):

$$|m=0\rangle = C\Sigma_i \mathrm{P}_i(|\uparrow_1\cdots\uparrow_{N/2}\downarrow_{N/2+1}\cdots\downarrow_N\rangle), \qquad (13)$$

where the P_i represent all permutations of the spins and C is a normalization constant. This state is highly entangled in a way that is robust to particle loss [16]. Even though the expectation values $\langle J_i\rangle$ vanish for this state, it still has maximal $\mathbf{J}^2$ eigenvalue. Loosely, this state represents a state of knowledge where the length of the spin vector is known and the z component is known to be zero, but the direction of the spin vector in the x-y plane is completely indeterminate. Similarly, the entangled states with $0<|m|<N/2$ can be imagined as residing on cones aligned along the z axis with projection m. The loss of pointing angle information from the measurement process is diagrammed in Fig. 1(B).

Along with their unique entanglement and uncertainty properties, Dicke states are also of interest for the important role they play in descriptions of collective radiation processes [4] and for their potential role in quantum information processing tasks [17,18,35].

B. Short-time limit

Even when working within the symmetric subspace, for a large number of spins the size of $\rho(t)$ may be too unwieldy for computational efficiency. Because it is often desirable to update our state description in real time (e.g., for optimal feedback procedures), finding simple but sufficient descriptors is of considerable importance.

We can derive a reduced model by employing a moment expansion for the observable of interest. Extracting the conditional expectation values of the first two moments of J_z from the SME gives the following scalar stochastic differential equations:

$$d\langle J_z\rangle(t) = \gamma\langle J_x\rangle(t)b(t)dt + 2\sqrt{M\eta}\langle\Delta J_z^2\rangle(t)dW(t), \quad (14)$$

$$d\langle\Delta J_z^2\rangle(t) = -4M\eta\langle\Delta J_z^2\rangle^2(t)dt - i\gamma\langle[\Delta J_z^2, J_y]\rangle(t)b(t)dt + 2\sqrt{M\eta}\langle\Delta J_z^3\rangle(t)dW(t). \quad (15)$$

Note that these equations are not closed because higher-order moments couple to them.

At short times, $t\ll 1/\eta M$, we can make this set of equations closed with the following approximations. If the spins are initially fully polarized along x, then by using the evolution equation for the x component, we can show $\langle J_x\rangle(t) \approx J\exp[-Mt/2]$. Making the Gaussian approximation at short times, the third-order terms $\langle\Delta J_z^3\rangle$ and $-i\gamma\langle[\Delta J_z^2, J_y]\rangle(t)b(t)$ can be neglected. The Holstein-Primakoff transformation makes it possible to derive this Gaussian approximation as an expansion in $1/J$ [36]. Both of the removed terms can be shown to be approximately $1/J\sqrt{J}$ smaller than the retained nonlinear term. Thus we can approximate the optimal solution with

$$d\langle J_z\rangle_s(t) = \gamma J\exp[-Mt/2]b(t)dt + 2\sqrt{M\eta}\langle\Delta J_z^2\rangle_s(t)dW_s(t), \quad (16)$$

$$d\langle\Delta J_z^2\rangle_s(t) = -4M\eta\langle\Delta J_z^2\rangle_s^2(t)dt, \quad (17)$$

where the s subscript denotes the short-time solution and $dW_s(t)\equiv 2\sqrt{M\eta}[y(t)dt-\langle J_z\rangle_s(t)dt]$. Also $b(t)$ is assumed to be of a form that keeps the total state nearly pointing along x. The differential equation for the variance $\langle\Delta J_z^2\rangle_s(t)$ is now deterministic. It can be solved to give

$$\langle\Delta J_z^2\rangle_s(t) = \frac{\langle\Delta J_z^2\rangle(0)}{1+4M\eta\langle\Delta J_z^2\rangle(0)t}. \quad (18)$$

The deterministically shrinking value of $\langle\Delta J_z^2\rangle_s(t)$ represents the squeezing about the initially fluctuating value of $\langle J_z\rangle_s(t)$ as shown in the first two frames of Figs. 1(A) and 1(B). If feedback is added, then the value of $\langle J_z\rangle_s(t)$ can be zeroed via Larmor precession due to a control field along y and the same centered spin-squeezed state can be prepared on every trial [6,7,12].

The resulting spin-squeezed states can be used in subsequent precision measurements [14,15]. It is also worth pointing out that a precision measurement can be performed *during* the production of the conditional spin squeezing. For example, we have shown that by properly estimating both the spin state and an unknown classical field simultaneously with continuous measurement and Kalman filtering techniques, the field estimation can be improved over conventional limits by the presence of the simultaneous squeezing [22,23].

C. Long-time limit

The approximations made in the previous section are no longer valid at times $t\gg 1/\eta M$. The third-order terms become non-negligible at long times; hence, the variance becomes stochastic. Subsequently, other high-order moments couple to the problem and we are forced to consider the stochastic differential equation for each. Eventually, any finite-numbered moment description is no longer useful and it initially appears that we must resort back to the full symmetric density matrix and the SME, Eq. (1) as our primary description.

Fortunately, we can take another approach and describe the state in terms of other sufficient statistics. Without a field, the only statistic of the photocurrent needed to describe the state at time t is its integral $\int_0^t y(s)ds$ (see the Appendix or [37]). Knowing that the state is only a function of this variable and the initial state (prior information) makes the experimental design of a real-time estimator experimentally convenient. For example, we could use an analog integrator to create this sufficient statistic from the photocurrent, then feed it into a possibly nonlinear device (like an FPGA [33]) to perform the estimation.

With the integrated photocurrent and the initial state

$$|\psi(0)\rangle = \sum_{m=-J}^{J} c_m|m\rangle, \quad (19)$$

we can calculate (see the Appendix) the conditional expectation value of any power of J_z with the expression

$$\mathrm{Tr}[J_z^k\tilde{\rho}(t)] = \sum_{m=-J}^{J} m^k|c_m|^2\exp\left[-2M\eta m^2 t + 4mM\eta\int_0^t y(s)ds\right], \quad (20)$$

where $\tilde{\rho}(t)$ is the unnormalized density matrix, and setting $k=0$ represents its trace, so

$$\langle J_z^k\rangle(t) = \mathrm{Tr}[J_z^k\tilde{\rho}(t)]/\mathrm{Tr}[J_z^0\tilde{\rho}(t)]. \qquad (21)$$

Consider the case when the system starts in the x-polarized spin-coherent state. To very good approximation (with reasonably large J) we can write for this state in the z basis,

$$|c_m|^2 \propto \exp\left[-\frac{m^2}{J}\right]. \qquad (22)$$

Using these coefficients, we now have the rule for mapping the photocurrent to the expectation of J_z:

$$\langle J_z\rangle(t) = \mathrm{Tr}[J_z^1\tilde{\rho}(t)]/\mathrm{Tr}[J_z^0\tilde{\rho}(t)]. \qquad (23)$$

Other than the minor approximation of the initial coefficients, using this estimate is essentially the same as using solution to the full SME, so we do not give it a new subscript.

To simplify further, we can change the sums to integrals, giving

$$\mathrm{Tr}[J_z^k\tilde{\rho}(t)] \simeq \int_{-J}^{J} m^k e^{-Am^2+2Bm}dm, \qquad (24)$$

with

$$A = \frac{1}{J} + 2M\eta t, \quad B = 2M\eta\int_0^t y(s)ds. \qquad (25)$$

This approximation produces an estimate

$$\langle J_z\rangle_i(t) = \frac{\int_{-J}^{J} me^{-Am^2+2Bm}dm}{\int_{-J}^{J} e^{-Am^2+2Bm}dm}, \qquad (26)$$

which performs suboptimally when the distribution of states becomes very narrow at long times. Interestingly, the integral approximation here numerically appears to give the same estimate as the one derived previously for short times when no field is present—i.e.,

$$\langle J_z\rangle_i(t) = \langle J_z\rangle_s(t). \qquad (27)$$

This is not entirely surprising as both of these estimators ignore the discreteness of the Dicke levels. Also, at long times, it turns out that both of these estimates appear to be numerically equivalent to the simplest of all estimates: averaging the photocurrent. In other words, one simple and intuitive approximation to the optimal $\langle J_z\rangle(t)$ would be

$$\langle J_z\rangle_a(t) = \frac{\int_0^t y(s)ds}{t}, \qquad (28)$$

which is an estimate one might guess from the form of the photocurrent, Eq. (4). From simulation, it appears that this estimate is the same as both $\langle J_z\rangle_i(t)$ and $\langle J_z\rangle_s(t)$ for $t \gg 1/\eta M$. Despite the nonoptimality of these simple estimators, they perform well enough to resolve the discretization of the Dicke levels at long times.

Unfortunately, the addition of a feedback field makes these simplified estimators inadequate at long times, and deriving simple reduced models with a field present is difficult, thus forcing us to use the full SME in our state based controller. Despite this difficulty, during our subsequent feedback analysis we assume sufficient control bandwidth that the SME can be evolved by the observer in real time.

III. MEASUREMENT EVOLUTION WITHOUT FEEDBACK

In this section, our goal is to describe how the estimates of the last section probabilistically evolve at long times into Dicke states via observation alone. First, we discuss steady-state and statistical properties of the SME, Eq. (1). Then, we examine the unconditional dynamical solution with $\eta=0$ which gives the average state preparation behavior when $\eta \neq 0$. We then consider in detail how individual trajectories behave when $\eta\neq 0$. Finally, we discuss the performance of the nonoptimal estimators relative to the optimal projective estimator.

A. Steady states of the SME and martingale properties

The fact that the SME eventually prepares eigenstates of J_z is rather intuitive from a projection postulate perspective because J_z is the quantity being measured. If we insert the pure Dicke state $\rho=|m\rangle\langle m|$ into the SME with no Hamiltonian (or only a field along z), we find that it is a steady state, $d\rho=0$, no matter what happens with the subsequent measurement record. Of course, this does not yet prove that the state will eventually be obtained, as we have not discussed the stability of attractors in stochastic systems.

Without a field present, the SME has several convenient properties. First of all, from the evolution equation for the variance notice that the variance is a stochastic process that decreases on average. In fact it is a supermartingale, in that for times $s\leqslant t$ we have

$$\mathrm{E}_s[\langle\Delta J_z^2\rangle(t)] \leqslant \langle\Delta J_z^2\rangle(s), \qquad (29)$$

where the notation $\mathrm{E}[x(t)]$ denotes the average of the stochastic variable $x(t)$ at time t and the s subscript represents conditional expectation given a particular stochastic trajectory up to the time s. Additionally, it can be shown [5] that the average variance obeys the equation

$$\mathrm{E}[\langle\Delta J_z^2\rangle(t)] = \frac{\langle\Delta J_z^2\rangle(0)}{1 + 4M\eta\langle\Delta J_z^2\rangle(0)[t + \xi(t)]}, \qquad (30)$$

where

$$\xi(t) = \int_0^t \frac{\mathrm{E}[\{\langle\Delta J_z^2\rangle(s) - \mathrm{E}[\langle\Delta J_z^2\rangle(s)]\}^2]}{\mathrm{E}[\langle\Delta J_z^2\rangle(s)]^2}ds \geqslant 0. \qquad (31)$$

A more explicit solution of $\xi(t)$ is not necessarily needed as its positivity ensures that $\langle\Delta J_z^2\rangle(t)$ stochastically approaches zero. This implies that a Dicke state is eventually prepared. The numerical simulation of Figs. 1 and 2 demonstrates this behavior for an initially x-polarized state. As expected, $\mathrm{E}[\langle\Delta J_z^2\rangle(t)]$ in Fig. 2(A) appears to be less than the short-

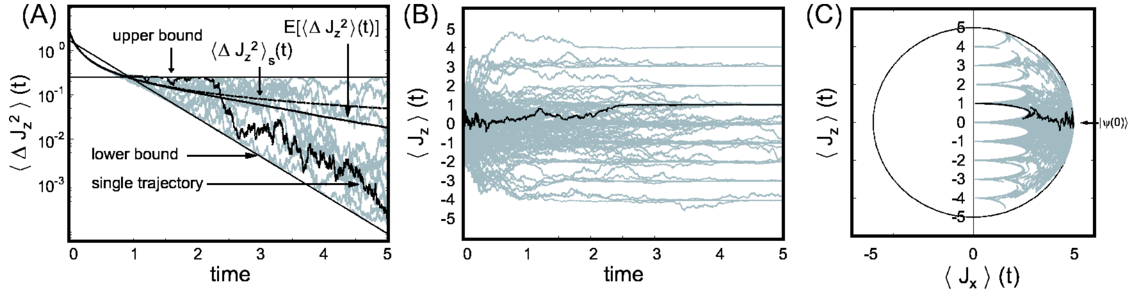

FIG. 2. Many open-loop moment trajectories[1] of the SSE, Eq. (5). The trajectory of Fig. 1 is darkened. (A) At short times, the evolution of the variance (shown on a log scale) is deterministic and given by $\langle \Delta J_z^2 \rangle_s(t)$. At long times, the variances become stochastic but bounded (above by $1/4$ and below by $\exp[-2(Mt-1)]/4$). The average of all 10 000 trajectories (only 10 are shown) gives. $E[\langle \Delta J_z^2 \rangle(t)]$. (B) The projective nature of the measurement is made clear by the evolution of 100 trajectories of $\langle J_z \rangle(t)$. The distribution of the final results is given by the first histogram of Fig. 1(A). (C) The evolution of the 100 trajectories all starting in an x-polarized CSS. When $\eta=1$, certain regions of Hilbert space are forbidden by the evolution.

time solution $\langle \Delta J_z^2 \rangle_s(t)$, Eq. (18), at long times.

Other useful properties of the stochastic evolution are evident from the moment equations. For example, we can show that

$$d\langle J_z^n \rangle = 2\sqrt{M\eta}(\langle J_z^{n+1} \rangle - \langle J_z^n \rangle \langle J_z \rangle) dW(t) \tag{32}$$

for integer n; hence,

$$d\mathrm{E}[\langle J_z^n \rangle] = 0 \tag{33}$$

and for times $s \leqslant t$ we have the *martingale* condition

$$\mathrm{E}_s[\langle J_z^n \rangle(t)] = \langle J_z^n \rangle(s). \tag{34}$$

This equation for $n=1$ gives us the useful identity

$$\mathrm{E}[\langle J_z \rangle(t) \langle J_z \rangle(s)] = \mathrm{E}[\langle J_z \rangle(s)^2] \tag{35}$$

for $s \leqslant t$. Also, we can rewrite the expression for $n=2$ as

$$\mathrm{E}_s[\langle J_z \rangle(t)^2 + \langle \Delta J_z^2 \rangle(t)] = \langle J_z \rangle(s)^2 + \langle \Delta J_z^2 \rangle(s). \tag{36}$$

This implies a sort of conservation of uncertainty as the diffusion in the mean, shown in Fig. 1(B), makes up for the decreasing value of the variance.

B. $\eta=0$

It is insightful to examine the behavior of the master equation with $\eta=0$ which corresponds to ignoring the measurement results and turns the SME, Eq. (1), into a deterministic unconditional master equation. We continue to consider only those initial states that are polarized. This is because these states are experimentally accessible (via optical pumping) and provide some degree of selectivity for the final prepared state. To see this, let us consider a spin-1/2 ensemble polarized in the x-z plane, making angle θ with the positive z axis, such that

$$\langle J_x \rangle(0) = \sin(\theta) N/2,$$

$$\langle J_y \rangle(0) = 0,$$

$$\langle J_z \rangle(0) = \cos(\theta) N/2,$$

$$\langle \Delta J_x^2 \rangle(0) = \cos^2(\theta) N/4,$$

$$\langle \Delta J_y^2 \rangle(0) = N/4,$$

$$\langle \Delta J_z^2 \rangle(0) = \sin^2(\theta) N/4. \tag{37}$$

Solving the unconditional moment equations and labeling them with u subscripts, we get

$$\langle J_x \rangle_u(t) = \sin(\theta)\exp(-Mt/2)N/2,$$

$$\langle J_y \rangle_u(t) = 0,$$

$$\langle J_z \rangle_u(t) = \cos(\theta) N/2,$$

$$\begin{aligned}\langle \Delta J_x^2 \rangle_u(t) = \sin^2(\theta)[&N^2 - N - 2N^2\exp(-Mt) \\ &+ (N^2 - N)\exp(-2Mt)]/8 \\ &+ N/4 \rightarrow \sin^2(\theta)(N^2 - N)/8 + N/4,\end{aligned}$$

$$\begin{aligned}\langle \Delta J_y^2 \rangle_u(t) &= \sin^2(\theta)[N^2 - N + (N - N^2)\exp(-2Mt)]/8 + N/4 \\ &\rightarrow \sin^2(\theta)(N^2 - N)/8 + N/4,\end{aligned}$$

$$\langle \Delta J_z^2 \rangle_u(t) = \sin^2(\theta) N/4. \tag{38}$$

Note that, because the unconditional solutions represent the average of the conditional solution—i.e., $\rho_u(t) = \mathrm{E}[\rho(t)]$—we have

$$\mathrm{E}[\langle J_z \rangle(t)] = \langle J_z \rangle_u(t) = \langle J_z \rangle(0) = \cos(\theta) N/2. \tag{39}$$

This also follows from the martingale condition for $\langle J_z \rangle(t)$. From the martingale condition for $\langle J_z^2 \rangle(t)$ we get

$$\begin{aligned}\mathrm{E}[(\langle J_z \rangle(t) - \mathrm{E}[\langle J_z \rangle(t)])^2] &= \langle \Delta J_z^2 \rangle(0) - \mathrm{E}[\langle \Delta J_z^2 \rangle(t)] \\ &\rightarrow \langle \Delta J_z^2 \rangle(0) = \sin^2(\theta) N/4.\end{aligned} \tag{40}$$

Thus, when $0 < \eta \leqslant 1$, we expect the final random conditional Dicke state on a given trial to fall within the initial z distribution. Given θ, the distribution will have spread $|\sin(\theta)|\sqrt{N}/2$ about the value $\cos(\theta)N/2$. Although the final state is generally random, starting with a polarized state clearly gives us some degree of selectivity for the final Dicke state because $\sqrt{N} \ll N$.

C. $0 < \eta \leqslant 1$

When $\eta \neq 0$, the measurement record is used to condition the state, and we can determine which Dicke state the system diffuses into. Given the task of preparing the state $|m_d\rangle$, the above analysis suggests the following experimental procedure. First, polarize the ensemble (via optical pumping) into an unentangled coherent state along any direction. Then rotate the spin vector (with a magnetic field) so that the z component is approximately equal to m_d. Finally, continuously measure z until a time $t \gg 1/\eta M$. The final estimate will be a random Dicke state in the neighborhood of m_d. When the trial is repeated, the final states will make up a distribution described by the initial moments of J_z $(\langle J_z\rangle(0), \langle \Delta J_z^2\rangle(0), \ldots)$. To reduce the effects of stray field fluctuations and gradients, a strong holding field could be applied along the z axis. Because this Hamiltonian commutes with the observable J_z, the final open-loop measurement results would be unchanged.

This process (with zero field) is shown schematically in Fig. 1 for $m_d = 0$ where the initial state is polarized along x. Because $\langle J_z\rangle(0) = 0$, the final state with the highest probability is the entangled Dicke state $m_d = 0$. In contrast, if $\langle J_z\rangle(0) = J$, the state would start in an unentangled CSS polarized along z and would not subsequently evolve.

One way of characterizing how close the state is to a Dicke state is through the variance $\langle \Delta J_z^2\rangle(t)$. Figure 2(A) displays many trajectories for the variance as a function of time. For times $t \ll 1/\eta M$ the variance is approximately deterministic and obeys the short-time solution of Eq. (18). During this period, the mean $\langle J_x\rangle(t)$ is decreasing at rate $M/2$. Before this mean has completely disappeared, a conditional spin-squeezed state is created. However, for larger times the mean and variance stochastically approach zero, and the state, while still entangled, no longer satisfies the spin squeezing criterion [16].

There are several features to notice about the approach to a Dicke state that are evident in Figs. 1 and 2. The variance at time $t = 1/\eta M$ is already of order unity. Thus, at this point, only a few neighboring m levels contain any population, as can be seen in Fig. 1(C). Also, it can be numerically shown that, for x-polarized initial states, the diffusion of the variance at long times $t \gg 1/\eta M$ is bounded above and below by

$$\exp[-2(\eta M t - 1)]/4 < \langle \Delta J_z^2\rangle(t) \leqslant 1/4, \tag{41}$$

which is evident from Fig. 2(A). These facts indicate that the population is divided among at most two levels at long times which "compete" to be the final winner. If we assume that only two neighboring levels are occupied and apply the SSE (with $\eta = 1$), the probability p to be in one level obeys the stochastic equation

$$dp = -2Mp(1-p)dW(t) \tag{42}$$

and the variance takes the form $\langle \Delta J_z^2\rangle(t) = p(1-p)$. As simple as it looks, this SDE is not analytically solvable [29,30]. The maximum variance is $1/4$ and it can be shown that, for $p \equiv 1 - \epsilon$, with ϵ small, the lower bound is of the exponential form stated above, so the two-level assumption seems to be a good one. The fact that occupied Hilbert space becomes small at long times is also evident in Fig. 2(C), where the allowed states are seen to be excluded from certain regions when $\eta = 1$. The arclike boundaries of the forbidden space are where the two-level competition occurs.

In practice, an experimentalist does not always have an infinite amount of time to prepare a state. Eventually spontaneous emission and other decoherence effects will destroy the dispersive QND approximation that the present analysis is based upon. Suppose our task were to prepare a Dicke state with, on average, a desired uncertainty, $\langle \Delta J_z^2\rangle_d \ll 1$, such that one level was distinguishable from the next. From Eq. (30), we see that the time that it would take to do this on average is given by

$$t_d = \left[\frac{1}{\langle \Delta J_z^2\rangle_d} - \frac{1}{\langle \Delta J_z^2\rangle(0)}\right] \Bigg/ 4M\eta. \tag{43}$$

Thus, if $\langle \Delta J_z^2\rangle_d \ll 1$ is our goal, then t_d is how long the state must remain coherent. The larger $\langle \Delta J_z^2\rangle(0)$ is, the more entangled the final states are likely to be $(m \approx 0)$ [16], and hence, by Eq. (43), the longer it takes to prepare the state for a given $\langle \Delta J_z^2\rangle_d$. Hence, we arrive at the intuitively satisfying conclusion that conditional measurement produces entangled states more slowly than unentangled states. Of course, Eq. (43) is an average performance limit. In a best case scenario, the variance would attain the lower bound of Eq. (41) where the state reduction happens exponentially fast.

D. Performance of suboptimal estimators

Now we consider the performance of the suboptimal estimators discussed previously, in particular the current average $\langle J_z\rangle_a(t)$ of Eq. (28). It makes sense to associate the overall "error" of this estimator, denoted V_a, to be the average squared distance of the estimator from the optimal estimator *plus* the average uncertainty of the optimal estimator itself, $\mathrm{E}[\langle \Delta J_z^2\rangle(t)]$. Using the martingale properties of the optimal estimate and the definition of the photocurrent gives this quantity as

$$V_a \equiv \mathrm{E}[(\langle J_z\rangle_a(t) - \langle J_z\rangle(t))^2] + \mathrm{E}[\langle \Delta J_z^2\rangle(t)] = \frac{1}{4M\eta t}. \tag{44}$$

This is just the error in estimating a constant masked by additive white noise with the same signal-to-noise ratio [23]. The optimal estimator is better than this suboptimal estimator at long times only through the quantity $\xi(t)$, Eq. (31).

In the open-loop experimental procedure described at the beginning of the last section, the above observation indicates that we can replace the optimal estimator with the photocurrent average and still resolve the projective behavior (given sufficient elimination of extraneous noise). The price paid for the simplicity of the averaging estimator is that it converges more slowly and it only works when a field is not present (hence without control).

IV. CLOSED-LOOP EVOLUTION

The primary problem with the open-loop state preparation scheme (and other approaches [17–19]) is that it is probabilistic. For a single measurement, there exists some degree of control, by adjusting the initial angle of rotation θ, but the final state is *a priori* unpredictable within the variance of the initial state. In this section, we show that the state preparation can be made deterministic with the use of feedback. Just as the control scheme of [6,7] produces deterministically centered spin-squeezed states, we present a simple feedback controller that will prepare the same desired Dicke state (particularly $m_d=0$) on every measurement trial.

We choose to work with y-axis magnetic field actuator corresponding to the Hamiltonian, $H(t)=\gamma b(t)J_y$. If the CSS initial state begins in the x-z plane, this will ensure that the vector $\langle\vec{J}\rangle(t)$ remains in this plane. This actuator is natural for the control of spin-squeezed states at short times, where the linear moments of $\langle\vec{J}\rangle(t)$ are large and allow intuitive rotation of the spin vector. However, at long times the field will mostly be affecting nonlinear terms in the moment expansion and the dynamics are less intuitive as can be seen by the structure near the z axis in Fig. 2(C). Still, we continue to give ourselves only these rotations to work with as they are the most experimentally accessible actuation variable.

In principle, the fact that Dicke states can be prepared deterministically with feedback should not be surprising. Given the aforementioned characteristics of the noncontrolled measurement one could imagine preparing a particular state by *alternating* measurement and control periods. For example, an initial measurement (lasting for a time $\Delta t \ll 1/\eta M$) would determine the fluctuation of $\langle J_z\rangle$ while the uncertainty $\langle\Delta J_z^2\rangle$ simultaneously decreased (on average). Then the measurement would be turned off and the state would be rotated with a control field to nullify the conditional quantity $\langle J_z\rangle - m_d$ (if preparing $|m_d\rangle$). The process of alternating measurement and control could then be repeated and would eventually clamp down on the desired state. Notice that, unlike the preparation of spin-squeezed states [6,7], this procedure could not be performed with a *single* measurement and control cycle. In other words, if we measure for a time $t \gg 1/\eta M$ and prepare a probabilistic Dicke state, then a single postmeasurement rotation cannot prepare a different desired Dicke state in the same basis.

With this intuitive picture in mind, now consider the continuous limit of this process, where the measurement and control are performed simultaneously. We wish to find a mapping from the photocurrent history to the control field that prepares our state of interest in a satisfactory manner on *every* trial. For simplicity, we work with $\eta=1$ and use the SSE of Eq. (5) for all simulations.[1] In selecting a controller, we could choose one of several strategies, including either direct current feedback or a feedback rule based on the state (i.e., what has been called Markovian and Bayesian feedback, respectively [27,38]). While direct current feedback possesses certain advantages, mainly simplicity that allows practical implementation, and is capable of working adequately at short times, any constant gain procedure would never prepare a Dicke state with confidence. If the current is directly fed back, a finite amount of noise will unnecessarily drive the system away from its target, even if the state starts there. Of course the gain could be ramped to zero in time, but unlike the short-time case, it is not clear how to tailor the gain intelligently.

Another alternative would be to prepare a spin-squeezed state with this approach and then turn off the feedback at some intermediate time. This would certainly enhance the probability of obtaining a certain Dicke state, but the process would remain probabilistic to some degree. For these reasons, we continue considering only state-based feedback, despite the fact that updating the state in real time is experimentally challenging.

A. Defining a cost

A useful first step in the design of any controller is to define the quantity that the ideal controller should minimize: the cost function. For example, consider a state preparation application where the controller aims to produce the desired target state $|\psi_d\rangle$. In this case, one possible cost function is the quantity

$$U_f \equiv 1 - \langle\psi_d|\rho|\psi_d\rangle \geq 0, \tag{45}$$

evaluated at the stopping time, which is zero iff the fidelity of the state with respect to the target is unity. In the current application, where we desire a final Dicke state $|m_d\rangle$, we wish to minimize a different quantity

$$U \equiv (\langle J_z\rangle - m_d)^2 + \langle\Delta J_z^2\rangle = \Sigma_m\langle m|\rho|m\rangle^2(m-m_d)^2 \geq 0, \tag{46}$$

which is zero iff $\rho=|m_d\rangle\langle m_d|$. Notice that U gives a higher penalty than U_f to states that are largely supported by Dicke states far removed from the target. In general, U will evolve stochastically and we may be more interested in the mean behavior, denoted $\mathrm{E}[U]$. In the uncontrolled case, it can be shown that this quantity remains constant, $\mathrm{E}[U(t)]=U(0)$. For the controlled case, we wish for $\mathrm{E}[U]\to 0$ as time advances, which, because $U\geq 0$, implies that every trajectory approaches the target state $|m_d\rangle$.

In general, the cost function could also include an integral of the quantity $U(t)$ instead of just the final value. As in classical control theory [23], it is also practical to include a function of $b(t)$ in the cost as a way of expressing our experimental feedback gain and bandwidth constraints. Analytically proceeding in this way by optimizing the average cost is too difficult for the current problem, but with this perspective in mind, we proceed by proposing controllers according to related considerations.

B. Control law 1

Now consider the average evolution of the above cost function, which is given by

$$d\mathrm{E}[U(t)] = -2\gamma\mathrm{E}\left[b(t)\left(\frac{\langle J_xJ_z + J_zJ_x\rangle(t)}{2} - m_d\langle J_x\rangle(t)\right)\right]dt. \tag{47}$$

Because we want this function to continuously decrease, the right-hand side should be negative at all times. If we have full access to the density matrix and minimal feedback delay, we could use the controller

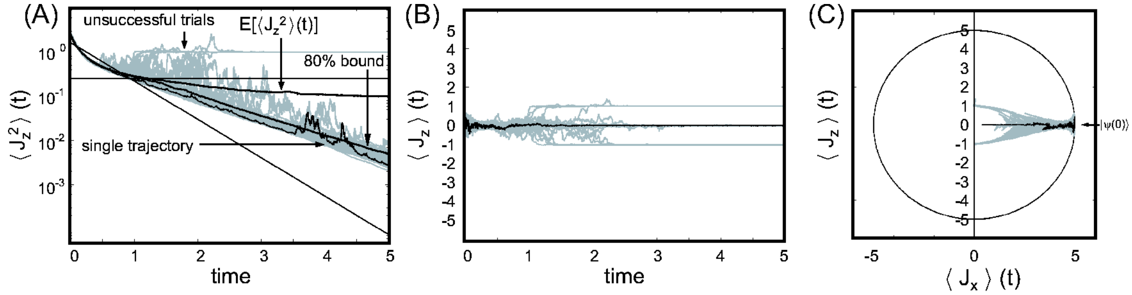

FIG. 3. One hundred closed-loop moment trajectories[1] of the SSE with feedback law $b(t)=\lambda\langle J_xJ_z+J_zJ_x\rangle(t)/2$ and $\lambda=10$ chosen from numerical considerations. (A), (B) If the control is successful, the quantity $\langle J_z^2\rangle(t)$ should go to zero on every trial. For this controller the number of successful trajectories is increased significantly (from 25% to 90%), but the remaining fraction is attracted to neighboring fixed points, causing the mean $\mathrm{E}[\langle J_z^2\rangle(t)]$ to saturate at a nonzero value. Although the successful fraction converges exponentially, the fastest converging trajectories are slower than in the open-loop case. This is evident in (C) as the converging trajectories have visibly not yet reached $\langle J_x\rangle=0$ at time $t=5$.

$$b_1(t) = \lambda\left(\frac{\langle J_xJ_z + J_zJ_x\rangle(t)}{2} - m_d\langle J_x\rangle(t)\right), \qquad (48)$$

where λ is a constant positive gain factor. This law guarantees that $d\mathrm{E}[U(t)]\leqslant 0$. Still, this does not yet prove that $U=0$ is obtained because $d\mathrm{E}[U(t)]=0$ for states other than the target state. Furthermore, even with this control law applied, all Dicke states *remain* fixed points.

Regardless of these issues, we proceed by analyzing the performance of this control law numerically with $m_d=0$. In principle, the gain could be chosen arbitrarily large. Here we choose to work with a gain that is large enough to be effective but small enough to keep the numerical simulation results valid.[1] The choice of a limited gain is a necessity in both simulation and experiment; thus, we wish to find a control law that works within this constraint. For the parameters used in our simulation, we use a gain of $\lambda=10$ which produces the results shown in Fig. 3.

In Fig. 3(A), we now plot the figure of merit for $m_d=0$, $U(t)=\langle J_z^2\rangle(t)$. In open-loop configuration, only 25% of all trajectories are attracted to $m=0$, whereas with this controller the percentage reaches 90%. Furthermore, most of these trajectories approach the state at an exponential rate close to M, as indicated by the curve under which 80% of the trajectories lie. Interestingly, this is at the expense of those trajectories that in open loop approached the target state at an exponential rate of $2M$. There is a trade-off by which the control slightly compromises the convergence of the best case trajectories.

Unfortunately, because all other Dicke states are still fixed points of the controlled SSE and the gain is finite, a small fraction (10%) of trajectories are attracted to those states neighboring the target state. Thus this controller does not appear to deterministically prepare all trajectories into the target state and the mean $\mathrm{E}[\langle J_z^2\rangle(t)]$ flattens at a level determined by the unsuccessful fraction of trials.

C. Control law 2

The obvious solution to the above problem is to try a controller that ensures the target state is the *only* fixed point of the SME on SSE. In this section we propose the control law

$$b_2(t) = \lambda[\langle J_z\rangle(t) - m_d], \qquad (49)$$

for which the state $|m_d\rangle$ is the only fixed point. However, unlike $b_1(t)$ this controller lacks the x symmetry that ensures $d\mathrm{E}[U(t)]\leqslant 0$. Also, while the symmetry of $b_1(t)$ will allow it to lock to both sides of the Bloch sphere, $b_2(t)$ will only lock to one side of the sphere.

Again, we proceed by numerically analyzing the performance of this controller for $m_d=0$, with the results displayed in Fig. 4. The gain is chosen in the same manner as before, which leads to the same reasonable choice of $\lambda=10$. In Fig. 4(C) the fundamental nature of the dynamics can be seen. Close to 90% of the trajectories are directly transported towards the target state, but the remaining "misses" on the first pass. Instead of being attracted towards other fixed points though, this unsuccessful fraction is *recycled* and rotated back onto the positive x axis where they can reattempt convergence onto the target state. These large excursions can be seen in Figs. 4(A) and 4(B) as well, but they do not appear to dominate the net flow. The average of 10 000 trajectories gives a quantity $\mathrm{E}[\langle J_z^2\rangle(t)]$ which appears to exponentially descend towards zero, implying that the state preparation has been made deterministic. As with the control of $b_1(t)$ there is again a trade-off: the trajectories that previously descended at the exponential rate of $2M$ converge more slowly, but still exponentially.

V. CONCLUSION

The purpose of this paper is to demonstrate the fact that the process of continuous projective measurement can be made deterministic with a theoretically simple and intuitive state-based control law. In the context of an atomic spin ensemble, the resulting Dicke states are highly entangled and otherwise difficult to reliably produce from an initially unentangled state.

However, there is much work to be done in the general field of quantum-state estimation and control, of which this is one example. In this pursuit, it is helpful to utilize and

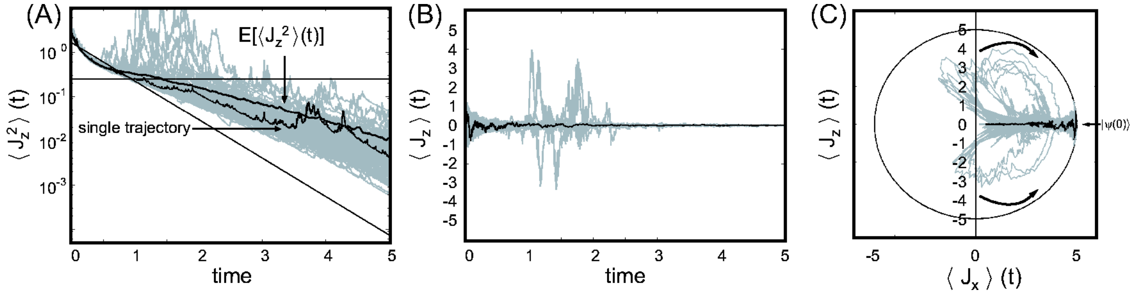

FIG. 4. One hundred closed-loop moment trajectories[1] of the SSE with feedback law $b(t)=\lambda\langle J_z\rangle(t)$ and $\lambda=10$ chosen from numerical considerations. (A) The average over 10 000 trajectories suggests that with this control law the mean $\mathrm{E}[\langle J_z^2\rangle(t)]$ descends to zero exponentially and the target state is deterministically prepared. (B) Despite a number of early excursions, all 100 trajectories shown converge to the desired value of $m=0$. (C) Those trajectories that do not descend to the goal directly (about 10 of 100) are recycled and rotated back into the attractive region of the target state. Again, the control slightly compromises the best-case convergence rate and the trajectories have a nonzero (but still decreasing) $\langle J_x\rangle$ at $t=5$.

adapt methods from the developed fields of classical stochastic estimation and control theory. In [28], for example, the problem of this paper is considered for a single spin with greater emphasis on technical notions of stochastic stability and convergence. Ultimately, we would like to discover constructive methods for deriving optimal control laws given a cost function and realistic actuators.

Even with an optimal control law in hand, there is no guarantee that experimental implementation will be possible. Any analysis should incorporate, among other constraints, nonunity detection efficiencies and finite controller resources (bandwidth, memory, etc). For experimental application of quantum feedback, the controller complexity needs to be reduced to the point where the delay is minimal compared to other dynamical time scales [33]. As in classical control, effective model reduction techniques are indispensable when it comes to implementation.

Despite these difficulties, the increasing number of physical systems that can be measured reliably at the quantum limit will surely hasten the effort to solve many of these technical challenges. By respecting the physical basis of measurement dynamics, experimentalists will be able to more efficiently use measurement itself, in tandem with more traditional techniques, to actuate quantum systems into desirable states.

ACKNOWLEDGMENTS

This work was supported by the NSF (Grant Nos. PHY-9987541 and EIA-0086038), the ONR (Grant No. N00014-00-1-0479), the ARO (Grant No. DAAD19-03-1-0073), and the Caltech MURI Center for Quantum Networks (Grant No. DAAD19-00-1-0374). J.K.S acknowledges support from the Hertz Foundation. We thank Andrew Doherty, J.M. Geremia, and Paige Randall for useful discussions. Additional information is available at http://minty.caltech.edu/Ensemble.

APPENDIX: SOLUTION OF THE SME WITHOUT A FIELD

An explicit solution to the SME, Eq. (1), can easily be found in the case $H(t)=0$. First, the SME is rewritten as

$$d\tilde{\rho}(t) = \mathcal{D}[\sqrt{M}J_z]\tilde{\rho}(t)dt + 2M\eta[J_z\tilde{\rho}(t) + \tilde{\rho}(t)J_z]y(t)dt. \tag{A1}$$

This equation, known as the *unnormalized* or *linear* SME, is equivalent to Eq. (1) with the identification

$$\rho(t) = \tilde{\rho}(t)/\mathrm{Tr}[\tilde{\rho}(t)]. \tag{A2}$$

Introducing the notation

$$\mathcal{G}_1\tilde{\rho} = J_z\tilde{\rho}J_z,$$

$$\mathcal{G}_2\tilde{\rho} = J_z^2\tilde{\rho} + \tilde{\rho}J_z^2,$$

$$\mathcal{G}_3\tilde{\rho} = J_z\tilde{\rho} + \tilde{\rho}J_z, \tag{A3}$$

Eq. (A1) can be written in the more suggestive form

$$d\tilde{\rho}(t) = M\left(\mathcal{G}_1 - \frac{1}{2}\mathcal{G}_2\right)\tilde{\rho}(t)dt + 2M\eta\mathcal{G}_3\tilde{\rho}(t)y(t)dt. \tag{A4}$$

Now note that Eq. (A4) is a linear Itô SDE [29] for $\tilde{\rho}(t)$, and moreover $\mathcal{G}_{1,2,3}$ all commute with each other in the sense that $\mathcal{G}_i\mathcal{G}_j\tilde{\rho}=\mathcal{G}_j\mathcal{G}_i\tilde{\rho}$. Such SDE's have a simple explicit solution [30]

$$\tilde{\rho}(t) = \exp\left[[M(1-\eta)\mathcal{G}_1 - M(1+\eta)\mathcal{G}_2/2]t + 2M\eta\mathcal{G}_3\int_0^t y(s)ds\right]\tilde{\rho}(0), \tag{A5}$$

as is easily verified by taking the time derivative of this expression, where care must be taken to use Itô's rule for the stochastic term.

Now consider an initial pure state of the form

$$|\psi(0)\rangle = \sum_{m=-J}^{J} c_m|m\rangle. \tag{A6}$$

The associated initial density matrix is then

$$\tilde{\rho}(0) = |\psi(0)\rangle\langle\psi(0)| = \sum_{m,m'=-J}^{J} c_m c_{m'}^{*} |m\rangle\langle m'|. \qquad (A7)$$

Substituting into Eq. (A5) gives

$$\tilde{\rho}(t) = \sum_{m,m'=-J}^{J} c_m c_{m'}^{*} \exp\left[\left\{M(1-\eta)mm' - \frac{1}{2}M(1+\eta)[m^2 + (m')^2]\right\}t + 2M\eta(m+m')\int_0^t y(s)ds\right]|m\rangle\langle m'|. \qquad (A8)$$

Hence

$$\mathrm{Tr}[J_z^k \tilde{\rho}(t)] = \sum_{m=-J}^{J} m^k |c_m|^2 \exp\left[-2M\eta m^2 t + 4mM\eta\int_0^t y(s)ds\right], \qquad (A9)$$

which is the result used in the text, Eq. (20).

---

[1] H. M. Wiseman, Quantum Semiclassic. Opt. **8**, 205 (1996).

[2] H. M. Wiseman, Phys. Rev. A **49**, 2133 (1994).

[3] R. H. Dicke, Phys. Rev. **93**, 99 (1954).

[4] L. Mandel and E. Wolf, *Optical Coherence and Quantum Optics* (Cambridge University Press, Cambridge, UK, 1997).

[5] S. L. Adler, D. C. Brody, T. A. Brun, and L. P. Hughston, J. Phys. A **34**, 8795 (2001).

[6] L. K. Thomsen, S. Mancini, and H. M. Wiseman, Phys. Rev. A **65**, 061801 (2002).

[7] L. K. Thomsen, S. Mancini, and H. M. Wiseman, J. Phys. B **35**, 4937 (2002).

[8] I. Bouchoule and K. Mølmer, Phys. Rev. A **66**, 043811 (2002).

[9] A. S. Sørensen and K. Mølmer, Phys. Rev. A **66**, 022314 (2002).

[10] A. Andre and M. D. Lukin, Phys. Rev. A **65**, 053819 (2002).

[11] L. M. Duan, J. I. Cirac, and P. Zoller, Phys. Rev. A **66**, 023818 (2002).

[12] J. M. Geremia, J. K. Stockton, and H. Mabuchi, Science **304**, 270 (2004).

[13] A. Kuzmich, L. Mandel, and N. P. Bigelow, Phys. Rev. Lett. **85**, 1594 (2000).

[14] D. J. Wineland, J. J. Bollinger, W. M. Itano, and D. J. Heinzen, Phys. Rev. A **50**, 67 (1994).

[15] D. Oblak, J. K. Mikkelsen, W. Tittel, A. K. Vershovski, J. L. Sorensen, P. G. Petrov, C. L. G. Alzar, and E. S. Polzik, e-print quant-ph/0312165.

[16] J. K. Stockton, J. Geremia, A. C. Doherty, and H. Mabuchi, Phys. Rev. A **67**, 022112 (2003).

[17] L. M. Duan and H. J. Kimble, Phys. Rev. Lett. **90**, 253601 (2003).

[18] A. S. Sørensen and K. Mølmer, Phys. Rev. Lett. **91**, 097905 (2003).

[19] R. G. Unanyan, M. Fleischhauer, N. V. Vitanov, and K. Bergmann, Phys. Rev. A **66**, 042101 (2002).

[20] A. C. Doherty, S. Habib, K. Jacobs, H. Mabuchi, and S. M. Tan, Phys. Rev. A **62**, 012105 (2000).

[21] V. Belavkin, Rep. Math. Phys. **43**, 405 (1999).

[22] J. M. Geremia, J. K. Stockton, A. C. Doherty, and H. Mabuchi, Phys. Rev. Lett. **91**, 250801 (2003).

[23] J. K. Stockton, J. Geremia, A. C. Doherty, and H. Mabuchi, Phys. Rev. A **69**, 032109 (2004).

[24] A. Andre, A. S. Sorensen, and M. D. Lukin, Phys. Rev. Lett. **92**, 230801 (2004).

[25] M. A. Armen, J. K. Au, J. K. Stockton, A. C. Doherty, and H. Mabuchi, Phys. Rev. Lett. **89**, 133602 (2002).

[26] C. Ahn, A. C. Doherty, and A. J. Landahl, Phys. Rev. A **65**, 042301 (2002).

[27] A. C. Doherty and K. Jacobs, Phys. Rev. A **60**, 2700 (1999).

[28] R. van Handel, J. K. Stockton, and H. Mabuchi, e-print quant-ph/0402136.

[29] B. Øksendal, *Stochastic Differential Equations*, 5th ed. (Springer-Verlag, Berlin, 1998).

[30] C. W. Gardiner, *Handbook of Stochastic Methods*, 2nd ed. (Springer, New York, 1985).

[31] G. A. Smith, S. Chaudhury, and P. S. Jessen, J. Opt. B: Quantum Semiclassical Opt. **5**, 323 (2003).

[32] A. Silberfarb and I. Deutsch, Phys. Rev. A **68**, 013817 (2003).

[33] J. Stockton, M. Armen, and H. Mabuchi, J. Opt. Soc. Am. B **19**, 3019 (2002).

[34] S. D. Bartlett and H. M. Wiseman, Phys. Rev. Lett. **91**, 097903 (2003).

[35] A. Cabello, Phys. Rev. A **65**, 032108 (2002).

[36] T. Holstein and H. Primakoff, Phys. Rev. **58**, 1098 (1940).

[37] D. C. Brody and L. P. Hughston, J. Math. Phys. **43**, 5254 (2002).

[38] H. M. Wiseman, S. Mancini, and J. Wang, Phys. Rev. A **66**, 013807 (2002).

[39] P. E. Kloeden, E. Platen, and H. Schurz, *Numerical Solution of SDE Through Computer Experiments* (Springer, New York, 1997).

PHYSICAL REVIEW A **70**, 053616 (2004)

Proposed magnetoelectrostatic ring trap for neutral atoms

Asa Hopkins,* Benjamin Lev, and Hideo Mabuchi
Norman Bridge Laboratory of Physics, 12-33, California Institute of Technology, Pasadena, California 91125, USA

(Received 6 February 2004; revised manuscript received 12 February 2004; published 22 November 2004)

We propose a trap for confining cold neutral atoms in a microscopic ring using a magnetoelectrostatic potential. The trapping potential is derived from a combination of a repulsive magnetic field from a hard drive atom mirror and the attractive potential produced by a charged disk patterned on the hard drive surface. We calculate a trap frequency of $[29.7, 42.6, 62.8]$ kHz and a depth of $[16.1, 21.8, 21.8]$ MHz for [^{133}Cs, ^{87}Rb, ^{40}K], and discuss a simple loading scheme and a method for fabrication. This device provides a one-dimensional potential in a ring geometry that may be of interest to the study of trapped quantum degenerate one-dimensional gases.

DOI: 10.1103/PhysRevA.70.053616 PACS number(s): 03.75.Be, 05.30.Jp, 03.75.Lm, 32.80.Pj

Traps are a standard tool for the study and manipulation of cold neutral atoms, allowing the investigation of fundamental quantum dynamics as well as providing a basis for quantum information processing. The manipulation of trapped atoms on "atom chips" allows the implementation of many different atom optics elements for trapping, waveguiding, interferometry, etc. [1,2]. Most atom chips use micron-sized current-carrying wires to generate the magnetic trapping fields. We propose to construct a magnetoelectrostatic ring trap, consisting of a hard drive atom mirror that provides a repulsive force on low-field seeking atoms [3] and electric pads that attract polarizable atoms via the Stark effect [4–6]. Schmiedmayer and Hinds and Hughes have proposed a range of such traps, including large-area two-dimensional traps, wire-based waveguides, and quantum-dot-like single state traps. Such traps could be used to construct beam splitters or to implement collisional quantum gates [7]. Here we propose a ring trap for cold neutral atoms constructed from a conducting disk placed above the atom mirror surface, which produces a trap with a deep ring potential around the edge of the disk.

Let us first examine the trapping potential from a charged conducting disk above a hard drive atom mirror. The hard drive's sinusoidal pattern of magnetization results in a repulsive potential—for atoms in weak-field seeking states—in the form of a decaying exponential [8]

$$U_{mag} = m_F g_F \mu_B B_0 \exp[-2\pi z/a]. \tag{1}$$

The amplitude depends on the remnant magnetization of the mirror, B_0, as well as the magnetic sublevel m_F and Landé g_F-factor of the atomic ground state. The decay length is proportional to the periodicity a of the magnetization pattern. A small externally applied magnetic field perpendicular to the magnetization of the hard disk eliminates zones of zero magnetic field which would allow Majorana spin-flip losses. The atom's low velocity allows the spin adiabatically to follow the magnetic field and thus the trapping potential depends only on the field magnitude.

In order to create a trap, the repulsive force from the mirror is balanced by an attractive force due to the dc Stark effect. The atomic potential due to an electric field is

$$U_{Stark} = -\frac{1}{2}\alpha |E|^2, \tag{2}$$

where we assume that we are working with atoms such as cesium or rubidium which possess only a scalar polarizability in the ground state. A charged conducting disk creates high electric fields near its edge, resulting in a strong short-range attractive potential.

The mirror is made out of an etched hard drive whose aluminum substrate is grounded. The boundary conditions consist of a ground at the mirror surface, and a constant potential on the surface of the thin conducting disk which is placed a distance d, typically on the order of a micron, above the mirror. The electric fields are calculated from the solution to the Poisson equation with these boundary conditions. The combined atomic potential due to the charged disk and mirror creates a trap above the conducting disk, which is deepest near the edge of the disk.

As an example, consider a conducting disk of radius 10 μm, placed $d = 0.6$ μm above a hard drive atom mirror. Let the hard drive have a field at its surface of 2 kG (a typical number for a commercial hard drive), and a periodicity of 3 μm in the magnetization. The trapping potential for cesium in the $F = 3$, $m_F = -3$ state near the edge of the disk has a depth of 16.1 MHz (770 μK) when the potential on the conducting disk is 14.2 V. For ^{87}Rb in the $F = 2$, $m_F = 2$ state, the trap has a depth of 21.8 MHz (1.05 mK) when 18.5 V is applied to the disk. These two atomic states will be used in all examples for the remainder of the paper. See Fig. 1 for the ^{133}Cs potential. The ^{87}Rb potential looks qualitatively the same, with a slightly deeper minimum. See Table I for trap parameters for a range of geometries for ^{133}Cs and ^{87}Rb, respectively. For ^{40}K, the optimal applied voltage is 4% larger than that for the ^{87}Rb trap, and trap frequencies scale up by a factor of $(m_{Rb}/m_K)^{1/2} = 1.48$ relative to the ^{87}Rb case.

The curvature of the trap is large enough that the atom is confined in the Lamb-Dicke regime. The Lamb-Dicke regime is defined as the regime in which η

---

*Electronic address: asa@caltech.edu

©2004 The American Physical Society

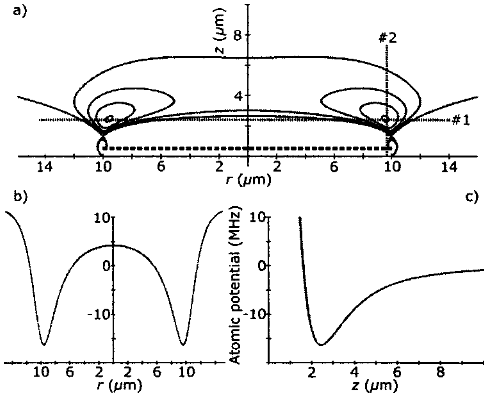

FIG. 1. The atomic potential for Cs with 14.2 V on the disk. (a) A cross section of the atomic potential in the plane containing the axis of the disk. The contour lines are spaced 4 MHz apart. The distance *r* along a diameter of the disk and the distance *z* above the disk are plotted on the horizontal and vertical axes, respectively. (b) The potential along slice no. 1 in (a). (c) The potential along slice no. 2 in (a).

$=(E_{recoil}/E_{trap})^{1/2}<1$. For the parameters of Fig. 1, the effective harmonic frequencies for [^{133}Cs, ^{87}Rb, ^{40}K] in the radial direction are $[29.7, 42.6, 62.8]$ kHz, and $[40.6, 56.8, 83.8]$ kHz in the direction perpendicular to the substrate. We obtain a Lamb-Dicke parameter of $\eta \leqslant 0.26$ for ^{133}Cs, $\eta \leqslant 0.30$ for ^{87}Rb, and $\eta \leqslant 0.37$ for ^{40}K. Significantly higher trap frequencies are possible with the use of custom magnetic materials, which can have remnant magnetic fields of up to 2.4 T [9]. For the same trap geometry as Fig. 1, but using this custom magnetic material with a correspondingly higher applied voltage, the harmonic frequencies for ^{133}Cs, for instance, are 103 kHz in the radial direction and 137 kHz in the perpendicular direction. The higher remnant magnetic field also allows the disk to be placed further from the hard drive while maintaining significant trap depth.

TABLE I. ^{133}Cs and ^{87}Rb trap parameters for several disk radii *r* and disk–hard drive separations *d*.

d (μm)	r (μm)	V	Trap depth (MHz)	Trap frequencies $\omega_r/2\pi$ (kHz)	$\omega_\perp/2\pi$ (kHz)
^{133}Cs					
0.6	5	13 3	17 0	24.4	44.1
0.6	10	14 2	16 1	29.7	40.6
0.6	20	14 8	15 4	30.6	37.0
1.0	5	9 4	8 5	18.0	31.1
1.0	10	10 2	8 2	21.2	28.0
1.0	20	10 8	8 1	22.1	26.3
^{87}Rb					
0.6	5	17 3	22 9	36.0	63.4
0.6	10	18 5	21 8	42.6	56.8
0.6	20	19 2	20 6	43.7	52.7
1.0	5	12 2	11 4	25.7	44.0
1.0	10	13 3	11 2	30.8	40.4
1.0	20	14 0	10 7	31.5	37.5

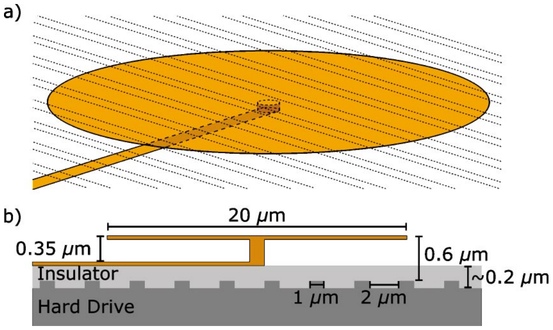

FIG. 2. (Color online) (a) Schematic of the magnetoelectrostatic ring trap drawn to scale. The disk is 20 μm in diameter, with a 1 μm wide lead connected via a central stem. The dotted lines show the hard drive atom mirror's 2:1 etch pattern with a 3 μm periodicity. (b) Cross section of the disk (with the vertical direction scaled up by a factor of 5), showing—from top to bottom—the disk, stem, lead, insulating layer, and etched hard drive.

A thin lead running along the hard drive surface may be used to connect the disk to a voltage source. The maximum possible voltage on the disk is limited by the breakdown electric field of the dielectric material separating the lead from the conducting hard drive surface. In order to minimize the perturbation that the lead produces on the atomic potential from the disk, the lead should be as narrow as is practical ($\sim$1 μm) and placed much closer to the hard drive surface than to the disk. At this location, the repulsive force from the mirror is much stronger and no trap forms due to the charge on the lead. In order to connect the lead to the disk, the disk is placed on a thin stem, with the lead connected to the bottom of the stem (see Fig. 2).

Three dimensional solutions to the Poisson equation indicate that the effect from the lead on the trapping potential is minimized if the stem connecting the lead to the disk is located at the center of the disk. For the previously used trap parameters and the lead placed 0.25 μm above the hard drive surface (0.35 μm below the surface of the disk), the trap minimum for a ^{133}Cs atom rises to $\sim$11.5 MHz above the lead, which is a $\sim$30% loss of trapping potential compared to the unperturbed trap. The width of the perturbation is a few μm, slightly wider than the lead. A shallower trap in which the electric pad is placed further from the mirror surface is perturbed less by the lead. Use of custom magnetic materials would allow deeper traps to be constructed further from the lead, thereby minimizing the height of the perturbation.

We intend to fabricate the device as follows. The hard drive atom mirror is etched in the manner described in Ref. [3], maintaining the 2:1 ratio of magnetization stripe spacing to minimize higher harmonics. The stripe periodicity will be $\leqslant 3$ μm. A deposition of an $\sim$200 nm thick insulating layer of silicon dioxide or silicon nitride is necessary to prevent shorting between the electric pads and the hard drive surface (see Fig. 2). This layer is thick enough to both support the voltage difference between the pads and underlying surface, and to help planarize the 100 nm deep corrugations of the etched hard drive. The $\sim$50 nm tall, $\sim$1 μm wide gold leads are patterned on the insulator surface using standard photolithography and thermal evaporation of the adhesion metal and gold layers [10,11]. To create the stems, the surface is spin-coated with photoresist to a predetermined thickness to achieve optimal disk to atom mirror spacing. Photolithography is again used to create vertical, cylindrical holes of 1 μm diameter in the photoresist located at the terminals of the gold leads. The gold stems are electroplated from the gold leads through the cylindrical guide holes to the top of the photoresist. A third photolithographic process and thermal evaporation patterns the 20 μm diameter gold disks attached to the tops of the stems. Finally, the photoresist is removed using standard techniques, leaving behind the mushroomlike structures. Field simulations show that to the percent level, leaving the photoresist under the disk does not disturb the electric field, and perturbations to the trap due to disk edge roughness or due to the hard drive trench corrugations are both negligible.

The trap is conservative once the voltage is established, and the kinetic energy of the atoms must be lowered for them to stay in the trap. A simple, but inefficient, method of loading this trap is to drop a cloud of cold atoms from a magneto-optical trap (MOT)—sub-doppler cooled to 10 μK—onto the device. The atoms are captured by turning on the voltage on the electric pads as the atoms are passing through their classical turning point above the atom mirror. Simulations indicate that this scheme can capture 1 to 2% of the dropped atoms. The fraction is small because the voltage ramp must be quite fast ($\sim 2\times 10^{-4}$ seconds) in order to remove enough energy from the atoms to trap them, while the atom cloud takes roughly 2×10^{-2} seconds to pass through the trapping volume. This scheme has many different parameters over which loading can be optimized, including the initial position, size and density of the MOT before it is dropped, and the shape and speed of the voltage ramp. Ramping up the voltage on the conducting disk is the simplest scheme for trapping the atoms, but it is possible that another procedure, involving atomic transitions or other degrees of freedom in the system, could be more effective and is currently being investigated.

Given this loading efficiency, a 10 micron-radius ring trap will capture roughly 30–50 atoms from a dropped cloud of 10^7 atoms and temperature 10 μK. In order to capture more atoms, disks can be arranged in an array covering a larger surface area. The volume of the trap deeper than 200 μK is 1 to 2×10^{-9} cm^3. Simulations indicate that these traps can be placed roughly 20 μm apart without significantly disturbing each other. Therefore, roughly 20% of the surface can be covered with the traps. Combining the loading efficiency with this surface coverage, roughly a few 10^3 atoms can be trapped. The leads can be routed through spaces between the disks with either a separate lead for each disk or a shared network of leads.

Several undesired effects, such as heating, fragmentation of Bose-Einstein condensates, and a reduction of trap lifetimes, have been detected in microtrap experiments involving atoms near room-temperature surfaces. The trap proposed here is insusceptible to heating due to technical noise on the currents in the microwires and to the fragmentation problems caused by the spatial variation of these currents [12,13]. However, the trap remains susceptible to atom loss due to spin flips induced by magnetic field fluctuations from thermal currents in the metal forming the electric pads, as detected in several experiments [14–16]. Surface effects in this system will most closely resemble those in Lin *et al.*, wherein the skin depth for the transition frequency between trapped and untrapped magnetic sublevels of the atoms is much larger than both the distance of the atoms from the metal surface and the thickness of the metal conductor. As reported in Lin *et al.*, at a distance of 2 μm this Johnson noise limits the lifetime of ^{87}Rb atoms above a 2 μm thick copper conductor to a few 100 ms—ample time for detecting atoms in the ring trap. The metal film used for the electric disk pad in the ring trap will be ten to a hundred times thinner than that used for the above experiment, and we expect this to further minimize the trap's loss rate [16,17].

There are several possibilities for minimizing or eliminating the perturbation due to the lead, or tuning it to be of a particular height, other than simply adjusting the trap geometry. The most versatile possibility is to add an additional photolithography step to insert another electric pad directly above the lead, separated by a thin insulation layer. The voltage applied to this separate pad can be used to compensate for the effects of the lead. In particular, the voltage on a pad the same width as the lead and placed 100 nm above it could be tuned to completely eliminate the perturbation (to within the percent-level accuracy of our calculations) or turn it into a dip rather than a bump. Complete elimination of any perturbation is possible by expanding such a pad to cover the entire surface, with a hole to allow the stem to reach from the lead to the disk. Another possibility is to charge the disk not with a lead but with an intrachamber electron beam. Such a system would be hard to charge and discharge quickly, requiring a loading scheme that does not require a rapid change to the charge distribution.

Several future improvements or extensions of this trapping concept are possible. For example, the decoherence effects due to the proximity of a conductor could be mitigated with the use of a dielectric magnetic film in place of the hard drive, and dielectric pads charged via an electron beam in place of the conducting disks. In addition, disks, rings, wires, and other shapes could be used to trap and manipulate the atoms just above the surface, and voltages adjusted to shift the atoms from one potential into another. Integration of these traps with magnetic microtraps based on current-carrying wires on the surface is also possible. Small single-atom traps with additional electrostatic pads to control the barrier heights could enable a system for quantum logic gates [7].

In the past several years, there has been much experimental and theoretical interest in trapped one-dimensional (1D) quantum degenerate gases (see Refs. [18–22] and the citations within). Trapped 1D gases require $k_BT,\mu \ll \hbar\omega_\perp$, where T is the temperature, μ is the chemical potential, and $\omega_\perp$ is the transverse trapping frequency. Various regimes of quantum degeneracy—of which a 1D gas of impenetrable bosons, the Tonks-Girardeau (TG) regime, is of particular interest—can be explored by changing the density of trapped atoms or by modifying the interactions between atoms via Feshbach resonances. In the latter case, a magnetic bias field for adjusting the *s*-wave scattering length, a, can be added parallel to the magnetization stripes of the atom mirror without affecting the potential of the magnetoelectrostatic ring trap. With respect to ^{87}Rb, a common alkali used for BEC, $k_B T/\hbar\omega_\perp$ is smaller than 0.05 for temperatures below 100 nK. The TG regime requires that the mean interparticle separation, $1/n$, be much larger than correlation length, $l_c = (\hbar/2mn\omega_\perp a)^{1/2}$, where m is the atom's mass, $n=N/L$ is the number density [21]. This constraint limits the number of ^{87}Rb atoms in the ring trap to $N \ll 2m\omega_\perp aL/\hbar = 250$ atoms for a device of circumference $L=2\pi\times 20$ μm, $\omega_\perp = 2\pi \times 40$ kHz, and an a unmodified by Feshbach resonances (the field at the trap minimum is $\sim$12 G). Overcoming the challenge of detecting so few atoms may be possible through the incorporation of microwire traps [22].

The ring geometry adds a unique element to the many-body physics of the 1D trap. Josephson effects in trapped BECs have been investigated theoretically for the case of a double well (see Ref. [23] and citations within) and investigated experimentally in an optical standing wave [24]. A BEC in this magnetoelectrostatic ring trap system with interspersed Josephson junctions formed from the addition of micron-sized perturbations to the trapping potential—such as those caused by wire leads, possibly tuned using additional pads—is reminiscent of superconducting electronic systems. The ratio of the chemical potential to the perturbation barrier height can be adjusted with the trap parameters such as d, r, atom number, and disk potential, as well as the use of additional electric pads, to cause the perturbation to act as either an impenetrable wall, a tunnel junction, or a scattering center. The utility of this 1D ring trap is highlighted by recent proposals for using a BEC in a double ring to create a SQUID-like device for neutral atoms [25] and for investigating quantum chaos in the system of the quantum kicked rotor [26].

This magnetoelectrostatic trap for cold neutral atoms—derived from balancing the repulsive force of an atom mirror with the attractive force from a charged disk—introduces a ring trapping geometry for cold neutral atoms. Fabrication of this trap is straightforward, and an array of such traps can trap a significant number of atoms. Furthermore, such a trap may allow the exploration of interesting many-body physics in a one-dimensional ring trap. This device is an example of the rich potential for developing atom optical elements through the integration of a hard drive atom mirror, charged pads, and microwires.

The authors thank Axel Scherer for helpful discussions. This work was supported by the Multidisciplinary University Research Initiative program under Grant No. DAAD19-00-1-0374. A.H. acknowledges financial support from the NSF.

---

[1] J. Reichel *et al.*, Appl. Phys. B: Lasers Opt. **72**, 81 (2001).
[2] R. Folman *et al.*, Adv. At., Mol., Opt. Phys. **48**, 263 (2002).
[3] B. Lev *et al.*, Appl. Phys. Lett. **83**, 395 (2003).
[4] J. Schmiedmayer, Eur. Phys. J. D **4**, 57 (1998).
[5] E. A. Hinds and I. G. Hughes, J. Phys. D **32**, R119 (1999).
[6] P. Kruger *et al.*, Phys. Rev. Lett. **91**, 233201 (2003).
[7] J. Schmiedmayer, R. Folman, and T. Calarco, J. Mod. Opt. **49**, 1375 (2002).
[8] G. Opat, S. Wark, and A. Cimmino, Appl. Phys. B: Photophys. Laser Chem. **B54**, 396 (1992).
[9] S. Xue, Seagate Technology (private communication).
[10] B. Lev, Quantum Inf. Comput. **3**, 450 (2003).
[11] M. J. Madou, *Fundamentals of Microfabrication* (CRC Press, New York, 2001).
[12] S. Kraft *et al.*, J. Phys. B **35**, 469 (2002).
[13] A. E. Leanhardt *et al.*, Phys. Rev. Lett. **90**, 100404 (2003).
[14] M. P. A. Jones *et al.*, Phys. Rev. Lett. **91**, 080401 (2003).
[15] D. M. Harber *et al.*, J. Low Temp. Phys. **133**, 229 (2003).
[16] Y. Lin *et al.*, Phys. Rev. Lett. **92**, 050404 (2004).
[17] C. Henkel *et al.*, Appl. Phys. B: Lasers Opt. **76**, 173 (2003).
[18] H. Moritz *et al.*, Phys. Rev. Lett. **91**, 250402 (2003).
[19] B. Laburthe Tolra *et al.*, cond-mat/0312003.
[20] M. Olshanii, Phys. Rev. Lett. **81**, 938 (1998).
[21] D. S. Petrov, G. V. Shlyapnikov, and J. T. M. Walraven, Phys. Rev. Lett. **85**, 3745 (2000).
[22] J. Reichel and J. H. Thywissen, cond-mat/0310330.
[23] J. E. Williams, Phys. Rev. A **64**, 013610 (2001).
[24] B. P. Anderson and M. A. Kasevich, Science **282**, 1686 (1998).
[25] B. P. Anderson, K. Dholakia, and E. M. Wright, Phys. Rev. A **67**, 033601 (2003).
[26] C. Zhang *et al.*, Phys. Rev. Lett. **92**, 054101 (2004).

PHYSICAL REVIEW A **70**, 062303 (2004)

Distinguishing between optical coherent states with imperfect detection

JM Geremia*
Physics and Control & Dynamical Systems, California Institute of Technology, Pasadena, California 91125, USA

(Received 26 July 2004; published 3 December 2004)

Several proposed techniques for distinguishing between optical coherent states are analyzed under a physically realistic model of photodetection. Quantum error probabilities are derived for the Kennedy receiver, the Dolinar receiver, and the unitary rotation scheme proposed by Sasaki and Hirota for subunity detector efficiency. Monte Carlo simulations are performed to assess the effects of detector dark counts, dead time, signal processing bandwidth, and phase noise in the communication channel. The feedback strategy employed by the Dolinar receiver is found to achieve the Helstrom bound for subunity detection efficiency and to provide robustness to these other detector imperfections making it more attractive for laboratory implementation than previously believed.

DOI: 10.1103/PhysRevA.70.062303 PACS number(s): 03.67.Hk, 03.65.Wj

I. INTRODUCTION

Communication is subject to quantum mechanical indeterminism even when the transmitted information is entirely classical. This potentially counterintuitive property results from the fact that information must be conveyed through a physical medium—a *communication channel*—that is unavoidably governed by quantum mechanics. From this perspective, the *sender* encodes information by preparing the channel into a well-defined quantum state $\hat{\rho}$ selected from a predetermined alphabet $\mathcal{A}\equiv\{\hat{\rho}_0,\ldots,\hat{\rho}_M\}$ of codewords. The *receiver*, following any relevant signal propagation, performs a measurement on the channel to ascertain which state was transmitted by the sender.

A quantum mechanical complication arises when the states in $\mathcal{A}$ are not orthogonal, as no measurement can distinguish between overlapping quantum states without some ambiguity [1–4]. This uncertainty in determining the channel state translates into a nonzero probability that the receiver will misinterpret the transmitted codeword and produce a communication error. While it would seem obvious that the sender should simply adopt an alphabet of orthogonal states, it is rarely practicable to communicate under such ideal conditions [5,6]. Even when it is possible for the sender to transmit orthogonal codewords, inevitable imperfections in the channel including decoherence and energy dissipation quickly damage that orthogonality. In some cases, the classical information capacity of a noisy channel is actually maximized by a nonorthogonal alphabet [7].

When developing a communication system to operate at the highest feasible rate given fixed channel properties and a constrained capability for state preparation, the objective is to minimize the communication error by designing a "good" receiver. Distinguishing between nonorthogonal states is a pervasive problem in quantum information theory [8,9] addressed mathematically by optimizing a state-determining measurement over all positive operator valued measures (POVMs) [3,10,11]. This general approach can be applied to communication; however, arbitrary POVMs are rarely straightforward to implement in the laboratory. Therefore, a "good" receiver must balance quantum mechanical optimality with implementability and robust performance under realistic experimental conditions.

For example, the optical field produced by a laser provides a convenient quantum system for carrying information. Of course, optical coherent states are not orthogonal and cannot be distinguished perfectly by photodetection. While the overlap between different coherent states can be reduced by employing large amplitudes, power limitations often restrict $\mathcal{A}$ to the small-amplitude regime where quantum effects dominate. This is especially true in situations (such as optical fibers) where the communication medium behaves nonlinearly at high power, as well as for long distance communication where signals are substantially attenuated, including deep space transmission.

Motivated by these experimental considerations, optimizing a communication process based on small-amplitude optical coherent states and photodetection has been an active subject since the advent of the laser [6,12–14]. Kennedy initially proposed a receiver based on simple photon counting to distinguish between two different coherent states [12]. However, the Kennedy receiver error probability lies above the quantum mechanical minimum [3] (or Helstrom bound) and this prompted Dolinar to devise a measurement scheme capable of achieving the quantum limit [13]. Dolinar's receiver, while still based on photon counting, approximates an optimal POVM by adding a local feedback signal to the channel; but, this procedure has often been deemed impractical [15] due to the need for real-time adjustment of the local signal following each photon arrival. As a result, Sasaki and Hirota later proposed an alternative receiver that applies an open-loop unitary transformation to the incoming coherent state signals to render them more distinguishable by simple photon counting [6,15,16].

However, recent experimental advances in real-time quantum-limited feedback control [17–19] suggest that the Dolinar receiver may be more experimentally practical than previously believed. The opinion that feedback should be avoided in designing an optical receiver is grounded in the now antiquated premise that real-time adaptive quantum

---

*Electronic mail: jgeremia@Caltech.EDU

©2004 The American Physical Society

measurements are technologically inaccessible. Most arguments in favor of passive devices have been based on idealized receiver models that assume, for example, perfect photon counting efficiency. A fair comparison between open- and closed-loop receivers should take detection error into account—feedback generally increases the robustness of the measurement device in exchange for the added complexity.

Here, we consider the relative performance of the Kennedy, Dolinar, and Sasaki-Hirota receivers under *realistic* experimental conditions that include (1) subunity quantum efficiency, where it is possible for the detector to miscount incoming photons, (2) nonzero dark counts, where the detector can register photons even in the absence of a signal, (3) nonzero dead time, or finite detector recovery time after registering a photon arrival, (4) finite bandwidth of any signal processing necessary to implement the detector, and (5) fluctuations in the phase of the incoming optical signal.

II. BINARY COHERENT STATE COMMUNICATION

An optical binary communication protocol can be implemented via the alphabet consisting of two pure coherent states $\hat{\rho}_0 = |\Psi_0\rangle\langle\Psi_0|$ and $\hat{\rho}_1 = |\Psi_1\rangle\langle\Psi_1|$. Without loss of generality, we will assume that logical 0 is represented by the vacuum,

$$\Psi_0(t) = 0, \tag{1}$$

and that logical 1 is represented by

$$\Psi_1(t) = \psi_1(t) exp[-i(\omega t + \varphi)] + \text{c.c.}, \tag{2}$$

where ω is the frequency of the optical carrier and φ is (ideally) a fixed phase. The envelope function $\psi_1(t)$ is normalized such that

$$\int_0^T |\psi_1(t)|^2 dt = \overline{N}, \tag{3}$$

where $\overline{N}$ is the mean number of photons to arrive at the receiver during the measurement interval $0 \leqslant t \leqslant T$. That is, $\hbar\omega|\psi_1(t)|^2$ is the instantaneous average power of the optical signal for logical 1.

This alphabet $\mathcal{A} = \{\hat{\rho}_0, \hat{\rho}_1\}$ is applicable to both amplitude and phase-shift keyed communication protocols as it is always possible to transform between the two by combining the incoming signal with an appropriate local oscillator. That is, amplitude keying with $\mathcal{A} = \{|0\rangle, |\alpha\rangle\}$ (for some coherent state $|\alpha\rangle$ with amplitude α) is equivalent to the phase-shift keyed alphabet $\{|-\frac{1}{2}\alpha\rangle, |\frac{1}{2}\alpha\rangle\}$ via a displacement, $\hat{D}[-\frac{1}{2}\alpha] \equiv exp[-\frac{1}{2}(\alpha\hat{a}^\dagger - \alpha^*\hat{a})]$, where $\hat{a}^\dagger$ and $\hat{a}$ are the creation and annihilation operators for the channel mode. Similarly, if $|\Psi_0\rangle \neq |0\rangle$, a simple displacement can be used to restore $|\Psi_0\rangle$ to the vacuum state.

A. The quantum error probability

The coherent states $\hat{\rho}_0$ and $\hat{\rho}_1$ are not orthogonal, so it is impossible for a receiver to identify the transmitted state without sometimes making a mistake. That is, the receiver attempts to ascertain which state was transmitted by performing a quantum measurement, Υ, on the channel. Υ is described by an appropriate POVM represented by a complete set of positive operators [20],

$$\sum_n \hat{\Upsilon}_n = \hat{\mathbb{1}}, \quad \hat{\Upsilon}_n \geqslant 0, \tag{4}$$

where n indexes the possible measurement outcomes. For binary communication, it is always possible (and optimal) for the receiver to implement the measurement as a decision between two hypotheses: (H_0), that the transmitted state is $\hat{\rho}_0$, selected when the measurement outcome corresponds to $\hat{\Upsilon}_0$, and (H_1), that the transmitted state is $\hat{\rho}_1$, selected when the measurement outcome corresponds to $\hat{\Upsilon}_1$.

Given the positive operators, $\hat{\Upsilon}_0 + \hat{\Upsilon}_1 = \hat{\mathbb{1}}$, there is some chance that the receiver will select the null hypothesis H_0 when $\hat{\rho}_1$ is actually present,

$$p(H_0|\hat{\rho}_1) = \text{tr}[\hat{\Upsilon}_0\hat{\rho}_1] = \text{tr}[(\hat{\mathbb{1}} - \hat{\Upsilon}_1)\hat{\rho}_1], \tag{5}$$

and it will sometimes select H_1 when $\hat{\rho}_0$ is present,

$$p(H_1|\hat{\rho}_0) = \text{tr}[\hat{\Upsilon}_1\hat{\rho}_0]. \tag{6}$$

The total receiver error probability depends upon the choice of $\hat{\Upsilon}_0$ and $\hat{\Upsilon}_1$ and is given by

$$p[\hat{\Upsilon}_0, \hat{\Upsilon}_1] = \xi_0 p(H_1|\hat{\rho}_0) + \xi_1 p(H_0|\hat{\rho}_1). \tag{7}$$

Here, $\xi_0 = p_0(\hat{\rho}_0)$ and $\xi_1 = p_0(\hat{\rho}_1)$ are the probabilities that the sender will transmit $\hat{\rho}_0$ and $\hat{\rho}_1$ respectively; they reflect the prior knowledge that enters into the hypothesis testing process implemented by the receiver, and in many cases $\xi_0 = \xi_1 = 1/2$.

Minimizing the receiver measurement over POVMs (over $\hat{\Upsilon}_0$ and $\hat{\Upsilon}_1$) leads to a quantity known as the *quantum error probability*,

$$P_H \equiv \min_{\hat{\Upsilon}_0, \hat{\Upsilon}_1} p[\hat{\Upsilon}_0, \hat{\Upsilon}_1], \tag{8}$$

also referred to as the Helstrom bound. P_H is the smallest physically allowable error probability, given the overlap between $\hat{\rho}_0$ and $\hat{\rho}_1$.

The Helstrom bound

Helstrom demonstrated that minimizing the receiver error probability

$$p[\hat{\Upsilon}_0, \hat{\Upsilon}_1] = \xi_0 \text{tr}[\hat{\Upsilon}_1\hat{\rho}_0] + \xi_1 \text{tr}[(\hat{\mathbb{1}} - \hat{\Upsilon}_1)\hat{\rho}_1] \tag{9}$$

$$= \xi_1 + \text{tr}[\hat{\Upsilon}_1(\xi_0\hat{\rho}_0 - \xi_1\hat{\rho}_1)] \tag{10}$$

is accomplished by optimizing

$$\min_{\hat{\Upsilon}_1} \text{tr}[\hat{\Upsilon}_1\hat{\Gamma}], \quad \hat{\Gamma} = \xi_0\hat{\rho}_0 - \xi_1\hat{\rho}_1, \tag{11}$$

over $\hat{\Upsilon}_1$ subject to $0 \leqslant \hat{\Upsilon}_1 \leqslant \hat{\mathbb{1}}$ [3]. Given the spectral decomposition

$$\hat{\Gamma} = \sum_n \lambda_n |n\rangle\langle n|, \qquad (12)$$

where the λ_n are the eigenvalues of $\hat{\Gamma}$, the resulting Helstrom bound can be expressed as [21]

$$P_H = \xi_1 + \sum_{\lambda_n < 0} \lambda_n. \qquad (13)$$

For pure states, where $\hat{\rho}_0 = |\Psi_0\rangle\langle\Psi_0|$ and $\hat{\rho}_1 = |\Psi_1\rangle\langle\Psi_1|$, $\hat{\Gamma}$ has two eigenvalues of which only one is negative,

$$\lambda_- = \frac{1}{2}\left(1 - \sqrt{1 - 4\xi_0\xi_1|\langle\Psi_0|\Psi_1\rangle|^2}\right) - \xi_1 > 0, \qquad (14)$$

and the quantum error probability is therefore [3]

$$P_H = \frac{1}{2}\left(1 - \sqrt{1 - 4\xi_0\xi_1|\langle\Psi_1|\Psi_0\rangle|^2}\right). \qquad (15)$$

The Helstrom bound is readily evaluated for coherent states by employing the relation [22]

$$|\alpha\rangle = e^{-|\alpha|^2/2}\sum_{n=0}^{\infty}\frac{\alpha^n}{\sqrt{n!}}|n\rangle, \qquad (16)$$

to compute the overlap between $|\Psi_1\rangle$ and $|\Psi_0\rangle$ [3,22],

$$c_0 \equiv \langle\Psi_1|\Psi_0\rangle = e^{-\bar{N}/2}. \qquad (17)$$

It is further possible to evaluate the Helstrom bound for imperfect detection. Coherent states have the convenient property that subunity quantum efficiency is equivalent to an ideal detector masked by a beam splitter with transmission coefficient $\eta \leqslant 1$, to give

$$P_H(\eta) = \frac{1}{2}\left(1 - \sqrt{1 - 4\xi_0\xi_1 c_0^{2\eta}}\right). \qquad (18)$$

This result and Eq. (15) indicate that there is a finite quantum error probability for all choices of $|\Psi_1\rangle$, even when an optimal measurement is performed.

B. The Kennedy receiver

Kennedy proposed a near-optimal receiver that simply counts the number of photon arrivals registered by the detector between $t=0$ and T. It decides in favor of H_0 when the number of clicks is zero, otherwise H_1 is chosen. This hypothesis testing procedure corresponds to the measurement operators

$$\hat{\Upsilon}_0 = |0\rangle\langle 0|, \qquad (19)$$

$$\hat{\Upsilon}_1 = \sum_{n=1}^{\infty} |n\rangle\langle n|, \qquad (20)$$

where $|n\rangle$ are the eigenvectors of the number operator $\hat{N} = \hat{a}^\dagger\hat{a}$.

The Kennedy receiver has the property that it always correctly selects H_0 when the channel is in $\hat{\rho}_0$, since the photon counter will never register photons when the vacuum state is present (ignoring background light and detector dark counts for now). Therefore, $p(H_1|\hat{\rho}_0) = 0$; however,

$$p(H_0|\hat{\rho}_1) \equiv \mathrm{tr}[\hat{\Upsilon}_0\hat{\rho}_1] = |\langle 0|\Psi_1\rangle|^2 \qquad (21)$$

is nonzero due to the finite overlap of all coherent states with the vacuum. The Poisson statistics of coherent state photon numbers allows for the possibility that zero photons will be recorded even when $\hat{\rho}_1$ is present.

Furthermore, an imperfect detector can misdiagnose $\hat{\rho}_1$ if it fails to generate clicks for photons that do arrive at the detector. The probability for successfully choosing H_1 when $\hat{\rho}_1$ is present is given by

$$p_\eta(H_1|\hat{\rho}_1) = \sum_{n=1}^{\infty}\sum_{k=1}^{\infty} p(n,k)|\langle n|\alpha\rangle|^2 \qquad (22)$$

where the Bernoulli distribution

$$p(n,k) = \frac{n!}{k!\,(n-k)!}\eta^k(1-\eta)^{n-k} \qquad (23)$$

gives the probability that a detector with quantum efficiency η will register k clicks when the actual number of photons is n. The resulting Kennedy receiver error

$$P_K(\eta) = 1 - p_\eta(H_1|\hat{\rho}_1) = \xi_1 c_0^{2\eta} \qquad (24)$$

asymptotically approaches the Helstrom bound for large signal amplitudes, but is larger for small photon numbers.

C. The Sasaki-Hirota receiver

Sasaki and Hirota proposed that it would be possible to achieve the Helstrom bound using simple photon counting by applying a unitary transformation to the incoming signal states prior to detection [6,15,16]. They considered rotations

$$\hat{U}[\theta] = \exp[\theta(|\Psi_0'\rangle\langle\Psi_1'| - |\Psi_1'\rangle\langle\Psi_0'|)], \qquad (25)$$

generated by the transformed alphabet $\mathcal{A}'$,

$$|\Psi_0'\rangle = |\Psi_0\rangle, \quad |\Psi_1'\rangle = \frac{|\Psi_1\rangle - c_0|\Psi_0\rangle}{\sqrt{1-c_0^2}}, \qquad (26)$$

obtained from Gram-Schmidt orthogalization of $\mathcal{A}$. The rotation angle $\theta \in \mathbb{R}$ is a parameter that must be optimized in order to achieve the Helstrom bound.

Application of $\hat{U}[\theta]$ on the incoming signal states (which belong to the original alphabet, $\mathcal{A}$) leads to the transformed states

$$\hat{U}[\theta]|\Psi_0\rangle = \left(\cos\,\theta + \frac{c_0\sin\,\theta}{\sqrt{1-c_0^2}}\right)|\Psi_0\rangle - \frac{\sin\,\theta}{\sqrt{1-c_0^2}}|\Psi_1\rangle \qquad (27)$$

and

$$\hat{U}[\theta]|\Psi_1\rangle = \frac{\sin\,\theta}{\sqrt{1-c_0^2}}|\Psi_0\rangle + \frac{\cos\,\theta\sqrt{1-c_0^2} - c_0\sin\,\theta}{\sqrt{1-c_0^2}}|\Psi_1\rangle. \qquad (28)$$

Since $|\Psi_0'\rangle$ is the vacuum state, hypothesis testing can still be performed by simple photon counting. However, unlike the Kennedy receiver, it is possible to misdiagnose $\hat{\rho}_0$ since $\hat{U}[\theta]|\Psi_0\rangle$ contains a nonzero contribution from $|\Psi_1\rangle$. The probability for a false-positive detection by a photon counter with efficiency, η, is given by

$$p_\eta^\theta(H_1|\hat{\rho}_0) = \sum_{n=1}^{\infty}\sum_{k=1}^{\infty} p(n,k)|\langle n|\hat{U}[\theta]|\Psi_0\rangle|^2 \tag{29}$$

$$= \frac{c_0^{2\eta}-1}{c_0^2-1}\sin^2\theta, \tag{30}$$

which is evaluated by recognizing that

$$\langle n|\hat{U}[\theta]|\Psi_0\rangle = \left[\cos\theta + \frac{c_0\sin\theta}{\sqrt{1-c_0^2}}\right]\delta_{n,0} - \frac{c_0\alpha^n\sin\theta}{\sqrt{n!\,(1-c_0^2)}}, \tag{31}$$

where α is the (complex) amplitude of $|\Psi_1\rangle$. The probability for correct detection can be similarly obtained to give

$$p_\eta^\theta(H_1|\hat{\rho}_1) = \sum_{n=1}^{\infty}\sum_{k=1}^{\infty} p(n,k)|\langle n|\hat{U}[\theta]|\Psi_1\rangle \tag{32}$$

$$= \frac{c_0^{2\eta}-1}{c_0^2-1}\left[c_0\sin\theta - \sqrt{1-c_0^2}\cos\theta\right]^2 \tag{33}$$

by employing the relationship

$$\langle n|\hat{U}[\theta]|\Psi_1\rangle = \left[c_0\cos\theta - \frac{c_0^2\alpha^n\sin\theta}{\sqrt{n!\,(1-c_0^2)}}\right] + \frac{\sin\theta}{\sqrt{1-c_0^2}}\delta_{n,0}. \tag{34}$$

The total Sasaki-Hirota receiver error is given by the weighted sum

$$P_{\mathrm{SH}}(\eta,\theta) = \xi_0 p_\eta^\theta(H_1|\hat{\rho}_0) + \xi_1[1 - p_\eta^\theta(H_1|\hat{\rho}_1)] \tag{35}$$

and can be minimized over $\theta \in \mathbb{R}$ to give

$$\theta = -\tan^{-1}\sqrt{\frac{\sqrt{1-4\xi_0\xi_1c_0^2}-1+2\xi_1c_0^2}{\sqrt{1-4\xi_0\xi_1c_0^2}+1-2\xi_1c_0^2}}. \tag{36}$$

For perfect detection efficiency, $\eta=1$, Eq. (35) is equivalent to the Helstrom bound; however, for $\eta<1$, it is larger.

D. The Dolinar receiver

The Dolinar receiver takes a different approach to achieving the Helstrom bound with a photon counting detector; it utilizes an adaptive strategy to implement a feedback approximation to the Helstrom POVM [13,23]. Dolinar's receiver operates by combining the incoming signal $\Psi(t)$ with a separate local signal,

$$U(t) = u(t)\exp[-i(\omega t + \phi)] + \text{c.c.}, \tag{37}$$

such that the detector counts photons with total instantaneous mean rate

$$\Phi(t) = |\psi(t) + u(t)|^2. \tag{38}$$

Here, $\psi(t)=0$ when the channel is in the state $\hat{\rho}_0$, and $\psi(t)=\psi_1(t)$ when the channel is in $\hat{\rho}_1$ [refer to Eqs. (1) and (2)].

The receiver decides between hypotheses H_0 and H_1 by selecting the one that is more consistent with the record of photon arrival times observed by the detector given the choice of $u(t)$. H_1 is selected when the ratio of conditional arrival time probabilities,

$$\Lambda = \frac{p_\eta[\hat{\rho}_1|t_1,\ldots,t_n,u(t)]}{p_\eta[\hat{\rho}_0|t_1,\ldots,t_n,u(t)]}, \tag{39}$$

is greater than 1; otherwise it is assumed that $\hat{\rho}_0$ was transmitted. The conditional probabilities $p_\eta[\hat{\rho}_i|t_1,\ldots,t_n,u(t)]$ reflect the likelihood that n photon arrivals occur precisely at the times $\{t_1,\ldots,t_n\}$, given that the channel is in the state $\hat{\rho}_i$, the feedback amplitude is $u(t)$, and the detector quantum efficiency is η.

We see that this decision criterion based on Λ is immediately related to the error probabilities

$$\Lambda = \frac{p_\eta[H_1|\hat{\rho}_1,u(t)]}{p_\eta[H_1|\hat{\rho}_0,u(t)]} = \frac{1-p_\eta[H_0|\hat{\rho}_1,u(t)]}{p_\eta[H_1|\hat{\rho}_0,u(t)]} \tag{40}$$

when $\Lambda>1$ (i.e., the receiver definitely selects H_1), and

$$\Lambda = \frac{p_\eta[H_0|\hat{\rho}_1,u(t)]}{p_\eta[H_0|\hat{\rho}_0,u(t)]} = \frac{p_\eta[H_0|\hat{\rho}_1,u(t)]}{1-p_\eta[H_1|\hat{\rho}_0,u(t)]} \tag{41}$$

when $\Lambda<1$ (i.e., the receiver definitely selects H_0). Similarly, the likelihood ratio Λ can be reexpressed in terms of the photon counting distributions frequently encountered in quantum optics by employing Bayes' rule,

$$\Lambda = \frac{p_\eta[t_1,\ldots,t_n|\hat{\rho}_1,u(t)]p_0(\hat{\rho}_1)}{p_\eta[t_1,\ldots,t_n|\hat{\rho}_0,u(t)]p_0(\hat{\rho}_0)} \tag{42}$$

$$= \frac{\xi_1}{\xi_0}\frac{p_\eta[t_1,\ldots,t_n|\hat{\rho}_1,u(t)]}{p_\eta[t_1,\ldots,t_n|\hat{\rho}_0,u(t)]}, \tag{43}$$

where the $p_\eta[t_1,\ldots,t_n|\hat{\rho}_i,u(t)]$ are the exclusive counting densities

$$p_\eta[t_1,\ldots,t_n|\hat{\rho}_i,u(t)] = \prod_{k=1}^{n+1} w_\eta[t_k|\hat{\rho}_i,u(t)]. \tag{44}$$

Here, $t_0=0$, $t_{n+1}=T$, and $w_\eta[t_k|\hat{\rho}_i,u(t)]$ is the exponential waiting time distribution

$$w[t_k|\hat{\rho}_i,u(t)] = \eta\Phi(t_k)\exp\left(-\eta\int_{t_{k-1}}^{k}\Phi(t')dt'\right) \tag{45}$$

for optical coherent states, or the probability that a photon will arrive at time t_k and that it will be the only click during the half-closed interval $(t_{k-1},t_k]$ [22].

1. Optimal control problem

The Dolinar receiver error probability

$$P_D[u(t)] = \xi_0 p_\eta[H_1|\hat{\rho}_0, u(t)] + \xi_1 p_\eta[H_0|\hat{\rho}_1, u(t)] \tag{46}$$

depends upon the amplitude of the locally applied feedback field, so the objective is to minimize P_D over $u(t)$. This optimization can be accomplished [23] via the technique of dynamic programming [24], where we adopt an effective state-space picture given by the conditional error probabilities

$$\mathbf{p}(t) = \begin{pmatrix} p_\eta[H_1|\hat{\rho}_0, u(t)](t) \\ p_\eta[H_0|\hat{\rho}_1, u(t)](t) \end{pmatrix} \tag{47}$$

and define the control cost as

$$\mathcal{J}[u(t)] \equiv P_D[u(t)] = \xi^{\mathrm{T}}\mathbf{p}. \tag{48}$$

The optimal control policy $u^*(t)$ is identified by solving the Hamilton-Jacobi-Bellman equation

$$\min_{u(t)}\left[\frac{\partial}{\partial t}\mathcal{J}[u(t)] + \boldsymbol{\nabla}_{\mathbf{p}}\mathcal{J}[u(t)]^{\mathrm{T}}\frac{\partial}{\partial t}\mathbf{p}(t)\right] = 0, \tag{49}$$

which is a partial differential equation for $\mathcal{J}$ based on the requirement that $\mathbf{p}(t)$ and $u(t)$ are smooth (continuous and differentiable) throughout the entire receiver operation. However, like all quantum point processes, our conditional knowledge of the system state evolves smoothly only *between* photon arrivals.

When a click is recorded by the detector, the system probabilities $\mathbf{p}$ can jump in a nonsmooth manner. Therefore, the photon arrival times divide the measurement interval $0 \leqslant t \leqslant T$ into segments that are only piecewise continuous and differentiable. Fortunately, the dynamic programming *optimality principle* [24] allows us to optimize $u(t)$ in a piecewise manner that begins by minimizing $\mathcal{J}[u(t)]$ on the final segment $[t_n, T]$. Of course, the system state at the beginning of this segment $\mathbf{p}(t_n)$ depends upon the detection history at earlier times and therefore the choice of $u(t)$ in earlier intervals. As such, the Hamilton-Jacobi-Bellman optimization for the final segment must hold for all possible starting states $\mathbf{p}(t_n) \in \mathbb{R}^2_{[0,1]}$. Once this is accomplished, $u(t)$ can be optimized on the preceding segment $[t_{n-1}, t_n)$ with the assurance that any final state for that segment will be optimally controlled on the next interval $[t_n, T]$. This procedure is iterated in reverse order for all of the measurement segments until the first interval $t=[0, t_1)$, where the initial value $\mathbf{p}(0) = (1 \quad 0)^{\mathrm{T}}$ can be unambiguously specified.

Solving the Hamilton-Jacobi-Bellman equation in each smooth segment between photon arrivals requires the time derivatives $\dot{\mathbf{p}}(t)$ which assume a different form when $\Lambda > 1$ versus when $\Lambda < 1$. Using Eqs. (40) and (41), the coherent state waiting time distribution, and

$$\Phi(t) \equiv \begin{pmatrix} \Phi_0(t) \\ \Phi_1(t) \end{pmatrix} = \begin{pmatrix} u(t) \\ u(t) + \psi_1(t) \end{pmatrix}, \tag{50}$$

we see that the smooth evolution of $\mathbf{p}(t)$ between photon arrivals is given by

$$\dot{p}_0(t) = \eta p_0(t)\left[\frac{d}{dt}\ln\Phi_0(t) - \Phi_0(t)\right],$$

$$\dot{p}_1(t) = \eta p_1(t)\left[\Phi_1(t) - \frac{d}{dt}\ln\Phi_1(t)\right] \tag{51}$$

when $\Lambda > 1$ and

$$\dot{p}_0(t) = \eta p_0(t)\left[\Phi_0(t) - \frac{d}{dt}\ln\Phi_0(t)\right],$$

$$\dot{p}_1(t) = \eta p_1(t)\left[\frac{d}{dt}\ln\Phi_1(t) - \Phi_1(t)\right] \tag{52}$$

when $\Lambda < 1$.

Performing the piecewise minimization in Eq. (49) over each measurement segment with initial states provided by the iterative point-process probabilities in Eq. (44) and combining the intervals (this is straightforward but eraser demanding) leads to the control policy

$$u_1^*(t) = -\psi_1(t)\left(1 + \frac{\mathcal{J}[u_1^*(t)]}{1 - 2\mathcal{J}[u_1^*(t)]}\right) \tag{53}$$

for $\Lambda > 1$, where $p_\eta[H_0|\hat{\rho}_1, u_1^*(t)] = 0$ and

$$\mathcal{J}[u_1^*(t)] = \xi_1 p_\eta[H_1|\hat{\rho}_0, u_1^*(t)] = \frac{1}{2}\left(1 - \sqrt{1 - 4\xi_0\xi_1 e^{-\eta\overline{n}(t)}}\right). \tag{54}$$

Here, $\overline{n}(t)$ represents the average number of photons expected to arrive at the detector by time t when the channel is in the state $\hat{\rho}_1$,

$$\overline{n}(t) = \int_0^t |\psi_1(t')|^2 dt'. \tag{55}$$

Conversely, the optimal control takes the form

$$u_0^*(t) = \psi_1(t)\left(\frac{\mathcal{J}[u_0^*(t)]}{1 - 2\mathcal{J}[u_0^*(t)]}\right) \tag{56}$$

for $\Lambda < 1$, where $p_\eta[H_1|\hat{\rho}_0, u_0^*(t)] = 0$ and

$$\mathcal{J}[u_0^*(t)] = \xi_1 p_\eta[H_0|\hat{\rho}_1, u_0^*(t)] = \frac{1}{2}\left(1 - \sqrt{1 - 4\xi_0\xi_1 e^{-\eta\overline{n}(t)}}\right). \tag{57}$$

2. Dolinar hypothesis testing procedure

The Hamilton-Jacobi-Bellman solution leads to a conceptually simple procedure for estimating the state of the channel. The receiver begins at $t=0$ by favoring the hypothesis that is more likely based on the prior probabilities $p_0(0) = \xi_0$ and $p_1(0) = \xi_1$.[1] Assuming that $\xi_1 \geqslant \xi_0$ (for $\xi_0 > \xi_0$, the opposite reasoning applies), the Dolinar receiver always selects H_1 during the initial measurement segment. The probability of deciding on H_0 is exactly zero prior to the first photon arrival such that an error only occurs when the channel is actually in $\hat{\rho}_0$.

---

[1] If $\xi_0 = \xi_1$, then neither hypothesis is *a priori* favored and the Dolinar receiver is singular with $P_D = 1/2$.

To see what happens when a photon does arrive at the detector, it is necessary to investigate the behavior of $\Lambda(t)$ at the boundary between two measurement segments. Substituting the optimal control policy $u^*(t)$, which alternates between $u_1^*(t)$ and $u_0^*(t)$, into the photon counting distribution leads to

$$\begin{aligned} p(t_1, \ldots, t_n | \hat{\rho}_i) = \eta^n \prod_{k=0}^{n+1} \Phi_i[u_{k|2}(0,t_1)] \\ \times \exp\biggl(-\eta \int_0^{t_1} \Phi_i[u_1(t'_{k-1},t'_k)] dt' \\ - \cdots - \eta \int_{t_n}^{T} \Phi_i[u_{n|2}(t'_n, T')] dt' \biggr). \quad (58) \end{aligned}$$

This expression can be used to show that the limit of $\Lambda(t)$ approaching a photon arrival time t_k from the left is the reciprocal of the limit approaching from the right,

$$\lim_{t \to t_k^-} \Lambda(t) = \left[\lim_{t \to t_k^+} \Lambda(t) \right]^{-1}. \quad (59)$$

That is, if $\Lambda > 1$ such that H_1 is favored during the measurement interval ending at t_k, the receiver immediately swaps its decision to favor H_0 when the photon arrives. Evidently, the optimal control policy $u^*(t)$ engineers the feedback such that the photon counter is least likely to observe additional clicks if it is correct based on its best knowledge of the channel state at that time. Each photon arrival invalidates the current hypothesis and the receiver completely reverses its decision on every click. This result implies that H_1 is selected when the number of photons n is even (or zero) and H_0 when the number of photons is odd.

Despite the discontinuities in the conditional probabilities $p_\eta[H_1|\hat{\rho}_0, u^*(t)]$ and $p_\eta[H_0|\hat{\rho}_1, u^*(t)]$ at the measurement segment boundaries, the total Dolinar receiver error probability

$$P_D(\eta,t) = \frac{1}{2}\left(1 - \sqrt{1 - \xi_0\xi_1 e^{-\eta\overline{n(t)}}}\right) \quad (60)$$

evolves smoothly since

$$\lim_{t \to t_k^-} \mathcal{J}[u^*(t)] = \lim_{t \to t_k^+} \mathcal{J}[u^*(t)] \quad (61)$$

at the boundaries. Recognizing that $\overline{n(t)} = \overline{N}$ leads to the final Dolinar receiver error

$$P_D(\eta) = \frac{1}{2}\left(1 - \sqrt{1 - 4\xi_0\xi_1 c_0^{2\eta}}\right), \quad (62)$$

which is equal to the Helstrom bound for all values of the detector efficiency $0 < \eta \leqslant 1$.

III. SIMULATIONS

Monte Carlo simulations of the Kennedy, Sasaki-Hirota, and Dolinar receivers were performed to verify the above quantum efficiency analysis and to analyze the effects of additional detector imperfections. Figure 1 shows benchmark simulation results for perfect photodetection. The three receivers perform as expected in the small-amplitude regime; both the Sasaki-Hirota and Dolinar protocols achieve the Helstrom bound while the Kennedy receiver is approximately a factor of 2 worse, at the shot-noise limit.[2] Statistics were accumulated for 10 000 Monte Carlo samples in which $\hat{\rho}_0$ and $\hat{\rho}_1$ were randomly selected with $\xi_0 = \xi_1 = 1/2$.

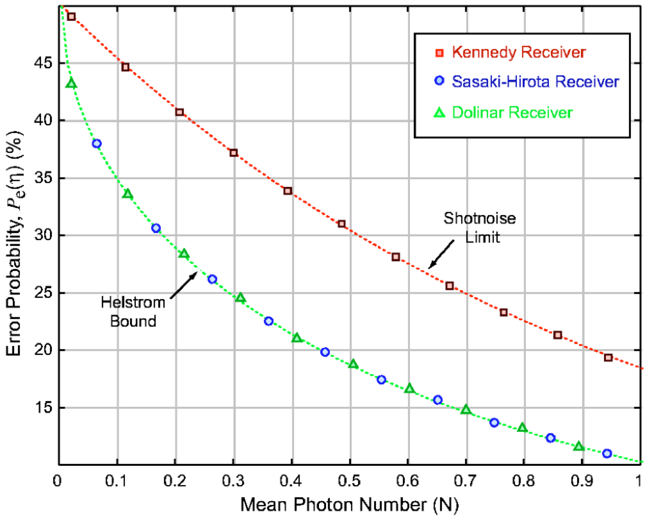

FIG. 1. Monte Carlo simulation of the Kennedy, Dolinar, and Sasaki-Hirota receivers as a function of the signal amplitude for perfect photon counting with $\xi_0 = \xi_1 = 1/2$. As expected, the Dolinar and Sasaki-Hirota protocols both achieve the Helstrom bound while the Kennedy receiver is approximately a factor of 2 worse.

Detector imperfections, however, will degrade the performance of each of the three receivers, and here we investigate the relative degree of that degradation for conditions to be expected in practice. The analysis is based on the observation that single photon counting in optical communications is often implemented with an avalanche photodiode (APD), as APDs generally provide the highest detection efficiencies. In the near infrared, for example, high-gain silicon diodes provide a quantum efficiency of $\eta \sim 50\%$. Additional APD nonidealities include a dead time following each detected photon during which the receiver is unresponsive, dark counts in the absence of incoming photons due to spontaneous breakdown events in the detector medium, a maximum count rate above which the detector saturates (and can be damaged), and occasional ghost clicks following a real photon arrival—a process referred to as "after pulsing." For the Dolinar receiver, which requires high-speed signal processing and actuation in order to modulate the adaptive feedback field, delays must also be considered. That is, the optical modulators used to adjust the phase and amplitude of the feedback signal as well as the digital signal processing technology necessary [25] for implementing all real-time computations display finite bandwidths.

---

[2] In some contexts, Eq. (24) is referred to as the *standard quantum limit* despite the fact that there is no measurement back action as $\hat{a}|\alpha\rangle = \alpha|\alpha\rangle$. We prefer the term *shot-noise limit* in order to avoid such confusion.

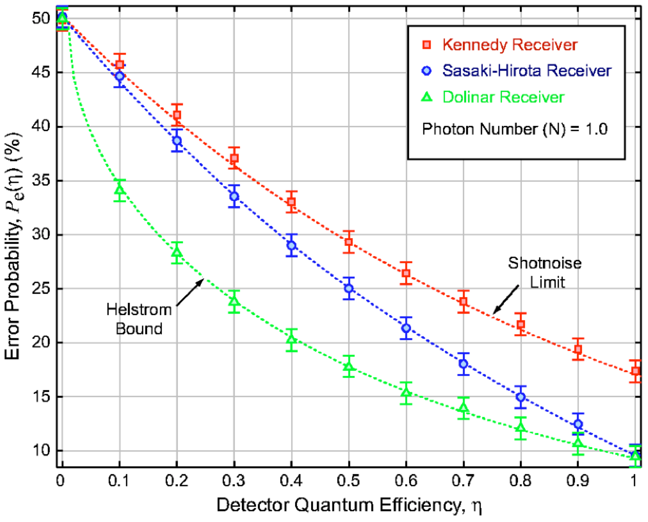

FIG. 2. Performance of the Kennedy, Sasaki-Hirota, and Dolinar receivers as a function of the detector quantum efficiency η. The simulations were performed for $\xi_0 = \xi_1 = 1/2$ and data points reflect the result of Monte Carlo simulations of the three receivers. Dotted lines correspond to the analytic results derived in Sec. II and illustrate that the Dolinar receiver achieves the Helstrom bound even for subunity quantum efficiency.

Figure 2 compares the error probabilities of the three receivers for subunity quantum efficiency but otherwise ideal detection. The mean photon number of the signal, $\Psi_1(t)$, in this simulation is $\bar{N}=1$ with $\Psi_0(t)=0$ and $\xi_0=\xi_1=1/2$. Data points in the figure were generated by accumulating statistics for 10 000 Monte Carlo simulations of the three receivers, and the dotted lines correspond to the error probabilities derived in Sec. II. The simulations agree well with the analytic expressions and it is evident that the Dolinar receiver is capable of achieving the Helstrom bound for $\eta < 1$ while the Sasaki-Hirota receiver performance lies between that of the Kennedy and Dolinar receivers.

Figure 3 compares the error probabilities for the three receivers with the additional detector and feedback nonidealities taken into account. Based on the performance data of the Perkin-Elmer SPCM-AQR-13 Si APD single photon counting module, we assumed a maximum count rate of 10^7 photons/s, a detector dead time of 50 ns, a dark count rate of 250 clicks/s, and an after-pulsing probability of 1%. For the Dolinar receiver, it was assumed that there was a 100 ns feedback delay resulting from a combination of digital processing time and amplitude/phase modulator bandwidth. The data points in Fig. 3 correspond to the error probabilities generated from 10 000 Monte Carlo simulations with $\xi_0=\xi_1=1/2$. The lower dotted line indicates the appropriate Helstrom bound as a function of the mean photon number $\bar{N}$ for a detector with quantum efficiency $\eta=0.5$, and the upper curve indicates the analogous Kennedy receiver error. Evidentally, technical imperfections can have a large negative effect on the performance of passive detection protocols like the Kennedy and Sasaki-Hirota receivers while the Dolinar receiver is more robust.

Unlike open-loop procedures, however, the feedback nature of the Dolinar receiver additionally requires precise knowledge of the incoming signal phase φ, so that $U^*(t)$ can be properly applied. Fluctuations in the index of refraction of the communication medium generally lead to some degree of phase noise in the incoming signal $\Psi(t)$. Adequately setting the phase of $U(t)$ necessarily requires that some light from the channel be used for phase-locking the local oscillator—a task that reduces the data transmission bandwidth. Therefore, operating a communication system based on the Dolinar receiver at the highest feasible rate requires that the number of photons diverted from the data stream to track phase variations in the channel be minimized. This optimization in turn requires knowledge of how signal phase noise propagates into the receiver error probability.

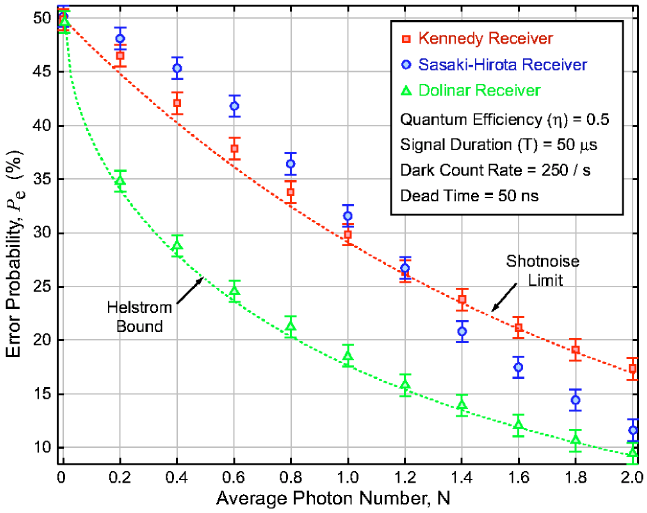

FIG. 3. Performance of the Kennedy, Sasaki-Hirota, and Dolinar receivers as a function of the mean number of photons in the signal under realistic experimental conditions, including a quantum efficiency of 50%, a dark-count rate of 250 clicks/s, an after-pulsing probability of 1%, and feedback delays of 100 ns.

Figure 4 shows the error probability $P_D(\delta\varphi)$ as a function of the phase difference $\delta\varphi$ between the incoming signal and the local oscillator. Data points correspond to results from 10 000 Monte Carlo simulations per photon number and phase angle, and the solid curves reflect numerical fits to the Monte Carlo points. An exact comparison between the open-loop and Dolinar receivers requires information regarding the specific phase-error density function for the actual communication channel being utilized. However, we do note that at $\bar{N}=1$ photon, the phase of the local oscillator could be as large as $\delta\varphi \sim 25°$ before its error probability increased to that of the Kennedy receiver. Additionally, it appears that the slope of $P_D(\delta\varphi)$ is zero at $\delta\varphi=0$ which implies that the Dolinar receiver conveniently displays minimal sensitivity to small phase fluctuations in the channel.

IV. DISCUSSION AND CONCLUSIONS

The Dolinar receiver was found to be robust to the types of detector imperfections likely to exist in any real implementation of a binary communication scheme based on optical coherent state signaling and photon counting. This ro-

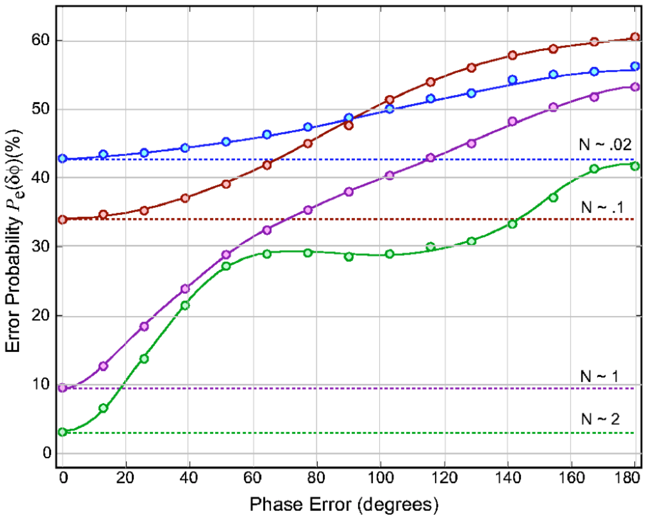

FIG. 4. Error probabilities for the Dolinar receiver as a function of the phase error in the signal state corresponding to logical 1 for different mean photon numbers. Monte Carlo data points were generated by accumulating statistics for 10 000 random bits. Solid lines are a fit to the data.

bustness seemingly results from the fact that the Dolinar receiver can correct itself after events that cause an open-loop receiver to irreversibly misdiagnose the transmitted state. For example, imperfect detection efficiency introduces a failure mode where the probability $p(H_0|\hat{\rho}_1)$ is increased above the value set by quantum mechanical vacuum fluctuations. However, the optimal structure of the Dolinar receiver feedback insures that it still achieves the quantum mechanical minimum because it has control over the counting rate. That is, if the Dolinar receiver selects the wrong hypothesis at some intermediate time $t_k < T$, the structure of the feedback ensures that the receiver achieves the highest allowable probability for invalidating that incorrect decision during the remainder of the measurement $t_k < t \leq T$.

In the opposite situation, where dark counts or background light produce detector clicks when there is no signal light in the channel, open-loop receivers will decide in favor of $\hat{\rho}_1$ without any possibility for self-correction. This type of error leads to an irreparable open-loop increase in $p(H_1|\hat{\rho}_0)$. But the Dolinar receiver has the potential to identify and fix such a mistake since selecting the wrong hypothesis at intermediate times increases the probability that a future click will invalidate the incorrect decision. When background light is present, poor phase coherence between stray optical fields and the signal provides no enhanced open-loop discrimination as there is no local oscillator to establish a phase reference; a received photon is a received photon (assuming that any spectral filtering failed to prevent the light from hitting the detector). The Dolinar receiver is better immune to such an error since incoherent addition of the stray field to the local oscillator will generally reduce the likelihood of a detector click, and even if so, that click will be inconsistent with the anticipated counting statistics.

Despite the previous belief that the Dolinar receiver is experimentally impractical due to its need for real-time feedback, we have shown that it is rather attractive for experimental implementation. Particularly, quantum efficiency scales out of a comparison between the Dolinar receiver error and the Helstrom bound, while this is not the case for known unitary rotation protocols. These results strongly suggest that real-time feedback, previously cited as the Dolinar receiver's primary drawback, in fact offers substantial robustness to many common imperfections that would be present in a realistic experimental implementation. Most importantly, simulations under these realistic conditions suggest that the Dolinar receiver can outperform the Kennedy receiver with currently available experimental technology, making it a viable option for small-amplitude, minimum-error optical communication.

ACKNOWLEDGMENTS

I would like to thank Hideo Mabuchi for countless insightful comments and suggestions regarding this work and to acknowledge helpful discussions with S. Dolinar and V. Vilnrotter. This work was supported by the Caltech MURI Center for Quantum Networks (Grant No. DAAD-19-00-1-0374) and the NASA Jet Propulsion Laboratory. For more information please visit http://minty.Caltech.edu

---

[1] J. von Neumann, *Mathematical Foundations of Quantum Mechanics* (Princeton University Press, Princeton, NJ, 1955).
[2] A. S. Holevo, J. Multivariate Anal. **3**, 337 (1973).
[3] C. W. Helstrom, *Quantum Detection and Estimation Theory*, Mathematics in Science and Engineering Vol. 123 (Academic Press, New York, 1976).
[4] C. A. Fuchs and A. Peres, Phys. Rev. A **53**, 2038 (1996).
[5] H. P. Yuen and J. H. Shapiro, IEEE Trans. Inf. Theory **IT-24**, 657 (1978).
[6] T. S. Usuda and O. Hirota, *Quantum Communication and Measurement* (Plenum, New York, 1995).
[7] C. A. Fuchs, Phys. Rev. Lett. **79**, 1162 (1997).
[8] A. Peres and W. K. Wootters, Phys. Rev. Lett. **66**, 1119 (1991).
[9] C. A. Fuchs, Ph.D. thesis, University of New Mexico, 1996, e-print quant-ph/9601020.
[10] E. B. Davies and J. T. Lewis, Commun. Math. Phys. **17**, 239 (1970).
[11] K. Kraus, *States, Effects, and Operations: Fundamental Notions of Quantum Theory*, Lecture Notes in Physics Vol. 190 (Springer-Verlag, Berlin, 1983).
[12] Kennedy, Research Laboratory of Electronics, MIT Technical Report No. 110, 1972 (unpublished).
[13] S. Dolinar, Tech. Rep. 111, Research Laboratory of Electronics, MIT Technical Report No. 111, 1973 (unpublished).
[14] V. P. Belavkin, O. Hirota, and L. Hudson, *Quantum Commu-*

nication and Measurement (Plenum, New York, 1995).

[15] R. Monmose, M. Osaki, M. Ban, M. Sasaki, and O. Hirota, in *Squeezed State and Uncertainty Relation*, NASA Proc. Ser. (U.S. GPO, Washington, D.C., 1996), pp. 307–312.

[16] M. Sasaki and O. Hirota, Phys. Rev. A **54**, 2728 (1996).

[17] M. A. Armen, J. K. Au, J. K. Stockton, A. C. Doherty, and H. Mabuchi, Phys. Rev. Lett. **89**, 133602 (2002).

[18] J. Geremia, J. K. Stockton, and H. Mabuchi, Science **304**, 270 (2004).

[19] JM Geremia, J. K. Stockton, and H. Mabuchi, e-print, quant-ph/0401107.

[20] A. Peres, Found. Phys. **20**, 1441 (1990).

[21] C. W. Helstrom, Info. Control **10**, 254 (1967).

[22] R. J. Glauber, Phys. Rev. **131**, 2766 (1963).

[23] S. Dolinar, Ph.D. thesis, Massachusetts Institute of Technology, 1976.

[24] D. P. Bertsekas, *Dynamic Programming and Optimal Control*, 2nd ed. (Athena Scientific, Belmont, MA, 2000), Vol. 1.

[25] J. Stockton, M. Armen, and H. Mabuchi, J. Opt. Soc. Am. B **19**, 3019 (2002).

VOLUME 93, NUMBER 14 PHYSICAL REVIEW LETTERS week ending 1 OCTOBER 2004

Determination of the Number of Atoms Trapped in an Optical Cavity

J. McKeever, J. R. Buck, A. D. Boozer, and H. J. Kimble
Norman Bridge Laboratory of Physics 12-33, California Institute of Technology, Pasadena, California 91125, USA

(Received 16 March 2004; published 27 September 2004)

The number of atoms trapped within the mode of an optical cavity is determined in real time by monitoring the transmission of a weak probe beam. Continuous observation of atom number is accomplished in the strong coupling regime of cavity quantum electrodynamics and functions in concert with a cooling scheme for radial atomic motion. The probe transmission exhibits sudden steps from one plateau to the next in response to the time evolution of the intracavity atom number, from $N \geq 3$ to $N = 2 \rightarrow 1 \rightarrow 0$ atoms, with some trapping events lasting over 1 s.

DOI: 10.1103/PhysRevLett.93.143601 PACS numbers: 42.50.Pq, 03.67.–a, 32.80.Pj

Cavity quantum electrodynamics (QED) provides a setting in which atoms interact predominantly with light in a single mode of an electromagnetic resonator [1,2]. Not only can the light from this mode be collected with high efficiency [3], but the associated rate of optical information for determining atomic position can greatly exceed the rate of free-space fluorescent decay employed for conventional imaging [4]. Moreover, the regime of strong coupling, in which coherent atom-cavity interactions dominate dissipation, offers a unique setting for the study of open quantum systems [5]. Dynamical processes enabled by strong coupling in cavity QED provide powerful tools in the emerging field of quantum information science (QIS), including for the realization of quantum computation [6] and distributed quantum networks [7].

With these prospects in mind, experiments in cavity QED have made great strides in trapping single atoms in the regime of strong coupling [4,8–10]. However, many protocols in QIS require multiple atoms to be trapped within the same cavity, with "quantum wiring" between internal states of the various atoms accomplished by way of strong coupling to the cavity field [6,11–13]. Clearly, the experimental ability to determine the number of trapped atoms coupled to a cavity is a critical first step toward the realization of diverse goals in QIS. Experimental efforts to combine ion trap technology with cavity QED are promising [14], but have not yet reached the regime of strong coupling.

In this Letter, we report measurements in which the number of atoms trapped inside an optical cavity is observed in real time. After initial loading of the intracavity dipole trap with $\bar{N} \approx 5$ atoms, the decay of atom number $N \geq 3 \rightarrow 2 \rightarrow 1 \rightarrow 0$ is monitored via the transmission of a near-resonant probe beam, with the transmitted light exhibiting a cascade of "stair steps" as successive atoms leave the trap. After the probabilistic loading stage, the time required for the determination of a particular atom number $N = 1, 2, 3$ is much shorter than the mean interval over which the N atoms are trapped. Hence, this scheme can be used to prepare a precise number of trapped intracavity atoms for subsequent experiments in QIS, for which the time scales $(g^{-1} \approx 10^{-8}\ \mathrm{s}) \ll (\tau \approx 3\ \mathrm{s})$, where τ is the atomic trapping time [9] and $\hbar g$ is the atom-field interaction energy. In addition, it requires none of the imaging optics or shielding needed for traditional fluorescence detection from single ions and atoms [15,16], which would be complicated by the presence of our short cavity.

As illustrated in Fig. 1, our experiment combines laser cooling, state-insensitive trapping, and strong coupling in cavity QED [9]. Cs atoms are released from a magneto-optical trap (MOT) several mm above the cavity, which is formed by the reflective surfaces of mirrors (M_1, M_2). Several atoms are cooled and loaded into an intracavity far-off-resonance trap (FORT) and are thereby strongly coupled to a single mode of the cavity. The single-photon Rabi frequency $2g_0$ for one atom at the peak of the Gaussian standing wave is given by $g_0/2\pi = 24$ MHz, and is based on the reduced dipole moment for the $6S_{1/2}, F = 4 \rightarrow 6P_{3/2}, F' = 4'$ transition of the $D2$ line in Cs at $\lambda_0 = 852.4$ nm. Decay rates for the $6P_{3/2}$ excited states and the cavity mode at $\omega_0 = 2\pi c/\lambda_0$ are $\gamma/2\pi = 2.6$ MHz and $\kappa/2\pi = 4.2$ MHz, respectively [17]. The fact that $g_0 \gg (\kappa, \gamma)$ places our system in the strong

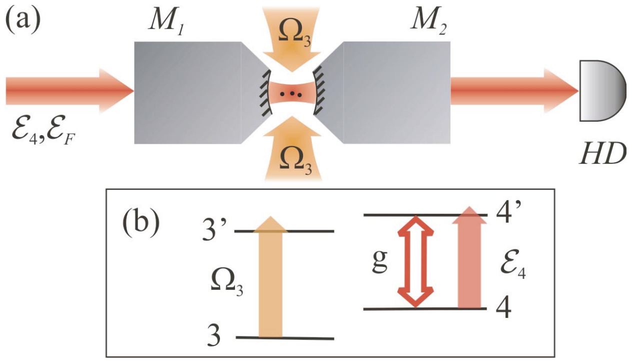

FIG. 1 (color online). Schematic of our experiment. Cs atoms are loaded into an intracavity FORT ($\mathcal{E}_F$) by way of the transverse cooling field Ω_3 and the cavity probe field $\mathcal{E}_4$. The transmitted $\mathcal{E}_4$ field is directed to a heterodyne detector (HD), allowing real-time determination of intracavity atom number.

© 2004 The American Physical Society

coupling regime of cavity QED, giving critical atom and photon numbers $n_0 \equiv \gamma^2/(2g_0^2) \approx 0.0057$, $N_0 \equiv 2\kappa\gamma/g_0^2 \approx 0.037$ [1].

The cavity length $l_0 = 42.2\ \mu$m is tuned such that it supports TEM_{00} modes simultaneously resonant with both the $F = 4 \rightarrow F' = 4'$ atomic transition at λ_0 and our FORT laser at $\lambda_F = 935.6$ nm. A weak probe laser $\mathcal{E}_4$ excites the cavity mode at λ_0 with the cavity output directed to detector HD, while a much stronger trapping laser $\mathcal{E}_F$ drives the mode at λ_F. In addition, the region between the cavity mirrors is illuminated by two orthogonal pairs of counter-propagating cooling beams in the transverse plane (denoted Ω_3), and for $\Omega_3 = 0$, no atoms are detected. Atoms arriving in the region of the cavity mode are exposed to the $(\mathcal{E}_4, \mathcal{E}_F, \Omega_3)$ fields continuously, with a fraction of the atoms cooled and loaded into the FORT by the combined actions of the $\mathcal{E}_4$ and Ω_3 fields [9]. For all measurements, the cavity detuning from the $4 \rightarrow 4'$ atomic resonance is $\Delta_C = 0$. The detuning of the $\mathcal{E}_4$ probe from the atom-cavity resonance is $\Delta_4 = +4$ MHz, and its intensity is set such that the mean intracavity photon number $\bar{n} = 0.02$ with no atoms in the cavity. The detuning of the Ω_3 transverse cooling field is $\Delta_3 = +25$ MHz from the $F = 3 \rightarrow F' = 3'$ resonance, with intensity $I_3 \approx 4 \times 10^1\ \mathrm{mW/cm^2}$.

The field $\mathcal{E}_F$ that drives the standing-wave, intracavity FORT is linearly polarized, so that all sublevels of the $6S_{1/2}$ ground manifold experience nearly equal ac-Stark shifts [18]. The peak value of the trapping potential is $-U_0/h = -47$ MHz, giving a trap depth $U_0/k_B = 2.2$ mK [19]. Importantly, all the $6P_{3/2}$ excited states likewise experience a *trapping* shift of about $-U_0$ (to within $\approx \pm 15\%$) [9,20,21], enabling continuous monitoring of trapped atoms in our cavity.

Figure 2(a) displays a typical record of the heterodyne current $i(t)$ resulting from one instance of FORT loading. Here, the current $i(t)$ is referenced to the amplitude of the intracavity field $|\langle \hat{a} \rangle|$ by way of the known propagation and detection efficiencies. The initial sharp drop in $|\langle \hat{a}(t) \rangle|$ shortly after $t = 0$ results from atoms that are cooled and loaded into the FORT by the combined action of the $(\mathcal{E}_4, \Omega_3)$ fields [9]. Falling atoms are not exposed to $\mathcal{E}_4$ until they reach the cavity mode, presumably leading to efficient trap loading for atoms that arrive at a region of overlap between the standing waves at (λ_0, λ_F) for the $(\mathcal{E}_4, \mathcal{E}_F)$ fields. The mean atomic free-fall time from our MOT is about $\tau_F = 0.03$ s, and trap loading occurs within a ± 10 ms window around $t = \tau_F$ [relative to $t = 0$ in Fig. 2(a)], giving a maximum total loading time of about 40 ms [8,9].

Subsequent to this loading phase, a number of features are apparent in the trace of Fig. 2(a), and are consistently present in all the data. Most notably, the transmission vs time consists of a series of flat "plateaus" in which the field amplitude is stable on long time scales [15,16]. Additionally, these plateaus reappear at nearly the same heights in all repeated trials of the experiment, as evidenced by the histogram of Fig. 2(b). We hypothesize that each of these plateaus represents a different number N of trapped atoms coupled to the cavity mode (arrows in Fig. 2). For detection bandwidth B, N can be measured in time $t_m \approx (2\pi B)^{-1}$, and for our parameters, the uncertainty p_{err} is dominated by the probability that an atom leaves during the interval t_m (for $N = 1$, $p_{\mathrm{err}} \approx 1\%$ for $B = 100$ Hz).

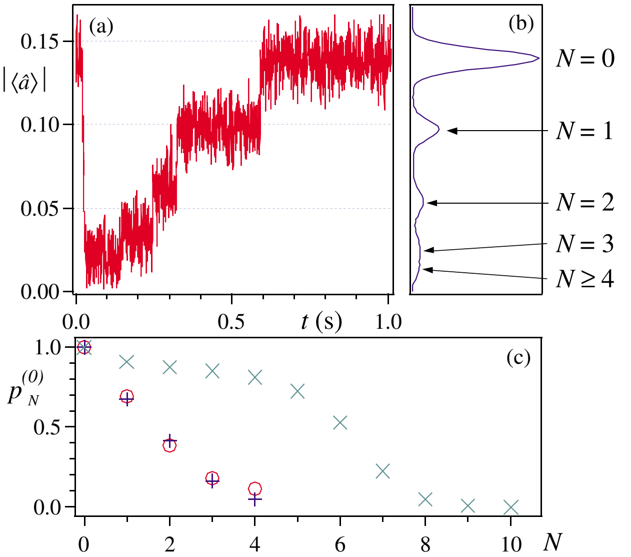

FIG. 2 (color online). (a) A typical detection record in which several $(N > 4)$ atoms are loaded into the trap. Heterodyne detection bandwidth $B = 1$ kHz. (b) Histogram of 500 such traces, binned with respect to the heterodyne signal $|\langle \hat{a} \rangle|$. A digital low-pass filter of bandwidth 100 Hz is applied to each trace prior to the computation of the histogram. (c) Comparison of the model prediction for $p_0^{(N)}(y = 0.5)$ (+) with the measured positions of the histogram peaks in (b) (○). Also shown (×) is $p_0^{(N)}(y = 0.1)$ to indicate the possibility to detect specific atom numbers for larger $\bar{N}$.

Consider first the one-atom case, which exhibits relatively large transmission and small variance compared to prior work [1,4,8,22,23]. For fixed drive $\mathcal{E}_4$, the intracavity field is a function of the coupling parameter $g^{(i,f)}(\mathbf{r}) = g_0 G_{i,f} \sin(k_0 z) \exp(-2\rho^2/w_0^2)$ where ρ is the transverse distance from the cavity axis (z), $k_0 = 2\pi/\lambda_0$, and $G_{i,f}$ relates to the Clebsch-Gordan coefficient for particular initial and final states (i, f) within the $F = 4$, $F' = 4'$ manifolds. Variations in g as a function of the atom's position $\mathbf{r}$ and internal state might be expected to lead to large variations of the intracavity field, both as a function of time and from atom to atom.

However, one atom in the cavity produces a reasonably well-defined intracavity intensity $I \propto |\langle \hat{a} \rangle|^2$ due to the interplay of two effects. The first is that for small probe detunings Δ_4, the intracavity intensity I_1 for one atom is suppressed by a factor f relative to the empty-cavity intensity I_0, where for weak excitation, $f \approx 4C_1^2 \gg 1$

with $C_1 = g^2/2\kappa\gamma$. A persistent, strongly reduced transmission thereby results, since the condition $[C_1^{(i,f)}(\mathbf{r})]^2 \gg 1$ is robust to large fluctuations in atomic position $\mathbf{r}$ and internal state. The second effect is that the $F = 4 \leftrightarrow F' = 4'$ transition cannot be approximated by a closed, two-level system, since the $F' = 4'$ excited states decay to both $F = 3, 4$ hyperfine ground levels [Fig. 1(b)]. An atom thus spends a fraction q of its time in the cavity QED manifold $(4, 4')$, and a fraction $p \approx 1 - q$ in the $(3, 3')$ manifold. In this latter case, the effective coupling is negligible ($C_1^{eff} \approx 4 \times 10^{-4}$), leading to an intensity $I \approx I_0$. Hence, the intracavity intensity $I(t)$ should approximate a random telegraph signal [15] switching between levels (I_0, I_1), with dwell times determined by $(\mathcal{E}_4, \Omega_3)$, which in turn set p [24]. Since $(\mathcal{E}_4, \Omega_3)$ drive their respective transitions near saturation, the time scale for optical pumping from one manifold to another is $\tau_P \sim 1\ \mu$s. This time scale represents a fundamental limit to the averaging time for detection, which in our case is $(1/2\pi B) \approx 160\ \mu\text{s} \gg \tau_p$. The fast modulation of $I(t)$ due to optical pumping processes thereby gives rise to an average detected signal corresponding to intensity $\bar{I}_1 \approx pI_0 + qI_1 \approx pI_0$.

This explanation for the $N = 1$ case can be extended to N intracavity atoms to provide a simple model for the stair steps of Fig. 2(a). For N atoms, the intracavity intensity should again take the form of a random telegraph signal, now switching between the levels (I_0, I_k), with high transmission I_0 during intervals when all N atoms happen to be pumped into the $(3, 3')$ manifold, and with low transmission $I_k \leq I_1$ anytime that $1 \leq k \leq N$ atoms reside in the $(4, 4')$ manifold, where $I_k \sim I_1/k^2$ for weak excitation with $\Delta_C = \Delta_4 = 0$. The intensities $\{I_k\}$ determine the transition rates $\{\gamma_{k\to k-1}\}$ between states with k and $k - 1$ atoms in the $(4, 4')$ manifold, while Ω_3 determines $\{\gamma_{k-1\to k}\}$ for $k - 1 \to k$ via transitions from the $(3, 3')$ manifold. For the hierarchy of states $k = 0, 1, \ldots, N$ with transition rates $\{\gamma_{k\to k-1}, \gamma_{k-1\to k}\}$, the steady-state populations $p_k^{(N)}$ can be obtained. With the physically motivated assignments $\gamma_{k-1\to k} = \gamma_{0\to 1}$ independent of k and $\gamma_{k\to k-1} = \gamma_{1\to 0}/k^2$ corresponding to $I_k \sim I_1/k^2$, we find that $p_0^{(N)} = 1/\sum_{k=0}^{N}(k!)^2 y^k$, where $y \equiv \gamma_{0\to 1}/\gamma_{1\to 0}$. Hence, for $I_k \ll I_0$, the prediction for the average intensity is $\bar{I}_N \approx p_0^{(N)} I_0$, which leads to a sequence of plateaus of increasing heights $\bar{I}_{N+1} \to \bar{I}_N \to \bar{I}_{N-1}$ as successive atoms leave the trap.

Figure 2(c) compares the prediction of this simple model with the measured values of peak positions in Fig. 2(b). The only adjustable parameter is the value $y = 0.5$, giving reasonable correspondence between the model and the measurements. Also shown are values $p_0^{(N)}$ for $y = 0.1$ to indicate that it might be possible to enhance the resolution for a particular range of atom number by framing a given few values $N_1, N_1 \pm 1$ in the transition region $p_0^{(N_1)} \approx 0.5$, where $N_1 \approx 6$ in Fig. 2(c). The parameter y would be adjusted via the strengths of the $(\mathcal{E}_4, \Omega_3)$ fields.

Although our simple model accounts for the qualitative features in Fig. 2, more detailed correspondence could be obtained using the full master equation for N intracavity atoms, including all Zeeman states and atomic motion [24]. We have made initial progress for the $N = 1$ case [25], and are working to extend the treatment to $N \geq 2$.

Figure 3 provides additional evidence for the correspondence between the plateaus in Fig. 2 and atom number. Here, the probe transmission data have been binned not only with respect to the value of $|\langle\hat{a}\rangle|$ as in Fig. 2(b), but also as a function of time. Definite plateaus for $|\langle\hat{a}\rangle|$ are again apparent, but now their characteristic time evolution can be determined. Clearly, the plateaus lying at higher values of $|\langle\hat{a}\rangle|$ correspond to times *later* in the trapping interval, in agreement with the expectation that N should always decrease with time after the trap-loading window. Moreover, none of the 500 traces in the data set includes a downward step in transmission after the initial trap loading.

Next we consider each atom number individually by integrating the plateau regions along the $|\langle\hat{a}(t)\rangle|$ axis for each time t. The dashed horizontal lines in Fig. 3 indicate the boundaries chosen to define the limits of integration for each value of N. We thereby obtain time-dependent "populations" $\Phi_N(t)$ for $N = 0, 1, 2$, and $\Phi_{\geq 3}(t) = \sum_{N=3}^{\infty} \Phi_N(t)$, [see Fig. 4(a)]. The qualitative behavior of these populations is sensible, since almost all trials begin with $N \geq 3$, eventually decaying to $N = 2, 1, 0$.

The quantities $\Phi_N(t)$ are approximately proportional to the fraction of experimental trials in which N atoms were trapped at time t, so long as the characteristic duration Δt_N of each plateau far exceeds the time resolution of the detection. If the bandwidth is too low, transient steps no longer represent a negligible fraction of the data, as is the case for transitions between the shortest-lived levels (e.g., $N = 3 \to 2$). We estimate that this ambiguity causes uncertainties in Φ_N at the 5%–10% level.

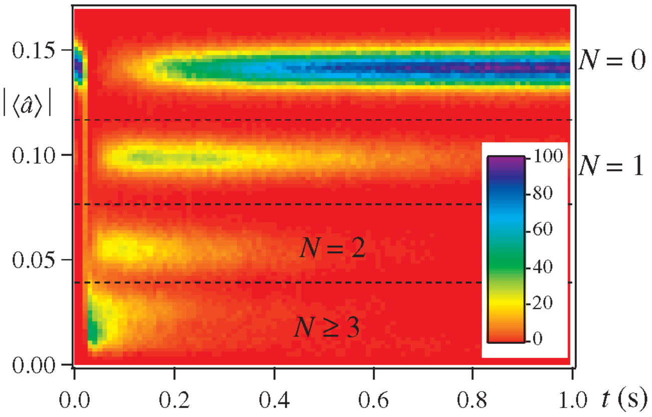

FIG. 3 (color online). Histogram of 500 traces such as the one in Fig. 2(a), binned with respect to both signal strength $|\langle\hat{a}\rangle|$ and time t. The signals are filtered first as in Fig. 2(b).

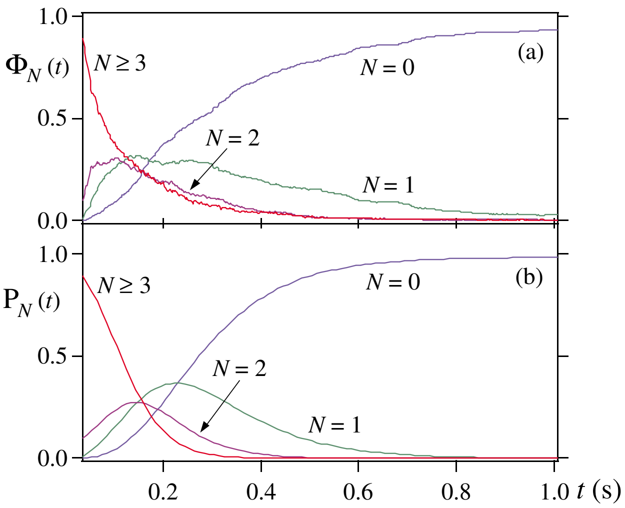

FIG. 4 (color online). (a) Experimentally determined N-atom populations $\Phi_N(t)$, normalized such that their sum is approximately unity throughout the interval shown. Here, the t axis begins at $t_0 = 0.034$ s. (b) The results of a simple model calculation $P_N(t)$ are fit to the data $\Phi_N(t)$ with one free parameter, the single-atom decay rate Γ.

Also shown [Fig. 4(b)] is the result of a simple birth-death model for predicting the time evolution of the populations, namely $\dot{P}_N(t) = -\Gamma[NP_N(t) - (N+1)P_{N+1}(t)]$, where $P_N(t)$ represents the probability of N atoms in the trap. We assume that there is one characteristic trap-decay rate Γ, and that each atom leaves the trap independently of all others. Initial conditions for $N = 0$, 1, and 2 are determined directly from the record of cavity transmission immediately after trap loading, $\Phi_N(t_0)$. Since the plateaus for higher values of N are not well resolved, we use a Poisson distribution for $N \geq 3$. The mean $\mu = 5.2$ is obtained by solving $\sum_{N=3}^{\infty} e^{-\mu}\mu^N/N! = \Phi_{N\geq3}(t_0)$. The value $\Gamma = 8.5\ \mathrm{s}^{-1}$ used in Fig. 4(b) then results from fitting the analytic solutions $\{P_N(t)\}$ to the data $\{\Phi_N(t)\}$. Although there is reasonable correspondence between Figs. 4(a) and 4(b), $\Phi_N(t)$ evolves more rapidly than does $P_N(t)$ at early times, and yet the data decay more slowly at long times. This suggests that there might be more than one time scale involved, possibly due to an inhomogeneity of decay rates from atom to atom or to a dependence of the decay rate on N. Indeed, we have observed nonexponential decay behavior in other measurements of single-atom trap lifetimes.

Our experiment represents a new method for the real-time determination of the number of atoms trapped and strongly coupled to an optical cavity. We emphasize that an exact number of atoms can be prepared in our cavity within ≈ 200 ms from the release of the MOT. Although the trap loading is not deterministic, N can be measured quickly compared to the subsequent trapping time $\tau \approx 3$ s [9]. These new techniques could assist in the realization of various protocols in quantum information science, including probabilistic schemes for entangling multiple atoms in a cavity [11–13]. Although our current investigation has centered on the case of small $N \leq 3$, there are reasonable prospects for an extension to higher values $N \lesssim 10$ [see Fig. 2(c)]. Moreover, the rate at which information about N is acquired can be substantially increased from the current value $\kappa|\langle\hat{a}\rangle|^2 \sim 10^5/\mathrm{s}$ toward the rate $g^2/\kappa \gtrsim 10^8/\mathrm{s} \gg \gamma$, with γ the rate for fluorescent imaging [4].

This work is supported by the Caltech MURI Center for Quantum Networks under ARO Grant No. DAAD19-00-1-0374, by the National Science Foundation, and by the Office of Naval Research.

---

[1] H. J. Kimble, Phys. Scr., T **76**, 127 (1998).

[2] See, for example, *Cavity Quantum Electrodynamics*, edited by P. R. Berman (Academic, San Diego, 1994).

[3] J. McKeever *et al.*, Science **303**, 1992 (2004).

[4] C. J. Hood *et al.*, Science **287**, 1447 (2000).

[5] H. Mabuchi and A. C. Doherty, Science **298**, 1372 (2002).

[6] T. Pellizzari, S. A. Gardiner, J. I. Cirac, and P. Zoller, Phys. Rev. Lett. **75**, 3788 (1995).

[7] H.-J. Briegel, S. J. van Enk, J. I. Cirac and P. Zoller, in *The Physics of Quantum Information*, edited by D. Bouwmeester, A. Ekert, and A. Zeilinger (Springer-Verlag, Berlin, 2000), p. 192.

[8] J. Ye, D.W. Vernooy and H. J. Kimble, Phys. Rev. Lett. **83**, 4987 (1999).

[9] J. McKeever *et al.*, Phys. Rev. Lett. **90**, 133602 (2003).

[10] P. Maunz *et al.*, Nature (London) **428**, 50 (2004).

[11] L. M. Duan and H. J. Kimble, Phys. Rev. Lett. **90**, 253601 (2003).

[12] J. Hong and H.-W. Lee, Phys. Rev. Lett. **89**, 237901 (2002).

[13] A. S. Sørensen and K. Mølmer, Phys. Rev. Lett. **90**, 127903 (2003).

[14] G. R. Guthöhrlein *et al.*, Nature (London) **414**, 49 (2001); A. B. Mundt *et al.*, Phys. Rev. Lett. **89**, 103001 (2002).

[15] R. J. Cook, in *Progress in Optics XXVIII*, edited by E. Wolf (Elsevier, Amsterdam, 1990), p. 361.

[16] S. Kuhr *et al.*, Science **293**, 278 (2001).

[17] Cavity finesse at λ_0 is $\mathcal{F} = 4.2 \times 10^5$, with each mirror reflectivity R given by $1 - R = 7.5 \times 10^{-6}$.

[18] K. L. Corwin, S. J. M. Kuppens, D. Cho, and C. E. Wieman, Phys. Rev. Lett. **83**, 1311 (1999).

[19] Peak FORT intensity is $I_0 = 3.4 \times 10^9\ \mathrm{W/m^2}$.

[20] H. Katori, T. Ido, and M. Kuwata-Gonokami, J. Phys. Soc. Jpn. **68**, 2479 (1999); T. Ido, Y. Isoya and H. Katori, Phys. Rev. A **61**, 061403 (2000).

[21] H. J. Kimble *et al.*, in *Laser Spectroscopy XIV*, edited by R. Blatt, J. Eschner, D. Leibfried, and F. Schmidt-Kaler (World Scientific, Singapore, 1999), p. 80.

[22] C. J. Hood, M. S. Chapman, T.W. Lynn, and H. J. Kimble, Phys. Rev. Lett. **80**, 4157 (1998).

[23] P.W. H. Pinkse, T. Fischer, P. Maunz, and G. Rempe, Nature (London) **404**, 365 (2000).

[24] Theoretical studies of the $N = 1$ case similar to Ref. [25] support these qualitative characteristics. Residual Zeeman splittings and the spatially dependent Ω_3 polarization are included in the simulations.

[25] A. D. Boozer *et al.*, Phys. Rev. A **70**, 023814 (2004).

Observation of the Vacuum Rabi Spectrum for One Trapped Atom

A. Boca, R. Miller, K. M. Birnbaum, A. D. Boozer, J. McKeever, and H. J. Kimble
Norman Bridge Laboratory of Physics 12-33, California Institute of Technology, Pasadena, CA 91125, USA

(Received 19 October 2004; published 3 December 2004)

The transmission spectrum for one atom strongly coupled to the field of a high finesse optical resonator is observed to exhibit a clearly resolved vacuum Rabi splitting characteristic of the normal modes in the eigenvalue spectrum of the atom-cavity system. A new Raman scheme for cooling atomic motion along the cavity axis enables a complete spectrum to be recorded for an individual atom trapped within the cavity mode, in contrast to all previous measurements in cavity QED that have required averaging over $10^3 - 10^5$ atoms.

DOI: 10.1103/PhysRevLett.93.233603 PACS numbers: 42.50.Pq, 03.67.–a, 32.80.Pj

A cornerstone of optical physics is the interaction of a single atom with the electromagnetic field of a high quality resonator. Of particular importance is the regime of strong coupling, for which the frequency scale g associated with reversible evolution for the atom-cavity system exceeds the rates (γ, κ) for irreversible decay of atom and cavity field, respectively [1]. In the domain of strong coupling, a photon emitted by the atom into the cavity mode is likely to be repeatedly absorbed and reemitted at the single-quantum Rabi frequency $2g$ before being irreversibly lost into the environment. This oscillatory exchange of excitation between atom and cavity field results from a normal-mode splitting in the eigenvalue spectrum of the atom-cavity system [2–4], and has been dubbed the vacuum Rabi splitting [3].

Strong coupling in cavity QED as evidenced by the vacuum Rabi splitting provides enabling capabilities for quantum information science, including for the implementation of scalable quantum computation [5,6], for the realization of distributed quantum networks [7,8], and more generally, for the study of open quantum systems [9]. Against this backdrop, experiments in cavity QED have made great strides over the past two decades to achieve strong coupling [10]. The vacuum Rabi splitting for single intracavity atoms has been observed with atomic beams in both the optical [11–13] and microwave regimes [14]. The combination of laser cooled atoms and large coherent coupling has enabled the vacuum Rabi spectrum to be obtained from transit signals produced by single atoms [15]. A significant advance has been the trapping of individual atoms in a regime of strong coupling [16,17], with the vacuum Rabi splitting first evidenced for single trapped atoms in Ref. [16] and the entire transmission spectra recorded in Ref. [18].

Without exception these prior single atom experiments related to the vacuum Rabi splitting in cavity QED [11–18] have required averaging over trials with many atoms to obtain quantitative spectral information, even if individual trials involved only single atoms (e.g., 10^5 atoms were required to obtain a spectrum in Ref. [14] and $>10^3$ atoms were needed in Ref. [18]). By contrast, the implementation of complex algorithms in quantum information science requires the capability for repeated manipulation and measurement of an individual quantum system, as has been spectacularly demonstrated with trapped ions [19,20] and recently with Cooper pair boxes [21].

With this goal in mind, in this Letter we report measurements of the spectral response of single atoms that are trapped and strongly coupled to the field of a high finesse optical resonator. By alternating intervals of probe measurement and of atomic cooling, we record a complete probe spectrum for one-and-the-same atom. The vacuum Rabi splitting is thereby measured in a quantitative fashion for each atom by way of a protocol that represents a first step towards more complex tasks in quantum infor-

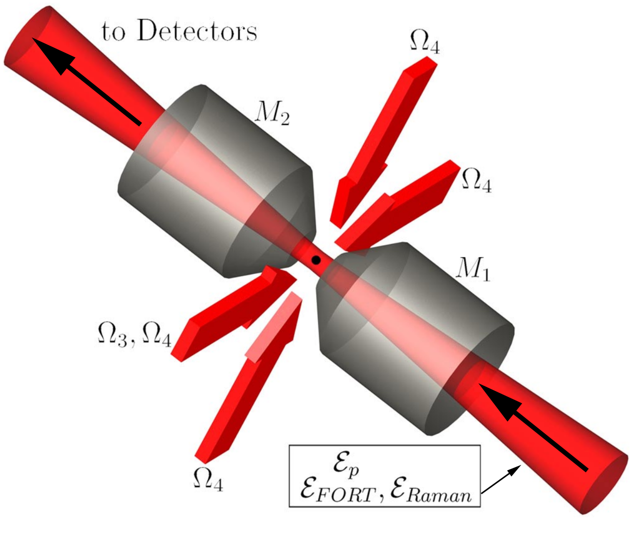

FIG. 1 (color online). A single atom is trapped inside an optical cavity in the regime of strong coupling by way of an intracavity FORT driven by the field $\mathcal{E}_{\mathrm{FORT}}$. The transmission spectrum $T_1(\omega_p)$ for the atom-cavity system is obtained by varying the frequency ω_p of the probe beam $\mathcal{E}_p$ and recording the output with single-photon detectors. Cooling of the radial atomic motion is accomplished with the transverse fields Ω_4, while axial cooling results from Raman transitions driven by the fields $\mathcal{E}_{\mathrm{FORT}}$, $\mathcal{E}_{\mathrm{Raman}}$. An additional transverse field Ω_3 acts as a repumper during probe intervals.

0031-9007/04/93(23)/233603(4)$22.50

© 2004 The American Physical Society

mation science. An essential component of our protocol is a new Raman scheme for cooling atomic motion along the cavity axis that leads to inferred atomic localization $\Delta z_{\mathrm{axial}} \simeq 33$ nm, $\Delta\rho_{\mathrm{transverse}} \simeq 5.5\ \mu$m.

A simple schematic of our experiment is given in Fig. 1 [22]. After release from a magneto-optical trap (MOT) located several mm above the Fabry-Perot cavity formed by mirrors (M_1, M_2), single Cesium atoms are cooled and loaded into an intracavity far-off-resonance trap (FORT) and are thereby strongly coupled to a single mode of the cavity. Our experiment employs the $6S_{1/2}, F = 4 \rightarrow 6P_{3/2}, F' = 5'$ transition of the $D2$ line in Cs at $\lambda_A = 852.4$ nm, for which the maximum single-photon Rabi frequency $2g_0/2\pi = 68$ MHz for $(F = 4, m_F = \pm4) \rightarrow (F' = 5', m'_F = \pm5)$. The transverse decay rate for the $6P_{3/2}$ atomic states is $\gamma/2\pi = 2.6$ MHz, while the cavity field decays at rate $\kappa/2\pi = 4.1$ MHz. Our system is in the strong coupling regime of cavity QED $g_0 \gg (\gamma, \kappa)$ [1].

The intracavity FORT is driven by a linearly polarized input field $\mathcal{E}_{\mathrm{FORT}}$ at $\lambda_F = 935.6$ nm [23], resulting in nearly equal ac-Stark shifts for all Zeeman states in the $6S_{1/2}, F = 3, 4$ manifold [24]. At an antinode of the field, the peak value of the trapping potential for these states is $U_0/h = -39$ MHz for all our measurements. Zeeman states of the $6P_{3/2}, F' = 5'$ manifold likewise experience a trapping potential, albeit with a weak dependence on m'_F [17]. The cavity length is independently stabilized to length $l_0 = 42.2\ \mu$m such that a TEM$_{00}$ mode at λ_{C_1} is resonant with the free-space atomic transition at λ_A and another TEM$_{00}$ mode at λ_{C_2} is resonant at λ_F [25].

As illustrated in Fig. 1, we record the transmission spectrum $T_1(\omega_p)$ for a weak external probe $\mathcal{E}_p$ of variable frequency ω_p incident upon the cavity containing one strongly coupled atom [26]. Our protocol consists of an alternating sequence of probe and cooling intervals. The probe beam is linearly polarized [27] and is matched to the TEM$_{00}$ mode around λ_{C_1}. $\mathcal{E}_p$ illuminates the cavity for $\Delta t_{\mathrm{probe}} = 100\ \mu$s, and the transmitted light is detected by photon counting [28]. During this interval a repumping beam Ω_3, transverse to the cavity axis and resonant with $6S_{1/2}, F = 3 \rightarrow 6P_{3/2}, F' = 4'$, also illuminates the atom. In successive probe intervals, the frequency ω_p is linearly swept from below to above the common atom-cavity resonance at $\omega_A \simeq \omega_{C_1}$. The frequency sweep for the probe is repeated eight times in $\Delta t_{\mathrm{tot}} = 1.2$ s, and then a new loading cycle is initiated.

Following each probe interval, we apply light to cool both the radial and axial motion for $\Delta t_{\mathrm{cool}} = 2.9$ ms. Radial cooling is achieved by the Ω_4 beams consisting of pairs of counter-propagating fields in a $\sigma_\pm$ configuration perpendicular to the cavity axis, as shown in Fig. 1. The Ω_4 beams are detuned $\Delta_4 \simeq 10$ MHz to the *blue* of the $4 \rightarrow 4'$ transition to provide blue Sisyphus cooling [29] for motion transverse to the cavity axis.

To cool the axial motion for single trapped atoms, we have developed a new scheme that employs $\mathcal{E}_{\mathrm{FORT}}$ and an auxiliary field $\mathcal{E}_{\mathrm{Raman}}$ that is frequency offset by $\Delta_{\mathrm{Raman}} = \Delta_{HF} + \delta$ and phase locked to $\mathcal{E}_{\mathrm{FORT}}$. Here, $\Delta_{HF} = 9.192\,632$ GHz is the hyperfine splitting between $6S_{1/2}, F = 3, 4$. $\mathcal{E}_{\mathrm{FORT}}$, $\mathcal{E}_{\mathrm{Raman}}$ drive Raman transitions between the $F = 3, 4$ levels with effective Rabi frequency $\Omega_E \sim 200$ kHz. By tuning δ near the $\Delta n = -2$ motional sideband (i.e., $-2\nu_0 \sim \delta = -1.0$ MHz, where ν_0 is the axial vibrational frequency at an antinode of the FORT), we implement sideband cooling via the $F = 3 \rightarrow 4$ transition, with repumping provided by the Ω_4 beams. The Raman process also acts as a repumper for population pumped to the $F = 3$ level by the Ω_4 beams. Each cooling interval is initiated by turning on the fields Ω_4, $\mathcal{E}_{\mathrm{Raman}}$ during Δt_{cool} and is terminated by gating these fields off before the next probe interval $\Delta t_{\mathrm{probe}}$.

Figure 2 displays normalized transmission spectra T_1 [26] for individual atoms acquired by alternating probe and cooling intervals. Clearly evident in each trace is a two-peaked structure that represents the vacuum Rabi splitting observed on an atom-by-atom basis. Also shown is the predicted transmission spectrum obtained from the steady-state solution to the master equation for one atom strongly coupled to the cavity, as discussed below. The quantitative correspondence between theory and experiment is evidently quite reasonable for each atom. Note that m_F-dependent Stark shifts for $F' = 5'$ in conjunction with optical pumping caused by $\mathcal{E}_p$ lead to the asymmetry of the peaks in Fig. 2 via an effective population-dependent shift of the atomic resonance frequency [30].

To obtain the data in Fig. 2, $N_{\mathrm{load}} = 61$ atoms were loaded into the FORT in 500 attempts, with the probabil-

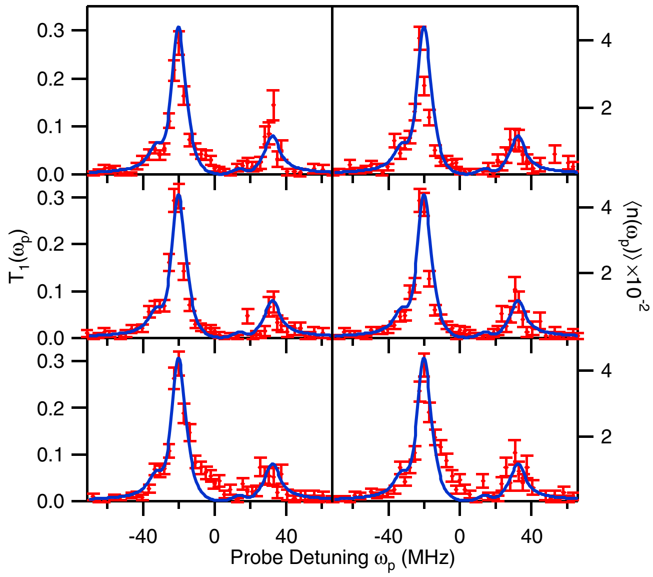

FIG. 2 (color online). Transmission spectrum $T_1(\omega_p)$ for six randomly drawn atoms [26]. In each case, $T_1(\omega_p)$ is acquired for one-and-the-same atom, with the two peaks of the vacuum Rabi spectum clearly evident. The error bars reflect the statistical uncertainties in the number of photocounts. The full curve is from the steady-state solution to the master equation.

ity that a given successful attempt involved two or more atoms estimated to be $P_{\text{load}}(N \geq 2) \lesssim 0.06$. Of the N_{load} atoms, $N_{\text{survive}} = 28$ atoms remained trapped for the entire duration Δt_{tot}. The six spectra shown in Fig. 2 were selected by a random drawing from this set of N_{survive} atoms. Our sole selection criterion for presence of an atom makes no consideration of the spectral structure of $T_1(\omega_p)$ except that there should be large absorption on line center, $T_1(\omega_p = \omega_{C_1}) \leq T_{\text{thresh}} \approx 0.2$ [26,31]. Note that an atom trapped in the FORT in the absence of the cooling and probing light has lifetime $\tau_0 \simeq 3$ s, which leads to a survival probability $p(\Delta t_{\text{tot}}) \simeq 0.7$.

In Fig. 3 we collect the results for $T_1(\omega_p)$ for all $N_{\text{survive}} = 28$ atoms, and display the average transmission spectrum $\bar{T}_1(\omega_p)$, as well as a scatter plot from the individual spectra. This comparison demonstrates that the vacuum Rabi spectrum observed for any particular atom represents with reasonable fidelity the spectrum that would be obtained from averaging over many atoms, albeit with fluctuations due to Poisson counting and optical pumping effects over the finite duration of the probe. The total acquisition time associated with the probe beam for the spectrum of any one atom is only 40 ms.

We have also acquired transmission spectra $T_1(\omega_p)$ for operating conditions other than those in Figs. 2 and 3, including intensities $|\mathcal{E}_p|^2$ varied by factors of 2, $\frac{1}{2}$, and $\frac{1}{4}$, and atom-cavity detunings $\Delta_{AC} = \omega_A - \omega_{C_1} = \pm 13$ MHz. We will describe these results elsewhere.

The full curves in Figs. 2 and 3 are obtained from the steady-state solution of the master equation including all transitions $(F = 4, m_F) \leftrightarrow (F' = 5', m'_F)$ with their respective coupling coefficients $g_0^{(m_F, m'_F)}$, as well as the two nearly degenerate modes of our cavity [23,27]. For the comparison of theory and experiment, the parameters $(g_0^{(m_F, m'_F)}, \gamma, \kappa, \Delta_{AC}, \omega_p - \omega_A, |\mathcal{E}_p|^2, U_0)$ are known in absolute terms without adjustment. However, we have no *a priori* knowledge of the particular FORT well into which the atom is loaded along the cavity standing wave, nor of the energy of the atom. The FORT shift and coherent coupling rate are both functions of atomic position $\mathbf{r}$, with $U(\mathbf{r}) = U_0 \sin^2(k_{C_2} z) \exp(-2\rho^2/w_{C_2}^2)$ and $g^{(m_F, m'_F)}(\mathbf{r}) = g_0^{(m_F, m'_F)} \psi(\mathbf{r})$, where $g_0^{(m_F, m'_F)} = g_0 G_{m_F, m'_F}$ with $G_{i,f}$ related to the Clebsch-Gordan coefficient for the particular $m_F \leftrightarrow m'_F$ transition. $\psi(\mathbf{r}) = \cos(k_{C_1} z) \exp(-\rho^2/w_{C_1}^2)$, where ρ is the transverse distance from the cavity axis z, and $k_{C_{1,2}} = 2\pi/\lambda_{C_{1,2}}$ [25].

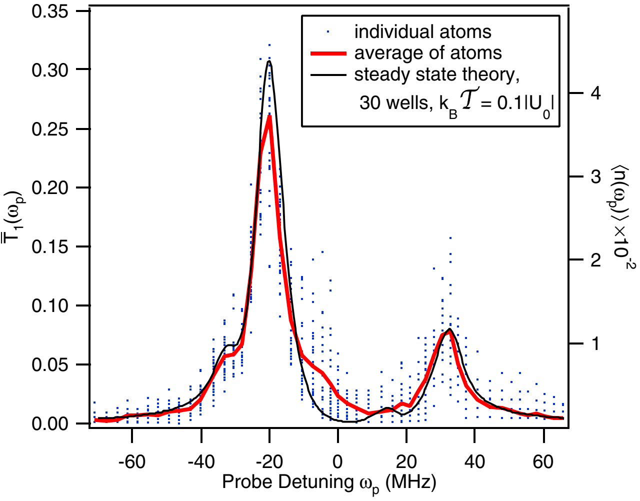

FIG. 3 (color online). Transmission spectrum $\bar{T}_1(\omega_p)$ (thick trace) resulting from averaging all 28 individual spectra $T_1(\omega_p)$ (dots) [26]. The thin trace is from the steady-state solution to the master equation, and is identical to that in Fig. 2. The only free parameters in the theory are the temperature and the range of FORT antinodes; the vertical scale is absolute.

As discussed in connection with Fig. 4 below, for the theoretical curves shown in Figs. 2 and 3, we have chosen only the 30 out of 90 total FORT wells for which $|\psi(\mathbf{r}_{\text{FORT}})| \geq 0.87$, where $\mathbf{r}_{\text{FORT}}$ is such that $U(\mathbf{r}_{\text{FORT}}) = U_0$. Furthermore, for these wells we have averaged $T_1(\omega_p)$ over a Gaussian distribution in position $\mathbf{r}$ consistent with a temperature $k_B\mathcal{T} = 0.1 U_0$ (~ 200 μK). Since all parameters are known except for those that characterize atomic motion, the good agreement between theory and experiment [32] allows us to infer that our cooling protocol together with the selection criterion $T_{\text{thresh}} = 0.2$ results in individual atoms that are strongly coupled in

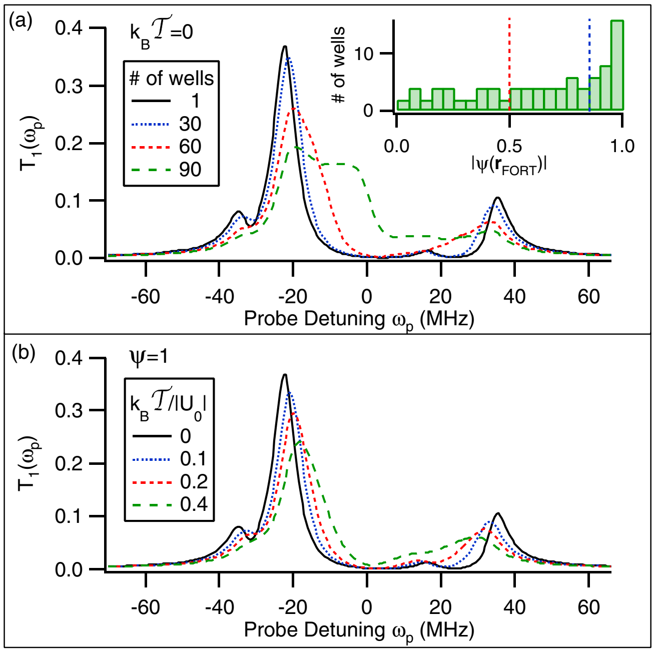

FIG. 4 (color online). Theoretical plots for $T_1(\omega_p)$ from the steady-state solution of the master equation. (a) For zero temperature, $T_1(\omega_p)$ is calculated from an average over various FORT antinodes along the cavity axis, with the inset showing the associated distribution of values for $|\psi(\mathbf{r}_{\text{FORT}})|$. (b) For an optimum FORT well (i.e., $|\psi(\mathbf{r}_{\text{FORT}})| = 1$), $T_1(\omega_p)$ is computed for various temperatures from an average over atomic positions within the well.

one of the "best" FORT wells (i.e., $|\psi(\mathbf{r}_{\text{FORT}})| \gtrsim 0.87$) with "temperature" $\sim 200\ \mu\text{K}$ [33].

In support of these assertions, Fig. 4(a) explores the theoretical dependence of $T_1(\omega_p)$ on the set of FORT wells selected, and hence on the distribution of values for $|\psi(\mathbf{r}_{\text{FORT}})|$ in the ideal case $\mathcal{T} = 0$. Extending the average beyond the 30 "best" FORT wells leads to spectra that are inconsistent with our observations in Figs. 2 and 3. Figure 4(b) likewise investigates the theoretical dependence of $T_1(\omega_p)$ on the temperature $\mathcal{T}$ for an atom at an antinode of the FORT with optimal coupling (i.e., $|\psi(\mathbf{r})| = 1$). For temperatures $\mathcal{T} \gtrsim 200\ \mu\text{K}$, the calculated spectra are at variance with the data in Figs. 2 and 3, from which we infer atomic localization $\Delta z \simeq 33$ nm in the axial direction and $\Delta x = \Delta y \simeq 3.9\ \mu\text{m}$ in the plane transverse to the cavity axis. Beyond these conclusions, a consistent feature of our measurements is that reasonable correspondence between theory and experiment is only obtained by restricting $|\psi(\mathbf{r})| \gtrsim 0.8$.

Our experiment represents an important advance in the quest to obtain single atoms trapped with optimal strong coupling to a single mode of the electromagnetic field. The vacuum Rabi splitting is the hallmark of strong coupling for single atoms and photons, and all measurements until now have required averaging over many atoms for its observation. By contrast, we are able to observe spectra $T_1(\omega_p)$ on an atom-by-atom basis with clearly resolved normal-mode splittings. These spectra contain detailed quantitative information about the coherent coupling $g(\mathbf{r})$ and FORT shifts for each atom. This information indicates that the coupling g is in a narrow range of near-maximal values. Our observations are made possible by the implementation of a new scheme to cool both the radial and axial atomic motion. The capabilities demonstrated in this Letter should provide the tools necessary to implement diverse protocols in quantum information science [5–9].

We gratefully acknowledge the contributions of T. Northup. This research is supported by the Caltech MURI Center for Quantum Networks, by the National Science Foundation, and by the Advanced Research and Development Activity (ARDA).

---

[1] H. J. Kimble, Phys. Scr., T **76**, 127 (1998).

[2] E. T. Jaynes and F. W. Cummings, Proc. IEEE **51**, 89 (1963).

[3] J. J. Sanchez-Mondragon, N. B. Narozhny, and J. H. Eberly, Phys. Rev. Lett. **51**, 550 (1983).

[4] G. S. Agarwal, Phys. Rev. Lett. **53**, 1732 (1984).

[5] T. Pellizzari, S. A. Gardiner, J. I. Cirac, and P. Zoller, Phys. Rev. Lett. **75**, 3788 (1995).

[6] L.-M. Duan and H. J. Kimble, Phys. Rev. Lett. **92**, 127902 (2004)

[7] J. I. Cirac, P. Zoller, H. J. Kimble, and H. Mabuchi, Phys. Rev. Lett. **78**, 3221 (1997).

[8] H.-J. Briegel *et al.*, in *The Physics of Quantum Information*, edited by D. Bouwmeester, A. Ekert, and A. Zeilinger (Springer, Berlin, 2000), p. 192.

[9] H. Mabuchi and A. C. Doherty, Science **298**, 1372 (2002).

[10] *Cavity Quantum Electrodynamics*, edited by P. Berman (Academic Press, San Diego, 1994).

[11] R. J. Thompson, G. Rempe, and H. J. Kimble, Phys. Rev. Lett. **68**, 1132 (1992).

[12] J. J. Childs *et al.*, Phys. Rev. Lett. **77**, 2901 (1996).

[13] R. J. Thompson, Q. A. Turchette, O. Carnal, and H. J. Kimble, Phys. Rev. A **57**, 3084 (1998).

[14] M. Brune *et al.*, Phys. Rev. Lett. **76**, 1800 (1996).

[15] C. J. Hood, M. S. Chapman, T. W. Lynn, and H. J. Kimble, Phys. Rev. Lett. **80**, 4157 (1998).

[16] J. Ye, D. W. Vernooy, and H. J. Kimble, Phys. Rev. Lett. **83**, 4987 (1999).

[17] J. McKeever *et al.*, Phys. Rev. Lett. **90** , 133602 (2003).

[18] P. Maunz *et al.*, quant-ph/0406136.

[19] M. Riebe *et al.*, Nature (London) **429**, 734 (2004).

[20] M. D. Barrett *et al.*, Nature (London) **429**, 737 (2004).

[21] A. Wallraff *et al.*, Nature (London) **431**, 162 (2004); I. Chiorescu *et al.*, *ibid.* **431**, 159 (2004).

[22] See J. McKeever, Ph.D thesis, California Institute of Technology, 2004 for more technical details.

[23] Birefringence in the mirrors leads to two nondegenerate cavity modes with orthogonal polarizations $\hat{l}_\pm$ and mode splitting $\Delta\nu_{C_1} = 4.4 \pm 0.2$ MHz. $\mathcal{E}_{\text{FORT}}$ ($\mathcal{E}_{\text{Raman}}$) is linearly polarized and aligned close to $\hat{l}_+$ ($\hat{l}_-$) for the higher (lower) frequency mode.

[24] K. L. Corwin *et al.*, Phys. Rev. Lett. **83**, 1311 (1999).

[25] At the cavity center $z = 0$, the mode waists $w_{C_{1,2}} = \{23.4, 24.5\}\ \mu\text{m}$ at $\lambda_{C_{1,2}} = \{852.4, 935.6\}$ nm.

[26] $T_1(\omega_p)$ is proportional to the ratio of photon flux transmitted by M_2 to the flux $|\mathcal{E}_p|^2$ incident upon M_1, with normalization $T_0(\omega_p = \omega_{C_1}) \equiv 1$ for the empty cavity. Figures 2 and 3 also show the corresponding intracavity photon number $\langle n(\omega_p)\rangle$.

[27] Relative to $\hat{l}_\pm$ [23], the linear polarization vector $\hat{l}_p$ for the probe field $\mathcal{E}_p$ is aligned along a direction $\hat{l}_p = \cos\theta\hat{l}_+ + \sin\theta\hat{l}_-$, where $\theta = 13\,°$ for Fig. 2; however, the theory is relatively insensitive to θ for $\theta \lesssim 15\,°$.

[28] The efficiency for photon escape from the cavity is $\alpha_{e2} = 0.6 \pm 0.1$. The propagation efficiency from M_2 to detectors (D_1, D_2) is $\alpha_P = 0.41 \pm .03$, with then each detector receiving half of the photons. The avalanche photodiodes (D_1, D_2) have quantum efficiencies $\alpha_P = 0.49 \pm 0.05$.

[29] D. Boiron *et al.*, Phys. Rev. A **53**, R3734 (1996).

[30] The ac-Stark shifts of the $(F' = 5', m_F')$ states are given by $\{m_F', U_{m_F'}\} = \{\pm 5, 1.18U\}, \{\pm 4, 1.06U\}, \{\pm 3, 0.97U\}, \{\pm 2, 0.90U\}, \{\pm 1, 0.86U\}, \{0, 0.85U\}$.

[31] Transmission spectra $T_1(\omega_p), \bar{T}_1(\omega_p)$ are insensitive over a range of selection criteria $0.02 \leq T_{\text{thresh}} \leq 0.73$.

[32] In Figs. 2 and 3 the discrepancy between experiment and the *steady-state* theory for $\bar{T}_1(\omega_p)$ around $\omega_p \sim 0$ can be accounted for by a *transient* solution to the master equation which includes optical pumping effects over the probe interval Δt_{probe}.

[33] Although the spectra are consistent with a thermal distribution, we do not exclude a more complex model involving probe-dependent heating and cooling effects.

arXiv:quant-ph/0401147 v2 24 Jan 2004

Single-Photon Generation from Stored Excitation in an Atomic Ensemble

C. W. Chou, S. V. Polyakov, A. Kuzmich,[*] and H. J. Kimble

Norman Bridge Laboratory of Physics 12-33
California Institute of Technology, Pasadena, CA 91125

(Dated: May 24, 2006)

Single photons are generated from an ensemble of cold Cs atoms via the protocol of Duan et al. [Nature **414**, 413 (2001)]. Conditioned upon an initial detection from field 1 at 852 nm, a photon in field 2 at 894 nm is produced in a controlled fashion from excitation stored within the atomic ensemble. The single-quantum character of the field 2 is demonstrated by the violation of a Cauchy-Schwarz inequality, namely $w(1_2, 1_2|1_1) = 0.24 \pm 0.05 \ngeq 1$, where $w(1_2, 1_2|1_1)$ describes detection of two events $(1_2, 1_2)$ conditioned upon an initial detection 1_1, with $w \to 0$ for single photons.

A critical capability for quantum computation and communication is the controlled generation of single-photon pulses into well-defined spatial and temporal modes of the electromagnetic field. Indeed, early work on the realization of quantum computation utilized single-photon pulses as quantum bits (*flying qubits*), with nonlinear interactions mediated by an appropriate atomic medium [1, 2]. More recently, a scheme for quantum computation by way of linear optics and photoelectric detection has been developed that again relies upon single-photon pulses as qubits [3]. Protocols for the implementation of quantum cryptography [4] and of distributed quantum networks also rely on this capability [5, 6], as do some models for scalable quantum computation [7].

Efforts to generate single-photon wavepackets can be broadly divided into techniques that provide photons "on demand" (e.g., quantum dots coupled to microcavities [8, 9, 10]) and those that produce photons as a result of conditional measurement on a correlated quantum system. For conditional generation, the detection of one photon from a correlated pair results in a one-photon state for the second photon, as was first achieved using "twin" photons from atomic cascades [11, 12] and parametric down conversion [13], with many modern extensions [14, 15, 16, 17]. Within the context of the collective enhancement of atom-photon interactions in optically thick atomic samples [18, 19], a remarkable protocol for scalable quantum networks [6] suggests a new avenue for producing single photons via conditional measurement.

Inspired by the protocol of Ref. [6], in this Letter we report a significant advance in the creation of single photons for diverse applications in quantum information science, namely the generation and storage of single quanta from an atomic ensemble. As illustrated in Figure 1, an initial *write* pulse of (classical) light creates a state of collective excitation in an ensemble of cold atoms as determined by photoelectric detection for the generated field 1. Although this first step is probabilistic, its success heralds the preparation of one excitation stored within the atomic medium. After a programmable delay δt, a *read* pulse converts the state of atomic excitation into a field excitation, thereby generating one photon in a well-defined spatial and temporal mode 2. The quantum character of the $(1, 2)$ fields is demonstrated by the observed violation of a Cauchy-Schwarz inequality for the ratio R of cross correlations to auto-correlations [11], namely $R = 53 \pm 2$ where $R \leq 1$ for any classical field [20, 21, 22].

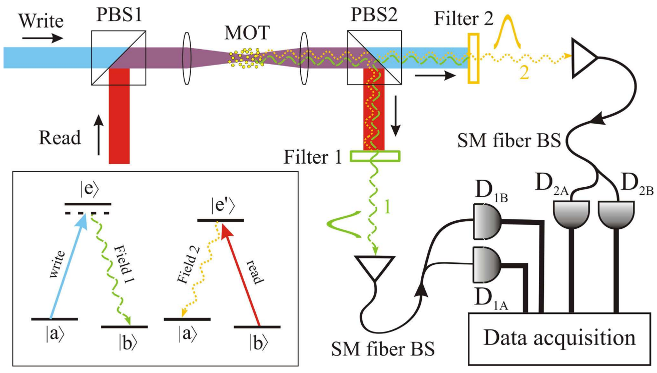

FIG. 1: Schematic of experiment for conditional generation of single photons. *Write* and *read* pulses sequentially propagate into a cloud of cold Cs atoms (MOT), generating the correlated output fields $(1, 2)$. A detection event for field 1 at $D_{1A,1B}$ leads to an approximate one-photon state for field 2, as confirmed with detectors $D_{2A,2B}$. (P)BS - (polarization) beam splitter, SM - single-mode. The inset illustrates the relevant atomic level scheme.

This greatly improved nonclassical correlation for photon pairs for the $(1, 2)$ fields enables the conditional generation of single photons as in Refs. [12, 13, 14, 15, 16, 17], but now with the photon 2 stored as an excitation in the atomic ensemble [15]. Given a first photon 1 from the *write* pulse, we trigger the emission of a second photon 2 with the *read* pulse. To demonstrate the single-photon character of the field 2, we measure the three-fold correlation function $w(1_2, 1_2|1_1)$ for detection of two photons $(1_2, 1_2)$ from field 2 given a detection event 1_1 from field 1, where $w(1_2, 1_2|1_1) = 1$ for coherent states and $w(1_2, 1_2|1_1) \geq 1$ for any classical field. Experimentally, we find $w(1_2, 1_2|1_1) = 0.34 \pm 0.06$ for $\delta t = 150$ ns, while $w(1_2, 1_2|1_1) = 0.24 \pm 0.05$ for $\delta t = 0$, thereby taking an important step toward the creation of ideal single photons for which $w(1_2, 1_2|1_1) \to 0$.

Figure 1 provides an overview of our experiment for producing correlated photons from an optically thick sample of four-level atoms in a magneto-optical trap (MOT) [20, 23]. The ground states $\{|a\rangle; |b\rangle\}$ correspond to the $6S_{1/2}, F = \{4; 3\}$ levels in atomic Cs, while the excited states $\{|e\rangle; |e'\rangle\}$ denote the $\{6P_{3/2}, F = 4; 6P_{1/2}, F = 4\}$ levels of the D_2, D_1 lines at $\{852; 894\}$ nm, respectively. We start the protocol for single photon generation by shutting off all light responsible for trapping and cooling for 1μs, with the trapping light turned off approximately 300 ns before the re-pumping light in order to empty the $F = 3$ hyperfine level in the Cs $6S_{1/2}$ ground state, thus preparing the atoms in $|a\rangle$. During the "dark" period, the jth trial is initiated at time $t_j^{(1)}$ when a rectangular pulse of laser light from the *write* beam, 150 ns in duration (FWHM) and tuned 10 MHz below the $|a\rangle \rightarrow |e\rangle$ transition, induces spontaneous Raman scattering to level $|b\rangle$ via $|a\rangle \rightarrow |e\rangle \rightarrow |b\rangle$. The *write* pulse is sufficiently weak so that the probability to scatter one Raman photon into a forward propagating wavepacket $\psi^{(1)}(\vec{r}, t_j^{(1)})$ is less than unity for each pulse. Detection of one photon from field 1 results in a "spin" excitation to level $|b\rangle$, with this excitation distributed in a symmetrized, coherent manner throughout the sample of N atoms illuminated by the *write* beam.

Given this initial detection, the stored atomic excitation can be converted into one quantum of light at a user controlled time $t_j^{(2)} = t_j^{(1)} + \delta t$. To implement this conversion, a rectangular pulse from the *read* beam, 120 ns in duration (FWHM) and resonant with the $|b\rangle \rightarrow |e'\rangle$ transition, illuminates the atomic sample. This pulse affects the transfer $|b\rangle \rightarrow |e'\rangle \rightarrow |a\rangle$ with the accompanying emission of a second Raman photon 2 on the $|e'\rangle \rightarrow |a\rangle$ transition described by the wavepacket $\psi^{(2)}(\vec{r}, t_j^{(2)})$, where the spatial and temporal structure of $\psi^{(1,2)}(\vec{r}, t)$ are discussed in more detail in Ref. [24]. The trapping and re-pumping light for the MOT are then turned back on to prepare the atoms for the next trial $j+1$, with the whole process repeated at 250 kHz.

The forward-scattered Raman light from the *write*, *read* pulses is directed to two sets of single-photon detectors ($D_{1A,1B}$ for field 1 and $D_{2A,2B}$ for field 2) [26]. Light from the (*write*, *read*) pulses is strongly attenuated (by $\simeq 10^6$) by the filters shown in Fig. 1, while the associated $(1, 2)$ photons from Raman scattering are transmitted with high efficiency ($\simeq 80\%$) [20]. Detection events from $D_{1A,1B}$ within the intervals $[t_j^{(1)}, t_j^{(1)} + T]$ and from $D_{2A,2B}$ within $[t_j^{(2)}, t_j^{(2)} + T]$ are time stamped (with a resolution of 2 ns) and stored for later analysis. $T = 200$ ns for all of our measurements.

For a particular set of operating conditions, we determine the single p_l and joint $p_{l,m}$ event probabilities from the record of detection events at $D_{1A,1B}, D_{2A,2B}$, where $(l, m) = 1$ or 2. For example, the total singles probability p_1 for events at D_{1A}, D_{1B} due to field 1 is found from the total number of detection events $n_{1A} + n_{1B}$ recorded by D_{1A}, D_{1B} during the intervals $[t_j^{(1)}, t_j^{(1)} + T]$ over M_{tot} repeated trials $\{j\}$, with then $p_1 = (n_{1A} + n_{1B})/M_{tot}$. To determine $p_{1,1}$ for joint detections at D_{1A}, D_{1B}, we count the total number of coincidences $N_{1A,1B}$ recorded by D_{1A}, D_{1B}, with then $p_{1,1} = N_{1A,1B}/M_{tot}$. $p_{2,2}$ is found in an analogous fashion using events from D_{2A}, D_{2B}. Joint detections between the $(1, 2)$ fields are described by $p_{1,2}$, which is determined by summing coincidence events between the four pairs of detectors for the $(1, 2)$ fields (e.g., between pairs D_{1A}, D_{2A}).

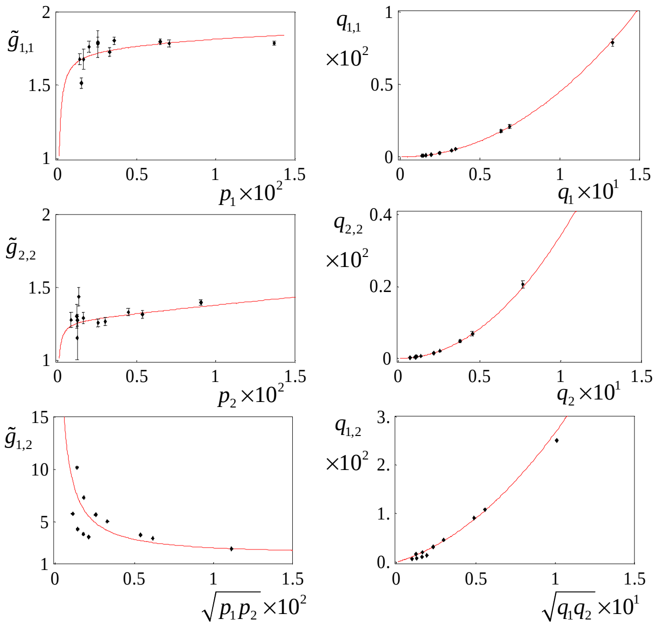

FIG. 2: Left column *(a) – (c)* Normalized intensity correlation functions $\tilde{g}_{1,1}, \tilde{g}_{2,2}, \tilde{g}_{1,2}$ versus observed detection probabilities $p_1, p_2, \sqrt{p_1 p_2}$, respectively. Right column *(d) – (f)* $q_{1,1}, q_{2,2}, q_{1,2}$ for joint detection versus $q_1, q_2, \sqrt{q_1 q_2}$ for single detection, with $q_l, q_{l,m}$ referenced to the output of the MOT. Statistical uncertainties are indicated by the error bars. The full curves are from the model calculation described in the text with $(\kappa_1, \kappa_2) = (0.17, 0.90)$ and $(|v_{1b}|^2, |v_{2b}|^2) = 0.006$.

From $(p_l, p_{l,m})$ we derive estimates of the normalized intensity correlation functions $\tilde{g}_{l,m}$, where $\tilde{g}_{l,m} = 1$ for coherent states. For example, the auto-correlation function $\tilde{g}_{1,1} = p_{1,1}/(p_{1A} p_{1B})$ for field 1, and similarly for the functions $\tilde{g}_{2,2}, \tilde{g}_{1,2}$ for the auto-correlation of field 2 and the cross correlation between fields $(1, 2)$. The first column in Figure 2 displays $\tilde{g}_{1,1}, \tilde{g}_{2,2}$, and $\tilde{g}_{1,2}$ as functions of p_1, p_2, and $\sqrt{p_1 p_2}$ [25]. A virtue of $\tilde{g}_{l,m}$ is its independence from the propagation and detection efficiencies. In the ideal case, the state for the fields $(1, 2)$ is [6, 22, 24]

$$|\Phi_{12}\rangle = |00\rangle + \sqrt{\chi}|11\rangle + \chi|22\rangle + O(\chi^{3/2}) \ , \qquad (1)$$

where $\sqrt{\chi}$ is the excitation amplitude for field 1 in each trial of the experiment. For $\chi \ll 1$, $\tilde{g}_{1,1} = \tilde{g}_{2,2} \simeq 2$ and $\tilde{g}_{1,2} = 1 + 1/\chi$. By contrast, for reasons that we will shortly address, our measurements in Fig. 2 give $\tilde{g}_{1,1} \simeq 1.7$ and $\tilde{g}_{2,2} \simeq 1.3$, with $\tilde{g}_{1,2}$ exhibiting a sharp rise with decreasing $\sqrt{p_1 p_2}$, but with considerable scatter.

To provide a characterization of the field generation that is independent of the efficiency of our particular detection setup, we convert the photodetection probabilities $(p_l, p_{l,m})$ to the quantities $(q_l, q_{l,m})$ for the field mode collected by our imaging system at the output of the MOT. Explicitly, for single events for fields $(1,2)$, we define $q_1 \equiv p_1/\alpha_1, q_2 \equiv p_2/\alpha_2$, while for joint events, $q_{1,1} \equiv p_{1,1}/\alpha_1^2, q_{2,2} \equiv p_{2,2}/\alpha_2^2, q_{1,2} \equiv p_{1,2}/\alpha_1\alpha_2$, where α_l gives the collection, propagation, and detection efficiency [26]. The second column in Fig. 2 displays the measured dependence of $q_{l,m}$ for joint events versus $q_1, q_2, \sqrt{q_1 q_2}$ for single events over a range of operating conditions. As expected from Eq. 1, $q_{1,1}, q_{2,2}$ exhibit an approximately quadratic dependence on q_1, q_2, while $q_{1,2}$ would be linear for $\sqrt{q_1 q_2} \ll 1$ in the ideal case.

In our experiment there are a number of imperfections that lead to deviations from the ideal case expressed by $|\Phi_{12}\rangle$ [6, 22, 24]. To capture the essential aspects, we have developed a simple model that assumes the total fields $(1,2)$ at the output of the MOT consist of contributions from $|\Phi_{12}\rangle$, together with background fields in coherent states $|v_{1,2}\rangle$. Operationally, increases in p_1, p_2 are accomplished by way of increases in the intensity of the *write* beam, with only minor adjustments to the *read* beam. Hence, we parameterize our model by taking $\chi = |v_w|^2$, with v_w as the (scaled) amplitude of the *write* beam. Since important sources of noise are light scattering from the *write* and *read* beams and background fluorescence from uncorrelated atoms in the sample [24], we assume that $v_{1,2} = \sqrt{\kappa_{1,2}} v_w$. We further allow for fixed incoherent backgrounds v_{1b}, v_{2b} to account for processes that do not depend upon increases in the *write* intensity.

With this model, it is straightforward to compute the quantities that appear in Figs. 2–4. The parameters $(\kappa_1, \kappa_2) = (0.17, 0.90)$ and $(|v_{1b}|^2, |v_{2b}|^2) = 0.006$ are obtained directly by optimizing the comparison between the model results and our measurements of normalized correlation functions (e.g., $\tilde{g}_{1,1}$ vs. $\tilde{g}_{1,2}$) without requiring absolute efficiencies. $\kappa_1 = 0.17$ implies that the photon number for "good" events associated with $|\Phi_{12}\rangle$ exceeds that for "bad" (background) events from $|v_1\rangle$ by roughly 6−fold for detection at D_{1A}, D_{1B}. For the curves in Fig. 2, we must also obtain the efficiencies β_l, η_l that convert expectation values for normally ordered photon number operators $\hat{n}_l$ for fields $l = (1,2)$ in the model into the various $(p_l, p_{l,m})$ and $(q_l, q_{l,m})$ (e.g., $p_l = \beta_l \langle \hat{n}_l \rangle, q_l = \eta_l \langle \hat{n}_l \rangle, q_{1,2} = \eta_1 \eta_2 \langle : \hat{n}_1 \hat{n}_2 : \rangle$). Ideally $\beta_l = \alpha_l$ and $\eta_l = 1$; we find instead $(\beta_l, \eta_l) = (0.013, 0.15)$, where we take $\beta_1 = \beta_2$ and $\eta_1 = \eta_2$ for simplicity. Among various candidates under investigation, values $\beta_l < \alpha_l, \eta_l < 1$ can arise from inherent mode mismatching for capturing collective emission from the atomic ensemble [24].

Independent of the absolute efficiencies, we can utilize the results from Fig. 2 to address directly the question of the nonclassical character of the $(1,2)$ fields by following the pioneering work of Clauser [11]. The correlation functions $\tilde{g}_{l,m}$ for fields for which the Glauber-Sudarshan phase-space function φ is well-behaved (i.e., *classical* fields) are constrained by the inequality $R \equiv [\tilde{g}_{1,2}]^2 / \tilde{g}_{1,1} \tilde{g}_{2,2} \leq 1$ [11, 22]. In Fig. 3 we plot the experimentally derived values for R as a function of the degree of cross-correlation $\tilde{g}_{1,2}$ [25]. As compared to previous measurements for which $R = 1.84 \pm 0.06$ [20] and $R = 1.34 \pm 0.05$ [21], we have now achieved $R \gg 1$, with $R = 53 \pm 2$ for the largest value of $\tilde{g}_{1,2}$. In Figs. 2 and 3 as well as 4 to follow, all points are taken with $\delta t = 150$ ns, except the points at $\tilde{g}_{1,2} \simeq 10$, which have $\delta t = 0$.

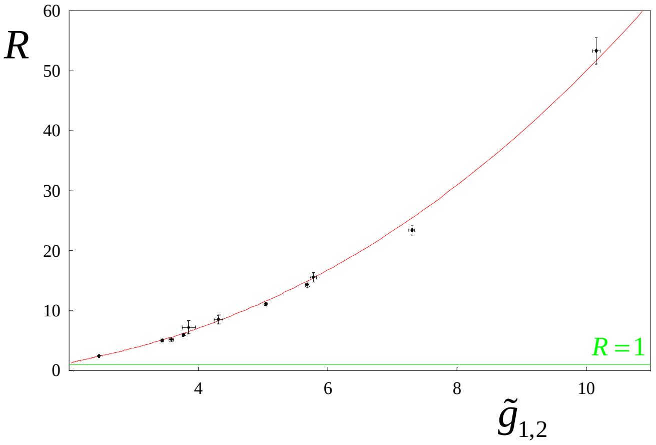

FIG. 3: Ratio $R \equiv [\tilde{g}_{1,2}]^2 / \tilde{g}_{1,1} \tilde{g}_{22}$ versus the normalized cross correlation $\tilde{g}_{1,2}$, where $R > 1$ for manifestly quantum (nonclassical) fields. The points are from our experiment with statistical uncertainties indicated by the error bars. The full curve is from the model calculation with (κ_1, κ_2) and $(|v_{1b}|^2, |v_{2b}|^2)$ as in Fig. 2.

This large degree of quantum correlation between the $(1,2)$ fields suggests the possibility of producing a single photon for field 2 by conditional detection of field 1. To investigate this possibility, we consider the three-fold correlation function $w(1_2, 1_2|1_1)$ for detection with the setup shown in Fig. 1, namely

$$w(1_2, 1_2|1_1) \equiv \frac{p^{(c)}(1_2, 1_2|1_1)}{[p^{(c)}(1_2|1_1)]^2}, \tag{2}$$

where $p^{(c)}(1_2, 1_2|1_1)$ is the conditional probability for detection of two photons $(1_2, 1_2)$ from field 2 conditioned upon the detection of an initial photon 1_1 for field 1, and $p^{(c)}(1_2|1_1)$ is the probability for detection of one photon 1_2 given a detection event 1_1 for field 1. Bayes' theorem allows the conditional probabilities in Eq. 2 to be written in terms of single and joint probabilities $p^{(k)}$ for k−fold detection, so that

$$w(1_2, 1_2|1_1) = \frac{p^{(1)}(1_1) p^{(3)}(1_1, 1_2, 1_2)}{[p^{(2)}(1_1, 1_2)]^2}. \tag{3}$$

Fields with a positive-definite φ must satisfy the Cauchy-Schwarz inequality $w(1_2, 1_2|1_1) \geq 1$. Indeed, for independent coherent states, $w = 1$, while for thermal beams, $w = 2$. By contrast, for the state $|\Phi_{12}\rangle$ of Eq. 1, $w = 4\chi \ll 1$ for small χ, approaching the ideal case $w \rightarrow 0$ for a "twin" Fock state $|1_1 1_2\rangle$.

From the record of photo-detection events at $D_{1A,1B}, D_{2A,2B}$, we calculate estimates of the various

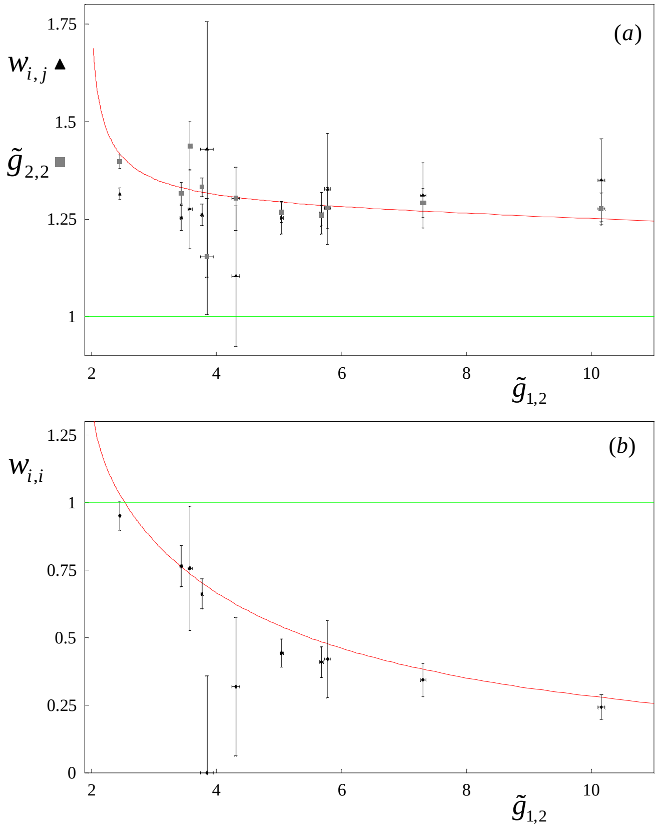

FIG. 4: Three-fold correlation function $w(1_2, 1_2|1_1)$ for detection event 1_1 for field 1 followed by two events $(1_2, 1_2)$ for field 2 versus the normalized cross correlation $\tilde{g}_{1,2}$. *(a)* $w_{i,j}(1_2, 1_2|1_1)$ for events $(1_1)_i$ and $(1_2, 1_2)_j$ from different trials $i \neq j$ together with points for $\tilde{g}_{2,2}$. $w_{i,j} = \tilde{g}_{2,2}$ for statistically independent trials. *(b)* $w_{i,i}(1_2, 1_2|1_1)$ for events from the same trial i. $w_{i,i} < 1$ for sub-Poissonian fields in support of the single-photon character of field 2. Statistical uncertainties are indicated by the error bars. The full curves are from the model calculation with (κ_1, κ_2) and $(|v_{1b}|^2, |v_{2b}|^2)$ as in Figs. 2, 3.

probabilities appearing in Eq. 3, with the results of this analysis shown in Fig. 4. Part (a) examines the quantity $w_{i,j}(1_2, 1_2|1_1)$ obtained from events taken from different trials $i \neq j$ for the $(1, 2)$ fields (i.e., detection 1_1 in trial i for field 1 followed by two detections $(1_2, 1_2)$ in trial j for field 2). In this case, the $(1, 2)$ fields should be statistically independent [22], so that $w_{i,j}(1_2, 1_2|1_1) = \tilde{g}_{2,2}$. Hence, we also superimpose $\tilde{g}_{2,2}$ from Fig. 2 and find reasonable correspondence within the statistical uncertainties (in particular, $w_{i,j}(1_2, 1_2|1_1) \gtrsim 1$), thereby validating our analysis techniques [25]. No corrections for dark counts or other backgrounds have been applied to the data in Fig. 4 (nor indeed to Figs. 2, 3).

Fig. 4 (b) displays $w_{i,i}(1_2, 1_2|1_1)$ for events from the same experimental trial i for the $(1, 2)$ fields. Significantly, as the degree of cross-correlation expressed by $\tilde{g}_{1,2}$ increases (i.e., decreasing χ), $w_{i,i}(1_2, 1_2|1_1)$ drops below the classical level of unity, indicative of the sub-Poissonian character of the conditional state of field 2. For $\delta t = 150$ ns, $w_{i,i}(1_2, 1_2|1_1) = 0.34 \pm 0.06$ for $\tilde{g}_{1,2} = 7.3$, while with $\delta t = 0$, $w_{i,i}(1_2, 1_2|1_1) = 0.24 \pm 0.05$ for $\tilde{g}_{1,2} = 10.2$. Beyond the comparison to our model shown the figure, empirically we find that $w_{i,i}(1_2, 1_2|1_1)$ is well approximated by $\tilde{g}_{1,1}\tilde{g}_{2,2}/\tilde{g}_{1,2}$, as in the ideal case of Eq. 1. However, independent of such comparisons, we stress that the observations reported in Fig. 4 represent a sizable nonclassical effect in support of the conditional generation of single photons for field 2.

In conclusion, our experiment represents an important step in the creation of an efficient source of single photons stored within an atomic ensemble, and thereby towards enabling diverse protocols in quantum information science [3, 4, 6, 7]. Our model supports the hypothesis that the inherent limiting behavior of $w_{i,i}(1_2, 1_2|1_1)$ below unity is set by the efficiency η_l, which leads to prohibitively long times for data acquisition for $\chi \lesssim 0.04$, corresponding to the smallest value of $w_{i,i}$ in Fig. 4. We are pursuing improvements to push $\eta_l \simeq 0.15 \to 1$, including in the intrinsic collection efficiency following the analysis of Ref. [24]. Dephasing due to Larmor precession in the quadrupole field of the MOT limits $\delta t \lesssim 300$ ns, which can be extended to several seconds in optical dipole or magnetic traps [23].

We gratefully acknowledge the contributions of A. Boca, D. Boozer, W. Bowen, and L.-M. Duan. This work is supported by ARDA, and by the Caltech MURI Center for Quantum Networks and by the NSF.

* School of Physics, Georgia Institute of Technology, Atlanta, Georgia 30332

[1] I. L. Chuang and Y. Yamamoto, Phys. Rev. A 52, 3489 (1995).
[2] Q. A. Turchette *et al.*, *Phys. Rev. Lett.* **75**, 4710-4713 (1995).
[3] E. Knill, R. Laflamme, and G. Milburn, *Nature* **409**, 46-52 (2001).
[4] N. Lutkenhaus, Phys. Rev. A **61**, 052304 (2000).
[5] H.-J. Briegel and S. J. van Enk, in *The Physics of Quantum Information*, eds. D. Bouwmeester, A. Ekert, and A. Zeilinger (Springer-Verlag, Berlin, 2000), **6.2** & **8.6**.
[6] L.-M. Duan, *et al.*, *Nature* **414**, 413 (2001).
[7] L.-M. Duan and H. J. Kimble, quant-ph/0309187.
[8] P. Michler *et al.*, Science **290**, 2282 (2000).
[9] E. Moreau *et al.*, Appl. Phys. Lett. **79**, 2865 (2001).
[10] M. Pelton *et al.*, Phys. Rev. Lett. **89**, 233602 (2002).
[11] J. F. Clauser, Phys. Rev. D **9**, 853 (1974).
[12] P. Grangier, G. Roger, and A. Aspect, Europhys. Lett. **1**, 173 (1986).
[13] C. K. Hong and L. Mandel, *Phys. Rev. Lett.* **56**, 58 (1986).

[14] A. I. Lvovsky *et al.*, *Phys. Rev. Lett.* **87**, 050402 (2001).
[15] T. B. Pittman, B. C. Jacobs, J. D. Franson, *Phys. Rev. A***66**, 042303 (2002).
[16] J. B. Altepeter *et al.*, *Phys. Rev. Lett.* **90**, 193601 (2003).
[17] A. B. U'Ren *et al.*, quant-ph/0312118.
[18] B. Julsgaard *et al.*, *Q. Inf. & Computation* **3**, 518 (2003).
[19] M. Lukin, *Rev. Mod. Phys.* **75**, 457 (2003).
[20] A. Kuzmich *et al.*, Nature **423**, 731 (2003).
[21] Wei Jiang *et al.*, quant-ph/0309175.
[22] See Supplementary Information accompanying Ref. [20].
[23] *Laser Cooling and Trapping*, H. J. Metcalf and P. van der Straten (Springer-Verlag, 1999).
[24] L.-M. Duan, J. I. Cirac, and P. Zoller, *Phys. Rev. A* **66**, 023818 (2002).
[25] As a consistency check, we have employed white light for measurements as in Figs. 2 − 4, and find that $\tilde{g}_{1,1} = 1.02 \pm 0.01, \tilde{g}_{2,2} = 1.01 \pm 0.01, \tilde{g}_{1,2} = 1.02 \pm 0.01, w_{i,i} = 0.99 \pm 0.2, w_{i,j} = 0.97 \pm 0.02$, where in all cases, these correlation functions should equal unity.
[26] The overall efficiencies $\alpha_{1,2} = \xi_{1,2} T_{1,2} \varsigma_{1,2}$, where $\xi_{1,2} = (0.41 \pm 0.04, 0.47 \pm 0.04)$ for light with the spatial shape of the *write*, *read* beams propagating from the MOT to the input beam splitters for detectors $(D_{1A,1B}, D_{2A,2B})$, which have quantum efficiencies $\varsigma_{1,2} \simeq (0.50, 0.40)$ (i.e., photon *in* to TTL pulse *out*). The efficiencies $T_{1,2} = 0.50$ for PBS2 in Fig. 1 account for the presumed unpolarized character of the $(1,2)$ fields in our experiment.

4. J. R. P. Geiger, P. Jonas, *Neuron* **28**, 927 (2000).
5. D. J. Linden, *Neuron* **22**, 661 (1999).
6. C. C. Lien, P. Jonas, *J. Neurosci.* **23**, 2058 (2003).
7. J. A. Connor, C. F. Stevens, *J. Physiol.* **213**, 31 (1971).
8. K. G. Chandy, G. A. Gutman, in *Handbook of Receptors and Channels*, R. A. North, Ed. (CRC Press, Boca Raton, FL, 1995), vol. 2.
9. O. Pongs *et al.*, *Ann. N. Y. Acad. Sci.* **868**, 344 (1999).
10. W. N. Zagotta, T. Hoshi, R. W. Aldrich, *Science* **250**, 568 (1990).
11. G. Yellen, *Q. Rev. Biophys.* **31**, 239 (1998).
12. D. W. Hilgemann, S. Feng, C. Nasuhoglu, *Sci. STKE* **2001**, RE19 (2001).
13. T. F. Freund, I. Katona, D. Piomelli, *Physiol. Rev.* **83**, 1017 (2003).
14. S. L. Shyng, C. G. Nichols, *Science* **282**, 1138 (1998).
15. D. W. Hilgemann, R. Ball, *Science* **273**, 956 (1996).
16. T. Baukrowitz *et al.*, *Science* **282**, 1141 (1998).
17. B. C. Suh, B. Hille, *Neuron* **35**, 507 (2002).
18. L. Wu, C. S. Bauer, X. G. Zhen, C. Xie, J. Yang, *Nature* **419**, 947 (2002).
19. H. H. Chuang *et al.*, *Nature* **411**, 957 (2001).
20. M. Fink *et al.*, *EMBO J.* **17**, 3297 (1998).
21. H. Watanabe *et al.*, *Nature* **424**, 434 (2003).
22. A. Villarroel, T. L. Schwarz, *J. Neurosci.* **16**, 1016 (1996).
23. S. Keros, C. J. McBain, *J. Neurosci.* **17**, 3476 (1997).
24. C. M. Colbert, E. Pan, *J. Neurosci.* **19**, 8163 (1999).
25. E. Honore, J. Barhanin, B. Attali, F. Lesage, M. Lazdunski, *Proc. Natl. Acad. Sci. U.S.A.* **91**, 1937 (1994).
26. Materials and methods are available as supporting material on *Science* Online.
27. J. López-Barneo, T. Hoshi, S. H. Heinemann, R. W. Aldrich, *Recept. Channels* **1**, 61 (1993).
28. H. H. Jerng, M. Shahidullah, M. Covarrubias, *J. Gen. Physiol.* **113**, 641 (1999).
29. T. Krauter, J. P. Ruppersberg, T. Baukrowitz, *Mol. Pharmacol.* **59**, 1086 (2001).
30. C. Antz *et al.*, *Nature Struct. Biol.* **6**, 146 (1999).
31. C. Antz *et al.*, *Nature* **385**, 272 (1997).
32. G. Yellen, *Nature* **419**, 35 (2002).
33. C. C. Lien, M. Martina, J. H. Schultz, H. Ehmke, P. Jonas, *J. Physiol.* **538**, 405 (2002).
34. J. Roeper *et al.*, *Nature* **391**, 390 (1998).
35. D. A. Doyle *et al.*, *Science* **280**, 69 (1998).
36. Y. Zhou, R. MacKinnon, *J. Mol. Biol.* **333**, 965 (2003).
37. F. I. Valiyaveetil, Y. Zhou, R. MacKinnon, *Biochemistry* **41**, 10771 (2002).
38. T. C. Hwang, R. E. Koeppe II, O. S. Andersen, *Biochemistry* **42**, 13646 (2003).
39. D. Oliver, B. Fakler, unpublished data.
40. P. Needleman, J. Turk, B. A. Jakschik, A. R. Morrison, J. B. Lefkowith, *Annu. Rev. Biochem.* **55**, 69 (1986).
41. L. Heginbotham, R. MacKinnon, *Neuron* **8**, 483 (1992).
42. K. L. Choi, R. W. Aldrich, G. Yellen, *Proc. Natl. Acad. Sci. U.S.A.* **88**, 5092 (1991).
43. We thank J. P. Adelman for comments on the manuscript, A. Blomenkamp and S. Eble for technical assistance, H. Kalbacher for the ball peptide, and S. H. Heinemann and R. Klinger for help with the PIP$_2$-binding assay.

Supporting Online Material
www.sciencemag.org/cgi/content/full/1094113/DC1
Materials and Methods
Figs. S1 to S4
References and Notes

1 December 2003; accepted 19 February 2004

Published online 18 March 2004;

10.1126/science.1094113
Include this information when citing this paper.

REPORTS

Real-Time Quantum Feedback Control of Atomic Spin-Squeezing

JM Geremia,* John K. Stockton, Hideo Mabuchi

Real-time feedback performed during a quantum nondemolition measurement of atomic spin-angular momentum allowed us to influence the quantum statistics of the measurement outcome. We showed that it is possible to harness measurement backaction as a form of actuation in quantum control, and thus we describe a valuable tool for quantum information science. Our feedback-mediated procedure generates spin-squeezing, for which the reduction in quantum uncertainty and resulting atomic entanglement are not conditioned on the measurement outcome.

Quantum systems evolve deterministically when no one is looking. Free from observation, knowledge of a quantum state at one point in time is in principle sufficient to predict its entire evolution. However, when a measurement is performed, quantum mechanics postulates that the observer will obtain a random postmeasurement outcome. Conveniently, measurement can produce states that are difficult to obtain by other means, such as Hamiltonian evolution, and thus provides a powerful tool for quantum state preparation. But standard quantum mechanics does not predict the outcomes of individual experiments, only their likelihood. Measurement-based state preparation is hindered by nondeterminism, and desirable (for example, entangled) quantum states often correspond to highly unlikely measurement outcomes. Here we demonstrate that quantum indeterminism can be reduced by suitable intrameasurement feedback, engineered to steer the outcome of an otherwise random quantum process toward a deterministic outcome.

The quantum system in our experiment was provided by a cloud of N atoms each with intrinsic angular momentum, $\hbar f$, because of a combination of nuclear spin, valence electron spin, and orbital angular momentum. The atoms were initially polarized such that their individual momenta were oriented along a common longitudinal direction, which we chose to be the x axis. The resulting atomic state displayed a net magnetization, $\mathbf{F}$, along x with magnitude $|\mathbf{F}| = \hbar\sqrt{F(F+1)}$, where $F = Nf$. The cartesian components of $\mathbf{F}$ are associated with noncommuting quantum operators, $\hat{F}_x$, $\hat{F}_y$ and $\hat{F}_z$, that obey the Heisenberg uncertainty relation

$$\Delta\hat{F}_y\Delta\hat{F}_z \geq \frac{1}{2}|\langle\hat{F}_x\rangle| \qquad (1)$$

This inequality has the interpretation that an ensemble of measurements (for similarly prepared atomic samples) performed on either $\hat{F}_y$ or $\hat{F}_z$ will yield a distribution of random shot-to-shot outcomes. For a large magnetization, the F_z (for example) measurement distribution is essentially Gaussian with mean $\langle\hat{F}_z\rangle$ and variance $\Delta\hat{F}_z^{\,2} \equiv \langle\hat{F}_z^{\,2}\rangle - \langle\hat{F}_z\rangle^2$. The fully polarized atomic state has $\langle\hat{F}_x\rangle = F$ and $\Delta\hat{F}_y = \Delta F_z = \sqrt{F/2}$, and is referred to as a coherent spin state (Fig. 1A)

It is possible to reduce the measurement variance in one of the transverse components below the coherent state value of $F/2$ at the expense of increased uncertainty in the orthogonal component, provided that Eq. 1 remains satisfied (Fig. 1A). Polarized states with this property are referred to as spin-squeezed states (*1*) and have received much attention for their potential to improve the sensitivity of spin-resonance measurements, including magnetometry (*2*, *3*) and atomic clocks (*4*, *5*). Spin-squeezing below the coherent state level is also of fundamental interest in quantum information science for achieving many-particle entanglement (*6*).

Although several different mechanisms have been explored for the preparation of squeezed atomic states (*7*, *8*), interest has focused on using quantum nondemolition (QND) measurements (*9*–*11*), in which the atomic system interacts coherently with an off-resonant optical probe. As a result, the z component of the atomic magnetization, F_z,

---

Physics and Control and Dynamical Systems, California Institute of Technology, Pasadena, CA 91125, USA.

*To whom correspondence should be addressed. E-mail: jgeremia@caltech.edu

becomes weakly entangled with the probe polarization, and photodetection gradually (*9*) provides the observer with information about the spin state (*12–14*). Continuous observation conditionally reduces ΔF_z^2 with respect to the QND measurement outcome in any individual measurement trajectory; however, the ensemble averaged uncertainty is not reduced, because the F_z measurement outcomes over many QND trajectories are distributed with a variance equal to ΔF_z^2 of the initial state.

Our experiment used real-time continuous quantum feedback (*15*) to steer the value of F_z toward a fiducial value in each QND measurement trajectory (*3*, *12*), and we were thus able to demonstrate unconditional spin-squeezing. Figure 1B provides a schematic of our experimental apparatus (*16*), which consisted of a spin-polarized cold atom cloud (prepared by laser cooling) and a Faraday polarimeter. As in previous experiments on atomic spin-squeezing, we used optical pumping initially to prepare approximate coherent spin states. The polarimeter photocurrent, which was proportional to F_z via Faraday rotation, provided our continuous QND measurement of atomic spin. With feedback enabled, the QND photocurrent modulated a y-axis magnetic field via proportional feedback to actuate the orientation of $\mathbf{F}$ by y-axis Larmor precession.

Figure 2A1 shows the DC-coupled polarimeter photocurrent for one open-loop (feedback disabled) QND measurement trajectory. Time $t = 0$ corresponds to the beginning of the measurement record after the atom sample preparation (*16*). The QND measurement was initiated at $t = 10$ μs by opening the probe laser shutter, and the value of F_z for each trajectory manifests itself as an offset in the photocurrent. We computed the QND value of F_z from the mean photocurrent, $y_1 = \overline{y(t)}$, for the window $50 \le t < 60$ μs. At $t = 60$ μs, the QND measurement was disabled for 10 μs by closing the probe shutter but was reenabled for the final 30 μs of the trajectory. This latter probe phase constitutes a second QND measurement, where F_z was determined from $y_2 = \overline{y(t)}$, for $70 \le t < 80$ μs.

The measurement trajectory in Fig. 2A1 illustrates conditional spin-squeezing, as the value of y_2 is seen to be correlated with y_1. The conditional uncertainty in F_z may be identified with the statistical uncertainty (due to optical noise) in determining the mean value y_1. With sufficient filtering (time averaging), this uncertainty is significantly reduced and spin-squeezing is obtained (*2*). However, on a shot-to-shot basis, y_1 randomly assumes different Gaussian-distributed values with variance $\Delta F_z^2 \approx F/2$. Figure 3A shows a histogram of $P(y_1)$, the probability of observing a given value of y_1 (generated from 500 trajectories). The measured variance of this distribution is given by ΔF_z^2 for the initial atomic state.

The outcome of the second QND measurement, y_2, can only be predicted with improved precision provided that the value of y_1 is already known: The squeezing is conditioned on the value of y_1. This can be seen from the probability distribution $P(y_2 - y_1)$ (Fig. 3B), which displays one-10th the variance of the initial spin projection. However, the average atomic state over many trajectories is not squeezed with respect to any fiducial value of F_z, such as zero, as indicated by $P(y_2)$ (dashed line in Fig. 3B). In Fig. 2A2, a precision-pulsed longitudinal magnetic field

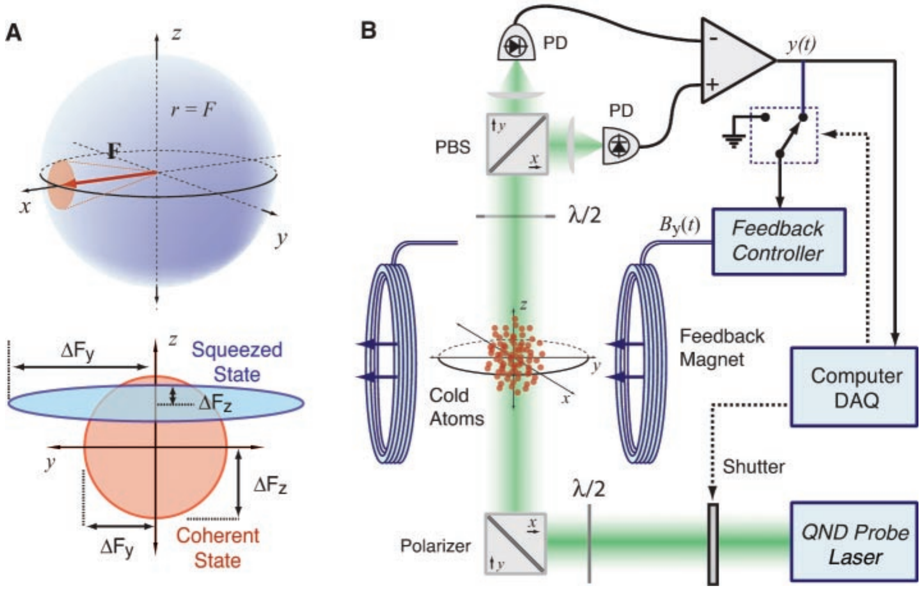

Fig. 1. (**A**) Graphical representation of atomic magnetization, including transverse uncertainty due to the Heisenberg uncertainty principle. (**B**) Schematic of our experimental apparatus. PD, photodetector; PBS, polarizing beam splitter; λ/2, half waveplate; $B_y(t)$, feedback control field; DAQ, data acquisition and control.

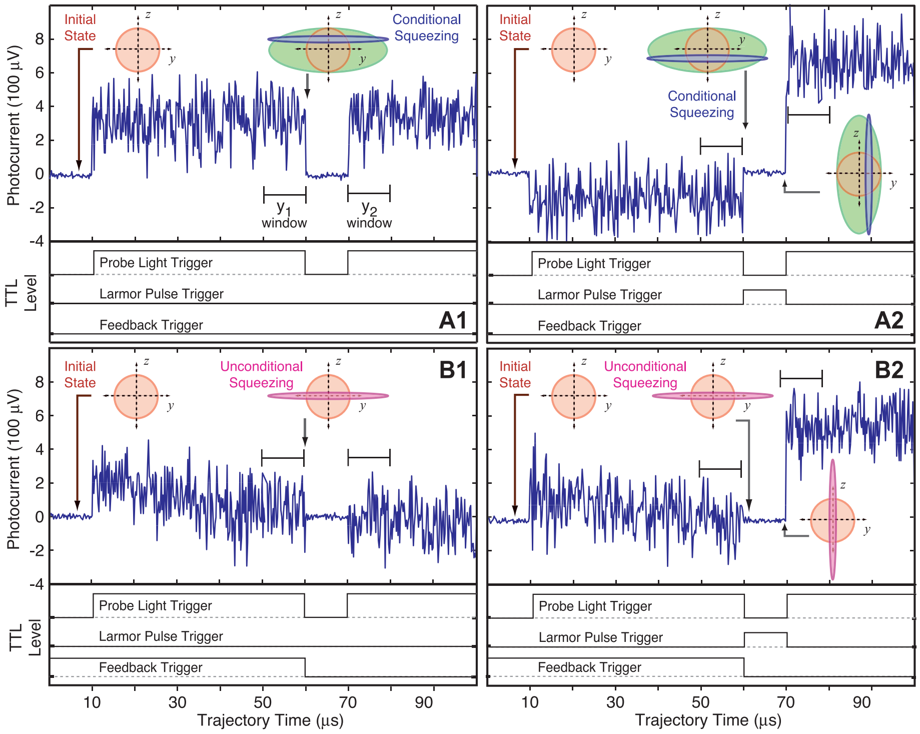

Fig. 2. Single-shot photocurrents for both open- (**A**) and closed- (**B**) loop QND measurements. The value of F_z for each trajectory was obtained by time-averaging the photocurrent over the indicated windows. TTL, computer-controlled digital trigger.

is applied during the 10-μs dark period to produce a 90° rotation around the x axis. The induced Larmor precession exchanges the transverse uncertainties ΔF_y and ΔF_z, making F_z the antisqueezed component. Consequently, y_2 is distributed with greater variance than y_1, as seen in the histogram in Fig. 3C.

In sharp contrast to the open-loop procedure, Fig. 2B1 demonstrates our deterministic ability to steer the value of F_z toward $y_1 = 0$, using intrameasurement feedback. Here the QND measurement reveals an initial offset in the photocurrent that corresponds to the random value of F_z for that trajectory. However, the photocurrent drives a y-axis feedback control field to rotate the atomic magnetization until $F_z = 0$. Feedback locks the orientation of the atomic magnetization onto the x axis despite the initial offset (illustrated by the squeezing ellipse centered on the origin in Fig. 2B1).

The QND measurement of y_2, after a 10-μs dark interval, demonstrates that the spin state is unconditionally squeezed: The feedback-stabilized value of $y_2 = 0$ can be predicted more precisely than the initial spin projection variance as confirmed by the $P(y_2)$ histogram in Fig. 3D. The variance of this distribution is approximately an order of magnitude smaller than the initial-state variance and reflects significant unconditional squeezing. Application of a 90° x-axis Larmor pulse between the two QND measurements again reveals the antisqueezed component of the atomic magnetization (Fig. 2B2).

Figure 3E displays the $P(y_2)$ variances of atomic states for different x-axis dark-period rotation angles. Although the initial spin-projection noise (red crosses) is independent of angle, the atomic states subject to QND measurement display the expected sinusoidal form that is characteristic of an elliptical noise distribution (*17*). The open-loop unconditioned variance, $P(y_2)$ (green squares), saturates to that of the optically pumped state, whereas the conditioned (blue triangles) and feedback (magenta circles) data display significant squeezing. Dotted horizontal lines depict the average uncertainty products (the square root of the minimum value times the maximum value) of their corresponding sinusoids; these uncertainty products respect Eq. 1 in that they lie above the measured variance of our approximate coherent spin state.

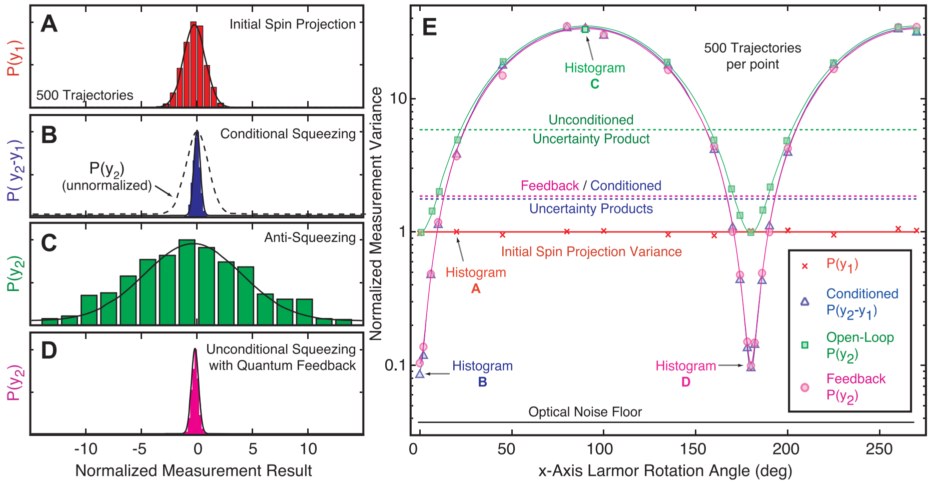

Fig. 3. QND measurement outcome distributions for (**A**) a coherent state, (**B**) conditional squeezing, (**C**) the antisqueezing, (**D**) deterministic squeezing via quantum feedback, and (**E**) rotation of the squeezing ellipse by Larmor precession.

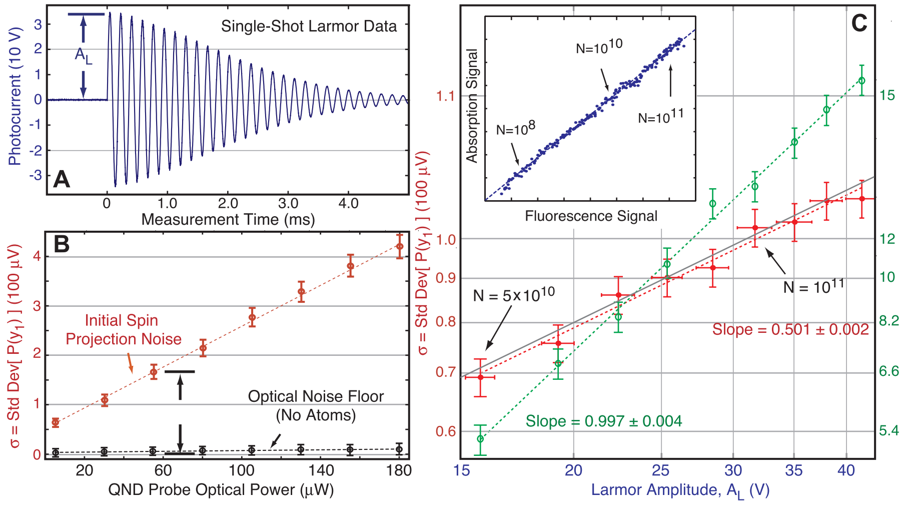

Fig. 4. (**A**) Induced atomic Larmor precession, (**B**) measurement uncertainty $\sigma = \text{std}[y_1]$ as a function of optical probe power, and (**C**) square root dependence of σ on atom number. Std Dev, sample standard deviation computed from 500 QND measurement trajectories.

Although ΔF_z^2 can only be determined by statistical analysis of many measurement trajectories, the QND nature of our procedure is manifest in individual trajectories of the experimental data. This is a key feature of our unmodulated, broadband, and continuous-time approach; it makes the principles of feedback control evident from basic features of the trajectory data. Figure 2 portrays a direct relation among the quantum spin state, the real-time measurement record, and the effects of feedback. Although spin-projection noise of the optically pumped atomic state gives rise to a random offset in the photocurrent of each trial, the conditional variance of the evolving spin state has no further influence on the measurement record (in terms of additional "spin noise"). The photocurrent noise is purely optical, and the decrease in statistical uncertainty accomplished by filtering rigorously corresponds to quantum-mechanical squeezing (*2*).

Care was taken to characterize possible systematic errors that could exaggerate the observed spin-squeezing in our experimental data. Stray magnetic fields were nulled (within a 100-μs line-locked window) with external computer-controlled Helmholtz coils. Imperfect polarimeter detector balancing was characterized by measuring the shot-to-shot photocurrent variance with no atoms in the probe beam path. This optical noise floor was found to lie well below the detected squeezing minima (Figs. 3E and 4B). Atomic depolarization due to probe-induced decoherence and ambient magnetic noise was characterized by observing the magnetization free-induction decay (Fig. 4A). Spin relaxation was estimated to be less than 6% over our 100-μs trajectories, as is also evident from the absence of any apparent "droop" in the open-loop optical signals (*16*).

The variance of the QND measurement, y_1, was measured for varying probe intensity and atom number to verify correct quantum noise–limited scaling. Figure 4B demonstrates good linearity between the probe optical power and the open-loop measurement uncertainty, $\sigma = \text{std}[P(y_1)]$. In Fig. 4C, σ is plotted on a logarithmic scale versus the maximum amplitude A_L of the atomic free-induction decay generated by y-axis Larmor precession. Because A_L is proportional to N, the slope-1/2 fit of σ versus A_L (red data points in Fig. 4C) indicates correct $\sqrt{N}$ scaling for ΔF_z. As a further verification, the Larmor amplitude was compared to an independent determination of atom number via fluorescence imaging with excellent linear scaling (green data points in Fig. 4C). The solid line in Fig. 4C indicates our predicted value for σ computed as $A_L/\sqrt{N}$ using the value of N determined from fluorescence imaging. We estimate our fluorescence data to be accurate to 10 to 20%, verified for varied imaging powers and detunings and by comparison to absorption data (Fig. 4C, inset). Combined with the visibility of the squeezing data in Fig. 3E, these calibrations strongly suggest quantum-limited performance.

It may be noted that an alternative procedure for deterministic spin-squeezing would be to produce a conditionally squeezed state, with a random offset, by open-loop QND measurement, and then to apply a pulsed *y*-axis magnetic field to recover the desired value of F_z. This procedure resembles a discrete form of feedback, but unless further verification measurements and correction steps were performed, the absence of true "loop closure" would render the procedure highly sensitive to technical uncertainties. The precise relation between the photocurrent and the orientation of the magnetization vector depend on a number of parameters, such as the exact number of atoms, that will not be known perfectly in practice. Hence, as noted previously (*3*, *12*), a single-pulse correction scheme will be substantially (even prohibitively) nonrobust.

Our results demonstrate the plausibility of emerging methodologies in quantum physics that use real-time feedback to influence the stochastic dynamics of quantum state reduction in the manner of directed diffusion. Through carefully engineered measurements and control laws, it may become possible to implement dynamics that are inherently unlikely or otherwise technically difficult to achieve. This approach offers great promise for optimizing applications, such as quantum noise–limited metrology, by incorporating techniques from mathematical filtering and control theories.

References and Notes

1. M. Kitagawa, M. Ueda, *Phys. Rev. A* **47**, 5138 (1993).
2. J. Geremia, J. K. Stockton, A. C. Doherty, H. Mabuchi, *Phys. Rev. Lett.* **91**, 250801 (2003).
3. J. K. Stockton, J. Geremia, A. C. Doherty, H. Mabuchi, www.arXiv.org/quant-ph/0309101.
4. D. J. Wineland, J. J. Bollinger, W. M. Itano, D. J. Heinzen, *Phys. Rev. A* **50**, 67 (1994).
5. D. Oblak *et al.*, www.arXiv.org/quant-ph/0312165.
6. A. Sørensen, K. Mølmer, *Phys. Rev. Lett.* **86**, 4431 (2001).
7. J. Hald, J. L. Sørensen, C. Schori, E. S. Polzik, *Phys. Rev. Lett* **83**, 1319 (1999).
8. K. Hammerer, K. Mølmer, E. Polzik, J. Cirac. www.arXiv.org/quant-ph/0312156.
9. M. Brune, S. Haroche, V. Lefevre, J. M. Raimond, N. Zagury, *Phys. Rev. Lett.* **65**, 976 (1990).
10. A. Kuzmich, L. Mandel, N. P. Bigelow, *Phys. Rev. Lett.* **85**, 1594 (2000).
11. B. Julsgaard, A. Kozhekin, E. S. Polzik, *Nature* **413**, 400 (2001).
12. L. K. Thomsen, S. Mancini, H. M. Wiseman, *Phys. Rev. A* **65**, 061801 (2002).
13. A. Silberfarb, I. H. Deutsch, *Phys. Rev. A* **68**, 013817 (2003).
14. G. A. Smith, S. Chaudhury, P. S. Jessen, *J. Opt. B Quant. Semiclass. Opt.* **5**, 323 (2003).
15. H. M. Wiseman, *Phys. Rev. A* **49**, 2133 (1994).
16. Details are provided in the supporting online material on *Science* Online.
17. L.-A. Wu, H. J. Kimble, J. L. Hall, H. Wu, *Phys. Rev. Lett.* **57**, 2520 (1986).
18. We thank P. Jessen, I. Deutsch, A. Silberfarb, H. Wiseman, K. Mølmer, M. Kasevich, V. Vuletik, R. van Handel, and particularly A. Doherty for numerous insightful conversations. Supported by NSF (grants PHY-9987541 and EIA-0086038), the Office of Naval Research (grant N00014-00-1-0479), and the Caltech MURI Center for Quantum Networks (grant DAAD19-00- 1-0374). J.K.S. acknowledges a Hertz fellowship.

Supporting Online Material
www.sciencemag.org/cgi/content/full/304/5668/270/DC1
Materials and Methods
Table S1
References

6 January 2004; accepted 2 March 2004

Plastic Deformation with Reversible Peak Broadening in Nanocrystalline Nickel

Zeljka Budrovic, Helena Van Swygenhoven, Peter M. Derlet, Steven Van Petegem, Bernd Schmitt

Plastic deformation in coarse-grained metals is governed by dislocation-mediated processes. These processes lead to the accumulation of a residual dislocation network, producing inhomogeneous strain and an irreversible broadening of the Bragg peaks in x-ray diffraction. We show that during plastic deformation of electrodeposited nanocrystalline nickel, the peak broadening is reversible upon unloading; hence, the deformation process does not build up a residual dislocation network. The results were obtained during in situ peak profile analysis using the Swiss Light Source. This in situ technique, based on well-known peak profile analysis methods, can be used to address the relationship between microstructure and mechanical properties in nanostructured materials.

In coarse-grained polycrystalline metals, plasticity is carried by dislocations generated by sources within the grains. Such dislocations propagate and interact with preexisting structures and also with each other, and can partly annihilate each other. At a given deformation level, all the dislocation segments that have not annihilated make up the final microstructure of the deformed state and are stored as extrinsic grain boundary (GB) dislocations, dislocation walls and subgrain boundaries, or individual dislocation segments (*1*).

There is a critical length scale below which a dislocation source can no longer operate (*2*) because the stress to bow out a dislocation approaches the theoretical shear stress. For face-centered cubic (fcc) metals the critical grain size is believed to lie between 20 and 40 nm, depending on the nature of the dislocations considered. Whether plasticity in nanocrystalline metals with mean grain sizes below 100 nm and an intrinsic grain size distribution is still carried by dislocations, and whether these dislocations are of the same nature as those observed in coarse-grained metals, are questions that remain unresolved (*3*). Postdeformation analysis in compressed or indented nanocrystalline Ni (nc-Ni) material does not indicate major dislocation debris (*4*), whereas deformation twinning is observed in ground nc-Al (*5*). In situ deformation in a transmission electron microscope (TEM) demonstrates some dislocation activity, often at the crack tip; however, the samples investigated are thinned for electron transparency, and the observed dislocation activity might therefore be a result of other dislocation sources such as surface defects (*4*, *6*–*8*). On the other hand, atomistic simulations suggest that GBs in the nanocrystalline regime promote sliding and act as both a source and sink for lattice dislocations that extend throughout the entire grain, leaving behind a stacking fault defect (*9*–*15*).

X-ray diffraction profile analysis is a well-known technique for microstructural analysis, where broadening of the peaks occurs for two reasons: (i) limitations in the spatial extent of the coherent scattering volumes (in our case the grain size), and (ii) the presence of inhomogeneous strain. The first type of broadening is independent of diffraction order, whereas the second is order dependent (*16*). Possible sources for inhomogeneous strain are lattice dislocations, but other sources can be of equal importance, especially in nanocrystalline structures. These sources may in-

---

Paul Scherrer Institute, CH-5232 Villigen PSI, Switzerland.

arXiv:quant-ph/0406050 v1 8 Jun 2004

Temporal Dynamics of Photon Pairs Generated by an Atomic Ensemble

S. V. Polyakov, C. W. Chou, D. Felinto and H. J. Kimble

Norman Bridge Laboratory of Physics 12-33
California Institute of Technology, Pasadena, CA 91125

The time dependence of nonclassical correlations is investigated for two fields $(1, 2)$ generated by an ensemble of cold Cesium atoms via the protocol of Duan et al. [Nature **414**, 413 (2001)]. The correlation function $R(t_1, t_2)$ for the ratio of cross to auto-correlations for the $(1, 2)$ fields at times (t_1, t_2) is found to have a maximum value $R^{\max} = 292 \pm 57$, which significantly violates the Cauchy-Schwarz inequality $R \leq 1$ for classical fields. Decoherence of quantum correlations is observed over $\tau_d \simeq 175$ ns, and is described by our model, as is a new scheme to mitigate this effect.

In recent years quantum measurement combined with conditional quantum evolution has emerged as a powerful paradigm for accomplishing diverse tasks in quantum information science [1, 2, 3, 4]. For example, Duan, Lukin, Cirac and Zoller (*DLCZ*) [4] have proposed a scheme for the realization of scalable quantum communication networks that relies upon entanglement created probabilistically between remotely located atomic ensembles. By utilizing successful measurements to condition subsequent steps in their protocol, *DLCZ* have developed a scheme that has built-in quantum memory, entanglement purification and resilience to realistic sources of noise, thereby enabling a quantum repeater architecture to overcome photon attenuation [5, 6].

Central to the *DLCZ* protocol is the ability to *write* and *read* collective spin excitations *into* and *out of* an atomic ensemble, with efficient conversion of discrete spin excitations to single-photon wavepackets. Observations of the resulting non-classical correlations between the optical fields generated from *writing* and *reading* such spin excitations have recently been reported by several groups, both at the single-photon level [7, 8, 9] as appropriate to the protocol of *DLCZ* and in a regime of large photon number $n \sim 10^3 - 10^7$ [10]. Generation and detection efficiencies have now been improved so that excitation stored within an atomic ensemble can be employed as a controllable source for single photons [8].

A critical aspect of such single-photon wavepackets is that they are emitted into well-defined spatio-temporal modes to enable quantum interference between emissions from separate ensembles (e.g., for entanglement based quantum cryptography [4]). However, with the exception of the verification of the time-delay implicit for the Raman processes employed [10], experiments to date have investigated neither the time or spatial dependence of quantum correlations for the emitted fields from the atomic ensemble. The high efficiencies achieved in Ref. [8] now enable such an investigation for the temporal properties of nonclassical correlations between emitted photon pairs, which we report in this Letter.

Specifically, we study the time dependence of quantum correlations for photons emitted from an ensemble of cold Cesium atoms, with photon pairs created sequentially by classically controlled *write* and *read* pulses. Large violations of the Cauchy-Schwartz inequality $R \leq 1$ for the ratio of cross to auto-correlations are observed for the generated fields, with $R^{\max} = 292 \pm 57 \nleq 1$. By contrast, previous measurements have reported violations $R \nleq 1$ only for detection events integrated over the entire durations of the *write* and *read* pulses ($R = 1.84 \pm 0.06$ in Ref. [7], $R = 1.34 \pm 0.05$ in Ref. [9], and $R = 53 \pm 2$ in Ref. [8]). We also map the decay of quantum correlations by varying the time delay between the *write* and *read* pulses, and find a decoherence time $\tau_d \simeq 175$ ns. We have developed a model to describe the decoherence and find good correspondence with our measurements. This model is utilized to analyze a new proposal that should extend the correlation times to beyond 10 μs, which would allow for entanglement between atomic ensembles on the scale of several kilometers.

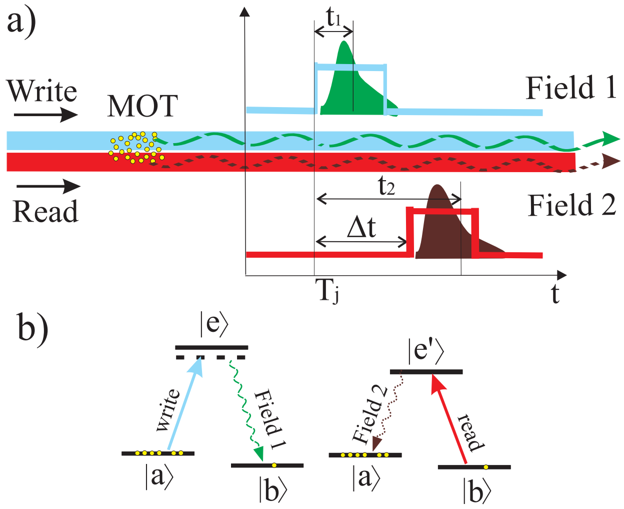

FIG. 1: (a) Schematic of experiment. *Write* and *read* pulses propagate into a cloud of cold Cs atoms (MOT) at times T_j and $T_j + \Delta t$ respectively, and generate the correlated output fields 1 and 2. Quantum correlations for these fields at times (t_1, t_2) are investigated by way of photoelectric detection. (b) The relevant atomic level scheme.

Our experimental procedure is illustrated in Figure 1. An initial *write* pulse at 852 nm creates a state of collective excitation in an ensemble of cold Cs atoms, as heralded by a photoelectric detection event from the Raman field 1. After a user-programmable delay Δt, a *read* pulse at 894 nm converts this atomic excitation into a field excitation of the Raman field 2. The (*write*, *read*) pulses are approximate coherent states with mean photon numbers (10^3,10^5), respectively, and are focussed into the MOT as TEM$_{00}$ Gaussian beams with orthogonal polarizations and beam waist $w_0 = 30$ μm. This scheme is implemented in an optically thick sample of four-level atoms, cooled and trapped in a magneto-optical trap (MOT) [11]. In particular, we utilize the ground hyperfine levels $6S_{1/2}, F = \{4; 3\}$ of atomic Cs (labelled $\{|a\rangle; |b\rangle\}$), and excited levels $\{6P_{3/2}, F = 4; 6P_{1/2}, F = 4\}$ of the D_2, D_1 lines at $\{852; 894\}$ nm (labelled $\{|e\rangle; |e'\rangle\}$).

Each attempt to generate a correlated pair of photons in the $(1, 2)$ fields is preceded by shutting off the trapping light for 700 ns. The re-pumping light is left on for an additional 300 ns in order to empty the $|b\rangle$ state, thus preparing the atoms in $|a\rangle$. The jth trial of a protocol is initiated at time T_j when a rectangular pulse from the *write* laser beam, 150 ns in duration (FWHM) and tuned 10 MHz below the $|a\rangle \rightarrow |e\rangle$ transition, induces spontaneous Raman scattering to level $|b\rangle$ via $|a\rangle \rightarrow |e\rangle \rightarrow |b\rangle$. The *write* pulse is sufficiently weak so that the probability to scatter one Raman photon into a forward propagating wavepacket is much less than unity for each pulse. Detection of one photon from field 1 results in a "spin" excitation to level $|b\rangle$, with this excitation distributed in a symmetrized, coherent manner throughout the sample of N atoms illuminated by the *write* beam [4]. Regardless of successful detection of a photon in field 1, we next address the atomic ensemble with a *read* pulse at a time $T_j + \Delta t$, where Δt is controlled by the user. The *read* light is a rectangular pulse, 120 ns in duration, tuned to resonance with the $|b\rangle \rightarrow |e'\rangle$ transition.

To investigate the photon statistics, we use four avalanche photodetectors, a pair for each field i, labelled as $D_{iA,iB}$, which are activated at $(T_j, T_j + \Delta t)$ with $i = (1, 2)$, respectively, for 200 ns for all experiments. The quantity $p_\tau(t_l, t_m)$ is defined as the joint probability for photoelectric detection from field l in the interval $[T_j + t_l, T_j + t_l + \tau]$ and for an event from field m in the interval $[T_j + t_m, T_j + t_m + \tau]$, where l and m equal 1 or 2. $p_\tau(t_l, t_m)$ is determined from the record of time-stamped detection events at $D_{1A,1B}, D_{2A,2B}$. In a similar fashion, $q_\tau(t_l, t_m)$ gives the joint probability for detection for fields (l, m) in the intervals $([T_j + t_l, T_j + t_l + \tau], [T_k + t_m, T_k + t_m + \tau])$ for two trials $k \neq j$.

Following Refs. [7, 8], we introduce the time-dependent ratio $R_\tau(t_1, t_2)$ of cross-correlation to auto-correlation for the $(1, 2)$ fields, where

$$R_\tau(t_1, t_2) \equiv \frac{[p_\tau(t_1, t_2)]^2}{p_\tau(t_1, t_1)p_\tau(t_2, t_2)} \, . \tag{1}$$

This ratio is constrained by the inequality $R_\tau(t_1, t_2) \leqslant 1$ for all fields for which the Glauber-Sudarshan phase-space function is well-behaved (i.e., *classical* fields) [7, 12]. Beyond enabling a characterization of the quantum character of the $(1, 2)$ fields in a model independent fashion, measurements of $R_\tau(t_1, t_2)$ also allow inferences of the quantum state for collective excitations of single spins within the atomic ensemble.

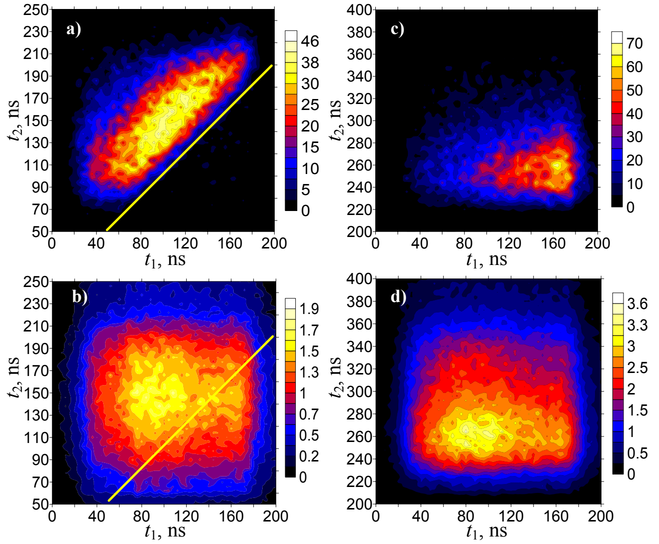

FIG. 2: Probability for joint detection from the fields $(1, 2)$ at times (t_1, t_2) with origin at the beginning of the *write* pulse. (a) $p_\tau(t_1, t_2)$, and (b) $q_\tau(t_1, t_2)$ for overlapped *write* and *read* pulses, $\Delta t = 50$ ns, with the solid line corresponding to $t_2 = t_1$. (c) $p_\tau(t_1, t_2)$ and (d) $q_\tau(t_1, t_2)$ for consecutive *write* and *read* pulses, $\Delta t = 200$ ns. In all cases, the bin size $\tau = 4$ ns, and the joint probabilities p_τ and q_τ have been scaled by 10^9.

The first step in the determination of $R_\tau(t_1, t_2)$ is the measurement of the joint probability $p_\tau(t_1, t_2)$ for the $(1, 2)$ fields, and for comparison, $q_\tau(t_1, t_2)$ for independent trials. In our experiment, we focus on two cases: (I) nearly simultaneous application of *write* and *read* pulses with offset $\Delta t = 50$ ns less than the duration of either pulse, and (II) consecutive application of *write* and *read* pulses with $\Delta t = 200$ ns longer than the *write*, *read* durations. Results for $p_\tau(t_1, t_2)$ and $q_\tau(t_1, t_2)$ are presented in Fig. 2 as functions of the detection times (t_1, t_2) for the fields $(1, 2)$. For both $\Delta t = 50$ and 200 ns, $p_\tau(t_1, t_2) \gg q_\tau(t_1, t_2)$, indicating the strong correlation between fields 1 and 2, with the maximal ratio $g^{\tau}_{1,2}(t_1, t_2) = p_\tau(t_1, t_2)/q_\tau(t_1, t_2) \gtrsim 30$, which is much greater than reported previously [7, 8, 9]. In Fig. 2, $\tau = 4$ ns, leading to statistical errors of about 8% for the largest values shown.

In case (I) for nearly simultaneous irradiation with *write* and *read* pulses, Fig. 2(a) shows that $p_\tau(t_1, t_2)$ peaks along the line $t_2 - t_1 = \delta t_{12} \simeq 50$ ns with a width $\Delta t_{12} \simeq 60$ ns, in correspondence to the delay δt_{12} and duration Δt_{12} for read-out associated with the transition $|b\rangle \rightarrow |e'\rangle \rightarrow |a\rangle$ given an initial transition $|a\rangle \rightarrow |e\rangle \rightarrow |b\rangle$ [10]. Apparently, the qualitative features of $p_\tau(t_1, t_2)$ depend only upon the time difference between photon detections in fields 1 and 2 (i.e., $p_\tau(t_1, t_2) \approx F(t_2 - t_1)$). In case ($II$) with the *read* pulse launched 200 ns after

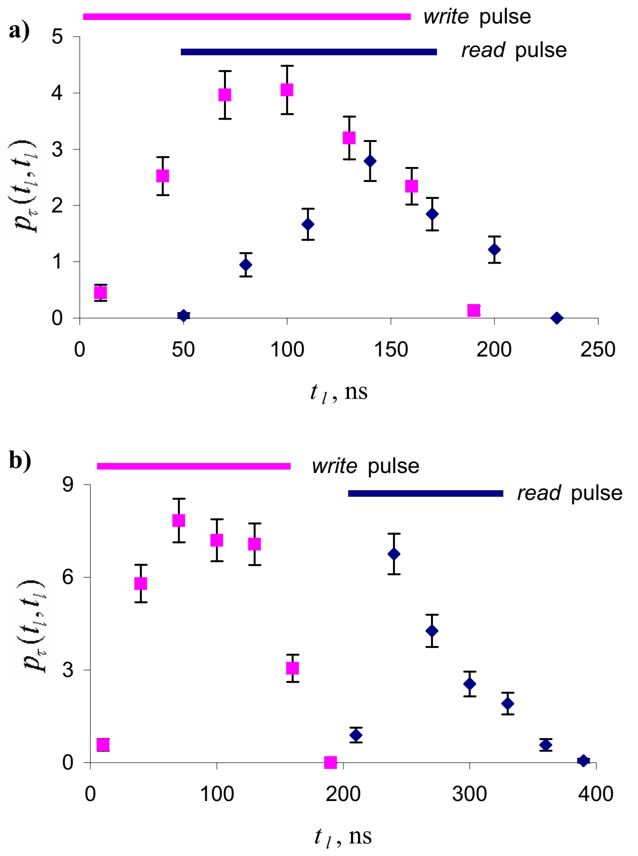

FIG. 3: Probability of joint detection $p_\tau(t_1, t_1)$ for field 1 (squares) and $p_\tau(t_2, t_2)$ for field 2 (diamonds) as functions of respective detection times t_1 and t_2. Bin size $\tau = 30$ ns. (a) Overlapping *write* and *read* pulses, $\Delta t = 50$ ns; (b) Consecutive *write* and *read* pulses, $\Delta t = 200$ ns.

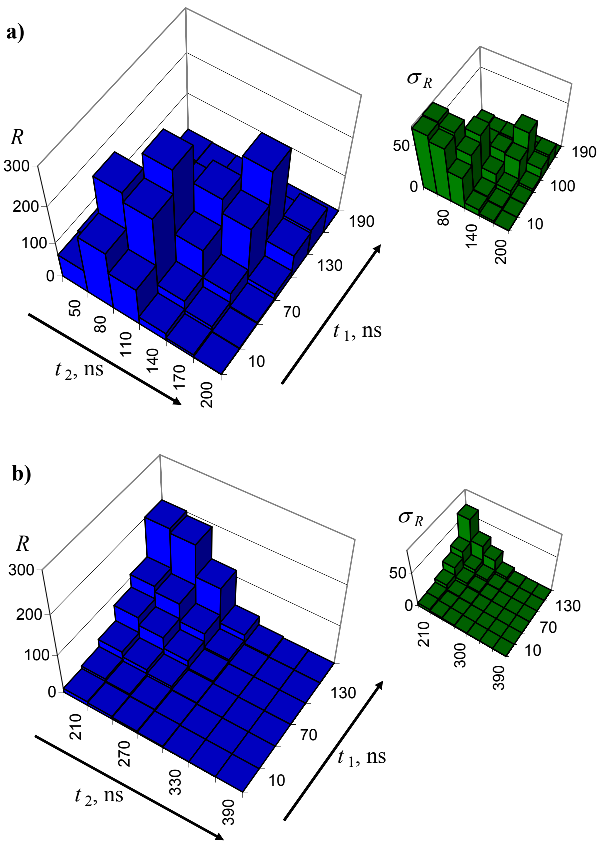

FIG. 4: The experimentally derived ratio $R_\tau(t_1, t_2)$ [Eq. 1] as a function of detection times (t_1, t_2) for the $(1, 2)$ fields, with $R_\tau \leq 1$ for classical fields. The left column gives $R_\tau(t_1, t_2)$ for $\Delta t = 50$ ns (top) and $\Delta t = 200$ ns (bottom), while the right column gives the associated statistical uncertainties. Bin size $\tau = 30$ ns.

the *write* pulse, excitation is "stored" in the atomic ensemble until the readout. The production of correlated photon pairs should now be distributed along $t_2 \simeq \delta t_{12}$ with width $\simeq \Delta t_{12}$. Instead, as shown in Fig. 2(c), $p_\tau(t_1, t_2)$ peaks towards the end of the *write* pulse (i.e., $t_1 \gtrsim 100$ ns), and near the beginning of the *read* pulse (i.e., $200 \lesssim t_2 \lesssim 300$ ns). Early events for field 1 lead to fewer correlated events for field 2, as $p_\tau(t_1, t_2)$ decays rapidly beyond the line $t_2 - t_1 = \tau_d \simeq 175$ ns. The marked contrast between $p_\tau(t_1, t_2)$ for $\Delta t = 50$ and 200 ns results in a diminished ability for the conditional generation of single photons from excitation stored within the atomic ensemble [8] and, more generally, for the implementation of the *DLCZ* protocol for increasing Δt. The underlying mechanism is decoherence within the ensemble, as will be discussed.

Fig. 2(b, d) displays $q_\tau(t_1, t_2)$ for independent trials $j \neq k$. $q_\tau(t_1, t_2)$ is expected to be proportional to the product of intensities of the fields 1 and 2, in reasonable correspondence to the form shown in Fig. 2(b, d) for our roughly rectangular *write*, *read* pulses, but distinctively different from $p_\tau(t_1, t_2)$ in (a, c).

To deduce $R_\tau(t_1, t_2)$ from Eq. 1, we next determine the joint detection probabilities $p_\tau(t_1, t_1)$ for field 1 and $p_\tau(t_2, t_2)$ for field 2 from the same record of photoelectric events as for Fig. 2 (a, c). Since the rate of coincidences for auto-correlations is roughly 10^2 times smaller than for cross-correlations for the $(1, 2)$ fields, we increase the bin size τ to 30 ns to accumulate enough events to reduce the statistical errors to acceptable levels. Fig. 3 shows the resulting time dependencies of $p_\tau(t_1, t_1)$ and $p_\tau(t_2, t_2)$ for cases (*I*, *II*). While the shape of $p_\tau(t_1, t_1)$ associated with the *write* pulse does not change with Δt, the profile of $p_\tau(t_2, t_2)$ from the *read* pulse is affected and exhibits a rise time that is ~ 3 times shorter for $\Delta t = 200$ ns than for $\Delta t = 50$ ns. This prompt rise in (b) is consistent with the observation that stored excitation is efficiently addressed at the beginning of the *read* pulse for non-overlapping *write*, *read* pulses, while the longer rise time in (a) results from continuous excitation and retrieval of atoms from the state $|b\rangle$ for the overlapping case.

We employ the data in Figs. 2, 3 together with Eq. 1 to construct the ratio $R_\tau(t_1, t_2)$, with the result presented in Fig. 4 [13]. Not unexpectedly, the trends

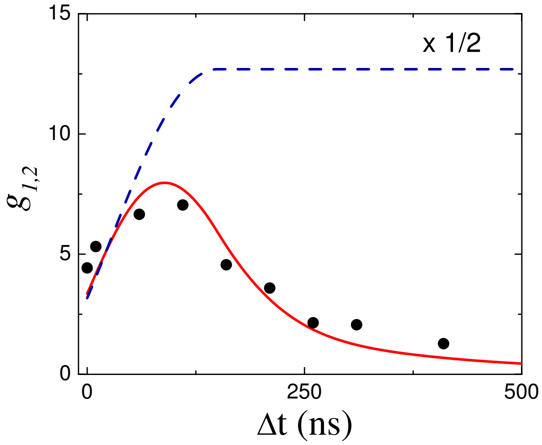

FIG. 5: Coherence time assessment. Experimentally acquired $g_{1,2}$ (black dots), theoretical description of the current experiment with $K = 1.1$ MHz (solid line), and the theoretical prediction for a spin polarized $m_F = 0$ MOT (dotted line).

for $R_\tau(t_1, t_2)$ closely resemble those of the joint probability $p_\tau(t_1, t_2)$ for correlated pair generation previously discussed. As for the violation of the Cauchy-Schwarz inequality $R_\tau(t_1, t_2) \leq 1$ for classical fields [7, 12], we observe maximal violations with $R_\tau^{\max} = 292 \pm 57$ for $\Delta t = 50$ ns and $R_\tau^{\max} = 202 \pm 60$ for $\Delta t = 200$ ns ($R_\tau = 198 \pm 33$ in the neighboring bin). The relatively large errors in $R_\tau(t_1, t_2)$ arise predominantly from the uncertainties in $p_\tau(t_1, t_1)$ and $p_\tau(t_2, t_2)$ (Fig. 3) [14].

The forms for $p_\tau(t_1, t_2)$ and $R_\tau(t_1, t_2)$ for the cases $\Delta t = 50$ and 200 ns imply a decoherence process operative on a time scale $\tau_d \sim 175$ ns. To investigate this decay, we have performed a separate set of experiments with the delay Δt varied $0 \leq \Delta t \leq 400$ ns. For each Δt we determine the normalized correlation function $g_{1,2}^\tau$ from the ratio of integrated coincidence counts to singles counts over the entire detection window (i.e., $\tau = 200$ ns), with the results presented in Fig. 5.

In Fig. 5, the initial growth of $g_{1,2}^\tau$ for small Δt is due to the finite time required to produce sequentially photons in the $(1, 2)$ fields, which is already evident in Fig. 2. More troublesome is the rapid decay of $g_{1,2}^\tau$. A likely candidate responsible for this decay is Larmor precession among the various Zeeman states of the $F = 3, 4$ hyperfine levels of the $6S_{1/2}$ ground level.

To investigate this possibility, we have extended the treatment of Ref. [15] to include the process involving the *read* beam as well as the full set of Zeeman states for the $F = 3, 4$ hyperfine levels. The sample of Cs atoms is assumed to be initially unpolarized and distributed over the same range of magnetic fields as for the MOT. With *write* and *read* pulses that approximate those used in our experiment, we obtain an expression for the probability $\tilde{p}_\tau(t_1, t_2)$ to generate a pair of photons at times (t_1, t_2) for fields 1 and 2 as a function of the offset Δt. By summing contributions for all (t_1, t_2) over the detection windows, we arrive at the joint probability $\tilde{p}_{1,2}(\Delta t)$ that we compare to the measured $g_{1,2}(\Delta t)$ by way of a single overall scaling parameter for all Δt, as the rate of single counts in fields $(1, 2)$ is measured not to depend on Δt (to within 20%) The result is the solid curve in Fig. 5 that evidently adequately describes the impact of Larmor precession on our experiment. The form of $\tilde{p}_{1,2}(\Delta t)$ strongly depends upon the inhomogeneity of Zeeman splitting across the MOT, which is described by the parameter $K = \mu_B g_{F_g} Lb/h$, where L is the MOT diameter, b is the gradient of the magnetic field for the MOT, and g_{F_g} is the Landé factor. The curve in Fig. 5 is the theoretical result for an initially unpolarized sample with $K = 1.1$ MHz as for our experiment (i.e., $L \approx 3.6$ mm and $b \approx 8.4$ G/cm).

An obvious remedy for this dephasing is to eliminate the magnetic field altogether, as by transferring the sample to a dipole-force trap [11]. Alternatively, we have developed a scheme that should allow for long coherence times even in the presence of the quadrupole field of the MOT by utilizing only magnetic-field insensitive states. The *write*, *read* beams are polarized $\sigma_\pm$ and are aligned along the $z-$axis of the MOT, which provides the quantization axis. Atoms within the approximately cylindrical volume illuminated by these beams are initially spin polarized into $F = 3, m_F = 0$ [16]. The $(1, 2)$ fields are selected to be $\sigma_\pm$, which results in spin excitation stored in $F = 4, m_F = 0$. The prediction of our model for this new protocol for the same experimental conditions as before but now with an initially spin polarized sample is shown as the dashed curve in Figure 5, resulting in an increase of more than 3× in $g_{1,2}^\tau$, and significantly extending the decoherence time to more than $\tau_d \sim 10\mu$s.

In conclusion, we have reported the first observations of the temporal dependence of the joint probability $p_\tau(t_1, t_2)$ for the generation of correlated photon pairs from an atomic ensemble, which is critical for the protocol of Ref. [4]. Our measurements of $p_\tau(t_1, t_2)$ are an initial attempt to determine the structure of the underlying two-photon wavepacket [17]. The nonclassical character of the emitted $(1, 2)$ fields has been tracked by way of time dependence of the ratio $R_\tau(t_1, t_2)$, with $R^{\max} = 292 \pm 57 \nleq 1$. Decoherence due to Larmor precession has been characterized and identified as a principal limitation of the current experiment. A new scheme for effectively eliminating this decay process has been proposed and analyzed, and could be important for the experimental realization of scalable quantum networks [4] as well as for an improved source for single photons [8].

This work is supported by ARDA, the Caltech MURI Center for Quantum Networks, and the NSF.

---

[1] C. H. Bennett, *et al.*, Phys. Rev. Lett. **70**, 1895 (1993).
[2] R. Raussendorf, H. J. and Briegel, Phys. Rev. Lett. **86**, 5188 (2001).
[3] E. Knill, R. Laflamme, and G. J. Milburn, Nature **409**, 46-52 (2001).
[4] L.-M. Duan *et al.*, Nature **414**, 413 (2001).
[5] H.-J. Briegel *et. al.* , Phys. Rev. Lett. **81**, 5932 (1998).
[6] S. J. Enk, J. I. Cirac, and P. Zoller, Science **279**, 205 (1998).
[7] A. Kuzmich *et al.*, Nature **423**, 731 (2003), and accompanying Supplementary Information.
[8] C. W. Chou *et al.*, Phys. Rev. Lett. **92**, 213601 (2004).
[9] Wei Jiang *et al.*, Phys. Rev. A **69**, 043819 (2004).
[10] C. H. van der Wal *et al.*, Science **301**, 196 (2003).
[11] *Laser Cooling and Trapping*, H. J. Metcalf and P. van der Straten (Springer-Verlag, 1999).
[12] J. F. Clauser, Phys. Rev. D **9**, 853 (1974).
[13] Before applying Eq. 1, we reprocess the data for $p_\tau(t_1, t_2)$ in Fig. 2 for $\tau = 30$ ns bin size.
[14] To verify the validity of our experimental procedures, we calculate $R(t_1, t_2)$ for detection events for the $(1, 2)$ fields from different trials $j \neq k$, for which $R(t_1^j, t_2^k)$ is expected to equal unity. This result is confirmed experimentally to within a statistical uncertainty of less than 4%.
[15] L. -M. Duan, J. I. Cirac, and P. Zoller, Phys. Rev. A **66**, 023818 (2002).
[16] Note that the beam waist $w_0 = 30\mu$m for the *write*, *read* fields is much smaller than the characteristic dimension $l > 1$mm of the MOT.
[17] K. M. Gheri, *et. al.*, Fortschr. Phys. **46**, 401 (1998).

PHYSICAL REVIEW A **72**, 052301 (2005)

Quantum computation via translation-invariant operations on a chain of qubits

Robert Raussendorf
California Institute of Technology, Institute for Quantum Information, Pasadena, California 91125, USA
(Received 17 June 2005; published 1 November 2005)

A scheme of universal quantum computation is described that does not require local control. All the required operations, an Ising-type interaction and spatially uniform simultaneous one-qubit gates, are translation invariant.

DOI: 10.1103/PhysRevA.72.052301 PACS number(s): 03.67.Lx

I. INTRODUCTION

Symmetry reduces complexity. In physical systems realizing quantum computers, the highest degree of symmetry is therefore not the most desirable. A quantum computer needs to be sufficiently simple and robust to be controllable in an experiment yet complex enough to be universal. One may therefore ask the question, "how much symmetry does a quantum computer allow for?" In fact, a number of physical systems considered for the realization of a quantum computer such as optical lattices [1] or arrays of microlenses [2] are translation invariant, and the above question acquires a practical aspect.

Quite surprisingly, it turns out that universal quantum computation can tolerate a fair amount of symmetry. Recently, a scheme of quantum computation using the rotation-invariant measurement of the total "spin" of two qubits as the only gate has been devised [3]. Furthermore, a translation-invariant computation scheme has been described [4].

The computational power of translation-invariant or nearly translation invariant quantum systems was revealed in Lloyd's [5] and Watrous' [6] work on quantum cellular automata (QCA). In Ref. [6] it was shown that a one-dimensional QCA can simulate any quantum Turing machine. Translation invariance is broken only by the initial state which encodes the program. The schemes in Refs. [5] and [7] allow one to simulate quantum circuits using a chain of qubits with a generic translation-invariant interaction. They require different species of qubits in a periodic arrangement and local addressability at one end-point of the chain. In the scheme in Ref. [8] such individual addressing is only required in the initialization. The method proposed in Ref. [4] is completely translation invariant in space. It requires homogeneous one- and two-local operations on five-level systems.

Here I describe a scheme for universal quantum computation via translation-invariant operations on a chain of qubits. No individual addressability is required. The scheme uses an Ising-type interaction and spatially uniform one-qubit gates. The qubits are all of the same species. Cold atoms in optical lattices [1], where the requirement of local control adds to the overall technological challenge, are a candidate for the realization of the presented scheme.

II. CONSTRUCTIVE ELEMENTS, UNIVERSALITY, AND SCALABILITY

I consider a one-dimensional chain of N qubits initialized in the state $|00\cdots 0\rangle$ which is repetitively updated according to the transition function

$$T=\left(\bigotimes_{i=1}^{N-1}\Lambda(Z)_{i,i+1}\right)\left(\bigotimes_{i=1}^{N}H_i\right). \tag{1}$$

That is, in each elementary step of the evolution first a Hadamard gate is applied to each qubit and second, conditional phase gates are simultaneously applied to all pairs of neighboring qubits. This QCA transition function has previously been discussed in Ref. [9].

Between the transitions one may apply translation-invariant unitary transformations of the form

$$U_A(\alpha)=\bigotimes_{i=1}^{N}\exp\left(i\frac{\alpha}{2}A_i\right), \tag{2}$$

with $A\in\{X,Y,Z\}$. (Note that the subscript "i" labels the site. The same operation is applied to each qubit.) These requirements are equivalent to bang-bang pulses of the form (2) and a permanent Ising-type interaction $\mathcal{H}=\Sigma_{i=1}^{N-1}|11\rangle_{i,i+1}\langle 11|$.

Let us first observe that

$$T^{N+1}=R, \tag{3}$$

where R is the reflection operator that sends the state of the qubit chain into its mirror image. Thus, despite the fact that the qubits at the end points need not be addressed, it is relevant that the chain *has* ends. (For adaption of the scheme to a ring of qutrits, see remark 1 in Sec. III). A proof of Eq. (3) is given in the Appendix.

Apart from its use in the computational scheme described here, the bit reversal operation R is interesting in its own. Recently, proposals for both approximate and perfect bit reversal in qubit chains with a Heisenberg and XY interaction have been made; see Refs. [10–12], and references therein. For perfect mirror reflection in an XY chain the coupling strength needs to vary with position [11], but only mildly [12].

Relation (3) represents a method to achieve spatial reflection in systems with an Ising-type interaction. Here, the interaction strength is independent of position, but additional stroboscopic pulses (2) are required to realize the uniform Hadamard transformations.

©2005 The American Physical Society

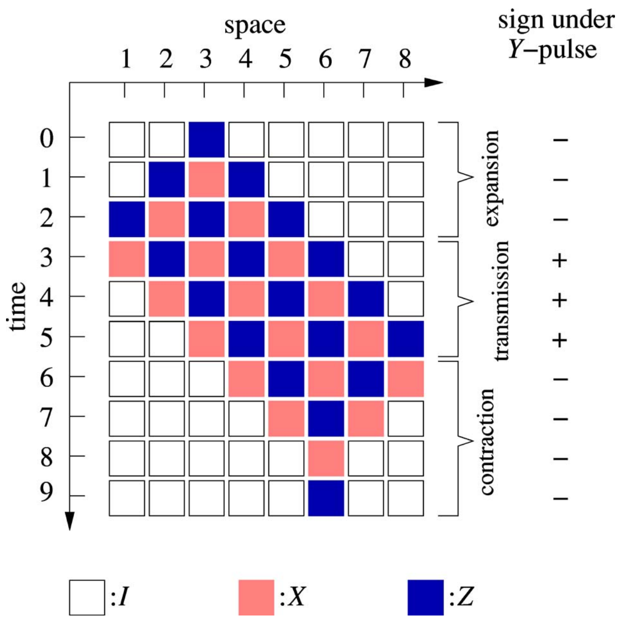

FIG. 1. (Color online) The evolution of a local Pauli observable Z_3 for a qubit chain of length $N=8$. The color-coded boxes denote Pauli operators X_i and Z_i, respectively, and each row of boxes represents a tensor product of such Pauli operators. Within the cycle that leads to reflection of the chain, each local observable undergoes the phases of expansion, transmission, and contraction. When expanding or contracting, the operators pick up a sign factor of −1 under conjugation by a Y pulse.

A. Universal set of gates

The key to the construction of a universal set of gates for the described automaton is displayed in Fig. 1. The $(N+1)$-fold repetition of the elementary transition function constitutes half a clock cycle of the automaton. Within this period each local Pauli observable goes through the phases of expansion, transmission, and contraction to the mirror image of the initial position. During expansion and contraction, the propagated observable is susceptible to a global Y pulse

$$Y \coloneqq U_Y(\pi) = \bigotimes_{i=1}^{N} Y_i. \tag{4}$$

Namely, it picks up a sign factor under conjugation. Contrarily, during the phase of transmission where the observables behave as left or right movers [9] a Y pulse has no effect. The duration of expansion, transmission and contraction phase depend on the initial position of the local Pauli observable. Therefore, each local Pauli observable shows a characteristic response to sequences of Y pulses within the half cycle. In this way, temporal control can be translated into spatial control. In the construction described below, suitably tailored sign flips of Pauli observables are used to reverse rotation angles. Depending on whether a rotation angle is reversed or not, two matching rotations will either cancel or amplify each others effect.

The degree of spatial control obtained suffices to simulate a quantum logic network. One constraint arises: every operation applied to the qubit chain is reflection symmetric. Therefore, qubit i cannot be addressed separately from its mirror image at location $\bar{i} \coloneqq N+1-i$. To cope with this constraint, the same network is simulated twice on the chain, once on the left side and once—as a mirror image—on the right. This doubles the required length of the chain and also influences the readout process, as will be discussed in Sec. II B.

To probe the available spatial control, consider the sequence

$$\begin{aligned} U_Z(\mathbf{c},\alpha) = {} & [TY^{c_N}TY^{c_{N-1}}T\cdots TY^{c_1}TY^{c_0}U_Z(-\alpha/2)] \\ & \times [TY^{c_N}TY^{c_{N-1}}T\cdots TY^{c_1}TY^{c_0}U_Z(\alpha/2)], \end{aligned} \tag{5}$$

where $\mathbf{c}=(c_0,\ldots,c_N)^T$ is a binary vector. To analyze the effect of this sequence, the Pauli operators Y^{c_i} are propagated backwards in time until they reach the U_Z gates. There they accumulate to $\bar{Y}$,

$$\bar{Y} = (T^{-N}Y^{c_N}T^{N})\cdots(T^{-1}Y^{c_1}T)Y^{c_0}. \tag{6}$$

Then,

$$U_Z(\mathbf{c},\alpha) = R\bar{Y}U_Z(-\alpha/2)R\bar{Y}U_Z(\alpha/2) = \bigotimes_{i=1}^{N} \exp[is_i(\alpha/2)Z_i], \tag{7}$$

where we have used that $R\bar{Y}R=\bar{Y}$ and

$$s_i = \begin{cases} 0 & \text{if } [\bar{Y},Z_i]=0, \\ 1 & \text{if } \{\bar{Y},Z_i\}=0. \end{cases} \tag{8}$$

In this way, temporal control has been converted into spatial control, provided that—for suitable choices of $\mathbf{c}$—the binary variables $s_i(\mathbf{c})$ do indeed vary with i.

The s_i are easily computed in the stabilizer formalism [13–15]. Following, Ref. [15] we write Pauli operators A in the form $i^{\delta}(-1)^{\epsilon}\tau_{\mathbf{a}}$, where $\mathbf{a}=\binom{\mathbf{z}}{\mathbf{x}}$ is a $2N$-component binary vector, $\mathbf{z}=(v_1,\ldots,v_N)^T$, $\mathbf{x}=(w_1,\ldots,w_N)^T$; $\delta,\epsilon\in\mathbb{Z}_2$, and $\tau_{\mathbf{a}}=\bigotimes_{i=1}^{N}Z_i^{v_i}X_i^{w_i}$. The evolution of A under conjugation by our Clifford unitary $T, A\rightarrow T(A)=TAT^{\dagger}$, may then be followed in terms of δ, ϵ, and $\mathbf{a}$. The scalars δ and ϵ have no influence on the sign factor $(-1)^{s_i}$ (8), and we need to consider the update of $\mathbf{a}$ only, $\mathbf{a}(t)\rightarrow\mathbf{a}(t+1)=C\mathbf{a}(t)$. Therein, C is a $2N\times 2N$ binary symplectic matrix which takes the form

$$C = \begin{pmatrix} \Gamma & I \\ I & 0 \end{pmatrix}. \tag{9}$$

Γ is the adjacency matrix of the interaction graph (the line graph). Further, denote by F the $2N\times 2N$-matrix $F=\binom{0I}{I0}$ and observe that $FC^{-1}=CF$. Now, the vector $\mathbf{s}=(s_1,\ldots,s_N)^T$ carrying the information about the sign flips under conjugation by $\bar{Y}$ is related to the vector $\mathbf{c}$ describing the temporal sequence of Y pulses, via $\mathbf{s}=M_Z\mathbf{c}$. The matrix M_Z encodes how temporal control is converted to spatial control. Its elements are given by

$$M_Z(i,t) = \mathbf{a}_{Z_i}^T F C^{-t} \mathbf{a}_Y = \mathbf{a}_{Z_i}^T C^t \mathbf{a}_Y. \tag{10}$$

The binary quantities $M_Z(i,t)$ can be defined for all $t(i=1\ldots N)$. But the matrix M_Z is the collection of $M_Z(i,t)$ only within the half-cycle $0 \leqslant t \leqslant N$.

For the interval $t \in [-1,N]$ (including $[0,N]$) the $M_Z(i,t)$ take the values

$$M_Z(i,t) = \theta(i-t-1) + \theta(t+i-N-1). \tag{11}$$

Therein, the addition is modulo 2 and the step function θ is equal to one for all non-negative arguments, and zero otherwise.

To prove Eq. (11) one may—in addition to M_Z—define a matrix M_X that encodes the sign factor acquired by the t-steps-backward-propagated observable X_i under conjugation with $\bar{Y}, M_X(i,t) \coloneqq \mathbf{a}_{X_i}^T C^t \mathbf{a}_Y$. Then, because of $TX_iT^{-1} = Z_i$ and $TZ_iT^{-1} = X_i \otimes_{j|\Gamma_{ij}=1} Z_j$, the $M_Z(i,t)$ and $M_X(i,t)$ obey the recursion relations

$$M_Z(i,t+1) = M_Z(i,t-1) + \sum_{j|\Gamma_{ij}=1} M_Z(j,t),$$

$$M_X(i,t+1) = M_Z(i,t). \tag{12}$$

The solution of the recursion relation for $M_Z(i,t)$ is unique once the boundary conditions on two consecutive time slices are specified. In the discussed case, the boundary conditions are $M_Z(i,-1) = M_Z(i,0) = 1$, for all $i = 1 \cdots N$. The expression on the right-hand side (RHS) of Eq. (11) obeys the recursion relation (12) in the interval $0 \leqslant t \leqslant N-1$ and the boundary conditions, and is thus the correct expression for M_Z.

To perform a z rotation on qubit i, one may apply a Y pulse at times $i-1$ and i. For $c_t = \delta(t,i-1) + \delta(t,i)$, with (11), one obtains $s_j = \delta(j,i) + \delta(j,N+1-i)$. Therefore, the pulse for a z rotation of qubit i is

$$e^{i(\alpha/2)Z_i} e^{i(\alpha/2)Z_{\bar{i}}} = [T^{N+1-i} YTYT^{i-1} U_Z(-\alpha/2)] \times [T^{N+1-i} YTYT^{i-1} U_Z(\alpha/2)], \tag{13}$$

with $\bar{i} = N+1-i$ the mirror site of i. In this way, two out of N z rotations can be selected. A further discrimination between two sites i and $\bar{i}$ is not possible because of the reflection symmetry of every sequence $U(\mathbf{c},\alpha) = RU(\mathbf{c},\alpha)R^{-1}$. As a result of this symmetry, each quantum algorithm is run on the qubit chain in two copies, one being the mirror image of the other. This accounts for a factor of two in spatial overhead.

From Eq. (13) the remaining universal gates can be deduced easily. Relation (13) is conjugated by T^{-1}. Using $T^{-1}Z_iT = X_i$, one finds

$$e^{i(\alpha/2)X_i} e^{i(\alpha/2)X_{\bar{i}}} = [T^{N-i} YTYT^{i} U_X(-\alpha/2)] \times [T^{N-i} YTYT^{i} U_X(\alpha/2)]. \tag{14}$$

Conjugating relation (14) again by T^{-1} and noting that $T^{-1}X_iT = Z_i \otimes_{j|\Gamma_{ij}=1} X_j \coloneqq K_i$ one obtains

$$e^{i(\alpha/2)K_i} e^{i(\alpha/2)K_{\bar{i}}} = [T^{N-1-i} YTYT^{i} U_X(-\alpha/2)T] \times [T^{N-1-i} YTYT^{i} U_X(\alpha/2)T]. \tag{15}$$

Now, the length of the chain is doubled a second time. Specifically, the logical qubits in state $|\psi\rangle$ are interlaced by ancilla qubits which remain in the state $|0\rangle$ throughout the computation

$$|\psi\rangle_{1,2,3,\ldots,n} \rightarrow |\psi'\rangle = |\psi\rangle_{1,3,5,\ldots,2n-1} \otimes |0\ldots0\rangle_{2,4,\ldots,2n-2}. \tag{16}$$

At this point it is suitable to introduce a logical coordinate $[j]$ that is related to the physical location within the qubit chain via $[j] = 2j-1$, for $1 \leqslant j \leqslant n$, such that, e.g., $|\psi'\rangle = |\psi\rangle_{[1],[2],\ldots,[n]} \otimes |0\ldots2\rangle_{2,4,\ldots,2n-2}$. Then, the action of the K_{2j} gate is equivalent to a two-qubit next-neighbor entangling gate

$$\exp\left(i\frac{\alpha}{2}K_{2j}\right)|\psi'\rangle \equiv \exp\left(i\frac{\alpha}{2}X_{[j]}X_{[j+1]}\right)|\psi'\rangle. \tag{17}$$

The gates (13)–(15) form a gate set that can be easily converted into the standard universal set [16].

B. Readout

As an example for global readout a measurement of the z-component of the total spin is considered. The measured observable is

$$S_Z = \sum_i Z_i. \tag{18}$$

This is a model for readout, e.g., of atomic qubits via resonance fluorescence spectroscopy, if the atoms are well within the Lamb-Dicke limit (their separation and fluctuation of position are much smaller than the optical wave length). In this case the underlying physics prohibits the extraction of local information. The readout method described below equally works for a scenario where a local readout could in principle be performed but is not pursued due to technological limitations. For specification of such a measurement model, see remark 3 in Sec. III.

With the capability to perform arbitrary unitary evolution on a quantum register the total spin observable S_Z acting on that register may be conjugated into any desired observable, and the standard network readout of the individual Z_i should be feasible. However, for the setting described here the readout procedure is, in the case of probabilistic algorithms, slightly complicated by the fact that two copies of the algorithm are run simultaneously and the readout measurement couples them.

For the readout each of the two circuits on the chain requires one additional logical qubit that is in the state $|0\rangle$ until the readout starts. The location of this qubit within the logical quantum register is denoted as $[0]$ which shall correspond to the physical position $2n+1$ in the qubit chain [see Fig. 2(a)]. The readout consists of three steps. First, S_Z is measured and the outcome m is recorded. Second, for all logical qubits $j = 1\ldots n$ the following procedure is performed. (2.1) Apply Controlled NOT (CNOT) gates $\Lambda(X)_{[j],[0]} \otimes \Lambda(X)_{[\bar{j}],\overline{[0]}}$ ($[0]$, $\overline{[0]}$ are the target qubits). (2.2) Measure the observable S_Z and record the outcome $m(j)$. (2.3) Apply the CNOT gates $\Lambda(X)_{[j],[0]} \otimes \Lambda(X)_{[\bar{j}],\overline{[0]}}$ again. Third, denote by

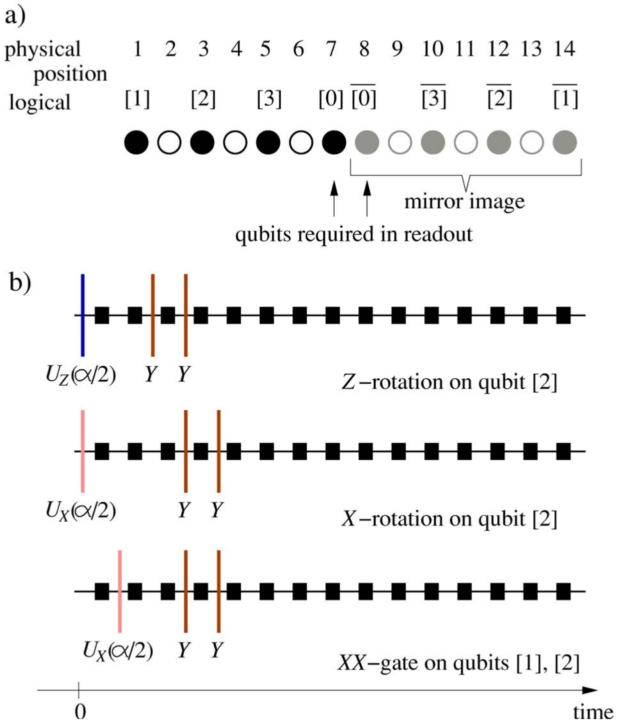

FIG. 2. (Color online) Arrangement of logical qubits within the chain (a) and pulse sequences for gates (b), for $n=3$. (a) Only every second physical qubit in the chain (●) is used as a logical qubit. The qubits in between (○) are ancillas. (b) Pulse sequences for the implementation of the universal gates, during the first half of a clock cycle. The second half-cycle is analogous, with $\alpha\rightarrow-\alpha$. The symbol ■ denotes application of the elementary transition function T. The vertical bars denote pulses (2).

$J=\{j_1,\ldots,j_{|J|}\}$ those $j\leqslant n$ for which $m-m(j)=2$. If $|J|<2$ the readout is finished. Otherwise, for all $k=2\ldots|J|$ perform the following procedure. (3.1) Apply the Toffoli gates $\Lambda_2(X)_{[j_1],[j_k];[0]}\otimes\Lambda_2(X)_{\overline{[j_1]},\overline{[j_k]};\overline{[0]}}$ ([0], $\overline{[0]}$ are the target qubits). (3.2) Measure S_Z and record the measurement outcome $m(j_1,j_k)$. (3.3) Apply the Toffoli gates $\Lambda_2(X)_{[j_1],[j_k];[0]}\otimes\Lambda_2(X)_{\overline{[j_1]},\overline{[j_k]};\overline{[0]}}$ again.

The conditional phase and Toffoli gates are their own inverse such that the above protocol amounts to a sequence of measurements where the first one is of S_Z and the following ones are of conjugated observables. These observables mutually commute because they are all diagonal in the computational basis, and the final state is a simultaneous eigenstate of them. The observables measured in step 2 are $Z_{[0]}Z_{[j]}+Z_{\overline{[0]}}Z_{\overline{[j]}}+\Sigma_{i\neq[0],\overline{[0]}}Z_i$. Since the qubits at locations [0] and $\overline{[0]}$ are individually in the state $|0\rangle$, and the observable $S_Z=\Sigma_i Z_i$ already has been measured in step 1, step 2 effectively acts as the measurement of the observables $Z_{[j]}+Z_{\overline{[j]}}$.

Similarly, step 3 amounts to the measurement of the observables $|11\rangle_{[j_1],[j_k]}\langle 11|+|11\rangle_{\overline{[j_1]},\overline{[j_k]}}\langle 11|$, $\forall k$. This measurement assigns a sharp value to $r_{[j_1]}r_{[j_k]}+\overline{r}_{[j_1]}\overline{r}_{[j_k]}$. Its purpose is, in combination with the information gathered in step 2, to discriminate between the two cases $\{r_{[j_1]}=r_{[j_k]},\overline{r}_{[j_1]}=\overline{r}_{[j_k]}\}$ and $\{r_{[j_1]}\neq r_{[j_k]},\overline{r}_{[j_1]}\neq\overline{r}_{[j_k]}\}$, for each k.

The state of the two quantum registers after the measurement, leaving out all the ancillas in the state $|0\rangle$, may be written as a superposition $\Sigma_\alpha c_\alpha|\mathbf{r}^{(\alpha)}\rangle|\underline{\mathbf{r}}^{(\alpha)}\rangle$ of computational basis states $|\mathbf{r}^{(\alpha)}\rangle|\underline{\mathbf{r}}^{(\alpha)}\rangle$, where $\mathbf{r}=(r_{[1]},\ldots,r_{[n]})^T$, $\underline{\mathbf{r}}=(r_{\overline{[1]}},\ldots,r_{\overline{[n]}})^T$. The measurements then impose constraints upon which basis states are admissible, i.e., occur with nonzero coefficients c_α. The constraints imposed by the measurements in step 2 read

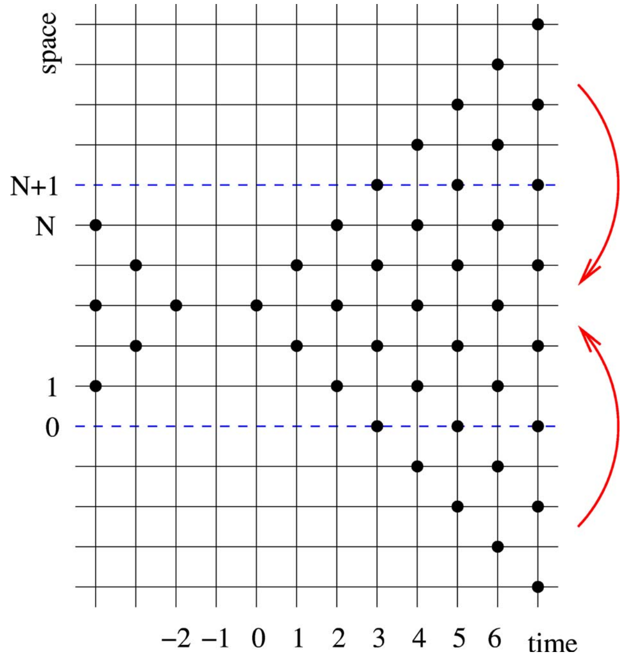

FIG. 3. (Color online) The solution for the recursion relations (A3) in free space. Each vertex in the lattice denotes a space-time point (i,t). The symbol ● indicates $v_i(t)=1$ and + $v_i(t)=0$. To obtain the solution for the case with boundary from the free space solution, the lattice is "folded back" to the space interval $[0,N+1]$.

$$\begin{gathered} r_{[j]}=\overline{r}_{[j]}=0 \text{ for } m-m(j)=0, \\ r_{[j]}+\overline{r}_{[j]} \mod 2=1 \text{ for } m-m(j)=2, \\ r_{[j]}=\overline{r}_{[j]}=1 \text{ for } m-m(j)=4, \end{gathered} \tag{19}$$

for all $j=1\ldots N$. The constraints that arise from the measurements in step 3 are

$$\begin{gathered} r_{[j_1]}+r_{[j_k]} \mod 2=0 \text{ for } m-m(j_1,j_k)=2, \\ r_{[j_1]}+r_{[j_k]} \mod 2=1 \text{ for } m-m(j_1,j_k)=0, \end{gathered} \tag{20}$$

for $[j_1],[j_k]\in J$, $k=2\ldots|J|$. The system (19) and (20) of linear equations has a unique solution if $J=\emptyset$ and two solutions otherwise. In the latter case, the two solutions $\mathbf{r}^{(1)}$ and $\mathbf{r}^{(2)}$ correspond to two states $|\mathbf{r}^{(1)}\rangle|\mathbf{r}^{(2)}\rangle$ and $|\mathbf{r}^{(2)}\rangle|\mathbf{r}^{(1)}\rangle$, and the state of the quantum register after readout is their reflection-symmetric linear combination. The solutions $\mathbf{r}^{(1)}$ and $\mathbf{r}^{(2)}$ are, modulo interchange, uniquely specified by the measurement outcomes m, $\{m(j)\}$ and $\{m(j_i,j_k)\}$. For a probabilistic algorithm, the automaton produces two potential solutions in each run.

C. Overhead

For the described method of universal computation via translation-invariant interaction it is relevant that the elementary transition function T repeated a sufficient number of times reduces to the identity operation. Such an elementary "clock cycle" takes $2(N+1)$ time steps where N is the length of the chain. But as described so far, one still ends up with a set of local and next-neighbor gates and thus pays the price of next-neighbor slowdown twice. This is not necessary. Before the resources are counted, a long-distance entangling gate is described. As compared to a logically equivalent composition of next-neighbor and local gates, it cuts the required operational resources by a factor of order n.

The natural gate set for the described scheme of quantum computation does not only contain local and next-neighbor gates, but all gates of the form

$$U_X(\alpha,L_1,L_2)=\exp\left(i\frac{\alpha}{2}\bigotimes_{l=L_1}^{L_2}X_{[l]}\right). \tag{21}$$

As before, the logical position $[l]$ corresponds to the physical location $2l-1$ in the chain. The sequence for implementing $U_X(\alpha,L_1,L_2)$ is

$$\begin{aligned}U_X(\alpha,L_1,L_2)=&[T^{t_3}YTYT^{t_2}U_X(-\alpha/2)T^{t_1}]\\&\times[T^{t_3}YTYT^{t_2}U_X(\alpha/2)T^{t_1}],\end{aligned} \tag{22}$$

with $t_1=L_2-L_1$, $t_2=L_1+L_2-2$ and $t_3=N-2L_1+2$. Now note that, with $|-\rangle:=-X|-\rangle$,

$$\begin{aligned}e^{i\pi|--\rangle_{l_1,l_2}\langle--|}=&U_X(\pi/2,l_1,l_2)U_X(-\pi/2,l_1+1,l_2)\\&\times U_X(\pi/2,l_1+1,l_2-1)\\&\times U_X(-\pi/2,l_1,l_2-1).\end{aligned} \tag{23}$$

Thus, a long-distance x-controlled spin flip can be implemented with four elementary gates (22). These four operations can be grouped into two pairs, with constant value of L_2 in each pair. Either pair of operations can be implemented in one clock cycle because the Y pulse sequences of the two operations coincide. An x-controlled spin flip thus takes two clock cycles irrespective of the distance between control and target qubit.

Now counting the resources, a quantum computation on n qubits in the described scheme requires a qubit chain of length $N=4n+2$. Each clock cycle takes $8n+6$ elementary time steps (applications of T), and each of the universal gates $\exp(i\alpha/2Z_l)$, $\exp(i\alpha/2X_l)$, and $e^{i\pi|--\rangle l_1,l_2\langle--|}$ takes at most two clock cycles. As compared to the network model, there arises a constant overhead of 4 in the spatial and a linear overhead of $16n$ in temporal resources.

III. CONCLUDING REMARKS

Universal quantum computation can be performed by translation-invariant operations on a chain of qubits initialized in the state $|00\cdots0\rangle$. The described method requires translation-invariant interaction of Ising type and spatially uniform local rotations. As compared to the network model, there occurs a constant spatial and a linear temporal overhead.

Three remarks are in order. (1) In the described setting translation invariance is broken by the finite extension of the qubit chain. To create a setting with perfect translational invariance, one may replace the qubits by qutrits, where the additional level $|2\rangle$ does not take part in any interaction, and consider a $N+1$-qubit ring geometry instead of a chain. Set $|\varphi(i)\rangle=|0\cdots0\rangle_{1\cdots i-1}|2\rangle_i|0\cdots0\rangle_{i+1\cdots N+1}$. With either the translation-invariant superposition $1/\sqrt{N+1}\Sigma_{i=1}^{N+1}|\varphi(i)\rangle$ or mixture $1/(N+1)\Sigma_{i=1}^{N+1}|\varphi(i)\rangle\langle\varphi(i)|$ as the initial state the scheme works as before.

(2) It may occur that a qubit chain capable of the required interaction has been created but its length N is unknown. It can be found out easily by repetitions of the following protocol: Initialize the chain in the state $|00\cdots0\rangle$, apply the transition function T t times and subsequently measure the spin observable $S_Z=\Sigma_{i=1}^{N}Z_i$. The received signal $\langle S_Z(t)\rangle$ carries a characteristic signature of N, namely $\langle S_Z(t)\rangle=N\delta(t \bmod N+1)$.

(3) Deviating from the setting discussed in Sec. II B, the available measurement may be such that local information could in principle be retrieved but is not retrieved, due to technological limitations. As an example, consider cold atoms in an optical lattice which are read out via resonance fluorescence spectroscopy and whose separation is larger than the wavelength of the probing laser. In this case, the readout can be modeled by the map

$$\rho\to\rho'(m)\sim\sum_{\{m_i\}|\Sigma_i m_i=m}P(\{m_i\})\rho P(\{m_i\}), \tag{24}$$

with the projectors $P(\{m_i\})=\otimes_{i=1}^{N}(1+m_iZ_i)/2$, and $m_i=\pm1\,\forall\, i=1\ldots N$. Every atom is individually measured but only the *global* signal $m=\Sigma_i m_i$ is recorded. For measurements of this type the readout procedure is the same as discussed in Sec. II and has the same efficiency.

ACKNOWLEDGMENTS

I thank Frank Verstraete, Luming Duan, GM Jeremia, Robin Blume-Kohout, Gavin Brennen, René Stock, and Sergey Bravyi for discussions. This work was supported by the Multidisciplinary University Research Initiative program under Grant No DAAD19-00-1-0374.

APPENDIX: BIT REVERSAL

Sufficiently many applications of the elementary transition function T reverse the order of qubits within the chain. As stated in Eq. (3), with R the spatial reflection,

$$T^{N+1}=R.$$

This phenomenon is related to the transmission of one-qubit states through chains described in Ref. [17]. Relation (3) is now proved. What needs to be shown is $T^{N+1}(X_p)=X_{\bar{p}}$ and $T^{N+1}(Z_p)=Z_{\bar{p}}$, for all $p=1,\ldots,N$. For this purpose, the vector space formulation [13–15] of the stabilizer formalism is used. In particular, I use the conventions and results of Ref. [15]. The evolution of the Pauli observables X_p, Z_p is followed in terms of the binary quantities **a** and ϵ, introduced in Sec. II below Eq. (8).

First, the recursion relation $\mathbf{a}(t+1)=C\mathbf{a}(t)$ is translated into a recursion relation for the **z** part of **a** alone and a relation that expresses **x** in terms of **z**. From Eq. (9), taking into account that Γ represents a line graph, the following recursion relations are obtained for $\mathbf{z}=(v_1,\cdots,v_N)^T$ and $\mathbf{x}=(w_1,\cdots,w_N)^T$:

$$\begin{gathered} v_1(t+1)=v_2(t)+v_1(t-1), \\ v_i(t+1)=v_{i-1}(t)+v_{i+1}(t)+v_i(t-1), \quad 1<i<N, \\ v_N(t+1)=v_{N-1}(t)+v_N(t-1), \\ w_i(t+1)=v_i(t),\ 1\leqslant i\leqslant N. \end{gathered} \tag{A1}$$

We seek the solution of these recursion relations for the time $t=N+1$, with boundary conditions

$$v_i(-1)=0, \quad v_i(0)=\delta(p-i), \quad \forall\, 1\leqslant i\leqslant N. \tag{A2}$$

The translation-invariance of the recursion relations (A1) is broken by the finite extension of the chain. The problem of solving these recursion relations is now reduced to the translation-invariant case of the infinite chain. Note that if a configuration $\{\tilde{v}_i(t)\}$ obeys the recursion relations

$$\tilde{v}_i(t+1)=\tilde{v}_{i-1}(t)+\tilde{v}_{i+1}(t)+\tilde{v}_i(t-1), \tag{A3}$$

then

$$v_i(t) := \sum_{l=-\infty}^{\infty} \tilde{v}_{i+2l(N+1)}+\tilde{v}_{-i+2l(N+1)} \tag{A4}$$

obeys the recursion relation (A1). The reduction of the case with spatial boundary to the case without boundary is illustrated in Fig. 3.

It is easily checked that

$$\tilde{v}_i(t)=[\theta(p-i+t)+\theta(r-i-t-1)]\delta(p-i+t \mod 2) \tag{A5}$$

is the solution of Eq. (A3) with the boundary conditions $\tilde{v}_i(-1)=0$, $\tilde{v}_i(0)=\delta(p-i)$, $\forall i$. If this expression is inserted into the RHS of Eq. (A4) one obtains a solution for $v_i(t)$ with boundary conditions (A2). It is observed that

$$\begin{gathered} v_i(t) \sim \delta(p-i+t \mod 2), \\ w_i(t) \sim \delta(p-i+t+1 \mod 2). \end{gathered} \tag{A6}$$

Next, the solution $v(t)$ (A4) and (A5) is evaluated for $t=N+1$. One obtains

$$v_i(N+1)=\delta[p-(N+1-i)]. \tag{A7}$$

This implies $T^{N+1}(Z_p)=\pm Z_{\bar{p}}$.

Next, the sign factor $(-1)^\epsilon$ in the above relation is worked out. Using the result of Ref. [15], the recursion relation for ϵ reads $\epsilon(t+1)=\epsilon(t)+\mathbf{z}(t)^T\Gamma_L\mathbf{z}(t)+\mathbf{x}(t)^T\mathbf{z}(t)$, with Γ_L the lower triangular part of Γ. With Eq. (A6), $\epsilon(t)\equiv\epsilon(0)=0$ such that $T^{N+1}(Z_p)=Z_{\bar{p}}$. Finally, with $T(X_p)=Z_p$, $T^{N+1}(X_p)=T^{-1}T^{N+1}T(X_p)=X_{\bar{p}}$.

[1] D. Jaksch, C. Bruder, J. I. Cirac, C. W. Gardiner, and P. Zoller, Phys. Rev. Lett. **81**, 3108 (1998).

[2] G. Birkl, F. B. J. Buchkremer, R. Dumke, and W. Ertmer, Opt. Commun. **191**, 67 (2001).

[3] T. Rudolph and S. S. Virmani, New J. Phys. **7**, 228 (2005).

[4] K. G. H. Vollbrecht, E. Solano, and J. I. Cirac, Phys. Rev. Lett. **93**, 220502 (2004); K. G. H. Vollbrecht and J. I. Cirac, quant-ph/0502143 (unpublished).

[5] S. Lloyd, Science **261**, 1569 (1993).

[6] J. Watrous, in *Proceedings of the 36th IEEE Symposium on Foundations of Computer Science* (IEEE Computer Society Press, Los Alamitos, California, 1995), p. 528.

[7] S. C. Benjamin, Phys. Rev. Lett. **88**, 017904 (2002).

[8] G. Ivanyos, S. Massar, and A. B. Nagy, quant-ph/0502142 (unpublished).

[9] B. Schumacher and R. F. Werner, quant-ph/0405174 (unpublished).

[10] S. Bose, Phys. Rev. Lett. **91**, 207901 (2003).

[11] C. Albanese, M. Christandl, N. Datta, and A. Ekert, Phys. Rev. Lett. **93**, 230502 (2004).

[12] P. Karbach and J. Stolze, quant-ph/0501007 (unpublished).

[13] D. Gottesman, *Stabilizer Codes and Quantum Error Correction*, Ph.D. thesis, California Institute of Technology, 1997 quant-ph/9705052.

[14] M. A. Nielsen and I. L. Chuang, *Quantum Computation and Quantum Information* (Cambridge University Press, Cambridge, 2000).

[15] J. Dehaene and B. De Moor, Phys. Rev. A **68**, 042318 (2003).

[16] P. O. Boykin *et al.*, Inf. Process. Lett. **75**, 101 (2000).

[17] G. K. Brennen and J. E. Williams, Phys. Rev. A **68**, 042311 (2003).

PHYSICAL REVIEW A **71**, 062313 (2005)

Long-range quantum entanglement in noisy cluster states

Robert Raussendorf, Sergey Bravyi, and Jim Harrington
Institute for Quantum Information, California Institute of Technology, Pasadena, California 91125, USA

(Received 9 December 2004; published 14 June 2005)

We describe a phase transition for long-range entanglement in a three-dimensional cluster state affected by noise. The partially decohered state is modeled by the thermal state of a short-range translation-invariant Hamiltonian. We find that the temperature at which the entanglement length changes from infinite to finite is nonzero. We give an upper and lower bound to this transition temperature.

DOI: 10.1103/PhysRevA.71.062313 PACS number(s): 03.67.Mn

I. INTRODUCTION

Nonlocality is an essential feature of quantum mechanics, put to the test by the famous Bell inequalities [1] and verified in a series of experiments (see, e.g., [2]). Entanglement [3] is an embodiment of this nonlocality which has become a central notion in quantum-information theory.

In realistic physical systems, decoherence represents a formidable but surmountable obstacle to the creation of entanglement among far distant particles. Devices such as quantum repeaters [4] and fault-tolerant quantum computers are being envisioned in which the entanglement length [5,6] is infinite, provided the noise is below a critical level. Here we are interested in the question of whether an infinite entanglement length can also be found in spin chains with a short-range interaction that are subjected to noise. A prerequisite for our investigation is the existence of systems with infinite entanglement length at zero temperature. An example of such behavior has been discovered by Verstraete, Martín-Delgado, and Cirac [7] with spin-1 chains in the Affleck-Kennedy-Lieb-Tasaki model [8], and by Pachos and Plenio with cluster Hamiltonians [9]; see also [10]. In this paper, we study the case of finite temperature. We present a short-range, translation-invariant Hamiltonian for which the entanglement length remains infinite until a critical temperature T_c is reached. The system we consider is a thermal cluster state in three dimensions. We show that the transition from infinite to finite entanglement length occurs in the interval $0.30\Delta \leqslant T_c \leqslant 1.15\Delta$, with Δ being the energy gap of the Hamiltonian.

We consider a simple three-dimensional (3D) cubic lattice $\mathcal{C}$ with one spin-1/2 particle (qubit) living at each vertex of the lattice. Let X_u, Y_u, and Z_u be the Pauli operators acting on the spin at a vertex $u \in \mathcal{C}$. The model Hamiltonian is

$$H = -\frac{\Delta}{2}\sum_{u\in\mathcal{C}} K_u, \quad K_u = X_u \prod_{v\in N(u)} Z_v. \tag{1}$$

Here $N(u)$ is a set of nearest neighbors of vertex u. The ground state of H obeys eigenvalue equations $K_u|\phi\rangle_{\mathcal{C}} = |\phi\rangle_{\mathcal{C}}$ and coincides with a cluster state [11]. We define a thermal cluster state at a temperature T as

$$\rho_{CS} = \frac{1}{\mathcal{Z}}\exp(-\beta H), \tag{2}$$

where $\mathcal{Z} = \mathrm{Tr}\, e^{-\beta H}$ is a partition function and $\beta \equiv T^{-1}$. Since all terms in H commute, one can easily get

$$\rho_{CS} = \frac{1}{2^{|\mathcal{C}|}}\prod_{u\in\mathcal{C}}[I + \tanh(\beta\Delta/2)K_u]. \tag{3}$$

Let $A,B \subset \mathcal{C}$ be two distant regions on the lattice. Our goal is to create as much entanglement between A and B as possible by doing local measurements on all spins not belonging to $A\cup B$. Denote α as the list of all outcomes obtained in these measurements and ρ_α^{AB} as the state of A and B conditioned on the outcomes α. Let $E[\rho]$ be some measure of bipartite entanglement. Following [5] we define the localizable entanglement between A and B as

$$E(A,B) = \max\sum_\alpha p_\alpha E[\rho_\alpha^{AB}], \tag{4}$$

where p_α is a probability to observe the outcome α and the maximum is taken over all possible patterns of local measurements. To specify the entanglement measure $E[\rho]$ it is useful to regard ρ_α^{AB} as an encoded two-qubit state with the first logical qubit residing in A and the second in B. We choose $E[\rho]$ as the maximum amount of two-qubit entanglement (as measured by entanglement of formation) contained in ρ. Thus $0 \leqslant E(A,B) \leqslant 1$ and an equality $E(A,B)=1$ implies that a perfect Bell pair can be created between A and B. Conversely, $E(A,B)=0$ implies that any choice of a measurement pattern produces a separable state.

In this paper we consider a finite 3D cluster

$$\mathcal{C} = \{u = (u_1,u_2,u_3): 1 \leqslant u_1, u_2 + 1 \leqslant l; 1 \leqslant u_3 \leqslant d\}$$

and choose a pair of opposite 2D faces as A and B:

$$A = \{u \in \mathcal{C}: u_3 = 1\}, \quad B = \{u \in \mathcal{C}: u_3 = d\},$$

so that the separation between the two regions is $d-1$. In Sec. II we show that[1]

$$\lim_{l,d\to\infty} E(A,B) = 1 \quad \text{for} \quad T < 0.30\Delta.$$

Further, we show in Sec. III that if $T > 1.15\Delta$ then $E(A,B) = 0$ for $d \geqslant 2$ and arbitrarily large l.

---

[1] References [15,16] consider a lattice with proportions of a cube, corresponding to $l=d$. However, numerical simulations indicate that $\lim_{l,d\to\infty} E(A,B)=1$ even if $l = C\ln(d)$; see remarks to Sec. II.

©2005 The American Physical Society

II. LOWER BOUND

We relate the lower bound on the transition temperature to quantum error correction. From Eq. (3) it follows that ρ_{CS} can be prepared from the perfect cluster state $|\phi\rangle_{\mathcal{C}}$ by applying the Pauli operator Z_u to each spin $u \in \mathcal{C}$ with a probability

$$p = \frac{1}{1+\exp(\beta\Delta)}. \tag{5}$$

Thus, thermal fluctuations are equivalent to independent local Z errors with an error rate p.

We use a single copy of ρ_{CS} and apply a specific pattern of local measurements which creates an encoded Bell state among sets of particles in A and B. For encoding we use the planar code, which belongs to the family of surface codes introduced by Kitaev. The 3D cluster state has, as opposed to its 1D counterpart [11], an intrinsic error correction capability which we use in the measurement pattern described below. Therein, the measurement outcomes are individually random but not independent; parity constraints exist among them. The violation of any of these indicates an error. Given sufficiently many such constraints, the measurement outcomes specify a syndrome from which typical errors can be reliably identified. The optimal error correction given this syndrome breaks down at a certain error rate (temperature), and the Bell correlations can no longer be mediated. This temperature is a lower bound to T_c, because in principle there may exist a more effective measurement pattern.

To describe the measurement pattern we use, let us introduce two cubic sublattices T_e, $T_o \subset \mathcal{C}$ with a double spacing. Each qubit $u \in \mathcal{C}$ becomes either a vertex or an edge in one of the sublattices T_e and T_o. The sets of vertices $V(T_e)$ and $V(T_o)$ are defined as

$$V(T_e) = \{u = (e,e,e) \in \mathcal{C}\},$$

$$V(T_o) = \{u = (o,o,o) \in \mathcal{C}\},$$

where e and o stand for even and odd coordinates. The sets of edges $E(T_e)$ and $E(T_o)$ are defined as

$$E(T_e) = \{u = (e,e,o),(e,o,e),(o,e,e) \in \mathcal{C}\},$$

$$E(T_o) = \{u = (o,o,e),(o,e,o),(e,o,o) \in \mathcal{C}\}.$$

The lattices T_e, T_o play an important role in the identification of error correction on the cluster state with a $\mathbb{Z}_2$ gauge model [12]. They are displayed in Fig. 2 below.

Let us assume that the lengths l and d are odd.[2] The Bell pair to be created between A and B will be encoded into subsets of qubits

$$L = \{u = (o,e,1),(e,o,1) \in \mathcal{C}\} \subset A,$$

$$R = \{u = (o,e,d),(e,o,d) \in \mathcal{C}\} \subset B.$$

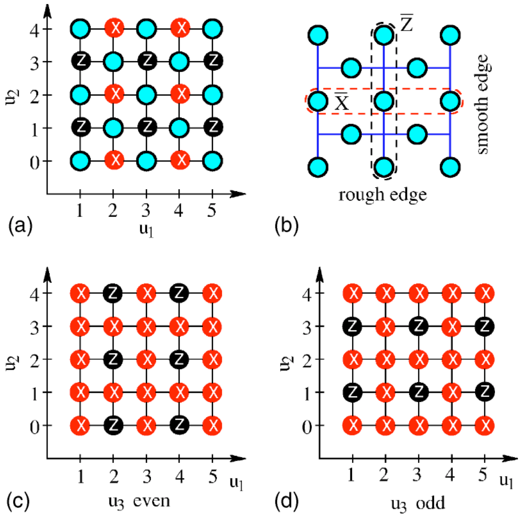

FIG. 1. (Color online) (a) Measurement pattern on the first and last slice of $\mathcal{C}$, for $l=5$. The resulting state is in the code space of the planar code. (The unmeasured qubits are displayed as shaded circles.) (b) Lattice for the planar code. (c) and (d) Measurement pattern for even and odd inner slices.

Each qubit $u \in \mathcal{C}$ is measured either in the Z or X basis unless it belongs to L or R. Denoting by M_X and M_Z local X and Z measurements, we can now present the measurement pattern:

$$\begin{aligned} &M_Z \quad \forall\ u \in V(T_e) \cup V(T_o), \\ &M_X \quad \forall\ u \in E(T_e) \cup E(T_o) \setminus (L \cup R). \end{aligned} \tag{6}$$

We denote the measurement outcome ±1 at vertex u by z_u or x_u, respectively. A graphic illustration of the measurement patterns for the individual slices is given in Fig. 1.

Before we consider errors, let us discuss the effect of this measurement pattern on a perfect cluster state. Consider some fixed outcomes $\{x_u\},\{z_u\}$ of local measurements and let $|\psi\rangle_{LR}$ be the reduced state of the unmeasured qubits L and R. We will now show that $|\psi\rangle_{LR}$ is, modulo local unitaries, an encoded Bell pair, with each qubit encoded by the planar code [13], the planar counterpart of the toric code [14]. The initial cluster state obeys eigenvalue equations $K_u|\phi\rangle_{\mathcal{C}}=|\phi\rangle_{\mathcal{C}}$. This implies for the reduced state

$$Z_{P,u}|\psi\rangle_{LR} = \lambda_{P,u}|\psi\rangle_{LR} \quad \forall\ u=(e,e,1), \tag{7}$$

where $Z_{P,u}=\otimes_{v\in N(u)\cap L}Z_v$ is a plaquette (z-type) stabilizer operator for the planar code [13]. The eigenvalue $\lambda_{P,u}$ depends upon the measurements outcomes as $\lambda_{P,u}=x_u z_{(u_1,u_2,2)}$. Note that in the planar code the qubits live on the edges of a lattice rather than on its vertices. The planar code lattice is distinct from the cluster lattice $\mathcal{C}$; see Figs. 1 and 2.

From the equation $\Pi_{v\in N(u)}K_v|\phi\rangle_{\mathcal{C}}=|\phi\rangle_{\mathcal{C}}$, for $u=(o,o,1)$, we obtain

$$X_{S,u}|\psi\rangle_{LR} = \lambda_{S,u}|\psi\rangle_{LR} \quad \forall\ u=(o,o,1), \tag{8}$$

where $X_{S,u}=\otimes_{v\in N(u)\cap L}X_v$ coincides with a site (x-type) stabilizer operator for the planar code [13], and

---

[2] There is no loss of generality here since one can decrease the size of the lattice by measuring all of the qubits on some of the 2D faces in the Z basis.

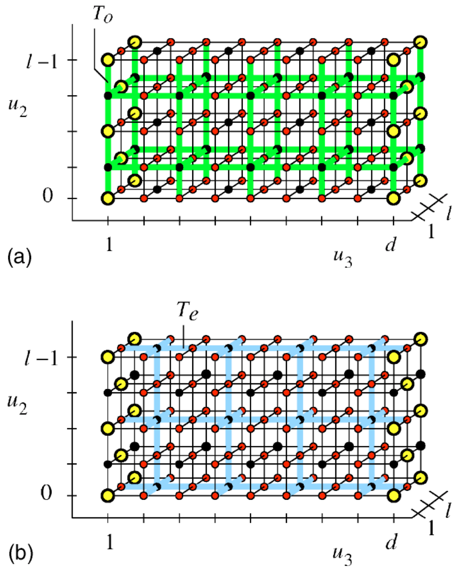

FIG. 2. (Color online) The measurement pattern on the cluster $\mathcal{C}$. The sublattices T_e and T_o are displayed (thick lines). For reference, the cluster lattice is also shown (thin lines) and the axis labeling shows the cluster coordinates. Cluster qubits measured in the Z basis (on the sites of T_o and T_e) are displayed in black, and qubits measured in the X basis (on the edges of T_o and T_e) are displayed in gray (red). The large circles to left and to the right denote the unmeasured qubits which form the encoded Bell pair. The measurement pattern has a bcc symmetry.

$\lambda_{S,u}=x_{(u_1,u_2,2)}z_u\prod_{v\in N_o(u)}z_v$, where N_o refers to a neighborhood relation on the sublattice T_o. The code stabilizer operators in Eqs. (7) and (8) are algebraically independent. There are $(l^2-1)/2$ code stabilizer generators for $(l^2+1)/2$ unmeasured qubits, such that there exists one encoded qubit on L. By direct analogy, there is also one encoded qubit located on R.

Next, we show that $|\psi\rangle_{LR}$ is an eigenstate of $\overline{X_L}\,\overline{X_R}$ and $\overline{Z_L}\,\overline{Z_R}$, where $\overline{X}$ and $\overline{Z}$ are the encoded Pauli operators X and Z, respectively, i.e., $|\psi\rangle_{LR}$ is an encoded Bell pair. The encoded Pauli operators [13] on L and R are $\overline{X_{L[R]}}=\otimes_{u_1\ \mathrm{odd}}X_{(u_1,u_2,1[d])}$ for any even u_2, and $\overline{Z_{L[R]}}=\otimes_{u_2\ \mathrm{even}}Z_{(u_1,u_2,1[d])}$ for any odd u_1. To derive the Bell correlations of $|\psi\rangle_{LR}$ let us introduce 2D slices

$$T_{XX}^{(u_2)}=\{u=(o,u_2,o)\in\mathcal{C}\}\subset T_o,$$

$$T_{ZZ}^{(u_1)}=\{u=(u_1,e,e)\in\mathcal{C}\}\subset T_e.$$

The eigenvalue equation $\prod_{v\in T_{XX}^{(u_2)}}K_v|\phi\rangle_{\mathcal{C}}=|\phi\rangle_{\mathcal{C}}$ with even u_2 implies for the reduced state

$$\overline{X_L}\,\overline{X_R}|\psi\rangle_{LR}=\lambda_{XX}|\psi\rangle_{LR}, \tag{9}$$

with $\lambda_{XX}=\prod_{v\in T_{XX}^{(u_2+1)}\cup T_{XX}^{(u_2-1)}}z_v\prod_{v\in T_{XX}^{(u_2)}\setminus(L\cup R)}x_v$. Here and hereafter it is understood that $x_u=z_u=1$ for all $u\notin\mathcal{C}$. Similarly, from $|\phi\rangle_{\mathcal{C}}=\prod_{v\in T_{ZZ}^{(u_1)}}K_v|\phi\rangle_{\mathcal{C}}$, for u_1 odd, we obtain for the reduced state

$$\overline{Z_L}\,\overline{Z_R}|\psi\rangle_{LR}=\lambda_{ZZ}|\psi\rangle_{LR}, \tag{10}$$

with $\lambda_{ZZ}=\prod_{v\in T_{ZZ}^{(u_1+1)}\cup T_{ZZ}^{(u_1-1)}}z_v\prod_{v\in T_{ZZ}^{(u_1)}}x_v$. Thus the eigenvalue equations (7)–(10) show that the measurement pattern of Eq. (6) projects the initial perfect cluster state into a state equivalent under local unitaries to the Bell pair, with each qubit encoded by the planar code.

It is crucial that the measurement outcomes $\{z_u\}$ and $\{x_v\}$ are not completely independent. Indeed, for any vertex $u\in T_o$ with $1<u_3<d$ the eigenvalue equation $\prod_{v\in N(u)}K_v|\phi\rangle_{\mathcal{C}}=|\phi\rangle_{\mathcal{C}}$ implies the constraint

$$\prod_{v\in N(u)}x_v\prod_{w\in N_o(u)}z_w=1. \tag{11}$$

Analogously, for any vertex $u\in T_e$ one has a constraint

$$\prod_{v\in N(u)}x_v\prod_{w\in N_e(u)}z_w=1, \tag{12}$$

where N_e refers to a neighborhood relat ion on the lattice T_e. Thus there exists one syndrome bit for each vertex of T_e and T_o (with an exception for the vertices of T_o with $u_3=1$ or $u_3=d$).

What are the errors detected by these syndrome bits? Since we have only Z errors (for generalization, see remark 1), only the X measurements are affected by them. Each X measured qubit is on an edge of either T_o or T_e. Thus, we can identify the locations of the elementary errors with $E(T_o)$ and $E(T_e)$. From Eqs. (11) and (12), each error located on an edge creates a syndrome at its end vertices.

Let us briefly compare with [12]. Therein, independent local X and Z errors were considered for storage whose correction runs completely independently. The X errors in this model correspond to our Z errors on qubits in $E(T_e)$, and the Z storage errors to our Z errors on qubits in $E(T_o)$, if the X and Z error correction phases in [12] are pictured as alternating in time.

The syndrome information provided by Eqs. (11) and (12) is not yet complete. There are two important issues to be addressed: (i) There are no syndrome bits at the vertices of T_o with $u_3=1$ or $u_3=d$; (ii) edges of T_e with $u_3=1$ or $u_3=d$ have only one end vertex, so errors that occur on these edges create only one syndrome bit. Concerning (i), to get the missing syndrome bits we will measure eigenvalues $\lambda_{P,u}$ and $\lambda_{S,u}$ for the plaquette and the site stabilizer operators living on the faces A and B [see Eqs. (7) and (8)]. Such measurements are local operations within A or within B, so they cannot increase entanglement between A and B. For any $u=(o,o,1)$ or $u=(o,o,d)$ it follows from Eq. (8) that

$$\begin{aligned}\lambda_{S,u}x_{(u_1,u_2,2)}z_u\prod_{v\in N_o(u)}z_v=1\quad\text{for}\quad u_3=1,\\ \lambda_{S,u}x_{(u_1,u_2,d-1)}z_u\prod_{v\in N_o(u)}z_v=1\quad\text{for}\quad u_3=d.\end{aligned} \tag{13}$$

For any vertex $u=(o,o,1)$ or $u=(o,o,d)$ there are several edges of the lattice T_o incident on u. It is easy to see that a single Z error that occurs on any of these edges changes a sign in Eqs. (13). Thus, these two constraints yield the syndrome bits living at the vertices $u=(o,o,1)$ and $u=(o,o,d)$, so the issue (i) is addressed. Concerning (ii), we make use of Eq. (7) and obtain

$$\lambda_{P,u} x_u z_{(u_1,u_2,2)} = 1 \quad \text{for any} \quad u=(e,e,1),$$
$$\lambda_{P,u} x_u z_{(u_1,u_2,d-1)} = 1, \quad \text{for any} \quad u=(e,e,d). \tag{14}$$

Since we have only Z errors, the eigenvalues $\lambda_{P,u}$ and the outcomes $z_{(u_1,u_2,2)}, z_{(u_1,u_2,d-1)}$ are not affected by errors. Thus the syndrome bits Eqs. (14) are equal to -1 if and only if an error has occurred on the edge $u=(e,e,1)$ or $u=(e,e,d)$ of the lattice T_e. Since each of these errors shows itself in a corresponding syndrome bit which is not affected by any other error, we can reliably identify these errors. This is equivalent to actively correcting them with unit success probability. We can therefore assume in the subsequent analysis that no errors occur on the edges $(e,e,1)$ and (e,e,d), which concludes the discussion of the issue (ii).

As in [14], we define an error chain $\mathcal{E}$ as a collection of edges where an elementary error has occurred. Each of the two lattices T_e and T_o has its own error chain. An error chain $\mathcal{E}$ shows a syndrome only at its boundary $\partial(\mathcal{E})$, and errors with the same boundary thus have the same syndrome. One may identify an error $\mathcal{E}$ only modulo a cycle D, $\mathcal{E}'=\mathcal{E}+D$, with $\partial(D)=0$.

There are homologically trivial and nontrivial cycles. A cycle D is trivial if it is a closed loop in T_o (T_e), and homologically nontrivial if it stretches from one rough face in T_o (T_e) to another. A rough face here is the 2D analog of a rough edge on a planar code [13]. The rough faces of T_o are on the upper and lower sides of $\mathcal{C}$, and the rough faces of T_e are on the front and back of $\mathcal{C}$ (recall that no errors occur on the left and right rough faces of T_e).

Let us now study the effect of error cycles on the identification of the state $|\psi\rangle_{LR}$ from the measurement outcomes. We only discuss the error chains on T_o here, which potentially affect the eigenvalue Eq. (9). The discussion of the error chains in T_e—which disturb the $\overline{Z_L}\,\overline{Z_R}$ correlations—is analogous. An individual qubit error on $v\in\mathcal{C}$ will modify the $\overline{X_L}\,\overline{X_R}$ correlation of $|\psi\rangle_{LR}$ if it affects either $\overline{X_L}$, $\overline{X_R}$ or λ_{XX}. That happens if $v\in T_{XX}^{(u_2)}$. Now, the vertices in $T_{XX}^{(u_2)}$ correspond to edges in T_o. If an error cycle D in T_o is homologically trivial, it intersects $T_{XX}^{(u_2)}$ in an even number of vertices; see Fig. 3. This has no effect on the eigenvalue Eq. (9). However, if the cycle is homologically nontrivial, i.e., if it stretches between the upper and lower face of $\mathcal{C}$, then it intersects $T_{XX}^{(u_2)}$ in an odd number of vertices. This does modify the eigenvalue Eq. (9) by a sign factor of (-1) on the left-hand side, which leads to a logical error. Therefore, for large system size, we require the probability of misinterpreting the syndrome by a nontrivial cycle to be negligible [12]:

$$\sum_{\mathcal{E}} \text{prob}(\mathcal{E}) \sum_{D \text{ nontrivial}} \text{prob}(\mathcal{E}+D|\mathcal{E}) \approx 0. \tag{15}$$

We have now traced back the problem of reconstructing an encoded Bell pair $|\psi\rangle_{LR}$ to the same setting that was found in [12] to describe fault-tolerant data storage with the toric code. Via the measurement pattern Eq. (6), we may introduce two lattices T_o, T_e such that (1) syndrome bits are located on the vertices of these lattices, (2) independent errors live on the edges and show a syndrome on their boundary, and (3) only the homologically nontrivial cycles give rise to a logical error. This error model can be mapped onto a random plaquette Z_2-gauge field theory in three dimensions [12,15] which undergoes a phase transition between an ordered low-temperature and a disordered high-temperature phase. In the limit of $l,d\to\infty$, full error correction is possible in the low-temperature phase.

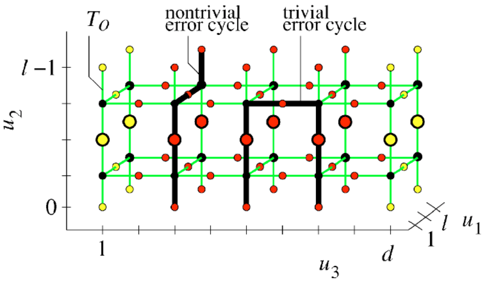

FIG. 3. (Color online) A homologically nontrivial and a homologically trivial error cycle on the lattice T_o. The nontrivial error cycle stretches from one rough face to the opposite one while the trivial error has both ends on the same face. Only the qubits belonging to T_o are shown and the qubits important for establishing the $\overline{X_A}\,\overline{X_B}$-correlation are displayed enlarged.

In our setting, the error probabilities for all edges are equal to p. For this case the critical error probability has been computed numerically in a lattice simulation [16], $p_c = 0.033\pm0.001$. This value corresponds, via Eq. (5), to $T_c = (0.296\pm0.003)\Delta$.

Remark 1. The error model equivalent to Eq. (3), i.e., Z errors only, is very restricted. We have a physical motivation for this model, but we would like to point out that the very strong assumptions we have made about the noise are not crucial to our result of the threshold error rate being nonzero. One may, for example, generalize the error model from a dephasing channel to a depolarizing channel, with $p_x=p_y=p_z=p'/3$. Then, two changes need to be addressed, those in the bulk and those on the faces L and R. Concerning the faces, the errors on the rough faces to the left and right of T_e can no longer be unambiguously identified by measurements of the code stabilizer (14), which raises the question of whether—for depolarizing errors—it may be these surface errors that set the threshold for long-range entanglement. This is not the case. To see this, note that two slices of 2D cluster states may be attached to the left and right of $\mathcal{C}$, at $u_3=0,-1$ and $u_3=d+1$, $d+2$. The required operations are assumed to be perfect. They do not change the localizable entanglement between the left and right sides of the cluster $\mathcal{C}$ because they act locally on the slices $-1,\ldots,1$ and $d,\ldots,d+2$, respectively. The subsets A and B of spins are relocated to the slices -1 and $d+2$, with the corresponding changes in the measurement pattern. The effect of this procedure is that

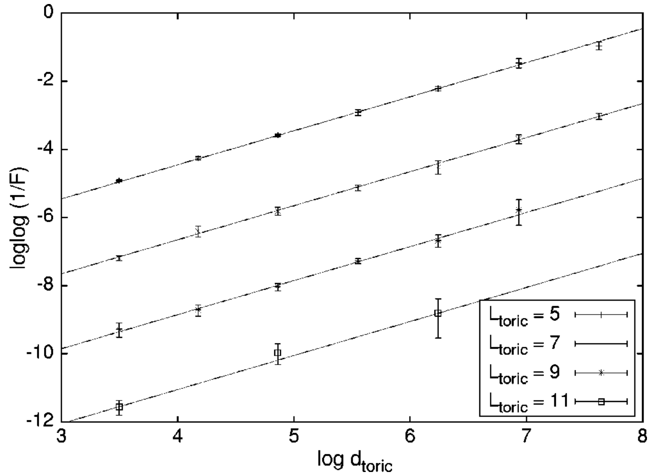

FIG. 4. This figure plots data for simulations of error correction on an $L\times L\times d_{\text{toric}}$ lattice, with periodic boundary conditions in the first two directions, for various L and d_{toric} $(d=2d_{\text{toric}}+1, l=2L)$. The error rate is $p=0.01$. The logarithms have are base e. Two standard deviations above and below the computed values (as given by statistical noise due to the sample sizes) are shown by the error bars. The solid lines each have slope 1, and they are spaced equally apart. This lends good support to the model of fidelity $F\sim\exp[-dk_1\exp(-lk_2)]$ for error rates below threshold.

the leftmost and rightmost slices of the enlarged cluster are error free,[3] and only the bulk errors matter.

Concerning the bulk, note that the cluster qubits measured in the Z basis serve no purpose and may be left out from the beginning. Then, the considered lattice for the initial cluster state has a bcc symmetry and double spacing. The lattices T_o, T_e remain unchanged. Further, X errors are absorbed in the X measurements and Y errors act like Z errors, such that we still map to the original $\mathbb{Z}_2$ gauge model [12] at the Nishimori line. The threshold for local depolarizing channels applied to this configuration is thus $p_c'=3/2p_c=4.9\%$. In addition, numerical simulations performed for the initial simple cubic cluster and depolarizing channel yield an estimate of the critical error probability of $p_c''=1.4\%$.

Remark 2. Finite-size effects. We carried out numerical simulations of error correction on an $l\times l\times d$ lattice with periodic boundary conditions (as opposed to the open boundary conditions of the planar codes within the cluster state). For differing error rates below the threshold value of 2.9% [15], we found good agreement for the fidelity F between the perfect and the error-corrected encoded Bell state with the model $F\sim\exp[-dk_1\exp(-lk_2)]$. Some data are shown in Fig. 4 corresponding to a Z error rate of 1.0%. Provided that planar codes and toric codes have similar behavior away from threshold, our simulations suggest that, in order to achieve constant fidelity, the length l specifying the surface code need only scale *logarithmically* with the distance d.

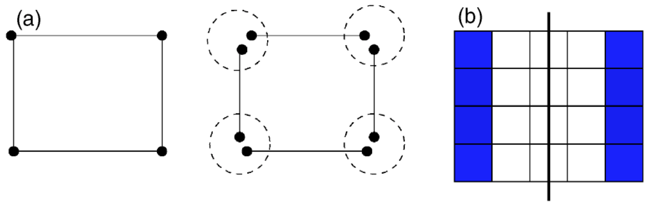

FIG. 5. (Color online) (a) Correspondence between physical and virtual qubits. Domains are shown by dashed lines. (b) A bipartite cut of a cubic lattice. The regions A and B are highlighted.

Remark 3. For even d, the construction presented above can be used to mediate an encoded conditional Z gate on distant encoded qubits located on slices 1 and d.

III. UPPER BOUND

In this section we analyze the high-temperature behavior of thermal cluster states and find an upper bound on the critical temperature T_c. Our analysis is based on the isomorphism between cluster states and the so-called valence bond solids (VBSs) pointed out by Verstraete and Cirac in [17] which can easily be generalized to a finite temperature.

With each physical qubit $u\in\mathcal{C}$ we associate a domain $u.*$ of $d(u)$ virtual qubits, where $d(u)=|N(u)|$ is the number of nearest neighbors of u [see Fig. 5(a)]. Let us label virtual qubits from a domain $u.*$ as $u.v$, $v\in N(u)$. Denote E to be the set of edges of the lattice $\mathcal{C}$ and define a thermal VBS state ρ_{VBS} as

$$\rho_{VBS}=\prod_{e=(u,v)\in E}\frac{1}{4}(I+\omega_e X_{u.v}Z_{v.u})(I+\omega_e Z_{u.v}X_{v.u}). \quad (16)$$

Here $\{\omega_e\}$ are arbitrary weights such that $0\leqslant\omega_e\leqslant1$. It should be emphasized that ρ_{VBS} is a state of virtual qubits rather than physical ones. Our goal is to convert ρ_{VBS} into ρ_{CS} by local transformations mapping a domain $u.*$ into a single qubit $u\in\mathcal{C}$. The following theorem is a straightforward generalization of the Verstraete and Cirac construction (here we put $\Delta/2=1$).

Theorem 1. Let ρ_{CS} be a thermal cluster state on the 3D cubic lattice $\mathcal{C}$ at a temperature $T\equiv\beta^{-1}$. Consider a thermal VBS state ρ_{VBS} as in Eq. (16) such that the weights ω_e satisfy

$$\prod_{v\in N(u)}\omega_{(u,v)}\geqslant\tanh(\beta)\quad\text{for each } u\in\mathcal{C}. \quad (17)$$

Then ρ_{VBS} can be converted into ρ_{CS} by applying a completely positive transformation $\mathcal{W}_u$ to each domain $u.*$,

$$\rho_{CS}=\mathcal{W}(\rho_{VBS}),\quad \mathcal{W}=\bigotimes_{u\in}\mathcal{W}_u. \quad (18)$$

Let us first discuss the consequences of this theorem. Note that each edge $e\in E$ of ρ_{VBS} carries a two-qubit state

$$\rho_e=\frac{1}{4}(I+\omega_e X_1Z_2)(I+\omega_e Z_1X_2). \quad (19)$$

The Peres-Horodecki partial transpose criterion [18,19] tells us that ρ_e is separable if and only if $\omega_e\leqslant\sqrt{2}-1$. Consider a bipartite cut of the lattice by a hyperplane of codimension 1 [see Fig. 5(b)]. We can satisfy Eq. (17) by setting $\omega_e = \tanh(\beta)$ for all edges crossing the cut and setting $\omega_e = 1$ for all other edges. Clearly, the state ρ_{VBS} is biseparable whenever $\tanh(\beta) \leqslant \sqrt{2}-1$. But biseparability of ρ_{VBS} implies biseparability of ρ_{CS}. We conclude that the localizable entanglement between the regions A and B is zero whenever $\tanh(\beta) \leqslant \sqrt{2}-1$, which yields the upper bound on T_c presented earlier.

---

[3] The following operations are required to attach a slice: (I) $\Lambda(Z)$ gates within the slice, (II) $\Lambda(Z)$ gates between the slice and its next neighboring slice, and (III) X and Z measurements within the slice (see Fig. 1). All these operations are assumed to be perfect, and the errors on slices 1 and d are not propagated to slices -1 and $d+2$ by the $\Lambda(Z)$ gates (II).

Remarks. We can also satisfy Eq. (17) by setting $\omega_e = \omega$ for all $e \in E$, with $\omega^6 = \tanh(\beta)$. This choice demonstrates that ρ_{CS} is completely separable for $\tanh(\beta) < (\sqrt{2}-1)^6$ (that is, $T \approx 200$). It reproduces the upper bound [20] of Dür and Briegel on the separability threshold error rate for cluster states.

In the remainder of this section we prove Theorem 1. Consider an algebra $\mathcal{A}_u$ of operators acting on some particular domain $u.*$. It is generated by the Pauli operators $Z_{u.v}$ and $X_{u.v}$ with $v \in N(u)$. The transformation $\mathcal{W}_u$ maps $\mathcal{A}_u$ into the one-qubit algebra generated by the Pauli operators Z_u and X_u. First, we choose

$$\mathcal{W}_u(\eta) = W_u^\dagger \eta W_u, \quad W_u = |0^{\otimes d(u)}\rangle\langle 0| + |1^{\otimes d(u)}\rangle\langle 1|.$$

One can easily check that

$$W_u^\dagger Z_{u.v} = Z_u W_u^\dagger \quad \text{and} \quad Z_{u.v} W_u = W_u Z_u, \tag{20}$$

for any $v \in N(u)$. As for commutation relations between W_u and $X_{u.v}$ one has

$$W_u^\dagger \left(\prod_{v \in N(u)} X_{u.v} \right) W_u = X_u,$$

$$W_u^\dagger \left(\prod_{v \in S} X_{u.v} \right) W_u = 0, \tag{21}$$

for any nonempty proper subset $S \subset N(u)$. Taking $\mathcal{W} = \otimes_{u \in \mathcal{C}} \mathcal{W}_u$ and using Eqs. (20) and (21) one can easily get

$$\mathcal{W}(\rho_{VBS}) = \frac{1}{4^{|E|}} \prod_{u \in \mathcal{C}} (I + \eta_u K_u), \quad \eta_u = \prod_{v \in N(u)} \omega_{(u,v)}. \tag{22}$$

We can regard the state in Eq. (22) as a thermal cluster state with a local temperature $\tanh(\beta_u) \equiv \eta_u$ depending upon u. The inequality of Eq. (17) implies that $\beta_u \geqslant \beta$ for all u. To achieve a uniform temperature distribution $\beta_u = \beta$ one can intentionally apply local Z errors with properly chosen probabilities.

IV. CONCLUSION

Thermal cluster states in three dimensions exhibit a transition from infinite to finite entanglement length at a nonzero transition temperature T_c. We have given a lower and an upper bound to T_c, $0.3\Delta \leqslant T_c \leqslant 1.15\Delta$ (Δ is the energy gap of the Hamiltonian). The reason for T_c being nonzero is an intrinsic error-correction capability of 3D cluster states. We have devised an explicit measurement pattern that establishes a connection between cluster states and surface codes. Using this, we have described how to create a Bell state of far separated encoded qubits in the low-temperature regime $T < 0.3\Delta$, making the entanglement contained in the initial thermal state accessible for quantum communication and computation.

ACKNOWLEDGMENTS

We would like to thank Hans Briegel and Frank Verstraete for bringing to our attention the problem of entanglement localization in thermal cluster states. This work was supported by the National Science Foundation under Grant No. EIA-0086038.

---

[1] J. S. Bell, Physics (Long Island City, N.Y.) **1**, 195 (1964).
[2] A. Aspect, P. Grangier, and G. Roger, Phys. Rev. Lett. **47**, 460 (1981).
[3] E. Schrödinger, Naturwiss. **23**, 807 (1935); **23**, 823 (1935); **23**, 844 (1935).
[4] H. J. Briegel, W. Dür, J. I. Cirac, and P. Zoller, Phys. Rev. Lett. **81**, 5932 (1998).
[5] F. Verstraete, M. Popp, and J. I. Cirac, Phys. Rev. Lett. **92**, 027901 (2004).
[6] D. Aharonov, e-print quant-ph/9910081.
[7] F. Verstraete, M. A. Martín-Delgado, and J. I. Cirac, Phys. Rev. Lett. **92**, 087201 (2004).
[8] I. Affleck, T. Kennedy, E. H. Lieb, and H. Tasaki, Commun. Math. Phys. **115**, 477 (1998).
[9] J. K. Pachos and M. B. Plenio, Phys. Rev. Lett. **93**, 056402 (2004).
[10] A. Kay *et al.*, e-print quant-ph/0407121.
[11] H. J. Briegel and R. Raussendorf, Phys. Rev. Lett. **86**, 910 (2001).
[12] E. Dennis, A. Kitaev, A. Landahl, and J. Preskill, e-print quant-ph/0110143.
[13] S. Bravyi and A. Kitaev, e-print quant-ph/9811052.
[14] A. Kitaev, e-print quant-ph/9707021.
[15] C. Wang, J. Harrington, and J. Preskill, Ann. Phys. (N.Y.) **303**, 31 (2003).
[16] T. Ohno, G. Arakawa, I. Ichinose, and T. Matsui, e-print quant-ph/0401101.
[17] F. Verstraete and J. I. Cirac, e-print quant-ph/0311130.
[18] A. Peres, Phys. Rev. Lett. **77**, 1413 (1996).
[19] M. Horodecki, P. Horodecki, and R. Horodecki, Phys. Lett. A **223**, 1 (1996).
[20] W. Dür and H. J. Briegel, Phys. Rev. Lett. **92**, 180403 (2004).

Quantum Information and Computation, Vol. 3, No. 5 (2003) 450–464
© Rinton Press

FABRICATION OF MICRO-MAGNETIC TRAPS FOR COLD NEUTRAL ATOMS

BENJAMIN LEV
Norman Bridge Laboratory of Physics 12-33, California Institute of Technology
Pasadena, California 91125, USA
benlev@caltech.edu

Received May 15, 2003
Revised July 31, 2003

Many proposals for quantum information processing require precise control over the motion of neutral atoms, as in the manipulation of coherent matter waves or the confinement and localization of individual atoms. Patterns of micron-sized wires, fabricated lithographically on a flat substrate, can conveniently produce large magnetic-field gradients and curvatures to trap cold atoms and to facilitate the production of Bose-Einstein condensates. The intent of this paper is to provide the researcher who has access to a standard clean-room enough information to design and fabricate such devices.

Keywords: atom optics, quantum computation, magnetic microtraps

Communicated by: D Wineland & E Polzik

1 Introduction

Cold samples of neutral atoms and Bose-Einstein condensates have become readily available using the techniques of laser cooling and trapping [1], and it has been widely recognized that cold atoms are a rich resource for experiments in quantum information science. For many proposals, however, quantum control of the atomic motional degrees of freedom is essential. For example, quantum computation in a cavity QED setting or through controlled cold collisions requires the ability to trap and control single atoms in the Lamb-Dicke regime [2, 3, 4]. In 1995, Weinstein and Libbrecht noted that micron-sized wires, fabricated on a substrate, are capable of producing the large magnetic field gradients and curvatures required for trapping atoms in the Lamb-Dicke regime [5]. Westervelt *et al.*, in 1998, succeeded in fabricating the wire patterns used in the trap designs of Weinstein and Libbrecht [6]. These microwire devices, now commonly known as atom chips [7], have been used to great success in atom optics and in the production of Bose-Einstein condensates (BEC), and are promising tools not just for quantum computation, but for atom interferometry, cavity QED, and the study of cold collisions as well [8, 7, 9, 10]. In this paper we describe techniques, which have been adapted from the standard lore of microfabrication, for fabricating this increasingly important tool for atomic physics and quantum optics.

Atom optical elements, such as mirrors, waveguides, splitters, traps, and conveyor belts have been demonstrated using atom chips [11, 12, 13, 14, 15, 16, 17]. Cesium cold collisions in the presence of light have been studied using a magnetic microtrap [18], and the use of fiber gap [19, 20] and microsphere cavities [20] for on-chip atom detection is being explored. Ion trap experiments are now using substrates with microfabricated electric pads for the purpose of controlling ion position [21, 22].

On-chip production of a BEC has been one of the most successful uses of the atom chip thus far [23, 24, 25]. Ioffe traps formed from microwires can produce extremely large trap compressions that enhance the efficiency of evaporative cooling. Consequently, condensate production time can be reduced from one minute to approximately ten seconds [23], and MOT loading can occur from a thermal vapor in a glass cell with a vacuum of only a few 10^{-10} Torr. All of the required magnetic fields can be produced on-chip [26, 27], removing the necessity of large, high power external coils. The atom chip greatly miniaturizes BEC production and will enable the integration of matter waves with chip-based atom optics and photonics.

Another exciting avenue of research involves the use of an atom chip to trap, in the Lamb-Dicke regime, one or more atoms in the mode of a high finesse cavity. The combination of magnetic microtraps and photonic bandgap (PBG) cavities would be an excellent cavity QED system for the implementation of scalable quantum computation, or for the study of continuous measurement and quantum-limited feedback. One technical proposal involves the integration of a PBG cavity with an Ioffe trap formed from microwires patterned on the same surface [28]. The combination of small mode volume and modest optical quality factor that should be obtainable with PBG structures would enable strong atom-cavity coupling. This would be an interesting alternative to present experiments that utilize a Far Off Resonance Trap (FORT) to confine atoms inside optical Fabry-Perot cavities [29]. Several PBG cavities, each with an independent microwire trap, could be fabricated on the same substrate and coupled together with a network of line-defect optical waveguides.

Atom chips exploit the interaction potential, $V = -\vec{\mu}\cdot\vec{B}$, between an atom's magnetic moment, $\vec{\mu}$, and a wire's magnetic field, $\vec{B}$, to trap or guide weak-field seeking states of a neutral atom. In general, the field's magnitude, gradient, and curvature scale as I/r, I/r^2, and I/r^3, respectively, where I is the wire's current and r is its characteristic dimension. Microscopic wire patterns maximize field gradients and curvatures while keeping power dissipation to a minimum. Experiments involve ultra-high vacuum chambers wherein atoms are trapped and cooled near the vicinity of the atom chip's confining magnetic potentials.

2 Fabrication Challenges and Constraints

Fabrication of atom chips poses several challenges in addition to those encountered in standard photolithography [30]. Many applications require the wires to be a couple microns wide by a few microns tall and spaced only a few microns from one another. One micron resolution is near the limit of standard photolithography, and much care must be taken to accurately produce these micron-sized wires. Wires with widths much less than a micron—though perhaps important for realizing potentials with sub-micron scale features—are of limited usefulness for creating large magnetic field gradients and curvatures since they become limited to the same maximum current density as micron-sized wires [31]. Further fabrication complications arise from the need to trap the atoms near the substrate's surface, and the need to connect the microwires to macroscopic leads without blocking optical access. A common technique for trapping atoms near the substrate surface, the mirror magneto-optical trap (MMOT), requires that this surface be an optical mirror as well as the support surface for the microwires (see figure 1) [8]. The substrate surface needs to be larger than 5 to 10 cm^2 to accommodate the reflected trapping beams as well as to allow the pads for macroscopic wire contacts to be outside of the mirror area and not blocking the optical access needed for the trapping, imaging, and pumping beams. Consequently, the wire pattern must be flawless over an exceptionally large surface area: during fabrication one must be extremely careful that no dust or surface defects break or short the wires.

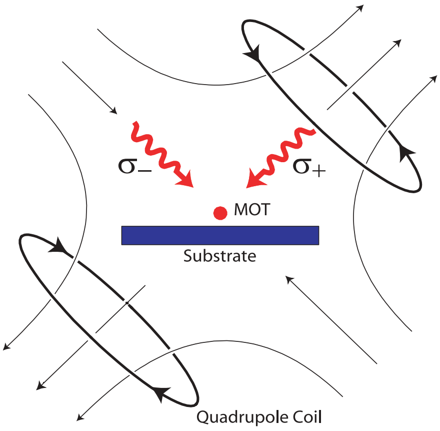

Fig. 1. Diagram of the mirror MOT experimental set-up. A quadrupole field and two 45° laser beams and one retroreflected grazing beam (perpendicular to the page and not shown) form a MOT 1.5 to 4 mm above the substrate.

The major fabrication challenge lies in increasing the height of the wires to a few microns. Even the smallest wires need to support up to an amp of current, and consequently, the cross-sectional area of the wire must be maximized. This reduces wire resistance and limits the heating that causes wire breakdown. Moreover, attention must be paid to the thermal conductivity of the substrate and mounting system to ensure sufficient power dissipation. Sapphire or polished aluminum nitride (AlN) substrates provide sufficient thermal conductivity, but are slightly trickier to use for fabrication than more standard substrates.

The use of microwires to create an Ioffe trap illustrates these challenges. The wire pattern shown in figures 2(a) and (b) creates a 3D harmonic trap when combined with a perpendicular homogenous bias field [5]. Unlike a quadrupole trap, the Ioffe trap has a non-zero field at the trap center and thus does not suffer from Majorana spin-flip losses. An atom is confined within the Lamb-Dicke regime when its recoil energy is less then the trap's vibrational level spacing ($\eta = (E_{recoil}/E_{vib})^{1/2} < 1$), and for a cesium atom this occurs when the trap curvature exceeds 2×10^6 G/cm^2. To achieve this extremely large field curvature in all three dimensions, the radius of the wire pattern in figure 2(a) must be smaller than ~ 30 μm. For a trap of inner radius 10 μm, outer radius 15 μm, and wire current $I = 1$ A, the curvature and Lamb-Dicke parameter, η, at the center of the trap in the axis perpendicular (plane parallel) to the substrate is 2×10^8 G/cm^2 (2×10^{10} G/cm^2) and $\eta = 0.38$ ($\eta = 0.11$). The closely spaced wires can only be a few microns wide, and even if fabricated to a height of 2 to 4 microns, the wires would need to support the large current density of $\sim 10^{11}$ A/m^2. The accommodation of laser beams for atom cooling, loading, and imaging constrains and complicates the atom chip's design. The trap minimum is only 7 μm from the substrate's surface, and the mirror patterned on the surface for use with the MMOT must neither short the Ioffe wires nor extend more than ~ 5 μm from the surface. The following sections describe the necessary fabrication tools and the techniques we use to overcome these challenges.

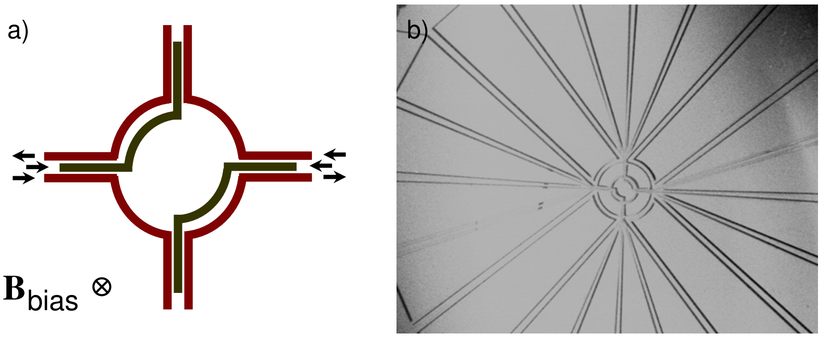

Fig. 2. The planar Weinstein and Libbrecht-style Ioffe trap. a) When combined with an opposing bias field, this wire pattern produces a 3D harmonic potential above the substrate with a non-zero field at the trap center [5]. b) A planar Ioffe trap with an on-chip bias coil fabricated with gold on sapphire using the lift-off method. In the sample shown here, the wire height is 1.5 μm and the minimum wire width is 10 μm. The gold between the wires forms a mirror for creating a mirror MOT.

3 The Elements of Atom Chip Fabrication

Microfabrication is a labor intensive process, often involving several weeks of trial and error to perfect the fabrication recipe. However, once the process works, five to ten atom chips can be produced over a span of two to three days. The intent of this paper is to provide the researcher who has access to a standard clean-room enough information to design and fabricate an atom chip. We will describe the use of fabrication instruments and techniques only insofar as they are relevant to atom chips. Fabrication is not an exact science, and the techniques described here may not be optimal, but nevertheless have proven successful for the chips we have fabricated.

In photolithography, UV light shone through a photomask casts shadows onto photoresist, a light sensitive polymer, which is coated on the surface of the substrate. Either positive or negative photoresist may be used, with the primary difference being that exposed areas of positive photoresist are removed after developing whereas exposed areas remain in a process using negative photoresist. The various fabrication techniques differ in how the wire metal and photoresist are used to create the wire patterns. For instance, the wire metal may be either thermally evaporated into the trenches created in the photoresist, or grown upward trough the trenches by electroplating onto a seed metallic layer underneath the photoresist. The photoresist and unwanted metal are removed leaving only the desired wire pattern. Generally, chip fabrication consists of six steps: creating a photomask containing the desired wire pattern, using photolithography to transfer the wire pattern to photoresist on a substrate, thermally evaporating wire material, increasing the wire height, preparing the surface mirror, and making contacts to macroscopic wires. The details and exact order of these steps vary depending on the specific requirements of the microwire pattern to be fabricated. For instance, wires wider than 30 μm or less than one micron in height may be fabricated with a much simpler technique than thinner or taller wires. This section discusses the steps common to all techniques. Procedures required to increase the wire's thickness pertain to individual fabrication techniques and will be discussed in the next section.

3.1 The photomask

The photomask is typically a 10 cm square piece of glass or transparent plastic on which is printed a positive or negative 1:1 image of the wire pattern. Wire patterns with widths or spacings less than $\sim$ 30 μm require a professionally made chrome mask: one in which the pattern is written with chromium on a glass plate. We have used the company Photronics, Inc. (telephone 619-992-8467) to make photomasks from AutoCAD drawings. Much care must be taken in producing the AutoCAD files since not all functions are properly converted to the company's file format. These masks are quite expensive, costing between \$600 and \$800, but have sub-micron resolution and are typically shipped within a week. It is possible to purchase a laser writer to produce in-house photomasks with resolution down to 0.8 μm. This can be a cost effective alternative to purchasing individual masks from companies.

Many commercial printing shops are capable of printing overhead transparencies with high enough resolution to serve as photomasks for wire patterns with features larger than $\sim$ 30 μm. The line edges are granular on a scale of a few microns, and the UV exposure time must be adjusted to account for the ink not being perfectly opaque. However, the one day turn-around, low cost of $\sim$ \$20, and ease of file preparation—only an .eps file is typically needed—make the transparency photomask quite an attractive alternative for large features.

3.2 The substrate

As mentioned earlier, the substrate material for the atom chip should be carefully chosen: it must be electrically insulating, highly polished, insusceptible to fractures upon localized heating, and an excellent thermal conductor. We have found that both sapphire and AlN substrates satisfy these requirements. Sapphire substrates 0.5 mm to 2 mm thick with surface areas of several cm^2 may be purchased from companies such as Meller Optics, Inc. (telephone 800-821-0180) for \$30 to \$40 apiece. A surface quality of 80-50 scratch-dig is sufficient for fabrication. The thermal conductivity of AlN, $\sim 170 - 180$ Wm^{-1}K^{-1} at 20°C, is $\sim$ 4.5 times higher than that of sapphire [31]. We measured that the max current density supported by microwires on AlN, $\sim 2 \times 10^{11}$ A/m^2, is a factor of two greater than for microwires patterned on sapphire. This was measured using electroplated gold wires of varying cross-sections patterned exactly the same way on both AlN and sapphire substrates. Specifically, we used several 3 μm and 20 μm wide wires whose heights ranged from one to three microns. The substrates were glued to room temperature copper blocks using EPO-TEK H77 (Epoxy Technology, telephone 978-667-3805), a thermally conductive epoxy.

Sapphire substrates are easier to use for fabrication because their transparency allows one to detect and avoid defects and dust during the photolithography process. Polished AlN substrates may be purchased in bulk for less than $\sim$ \$75, and unlike sapphire, AlN substrates can be cleaved with a diamond scorer to any shape desired. The polished AlN still has a considerable amount of surface roughness—one micron wide plateaus a few hundred nanometers tall are typical—but we found that it is nevertheless possible to fabricate on this surface perfect three micron wide wires spaced less than three microns from one another. The surface bumps simply map directly onto the upper surface of the wires.

3.3 Substrate cleaning

Before the photolithography process may begin, the surface of the substrate must be cleaned to remove all organic material and dust. Although some of the following steps may seem unnecessary and "overkill," investing the time to thoroughly clean minimizes the chance that after many hours of work, one discovers that a piece of dirt has broken or shorted a wire. The first step is to immerse the substrate in a beaker of "piranha etch," sulfuric acid and hydrogen peroxide in a 10:1 volume ratio brought to 100°C on a hot plate for $\sim$ 5 min. Teflon coated, flat tipped tweezers are ideal for manipulating substrates. After the etch, the substrate should be placed in a beaker of acetone, heated again to 100°C for a few minutes, and finally inserted into an ultrasound cleaner for few more minutes. In extreme cases of substrate grime, a cotton tipped dowel can be used to manually wipe away the dirt. Acetone leaves a thin film—and sometimes even particulate—when allowed to dry on a substrate's surface. It is imperative that one spray isopropanol (IPA) onto the substrate as it is removed from the acetone bath. This rinses the surface of acetone and wets it with IPA which does not quickly dry. The substrate must then be rinsed with methanol, which is relatively clean and does not leave a film, and quickly blown dry with an air or nitrogen gun. It is crucial that the air jet is aimed almost parallel to the surface so that the methanol is blown-off rather than dried on the substrate. When done correctly, the only remaining dirt particles will be along the edge of the substrate that is downwind of the air jet, and not in the center fabrication region. If the substrate is reasonably clean after the piranha etch, then the acetone step (which may actually add some dirt particulate) may be skipped, and the substrate should instead be immersed in IPA and placed inside an ultrasound cleaner.

3.4 Thermal evaporation

Certain fabrication techniques, to be discussed below, require that a 100 nm metal layer be thermally evaporated before coating the surface with photoresist. We take this opportunity to discuss the thermal evaporation process. We use gold for the wires because of its high electrical conductivity, resistance to corrosion, and ease of evaporation, electroplating, and wet etching. To successfully deposit gold on a substrate's surface, one must first evaporate a 50 Å metallic layer that promotes adhesion between the gold and the sapphire or AlN. We typically use chromium, but titanium may also be used. The magnetic effects from the thin layer of chromium are negligible. In a thermal evaporator, the substrate is mounted in a vacuum chamber facing a tungsten crucible positioned a few tens of centimeters below. The crucible, known as a boat, can hold 10 to 20 pieces of $\sim$ 2 mm long and 0.5 mm diameter gold wire. Current flows through the boat, melting the gold and spewing it upwards toward the substrate. A calibrated crystal monitor measures the deposition rate. One to two boats are sufficient to deposit 100 to 200 nm of gold, and this costs \$10 to \$15 per boat. There are typically only four sets of electrical feedthroughs in the evaporator's vacuum chamber, and to deposit more gold, one needs to bring the chamber up to atmosphere, reload the boats with gold, and pump back down to base pressure—a process that takes about an hour. The substrate mounting area allows several substrates to be coated at once. Evaporating less than

1 μm of gold is reasonable, but depositing more than 1 μm becomes too expensive and time consuming, and the quality of the gold surface begins to diminish. Moreover, the vacuum chamber eventually becomes hot which may result in the failure of the crystal monitor or the burning of photoresist.

3.5 Photoresist spinning and baking

Photoresist does not always adhere well to the substrate's surface. Before coating with photoresist, the substrate should be baked on a hot plate at $\sim 150^\circ$C for a few minutes to remove surface moisture. Hexamethyldisilazane (HMDS) should be used with sapphire substrates to promote adhesion (this is unnecessary for AlN). Only a few monolayers of HMDS are required: after baking, place the sapphire in a dish next to several drops of HMDS and cover for a few minutes. Note that both HMDS and photoresist are carcinogenic and should be handled with care.

Spinning photoresist onto a substrate is a relatively straightforward process. The substrate, with beads of photoresist dripped onto its surface, is spun by a vacuum chuck to a few thousand rpm for several tens of seconds. A faster rotation results in a thinner film of photoresist. Typically, a film thickness of a few microns is possible with standard photoresists, and there exists special resists that are four to twenty microns thick. These thick resists are often important for making tall wire structures. The thickness of a photoresist may be increased beyond its specification by dripping resist onto its surface during rotation. After spin-coating, the photoresist needs to be baked on a hot plate to prepare the polymer for UV exposure. The exact temperature and bake duration are often crucial to the success of the fabrication. We would like to note that it is possible to layer microwire patterns on top of one another by fabricating each new wire layer on top of a spin-coated insulator such as polyimide [32].

3.6 UV exposure

The central step in photolithography is the UV exposure of the photoresist. An instrument known as a mask aligner allows one to accurately position the photomask flush to the substrate's photoresist-coated surface, and a built-in UV lamp exposes the photoresist for a specified amount of time. Essential for photomask and substrate registration is an optical microscope mounted on the mask aligner. This enables one to simultaneously view the wire patterns on the mask and the underlying substrate. Dust particles or scratches often remain on the substrate even after a thorough cleaning. If these defects are sparse, then the substrate may be translated such that the wires avoid all defects. Aligning the chip's wire pads along one or more edges of the substrate further constrains the relative position of the photomask to the substrate. It should be noted that it is difficult to properly develop the pads (or other wire features) less than a millimeter from the edge due to photoresist beading. Certain fabrication recipes require the photoresist to be baked and exposed again before developing.

It is good practice to clean the chrome photomasks after every use. Photoresist can stick to the surface, and if left for days, will produce hard to remove specs that can block the UV light, creating unwanted features or breaks in the patterned wires. Immersing in a dish of acetone and rinsing with IPA and methanol is sufficient for routine cleaning. Some chrome masks can withstand ultrasound cleaning as well as being wiped with a soft, lint-free cloth, and this seems to be the only way to remove encrusted grime or particulate.

3.7 Developing

To remove the photoresist regions defined by the UV exposure, the substrate must be immersed and slightly agitated in a beaker of developer for a few tens of seconds followed by a water rinse. The exact developing time depends on the previous fabrication steps, but it is generally possible, especially with the transparent sapphire substrates, to see a characteristic change in opacity of the photoresist as it becomes fully developed. For instance, when using a positive process, one first sees the exposed photoresist turn hazy, revealing the wire pattern. After a few seconds, the hazy region sloughs off exposing the bare substrate and leaving darker, patterned regions of photoresist. If a mistake is made at any point in the photolithography process, the substrate can be reused by removing the photoresist in a beaker of acetone and cleaning the substrate as mentioned above, starting with the ultrasound.

3.8 Ozone dry stripping

Certain fabrication processes require the substrate surface to be etched in an ozone dry stripper. This uses UV light, ozone, and heat to remove thin films of unwanted organic material, photoresist, or HMDS that may prevent the deposition of thermally evaporated or electroplated gold.

3.9 Wire contacts

Wire bonding and ultrasonic fluxless soldering are useful methods for attaching macroscopic wires to the substrate's contact pads. Wire bonding is the standard method for making contacts to micro- or nanofabricated devices. The wire bonder attaches each end of a thin thread of gold wire to a pad using a heated, ultrasonically vibrating tip. The thin wire may be stretched over several millimeters between the pad on the substrate and a pad on the substrate support structure. The pads on the support structure may then be connected to standard wire contact pins. Because the wire threads are prone to break and cannot individually support more than a few hundred mA of current, it is necessary to make several redundant bonds per pad. This process can be quite time consuming. As an alternative, ultrasonic soldering irons are capable of attaching regular wires to sapphire or AlN using fluxless solder. Attaching wires is nearly as simple as standard soldering, and the fluxless solder is vacuum compatible to at least 10^{-9} Torr. Unfortunately, the solder material forms mounds on the substrate's surface that can limit optical access.

3.10 The mirror

Finally, we would like to discuss methods for making the atom chip's surface mirror-like. The most straightforward method involves simply patterning gold on the entire chip's surface except for thin, $> 10\ \mu$m, wide gaps around the actual wires [7]. This technique does not add any additional steps to the fabrication procedure, but it does increase the likelihood that surface defects will short the wires through contacts to the large mirrored areas. The mirror gaps that define the wires imprint defects onto the reflected mirror MOT beams, but we have nevertheless been able to trap more than a million cesium atoms with this less than perfect mirror. Another technique involves coating the chip's surface with an insulator and then applying a mirror coating. For example, several layers of polymethyl methacrylate (PMMA) can be spun onto the substrate. Swabbing with acetone removes the PMMA covering the wire pads near the substrate's edge, and the mirror is created by using a mask to thermally evaporate gold only onto the PMMA-coated region. Epoxying a silver mirror (with EPO-TEK 353) to the surface also forms a good mirror, and it eliminates any corrugations on the mirror surface caused by the underlying wires [11]. Unfortunately, the minimum distance between the atoms and the wires is set by the mirror and epoxy thickness. An improved mirror can be made by epoxying a dialectic mirror onto the surface. Vacuums of 2×10^{-10} Torr, in a chamber baked to 150°C, have been achieved despite using this glue and dielectric coating.

4 Specific fabrication techniques: wet etching, ion milling, lift-off method, and electroplating

The minimum required wire dimensions vary significantly depending on the the atom chip's application, and an optimal fabrication technique should be chosen accordingly. This section describes the recipe and relative merit of each fabrication method.

4.1 Wet etching and ion milling

The simplest chip to fabricate has wire widths no smaller than 30–40 μm and wire heights less than 1 μm. A transparency mask should be used for the photolithography (see Section 3.1). The wire height is set by a thermally evaporated gold layer and the photoresist masks the gold intended for wires from the wet etch solution (see figure 3(a)). To begin the procedure, the cleaned substrate should be placed in the ozone dry stripper for five minutes at 65°C to ensure that no organic material will prevent the adhesion of chromium and gold. The thermal evaporation step follows, with the thickness of the gold layer determined by chip's current density requirements. Because the photoresist adheres well to gold, only a 5 min bake at 180°C is necessary for adhesion. Wet etching removes exposed gold, and the photoresist should be patterned such than it covers the areas intended for wires, i.e. the photoresist should be a positive image of the wire pattern. A photomask on which the wires are opaque, used in conjunction with positive photoresist, will produce a positive image of the wire pattern. We use the photoresist AZ5214 (Clariant), which can serve as both a negative and positive photoresist depending on the bake and exposure procedure. The positive process recipe is as follows: spin coat at 5000 rpm for 50 s, bake at 95°C for 2 min, expose for 10 to 20 s, and develop in AZ327 MIF (or some similar developer) for 30 s. All of the above times are approximate and will vary depending on the UV light intensity of the specific mask aligner and on various environmental conditions. It may be necessary to try various exposure and bake times to find the optimal recipe. These exposure times are based on the 16 mW/cm^2 UV intensity of our mask aligner. To remove the gold not covered by photoresist, submerge the substrate in gold etch solution (Gold Etchant TFA, Transene Company, Inc., telephone 978-777-7860) for a few tens of seconds until only the dull gray of the chromium layer remains. Finally, remove the chromium layer with chrome etchant (CR-7S, Cyantek, Co., telephone 510-651-3341). Figures 4(a) and (b) show a substrate patterned in this manner. The wet etch dissolves the gold isotropically, and the decrease in wire width is insignificant for wires larger than 10 to 20 μm. Of course, transparency masks cannot be used for features smaller than a few tens of microns.

Ion milling can be useful alternative to wet etching. Instead of removing the unwanted gold with an etch solution, argon ions anisotropically bombard the surface, removing the gold not covered by photoresist (see figure 3(b)). This method can produce very narrow features,

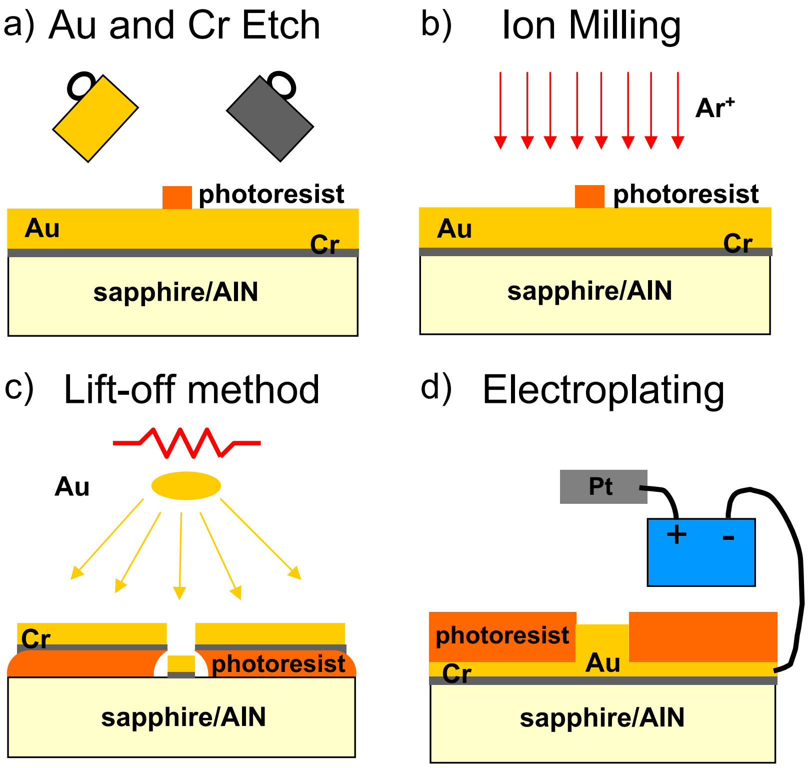
a) Au and Cr Etch
photoresist
Au
Cr
sapphire/AlN
b) Ion Milling
Ar+
photoresist
Au
Cr
sapphire/AlN
c) Lift-off method
Au
Cr
photoresist
sapphire/AlN
d) Electroplating
Pt
+
-
photoresist
Au
Cr
sapphire/AlN

Fig. 3. Fabrication techniques. (a) Patterned positive photoresist masks the gold layer from the gold and chromium wet etch. (b) The argon ions mill away the gold not covered by positive photoresist. (c) Gold is thermally evaporated into the trenches patterned in the negative photoresist. The undercut allows the photoresist and unwanted gold to separate from the substrate without peeling away the gold in the trenches. (d) Wires are defined by gaps in the positive photoresist, and the walls of the photoresist guide the wires as they are electroplated. After electroplating, acetone removes the photoresist and gold and chromium etches remove the seed layer.

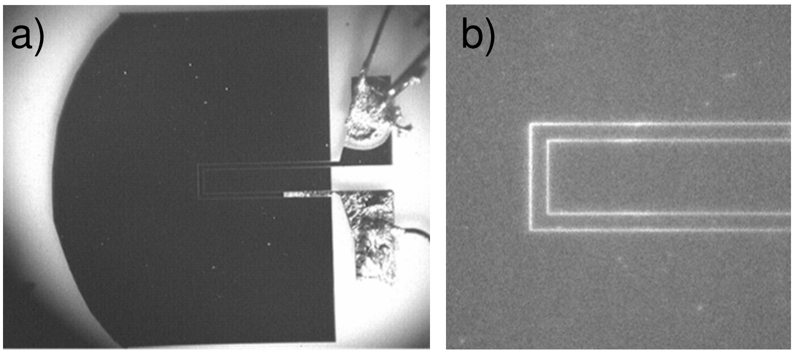

Fig. 4. Gold wire patterned using the wet etch technique. (a) This atom chip contains a quadrupole trap in the U configuration. The gold wire, patterned on sapphire and surrounded by a gold mirror, is 300 μm wide and 1 μm tall. (b) Close-up of the wire region. The gold appears darker than the uncovered sapphire substrate.

limited only by photoresist resolution, with heights determined by the thermally evaporated gold layer. The photoresist is also milled, but this is of no consequence as long as it is thicker than the gold layer. The substrate may become quite hot during the ion etching, and one needs to be careful that the substrate does not overheat, causing the photoresist to become hard and difficult to remove. We have used ion milling to make atom chips as well as to etch a common hard drive for use as a magnetic atom mirror [17].

4.2 ***The lift-off method***

The quick and easy wet etch technique is unfortunately not suitable for wire widths smaller than 10 μm, and ion milling machines are not readily available. The lift-off method should be used for the case in which the wires need not be taller than 1 μm but less than 10 μm wide. In contrast to the wet etch technique, the photoresist in this method is used as a mask for the deposition of thermally evaporated gold. Trenches are created in a negative photoresist using a photomask with opaque wires, and evaporated gold deposits both into the trenches, adhering to the substrate, and onto the surface of the photoresist (see figure 3(c)). If done properly, the walls of the trenches have an overhang—which looks like an undercut when viewed from above—that prevents the unwanted gold on the photoresist from connecting to the gold in the trenches. An acetone bath dissolves the photoresist, allowing the unwanted gold to lift-off leaving the wire pattern formed from the gold in the trenches.

After cleaning the substrate, the AZ5214 is spun on the substrate for 45 s at 5000 rpm. The maximum height of the thermally evaporated wires is set by the thickness of the photoresist since lift-off will not work once the top of the gold connects with the gold on the overhang. We have been able to achieve lift-off with wires 1.5 μm tall by spinning the photoresist on at 2000 rpm and thermally evaporating many boats of gold over a period of three to four hours. The photoresist should then be baked for 45 s at 100°C, UV exposed with the photomask for 10 s, baked again for 45 s at 123°C, UV exposed with no mask for 2.1 min, and developed for 25 to 35 s. Developing is finished when one can see the wire pattern in the photoresist. A successful undercut can be seen in a microscope as a bright outline of the edges of the trenches. Before thermal evaporation, the substrate should be placed in the ozone dry stripper at 65°C for 5 minutes. This removes unwanted material that could prevent gold adhesion, and does not seem to hamper photoresist removal as in the electroplating process described below. To promote lift-off, the acetone bath should be heated on a hot plate, and the substrate, while inside the beaker, should be sprayed with an acetone squirt bottle. It is very important that all of the gold-coated photoresist be pealed away before the substrate is removed from the acetone. Otherwise, once dried, the unwanted gold flakes become extremely difficult to separate from the surface. Difficulty in achieving lift-off may be overcome by briefly exposing the substrate to ultrasound. This is risky, however, since the gold wires might be stripped-off as well. Figure 2(b) shows an atom chip fabricated with the lift-off method.

4.3 Electroplating

The above methods rely on thermal evaporation to achieve the required wire thickness. This limits the wire heights to ~ 1 μm. Electroplating the wires can increase the wire height considerably: for example, we have made 3 μm wide wires, 4 μm tall. Thick photoresist spun and patterned on a thin gold seed layer provide a template for the growth of the wires. The walls of the photoresist maintain a constant wire width as the wire height increases (see figure 3(d)). An acetone wash followed by a brief wet etch removes the photoresist and gold seed layer. Electroplating is a tricky process that does not always produce reliable results. We provide here a general guideline for the process, and with this process we have typically been able to achieve a 75% yield with a wire height accuracy of ± 0.5 μm.

Fabrication begins with cleaning and ozone dry stripping the substrate, followed by the thermal evaporation of a 100 to 150 nm seed layer of gold along with a 50 Å chromium adhesion layer. For proper wire guiding, the photoresist must always be taller than the electroplated wires, and a photoresist thicker than the one used in the aforementioned techniques is necessary. Clariant's AZ9200 series photoresists are 4 to 24 microns thick, and can achieve aspect ratios of 5 to 7 with resolutions of < 1 μm to 3.5 μm depending on the resist thickness. After spin coating, the photoresist should be UV exposed for 60 s (or longer depending on the photoresist thickness) using a photomask with transparent wire patterns. The resist is developed in a 1:4 solution of AZ400K and water for a minute or more: the exposed photoresist will turn hazy before dissolving away. The gold seed layer also acts as the cathode in the electroplating process, and some of the photoresist must be whipped away with acetone—or a blank spot designed in the photoresist—to serve as a contact for the cathode lead. An ozone dry etch is then used to remove any layers of HMDS, photoresist, or organics that might mask regions of the gold from the electroplating solution. The time and temperature of this process is crucial: too long of an exposure at too high of a temperature will make the photoresist difficult to remove between closely spaced wires, and too short of an exposure will not remove enough unwanted masking material. For example, we found that an 18 s room-temperature ozone dry etch was optimal for removing unwanted material while also enabling the removal of photoresist between wires spaced by 3 μm.

We use a sodium gold sulfite solution (TG-25E, Technic, Inc. telephone 714-632-0200) for the electroplating. The solution is temperature controlled on a hot plate to 60°C and agitated with a magnetic stirrer. The anode is a platinum foil, and the substrate is connected to the power supply with a standard mini alligator clip. This clip can be dipped into the bath to enable the complete submersion of the substrate. We usually use a current of 0.1 to 0.2 mA to electroplate. Higher currents seem to produce rougher wire surfaces. The solution should remain clear to slightly yellowish during the process, and something is wrong if the solution starts to turn brown. The substrate should be gently agitated while electroplating to promote even plating and suppress the formation of ~ 5 μm tall towers of gold. Typically, it takes 10 to 30 minutes to electroplate several microns of gold at this current setting.

After electroplating, the photoresist should be removed in a room-temperature acetone bath. Sometimes it is difficult to remove the photoresist between wires spaced only several microns from one another, and in these cases the substrate—while in the acetone—should be placed in an ultrasound for a few minutes. The gold should not peel away since it is attached to the entire substrate surface. After rinsing the acetone away with IPA and methanol, the gold seed layer is removed with a ~ 15 s wet etch. The chromium adhesion layer should also be wet etched away. Occasionally, the air jet does not remove all of the methanol from the substrate, and tiny drops of methanol can sometimes dry on leeward side of the wires. This dried methanol acts as a mask for the gold etch, leaving small puddles of the seed layer that can short adjacent wires. These puddles can be removed by rinsing with methanol, blow-drying from a different angle, and briefly wet etching a second time. The surface reflectance of the gold is typically diminished after the wet etch, and a mirror fabricated with this gold may not be ideal.

A surface profilometer, commonly known as an alpha step machine, is quite useful for quickly measuring the height of the wires. Inevitably, a few substrates must be spent optimizing the electroplating process for a specific wire height. Figures 5(a) and (b) show an atom chip-based BEC interferometer that we fabricated by electroplating on an AlN substrate [33]. The smallest features are five, 1 mm long wires that are each 3 μm wide, 4 μm tall, and spaced less than 3 μm from one another.

5 Conclusion

The techniques described in this paper provide a basic starting point for the design and fabrication of these atom chips. The precise control of atomic position enabled by these chips is quite crucial to many areas of research. Moreover, these devices allow an incredible miniaturization of experiments involving cold atoms. From constructing atom optical elements to studies of BECs and cavity QED, atom chips are proving invaluable to the fields of atomic physics, quantum optics, and quantum computation.

Acknowledgements

We would like to thank Michael Roukes and Axel Scherer for use of their clean room facilities. Eyal Buks and Darrell Harrington were invaluable in teaching us the basics of photolithography. We also thank Marko Loncar for instruction in ion milling, and Jakob Reichel and Chungsok Lee for their advice regarding electroplating. This work was performed in the group of Hideo Mabuchi and supported by the Multidisciplinary University Research Initiative program under Grant No. DAAD19-00-1-0374.

References

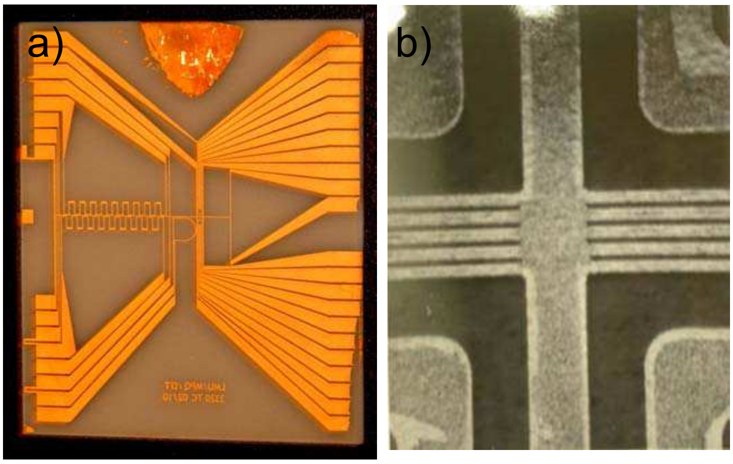

Fig. 5. An atom chip-based BEC interferometer fabricated by electroplating onto a AlN substrate. a) The chip will produce a BEC and transport it to the center region where b) five wires 3 μm wide, 4 μm tall, and spaced by 3 μm will split the BEC in a double well potential.

1. H. Metcalf and P. van der Straten (1999), *Laser Cooling and Trapping*, Springer-Verlag (New York).
2. T. Pellizzari, S. A. Gardiner, J. I. Cirac, and P. Zoller (1995), *Decoherence, continuous observation, and quantum computing: a cavity QED model*, Phys. Rev. Lett., **75**, 3788.
3. T. Calarco, E. A. Hinds, D. Jaksch, J. Schmiedmayer, J. I. Cirac, and P. Zoller (2000), *Quantum gates with neutral atoms: Controlling collisional interactions in time-dependent traps*, Phys. Rev. A, **61**, 022304.
4. R. Raussendorf and H. Briegel (2001), *A one-way quantum computer*, Phys. Rev. Lett., **86**, 5188.
5. J. D. Weinstein and K. G. Libbrecht (1995), *Microscopic magnetic traps for neutral atoms*, Phys. Rev. A, **52**, 4004.
6. M. Drndić, K. S. Johnson, J. H. Thywissen, M. Prentiss, and R. M. Westervelt (1998), *Micro-electromagnets for atom minipulation*, Appl. Phys. Lett., **72**, 2906.
7. R. Folman, P. Krüger, D. Cassettari, B. Hessmo, T. Maier, and J. Schmiedmayer (2000), *Controlling cold atoms using nanofabricated surfaces: atom chips*, Phys. Rev. Lett., **84**, 4749.
8. J. Reichel, W. Hänsel, and T. W. Hänsch (1999), *Atomic micromanipulation with magnetic surface traps*, Phys. Rev. Lett., **83**, 3398.
9. D. Müller, D. Anderson, R. Grow, P. Schwindt, and E. Cornell (1999), *Guiding neutral atoms around curves with lithographically patterned current-carrying wires*, Phys. Rev. Lett., **83**, 5194.
10. N.H. Dekker, C.S. Lee, V. Lorent, J.H. Thywissen, S.P. Smith, M. Drndić, R.M. Westervelt, and M. Prentiss (2000), *Guiding neutral atoms on a chip*, Phys. Rev. Lett., **84**, 1124.
11. J. Reichel, W. Hänsel, P. Hommelhoff, and T. W. Hänsch (2001), *Applications of integrated magnetic microtraps*, Appl. Phys. B, **72**, 81.
12. R. Folman, P. Krüger, J. Schmiedmayer, J. Denschlag, and C. Henkel (2002), *Microscopic atom optics: From wires to an atom chip*, Adv. At. Mol. Opt. Phys., **48**, 263.
13. D. Müller, E. Cornell, M. Prevedelli, P. Schwindt, Y. Wang, and D. Anderson (2001), *Magnetic switch for integrated atom optics*, Phys. Rev. A, **63**, 041602.
14. E. A. Hinds and I. G. Hughes (1999), *Magnetic atom optics: mirrors, guides, traps, and chips for atoms*, J. Phys. D: Appl. Phys., **32**, R119.

15. K. S. Johnson, M. Drndic, J. H. Thywissen, G. Zabow, R. M. Westervelt, and M. Prentiss (1998), *Atomic deflection using an adaptive microelectromagnet mirror*, Phys. Rev. Lett., **81**, 1137.
16. A. I. Sidorov, R. J. McLean, F. Scharnberg, D. S. Gough, T. J. Davis, B. J. Sexton, G. I. Opat, and P. Hannaford (2002) *Permanent-magnet microstructures for atom optics*, Acta Physica Polonica B, **33**, 2137.
17. B. Lev, Y. Lassailly, C. Lee, A. Scherer, and H. Mabuchi (2003), *Atom mirror etched from a hard drive*, Appl. Phys. Lett., **83**, 395.
18. B. Lev and H. Mabuchi (2003), in preparation.
19. P. Horak, B. Klappauf, A. Haase, R. Folman, J. Schmiedmayer, P. Domokos, and E. A. Hinds (2002), *Towards single-atom detection on a chip*, quant-ph/0210090.
20. R. Long, T. Steinmetz, P. Hommelhoff, W. Hänsel, T. W. Hänsch, and J. Reichel (2003), *Magnetic microchip traps and single-atom detection*, Phil. Trans. R. Soc. Lond. A, **361**, 1.
21. D. Kielpinski, C. Monroe, and D. J. Wineland (2002), *Architecture for a large-scale ion-trap quantum computer*, Nature, **417**, 709.
22. M. A. Rowe, A. Ben-Kish, B. Demarco, D. Leibfried, V. Meyer, J. Beall, J. Britton, J. Hughes, W. M. Itano, B. Jelenković, C. Langer, T. Rosenband, and D. J. Wineland (2002), *Transport of quantum states and seperation of ions in a dual RF ion trap*, Quantum Inf. Comput., **2**, 257.
23. W. Hänsel, P. Hommelhoff, T. W. Hänsch, and J. Reichel (2001), *Bose-Einstein condensation on a microelectronic chip* , Nature, **413**, 498.
24. H. Ott, J. Fortagh, G. Schlotterbeck, A. Grossmann, and C. Zimmermann (2001), *Bose-Einstein condensation in a surface microtrap*, Phys. Rev. Lett., **87**, 230401.
25. A. E. Leanhardt, Y. Shin, A. P. Chikkatur, D. Kielpinski, W. Ketterle, and D. E. Pritchard, (2003), *Bose-Einstein condensates near a microfabricated surface*, Phys. Rev. Lett., **90**, 100404.
26. R. Folman and J. Schmiedmayer (2003), private communication.
27. D. Cassettari, B. Hessmo, R. Folman, T. Maier, and J. Schmiedmayer (2000), *Beam splitter for guided atoms*, Phys. Rev. Lett., **85**, 5483.
28. H. Mabuchi, M. Armen, B. Lev, M. Loncar, J. Vučković, H. J. Kimble, J. Preskill, M. Roukes, and A. Scherer (2001), *Quantum networks based on cavity QED*, Quantum Inf. Comput., **1**, 7.
29. J. McKeever, J. R. Buck, A. D. Boozer, A. Kuzmich, H. C. Nägerl, D. M. Stamper-Kurn, and H. J. Kimble (2003), *State-insensitive cooling and trapping of single atoms in an optical cavity*, Phys. Rev. Lett., **90**, 133602.
30. M. J. Madou (2001), *Fundamentals of microfabrication*, CRC Press (New York).
31. J. Reichel (2002), *Microchip traps and Bose-Einstein condensation*, Appl. Phys. B, **75**, 469.
32. M. Drndić, C. S. Lee, and R. M. Westervelt (2001), *Three-dimensional microelectromagnet traps for neutral and charged particles*, Phys. Rev. B, **63**, 085321.
33. Wire pattern designed by T. Steinmetz and P. Hommelhoff at the Max-Plank-Institut für Quantenoptik in Garching and the Ludwig-Maximilians-Universität in Munich.

arXiv:quant-ph/0510135 v1 17 Oct 2005

A fault-tolerant one-way quantum computer

R. Raussendorf[1], J. Harrington[2] and K. Goyal[1]
[1]*Institute for Quantum Information, California Institute of Technology, Pasadena, CA 91125*
[2]*Los Alamos National Laboratory, Biological and Quantum Physics, MS D454, Los Alamos, NM 87545*

January 11, 2006

We describe a fault-tolerant one-way quantum computer on cluster states in three dimensions. The presented scheme uses methods of topological error correction resulting from a link between cluster states and surface codes. The error threshold is 1.4% for local depolarizing error and 0.11% for each source in an error model with preparation-, gate-, storage- and measurement errors.

1 Introduction

A quantum computer as a physical device has to cope with imperfections of its hardware. Fortunately, it turns out that arbitrary large quantum computations can be performed with arbitrary accuracy, provided the error level of the elementary components of the quantum computer is below a certain threshold. This is the content of the threshold theorem for quantum computation [1, 2, 3, 4]. The threshold theorem also provides lower bounds to the error threshold which are in the range between 10^{-10} and 10^{-4}, depending on the error model. It thus appears that there is a gap between the required and the currently available accuracy of quantum operations, and it invites narrowing from both the experimental and the theoretical side. In this context, significant progress has been made in [5] where a threshold estimate in the percent range has been demonstrated. For experimentally viable quantum computation there is a further desideratum besides a high error threshold. With the exception of certain schemes for topological quantum computation [6, 7, 8], the price for fault-tolerance is an overhead in quantum resources. This overhead should be moderate.

Here we describe a fault-tolerant version of the one-way quantum computer ($QC_\mathcal{C}$). The $QC_\mathcal{C}$ is a scheme for universal quantum computation by one-qubit measurements on cluster states [9]. Cluster states [10] consist of qubits arranged on a two- or three-dimensional lattice and may be created by a nearest-neighbor Ising interaction. Thus, for the $QC_\mathcal{C}$, only nearest-neighboring qubits need interact and furthermore, only once at the beginning of the computation. For this scenario in three dimensions we present methods of error correction and a threshold value.

The existence of an error threshold for the $QC_\mathcal{C}$ has previously been established [11, 12, 13] and threshold estimates have been obtained [12, 13], by mapping to the circuit model. Here we take a different path. We make use of topological error correction capabilities that the cluster states naturally provide [14] and which can be linked to surface codes [6, 15]. The main design tool upon which we base our construction are engineered lattice defects which are topologically entangled.

The picture is the following: quantum computation is performed on a three-dimensional cluster state via a temporal sequence of one-qubit measurements. The cluster lattice is subdivided into three regions, V, D and S. The set S comprises the ‘singular’ qubits which are measured in an adaptive basis. The quantum computation happens essentially there. The sets V and D are to distribute the correct quantum correlations among the qubits of S. V stands for ‘vacuum’, the quantum correlations can propagate and spread freely in V. D stands for ‘defect’. Quantum correlations cannot penetrate the defect regions. They either end in them or wrap around them. In both cases,

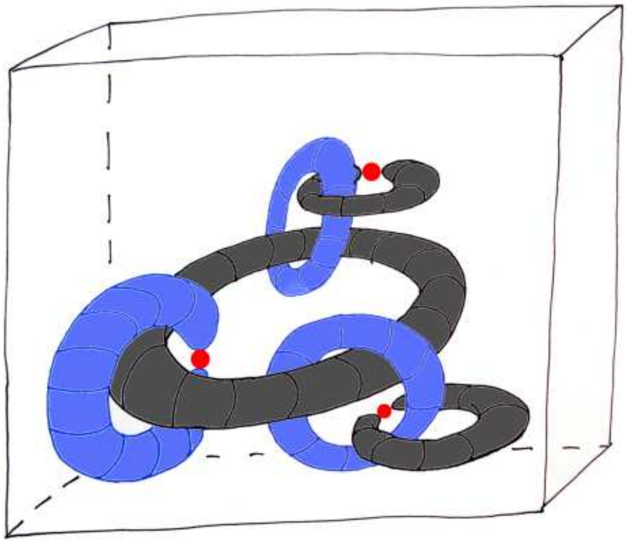

Figure 1: Topological error correction for the $QC_\mathcal{C}$. The three-dimensional cluster state, shown as a block, is structured by lattice defects which exist in two kinds: primal and dual. The defects wind around another. Some of them hold singular qubits (red) which realize the non-Clifford part of the quantum computation.

the defects *guide* the quantum correlations. V and D are distinguished by the bases in which the respective cluster qubits are measured. The region V fills most of the cluster. Embedded in V are the defects (D) most of which take the shape of loops. These loops are topologically entangled with another. Further, there are defects in the shape of ear clips which each hold an S-qubit in their opening. Such a defect and the belonging S-qubit form again a loop. These are the only locations where the S-qubits occur. See Fig. 1.

There are two codes upon which we base our construction, the planar code [15] and the concatenated $[15, 3, 1]$ quantum Reed-Muller code [16, 17]. Both codes individually have their strengths and weaknesses, but they can be advantageously combined. The planar code has a relatively high error threshold of about 11% [18], and the symmetries of its stabilizer fit well with cluster states. Moreover, fault-tolerant data storage with the planar code and the creation of long range entanglement among planar code qubits are easily accomplished in three-dimensional cluster states, via a bcc-symmetric pattern of one-qubit measurements. Therefore, it is suggestive to base fault-tolerant cluster state computation on this code. However, the planar code is not well suited to non-Clifford operations which are essential for universal quantum computation.

Now, in cluster- and graph state quantum computation, the non-Clifford part of the circuit is implemented by destructive measurements of the observables $(X \pm Y)/\sqrt{2}$ (The Clifford part is implemented by X-, Y- and Z-measurements.). The Reed-Muller quantum code is well suited for fault-tolerant quantum computation via local measurements because the measurements of the encoded observables $(\overline{X} \pm \overline{Y})/\sqrt{2}$ (and of $\overline{X}$, $\overline{Y}$, $\overline{Z}$ besides) are accomplished fault-tolerantly by the respective measurements on the bare level—and bare level measurements is what we are allowed to do in the $QC_\mathcal{C}$. If we could assume we had given a graph state state as algorithmic resource where each cluster qubit was encoded with the concatenated Reed-Muller code and where noise acted locally on the bare level, then fault-tolerant quantum computation were trivial to achieve. However, is not obvious how to create such an encoded graph state affected by local noise only. But this is just what the topological error correction in cluster states can do.

This paper is organized as follows. In Section 2, we introduce the ingredients required for the error correction mechanisms we use, namely cluster states, the planar code and the 15-qubit Reed-Muller quantum code. In Section 3 the measurement pattern used for fault-tolerant cluster state quantum computation is described, and in Sections 5 - 6 it is explained. Specifically, in Section 5 we describe the physical objects relevant for the discussed scheme—defects, cluster state quantum correlations, errors and syndrome bits—in the language of homology. In Section 6 we introduce the techniques for structuring quantum correlations via topological entanglement of lattice defects. Our error models are stated in Section 7.1 and the fault-tolerance threshold is derived in Section 7.2. The overhead is estimated in Section 8. We discuss our results in Section 9.

2 Cluster states and quantum codes

This section is a brief review of the ingredients for the described fault-tolerant $QC_{\mathcal{C}}$.

Cluster states. A cluster state is a stabilizer state of qubits, where each qubit occupies a site on a d-dimensional lattice $\mathcal{C}$. Each site $a \in \mathcal{C}$ has a neighborhood $N(a)$ which consists of the lattice sites with the closest spatial distance to a. Then, the cluster state $|\phi\rangle_{\mathcal{C}}$ is—up to a global phase—uniquely defined via the generators K_a of its stabilizer

$$K_a := X_a \bigotimes_{b \in N(a)} Z_b, \;\; \forall a \in \mathcal{C}, \tag{1}$$

i.e., $|\phi\rangle_{\mathcal{C}} = K_a |\phi\rangle_{\mathcal{C}}$. Here, X_a and Z_b are a shorthand for the Pauli operators $\sigma_x^{(a)}$ and $\sigma_z^{(b)}$ that we use throughout the paper. We refer to the generators K_a of the cluster state stabilizer as the elementary cluster state quantum correlations.

In this paper, we will use as the lattice underlying the cluster state a bcc-symmetric lattice in tree dimensions. That is, the location of cluster qubits is given by lattice vectors

$$\begin{array}{ll} \{(o[\text{dd}], e[\text{ven}], e), (e, o, e), (e, e, o)\}, & \text{odd qubits}, \\ \{(e, o, o), (o, e, o), (o, o, e)\}, & \text{even qubits}. \end{array} \tag{2}$$

We sub-divide the set of qubits into two subsets, the even and the odd qubits. For even (odd) qubits the sum of the coordinates of their respective lattice site is even (odd).

Note that instead of with a bcc-symmetric lattice we could have equivalently started with a cluster state on an sc-symmetric lattice, because a cluster state on the latter is mapped to a cluster state on the former by Z-measurements on the qubits (e, e, e) and (o, o, o); see [9].

The $[15, 3, 1]$ quantum Reed-Muller code. By this we denote a 15 qubit CSS-code based on the (classical) punctured Reed-Muller code $\mathcal{R}(1, 4)^*$ [19]. Its stabilizer generator matrix has the form

$$G_{RM} = \left(\begin{array}{c|c} G_X & 0 \\ 0 & G_Z \end{array} \right), \tag{3}$$

where

$$G_X = \begin{pmatrix} 1 & 0 & 1 & 0 & 1 & 0 & 1 & 0 & 1 & 0 & 1 & 0 & 1 & 0 & 1 \\ 0 & 1 & 1 & 0 & 0 & 1 & 1 & 0 & 0 & 1 & 1 & 0 & 0 & 1 & 1 \\ 0 & 0 & 0 & 1 & 1 & 1 & 1 & 0 & 0 & 0 & 0 & 1 & 1 & 1 & 1 \\ 0 & 0 & 0 & 0 & 0 & 0 & 0 & 1 & 1 & 1 & 1 & 1 & 1 & 1 & 1 \end{pmatrix}, \tag{4}$$

and G_Z is given by ${G_X}^{\perp} = G_Z \oplus (1, 1, ..., 1, 1)$.

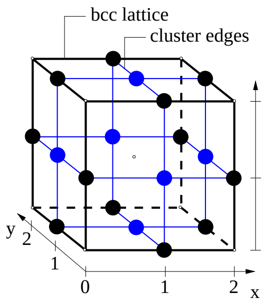

Figure 2: Elementary cell of the bcc lattice. Qubits live on the faces and edges of the elementary cell. Syndrome bits are located in the cube and on the sites. Each elementary cell has a volume of $2 \times 2 \times 2$ in cluster units. Black: elementary cell of the bcc lattice, blue: edges of the cluster graph.

This code has the fairly rare property that the encoded non-Clifford gate $\overline{U}_z(\pi/4) = \exp(-i\pi/8\overline{Z})$ is local [16, 17], i.e.,

$$\exp\left(-i\frac{\pi}{8}\,\overline{Z}\right) \cong \bigotimes_{i=1}^{15} \exp\left(i\frac{\pi}{8}\,Z_i\right). \tag{5}$$

This property has been used in magic state distillation [17]. In the computational scheme described here we use it to fault-tolerantly measure the encoded observables $\frac{\overline{X}\pm\overline{Y}}{\sqrt{2}}$ via *local* measurements of observables $\frac{X_i \pm Y_i}{\sqrt{2}}$.

Surface codes. For the surface codes [6, 15] physical qubits live on the edges of a two-dimensional lattice. The support of a physical error must stretch across a constant fraction (typically 1/2) of the lattice to cause a logical error. The protection against errors is topological.

The stabilizer generators of the code are associated with the faces f and the vertices v of the lattice,

$$S_X(v) = \bigotimes_{e|\, v \in \{\partial e\}} X_e, \;\; S_Z(f) = \bigotimes_{e \in \{\partial f\}} Z_e. \tag{6}$$

Therein, ∂ is the boundary operator. The number of qubits that can be stored depends on the boundary conditions of the code lattice. The code resulting from periodic boundary conditions, the 'toric code' [6], can store two qubits.

As an example we would briefly like to discuss the planar code [15] which encodes one qubit; see Fig. 3a. This example exhibits many features of our subsequent constructions one dimension higher up: Errors are identified with 1-chains and show a syndrome only at their end points. Homologically equivalent chains correspond to physically equivalent errors. Error chains can end in the system boundary without leaving a syndrome.

Specifically, Pauli operators Z_i live on the edges of the primal (=shown) lattice, and Pauli operators X_j live on edges of the dual lattice. The encoded Z-operator is a tensor product of individual Z_i operators corresponding to a primal 1-chain stretching from left to right across the code lattice. The encoded X-operator corresponds to a 1-chain of the dual lattice that stretches from top to bottom.

The code stabilizer is modified at the system boundary. For example, a face to the left or right of the lattice has only three elementary 1-chains in its boundary, instead of four. Such boundary is called a 'rough edge'. Where no modification of the faces occurs the system boundary is a 'smooth edge'. 'Smooth' on the primal lattice is 'rough' on the dual, and vice versa. Error chains can end in a rough edge of their respective lattice without leaving a syndrome, but not in a smooth edge.

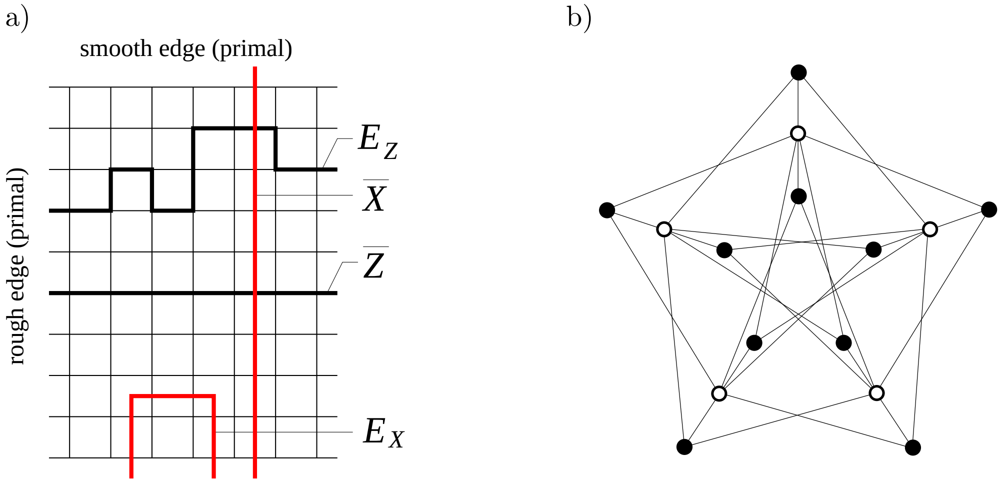

Figure 3: Codes. a) Planar code. The encoded Pauli observables $\overline{X}$ and $\overline{Z}$, two errors and the different boundary types 'smooth' and 'rough' are shown. The errors E_X, E_Z end in their respective rough boundary. E_X corresponds to a trivial 1-cycle on the dual lattice and has no effect on the encoded state. E_Z corresponds to an non-trivial 1-cycle on the primal lattice. It leaves no syndrome but causes a logical Z-error. b) Bi-colorable graph state locally unitary equivalent to the $\overline{|+\rangle}$-state of the 15-qubit quantum Reed-Muller code.

The surface codes will occur rather implicitly in our constructions. The reason is that here we do not use such codes to encode logical qubits. Instead, we use them to appropriately "wire" a subset of the cluster qubits, the S-qubits. The link between surface codes and cluster states has been established in [14], for the purpose of creating long range entanglement in noisy 3D cluster states via local measurements. It has been found that the error correction implemented by the local measurements is described—like fault-tolerant data storage with the toric code—by the so-called *Random plaquette* $\mathbb{Z}_2$*-gauge model in three dimensions* (RPGM) [18]. The three-dimensional cluster state is like a surface code, one dimension higher up. The third dimension, which is temporal in data storage with the toric code, is spatial for the cluster state. The extra spatial dimension can be used to fault-tolerantly mediate interaction among qubits. The creation of an encoded Bell state over large distances [14] is the simplest example. The long-range quantum correlations are engineered by the suitable choice of boundary conditions.

Why are the above two codes chosen? For the fault-tolerant scheme of quantum computation described in this paper we require a quantum code with the following three properties: 1) The code is of CSS-type, 2) The code satisfies Eq. (5), and 3) The code fits with cluster states. For some arrangement of qubits on a translation-invariant two-dimensional lattice, the code has a translation-invariant set of stabilizer generators and these generators each have a small support on the lattice.

The Reed-Muller code has properties 1 and 2 but not 3. The surface codes have properties 1 and 3 but not 2. Thus, neither of the codes alone suffices. But their combination does, as is described in the subsequent sections.

3 The measurement pattern

As pointed out in the introduction, we subdivide the cluster C into the three disjoint subsets V, D and S. S is the the set of qubits where the non-Clifford part of the quantum computation is performed, and V and D are to connect the qubits of S in the proper way. We have not yet explained what the defects are, and we will do so only in the next section. For the moment it suffices to note that the defects are located on the subset D of the cluster, and that D is the union of the two disjoint subsets D_1 and D_2. The measurement pattern on D, S and V is given by

$$\begin{array}{ll} \text{Defect qubits } a \in D: & \text{Measurement of } \left\{ \begin{array}{l} X_a \\ Z_a \end{array} \right., \quad \text{if } \left\{ \begin{array}{l} a \in D_2 \\ a \in D_1 \end{array} \right., \\ \text{Singular qubits } a \in S: & \text{Measurement of } \dfrac{X_a \pm Y_a}{\sqrt{2}}, \\ \text{Vacuum qubits } a \in V: & \text{Measurement of } X_a. \end{array} \tag{7}$$

Now we have to explain why we choose this measurement pattern, which is best done using the language of homology.

4 Involving the Reed-Muller quantum code

In this section we explain the role of the Reed-Muller code for the described computational scheme. Consider a cluster state $|\phi\rangle_{\mathcal{C}_2}$ on a two-dimensional cluster $\mathcal{C}_2$. It is a resource for universal quantum computation by measurements of the local observables X, Z and $\frac{X \pm Y}{\sqrt{2}}$, [9]. Denote by $Q \subset \mathcal{C}_2$ the set of qubits which are measured in the eigenbasis of $\frac{X \pm Y}{\sqrt{2}}$. These measurements implement the non-trivial part of a quantum circuit. The measurements of X and Z on the qubits $\mathcal{C}_2 \backslash Q$ implement the Clifford part. They are performed simultaneously in the first round of measurements. $|\Psi_\text{algo}\rangle_Q$ is the state of the unmeasured qubits after the first measurement round. It is an algorithm-specific stabilizer state, hence the subscript "algo". Since it is a stabilizer state, it is easy to create and one may start with this state as an algorithm-specific resource instead of the universal cluster state. Quantum computation with this state proceeds by measuring local observables $\frac{X \pm Y}{\sqrt{2}}$.

Now suppose an encoded version of this state, $|\overline{\Psi}_\text{algo}\rangle_S$, was given. The state were not perfect but only affected by local noise on the bare level. Of course, a question that arises immediately is how such a state is obtained. The main part of work in this paper goes into answering this question, see subsequent sections. Now, with $|\overline{\Psi}_\text{algo}\rangle_S$ given, one could perform fault-tolerant quantum computation by fault-tolerant measurement of the encoded observables $\frac{\overline{X} \pm \overline{Y}}{\sqrt{2}}$. This is not what we have in mind, because we are seeking a scheme of fault-tolerant quantum computation by *local* measurements. Here lies the reason for involving the (concatenated) Reed-Muller code: For this code, the fault-tolerant measurement of the observables $\frac{\overline{X} \pm \overline{Y}}{\sqrt{2}}$ proceeds by local measurements of observables $\frac{X \pm Y}{\sqrt{2}}$. The reason for this is property (5). If J is a set such that $g_X(J) := \bigotimes_{j \in J} X_j$ is in the RM code stabilizer, then also

$$g_\pm(J) := \bigotimes_{j \in J} \frac{X_j \pm Y_j}{\sqrt{2}} \in \text{RM code stabilizer}. \tag{8}$$

The relevant encoded observables are given by

$$\frac{\overline{X} \pm \overline{Y}}{\sqrt{2}} = \bigotimes_j \frac{X_j \mp Y_j}{\sqrt{2}}. \tag{9}$$

The "∓" is for the total number of concatenation levels being odd. If the number is even, replace "∓" by "±". Therefore, if all the bare qubits belonging to an encoded qubit are individually measured in the eigenbasis of $\frac{X_j - Y_j}{\sqrt{2}}$, then the eigenvalue found in a measurement of the encoded observable $\frac{\overline{X} + \overline{Y}}{\sqrt{2}}$ and the eigenvalues of the stabilizer generators $g_+(J)$ can be deduced from the individual measurement outcomes. This is all what is needed for fault-tolerant measurement of the encoded observable $\frac{\overline{X} + \overline{Y}}{\sqrt{2}}$.

The Z-part of the code stabilizer is lost in the local measurement, but it is not needed for the fault-tolerant measurement of $\frac{\overline{X \pm Y}}{\sqrt{2}}$. This can be seen as follows. For simplicity assume a local depolarizing error $p/3\,([X_j]+[Y_j]+[Z_j]) = \frac{p}{3\sqrt{2}}\left([X_j+Y_j]+[X_j-Y_j]+\sqrt{2}[Z_j]\right)$ for all qubits j. The brackets "$[\cdot]$" indicate a super-operator. W.l.o.g. assume that the local measurements are in the eigenbasis of $\frac{X_j-Y_j}{\sqrt{2}}$. Then, the error $\frac{X_j-Y_j}{\sqrt{2}}$ is absorbed in the measurement and has no effect. The second error $\frac{X_j+Y_j}{\sqrt{2}} = i\frac{X_j-Y_j}{\sqrt{2}}Z_j \cong Z_j$, so all remaining errors are equivalent to Z-errors. Such errors are identified by the stabilizer elements $\{g_+(J)\}$.

To summarize, the Reed-Muller code is involved to perform the fault-tolerant measurement of the encoded observables locally on the bare level. The eigenvalues corresponding to the encoded observable and to the relevant stabilizer generators are simultaneously inferred from the measurement outcomes. Error correction proceeds by classical post-processing of these quantities.

5 Involving a topological quantum code - Homology

The remaining question is how we actually create the state $|\overline{\Psi}_{\text{algo}}\rangle_S$ with only local error from a three-dimensional cluster state. To accomplish this task we involve topological error correction.

5.1 Errors and correlations as chains

The physical objects of our discussion—cluster state correlations and error operators—may be identified with faces and edges of an underlying lattice. Compositions of such faces or edges are called 2-chains and 1-chains, respectively. For the chains homology provides an equivalence relation; namely, two chains are homologically equivalent if they differ by the boundary of a third chain one dimension higher up [20, 21, 22]. Homology plays a role in our constructions because homological equivalence of the underlying chains implies physical equivalence of the associated physical objects.

First we introduce the two simple cubic sub-lattices $\mathcal{L}$ and $\overline{\mathcal{L}}$ whose vertices are at locations

$$\begin{array}{lcl} \mathcal{L} & : & \{(e,e,e)\}, \\ \overline{\mathcal{L}} & : & \{(o,o,o)\}. \end{array} \tag{10}$$

One lattice can be obtained from the other via translation by a vector $(\pm 1, \pm 1, \pm 1)$. $\mathcal{L}$ and $\overline{\mathcal{L}}$ are dual to another in the sense that the faces of $\mathcal{L}$ are the edges of $\overline{\mathcal{L}}$, the cubes of $\mathcal{L}$ are the vertices of $\overline{\mathcal{L}}$, and vice versa. We denote by $*$ the duality transformation that maps primal edges into the corresponding dual faces ($*e = \overline{f}$), and so forth.

We denote by $\mathcal{B}(C_0) := \{v_k\}$ the set of vertices in $\mathcal{L}$, by $\mathcal{B}(C_1) = \{e_l\}$ the set of edges in $\mathcal{L}$, by $\mathcal{B}(C_2) = \{f_m\}$ the set of faces in $\mathcal{L}$, and by $\mathcal{B}(C_3) = \{q_n\}$ the set of elementary cells [or cubes] of $\mathcal{L}$. We may now define chains in $\mathcal{L}$ [20]. $\mathcal{B}(C_0)$ forms a basis for the set C_0 of so called 0-chains c_0, $\mathcal{B}(C_1)$ forms a basis for the set C_1 of 1-chains c_1, and so forth. Specifically, the chains are given by

$$c_0 = \textstyle\sum_k z_k v_k, \quad c_1 = \sum_l z_l e_l, \quad c_2 = \sum_m z_m f_m, \quad c_3 = \sum_n z_n q_n. \tag{11}$$

where $z_k, z_l, z_m, z_n \in \mathbb{Z}_2$. The sets C_0, C_1, C_2 and C_2 are, in fact, abelian groups under component-wise addition, e.g. $c_1 + c_1' = \sum_l z_l e_l + \sum_l z_l' e_l = \sum_l (z_l + z_l') e_l$. For each $i = 1..3$, there exists a homomorphism ∂_i mapping C_i to C_{i-1}, with the composition $\partial_{i-1} \circ \partial_i = 0$. Then,

$$\mathcal{L} = \{C_3, C_2, C_1, C_0\} \tag{12}$$

is called a chain complex, and ∂ is called boundary operator. It maps an i-chain c_i to its boundary, which is an $i-1$-chain. In the same way, $\overline{\mathcal{L}}$ can be defined as a dual chain complex, $\overline{\mathcal{L}} = \{\overline{C}_3, \overline{C}_2, \overline{C}_1, \overline{C}_0\}$, with chains $\overline{c}_3$, $\overline{c}_2$, $\overline{c}_1$ and $\overline{c}_0$.

Now, considering a space $\mathcal{C}$, two chains c_n, $c_n' \in C_n(\mathcal{C})$ are homologically equivalent if $c_n' = c_n + \partial c_{n+1}$ for some $c_{n+1} \in C_{n+1}(\mathcal{C})$ [20]. Of interest for topological error-correction is the notion of *relative homology*. Consider a pair of spaces $(\mathcal{C}, D)$ with $D \subset \mathcal{C}$. Then, two chains c_n, c_n' are called equivalent w.r.t relative homology, $c_n' \cong_{\mathrm{r}} c_n$, if $c_n' = c_n + \partial c_{n+1} + \gamma_n$ for some $c_{n+1} \in C_{n+1}(\mathcal{C})$, $\gamma_n \in C_n(D)$; see [21]. Relative cycles may end in D.

Below we describe how the cluster state quantum correlations may be identified with the 2-chains, the errors with the 1-chains and the syndrome with the 0-chains of $\mathcal{L}$ and $\overline{\mathcal{L}}$. All these objects appear in two kinds, 'primal' and 'dual', depending on whether they are defined with respect to $\mathcal{L}$ or $\overline{\mathcal{L}}$.

Cluster state correlations. We define primal such correlations, $K(c_2)$, and dual ones, $K(\overline{c}_2)$, which can be identified with 2-chains in $\mathcal{L}$ and $\overline{\mathcal{L}}$, respectively, by

$$K(c_2) := \prod_{f \in \{c_2\}} K_f, \;\; K(\overline{c}_2) := \prod_{\overline{f} \in \{\overline{c}_2\}} K_{\overline{f}}. \tag{13}$$

Therein, e.g. the set $\{c_2\}$ is defined via a mapping $c_2 = \sum_m z_m f_m \longrightarrow \{c_2\} = \{f_m | z_m = 1\}$. Further, we introduce the notion $O(c) := \bigotimes_{a \in \{c\}} O_a$, for all $c \in C$ and $O \in \{X, Z\}$. It is now easily verified that

$$K(c_2) = X(c_2) Z(\partial c_2), \; K(\overline{c}_2) = X(\overline{c}_2) Z(\partial \overline{c}_2). \tag{14}$$

Errors. We will mainly discuss (correlated) probabilistic noise. Then, it is sufficient to restrict the attention to Pauli phase flips Z, because $X_a \cong \bigotimes_{b \in N(a)} Z_b$ etc. We combine Z-errors on odd (even) qubits to primal (dual) error chains $E(c_1)$ ($E(\overline{c}_1)$),

$$E(c_1) := Z(c_1), \;\; E(\overline{c}_1) := Z(\overline{c}_1). \tag{15}$$

Syndrome. The first type of correlations we discuss are those for error correction in V. They are characterized by the property that the corresponding 2-chains have no boundary. I.e., we consider $K(c_2)$, $K(\overline{c}_2)$ with $\{c_2\}, \{\overline{c}_2\} \in V$ and $\partial c_2 = \partial \overline{c}_2 = 0$. With (13), these correlations take the form $K(c_2) = X(c_2)$, $K(\overline{c}_2) = X(\overline{c}_2)$. They are measured by the X-measurements in V, see (7), and are used to identify errors occurring on the qubits $\{c_2\}$, $\{\overline{c}_2\}$.

The group of 2-chains in the kernel of ∂ we denote by $Z_2(\mathcal{L})$. Since $\partial\partial = 0$, a subgroup of those, $B_2(\mathcal{L})$, is formed by the 2-chains which are themselves a boundary of a 3-chain. Denote by q ($\overline{q}$) a 3-chain from the basis $\mathcal{B}(C_3)$ ($\mathcal{B}(\overline{C}_3)$). It represents an individual cell [or cube] of the primal lattice $\mathcal{L}$ (dual lattice $\overline{\mathcal{L}}$). The associated quantum correlations are

$$K_q := K(\partial q) = X(\partial q), \;\; K_{\overline{q}} := K(\partial \overline{q}) = X(\partial \overline{q}). \tag{16}$$

When being measured, each of these correlations yields a syndrome bit $Sy(q)$, $Sy(\overline{q})$ which, we say, is located at q or $\overline{q}$, respectively. Because the lattices $\mathcal{L}$ and $\overline{\mathcal{L}}$ are dual to another, we may identify the cell q in $\mathcal{L}$ with a vertex $\overline{v}$ in $\overline{\mathcal{L}}$, and vice versa. In this way, the syndrome bits become located at vertices of the lattices $\mathcal{L}$ and $\overline{\mathcal{L}}$. The syndrome resulting from the quantum correlations (16) are those which enable topological error correction [18].

Syndrome and errors. Let $E(c_1)$ denote a primal error chain, $\overline{q} \in \mathcal{B}(\overline{C}_3)$ a cell in the dual lattice $\overline{\mathcal{L}}$ and $v \in \mathcal{B}(C_0) = *\overline{q}$. $K(\overline{q})$ detects the error $E(c_1)$ if $|\{c_1\} \cap \{\partial \overline{q}\}| = \text{odd}$. Equivalently, $K(\overline{q})$ detects $E(c_1)$ if $v \in \{\partial c_1\}$. Thus, error chains show a syndrome only at their ends.

Correlations and errors. Primal cluster state correlations are affected by dual error chains and dual correlations are affected by primal error chains. Primal correlations are not affected by primal error chains, and dual correlations are not affected by dual error chains.

To see this, note that a primal correlation $K(c_2)$ consists of Pauli operators X on even qubits and Pauli operators Z on odd qubits. A dual error chain $E(\overline{c}_1)$ consists of operators Z on even qubits. Then, $E(\overline{c}_1)K(c_2) = (-1)^{|\{\overline{c}_1\} \cup \{c_2\}|}\, K(c_2)E(\overline{c}_1)$. If $|\{\overline{c}_1\} \cup \{c_2\}|$ is odd, the correlation $K(c_2)$ is conjugated to $-K(c_2)$ by the error. If it is even, then the correlation remains unchanged. This situation has a geometric interpretation. $|\{\overline{c}_1\} \cup \{c_2\}|$ is the number of intersection points between the primal 2-chain c_2 and the dual 1-chain $\overline{c}_1$. If the number of intersections is odd (even) then the correlation is (is not) affected by the error. For dual correlations and primal errors the situation is the same. Further, a primal error chain consists of Pauli operators Z on odd qubits. Thus, $[K(c_2), E(c_1)] = 0$ always. Similarly, $[K(\overline{c}_2), E(\overline{c}_1)] = 0$, $\forall\, \overline{c}_1, \overline{c}_2$.

Defects. The purpose of defects is to structure the space underlying the pair of lattices $\mathcal{L}, \overline{\mathcal{L}}$. Practically, a defect can be thought of as a set of qubits that are removed from the initial cluster $\mathcal{C}$ before the remaining qubits are entangled. For the chain complexes C, $\overline{C}$, a defect is a set d of missing edges. What defines a defect as an entity is that the belonging edges are connected. As all the other objects, defects are either primal or dual,

$$d \subset \mathcal{B}(C_1),\ \overline{d} \subset \mathcal{B}(\overline{C}_1). \tag{17}$$

The sets d, $\overline{d}$ of defect qubits are not arbitrary. Seen from afar they take the shape of doughnuts. These doughnut-shaped defects will be topologically entangled with another, and the way they are entangled encodes the quantum algorithm to be performed. From the viewpoint of quantum logic, what matters about the doughnuts is that they are loops. Their 'thickness' is required for fault-tolerance.

We now briefly explain how the above definition of a defect as a set of missing cluster qubits fits with the measurement pattern (7). Formally, each defect d will be assigned a set $D(d)$ of locations on the cluster. This set is subdivided into a set of edge- and a set of face qubits, $D_1(d)$ and $D_2(d)$. Here, the notions of 'edge' and 'face' are in reference to the lattice the defect belongs to. If the defect is primal (dual) then the edges and faces are taken with respect to the primal (dual) lattice. For primal defects, the sets $D_1(d)$ and $D_2(d)$ are defined as

$$D_1(d) := d,\ D_2(d) = \{f \in \mathcal{B}(C_2) |\, \{\partial f\} \cap d = \{\partial f\}\}\,. \tag{18}$$

For dual defects, replace f by $\overline{f}$ and C_2 by $\overline{C}_2$ in the above definition. The whole defect region D splits into an edge part D_1 and a face part D_2, $D = D_1 \cup D_2$ where

$$D_1 = \bigcup_d D_1(d),\ D_2 = \bigcup_d D_2(d). \tag{19}$$

Now the measurement pattern (7) becomes understandable: the edge qubits in the defects are measured in the Z-basis which effectively removes them from the cluster [10]. In this way, the quantum state on the exterior of the defect becomes disentangled from the state with support on interior of the defect. Thereby, a defect is created in the cluster lattice. Note that the qubits on faces whose entire boundary is in $D_1(d)$ become disentangled individually. If no errors were present we could leave these qubits alone. However, their measurement in the X-basis provides additional syndrome and so it is advantageous to measure them.

Correlations and defects. In the proximity of a primal defect, edges in the boundary of a primal 2-chain are removed, see (17). Therefore, primal correlations can end in primal defects. Dual defects do not remove primal edges, and thus primal correlations cannot end in dual defects. Analogously, dual correlations can end in dual defects, but not in primal defects.

	This object does ...				
to this one↓	dual corr.	primal defect	dual defect	primal err. cy.	dual err. cy.
correlation	nothing	bound	repel	nothing	affect
dual correlation		repel	bound	affect	nothing
primal defect			encircle	pairwise end	encircle
dual defect				encircle	pairwise end
primal err. cy.					nothing

Table 1: This table shows who does what to whom. 'A bounds B' is synonymous with 'B ends in A'. The displayed objects do not interact with themselves.

Syndrome and defects. In the presence of a primal defect d the correlations $\{K_{\overline{q}} = K(\partial \overline{q}) |\, \overline{q} \in \mathcal{B}(\overline{c}_3) \wedge \partial \overline{q} \cap d \neq \emptyset\}$ do not commute with the measurements (7), such that the syndrome at the locations

$$D_0 = \{v \in \partial e |\, e \in d\} \tag{20}$$

is lost. Note, however, that for each defect d there will be one syndrome bit associated with the defect as a whole. There exists a 2-cycle $\overline{c}_2(d)$, $\{\overline{c}_2(d)\} \subset V$, that wraps around d, and $K(\overline{c}_2(d)) = X(\overline{c}_2(d))$. When the qubits in V are measured in the X-basis, this correlation yields an additional syndrome bit. Dual defects act analogously on the dual lattice.

Errors and defects. Because the local syndrome is lost at the surface of a defect, primal error chains can potentially end in primal defects. However, there is a dual correlation $K(\overline{c}_2(d)) = X(\overline{c}_2(d))$ wrapping around a primal defect, and this correlation detects a primal error chain $E(c_1)$ if the number of intersection points between $\overline{c}_2(d)$ and c_1 is odd. Thus, primal error chains can *pairwise* end in primal defects.

Primal error chains cannot end in dual defects, because dual defects do not remove primal syndrome. Similarly, dual error chains can pairwise end in dual defects, and they cannot end in primal defects.

The relations among cluster state correlations, errors and defects are summarized in Tab. 1.

5.2 Homological and physical equivalence

We have so far identified physical objects—correlations and errors—with chains of a chain complex. In this section we point out that it is the homology class of the chain rather than the chain itself which characterizes the respective physical object. The equivalence of two chains under relative homology implies the physical equivalence of the corresponding physical operators.

1. Cluster state correlations. We regard two cluster state correlations $K(c_2)$, $K(c_2')$ as physically equivalent if they yield the same stabilizer element for the state $|\overline{\Psi}_{\text{algo}}\rangle_S$ after the measurement of the qubits in V and D. This requires two things. First, $K(c_2)$ and $K(c_2')$ need to be simultaneously measurable. With O_a the locally measured observables (7) we require $[K(c_2), O_a] = 0\ \forall a \in V \cup D \Longleftrightarrow [K(c_2'), O_a] = 0\ \forall a \in V \cup D$. Second, the two operators must agree on S, $K(c_2)|_S = K(c_2')|_S$. Then, the following statement holds: If $c_2' \cong_{\text{r}} c_2$ w.r.t. $(V \cup D, D)$ then $K(c_2') \cong K(c_2)$.
Proof: There exists $c_3 \in C_3 |\, \{\partial c_3\} \subset V \cup D_2$ and $\gamma_2 \in C_2 |\, \{\gamma_2\} \subset D_2$ such that $c_2' = c_2 + \partial c_3 + \gamma_2$. 1. Simultaneous measurability: $K(\gamma_2) = \left(\bigotimes_{a \in D_2(\gamma_2)} X_a\right)\left(\bigotimes_{b \in D_1(\gamma_2)} Z_b\right)$, where $D_1(\gamma_2) \subset D_1$ and $D_2(\gamma_2) \subset D_2$. Therefore, with (7), $[K(\gamma_2), O_a] = 0\ \forall a \in V \cup D$ (*). Similarly, $K(\partial c_3) = X(\partial c_3)$ such that, with (7), $[K(\partial c_3), O_a] = 0\ \forall a \in V \cup D$ (**). Since $K(c_2') = K(c_2)K(\partial c_3)K(\gamma_2)$, (*) and (**) imply simultaneous measurability of $K(c_2)$ and $K(c_2')$ on $V \cup D$. 2. Same restriction to S: $K(\partial c_3)$ and $K(\gamma_2)$ don't act on S, hence $K(c_2)|_S = K(c_2')|_S$. $\square$

2. Errors. Two errors $E(c_1)$ and $E(c_1')$ are physically equivalent if they cause the same damage to the computation. That is, they have the same logical effect and leave the same syndrome. Then, the following statement holds: If $c_1' \cong_r c_1$ w.r.t. $(V \cup D, D)$ then $E(c_1') \cong E(c_1)$.
Proof: There exist $c_2 \in C_2$, $\gamma_1 \in C_1$, with $\{c_2\} \subset V \cup D_2$, $\{\gamma_1\} \subset D_1$, such that $c_1' = c_1 + \partial c_2 + \gamma_1$. Now, a Pauli spin flip error X is absorbed in a subsequent X-measurement and has no effect on the computation, $\frac{I \pm X}{2} X = \pm \frac{I \pm X}{2} I$. Thus, with (7), $X_a \cong I_a$ for all $a \in V \cup D_2$. Similarly, $Z_b \cong I_b$ for all $b \in D_1$. Then, $E(c_1 + \partial c_2 + \gamma_1) = E(c_1) Z(\partial c_2) Z(\gamma_1) = E(c_1) K(c_2) X(c_2) Z(\gamma_1) \cong E(c_1)$. □

6 Constructive techniques

The purpose of the measurements in V and D is to create on S the Reed-Muller-encoded algorithm-specific resource $|\overline{\Psi}_\text{algo}\rangle_S$ described in Section 4. In Section 6.1, we specify the location of S-qubits with respect to the lattice defects and then, in Section 6.2, we give a construction for a topologically protected circuit providing $|\overline{\Psi}_\text{algo}\rangle_S$.

6.1 Location of the S-qubits

The S-qubits have very particular locations within the cluster. Besides the defects in the shape of doughnuts that we have already introduced the cluster also supports defects shaped like ear clips. The opening of these ear clip defects is only one cluster qubit wide. If this one cluster qubit were a defect qubit ($q \in D$) too, the ear clips would become doughnuts. But the particular cluster qubit is not in D, it is an S-qubit. The situation is displayed graphically in Fig. 4a.

The appropriate stabilizer generators among the S-qubits are induced from the cluster state correlations associated with relative 2-cycles, by measurement of the V- and D-qubits. As everything else in this computational scheme, the S-qubits occur in the two kinds 'primal' and 'dual'. We call an S-qubit q primal, $q \in S_p$, if it lives on the a face of the primal lattice, and we call it dual, $q \in S_d$, if it lives on a face of the dual lattice.

We now discuss how primal and dual correlations affect the S-qubits. Consider, for example the correlation $K(c_2)$ corresponding to a primal relative 2-chain c_2. A primal S-qubit at location q may lie within c_2, but never in its boundary, $\{\partial c_2\} \cap q = \emptyset$. A dual S-qubit q' may lie in the boundary of a primal 2-chain c_2 but never in c_2 itself, $\{c_2\} \cap q' = \emptyset$. We therefore conclude that

> *A primal correlation $K(c_2)$ acts on a primal S-qubit by one of the two Pauli-operators X, I and on a dual S-qubit by one of the two operators Z, I. A dual correlation $K(\overline{c}_2)$ acts on a primal S-qubit by one of the two Pauli-operators Z, I and on a dual S-qubit by one of the two operators X, I.* (21)

For finding the extended relative 2-cycles on the primal lattice, we thus regard S_p as part of V and S_d as part of D. Analogously, for finding the extended relative 2-cycles on the dual lattice, we regard S_p as part of D and S_d as part of V. In this way, the problem of finding the extended primal 2-cycles on a cluster with S-qubits is reduced to the same problem without S-qubits.

6.2 Creating $|\overline{\Psi}_\text{algo}\rangle$ among the S-qubits

The construction of a topologically protected circuit providing $|\overline{\Psi}_\text{algo}\rangle_S$ proceeds in three steps. First we show that $|\overline{\Psi}_\text{algo}\rangle_S$ is local unitarily equivalent to a bi-colorable graph state, by local Hadamard-transformations. Second, we show how to create a bi-colorable graph state. Third, we take care of the Hadamard-transformations.

Equivalence of $|\overline{\Psi}_\text{algo}\rangle$ to a bi-colorable graph state. Denote by $|\Psi\rangle_{\mathcal{C}_2}$ the state after the first measurement round (X- and Z-measurements) in a $QC_\mathcal{C}$-computation on a cluster state $|\phi\rangle_{\mathcal{C}_2}$, cf.

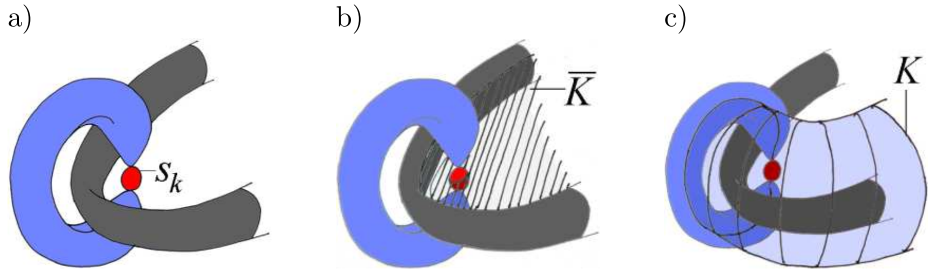

Figure 4: a) Location of a singular qubit (dual, held by a primal defect). b,c) The correlations $\overline{K}$, K affect the S-qubit by a Pauli-operator X in (b), and by Z in (c).

Section 4. Denote by $\mathcal{C}_X$, $\mathcal{C}_Z$ the subsets of $\mathcal{C}_2 \backslash Q$ whose qubits are measured in the X- or Z-basis, respectively. Further, denote by $\mathcal{C}_{\text{even}}$, $\mathcal{C}_{\text{odd}}$ the sets of even and odd qubits in $\mathcal{C}_2$ (checkerboard pattern). The state $|\Psi\rangle_{\mathcal{C}_2}$ is given by

$$|\Psi\rangle_{\mathcal{C}_2} \sim \left(\bigotimes_{a \in \mathcal{C}_X} \frac{I \pm X_a}{2} \right) \left(\bigotimes_{b \in \mathcal{C}_Z} \frac{I \pm Z_b}{2} \right) |\phi\rangle_{\mathcal{C}_2} \tag{22}$$

and has the form $|\Psi\rangle_{\mathcal{C}_2} = |\Psi_{\text{algo}}\rangle_Q \otimes |\text{rest}\rangle_{\mathcal{C}_2 \backslash Q}$. Further, $|\phi\rangle_{\mathcal{C}_2}$ is local unitary equivalent to some CSS-state, $|\phi\rangle_{\mathcal{C}_2} = \left(\bigotimes_{i \in \mathcal{C}_{\text{odd}}} H_i \right) |CSS\rangle_{\mathcal{C}_2}$. Then, with (22) and $\mathcal{C}_X' := (\mathcal{C}_X \cap \mathcal{C}_{\text{even}}) \cup (\mathcal{C}_Z \cap \mathcal{C}_{\text{odd}})$, $\mathcal{C}_Z' := (\mathcal{C}_Z \cap \mathcal{C}_{\text{even}}) \cup (\mathcal{C}_X \cap \mathcal{C}_{\text{odd}})$, $|\Psi\rangle_{\mathcal{C}_2} \sim \left(\bigotimes_{i \in \mathcal{C}_{\text{odd}}} H_i \right) \left(\bigotimes_{a \in \mathcal{C}_X'} \frac{I \pm X_a}{2} \circ \bigotimes_{b \in \mathcal{C}_Z'} \frac{I \pm Z_b}{2} |CSS\rangle_{\mathcal{C}_2} \right) = \left(\bigotimes_{i \in \mathcal{C}_{\text{odd}}} H_i \right) |CSS'\rangle_{\mathcal{C}_2}$. Thus, also the state $|\Psi_{\text{algo}}\rangle$ is l.u. equivalent to a CSS-state,

$$|\Psi_{\text{algo}}\rangle_Q = \left(\bigotimes_{q \in \mathcal{C}_{\text{odd}} \cap Q} H_q \right) |CSS''\rangle_Q. \tag{23}$$

Now, we consider the concatenated-Reed-Muller-encoded resource $|\overline{\Psi}_{\text{algo}}\rangle_S$, which may obtained from the bare state $|\Psi_{\text{algo}}\rangle_Q$ via encoding, $|\overline{\Psi}_{\text{algo}}\rangle_S = \left(\bigotimes_{q \in Q} \text{Enc}_q \right) |\Psi_{\text{algo}}\rangle_Q$. The encoding procedure Enc takes every qubit $q \in Q$ to a set $S(q)$ of qubits, $\bigcup_{q \in Q} S(q) = S$. It has the property that $\text{Enc}_q \circ H_q = \left(\bigotimes_{i \in S(q)} H_i \right) \circ \text{Enc}_q'$. Therein, Enc' is an encoding procedure for the code conjugated to the Reed-Muller-code, i.e., for the code with the X- and the Z-block of the stabilizer interchanged. This code is of CSS type, like the Reed-Muller code itself. The encoding procedure changes when passing through the Hadamard-gate because the encoded Hadamard-gate is not local for the Reed-Muller quantum code.

At any rate, the state $|\overline{\Psi}_{\text{algo}}\rangle_S$ is l.u. equivalent to a CSS-state encoded with CSS-codes, i.e., to a larger CSS-state, $|\overline{\Psi}_{\text{algo}}\rangle_S = \left(\bigotimes_{q \in \mathcal{C}_{\text{odd}} \cap Q} \bigotimes_{i \in S(q)} H_i \right) |CSS'''\rangle_S$. Every CSS-state is l.u. equivalent to a bi-colorable graph state [23], by a set of local Hadamard-transformations. Thus, we finally obtain

$$|\overline{\Psi}_{\text{algo}}\rangle_S = \bigotimes_{i \in S_H} H_i \, |\Gamma\rangle_S. \tag{24}$$

Therein, S_H is some subset of S and $|\Gamma\rangle_S$ is a bi-colorable graph state with adjacency matrix of the corresponding graph

$$\Gamma = \begin{pmatrix} 0 & G^T \\ G & 0 \end{pmatrix}. \tag{25}$$

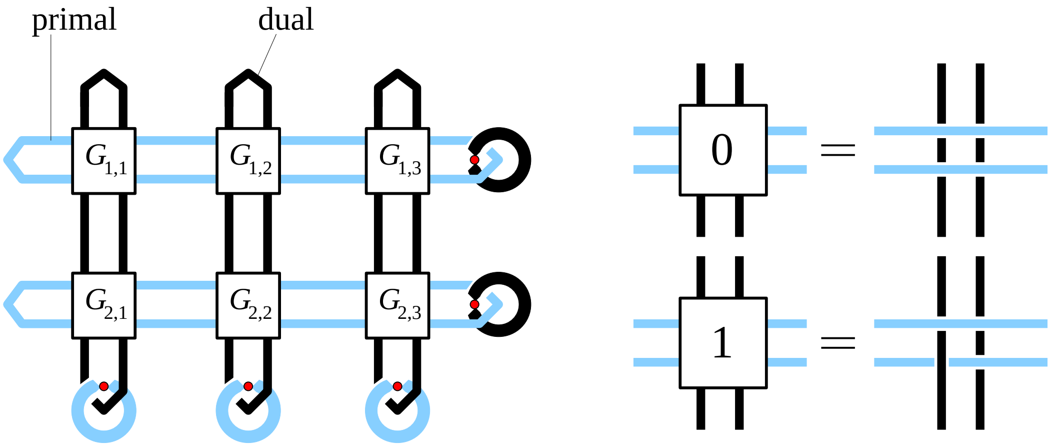

Figure 5: Creation of an arbitrary bi-colorable graph state. The singular qubits are displayed as red circles. G denotes the sub-matrix of the adjacency matrix Γ which encodes the edges between primal and dual vertices.

Circuit for a bi-colorable graph state. The circuit layout for the topologically protected creation of an arbitrary bi-colorable graph state is shown in Fig. 5. The circuit consists of a set of horizontal primal and a set vertical dual defects. Each primal defect comes close to each dual defect once, and the two defects may be linked in that region. The form of this junction is decided by a corresponding element of the graph state adjacency matrix G. If $G_{i,j} = 1$ then the defects are linked and otherwise they are not. In addition, each of the loop defects is linked with an ear-clip shaped defect which holds an S-qubit. The graph state in question is formed among these qubits after the remaining qubits have been measured.

An explanation of the circuit in Fig. 5, for the specific example of a line graph, is given in Fig. 6. From this example it should be clear how the circuit works in general. For the line graph we have the adjacency sub-matrix

$$G_{\text{line}} = \begin{array}{cc} \begin{pmatrix} 1 & 1 & 0 \\ 0 & 1 & 1 \end{pmatrix} & \begin{matrix} b \\ d \end{matrix} \\ \begin{matrix} a & c & e \end{matrix} & \end{array} . \tag{26}$$

This implies, for example, that in the circuit of Fig. 6a the dual defect winding around the dual S-qubit a will be linked with the primal defect winding around the primal S-qubit b. Now we explain how the stabilizer element $K_b = Z_a X_b Z_c$ for the graph state $|\Gamma_{\text{line}}\rangle$ emerges. The other stabilizer generators emerge in the same way.

Consider the relative 2-cycle $c_2(b)$ and imagine it being built up step by step. We start around the S-qubit b. Because $c_2(b)$ is primal and b is primal, $K(c_2(b))$ affects qubit b by a Pauli-operator X, see Eq. (21). Also, $c_2(b)$ is bounded by the primal defect encircling b.

We move further to the left. At some point, $c_2(b)$ approaches a dual defect. Primal correlations cannot end in dual defects. Therefore, $c_2(b)$ bulges out and forms a tube wrapping around the dual defect, leading downwards. It ends in the primal defect holding the dual S-qubit c. $K(c_2(b))$ affects qubit c by a Pauli-operator Z. Back at the junction, $c_2(b)$ continues to expand to the left. It approaches a second dual defect where it forms another tube. In result, the dual S-qubit a is affected by a Pauli-operator Z. Further to the left, the primal defect closes up and bounds $K(c_2(b))$.

$K(c_2(b))$ takes the form $X_b Z_a Z_c \bigotimes_{d \in V(b) V} X_d$ for some set $V(b) \subset V$. All qubits in V are measured in the X-basis (7) such that after these measurements the correlation $K_b = \pm Z_a X_b Z_c$ remains. This is a stabilizer generator for the graph state in Fig. 6b since (a, b) and (c, b) are the

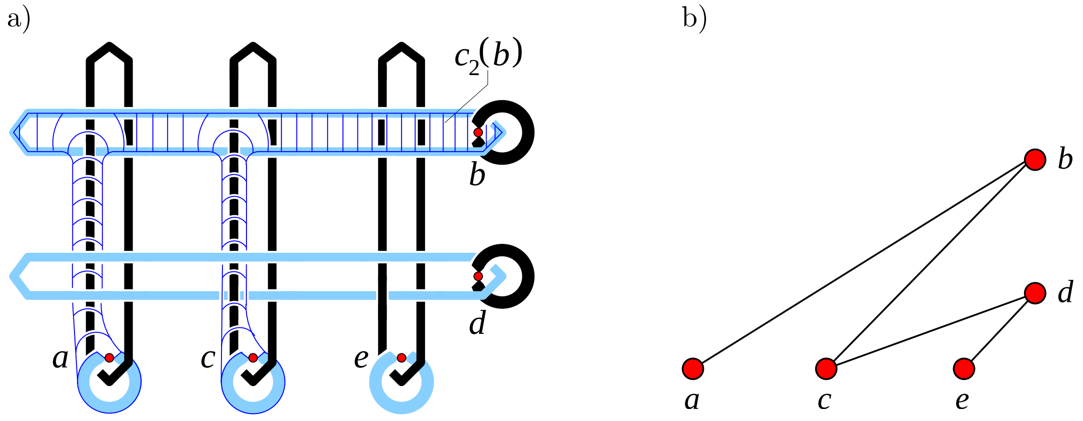

Figure 6: Explanation of the circuit in Fig. 5 for a particular example, the line graph. a) The relative 2-cycle $c_2(b)$ which gives rise to the graph-state stabilizer $K_b = Z_a X_b Z_c$. b) Graph corresponding to the created graph state.

only edges of the line graph ending in the vertex b. For every edge in the graph there is a link among defect loops in the circuit.

The proof for the programmable circuit of Fig. 5 realizing a general bi-colorable graph state is similar. As an outline, each stabilizer generator is associated with a doughnut-shaped defect in the circuit. Such a defect bounds a correlation, and this correlation affects one S-qubit by X. Further, because the considered defect is linked with other defects of the opposite kind, the correlation surface forms tubes. These tubes affect one other S-qubit each—the neighbors of the first—by Pauli-operators Z.

Implementing the local Hadamard-transformations. The equivalence between the graph state $|\Gamma\rangle_S$ and the encoded algorithm specific resource $|\overline{\Psi}_{\text{algo}}\rangle_S$ is by Hadamard-transformations on some subset S_H of S-qubits. Wherever such a Hadamard-transformation needs to be applied, attach an extra loop to the circuit in Fig. 5,

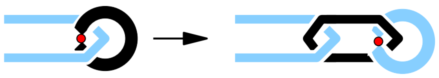

. (27)

7 Error sources, error correction and fault-tolerance threshold

7.1 Two error models

Below we describe two error models, a simple one and a more realistic one.

Error Model 1. *The cluster state is created only on those cluster qubits which are needed for the computation, i.e., on* $V \cup S$. *The defect qubits of* D *are left out.*

1. *The noise is described by independent partially depolarizing channels acting on each cluster qubit. The noisy state* $\rho_{\mathcal{C}}$ *is given by* $\rho_{\mathcal{C}} = \bigotimes_{a \in \mathcal{C}} T_a(p_1)\, |\phi\rangle_{\mathcal{C}}\langle\phi|$, *with*

$$T_a^{(1)}(p_1) = (1-p_1)[I_a] + \frac{p_1}{3}\left([X_a] + [Y_a] + [Z_a]\right). \tag{28}$$

2. *The classical computation for syndrome processing is instantaneous.*

The reason for considering this error model first is its simplicity. We would like to separate the intricacies inherent in the presented error-correction scheme from additional difficulties incurred by a realistic error model. The basic justification for such an approach is this: The error correction used here is topological. Therefore, a threshold should exist regardless of whether independent errors are strictly local or only local in the sense of having a support of bounded size.

The most straightforward method to create a cluster state is from a product state $\bigotimes_a |+\rangle_a$ via a (constant depth) sequence of $\Lambda(Z)$-gates [10]. If these gates are erroneous, then Error Model 1 does not apply in general.[1] Specifically, one may raise the following objections to Error Model 1:

- No correlated errors are included in Error Model 1. Creating the cluster state via a sequence of gates will, however, lead to correlated errors in the output cluster state.
- Storage errors accumulate in time. There is temporal order among the measurements such that the computation takes a certain time t_{comp} which cannot be bounded by a constant for all possible computations. As a consequence, for the qubits measured in the final round the local noise rate increases monotonically with t_{comp} and exceeds the error threshold.
- To leave the D-qubits out is a deviation from the originally envisioned setting: the cluster state on $S \cup V$ is algorithm-specific.[2]

To account for these inadequacies, we consider a second error model.

Error Model 2. *A cluster state on a bcc-symmetric lattice is created in four steps of nearest-neighbor $\Lambda(Z)$-gates. The gate sequence is as shown in Fig. 7. Errors occur due to the erroneous preparation of the initial $|+\rangle$-qubits, erroneous $\Lambda(Z)$-gates in the process of creating the cluster state, storage and measurement.*

1. *The computation is split up into steps which performed on sub-clusters $\mathcal{C}_k$. In each step, unmeasured qubits remaining from the previous step—the hand-over qubits—are loaded into a cluster state on a sub-cluster. Subsequently, all but a few cluster qubits (the new hand-over qubits) are measured. The steps have their temporal depth adjusted such that each qubit, after being locally prepared and entangled, waits at most a constant number t_0 of time steps until its measurement occurs, $t_0 \geq 1$. Error in storage is described by a partially depolarizing noise with error probability p_S per time step.*
2. *The erroneous preparation of initial $|+\rangle$-qubits is modeled by the perfect procedure followed by local depolarizing noise* (28)*, with probability p_P. Measurement is described by perfect measurement preceded by partially depolarizing noise with error probability p_M. The erroneous $\Lambda(Z)$-gates are modeled by the perfect gate followed by a 2-qubit depolarizing channel*

$$T^{(2)}_{e,f}(p_2) = (1-p_2)[I_{e,f}] + \frac{p_2}{15}\left([I_e \otimes X_f] + ... + [Z_e \otimes Z_f]\right). \tag{29}$$

3. *Classical syndrome processing is instantaneous.*

---

[1] There may be situations in which the error Model 1 is in fact a good approximation. For example, consider a scenario in which the cluster state is purified before being measured for computation. Of course, the gates in a purification protocol would be erroneous, too, such that the purified state is not perfect. In effect, the errors of the initial state were replaced by the errors of the purification protocol. There exist purification protocols [24] in which the gates act transversally on two copies of the cluster state (one of which is subsequently measured). As a result, the errors introduced by the purification are approximately local, as in Error Model 1. The purification protocol [24] in its current form has a problem of its own, though; due to the exponentially decreasing efficiency of post-selection, it is not scalable in the size of the state. But chances are that this can be repaired.

[2] For the creation of the cluster state this makes little or no difference: fewer gate operations are needed than for the creation of $|\phi\rangle_{\mathcal{C}}$. For parallelized procedures that make use of the translation invariance of $\mathcal{C}$, it should not be too difficult to remove the superfluous D-qubits from the lattice before the remaining qubits are entangled.

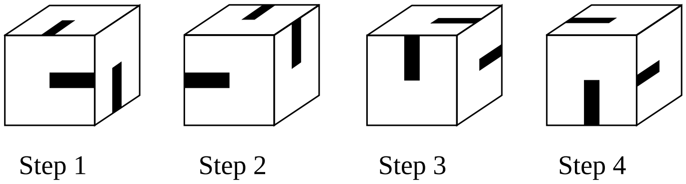

Figure 7: Steps of $\Lambda(Z)$-gates for the creation of a cluster state on a bcc-symmetric lattice, for the sub-clusters $\mathcal{C}_k$. For k odd, the sequence is $1 \rightarrow 2 \rightarrow 3 \rightarrow 4$, and for k even it is $3 \rightarrow 4 \rightarrow 1 \rightarrow 2$.

In the subsequent sections we compute a fault-tolerance threshold for both error models. In Error Model 2, storage error will cause the minimum damage for the smallest possible value of t_0, which is $t_0 = 1$. In this case, each sub-cluster carries a subset of S-qubits with no mutual temporal dependence. All qubits in V and D, except the hand-over qubits (See Appendix A), are measured immediately after being entangled. The measurement of the S-qubits has to wait one time step. *Henceforth we set* $t_0 = 1$.

7.2 Methods for error correction and the threshold value

There are different methods of error correction associated with the different regions V, S and D of the cluster. In D, there are as many inequivalent errors as there are syndrome bits, such that the error correction is trivial. The error correction in V is based on the random plaquette $\mathbb{Z}_2$-gauge model in three dimensions [18]. The error correction in S is carried out using the (concatenated) quantum Reed-Muller code.

Error correction in D. In the domain $D(d)$ of the defect only Z-errors matter for face qubits and only X-errors matter for edge qubits. Any other errors may be absorbed into the subsequent measurements (7). The X-errors on edges may be relocated to Z errors on the neighboring face qubits via $X_e \cong K_e X_e$, such that we need to consider Z-errors on face qubits only. For each face in d we learn one syndrome bit, yielding a unique syndrome for each error configuration.

However, if an error X_e on an edge qubit e in the surface of defect d is relocated, the equivalent error $K_e X_e$ may partially be outside $D(d)$. After error correction in $D(d)$, an individual Z-error on a face qubit in V is left next to $D(d)$. This affects the error correction in V near D; see below.

Error correction in V. First consider a scenario where the entire cluster consists of the region V (*i.e.*, there are no defects and no singular qubits). Error correction on the primal lattice $\mathcal{L}$ and the dual lattice $\overline{\mathcal{L}}$ run separately. Here we consider error correction on the primal lattice only; error correction on the dual lattice is analogous.

The error chains live on the edges of the lattice $\mathcal{L}$ and leave a syndrome at the end points, which are vertices of $\mathcal{L}$. This is exactly the scenario which has been considered for topological quantum memory in [18], and subsequently the results of [18] that we need in the present context are briefly summarized. The connection between topological error correction and cluster states has been made in [14] for the purpose of creating long-range entanglement in the presence of noise.

Given a particular syndrome and an error chain $E(c_1)$ compatible with this syndrome, we are interested in the total probability $P(c_1)$ of the *homology class* of c_1,

$$P(c_1) = \sum_{z_1 \in Z_1} p(c_1 + z_1), \tag{30}$$

where $p(c_1')$ is the probability of an individual error chain $E(c_1')$, and the sum is over all 1-cycles.

For error correction we infer that the physical error which occurred was from the homology class with the largest probability.

If the errors on the lattice edges occur independently with a probability q then the problem of computing $P(c_1)$ for a given chain c_1 can be mapped onto a problem from statistical mechanics, namely the random plaquette $\mathbb{Z}_2$-gauge model in three dimensions [18]. The crossover from high fidelity error correction at small error rates to low fidelity error correction at high error rates corresponds to a phase transition in this model. A numerical estimate of the critical error rate is $q_c = 0.033 \pm 0.001$ [25].

As far as is known, the classical operational resources required to find the most likely error homology class consistent with a given syndrome scales exponentially in the number of error locations. The assumption of the classical processing being instantaneous cannot be justified under these conditions. However, it is possible to trade threshold value for efficiency in the error correction procedure. A reasonable approximation to the maximum probability for a homology class of errors is the probability of the lowest weight admissible chain. The minimum-weight perfect matching algorithm [26, 27] computes this chain using only polynomial operational resources. A numerical estimate to the threshold with this algorithm for error correction is $q'_c = 0.0293 \pm 0.0002$ [28].

Remark: The topological error threshold is estimated in numerical simulations of finite-size systems. For this purpose, the probability of logical error is plotted vs. the physical error parameter for various system sizes. For sufficiently large lattices (such that finite-size effects are small), we expect these curves to follow a universal scaling ansatz near the threshold such that they share a common intersection point and their slopes are proportional to a common power of the lattice size. As the system size is increased to infinity, we then expect the curves to approach a step function which transitions at the threshold value of the physical error parameter.

The above quoted threshold value is for independent errors on the edges of $\mathcal{L}$. Do the models for the physical error sources of Section 7.1 lead to such independent errors? The answer is 'yes' for error Model 1 and 'no' for error Model 2. For the latter, we need to consider a modified RPGM with correlated errors among next-to-nearest neighbors. Specifically, for Error Model 1 the relation between the local rate p_1 of the physical depolarizing error and the error parameter q that shows up in the RPGM is

$$q = \frac{2}{3} p_1, \qquad \text{for Error Model 1.} \tag{31}$$

Given a threshold of $q = 2.93\%$ [28] for error correction via the minimum weight perfect matching algorithm in the bulk, then the corresponding depolarizing error rate that can be tolerated is

$$p_{1,\text{c}} = 4.4 \times 10^{-2}, \quad (\text{in } V). \tag{32}$$

For Error Model 2, first consider the case where only the $\Lambda(Z)$-gates are erroneous, $p_P = p_S = p_M = 0$. Then, in addition to local errors with a rate q_1 there exist correlated errors with error rate q_2 for each pair of opposite edges in all faces of $\mathcal{L}$. That is, with a probability q_2 simultaneous errors are introduced on opposite edges of the faces in $\mathcal{L}$. The local noise specified by q_1 and the two-local noise specified by q_2 are independent processes. The relations between the error parameter p_2 of the $\Lambda(Z)$-gates and the parameters q_1, q_2 of the RPGM with correlated errors are

$$\begin{aligned} q_1 &= \frac{32}{15} p_2 \left(1 - \frac{8}{15} p_2\right) \left(\frac{64}{225} p_2^2 + \left(1 - \frac{8}{15} p_2\right)^2\right), \\ q_2 &= \frac{1}{2} - \sqrt{\frac{1}{4} - \frac{4}{15} p_2} = \frac{4}{15} p_2 + O(p_2^2). \end{aligned} \tag{33}$$

The correlation of errors on sites separated by a distance of two arises through error propagation in the creation of the cluster state. Correlations among errors on next-neighboring sites play no role because such errors live on different lattices ($\mathcal{L}$ and $\overline{\mathcal{L}}$) and are corrected independently.

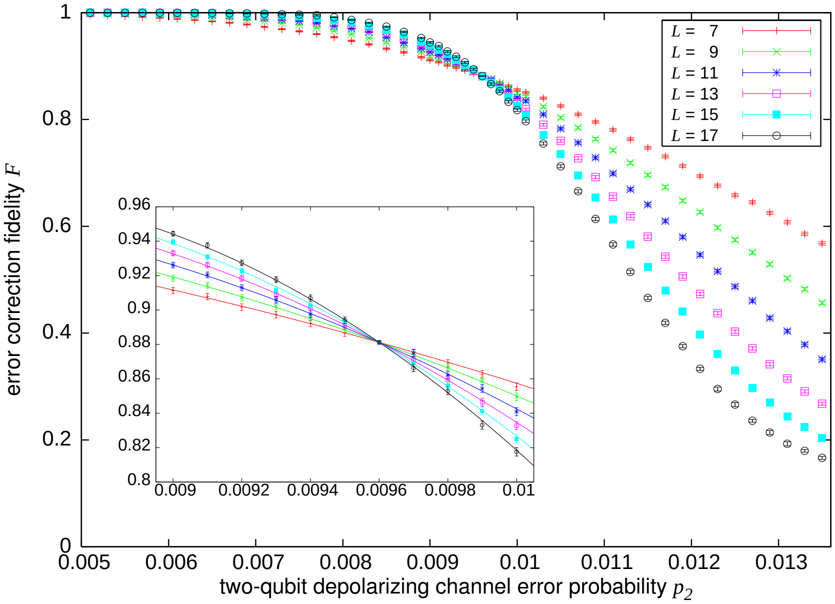

Figure 8: Threshold estimation in lattices of finite size, for periodic boundary conditions. Here, with $\Lambda(Z)$-gates as the only error source, we find a threshold of $p_{2,\text{c}} = 9.6 \times 10^{-3}$. In the inset, best fits to the universal scaling ansatz are drawn. Error bars denote two standard deviations due to finite sampling size.

The only effect of $p_P, p_S, p_M > 0$ is an enhanced local error rate q_1. We give the relations to leading order only; they read

$$\begin{aligned} q_1 &= \frac{32}{15}p_2 + \frac{2}{3}\left(p_P + p_S + p_M\right), \\ q_2 &= \frac{4}{15}p_2, \end{aligned} \qquad \text{for error Model 2.} \tag{34}$$

See Fig. 8 for a simulation of error correction under faulty $\Lambda(Z)$-gates as the only error source, which gives rise to correlated noise between neighboring edge qubits. If we define $x = (p_2 - p_{2,c})L^{1/\nu_0}$ then the universal scaling ansatz states that fidelity F should be a function dependent only on the scaling parameter x in the vicinity of the threshold [28]. We find very good agreement (with $R^2 > .9991$) for $F = A + Bx + Cx^2$, where we fit for constants A, B, C, $p_{2,c}$, and ν_0. This gives very tight bounds on the critical probability $p_{2,c} = 9.6 \times 10^{-3}$. Interestingly, we also find $\nu_0 = 1.00 \pm 0.02$, which indicates that this model belongs to the same universality class as the purely local error model of the 3D-RPGM [28].

In Fig. 9 the threshold trade-off curve between $p_P + p_S + p_M$ and p_2 is displayed. Numerically, we obtain for the thresholds in the bulk

$$\begin{aligned} p_P = p_S = p_M &= 1.46 \times 10^{-2}, &&\text{for } p_2 = 0, \\ p_2 &= 0.96 \times 10^{-2}, &&\text{for } p_P = p_S = p_M = 0, \\ p_i &= 0.58 \times 10^{-2}, &&\text{for } p_P = p_S = p_M = p_2. \end{aligned} \tag{35}$$

Error correction in V near D. In the presence of defects there are two modifications to error processes in V. First, the length scale for the minimum extension of a non-trivial error cycle shrinks. Second, there is a surface effect; the effective error rate for qubits in V next to the surface of defects is enhanced by a constant factor.

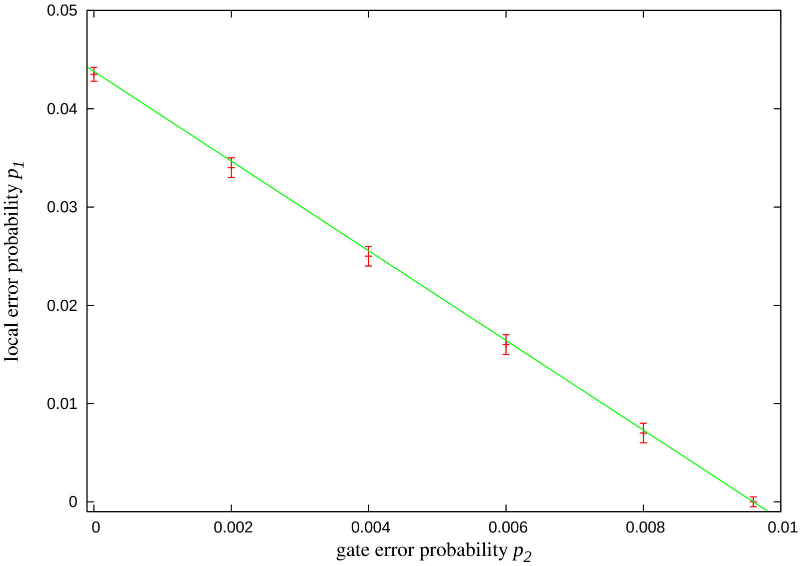

Figure 9: Trade-off curve for the threshold value in the presence of local and two-local errors. Horizontal axis: two-qubit gate error p_2, vertical axis: local error rate $p_P + p_S + p_M$.

1. Length scale for non-trivial errors: For comparison, consider a cluster cube of finite size $2L \times 2L \times 2L$. A non-trivial error cycle must stretch across the entire cube and thus has a weight of at least L. The lowest weight errors which are misinterpreted by the error correction procedure occur with a probability $q^{L/2}$. The total error probability incurred by such errors may therefore be expected to decrease exponentially fast in L, which is confirmed in numerical simulations [14].

In the presence of defects, the dominant sources for logical error are 1-chains that either wind around a defect or that begin and end in a defect and intersect a correlation surface (2-chain) in between; see Fig. 10. The relevant length scales are thus the thickness (circumference) and the diameter of the defects. They are much smaller than L.

Specifically, consider a defect with circumference u and length l which bounds a correlation surface c_2, such that $|\{\partial c_2\}| = l$. An error cycle winding around the defect has a weight of at least $u + 8 \approx u$, and there are l such minimum weight cycles. Therefore, the probability $p_E(u,l)$ for affecting $K(c_2)$ by an error is, to lowest contributing order,

$$p_E(u,l) = l \frac{u!}{(u/2)!^2} q^{u/2} \approx l \exp\left(\frac{\ln 4q}{2} u\right) \frac{1}{\sqrt{\pi/2\, u}}. \tag{36}$$

In the range of validity for the above expansion in powers of q, the error is still exponentially suppressed in the relevant length scale u.

2. Surface effects: As discussed above, the error level is enhanced for qubits in V near the surface of a defect. If the defect is primal (dual), the enhancement occurs on dual (primal) qubits. This effect will—if anything—lower the threshold. But there is another effect: the presence of the defect changes the boundary conditions. In case of a primal defect, the boundary conditions on the defect surface become rough for the primal lattice and smooth for the dual lattice. Dual error chains cannot end in a primal defect, as we noted earlier. For the dual lattice, there is excess syndrome available at the defect surface. This effect will—if anything—increase the threshold. Our intuition is that neither effect has an impact on the threshold value. The threshold should, if the perturbations at the boundary are not too strong, still be set by the bulk.

We have performed numerical simulations for lattices of size $L \times L \times 2L$, where half of the lattice belongs to V and the other half to the defect region D. The error rate is doubled near

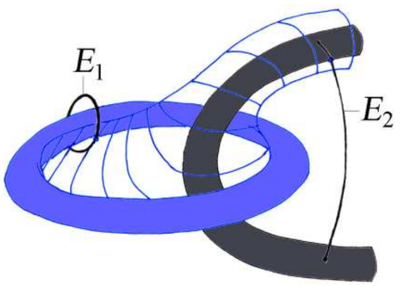

Figure 10: Sources for logical error in the presence of defects.

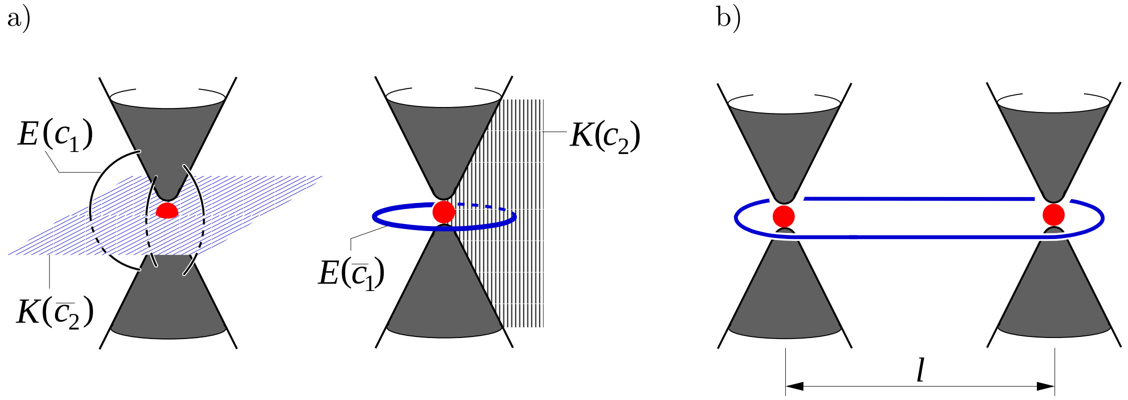

Figure 11: Topological error correction in the presence of defects. a) Short error cycles intersect with the correlation surfaces and thereby jeopardize the topological error correction. b) Correlated errors on S-qubits are suppressed exponentially in the qubit separation l.

the mutual boundary of the regions and there is no remaining error in D. Simulations are feasible with reasonable effort up to $L \approx 20$. We find that finite-size effects (due to the smooth boundary conditions) are still noticeable up to these lattice sizes, but the intersection point of fidelity curves for nearby lattice sizes is slowly converging to a threshold value around that of the bulk ($\sim 2.9\%$).

Error correction in V near a junction between D and S. Near an S-qubit there exist relative error cycles of small length, see Fig. 11a, and the topological error correction breaks down. As a result, the effective error on an S-qubit is enhanced by its surrounding. To compute the effective error probabilities, we replace every low-weight error-chain $E(\gamma)$ that results in a logical error *after error correction* by an equivalent error $E_S(\gamma)$ acting on the S-qubits. The error correction converts $E(\gamma)$ into $E(c_1(\gamma))$ with $c_1(\gamma)$ a relative 1-cycle. 'Equivalent' means that $E(c_1(\gamma))$ and $E_S(\gamma)$ act in the same way on the stabilizer generators $\{K_{\overline{\Psi},s} |\ s \in S\}$ of the induced state $|\overline{\Psi}_{\text{algo}}\rangle_S$, i.e., $[E(c_1(\gamma))E_S(\gamma), K_{\overline{\Psi},s}] = 0$ for all $s \in S$. The relevant correlations to check are $K(\overline{c}_2)$ and $K(c_2)$ displayed in Fig. 11a.

It is important to note that the effective error on the S-qubits is *local*. This arises because only error chains causing a 1-qubit error may have small length. Error chains causing a correlated error on the S-qubits are suppressed exponentially in the qubit separation. See Fig. 11b.

We compute the effective error channel on the S-qubit to first order in the error probabilities only. For error Model 1 the error enhancement only affects sub-leading orders of p_1,

$$T_s^{(1)} = (1-p_1)[I_s] + \frac{p_1}{3}\left([X_s] + [Y_s] + [Z_s]\right). \tag{37}$$

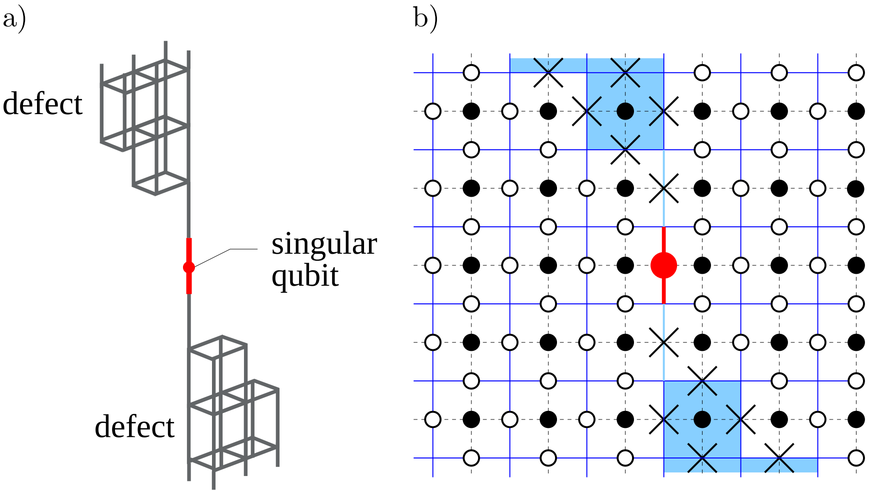

Figure 12: Shape of the defect near an S-qubit (red). a) Three-dimensional view. b) Cross-section through the cluster. Edges which belong to the defect are marked as "×". Black dashed lines connect neighbors on the cluster. Blue underlay: faces in the defect. Even/odd qubits: •/∘.

For Error Model 2 the effective error channel on an S-qubit is not universal but depends on the precise shape of the defect double-tip near the S-qubit. For our calculation we use the defect shape displayed in Fig. 12. The defect is one-dimensional nearest to the S-qubit, and farther away becomes three-dimensional. The effective error channel then is

$$\begin{aligned}\tilde{T}_s^{(1)} &= \left(1-\frac{2}{3}p_P-\frac{7}{3}p_S-\frac{7}{3}p_M-\frac{94}{15}p_2\right)[I_s]+\left(2p_2+\frac{5}{3}p_S+\frac{5}{3}p_M\right)[X_s]+\\ &+\left(\frac{2}{5}p_2+\frac{1}{3}p_S+\frac{1}{3}p_M\right)[Y_s]+\left(\frac{2}{3}p_P+\frac{1}{3}p_S+\frac{1}{3}p_M+\frac{58}{15}p_2\right)[Z_s].\end{aligned} \tag{38}$$

The individual contributions to (38) are listed in Appendix B.

Error correction in S. The S-qubits are protected by the concatenated Reed-Muller code. This code corrects for the errors (37)/(38) that remain after error correction in V and D.

The S-qubits are all measured in the eigenbases of $\frac{X\pm Y}{\sqrt{2}}$. Then, an X- or a Y-error is equivalent to a Z-error with half the probability. This is easily verified for the case where X- and Y-errors occur with the same probability. W.l.o.g. assume the measurement basis is $\frac{X+Y}{\sqrt{2}}$. Then $[X]+[Y]=\frac{[X+Y]}{\sqrt{2}}+\frac{[X-Y]}{\sqrt{2}}=\frac{[X+Y]}{\sqrt{2}}([I]+[Z])\cong[Z]$. But the statement is, to leading and next-to-leading order in the error probability, also true when X- and Y-errors do not occur with equal probability; see Appendix C. We may thus convert the X- and Y-errors in (37) and (38) into Z-errors. The corresponding error probability p_Z is

$$\begin{aligned} p_Z &= \frac{2}{3}p_1, && \text{for error Model 1,}\\ p_Z &= \frac{76}{15}p_2+\frac{2}{3}p_P+\frac{4}{3}p_M+\frac{4}{3}p_S, && \text{for error Model 2.}\end{aligned} \tag{39}$$

The fault-tolerance threshold of the concatenated $[15,1,3]$-Reed-Muller code for independent Z-errors with probability p_Z is 1.09×10^{-2}. As we discuss all Reed-Muller error correction to leading order only, we take the leading order estimate

$$p_{Z,\mathrm{c}}=\frac{1}{105}\approx 0.95\times10^{-2}. \tag{40}$$

For Error Model 1, from (39) and (40) we obtain the threshold

$$p_{1,\mathrm{c}} = \frac{1}{70} \approx 1.4 \times 10^{-2}, \qquad (\text{in } S). \tag{41}$$

For error Model 2 we obtain

$$\begin{aligned} p_{P,\mathrm{c}} = p_{S,\mathrm{c}} = p_{M,\mathrm{c}} &= \frac{1}{350} \approx 0.29 \times 10^{-2}, && \text{for } p_2 = 0, \\ p_{2,\mathrm{c}} &= \frac{1}{532} \approx 0.19 \times 10^{-2}, && \text{for } p_P = p_S = p_M = 0, \qquad (\text{in } S). \\ p_{i,\mathrm{c}} &= \frac{1}{882} \approx 0.11 \times 10^{-2}, && \text{for } p_P = p_S = p_M = p_2, \end{aligned} \tag{42}$$

The topological error correction in V and the Reed-Muller error correction in S run separately, and all that remains is to check which mechanism breaks down first. By comparison of Equation (32) with (41) and Equation (35) with (42), we find for both error models that the Reed-Muller error correction collapses first. It therefore sets the overall threshold. In Error Model 1, the critical error probability for local depolarizing error is 1.4×10^{-2}. In Error Model 2, for the case where preparation, gate, storage and measurement errors each have equal strength, the error threshold for the individual processes is 1.1×10^{-3}.

8 Overhead

Denote by N the number of qubits in the algorithm-specific resource state $|\Psi_{\text{algo}}\rangle_Q$. N is also the number of non-Clifford one-qubit rotations in a quantum circuit realizing the algorithm "algo". What is the number N_{ft} of cluster qubits required to perform the same computation fault-tolerantly?

The qubit overhead factor for Reed-Muller error correction is

$$O_{\text{RM}} = \left(\frac{\log N}{\log p_\mathrm{c}/p} \right)^{\gamma}, \tag{43}$$

where $\gamma = \log_2 15 \approx 3.91$, and p is the actual and p_c the critical Reed-Muller error rate. The set S consists of $|S| = N O_{\text{RM}}$ qubits.

We need to determine the additional overhead due to topological error correction. We choose a separation r between strands of a defect loop, and a strand diameter of $r/2$.

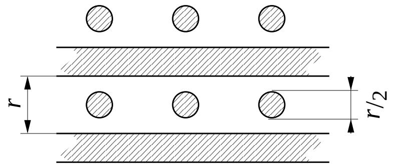

The dimensions of the cluster thus are width, depth $\leq 3/2\, r N O_{\text{RM}}$, height $= 4r$. The most likely errors then occur with a probability of $\exp(-\kappa(p) r)$, (36), and there are less than $3r(NO_{\text{RM}})^2$ locations for them (primal+dual). We require that $3r(NO_{\text{RM}})^2 \exp(-\kappa(p)r) \approx 1$, such that in the large N limit

$$r \approx \frac{2}{\kappa(p)} \ln N. \tag{44}$$

Double-logarithmic corrections are omitted. The total number of qubits is given by $N_{\text{ft}} = \text{width} \times \text{depth} \times \text{height} \leq 9r^3 (NO_{\text{RM}})^2$, such that

$$N_{\text{ft}} \sim N^2 \left(\log N\right)^{3+2\gamma}. \tag{45}$$

The overhead is polynomial. The values of the exponents in the above expression may be reduced in more resourceful adaptations of the presented scheme.

9 Discussion

We have described a scheme for fault-tolerant cluster state universal quantum computation which employs topological error correction. This is possible because of a link between cluster states and surface codes. In addition to the topological method, we make use of a Reed-Muller quantum code which ensures that non-Clifford operations can be performed fault-tolerantly by local measurements.

The error threshold is 1.4% for an ad-hoc error model with local depolarizing error and 0.11% for a more detailed error model with preparation-, gate-, storage- and measurement errors. We have not tried to optimize for either threshold value or overhead here; the foremost purpose of this paper is to explain the techniques. With regard to a high threshold, the obvious bottleneck is the Reed-Muller code. The error threshold imposed by this code on the cluster region S is—depending on the error model—a factor of 3 to 5 times worse than the threshold obtained from the topological error correction in V. To increase the threshold one may replace this code by another CSS code with property (5) that has a higher error threshold, provided such a code exists. Alternatively, one may probe the Reed-Muller code in error detection, as in magic state distillation [17]. The error detection threshold is 14%, which indicates that there is some room for improvement.

Part of the investigations in this paper are numerical simulations, and we would like to comment on their impact on the threshold value. Numerics are encapsulated only in the threshold estimate for topological error correction which is much higher than the overall threshold. Our final threshold estimate stems from the Reed-Muller code and is analytical.

Acknowledgments: We would like to thank Sergey Bravyi, Frank Verstraete, Alex McCauley, Hans Briegel and John Preskill for discussions. JH is supported by ARDA under an Intelligence Community Postdoctoral Fellowship. KG is supported by DOE Grant No. DE-FG03-92-ER40701. RR is supported by MURI under Grant No. DAAD19-00-1-0374 and by the National Science Foundation under contract number PHY-0456720. Additional support was provided by the Austrian Academy of Sciences.

References

[1] E. Knill, R. Laflamme, W.H. Zurek, Proc. Roy. Soc. London A **454**, 365 (1998).

[2] D. Aharonov and M. Ben-Or, Proc. 29th Ann. ACM Symp. on Theory of Computing, 176 (New York, ACM, 1998); D. Aharonov, M. Ben-Or, quant-ph/9906129 (1999).

[3] D. Gottesman, PhD thesis, Caltech (1997), quant-ph/9705052.

[4] P. Aliferis, D. Gottesman, J. Preskill, quant-ph/0504218.

[5] E. Knill, Nature **434**, 39 (2005).

[6] A. Kitaev, Ann. Phys. **303**, 2 (2003); quant-ph/9707021.

[7] J. Preskill, quant-ph/9712048.

[8] C. Mochon, Phys. Rev. A **67**, 022315 (2003).

[9] R. Raussendorf and H.-J. Briegel, Phys. Rev. Lett. **86**, 5188, (2001).

[10] H.-J. Briegel and R. Raussendorf, Phys. Rev. Lett. **86**, 910, (2001).

[11] R. Raussendorf, PhD thesis, University of Munich (2003).

[12] M.A. Nielsen, C.M. Dawson, Phys. Rev. A **71**, 052312 (2005); C.M. Dawson, H.L. Haselgrove, and M.A. Nielsen, quant-ph/0509060.

[13] P. Aliferis, D. Leung, quant-ph/0503130.

[14] R. Raussendorf, S. Bravyi, J. Harrington, Phys. Rev. A **71**, 062313 (2005).

[15] S. Bravyi and A. Kitaev, quant-ph/980092.

[16] E. Knill, R. Laflamme, W. Zurek, quant-ph/9610011.

[17] S. Bravyi and A. Kitaev, Phys. Rev. A **71**, 022316 (2005).

[18] E. Dennis, A. Kitaev, A. Landahl and J. Preskill, quant-ph/0110143.

[19] F.J. MacWilliams, N.J.A. Sloane, *The Theory of Error-Correcting Codes*, North-Holland Publishing Company, Amsterdam (1977).

[20] J.W. Vick, *Homology theory: an introduction to algebraic topology*, Springer, New York (1994), originally published: Academic Press, New York (1973).

[21] A. Hatcher, *Algebraic Topology*, Cambridge University Press, Cambridge (2002).

[22] M. Nakahara, *Geometry, Topology and Physics*, IOP Publishing Ltd, Bristol (1990).

[23] E. Rains, private communication. See: K. Chen and H.-K. Lo, quant-ph/0404133, and H. Aschauer, W. Dür and H.-J. Briegel, Phys. Rev. A **71**, 012319 (2005).

[24] W. Dür, H. Aschauer and H.-J. Briegel, Phys. Rev. Lett. **91**, 107903 (2003).

[25] T. Ohno, G. Arakawa, I. Ichinose, and T. Matsui, quant-ph/0401101.

[26] J. Edmonds, Canadian J. Math., **17**, 449 (1965).

[27] W. Cook and A. Rohr, INFORMS Journal on Computing **11**, 138, (1999).

[28] C. Wang, J. Harrington, and J. Preskill, Ann. Phys. (N.Y.) **303**, 31 (2003).

The appendices are relevant for Error Model 2 only.

A Connecting sub-clusters

The cluster $\mathcal{C}$ consists of a set of sub-clusters $\mathcal{C}_k$, $\mathcal{C} = \bigcup_k \mathcal{C}_k$ which are prepared in sequence. Two successive sub-clusters $\mathcal{C}_k$, $\mathcal{C}_{k+1}$ have an overlap, $\mathcal{C}_k \cap \mathcal{C}_{k+1} = H_k \subset V \cup D$. H_k is a set of locations for hand-over qubits. Each graph edge (corresponding to a $\Lambda(Z)$-gate in cluster state creation) can be unambiguously assigned to one sub-cluster. The set of edges ending in one vertex either belongs to one or to two sub-clusters. In the latter case, the vertex is the location for a hand-over qubit.

If k is odd, the cluster state creation procedure on $\mathcal{C}_k$ is the sequence $1 \rightarrow 2 \rightarrow 3 \rightarrow 4$. If k is even, the sequence is $3 \rightarrow 4 \rightarrow 1 \rightarrow 2$. As shown in Fig. 13b, connecting the sub-clusters proceeds smoothly. Consider, for example, the sub-cluster $\mathcal{C}_1$. With the exception of a subset of the hand-over qubits to $\mathcal{C}_2$, the qubits in $\mathcal{C}_1$ are prepared at $t = 0$, entangled in steps 1 to 4, and measured at $t = 5, 6$. Specifically, the V- and D-qubits are measured at time $t = 5$, while the S-qubits are measured at time $t = 6$ with measurement bases adapted according to previous measurement outcomes. The sub-clusters $\mathcal{C}_k$ are chosen such that there is no temporal order among

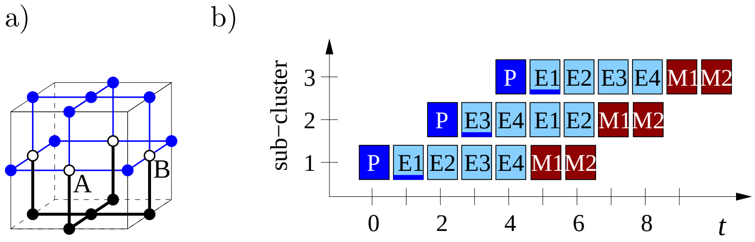

Figure 13: Connecting sub-clusters. a) Elementary cell of $\mathcal{L}$. The old sub-cluster is displayed in blue, the new in black; "∘"; hand-over qubits, "•": qubits within one sub-cluster. b) Temporal order of operations. "P": $|+\rangle$-preparation, "E1-E4": steps of parallel $\Lambda(Z)$-gates, M1, M2: measurement.

the measurements on qubits within $S \cap \mathcal{C}_k$, for all k. Then, the S-qubits wait for one time step in which a storage error may occur.

The hand-over qubits stay in the computation no longer than the other V- and D-qubits. They form two subsets, $H_1 = A \cup B$; see Fig. 13a. The qubits in A are prepared at $t = 0$, entangled in time steps 1 to 4 and measured in at $t = 5$. They cause no change in the error model.

The qubits in B are not acted upon by a gate until time step 2 (since the potential interaction partner of step 1 isn't there yet), so they are prepared at time $t = 1$. The final interaction involving the B-qubits is in step 5, and they are measured in step 6. Between preparation and measurement, the B-qubits are in the computation for four time steps in each of which they are acted upon by a gate. No additional storage error occurs. There is one modification due to the B-qubits. The temporal order of $\Lambda(Z)$-gates involving the qubits $b \in B$ is changed. As a result, the correlated errors on the edge qubits of the faces $\{c_2\} = b$ are not among pairs of opposite edge qubits but among pairs of neighboring edge qubits. So, the error rates q_1 and q_2 in (34) are unchanged, but q_2 characterizes a slightly different process.

We expect this to be a minor effect. The overall threshold is still set by the threshold for Reed-Muller error-correction, which is some five times smaller than the simulated threshold for topological error correction.

B Effective error channel on the S-qubits

The effective error on an S-qubit stems from the S-qubit itself and its immediate surrounding shown in Fig. 14 and from the two edge-qubits in the one-dimensional section of the defect, which are not protected by any syndrome. Of the latter each contributes an error

$$E_{\text{defect}} = \left(\frac{4}{5}p_2 + \frac{2}{3}p_S + \frac{2}{3}p_M\right)[X_s]. \tag{46}$$

The preparation error does not contribute, because the corresponding Z-error on the defect qubit is absorbed in the Z-measurement.

The effective error of the center qubit $s \in S$ stems from operations that act on s directly, from X- or Y-errors propagated to s by the $\Lambda(Z)$-gates and from short nontrivial cycles. Specifically, there are four non-trivial cycles of length 3. One of them is denoted as $E(c_1)$ in Fig. 14. Because of the correlations in the forward-propagated errors these cycles have weight 2 and cause inconclusive syndrome at lowest order in the error probability. There are further error cycles of length 3, such as $E(c_1')$ in Fig 14. But they have weight 3 even for Error Model 2 and do not contribute to the lowest order error channel. We perform a count including all error sources in the cluster region displayed in Fig. 14, right. There is one convention that enters into the count. Namely, the error $Z_aZ_bZ_cZ_d$ (see Fig. 14) is a non-trivial error cycle such that the errors Z_aZ_b and Z_cZ_d have the same weight

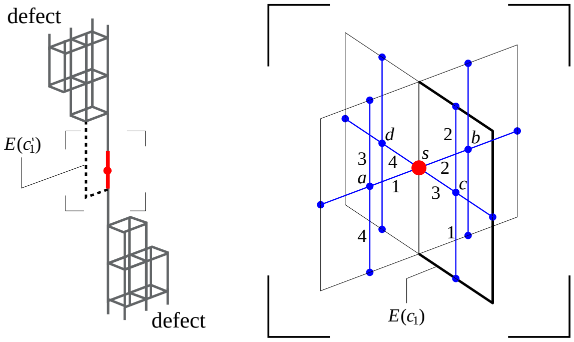

Figure 14: Lattice around an S-qubit. Left: Location of the S-qubit (red) and the defect (gray). $E(c_1')$ is an error cycle of length 3 and weight 3 for Error Models 1 and 2. Right: Detail. $E(c_1)$ is a non-trivial error cycle of length 3 which has weight 2 in error Model 2. Red: S-qubit, black: lattice $\mathcal{L}$ for topological error correction. The cluster edges (blue) correspond to $\Lambda(Z)$-gates whose temporal order is as indicated.

and the same syndrome but different effect on the computation, X_s vs. I_s. When the corresponding syndrome occurs, we assert that a logical X-error occurred and correct for it. We obtain

$$E_{\text{central}} = \left(\frac{2}{5}p_2 + \frac{1}{3}p_S + \frac{1}{3}p_M\right)([X_s] + [Y_s]) + \left(\frac{2}{3}p_P + \frac{1}{3}p_S + \frac{1}{3}p_M + \frac{58}{15}p_2\right)[Z_s]. \tag{47}$$

The sources (46) and (47) combined, $E_{\text{central}} + 2 \times E_{\text{defect}}$, lead to the local error channel (38).

C Conversion of X- and Y-errors on S-qubits

Here we show that an X- or Y-error on an individual S-qubit s with probability p is equivalent to a Z-error on that qubit with probability $p/2$, $p[X_s] \cong p[Y_S] \cong p/2\,[Z_s]$. The qubit s may be measured in the eigenbasis of $\frac{X+Y}{\sqrt{2}}$ or of $\frac{X-Y}{\sqrt{2}}$. W.l.o.g. assume the qubit s is measured in the eigenbasis of $\frac{X+Y}{\sqrt{2}}$. Then, $X_s = \frac{X_s+Y_s}{\sqrt{2}}\frac{I_s-iZ_s}{\sqrt{2}} \cong \frac{I_s-iZ_s}{\sqrt{2}}$. The X-error is equivalent to a coherent Z-error and we need to check whether the coherences matter. More generally, for the described scenario with the subsequent measurement a probabilistic local error channel $(1-p_X-p_Y-p_Z)[I_s] + p_X[X_s] + p_Y[Y_s] + p_Z[Z_s]$ is equivalent to a channel with coherent errors

$$\rho \longrightarrow (1-q)\rho + qZ_s\rho Z_s + i\tilde{q}\left(\rho Z_s - Z_s\rho\right), \tag{48}$$

with

$$q = p_Z + \frac{p_X + p_Y}{2}, \quad \tilde{q} = \frac{p_X - p_Y}{2}. \tag{49}$$

Now assume that all S-qubits are affected individually by the error channel (48). The Reed-Muller error correction at successive levels maps these channels to channels of the same form, one coding level higher up. The parameters q_l, $\tilde{q}_l$ at coding level l obey recursion relations which, up to fourth order, read

$$\begin{aligned} q_{l+1} &= 105\,q_l^2\,(1-q_l)^{13} + 35\,q_l^3\,(1-q_l)^{12} + 1260\,q_l^4\,(1-q_l)^{11} + 630\,\tilde{q}_l^4\,(1-q_l)^{11}, \\ \tilde{q}_{l+1} &= 70\,\tilde{q}_l^3\,(1-q_l)^{12} - 1680\,\tilde{q}_l^3 q_l\,(1-q_l)^{11}. \end{aligned} \tag{50}$$

If we compare (50) to the recursion relation of q for probabilistic Z-error, a deviation first shows up at fourth order. The discussion of Reed-Muller error correction in this paper is confined to leading order. The leading order result for the threshold, $q_c = 1/105$, is not affected by the coherences in the error (48). Probabilistic X-and Y-errors influence the threshold by contributing half their weight to the probability of an effective Z-error; see (49).

Efficient Quantum Computation with Probabilistic Quantum Gates

L.-M. Duan[1] and R. Raussendorf[2]

[1]*FOCUS Center and MCTP, Department of Physics, University of Michigan, Ann Arbor, Michigan 48109-1120, USA*
[2]*Institute for Quantum Information, California Institute of Technology, Pasadena, California 91125, USA*

(Received 28 February 2005; published 17 August 2005)

With a combination of the quantum repeater and the cluster state approaches, we show that efficient quantum computation can be constructed even if all the entangling quantum gates only succeed with an arbitrarily small probability p. The required computational overhead scales efficiently both with $1/p$ and n, where n is the number of qubits in the computation. This approach provides an efficient way to combat noise in a class of quantum computation implementation schemes, where the dominant noise leads to probabilistic signaled errors with an error probability $1 - p$ far beyond any threshold requirement.

DOI: 10.1103/PhysRevLett.95.080503 PACS numbers: 03.67.Lx, 03.67.Pp, 03.67.Mn

The celebrated threshold theorem in quantum computation has assured that, if the amount of noise per quantum gate is less than a small value, reliable quantum computation can be efficiently performed [1]. In terms of implementation, however, the experimental noise is typically orders of magnitude large than the required threshold value. To overcome this problem, a practical route to noise reduction is by exploitation of certain properties of the noise. In carefully designed implementation schemes, the dominant noise leads to specific types of errors only, which can be corrected much more efficiently. Here, we consider an important noise model, which is relevant for several experimental approaches to quantum computation with the use of photons or trapped atoms or ions as the qubits [2–11]. In these schemes, the dominant noise leads to significant failure probability for the entangling gates only, and a gate failure is always signaled through built-in fast photon detections during the gate operation. The success probability p for each entangling gate is rather small for some typical experimental systems [4,10,11]. It is hard to use the standard methods of error correction in the considered scenario, because the error probability $1 - p$ (close to the unity) is simply too large.

Naively, if a gate succeeds only with a certain probability p, one cannot have efficient computation, as the overall success probability (efficiency) scales down exponentially as p^n with the number n of gates. However, in this Letter we show that efficient quantum computation can be constructed with the required computational overhead (such as the computation time or the repetition number of the entangling gates) scaling up slowly (polynomially) with both n and $1/p$. The demonstration of this result combines the ideas from the quantum repeater schemes [12,13] and the cluster state approach to computation [14,15]. It has been shown in quantum repeater schemes that, with probabilistic entangling operations, one can construct scalable quantum communication and Greenberger-Horne-Zeilinger correlations [13,16]. Recently, it has also been demonstrated in the context of linear optics computation [2] that the threshold requirement on the probability p for the entangling gates can be significantly improved using the cluster state approach to quantum computation [3,5,7,8]. In particular, Ref. [8] shows that for construction of one-dimensional (1D) cluster states, to get efficient scaling with n, in principle no threshold value is needed on p, although in practice p is still required to be sufficiently large as the computational overhead in that scheme has inefficient (superexponential) scaling with $1/p$. Compared with these previous results, here we have the following two advances: (i) We propose a probabilistic computation scheme which has efficient scaling with both n and $1/p$. This improvement is substantial as in current experiments $1/p$ is large [10,11]. (ii) Through explicit construction, we also demonstrate efficient scaling of the computational overhead for generation of the two-dimensional (2D) cluster states which are critical for realization of universal quantum computation.

To be more specific, we assume in this Letter that one can reliably perform two-qubit controlled phase flip (CPF) gates with a small success probability p, although the basic ideas here also apply for other kinds of entangling gates. We neglect the noise for all the single-bit operations, which is well justified for typical atomic or optical experiments. Our basic steps are as follows: First, we show how to efficiently prepare 1D cluster state from probabilistic CPF gates. Then, we give a construction to efficiently generate 2D cluster states from 1D chains. Efficient preparation of 2D cluster states, together with simple single-bit operations, realizes universal quantum computation.

With respect to a given lattice geometry, the cluster state is defined as coeigenstates of all the operators $A_i = X_i \prod_j Z_j$, where i denotes an arbitrary lattice site and j runs over all the nearest neighbors of the site i. The X_i and Z_j denote, respectively, the Pauli spin and phase flip operators on the qubits at the sites i, j. In our construction of lattice cluster states with probabilistic CPF gates, we will make use of the following three properties of the cluster states: (i) If we have two chains of cluster states each with n qubits, we can join them to form a 1D cluster

© 2005 The American Physical Society

state of $2n$ qubits by successfully applying a CPF gate on the end qubits of the two chains. (ii) If we destroy the state of an end qubit of an n-qubit cluster chain, for instance, through an unsuccessful attempt of the CPF gate, we can remove this bad qubit by performing a Z measurement on its neighboring qubit, and recover a cluster state of $n-2$ qubits. (iii) We can shrink a cluster state by performing X measurements on all the connecting qubits [see Fig. 1(c)]. These three properties of the cluster states, illustrated in Fig. 1, can be conveniently explained from their above definition [15,17].

If we have generated two sufficiently long cluster chains each of n_0 qubits, we can just try to connect them through a probabilistic CPF gate. If this attempt fails, through the property (ii), we can recover two (n_0-2)-qubit cluster chains through a Z measurement, and try to connect them again. As one continues with this process, the average number of the qubits in the connected chain is then given by $n_1=\sum_{i=0}^{n_0/2}2(n_0-2i)p(1-p)^i\simeq 2n_0-4(1-p)/p$, where the last approximation is valid when $e^{-n_0p/2}\ll 1$. So the average chain length goes up if $n_0>n_c\equiv 4(1-p)/p$. We can iterate these connections to see how the computation overhead scales with the qubit number n. We measure the computation overhead in terms of the total computation time and the total number of attempts for the CPF gates. For the rth $(r\geq 1)$ round of successful connection, the chain length n_r, the total preparation time T_r, and the total number of attempts M_r scale up, respectively, by the recursion relations $n_r=2n_{r-1}-n_c$, $T_r=T_{r-1}+t_a/p$, and $M_r=2M_{r-1}+1/p$. In writing the recursion relation for T_r, we have assumed that two cluster chains for each connection are prepared in parallel, and we neglect the time for single-bit operations (t_a denotes the time for each attempt of the CPT gate). From the above recursion relations, we conclude that if we can prepare cluster chains of n_0 $(n_0>n_c)$ qubits in time T_0 with M_0 attempts of the probabilistic gates, for a large cluster state, the preparation time T and the number of attempts M scale with the chain length n as $T(n)=T_0+(t_a/p)\log_2[(n-n_c)/(n_0-n_c)]$ and $M(n)=(M_0+1/p)(n-n_c)/(n_0-n_c)-1/p$.

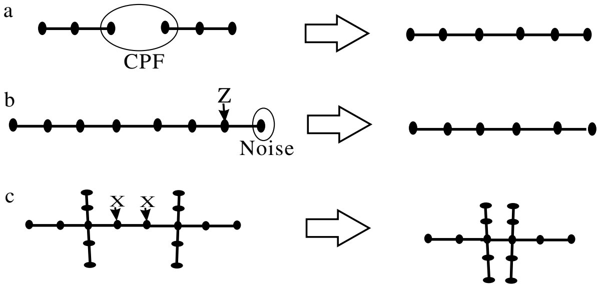

FIG. 1. Illustration of the three properties of the cluster states which are important for our construction of such states with the probabilistic entangling gates: (a) extend cluster states with CPF gates; (b) recover cluster states by removing bad qubits; (c) shrink cluster states for more complicated links.

In the above, we have shown that if one can prepare cluster chains longer than some critical length n_c, one can generate large scale 1D cluster states very efficiently. The problem then reduces to how to efficiently prepare cluster chains up to the critical length n_c. If one wants to prepare an n-qubit cluster chain, we propose to use a repeater protocol which divides the task into $m=\log_2 n$ steps: For the ith $(i=1,2,\ldots,m)$ step, we attempt to build a 2^i-bit cluster state by connecting two 2^{i-1}-bit cluster chains through a probabilistic CPF gate. If such an attempt fails, we discard all the qubits and restart from the beginning [18]. For the ith step, the recursion relations for the preparation time T_i and the number of attempts M_i are given by $T_i=(1/p)(T_{i-1}+t_a)$ [19] and $M_i=(1/p)(2M_{i-1}+1)$, which, together with $T_1=t_a/p$ and $M_1=1/p$, give the scaling rules $T(n)\simeq t_a(1/p)^{\log_2 n}$ and $M(n)\simeq(2/p)^{\log_2 n}/2$. The cost is more significant, but it is still a polynomial function of n. To construct a n-qubit cluster chain, in total we need $n-1$ successful CPF gates. In a direct protocol, we need all these attempts to succeed simultaneously, which gives the scaling $T(n)\propto M(n)\propto(1/p)^{n-1}$. By dividing the task into a series of independent pieces, we improve the scaling with n from exponential to polynomial (for $n\leq n_c$).

To generate a cluster chain of a length $n>n_c$, we simply combine the above two protocols. First, we use the repeater protocol to generate n_0-qubit chains with $n_0>n_c$. Then it is straightforward to use the connect-and-repair protocol to further increase its length. For instance, with $n_0=n_c+1$ (which is a reasonable close-to-optimal choice), the overall scaling rules for T and M are (for $n>n_c$)

$$T(n)\simeq t_a(1/p)^{\log_2(n_c+1)}+(t_a/p)\log_2(n-n_c),\qquad(1)$$

$$M(n)\simeq(2/p)^{\log_2(n_c+1)}(n-n_c)/2.\qquad(2)$$

As the critical length is $n_c\simeq 4/p$, T and M in our protocol scale with $1/p$ as $(1/p)^{\log_2(4/p)}$, which is much more efficient than the superexponential scaling $(1/p)^{4/p}$ in the previous work.

We have shown that for any success probability p of the probabilistic entangling gate, 1D cluster states of arbitrary length can be created efficiently. For universal quantum computation, however, such 1D cluster states are not sufficient. They need to be first connected and transformed into 2D cluster states (for instance, with a square lattice geometry) [15]. It is not obvious that such a connection can be done *efficiently*. First, in the connect-and-repair protocol, when an attempt fails, we need to remove the end qubits and all of their neighbors. This means that in a 2D geometry the lattice shrinks much faster to an irregular shape in the events of failure. Furthermore, a more important obstacle is that we need to connect much more boundary qubits if we want to join two 2D cluster states. For instance, for a square lattice of n qubits, the number of boundary qubits scales as $\sqrt{n}$ (which is distinct from a 1D chain). If we need to connect all the corresponding boundary qubits of the two parts, the overall success probability is exponentially small.

To overcome this problem, we introduce a method which enables efficient connection by attaching a long leg (a 1D cluster chain) to each boundary qubit of the 2D lattice. The protocol is divided into the following steps: First, we try to build a "+-shape" cluster state by probabilistically connecting two cluster chains each of length $2n_l + 1$ (the value of n_l will be specified below). This can be done through the probabilistic CPF gate together with a simple Hardmard gate H and an X measurement, as shown in Fig. 2(a) and explained in its caption. With on average $1/p$ repetitions, we get a +-shape state with the length of each of the four legs given by n_l. We use the +-shape state as the basic building blocks of large scale 2D cluster states. In the +-shape state, we have attached four long legs to the center qubit. The leg qubits serve as ancilla to generate near-deterministic connection from the probabilistic CPF gates. The critical idea here is that if we want to connect two center qubits, we always start the connection along the end qubits of one of the legs (see illustration in Fig. 2). If such an attempt fails, we can delete two end qubits and try the connection again along the same legs. If the leg is sufficiently long, we can almost certainly succeed before we reach (destroy) the center qubits. When we succeed, and if there are still redundant leg qubits between the two center ones, we can delete the intermediate leg qubits by performing simple single-bit X measurements on all of them [see Figs. 1(c) and 2 for the third property of the cluster state]. With such a procedure, we can continuously connect the center qubits and form any complex lattice geometry [see the illustration for construction of the square lattice state in Figs. 2(b) and 2(c)]. What is important here is that after each time of connection of the center qubits, in the formed new shape, we still have the same length of ancillary legs on all the boundary qubits, which enables the succeeding near-deterministic connection of these new shapes.

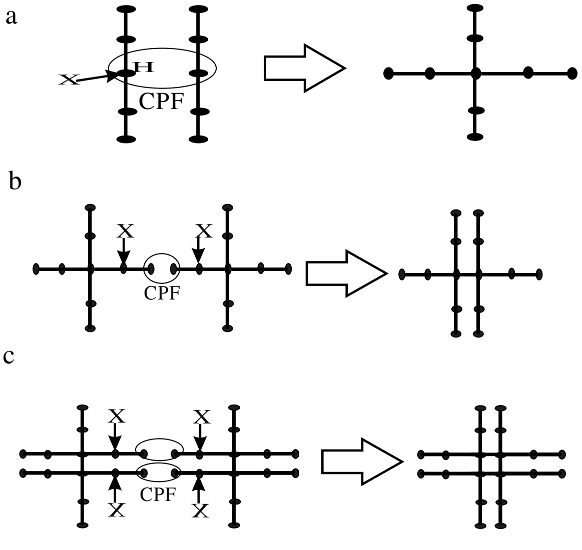

FIG. 2. Illustration of the steps for construction of the 2D square lattice cluster states from a set of cluster chains. (a) Construction of the basic +-shape states from cluster chains by applying first a Hardmard gate H on the middle qubit of one chain, and then a CPF gate to connect the two middle qubits, and finally a X measurement on one middle qubit to remove it. (b),(c) Construction of the square lattice cluster state from the +-shape states through probabilistic CPF gates along the legs and X measurements to remove the remaining redundant qubits.

Now we investigate for the 2D case how the computational overhead scales with the size of the cluster state. If the ancillary legs have length n_l, for each connection of two center qubits, we can try at most $n_l/2$ times of the probabilistic CPF gates, and the overall success probability is given by $p_c = 1 - (1 - p)^{n_l/2}$. If we want to build a square lattice cluster state of N qubits, we need about $2N$ times of connections of the center qubits (there are about $2N$ edges in an N-vertex square lattice). The probability for all these connections to be successful is given by p_c^{2N}. We require that this overall success probability is sufficiently large with $p_c^{2N} \geq 1 - \epsilon$, where ϵ is a small number characterizing the overall failure probability. From that requirement, we figure out that $n_l \simeq (2/p)\ln(2N/\epsilon)$. To construct a square lattice cluster state of N qubits, we need to consume N +-shape states, and each of the latter requires on average $2/p$ cluster chains with a length of $2n_l + 1$ qubits. So we need in total $(2N/p)(2n_l + 1)$-bit cluster chains, which can be prepared in parallel with $(2N/p)M(2n_l + 1)$ CPF attempts within a time period $T(2n_l + 1)$ [see Eqs. (1) and (2) for expressions of the $M(n)$ and $T(n)$]. This gives the resources for preparation of all the basic building blocks (the chains). Then we need to connect these blocks to form the square lattice. We assume that the connection of all the building blocks are done in parallel. The whole connection takes on average $2N/p$ CPF attempts, and consumes a time at most $t_a/p\ln(2N/\epsilon)$. Summarizing these results, the temporal and the operational resources for preparation of an N-bit square lattice cluster state are approximately given by

$$T(N) \simeq t_a(1/p)^{\log_2(4/p-3)} + \frac{t_a}{p}\log_2\left(\frac{4}{p}[\ln(2N/\epsilon) - 1]\right) + \frac{t_a}{p}\ln(2N/\epsilon), \tag{3}$$

$$M(N) \simeq (2/p)^{2+\log_2(4/p-3)}N[\ln(2N/\epsilon) - 1] + 2N/p. \tag{4}$$

In the 2D case, the temporal and the operational overheads still have very efficient scaling with the qubit number N, logarithmically for $T(N)$ and $N\ln(N)$ for $M(N)$. Their scalings with $1/p$ are almost the same as in the 1D case except an additional factor of $1/p^2$ for $M(N)$. Through some straightforward variations of the above method, it is also possible to efficiently prepare any complicated graph state using probabilistic CPF gates [17]. This shows that in principle we do not need to impose any threshold on the success probability of the CPF gates for efficient quantum computation.

Before ending the Letter, we would like to add a few remarks on other sources of noise that have not been taken into account in the above discussions. If each CPF gate has some small additional infidelity error, one might wonder whether such an error scales up with the large number of attempts $M(N)$. That is actually not the case. Most of the CPF attempts have failed, and all the failed CPF gates have no contribution to the final state infidelity. In practice, we may be more concerned about the temporal overhead $T(N)$ than the operational overhead $M(N)$. Each qubit has a finite coherence time and we need to finish all the CPF attempts within such a time scale. For typical probabilistic entangling experiments with atoms [10,11], the time t_a for each CPF attempt is about 100 ns, while the qubit coherence time is usually longer than 1 s. If we take the success probability $p \sim 0.1$, Eq. (3) gives $T(N) \sim 1.6 \times 10^5 t_a \sim$ 16 ms for any large N [20], which is still well within the qubit coherence time.

In summary, we have shown that cluster states in two dimensions can be generated using probabilistic CPF gates with efficient scaling in both the qubit number and the inverse of the success probability. This result opens up a prospect to realize efficient quantum computation with probabilistic entangling gate operations. Such a prospect is relevant for several experimental systems involving atoms, ions, or photons [2,4,10,11], with ongoing efforts towards probabilistic quantum information processing.

L. M. D. thanks Chris Monroe for helpful discussions. This work was supported by NSF grants (0431476 and EIA-0086038), the ARDA under ARO contracts, the A. P. Sloan Foundation, and the visitor program of MCTP.

Note added.—Recently, we became aware that in the latest version of Ref. [8] the authors have also made some interesting improvement of their construction efficiency of the 1D cluster state to overcome the inefficient scaling.

---

[1] M. A. Nielsen and I. L. Chuang, *Quantum Computation and Quantum Information* (Cambridge University Press, Cambridge, England, 2000).

[2] E. Knill, R. Laflamme, and G. Milburn, Nature (London) **409**, 46 (2001).

[3] N. Yoran and B. Reznik, Phys. Rev. Lett. **91**, 037903 (2003).

[4] L.-M. Duan and H. J. Kimble, Phys. Rev. Lett. **92**, 127902 (2004); **90**, 253601 (2003); L.-M. Duan, B. Wang, and H. J. Kimble, quant-ph/0505054.

[5] M. A. Nielsen, Phys. Rev. Lett. **93**, 040503 (2004).

[6] L.-M. Duan, B. B. Blinov, D. L. Moehring, and C. Monroe, Quantum Inf. Comput. **4**, 165 (2004).

[7] D. E. Browne and T. Rudolph, quant-ph/0405157.

[8] S. D. Barrett and P. Kok, Phys. Rev. A **71**, 060310(R) (2005).

[9] X. Zou and W. Mathis, quant-ph/0401042; Y. L. Lim, A. Beige, and L. C. Kwek, quant-ph/0408043.

[10] B. B. Blinov, D. L. Moehring, L.-M. Duan, and C. Monroe, Nature (London) **428**, 153 (2004).

[11] A. Kuzmich *et al.*, Nature (London) **423**, 731 (2003); C. H. van der Wal *et al.*, Science **301**, 196 (2003); W. Jiang *et al.*, Phys. Rev. A **69**, 043819 (2004); D. N. Matsukevich and A. Kuzmich, Science **306**, 663 (2004).

[12] H.-J. Briegel, W. Dür, J. I. Cirac, and P. Zoller, Phys. Rev. Lett. **81**, 5932 (1998).

[13] L. M. Duan, M. D. Lukin, J. I. Cirac, and P. Zoller, Nature (London) **414**, 413 (2001).

[14] H. J. Briegel and R. Raussendorf, Phys. Rev. Lett. **86**, 910 (2001).

[15] R. Raussendorf and H. J. Briegel, Phys. Rev. Lett. **86**, 5188 (2001).

[16] L.-M. Duan, Phys. Rev. Lett. **88**, 170402 (2002).

[17] R. Raussendorf, D. E. Browne, and H. J. Briegel, Phys. Rev. A **68**, 022312 (2003).

[18] If we do not immediately discard all the qubits, but instead do some repairing and reconnection as described in the previous paragraph, the protocol will be somewhat more efficient. But for $n \leq n_r$, such repairing has no significant influence on the basic scaling rules.

[19] For this recursion relation on T_i, we have assumed that we use only one copy of the system with n qubits (no ancillary qubits) and that, if we fail, we start over from the first step. However, if we allow very many copies of such n-qubit systems on which we operate in parallel, in principle we can get much more efficient scaling for T_i. We try the chain connection in parallel in all these n-qubit systems, discard the systems with failure events, and continue the next-step connection for the systems where all the previous connections are successful. In this way, one connection (one length doubling of the qubit chain) takes only one time step t_a, so we have $T_i = T_{i-1} + t_a$. This recursion relation will lead to a significant improvement in the total required preparation time: the scaling of $T(N)$ [or $T(n)$] with $1/p$ in Eq. (3) [or Eq. (1)] changes from $(1/p)^{\log_2(4/p)}$ to $(1/p)\log_2(4/p)$. Of course, the cost for this improvement is probably too expensive for practical experiments: to prepare n-qubit cluster states with the above parallel operations, we need to have roughly $n(1/p)^{\log_2(4/p)}$ ancillary qubits.

[20] For the quoted number, $T(N)$ is basically independent of N for $N/\epsilon < 10^{7000}$ due to the slow logarithmic scaling $\ln(2N/\epsilon)$.

PHYSICAL REVIEW A **72**, 022301 (2005)

Quantum cellular automaton for universal quantum computation

Robert Raussendorf
Institute for Quantum Information, California Institute of Technology, Pasadena, California 91125, USA

(Received 14 March 2005; revised manuscript received 11 May 2005; published 1 August 2005)

This paper describes a quantum cellular automaton capable of performing universal quantum computation. The automaton has an elementary transition function that acts on Margolus cells of 2×2 qubits, and both the "quantum input" and the program are encoded in the initial state of the system.

DOI: 10.1103/PhysRevA.72.022301 PACS number(s): 03.67.Lx

I. INTRODUCTION

A number of physical systems that are considered for the realization of a universal quantum computer, such as optical lattices [1] or arrays of microlenses [2], possess a translation symmetry in the arrangement of qubits and their mutual interaction. Quantum cellular automata (QCA) represent a suitable framework to explore the computational power of such physical systems, because they respect this symmetry. *A priori*, translation invariance may be regarded as a severe limitation since it constrains the degree of control that can be exerted to the quantum system. However, it has been demonstrated that one-dimensional QCA can efficiently simulate any quantum Turing machine [3].

Further it has been shown that there exists a universal QCA which can simulate any other automaton with linear slow down [4], and that every reversible QCA can be represented in a generalized Margolus partitioning scheme [5]. Proposals with an emphasis on experimental viability have outlined how generic physical systems can be used as quantum computation devices if equipped with a minimal amount of external control. Among the described mechanisms are global control via sequences of resonant light pulses [6] or modulation of a coupling constant [7,8], and individual control over one of the elementary cells [9].

At this point, one may abandon all algorithm-specific control during the process of computation and ask "How intricate do quantum cellular automata have to be such that they can perform useful tasks in quantum information processing?." A quick answer may be "Simple, by definition." However, when QCAs are tuned for algorithmic application, it may occur that—while the simple composition is retained—the elementary cells and neighborhood schemes become complicated. An interesting facet of the answer to the above question has been provided in Ref. [10], where a very simple QCA for quantum data transmission has been devised (also see Ref. [5]). Motivated by a recent result [11], where universal computation via autonomous evolution of a 10-local Hamiltonian is described, here we consider quantum computation in the cellular automaton scenario. We explicitly construct a computationally universal two-dimensional QCA whose transition rule is based on a four-qubit unitary.

II. CONSTRUCTION OF THE AUTOMATON

Consider a two dimensional lattice of size $2s\times 2r$ with periodic boundary conditions, i.e., a torus. Each lattice site carries a qubit. The transition rule for the QCA is described in terms of a Margolus partitioning [12]. The lattice is partitioned into cells of size 2×2, and there is a separate partitioning for the time t being even or odd, respectively. One may choose a coordinate system on the torus with axes parallel to what were the boundaries before identification. For t even, the qubits in the upper left corner of each cell have both coordinates even, and for t odd they have both coordinates odd. Thus, a cell in step t overlaps with four cells of step $t-1$.

The transition of the QCA from time t to $t+1$ proceeds by simultaneously applying a unitary transition function τ to each cell. For a suitable choice of the 4-qubit unitary τ one can perform universal quantum computation with the described QCA. Specifically, a quantum logic network of local and next-neighbor unitary gates with width $2s$ and depth r can be simulated.

With a labeling of particles as illustrated in Fig. 1(a), the following elementary transition function is chosen:

$$\tau = S(1,3)S(2,4)H_1\exp\left(-i\frac{\pi}{8}\frac{1-Z_3}{2}Z_1\right)\times\exp\left(i\pi\frac{1-Z_4}{2}\frac{1-Z_1}{2}\frac{1-Z_2}{2}\right). \tag{1}$$

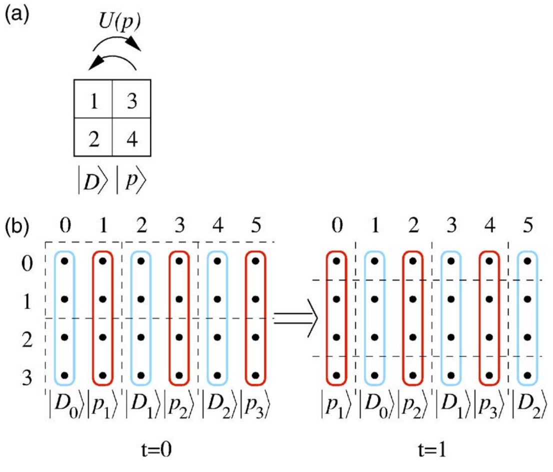
(a)
U(p)
1
3
2
4
|D⟩ |p⟩
(b)
0 1 2 3 4 5
0
1
2
3
|D_0⟩|p_1⟩|D_1⟩|p_2⟩|D_2⟩|p_3⟩
t=0
0 1 2 3 4 5
|p_1⟩|D_0⟩|p_2⟩|D_1⟩|p_3⟩|D_2⟩
t=1

FIG. 1. (Color online) Transition of the QCA from t to $t+1$. (a) Margolus cell of 2×2 qubits, with the part $|D\rangle_{12}$ of a data and $|p\rangle_{34}$ of the program column. (b) Before and after the first transition. The program columns move left and the data columns move right. The dashed lines indicate the partitioning into Margolus cells.

1050-2947/2005/72(2)/022301(4)/$23.00

©2005 The American Physical Society

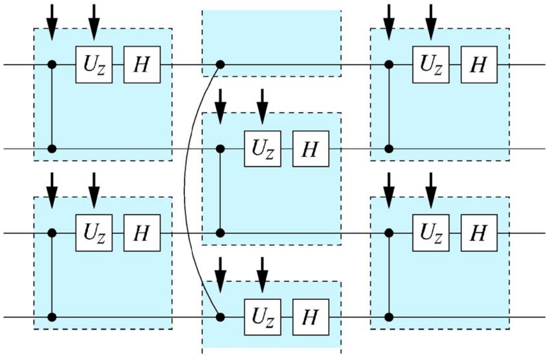

FIG. 2. (Color online) The quantum logic network simulated by the QCA. The gates in each shaded box result from one application of the elementary transition function. The arrows denote classically controlled gates which are triggered by the program registers. In the second time slice of the displayed network, the two half-neighborhoods at the lower and upper end form a neighborhood, due to the toric topology.

Therein, $S(a,b)$ denotes a SWAP gate between qubit a and b, H_1 is a Hadamard transformation on qubit 1, and Z_c denotes a Pauli phase flip operator applied to qubit c.

If $|p\rangle_{34}$ is a state in the computational basis, it effectively stores two classical bits, $p^{(3)}$ and $p^{(4)}$. Then, the transition function τ amounts to a classically controlled unitary operation $U(p)$ applied to $|D\rangle_{12}$. The bit $p^{(4)}$ triggers a $\Lambda(Z)$ gate applied to $|D\rangle_{12}$, and $p^{(3)}$ a $\pi/4$-phase gate $\exp(-i\pi/8Z_1)$ applied to qubit 1 of $|D\rangle_{12}$. In this way, $|p\rangle$ encodes an elementary step of a program, carried out on the two-qubit "data" $|D\rangle_{12}$. The SWAP gates allow the quantum data and the program to pass by another, such that $|D\rangle_{12}$ can interact with subsequent program registers.

The sets of qubits on the torus with the same first coordinate x, $0 \leqslant x \leqslant 2r-1$, are called columns. At time $t=0$ all even columns contain data registers $|D_i\rangle$, and all odd columns contain program registers $|p_j\rangle$. The initial state of the automaton is

$$|\psi(0)\rangle = \bigotimes_{i=0}^{r-1} |D_i(0)\rangle_{2i} |p_{i+1}\rangle_{2i+1}. \tag{2}$$

Here and in the following the labels inside the kets specify the state and the ones outside specify the location of the support within the lattice, i.e., the column. For example, $|D_1(0)\rangle_2$ is data register number 1 at time $t=0$, located on column 2. Of all data registers only $|D_0\rangle$ is used, the others are auxiliary. When the QCA starts to run, the data registers move right (counter-clockwise, as seen from top) and the program registers move left (clockwise), by one column in each time step. When passing the data registers, the program registers $|p\rangle$ control unitary transformations $U(p)$ acting upon the data registers $|D\rangle$. In this way, a program specified by the data $p_1,\ldots,p_r$, with p_1 encoding the first and p_r the last step, is carried out on the quantum data register $|D_0\rangle$. The program that is carried out corresponds to a quantum logic network of local and next-neighbor gates in a particular arrangement; see Fig. 2. Such networks are sufficient for universal quantum computation, as is discussed in detail further below. The same program steps that are applied to the register $|D_0\rangle$ are also carried out on the auxiliary data registers $|D_i\rangle$, $1 \leqslant i \leqslant r-1$, but in scrambled order. Therefore, these registers are not used.

In the course of computation, both data and program travel across half the torus. When the automaton has run for r time steps, the computation is finished and the register $|D_0(r)\rangle_r$ can be read out from column r, via local measurements.

Let $\tau_{i,j}$ denote the elementary transition function (1) applied to the cell (i,j). Therein, i is the column coordinate of the upper left qubit in the cell, and j the respective coordinate within the column. Then, the unitary transition function T_i, acting upon two consecutive columns i, $i+1$, is

$$T_i = \bigotimes_{j=0}^{s-1} \tau_{i,[2j+i]_{2s}}. \tag{3}$$

Therein, $[2j+i]_{2s}$ is a shorthand for $2j+i \bmod 2s$ that will be used throughout the remainder of the paper.

If $|p\rangle$ is a state in the computational basis, then

$$T_i(|D\rangle_i \otimes |p\rangle_{i+1}) = |p\rangle_i \otimes [U(p)|D\rangle]_{i+1}. \tag{4}$$

Therein, $U(p)$ is a unitary transformation chosen by p containing a Hadamard—and possibly a $\Lambda(Z)$—and a $\pi/4$-phase gate, in accordance with (1).

The global transition function $T:|\psi(t)\rangle \rightarrow |\psi(t+1)\rangle$ is, for even t given by $T_e = \otimes_{i=0}^{r-1} T_{2i}$, and for odd t by $T_o = \otimes_{i=0}^{r-1} T_{2i+1}$. In both cases it can be written in the form

$$T = \bigotimes_{i=0}^{r-1} T_{[2i+t]_{2r}}. \tag{5}$$

Now, the state $|\psi(t)\rangle$ of the QCA at time t is

$$|\psi(t)\rangle = \bigotimes_{i=0}^{r-1} |D_i(t)\rangle_{[2i+t]_{2r}} \otimes |p_{[i+t+1]_r}\rangle_{[2i+t+1]_{2r}}, \tag{6}$$

with the data register i at time t given by

$$|D_i(t)\rangle = \left(\prod_{k=1}^{t} U(p_{[i+k]_r}) \right) |D_i(0)\rangle. \tag{7}$$

The unitaries $U(p_{[i+k]_r})$ are ordered in ascending order with k, i.e., $U(p_{[i+1]_r})$ acts first. For $i=0$ and $t=r$, in particular, one finds that

$$|D_0(r)\rangle = \left(\prod_{k=1}^{r} U(p_k) \right) |D_0(0)\rangle \tag{8}$$

is the output quantum register, with the unitaries $U(p_1)\cdots U(p_r)$ applied in the correct order to the quantum register in its input state, $|D_0(0)\rangle$.

Before proving (6), let us recover therein some features of the QCA that were stated before. It is easy to see that—apart from being moved—the program registers remain unchanged throughout the evolution, and that there is no entanglement across columns. The data registers indeed move right, and the program registers left (with $i+t+1=i'$, $|p_{[i+t+1]_r}\rangle_{[2i+t+1]_{2r}} = |p_{[i']_r}\rangle_{[2i'-t-1]_r}$). After r time steps, the output quantum register $|D_0(r)\rangle$ can be read out from column r.

Equation (6) is proved by induction. First note that for $t=0$ it reduces to (2). Further,

$$\begin{aligned} T|\psi(t)\rangle &= \bigotimes_{i=0}^{r-1} T_{[2i+t]_{2r}}|D_i(t)\rangle_{[2i+t]_{2r}}|p_{[i+t+1]_r}\rangle_{[2i+t+1]_{2r}} \\ &= \bigotimes_{i=0}^{r-1}(U(p_{[i+t+1]_r})|D_i(t)\rangle)_{[2i+t+1]_{2r}} \\ &\quad \otimes |p_{[i+t+1]_r}\rangle_{[2i+t]_{2r}} \\ &= \bigotimes_{i=0}^{r-1}|D_i(t+1)\rangle_{[2i+(t+1)]_{2r}} \\ &\quad \otimes |p_{[i+(t+1)+1]_r}\rangle_{[2i+(t+1)+1]_{2r}} \\ &= |\psi(t+1)\rangle. \end{aligned} \tag{9}$$

Here, the first line follows by the definitions of T and $|\psi(t)\rangle$, (5) and (6), and the second follows by (4). The third line follows by (7) and, for the $|p\rangle$ part, the substitution $i \rightarrow i+1$ under which the product is invariant. □

Finally, it is shown that the quantum logic network simulated by the described QCA is indeed universal, as stated. The controlled-NOT (CNOT), the Hadamard and the $\pi/4$ phase gate $\exp(-i\pi/8Z)$ form a universal gate set [13]. For the described QCA, one can independently apply the Hadamard, the $\pi/4$ phase gate and the identity to the simulated logical qubits, by choosing the following sequences of $p^{(3)}$ bits:

$$\mathbf{p}^{(3)} = \begin{cases} 0\,000\,000\,000, & \text{for } U = I, \\ 0\,101\,101\,101, & \text{for } U = H, \\ 1\,000\,000\,000, & \text{for } U = U_z[\pi/4]. \end{cases} \tag{10}$$

with all $p^{(4)}$ bits zero. In the way they are constructed here (no claim that this is close to optimal), the one-qubit operations from the universal set require 10 successive applications of $p^{(3)}$-controlled gates and thus 20 time steps of the QCA. A next-neighbor CNOT gate that acts within this cycle can be constructed from a $\Lambda(Z)$ and two Hadamard gates. The long-distance CNOT gates may then be constructed with the help of next-neighbor SWAP gates, which themselves consist of three next-neighbor CNOT gates. This completes our construction of a QCA capable of performing universal quantum computation.

Two remarks, (1) the described QCA may, with some right, be called a deterministic programmable quantum gate array, but this notion is already in use for a construction that has been proven not to exist [14]. Our QCA is consistent with this result. The program information is classical and all program states $\otimes_{i=1}^{r}|p_i\rangle_{2i-1}$ are orthogonal, as required in Ref. [14]. Further, from the viewpoint of temporal complexity, the described QCA is—within a constant—as efficient as a quantum logic network with local and next-neighbor gates. These issues have also been addressed in Ref. [15].

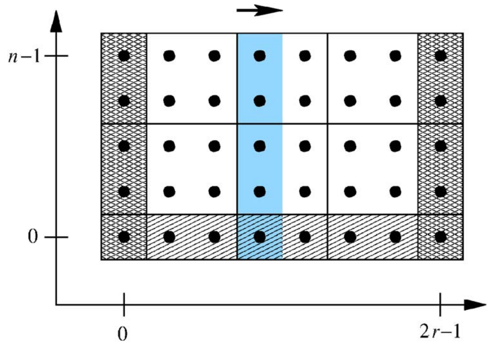

FIG. 3. (Color online) Boundary specifications for the described QCA on a planar sheet. The 2×2 cells displayed in white are acted upon by τ, as usual. To the hatched 1×2 cells a SWAP gate is applied, and to the cross-hatched cells the identity operation. The column in gray underlay represents a data register moving right.

(2) That the described QCA lives on a torus simplifies the discussion, but is not essential. A planar sheet of size $n\times2r$ is sufficient for simulation of the discussed networks of r time steps and n qubits. Figure 3 specifies the operations on the boundary that differ from τ. When this modified QCA is run, in the bulk the data registers still move right and the program registers left. On the left and right boundary, however, the registers are reflected. As a consequence, on the left-hand side of the lattice, reflected program registers are acted upon by left-moving program registers as if they were data. More severely, on the right-hand side of the cluster, reflected data registers act upon right-moving data registers as program. Therefore, the state of the QCA is no longer a tensor product of the column states, but instead an entangled state supported by many columns grows from the right, by one column in each time step. However, none of that has an impact on the data register $|D_0\rangle$, which—as before—can be read out from column r after r transitions of the automaton.

III. CONCLUSION

This paper describes a quantum cellular automaton for universal quantum computation. The transition function from one time step to the next is generated by a four-qubit unitary transformation acting on Margolus cells of size 2×2. The program is encoded in the initial state of the system, and the automaton is left to its autonomous evolution from initialization to readout.

Coming back to our initially posed question, it is found that QCAs performing complex tasks in quantum information processing can indeed be constructed for compact cells and neighborhood schemes.

ACKNOWLEDGMENTS

The author would like to thank Pawel Wocjan and Sergey Bravyi for discussions. This work was supported by the National Science Foundation under Grant No. EIA-0086038.

[1] D. Jaksch, C. Bruder, J. I. Cirac, C. W. Gardiner, and P. Zoller, Phys. Rev. Lett. **81**, 3108 (1998).

[2] G. Birkl, F. B. J. Buchkremer, R. Dumke, and W. Ertmer, Opt. Commun. **191**, 67 (2001).

[3] J. Watrous, Proceedings of the 36th IEEE Symposium on Foundations of Computer Science, 1995, p. 528.

[4] W. van Dam, Masters thesis, University of Nijmegen, 1996.

[5] B. Schumacher and R. F. Werner, e-print quant-ph/0405174.

[6] S. Lloyd, Science **261**, 1569 (1993).

[7] S. C. Benjamin, Phys. Rev. A **64**, 054303 (2001).

[8] J. Levy, Phys. Rev. Lett. **89**, 147902 (2002).

[9] S. C. Benjamin, Phys. Rev. Lett. **88**, 017904 (2002).

[10] G. K. Brennen and J. E. Williams, Phys. Rev. A **68**, 042311 (2003).

[11] D. Janzing and P. Wocjan, Quant. Inf. Proc. **2**(2), 129 (2005).

[12] T. Toffoli and M. Margolus, Physica D **45**, 229 (1990).

[13] P. O. Boykin *et al.*, Inf. Process. Lett. **75**, 101 (2000).

[14] M. A. Nielsen and I. L. Chuang, Phys. Rev. Lett. **79**, 321 (1997).

[15] A. Yu. Vlasov, Proc. International Conference Physics and Control, St. Petersburg (2003), p. 861; e-print quant-ph/0311196; e-print quant-ph/0503230.

QUANTUM NETWORKS BASED ON CAVITY QED

H. MABUCHI, M. ARMEN, B. LEV, M. LONCAR, J. VUCKOVIC, H. J. KIMBLE,
J. PRESKILL, M. ROUKES, A. SCHERER
California Institute of Technology, Mail Code 12-33, Pasadena, CA, 91125, U.S.A.

S. J. VAN ENK
Lucent Technologies Bell Labs, 600-700 Mountain Ave., Murray Hill, NJ, 07974, U.S.A.

We review an ongoing program of interdisciplinary research aimed at developing hardware and protocols for quantum communication networks. Our primary experimental goals are to demonstrate *quantum state mapping* from storage/processing media (internal states of trapped atoms) to transmission media (optical photons), and to investigate a nanotechnology paradigm for cavity QED that would involve the integration of magnetic microtraps with photonic bandgap structures.

1 Introduction

No one can dispute that we live in an age of information; living in such an age, we experience an ever-increasing need for technology that allows us to share information in a secure, efficient, and reliable way. Quantum technologies show great potential for revolutionizing the methods by which we collect and distribute information, in diverse engineering contexts that range from computer architecture to the Internet. Seminal theoretical research in the field has identified a portfolio of tasks for which quantum methods are provably superior to their classical counterparts. For example, it has recently been shown that the communication complexity of a fundamental task such as appointment-scheduling can be drastically reduced through the use of quantum resources [1]. It is also known that the elementary protocol of quantum state teleportation [2] could provide a means for distributing cryptographic key with absolute and verifiable security [3], and that related methods could be used

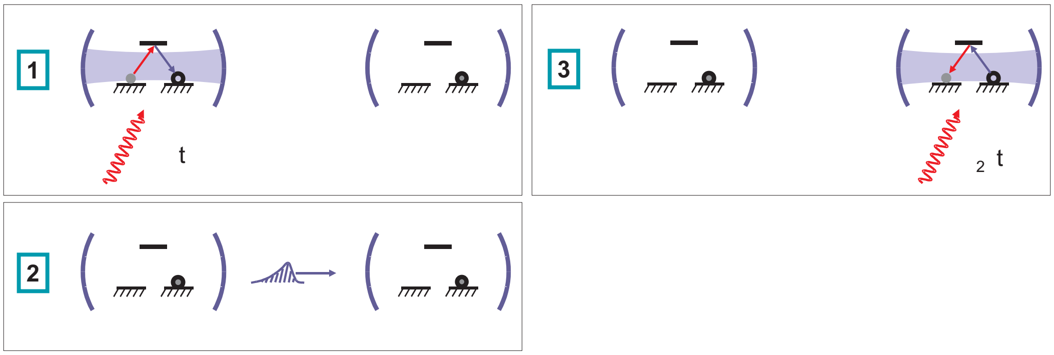

Figure 1. Transmission of quantum information between nodes in a quantum network. A qubit is initially stored in the internal state of an atom trapped within a high-finesse optical cavity, at the sending node (each node contains multiple atoms). 1: the atomic state is mapped to that of an optical photon via cavity QED, 2: the photon travels through a fiber to the receiving node, 3: the photonic state is mapped into that of a trapped atom at the receiving node. Multiple nodes connected in this fashion form a *quantum network*.

to enhance the capacity of noisy communication channels [4].

An ongoing program of research at Caltech focuses on development of the hardware and error correction protocols required to construct a *quantum network* (see Fig. 1). Here quantum nodes with memory and local processing capabilities will be connected by quantum communication channels that allow robust transmission of coherent quantum information among nodes of the network. Such a network would be capable of performing distributed quantum computations [5]. In our proposed implementation, trapped neutral atoms will provide quantum memory at each node of the network, and optical cavities will be utilized both to perform quantum gates and to transfer quantum information between nodes [6]. With a long-term view towards developing integrated and robust hardware for quantum nodes, much of our work is aimed at exploring a revolutionary new technical paradigm for cavity QED based on magnetic microtraps and optical photonic bandgap structures [7]. In the following sections, we first provide an overview of this new technical paradigm and then describe the quantum repeater protocol that will enable robust quantum communication in the presence of channel decoherence.

2 Nanotechnology for optical cavity QED with neutral atoms

During the past decade, advances in semiconductor crystal growth technique have led to the rapid development of optical microcavity devices. With the ultrahigh precision that can now be obtained over layer thicknesses, high reflectivity mirrors can easily be grown by depositing alternating layers of high- and low-index materials to define high-Q cavities in the vertical dimension. Recently, it has also become possible to microfabricate high reflectivity mirrors with *horizontal* orientation by etching periodic arrays of holes into a semiconductor substrate. These "photonic crystals" can be designed to fully suppress horizontal light propagation within certain frequency bands, called photonic bandgaps (see Fig. 2) [8,9].

When combined with high index-contrast slabs, in which the propagation of light is already confined to a plane, photonic bandgap mirrors can be used to confine light within "nanocavities" of extremely small volume. Such cavities can be produced simply by introducing defects into the photonic bandgap structure, for example by omitting one hole from the periodic array. The resonance wavelength of such a cavity can be lithographically defined by adjusting the precise geometry of the holes immediately surrounding the defect. In previous work this strategy has been employed to construct microcavity semiconductor lasers [10] with mode volumes as small as $2.5\,(\lambda/2n_{\mathrm{slab}})^3$.

Using the same fabrication techniques, it is also possible to guide, bend, filter, and sort light in 2-D photonic crystals. Such photonic waveguides could clearly be used as optical channels between nanocavities, and could also be used to define simple interferometers to combine cavity inputs/outputs. Tapered photonic waveguides could be pigtailed to standard optical fibers, as a means of bringing light into or out of the semiconductor slab. Using the techniques described above, we can easily envision fabricating semiconductor wafers in which multiple interconnected optical cavities are embedded at an areal density $\sim 10^6$ cm^{-2}. Such arrays of PBG nanocavities could replace the Fabry-Perot cavities that have been used in previous experiments on optical cavity QED with neutral atoms.

The basic parameter that measures coupling strength between an atom and an optical cavity is the so-called "vacuum Rabi frequency" $g \equiv \frac{d \cdot E_1}{2\hbar}$, where d is the atomic dipole-transition matrix element and E_1 is the electric field per photon in the cavity. To achieve

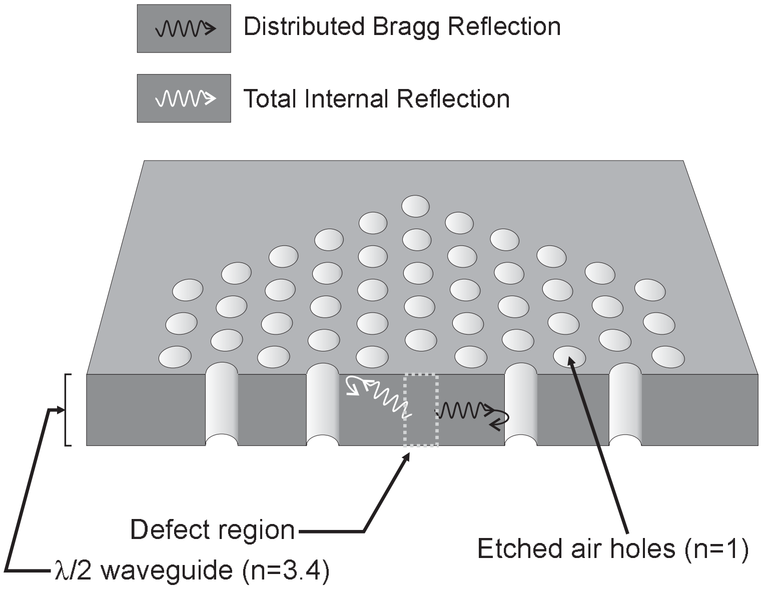

Figure 2. Schematic cross-section of the photonic crystal structure.

strong coupling we must have g sufficiently large compared to both the atomic dipole decay rate $\gamma_\perp$ and the cavity field decay rate κ. For the purpose of quantum information processing, we require that both the critical photon number m_0 and the critical atom number N_0 be less than one, where $m_0 = \frac{\gamma_\perp^2}{2g^2}$ and $N_0 = \frac{2\kappa\gamma_\perp}{g^2}$. As the dipole matrix element d is fixed by atomic structure, the only way to increase $g/\gamma_\perp$ is to construct cavities in which E_1 is as large as possible.

We have performed numerical calculations (via finite-difference time-domain modeling [12]) of the mode properties for several possible PBG defect cavities. In one case we have obtained $V_{\text{eff}} = 0.09\,(\lambda/2)^2$ together with $Q \approx 1.6 \times 10^4$. This particular geometry incorporates a central "defect" hole of reduced diameter $\sim$ 108 nm. To couple most strongly with the cavity field, an atom should be trapped at the center of this hole. While further optimization of the geometry may still be possible, these parameters already lead to $g \approx 5.6$ GHz with $\kappa = 11$ GHz, or $m_0 \approx 5.4 \times 10^{-8}$ photons and $N_0 \approx 1.8 \times 10^{-3}$ atoms.

In addition to the creation of semiconductor nanostructures, modern microfabrication techniques also allow the patterning of conducting wires and ferromagnetic materials at the $1 - 10$ μm scale. As a result, it should be possible to construct magnetic microtraps with field gradients on the order of 10^8 G/cm and field curvatures $\sim 10^8$ G/cm^2 [14,15]. With this magnitude of field curvature, *e.g.*, an Ioffe configuration trap would hold a Cs atom with $\eta \sim 0.35$ in the axial coordinate and $\eta \sim 0.035$ in the radial coordinates [14], and provide a well-defined bias field ~ 1 G at the trap center.

Our initial integration scheme will be to deposit micron-scale wires on the surface of a photonic crystal membrane, such that each PBG cavity is surrounded by a concentric microtrap. Fig. 3 shows one possible configuration. Current-carrying wires arranged in a

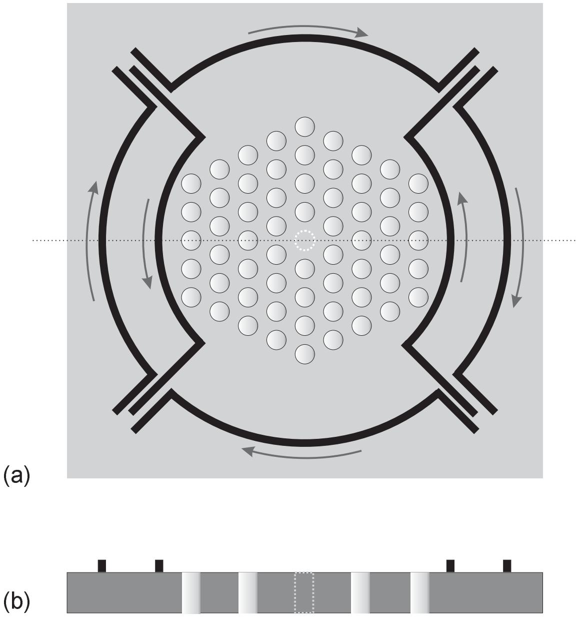

Figure 3. Schematic of an integrated PBG cavity and planar magnetic microtrap. (a) Top view showing arrangement of the current-carrying wires. Arrows indicate the direction of current flow. (b) Cross-section through the defect cavity (as indicated by the dashed line in (a)), showing wire deposition on the surface of the semiconductor slab.

suitable modification of Weinstein and Libbrecht's 'Ioffe *c*' configuration [14] can project a magnetic field with a stable minimum at the geometric center of the PBG cavity, such that one or more atoms could be confined within the defect hole and (as discussed above) would therefore experience strong coupling. A similar geometry can be envisioned for a microtrap based on permanent magnets, rather than current-carrying wires. This would involve the use of techniques for electroplating ferromagnetic material (such as nickel [16]) into selected holes around the perimeter of each PBG cavity.

3 Quantum repeater architecture

Any quantum communication scheme will have to deal with losses and other noise (such as phase shifts) in the quantum channel connecting the sending and receiving nodes. Unfortunately, standard quantum error correction schemes as developed for quantum computing will not be practical for two reasons. First, such schemes typically work only if the error probability is sufficiently small, and second, they would require a large overhead in qubits to protect a single qubit against one error. Here we review an error correction protocol that solves for photon absorption errors to all orders (i.e., it works irrespective of the error rate) and that nevertheless requires only a moderate overhead in resources. Subsequently we describe a quantum repeater scheme that allows one to reinforce the quantum signal at intermediate nodes, thus allowing communication over long distances.

Quantum error correction schemes require entangled states of at least 5 qubits to protect one qubit against a single general error. In the specific physical setup described in the present proposal, however, not all possible errors are equally likely to occur. In particular, whereas photon absorption is a common error, the inverse process, the spontaneous creation of a photon with a particular polarization and optical frequency is extremely unlikely. This fact allows one to encode the quantum information in such a way that the photon absorption error can be corrected to all orders with just two entangled atoms per node. Without going into the technical details (see [17,18]), we present here just the basic ideas.

1. The logical $|0\rangle$ and $|1\rangle$ are encoded in the absence and presence of a photon in a particular mode, respectively, so that the error $|0\rangle \mapsto |1\rangle$ has been eliminated.

2. We use an *auxiliary* qubit in the sending node that contains no information about the actual qubit we wish to communicate, to send a photon. This way, if that photon is absorbed, no information will be lost. This part of the protocol is repeated until we know that the photon arrived. Only then do we involve the qubit that contains the actual information.

3. In order to detect photon absorption, we do not have to monitor the environment. The auxiliary atom in the sending node is used twice: its state is communicated in two transmissions to two atoms in the receiving node. Between the two transmissions a NOT operation is applied (i.e., we interchange $|0\rangle \leftrightarrow |1\rangle$) to the sending atom. The two atoms receiving the information should, therefore, be in different states. Photon absorption can thus be unambiguously detected by measuring whether the two atoms are in the state $|0\rangle|0\rangle$.

4. As a bonus, the application of the NOT operation symmetrizes and thereby corrects for all systematic phase errors.

Two atoms per node are sufficient to achieve a high communication fidelity F (defined as the overlap between the actual and desired final state). If there is need for further correction of the remaining phase errors, one extra atom per node is needed [18].

The probability of photon absorption increases exponentially with the length of the communication channel. Thus, while the above error correction scheme in principle works just as well for large-distance communication, it would require an exponentially large number of transmissions. In order to reduce the number of transmissions, we need, just as for classical communication, intermediate nodes—quantum repeaters—where the signal is "amplified." Of course, since true amplification of quantum signals is not possible, the procedure used is more subtle than in the classical case, and is in fact a variant of standard entanglement purification schemes [19], modified to encompass the restrictions on the amount of physical resources.

Several quantum repeater schemes have been discussed in Ref. [20]. The most efficient scheme takes the form of a concatenated error correction code. It makes use of two simple sub-procedures.

1. Two pairs of imperfect EPR pairs of entangled qubits can be used to distill a single pair of *higher* fidelity between nodes A and B.

2. Two pairs of imperfect entangled states connecting nodes A with B, and B with C, resp., can be used to create a single EPR pair of *lower* fidelity between nodes A and C.

When one has more than one intermediate mode, repeating procedure 2 would lead to a fidelity that decreases exponentially with the total number of nodes. In order to achieve a certain minimum final fidelity, one has to periodically purify the entangled states obtained thus far with procedure 1. The whole protocol is then a concatenated procedure in that the purification has to be repeated at different levels: starting at the lowest level one purifies all EPR pairs between adjacent modes, at the next level one purifies the lower-fidelity EPR pairs between more distant nodes as gotten by procedure 2, and so on.

Acknowledgments

This research has been supported by the Caltech MURI Center for Quantum Networks.

References

1. H. Buhrman, R. Cleve, and A. Wigderson, LANL e-print quant-ph/9802040, http://xxx.lanl.gov.
2. C. H. Bennett, G. Brassard, C. Crepeau, R. Jozsa, A. Peres, and W. K. Wootters, Phys. Rev. Lett. **70**, 1895 (1993).
3. H.-K. Lo and H. F. Chau, Science **283**, 2050 (1999).
4. C. H. Bennett, P. W. Shor, J. A. Smolin, and A. V. Thapliyal, Phys. Rev. Lett. 85, 3081 (1999).
5. R. de Wolf, in press (2000).
6. J. I. Cirac, P. Zoller, H. J. Kimble, and H. Mabuchi, Phys. Rev. Lett. **78**, 3221 (1997).
7. J. Vuckovic, M. Loncar, H. Mabuchi, and A. Scherer, submitted to Phys. Rev. A (2000).
8. E. Yablonovitch, Phys. Rev. Lett. **58**, 2059 (1987).
9. S. John, Phys. Rev. Lett. **58**, 2486 (1987).
10. O. Painter, R. K. Lee, A. Scherer, A. Yariv, J. D. O'Brien, P. D. Dapkus, and I. Kim, Science **284**, 1819 (1999).
11. J. D. Joannopoulos, R. D. Meade, and J. N. Winn, *Photonic Crystals* (Princeton University Press, 1995).
12. J. Vuckovich, O. Painter, Y. Xu, A. Yariv, and A. Scherer, IEEE J. of Quantum Electronics **35**, 1168 (1999).
13. R. K. Lee, O. J. Painter, B. Kitzke, A. Scherer, and A. Yariv, Electronics Lett. **35**, 569 (1999).
14. J. D. Weinstein and K. G. Libbrecht, Phys. Rev. A **52**, 4004-4009 (1995).
15. M. Drndic, K. S. Johnson, J. H. Thywissen, M. Prentiss, and R. M. Westervelt, Appl. Phys. Lett. **72**, 2906-2908 (1998).
16. M. Todorovic, S. Schultz, J. Wong, and A. Scherer, Appl. Phys. Lett. **74**, 2516 (1999).
17. S.J. van Enk, J.I. Cirac and P. Zoller, Phys. Rev. Lett. **78**, 4293 (1997).
18. S.J. van Enk, J.I. Cirac and P. Zoller, Science **279**, 205 (1998).
19. C.H. Bennett, G. Brassard, S. Popescu, B. Schumacher, J.A. Smolin and W.K. Wootters, Phys. Rev. Lett. **76**, 722 (1996); D. Deutsch, A. Ekert, C. Macchiavello, S. Popescu and A. Sanpera, Phys. Rev. Lett. **77**, 2818 (1996).
20. W. Dür, H.J. Briegel, J.I. Cirac and P. Zoller, Phys. Rev. A **59**, 169 (1999).

PHYSICAL REVIEW A, VOLUME 64, 062301

Achievable rates for the Gaussian quantum channel

Jim Harrington* and John Preskill†
Institute for Quantum Information, California Institute of Technology, Pasadena, California 91125

(Received 17 May 2001; published 8 November 2001)

We study the properties of quantum stabilizer codes that embed a finite-dimensional protected code space in an infinite-dimensional Hilbert space. The stabilizer group of such a code is associated with a symplectically integral lattice in the phase space of $2N$ canonical variables. From the existence of symplectically integral lattices with suitable properties, we infer a lower bound on the quantum capacity of the Gaussian quantum channel that matches the one-shot coherent information optimized over Gaussian input states.

DOI: 10.1103/PhysRevA.64.062301 PACS number(s): 03.67.Lx

I. INTRODUCTION

A central problem in quantum information theory is to determine the quantum capacity of a noisy quantum channel—the maximum rate at which coherent quantum information may be transmitted through the channel and recovered with arbitrarily good fidelity [1,2]. A general solution to the corresponding problem for classical noisy channels was found by Shannon in the pioneering paper that launched classical information theory [3,4]. With the development of the theory of quantum error correction [5,6], considerable progress has been made toward characterizing the quantum channel capacity [7], but it remains less well understood than the classical capacity.

The asymptotic coherent information has been shown to provide an upper bound on the capacity [8,9] and a matching lower bound has been conjectured, but not proven [10]. Unfortunately, the coherent information is not subadditive [11], so that its asymptotic value is not easily computed. Therefore, it has been possible to verify the coherent information conjecture in just a few simple cases [12].

One quantum channel of considerable intrinsic interest is the Gaussian quantum channel, which might also be simple enough to be analytically tractable, thus providing a fertile testing ground for the general theory of quantum capacities. A simple analytic formula for the capacity of the Gaussian classical channel was found by Shannon [3,4]. The Gaussian quantum channel was studied by Holevo and Werner [13], who computed the one-shot coherent information for Gaussian input states, and derived an upper bound on the quantum capacity.

Lower bounds on the quantum capacity of the Gaussian quantum channel were established by Gottesman, Kitaev, and Preskill [14]. They developed quantum error-correcting codes that protect a finite-dimensional subspace of an infinite-dimensional Hilbert space, and showed that these codes may be used to transmit high-fidelity quantum information at a nonzero asymptotic rate. In this paper, we continue the study of the Gaussian quantum channel begun in [14]. Our main result is that the coherent information computed by Holevo and Werner is in fact an achievable rate. This result lends nontrivial support to the coherent information conjecture.

We define the Gaussian quantum channel and review the results of Holevo and Werner [13] in Sec. II. In Sec. III, we describe the stabilizer codes for continuous quantum variables introduced in [14], which are based on the concept of a symplectically integral lattice embedded in phase space. In Secs. IV and V, we apply these codes to the Gaussian quantum channel, and calculate an achievable rate arising from lattices that realize efficient packings of spheres in high dimensions. This achievable rate matches the one-shot coherent information I_Q of the channel in cases where 2^{I_Q} is an integer. Rates achieved with concatenated coding are calculated in Sec. VI; these fall short of the coherent information but come close. In Sec. VII, we consider the Gaussian classical channel, and again find that concatenated codes achieve rates close to the capacity. Section VIII contains some concluding comments about the quantum capacity of the Gaussian quantum channel.

II. THE GAUSSIAN QUANTUM CHANNEL

The Gaussian quantum channel is a natural generalization of the Gaussian classical channel. In the classical case, we consider a channel such that the input x and the output y are real numbers. The channel applies a displacement to the input by distance ξ,

$$y = x + \xi, \tag{1}$$

where ξ is a Gaussian random variable with mean zero and variance σ^2; the probability distribution governing ξ is

$$P(\xi) = \frac{1}{\sqrt{2\pi\sigma^2}} e^{-\xi^2/2\sigma^2}. \tag{2}$$

Similarly, acting on a quantum system described by canonical variables q and p that satisfy the commutation relation $[q,p] = i\hbar$, we may consider a quantum channel that applies a phase-space displacement described by the unitary operator

$$D(\alpha) = \exp(\alpha a^\dagger + \alpha^* a), \tag{3}$$

where α is a complex number, $[a, a^\dagger] = 1$, and q, p may be expressed in terms of a and $a^\dagger$ as

---

*Email address: jimh@theory.caltech.edu
†Email address: preskill@theory.caltech.edu

1050-2947/2001/64(6)/062301(10)/$20.00

©2001 The American Physical Society

$$q=\sqrt{\frac{\hbar}{2}}(a+a^{\dagger}), \quad p=-i\sqrt{\frac{\hbar}{2}}(a-a^{\dagger}). \tag{4}$$

This quantum channel is Gaussian if α is a complex Gaussian random variable with mean zero and variance $\tilde{\sigma}^2$. In that case, the channel is the superoperator (trace-preserving completely positive map) $\mathcal{E}$ that acts on the density operator ρ according to

$$\rho\rightarrow\mathcal{E}(\rho)=\frac{1}{\pi\tilde{\sigma}^2}\int d^2\alpha\, e^{-|\alpha|^2/\tilde{\sigma}^2}D(\alpha)\rho D(\alpha)^{\dagger}. \tag{5}$$

In other words, the position q and momentum p are displaced independently,

$$q\rightarrow q+\xi_q, \quad p\rightarrow p+\xi_p, \tag{6}$$

where ξ_q and ξ_p are real Gaussian random variables with mean zero and variance $\sigma^2=\hbar\tilde{\sigma}^2$.

To define the capacity, we consider a channel's nth extension. In the classical case, a message is transmitted consisting of the n real variables

$$\vec{x}=(x_1,x_2,\ldots,x_n), \tag{7}$$

and the channel applies the displacement

$$\vec{x}\rightarrow\vec{x}+\vec{\xi}, \quad \vec{\xi}=(\xi_1,\xi_2,\ldots,\xi_n), \tag{8}$$

where the ξ_i's are independent Gaussian random variables, each with mean zero and variance σ^2. A code consists of a finite number m of n-component input signals

$$\vec{x}^{(a)}, \quad a=1,2,\ldots,m \tag{9}$$

and a decoding function that maps output vectors to the index set $\{1,2,\ldots,m\}$. We refer to n as the *length* of the code.

If the input vectors were unrestricted, then for fixed σ^2 we could easily construct a code with an arbitrarily large number of signals m and a decoding function that correctly identifies the index (a) of the input with an arbitrarily small probability of error; even for $n=1$, we merely choose the distance between signals to be large compared to σ. To obtain an interesting notion of capacity, we impose a constraint on the *average power* of the signal,

$$\frac{1}{n}\sum_i (x_i^{(a)})^2\leq P, \tag{10}$$

for each a. We say that a rate R (in bits) is achievable with power constraint P if there is a sequence of codes satisfying the constraint such that the βth code in the sequence contains m_β signals with length n_β, where

$$R=\lim_{\beta\rightarrow\infty}\frac{1}{n_\beta}\log_2 m_\beta, \tag{11}$$

and the probability of a decoding error vanishes in the limit $\beta\rightarrow\infty$. The capacity of the channel with power constraint P is the supremum of all achievable rates.

The need for a constraint on the signal power to define the capacity of the Gaussian classical channel may be understood on dimensional grounds. The classical capacity (in bits) is a dimensionless function of the variance σ^2, but σ^2 has dimensions. Another quantity with the dimensions of σ^2 is needed to construct a dimensionless variable, and the power P fills this role.

In contrast, no power constraint is needed to define the quantum capacity of the quantum channel. Rather, Planck's constant $\hbar$ enables us to define a dimensionless variance $\tilde{\sigma}^2=\sigma^2/\hbar$, and the capacity is a function of this quantity. In the quantum case, a code consists of an encoding superoperator that maps an m-dimensional Hilbert space $\mathcal{H}_m$ into the infinite-dimensional Hilbert space $\mathcal{H}^{\otimes N}$ of N canonical quantum systems, and a decoding superoperator that maps $\mathcal{H}^{\otimes N}$ back to $\mathcal{H}_m$. We say that the rate R (in qubits) is achievable if there is a sequence of codes such that

$$R=\lim_{\beta\rightarrow\infty}\frac{1}{N_\beta}\log_2 m_\beta, \tag{12}$$

where arbitrary states in $\mathcal{H}_m$ may be recovered with a fidelity that approaches 1 as $\beta\rightarrow\infty$. The quantum capacity C_Q of the channel is defined as the supremum of all achievable rates.

Holevo and Werner [13] studied a more general Gaussian channel that includes damping or amplification as well as displacement. However, we will confine our attention in this paper to channels that apply only displacements. Holevo and Werner derived a general upper bound on the quantum capacity by exploiting the properties of the "diamond norm" (norm of complete boundedness) of a superoperator. The diamond norm is defined as follows: First, we define the trace norm of an operator X as

$$\|X\|_{\mathrm{tr}}\equiv\mathrm{tr}\sqrt{X^{\dagger}X}, \tag{13}$$

which for a self-adjoint operator is just the sum of the absolute values of the eigenvalues. Then a norm of a superoperator $\mathcal{E}$ may be defined as

$$\|\mathcal{E}\|_{\mathrm{so}}=\sup_{X\neq0}\frac{\|\mathcal{E}(X)\|_{\mathrm{tr}}}{\|X\|_{\mathrm{tr}}}. \tag{14}$$

The superoperator norm is not stable with respect to appending an ancillary system on which $\mathcal{E}$ acts trivially. Thus, we define the diamond norm of $\mathcal{E}$ as

$$\|\mathcal{E}\|_{\diamond}=\sup_n\|\mathcal{E}\otimes I_n\|_{\mathrm{so}}, \tag{15}$$

where I_n denotes the n-dimensional identity operator. (This supremum is always attained for some n no larger than the dimension of the Hilbert space on which $\mathcal{E}$ acts.) Holevo and Werner showed that the quantum capacity obeys the upper bound

$$C_Q(\mathcal{E})\leq\log_2\|\mathcal{E}\circ T\|_{\diamond}, \tag{16}$$

where T is the transpose operation defined with respect to some basis. In the case of the Gaussian quantum channel, they evaluated this expression, obtaining

$$C_Q(\sigma^2) \leqslant \log_2(\hbar/\sigma^2) \tag{17}$$

for $\hbar/\sigma^2 > 1$, and $C_Q(\sigma^2)=0$ for $\hbar/\sigma^2 \leqslant 1$.

Holevo and Werner [13] also computed the *coherent information* of the Gaussian quantum channel for a Gaussian input state. To define the coherent information of the channel $\mathcal{E}$ with input density operator ρ, one introduces a reference system R and a *purification* of ρ, a pure state $|\Phi\rangle$ such that

$$\mathrm{tr}_R(|\Phi\rangle\langle\Phi|)=\rho. \tag{18}$$

Then the coherent information I_Q is

$$I_Q(\mathcal{E},\rho)=S(\mathcal{E}(\rho))-S(\mathcal{E}\otimes I_R(|\Phi\rangle\langle\Phi|)), \tag{19}$$

where S denotes the Von Neumann entropy,

$$S(\rho)=-\mathrm{tr}(\rho \log_2 \rho). \tag{20}$$

It is *conjectured* [10,8,9] that the quantum capacity is related to the coherent information by

$$C_Q(\mathcal{E})=\lim_{n\to\infty}\frac{1}{n}C_n(\mathcal{E}), \tag{21}$$

where

$$C_n(\mathcal{E})=\sup_\rho I_Q(\mathcal{E}^{\otimes n},\rho). \tag{22}$$

Unlike the mutual information that defines the classical capacity, the coherent information is not subadditive in general, and therefore, the quantum capacity need not coincide with the "one-shot" capacity C_1. Holevo and Werner showed that for the Gaussian quantum channel, the supremum of I_Q over Gaussian input states is

$$(I_Q)_{\max}=\log_2(\hbar/e\sigma^2), \tag{23}$$

(where $e=2.71828, \ldots,$) for $\hbar/e\sigma^2>1$, and $(I_Q)_{\max}=0$ for $\hbar/e\sigma^2 \leqslant 1$. According to the coherent-information conjecture, Eq. (23) should be an achievable rate.

III. QUANTUM ERROR-CORRECTING CODES FOR CONTINUOUS QUANTUM VARIABLES

The lattice codes developed in [14] are stabilizer codes [15,16] that embed a finite-dimensional code space in the infinite-dimensional Hilbert space of N "oscillators," a system described by $2N$ canonical variables $q_1,q_2, \ldots q_N,p_1,p_2, \ldots ,p_N$. That is, the code space is the simultaneous eigenstate of $2N$ commuting unitary operators, the generators of the code's stabilizer group. Each stabilizer generator is a *Weyl operator*, a displacement in the $2N$-dimensional phase space.

Such displacements may be parametrized by $2N$ real numbers $\alpha_1,\alpha_2, \ldots ,\alpha_N,\beta_1,\beta_2, \ldots ,\beta_N$, and expressed as

$$U(\alpha,\beta)=\exp\left[i\sqrt{2\pi}\left(\sum_{i=1}^{N}\alpha_i p_i+\beta_i q_i\right)\right]. \tag{24}$$

Two such operators obey the commutation relation

$$U(\alpha,\beta)U(\alpha',\beta')=e^{2\pi i\omega(\alpha\beta,\alpha'\beta')}U(\alpha',\beta')U(\alpha,\beta), \tag{25}$$

where

$$\omega(\alpha\beta,\alpha'\beta')\equiv\alpha\cdot\beta'-\alpha'\cdot\beta \tag{26}$$

is the symplectic form. Thus, Weyl operators commute if and only if their symplectic form is an integer.

The $2N$ generators of a stabilizer code are commuting Weyl operators

$$U(\alpha^{(a)},\beta^{(a)}), \quad a=1,2, \ldots ,2N. \tag{27}$$

Thus, the elements of the stabilizer group are in one-to-one correspondence with the points of a lattice $\mathcal{L}$ generated by the $2N$ vectors $v^{(a)}=(\alpha^{(a)},\beta^{(a)})$. These vectors may be assembled into the generator matrix M of $\mathcal{L}$ given by

$$M=\begin{pmatrix} v^{(1)} \\ v^{(2)} \\ \cdot \\ \cdot \\ v^{(2N)} \end{pmatrix}. \tag{28}$$

Then the requirement that the stabilizer generators commute, through Eq. (25), becomes the condition that the antisymmetric matrix

$$A=M\omega M^T \tag{29}$$

has integral entries, where M^T denotes the transpose of M, ω is the $2N\times 2N$ matrix

$$\omega=\begin{pmatrix} 0 & I_N \\ -I_N & 0 \end{pmatrix}, \tag{30}$$

and I_N is the $N\times N$ identity matrix. If the generator matrix M of a lattice $\mathcal{L}$ has the property that A is an integral matrix, then we will say that the lattice $\mathcal{L}$ is *symplectically integral*.

Encoded operations that preserve the code subspace are associated with the code's *normalizer* group, the group of phase-space translations that commute with the code stabilizer. The generator matrix of the normalizer is a matrix $M^\perp$ that may be chosen to be

$$M^\perp=A^{-1}M, \tag{31}$$

so that

$$M^\perp\omega M^T=I; \tag{32}$$

and

$$(M^\perp)\omega(M^\perp)^T=(A^{-1})^T. \tag{33}$$

We will refer to the lattice generated by $M^{\perp}$ as the *symplectic dual* $\mathcal{L}^{\perp}$ of the lattice $\mathcal{L}$.

Another matrix that generates the same lattice as M (and therefore defines a different set of generators for the same stabilizer group) is

$$M' = RM, \tag{34}$$

where R is an integral matrix with $\det R = \pm 1$. This replacement changes the matrix A according to

$$A \to RAR^T. \tag{35}$$

By Gaussian elimination, an R may be constructed such that

$$A = \begin{pmatrix} 0 & D \\ -D & 0 \end{pmatrix}, \tag{36}$$

and

$$(A^{-1})^T = \begin{pmatrix} 0 & D^{-1} \\ -D^{-1} & 0 \end{pmatrix}, \tag{37}$$

where D is a positive diagonal integral $N \times N$ matrix. In the important special case of a *symplectically self-dual* lattice, both A and $(A^{-1})^T$ are integral matrices; therefore $D = D^{-1}$ and the standard form of A is

$$A = \begin{pmatrix} 0 & I_N \\ -I_N & 0 \end{pmatrix} = \omega. \tag{38}$$

Hence, the generator matrix of a symplectically self-dual lattice may be chosen to be a real symplectic matrix: $M \omega M^T = \omega$.

If the lattice is rotated, then the generator matrix is transformed as

$$M \to MO, \tag{39}$$

where O is an orthogonal matrix. Therefore, it is convenient to characterize a lattice with its Gram matrix

$$G = MM^T, \tag{40}$$

which is symmetric, positive, and rotationally invariant. In the case of a symplectically self-dual lattice, the Gram matrix G may be chosen to be symplectic, and two symplectic Gram matrices G and G' describe the same lattice if

$$G' = RGR^T, \tag{41}$$

where R is symplectic and integral. Therefore, the moduli space of symplectically self-dual lattices in $2N$ dimensions may be represented as

$$\mathcal{A}_N = H(2N)/Sp(2N,\mathbb{Z}), \tag{42}$$

where $H(2N)$ denotes the space of real symplectic positive $2N \times 2N$ matrices of determinant 1 and $SP(2N,\mathbb{Z})$ denotes the space of integral symplectic $2N \times 2N$ matrices. The space $\mathcal{A}_N$ may also be identified as the moduli space of principally polarized abelian varieties in complex dimension N [17].

The encoded operations that preserve the code space but act trivially within the code space comprise the quotient group $\mathcal{L}^{\perp}/\mathcal{L}$. The order of this group, the ratio of the volume of the unit cell of $\mathcal{L}$ to that of $\mathcal{L}^{\perp}$, is m^2, where m is the dimension of the code space. The volume of the unit cell of $\mathcal{L}$ is $|\det M| = |\det A|^{1/2}$ and the volume of the unit cell of $\mathcal{L}^{\perp}$ is $|\det M^{\perp}| = |\det A|^{-1/2}$; therefore, the dimension of the code space is

$$m = |\mathrm{Pf}\, A| = |\det M| = \det D, \tag{43}$$

where $\mathrm{Pf}\, A$ denotes the Pfaffian of A, the square root of its determinant. Thus, a symplectically self-dual lattice, for which $|\det M| = |\det M^{\perp}| = 1$, corresponds to a code with a one-dimensional code space. Given a $2N \times 2N$ generator matrix M of a symplectically self-dual lattice, we can rescale it as

$$M \to \sqrt{\lambda} M, \tag{44}$$

where λ is an integer, to obtain the generator matrix of a symplectically integral lattice corresponding to a code of dimension

$$m = \lambda^N. \tag{45}$$

The rate of this code, then, is

$$R = \log_2 \lambda. \tag{46}$$

When an encoded state is subjected to the Gaussian quantum channel, a phase-space displacement

$$(\vec{q},\vec{p}) \to (\vec{q},\vec{p}) + (\vec{\xi}_q, \vec{\xi}_p) \tag{47}$$

is applied. To diagnose and correct this error, the eigenvalues of all stabilizer generators are measured, which determines the value of $(\vec{\xi}_q, \vec{\xi}_p)$ modulo the normalizer lattice $\mathcal{L}^{\perp}$. To recover, a displacement of minimal length is applied that returns the stabilizer eigenvalues to their standard values, and so restores the quantum state to the code space. We may associate with the origin of the normalizer lattice its *Voronoi cell*, the set of points in $\mathbb{R}^{2N}$ that are closer to the origin than to any other lattice site. Recovery is successful if the applied displacement lies in this Voronoi cell. Thus, we may estimate the likelihood of a decoding error by calculating the probability that the displacement lies outside the Voronoi cell.

IV. ACHIEVABLE RATES FROM EFFICIENT SPHERE PACKINGS

One way to establish an achievable rate for the Gaussian quantum channel is to choose a normalizer lattice $\mathcal{L}^{\perp}$ whose shortest nonzero vector is sufficiently large. In this section, we calculate an achievable rate by demanding that the Voronoi cell surrounding the origin contain all typical displacements of the origin in the limit of large N. In Sec. V, we will use a more clever argument to improve our estimate of the rate.

The volume of a sphere with unit radius in n dimensions is

$$V_n=\frac{\pi^{n/2}}{\Gamma\left(\frac{n}{2}+1\right)},\tag{48}$$

and from the Stirling approximation we find that

$$V_n\leqslant\left(\frac{2\pi e}{n}\right)^{n/2}.\tag{49}$$

It was shown by Minkowski [18,19], that lattice sphere packings exist in n dimensions that fill a fraction at least $1/2^{(n-1)}$ of space. Correspondingly, if the lattice is chosen to be unimodular, so that its unit cell has unit volume, then kissing spheres centered at the lattice sites may be chosen to have a radius r_n such that

$$V_n(r_n)^n\geqslant 2^{-(n-1)},\tag{50}$$

or

$$r_n^2\geqslant\frac{1}{4}(2/V_n)^{2/n}\geqslant\frac{n}{8\pi e}.\tag{51}$$

This lower bound on the efficiency of sphere packings has never been improved in the nearly 100 years since Minkowski's result. More recently, Buser and Sarnak [17] have shown that this same lower bound applies to lattices that are symplectically self dual.

Now consider the case of $n=2N$-dimensional phase space. For sufficiently large n, the channel will apply a phase-space translation by a distance that with high probability will be less than $\sqrt{n(\sigma^2+\varepsilon)}$, for any positive ε. Therefore, a code that may correct a shift this large will correct all likely errors. What rate can such a code attain? If the code is a lattice stabilizer code, and the dimension of the code space is m, then the unit cell of the code's normalizer lattice has volume

$$\Delta=\frac{1}{m}\times(2\pi\hbar)^N.\tag{52}$$

Nonoverlapping spheres centered at the sites of the normalizer lattice may be chosen to have radius $r=\sqrt{n(\sigma^2+\varepsilon)}$, where

$$\left(\frac{2\pi e}{n}\right)^{n/2}[n(\sigma^2+\varepsilon)]^{n/2}\geqslant\frac{1}{m}\times 2^{-n}\times(2\pi\hbar)^{n/2},\tag{53}$$

or

$$m\geqslant\left(\frac{\hbar}{4e(\sigma^2+\varepsilon)}\right)^N.\tag{54}$$

The error probability becomes arbitrarily small for large N if Eq. (54) is satisfied, for any positive ε. We conclude that the rate

$$R\equiv\frac{1}{N}\log_2 m=\log_2\left(\frac{\hbar}{4e\sigma^2}\right),\tag{55}$$

is achievable, provided $\hbar/4e\sigma^2\geqslant 1$. However, as noted in Sec. III, the rates that may be attained by this construction (rescaling of a symplectically self-dual lattice) are always of the form $\log_2\lambda$, where λ is an integer.

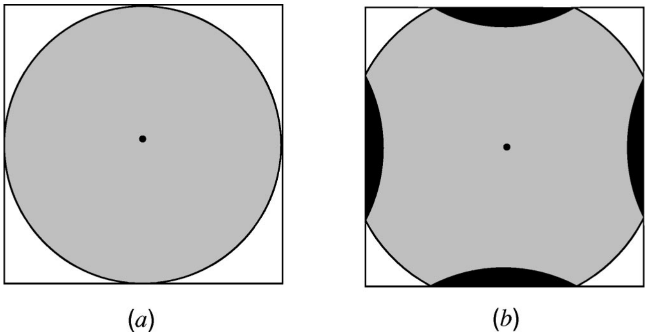

FIG. 1. Two ways to estimate the rate achieved by a lattice code. Each site of the normalizer lattice has a Voronoi cell (represented here by a square) containing all points that are closer to that site than any other site. Displacements that move a site to a position within its Voronoi cell may be corrected. The volume of the Voronoi cell determines the rate of the code. In (a), the ball containing typical displacements lies within the cell, so that the error probability is small. In (b), the ball of typical displacements is not completely contained within the cell, but the region where neighboring balls overlap (shown in black) has a small volume, so that the error probability is still small.

V. IMPROVING THE RATE

The achievable rate found in Eq. (55) falls two qubits short of the coherent information Eq. (23). We will now show that this gap may be closed by using tighter estimates of the error probability. We established Eq. (55) by filling phase space with nonoverlapping spheres, which is overly conservative. It is acceptable for the spheres to overlap, as long as the overlaps occupy an asymptotically negligible fraction of the total volume, as suggested in Fig. 1.

Our improved estimate applies another result obtained by Buser and Sarnak [17]. They note that the moduli space of symplectically self-dual lattices is compact and equipped with a natural invariant measure. Therefore, it makes sense to consider averaging over all lattices. Denote by $\langle\cdot\rangle$ the average over all symplectically self-dual lattices with specified dimension $n=2N$, and let $f(x)$ denote an integrable rotationally invariant function of the vector x (that is a function of the length $|x|$ of x). Then, Buser and Sarnak [17] show that

$$\left\langle\sum_{x\in\mathcal{L}\setminus\{0\}}f(x)\right\rangle=\int f(x)d^nx.\tag{56}$$

(Note that the sum is over all *nonzero* vectors in the lattice $\mathcal{L}$.) It follows that there must exist a *particular* symplectically self-dual lattice $\mathcal{L}$ such that

$$\sum_{x\in\mathcal{L}\setminus\{0\}}f(x)\leqslant\int f(x)d^nx.\tag{57}$$

The statement that a *unimodular* lattice exists that satisfies Eq. (57) is the well-known Minkowski-Hlawka theorem [19]. Buser and Sarnak established the stronger result that the lattice may be chosen to be symplectically self dual.

We may use this result to bound the probability of a decoding error, and establish that a specified rate is achievable. Our argument will closely follow de Buda [20], who performed a similar analysis of lattice codes for the Gaussian classical channel. However, the quantum case is considerably easier to analyze, because we can avoid complications arising from the power constraint [21–23].

A decoding error occurs if the channel displaces the origin to a point outside the Voronoi cell centered at the origin. The Voronoi cell has a complicated geometry, so that the error probability is not easy to analyze. But, we may simplify the analysis with a trick [20]. Imagine drawing a sphere with radius

$$a=\sqrt{n(\sigma^2+\varepsilon)} \tag{58}$$

around each lattice site, where $\varepsilon>0$; this value of a is chosen so that the typical displacement introduced by the channel has a length less than a; the probability of a shift larger than a thus becomes negligible for large n. It may be that these spheres overlap. However, a vector that is contained in the sphere centered at the origin, and is not contained in the sphere centered at any other lattice site, must be closer to the origin than any other lattice site. Therefore, the vector is contained in the origin's Voronoi cell, and is a shift that may be corrected successfully. (See Fig. 1.)

Hence (ignoring the possibility of an atypical shift by $\xi>a$) we can upper bound the probability of error by estimating the probability that the shift moves any other lattice site into the sphere of radius a around the origin. We then find

$$P_{\text{error}}\leqslant\sum_{x\in\mathcal{L}^{\perp}\setminus\{0\}}\int_{|r|\leqslant a}P(x-r)d^nr, \tag{59}$$

where $P(\xi)$ denotes the probability of a displacement by ξ.

The Buser-Sarnak theorem [17] tells us that there exists a lattice whose unit cell has volume Δ, and which is related by rescaling to a symplectically self-dual lattice, such that

$$P_{\text{error}}\leqslant\frac{1}{\Delta}\int d^nx\int_{|r|\leqslant a}P(x-r)d^nr; \tag{60}$$

by interchanging the order of integration, we find that

$$P_{\text{error}}\leqslant\frac{1}{\Delta}V_na^n, \tag{61}$$

the ratio of the volume of the n-dimensional sphere of radius a to the volume of the unit cell.

Now the volume Δ of the unit cell of the normalizer lattice $\mathcal{L}^{\perp}$, and the dimension m of the code space, are related by

$$\Delta=(2\pi\hbar)^Nm^{-1}=(2\pi\hbar\times2^{-R})^N, \tag{62}$$

where R is the rate, and we may estimate the volume of the sphere as

$$V_na^n\leqslant\left(\frac{2\pi e}{n}\right)^{n/2}[n(\sigma^2+\varepsilon)]^{n/2}, \tag{63}$$

where $n=2N$. Thus, we conclude that

$$P_{\text{error}}\leqslant\left(\frac{e(\sigma^2+\varepsilon)}{\hbar}\times2^R\right)^N. \tag{64}$$

Therefore, the error probability becomes small for large N for any rate R such that

$$R<\log_2\left(\frac{\hbar}{e(\sigma^2+\varepsilon)}\right), \tag{65}$$

where ε may be arbitrarily small. We conclude that the rate

$$R=\log_2\left(\frac{\hbar}{e\sigma^2}\right) \tag{66}$$

is achievable in the limit $N\to\infty$, provided that $\hbar/e\sigma^2>1$. This rate matches the optimal value Eq. (23) of the one-shot coherent information for Gaussian inputs. We note, again, that the rates that we obtain from rescaling a symplectically self-dual lattice are restricted to $R=\log_2\lambda$, where λ is an integer. Thus, for specified σ^2, the achievable rate that we have established is really the maximal value of

$$R=\log_2\lambda,\quad \lambda\in\mathbb{Z}, \tag{67}$$

such that the positive integer λ satisfies

$$\lambda<\frac{\hbar}{e\sigma^2}. \tag{68}$$

VI. ACHIEVABLE RATES FROM CONCATENATED CODES

Another method for establishing achievable rates over the Gaussian quantum channel was described in [14], based on *concatenated coding*. In each of N "oscillators" described by canonical variables p_i and q_i, a d-dimensional system ("qudit") is encoded that is protected against sufficiently small shifts in p_i and q_i. The encoded qudit is associated with a square lattice in two-dimensional phase space. Then, a stabilizer code is constructed that embeds a k-qudit code space in the Hilbert space of N qudits; these k encoded qudits are protected if a sufficiently small fraction of the N qudits are damaged. Let us compare the rates achieved by concatenated codes to the rates achieved with codes derived from efficient sphere packings.

We analyze the effectiveness of concatenated codes in two stages. First, we consider how likely each of the N qudits is to sustain damage if the underlying oscillator is subjected to the Gaussian quantum channel. The area of the unit cell of the two-dimensional square normalizer lattice that represents the encoded operations acting on the qudit is $2\pi\hbar/d$, and the minimum distance between lattice sites is $\delta=\sqrt{2\pi\hbar/d}$. A displacement of q by $a\delta$, where a is an integer, is the operation X^a acting on the code space, and a displacement of p by $b\delta$ is the operation Z^b, where X and Z are the Pauli operators acting on the qudit; these act on a basis $\{|j\rangle, j=0,1,2,\ldots,d-1\}$ for the qudit according to

$$X:|j\rangle \to |j+1 \pmod d\rangle,$$
$$Z:|j\rangle \to \omega^j|j\rangle, \tag{69}$$

where $\omega=\exp(2\pi i/d)$.

Shifts in p or q may be corrected successfully provided that they satisfy

$$|\Delta q|<\delta/2=\sqrt{\frac{\pi\hbar}{2d}}, \quad |\Delta p|<\delta/2=\sqrt{\frac{\pi\hbar}{2d}}. \tag{70}$$

If the shifts in q and p are Gaussian random variables with variance σ^2, then the probability that a shift causes an uncorrectable error is no larger than the probability that the shift exceeds $\sqrt{\pi\hbar/2d}$, or

$$p_X,p_Z \leq 2\frac{1}{\sqrt{2\pi\sigma^2}}\int_{\sqrt{\pi\hbar/2d}}^{\infty} dx\, e^{-x^2/2\sigma^2}$$
$$=\mathrm{erfc}(\sqrt{\pi\hbar/4d\sigma^2}), \tag{71}$$

where erfc denotes the complementary error function. Here, p_X is the probability of an "X error" acting on the qudit, of the form X^a for $a\not\equiv 0 \pmod d$, and p_Z denotes the probability of a "Z error" of the form Z^b for $b\not\equiv 0 \pmod d$. The X and Z errors are uncorrelated, and errors with $a,b=\pm 1$ are much more likely than errors with $|a|,|b|>1$. By choosing $d\sim\hbar/\sigma^2$, we may achieve a small error probability for each oscillator.

The second stage of the argument is to determine the rate that may be achieved by a qudit code if p_X,p_Z satisfy Eq. (71). We will consider codes of the Calderbank-Shor-Steane (CSS) type, for which the correction of X errors and Z errors may be considered separately [24,25]. A CSS code is a stabilizer code, in which each stabilizer generator is either a tensor product of I's and powers of Z (measuring these generators diagnoses the X errors) or a tensor product of I's and powers of X (for diagnosing the Z errors).

We can establish an achievable rate by averaging the error probability over CSS codes; we give only an informal sketch of the argument. Suppose that we fix the block size N and the number of encoded qudits k. Now select the generators of the code's stabilizer group at random. About half of the $N-k$ generators are of the Z type and about half are of the X type. Thus, the number of possible values for the eigenvalues of the generators of each type is about

$$d^{\,(N-k)/2}. \tag{72}$$

Now, we can analyze the probability that an uncorrectable X error afflicts the encoded quantum state (the probability of an uncorrectable Z error is analyzed in exactly the same way). Suppose that X errors act independently on the N qudits in the block, with a probability of error per qudit of p_X. Thus, for large N, the typical number of damaged qudits is close to p_XN. A damaged qudit may be damaged in any of $d-1$ different ways [X^a, where $a=1,2,\ldots,(d-1)$]. We will suppose, pessimistically, that all $d-1$ shifts of the qudit are equally likely. The actual situation that arises in our concatenated coding scheme is more favorable—small values of $|a|$ are more likely—but our argument will not exploit this feature.

Thus, with high probability, the error that afflicts the block will belong to a typical set of errors that contains a number of elements close to

$$N_{\rm typ}\sim\binom{N}{Np_X}(d-1)^{Np_X}\sim d^{N[H_d(p_X)+p_X\log_d(d-1)]}, \tag{73}$$

where

$$H_d(p)=-p\log_d p-(1-p)\log_d(1-p). \tag{74}$$

If a particular typical error occurs, then recovery will succeed as long as there is no other typical error that generates the same error syndrome. It will be highly unlikely that another typical error has the same syndrome as the actual error, provided that the number of possible error syndromes $d^{(N-k)/2}$ is large compared to the number of typical errors. Therefore, the X errors may be corrected with high probability for

$$\frac{1}{2}\left(1-\frac{k}{N}\right)>\frac{1}{N}\log_d N_{\rm typ}\sim H_d(p_X)+p_X\log_d(d-1), \tag{75}$$

or for a rate R_d in qudits satisfying

$$R_d\equiv\frac{k}{N}<1-2H_d(p_X)-2p_X\log_d(d-1). \tag{76}$$

Similarly, the Z errors may be corrected with high probability by a random CSS code if the rate satisfies

$$R_d<1-2H_d(p_Z)-2p_Z\log_d(d-1). \tag{77}$$

Converted to qubits, the rate becomes

$$R=(\log_2 d)R_d. \tag{78}$$

Under these conditions, the probability of error averaged over CSS codes becomes arbitrarily small for N large. It follows that there is a particular sequence of CSS codes with rate approaching Eqs. (76)–(78), and error probability going to zero in the limit $N\to\infty$.

For given σ^2, the optimal rate that may be attained by concatenating a code that encodes a qudit in a single oscillator with a random CSS code, is found by estimating p_X and p_Z using Eq. (71) and then choosing d to maximize the rate R given by Eqs. (76)–(78). The results are shown in Fig. 2. This rate (in qubits) may be expressed as

$$R=\log_2(C^2\hbar/\sigma^2), \tag{79}$$

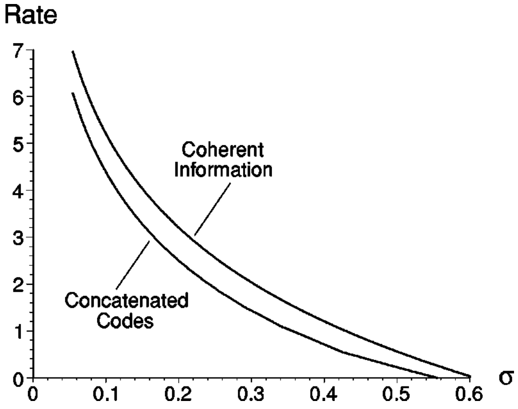

FIG. 2. Rates achieved by concatenated codes, compared to the one-shot coherent information optimized over Gaussian input states. Here, σ is the standard deviation of the magnitude of the phase-space displacement introduced by the channel, in units with $\hbar = 1$. The rate is in units of qubits per oscillator.

where C^2 is a slowly varying function of $\sigma^2/\hbar$ plotted in Fig. 3. It turns out that this rate is actually fairly close to $\log_2 d$; that is, the optimal dimension d of the qudit encoded in each oscillator is approximately $C^2\hbar/\sigma^2$. With this choice for d, the error rate for each oscillator is reasonably small, and the random CSS code reduces the error probability for the encoded state to a value exponentially small in N at a modest cost in rate. The rate achieved by concatenating coding lies strictly below the coherent information I_Q, but comes within one qubit of I_Q for $\sigma^2 > 1.88\times 10^{-4}$.

Both the concatenated codes and the codes derived from efficient sphere packings are stabilizer codes, and therefore, both are associated with lattices in $2N$-dimensional phase space. But while the sphere-packing codes have been chosen so that the shortest nonzero vector on the lattice is large relative to the size of the unit cell, the concatenated codes correspond to sphere packings of poor quality. For the concatenated codes, the shortest vector of the normalizer lattice has length ℓ, where

$$\ell^2 = 2\pi\hbar/d, \tag{80}$$

and the rate R is close to $\log_2 d$. The efficient sphere packings have radius $r = \ell/2$ close to $\sqrt{n\sigma^2}$, or

$$\ell^2 = \frac{8N\hbar}{e} \times 2^{-R}. \tag{81}$$

Hence, if we compare sphere-packing codes and concatenated codes with comparable rates, the sphere-packing codes have minimum distance that is larger by a factor of about $\sqrt{4N/\pi e}$. The concatenated codes achieve a high rate not because the minimum distance of the lattice is large, but rather because the decoding procedure exploits the hierarchical structure of the code.

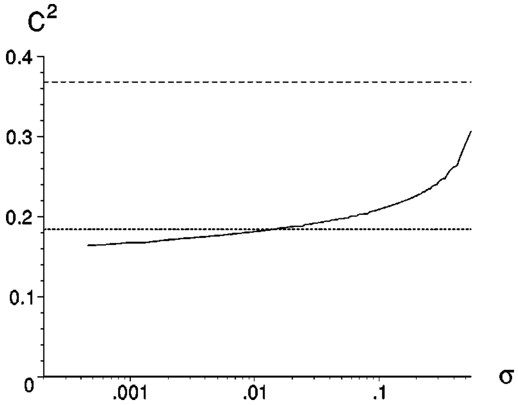

FIG. 3. The slowly varying function C^2, defined by $R = \log_2(C^2/\sigma^2)$, where R is the rate achievable with concatenated codes. Units have been chosen such that $\hbar = 1$. The horizontal lines are at $C^2 = 1/e$, corresponding to a rate equal to the coherent information, and at $C^2 = 1/2e$, corresponding to one qubit below the coherent information.

VII. THE CLASSICAL GAUSSIAN CHANNEL

We have found that quantum stabilizer codes based on efficient sphere packings can achieve rates for the Gaussian quantum channel that match the one-shot coherent information, and that concatenated codes achieve rates that are below, but close to, the coherent information. Now, as an aside, we will discuss the corresponding statements for the classical Gaussian channel. We will see, in particular, that concatenated codes achieve rates that are close to the classical channel capacity.

Shannon's expression for the capacity of the classical Gaussian channel may be understood heuristically as follows [3,4]. If the input signals have average power P, which is inflated by the Gaussian noise to $P + \sigma^2$, then if n real variables are transmitted, the total volume occupied by the space of output signals is the volume of a sphere of radius $\sqrt{n(P+\sigma^2)}$, or

$$V_{tot} = V_n[n(P+\sigma^2)]^{n/2}. \tag{82}$$

We will decode a received message as the signal state that is the minimal distance away. Consider averaging over all codes that satisfy the power constraint and have m signals. When a message is received, the signal that was sent will typically occupy a decoding sphere of radius $\sqrt{n(\sigma^2+\varepsilon)}$ centered at the received message, which has volume

$$V_{\text{decoding sphere}} = V_n[n(\sigma^2+\varepsilon)]^{n/2}. \tag{83}$$

A decoding error may arise if another one of the m signals, aside from the one that was sent, is also contained in the decoding sphere. The probability that a randomly selected signal inside the sphere of radius $\sqrt{n(P+\sigma^2)}$ is contained in a particular decoding sphere of radius $\sqrt{n(\sigma^2+\varepsilon)}$ is the ratio of the volume of the spheres, so the probability of a decoding error may be upper bounded by m times that ratio, or

$$P_{\text{error}} < m\left(\frac{\sigma^2+\varepsilon}{\sigma^2+P}\right)^{n/2} = \left(2^{2R}\frac{\sigma^2+\varepsilon}{\sigma^2+P}\right)^{n/2}, \tag{84}$$

where R is the rate of the code. If the probability of error averaged over codes and signals satisfies this bound, there is a particular code that satisfies the bound when we average only over signals. If $P_{\rm error}<\delta$ when we average over signals, then we can discard at most half of all the signals (reducing the rate by at most $1/n$ bits) to obtain a new code with $P_{\rm error}<2\delta$ for *all* signals. Since ε may be chosen arbitrarily small for sufficiently large n, we conclude that there exist codes with arbitrarily small probability of error and rate R arbitrarily close to

$$C=\frac{1}{2}\log_2\left(1+\frac{P}{\sigma^2}\right), \tag{85}$$

which is the Shannon capacity. Conversely, for any rate exceeding C, the decoding spheres inevitably have nonnegligible overlaps, and the error rate cannot be arbitrarily small.

Suppose that, instead of Shannon's random coding, we use a lattice code based on an efficient packing of spheres. In this case, the power constraint may be imposed by including as signals all lattice sites that are contained in an n-dimensional ball of radius $\sqrt{nP}$, and the typical shifts by distance $\sqrt{n\sigma^2}$ must be correctable. Thus, decoding spheres of radius $\sqrt{n\sigma^2}$ are to be packed into a sphere of total radius $\sqrt{n(P+\sigma^2)}$. Suppose that the lattice is chosen so that nonoverlapping spheres centered at the lattice sites fill a fraction at least $2^{-(n-1)}$ of the total volume; the existence of such a lattice is established by Minkowski's estimate [18,19]. Then the number m of signals satisfies

$$mV_n(n\sigma^2)^{n/2}\geqslant 2^{-(n-1)}V_n[n(P+\sigma^2)]^{n/2}, \tag{86}$$

or

$$m\geqslant 2^{-n}\left(1+\frac{P}{\sigma^2}\right)^{n/2}, \tag{87}$$

corresponding to the rate

$$R\equiv\frac{1}{n}\log_2 m=\frac{1}{2}\log_2\left(1+\frac{P}{\sigma^2}\right)-1, \tag{88}$$

which is one bit less than the Shannon capacity.

Much as in the discussion of quantum lattice codes in Sec. V, an improved estimate of the achievable rate is obtained if we allow the decoding spheres to overlap [20–23]. In fact, there are classical lattice codes with rate arbitrarily close to the capacity, such that the probability of error, *averaged* over signals, is arbitrarily small [23]. Unfortunately, though, because of the power constraint, the error probability depends on which signal is sent, and the trick of deleting the worst half of the signals would destroy the structure of the lattice. Alternatively, it may be shown that for any rate

$$R<\frac{1}{2}\log_2(P/\sigma^2), \tag{89}$$

there are lattice codes with maximal probability of error that is arbitrarily small [20]. This achievable rate approaches the capacity for large P/σ^2.

Now consider the rates that may be achieved for the Gaussian classical channel with concatenated coding. A d-state system (dit) is encoded in each of n real variables. If each real variable takes one of d possible values, with spacing $2\Delta x$ between the signals, then a shift by Δx may be corrected. By replacing the sum over d values by an integral, which may be justified for large d, we find an average power per signal

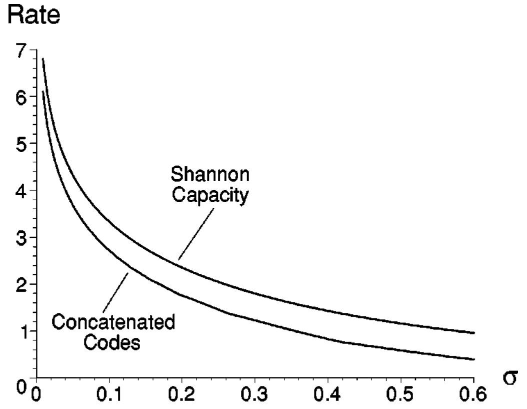

FIG. 4. Rates for the Gaussian classical channel achievable with concatenated codes, compared to the Shannon capacity. Here, σ is the standard deviation of the displacement, in units with the power $P=1$. The rate is in units of bits per signal.

$$P\sim\frac{1}{2d\Delta x}\int_{-d\Delta x}^{d\Delta x}x^2dx=\frac{1}{3}(d\Delta x)^2; \tag{90}$$

thus, the largest correctable shift may be expressed in terms of the average power as

$$\Delta x=\sqrt{3P}/d. \tag{91}$$

For the Gaussian channel with mean zero and variance σ^2, the probability p of an error in each real variable transmitted is no larger than the probability of a shift by a distance exceeding Δx, or

$$p\leqslant \mathrm{erfc}(\sqrt{3P/2d^2\sigma^2}), \tag{92}$$

where erfc denotes the complementary error function.

We reduce the error probability further by encoding $k<n$ dits in the block of n dits. Arguing as in Sec. VI, we see that a random code for dits achieves an asymptotic rate in bits given by

$$R=(\log_2 d)[1-H_d(p)-p\log_d(d-1)]. \tag{93}$$

Given σ^2, using the expression Eq. (92) for p, and choosing d to optimize the rate in Eq. (93), we obtain a rate close to the Shannon capacity, as shown in Fig. 4. As for the concatenated quantum code, the rate of the concatenated classical code is close to $\log_2 d$, where $d\sim C(\sigma^2)\sqrt{P/\sigma^2}$, and $C(\sigma^2)$ is a slowly varying function.

VIII. CONCLUSIONS

We have described quantum stabilizer codes, based on symplectically integral lattices in phase space, that protect quantum information carried by systems described by continuous quantum variables. With these codes, we may establish lower bounds on the capacities of continuous-variable quantum channels.

For the Gaussian quantum channel, the best rate we know how to achieve with stabilizer coding matches the one-shot coherent information optimized over Gaussian inputs, at least when the value of the coherent information is $\log_2$ of an integer. That our achievable rate matches the coherent information only for isolated values of the noise variance σ^2 seems to be an artifact of our method of analysis, rather than indicative of any intrinsic property of the channel. Hence, it is tempting to speculate that this optimal one-shot coherent information actually is the quantum capacity of the channel.

Conceivably, better rates may be achieved with *nonadditive* quantum codes that cannot be described in terms of symplectically integral lattices. We do not know much about how to construct these codes, or about their properties.

In the case of the depolarizing channel acting on qubits, Shor and Smolin discovered that rates exceeding the one-shot coherent information could be achieved. Their construction used concatenated codes, where the ‘‘outer code’’ is a random stabilizer code, and the ‘‘inner code’’ is a degenerate code with a small block size [11]. The analogous procedure for the Gaussian channel would be to concatenate an outer code based on a symplectically integral lattice with an inner code that encodes one logical oscillator in a block of several oscillators. This inner code, then, embeds an infinite-dimensional code space in a larger infinite-dimensional space, as do codes constructed by Braunstein [26] and Lloyd and Slotine [27]. However, we have not been able to find concatenated codes of this type that achieve rates exceeding the one-shot coherent information of the Gaussian channel.

ACKNOWLEDGMENTS

We thank Dave Beckman, Anne-Marie Bergé, Bob McEliece, Michael Postol, Eric Rains, Peter Shor, and Edward Witten for helpful discussions and correspondence. This work was supported in part by the Department of Energy under Grant No. DE-FG03-92-ER40701, by the National Science Foundation under Grant No. EIA-0086038, and by the Caltech MURI Center for Quantum Networks under ARO Grant No. DAAD19-00-1-0374.

[1] M.A. Nielsen and I.L Chuang, *Quantum Computation and Quantum Information* (Cambridge University Press, Cambridge, 2000).

[2] J. Preskill, *Lecture Notes for Physics 229: Quantum Information and Computation*, http://www.theory.caltech;edu/people/preskill/ph229 (1998).

[3] C. Shannon, Bell Syst. Tech. J. **27**, 379 (1948).

[4] T.M. Cover and J.A. Thomas, *Elements of Information Theory* (Wiley, New York, 1991).

[5] P.W. Shor, Phys. Rev. A **52**, 2493 (1995).

[6] A. Steane, Phys. Rev. Lett. **77**, 793 (1996).

[7] C.H. Bennett, D.P. DiVincenzo, J.A. Smolin, and W.K. Wootters, Phys. Rev. A **54**, 3824 (1996).

[8] B.W. Schumacher and M.A. Nielsen, Phys. Rev. A **54**, 2629 (1996).

[9] H. Barnum, M.A. Nielsen, and B. Schumacher, Phys. Rev. A **57**, 4153 (1998).

[10] S. Lloyd, Phys. Rev. A **56**, 1613 (1997).

[11] P.W. Shor and J.A. Smolin, e-print quant-ph/9604006; D.P. DiVincenzo, P.W. Shor, and J.A. Smolin, Phys. Rev. A **57**, 830 (1998).

[12] C.H. Bennett, D.P. DiVincenzo, and J.A. Smolin, Phys. Rev. Lett. **78**, 3217 (1997), quant-ph/9701015.

[13] A.S. Holevo and R.F. Werner, e-print quant-ph/9912067.

[14] D. Gottesman, A. Kitaev, and J. Preskill, Phys. Rev. A (to be published), e-print quant-ph/0008040.

[15] D. Gottesman, Phys. Rev. A **54**, 1862 (1996).

[16] A.R. Calderbank, E.M. Rains, P.W. Shor, and N.J.A. Sloane, Phys. Rev. Lett. **78**, 405 (1997).

[17] P. Buser and P. Sarnak, Invent. Math. **117**, 27 (1994).

[18] J.H. Conway and N.J.A. Sloane, *Sphere Packings, Lattices and Groups* (Springer, New York, 1999).

[19] J.W.S. Cassels, *An introduction to the Geometry of Numbers* (Springer-Verlag, New York, 1971).

[20] R. de Buda, IEEE Trans. Inf. Theory **IT-21**, 441 (1975).

[21] R. de Buda, IEEE J. Sel. Areas Commun. **7**, 893 (1989).

[22] T. Linder, C. Schleger, and K. Zeger, IEEE Trans. Inf. Theory **39**, 1735 (1993).

[23] R. Urbanke and B. Rimoldi, IEEE Trans. Inf. Theory **44**, 273 (1998).

[24] A.R. Calderbank and P.W. Shor, Phys. Rev. A **54**, 1098 (1996).

[25] A. Steane, Proc. R. Soc. London, Ser. A **452**, 2551 (1996).

[26] S. Braunstein, Phys. Rev. Lett. **80**, 4084 (1998).

[27] S. Lloyd and J.E. Slotine, Phys. Rev. Lett. **80**, 4088 (1998).

PHYSICAL REVIEW A, VOLUME 64, 012310

Encoding a qubit in an oscillator

Daniel Gottesman,^{1,2,*} Alexei Kitaev,^{1,†} and John Preskill^{3,‡}
^{1}*Microsoft Corporation, One Microsoft Way, Redmond, Washington 98052*
^{2}*Computer Science Division, EECS, University of California, Berkeley, California 94720*
^{3}*Institute for Quantum Information, California Institute of Technology, Pasadena, California 91125*

(Received 9 August 2000; published 11 June 2001)

Quantum error-correcting codes are constructed that embed a finite-dimensional code space in the infinite-dimensional Hilbert space of a system described by continuous quantum variables. These codes exploit the noncommutative geometry of phase space to protect against errors that shift the values of the canonical variables q and p. In the setting of quantum optics, fault-tolerant universal quantum computation can be executed on the protected code subspace using linear optical operations, squeezing, homodyne detection, and photon counting; however, nonlinear mode coupling is required for the preparation of the encoded states. Finite-dimensional versions of these codes can be constructed that protect encoded quantum information against shifts in the amplitude or phase of a d-state system. Continuous-variable codes can be invoked to establish lower bounds on the quantum capacity of Gaussian quantum channels.

DOI: 10.1103/PhysRevA.64.012310 PACS number(s): 03.67.Lx

I. INTRODUCTION

Classical information can be carried by either a discrete (digital) signal or a continuous (analog) signal. Although in principle an analog signal can be processed, digital computing is far more robust—a digital signal can be readily restandardized and protected from damage caused by the gradual accumulation of small errors.

Quantum information can also be carried by either a discrete (finite-dimensional) system, such as a two-level atom or an electron spin, or by a continuous (infinite-dimensional) system, such as to a harmonic oscillator or a rotor. Even in the finite-dimensional case, quantum information is in a certain sense continuous — a state is a vector in a Hilbert space that can point in any direction. Nevertheless, we have known for nearly five years that cleverly encoded quantum states can be restandardized and protected from the gradual accumulation of small errors, or from the destructive effects of decoherence due to uncontrolled interactions with the environment [1,2].

One is tempted to wonder whether we can go still further and protect the quantum state of a system described by *continuous quantum variables*. Probably this is too much to hope for, since even the problem of protecting analog classical information seems to pose insuperable difficulties.

In this paper we achieve a more modest goal: we describe quantum error-correcting codes that protect a state of a *finite-dimensional* quantum system (or ‘‘qudit’’) that is encoded in an infinite-dimensional system. These codes may be useful for implementing quantum computation and quantum communication protocols that use harmonic oscillators or rotors that are experimentally accessible.

We also explain how encoded quantum states can be processed fault tolerantly. Once encoded states have been prepared, a universal set of fault-tolerant quantum gates can be implemented using, in the language of quantum optics, linear optical operations, squeezing, homodyne detection, and photon counting. However, for preparation of the encoded states, nonlinear couplings must be invoked.

Our continuous-variable quantum error-correcting codes are effective in protecting against sufficiently weak diffusive phenomena that cause the position and momentum of an oscillator to drift, or against losses that cause the amplitude of an oscillator to decay. By concatenating with conventional finite-dimensional quantum codes, we can also provide protection against errors that heavily damage a (sufficiently small) subset of all the oscillators in a code block. A different scheme for realizing robust and efficient quantum computation based on linear optics has been recently proposed by Knill, Laflamme, and Milburn [3,4].

We begin in Sec. II by describing codes that embed an n-state quantum system in a larger d-state system, and that protect the encoded quantum information against shifts in the amplitude or phase of the d-state system. A realization of this coding scheme based on a charged particle in a magnetic field is discussed in Sec. III. Our continuous-variable codes are obtained in Sec. IV by considering a $d \rightarrow \infty$ limit. Formally, the code states of the continuous-variable codes are nonnormalizable states, infinitely squeezed in both position and momentum; in Sec. V we describe the consequences of using more realistic approximate code states that are finitely squeezed. In Sec. VI we outline the theory of more general continuous-variable codes based on lattice sphere packings in higher dimensional phase space.

We discuss in Sec. VII how continuous-variable codes protect against quantum diffusion, amplitude damping, and unitary errors. In Sec. VIII we establish a lower bound on the quantum capacity of the Gaussian quantum channel.

We then proceed to develop schemes for fault-tolerant manipulation of encoded quantum information, starting in Sec. IX with a discussion of the symplectic operations that can ^{3}be implemented with linear optics and squeezing. In Sec. X we discuss the measurement of the error syndrome

---

[*] Email address: gottesma@eecs.berkeley.edu

[†] Email address: kitaev@microsoft.com

[‡] Email address: preskill@theory.caltech.edu

©2001 The American Physical Society

and error recovery, which can be achieved with symplectic operations and homodyne detection. Completion of the fault-tolerant universal gate set by means of photon counting is described in Sec. XI, and the preparation of encoded states is explained in Sec. XII. Finally, Sec. XIII contains some further remarks about the physical realization of our coding schemes, and Sec. XIV contains concluding comments.

II. SHIFT-RESISTANT QUANTUM CODES

An unusual feature of our codes is that they are designed to protect against a different type of error than has been considered in previous discussions of quantum coding. This distinction is more easily explained if we first consider not the case of a continuous quantum variable, but instead the (also interesting) case of a ''qudit,'' a d-dimensional quantum system. Quantum codes can be constructed that encode k protected qudits in a block of N qudits, so that the encoded qudits can be perfectly recovered if up to t qudits are damaged, irrespective of the nature of the damage [5–8]. Error recovery will be effective if errors that act on many qudits at once are rare. More precisely, a general error superoperator acting on N qudits can be expanded in terms of a basis of operators, each of definite ''weight'' (the number of qudits on which the operator acts nontrivially). Encoded information is well protected if the error superoperator has nearly all its support on operators of weight t or less.

But consider instead a different situation, in which the amplitude for an error to occur on each qudit is not small, but the errors are of a restricted type. The possible errors acting on a single qudit can be expanded in terms of a unitary operator basis with d^2 elements, the ''Pauli operators:''

$$X^aZ^b, \quad a,b=0,1,2,\ldots,d-1. \tag{1}$$

Here X and Z are generalizations of the Pauli matrices σ_x and σ_z, which act in a particular basis $\{|j\rangle, j=0,1,2,\ldots,d-1\}$ according to

$$X:|j\rangle\rightarrow|j+1 \pmod d\rangle,$$
$$Z:|j\rangle\rightarrow\omega^j|j\rangle, \tag{2}$$

where $\omega=\exp(2\pi i/d)$. Note that it follows that

$$ZX=\omega XZ. \tag{3}$$

For N qudits, there is a unitary operator basis with d^{2N} elements consisting of all tensor products of single-qudit Pauli operators.

We will now imagine that errors with $|a|,|b|$ small compared to d are common, but errors with large $|a|$ and $|b|$ are rare. This type of error model could be expected to apply in the case of a continuous quantum variable, which is formally the $d\rightarrow\infty$ limit of a qudit. For example, decoherence causes the position q and momentum p of a particle to diffuse with some nonzero diffusion constant. In any finite time interval q and p will drift by some amount that may be small, but is certainly not zero. How can we protect encoded quantum information under these conditions?

Fortunately, the general ''stabilizer'' framework [9,10] for constructing quantum codes can be adapted to this setting. In this framework, one divides the elements of a unitary operator basis into two disjoint and exhaustive classes: the set $\mathcal{E}$ of ''likely errors'' that we want to protect against, and the rest; the ''unlikely errors.'' A code subspace is constructed as the simultaneous eigenspace of a set of commuting ''stabilizer generators,'' that generate an Abelian group, the ''code stabilizer.'' The code can reverse errors in the set $\mathcal{E}$ if, for each pair of errors E_a and E_b, either $E_a^\dagger E_b$ lies in the stabilizer group, or $E_a^\dagger E_b$ fails to commute with some element of the stabilizer. (In the latter case, the two errors alter the eigenvalues of the generators in distinguishable ways; in the former case they do not, but we can successfully recover from an error of type a by applying either $E_a^\dagger$ or $E_b^\dagger$.) In typical discussions of quantum coding, $\mathcal{E}$ is assumed to be the set of all tensor products of Pauli operators with weight up to t (those that act trivially on all but at most t qudits). But the same principles can be invoked to design codes that protect against errors in a set $\mathcal{E}$ with other properties.

Quantum codes for continuous variables have been described previously by Braunstein [11] and by Lloyd and Slotine [12]. For example, one code they constructed can be regarded as the continuous limit of a qudit code of the type originally introduced by Shor in the binary ($d=2$) case, an $[[N=9,k=1,2t+1=3]]$ code that protects a single qudit encoded in a block of 9 from arbitrary damage inflicted on any one of the 9. The 8 stabilizer generators of the code can be expressed as

$$Z_1Z_2^{-1},Z_2Z_3^{-1},Z_4Z_5^{-1},Z_5Z_6^{-1},Z_7Z_8^{-1},Z_8Z_9^{-1},$$
$$(X_1X_2X_3)\cdot(X_4X_5X_6)^{-1},(X_4X_5X_6)\cdot(X_7X_8X_9)^{-1}, \tag{4}$$

and encoded operations that commute with the stabilizer and hence act on the encoded qudit can be chosen to be

$$\bar{Z}=Z_1Z_4Z_7,$$
$$\bar{X}=X_1X_2X_3. \tag{5}$$

In the $d\rightarrow\infty$ limit, we obtain a code that is the simultaneous eigenspace of eight commuting operators acting on nine particles, which are

$$q_1-q_2,q_2-q_3,q_4-q_5,q_5-q_6,q_7-q_8,q_8-q_9,$$
$$(p_1+p_2+p_3)-(p_4+p_5+p_6),$$
$$(p_4+p_5+p_6)-(p_7+p_8+p_9). \tag{6}$$

Logical operators that act in the code space are

$$\bar{q}=q_1+q_4+q_7,$$
$$\bar{p}=p_1+p_2+p_3. \tag{7}$$

This code is designed to protect against errors in which one of the particles makes a large jump in q or p (or both), while the others hold still. But it provides little protection against small diffusive motions of all the particles, which allow $\overline{q}$ and $\overline{p}$ to drift.

Entanglement purification protocols for continuous variable systems have also been proposed — good entangled states can be distilled from noisy entangled states via a protocol that requires two-way classical communication [13,14]. These purification protocols work well against certain sorts of errors, but their reliance on two-way classical communication makes them inadequate for accurately preserving unknown states in an imperfect quantum memory, or for robust quantum computation.

Returning to qudits, let us consider an example of a quantum code that can protect against small shifts in both amplitude and phase, but not against large shifts. It is already interesting to discuss the case of a system consisting of a single qudit, but where the dimension n of the encoded system is (of course) less than d. For example, a qudit $(n=2)$ can be encoded in a system with dimension $d=18$, and protected against shifts by one unit in the amplitude or phase of the qudit; that is, against errors of the form X^aZ^b where $|a|,|b|\leqslant 1$. The stabilizer of this code is generated by the two operators

$$X^6, \quad Z^6, \tag{8}$$

and the commutation relations of the Pauli operators with these generators are

$$(X^aZ^b)\cdot X^6=\omega^{6b}X^6\cdot(X^aZ^b),$$

$$(X^aZ^b)\cdot Z^6=\overline{\omega}^{6a}Z^6\cdot(X^aZ^b). \tag{9}$$

Therefore, a Pauli operator commutes with the stabilizer only if a and b are both multiples of $3=18/6$; this property ensures that the code can correct single shifts in both amplitude and phase. Logical operators acting on the encoded qudit are

$$\overline{X}=X^3, \quad \overline{Z}=Z^3, \tag{10}$$

which evidently commute with the stabilizer and are not contained in it.

Since the code words are eigenstates of Z^6 with eigenvalue one, the only allowed values of j are multiples of three. And since there are also eigenstates of X^6 with eigenvalue one, the code words are invariant under a shift in j by six units. A basis for the two-dimensional code space is

$$|\overline{0}\rangle=\frac{1}{\sqrt{3}}(|0\rangle+|6\rangle+|12\rangle),$$

$$|\overline{1}\rangle=\frac{1}{\sqrt{3}}(|3\rangle+|9\rangle+|15\rangle). \tag{11}$$

If an amplitude error occurs that shifts j by ± 1, the error can be diagnosed by measuring the stabilizer generator Z^6, which reveals the value of j modulo 3; the error is corrected by adjusting j to the nearest multiple of 3. Phase errors are shifts in the Fourier transformed conjugate basis, and can be corrected similarly.

This code is actually *perfect*, meaning that each possible pair of eigenvalues of the generators X^6 and Z^6 is a valid syndrome for correcting a shift. There are nine possible errors $\{X^aZ^b,|a|,|b|\leqslant 1\}$, and the Hilbert space of the qudit contains nine copies of the two-dimensional code space, one corresponding to each possible error. These ''error spaces'' just barely fit in the qudit space for $d=18=9\cdot 2$.

Similar perfect codes can be constructed that protect against larger shifts. For $d=r_1r_2n$, consider the stabilizer generators

$$X^{r_1 n}, \quad Z^{r_2 n}. \tag{12}$$

There is an encoded *qunit*, acted on by logical operators

$$\overline{X}=X^{r_1},$$

$$\overline{Z}=Z^{r_2}, \tag{13}$$

which evidently commute with the stabilizer and satisfy

$$\overline{ZX}=\omega^{r_1r_2}\overline{XZ}=e^{2\pi i/n}\overline{XZ}. \tag{14}$$

The commutation relations of the Pauli operators with the generators are

$$(X^aZ^b)\cdot X^{r_1n}=\omega^{r_1nb}X^{r_1n}\cdot(X^aZ^b)=e^{2\pi ib/r_2}X^{r_1n}\cdot(X^aZ^b),$$

$$(X^aZ^b)\cdot Z^{r_2n}=\overline{\omega}^{r_2na}Z^{r_2n}\cdot(X^aZ^b)=e^{-2\pi ia/r_1}Z^{r_2n}\cdot(X^aZ^b). \tag{15}$$

The phases are trivial only if a is an integer multiple of r_1 and b an integer multiple of r_2. Therefore, this code can correct all shifts with

$$|a|<\frac{r_1}{2},$$

$$|b|<\frac{r_2}{2}. \tag{16}$$

The number of possible error syndromes is $r_1r_2=d/n$, so the code is perfect.

Expressed in terms of Z eigenstates, the code words contain only values of j that are multiples of r_1 (since $Z^{r_2n}=1$), and are invariant under a shift of j by r_1n (since $X^{r_1n}=1$). Hence a basis for the n-dimensional code subspace is

$$|\overline{0}\rangle = \frac{1}{\sqrt{r_2}}(|0\rangle + |nr_1\rangle + \ldots + |(r_2-1)nr_1\rangle),$$

$$|\overline{1}\rangle = \frac{1}{\sqrt{r_2}}(|r_1\rangle + \ldots + |((r_2-1)n+1)r_1\rangle),$$

$$\vdots$$

$$|\overline{n}-\overline{1}\rangle = \frac{1}{\sqrt{r_2}}(|(n-1)r_1\rangle + \ldots + |(r_2 n-1)r_1\rangle). \quad (17)$$

If the states undergo an amplitude shift, the value of j modulo r_1 is determined by measuring the stabilizer generator $Z^{r_2 n}$, and the shift can be corrected by adjusting j to the nearest multiple of r_1. The code words have a similar form in the Fourier transformed conjugate basis (the basis of X eigenstates), but with r_1 and r_2 interchanged. Therefore, amplitude shifts by less than $r_1/2$ and phase shifts by less than $r_2/2$ can be corrected.

III. A QUDIT IN A LANDAU LEVEL

A single electron in a uniform magnetic field in two dimensions provides an enlightening realization of our codes. General translations in a magnetic field are noncommuting, since an electron transported around a closed path acquires an Aharonov-Bohm phase $e^{ie\Phi}$, where Φ is the magnetic flux enclosed by the path. Two translations T and S commute only if the operator $TST^{-1}S^{-1}$ translates an electron around a path that encloses a flux $\Phi = k\Phi_0$, where $\Phi_0 = 2\pi/e$ is the flux quantum and k is an integer.

Translations commute with the Hamiltonian H, and two translations T_1 and T_2 form a maximally commuting set if they generate a lattice that has a unit cell enclosing one quantum of flux. Simultaneously diagonalizing H, T_1, and T_2, we obtain a Landau level of degenerate energy eigenstates, one state corresponding to each quantum of magnetic flux. Then T_1 and T_2^n are the stabilizer generators of a code, where $\overline{Z} = T_1^{1/n}$ and $\overline{X} = T_2$ are the logical operators on a code space of dimension n.

Suppose the system is in a periodically identified box (a torus), so that $T_1^{r_1} = (T_2^n)^{r_2} = 1$ are translations around the cycles of the torus. The number of flux quanta through the torus, and hence the degeneracy of the Landau level, is nr_1r_2. The code, then, embeds an n-dimensional system in a system of dimension $d = r_1r_2n$.

In this situation, the logical operations $\overline{X}$ and $\overline{Z}$ can be visualized as translations of the torus in two different directions; the stabilizer generator $\overline{X}^n$ is a translation by a fraction $1/r_2$ of the length of the torus in one direction, and the stabilizer generator $\overline{Z}^n$ is a translation by $1/r_1$ of the length in the other direction. Therefore, for any state in the code space, the wave function of the electron in a cell containing n flux quanta is periodically repeated altogether r_1r_2 times to fill the entire torus. Our code can be regarded as a kind of ‘‘quantum repetition code’’—identical ‘‘copies’’ of the wave function are stored in each of the r_1r_2 cells. But of course there is only one electron, so if we detect the electron in one cell its state is destroyed in all the cells.

This picture of the state encoded in a Landau level cautions us about the restrictions on the type of error model that the code can fend off successfully. If the environment strongly probes one of the cells and detects nothing, the wave function is suppressed in that cell. This causes a $\overline{X}$ error in the encoded state with a probability of about $1/2r_2$, and a $\overline{Z}$ error with a probability of about $1/2r_1$. The code is more effective if the typical errors gently deform the state in each cell, rather than strongly deforming it in one cell.

IV. CONTINUOUS VARIABLE CODES FOR A SINGLE OSCILLATOR

Formally, we can construct quantum codes for systems described by continuous quantum variables by considering the large-d limit of the shift-resistant codes described in Sec. II. We might have hoped to increase d to infinity while holding r_1/d and r_2/d fixed, maintaining the ability to correct shifts in both amplitude and phase that are a fixed fraction of the ranges of the qudit. However, since the perfect codes satisfy

$$\frac{r_1}{d} = \frac{1}{nr_2}, \quad \frac{r_2}{d} = \frac{1}{nr_1}, \quad (18)$$

this is not possible. Nonetheless, interesting codes can be obtained as the amplitude and phase of the qudit approach the position q and momentum p of a particle—we can hold fixed the size of the shifts Δq and Δp that can be corrected, as the ranges of q and p become unbounded.

Another option is to take $d \to \infty$ with $r_1/d \equiv 1/m$ fixed and $r_2 = m/n$ fixed, obtaining a *rotor* $Z = e^{i\theta}$ (or a particle in a periodically identified finite box) that can be protected against finite shifts in both the orientation θ of the rotor and its (quantized) angular momentum L. The stabilizer of this code is generated by

$$Z^{r_2 n} \to e^{i\theta m},$$

$$X^{r_1 n} = X^{d/r_2} \to e^{-2\pi i L(n/m)} \quad (19)$$

and the logical operations are

$$\overline{Z} = e^{i\theta m/n},$$

$$\overline{X} = e^{-2\pi i L/m}. \quad (20)$$

Since $\overline{X}$ shifts the value of θ by $2\pi/m$, and $\overline{Z}$ shifts the value of L by $m/n = r_2$, this code can correct shifts in θ with $\Delta\theta < \pi/m$ and shifts in L with $|\Delta L| < m/2n$.

Alternatively, we can consider a limit in which r_1 and r_2 both become large. We may write $r_1 = \alpha/\varepsilon$ and $r_2 = 1/n\alpha\varepsilon$, where $d = nr_1r_2 = 1/\varepsilon^2$, obtaining a code with stabilizer generators

$$Z^{r_2 n} \to (e^{2\pi i q\varepsilon})^{(1/\alpha\varepsilon)} = e^{2\pi i q/\alpha},$$

$$X^{r_1 n} \to (e^{-ip\varepsilon})^{(n\alpha/\varepsilon)} = e^{-inp\alpha}, \tag{21}$$

and logical operations

$$\bar{Z} = e^{2\pi i q/n\alpha}, \quad \bar{X} = e^{-ip\alpha}, \tag{22}$$

where α is an arbitrary real number. Using the identity $e^A e^B = e^{[A,B]} e^B e^A$ (which holds if A and B commute with their commutator) and the canonical commutation relation $[q,p]=i$, we verify that

$$\overline{ZX} = \omega \overline{XZ}, \quad \omega = e^{2\pi i/n}. \tag{23}$$

Since $\bar{X}$ translates q by α and $\bar{Z}$ translates p by $2\pi/n\alpha$, the code protects against shifts with

$$|\Delta q| < \frac{\alpha}{2},$$

$$|\Delta p| < \frac{\pi}{n\alpha}. \tag{24}$$

Note that the shifts in momentum and position that the code can correct obey the condition

$$\Delta p \Delta q < \frac{\pi}{2n}\hbar. \tag{25}$$

In typical situations, errors in q and p are of comparable magnitude, and it is best to choose $\alpha = \sqrt{2\pi/n}$ so that

$$\bar{Z} = \exp\left(iq\sqrt{\frac{2\pi}{n}} \right), \quad \bar{X} = \exp\left(-ip\sqrt{\frac{2\pi}{n}} \right). \tag{26}$$

Formally, the code words are coherent superpositions of infinitely squeezed states, e.g., (up to normalization)

$$|\bar{Z} = \omega^j\rangle = \sum_{s=-\infty}^{\infty} |q = \alpha(j+ns)\rangle,$$

$$|\bar{X} = \bar{\omega}^j\rangle = \sum_{s=-\infty}^{\infty} \left| p = \frac{2\pi}{n\alpha}(j+ns) \right\rangle. \tag{27}$$

(See Fig. 1.) Of course, realistic code words will be normalizable finitely squeezed states, rather than nonnormalizable infinitely squeezed states. But squeezing in at least one of p and q is required to comfortably fulfill condition (25).

The Wigner function associated with the code word wave function $\psi^{(j)}(q) \equiv \langle q | \bar{Z} = \omega^j \rangle$ is a sum of delta functions positioned at the sites of a lattice in phase space, where three quarters of the delta functions are positive and one quarter are negative. Explicitly, we have

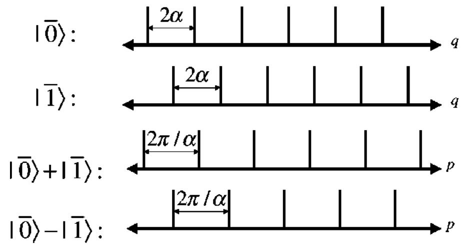

$|\bar{0}\rangle$:
2α
q
$|\bar{1}\rangle$:
2α
q
$|\bar{0}\rangle + |\bar{1}\rangle$:
2π/α
p
$|\bar{0}\rangle - |\bar{1}\rangle$:
2π/α
p

FIG. 1. Code words of the $n=2$ code. The states $|\bar{0}\rangle$, $|\bar{1}\rangle$ are superpositions of q eigenstates, periodically spaced with period 2α; the two basis states differ by a displacement in q by α. The states $(|0\rangle \pm |1\rangle)/\sqrt{2}$ are superpositions of p eigenstates, periodically spaced with period $2\pi/\alpha$; the two basis states differ by a displacement in p by π/α.

$$W^{(j)}(q,p) \equiv \frac{1}{2\pi}\int_{-\infty}^{\infty} dx\, e^{ipx} \psi^{(j)}(q+x/2)^* \psi^{(j)}(q-x/2)$$

$$\propto \sum_{s,t=-\infty}^{\infty} (-1)^{st} \delta\left(p - \frac{\pi}{n\alpha}s \right) \delta\left(q - \alpha j - \frac{n\alpha}{2}t \right); \tag{28}$$

the δ functions are negative on the sublattice with s,t odd. If we integrate over p, the oscillating sign causes the terms with odd t to cancel in the sum over s, and the surviving positive δ functions have support at $q = (n \times \text{integer} + j)\alpha$. If we integrate over q, the terms with odd s cancel in the sum over t, and the surviving positive δ functions have support at $p = (2\pi/n\alpha) \times \text{integer}$. Wigner functions for the $\bar{X}$ eigenstates are similar, but with the roles of q and p interchanged.

It is also of interest to express the encoded states in terms of the basis of coherent states. Consider for example the encoded state with $\bar{X} = 1$, which is the unique simultaneous eigenstate with eigenvalue one of the operators $e^{2\pi i q/\alpha}$ and $e^{-ip\alpha}$. In fact starting with any state $|\psi\rangle$, we can construct the encoded state (up to normalization) as

$$\left(\sum_{s=-\infty}^{\infty} e^{-isp\alpha} \right) \left(\sum_{t=-\infty}^{\infty} e^{2\pi i t q/\alpha} \right) |\psi\rangle$$

$$= \sum_{s,t} \exp[i(-sp\alpha + 2\pi t q/\alpha + \pi st)] |\psi\rangle. \tag{29}$$

In particular, if we choose $|\psi\rangle$ to be the ground state $|0\rangle$ of the oscillator, then the operator $\Sigma_{s,t} \exp[i(-sp\alpha + 2\pi t q/\alpha + \pi st)]$ displaces it to a coherent state centered at the point $(q,p) = (s\alpha, 2\pi t/\alpha)$ in the quadrature plane. Thus the encoded state is an equally weighted superposition of coherent states, with centers chosen from the sites of a lattice in the quadrature plane whose unit cell has area 2π. Since the coherent states are overcomplete , the expansion is not unique; indeed, if we choose $|\psi\rangle$ to be a coherent state rather than the vacuum, then the lattice is rigidly translated, but the encoded state remains invariant.

We can envision the stabilizer of the code as a lattice of translations in phase space that preserve the code words; the lattice generated by the translations $e^{2\pi i q/\alpha}$ and $e^{-inp\alpha}$. In fact, this lattice need not be rectangular—we can encode an n-dimensional system in the Hilbert space of a single oscillator by choosing *any* two variables Q and P that satisfy the canonical commutation relation $[Q,P]=i$, and constructing the code space as the simultaneous eigenstate of $e^{2\pi iQ}$ and e^{-inP}. The unit cell of the lattice has area $2\pi\hbar n$, in keeping with the principle that each quantum state ‘‘occupies’’ an area $2\pi\hbar$ in the phase space of a system with one continuous degree of freedom.

V. FINITE SQUEEZING

Strictly speaking, our code words are nonnormalizable states, infinitely squeezed in both q and p. In practice, we will have to work with approximate code words that will be finitely squeezed normalizable states. We need to consider how using such approximate code words will affect the probability of error.

We will replace a position eigenstate $\delta(0)$ by a normalized Gaussian of width Δ centered at the origin,

$$|\psi_0\rangle=\int_{-\infty}^{\infty}\frac{dq}{(\pi\Delta^2)^{1/4}}e^{-1/2\,q^2/\Delta^2}|q\rangle$$

$$=\int_{-\infty}^{\infty}\frac{dp}{(\pi/\Delta^2)^{1/4}}e^{-1/2\,\Delta^2p^2}|p\rangle. \qquad (30)$$

A code word, formally a coherent superposition of an infinite number of δ functions, becomes a sum of Gaussians weighted by a Gaussian envelope function of width κ^{-1}; in the special case of a two-dimensional code space, the approximate code words become

$$|\tilde{0}\rangle=N_0\sum_{s=-\infty}^{\infty}e^{-1/2\,\kappa^2(2s\alpha)^2}T(2s\alpha)|\psi_0\rangle,$$

$$|\tilde{1}\rangle=N_1\sum_{s=-\infty}^{\infty}e^{-1/2\,\kappa^2[(2s+1)\alpha)]^2}T[(2s+1)\alpha]|\psi_0\rangle, \qquad (31)$$

where $T(a)$ translates q by a, $N_{0,1}$ are normalization factors, and we use, e.g., $|\tilde{0}\rangle$ rather than $|\overline{0}\rangle$ to denote the approximate code word. We will assume that $\kappa\alpha$ and Δ/α are small compared to one, so that $N_0\approx N_1\approx(4\kappa^2\alpha^2/\pi)^{1/4}$; then in momentum space, the approximate code word becomes, e.g.,

$$(|\tilde{0}\rangle+|\tilde{1}\rangle)/\sqrt{2}\approx\left(\frac{\kappa^2\alpha^2}{\pi}\right)^{1/4}\int_{-\infty}^{\infty}\frac{dp}{(\pi/\Delta^2)^{1/4}}e^{-\frac{1}{2}\Delta^2p^2}$$

$$\times\sum_{s=-\infty}^{\infty}e^{-1/2\,\kappa^2(s\alpha)^2}e^{ip(\alpha s)}|p\rangle. \qquad (32)$$

By applying the Poisson summation formula,

$$\sum_{m=-\infty}^{\infty}e^{-\pi a(m-b)^2}=(a)^{-1/2}\sum_{s=-\infty}^{\infty}e^{-\pi s^2/a}e^{2\pi isb}, \qquad (33)$$

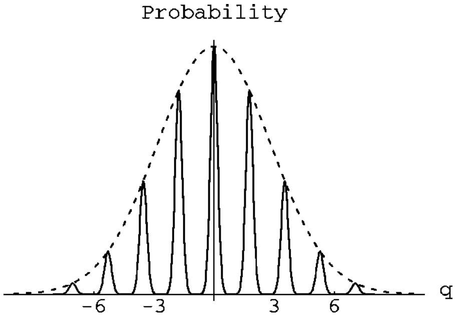

FIG. 2. Probability distribution in position space $P(q)=\frac{1}{2}|\langle q|(|\tilde{0}\rangle+|\tilde{1}\rangle)|^2$ for an approximate code word with $\Delta=\kappa=0.25$. The dashed line is the distribution’s Gaussian envelope.

this approximate code word can be rewritten as

$$(|\tilde{0}\rangle+|\tilde{1}\rangle)/\sqrt{2}\approx\left(\frac{\kappa^2\alpha^2}{\pi}\right)^{1/4}\int_{-\infty}^{\infty}\frac{dp}{(\pi/\Delta^2)^{1/4}}e^{-1/2\,\Delta^2p^2}\frac{\sqrt{2\pi}}{\kappa\alpha}$$

$$\times\sum_{m=-\infty}^{\infty}\exp\left[-\frac{1}{2}\left(p-\frac{2\pi}{\alpha}m\right)^2\Big/\kappa^2\right]|p\rangle$$

$$=\int_{-\infty}^{\infty}\frac{dp}{(\pi\kappa^2)^{1/4}}\left(\frac{4\pi\Delta^2}{\alpha^2}\right)^{1/4}\sum_{m=-\infty}^{\infty}e^{-1/2\Delta^2p^2}$$

$$\times\exp\left[-\frac{1}{2}\left(p-\frac{2\pi}{\alpha}m\right)^2\Big/\kappa^2\right]|p\rangle, \qquad (34)$$

again a superposition of Gaussians weighted by a Gaussian envelope. (See Fig. 2.)

The approximate code words $|\tilde{0}\rangle,|\tilde{1}\rangle$ have a small overlap if Δ is small compared to α, and κ is small compared to π/α. For estimating the error probability caused by the overlap, let’s consider the special case where q and p are treated symmetrically, $\alpha=\sqrt{\pi}$ and $\kappa=\Delta$, then

$$|\langle q|\tilde{0}\rangle|^2\approx\frac{2}{\sqrt{\pi}}\sum_{s=-\infty}^{\infty}e^{-4\pi\Delta^2s^2}\exp[-(q-2s\sqrt{\pi})^2/\Delta^2] \qquad (35)$$

and

$$\frac{1}{2}|\langle p|\tilde{0}\rangle+\langle p|\tilde{1}\rangle|^2\approx\frac{2}{\sqrt{\pi}}\sum_{m=-\infty}^{\infty}e^{-\Delta^2p^2}$$

$$\times\exp[-(p-2m\sqrt{\pi})^2/\Delta^2]. \qquad (36)$$

To perform error recovery, we measure the value of q and p modulo $\sqrt{\pi}$ and then correct for the observed shift. In the state $|\tilde{0}\rangle$, the probability of failure is the probability that q is closer to an odd multiple of $\sqrt{\pi}$ than an even multiple, and in the state $(|\tilde{0}\rangle+|\tilde{1}\rangle)/\sqrt{2}$, the error probability is the probability that p is closer to an odd multiple of $\sqrt{\pi}$ than an even multiple. For both the amplitude and phase errors, the intrinsic error probability arising from the imperfections of the approximate code words becomes exponentially small for small Δ. Using the asymptotic expansion of the error function,

$$\int_x^\infty dt e^{-t^2} = \left(\frac{1}{2x}\right) e^{-x^2}[1 - O(1/x^2)], \tag{37}$$

we may estimate the error probability by summing the contributions from the tails of all the Gaussians, obtaining

$$\begin{aligned} \text{Error Prob} &< \frac{2}{\sqrt{\pi}} \left(\sum_{n=-\infty}^{\infty} e^{-4\pi\Delta^2 n^2} \right) 2 \int_{\sqrt{\pi}/2}^{\infty} dq e^{-q^2/\Delta^2} \\ &\sim \frac{2}{\sqrt{\pi}} \frac{1}{2\Delta} 2\Delta \frac{\Delta}{\sqrt{\pi}} e^{-\pi/4\Delta^2} \\ &= \frac{2\Delta}{\pi} e^{-\pi/4\Delta^2}. \end{aligned} \tag{38}$$

This error probability is about 1% for $\Delta \sim .5$, and is already less than 10^{-6} for a still modest value $\Delta \sim .25$. Using finitely squeezed approximate code words does not badly compromise the error-correcting power of the code, since a gentle spreading in p and q is just the kind of error the code is intended to cope with.

The mean photon number of a finitely squeezed approximate code word is

$$\langle a^\dagger a \rangle + 1/2 = \frac{1}{2} \langle p^2 + q^2 \rangle \approx \Delta^{-2} \tag{39}$$

for small Δ. Therefore, an error probability of order 10^{-6} can be achieved with Gaussian approximate code words that have mean photon number of about $(.25)^{-2} \sim 16$.

More generally, a finitely squeezed code word $|\psi\rangle$ can be regarded as a perfect code word $|\xi\rangle$ that has undergone an error; we may write

$$|\psi\rangle = \int du dv\, \eta(u,v) e^{i(-up+vq)} |\xi\rangle, \tag{40}$$

where $\eta(u,v)$ is an error ''wave function.'' In the special case of a Gaussian finitely squeezed code word, we have

$$\eta(u,v) = \frac{1}{\sqrt{\pi \kappa \Delta}} \exp\left(-\frac{1}{2}(u^2/\Delta^2 + v^2/\kappa^2) \right), \tag{41}$$

where Δ and κ are the squeezing parameters defined above.

If $\eta(u,v)$ vanishes for $|u| > \alpha/2$ or $|v| > \pi/(n\alpha)$, then the error is correctable. In this case, the interpretation of $\eta(u,v)$ as a wave function has a precise meaning, since there is an unambiguous decomposition of a state into code word and error. Indeed, if $|\xi_1\rangle$, $|\xi_2\rangle$ are perfect code words and $|\psi_1\rangle$, $|\psi_2\rangle$ are the corresponding finitely squeezed code words with error wave functions η_1, η_2, then

$$\langle \psi_1 | \psi_2 \rangle = \langle \xi_1 | \xi_2 \rangle \langle \eta_1 | \eta_2 \rangle, \tag{42}$$

where

$$\langle \eta_1 | \eta_2 \rangle = \int du dv\, \eta_1(u,v)^* \eta_2(u,v). \tag{43}$$

VI. CONTINUOUS VARIABLE CODES FOR MANY OSCILLATORS

The continuous variable codes described in Sec. IV are based on simple lattices in the two-dimensional phase space of a single particle. We can construct more sophisticated codes from lattices in the $2N$-dimensional phase space of N particles. Then codes of higher quality can be constructed that take advantage of efficient packings of spheres in higher dimensions.

For a system of N oscillators, a tensor product of Pauli operators can be expressed in terms of the canonical variables q_i and p_i as

$$U_{\alpha\beta} = \exp\left[i\sqrt{2\pi} \left(\sum_{i=1}^{N} \alpha_i p_i + \beta_i q_i \right) \right], \tag{44}$$

where the α_i's and β_i's are real numbers. (In this setting, the Pauli operators are sometimes called ''Weyl operators.'') Two such operators commute up to a phase:

$$U_{\alpha\beta} U_{\alpha'\beta'} = e^{2\pi i[\omega(\alpha\beta,\alpha'\beta')]} U_{\alpha'\beta'} U_{\alpha\beta}, \tag{45}$$

where

$$\omega(\alpha\beta, \alpha'\beta') \equiv \alpha \cdot \beta' - \alpha' \cdot \beta \tag{46}$$

is the symplectic form. Thus two Pauli operators commute if and only if their symplectic form is an integer.

Now a general continuous variable stabilizer code is the simultaneous eigenspace of commuting Pauli operators, the code's stabilizer generators. If the continuous variable phase space is $2N$-dimensional and the code space is a finite-dimensional Hilbert space, then there must be $2N$ independent generators. The elements of the stabilizer group are in one-to-one correspondence with the points of a lattice $\mathcal{L}$ in phase space, via the relation

$$U(k_1, k_2, \ldots k_{2N}) = \exp\left[i\sqrt{2\pi} \left(\sum_{a=1}^{2N} k_a v_a \right) \right]. \tag{47}$$

Here $\{v_a, a = 1,2, \ldots, 2N\}$ are the basis vectors of the lattice (each a linear combination of q's and p's), the k_a's are arbitrary integers, and $U(k_1, k_2, \ldots k_{2N})$ is the corresponding element of the stabilizer. For the stabilizer group to be Abelian, the symplectic inner product of any pair of basis vectors must be an integer; that is, the antisymmetric $2N \times 2N$ matrix

$$A_{ab} = \omega(v_a, v_b) \tag{48}$$

has integral entries. The lattice $\mathcal{L}$ has a $2N \times 2N$ generator matrix M whose rows are the basis vectors,

$$M=\begin{pmatrix} v_1 \\ v_2 \\ \cdot \\ \cdot \\ v_{2N} \end{pmatrix}. \tag{49}$$

In terms of M, the matrix A can be expressed as

$$A=M\omega M^T, \tag{50}$$

where ω denotes the $2N\times 2N$ matrix

$$\omega=\begin{pmatrix} 0 & I \\ -I & 0 \end{pmatrix}, \tag{51}$$

and I is the $N\times N$ identity matrix.

The generator matrix of a lattice is not unique. The replacement

$$M\rightarrow M'=RM \tag{52}$$

leaves the lattice unmodified, where R is an invertible integral matrix with determinant ± 1 (whose inverse is also integral). Under this replacement, the matrix A changes according to

$$A\rightarrow A'=RAR^T. \tag{53}$$

By Gaussian elimination, an R can be constructed such that the antisymmetric matrix A is transformed to

$$A'=\begin{pmatrix} 0 & D \\ -D & 0 \end{pmatrix}, \tag{54}$$

where D is a positive diagonal $N\times N$ matrix.

There are also Pauli operators that provide a basis for the operations acting on the code subspace—these are the Pauli operators that commute with the stabilizer but are not contained in the stabilizer. The operators that commute with the stabilizer themselves form a lattice $\mathcal{L}^\perp$ that is dual (in the symplectic form) to the stabilizer lattice. The basis vectors of this lattice can be chosen to be $\{u_b, b=1,2,3,\ldots,2N\}$ such that

$$\omega(u_a,v_b)=\delta_{ab}; \tag{55}$$

then the generator matrix

$$M^\perp=\begin{pmatrix} u_1 \\ u_2 \\ \cdot \\ \cdot \\ u_{2N} \end{pmatrix} \tag{56}$$

of $\mathcal{L}^\perp$ has the property

$$M^\perp\omega M^T=I. \tag{57}$$

It follows from Eq. (48) and Eq. (55) that the $\mathcal{L}$ basis vectors can be expanded in terms of the $\mathcal{L}^\perp$ basis vectors as

$$v_a=\sum_b A_{ab}u_b, \tag{58}$$

or

$$M=AM^\perp, \tag{59}$$

and hence that

$$\omega(u_a,u_b)=(A)^{-1}_{ba}, \tag{60}$$

or

$$M^\perp\omega(M^\perp)^T=(A^{-1})^T. \tag{61}$$

If the lattice basis vectors are chosen so that A has the standard form Eq. (54), then

$$(A^{-1})^T=\begin{pmatrix} 0 & D^{-1} \\ -D^{-1} & 0 \end{pmatrix}. \tag{62}$$

In the special case of a self-dual lattice, corresponding to a code with a one-dimensional code space, both A and A^{-1} must be integral; hence $D=D^{-1}$ and the standard form of A is

$$A=\begin{pmatrix} 0 & I \\ -I & 0 \end{pmatrix}=\omega. \tag{63}$$

Since the code subspace is invariant under the translations in $\mathcal{L}$, we can think of the encoded information as residing on a torus, the unit cell of $\mathcal{L}$. The encoded Pauli operators $\{\bar{X}^a\bar{Z}^b\}$ are a lattice of translations on this torus, corresponding to the coset space $\mathcal{L}^\perp/\mathcal{L}$. The number of encoded Pauli operators is the ratio of the volume of the unit cell of $\mathcal{L}$ to the volume of the unit cell of $\mathcal{L}^\perp$, namely the determinant of A, which is therefore the square of the dimension of the Hilbert space of the code. Thus the dimension of the code space is

$$n=|\mathrm{Pf}A|=\det D, \tag{64}$$

where PfA denotes the *Pfaffian*, the square root of the determinant of the antisymmetric matrix A.

The stabilizer lattice unit cell has volume $|\mathrm{Pf}A|$ in units with $h=2\pi\hbar=1$, and the unit cell of the lattice of encoded operations has volume $|\mathrm{Pf}A|^{-1}$ in these units. So the code fits an n-dimensional code space into n units of phase space volume, as expected.

Codes of the CSS type (those analogous to the binary quantum codes first constructed by Calderbank and Shor [15] and by Steane [16]) are constructed by choosing one lattice $\mathcal{L}_q$ describing stabilizer generators that are linear combinations of the q's, and another lattice $\mathcal{L}_p\subset\mathcal{L}_q^\perp$ describing stabilizer generators that are linear combinations of the p's.

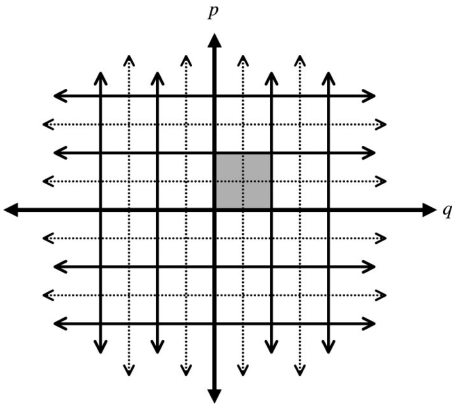

FIG. 3. The stabilizer lattice and its dual for an $n=2$ code of a single oscillator. Solid lines indicate the stabilizer lattice; solid and dotted lines together comprise the dual lattice. In units of $(2\pi\hbar)^2$, the unit cell of the stabilizer lattice (shaded) has area 2, and the unit cell of its dual has area 1/2.

(Here $\mathcal{L}_q^{\perp}$ denotes the *Euclidean* dual of the lattice $\mathcal{L}_q$.) The generator matrix of a CSS code has the form

$$M=\begin{pmatrix} M_q & 0 \\ 0 & M_p \end{pmatrix}, \tag{65}$$

where M_q and M_p are $N\times N$ matrices, and the integral matrix A has the form

$$A=\begin{pmatrix} 0 & M_qM_p^T \\ -M_pM_q^T & 0 \end{pmatrix}. \tag{66}$$

For single-oscillator codes described in Sec. IV, A is the 2×2 matrix

$$A=\begin{pmatrix} 0 & n \\ -n & 0 \end{pmatrix}, \tag{67}$$

where n is the code's dimension. For a single-oscillator CSS code, the lattice is rectangular, as shown in Fig. 3.

The closest packing of circles in two dimensions is achieved by the hexagonal lattice. The generator matrix for a hexagonally encoded qunit can be chosen to be

$$M=\left(\frac{2}{\sqrt{3}}\,n\right)^{1/2}\begin{pmatrix} 1 & 0 \\ 1/2 & \sqrt{3}/2 \end{pmatrix}, \tag{68}$$

and the dual lattice is generated by

$$M^{\perp}=\frac{1}{n}\,M. \tag{69}$$

The shortest vector of the dual lattice has length $(2/n\sqrt{3})^{1/2}$, compared to length $1/\sqrt{n}$ for the square lattice. Therefore the size of the smallest uncorrectable shift is larger for the hexagonal code than for the square lattice code, by the factor $(2/\sqrt{3})^{1/2}\approx 1.07457$.

An important special class of quantum codes for many oscillators are the *concatenated codes*. In particular, we can encode a qudit in each of N oscillators using the code of Sec. IV. Then we can use a binary stabilizer code that encodes k qudits in a block of N oscillators, and protects against arbitrary errors on any t oscillators, where $2t+1$ is the binary code's distance. The concatenated codes have the important advantage that they can protect against a broader class of errors than small diffusive shifts applied to each oscillator — if most of the oscillators undergo only small shifts in p and q, but a few oscillators sustain more extensive damage, then concatenated codes still work effectively.

For example, there is a binary [[7,1,3]] quantum code, well suited to fault-tolerant processing, that encodes one logical qudit in a block of seven qudits and can protect against heavy damage on any one of the seven [2]. Given seven oscillators, we can encode a qudit in each one that is resistant to quantum diffusion, and then use the [[7,1,3]] block code to protect one logical qudit against severe damage to any one of the oscillators.

For $n\geqslant 5$, there is a [[5,1,3]] polynomial code [17], also well suited to fault-tolerant processing, encoding one qunit in a block of 5. (Actually, [[5,1,3]] quantum codes exist for $n<5$ as well [6,7], but these codes are less conducive to fault-tolerant computing.) The larger value of n increases the vulnerability of each qunit to shift errors. Hence, whether the [[7,1,3]] binary code or the [[5,1,3]] should be preferred depends on the relationship of the size of the typical shift errors to the rate of large errors.

VII. ERROR MODELS

What sort of errors can be corrected by these codes? The codes are designed to protect against errors that shift the values of the canonical variables p and q. In fact the Pauli operators are a complete basis, so the action of a general superoperator $\mathcal{E}$ acting on the input density matrix ρ of a single oscillator can be expanded in terms of such shifts, as in

$$\mathcal{E}(\rho)=\int d\alpha d\beta d\alpha' d\beta' C(\alpha,\beta;\alpha'\beta') \times e^{i(\alpha p+\beta q)}\rho e^{-i(\alpha' p+\beta' q)}. \tag{70}$$

If the support of $C(\alpha,\beta;\alpha',\beta')$ is concentrated on sufficiently small values of its arguments, then the input ρ can be recovered with high fidelity.

A useful model of decoherence is the special case of a ''Pauli channel'' in which $C(\alpha,\beta;\alpha',\beta')$ is diagonal and the superoperator can be expressed as

$$\mathcal{E}(\rho)=\int d\alpha d\beta P(\alpha,\beta)e^{i(\alpha p+\beta q)}\rho e^{-i(\alpha p+\beta q)}. \tag{71}$$

Since $\mathcal{E}$ is positive and trace preserving, we infer that $P(\alpha,\beta)\geqslant 0$ and

$$\int d\alpha d\beta P(\alpha,\beta)=1. \tag{72}$$

Thus, we may interpret $P(\alpha,\beta)$ as a probability distribution: the phase space translation

$$(q,p)\rightarrow(q-\alpha,p+\beta) \tag{73}$$

is applied with probability $P(\alpha,\beta)$.

Weak interactions between an oscillator and its environment drive a diffusive process that can be well modeled by a Pauli channel. If the environment quickly ''forgets'' what it learns about the oscillator, the evolution of the oscillator can be described by a master equation. Over a short time interval dt, the shifts applied to the oscillator may be assumed to be small, so that the Pauli operator can be expanded in powers of α and β. Suppose that the shifts are symmetrically distributed in phase space such that

$$\begin{aligned}\langle\alpha\rangle=\langle\beta\rangle=0,\\ \langle\alpha^2\rangle=\langle\beta^2\rangle,\\ \langle\alpha\beta\rangle=0,\end{aligned} \tag{74}$$

where $\langle\cdot\rangle$ denotes the mean value determined by the probability distribution $P(\alpha,\beta)$. Suppose further that the shifts are diffusive, so that the mean square displacement increases linearly with dt; we may write

$$\langle\alpha^2\rangle=\langle\beta^2\rangle=D\,dt, \tag{75}$$

where D is a diffusion constant. We then obtain

$$\begin{aligned}\rho(t+dt)&=\int d\alpha d\beta P(\alpha,\beta)e^{i(\alpha p+\beta q)}\rho e^{-i(\alpha p+\beta q)}\\ &=\rho(t)+D\,dt\left(p\rho p-\frac{1}{2}p^2\rho-\frac{1}{2}\rho p^2\right)\\ &\quad+D\,dt\left(q\rho q-\frac{1}{2}q^2\rho-\frac{1}{2}\rho q^2\right)+O(dt^{3/2}),\end{aligned} \tag{76}$$

or

$$\dot{\rho}=-\frac{D}{2}[p,[p,\rho]]-\frac{D}{2}[q,[q,\rho]]. \tag{77}$$

The interpretation of D as a diffusion constant can be confirmed by computing

$$\frac{d}{dt}\mathrm{tr}(p^2\rho)=D=\frac{d}{dt}\mathrm{tr}(q^2\rho); \tag{78}$$

the mean square values of p and q increase with time as Dt.

More generally, the master equation contains a diffusive term determined by the covariance of the distribution $P(\alpha,\beta)$, and perhaps also a nondissipative drift term determined by the mean of $P(\alpha,\beta)$. Our quantum error-correcting codes can successfully suppress decoherence caused by quantum diffusion, if the recovery operation is applied often enough; roughly, the time interval Δt between error correction steps should be small compared to the characteristic diffusion time D^{-1}.

Interactions with the environment might also damp the amplitude of the oscillator, as described by the master equation

$$\dot{\rho}=\Gamma\left(a\rho a^\dagger-\frac{1}{2}a^\dagger a\rho-\frac{1}{2}\rho a^\dagger a\right); \tag{79}$$

here $a=(q+ip)/\sqrt{2}$ is the annihilation operator and Γ is a decay rate. This master equation cannot be obtained from a Pauli channel, but as for quantum diffusion, the effects of amplitude damping over short-time intervals can be expressed in terms of small phase-space displacements.

The master equation for amplitude damping can be obtained as the $dt\rightarrow 0$ limit of the superoperator

$$\begin{aligned}\rho(t+dt)=\mathcal{E}(\rho(t))&=(\sqrt{\Gamma dt}a)\rho(t)(\sqrt{\Gamma dt}a^\dagger)\\ &\quad+\left(I-\frac{\Gamma dt}{2}a^\dagger a\right)\rho(t)\left(I-\frac{\Gamma dt}{2}a^\dagger a\right).\end{aligned} \tag{80}$$

For dt small, the annihilation operator can be expanded in terms of Pauli operators as

$$\begin{aligned}\sqrt{\Gamma dt}a\approx&-\frac{i}{2}(e^{i\sqrt{\Gamma dt/2}q}-e^{-i\sqrt{\Gamma dt/2}q})\\ &+\frac{1}{2}(e^{i\sqrt{\Gamma dt/2}p}-e^{-i\sqrt{\Gamma dt/2}p}).\end{aligned} \tag{81}$$

Thus, if the time interval Δt between error correction steps is small compared to the damping time Γ^{-1}, the displacements applied to code words are small, and error correction will be effective.

Aside from decoherence, we also need to worry about ''unitary errors.'' For example, an inadvertent rotation of the phase of the oscillator induces the unitary transformation

$$\mathrm{U}(\theta)\equiv\exp(i\theta a^\dagger a). \tag{82}$$

Like any unitary transformation, this phase rotation can be expanded in terms of Pauli operators. It is convenient to introduce the notation for the phase-space displacement operator

$$D(\gamma)\equiv\exp(\gamma a-\gamma^* a^\dagger)=\exp i\sqrt{2}[(\mathrm{Im}\gamma)q-(\mathrm{Re}\gamma)p], \tag{83}$$

where γ is a complex number. The displacements satisfy the identity

$$\mathrm{tr}(D(\gamma)D(\eta)^\dagger)=\pi\delta^2(\gamma-\eta), \tag{84}$$

so the operator $U(\theta)$ can be expanded in terms of displacements as

$$U(\theta)=\frac{1}{\pi}\int d^2\gamma\, u_\theta(\gamma)D(\gamma), \tag{85}$$

where

$$u_\theta(\gamma)=\mathrm{tr}(U(\theta)D(\gamma)^\dagger). \tag{86}$$

Evaluating the trace in the coherent state basis, we find that

$$u_\theta(\gamma)=\frac{ie^{i\theta/2}}{2\sin(\theta/2)}\exp\left(-\frac{i}{2}|\gamma|^2\cot(\theta/2)\right). \tag{87}$$

For small θ, the coefficient

$$u_\theta(\gamma)\approx\frac{i}{\theta}\exp\left(-\frac{i}{\theta}|\gamma|^2\right) \tag{88}$$

has a rapidly oscillating phase, and can be regarded as a distribution with support concentrated on values of γ such that $|\gamma|^2\sim\theta$; indeed, formally

$$\lim_{\theta\to 0}u_\theta(\gamma)=\pi\delta^2(\gamma). \tag{89}$$

Thus a rotation by a small angle θ can be accurately expanded in terms of small displacements—error correction is effective if an oscillator is slightly overrotated or underrotated.

VIII. THE GAUSSIAN QUANTUM CHANNEL

At what rate can error-free digital information be conveyed by a noisy continuous signal? In classical information theory, an answer is provided by Shannon's noisy channel coding theorem for the Gaussian channel [18]. This theorem establishes the capacity that can be attained by a signal with specified average power, for a channel with specified bandwidth and specified Gaussian noise power. The somewhat surprising conclusion is that a nonzero rate can be attained for any nonvanishing value of the average signal power.

A natural generalization of the Gaussian classical channel is the *Gaussian quantum channel*. The Gaussian quantum channel is a Pauli channel: N oscillators are transmitted, and the q and p displacements acting on the oscillators are independent Gaussian random variables with mean 0 and variance σ^2. A code is an M-dimensional subspace of the Hilbert space of the N oscillators, and the rate R of the code (in qudits) is defined as

$$R=\frac{1}{N}\log_2 M. \tag{90}$$

The quantum-information capacity C_Q of the channel is the maximal rate at which quantum information can be transmitted with fidelity arbitrarily close to one.

The need for a constraint on the signal power to define the capacity of the Gaussian classical channel can be understood on dimensional grounds. The classical capacity (in bits) is a dimensionless function of the variance σ^2, but σ^2 has dimensions. Another quantity with the same dimensions as σ^2 is needed to construct a dimensionless variable, and the power fulfills this role. But no power constraint is needed to define the quantum capacity of the quantum channel. The capacity (in qudits) is a function of the dimensionless variable $\hbar/\sigma^2$, where $\hbar$ is Planck's constant.

An upper bound on the quantum capacity of the Gaussian quantum channel was derived by Holevo and Werner [19]; they obtained (reverting now to units with $\hbar=1$)

$$C_Q\leqslant\log_2(1/\sigma^2), \tag{91}$$

for $0<\sigma^2<1$, and $C_Q=0$ for $\sigma^2\geqslant 1$. They also computed the coherent information I_Q of the Gaussian quantum channel, and maximized it over Gaussian signal states, finding [19]

$$(I_Q)_{\max}=\log_2(1/e\sigma^2), \tag{92}$$

for $0<\sigma^2<1/e$ (where $e=2.718\,28\ldots$). The coherent information is *conjectured* to be an attainable rate [1–3]; if this conjecture is true, then Eq. (92) provides a lower bound on C_Q.

Using our continuous variable codes, rigorous lower bounds on C_Q can be established. For σ^2 sufficiently small, a nonzero attainable rate can be established asymptotically for large N by either of two methods. In one method, the $n=2$ code described in Sec. IV is invoked for each oscillator, and concatenated with a binary quantum code. In the other method, which more closely follows Shannon's construction, a code for N oscillators is constructed as in Sec. VI, based on a close packing of spheres in $2N$-dimensional phase space. However (in contrast to the classical case), neither method works if σ^2 is too large. For large σ^2, encodings can be chosen that protect against q shifts or against p shifts, but not against both.

To establish an attainable rate using concatenated coding (the method that is easier to explain), we first recall a result concerning the quantum capacities of binary channels [15,20]. If X and Z errors are independent and each occur with probability p_e, then binary CSS codes exist that achieve a rate

$$R>1-2H_2(p_e)\equiv 1+2p_e\log_2 p_e+2(1-p_e)\log_2(1-p_e); \tag{93}$$

this rate is nonzero for $p_e<.1100$.

Now, for the Gaussian quantum channel, if we use the $n=2$ continuous variable code, errors afflicting the encoded qudit are described by a binary channel with independent X and Z errors. Since the code can correct shifts in q or p that satisfy $\Delta q,\Delta p<\sqrt{\pi}/2$, the error probability is

$$p_e<2\frac{1}{\sqrt{2\pi\sigma^2}}\int_{\sqrt{\pi}/2}^{\infty}dx\,e^{-x^2/2\sigma^2}. \tag{94}$$

Since the expression bounding p_e in Eq. (94) has the value .110 for $\sigma\approx.555$, we conclude that the Gaussian quantum channel has nonvanishing quantum capacity C_Q provided that

$$\sigma<.555. \tag{95}$$

One might expect to do better by concatenating the *hexagonal* $n=2$ single-oscillator code with a binary stabilizer code, since the hexagonal code can correct larger shifts than the code derived from a square lattice. For the Gaussian quantum channel, the symmetry of the hexagonal lattice ensures that X, Y, and Z errors afflicting the encoded qudit are equally likely. A shift is correctable if it lies within the ''Voronoi cell'' of the dual lattice, the cell containing all the points that are closer to the origin than to any other lattice site. By integrating the Gaussian distribution over the hexagonal Voronoi cell, we find that the probability $p_{e,\text{total}}$ of an uncorrectable error satisfies

$$p_{e,\text{total}} < 1 - \frac{12}{2\pi\sigma^2}\int_0^r dx \int_0^{x/\sqrt{3}} dy e^{-(x^2+y^2)/2\sigma^2}, \qquad (96)$$

where $r=(\pi/2\sqrt{3})^{1/2}$ is the size of the smallest uncorrectable shift. For a binary quantum channel with equally likely X, Y, and Z errors, it is known [21] that there are stabilizer codes achieving a nonvanishing rate for $p_{e,\text{total}}<.1905$; our bound on $p_{e,\text{total}}$ reaches this value for $\sigma\approx .547$.

Somewhat surprisingly, for very noisy Gaussian quantum channels, square lattice codes concatenated with CSS codes seem to do better than hexagonal codes concatenated with stabilizer codes. The reason this happens is that a CSS code can correct independent X and Z errors that occur with total probability $p_{e,\text{total}}=p_X+p_Z-p_X\cdot p_Z$, which approaches $0.2079>0.1905$ as $p_X=p_Z\rightarrow 0.1100$. For a given value of σ, the qudit encoded in each oscillator will have a lower error probability if the hexagonal code is used. But if the square lattice is used, a higher qudit error rate is permissible, and this effect dominates when the channel is very noisy.

We remark that this analysis is readily extended to more general Gaussian quantum channels. We may consider Pauli channels acting on a single oscillator in which the probability distribution $P(\alpha,\beta)$ is a more general Gaussian function, not necessarily symmetric in p and q. In that case, a symplectic transformation (one preserving the commutator of p and q) can be chosen that transforms the covariance matrix of the Gaussian to a multiple of the identity; therefore, this case reduces to that already discussed above. We may also consider channels acting on N oscillators that apply shifts in the $2N$-dimensional phase space, chosen from a Gaussian ensemble. Again there is a symplectic transformation that diagonalizes the covariance matrix; therefore, this case reduces to N independent single oscillator channels, each with its own value of σ^2.

IX. SYMPLECTIC OPERATIONS

To use these codes for fault-tolerant quantum computation, we will need to be able to prepare encoded states, perform error recovery, and execute quantum gates that act on the encoded quantum information. The most difficult task is encoding; we will postpone the discussion of encoding until after we have discussed encoded operations and error recovery.

Suppose, for example, that we have N oscillators, each encoding a qunit. We wish to apply $U(n^N)$ transformations that preserve the code subspace of the N qunits. As is typical of quantum codes, we will find that there is a discrete subgroup of $U(n^N)$ that we can implement ''easily;'' but to complete a set of universal gates we must add further transformations that are ''difficult.'' In the case of our continuous variable codes, the easy gates will be accomplished using linear optical elements (phase shifters and beam splitters), along with elements that can ''squeeze'' an oscillator. For the ''difficult'' gates we will require the ability to count photons.

The easy gates are the gates in the Clifford group. In general, the Clifford group of a system of N qunits is the group of unitary transformations that, acting by conjugation, take tensor products of Pauli operators to tensor products of Pauli operators (one says that they preserve the ''Pauli group''). Since for N oscillators the tensor products of Pauli operators have the form (44), the Clifford group transformations, acting by conjugation, are linear transformations of the p's and q's that preserve the canonical commutation relations. Such transformations are called symplectic transformations. The symplectic group has a subgroup that preserves the photon number

$$(\text{total photon number})=\sum_{i=1}^{N} a_i^\dagger a_i . \qquad (97)$$

The transformations in this subgroup can be implemented with linear optics [22]. The full symplectic group also contains ''squeeze operators'' that take an a to a linear combination of a's and $a^\dagger$'s; equivalently, the squeeze operators rescale canonical operators by a real number λ along one axis in the quadrature plane, and by λ^{-1} along the conjugate axis, as in (for example)

$$q_1\rightarrow\lambda q_1, \quad p_1\rightarrow\lambda^{-1}p_1 . \qquad (98)$$

With squeezing and linear optics, we can in principle implement any symplectic transformation.

Aside from the symplectic transformations, we will also assume that it is easy to do displacements that shift q and p by constants. A displacement of q_1 by c is actually the limiting case of a symplectic transformation on two oscillators q_1 and q_2:

$$q_1\rightarrow q_1+\varepsilon q_2, \quad p_1\rightarrow p_1+\varepsilon p_2$$
$$q_2\rightarrow q_2-\varepsilon q_1, \quad p_2\rightarrow p_2-\varepsilon p_1, \qquad (99)$$

where $\varepsilon\rightarrow 0$ with $\varepsilon q_2=c$ held fixed.

Since for the code with stabilizer generators (21) the Pauli operators acting on our encoded qunits are $\overline{X}=e^{ip\alpha}$ and $\overline{Z}=e^{2\pi i q/n\alpha}$, the Clifford group transformations acting on N qunits constitute a subgroup of the symplectic transformations (including shifts) acting on N oscillators, the subgroup that preserves a specified lattice in phase space. Thus we can do any encoded Clifford group gate we please by executing an appropriate symplectic transformation (possibly including a shift).

A similar comment applies to the case of a qunit encoded in a qudit. Since the logical Pauli operators are $\overline{X}=X^{r_1}$ and $\overline{Z}=Z^{r_2}$, each Clifford group transformation in the

n-dimensional code space is also a Clifford group transformation on the underlying qudit.

But we must also be sure that our implementation of the Clifford group is *fault tolerant*. In previous discussions of quantum fault tolerance for $[[N,k,2t+1]]$ codes, the central theme has been that propagation of error from one qudit to another in the same code block must be very carefully controlled [23,24]. For shift-resistant codes the main issue is rather different. Since each qudit typically has a (small) error anyway, propagation of error from one qudit to another is not necessarily so serious. But what must be controlled is *amplification* of errors—gates that turn small errors into large errors should be avoided.

The Clifford group can be generated by gates that are fault-tolerant in this sense. The Clifford group for qunits can be generated by three elements. The SUM gate is a two-qunit gate that acts by conjugation on the Pauli operators according to

$$\text{SUM}: \quad X_1^a X_2^b \to X_1^a X_2^{b-a}, \quad Z_1^a Z_2^b \to Z_1^{a+b} Z_2^b. \tag{100}$$

Here qunit 1 is said to be the control of the SUM gate, and qunit 2 is said to be its target; in the binary $(n=2)$ case, SUM is known as controlled-NOT, or CNOT. The Fourier gate F acts by conjugation as

$$F: \quad X \to Z, \quad Z \to X^{-1}; \tag{101}$$

for $n=2$ the Fourier Transform is called the Hadamard gate. The phase gate P acts as

$$P: \quad X \to (\eta) XZ, \quad Z \to Z, \tag{102}$$

where the n-dependent phase η is $\omega^{1/2}$ if n is even and 1 if n is odd. Any element of the Clifford group can be expressed as a product of these three generators. (In Ref. [8] another gate S was included among the generators of the Clifford group, but in fact the S gate can be expressed as a product of SUM gates.)

For an n-dimensional system encoded in a continuous variable system, these Clifford group generators can all be realized as symplectic transformations. In the case where the stabilizer generators are symmetric in q and p,

$$\bar{X} = \exp\left(-ip\sqrt{\frac{2\pi}{n}}\right), \quad \bar{Z} = \exp\left(iq\sqrt{\frac{2\pi}{n}}\right), \tag{103}$$

the required symplectic transformations are

$$\begin{aligned} \text{SUM}: q_1 &\to q_1, \quad p_1 \to p_1 - p_2, \\ q_2 &\to q_1 + q_2, \quad p_2 \to p_2, \\ F: \quad q &\to p, \quad p \to -q, \\ P: \quad q &\to q, \quad p \to p - q + c, \end{aligned} \tag{104}$$

where the n-dependent shift c is 0 for n even and $\sqrt{\pi/2n}$ for n odd. Under these symplectic transformations, small deviations of q and p from the stabilizer lattice remain small; in this sense the transformations are fault tolerant.

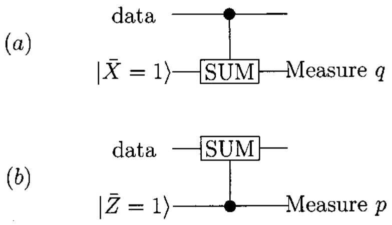

FIG. 4. Measurement of the error syndrome. (a) To diagnose the q shift, an ancilla is prepared in the encoded $\bar{X}=1$ state, a SUM gate is executed with the data as control and the ancilla as target, and the position of the ancilla is measured. (b) To diagnose the p shift, the ancilla is prepared in the $\bar{Z}=1$ state, a SUM gate is executed with the ancilla as control and the data as target, and the momentum of the ancilla is measured.

X. ERROR RECOVERY

If we are willing to destroy the encoded state, then measuring the encoded $\bar{X}$ or $\bar{Z}$ is easy—we simply conduct a homodyne measurement of the q or p quadrature of the oscillator. For example, suppose that we measure q for a state in the code subspace. If there are no errors and the measurement has perfect resolution, the only allowed values of q will be integer multiples of α. If there are errors or the measurement is imperfect, classical error correction can be applied to the outcome, by adjusting it to the nearest $\alpha \cdot k$, where k is an integer. Then the outcome of the measurement of $\bar{Z}$ is ω^k.

To diagnose errors in a coded data state, we must measure the stabilizer generators. This measurement can be implemented by ‘‘feeding’’ the errors from the code block to a coded ancilla, and then measuring the ancilla destructively, following the general procedure proposed by Steane [25] (see Fig. 4). For example, to measure the generator $e^{2\pi i q/\alpha}$ (i.e., the value of q modulo α), we prepare the ancilla in the state $(|\bar{0}\rangle + |\bar{1}\rangle)/\sqrt{2}$, the equally weighted superposition of all $|q = s\cdot\alpha\rangle$, s being an integer. Then a SUM gate is executed with the data as control and the ancilla as target—acting according to

$$q_2 \to q_1 + q_2, \tag{105}$$

where q_1, q_2 are the values of q for the data and ancilla respectively, prior to the execution of the SUM gate. By measuring q of the ancilla, the value of $q_1 + q_2$ is obtained, and this value modulo α determines the shift that should be applied to the data to recover from the error.

Similarly, to measure the stabilizer generator $e^{inp\alpha}$, we prepare the ancilla in the state $|\bar{0}\rangle$, the equally weighted superposition of all $|p = s\cdot 2\pi/n\alpha\rangle$, s being an integer. Then a SUM gate is executed with the ancilla as control and the data as target. Finally, the p quadrature of the ancilla is measured. The outcome reveals the value of $p_2 - p_1$ prior to the SUM gate, where p_1 is the momentum of the data, and p_2 is the momentum of the ancilla. The measured value modulo $2\pi/n\alpha$ then determines the shift that should be applied to the data to recover from the error.

Of course, the ancilla used in the syndrome measurement can also be faulty, resulting in errors in the syndrome and imperfect recovery. Similarly, the measurement itself will not have perfect resolution, and the shift applied to recover will not be precisely correct. Furthermore, as is discussed in Sec. V, the ideal code words are unphysical nonnormalizable states, so that the encoded information will always be carried by approximate code words. For all these reasons, deviations from the code subspace are unavoidable. But if a fresh supply of ancilla oscillators is continuously available, we can prevent these small errors from accumulating and eventually damaging the encoded quantum information.

XI. UNIVERSAL QUANTUM COMPUTATION

Symplectic transformations together with homodyne measurements are adequate for Clifford group computation and for error recovery (assuming we have a supply of encoded states). But to achieve universal computation in the code space, we need to introduce additional operations. Fortunately, the quantum optics laboratory offers us another tool that can be used to go beyond the symplectic computational model—the ability to count photons.

There are a variety of ways in which photon counting can be exploited to complete a universal set of fault-tolerant gates. We will describe two possible ways, just to illustrate how universal fault-tolerant quantum computation might be realized with plausible experimental tools. For this discussion, we will consider the binary case $n=2$.

A. Preparing a Hadamard eigenstate

We can complete the universal gate set if we have the ability to prepare eigenstates of the Hadamard operator H [26,27]. For this purpose it suffices to be able to *destructively* measure H of an encoded qudit. Assuming we are able to prepare a supply of the encoded $\overline{Z}$ eigenstate $|\overline{0}\rangle$, we can make an encoded Einstein-Podolsky-Rosen (EPR) pair using symplectic gates. Then by destructively measuring H for one encoded qudit in the pair, we prepare the other qudit in an encoded eigenstate of H with the known eigenvalue.

But how can we destructively measure H? The Hadamard gate acts by conjugation on the encoded Pauli operators according to

$$H: \quad \overline{X} \rightarrow \overline{Z}, \quad \overline{Z} \rightarrow \overline{X}. \tag{106}$$

If we use the code that treats q and p symmetrically so that $\overline{X}= \exp(-ip\sqrt{\pi})$ and $\overline{Z}= \exp(iq\sqrt{\pi})$, then the Hadamard gate can be implemented by the symplectic transformation.

$$q \rightarrow p, \quad p \rightarrow -q \tag{107}$$

(recalling that $\overline{X}^2=\overline{Z}^2=I$ on the code subspace). This transformation is just the Fourier transform

$$F: \quad \exp\left(i\frac{\pi}{2} a^\dagger a \right) \tag{108}$$

(where $a^\dagger a$ is the photon number), which describes the natural evolution of the oscillator for one quarter cycle. Thus the phase of the Hadamard operator is simply the photon number modulo four; we can measure the eigenvalue of the encoded Hadamard transformation by counting photons.

In fact the photon number in the code space is even—all code words are invariant under a 180° rotation in the quadrature plane. Because of this feature, the preparation of the Hadamard eigenstate has some fault tolerance built in; if the photon count is off by one, the number will be odd and an error will be detected. In that case we reject the state we have prepared and make a new attempt. If the photon number is large, then obtaining a reliable determination of the photon number modulo four will require highly efficient photodetection. But on the other hand, the photon number need not be very large — the mean value of $a^\dagger a$ is about Δ^{-2}, where Δ is the squeeze factor, and we have seen that the intrinsic error rate due to imperfect squeezing is quite small for $\Delta \sim 1/4$, or $\langle a^\dagger a\rangle \sim 16$.

An alternative to preparing an encoded EPR pair and destructively measuring one member of the pair is to prepare $|\overline{0}\rangle$ and then perform a quantum nondemolition measurement of the photon number modulo 4. This might be done by coupling the oscillator to a two-level atom as proposed in Ref. [28]. Indeed, since only one bit of information needs to be collected (the photon number is either 0 or 2 modulo 4), the measurement could be made in principle by reading out a single atom. Suppose that the coupling of oscillator to atom is described by the perturbation

$$H' = \lambda a^\dagger a \sigma_z , \tag{109}$$

where $\sigma_z = -1$ in the atomic ground state $|g\rangle$ and $\sigma_z = 1$ in the atomic excited state $|e\rangle$. By turning on this coupling for a time $t=\pi/4\lambda$, we execute the unitary transformation

$$\mathrm{U}= \exp[-i(\pi/4)a^\dagger a \sigma_z]. \tag{110}$$

Then the atomic state $(|g\rangle+|e\rangle)/\sqrt{2}$ evolves as

$$\mathrm{U}: \frac{1}{\sqrt{2}}(|g\rangle+|e\rangle) \rightarrow \frac{1}{\sqrt{2}} e^{ia^\dagger a \pi/4}(|g\rangle + e^{-ia^\dagger a \pi/2}|e\rangle). \tag{111}$$

By measuring the atomic state in the basis $(|g\rangle \pm |e\rangle)/\sqrt{2}$, we read out the value of the photon number modulo 4 (assumed to be either 2 or 4). Since this is a nondemolition measurement, it can be repeated to improve reliability. By measuring the photon number mod 4 many times (perhaps with rounds of error correction in between the measurements), we obtain a Hadamard eigenstate with excellent fidelity.

How does the ability to construct the Hadamard eigenstate enable us to achieve universal quantum computation? We can make contact with constructions that have been described previously in the literature by observing that the Hadamard eigenstate can be transformed by applying symplectic gates to the ‘‘π/8-phase state.’’ First note that the two Hadamard eigenstates can be converted to one another by applying the encoded gate $\overline{XZ}$, which can be implemented

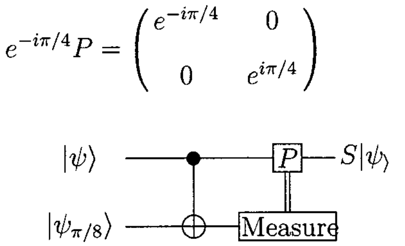
$e^{-i\pi/4}P = \begin{pmatrix} e^{-i\pi/4} & 0 \\ 0 & e^{i\pi/4} \end{pmatrix}$
$|\psi\rangle$
P
$S|\psi\rangle$
$|\psi_{\pi/8}\rangle$
Measure

FIG. 5. Implementation of the S gate. An ancilla is prepared in the state $|\psi_{\pi/8}\rangle$, and a CNOT gate is executed with the data as control and the ancilla as target; then the ancilla is measured in the basis $\{|0\rangle, |1\rangle\}$. A P gate is applied to the data conditioned on the measurement outcome.

by shifting both p and q. Therefore it is sufficient to consider the eigenstate corresponding to the eigenvalue 1,

$$|\psi_{H=1}\rangle = \cos(\pi/8)|0\rangle + \sin(\pi/8)|1\rangle. \tag{112}$$

By applying the symplectic single-qudit gate

$$H\cdot P^{-1} \equiv \frac{1}{\sqrt{2}}\begin{pmatrix} 1 & 1 \\ 1 & -1 \end{pmatrix}\cdot\begin{pmatrix} 1 & 0 \\ 0 & -i \end{pmatrix} = \frac{1}{\sqrt{2}}\begin{pmatrix} 1 & -i \\ 1 & i \end{pmatrix}, \tag{113}$$

we obtain the $\pi/8$ state

$$|\psi_{\pi/8}\rangle = \frac{1}{\sqrt{2}}(e^{-i\pi/8}|0\rangle + e^{i\pi/8}|1\rangle). \tag{114}$$

Now this $\pi/8$ state can be used to perform the nonsymplectic phase gate

$$S = \begin{pmatrix} e^{-i\pi/8} & 0 \\ 0 & e^{i\pi/8} \end{pmatrix}, \tag{115}$$

which completes the universal gate set [29,30]. The gate is constructed by executing the circuit shown in Fig. 5. We perform a CNOT gate with the arbitrary single-qudit state $|\psi\rangle = a|0\rangle + b|1\rangle$ as the control, and the $\pi/8$ phase state as the target; then the target qudit is measured in the basis $\{|0\rangle,|1\rangle\}$. If the measurement outcome is $|0\rangle$ (which occurs with probability 1/2), then the control qudit has become $ae^{i\pi/8}|0\rangle + be^{-i\pi/8}|1\rangle = S|\psi\rangle$ and we are done. If the measurement outcome is $|1\rangle$, then the control qudit has become $ae^{-i\pi/8}|0\rangle + be^{i\pi/8}|1\rangle$, and we obtain $S|\psi\rangle$ by applying the symplectic single-qudit gate

$$e^{-i\pi/4}P = \begin{pmatrix} e^{-i\pi/4} & 0 \\ 0 & e^{i\pi/4} \end{pmatrix}. \tag{116}$$

Completing the universal gate set by measuring the Hadamard transformation has some drawbacks. For one thing, while photon number modulo four corresponds to the Hadamard eigenvalue in the ideal code space, this correspondence will not apply to approximate code words unless they are of a special type.

Recall that the imperfections of the code words arising from finite squeezing can be described by an ‘‘embedded error’’ $|\eta\rangle$ as in Eq. (40); a Gaussian approximate code word has a Gaussian embedded error

$$\eta(u,v) = \frac{1}{\sqrt{\pi\Delta\kappa}}\exp\left(-\frac{1}{2}(u^2/\Delta^2 + v^2/\kappa^2)\right), \tag{117}$$

where Δ is the width in q and κ is the width in p. Symplectic gates act separately on the encoded qudit and the ‘‘embedded error’’ $|\eta\rangle$; for example, the Fourier transform gate and the SUM gate act on the error according to

$$F:|u,v\rangle \rightarrow |v,-u\rangle,$$

$$\text{SUM}:|u_1,v_1;u_2,v_2\rangle \rightarrow |u_1,v_1+v_2;u_2-u_1,v_2\rangle. \tag{118}$$

By measuring the photon number modulo 4, we actually measure the *product* of the eigenvalue of the Hadamard gate acting on the code word and the eigenvalue of F acting on the embedded error. The latter always equals 1 *if* we use symmetrically squeezed code words, with $\Delta = \kappa$.

Symmetric squeezing is not in itself sufficient to ensure that the measurement of the photon number modulo 4 will prepare the desired encoded Hadamard eigenstate. We also need to consider how the embedded error is affected by the preparation of the EPR pair that precedes the measurement. To prepare the EPR pair, we use the SUM gate. Suppose that we start with two symmetrically squeezed states. Then the SUM gate yields the error wave function

$$\eta'(u_1,v_1;u_2,v_2) = \exp\{-[u_1^2 + (v_1-v_2)^2 + (u_1+u_2)^2 + v_2^2]/\Delta^2\}. \tag{119}$$

Not only is it not symmetric, but the error is entangled between the two oscillators. The Fourier transform measurement will not give the desired result when applied to either oscillator.

To ameliorate this problem, we could perform error correction after the preparation of the EPR pair and before the measurement, where the error correction protocol has been designed to produce symmetrically squeezed states. Or we could avoid preparing the EPR state by using the nondemolition measurement of photon number modulo 4, as described above.

B. Preparing a cubic phase state

Now we will describe another way to use photon counting to implement nonsymplectic gates, which is less sensitive to the code word quality. Again, we will complete the universal gate set by constructing the $\pi/8$ phase gate S.

For our binary ($n = 2$) code, the code subspace has the basis

$$|\overline{0}\rangle = \sum_{s=-\infty}^{+\infty} |q = 2s\alpha\rangle,$$

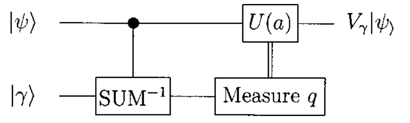

FIG. 6. Implementation of the cubic phase gate. An ancilla is prepared in the state $|\gamma\rangle$, and a SUM^{-1} gate is executed with the data as control and the ancilla as target; then the position of the ancilla is measured. A symplectic gate $\mathrm{U}(a)$ is then applied to the data, conditioned on the outcome a of the measurement.

$$|\overline{1}\rangle=\sum_{s=-\infty}^{+\infty}|q=(2s+1)\alpha\rangle. \tag{120}$$

(For now we ignore the embedded error due to imperfect squeezing; it will be taken into account later.) An S gate acting on the encoded qudit is implemented (up to an irrelevant overall phase) by the unitary operator

$$W=\exp\left(\frac{i\pi}{4}[2(q/\alpha)^3+(q/\alpha)^2-2(q/\alpha)]\right). \tag{121}$$

Indeed, we can check that

$$2x^3+x^2-2x(\mathrm{mod}8)=\begin{cases}0, & \text{if } x=2s\ ,\\ 1, & \text{if} x=2s+1\ .\end{cases} \tag{122}$$

The operator W is the product of a symplectic gate and the cubic phase gate

$$V_\gamma=\exp(i\gamma q^3), \tag{123}$$

where $\gamma=\pi/(2\alpha^3)$. But how do we implement the cubic gate? In fact, if we are able to prepare a ‘‘cubic phase state’’

$$|\gamma\rangle=\int dx e^{i\gamma x^3}|x\rangle, \tag{124}$$

then we can perform the gate V_γ by executing the circuit shown in Fig. 6.

To understand how the circuit works, consider the more general problem of implementing a phase gate that acts on the position eigenstates according to

$$V_\phi:|q\rangle\rightarrow e^{i\phi(q)}|q\rangle \tag{125}$$

(where $\phi(q)$ is a real-valued function), using the prepared phase state

$$|\phi\rangle=\int dx e^{i\phi(x)}|x\rangle. \tag{126}$$

If we perform the gate SUM^{-1} with position eigenstate $|q\rangle$ as control and $|\phi\rangle$ as target, and then measure the position of the target obtaining the outcome $|a\rangle$, the state of the control oscillator has become $e^{i\phi(q+a)}|q\rangle$. We can therefore complete the construction of V_ϕ by applying the transformation

$$\mathrm{U}(a)=e^{i[\phi(q)-\phi(q+a)]}. \tag{127}$$

If the function $\phi(q)$ is cubic, then the argument of the exponential is quadratic and hence $\mathrm{U}(a)$ is a symplectic transformation.

Now the problem of implementing universal quantum computation in the code subspace has been reduced to the problem of preparing the cubic phase state $|\gamma\rangle$. We can accomplish this task by preparing an EPR pair, and then performing a suitable photon counting measurement (a nonideal homodyne measurement) on one member of the pair.

Of course, the EPR pair will not be perfect. To be definite, let us suppose (although this assumption is not really necessary) that it is a Gaussian state

$$|\psi_{\sigma_p,\sigma_q}\rangle=\left(\frac{\sigma_p}{\pi\sigma_q}\right)^{1/2}\int dq_1dq_2\exp\left[-\frac{1}{2}\sigma_p^2\left(\frac{q_1+q_2}{2}\right)^2\right]\times\exp\left[-\frac{1}{2}(q_1-q_2)^2/\sigma_q^2\right]|q_1,q_2\rangle \tag{128}$$

with $\sigma_p,\sigma_q\ll 1$.

Now suppose that the second oscillator is mixed with a coherent light beam, resulting in a large shift in momentum,

$$|\psi\rangle\rightarrow e^{iwq}|\psi\rangle,\quad w\gg\sigma_q^{-1},\sigma_p^{-1}; \tag{129}$$

then the photon number is measured and n photons are detected. Thus the state of the first oscillator becomes (up to normalization)

$$|\psi_1^{(n)}\rangle\approx\left(\frac{\sigma_p}{\pi\sigma_q}\right)^{1/2}\int dq_1|q_1\rangle e^{-1/2\,\sigma_p^2q_1^2}\times\int dq_2\varphi_n^*(q_2)e^{iwq_2}e^{-1/2(q_1-q_2)^2/\sigma_q^2}, \tag{130}$$

where $|\varphi_n\rangle$ denotes the photon number eigenstate, the eigenstate with eigenvalue $n+\frac{1}{2}$ of the Hamiltonian $H=\frac{1}{2}(p^2+q^2)$.

We can evaluate the q_2 integral in Eq. (130) by appealing to the semiclassical approximation. For q_2 in the classically allowed region and far from the classical turning points, we may write

$$\varphi_n^*(q_2)\sim\frac{1}{\sqrt{2\pi p(q_2)}}\exp\left(-i\int^{q_2}dxp(x)\right)+\frac{1}{\sqrt{2\pi p(q_2)}}\exp\left(+i\int^{q_2}dxp(x)\right), \tag{131}$$

where

$$p(x)=\sqrt{2n+1-x^2}. \tag{132}$$

For $w\gg\sigma_q^{-1}$, the rapid phase oscillations strongly suppress the contribution to the integral arising from the left-moving part of $\varphi^{(n)}(q_2)$. A contribution from the right-moving part survives provided that

$$|p(q_1)-w|<\sigma_q^{-1}. \tag{133}$$

When this condition is satisfied, it is a reasonable approximation to replace the Gaussian factor $e^{-1/2(q_1-q_2)^2/\sigma_q^2}$ in the q_2 integral by $\sqrt{2\pi\sigma_q^2}\,\delta(q_1-q_2)$, so that we obtain

$$|\psi_1^{(n)}\rangle \approx (2\sigma_p\sigma_q)^{1/2}\int dq_1|q_1\rangle e^{-1/2\sigma_p^2 q_1^2}\frac{1}{\sqrt{2\pi p(q_1)}}$$

$$\times\exp\left(-i\int^{q_1}dx[p(x)-w]\right). \tag{134}$$

The probability that n photons are detected is given by the norm of this $|\psi_1^{(n)}\rangle$. The values of n that occur with appreciable probability satisfy Eq. (133) for some q_1 with $|q_1| < \sigma_p^{-1}$; thus typical measurement outcomes are in the range

$$n+\frac{1}{2}\sim\frac{1}{2}(w\pm\sigma_q^{-1})^2+\frac{1}{2}\sigma_p^{-2}, \tag{135}$$

with a flat probability distribution

$$\mathrm{Prob}(n)=\langle\psi_1^{(n)}|\psi_1^{(n)}\rangle\sim\frac{\sigma_q}{w}. \tag{136}$$

Heuristically, after the momentum shift is applied, the oscillator that is measured has momentum of order $w\pm\sigma_q^{-1}$, and position of order σ_p^{-1}, so that the value of the energy is $n+\frac{1}{2}=\frac{1}{2}(p^2+q^2)\sim\frac{1}{2}(w\pm\sigma_q^{-1})^2+\frac{1}{2}\sigma_p^{-2}$.

For a particular typical outcome of the photon-counting measurement, since $|\psi_1^{(n)}\rangle$ has its support on $|q_1|<\sigma_p^{-1}\ll w$, we can Taylor expand $p(x)$ about $x=q_1$ to express $|\psi_1^{(n)}\rangle$ as

$$\psi_1^{(n)}(q_1)\propto\exp\left(-i\int^{q_1}(\sqrt{(2n+1)-x^2}-w)dx\right)$$

$$\propto\exp\left(\frac{i}{6\sqrt{2n+1}}q_1^3-i(\sqrt{2n+1}-w)q_1\right.$$

$$\left.+O(q_1^5/w^3)\right). \tag{137}$$

This is a cubic phase state to good precision if w is large enough.

The coefficient γ' of q_1^3 in the phase of ψ_1 is of order $n^{-1/2}$, while the phase γ of the operator V_γ that we wish to execute is of order one. However, we can construct V_γ from $V_{\gamma'}$ as

$$V_\gamma=(S_{\gamma/\gamma'})^{-1}V_{\gamma'}(S_{\gamma/\gamma'}), \tag{138}$$

where S_r is a squeeze operation that acts according to

$$S_r: q\rightarrow(r)^{1/3}q,$$

$$p\rightarrow(r)^{-1/3}p. \tag{139}$$

Alternatively, we could squeeze the phase state $|\gamma'\rangle$ before we use it to implement the cubic phase gate.

Is this procedure fault tolerant? Before considering the errors introduced during the implementation of the cubic phase gate, we should check that the gate does not catastrophically amplify any preexisting errors. In general, a phase gate can transform a small position shift error into a potentially dangerous momentum shift error. Commuting $V(\phi)=e^{i\phi(q)}$ through the shift operator e^{-iup}, we find

$$e^{i\phi(q)}e^{-iup}=e^{-iup}e^{if_u(q)}e^{i\phi(q)}, \tag{140}$$

where $f_u(q)=\phi(q+u)-\phi(q)$; the operator $e^{if_u(q)}$ can be expanded in terms of momentum shift operators of the form e^{ivq} by evaluating the Fourier transform

$$\tilde{f}_u(v)=\int\frac{dq}{2\pi}e^{i(f_u(q)-vq)}. \tag{141}$$

Assuming we use a code where the parameter α is of order one, uncorrectable errors will be likely if $\tilde{f}_u(v)$ has significant support on values of v that are order one.

Suppose that $V(\phi)$ acts on an approximate code word whose wave function is concentrated on values of q in the domain $|q|<L$. Phase cancellations will strongly suppress $\tilde{f}_u(v)$, unless the stationary phase condition $f_u'(q)=v$ is satisfied for some value of q in the domain of the approximate code word. Therefore, $V(\phi)$ can propagate a preexisting position shift u to a momentum shift error of magnitude

$$|v|\sim\max_{|q|\leqslant L}|f_u'(q)|. \tag{142}$$

The cubic phase gate needed to implement the encoded S gate is $W=e^{i\phi(q)}$, where $\phi(q)=\pi q^3/2\alpha^3$, so that $f_u(q)=3\pi uq^2/2\alpha^3+\cdots$ (ignoring small terms linear and constant in q), and $f_u'(q)=3\pi uq/\alpha^3$; the gate transforms the position shift u to a momentum shift

$$v\sim3\pi Lu/\alpha^3. \tag{143}$$

For α of order one, then, to ensure that v is small we should use approximate code words with the property that the typical embedded position shift u satisfies

$$|u|\ll L^{-1}. \tag{144}$$

In particular, if the approximate code word's embedded errors are Gaussian, where κ is the typical size of a momentum shift and Δ is the typical size of a position shift, we require

$$\Delta\ll\kappa. \tag{145}$$

We assume that shift errors due to other causes are no larger than the embedded error.

In the circuit Fig. 6 that implements the cubic phase gate, position shift errors in either the encoded state $|\psi\rangle$ or the ancilla state $|\gamma\rangle$ might cause trouble. A shift by u in $|\psi\rangle$ is transformed to a phase error $e^{if_u(q)}$, and a shift by u in $|\gamma\rangle$ infects $|\psi\rangle$ with a phase error $e^{if_u(q+a)}$. Therefore, we should require that position shift errors in both $|\psi\rangle$ and $|\gamma\rangle$ satisfy the criterion (144), where L is the larger of the two wave packet widths.

When a cubic phase state is prepared by measuring half of an EPR pair, the packet width is of order σ_p^{-1} and typical position shift errors have $u \sim \sigma_q$. However, we must also take into account that either the encoded state or the ancilla must be squeezed as in Eq. (139). Suppose that the ancilla is squeezed, by a factor of order $n^{1/6} \sim w^{1/3}$; the wave packet is rescaled so that, after squeezing, the width L' and the typical shifts u' are given by

$$L' \sim \sigma_p^{-1} w^{-1/3}, \quad u' \sim \sigma_q w^{-1/3}. \tag{146}$$

Then the condition $|u'| \ll L'^{-1}$ is satisfied provided that $\sigma_q \ll \sigma_p w^{2/3}$. We also require that the rescaled packet has a large width compared to 1, or $\sigma_p \ll w^{-1/3}$.

For the derivation of Eq. (137), we used the approximations $w\sigma_q \gg 1$ and $w\sigma_p \gg 1$. We also need to check that the remainder terms in the Taylor expansion give rise to a phase error that is acceptably small. This error has the form $e^{if(q_1)}$, where $f(q_1) = O(q_1^5/w^3)$, corresponding to a momentum shift

$$v \sim f'(q_1) \sim \sigma_p^{-4} w^{-3}. \tag{147}$$

Squeezing amplifies this momentum shift error to $v' \sim v w^{1/3} \sim \sigma_p^{-4} w^{-8/3}$, which will be small compared to 1 provided that $\sigma_p \gg w^{-2/3}$. To summarize, our implementation of the cubic phase gate works well if the approximate code words have embedded errors satisfying $\Delta \ll \kappa$, and if widths σ_q and σ_p of the approximate EPR state satisfy $w \gg \sigma_q^{-1}$ and

$$w^{-1/3} \gg \sigma_p \gg w^{-2/3}. \tag{148}$$

Finally, how accurately must we count the photons? An error Δn in the photon number results in a phase error e^{ivq_1} with $|v| \sim n^{-1/2} \Delta n$ in $\psi_1^{(n)}(q_1)$, which will be amplified by squeezing to $|v'| \sim |v| w^{1/3} \sim n^{-1/3} \Delta n$. Therefore, the precision of the photon number measurement should satisfy

$$\Delta n \ll n^{1/3} \tag{149}$$

to ensure that this error is acceptably small.

C. Purification

Either of the above two methods could be used to implement a nonsymplectic phase transformation that completes the universal gate set. Of course, experimental limitations might make it challenging to execute the gate with very high fidelity. One wonders whether it is possible to refine the method to implement fault-tolerant universal gates of improved fidelity.

In fact, such refinements are possible. We have seen that we can reach beyond the symplectic transformations and achieve universal quantum computation if we have a supply of appropriate ‘‘nonsymplectic states’’ that cannot be created with the symplectic gates. If the nonsymplectic states have the right properties, then we can carry out a purification protocol to distill from our initial supply of noisy nonsymplectic states a smaller number of nonsymplectic states with much better fidelity [31,32].

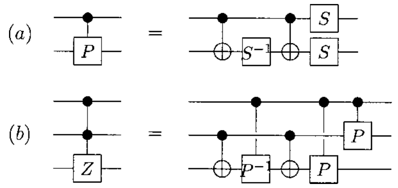

FIG. 7. Construction of the three-qudit gate $\Lambda^2(Z)$. (a) A $\Lambda(P)$ gate can be constructed (up to an overall phase) from two S gates, an S^{-1} gate, and two CNOT’S. The circuit is executed from left to right. (b) A $\Lambda^2(Z)$ gates can be constructed from two $\Lambda(P)$ gates, a $\Lambda(P^{-1})$ gate, and two CNOT’S.

An example of a nonsymplectic state that admits such a purification protocol is a variant of the state originally introduced by Shor [23], the three-qudit state

$$2^{-3/2} \sum_{a,b,c \in \{0,1\}} (-1)^{abc} |a\rangle_1 |b\rangle_2 |c\rangle_3; \tag{150}$$

it can be characterized as the simultaneous eigenstate of three commuting symplectic operators: $\Lambda(Z)_{1,2} X_3$ and its two cyclic permutations, where $\Lambda(Z)$ is the two-qudit conditional phase gate

$$\Lambda(Z): |a,b\rangle \to (-1)^{ab} |a,b\rangle. \tag{151}$$

As Shor explained, this nonsymplectic state can be employed to implement the Toffoli gate

$$T: |a,b,c\rangle \to |a,b,c \oplus ab\rangle, \tag{152}$$

and so provides an alternative way to complete the universal gate set.

To purify our supply of nonsymplectic states, symplectic gates are applied to a pair of nonsymplectic states and then one of the states is measured. Based on the outcome of the measurement, the other state is either kept or discarded. If the initial ensemble of states approximates the nonsymplectic states with adequate fidelity, then as purification proceeds, the fidelity of the remaining ensemble converges rapidly toward one.

The details of the purification protocol will be described elsewhere; here we will only remark that these Shor states can be readily created using symplectic gates and $\pi/8$-phase gates. The Shor state is obtained if we apply the transformation

$$\Lambda^2(Z): |a,b,c\rangle \to (-1)^{abc} |a,b,c\rangle \tag{153}$$

to the state

$$H_1 H_2 H_3 |0,0,0\rangle = 2^{-3/2} \sum_{a,b,c \in \{0,1\}} |a,b,c\rangle. \tag{154}$$

As shown in Fig. 7, $\Lambda^2(Z)$ can be applied by executing a circuit containing 5 S gates, 4 S^{-1} gates, and 8 CNOT gates.

Therefore, if we can apply symplectic gates accurately, and are also able to create a supply of $\pi/8$ states of reasonable fidelity (or can otherwise implement S gates of reasonable fidelity), then we can use the purification protocol to implement Toffoli gates with very good fidelity.

XII. ENCODING

Now we have discussed how to execute universal quantum computation fault tolerantly, and how to perform error recovery. But the discussion has all been premised on the assumption that we can prepare encoded states. It is finally time to consider how this can be done. In fact, preparing simultaneous eigenstates of the stabilizer generators $\exp(2\pi iq/\alpha)$ and $\exp(-inp\alpha)$ is a challenging task.

For the $[[N,k]]$ stabilizer codes that have been discussed previously, encoding is not intrinsically difficult in that it can be accomplished with Clifford group gates. Acting by conjugation, Clifford group transformations take tensor products of Pauli matrices to tensor products of Pauli operators. In particular, there is a Clifford group transformation that takes the state $|0\rangle^{\otimes N}$ (the simultaneous eigenstate with eigenvalue one of all N single-qudit Z's) to the encoded $|\overline{0}\rangle^{\otimes k}$ (the simultaneous eigenstate with eigenvalue one of $(N-k)$ stabilizer generators and k encoded $\overline{Z}$'s).

Where our codes are different, in both their finite-dimensional and infinite-dimensional incarnations, is that a *single* qudit or oscillator is required to obey *two* independent stabilizer conditions—i.e., to be the simultaneous eigenstate of two independent Pauli operators. Hence there is no Clifford group encoder. In the continuous variable case, the problem can be stated in more familiar language: the symplectic transformations take Gaussian (coherent or squeezed) states to Gaussian states. Hence no symplectic transformation can take (say) the oscillator's ground state to a state in the code subspace.

So encoding requires nonsymplectic operations, and as far as we know it cannot be accomplished by counting photons either—we must resort to a nonlinear coupling between oscillators, such as a $\chi^{(3)}$ coupling. We will describe one possible encoding scheme: First, we prepare a squeezed state, an eigenstate of the momentum with $p=0$. This state is already an eigenstate with eigenvalue one of the stabilizer generator $e^{inp\alpha}$, but not an eigenstate of $e^{2\pi iq/\alpha}$; rather its value of q is completely indefinite. To obtain an encoded state, we must project out the component with a definite value of q modulo α.

This can be achieved by coupling the oscillator to another oscillator that serves as a meter, via the perturbation of the Hamiltonian

$$H'=\lambda q(b^{\dagger}b), \tag{155}$$

where b is the annihilation operator of the meter.[1] This perturbation modifies the frequency of the meter,

$$\Delta\omega_{\text{meter}}=\lambda q; \tag{156}$$

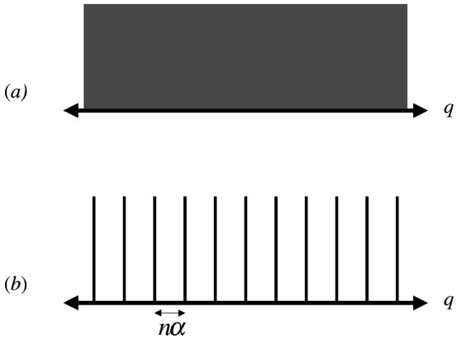

FIG. 8. Preparation of an encoded state. (a) An eigenstate of p is prepared, which has an indefinite value of q. (b) The value of q modulo $n\alpha$ is measured, projecting out a state that differs from the encoded $\overline{Z}$ eigenstate by a shift in q.

then if this coupling is turned on for a time $t=2\pi/\lambda n\alpha$, the phase of the meter advances by

$$\Delta\theta_{\text{meter}}=2\pi q/n\alpha. \tag{157}$$

By reading out the phase, we can determine the value of q modulo $n\alpha$, and apply a shift if necessary to obtain the state with $q\equiv 0 \pmod{n\alpha}$, the known state $|\overline{0}\rangle$ in the code subspace. (See Fig. 8.)

Of course, in practice the state squeezed in p prepared in the first step will be only finitely squeezed, and the measurement of q modulo $n\alpha$ will have imperfect resolution. If the squeezed state is Gaussian and the measurement has a Gaussian acceptance, then this procedure will produce an approximate code word of the sort described in Sec. V.

If we are able to prepare ''good enough'' encoded states, we can distill better ones. The distillation protocol is similar to the error recovery procedure, but where the ancilla used for syndrome measurement may be fairly noisy. We might improve the convergence of the distillation procedure by discarding the data oscillator if the measurement of the ancilla oscillator yields a value of q or p that is too distant from the values allowed by the code stabilizer.

So far, we have described how to prepare encoded states for the ''single-oscillator'' codes described in Sec. IV. To prepare an encoded state for one of the N-oscillator codes described in Sec. VI, we proceed in two steps. First we prepare each of N oscillators in a single-oscillator encoded state. Then we apply a symplectic transformation to obtain the encoded state of the N-oscillator code.

A particular known encoded state of a lattice stabilizer code can itself be regarded as a code with an $(n=1)$-dimensional code space. Hence it can be characterized by a *self-dual* symplectic lattice. For example, the $\overline{X}=1$ state of a qunit encoded in a single oscillator is the simultaneous eigenstate with eigenvalue of one of the operators $e^{-ip\alpha}$ and $e^{2\pi iq/\alpha}$—the state associated with the self-dual lattice whose basis vectors are $p\alpha/\sqrt{2\pi}$ and $q\sqrt{2\pi}/\alpha$.

One encoded state can be transformed to another by symplectic gates if there is a symplectic linear transformation that takes the self-dual lattice associated with the first state to the self-dual lattice associated with the second. In fact, such a symplectic transformation exists for any pair of self-dual lattices.

---

[1] There is an extensive literature on the experimental realization and applications of this kind of coupling; see [33].

A linear transformation acting on the p's and q's modifies the generator matrix M of a lattice according to

$$M \to MS; \tag{158}$$

this transformation is symplectic if

$$S\omega S^T = \omega, \tag{159}$$

where

$$\omega = \begin{pmatrix} 0 & I \\ -I & 0 \end{pmatrix}. \tag{160}$$

We saw in Sec. VI that we can always choose the generator matrix M of a self-dual lattice so that the matrix A has the form

$$A \equiv M\omega M^T = \omega; \tag{161}$$

that is, so that M is a symplectic matrix. Therefore, the generator matrices M_1 and M_2 of two self-dual lattices can each be chosen to be symplectic; then the linear transformation

$$S = M_1^{-1} M_2 \tag{162}$$

that takes one lattice to the other is also symplectic. Thus, while the task of preparing the encoded states of the single-oscillator codes can be accomplished only by introducing a nonlinear coupling between oscillators, proceeding from single-oscillator encoded states to many-oscillator encoded states can be achieved with linear optical operations and squeezing.

XIII. PHYSICAL FAULT TOLERANCE?

In a physical setting, making use of the continuous variable quantum error-correcting codes proposed here (or ‘‘digital’’ quantum codes that have been proposed previously) is a daunting challenge. We must continually measure the stabilizer operators (the ‘‘error syndrome’’) to diagnose the errors; to recover we must apply frequent shifts of the canonical variables that are conditioned on the measurement outcomes. Cold ancilla oscillators must be provided that are steadily consumed by the syndrome measurements. The ancillas must be discarded (or refreshed) to rid the system of excess entropy that has been introduced by the accumulated errors.

An alternative to this complex scheme was suggested in Ref. [34]. Perhaps we can engineer a quantum system whose (degenerate) ground state is the code subspace. Then the natural coupling of the system to its environment will allow the system to relax to the code space, removing errors introduced by quantum and thermal noise, or through the imperfect execution of quantum gates. Such a system, if it could be built, would be a highly stable quantum memory.

Continuous variable coding suggests possible approaches to implementing this type of physical fault tolerance. For example, the Hamiltonian

$$H = 2 - [\cos p + \cos(2\pi n q)] \tag{163}$$

has an n-fold degenerate (but nonnormalizable) ground state that is just the code space of a continuous variable code. (The operators $\cos p$ and $\cos 2\pi nq$ commute and can be simultaneously diagonalized.) The low-lying states of a real system whose Hamiltonian is a reasonable approximation to H would resemble the approximate code words described in Sec. V.

One possible way to realize physical fault tolerance is suggested by the codes for an electron in a Landau level, described in Sec. III. The wave functions in the code space are doubly periodic with a unit cell that encloses n flux quanta, where n is the code's dimension. If we turn on a tunable periodic potential whose unit cell matches that of the code, then the Landau level is split into n energy bands, and the code words are the states with vanishing Bloch momentum. Therefore, an encoded state could be prepared by turning on the potential, waiting for dissipative effects to cause the electrons to relax to the bottom of the lowest band, and then adiabatically turning off the potential. If dissipative effects cause electrons to relax to the bottom of a band on a timescale that is short compared to spontaneous decay from one band to another, then more general encoded states could be prepared by a similar method. Furthermore, turning on the potential from time to time would remove the accumulated Bloch momentum introduced by errors, allowing the electron to relax back to the code space.

XIV. CONCLUDING COMMENTS

We have described codes that protect quantum states encoded in a finite-dimensional subspace of the Hilbert space of a system described by continuous quantum variables. With these codes, continuous variable systems can be used for robust storage and fault-tolerant processing of quantum information.

For example, the coded information could reside in the Hilbert space of a single-particle system described by canonical quantum variables q and p. In practice, these variables might describe the states of a mode of the electromagnetic field in a high-finesse microcavity, or the state of the center of mass motion of an ion in a trap. Or the continuous Hilbert space could be the state space of a rotor described by an angular variable θ and its conjugate angular momentum L; in practice, these variables might be the phase and charge of a superconducting quantum dot. Our coding scheme can also be applied to a charged particle in a magnetic field.

Our codes are designed to protect against small errors that occur continually—diffusive drifts in the values of the canonical variables. The codes are less effective in protecting against large errors that occur rarely. In some settings, we may desire protection against both kinds of errors. One way to achieve that would be to *concatenate* our continuous-variable codes with conventional finite-dimensional quantum codes.

When we consider how to manipulate continuous-variable quantum information fault tolerantly, the issues that arise are rather different than in previous discussions of quantum fault tolerance. With continuous variable codes, propagation of error from one oscillator to another is not necessarily a serious problem. More damaging are processes that amplify a small shift of the canonical variables to a large shift. We have described how to implement a universal set of fault-tolerant quantum gates; with these, harmful error amplification can be avoided as the encoded state is processed.

Apart from encouraging the intriguing possibility that continuous quantum variables might prove useful for the construction of robust quantum memories and computers, these new quantum codes also have important theoretical applications. In this paper we have discussed an application to the theory of the quantum capacity of the Gaussian quantum channel. Furthermore, quantum codes can be invoked to investigate the efficacy of quantum cryptographic protocols, even in cases where the protocol makes no direct use of the encoded states [35]. With continuous-variable codes, we can demonstrate the security of key distribution protocols based on the transmission of continuous variable quantum information. This application is discussed in a separate paper [36].

ACKNOWLEDGMENTS

We gratefully acknowledge helpful discussions with Isaac Chuang, Sumit Daftuar, David DiVincenzo, Andrew Doherty, Steven van Enk, Jim Harrington, Jeff Kimble, Andrew Landahl, Hideo Mabuchi, Harsh Mathur, Gerard Milburn, Michael Nielsen, and Peter Shor. This work was supported in part by the Department of Energy under Grant No. DE-FG03-92-ER40701, and by the Caltech MURI Center for Quantum Networks under ARO Grant No. DAAD19-00-1-0374. Some of this work was done at the Aspen Center for Physics.

[1] P. W. Shor, Phys. Rev. A **52**, R2493 (1995).
[2] A. Steane, Phys. Rev. Lett. **77**, 793 (1996).
[3] E. Knill, R. Laflamme, and G. Milburn, Nature (London) (London) **409**, 46-52 (2001); e-print quant-ph/0006088.
[4] E. Knill, R. Laflamme, and G. Milburn, e-print quant-ph/0006120.
[5] E. Knill, e-print quant-ph/9608048; E. Knill, e-print quant-ph/9608049.
[6] H. F. Chau, Phys. Rev. A **55**, R839 (1997); H. F. Chau, *ibid.* **56**, R1 (1997).
[7] E. M. Rains, e-print quant-ph/9703048.
[8] D. Gottesman, Lect. Notes. Comp. Sci. **1509**, 302 (1999).
[9] A. R. Calderbank, E. M. Rains, P. W. Shor, and N. J. A. Sloane, Phys. Rev. Lett. **78**, 405 (1997).
[10] D. Gottesman, Phys. Rev. A **54**, 1862 (1996).
[11] S. Braunstein, Phys. Rev. Lett. **80**, 4084 (1998).
[12] S. Lloyd and J. E. Slotine, Phys. Rev. Lett. **80**, 4088 (1998).
[13] S. Parker, S. Bose, and M. B. Plenio, Phys. Rev. A **61**, 032305 (2000).
[14] L. M. Duan, G. Giedke, J. I. Cirac, and P. Zoller, Phys. Rev. Lett. **84**, 4002 (2000); L. M. Duan, G. Giedke, J. I. Cirac, and P. Zoller, Phys. Rev. A **62**, 032304 (2000).
[15] A. R. Calderbank and P. W. Shor, Phys. Rev. A **54**, 1098 (1996).
[16] A. Steane, Proc. R. Soc. London, Ser. A **452**, 2551 (1996).
[17] D. Aharonov and M. Ben-Or, in *Proceedings of the 29th Annual ACM Symposium on Theory of Computing* (ACM, New York, 1998), p. 176, e-print quant-ph/9611025; D. Aharonov and M. Ben-Or, e-print quant-ph/9906129.
[18] T. M. Cover and J. A. Thomas, *Elements of Information Theory* (Wiley, New York, 1991).
[19] A. S. Holevo and R. F. Werner, e-print quant-ph/9912067.
[20] S. Lloyd, Phys. Rev. A **56**, 1613 (1997).
[21] B. W. Schumacher and M. A. Nielsen, Phys. Rev. A **54**, 2629 (1996).
[22] H. Barnum, M. A. Nielsen, and B. Schumacher, Phys. Rev. A **57**, 4153 (1998).
[23] P. W. Shor, in *Proceedings of the 37th Annual Symphony on Foundations of Computer Science* (IEEE, Los Alamitos, CA, 1996), p. 56.
[24] D. Gottesman, Phys. Rev. A **57**, 127 (1998).
[25] A. Steane, Phys. Rev. Lett. **78**, 2252 (1997).
[26] E. Knill, R. Laflamme, and W. H. Zurek, Proc. R. Soc. London, Ser. A **454**, 365 (1998).
[27] D. Gottesman and I. Chuang, Nature (London) **402**, 390 (1999),
[28] S. Schneider, H. M. Wiseman, W. J. Munro, and G. J. Milburn, Fortschr. Physik **46**, 391 (1998).
[29] P. O. Boykin, T. Mor, M. Pulver, V. Roychowdhury, and F. Vatan, Inf. Process. Lett. **75**, 101 (2000).
[30] X. Zhou, D. W. Leung, and I. L. Chuang, Phys. Rev. A **62**, 052316 (2000).
[31] A. Yu. Kitaev (unpublished).
[32] E. Dennis, e-print quant-ph/9905027.
[33] V. Giovannetti, S. Mancini, and P. Tombesi, e-print quant-ph/0005066, and references therein.
[34] A. Yu. Kitaev, e-print quant-ph/9707021.
[35] P. W. Shor and J. Preskill, Phys. Rev. Lett. **85**, 441 (2000).
[36] D. Gottesman and J. Preskill, Phys. Rev. A **63**, 022309 (2001).

APPLIED PHYSICS LETTERS VOLUME 79, NUMBER 26 24 DECEMBER 2001

High quality two-dimensional photonic crystal slab cavities

Tomoyuki Yoshie,[a] Jelena Vučković, and Axel Scherer
Department of Electrical Engineering, California Institute of Technology, Pasadena, California 91125

Hao Chen and Dennis Deppe
Microelectronics Research Center, Department of Electrical and Computer Engineering,
The University of Texas at Austin, Austin, Texas 78712-1084

(Received 18 September 2001; accepted for publication 24 October 2001)

We have fabricated and characterized donor-mode nanocavities formed by a single defect cavity defined within a two-dimensional photonic crystal slab. Quantum dots emitting in the 1.1–1.3 micron range were used as luminescence sources, and a design using fractional edge dislocations was used to demonstrate well-confined dipole modes with high quality factors. By applying the fractional dislocation geometry, the measured quality factor could be increased to values as high as 2800. This compares with typical quality factors of around 1500 measured from more conventional shallow donor mode cavities with larger mode volumes. © *2001 American Institute of Physics.* [DOI: 10.1063/1.1427748]

The combination of high quality factors (Q) and small mode volumes are two important attributes for high performance nanocavities. High Q microcavities will become very important for control of optical emission processes[1] for strong coupling experiments and many other industrial applications of novel light emitters. State of the art lithography and etching enables us to construct microcavities with many different kinds of geometries such as micropillars,[2,3] microdisks,[4] AlO_x-apertured vertical cavities,[5] and photonic band-gap cavities.[6] Photonic crystal nanocavities[7–9] have recently attracted much attention because such cavities are predicted to provide the desired combination of both small mode volume and high Q values. Our photonic crystal cavities are constructed in thin slabs, which are perforated with triangular hole arrays and used to define photonic crystal mirrors. In the simplest defect cavity designs, regardless of whether we increase the number of defects forming the cavity, it has so far not been possible to demonstrate both small mode volume and high Q. The maximum Q for donor cavities is around 1500 from extended modes in empty lattice photonic crystal cavities.[10] Previous work to obtain higher Q values has focused on thin slabs patterned within hexagonal hole patterns missing several holes within a photonic crystal lattice. However, those cavities are not suitable for many applications since they have relatively large mode volumes and many modes exist within the semiconductor emission range. Typical well-confined donor mode cavities have small mode volumes, but also suffer from relatively low Q values, which are limited by vertical scattering losses. To address the problem, Vučković *et al.*[11] recently predicted by 3D-FDTD (finite difference time domain) calculations that single defect cavities with fractional edge dislocations can have well-localized modes with surprisingly high Q values of as high as 30 000. In this letter, we report the experimental demonstration that by using fractional edge dislocations in photonic crystal cavities, it is possible to measure microcavities with high Q's as well as small mode volumes.

In Fig. 1, we describe the structure used in this work. The schematic of our single defect photonic crystal nanocavity is constructed within a thin slab of GaAs, which is perforated with a triangular lattice of holes. A single smaller hole replaces a larger hole within the center of this slab to define the optical cavity. This cavity supports doubly degenerate shallow donor states. In our design, we have modified this geometry in two important ways: (1) In the x direction, in line with the smaller hole, ellipsoids rather than circles are fabricated at lattice spacing (a) with an elongated major axis of $2r+s=2r(1+p/2a')$ where r is a radius of original hole, $a'=\sqrt{3}a/2$ is an original distance of vicinal lattice array in y direction, and p/a is an elongation parameter. (2) Holes are moved away from the x axis by $p/2$ toward $+y$ or $-y$ direction. In $+y$ or $-y$ direction, the minor axis of ellipsoids is still $2r$. These two operations correspond to adding a fractional edge dislocation in the y direction. It also should be noted that Vučković *et al.*[11] used the major axis of ellipsoids of $2r+p$ which is bigger than the value $2r(1+p/2a')$ used in this letter.

We used self-assembled grown quantum dots as the light-emitting material grown on (001) GaAs by molecular

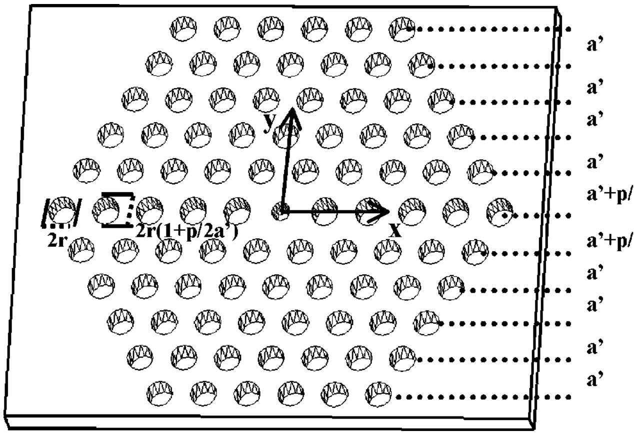

FIG. 1. Schematic of two-dimensional photonic crystal slab cavity with fractional edge dislocation.

---

[a] Electronic mail: yoshie@its.caltech.edu

Downloaded 03 Jan 2002 to 131.215.133.150. Redistribution subject to AIP license or copyright, see http://ojps.aip.org/aplo/aplcr.jsp

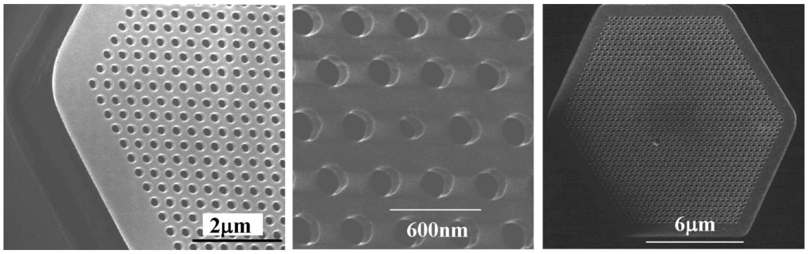

FIG. 2. Scanning electron microscopy image of photonic crystal slab with fractional edge dislocation.

beam epitaxy. Three stacked InAs quantum dot (QD) layers (QDs density: $3\times10^{10}\,\text{dots/cm}^2$) were clad by $Al_{0.16}Ga_{0.84}As$ layers on top of a 400 nm $Al_{0.94}Ga_{0.06}As$ layer. A GaAs cap layer is then added to protect the top on the final layer. The cavity thickness (d) is 240 nm. The ground state emission of QDs used in this report showed linewidths as narrow as 40 meV. The ground state emission at room temperature is peaked around 1240 nm.

The patterns to form hexagonal-arrayed photonic crystal defect cavity[12] were lithographically defined. Photonic crystal cavities are surrounded by twenty layers of photonic crystal for good optical confinement in plane. The lattice spacing (a) used in this work is lithographically controlled to 370 nm ($d/a=0.65$). After lithography, the beam-written patterns were transferred through the active membrane by using an Ar^+ ion beam assisted with a Cl_2 jet, and the $Al_{0.94}Ga_{0.06}As$ layer under cavities was subsequently oxidized in steam to define a perforated dielectric slab structure on top of an AlO_x cladding layer. Then, the AlO_x layer was completely dissolved in potassium hydroxide solution. Figure 2 shows images taken by scanning electron microscopy (SEM) for photonic crystal cavities containing a single donor defect with fractional edge dislocations. We fabricated samples with four different p/a values ($p=0, 0.10, 0.15$, and $0.20a$). The value of the hole radii defining the photonic crystals r ranged from 0.28 to $0.29a$, whereas the radius of the smaller hole defining the cavity ranged and from 0.20 to $0.23a$. In the four samples, the geometry parameters have slight fluctuations, but the imperfections could be measured by careful SEM characterization and compared to model results.

Local microphotoluminescence pumping of the center of cavity, and measuring the luminescence normal to the surface, allows us to quickly compare the performance of different cavity designs. The 830 nm pump laser light was absorbed by the InAs quantum dots and the wetting layers, and the pump light could be focused onto the sample with a spot diameter of 2 μm. Light emission from the photonic crystal slab surface was then detected by an optical spectrum analyzer. The peak pumping power was 1.4 mW, which corresponds to a power density of $45\,\text{kW/cm}^2$.

Figure 3 shows the p/a dependence of photoluminescence spectrum measured from four cavities with almost the same r/a and r'/a. In this case, we selected a 2 nm bandwidth for the spectrum measurement to detect weak emission from the samples. The shallow donor (SD1 and SD2) peaks have distinct y and x polarizations, respectively. By considering polarization dependence and simulation results, SD1 and SD2 were found to match numerically predicted shallow donor modes. We believe that the degeneracy of shallow donor modes for $p/a=0$ are lifted because of fabrication fluctuations in our quantum dot nanocavities. In Fig. 3, it can be observed that, for $p/a=0$, only two donor modes are seen, whereas a group of peaks labeled as (X) emerge just above SD2 resonance in cavities with higher p/a asymmetries. All the peaks shift toward longer wavelengths as p/a increases. However, the shift of SD1 resonance seems to be more pronounced than that of SD2 resonance. This can be understood by assuming that the added edge dislocation overlaps better with the SD1 mode than with the SD2 mode. Figure 4 shows the influence of p/a asymmetry on the Q as well as the normalized resonance energy (a/λ) taken from SD1 resonances. The SD1 resonance energy monotonically decreases almost linearly as p/a increases for the same reason as described above. Though the shift is small, the SD2 frequency dependence also has the same trend. On the other hand, Q continues to increase as p/a increases for this plot. In our samples, a maximum Q was obtained at $p/a=0.20$. Typical spectra taken from the nanocavities are shown in Fig. 5,

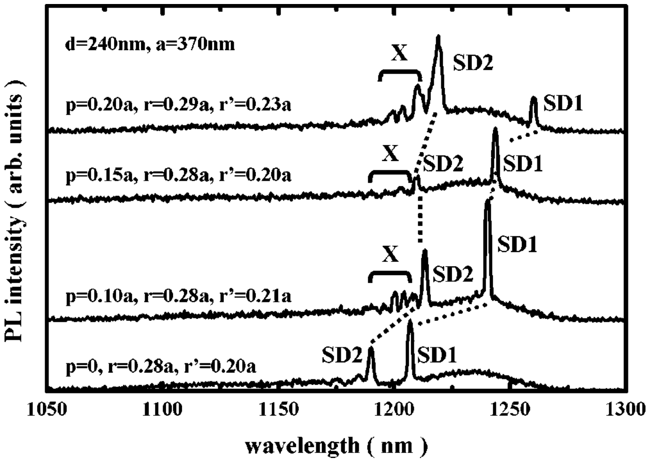

FIG. 3. PL spectrum of samples with different elongation parameter (p/a) ranging from 0 to 0.20.

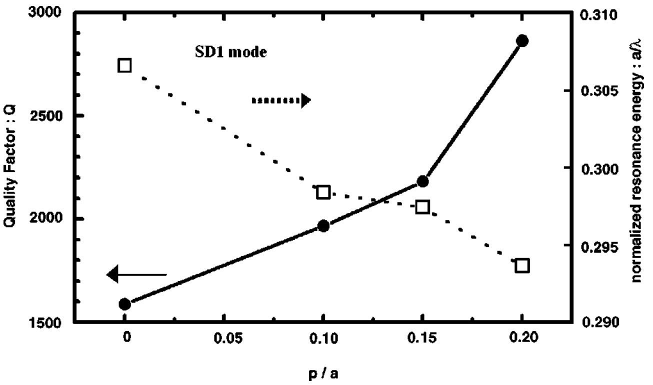

FIG. 4. Elongation parameter (p/a) dependence of Q and frequency (a/λ).

Downloaded 03 Jan 2002 to 131.215.133.150. Redistribution subject to AIP license or copyright, see http://ojps.aip.org/aplo/aplcr.jsp

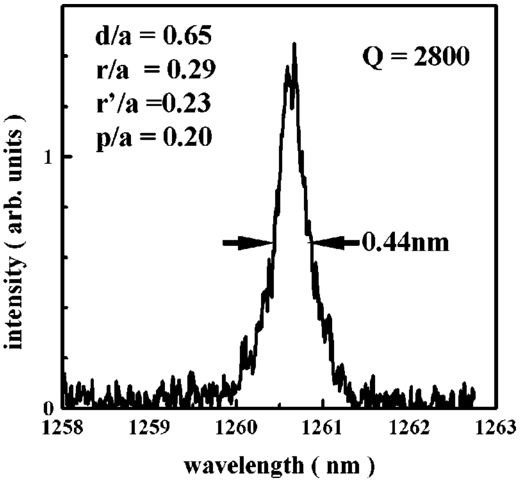

FIG. 5. PL spectra of the sample with *Q* of 2800.

where the resolution width of the spectrometer was set to 0.2 nm. The measured *Q* was as high as 2800. Therefore, by adding fractional edge dislocation, we could increase the measured *Q* to twice the value measured from a symmetric cavity. To compare the measured *Q* with our simulation results, we have carefully measured the geometries of our fabricated structures, and modeled these with our three-dimensional FDTD code. Indeed, we find that the calculated *Q* values for our experimentally realized geometries (of 4400) are much closer to the measured values, and that the simulated mode volume is $0.43(\lambda/n)^3$.

To confirm that the measured mode is localized to the defect region, we also changed the spatial location of pumping position to several points ten lattice layers away from the central hole.[12] We could not see the SD1 resonance in such measurements, which leads us to believe that the shallow donor modes are well confined. This is a strong indicator that the measured cavity mode has both a high *Q* as well as a small mode volume.

In order to verify whether the resonances appear in an appropriate range of emission, we have compared the observed spectra with spectra obtained by 3D-FDTD simulations, as shown in Fig. 6. For the simulation, spectral intensities in several points in the middle of the slab were added. Therefore, the spectra reflects on confined modes in the slab while the detected spectra reflects on leaky part of modes. That is why we also observe inhomogeneous emission from the QD layer in the spectrum. The SD1 and SD2 resonance frequencies are very similar to values predicted by the simulation. As the QD emission covers only the SD1, SD2, and air band region we did not see any prominent peaks around $a/\lambda = 0.33$, which is shown in the simulated Fourier spectra. However, we believe those modes do not leak into air significantly since they are guided modes and the original intensity of the QD emission in this frequency range is too weak to be observed. Therefore, we conclude that the measured spectra showed a good agreement with the simulated one. Though our predictions indicate that *Q* values of 30 000 are possible in geometries similar with the ones presented here, our measurement results are enough to show the advantage of using the fractional edge dislocation over the conventional designs. We believe it will become feasible to obtain the high *Q* predicted once the optimum photonic crystal parameters are precisely fabricated, and we are presently working on more precise fabrication accuracy and similar designs to obtain even higher measured quality factors.

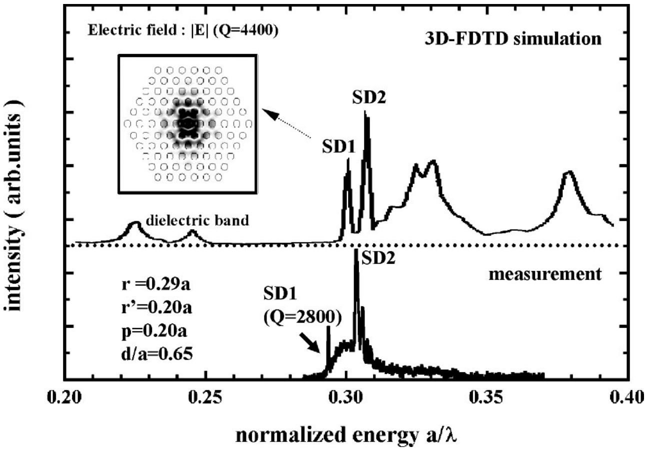

FIG. 6. Simulated Fourier spectrum of optical modes around a band gap.

In summary, we have characterized donor modes supported in single defect nanocavities defined within, two-dimensional photonic crystal slabs with fractional edge dislocations. The mode modulated by the dislocation was found to be well-confined around the single defect as predicted. High quality factors of up to 2800 were measured by luminescence from quantum dot emitters at 1.2 μm. These values were significantly higher than the values of 1500 measured for the simpler symmetric shallow donor mode cavities without the fractional edge dislocation. Our measured *Q* values were limited by fabrication precision and fine design optimization, and these results indicate that further improvement of *Q* is very likely in these kinds of geometries.

The authors gratefully appreciate many valuable suggestions from Marko Lončar. This work was supported by the NSF under Grant No. ECS-9912039, the DARPA under contract MDA972-00-1-0019, and the ARO under contract DAAD19-00-1-0374.

[1] E. M. Purcell, Phys. Rev. **69**, 681 (1946).
[2] A. Scherer, J. L. Jewell, Y. H. Lee, J. P. Harbison, and L. T. Florez, Appl. Phys. Lett. **55**, 2724 (1989).
[3] J. M. Gerard, D. Barrier, J. Y. Marzin, R. Kuszelewicz, L. Manin, E. Costard, V. Thierry-Mieg, and T. Rivera, Appl. Phys. Lett. **69**, 449 (1996).
[4] A. F. J. Levi, R. E. Slusher, S. L. McCall, T. Tanbun-Ek, D. L. Coblentz, and S. J. Pearton, Electron. Lett. **28**, 1010 (1992).
[5] D. G. Deppe, L. A. Graham, and D. L. Huffaker, IEEE J. Quantum Electron. **35**, 1502 (1999).
[6] E. Yablonovitch, T. J. Gmitter, R. D. Meade, A. M. Rappe, K. D. Brommer, and J. D. Joannopoulos, Phys. Rev. Lett. **67**, 3380 (1991).
[7] R. D. Meade, A. Devenyi, J. D. Joannopoulos, O. L. Alerhand, D. A. Smith, and K. Kash, J. Appl. Phys. **75**, 4753 (1994).
[8] O. Painter, J. Vučković, and A. Scherer, J. Opt. Soc. Am. B **16**, 275 (1999).
[9] O. J. Painter, R. K. Lee, A. Scherer, A. Yariv, J. D. O'Brien, P. D. Dapkus, and I. Kim, Science **284**, 1819 (1999).
[10] J. Hwang, H. Ryu, D. Song, I. Han, H. Song, H. Park, Y. Lee, and D. Jang, Appl. Phys. Lett. **76**, 2982 (2000).
[11] J. Vučković, M. Lončar, A. Scherer, and H. Mabuchi, Phys. Rev. E (in press).
[12] T. Yoshie, A. Scherer, H. Chen, D. Hufferker, and D. Deppe, Appl. Phys. Lett. **79**, 114 (2001).

Downloaded 03 Jan 2002 to 131.215.133.150. Redistribution subject to AIP license or copyright, see http://ojps.aip.org/aplo/aplcr.jsp

PHYSICAL REVIEW D, VOLUME 65, 022002

Conversion of conventional gravitational-wave interferometers into quantum nondemolition interferometers by modifying their input and/or output optics

H. J. Kimble,[1] Yuri Levin,[2,*] Andrey B. Matsko,[3] Kip S. Thorne,[2] and Sergey P. Vyatchanin[4]
[1]*Norman Bridge Laboratory of Physics 12-33, California Institute of Technology, Pasadena, California 91125*
[2]*Theoretical Astrophysics, California Institute of Technology, Pasadena, California 91125*
[3]*Department of Physics, Texas A&M University, College Station, Texas 77843-4242*
[4]*Physics Faculty, Moscow State University, Moscow, 119899, Russia*

(Received 11 August 2000; published 26 December 2001)

The LIGO-II gravitational-wave interferometers (ca. 2006–2008) are designed to have sensitivities near the standard quantum limit (SQL) in the vicinity of 100 Hz. This paper describes and analyzes possible designs for subsequent LIGO-III interferometers that can beat the SQL. These designs are identical to a conventional broad band interferometer (without signal recycling), except for new input and/or output optics. Three designs are analyzed: (i) a *squeezed-input interferometer* (conceived by Unruh based on earlier work of Caves) in which squeezed vacuum with frequency-dependent (FD) squeeze angle is injected into the interferometer's dark port; (ii) a *variational-output* interferometer (conceived in a different form by Vyatchanin, Matsko and Zubova), in which homodyne detection with FD homodyne phase is performed on the output light; and (iii) a *squeezed-variational interferometer* with squeezed input and FD-homodyne output. It is shown that the FD squeezed-input light can be produced by sending ordinary squeezed light through two successive Fabry-Pérot filter cavities before injection into the interferometer, and FD-homodyne detection can be achieved by sending the output light through two filter cavities before ordinary homodyne detection. With anticipated technology (power squeeze factor $e^{-2R}=0.1$ for input squeezed vacuum and net fractional loss of signal power in arm cavities and output optical train $\epsilon_*=0.01$) and using an input laser power I_o in units of that required to reach the SQL (the planned LIGO-II power, $I_{\rm SQL}$), the three types of interferometer could beat the amplitude SQL at 100 Hz by the following amounts $\mu\equiv\sqrt{S_h}/\sqrt{S_h^{\rm SQL}}$ and with the following corresponding increase $\mathcal{V}=1/\mu^3$ in the volume of the universe that can be searched for a given noncosmological source: *Squeezed input*—$\mu\simeq\sqrt{e^{-2R}}\simeq 0.3$ and $\mathcal{V}\simeq 1/0.3^3\simeq 30$ using $I_o/I_{\rm SQL}=1$. *Variational-output*—$\mu\simeq\epsilon_*^{1/4}\simeq 0.3$ and $\mathcal{V}\simeq 30$ but only if the optics can handle a ten times larger power: $I_o/I_{\rm SQL}\simeq 1/\sqrt{\epsilon_*}=10$. *Squeezed varational*—$\mu=1.3(e^{-2R}\epsilon_*)^{1/4}\simeq 0.24$ and $\mathcal{V}\simeq 80$ using $I_o/I_{\rm SQL}=1$; and $\mu\simeq(e^{-2R}\epsilon_*)^{1/4}\simeq 0.18$ and $\mathcal{V}\simeq 180$ using $I_o/I_{\rm SQL}=\sqrt{e^{-2R}/\epsilon_*}\simeq 3.2$.

DOI: 10.1103/PhysRevD.65.022002 PACS number(s): 04.80.Nn, 03.65.Ta, 42.50.Dv, 95.55.Ym

I. INTRODUCTION AND SUMMARY

In an interferometric gravitational-wave detector, laser light is used to monitor the motions of mirror-endowed test masses, which are driven by gravitational waves $h(t)$. The light produces two types of noise: photon *shot noise*, which it superposes on the interferometer's output signal, and fluctuating *radiation-pressure noise*, by which it pushes the test masses in random a manner that can mask their gravity-wave-induced motion. The shot-noise spectral density scales with the light power I_o entering the interferometer as $S_h^{\rm shot}\propto 1/I_o$; the radiation-pressure noise scales as $S_h^{\rm rp}\propto I_o$.

In the first generation of kilometer-scale interferometers [e.g., the Laser Interferometric Gravitational Wave Observatory's LIGO-I interferometers, 2002–2003 [1]], the laser power will be low enough that shot-noise dominates and radiation-pressure noise is unimportant. Tentative plans for the next generation interferometers (LIGO-II, ca. 2006–2008) include increasing I_o to the point that, $S_h^{\rm rp}=S_h^{\rm shot}$ at the interferometers' optimal gravitational-wave frequency, $\Omega/2\pi\sim 100$ Hz. The resulting net noise $S_h=S_h^{\rm rp}+S_h^{\rm shot}=2S_h^{\rm shot}$ is the lowest that can be achieved with conventional interferometer designs. Further *increases* of light power will drive the radiation-pressure on upward, increasing the net noise, while *reductions* of light power will drive the shot noise upward, also increasing the net noise.

This minimum achievable noise is called the "standard quantum limit" (SQL) [2] and is denoted $S_h^{\rm SQL}\equiv h_{\rm SQL}^2$. It can be regarded as arising from the effort of the quantum properties of the light to enforce the Heisenberg uncertainty principle on the interferometer test masses, in just the manner of the Heisenberg microscope. Indeed, a common derivation of the SQL is based on the uncertainty principle for the test masses' position and momentum [3]: The light makes a sequence of measurements of the difference x of test-mass positions. If a measurement is too accurate, then by state reduction it will narrow the test-mass wave function so tightly (Δx very small) that the momentum becomes highly uncertain (large Δp), producing a wave function spreading that is so rapid as to create great position uncertainty at the time of the next measurement. There is an optimal accuracy for the first measurement—an accuracy that produces only a factor $\sqrt{2}$ spreading and results in optimal predictability for the next measurement. This optimal accuracy corresponds to $h_{\rm SQL}$.

---

[*] Present address: Department of Astronomy, University of California, Berkeley, California 94720.

©2001 The American Physical Society

Despite this *apparent* intimate connection of the SQL to test-mass quantization, it turns out that the test-mass quantization has *no influence whatsoever* on the output noise in gravitational-wave interferometers [4]. The sole forms of quantum noise in the output are photon shot noise and photon radiation-pressure noise.[1]

Braginsky (the person who first recognized the existence of the SQL for gravitational-wave detectors and other high-precision measuring devices [5]) realized, in the mid 1970s, that the SQL can be overcome, but to do so would require significant modifications of the experimental design. Braginsky gave the name quantum nondemolition (QND) to devices that can beat the SQL; this name indicates the ability of QND devices to prevent their own quantum properties from demolishing the information one is trying to extract [6].

The LIGO-I interferometers are now being assembled at the LIGO sites, in preparation for the first LIGO gravitational-wave searches. In parallel, the LIGO scientific community (LSC) is deeply immersed in research and development for the LIGO-II interferometers [7], and a small portion of the LSC is attempting to invent practical designs for the third generation of interferometers, LIGO-III. This paper is a contribution to the LIGO-III design effort.

In going from LIGO-II to LIGO-III, a large number of noise sources must be reduced. Perhaps the most serious are the photon shot noise and radiation pressure noise (‘‘optical noise’’), and thermal noise in the test masses and their suspensions [7,8]. In this paper we shall deal solely with the shot noise and radiation pressure noise (and the associated SQL); we shall tacitly assume that all other noise sources, including thermal noise, can be reduced sufficiently to take full advantage of the optical techniques that we propose and analyze.

Because LIGO-II is designed to operate at the SQL, in moving to LIGO-III there are just two ways to reduce the optical noise: increase the masses m of the mirrored test masses (it turns out that $h_{\rm SQL}^2 \propto 1/m$), or redesign the interferometers so they can perform QND. The transition from LIGO-I to LIGO-II will already (probably) entail a mass increase, from $m=11$ kg to $m=30$ kg, in large measure because the SQL at 11 kg was unhappily constraining [7]. Any large further mass increase would entail great danger of unacceptably large noise due to energy coupling through the test-mass suspensions and into or from the overhead supports (the seismic isolation system); a larger mass would also entail practical problems due to the increased test-mass dimensions. Accordingly, there is strong motivation for trying to pursue the QND route.

Our Caltech and Moscow University research groups are jointly exploring three approaches to QND interferometer design:

First: The conversion of conventional interferometers into QND interferometers by modifying their input and/or output optics (this paper). This approach achieves QND by creating and manipulating correlations between photon shot noise and radiation pressure noise; see below. It is the simplest of our three approaches, but has one serious drawback: an uncomfortably high light power, $W_{\rm circ} \gtrsim 1$ MW, that must circulate inside the interferometers' arm cavities [9]. It is not clear whether the test-mass mirrors can be improved sufficiently to handle this high a power in a sufficiently noise-free way.

Second: A modification of the interferometer design (including using two optical cavities in each arm) so as to make its output signal be proportional to the relative speeds of the test masses rather than their relative positions [10,11]. Since the test-mass speed is proportional to momentum, and momentum (unlike position) is very nearly conserved under free test-mass evolution on gravity-wave time scales (~ 0.01 sec), the relative speed is very nearly a ‘‘QND observable’’ [12] and thus is beautifully suited to QND measurements. Unfortunately, the resulting *speed-meter interferometer*, like our input-output-modified interferometers, suffers from a high circulating light power [9], $W_{\rm circ} \gtrsim 1$ MW.

Third: Radical redesigns of the interferometer aimed at achieving QND performance with $W_{\rm circ}$ well below 1 MW [13]. These, as currently conceived by Braginsky, Gorodetsky and Khalili, entail transfering the gravitational-wave signal to a single, small test mass via light pressure, and using a local QND sensor to read out the test mass's motions relative to a local inertial frame.

In this paper we explore the first approach. The foundation for this approach is the realization that: (i) photon shot noise and radiation-pressure noise together enforce the SQL *only if they are uncorrelated*; see, e.g., Ref. [4]; (ii) whenever carrier light with side bands reflects off a mirror (in our case, the mirrors of an interferometer's arm cavities), the reflection *ponderomotively squeezes* the light's side bands, thereby creating correlations between their radiation-pressure noise in one quadrature and shot noise in the other; (iii) these correlations are not accessed by a conventional interferometer because of the particular quadrature that its photodiode measures; (iv) however, these correlations *can* be accessed by (conceptually) simple modifications of the interferometer's input and/or output optics, and by doing so one can beat the SQL. These correlations were first noticed explicitly by Unruh [14], but were present implicitly in Braginsky's

---

[1] In brief, the reasons for this are the following: The interferometer's measured output, in general, is one quadrature of the electric field [the b_ζ of Eqs. (54) and (10) below], and this output observable commutes with itself at different times by virtue of Eqs. (7) with $a \rightarrow b$. This means that the digitized data points (collected at a rate of 20 kHz) are mutually commuting Hermitian observables. One consequence of this is that reduction of the state of the interferometer due to data collected at one moment of time will not influence the data collected at any later moment of time. Another consequence is that, when one Fourier analyzes the interferometer output, one puts all information about the initial states of the test masses into data points near zero frequency, and when one then filters the output to remove low-frequency noise (noise at $f=\Omega/2\pi \lesssim 10$ Hz), one thereby removes from the data all information about the test-mass initial states; the only remaining test-mass information is that associated with Heisenberg-picture changes of the test-mass positions at $f \gtrsim 10$ Hz, changes induced by external forces: light pressure (which is quantized) and thermal- and seismic-noise forces (for which quantum effects are unimportant). See Ref. [4] for further detail.

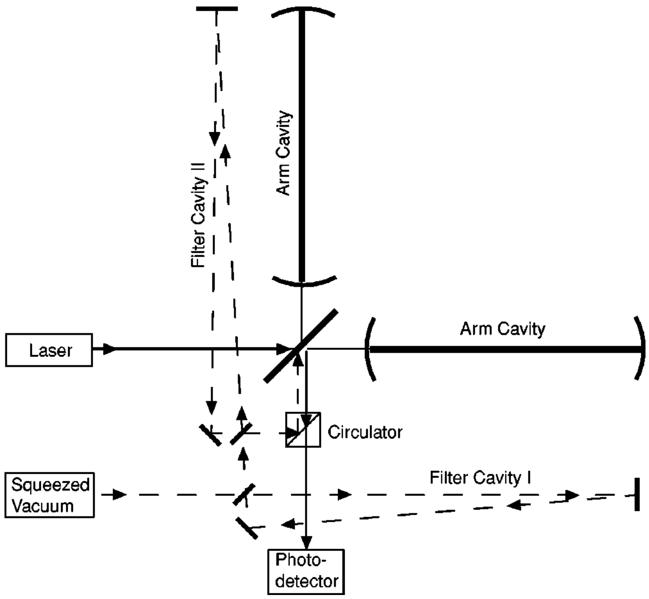

FIG. 1. Schematic diagram of a squeezed-input interferometer.

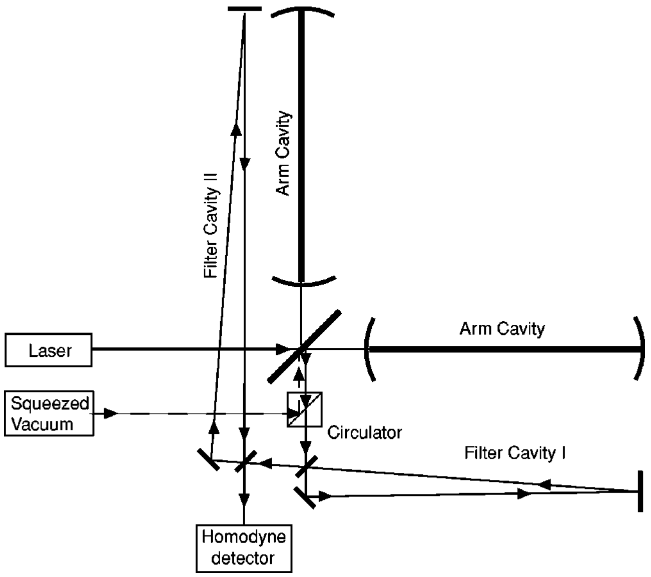

FIG. 2. Schematic diagram of a squeezed-variational interferometer. A variational-output interferometer differs from this solely by replacing the input squeezed vacuum by ordinary vacuum.

earlier identification of the phenomenon of ponderomotive squeezing [15,16].

In this paper we study three variants of QND interferometers that rely on ponderomotive-squeeze correlations:

(i) *Squeezed-input interferometer*. Unruh [14] (building on earlier work of Caves [17]) invented this design nearly 20 years ago, and since then it has been reanalyzed by several other researchers [18,19]. In this design, squeezed vacuum is sent into the dark port of the interferometer (“modified input”) and the output light is monitored with a photodetector as in conventional interferometers.

For a broad-band squeezed-input interferometer, the squeeze angle must be a specified function of frequency that changes significantly across the interferometer’s operating gravity-wave band. (This contrasts with past experiments employing squeezed light to enhance interferometry [20,21], where the squeeze angle was constant across the operating band.) Previous papers on squeezed-input interferometers have ignored the issue of how, in practice, one might achieve the required frequency-dependent (FD) squeeze angle. In Sec. V C, we show that it can be produced via ordinary, frequency-independent squeezing (e.g., by nonlinear optics [22]), followed by filtration through two Fabry-Pérot cavities with suitably adjusted bandwidths and resonant-frequency offsets from the light’s carrier frequency. A schematic diagram of the resulting squeezed-input interferometer is shown in Fig. 1 and is discussed in detail below. Our predicted performance for such an interferometer agrees with that of previous research.

(ii) *Variational-output interferometer*. Vyatchanin, Matsko and Zubova invented this design conceptually in the early 1990s [23–25]. It entails a conventional interferometer input (ordinary vacuum into the dark port), but a modified output: instead of photodetection, one performs homodyne detection with a homodyne phase that depends on frequency in essentially the same way as the squeeze angle of a squeezed-input interferometer. Vyatchanin, Matsko and Zubova did not know how to achieve FD homodyne detection in practice, so they proposed approximating it by homodyne detection with a time-dependent (TD) homodyne phase. Such TD homodyne detection can beat the SQL, but (by contrast with FD homodyne) it is not well-suited to gravitational-wave searches, where little is known in advance about the gravitational waveforms or their arrival times. In this paper (Sec. V and Appendix C), we show that the desired FD homodyne detection can be achieved by sending the interferometer’s output light through two successive Fabry-Pérot cavities that are essentially identical to those needed in our variant of a squeezed-input interferometer, and by then performing conventional homodyne detection with fixed homodyne angle. A schematic diagram of the resulting variational-output interferometer is shown in Fig. 2.

(iii) *Squeezed-variational interferometer*. This design (not considered in the previous literature[2]) is the obvious combination of the first two; one puts squeezed vacuum into the dark port and performs FD homodyne detection on the output light. The optimal performance is achieved by squeezing the input at a fixed (frequency-independent) angle; filtration cavities are needed only at the output (for the FD homodyne detection) and not at the input; cf. Fig. 2.

In Sec. IV we compute the spectral density of the noise for all three designs, ignoring the effects of optical losses. We find (in agreement with previous analyses [18,19]) that, when the FD squeeze angle is optimized, the squeezed-input interferometer has its shot noise and radiation-pressure noise both reduced in amplitude (at fixed light power) by e^{-R}, where R is the (frequency-independent) squeeze factor; see Fig. 2 below. This enables a lossless squeezed-input interferometer to beat the SQL by a factor e^{-R} (when the power is optimized) but no more. By contrast, the lossless, variational-output interferometer, with optimized FD homodyne phase, can have its radiation-pressure noise completely removed from the output signal, and its shot noise will scale with light power as $1/\sqrt{I_o}$ as for a conventional interferometer. As a result, the lossless variational-output interferometer can beat the SQL in amplitude by $\sqrt{I_{\rm SQL}/2I_o}$, where $I_{\rm SQL}$ is the light power required by a conventional interferometer to reach the SQL. The optimized, lossless, squeezed-variational interferometer has its radiation-pressure noise completely removed, and its shot noise reduced by e^{-R}, so it can beat the SQL in amplitude by $e^{-R}\sqrt{I_{\rm SQL}/2I_o}$.

---

[2] A design similar to it has previously been proposed and analyzed [24] for a simple optical meter, in which the position of a movable mirror (test mass) is monitored by measuring the phase or some other quadrature of a light wave reflected from the mirror. In this case it was shown that the SQL can be beat by a combination of phase-squeezed input light and TD homodyne detection.

Imperfections in squeezing, in the filter cavities, and in the homodyne local-oscillator phase will produce errors $\Delta\lambda$ in the FD squeeze angle $\lambda(\Omega)$ of a squeezed-input or squeezed-variational interferometer, and $\Delta\zeta$ in the FD homodyne phase $\zeta(\Omega)$ of a variational-output or squeezed-variational interferometer. At the end of Sec. VI E, we shall show that, to keep these errors from seriously compromising the most promising interferometer's performance, $|\Delta\lambda|$ must be no larger than ~ 0.05 radian, and $|\Delta\zeta|$ must be no larger than ~ 0.01 radian. This translates into constraints of order five percent on the accuracies of the filter cavity finesses and about 0.01 on their fractional frequency offsets and on the homodyne detector's local-oscillator phase.

The performance will be seriously constrained by unsqueezed vacuum that leaks into the interferometer's optical train at all locations where there are optical losses, whether those losses are fundamentally irreversible (e.g., absorption) or reversible (e.g., finite transmissivity of an arm cavity's end mirror). We explore the effects of such optical losses in Sec. VI. The dominant losses and associated noise production occur in the interferometer's arm cavities and FD filter cavities. The filter cavities' net losses and noise will dominate unless the number of bounces the light makes in them is minimized by making them roughly as long as the arm cavities. This suggests that they be 4 km long and reside in the beam tubes alongside the interferometer's arm cavities. To separate the filters' inputs and outputs, they might best be triangular cavities with two mirrors at the corner station and one in the end station.

Our loss calculations reveal the following:

The *squeezed-input* interferometer is little affected by losses in the interferometer's arm cavities or in the output optical train, so long as the fractional energy loss ϵ is small compared to the squeeze factor e^{-2R}, as is likely to be the case. However, losses in the input optical train (most seriously the filter cavities and a circulator) influence the noise by constraining the net squeeze factor e^{-2R} of the light entering the arm cavities. The resulting noise, expressed in terms of e^{-2R}, is the same as in a lossless squeezed-input interferometer (discussed above): With the light power optimized so $I_o = I_{\rm SQL}$, the squeezed-input interferometer can beat the amplitude SQL by a factor $\mu \equiv \sqrt{S_h}/\sqrt{S_h^{\rm SQL}} \simeq \sqrt{e^{-2R}} \simeq 0.3$ (where $e^{-2R} \simeq 0.1$ is a likely achievable value of the power squeeze factor).

The *variational-output* and *squeezed-variational* interferometers are strongly affected by losses in the interferometer's arm cavities and in the output optical train (most seriously: a circulator, the two filter cavities, the mixing with the homodyne detector's local-oscillator field, and the photodiode inefficiency). The net fractional loss ϵ_* of signal power and (for squeezed-variational) the squeeze factor e^{-2R} for input power together determine the interferometer's optimized performance: The amplitude SQL can be beat by an amount $\mu = (e^{-2R}\epsilon_*)^{1/4}$, and the input laser power required to achieve this optimal performance is $I_o/I_{\rm SQL} \simeq \sqrt{e^{-2R}/\epsilon_*}$. In particular, the variational-output interferometer (no input squeezing; $e^{-2R}=1$), with the possibly achievable loss level $\epsilon_* = 0.01$, can beat the SQL by the same amount as our estimate for the squeezed-input interferometer, $\mu \simeq \epsilon_*^{1/4} \simeq 0.3$, but requires ten times higher input optical power, $I_o/I_{\rm SQL} \simeq 1/\sqrt{\epsilon_*} \simeq 10$—which could be a very serious problem. By contrast, the squeezed-variational interferometer with the above parameters has an optimized performance $\mu \simeq (0.1\times 0.01)^{1/4} \simeq 0.18$ (substantially better than squeezed-input or variational-output), and achieves this with an optimizing input power $I_o/I_{\rm SQL} = \sqrt{0.1/0.01} \simeq 3.2$. If the input power is pulled down from this optimizing value to $I_o/I_{\rm SQL} = 1$ so it is the same as for the squeezed-input interferometer, then the squeezed-variational performance is debilitated by a factor 1.3, to $\mu \simeq 0.24$, which is still somewhat better than for squeezed-input.

It will require considerable research and development to actually achieve performances at the above levels, and there could be a number of unknown pitfalls along the way. For example, ponderomotive squeezing, which underlies all three of our QND configurations, has never yet been seen in the laboratory and may entail unknown technical difficulties.

Fortunately, the technology for producing squeezed vacuum via nonlinear optics is rather well developed [22] and has even been used to enhance the performance of interferometers [20,21]. Moreover, much effort is being invested in the development of low-loss test-mass suspensions, and this gives the prospect for new (ponderomotive) methods of generating squeezed light that may perform better than traditional nonlinear optics. These facts, plus the fact that, in a squeezed-input configuration, the output signal is only modestly squeezed and thus is not nearly so delicate as the highly-squeezed output of an optimally performing squeezed-variational configuration, make us feel more confident of success with squeezed-input interferometers than with squeezed-variational ones.

On the other hand, the technology for a squeezed-variational interferometer is not much different from that for a squeezed-input one: Both require input squeezing and both require filter cavities with roughly the same specifications; the only significant differences are the need for conventional, frequency-independent homodyne detection in the squeezed-variational interferometer, and its higher-degree of output squeezing corresponding to higher sensitivity. Therefore, the squeezed-variational interferometer may turn out to be just

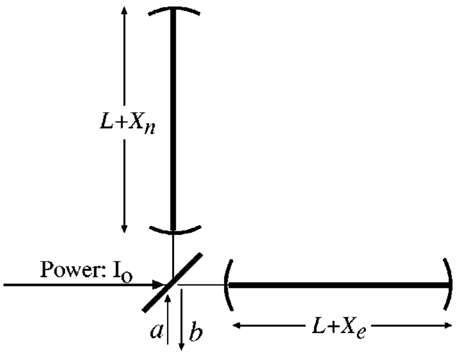

FIG. 3. Gravitational-wave interferometer with two inputs (the carrier which has power I_o entering the bright port, and quantum field a entering the dark port) and one relevant output (the quantum field b leaving the dark port).

as practical as the squeezed-input, and may achieve significantly better overall performance at the same laser power.

This paper is organized as follows: In Sec. II we sketch our mathematical description of the interferometer, including our use of the Caves-Schumaker [26,27] formalism for two-photon quantum optics, including light squeezing (cf. Appendix A); and we write down the interferometer's input-output relation in the absence of losses [Eq. (16); cf. Appendix B for derivation]. In Sec. III, relying on our general lossless input-output relation (16), we derive the noise spectral density $S_h(f)$ for a conventional interferometer and elucidate thereby the SQL. In Sec. IV, we describe mathematically our three QND interferometer designs and, using our lossless input-output relation (16), derive their lossless noise spectral densities. In Sec. V, we show that FD homodyne detection can be achieved by filtration followed by conventional homodyne detection, and in Appendix C we show that the required filtration can be achieved by sending the light through two successive Fabry-Pérot cavities with suitably chosen cavity parameters. We list and discuss the required cavity parameters in Sec. V. In Sec. VI, we compute the effects of optical losses on the interferometers' noise spectral density; our computation relies on an input-output relation (97) and (101) derived in Appendix B. In Sec. VII we discuss and compare the noise performances of our three types of inteferometers. Finally, in Sec. VIII we briefly recapitulate and then list and briefly discuss a number of issues that need study, as foundations for possibly implementing these QND interferometers in LIGO-III.

This paper assumes that the reader is familiar with modern quantum optics and its theoretical tools as presented, for example, in Refs. [28].

II. MATHEMATICAL DESCRIPTION OF THE INTERFEROMETER

A. Input and output fields

Figure 3 shows the standard configuration for a gravitational-wave interferometer. In this subsection we focus on the beam splitter's input and output. In our equations we idealize the beam splitter as infinitesimally thin and write the input and output fields as functions of time (not time and position) at the common centers of the beams as they strike the splitter.

At the beam splitter's bright port the input is a carrier field, presumed to be in a perfectly coherent state with power $I_o \sim 10$ kW (achieved via power recycling [29]), angular frequency $\omega_o \simeq 1.78\times 10^{15}$ sec^{-1} (1.06 micron light), and excitation confined to the $\cos(\omega_o t)$ quadrature [i.e., the mean field arriving at the beam splitter is proportional to $\cos(\omega_o t)$].

At the dark port the input is a (quantized) electromagnetic field with the positive-frequency part of the electric field given by the standard expression

$$E_{\rm in}^{(+)} = \int_0^\infty \sqrt{\frac{2\pi\hbar\omega}{\mathcal{A}c}}\, a_\omega e^{-i\omega t}\frac{d\omega}{2\pi}. \tag{1}$$

Here $\mathcal{A}$ is the effective cross sectional area of the beam and a_ω is the annihilation operator, whose commutation relations are

$$[a_\omega, a_{\omega'}] = 0, \quad [a_\omega, a_{\omega'}^\dagger] = 2\pi\delta(\omega-\omega'). \tag{2}$$

Throughout this paper we use the Heisenberg picture, so $E^{(+)}$ evolves with time as indicated. However, our creation and annihilation operators a_ω and $a_\omega^\dagger$ are fixed in time, with their usual Heisenberg-picture time evolutions always factored out explicitly as in Eq. (1).

We split the field (1) into side bands about the carrier frequency ω_o, $\omega = \omega_o \pm \Omega$, with side-band frequencies Ω in the gravitational-wave range $\sim$60 to $\sim$6000 sec^{-1} (10 to 1000 Hz), and we define

$$a_+ \equiv a_{\omega_o+\Omega}, \quad a_- \equiv a_{\omega_o-\Omega}. \tag{3}$$

As in Eq. (2), we continue to use a prime on the subscript to denote frequency Ω': $a_{+'} \equiv a_{\omega_o+\Omega'}$. Correspondingly, the commutation relations (2) imply for the only nonzero commutators

$$[a_+, a_{+'}^\dagger] = 2\pi\delta(\Omega-\Omega'), \quad [a_-, a_{-'}^\dagger] = 2\pi\delta(\Omega-\Omega'); \tag{4}$$

and expression (1) for the dark-port input field becomes

$$E_{\rm in}^{(+)} = \sqrt{\frac{2\pi\hbar\omega_o}{\mathcal{A}c}}\, e^{-i\omega_o t}\int_0^\infty (a_+ e^{-i\Omega t} + a_- e^{+i\Omega t})\frac{d\Omega}{2\pi}. \tag{5}$$

Here (and throughout this paper) we approximate $\omega_0 \pm \Omega \simeq \omega_o$ inside the square root, since $\Omega/\omega_o \sim 3\times 10^{-13}$ is so small; and we formally extend the integrals over Ω to infinity, for ease of notation.

Because the radiation pressure in the optical cavities produces squeezing, and because this ponderomotive squeezing is central to the operation of our interferometers, we shall find it convenient to think about the interferometer not in terms of the single-photon modes, whose annihilation operators are a_+ and a_-, but rather in terms of the correlated two-photon modes (Appendix A and Refs. [26,27]) whose field amplitudes are

$$a_1 = \frac{a_+ + a_-^\dagger}{\sqrt{2}}, \quad a_2 = \frac{a_+ - a_-^\dagger}{\sqrt{2}i}. \tag{6}$$

The commutation relations (4) imply the following values for the commutators of these field amplitudes and their adjoints:

$$[a_1, a_{2'}^\dagger] = -[a_2, a_{1'}^\dagger] = i2\pi\delta(\Omega - \Omega') \tag{7a}$$

and all others vanish [though some would be of order (Ω/ω_o) if we had not approximated $\omega_o \pm \Omega \simeq \omega_o$ inside the square root in Eq. (5); cf. [26,27]]:

$$[a_1, a_{1'}] = [a_1, a_{1'}^\dagger] = [a_1^\dagger, a_{1'}^\dagger] = [a_1, a_{2'}] = [a_1^\dagger, a_{2'}^\dagger] = 0, \tag{7b}$$

and similarly with $1 \leftrightarrow 2$. In terms of these two-photon amplitudes, Eq. (5) and $E^{(-)} = E^{(+)\dagger}$ imply that the full electric field operator for the dark-port input is

$$\begin{aligned} E_{\text{in}} &= E_{\text{in}}^{(+)} + E_{\text{in}}^{(-)} \\ &= \sqrt{\frac{4\pi\hbar\omega_o}{\mathcal{A}c}}\left[\cos(\omega_o t)\int_0^\infty (a_1 e^{-i\Omega t} + a_1^\dagger e^{+i\Omega t})\frac{d\Omega}{2\pi}\right. \\ &\quad \left. + \sin(\omega_o t)\int_0^\infty (a_2 e^{-i\Omega t} + a_2^\dagger e^{+i\Omega t})\frac{d\Omega}{2\pi}\right]. \end{aligned} \tag{8}$$

Thus, we see that a_1 is the field amplitude for photons in the $\cos\omega_o t$ quadrature and a_2 is that for photons in the $\sin\omega_o t$ quadrature [26,27]. These and other quadratures will be central to our analysis.

The output field at the beam splitter's dark port is described by the same equations as the input field, but with the annihilation operators a replaced by b; for example,

$$\begin{aligned} E_{\text{out}} &= \sqrt{\frac{4\pi\hbar\omega_o}{\mathcal{A}c}}\left[\cos(\omega_o t)\int_0^\infty (b_1 e^{-i\Omega t} + b_1^\dagger e^{+i\Omega t})\frac{d\Omega}{2\pi}\right. \\ &\quad \left. + \sin(\omega_o t)\int_0^\infty (b_2 e^{-i\Omega t} + b_2^\dagger e^{+i\Omega t})\frac{d\Omega}{2\pi}\right]. \end{aligned} \tag{9}$$

We shall find it convenient to introduce explicitly the cosine and sine quadratures of the output field, $E_1(t)$ and $E_2(t)$, defined by

$$\begin{aligned} E_{\text{out}} &= E_1(t)\cos(\omega_o t) + E_2(t)\sin(\omega_o t); \\ E_j(t) &= \sqrt{\frac{4\pi\hbar\omega_o}{\mathcal{A}c}}\int_0^\infty (b_j e^{-i\Omega t} + b_j^\dagger e^{+i\Omega t})\frac{d\Omega}{2\pi}. \end{aligned} \tag{10}$$

B. Interferometer arms and gravitational waves

LIGO's interferometers are generally optimized for the waves from inspiraling neutron-star and black-hole binaries—sources that emit roughly equal power into all logarthmic frequency intervals $\Delta\Omega/\Omega \sim 1$ in the LIGO band ~ 10 Hz $\lesssim f \equiv \Omega/2\pi \lesssim 1000$ Hz. Optimization turns out to entail making the lowest point in the interferometer's dimensionless noise spectrum $f \times S_h(f)$ as low as possible. Because of the relative contributions of shot noise, radiation pressure noise, and thermal noise, this lowest point turns out to be at $f \equiv \Omega/2\pi \simeq 100$ Hz. To minimize the noise at this frequency, one makes the end mirrors of the interferometer's arm cavities (Fig. 3) as highly reflecting as possible (we shall idealize them as perfectly reflecting until Sec. VI), and one gives their corner mirrors transmisivities $T \simeq 0.033$, so the cavities' half bandwidths are

$$\gamma \equiv \frac{Tc}{4L} \simeq 2\pi \times 100 \ \text{Hz}. \tag{11}$$

Here $L = 4$ km is the cavities' length (the interferometer "arm length"). We shall refer to γ as the interferometer's *optimal frequency,* and when analyzing QND interferometers, we shall adjust their parameters so as to beat the SQL by the maximum possible amount at $\Omega = \gamma$. In Table I we list γ, L and other parameters that appear extensively in this paper, along with their fiducial numerical values.

TABLE I. Interferometer parameters and their fiducial values.

Parameter	Symbol	Fiducial value
light frequency	ω_o	$1.8\times10^{15}\ \text{s}^{-1}$
arm cavity $\frac{1}{2}$-bandwidth	γ	$2\pi\times100\ \text{s}^{-1}$
gravitational wave frequency	Ω	—
mirror mass	m	30 kg
arm length	L	4 km
light power to beam splitter	I_o	—
light power to reach SQL	I_{SQL}	1.0×10^4 W
gravitational wave SQL	h_{SQL}	$2\times10^{-24}\ (\gamma/\Omega)\text{Hz}^{-1/2}$
opto-mechanical coupling const	$\mathcal{K}$	$\dfrac{(I_o/I_{\text{SQL}})2\gamma^4}{\Omega^2(\gamma^2+\Omega^2)}$
fractional signal-power loss	ϵ_*	0.01
max power squeeze factor	e^{-2R}	0.1

In this and the next few sections we assume, for simplicity, that the mirrors and beam splitter are lossless; we shall study the effects of losses in Sec. VI below. We assume that the carrier light (frequency ω_o) exites the arm cavities precisely on resonance.

We presume that all four mirrors ("test masses") have masses $m \simeq 30$ kg, as is planned for LIGO-II.

We label the two arms n for north and e for east, and denote by X_n and X_e the changes in the lengths of the cavities induced by the test-mass motions. We denote by

$$x \equiv X_n - X_e \tag{12}$$

the changes in the arm-length difference, and we regard x as a quantum mechanical observable (though it could equally well be treated as classical [4]). In the absence of external forces, we idealize x as behaving like a free mass (no pendular restoring forces). This idealization could easily be relaxed, but because all signals below ~ 10 Hz are removed in the data analysis, the pendular forces have no influence on the interferometer's ultimate performance.

The arm-length difference evolves in response to the gravitational wave and to the back-action influence of the light's fluctuating radiation pressure. Accordingly, we can write it as

$$x(t)=x_o+\frac{p_o}{m/4}t+\int_{-\infty}^{+\infty}(Lh+x_{\mathrm{BA}})e^{-i\Omega t}\frac{d\Omega}{2\pi}. \tag{13}$$

Here x_o is the initial value of x when a particular segment of data begins to be collected, p_o is the corresponding initial generalized momentum, $m/4$ is the reduced mass[3] associated with the test-mass degree of freedom x, h is the Fourier transform of the gravitational-wave field

$$h(t)=\int_{-\infty}^{+\infty}he^{-i\Omega t}\frac{d\Omega}{2\pi}, \tag{14}$$

and x_{BA} is the influence of the radiation-pressure back action. Notice our notation: x, x_{BA}, and h are the Ω-dependent Fourier transforms of $x(t)$, $x_{\mathrm{BA}}(t)$, and $h(t)$.

Elsewhere [4] we discuss the fact that x_o and p_o influence the interferometer output only near zero frequency $\Omega\sim 0$, and their influence is thus removed when the output data are filtered. For this reason, we ignore them and rewrite $x(t)$ as

$$x(t)=\int_{-\infty}^{+\infty}(Lh+x_{\mathrm{BA}})e^{-i\Omega t}\frac{d\Omega}{2\pi}. \tag{15}$$

C. Output field expressed in terms of input

Because we have idealized the beam splitter as infinitesimally thin, the input field emerging from it and traveling toward the arm cavities has the coherent laser light in the same $\cos\omega_o t$ quadrature as the dark-port field amplitude a_1. We further idealize the distances between the beam splitter and the arm-cavity input mirrors as integral multiples of the carrier wavelength $\lambda_o=2\pi c/\omega_o$ and as small compared to $2\pi c/\gamma\sim 300$ m. (These idealizations could easily be relaxed without change in the ultimate results.)

Relying on these idealizations, we show in Appendix B that the annihilation operators b_j for the beam splitter's output quadrature fields $E_j(t)$ are related to the input annihilation operators a_j and the gravitational-wave signal h by the linear relations

$$b_1=\Delta b_1=a_1e^{2i\beta},$$

$$b_2=\Delta b_2+\sqrt{2\mathcal{K}}\frac{h}{h_{\mathrm{SQL}}}e^{i\beta},\quad \Delta b_2=(a_2-\mathcal{K}a_1)e^{2i\beta}. \tag{16}$$

Here and below, for any operator A, $\Delta A\equiv A-\langle A\rangle$. This input-output equation and the quantities appearing in it require explanation.

The quantities Δb_j are the noise-producing parts of b_j, which remain when the gravitational-wave signal is turned off. The a_j impinge on the arm cavities at a frequency $\omega_o+\Omega$ that is off resonance, so they acquire the phase shift 2β upon emerging, where

$$\beta\equiv\arctan(\Omega/\gamma). \tag{17}$$

If the test masses were unable to move, then Δb_j would just be $a_je^{2i\beta}$; however, the fluctuating light pressure produces the test-mass motion x_{BA}, thereby inducing a phase shift in the light inside the cavity, which shows up in the emerging light as the term $-\mathcal{K}a_1$ in b_2. (cf. Appendix B). The quantity

$$\mathcal{K}\equiv\frac{(I_o/I_{\mathrm{SQL}})2\gamma^4}{\Omega^2(\gamma^2+\Omega^2)} \tag{18}$$

is the coupling constant by which this radiation-pressure back-action converts input a_1 into output Δb_2. In this coupling constant, I_{SQL} is the input laser power required, in a conventional interferometer (Sec. III), to reach the standard quantum limit:

$$I_{\mathrm{SQL}}=\frac{mL^2\gamma^4}{4\omega_o}\simeq 1.0\times 10^4\ \mathrm{W}. \tag{19}$$

In Eq. (16), the gravitational-wave signal shows up as the classical piece $\sqrt{2\mathcal{K}}h/h_{\mathrm{SQL}}$ of b_2. Here, as we shall see below,

$$h_{\mathrm{SQL}}\equiv\sqrt{\frac{8\hbar}{m\Omega^2L^2}}\simeq 2\times 10^{-24}\frac{\gamma}{\Omega}\ \mathrm{Hz}^{-1/2} \tag{20}$$

is the standard quantum limit for the square root of the single-sided spectral density of $h(t)$, $\sqrt{S_h}$.

III. CONVENTIONAL INTERFEROMETER

In an (idealized) conventional interferometer, the beamsplitter's output quadrature field $E_2(t)$ is measured by means of conventional photodetection.[4] The Fourier transform of this measured quadrature is proportional to the field amplitude $b_2 = \Delta b_2 + \sqrt{2\mathcal{K}}(h/h_{\rm SQL})e^{i\beta}$; cf. Eqs. (10) and (16). Correspondingly, we can think of $b_2 = b_2(\Omega)$ as the quantity measured, and when we compute, from the output, the Fourier transform $h = h(\Omega)$ of the gravitational-wave signal, the noise in that computation will be

---

[3] In each arm of the interferometer, the quantity measured is the difference between the positions of the two mirrors' centers of mass; this degree of freedom behaves like a free particle with reduced mass $m_r=m\times m/(m+m)=m/2$. The interferometer output is the difference, between the two arms, of this free-particle degree of freedom; that difference behaves like a free particle with reduced mass $m_r/2=m/4$.

[4] Here and throughout this paper we regard some particular quadrature $E_\zeta(t)$ as being measured directly. This corresponds to superposing on $E_\zeta(t)$ carrier light with the same quadrature phase as E_ζ and then performing direct photodetection, which produces a photocurrent whose time variations are proportional to $E_\zeta(t)$. For a conventional interferometer the carrier light in the desired quadrature, that of $E_2(t)$, can be produced by operating with the dark port biased slightly away from the precise dark fringe. In future research it might be necessary to modify the QND designs described in this paper so as to accommodate the modulations that are actually used in the detection process; see Sec. VIII and especially footnote 13.

$$h_n(\Omega) = \frac{h_{\rm SQL}}{\sqrt{2\mathcal{K}}}\Delta b_2 e^{-i\beta}. \tag{21}$$

This noise is an operator for the Fourier transform of a random process, and the corresponding single-sided spectral density $S_h(f)$ associated with this noise is given by the standard formula [3,26,27]

$$\frac{1}{2}2\pi\delta(\Omega - \Omega')S_h(f) = \langle {\rm in}|h_n(\Omega)h_n^\dagger(\Omega')|{\rm in}\rangle_{\rm sym}. \tag{22}$$

Here $f = \Omega/2\pi$ is frequency, $|{\rm in}\rangle$ is the quantum state of the input light field (the field operators a_1 and a_2), and the subscript "sym" means "symmetrize the operators whose expectation value is being computed," i.e., replace $h_n(\Omega)h_n^\dagger(\Omega')$ by $\frac{1}{2}(h_n(\Omega)h_n^\dagger(\Omega') + h_n^\dagger(\Omega')h_n(\Omega))$. Note that when Eq. (21) for h_n is inserted into Eq. (22), the phase factor $e^{-i\beta}$ cancels, i.e., it has no influence on the noise S_h. This allows us to replace Eq. (21) by

$$h_n(\Omega) = \frac{h_{\rm SQL}}{\sqrt{2\mathcal{K}}}\Delta b_2. \tag{23}$$

For a conventional interferometer, the dark-port input is in its vacuum state, which we denote by

$$|{\rm in}\rangle = |0_a\rangle. \tag{24}$$

For this vacuum input, the standard relations $a_+|0_{\rm a}\rangle = a_-|0_{\rm a}\rangle = 0$, together with Eqs. (6) and (7), imply [26,27]

$$\langle 0_a|a_j a_{k'}^\dagger|0_a\rangle_{\rm sym} = \frac{1}{2}2\pi\delta(\Omega - \Omega')\delta_{jk}. \tag{25}$$

Comparing this relation with Eq. (22) and its generalization to multiple random processes, we see that (when $|{\rm in}\rangle = |0_a\rangle$) $a_1(\Omega)$ and $a_2(\Omega)$ can be regarded as the Fourier transforms of classical random processes with single-sided spectral densities and cross-spectral density given by [4]

$$S_{a_1}(f) = S_{a_2}(f) = 1, \quad S_{a_1a_2}(f) = 0. \tag{26}$$

Combining Eqs. (16) and (23)–(25) [or, equally well, Eqs. (16), (23), and (26)], we obtain for the noise spectral density of the conventional interferometer

$$S_h = \frac{h_{\rm SQL}^2}{2}\left(\frac{1}{\mathcal{K}} + \mathcal{K}\right). \tag{27}$$

This spectral density is limited, at all frequencies Ω, by the standard quantum limit

$$S_h \geqslant h_{\rm SQL}^2 = \frac{8\hbar}{m\Omega^2 L^2}. \tag{28}$$

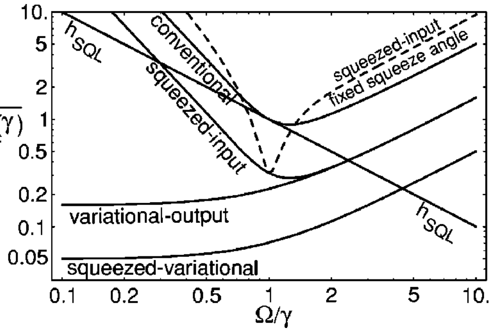

FIG. 4. The square root of the spectral density $\sqrt{S_h}$ of the gravitational-wave noise for several interferometer designs, as a function of angular frequency Ω, with *optical losses assumed negligible*; $\sqrt{S_h}$ is measured in units of the standard quantum limit at frequency $\Omega = \gamma$, and Ω is measured in units of γ. The noise curves shown are: (i) the standard quantum limit itself, $h_{\rm SQL}(\Omega)$ [Eq. (20)]; (ii) the noise for a *conventional* interferometer with laser power $I_o = I_{\rm SQL}$ [Eq. (29)]; (iii) the noise for a *squeezed-input* interferometer with $I_o = I_{\rm SQL}$, squeeze factor $e^{-2R} = 0.1$, and (a) optimized FD squeeze angle $\lambda = -\Phi(\Omega)$ [Eq. (49); solid curve], (b) optimized frequency-independent squeeze angle [Eq. (52); dashed curve]; (iv) the noise for a *variational-output* interferometer with $I_o = 10I_{\rm SQL}$ and optimized frequency-dependent homodyne phase $\zeta = \Phi(\Omega)$ [Eq. (58)]; and (v) the noise for a *squeezed-variational* interferometer with $I_o = 10I_{\rm SQL}$, input squeeze factor $e^{-2R} = 0.1$, and optimized input squeeze angle $\lambda = \pi/2$ and output homodyne phase $\zeta = \Phi(\Omega)$ [Eq. (73)].

Recall that $\mathcal{K}$ is a function of frequency Ω and is proportional to the input laser power I_o [Eq. (18)]. In our conventional interferometer, we adjust the laser power to $I_o = I_{\rm SQL}$ [Eq. (19)], thereby making $\mathcal{K}(\Omega = \gamma) = 1$, which minimizes S_h at the interferometer's optimal frequency $\Omega = \gamma$. The noise spectral density then becomes [cf. Eqs. (27) and (18)]

$$S_h = \frac{4\hbar}{mL^2\Omega^2}\left[\frac{2\gamma^4}{\Omega^2(\gamma^2 + \Omega^2)} + \frac{\Omega^2(\gamma^2 + \Omega^2)}{2\gamma^4}\right]. \tag{29}$$

This optimized conventional noise is shown as a curve in Fig. 4, along with the standard quantum limit $h_{\rm SQL}$ and the noise curves for several QND interferometers to be discussed below. This conventional noise curve is currently a tentative goal for LIGO-II, when operating without signal recycling [7].

IV. STRATEGIES TO BEAT THE SQL, AND THEIR LOSSLESS PERFORMANCE

A. Motivation: Ponderomotive squeezing

The interferometer's input-output relations $\Delta b_1 = a_1 e^{2i\beta}$, $\Delta b_2 = (a_2 - \mathcal{K}a_1)e^{2i\beta}$ can be regarded as consisting of the uninteresting phase shift $e^{2i\beta}$, and a rotation in the $\{a_1, a_2\}$ plane (i.e., $\{\cos\omega_o t, \sin\omega_o t\}$ plane), followed by a squeeze:

$$b_j = S^\dagger(r,\phi)R^\dagger(-\theta)a_j e^{2i\beta}R(-\theta)S(r,\phi). \tag{30}$$

Here $R(-\theta)$ is the rotation operator and $S(r,\phi)$ the squeeze operator for two-photon quantum optics; see Appendix A for a very brief summary, and Refs. [26,27] for extensive detail. The rotation angle θ, squeeze angle ϕ and squeeze factor r are given by

$$\theta = \arctan(\mathcal{K}/2), \quad \phi = \frac{1}{2}\operatorname{arccot}(\mathcal{K}/2), \quad r = \operatorname{arcshinh}(\mathcal{K}/2). \tag{31}$$

Note that, because the coupling constant $\mathcal{K}$ depends on frequency Ω [Eq. (18)], the rotation angle, squeeze angle, and squeeze factor are frequency dependent. This frequency dependence will have major consequences for the QND interferometer designs discussed below.

The rotate-and-squeeze transformation (30) for the two-photon amplitudes implies corresponding rotate-and-squeeze relations for the one-photon creation and annihilation operators

$$b_\pm = S^\dagger(r,\phi) R^\dagger(-\theta) a_\pm e^{\pm 2i\beta} R(-\theta) S(r,\phi). \tag{32}$$

Denote by $|0_{a_+}\rangle$ the vacuum for the *in* mode at frequency $\omega_o+\Omega$, by $|0_{a_-}\rangle$ that for the *in* mode at $\omega_o-\Omega$, and by $|0_{a_\pm}\rangle$ the vacuum for one or the other of these modes; and denote similarly the vacuua for the *out* modes, $|0_{b\pm}\rangle$. Then $|0_{a_\pm}\rangle$ is the state annihilated by $a_\pm$ and $|0_{b_\pm}\rangle$ is that annihilated by $b_\pm$. Correspondingly, the rotate-squeeze relation (32) implies that

$$b_\pm |0_{b_\pm}\rangle = S^\dagger R^\dagger a_\pm e^{\pm 2i\beta} RS |0_{b_\pm}\rangle = 0, \tag{33}$$

where the parameters of the squeeze and rotation operators are those given in Eqs. (31) and (32). This equation implies that $e^{\pm 2i\beta}RS|0_{b_\pm}\rangle$ is annihilated by $a_\pm$ and therefore is the *in* vacuum $|0_{a_\pm}\rangle$ for the *in* mode $\omega_o \pm \Omega$:

$$e^{\pm 2i\beta} RS |0_{b_\pm}\rangle = |0_{a_\pm}\rangle. \tag{34}$$

Applying $R^\dagger$ and noting that $R^\dagger|0_{a_\pm}\rangle = |0_{a_\pm}\rangle$ (the vacuum is rotation invariant), we obtain

$$|0_{a_\pm}\rangle = e^{\pm 2i\beta} S(r,\phi) |0_{b_\pm}\rangle. \tag{35}$$

Thus, *the* in *vacuum is equal to a squeezed* out *vacuum, aside from an uninteresting, frequency-dependent phase shift*. The meaning of this statement in the context of a conventional interferometer is the following.

For a conventional interferometer, the *in* state is

$$|\text{in}\rangle = |0_{a_\pm}\rangle = e^{\pm 2i\beta} S(r,\phi) |0_{b_\pm}\rangle; \tag{36}$$

and because we are using the Heisenberg picture where the state does not evolve, the light emerges from the interferometer in this state. However, in passing through the interferometer, the light's quadrature amplitudes evolve from a_j to b_j. Correspondingly, at the output we should discuss the properties of the unchanged state in terms of a basis built from the *out* vacuum $|0_{b_\pm}\rangle$. Equation (35) says that in this *out* language, the light has been squeezed at the angle ϕ and squeeze-factor r given by Eq. (31). This squeezing is produced by the back-action force of fluctuating radiation pressure on the test masses. That back action has the character of a ponderomotive nonlinearity first recognized by Braginsky and Manukin [15].[5] The correlations inherent in this squeezing form the foundation for the QND interferometers discussed below.

One can also deduce this ponderomotive squeezing from the in-out relations $\Delta b_1 = a_1 e^{2i\beta}$, $\Delta b_2 = (a_2 - \mathcal{K} a_1) e^{2i\beta}$ [Eq. (16)], the expressions

$$\frac{1}{2} 2\pi\delta(\Omega-\Omega') S_{b_j}(f) = \langle \text{in}|\Delta b_j \Delta b_{j'}{}^\dagger|\text{in}\rangle_{\text{sym}},$$

$$\frac{1}{2} 2\pi\delta(\Omega-\Omega') S_{b_1 b_2}(f) = \left\langle \text{in}\left| \frac{1}{2}(\Delta b_1 \Delta b_{2'}{}^\dagger + \Delta b_1^\dagger \Delta b_{2'}) \right|\text{in}\right\rangle_{\text{sym}} \tag{37}$$

for the spectral densities and cross spectral densities of b_1 and b_2, and the spectral densities $S_{a_1} = S_{a_2} = 1$, $S_{a_1 a_2} = 0$ [Eqs. (26)]. These imply that for a conventional interferometer

$$S_{b_1} = 1, \quad S_{b_2} = 1 + \mathcal{K}^2, \quad S_{b_1 b_2} = -\mathcal{K}. \tag{38}$$

Rotating Δb_j through the angle $\phi = \frac{1}{2}\operatorname{arccot}(\mathcal{K}/2)$ to obtain

$$b_1' = b_1 \cos\phi + b_2 \sin\phi, \quad b_2' = b_2 \cos\phi - b_1 \sin\phi, \tag{39}$$

and using Eqs. (37) and (38), we obtain

$$S_{b_1'} = e^{-2r} = \left(\sqrt{1+(\mathcal{K}/2)^2} - \mathcal{K}/2\right)^2 \simeq 1/\mathcal{K} \quad \text{if} \quad \mathcal{K} \gg 1,$$

$$S_{b_2'} = e^{+2r} = \left(\sqrt{1+(\mathcal{K}/2)^2} + \mathcal{K}/2\right)^2, \quad S_{b_1' b_2'} = 0, \tag{40}$$

which represents a squeezing of the input vacuum noise in the manner described formally by Eqs. (36) and (31).

This ponderomotive squeezing is depicted by the noise ellipse of Fig. 5. For a conventional interferometer (b_2 measured via photodetection[6]), the signal is the arrow along the b_2 axis, and the square root of the noise spectral density S_{b_2} is the projection of the noise ellipse onto the b_2 axis. For a detailed discussion of this type of graphical representation of noise in two-photon quantum optics see, e.g., Ref. [26].

---

[5] Recently it has been recognized that this ponderomotive nonlinearity acting on a movable mirror in a Fabry-Pérot resonator may provide a practical method for generating bright squeezed light [30].

[6] See footnote 4.

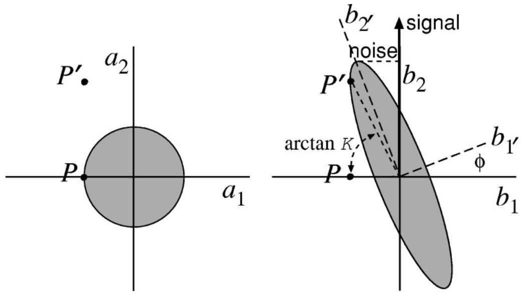

FIG. 5. Noise ellipses for a conventional interferometer. *Left:* Noise for vacuum that enters the interferometer's dark port. *Right:* Noise for ponderomotively squeezed vacuum that exits at the dark port along with the gravitational-wave signal; the ponderomotive squeeze has moved the point P to the new point P' [$b_1 = a_1$, $b_2 = a_2 - \mathcal{K} a_1$, Eqs. (16)]. These noise ellipses have dimensions and shapes described by the noise spectral densities (26), (38) and (40), and by the squeeze equations (36) and (31). The minor radius of the output noise ellipse is $\sqrt{S_{b_1'}} = e^{-r}$, and its major radius is $\sqrt{S_{b_2'}} = e^{+r}$, where r is the squeeze factor; cf. Eqs. (31) and (40). The conventional interferometer measures b_2, which contains the indicated noise [cf. Eq. (23)] and the indicated signal [$\delta b_2 = \sqrt{2\mathcal{K}} h / h_{\rm SQL}$; cf. Eq. (16)]. For a detailed discussion of noise ellipses in 2-photon quantum optics see, e.g., Ref. [26].

B. Squeezed-input interferometer

Interferometer designs that can beat the SQL (28) are sometimes called "QND interferometers." Unruh [14] has devised a QND interferometer design based on (i) putting the input electromagnetic fluctuations at the dark port (a_1 and a_2) into a squeezed state, and (ii) using standard photodetection to measure the interferometer's output field. We shall call this a *squeezed-input interferometer*. The squeezing of the input has been envisioned as achieved using nonlinear crystals [20,21], but one might also use ponderomotive squeezing.

The squeezed-input interferometer is identical to the conventional interferometer of Sec. III, except for the choice of the *in* state $|\text{in}\rangle$ for the dark-port field. Whereas a conventional interferometer has $|\text{in}\rangle = |0_a\rangle$, the squeezed-input interferometer has

$$|\text{in}\rangle = S(R,\lambda)|0_a\rangle, \tag{41}$$

where R is the largest squeeze factor that the experimenters are able to achieve ($e^{-2R} \sim 0.1$ in the LIGO-III time frame), and $\lambda = \lambda(\Omega)$ is a squeeze angle that depends on side-band frequency. One adjusts $\lambda(\Omega)$ so as to minimize the noise in the output quadrature amplitude b_2, which (i) contains the gravitational-wave signal and (ii) is measured by standard photodetection. As we shall see, the optimized λ is strongly frequency dependent. By contrast, we shall idealize the squeeze factor R as independent of side-band frequency Ω except when otherwise stated (Secs. IV D and VI F).

The gravitational-wave noise for such an interferometer is proportional to

$$\langle \text{in}|h_n h_{n'}|\text{in}\rangle = \langle 0_a|h_{ns} h_{ns'}|0_a\rangle \tag{42}$$

[Eq. (22)], where h_{ns} is the *squeezed* gravitational-wave noise operator

$$h_{ns} = S^\dagger(R,\lambda) h_n S(R,\lambda) \tag{43}$$

and $h_n' \equiv h_n(\Omega')$. By inserting expression (21) for h_n into Eq. (43) and then combining the interferometer's ponderomotive squeeze relation $\Delta b_2 = (a_2 - \mathcal{K} a_1) e^{2i\beta}$ with the action of the squeeze operator on a_1 and a_2 [Eq. (A8)], we obtain

$$\begin{aligned} h_{ns} = &-\frac{h_{\rm SQL}}{\sqrt{2\mathcal{K}}}\sqrt{(1+\mathcal{K}^2)}\, e^{i\beta} \\ &\times(a_1\{\cosh R \cos\Phi - \sinh R \cos[\Phi - 2(\Phi+\lambda)]\} \\ &- a_2\{\cosh R \sin\Phi - \sinh R \sin[\Phi - 2(\Phi+\lambda)]\}), \end{aligned} \tag{44}$$

where

$$\Phi \equiv \operatorname{arccot} \mathcal{K}. \tag{45}$$

We can read the spectral density of the gravitational-wave noise off of Eq. (44) by recalling that in the $|0_a\rangle$ vacuum state [which is relevant because of Eq. (42)], a_1 and a_2 can be regarded as random processes with spectral sensities $S_{a_1} = S_{a_2} = 1$ and vanishing cross spectral density [Eqs. (26)]:

$$S_h = \frac{h_{\rm SQL}^2}{2}\left(\frac{1}{\mathcal{K}} + \mathcal{K}\right)(\cosh 2R - \cos[2(\lambda+\Phi)]\sinh 2R). \tag{46}$$

It is straightforward to verify that this noise is minimized by making it proportional to $\cosh 2R - \sinh 2R = e^{-2R}$, which is achieved by choosing for the input squeeze angle

$$\lambda(\Omega) = -\Phi(\Omega) \equiv -\operatorname{arccot} \mathcal{K}(\Omega). \tag{47}$$

The result is

$$S_h = \frac{h_{\rm SQL}^2}{2}\left(\frac{1}{\mathcal{K}} + \mathcal{K}\right) e^{-2R}. \tag{48}$$

This says that *the squeezed-input interferometer has the same noise spectral density as the conventional interferometer, except for an overall reduction by* e^{-2R}, where R is the squeeze factor for the dark-port input field (a result deduced by Unruh [14] and later confirmed by Jaekel and Reynaud [18] using a different method); see Fig. 4. This result implies that the squeezed-input interferometer can beat the amplitude SQL by a factor e^{-R}.

When the laser power I_o of the squeezed-input interferometer is optimized for detection at the frequency $\Omega = \gamma$ ($I_o = I_{\rm SQL}$ as for a conventional interferometer), the noise spectrum becomes

$$S_h = \frac{4\hbar}{mL^2\Omega^2}\left[\frac{2\gamma^4}{\Omega^2(\gamma^2+\Omega^2)} + \frac{\Omega^2(\gamma^2+\Omega^2)}{2\gamma^4}\right] e^{-2R}. \tag{49}$$

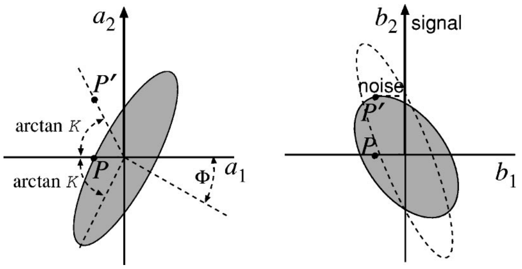

FIG. 6. Noise ellipses for a squeezed-input interferometer. *Left:* Noise for squeezed vacuum that enters the interferometer's dark port. The field is squeezed at the angle $\lambda = -\Phi$. *Right:* Noise for the field that exits at the dark port along with the gravitational-wave signal. This output field results from the interferometer's ponderomotive squeezing of the input field [e.g., point P goes to point P' in accord with $b_1 = a_1$, $\quad b_2 = a_2 - \mathcal{K} a_1$; Eqs. (16)]. If the input field had been vacuum as in a conventional interferometer (Fig. 5), then the output would have been squeezed in the manner of the dashed ellipse. The two squeezes (input and ponderomotive) result in the shaded ellipse, whose projection along the axis measured by the photodetector (b_2 axis) has been minimized by the choice of squeeze angle, $\lambda = -\Phi$.

This optimized noise is shown in Fig. 4 for $e^{-2R} = 0.1$, along with the noise spectra for other optimized interferometer designs.

In previous discussions of this squeezed-input scheme [14,18,19], no attention has been paid to the practical problem of how to produce the necessary frequency dependence

$$\lambda(\Omega) = -\Phi(\Omega) = -\operatorname{arccot} \frac{2\gamma^4}{\Omega^2(\gamma^2 + \Omega^2)} \tag{50}$$

of the squeeze angle. In Sec. V C, we shall show that this $\lambda(\Omega)$ can be achieved by squeezing at a frequency-independent squeeze angle (using, e.g., a nonlinear crystal for which the squeeze angle will be essentially frequency-independent because the gravity-wave bandwidth, <1000 Hz, is so small compared to usual optical bandwidths) and then filtering through two Fabry-Pérot cavities. This squeezing and filtering must be performed before injection into the interferometer's dark port; see Fig. 1 for a schematic diagram.

The signal and noise for this squeezed-input interferometer are depicted in Fig. 6.

We comment, in passing, on two other variants of a squeezed-input interferometer:

(i) If, for some reason, the filter cavities cannot be implemented successfully, one can still inject squeezed vacuum at the dark port with a frequency-independent phase that is optimized for the lowest point in the noise curve, $\Omega = \gamma$; i.e., (with the input power optimized to $I_o = I_{\rm SQL}$):

$$\lambda = -\Phi(\gamma) = -\pi/4; \tag{51}$$

cf. Eq. (50). In this case the noise spectrum is

$$S_h = \frac{h_{\rm SQL}^2}{2}\left(\frac{1}{\mathcal{K}} + \mathcal{K}\right)[(\cosh R \cos\Phi - \sinh R \sin\Phi)^2 + (\cosh R \sin\Phi - \sinh R \cos\Phi)^2] \tag{52}$$

[Eq. (46), translated into gravitational-wave noise via Eq. (23)]. This noise spectrum is shown as a dashed curve in Fig. 4, for $e^{-2R} = 0.1$. The SQL is beat by the same factor $\mu = \sqrt{e^{-2R}} \simeq 0.32$ as in the case of a fully optimized squeezed-input interferometer, but the frequency band over which the SQL is beat is significantly smaller than in the optimized case, and the noise is worse than for a conventional interferometer outside that band.

(ii) Caves [17], in a paper that preceeded Unruh's and formed a foundation for Unruh's ideas, proposed a squeezed-input interferometer with the squeeze angle set to $\lambda = \pi/2$ independent of frequency. In this case, Eq. (46), translated into gravitational-wave noise via Eq. (23), says that

$$S_h = \frac{h_{\rm SQL}^2}{2}\left(\frac{1}{e^{2R}\mathcal{K}} + e^{2R}\mathcal{K}\right). \tag{53}$$

Since $\mathcal{K}$ is proportional to the input laser power I_o, Caves' interferometer produces the same noise spectral density as a conventional interferometer [Eq. (27)] but with an input power that is reduced by a factor e^{-2R}. This is a well-known result.

C. Variational-output interferometer

Vyatchanin, Matsko and Zubova [23–25] have devised a QND interferometer design based on (i) leaving the dark-port input field in its vacuum state, $|{\rm in}\rangle = |0_a\rangle$, and (ii) changing the output measurement from standard photodetection (measurement of b_2) to homodyne detection at an appropriate, frequency-dependent (FD) homodyne phase $\zeta(\Omega)$ – i.e., measurement of

$$b_\zeta = b_1 \cos\zeta + b_2 \sin\zeta. \tag{54}$$

In their explorations of this idea, Vyatchanin, Matsko and Zubova [23–25] did not identify any practical scheme for achieving such a FD homodyne measurement, so they approximated it by homodyne detection with a homodyne phase that depends on time rather than frequency—a technique that they call a ''quantum variational measurement.''

In Sec. V below, we show that the optimized FD homodyne measurement can, in fact, be achieved by filtering the interferometer output through two Fabry-Pérot cavities and then performing standard, balanced homodyne detection at a frequency-independent homodyne phase; see Fig. 2 for a schematic diagram. We shall call such an scheme a *variational-output interferometer*. The word ''variational'' refers to (i) the fact that the measurement entails monitoring a frequency-varying quadrature of the output field, as well as (ii) the fact that the goal is to measure variations of the classical force acting on the interferometer's test mass (the original Vyatchanin-Matsko-Zubova motivation for the word).

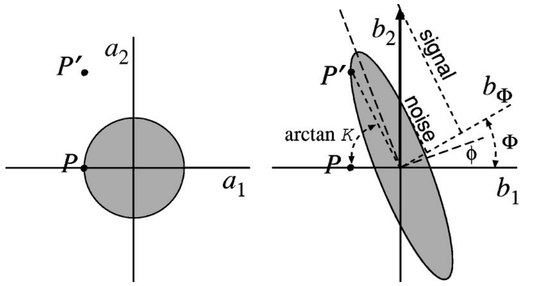

FIG. 7. Noise ellipses for a variational-output interferometer. *Left:* Noise for the ordinary vacuum that enters the interferometer's dark port. *Right:* Noise for the field that exits at the dark port along with the gravitational-wave signal. These noise ellipses are the same as for a conventional interferometer, Fig. 5, but here the quantity measured is the quadrature amplitude b_Φ with frequency dependent phase $\Phi \equiv \operatorname{arccot} \mathcal{K}$. It is informative to compare the measured phase Φ with the angle of ponderomotive squeeze $\phi = \frac{1}{2}\operatorname{arccot}(\mathcal{K}/2)$. They are related by $\tan\Phi = \frac{1}{2}\tan 2\phi = \tan\phi/(1-\tan^2\phi)$, so Φ is always larger than ϕ; but for large $\mathcal{K}$ (strong beating of the SQL), they become small and nearly equal.

The monitored FD amplitude b_ζ [Eq. (54)] can be expressed in terms of the interferometer's dark-port input amplitudes a_1, a_2 and the Fourier transform of the gravitational-wave field h as

$$b_\zeta = \sin\zeta \left(\sqrt{2\mathcal{K}}\,\frac{h}{h_{\rm SQL}} e^{i\beta} + [a_2 + (\cot\zeta - \mathcal{K})a_1] e^{2i\beta} \right); \tag{55}$$

cf. Eqs. (16) and (54). Correspondingly, the operator describing the Fourier transform of the interferometer's gravitational-wave noise is

$$h_n(\Omega) = \frac{h_{\rm SQL}}{\sqrt{2\mathcal{K}}} e^{i\beta}[a_2 + a_1(\cot\zeta - \mathcal{K})]; \tag{56}$$

cf. Eq. (23).

The radiation-pressure-induced back action of the measurement on the interferometer's test masses is embodied in the $-\mathcal{K}a_1$ term of this equation; cf. Eq. (16) and subsequent discussion. It should be evident that *by choosing*

$$\zeta = \Phi \equiv \operatorname{arccot} \mathcal{K}, \tag{57}$$

we can completely remove the back-action noise from the measured interferometer output; cf. Fig. 7. This optimal choice of the FD homodyne phase, together with the fact that the input state is vacuum, $|\text{in}\rangle = |0_a\rangle$, leads to the gravitational-wave noise

$$S_h = \frac{h_{\rm SQL}^2}{2}\frac{1}{\mathcal{K}} = \frac{1}{I_o/I_{\rm SQL}} \left(\frac{4\hbar}{mL^2\Omega^2} \right) \frac{\Omega^2(\gamma^2+\Omega^2)}{2\gamma^4}. \tag{58}$$

Cf. Eqs. (22) and (25).

This noise for an optimized variational-output interferometer is entirely due to shot noise of the measured light, and continues to improve $\propto 1/I_o$ even when the input light power I_o exceeds $I_{\rm SQL}$. Figure 4 shows this noise, along with the noise spectra for other optimized interferometer designs.

It is interesting that the optimal frequency-dependent homodyne phase Φ for this variational-output interferometer is the same, aside from sign, as the optimal frequency-dependent squeeze angle for the squeezed-input interferometer; cf. Eq. (47).

D. Comparison of squeezed-input and variational-output interferometers

The squeezed-input and variational-output interferometers described above are rather idealized, most especially because they assume perfect, lossless optics. When we relax that assumption in Sec. VI below, we shall see that, for realistic squeeze factors e^{-2R} and losses ϵ_*, the two interferometers have essentially the same performance, but the variational-output intefermometer requires ~ 10 times higher input power I_o. In this section we shall seek insight into the physics of these interferometers by comparing them in the idealized, lossless limit.

Various comparisons are possible. The noise curves in Fig. 4 illustrate one comparison: When the FD homodyne angle has been optimized, a lossless variational-output interferometer reduces shot noise below the SQL and completely removes back-action noise; by contrast, when the FD squeeze angle has been optimized, a squeezed-input interferometer reduces shot noise and reduces but does not remove back-action noise; cf. Eqs. (58) and (48).

In variational-output interferometers, after optimizing the FD homodyne angle, the experimenter has further control of just one input/output parameter: the laser intensity or equivalently $I_o/I_{\rm SQL} = \mathcal{K}(\Omega = \gamma)$. When $I_o/I_{\rm SQL}$ is increased, the shot noise decreases; independent of its value, the back-action noise has already been removed completely; cf. Eq. (58). By contrast, in squeezed-input interferometers, after optimizing the FD squeeze phase, the experimenter has control of two parameters: $I_o/I_{\rm SQL}$, which moves the minimum of the noise curve back and forth in frequency but does not lower its minimum [17], and the squeeze factor R, which reduces the noise by e^{-2R}; cf. Eq. (48).

Present technology requires that R be approximately constant over the LIGO frequency band. However, in the same spirit as our assumption that the FD homodyne phase can be optimized at all frequencies, it is instructive to ask what can be achieved with an unconstrained, frequency-dependent (FD) squeeze factor $R(\Omega)$, when coupled to an unconstrained FD squeeze angle $\lambda(\Omega)$.

One instructive choice is $\lambda(\Omega) = -\operatorname{arccot}\mathcal{K}$ as in our previous, optimized interferometer [Eq. (47)], and $e^{-2R(\Omega)} = 1/(1+\mathcal{K}^2)$. In this case, the squeezed-input interferometer has precisely the same noise spectrum as the lossless variational-output interferometer

$$S_h = \frac{h_{\rm SQL}^2}{2\mathcal{K}}; \tag{59}$$

[Eq. (58)], and achieves it with precisely the same laser power.

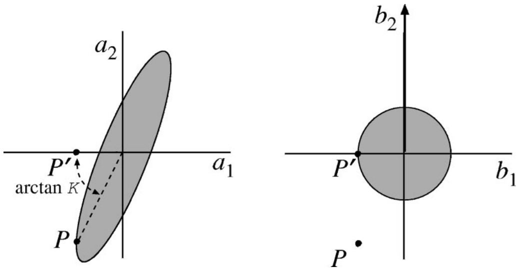

FIG. 8. Noise ellipses for a squeezed-input interferometer whose input squeeze is inverse to the interferometer's ponderomotive squeeze (“IIS interferomter”).

Another instructive choice is an input squeeze that is inverse to the interferometer's ponderomotive squeeze (a configuration we shall call “inversely input squeezed” or IIS): Let the dark-port input field before squeezing be described by annihilation operators $c_{\pm}$, so

$$c_{\pm}|\text{in}\rangle = 0, \tag{60}$$

i.e., the pre-squeeze field is vacuum. Then, denoting by c_1, c_2 the quadrature amplitudes of this pre-squeeze field, the IIS input squeezing is

$$a_1 = c_1, \quad a_2 = c_2 + \mathcal{K} c_1, \tag{61}$$

where $\mathcal{K}(\Omega)$ is the interferometer's frequency-dependent coupling constant (18). The interferometer's ponderomotively squeezed output noise is then

$$\Delta b_1 = a_1 e^{2i\beta} = c_1 e^{2i\beta}, \quad \Delta b_2 = (a_2 - \mathcal{K} a_1) e^{2i\beta} = c_1 e^{2i\beta} \tag{62}$$

[cf. Eq. (16)], i.e., the noise of the output light is that of the vacuum with a phase shift, but since the vacuum state is insensitive to phase, it is actually just the noise of the vacuum.

Figure 8 illustrates this: The IIS input light is squeezed in a manner that gets perfectly undone by the ponderomotive squeeze, so the output light has no squeeze at all. The fact that the input squeeze is inverse to the ponderomotive squeeze shows up in this diagram as an input noise ellipse that is the same as the output ellipse of the ponderomotively squeezed vacuum, Fig. 5, except for a reflection in the horizontal axis.

Because the output of the IIS interferometer is b_2 (ordinary photodetection) and the output light's state is the ordinary vacuum, its gravitational-wave noise is

$$S_h = \frac{h_{\text{SQL}}^2}{2\mathcal{K}}; \tag{63}$$

cf. Eqs. (23), (22) and (26) (with a_j replaced by b_j). Notice that this is identically the same noise spectral density as for our previous example [Eq. (59)] and as for a variational-output interferometer, and it is achieved in all three cases with the same light power.

The fact that our two squeezed-input examples produce the same noise spectrum using different squeeze angles and squeeze factors should not be surprising. The noise spectrum is a single function of Ω and it is being shaped jointly by the two squeeze functions $\lambda(\Omega)$ and $R(\Omega)$.

The fact that the IIS interferometer and the variational output interferometer produce the same noise spectra results from a *reciprocity* between the IIS and the variational-output configurations: The IIS interferometer has its input squeezed at the angle $-\Phi = -\text{arccot}\,\mathcal{K}$ and it has vacuum-noise output, whereas the variational-output interferometer has vacuum-noise input and is measured at the homodyne angle $+\Phi = +\text{arccot}\,\mathcal{K}$.

Note that the IIS interferometer has a different input squeeze angle [$\lambda(\Omega) = -1/2\,\text{arccot}(\mathcal{K}/2)$; cf. Eq. (31)] from that of the *angle-optimized* squeezed-input interferometer of Sec. IV B [$\lambda(\Omega) = -\text{arccot}\,\mathcal{K}$; cf. Eq. (47)]. This difference shows clearly in the noise ellipses of Fig. 8 (the IIS interferometer) and Fig. 6 (the angle-optimized interferomter). Moreover, this difference implies that by optimizing the IIS interferometer's squeeze angle (changing it to $\lambda(\Omega) = -\text{arccot}\,\mathcal{K}$), while keeping its squeeze factor unchanged [$R(\Omega) = \text{arcshinh}(\mathcal{K}/2)$; cf. Eq. (31)], we can improve its noise performance slightly. The improvement is from Eq. (63) to

$$S_h = \frac{h_{\text{SQL}}^2}{2\mathcal{K}} \left[\frac{1+\mathcal{K}^2}{1+\frac{1}{2}(\mathcal{K}^2 + \mathcal{K}\sqrt{\mathcal{K}^2+4})} \right] \tag{64}$$

[which can be derived by setting $\lambda(\Omega) = -\Phi = -\text{arccot}\,\mathcal{K}$ and $R(\Omega) = \text{arcshinh}(\mathcal{K}/2)$ in Eq. (46), or by inserting $R(\Omega) = \text{arcshinh}(\mathcal{K}/2)$ into Eq. (48)—note that (48) is valid for any angle-optimized, squeezed-input interferometer but not for the IIS interferometer]. The improvement factor in square brackets is quite modest; it lies between 0.889 and unity.

We reiterate, however, that the above comparison of interferometer designs is of pedagogical interest only. In the real world, the noise of a QND interferometer is strongly influenced by losses, which we consider in Sec. VI below.

E. Squeezed-variational interferometer

The squeezed-input and variational-output techniques are complementary. By combining them, one can beat the SQL more strongly than using either one alone. We call an interferometer that uses the two techiques simultaneously a *squeezed-variational interferometer*.

The dark-port input of such an interferometer is squeezed by the maximum achievable squeeze factor R at a (possibly frequency dependent) squeeze angle $\lambda(\Omega)$, so

$$|\text{in}\rangle = S(R,\lambda)|0_a\rangle. \tag{65}$$

The dark-port output is subjected to FD homodyne detection with (possibly frequency dependent) homodyne angle $\zeta(\Omega)$; i.e., the measured quantity is the same output quadrature as for a variational-output interferometer, b_ζ [Eq. (55)], so the gravitational-wave noise operator is also the same

$$h_n(\Omega)=\frac{h_{\rm SQL}}{\sqrt{2\mathcal{K}}}e^{i\beta}[a_2+a_1(\cot\zeta-\mathcal{K})]e^{i\beta} \tag{66}$$

[Eq. (56)].

As for a squeezed-input interferometer, the gravitational-wave noise is proportional to

$$\langle \mathrm{in}|h_n h_{n'}|\mathrm{in}\rangle=\langle 0_a|h_{ns}h_{ns'}|0_a\rangle \tag{67}$$

[Eq. (22)], where h_{ns} is the squeezed gravitational-wave noise operator

$$h_{ns}=S^{\dagger}(R,\lambda)h_n S(R,\lambda). \tag{68}$$

By inserting expression (66) for h_n into Eq. (68) and invoking the action of the squeeze operator on a_1 and a_2 [Eq. (A8)], we obtain

$$\begin{aligned}h_{ns}=&-\frac{h_{\rm SQL}}{\sqrt{2\mathcal{K}}}\sqrt{1+\tilde{\mathcal{K}}^2}e^{i\beta}\\&\times(a_1\{\cosh R\cos\tilde{\Phi}-\sinh R\cos[\tilde{\Phi}-2(\tilde{\Phi}+\lambda)]\}\\&-a_2\{\cosh R\sin\tilde{\Phi}-\sinh R\sin[\tilde{\Phi}-2(\tilde{\Phi}+\lambda)]\}),\end{aligned} \tag{69}$$

where

$$\tilde{\mathcal{K}}=\mathcal{K}-\cot\zeta,\quad \tilde{\Phi}=\mathrm{arccot}\,\tilde{\mathcal{K}}. \tag{70}$$

As for a squeezed-input interferometer [see passage following Eq. (45)], we can read the gravitational-wave spectral density off of Eq. (69) by regarding a_1 and a_2 as random processes with unit spectral densities and vanishing cross spectral density. The result is

$$S_h=\frac{h_{\rm SQL}^2}{2\mathcal{K}}(1+\tilde{\mathcal{K}}^2)\{e^{-2R}+\sinh 2R[1-\cos 2(\tilde{\Phi}+\lambda)]\}. \tag{71}$$

This noise is minimized by setting the input squeeze angle λ and output homodyne phase ζ to

$$\lambda=\pi/2,\quad \zeta=\Phi=\mathrm{arccot}\,\mathcal{K}, \tag{72}$$

which produces $\tilde{\mathcal{K}}=0$ and $\lambda=\tilde{\Phi}=\pi/2$, so

$$S_h=\frac{h_{\rm SQL}^2}{2\mathcal{K}}e^{-2R}=\frac{e^{-2R}}{I_o/I_{\rm SQL}}\left(\frac{4\hbar}{mL^2\Omega^2}\right)\frac{\Omega^2(\gamma^2+\Omega^2)}{2\gamma^4}; \tag{73}$$

see Fig. 4.

Equation (72) says that, to optimize the (lossless) squeezed-variational interferometer, one should squeeze the dark-port input field at the frequency-independent squeeze angle $\zeta=\pi/2$ (which ends up squeezing the interferometer's shot noise), and measure the output field at the same FD homodyne phase $\zeta=\Phi$ as for a variational-output interferometer; see Fig. 9. Doing so produces an output, Eq. (73), in which the radiation-pressure-induced back-action noise has been completely removed, and the shot noise has been reduced by the input squeeze factor e^{-2R}.

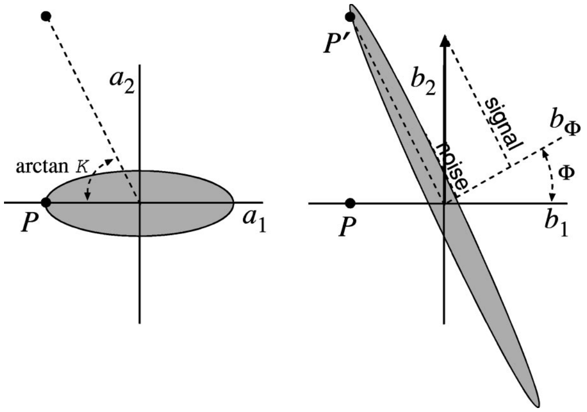

FIG. 9. Noise ellipses for a squeezed-variational interferometer. *Left:* Noise for the squeezed vacuum that enters the interferometer's dark port. *Right:* Noise for the field that exits at the dark port along with the gravitational-wave signal.

Because the optimal input squeeze angle is frequency independent, the squeezed variational interferometer needs no filter cavities on the input. However, they are needed on the output to enable FD homodyne detection; see Fig. 2 for a schematic diagram.

V. FD HOMODYNE DETECTION AND SQUEEZING

Each of the QND schemes discussed above requires homodyne detection with a frequency-dependent phase (FD homodyne detection) and/or input squeezed vacuum with a frequency-dependent squeeze angle (FD squeezed vacuum). In this section we sketch how such FD homodyne detection and squeezing can be achieved.

A. General method for FD homodyne detection

The goal of FD homodyne detection is to measure the electric-field quadrature

$$E_\zeta(t)=\sqrt{\frac{4\pi\hbar\omega_o}{\mathcal{A}c}}\int_0^\infty(b_\zeta e^{-i\Omega t}+b_\zeta^\dagger e^{+i\Omega t})\frac{d\Omega}{2\pi}, \tag{74}$$

for which the quadrature amplitude is

$$b_\zeta=b_1\cos\zeta+b_2\sin\zeta,\quad \zeta=\zeta(\Omega); \tag{75}$$

cf. Eqs. (10) and (54). If ζ were frequency independent, the measurement could be made by conventional balanced homodyne detection, with homodyne phase ζ. In this subsection we shall show that, *when ζ depends on frequency, the measurement can be achieved in two steps: first send the light through an appropriate filter (assumed to be lossless), and then perform conventional balanced homodyne detection.*

The filter puts onto the light a phase shift α that depends on frequency. Let the phase shift be α_+ for light frequency $\omega_o+\Omega$, and α_- for $\omega_0-\Omega$. The input to the filter has amplitudes (annihilation operators) $b_\pm$ at these two sidebands, and the filter output has amplitudes (denoted by a tilde)

$$\tilde{b}_\pm = b_\pm e^{i\alpha_\pm}. \tag{76}$$

The corresponding quadrature amplitudes are

$$b_1 = \frac{b_+ + b_-^\dagger}{\sqrt{2}}, \quad b_2 = \frac{b_+ - b_-^\dagger}{\sqrt{2}i} \tag{77}$$

at the input [Eqs. (6)], and the analogous expression with tildes at the output. Combining Eqs. (77) with and without tildes, and Eq. (76), we obtain for the output quadrature amplitudes in terms of the input

$$\tilde{b}_1 = e^{i\alpha_\mathrm{m}}(b_1 \cos\alpha_\mathrm{p} - b_2 \sin\alpha_\mathrm{p}),$$

$$\tilde{b}_2 = e^{i\alpha_\mathrm{m}}(b_2 \cos\alpha_\mathrm{p} + b_2 \sin\alpha_\mathrm{p}). \tag{78}$$

Here

$$\alpha_\mathrm{m} = \frac{1}{2}(\alpha_+ - \alpha_-), \quad \alpha_\mathrm{p} = \frac{1}{2}(\alpha_+ + \alpha_-). \tag{79}$$

The light with the output amplitudes $\tilde{b}_1$, $\tilde{b}_2$ is then subjected to conventional balanced homodyne detection with frequency-independent homodyne angle θ, which measures an electric-field quadrature with amplitude

$$\begin{aligned}\tilde{b}_\theta &= \tilde{b}_1 \cos\theta + \tilde{b}_2 \sin\theta \\ &= e^{i\alpha_\mathrm{m}}[b_1 \cos(\theta - \alpha_\mathrm{p}) + b_2 \sin(\theta - \alpha_\mathrm{p})].\end{aligned} \tag{80}$$

If we adjust the filter and the constant homodyne phase so that

$$\theta - \alpha_\mathrm{p} \equiv \theta - \frac{1}{2}(\alpha_+ + \alpha_-) = \zeta(\Omega), \tag{81}$$

then, aside from the frequency-dependent phase shift α_m, the output quadrature amplitude will be equal to our desired FD amplitude:

$$\tilde{b}_\theta = e^{i\alpha_\mathrm{m}} b_\zeta. \tag{82}$$

The phase shift $\alpha_\mathrm{m}(\Omega)$ is actually unimportant; it can be removed from the signal in the data analysis [as can be the phase shift $\beta(\Omega)$ produced by the interferometer's arm cavities].

To recapituate: *FD homodyne detection with homodyne phase* $\zeta(\Omega)$ *can be achieved by filtering and conventional homodyne detection, with the filter's phase shifts* $\alpha_\pm$ *(at* $\omega = \omega_o \pm \Omega$*) and the constant homodyne phase* θ *adjusted to satisfy Eq. (81).*

B. Realization of the filter

The desired FD homodyne phase is

$$\begin{aligned}\zeta = \Phi(\Omega) = \operatorname{arccot}\mathcal{K} &= \operatorname{arccot}\left(\frac{\Lambda^4}{\Omega^2(\gamma^2+\Omega^2)}\right) \\ &= \arctan\left(\frac{\Omega^2(\gamma^2+\Omega^2)}{\Lambda^4}\right),\end{aligned} \tag{83}$$

where

$$\Lambda^4 = (I_o/I_\mathrm{SQL})2\gamma^4 \tag{84}$$

[cf. Eqs. (18) and (45)]. Recall that $\gamma \simeq 2\pi \times 100$ Hz is the optimal frequency of operation of the interferometer, and to beat the SQL by a moderate amount will require $I_o/I_\mathrm{SQL} \sim 10$ so $\Lambda^4 \sim 20\gamma^4$, i.e., $\Lambda \sim 2\gamma$.

In Appendix C we show that this desired FD phase can be achieved by filtering the light with two successive lossless Fabry-Pérot filter cavities, followed by conventional homodyne detection at homodyne angle

$$\theta = \pi/2 \tag{85}$$

[i.e., homodyne measurement of $\tilde{b}_2$ at the filter output; cf. Eq. (80)].[7] The two filter cavities (denoted I and II) produce phase shifts $\alpha_{\mathrm{I}\pm}$ and $\alpha_{\mathrm{II}\pm}$ on the $\omega_o \pm \Omega$ side bands, so upon emerging from the second cavity, the net phase shifts are

$$\alpha_\pm = \alpha_{\mathrm{I}\pm} + \alpha_{\mathrm{II}\pm}. \tag{86}$$

Each cavity ($J = \mathrm{I}$ or II) is characterized by two parameters: its decay rate (bandwidth) $2\delta_J$ (with $J = \mathrm{I}$ or II), and its fractional resonant-frequency offset from the light's carrier frequency ω_o,

$$\xi_J \equiv \frac{\omega_o - \omega_{\mathrm{res}\,J}}{\delta_J}. \tag{87}$$

Here $\omega_{\mathrm{res}\,J}$ is the resonant frequency of cavity J. In terms of these parameters, the phase shifts produced in the $\omega_o \pm \Omega$ side bands by cavity J are

$$\alpha_{J\pm} = \arctan(\xi_J \pm \Omega/\delta_J). \tag{88}$$

The filters' parameters must be adjusted so that the net phase shift (86), together with the final homodyne angle $\theta = \pi/2$, produce the desired FD phase, Eqs. (81) and (83).

In Appendix C we derive the following values for the filter parameters ξ_I, δ_I, ξ_II, and δ_II as functions of the parameters Λ and γ that appear in the desired FD homodyne phase. Define the following four functions of Λ and γ:

$$P \equiv \frac{4\Lambda^4}{\gamma^4}, \quad Q \equiv 1 + \sqrt{\frac{1+P^2}{2}}, \tag{89a}$$

---

[7] The fact that only two cavities are needed to produce the desired FD homodyne phase (83) is a result of the simple quadratic form of $\tan\Phi(\Omega^2)$. If the desired phase were significantly more complicated, a larger number of filter cavities would be needed; cf. Eq. (C3) and associated analysis. It would be interesting to explore what range of FD homodyne phases can be achieved, with what accuracy, using what number of cavities.

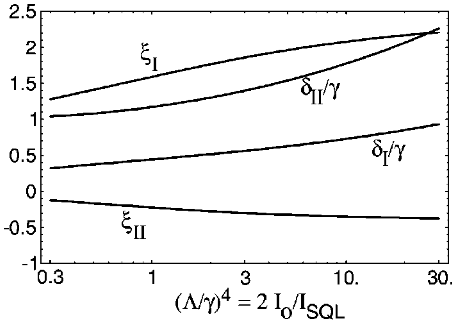

FIG. 10. The parameters characterizing the two Fabry-Pérot cavities that are used, together with conventional homodyne detection at phase $\theta=\pi/2$, to produce FD homodyne detection at the desired frequency-dependent phase (83). The quantities ξ_{I} and ξ_{II} are the filters' fractional frequency offsets from the light's carrier frequency (87); $\delta_{\mathrm{I}}/\gamma$ and $\delta_{\mathrm{II}}/\gamma$ are the filters' half bandwidths in units of the half-bandwidth of the interferometer's identical arm cavities. The functional forms of these parameters are Eqs. (89).

$$A_+\equiv Q+\sqrt{\frac{Q}{P}},\quad A_-\equiv Q-\sqrt{\frac{Q}{P}}. \tag{89b}$$

Then in terms of these functions, the filter parameters are

$$\xi_{\mathrm{I}}=\frac{1}{2A_+}+\sqrt{1+\frac{1}{(2A_+)^2}}, \tag{89c}$$

$$\xi_{\mathrm{II}}=\frac{1}{2A_-}-\sqrt{1+\frac{1}{(2A_-)^2}}, \tag{89d}$$

$$\frac{\delta_{\mathrm{I}}}{\gamma}=\sqrt{\frac{P}{8\xi_{\mathrm{I}}\sqrt{Q}}}, \tag{89e}$$

$$\frac{\delta_{\mathrm{II}}}{\gamma}=\sqrt{\frac{P}{8(-\xi_{\mathrm{II}})\sqrt{Q}}}. \tag{89f}$$

Note that, when the cavity half-bandwidths δ_J are expressed in terms of the half-bandwidth γ of the interferometer's arm cavities, as in Eqs. (89e) and (89f), then the filter parameters depend on only one characteristic of the desired FD homodyne phase: the quantity $(\Lambda/\gamma)^4=2I_o/I_{\mathrm{SQL}}$. Figure 10 depicts the filter parameters as functions of this quantity.

As Fig. 10 shows, the half-bandwidths of the two filter cavities are within a factor ~ 2 of that of the interferometer's arm cavities. This is so for the entire range of laser powers, I_o/I_{SQL}, that are likely to be used in QND interferometers, at least in the early years (e.g., LIGO-III; ca. 2008–2010). Moreover, the filter cavities' fractional frequency offsets ξ_J are of order unity $(-0.5<\xi_J\lesssim 2)$. Thus, the desired properties of the filter cavities are not much different from those of the interferometer's arm cavities.

In Sec. VI below, we shall see that the most serious limitation on the sensitivities of variational-output and squeezed-variational interferometers is optical loss in the filter cavities. To minimize losses, the cavities should be very long (so the cavities' stored light encounters the mirrors a minimum number of times). This suggests placing the filter cavities in the interferometer's 4-km-long arms, alongside the interferometer's arm cavities.

C. Squeezing with frequency-dependent squeeze angle

Just as the variational-output and squeezed-variational interferometers require homodyne detection at a FD phase, so a squeezed-input interferometer requires squeezing at a FD angle $\lambda(\Omega)$.

The nonlinear-optics techniques currently used for squeezing will produce a squeeze angle that is nearly constant over the very narrow frequency band of gravitational-wave interferometers, $|\omega-\omega_o|\lesssim(\text{a few})\times\gamma\sim 10^{-12}\omega_o$. What we need is a way to change the squeeze angle from its constant nonlinear-optics-induced value to the desired frequency-dependent value, $\lambda=-\Phi(\Omega)$ [Eq. (50)].

Just as FD homodyne detection can be achieved by sending the light field through appropriate filters followed by a frequency-independent homodyne device, so also FD squeezing can be achieved by squeezing the input field in the standard frequency-independent way, and then sending it through appropriate filters. Moreover, since the necessary squeeze angle (50) has the same frequency dependence $-\Phi(\Omega)$ as the homodyne phase (57) and (18) (aside from sign and the value of a multiplicative constant in $\mathcal{K}$), the filters needed in FD squeezing are nearly the same as those needed in FD homodyne detection: The filtering can be achieved by sending the squeezed input field through two Fabry-Pérot cavities before injecting it into the interferometer, and the cavity parameters are given by Eqs. (89a)–(89f), with certain sign changes and with $P=8$:

$$Q\equiv 1+\sqrt{\frac{65}{2}},\quad A_\pm\equiv -Q\pm\sqrt{\frac{Q}{8}}, \tag{90a}$$

$$\xi_{\mathrm{I}}=\frac{1}{2A_+}-\sqrt{1+\frac{1}{(2A_+)^2}}, \tag{90b}$$

$$\xi_{\mathrm{II}}=\frac{1}{2A_-}+\sqrt{1+\frac{1}{(2A_-)^2}}. \tag{90c}$$

$$\frac{\delta_{\mathrm{I}}}{\gamma}=\sqrt{\frac{1}{(-\xi_{\mathrm{I}})\sqrt{Q}}}, \tag{90d}$$

$$\frac{\delta_{\mathrm{II}}}{\gamma}=\sqrt{\frac{1}{\xi_{\mathrm{II}}\sqrt{Q}}}. \tag{90e}$$

The details of the calculations are essentially the same as Appendix C, but with Eq. (C1) changed into the following expression for the initial frequency-independent squeeze angle θ and the cavities' frequency-dependent phase shifts $\alpha_{J\pm}$:

$$\tan\Phi(\Omega)\equiv-\frac{\Omega^2(\gamma^2+\Omega^2)}{2\gamma^4}$$
$$=\tan\left(\theta-\frac{\alpha_{I+}+\alpha_{I-}+\alpha_{II+}+\alpha_{II-}}{2}\right). \quad (91)$$

VI. INFLUENCE OF OPTICAL LOSSES ON QND INTERFEROMETERS

A. The role of losses

It is well known that, when one is working with squeezed light, any source of optical loss (whether fundamentally irreversible or not) can debilitate the light's squeezed state. This is because, wherever the squeezed light can leave one's optical system, vacuum field can (and must) enter by the inverse route; and the entering vacuum field will generally be unsqueezed [31].

All of the QND interferometers discussed in this paper rely on squeezed-light correlations in order to beat the SQL—with the squeezing always produced ponderomotively inside the interferometer and, in some designs, also present in the dark-port input field. Thus, optical loss is a serious issue for all the QND interferometers.

In this section we shall study the influence of optical losses on the optimized sensitivities of our three types of QND interferometers.

B. Sources of optical loss

The sources of optical loss in our interferometers are the following:

(i) For light inside the interferometer's arm cavities and inside the Fabry-Pérot filter cavities: scattering and absorption on the mirrors and finite transmissivity through the end mirrors. We shall discuss these quantitatively at the end of the present subsection. (In addition, wave front errors and birefringence produced in the arm cavities and filters, e.g., via power-dependent changes in the shapes and optical properties of the mirrors, will produce mode missmatching and thence losses in subsequent elements of the output optical train.)

(ii) For squeezed vacuum being injected into the interferometer: fractional photon losses $\epsilon_{\rm circ}$ in the *circulator*[8] used to do the injection, in the beam splitter $\epsilon_{\rm bs}$, and in mode-matching into the interferometer $\epsilon_{\rm mm}$.

(iii) For the signal light traveling out of the interferometer: In addition to losses in the arm cavities and filter cavities, also fractional photon losses in the beam splitter $\epsilon_{\rm bs}$, in the circulator $\epsilon_{\rm circ}$, in mode matching into each of the filter cavities $\epsilon_{\rm mm}$, in mode matching with the local-oscillator light used in the homodyne detection $\epsilon_{\rm lo}$, and in the photodiode inefficiency $\epsilon_{\rm pd}$.

It is essential to pursue research and development with the aim of driving these fractional photon losses down to

$$\epsilon_{\rm circ}\sim\epsilon_{\rm bs}\sim\epsilon_{\rm mm}\sim\epsilon_{\rm lo}\sim\epsilon_{\rm pd}\sim 0.001. \quad (92)$$

These loss levels are certainly daunting. However, it is well to keep in mind that attaining the absolute lowest loss levels will likely be an essential component of any advanced interferometer that attempts to challenge and surpass the SQL. In the current case, discussions with Stan Whitcomb and the laboratory experience of one of the authors (H.J.K.) lead us to suggest that it may be technically plausible to achieve the levels of Eq. (92) in the LIGO-III time frame, though a vigorous research effort will be needed to determine the actual feasibility.

The arm cavities are a dangerous source of losses because the light bounces back and forth in them so many times. We denote by $\mathcal{L}$ the probability that a photon in an arm cavity gets lost during one round-trip through the cavity, due to scattering and absorption in each of the two mirrors and transmission through the end mirror. With much research and development by the LIGO-III time frame this *loss coefficient* per round trip may be as low as

$$\mathcal{L}\sim 20\times 10^{-6}. \quad (93)$$

A fraction

$$\epsilon\equiv\frac{2\mathcal{L}}{T}=\frac{\mathcal{L}}{2\gamma L/c}\simeq 0.0012 \quad (94)$$

of the carrier photons that impinge on each arm cavity gets lost in the cavity [cf. Eq. (B25) on resonance so $\mathcal{E}=\epsilon$]. (Note the absence of any subscript on this particular ϵ.) For sideband light the net fractional loss [denoted $\mathcal{E}(\Omega)$; Eq. (100) below] is also of order ϵ.

Each filter cavity, $J=$I or II, has an analogous loss coefficient $\mathcal{L}_J\simeq\mathcal{L}$ and fractional loss of resonant photons

$$\epsilon_J\equiv\frac{2\mathcal{L}_J}{T_J}\simeq\frac{\mathcal{L}}{2\delta_J L_J/c}. \quad (95)$$

Because (as we shall see), the filter cavities' losses place severe limits on the interferometer sensitivity, we shall minimize their net fractional loss in our numerical estimates by making the filter cavities as long as possible: $L_J=L=4$ km. Then the ratio of Eqs. (95) and (94) gives

$$\epsilon_J=\epsilon(\gamma/\delta_J)\sim(0.5\ \text{to}\ 2)\epsilon. \quad (96)$$

C. Input-output relation for lossy interferometer

We show in Appendix B that, accurate to first order in the arm-cavity losses (and ignoring beam-splitter losses which we shall deal with separately below), the relation between the input to the interferometer's beam splitter (field amplitudes a_j) and the output from the beam splitter (field amplitudes b_j) takes the following form:

---

[8] The circulator is a four-port optical device that separates spatially the injected input and the returning output from the interferometer; see Fig. 1. It can be implemented via a Faraday rotator in conjunction with two linear polarizers.

$$b_1=\Delta b_1, \quad b_2=\Delta b_2+\sqrt{2\mathcal{K}_*}\,\frac{h}{h_{\mathrm{SQL}}}e^{i\beta_*} \tag{97}$$

[cf. the last sentence of Appendix B; also the lossless input-output relation (16) and Fig. 3]. Here, accurate to first order in ϵ,

$$\beta_*\equiv\arctan\left(\frac{\Omega/\gamma}{1+\epsilon/2}\right)=\beta-\frac{\epsilon/2}{\Omega/\gamma+\gamma/\Omega} \tag{98}$$

is the loss-modified[9] phase β [Eq. (17)], and the coupling coefficient is reduced slightly by the losses:[10]

$$\mathcal{K}_*\equiv\frac{(I_o/I_{\mathrm{SQL}})2\gamma^4}{\Omega^2[\gamma^2(1+\epsilon/2)^2+\Omega^2]}=\mathcal{K}\left(1-\frac{1}{2}\mathcal{E}\right) \tag{99}$$

[cf. Eq. (18)], where

$$\mathcal{E}=\frac{2\gamma^2}{\gamma^2+\Omega^2}\epsilon=\frac{2\epsilon}{1+(\Omega/\gamma)^2} \tag{100}$$

is the net fractional loss of sideband photons in the arm cavities [cf. Eq. (B25)]. Accurate to first order in the losses, the output quadrature noise operators in Eq. (97) have the form

$$\begin{aligned}\Delta b_1&=a_1e^{2i\beta}\left(1-\frac{1}{2}\mathcal{E}\right)+\sqrt{\mathcal{E}}e^{i\beta}n_1,\\ \Delta b_2&=a_2e^{2i\beta}\left(1-\frac{1}{2}\mathcal{E}\right)+\sqrt{\mathcal{E}}e^{i\beta}n_2\\ &\quad-\mathcal{K}_*(a_1+\sqrt{\epsilon/2}\,n_1)e^{2i\beta_*}\end{aligned} \tag{101}$$

[cf. last sentence of Appendix B and cf. Eq. (16)]. Here n_1 and n_2 are the net quadrature field amplitudes that impinge on the interferometer's arm cavities at their various sites of optical loss. We shall call n_j the quadrature amplitudes of the arm cavities' *loss-noise field*. They are complete analogs of the input and output fields' quadrature amplitudes a_j and b_j: they are related to the loss-noise field's annihilation and creation operators $n_\pm$ and $n_\pm^\dagger$ in the standard way [analog of Eqs. (6)], they have the standard commutation relations [analog of Eqs. (7)], and they commute with the dark-port input field amplitudes a_j.

Equations (101) have a simple physical interpretation. The dark-port input field a_j at frequency $\omega_o\pm\Omega$ gets attenuated by a fractional amount $\mathcal{E}/2$ while in the interferometer (corresponding to a photon-number fractional loss $\mathcal{E}$), and the lost field gets replaced, in the output light, by a small bit of loss-noise field $\sqrt{\mathcal{E}}n_j$. The phase shift β that the interferometer cavities put onto the loss-noise field is half that put onto the dark-port input field because of the different routes by which the a_j and n_j get into the arm cavities.

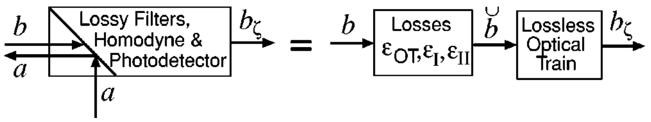
b
a
Lossy Filters, Homodyne & Photodetector
a
b_ζ
=
b
Losses
$\varepsilon_{\mathrm{OT}},\varepsilon_{\mathrm{I}},\varepsilon_{\mathrm{II}}$
$\breve{b}$
Lossless Optical Train
b_ζ

FIG. 11. The output light b is sent through a lossy output optical train, including a beam splitter, circulator, cavity filters I and II, a mixer with local oscillator light and a photodiode. The result (aside from an unimportant phase shift α_{m}) is the desired measured quantity $b_{\zeta(\Omega)}$. This actual process, sketched on the left side of the equality sign, is mathematically equivalent to the idealized process sketched on the right side: The cavities' loss effects are introduced first, producing $\breve{b}$, which is then sent through an idealized, lossless optical train including the filters.

The radiation-pressure back-action force on the test mass is produced by a beating of the laser's carrier light against the in-phase quadrature of the inside-cavity noise field $a_1+\sqrt{\epsilon/2}\,n_1$. Thus, it is $a_1+\sqrt{\epsilon/2}\,n_1$ that appears in the output light's back-action noise (last term of Δb_2).

D. Noise from losses in the output optical train and the homodyne filters

The output quadrature operators b_j get fed through an output optical train including the beam splitter, circulator (if present), filter cavities (if present in the output as opposed to the input), local-oscillator mixer, and photodiode. Losses in all these elements will modify the Δb_j. In analyzing these modifications, we shall not assume, initially, that the FD homodyne phase is $\Phi(\Omega)$; rather, we shall give it an arbitrary value $\zeta(\Omega)$ (as we did in our lossless analysis, Sec. IV C), and shall optimize ζ at the end. The optimal ζ will turn out to be affected negligibly by the losses; i.e., it will still be $\Phi(\Omega)\equiv\operatorname{arccot}\mathcal{K}$.

By analogy with the effects of arm-cavity losses [factors $\mathcal{E}$ in Eqs. (101)], the effects of the optical-train losses on the output fields b_j can be computed in the manner sketched in Fig. 11: The process of sending the quadrature amplitudes b_j through the optical train is equivalent to (i) sending b_j through a "loss device" to obtain loss-modified fields $\breve{b}_j$, and then (ii) sending $\breve{b}_j$ through the lossless optical train.[11]

Because the filter cavities have frequency offsets ξ_J that make their losses different in the upper and lower side bands, the influence of the losses is most simply expressed in terms of the annihilation operators for the side bands $\breve{b}_\pm$, rather than in terms of the quadrature amplitudes $\breve{b}_j$. In terms of $b_\pm$, the equation describing the influence of losses is identical to that in the case of the arm cavities with fixed mirrors, Eqs. (101) with $\mathcal{K}=0$:

---

[9] The loss modification, i.e., the difference between β_* and β, turns out to influence the gravitational-wave noise only at second order in ϵ and thus is unimportant; see footnote 12 below.

[10] As is discussed in footnote 16, in Eq. (99) for $\mathcal{K}_*$, strictly speaking, I_o is not the input power to the interferometer, but rather is the input power reduced by the losses that occur in the input optics, beamsplitter, and arm cavities. We ignore this delicacy since its only effect in our final formulas is a slight renormalization of I_o.

[11] Yanbei Chen [32] has shown that it does not matter whether the losses are placed before or after the lossless train.

$$\breve{b}_\pm = \left(1 - \frac{1}{2}\sum_J \mathcal{E}_{J\pm}\right) b_\pm + \sum_J \sqrt{\mathcal{E}_{J\pm}}\, n_{J\pm}. \tag{102}$$

Here (i) the sum is over the two filter cavities $J=\mathrm{I}$ and II (which must be treated specially) and over the rest of the output optical train, denoted $J=\mathrm{OT}$; (ii) $\mathcal{E}_J$ is the net fractional loss of photons in element J; (iii) $n_{J\pm}$ is the annihilation operator for the loss-noise field introduced by element J; (iv) for each filter I or II, the analog of the phase factor 2β of Eq. (101) gets put onto the light in the subsequent lossless filter and thus is absent here; and (v) we have absorbed a phase factor into the definition of $n_{J\pm}$.

The net fractional photon loss in a filter cavity must be identical to that in an arm cavity, Eq. (100), if written in terms of the cavity's half bandwidth (γ for arm cavity, δ_J for filter cavity) and the difference between the field's frequency $\omega=\omega_o\pm\Omega$ and the cavity's resonant frequency ω_{res} ($\omega-\omega_{\mathrm{res}}=\pm\Omega$ for arm cavity; $\omega-\omega_{\mathrm{res}}=\xi_J\delta_J\pm\Omega$ for filter cavity). Therefore, Eq. (100) implies that

$$\mathcal{E}_{J\pm} = \frac{2\epsilon_J}{1+(\xi_J\pm\Omega/\delta_J)^2} \quad \text{for} \quad J=\mathrm{I,II}. \tag{103}$$

For the remainder of the optical train, the net fractional photon loss $\mathcal{E}_{\mathrm{OT}}$ is the sum of the contributions from the various elements and is independent of frequency:

$$\mathcal{E}_{\mathrm{OT}\pm} = \mathcal{E}_{\mathrm{OT}} = \epsilon_{\mathrm{bs}} + \epsilon_{\mathrm{circ}} + 2\epsilon_{\mathrm{mm}} + \epsilon_{\mathrm{lo}} + \epsilon_{\mathrm{pd}} \sim 0.006. \tag{104}$$

By expressing $b_\pm$ and $n_{J\pm}$ in terms of b_j and n_{Jj} (for $j=1,2$) via the analog of Eq. (6), inserting these expressions into Eq. (102), then computing $\breve{b}_j$ via the analog of Eq. (6), we obtain

$$\breve{b}_1 = \left(1-\frac{1}{2}\mathcal{E}_{\mathrm{OTF}}\right) b_1 - \frac{i}{4}\sum_J (\mathcal{E}_{J+}-\mathcal{E}_{J-}) b_2 + \frac{1}{2}\sum_J \left[\left(\sqrt{\mathcal{E}_{J+}}+\sqrt{\mathcal{E}_{J-}}\right) n_{J1} + i\left(\sqrt{\mathcal{E}_{J+}}-\sqrt{\mathcal{E}_{J-}}\right) n_{J2}\right], \tag{105a}$$

$$\breve{b}_2 = \left(1-\frac{1}{2}\mathcal{E}_{\mathrm{OTF}}\right) b_2 + \frac{i}{4}\sum_J (\mathcal{E}_{J+}-\mathcal{E}_{J-}) b_1 + \frac{1}{2}\sum_J \left[\left(\sqrt{\mathcal{E}_{J+}}+\sqrt{\mathcal{E}_{J-}}\right) n_{J2} - i\left(\sqrt{\mathcal{E}_{J+}}-\sqrt{\mathcal{E}_{J-}}\right) n_{J1}\right]. \tag{105b}$$

Here

$$\begin{aligned}\mathcal{E}_{\mathrm{OTF}} &\equiv \frac{1}{2}\sum_J (\mathcal{E}_{J+}+\mathcal{E}_{J-}) \\ &= \mathcal{E}_{\mathrm{OT}} + \frac{1}{2}(\mathcal{E}_{\mathrm{I}+}+\mathcal{E}_{\mathrm{I}-}+\mathcal{E}_{\mathrm{II}+}+\mathcal{E}_{\mathrm{II}-}) \\ &\simeq \mathcal{E}_{\mathrm{OT}} + \epsilon \sum_{J=\mathrm{I,II}} \sum_{s=+,-} \frac{\gamma/\delta_J}{1+(\xi_J+s\Omega/\delta_J)^2}\end{aligned} \tag{106}$$

is the net, Ω-dependent loss factor for the entire output optical train including the filter cavities. From Eqs. (94), (104) and (106) and Fig. 10, we infer that

$$\mathcal{E}_{\mathrm{OTF}} \sim 0.009 \tag{107}$$

with only a weak dependence on frequency, which we shall neglect.

In Eqs. (105a), (105b) the terms $i\times$ (quantity linear in $\mathcal{E}_{J\pm}$)b_j [the b_2 term in $\breve{b}_1$ and the b_1 term in $\breve{b}_2$] will contribute amounts second order in the losses ($\propto\mathcal{E}_J^2$) to the signal and/or noise, and thus can be neglected. We shall flag our neglect of these terms below, when they arise.

E. Computation of noise spectra for variational-output and squeezed-variational interferometers

The output of a squeezed-variational interferometer or variational-output interferometer is the frequency-dependent quadrature b_ζ depicted in Fig. 11. This quantity, when split into signal $\propto h$ plus noise $\propto\Delta\breve{b}_\zeta$, takes the following form:

$$\begin{aligned}b_\zeta &= \breve{b}_1\cos\zeta + \breve{b}_2\sin\zeta \\ &= \sin\zeta\left[\sqrt{2\mathcal{K}_*}\left(1-\frac{1}{2}\mathcal{E}_{\mathrm{OTF}}\right)\frac{h}{h_{\mathrm{SQL}}}e^{i\beta_*} + \frac{\Delta\breve{b}_\zeta}{\sin\zeta}\right];\end{aligned} \tag{108}$$

cf. Eqs. (97) and (105a), (105b). Here we have omitted an imaginary part of the factor $1-\frac{1}{2}\mathcal{E}_{\mathrm{OTF}}$ [arising from the b_2 term in $\breve{b}_1$, Eq. (105a)] because its modulus is second order in the losses ($\propto\mathcal{E}_J^2$) and therefore it contributes negligibly to the signal strength.

Equation (108) implies that the gravitational-wave noise operator is

$$h_n = \left(1+\frac{1}{2}\mathcal{E}_{\mathrm{OTF}}+\frac{1}{4}\mathcal{E}\right)\frac{h_{\mathrm{SQL}}}{\sqrt{2\mathcal{K}}}e^{-i\beta_*}(\Delta\breve{b}_2+\Delta\breve{b}_1\cot\zeta), \tag{109}$$

where we have used Eq. (99) for $\mathcal{K}_*$.

For a squeezed-variational interferometer, the dark-port input field a_j is in a squeezed state, with squeeze factor R and squeeze angle $\lambda(\Omega)$ (which, after optimization, will turn out to be $\lambda=\pi/2$ as for a lossless interferometer). For a variational-output interferometer, a_j is in its vacuum state, which corresponds to squeezing with $R=0$ so we lose no generality by assuming a squeezed input. Since all the noise fields except a_j are in their vacuum states, the light's full input state is

$$|\text{in}\rangle = |0_n\rangle \otimes |0_{n_{\text{OT}}}\rangle \otimes |0_{n_{\text{I}}}\rangle \otimes |0_{n_{\text{II}}}\rangle \otimes S(R,\lambda)|0_a\rangle, \quad (110)$$

where the notation should be obvious.

The gravitational-wave noise is proportional to

$$\langle \text{in}|h_n h_{n'}|\text{in}\rangle = \langle 0|h_{ns} h_{ns'}|0\rangle \quad (111)$$

where $|0\rangle$ is the vacuum state of all the noise fields a, n, n_{OT}, n_{I}, and n_{II}; and h_{ns} is the usual squeezed noise operator

$$h_{ns} = S^{\dagger}(R,\lambda) h_n S(R,\lambda). \quad (112)$$

We bring this squeezed-noise operator into an explicit form by (i) inserting Eq. (109) into Eq. (112), then (ii) replacing the $\Delta\breve{b}_j$'s by expressions (105a), (105b) [with Δ put onto all the b's, i.e., with the signal removed], then (iii) replacing the Δb_j's by expressions (101), and then (iv) invoking Eqs. (A8) for the action of the squeeze operators on the a_j's. The result is

$$\begin{aligned} h_{ns} = {} & \left(1 - \frac{1}{4}\mathcal{E}\right) \times [\text{Eq. (69)}] \\ & + \frac{h_{\text{SQL}}}{\sqrt{2\mathcal{K}}} \Bigg\{ (-\mathcal{K} e^{i\beta}\sqrt{\epsilon/2} + \sqrt{\mathcal{E}} \cot\zeta) e^{i\beta} n_1 + \sqrt{\mathcal{E}} e^{i\beta} n_2 \\ & + \frac{1}{2}\sum_J [(\sqrt{\mathcal{E}_{J+}} + \sqrt{\mathcal{E}_{J-}})\cot\zeta - i(\sqrt{\mathcal{E}_{J+}} - \sqrt{\mathcal{E}_{J-}})] n_{J1} \\ & + \frac{1}{2}\sum_J [\sqrt{\mathcal{E}_{J+}} + \sqrt{\mathcal{E}_{J-}} + i(\sqrt{\mathcal{E}_{J+}} - \sqrt{\mathcal{E}_{J-}})\cot\zeta] n_{J2} \Bigg\} \end{aligned} \quad (113)$$

where we have omitted terms, arising from b_2 in Eq. (105a) and from b_1 in Eq. (105b), which contribute amounts $\mathcal{O}(\mathcal{E}_J^2)$ to S_h; and we have omitted a term[12] proportional to $\beta_* - \beta$ which contributes an amount $\mathcal{O}(\epsilon^2)$.

By virtue of Eq. (111) and the argument preceding Eqs. (26), we can regard all of the quadrature noise operators a_j, n_j, n_{Jj} in this h_{ns} as random processes with unit spectral densities and vanishing cross-spectral densities. Correspondingly, the gravitational-wave noise is the sum of the squared moduli of the coefficients of the quadrature noise operators in Eq. (113):

$$\begin{aligned} S_h = \frac{h_{\text{SQL}}^2}{2\mathcal{K}} \Bigg[& \left(1 - \frac{1}{2}\mathcal{E}\right)(1 + \tilde{\mathcal{K}}^2) \\ & \times \{e^{-2R} + \sinh 2R[1 - \cos 2(\tilde{\Phi} + \lambda)]\} \\ & + \mathcal{K}^2 \frac{\epsilon}{2} + (1 - \tilde{\mathcal{K}}\cot\zeta)\mathcal{E} + (1 + \cot^2\zeta)\mathcal{E}_{\text{OTF}} \Bigg] \end{aligned} \quad (114)$$

where

$$\tilde{\mathcal{K}} = \mathcal{K} - \cot\zeta, \quad \tilde{\Phi} = \operatorname{arccot}\tilde{\mathcal{K}} \quad (115)$$

[Eq. (70)]. In Eq. (114), the first two lines come from a_1 and a_2 [squeezed vacuum entering the dark port; cf. Eq. (71)] modified by losses in the arm cavities [the factor $1 - \mathcal{E}/2$)]; the first two terms on the third line come from n_1 and n_2 [shot noise due to vacuum entering at loss points in the arm cavities]; and the last term comes from n_{J1} and n_{J2} [shot noise due to vacuum entering at loss points in the output optical train, including the filters].

As for the lossless interferometer [Eqs. (72) and (73)], the noise (114) is minimized by setting the input squeeze angle λ and output homodyne phase ζ to

$$\lambda = \pi/2, \quad \zeta = \Phi \equiv \operatorname{arccot}\mathcal{K} \quad (116)$$

[aside from a neglible correction $\delta\zeta = (\mathcal{E} + 2\mathcal{E}_{\text{OTF}})e^{-2R}/(\mathcal{K} + \mathcal{K}^{-1})$]. This optimization produces $\tilde{\mathcal{K}} = 0$ and $\lambda = \tilde{\Phi} = \pi/2$, so

$$S_h = \frac{h_{\text{SQL}}^2}{2}\left[\frac{\left(1 - \frac{1}{2}\mathcal{E}\right)e^{-2R} + \mathcal{E} + \mathcal{E}_{\text{OTF}}}{\mathcal{K}} + \mathcal{K}\left(\frac{\epsilon}{2} + \mathcal{E}_{\text{OTF}}\right)\right]. \quad (117)$$

Note that the optimization has entailed a squeezed input with frequency-independent squeeze phase, as in the lossless interferometer; so no filters are needed in the input. The output filters must produce a FD homodyne angle $\zeta = \Phi(\Omega)$ that is the same as in the lossless case and therefore can be achieved by two long, Fabry-Pérot cavities.

It is instructive to compare the noise (117) for a lossy squeezed-variational interferometer with that of Eq. (73) for one without optical losses. In the absence of losses, the output's FD homodyne detection can completely remove the radiation-pressure back-action noise from the signal; only the shot noise, $\propto 1/\mathcal{K} \propto 1/I_o$, remains. Losses in the interferometer's arm mirrors prevent this back-action removal from being perfect: they enable a bit of vacuum field n to leak into the arm cavities, and this field produces radiation-pressure noise that remains in the output after the FD homodyne detection (the $\mathcal{K}\epsilon/2$ term in Eq. (117)].

The $\mathcal{K}\mathcal{E}_{\text{OTF}}$ noise in Eq. (117) has the same dependence on laser power, $\propto \mathcal{K} \propto I_o$, as the radiation-pressure noise. Nevertheless, it is actually shot noise, not radiation pressure noise. It is produced by the vacuum loss-noise fields that leak into the output signal light when it encounters each lossy optical element. Those fields' shot noise gets weighted by the factor

---

[12] This term is an imaginary part, $2i(\beta_* - \beta)\mathcal{K} = -\frac{1}{2}i\epsilon\mathcal{K}\sin 2\beta$, of the quantity $\tilde{\mathcal{K}}$, which enters Eq. (69) via Eq. (70). Because this imaginary part produces a correction to the loss-free part of h_n that is 90° out of phase with the loss-free part and is of order ϵ, it produces a correction to S_h that is quadratic in ϵ and thus negligible.

$\cot\zeta = \cot\Phi = \mathcal{K}$ in the homodyne process, which accounts for their proportionality to $\mathcal{K} \propto I_o$.

A reasonable estimate for the amount of input-light squeezing that might be achieved in LIGO-III is [33]

$$e^{-2R} \simeq 0.1. \tag{118}$$

By contrast, Eqs. (94), (96), (100) and (106) suggest

$$(\mathcal{E} + \mathcal{E}_{\rm OTF}) \sim 0.01. \tag{119}$$

This motivates our neglecting $\mathcal{E} + \mathcal{E}_{\rm OTF}$ compared to e^{-2R} in expression (117), and rewriting the noise (117) as

$$S_h \simeq \frac{h_{\rm SQL}^2}{2}\left[\frac{e^{-2R}}{\mathcal{K}} + \mathcal{K}\epsilon_*\right], \tag{120}$$

where

$$\epsilon_* \equiv \frac{\epsilon}{2} + \mathcal{E}_{\rm OTF} \sim 0.0010; \tag{121}$$

cf. Eqs. (94) and (107).

Equation (120) is our final form for the noise spectrum of a lossy squeezed-variational interferometer. When we set the input squeeze factor to unity, $e^{-2R} = 1$, it becomes the noise spectrum for a lossy variational-output interferometer:

$$S_h \simeq \frac{h_{\rm SQL}^2}{2}\left[\frac{1}{\mathcal{K}} + \mathcal{K}\epsilon_*\right]. \tag{122}$$

Errors $\Delta\lambda = \lambda - \pi/2$ in the input squeeze angle and $\Delta\zeta = \zeta - \operatorname{arccot}\mathcal{K}$ in the output homodyne phase will increase the noise spectral density. By performing a power series expansion of expression (114), we obtain for the noise increase

$$\begin{aligned}\Delta S_h &= \frac{h_{\rm SQL}^2}{\mathcal{K}}\left[\sinh 2R\,\Delta\lambda^2 - 2(1+\mathcal{K}^2)\sinh 2R\,\Delta\lambda\,\Delta\zeta \right.\\ &\qquad \left. + \frac{(1+\mathcal{K})^2 e^{2R}}{2}\Delta\zeta^2\right]\\ &\simeq \frac{h_{\rm SQL}^2}{2\mathcal{K}} e^{2R}[\Delta\lambda - (1+\mathcal{K}^2)\Delta\zeta]^2,\end{aligned} \tag{123}$$

where the second expression is accurate in the limit $e^{2R} \gg e^{-2R}$. Numerical evaluations show that, for $e^{-2R} = 0.1$ and $\epsilon_* = 0.01$ (see above), and for $\mathcal{K} \sim 1$ to 3 (the range of greatest interest; cf. Sec. VII), $\Delta\sqrt{S_h}$ will be less than $\frac{1}{4}\sqrt{S_h}$ so long as: (i) the input squeeze angle is accurate to $|\Delta\lambda| \lesssim 0.05$, and (ii) the FD output homodyne phase is accurate to $|\Delta\zeta| \lesssim 0.01$. At $\mathcal{K} = 1$ the FD phase's required accuracy is reduced to $|\Delta\zeta| \lesssim 0.04$. The FD phase ζ is determined by the filter cavities' half bandwidths δ_J and fractional frequency offsets ξ_J, and the local oscillator phase or equivalently the final, conventional homodyne detector's homodyne phase θ. The filter cavities' half bandwidths δ_J (or equivalently their finesses) are fixed by the mirror coatings. Coating-produced errors in δ_J can be compensated to some degree by tuning the fractional frequency offsets ξ_J (via adjusting the mirror positions) and by tuning the local oscillator phase or equivalently θ. Finesse errors as large as five per cent, $|\Delta\delta_J|/\delta_J \lesssim 0.05$, can be compensated to yield the required $|\Delta\zeta| \lesssim 0.01$ by tuning the offsets and homodyne phase to one percent accuracy, $|\Delta\xi_J| \lesssim 0.01$, $\Delta\theta \lesssim 0.01$ [Eqs. (83), (C1), (C2) and Fig. 10]. These requirements are challenging.

F. Computation of the noise spectrum for a squeezed-input interferometer

For a squeezed-input interferometer, as for squeezed-variational, the losses in the input optical train (including the filter cavities) influence the noise only through their impact on the squeeze factor $e^{-2R} \sim 0.1$ of the dark-port vacuum when it enters the arm cavities—an impact that may make R frequency dependent, $R = R(\Omega)$. By contrast, losses in the arm cavities and in the output optical train will produce noise in much the same manner as they do for a squeezed-variational interferometer. More specifically:

The effect of arm-cavity and output-train losses on the squeezed noise operator h_{ns} can be read off of the squeezed-variational formula (113) as follows: (i) Set $\zeta = \pi/2$ so the quantity measured is $\breve{b}_2$ [no output filtering; Eq. (108)]; (ii) correspondingly set $\cot\zeta = 0$, $\tilde{\mathcal{K}} = \mathcal{K}$, and $\tilde{\Phi} = \Phi \equiv \operatorname{arccot}\mathcal{K}$ [Eqs. (115)]; (iii) in the sum over J include only $J = \mathrm{OT}$ and not $J = \mathrm{I}$, II since there are no output filters. The result is

$$\begin{aligned}h_{ns} &= \left(1 - \frac{1}{4}\mathcal{E}\right) \times [\text{Eq. (44)}] + \frac{h_{\rm SQL}}{\sqrt{2\mathcal{K}}}(-\mathcal{K}\sqrt{\epsilon/2}\,e^{2i\beta}n_1\\ &\qquad + \sqrt{\mathcal{E}}e^{i\beta}n_2 + \sqrt{\mathcal{E}_{\rm OT'}}\,n_{\rm OT'2}).\end{aligned} \tag{124}$$

Here the prime on the subscript OT indicates that we must omit losses due to mode matching into the output filters and mixing with the local oscillator, since there are no output filters or homodyne detection. Correspondingly,

$$\mathcal{E}_{\rm OT'} = \epsilon_{\rm bs} + \epsilon_{\rm circ} + \epsilon_{\rm pd} \sim 0.003 \tag{125}$$

is the net fractional photon loss in the output optical train.

Treating the quadrature noise operators as random processes with unit spectral density and vanishing cross spectral densities, we read off S_h from Eq. (124):

$$\begin{aligned}S_h &= \frac{h_{\rm SQL}^2}{2}\left[\frac{\mathcal{E} + \mathcal{E}_{\rm OT'}}{\mathcal{K}} + \frac{\epsilon}{2}\mathcal{K} + \left(1 - \frac{1}{2}\mathcal{E}\right)\left(\frac{1}{\mathcal{K}} + \mathcal{K}\right)\right.\\ &\qquad \left. \times \{\cosh 2R - \cos[2(\lambda + \Phi)]\sinh 2R\}\right].\end{aligned} \tag{126}$$

As in the lossles case, the noise is minimized by squeezing the dark-port input at the FD angle $\lambda(\Omega) = -\Phi \equiv -\operatorname{arccot}\mathcal{K}$ [Eq. (47)]. The result is

$$S_h = \frac{h_{\rm SQL}^2}{2}\left[\left(1 - \frac{1}{2}\mathcal{E}\right)\left(\frac{1}{\mathcal{K}} + \mathcal{K}\right)e^{-2R} + \frac{\mathcal{E} + \mathcal{E}_{\rm OT}}{\mathcal{K}} + \frac{\epsilon}{2}\mathcal{K}\right]. \tag{127}$$

For our estimated squeezing $e^{-2R} \sim 0.1$ and losses $\mathcal{E}_{\rm OT'} \sim \mathcal{E} \sim \epsilon \lesssim 0.003$ in the LIGO-III time frame, the loss parameters

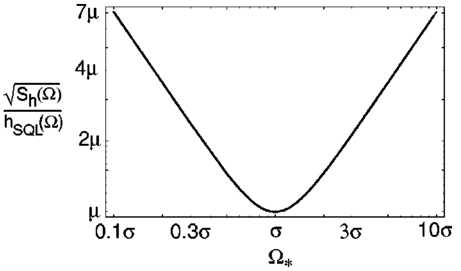

FIG. 12. Universal noise curve for conventional and QND interferometers [Eqs. (130)].

are small compared to the squeeze, and thus contribute negligibly to the noise, so S_h is well approximated by the lossless formula

$$S_h \simeq \frac{h_{\rm SQL}^2}{2}\left(\frac{1}{\mathcal{K}}+\mathcal{K}\right)e^{-2R}. \tag{128}$$

However, it is important to keep in mind that the input squeeze factor e^{-2R} is constrained not only by the physics of the squeezing apparatus, but also by frequency dependent losses in the input optical train and mode matching into the arm cavities.

By expanding expression (126) in powers of $\Delta\lambda=\lambda+\operatorname{arccot}\mathcal{K}$, we see that the fractional increase in noise due to errors in the FD squeeze angle is

$$\Delta\sqrt{\frac{S_h}{\sqrt{S_h}}}=e^{2R}\sinh 2R\,\delta\lambda^2\simeq\frac{e^{4R}}{2}\Delta\lambda^2. \tag{129}$$

For $e^{-2R}=0.1$, this fractional noise increase will be less than 1/4 so long as $\Delta\lambda$ is less than 0.07. This translates into accuracies of ~ 7 percent for the prefilter squeeze angle, ~ 15 percent for the filter cavities' fractional frequency offsets ($|\Delta\xi_J|\lesssim 0.15$), and ~ 10 percent for the cavities' half bandwidths or equivalently their finesses ($\Delta\delta_J/\delta_J\lesssim 0.1$). These constraints are significantly less severe than those for a squeezed-variational interferometer (end of Sec. VI E); but, as we shall see, the potential performance of this squeezed-input interferometer is poorer by a factor ~ 1.5–2 than that of the squeezed-variational one.

VII. DISCUSSION OF THE INTERFEROMETERS' NOISE SPECTRA

The noise spectra for our three lossy QND interferometers, Eqs. (120), (122) and (128), all have the same universal form—a form identical to that for a conventional broadband interferometer, Eq. (27). Only the parameters μ and σ characterizing the noise differ from one interferometer to another. This universal form can be written as

$$\frac{\sqrt{S_h(\Omega)}}{h_{\rm SQL}(\Omega)}=\mu\sqrt{\frac{1}{2}\left(\frac{\Omega_*^2}{\sigma^2}+\frac{\sigma^2}{\Omega_*^2}\right)}, \tag{130a}$$

where Ω_* is the following function of angular frequency

$$\Omega_*\equiv\frac{\Omega}{\gamma}\sqrt{\frac{1+\Omega^2/\gamma^2}{2}} \tag{130b}$$

and $h_{\rm SQL}(\Omega)$ is given by Eq. (20). Notice that $\Omega_*=1$ when $\Omega=\gamma\simeq 100$ Hz; $\Omega_*=(\Omega/\gamma)/\sqrt{2}$ when $\Omega\ll\gamma$, and $\Omega_*=(\Omega/\gamma)^2/\sqrt{2}$ when $\Omega\gg\gamma$.

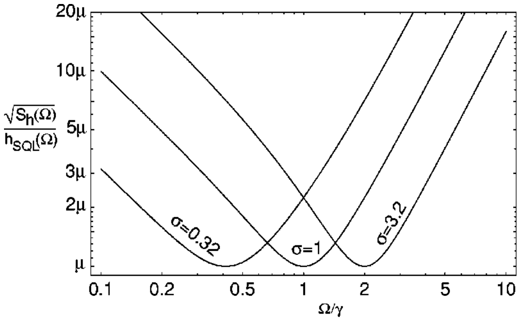

FIG. 13. Universal noise curve plotted as a function of angular frequency Ω for various values of the dimensionless frequency parameter σ.

This universal noise curve is plotted as a function of Ω_* in Fig. 12. Its two parameters are the minimum value μ of the noise, i.e., the minimum amplitude noise in units of the SQL, and the dimensionless frequency σ (in units of Ω_*) at which the noise takes on this minimum value.

Figure 13 shows this universal noise curve plotted as a function of angular frequency Ω. Notice that, because of the relation (130b) between Ω_* and Ω, the shape of the noise curve depends modestly on the location σ of its minimum.

The values of the parameters μ and σ for our various interferometer configurations are shown in Table II. Notice the following details of this table: (i) The minimum noise μ (the optimal amount by which the SQL can be beat) is independent of the laser input power I_o in all cases; it depends only on the level of input squeezing e^{-2R} and the level of losses ϵ_*. (ii) For our estimated loss level and squeeze level, the squeezed-input interferometer and variational-output in-

TABLE II. The values of the parameters $\mu=$(minimum noise) and $\sigma=$(frequency of minimum) for various interferometer ("IFO") configurations: Conv = Conventional broadband [Eq. (27)], SI = Squeezed-Input [Eq. (128)], VO = Variational-Output [Eq. (122)], and SV = Squeezed-Variational [Eq. (120)]. The numerical values are for $e^{-2R}=0.1$ and $\epsilon_*=0.01$.

IFO	μ	σ
Conv.	1	$\sqrt{I_o/I_{\rm SQL}}$
SI	$\sqrt{e^{-2R}}\simeq 0.32$	$\sqrt{I_o/I_{\rm SQL}}$
VO	$\epsilon_*^{1/4}\simeq 0.32$	$\sqrt{\frac{I_o/I_{\rm SQL}}{1/\sqrt{\epsilon_*}}}\simeq\sqrt{\frac{I_o/I_{\rm SQL}}{10}}$
SV	$(e^{-2R}\epsilon_*)^{1/4}\simeq 0.18$	$\sqrt{\frac{I_o/I_{\rm SQL}}{\sqrt{e^{-2R}/\epsilon_*}}}\simeq\sqrt{\frac{I_o/I_{\rm SQL}}{3.2}}$

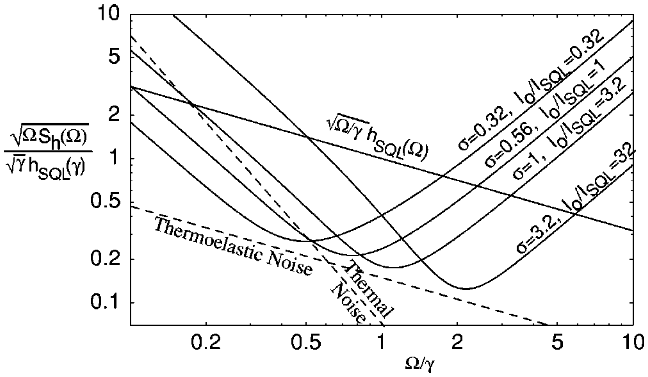

FIG. 14. Noise curves for SQL interferometers with noise minima $\mu=0.18$ and various values of the frequency parameter σ. The vertical axis is weighted by $\sqrt{\Omega/\gamma}$ so the curves give an indication of the relative noise in searches for waves from inspiraling binaries; see text. The noise curves are labeled by the power $I_o/I_{\rm SQL}$ required by a squeezed-variational interferometer to achieve the given σ.

terferometer achieve the same $\mu\simeq0.32$, while the squeezed-variational interferometer achieves a moderately lower $\mu\simeq0.18$. (iii) The frequency $\Omega_*=\sigma$ at which the minimum noise is achieved is proportional to $\sqrt{I_o/I_{\rm SQL}}$. (Recall that $I_{\rm SQL}$ is the input power required for a conventional interferometer to reach the SQL *at the angular frequency* $\Omega=\gamma\simeq2\pi\times100$ Hz, i.e., at $\Omega_*=1$; to do so, the conventional interferometer must have $\sigma=1$.) (iv) For $I_o=I_{\rm SQL}$, the squeezed-input interferometer has $\sigma=1$, but the variational-output and squeezed-variational interferometers have $\sigma<1$, which means that the minimum of the noise curve is at $\Omega<\gamma\simeq100$ Hz. To push σ up to unity, i.e., to push the noise-curve minimum up to $\Omega=\gamma$, requires $I_o/I_{\rm SQL}=1/\sqrt{\epsilon_*}\simeq10$ in a variational-output interferometer, and $I_o/I_{\rm SQL}=\sqrt{e^{-2R}/\epsilon_*}\simeq3.2$ in a squeezed-variational interferometer.

The importance of pushing σ up to unity or higher is explained in Fig. 14. This figure requires some discussion:

The most promising gravitational waves for LIGO are those from the last few minutes of inspiral of black-hole–black-hole binaries, black-hole–neutron-star binaries, and neutron-star–neutron-star binaries. The amplitude signal-to-noise ratio S/N produced by these waves is given by

$$\frac{S^2}{N^2}=4\int_0^\infty\frac{|\tilde h|^2}{S_h}\frac{d\Omega}{2\pi}=4\int_{-\infty}^\infty\frac{|\Omega\tilde h|^2}{\Omega S_h}\frac{d\ln\Omega}{2\pi}, \tag{131}$$

where $\tilde h$ is the Fourier transform of the waveform $h(t)$. For the inspiraling binary $|\Omega\tilde h|$ is nearly independent of frequency throughout the LIGO band [34], so the signal-to-noise ratio is optimized by making $\Omega S_h(\Omega)$ as small as possible over as wide a range of $\ln\Omega$ as possible.

Figure 14 plots $\sqrt{\Omega S_h(\Omega)}$ as a function of Ω/γ using logarithmic scales on both axes, and using the minimum-noise parameter $\mu=0.18$ corresponding to our fiducial squeezed-variational interferometer (though the specific value of μ is irrelevant to our present discussion). From the shapes of the curves it should be evident that *the larger is the frequency of the noise minimum, i.e. the larger is* σ *at fixed* μ*, the larger will be the* S/N *for inspiraling binaries.*

A second factor dictates using large σ, in particular $\sigma\gtrsim1$. This is thermal noise in the interferometer's test-mass suspension fibers. The thermal noise scales with frequency as $\sqrt{\Omega S_h^{\rm thermal}(\Omega)}\propto\Omega^{-2}$ or $\propto\Omega^{-5/2}$ depending on the nature of the dissipation [35]; see the steep dashed curve in Fig. 14. It seems realistic to expect, in LIGO-III, that this thermal noise will be at approximately the level shown in the figure, so it compromises the performance of QND interferometers at $\Omega\lesssim0.5\gamma\simeq50$ Hz [7,36]. Correspondingly, to avoid the thermal noise significantly debilitating the S/N for inspiraling binaries, it will be necessary to have $\sigma\gtrsim1$.

Because σ scales as $\sqrt{I_o/I_{\rm SQL}}$ for all interferometer designs, large σ entails large laser power. In particular, $\sigma\gtrsim1$ requires $I_o\gtrsim I_{\rm SQL}$; cf. Table II. For our fiducial parameters (Table I), $I_{\rm SQL}=10$ kW, which corresponds to an optical power circulating in each of the interferometer's arm cavities

$$W_{\rm circ}^{\rm SQL}=\frac{I_{\rm SQL}/2}{\gamma L/c}=\frac{mcL\gamma^3}{8\omega_o}=0.62\ \ {\rm MW}. \tag{132}$$

To construct mirrors capable of handling this huge power will be an enormous technical challenge (even though this is approximately the circulating power contemplated for LIGO-II). To operate with a circulating power much larger than this might not be possible. Therefore, it may be important in LIGO-III to achieve $\sigma\gtrsim1$ while keeping $I_o/I_{\rm SQL}$ not much larger than unity.

The squeezed-input interferometer, with its $\sigma=\sqrt{I_o/I_{\rm SQL}}$ (Table II) is the most attractive from this point of view [and also in terms of its required filter and squeeze-phase accuracies; cf. end of Sec. VI F]; and the variational-output with its $\sigma=\sqrt{\sqrt{\epsilon_*}I_o/I_{\rm SQL}}\simeq\sqrt{0.1I_o/I_{\rm SQL}}$ is the least attractive. The squeezed-variational interferometer, with $\sigma=\sqrt{\sqrt{\epsilon_*/e^{-2R}}I_o/I_{\rm SQL}}\simeq\sqrt{0.32I_o/I_{\rm SQL}}$ requires a modestly higher laser power to reach $\sigma=1$ than the squeezed-input [and requires better filter and squeeze-phase accuracies], but it is capable of a lower noise minimum, $\mu\simeq(e^{-2R}\epsilon_*)^{1/4}\simeq0.18$ vs $\mu=\sqrt{e^{-2R}}\simeq0.32$ for squeezed-input.

This suggests a research and development strategy: Focus on input squeezing as a key foundation for LIGO-III (it is needed both for squeezed-input and squeezed-variational interferometers), and in parallel (i) develop the technology and techniques for the FD homodyne detection required by squeezed-variational configurations, (ii) work to drive down optical losses to the levels $\epsilon\sim\epsilon_{\rm circ}\sim\epsilon_{\rm bs}\sim\epsilon_{\rm mm}\sim\epsilon_{\rm lo}\sim\epsilon_{\rm pd}\sim0.001$ [Eq. (92)], and (since ponderomotive squeezing, which underlies all our QND interferometers, has never been seen) (iii) carry out experiments in a small test appratus to demonstrate ponderomotive squeezing and to search for unexpected obstacles and imperfections in it.

If both input squeezing and FD homodyne detection can be implemented successfully, then the squeezed-variational interferometer is likely to achieve better performance than any other configuration discussed in this paper, despite its apparent need for higher laser power (e.g., $I_o/I_{\rm SQL}\simeq3.2$ to achieve $\sigma=1$ compared to $I_o/I_{\rm SQL}=1$ for squeezed input, with our fiducial parameters). If powers as high as $I_o/I_{\rm SQL} \simeq 3.2$ cannot be handled, then we can operate the squeezed-variational interferometer with a lower power without much loss of performance.

Consider, for example, $\sqrt{S_h}/h_{\rm SQL}$ evaluated at $\Omega=\sigma \simeq 2\pi\times 100$ Hz, as a function of $I_o/I_{\rm SQL}$ in a squeezed-variational interferometer with our fiducial $e^{-2R}=0.1$ and $\epsilon_*=0.01$. The optimal $I_o/I_{\rm SQL}=3.2$ produces $\sqrt{S_h(\gamma)}/h_{\rm SQL}=0.18$; pushing $I_o/I_{\rm SQL}$ down by a factor 2, to 1.6, increases the noise at $\Omega=\gamma$ by only 10 percent, to 0.20; pushing down all the way to $I_o/I_{\rm SQL}=1$ increases the noise to only $\sqrt{S_h(\gamma)}/h_{\rm SQL}=0.23$, which is still significantly lower noise than the optimized squeezed-input interferometer (0.32 at $I_o/I_{\rm SQL}=1$).

It is worth recalling that for noncosmological sources (sources at distance $\ll 3$ Gpc), the volume of the universe that can be searched for a given type of source scales as the inverse cube of the amplitude noise, so a noise level $\sqrt{S_h}/h_{\rm SQL}=0.18$ corresponds to search-volume increase of $1/0.18^3 \simeq 180$ over a SQL-limited interferometer, i.e., over LIGO-II.

VIII. CONCLUSIONS

In this paper we have explored three candidate ideas for QND LIGO-III interferometers: squeezed-input, variational-output, and squeezed variational. The squeezed-input and squeezed-variational interferometers both look quite promising. For our estimated levels of optical loss and levels of squeezing, and for an input laser power $I_o/I_{\rm SQL}=1$ (the LIGO-II level), the squeezed-input interferometer could achieve a noise $\mu \simeq 0.32$ of the SQL, with a corresponding increase $\mathcal{V} \simeq 1/0.32^3 \simeq 30$ over LIGO-II in the volume of the universe that could be searched for a given source, at noncosmological distances. The squeezed-variational interferometer could achieve $\mu \simeq 0.23$ of the SQL with a search-volume increase over LIGO-II of $\mathcal{V} \simeq 80$. If the optics can handle a laser power $I_o/I_{\rm SQL} \simeq 3.2$, then the squeezed-variational interferometer could reach $\mu \simeq 0.18$ of the SQL and a search-volume increase of $\mathcal{V} \simeq 180$. These numbers scale with the losses, squeezing, and laser power as shown in Table II.

The squeezed-input and squeezed-variational designs are therefore sufficiently promising to merit serious further study. Some of the issues that need theoretical analysis are:

(i) How can one incorporate into these interferometer designs the various light modulations that are required, in a real gravitational-wave interferometer, to (i) make the interferometer be shot-noise limited (put the gravitational-wave signal into ~ 100 Hz sidebands of a MHz modulation[13]), (ii) control the mirror positions and orientations, etc. [37].

(ii) What accuracies and other characteristics are needed for the interferometers' new elements: the circulator, filter cavities,[14] and input squeezing? How can these be achieved? For example, how stable must be the local oscillator for the conventional homodyne detector, and can it be achieved simply by tapping some light off the interferometer's output or input beam?

(iii) If the filter cavities are placed in the same long vacuum tubes as the interferometer's arm cavities (with their enormous circulating power), what will be the nature and level of noise due to scattering of light from the test-mass cavites to the filter cavities? (We thank Eanna Flanagan for raising this issue.)

(iv) Can the filter cavities be made to serve multiple purposes? For example, is it possible to use a single optical cavity for both filters, e.g., with the two filters based on two different polarization states (for which the filter might be made to behave differently via birefringence), or with the two filters based on different, adjacent longitudinal modes? As another example, could an output filter cavity be used as a source of ponderomotively squeezed vacuum for input into the interferometer's dark port?[15]

(v) Signal recycling via resonant-sideband extraction (RSE) [38] is likely to be a standard tool in LIGO-II [7]. How can one best implement RSE simultaneously with the FD homodyne detection (and input squeezing) of a variational-output (or squeezed-variational) interferometer? [37] How can one best achieve the FD homodyne's filtration [which will entail a different frequency dependence $\Phi(\Omega)$ from that in this paper's non-RSE designs]?

(vi) In this paper's analysis we have made a number of simplifying approximations [e.g., our approximating the phase of the coefficient of f_j in Eq. (B24) by 2β an approximation that fails by a frequency-dependent amount which can be nearly as large as one per cent]. At what level of sensitivity do these approximations become problematic (e.g., for our proposed two-cavity way of achieving the necessary FD homodyne detection), and how can the resulting problems be overcome?

(vii) Our analysis is based on the crucial assumption that the interferometer's output is strictly linear in its input [4]. Matsko and Vyatchanin [39] have shown that this is not quite correct. In the interferometer's arms the back-action-induced mirror displacement X produces a phase shift of reflected light given by $e^{-2i\Omega X/c}$, which our linearized analysis approximates as $1-2i\Omega X/c$ [cf. Eq. (B10)]; when the better approximation $1-2i\Omega X/c-2(\Omega X/c)^2$ is used, the result is additional, nonlinear noise, which limits the cancellation of the back-action noise by the shot noise and produces a limit [39]

---

[13] LIGO scientists are currently exploring the possibility of achieving shot-noise-limited performance in LIGO-II without this modulation-demodulation. The modulation-demodulation may, in fact, be replaced in LIGO-II by homodyne detection at the interferometer output, making it more nearly like our paper's LIGO-III designs.

[14] The filter cavities will require a mechanical stability far less than that of the arm cavities, since the carrier power in the output light is small and filter mirror displacements of magnitude $\sim hL$ therefore do *not* imprint a significant signal on the light.

[15] For ponderomotively squeezed vacuum, the squeeze angle is frequency dependent, with $d\phi/d\Omega$ of the opposite sign to that needed by a squeezed-input interferometer. This must be compensated by a filtering different from that discussed in Sec. V.

$$S_h^{\rm NL}\sim\frac{h^2_{\rm SQL}}{2\mathcal{N}^{1/5}_{\rm SQL}}\sim 5\times 10^{-5}h^2_{\rm SQL} \tag{133}$$

on the sensitivity that any of our QND designs can achieve. Here

$$\mathcal{N}_{\rm SQL}=\frac{I_{\rm SQL}}{\hbar\,\omega_o\gamma}=\frac{1}{2}\left(\frac{Tc/4\omega_o}{\sqrt{\hbar/m\gamma}}\right)^2\simeq 2\times 10^{20} \tag{134}$$

is the number of quanta entering a SQL interferometer in time $\gamma^{-1}\sim 2$ ms. The nonlinear limitation (133) is sufficiently far below the SQL that we need not be concerned about it. Are there any other, more serious sources of nonlinearity that might compromise the performance of these interferometers?

Experimental studies are also needed as foundations for any possible implementation of variational-output or squeezed-variational interferometers [40]. Examples are

(i) Studies of the debilitating effects of very high circulating powers, $W_{\bigcirc}\sim$ a few MW, and how to control them.

(ii) A continuation of efforts to achieve large squeezing, robustly, via nonlinear optics [33], and exploration of the possibility to do so ponderomotively [41–44].

(iii) A continuation of efforts to achieve low levels of losses in optical cavities and interferometers, so as to minimize the contamination of squeezed light by ordinary vacuum [45].

(iv) Prototyping of FD homodyne detection by the technique proposed in this paper: filtration followed by conventional homodyne detection.

In the meantime, and in parallel with such studies, it is important to push hard on the effort to find practical QND designs that entail circulating light powers well below 1 MW [13], and that might be much less constrained by optical losses than the designs explored in this paper.

ACKNOWLEDGMENTS

For helpful discussions or email, one or more of the authors thank Vladimir Braginsky, Alessandra Buonanno, Carlton Caves, Yanbei Chen, Eanna Flanagan, Mikhail Gorodetsky, Farid Khalili, Patricia Purdue, Stan Whitcomb, Bill Unruh, and members of the Caltech QND Reading Group—most especially Constantin Brif, Bill Kells and John Preskill. We also thank Buonanno and Chen for pointing out several errors in the manuscript. This paper was supported in part by NSF grants PHY-9503642 (S.P.V.), PHY-9722674 (H.J.K.), PHY-9732445 (A.B.M.), PHY-9800097 (S.P.V.) and PHY-9900776 (K.S.T. and Y.L.), by the Office of Naval Research (H.J.K. and A.B.M.), by DARPA via the QUIC (Quantum Information and Computing) program administered by ARO (H.J.K.), by the Institute for Quantum Information (IQI) funded by the NSF-ITR program (H.I.K.), by the Caltech MURI on quantum networks administered by the Army Research Office (H.J.K.), and by the Russian Foundation for Fundamental Research grants No. 96-02-16319a and No. 97-02-0421g (S.P.V.).

APPENDIX A: ROTATION AND SQUEEZE OPERATORS

In this paper we make extensive use of squeeze operators and some use of rotation operators. In this appendix we list properties of these operators that are useful in verifying statements made in the text. This appendix is based on the formalism for 2-photon quantum optics developed by Caves and Schumaker [26,27].

The rotation operator $R(\theta)$, which acts on the Hilbert space of the modes with frequencies $\omega=\omega_o\pm\Omega$, is defined by

$$R(\theta)=\exp[-i\theta(a^\dagger_+a_+ + a^\dagger_-a_-)] \tag{A1}$$

[Eq. (4.33) of [26]]; here $a_\pm$ are the annihilation operators, and $a^\dagger_\pm$ the creation operators for photons in these modes. This operator is unitary and has the inverse

$$R^{-1}(\theta)=R^\dagger(\theta)=R(-\theta). \tag{A2}$$

The effect of a rotation on the modes' annihilation operators is

$$R(\theta)a_\pm R^\dagger(\theta)=a_\pm e^{i\theta} \tag{A3}$$

[Eq. (4.35) of [26]], and its effect on the two-photon quadrature amplitudes [Eqs. (6)] is

$$R(\theta)a_1R^\dagger(\theta)=a_1\cos\theta-a_2\sin\theta,$$

$$R(\theta)a_2R^\dagger(\theta)=a_1\sin\theta+a_2\cos\theta \tag{A4}$$

[Eq. (4.36) of [26]].

The squeeze operator also acts on the Hilbert space of modes with frequencies $\omega=\omega_o\pm\Omega$, and is defined by

$$S(r,\phi)=\exp[r(a_+a_-e^{-2i\phi}-a^\dagger_+a^\dagger_-e^{2i\phi})] \tag{A5}$$

[Eq. (4.9) of [26]; Eq. (1.8) of [27]]. This squeeze operator is unitary and its inverse is

$$S^{-1}(r,\phi)=S^\dagger(r,\phi)=S(-r,\phi)=S(r,\phi+\pi/2) \tag{A6}$$

[Eq. (1.9) of [27]]. The effect of a squeeze on the modes' annihilation operators is

$$S(r,\phi)a_\pm S^\dagger(r,\phi)=a_\pm\cosh r+a^\dagger_\mp e^{2i\phi}\sinh r \tag{A7}$$

[Eq. (4.10) of [26]]. From this equation and the definition (6) of the quadrature amplitudes, we infer the effect of a squeeze on those amplitudes

$$S(r,\phi)a_1S^\dagger(r,\phi)=a_1(\cosh r+\sinh r\cos 2\phi)+a_2\sinh r\sin 2\phi,$$

$$S(r,\phi)a_2S^\dagger(r,\phi)=a_2(\cosh r-\sinh r\cos 2\phi)+a_1\sinh r\sin 2\phi. \tag{A8}$$

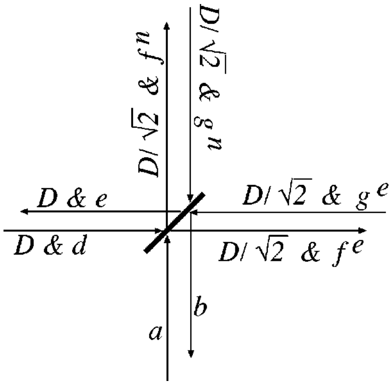

FIG. 15. Field amplitudes entering and leaving the beam splitter (which here is idealized as lossless). The various amplitudes are defined in Eqs. (B1)–(B4).

APPENDIX B: INPUT-OUTPUT RELATIONS FOR INTERFEROMETERS

In this appendix we shall derive the input-output relations for the fields a_j and b_j that enter and leave the interferometer's dark port. From the outset we shall include optical losses in our derivation, thereby obtaining the lossy input-output relations (97) and (101); the lossless input-output relations (16) then follow by setting $\epsilon=0$.

1. Fields at beam splitter

We describe the field amplitudes entering and leaving the beam splitter by the notation shown in Fig. 15 (cf. Fig. 3). We idealize the beam splitter as lossless in this appendix, and deal with its losses in the body of the paper in the manner sketched in Fig. 11. The amplitudes $D\&d$ of the field entering the beam splitter from the laser are defined by the following formulas for the positive-frequency part of the electric field

$$E_{\rm in}^{(+)}=\sqrt{\frac{2\pi\hbar\omega_o}{\mathcal{A}c}}e^{-i\omega_o t}\left[D+\int_0^\infty(d_+e^{-i\Omega t}+d_-e^{+i\Omega t})\frac{d\Omega}{2\pi}\right] \tag{B1}$$

[cf. Eq. (5)] and for the total electric field

$$\begin{aligned}E_{\rm in}=&\sqrt{\frac{4\pi\hbar\omega_o}{\mathcal{A}c}}\\&\times\left\{\cos(\omega_o t)\left[\sqrt{2}D+\int_0^\infty(d_1e^{-i\Omega t}+d_1^\dagger e^{+i\Omega t})\frac{d\Omega}{2\pi}\right]\right.\\&\left.+\sin(\omega_o t)\int_0^\infty(d_2e^{-i\Omega t}+d_2^\dagger e^{+i\Omega t})\frac{d\Omega}{2\pi}\right\}.\end{aligned} \tag{B2}$$

Thus, D is the classical amplitude of the laser light (carrier with frequency ω_o), $d_\pm$ are the annihilation operators for the $\omega_o\pm\Omega$ sidebands, and d_1 and d_2 are the quadrature amplitudes for the side bands. [Notice that the factor out front is a $\sqrt{2\pi}$ in Eq. (B1) but $\sqrt{4\pi}$ in Eq. (B2), and notice the $\sqrt{2}D$ in Eq. (B2).] The light power I_o impinging on the beam splitter is related to the classical amplitude D by

$$I_o=\frac{\overline{E_{\rm in}^2}}{4\pi}\mathcal{A}c=\hbar\omega_oD^2, \tag{B3}$$

where the overbar means time average. (Note that D^2 has dimensions Hz = 1/sec.)

For all other fields the classical amplitude and sideband amplitudes are as indicated in the figure; for example, the field going toward the east cavity has classical amplitude $D/\sqrt{2}$ and quadrature amplitudes f_1^e, f_2^e.

With an appropriate choice of conventions [46], the fields' junction conditions at the splitter are

$$f_j^n=\frac{d_j+a_j}{\sqrt{2}},\quad f_j^e=\frac{d_j-a_j}{\sqrt{2}},$$

$$b_j=\frac{g_j^n-g_j^e}{\sqrt{2}},\quad e_j=\frac{g_j^n+g_j^e}{\sqrt{2}}. \tag{B4}$$

Here $j=1$ or 2.

2. Arm cavities and fields

The east and north arm cavities are presumed to be identical, with power reflection and transmission coefficients R and T for the front mirror, and $\tilde{R}$ and $\tilde{T}$ for the back mirror. The amplitude reflection and transmission coefficients are chosen be real, with signs $\{+\sqrt{T},-\sqrt{R}\}$, $\{+\sqrt{\tilde{T}},-\sqrt{\tilde{R}}\}$ for light that impinges on a mirror from outside the cavity; and $\{+\sqrt{T},+\sqrt{R}\}$, $\{+\sqrt{\tilde{T}},+\sqrt{\tilde{R}}\}$ for light that impinges from inside the cavity.

The dominant optical losses are for light impinging on mirrors from inside the cavity (cf. Sec. VI B). The influence of the losses on the interferometer's signal and noise are independent of the physical nature of the losses—whether it is light scattering off a mirror, absorption in the mirror, or transmission through the end mirror. (We ignore the effects of mirror heating.) For computational simplicity, we model all the losses as due to finite transmissivity $\mathcal{L}=\tilde{T}\neq 0$ of the end mirror, and correspondingly we set

$$R+T=1,\quad \tilde{R}+\tilde{T}=1. \tag{B5}$$

The fractional loss of photons in each round trip in the cavity is then $\tilde{T}$, and the net fractional loss of photons in the arm cavities is

$$\epsilon=\frac{2\mathcal{L}}{T}=\frac{2\tilde{T}}{T} \tag{B6}$$

cf. Eqs. (93) and (94). Recall that $T\simeq 0.033$ and $\epsilon\sim 0.0012$, and also that $\Omega\sim\gamma=Tc/4L$ [Eqs. (11), (94)]; correspondingly, we shall make the approximations

$$\tilde{T}\ll T=4\gamma L/c\sim\Omega L/c\ll 1 \tag{B7}$$

throughout our analysis.

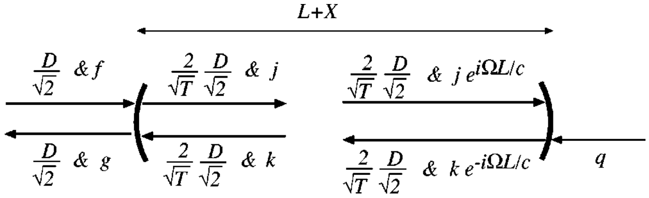
$L+X$
$\frac{D}{\sqrt{2}}$ & f
$\frac{2}{\sqrt{T}}\frac{D}{\sqrt{2}}$ & j
$\frac{2}{\sqrt{T}}\frac{D}{\sqrt{2}}$ & $j\,e^{i\Omega L/c}$
$\frac{D}{\sqrt{2}}$ & g
$\frac{2}{\sqrt{T}}\frac{D}{\sqrt{2}}$ & k
$\frac{2}{\sqrt{T}}\frac{D}{\sqrt{2}}$ & $k\,e^{-i\Omega L/c}$
q

FIG. 16. Field amplitudes entering and leaving an arm cavity. The cavity's front-port input and output amplitudes D, f, and g are defined in Eqs. (B3) and (B4) and Fig. 15, and its back-port input q is defined in Eq. (B11).

Figure 16 shows an arm cavity and the amplitudes of the fields that impinge on or depart from its mirrors. The amplitudes are those at the (front or back) mirror location, and the mirrors, like the beam splitter, are idealized as infinitesimally thin.

For pedagogical simplicity, the distance from the beam splitter to the front mirror of each arm cavity is set to an integral multiple of the carrier wavelength and is assumed to be far smaller than c/Ω (the wavelength associated with the sidebands). This means that there are no net phase shifts of the light in traveling between the beam splitter and the cavity's front mirror; i.e., the field amplitudes $D/\sqrt{2}\&f$ (or $D/\sqrt{2}\&g$) arriving at (or departing from) the mirror are the same as those departing from (or arriving at) the beam splitter; cf. Figs. 16 and 15.

The cavity's length is adjusted to an integral number of carrier wavelengths so there is no carrier phase shift from one end of the cavity to the other, and inside the cavity the carrier amplitude is amplified by the standard resonance factor $2/\sqrt{T}$. (Losses are small enough to be of little importance for the carrier.) Because the side bands inside the cavity have a frequency dependence $g_j e^{-i\Omega t}\cos(\omega_o t)$ at the front mirror location [cf. Eq. (B2)], they propagate down the cavity as $g_j e^{-i\Omega(t-z)}\cos[\omega_o(t-z)]$ and upon reaching the back mirror (where $\cos[\omega_o(t-z)]=\cos[\omega t]$), they have acquired the phase shift indicated in the figure, $g_j e^{i\Omega L/c}$; and similarly for the k_j field propagating in the other direction.

The standard junction conditions at the front mirror imply that

$$j_j=\sqrt{T}f_j+\sqrt{R}k_j\,,\quad g_j=-\sqrt{R}f_j+\sqrt{T}k_j\,. \tag{B8}$$

We denote by $X(t)$ the change of arm length produced by radiation pressure and the gravitational waves, and by X its Fourier transform. The oscillating $X(t)$ pumps carrier light into the side bands. More specifically, in traveling from the front mirror $z=0$ to the perturbed position $z=L+X(t)$ of the back mirror, then reflecting and propagating to the unperturbed location $z=L$, the carrier field acquires the form[16]

$$\begin{aligned}E_{\text{carrier}}&=\sqrt{\frac{4\pi\hbar\omega_o}{\mathcal{A}c}}\sqrt{\frac{2}{T}}\sqrt{2}D\cos(\omega_o[t-2X(t)/c])\\&=\sqrt{\frac{4\pi\hbar\omega_o}{\mathcal{A}c}}\sqrt{\frac{4}{T}}D\biggl(\cos\omega_o t\\&\quad+\sin\omega_o t\frac{2\omega_o}{c}\int_{-\infty}^{+\infty}Xe^{-i\Omega t}\frac{d\Omega}{2\pi}\biggr).\end{aligned} \tag{B9}$$

Comparing with the standard expression for the field at the location of the unperturbed end mirror [Eq. (B2) with the amplitude changes indicated in the lower right of Fig. 16, $D\to(2/\sqrt{2})(D/\sqrt{2})$ and $d_j\to k_j e^{-i\Omega L/c}$], we obtain the following expression for the field fed from the carrier D into the sideband amplitudes k_j:

$$\delta k_1=0,\quad \delta k_2=\frac{2}{\sqrt{T}}D\frac{2\omega_o}{c}X. \tag{B10}$$

This acts as a source term in the standard junction condition for the back mirror:

$$k_j e^{-i\Omega L/c}=\sqrt{\tilde{R}}j_j e^{i\Omega L/c}+\sqrt{\tilde{T}}q_j+\delta k_j\,. \tag{B11}$$

Note that q_j is the noise-producing vacuum fluctuation that leaks into the cavity as a result of the optical losses.

3. Cavity's internal field and radiation-pressure fluctuations

By combining the front-mirror and back-mirror junction conditions (B8) and (B11) we obtain for the side-band amplitude in the cavity

$$j_j=\frac{\sqrt{T}f_j+\sqrt{R}e^{i\Omega L/c}(\sqrt{\tilde{T}}q_j+\delta k_j)}{1-\sqrt{R\tilde{R}}e^{2i\Omega L/c}}. \tag{B12}$$

Equations (B7) and $\sqrt{R}=\sqrt{1-T}=\sqrt{1-0.033}\simeq 1$ allow us to make the approximations $\sqrt{R}e^{i\Omega L/c}\simeq 1$ in the numerator and [using Eq. (11)]

$$1-\sqrt{R\tilde{R}}e^{2i\Omega L/c}\simeq(2L/c)(\gamma_*-i\Omega), \tag{B13}$$

$$\gamma_*\equiv\gamma(1+\epsilon/2) \tag{B14}$$

in the denominator (accurate to better than 1 percent for all Ω of interest to us), thereby bringing Eq. (B12) into the form

$$j_j=\frac{\sqrt{T}(f_j+\sqrt{\epsilon/2}q_j)+\delta k_j}{(2L/c)(\gamma_*-i\Omega)}, \tag{B15}$$

where we have used $\tilde{T}=1/2\epsilon T$. The cavity's internal electric field E_{int} is expression (B2) with $D\to(2/\sqrt{T})(D/\sqrt{2})$ [Eq. (B9)] and $d_j\to j_j$ [expression (B15)]; cf. Fig. 16. The power circulating in the cavity is this $(\overline{E_{\rm int}^2/4\pi})\mathcal{A}c$, and consists of two parts, a steady classical piece

---

[16] Here we have neglected the attenuation of the carrier field due to the arm-cavity losses. This neglect is in the same spirit as our ignoring attenuation in the input optics, in the beam splitter, and in mode matching into the arm cavities. Including these attenuations would simply change D in Eq. (B9) to $D\times(1-1/2$ power attenuation factor)—i.e., $D\times(1-1/2\epsilon)$ for the effect of arm-cavity losses. Equivalently, it would dictate replacing I_o by I_o $(1-$ power attenuation factor) in $\mathcal{K}$, $\mathcal{K}_*$, and all our formulas for the gravitational-wave noise.

$$W_{\rm circ} = \frac{1}{2}\frac{4D^2}{T}\hbar\omega_o = \frac{2}{T}I_o = \frac{I_o/2}{\gamma L/c}, \tag{B16}$$

and a fluctuating piece

$$\delta W_{\rm circ} = \int_0^\infty \frac{\sqrt{I_o\hbar\omega_o}(f_1+\sqrt{\epsilon/2}q_1)}{(L/c)(\gamma_*-i\Omega)}e^{-i\Omega t}\frac{d\Omega}{2\pi} + \text{H.c.}, \tag{B17}$$

where H.c. means Hermitian conjugate (adjoint) of the previous term.

4. Mirror motion

The circulating-power fluctuations (B17) produce a fluctuating radiation-pressure (back-action) force

$$F_{\rm BA} = 2\,\delta W_{\rm circ}/c \tag{B18}$$

on each mirror. This force is equal and opposite on the cavity's two mirrors and, along with the gravitational waves, it produces the following acceleration of the mirror separation:

$$\frac{d^2X(t)}{dt^2} = \frac{1}{2}\eta_{ne}L\frac{d^2h(t)}{dt^2} + \frac{4\,\delta W_{\rm circ}(t)}{mc}. \tag{B19}$$

Here $h(t)$ is the gravitational-wave field (projected onto the interferometer's arms), and η_{ne} is $+1$ for the north arm and -1 for the east arm (one arm is stretched while the other is squeezed).

Below we will need an expression for the (Fourier transform of the) arm-length difference, $x = X_n - X_e$. It can be obtained by Fourier transforming the equation of motion (B19), solving for X (i.e., X_n or X_e), inserting expression (B17) for $\delta W_{\rm circ}$, and then taking the difference of the north and east arms. The result is

$$x = Lh + x_{\rm BA} \tag{B20}$$

[cf. Eq. (15)], where

$$x_{\rm BA} = \frac{-4\sqrt{2I_o\hbar\omega_o}(a_1+\sqrt{\epsilon/2}n_1)}{m\Omega^2L(\gamma_*-i\Omega)} = -\sqrt{\mathcal{K}_*/2}\,L\,h_{\rm SQL}(a_1+\sqrt{\epsilon/2}n_1)e^{i\beta_*}. \tag{B21}$$

Here we have introduced the quadrature amplitude for the difference of the arms' noise fields

$$n_j \equiv \frac{q_j^n - q_j^e}{\sqrt{2}} \tag{B22}$$

and have used Eq. (B4) for f_1^n and f_1^e, and Eqs. (99), (98), (19) and (20) for the coupling constant $\mathcal{K}_*$, the phase β_*, the SQL power $I_{\rm SQL}$ and the standard quantum limit $h_{\rm SQL}$.

Below we shall also need the following expression for the difference of the two arms' sideband fields produced by the mirror motions' coupling to the carrier:

$$\frac{\delta k_2^n - \delta k_2^e}{\sqrt{2}} = 2\sqrt{\frac{2}{T}}\sqrt{\frac{I_o}{\hbar\omega_o}}\frac{\omega_o x}{c}. \tag{B23}$$

This follows from Eqs. (B10), (B3) and (12).

5. Cavity output

The field exiting from the (north or east) cavity is obtained by combining Eqs. (B8), (B11) and (B12):

$$g_j = \frac{\sqrt{\tilde{R}}e^{2i\Omega L/c} - \sqrt{R}}{1-\sqrt{R\tilde{R}}e^{2i\Omega L/c}} \times f_j + \frac{(\sqrt{T\tilde{T}}q_j + \sqrt{T}\delta k_j)e^{i\Omega L/c}}{1-\sqrt{R\tilde{R}}e^{2i\Omega L/c}}. \tag{B24}$$

Inserting Eq. (B13) for the denominator and analogous expressions for the numerator, and discarding terms that are higher order than linear in the losses, we bring Eq. (B24) into the form

$$g_j = \left(1-\frac{1}{2}\mathcal{E}\right)e^{2i\beta}f_j + \sqrt{\mathcal{E}}e^{i\beta}q_j + \sqrt{\frac{(c/2L)^2T}{\gamma_*^2+\Omega^2}}e^{i\beta_*}\delta k_j, \tag{B25}$$

where β_* is given by Eq. (98) and $\mathcal{E}$ by Eq. (100).

6. Beam splitter output

By combining Eqs. (B4), (B25), and (B22), we obtain for the dark-port output of the beam splitter

$$b_j = \left(1-\frac{1}{2}\mathcal{E}\right)a_je^{2i\beta} + \sqrt{\mathcal{E}}n_1e^{i\beta} + \sqrt{\frac{(c/2L)^2T}{\gamma_*^2+\Omega^2}}\left(\frac{\delta k_j^n - \delta k_j^e}{\sqrt{2}}\right)e^{i\beta_*}. \tag{B26}$$

Inserting $\delta k_1^{n,e}=0$ [Eq. (B10)] and our expression (B23) for the difference of the δk_2's, and inserting Eqs. (B20) for x and Eqs. (99), (20), (B14) for $\mathcal{K}_*$, $h_{\rm SQL}$, γ_*, we obtain for the output fields:

$$b_1 = \left(1-\frac{1}{2}\mathcal{E}\right)a_1e^{2i\beta} + \sqrt{\mathcal{E}}n_1e^{i\beta}, \tag{B27a}$$

$$b_2 = \left(1-\frac{1}{2}\mathcal{E}\right)a_2e^{2i\beta} + \sqrt{\mathcal{E}}n_2e^{i\beta} + \sqrt{2\mathcal{K}_*}\left(\frac{h+x_{\rm BA}/L}{h_{\rm SQL}}\right)e^{i\beta_*}. \tag{B27b}$$

By inserting expression (B21) for the back-action-induced mirror displacement $x_{\rm BA}$, we obtain the input-output relations quoted in the text: Eqs. (97) and (101) with losses, and Eqs. (16) in the lossless limit.

APPENDIX C: FILTER PARAMETERS

In our discussion of FD homodyne detection (Sec. V), we derived the following requirement for the conventional homodyne phase θ and the filter parameters ξ_J and δ_J (with $J = \mathrm{I}$ and II):

$$\tan\Phi(\Omega)\equiv\frac{\Omega^2(\gamma^2+\Omega^2)}{\Lambda^4}=\tan\left(\theta-\frac{\alpha_{\mathrm{I}+}+\alpha_{\mathrm{I}-}+\alpha_{\mathrm{II}+}+\alpha_{\mathrm{II}-}}{2}\right) \tag{C1}$$

[Eqs. (81), (86), and (83)], where

$$\alpha_{J\pm}=\arctan(\xi_J\pm\Omega/\delta_J) \tag{C2}$$

[Eq. (88)]. In this appendix, we shall show that this requirement is satisfied by the parameter choices asserted in the text: Eqs. (85) and (89).

We initially regard the parameters θ, ξ_J, and δ_J as unknown. By inserting Eq. (C2) into Eq. (C1) and invoking some trigonometric identities, we obtain the requirement

$$\frac{(R_0-I_0\cot\theta)+(R_2-I_2\cot\theta)\Omega^2+R_4\Omega^4}{(R_0\cot\theta+I_0)+(R_2\cot\theta+I_2)\Omega^2+R_4\cot\theta\Omega^4}=\frac{\gamma^2\Omega^2+\Omega^4}{\Lambda^4}. \tag{C3}$$

Here $R_0+R_2\Omega^2+R_4\Omega^4$ is the real part and $I_0+I_2\Omega^2$ is the imaginary part of $(1+i\tan\alpha_{\mathrm{I}+})(1+i\tan\alpha_{\mathrm{I}-})(1+i\tan\alpha_{\mathrm{II}+})(1+i\tan\alpha_{\mathrm{II}-})$. More specifically,

$$R_0=1-\xi_{\mathrm{I}}^2-\xi_{\mathrm{II}}^2-4\xi_{\mathrm{I}}\xi_{\mathrm{II}}+\xi_{\mathrm{I}}^2\xi_{\mathrm{II}}^2, \tag{C4a}$$

$$R_2=(1-\xi_{\mathrm{I}}^2)/\delta_{\mathrm{II}}^2+(1-\xi_{\mathrm{II}}^2)/\delta_{\mathrm{I}}^2, \tag{C4b}$$

$$R_4=1/(\delta_{\mathrm{I}}^2\delta_{\mathrm{II}}^2), \tag{C4c}$$

$$I_0=2(\xi_{\mathrm{I}}+\xi_{\mathrm{II}})(1-\xi_{\mathrm{I}}\xi_{\mathrm{II}}), \tag{C4d}$$

$$I_2=2\xi_{\mathrm{II}}/\delta_{\mathrm{I}}^2+2\xi_{\mathrm{I}}/\delta_{\mathrm{II}}^2. \tag{C4e}$$

To get rid of the Ω^4 term in the denominator of Eq. (C3), we must set

$$\theta=\pi/2,\quad \text{so}\quad \cot\theta=0. \tag{C5}$$

(We cannot set $R_4=0$ since that would require an infinite bandwidth for one or both of the filters.) To get rid of the Ω^2 term in the denominator and the constant term in the numerator, and to make the Ω^2 and Ω^4 terms in the numerator have the correct coefficients, we must set

$$I_2=0, \tag{C6a}$$

$$R_0=0, \tag{C6b}$$

$$R_2^2/(I_0R_4)=\gamma^4/\Lambda^4\equiv 4/P, \tag{C6c}$$

$$R_2/R_4=\gamma^2. \tag{C6d}$$

Here we have used definition (89a) of the constant P.

Equations (C6) are four equations for the four unkown filter parameters: the fractional frequency offsets ξ_{I}, ξ_{II} and the half bandwidths δ_{I}, δ_{II}. In the next four paragraphs we shall explore the consequences of these four equations, arriving finally at the solution (89) for ξ_{I}, ξ_{II}, δ_{I}, and δ_{II} given in the text.

Equation (C6a) implies that

$$\delta_{\mathrm{I}}^2/\delta_{\mathrm{II}}^2=-\xi_{\mathrm{II}}/\xi_{\mathrm{I}}. \tag{C7}$$

Equation (C6b) implies that $(1-\xi_{\mathrm{I}}\xi_{\mathrm{II}})^2=(\xi_{\mathrm{I}}+\xi_{\mathrm{II}})^2$. It turns out that one of the frequency offsets is positive and the other is negative (cf. Fig. 10); we choose ξ_{I} to be the positive one. It also turns out that $\xi_{\mathrm{I}}+\xi_{\mathrm{II}}$ is positive (cf. Fig. 10). Consequently, we can take the square root of the above equation to obtain

$$1-\xi_{\mathrm{I}}\xi_{\mathrm{II}}=\xi_{\mathrm{I}}+\xi_{\mathrm{II}}, \tag{C8}$$

which enables us to express the frequency offsets in terms of each other:

$$\xi_{\mathrm{I}}=\frac{1-\xi_{\mathrm{II}}}{1+\xi_{\mathrm{II}}},\qquad \xi_{\mathrm{II}}=\frac{1-\xi_{\mathrm{I}}}{1+\xi_{\mathrm{I}}}. \tag{C9}$$

Equation (C6c), when combined with Eqs. (C7) and (C8), implies that

$$\frac{8}{P}=\frac{\left[\sqrt{\frac{-\xi_{\mathrm{II}}}{\xi_{\mathrm{I}}}}(1-\xi_{\mathrm{I}}^2)+\sqrt{\frac{-\xi_{\mathrm{I}}}{\xi_{\mathrm{II}}}}(1-\xi_{\mathrm{II}}^2)\right]^2}{(\xi_{\mathrm{I}}+\xi_{\mathrm{II}})^2}. \tag{C10}$$

We shall now combine this equation with Eqs. (C9) to obtain Eqs. (89) for the frequency offsets ξ_{I} and ξ_{II} in terms of $P=4\gamma^4/\Lambda^4$. Our first step is to define $A_\pm$ by Eqs. (89c) and (89d), which are equivalent to

$$A_+\equiv\frac{\xi_{\mathrm{I}}}{\xi_{\mathrm{I}}^2-1},\qquad A_-\equiv\frac{\xi_{\mathrm{II}}}{\xi_{\mathrm{II}}^2-1}. \tag{C11}$$

Note that the relation (C9) between ξ_{I} and ξ_{II} is equivalent to

$$4A_+A_-=1. \tag{C12}$$

By using Eqs. (C9), (C11) and (C12), we can reexpress the right side of Eq. (C10) solely in terms of A_+:

$$\frac{8}{P}=\frac{(4A_+^2-1)^2}{A_+(4A_+^2+1)}. \tag{C13}$$

It is convenient to define Q by Eqs. (89b), which are equivalent to

$$A_++A_-\equiv 2Q/P. \tag{C14}$$

Using Eqs. (C12) and (C14), we can rewrite Eq. (C13) in terms of Q instead of A_+:

$$\frac{2}{P}=\frac{2Q}{P}-\frac{P}{2Q}, \tag{C15}$$

which can be solved for Q as a function of P

$$Q=\frac{1+\sqrt{1+P^2}}{2}. \tag{C16}$$

This is the relation asserted in the text, Eq. (89a), and it completes our derivation of Eqs. (89a)–(89d) for the frequency offsets $\xi_{\rm I}$ and $\xi_{\rm II}$ in terms of P.

Turn, finally, to the consequences of Eq. (C6d), which says

$$\gamma^2=\delta_{\rm I}^2(1-\xi_{\rm I}^2)+\delta_{\rm II}^2(1-\xi_{\rm II}^2). \tag{C17}$$

By eliminating $\delta_{\rm II}$ with the aid of Eq. (C7), we obtain

$$\gamma^2=\delta_{\rm I}^2\xi_{\rm I}\left(\frac{1-\xi_{\rm I}^2}{\xi_{\rm I}}-\frac{1-\xi_{\rm II}^2}{\xi_{\rm II}}\right). \tag{C18}$$

Using Eqs. (C11), (C12), and (89b), we can rewrite this as

$$\frac{\delta_{\rm I}}{\gamma}=\sqrt{\frac{P}{8\xi_1\sqrt{Q}}}, \tag{C19}$$

which is the formula for the half bandwidth $\delta_{\rm I}$ given in the text, Eq. (89e). The corresponding formula for $\delta_{\rm II}$, Eq. (89f), follows directly from Eqs. (C19) and (C7).

[1] http://www.ligo.caltech.edu/.

[2] V. B. Braginsky and F. Ya. Khalili, Rev. Mod. Phys. **68**, 1 (1996).

[3] V. B. Braginsky and F. Ya. Khalili, *Quantum Measurement* (Cambridge University Press, Cambridge, England, 1992). Note: In this reference the spectral densities are double sided and thus are 1/2 the single-sided spectral densities used in the present paper.

[4] V. B. Braginsky, M. L. Gorodetsky, F. Ya. Khalili, A. B. Matsko, K. S. Thorne, and S. P. Vyatchanin, gr-qc/0109003.

[5] V. B. Braginsky, Sov. Phys. JETP **26**, 831 (1968); V. B. Braginsky, in *Physical Experiments with Test Bodies*, NASA Technical Translation TT F-672 (U.S. Technical Information Service, Springfied, VA, 1972).

[6] V. B. Braginsky and Yu. I. Vorontsov, Sov. Phys. Usp. **17**, 644 (1975).

[7] E. Gustafson, D. Shoemaker, K. Strain, and R. Weiss, ''LSC White Paper on Detector Research and Development,'' LIGO Document Number T990080-00-D (Caltech/MIT, 1999).

[8] See, e.g., S. Rowan *et al.*, Phys. Lett. A **233**, 303 (1997); V. B. Braginsky, M. L. Gorodetsky, and S. P. Vyatchanin, *ibid.* **264**, 1 (1999), and references therein.

[9] For a very general demonstration that ~1 MW is the minimum circulating power that is required to beat the standard quantum limit in a wide variety of QND interferometer designs, see V. B. Braginsky, M. L. Gorodetsky, F. Ya. Khalili, and K. S. Thorne, in *Proceedings of the Third Edoardo Amaldi Meeting on Gravitational Waves*, edited by S. Meshkov (AIP Press, Melville, NY, 2000), p. 180.

[10] V. B. Braginsky, M. L. Gorodetsky, F. Ya. Khalili, and K. S. Thorne, Phys. Rev. D **61**, 044002 (2000).

[11] P. Purdue, Phys. Rev. D (to be published), gr-qc/0111042.

[12] C. M. Caves, K. S. Thorne, R. W. P. Drever, V. D. Sandberg, and M. Zimmermann, Rev. Mod. Phys. **52**, 341 (1980); V. B. Braginsky, Yu. I. Vorontsov, and K. S. Thorne, Science **209**, 547 (1980); C. M. Caves, in *Quantum Optics, Experimental Gravity, and Measurement Theory*, edited by P. Meystre and M. O. Scully (Plenum, New York, 1982), p. 567. See also W. G. Unruh, Phys. Rev. D **19**, 2888 (1979).

[13] V. B. Braginsky, M. L. Gorodetsky, and F. Ya. Khalili, Phys. Lett. A **232**, 340 (1997); **246**, 485 (1998); V. B. Braginsky and F. Ya. Khalili, *ibid.* **257**, 241 (1999).

[14] W. G. Unruh, in *Quantum Optics, Experimental Gravitation, and Measurement Theory*, edited by P. Meystre and M. O. Scully (Plenum, New York, 1982), p. 647.

[15] V. B. Braginsky and A. B. Manukin, Zh. Éksp. Teor. Fiz. **52**, 987 (1967) [Sov. Phys. JETP **25**, 653 (1967)].

[16] A similar effect has been considered by A. V. Gusev and V. N. Rudenko, Zh. Eksp. Teor. Fiz. **76**, 1488 (1979).

[17] C. M. Caves, Phys. Rev. D **23**, 1693 (1981).

[18] M. T. Jaekel and S. Reynaud, Europhys. Lett. **13**, 301 (1990).

[19] A. F. Pace, M. J. Collett, and D. F. Walls, Phys. Rev. A **47**, 3173 (1993).

[20] M. Xiao, L.-A. Wu, and H. J. Kimble, Phys. Rev. Lett. **59**, 278 (1987).

[21] P. Grangier, R. E. Slusher, B. Yurke, and A. LaPorta, Phys. Rev. Lett. **59**, 2153 (1987).

[22] See, e.g., the following special issues of journals dealing with squeezing via nonlinear optics: J. Opt. Soc. Am. B **4**, 1453 (1987); and *Quantum Noise Reduction in Optical Systems*, edited by C. Fabre and E. Giacobino [Appl. Phys. B **55**, 189ff (1992)].

[23] S. P. Vyatchanin and A. B. Matsko, JETP **77**, 218 (1993); S. P. Vyatchanin and E. A. Zubova, Phys. Lett. A **203**, 269 (1995); S. P. Vyatchanin, *ibid.* **239**, 201 (1998).

[24] S. P. Vyatchanin and A. B. Matsko, JETP **82**, 1007 (1996).

[25] S. P. Vyatchanin and A. B. Matsko, JETP **83**, 690 (1996).

[26] C. M. Caves and B. L. Schumaker, Phys. Rev. A **31**, 3068 (1985).

[27] B. S. Schumaker and C. M. Caves, Phys. Rev. A **31**, 3093 (1985).

[28] D. F. Walls and G. J. Milburn, *Quantum Optics* (Springer-Verlag, Berlin, 1994); L. Mandel and E. Wolf, *Optical Coherence and Quantum Optics* (Cambridge University Press, Cambridge, England, 1995). Some readers may also find useful background in C. W. Gardiner, *Quantum Noise* (Springer-Verlag, Berlin, 1991).

[29] R. W. P. Drever *et al.*, in *Quantum Optics, Experimental Gravity and Measurement Theory*, edited by P. Meystre and M. O. Scully (Plenum, New York, 1981), p. 503.

[30] C. Fabre, M. Pinard, S. Bourzeix, A. Heidmann, E. Giacobino, and S. Reynaud, Phys. Rev. A **49**, 1337 (1994); S. Mancini and P. Tombesi, *ibid.* **49**, 4055 (1994); A. Heidmann and S. Reynaud, *ibid.* **50**, 4237 (1994); M. Pinard, C. Fabre, and A. Heidmann, *ibid.* **51**, 2443 (1995).

[31] H. J. Kimble, in *Fundamental Systems in Quantum Optics*, Les Houches Session LIII, 1990, edited by J. Dalibard, J. M. Raimond, and J. Zinn-Justin (Elsevier, Amsterdam, 1992), pp. 549–674.

[32] Y. Chen (private communication).

[33] For example, although the detected degree of squeezing e^{-2R} in L.-A. Wu, M. Xiao, and H. J. Kimble, J. Opt. Soc. Am. B **4**, 1465 (1987) was only -4.3 dB, the inferred degree of squeezing was much larger: after making an absolute accounting for passive linear losses, these authors inferred a degree of squeezing corresponding to approximately -12 dB, which provides a benchmark for how well the basis nonlinear optical process of parametric down conversion conforms to simple theoretical models [31]. Somewhat more recently, E. S. Polzik, J. Carri, and J. H. Kimble, Appl. Phys. B: Photophys. Laser Chem. **B55**, 279 (1992), have recorded quantum noise reductions of -6 dB directly in the observed homodyne current. In this case the degree of squeezing was limited not by passive linear losses, but instead by nonlinear light induced absorption in the potassium niobate crystal used for parametric down conversion. Quite recently, K. Schneider, M. Lang, J. Mlynek, and S. Schiller, Opt. Express **2**, 59 (1998), have reported 6.5 dB of vacuum squeezing from a below-threshold optical parametric oscillator, with comparable levels reported by P. K. Lam *et al.*, J. Opt. B: Quantum Semiclassical Opt. **1**, 469 (1999).

[34] Equation (44) of K. S. Thorne, in *300 Years of Gravitation*, edited by S. W. Hawking and W. Israel (Cambridge University Press, Cambridge, England, 1987).

[35] P. R. Saulson, Phys. Rev. D **42**, 2437 (1990).

[36] V. B. Braginsky, V. P. Mitrofanov, and K. V. Tokmakov, Phys. Lett. A **218**, 164 (1996); K. Tokmakov, V. Mitrofanov, V. Braginsky, S. Rowan, and J. Hough, in *Proceedings of the Third Edoardo Amaldi Conference on Gravitational Waves*, edited by S. Meshkov (AIP Press, Melville, NY, 2000), p. 445.

[37] For analyses of the compatibility of input squeezing, modulations, and signal recycling, see S. Song, Ph.D. thesis, University of Southern California, 1994; and J. Geabanacloche and G. Leuchs, J. Mod. Opt. **34**, 793 (1987).

[38] J. Mizuno, K. A. Strain, P. G. Nelson, J. M. Chen, R. Schilling, A. Rudiger, W. Winkler, and K. Danzmann, Phys. Lett. A **175**, 273 (1993).

[39] Equation (133) can be derived by the techniques used in Ref. [25]; see especially Eqs. (13)–(15) of [25].

[40] The experimental challenge simply to reach the SQL for mirror position is daunting. Two recent experiments that addressed this challenge with small masses but were impeded by thermal noise are reported in Refs. [42] and [43].

[41] A. Dorsel, J. D. McCullen, P. Meystre, E. Vignes, and H. Walther, Phys. Rev. Lett. **51**, 1550 (1983).

[42] Y. Hadjar, P. F. Cohadon, C. J. Aminoff, M. Pinard, and A. Heidmann, Europhys. Lett. **47**, 545 (1999).

[43] I. Tittonen *et al.*, Phys. Rev. A **59**, 1038 (1999).

[44] K. Jacobs, I. Tittonen, H. M. Wiseman, and S. Schiller, Phys. Rev. A **60**, 538 (1999).

[45] For a detailed discussion of losses and various efficiency factors associated with the spatial overlap of fields in interferometry with squeezed light, see Min Xiao, Ph.D. thesis, University of Texas at Austin, 1988, Chap. 4, Sec. II A.

[46] A. E. Siegman, *An Introduction to Lasers and Masers* (McGraw-Hill, New York, 1971), Appendix C, Eq. (14).

PHYSICAL REVIEW A, VOLUME 64, 013407

Cooling of a single atom in an optical trap inside a resonator

S. J. van Enk,[1,*] J. McKeever,[1] H. J. Kimble,[1] and J. Ye[2]
[1]*Norman Bridge Laboratory of Physics, California Institute of Technology 12-33, Pasadena, California 91125*
[2]*JILA, Campus Box 440, University of Colorado and National Institute of Standards and Technology, Boulder, Colorado 80309-0440*

(Received 31 May 2000; revised manuscript received 21 February 2001; published 6 June 2001)

We present detailed discussions of cooling and trapping mechanisms for an atom in an optical trap inside an optical cavity, as relevant to recent experiments. The interference pattern of cavity QED and trapping fields in space makes the trapping wells, in principle, distinguishable from one another. This adds considerable flexibility to creating effective trapping and cooling conditions and to detection possibilities. Friction and diffusion coefficients are calculated in and beyond the low excitation limit and full three-dimensional simulations of the quasiclassical motion of a Cs atom are performed.

DOI: 10.1103/PhysRevA.64.013407 PACS number(s): 32.80.Pj, 42.50.Vk, 42.50.Lc

I. INTRODUCTION

A recent experiment [1] succeeded in trapping a single atom with single photons inside an optical cavity and in monitoring the atomic motion with the resolution approaching the standard quantum limit for position measurements. Yet a second experiment [2] has likewise reported single-atom trapping at the few-photon level, although in this case the trapping potential and diffusion are in fact well approximated by a free-space semiclassical theory [3].

One future objective for such experiments is to use atoms trapped in cavities for quantum communication purposes, with atoms serving as quantum memories and photons as the transporters of quantum information [4,5]. While the single-photon trapping experiments provide a new paradigm for quantum measurement and control, they are, nevertheless, not entirely suitable for the purpose of distributed quantum networks where qubits will be communicated among quantum nodes. The reason is the short trapping lifetime of the atoms as well as limited operation flexibility. A better strategy might be to use the cavity QED field for quantum state entanglement and distribution while an additional (external) trapping mechanism provides the necessary confinement of the atomic center-of-mass motion. For instance, in another recent experiment from the Caltech group [6], mean trapping times of ~ 28 ms (as compared to mean trapping times of <1 msec in the experiments [1,2]) were achieved by employing a far-off resonant trapping (FORT) beam along the cavity axis. In that experiment the trapping lifetime was limited due to intensity fluctuations of the intracavity FORT beam [7]. Here we consider the situation of current improved experiments [8] in which a single atom is held inside an optical cavity in a stable FORT beam of minimum intensity fluctuations.

Several mechanisms for cooling inside optical resonators have been discussed before [9–11]. Here we discuss in detail how the combination of an external trapping potential and the cavity QED field adds flexibility in predetermining where and to what degree atoms will be trapped and cooled. Moreover, our calculations go beyond the weak driving limit discussed in [10]. That is, we allow the ‘‘probe’’ field driving the cavity to be so strong as to appreciably modify the dynamical behavior of, rather than merely probe, the atom-cavity system.

This paper is organized as follows. In Sec. II we describe the physical situation of an atom trapped in an optical potential and strongly interacting with a cavity QED field. We give the evolution equations for both internal and external atomic degrees of freedom and for the quantized cavity mode. Section III contains an exposition on how we calculated friction and diffusion coefficients from the forces acting on the atom. Section IV contains the main results of this paper: we discuss simple pictures for cooling mechanisms, based on the dressed state structure of the atom-cavity system, and give numerical results for the typical cooling and diffusion rates, and hence ‘‘temperatures’’ for single atoms under various trapping conditions. We also study the saturation behavior under strong driving conditions and perform simulations of the full three-dimensional (3D) motion of atoms trapped in particular wells that show how the probe field transmission is correlated with the atomic motion and how trapping times can be prolonged by strong cooling. Section IV F concludes with a brief discussion of a slightly different trapping scheme. The summary highlights the main results.

II. DESCRIPTION OF PROBLEM

We consider a single two-level atom coupled to a single-quantized-cavity mode and coupled to a (classical) far-off resonant trapping beam. In most of the paper we assume that the FORT shifts the atomic excited state $|e\rangle$ *up* and the ground state $|g\rangle$ *down* by an amount $S_F(\vec{r})$ (i.e., the energy of the ground state is $E_g - S_F$, that of the excited state $E_e + S_F$), as this is the situation pursued in previous and current experiments [6,8]. In Sec. IV F, however, we will also study the different situation where both ground and excited states are shifted *down* by S_F (see, e.g., [12]). The FORT beam coincides with one of the longitudinal modes of the cavity and its wavelength λ_F is longer than that of the main cavity mode of interest for cavity QED, λ_0. In fact, in the experiments [6,8] the cavity length L is $104\lambda_0/2 = 102\lambda_F/2$.

The position-dependent ac-Stark shift due to the FORT field is of the form

$$S_F(\vec{r}) = S_0 \sin^2(k_F z) \exp(-2\rho^2/w_0^2), \tag{1}$$

---

[*] Present address: Bell Laboratories, Lucent Technologies, 600–700 Mountain Ave., Murray Hill, NJ 07980.

©2001 The American Physical Society

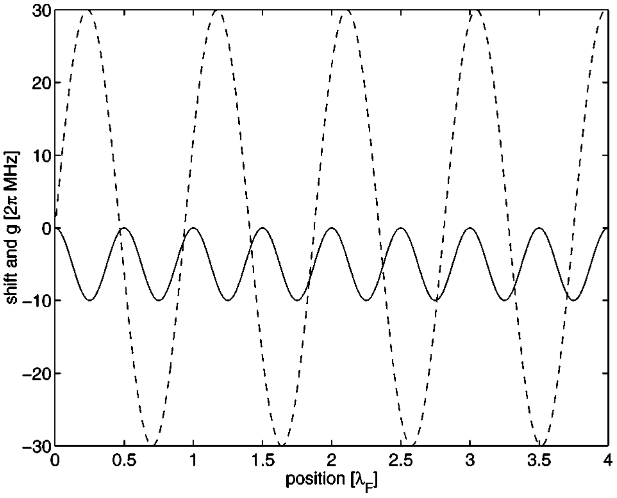

FIG. 1. The FORT-induced shift of the ground state on axis ($\rho=0$) in the case where $S_0/(2\pi)=10$ MHz and the cavity-QED coupling rate g (dashed curve), with $g_0=3S_0$, as functions of position along the cavity axis measured in units of the FORT wavelength λ_F, with $z=0$ at the left cavity boundary. The cavity length is $L=15\lambda_F$.

with $S_0>0$ the maximum shift, $k_F=2\pi/\lambda_F$ the wave vector of the FORT field, w_0 the size of the Gaussian mode of the cavity, while z and ρ give the coordinate along, and the distance perpendicular to, the cavity axis, respectively. The quantized cavity mode is assumed to have the same transverse dimensions[1] w_0 so that the atom-cavity coupling is determined by

$$g(\vec{r})=g_0\sin(kz)\exp(-\rho^2/w_0^2), \tag{2}$$

with g_0 the maximum coupling rate and $k=2\pi/\lambda_0$ the wave vector of the cavity mode. Under conditions where the cavity is not driven too strongly, the atom will be trapped around the antinodes of the red-detuned FORT field. Thanks to the fact that $\lambda_0\neq\lambda_F$, the atom will experience a different coupling strength to the cavity mode in each different well. Figure 1 shows the axial pattern arising from the FORT and cavity fields. For illustrative purposes we choose here (and in the rest of this paper) a cavity of length $L=16\lambda_0=15\lambda_F$. This does not influence the basic physics involved: in particular we note that the precise value of λ_F is largely irrelevant on the time scales considered here, as the FORT field is detuned far from atomic resonance. The choice of $L=16\lambda_0=15\lambda_F$ just means that only eight wells out of 30 are qualitatively and quantitatively different.

This is illustrated in Fig. 2 where we plot the value of the cavity QED coupling g at the antinodes of the FORT (i.e., the bottom of the trapping potential). In particular, there are two antinodes in which $g=0$, and 4 in which $|g|$ attains its maximum.

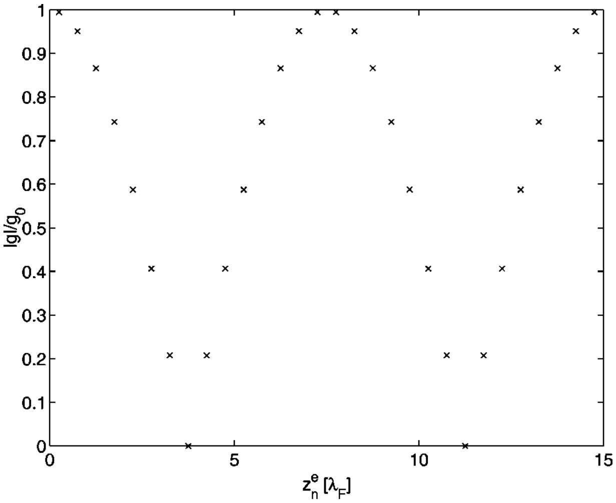

FIG. 2. The values of $|g|/g_0$ at the locations of the antinodes of the FORT, i.e., at the points $z_n=(n/2-1/4)\lambda_F$ for $n=1,\dots,30$. There are eight quantitatively different wells.

The cavity is driven by an external classical field $\mathcal{E}(t)=\mathcal{E}_0\exp(i\omega_p t)$, at a frequency ω_p, which is used to probe the atom-cavity system and which may cool the atom at the same time. In the following, the strength of the driving field is indicated by the number of cavity photons N_e that would be present if there were no atom in the cavity, rather than by $\mathcal{E}_0$. This closely follows the experimental procedure for determining the driving strength. The relation between the two is

$$N_e=\frac{\mathcal{E}_0^2}{\kappa^2+\Delta_c^2}, \tag{3}$$

with $\Delta_c=\omega_c-\omega_p$ the detuning of the probe from the cavity frequency $\omega_c=kc$. The Hamiltonian for the internal atomic degrees of freedom and the quantized cavity mode is, in a frame rotating at the probe frequency ω_p, given by

$$H=\hbar\Delta_c a^\dagger a+\hbar\Delta_a\sigma^+\sigma^-+2\hbar S_F(\vec{r})(\sigma^+\sigma^--1/2)+\hbar\mathcal{E}_0(a^\dagger+a)+\hbar g(\vec{r})(a^\dagger\sigma^-+\sigma^+a). \tag{4}$$

Here $\Delta_a=\omega_a-\omega_p$ is the detuning of the atomic resonance from the probe frequency. In all numerical examples given below the cavity frequency is chosen to coincide with the atomic frequency, so that $\Delta_c=\Delta_a$. The quantity $\Delta_p\equiv-\Delta_a$ is then referred to as the probe detuning. Note here that without a FORT the optimum cavity and atom detunings are not equal [9–11]. In our case, however, the FORT effectively changes the atomic frequency in a position-dependent way and thus the precise value of the atomic detuning relative to the cavity detuning is largely irrelevant. Indeed, optimum cooling conditions will exist in certain wells but not in others, which is one feature that allows one to distinguish various wells.

Coupling the atom and the cavity to the remaining modes of the electromagnetic field leads by a standard procedure to the master equation for the density operator of the coupled atom-cavity system,

---

[1] It is in fact the Rayleigh ranges of the beams that are identical, so that $w_0^{\mathrm{FORT}}/w_0^{\mathrm{cav}}=\sqrt{\lambda_0/\lambda_F}\approx0.99$.

$$\frac{d\rho}{dt} = -i[H,\rho]/\hbar - \kappa\{a^\dagger a,\rho\} + 2\kappa a\rho a^\dagger + - \frac{\Gamma}{2}\{\sigma^+\sigma^-,\rho\} + \frac{3\Gamma}{8\pi}\int d^2\hat{k}\sum_{\hat{\epsilon}} (\hat{d}\cdot\hat{\epsilon})^2 \exp(-i\vec{k}\cdot\vec{r}) \times \sigma^-\rho\sigma^+ \exp(i\vec{k}\cdot\vec{r}), \tag{5}$$

with Γ the spontaneous decay rate and κ the cavity decay rate. We are mainly interested in the strong-coupling regime, where $g_0 \gg \Gamma,\kappa$.

We treat the external (center-of-mass) degrees of freedom of the atom classically, an approximation justified at the end of Sec. IV C. For a discussion of various interesting effects arising from the quantized external motion of an atom in a cavity QED field, we refer the reader to [13].

In the quasiclassical approximation (i.e., where we retain the full quantum character of the internal degrees of freedom and of the cavity mode; see [3] for a full discussion of this approximation), the integral in Eq. (5) can be evaluated to give the simpler result

$$\frac{d\rho}{dt} = -i[H,\rho]/\hbar - \kappa\{a^\dagger a,\rho\} + 2\kappa a\rho a^\dagger - \frac{\Gamma}{2}\{\sigma^+\sigma^-,\rho\} + \Gamma\sigma^-\rho\sigma^+. \tag{6}$$

The force acting on the atom consists of two parts, one due to spontaneous emission, whose mean vanishes on average, and the other part is represented by the operator

$$\vec{F} \equiv -\vec{\nabla}H = -2\hbar\vec{\nabla}S_F(\sigma^+\sigma^- - 1/2) - \hbar\vec{\nabla}g(a^\dagger\sigma^- + \sigma^+ a), \tag{7}$$

which has contributions arising from the FORT potential and from the interaction with the cavity mode. It was only the latter part that was considered in [10] and that leads to 1D cooling to temperatures of the order $k_BT \sim \min(\hbar\kappa,\hbar\Gamma/2)$. See also Refs. [14] for similar calculations on single atoms moving in cavity QED field, and Refs. [15,16] for calculations of diffusion of atoms in optical traps in free space.

It can be shown [17] starting from a fully quantized description, that the semiclassical motion of the atom is described by a Fokker-Planck equation for the Wigner distribution function containing (position-dependent) friction and diffusion coefficients. Equivalently, we may use stochastic equations for the classical atomic position and velocity variables $\vec{r}$ and $\vec{v}$ of the form

$$d\vec{r} = \vec{v}\,dt,$$

$$d\vec{v} = \frac{\langle\vec{F}\rangle}{m}dt - \beta\vec{v}\,dt + B\,d\vec{W}, \tag{8}$$

where $\langle . \rangle$ denotes an expectation value, β is the friction tensor (with dimensions of a rate), m the mass of the atom, B is a tensor such that $D = BB^T/2$ is the velocity diffusion tensor (with dimension $\mathrm{m}^2/\mathrm{s}^3$), and $d\vec{W}$ is a three-dimensional Wiener process that satisfies $dW_i dW_j = \delta_{ij}dt$ [18]. Starting with the expression (7) for the force operator, we can calculate β and D by the procedure outlined in the next section.

III. FRICTION AND DIFFUSION

Reference [10] employs Heisenberg equations of motion for various field and atomic operators to find friction and diffusion coefficients. These equations are not closed and, consequently, an approximation has to be made in order to find solutions. The natural assumption is to consider the weak driving limit (i.e., $\mathcal{E}_0 \ll \kappa$) and truncate the available Hilbert space to that part containing no more than a single cavity photon. This allows one to close the Heisenberg equations [10]. Here we employ a different method (using the density matrix equations) to calculate friction and diffusion coefficients that does not require us to stay within the weak driving limit, but in addition we used Ref. [10]'s procedure here to obtain results in the weak driving limit for verification purposes. In any case, it is still true that the most interesting regime is where only one or few photons are involved. Note that given the strong coupling between atom and cavity field, even a single photon is sufficient to lead to regimes far beyond the weak driving limit. In our examples we truncated the Hilbert space to photon numbers of around 4 or smaller. We refer to [19] for an exposition on how to represent operators in truncated Hilbert spaces of precisely this form in a numerically convenient manner.

The master equation (6) is written as

$$\frac{d\rho}{dt} = \mathcal{L}\rho. \tag{9}$$

Numerically, the Liouvillian superoperator $\mathcal{L}$ is converted into a premultiplication operator by methods explained in [19]. In order to find friction and diffusion coefficients we apply a simple procedure, which yields these coefficients at zero velocity: this is sufficient for our purposes as the atom we are interested in, Cs, is relatively heavy. More precisely, the relevant dimensionless parameters determining the velocity dependence of friction and diffusion coefficients are kv/Γ and kv/κ (see for instance [20]), and both are very small in all our simulations. In particular, $\Gamma/k \sim 4.3$ m/s and $\kappa/k \sim 3.4$ m/s, while velocities in the trapping regime we are interested in (where atoms are localized in wells at low temperatures for times $\gg \kappa^{-1},\Gamma^{-1}$) are around the Doppler limit velocity

$$v_D = \sqrt{\frac{\hbar\Gamma/2}{m}} \approx 8.8\ \text{cm/s}. \tag{10}$$

Also note that the standard procedure of continued fractions to calculate the full velocity dependence is not directly applicable to the present case, as the potential through which the atom is moving is not periodic ($\lambda_F \neq \lambda_0$).

For an atom moving at velocity $\vec{v}$ we write

$$\frac{d}{dt} = \frac{\partial}{\partial t} + \vec{v}\cdot\vec{\nabla}, \tag{11}$$

and expand Eq. (9) in powers in $\vec{v}$ and solve for the steady state. The zeroth-order solution is then the steady state ρ_0 at zero velocity:

$$\mathcal{L}\rho_0 = 0, \tag{12}$$

while the first-order term ρ_1 is determined by

$$\mathcal{L}\rho_1 = \vec{v} \cdot \vec{\nabla}\rho_0. \tag{13}$$

The zeroth-order force is the steady-state force for an atom at rest, and is given by

$$\vec{F}_0 = -\mathrm{Tr}(\rho_0 \vec{\nabla} H). \tag{14}$$

Similarly, the friction coefficients follow from the first-order term in the force

$$\vec{F}_1 = -\mathrm{Tr}(\rho_1 \vec{\nabla} H), \tag{15}$$

by identifying

$$\vec{F}_1 \equiv -\beta m \vec{v}, \tag{16}$$

where β is a 3×3 tensor. In our case [6], the gradients along the cavity axis are larger in magnitude than those in the transverse directions by roughly a factor $kw_0 \approx 150$ (and around the cavity axis where the atoms spend most of their time the radial gradients are even smaller, of course). Since the friction coefficient scales with the product of two gradients [cf. Eqs. (13) and (15)], the largest element of the tensor β is the zz component. Next largest in magnitude are the off-diagonal components such as β_{xz} and β_{zx}. Their effects, however, can be safely neglected in our case: first, the force in the z direction proportional to $-\beta_{zx}v_x$ is smaller than the friction force $-\beta_{zz}v_z$ by roughly a factor kw_0. Second, the force in the x direction $-\beta_{xz}v_z$ is not a friction force (as it is not proportional to v_x), and its contribution is averaged out because the oscillations in v_z are faster than those in the x direction by another factor kw_0. Finally, the purely radial friction rates such as β_{xx} are too small ($\ll 1\ \mathrm{s}^{-1}$ on average) to have any influence on the time scales considered here. Thus we take only β_{zz} into account.

The diffusion coefficient, again at zero velocity, is calculated as follows. The standard method is to use the quantum regression theorem, and a particularly useful (for numerical purposes) interpretation of that theorem is given in [19]. The momentum diffusion tensor D_p is given by

$$D_p = \lim_{t\to\infty} \mathrm{Re} \int_0^\infty d\tau \langle \vec{F}(t)\vec{F}(t-\tau)\rangle - \langle \vec{F}(t)\rangle\langle \vec{F}(t-\tau)\rangle, \tag{17}$$

and its relation to the velocity diffusion tensor is $D = D_p/m^2$. Before eliminating any degrees of freedom, the total system in fully quantized form is described by a time-independent Hamiltonian, which we denote by H_{tot}. In that case the time evolution of all operators is determined by $\exp(-iH_{\mathrm{tot}}t)$, and two-time averages of the form $\langle A(t)B(t-\tau)\rangle$ as appearing in Eq. (17) can be written as

$$\langle A(t)B(t-\tau)\rangle = \mathrm{Tr}[A\exp(-iH_{\mathrm{tot}}\tau)B\rho_{\mathrm{tot}}(t)\exp(iH_{\mathrm{tot}}\tau)], \tag{18}$$

with ρ_{tot} the density matrix of the total system. This expression formally contains the evolution of a density matrix over a time interval τ starting from an initial density matrix $\rho_{\mathrm{init}} \equiv B\rho_{\mathrm{tot}}(t)$. The quantum regression theorem now states that Eq. (18) is still valid for the reduced density matrix that evolves under the Liouvillian $\mathcal{L}$. That is, instead of Eq. (18) we may use

$$\langle A(t)B(t-\tau)\rangle = \mathrm{Tr}[A\exp(\mathcal{L}\tau)B\rho(t)]. \tag{19}$$

In our case, $\mathcal{L}$ is a time-independent operator and hence the right-hand side of Eq. (19) can be evaluated by expanding $\exp(\mathcal{L}\tau)$ in an exponential time series, as in the methods developed in [19]. This then is the method we use here to evaluate the friction and diffusion tensors, and the results have been checked in the low-intensity limit by applying the different methods from [10] to the same problem.

Diffusion due to spontaneous emission is not obtained this way (as the bath of vacuum modes has been eliminated already), but can be obtained by standard methods and gives an independent additional three components $(D_p)_{ii}^{SE} = N_i\hbar^2k^2\Gamma/2\langle\sigma^+\sigma^-\rangle_0$ for $i=x,y,z$, with $\langle . \rangle_0$ denoting a steady-state value and with the dimensionless factor N_i depending on polarization. When the two-level system is formed by two Zeeman levels that are connected by circularly polarized light propagating in the z direction, we have $N_z = 2/5$, and $N_x = N_y = 3/10$.

Since the diffusion coefficients, just as the friction coefficients, scale as the square of a gradient, the largest component is D_{zz}. Off-diagonal elements such as D_{xz} and D_{zx} are, again, smaller by roughly a factor $kw_0 \approx 150$, while the diagonal radial components such as D_{xx} are in fact largely determined by spontaneous emission, and are of similar or larger magnitude than the off-diagonal elements. The proper way to take into account the off-diagonal elements of the diffusion tensor D is to diagonalize D, and consider three independent diffusion processes along the axes of the basis that diagonalizes D with the eigenvalues of D as diffusion coefficients. Using the fact that D_{zz} is large we can calculate both eigenvalues and eigenbasis perturbatively. The eigenvalues to first order are given by

$$\begin{aligned} D_{x'x'} &= D_{xx} - \frac{D_{xz}D_{zx}}{D_{zz}} + \cdots \\ D_{z'z'} &= D_{zz} + \frac{D_{xz}D_{zx}}{D_{zz}} + \cdots, \end{aligned} \tag{20}$$

where the $\cdots$ stands for terms of higher order in $1/(kw_0)$, while the axes change as

$$\begin{aligned} \hat{z}' &= \hat{z} + \hat{x}\frac{D_{xz}}{D_{zz}} + \cdots \\ \hat{x}' &= \hat{x} + \hat{z}\frac{D_{zx}}{D_{zz}} + \cdots. \end{aligned} \tag{21}$$

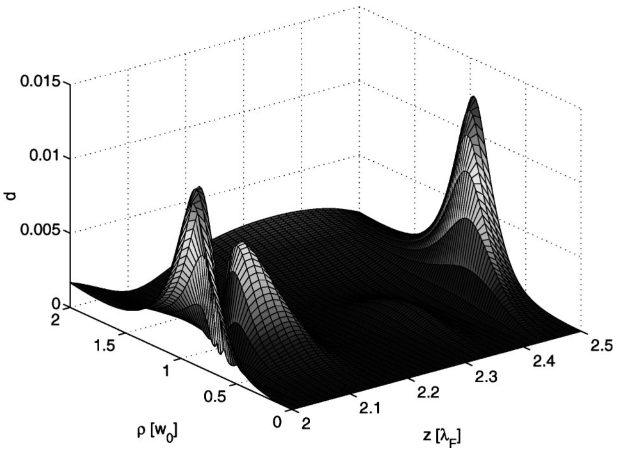

FIG. 3. For parameters to be used later, $S_0/(2\pi)=50$ MHz, and $\Delta_p/(2\pi)=-10$ MHz, $N_e=0.01$ we plot here the ratio $d=D_{zx}^2/(D_{zz}D_{xx})$ as a function of position.

The fact that $\hat{z}'$ is slightly tilted toward the x direction implies that a small part of the large diffusion coefficient $D_{z'z'}$ will contribute to diffusion in the x direction. This increase, however, is almost exactly compensated for by the decrease in $D_{x'x'}$. In particular, the velocity in the x direction undergoes the following Wiener process:

$$dv_x=\sqrt{2D_{x'x'}+2D_{z'z'}\frac{D_{zx}^2}{D_{zz}^2}+\cdots}\,dW. \tag{22}$$

In our case it turns out that $D_{xx}D_{zz}\gg D_{zx}^2$ (see Fig. 3), so that effects due to the off-diagonal elements of the diffusion tensor can in fact be neglected. The figure also shows that the previous considerations about the relative sizes of the various components of D do not just hold on average, but also locally.

Thus, friction is appreciable only along the cavity axis, while diffusion has two main contributions: from spontaneous emission in all three directions, and a large diffusion along the cavity axis from fluctuations in the FORT and cavity QED forces.

IV. NUMERICAL RESULTS

The following results pertain to a Cs atom, with the ground state given by $|6S_{1/2};F=4;m_F=4\rangle$ and the excited state by $|6P_{3/2};F=5;m_F=5\rangle$, so that $\lambda_0=852.4$ nm and $\Gamma/(2\pi)=5.2$ MHz. The cavity parameters are $\kappa/(2\pi)=4$ MHz and $g_0/(2\pi)=30$ MHz, and $w_0=20$ μm, which are typical of the experiments discussed in [6]. Furthermore, the values for S_0 examined here are $S_0/(2\pi)=10{,}50$ MHz. Both of these values are close to those explored in the actual experiment [6], and they contrast the behavior of atoms in shallow ($S_0<g_0$) and deep ($S_0>g_0$) wells. Typical values for N_e range from 10^{-3} to 0.1.

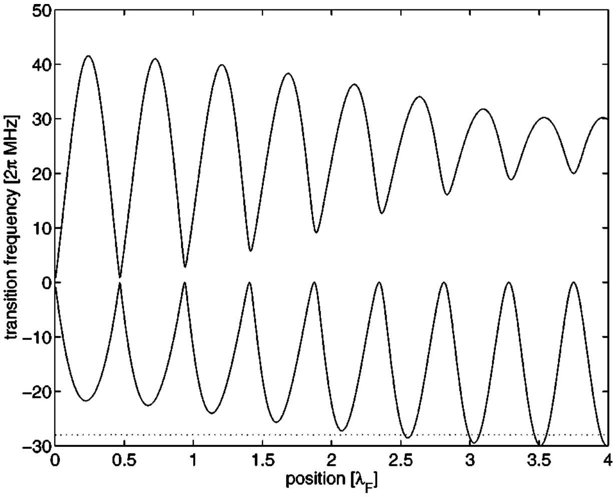

FIG. 4. Transition frequencies $\Delta_\pm$ relative to the bare atomic frequency from the ground state to the lower two excited dressed states as functions of the position of the atom along the cavity axis (i.e., $\rho=0$) . Here $S_0/(2\pi)=10$ MHz. Also indicated by the dotted line is the probe detuning used in Fig. 9, $\Delta_p/(2\pi)=-28$ MHz.

A. Dressed-state structure

We first focus on the atomic motion along the cavity axis. The simplest way to get a feeling for the results for β_{zz} and D_{zz} as a function of the probe detuning Δ_p is to first consider the eigenenergies of the dressed atom-cavity states. When we neglect dissipation for the moment, and take the limit of no driving ($N_e=0$), we can easily find the energies of the lower dressed states $|\psi_\pm\rangle$ containing at most one excitation: the state containing no excitation is the ground state with an energy of $E_0=-\hbar S_F(\vec{r})$, while the energies of the two dressed states in the manifold of states containing a single excitation are

$$E_\pm=\hbar\omega_a\pm\hbar\sqrt{g(\vec{r})^2+S_F(\vec{r})^2}, \tag{23}$$

if the atom and cavity are on resonance. The excited dressed states are given by

$$|\psi_-\rangle=(\sin\theta)|g,1\rangle+(\cos\theta)|e,0\rangle, \tag{24}$$

with

$$\sin\theta=\frac{g}{\sqrt{g^2+(\sqrt{g^2+S_F^2}-S_F)^2}},$$

$$\cos\theta=\frac{S_F-\sqrt{g^2+S_F^2}}{\sqrt{g^2+(\sqrt{g^2+S_F^2}-S_F)^2}}. \tag{25}$$

In Fig. 4 (10 MHz FORT) and 5 (50 MHz FORT) we plot the transition frequencies (relative to ω_a) from the ground state to these two excited states as functions of position, i.e.,

$$\Delta_\pm=S_F(\vec{r})\pm\sqrt{g(\vec{r})^2+S_F(\vec{r})^2}. \tag{26}$$

This expression along with the figures explicitly shows that the main features of the atom-cavity system are determined by the ratio S_0/g_0. It furthermore shows an important difference with the situation of trapping with a FORT in free

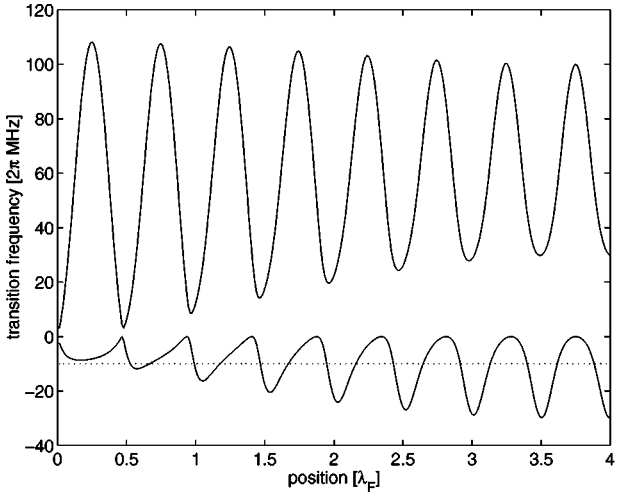

FIG. 5. Same as previous figure but for $S_0/(2\pi)=50$ MHz. Also indicated by the dotted line is the probe detuning used in Fig. 10, $\Delta_p/(2\pi)=-10$ MHz.

space. The fact that the excited state shifts *up* while the ground state shifts *down* implies that ground and excited states are trapped in different positions in free space. In the presence of the quantized cavity field, however, both the lower excited dressed state and the ground state are now shifted *down*. This may improve trapping and cooling conditions, as detailed below.

B. Cooling mechanisms

We now take a closer look at cooling mechanisms. In the regime of weak driving, we will find that the friction coefficient β_{zz} is positive (corresponding to cooling) when the probe field is tuned slightly (by an amount $\sim\kappa,\Gamma/2$) below the transition to the relevant dressed state while for blue detuning the friction coefficient is negative, leading to exponential heating of the atom's velocity. This can be understood by analogy with Doppler cooling: by tuning below resonance, the process of stimulated absorption followed by spontaneous emission leads to a loss of energy, while the maximum cooling rate is achieved by maximizing the product of excitation rate and detuning. Now looking back to Figs. 4 and 5 one sees that the variation of Δ_+ with position is larger than that of Δ_-, because both the ground state and the lower excited dressed state shift down, while the upper excited dressed state shifts upward. Generally speaking, for cooling purposes it is better to tune to the *lower* excited state so as to have smaller spatial variations in cooling rates. More importantly, the upper-excited-state energies decrease with increasing radial distance, whereas the lower-excited-state energy increases. Thus, for the upper state the probe detuning changes from red to blue, so that an atom cooled on axis will in fact be heated if it moves away radially. For the lower dressed state the probe detuning becomes more red, so that an atom that is optimally cooled on axis will still be cooled away from the axis, but at a lower rate.

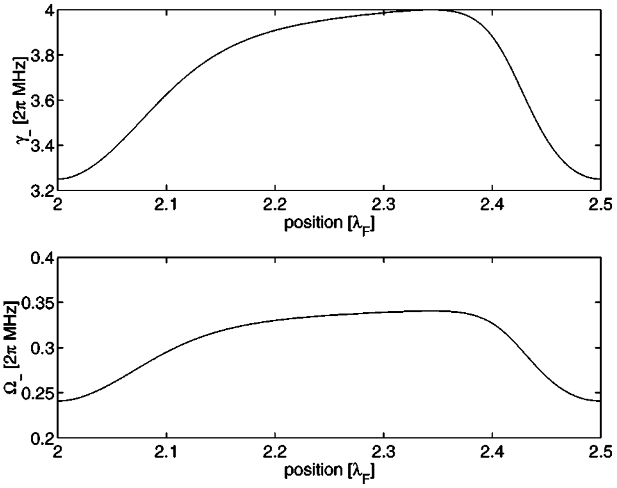

FIG. 6. Decay rate and excitation rate of the lower dressed state as functions of position along the cavity axis ($\rho=0$). Here and in Figs. 7 and 8, we chose the following parameters: $N_e=0.001$, $S_0/(2\pi)=50$ MHz, $\Delta_p/(2\pi)=-10$ MHz.

The most popular explanation for intracavity cooling [10] exploits analogies with Sisyphus cooling [21], although another explanation for cavity-based cooling based on asymmetries in coherent scattering was recently put forward in [11]. Here we illustrate the Sisyphus picture for cooling inside optical wells within an optical resonator, using a very simple dressed-state picture, that makes use of only the lower dressed state and the ground state, relevant in the low-excitation limit. We choose one particular well, from $z=2.0\lambda_F$ to $z=2.5\lambda_F$, and one particular set of parameters given in the caption of Fig. 6. In that figure we plot the decay rate γ_- of the lower dressed state and the excitation rate from ground to the dressed state, Ω_-, as functions of position. In the weak driving limit the decay rate is given by

$$\gamma_- = \langle \psi_- | \kappa a^\dagger a + \Gamma \sigma^+ \sigma^-/2 | \psi_- \rangle = (\sin^2\theta)\kappa + (\cos^2\theta)\Gamma/2, \tag{27}$$

and the excitation rate by

$$\Omega_- = |\langle g,0|\mathcal{E}_0(a^\dagger + a)|\psi_-\rangle| = \mathcal{E}_0|\sin\theta|. \tag{28}$$

These two quantities, together with the detuning of the probe field from (dressed-state) resonance determine the steady-state population in the lower dressed state, according to

$$n_- = \frac{\Omega_-^2}{(\Delta_- - \Delta_p)^2 + \gamma_-^2}. \tag{29}$$

The population n_- is plotted in Fig. 7, along with the transition frequency Δ_-. These two quantities are sufficient to understand the Sisyphus cooling mechanism.

Since an atom in the ground state is moving in a conservative potential around the equilibrium position $z=2.25\lambda_F$, the following Sisyphus picture should be taken as to apply to the motion of the atom in addition to that conservative motion [see Eq. (30)]. Suppose, for example, that the atom is at position $z=2.2\lambda_F$ and moving toward the right (cf. Fig. 7). The probability to be in the excited state now decreases (according to the lower part of Fig. 7), while the energy of the excited state relative to the ground state is increasing: in

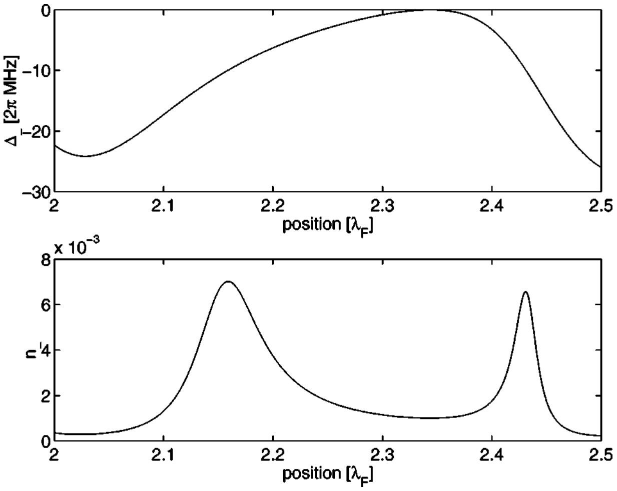

FIG. 7. Transition frequency to and populations in the lower dressed state as functions of position along the cavity axis. Note that the equilibrium position of the atom is around $z = 2.25\lambda_F$.

other words, an atom in the excited state is climbing uphill (again, in relation to the ground state), but will likely make the down transition to the ground state, thus leading to cooling at that particular position. Similarly, at $z = 2.4\lambda_F$ an atom moving to the left is going uphill while having an increased chance of decaying to the ground state, again leading to cooling. This picture in fact shows that the cooling rate is expected to be proportional to the gradient of n_- and the gradient of Δ_-. More precisely, the force on the atom at position z is approximately given by

$$F_z \approx \hbar \frac{dS_F}{dz} - \hbar n_-(z - v/\gamma_-) \frac{d\Delta_-}{dz} \approx \hbar \frac{dS_F}{dz} - \hbar n_-(z) \frac{d\Delta_-}{dz} + \frac{\hbar v}{\gamma_-} \frac{dn_-}{dz} \frac{d\Delta_-}{dz}, \tag{30}$$

where the argument of n_- indicates the lag between the atom reaching a position z and reaching its steady state, with the lag time scale determined by the inverse decay rate from the dressed state. From the second line we see that the friction coefficient β_{zz} is approximated by

$$R \equiv -\frac{\hbar}{m\gamma_-} \frac{dn_-}{dz} \frac{d\Delta_-}{dz}. \tag{31}$$

Indeed, Fig. 8 shows the similar behavior of β_{zz} and R as functions of position.

C. Friction, diffusion and equilibrium rms velocities

In Figs. 9–10 we give examples of friction and diffusion coefficients for both the 10 and 50 MHz FORTs, as functions of the atomic position. They illustrate the point that in the low-excitation limit red (blue) detuning leads to cooling (heating) (cf. Figs. 4 and 5). They, moreover, clearly show how all wells are quantitatively different, with cooling rates and diffusion strengths differing by orders of magnitude over the various wells, and with β_{zz} being negative in some wells, and always positive in others. This of course also implies that the temperatures reached by atoms in thermal equilibrium vary with position.

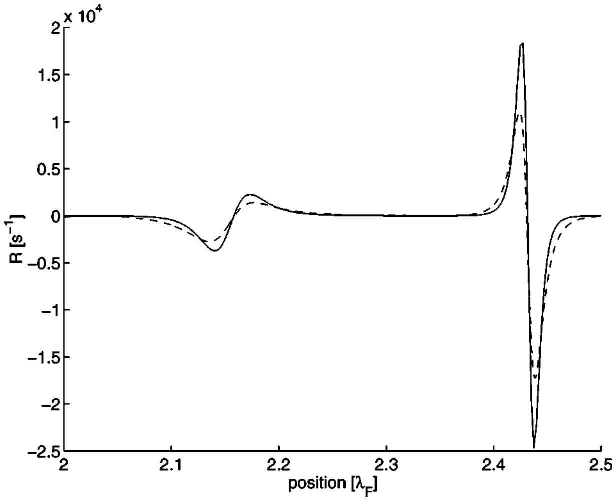

FIG. 8. Cooling rate β_{zz} (solid curve) and the product of gradients of dressed-state population and transition frequency R (dashed curve) as functions of position along the cavity axis. The similarity between the two curves confirms the validity of the Sisyphus cooling picture.

For the case of the shallow FORT we consider weak driving ($N_e = 0.001$), whereas for the deeper FORT the driving field is taken to be stronger by an order of magnitude. The stronger driving field increases cooling rates while the fact that deeper wells trap the atoms better means that correspondingly larger diffusion rates still can be tolerated.

The stable equilibrium points z_n^e are located around the maxima of S_F, i.e., around $z_n = (n - 1/2)\lambda_F/2$ for integer n, because it is the FORT that gives the main contribution to the total force (even for the smallest value of $S_0 = 2\pi \times 10$ MHz considered here). The cavity QED field gives

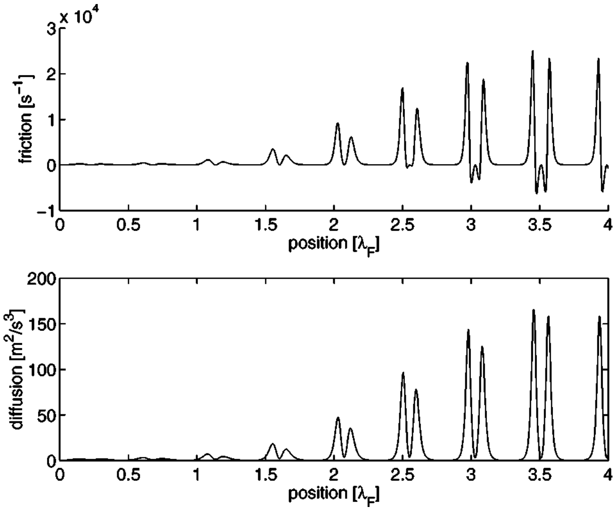

FIG. 9. Friction and velocity diffusion coefficients β_{zz} and D_{zz} as functions of the atomic position (in units of λ_F) along the cavity axis. Here $N_e = 0.001$, $S_0/(2\pi) = 10$ MHz, and $\Delta_p = -28 \times 2\pi$ MHz. Compare Fig. 4.

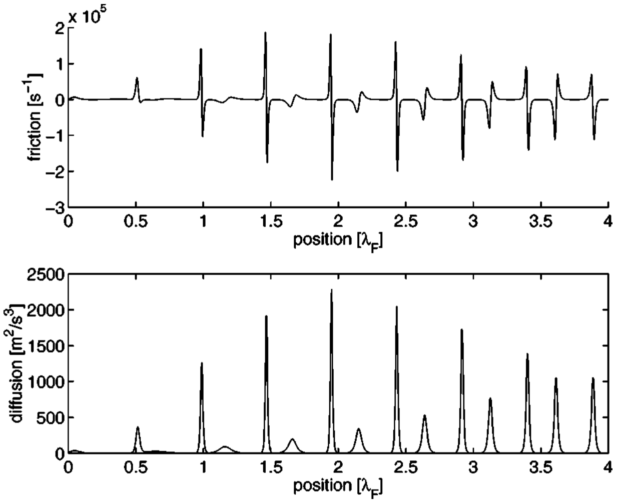

FIG. 10. Same as previous figure but for $N_e = 0.01$, $S_0/(2\pi) = 50$ MHz, and $\Delta_p = -10\times 2\pi$ MHz.

only a small correction to the force and hence to the equilibrium position. In each equilibrium point, we can define a measure for the expected rms velocity of the atom along the z axis in thermal equilibrium by considering averages over local wells

$$v^z_{\rm rms} = \sqrt{\frac{\overline{D_{zz}}}{\overline{\beta_{zz}}}} \quad \text{if} \quad \overline{\beta_{zz}} > 0, \tag{32}$$

in terms of the friction and diffusion coefficients. This averaging procedure gives a sensible measure for the rms velocity only if the atom indeed samples the whole well. This condition is fulfilled for the relatively shallow wells originating from $S_0 = 2\pi\times 10$ MHz, and Fig. 11 uses this averaging procedure. For the 50 MHz FORT, however, we averaged over only part of the well, namely, a region of size $\lambda_F/10$ symmetrically around the equilibrium point. This choice is rather arbitrary, and thus Fig. 12 just gives an indication of what rms velocities to expect of atoms trapped in the corresponding wells, although the simulations in fact do confirm these values.

We see here that depending on the probe detuning, the atom will be cooled to low temperatures either in all wells, or only in wells where g is large in the equilibrium point, or only in wells where g is small. This shows the flexibility that a FORT beam adds: one can predetermine to a certain degree in which well the atom will be trapped (and cooled) for longer times and in which it will not be.

Under the current conditions $\kappa > \Gamma/2$ the lowest temperatures achievable are determined by the Doppler velocity v_D. More precisely, the lower limit on rms velocities along the cavity axis is expected to be

$$v^z_D = \sqrt{0.7\frac{\hbar\Gamma}{2m}}, \tag{33}$$

where the factor $0.7 = (1+2/5)/2$ comes from the fact that in our case the diffusion due to spontaneous emission in the z direction is two-fifths of the full 3D value. We tested that for

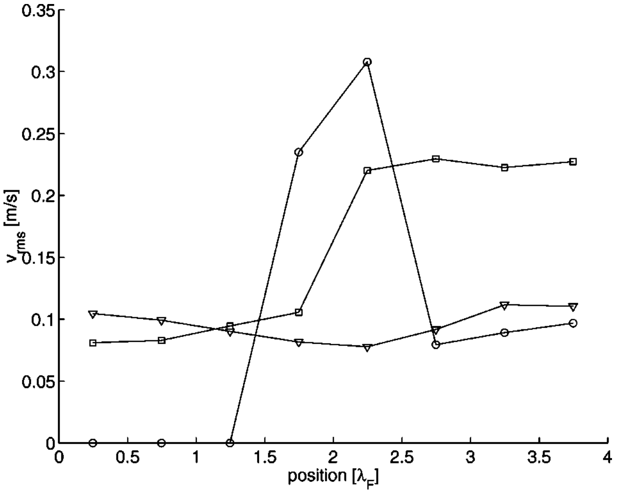

FIG. 11. The values of $v^z_{\rm rms}$ in the eight equilibrium points as defined in Eq. (32) by averaging over the entire well. In all cases $S_0 = 2\pi\times 10$ MHz. Triangles correspond to a detuning $\Delta_p/(2\pi) = -28$ MHz, squares to $\Delta_p/(2\pi) = -23$ MHz, and circles to $\Delta_p/(2\pi) = 15$ MHz. Note the points on the latter curve on the axis indicate that the friction coefficient is negative, so that there is in fact no cooling and $v^z_{\rm rms}$ is not defined. They do not indicate cooling to $v_{\rm rms} = 0$.

smaller κ the rms velocities indeed do become even smaller, now determined by $\sqrt{\hbar\kappa/m}$, thus confirming predictions of [10].

Finally, we note that the quasiclassical approximation used throughout this paper is justified as neither the recoil limit is reached nor the resolved-sideband limit, i.e.,

$$\hbar\Gamma/2 \gg (\hbar k)^2/m,$$

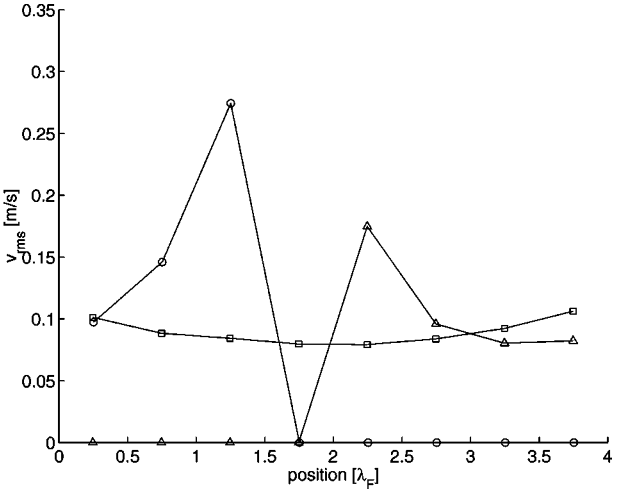

FIG. 12. As previous figure, but for $S_0 = 2\pi\times 50$ MHz and $N_e = 0.01$, and where the average is taken over a region of size $\lambda_F/10$ around the equilibrium point. The probe detunings were $\Delta_p/(2\pi) = -10, -5100$ MHz for the squares, triangles, and circles, respectively. Note the points on the axis indicate that the friction coefficient is negative, so that there is in fact no cooling and $v^z_{\rm rms}$ is not defined. They do not indicate cooling to $v_{\rm rms} = 0$.

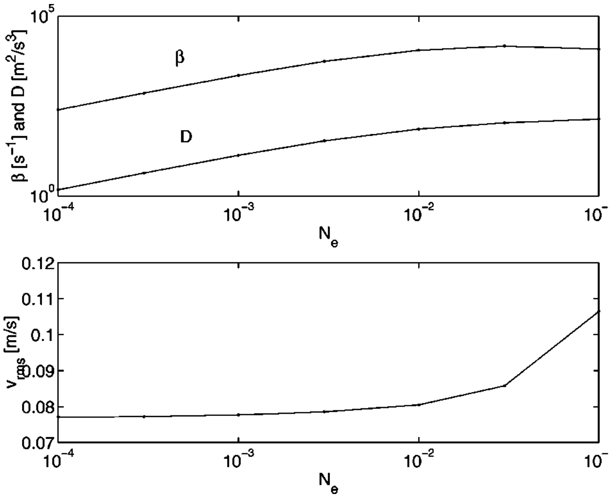

FIG. 13. The average values of D_{zz} and β_{zz} as functions of the driving field strength N_e in the well extending from $z=2\lambda_F$ to $z=2.5\lambda_F$, for the 10 MHz FORT, where $\Delta_p=-28\times 2\pi$ MHz. In the lower part the corresponding values for the rms velocity $v^z_{\rm rms}$ are plotted as a function of N_e.

$$\hbar\Gamma/2 \gg h\nu_{\rm osc}, \tag{34}$$

with $\nu_{\rm osc}$ the oscillation frequency of the atom in a well (see below), although in some cases the latter condition is only marginally fulfilled, namely, when $\nu_{\rm osc}=600$ kHz, which is only a factor 4 smaller than $\Gamma/(4\pi)$.

D. Saturation behavior

We now briefly turn to the question of the nonlinear behavior of the atom-cavity system with increasing excitation. In the absence of saturation effects, both friction and diffusion coefficients would increase linearly with N_e. For the same parameters as Fig. 9, Fig. 13 shows nonlinearities setting in around $N_e=0.01$. The friction coefficient even starts to *decrease* around $N_e=0.1$ as a result of the local values of β_{zz} becoming negative where they were positive in the weak driving limit. The concomitant effect on the $v^z_{\rm rms}$ is shown as well.

E. Simulations

We also performed Monte Carlo simulations of the 3D motion in given wells by solving the Langevin equations (8) for position and velocity (see also [14]). The experimental procedure switches the FORT field on only when an atom has been detected and when it consequently has partly fallen through the cavity already [6]. We accordingly fix initial conditions as follows: We start the atom on the cavity axis, and we fix the downward velocity to be $v_x=10$ cm/s. Furthermore, we chose $v_z=0$ cm/s, and the initial position along the z axis to be $\lambda_F/8$ away from the equilibrium point. The initial position and velocity were fixed so that all variations in trapping times and rms velocities are solely due to the random fluctuations of the forces acting on the atom, rather than from random initial conditions. Experimentally these two are mixed of course.

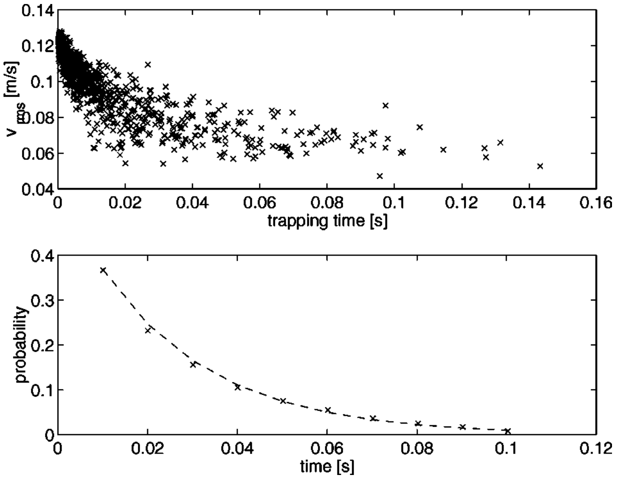

FIG. 14. In the upper part of the plot each data point gives the trapping time and the average $v_{\rm rms}$ resulting from a single trajectory. Identical initial conditions were chosen for each trajectory: each atom started at $z=2.125\lambda_F$ with $v_z=0$ and $v_x=10$ cm/s (downward). Other parameters were: $N_e=0.001$, $\Delta_p=-28\times 2\pi$ MHz, $S_0=10\times 2\pi$ MHz. The lower part gives a histogram of the probability $P(T)$ for an atom to be trapped longer than a time T. A fit of the tail of this distribution to an exponential $\propto \exp(-T/\tau)$ gives $\tau=25\pm 2$ ms.

Since atoms with these initial conditions do not possess angular momentum around the z axis, this in some sense represents a favorable case (although the atoms are not put in the bottom of the well). However, in the course of their evolution the atoms do acquire angular momentum so that this is in fact not a severe restriction. For more detail see below (Fig. 22).

In Fig. 14 we plot the results of simulations of 1000 trajectories for an atom in the shallow well of 10 MHz. We plot the average rms velocity along the cavity axis as a function of trapping time for each trajectory. Here we defined the ''trapping time'' as the time spent by the atom in one particular given well of size $\lambda_F/2$. The actual trapping time inside the cavity may be longer, obviously, as the atom may subsequently get trapped in different wells. For very short trapping times, $v_{\rm rms}$ is determined by the initial condition, but for longer times lower temperatures corresponding to those calculated in Fig. 11 are reached. Note, however, that the simulations were done in 3D, and as such do not necessarily give the same temperatures as predicted for on-axis (1D) motion in Figs. 11 and 12. Nevertheless, the effect of the atoms' radial motion is apparently not strong, and in fact atoms leave the well while still being trapped radially. This is partly due to the fact that all (especially heating) rates in the radial direction are smaller by a factor $kw_0 \approx 150$ than those in the axial direction.

About half of the atoms is basically not trapped at all. The remaining atoms have a probability $P(T)$ to be trapped longer than a time T, with $P(T)$ decaying exponentially with T. The average trapping time for these parameters is found to be $\tau \approx 25$ ms, as shown in Fig. 14.

In Figs. 15 and 16 we plot for the same 10 MHz FORT an example of a single trajectory, after the atom has spent 4 ms

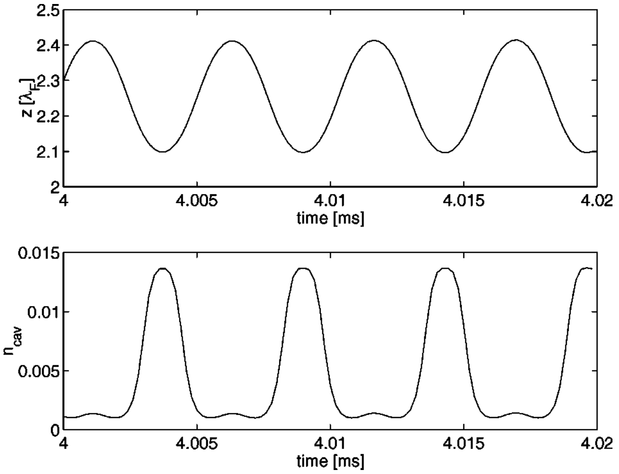

FIG. 15. Snapshot of a single trajectory, with parameters as in Fig. 14. The upper plot gives the z coordinate of the atom as a function of time, the lower plot gives the transmission (in fact the number of photons $\langle a^\dagger a\rangle$ inside the cavity) in that same time interval. Note the time scales here differ by two orders of magnitude from those of Fig. 16.

in the trap. The oscillation frequencies along the z and the radial directions differ by two orders of magnitude (since $kw_0 \approx 150$): in the z direction the oscillation rate is ~ 200 kHz, in the radial direction ~ 2.2 kHz. The photon transmission follows both these oscillations so that in principle the atomic motion in both axial and radial direction is detectable. Experimentally, though, the oscillations along the cavity axis may be too fast to be accessible. In particular, the average rate at which photons leaking out through one end of the cavity are detected is at most (the efficiency is less than 100%) equal to the cavity decay rate multiplied by the average number of photons inside the cavity. For the parameters of Fig. 15 this amounts to a rate $\sim 0.01 \times \kappa \approx 2.5 \times 10^5$/sec, which corresponds to just about one photon per oscillation period.

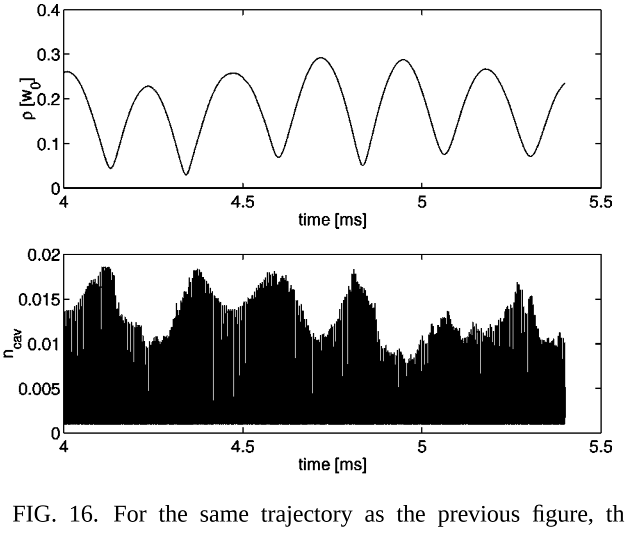

FIG. 16. For the same trajectory as the previous figure, the upper plot gives the radial distance to the cavity axis, ρ in units of w_0 as a function of time, the lower plot gives again the number of photons inside the cavity during that same time interval. The atom has a nonzero angular momentum along z and does not cross the z axis.

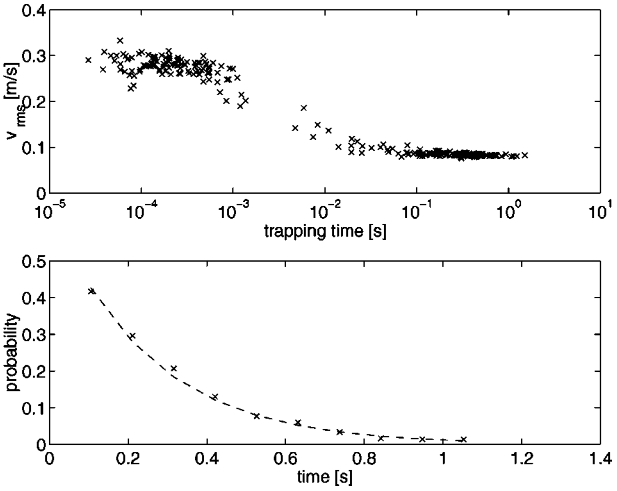

FIG. 17. As Fig. 14 but for $N_e = 0.01$, $\Delta_p = -10 \times 2\pi$ MHz, $S_0 = 50 \times 2\pi$ MHz. The mean trapping time is $\tau = 250 \pm 20$ ms.

The figures show that when the atom is in a position where it is not coupled to the cavity ($g = 0$), the number of photons in the cavity drops to $N_e = 0.001$. Similarly, when the atom moves away radially, the transmission drops.

To make a direct comparison with the trapping times achieved in the experiment [6], we now turn to the case of a 50 MHz FORT. We plot rms velocities vs trapping times for 300 trajectories for an atom trapped in the well ranging from $z = 2\lambda_F$ to $z = 2.5\lambda_F$.

For the parameters of Fig. 17 the atom is either trapped for long times (>10 ms) or only for a short time (<1 ms), both with about 50% probability. In the latter case the rms velocity is determined just by the (arbitrarily chosen) initial condition and is around 30 cm/s, but for longer trapping times the effects of cooling are visible. Thermal equilibrium is reached with $v_{\rm rms} \sim 8$ cm/s, thus confirming the results of Fig. 12. The distribution of trapping times again follows an exponential law, and the average trapping time, as determined from the tail of the distribution, is $\tau \approx 250$ ms, which is ten times longer than for the (fluctuating) 50 MHz FORT used in [6]. This shows the great potential of holding single atoms in the cavity for extended periods of time if the intensity fluctuations of the FORT beam can be minimized. Experimental efforts along this path are currently underway.

Also for this case we plot snapshots for a single trajectory (Fig. 18), taken after the atom has spent 25 ms in the trap. Compared to the 10 MHz FORT, the oscillations of the atom along the cavity axis and in the radial direction become faster by about a factor of 3. The axial oscillation frequency is about 600 kHz, while along the radial direction the oscillations occur at a rate 6.2 kHz, i.e., again slower by two orders of magnitude. In this case, the photon transmission still follows directly the axial oscillations but no longer follows the radial excursions of the atom, as now the fluctuations in the magnitude of g at the atom's position along the cavity axis are in fact larger than those due to the radial excursions of the atom. This is partly due to the fact that in the simulations here the driving field is stronger than for the

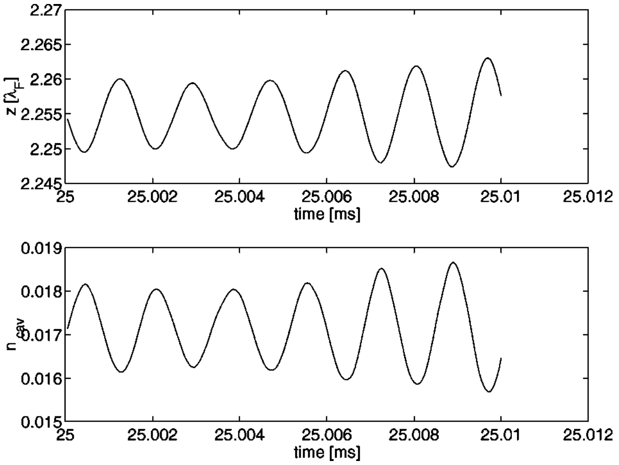

FIG. 18. Snapshot of a single trajectory, with parameters as in Fig. 17. The upper plot gives the z coordinate of the atom as a function of time (with the atom released with standard initial conditions at $t=0$). The lower plot gives the transmission (in fact the number of photons inside the cavity) in that same time interval. Note the time scales here differ by two orders of magnitude from those of Fig. 19.

10 MHz example above so that fluctuations in the atomic motion occur at a shorter time scale, and partly simply because the radial excursions are small. Figure 19(c) shows that it is primarily the axial fluctuations that determine the variations in the numbers of photons inside the cavity.

Generally speaking, the axial excursions determine (local) minimum and maximum transmission levels (as in Fig. 15). When these minima and/or maxima depend on the radial position, then the radial motion could, in principle, be visible in the cavity transmission level. This depends in turn on whether the axial fluctuations on the time scale of the transverse motion are sufficiently small so as not to hide the radial dependence. There seems to be no simple general rule how this interplay between radial and axial motions depends on detunings, driving strength, and the particular well.

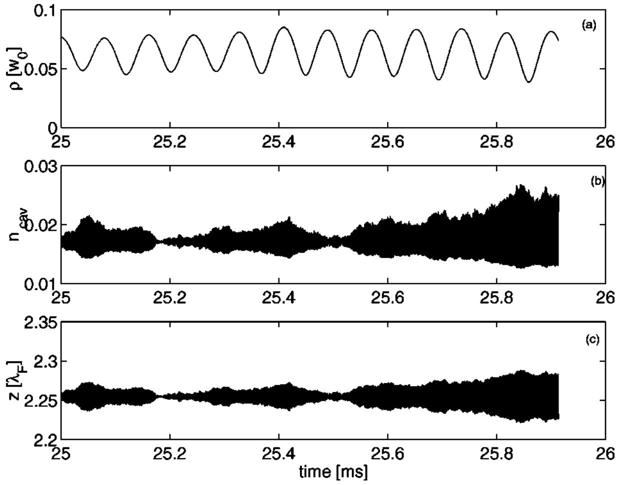

FIG. 19. For the same trajectory as the previous figure, (a) the radial distance to the cavity axis, ρ in units of w_0 as a function of time, (b) the number of photons inside the cavity during that same time interval, and (c) the position along the cavity axis in units of λ_F.

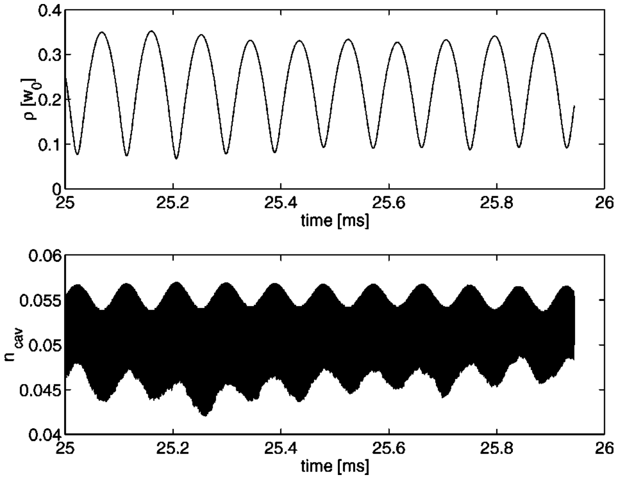

FIG. 20. For an atom in the well ranging from $z=0$ to $z=\lambda_F/2$, for $N_e=0.01$, $\Delta_p=-10\times 2\pi$ MHz, and $S_0=50\times 2\pi$ MHz, the upper plot gives the radial distance to the cavity axis, ρ in units of w_0 as a function of time, the lower plot gives the number of photons inside the cavity during that same time interval.

In contrast, in a different well, the one ranging from $z=0.0$ to $z=0.5\lambda_F$, the photon number in the cavity does follow the radial motion, as the radial excursions become larger (Fig. 20). Perhaps more importantly, the average transmission level is higher by more than a factor 2 compared to the previous case, as a result of g being larger in this well (cf. Fig. 2). This shows how, in principle, different wells may be experimentally distinguished via the transmission of the probe field through the cavity.

We also simulated the motion of an atom trapped under more adverse conditions, namely for an atom in the well $[z=\lambda_F\rightarrow 1.5\lambda_F]$ at a probe detuning $\Delta_p/(2\pi)=-5$ MHz. According to Fig. 12, the atom is not cooled on axis under these conditions (i.e. the average friction coefficient around the equilibrium point on the z axis is negative). This is confirmed by Fig. 21: the mean trapping time for an atom starting at $z=1.125\lambda_F$ is now very short, about 1.6 ms, while the average rms velocity is $v_{\rm rms}^z\approx 28$ cm/s, as determined essentially by the initial condition.

Finally, we consider the influence of different initial conditions on trapping and cooling. All the results so far were obtained by considering atoms that initially are moving on axis. Thus, they have no angular momentum along the z axis, nor any radial potential energy. Figure 22 shows a plot of rms velocities vs trapping times for atoms trapped under the same conditions as for Fig. 17) (i.e., in the well from $z=2\lambda$ to $z=2.5\lambda$, for $\Delta_p=-10\times 2\pi$ MHz, $N_e=0.01$, and $S_0=50\times 2\pi$ MHz), but with different (nonzero) values for the initial angular momentum.

Obviously, the more initial potential energy the atom has, the less likely it is to be trapped. In fact, the angular momentum does not play any role here, as confirmed by similar calculations with initial conditions chosen such that the atoms have no initial angular momentum but have the same potential energy. The results are the same in that case. For

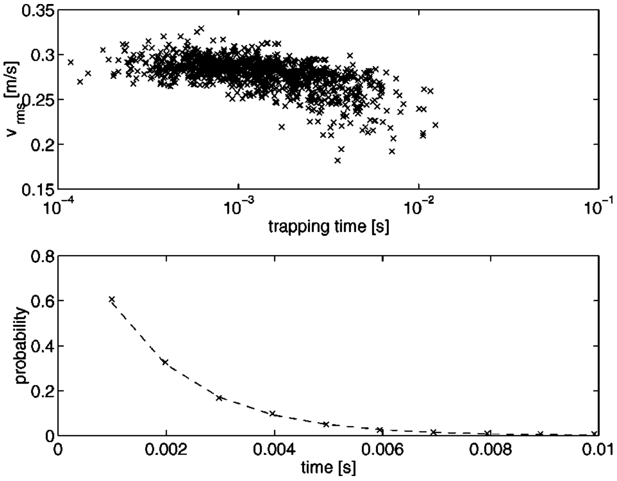

FIG. 21. As Fig. 14 but for $N_e=0.01$, $\Delta_p=-5\times 2\pi$ MHz, $S_0=50\times 2\pi$ MHz. The initial position of the atom is $z=1.125\lambda_F$. The mean trapping time is $\tau=1.6\pm 0.1$ ms.

atoms starting at $y=0.2w_0$ the trapping times and rms velocities are basically not affected, and the trapping time is still around 250 ms. But for atoms starting at $y=0.5w_0$ the effect of their increased potential energy leads to clearly shorter trapping times (by roughly a factor of 2), and for atoms starting at $y=w_0$ this effect is even more pronounced with a decrease in trapping time of about a factor of 10.

F. A different trapping structure

We now consider a different case where the atomic excited state is assumed to be shifted *down* by the FORT field, just as the ground state is (see, for instance [12]). This can be achieved by using a FORT that is (red) detuned in such a way that the excited atomic state is relatively closer to resonance with a higher-lying excited state than with the ground state. This situation at first sight looks even more appealing for trapping purposes, as now both excited and ground state will be trapped in the same positions. Moreover, fluctuations in the force due to the FORT are diminished.

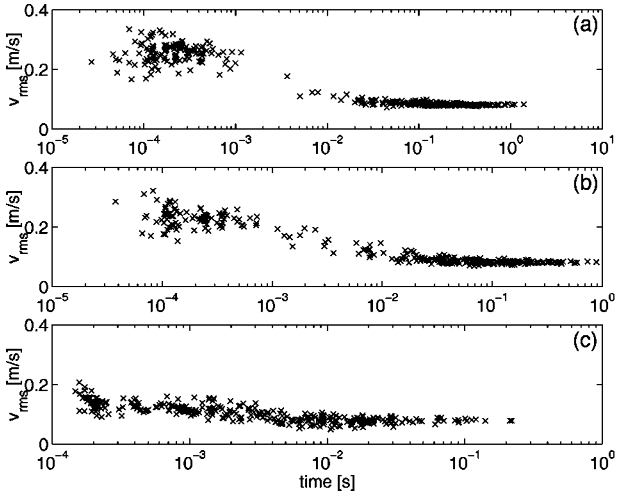

FIG. 22. rms velocities vs trapping times for atoms trapped under the same conditions as for Fig. 17 but with different initial radial conditions for y. In particular, for plot (a) the initial conditions on y is $y=0.2w_0$. for (b) $y=0.5w_0$ and for (c) $y=w_0$. Since $v_x=-10$ cm/s, the atoms have different angular momenta along z in these cases, and different initial potential energies.

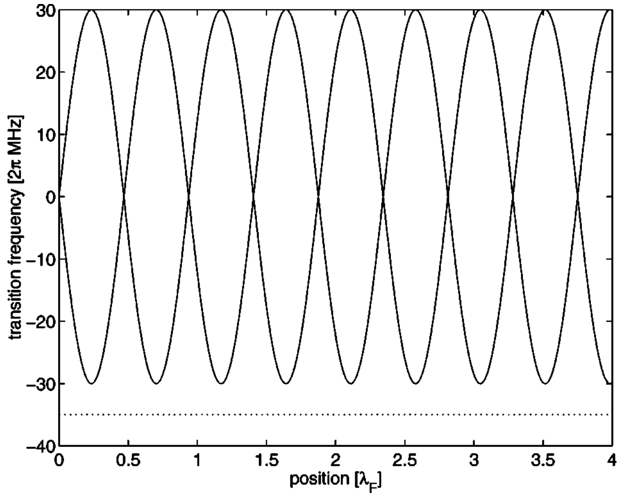

FIG. 23. Transition frequencies $\Delta_\pm$ for the case where the atomic excited state is assumed to be shifted down by the FORT field by the same amount S_F as is the ground state, for the 50 MHz FORT. A detuning of -35 MHz is indicated by the dotted line.

We consider only the 50 MHz FORT here, and compare this case to the previous 50 MHz FORT case, and in particular we refer the reader back to Figs. 5, 10, and 17. For ease of comparison we keep λ_F the same, and assume for simplicity that the excited state is shifted down by an amount S_F, so that the shifts of the ground and excited state are in fact identical.

The fact that ground and excited states have the same potential, implies that the transition frequencies to the dressed states are simply periodic in space with period λ_0, as shown in Fig. 23, rather than aperiodic as in Fig. 5.

Similarly, the fluctuations in the force due to the FORT now vanish, as both ground and excited state undergo the same shift, so that the diffusion coefficient is periodic with period λ_0. Also the friction force arises only from the cavity QED part and is periodic. Yet, the different wells are not equivalent. The forces are, just as before, driven by both cavity QED field and the FORT, and the value of g at the antinode of the FORT still varies over the different wells. This is illustrated in Fig. 24 where the rms velocities in the eight different wells are shown, along with friction and diffusion coefficients. Since in this example the probe field is detuned below the lower dressed state, one has cooling everywhere in space.

The simulations show that the mean trapping time is smaller, although the rms velocities are just as small as before. The reason is the less favorable cooling condition away from the cavity axis. In particular, for the parameters used here the expected rms velocity $v^z_{\rm rms}$ steadily increases to 90 cm/s at a radial distance $\rho=2w_0$, while for the simulations of Figs. 17, $v^z_{\rm rms}$ is increasing only slowly to 12 cm/s. This large difference can be understood by noting the difference in dressed state structures between the two cases. For the

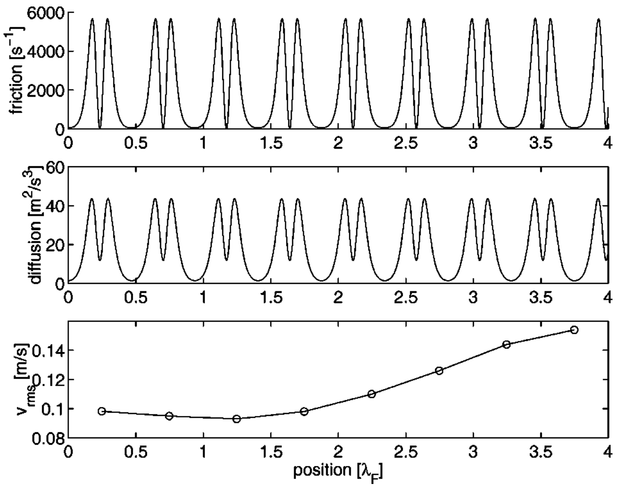

FIG. 24. Friction and diffusion coefficients, and the resulting rms velocity as functions of position along the cavity axis for the trapping structure of Sec. IV F. Here $\Delta_p/(2\pi) = -35$ MHz, and $N_e = 0.01$.

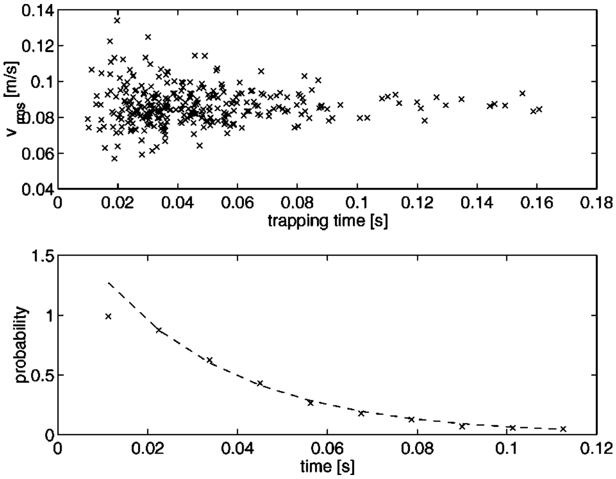

FIG. 25. As Fig. 14, but for the different trapping structure of Sec. IV F. The initial position was $z = 0.125\lambda_F$, and further parameters were $N_e = 0.01$, $\Delta_p = -35 \times 2\pi$ MHz, $S_0 = 50 \times 2\pi$ MHz. The mean trapping time is $\tau = 28 \pm 2$ ms.

case of Fig. 5, the transition frequency to the lower dressed state around the equilibrium position $z \approx 2.25\lambda_F$ does not change much with increasing radial distance, so that the probe field in that trapping region is always detuned below resonance by an amount that stays more or less constant. For the dressed state structure of Fig. 23, however, the probe detuning increases from $\geqslant 5$ MHz to $\geqslant 35$ MHz below resonance, thus leading to much worse cooling conditions. In other words, the presence of opposite level shifts due to the FORT makes the spatial variation of the transition frequency to the lower dressed state *smaller*: compare $\Delta_- = S_F - \sqrt{S_F^2 + g^2}$ to $\Delta_- = -g$, especially when $g \ll S_F$.

The alternative trapping potential is, therefore, not necessarily more favorable for trapping purposes. On the other hand, *all* atoms are captured now and are trapped for at least 10 ms. This can be understood from the simple fact that here the friction coefficient is positive in the *entire* well (Fig. 25).

V. SUMMARY

We analyzed cooling limits and trapping mechanisms for atoms trapped in optical traps inside optical cavities. The main distinguishing feature from previous discussions on cooling of atoms inside cavities is the presence of the external trapping potential with a different spatial periodicity as compared to the cavity QED field. This not only provides better cooling and trapping conditions but the different spatial period makes the various potential wells qualitatively different. Atoms can be trapped in regions of space where the coupling to the cavity QED field is maximum, minimum or somewhere in between. Depending on the laser detuning, cooling may take place only in wells where the atom is minimally coupled to the cavity QED field, or where it is maximally coupled. This allows one, in principle, to distinguish to a certain degree the different atomic positions along the cavity axis, namely, by comparing

(1) the average transmission level,
(2) the fluctuations of the cavity transmission,
(3) the total trapping time

which reflect, respectively, the average atom-cavity coupling, the temperature of the atom and under certain conditions the radial motion, and the overall cooling and trapping conditions. This is an important additional tool useful for eventual control of coherent evolution of the atomic center-of-mass degrees of freedom, as relevant to performing quantum logic operations.

ACKNOWLEDGMENTS

We thank Andrew Doherty, Klaus Mølmer, and David Vernooy for helpful discussions and comments. This work was funded by the National Science Foundation, by the Caltech MURI on Quantum Networks administered by the U.S. Army Research Office, by DARPA through the QUIC (Quantum Information and Computation) program, and by the Office of Naval Research.

---

[1] C.J. Hood, T.W. Lynn, A.C. Doherty, A.S. Parkins, and H.J. Kimble, Science **287**, 1447 (2000).
[2] P.W.H. Pinkse, T. Fischer, P. Maunz, and G. Rempe, Nature (London) **404**, 365 (2000).
[3] A.C. Doherty, C.J. Hood, T.W. Lynn, and H.J. Kimble, Phys. Rev. A **63**, 013401 (2001).
[4] J.I. Cirac, P. Zoller, H.J. Kimble, and H. Mabuchi, Phys. Rev. Lett. **78**, 3221 (1997).
[5] S.J. van Enk, J.I. Cirac, and P. Zoller, Phys. Rev. Lett. **78**, 4293 (1997); Science **279**, 205 (1998).
[6] J. Ye, D.W. Vernooy, and H.J. Kimble, Phys. Rev. Lett. **83**, 4987 (1999).

[7] C.W. Gardiner, J. Ye, H.C. Nägerl, and H.J. Kimble, Phys. Rev. A **61**, 045801 (2000).

[8] H. C. Nägerl, D. Stamper-Kurn, J. Ye, and H.J. Kimble (to be published).

[9] T.W. Mossberg, M. Lewenstein, and D.J. Gauthier, Phys. Rev. Lett. **67**, 1723 (1991).

[10] P. Horak, G. Hechenblaikner, K.M. Gheri, H. Stecher, and H. Ritsch, Phys. Rev. Lett. **79**, 4974 (1997). G. Hechenblaikner, M. Gangl, P. Horak, and H. Ritsch, Phys. Rev. A **58**, 3030 (1998).

[11] V. Vuletic and S. Chu, Phys. Rev. Lett. **84**, 3787 (2000), and references therein.

[12] H. J. Kimble, C. J. Hood, T. W. Lynn, H. Mabuchi, D. W. Vernooy, and J. Ye, in *Laser Spectroscopy XIV*, edited by R. Blatt *et al.* (World Scientific, Singapore, 1999).

[13] For a review of older work on quantized atomic motion in the context of cavity QED, see P. Meystre, Prog. Opt. **XXX**, 263 (1992); For a more recent review, see H. Walther, Phys. Scr. **T76**, 138 (1998); see also D.W. Vernooy and H.J. Kimble, Phys. Rev. A **56**, 4287 (1997), and references therein, in particular [3]–[18].

[14] A.C. Doherty, A.S. Parkins, S.M. Tan, and D.F. Walls, Phys. Rev. A **56**, 833 (1997); **57**, 4804 (1998).

[15] R. Taieb, R. Dum, J.I. Cirac, P. Marte, and P. Zoller, Phys. Rev. A **49**, 4876 (1994).

[16] S. Marksteiner, K. Ellinger, and P. Zoller, Phys. Rev. A **53**, 3409 (1996).

[17] J. Dalibard and C. Cohen-Tannoudji, J. Phys. B **18**, 1661 (1985).

[18] C. W. Gardiner, *Handbook of Stochastic Methods*, 2nd ed. (Springer, Berlin, 1997).

[19] S.M. Tan, J. Opt. B: Quantum Semiclassical Opt. **1**, 424 (1999).

[20] G.S. Agarwal and K. Mϕlmer, Phys. Rev. A **47**, 5158 (1993).

[21] J. Dalibard and C. Cohen-Tannoudji, J. Opt. Soc. Am. B **2**, 1707 (1985).

arXiv:quant-ph/0012001 v3 12 Dec 2000

Quantum versus Classical Domains for Teleportation with Continuous Variables

Samuel L. Braunstein[†], Christopher A. Fuchs[‡], H. J. Kimble[*], and P. van Loock[†]
[†]*Informatics, Bangor University, Bangor LL57 1UT, UK*
[‡] *Bell Labs, Lucent Technologies, 600-700 Mountain Ave., Room 2C-420, Murray Hill, NJ 07974, USA*
[*]*Norman Bridge Laboratory of Physics 12-33, California Institute of Technology, Pasadena, California 91125, USA*
(May 25, 2006)

Fidelity $F_{classical} = \frac{1}{2}$ has been established as setting the boundary between classical and quantum domains in the teleportation of coherent states of the electromagnetic field (S. L. Braunstein, C. A. Fuchs, and H. J. Kimble, J. Mod. Opt. **47**, 267 (2000)). Two recent papers by P. Grangier and F. Grosshans (`quant-ph/0009079` and `quant-ph/0010107`) introduce alternate criteria for setting this boundary and as a result claim that the appropriate boundary should be $F = \frac{2}{3}$. Although larger fidelities would lead to enhanced teleportation capabilities, we show that the new conditions of Grangier and Grosshans are largely unrelated to the questions of entanglement and Bell-inequality violations that they take to be their primary concern. With regard to the quantum-classical boundary, we demonstrate that fidelity $F_{classical} = \frac{1}{2}$ remains the appropriate point of demarcation. The claims of Grangier and Grosshans to the contrary are simply wrong, as we show by an analysis of the conditions for nonseparability (that complements our earlier treatment) and by explicit examples of Bell-inequality violations.

I. INTRODUCTION

As proposed by Bennett *et al.* [1], the protocol for achieving quantum teleportation is the following. Alice is to transfer an unknown quantum state $|\psi\rangle$ to Bob, using as the sole resources some previously shared *quantum entanglement* and a *classical channel* capable of communicating measurement results. Physical transport of $|\psi\rangle$ from Alice to Bob is excluded at the outset. Ideal teleportation occurs when the state $|\psi\rangle$ enters Alice's sending station and the *same* state $|\psi\rangle$ emerges from Bob's receiving station.

Of course, in actual experiments [2–5], the ideal case is *unattainable* as a matter of principle. The question of operational criteria for gauging success in an experimental setting, therefore, cannot be avoided. We have proposed previously that a minimal set of conditions for claiming success in the laboratory are the following [6].

1. An unknown quantum state (supplied by a third party Victor) is input physically into Alice's station from an outside source.
2. The "recreation" of this quantum state emerges from Bob's receiving terminal available for Victor's independent examination.
3. There should be a quantitative measure for the quality of the teleportation and based upon this measure, it should be clear that shared entanglement enables the output state to be "closer" to the input state than could have been achieved if Alice and Bob had utilized a classical communication channel alone.

In Ref. [6], it was shown that the fidelity F between input and output states is an appropriate measure of the degree of similarity in Criterion 3. For an input state $|\psi_{in}\rangle$ and output state described by the density operator $\hat{\rho}_{out}$, the fidelity is given by [7]

$$F = \langle\psi_{in}|\hat{\rho}_{out}|\psi_{in}\rangle \ . \tag{1}$$

To date only the experiment of Furusawa *et al.* [4] has achieved unconditional experimental teleportation as defined by the three criteria above [6,8,9]. This experiment was carried out in the setting of continuous quantum variables with input states $|\psi_{in}\rangle$ consisting of coherent states of the electromagnetic field, with an observed fidelity $F_{\rm exp} = 0.58 \pm 0.02$ having been attained. This benchmark is significant because it can be demonstrated [4,6] that quantum entanglement is the critical ingredient in achieving an average fidelity greater than $F_{classical} = \frac{1}{2}$ *when* the input is an absolutely random coherent state [10].

Against this backdrop, Grangier and Grosshans [11,12] have recently suggested that the appropriate boundary between the classical and quantum domains in the teleportation of coherent states should be a fidelity $F = \frac{2}{3}$. Their principal concern is the distinction between "entanglement" and "non-separability," where by the latter term, they mean "the physical properties associated with non-locality and the violation of Bell's inequalities (BI)."[*] They claim that "due to imperfect transmissions,

---

[*]Since the terms "entanglement" and "nonseparability" are used interchangeably in the quantum information community, we will treat them as synonyms to eliminate further confusion. We will refer to violations of Bell's inequalities explicitly whenever a distinction must be made between entanglement and local realism *per se.* The only exceptions will be when we quote directly from Grangier and Grosshans [11,12].

... it becomes possible to violate the classical boundary *(i.e., $F = \frac{1}{2}$)* of teleportation without any violation of BI." [11] However, rather than addressing the issue in a direct manner, they then propose the violation of a certain "Heisenberg-type inequality (HI)" as "a more effective – and in some sense 'necessary' – way to characterize shared entanglement." It is this that leads to their condition $F > \frac{2}{3}$ as being necessary for the declaration of successful teleportation. In support of this threshold, they further relate their criterion based on the HI to ones previously introduced in the quantum nondemolition measurement (QND) literature. Finally, in Ref. [12], Grangier and Grosshans find that $F > \frac{2}{3}$ is also required by a criterion they introduce having to do with a certain notion of reliable "information exchange" [12].

The purpose of the present paper is to demonstrate that the conclusions of Grangier and Grosshans concerning the proposed quantum-classical boundary $F = \frac{2}{3}$ are unwarranted and, by explicit counter example, incorrect. Our approach will be to investigate questions of nonseparability and violations of Bell inequalities for the particular entangled state employed in the teleportation protocol of Ref. [13]. Of significant interest will be the case with losses, so that the relevant quantum states will be mixed quantum states. Our analysis supports the following conclusions.

1. Although the argument of Grangier and Grosshans is claimed to be based upon "EPR non-separability of the entanglement resource" [12] [by which they mean a potential violation of a BI], they offer no quantitative connection (by constructive proof or otherwise) between the criteria they introduce (including the threshold $F = \frac{2}{3}$) [11,12] and the actual violation of any Bell inequality. Nothing in their analysis provides a warranty that $F > \frac{2}{3}$ would preclude a description in terms of a local hidden-variables theory. They offer only the suggestion that "$F > \frac{2}{3}$ would be much safer" [11].
2. By application of the work of Duan *et al.* [14], Simon [15], and Tan [16], we investigate the question of entanglement. We show that the states employed in the experiment of Ref. [4] are nonseparable, as was operationally confirmed in the experiment. Moreover, we study the issue of nonseparability for mixed states over a broad range in the degree of squeezing for the initial EPR state, in the overall system loss, and in the presence of thermal noise. This analysis reveals that EPR mixed states that are nonseparable do indeed lead to a fidelity of $F > F_{classical} = \frac{1}{2}$ for the teleportation of coherent states. Hence, in keeping with Criterion 3 above, the threshold fidelity for employing entanglement as a quantum resource is precisely the same as was deduced in the previous analysis of Ref. [6]. Within the setting of Quantum Optics, this threshold coincides with the standard benchmark for manifestly quantum or nonclassical behavior, namely that the Glauber-Sudarshan phase-space function becomes nonpositive-definite, here for any bipartite nonseparable state [17]. By contrast, the value $F = \frac{2}{3}$ championed by Grangier and Grosshans is essentially unrelated to the threshold for entanglement (nonseparability) in the teleportation protocol, as well as to the boundary for the nonclassical character of the EPR state.
3. By application of the work of Banaszek and Wodkiewicz [18,19], we explore the possibility of violations of Bell inequalities for the EPR (mixed) states employed in the teleportation of continuous quantum-variables states. We find direct violations of a CHSH inequality [20] over a large domain. Significant relative to the claims of Grangier and Grosshans is a regime both of entanglement (nonseparability) and of violation of a CHSH inequality for which the teleportation fidelity $F < \frac{2}{3}$ and for which the criterion of the Heisenberg inequalities of Ref. [11] fails. Hence, teleportation with $\frac{1}{2} < F < \frac{2}{3}$ is possible with EPR (mixed) states which do not admit a local hidden variables description. In contradistinction to the claim of Grangier and Grosshans, $F > \frac{2}{3}$ does not provide a relevant criterion for delineating the quantum and classical domains with respect to violations of Bell's inequalities.
4. By adopting a protocol analogous to that employed in *all* previous experimental demonstrations of violations of Bell's inequalities [21–23], scaled correlation functions can be introduced for continuous quantum variables. In terms of these scaled correlations, the EPR mixed state used for teleportation violates a generalized version of the CHSH inequality, though non-ideal detector efficiencies require a "fair sampling" assumption for this. These violations set in for $F > \frac{1}{2}$ and have recently been observed in a setting of low detection efficiency [24]. This experimental verification of a violation of a CHSH inequality (with a fair sampling assumption) again refutes the purported significance of the threshold $F = \frac{2}{3}$ promoted by Grangier and Grosshans.

Overall, we find no support for the claims of Grangier and Grosshans giving special significance to the threshold fidelity $F = \frac{2}{3}$ in connection to issues of separability and Bell-inequality violations. Instead, as we will show, it is actually the value $F_{classical} = \frac{1}{2}$ that heralds entrance into the quantum domain with respect to the very same issues. Their claims based upon a Heisenberg-type inequality and a criterion for "information exchange" are essentially unrelated to the issue of a quantum-classical boundary.

All this is not to say that teleportation of coherent states with increasing degrees of fidelity beyond $F_{classical} = \frac{1}{2}$ to $F > \frac{2}{3}$ is not without significance. In fact, as tasks of ever increasing complexity are to be accomplished, there will be corresponding requirements to improve the fidelity of teleportation yet further. Moreover, there are clearly diverse quantum states other than coherent states that one might desire to teleport, including squeezed states, quantum superpositions, entangled states [16], and so on. The connection between the "intricacy" of such states and the requisite resources for achieving high fidelity teleportation has been discussed in Ref. [13], including the example of the superposition of two coherent states,

$$|\alpha\rangle + |-\alpha\rangle \ , \tag{2}$$

which for $|\alpha| \gg 1$ requires an EPR state with an extreme degree of quantum correlation.

Similiarly, Heisenberg-type inequalities are in fact quite important for the inference of the properties of a *system* given the outcomes of measurements made on a *meter* following a *system-meter* interaction. Such quantities are gainfully employed in Quantum Optics in many settings, including realizations of the original EPR *gedanken* experiment [25–27] and of back-action evading measurement and quantum non-demolition detection [28].

Our only point is that the claim of Grangier and Grosshans that $F = \frac{2}{3}$ is required for the "successful quantum teleportation of a coherent state" [12] is incorrect. They simply offer no quantitative analysis directly relevant to either entanglement or Bell-inequality violation issues. In contrast, the prior treatment of Ref. [6] demonstrates that in the absence of shared entanglement between Alice and Bob, there is an upper limit for the fidelity for the teleportation of randomly chosen coherent states given by $F_{classical} = \frac{1}{2}$. Nothing in the work of Grangier and Grosshans calls this analysis into question.

This, however, leads to something we would like to stress apart from the details of any particular teleportation criterion. There appears to be a growing confusion in the community that equates quantum teleportation experiments with fundamental tests of quantum mechanics. The purpose of such tests is generally to compare quantum mechanics to other potential theories, such as locally realistic hidden-variable theories [11,29,30]. In our view, experiments in teleportation have nothing to do with this. They instead represent investigations *within* quantum mechanics, demonstrating only that a particular task can be accomplished with the resource of quantum entanglement and cannot be accomplished without it. This means that violations of Bell's inequalities are largely irrelevant as far as the original proposal of Bennett *et al.* [1] is concerned, as well as for experimental implementations of that protocol. In a theory which allows states to be cloned, there would be no need to discuss teleportation at all – unknown states could be cloned and transmitted with fidelity arbitrarily close to one.

These comments notwithstanding, Grangier and Grosshans did nevertheless attempt to link the idea of Bell-inequality violations with the fidelity of teleportation. It is to the details of that linkage that we now turn. The remainder of the paper is organized as follows. In Section II, we extend the prior work of Ref. [6] to a direct treatment of the consequences of shared entanglement between Alice and Bob, beginning with an explicit model for the mixed EPR states used for teleportation of continuous quantum variables. In Section III we review the criteria Grangier and Grosshans introduced in preparation for showing their inappropriateness as tools for the questions at hand. In Section IV, we demonstrate explicitly the relationship between entanglement and fidelity, and find the same threshold $F_{classical} = \frac{1}{2}$ as in our prior analysis [6]. The value $F = \frac{2}{3}$ is shown to have no particular distinction in this context. In Sections V and VI, we further explore the role of entanglement with regard to violations of a CHSH inequality and provide a quantitative boundary for such violations. Again, $F_{classical} = \frac{1}{2}$ appears as the point of entry into the quantum domain, with the point $F = \frac{2}{3}$ having no particular distinction. Our conclusions are collected in Section VII. Of particular significance, we point out that the teleportation experiment of Ref. [4] did indeed cross from the classical to the quantum domain, just as advertised previously.

II. THE EPR STATE

The teleportation protocol we consider is that of Braunstein and Kimble [13], for which the relevant entangled state is the so-called two-mode squeezed state. This state is given explicitly in terms of a Fock-state expansion for two-modes $(1, 2)$ by [31,32]

$$|EPR\rangle_{1,2} = \frac{1}{\cosh r} \sum_{n=0}^{\infty} (\tanh r)^n |n\rangle_1 |n\rangle_2 \ , \tag{3}$$

where r measures the amount of squeezing required to produce the entangled state. Note that for simplicity we consider the case of two single modes for the electromagnetic field; the extension to the multimode case for fields of finite bandwidth can be found in Ref. [33].

The pure state of Eq. (3) can be equivalently described by the corresponding Wigner distribution $W_{\rm EPR}$ over the two modes $(1, 2)$,

$$\begin{aligned} &W_{\rm EPR}(x_1, p_1; x_2, p_2) \\ &= \frac{4}{\pi^2} \frac{1}{\sigma_+^2 \sigma_-^2} \ \exp\Big(- [(x_1 + x_2)^2 + (p_1 - p_2)^2]/\sigma_+^2 \\ &\quad -[(x_1 - x_2)^2 + (p_1 + p_2)^2]/\ \sigma_-^2 \Big) \ , \end{aligned} \tag{4}$$

where $\sigma_\pm$ are expressed in terms of the squeezing parameter by

$$\begin{aligned}\sigma_+^2 &= e^{+2r},\\ \sigma_-^2 &= e^{-2r},\end{aligned} \tag{5}$$

with $\sigma_+^2\sigma_-^2 = 1$. Here, the canonical variables (x_j, p_j) are related to the complex field amplitude α_j for mode $j = (1, 2)$ by

$$\alpha_j = x_j + ip_j. \tag{6}$$

In the limit of $r \to \infty$, Eq. (4) becomes

$$C\,\delta(x_1 - x_2)\,\delta(p_1 + p_2) \tag{7}$$

which makes a connection to the original EPR state of Einstein, Podolsky, and Rosen [25].

Of course, $W_{\rm EPR}$ as given above is for the ideal, lossless case. Of particular interest with respect to experiments is the inclusion of losses, as arise from, for example, finite propagation and detection efficiencies. Rather than deal with any detailed setup (e.g., as treated in explicit detail in Ref. [26]) here we adopt a generic model of the following form. Consider two identical beam splitters each with a transmission coefficient η, one for each of the two EPR modes. We take $0 \leq \eta \leq 1$, with $\eta = 1$ for the ideal, lossless case. The input modes to the beam splitter 1 are taken to be $(1', a')$, while for beam splitter 2, the modes are labeled by $(2', b')$. Here, the modes $(1', 2')$ are assumed to be in the state specified by the ideal $W_{\rm EPR}$ as given in Eq. (4) above, while the modes (a', b') are taken to be independent thermal (mixed) states each with Wigner distribution

$$W(x,p) = \frac{1}{\pi(\bar{n}+\frac{1}{2})}\exp\{-(x^2+p^2)/(\bar{n}+1/2)\}, \tag{8}$$

where $\bar{n}$ is the mean thermal photon number for each of the modes (a', b').

The overall Wigner distribution for the initial set of input modes $(1', 2'), (a', b')$ is then just the product

$$W_{\rm EPR}(x_{1'}, p_{1'}; x_{2'}, p_{2'})W(x_{a'}, p_{a'})W(x_{b'}, p_{b'})\ . \tag{9}$$

The standard beam-splitter transformations lead in a straightforward fashion to the Wigner distribution for the output set of modes $(1, 2), (a, b)$, where, for example,

$$\begin{aligned}x_1 &= \sqrt{\eta}x_{1'} - \sqrt{1-\eta}x_{a'},\\ x_a &= \sqrt{\eta}x_{a'} + \sqrt{1-\eta}x_{1'}.\end{aligned} \tag{10}$$

We require $W_{\rm EPR}^{out}$ for the $(1, 2)$ modes alone, which is obtained by integrating over the (a, b) modes. A straightforward calculation results in the following distribution for the mixed output state:

$$\begin{aligned}&W_{\rm EPR}^{out}(x_1, p_1; x_2, p_2)\\ &= \frac{4}{\pi^2}\frac{1}{\bar\sigma_+^2\bar\sigma_-^2}\ \exp\Big(-[(x_1+x_2)^2+(p_1-p_2)^2]/\bar\sigma_+^2\\ &\qquad -[(x_1-x_2)^2+(p_1+p_2)^2]/\ \bar\sigma_-^2\Big),\end{aligned} \tag{11}$$

where $\bar\sigma_\pm$ are given by

$$\begin{aligned}\bar\sigma_+^2 &= \eta e^{+2r} + (1-\eta)(1+2\bar{n}),\\ \bar\sigma_-^2 &= \eta e^{-2r} + (1-\eta)(1+2\bar{n}).\end{aligned} \tag{12}$$

Note that $W_{\rm EPR}^{out}$ as above follows directly from $W_{\rm EPR}$ in Eq. (4) via the simple replacements $\sigma_\pm \longrightarrow \bar\sigma_\pm$. Relevant to the discussion of Bell inequalities in Sections V and VI is the fact that $\bar\sigma_+^2\bar\sigma_-^2 > 1$ for any $r > 0$ and $\eta < 1$.

III. THE CRITERIA OF GRANGIER AND GROSSHANS

The two recent papers of Grangier and Grosshans argue that "fidelity value larger than $\frac{2}{3}$ is actually required for successful teleportation" [11,12]. In this section, we recapitulate the critical elements of their analysis and state their criteria in the present notation. In subsequent sections we proceed further with our own analysis of entanglement and possible violations of Bell's inequalities for the EPR state of Eq. (11).

Beginning with Ref. [11], Eq. (21), Grangier and Grosshans state the following:

> "As a criteria for non-separability [by which they mean violations of Bell's inequalities], we will use the EPR argument: two different measurements prepare two different states, in such a way that the product of conditional variances (with different conditions) violates the Heisenberg principle."

This statement takes a quantitative form in terms of the following conditional variances expressed in the notation of the preceding section for EPR beams $(1, 2)$:

$$\begin{aligned}V_{x_i|x_j} &= \langle\Delta x_i^2\rangle - \frac{\langle x_i x_j\rangle^2}{\langle\Delta x_j^2\rangle},\\ V_{p_i|p_j} &= \langle\Delta p_i^2\rangle - \frac{\langle p_i p_j\rangle^2}{\langle\Delta p_j^2\rangle}.\end{aligned} \tag{13}$$

with $(i, j) = (1, 2)$ and $i \neq j$. Note that, for example, $V_{x_2|x_1}$ gives the error in the knowledge of the canonical variable x_2 based upon an estimate of x_2 from a measurement of x_1, and likewise for the other conditional variances. These variances were introduced in Refs. [26,27] in connection with an optical realization of the original *gedanken* experiment of Einstein, Podolsky, and Rosen [25]. An apparent violation of the uncertainty principle arises if the product of inference errors is below the uncertainty product for one beam alone. For example, $V_{x_2|x_1}V_{p_2|p_1} < \frac{1}{16}$ represents such an apparent violation since $\Delta x_2^2 \Delta p_2^2 \geq \frac{1}{16}$ is demanded by the canonical commutation relation between x_2 and p_2, with here $\Delta x_{1,2}^2 = \frac{1}{4} = \Delta p_{1,2}^2$ for the vacuum state [26,27].

Grangier and Grosshans elevate this concept of inference at a distance from the EPR analysis to "a criteria for non-separability [i.e., violation of Bell's inequalities]." Specifically, they state that "the classical limit of no apparent violation of HI" [and hence the domain of local realism] is determined by the conditions

$$V_{x_2|x_1}V_{p_2|p_1} \geq \frac{1}{16}, \quad \text{and} \quad V_{x_1|x_2}V_{p_1|p_2} \geq \frac{1}{16}. \tag{14}$$

As shown in Refs. [26,27] for the states under consideration, the conditional variances of Eq. (13) are simply related to the following (unconditional) variances

$$\begin{aligned}\Delta x_{\mu_{ij}}^2 &= \langle (x_i - \mu_{ij} x_j)^2 \rangle, \\ \Delta p_{\nu_{ij}}^2 &= \langle (p_i - \nu_{ij} p_j)^2 \rangle.\end{aligned} \tag{15}$$

If we use a measurement of x_j to estimate x_i, then $\Delta x_{\mu_{ij}}^2$ is the variance of the error when the estimator is chosen to be $\mu_{ij} x_j$, and likewise for $\Delta p_{\nu_{ij}}^2$. For an optimal estimate, the parameters (μ_{ij}, ν_{ij}) are given by [26,27]

$$\mu_{ij}^{\text{opt}} = \frac{\langle x_i x_j \rangle}{\langle \Delta x_j^2 \rangle}, \quad \nu_{ij}^{\text{opt}} = \frac{\langle p_i p_j \rangle}{\langle \Delta p_j^2 \rangle}, \tag{16}$$

and in this case,

$$V_{x_i|x_j} = \Delta x^2_{\mu_{ij}^{\text{opt}}}, \text{ and } V_{p_i|p_j} = \Delta p^2_{\nu_{ij}^{\text{opt}}}. \tag{17}$$

The "non-separability" condition of Grangier and Grosshans in Eq. (14) can then be re-expressed as

$$\Delta x_{\mu_{21}}^2 \Delta p_{\nu_{21}}^2 \geq \frac{1}{16}, \quad \text{and} \quad \Delta x_{\mu_{12}}^2 \Delta p_{\nu_{12}}^2 \geq \frac{1}{16}, \tag{18}$$

where we assume the optimized choice and drop the superscript 'opt'. Again, Grangier and Grosshans take this condition of "no apparent violation of HI" as the operational signature of "nonseparability criteria" [violations of Bell inequalities], and hence, by their logic, to delineate the classical boundary for teleportation [11].

To make apparent the critical elements of the discussion, we next assume symmetric fluctuations as appropriate to the EPR state of Eq. (11), $\mu_{ij} = \mu_{ji} \equiv \mu$ and $\nu_{ij} = \nu_{ji} \equiv \nu$, with $\mu = -\nu$. Note that within the context of our simple model of the losses, the optimal value of μ is given by

$$\mu = \frac{\eta \sinh 2r}{(1-\eta) + \eta \cosh 2r}, \tag{19}$$

where in the limit $r \gg 1$, $\mu \to 1$. For this case of symmetric fluctuations, the HI of Eq. (18) becomes

$$\Delta x_\mu^2 \Delta p_\mu^2 \geq \frac{1}{16}, \tag{20}$$

where

$$\begin{aligned}\Delta x_\mu^2 &= \langle (x_1 - \mu x_2)^2 \rangle = \langle (x_2 - \mu x_1)^2 \rangle, \\ \Delta p_\mu^2 &= \langle (p_1 + \mu p_2)^2 \rangle = \langle (p_2 + \mu p_1)^2 \rangle.\end{aligned} \tag{21}$$

Note that in general the inequality

$$V_1 V_2 \geq \frac{a^2}{4} \tag{22}$$

implies that

$$V_1 + V_2 \geq V_1 + \frac{a^2}{4V_1} \geq a, \tag{23}$$

so that the criterion of Eq. (20) for *classical* teleportation leads to

$$\Delta x_\mu^2 + \Delta p_\mu^2 \geq \frac{1}{2}. \tag{24}$$

Hence, the requirement of Grangier and Grosshans for *quantum* teleportation is that

$$\Delta x_\mu^2 + \Delta p_\mu^2 < \frac{1}{2}, \tag{25}$$

which for $r \gg 1$ becomes

$$\Delta x^2 + \Delta p^2 < \frac{1}{2}. \tag{26}$$

Here, $(\Delta x^2, \Delta p^2)$ are as defined in Eq. (21), now with $\mu = 1$;

$$\begin{aligned}\Delta x^2 &= \langle (x_1 - x_2)^2 \rangle, \\ \Delta p^2 &= \langle (p_1 + p_2)^2 \rangle,\end{aligned} \tag{27}$$

where from Eq. (11), we have that $\Delta x^2 + \Delta p^2 = \bar{\sigma}_-^2$ for the EPR beams $(1,2)$. The claim of Grangier and Grosshans [11] is that the inequality of Eq. (20) serves as "the condition for no useful entanglement between the two beams," where by 'useful' they refer explicitly to "the existence of quantum non-separability [violation of Bell's inequalities]." The inequalities of Eqs. (18) and (20) are also related to criteria developed within the setting of quantum nondemolition detection (QND) [28], as discussed in the next section.

In a second paper [12], Grangier and Grosshans introduce an alternative criteria for the successful teleportation of coherent states, namely that

> "the information content of the teleported quantum state is higher than the information content of any (classical or quantum) copy of the input state, that may be broadcasted classically."

To quantify the concept of "information content" they introduce a "generalized fidelity" describing not the overlap of quantum states as is standard in the quantum information community, but rather the conditional probability $P(\alpha|I)$ that a particular coherent state $|\alpha\rangle$ was actually sent given "the available information I." In effect, Grangier and Grosshans consider the following protocol. Victor sends to Alice some unknown coherent state $|\alpha_0\rangle$, with Alice making her best attempt to determine this state [34], and sending the resulting measurement outcome to Bob as in the standard protocol. Bob then does one of two things. In the first instance, he forwards only this classical message with Alice's measurement outcome to Victor without reconstructing a quantum state. In the second case, he actually generates a quantum state conditioned upon Alice's message and sends this state to Victor, who must then make his own measurement to deduce whether the teleported state corresponds to the one that he initially sent. For successful teleportation, Grangier and Grosshans demand that the information gained by Victor should be greater in the latter case where quantum states are actually generated by Bob than in the former case where only Alice's classical measurement outcome is distributed. It is straightforward to show that Eq. (26) given above is sufficient to ensure that this second criteria is likewise satisfied for the teleportation of a coherent state $|\alpha\rangle$, albeit with the same caveat expressed in [10], namely that neither the set S of initial states $\{|\psi_{in}\rangle\}$ nor the distribution $P(|\psi_{in}\rangle)$ over these states is specified.

We now turn to an evaluation of these criteria of Grangier and Grosshans placing special emphasis on the issues of entanglement and violations of Bell's inequalities, specifically because these are the concepts Grangier and Grosshans emphasize in their work [11,12].

IV. ENTANGLEMENT AND FIDELITY

A. Nonseparability of the EPR beams

To address the question of the nonseparability of the EPR beams, we refer to the papers of Duan *et al.* and of Simon [14,15], as well as related work by Tan [16]. For the definitions of (x_i, p_i) that we have chosen for the EPR beams $(1, 2)$, a sufficient condition for nonseparability (without an assumption of Gaussian statistics) is that

$$\Delta x^2 + \Delta p^2 < 1, \tag{28}$$

where Δx^2 and Δp^2 are defined in Eq. (27). This result follows from Eq. (3) of Duan *et al.* with $a = 1$ (and from a similar more general equation in Simon) [35]. Note that Duan *et al.* have $\Delta x_i^2 = \frac{1}{2} = \Delta p_i^2$ for the vacuum state, while our definitions lead to $\Delta x_i^2 = \frac{1}{4} = \Delta p_i^2$ for the vacuum state, where for example, $\Delta x_1^2 = \langle {x_1}^2 \rangle$, and that all fields considered have zero mean.

Given the Wigner distribution $W_{\rm EPR}^{out}$ as in Eq. (11), we find immediately that

$$\begin{aligned}\Delta x^2 + \Delta p^2 &= 2\frac{\bar{\sigma}_-^2}{2} \\ &= \eta e^{-2r} + (1-\eta)(1+2\bar{n}).\end{aligned} \tag{29}$$

For the case $\bar{n} = 0$, the resulting state is *always entangled for any* $r > 0$ *even for* $\eta \ll 1$, in agreement with the discussion in Duan *et al.* [14]. For nonzero $\bar{n}$, the state is entangled so long as

$$\bar{n} < \frac{\eta[1-\exp(-2r)]}{2(1-\eta)}. \tag{30}$$

We emphasize that in the experiment of Furusawa *et al.* [4] for which $\bar{n} = 0$ is the relevant case, the above inequality guarantees that teleportation was carried out with entangled (i.e., nonseparable) states for the EPR beams, independent of any assumption about whether these beams were Gaussian or pure states [36].

By contrast to the condition for entanglement given in Eq. (28), Grangier and Grosshans require instead the more stringent condition of Eq. (25) for successful teleportation. Although they would admit that the EPR beams are indeed entangled whenever Eq. (28) is satisfied,[†] they would term entanglement in the domain

$$\frac{1}{2} \leq \Delta x^2 + \Delta p^2 < 1$$

as not "useful" [11].

With regard to the QND-like conditions introduced by Grangier and Grosshans [11], we note that more general forms for the nonseparability condition of Eq. (28) are given in Refs. [14,15]. Of particular relevance is a condition for the variances of Eq. (15) for the case of symmetric fluctuations as for EPR state in Eq. (11), $\mu_{ij} = \mu_{ji} \equiv \mu$ and $\nu_{ij} = \nu_{ji} \equiv \nu$, with $\mu = -\nu$. Consider for example the first set of variances in Eq. (21), namely

$$\Delta x_\mu^2 = \langle (x_2 - \mu x_1)^2 \rangle \quad \text{and} \quad \Delta p_\mu^2 = \langle (p_2 + \mu p_1) \rangle^2, \tag{31}$$

as would be appropriate for an inference of (x_2, p_2) from a measurement (at a distance) of (x_1, p_1). In this case, a sufficient condition for entanglement of the EPR beams $(1, 2)$ may be obtained using Eq. (11) of Ref. [15] yielding

$$\Delta x_\mu^2 + \Delta p_\mu^2 < \frac{(1+\mu^2)}{2}, \tag{32}$$

[†] Grangier was in fact unaware of Refs. [14,15] when Ref. [11] was originally posted, having had this work pointed out by us.

which reproduces Eq. (28) for $\mu = 1$. This equation for nonseparability implies that

$$\Delta x_\mu^2 \Delta p_\mu^2 < \frac{(1+\mu^2)^2}{16}, \tag{33}$$

which is in the form of a Heisenberg-type inequality. Note that this inequality is satisfied for any $r > 0$ and $0 < \eta \leq 1$ for $\bar{n} = 0$. As discussed in Refs. [26,27], μ must be chosen in correspondence to the degree of correlation between the EPR beams, with $0 < \mu \leq 1$. An explicit expression for our current model given in Eq. (19). By constrast, in applying their QND-like conditions, Grangier and Grosshans demand to the contrary the Heisenberg-type inequality

$$\Delta x_\mu^2 \Delta p_\mu^2 < \frac{1}{16}. \tag{34}$$

Within the setting our current model, this condition can only be satisfied for efficiency $\eta > \frac{1}{2}$ [37]. Although this criterion has been found to be useful in the analysis of back-action evading measurement for quantum nondemolition detection, it apparently has no direct relevance to the question of entanglement, for $\mu = 1$ or otherwise.

Certainly, $\mu = 1$ is the case relevant to the actual teleportation protocol of Ref. [13]. However, Alice and Bob are surely free to explore the degree of correlation between their EPR beams and to test for entanglement by any means at their disposal, including simple measurements with $\mu \neq 1$.

Although the boundary expressed by the nonseparability conditions of Eqs. (28) and (32) are perhaps not so familiar in Quantum Optics, we stress that these criteria are associated quite directly with the standard condition for nonclassical behavior adopted by this community. Whenever Eqs. (28) and (32) are satisfied, the Glauber-Sudarshan phase-space function becomes nonpositive [17], which for almost forty years has heralded entrance into a manifestly quantum or nonclassical domain. It is difficult to understand how Grangier and Grosshans propose to move from $\Delta x^2 + \Delta p^2 = 1$ to $\Delta x^2 + \Delta p^2 = \frac{1}{2}$ without employing quantum resources in the teleportation protocol (as is required when the Glauber-Sudarshan P-function is not positive definite). Their own work offers no suggestion of how this is to be accomplished.

B. Fidelity

Turning next to the question of the relationship of entanglement of the EPR beams [as quantified in Eq. (28)] to the fidelity attainable for teleportation *with these beams*, we recall from Eq. (2) of Ref. [4] that

$$F = \frac{1}{1+\bar{\sigma}_-^2}, \tag{35}$$

where this result applies to teleportation of coherent states [38,39]. When combined with Eq. (29), we find that

$$F = \frac{1}{1+(\Delta x^2 + \Delta p^2)}, \tag{36}$$

The criterion of Eq. (28) for nonseparability then guarantees that nonseparable EPR states as in Eqs. (4,11)(be they mixed or pure) are sufficient to achieve

$$F > F_{classical} = \frac{1}{2}, \tag{37}$$

whereas separable states must have $F \leq F_{classical} = \frac{1}{2}$, although we emphasize that this bound applies for the average fidelity for coherent states distributed over the entire complex plane [6,39].

We thereby demonstrate that the condition $F > F_{classical} = \frac{1}{2}$ *for quantum teleportation as established in Ref. [6] coincides with that for nonseparability (i.e., entanglement) of Refs. [14,15] for the EPR state of Eq. (11).* Note that for $\bar{n} = 0$, we have

$$F = \frac{1}{2 - \eta(1 - e^{-2r})}, \tag{38}$$

so that the entangled EPR beams considered here (as well as in Refs. [11,12]) provide a sufficient resource for beating the limit set by a classical channel alone for any $r > 0$, so long as $\eta > 0$. In fact, the quantities $(\Delta x^2, \Delta p^2)$ are readily measured experimentally, so that the entanglement of the EPR beams can be operationally verified, as was first accomplished in Ref. [26], and subsequently in Ref. [4]. We stress that independently of any further assumption, the condition of Eq. (28) is sufficient to ensure entanglement for pure or mixed states [40,41].

The dependence of fidelity F on the degree of squeezing r and efficiency η as expressed in Eq. (38) is illustrated in Figure 1. Here, in correspondence to an experiment with fixed overall losses and variable parametric gain in the generation of the EPR entangled state, we show a family of curves in Figure 1 each of which is drawn for constant η as a function of r. Clearly, $F > F_{classical} = \frac{1}{2}$ and hence nonseparability results in each case. The only apparent significance of $F = \frac{2}{3}$ as championed by Grangier and Grosshans (and which results for $\Delta x^2 + \Delta p^2 = \frac{1}{2}$) is to bound F for $\eta = 0.5$.

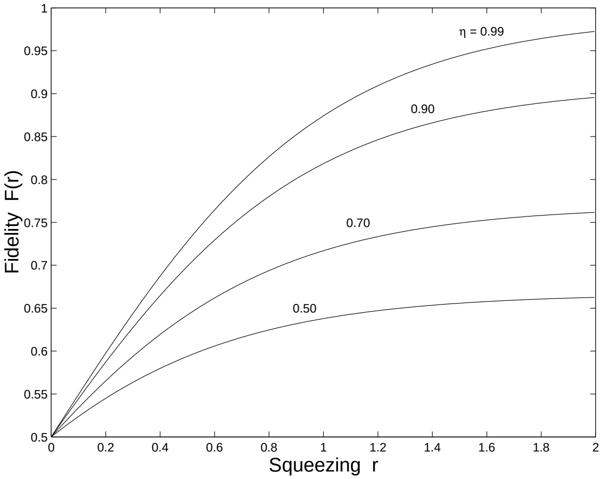

FIG. 1. Fidelity F as given by Eq. (38) versus the degree of squeezing r for fixed efficiency η. From top to bottom, the curves are drawn with $\eta = \{0.99, 0.90, 0.70, 0.50\}$ in correspondence to increasing loss $(1-\eta)$. Note that $F_{classical} = \frac{1}{2}$ provides a demarcation between separable and nonseparable states (mixed or otherwise), while $F = \frac{2}{3}$ is apparently of no particular significance, the contrary claims of Ref. [11,12] notwithstanding. Note that for $\eta = 1$, $r = \frac{\ln 2}{2} = 0.3466$ gives $F = \frac{2}{3}$, corresponding to -3dB of squeezing. In all cases, $\bar{n} = 0$.

As for the criterion of "information content" introduced by Grangier and Grosshans [12], we note it can be easily understood from the current analysis and the original discussion in Ref. [13]. Each of the interventions by Alice and Bob represent one unit of added vacuum noise that will be convolved with the initial input state in the teleportation protocol (the so-called *quduties*). Grangier and Grosshans compare the following two situations: (i) Bob passes directly the classical information that he receives to Victor and (ii) Bob generates a quantum state in the usual fashion that is then passed to Victor. Grangier and Grosshans would demand that Victor should receive the same information in these two cases, which requires that $\bar{\sigma}_-^2 = \Delta x^2 + \Delta p^2 < \frac{1}{2}$, and hence $F > \frac{2}{3}$. That is, as the degree of correlation between the EPR beams is increased, there comes a point for which $\Delta x^2 + \Delta p^2 = \frac{1}{2}$, and for which each of Alice and Bob's excess noise has been reduced from 1 quduty each to $\frac{1}{2}$ quduty each. At this point, Grangier and Grosshans would (arbitrarily) assign the entire resulting noise of $\frac{1}{2} + \frac{1}{2} = 1$ quduties to Alice, with then the perspective that Bob's state recreation adds no noise. Of course one could equally well make the complementary assignment, namely 1 quduty to Bob and none to Alice (again in the case with $\bar{\sigma}_-^2 = \frac{1}{2}$). The point that seems to be missed by Grangier and Grosshans is that key to quantum teleportation is the transport of quantum states. Although they correctly state that "there is *no* extra noise associated to the reconstruction: given a measured β, one can exactly reconstruct the coherent state $|\beta\rangle$, by using a deterministic translation of the vacuum." Bob can certainly make such a state deterministically, but it is an altogether different matter for Victor to receive a classical number from Bob in case (i) as opposed to the actual quantum state in (ii). In this latter case apart from having a physical state instead of a number, Victor must actually make his own measurement with the attendant uncertainties inherent in $|\beta\rangle$ then entering. Analogously, transferring measurement results about a qubit, without recreating a state at the output (i.e., without sending an actual *quantum state* to Victor), is not what is normally considered to constitute quantum teleportation relative to the original protocol of Bennett *et al.* [1].

Turning next to the actual experiment of Ref. [4], we note that a somewhat subtle issue is that the detection efficiency for Alice of the unknown state was not 100%, but rather was $\eta_A^2 = 0.97$. Because of this, the fidelity for classical teleportation (i.e., with vacuum states in place of the EPR beams) did not actually reach $\frac{1}{2}$, but was instead $F_0 = 0.48$. This should not be a surprise, since there is nothing to ensure that a given classical scheme will be optimal and actually reach the bound $F_{classical} = \frac{1}{2}$. Hence, the starting point in the experiment with $r = 0$ had $F_0 < F_{classical}$; the EPR beams with $r > 0$ (which were in any event entangled by the above inequality) then led to increases in fidelity from F_0 upward, exceeding the classical bound $F_{classical} = \frac{1}{2}$ for a small (but not infinitesimal) degree of squeezing. Note that the whole effect of the offset $F_0 = 0.48 < \frac{1}{2}$ can be attributed to the lack of perfect (homodyne) efficiency at Alice's detector for the unknown state. In the current discussion for determining the classical bound in the *optimal* case, we set Alice's detection efficiency instead to $\eta_A^2 = 1$, then as shown above, classical teleportation will achieve $F = \frac{1}{2}$.

Independent of such considerations, we reiterate that the nonseparability condition of Refs. [14,15] applied to the EPR state of Eqs. (4) and (11) leads to the same result $F_{classical} = \frac{1}{2}$ [Eqs. (36) and (37)] as did our previous analysis based upon teleportation with only a classical communication channel linking Alice and Bob [6]. This convergence further supports $F_{classical} = \frac{1}{2}$ as the appropriate quantum-classical boundary for the teleportation of coherent states, the claims of Grangier and Grosshans notwithstanding. Relative to the original work of Bennett *et al.* [1], exceeding the bound $F_{classical} = \frac{1}{2}$ for the teleportation of coherent can be accomplished with a classical channel and entangled (i.e., nonseparable) EPR states, be they mixed or pure, as is made clear by the above analysis and as has been operationally confirmed [4].

We should however emphasize that the above conclusions concerning nonseparability and teleportation fidelity apply to the specific case of the EPR state as in Eq. (11), for which inequality Eq. (28) represents both a necessary and sufficient criterion for nonseparability according to Refs. [14,15]. More generally, for arbitrary entangled states, nonseparability does not necessarily lead to $F > \frac{1}{2}$ in coherent-state teleportation [40,41].

V. BELL'S INEQUALITIES

The papers by Banaszek and Wodkiewicz [18,19] provide our point of reference for a discussion of Bell's inequalities. In these papers, the authors introduce an appropriate set of measurements that lead to a Bell inequality of the CHSH type. More explicitly, Eq.(4) of Ref. [18] gives the operator $\hat{\Pi}(\alpha;\beta)$ whose expectation values are to be measured. Banaszek and Wodkiewicz point out that the expectation value of $\hat{\Pi}(\alpha;\beta)$ is closely related the Wigner function of the field being investigated, namely

$$W(\alpha;\beta) = \frac{4}{\pi^2}\Pi(\alpha;\beta) \ , \tag{39}$$

where $\Pi(\alpha;\beta) = \langle\hat{\Pi}(\alpha;\beta)\rangle$.

For the entangled state shared by Alice and Bob in the teleportation protocol, we identify $W^{out}_{\rm EPR}$ as the relevant Wigner distribution for the modes $(1,2)$ of interest, so that

$$\begin{aligned} &\Pi^{out}_{\rm EPR}(x_1,p_1;x_2,p_2) \\ &= \frac{1}{\bar{\sigma}^2_+\bar{\sigma}^2_-}\exp\{-[(x_1+x_2)^2+(p_1-p_2)^2]/\bar{\sigma}^2_+ \\ &\quad -[(x_1-x_2)^2+(p_1+p_2)^2]/\ \bar{\sigma}^2_-\} \quad . \end{aligned} \tag{40}$$

Banaszek and Wodkiewicz show that $\Pi^{out}_{\rm EPR}(x_1,p_1;x_2,p_2)$ gives directly the correlation function that would otherwise be obtained from a particular set of observations over an ensemble representing the field with density operator $\hat{\rho}$, where the actual measurements to be made are as described in Refs. [18,19]. In simple terms, $\hat{\Pi}^{out}_{\rm EPR}(0,0;0,0)$ is the parity operator for separate measurements of photon number on modes $(1,2)$, with then nonzero (x_i,p_i) corresponding to a "rotation" on the individual mode i that precedes its parity measurement.

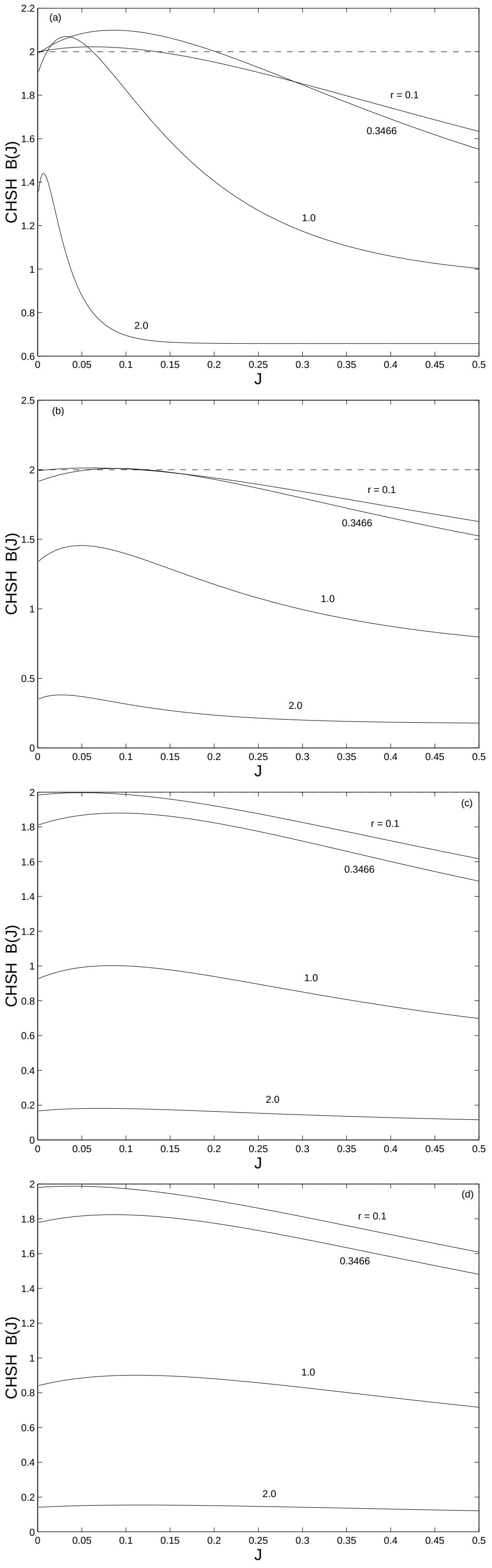

FIG. 2. The function $\mathcal{B}(\mathcal{J})$ from Eq. (41) as a function of $\mathcal{J}$ for various values of (r,η). Recall that $\mathcal{B} > 2$ heralds a direct violation of the CHSH inequality, with the dashed line $\mathcal{B} = 2$ shown. In each of the plots (a)-(d) a family of curves is drawn for fixed efficiency η and four values of $r = \{0.1, \frac{\ln 2}{2}, 1.0, 2.0\}$. (a) $\eta = 0.99$, (b) $\eta = 0.90$, (c) $\eta = 0.70$, (d) $\eta = 0.50$; in all cases, $\bar{n} = 0$.

The function constructed by Banaszek and Wodkiewicz to test for local hidden variable theories is denoted by $\mathcal{B}$ and is defined by

$$\begin{aligned}&\mathcal{B}(\mathcal{J}) \\ &= \Pi_{\mathrm{EPR}}^{out}(0,0;0,0) + \Pi_{\mathrm{EPR}}^{out}(\sqrt{\mathcal{J}},0;0,0) \\ &\quad + \Pi_{\mathrm{EPR}}^{out}(0,0;-\sqrt{\mathcal{J}},0) - \Pi_{\mathrm{EPR}}^{out}(\sqrt{\mathcal{J}},0;-\sqrt{\mathcal{J}},0)\ ,\end{aligned} \tag{41}$$

where $\mathcal{J}$ is a positive (real) constant. As shown in Ref. [18,19], any local theory must satisfy

$$-2 \leq \mathcal{B} \leq 2\ . \tag{42}$$

As emphasized by Banaszek and Wodkiewicz for the lossless case, $\Pi_{\mathrm{EPR}}^{out}(0,0;0,0) = 1$ "describes perfect correlations ... as a manifestation of ... photons always generated in pairs."

There are several important points to be made about this result. In the first place, in the ideal case with no loss ($\eta = 1$), there is a violation of the Bell inequality of Eq. (42) for any $r > 0$. Further, this threshold for the onset of violations of the CHSH inequality coincides with the threshold for entanglement as given in Eq. (28), which likewise is the point for surpassing $F_{classical} = \frac{1}{2}$ as in Eqs. (36,37) and as shown in our prior analysis of Ref. [6] which is notably based upon a quite different approach.

Significantly, there is absolutely nothing special about the point $r = \frac{\ln 2}{2} \approx 0.3466$ (i.e., the point for which $\exp[-2r] = 0.5$ and for which $F = \frac{2}{3}$ for the teleportation of coherent states), in contradistinction to the claims of Grangier and Grosshans to the contrary [11,12]. Instead, any $r > 0$ leads to a nonseparable EPR state, to a violation of a Bell inequality, and to $F > F_{classical} = \frac{1}{2}$ for the teleportation of coherent states. There is certainly no surprise here since we are dealing with pure states for $\eta = 1$ [42].

We next examine the case with $\eta < 1$, which is clearly of interest for any experiment. Figure 2 illustrates the behavior of $\mathcal{B}$ as a function of $\mathcal{J}$ for various values of the squeezing parameter r and of the efficiency η. Note that throughout our analysis in this section, we make no attempt to search for optimal violations, but instead follow dutifully the protocol of Banaszek and Wodkiewicz as expressed in Eq. (41) for the case with losses as well.

From Figure 2 we see that for any particular set of parameters (r, η), there is an optimum value $\mathcal{J}_{\max}$ that leads to a maximum value for $\mathcal{B}(\mathcal{J}_{\max})$, which is a situation analogous to that found in the discrete variable case. By determining the corresponding value $\mathcal{J}_{\max}$ at each (r, η), in Figure 3 we construct a plot that displays the dependence of $\mathcal{B}$ on the squeezing parameter r for various values of efficiency η. Note that all cases shown in the figure lead to fidelity $F > F_{classical}$.

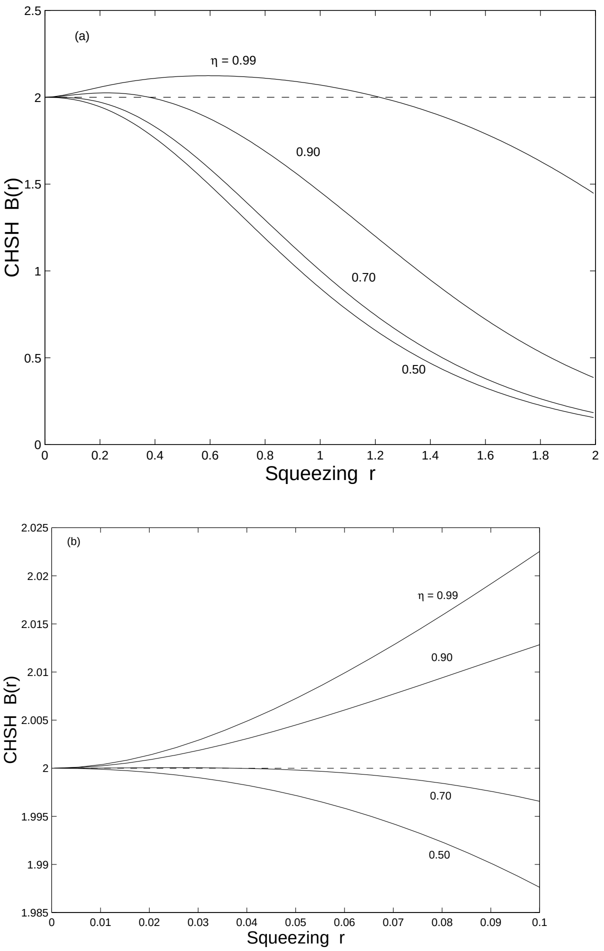

FIG. 3. (a) The quantity $\mathcal{B}$ from Eq. (41) as a function of r for various values of efficiency $\eta = \{0.99, 0.90, 0.70, 0.50\}$ as indicated. At each point in (r, η), the value of $\mathcal{J}$ that maximizes $\mathcal{B}$ has been chosen. Recall that $\mathcal{B} > 2$ heralds a direct violation of the CHSH inequality, with the dashed line $\mathcal{B} = 2$ shown. Also note that $F > \frac{1}{2}$ for all $r > 0$. (b) An expanded view of $\mathcal{B}$ in the small r region $r \leq 0.1$. Note that in the case $\eta = 0.70$, $\mathcal{B} > 2$ for small r. In all cases, $\bar{n} = 0$.

For $\frac{2}{3} < \eta \leq 1$ there are regions in r that produce direct violations of the Bell inequality considered here, namely $\mathcal{B} > 2$ [43]. In general, these domains with $\mathcal{B} > 2$ contract toward smaller r with increasing loss $(1-\eta)$. In fact as r increases, η must become very close to unity in order to preserve the condition $\mathcal{B} > 2$, where for $r \gg 1$,

$$2(1-\eta)\cosh(2r) \ll 1. \tag{43}$$

This requirement is presumably associated with the EPR state becoming more "nonclassical" with increasing r and hence more sensitive to dissipation [44]. Stated somewhat more quantitatively, recall that the original state $|EPR\rangle_{1,2}$ of Eq. (3) is expressed as a sum over correlated photon numbers for each of the two EPR beams $(1,2)$. The determination of $\mathcal{B}$ derives from (displaced) parity measurements on the beams $(1,2)$ (i.e., projections onto odd and even photon number), so that $\mathcal{B}$ should be sensitive to the loss of a single photon. The mean photon number $\bar{n}_i$ for either EPR beam goes as $\sinh^2 r$, with then the probability of losing no photons after encountering the beam-splitter with transmission η scaling as roughly $p_0 \sim [\eta]^{\bar{n}_i}$. We require that the total probability for the loss of one or more photons to be small, so that

$$(1 - p_0) \ll 1, \tag{44}$$

and hence for $(1-\eta) \ll 1$ and $r \gg 1$ that

$$(1-\eta)\bar{n}_i \sim (1-\eta)\exp(2r) \ll 1, \tag{45}$$

in correspondence to Eq. (43) [45].

On the other hand, note that small values of r in Figure 3 lead to direct violations of the CHSH inequality $\mathcal{B} > 2$ with much more modest efficiencies [44]. In particular, note that for $r = \frac{\ln 2}{2} \approx 0.3466$ and $\eta = 0.90$, $F < \frac{2}{3}$ [from Eq. (38)]. This case and others like it provide examples for which mixed states are nonseparable and yet directly violate a Bell inequality, but for which $F \leq \frac{2}{3}$. Such mixed states do not satisfy the criteria of Grangier and Grosshans (neither with respect to their Heisenberg-type inequality nor with respect to their information exchange), yet they are states for which $\frac{1}{2} < F \leq \frac{2}{3}$ and $\mathcal{B} > 2$, which in and of itself calls the claims of Grangier and Grosshans into question. There remains the possibility that $F > \frac{2}{3}$ might be sufficient to warranty that mixed states in this domain would satisfy that $\mathcal{B} > 2$, and hence to exclude a description of the EPR state in terms of a local hidden variables theory.

To demonstrate that this is emphatically not the case, we examine further the relationship between the quantity $\mathcal{B}$ relevant to the CHSH inequality and the fidelity F. Figure 4 shows a parametric plot of $\mathcal{B}$ versus F for various values of the efficiency η. The curves in this figure are obtained from plots as in Figures 1 and 3 by eliminating the common dependence on r. From Figure 4, we are hard pressed to find any indication that the value $F = \frac{2}{3}$ is in any fashion noteworthy with respect to violations of the CHSH inequality. In particular, for efficiency $\eta \simeq 0.90$ most relevant to current experimental capabilities, the domain $F > \frac{2}{3}$ is one largely devoid of instances with $\mathcal{B} > 2$, in contradistinction to the claim of Grangier and Grosshans that this domain is somehow "safer" [11] with respect to violations of Bell's inequalities. Moreover, contrary to their dismissal of the domain $\frac{1}{2} < F \leq \frac{2}{3}$ as not being manifestly quantum, we see from Figure 4 that there are in fact regions with $\mathcal{B} > 2$. Overall, the conclusions of Grangier and Grosshans [11] related to the issues of violation of a Bell inequality and of teleportation fidelity are simply not supported by an actual quantitative analysis.

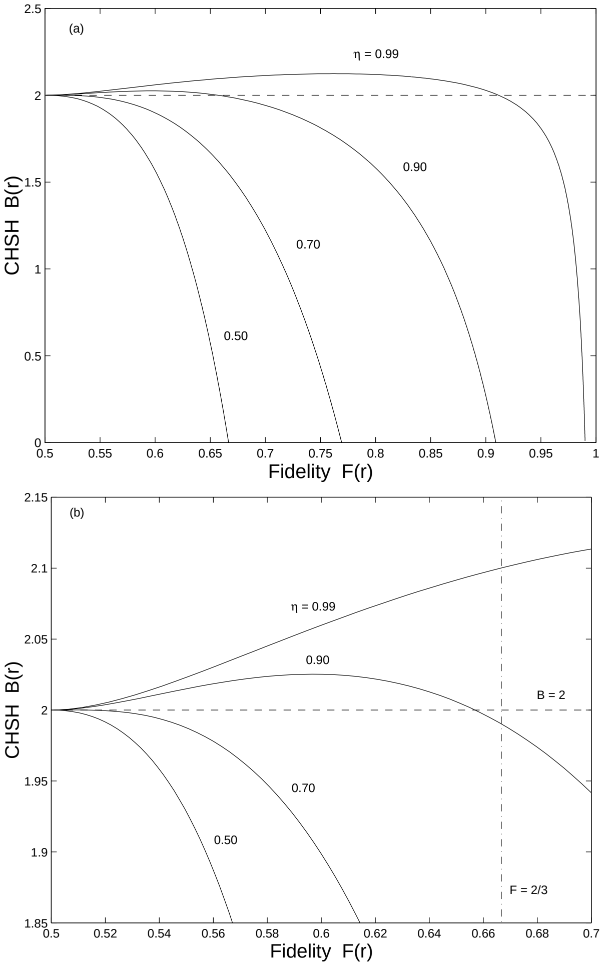

FIG. 4. (a) A parametric plot of the CHSH quantity $\mathcal{B}$ [Eq. (41)] versus fidelity F [Eq. (38)]. The curves are constructed from Figures 1 and 3 by eliminating the r dependence, now over the range $0 \leq r \leq 5$, with r increasing from left to right for each trace. The efficiency η takes on the values $\eta = \{0.99, 0.90, 0.70, 0.50\}$ as indicated; in all cases, $\bar{n} = 0$. Recall that $\mathcal{B} > 2$ heralds a direct violation of the CHSH inequality, with the dashed line $\mathcal{B} = 2$ shown. (b) An expanded view around $\mathcal{B} = 2$. Note that $\mathcal{B} > 2$ is impossible for $F \leq F_{classical} = \frac{1}{2}$, but that $\mathcal{B} > 2$ for $F > F_{classical}$ in various domains (including for $\eta = 0.70$ at small r). The purported boundary $F = \frac{2}{3}$ proposed by Grangier and Grosshans [11,12] is seen to have no particular significance. Contrary to their claims, $F = \frac{2}{3}$ provides absolutely no warranty that $\mathcal{B} > 2$ for $F > \frac{2}{3}$, nor does it preclude $\mathcal{B} > 2$ for $F < \frac{2}{3}$.

While the above results follow from the particular form of the CHSH inequality introduced by Banaszek and Wodkiewicz [18,19], we should note that another quite different path to a demonstration of the inadequacy of local realism for continous quantum varialbes has recently been proposed by Ralph, Munro, and Polkinghorne [46]. These authors consider a novel scheme involving measurements of quadrature-phase amplitudes for two entangled beams (A, B). These beams are formed by combining *two* EPR states (i.e., a total of four modes, two for each beam). Relevant to our discussion is that maximal violations of a CHSH inequality (i.e., $\mathcal{B} = 2\sqrt{2}$) are predicted for $r \ll 1$, with then a decreasing maximum value of $\mathcal{B}$ for increasing r. Once again, the threshold for onset of the violation of a Bell's inequality coincides with the threshold for entanglement of the relevant fields [i.e., Eq. (28)], with no apparent significance to the boundary set by the Heisenberg-type inequality Eq. (26) of Grangier and Grosshans.

To conclude this section, we would like to inject a note of caution concerning any discussion involving issues of testing Bell's inequalities and performing quantum teleportation. We have placed them in juxtaposition here to refute the claims of Grangier and Grosshans related to a possible connection between the bound $F = \frac{2}{3}$ and violation of Bell's inequalities (here, via the behavior of the CHSH quantity $\mathcal{B}$). However, in our view there is a conflict between these concepts, with an illustration of this point provided by the plot of the CHSH quantity $\mathcal{B}$ [Eq. (42)] versus fidelity F [Eq. (38)] in Figure 4. For example, for $\eta = 0.90$, $\mathcal{B} > 2$ over the range $0.50 < F \lesssim 0.66$, while $\mathcal{B} < 2$ for larger values of F. Hence, local hidden variables theories are excluded for modest values of fidelity $0.50 < F \lesssim 0.66$, but not for larger values $F \gtrsim 0.66$. This leads to the strange conclusion that quantum resources are required for smaller values of fidelity but not for larger ones. The point is that the nonseparable states that can enable quantum teleportation, can *in a different context* also be used to demonstrate a violation of local realism. Again, the juxtaposition of these concepts in this section is in response to the work of Ref. [11], which in any event offers no quantitative evidence in support of their association.

VI. BELL'S INEQUALITIES FOR SCALED CORRELATIONS

The conclusions reached in the preceding section about violations of the CHSH inequality by the EPR (mixed) state for modes $(1, 2)$ follow directly from the analysis of Banaszek and Wodkiewicz [18,19] as extended to account for losses in propagation. Towards the end of making these results more amenable to experimental investigation, recall that the more traditional versions of the Bell inequalities formulated for spin $\frac{1}{2}$ particles or photon polarizations are based upon an analysis of the expectation value

$$E(\vec{a}, \vec{b}) \tag{46}$$

for detection events at locations $(1, 2)$ with analyzer settings along directions $(\vec{a}, \vec{b})$. As emphasized by Clauser and Shimony, actual experiments do not measure directly $E(\vec{a}, \vec{b})$ but rather record a reduced version due to "imperfections in the analyzers, detectors, and state preparation [20]." Even after more than thirty years of experiments, no *direct* violation of the CHSH inequality has been recorded, where by *direct* we mean without the need for post-selection to compensate for propagation and detection efficiencies (also called *strong violations*) [22,23]. Rather, only subsets of events that give rise to coincidences are included for various polarization settings. This "problem" is the so-called detector efficiency loophole that several groups are actively working to close.

Motivated by these considerations, we point out that an observation of violation of a Bell-type inequality has recently been reported [24], based in large measure upon the earlier proposal of Ref. [47], as well as that of Refs. [18,19]. This experiment was carried out in a pulsed mode, and utilized a source that generates an EPR state of the form given by Eq. (11) in the limit $r \ll 1$. Here, the probability $P(\alpha_1, \alpha_2)$ of detecting a coincidence event between detectors (D_1, D_2) for the EPR beams $(1, 2)$ is given by

$$P(\alpha_1, \alpha_2) = M[1 + V \cos(\phi_1 - \phi_2 + \theta)], \tag{47}$$

with then the correlation function E relevant to the construction of a CHSH inequality $-2 \leq S \leq 2$ given by

$$E(\phi_1, \phi_2) = V \cos(\phi_1 - \phi_2 + \theta), \tag{48}$$

where the various quantities are as defined in association with Eqs. (2,3) in Ref. [24]. Note that the quantity M represents an overall scaling that incorporates losses in propagation and detection. Significantly, Kuzmich *et al.* demonstrated a violation of a CHSH inequality ($S_{\rm exp} = 2.46 \pm 0.06$) in the limit $r \ll 1$ and with inefficient propagation and detection $\eta \ll 1$, albeit with the so-called "detection" or "fair-sampling" loophole.

In terms of our current discussion, this experimental violation of a CHSH inequality is only just within the nonseparability domain $\Delta x^2 + \Delta p^2 < 1$ (by an amount that goes as $\eta r \ll 1$), yet it generates a large violation of a CHSH inequality. If this same EPR state were employed for the teleportation of coherent states, the fidelity obtained would likewise be only slightly beyond the quantum-classical boundary $F_{classical} = \frac{1}{2}$. It would be far from the boundary $F = \frac{2}{3}$ offered by Grangier and Grosshans as the point for "useful entanglement," yet it would nonetheless provide an example of teleportation with fidelity $F > \frac{1}{2}$ and of a violation of a CHSH inequality. Of course, the caveat would be the aforementioned "fair-sampling" loophole, but this same restriction accompanies all previous experimental demonstrations of violations of Bell's inequalities. Once again, we find no support for the purported significance of the criteria offered by Grangier and Grosshans [11,12].

VII. CONCLUSIONS

Beyond the initial analysis of Ref. [6], we have examined further the question of the appropriate point of demarcation between the classical and quantum domains for the teleportation of coherent states. In support of our previous result that fidelity $F_{classical} = \frac{1}{2}$ represents the bound attainable by Alice and Bob if they make use only of a classical channel, we have shown that the nonseparability criteria introduced in Refs. [14,15] are sufficient to ensure fidelity beyond this bound for teleportation with the EPR state of Eq. (11), which is in general a mixed state. Significantly, the threshold for entanglement for the EPR beams as quantified by these nonseparability criteria coincides with the standard boundary between classical and quantum domains employed in Quantum Optics, namely that the Glauber-Sudarshan phase-space function becomes non-positive definite [17].

Furthermore, we have investigated possible violations of Bell's inequalities and have shown that the threshold for the onset of such violations again corresponds to $F_{classical} = \frac{1}{2}$. For thermal photon number $\bar{n} = 0$ as appropriate to current experiments, direct violations of a CHSH inequality are obtained over a large domain in the degree of squeezing r and overall efficiency η. Significant relative to the claims of Grangier and Grosshans [11,12] is that there is a regime for nonseparability and violation of the CHSH inequality for which $F < \frac{2}{3}$ and for which their Heisenberg inequalities are not satisfied. Moreover, the experiment of Ref. [24] has demonstrated a violation of the CHSH inequality in this domain for $(r, \eta) \ll 1$ (i.e., F would be only slightly beyond $\frac{1}{2}$), albeit with the caveat of the "fair-sampling" loophole. We conclude that fidelity $F > \frac{2}{3}$ offers absolutely no warranty or "safety" relative to the issue of violation of a Bell inequality (as might be desirable, for example, in quantum cryptography), in direct disagreement with the assertions by Grangier and Grosshans. Quite the contrary, larger r (and hence larger F) leads to an exponentially decreasing domain in allowed loss $(1 - \eta)$ for violation of the CHSH inequality, as expressed by Eq. (43) [45].

Moreover, beyond the analysis that we have presented here, there are several other results that support $F_{classical} = \frac{1}{2}$ as being the appropriate boundary between quantum and classical domains. In particular, we note that any nonseparable state and hence also our mixed EPR state is always capable of teleporting perfect entanglement, i.e., one half of a pure maximally entangled state. This applies also to those nonseparable states which lead to fidelities $\frac{1}{2} < F \leq \frac{2}{3}$ in coherent-state teleportation. According to Refs. [11,12], this would force the conclusion that there is entanglement that is capable of teleporting truly nonclassical features (i.e., entanglement), but which is not "useful" for teleporting rather more classical states such as coherent states. Further, in Ref. [48] it has been shown that entanglement swapping can be achieved with two pure EPR states for *any nonzero squeezing* in both initial states. Neither of the initial states has to exceed a certain amount of squeezing in order to enable successful entanglement swapping. This is another indication that $F = \frac{2}{3}$, which is exceedable in coherent-state teleportation only with more than 3 dB squeezing, is of no particular significance.

We also point out that Giedke et al. have shown that for all bipartite Gaussian states, nonseparability implies distillability [49,50]. This result applies to those nonseparable states for which $\frac{1}{2} < F \leq \frac{2}{3}$ in coherent state teleportation, which are otherwise dismissed by Grangier and Grosshans as not "useful." To the contrary, entanglement distillation could be applied to the mixed EPR states employed for teleportation in this domain (and in general for $F > \frac{1}{2}$) [51], leading to enhanced teleportation fidelities and to expanded regions for violations of Bell's inequalities for the distilled subensemble.

By contrast, there appears to be no support for the claims of Grangier and Grosshans [11,12] that their so-called Heisenberg inequality and information exchange are somehow "special" with respect to the issues of separability and violations of Bell's inequalities. They have neither found fault in the prior analysis of Ref. [6], nor with the application of the work on nonseparability [14–16] to the current problem. They have likewise provided no analysis that directly supports their assertion that their Heisenberg inequality is in any way significant to the possibility that "the behavior of the *observed* quantities can be mimicked by a *classical* and *local* model." [11] Rather, they attempt to set aside by *fiat* a substantial body of evidence in favor of the boundary $F_{classical} = \frac{1}{2}$ for the teleportation of coherent states with a lack of rigor indicated by their claim that "$F = \frac{2}{3}$ would be much safer." [11]

However, having said this, we emphasize that there is no criterion for quantum teleportation that is sufficient to all tasks. For the special case of teleportation of coherent states, the boundary between classical and quantum teleportation is fidelity $F_{classical} = \frac{1}{2}$, as should by now be firmly established. Fidelity $F > \frac{2}{3}$ will indeed enable certain tasks to be accomplished that could not otherwise be done with $\frac{1}{2} < F \leq \frac{2}{3}$. However, $F = \frac{2}{3}$ is in no sense an important point of demarcation for entrance into the quantum domain. There is instead a hierarchy of fidelity thresholds that enable ever more remarkable tasks to be accomplished via teleportation within the quantum domain, with no one value being sufficient for all possible purposes. For example, if the state to be teleported were some intermediate result from a large-scale quantum computation as for Shor's algorithm, then surely the relevant fidelity threshold would be well beyond any value currently accessible to experiment, $F \sim 1 - \epsilon$, with $\epsilon \lesssim 10^{-4}$ to be compatible with current work in fault tolerant architectures. We have never claimed that $F = \frac{1}{2}$

endows special powers for all tasks such as these, only that it provides an unambiguous point of entry into the quantum realm for the teleportation of coherent states.

HJK gratefully acknowledges critical input from A. C. Doherty, H. Mabuchi, E. S. Polzik, and J. P. Preskill, and support from the NSF (Grant No. PHY-9722674), the Institute for Quantum Information (IQI) funded by the NSF-ITR Program, and the ONR. SLB and PvL are funded in part under project QUICOV as part of the IST-FET-QJPC programme. PvL acknowledges support by a DAAD Doktorandenstipendium (HSP III)

---

[1] C. H. Bennett, G. Brassard, C. Crépeau, R. Jozsa, A. Peres, and W. K. Wootters, Phys. Rev. Lett. **70**, 1895 (1993).

[2] D. Bouwmeester, J.-W. Pan, K. Mattle, M. Eibl, H. Weinfurter, and A. Zeilinger, Nature **390**, 575–579 (1997).

[3] D. Boschi, S. Branca, F. De Martini, L. Hardy, and S. Popescu, Phys. Rev. Lett. **80**, 1121–1125 (1998).

[4] A. Furusawa, J. L. Sørensen, S. L. Braunstein, C. A. Fuchs, H. J. Kimble, and E. S. Polzik, Science **282**, 706 (1998).

[5] M. A. Nielsen, E. Knill, and R. Laflamme, Nature **396**, 52 (1998).

[6] S. L. Braunstein, C. A. Fuchs, and H. J. Kimble, J. Mod. Opt. **47**, 267 (2000).

[7] B. Schumacher, Phys. Rev. A **51**, 2738 (1995).

[8] S. L. Braunstein and H. J. Kimble, Nature **394**, 840–841 (1998).

[9] S. L. Braunstein, C. M. Caves, R. Jozsa, N. Linden, S. Popescu, and R. Schack, Phys. Rev. Lett. **83**, 1054 (1999).

[10] The fidelity F as defined in Eq. (1) is for teleportation of some particular state $|\psi_{in}\rangle$. However, as we have emphasized in Ref. [6], useful criteria for achieving teleportation are anchored in a set S of states $\{|\psi_{in}\rangle\}$ and a distribution over these states $P(|\psi_{in}\rangle)$. Teleportation of an *unknown* state then proceeds by Victor drawing a state $|\psi_{in}\rangle$ from S with probability $P(|\psi_{in}\rangle)$. Alice and Bob are privy to S and to $P(|\psi_{in}\rangle)$, but not to the particular state selected and sent by Victor in each trial. In this general case, an average fidelity $\bar{F}$ over the distribution P becomes the benchmark for gauging success of the teleportation protocol.

[11] P. Grangier and F. Grosshans, `quant-ph/0009079`.

[12] P. Grangier and F. Grosshans, `quant-ph/0010107`. Note that there are both an original and revised versions of this preprint.

[13] S. L. Braunstein and H. J. Kimble, Phys. Rev. Lett. **80**, 869–872 (1998).

[14] L.-M. Duan, G. Giedke, J. I. Cirac, and P. Zoller, Phys. Rev. Lett. **84**, 2722 (2000).

[15] R. Simon, Phys. Rev. Lett. **84**, 2726 (2000).

[16] S. M. Tan, Phys. Rev. **60**, 2752 (1999).

[17] This result can be found in Ref. [15]. Note that it in the context of the current discussion, it applies to *multimode* fields.

[18] K. Banaszek and K. Wodkiewicz, Phys. Rev. A **58**, 4345 (1998).

[19] K. Banaszek and K. Wodkiewicz, Phys. Rev. Lett. **82**, 2009 (1999).

[20] J. F. Clauser and A. Shimony, Rep. Prog. Phys. **41**, 1881 (1978).

[21] M. O. Scully and A. S. Zubairy, *Quantum Optics* (Cambridge University Press, Cambridge, UK, 1997), Chapter 18.

[22] P. G. Kwiat, P. H. Eberhard,A. M. Steinberg, and R. Y. Chiao, Phys. Rev. A **49**, 3209 (1994).

[23] E. S. Fry, T. Walther, and S. Li, Phys. Rev. A **52**, 4381 (1995).

[24] A. Kuzmich, I. A. Walmsley, and L. Mandel, Phys. Rev. Lett. **85**, 1349 (2000).

[25] A. Einstein, B. Podolsky and N. Rosen, Phys. Rev. **47**, 777 (1935).

[26] Z. Y. Ou, S. F. Pereira, H. J. Kimble, K. C. Peng, Phys. Rev. Lett. **68**, 3663(1992); Z. Y. Ou, S. F. Pereira, H. J. Kimble, Appl. Phys. B **55**, 265 (1992).

[27] M. Reid, Phys. Rev. A **40**, 913 (1989).

[28] P. Grangier, J. A. Levenson, and J.-P. Poziat, Nature **396**, 537 (1998).

[29] C. M. Caves, private communication.

[30] K. Wodkiewicz, private communication.

[31] D. F. Walls and G. J. Milburn, *Quantum Optics* (Springer Verlag, Berlin, 1994), Eq. (5.64).

[32] S. J. van Enk, Phys. Rev. **A60**, 5095 (1999).

[33] P. van Loock, S. L. Braunstein, and H. J. Kimble, Phys. Rev. A **62**, 022309 (2000).

[34] E. Arthurs and J. L. Kelly, Jr., Bell Syst. Tech. J. **44**, 725–729 (1965).

[35] Note that the violation of the inequality $\Delta x^2 + \Delta p^2 \geq 1$ of Refs. [14,15] implies the violation of the product inequality $\Delta x^2 \Delta p^2 \geq 1/4$ of Ref. [16], but *not vice versa*.

[36] For the experiment of Ref. [4], the measured variances were $\Delta x^2 \approx (0.8 \times \frac{1}{2}) \approx \Delta p^2$, so that $\Delta x^2 + \Delta p^2 \approx 0.8 < 1$.

[37] P. Grangier, private communication.

[38] Eq. (35) is written in the notation of the current paper. It follows from Eq. (2) of Ref. [4] for the case gain $g = 1$, Alice's detection efficiency $\eta_A^2 = 1$ (denoted η^2 in [4]), and with the replacement of efficiencies $(\xi_1^2 = \xi_2^2)$ from [4] $\rightarrow \eta$ here.

[39] The expressions of Eqs. (32-35) are strictly applicable only for the case gain $g = 1$ for teleportation of coherent states uniformly distributed over the entire complex plane. More generally, when working with a restricted alphabet of states (e.g., coherent amplitudes selected from a Gaussian distribution), the optimal gain is not unity when referenced to the fidelity averaged over the input alphabet. In fact as shown in Ref. [6], the optimal gain is $g = 1/(1 + \lambda)$ for an input alphabet of coherent states distributed according to $p(\beta) = (\lambda/\pi)exp(-\lambda|\beta|^2)$. When incorporated into the current analysis, we find that nonseparable EPR states are sufficient to achieve $F > (1 + \lambda)/(2 + \lambda)$ (again with optimal gain $g \neq 1$) although F is no longer a monotonic function of r as

in Figure 1. This result is in complete correspondence with our prior result that $F_{classical} = (1+\lambda)/(2+\lambda)$ is the bound for teleportation when only a classical channel is employed. To simplify the discussion, here we set $\lambda = 0$ throughout, with then the optimal gain $g = 1$ and $F_{classical} = \frac{1}{2}$.

[40] Note that for the noisy EPR states considered here with Gaussian statistics, Eqs. (36) and (37) are both necessary and sufficient conditions. However, this is not generally the case for states with Gaussian statistics; there are in fact nonseparable Gaussian states for which Eq. (28) is not true. Close examination of Ref. [14] shows that their results concerning necessary and sufficient conditions for states with Gaussian statistics apply only to Gaussian states in a particular standard form. Explicit counter examples can be constructed from Ref. [41].

[41] P. van Loock and S. L. Braunstein, Phys. Rev. Lett. **84**, 3482 (2000). Fig. 1 demonstrates nonseparable bipartite Gaussian states which nonetheless do not achieve $F > 1/2$. For example, if the *Gaussian* states in this paper are used for coherent-state teleportation, they yield an optimum fidelity $F_{\text{opt}} = \left\{1 + e^{-2r}\right\}^{-1/2} \times \left\{1 + N/[2e^{+2r} + (N-2)e^{-2r}]\right\}^{-1/2}$. For any $r > 0$, $F_{\text{opt}} > \frac{1}{2}$, *only provided* $N \leq 29$. In fact, if the excess noise due to the teleportation process is extracted according to $F = 1/(2\sqrt{\sigma_x \sigma_p})$ with σ_x and σ_p being the Q-function variances of the teleported mode, one finds that the inequality $\Delta x^2 + \Delta p^2 < 1$ of Refs. [14] is satisfied for any $r > 0$ only if $N \leq 17$, but that the product inequality $\Delta x^2 \Delta p^2 < 1/4$ of Ref. [16] is satisfied for any $r > 0$ and any N. Significantly, this demonstrates that not all sufficient criteria are identical to each other. Note that in this example the excess noises in x and p are not equal, which makes these criteria differ from each other. Of course, the necessary nonseparability criteria of Refs. [14,15] would give identical results, revealing the nonseparability in the above example for any $r > 0$ and any N.

[42] N. Gisin and A. Peres, Phys. Lett. A **162**, 15 (1992).

[43] The value $\eta = \frac{2}{3}$ is significant in that $\mathcal{B} > 2$ is not possible for efficiency $\eta \leq \frac{2}{3}$. This same threshold efficiency was also found by P. H. Eberhard, Phys. Rev. A **47**, R747 (1993) in a somewhat different context .

[44] H. Jeong, J. Lee, and M. S. Kim, Phys. Rev. A **61**, 052101 (2000); `quant-ph/0003077`. These authors provide the analytical solution of the master equation for the two-mode squeezed state of Eq. (3) in contact with a thermal reservoir. Their conclusions based upon this dynamical model are in complete accord with ours that follow from the conceptually more straightforward beamsplitter model of Eq. (10).

[45] We stress that these conclusions relate to the particular measurement strategy proposed in Refs. [18,19], which certainly might be expected not to be optimal in the presence of loss. It is quite possible that for fixed η as r grows, there could be larger domains and magnitudes for violation of the CHSH inequality if a different set of observables were chosen, including general POVMs.

[46] T. C. Ralph, W. J. Munro, and R. E. S. Polkinghorne, Phys. Rev. Lett. **85**, 2035 (2000).

[47] P. Grangier, M. J. Potasek, and B. Yurke, Phys. Rev. A **38**, R3132 (1988).

[48] P. van Loock and S. L. Braunstein, Phys. Rev. A **61**, 10302(R) (2000).

[49] G. Giedke, L-M. Duan, J. I. Cirac, and P. Zoller, `quant-ph/0007061`.

[50] R. F. Werner and M. M. Wolf, `quant-ph/0009118`.

[51] L.-M. Duan, G. Giedke, J. I. Cirac, and P. Zoller, Phys. Rev. Lett. **84**, 4002 (2000) and Phys. Rev. A **62**, 032304 (2000).

arXiv:quant-ph/0101103 v1 22 Jan 2001

Characterization of high finesse mirrors: loss, phase shifts and mode structure in an optical cavity

Christina J. Hood and H. J. Kimble
Norman Bridge Laboratory of Physics 12-33, California Institute of Technology, Pasadena, CA 91125

Jun Ye
JILA, National Institute of Standards and Technology and University of Colorado, Boulder, CO 80309

(Dated: May 27, 2006)

An extensive characterization of high finesse optical cavities used in cavity QED experiments is described. Different techniques in the measurement of the loss and phase shifts associated with the mirror coatings are discussed and their agreement shown. Issues of cavity field mode structure supported by the dielectric coatings are related to our effort to achieve the strongest possible coupling between an atom and the cavity.

I. INTRODUCTION

For many contemporary physics experiments, measurement enhancement via an optical cavity is a useful tool. Indeed, an optical cavity allows one to extend the interaction length between matter and field, to build up the optical power, to maintain a well-defined mode structure, and to study the extreme nonlinear optics and quantum mechanics associated with the large field of a single photon for small cavity volumes [1]. In most situations, a better understanding of cavity and mirror properties is important for achieving improved sensitivity and for elimination of systematic errors. For example, in cavity QED, one needs to know the mode structure of the intracavity field in order to develop the optimum strategy of atom-cavity coupling; for frequency metrology, accurate determination of phase shifts of the resonant fields can provide precision frequency markers; and in quantitative spectroscopy, knowledge of the mirror loss sets the accuracy scale of absorption measurement. On the technology development side, the knowledge gained from careful mirror characterization could provide guidelines for the optic coating community to develop in situ measurement and control capabilities of the coating process.

The work presented in this paper is motivated by the ever-increasing demand for a high coherent coupling rate between an atom and the field, as well as of a decreasing cavity loss rate. The aim is to have coherent (reversible) evolution dominating over dissipative processes, and thereby to explore manifestly quantum dynamics in real time, which in turn should lead eventually to the investigation of the strong conditioning of system evolution on measurement results and the realization of quantum feedback control. An important feature associated with strong coupling is that system dynamics are readily influenced by single quanta. Thus single-atom and single-photon cavity QED provides an ideal stage where the dynamical processes of individual quantum systems can be isolated and manipulated. A collection of such coherent systems could help to realize a distributed quantum networks for computation and communication [2]. At each node the quantum information is stored by one or a collection of entangled atoms. Photons serve as the communication link which in turn entangle the whole network. Within this context, technical advances in optical cavity quantum electrodynamics have become increasingly important. Some significant developments down this road have been achieved by the group at Caltech [3, 4, 5, 6, 7, 8], where in Ref. [8] the one-photon Rabi frequency is $\Omega_1/2\pi = 220$MHz, in comparison with the atomic decay rate $\gamma_\perp = 2.6$MHz and the cavity decay rate $\kappa/2\pi = 14.2$MHz.

The strong coupling condition $\Omega_1 \gg (\gamma_\perp, \kappa)$ is achieved by using a small cavity length, of the order of 10μm. Precise measurement of the length of a short optical cavity facilitates the determination of mirror coating characteristics. A 10μm cavity length translates to a free-spectral-range (FSR) of 15 THz, or a wavelength difference of a few tens of nanometers (for example, it is 36 nm for a center wavelength of 852 nm) for neighboring cavity modes. Therefore a straightforward 6-digit measurement of the wavelengths (Burleigh wavemeter) of the cavity modes acquires a precision of the order of 5 x 10^{-5} for accurate determination of the equivalent optical length of the cavity, from which details of the index of refraction and layer thickness of materials in the mirror stack can be inferred.

The low loss rate of the cavity field is made possible by high quality mirror coatings that lead to scatter and absorption losses in the 10^{-6} range [9, 10]. The cavity finesse and overall cavity transmission can be measured directly to determine the mirror losses, l, and transmission, T. This information can be combined with the FSR measurement in two useful ways: Firstly, the FSR measurement is sensitive to the difference in refractive index $n_H - n_L$ of the materials making up the multilayer mirror stack, whereas the transmission T depends on the ratio n_H/n_L, as will be shown later. As a result, a precise measurement of both the FSR and T can be used to determine the values of n_H and n_L independently. Moreover, by mapping out the wavelength dependence of the FSR, the thickness of layers in the mirror stack can be determined. Secondly, if one of the refractive indices (here n_L) is well known, then the FSR measurement determines n_H, and an independent value for the mirror transmission T can then be calculated from n_H and n_L, and compared to the experimentally measured result. Indeed, the work presented in this paper shows that we are able to make complementary and mutually-confirming measurements of the cavity properties by the two approaches, i.e., measurements of the direct cavity loss and the dispersion of the cavity modes.

Coming back to the cavity QED experiments, we note that knowledge of the cavity properties is of importance in two particular ways: 1. Mirror absorption/scatter losses are a critical limiting factor in the loss rate from our cavity QED system - for our current cavities the loss rate from photon scattering due to mirror imperfections is similar in size to the atomic spontaneous emission rate. To build robust quantum computing/communications devices from cavity QED components, it is necessary to improve the ratio of mirror transmission to mirror losses. 2. The standing-wave light field inside the cavity penetrates into the mirror coatings, giving a larger mode-volume V_{mode} than would be expected naively from the physical distance between the mirror surfaces. Since $\Omega_1 \propto 1/\sqrt{V_{\mathrm{mode}}}$, as our micro-cavities are pushed to shorter lengths, this leakage field will have a non-negligible effect on the achievable coupling strength $g_0 = \Omega_1/2$.

II. DIRECT TRANSMISSION AND LOSS MEASUREMENTS

All of the mirrors described in this paper were fabricated by Research Electro-Optics in Boulder, Colorado[10]. More specifically, the measurements were made for the particular coating run REO #T95 and involved mirrors with radius of curvature R = 10 and 20 cm. The coating run had a design transmission of Tth=7ppm at a center wavelength of 852nm, from which a cavity finesse of $\mathcal{F}$=370,000 was expected. It was somewhat surprising therefore to measure a finesse of $\mathcal{F}$=480,000 at the targeted wavelength, and this prompted us to make more detailed measurements of the mirror properties, and design a model to match these measurements.

Firstly, losses were measured directly with a $40\mu m$ length cavity of 20cm radius of curvature mirrors in the usual way by recording resonant cavity transmission, reflection and finesse. If we denote the transmission of mirrors 1 and 2 by T_1 and T_2, respectively, and the (absorption + scatter) loss per mirror as $l_i = (A+S)_i$, then the total cavity losses $\mathcal{L} = T_1+T_2+l_1+l_2$ can be determined from the cavity finesse $\mathcal{F} = FSR/2\kappa$, with FSR as the cavity free spectral range and κ as the HWHM for the TEM$_{00}$ mode of the cavity; equivalently, $\mathcal{F} = 2\pi/\mathcal{L}$. The cavity linewidth $\beta = 2\kappa$ can be determined from a ring-down measurement or using a modulation sideband as a frequency marker with the cavity length scanned, which is the technique employed here. The cavity transmission $I_{trans} = \frac{4T_1T_2}{(T_1+T_2+l_1+l_2)^2}$ can then be used to determine l_1+l_2, if T_1 and T_2 are known independently. In practice this is a difficult measurement to make, because the overall transmission I_{trans} depends on the mode-matching into the cavity being perfect. A variation of this protocol that does not require perfect mode-matching can be derived, by comparing the cavity reflection and transmission values with the cavity locked on resonance and off resonance.

The rudiments of this protocol are as follows. First of all, the total loss ($\mathcal{L} = T_1 + T_2 + l_1 + l_2$) is always measured first with the determination of the cavity FSR and linewidth. Now let us denote the input power as P_{in}, the reflected power P_r , and the transmitted power P_t. There is also a mode matching factor ϵ, meaning that of the input power of P_{in}, only ϵP_{in} is useful for coupling to the cavity TEM$_{00}$ mode, $(1-\epsilon)P_{in}$ is wasted. We have the following equations (the assumption of two equal mirrors is reasonable since the two mirrors are produced in the same coating run)

$$\mathcal{F} = \frac{2\pi}{T_1+T_2+l_1+l_2} = \frac{\pi}{l+T} \tag{1}$$

$$\frac{P_t}{\epsilon P_{in}} = 4T_1T_2(\frac{\mathcal{F}}{2\pi})^2 = T^2(\frac{\mathcal{F}}{\pi})^2 \tag{2}$$

$$\frac{P_r-(1-\epsilon)P_{in}}{\epsilon P_{in}} = (l_1+l_2+T_1-T_2)^2(\frac{\mathcal{F}}{2\pi})^2 = l^2(\frac{\mathcal{F}}{\pi})^2 \tag{3}$$

Remember that $(1-\epsilon)P_{in}$ is the "useless" power that is reflected directly off of the input mirror, and must be subtracted from P_r to leave the reflected power we wish to measure, that is, the sum of the field leaked from the cavity storage and the field (mode-matched) directly reflected off the input mirror. This cavity contrast is a direct result of the mirror properties. Division of equation 2 by 3 gives

$$\frac{P_t}{P_r-P_{in}} = \frac{T^2(\frac{\mathcal{F}}{\pi})^2}{l^2(\frac{\mathcal{F}}{\pi})^2-1} \tag{4}$$

Equation 4, combined with 1, will determine completely T and l .

In the actual experiment, this direct measurement approach found that (from finesse we have $l+T = 7.2ppm$) $P_{in} = 54\mu W$, $P_r = 42.6\mu W$ and $P_t = 4.82\mu W$ and therefore $l = 2.9ppm$ and $T = 4.3ppm$, with measurement uncertainties below 5%.

Another way to measure the (T, l) is by sweeping out all the high order spatial modes and carefully noting the transmission and reflection powers at each spatial mode. One measures the total input power and also sums together the powers of every matched mode for transmission and reflection. These three powers can be used in

Eq. 2 and 3 to calculate the partition between T and l. That measurement produced $l = 3ppm$, and $T = 4.2ppm$. The value of T should be a bit lower in this case because it is not possible to include all higher order modes in the measurement, some of them are simply impossible to resolve due to their weakness.

Other cavities measured with mirrors from the same coating run had higher finesse, very likely due to a lower density of surface defects. To construct a cavity of minimal mode volume for the intended maximal coherent coupling rate, we need to have the distance between two mirrors (radius of curvature $R = 10cm$) on the order of $10\mu m$ or below. To avoid contact between the outer edges of the two mirrors, the mirrors were fabricated with cone-shaped fronts, reducing the substrate radius from 3 mm to 1 mm. We notice this extra machine process might have introduced some additional surface defects on some mirrors. However, the highest finesse achieved with cone-shaped mirrors was comparable to unmodified pieces, at $\mathcal{F}$=480,000±10,000, corresponding to losses $l = 2.2ppm$ if mirror transmission $T = 4.3ppm$ as determined from the above measurements.

III. TECHNICAL DETAILS OF THE MODEL

In this section we derive a model for the coating properties. A transfer-matrix formalism was used to calculate the input-output propagation of a plane-wave field through the 37 layer stack of alternating high index (Ta_20_5, n_H=2.0411) and low index (SiO_2, n_L=1.455) dielectric layers (these dielectric constants are assumed to be constant with wavelength). The substrate refractive index (supplied by REO) used was n_{sub} =1.5098. That is, the transfer of the field through each $\lambda/4$ layer is represented by a matrix, and the response of the entire mirror (or cavity) is determined by the product of these individual matrices.

Following the treatment of Hecht [11] for normal incidence, we take the matrix representing layer j to be given by $\mathrm{M}_j = \begin{bmatrix} \cos(kh_j) & (i\sin(kh_j))/Y_j \\ iY_j\sin(kh_j) & \cos(kh_j) \end{bmatrix}$. Here M_j relates the electric and magnetic fields (E, H) of the input and output via

$$\begin{bmatrix} E_{out} \\ H_{out} \end{bmatrix} = [M] \begin{bmatrix} E_{in} \\ H_{in} \end{bmatrix}. \tag{5}$$

$k = 2\pi/\lambda$ is the free-space wavevector of the incident light, $h_j = n_j$ x (layer thickness) with n_j the refractive index, and $Y_j = \sqrt{\frac{\epsilon_0}{\mu_0}} n_j$ with (ϵ_0, μ_0) the electric and magnetic constants in SI units. For an exact $\lambda/4$ layer (and for light at the design wavelength of the coating), this simplifies to $\mathrm{M}_j = \begin{bmatrix} 0 & i/Y_j \\ iY_j & 0 \end{bmatrix}$. A multilayer stack is represented by multiplying the matrices of the individual layers: For light incident on layer 1, the matrix for the entire structure of q layers is defined as the product $M = M_1 M_2 ... M_q$. For our mirror stack, this gives $M = (M_{Ta_2O_5} M_{SiO_2})^{18} M_{Ta_2O_5}$. Note that at the coating center (where there is an exact $\lambda/4$ layer), $M_{Ta_2O_5} M_{SiO_2} = \begin{bmatrix} -\frac{n_L}{n_H} & 0 \\ 0 & -\frac{n_H}{n_L} \end{bmatrix}$, so the system matrix has the simple form $M = \begin{bmatrix} 0 & \frac{i}{Y_H}(\frac{n_L}{n_H})^{18} \\ iY_H(\frac{n_H}{n_L})^{18} & 0 \end{bmatrix}$.

For a field incident from material with index n_0 and exiting into material with index n_s, the resulting transmission coefficient is given by

$$t = 2Y_0/(Y_0 M_{11} + Y_0 Y_S M_{12} + M_{21} + Y_S M_{22}), \tag{6}$$

with transmission $T = \frac{n_s}{n_0}|t|^2$ (the factor $\frac{n_s}{n_0}$ accounts for the change in the amplitude of the electric field in the dielectric, thereby conserving the net energy flux). At the center wavelength of the coating then,

$$T = \frac{n_s}{n_0}|-2i/[(n_S/n_H)(n_L/n_H)^{18} + (n_H/n_0)(n_H/n_L)^{18}]|^2. \tag{7}$$

We can make a further simplification: as $(n_L/n_H)^{18} = 0.0018$ and $(n_H/n_L)^{18}$ =557, the first term in the denominator of the above equation is only a 10^{-6} correction, so the final result for T at the coating center becomes

$$T = 4n_S n_0 (n_L)^{36}/(n_H)^{38}, \tag{8}$$

and the transmission is determined by the *ratio* of the refractive indices.

This calculation reproduced the target reflectivity of Tth=7.3ppm for the coating run #T95, and T^{th}=14.6ppm for another REO coating run #D1306 where the number of layers was reduced to 35. The model and measured (REO spectrophotometer data) "coating curves" are shown in Fig. 1 for the #D1306 coating run.

For a fixed cavity length the resonance wavelengths of the cavity can be calculated simply with the same transfer-matrix formalism, using a matrix for the entire system, $M_{total} = M M_{gap} M$, (a product of two mirrors plus a fixed-length vacuum gap in between). The calculation steps through a series of wavelengths calculating the cavity transmission T at each, and by finding places of maximum transmission finds the vacuum wavelengths of the cavity resonances.

Conversely, for a given set of measured cavity-resonance wavelengths, it is possible to determine the effective cavity length precisely. With a commercial wavelength-meter that gives 6-digit wavelength measurement, we typically measure the cavity resonance within an uncertainty of 0.01 nm. Error propagation analysis gives an uncertainty for the determination of the effective cavity length (tens of microns) on the order of $0.05 - 0.1$ nm. The parameters of the model (index contrast, layer thickness) are set by comparison to such measurements. Hence, armed with the detailed knowledge of the mirrors provided from the model, the physical cavity length can be determined precisely from a single measurement of resonance, for example, when the cavity is locked to a laser of known frequency (in our case a cesium transition at 852.359nm). Close to the center of the design wavelength of the coating, the effective cavity length (on resonance) is roughly $L_{eff} = L + 1.633\lambda/2$ with L (the physical distance between the mirror surfaces) an integer number of $\lambda/2$. The physical cavity length can therefore be determined, with an uncertainty of ~ 0.5 nm, limited by the overall parameter-fitting in the model. Further details of the wavelength-dependence are provided by reference to the model.

IV. FREE-SPECTRAL RANGE (FSR) MEASUREMENTS

To determine the parameters of the model (index contrast, layer thickness), a series of precise measurements of the cavity FSR (frequency between successive cavity resonances) was made[12, 13, 14]. At fixed cavity length a Ti-Sapphire laser was tuned to find successive resonant wavelengths (λ_1, λ_2) of the cavity, and an experimentally determined length was then defined by $L_{expt} = \lambda_1\lambda_2/2(\lambda_1 - \lambda_2)$.

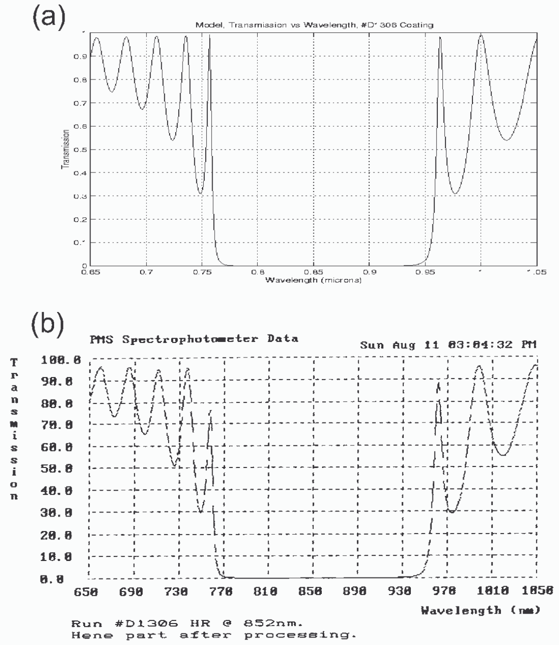

FIG. 1: (a) Calculated and (b) Measured transmission of coating as a function of wavelength, for a 35 layer $\lambda/4$ stack with n_H=2.0411, n_L=1.455, and center wavelength 850nm.

This length comprises the actual physical length between the two mirror surfaces, L, plus a contribution from leakage of the mode into the mirror stack, which gives rise to an additional phase shift at the coatings, to give a length $L_{eff} > L$. In addition, the leakage into the coatings increases with wavelength as (λ_1, λ_2) move away from the coating design wavelength, so this gives another additional contribution to the round-trip phase and hence to the measured length L_{expt}.

As discussed in Ref. [12], if λ_1 and λ_2 were closely spaced compared to the scale on which the coating properties vary (so that coating dispersion could be neglected) then near the design wavelength of the coating, we would have $L_{expt} = L_{eff} = L + (\frac{1}{n_H - n_L}) \times \lambda_c/2$ where n_H and n_L are the high and low index materials of the stack, and $\lambda_c = 2\lambda_1\lambda_2/(\lambda_1 + \lambda_2)$ is the average (in frequency) of wavelengths λ_1 and λ_2. We thereby have a dependence of the free spectral range on $(\frac{1}{n_H - n_L})$, which combined with the transmission (which depends on n_L/n_H) can fix n_H and n_L. For these materials, this gives $L_{eff} = L + 1.633\lambda_c/2$. However, for our measurements with short cavities, λ_1 and λ_2 are separated by $\simeq$30nm, so $L_{expt} > L_{eff}$. But we can still use the complete model to fit to the measured values (λ_1, λ_2) and determine parameters of the coating. Finally, by mapping out this wavelength dependence of the free-spectral range to find $min(L_{expt})$, we find the center wavelength of the coating.

In the model, the refractive indices used are adjusted to obtain the same pairs (λ_1, λ_2) as measured. Then, the layer thickness in the model is adjusted to agree with the measured coating center wavelength. By using the additional information of the measured mirror transmission T from Section II, we can now either:

1. Derive independent values for the refractive indices and layer thickness, or

2. Assuming one index is known, use the refractive indices and layer thickness information to give an independent value for the mirror transmission, which can be compared to the measurement of Section II.

That the dispersion (FSR) measurement alone is sufficient to determine the loss-less part of the mirror properties represents some useful information for the mirror coating technician: the index difference $n_H - n_L$ and the optical thickness of the coating layers can be simply measured in this way without interference from absorption/scatter losses. And, if n_L is known, this also gives a simple way of finding the mirror transmission. Adding in a direct measurement of mirror transmission yields values for n_H and n_L separately.

Data obtained from these measurements are shown in Figure 2, where L_{expt} is plotted as a function of wavelength, for a 10 μm cavity with 10 cm radius of curvature mirrors. The circles are measured data, and the curves the calculation from the model, with parameters chosen to best fit the data. This data was taken by setting the cavity to a series of different lengths, and recording a pair of resonant wavelengths (λ_1, λ_2) at each length. The x axis is center wavelength $\lambda_c = 2\lambda_1\lambda_2/(\lambda_1 + \lambda_2)$, the y axis the measured cavity length $L_{expt} = \lambda_1\lambda_2/2(\lambda_1 - \lambda_2)$ shown in units of $\lambda_1/2$: for each pair (λ_1, λ_2), the length is such that $L_{expt}/(\lambda_1/2) = 24.xx$. Dividing by λ_2 instead would exactly give 23.xx, since by rearranging the formula for L_{expt} we see that $L_{expt}/(\lambda_1/2) \equiv L_{expt}/(\lambda_2/2)+1$. Due to a finite drift in the cavity length, each measurement of λ was made to only 5 digits resolution (e.g. 852.59±0.01nm), leading to the uncertainty in L_{expt} shown. Uncertainty in λ_c is ± 0.03nm and cannot be seen on this scale.

Two theory curves are shown. The solid curve shows a model with n_L assumed to be fixed at its nominal value of n_L=1.455. To best fit the data, n_H was *increased* to n_H=2.0676 (a factor of 1.3%). In addition, the center wavelength was shifted to 847nm (by reducing the thickness of each $\lambda/4$ layer by 0.6%). Discussions with REO confirmed that 1.3% is a known offset in n_H for the particular coating machine which produced this run, and also that a few nm uncertainty in the center wavelength is typical. With these parameters, the inferred mirror transmission is $T_{\rm inf}$ =4.6±0.2 ppm, agreeing well with the measured value $T_{\rm exp}$ =4.3 ppm from Section II. The dotted curve (which overlaps the solid curve) shows the model when both n_L and n_H are allowed to vary. Their values are chosen to match both the FSR measurement shown, and to give a mirror transmission to match exactly the experimentally determined value $T_{\rm exp}$ = 4.3 ppm. Parameters which satisfy these criteria are n_H =2.0564 (0.75% increase) and n_L=1.4440 (0.76% decrease). Our direct measurement of T in Section II had a large uncertainty, which limits the absolute determination of n_H and n_L to about this 1% level. However, a more precise measurement could in principle determine the indices at the 0.1% level. One application might be to measure T and the FSR as a function of position across a mirror substrate, thereby mapping out stress induced variations in the refractive indices at the 0.1% level with a spatial resolution of $\sim$ 10 μm.

In this data set the correction for the Gaussian phase difference between the actual resonator mode and the plane-wave of the model has been neglected. After the propagation distance from the mode waist to the mirror surfaces, a Gaussian beam will have acquired less phase than a plane wave traveling the same distance. For a 10 μm cavity with 10 cm radius of curvature mirrors, this gives a 2% correction, corresponding to a shift in L_{expt} by $\simeq$ 0.0045 cavity orders (that is, $\Delta L \simeq +\frac{\lambda}{2} \times 0.0045$). Lowering the refractive index contrast of the model to shift the calculated curve by this amount would increase the inferred mirror transmission by $\lesssim$ 0.1 ppm. For our second cavity (44 μm, 20 cm radius of curvature mirrors), the correction is 0.0066 cavity orders.

The mirror phase shift (FSR measurement) is only sensitive to the transmission (index contrast) and center wavelength (layer thickness). Therefore, if absorption/scatter losses are added to the model (by introducing an imaginary component to the refractive index) the cavity resonance wavelengths do not change. More precisely, adding a scattering loss at the mirror surfaces has exactly zero effect on the FSR and mirror transmission. Adding losses *within* the coatings has a small effect: increasing the mirror absorption from 0.5ppm to 2ppm (an experimentally reasonable range) changes the mirror transmission by a factor of $\simeq 10^{-5}T$, clearly negligible, and again there is no effect on the FSR measurement. As a result, this measurement (with n_L assumed fixed) provided a very simple and sensitive inference of the mirror transmission of $T_{\rm inf}$ =4.6±0.2 ppm, which is *unaffected* by absorption/scatter losses.

The same measurement and fitting procedure was used on another cavity with mirrors from the same coating run. This 44 μm cavity made from 20 cm radius of curvature mirrors gave a transmission of $T_{\rm inf}$ =4.5±0.2 ppm, with a center wavelength of 848 nm.(This was the cavity used for the direct measurements of Section II which gave T=4.3 ppm).

One other factor which has been ignored so far is the effect of fluctuations in the $\lambda/4$ layer thickness. Discussions with REO suggested that a 1% variation in thickness was reasonable, so a Gaussian-distributed variation (of standard deviation 1%) was added to the layer thicknesses of the model. For cavity calculations, identical mirrors were used for both sides of the cavity. The principal effect of this variation is to shift the center wavelength of the coating - over several realizations of random coatings, this resulted in an rms shift of the center wavelength by ±1.2 nm. So, the measured shift of center wavelength in the coating (from 852 nm to 847 nm) is probably due partly to a systematic offset, and partly to fluctuations. The mirror transmission is also affected: the value of the

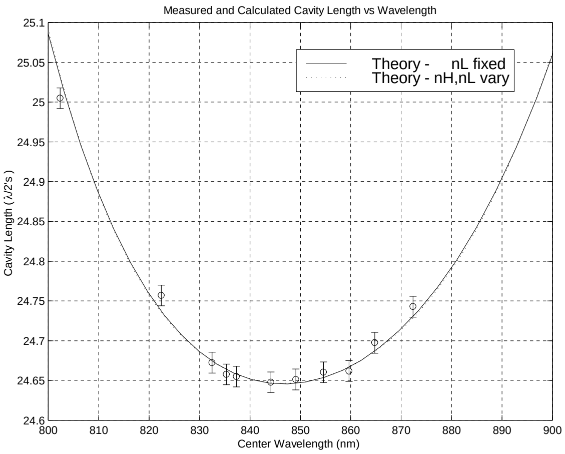

FIG. 2: The cavity length L_{expt} measured from the Free-Spectral Range (FSR) varies about the design wavelength of the coating. Fitting a model to these data points gives a measure of mirror transmission (from fitting of the difference $n_H - n_L$) and center wavelength (from fitting layer thickness).

transmission is on average *increased* slightly, by 0.6% in the case studied, from 4.55 ppm to 4.58 ppm at the center of the coating. At the level of our current measurements this is another negligible effect, but with a more precise measurement aimed at determining n_H and n_L, the possibility of a systematic offset from this mechanism should be considered. Lastly, the FSR measurement is mostly effected via the change in center wavelength of the coating - the value of $min(L_{expt(simulated)})$ has a mean the same as without the added fluctuations, and varies by only 0.0014 mode orders rms, again negligible for our purposes.

Another useful result of these calculations is that the free spectral range of the cavity is well known, so that resonant wavelengths of the cavity can be accurately predicted. This is important for choosing a diode laser of correct center wavelength to match the mode, for applications such as cavity locking or dipole-force traps. With the idea of using a laser of >920 nm wavelength to form an intracavity dipole-force trap,[15] this knowledge was particularly important: our Ti:Sapphire laser tuned only as high as 890nm so cavity resonances in this wavelength range could not be measured, only predicted. With the parameters chosen above for the model, the following theoretical and experimental resonance wavelengths resulted:

theory	787.208nm	818.659	853.255	890.798	930.683
experiment	787.170nm	818.651	853.255	890.800	N/A

The experimental value for the cavity resonance can then confidently be predicted to be 930.7±0.05nm, and a diode laser chosen accordingly.

V. LIMITATIONS TO MODE VOLUME

In a similar calculation to the one described above, it is possible to calculate the field distribution of light inside the resonant cavity, by describing each layer separately with a left and right travelling plane wave, then matching electromagnetic boundary conditions between layers. An example of this kind of calculation is shown in Figure 3, where refractive index and field distribution (modulus of the electric-field) are plotted as a function of distance for a cavity with length $L_{eff} = 3\lambda/2$. The coupling strength g_0 of an atom placed in the center of the cavity mode is proportional to $\frac{1}{\sqrt{V_m}}$, where V_m the cavity mode volume is found by integrating the field $(D \cdot E)$ over the standing wave and Gaussian transverse mode profile. Large coupling is achieved by making a short cavity with a small mode waist (short radius of curvature mirrors).

For a cavity of physical length L, the "leakage" of the mode into the $\lambda/4$ mirror stack (look at the tails of the mode in Fig. 3) that increases L to L_{eff} also increases the cavity mode volume. For our materials at 852nm, $L_{eff} = L + 1.633\lambda/2$, so for a cavity with physical distance between mirror surfaces $L = \lambda/2$, the cavity mode volume ends up being 2.63 times larger than might otherwise have been expected, and hence the atom-cavity coupling g_0 is 0.6 times smaller than the naive estimate based on the physical separation of the mirror surfaces.

This effect is proportionately larger as the cavity length gets shorter. In Figure 4, the expected g_0 is plotted for a cavity formed with two 20cm radius of curvature mirrors, as a function of the physical distance L between the mirrors. The two curves show a real mirror (with g_0 reduced by leakage into the coatings) and an idealized mirror with no leakage (perfect reflectors at $\pm L/2$). The transverse (Gaussian waist) dimension is calculated by simple Gaussian beam propagation, which is not strictly accurate for length scales less than a few microns; however any error in this should be roughly the same for both the ideal and actual mirror cases, so the ratio of these should remain sensibly correct. The cavity is assumed resonant at an integer number of half-wavelengths of light at the 852nm Cs D2 transition; that is, each $\lambda/2$ is a distance of 0.426 microns.

The discrepancy between the expected and achieved coupling g is large even for our longer cavities - 5% for a 10μm cavity. However, in the lab this is largely compensated by the fact that we never measure the actual physical distance L between mirror surfaces, but instead $L_{expt} = \lambda_1\lambda_2/2(\lambda_1 - \lambda_2)$, which is close to L_{eff}, and so incorporates the same offset of mirror penetration that determines g_0. This method of length measurement breaks down eventually due to the dispersion of the mirror coatings: Eventually if λ_1 is at the center of the coating, λ_2 will be so far separated in wavelength that it reaches the edges of the mirror coating stopband, and the observed round-trip phase has then more to do with the structure of the dielectric coatings than it does with the vacuum gap between the surfaces of the cavity mirrors. That is to say, our measured L_{expt} becomes increasingly different from L_{eff} and introduces an offset in estimating the mode volume as the cavity length approaches the scale of the wavelength.

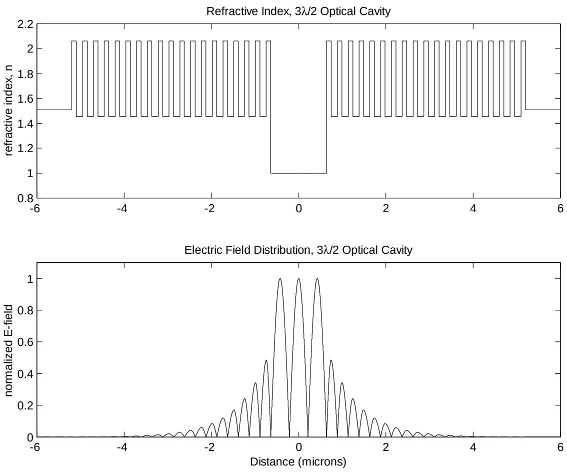

FIG. 3: Mirror refractive index stack design, and resulting electric field distribution for a resonant $3\lambda/2$ cavity made from dielectric mirrors.

At $L = 20\lambda/2$ physical length (the regime of our present cavities) the difference between the coupling coefficient g_0 inferred from L_{expt} and that found by integrating $D \cdot E$ over the mode volume is <0.1%. At $L = 10\lambda/2$ (4.26μm) it would be a 1% error, at $5\lambda/2$ an 8% error. Note however that knowledge of these offsets means that when calculating g_0 from L_{expt} we can compensate for this effect. Measurements of L_{expt} for cavities any shorter than $5\lambda/2$ would be impossible since λ_2 has reached the edge of the mirror stopband. To align shorter cavities a new method for length measurement will need to be developed, such as measuring the frequency spacing of transverse modes.

We are now in a position to estimate parameters for the best Fabry-Perot cavity that will be experimentally feasible in the near future using this type of mirrors. First consider a $L = \lambda/2$ cavity with 20cm radius of curvature mirrors. If the mirror transmission and losses were each reduced to $T = l =$0.5ppm to yield a cavity finesse of $\mathcal{F} = 3.14 \times 10^6$, then this cavity has parameters $(g_0, \kappa, \gamma_\perp)/2\pi = (647, 56, 2.6)$MHz, which gives critical photon number $n_0 = \gamma_\perp^2/2g_0^2 = 8.1 \times 10^{-6}$ and critical atom number $N_0 = 2\kappa\gamma_\perp/g_0^2 = 7.0 \times 10^{-4}$. To make a cavity of this length the 20cm mirrors would have to be reduced to a diameter of 0.5mm rather than 1mm. At this size there would still be a 0.11μm gap between the mirror edges for the $L = \lambda/2$ (0.426 micron) cavity length, which should make it possible to still get atoms into and out of the cavity (as in Ref. [3, 4, 5, 6, 7, 8]), and to align the mirrors.

If the mirror diameter could be reduced to 350μm (without adversely affecting the cavity losses), then 10cm radius of curvature mirrors could be used, with a 0.12μm gap at the edges. Due to the tighter radius of curvature, $g_0/2\pi$ would be increased to 770MHz in this case. Now speculating that "dream" mirrors of $T =$0.2ppm transmission, $l =$0.2ppm loss might be possible ($\mathcal{F} = 7.85 \times 10^6$), we could aim for the ultimate goal of $(g_0, \kappa, \gamma_\perp)/2\pi = (770, 22, 2.6)$ MHz, in which case $n_0 = 5.7 \times 10^{-6}$ photons, and $N_0 = 1.9 \times 10^{-4}$ atoms.

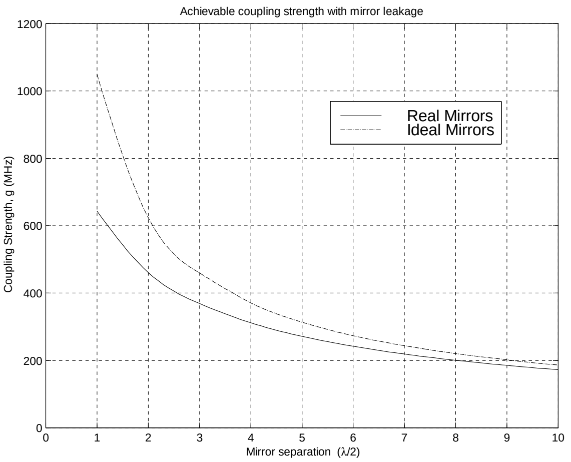

FIG. 4: Coupling coefficient g_0 (expressed in cycles per second) versus the physical separation L of the surfaces of two mirrors forming a Fabry-Perot resonator. Due to penetration of the standing-wave mode into the mirror coatings, the cavity mode volume achieved with real mirrors is larger (and hence the coupling strength smaller) than for an ideal mirror with the same spacing between mirror surfaces but no penetration.

In conclusion, we have presented two measurement approaches, one based upon direct loss and the other on cavity dispersion, that produce the same quantitative determination of the mirror coating properties. The dispersion measurement is more informative, as it has the potential to determine the complete characteristics of a mirror. A model has been derived to link the mirror properties to the physical parameters of coating layers. Issues relevant to optical cavity QED, such as the cavity field mode structure, have been discussed.

First and foremost, we thank Research Electro-Optics, Inc. for providing the best quality mirrors and coatings that have made our work possible. In particular, the critical and ongoing contributions of R. Lalezari and J. Sandburg to our reserach program in cavity QED are gratefully acknowledged. Our Caltech colleagues David Vernooy and Theresa Lynn made important contributions to the work presented here. Funding has been provided in part by DARPA through the QUIC (Quantum Information and Computing) program administered by the US Army Research Office, the Office of Naval Research, the National Science Foundation, and the National Institute of Standards and Technology.

---

[1] H.J. Kimble, *Cavity Quantum Electrodynamics*, Ed., P.R. Berman, pp.203-266, Academic Press (1994).

[2] S.J. van Enk, J.I. Cirac, and P. Zoller, Science **279**, 205 (1998).

[3] H. Mabuchi, Q. Turchette, M.S. Chapman, and H.J. Kimble, Opt. Lett. **21**, 1393 (1996).

[4] C.J. Hood, M.S. Chapman, T.W. Lynn, and H.J. Kimble, Phys. Rev. Lett. **80**, 4157 (1998).

[5] H. Mabuchi, J. Ye, and H.J. Kimble, Appl. Phys. B **68**, 1095 (1999).

[6] J. Ye, C.J. Hood, T.W. Lynn, H. Mabuchi, D.W. Vernooy, and H.J. Kimble, IEEE Trans. Instru. & Meas. **48**, 608 (1999).

[7] J. Ye, D.W. Vernooy, and H.J. Kimble, Phys. Rev. Lett. **83**, 4987 (1999).

[8] C.J. Hood, T.W. Lynn, A.C. Doherty, A.S. Parkins, and H.J. Kimble, Science **287**, 1447 (2000).

[9] G. Rempe, R. J. Thompson, H. J. Kimble, and R. Lalezari,Opt. Lett. **17**, 363 (1992).

[10] Research Electro-Optics, Inc., 1855 South 57th Court, Boulder, Colorado 80301.

[11] Hecht, *Optics*, pp.373-375, Addison-Wesley Publishing (1987).

[12] For a derivation of the $(\frac{1}{n_H - n_L})$ effective length correction, see R.G. DeVoe, C. Fabre, K. Jungmann, J. Hoffnagle, and R.G. Brewer, Phys. Rev. A. **37**, 1802 (1988).

[13] W. Lichten, J. Opt. Soc. Am. A **2**, 1869 (1985).

[14] H. P. Layer, R. D. Deslattes, and W.G. Schewietzer, Jr., Applied Optics **15**, 734 (1976).

[15] H. J. Kimble, C. J. Hood, T. W. Lynn, H. Mabuchi, D. W. Vernooy, and J. Ye, in Laser Spectroscopy XIV, R. Blatt, J. Eschner, D. Leibfried, and F. Schmidt-Kaler, Eds., World Scientific, Singapore, p. 80 (1999).

PHYSICAL REVIEW E, VOLUME 65, 016608

Design of photonic crystal microcavities for cavity QED

Jelena Vučković, Marko Lončar, Hideo Mabuchi, and Axel Scherer
California Institute of Technology, Mail Code 136-93, Pasadena, California 91125

(Received 28 December 2000; revised manuscript received 19 July 2001; published 21 December 2001)

We discuss the optimization of optical microcavity designs based on two-dimensional photonic crystals for the purpose of strong coupling between the cavity field and a single neutral atom trapped within a hole. We present numerical predictions for the quality factors and mode volumes of localized defect modes as a function of geometric parameters, and discuss some experimental challenges related to the coupling of a defect cavity to gas-phase atoms.

DOI: 10.1103/PhysRevE.65.016608 PACS number(s): 42.70.Qs, 42.60.Da, 12.20.−m, 03.67.−a

I. INTRODUCTION

A variety of passive and active optical devices can be constructed by introducing point or line defects into a periodic array of holes perforating an optically thin semiconductor slab. In such structures, light is confined within the defect regions by the combined action of distributed Bragg reflection and internal reflection. This technique has been employed in making a microcavity semiconductor (In-Ga-As-P) laser [1] (emitting at $\lambda = 1.55\ \mu\text{m}$), and for demonstrating Si optical waveguides with sharp bends [2]. One can thus easily envision the fabrication of integrated optical "networks" on a single chip, with numerous microcavity-based active devices linked by passive waveguide interconnects.

The combination of high quality factor and extremely low mode volume that should be obtainable in point-defect microcavities makes the photonic crystal (PC) paradigm especially attractive for experiments in cavity quantum electrodynamics (cavity QED) [3], with potential applications in quantum information technology. The primary focus of this paper will be to discuss the optimization of microcavity designs for cavity QED with strong coupling between defect modes and gas-phase neutral atoms. This new paradigm for cavity QED poses formidable technical challenges with regard to atom trapping and the characterization of surface effects, so we include some discussion of these issues and of our current approaches to addressing them.

In Sec. II of this paper we begin by analyzing elementary microcavities formed by changing either the refractive index or radius of a single defect hole. We discuss in detail some problems in previous finite-difference time-domain (FDTD) calculations done by our group [4], as intuitions gained from the resolution of these problems are important in the microcavity design optimization for cavity QED. In Sec. III we present our designs of microcavities optimized for strong coupling between the cavity field and an atom trapped within a hole of the PC. Based on numerical analysis using the three-dimensional (3D) finite-difference time-domain (FDTD) method, we predict that quality factors over 3×10^4 can be achieved in these structures. We also discuss in this section the difficulty of estimating surface interactions between a trapped atom and the semiconductor substrate, and propose a technical strategy for confining gas-phase atoms within a defect microcavity. Finally, in Sec. IV we describe a procedure that we have developed for microcavity fabrication.

II. SINGLE DEFECT HOLE

The microcavities analyzed in this paper are formed by introducing point defects into a dielectric slab patterned with a hexagonal array of air holes. The thickness of the slab is d and its refractive index is equal to 3.4. The spacing between holes is denoted by a and the hole radius by r, as shown in Fig. 1. We use λ to specify the optical wavelength in air. In our calculations of microcavity quality factors, the boundary for separation of vertical from lateral loss (i.e., the vertical quality factor $Q_\perp$ from the lateral quality factor $Q_{||}$) was positioned approximately at $\lambda/2$ from the surface of the membrane. As the number of PC layers around a defect is increased, $Q_{||}$ increases and the total quality factor Q approaches $Q_\perp$. We will adopt a coordinate convention in which $x=0$, $y=0$, $z=0$ denotes the center of the cavity and $z=0$ is the middle plane of the slab.

The simplest method of forming a microcavity within the structure shown in Fig. 1 is to change the radius or index of refraction of a single hole. The former method is more interesting from the perspective of fabrication, since the lithographic tuning of geometric parameters of individual holes is a simple process, but in this section we will consider both methods. By increasing the radius of a single hole an acceptor defect state is excited, i.e., pulled into the band gap from the dielectric band. On the other hand, by decreasing the radius of an individual hole (or by tuning its refractive index between 1 and the refractive index of the slab) a donor defect state is pulled into the band gap from the air band [5]. Ac-

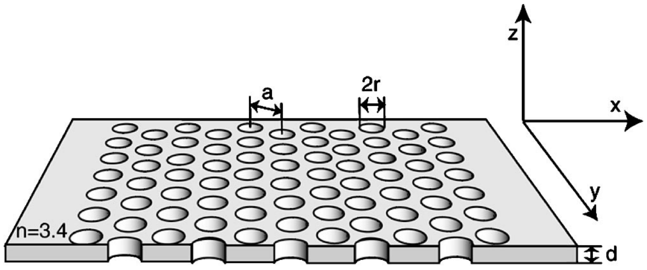

FIG. 1. Optically thin slab patterned with a hexagonal array of air holes.

©2001 The American Physical Society

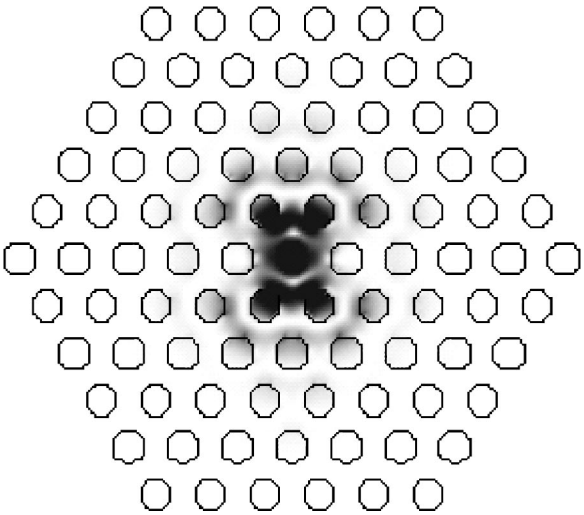

FIG. 2. Electric field intensity pattern of the *x*-dipole mode. Parameters of the structure are $r/a=0.3$, $d/a=0.6$, and in the used discretization $a=15$. The refractive index of the slab is 3.4 and of the defect is 2.4. The plotted intensity patterns are for the x-y plane at the middle of the slab.

ceptors tend to concentrate their electric field energy density in regions where the larger (semiconductor) refractive index was located in the unperturbed PC, while the electric field energy density of donors is concentrated in regions where there was air in the unperturbed PC. Since the electric field intensity in air regions is small in the case of acceptor defects, these are not good candidates for strong coupling with a single gas-phase atom that would be trapped within a hole. In this paper we will thus focus on donor states. For a discussion of acceptor states excited in an optically thin slab perforated with a hexagonal PC array, readers are referred to Ref. [6].

A. Changing the refractive index of a single hole

Microcavity formation by alteration of the refractive index of a single defect hole in a hexagonal PC has been analyzed previously by our group [4]. In that analysis we predicted that dipole-like donor states (such as the *x*-dipole mode shown in Fig. 2) with quality factors up to 3×10^4 should exist. We now believe that the quality factors of such microcavities are limited to several thousand, for reasons discussed below. This discussion reveals the extreme sensitivity of microcavity quality factors to small distortions to the local PC geometry, which will later be used as a powerful design tool in optimization for cavity QED.

In our previous work, mirror boundary conditions were applied in the *x*, *y*, and *z* directions to achieve an eightfold reduction in the computational grid size. We have since realized that the manner in which even (symmetric) mirror boundary conditions are implemented in our finite-difference time-domain (FDTD) code results in numerical output that properly corresponds to an analyzed structure with slight deformations relative to the intended structure. For example, the set of mirror boundary conditions used to select the *x*-dipole mode in a defect cavity leads to a deformation of the structure as shown in Fig. 3. Holes on the *x* axis are elongated in the *y* direction by one point but the distance between holes in the *x* and *y* directions is preserved. Because hole-to-hole distances are preserved under this deformation, the half-spaces $y>1/2$ and $y<-1/2$ actually maintain the unperturbed PC geometry when holes in the central row are elongated by 1/2 points in both the $\pm y$ directions. The symmetry of the PC surrounding the defect is therefore broken, and this contributes to artificially high quality factors for *x*-dipole modes. An even mirror boundary condition (BC) was also applied in the *z* direction in our previous analysis, causing a slight error in the thickness of the slab. The correct d/a ratios of the structures analyzed in Ref. [4] would be 0.6, 0.46, and 1, instead of the values 0.53, 0.4, and 0.93, as noted there.

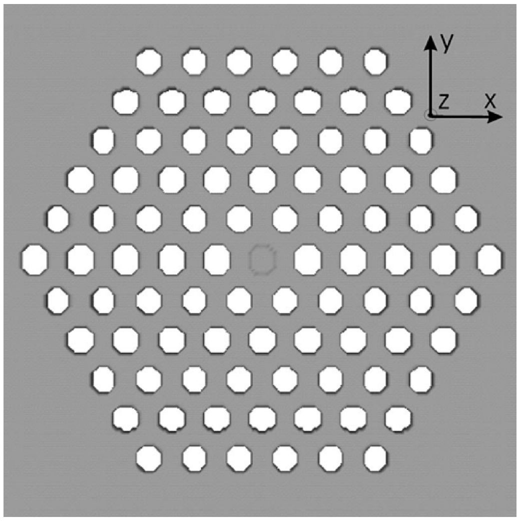

FIG. 3. Deformation of the analyzed structure introduced by the application of mirror boundary conditions along the *x* and *y* axes and through the center of the defect. The applied mirror boundary conditions select the *x*-dipole mode, whose electric field pattern is shown in Fig. 2. Holes on the *x* axis (in the central row, containing the defect) are elongated by one point in the *y* direction. The refractive index of the defect is $n_{\text{defect}}=2.4$. Parameters of the structure are $r/a=0.3$, $d/a=0.6$, and in the used discretization $a=15$.

1. Perfectly symmetric cavity

We reanalyzed the structure with $r/a=0.3$, $d/a=0.6$, $n_{\text{defect}}=2.4$, $n_{\text{slab}}=3.4$, five layers of holes around the defect, and $a=15$ grid points. For this set of parameters, the predicted $Q_{\perp}$ in Ref. [4] for the *x*-dipole mode was 3×10^4. In the present analysis, even mirror boundary conditions were applied to the lower boundary in the *z* direction only, to reduce the computation size by one-half and to eliminate TM-like modes. Absorbing boundary conditions were applied to all boundaries in *x* and *y* directions and to the upper boundary in the *z* direction. Under these BC's the intended symmetry of the defect structure was achieved. The initial field distribution was chosen in such a way as to excite *x* or *y* dipole modes selectively. For the *x*-dipole mode we now calculate $Q_{||}=2260$, $Q_{\perp}=1730$, and $a/\lambda=0.3137$, and for the *y*-dipole mode we calculate $Q_{||}=1867$, $Q_{\perp}=1007$, and $a/\lambda=0.3182$.

The difference between parameters computed for the x- and y-dipole modes comes partly from the asymmetry of the structure introduced by imperfect discretization. In a two-dimensional (2D) PC with infinite slab thickness, these two modes should be degenerate [4]. In the thin slab, however, the y-dipole mode suffers more vertical scattering at the edges of holes and, therefore, has a lower $Q_\perp$. For a nonsymmetric applied initial field distribution leading to excitation of both x- and y-dipole modes, we calculated $Q_{||}=2070$, $Q_\perp=1290$, and $a/\lambda=0.316$. This mode can be represented as a superposition of the x and y dipole, with weighting factors depending on the initial field. Its quality factor and resonant frequency depend on these weighting factors.

2. Asymmetric cavity

Our explanation for the discrepancy between our current and previous results leads us to ask whether a "real" (intentional) elongation of the central row of holes along the y axis may actually improve the quality factor (Q) of the x-dipole mode. A possible disadvantage of this approach is the excitation of acceptor states caused by enlarging holes in the central row. We have therefore analyzed how a/λ and Q of the x-dipole mode in this structure changes as a function of the elongation parameter p. Holes on the x axis (including the defect) are elongated in both the $\pm y$ directions by $p/2$ points, in such away that hole-to-hole distances are preserved and the half-spaces $y>p/2$ and $y<-p/2$ maintain the unperturbed PC geometry. The structure parameters are $r/a=0.3$, $d/a=0.6$, $n=3.4$, $n_{\text{defect}}=2.4$, and five layers of holes surround the defect. The periodicity a used in these calculations is equal to 15 grid points, and the elongation step $\Delta p=1$ corresponds to $a/15$. The results are shown in Fig. 4. It is interesting that the frequency of the mode decreases as p increases, even though the amount of the low refractive index material increases. However, the net amount of low refractive index material does not matter; what does matter is where the low refractive index is positioned relative to the unperturbed PC. The explanation of the decrease in frequency is very simple if we recall the x-dipole mode pattern shown in Fig. 2. This is a donor type defect mode, which concentrates its electric field energy density in low refractive index regions of the unperturbed PC. As p increases, layers of PC holes are moved away from the defect in the y direction. For example, the nth layer of holes parallel to the x axis will be positioned at $y=\pm na\sqrt{3}/2\pm p/2$, instead of $y=\pm na\sqrt{3}/2$. Therefore a large refractive index material will be positioned at places where the mode expects to "see" air, leading to a decrease in the mode's frequency. By tuning the mode's frequency across the band gap, we can also tune its Q factor, as noted previously [6]. For $p=3$, $Q_\perp$ reaches the value of 20 000. The analyzed x-dipole mode mostly resonates in the direction of the y axis, i.e., in the ΓX direction of the photonic crystal. The tuning of the elongation parameter p is, therefore, analogous to tuning of a spacer in the micropost cavity, which leads to tuning of the mode's frequency and Q factor. A more detailed explanation of the effect of elongations on Q factors is given in The Appendix.

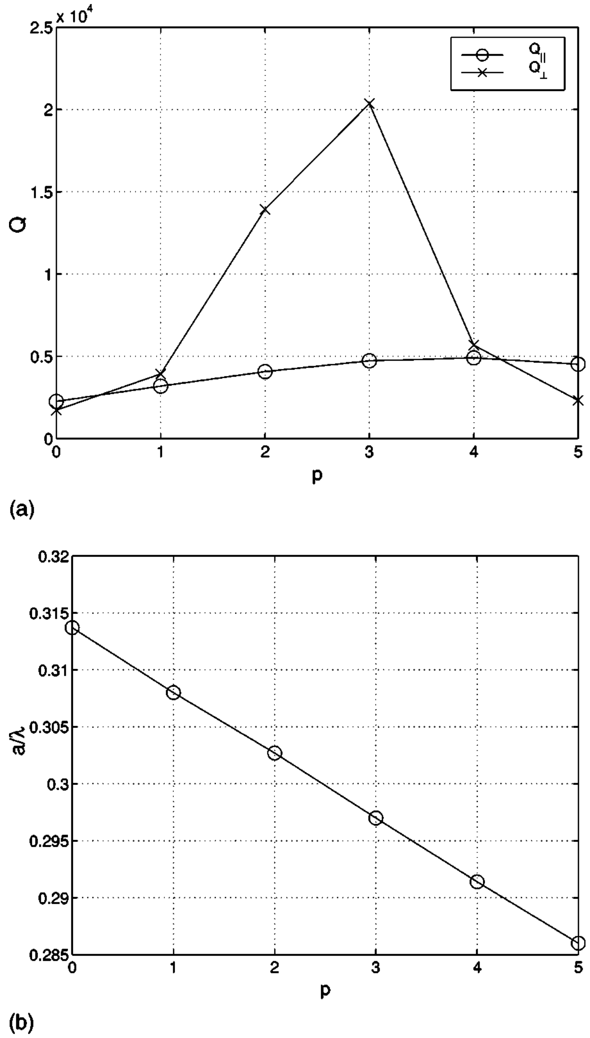

FIG. 4. (a) Q factors and (b) frequencies of x-dipole modes in the structure shown in Fig. 3 as a function of the elongation parameter p. The structure parameters are $r/a=0.3$, $d/a=0.6$, $n=3.4$, $n_{\text{defect}}=2.4$, $a=15$, and five layers of holes surround the defect.

By increasing the number of PC periods around the defect, the total quality factor Q approaches $Q_\perp$, as shown in Fig. 5. It is important to note that $Q_{||}$ does not increase exponentially with the number of PC layers around the defect, as noted previously in Ref. [4]. Instead, it saturates at a large number of PC layers. The reason is in the choice of a boundary for separation of $Q_\perp$ from $Q_{||}$, positioned at approximately $\lambda/2$ from the surface of the membrane. From the radiation pattern of the x-dipole mode we can see that some portion of the out-of-plane loss mostly in the x direction still gets collected in $Q_{||}$. This loss cannot be suppressed by increasing the number of PC layers around the defect, and it determines a value at which $Q_{||}$ saturates. However, much larger out-of-plane loss is collected in $Q_\perp$, which ultimately determines the total quality factor Q.

Therefore, the dramatic improvement in Q factors of dipole modes over single defect microcavities can be obtained by introducing a novel type of PC lattice defect, consisting of the elongation of holes along the symmetry axes. We call it fractional edge dislocation, by analogy with edge dislocations in solid state physics. Edge dislocations are formed by

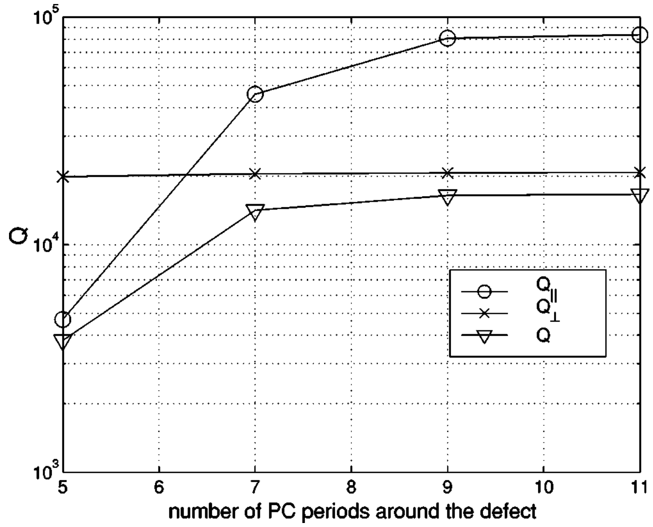

FIG. 5. Q factor for $p=3$, in the structure shown in Fig. 3, as a function of the number of PC periods around the defect. The structure parameters are $r/a=0.3$, $d/a=0.6$, $n=3.4$, $n_{\mathrm{defect}}=2.4$, and $a=15$.

introducing extra atomic planes into the crystal lattice. On the other hand, we here insert only fractions of atomic planes along the symmetry axes of a photonic crystal.

Unfortunately, at this time, we do not know how to control the refractive index of a single PC hole during the fabrication. For that reason in the next section we will consider alternative methods of forming single defect microcavities, which are much easier to construct by microfabrication.

Even after the elongation of holes on the x axis by 1 point, Q factors of 30 000 were not obtained. This means that the application of mirror BC's at $x=0$ and $y=0$ planes causes additional effects that lead to the overestimation of quality factors. One of the reasons may be that the excited dipole mode does not have a symmetry described by the applied discretized mirror BC's. This may be partly due to the structure imperfection caused by discretization. In order to avoid problems caused by BC's all the calculations in this paper were done by applying the even mirror symmetry to the $z=0$ plane only, in order to select TE-like modes and to reduce the computation size by one-half. Absorbing boundary conditions are applied to all boundaries in the x and y directions and to the upper boundary in the z direction. To prove that the application of mirror BC's at the lower z boundary does not change Q, we also analyzed entire structures with absorbing BC's applied to all boundaries and obtained the same results as in the analysis of one-half of the structure.

B. Reducing the radius of a single hole

Microcavities analyzed in this section are formed by reducing the radius of a single hole to r_{def}. We calculate parameters of excited dipole modes for a range of microcavity parameters and the results are shown in Table I. For all tabulated results, five layers of holes surround the defect and $a=20$. Calculated Q's are not very impressive, but they do provide us with a good starting point for further optimization. Why did we decide to use a relatively small r/a ratio for the PC? According to our calculations, increasing r/a within the analyzed range leads to increases in the band gap and reduction of lateral losses. However, vertical scattering at the edges of holes also increases and $Q_{\perp}$ drops. It is therefore important to find an optimum r/a which leads to small vertical losses but preserves good lateral confinement, in order not to increase the mode volume too much.

TABLE I. Q factors of dipole modes excited in microcavities formed by decreasing the radius of a single PC hole.

r/a	r_{def}/a	d/a	a/λ	$Q_{\|}$	$Q_{\perp}$
0.275	0.15	0.75	0.286	778	920
0.275	0.2	0.75	0.297	470	2078
0.25	0.15	0.75	0.277	230	1840
0.25	0.2	0.75	0.284	116	3190

The band diagram for TE-like modes of a thin slab ($n=3.4$, $d/a=0.75$) surrounded by air on both sides and patterned with a hexagonal array of air holes ($r/a=0.275$) is shown in Fig. 6. These PC parameters are used in most of the calculations in the next section. From the comparison of the dipole mode frequencies tabulated in Table I and the band diagram shown in Fig. 6, it can be confirmed that as the cavity mode's frequency approaches the bottom of the air band, vertical losses decrease, but lateral losses increase, which in turn leads to an increase in the mode volume. Our goal in the next section will be to reduce vertical losses and improve Q factors even further, while preserving small mode volumes. For this purpose, we will explore fractional edge dislocations. In Fig. 4, one can observe that an increase in the elongation parameter p can be used to tune the $Q_{\perp}$ factor of a mode, but also leads to a decrease in the dipole mode's frequency. This implies that by increasing p, the mode is pulled deeper into the band gap, away from the air band edge, which leads to its better latteral confinement. Therefore, we can simultaneously achieve a reduction in vertical losses and an improvement in lateral confinement (i.e., an increase in both $Q_{\perp}$ and $Q_{\|}$, and a reduction in the mode volume).

III. CAVITIES FOR STRONG COUPLING

In this section we consider the design of PC microcavities to achieve strong coupling between the cavity field and a single gas-phase atom, that is, an atom located in free space rather than contained as an impurity in the dielectric slab. Our long-term goal is to investigate photonic band-gap structures for single-atom cavity quantum electrodynamics in the strong coupling regime [3]. For this purpose the microcavity mode quality factor (Q) has to be as large as possible and the mode volume (V_{mode}) as small as possible. These two design rules are also followed when designing PC microcavities for semiconductor lasers. However, in a cavity for strong coupling, an atom must be trapped at the point where it interacts most strongly with the cavity field. Therefore an additional design goal is imposed in this case: the cavity mode should have the E-field intensity as high as possible in the air re-

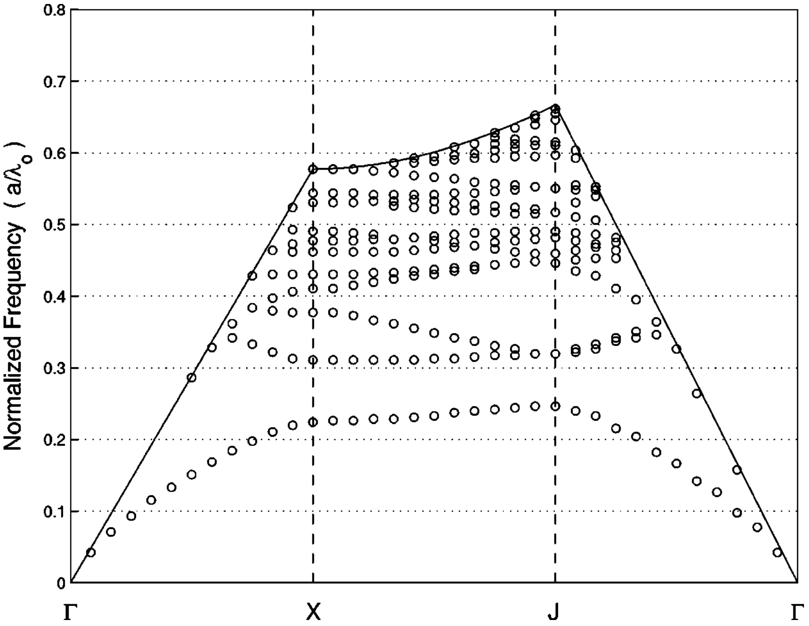

FIG. 6. Band diagram for TE-like modes of a thin slab ($n = 3.4$, $d/a = 0.75$) surrounded by air on both sides and patterned with a hexagonal array of air holes ($r/a = 0.275$).

gion. When designing a laser cavity, the problem is the opposite: one tends to maximize the overlap between the gain region and the cavity field and, therefore, wants to have the strongest E-field in the semiconductor region.

Mode volume (V_{mode}), critical atom (N_0) and photon (m_0) numbers are defined as follows:

$$V_{\mathrm{mode}} = \frac{\int\int\int \epsilon(r)|E|^2 dV}{\max[\epsilon(r)|E|^2]}, \tag{1}$$

$$N_0 = \frac{2\kappa\gamma_\perp}{g^2}, \tag{2}$$

$$m_0 = \left(\frac{\gamma_\perp}{2g}\right)^2, \tag{3}$$

where κ is the cavity field decay rate, proportional to the ratio of the angular frequency of the mode (ω_0) and the mode quality factor (Q):

$$\kappa = \frac{\omega_0}{4\pi Q}, \tag{4}$$

$\gamma_\perp$ is the atomic dipole decay rate (2.6 MHz for cesium) and g is the coupling parameter at the point where we want to put an atom:

$$g(r) = g_0 \frac{\epsilon(r)|E|}{\max[\epsilon(r)|E|]}, \tag{5}$$

g_0 denotes the vacuum Rabi frequency:

$$g_0 = \gamma_\perp \sqrt{\frac{V_0}{V_{\mathrm{mode}}}}, \tag{6}$$

$$V_0 = \frac{c\lambda^2}{8\pi\gamma_\perp}. \tag{7}$$

Strong coupling is possible if both N_0 and m_0 are smaller than 1. Therefore, in order to predict whether the strong coupling can occur, we must calculate upper limits of N_0 and m_0 and compare them to 1. In other words, it is acceptable if calculated critical numbers are overestimated. As the number of PC layers around the defect increases, the total quality factor Q approaches $Q_\perp$ and V_{mode} drops due to the better lateral confinement. Hence we can calculate N_0 and m_0 by assuming $Q = Q_\perp$ and using V_{mode} calculated for five PC layers around the defect.

For all calculations in this section, the refractive index of the slab is $n = 3.4$, five layers of holes surround the central hole, and $a = 20$. The elongation step $\Delta p = 1$ corresponds to $a/20$, i.e., 5% of the lattice periodicity a. The material and PC properties are chosen in such a way that cavities operate at $\lambda = 852$ nm (the wavelength corresponding to the D2 atomic transition in ^{133}Cs).

A. Single defect with fractional edge dislocations

Let us study microcavities formed by reducing the radius of a single hole and simultaneously applying the fractional edge dislocation (of order p) along the x axis. We will calculate the dependence of the x-dipole mode properties on parameter p. Parameters of the unperturbed PC are $r/a = 0.275$, $d/a = 0.75$, $a = 20$, and the defect hole radius is $r_{\mathrm{def}}/a = 0.2$. The critical atom (N_0) and photon (m_0) numbers are shown as a function of the elongation parameter p for the x-dipole mode in Fig. 7. V_{mode} did not change significantly with p and it was approximately equal to $0.1(\lambda/2)^3$ for all structures. When p increases, the frequency of the mode moves away from the band edge, towards the center of the band gap, $Q_{||}$ increases, and $Q_\perp$ peaks at the value of 1×10^4 for $p = 2$.

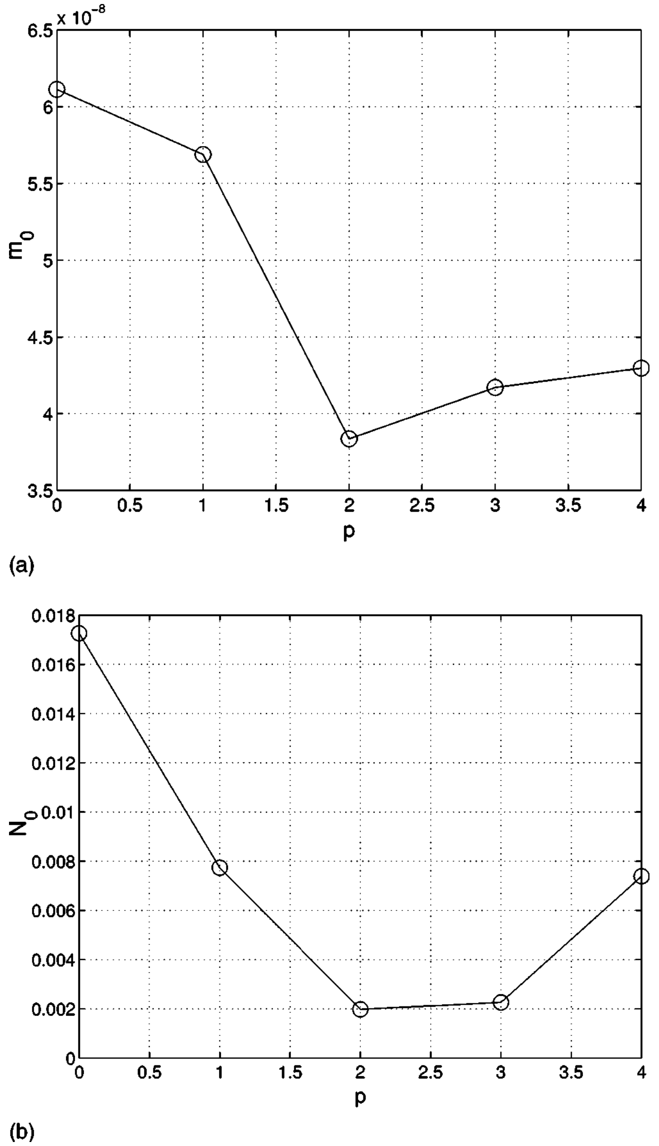

FIG. 7. Parameters of the x-dipole mode in the single defect structure $(r/a=0.275,\ d/a=0.75,\ r_{\mathrm{def}}/a=0.2,\ n=3.4,$ and $a=20)$ as a function of the elongation parameter p: (a) m_0 and (b) N_0.

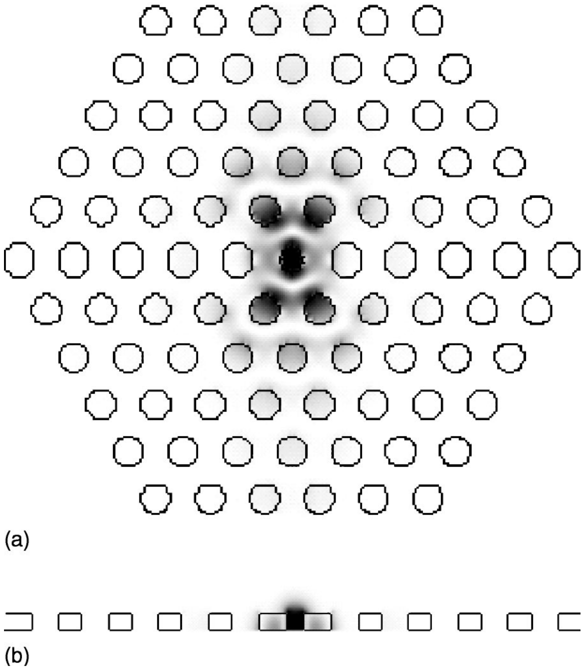

FIG. 8. Electric field intensity pattern of the x-dipole mode excited in the microcavity formed by reducing the radius of a single hole and simultaneously elongating holes on the x axis by two points. (a) Slice through the middle of the membrane, in the x-y plane; (b) x-z half-plane $(z>0)$.

From the electric field intensity pattern of the x-dipole mode shown in Fig. 8, one can see that the electric field intensity is very strong within the defect hole. Therefore, an atom trapped there should interact very strongly with the cavity field. From the calculated critical atom and photon numbers, it then should be possible to achieve very strong coupling. At $\lambda=852$ nm the parameters of such a cavity are $r=70$ nm, $d=190$ nm, $a=250$, and $r_{def}=50$ nm. Due to extremely small mode volumes in these cavities, strong coupling is possible even for moderate values of Q, as $Q_\perp$ did not exceed $\sim 1\times 10^4$ in the parameter range of Fig. 7. Furthermore, m_0 is much smaller than N_0, which means that we can try to improve Q factors further at the expense of increasing V_{mode}. Q factors above 1×10^4 and similar values of m_0 and N_0 can also be obtained for the cavity consisting of a single defect with $r_{def}/a=0.2$ and a fractional edge dislocation of order p, produced in the photonic crystal whose parameters are $r/a=0.3$, $d/a=0.65$, and $n=3.4$.

B. Tuning holes around the defect

Dipole modes are particularly sensitive to the geometry of holes closest to the defect. By tuning these holes we can induce frequency splitting of dipole modes and dramatically influence their Q factors. In Ref. [4], the variation of two nearest neighbor holes along the x axis was analyzed. Here we will test the influence of changing four holes closest to the defect in the ΓJ directions. The analyzed structure is shown in Fig. 9. The radius of the central hole is reduced to r_2 and the radii of the four closest holes in the ΓJ directions are reduced to r_1. These four holes are simultaneously moved away from defect, by $r-r_1$ in the ΓJ directions, which preserves the distance between them and the next nearest neighbors in the same directions. This design will improve the Q factor of the y-dipole mode and spoil the Q of the x-dipole mode. We analyzed structures with various parameters, but our best result was obtained for $r/a=0.275$, $d/a=0.75$, $r_2/a=0.2$, $r_1/a=0.225$, and $a=20$. The electric field intensity pattern of the excited y-dipole mode is shown in Fig. 10, and its calculated parameters are $a/\lambda=0.289$ and $Q_\perp=4890$. From Table I we can see that a dipole mode excited in a single defect microcavity with this r_2/a, r/a, d/a had $Q_\perp=2078$. Therefore the tuning of four holes can lead to a substantial increase in Q of the x dipole mode. The disadvantages of this design include the excitation of defect modes other than dipoles (coming from variation of several holes).

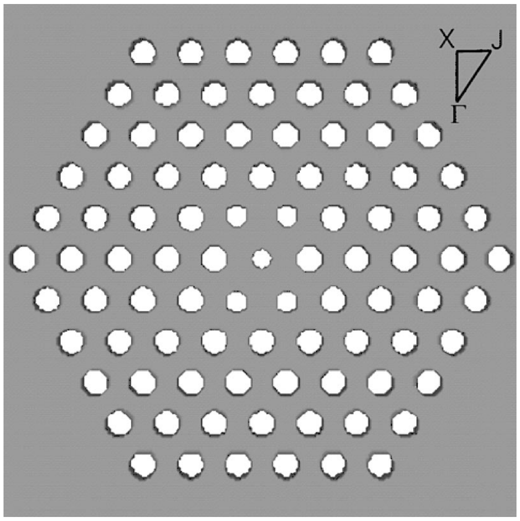

FIG. 9. Tuning four holes closest to the defect in the Γ J directions. Their radii are reduced to r_1 and they are simultaneously moved away from the defect in the Γ J directions by $r-r_1$. The radius of the central hole is r_2.

Let us try to improve Q of this cavity even further by also employing the idea of elongation of holes along desired directions. Our mode of choice is the y dipole and we will elongate holes sitting on the y axis by p points in the x direction in such a way that the half-spaces $x>p/2$ and $x<-p/2$ remain the unperturbed PC geometry. The dependence of N_0 (which decreases with Q) on parameter p is shown in Fig. 11. V_{mode} did not change significantly with p and was in the range between $0.09(\lambda/2)^3$ and $0.12(\lambda/2)^3$. The calculated m_0 was around 5×10^{-8} for all structures. Again, a very strong coupling is achievable by this design, and we note that $Q_\perp$ at the point $p=2$ achieves a value of $\approx3.3\times10^4$.

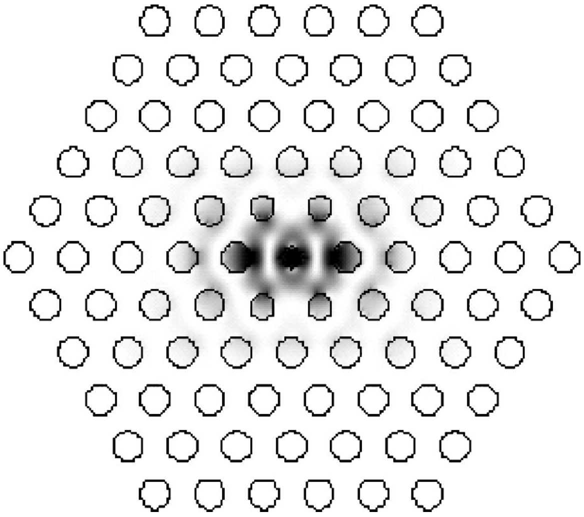

FIG. 10. Electric field intensity pattern of the y-dipole mode excited in the cavity where four holes closest to the defect in the Γ J directions are tuned. Their radii are reduced to $r_1/a=0.225$ and they are simultaneously moved away from the defect in the Γ J directions by $r-r_1$. The radius of the central hole is $r_2/a=0.2$. PC parameters are $r/a=0.275$, $d/a=0.75$, $a=20$, and $n=3.4$.

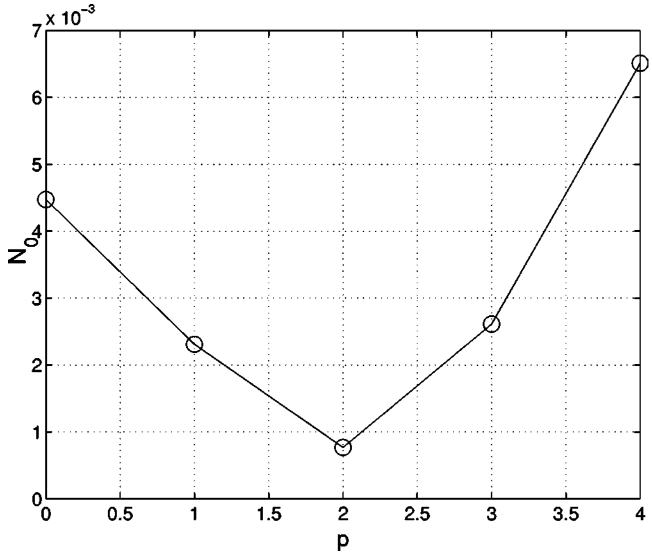

FIG. 11. N_0 of the x-dipole mode in the structure where four holes in the Γ J directions are tuned (as shown in Figs. 9 and 10) as a function of the elongation parameter p. Holes on the y axis are elongated by p points in the x direction in such a way that the half-spaces $x>p/2$ and $x<-p/2$ remain the unperturbed PC geometry.

C. Atomic physics

Given that microcavities with strong coupling parameters can be designed and fabricated, two further technical issues must be addressed in order to establish the feasibility of cavity QED with neutral atoms in PC's. First, we must identify a method for stably trapping an individual atom within a hole of the PC. Second, accurate estimates or measurements must be made of the surface interaction between such a trapped atom and the semiconductor substrate. Although definitive solutions to these challenges are the subject of future work, we include in this section a brief discussion of each topic.

In addition to the creation of photonic crystals, modern microfabrication techniques enable the patterning of either conductive wires or ferromagnetic materials at the micron scale and below. As a result, it should be possible to construct magnetic microtraps with field curvatures $\sim10^8$ G/cm^2 [7–10]. With this magnitude of field curvature an Ioffe trap could hold a Cs atom with Lamb-Dicke parameter $\eta\sim0.035$ in the radial direction, yielding $\Delta x\sim10$ nm in the ground state of the trapping potential and enabling resolved-sideband laser cooling as a means of putting single atoms in the ground state.

We are currently investigating fabrication and laser cooling techniques for an atom-trapping scheme in which micron-scale wires would be deposited on the surface of the PC semiconductor substrate, such that the circular wire pattern of an Ioffe microtrap are arranged concentrically around a defect microcavity. The trap designs discussed in Ref. [7] have a sufficiently large inner diameter not to disturb the photonic band-gap structure of the defect cavity. Such a wire arrangement would project a magnetic field with a stable minimum at the geometric center of the microcavity, such that one or more atoms could be confined within the defect hole and would therefore experience strong coupling. A similar geometry could be envisioned for microtraps based on permanent magnets rather than current-carrying wires, which would have significant advantages in terms of heat load to the PC substrate.

A neutral atom trapped within a hole of a PC structure will experience surface (van der Waals) interactions that are quite difficult to estimate. The significance of such interactions is twofold. The sensitive dependence of the ground state energy shift on an atom's position will lead to mechanical forces that must be compensated by the trap design. Differential shifting of the atomic ground and excited states on the cavity QED transition must also be accounted for, as this will introduce a position-dependent detuning relative to the fixed microcavity resonance. Although van der Waals shifts can be computed for alkali atoms near dielectric or metallic boundaries with simple symmetry [11,12], the case of an atom in a PC hole is far more complex. The local geometry seen by a trapped atom will be that of a cylindrical hole with finite extent, and a proper calculation must take into account the overall modification of vacuum modes due to the extended photonic crystal. Furthermore, the resonant frequencies of many atomic transitions that connect to low-lying states, and therefore contribute strongly to their van der Waals shifts, are above the band gap of the semiconductor substrate. Such transitions will ''see'' an absorptive surface while those below the band gap will see a dielectric surface. This set of factors brings the complexity of the desired calculation well beyond that of existing analytic results in the literature. It should be noted that experimental measurements of the van der Waals shifts in our proposed system would be of significant interest for the general subject of quantum electrodynamics of semiconductors.

We are pursuing a numerical strategy for estimating the magnitude of surface interactions. In a linear response approximation, it should be possible to compute leading-order contributions to the van der Waals shifts from FDTD simulations of the electromagnetic field created by an oscillating dipole source in the photonic crystal structure. While the nature of the code does not allow us to compute directly the backaction of the scattered field on the source dipole, we believe that elementary field theory can be used to relate the simulated field to van der Waals shifts. Our findings will be reported in a forthcoming publication.

D. Coupled dipole defect modes

The significance of surface effects that could perturb atomic radiative structure within the small defect hole is still unknown. For that reason we will try to investigate ways of increasing the radius of the hole where the coupling between the atom and the cavity field should occur. Let us now analyze the cavity design where the strong E-field intensity can be achieved in the center of an unperturbed hole. The idea is to use coupling of two dipole defect states.

Resonant modes of the microcavity formed by coupling two single defects are presented in Fig. 12. Based on the resultant electric field intensity in the central, unperturbed hole, we call them constructively or destructively coupled defect states. They have different frequencies as well as Q factors. We will analyze properties of the constructively coupled state, since the central, unperturbed hole would be a good place for an atom.

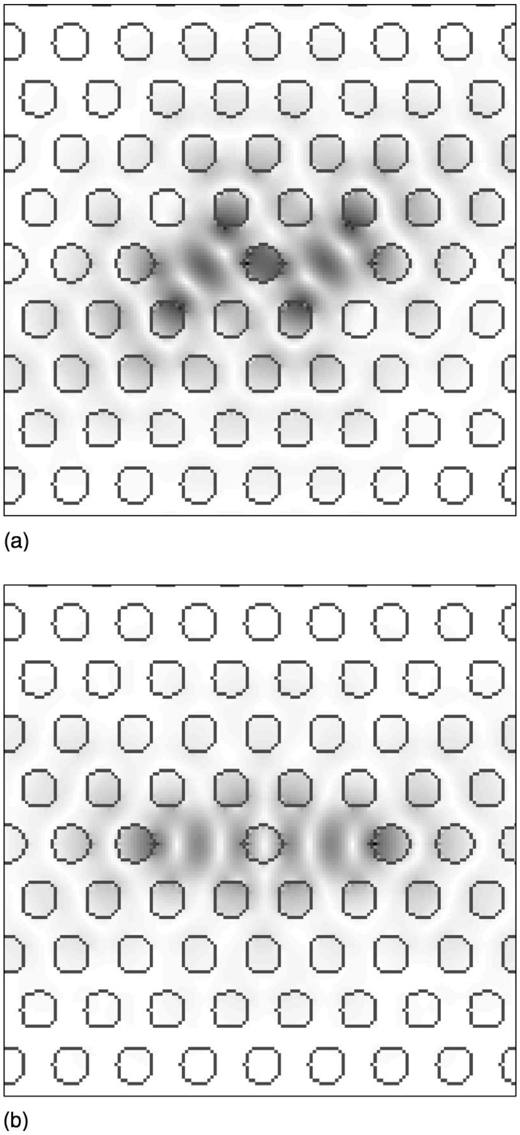

FIG. 12. Electric field intensity patterns of the coupled dipole modes: (a) constructively and (b) destructively coupled defect states.

We analyzed a series of structures with different parameters. The best results were obtained for two coupled defects with $r_{\mathrm{def}}/a = 0.2$ in a PC with the following parameters: $d/a = 0.75$, $r/a = 0.275$, $n = 3.4$, and $a = 20$. Holes in the ΓX direction, in columns containing defects, are elongated by two points in the x direction. The mode pattern of the constructively coupled defect state is shown in Fig. 13. Parameters of the mode are $a/\lambda = 0.29$, $Q_{\perp} = 6100$, $V_{\mathrm{mode}} = 0.19(\lambda/2)^3$, $m_0 = 1.5\times 10^{-7}$, and $N_0 = 0.0135$. An atom can now be trapped in the central hole of an unperturbed radius. For $\lambda = 852$ nm, this radius is $r = 68$ nm, which is a

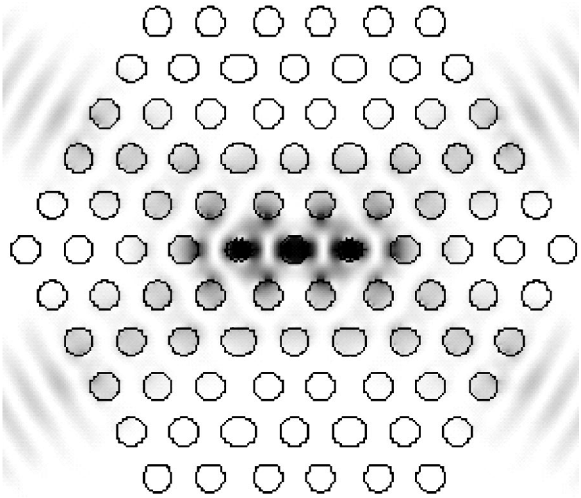

FIG. 13. Electric field intensity patterns of the constructively coupled dipole modes in the structure with the following parameters: $r_{def}/a=0.2$, $d/a=0.75$, $r/a=0.275$, $n=3.4$, and $a=20$. Holes in columns containing defects are elongated by two points in the x direction.

significant improvement over the previous design, where an atom must be trapped within a 50 nm radius hole. Again, a strong coupling is achievable in this cavity.

An alternative way of forming the coupled defects state is represented in Fig. 14. We used the same PC parameters as previously: $r_{\mathrm{def}}/a=0.2$, $d/a=0.75$, $r/a=0.275$, $n=3.4$, and $a=20$. Holes in rows containing defects are elongated by two points in the y direction. The mode pattern of the constructively coupled defect state is shown in Fig. 14. Parameters of the mode are $a/\lambda=0.288$, $Q_{\perp}=12\,120$, $V_{\mathrm{mode}}=0.14(\lambda/2)^3$, $m_0=1.4\times10^{-7}$, and $N_0=0.0063$. Strong coupling is achievable for an atom trapped in any of the two central holes of the unperturbed radius (positioned between the defects). For $\lambda=852$ nm this radius is again $r=68$ nm.

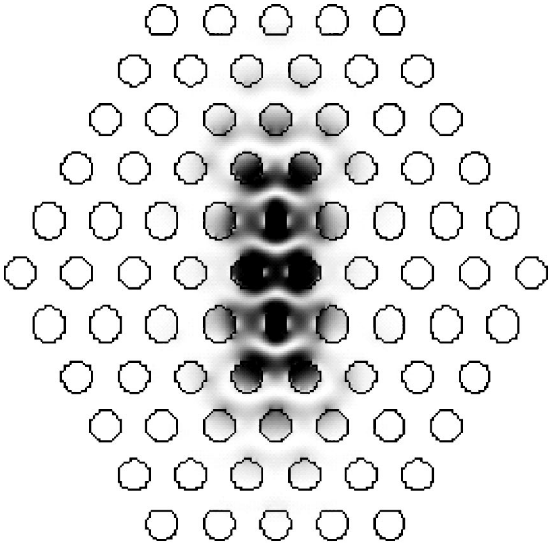

FIG. 14. Electric field intensity patterns of the constructively coupled dipole modes in the structure with the following parameters: $r_{def}/a=0.2$, $d/a=0.75$, $r/a=0.275$, $n=3.4$, and $a=20$. Holes in rows containing defects are elongated by two points in the y direction.

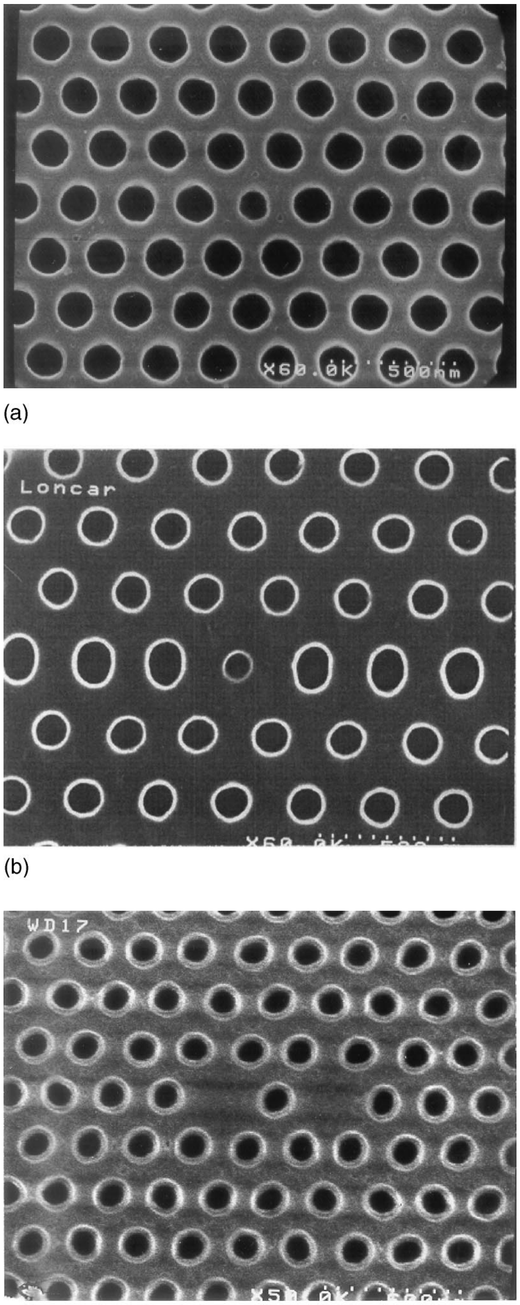

(a)

(b)

(c)

FIG. 15. SEM pictures showing the top views of the fabricated structures.

IV. FABRICATION

We have recently developed the fabrication procedure for making these cavities in $Al_xGa_{1-x}As$. The material and PC properties are chosen in such a way that cavities operate at $\lambda=852$ nm (the wavelength corresponding to the atomic D2 transition in ^{133}Cs).

The fabrication process starts by the spinning of 100 nm thick high molecular weight PMMA (polymethylmethacrylate) on top of the wafer. The PMMA layer is subsequently baked on a hot plate at 150 °C for 20 min. A desired 2D PC pattern is beamwritten on the PMMA by electron beam lithography in a Hitachi S-4500 electron microscope. The exposed PMMA is developed in a 3:7 solution of 2-ethoxyethanol:methanol for 30 s. The pattern is then transferred into the $\mathrm{Al}_x\mathrm{Ga}_{1-x}\mathrm{As}$ layer using the Cl_2 assisted ion beam etching. After that, the sacrificial AlAs layer is dissolved in hydrofluoric acid (HF) diluted in water. HF attacks AlAs very selectively over $\mathrm{Al}_x\mathrm{Ga}_{1-x}\mathrm{As}$ for $x<0.4$ [13]. Therefore the percentage of Al in our $\mathrm{Al}_x\mathrm{Ga}_{1-x}\mathrm{As}$ layer is around 30%. Finally, the remaining PMMA may be dissolved in acetone.

Three scanning electron microscopy (SEM) pictures showing top views of fabricated microcavity structures are shown in Fig. 15. We are currently working to measure the passive optical properties of such microcavities in order to validate our theoretical predictions.

V. CONCLUSION

In conclusion, we have theoretically demonstrated that PC cavities can be designed for strong interaction with atoms trapped in one of the PC holes. At present we are working on further optimization of the design and the characterization of fabricated structures.

Critical issues for further investigation include efficient coupling of light in and out of the PC microcavity, as well as accurate estimation of surface effects that could perturb atomic radiative structure within the small defect hole. The extremely small mode volume in these structures also poses an interesting theoretical question of how standard cavity QED models must be modified when the single-photon Rabi frequency exceeds the atomic hyperfine spacing.

ACKNOWLEDGMENT

This work was supported by the Caltech MURI Center for Quantum Networks.

APPENDIX: THE EFFECT OF FRACTIONAL EDGE DISLOCATIONS

Any wavefront can be considered as a source of secondary waves that combine to produce distant wavefronts, according to the Huygens principle. Let us assume that we know the field distribution across the plane *S*, positioned in the near field, above the free-standing membrane and parallel to the membrane surface. The far fields can be considered as arising from the equivalent current sheets on this plane. Therefore, we can calculate the far field distribution and the total averaged radiated power into the half-space above the plane *S* [14]:

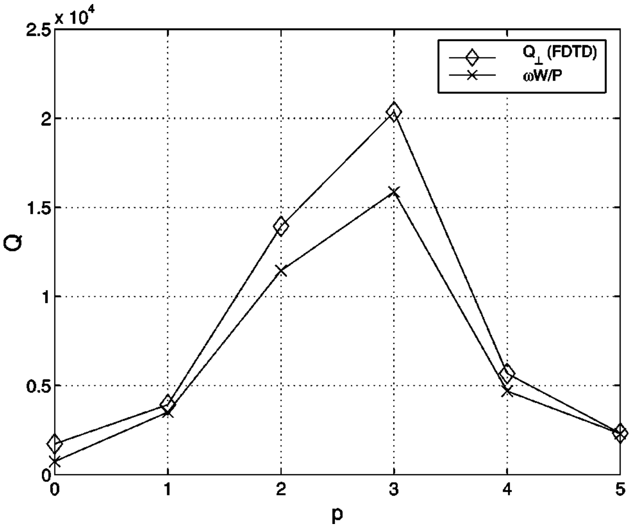

FIG. 16. Q factor computed using the FDTD method and from the expression (A1), for the structure analyzed in Sec. II A 2.

$$P=\frac{\eta}{8\lambda^2}\int_0^{\pi/2}\int_0^{2\pi}d_\theta d_\phi \sin(\theta)K(\theta,\phi),$$

$$K(\theta,\phi)=\left|N_\theta+\frac{L_\phi}{\eta}\right|^2+\left|N_\phi-\frac{L_\theta}{\eta}\right|^2, \tag{A1}$$

$$\eta=\sqrt{\frac{\mu_0}{\epsilon_0}},$$

where $\vec{N}$ and $\vec{L}$ represent radiation vectors, whose components in the rectangular coordinate system are proportional to Fourier transforms of tangential field components at the plane S [15]:

$$N_x=-FT_2(H_y)|_{\vec{k}_\parallel}, \tag{A2}$$

$$N_y=FT_2(H_x)|_{\vec{k}_\parallel}, \tag{A3}$$

$$L_x=FT_2(E_y)|_{\vec{h}_\parallel}, \tag{A4}$$

$$L_y=-FT_2(E_x)|_{\vec{k}_\parallel}, \tag{A5}$$

$$\vec{k}_\parallel=\frac{2\pi}{\lambda}\sin\theta(x\cos\phi+\hat{y}\sin\phi), \tag{A6}$$

$$FT_2(f(x,y))=\int\int_S d_x d_y f(x,y)e^{i(k_x x+k_y y)}. \tag{A7}$$

Therefore, just by knowing the Fourier transforms of the tangential field components at the plane S, we can evaluate the time-averaged radiated power P. From the previous expressions it is clear that the wave vector of interest $\vec{k}_\parallel$ lies within the light cone for any values of angles θ and ϕ in the circular polar coordinate system (i.e., $|\vec{k}_\parallel|\leqslant 2\pi/\lambda$). This implies that the radiated power P depends only on the wavevector components located within the light cone. It is also clear that by suppressing the Fourier components within the light cone, one can reduce P. Having in mind that for the x-dipole mode the E_y and H_x fields are odd with respect to both x and y symmetry axes, N_y and L_x do not contribute significantly to the integral in expression (A1) (they are both equal to zero at any point in the k space with either k_x or k_y equal to zero). On the other hand, E_x and H_y field components are even with respect to both x and y axes and their Fourier transforms are generally nonzero at small wave-vector values. However, by tuning the elongation factor p, one can balance the energy in the positive and negative field lobes and minimize the Fourier components of E_x and H_y within the light cone. This also leads to a decrease in the radiated power P. We can conclude that the improvement in the Q factor after the application of fractional edge dislocations is due to the suppression of the wave-vector components composing the defect mode, which are located within the light cone. A more detailed explanation of this phenomenon and how it can be used to improve Q factors of other types of modes will be presented in our forthcoming publications [15].

The Q factor of a mode can be expressed as $Q = \omega(W/P)$, where W is the total energy of a mode in the half-space $z \geqslant 0$. The comparison between the Q factor calculated using the method presented in this appendix, and $Q_{\perp}$ previously estimated using the FDTD, for the structure from the Sec. II A 2, is shown in Fig. 16. The plane S is positioned directly above the surface of the membrane in this case. From Fig. 5 follows that the total Q factor saturates at about 17 000, when the number of PC layers around the defect increases in the structure with $p = 3$. This is very close to the maximum Q value estimated from the expression (A1).

[1] O. Painter, R. Lee, A. Scherer, A. Yariv, J. O'Brien, P. Dapkus, and I. Kim, Science **284**, 1819 (1999).

[2] M. Lončar, D. Nedeljković, T. Doll, J. Vučković, A. Scherer, and T.P. Pearsall, Appl. Phys. Lett. **77**, 1937 (2000).

[3] H.J. Kimble, in *Cavity Quantum Electrodynamics*, edited by P. Berman (Academic, San Diego, 1994).

[4] O. Painter, J. Vučković, and A. Scherer, J. Opt. Soc. Am. B **16**, 275 (1999).

[5] E. Yablonovitch, T. Gmitter, R. Meade, A. Rappe, K. Brommer, and J. Joannopoulos, Phys. Rev. Lett. **67**, 3380 (1991).

[6] J. Vučković, M. Lončar, and A. Scherer, Proc. SPIE (to be published).

[7] J.D. Weinstein and K.G. Libbrecht, Phys. Rev. A **52**, 4004 (1995).

[8] M. Drndić, C.S. Lee, and R.M. Westervelt, Phys. Rev. B **63**, 085321 (2001).

[9] J. Reichel, W. Hansel, P. Hommelhoff, and T.W. Hansch, Appl. Phys. B: Lasers Opt. **B72**, 81 (2001).

[10] M. Bartenstein *et al.*, Int. J. Quantum Chem. **36**, 1364 (2000).

[11] G. Barton, Proc. R. Soc. London, Ser. A **453**, 2461 (1997).

[12] M. Chevroliier, M. Fichet, M. Oria, G. Rahmat, D. Bloch, and M. Ducloy, J. Phys. II **2**, 631 (1992).

[13] E. Yablonovitch, D. Hwang, T. Gmitter, L. Florez, and J. Harbison, Appl. Phys. Lett. **56**, 2419 (1990).

[14] S. Ramo, J. Whinnery, and T.V. Duzer, *Fields and Waves in Communication Electronics* (Wiley, New York, 1994).

[15] J. Vučković, M. Lončar, H. Mabuchi, and A. Scherer (unpublished).

Optimization of the Q Factor in Photonic Crystal Microcavities

Jelena Vučković, Marko Lončar, Hideo Mabuchi, and Axel Scherer

***Abstract*—We express the quality factor of a mode in terms of the Fourier transforms of its field components and prove that the reduction in radiation loss can be achieved by suppressing the mode's wavevector components within the light cone. Although this is intuitively clear, our analytical proof gives us insight into how to achieve the Q factor optimization, without the mode delocalization. We focus on the dipole defect mode in free-standing membranes and achieve $Q > 10^4$, while preserving the mode volume of the order of one half of the cubic wavelength of light in the material. The derived expressions and conclusions can be used in the optimization of the Q factor for any type of defect in planar photonic crystals.**

***Index Terms*—FDTD methods, Fourier transforms, integrated optics, optical resonators, optics, optoelectronic devices, Q factor.**

I. INTRODUCTION

ONE OF the greatest challenges in photonic crystal research is the construction of optical microcavities with small mode volumes and large quality factors, for efficient localization of light. Beside standard applications of these structures (such as lasers or filters), they can potentially be used for cavity QED experiments, or as building blocks for quantum networks. Although three-dimensional (3-D) photonic crystals offer the opportunity to manipulate light in all three dimensions in space, many research groups have focused their efforts on planar photonic crystals (i.e., two-dimensional (2-D) photonic crystals of finite depth) in recent years [1]–[13]. The fabrication procedures of planar photonic crystals are much simpler than those of their 3-D counterparts, but their light confinement is only "quasi-3D" and resulting from the combined action of the 2-D photonic crystal and internal reflection. The imperfect confinement in the third dimension produces some unwanted out-of-plane loss (radiation loss), which is usually a limiting factor in the performance of these structures. The problem of the Q factor optimization in planar photonic crystal microcavities has been addressed recently by several groups [2], [14]–[17]. The cavities that we proposed have a potential for achieving $Q > 10^4$ together with the mode volume of the order of one half of the cubic wavelength of light in the material [2], [16]. We have also recently demonstrated an experimental Q factor of 2800 in this type of structure, for which the theoretically predicted Q was around 4000 [18]. In our earlier work [2], we have only briefly addressed the mechanism behind the reduction of radiation loss in our structures: the suppression of wavevector components of the defect mode that are positioned within the light cone. In this paper, we discuss this phenomenon in detail and derive the analytical expression relating the Q factor of a mode to the Fourier transform of the mode pattern. We also show how to suppress the wavevector components within the light cone, without delocalizing a mode. Although our study focuses only on the dipole mode, the derived relations are universal and conclusions can be used in the optimization of the Q factor for any type of mode and defect in planar photonic crystals.

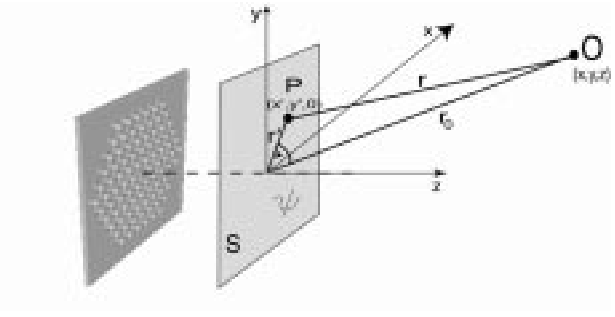

Fig. 1. Estimating the radiation field at the observation point O from the known near field at the surface S.

II. RELATION BETWEEN THE Q FACTOR AND THE FOURIER TRANSFORM OF A MODE

The 3-D finite difference time-domain (FDTD) analysis can provide us with the near-field distribution of the analyzed microcavity. FDTD analysis of the far field would require large amounts of computer memory and would be computationally inefficient. However, we can compute the far field starting from the known near-field distribution. Any wavefront can be considered as a source of secondary waves that add to produce distant wavefronts, according to Huygens principle. Let us assume that we know the field distribution across the surface S, positioned in the near field and above the free-standing membrane, as in Fig. 1. Our goal is to estimate the far field at the observation point O. The far fields can be considered as arising from the equivalent current sheets at the surface S [19]. For example, let S be the plane positioned at $z = 0$, parallel to the surface of the membrane, and at a small distance Δz from it. This choice of surface S will allow us to relate the Q factor of a mode to the Fourier transform of its field pattern. The equivalent sources in

Manuscript received September 18, 2001; revised January 8, 2002. This work was supported by the Caltech MURI Center for Quantum Networks.

J. Vučković is with the Edward L. Ginzton Laboratory, Stanford University, Stanford, CA 94305-4085 USA.

M. Lončar, H. Mabuchi, and A. Scherer are with the California Institute of Technology, Pasadena, CA 91125 USA.

Publisher Item Identifier S 0018-9197(02)05687-7.

0018-9197/02$17.00 © 2002 IEEE

the plane S can be represented in terms of the surface electric ($\vec{J}_s$) and magnetic ($\vec{M}_s$) currents

$$\vec{J}_s = \hat{n} \times \vec{H} = -\hat{x}H_y + \hat{y}H_x \tag{1}$$

$$\vec{M}_s = -\hat{n} \times \vec{E} = \hat{x}E_y - \hat{y}E_x \tag{2}$$

where $\hat{n}$ is a normal to the surface S, and $\vec{E}$ and $\vec{H} = \vec{B}/\mu_0$ are the electric and magnetic fields, respectively. In a homogeneous, isotropic medium above S, a retarded potential $\vec{A}$ and a second retarded potential $\vec{F}$ can be estimated from the previously introduced surface currents

$$\vec{A} = \mu_0 \int_S \frac{\vec{J}_s e^{-ikr}}{4\pi r}\, dS \tag{3}$$

$$\vec{F} = \epsilon_0 \int_S \frac{\vec{M}_s e^{-ikr}}{4\pi r}\, dS \tag{4}$$

where k is defined as $k = 2\pi/\lambda = \omega/c$ (λ is the mode wavelength measured in air) and r is the distance between the point where the potentials are evaluated and the surface element dS (i.e., between the points O and P).

From Fig. 1, it follows that $r \approxeq r_0 - r' \cos(\psi)$. Let us now introduce the radiation vectors $\vec{L}$ and $\vec{N}$

$$\vec{N} = \int_S \vec{J}_s e^{ikr' \cos(\psi)}\, dS \tag{5}$$

$$\vec{L} = \int_S \vec{M}_s e^{ikr' \cos(\psi)}\, dS. \tag{6}$$

Then we have

$$\vec{A} = \mu_0 \frac{e^{-ikr_0}}{4\pi r_0} \vec{N} \tag{7}$$

$$\vec{F} = \epsilon_0 \frac{e^{-ikr_0}}{4\pi r_0} \vec{L}. \tag{8}$$

From Fig. 1, we also have

$$kr' \cos(\psi) = \frac{k}{r_0}(xx' + yy') \tag{9}$$

where $(x', y', 0)$ are the coordinates of the point P in the plane S, and (x, y, z) are the coordinates of the observation point O.

From (5) and (6), it follows that radiation vectors $\vec{N}$ and $\vec{L}$ represent the 2-D Fourier transforms of the surface currents $\vec{J}_s$ and $\vec{M}_s$, evaluated at the value of the wavevector $\vec{k}_{||} = k(x/r_o\hat{x} + y/r_o\hat{y})$ (in rectangular coordinates), i.e., $\vec{k}_{||} = k\sin\theta(\cos\phi\hat{x} + \sin\phi\hat{y})$ in circular polar coordinates

$$\vec{N} = FT_2(\vec{J}_s)\Big|_{\vec{k}_{||} = k(x/r_0,\, y/r_0)} \tag{10}$$

$$\vec{L} = FT_2(\vec{M}_s)\Big|_{\vec{k}_{||} = k(x/r_0,\, y/r_0)} \tag{11}$$

$$FT_2(f(x, y)) = \iint d_x\, d_y f(x, y) e^{i\vec{k}_{||}\cdot(x, y)}$$
$$= \iint d_x\, d_y f(x, y) e^{i(k_x x + k_y y)}. \tag{12}$$

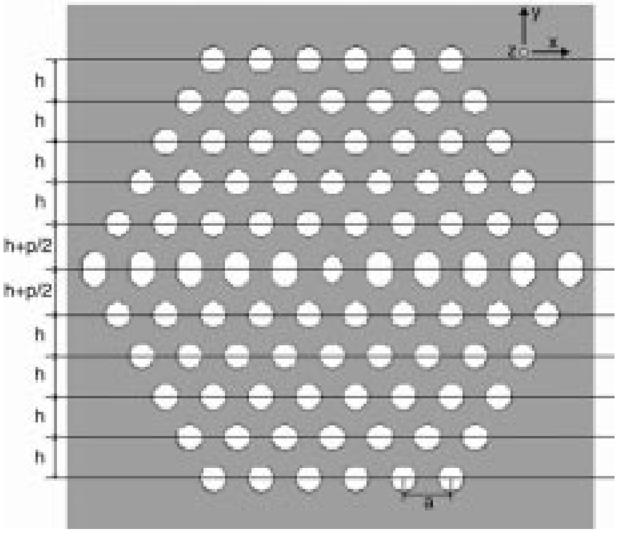

Fig. 2. Microcavity structure consisting of a single defect (produced by reducing the radius of the central hole to $r_{def}/a = 0.2$ from $r/a = 0.275$) and a fractional edge dislocation of order $p = 4$ along the x axis. The applied discretization is 20 pixels per periodicity a.

Components of radiation vectors can, therefore, be expressed in terms of the Fourier transforms of the field components at the surface S

$$N_x = -FT_2(H_y)|_{\vec{k}_{||}} \tag{13}$$

$$N_y = FT_2(H_x)|_{\vec{k}_{||}} \tag{14}$$

$$L_x = FT_2(E_y)|_{\vec{k}_{||}} \tag{15}$$

$$L_y = -FT_2(E_x)|_{\vec{k}_{||}} \tag{16}$$

$$\vec{k}_{||} = k\left(\frac{x}{r_0}, \frac{y}{r_0}\right) = k\sin\theta(\cos\phi\hat{x} + \sin\phi\hat{y}). \tag{17}$$

It is important to note that, for any observation point O, the previously introduced wavevector $\vec{k}_{||}$ lies within the light cone (i.e., $|\vec{k}_{||}| \leq k$, where $k = 2\pi/\lambda$). *Therefore, radiation vectors are purely determined by Fourier components located within the light cone.*

Far fields can be expressed in terms of retarded potentials as

$$\vec{E} = -i\omega\vec{A} - \frac{i\omega}{k^2}\nabla(\nabla \cdot \vec{A}) - \frac{1}{\epsilon_0}\nabla \times \vec{F} \tag{18}$$

$$\vec{H} = -i\omega\vec{F} - \frac{i\omega}{k^2}\nabla(\nabla \cdot \vec{F}) - \frac{1}{\mu_0}\nabla \times \vec{A}. \tag{19}$$

Under the assumption that all terms in fields decaying faster than $1/r_o$ can be neglected, the electric field components at an arbitrary point O are

$$E_\theta = \eta H_\phi = -i\frac{e^{-ikr_o}}{2\lambda r_o}(\eta N_\theta + L_\phi) \tag{20}$$

$$E_\phi = -\eta H_\theta = i\frac{e^{-ikr_o}}{2\lambda r_o}(-\eta N_\phi + L_\theta) \tag{21}$$

$$\eta = \sqrt{\frac{\mu_o}{\epsilon_o}} \tag{22}$$

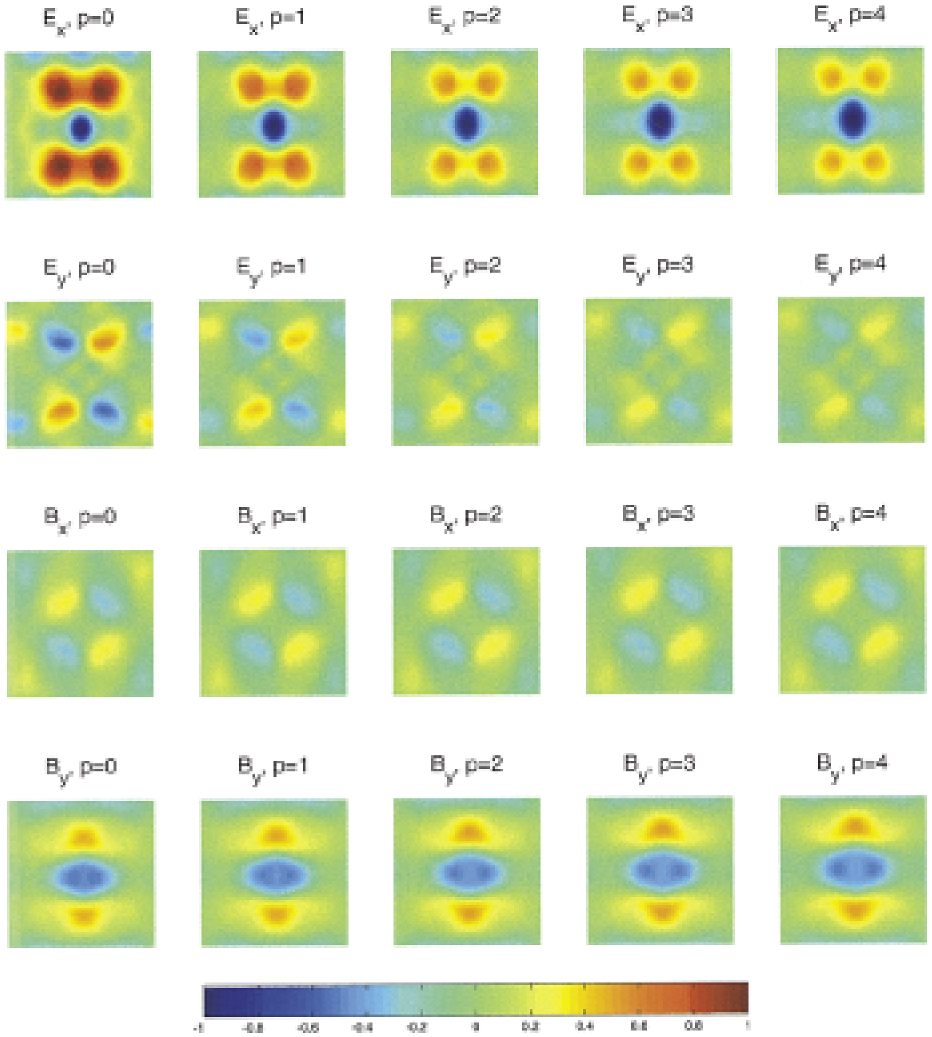

Fig. 3. Field components of the x-dipole mode at the surface S positioned at approximately $d/4$ from the surface of the membrane. The analyzed structure is shown in Fig. 2.

where (r_o, θ, ϕ) represent the coordinates of the point O in the spherical polar coordinate system. The radiation intensity (power per unit solid angle) is then equal to [19]

$$K(\theta, \phi) = \frac{\eta}{8\lambda^2}\left(\left|N_\theta + \frac{L_\phi}{\eta}\right|^2 + \left|N_\phi - \frac{L_\theta}{\eta}\right|^2\right) \tag{23}$$

and the total averaged power radiated into the half-space $z > 0$ is given by

$$P_1 = \int_0^{\pi/2}\int_0^{2\pi} d_\theta\, d_\phi \sin(\theta) K(\theta, \phi). \tag{24}$$

The radiation vectors in spherical polar coordinates can be expressed from their components in rectangular coordinates

$$N_\theta = (N_x \cos\phi + N_y \sin\phi)\cos\theta \tag{25}$$

$$N_\phi = -N_x \sin\phi + N_y \cos\phi \tag{26}$$

where N_x, N_y, L_x, and L_y were previously given as the 2-D Fourier transforms of the appropriate field components tangential to the surface S. Hence, just by knowing the Fourier transforms of the tangential field components at the plane S, we can evaluate the total averaged power radiated and the far-field distribution. Furthermore, the radiated power depends only on the wavevector components located within the light cone. Therefore, the reduction in radiation loss and the improvement in the Q factor can be achieved by suppressing the Fourier components within the light cone or by redistributing them outside the light cone.

In the case when most of the radiated power is collected at vertical incidence (i.e., at small θ), (24) can be simplified as follows:

$$\begin{aligned} P_2 &= \frac{\eta}{8\lambda^2 k^2} \iint\limits_{|\vec{k}_{||}|\le k} d\vec{k}\left(\left|N_x + \frac{L_y}{\eta}\right|^2 + \left|N_y - \frac{L_x}{\eta}\right|^2\right) \\ &= \frac{\eta}{8\lambda^2 k^2} \iint\limits_{|\vec{k}_{||}|\le k} d\vec{k}\left(\left|FT_2(H_y) + \frac{1}{\eta}FT_2(E_x)\right|^2 \right. \\ &\quad \left. + \left|FT_2(H_x) - \frac{1}{\eta}FT_2(E_y)\right|^2\right). \end{aligned} \tag{27}$$

The integral of the cross terms in (27) gives approximately one half of the radiated power. This can be proved easily by starting from the expansion of fields in terms of the Fourier components and the expression for the radiated power as the integral of the z component of the Poynting vector $\vec{\Gamma}$ over the surface S. This leads to the following expression for the averaged radiated power:

$$P_3 = 2\,\frac{\eta}{8\lambda^2 k^2} \iint\limits_{|\vec{k}_{||}| \le k} d\vec{k} \left(|FT_2(H_x)|^2 + |FT_2(H_y)|^2 + \frac{1}{\eta^2}\,|FT_2(E_x)|^2 + \frac{1}{\eta^2}\,|FT_2(E_y)|^2 \right). \quad (28)$$

It is important to note that, if some field component $u(x, y)$ is odd with respect to the x coordinate [i.e., $u(x, y) = -u(-x, y)$], then its Fourier transform must be equal to zero for any point in the Fourier space with $k_x = 0$. Similarly, any field component which is odd with respect to the y coordinate has a Fourier transform which is zero for any point with $k_y = 0$.

Let us introduce the radiation factor RF which is directly proportional to the radiated power P

$$RF_i = \frac{P_i}{W}, \qquad i = 1, 2, 3, \ldots \quad (29)$$

where W represents the total energy of a mode in the half-space above the middle of the membrane. The radiation Q factor of a mode (which is a measure of the radiation, out-of-plane loss) can be expressed as

$$Q = \omega\,\frac{W}{P} = \frac{\omega}{RF}. \quad (30)$$

III. EFFECT OF FRACTIONAL EDGE DISLOCATIONS ON THE Q FACTOR OF THE DIPOLE MODE IN FREE-STANDING MEMBRANES

We have recently proposed the design and fabrication of optical microcavities in free-standing membranes with $Q > 10^4$ for the dipole mode, and mode volumes of the order of one half of the cubic wavelength of light (measured in the material) [2], [16]. The dramatic improvement in Q factors over single defect microcavities (without a significant increase in the mode volume) was obtained by introducing a novel type of photonic crystal lattice defect, consisting of the elongation of holes along the symmetry axes. We call this type of defect a *fractional edge dislocation*, by analogy with edge dislocations in solid state physics. Edge dislocations are formed by introducing extra atomic planes into the crystal lattice. On the other hand, we insert here only fractions of the atomic planes along the symmetry axes of the photonic crystal, as shown in Fig. 2. Hole-to-hole distances are preserved under this deformation, and the half-spaces $y > p/2$ and $y < -p/2$ maintain the unperturbed photonic crystal geometry.

We consider again some of the microcavities that we proposed in [2]. The unperturbed photonic crystal parameters are $r/a = 0.275$, $d/a = 0.75$, and $n = 3.4$, where r, a, d, and n represent the hole radius, the periodicity of the triangular lattice, the thickness of the slab, and the refractive index of the semiconductor material, respectively. The choice of photonic crystal parameters is discussed in more detail in our previous work [2], [20]. Briefly, we limit the r/a ratio to rather modest values of around 0.3, in order to minimize the out-of-plane losses produced by the vertical scattering at the edges of holes. Since the reduction in r/a leads to a decrease in the size of the bandgap, it is important not to reduce the hole radius too much, in order to preserve the lateral confinement and small mode volume (e.g., we do not use r/a below 0.275). The d/a ratio of our structures is usually between 0.65 and 0.75, and we were able to design microcavities with very high Q factors at both ends of this range, without a significant change in the mode volume [2], [20]. The reasons for choosing this thickness range are the following: if the slab is too thin, the mode is not confined well within it vertically, and it interacts more strongly with the substrate (positioned at around $\lambda/2$ underneath the bottom membrane surface in our structures [2]), which reduces its Q factor. Furthermore, the fabrication of thin suspended membranes is difficult, and these structures are not robust. On the other hand, if d/a is too large, the structure is multimode in the vertical direction, which is also undesirable. In the FDTD method, we apply the discretization of 20 pixels per periodicity a. Therefore, a fractional edge dislocation of order $p = 1$ corresponds to the insertion of extra material whose thickness is equal to $1/20a$. In the microcavity of our interest, the central hole radius is decreased to $r_{\text{def}}/a = 0.2$ and a fractional edge dislocation of order p is applied along the x axis, as shown in Fig. 2. The dipole mode's frequency decreases as a function of the elongation parameter p [2], [20], and it is desirable to start in the elongation process with a mode whose frequency is close to the edge of the air band, allowing enough space to achieve the optimum $Q_{\perp}$ within the bandgap when the structure is tuned. In that case, the lateral

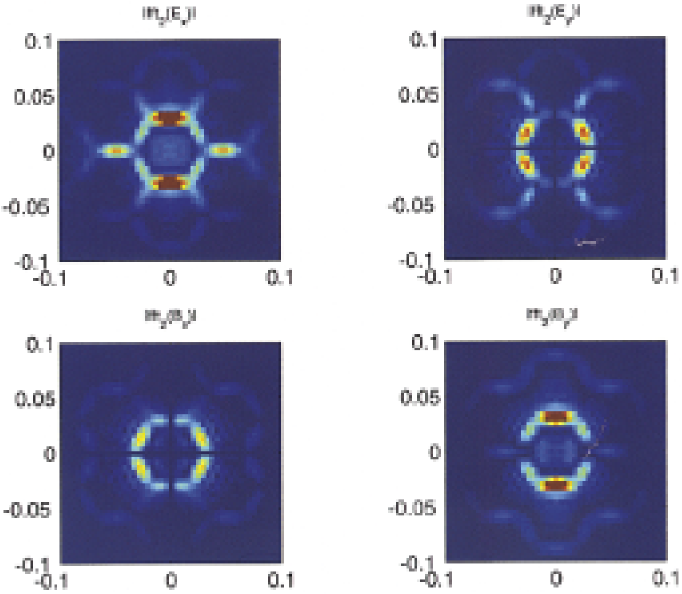

Fig. 4. Fourier components of the x-dipole mode in the structure from Fig. 2. A fractional edge dislocation is of the order $p = 0$ in this case. The light cone can be represented as a disk with the radius approximately equal to 0.015 located in the center of each square. The horizontal and vertical axes correspond to $k_x/2\pi$ and $k_y/2\pi$, respectively.

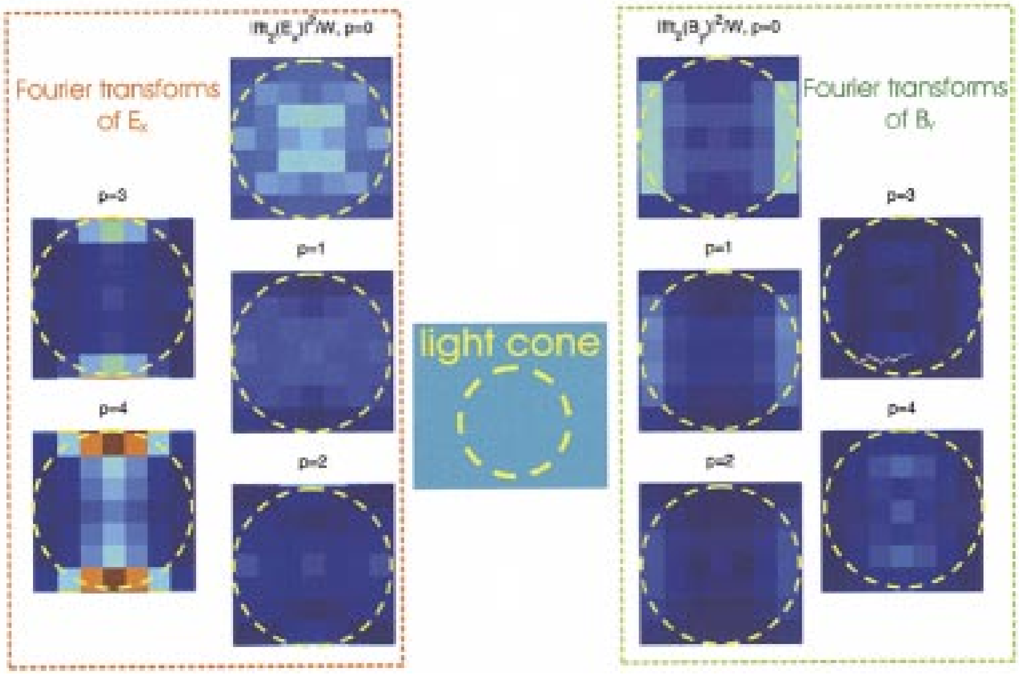

Fig. 5. The 2-D Fourier transforms of the even field components of the x-dipole mode in the structure shown in Fig. 2, as a function of the elongation parameter p. The light cone can be represented as a disk inscribed into the square. Clearly, the intensities of the Fourier transforms within the light cone are minimized for $p = 2$, where the Q factor reaches its maximum.

confinement is preserved and $Q_{||}$ can be improved by increasing the number of photonic crystal layers around the defect. This is one of the reasons for reducing the defect hole radius to only $0.2a$. The other reason is our long-term goal, a photonic crystal cavity QED with neutral atoms [2], for which we need a strong field intensity within an air hole large enough to place a neutral atom, without significant surface effects. Field components of the x-dipole mode in the analyzed structure are shown in Fig. 3, as a function of the elongation parameter p. For the x-dipole mode, the E_x and B_y components are even, while the E_y and B_x components are odd with respect to both symmetry axes x and y. Therefore, it is expected that E_y and B_x (i.e., L_x and N_y) do not contribute significantly to the radiated power in this case, since their Fourier transforms are equal to zero along both the k_x and k_y axes. This is also illustrated in Fig. 4. Therefore, in the case of the analyzed x-dipole mode we can approximate the expression (28) even further as

$$P_4 = 2\,\frac{\eta}{8\lambda^2 k^2} \iint\limits_{|\vec{k}_{||}|\leq k} d_{k_x} d_{k_y} \cdot \left(|FT_2(H_y)|^2 + \frac{1}{\eta^2}\,|FT_2(E_x)|^2 \right). \quad (31)$$

In order to minimize the radiated power, it is necessary to minimize (within the light cone) the Fourier transforms of the even field components E_x and B_y. In the general case, these Fourier transforms are nonzero at small values of $|\vec{k}_{||}|$ (i.e., in the light cone). However, they can be minimized by balancing the intensities of positive and negative field lobes. Indeed, we can observe in Fig. 3 that, by varying the elongation parameter p, we also tune the sizes of the central (negative) lobes in E_x and B_y, as well as the intensity distribution between the positive and negative lobes. Therefore, the tuning in p is expected to lead to tuning in the Fourier transforms of the even field components, and subsequently to tuning in radiated powers.

The Fourier components of the x-dipole mode in the structure with $p = 0$ are shown in Fig. 4. When the elongation parameter p changes in the analyzed range from 0 to 4, peaks in the Fourier space preserve their position, but their intensities are tuned. This can be observed in Fig. 5. Clearly, Fourier components within the light cone are minimized for $p = 2$, where the Q factor reaches its maximum. Therefore, the optimization of the Q factor of the dipole mode (after the application of fractional edge dislocations) is a result of suppression of the wavevector components within the light cone. This suppression is a product of balancing between the energies of the positive and negative field lobes of the even field components. The balancing is obtained by tuning the sizes of the negative lobes with insertion of extra material along the symmetry axis. The Q factor optimization is achieved in this case without a significant mode delocalization.

In our FDTD calculations [2], the total Q factor is separated into the lateral ($Q_{||}$) and vertical ($Q_{\perp}$) quality factors. $Q_{\perp}$ is a measure of radiation loss, while $Q_{||}$ corresponds to the loss through the mirrors in the lateral directions, which can be reduced by adding more layers of photonic crystal. The boundary for separation of vertical from lateral loss (i.e., $Q_{\perp}$ from $Q_{||}$) is positioned approximately at $\lambda/2$ from the surface of the membrane, as suggested in our early work [21]. We have discussed in our recent publication [2] that this choice of boundary excludes some small portion of radiation loss from $Q_{\perp}$, and the total Q factor of the analyzed dipole mode achievable by increasing the

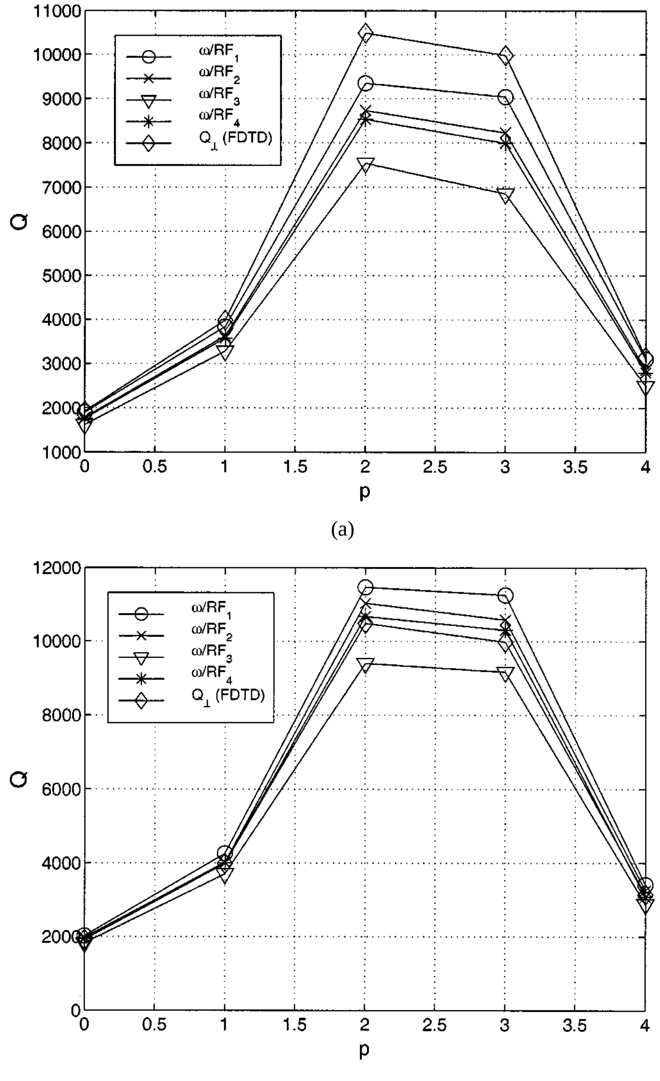

(a)

(b)

Fig. 6. Q factors estimated from the FDTD, or from the Fourier transforms of the tangential field components. The plane S is positioned (a) directly above the surface of the membrane, at a distance equal to $d/4$ from it, and (b) at a distance equal to $\lambda/2$ from the surface of the membrane.

number of the PC layers around the defect (also referred to as the limit of total Q factor) is somewhat smaller than $Q_\perp$. For this reason, we now believe that a better choice of boundary for separation of $Q_\perp$ from $Q_{||}$ would be the one positioned directly above the surface of the membrane. However, for the purpose of comparing our new results [2] with our earlier work [21], we preserve this boundary positioned at $\lambda/2$ from the surface of the membrane.

The radiation Q factors are evaluated using the method presented in this paper, and results are shown in Fig. 6. The plane S (above which we integrate the radiated power) is positioned directly above and at $\lambda/2$ above the surface of the membrane, in Fig. 6(a) and (b), respectively. Therefore, in the latter case, we expect a better agreement between the radiation Q factors (ω/RF) estimated using our new method and $Q_\perp$ estimated from the FDTD calculations, but in the former case the newly calculated Q factors are a better approximation of the limit of the total Q factors. In Fig. 6(a), $Q_\perp$ factors are larger than Q factors calculated as ω/RF, because ω/RF includes practically all radiation (out-of-plane) loss, while $Q_\perp$ includes only the radiation loss above $\lambda/2$ from the surface of the membrane. In Fig. 6(b), both the plane S and the boundary for separation of $Q_\perp$ from $Q_{||}$ are positioned at $\lambda/2$ from the membrane surface, and a better agreement with $Q_\perp$ from the FDTD simulations is observed. However, $Q_\perp$ is somewhat smaller, due to numerical inaccuracy. Radiation factors RF_2, RF_3, and RF_4 are estimated under the assumption that most of the radiation is collected at vertical incidence. This is not really true in the case of the x-dipole, for which reason there is an offset between the Q factors evaluated from RF_i, $i = 2, 3, 4$, and Q estimated from RF_1, which does not make any assumptions regarding the direction of radiation.

IV. CONCLUSION

We have presented a method for estimating the Q factor of a mode and its radiation loss from the known Fourier transform of the near-field distribution. By applying this approach to high Q structures that we have proposed recently [2], we have proven that the optimization of the Q factor of the dipole defect mode (after the application of fractional edge dislocations) results from the suppression of the wavevector components within the light cone. This suppression is a result of balancing between the positive and negative lobes in the even field components. The balancing is obtained by tuning the sizes of the negative lobes with insertion of extra material along the symmetry axis. Although our analysis focuses on the dipole mode only, a similar approach can be applied to any type of microcavity formed in planar photonic crystals.

ACKNOWLEDGMENT

One of the authors, J. Vučković, would like to thank Prof. Y. Yamamoto, Stanford University, Stanford, CA, for many fruitful discussions.

REFERENCES

[1] M. Lončar, D. Nedeljković, T. Doll, J. Vučković, A. Scherer, and T. P. Pearsall, "Waveguiding at 1500nm using photonic crystal structures in silicon on insulator wafers," *Appl. Phys. Lett.*, vol. 77, pp. 1937–1939, Sept. 2000.

[2] J. Vučković, M. Lončar, H. Mabuchi, and A. Scherer, "Design of photonic crystal microcavities for cavity QED," *Phys. Rev. E*, vol. 65, no. 016 608, Jan. 2001.

[3] O. Painter, R. Lee, A. Scherer, A. Yariv, J. O'Brien, P. Dapkus, and I. Kim, "Two-dimensional photonic band-gap defect mode laser," *Science*, vol. 284, pp. 1819–1821, June 1999.

[4] T. Yoshie, A. Scherer, H. Chen, D. Huffaker, and D. Deppe, "Optical characterization of two-dimensional photonic crystal cavities with indium arsenide quantum dot emitters," *Appl. Phys. Lett.*, vol. 79, no. 1, pp. 114–116, July 2001.

[5] P. Villeneuve, S. Fan, S. Johnson, and J. Joannopoulos, "Three dimensional photon confinement in photonic crystals of low-dimensional periodicity," *Proc. Inst. Elect. Eng.*, pt. J, vol. 145, pp. 384–390, Dec. 1998.

[6] D. Labilloy, H. Benisty, C. Weisbuch, C. Smith, T. Krauss, R. Houdre, and U. Oesterle, "Finely resolved transmission spectra and band structure of two-dimensional photonic crystals using emission from InAs quantum dots," *Phys. Rev. B*, vol. 59, pp. 1649–1652, Jan. 1999.

[7] S. Noda, A. Chutinan, and M. Imada, "Trapping and emission of photons by a single defect in a photonic bandgap structure," *Nature*, vol. 407, no. 6804, pp. 608–610, Oct. 2000.

[8] M. Boroditsky, R. Vrijen, T. Krauss, R. Coccioli, R. Bhat, and E. Yablonovitch, "Spontaneous emission extraction and Purcell enhancement from thin-film 2-D photonic crystals," *J. Lightwave Technol.*, vol. 17, pp. 2096–2112, Nov. 1999.

[9] J. K. Hwang, H. Y. Ryu, D. S. Song, I. Y. Han, H. W. Song, H. K. Park, Y. H. Lee, and D. H. Jang, "Room-temperature triangular-lattice two-dimensional photonic band gap lasers operating at 1.54 μm," *Appl. Phys. Lett.*, vol. 76, no. 21, pp. 2982–2984, May 2000.

[10] T. Baba, N. Fukaya, and A. Motegi, "Clear correspondence between theoretical and experimental light propagation characteristics in photonic crystal waveguides," *Electron. Lett.*, vol. 37, no. 12, pp. 761–762, June 2001.

[11] C. J. M. Smith, T. F. Krauss, H. Benisty, M. Rattier, C. Weisbuch, U. Oesterle, and R. Houdre, "Clear correspondence between theoretical and experimental light propagation characteristics in photonic crystal waveguides," *J. Opt. Soc. Amer. B*, vol. 17, no. 12, pp. 2043–2051, Dec. 2000.

[12] C. Monat, C. Seassal, X. Letartre, P. Viktorovitch, P. Regreny, M. Gendry, P. Rojo-Romeo, G. Hollinger, E. Jalaguier, S. Pocas, and B. Asper, "InP 2D photonic crystal microlasers on silicon wafer: Room temperature operation at 1.55 μm," *Electron. Lett.*, vol. 37, no. 12, pp. 764–766, June 2001.

[13] N. Kawai, K. Inoue, N. Carlsson, N. Ikeda, Y. Sugimoto, K. Asakawa, and T. Takemori, "Confined band gap in an air-bridge type of two-dimensional AlGaAs photonic crystal," *Phys. Rev. Lett.*, vol. 86, no. 11, pp. 2289–2292, Mar. 2001.

[14] S. G. Johnson, S. Fan, A. Mekis, and J. D. Joannopoulos, "Multipole-cancellation mechanism for high-Q cavities in the absence of a complete photonic band gap," *Appl. Phys. Lett.*, vol. 78, no. 22, pp. 3388–3390, May 2001.

[15] E. Miyai and and K. Sakoda, "Quality factor for localized defect modes in a photonic crystal slab upon a low-index dielectric substrate," *Opt. Lett.*, vol. 26, no. 10, pp. 740–742, May 2001.

[16] J. Vučković, M. Lončar, H. Mabuchi, and A. Scherer, "Photonic crystal microcavities for strong coupling between an atom and the cavity field," in *Proc. LEOS 2000*, Rio Grande, Puerto Rico, Nov. 2000.

[17] H. Y. Ryu, S. H. Kim, H. G. Park, J. K. Hwang, and Y. H. Lee, "Square-lattice photonic gand-gap sincle-cell laser operating in the lowest-order whispering gallery mode," , vol. 80, no. 21, pp. 3883–3885, May, 2002.

[18] T. Yoshie, J. Vučković, A. Scherer, H. Chen, and D. Deppe, "High quality two-dimensional photonic crystal slab cavities," *Appl. Phys. Lett.*, vol. 79, no. 26, pp. 4289–4291, Dec. 2001.

[19] S. Ramo, J. R. Whinnery, and T. Van Duzer, *Fields and Waves in Communication Electronics*. New York: Wiley, 1994.

[20] J. Vučković, "Photonic crystal structures for efficient localization or extraction of light," Ph.D. dissertation, California Inst. of Technology, Pasadena, 2002.

[21] O. Painter, J. Vučković, and A. Scherer, "Defect modes of a two-dimensional photonic crystal in an optically thin dielectric slab," *J. Opt. Soc. Amer. B*, vol. 16, no. 2, pp. 275–285, Feb. 1999.

Jelena Vučković received the Ph.D. degree in electrical engineering from the California Institute of Technology (Caltech), Pasadena, in 2002, for her work on photonic crystal-based optical and quantum optical devices.

She is presently a post-doctoral scholar in the Mesoscopic Quantum Optics Group at Stanford University, Stanford, CA, working on a single photon source based on a single quantum dot coupled to a micropost microcavity. Her research interests include photonic crystals, semiconductor cavity QED, quantum optics, and nanofabrication techniques.

Marko Lončar was born in Dubrovnik, Croatia, in 1974. He received the Diploma in engineering from the University of Belgrade, Yugoslavia, in 1997 and the M.S. degree in electrical engineering from California Institute of Technology (Caltech), Pasadena, in 1998. He is currently working toward the Ph.D. degree in electrical engineering at Caltech.

His research interests include design and fabrication of nano-optics devices and ultrasmall device processing techniques.

Hideo Mabuchi received the A.B. degree from Princeton University, Princeton, NJ, in 1992 and the Ph.D. degree in physics from the California Institute of Technology (Caltech), Pasadena, in 1998.

He has been on the Caltech faculty since 1998, currently as Associate Professor of Physics. His experimental and theoretical research span a range of topics from quantum measurement and quantum feedback to molecular biophysics.

Dr. Mabuchi is an Office of Naval Research Young Investigator and a John D. and Catherine T. MacArthur Foundation Fellow.

Axel Scherer received the B.S., M.S., and Ph.D. degrees from the New Mexico Institute of Mining and Technology in 1981, 1982 and 1985, respectively.

From 1985 until 1993 he worked in the Quantum Device Fabrication Group at Bellcore. Currently he is the Bernard E. Neches Professor of Electrical Engineering, Applied Physics, and Physics at the California Institute of Technology, Pasadena, specializing in device microfabrication. His research interests include design and fabrication of functional photonic, nanomagnetic, and microfluidic devices.

Distinguishing Separable and Entangled States

A. C. Doherty,[1] Pablo A. Parrilo,[2,3] and Federico M. Spedalieri[1]
[1]*Institute for Quantum Information, California Institute of Technology, Pasadena, California 91125*
[2]*Institut für Automatik, ETH Zürich, CH-8092, Switzerland*
[3]*Department of Control and Dynamical Systems, California Institute of Technology, Pasadena, California 91125*

(Received 12 December 2001; published 23 April 2002)

We show how to design families of operational criteria that distinguish entangled from separable quantum states. The simplest of these tests corresponds to the well-known Peres-Horodecki positive partial transpose (PPT) criterion, and the more complicated tests are strictly stronger. The new criteria are tractable due to powerful computational and theoretical methods for the class of convex optimization problems known as semidefinite programs. We successfully applied the results to many low-dimensional states from the literature where the PPT test fails. As a by-product of the criteria, we provide an explicit construction of the corresponding entanglement witnesses.

DOI: 10.1103/PhysRevLett.88.187904 PACS numbers: 03.67.–a, 03.65.Ca, 03.65.Ud

Entanglement is one of the most striking features of quantum mechanics. Not only is it at the heart of the violation of Bell inequalities [1], but it has lately been recognized as a very useful resource in the field of quantum information. Entanglement can be used to perform several important tasks such as teleportation, quantum key distribution, and quantum computation [2]. Despite its widespread importance, there is no procedure that can tell us whether a given state is entangled or not, and considerable effort has been dedicated to this problem [3,4]. In this Letter we apply powerful tools of optimization theory for problems known as semidefinite programs to construct a hierarchy of tests for entanglement.

A bipartite mixed state ρ is said to be separable [5] (not entangled) if it can be written as a convex combination of pure product states

$$\rho = \sum p_i |\psi_i\rangle\langle\psi_i| \otimes |\phi_i\rangle\langle\phi_i|, \tag{1}$$

where $|\psi_i\rangle$ and $|\phi_i\rangle$ are state vectors on the spaces $\mathcal{H}_A$ and $\mathcal{H}_B$ of subsystems A and B, respectively, and $p_i > 0$, $\sum_i p_i = 1$. If a state admits such a decomposition, it can be created by local operations and classical communication, and hence it cannot be an entangled state.

Several operational criteria have been proposed to identify entangled states. Typically these are based on simple properties obeyed by all separable states and are thus necessary but not sufficient conditions for separability (although some sufficient conditions for separability are known [6]). The most famous of these criteria is based on the partial transposition and was first introduced by Peres [7]. It was shown by Horodecki *et al.* [8] to be both necessary and sufficient for separability in $\mathcal{H}_2 \otimes \mathcal{H}_2$ and $\mathcal{H}_2 \otimes \mathcal{H}_3$. If ρ has matrix elements $\rho_{ik,jl} = \langle i| \otimes \langle k|\rho|j\rangle \otimes |l\rangle$ then the partial transpose ρ^{T_A} is defined by $\rho^{T_A}_{ik,jl} = \rho_{jk,il}$. If a state is separable, then it must have a positive partial transpose (PPT). To see this, consider the decomposition (1) for ρ. Partial transposition takes $|\psi_i\rangle\langle\psi_i|$ to $|\psi_i^*\rangle\langle\psi_i^*|$, so the result of this operation is another valid density matrix and must be positive. Thus any state for which ρ^{T_A} is not positive semidefinite is necessarily entangled. This criterion has the advantage of being very easy to check, but there are PPT states that are nonetheless entangled as was first demonstrated in [9].

Our separability criteria will also be based on simple computationally checkable properties of separable states. Let $\tilde{\rho}$, defined on $\mathcal{H}_A \otimes \mathcal{H}_B \otimes \mathcal{H}_A$, be given by

$$\tilde{\rho} = \sum p_i |\psi_i\rangle\langle\psi_i| \otimes |\phi_i\rangle\langle\phi_i| \otimes |\psi_i\rangle\langle\psi_i|. \tag{2}$$

First, $\tilde{\rho}$ is an extension of ρ (that is, the partial trace over the third party C is equal to ρ, $\mathrm{Tr}_C[\tilde{\rho}] = \rho$). Second, the state is symmetric under interchanging the two copies of $\mathcal{H}_A$. To put this more formally we define the swap operator P such that $P|i\rangle \otimes |k\rangle \otimes |j\rangle = |j\rangle \otimes |k\rangle \otimes |i\rangle$. We have $P^2 = I$, and $\pi = (I + P)/2$ is a projector onto the symmetric subspace. Since $\pi\tilde{\rho}\pi = \tilde{\rho}$, the extension $\tilde{\rho}$ has support only on this subspace. Finally the extension $\tilde{\rho}$ is a tripartite separable state. This means that it will have positive partial transposes with respect to any of the parties, and in particular we have $\tilde{\rho}^{T_A} \geq 0$ and $\tilde{\rho}^{T_B} \geq 0$.

We may now formulate an explicit separability criterion based on the existence of the extension discussed above. *If the state ρ on $\mathcal{H}_A \otimes \mathcal{H}_B$ is separable then there is an extension $\tilde{\rho}$ on $\mathcal{H}_A \otimes \mathcal{H}_B \otimes \mathcal{H}_A$ such that $\pi\tilde{\rho}\pi = \tilde{\rho}$, $\tilde{\rho}^{T_A} \geq 0$, and $\tilde{\rho}^{T_B} \geq 0$.* Note that the symmetry of the extension means that if $\tilde{\rho}^{T_A} \geq 0$ then $\tilde{\rho}^{T_C} \geq 0$, so including this would not make a stronger test. We may generalize this criterion to an arbitrary number of copies of both $\mathcal{H}_A$ and $\mathcal{H}_B$. *If the state ρ on $\mathcal{H}_A \otimes \mathcal{H}_B$ is separable then there is an extension $\tilde{\rho}$ with support only on the symmetric subspace of $\mathcal{H}_A^{\otimes k} \otimes \mathcal{H}_B^{\otimes l}$ such that $\tilde{\rho}$ has a positive partial transpose for all partitions of the $k + l$ parties into two groups.* Since the extensions are required to be symmetric, it is only necessary to test the possible partitions into two groups that are not related by permuting copies of $\mathcal{H}_A$ and $\mathcal{H}_B$. Including testing for positivity of the extension itself, there are $\lceil (k + 1)(l + 1)/2 \rceil$ distinct positivity checks to be satisfied by $\tilde{\rho}$.

© 2002 The American Physical Society

These results generate a hierarchy of necessary conditions for separability. The first is the usual PPT test for a bipartite density matrix ρ. If the test fails, the state is entangled; if the test is passed, the state could be separable or entangled. In the latter case we look for an extension $\tilde{\rho}$ of ρ to three parties such that $\pi\tilde{\rho}\pi = \tilde{\rho}$ satisfies the PPT test for all possible partial transposes. If no such extension exists, then ρ must be entangled. If such an extension is possible, the state could be separable or entangled, and we need to consider an extension to four parties, and so on.

Each test in this sequence is at least as powerful as the previous one. We can see this by showing that, if there is a PPT extension $\tilde{\rho}_n$ to n parties, then there must be a PPT extension $\tilde{\rho}_{n-1}$ to $n-1$ parties. Let $\tilde{\rho}_{n-1} = \mathrm{Tr}_X[\tilde{\rho}_n]$, X being one of the copies of A or B. Then $\tilde{\rho}_{n-1}$ will inherit from $\tilde{\rho}_n$ the property of having its support on the symmetric subspace. Let's assume that it is not PPT. Then there is a subset $\mathcal{I}$ of the parties such that $\tilde{\rho}_{n-1}^{T_{\mathcal{I}}}$ has a negative eigenvalue, where $T_{\mathcal{I}}$ represents the partial transpose with respect to all the parties in subset $\mathcal{I}$. Let $|e\rangle$ be the corresponding eigenvector and let $\{|i\rangle\}$ be a basis of the system X over which the partial trace was performed. Since $\tilde{\rho}_n$ is PPT, then $\langle e|\langle i|\tilde{\rho}_n^{T_{\mathcal{I}}}|e\rangle|i\rangle \geq 0$, for all i. Then

$$\sum_i \langle e|\langle i|\tilde{\rho}_n^{T_{\mathcal{I}}}|e\rangle|i\rangle = \langle e|\mathrm{Tr}_X[\tilde{\rho}_n^{T_{\mathcal{I}}}]|e\rangle \geq 0. \qquad (3)$$

Since $X \notin \mathcal{I}$, we can commute the trace and the partial transpose, and, using $\tilde{\rho}_{n-1} = \mathrm{Tr}_X[\tilde{\rho}_n]$, we have $\langle e|\tilde{\rho}_{n-1}^{T_{\mathcal{I}}}|e\rangle \geq 0$, which contradicts the fact that $|e\rangle$ is an eigenvector of $\tilde{\rho}_{n-1}^{T_{\mathcal{I}}}$ with negative eigenvalue.

The problem of searching for the extension can be solved efficiently, since it can be stated as a particular case of the class of convex optimizations known as *semidefinite programs* (SDP) [10]. A SDP corresponds to the optimization of a linear function, subject to a linear matrix inequality (LMI). A typical SDP will be

$$\begin{aligned} &\text{minimize} \quad c^T \mathbf{x}, \\ &\text{subject to} \quad F(\mathbf{x}) \geq 0, \end{aligned} \qquad (4)$$

where c is a given vector, $\mathbf{x} = (x_1, \ldots, x_m)$, and $F(\mathbf{x}) = F_0 + \sum_i x_i F_i$, for some fixed n-by-n Hermitian matrices F_j. The inequality in the second line of (4) means that the matrix $F(\mathbf{x})$ is positive semidefinite. The vector $\mathbf{x}$ is the variable over which the minimization is performed. In the particular instance in which $c = 0$, there is no function to minimize and the problem reduces to whether or not it is possible to find $\mathbf{x}$ such that $F(\mathbf{x})$ is positive semidefinite. This is termed a feasibility problem. The convexity of SDPs has made it possible to develop sophisticated and reliable analytical and numerical methods for them [10].

The separability criteria we introduced above may all be formulated as semidefinite programs. For brevity we will explicitly consider only the problem of searching for an extension of ρ to three parties. We will also relax the symmetry requirements on the extension $\tilde{\rho}$, and we will ask only $P\tilde{\rho}P = \tilde{\rho}$. This increases the size of the SDP, but simplifies the setup. Let $\{\sigma_i^A\}_{i=1,\ldots,d_A^2}$ and $\{\sigma_j^B\}_{j=1,\ldots,d_B^2}$ be bases for the space of Hermitian matrices that operate on $\mathcal{H}_A$ and $\mathcal{H}_B$, respectively, such that they satisfy

$$\mathrm{Tr}(\sigma_i^X \sigma_j^X) = \alpha\delta_{ij} \quad \text{and} \quad \mathrm{Tr}(\sigma_i^X) = \delta_{i1}, \qquad (5)$$

where X stands for A or B, and α is some constant—the generators of SU(n) could be used to form such a basis. We can then expand ρ in the basis $\{\sigma_i^A \otimes \sigma_j^B\}$, and write $\rho = \sum_{ij} \rho_{ij} \sigma_i^A \otimes \sigma_j^B$, with $\rho_{ij} = \alpha^{-2}\mathrm{Tr}[\rho\sigma_i^A \otimes \sigma_j^B]$. We can write the extension $\tilde{\rho}$ in a similar way

$$\begin{aligned} \tilde{\rho} = &\sum_{\substack{ij \\ i<k}} \tilde{\rho}_{kji}\{\sigma_i^A \otimes \sigma_j^B \otimes \sigma_k^A + \sigma_k^A \otimes \sigma_j^B \otimes \sigma_i^A\} \\ &+ \sum_{kj} \tilde{\rho}_{kjk} \sigma_k^A \otimes \sigma_j^B \otimes \sigma_k^A, \end{aligned} \qquad (6)$$

where we have explicitly used the symmetry between the first and third party. We also need to satisfy $\mathrm{Tr}_C(\tilde{\rho}) = \rho$. Using (5), and the fact that the $\sigma_i^A \otimes \sigma_j^B$ form a basis of the space of Hermitian matrices on $\mathcal{H}_A \otimes \mathcal{H}_B$, we obtain $\tilde{\rho}_{ij1} = \rho_{ij}$. The remaining components of $\tilde{\rho}$ will be the variables in our SDP. The LMIs come from requiring that the state $\tilde{\rho}$ and its partial transposes be positive semidefinite. For example, the condition $\tilde{\rho} \geq 0$ will take the form $F(\mathbf{x}) = F_0 + \sum_i x_i F_i \geq 0$ if we define

$$\begin{aligned} F_0 &= \sum_j \rho_{1j}\sigma_1^A \otimes \sigma_j^B \otimes \sigma_1^A + \sum_{i=2,j=1} \rho_{ij}\{\sigma_i^A \otimes \sigma_j^B \otimes \sigma_1^A + \sigma_1^A \otimes \sigma_j^B \otimes \sigma_i^A\}, \\ F_{iji} &= \sigma_i^A \otimes \sigma_j^B \otimes \sigma_i^A, \qquad i \geq 2, \\ F_{ijk} &= (\sigma_i^A \otimes \sigma_j^B \otimes \sigma_k^A + \sigma_k^A \otimes \sigma_j^B \otimes \sigma_i^A), \qquad k > i \geq 2. \end{aligned}$$

The coefficients $\tilde{\rho}_{ijk}(k \neq 1, k \geq i)$ play the role of the variable $\mathbf{x}$. There are $m = (d_A^4 d_B^2 - d_A^2 d_B^2)/2$ components of $\mathbf{x}$, where d_I is the dimension of $\mathcal{H}_I$. Each F is a square matrix of dimension $n = d_A^2 d_B$. Positivity of the partial transposes T_A and T_B leads to two more LMIs, $\tilde{\rho}^{T_A} \geq 0$ and $\tilde{\rho}^{T_B} \geq 0$. The F matrices for these two LMIs are related to the matrices F_{ijk} by the appropriate partial transposition. We can write these three LMIs as one, if we define the matrix $G = \tilde{\rho} \oplus \tilde{\rho}^{T_A} \oplus \tilde{\rho}^{T_B}$, so for example, $G_0 = F_0 \oplus F_0^{T_A} \oplus F_0^{T_B}$ (a block-diagonal matrix $C = A \oplus B$ is positive semidefinite if, and only if, both A and B are positive semidefinite). So the feasibility problem reduces to attempting to find $\tilde{\rho}_{ijk}(k \neq 1, k \geq i)$ with $G \geq 0$. In fact, the SDP corresponding to minimizing t subject to $tI_{ABA} + G \geq 0$ is always feasible and performs better numerically. A positive optimum gives a value of p^* such that $(1-p)\rho + pI_{AB}/d_A d_B$ is entangled for all $0 \leq p < p^*$. Looking for an extension on $\mathcal{H}_A^{\otimes k} \otimes \mathcal{H}_B^{\otimes l}$ is a semidefinite program with $m = \binom{d_A+k-1}{k}^2\binom{d_B+l-1}{l}^2 - d_A^2 d_B^2$ variables and a matrix G with $\lceil (k+1)(l+1)/2 \rceil$ blocks of dimension at most $\binom{d_A+\lceil k/2\rceil-1}{\lceil k/2\rceil}^2\binom{d_B+\lceil l/2\rceil-1}{\lceil l/2\rceil}^2$.

Numerical SDP solvers are described in detail in [10]. Typically they involve the solution of a series of least squares problems, each requiring a number of operations scaling with a problem size as $O(m^2n^2)$. For SDPs with a block structure these break into independent parts, each with a value of n determined by the block size. The number of iterations required is known to scale no worse than $O(n^{1/2})$. Thus for any fixed value of (k, l) the computation involved in checking our criteria scales no worse than $O(d_A^{13k/2} d_B^{13l/2})$ which is polynomial in the system size.

Using the SDP solver SeDuMi [11], we applied the first criterion ($k = 2, l = 1$) to several examples of PPT entangled states with $d_A = 2$, $d_B = 4$ or $d_A = 3$, $d_B = 3$. On a 500 MHz desktop computer a single state could be tested in under a second for $d_A = 2$, $d_B = 4$ and in about eight seconds for $d_A = 3$, $d_B = 3$. For the one and two parameter families of PPT entangled states described in [3,9,12] we performed a systematic search of the parameter space, in each case testing hundreds or thousands of different states. We checked 4000 randomly chosen examples of the seven parameter family of PPT entangled states in [13]. We also checked the PPT entangled states constructed from unextendable product bases in [14]. We did not find any PPT entangled state with an extension of the required form, thus verifying the entanglement of all these states. Very close to the separable states the test was inconclusive due to numerical uncertainties. Uncertainties and one example are discussed more fully below.

A very useful property of a SDP is the existence of the dual problem. If a problem can be stated as a SDP like (4), usually called the primal problem, then the dual problem corresponds to another SDP that can be written as

$$\begin{aligned} \text{maximize} \quad & -\operatorname{Tr}[F_0 Z] \\ \text{subject to} \quad & Z \geq 0 \\ & \operatorname{Tr}[F_i Z] = c_i\,, \end{aligned} \tag{7}$$

where the matrix Z is Hermitian and is the variable over which the maximization is performed. For any feasible solutions of the primal and dual problems we have

$$c^T \mathbf{x} + \operatorname{Tr}[F_0 Z] = \operatorname{Tr}[F(\mathbf{x})Z] \geq 0\,, \tag{8}$$

where the last inequality follows from the fact that both $F(\mathbf{x})$ and Z are positive semidefinite. Then, for the particular case of a feasibility problem ($c = 0$), Eq. (8) will read $\operatorname{Tr}[F_0 Z] \geq 0$. This result can be used to give a certificate of infeasibility for the primal problem: *if there exists* Z *such that* $Z \geq 0$, $\operatorname{Tr}[F_i Z] = 0$, *that satisfies* $\operatorname{Tr}[F_0 Z] < 0$, *then the primal problem must be infeasible.*

In the context of entanglement, the role of the "certificate" is played by observables known as *entanglement witnesses* (EW) [8,15]. An EW for a state ρ satisfies

$$\operatorname{Tr}[\rho_{\text{sep}} W] \geq 0 \quad \text{and} \quad \operatorname{Tr}[\rho W] < 0\,, \tag{9}$$

where ρ_{sep} is any separable state. If our primal SDP is infeasible (which means that the state ρ must be entangled), the dual problem provides a certificate of that infeasibility that can be used to construct an EW for ρ.

First, we note that, due to the block diagonal structure of the LMI, we can restrict any feasible dual solution Z to have the same structure, i.e., $Z = Z_0 \oplus Z_1^{T_A} \oplus Z_2^{T_B}$ where the Z_i are operators on $\mathcal{H}_A \otimes \mathcal{H}_B \otimes \mathcal{H}_A$. Second, we have $\operatorname{Tr}[G_0 Z] = \operatorname{Tr}[F_0(Z_0 + Z_1 + Z_2)]$. We defined F_0 as a linear function of ρ so that $F_0 = \Lambda(\rho)$, where Λ is a linear map from $\mathcal{H}_A \otimes \mathcal{H}_B$ to $\mathcal{H}_A \otimes \mathcal{H}_B \otimes \mathcal{H}_A$. We can now define an operator $\tilde{Z}$ on $\mathcal{H}_A \otimes \mathcal{H}_B$ through the adjoint map Λ^* such that $\tilde{Z} = \Lambda^*(Z_0 + Z_1 + Z_2)$ and

$$\operatorname{Tr}[\rho \tilde{Z}] = \operatorname{Tr}[\Lambda(\rho)(Z_0 + Z_1 + Z_2)] = \operatorname{Tr}[G_0 Z]\,. \tag{10}$$

If ρ_{sep} is any separable state, we know that the primal problem is feasible (the extension $\tilde{\rho}$ exists). Then, using $\operatorname{Tr}[G_0 Z] \geq 0$ and (10), we have $\operatorname{Tr}[\rho_{\text{sep}} \tilde{Z}] \geq 0$ for *any* $\tilde{Z}$ obtained from a dual feasible solution. For this particular problem, if the primal is not feasible (which means ρ is an entangled state), a feasible dual solution Z_{EW} that satisfies $\operatorname{Tr}[G_0 Z_{\text{EW}}] < 0$ always exists. Using (10) we can see that the corresponding operator $\tilde{Z}_{\text{EW}}$ satisfies $\operatorname{Tr}[\rho \tilde{Z}_{\text{EW}}] < 0$ which together with $\operatorname{Tr}[\rho_{\text{sep}} \tilde{Z}_{\text{EW}}] \geq 0$ means that $\tilde{Z}_{\text{EW}}$ is an entanglement witness for ρ.

In numerical work, if the SDP solver cannot find an extension $\tilde{\rho}$ it constructs the matrices Z_i. Evaluating $\operatorname{Tr}[\rho \tilde{Z}_{\text{EW}}]$ and verifying the three positivity conditions provide an *independent* check of the result. Unless this check is not conclusive—for example, if $\operatorname{Tr}[\rho \tilde{Z}_{\text{EW}}]$ is not significantly different from zero—we are able to definitively conclude that no $\tilde{\rho}$ exists.

If W is an EW, then for any product state $|xy\rangle$ we have

$$E(x, y) = \langle xy|W|xy\rangle = \sum_{ijkl} W_{ijkl} x_i^* y_j^* x_k y_l \geq 0\,, \tag{11}$$

where $\{x_i, y_i\}$ are the components of $|x\rangle$, $|y\rangle$ in some basis, and W_{ijkl} are the matrix elements of W in the same basis. Equation (11) states that the biquadratic Hermitian form E associated with W must be positive semidefinite (PSD). It is not hard to show that all of the EWs generated by Eq. (10) satisfy the relation

$$\begin{aligned} \langle xyx|\tilde{Z}_{\text{EW}} \otimes I|xyx\rangle &= \langle xyx|(Z_0 + Z_1 + Z_2)|xyx\rangle \\ &= \langle xyx|Z_0|xyx\rangle + \langle x^* yx|Z_1^{T_A}|x^* yx\rangle \\ &\quad + \langle xy^* x|Z_2^{T_B}|xy^* x\rangle\,. \end{aligned} \tag{12}$$

Since Z_0, $Z_1^{T_A}$, and $Z_2^{T_B}$ are positive by construction the biquadratic Hermitian form $E(x, y)\langle x\,|\,x\rangle$ has a decomposition as a sum of squared (SOS) magnitudes. This guarantees that $E(x, y)$ is PSD. It can be shown that our first separability criterion detects all entangled states that possess an EW such that E may be written in this form. The dual program to our initial SDP may be interpreted as a search for an entanglement witness of this type. Equally, the Peres-Horodecki criterion detects the entanglement of those states which possess entanglement witnesses for which (11) may be written directly as a SOS—the decomposable entanglement witnesses [16] such that $W = P + Q^{T_A}$ for some PSD P and Q. In general, if there is no EW W such that (11) is a SOS, we can search over W for which (11) is a SOS when multiplied by $\langle x \,|\, x\rangle^{k-1}\langle y \,|\, y\rangle^{l-1}$ for some $k,\ l \geq 1$. By duality, this corresponds to our (k, l) separability criterion.

As an example illustrating the methodology, consider the state described in [3], Section 4.6, given by

$$\rho_\alpha = \frac{2}{7}|\psi_+\rangle\langle\psi_+| + \frac{\alpha}{7}\sigma_+ + \frac{5-\alpha}{7}P\sigma_+P\,, \quad (13)$$

with $0 \leq \alpha \leq 5$, $|\psi_+\rangle = \frac{1}{\sqrt{3}}\sum_{i=0}^{2}|ii\rangle$, and $\sigma_+ = \frac{1}{3}(|01\rangle\langle 01| + |12\rangle\langle 12| + |20\rangle\langle 20|)$. Notice that ρ_α is invariant under the simultaneous change of $\alpha \longrightarrow 5 - \alpha$ and interchange of the parties. The state is separable for $2 \leq \alpha \leq 3$ and not PPT for $\alpha > 4$ and $\alpha < 1$. Numerically, entanglement witnesses could be constructed for ρ_α in the range $3 + \epsilon < \alpha \leq 4$ (and $1 \leq \alpha < 2 - \epsilon$) with $\epsilon \geq 10^{-8}$. A witness for $\alpha > 3$ can be extracted from these by inspection

$$\begin{aligned}\tilde{Z}_{\mathrm{EW}} = {}& 2(|00\rangle\langle 00| + |11\rangle\langle 11| + |22\rangle\langle 22|) + |02\rangle \\ & \times \langle 02| + |10\rangle\langle 10| + |21\rangle\langle 21| - 3|\psi_+\rangle\langle\psi_+|\,.\end{aligned}$$

This observable is non-negative on separable states:

$$\begin{aligned}2\langle xy|\tilde{Z}_{\mathrm{EW}}|xy\rangle\langle x \,|\, x\rangle = {}& |2x_0x_1y_2^* - x_2x_0y_1^* - x_1x_2y_0^*|^2 + |2x_0x_0^*y_0 - 2x_1x_0^*y_1 + x_1x_1^*y_0 - x_2x_0^*y_2|^2 \\ & + |2x_0x_0^*y_2 - 2x_1x_2^*y_1 + x_2x_2^*y_2 - x_0x_2^*y_0|^2 + |2x_0x_1^*y_0 - 2x_2x_2^*y_1 + x_2x_1^*y_2 - x_1x_1^*y_1|^2 \\ & + 3|x_2x_0y_1^* - x_1x_2y_0^*|^2 + 3|x_1x_1^*y_0 - x_2x_0^*y_2|^2 + 3|x_2x_2^*y_2 - x_0x_2^*y_0|^2 + 3|x_2x_1^*y_2 - x_1x_1^*y_1|^2 \\ \geq {}& 0\,.\end{aligned}$$

The expected value on the original state is $\mathrm{Tr}[\tilde{Z}_{\mathrm{EW}}\rho_\alpha] = \frac{1}{7}(3 - \alpha)$, demonstrating entanglement for all $\alpha > 3$.

The reformulation of our separability tests as a search for SOS decompositions of the forms $E(x, y)$ provides connections with existing results in real algebra (see [17] for a discussion of the SDP-based approach in a general setting). By Artin's positive solution to Hilbert's 17th problem, for any real PSD form $f(\mathbf{x})$ there exists a SOS form $h(\mathbf{x})$, such that the product $f(\mathbf{x})h(\mathbf{x})$ is SOS [18]. Finding such an $h(\mathbf{x})$ and SOS decomposition proves that f is PSD. For a fixed SOS form $h(x, y)$, we may write a SDP that attempts to find EWs such that $h(x, y)E(x, y)$ is SOS. In our hierarchy of criteria the form h is restricted to be $\langle x \,|\, x\rangle^{k-1}\langle y \,|\, y\rangle^{l-1}$. While it is conceivable that every PSD bi-Hermitian form is SOS when multiplied by appropriate factors of this type, currently we do not have a proof. Deciding whether a form is positive is computationally hard and so this connection to positive forms also promises to shed light on the computational complexity of the separability problem.

In this Letter we introduced a hierarchy of separability tests that are computationally tractable and strictly stronger than the PPT criterion. Only the second step in this sequence of tests was required to detect the entanglement of a wide class of known PPT entangled states. The method is based on the application of semidefinite programs. By exploiting the duality property of these problems, we showed how to construct entanglement witnesses for states that fail any separability test in the sequence. Finally, the wide range of applications of semidefinite programming, along with the work reported here and in [19], suggests that it may become a useful tool in quantum information and in quantum theory in general.

It is a pleasure to acknowledge conversations with Hideo Mabuchi, John Doyle, John Preskill, and Patrick Hayden.

This work was supported by the Caltech MURI Center for Quantum Networks, the NSF Institute for Quantum Information, and the Caltech MURI Center for Uncertainty Management for Complex Systems.

[1] J. S. Bell, Physics (Long Island City, N.Y.) **1**, 195 (1964).
[2] M. N. Nielsen and I. L. Chuang, *Quantum Computation and Quantum Information* (Cambridge University Press, Cambridge, 2000).
[3] M. Horodecki, P. Horodecki, and R. Horodecki, quant-ph/0109124.
[4] M. Lewenstein *et al.,* J. Mod. Opt. **47**, 2841 (2000).
[5] R. F. Werner, Phys. Rev. A **40**, 4277 (1989).
[6] S. L. Braunstein *et al.,* Phys. Rev. Lett. **83**, 1054 (1999).
[7] A. Peres, Phys. Rev. Lett. **77**, 1413 (1996).
[8] M. Horodecki, P. Horodecki, and R. Horodecki, Phys. Lett. A **223**, 1 (1996).
[9] P. Horodecki, Phys. Lett. A **232**, 333 (1997).
[10] L. Vandenberghe and S. Boyd, SIAM Rev. **38**, 49 (1996).
[11] J. Sturm, *SeDuMi version 1.05* 2001, available from http://fewcal.kub.nl/sturm/software/sedumi.html.
[12] P. Horodecki and M. Lewenstein, Phys. Rev. Lett. **85**, 2657 (2000).
[13] D. Bruss and A. Peres, Phys. Rev. A **61**, 030301(R) (2000).
[14] C. H. Bennett *et al.,* Phys. Rev. Lett. **82**, 5385 (2000).
[15] B. M. Terhal, Phys. Lett. A **271**, 319 (2000).
[16] M. Lewenstein, B. Kraus, J. I. Cirac, and P. Horodecki, Phys. Rev. A **62**, 052310 (2000).
[17] P. A. Parrilo, http://www.cds.caltech.edu/~pablo/pubs.
[18] B. Reznick, *Contemporary Mathematics* (American Mathematical Society, Providence, 2000), Vol. 253, pp. 251–272.
[19] E. M. Rains, quant-ph/0008047; K. Audenaert and B. D. Moor, quant-ph/0109155.

PHYSICAL REVIEW A, **66**, 023818 (2002)

Three-dimensional theory for interaction between atomic ensembles and free-space light

L. -M. Duan,[1,2,*] J. I. Cirac,[3] and P. Zoller[4]
[1]*Institute for Quantum Information, MC 107-81, California Institute of Technology, Pasadena, California 91125-8100*
[2]*Laboratory of Quantum Information, USTC, Hefei 230026, China*
[3]*Max Planck Institut fuer Quantenoptik, Hans Kopfermannstrasse 1, D-85748 Garching, Germany*
[4]*Institut fuer Theoretische Physik, Universitaet Innsbruck, A-6020 Innsbruck, Austria*

(Received 4 May 2002; published 27 August 2002)

Atomic ensembles have shown to be a promising candidate for implementations of quantum information processing by many recently discovered schemes. All these schemes are based on the interaction between optical beams and atomic ensembles. For description of these interactions, one assumed either a cavity-QED model or a one-dimensional light propagation model, which is still inadequate for a full prediction and understanding of most of the current experimental efforts that are actually taken in the three-dimensional free space. Here, we propose a perturbative theory to describe the three-dimensional effects in interaction between atomic ensembles and free-space light with a level configuration important for several applications. The calculations reveal some significant effects that were not known before from the other approaches, such as the inherent mode-mismatching noise and the optimal mode-matching conditions. The three-dimensional theory confirms the collective enhancement of the signal-to-noise ratio which is believed to be one of the main advantages of the ensemble-based quantum information processing schemes, however, it also shows that this enhancement needs to be understood in a more subtle way with an appropriate mode-matching method.

DOI: 10.1103/PhysRevA.66.023818 PACS number(s): 42.50.Gy, 03.67.−a

I. INTRODUCTION

Recently, many interesting schemes have been proposed that use atomic ensembles with a large number of identical atoms as the basic system for quantum state engineering and for quantum information processing. For instance, one can use atomic ensembles for generation of substantial spin squeezing [1–3] and continuous variable entanglement [4–6], for storage of quantum light [7–11], for realization of scalable long-distance quantum communication [12], and for efficient preparation of many-party entanglement [13]. The experimental candidates of atomic ensembles can be either some cold or ultracold atoms in a trap [2,10], or a cloud of room-temperature atomic gas contained in a glass cell with coated walls [3,6,11]. The schemes based on atomic ensembles have some special advantages compared with the quantum information schemes based on the control of single particles: first, laser manipulation of atomic ensembles without separately addressing the individual atoms is normally easier than the coherent control of single particles; second, and more important, atomic ensembles with suitable level configurations could have some kinds of collectively enhanced coupling to certain optical mode (called the signal light mode) due to the many-atom interference effects. Thanks to this enhanced coupling, we can obtain collective enhancement of the signal-to-noise ratio (that is, the ratio between the controllable coherent interaction and the uncontrollable noisy interactions) compared with the single-particle case if we choose to manipulate the appropriate atomic and optical modes. This collective enhancement plays an important role in all the recent schemes based on the atomic ensembles.

To describe the interaction between atomic ensembles and optical beams, in particular, to understand the collective enhancement of the signal-to-noise ratio, normally one assumes a simple cavity-QED model [7,8,12,1] or a one-dimensional light propagation model [9,4] with an independent spontaneous emission rate for each atom. In contrast to this, most of the current experiments are done with free-space atomic ensembles coupling directly to the three-dimensional optical beams [3,6,10,11]. It is not obvious that the predictions from the simple models will always be valid for this real, much more complicated, experimental situations. To fully predict and understand the real experiments, one needs to answer various questions associated with the three-dimensional interaction effects, for instance, what is the inherent mode structure of the signal light when we have a definite geometry of the atomic ensemble? Can we achieve a good mode matching with the matching efficiency in principle arbitrarily close to one? What is the noise magnitude associated with density fluctuation (induced by the random initial distribution of the atom positions and the random atomic motion) of the atomic ensemble? In the three-dimensional configuration, is there still the collective enhancement of the signal-to-noise ratio?

In this paper, we will try to provide answers to the above important questions for a Raman-type Λ-level configuration that is useful for scalable long-distance quantum communication [12] and for many-party entanglement generation [13]. In general, it is very challenging to build a full quantum theory from the first principles to describe the interaction between the many-atom ensemble and the infinite-mode optical field and to give definite answers to the above-listed questions. In this paper, we will use a perturbative approach by assuming that the Raman pumping laser is very weak. There are several motivations to use a perturbative approach: first, the schemes in Refs. [12,13] for scalable quantum com-

---

[*] Email address: lmduan@caltech.edu

©2002 The American Physical Society

munication and for many-party entanglement generation can work in the weak-pumping limit, so the perturbative approach describes a useful realistic situation. Second, the perturbative calculations allow us to investigate the three-dimensional effects and to give definite answers to the questions listed above from the first principles without any doubtful approximation. Finally, we expect that the three-dimensional effects should be at least to some extent independent of the power of the pumping laser, so the perturbative calculations could give at least some indications for the three-dimensional interaction picture in other regions.

The calculations reveal some significant results that are unexpected from the simple models, for instance, it turns out that due to the density fluctuation of the atomic ensemble, there will be two sources of noise for the light–atomic-ensemble interaction: one is the spontaneous emission loss and the other is the inherent mode-mismatching noise (here, by ‘‘inherent,’’ we mean that this mode mismatching is not from any technical imperfection). Thus, we need to use two quantities to describe the signal-to-noise ratios, and need to keep a balance between these two sources of noise by appropriate mode-matching methods to optimize the setup for applications. The intuitive mode-matching method will result in a quite large inherent mode mismatching noise. It is better to use some other mode-matching methods that reduce the mode-matching noise at the cost of increasing the spontaneous emission loss. This can optimize the setup for some applications, such as the ones in Refs. [12,13], since there the spontaneous emission loss has a far less important influence. The calculations in this paper also demonstrate that in the realistic three-dimensional configuration, one can still obtain large collective enhancement of the signal-to-noise ratio for atomic ensembles compared with the single-atom case, which is an important feature of this kind of systems.

It is also helpful to make a comparison between the collective enhancement of the signal-to-noise ratio we consider here and some other collective optical effects, such as the super-radiance. The similarity lies in that both phenomena involve many-atom interference. However, there are also important differences. For super-radiance, it is a stimulated emission effect, and the enhancement is in the emission speed. At the initial stage, coherence is built between different atoms from the spontaneous emissions. After the coherence has been built, super-radiance can be understood even from a classical interference picture. For the light–atomic-ensemble interaction considered here, we are still completely in the spontaneous emission region that needs a full quantum description, and the enhancement is not in the emission speed, but in the signal-to-noise ratio when we only manipulate and measure a definite atomic mode (called the symmetric collective atomic mode) and a definite signal light mode (which is the optical mode collinear with the Raman pumping light). The coupling between the above atomic and the optical modes are coherent for different atoms (which means, for this coupling there is a certain phase relation between different atoms), while the coupling of these two modes to other atomic and other optical modes (called the noise modes) are inherent with random phase relations between different atoms (the randomness comes from the random atom positions). We have collective enhancement of the signal-to-noise ratio since the coherent coupling interferes constructively for different atoms. Of course, in the three-dimensional free space, there are infinite optical modes, and the signal light mode changes continuously to other noisy optical modes when we continuously vary the solid angle. Due to the continuous change from the coherent coupling to the inherent coupling, we have nontrivial mode-matching problem, and we get some inherent mode-mismatching noise.

We also would like to mention that there are some early important works on the transverse effects of the Raman interaction by using the three-dimensional light propagation equations [14]. However, it is not clear to us how to use this approach to describe the collective enhancement of the signal-to-noise ratio, and in particular, how to give definite answers to the questions listed above. There is also some unpublished effort to try to figure out the three-dimensional effects in another light-atom interaction configuration [15]. The interaction picture is not yet clear to us.

This paper is arranged as follows: in Sec. II, we explain the interaction scheme and the basic ideas of the applications of this interaction scheme for quantum information processing. With the applications in mind, we can focus our efforts on the most relevant quantities that we need to calculate. We will also explain in this section the basic interaction picture between the light and the atomic ensemble from our calculations. Then, in the next section, we will describe the theoretical model for this light-atom interaction from the first principles, and solve this model by using a perturbative approach. In Sec. IV, we will discuss the properties of this solution, in particular, we will define and calculate the mode structure of the signal light, the spontaneous emission inefficiency, and the inherent mode-mismatching noise. Section V is devoted to the discussion of the appropriate mode matching methods for real experiments. We show that by appropriate mode matching methods, we can keep a balance between the two sources of noise mentioned above in order to optimize this setup for applications. Finally, in Sec. VI we summarize the results.

II. THE INTERACTION SCHEME AND ITS APPLICATIONS

The basic element of our system is an atomic ensemble, that consists of a cloud of N_a identical atoms with the relevant level structure shown in Fig. 1. A pair of metastable lower states $|g\rangle$ and $|s\rangle$ can correspond, for instance, to hyperfine or Zeeman sublevels of electronic ground state of alkali atoms. The relevant coherence between the levels $|g\rangle$ and $|s\rangle$ can be maintained for a long time, as has been demonstrated both experimentally [6,10,11] and theoretically [7–9]. All the atoms are initially prepared in the ground state $|g\rangle$ through optical pumping.

The ensemble is then illuminated by a weak pumping laser pulse that couples the transition $|g\rangle \rightarrow |e\rangle$ with a large detuning Δ, and we look at the spontaneous emission light from the transition $|e\rangle \rightarrow |s\rangle$, whose polarization and/or frequency are assumed to be different from the pumping laser.

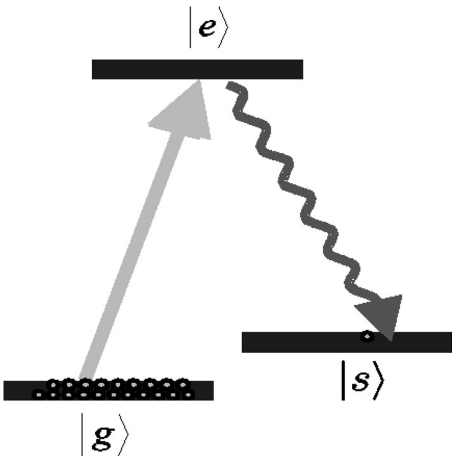

FIG. 1. The relevant atomic level structure with $|g\rangle$, $|s\rangle$, a pair of ground or metastable states, and $|e\rangle$, the excited state.

There are two interaction configurations: in the first configuration, the pumping laser is shined on all the atoms so that each atom has an equal small probability to be excited into the state $|s\rangle$ through the Raman transition. In the second configuration, as is reported in the experiment [6], the pumping laser is focused with a transverse area smaller than the transverse area of the atomic ensemble, so only part of the atoms are illuminated by the laser at each instant. However, during the light-atom interaction period, all the atoms in the ensemble are moving fast, and they frequently enter and leave the interaction region. As a result, each atom still has an equally small probability to be excited into the state $|s\rangle$.

As we will show in the next section, after the atomic gas interacts with a weak pumping laser, there will be a special atomic mode s_s, called the symmetric collective atomic mode, and a special optical spontaneous emission mode a_s (which couples to the transition $|e\rangle\rightarrow|s\rangle$), called the signal light mode. The symmetric collective atomic mode s_s and the signal light mode a_s are defined, respectively, by

$$s_s \equiv (1/\sqrt{N_a})\sum_{i=1}^{N_a} |g\rangle_i\langle s|, \tag{1}$$

$$a_s = \int f_{\mathbf{k}}^{*} a_{\mathbf{k}} d^3\mathbf{k}, \tag{2}$$

where $a_{\mathbf{k}}$ represents the plane-wave mode with the wave vector $\mathbf{k}$ (we have used the plane-wave modes as the eigenmodes for the expansion of the optical spontaneous emission field). The operators $a_{\mathbf{k}}$ satisfy the standard commutation relations $[a_{\mathbf{k}}, a_{\mathbf{k}'}^{\dagger}] = \delta(\mathbf{k}-\mathbf{k}')$, and $f_{\mathbf{k}}^{*}$ is the normalized signal mode function whose explicit form will be specified in Sec. IV. We just need to mention here that a_s represents the spontaneous emission light that is basically collinear with the pumping laser, with a distribution only over a very small solid angle. The particularity of the modes s_s and a_s comes from the fact that they are dominantly correlated with each other, which means, if an atom is excited to the symmetric collective mode s_s, the accompanying spontaneous emission photon will most probably go to the signal light mode a_s, and vice versa. There are still many other atomic modes in the ensemble and infinite other optical modes in the spontaneous emission field, and these atomic and optical modes are correlated with each other in a complicated way. However, the correlation between the good modes s_s and a_s is quite "pure," and these two modes are only weakly correlated with the other atomic and optical modes that contribute to noise. The correlation between the atomic mode s_s and other optical modes contributes to the spontaneous emission loss, and the correlation between the signal mode a_s and other atomic modes contributes to the inherent mode-mismatching noise. The interaction picture for this system is schematically shown in Fig. 2.

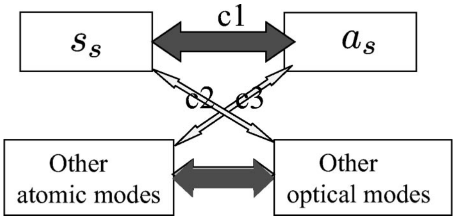

FIG. 2. For a many-atom ensemble, The intuitive interaction picture between the atomic modes and the free-space optical modes, where $c1$ represents the "good" correlation between the collective atomic mode and the signal light mode, $c2$ represents the spontaneous emission loss, and $c3$ represents the inherent mode-mismatching noise. Broader connections stand for stronger correlations between the excitations in the corresponding modes.

The applications of this system for quantum information processing exactly comes from the almost pure correlation between the modes s_s and a_s. If we neglect the weak correlations between the good modes s_s, a_s and the other noisy atomic and optical modes, that is, if we neglect the two sources of noise illustrated in Fig. 2, then all the noisy modes can be traced over, and we get effectively a two-mode problem. The excitations in the modes s_s and a_s can be both separately measured. For the signal mode a_s, this is done through a single-photon detector with an appropriate mode-matching; and for the atomic mode s_s, this can be done by first mapping the atomic excitation to an excitation in the signal mode through a repumping laser pulse [12], and then detecting it again through a single-photon detector. Using the almost pure correlation between the modes s_s and a_s, one can generate some preliminary entanglement between two distant atomic ensembles by only linear optics means, which forms the important first step for applications of this setup for different kinds of quantum information processing tasks detailed in Refs. [12,13]. Here, we will briefly explain the basic ideas on how to entangle atomic ensembles using the correlation between the modes s_s and a_s. This explanation helps us to define the most relevant quantities for the applications that we need to calculate.

The setup for entanglement generation between the two distant atomic ensembles L and R is shown in Fig. 3. We apply simultaneously two short Raman pumping pulses on the ensembles L and R, respectively, so that for each ensemble the light scattered to the signal mode a_s has a mean photon number much smaller than 1. The signal modes are then coupled to optical channels (such as fibers) through

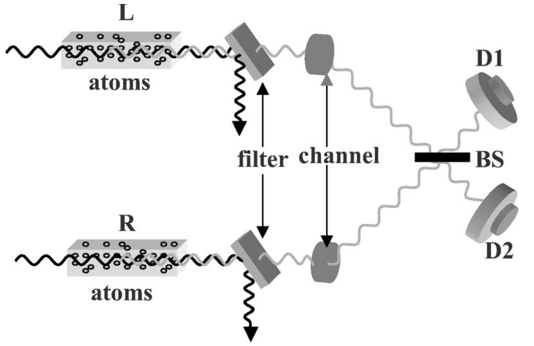

FIG. 3. The schematic setup for generating entanglement between two distant atomic ensembles *L* and *R*.

mode matching after the filters, which are polarization and frequency selective to filter the pumping light. The signal pulses after the transmission channels interfere at a 50%-50% beam splitter (BS), with the outputs detected respectively by two single-photon detectors $D1$ and $D2$. If either $D1$ or $D2$ registers one photon, the process is finished. Otherwise, we first apply a repumping laser pulse to the transition $|s\rangle \rightarrow |e\rangle$ on the ensembles *L* and *R* to set the atoms back to the ground state $|g\rangle$, then the same Raman driving pulses as the first round are applied to the transition $|g\rangle \rightarrow |e\rangle$ and we detect again the photon number of the signal modes after the beam splitter. This process is repeated until finally we have a click in either $D1$ or $D2$ detector.

We show now how the entanglement is generated between the ensembles *L* and *R* if we successfully register one photon in $D1$ or $D2$ detector. To understand this, let us first look at one ensemble. Before the Raman pumping pulse, the collective atomic mode s_s and the signal light mode a_s are in vacuum states, which are denoted respectively by $|0_a\rangle$, $|0_p\rangle$. If we neglect the small noisy correlations, after the weak pumping, the state of the modes s_s and a_s has the following form (see the next section for the detailed derivation):

$$|\phi\rangle = |0_a\rangle|0_p\rangle + \sqrt{p_c} s_s^\dagger a_s^\dagger |0_a\rangle|0_p\rangle + o(p_c), \tag{3}$$

where $p_c \ll 1$ is the probability for one atom excited to the collective atomic mode s_s, and $o(p_c)$ represents the high-order terms with more excitations whose probabilities are equal to or smaller than p_c^2.

In Fig. 3, the pumping pulses excite both ensembles simultaneously, the whole system is thus described by the state $|\phi\rangle_L \otimes |\phi\rangle_R$, where $|\phi\rangle_L$ and $|\phi\rangle_R$ are given by Eq. (1) with all the operators and states distinguished by the subscript *L* or *R*, respectively. The two signal light modes are superposed at the beam splitter, and a photodetector click in either $D1$ or $D2$ measures, respectively, the operators $a_+^\dagger a_+$ or $a_-^\dagger a_-$ with $a_\pm = (a_{sL} \pm e^{i\varphi} a_{sR})/\sqrt{2}$. Here, φ denotes the difference of the phase shifts in the two-side optical channels. Conditional on the detector click, we should apply a projection operator a_+ or a_- onto the whole state $|\phi\rangle_L \otimes |\phi\rangle_R$. If we neglect the high-order corrections in Eq. (3), the projected state of the ensembles *L* and *R* thus has the form

$$|\Psi_\varphi\rangle_{LR}^{\pm} = (s_{sL}^\dagger \pm e^{i\varphi} s_{sR}^\dagger)/\sqrt{2}|0_a\rangle_L|0_a\rangle_R, \tag{4}$$

which is maximally entangled in the excitation number basis. The generation of this kind of state forms the basis of further applications in quantum information processing [12,13]. If we take into account the high-order terms in Eq. (3), the fidelity between the actually generated state and the ideal state (4) will decrease by an amount proportional to p_c, and this decrease will contribute to the final fidelity imperfection of the schemes in Refs. [12,13]. For the applications described by these schemes, we need to fix the fidelity imperfection to be small, which means that we should keep a small excitation probability p_c by controlling the intensity of the Raman pumping laser.

Now we look at the influence of the two types of noisy correlations illustrated in Fig. 2. The spontaneous emission loss can be quantified by the probability p_{spon} of the event that the scattered photon goes to some other optical modes instead of the signal mode a_s while the accompanying atom is excited to the collective atomic mode s_s. Without the spontaneous emission loss, for each round of Raman pumping, we succeed with a probability $2p_c$ to get a detector click, which prepares the entangled state (4). However, the spontaneous emission loss means that even if an atom is excited to the mode s_s (which has a probability p_c for each ensemble), the accompanying photon, with a probability $1-p_{\mathrm{spon}}$, cannot be registered. For entanglement generation, the fidelity imperfection to the ideal state (4) is given by the excitation probability of the atomic mode s_s, which is now $p_c/(1-p_{\mathrm{spon}})$ instead of p_c [we always use p_c to denote the possibility of the good event described by Eq. (3)]. To fix the fidelity imperfection to be small, in the presence of the spontaneous emission loss, we need to further decrease the excitation probability p_c by a factor of $1-p_{\mathrm{spon}}$, which means that we have a smaller probability to register one signal photon. So, as a result of this noise, the preparation efficiency (the success probability of the scheme) is decreased by a factor of $1-p_{\mathrm{spon}}$ when we fix the fidelity imperfection.

The inherent mode-mismatching noise can be quantified by the probability p_{mode} of the event that an atom is excited to some other atomic modes instead of the collective mode s_s while the accompanying photon goes to the right signal mode a_s. In this case, we can register a photon from the single-photon detectors, but the atomic mode s_s will be actually still in the initial vacuum state $|0_a\rangle$. So, this noise will add some vacuum component to the generated state between the ensembles *L* and *R*. In the presence of this noise, the generated state between the ensembles *L* and *R* is mixed with the form

$$\rho_{LR}(c_0,\varphi) = \frac{1}{c_0+1}(c_0|0_a0_a\rangle_{LR}\langle 0_a0_a| + |\Psi_\varphi\rangle_{LR}^{+}\langle\Psi_\varphi|), \tag{5}$$

where the vacuum coefficient c_0 is basically given by the conditional probability p_{mode} for this noise contribution. Actually, as has been shown in Ref. [12], there are other sources of noise which can contribute to the vacuum coefficient c_0, such as the detector dark counts, and the detector inefficiency in the succeeding entanglement connection scheme detailed in Ref. [12]. It has also been shown there that the vacuum

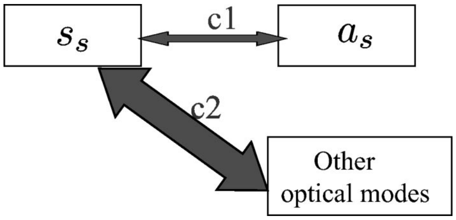

FIG. 4. The intuitive interaction picture for the single-atom case with the corresponding symbols having the same meaning as Fig. 2. There is only one atomic mode, but the spontaneous emission loss represented by $c2$ becomes much larger compared with the good correlation $c1$.

component noise will be finally automatically purified, and thus has no influence on the final communication fidelity. However, it has a more significant influence on the efficiency than the spontaneous emission loss. For applications in Refs. [12,13], to get a better overall efficiency, it is better to keep a balance between the mode-mismatching noise p_{mode} and the spontaneous emission inefficiency p_{spon}, with p_{mode} significantly smaller than p_{spon}.

It is helpful to make a comparison here with the single-atom case. For a single atom interacting with the free-space light with the same level configuration as shown in Fig. 1, there is only one atomic mode given by $s=|g\rangle\langle s|$, but there are still infinite optical modes. We can still identify the forward scattered optical mode a_s as the signal mode. The interaction picture is then shown intuitively by Fig. 4. For a single atom, there is no inherent mode-mismatching noise, but the spontaneous emission inefficiency becomes much larger. If the atom is excited to the level $|s\rangle$ (that is, to the mode s) through the Raman laser pumping, the accompanying photon has a probability to go to all the possible directions [16], and thus has only a very small possibility to go to the signal mode a_s. We will calculate in the following sections the spontaneous emission inefficiencies for the signal atom case as well as for the atomic ensemble case, and compare them with the different mode-matching methods to see whether there is collective enhancement of the signal-to-noise ratio for the many-atom ensemble.

III. THE THEORETICAL MODEL FOR THE LIGHT–ATOMIC-ENSEMBLE INTERACTION AND ITS SOLUTION

We will now go to the detailed description of the light–atomic-ensemble interaction. From this description, we will calculate the signal-light mode structure $f_{\mathbf{k}}$, the spontaneous emission inefficiency p_{spon}, and the inherent mode-mismatching noise p_{mode}. In the interaction configuration shown by Fig. 1, the Raman pumping laser can be described classically by neglecting its small quantum variance, and is assumed to be propagating basically along the z direction. So, we can write its amplitude as $\varepsilon_{ge}(\mathbf{r},t)=u(\mathbf{r},t)e^{i(k_0 z-\omega_0 t)}$, where $\omega_0=k_0c=2\pi c/\lambda_0$ is the carrier frequency and $u(\mathbf{r},t)$ is a slowly varying function of the coordinate $\mathbf{r}$ and the time t. The field ε_{se} coupling to the transition $|e\rangle\rightarrow|s\rangle$ should be described quantum mechanically, and we expand it into plane wave modes $\varepsilon_{se}(\mathbf{r},t)\propto\int a_{\mathbf{k}}e^{i(\mathbf{k}\cdot\mathbf{r}-\omega_{\mathbf{k}}t)}d^3\mathbf{k}$ with $\omega_{\mathbf{k}}=|\mathbf{k}|c$, and $a_{\mathbf{k}}$, the corresponding annihilation operator. Then, the Hamiltonian describing the light-atom interaction has the following form in the interaction picture (setting $\hbar=1$)

$$H(t)=\Delta\sum_{i=1}^{N_a}\sigma_{ee}^{i}+\Bigg\{g_{eg}\sum_{i=1}^{N_a}\sigma_{eg}^{i}u(\mathbf{r}_i,t)e^{ik_0z}+\sum_{i=1}^{N_a}\sigma_{se}^{i}\int g_{se}^{\mathbf{k}}a_{\mathbf{k}}^{\dagger}e^{-i[\mathbf{k}\cdot\mathbf{r}_i-(\omega_{\mathbf{k}}-\omega_0+\omega_{sg})t]}d^3\mathbf{k}+\mathrm{H.c.}\Bigg\},\tag{6}$$

where the detuning $\Delta=\omega_{eg}-\omega_0$ with $\omega_{eg}=\omega_e-\omega_g$, the frequency difference between the atomic levels, $\sigma_{\mu\nu}^{i}=|\mu\rangle_i\langle\nu|$ $(\mu,\nu=g,e,s)$ are the transition operators of the ith atom, $\mathbf{r}_i$ is the coordinate of the ith atom, and $g_{eg},g_{se}^{\mathbf{k}}$ are the coupling coefficients that are proportional to the dipole moments of the corresponding transitions. The coefficient $g_{se}^{\mathbf{k}}$ depends in general on the direction of the wave vector $\mathbf{k}$ by the dipole pattern. In Eq. (6), the carrier frequency of the spontaneous emission field $\varepsilon_{se}(\mathbf{r},t)$ is given by $\omega_0-\omega_{sg}$, and its relevant frequency width can be estimated by the natural width Γ of the excited level $|e\rangle$, which means that the modes $a_{\mathbf{k}}$ with the frequency difference between $\omega_{\mathbf{k}}$ and $\omega_0-\omega_{sg}$ much larger than the width Γ will have negligible influence on the system dynamics. We neglect in Eq. (6) the spontaneous emission back to the level $|g\rangle$ since it is not important for our purpose (with the detection method specified in Sec. II), and has no influence on all of our results.

If both the natural width Γ and the frequency spreading of the pumping laser $u(\mathbf{r},t)$ are significantly smaller than the detuning Δ, we can adiabatically eliminate the upper level $|e\rangle$ through the standard technique, and the resulting adiabatic Hamiltonian is given by

$$H(t)=-\Bigg\{\sum_{i=1}^{N_a}\sigma_{sg}^{i}u(\mathbf{r}_i,t)\int\frac{g_{eg}g_{se}^{\mathbf{k}}}{\Delta}a_{\mathbf{k}}^{\dagger}e^{-i[\Delta\mathbf{k}\cdot\mathbf{r}_i-\Delta\omega_{\mathbf{k}}t]}\times d^3\mathbf{k}+\mathrm{H.c.}\Bigg\}-\frac{|g_{eg}|^2}{\Delta}\sum_{i=1}^{N_a}\sigma_{gg}^{i}|u(\mathbf{r}_i,t)|^2,\tag{7}$$

where $\Delta\omega_{\mathbf{k}}=\omega_{\mathbf{k}}-(\omega_0-\omega_{sg})$ and $\Delta\mathbf{k}=\mathbf{k}-k_0\mathbf{z}_0$ with $\mathbf{z}_0$, the unit vector in the z direction. We have neglected in Eq. (7) the Stark shift of the level $|s\rangle$ since it is much smaller than the other terms. (The spontaneous emission field is much weaker than the pumping field). The last term in Eq. (7) [the Stark shift of the level $|g\rangle$] can be eliminated if we make a phase rotation of the basis $\{|g\rangle,|s\rangle\}$ which will transform σ_{sg}^{i} to $\sigma_{sg}^{i}e^{i(|g_{eg}|^2/\Delta)\int_0^t|u(\mathbf{r}_i,\tau)|^2d\tau}$. Thus, we can simply drop off the last term, and replace $u(\mathbf{r}_i,t)$ by $u'(\mathbf{r}_i,t)=u(\mathbf{r}_i,t)e^{i(|g_{eg}|^2/\Delta)\int_0^t|u(\mathbf{r}_i,\tau)|^2d\tau}$. In the following, for simplicity of the symbol, we will denote $u'(\mathbf{r}_i,t)$ still by $u(\mathbf{r}_i,t)$, and denote $-g_{eg}g_{se}^{\mathbf{k}}/\Delta$ by a single coefficient $g_{\mathbf{k}}$.

At the beginning, all the atoms are in the ground state $|g\rangle$, and all the optical modes $a_{\mathbf{k}}$ are in the vacuum state. We denote this initial state of all the atomic and optical modes by

$|\mathrm{vac}\rangle$. Then, if the Raman pumping laser $u(\mathbf{r},t)$ is short and weak enough, we can expand the final state $|\Psi_f\rangle$ into a perturbative expansions. To the second order of the perturbation, the final state has the form

$$|\Psi_f\rangle=\left\{1-i\int_0^{t_0}H(\tau)d\tau -\frac{1}{2}T\left[\int_0^{t_0}\int_0^{t_0}H(\tau_1)H(\tau_2)d\tau_1 d\tau_2\right]\right\}|\mathrm{vac}\rangle, \tag{8}$$

where t_0 is the duration of the Raman pulse, and $T[\cdots]$ denotes the time-ordered product.

At this point, we should note that for an atomic vapor, the atom positions $\mathbf{r}_i$ are randomly distributed, and during the light-atom interaction, the atoms are moving fast in the room temperature [17]. Therefore, we should treat $\mathbf{r}_i$ in the Hamiltonian (7) as stochastic variables. We make the following two assumptions about the properties of these variables: (i) For different atoms *i* and *j*, $\mathbf{r}_i$ and $\mathbf{r}_j$ do not correlate with each other; (ii) Different stochastic variables $\mathbf{r}_i$ obey the same probability distribution that is determined by the geometry of the atomic cell. Note that these two assumptions are well satisfied by the room-temperature atomic gas. If the atom positions $\mathbf{r}_i$ behave as classical random variables, we should take an average of the final state $|\Psi_f\rangle$ over the joint probability distribution of these variables, and the resulting state becomes mixed with

$$\rho_f=\langle|\Psi_f\rangle\langle\Psi_f|\rangle_{\{\mathbf{r}_i\}}, \tag{9}$$

where the symbol $\langle\cdots\rangle_{\{\mathbf{r}_i\}}$ denotes the average over all the variables $\mathbf{r}_i$.

To take the average in Eq. (9), first we note that the Hamiltonian (7) can be written as

$$H(t)=\sum_{i=1}^{N_a}H_i(\mathbf{r}_i,t) \tag{10}$$

with

$$H_i(\mathbf{r}_i,t)=\sigma_{sg}^i\int g_{\mathbf{k}}a_{\mathbf{k}}^\dagger e^{i\Delta\omega_{\mathbf{k}}t}\{u(\mathbf{r}_i,t)e^{-i\Delta\mathbf{k}\cdot\mathbf{r}_i}\}d^3\mathbf{k}. \tag{11}$$

Only the term in the large bracket of the Hamiltonian H_i depends on the variable $\mathbf{r}_i$. By the property (i) of the variables $\mathbf{r}_i$, we have

$$\langle H_iH_j\rangle_{\{\mathbf{r}_i\}}=\langle H_i\rangle_{\{\mathbf{r}_i\}}\langle H_j\rangle_{\{\mathbf{r}_i\}}+\delta_{ij}\{\langle H_i^2\rangle_{\{\mathbf{r}_i\}}-\langle H_i\rangle_{\{\mathbf{r}_i\}}^2\}. \tag{12}$$

By the property (ii) of the variables $\mathbf{r}_i$, we know that $\langle u(\mathbf{r}_i,t)e^{-i\Delta\mathbf{k}\cdot\mathbf{r}_i}\rangle_{\{\mathbf{r}_i\}}$ becomes independent of the atom index *i*, so the average of the Hamiltonian $H(t)$ has the simple form

$$\langle H(t)\rangle_{\{\mathbf{r}_i\}}=\sqrt{N_a}s_s\int g_{\mathbf{k}}a_{\mathbf{k}}^\dagger e^{i\Delta\omega_{\mathbf{k}}t}\langle u(\mathbf{r}_i,t)e^{-i\Delta\mathbf{k}\cdot\mathbf{r}_i}\rangle_{\{\mathbf{r}_i\}}d^3\mathbf{k}, \tag{13}$$

where s_s is the symmetrical collective atomic operators defined in Eq. (1). We will write the initial vacuum state $|\mathrm{vac}\rangle$ as a tensor product of the atomic part $|\mathrm{vac}\rangle_a$ and the optical part $|\mathrm{vac}\rangle_p$, and denote the atomic state $\sigma_{sg}^i|\mathrm{vac}\rangle_a$ simply by $|s\rangle_i$. With this notation, a combination of Eqs. (8)–(13) yields the following form for the averaged state ρ_f:

$$\rho_f=(1-p_2-p_c)|\Psi_{\mathrm{eff}}\rangle\langle\Psi_{\mathrm{eff}}|+p_2\rho_n+o(p_2), \tag{14}$$

where the effective pure state $|\Psi_{\mathrm{eff}}\rangle$ (notnormalized) is

$$|\Psi_{\mathrm{eff}}\rangle=\left(1-i\int_0^{t_0}\langle H(\tau)\rangle_{\{\mathbf{r}_i\}}d\tau\right)|\mathrm{vac}\rangle, \tag{15}$$

with $\langle\Psi_{\mathrm{eff}}|\Psi_{\mathrm{eff}}\rangle=1+p_c$, and the noise component $p_2\rho_n$ is given by

$$p_2\rho_n=\sum_{i=1}^{N_a}|s\rangle_i\langle s|\otimes\int_0^{t_0}\int_0^{t_0}d\tau_1 d\tau_2\int d^3\mathbf{k}\int d^3\mathbf{k}'g_{\mathbf{k}}g_{\mathbf{k}'}^*e^{i(\Delta\omega_{\mathbf{k}}\tau_1-\Delta\omega_{\mathbf{k}'}\tau_2)}a_{\mathbf{k}}^\dagger|\mathrm{vac}\rangle_p\langle\mathrm{vac}|a_{\mathbf{k}'} \times\{\langle u(\mathbf{r}_i,\tau_1)u^*(\mathbf{r}_i,\tau_2)e^{-i(\mathbf{k}-\mathbf{k}')\cdot\mathbf{r}_i}\rangle_{\{\mathbf{r}_i\}}-\langle u(\mathbf{r}_i,\tau_1)e^{-i\Delta\mathbf{k}\cdot\mathbf{r}_i}\rangle_{\{\mathbf{r}_i\}}\langle u(\mathbf{r}_i,\tau_2)e^{i\Delta\mathbf{k}'\cdot\mathbf{r}_i}\rangle_{\{\mathbf{r}_i\}}\}, \tag{16}$$

with the value of p_2 determined by the normalization of ρ_n, i.e., by $\mathrm{tr}(\rho_n)=1$. In Eq. (14), $o(p_2)$ represents the higher-order terms compared with the magnitude of p_2 and p_c, which will be neglected in the following. We also ignored the second-order cross terms proportional to $\sigma_{sg}^i a_{\mathbf{k}}^\dagger|\mathrm{vac}\rangle\langle\mathrm{vac}|$ or $|\mathrm{vac}\rangle\langle\mathrm{vac}|\sigma_{gs}^i a_{\mathbf{k}}$ in writing Eq. (14), since they have no contributions to the quantities we will calculate below. The solution (14) serves as the starting point for discussions of various properties of this system in the following section.

IV. PROPERTIES OF THE LIGHT–ATOMIC-ENSEMBLE INTERACTION

Now, let us analyze the properties of the light–atomic-ensemble interaction revealed by the solution (14). First, we look at the effective pure state $|\Psi_{\mathrm{eff}}\rangle$ by neglecting the noise component $p_2\rho_n$. The state $|\Psi_{\mathrm{eff}}\rangle$ has exactly the same form as the ideal state (3) that is the starting point for all the applications. To see this clearly, we can write $|\Psi_{\mathrm{eff}}\rangle$ as $|\Psi_{\mathrm{eff}}\rangle=(1+\sqrt{p_c}s_s^\dagger a_s^\dagger)|\mathrm{vac}\rangle$, by defining the signal mode

$$\begin{aligned} a_s^\dagger &\equiv \int f_{\mathbf{k}} a_{\mathbf{k}}^\dagger d^3\mathbf{k} \\ &\equiv -i\frac{\sqrt{N_a}}{\sqrt{p_c}}\int d^3\mathbf{k}\int_0^{t_0} d\tau g_{\mathbf{k}} a_{\mathbf{k}}^\dagger e^{i\Delta\omega_{\mathbf{k}}\tau} \\ &\quad\times\langle u(\mathbf{r}_i,\tau)e^{-i\Delta\mathbf{k}\cdot\mathbf{r}_i}\rangle_{\{\mathbf{r}_i\}}, \end{aligned} \tag{17}$$

where the value of p_c is determined by the normalization of the operator $a_s^\dagger$, i.e., by the condition $[a_s, a_s^\dagger]=1$.

We are particularly interested in the spatial structure of the signal mode $a_s^\dagger$, since one needs to know this spatial structure to design mode matching in practical experiments. The integration $\int d^3\mathbf{k}$ can be expressed as $\int d^3\mathbf{k} = \int_{\omega_0-\omega_{sg}-\delta/2}^{\omega_0-\omega_{sg}+\delta/2} d\omega \int_{4\pi} d\Omega$, where $d\Omega=\sin\theta d\theta d\varphi$ represents the infinitesimal solid angle and δ is the bandwidth of the spontaneous emission field which is in the order of the natural width Γ of the excited level $|e\rangle$. The spatial structure of the mode $a_s^\dagger$ is determined by the superposition coefficient $f_{\mathbf{k}}=f(\omega,\Omega)$ as a function of the solid angle Ω. Typically, the size L of the atomic ensemble (centimeter long or less) satisfies the condition $\Gamma L/c \ll 1$, and $\omega_{sg}L/c \ll 1$ (ω_{sg} is either around GHz or zero, depending on whether one uses the hyperfine level or the Zeeman sublevel for the $|s\rangle$ state). In this case, $\Delta\mathbf{k}\cdot\mathbf{r}_i=(\mathbf{k}-k_0\mathbf{z}_0)\cdot\mathbf{r}_i \simeq k_0(\mathbf{k}/|\mathbf{k}|-\mathbf{z}_0)\cdot\mathbf{r}_i$, which only depends on the direction of $\mathbf{k}$, and becomes independent of the frequency ω. We assume that the Raman pumping field can be factorized as $u(\mathbf{r},t)=u_\perp(\mathbf{r})\mu_l(z,t)$, where $\mu_l(z,t)$ is a slowly changing function of the coordinate, and can be well approximated as a constant along the size of the atomic ensemble. With this condition, the superposition function $f(\omega,\Omega)$ is factorized as a product of the frequency part $f_\omega(\omega)$ and the spatial part $f_\Omega(\Omega)$, and the spatial part $f_\Omega(\Omega)$ becomes independent of the emission frequency ω and the interaction time t_0. To have a more explicit expression of the spatial structure $f_\Omega(\Omega)$ of the signal mode $a_s^\dagger$, we assume that the atoms are distributed by the normalized distribution function $p_{\text{dis}}(\mathbf{r})$ [with $\int p_{\text{dis}}(\mathbf{r})d^3\mathbf{r}=1$], which is determined by the geometry of the ensemble. As we mentioned before, the interaction coefficient $g_{\mathbf{k}}$ normally also depends on the direction of the wave vector $\mathbf{k}$ in the form of a dipole pattern, but it varies very slowly with the angle Ω compared with other contributions in $f_\Omega(\Omega)$, so we drop it off when considering the spatial structure of the signal mode. Under this circumstance, $f_\Omega(\Omega)$ is simply expressed as

$$\begin{aligned} f_\Omega(\Omega) &= \langle u_\perp(\mathbf{r})e^{-i\Delta\mathbf{k}\cdot\mathbf{r}_i}\rangle_{\{\mathbf{r}_i\}} \\ &= \int d^3\mathbf{r}\, u_\perp(\mathbf{r}) p_{\text{dis}}(\mathbf{r}) \\ &\quad\times e^{ik_0 z(1-\cos\theta)-ik_0\sin\theta(x\cos\varphi+y\sin\varphi)}. \end{aligned} \tag{18}$$

To further simplify this expression, we assume a Gaussian pump beam with $u_\perp(\mathbf{r})=e^{-(x^2+y^2)/r_0^2}$, and a Gaussian form for the transverse part of the atomic distribution function with [18]

$$\begin{aligned} p_{\text{dis}}(\mathbf{r}) &= \frac{1}{\pi L R_0^2} e^{-(x^2+y^2)/R_0^2} \quad (-L/2 \leqslant z \leqslant L/2), \\ p_{\text{dis}}(\mathbf{r}) &= 0, \qquad (z<-L/2,\text{or},z>L/2), \end{aligned} \tag{19}$$

where r_0 and R_0 characterize the radius of the pump beam and the radius of the atomic ensemble, respectively, and L is the length of the ensemble. In this case, we have an analytic expression for the signal mode function

$$f_\Omega(\Omega) = \frac{r_0^2}{r_0^2+R_0^2} e^{-(1/4)k_0^2 r_0^2 R_0^2 \sin^2\theta/(r_0^2+R_0^2)} \text{sinc}\left(k_0 L \sin^2\frac{\theta}{2}\right), \tag{20}$$

where the function sinc is defined as $\text{sinc}(x)\equiv\sin(x)/x$. From this expression, we see that the signal photon mainly goes to the forward direction. The signal mode is inside a small cone around $\theta=0$ with $\Delta\theta$ characterized by $\min[\sqrt{r_0^2+R_0^2}/(k_0 r_0 R_0), 1/\sqrt{k_0 L}]$.

We have shown that the first component of the solution (14) exactly contributes to the ideal coherent process, and have specified the spatial structure of the signal mode. Now we analyze the contributions of the noise described by the second component of Eq. (14). From Eq. (14), we see that the noise component $p_2\rho_n$ is expressed as a tensor product of the atomic density operator $\rho_n^a=\sum_{i=1}^{N_a}|s\rangle_i\langle s|$ and the remaining optical density operator ρ_n^p. Besides the symmetric collective atomic mode s_s and the signal optical mode a_s, there are many other noise modes contributing to the atomic density operator ρ_n^a and the optical density operator ρ_n^p. These noise modes correlate with each other in a complicated way, however, these correlations do not contribute to the noise of the relevant dynamics if the two signal modes are not involved in the correlations, since the reduced density operator of the modes s_s and a_s, which describes the relevant dynamics, will not be influenced by these correlations after we take trace over all the noise modes. Nevertheless, the correlations between the good modes and the noisy mode will have influence on the relevant dynamics, and these contribute to the two sources of noise we have mentioned before: the spontaneous emission loss and the inherent mode-matching inefficiency. These two sources of noise are described quantitatively by the conditional probabilities p_{spon} and p_{mode}, respectively. The p_{spon} represents the probability that an atom is excited to the right mode s_s, but the accompanying photon does not go to the signal mode a_s. From the solution (14) to the whole density operator ρ_f, this possibility can be expressed as

$$p_{\text{spon}} = 1 - \frac{\text{tr}(\langle 0_a 0_p | a_s s_s \rho_f s_s^\dagger a_s^\dagger | 0_a 0_p\rangle)}{\text{tr}(\langle 0_a | s_s \rho_f s_s^\dagger | 0_a\rangle)}, \tag{21}$$

where $\text{tr}(\cdots)$ represents the trace over all the remaining atomic and optical modes involved in the operator ρ_f. Similarly, p_{mode} represents the probability that a photon is emitted to the signal mode a_s, but the accompanying atomic excitation is not in the right mode s_s, and this possibility can be expressed from the density operator ρ_f as

$$p_{\text{mode}}=1-\frac{\text{tr}(\langle 0_a 0_p|a_s s_s \rho_f s_s^\dagger a_s^\dagger|0_a 0_p\rangle)}{\text{tr}(\langle 0_p|a_s \rho_f a_s^\dagger|0_p\rangle)}. \tag{22}$$

In the following, we need to calculate these two probabilities to quantify the noise magnitudes.

From the solution (14), we can derive the probability $\text{tr}(\langle 0_a|s_s\rho_f s_s^\dagger|0_a\rangle)$ for one atomic excitation in the mode s_s, the possibility $\text{tr}(\langle 0_p|a_s\rho_f a_s^\dagger|0_p\rangle)$ for one photon in the mode a_s, and the joint possibility $\text{tr}(\langle 0_a 0_p|a_s s_s\rho_f s_s^\dagger a_s^\dagger|0_a 0_p\rangle)$ for one atom in the mode s_s and one photon in the mode a_s. They are respectively given by

$$\text{tr}(\langle 0_a|s_s\rho_f s_s^\dagger|0_a\rangle)=p_c+p_2/N_a, \tag{23}$$

$$\text{tr}(\langle 0_p|a_s\rho_f a_s^\dagger|0_p\rangle)=p_c+\chi p_c, \tag{24}$$

$$\text{tr}(\langle 0_a 0_p|a_s s_s\rho_f s_s^\dagger a_s^\dagger|0_a 0_p\rangle)=p_c+\chi p_c/N_a, \tag{25}$$

where p_2 and p_c are obtained, respectively, from the normalization of ρ_n and $a_s^\dagger$ [see Eq. (16) and Eq. (17)], and the ratio χ is defined as

$$\chi=N_a\text{tr}(\langle 0_p|a_s\rho_n^p a_s^\dagger|0_p\rangle)/p_c, \tag{26}$$

with ρ_n^p, the optical part of the noise component $p_2\rho_n$ as we have specified before.

From the above equations, we see that we only need to calculate the two ratios p_c/p_2 and χ to determine the noise probabilities p_{spon} and p_{mode}. As we have mentioned before, the shape $u(\mathbf{r},t)$ of the pump beam is typically decomposed as $u(\mathbf{r},t)=u_\perp(\mathbf{r})\mu_l(z,t)$ with $\mu_l(z,t)$ approximately independent of z along the size of the atomic ensemble. In this case, the two ratios p_c/p_2 and χ have much simplified expressions, which, become independent of the interaction details, such as the interaction time or the bandwidth of the coupling field, and depend only on some spatial integrations determined by the geometry of the atomic ensemble and the pump beam. For simplicity, we also neglect the slow variation of the coupling coefficient $g_{\mathbf{k}}$ with the direction of $\mathbf{k}$. Under these conditions, the ratios p_c/p_2 and χ are given respectively by

$$\frac{p_c}{p_2}=\frac{\int_{4\pi}d\Omega\{|\langle u_\perp(\mathbf{r}_i)e^{-i\Delta\mathbf{k}\cdot\mathbf{r}_i}\rangle_{\{\mathbf{r}_i\}}|^2\}}{\int_{4\pi}d\Omega\{\langle|u_\perp(\mathbf{r}_i)|^2\rangle_{\{\mathbf{r}_i\}}-|\langle u_\perp(\mathbf{r}_i)e^{-i\Delta\mathbf{k}\cdot\mathbf{r}_i}\rangle_{\{\mathbf{r}_i\}}|^2\}}, \tag{27}$$

$$\begin{aligned}\chi=&\left[\int_{4\pi}d\Omega\{|\langle u_\perp(\mathbf{r}_i)e^{-i\Delta\mathbf{k}\cdot\mathbf{r}_i}\rangle_{\{\mathbf{r}_i\}}|^2\}\right]^{-2}\int_{4\pi}d\Omega\int_{4\pi}d\Omega'\{\langle|u_\perp(\mathbf{r}_i)|^2e^{-i(\mathbf{k}-\mathbf{k}')\cdot\mathbf{r}_i}\rangle_{\{\mathbf{r}_i\}}\\&\times\langle u_\perp^*(\mathbf{r}_i)e^{i\Delta\mathbf{k}\cdot\mathbf{r}_i}\rangle_{\{\mathbf{r}_i\}}\langle u_\perp(\mathbf{r}_i)e^{-i\Delta\mathbf{k}'\cdot\mathbf{r}_i}\rangle_{\{\mathbf{r}_i\}}\}-1.\end{aligned} \tag{28}$$

Similar to the case for calculating the signal mode structure $f_\Omega(\Omega)$, we also assume a Gaussian pump beam and a Gaussian form for the transverse atomic distribution function as is shown by Eq. (19). In this case, we have the following analytic expressions for these two ratios:

$$\frac{p_c}{p_2}\simeq\frac{r_0^2(r_0^2+2R_0^2)}{2(r_0^2+R_0^2)^2}\int_0^\pi\sin\theta d\theta\left\{e^{-(1/2)k_0^2r_0^2R_0^2\sin^2\theta/(r_0^2+R_0^2)}\times\text{sinc}^2\left(k_0L\sin^2\frac{\theta}{2}\right)\right\}, \tag{29}$$

$$\begin{aligned}\chi=&\frac{(r_0^2+R_0^2)^2}{r_0^2(r_0^2+2R_0^2)}\left[\int_0^\pi\sin\theta d\theta\left\{e^{-(1/2)k_0^2r_0^2R_0^2\sin^2\theta/(r_0^2+R_0^2)}\text{sinc}^2\left(k_0L\sin^2\frac{\theta}{2}\right)\right\}\right]^{-2}\\&\times\int_0^\pi\int_0^\pi\sin\theta\sin\theta'd\theta d\theta'\left\{\frac{1}{2\pi}\int_0^{2\pi}e^{-(1/4)k_0^2r_0^2R_0^2(\sin^2\theta+\sin^2\theta'-2\sin\theta\sin\theta'\cos\varphi)/(r_0^2+2R_0^2)}d\varphi\right.\\&\left.\times e^{-(1/4)k_0^2r_0^2R_0^2(\sin^2\theta+\sin^2\theta')(r_0^2+R_0^2)}\text{sinc}\left[k_0L\left(\sin^2\frac{\theta}{2}-\sin^2\frac{\theta}{2}\right)\right]\text{sinc}\left(k_0L\sin^2\frac{\theta}{2}\right)\text{sinc}\left(k_0L\sin^2\frac{\theta'}{2}\right)\right\}-1.\end{aligned} \tag{30}$$

In writing Eq. (29), we have assumed $k_0L \gg 1$ and have neglected the term which is about $1/k_0L$ times smaller.

From the two ratios p_c/p_2 and χ, the spontaneous emission loss and the inherent mode-matching inefficiency are directly written as

$$p_{\mathrm{spon}} \simeq (1+N_a p_c/p_2)^{-1}, \tag{31}$$

$$p_{\mathrm{mode}} \simeq \chi/(1+\chi). \tag{32}$$

The approximations in Eqs. (31) and (32) are valid under the condition $N_a \gg 1$ (we neglected the terms that are $1/N_a$ times smaller). To minimize the two sources of noise p_{spon} and p_{mode}, it is better to have a large $N_a p_c/p_2$ and a small χ. We will discuss the details in the following section on how to minimize these two noise by using different kinds of mode-matching methods.

At the end of this section, we would like to make a brief comparison with the single-atom case. For the case of a single atom, if the position of this atom is also fluctuating in the space, the above calculation is still valid but with $N_a = 1$. From Eqs. (21)–(26), we see that in the case of $N_a = 1$, we always have $p_{\mathrm{mode}} = 0$. Thus, for the case of a single atom, the spontaneous emission loss is the only source of noise, as has been shown intuitively in Fig. 4. However, in this case, the spontaneous emission inefficiency p_{spon}, which can be approximated by $p_{\mathrm{spon}} \simeq 1-(1+\chi)p_c/p_2$ since $p_c \ll p_2$, becomes much larger. If we compare the efficiency (defined as $1-p_{\mathrm{spon}}$) from the spontaneous emission noise between the single-atom case and the atomic-ensemble case, we see that this efficiency is increased by about a factor of N_a for the atomic ensemble. This is what we called the collective enhancement of the signal-to-noise ratio for the many-atom ensemble.

V. MODE-MATCHING METHODS

The first mode-matching method is to choose the signal mode as the mode for detection, with the mode function exactly given by the inherent spatial structure (20) of the signal light. The mode function (20) is similar to a Gaussian function, especially when $k_0 r_0^2 > L$ and $k_0 R_0^2 > L$. [It would be an exact Gaussian function if the axial distribution of $p_{\mathrm{dis}}(\mathbf{r})$ is Gaussian.] One can couple a Gaussian mode into a single-mode optical fiber with a good technical mode-matching efficiency. For this case with an exact mode matching, the two noise probabilities p_{spon} and p_{mode} are exactly given by Eqs. (29)–(32). We now go to the calculations of these two noise probabilities. For this purpose, we need to understand first how to get a large $N_a p_c/p_2$ and a small χ to minimize the noise p_{spon} and p_{mode}.

First, we give an estimation of the ratio $N_a p_c/p_2$. It has a definite physical meaning. From Eq. (29), we see that the integration function is significantly different from zero only when the integration variable θ falls into a small cone with $0 \leqslant \theta < \theta_f$, where θ_f is estimated by $\theta_f \sim \min(1/\sqrt{k_0L}, 1/k_0 r_{eff} t)$ with $r_{eff} \equiv r_0 R_0/\sqrt{r_0^2+R_0^2}$. Thus, the result of the integration can be estimated by θ_f^2. We also know that the total atom number can be approximated by $N_a \sim n_a \pi R_0^2 L$, where n_a denotes the average atom number density. From this, we see that the ratio $N_a p_c/p_2$ is estimated by

$$\frac{N_a p_c}{p_2} \sim \min\left(\frac{1}{2} n_a \lambda_0 r_{eff}^2, \frac{1}{4\pi} n_a \lambda_0^2 L\right). \tag{33}$$

If we assume that the two bounds for $N_a p_c/p_2$ are comparable, which means that $1/\sqrt{k_0L} \sim 1/k_0 r_{eff}$, or the Fresnel number defined as $F \equiv \pi r_{eff}^2/\lambda_0 L$ is in the order of 1, we have $N_a p_c/p_2 \sim n_a \lambda_0^2 L/(4\pi) \sim d_o/(4\pi)$, where the on-resonance optical depth d_o is simply defined as $d_o \equiv n_a \lambda_0^2 L$. Therefore, to have a small spontaneous emission inefficiency p_{spon}, we need to use an optically dense ensemble with $d_o \gg 1$ (the off-resonance optical depth can still be much smaller than 1 due to the large detuning).

Next, we consider how to minimize the ratio χ by choosing appropriate interaction configurations. From Eq. (30), we see that χ increase with the ratio R_0/r_0. This can be intuitively understood as follows: the noise characterized by p_{mode} and χ comes from the density fluctuation of the atomic ensemble. With a larger R_0, the atoms have more space to move around, and one thus has a relatively larger density function and a larger noise ratio χ [19]. Thus, to minimize χ, we choose a configuration with $r_0 \gg R_0$ in the following, which means the pumping laser is shined on all the atoms with a broad cross section. In this case, the effective radius $r_{eff} \simeq R_0$.

Now we would like to calculate the noise probabilities p_{spon} and p_{mode} in a more accurate way in the case of exact mode matching. This requires us to carry out the complicated integrations in Eqs. (29) and (30), which is only possible by using numerical methods. The spontaneous emission inefficiency p_{spon} depends on the optical depth $d_o = n_a \lambda_0^2 L$. We have numerically calculated the value of p_{spon} versus the optical depth d_o under different geometries of the atomic ensemble. The geometry of the ensemble is described by the Fresnel number $F \equiv \pi R_0^2/\lambda_0 L$. The calculation result is shown in Fig. 5. From the figure, we see that the spontaneous emission inefficiency is insensitive to the geometry of the ensemble. The two curves with $F=1$ and $F=10$ basically overlap. With a much smaller $F=0.1$, the inefficiency p_{spon} increases by about a factor of 2. On the other hand, p_{spon} is sensitive to the optical depth d_o. It decreases with $1/d_o$ approximately linearly, which confirms the rough estimation from the above. From the curves, we can write p_{spon} approximately as $p_{\mathrm{spon}} = 1/(1+d_o/26)$ for the Fresnel number F from 1 to 10. In the above numerical calculation, we assumed some typical values for the parameters with $\lambda_0 \sim 0.8$ μm and $L \sim 1$ cm, but actually the result is very insensitive to the parameter k_0L as long as it is still much larger than 1. For an atomic cell with a typical number density $n_a \sim 10^{12}/$ cm^3 and length $L \sim 1$ cm, the optical depth $d_o \sim 6.4 \times 10^3$, and we have a spontaneous emission inefficiency $p_{\mathrm{spon}} \sim 0.4\%$, which is very small.

The inherent mode-matching inefficiency p_{mode} is determined by the geometry of the ensemble, and does not depend on the value of the optical depth. We have numerically cal-

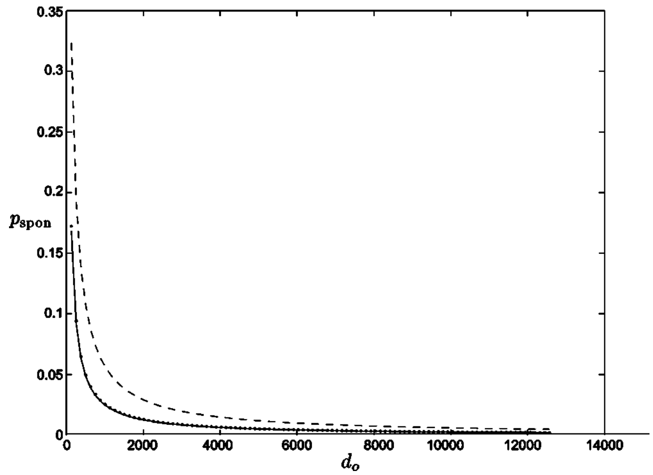

FIG. 5. The spontaneous emission inefficiency $p_{\rm spon}$ versus the on-resonance optical depth d_o of the ensemble under different geometries characterized by the Fresnel number F. We have $F=10$ for the solid curve, $F=1$ for the dotted curve, and $F=0.1$ for the dashed curve.

culated the value of $p_{\rm mode}$. It turns out that $p_{\rm mode}$ is actually also insensitive to the geometric parameters k_0L and F as long as they are still in the typical region. For instance, we have $p_{\rm mode}\simeq 24\%$ for $F=1$, $p_{\rm mode}\simeq 25\%$ for $F=10$, and $p_{\rm mode}\simeq 23\%$ for $F=0.1$. In each case, we change the length L from 0.3 cm to 3 cm (with $\lambda_0 \sim 0.8\ \mu$m), and the value of $p_{\rm mode}$ basically does not change at all. Note that the typical inherent mode-matching inefficiency $p_{\rm mode}\simeq 24\%$ is quite large, and we cannot efficiently reduce it by controlling the geometry of the ensemble. As we have mentioned before, the mode mismatching noise has a more significant influence on the efficiency of the application schemes than the spontaneous emission noise. The large inherent mode-matching inefficiency is a disadvantage of the exact mode-matching method.

To reduce the inefficiency $p_{\rm mode}$, we consider the following simple improvement to the exact mode-matching method. After the light–atomic-ensemble interaction, the scattered light is focused by a lens, and we apply an aperture on the focal plane of the lens to collect the signal light only from a small cone in the forward direction with $0 \leqslant \theta \leqslant \theta_D$, where the detection angle θ_D can be controlled by the size of the aperture. We call this kind of mode matching the filtered exact mode matching. By the exact mode matching, we detect the photon scattered to the signal mode; and by the filtered exact mode matching, we only detect the scattered photon that is in the signal mode and at the same time lies in the filtering cone with $0 \leqslant \theta \leqslant \theta_D$. Due to the additional restriction, we now have a less probability of success to register the photon. The spontaneous emission inefficiency $p_{\rm spon}$ should increase, but through this scarification, we can significantly reduce the noise $p_{\rm mode}$, which means, if we register the photon with this additional restriction, we are more confident that the accompanying atomic excitation will go to the collective atomic mode s_s. To calculate $p_{\rm spon}$ and $p_{\rm mode}$ for the filtered exact mode matching, we can still use Eqs. (21)–(26), but the signal mode a_s should be confined inside the small cone with $0 \leqslant \theta \leqslant \theta_D$. Inside this filtering cone, the signal mode has the same mode structure as given by Eq. (20). With this modified signal mode, we find that $p_{\rm mode}$ is still given by Eqs. (32) and (30), but all the integrations of θ and θ' in Eq. (30) can only be taken from 0 to the filtering angle θ_D instead of from 0 to π. The spontaneous emission inefficiency $p_{\rm spon}$ now has the following expression:

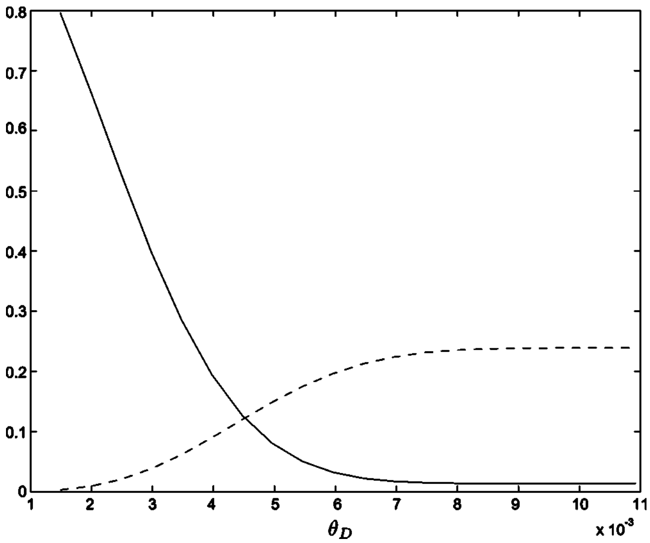

FIG. 6. The spontaneous emission inefficiency $p_{\rm spon}$ (solid curve) and the inherent mode mismatching probability $p_{\rm mode}$ (dashed curve) versus the filtering angle θ_D with the Fresnel number $F=1$.

$$p_{\rm spon} \simeq 1 - \frac{N_a p_c|_{\theta \leqslant \theta_D}}{N_a p_c + p_2}, \tag{34}$$

where we have assumed $N_a \gg 1$ for the approximation, and the symbol $p_c|_{\theta \leqslant \theta_D}$ means that the integration of θ in p_c can only be taken from 0 to θ_D. From Eq. (34), we need to calculate two ratios, p_c/p_2 and $p_c|_{\theta \leqslant \theta_D}/p_2$, for $p_{\rm spon}$. The ratio p_c/p_2 is exactly given by Eq. (29), and the ratio $p_c|_{\theta \leqslant \theta_D}/p_2$ has the same form as Eq. (29), but the integration of θ is only from 0 to θ_D.

We have numerically calculated the noise probabilities $p_{\rm spon}$ and $p_{\rm mode}$ versus the filtering angle θ_D, and the result is shown in Fig. 6 with the Fresnel number $F=1$ and the optical depth $d_o \sim 1.9 \times 10^3$. From the figure, we see that by decreasing the filtering angle θ_D, we can significantly reduce the noise $p_{\rm mode}$. The cost is that at the same time the inefficiency $p_{\rm spon}$ significantly increases. However, as we have mentioned before, though both of the noises $p_{\rm spon}$ and $p_{\rm mode}$ can be corrected in the application schemes in Refs. [12,13], the mode-mismatching noise $p_{\rm mode}$ has a more severe influence on the final efficiency of the schemes than the spontaneous emission noise $p_{\rm spon}$. Thus, for these applications, it is worth choosing an appropriate filtering angle θ_D with $p_{\rm mode}$ significantly smaller than $p_{\rm spon}$. For instance, if we choose the angle $\theta_D \simeq 0.002$, the mode-mismatching noise $p_{\rm mode} \simeq 0.9\%$, which is basically negligible compared with other sources of noise. At the same time, $p_{\rm spon}$

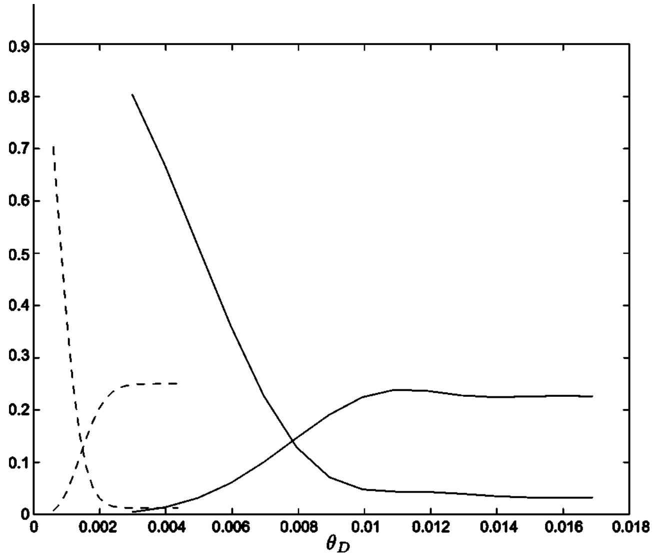

FIG. 7. The spontaneous emission inefficiency p_{spon} and the inherent mode-mismatching probability p_{mode} versus the filtering angle θ_D with the Fresnel number $F=10$ (the two dashed curves) and $F=0.1$ (the two solid curves). The spontaneous emission inefficiency increases with the decrease of the angle θ_D while the mode-mismatching noise decreases.

$\simeq 66.6\%$, which seems to be quite large. However, to overcome this noise, we need only to increase the repetitions of the entanglement generation scheme in Refs. [12,13] by another factor of 3 [given by $1/(1-p_{\mathrm{spon}})$], which is actually only a moderate cost. This choice would be much better than the case without any filtering, where we have an inherent mode-mismatching noise $p_{\mathrm{mode}}\simeq 24\%$. For the purpose of guiding the choice of the best experimental configuration, we list several important values of p_{spon} and p_{mode} versus the angle θ_D in the following table:

θ_D	0.0015	0.0020	0.0025	0.0040	0.0055
p_{mode}	0.31%	0.92%	2.05%	8.98%	17.5%
p_{spon}	79.6%	66.6%	52.9%	19.5%	5.02%

We have also calculated the noise probabilities p_{spon} and p_{mode} versus the angle θ_D under different geometries of the ensemble characterized by the Fresnel number F. For $F=10$ and $F=0.1$, the results are shown in Fig. 7. In all the calculations, we assumed the same optical depth $d_o\sim 1.9\times 10^3$ and the cell length $L\sim 1$ cm. The qualitative properties of the curves for different Fresnel numbers are quite similar, but one needs to shift the appropriate angle θ_D. With a large Fresnel number F, one needs to choose a smaller angle θ_D. The appropriate filtering angle θ_D changes by a factor of 2–3 if the Fresnel number changes by a factor of 10.

Finally, we describe a mode-matching method that is the simplest for implementation. For this method, we still use an aperture to select the scattered light from the small cone with $0\leqslant\theta\leqslant\theta_D$. But now we do not use any technical mode matching to choose only the signal mode with the right mode structure $f_\Omega(\Omega)$ for detection. Instead, we detect the photon in all the modes that lie in the small cone with $0\leqslant\theta\leqslant\theta_D$. We call this the simple filtering method. This seems to be a bad mode-matching method, since one does not make any distinction between the modes in this small cone. If the registered photon does not come from the right mode a_s, the accompanying atomic excitation will be most probably not in the collective mode s_s, and one thus has a significantly larger inherent mode-mismatching noise p_{mode}. However, the observation here is that if θ_D is sufficiently small, basically only the signal mode exists in this small cone, and all the other modes make negligible contributions. The important question is how small the angle θ_D should be to guarantee a small p_{mode}. Note that for the simple filtering method, the spontaneous emission inefficiency p_{spon} can be calculated in the same way as the filtered exact mode-matching method by the use of Eq. (34). But we have a different expression for p_{mode}, which in this case is defined as the probability that the accompanying atomic excitation does not go to the collective mode s_s when one photon (from any optical modes) is detected in the small cone with $0\leqslant\theta\leqslant\theta_D$. This possibility can be expressed as

$$p_{\mathrm{mode}}\simeq 1-\frac{p_c|_{\theta\leqslant\theta_D}+(1/N_a)\mathrm{tr}(p_2\rho_n)|_{\theta\leqslant\theta_D}}{p_c|_{\theta\leqslant\theta_D}+\mathrm{tr}(p_2\rho_n)|_{\theta\leqslant\theta_D}}, \tag{35}$$

where the trace $\mathrm{tr}(\cdots)$ is over all the atomic and the optical modes, and the symbol $|_{\theta\leqslant\theta_D}$ has the same meaning that the integrations of θ in p_c and $\mathrm{tr}(p_2\rho_n)$ are only from 0 to θ_D. In the limit of $N_a\gg 1$, p_{mode} can still be written in the form $p_{\mathrm{mode}}\simeq\chi_s/(1+\chi_s)$, with

$$\begin{aligned}\frac{1}{\chi_s+1}&=\frac{p_c|_{\theta\leqslant\theta_D}}{\mathrm{tr}(p_2\rho_n)|_{\theta\leqslant\theta_D}+p_c|_{\theta\leqslant\theta_D}}\\&=\frac{1}{(1-\cos\theta_D)}\int_0^{\theta_D}\sin\theta d\theta\left\{e^{-(1/2)k_0^2R_0^2\sin^2\theta}\right.\\&\quad\left.\times\mathrm{sinc}^2\left(k_0L\sin^2\frac{\theta}{2}\right)\right\}.\end{aligned} \tag{36}$$

In writing Eq. (36), we have assumed the same kind of atomic distribution function $p_{\mathrm{dis}}(\mathbf{r})$ and the pump mode function $u_\perp(\mathbf{r})$ as we have specified before. We can use Eqs. (36) to numerically calculate the mode mismatching probability p_{mode} versus the filtering angle θ_D for the simple filtering method. The result, together with the curve for p_{spon} versus θ_D, is shown in Fig. 8 for the Fresnel number $F=1$. In the calculation, we assumed the same optical depth $d_o\sim 1.9\times 10^3$. From the figure, we see that if θ_D is large, the mode-mismatching probability p_{mode} is very large, but as θ_D decreases, p_{mode} can still tend to zero. This confirms our intuitive observation. With the same parameters, for the simple filtering method, we should further decrease the filtering angle θ_D by a factor of 2–3 to get the optimal configuration compared with the filtered exact mode-matching method. Of course, due to the decrease of the optimal θ_D, the corresponding spontaneous emission inefficiency p_{spon} significantly increases. To guide the experimental choice of

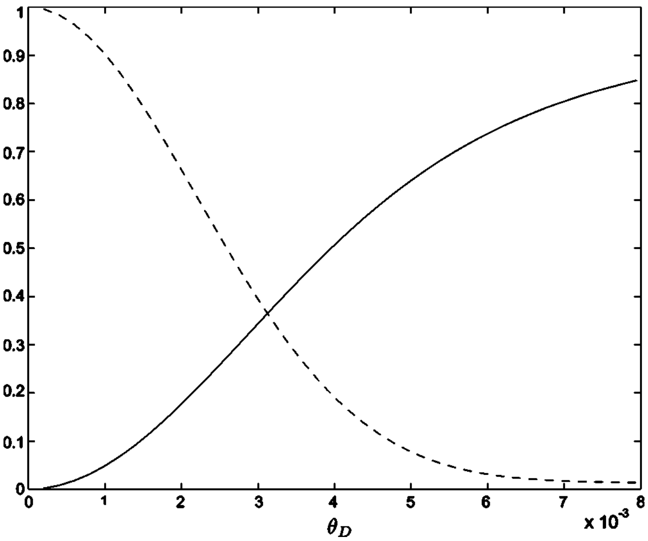

FIG. 8. The spontaneous emission inefficiency p_{spon} (dashed curve) and the inherent mode-mismatching probability p_{mode} (solid curve) versus the filtering angle θ_D with the Fresnel number $F=1$ for the simple filtering method.

the optimal θ_D, we also list some important values of p_{spon} and p_{mode} for the simple filtering method

θ_D	0.0006	0.0010	0.0014	0.0020	0.0032
p_{mode}	1.76%	4.78%	9.10%	17.5%	37.4%
p_{spon}	96.4%	90.3%	82.0%	66.6%	35.1%

For the simple filtering method, we also calculated the noise probabilities p_{spon} and p_{mode} under different geometries of the ensemble. For the Fresnel number $F=10$ and $F=0.1$, the results are shown in Fig. 9. We assumed the same optical depth and the cell length in these calculations. Since the qualitative picture revealed by this figure is quite similar to the case of the filtered exact mode matching, we do not need to discuss its properties in details.

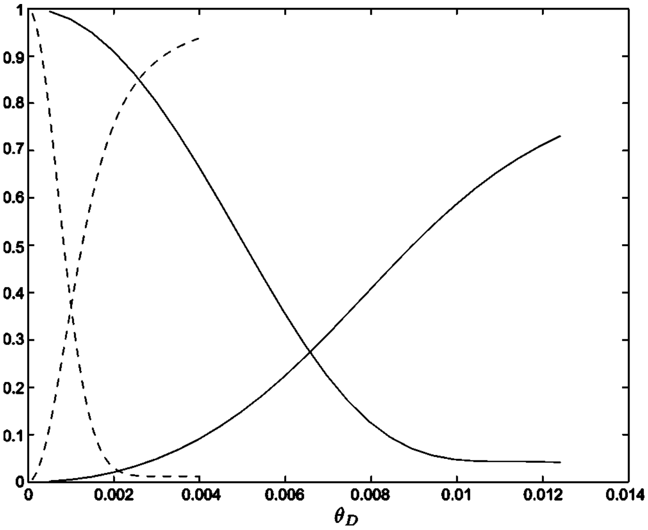

FIG. 9. The spontaneous emission inefficiency p_{spon} and the inherent mode-mismatching probability p_{mode} versus the filtering angle θ_D with the Fresnel number $F=10$ (the two dashed curves) and $F=0.1$ (the two solid curves) for the simple filtering method.

For experimental realizations, the simple filtering method can be much easier than other mode-matching methods. The calculation here shows that the price we need to pay for this simplification is to choose a smaller filtering angle with a significantly increased spontaneous emission inefficiency. Note that for the application schemes in Refs. [12,13], this price seems to be still acceptable. For instance, if we choose $\theta_D \simeq 0.001$, the mode-mismatching noise $p_{\mathrm{mode}} \simeq 4.8\%$ has already been small. In this case, the additional repetitions of the entanglement generation scheme in Refs. [12,13] is given by the factor $1/(1-p_{\mathrm{spon}}) \simeq 10$, which is not too much.

VI. SUMMARY

In summary, we have developed a theory in the weak-pumping limit to describe the three-dimensional effects in the interaction between the free-space light and the many-atom ensemble. The calculations demonstrate some interesting results that are not known from the other approaches. first, it shows that the signal light has an inherent spatial mode structure, which is determined together by the geometry of the ensemble and the mode structure of the pump beam. Second, it reveals that there will be two sources of noise during the light-atom interaction. One is the spontaneous emission inefficiency, that is inversely proportional to the on-resonance optical depth of the ensemble, and the other is the inherent mode-mismatching noise, that arises from the density fluctuation of the ensemble, and should be fully determined by the geometry of the ensemble for room-temperature atomic cells. It turns out that the inherent mode-mismatching noise is quite large if one collects the signal light through the exact mode-matching method, and one cannot efficiently reduce this noise by optimizing the geometry of the ensemble since in the typical parameter region, this noise is insensitive to the cell geometry. Finally, we show an effective way to reducing the inherentmode-mismatching noise by adding an aperture to select the light only from a small emission cone. By this means, we can efficiently reduce the mode-mismatching noise at the price of increasing the spontaneous emission inefficiency. It is worth doing this since the spontaneous emission inefficiency is far less important for some application schemes. There are two methods for this purpose: the filtered exact mode-matching method and the simple filtering method. Both methods can reduce the inherent mode-matching noise if one chooses an appropriate filtering angle.

The calculations in this paper show that there is a large collective enhancement of the signal-to-noise ratio if one compares the many-atom ensemble with the single-atom case, which confirms the prediction from some simple theoretical models, and demonstrates the validity of this important observation for the complicated realistic situations.

At the end of this paper, we should mention that the calculations here also show that for any mode-matching method, we cannot make both the spontaneous emission inefficiency p_{spon} and the inherent mode-mismatching noise p_{mode} negligible for the room-temperature atomic cell even if the cell has a large on-resonance optical depth. This result does not have much influence on the application schemes in Refs. [12,13] since they are inherently robust to the noise p_{spon} and p_{mode}. As a consequence of this inherent robustness, a non-negligible but, not huge, noise only has a moderate influence on the efficiency of the schemes. However, for any of the application schemes of atomic ensembles that are not inherently robust, such as the quantum light memory scheme [7–9] or the continuous variable teleportation scheme [4–6], a non-negligible noise will decrease the scheme fidelity. The calculations here do not directly apply to these schemes, since they work out of the perturbation region. However, it indeed raises the interesting question whether there is some theoretical limit on the best achievable fidelity of these schemes if one uses free-space atomic cells for their implementation.

ACKNOWLEDGMENTS

L.M.D. thanks Jeff Kimble and Alex Kuzmich for discussions. Work of L.M.D was supported by the Caltech MURI Center for Quantum Networks under ARO Grant No. DAAD19-00-1-0374, by the National Science Foundation under Grant No. EIA-0086038, and also by the Chinese Science Foundation and Chinese Academy of Sciences. Work at the University of Innsbruck was supported by the Austrian Science Foundation and EU networks.

---

[1] A. Kuzmich, N.P. Bigelow, and L. Mandel, Europhys. Lett. **42**, 481 (1998).

[2] J. Hald, J.L. Sorensen, C. Schori, and E.S. Polzik, Phys. Rev. Lett. **83**, 1319 (1999).

[3] A. Kuzmich, L. Mandel, and N.P. Bigelow, Phys. Rev. Lett. **85**, 1594 (2000).

[4] L.-M. Duan, J.I. Cirac, P. Zoller, and E.S. Polzik, Phys. Rev. Lett. **85**, 5643 (2000).

[5] A. Kuzmich and E.S. Polzik, Phys. Rev. Lett. **85**, 5639 (2000).

[6] B. Julsgaard, A. Kozhekin, and E.S. Polzik, Nature (London) **413**, 400 (2001).

[7] M.D. Lukin, S.F. Yelin, and M. Fleischhauer, Phys. Rev. Lett. **84**, 4232 (2000).

[8] L. -M. Duan, J. I. Cirac, and P. Zoller (unpublished).

[9] M. Fleischhauer and M.D. Lukin, Phys. Rev. Lett. **84**, 5094 (2000).

[10] C. Liu, Z. Dutton, C.H. Behroozi, and L.V. Hau, Nature (London) **409**, 490 (2001).

[11] D.F. Phillips, *et al.*, Phys. Rev. Lett. **86**, 783 (2001).

[12] L.-M. Duan, M. Lukin, J.I. Cirac, and P. Zoller, Nature (London) **414**, 413 (2001).

[13] L.-M. Duan, Phys. Rev. Lett. **88**, 170402 (2002), e-print quant-ph/0201128.

[14] M.G. Raymer, I.A. Walmsley, J. Mostowski, B. Sobolewska, Phys. Rev. A **32**, 332 (1985).

[15] A. Sorensen (unpublished); L. -M. Duan *et al.* (unpublished).

[16] C. Cabrillo, J.I. Cirac, P. G-Fernandez, and P. Zoller, Phys. Rev. A **59**, 1025 (1999).

[17] Note that for rapidly moving atoms, we also have the effect of Doppler shifts which are not included in the Hamiltonian (6). However, the Doppler shifts are not important for the off-resonant coupling considered here (they are still significantly smaller than the detuning). In addition, the Doppler shifts will cancel for the spontaneous emission modes that are nearly collinear with the pumping laser (including the important signal light mode).

[18] The noise properties in subsequent discussions will depend on the ratio of the transverse length scales for the atomic cell and for the pump beam, but they are insensitive to the detailed form of the atomic distribution function. Here, for simplicity of the calculation, we assume a Gaussian form for the atomic transverse distribution function. But we expect that all the results will be basically still valid if the transverse distribution is not in the Gaussian form, but instead, is uniform within the cell radius R_0 and zero outside.

[19] Note that this is a valid picture for room-temperature atomic cells. However, for ultracold atoms, each atom will be localized in a small space, and the density fluctuation basically will not depend on the size and geometry of the ensemble. Thus, for cold atoms, one may have a different interaction picture and a smaller noise ratio.

Entangling Many Atomic Ensembles through Laser Manipulation

L.-M. Duan[1,2,*]
[1]Institute for Quantum Information, California Institute of Technology, Mail Code 107-81, Pasadena, California 91125-8100
[2]Laboratory of Quantum Information, USTC, Hefei 230026, China

(Received 28 January 2002; published 11 April 2002)

We propose an experimentally feasible scheme to generate the Greenberger-Horne-Zeilinger–type of maximal entanglement between many atomic ensembles based on laser manipulation and single-photon detection. The scheme, with inherent fault tolerance to the dominant noise and efficient scaling of the efficiency with the number of ensembles, allows one to maximally entangle many atomic ensembles within the reach of current technology. Such a maximum entanglement of many ensembles has wide applications in the demonstration of quantum nonlocality, high-precision spectroscopy, and quantum information processing.

DOI: 10.1103/PhysRevLett.88.170402 PACS numbers: 03.65.Ud, 03.67.–a, 42.50.Gy

Quantum entanglement links two or more distant subsystems in a profound quantum mechanical way. Such a link has found wide applications in the demonstration of quantum nonlocality [1,2], high-precision spectroscopy [3], and quantum information processing including computation, communication, and cryptography [4,5]. There were great experimental efforts recently to get more and more subsystems entangled [6–9], since, with more subsystems entangled, quantum nonlocality becomes more striking [1,2], and the entanglement is more useful for various applications [3–5]. In most of the experimental efforts, the subsystems are taken as single particles, and until now three to four atoms or photons have been entangled with a linear ion trap [8], with a spontaneous parametric down converter [6,9], or with a high-Q cavity [7]. There are also proposals to entangle indistinguishable atoms in Bose-Einstein condensates [10], or to weakly entangle two macroscopic atomic ensembles [11], and the latter has been demonstrated in a recent exciting experiment [12].

In all the experimental efforts, it is hard to continuously increase the number of the entangled subsystems due to the fast exponential decrease of the preparation efficiency [6,7,9] or due to noise and imperfections in the setup [7,8]. Here, we propose a scheme to generate the GHZ type of maximal entanglement between many atomic ensembles with the following features: First, the scheme has built-in fault tolerance and is robust to realistic noise and imperfections. As a result, the physical requirements of the scheme are moderate and well fit the experimental technique. Second, the preparation efficiency of the Greenberger-Horne-Zeilinger (GHZ) entanglement decreases only with the number of ensembles by a slow polynomial law. Such an efficient scaling makes it possible to maximally entangle many (such as tens of) ensembles with the current technology. Our scheme is based on Raman-type laser manipulation of the ensembles and single-photon detection which postselects the desired entangled state in a probabilistic fashion. In contrast to the belief that entangling schemes based on postselections will necessarily suffer from the fast exponential degradation of the efficiency, we design a scheme which circumvents this problem by making use of quantum memory available in atomic internal levels.

The basic element of our system is an ensemble of many identical alkali atoms, whose experimental realization can be either a room-temperature atomic gas [12,13] or a sample of cold trapped atoms [14,15]. The relevant level structure of the atom is shown in Fig. 1. From the three levels $|g\rangle, |h\rangle, |v\rangle$, we can define two collective atomic operators $s = (1/\sqrt{N_a})\sum_{i=1}^{N_a} |g\rangle_i\langle s|$ with $s = h, v$, where $N_a \gg 1$ is the total atom number. The atoms are initially prepared through optical pumping to the ground state $|g\rangle$, which is effectively a vacuum state $|\mathrm{vac}\rangle$ of the operators h, v. The h, v behave similar to independent bosonic mode operators as long as most of the atoms remain in the state $|g\rangle$. A basis of the "polarization" qubit (in analogy to the language for photons) can be defined from the states $|H\rangle = h^\dagger|\mathrm{vac}\rangle$ and $|V\rangle = v^\dagger|\mathrm{vac}\rangle$, which have an experimentally demonstrated long coherence time [12–15]. Single-bit

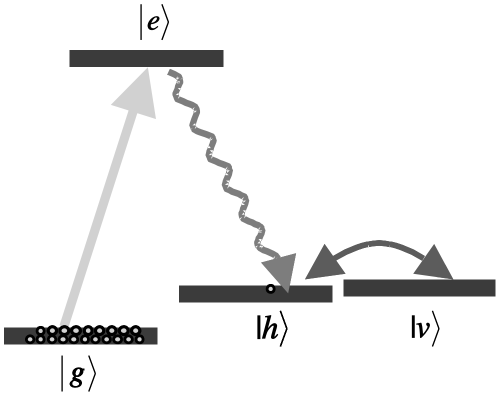

FIG. 1. The relevant atomic level structure with $|g\rangle$ the ground state, $|e\rangle$ the excited state, and $|h\rangle$ and $|v\rangle$ the two metastable states (e.g., Zeeman or hyperfine sublevels) for storing a qubit of information. The three levels, $|g\rangle$, $|e\rangle$, and $|h\rangle$ can be coupled through a Raman process which is useful for measurement of the collective atomic excitation in the state $|h\rangle$ [16] and for generating preliminary entanglement between two ensembles [17].

© 2002 The American Physical Society

rotations in this basis can be done with high precision by shining Raman pulses or radio-frequency pulses on all the atoms. The excitations in the mode h can be transferred to optical excitations [16] and then detected by single-photon detectors. Such a transfer has a high efficiency even for a free-space ensemble due to the collectively enhanced coherent interaction as has been demonstrated both in theory [16] and in experiments [13,14].

The first step for generation of many-party entanglement is to share an excitation between the modes h_i, h_j in two distant ensembles i, j. This can be readily done through a scheme in the recent quantum repeater proposal [17], where one prepares the state $(h_i^\dagger + e^{i\phi_{ij}} h_j^\dagger)/\sqrt{2}|\text{vac}\rangle$ [18], with $\phi_{ij} = \phi_j - \phi_i$, an unknown phase difference fixed by the optical channel connecting the i, j ensembles. This state, after a single-bit rotation, can be transferred to the useful form,

$$|\Psi_{i,j}\rangle = (h_i^\dagger + e^{i\phi_{i,j}} v_j^\dagger)/\sqrt{2}|\text{vac}\rangle. \tag{1}$$

The basic idea of the preparation scheme in Ref. [17] is as follows: One excites the ensembles i and j, respectively, through a short weak Raman pulse applied to the transition $|g\rangle \to |e\rangle$ so that the forward-scattered Stokes light from the transition $|e\rangle \to |h\rangle$ has a mean photon number much smaller than 1. The forward-scattered Stokes lights from the two ensembles are then interfered at a beam splitter and further detected by two single-photon detectors. If we successfully get a detector click, we do not know from which ensemble this registered photon comes; due to this indistinguishability, the accompanying collective atomic excitation should be distributed over the ensembles i and j with an equal probability amplitude, and we get the state described previously. This preparation scheme has the following two features: First, the preparation succeeds only with a controllable small probability p_0 for each Raman driving pulse, and needs to be repeated in average $1/p_0$ times for the final successful state generation, with the total preparation time $t_0 \sim 1/(p_0 f_p)$, where f_p is the repetition frequency of the Raman pulses. Second, the scheme, with inherent resilience to noise, is well based on the current technology of laser manipulation. We can safely use it as our first step, to generate the state (1) with a fidelity $F = 1 - p_0$ very close to the unity by controlling the probability p_0. For instance, with a typical repetition frequency $f_p = 10$ MHz, one may prepare the state (1) with a fidelity $F = 1 - p_0 \approx 99\%$ in a time $t_0 \sim 10\ \mu$s.

Based on the preparation of the state (1), now we show how to generate effective many-party entanglement between n such atomic ensembles. We prepare the state (1) between the i and $i + 1$ ensembles for each i from 1 to n, and get the following state:

$$|\Psi\rangle = (1/\sqrt{2^n})\prod_{i=1}^{n}(h_i^\dagger + e^{i\phi_{i,i+1}} v_{i+1}^\dagger)|\text{vac}\rangle, \tag{2}$$

where for convenience we have assumed the notation $n + 1 \equiv 1$ for the subscripts, and have used the same symbol $|\text{vac}\rangle$ to denote the vacuum of the whole n ensembles. In the expansion of the state (1), there are only two components which have one excitation on each ensemble. This component state is given by

$$|\Psi_{\text{eff}}\rangle = (1/\sqrt{2})\left(\prod_{i=1}^{n} h_i^\dagger + e^{i\phi_t}\prod_{i=1}^{n} v_i^\dagger\right)|\text{vac}\rangle, \tag{3}$$

with $\phi_t = \sum_{i=1}^{n}\phi_{i,i+1}$, which is exactly the n-party GHZ-type maximally entangled state in the polarization basis. Note that, for any practical application of the GHZ entanglement [1–4], the state preparation should be succeeded by a measurement of the polarization of the excitation on each ensemble, which can be done for our system by combining single-bit rotations, such as Hadamard transformations, with the number detection of the mode h_i through single-photon detectors. If in this measurement we keep only the results for which an excitation appears on each ensemble (i.e., postselect the case when the detector on each side registers a click), the states (2) and (3) become effectively equivalent since the other components in the state (2) have no contributions to the measurement. Through this postselection technique, we can simply prepare the state (2), which, whenever we put it into applications, yields effectively the GHZ entanglement described by the effective state (3). Here and in the following, we label a component of the full state as the effective state if only this component has contributions to the application measurements (which are the measurements required for the detection or application of the generated state). The effective state is the state postselected by the application measurements.

For applications of the GHZ entanglement, we need also to know the phase ϕ_t in the effective state (3), which is fixed by the whole setup and in principle can be measured. However, a better way is to directly cancel this unknown phase ϕ_t with the following method. Assume that we have an even number n of the ensembles. The pair of ensembles i and $i' = n + 2 - i$ are put in near proximity so that the ensembles $i, i + 1$ and $i', (i + 1)'$ can be connected through the same optical channel, which fixes the phases to satisfy the relation $\phi_{i,i+1} = \phi_{i',(i+1)'} = -\phi_{(i+1)',i'}$ [19]. With this relation, the accumulated phase ϕ_t is exactly canceled to zero.

The above preparation scheme of the effective GHZ entanglement is robust to realistic noise and imperfections. The dominant noise in this system is the photon detector inefficiency, the transferring inefficiency (induced by the spontaneous emission loss) of the excitation from the atomic mode h_i to the optical mode, and the small decay of the atomic excitation in each ensemble. All the above noise is well described by loss of excitations with an overall loss probability denoted by η. Note that, by including the detector inefficiency, we have automatically taken into account that the single-photon detectors cannot perfectly distinguish between single and two photons. It is easy to see that loss of excitations has influence only on the success probability to register an excitation from each ensemble. Whenever the excitation is registered, its polarization is still perfectly entangled as shown by the effective state (3).

Now we consider the efficiency of this scheme, which can be described by the total time needed to successfully register the effective GHZ entanglement. The preparation of the factor state (1) is probabilistic; however, due to the available quantum memory provided by the metastable atomic modes h, v, the preparation time t_1 of the state (2) is at most nt_0 if its factor states are prepared one after the other, and can be reduced to $t_1 \sim t_0$ (in the case of $n < 1/p_0$) if its factor states are prepared independently at the same time. In contrast to this, in the case of no quantum memory, one would need about $1/p_0^n$ repeats of the Raman pulses for a successful preparation of the state (2), and a total time $t_0/p_0^{n-1} \gg t_0$. After preparation of the state (2), the projection efficiency (success probability) from the state (2) to the effective GHZ state (3) is given by $(1-\eta)^n/2^{n-1}$, where we have assumed the same loss probability η for each ensemble. So the total time for registering the n-party GHZ entanglement is $T \sim t_0 2^{n-1}/(1-\eta)^n$, which increases with the number of ensembles exponentially by the factor $2/(1-\eta)$. Note that this increase has been much slower than the case for spontaneous parametric down-conversion, where the exponential increasing factor is about 2 orders larger due to the absence of quantum memory [6,9].

We can in fact further improve the scheme to get a much more efficient scaling of the efficiency, with the time T increasing with the party number n only polynomially. The improved scheme is divided into the following three steps.

(i) We start with two pairs of ensembles 1, 2 and 3, 4, prepared in the state $|\Psi_{1,2}\rangle \otimes |\Psi_{3,4}\rangle$ with $|\Psi_{i,j}\rangle$ in the form of Eq. (1). We then connect these two disjoint pairs by preparing the state $|\Psi_{2,3}\rangle$. The ensembles 2 and 3 will not be involved any more in the following steps for state preparation, so we can immediately put them into applications by doing the same type of measurements on them as if we had generated n-party GHZ entanglement. In these measurements, if one excitation is registered from each ensemble 2 and 3, we succeed and will go on with the next step. Otherwise, we simply repeat the above process until we succeed. Upon success, only the component $|\Psi_{1-4}\rangle$ of the state $|\Psi_{1,2}\rangle \otimes |\Psi_{3,4}\rangle \otimes |\Psi_{2,3}\rangle$ has contributions to the measurement with

$$|\Psi_{1-4}\rangle = (1/\sqrt{2})(h_1^\dagger h_2^\dagger h_3^\dagger + v_2^\dagger v_3^\dagger v_4^\dagger)|\text{vac}\rangle, \tag{4}$$

where for simplicity we have neglected the phase $\phi_{i,i+1}$, since they will finally cancel each other with the method described previously. If loss of excitations with a loss probability η is taken into account for detections on the ensembles 2, 3, a registered click might result from two excitations, and in this case there will be no excitation in the ensembles 1 and 4. So with the loss, upon success of step (i), instead of $|\Psi_{1-4}\rangle$ the effective state of the ensembles 1–4 is actually described by

$$\rho_{1-4} = (|\Psi_{1-4}\rangle\langle\Psi_{1-4}| + c_1\rho_{\text{vac}})/(1+c_1), \tag{5}$$

with the vacuum coefficient $c_1 = 2\eta$, where ρ_{vac} stands for the vacuum component with no excitation in the undetected ensembles 1 and 4. The probability of a successful detection on both of the ensembles 2 and 3 is given by $p_1 = (1-\eta)^2(1+2\eta)/4$, which means that we need to repeat the process in average $1/p_1$ times for the final success of step (i).

(ii) In step (ii) we further extend the number of entangled ensembles in the effective state (5). Assume that we have applied the method of step (i) in parallel to the two disjoint sets of ensembles 1–4 and 5–8, with their effective states [each in the form of Eq. (5)] denoted by ρ_{1-4} and ρ_{5-8}, respectively. We connect these two sets by first preparing the state $|\Psi_{4,5}\rangle$ [in the form of Eq. (1)] and then putting the ensembles 4, 5 into application measurements as described in step (i). Upon success of these measurements with one excitation registered from each ensemble, the postselected state of the ensembles 1–8 is effectively described by ρ_{1-8} which is similar to Eq. (5), but with an increased vacuum coefficient and with $|\Psi_{1-4}\rangle$ replaced by $|\Psi_{1-k}\rangle = (1/\sqrt{2})(\prod_{i=1}^{k-1} h_i^\dagger + \prod_{i=2}^{k} v_i^\dagger)|\text{vac}\rangle$, $(k = 8)$. Whenever the measurement fails, we repeat the whole state preparation from step (i). The above connection process can be continued with the number n of effectively entangled ensembles doubled for each time of connection. After i times connection, we have $n = 2^{i+1}$. The success probability and the new vacuum coefficient of the ith connection are denoted, respectively, by p_i and c_i, which satisfy the following recursion relations with the previous vacuum coefficient c_{i-1} through $p_i = (1-\eta)^2(1+2\eta+2c_{i-1})/[4(1+c_{i-1})^2]$, and $c_i = 2c_{i-1} + 2\eta$. From these recursion relations, we have $c_i = 2\eta(2^i - 1)$, which, after substituted into p_i, yields an explicit expression for the repetition number $1/p_i$ of the ith connection.

(iii) After a desired number $n = 2^{i+1}$ of the ensembles have been entangled in the effective state ρ_{1-n}, we close the loop in the last step by first preparing the state $|\Psi_{n,1}\rangle$ [in the form of Eq. (1)] and then putting the last two ensembles $n, 1$ into application measurements. As usual, we keep the results only when one excitation appears from each detected ensemble, and this automatically eliminates contributions from the vacuum component in the state ρ_{1-n}. So the effective state of the whole set of ensembles postselected by all the application measurements is still described by the exact GHZ state (3), and the application measurement results should reveal perfect GHZ entanglement between the n ensembles in the polarization degree of freedom. The application measurements on the ensembles $n, 1$ in the last step succeeds with a probability $p_l = (1-\eta)^2/[2(1+c_i)]$, so the whole process needs to be repeated in average $1/p_l$ times.

Now we calculate in this improved scheme how much time is needed in total for a successful detection of the n-party GHZ entanglement. This time is given by $T_{\mathrm{imp}} = t_0/[p_l p_1 \prod_{j=2}^{i} p_j]$, where t_0 is the preparation time of the state (1). We consider two limiting cases. In the first case with a negligible loss probability η for each ensemble, we have $p_l = 2p_j = 1/2$ and $T_{\mathrm{imp}} = 2^{2i+1} t_0 = n^2 t_0/2$, which increases with the number n of entangled ensembles by the slow quadratic law. In the second case with a considerably large loss probability η, the total time T_{imp} is approximated by $T_{\mathrm{imp}} \sim t_0[2\eta n/(1-\eta)^2](n/2)^{\log_2[2\eta\sqrt{n}/(1-\eta)^2]}$, which increases with n faster, but still polynomially (or, more accurately, subexponentially). The basic reason for the improvement from the exponential scaling to the much slower polynomial scaling is because we have divided the whole preparation process into many small steps, checking in each step whether the preparation is successful, and repeating this small step instead of the whole process if it fails.

Finally, we briefly discuss the practical implication of this proposal. With the improved scheme, for example, we can generate high-fidelity GHZ entanglement over $n = 16$ ensembles in a time $T_{\mathrm{imp}} \sim 50$ ms with a notable loss $\eta \approx 1/3$ and a typical choice $t_0 \sim 10\ \mu$s. With such a short preparation time T_{imp}, the noise that we have not included, such as the nonstationary phase drift induced by the pumping phase or by the optical channel, is negligible. As long as the number n of the ensembles is not huge, we can also safely neglect the single-bit rotation error (below 10^{-4} with the use of accurate polarization techniques for Zeeman sublevels [20]) and the dark count probability (about 10^{-5} in a typical detection time window 0.1 μs) of single-photon detectors. Because of the efficient scaling of this scheme, one can use it to steadily increase the number of entangled ensembles, and it seems reasonable to generate GHZ entanglement over tens of ensembles with the current technology. Such an extraordinary possibility opens up prospects for many exciting experiments and applications.

This work was supported in part by the Caltech MURI Center for Quantum Networks under ARO Grant No. DAAD19-00-1-0374, by the National Science Foundation under Grant No. EIA-0086038, and also by the Chinese Science Foundation and Chinese Academy of Sciences.

*Email address: lmduan@caltech.edu

[1] D. M. Greenberger, M. A. Horne, A. Shimony, and A. Zeilinger, Am. J. Phys. **58**, 1131 (1990).
[2] N. D. Mermin, Phys. Rev. Lett. **65**, 1838 (1990).
[3] J. J. Bollinger, W. M. Itano, D. Wineland, and D. Heinzen, Phys. Rev. A **54**, 4649 (1996).
[4] D. Gottesman and I. L. Chuang, Nature (London) **402**, 390 (1999).
[5] M. A. Nielsen and I. L. Chuang, *Quantum Computation and Quantum Information* (Cambridge University Press, Cambridge, England, 2000).
[6] D. Bouwmeester *et al.,* Phys. Rev. Lett. **82**, 1345 (1999).
[7] A. Rauschenbeutel *et al.,* Science **288**, 2024 (2000).
[8] C. A. Sackett *et al.,* Nature (London) **404**, 256 (2000).
[9] J.-W. Pan *et al.,* Phys. Rev. Lett. **86**, 4435 (2001).
[10] A. Sorensen, L. M. Duan, J. I. Cirac, and P. Zoller, Nature (London) **409**, 63 (2001).
[11] L. M. Duan, J. I. Cirac, P. Zoller, and E. S. Polzik, Phys. Rev. Lett. **85**, 5643 (2000).
[12] B. Julsgaard, A. Kozhekin, and E. S. Polzik, Nature (London) **413**, 400 (2001).
[13] D. F. Phillips *et al.,* Phys. Rev. Lett. **86**, 783 (2001).
[14] C. Liu, Z. Dutton, C. H. Behroozi, and L. V. Hau, Nature (London) **409**, 490 (2001).
[15] J.-F. Roch *et al.,* Phys. Rev. Lett. **78**, 634 (1997).
[16] M. Fleischhauer and M. D. Lukin, Phys. Rev. Lett. **84**, 5094 (2000).
[17] L. M. Duan, M. D. Lukin, J. I. Cirac, and P. Zoller, Nature (London) **414**, 413 (2001).
[18] Reference [17] shows that the generated state will be mixed with a small vacuum component if we take into account the detector dark counts. However, this vacuum component is typically very small since the normal dark count rate (100 Hz) is much smaller than the repetition frequency (10 MHz, for instance) of the Raman pulses; in addition, this component will be finally automatically eliminated in our scheme since its effect is the same as the effect of detector inefficiency in the application measurements, which we will analyze below. So, for simplicity, we write a pure state here by neglecting this small component.
[19] Remember the notation $n + 1 \equiv 1$. The index i and $i' = n + 2 - i$ actually denote the same ensemble for $i = 1$ and $n/2 + 1$. So, as a special case of the relation $\phi_{i,i+1} = -\phi_{(i+1)',i'}$, we have $\phi_{1,2} = -\phi_{n,1}$ and $\phi_{n/2,n/2+1} = -\phi_{n/2+1,n/2+2}$.
[20] D. Budker, V. Yashuk, and M. Zolotorev, Phys. Rev. Lett. **81**, 5788 (1998).

Photonic Crystals for Confining, Guiding, and Emitting Light

Axel Scherer, Oskar Painter, Jelena Vuckovic, Marko Loncar, and Tomoyuki Yoshie

***Abstract*—We show that by using the photonic crystals, we can confine, guide, and emit light efficiently. By precise control over the geometry and three-dimensional design, it is possible to obtain high quality optical devices with extremely small dimensions. Here we describe examples of high-Q optical nanocavities, photonic crystal waveguides, and surface plasmon enhanced light-emitting diode (LEDs).**

***Index Terms*—Finite-difference time-domain (FDTD) methods, light-emitting diodes (LEDs), microcavities, nanooptics, photonic bandgap (PBG) materials, photonic crystal waveguides, photonic crystals, quantum-well laser, semiconductor device fabrication, spontaneous emission, surface plasmons.**

I. PHOTONIC CRYSTAL NANOCAVITIES

THE PAST rapid emergence of optical microcavity devices, such as vertical-cavity surface-emitting lasers (VCSELs) [1] and [2] can be largely attributed to the high precision over the layer thickness control available during semiconductor crystal growth. High reflectivity mirrors can, thus, be grown with subnanometer accuracy to define high-Q cavities in the vertical dimension. Recently, it has also become possible to *microfabricate* high reflectivity mirrors by creating two- and three-dimensional periodic structures. These periodic "photonic crystals" [3] and [4] can be designed to open up frequency bands within which the propagation of electromagnetic waves is forbidden irrespective of the propagation direction in space and define photonic bandgaps. When combined with high index contrast slabs in which light can be efficiently guided, microfabricated two-dimensional photonic bandgap (PBG) mirrors provide us with the geometries needed to confine and concentrate light into extremely small volumes and to obtain very high field intensities. Here we show that it is possible to use these "artificially" microfabricated crystals in functional optical devices, such as lasers, modulators, add–drop filters, polarizers and detectors.

Fabrication of optical structures has evolved to a precision which allows us to control light within etched nanostructures [5]. For example, subwavelength nano-optic cavities can be used for efficient and flexible control over the emission wavelength [6] and [7]. Similarly, nanofabricated optical waveguides can be used for efficient coupling of light between devices. This new capability allows the reduction of the size of optical components and leads to their integration in large numbers, much in the same way as electronic components have been integrated for improved functionality to form microchips. As high-Q optical and electronic cavity sizes approach a cubic half-wavelength the spatial and spectral densities (both electronic and optical) increase to a point where the light-matter coupling becomes so strong that spontaneous emission is replaced by the coherent exchange of energy between the two systems [8]–[11].

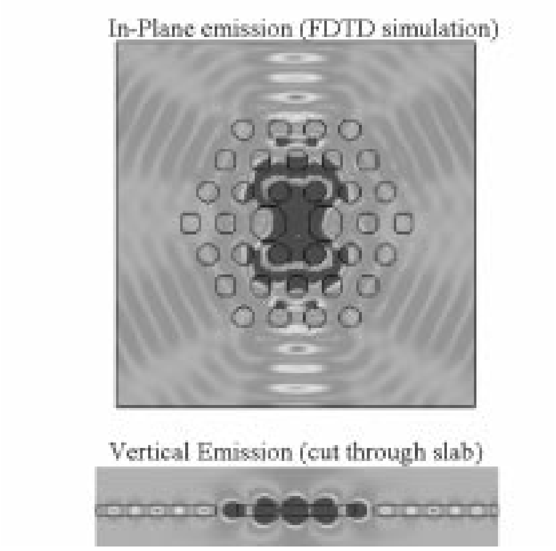

Fig. 1. Field intensity of light leakage from a single defect surrounded by three periods of photonic crystal and slightly enlarged holes in the horizontal direction. Light preferentially emits in the y dipole.

We can use the lithographic control over the wavelength and polarization supported within photonic crystal cavities to construct compact nanophotonic laser (see Fig. 1) and detector arrays, as well as all-optical gates and routers. We have already demonstrated room temperature lasing in the smallest optical cavities, with mode volumes down to 2.5 $(\lambda/2n_{\mathrm{slab}})^3$, or 0.03 μm^3 in InGaAsP emitting at 1.55 μm. We have also been able to tune the emission wavelength of these lasers from 1450 nm to 1620 nm within a 10 × 10 laser array in an area of 100 μm × 100 μm by local lithographic modification of the cavity lengths (see Fig. 2) [5]. As the mode volumes of nanocavities are decreased, the coupling efficiency between the spontaneous emission [12] within the cavity and the lasing mode can be significantly improved. We have calculated spontaneous emission coupling factors (β) above 85% [13] for optimized photonic crystal lasers constructed in active quantum-well (QW) material. This spontaneous emission coupling efficiency can be even higher if the linewidth of the

---

Manuscript received February 27, 2002; revised March 1, 2002. This work was supported in part by the Air Force Office of Scientific Research (AFOSR) under the Defense Advanced Research Projects Agency (DARPA)/Quantum Information Science and Technology (QuIST) Program, and in part by the National Science Foundation (NSF) under Grant ECS-9912039, and the Army Research Office (ARO) under a Multidisciplinary University Research Initiative (MURI) Grant DAAD 190010374.

The authors are with the California Institute of Technology (Caltech), Pasadena, CA 91125 USA.

Publisher Item Identifier S 1536-125X(02)04953-0.

1536-125X/02$17.00 © 2002 IEEE

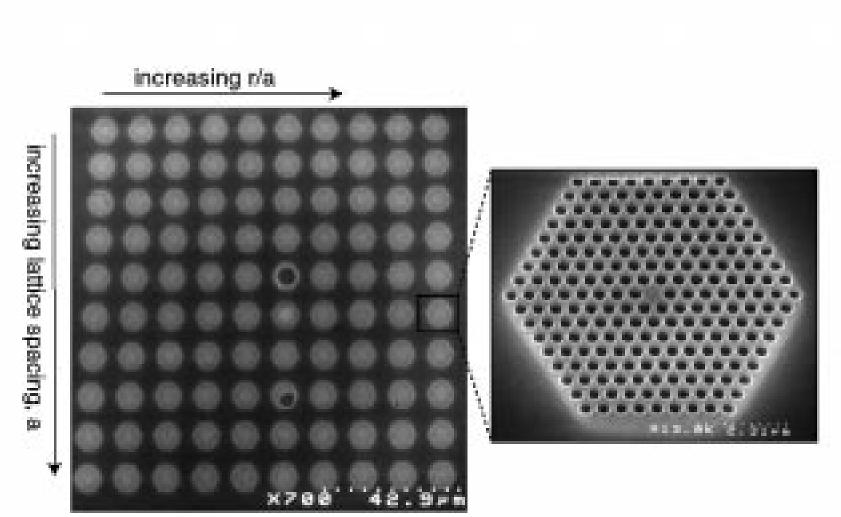

Fig. 2. 10 × 10 multiwavelength laser array within a 100 × 100 μ area. Each laser emits at a lithographically controlled wavelength.

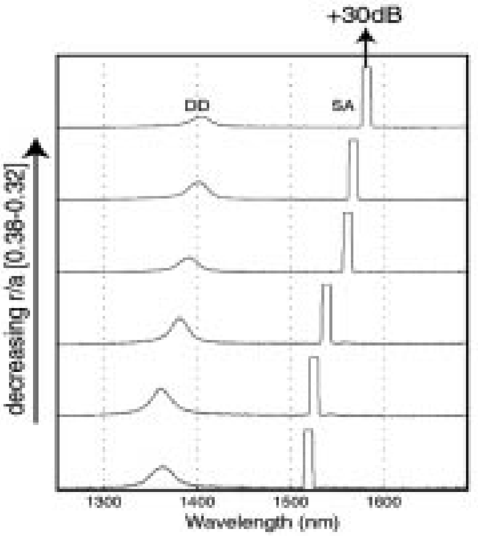

Fig. 3. Sample spectra taken from lasers defined within the 10 × 10 array.

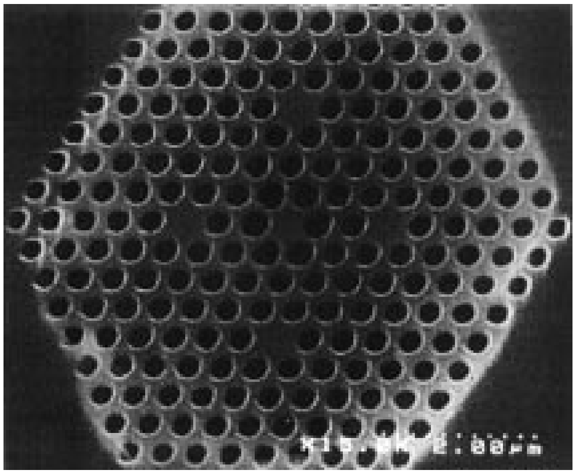

Fig. 4. Five photonic crystal cavities coupled together lithographically by arrangement in the same slab.

semiconductor emission is narrowed, as will be the case when using quantum dot active material. Therefore, single defect photonic crystal lasers represent in many ways the ultimate evolution of VCSELs, since control over both vertical and lateral spontaneous emission is possible. With most of the spontaneous emission funneled into a single optical mode, the photonic crystal laser can be modulated at much higher frequencies even close to threshold. The photonic crystal provides us with the unique opportunity of coupling light emitted by one cavity, and using it to optically pump another with negligible diffraction losses. Photonic crystals are also the perfect medium for constructing what have been termed “photonic molecules,” or interconnected cavities which can share and exchange photons. Finally, we have shown that the emission wavelength of light from these photonic crystal lasers can be varied by simple adjustments of the lithographic pattern during their fabrication. Thus, single mode lasers emitting at 1450 nm can be fabricated only microns apart from lasers emitting at 1600 nm, and could share the same waveguide slab. Photonic crystals provide us with the opportunity of constructing very compact laser sources with designed frequencies (Fig. 3) and polarization as well as wavelength and polarization sensitive detector arrays. Moreover, they can form very flexible platforms for connecting optical sources, detectors, routers, modulators, polarizers and filters in very compact microfabricated systems.

Another unique feature of active photonic crystal cavities (see Fig. 4), which arises from their ability to limit the number of modes supported within the laser, is the ability to build high contrast modulators.

Fig. 5 shows an example of such a single defect photonic crystal cavity, which supports a few modes within the same cavity. Depending on the diameter of the pump beam, (shown on the left-hand side of the figure), we find that different modes are excited, and these in turn exhibit different spectra. Finite-difference time-domain simulations of the expected geometric distribution of the field intensities within these modes are also shown, and the relative overlap of the pump beam with the expected mode geometries matches well to the observations.

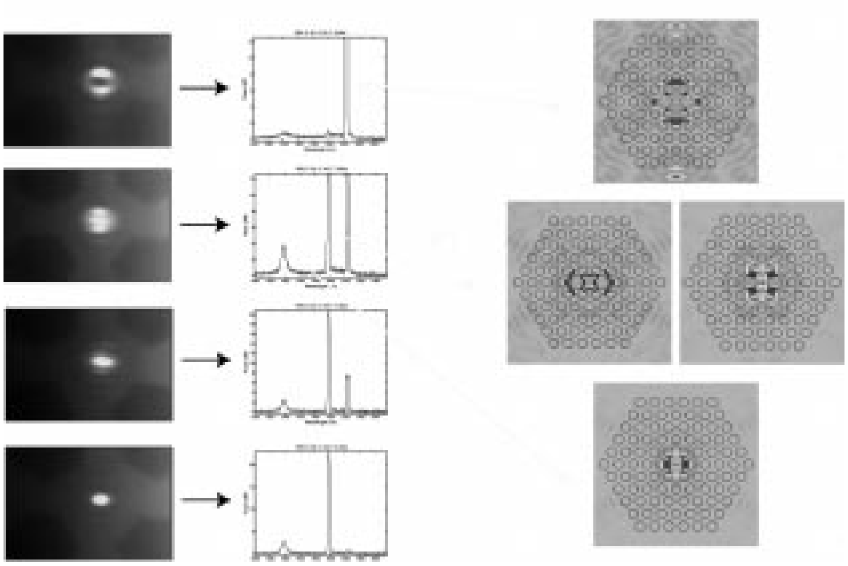

Fig. 5. Geometries of modes supported by a single defect photonic crystal cavity. We show the measured spectra and the modeled field distributions of the modes.

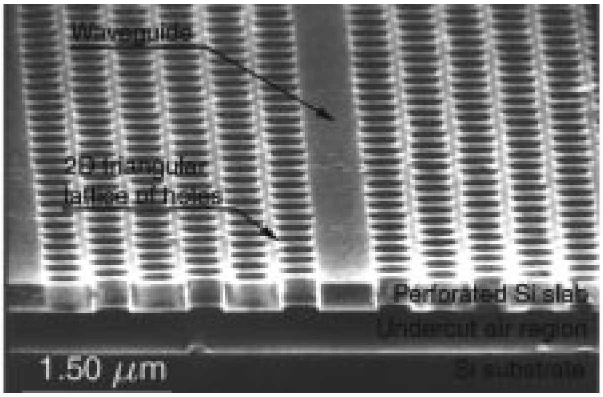

Fig. 6. Photonic crystal waveguide defined into a SOI wafer.

II. PHOTONIC CRYSTAL WAVEGUIDES

We have shown above that it is possible to generate light and modulate it with simple high-Q optical resonator cavities. However, if a nanophotonic system is to be constructed, it is also necessary to guide light from one device to another. We have conducted extensive tests on optical waveguides based on photonic crystals to explore the opportunities of using this geometry to efficiently guide light, especially around very sharp bends [18]. In the simplest geometry, a photonic crystal waveguide can be constructed by lithographically removing a line of holes from a perfect photonic crystal. This geometry provides the opportunity for light to propagate through the photonic crystal (Fig. 6) [15]–[17].

Although it is difficult to couple light into such structures, we have been able to measure light guiding in such photonic crystal waveguides through sharp bends. We have both calculated (see Fig. 8) and experimentally obtained [19] the dispersion diagram of such waveguides, and have found that several modes can propogate within them, making them less desirable for many telecommunication applications. More recently, we have developed new single mode photonic crystal waveguide designs, in which the dispersion properties can be controlled [20]. Fig. 7 shows modified waveguide designs, fabricated in silicon-on-insulator (SOI) material, in which only one waveguiding mode is supported at desired frequency. Photonic crystal waveguides offer the opportunities to ensure mode-matching between an optical cavity and the waveguide, but much work still needs to be done to determine the dispersive character of such structures with periodic edges.

Very interesting structures can also be defined by using waveguides with periodic cavities [Fig. 7(b)], or coupled resonant cavity structures [21]. In our fabricated structures, we expect to define geometries with designed dispersive characteristics.

III. SURFACE PLASMON LIGHT EMITTERS

Surface plasmons (SP), also called surface plasmons polaritons are electromagnetic surface waves that propagate along metallic surfaces, have their intensity maximum at the surface and exponentially decaying fields perpendicular to it. The condition for occurrence of such localized waves at the boundary between two media is that the two materials joined the boundary must have opposite signs of the real part of the dielectric constant (otherwise, a strong field localization at the surface cannot be obtained). This is possible at the interface between a metal operating at frequencies below the plasma frequency and any dielectric.

Numerical electromagnetic calculations in metals which are capable of manipulating radiation at the nanometer scale are very demanding. An important tool is the use of FDTD [23] and [24] methods for metal/dielectric media developed in Scherer's group to analyze theoretically the electromagnetic fields within a microcavity. In order to analyze metals as well as dielectric materials at optical frequencies, it is necessary to make certain changes [25] to Yee's standard FDTD scheme [26]. Electromagnetic fields in metals are described by adding a current term to Maxwell curl equations via a Drude model. Fig. 9 illustrates results of FDTD calculations which yield the photonic band structure and the electromagnetic field profile for a metal-clad micro-

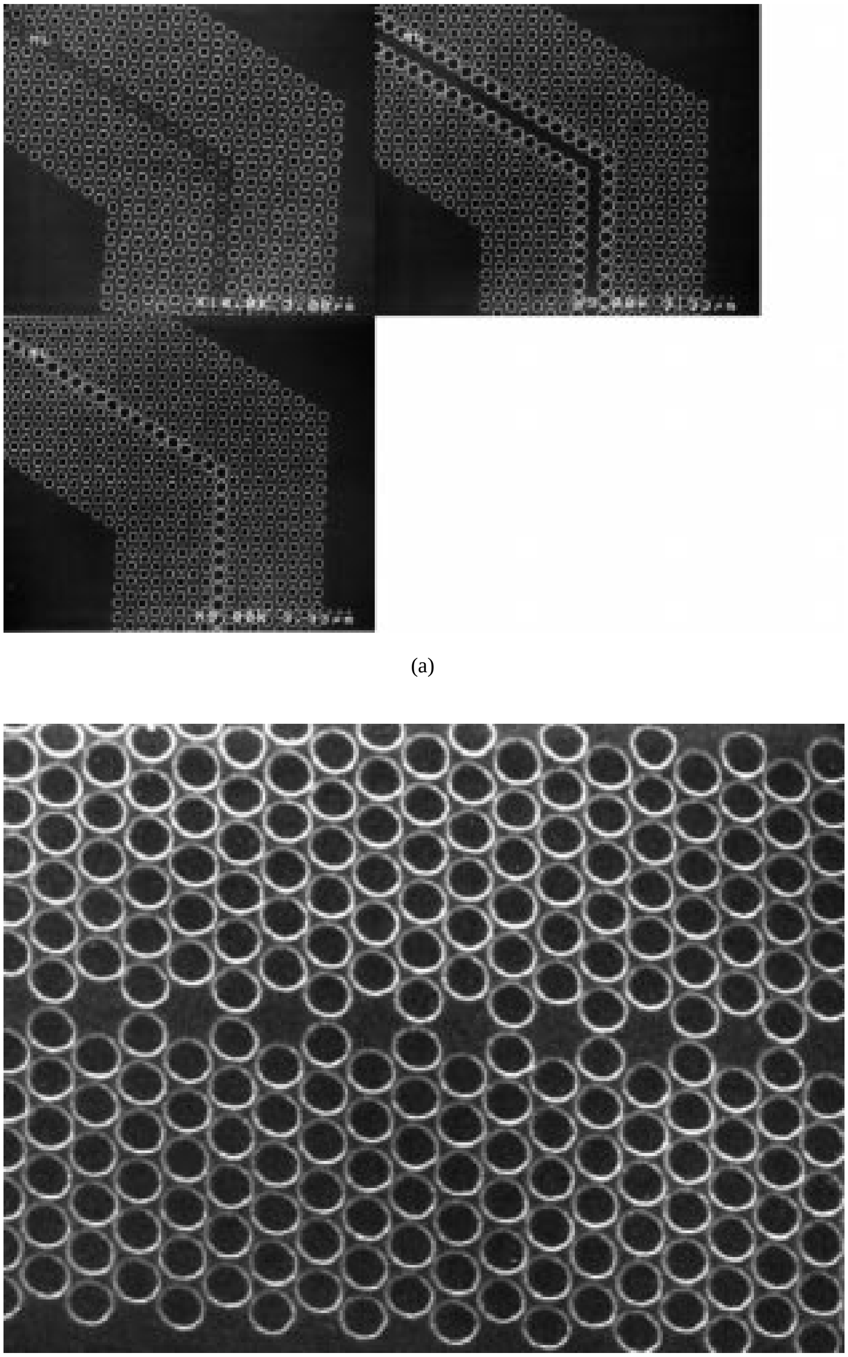

(a)

(b)

Fig. 7. (a) Novel photonic band gap (PBG) waveguide designs. (b) Coupled resonator waveguide.

cavity light-emitting diode [19]. In the frequency range where the cavity thickness is of the order of wavelength of less, coupled surface plasmon modes of the top and bottom surfaces can exist and can be used to efficiently extract light from the semiconductor slab. Very small discretization steps of ~1 nm must be used for the finite difference algorithm to describe the propagation of electromagnetic waves in metals, and this in turn requires large computational volumes. We have developed distributed FDTD algorithms which are supported on multiprocessor computer clusters to manage the large memory requirements.

IV. SP ENHANCED LIGHT-EMITTING DIODES (SP-LEDS)

Much scientific work has been focused on improving the extraction efficiency of light emitting diodes (LEDs). Many interesting approaches have been proposed to accomplish this, such as the use of thin light emitting layers with surface texturing, resonant cavities or photon recycling. External quantum efficiencies of 31% were achieved by employing reflection from a bottom metal mirror together with a textured top semiconductor surface. Apart from efforts to improve light extraction from a

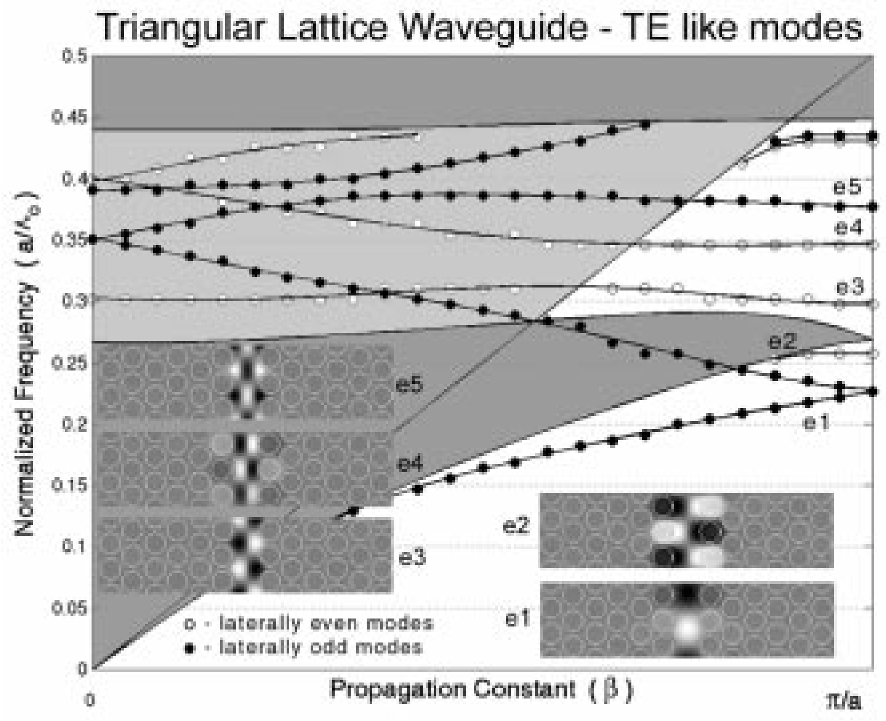

Fig. 8. Dispersion diagram for vertically even TE-like guided modes in the single-line defect PBG waveguide based on the triangular lattice. Insets show field patters of $\mathbf{B_z}$of a surface plasmon wave.

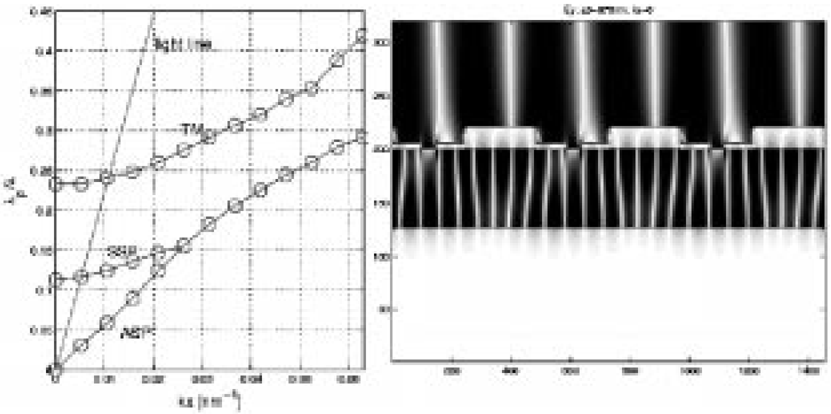

Fig. 9. Band diagram (left) and transverse magnetic (TM) field profile (right) for p-polarized light of a metal clad microcavity. The core is assumed to be made of 150-nm thick GaAs (refractive index $n = 3.5$). Top and bottom metal layers are made of silver with the following parameters: $h\omega_p = 8.8$ eV and $hv = 0.05$ eV. The top layer is only 40-nm thick and the bottom layer is 200 nm thick. The analyzed structure is surrounded by air on top and bottom and the slab is infinite in lateral dimension. Only the bottom three bands are shown, since they are within the frequency range of interest.

semiconductor device, it is also possible to enhance the light emission rate within a semiconductor. This approach is based on Purcell's prediction in 1946 [12] that the radiation rate of an atom placed within a wavelength-sized cavity can be changed. A 12-fold enhancement of spontaneous emission was recently measured in a semiconductor optical microcavity at low temperatures. Metallic structures were identified as candidates for very large decay rate enhancement—much larger than the one achievable by semiconductor photonic crystals. Unfortunately, much of the previous work on surface plasmon emitters was limited by the need to efficiently extract the light generated within such structures.

In order to build an ideal, highly efficient LED, it is desirable to improve both the extraction efficiency and simultane-

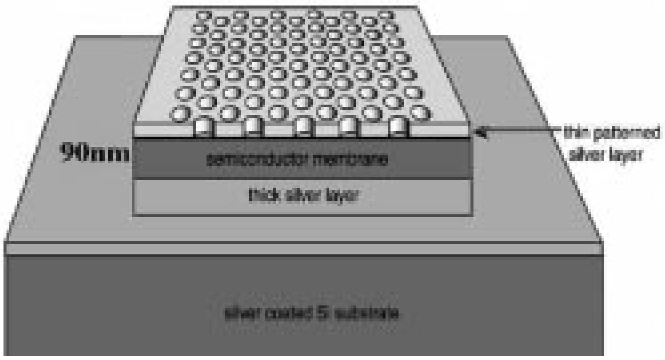

Fig. 10. Design of the surface plasmon LED structure.

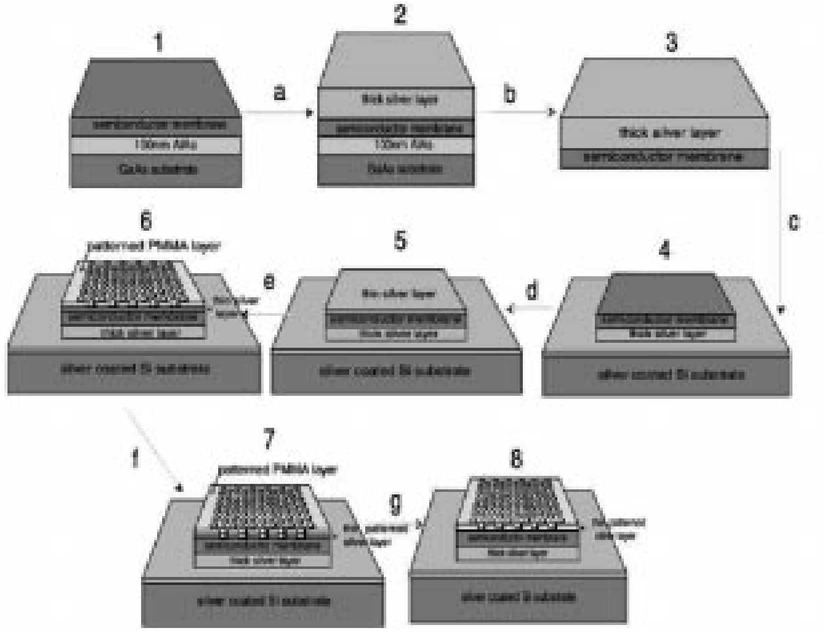

Fig. 11. Fabrication sequence for constructing a SP-LED.

ously enhance the spontaneous emission rate. Metallic photonic crystals have attracted significant scientific attention in recent years for both of these purposes. In 1996, Bill Barnes at the University of Exeter observed a PBG for surface modes on a silver surface textured with a hexagonal array of dots. Two years later, researchers at NEC and their collaborators observed sharp peaks in the transmission of light through a metallic layer patterned with a hexagonal array of subwavelength holes. Both experimental results were attributed to the peculiar properties of surface plasmons polaritons—modes that exist at the interface of two media with opposite signs of the real part of dielectric constant.

In order to couple the emission to SP waves from a single metal–semiconductor surface, it is typically necessary to position the QW very close to that metal surface and within the fringing field depth of the SP. However, the nonradiative transfer between a QW and the metal increases as their distance decreases. The question is then how much of the observed large reduction in lifetime at small distances is due to the coupling to SP waves, and what portion of it comes from other nonradiative processes. The only part that can be possibly extracted outside of the structure by properly designing an "antenna" (i.e., by structuring the surface of metal) is the portion coupled to SP waves. To reduce the nonradiative transfer, we decided to position the QW further from the metal surface (at distances of 40 to 50 nm). However, the intensity of SP waves decreases exponentially as a function of distance from the metallic surface. In order to increase the field intensity at the position of the QW even more, it is possible to use the coupled surface plasmon modes of two closely spaced metallic interfaces.

The analyzed structure consists of a 90-nm thick-semiconductor layer sandwiched between two silver films. A single 8 nm thick InGaAs quantum well is positioned in the middle of the semiconductor membrane. The fabrication sequence is summarized in Fig. 11 and a scanning electron micrograph of a completed surface plasmon LED is shown in Fig. 12. The main emission peak is at the wavelength of 990 nm, corresponding to conduction-to-heavy hole (C–HH) band transitions. Another peak can be observed at 930 nm, corresponding to conduction-to-light hole (C–LH) band transitions. If a periodic pattern is defined in the top semitransparent metal layer by lithography (Fig. 10), it is possible to efficiently couple out the light emitted from the semiconductor and to simultaneously enhance the spontaneous emission rate. For the analyzed designs, we theoretically estimate extraction efficiencies as high as 37% and Purcell factors (Fp) of up to 4.5 [22]. We have experimentally measured photoluminescence intensities of up to 46 times higher in fabricated structures compared to unprocessed wafers. The increased light emission is due to an increase in the efficiency and an increase in the pumping intensity resulting

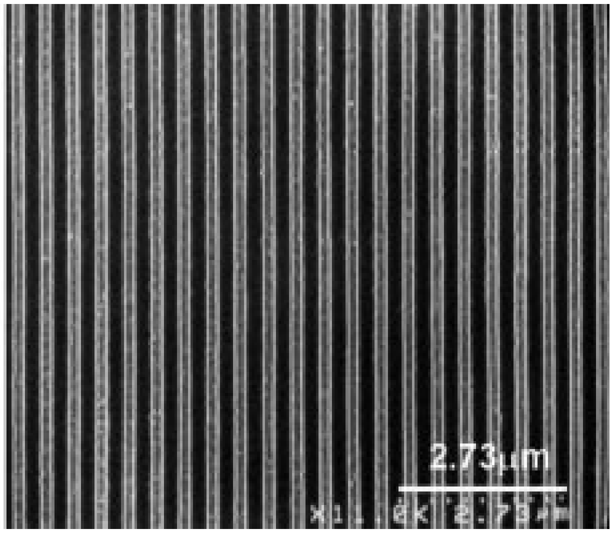

Fig. 12. Scanning electron micrograph of a surface plasmon enhanced LED showing the metal grating pattern which is used to couple out the radiation.

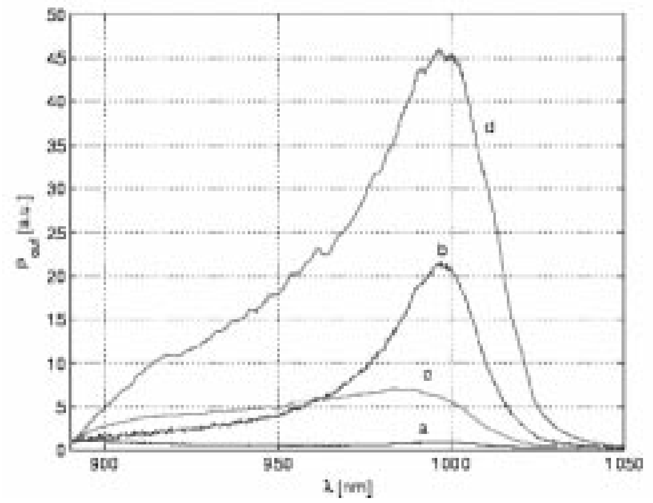

Fig. 13. Luminescence spectra from a surface plasmon enhanced LED at various stages of fabrication (see text).

TABLE I

PARAMETERS OF GRATINGS USED FOR EXTRACTING THE EMISSION FROM THE METAL CLAD MICROCAVITY. a IS THE GRATING PERIODICITY, s IS THE GAP BETWEEN SILVER STRIPES, θ IS THE ANGLE OF THE OUTCOUPLED PHOTON WITH RESPECT TO NORMAL, AND η IS THE NORMALIZED DIFFRACTION EFFICIENCY INTO THE nTH ORDER OF A GRATING. THE OUTCOUPLING HAPPENS THROUGH THE nTH ORDER OF A GRATING

a [nm]	n	θ(at 986nm)	θ(at 930nm)	s[nm]	η
250	-1	6°	25°	160	0.82
480	-2	3.5°	15.3°	160	0.19
650	-3	30°	9°	160	0.06
650	-3	30°	9°	100	0.11

from trapping of pump photons within the microcavity. The measured photoluminescence spectra are shown in Fig. 13. The spectra labels correspond: (a) the unprocessed wafer; (b) the half-processed wafer (i.e., 90-nm-thick semiconductor membrane on top of a thick, nontransparent silver layer); (c) the unpatterned metal-clad microcavity (i.e., a semiconductor membrane sandwiched between two metal films, without patterning of the top silver layer); and (d) the fully processed structure (where silver stripes are defined in the top silver layer, with the grating periodicity of 250 nm and the 160 nm gap between silver stripes). From the calculated values shown in Table I, we conclude that the grating with periodicity of 250 nm will have the best performance, since it has the largest diffraction efficiency. The grating with periodicity of 650 nm and a gap between stripes of $s = 160$ nm will have the worst performance, which can be somewhat improved by reducing the gap to 100 nm.

For all fully processed wafers, including the unpatterned metal clad microcavity, the full-width at half-maximum (FWHM) of the emission spectra is in the range of 60 to 110 nm. Therefore, their quality factors are between 10 and 15. For the half-processed wafer, a FWHM is 32 nm. Because of a bulk emission tail at lower wavelengths, a luminescence peak at 930 nm for unprocessed wafers cannot be clearly resolved. The spectra of unprocessed, half-processed and fully processed wafers are shown in Fig. 13. The PL peak of the unprocessed wafer at 986 nm was normalized to 1. A GaAs filter was applied in front of the detector to cutoff wavelengths below 890 nm. As can be seen from the luminescence curves, it is possible to increase the luminescence intensity of a diode 48 times over a grown heterostructure by introducing a metal clad waveguide with a semitransparent patterned surface plasmon extractor. More interestingly, when comparing curve (b), the half-processed wafer on top of a silver mirror, with curve (d), the fully processed and metalized structure, much higher light extraction is obtained through the top metal layer. Such a structure is ideally suited for electrical pumping, since the metal layers can be used for both light extraction as well as carrier injection. Moreover, our calculations predict that efficient collimated light emission can be generated from surface plasmon LEDs (Fig. 14). Here we propose to optimize this diode structure for electrical pumping, which is expected to lead to highly efficient LEDs with very fast modulation speeds. Our preliminary tests have indicated that in our structures, the spontaneous emission rate is increased by approximately five fold (at room temperature) over conventional LED material.

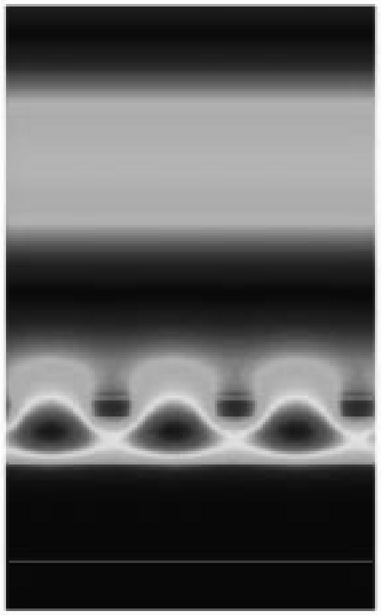

Fig. 14. FDTD calculation of TE field intensities emitted from a surface plasmon LED with a 250-nm-period grating. Collimated light emission is observed in the time evolution of the field.

V. CONCLUSION

Microfabricated structures with dimensions smaller than the wavelength of light allow the efficient confining and guiding of light. High index contrast systems allow such structures to be defined with very small sizes, and, thus, leads to integration of several optical components into more functional systems. Although more complex three-dimensional geometries will eventually be developed [27], one very promising geometry is the two-dimensional photonic crystal, into which cavities, waveguides and dispersive elements can be embedded. The most important advantage of this geometry lies in the opportunity to lithographically couple devices together with minimal diffraction losses and excellent coupling efficiencies. We believe that photonic crystals will be extremely useful for the definition of integrated optical systems, as well as for the definition of extremely small optical cavities, which would be applicable toward strong coupling experiments with quantum dot or atom emitters. On the other hand, metallic structures with high index contrast offer the opportunity to harness surface plasmons, and we show that even with a very simple design it is possible to construct very efficient surface LEDs.

REFERENCES

[1] J. L. Jewell, J. P. Harbison, A. Scherer, Y. H. Lee, and L. T. Florez, "Vertical cavity surface emitting lasers: Growth, design, fabrication, measurements," *IEEE J. Quantum Electron.*, vol. 27, p. 1332, 1991.

[2] A. Scherer, J. L. Jewell, and J. P. Harbison, "Lasing in sub-micron wide vertical cavity microlasers," *Opt. Photonics News*, vol. 2, p. 9, 1991.

[3] E. Yablonovitch, "Inhibited spontaneous emission in solid state physics and electronics?," *Phys. Rev. Lett., E*, vol. 58, no. 20, p. 2059, 1987.

[4] S. John, "Strong localization of photons in certain disordered dielectric superlattices," *Phys. Rev. Lett.*, vol. 58, no. 23, p. 2486, 1987.

[5] O. Painter *et al.*, "Lithographic tuning of a two-dimensional photonic crystal laser array," *IEEE Photonic Tech. L*, vol. 12, no. 9, pp. 1126–1128, Sept. 2000.

[6] O. Painter *et al.*, "Room temperature photonic crystal defect lasers at near-infrared wavelengths in InGaAsP," *J. Lightwave Technol.*, vol. 17, no. 11, pp. 2082–2088, Nov. 1999.

[7] T. Yoshie, S. Scherer, H. Chen, D. Huffaker, and D. Deppe, "Optical chasracterization of two-dimensional photonic crystal cavities with indium arsenide quantum dot emitters," *Appl. Phys. Lett.*, vol. 79, no. 1, pp. 114–116, July 2001.

[8] H. Yokoyama, "Physics and device applications of optical microcavities," *Science*, vol. 256, pp. 66–70, 1992.

[9] Y. Yamamoto and S. Machida, "Microcavity semiconductor laser with enhanced spontaneous emission," *Phys. Rev. A, Gen. Phys.*, vol. 44, no. 1, p. 657, 1991.

[10] L. A. Graham, D. L. Huffaker, and D. G. Deppe, "Spontaneous lifetime control in a native oxide apertured microcavity," *Appl. Phys. Lett.*, vol. 74, no. 17, p. 2408, 1999.

[11] G. P. Agrawal and N. K. Dutta, *Semiconductor Lasers*. New York: Van Nostrand, 1993.

[12] E. M. Purcell, "Spontaneous emission probabilities at radio frequencies," *Phys. Rev.*, vol. 69, p. 681, 1946.

[13] J. Vuckovic, O. Painter, Y. Xu, A. Yariv, and A. Scherer, "Finite difference time domain calculations of the spontaneous emission coupling factor in optical microcavities," *IEEE J. Quantum Electron.*, vol. 35, pp. 1168–1175, Aug. 1999.

[14] O. Painter, R. K. Lee, and A. Scherer, "Two-dimensional photonic band-gap defect mode laser," *Science*, vol. 284, no. 5421, pp. 1819–1821, June 11, 1999.

[15] M. Loncar *et al.*, "Design and fabrication of silicon photonic crystal optical waveguides," *J. Lightwave Technol.*, vol. 18, pp. 1402–1411, Oct. 2000.

[16] J. D. Joannopoulos, R. D. Meade, and J. N. Winn, *Photonic Crystals*. Princeton, NJ: Princeton Univ. Press, 1995.

[17] S.-Y. Lin, E. Chow, V. Hietala, P. R. Villeneuve, and J. D. Joannopoulos, "Experimental demonstration of guiding and bending of electromagnetic waves in a photonic crystal," *Science*, vol. 282, p. 274, 1998.

[18] M. Loncar, D. Nedeljkovic, and T. Doll, "Waveguiding in planar photonic crystals," *Appl. Phys. Lett.*, vol. 77, no. 13, pp. 1937–1939, 1999.

[19] M. Loncar *et al.*, "Experimental and theoretical confirmation of Block-mode light propagation in planar photonic crystal waveguides," *Appl. Phys. Lett.*, vol. 80, no. 10, pp. 1689–1691, Mar. 2002.

[20] M. Loncar, J. Vuckovic, and A. Scherer, "Methods for controlling positions of guided modes of photonic-crystal waveguides," *J. Opt. Soc. Amer. B, Opt. Phys.*, vol. 18, no. 9, pp. 1362–1368, Sept. 2001.

[21] A. Yariv *et al.*, "Coupled-resonator optical waveguide: A proposal and analysis," *Opt. Lett.*, vol. 24, no. 11, pp. 711–713, June 1, 1999.

[22] J. Vuckovic, M. Loncar, and A. Scherer, "Surface plasmon enhanced light-emitting diode," *IEEE J. Quantum Electron.*, vol. 36, pp. 1131–1144, Oct. 2000.

[23] B. D'Urso, O. Painter, J. O'Brien, T. Tombrello, A. Yariv, and A. Scherer, "Modal reflectivity in finite-depth 2-D photonic crystal microcavities," *J. Opt. Soc. Am. B, Opt. Phys.*, vol. 15, no. 3, p. 1155, 1998.

[24] A. Scherer *et al.*, "InGaAsP photonic band gap crystal membrane microresonators," *J. Vac. Sci. Technol. B, Microelectron.*, vol. 16, no. 6, pp. 3906–3910, Nov.–Dec. 1998.

[25] S. A. Cummer, "An analysis of new and existing FDTD methods for isotropic cold plasma and a method for improving their accuracy," *IEEE Trans. Antennas Propagat.*, vol. AP45, p. 392, 1997.

[26] K. S. Yee, "Numerical solution to initial boundary value problems involving Maxwell's equations in isotropic media," *IEEE Trans. Antennas Propagat.*, vol. AP14, p. 302, 1966.

[27] C. C. Cheng *et al.*, "Nanofabricated three dimensional photonic crystals operating at optical wavelengths," *Phys. Scr.*, vol. T68, pp. 17–20, 1996.

Axel Scherer, photograph and biography not available at the time of publication.

Oskar Painter, photograph and biography not available at the time of publication.

Jelena Vuckovic, photograph and biography not available at the time of publication.

Marko Loncar, photograph and biography not available at the time of publication.

Tomoyuki Yoshie, photograph and biography not available at the time of publication.

PHYSICAL REVIEW A, VOLUME 65, 012322

Robustness of adiabatic quantum computation

Andrew M. Childs* and Edward Farhi†
Center for Theoretical Physics, Massachusetts Institute of Technology, Cambridge, Massachusetts 02139

John Preskill‡
Institute for Quantum Information, California Institute of Technology, Pasadena, California 91125

(Received 23 August 2001; published 14 December 2001)

We study the fault tolerance of quantum computation by adiabatic evolution, a quantum algorithm for solving various combinatorial search problems. We describe an inherent robustness of adiabatic computation against two kinds of errors, unitary control errors and decoherence, and we study this robustness using numerical simulations of the algorithm.

DOI: 10.1103/PhysRevA.65.012322 PACS number(s): 03.67.Lx, 03.65.Yz

I. INTRODUCTION

The method of quantum computation by adiabatic evolution has been proposed as a general way of solving combinatorial search problems on a quantum computer [1]. Whereas a conventional quantum algorithm is implemented as a sequence of discrete unitary transformations that form a quantum circuit involving many energy levels of the computer, the adiabatic algorithm works by keeping the state of the quantum computer close to the instantaneous ground state of a Hamiltonian that varies continuously in time. Therefore, an imperfect quantum computer implementing a conventional quantum algorithm might experience different sorts of errors than an imperfect adiabatic quantum computer. In fact, we claim that an adiabatic quantum computer has an inherent robustness against errors that might enhance the usefulness of the adiabatic approach.

The adiabatic algorithm works by applying a time-dependent Hamiltonian that interpolates smoothly from an initial Hamiltonian whose ground state is easily prepared to a final Hamiltonian whose ground state encodes the solution to the problem. If the Hamiltonian varies sufficiently slowly, then the quantum adiabatic theorem guarantees that the final state of the quantum computer will be close to the ground state of the final Hamiltonian, so a measurement of the final state will yield a solution of the problem with high probability. This method will surely succeed if the Hamiltonian changes slowly. But how slow is slow enough?

Unfortunately, this question has proved difficult to analyze in general. Some numerical evidence suggests the possibility that the adiabatic algorithm might efficiently solve computationally interesting instances of hard combinatorial search problems, outperforming classical methods [1–4]. Whether the adiabatic algorithm provides a definite speedup over classical methods remains an interesting open question. As we will discuss in Sec. II, the time required by the algorithm for a particular instance can be related to the minimum gap Δ between the instantaneous ground state and the rest of the spectrum. Roughly speaking, the required time goes like Δ^{-2}. Thus, if Δ^{-2} increases only polynomially with the size of the problem, then so does the time required to run the algorithm. However, determining Δ has not been possible in general.

Our objective in this paper is not to explore the computational power of the adiabatic model, but rather to investigate its intrinsic *fault tolerance*. Since quantum computers are far more susceptible to making errors than classical digital computers, fault tolerant protocols will be necessary for the operation of large-scale quantum computers. General procedures have been developed that allow any quantum algorithm to be implemented fault tolerantly on a universal quantum computer [5], but these involve a substantial computational overhead. Therefore, it would be highly advantageous to weave fault tolerance into the design of our quantum hardware.

We therefore will regard adiabatic quantum computation not as a convenient language for describing a class of quantum circuits, but as a proposed physical implementation of quantum information processing. We do not cast the algorithm into the conventional quantum computing paradigm by approximating it as a sequence of discrete unitary transformations acting on a few qubits at a time. Instead, suppose we can design a physical device that implements the required time-dependent Hamiltonian with reasonable accuracy. We then imagine implementing the algorithm by slowly changing the parameters that control the physical Hamiltonian. How well does such a quantum computer resist decoherence, and how well does it perform if the algorithm is imperfectly implemented?

Regarding resistance to decoherence, we can make a few simple observations. The phase of the ground state has no effect on the efficacy of the algorithm, and therefore dephasing in the energy eigenstate basis is presumably harmless. Only the interactions with the environment that induce transitions between eigenstates of the Hamiltonian might cause trouble. In principle, these may be well controlled by running the algorithm at a temperature that is small compared to the minimum gap Δ. (We use units in which Boltzmann's constant $k_B=1$, so that temperature has units of energy.) If Δ decreases slowly as the size of the problem increases, then the resources required to run at a sufficiently low tempera-

---

*Electronic address: amchilds@mit.edu

†Electronic address: farhi@mit.edu

‡Electronic address: preskill@theory.caltech.edu

©2001 The American Physical Society

ture may be reasonable. Since the adiabatic method is only efficient if Δ is not too small, we conclude that whenever the method works on a perfectly functioning quantum computer, it is robust against decoherence.

In addition to environmental decoherence, we must also consider the consequences of imperfect implementation. Our chosen algorithm may call for the time-dependent Hamiltonian $H(t)$, but when we run the algorithm, the actual Hamiltonian will be $H(t)+K(t)$, where $K(t)$ is an "error." An interesting feature of adiabatic quantum computation is that $K(t)$ need not remain small during the evolution in order for the algorithm to work effectively. A reasonably large excursion away from the intended Hamiltonian is acceptable, as long as $K(t)$ is slowly varying and has initial and final values that are not too large. A very rapidly fluctuating $K(t)$ may also be acceptable, if the characteristic frequency of the fluctuations is large compared to the energy scale of $H(t)$.

In this paper, we use numerical simulations to investigate the sensitivity of an adiabatic computer to decohering transitions and to a certain class of unitary perturbations induced by a Hamiltonian $K(t)$. The results are consistent with the idea that the algorithm remains robust as long as the temperature of the environment is not too high and $K(t)$ varies either sufficiently slowly or sufficiently rapidly. Thus, the adiabatic model illustrates the principle that when the characteristics of the noise are reasonably well understood, it may be possible to design suitable quantum hardware that effectively resists the noise. However, note that some of the effects of decoherence and unitary control error may not be significant for the small problems we are able to study—especially in the case of decoherence, where the time required by the simulation restricts us to systems with only four qubits—and hence, our data may not be indicative of the performance of the algorithm working on larger inputs.

A technique closely related to adiabatic computation was described by Kadowaki and Nishimori [6] and has been tested experimentally (in conjunction with a cooling procedure) by Brooke *et al.* [7]. In a different guise, the principles that make quantum adiabatic evolution robust also underlie the proposal by Kitaev [8] to employ nonabelian anyons for fault-tolerant quantum computation. The fact that adiabatic evolution incorporates a kind of intrinsic fault tolerance has also been noted in [9–14].

In Sec. II we review the adiabatic model of quantum computation, and in Sec. III we describe the specific combinatorial search problem (three-bit exact cover) that we use in our simulations. Sections IV and V report our numerical results on decoherence and unitary control error, and Sec. VI summarizes our conclusions.

II. ADIABATIC QUANTUM COMPUTATION

We briefly review the adiabatic model of quantum computation introduced in [1]. Let $h(z)$ be a function of n bits $z=(z_1,z_2,z_3,\ldots,z_n)$, and consider the computational problem of finding a value of z that minimizes $h(z)$. We will typically be interested in the case where this value of z is unique. We may associate with this function the Hermitian operator

$$H_P=\sum_{z=0}^{2^n-1} h(z)|z\rangle\langle z|, \tag{1}$$

so that the computational basis state $|z\rangle$ is an eigenstate of H_P with eigenvalue $h(z)$. Then the problem is to determine which state $|z\rangle$ is the ground state (eigenstate with lowest eigenvalue) of H_P. We refer to H_P as the *problem Hamiltonian.*

The strategy for finding the ground state of H_P is to prepare the ground state of some other *beginning Hamiltonian* H_B and slowly interpolate to H_P. A simple choice for the interpolation is given by the one-parameter family of Hamiltonians

$$\tilde{H}(s)=(1-s)H_B+sH_P \tag{2}$$

that interpolates between H_B and H_P as s varies from 0 to 1. We prepare the ground state of H_B at time $t=0$, and then the state evolves from $t=0$ to T according to the Schrödinger equation,

$$i\frac{\mathrm{d}}{\mathrm{d}t}|\psi(t)\rangle=H(t)|\psi(t)\rangle, \tag{3}$$

where the Hamiltonian is

$$H(t)=\tilde{H}(t/T). \tag{4}$$

At time T (the *run time* of the algorithm), we measure the state in the computational basis. If we let $|\varphi\rangle$ denote the (unique) ground state of H_P for a given instance of the problem, then the *success probability* of the algorithm for this instance is

$$\mathrm{Prob}(T)\equiv|\langle\varphi|\psi(T)\rangle|^2. \tag{5}$$

Does the algorithm work? According to the quantum adiabatic theorem [15,16], if there is a nonzero gap between the ground state and the first excited state of $\tilde{H}(s)$ for all $s\in[0,1]$, then Prob(T) approaches 1 in the limit $T\to\infty$. Furthermore, level crossings are nongeneric in the absence of symmetries, so a nonvanishing gap is expected if H_B does not commute with H_P. Thus, the success probability Prob(T) of the algorithm will be high if the evolution time T is large enough. The question is: how large a T is large enough so that Prob(T) is larger than some fixed constant?

We can reformulate this question in terms of

$$\Delta=\min_{s\in[0,1]}[E_1(s)-E_0(s)] \tag{6}$$

and

$$\mathcal{E}=\max_{s\in[0,1]}\left|\langle 1,s|\frac{\mathrm{d}\tilde{H}}{\mathrm{d}s}|0,s\rangle\right|, \tag{7}$$

where $E_0(s)$ is the lowest eigenvalue of $\tilde{H}(s)$, $E_1(s)$ is the second-lowest eigenvalue, and $|0,s\rangle$, $|1,s\rangle$ are the corresponding eigenstates. By calculating the transition probability to lowest order in the adiabatic expansion [16], one finds that the probability of a transition from ground state to first excited state is small provided that the run time T satisfies

$$T \gg \frac{\mathcal{E}}{\Delta^2}. \tag{8}$$

If the spectrum consists of only two levels, then this condition is sufficient to ensure that the system remains in the ground state with high probability. In general, the required run time T will be bounded by a polynomial in n so long as Δ and $\mathcal{E}$ are polynomially bounded. For the problems we are interested in, $\mathcal{E}$ is polynomially bounded, so we only have to consider the behavior of Δ.

By rescaling the time, we can think of the evolution as taking place in the unit time interval between $s=0$ and 1, but in this case, the energy eigenvalues are rescaled by the factor T. Roughly speaking, we can think of $d\tilde{H}(s)/ds$ as a perturbation that couples the levels of the instantaneous Hamiltonian $\tilde{H}(s)$, and has the potential to drive a transition from $|0,s\rangle$ to $|1,s\rangle$. But if T is large, the effects of this perturbation are washed out by the rapid oscillations of the relative phase $\exp\{-iT\int_0^s ds'[E_1(s')-E_0(s')]\}$.

Note that the Hamiltonian may be regarded as reasonable only if it is "local," that is, if it can be expressed as a sum of terms, where each term acts on a bounded number of qubits (a number that does not grow with n). Indeed, in this case, the Hamiltonian evolution may be accurately and efficiently simulated by a universal quantum computer [17]. Many combinatorial search problems (e.g., 3SAT) can be formulated as a search for a minimum of a function that is local in this sense. Along with a local choice of H_B, this results in a full $H(t)$ that is also local.

A direct physical implementation of the continuously varying $H(t)$ would presumably be possible only under a somewhat stronger locality condition. We might require that each qubit is coupled to only a few other qubits, or perhaps that the qubits can be physically arranged in such a way that the interactions are spatially local. Fortunately, there are interesting computational problems that have such forms, such as 3SAT restricted to having each bit involved in only three clauses or the problem of finding the ground state of a spin glass on a cubic lattice [18]. However, for the purposes of our simulation, we will only consider small instances, and since we do not have a specific physical implementation in mind, we will not concern ourselves with the spatial arrangement of the qubits.

III. AN EXAMPLE: THE EXACT COVER PROBLEM

For definiteness, we study the robustness of the adiabatic algorithm via its performance on the problem known as "three-bit exact cover" (EC3). An n-bit instance of EC3 consists of a set of clauses, each of which specifies three of the n bits. A clause is said to be satisfied if and only if exactly one of its bits has the value 1. The problem is to determine if any of the 2^n assignments of the n bits satisfies all of the clauses.

For this problem, the function $h(z)$ is a sum

$$h(z)=\sum_C h_C(z_{i_C},z_{j_C},z_{k_C}) \tag{9}$$

of three-bit clauses, where

$$h_C(z_{i_C},z_{j_C},z_{k_C})=\begin{cases} 0, & (z_{i_C},z_{j_C},z_{k_C}) \quad \text{satisfies clause } C \\ 1, & (z_{i_C},z_{j_C},z_{k_C}) \quad \text{violates clause } C. \end{cases} \tag{10}$$

The value of the function $h(z)$ is the number of clauses that are violated; in particular, $h(z)=0$ if and only if z is an assignment that satisfies all the clauses.

To solve EC3 by the adiabatic algorithm, a sensible choice for the beginning Hamiltonian is

$$H_B=\sum_C H_{B,C}, \tag{11}$$

where

$$H_{B,C}=\frac{1}{2}(1-\sigma_x^{(i_C)})+\frac{1}{2}(1-\sigma_x^{(j_C)})+\frac{1}{2}(1-\sigma_x^{(k_C)}), \tag{12}$$

which has the ground-state

$$|\psi(0)\rangle=\frac{1}{2^{n/2}}\sum_{z=0}^{2^n-1}|z\rangle. \tag{13}$$

The resulting $H(t)$ is local in the sense that it is a sum of terms, each of which acts on only a few qubits. A stronger kind of locality may be imposed by restricting the instances so that each bit is involved in at most a fixed number of clauses. The computational complexity of the problem is unchanged by this restriction.

Numerical studies of the adiabatic algorithm applied to this problem were reported in [2,4]. Instances of EC3 with n bits were generated by adding random clauses until there was a unique satisfying assignment, giving a distribution of instances that one might expect to be computationally difficult to solve. The results for a small number of bits ($n \leq 20$) were consistent with the possibility that the adiabatic algorithm requires a time that grows only as a polynomial in n for typical instances drawn from this distribution. If this is the case, then the gap Δ does not shrink exponentially. Although the typical spacing between levels must be exponentially small, since there are an exponential number of levels in a polynomial range of energies, it is possible that the gap at the bottom is larger. For example, Fig. 1 shows the spectrum of a randomly generated seven-bit instance of EC3. The gap at the bottom of the spectrum is reasonably large compared to the typical spacing. This feature is not specific to this one instance, but is characteristic of randomly generated instances, at least for $n \lesssim 10$, beyond which the repeated matrix diagonalization required to create a picture of the spectrum becomes computationally costly. A large gap makes an in-

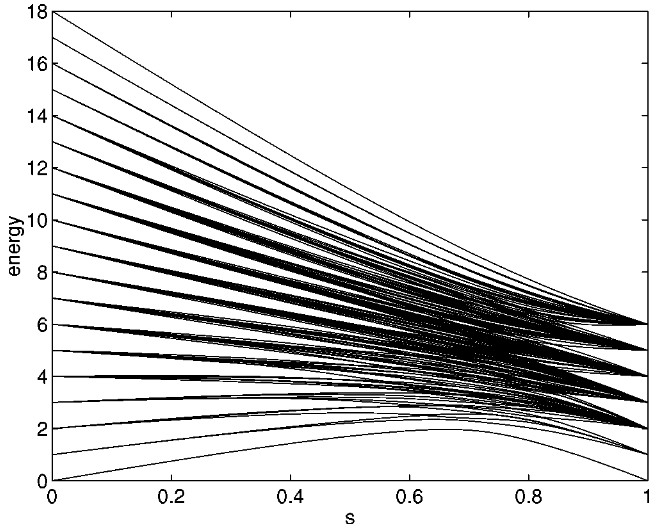

FIG. 1. Spectrum of a randomly generated $n=7$ bit instance of EC3 with a unique satisfying assignment. Note that the energy gap between the ground state and the first excited state is significantly larger than all other gaps. An expanded view would show that there are no level crossings anywhere in the spectrum (except for the degeneracies at $s=0$ and 1).

stance readily solvable by the adiabatic algorithm, and also provides robustness against thermal transitions out of the ground state.

IV. DECOHERENCE

Perhaps the most significant impediment to building a large-scale quantum computer is the problem of decoherence. No quantum device may be perfectly isolated from its environment, and interactions between a device and its environment will inevitably introduce noise. Fortunately, such effects can be countered using fault-tolerant protocols, but as we have already mentioned, these protocols may be costly. Therefore, we would like to consider quantum systems with inherent resistance to decohering effects. If the ground state of our adiabatic quantum computer is separated from the excited states by a sizable energy gap, then we expect it to exhibit such robustness. Here, we consider how the adiabatic algorithm for EC3 is affected by decoherence.

First, we briefly review the master equation formalism for describing the decohering effects of an environment on a quantum system. Suppose that our quantum computer is a collection of spin-1/2 particles interacting with each other according to the Hamiltonian H_S and weakly coupled to a large bath of photons. The total Hamiltonian of the quantum computer and its environment is

$$H=H_S+H_E+\lambda V, \tag{14}$$

where H_E is the Hamiltonian of its environment, V is an interaction that couples the quantum computer and the photon bath, and λ is a coupling constant. We may describe the state of the quantum computer alone by the density matrix ρ found by tracing over the environmental degrees of freedom. In general, the time evolution of ρ is complicated, but under reasonable assumptions, we may approximate its evolution using a Markovian master equation.

One way of deriving such a master equation is to consider the weak coupling limit, in which $\lambda \ll 1$ [19]. If the environment is very large and only weakly coupled to the quantum computer, it will be essentially unchanged by the interaction. Furthermore, in this limit, we expect the evolution of the quantum computer to be Markovian, or local in time, if we filter out high-frequency fluctuations by some coarse-graining procedure. Assuming that the combined state of the quantum computer and its environment begins in a product state $\rho(0)\otimes\rho_E$, Davies derives the master equation

$$\frac{\mathrm{d}\rho}{\mathrm{d}t}=-i[H_S,\rho]+\lambda^2 K^\natural \rho, \tag{15}$$

where

$$K\rho=-\int_0^\infty \mathrm{d}x\, \mathrm{Tr}_E[U(-x)VU(x),[V,\rho\otimes\rho_E]], \tag{16}$$

$$K^\natural \rho=\lim_{x\to\infty}\frac{1}{x}\int_0^x \mathrm{d}y\, U(-y)\{K[U(y)\rho U(-y)]\}U(y), \tag{17}$$

with

$$U(x)=e^{-ix(H_S+H_E)}, \tag{18}$$

where we have (temporarily) assumed that H_S is time independent. Although the $\natural$ operation defined by Eq. (17) does not appear in some formulations of the Markovian master equation, it appears to be essential for the equation to properly describe the weak-coupling limit [20], and in particular, for it to capture the physics of relaxation to thermal equilibrium. The master equation (15) has the property that if the environment is in thermal equilibrium at a given temperature, then the decohering transitions drive the quantum computer towards the Gibbs state of H_S at that temperature. While not an exact description of the dynamics, Eq. (15) should provide a reasonable caricature of a quantum computer in a thermal environment.

Note that Eq. (15) is derived assuming a time-independent Hamiltonian H_S; with a time-varying $H_S(t)$, we should expect the generator of time evolution at any particular time to depend on the Hamiltonian at all previous times [21]. However, if $H_S(t)$ is slowly varying, then it is a good approximation to imagine that the generator at any particular time depends only on H_S at that time [22]. In particular, since we are interested in nearly adiabatic evolution, $H_S(t)$ varies slowly, so Eq. (15) remains a good approximation, where at any given time t we compute $K^\natural$ using only $H_S(t)$. Note that with $H_S(t)$ time dependent, $U(x)$ defined by Eq. (18) is not the time evolution operator; it depends on the time t only implicitly through $H_S(t)$.

For a system of spins coupled to photons, we choose the interaction

$$V=\sum_i \int_0^\infty d\omega[g(\omega)a_\omega\sigma_+^{(i)}+g^*(\omega)a_\omega^\dagger\sigma_-^{(i)}], \tag{19}$$

where Σ_i is a sum over the spins, $\sigma_\pm^{(i)}$ are raising and lowering operators for the ith spin, a_ω is the annihilation operator for the photon mode with frequency ω, and $\lambda g(\omega)$ is the product of the coupling strength and spectral density for that mode. Note that if the coupling strength is frequency dependent, we may absorb that dependence into $g(\omega)$, leaving λ as a frequency-independent parameter. With this specific choice for V, we can perform the integrals and trace in Eqs. (15–18). If we assume that all spacings between eigenvalues of H_S are distinct, the resulting expression simplifies considerably, and we find

$$\begin{aligned}\frac{\mathrm{d}\rho}{\mathrm{d}t}=&-i[H_S,\rho]-\sum_{i,a,b}[N_{ba}|g_{ba}|^2\langle a|\sigma_-^{(i)}|b\rangle\langle b|\sigma_+^{(i)}|a\rangle\\&+(N_{ab}+1)|g_{ab}|^2\langle b|\sigma_-^{(i)}|a\rangle\langle a|\sigma_+^{(i)}|b\rangle]\{(|a\rangle\langle a|\rho)\\&+(\rho|a\rangle\langle a|)-2|b\rangle\langle a|\rho|a\rangle\langle b|\},\end{aligned} \tag{20}$$

where the states $|a\rangle$ are the time-dependent instantaneous eigenstates of H_S with energy eigenvalues ω_a,

$$N_{ba}=\frac{1}{\exp[\beta(\omega_b-\omega_a)]-1} \tag{21}$$

is the Bose-Einstein distribution at temperature $1/\beta$, and

$$g_{ba}=\begin{cases}\lambda g(\omega_b-\omega_a), & \omega_b>\omega_a,\\ 0, & \omega_b\leqslant\omega_a.\end{cases} \tag{22}$$

We simulated the effect of thermal noise by numerically integrating the master Eq. (20) with a Hamiltonian H_S given by Eq. (4) and with the initial pure state density matrix $\rho(0)=|\psi(0)\rangle\langle\psi(0)|$ given by Eq. (13). For simplicity, we chose $g(\omega)=1$ for $\omega\geqslant 0$ and zero otherwise. Although we would expect that $g(\omega)\to 0$ as $\omega\to\infty$, for the small systems we are able to simulate, it should be a reasonable approximation to treat $g(\omega)$ as constant and tune the overall coupling strength using λ^2.

How should we expect the success probability $\langle\varphi|\rho(T)|\varphi\rangle$, where $|\varphi\rangle$ is the ground state of H_P, to depend on the run time T and the temperature? If the run time T is sufficiently long, then regardless of its initial state, the quantum computer will come to thermal equilibrium. At the time of the final readout, it will be close to the Gibbs state

$$\lim_{T\to\infty}\rho(T)=\frac{e^{-\beta H_P}}{\mathrm{Tr}\,e^{-\beta H_P}}\equiv\rho_P \tag{23}$$

of the problem Hamiltonian H_P, and the success probability will be approximately $\langle\varphi|\rho_P|\varphi\rangle$. This probability may be appreciable if the temperature is small compared to the gap between the ground state and first excited state of H_P. Thus, one way to find the ground state of H_P is to prepare the computer in any initial state, put it in a cold environment, wait a long time, and measure. However, this thermal relaxation method is not an efficient way to solve hard optimization problems. Although it may work well on some instances of a given problem, this method will not work in cases where the computer gets stuck in local minima from which downward transitions are unlikely. In such cases, the time for equilibration is expected to be exponentially large in n.

Consider an instance with a long equilibration time so that cooling alone is not an efficient way to find the ground state of H_P. It is possible that the minimum gap Δ associated with the quantum algorithm is not small, and the idealized quantum computer, running without decohering effects, would find the ground state of H_P in a short time. In this situation, if we include the coupling of the system to the environment and we run at a temperature much below Δ, then thermal transitions are never likely, and the adiabatic algorithm should perform nearly as well as in the absence of decoherence. But if the temperature is comparable to Δ, then the performance may be significantly degraded.

On the other hand, consider an instance for which the equilibration time is short, so that cooling alone is a good algorithm. Furthermore, suppose that the adiabatic algorithm would find the ground state of H_P in a short time in the absence of decohering effects. In this case, the combined effects of cooling and adiabatic evolution will surely find the ground state of H_P in a short time. But note that Δ alone does not control the success of the algorithm. Even if $H(t)$ changes too quickly for the evolution to be truly adiabatic so that a transition occurs where the gap is smallest, the system may be cooled back into its ground state at a later time.

Typical results of the simulation are shown in Fig. 2 for two $n=4$ bit instances of EC3 with unique satisfying assignments. These two instances have minimum gaps of $\Delta\approx 0.301$ and $\Delta\approx 0.425$. For each instance, we plot the success probability as a function of the run time T. With $\lambda^2=0.1$, we consider five temperatures: 1/10, 1/2, 1, 2, and 10. We also present the data with no decoherence ($\lambda^2=0$) for comparison.

Unfortunately, the time required to integrate Eq. (20) grows very rapidly with n. Whereas a state vector contains 2^n entries, the density matrix contains 4^n entries; and in addition, calculating $\mathrm{d}\rho/\mathrm{d}t$ at each timestep requires evaluating a double sum over 2^n energy eigenstates. For this reason, we were only able to consider instances with $n\leqslant 4$.

The results are consistent with our general expectations. In the absence of decoherence, the success probability becomes appreciable for sufficiently long run times. This probability rises faster for the problem with a larger gap. When we add decoherence at high temperature, the success probability never becomes very large (note the lowest curves in Fig. 2). As the temperature is decreased to a value of order one, the presence of decoherence has a less significant effect on the success probability. In fact, for sufficiently low temperatures, the success probability may actually be higher in the presence of decoherence than when there is no decoherence. This is because the primary effect of decoherence at low temperature is to drive transitions towards the ground state, improving performance.

However, these results do not illustrate a definitive connection between the minimum gap Δ and the temperature

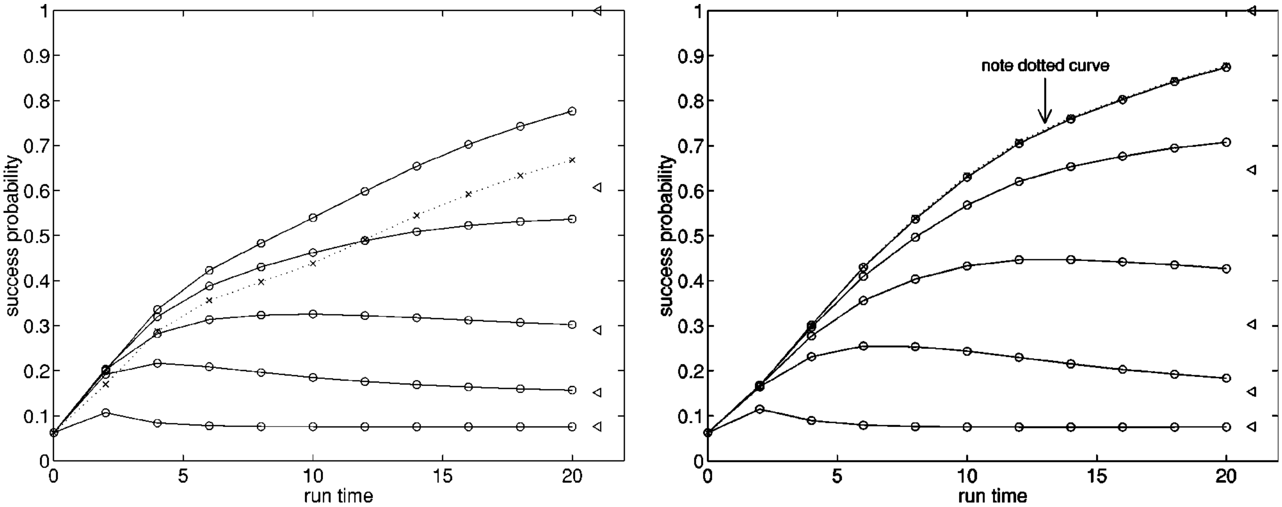

FIG. 2. The success probability as a function of run time T for two instances of EC3 with $n=4$ bits. The instance on the left has a gap of $\Delta_1\approx 0.301$ and the instance on the right has a gap of $\Delta_2\approx 0.425$. The dotted line shows the behavior of the algorithm with no decoherence, i.e., $\lambda^2=0$. Note that in the figure on the right, the dotted curve is partially obscured but can be seen slightly above the topmost solid curve. The solid lines show the behavior of the algorithm in the presence of decoherence with $\lambda^2=0.1$ for five different temperatures. The triangles at the far right show the thermal success probabilities $\langle\varphi|\rho_P|\varphi\rangle$ at each of these temperatures. From top to bottom, the temperatures are 1/10, 1/2, 1, 2, and 10.

above which the algorithm no longer works. These simple $n=4$ bit instances fall into the second category discussed above: the equilibration time is short, so cooling alone is a good algorithm. In other words, no sharp distinction can be drawn between the run time required for the adiabatic algorithm to perform well in the absence of decoherence and the run time required for equilibration. Accordingly, the dependence of the success probability on temperature and run time is similar for the two instances shown in Fig. 2, even though the minimum gaps for these instances are somewhat different.

V. UNITARY CONTROL ERROR

We now consider how the performance of the adiabatic algorithm for EC3 is affected by adding three different kinds of perturbations to the Hamiltonian. Each perturbation we consider is a sum of single-qubit terms, where each term can be interpreted as a magnetic field pointing in a random direction. To simplify our analysis, we assume that the magnitude of the magnetic field is the same for all qubits, but its direction varies randomly from qubit to qubit. The perturbations we consider are

$$\tilde{K}_1(s)=C_1 s\sum_{i=1}^{n}\hat{m}_i\cdot\vec{\sigma}^{(i)}, \tag{24}$$

$$\tilde{K}_2(s)=C_2\sin(\pi s)\sum_{i=1}^{n}\hat{m}_i\cdot\vec{\sigma}^{(i)}, \tag{25}$$

$$\tilde{K}_3(s)=\frac{1}{2}\sin(C_3\pi s)\sum_{i=1}^{n}\hat{m}_i\cdot\vec{\sigma}^{(i)}, \tag{26}$$

which are added to Eq. (2) and give a time-dependent Hamiltonian according to Eq. (4). Each $\hat{m}_i$ is a randomly generated real three-component vector with unit length, C_1 and C_2 are real numbers, and C_3 is a nonnegative integer.

The adiabatic algorithm was simulated by numerically solving the time-dependent Schrödinger equation with initial state $|\psi(0)\rangle$ given by Eq. (13) and Hamiltonian $\tilde{H}(t/T)+\tilde{K}_j(t/T)$ for a given $j\in\{1,2,3\}$. As in [2–4], we used a fifth-order Runge-Kutta method with variable step size, and checked the accuracy by verifying that the norm of the state was maintained to one part in a thousand. For a specified value of n, we randomly generated an instance of EC3 with a unique satisfying assignment. Then we randomly generated several different values of the magnetic field directions $\{\hat{m}_i\}$. For each instance of the problem and the magnetic field, the run time was chosen so that the success probability without the perturbation was reasonably high. With this run time fixed, we then determined the success probability for varying values of the relevant C_j.

First, we consider the perturbation K_1. Since it turns on at a constant rate, this perturbation can be thought of as an error in H_P. Note that with $C_1\neq 0$, the final Hamiltonian is not simply H_P, so the algorithm will not work exactly even in the adiabatic limit $T\rightarrow\infty$. This perturbation is potentially dangerous because of the way its effect scales with the number of bits n. Indeed, consider the case where H_P can be separated into a sum of Hamiltonians acting separately on each qubit. If adding K_1 reduces the overlap of the ground-state $|\varphi\rangle$ of H_P with the perturbed ground-state $|\varphi'\rangle$ by some fixed value ϵ for each of the n qubits, then the total overlap is $(1-\epsilon)^n$, which is exponentially small in the number of bits. Thus, the algorithm clearly fails in this factorized case. In general, if the magnitude of K_1 is independent of n, then we expect the algorithm to fail. However, if the magni-

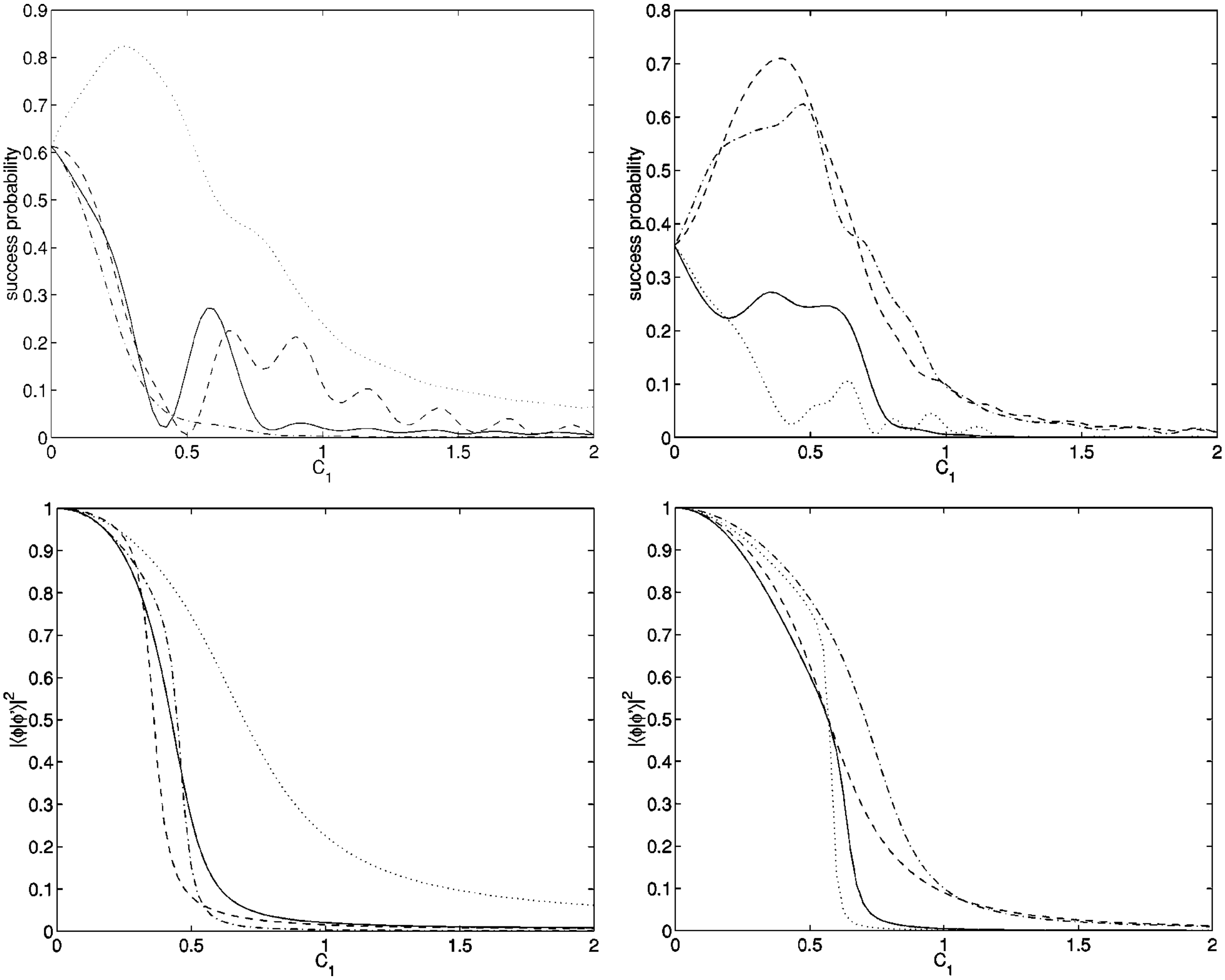

FIG. 3. (Top) The success probability of the adiabatic algorithm for two randomly generated instances of EC3 with $n=7$ bits (left) and $n=10$ bits (right) under the perturbation K_1 defined by Eq. (24) for four different sets of magnetic-field directions. For each n, the run time is the same for each random perturbation. (Bottom) The corresponding overlaps $|\langle\varphi|\varphi'\rangle|^2$ of the ground-state $|\varphi\rangle$ of H_P with the perturbed ground-state $|\varphi'\rangle$ at $s=1$.

tude of K_1 falls as $1/n$ or faster, then the shift of the ground state may be small enough (as it would be in the factorized case) that the algorithm is not significantly affected. Note that for any n there is some value of C_1 that is small enough that the disadvantage of reduced overlap with the ground state of H_P may be overcome if the perturbation happens to increase the minimum gap Δ. For this reason, we expect to sometimes see an increase in success probability for small C_1 that goes away as C_1 is increased.

The effect of the perturbation K_1 is shown in Fig. 3 for $n=7$ and 10 bit instances of EC3, with four different randomly generated sets of magnetic-field directions for each instance. The run time is chosen such that for $C_1=0$, the success probability is around 1/2. The top plots show that for small C_1, the success probability is not strongly suppressed; in fact, in some cases it is significantly enhanced. For large enough C_1, the success probability is heavily suppressed. The bottom plots show the overlap $|\langle\varphi|\varphi'\rangle|^2$ between the ground state of H_P and the actual ground state in the presence of the perturbation. As we expect, the suppression of the success probability is correlated with the amount of overlap. We also studied a similar perturbation in which s is replaced by $1-s$, which may be thought of as an error in H_B. Unsurprisingly, the results were qualitatively similar.

Next, we consider the low-frequency perturbation K_2. The period of oscillation is chosen such that the perturbation vanishes at $t=0$ and T, so the perturbation does not affect the algorithm in the adiabatic limit. Since the success probability is quite sensitive to the value of the minimum gap Δ, and it is not *a priori* obvious whether a perturbation will increase or decrease Δ, we can guess that turning on a nonzero value of C_2 may either increase the success probability or decrease it. In fact, it would be surprising if Δ decreased for all perturbations K_2. The Hamiltonian $\widetilde{H}(s)+\widetilde{K}_2(s)$ is another way to interpolate from H_B to H_P, and we know of no reason why the choice $\widetilde{K}_2=0$ should always be optimal, even when the number of bits is large and C_2 is not decreasing with n.

Figure 4 shows the effect of the perturbation K_2, using the same instances, magnetic field directions, and run times as in Fig. 3. The top plots show the success probability as a function of C_2. As in the case of K_1, some perturbations may

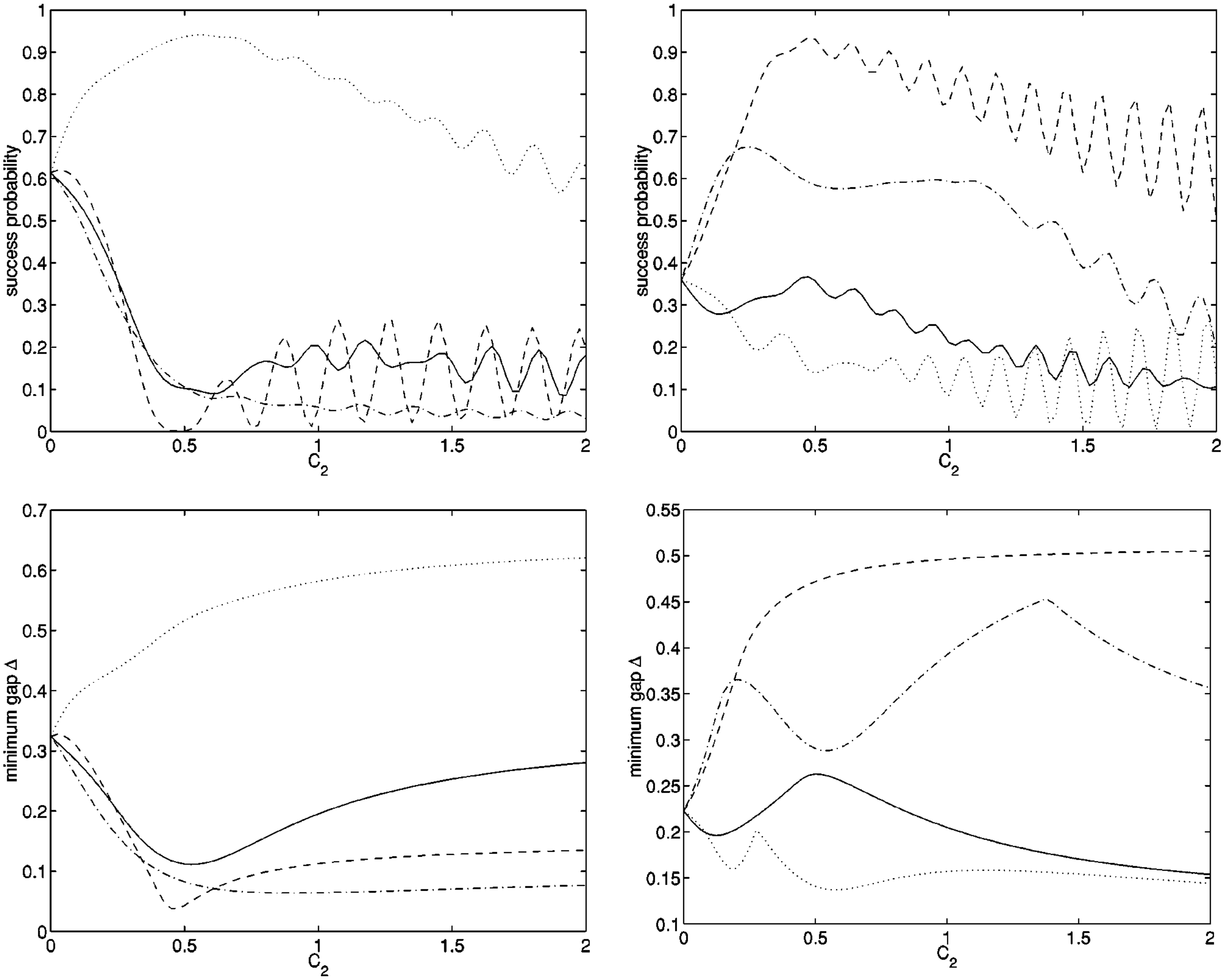

FIG. 4. (Top) The success probability of the adiabatic algorithm for the same instances used in Fig. 3 under the perturbation K_2 defined by Eq. (25). The four different magnetic field directions for each instance are also the same as in Fig. 3. (Bottom) The minimum gap Δ in the perturbed problem.

raise the success probability and some suppress it. Perhaps unsurprisingly, a particular set of magnetic field directions that raises the success probability under K_1 is also likely to help when K_2 is applied. But unlike K_1, K_2 may improve the success probability even with $C_2 \simeq 2$, where the size of the perturbation is comparable to the size of the unperturbed Hamiltonian. The bottom plots show the minimum gap Δ when the perturbation is added. Note that there is a strong correlation between the success probability and Δ.

For both perturbations K_1 and K_2, similar results have been observed (with fewer data points) for instances with as many as $n=14$ bits. Figures 3 and 4 present typical data. For example, for a given instance, typically one or two out of four sets of randomly chosen magnetic-field directions led to an improvement in the success probability for some values of C_1 and C_2, compared to the unperturbed case.

Finally, we consider the perturbation K_3, in which the magnitude of the oscillating component is fixed, but we may vary its frequency by varying C_3. As for K_2, the frequency is chosen so that the perturbation vanishes at $t=0$ and T. We expect that for C_3 of order one, the perturbation will be likely to excite a transition, and that the success probability will be small. But since both H_B and H_P have a maximum eigenvalue of order n, we may anticipate that for

$$C_3 \gg \frac{nT}{\pi}, \tag{27}$$

the perturbation will be far from any resonance. Then the probability that the perturbation drives a transition will be low, and the success probability should be comparable to the case where the perturbation vanishes.

Some representative plots of the dependence of the success probability on C_3 are shown in Fig. 5. Each plot corresponds to a particular randomly generated instance of EC3 (with either $n=8$ bits or $n=10$ bits) and a randomly generated set of magnetic field directions. In the top row of plots, the run time is chosen so that the success probability is around 1/8 with the perturbation absent (i.e., $C_3=0$). In the bottom row, the run time is doubled. All of the data exhibit

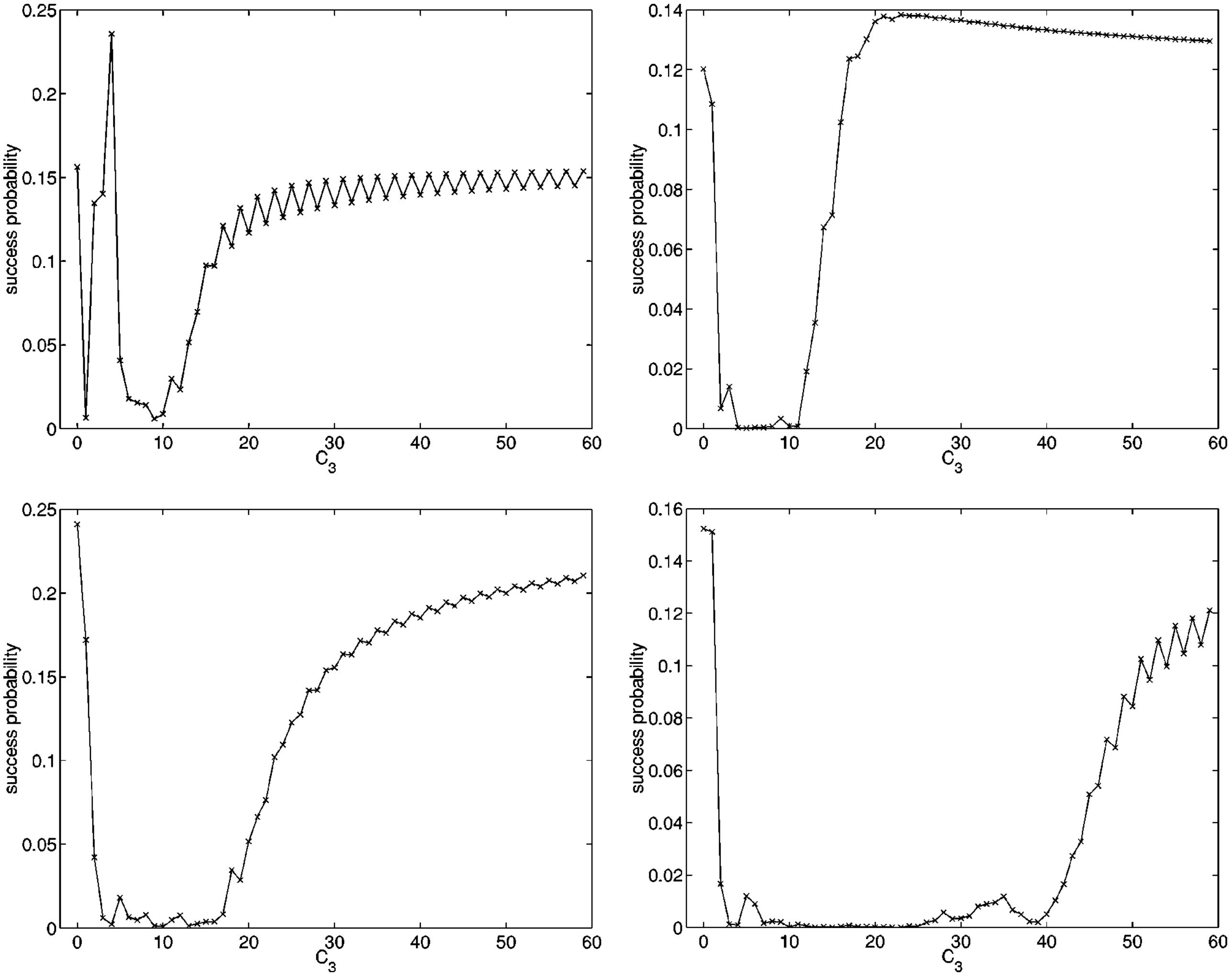

FIG. 5. The success probability as a function of the frequency C_3 of the perturbation K_3 defined in Eq. (26). The data in each plot were obtained for a randomly generated instance of EC3 with randomly generated magnetic-field directions. The data in the left column are for two instances with $n=8$ bits, and the data in the right column are for two instances with $n=10$ bits. For the top row, the run time is chosen so that the success probability is around 1/8 for $C_3=0$, and for the bottom row, the run time is twice as long. The leftmost points in each plot correspond to $C_3=0$, so the perturbation is absent for all t. C_3 takes integer values, so the lines are included only to guide the eye.

the expected qualitative trend. The leftmost point corresponds to $C_3=0$. For the smallest values of $C_3>0$, the success probability may not be too badly damaged; for somewhat larger values of C_3, it is heavily suppressed; and for sufficiently large C_3, it recovers to a value near the success probability in the absence of the perturbation. The value of nT/π is around 19 and 39 for the upper and lower $n=8$ plots and is around 38 and 76 for the upper and lower $n=10$ plots, so the estimate (27) turns out to be reasonable.

Another conspicuous feature of the plots in Fig. 5 is that the success probability tends to oscillate between even and odd values of C_3, though whether even or odd values are favored varies from case to case. This occurs because the perturbation's time average vanishes for C_3 even, so that its integrated effect is weaker than for C_3 odd. Since a small perturbation might either help or hurt, the success probability is slightly enhanced for odd C_3 in some cases, and is slightly suppressed in other cases.

VI. CONCLUSIONS

We have conducted numerical simulations to investigate the fault tolerance of adiabatic quantum computation, and our results are consistent with the claim that this algorithm is robust against decoherence and certain kinds of random unitary perturbations. Thus, if a physical system could be engineered with interactions reasonably well described by a Hamiltonian that smoothly interpolates from an initial H_B to a final H_P corresponding to an interesting combinatorial search problem, and if the gap remains large throughout the interpolation, that system might be a powerful computational device.

Although we have viewed unitary perturbations as noise, the fact that they sometimes raise the success probability suggests a possible way to speed up the adiabatic algorithm. The algorithm finds the ground state of H_P by starting the system in the ground state of H_B. The quantum state evolves as the system Hamiltonian smoothly interpolates from H_B to H_P. However, there are many possible choices for H_B and many smooth paths from a given H_B to H_P. The choices (11) and (2) are convenient but arbitrary, so choosing an alternate route to H_P might speed up the algorithm. An example of this is seen in [23], where it is shown that optimizing the time-dependent coefficients of H_B and H_P allows the adiabatic algorithm to achieve a square-root speedup for an unordered search problem. More generally, the interpolating Hamiltonian might involve terms that have nothing to do with H_B or H_P, but that increase Δ and therefore improve performance. For example, the perturbation K_2 sometimes increases the success probability, as seen in Fig. 4. Rather than being thought of as a source of error, such a perturbation could be applied intentionally and might sometimes enhance the effectiveness of the adiabatic algorithm.

ACKNOWLEDGMENTS

We thank Todd Brun, Evan Fortunato, Jeffrey Goldstone, Sam Gutmann, Jeff Kimble, Alesha Kitaev, and Seth Lloyd for helpful discussions. A.M.C. gratefully acknowledges the support of the Fannie and John Hertz Foundation. This work was supported in part by the Department of Energy under Grant No. DE-FG03-92-ER40701 and Grant No. DE-FC02-94-ER40818, by the National Science Foundation under Grant No. EIA-0086038, by the Caltech MURI Center for Quantum Networks under ARO Grant No. DAAD19-00-1-0374, by the National Security Agency (NSA) and Advanced Research and Development Activity (ARDA) under Army Research Office (ARO) Contract No. DAAD19-01-1-0656, and by an IBM Faculty Partnership Award.

[1] E. Farhi, J. Goldstone, S. Gutmann, and M. Sipser, e-print quant-ph/0001106.
[2] E. Farhi, J. Goldstone, and S. Gutmann, e-print quant-ph/0007071.
[3] A.M. Childs, E. Farhi, J. Goldstone, and S. Gutmann, e-print quant-ph/0012104.
[4] E. Farhi, J. Goldstone, S. Gutmann, J. Lapan, A. Lundgren, and D. Preda, Science **292**, 472 (2001).
[5] P. W. Shor, in *Proceedings of the 37th Annual Symposium on Foundations of Computer Science* (IEEE Press, Los Alamitos, CA, 1996), pp. 56–65.
[6] T. Kadowaki and H. Nishimori, Phys. Rev. E **58**, 5355 (1998).
[7] J. Brooke, D. Bitko, T.F. Rosenbaum, and G. Aeppli, Science **284**, 779 (1999).
[8] A.Yu. Kitaev, e-print quant-ph/9707021.
[9] J. Preskill, in *Introduction to Quantum Computation and Information*, edited by H.-K. Lo, S. Popescu, and T. Spiller (World Scientific, Singapore, 1998).
[10] W. Ogburn and J. Preskill, Lect. Notes Comput. Sci. **1509**, 341 (1999).
[11] P. Zanardi and M. Rasetti, Phys. Lett. A **264**, 94 (1999).
[12] A. Ekert, M. Ericsson, P. Hayden, H. Inamori, J.A. Jones, D.K.L. Oi, and V. Vedral, e-print quant-ph/0004015.
[13] S. Lloyd, e-print quant-ph/0004010.
[14] M.H. Freedman, A. Kitaev, M.J. Larsen, and Z. Wang, e-print quant-ph/0101025.
[15] T. Kato, Phys. Soc. Jap. **5**, 435 (1950).
[16] A. Messiah, *Quantum Mechanics* (North-Holland, Amsterdam, 1961), Vol. II.
[17] S. Lloyd, Science **273**, 1073 (1996).
[18] F. Barahona, J. Phys. A **15**, 3241 (1982).
[19] E.B. Davies, Commun. Math. Phys. **39**, 91 (1974).
[20] R. Dümcke and H. Spohn, Z. Phys. B: Condens. Matter **34**, 419 (1979).
[21] E.B. Davies and H. Spohn, J. Stat. Phys. **19**, 511 (1978).
[22] G. Lindblad, *Non-Equilibrium Entropy and Irreversibility* (Reidel, Dordrecht, 1983), pp. 65–71.
[23] J. Roland and N.J. Cerf, e-print quant-ph/0107015.

PHYSICAL REVIEW D, VOLUME 65, 065022

Measurability of Wilson loop operators

David Beckman,[1,*] Daniel Gottesman,[2,†] Alexei Kitaev,[1,‡] and John Preskill[1,§]
[1]*Institute for Quantum Information, California Institute of Technology, Pasadena, California 91125*
[2]*Computer Science Division, EECS, University of California, Berkeley, California 94720*

(Received 23 October 2001; published 5 March 2002)

We show that the nondemolition measurement of a spacelike Wilson loop operator $W(C)$ is impossible in a relativistic non-Abelian gauge theory. In particular, if two spacelike-separated magnetic flux tubes both link with the loop C, then a nondemolition measurement of $W(C)$ would cause electric charge to be transferred from one flux tube to the other, a violation of relativistic causality. A destructive measurement of $W(C)$ is possible in a non-Abelian gauge theory with suitable matter content. In an Abelian gauge theory, many cooperating parties distributed along the loop C can perform a nondemolition measurement of the Wilson loop operator if they are equipped with a shared entangled ancilla that has been prepared in advance. We also note that Abelian electric charge (but not non-Abelian charge) can be transported superluminally, without any accompanying transmission of information.

DOI: 10.1103/PhysRevD.65.065022 PACS number(s): 11.15.−q

I. INTRODUCTION AND SUMMARY

What measurements are possible in a gauge field theory? Since the interactions of the elementary constituents of matter are described by gauge theory, hardly any question could be more fundamental. Yet definitive answers are elusive.

The Wilson loop operators associated with closed spacelike paths provide a complete characterization of a gauge-field configuration in terms of gauge-invariant quantities [1,2]. Therefore, in formulations of gauge theories, Wilson loops are often taken to be the basic observables. But we will show that nondemolition measurements of spacelike Wilson loops are impossible in a non-Abelian gauge theory that respects relativistic causality. We reach this conclusion by arguing that any procedure for nondemolition measurement of a spacelike non-Abelian Wilson loop would allow information to be transmitted outside the forward light cone.

Causality places no such restriction on the measurability of an Abelian Wilson loop (one evaluated in a one-dimensional irreducible representation of the gauge group), and indeed we find that nondemolition measurement of an Abelian Wilson loop is possible. We also find that, in gauge theories with suitable matter content, *destructive* measurements of non-Abelian Wilson loops are possible. By destructive measurements we mean ones that, in contrast to nondemolition measurements, inflict damage on Wilson loop eigenstates.

In a quantum field theory in flat spacetime, described in the Schrödinger picture, what do we mean by a nondemolition ‘‘measurement’’ of an observable defined on a time slice? Typically, such a measurement requires the cooperation of many parties who are distributed over the slice, and is a three-step process. In the first step (which might not be necessary), a suitable entangled quantum state (the ‘‘ancilla’’) is prepared and distributed to the parties. Second, each party performs a local operation on her local field variables and her part of the entangled ancilla. Third, classical or quantum information extracted by the parties in the second step is shipped to a central location where the readout of the result is completed.

Although the outcome of the measurement is not known until the third step is completed, the coherence of a superposition of eigenstates of the observable with distinct eigenvalues is already destroyed in the second step, which is carried out on the time slice where the operator is defined. At that time, the density operator ρ encoding the quantum state of the field theory is transformed according to

$$\rho \to \mathcal{E}(\rho) \equiv \sum_a E_a \rho E_a , \tag{1}$$

where $\{E_a\}$ is the set of orthogonal projectors onto the eigenspaces of the observable. The term ‘‘nondemolition’’ means that if the state prior to the measurement is an eigenstate of the observable, then the state will be unaffected by the measurement.

Any permissible way in which a quantum state can change is described by a *quantum operation*, a completely positive trace-nonincreasing linear map of density operators to density operators [3,4]. The orthogonal measurement $\mathcal{E}$ in Eq. (1), summed over its possible outcomes, is a special type of quantum operation. It is natural to ask, what are the quantum operations that can really be executed on a time slice in a relativistic quantum theory? The general answer is not known, but it *is* known that many operations are unphysical because they run afoul of relativistic causality [5–11]. Consider, as in Fig. 1, two parties Alice and Bob who perform spacelike-separated actions. Just prior to the implementation of $\mathcal{E}$, Alice performs a local operation on the fields in her vicinity, and just after the implementation of $\mathcal{E}$, Bob performs a local measurement of the fields in his vicinity. If Bob is able to acquire any information about what local operation Alice chose to apply, then Alice has successfully sent a superluminal signal to Bob. If an operation allows such superluminal signaling, we say that the operation is *acausal*; oth-

---

[*] Email address: beckman@caltech.edu
[†] Email address: gottesma@eecs.berkeley.edu
[‡] Email address: kitaev@iqi.caltech.edu
[§] Email address: preskill@theory.caltech.edu

©2002 The American Physical Society

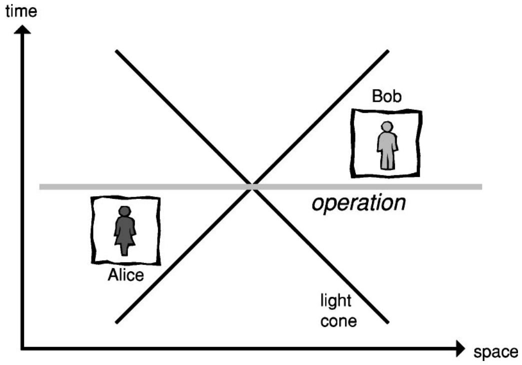

FIG. 1. Causality criterion for quantum operations. First Alice applies a local operator in her vicinity, then the quantum operation is executed, and finally Bob makes a local measurement that is spacelike separated from Alice's action. If Bob's measurement result allows him to acquire information about what local operator Alice applied, then the quantum operation is not *causal* and hence not physically implementable.

erwise, it is causal. Physically realizable operations must be causal. We will apply this causality criterion to non-Abelian gauge theories, and will argue that nondemolition measurement of a Wilson loop operator is an acausal operation.

In discussing the locality properties of a field theory, it is convenient to use the concept of a ''reduced'' density operator that encodes the observations that are accessible to an agent acting in a bounded spatial region. This density operator is obtained from a density operator for the full system by ''tracing out'' the degrees of freedom in the unobserved region. In a gauge theory, performing a partial trace involves potential subtleties arising from the Gauss law constraint satisfied by physical states. For conceptual clarity, we will sidestep these difficulties by founding our discussion on the concept of charge super-selection sectors [12]. Strictly speaking, our analysis applies to the ''free-charge'' phase of a weakly coupled gauge theory with non-Abelian gauge group G; the local symmetry is unbroken and G charges are unconfined. The same argument, though, shows that Wilson loop measurement would allow superluminal signaling in a confining gauge theory, where the separation between the communicating parties is small compared to the confinement distance scale.

The protocol by which Alice can exploit measurement of the spacelike Wilson loop operator $W(C)$ to send a signal to Bob is illustrated in Fig. 2. First Alice and Bob, acting on the weakly-coupled ground state with gauge-invariant local probes, both create *magnetic flux tubes*. Bob's flux tube links with the loop C; Alice encodes one bit of classical information by placing her tube in one of two possible positions, either linking with C or not. In the framework of lattice gauge theory, we may imagine that Bob has control of a single lattice link l_B contained in the loop C, and he creates his ''flux tube'' by manipulating his link—exciting the lattice plaquettes that contain l_B to a particular nontrivial conjugacy class of G, as illustrated in Fig. 3. Similarly, Alice controls a single link l_A and she encodes a bit by either exciting her link or not. Of course, since Alice and Bob act locally and the theory respects a charge superselection rule, the flux tubes created by Alice and Bob have trivial electric charge.

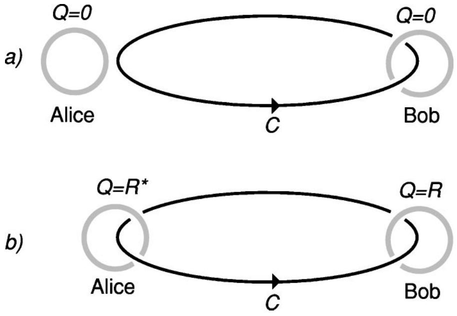

FIG. 2. Nondemolition measurement of the Wilson loop operator $W(C)$ [more precisely decoherence in the basis of eigenstates of $W(C)$] allows Alice to signal Bob. Alice and Bob, with gauge-invariant probes, can prepare magnetic flux tubes that carry trivial electric charge. In (a), Bob's tube links with the loop C but Alice's does not; when $W(C)$ is measured, neither tube is affected. In (b), Alice moves her tube into position so that it too links with C; when $W(C)$ is measured, then (with nonvanishing probability), Bob's tube and Alice's acquire nontrivial and opposite electric charges. By measuring the charge of his tube, Bob can tell how Alice positioned her loop and so receive a message from Alice.

If either Bob's tube or Alice's tube links with the loop C, but not both, then the configuration is an eigenstate of $W(C)$ (or close to an eigenstate in the weakly-coupled case) and will be unaffected (or little affected) by the measurement of $W(C)$. But if both tubes link with C, the configuration is not an eigenstate, and will be altered by the measurement. We will see that, with nonvanishing probability, the measurement will generate equal and opposite nonzero electric charges on Alice's tube and Bob's. Then, by measuring the charge on his tube, Bob can infer (with a success probability better than a random guess) whether Alice's tube linked with C or not, and so receive a superluminal signal.

In a non-Abelian gauge theory, a magnetic flux tube can carry a peculiar kind of electric charge that has no localized source, which has been called Cheshire charge [13,14]. (The property that the *charge* of an excitation in a non-Abelian gauge theory need not be the integral of a local density is analogous to the property that the *energy* of an object in general relativity need not be the integral of a local density.)

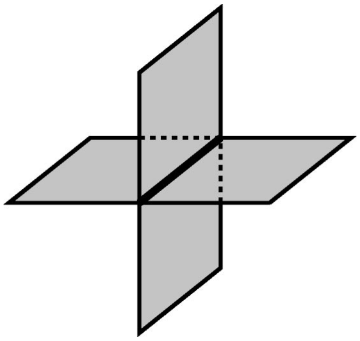

FIG. 3. A small ''magnetic flux tube'' in lattice gauge theory. By manipulating her link, Alice excites the plaquettes that contain the link, creating a magnetic flux tube. The links dual to these plaquettes form a closed loop on the dual lattice.

Our protocol for superluminal signaling is based on the observation that Wilson loop measurement causes Cheshire charge to be transferred from Alice's flux tube to Bob's. Cheshire charge, while conceptually elusive, is physically genuine and readily detected in principle.

Our conclusion that Wilson loop measurement is an acausal operation does not hold in the case of an Abelian gauge theory. Indeed, we will show that a nondemolition measurement of $W(C)$ is possible in an Abelian gauge theory that includes charged matter. In our analysis of this case, we adopt the convenient idealization that the parties who perform the measurement are equipped with gauge-invariant ancilla variables that are not themselves described by the gauge theory. We will also see that a *destructive* measurement of a non-Abelian Wilson loop (a measurement that determines the value of the Wilson loop but in doing so damages Wilson loop eigenstates) is possible in a gauge theory that includes suitable charged matter. In particular, if the matter transforms faithfully under the gauge group, then the Wilson loop can be measured destructively in any representation of the gauge group.

The conclusion that nondemolition measurement of spacelike Wilson loops is impossible in a non-Abelian gauge theory seems surprising and somewhat troubling, as it leaves us without a fully satisfactory way to characterize the configurations of a quantized relativistic gauge theory in terms of measurable quantities. Related difficulties arise in quantum theories of gravity. That nondemolition measurement of a Wilson loop operator would allow superluminal signaling has been anticipated by Sorkin [8].

We formulate the properties of magnetic flux tubes in Sec. II, and analyze a protocol for superluminal signaling enabled by Wilson loop measurement in Sec. III. In Sec. IV, we defend the legitimacy of the magnetic flux tubes that are used in our signaling protocol, through explicit constructions within the formalism of lattice gauge theory. In Sec. V, we explore the consequences of including charged matter fields in the gauge theory, and show that destructive measurement of a spacelike Wilson loop is possible. The Abelian case is discussed in Sec. VI, and we show that in an Abelian gauge theory with charged matter, nondemolition measurement of a Wilson loop is possible. The pure Abelian gauge theory (without matter) is considered in Sec. VII; in that case nondemolition measurement of homologically trivial Wilson loops is possible, but homologically nontrivial Wilson loops are unmeasurable and there is an associated superselection rule. We take up the related question of whether electric charges can travel faster than light in Sec. VIII, concluding that superluminal transport of Abelian charge, but not non-Abelian charge, is possible. Section IX contains some concluding comments.

II. WILSON LOOPS, MAGNETIC FLUX, AND ELECTRIC CHARGE

In a theory with gauge group G, the effect of parallel transport of a charged object around a closed path C that begins and ends at the point x_0 can be encoded in a group element $a(C,x_0)\in G$ given by

$$a(C,x_0)=P\exp\left(i\int_{C,x_0}A\right). \tag{2}$$

Here A is the gauge potential and P denotes path ordering; the state $|q\rangle$ of a charged object carried along C is modified according to

$$|q\rangle\rightarrow D^{(R)}(a(C,x_0))|q\rangle, \tag{3}$$

if $|q\rangle$ transforms as the unitary irreducible representation $D^{(R)}$ of G. The element $a(C,x_0)\in G$ depends on a "gauge choice" at the point x_0; that is, on how a basis is chosen in the representation $D^{(R)}$. A basis-independent characterization of the gauge holonomy is obtained if we evaluate the trace in the representation $D^{(R)}$, obtaining the Wilson loop operator associated with C given by

$$W^{(R)}(C)=\chi^{(R)}(a(C,x_0)), \tag{4}$$

where $\chi^{(R)}$ denotes the character of the representation $D^{(R)}$. The Wilson loop operator does not depend on how the point x_0 on the loop C is chosen. In much of what follows, we will assume for notational simplicity that the unbroken gauge group G is finite; however, our arguments can be easily extended to the case of compact Lie groups.

By acting with a gauge-invariant source on the weakly-coupled ground state of the gauge theory, Alice (or Bob) can create a "color magnetic flux tube" or "cosmic string" that carries trivial "color electric" charge. This tube is an eigenstate of the Wilson loop operator $W^{(R')}(C_A)$, where C_A is a loop that links once with the tube, for any irreducible representation (R') of the gauge group G; hence the tube can be labeled by a conjugacy class α of G.

When we say that the tube has trivial gauge charge, we mean that it transforms as the trivial representation of G under global gauge transformations. To understand this property it is helpful to specify a basepoint $x_{0,A}$ on the loop C_A and to fix the gauge at this point. Then the effect of parallel transport around the loop C_A, beginning and ending at $x_{0,A}$, can be encoded (in this particular gauge) in a group element $a(C_A,x_{0,A})\equiv a$. If the tube is associated with a particular group element a, we call its quantum state a "flux eigenstate," denoted $|a\rangle$. But under a gauge transformation $g\in G$ at $x_{0,A}$, this flux eigenstate is transformed as

$$a\rightarrow gag^{-1}. \tag{5}$$

Thus a flux eigenstate is not a gauge singlet in general, if G is non-Abelian. A gauge-singlet quantum state of the flux tube is a coherent superposition of the flux eigenstates belonging to conjugacy class α,

$$|\alpha,0\rangle=\frac{1}{\sqrt{|\alpha|}}\left(\sum_{a\in\alpha}|a\rangle\right), \tag{6}$$

where $|\alpha|$ denotes the number of members of the class.

Other possible states of the flux tube can carry nontrivial electric charge. For example, the state

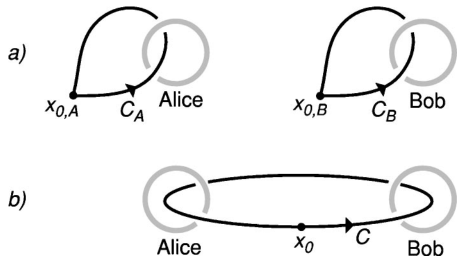

FIG. 4. Loops linked with flux tubes. The flux tube configuration created locally by Alice and by Bob is an eigenstate of the Wilson loop operators associated with the paths C_A and C_B, shown in (a), but not an eigenstate of the Wilson loop operator C that links with both tubes, shown in (b).

$$|\alpha,R\rangle = N_{\alpha,R}\left(\sum_{g\in G}\chi^{(R)}(g)^*|gag^{-1}\rangle\right) \tag{7}$$

(where $N_{\alpha,R}$ is a normalization factor and $a\in\alpha$) transforms as the nontrivial irreducible representation (R) under global gauge transformations. To verify this, first construct the operator

$$E^{(R)} = \frac{n_R}{|G|}\sum_{g\in G}\chi^{(R)}(g)U(g), \tag{8}$$

where $|G|$ denotes the order of the group, n_R is the dimension of the irreducible representation (R), and $U(g)$ is the global gauge transformation that conjugates the flux by g,

$$U(g):|a\rangle \to |gag^{-1}\rangle. \tag{9}$$

Using the group orthogonality relations

$$\frac{n_R}{|G|}\sum_{g\in G}\chi^{(R)}(g)^*\chi^{(R')}(gh) = \delta^{RR'}\chi^{(R)}(h), \tag{10}$$

we find that $E^{(R)}$ is the orthogonal projection onto the space transforming as (R), which satisfies

$$E^{(R)}E^{(R')} = \delta^{RR'}E^{(R)}. \tag{11}$$

Applying the orthogonality relations once more, we see that

$$E^{(R)}|\alpha,R\rangle = |\alpha,R\rangle; \tag{12}$$

thus $|\alpha,R\rangle$ transforms as (R). The "Cheshire charge" carried by the flux tube in this state can be detected through, for example, the Aharonov-Bohm interactions of the tube with other, distant, flux tubes [13,14].

Suppose that Alice and Bob, acting locally, each create flux tubes with zero electric charge, where the flux of Alice's tube belongs to conjugacy class α and the flux of Bob's belongs to conjugacy class β. (The process of preparing the flux tubes will be discussed in more detail in Sec. IV.) To describe the quantum state of this configuration, we may choose loops C_A and C_B that link with the tubes, and fix the gauge at basepoints $x_{0,A}$ and $x_{0,B}$ as illustrated in Fig. 4(a). Up to a normalization factor, the quantum state of the two tubes can be expressed as

$$\left(\sum_{h\in G}|hah^{-1}\rangle_A\right)\otimes\left(\sum_{g\in G}|gbg^{-1}\rangle_B\right), \tag{13}$$

where $a\in\alpha$ and $b\in\beta$. This configuration is a direct product of the state of Alice's tube with the state of Bob's tube, a simultaneous eigenstate of the commuting Wilson loop operators $W(C_A)$ and $W(C_B)$.

But because multiplication of conjugacy classes is ill-defined, this state is not an eigenstate of $W(C)$, where C is the loop shown in Fig. 4(b) that links with both tubes. Rather, if Alice's tube is an eigenstate of $W(C_A)$ and Bob's tube is an eigenstate of $W(C_B)$, then an eigenstate of $W(C)$ is not a product state but an entangled state of the form (up to normalization)

$$\sum_{g\in G}|gag^{-1}\rangle_A\otimes|gbg^{-1}\rangle_B. \tag{14}$$

This state has zero total charge, as it is invariant under a global gauge transformation applied to both tubes. But it is not invariant under a gauge transformation that acts on just one of the tubes; it can be expanded in a basis in which Alice's tube and Bob's have definite and opposite charges. Using the group orthogonality relations in the form

$$\sum_R\frac{n_R}{|G|}\chi^{(R)}(g) = \delta_{g,e} \tag{15}$$

(where e is the identity element), we may rewrite the state as a sum over irreducible representations

$$\sum_R\frac{n_R}{|G|}\left(\sum_{h,g\in G}\chi^{(R)}(gh^{-1})^*|hah^{-1}\rangle_A\otimes|gbg^{-1}\rangle_B\right). \tag{16}$$

The expression in parentheses transforms as (R) under gauge transformations acting on Bob's tube and as the conjugate representation (R^*) under gauge transformations acting on Alice's tube, as we can verify by applying $I\otimes E^{(R)}$ and $E^{(R^*)}\otimes I$.

Thus, when two flux tubes are prepared in a quantum state that is an eigenstate of the Wilson loop operator $W(C)$, where C links with both flux tubes, then the flux tubes carry correlated nontrivial electric charges. This property is the basis of our claim that Wilson loop measurement is acausal, as we elaborate in the next section.

III. NONDEMOLITION MEASUREMENT OF NON-ABELIAN WILSON LOOPS IS ACAUSAL

For a *static* gauge field configuration, it is possible in principle to measure $W^{(R)}(C)$ [and hence the conjugacy class of the group element $a(C,x_0)$] by performing interference experiments with projectiles that transform as $D^{(R)}$ [15]. But what if the loop C lies in a time slice and the gauge field is *dynamical*? In a relativistic field theory, no projectile can follow a spacelike world line, so that a direct measurement of the effect of parallel transport along C is not feasible.

However, it seems conceivable that a less direct measurement strategy might succeed. When we speak of a ''measurement'' of an operator whose support is on a spacelike slice, we need not require that the result be instantaneously known by anyone. We might imagine instead that, in order to measure $W^{(R)}(C)$ at time $t=0$, many parties distributed along the loop C perform local operations at $t=0$. Later, the data collected by the parties can be assembled and processed at a central laboratory, where the outcome of the measurement of $W^{(R)}(C)$ can be determined. In such a protocol, we should allow the parties to share any entangled quantum state that they might have prepared prior to $t=0$, and we should allow them to ship quantum information (rather than just classical data) to the central laboratory after they have performed their local operations. Of course, the quantum or classical variables that are sent to the central laboratory for analysis are not the variables of the underlying field theory; they are ancilla variables that are assumed to be available to assist with the measurement.

Just prior to the measurement at time $t=0$, the quantum state of the gauge theory is ρ, a density operator that acts on the physical gauge-invariant subspace. Even though the measurement result may not be known until later, the operations performed at $t=0$ modify the state ρ immediately. If the local operations performed at $t=0$ are to achieve a measurement of $W^{(R)}(C)$, then the coherence of a superposition of eigenstates of ρ with different eigenvalues must be destroyed. At $t=0$, then, the quantum state is modified according to

$$\rho\to\mathcal{E}_{W(C)}(\rho)\equiv\sum_{w} E_w\rho E_w, \tag{17}$$

where E_w is the orthogonal projector onto the subspace of states with

$$W^{(R)}(C)=w. \tag{18}$$

This operation describes a projective measurement of $W^{(R)}(C)$ with an unknown outcome.

The operation $\mathcal{E}_{W(C)}$ is actually weaker than a measurement of $W^{(R)}(C)$; conceivably decoherence in the basis of eigenstates of an observable can be accomplished even if the measurement outcome is *never* recorded. But if any record of the value of $W^{(R)}(C)$ is written at $t=0$ (even one that cannot be read until later), then decoherence as described by Eq. (17) must occur.

We will show that $\mathcal{E}_{W(C)}$ can be used to send superluminal signals, and so establish that $\mathcal{E}_{W(C)}$ cannot be implemented in a gauge theory that respects relativistic causality.

To devise a superluminal signaling protocol, Alice and Bob use local gauge-invariant probes to prepare uncharged flux tubes belonging to classes α and β respectively, as described in Sec. II. Bob moves his flux tube, which will receive the message, into position so that it links once with the loop C; Alice encodes one bit of information by choosing to place her flux tube in one of two possible positions, either linking with C or not. If Alice chooses to place her tube where it does not link with C, then the configuration is an eigenstate of $W^{(R)}(C)$ and will be unaffected when the Wilson loop is measured. But if Alice moves her flux tube into position to link with C, then the configuration is no longer an eigenstate of $W^{(R)}(C)$, and it *is* affected by the operation $\mathcal{E}_{W(C)}$. In fact, after the operation, though the total charge of the system remains zero, there is a nonzero probability that Alice's tube and Bob's tube carry equal and opposite nonzero charges. This charge can be detected by Bob. For example, he can determine whether his tube has vacuum quantum numbers by allowing it to shrink and observing whether it will annihilate and disappear—if the tube is charged, a stable charged particle will be left behind.

Thus, if there were a way to implement the operation $\mathcal{E}_{W(C)}$ at $t=0$, then by observing whether his flux tube is charged after $t=0$, Bob would be able to infer (with a probability of success better than a random guess) whether Alice moved her tube into position or not. Therefore Alice can transmit classical information to Bob over a noisy channel with nonzero capacity; she is able to send a superluminal signal to Bob. By the same method, Bob can send a signal to Alice.

To understand this charge transfer process in more detail, let us consider a specific example. Suppose that G is the *quaternionic group* of order eight, whose two-dimensional faithful unitary irreducible representation is

$$\{\pm I,\pm i\sigma_1,\pm i\sigma_2,\pm i\sigma_3\}, \tag{19}$$

where $\sigma_1,\sigma_2,\sigma_3$ are the Pauli matrices. Suppose that Alice and Bob both have tubes carrying flux in the class $\alpha=\beta=\{\pm i\sigma_1\}$. For tubes in this class, the quantum state with trivial charge is

$$|+\rangle=\frac{1}{\sqrt{2}}(|i\sigma_1\rangle+|-i\sigma_1\rangle), \tag{20}$$

and there is also a state of nontrivial charge

$$|-\rangle=\frac{1}{\sqrt{2}}(|i\sigma_1\rangle-|-i\sigma_1\rangle). \tag{21}$$

The state $|-\rangle$ transforms as the nontrivial one-dimensional representation of G in which $\pm I$, $\pm i\sigma_1$ are represented by 1 and $\pm i\sigma_2$, $\pm i\sigma_3$ are represented by -1.

If Alice and Bob each have a charge-zero flux tube, the quantum state of their two tubes is a product state

$$|\psi\rangle_{\text{init}}=|+\rangle_A\otimes|+\rangle_B. \tag{22}$$

But if the loop C links once with each tube, then the value of $W^{(R)}(C)$ in the two-dimensional irreducible representation (R) can be either 2 or -2. If the initial state $|\psi\rangle_{\text{init}}$ is projected onto the state with $W^{(R)}(C)=2$, Alice's tube becomes entangled with Bob's; the resulting state is

$$|\psi\rangle_{\text{fin},2}=\frac{1}{\sqrt{2}}(|i\sigma_1\rangle_A\otimes|-i\sigma_1\rangle_B+|-i\sigma_1\rangle_A\otimes|i\sigma_1\rangle_B). \tag{23}$$

Bob's final density operator, obtained by tracing over the state of Alice's tube, is

$$\rho_{B,\mathrm{fin},2}=\frac{1}{2}(|i\sigma_1\rangle\langle i\sigma_1|+|-i\sigma_1\rangle\langle -i\sigma_1|), \tag{24}$$

an *incoherent mixture* of the two flux eigenstates. Similarly, if $|\psi\rangle_{\mathrm{init}}$ is projected onto the state with $W^{(R)}(C)=-2$, the resulting state is

$$|\psi\rangle_{\mathrm{fin},-2}=\frac{1}{\sqrt{2}}(|i\sigma_1\rangle_A\otimes|i\sigma_1\rangle_B+|-i\sigma_1\rangle_A\otimes|-i\sigma_1\rangle_B), \tag{25}$$

and again Bob's final density operator is

$$\rho_{B,\mathrm{fin},-2}=\rho_{B,\mathrm{fin},2}. \tag{26}$$

Each of the two flux eigenstates is an equally weighted coherent superposition of the charge eigenstates $|+\rangle_B$ and $|-\rangle_B$. Thus if Bob were to measure the charge of his tube after the operation $\mathcal{E}_{W(C)}$ acts at $t=0$, he would find the charge to be $(-)$ with probability 1/2 if Alice's tube linked with the loop *C*, while he would never find the charge to be $(-)$ if Alice's tube did not link with *C*. Alice has sent a superluminal signal to Bob.

We can easily generalize this construction to an arbitrary finite gauge group *G*. If Alice's tube initially carries flux in the conjugacy class α and has trivial charge, while Bob's carries flux in the class β and has trivial charge, then the initial state of their tubes is a product state

$$|\psi\rangle_{\mathrm{init}}=\frac{1}{\sqrt{|\alpha|\cdot|\beta|}}\sum_{a\in\alpha}\sum_{b\in\beta}|a\rangle_A\otimes|b\rangle_B. \tag{27}$$

This state can be expanded in terms of eigenstates of

$$W^{(R)}(C)=\chi^{(R)}(ab). \tag{28}$$

Suppose that for fixed $a\in\alpha$ there are n_i distinct elements $b_{i,\mu}^{(a)}\in\beta$, $\mu=1,2,\ldots,n_i$, such that $\chi^{(R)}(ab)=w_i$. (This number n_i is independent of how the class representative *a* is chosen.) Then the component of $|\psi\rangle_{\mathrm{init}}$ with $W^{(R)}(C)=w_i$ is the (unnormalized) entangled state

$$|\psi\rangle_{w_i}=\frac{1}{\sqrt{|\alpha|\cdot|\beta|}}\sum_{a\in\alpha}|a\rangle_A\otimes\sum_{\mu=1}^{n_i}|b_{i,\mu}^{(a)}\rangle_B. \tag{29}$$

This state is invariant under a global gauge transformation acting as

$$a\to gag^{-1},\quad b\to gbg^{-1}, \tag{30}$$

so that its total charge is trivial. We see that if $W^{(R)}(C)$ is measured, the outcome w_i occurs with probability

$$\mathrm{Prob}(w_i)={}_{w_i}\langle\psi|\psi\rangle_{w_i}=n_i/|\beta|; \tag{31}$$

it is obvious from the definition of n_i that these probabilities sum to unity. Furthermore, if the state $|\psi\rangle_{w_i}$ is prepared by the measurement of the Wilson loop, and Bob subsequently measures the charge of his tube, he will find the charge to be trivial with probability

$$\mathrm{Prob}(0|w_i)=\frac{{}_{w_i}\langle\psi|(I_A\otimes|\beta,0\rangle\langle\beta,0|)|\psi\rangle_{w_i}}{{}_{w_i}\langle\psi|\psi\rangle_{w_i}}$$

$$=n_i/|\beta|=\mathrm{Prob}(w_i). \tag{32}$$

(Here $|\beta,0\rangle$ denotes the charge-0 state of a string whose flux is in conjugacy class β.) Therefore, if Alice's and Bob's tubes both link once with the loop *C* when the operation $\mathcal{E}_{W(C)}$ is applied, then afterwards Bob will find his tube carries trivial charge with probability

$$\mathrm{Prob}(0)=\sum_i \mathrm{Prob}(0|w_i)\cdot\mathrm{Prob}(w_i)$$

$$=\sum_i (\mathrm{Prob}(w_i))^2=\sum_i (n_i/|\beta|)^2. \tag{33}$$

We see that, unless the initial configuration is an eigenstate of $W^{(R)}(C)$, we have $\mathrm{Prob}(0)<1$. We conclude that Bob's tube is charged with nonzero probability if Alice's tube linked with *C*, and it is guaranteed to be uncharged if Alice's tube did not link with *C*. Alice can send a superluminal signal to Bob. (Of course, since Alice's tube has an electric charge equal and opposite to that of Bob's tube, Bob can also send a superluminal signal to Alice, with the same probability of success.)

The argument also applies to compact Lie groups. For example if the gauge group is

$$G=SU(2)=\{g(\hat{n},\theta)=\exp[-i(\theta/2)\hat{n}\cdot\vec{\sigma}],$$

$$\hat{n}\in S^2,\quad \theta\in[0,2\pi]\}, \tag{34}$$

then conjugacy classes are labeled by θ. If a flux tube has trivial charge, its quantum state can be expressed as

$$|0,f\rangle=\int d\theta f(\theta)\int d\hat{n}|g(\hat{n},\theta)\rangle, \tag{35}$$

where *f* is any square integrable class function. If the loop *C* links with Alice's tube and Bob's, then the product state

$$|\psi\rangle_{\mathrm{init}}=|0,f_1\rangle_A\otimes|0,f_2\rangle_B \tag{36}$$

is in general not an eigenstate of the operator $W^{(R)}(C)$; hence measurement of $W^{(R)}(C)$ would induce a detectable transfer of charge from Alice's tube to Bob's.

The argument also applies in any spatial dimension $d\geqslant 2$. In $d=2$ dimensions, the flux tubes may be replaced by pairs of pointlike vortices; in $d>3$ dimensions, the tubes become membranes of codimension 2.

In our discussion, we have ignored the effects of magnetic and electric quantum fluctuations—in particular we have not considered whether gauge charges might be confined or screened by the Higgs mechanism. We have implicitly assumed that the *G* gauge symmetry is unbroken, and (if *G* electric charges are confined) that the separation between Alice and Bob is small compared to the characteristic distance scale of electric confinement.

We should note that in the case of a continuous gauge group, an ultraviolet regulator is implicitly invoked to define the Wilson loop. The Wilson loop detects the magnetic flux that links with C. If we think of C as a wire of infinitesimal thickness, then $W(C)$ will be dominated by very-short-wavelength fluctuations of the gauge field near the wire. To suppress these fluctuations, we allow the wire to have a nonzero thickness a, removing the contributions of fluctuations with wavelength below a. In $3+1$ spacetime dimensions, the fluctuations near the wire are unimportant provided that

$$e^2 \log(L/a) \ll 1, \tag{37}$$

where e^2 is the gauge coupling constant (renormalized at distance scale a) and L is the characteristic size of the loop C.

IV. FLUX TUBES ON THE LATTICE

Our argument that Wilson loop measurement would allow Alice to send a superluminal signal to Bob had two crucial elements: that Alice and Bob are capable of creating uncharged magnetic flux tubes, and that Bob can detect the charge on his tube. Let us examine more deeply whether the preparation of the flux tube is really possible in principle.

In considering whether flux tubes are legitimate objects, it is helpful to think about a scenario in which an underlying continuous gauge symmetry is spontaneously broken to a finite non-Abelian subgroup. To be specific, a generic vacuum expectation value of a Higgs field in the five-dimensional irreducible representation of $SU(2)$ breaks the gauge symmetry to the quaternionic group considered in Sec. III. In this Higgs phase, there are locally stable cosmic strings that carry nontrivial magnetic flux; these serve as the flux tubes needed for the signaling protocol. Alice and Bob both require closed loops of string that have vacuum quantum numbers; in principle, these could be created in, for example, a hard collision between particles.

Wilson loop measurement can change the transformation properties of a string loop under global gauge transformations—it transfers charge to the loop. This charge, like any charge in a discrete gauge theory, can be detected through the Aharonov-Bohm interactions of the string loop with other string loops [13,14].

In a confining gauge theory like quantum chromodynamics, a flux tube is not locally stable, but it is still possible to engineer one, at least if it is small compared to the confinement distance scale. To be as concrete as possible, we will describe how a flux tube can be created in a gauge theory defined on a spatial lattice (but with continuous time). In this framework, Bob (or Alice) can prepare a flux tube with zero charge by acting on a single link variable with a gauge-invariant local operator, as indicated in Fig. 3.

In our description of the construction of this operator, we will again find it convenient to suppose that the gauge group G is a finite group of order $|G|$, though there are no serious obstacles to generalizing the discussion to the case of Lie groups. Residing on the lattice links are variables that take values in the G group algebra, a Hilbert space of dimension $|G|$ for which an orthonormal basis can be chosen as $\{|g\rangle, g\in G\}$. A local gauge transformation associates a group element with each lattice site. Each link has an orientation, and if a link connecting sites x and y is oriented so that it points from y to x, then gauge transformations $U_x(h)$ and $U_y(k)$ at site x and y act on the link variable according to

$$\begin{aligned} U_x(h)&:|g\rangle_{xy}\rightarrow|hg\rangle_{xy},\\ U_y(k)&:|g\rangle_{xy}\rightarrow|gk^{-1}\rangle_{xy}. \end{aligned} \tag{38}$$

Physical states are invariant under all local gauge transformations. Physical observables preserve the space of physical states, and hence must commute with the local gauge transformations.

Now consider an operator $H_l(a)$ that acts on a particular link l as

$$H_l(a):|g\rangle_l\rightarrow|ag\rangle_l. \tag{39}$$

Note that $H_l(a)$ is not a gauge transformation, since it acts only on a single link, rather than all of the links that meet at a site. This operator does not commute with local gauge transformations; rather if l is oriented so that it points toward the site x, we have

$$U_x(h)H_l(a)U_x(h)^{-1}:|g\rangle_l\rightarrow|hah^{-1}\cdot g\rangle_l, \tag{40}$$

or

$$U_x(h)H_l(a)U_x(h)^{-1}=H_l(hah^{-1}). \tag{41}$$

But if we define an operator by summing $H_l(a)$ over a conjugacy class of G,

$$H_l(\alpha)=\frac{1}{|\alpha|}\left(\sum_{a\in\alpha}H_l(a)\right), \tag{42}$$

then $H_l(\alpha)$ *does* commute with $U_x(h)$ and is therefore a gauge-invariant operator. This is the operator that Alice applies to her link to create a local flux tube excitation [16,17]. Of course, by acting on several adjacent links, Alice can create a larger flux tube if she wishes.

If Alice applies this operator to her link and Bob applies it to his link, then the state they prepare (acting on the weak-coupling vacuum) is not an eigenstate of the Wilson loop operator $W(C)$, where C contains both links. There *is* an eigenstate of $W(C)$ in which Alice's link is excited to conjugacy class α and Bob's to class β, and of course this state can be created by a gauge-invariant operator acting on the perturbative vacuum. But the operator cannot be local, since it creates charges on Alice's link and Bob's. It is instructive to construct the nonlocal gauge-invariant operator that creates this state.

For this purpose, it is convenient to choose a basepoint lattice site x_0, and to choose oriented lattice paths P_A and P_B that connect Alice's link A and Bob's link B to the basepoint,

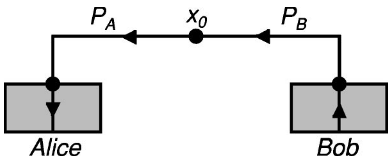

FIG. 5. A nonlocal operator that creates correlated excitations at distantly separated links of a lattice gauge theory. An arbitrary basepoint x_0 is chosen, together with arbitrary paths P_A and P_B that connect Alice's link and Bob's link to the basepoint. By acting on the links, the operator excites the lattice plaquettes (shaded) that contain the links. The nonlocality is necessary because Alice's excitation and Bob's excitation carry nontrivial and opposite electric charges.

as shown in Fig. 5. Let g_P denote the path-ordered product of link variables associated with the path P,

$$g_P = \prod_{l \in P} g_l, \tag{43}$$

with later links along the path appearing further to the left. Then we may define a generalization of the operator H_l that depends on the path and the basepoint. Acting on Alice's link l_A we have

$$H_{l_A}(a,P_A,x_0) : |g\rangle_{l_A} \to |g \cdot g_{P_A} a g_{P_A}^{-1}\rangle_{l_A}, \tag{44}$$

and acting on Bob's link l_B we have

$$H_{l_B}(b,P_B,x_0) : |g\rangle_{l_B} \to |g_{P_B}^{-1} b g_{P_B} \cdot g\rangle_{l_B}. \tag{45}$$

Hence $H_{l_B}(b,P_B,x_0)$, like $H_{l_B}(b)$, excites the plaquettes that contain Bob's link. But while $H_{l_B}(b)$ left-multiplies the link variable by b, $H_{l_B}(b,P_B,x_0)$ left-multiplies by the conjugate group element $g_{P_B}^{-1} b g_{P_B}$. In a fixed gauge, the operator $H_{l_B}(b,P_B,x_0)$ creates an excitation such that the effect of gauge parallel transport about a closed path that begins and ends at x_0 and passes through link l_B is encoded in the group element b. $H_{l_A}(a,P_A,x_0)$ is defined similarly, but acts by right multiplication because of the way we have chosen the orientation of the link l_A.

The operator $H_{l_A}(a,P_A,x_0)$ commutes with local gauge transformations acting in the vicinity of Alice's link l_A, and $H_{l_B}(b,P_B,x_0)$ commutes with gauge transformations acting in the vicinity of Bob's link l_B. But they do not commute with gauge transformations acting at the basepoint x_0; rather we have

$$U_{x_0}(g) H_{l_A}(a,P_A,x_0) U_{x_0}(g)^{-1} = H_{l_A}(gag^{-1},P_A,x_0),$$

$$U_{x_0}(g) H_{l_B}(b,P_B,x_0) U_{x_0}(g)^{-1} = H_{l_B}(gbg^{-1},P_B,x_0). \tag{46}$$

Again, we can obtain a gauge-invariant operator by summing a or b over a conjugacy class, e.g.,

$$H_{l_B}(\beta,P_B,x_0) = \frac{1}{|\beta|}\left(\sum_{b \in \beta} H_{l_B}(b,P_B,x_0)\right). \tag{47}$$

In fact, it is clear from the definitions that $H_{l_B}(\beta,P_B,x_0) = H_{l_B}(\beta)$; it is really a local operator in disguise.

But we can also construct a gauge-invariant operator that acts simultaneously on Alice's link and Bob's, and that really is nonlocal [16,17]:

$$\frac{1}{|G|}\left(\sum_{g \in G} H_{l_A}(gag^{-1},P_A,x_0) \cdot H_{l_B}(gbg^{-1},P_B,x_0)\right). \tag{48}$$

This operator, acting on the weak-coupling vacuum, creates a state in which Alice's link and Bob's are correlated, as in Eq. (14). This gauge-invariant operator does not depend on how the basepoint x_0 is chosen; we are free to slide the basepoint along the path connecting Alice's link and Bob's however we please.

The communication protocol explained in Sec. III can be described this way: Alice and Bob apply the local operators $H_{l_A}(\alpha)$ and $H_{l_B}(\beta)$ to create link excitations that are uncorrelated with one another. Then the Wilson loop measurement operation $\mathcal{E}_{W(C)}$ is applied, where the loop C contains the links l_A and l_B. This operation establishes a correlation between the links. It transforms a state that can be created by local operators to a state that can be created only by a nonlocal operator like that in Eq. (48). Such a transformation cannot occur on a time slice in a theory that respects relativistic causality. We conclude that the nondemolition measurement of the non-Abelian Wilson loop operator is not physically realizable.

Now, the operator $H_l(\alpha)$ is a gauge-invariant local operator, but it is not unitary, so we should clarify what it means to say that Alice or Bob applies this operator to a state. In fact, if A is any bounded operator that does not annihilate the state $|\psi\rangle$, we can apply the operation

$$|\psi\rangle \to \frac{A|\psi\rangle}{\sqrt{\langle\psi|A^\dagger A|\psi\rangle}} \tag{49}$$

with a nonzero probability of success by making a suitable measurement. First note that we may assume without loss of generality that the eigenvalues of $A^\dagger A$ are no larger than one—if not, we merely rescale A without modifying the operation equation (49). Then let $\{|0\rangle,|1\rangle\}$ be an orthonormal basis for a two-dimensional "ancilla" space, and consider the transformation

$$U: |0\rangle \otimes |\psi\rangle \to |0\rangle \otimes A|\psi\rangle + |1\rangle \otimes B|\psi\rangle, \tag{50}$$

where

$$A^\dagger A + B^\dagger B = I. \tag{51}$$

This transformation is norm-preserving and so has a unitary extension. Hence we apply the unitary U to $|0\rangle \otimes |\psi\rangle$ and then measure the ancilla by projecting onto the basis $\{|0\rangle,|1\rangle\}$. The outcome $|0\rangle$ is obtained with probability

$\langle\psi|A^\dagger A|\psi\rangle$, in which case Eq. (49) is applied. If the outcome $|1\rangle$ is found, then Alice may discard the state and make another attempt. As long as $A|\psi\rangle\neq 0$, Alice can repeat the procedure until she gets the desired outcome.

Clearly, the gauge-invariant bounded operator analogous to $H_l(\alpha)$ can also be constructed in the case where G is a Lie group. For example if the gauge group is $SU(2)$, then associated with the group element $g(\hat{n},\theta)=\exp(-i(\theta/2)\hat{n}\cdot\vec{\sigma})$ is the transformation

$$H_l(g(\hat{n},\theta)):|h\rangle_l\rightarrow|g(\hat{n},\theta)h\rangle_l, \tag{52}$$

where $h\in SU(2)$. This transformation can be expressed as

$$H_l(g(\hat{n},\theta))=e^{-i\theta\hat{n}\cdot\vec{E}_l}, \tag{53}$$

where the electric field $\vec{E}_l$ is the angular momentum conjugate to the $SU(2)$ rotor h at link l. The bounded operator

$$H_l(f)=\int d\theta f(\theta)\int d\hat{n}e^{i\theta\hat{n}\cdot\vec{E}_l} \tag{54}$$

(where f is any integrable function) is gauge-invariant. Indeed, it is a function of the gauge-invariant observable $\vec{E}_l^2$ that acts on the link l.

As we have also explained in Sec. III, the common-sense reason that the state created by the nonlocal operator in Eq. (48) cannot be created with local operators is that Alice's link and Bob's carry (correlated) nonzero electric charges. In quantum chromodynamics, as in a discrete gauge theory, Wilson loop measurement can cause color charge to be transferred to a flux tube. This color charge is surely detectable; like any color charge, it acts as a source for a measurable color electric field.

V. MATTER FIELDS AND THE DESTRUCTIVE MEASUREMENT OF WILSON LOOPS

We have shown that the nondemolition measurement of a non-Abelian Wilson loop conflicts with relativistic causality. But there are further questions that we wish to address. Can the Wilson loop be measured *destructively*? What about the Abelian case? To formulate our answers, we will continue to use the formalism of lattice gauge theory. Furthermore, to ensure that the agents who are to perform measurements are as well equipped as possible, we will include in the theory matter fields that couple to the gauge fields.

Our matter fields reside on the sites of the lattice, and like the link variables, take values in the group algebra. The basis for the Hilbert space at a site x will be denoted $\{|\phi\rangle_x,\phi\in G\}$. Under the local gauge transformation $U_x(g)$ acting at the site x, the matter variable transforms as the regular representation of G (which contains all irreducible representations of G),

$$U_x(g):|\phi\rangle_x\rightarrow|g\phi\rangle_x. \tag{55}$$

In addition to the gauge symmetry, the matter field at site x also transforms under a *global* symmetry transformation $V_x(h)$, acting on ϕ from the right, that commutes with gauge transformations:

$$V_x(h):|\phi\rangle_x\rightarrow|\phi h^{-1}\rangle_x. \tag{56}$$

The interpretation of this global symmetry is that our matter fields have both "color" and "flavor" degrees of freedom. The regular representation of G decomposes into irreducible representations, with the dimension-n_R representation (R) occurring n_R times. Gauge transformations mix the n_R states that span (R) (the colors), while global transformation mix the n_R copies of (R) (the flavors).

Let xy denote a link connecting the neighboring sites x and y on the lattice, with orientation pointing from y to x, and let $U_{xy}\in G$ be the gauge-field variable associated with this oriented link. We may also assign to this link the gauge-invariant variable

$$u_{xy}=\phi_x^{-1}U_{xy}\phi_y, \tag{57}$$

the "covariant derivative" of the matter field. Without changing the physical content of the theory, we can replace the link variables $\{U_l\}$ by the new gauge-invariant variables $\{u_l\}$. But after this replacement, the physical Hilbert constraint can be trivially constructed: at each site x, the state of the matter field is required to be the gauge-invariant uniform superposition state

$$\frac{1}{\sqrt{|G|}}\sum_{\phi\in G}|\phi\rangle_x. \tag{58}$$

Since the matter fields are completely constrained by gauge invariance, they have no role in dynamics and they too can be eliminated, leaving only the gauge-invariant local variables $\{u_l\}$.

Although the new variables are gauge invariant, they transform nontrivially under the global transformations, according to

$$V_x(h):|u\rangle_{xy}\rightarrow|hu\rangle_{xy}, \tag{59}$$

$$V_y(k):|u\rangle_{xy}\rightarrow|uk^{-1}\rangle_{xy}. \tag{60}$$

Thus physical states can carry global G charges.

A gauge-invariant unitary operator acting on the link xy can be defined as

$$H_{xy}(a):|u\rangle_{xy}\rightarrow|au\rangle_{xy}. \tag{61}$$

Acting on the weakly coupled vacuum, this operator produces a flux tube excitation at the link. The flux tube at xy has Cheshire charge that is exactly compensated by charge localized at the site x. An operator $H_{xy}(\alpha)$ that creates an excitation with trivial Cheshire charge can be constructed and applied as described in Sec. IV.

Since the variables $\{u_l\}$ are local and preserve the physical Hilbert space, it is reasonable to postulate that they are observable. Physically, the measurement of u_{xy} has a simple interpretation in terms of the effect of parallel transport of a colored object from site y to the neighboring site x. Of course, we are free to adopt arbitrary color conventions at each site, and the way we describe the effect of parallel transport depends on these conventions. However, if we have multiple flavors at our disposal, we can use the flavors to record our conventions, so that in effect (gauge-dependent) statements about color transport can be translated into (gauge-invariant) statements about flavors.

To be concrete, suppose that (R) is a three-dimensional irreducible representation; our ''quarks'' come in three colors (red, yellow, blue) and three flavors (up, down, strange). At each site, we adopt conventions for color and flavor, and we prepare standard quarks in three mutually orthogonal colors and three mutually orthogonal flavors that lock these conventions together: the up quark is red, the down quark is yellow, the strange quark is blue. Then standard quarks prepared at site y are covariantly transported to site x, and compared to the standard quarks that have been prepared at that site. Thus the effect of the transport can be equivalently described as either a rotation in the color space (U_{xy}) or in the flavor space (u_{xy}). Performing this experiment for each irreducible transformation of G assigns a unique group element u_{xy} to the link xy, for these particular conventions. A modification of the conventions can be interpreted as a rotation in the flavor space, under which the variable u_{xy} transforms.

Now consider a large loop C on the spatial lattice, and suppose that many parties distributed along the loop are to measure the Wilson loop

$$W^{(R)}(C) \equiv \chi^{(R)}\left(\prod_{l\in C} U_l\right) = \chi^{(R)}\left(\prod_{l\in C} u_l\right) \tag{62}$$

in representation (R). Since all the matter fields cancel out, the Wilson loop can be expressed in terms of the gauge-invariant variables $\{u_l\}$. Each party has access to a single link along the loop, and using n_R flavors of quarks in representation (R), determines the value of the $n_R \times n_R$ matrix $D^{(R)}(u)$ at that link, for a particular choice of flavor conventions. Each party then reports her value of $D^{(R)}(u)$ to the central authority for post-processing, the matrices are multiplied together, and the trace is evaluated. The result, which does not depend on the local flavor conventions, is the value of the Wilson loop.

Thus, distributed parties, each acting locally, can measure the Wilson loop operator. But in doing so, they collect much additional information aside from the value of the Wilson loop. In particular, an eigenstate of $W^{(R)}(C)$ need not have a definite value of each $D^{(R)}(u_l)$ along the loop. Therefore, the localized measurement procedure typically disturbs the quantum state of the field, even if the initial state before the measurement is a Wilson loop eigenstate. Rather than a localized *nondemolition* measurement (which we have already seen is impossible) it is a localized *destructive* measurement. Note also that distributed parties can measure destructively each of several Wilson loop operators $W^{(R_i)}(C_i), i = 1,2,3,\ldots,n$, all on the same time slice, and hence the product $\Pi_i W^{(R_i)}(C_i)$. In this respect, the destructive measurement is compatible with the Wilson loop algebra. Of course, we may not be able to measure more than one of the $W^{(R_i)}(C_i)$ if the C_i are on different time slices, since a measurement on an earlier slice may interfere with a measurement on a later slice.

We have assumed that the matter fields transform as the regular representation Eq. (55) of the gauge group G. What about more general choices for the representation content of the matter? Provided that the matter transforms as a faithful representation of the gauge group, one can show that the destructive measurement of $W^{(R)}(C)$ is still possible in any representation (R).

We reach this conclusion by noting that matter in the regular representation can be *simulated* using matter that transforms faithfully, augmented by ancilla degrees of freedom. We will give only a brief sketch of the argument. First we recall that if (R_m) is a faithful representation, and (R) is any irreducible representation, then (R) is contained in $(R_m)^{\otimes n}$ for some n. Therefore, if our fundamental matter fields transform as (R_m), then we can build composite objects that transform as (R) from n fundamental constituents.

Next we observe that if the theory contains only a single matter field that transforms as (R), we can use ancilla variables to attach an effective flavor index to the field. To understand the point heuristically, consider the case of ''quarks'' that come in three colors but only one flavor. Rather than using ''natural'' flavors to keep track of our color conventions, we can use ''artificial'' flavors instead, labeling red, yellow, and blue quarks with the three mutually orthogonal states (up, down, strange) of the ancilla. When quarks are transported from one site to a neighboring site, the attached value of the ancilla is transported along with the color; hence artificial flavors, just like natural flavors, allow us to describe local gauge transport in terms of gauge-invariant quantities. Since we can construct composite matter fields in any representation (R) of G, and we can use ancillas to ensure that matter transforming as (R) comes in n_R flavors, our simulated matter transforms as the regular representation; thus we can measure destructively a Wilson loop in any representation.

What about the case of a pure gauge theory (one containing no charged matter at all)? The gauge variables themselves can simulate matter that transforms according to the adjoint representation

$$D(g): |h\rangle \rightarrow |ghg^{-1}\rangle, \tag{63}$$

which is a faithful representation of $G/Z(G)$, where $Z(G)$ denotes the center of G. Thus, by building composite fields and manipulating ancillas, we can simulate matter that transforms as the regular representation of $G/Z(G)$. Therefore, $W^{(R)}(C)$ can be measured destructively for any representation (R) of $G/Z(G)$, or equivalently for any representation of G that represents the center of G trivially.

We have seen that the nondemolition measurement of a non-Abelian Wilson loop is an example of an acausal measurement that can be made causal (and in fact localizable) if additional information is collected simultaneously. Other examples were noted in [11].

VI. NONDEMOLITION MEASUREMENT OF ABELIAN WILSON LOOPS IS LOCALIZABLE

The causality problem arose for the nondemolition measurement of non-Abelian Wilson loops because multiplication of conjugacy classes is ill-defined. Since this problem does not arise if G is Abelian, one might expect that a space-like Wilson loop operator should be measurable in an Abelian gauge theory (or more generally, if the Wilson loop is evaluated in a one-dimensional irreducible representation of the gauge group). We will see that this is the case.

To be concrete, consider a lattice theory (containing charged matter) with gauge group $G=U(1)$. Gauge variables $U_l \in U(1)$ reside at each link l of the lattice, and matter variables $\phi_x \in U(1)$ reside at each site x. As we have seen, the gauge and matter variables can be eliminated in favor of gauge-invariant variables $u_{xy}=\phi_x^{-1}U_{xy}\phi_y$, and the Wilson loop operator is

$$W(C)\equiv\prod_{l\in C} U_l=\prod_{l\in C} u_l. \tag{64}$$

To perform a destructive measurement of $W(C)$, parties distributed along the loop C could each measure the local value of u; then the results can be multiplied together later to determine the value of the Wilson loop.

To perform a nondemolition measurement of $W(C)$, the procedure must be modified so that only the value of the Wilson loop, and no further information, is collected. Imagine, then, that n parties have been distributed along the loop C, each with access to one of the links of C. And suppose the party who resides at link l can manipulate not only the gauge-invariant field variable u_l, but also a gauge-invariant *ancilla* variable $\tilde{u}_l \in U(1)$ that will be used to assist with the measurement. Some time ago, the parties prepared an entangled state of their ancilla variables,

$$|\text{initial}\rangle_{\text{anc}}=\int\prod_{l=1}^{n}(d\tilde{u}_l)|\tilde{u}_1,\tilde{u}_2,\ldots,\tilde{u}_n\rangle\,\delta\!\left(\prod_{l=1}^{n}\tilde{u}_l-I\right). \tag{65}$$

This state is a coherent superposition of all possible states for the ancilla variables, subject only to one global constraint on the product of all the $\tilde{u}_l$'s. Now each party applies a local unitary transformation to her lattice field variable and her part of the ancilla:

$$|u_l,\tilde{u}_l\rangle\rightarrow|u_l,u_l\tilde{u}_l\rangle, \tag{66}$$

a rotation of the ancilla rotor controlled by the value of the lattice rotor. This is achieved by turning on a Hamiltonian that couples u_l and $\tilde{u}_l$.

The operation Eq. (66) modifies the constraint on the ancilla variables, which becomes

$$\prod_l \tilde{u}_l=W(C). \tag{67}$$

Now each party can measure the value of her $\tilde{u}_l$, and broadcast the result to the central authority. The measurement outcomes are random, so that each individual measurement reveals no information about the state of the lattice variables. When the results are accumulated, the value of $W(C)$ can be inferred by evaluating $\Pi_l\tilde{u}_l$, but no further information about the field configuration is acquired. (This type of local measurement making use of a shared entangled ancilla was described in [7], and was shown to be the basis of a separation between classical and quantum multiparty communication complexity in [18].)

Of course, the transformation equation (66) that couples the ancilla to the field variables can also be described in a conjugate basis, which may clarify its meaning. We may write $u=e^{-i\theta}$, $\tilde{u}=e^{-i\tilde{\theta}}$, and define the angular momentum $\tilde{Q}$ conjugate to $\tilde{\theta}$ by

$$e^{-i\tilde{Q}\tilde{\xi}}|\tilde{\theta}\rangle=|\tilde{\theta}+\tilde{\xi}\rangle. \tag{68}$$

Then Eq. (66) becomes

$$|\theta,\tilde{Q}\rangle\rightarrow(e^{-i\theta})^{\tilde{Q}}|\theta,\tilde{Q}\rangle. \tag{69}$$

Thus we may regard $\tilde{Q}$ as a fictitious electric charge, whose transport properties are governed by the connection u—the parties implement Eq. (69) by “parallel transporting” their ancilla charges by one lattice spacing in the effective gauge field defined by u. The (unnormalizable) initial state of the ancilla can be written

$$|\text{initial}\rangle_{\text{anc}}=\sum_{\tilde{Q}=-\infty}^{\infty}|\tilde{Q},\tilde{Q},\tilde{Q},\ldots,\tilde{Q}\rangle, \tag{70}$$

which is transformed to

$$|\text{initial}\rangle_{\text{anc}}=\sum_{\tilde{Q}=-\infty}^{\infty}[W(C)]^{\tilde{Q}}|\tilde{Q},\tilde{Q},\tilde{Q},\ldots,\tilde{Q}\rangle. \tag{71}$$

Since the charges held by the parties are perfectly correlated, only the global information about transport around the entire loop C becomes imprinted on the ancilla state. This information, encoded in relative phases in the $\tilde{Q}$-basis, can be read out via measurements in the conjugate $\tilde{\theta}$-basis. Note that it is important that the ancilla variables carry fictitious rather than genuine electric charges—otherwise states with different values of the total charge would reside in distinct superselection sectors and the relative phases in Eq. (71) would be unobservable. We also note that while to measure the Wilson loop perfectly we must prepare the ancilla in the unnormalizable (and hence unphysical) state Eq. (70), a measurement with arbitrarily good precision can be achieved using a normalizable approximation to this state.

The key to this procedure for measuring the Wilson loop is that the $W(C)$ can be expressed in terms of the local gauge-invariant variables $\{u_l\}$ as in Eq. (64). This property has a clear physical interpretation. The matter field represents a medium laid out along the loop C that becomes superconducting on the time slice where the measurement of

$W(C)$ is to be carried out: $\phi = e^{-i\theta}$ is a superconducting order parameter with phase θ. Though the phase and the gauge field A_μ are not locally observable, the covariant derivative

$$D_\mu \theta = \partial_\mu \theta + A_\mu \tag{72}$$

is observable—it is proportional to the local current density. By coupling the local current to our entangled ancilla, we have modified the state of the ancilla in a manner that is sensitive to the value of the quantity

$$\exp\left[i \oint_C D_\mu \theta dx^\mu \right] = W(C); \tag{73}$$

the equality is obtained from the property that $\phi = e^{-i\theta}$ is a single-valued function.

Even without the entangled ancilla, parties distributed along the loop could determine the value of $W(C)$ by measuring the local value of $D_\mu \theta$, and broadcasting their results. In that case, not just $W(C)$ but also the covariant derivative of θ would be determined by their measurement outcomes. By invoking the entangled ancilla, we have emphasized that it is possible to measure $W(C)$ without learning anything else about the state of the lattice system, that is, to perform a nondemolition measurement of $W(C)$.

It is clear that the technique we have described could be applied in principle to perform a nondemolition measurement of the Wilson loop operator in any one-dimensional representation of the gauge group. But as we have shown must be so, it fails in the non-Abelian case. We can introduce matter fields such that $u_{xy} = \phi_x^{-1} U_{xy} \phi_y$ is a gauge-invariant quantity, but since the u's do not commute with the $\tilde{u}$'s, the transformation equation (66) will not in that case simply modify the constraint on the ancilla variables as in Eq. (67).

VII. WILSON LOOPS IN THE PURE ABELIAN GAUGE THEORY

Our procedure for the nondemolition measurement of an Abelian Wilson loop uses charged matter coupled to the gauge fields. Let us now consider whether the nondemolition measurement is possible in the pure Abelian gauge theory. When there is no charged matter, we cannot replace the gauge variables on links by gauge-invariant variables that are locally measurable.

A. Homologically trivial loops

Consider first the case of a homologically trivial loop C, the boundary of a two-dimensional surface S. In the Abelian gauge theory, the Wilson loop operator $W(C)$ can be interpreted as $e^{i\Phi}$ where Φ is the magnetic flux linking the loop. In the lattice formulation of the theory, the surface S is the union of elementary cells that tessellate the surface. Suppose there are N such cells, labeled by an index Σ taking values $\Sigma = 1,2,3, \ldots, N$. Then the Wilson loop operator can be expressed as

$$W(C) \equiv \prod_{l \in C} U_l = \prod_{\Sigma \in S} U_\Sigma , \tag{74}$$

where U_Σ is the value of the Wilson operator $W(\partial\Sigma)$ for the boundary $\partial\Sigma$ of the cell Σ. Therefore, a destructive measurement of $W(C)$ can be carried out by a collection of parties occupying the surface S. Each party measures the local "magnetic field" U_Σ and reports her result to the central authority. The results can then be accumulated to determine the value of $W(C)$.

This destructive measurement differs from a nondemolition measurement of $W(C)$ in that too much information is collected—not just the total flux through the surface, but also the local distribution of magnetic flux is determined by the measurement. In a nondemolition measurement of $W(C)$, a superposition of two different magnetic field configurations with the same value of $W(C)$ would not decohere, but if the local field is measured this superposition does decohere. Yet as in our previous discussion, a nondemolition measurement can be achieved if ancilla variables are prepared in an appropriate state that is distributed to the parties in advance. Suppose that each of the N parties can access both the gauge-invariant local magnetic field variable $U_\Sigma \in U(1)$ and an ancilla variable $\tilde{U}_\Sigma \in U(1)$. The ancilla has been prepared in the shared initial state

$$|\text{init}\rangle_{\text{anc}} = \int \prod_{\Sigma=1}^{N} (d\tilde{U}_\Sigma) |\tilde{U}_1, \tilde{U}_2, \ldots, \tilde{U}_N\rangle \delta\left(\prod_{\Sigma=1}^{N} \tilde{U}_\Sigma - I \right), \tag{75}$$

a coherent superposition of all possible states for the ancilla variables, subject only to one global constraint on the product of all the $\tilde{U}_\Sigma$'s. To perform the nondemolition measurement, each party applies a local unitary transformation to her magnetic flux variable and her part of the ancilla:

$$|U_\Sigma, \tilde{U}_\Sigma\rangle \rightarrow |U_\Sigma, U_\Sigma \tilde{U}_\Sigma\rangle, \tag{76}$$

a rotation of the ancilla rotor controlled by the value of the lattice rotor. This operation modifies the constraint on the ancilla variables, which has become

$$\prod_\Sigma \tilde{U}_\Sigma = \prod_\Sigma U_\Sigma = W(C). \tag{77}$$

Now each party can measure the value of her $\tilde{U}_\Sigma$, and broadcast the result to the central authority. The measurement outcomes are random, so that each individual measurement reveals no information about the state of the lattice variables. When the results are accumulated, the value of $W(C)$ can be inferred by evaluating $\Pi_\Sigma \tilde{U}_\Sigma$, but no further information about the gauge field configuration is acquired.

B. Homologically nontrivial loops

Now consider the case of a homologically nontrivial loop C, which is not the boundary of any surface. For example, suppose that the theory lives on a d-dimensional spatial torus (a rectangular box with opposite sides identified), and that the loop C is a nontrivial cycle that winds around the torus.

The gauge-invariant local operators of the theory are the magnetic flux operators U_Σ acting on the elementary lattice cells, and the "electric field" operators that act on elementary links. The electric field E_l at the link l is the "angular momentum" conjugate to the link rotor variable U_l; it generates rotations of U_l

$$\exp(-i\theta E_l):|U\rangle_l \rightarrow |e^{-i\theta}U\rangle_l . \tag{78}$$

Each party residing on the lattice is empowered to apply or measure the local operators in her vicinity.

But the homologically nontrivial Wilson loop operator is not included in the algebra generated by these local operations. Hence $W(C)$, where C is a nontrivial cycle, is completely inaccessible to the local residents of the lattice. They cannot measure this operator, either destructively nor nondestructively, nor can they apply it to a state. The homologically nontrivial Wilson loop is not an observable of the pure gauge theory.

Although the inhabitants of this world are unable to measure $W(C)$, they are able to change its value. The link rotation $e^{-i\theta E_l}$ has a nontrivial commutation relation with $W(C)$ if $l\in C$:

$$e^{-i\theta E_l}W(C)=e^{-i\theta}W(C)e^{-i\theta E_l}. \tag{79}$$

(Here the orientation of the link l used to define E_l is assumed to be aligned with the orientation of C at link l.) Thus any party with access to a link l of C can rotate the value of $W(C)$, whether or not $W(C)$ is the boundary of a surface.

Like Wilson loop operators, electric field operators are of two types with differing locality properties. If C is a fundamental nontrivial cycle, we can construct an electric field operator E_C that rotates $W(C)$ but has no effect on homologically trivial Wilson loops. Associated with the cycle C of the torus is a closed orientable hypersurface S that crosses C exactly once; dual to this surface is a set of oriented lattice links S^*, as illustrated in Fig. 6. The electric field conjugate to $W(C)$ is

$$E_C=\sum_{l\in S^*} E_l . \tag{80}$$

This nonlocal operator generates a rotation of the homologically nontrivial Wilson loop $W(C)$, but since any homologically trivial closed loop crosses S as many times with a $+$ orientation as with a $-$ orientation, homologically trivial Wilson loop operators commute with E_C.

The "nonlocal electric field" E_C can be measured—all parties residing at links contained in S^* can measure the local electric field and the results can be summed. But while the inhabitants of the lattice are able to measure E_C, they are unable to change its value. The Hilbert space of the theory divides into superselection sectors, each labeled by the values of $E_{C_i}\in Z$, where the C_i's are the cycles that generate the homology group of the spatial manifold.

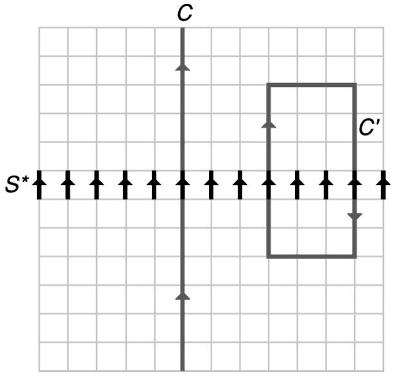

FIG. 6. The nonlocal electric field operator dual to a homologically nontrivial Wilson loop operator $W(C)$, in an Abelian lattice gauge theory in two spatial dimensions. Here a two-torus is represented as a square with opposite sides identified, C is a nontrivial oriented cycle that winds around the torus, and S^* is the set of oriented links dual to a closed "surface" that crosses C once. Any homologically trivial closed loop (like C') crosses S^* as many times with a $+$ orientation as with a $-$ orientation. Thus the electric field operator on S^* commutes with $W(C')$, but has a nontrivial commutation relation with $W(C)$.

It is obvious that similar conclusions apply to any Abelian pure gauge theory. If the theory is defined on a manifold with nontrivial homology, then the algebra of observables has a different structure in the theory with charged matter than in the pure gauge theory without matter. In the pure gauge theory, the homologically nontrivial Wilson loops are not observables at all, and consequently, the theory divides into sectors with different values of the nonlocal electric field.

VIII. SUPERLUMINAL CHARGE TRANSPORT

The main conclusion of this paper is that the observables of Abelian and non-Abelian gauge theories have fundamentally different properties—in particular, the nondemolition measurement of a Wilson loop is acausal in the non-Abelian case and localizable in the Abelian case. We can further appreciate the distinction between Abelian and non-Abelian gauge theories by thinking about not what operators can be *measured*, but rather what operators can be *applied* to a state by a group of parties each of whom acts locally.

To dramatize the question, imagine two parties Alice and Bob, many light years apart, who share a "superluminal charge transport line" (SCTL). Alice places a single electrically charged particle, an electron, at her end of the SCTL (the point y); then her charge mysteriously disappears, and in an instant reappears at Bob's end of the SCTL (the point x). The electron has been transmitted through the SCTL far more rapidly than Alice could send a light signal to Bob. Is such a device physically possible?

Yes. We can understand how the SCTL works by characterizing it with a gauge-invariant unitary operator that it applies to a state. In our lattice formulation of an Abelian lattice gauge theory with matter, consider a connected path of links P that begins at y and ends at x. Associated with this path is the gauge-invariant operator

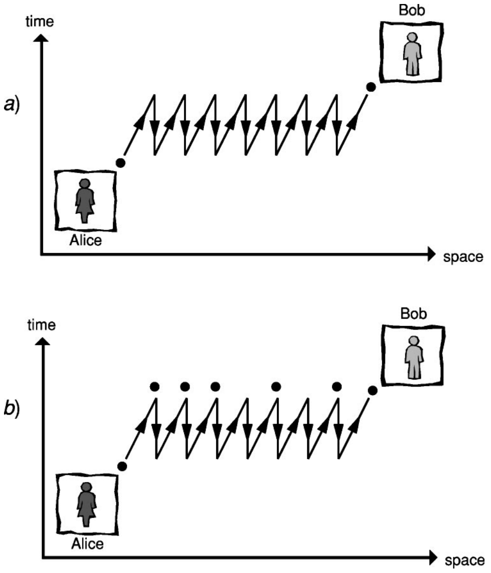

FIG. 7. (a) ‘‘Sawtooth protocol’’ for superluminal transmission of an electron from Alice to Bob, assisted by many intervening parties. Each party (except Alice and Bob) produces an electron-positron pair and keeps the positron, and each (except Bob) passes an electron to the party on her right. Then all pairs annihilate. Thus a charged particle sent by Alice is received by Bob almost instantaneously, even though Bob is many light years away. (b) The protocol fails to achieve superluminal transport of non-Abelian charge. All intervening parties produce color-singlet pairs of charges, but when each party unites her antiparticle with the particle created by her neighbor, the pairs fail to annihilate completely. Though the procedure conserves color, the color of the charge received by Bob is uncorrelated with the color of the particle that had been in Alice’s possession. In both the Abelian and non-Abelian cases, no information is transmitted from Alice to Bob, so that causality is not violated.

$$\phi_x^{-1}\left(\prod_{l\in P} U_l\right)\phi_y=\prod_{l\in P} u_l\,. \tag{81}$$

Acting on the weakly coupled ground state of the theory, this operator creates a pair of equal and opposite charges at the sites x and y. Acting on a state with a charged particle at site y, it annihilates the particle at y while creating a particle of like charge at x, in effect transporting the particle from y to x. The applied operator factorizes as a product of gauge-invariant unitary operators u_l, each acting on a single lattice link. Therefore, many parties acting simultaneously, each manipulating only the link in her own vicinity, are able to operate the SCTL.

More physically, we can envision the operation of the SCTL as in Fig. 7. Many parties are distributed along the SCTL. At a pre-arranged time, each party creates an electron-positron pair. Retaining the positron, she passes the electron to her right, while receiving an electron from the party on her left. Then she brings electron and positron together to annihilate. Claire, the party closest to Alice, receives an electron from Alice and annihilates it with Claire’s positron, while Diane, the party closest to Bob, hands her electron to Bob. After all pairs annihilate, the sole remaining electron, initially in Alice’s hands, has been delivered to Bob. The closer the parties are to one another, the faster the procedure can be completed.

Even though the charge transfer is virtually instantaneous, the Gauss law is satisfied at all times. If we draw surfaces around Alice and Bob, then while the SCTL is operating one unit of charge leaves Alice’s surface and one unit enters Bob’s. Furthermore, even though the charge moves superluminally, the process does not violate causality, since no information is transmitted from Alice to Bob. Indeed, if Felicity, a party in the middle of the SCTL, were to disobey orders and fail to create an electron-positron pair, then Felicity would ‘‘intercept’’ the charge sent by Alice, and Felicity’s neighbor on the right would share a distantly separated electron-positron pair with Bob. When Bob receives the electron, all he learns is that his left neighbor has performed as expected, but he learns nothing about the activities of Alice.

While an Abelian charge really carries no information, non-Abelian charge is much more interesting—its orientation in a representation space can encode a message. Thus it is easy to see that a non-Abelian SCTL, were one to exist, would violate causality. To be explicit, consider the following protocol that enables Bob to send classical information to Alice (based on ideas similar to those used to show that Wilson loop measurement is acausal). First, Alice produces a particle-antiparticle pair, where the particle transforms as representation (R) of G and the antiparticle as representation (R^*). The total charge of the pair is trivial. If $\{|e_i\rangle, i=1,2,3,\dots n_R\}$ denotes a basis for the representation (R), and $\{|e_i^*\rangle\}$ denotes the conjugate basis for (R^*), then the singlet state prepared by Alice is

$$\frac{1}{\sqrt{n_R}}\sum_i |e_i\rangle\otimes|e_i^*\rangle. \tag{82}$$

Alice keeps the antiparticle, and sends the particle through the SCTL to Bob. Bob has a loop of magnetic flux that he has prepared in the charge-zero state $|\alpha,0\rangle$ associated with conjugacy class α of G, as in Eq. (6). To convey a bit of information to Alice, Bob either does nothing to the charged particle he received from Alice (sending 0) or lassoes it with his flux tube (sending 1), and returns the charge through the SCTL to Alice. Now if Bob did nothing, Alice recovers a singlet pair, but if Bob lassoed the charge, then the state of the pair has become entangled with the state of Bob’s tube:

$$\frac{1}{\sqrt{n_R}}\frac{1}{\sqrt{|\alpha|}}\sum_{a\in\alpha}\sum_{i,j}|e_i\rangle\otimes|e_j^*\rangle D_{ij}(a)\otimes|a\rangle. \tag{83}$$

Alice then unites the particles and observes whether the pair annihilates. In the state Eq. (83), the probability of annihilation is determined by the overlap of the pair’s state with the singlet state, and is readily seen to be

$$\text{Prob}=\left|\frac{1}{n_R}\chi^{(R)}(\alpha)\right|^2, \tag{84}$$

where $\chi^{(R)}(\alpha)$ is the character of class α in representation (R). As long as the representation (R) is not one-dimensional, the class α can be chosen so that this probability is less than one. Therefore, Alice observes annihilation with certainty if Bob sends 0 and observes annihilation with probability less than unity if Bob sends 1—thus Bob can signal Alice.

The capacity of the SCTL is easily estimated. Suppose that Alice will signal Bob by transmitting N particles (where N is even) each transforming as the representation (R) or its conjugate representation (R^*). She can prepare and send a state of $N/2$ particles and $N/2$ antiparticles, in any one of A_N distinct singlet states. These states are mutually orthogonal and in principle they can be readily distinguished by Bob. Therefore, Alice is able to send $\log_2 A_N$ bits to Bob by using the SCTL N times. But the number of singlets is

$$A_N=\frac{(n_R)^N}{P(N)}, \tag{85}$$

where $P(N)$ grows no faster than a polynomial with N. Thus, asymptotically Alice can send $\log_2 n_R$ bits of information per transmission. This rate is just what we would have guessed naively, ignoring that observables must be gauge invariant.

Since the non-Abelian SCTL is acausal, it ought not to be physically realizable. What goes wrong if we try the same procedure that succeeded in the Abelian case? The trouble is that if Claire produces a singlet pair, and Diane does the same, then when Claire's particle unites with Diane's antiparticle, the charges might be unable to annihilate. In fact, if Claire's particle transforms as the representation (R) and Diane's as (R^*), then the probability that the pair annihilates, determined by its overlap with the single state, is $1/n_R^2$. Thus, while in the Abelian case the outcome of the procedure is that only a single electron survives, which is in Bob's possession, in the non-Abelian case many relic charges remain strewn along the path of the would-be SCTL. Though the procedure conserves charge, the orientation in the representation space of the charge that Bob receives is actually uncorrelated with the orientation of the charge that Alice sent, and no information is transmitted.

Finally, in the non-Abelian theory as in the Abelian theory, the operator that propagates a charged particle from y to x can be factorized as in Eq. (81) into local factors. So why can't this operator be applied by many parties, each acting locally? We must recall that the operators of the theory are not the group elements $u_l \in G$ themselves, but rather the matrix elements $D_{ij}^{(R)}(u_l)$ of representations of the group. In the Abelian case, the character of a product of group elements can be written as a product of characters, where each character is a unitary operator. But in the non-Abelian case, the ''factorized'' operator is really a product of matrices. The contraction of indices in this matrix product cannot be achieved by many parties acting locally; rather it requires a nonlocal conspiracy.

IX. CONCLUSIONS

In the standard formulation of algebraic relativistic quantum field theory [12], an algebra of ''local'' operators on Hilbert space is associated with each bounded open region of spacetime, such that two local operators commute if they are associated with regions that are spacelike separated. A local operator is designated as a ''local observable'' if it preserves the superselection sectors of the theory. One might be tempted to postulate that a quantum operation is physically possible in principle if and only if it can be expanded in terms of these local observables.

We find this viewpoint untenable, because causality places more stringent constraints on the allowed operations [11]. The problem of characterizing which quantum operations are compatible with causality is especially subtle, interesting, and physically relevant in relativistic quantum field theories with local gauge symmetry.

One form of the question is: what operators can justifiably be called ''observables?'' We have focused our attention on the measurability of the Wilson loop because of its prominent place in the operator algebra of a gauge theory. The answer we have found is rather elaborate. In a gauge theory that includes charged matter that transforms faithfully, a *destructive* measurement of a spacelike Wilson loop $W^{(R)}(C)$ is physically possible for any representation (R) of the gauge group. The term ''destructive'' means that many cooperating parties acting together can ascertain the value of the Wilson loop, but only by collecting additional information in the process, and at the price of damaging Wilson loop eigenstates. In a pure gauge theory (one with no charged matter), the destructive measurement of $W^{(R)}(C)$ is possible for any (R) that represents the center of the gauge group trivially. A nondemolition measurement of the Wilson loop (one that leaves Wilson loop eigenstates intact) is possible in an Abelian gauge theory but not in a non-Abelian gauge theory.

Nondemolition measurement of a non-Abelian Wilson loop is impossible because it would conflict with relativistic causality. Two distantly separated parties (Alice and Bob) can each produce excitations locally (magnetic flux tubes), preparing a state that is not an eigenstate of the Wilson loop operator $W(C)$, where C is a loop that passes through both excitations. Projecting onto a Wilson loop eigenstate, whatever the outcome, entangles Alice's excitation with Bob's, modifying the excitations in a manner that either party can discern locally. Such instantaneous preparation of quantum entanglement would enable spacelike-separated Alice and Bob to communicate.

In quantum field theory in general, and in gauge theories in particular, characterizing the physically allowed quantum operations seems to be an open problem. Further progress on this question is bound to elucidate the physical content of relativistic quantum theory.

ACKNOWLEDGMENTS

We thank Steve Giddings, Anton Kapustin, Michael Nielsen, Edward Witten, and especially Mark Srednicki for helpful discussions and comments. This work was supported in part by the Department of Energy under Grant No. DE-FG03-92-ER40701, by the National Science Foundation under Grant No. EIA-0086038, by the Caltech MURI Center for Quantum Networks under ARO Grant No. DAAD19-00-1-0374, by IBM, and by the Clay Mathematics Institute. Some of this work was done at the Aspen Center for Physics.

[1] R. Giles, Phys. Rev. D **24**, 2160 (1981).
[2] R. Gambini and J. Pullin, *Loops, Knots, Gauge Theories and Quantum Gravity* (Cambridge University Press, Cambridge, England, 1996).
[3] M. A. Nielsen and I. L. Chuang, *Quantum Computation and Quantum Information* (Cambridge University Press, Cambridge, England, 2000).
[4] J. Preskill, Lecture Notes for Physics 229: Quantum Information and Computation, http://www.theory.caltech.edu/people/preskill/ph229
[5] Y. Aharonov and D. Z. Albert, Phys. Rev. D **21**, 3316 (1980).
[6] Y. Aharonov and D. Z. Albert, Phys. Rev. D **24**, 359 (1981).
[7] Y. Aharonov, D. Z. Albert, and L. Vaidman, Phys. Rev. D **34**, 1805 (1986).
[8] R. D. Sorkin, in *Directions in General Relativity, Vol. 2*, edited by B. L. Hu and T. A. Jacobson (Cambridge University Press, Cambridge, England, 1993), gr-qc/9302018.
[9] S. Popescu and L. Vaidman, Phys. Rev. A **49**, 4331 (1994).
[10] D. Beckman, Ph.D. thesis, Caltech, 2001.
[11] D. Beckman, D. Gottesman, M. Nielsen, and J. Preskill, Phys. Rev. A **64**, 052309 (2001).
[12] R. Haag, *Local Quantum Physics: Fields, Particles, Algebras* (Springer-Verlag, Berlin, 1992).
[13] J. Preskill and L. Krauss, Nucl. Phys. **B341**, 50 (1990).
[14] M. Alford, K. Benson, S. Coleman, J. March-Russell, and F. Wilczek, Phys. Rev. Lett. **64**, 1632 (1990).
[15] M. Alford, S. Coleman, and J. March-Russell, Nucl. Phys. **B351**, 735 (1991).
[16] M. G. Alford, K.-M. Lee, J. March-Russell, and J. Preskill, Nucl. Phys. **B384**, 251 (1992).
[17] A. Yu. Kitaev, ''Fault-tolerant quantum computation by anyons,'' quant-ph/9707021.
[18] H. Buhrman, W. van Dam, P. Hoyer, and A. Tapp, Phys. Rev. A **60**, 2737 (1999).

Controlling Spin Exchange Interactions of Ultracold Atoms in Optical Lattices

L.-M. Duan,[1] E. Demler,[2] and M. D. Lukin[2]

[1]*Institute for Quantum Information, California Institute of Technology, mc 107-81, Pasadena, California 91125, USA*
[2]*Physics Department, Harvard University, Cambridge, Massachusetts 02138, USA*

(Received 25 October 2002; published 26 August 2003)

We describe a general technique that allows one to induce and control strong interaction between spin states of neighboring atoms in an optical lattice. We show that the properties of spin exchange interactions, such as magnitude, sign, and anisotropy, can be designed by adjusting the optical potentials. We illustrate how this technique can be used to efficiently "engineer" quantum spin systems with desired properties, for specific examples ranging from scalable quantum computation to probing a model with complex topological order that supports exotic anyonic excitations.

DOI: 10.1103/PhysRevLett.91.090402 PACS numbers: 03.75.Nt, 03.67.–a, 42.50.–p, 73.43.–f

Recent observations of the superfluid to Mott insulator transition in a system of ultracold atoms in an optical lattice open fascinating prospects for studying many-body phenomena associated with strongly correlated systems in a highly controllable environment [1–4]. For instance, the recent studies have shown that, with spinor bosonic or fermionic atoms in optical lattices, it may be possible to observe complex quantum phase transitions [5,6], to probe novel superfluidity mechanisms [7,8], or to demonstrate the spin-charge separation predicted from the Luttinger liquid model [9].

This Letter describes a general technique to control many-body spin Hamiltonians using ultracold atoms. Specifically, we show that, when two-state bosonic or fermionic atoms are confined in an optical lattice, the interaction between spins of the particles can be controlled by adjusting the intensity, frequency, and polarization of the trapping light. The essential idea is to induce and control virtual spin-dependent tunneling between neighboring atoms in the lattice that results in a controllable Heisenberg exchange interaction. By combining this simple experimental technique with the design of the lattice geometry, it is possible to engineer many interesting spin Hamiltonians corresponding to strongly correlated systems.

Such techniques are of particular significance since quantum magnetic interactions are central to understanding complex orders and correlations [10]. We illustrate this with several examples: (i) We show that one of the generated Hamiltonians provides us an easy way to realize the so-called cluster states in two or three dimensions [11], which are useful for an implementation of scalable quantum computation with neutral atoms; (ii) we show that the realized Hamiltonian has a rich phase diagram, opening up the possibility to observe various quantum magnetic phase transitions in a controllable way; (iii) finally, we show how to implement an exactly solvable spin Hamiltonian recently proposed by Kitaev [12], which supports Abelian and non-Abelian anyonic excitations with exotic fractional statistics. Abelian anyons could also exist in a fast rotating condensate [13].

We consider an ensemble of ultracold bosonic or fermionic atoms confined in an optical lattice formed by several standing-wave laser beams. We are interested in the Mott insulator regime, and the atomic density of roughly one atom per lattice site. Each atom is assumed to have two relevant internal states, which are denoted with the effective spin index $\sigma = \uparrow, \downarrow$, respectively. We assume that the atoms with spins $\sigma = \uparrow, \downarrow$ are trapped by independent standing-wave laser beams through polarization (or frequency) selection. Each laser beam creates a periodic potential $V_{\mu\sigma}\sin^2(\vec{k}_\mu \cdot \vec{r})$ in a certain direction μ, where $\vec{k}_\mu$ is the wave vector of light. For sufficiently strong periodic potential and low temperatures, the atoms will be confined to the lowest Bloch band as has been confirmed from experiments [1], and the low energy Hamiltonian is then given by

$$H = -\sum_{\langle ij \rangle \sigma} (t_{\mu\sigma} a_{i\sigma}^\dagger a_{j\sigma} + \text{H.c.}) + \frac{1}{2}\sum_{i,\sigma} U_\sigma n_{i\sigma}(n_{i\sigma} - 1) + U_{\uparrow\downarrow}\sum_i n_{i\uparrow} n_{i\downarrow}, \tag{1}$$

Here $\langle i, j \rangle$ denotes the near neighbor sites in the direction μ, $a_{i\sigma}$ are bosonic (or fermionic) annihilation operators, respectively, for bosonic (or fermionic) atoms of spin σ localized on-site i, and $n_{i\sigma} = a_{i_\sigma}^\dagger a_{i_\sigma}$.

For the cubic lattice ($\mu = x, y, z$) and using a harmonic approximation around the minima of the potential [3], the spin-dependent tunneling energies and the on-site interaction energies are given by $t_{\mu\sigma} \approx (4/\sqrt{\pi}) E_R^{1/4} (V_{\mu\sigma})^{3/4} \times \exp[-2(V_{\mu\sigma}/E_R)^{1/2}]$, $U_{\uparrow\downarrow} \approx (8/\pi)^{1/2}(k a_{s\uparrow\downarrow}) \times (E_R \overline{V}_{1\uparrow\downarrow}\overline{V}_{2\uparrow\downarrow}\overline{V}_{3\uparrow\downarrow})^{1/4}$. Here $\overline{V}_{\mu\uparrow\downarrow} = 4V_{\mu\uparrow}V_{\mu\downarrow}/(V_{\mu\uparrow}^{1/2} + V_{\mu\downarrow}^{1/2})^2$ is the spin average potential in each direction, $E_R = \hbar^2 k^2/2m$ is the atomic recoil energy, and $a_{s\uparrow\downarrow}$ is the scattering length between the atoms of different spins. For bosonic atoms $U_\sigma \approx (8/\pi)^{1/2}(k a_{s\sigma})(E_R V_{1\sigma} V_{2\sigma} V_{3\sigma})^{1/4}$ ($a_{s\sigma}$ are the corresponding scattering lengths). For fermionic atoms, U_σ is on the order of Bloch band separation $\sim 2\sqrt{V_{\mu\sigma} E_R}$, which is typically much larger than $U_{\uparrow\downarrow}$ and can be taken to be infinite. In writing Eq. (1), we have neglected overall energy shifts $\sum_{i\mu}(\sqrt{E_R V_{\mu\uparrow}} - \sqrt{E_R V_{\mu\downarrow}})(n_{i\uparrow} - n_{i\downarrow})/2$, which can be easily compensated

0031-9007/03/91(9)/090402(4)$20.00 © 2003 The American Physical Society

by a homogeneous external magnetic field applied in the z direction.

From the above expressions, we observe that $t_{\mu\sigma}$ depend sensitively (exponentially) upon the ratios $V_{\mu\sigma}/E_R$, while $U_{\uparrow\downarrow}$ and U_σ exhibit only weak dependence. We can easily introduce spin-dependent tunneling $t_{\mu\sigma}$ by varying the potential depth $V_{\mu\uparrow}$ and $V_{\mu\downarrow}$ with control of the intensity of the trapping laser. We now show that this simple experimental method provides us a powerful tool to engineer many-body Hamiltonians. We are interested in the regime where $t_{\mu\sigma} \ll U_\sigma, U_{\uparrow\downarrow}$ and $\langle n_{i\uparrow}\rangle + \langle n_{i\downarrow}\rangle \simeq 1$, which corresponds to an insulating phase. In this regime, the terms proportional to tunneling $t_{\mu\sigma}$ can be considered via perturbation theory. We use a simple generalization of the Schriffer-Wolf transformation [14] (see another method in [8]) and, to the leading order in $t_{\mu\sigma}/U_{\uparrow\downarrow}$, Eq. (1) is equivalent to the following effective Hamiltonian:

$$H = \sum_{\langle i,j\rangle}[\lambda_{\mu z}\sigma_i^z\sigma_j^z \pm \lambda_{\mu\perp}(\sigma_i^x\sigma_j^x + \sigma_i^y\sigma_j^y)]. \tag{2}$$

Here $\sigma_i^z = n_{i\uparrow} - n_{i\downarrow}$, $\sigma_i^x = a_{i\uparrow}^\dagger a_{i\downarrow} + a_{i\downarrow}^\dagger a_{i\uparrow}$, and $\sigma_i^y = -i(a_{i\uparrow}^\dagger a_{i\downarrow} - a_{i\downarrow}^\dagger a_{i\uparrow})$ are the usual spin operators. The + and − signs before $\lambda_{\mu\perp}$ in Eq. (4) correspond, respectively, to the cases of fermionic and bosonic atoms. The parameters $\lambda_{\mu z}$ and $\lambda_{\mu\perp}$ for the bosonic atoms are given by

$$\lambda_{\mu z} = \frac{t_{\mu\uparrow}^2 + t_{\mu\downarrow}^2}{2U_{\uparrow\downarrow}} - \frac{t_{\mu\uparrow}^2}{U_\uparrow} - \frac{t_{\mu\downarrow}^2}{U_\downarrow}, \qquad \lambda_{\mu\perp} = \frac{t_{\mu\uparrow}t_{\mu\downarrow}}{U_{\uparrow\downarrow}}. \tag{3}$$

For fermionic atoms, the expression for $\lambda_\perp$ is the same as in (3), but in the expression for λ_z the last two terms vanish since $U_\sigma \gg U_{\uparrow\downarrow}$. In writing Eq. (2), we neglected the term $\sum_{i\mu}4(t_{\mu\uparrow}^2/U_\uparrow - t_{\mu\downarrow}^2/U_\downarrow)\sigma_i^z$, which can be easily compensated by an applied external magnetic field.

The Hamiltonian (2) represents the well-known anisotropic Heisenberg model (XXZ model), which arises in the context of various condensed matter systems [10]. However, the approach involving ultracold atoms has a unique advantage in that the parameters $\lambda_{\mu z}$ and $\lambda_{\mu\perp}$ can be easily controlled by adjusting the intensity of the trapping laser beams. They can also be changed within a broad range by tuning the ratio between the scattering lengths $a_{s\uparrow\downarrow}$ and $a_{s\sigma}$ ($\sigma = \uparrow, \downarrow$) by adjusting an external magnetic field through Feshbach resonance [15]. Therefore, even with bosonic atoms alone, it is possible to realize the entire class of Hamiltonians in the general form (2) with an arbitrary ratio $\lambda_{\mu z}/\lambda_{\mu\perp}$. This is important since bosonic atoms are generally easier to cool. In Fig. 1(a), we show the phase diagram of the Hamiltonian (2) on a bipartite lattice as a function of $\beta_t = t_\uparrow/t_\downarrow + t_\downarrow/t_\uparrow$ and $U_{\uparrow\downarrow}/U_\sigma$ [16] for the case when $U_\uparrow = U_\downarrow$ and $t_{\mu\sigma}$ is independent of the spatial direction μ. Certain lines on this phase diagram correspond to well-known spin systems: When $U_{\uparrow\downarrow}/U_\sigma = 1/2$ we have an XY model; when $\beta_t = \infty$ ($t_\uparrow$ or $t_\downarrow$ is zero) we have an Ising model; for $\beta_t = \pm(1/2 - U_{\uparrow\downarrow}/U_\sigma)^{-1}$ we have an SU(2) symmetric antiferromagnetic or ferromagnetic systems, respectively.

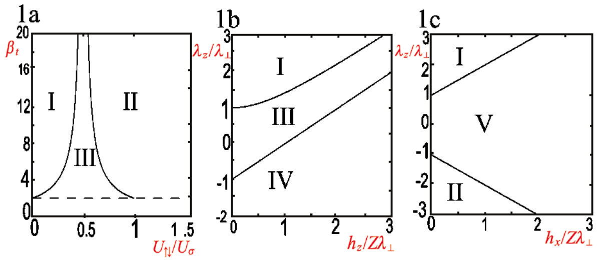

FIG. 1 (color online). Phase diagrams of the Hamiltonians (2) for bosonic and fermionic atoms: (a) at zero magnetic field, (b) with a longitudinal field h_z, and (c) (for bosons only) with a transverse field h_x. Each phase is characterized by the following order parameter: I, z-Néel order; II, z-ferromagnetic order; III, xy-Néel order for fermionic atoms and xy-ferromagnetic order for bosonic atoms; IV and V, spin polarization in the direction of applied field, z and x, respectively.

Before proceeding, we estimate the typical energy scales and discuss the influence of imperfections and noise. For Rb atoms with a lattice constant $\pi/|\vec{k}| \sim 426$ nm, the typical tunneling rate $t/\hbar$ can be chosen from zero to a few kHz [1]. The on-site interaction $U/\hbar$ corresponds to a few kHz at zero magnetic field, but can be much larger near the Feshbach resonance. The energy scale for magnetic interaction is about $t^2/\hbar U \sim 0.1$ kHz (corresponding to a time scale of 10 ms) with a conservative choice of $U \sim 2$ kHz and $(t/U)^2 \sim 1/20$. These energy scales are clearly compatible with current experiments [1]. We further note that the present system should be quite robust to realistic noise and imperfections. First of all, the next order correction to the Hamiltonian (2) is proportional to $(t/U)^2$, which is small in the Mott regime. Second, since the atoms only virtually tunnel to the neighboring sites with a small probability $(t/U)^2$, the dephasing rate and the inelastic decay rate are significantly reduced compared with the cold collision scheme [17,18]. Finally, the spontaneous emission noise rate can be made very small by using a blue-detuned optical lattice or by increasing the detuning. In a blue-detuned lattice, even with a moderate detuning $\Delta \sim 5$ GHz, the effective spontaneous emission rate is estimated to be of the order of Hz, which is significantly smaller than $t^2/(\hbar U)$.

We now illustrate the ability to engineer many-body spin Hamiltonians with specific examples. For the first example, we set $V_{\mu\downarrow}/V_{\mu\uparrow} \gg 1$, so that $t_{\mu\downarrow}$ becomes negligible while $t_{\mu\uparrow}$ remains finite. In this case, the Hamiltonian (2) reduces to the Ising model $H = \sum_{\langle i,j\rangle}\lambda_{\mu z}\sigma_i^z\sigma_j^z$, with $\lambda_{\mu z} = t_{\mu\uparrow}^2/(0.5/U_{\uparrow\downarrow} - 1/U_\uparrow)$. Though this Hamiltonian has quite trivial properties for its ground states and excitations, its realization in optical lattices can be very useful for a dynamical generation of the so-called cluster states [11]. Specifically, we note that this Ising interaction can be easily turned on and off by adjusting the potential depth $V_{\mu\uparrow}$. If we first prepare each atom in the lattice into the superposition state $(|\uparrow\rangle + |\downarrow\rangle)/\sqrt{2}$, and then lower $V_{\mu\uparrow}$ for a time T with $\lambda_{\mu z}T = \pi/4 \bmod \pi/2$, the final state is a cluster state with its dimension determined by the dimension of the lattice [11]. The d-dimensional ($d \geq 2$) cluster states have important applications for implementation of scalable quantum computation with neutral atoms: After its preparation, one can implement universal quantum computation simply via a series of single-bit measurements only [11]. The use of such cluster states can significantly alleviate the stringent requirements on separate addressing of the neighboring atoms in the proposed quantum computation schemes [17,19]. Although the present approach is somewhat slower that the cold collision scheme [17], it allows one to take advantage of its simplicity and the reduced dephasing rate.

As our second example, we explore the rich phase diagram of the Hamiltonian (2) in the presence of magnetic fields. For simplicity, we assume a bipartite lattice and identical spin exchange constants for all links. Figure 1(b) shows the mean-field phase diagram for bosonic particles in the presence of a longitudinal field h_z. This diagram was obtained by comparing energies of the variational wave functions of two kinds: (i) the Néel state in the z direction $\langle \vec{\sigma}_i \rangle = (-1)^i \vec{e}_z$; (ii) canted phase with ferromagnetic order in the xy plane and finite polarization in the z direction $\langle \vec{\sigma}_i \rangle = \vec{e}_x \cos\theta + \vec{e}_z \sin\theta$. Here, θ is a variational parameter, and $\vec{e}_{z,x}$ are unit vectors in the directions z, x. Transition between the z-Néel and the canted phases is a first order spin-flop transition [20] at $h_z = Z(\lambda_z^2 - \lambda_\perp^2)^{1/2}$ (Z is the number of neighboring atoms of each lattice site), and transition between the xy-Néel phase and the z polarized phase is a second order transition of the XY type at $h_z = Z(\lambda_z + \lambda_\perp)$. In the absence of transverse magnetic field, one can use the existence of two sublattices to change the sign of $\lambda_\perp$ using the transformation $\sigma_i^{x,y} \to (-)^i \sigma_i^{x,y}$. Hence, fermionic atoms in the longitudinal magnetic field have the same phase diagram as shown in Fig. 1(b), except that their canted phase has transverse Néel rather than transverse ferromagnetic order. Results of a similar mean-field analysis of the Hamiltonian (2) for bosonic atoms with a transverse magnetic field h_x are shown in Fig. 1(c). For fermionic atoms in a transverse field, there is one more phase with a Néel order along y direction.

The third example involves the anisotropic spin model on a 2D hexagonal lattice proposed recently by Kitaev [12]. In this model, interactions between nearest neighbors are of the XX, the YY, or the ZZ type, depending on the direction of the link:

$$H = \sum_{\nu = x,y,z; \langle i,j \rangle \in D_\nu} \lambda_\nu \sigma_i^\nu \sigma_j^\nu, \tag{4}$$

where the symbol $\langle i, j \rangle \in D_\nu$ denotes the neighboring atoms in the D_ν ($\nu = x, y, z$) direction [see Fig. 2(b)].

To implement this model using ultracold atoms, we first raise the potential barriers along the vertical direction Z in the three-dimensional optical lattice so that the tunneling and the spin exchange interactions in Z direction are completely suppressed [1,9]. In this way, we get an effective 2D configuration with a set of independent identical 2D lattice in the X-Y plane. We then apply in the X-Y plane three trapping potentials (identical for all spin states) of the forms

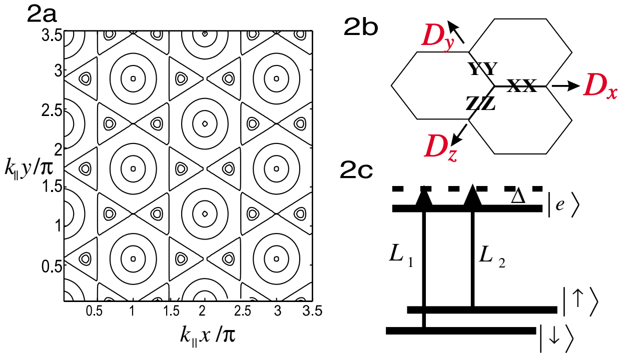

FIG. 2 (color online). (a) The contours with the three potentials in the form of Eq. (5). The minima are at the centers of the triangles when $\varphi_0 = \pi/2$. (b) The illustration of the model Hamiltonian (4). (c) The schematic atomic level structure and the laser configuration to induce spin-dependent tunneling.

$$V_j(x, y) = V_0 \sin^2[k_{\|}(x \cos\theta_j + y \sin\theta_j) + \varphi_0], \tag{5}$$

where $j = 1, 2, 3$, and $\theta_1 = \pi/6$, $\theta_2 = \pi/2$, $\theta_3 = -\pi/6$. Each of the potentials is formed by two blue-detuned interfering traveling laser beams above the X-Y plane with an angle $\varphi_{\|} = 2\arcsin(1/\sqrt{3})$, so that the wave vector $k_{\|}$ projected onto the X-Y plane has the value $k_{\|} = k \sin(\varphi_{\|}/2) = k/\sqrt{3}$. We choose the relative phase $\varphi_0 = \pi/2$ in Eq. (5) so that the maxima of the three potentials overlap. In this case, the atoms are trapped at the minima of the potentials, which form a hexagonal lattice as shown by the centers of the triangles in Fig. 2(a). We assume that there is one atom per each lattice site, and this atom interacts with the three neighbors in different directions through virtual tunneling with a potential barrier given by $V_0/4$.

In such a hexagonal lattice, we wish to engineer anisotropic Heisenberg exchange for each tunneling direction (denoted by D_x, D_y, and D_z, respectively). To this end, we apply three blue-detuned standing-wave laser beams in the X-Y plane along these tunneling directions:

$$V_{\nu\sigma}(x, y) = V_{\nu\sigma} \sin^2[k(x \cos\theta'_\nu + y \sin\theta'_\nu)], \tag{6}$$

where $\nu = x, y, z$, and $\theta'_x = -\pi/3$, $\theta'_y = \pi$, $\theta'_z = \pi/3$. In general, we require that the potential depth $V_{\nu\sigma}$ depend on the atomic spin state as

$$V_{\nu\sigma} = V_{\nu+} |+\rangle_\nu \langle +| + V_{\nu-} |-\rangle_\nu \langle -|, \qquad (\nu = x, y, z), \tag{7}$$

where $|+\rangle_\nu$ ($|-\rangle_\nu$) is the eigenstate of the corresponding Pauli operator σ^ν with the eigenvalue $+1$ ($-$ 1).

The spin-dependent potentials in the form of Eqs. (6) and (7) can be realized, for instance, with the specific atomic level configuration shown in Fig. 2(c). Here, $\sigma = \uparrow, \downarrow$ denote two hyperfine levels of the atom with different energies. They are coupled to the common excited level $|e\rangle$ with a blue detuning Δ, respectively, through the laser beams L_1 and L_2 with frequencies matching the corresponding transitions. The quantization axis is chosen to be perpendicular to the X-Y plane, and the phase-locked laser beams L_1 and L_2 are both polarized along this direction. In the tunneling direction D_z, we only apply the L_1 laser beam, which induces the potential $V_{z\sigma}(x, y)$ with the desired form (7) of its depth $V_{z\sigma}$. In the tunneling direction D_x or D_y, we apply both lasers L_1 and L_2, but with different relative phases, which realize the desired potential depth $V_{x\sigma}$ or $V_{y\sigma}$ of the form (7) in the corresponding direction.

The potentials (6) and (7) do not have influence on the equilibrium positions of the atoms, but they change the potential barrier between the neighboring atoms in the D_ν direction from $V_0/4$ to $V'_{\nu\sigma} = V_0/4 + V_{\nu\sigma}$. The parameters $V_{\nu+}$ and $V_{\nu-}$ in Eq. (7) can be tuned by varying the laser intensity of L_1 and L_2 in the D_ν direction, and one can easily find their appropriate values so that, in the D_ν direction, the atom can virtually tunnel with a rate $t_{+\nu}$ only when it is in the eigenstate $|+\rangle_\nu$. Hence, it follows from Eqs. (2) and (3) that the effective Hamiltonian for our system is given by Eq. (4) with $\lambda_\nu \approx -t_{+\nu}^2/(2U)$ for bosonic atoms with $U_{\uparrow\downarrow} \approx U_\uparrow \approx U_\downarrow \approx U$. After compensating effective magnetic fields, we find exactly the model described by the Hamiltonian (4).

The model (4) is exactly solvable due to the existence of many conserved operators, and it has been shown to possess very interesting properties [12]. In particular, it supports both Abelian and non-Abelian anyonic excitations, depending on the ratios between the three parameters λ_ν. In the region where $2\lambda_\nu/(\lambda_x + \lambda_y + \lambda_z) \leq 1$ $(\nu = x, y, z)$, the excitation spectrum of the Hamiltonian (4) is gapless, but a gap opens when perturbation magnetic fields are applied in the x, y, z directions, and the excitations in this case obey non-Abelian fractional statistics. Out of this region, except at some trivial points with $\lambda_x\lambda_y\lambda_z = 0$, the Hamiltonian (4) has gapped excitations which satisfy Abelian fractional statistics. Thus, the present implementation opens up an exciting possibility to realize experimentally the exotic Abelian and non-Abelian anyons.

Now we briefly discuss the techniques for probing the resulting states. To detect the quantum phase transitions in the *XXZ* model with magnetic fields or in Kitaev's model, one can probe the excitation spectra via Bragg or Raman spectroscopy. In general, different quantum phases are characterized by specific dispersion relations (for instance, in Kitaev's model, one phase is gapped while the other is gapless). If the two probe light beams have the momentum and frequency differences which match those of the dispersion relation in the corresponding phase, a resonant absorption of the probe light could be observed [21]. The direct observation of the fractional statistics in Kitaev's model can be based on atomic interferometry with a procedure similar to that described in Ref. [13]: One generates a pair of anyonic excitations with a spin-dependent laser focused on two lattice sites, rotates one anyon around the other, and then brings them together for fusion which gives different results depending on the anyonic statistics. Other methods for detecting complex quantum states of atoms have also been developed recently [22].

In summary, we have described a general technique to engineer many-body spin Hamiltonians.

We thank J. I. Cirac, D. DiVincenzo, W. Hofstetter, A. Kitaev, and P. Zoller for helpful discussions. This work was supported by NSF (EIA-0086038, DMR-0132874, and PHY-0134776), and by Sloan and Packard Foundations. L. M. D. also acknowledges support from the MURI Center DAAD19-00-1-0374, the CNSF, the CAS, and the "97.3" project 2001CB309300.

[1] M. Greiner *et al.*, Nature (London) **415**, 39 (2002).
[2] C. Orzel *et al.*, Science **291**, 2386 (2001).
[3] D. Jaksch *et al.*, Phys. Rev. Lett. **81**, 3108 (1998).
[4] M. P. A. Fisher *et al.*, Phys. Rev. B **40**, 546 (1989).
[5] E. Demler and F. Zhou, Phys. Rev. Lett. **88**, 163001 (2002).
[6] K. Gross *et al.*, Phys. Rev. A **66**, 033603 (2002).
[7] W. Hofstetter *et al.*, Phys. Rev. Lett. **89**, 220407 (2002).
[8] A. B. Kuklov and B.V. Svistunov, Phys. Rev. Lett. **90**, 100401 (2003).
[9] A. Recati, P. O. Fedichev, W. Zwerger, and P. Zoller, Phys. Rev. Lett. **90**, 020401 (2003); B. Paredes and J. I. Cirac, Phys. Rev. Lett. **90**, 150402 (2003).
[10] A. Auerbach, *Interacting Electrons and Quantum Magnetism* (Springer-Verlag, New York, 1994).
[11] H. J. Briegel and R. Raussendorf, Phys. Rev. Lett. **86**, 910 (2001); **86**, 5188 (2001).
[12] A. Kitaev (to be published).
[13] B. Paredes *et al.*, Phys. Rev. Lett. **87**, 10402 (2001).
[14] A. C. Hewson, *The Kondo Problem to Heavy Fermions* (Cambridge University Press, Cambridge, England, 1997).
[15] See, e.g., E. A. Donley *et al.*, cond-mat/0204436.
[16] We note that, under the conditions of Ref. [1], an inhomogeneous Mott state can be created due to overall trapping potential. This can result in a domain structure involving new, coexisting phases, which will be discussed elsewhere.
[17] D. Jaksch *et al.*, Phys. Rev. Lett. **82**, 1975 (1999).
[18] O. Mandel *et al.*, cond-mat/0301169.
[19] G. K. Brennen *et al.*, Phys. Rev. Lett. **82**, 1060 (1999).
[20] M. E. Fisher and D. R. Nelson, Phys. Rev. Lett. **32**, 1350 (1974).
[21] W. Ketterle and S. Inouye, cond-mat/0101424.
[22] E. Altman, E. Demler, and M. D. Lukin, cond-mat/0306226.

APPLIED PHYSICS LETTERS VOLUME 82, NUMBER 11 17 MARCH 2003

Near-field scanning optical microscopy of photonic crystal nanocavities

Koichi Okamoto,[a] Marko Lončar, Tomoyuki Yoshie, and Axel Scherer
Department of Electrical Engineering, California Institute of Technology, Pasadena, California 91125-9300

Yueming Qiu and Pawan Gogna
In Situ Technology and Experiments System Section, Jet Propulsion Laboratory, California Institute of Technology, MS 302-306, 4800 Oak Grove Drive, Pasadena, California 91109

(Received 23 September 2002; accepted 20 January 2003)

Near-field scanning optical microscopy was used to observe high-resolution images of confined modes and photonic bands of planar photonic crystal (PPC) nanocavities fabricated in active InGaAsP material. We have observed the smallest optical cavity modes, which are intentionally produced by fractional edge dislocation high-*Q* cavity designs. The size of the detected mode was roughly four by three lattice spacings. We have also observed extended dielectric-band modes of the bulk PPC surrounding the nanocavity by geometrically altering the bands in emission range and eliminating localized modes out of the emission range. © *2003 American Institute of Physics.* [DOI: 10.1063/1.1559646]

Photonic crystals,[1] and planar photonic crystals (PPC) in particular, have recently attracted attention as a promising platform for realization of compact and efficient nanocavities[2,3] and lasers.[4–8] In most of these reports, microphotoluminescence was used to characterize the structures. On the other hand, near-field scanning optical microscopy (NSOM) has recently been used as a powerful alternative method to analyze local electromagnetic field distributions in fabricated nanophotonic structures.[9–17] Gérard *et al.* [14] reported NSOM measurements of active PPC with spectral emission in the infrared region and Shin *et al.*[15] reported the near-field investigation of the lasing modes in PPC lasers. However, in both studies, uncoated optical fibers were used and, therefore, it was not possible to obtain high spatially resolved near-field images of the field distribution inside the cavity. Also, both studies analyzed large hexagonal cavities (empty lattice cavities), which support many modes with rather large mode volumes. In this letter, we report the results of NSOM of very small PPC cavities based on fractional edge dislocations.[2,3,8] The metal-coated fiber tip enables us to distinguish between localized cavity modes and propagating far-field modes, and to obtain more precise mode profiles when the tip probes into holes of PPCs. The best resolution in our system is as small as 50 nm.

The experimental setup for the NSOM measurement is shown in Fig. 1. We used a twin-SNOM system manufactured by OMICRON, capable of both illumination mode (I-mode) and the collection mode (C-mode) measurements. For the I mode, continuous-wave light from a He–Ne laser (633 nm) was used to pump the structures through the optical fiber tip. The photoluminescence (PL) signal was detected through the reflective objective lens. The excitation power of the He–Ne laser, before coupling into the optical fiber, was 1 mW. For the C mode, a 780 nm diode laser, operated with 20 ns long pulses of 2 μs periodicity, was focused on the sample through the refractive objective lens and the optical fiber tip was used to detect the PL signal. The excitation pump beam spot was several tens of μm^2. In both modes, the PL signals were distinguished from the reflected light of the excitation laser by using the colored glass filter with a cutoff wavelength of 850 nm, and detected with a high-sensitivity (fW) InGaAs photodetector. The optical fiber tip was metal coated and the aperture size at the end of the tip was 150 nm. The fiber tip is positioned at the dither piezodevice and shear-force detector in order to control the distance between the tip and the sample surface ($\approx$10 nm) and to obtain a topographic image of the sample.

The PPC nanocavities described in this work are very similar to those used to realize low-threshold lasers described in our previous publication.[8] The most important difference from the cavities analyzed in Ref. 8 is the omission of central defect hole, and therefore *Q* factors are limited to about 1000, according to our theoretical predictions. Optical emission in our structures was obtained from four 9 nm thick InGaAsP quantum well (QW) layers ($\text{Eg}=1.55\ \mu\text{m}$) separated by 20 nm thick InGaAsP barrier layers ($\text{Eg}=1.22\ \mu\text{m}$), and placed in the center of a 330 nm thick InGaAsP slab, grown on the top of InP substrate. The emission from QWs was found to be in the range of 1300 to 1650 nm. The PPC structure is a free-standing membrane patterned with triangular lattice of holes within which cavity based on fractional edge dislocation is defined. Details of the fabrication procedures are presented in Ref. 8.

Figure 2(a) shows the topographic image of the entire structure obtained by the shear-force microscopy. The PPC structure in the center of the membrane as well as the unpatterned edges of the membrane can be seen. In Fig. 2(b), we show the near-field optical image of the same sample obtained using NSOM I mode. A bright region corresponds to the light localized in the Fabry–Perot (FP) resonator formed between the edge of the membrane and the edge of the PPC region in Fig. 2(b). We have confirmed this by conducting micro-PL measurements on this $\approx$2.1 μm long resonator, and FP resonances were detected in the spectrum when the structure was pumped close to the edge [Fig. 2(c)].

---

[a] Electronic mail: kokamoto@caltech.edu

© 2003 American Institute of Physics

Downloaded 07 Jun 2006 to 131.215.106.183. Redistribution subject to AIP license or copyright, see http://apl.aip.org/apl/copyright.jsp

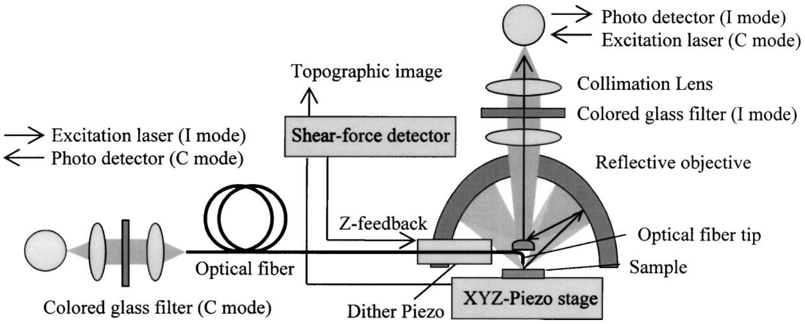

FIG. 1. Experimental setup for the NSOM measurement with illumination mode and collection mode.

Close inspection of Fig. 2(b) also reveals presence of the light localized at the center of the PPC structure. In order to investigate the origin of this signal, we have increased the spatial resolution of our NSOM and analyzed only the central region of the structure, where a nanocavity based on fractional edge dislocations exists. In Fig. 3(a), we show the scanning electron microscope (SEM) image of this central region of the device shown in Fig. 2. The periodicity of the lattice is $a=420$ nm, radius of holes is $r=135$ nm, and thickness of the slab is $d=330$ nm. This PPC geometry, with $r/a=0.32$ and $d/a=0.79$, has a band gap in the frequency range approximately $a/\lambda \in (0.25, 0.33)$, that is in the wavelength range $\lambda \in (1270$ nm, 1680 nm$)$. The elongation in this cavity was $p/a=15\%$.[2,8] The cavity based on fractional edge dislocations supports two prominent resonances. These resonances correspond to doubly degenerate dipole modes of the simple single defect cavity,[4] and the introduced asymmetry due to the dislocation lifts the degeneracy. The two dipole modes are linearly but orthogonally polarized, and the mode positioned at a longer wavelength can have very high Q. Figure 3(b) shows the results of micro-PL analysis of this structure. Two peaks positioned around $\lambda=1450$ nm correspond to the localized dipole modes, whereas peaks above $\lambda=1600$ nm correspond to dielectric band modes.

Figures 3(c) and 3(d) show an enlargement of the central region from Figs. 2(a) and 2(b), respectively. The bright spot seen in NSOM-PL image [Fig. 3(d)] is located at the center of the PPC structure, matching the position of the defect cavity, as shown in topographic image [Fig. 3(c)]. We have attributed this optical signal to two dipole eigenmodes of our cavity. The size of the bright spot is roughly $4.4a$ by $3a$. This small spot size is an indication of a small mode volume, as expected from the localized cavity modes. The NSOM images should be a superposition of two orthogonal dipole modes. These NSOM-PL results are obtained by using I mode and, therefore, the size of the bright spot is expected to contain information on the diffusion properties of free carriers excited by the pump beam, in addition to the information on the optical mode size. Therefore, we believe that by using I mode, we actually overestimate the size of the optical mode due to the free-carrier diffusion. However, the small size of the detected light signal is a clear indication of presence of well-confined modes in the center of our cavity. In Figs. 3(e) and 3(f), we show NSOM images without and with a cutoff colored glass filter, respectively, this time for a cavity with elongation $p/a=20\%$. When the filter was not used [Fig. 3(e)], an interference pattern was observed. We have attributed this to the reflection of the pump He–Ne laser light from the sample surface. On the other hand, when a filter was used, a very different result was obtained and, clearly, localized defect modes could be observed. Figure 4 shows the polarization dependence of the optical modes detected in cavity with $p/a=25\%$, obtained using both micro-PL and NSOM approaches. As predicted by theory, two dipole modes are linearly polarized, with orthogonal polarizations. The intensities of the NSOM images with 0°, 60°, and 90° $(\pm 15°)$ polarizers are in very good agreement with spectra obtained using microphotoluminescence. Therefore, we conclude that optical modes detected with NSOM correspond to confined cavity modes.

Figure 5 shows the topographic images and the corresponding NSOM images for different PPC structures, this

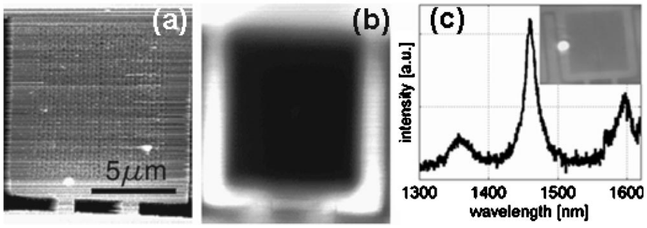

FIG. 2. (a) Topographic image of the whole structure by the shear-force microscopy. (b) Near-field PL image. (c) FP resonances detected using microphotoluminescence when structure was pumped close to the edge. Inset shows pump spot on the structure.

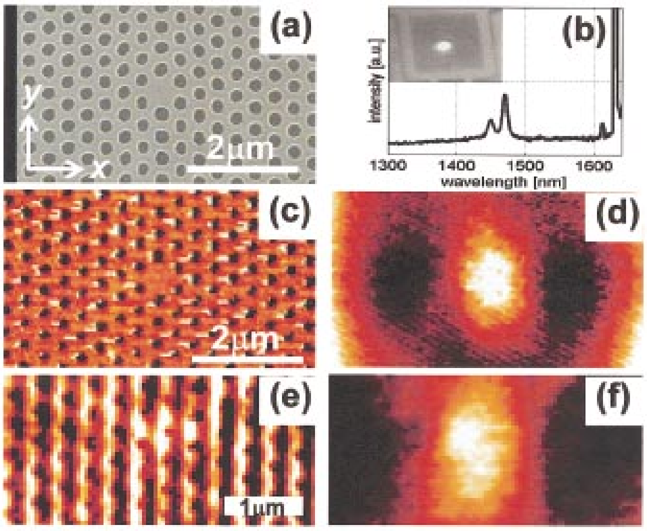

FIG. 3. (Color) (a) SEM image of the tested cavity with $p/a=15\%$. (b) Resonances detected using micro-PL setup. Confined modes (around 1450 nm) and extended dielectric band modes (above 1600 nm) can be seen. (c) Topographic and (d) near-field optical image. Detected optical field corresponds to the confined cavity modes. (e) Near-field image of the cavity with $p/a=20\%$ obtained without and (f) with a colored glass filter.

Downloaded 07 Jun 2006 to 131.215.106.183. Redistribution subject to AIP license or copyright, see http://apl.aip.org/apl/copyright.jsp

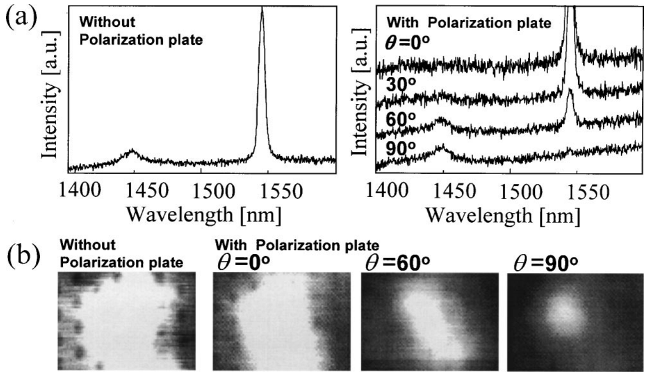

FIG. 4. (a) Micro-PL spectra and (b) near-field images taken from a sample with a parameter $p/a=25\%$ with and without a polarization plate. A polarization parameter θ is a clockwise angle from x axis defined in Fig. 3(a).

time with slightly larger holes and with the central defect hole present. Therefore, we expect dipole eigenmodes of this cavity to be moved toward shorter wavelengths. In the tested sample, they were completely pushed outside the emission range of QWs, and no localized cavity modes could be observed in the micro-PL experiment. However, we could observe several peaks that correspond to the dielectric bands of bulk PPC [Figs. 5(c) and 5(f)]. The NSOM images obtained using C-mode and shown in Figs. 5(a) and 5(b) show light localization in the dielectric region between the PPC holes. Also, positions of the air holes appear dark in this NSOM image. Therefore, we have attributed this result to the existence of the dielectric band modes in the emission region of QW material. Similar results were predicted by theory.[10] Also, spectra obtained using microphotoluminescence [Fig. 5(c)] show the presence of dielectric bands at $\lambda = 1555$ nm. We would like to point out that dielectric band modes, also observed in Fig. 3(b) were not detected using NSOM I mode [Figs. 3(d) and 3(f)]. We believe that it is due to localized pumping in the case of I mode (as opposed to the large pumping spot in C mode) and dielectric band modes that extend over large areas in PPC could not be excited. We have tested another geometries in PPC structures, and the NSOM results are shown in Figs. 5(d) and 5(e). Strong light intensity is observed at the positions of the air holes, this time. This phenomenon could be attributed to the presence of air-band modes in the emission region of the QW material. However, we were not able to observe air-band modes in our micro-PL experiments, and only dielectric band modes were observed [Fig. 5(f)]. At present, experiments are underway to explain this phenomenon.

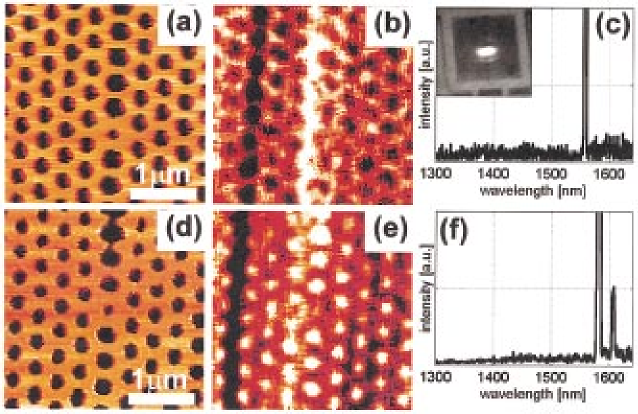

FIG. 5. (Color) (a) Topographic image and (b) near-field PL image (C mode) of PPC structure with bigger holes $(p/a=25\%)$. (d) Topographic and (e) near-field image of another structure. (c) and (f) show spectra obtained by microphotoluminescence from structures shown in (a) and (d), respectively.

In conclusion, we have observed localized defect modes of the compact PPC nanocavities. In addition to localized cavity modes, we have experimentally observed dielectric band modes in bulk PPCs. We conclude that NSOM is a powerful tool for the investigation of local profiles of confined modes in nanocavities.

This work was supported by the Japan Society for the Promotion of Science (12002454), Caltech MURI Center for Quantum Networks, DARPA (MDA 972-00-1-0019), and AFOSR (F49620-01-6-0497). Two of the authors (Y.Q. and P.G.) acknowledge the partial support from the Cross Enterprise Technology Development Program at the Jet Propulsion Laboratory (under a contract with the National Aeronautics and Space Administration).

[1] E. Yablonvitch, Phys. Rev. Lett. **58**, 2059 (1987); S. John, *ibid.* **58**, 2486 (1987).
[2] J. Vučković, M. Lončar, H. Mabuchi, and A. Scherer, Phys. Rev. E **65**, 016608 (2001).
[3] T. Yoshie, J. Vučković, A. Scherer, H. Chen, and D. Deppe, Appl. Phys. Lett. **79**, 4289 (2001).
[4] O. Painter, R. K. Lee, A. Scherer, A. Yariv, J. D. O'Brien, P. D. Dapkus, and I. Kim, Science **284**, 1819 (1999).
[5] H. G. Park, J. K. Hwang, J. Huh, H. Y. Ryu, and Y.-H. Lee, Appl. Phys. Lett. **79**, 3032 (2001).
[6] H.-Y. Ryu, S.-H. Kim, H.-G. Park, J.-K. Hwang, Y.-H. Lee, and J.-S. Kim, Appl. Phys. Lett. **80**, 3883 (2002).
[7] T. Yoshie, O. B. Shchekin, H. Chen, D. G. Deppe, and A. Scherer, Electron. Lett. **38**, 967 (2002).
[8] M. Lončar, T. Yoshie, A. Scherer, P. Gogna, and Y. Qiu, Appl. Phys. Lett. **81**, 2680 (2002).
[9] M. L. M. Balisteri, D. J. W. Klunder, F. C. Blom, A. Driessen, W. J. M. Hoekstra, J. P. Korterik, L. Kuipers, and N. F. van Hulst, Opt. Lett. **24**, 1829 (1999).
[10] G. W. Bryant, E. L. Shirley, L. S. Goldner, E. B. McDaniel, J. W. P. Hsu, and R. J. Tonucci, Phys. Rev. B **58**, 2131 (1998).
[11] S. Fan, A. Ian, and J. D. Joannopoulos, Appl. Phys. Lett. **75**, 3461 (1999).
[12] D. Mulin, C. Girard, G. Colas des Francs, M. Spajer, and D. Courjon, J. Microsc. **202**, 110 (2000).
[13] A. L. Campillo, J. W. P. Hsu, C. A. White, and A. Rosenberg, J. Appl. Phys. **89**, 2801 (2001).
[14] D. Gérard, L. Berguiga, F. de Fornel, L. Salomon, C. Seassal, X. Letartre, and P. Viktorovitch, Opt. Lett. **27**, 173 (2002).
[15] D.-J. Shin, S.-H. Kim, J.-K. Hwang, H.-Y. Ryu, H.-G. Park, D.-S. Song, and Y.-H. Lee, IEEE J. Quantum Electron. **38**, 857 (2002).
[16] T. Baba, H. Yamada, and A. Sakai, Appl. Phys. Lett. **77**, 1584 (2000).
[17] P. Kramper, A. Birner, M. Agio, C. M. Soukoulis, F. Müller, U. Gösele, J. Mlynek, and V. Sandoghdar, Phys. Rev. B **64**, 023102 (2001).

Downloaded 07 Jun 2006 to 131.215.106.183. Redistribution subject to AIP license or copyright, see http://apl.aip.org/apl/copyright.jsp

ACADEMIC PRESS

Available online at www.sciencedirect.com
SCIENCE DIRECT®

Annals of Physics 303 (2003) 31–58

ANNALS
of
PHYSICS

www.elsevier.com/locate/aop

Confinement-Higgs transition in a disordered gauge theory and the accuracy threshold for quantum memory[☆]

Chenyang Wang, Jim Harrington, and John Preskill*

Institute for Quantum Information, California Institute of Technology, Pasadena, CA 91125, USA

Received 18 July 2002

Abstract

We study the $\pm J$ random-plaquette Z_2 gauge model (RPGM) in three spatial dimensions, a three-dimensional analog of the two-dimensional $\pm J$ random-bond Ising model (RBIM). The model is a pure Z_2 gauge theory in which randomly chosen plaquettes (occurring with concentration p) have couplings with the "wrong sign" so that magnetic flux is energetically favored on these plaquettes. Excitations of the model are one-dimensional "flux tubes" that terminate at "magnetic monopoles" located inside lattice cubes that contain an odd number of wrong-sign plaquettes. Electric confinement can be driven by thermal fluctuations of the flux tubes, by the quenched background of magnetic monopoles, or by a combination of the two. Like the RBIM, the RPGM has enhanced symmetry along a "Nishimori line" in the p–T plane (where T is the temperature). The critical concentration p_c of wrong-sign plaquettes at the confinement-Higgs phase transition along the Nishimori line can be identified with the accuracy threshold for robust storage of quantum information using topological error-correcting codes: if qubit phase errors, qubit bit-flip errors, and errors in the measurement of local check operators all occur at rates below p_c, then encoded quantum information can be protected perfectly from damage in the limit of a large code block. Through Monte-Carlo simulations, we measure p_{c0}, the critical concentration along the $T = 0$ axis (a lower bound on p_c), finding $p_{c0} = .0293 \pm .0002$. We also measure the critical concentration of antiferromagnetic bonds in the two-dimensional RBIM on the $T = 0$ axis, finding $p_{c0} = .1031 \pm .0001$. Our value of p_{c0} is incompatible with the value of $p_c = .1093 \pm .0002$ found in earlier numerical studies of the RBIM, in disagreement with the conjecture that the phase boundary of the RBIM is

---

[☆] CALT-68-2374.

[*] Corresponding author.

E-mail addresses: chenyang@stanford.edu (C. Wang), jimh@caltech.edu (J. Harrington), preskill@theory.caltech.edu (J. Preskill).

0003-4916/02/$ - see front matter © 2002 Elsevier Science (USA). All rights reserved.
PII: S0003-4916(02)00019-2

vertical (parallel to the T axis) below the Nishimori line. The model can be generalized to a rank-r antisymmetric tensor field in d dimensions, in the presence of quenched disorder.

© 2002 Elsevier Science (USA). All rights reserved.

---

1. Introduction

Spin systems with quenched randomness have been extensively studied, leading to valuable insights that apply to (for example) spin glass materials, quantum Hall systems, associative memory, error-correcting codes, and combinatorial optimization problems [1–3]. Gauge systems with quenched randomness, which have received comparatively little attention, will be studied in this paper.

The gauge models we consider are intrinsically interesting because they provide another class of simple systems with disorder-driven phase transitions. But our investigation of these models has a more specific motivation connected to the theory of quantum error correction.

In practice, coherent quantum states rapidly decohere due to uncontrollable interactions with the environment. But in principle, if the quantum information is cleverly encoded [6,7], it can be stabilized and preserved using fault-tolerant recovery protocols [8]. Kitaev [4,5] proposed a particularly promising class of quantum error-correcting codes (*surface codes*) in which the quantum processing required for error recovery involves only *local* interactions among qubits arranged in a two-dimensional block, and the protected information is associated with global topological properties of the quantum state of the block. If the error rate is small, then the topological properties of the code block are well protected, and error recovery succeeds with a probability that rapidly approaches one in the limit of a large code block. But if the error rate is above a critical value, the *accuracy threshold*, then quantum error correction is ineffective.

In [9], a precise connection was established between the accuracy threshold achievable with surface codes and the confinement-Higgs transition in a three-dimensional Z_2 lattice gauge model with quenched randomness. The model has two parameters: the temperature T and the concentration p of "wrong-sign" plaquettes. On wrong-sign plaquettes (which are analogous to antiferromagnetic bonds in a spin system) it is energetically favorable for the Z_2 magnetic flux to be nontrivial. In the mapping between quantum error recovery and the gauge model, the quenched fluctuations correspond to the actual errors introduced by the environment; these impose sites of frustration, *magnetic monopoles*, corresponding to an "error syndrome" that can be measured by executing a suitable quantum circuit. Thermally fluctuating magnetic flux tubes, which terminate at magnetic monopoles, correspond to the ensemble of possible error patterns that could generate a particular error syndrome. (The temperature T is tied to the strength p of the quenched fluctuations through a *Nishimori relation* [10].) When the disorder is weak and the temperature low (corresponding to a small error rate), the system is in a magnetically ordered Higgs phase. In the surface code, magnetic order means that all likely error patterns that might have produced the observed error syndrome are topologically equivalent, so that the topologically encoded information resists damage. But at a critical value p_c of the disorder strength (and a temperature determined by Nishimori's relation), magnetic flux tubes condense and the system enters the magnetically disordered confinement phase. In the surface code, magnetic disorder means that the error syndrome cannot point to likely error patterns belonging to a unique topological class; therefore topologically encoded information is vulnerable to damage.

Although the code block is two dimensional, the gauge model is three dimensional because one dimension represents *time*. Time enters the analysis of recovery because measurements of the error syndrome might themselves be faulty; therefore measurements must be repeated on many successive time slices if they are to provide reliable information about the errors that have afflicted the code block. If qubit phase errors, qubit bit-flip errors, and errors in the measurement of local check operators all occur at rates below p_c, then encoded quantum information can be protected perfectly from damage in the limit of a large code block. As we consider more and more reliable measurements of the syndrome, the corresponding three-dimensional gauge model becomes more and more anisotropic, reducing in the limit of perfect measurements to the two-dimensional random-bond Ising model.

The numerical value p_c of the accuracy threshold is of considerable interest, since it characterizes how reliably quantum hardware must perform in order for a quantum memory to be robust. In the three-dimensional Z_2 gauge model, p_c is the value of the wrong-sign plaquette concentration where the confinement-Higgs boundary crosses the Nishimori line in the p–T plane. A lower bound on p_c is provided by the critical concentration p_{c0} on the $T = 0$ axis. In [9], an analytic argument established that $p_{c0} \geqslant .0114$. In this paper we report on a numerical calculation that finds $p_{c0} = .0293 \pm .0002$.

In the case where the error syndrome can be measured flawlessly, the critical error rate is given by the critical antiferromagnetic bond concentration on the Nishimori line of the two-dimensional random-bond Ising model (RBIM). Numerical calculations performed earlier by other authors [11,12] have established $p_c = .1093 \pm .0002$. According to a conjecture of Nishimori [13] and Kitatani [14], this value of p_c should agree with the critical bond concentration p_{c0} of the 2D RBIM on the $T = 0$ axis. The same reasoning that motivates this conjecture for the RBIM indicates that $p_c = p_{c0}$ for the 3D random-plaquette gauge model (RPGM) as well. However, we have calculated p_{c0} in the 2D RBIM numerically, finding $p_{c0} = .1031 \pm .0001$. Our value of p_{c0} agrees with an earlier numerical calculation by Kawashima and Rieger [23], but disagrees with the conjecture that $p_c = p_{c0}$.

In Section 2 we describe in more detail the properties of the 2D RBIM and the 3D RPGM, emphasizing the importance of the Nishimori line and the inferences that can be made about the behavior of order parameters on this line. Section 3 reviews the connection between the models and error recovery using surface codes. Our numerical results for p_{c0} and for the critical exponent ν_0 at the $T = 0$ critical point are presented in Section 4. Section 5 summarizes our conclusions.

2. Models

2.1. Random-bond Ising model

The two-dimensional $\pm J$ random-bond Ising model (RBIM) has a much studied multicritical point at which both the temperature and the strength of quenched disorder are nonzero. This model is an Ising spin system on a square lattice, with a variable $S_i = \pm 1$ residing at each lattice site i. Its Hamiltonian is

$$H = -J \sum_{\langle ij \rangle} \tau_{ij} S_i S_j, \tag{1}$$

where J is the strength of the coupling between neighboring spins, and $\tau_{ij} = \pm 1$ is a quenched random variable. (That is, τ_{ij} depends on what *sample* of the system is selected from a certain ensemble, but is not subject to thermal fluctuations.) The τ_{ij}'s are independently and identically distributed, with the antiferromagnetic choice $\tau_{ij} = -1$ (favoring that neighboring spins antialign) occurring with probability p, and the ferromagnetic choice $\tau_{ij} = +1$ (favoring that neighboring spins align) occurring with probability $1 - p$. We refer to p as the concentration of antiferromagnetic bonds, or simply the bond concentration.

The free energy F of the model at inverse temperature β, averaged over samples, is

$$[\beta F(K, \tau)]_{K_p} = -\sum_{\tau} P(K_p, \tau) \ln Z(K, \tau), \tag{2}$$

where

$$Z(K, \tau) = \sum_{S} \exp\left(K \sum_{\langle ij \rangle} \tau_{ij} S_i S_j \right) \tag{3}$$

is the partition function for sample τ (with $K = \beta J$), and

$$P(K_p, \tau) = (2 \cosh K_p)^{-N_{\mathrm{B}}} \times \exp\left(K_p \sum_{\langle ij \rangle} \tau_{ij} \right) \tag{4}$$

is the probability of the sample τ; here

$$\frac{p}{1-p} = \mathrm{e}^{-2K_p} \tag{5}$$

and N_{B} is the number of bonds.

The partition function $Z(K, \tau)$ is invariant under the change of variable

$$S_i \rightarrow \sigma_i S_i, \quad \tau_{ij} \rightarrow \sigma_i \sigma_j \tau_{ij}, \tag{6}$$

where $\sigma_i = \pm 1$. Thus τ itself has no invariant meaning—samples τ and τ' that differ by the change of variable have equivalent physics. The only invariant property of τ that cannot be modified by such a change of variable is the *distribution of frustration* that τ determines. If an odd number of the bonds contained in a specified plaquette have $\tau = -1$ then that plaquette is frustrated—an *Ising vortex* resides at the plaquette. For purposes of visualization, we sometimes will find it convenient to define the spin model on the dual lattice so that the spins reside on plaquettes and the Ising vortices reside on sites. Then excited bonds with $\tau_{ij}S_iS_j = -1$ form one-dimensional chains that terminate at the frustrated sites.

Changes of variable define an equivalence relation on the set of 2^{N_B} τ configurations: there are the 2^{N_S} elements of each equivalence class (the number of changes of variable, where N_S is the number of sites) and there are 2^{N_S} classes (the number of configurations for the Ising vortices—note that $N_\mathrm{B} = 2N_\mathrm{S}$ for a square lattice on the 2-torus, and that the number of plaquettes is $N_\mathrm{P} = N_\mathrm{S}$). Denote a distribution of Ising vortices, or equivalently an equivalence class of τ's, by η. The probability $P(K_p, \eta)$ of η is found by summing $P(K_p, \tau)$ over all the representatives of the class; hence

$$\begin{aligned}(2\cosh K_p)^{N_\mathrm{B}} P(K_p,\eta) &= (2\cosh K_p)^{N_\mathrm{B}} \sum_{\tau\in\eta} P(K_p,\tau)\\ &= \sum_{\sigma} \exp\left(K_p \sum_{\langle ij\rangle} \tau_{ij}\sigma_i\sigma_j\right) = Z(K_p,\eta). \qquad (7)\end{aligned}$$

Apart from a normalization factor, the probability of a specified distribution of frustration is given by the partition function of the model, but with $K = \beta J$ replaced by K_p.

In this model, we can define an order parameter that distinguishes the ferromagnetic and paramagnetic phases. Let

$$m^2(K, K_p) = \lim_{|i-j|\to\infty} \left[\langle S_iS_j\rangle_K\right]_{K_p}, \qquad (8)$$

where $\langle\cdot\rangle_K$ denotes the average over thermal fluctuations, $[\cdot]_{K_p}$ denotes the average over samples, and $|i-j|$ denotes the distance between site i and site j; then in the ferromagnetic phase $m^2 > 0$ and in the paramagnetic phase $m^2 = 0$. But the two-point correlation function $\langle S_iS_j\rangle_K$ is not invariant under the change of variable Eq. (6), so how should m^2 be interpreted?

Following [9], denote by E the set of bonds that are antiferromagnetic ($\tau_{ij} = -1$), denote by E' the set of excited bonds with $\tau_{ij}S_iS_j = -1$, and denote by D the set of bonds with $S_iS_j = -1$ (those such that the neighboring spins antialign)—see Fig. 1. Then $D = E + E'$ is the disjoint union of E and E' (containing bonds in E or E' but not both). Furthermore, D contains an even number of the bonds that meet at any given site; that is, D is a *cycle*, a chain of bonds that has no boundary points. The quantity S_iS_j just measures whether a line connecting i and j crosses D an even number ($S_iS_j = 1$) or an odd number ($S_iS_j = -1$) of times.

Now D consists of disjoint "domain walls" that form closed loops. If loops that are arbitrarily large appear with appreciable weight in the thermal ensemble, then the two-point function $\langle S_iS_j\rangle_K$ decays like $\exp(-|i-j|/\xi)$—fluctuations far from the sites i and j contribute to the correlation function. Thus the spins are disordered and $m^2 = 0$. But if large loops occur only with negligible probability, then only fluctuations localized near i and j contribute significantly; the spin correlation persists at

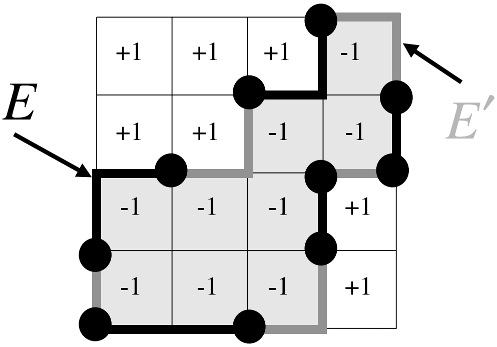

Fig. 1. The chain E of antiferromagnetic bonds (darkly shaded) and the chain E' of excited bonds (lightly shaded), in the two-dimensional random-bond Ising model. Ising spins taking values in $\{\pm 1\}$ reside on plaquettes; Ising vortices (boundary points of E) are located on the sites marked by filled circles. The bonds of E' comprise a one-dimensional defect that connects the vortices. The cycle $D = E + E'$ encloses a domain of spins with the value -1.

large distances and $m^2 > 0$. Thus, the order parameter probes whether the chain E' of excited bonds can wander far from the chain E of ferromagnetic bonds; that is, whether $D = E + E'$ contains arbitrarily large connected closed loops, for typical thermal fluctuations and typical samples.

Nishimori [10] observed that the model has enhanced symmetry properties along a line in the p–T plane (the *Nishimori line*) defined by $K = K_p$ or $\exp(-2\beta J) = p/(1-p)$. In this case, the antiferromagnetic bond chain E and the excited bond chain E' are generated by sampling the same probability distribution, subject to the constraint that both chains have the same boundary points. This feature is preserved by renormalization group transformations, so that renormalization group flow preserves Nishimori's line [15]. The *Nishimori point* (p_c, T_c) where the Nishimori line crosses the ferromagnetic-paramagnetic phase boundary, is a renormalization group fixed point, the model's multicritical point.

When the temperature T is above the Nishimori line, excited bonds have a higher concentration than antiferromagnetic bonds, so we may say that thermal fluctuations play a more important role than quenched randomness in disordering the spins. When T is below the Nishimori line, antiferromagnetic bonds are more common than excited bonds, and the quenched randomness dominates over thermal fluctuations. Right on the Nishimori line, the effects of thermal fluctuations and quenched randomness are in balance [16].

By invoking the change of variable Eq. (6), various properties of the model on the Nishimori line can be derived [3,10]. For example, the internal energy density (or "average bond") can be computed analytically,

$$[\tau_{ij}\langle S_i S_j\rangle_{K_p}]_{K_p} = 1 - 2p, \tag{9}$$

where i and j are neighboring sites; averaged over thermal fluctuations and samples, the concentration of excited bonds is p as one would expect (and the internal energy has no singularity at the Nishimori point). Furthermore, after averaging over disorder, the $(2m-1)$st power of the k-spin correlator has the same value as the $(2m)$th power, for any positive integer m:

$$\left[\langle S_{i_1}S_{i_2}\cdots S_{i_k}\rangle_{K_p}^{2m-1}\right]_{K_p} = \left[\langle S_{i_1}S_{i_2}\cdots S_{i_k}\rangle_{K_p}^{2m}\right]_{K_p}. \tag{10}$$

It follows in particular that the spin-glass order parameter

$$q^2(K_p,K_p) \equiv \lim_{|i-j|\to\infty}\left[\langle S_iS_j\rangle_{K_p}^2\right]_{K_p} \tag{11}$$

coincides with the ferromagnetic order parameter $m^2(K_p,K_p)$ along the Nishimori line, reflecting the property that thermal fluctuations and quenched randomness have equal strength on this line.

Comparing Eqs. (2) and (7), we see that for $K = K_p$ the free energy of the model coincides with the *Shannon entropy* of the distribution of vortices, apart from a non-singular additive term:

$$[\beta F(K_p,\tau)]_{K_p} = -\sum_{\eta} P(K_p,\eta)\ln P(K_p,\eta) - N_{\rm B}\ln(2\cosh K_p). \tag{12}$$

Since the free energy is singular at the Nishimori point $(p_{\rm c}, T_{\rm c})$, it follows that the Shannon entropy of frustration (which does not depend on the temperature) is singular at $p = p_{\rm c}$ [13]. This property led Nishimori to suggest that the boundary between the ferromagnetic and paramagnetic phases occurs at $p = p_{\rm c}$ at sufficiently low temperature, and thus that the phase boundary is vertical in the p–T plane below the Nishimori point, as in Fig. 2a. Later, Kitatani [14] arrived at the same conclusion by a different route, showing that the verticality of the phase boundary follows from

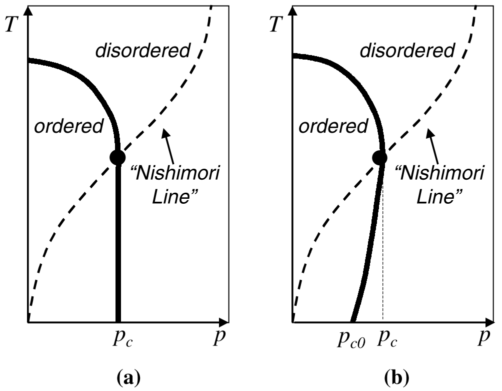

(a) (b)

Fig. 2. The phase diagram of the random-bond Ising model (shown schematically), with the temperature T on the vertical axis and the concentration p of antiferromagnetic bonds on the horizontal axis. The solid line is the boundary between the ferromagnetic (ordered) phase and the paramagnetic (disordered) phase. The dotted line is the Nishimori line $e^{-2\beta J} = p/(1-p)$, which crosses the phase boundary at the Nishimori point (the heavy black dot). It has been conjectured, but not proven, that the phase boundary from the Nishimori point to the p-axis is *vertical*, as in (a). The numerics reported in Section 4 favor the reentrant phase diagram shown in (b). The deviation of the critical bond concentration $p_{\rm c}$ on the Nishimori line from the critical bond concentration $p_{\rm c0}$ on the $T = 0$ axis has been exaggerated in (b) for clarity.

an "appropriate condition." These arguments, while suggestive, do not seem compelling to us. There is no known rigorous justification for Kitatani's condition, and no rigorous reason why the ferro-para boundary must coincide with the singularity in the entropy of frustration, even at low temperature. Hence we regard the issue of the verticality of the phase boundary as still unsettled. Nishimori did argue convincingly that the phase boundary cannot extend to any value of p greater than p_c [10], and Le Doussal and Harris argued that the *tangent* to the phase boundary is vertical at the Nishimori point [15], but these results leave open the possibility of a "reentrant" boundary that slopes back toward the T axis below the Nishimori point, as in Fig. 2b.

The RBIM can also be defined in d dimensions. Much of the above discussion still applies, with minor modifications. Consider, for example, $d = 3$. On the dual lattice, spins reside on lattice cubes and the bonds become plaquettes shared by two neighboring cubes. The set of antiferromagnetic bonds E is dual to a two-dimensional surface, and its boundary ∂E consists of one-dimensional loops—the Ising *strings* where the spins are frustrated. The set of excited bonds E' is dual to another two-dimensional surface that is also bounded by the Ising strings: $\partial E' = \partial E$. The spins are disordered if the two-cycle $D = E + E'$ contains arbitrarily large closed connected surfaces for typical thermal fluctuations and typical samples. Similarly, in d dimensions, frustration is localized on closed surfaces of dimension $d - 2$, and the thermally fluctuating defects are dimension-$(d - 1)$ surfaces that terminate on the locus of frustration. For any d, the model has enhanced symmetry along the Nishimori line $K = K_p$, where antiferromagnetic bonds and excited bonds are drawn from the same probability distribution.

In the absence of quenched disorder, the two-dimensional Ising model is mapped to itself by a duality relation that can be used to infer properties of the critical theory. When quenched disorder is introduced, however, the two-dimensional random bond Ising model is mapped under duality to a model with Boltzmann weights that are not positive definite [17], so that it is not easy to draw any firm conclusions.

2.2. Random-plaquette gauge model

In the d-dimensional RBIM, excitations have codimension 1 and terminate on a closed surface of codimension 2. The Z_2 random-plaquette gauge model (RPGM) is defined in an entirely analogous manner, except that the excitations are codimension-2 objects ("magnetic flux tubes") that terminate on codimension-3 objects ("magnetic monopoles").

More concretely, the variables of the model are $U_l = \pm 1$ residing on each link l of the lattice, and the Hamiltonian is

$$H = -J \sum_{P} \tau_{\mathrm{P}} U_{\mathrm{P}}, \tag{13}$$

where J is the coupling strength,

$$U_{\mathrm{P}} = \prod_{l \in P} U_l \tag{14}$$

is the Z_2-valued "magnetic flux" through the plaquette P, and $\tau_P = \pm 1$ is a quenched random variable. The τ_P's are independently and identically distributed, with the "wrong-sign" choice $\tau_P = -1$ (favoring nontrivial flux) occurring with probability p, and the "right-sign" choice $\tau_P = +1$ (favoring trivial flux) occurring with probability $1 - p$. We refer to p as the concentration of wrong-sign plaquettes, or simply the plaquette concentration.

The free energy F of the model at inverse temperature β, averaged over samples, is

$$[\beta F(K,\tau)]_{K_p} = -\sum_{\tau} P(K_p,\tau) \ln Z(K,\tau), \tag{15}$$

where

$$Z(K,\tau) = \sum_{U} \exp\left(K \sum_{P} \tau_P U_P\right) \tag{16}$$

is the partition function for sample τ (with $K = \beta J$), and

$$P(K_p,\tau) = (2\cosh K_p)^{-N_P} \times \exp\left(K_p \sum_{P} \tau_P\right) \tag{17}$$

is the probability of the sample τ; here

$$\frac{p}{1-p} = e^{-2K_p} \tag{18}$$

and N_P is the number of plaquettes.

The partition function $Z(K,\tau)$ is invariant under the change of variable

$$U_l \to \sigma_l U_l, \quad \tau_P \to \sigma_P \tau_P, \tag{19}$$

where $\sigma_l = \pm 1$ and $\sigma_P = \prod_{l \in P} \sigma_l$. While τ itself has no invariant meaning, τ determines a distribution of frustration that cannot be altered by a change of variable. If an odd number of the plaquettes contained in a specified cube have $\tau = -1$ then that cube is frustrated—a Z_2 *magnetic monopole* resides in the cube. For purposes of visualization, we will sometimes find it convenient to define the gauge model on the dual lattice so that the gauge variables U_l reside on plaquettes, the magnetic flux on bonds, and the magnetic monopoles on sites. Then excited bonds with $\tau_P U_P = -1$ form one-dimensional strings that terminate at monopoles.

We can define an order parameter that distinguishes the Higgs (magnetically ordered) phase and the confinement (magnetically disordered) phase. Consider the Wilson loop operator associated with a closed loop C (on the original lattice, not the dual lattice):

$$W(C) = \prod_{l \in C} U_l \tag{20}$$

and consider the behavior of the expectation value of $W(C)$, averaged over thermal fluctuations and over samples. In the Higgs phase, for a large loop C the Wilson loop operator decays exponentially with the perimeter of the loop,

$$[\langle W(C) \rangle_K]_{K_p} \sim \exp[-\mu \cdot \text{Perimeter}(C)] \tag{21}$$

while in the confinement phase it decays exponentially with the area of the minimal surface bounded by C,

$$[\langle W(C)\rangle_K]_{K_p} \sim \exp[-\kappa\cdot\mathrm{Area}(C)]. \tag{22}$$

The interpretation is that on the dual lattice the wrong-sign plaquettes correspond to a one-chain E bounded by magnetic monopoles, and the excited plaquettes correspond to another one-chain E' with the same boundary; hence $D = E + E'$ is a cycle, a sum of disjoint closed "flux tubes." If arbitrarily large loops of flux appear with appreciable weight in the thermal ensemble for typical samples, then magnetic fluctuations spanning the entire surface bounded by C contribute to the expectation value of $W(C)$, and the area-law decay results. If large flux tubes are suppressed, then only the fluctuations localized near the loop are important, and the perimeter-law decay applies. Thus, the Wilson-loop order parameter probes whether the chain E' of excited plaquettes can wander far from the chain E of wrong-sign plaquettes; that is, whether $D = E + E'$ contains arbitrarily large connected closed loops.

The one-chain E bounded by the magnetic monopoles is analogous to a Z_2-valued *Dirac string*—the change of variable Eq. (19) deforms the strings while leaving invariant the boundary of E (the locations of the monopoles). One should notice that these strings are *not* invisible to our Wilson loop operator; that is $W(C)$ is not invariant under the change of variable. It is possible to modify $W(C)$ to obtain an invariant object [18], but that would not be appropriate if the order parameter is supposed to probe the extent to which the thermally fluctuating defects (the excited plaquettes) depart from the quenched disorder (the Dirac strings).

Like the RBIM, the RPGM has enhanced symmetry on the Nishimori line $K = K_p$, and the change of variable Eq. (19) may be invoked to derive properties of the model on this line. The Nishimori line is preserved by renormalization group flow, and crosses the confinement-Higgs boundary at a multicritical point (p_c, T_c). The internal energy (or average plaquette) can be computed on this line,

$$\left[\tau_P\langle U_P\rangle_{K_p}\right]_{K_p} = 1 - 2p \tag{23}$$

(excited plaquettes have concentration p) and for each positive integer m, the $(2m-1)$'st power of $W(C)$ and the $2m$'th power are equal when averaged over samples,

$$\left[\langle W(C)\rangle_{K_p}^{2m-1}\right]_{K_p} = \left[\langle W(C)\rangle_{K_p}^{2m}\right]_{K_p}. \tag{24}$$

Furthermore, the free energy on the Nishimori line, apart from a nonsingular additive term, is equal to the Shannon entropy of the distribution of magnetic monopoles, so that the latter is singular at $p = p_c$.

In principle, the RPGM could have what might be called a "gauge glass" phase. In this phase, the Wilson loop, averaged over thermal and quenched fluctuations, has area-law behavior,

$$[\langle W(C)\rangle_K]_{K_p} \sim \exp[-\kappa\cdot\mathrm{Area}(C)], \tag{25}$$

but the *square* of its thermal expectation value, averaged over quenched fluctuations, has perimeter-law behavior:

$$\left[\langle W(C)\rangle_K^2\right]_{K_p} \sim \exp\left[-\mu \cdot \text{Perimeter}(C)\right]. \tag{26}$$

This means that thermal fluctuations do not induce magnetic disorder for each typical sample, but that the magnetic fluctuations are large when we compare one sample to another. However, the identity Eq. (24) shows that, along the Nishimori line $K = K_p$, there can be no gauge glass phase. Since $\langle W(C)\rangle$ and $\langle W(C)\rangle^2$ have the same average over samples, both order parameters cross from perimeter to area law at the same point on the Nishimori line. (Nishimori [10] used the analogous argument to show that there is no spin glass behavior in the RBIM along the Nishimori line.)

Another useful identity that can be derived using the change of variable is

$$[\langle W(C)\rangle_K]_{K_p} = [\langle W(C)\rangle_K \langle W(C)\rangle_{K_p}]_{K_p}. \tag{27}$$

Since $-1 \leqslant W(C) \leqslant 1$, it follows that

$$\left|[\langle W(C)\rangle_K]_{K_p}\right| \leqslant \left[\left|\langle W(C)\rangle_{K_p}\right|\right]_{K_p}. \tag{28}$$

From this inequality, we may infer that if the point on the Nishimori line with concentration p is in the confinement phase, then the point (p, T) is in the confinement phase for any temperature T. (Again, the reasoning is exactly analogous to Nishimori's argument for the RBIM [10].) Since there is no gauge-glass behavior on the Nishimori line, if a point on the Nishimori line is in the confinement phase, then $\langle W(C)\rangle_{K_p}$ already exhibits area-law decay before averaging over samples. Therefore the right-hand side of Eq. (28) shows area-law decay and so must the left-hand side. We conclude that, as for the RBIM, the phase boundary of the RPGM below the Nishimori line must either be vertical (parallel to the T axis as in Fig. 2a) or reentrant (tipping back toward the T axis as T decreases as in Fig. 2b).

2.3. Further generalizations

In d dimensions, the magnetic order parameter of the RBIM explores whether a thermally excited chain E' of codimension 1 (domain walls) deviates far from a quenched codimension-1 chain E (antiferromagnetic bonds), where both E and E' have the same codimension-2 boundary (the Ising vortices). Similarly, the RPGM can be defined in d dimensions, and its Wilson-loop order parameter probes whether a thermally excited chain E' of codimension 2 (flux tubes) deviates far from a quenched codimension-2 chain E (Dirac strings), where both E and E' have the same codimension-3 boundary (the magnetic monopoles).

This concept admits further generalizations. In d-dimensions, we may consider the lattice theory of a "rank-r antisymmetric tensor field" with quenched disorder. Then variables reside on the r-cells of the lattice, and the Hamiltonian is expressed in terms of a field strength defined on $(r+1)$-cells. The sign of the coupling is determined by a random variable τ taking values ± 1 on $(r+1)$-cells; cells with the "wrong sign" have concentration p. On the dual lattice, τ corresponds to a codimension-$(r+1)$ chain E, and the excited cells to a codimension-$(r+1)$ chain E', where E and E' are bounded by the same codimension-$(r+2)$ chain of frustration. An operator analogous to the Wilson loop can be defined that detects the flux through the dimension-$(r+1)$ "surface" bounded by a dimension-r "loop" C; this operator serves as the order parameter for an order-disorder transition. The order parameter probes whether the thermally fluctuating codimension-$(r+1)$ chain E' deviates far from the quenched codimension-$(r+1)$ chain E.

For any d and r, the model has enhanced symmetry on the Nishimori line, where $K = K_p$. Properties of the model on this line can be derived, analogous to those discussed above for the RBIM and the RPGM.

3. Accuracy threshold for quantum memory

How the RBIM and RPGM relate to the performance of topological quantum memory was extensively discussed in [9]. Here we will just briefly reprise the main ideas.

3.1. Toric codes

Quantum information can be protected from decoherence and other possible sources of error using quantum error-correcting codes [6,7] and fault-tolerant error recovery protocols [8]. Topological codes (or *surface codes*) are designed so that the quantum processing needed to control errors has especially nice locality properties [4,5].

Specifically, consider a system of $2L^2$ qubits (a qubit is a two-level quantum system), with each qubit residing at a link of an $L \times L$ square lattice drawn on a two-dimensional *torus*. (Other examples of surface codes, including codes defined on planar surfaces, are discussed in [9].) This system can encode two qubits of quantum information that are well protected from noise if the error rate is low enough. The two-qubit code space, where the protected information resides, can be characterized as a simultaneous eigenspace with eigenvalue one of a set of check operators (or "stabilizer generators"); check operators are associated with each site and with each elementary cell (or "plaquette") of the lattice, as shown in Fig. 3. We use the notation

$$I = \begin{pmatrix} 1 & 0 \\ 0 & 1 \end{pmatrix}, \quad X = \begin{pmatrix} 0 & 1 \\ 1 & 0 \end{pmatrix}, \tag{29}$$

$$Y = \begin{pmatrix} 0 & -i \\ i & 0 \end{pmatrix}, \quad Z = \begin{pmatrix} 1 & 0 \\ 0 & -1 \end{pmatrix} \tag{30}$$

for the 2×2 identity and Pauli matrices. The check operator at site i acts nontrivially on the four links that meet at the site; it is the tensor product

$$X_i = \otimes_{l \ni s} X_l \tag{31}$$

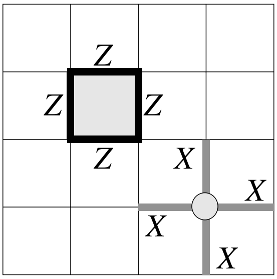

Fig. 3. The check operators of the toric code. Each plaquette operator is a tensor product of Z's acting on the four links contained in the plaquette. Each site operator is a tensor product of X's acting on the four links that meet at the site.

acting on those four qubits, times the identity acting on the remaining qubits. The check operator at plaquette P acts nontrivially on the four links contained in the plaquette, as the tensor product

$$Z_{\mathrm{P}} = \otimes_{l \in P} Z_l, \tag{32}$$

times the identity on the remaining links.

The check operators can be simultaneously diagonalized, and the toric code is the space in which each check operator acts trivially. Because of the periodic boundary conditions on the torus, the product of all L^2 site operators or all L^2 plaquette operators is the identity—each link operator occurs twice in the product, and $X^2 = Z^2 = I$. There are no further relations among these operators; therefore, there are $2 \cdot (L^2 - 1)$ independent check operators constraining the $2L^2$ qubits in the code block, and hence two encoded qubits (the code subspace is four dimensional).

Since the check operators are spatially local, it is useful to think of a site or plaquette where the check operator has the eigenvalue -1 as the position of a localized excitation or "defect." The code space contains states with no defects, which are analogous to vacuum states of a Z_2 gauge theory on the torus: $Z_{\mathrm{P}} = 1$ means that there is no Z_2 magnetic flux at plaquette P, and $X_i = 1$ means that there is no Z_2 electric charge at site i. (This Z_2 gauge theory on the two-torus should not be confused with the three-dimensional Z_2 gauge theory, described in Section 3.3, that arises in the analysis of the efficacy of error correction!)

Consider applying to the vacuum state an operator that is a tensor product of Pauli matrices $\{Z_l\}$ acting on each of a set of links forming a connected chain $\{l\}$. This operator creates isolated site defects at the ends of the chain. Similarly, if we apply to the vacuum a tensor product of Pauli matrices $\{X_l\}$ acting on a connected chain of the dual lattice, isolated plaquette defects are created at the ends of the chain, as in Fig. 4. A general "Pauli operator" (tensor product of Pauli matrices) can be expressed as tensor product of X_l's and I_l's times a tensor products of Z_l's and I_l's; this operator preserves the code space if and only if the links acted upon by Z's comprise a *cycle* of the lattice (a chain with no boundary) and the links acted upon by X's comprise a cycle of the dual lattice.

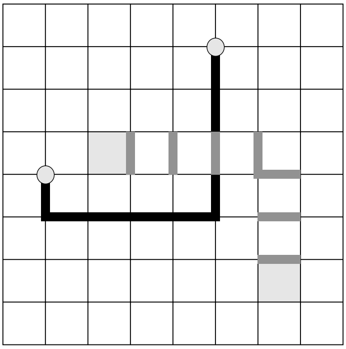

Fig. 4. Site defects and plaquette defects in the toric code. Applied to the code space, Z's acting on a connected chain of links (darkly shaded) create site defects (electric charges) at the ends of the chain. Similarly, X's applied to a connected chain of dual links (lightly shaded) create plaquette defects (magnetic fluxes) at the ends of the chain.

Cycles on the torus are of two types. A *homologically trivial* cycle is the boundary of a region that can be tiled by plaquettes. A product of Z's acting on the links of the cycle can be expressed as a product of the enclosed plaquette operators, which acts trivially on the code space. A *homologically nontrivial* cycle wraps around the torus and is not the boundary of anything. A product of Z's acting on the links of the cycle preserves the code space, but acts nontrivially on the encoded quantum information. Associated with the two fundamental nontrivial cycles of the torus are encoded operations $\bar{Z}_1$ and $\bar{Z}_2$ acting on the two encoded qubits. Similarly, associated with the two dual cycles of the dual lattice are the corresponding encoded operations $\bar{X}_1$ and $\bar{X}_2$, as shown in Fig. 5.

A general error acting on the code block can be expanded in terms of Pauli operators. Therefore, we can characterize the efficacy of error correction by considering how well we can protect the encoded state against Pauli operator errors. With the toric code, X errors (bit flips) and Z errors (phase flips) can be corrected indepen-

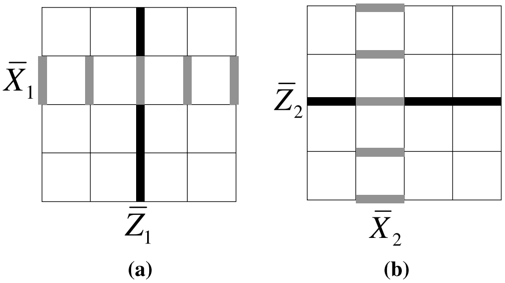

Fig. 5. Basis for the operators that act on the two encoded qubits of the toric code. (a) The encoded $\bar{Z}_1$ is a tensor product of Z's acting on lattice links comprising a cycle of the torus, and the encoded $\bar{X}_1$ is a tensor product of X's acting on dual links comprising the complementary cycle. (b) $\bar{Z}_2$ and $\bar{X}_2$ are defined similarly.

dently; this suffices to protect against general Pauli errors, since a Y error is just a bit flip and a phase flip acting on the same qubit. We may therefore confine our attention to Z errors; the X errors may be dealt with in essentially the same way, but with the lattice replaced by its dual.

3.2. Perfect measurements and the random-bond Ising model

To be concrete, suppose that the Z errors are independently and identically distributed, occurring with probability p on each qubit. Noise produces an *error chain* E, a set of qubits acted upon by Z. To diagnose the errors, the code's local check operators are measured at each lattice site, the measurement outcomes providing a "syndrome" that we may use to diagnose errors. However, the syndrome is highly ambiguous. It does not completely characterize where the errors occurred; rather it only indicates whether the number of damaged qubits adjacent to each site is even or odd. That is, the measurement determines the *boundary* ∂E of the error chain E.

To recover from the damage, we choose a *recovery chain* E' that has the same boundary as the measured boundary of E, and apply Z to all the qubits of E'. Since $\partial E = \partial E'$, the chain $D = E + E'$ is a cycle with $\partial D = 0$. Now, if D is homologically trivial, then the recovery successfully protects the two encoded qubits—the effect of the errors together with the recovery step is just to apply a product of check operators, which has trivial action on the code space. But if D is homologically nontrivial, then recovery fails—the encoded quantum information suffers an error.

Error recovery succeeds, then, if we can guess the homology class of the randomly generated chain E, knowing only its boundary ∂E—we succeed if our guess $E' = E + D$ differs from E by a homologically trivial cycle D. If the error rate p is below a certain critical value p_c called the *accuracy threshold*, it is possible to guess correctly, with a probability of failure that approaches zero for a sufficiently large linear size L of the lattice. But if p is above p_c, the failure probability approaches a nonzero constant as $L \to \infty$. The numerical value of p_c is of considerable interest, since it characterizes how reliably quantum hardware must perform for a quantum memory to be robust.

Let $\mathrm{prob}(E)$ denote the probability that the error chain is E, and let $\mathrm{prob}[(E+D)|E]$ denote the normalized conditional probability for error chains $E' = E + D$ that have the same boundary as E. Then, the probability of error per qubit lies below threshold if and only if, in the limit $L \to \infty$,

$$\sum_E \mathrm{prob}(E) \cdot \sum_{D\ \mathrm{nontrivial}} \mathrm{prob}[(E+D)|E] = 0. \tag{33}$$

Eq. (33) says that error chains that differ from the actual error chain by a homologically nontrivial cycle have probability zero. Therefore, the outcome of the measurement of the check operators is sure to point to the correct homology class, in the limit of an arbitrarily large code block.

This criterion is identical to the criterion for long-range order in the two-dimensional RBIM, along the Nishimori line. The error chain E can be identified with the chain of antiferromagnetic bonds of a sample, bounded by Ising vortices that are pinned down by the measurement of the local check operators. The ensemble of all the chains $\{E'\}$ with a specified boundary can be interpreted as a thermal ensemble. If the temperature T and the error rate p obey Nishimori's relation, then the chain E' and the chain E have the same bond concentration. At low temperature along the Nishimori line, the cycle $D = E + E'$ contains no large connected loops for typical samples and typical thermal fluctuations—the spin system is magnetically ordered and error recovery succeeds with high probability. But at higher temperature, the quenched chain E and the thermal chain E' fluctuate more vigorously. At the Nishimori point, D contains loops that "condense," disordering the spins and compromising the effectiveness of error correction. Thus, the critical concentration p_c at the Nishimori point of the two-dimensional RBIM coincides with the accuracy threshold for quantum memory using toric codes (where p_c is the largest acceptable probability for either an X error or a Z error).

The optimal recovery procedure is to choose a recovery chain E' that belongs to the most likely homology class, given the known boundary of the chain $\partial E' = \partial E$. For $p < p_c$, the probability distribution has support on a single class in the limit $L \to \infty$, and the optimal recovery procedure is sure to succeed. In the language of the RBIM, for a given sample with antiferromagnetic chain E, a chain E' of excited bonds can be classified according to the homology class to which the cycle $D = E + E'$ belongs, and a free energy can be defined for each homology class. For $p < p_c$ along the Nishimori line, the trivial homology class has lowest free energy, and the free energy cost of choosing a different class diverges as $L \to \infty$.

An alternative recovery procedure is to choose the single most likely recovery chain E', rather than a chain that belongs to the most likely *class*. In the language of the RBIM, this most likely recovery chain E' for a given sample is the set of excited links that minimizes energy rather than free energy. This energy minimization procedure is sure to succeed if the error rate is $p < p_{c0}$, where p_{c0} is the critical bond concentration of the RBIM at $T = 0$. Since minimizing energy rather than free energy need not be optimal, we see that $p_{c0} \leqslant p_c$. However, the energy minimization procedure has advantages: it can be carried out efficiently using the Edmonds perfect matching algorithm [19,20], and without any prior knowledge of the value of p.

3.3. Imperfect measurement and the random-plaquette gauge model

But the RBIM applies only to an unrealistic situation in which the outcomes of measurements of check operators are known with perfect accuracy. Since these are four-qubit measurements, they must be carried out with a quantum computer and are themselves degraded by noise. To obtain reliable information about the positions of the Ising vortices, we must repeat the measurements many times, assembling a measurement history from which we can infer the world lines of the vortices in three-dimensional spacetime.

To visualize the world lines in three dimensions, consider a three-dimensional simple cubic lattice on $T^2 \times R$, where T^2 is the two-torus and R is the real line. The error operation acts at each integer-valued time t, and check operators are measured between each t and $t+1$. Qubits in the code block are associated with timelike plaquettes, those lying in the tx and ty planes. A qubit error that occurs at time t is associated with a horizontal (spacelike) bond that lies in the time slice labeled by t. An error in the measurement of a check operator at site j between time t and time $t+1$ is associated with the vertical (timelike) bond connecting site j at time t and site j at time $t+1$. Qubit errors on horizontal bonds occur with probability p, and measurement errors on vertical links occur with probability q. The set of all errors, both horizontal and vertical, defines a one-chain E, shown darkly shaded in Fig. 6. The set of all syndrome measurements with nontrivial outcomes (those where the observed value of the check operator is -1 rather than $+1$) defines a (vertical) one-chain S, shown lightly shaded in Fig. 6. The chains E and S share the same boundary; therefore the (possibly faulty) measurements of the check operators reveal the boundary of the error chain E.

Error recovery succeeds if we can guess the homology class of the error chain E, given knowledge of its boundary ∂E; that is, we succeed if our guess $E' = E + D$ differs from E by a cycle D that is homologically trivial on $T^2 \times R$. Thus, the accuracy threshold can be mapped to the confinement-Higgs transition of the RPGM. The error one-chain E on the dual lattice becomes the set of wrong-sign plaquettes on the lattice; its boundary points are magnetic monopoles, whose locations are determined by the measurements of local check operators. Since q need not equal p, the gauge model can be anisotropic—on the original lattice, the concentration of spacelike

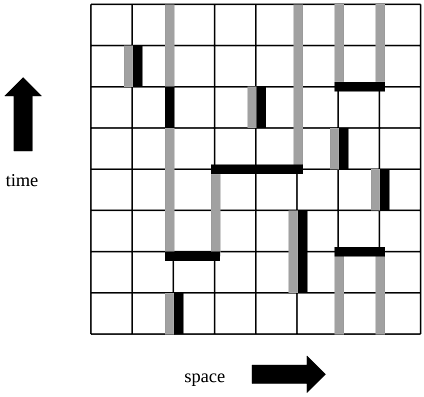

Fig. 6. An error history shown together with the syndrome history that it generates, for the toric code. For clarity, the three-dimensional history of the two-dimensional code block has been compressed to two dimensions. Qubits reside on plaquettes, and four-qubit check operators are measured at each vertical link. Links where errors have occurred are darkly shaded, and links where the syndrome is nontrivial are lightly shaded. Errors on horizontal links indicate where a qubit flipped between successive syndrome measurements, and errors on vertical links indicate where the syndrome measurement was wrong. Vertical links that are shaded both lightly and darkly are locations where a nontrivial syndrome was found erroneously. The chain S of lightly shaded links (the syndrome) and the chain E of darkly shaded links (the errors) both have the same boundary.

wrong-sign plaquettes is q (spacelike plaquettes are dual to timelike bonds) and the concentration of timelike wrong-sign plaquettes is p (timelike plaquettes are dual to spacelike bonds). The ensemble of error chains $\{E'\}$ that have the same boundary as E becomes the thermal ensemble determined by an anisotropic Hamiltonian, with the coupling K_{space} on spacelike plaquettes obeying the Nishimori relation $K_{\text{space}} = K_q$ and the coupling K_{time} on timelike plaquettes the relation $K_{\text{time}} = K_p$.

For small p and q, the cycle $D = E + E'$ contains no large connected loops for typical samples and typical thermal fluctuations—the gauge system is magnetically ordered and error recovery succeeds with high probability. But there is a critical curve in the (p, q) plane where the magnetic flux tubes "condense," magnetically disordering the system and compromising the effectiveness of error correction. For the sort of error model described in [9], the qubit error rate and the measurement error rate are comparable, so the isotropic model with $p = q$ provides useful guidance. For that case, the critical concentration p_c at the Nishimori point of the three-dimensional RPGM coincides with the accuracy threshold for quantum memory using toric codes (where p_c is the largest acceptable probability for an X error, a Z error, or a measurement error). In the extreme anisotropic limit $q \to 0$, flux on spacelike plaquettes is highly suppressed, and the timelike plaquettes on each time slice decouple, with each slice described by the RBIM.

For both the 2D RBIM and the 3D (isotropic) RPGM, we may infer (as Nishimori argued for the RBIM [10]) that the phase boundary lies in the region $p \leqslant p_c$, i.e., does not extend to the right of the Nishimori point. From the perspective of the error recovery procedure, this property reflects that the best hypothesis about the error chain, when its boundary is known, is obtained by sampling the distribution $\text{prob}[(E + D)|E]$. Thus, for each value of p, the fluctuations of D are best controlled (the spins or gauge variables are least disordered) by choosing the temperature on the Nishimori line. For $p > p_c$ the magnetization of the 2D RBIM vanishes on the Nishimori line, and so must vanish for all T. A similar remark applies to the Wilson-loop order parameter of the 3D RPGM.

In particular, the critical value of p on the $T = 0$ axis (denoted p_{c0}) provides a lower bound on p_c. Rigorous arguments in [9] established that $p_{c0} \geqslant .0373$ in the 2D RBIM and $p_{c0} \geqslant .0114$ in the 3D RPGM. (A similar lower bound for the 2D RBIM was derived by Horiguchi and Morita many years ago [21].) We have estimated the value of p_{c0} using numerical simulations that we will now describe.

4. Numerics

4.1. Method

For the RBIM in two dimensions (but not in higher dimensions), and for the RPGM in three dimensions (but not in higher dimensions), it is numerically tractable to study the phase transition on the $T = 0$ axis. Specifically, for the RBIM, we proceed as follows: Consider an $L \times L$ lattice on the torus, and generate a sample by choosing a random τ_{ij} at each bond (where $\tau_{ij} = -1$ occurs with probability p).

Consider, for this sample, the one-chain E on the dual lattice containing bonds with $\tau_{ij} = -1$, and compute its boundary ∂E to locate the Ising vortices.

Then, to find the ground state of the Hamiltonian for this sample, construct the one-chain E' of the dual lattice, bounded by the Ising vortices, with the minimal number of bonds. This minimization can be carried out in a time polynomial in L using the Edmonds perfect matching algorithm [19,20]. (If the ground state is not unique, choose a ground state at random.) Now examine the one-cycle $D = E + E'$ on the torus and compute whether its homology class is trivial. If so, we declare the sample a "success"; otherwise the sample is a "failure." Repeat for many randomly generated samples, to estimate the probability of failure $P_{\text{fail}}(p)$.

We expect $P_{\text{fail}}(p)$ to be discontinuous at $p = p_{c0}$ in the infinite volume limit. For $p < p_{c0}$, large loops in D are heavily suppressed, so that P_{fail} falls exponentially to zero for L sufficiently large compared to the correlation length ξ. But for $p > p_{c0}$, arbitrarily large loops are not suppressed, so we anticipate that the homology class is random. Since there are four possible classes, we expect P_{fail} to approach 3/4 as $L \to \infty$.

This expectation suggests a finite-size scaling ansatz for the failure probability. Let the critical exponent ν_0 characterize the divergence of the correlation length ξ at the critical point $p = p_{c0}$:

$$\xi \sim |p - p_{c0}|^{-\nu_0}. \tag{34}$$

For a sufficiently large linear size L of the sample, the failure probability should be controlled by the ratio L/ξ; that is, it is a function of the scaling variable

$$x = (p - p_{c0})L^{1/\nu_0}. \tag{35}$$

Thus the appropriate ansatz is

$$P_{\text{fail}} \sim \frac{3}{4} f(x), \tag{36}$$

where the function f has the properties

$$\lim_{x\to-\infty} f(x) = 0, \quad \lim_{x\to\infty} f(x) = 1. \tag{37}$$

Though the scaling ansatz should apply asymptotically in the limit of large L, there are systematic corrections for finite L that are not easily estimated.

According to Eq. (36), the failure probability at $p = p_{c0}$ has a universal value $(3/4)f(0)$ that does not depend on L. Thus, by plotting P_{fail} vs. p for various values of L, we can estimate p_{c0} by identifying the value of p where all the curves cross. To find ν_0, we observe that

$$\log\left(\left.\frac{\partial P_{\text{fail}}}{\partial p}\right|_{p=p_{c0}}\right) = \frac{1}{\nu_0}\log L + \text{constant}. \tag{38}$$

Hence, if we estimate the slope of P_{fail} at $p = p_{c0}$, we can extract ν_0 from a linear fit to a plot of log(slope) vs. $\log L$.

The three-dimensional RPGM can be analyzed by the same method. A sample is generated by randomly choosing τ_P on each plaquette of an L^3 cubic lattice on the

3-torus. The wrong-sign plaquettes define a one-chain E on the dual lattice, whose boundary defines the locations of the magnetic monopoles. The ground state of the sample is constructed by finding the one-chain E' with the same boundary that has the minimal length, and the one-cycle $D = E + E'$ is examined to determine if it is homologically trivial. Since there are eight homology classes on the 3-torus, the scaling ansatz becomes

$$P_{\text{fail}} \sim \frac{7}{8}\tilde{f}(x), \tag{39}$$

and p_{c0} and ν_0 are estimated as described above.

For the RBIM in three dimensions, or the RPGM in four dimensions, E and E' become two-chains. To construct the ground state, then, we must find the minimal two-dimensional surface that has a specified boundary. Unfortunately, this problem is known to be NP-hard [22] and so appears to be computationally intractable.

Detailed numerical studies of the two-dimensional RBIM in the vicinity of the Nishimori point have been done earlier by other authors [11,12], using methods that are not very effective at low temperature. The $T = 0$ phase transition has been studied using methods related to ours [20,23], but with less numerical accuracy. As far as we know, numerical studies of the RPGM have not been previously attempted.

4.2. Random-bond Ising model

We measured P_{fail} by generating 10^6 samples for each value of L from 2 to 36, and for each value of p increasing in increments of .001 from .100 to .107; in addition we generated 10^6 samples at $L = 37, 38, 40, 42$ for $p = .102, .103, .104$. Values of P_{fail} for even L lie slightly but systematically above the values for odd L at the same p; therefore we analyzed the data for even and odd L separately. Data for $L = 16, 20, 24, 28, 32, 36$ are shown in Fig. 7, and data for $L = 15, 19, 23, 27, 31, 35$ are shown in Fig. 8. Crudely, the point of concordance of the data sets provides an estimate of p_{c0}, while the trend of the data with L determines the exponent ν_0.

We did a global fit of the data to the form

$$P_{\text{fail}} = A + Bx + Cx^2, \tag{40}$$

where $x = (p - p_{c0})L^{1/\nu_0}$, adopting a quadratic approximation to the scaling function $f(x)$ in the vicinity of $x = 0$. (In the range of x we considered, the quadratic term is small but not quite negligible.) For even L ranging from 22 to 42, our fit found

$$\begin{aligned} p_{c0} &= .10330 \pm .00002, \\ \nu_0 &= 1.49 \pm .02, \end{aligned} \tag{41}$$

where the quoted errors are one-sigma statistical errors. For odd L ranging from 21 to 37, our fit found

$$\begin{aligned} p_{c0} &= .10261 \pm .00003, \\ \nu_0 &= 1.46 \pm .02. \end{aligned} \tag{42}$$

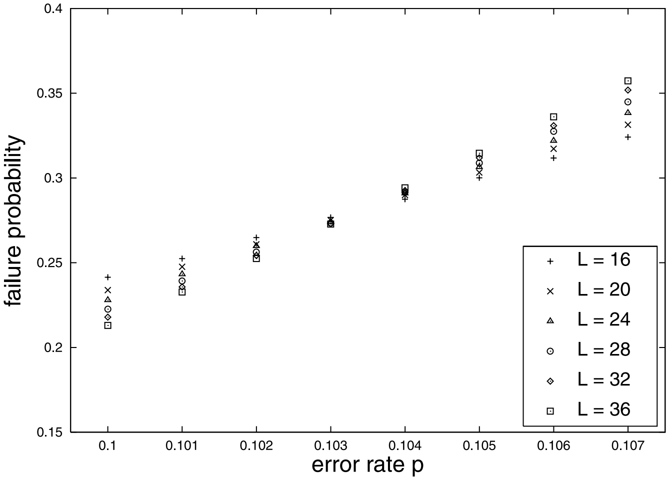

Fig. 7. The failure probability P_{fail} as a function of the error probability p for linear size $L = 16, 20, 24, 28, 32, 36$, in the two-dimensional random-bond Ising model. Each data point was generated by averaging 10^6 samples.

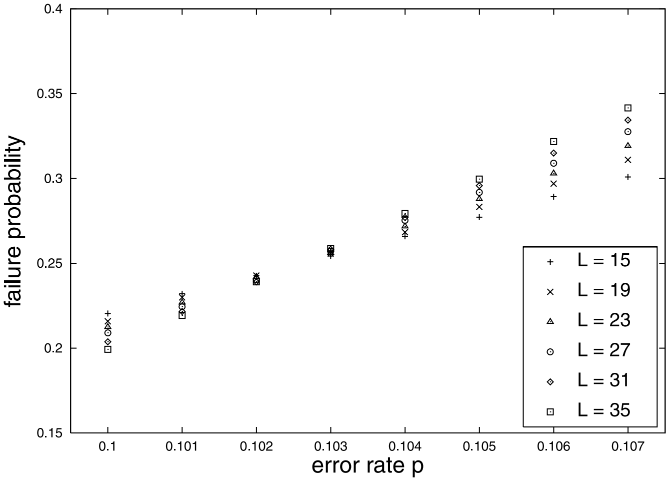

Fig. 8. The failure probability P_{fail} as a function of the error probability p for linear size $L = 15, 19, 23, 27, 31, 35$, in the two-dimensional random-bond Ising model. Each data point was generated by averaging 10^6 samples.

The discrepancy between the values of p_{c0} for even and odd L indicates a nonnegligible finite-size effect.

On closer examination, we see evidence for small but detectable violations of our scaling ansatz in both the even and odd data sets. These violations are very well accounted for by the modified ansatz

$$P_{\text{fail}} = A + Bx + Cx^2 + \begin{cases} D_{\text{even}} \cdot L^{-1/\mu_{\text{even}}} & (L \text{ even}), \\ D_{\text{odd}} \cdot L^{-1/\mu_{\text{odd}}} & (L \text{ odd}), \end{cases} \tag{43}$$

which includes a nonuniversal additive correction to P_{fail} at criticality, different for even and odd sizes. Fitting the modified ansatz to the data for even L ranging from 2 to 42, we find

$$\begin{aligned} p_{c0} &= .10309 \pm .00003, \\ \nu_0 &= 1.461 \pm .008, \\ D_{\text{even}} &= 0.165 \pm .002, \\ \mu_{\text{even}} &= 0.71 \pm .01. \end{aligned} \tag{44}$$

Fitting to the data for odd L ranging from 3 to 37, we find

$$\begin{aligned} p_{c0} &= .10306 \pm .00008, \\ \nu_0 &= 1.463 \pm .006, \\ D_{\text{odd}} &= -.053 \pm .003, \\ \mu_{\text{odd}} &= 2.1 \pm .3. \end{aligned} \tag{45}$$

In Fig. (9) we show the data for all values of L and p; using the values of p_{c0}, ν_0, D, and μ found in our fits, we have plotted P_{fail}, with the nonuniversal correction of Eq. (43) subtracted away, as a function of the scaling variable $x = (p - p_{c0})L^{1/\nu_0}$. All of the data lie on a single line, indicating that residual scaling violations are quite small. Furthermore, the agreement between the values of p_{c0} and ν_0 extracted from the even and odd data sets, which were fit independently, indicates that our extrapolation to large L

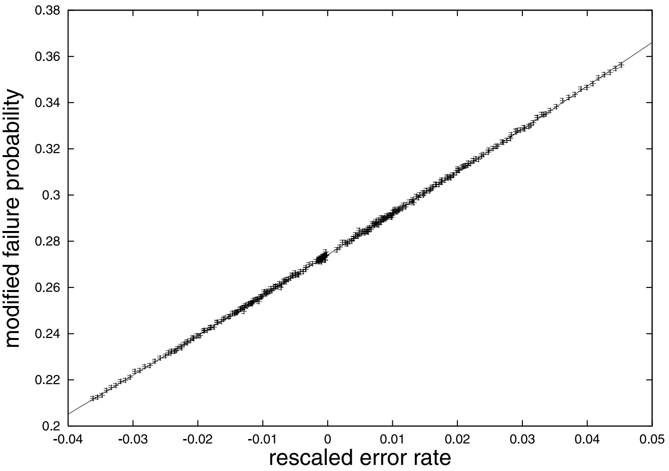

Fig. 9. The failure probability P_{fail}, with the nonuniversal correction of Eq. (43) subtracted away, as a function of the scaling variable $x = (p - p_{c0})L^{1/\nu_0}$ for the two-dimensional random-bond Ising model, where p_{c0} and ν_0 are determined by the best fit to the data. A two-sigma error bar is shown for each point. The data for values of L from 2 to 42 lie on a single line, indicating that the (small) scaling violations are well accounted for by our ansatz.

is reasonable, and that the statistical errors in Eqs. (44) and (45) do not seriously underestimate the actual errors in our measurement. A plausible conclusion is that

$$\begin{aligned} p_{c0} &= .1031 \pm .0001, \\ \nu_0 &= 1.46 \pm .01. \end{aligned} \tag{46}$$

An earlier measurement reported by Kawashima and Rieger found [23]

$$\begin{aligned} p_{c0} &= .104 \pm .001, \\ \nu_0 &= 1.30 \pm .02; \end{aligned} \tag{47}$$

their value of p_{c0}, but not of ν_0, is compatible with ours. An important reason why our value of p_{c0} has a smaller statistical error than theirs is that they computed a different observable (the domain wall energy) for which the finite-size scaling analysis is more delicate than for the failure probability (another critical scaling exponent is involved).

In a recent study of the Nishimori point, Merz and Chalker found [12]

$$\begin{aligned} p_c &= .1093 \pm .0002, \\ \nu &= 1.50 \pm .03. \end{aligned} \tag{48}$$

There is a clear discrepancy between the values of p_c and p_{c0}, in disagreement with the conjecture of Nishimori [13] and Kitatani [14]. Evidence for a reentrant phase diagram has also been found by Nobre [24], who reported

$$p_{c0} = .1049 \pm .0003. \tag{49}$$

In principle, the phase transitions at $T = 0$ and at the Nishimori point could be in different universality classes, so that the critical exponents ν_0 and ν could have different values. However, our measurement of ν_0 at $T = 0$ is consistent with the value of ν at the Nishimori point reported by Merz and Chalker [12].

4.3. Random-plaquette gauge model

We measured P_{fail} by generating 10^6 samples for each value of L from 9 to 14, and for each value of p increasing in increments of .0004 from .02805 to .03005; in addition we generated 10^6 samples at $L = 15, 16$ for $p = .02845, .02925, .03005$. Values of P_{fail} for even L lie slightly but systematically above the values for odd L at the same p; therefore we analyzed the data for even and odd L separately. Data for even L are shown in Fig. 10. Crudely, the point of concordance of the data sets provides an estimate of p_{c0}, while the trend of the data with L determines the exponent ν_0.

We did a global fit of the data to the form

$$P_{\text{fail}} = A + Bx + Cx^2, \tag{50}$$

where $x = (p - p_{c0})L^{1/\nu_0}$, adopting a quadratic approximation to the scaling function $f(x)$ in the vicinity of $x = 0$. For L ranging from 9 to 16, our fit found

$$\begin{aligned} p_{c0} &= .02937 \pm .00002, \quad \nu_0 = 0.974 \pm .026 \ (L \text{ even}), \\ p_{c0} &= .02900 \pm .00001, \quad \nu_0 = 1.025 \pm .016 \ (L \text{ odd}), \end{aligned} \tag{51}$$

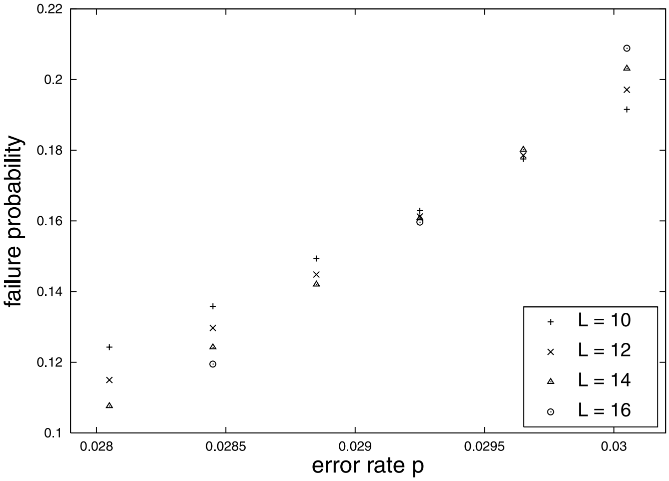

Fig. 10. The failure probability P_{fail} as a function of the error probability p for linear size $L = 10, 12, 14, 16$, in the three-dimensional random-plaquette gauge model. Each data point was generated by averaging 10^6 samples.

where the quoted errors are one-sigma statistical errors. The results for even and odd L are incompatible, indicating a nonnegligible finite-size effect.

We believe that our analysis for even L is likely to be more reliable; finite size effects are enhanced for odd L, the case in which the failure probability is smaller. All of the even L data are shown in Fig. 11, with P_{fail} plotted as a function of

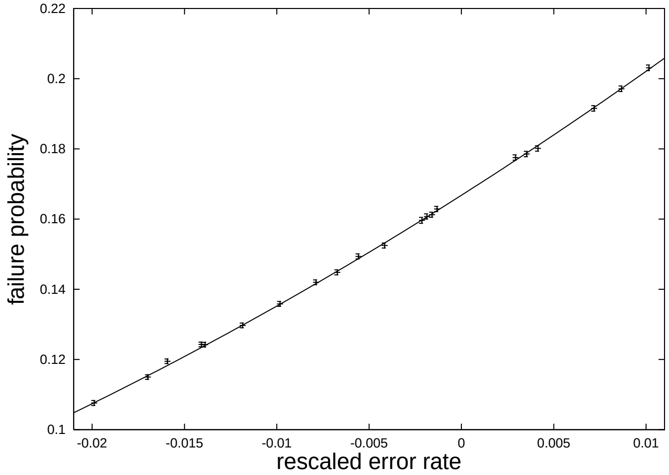

Fig. 11. The failure probability P_{fail} as a function of the scaling variable $x = (p - p_{c0})L^{1/\nu_0}$ for the random-plaquette gauge model, where p_{c0} and ν_0 are determined by the best fit to the data. A two-sigma error bar is shown for each point. The data for all even values of L from 10 to 16 lie on a single curve, indicating that scaling violations are small.

$x = (p - p_{c0})L^{1/\nu_0}$, where p_{c0} and ν_0 are determined by our fit. The data fit a single curve, indicating that scaling violations are small. (Scaling violations are more discernable in the odd L data set.) A reasonable conclusion is that

$$\begin{aligned} p_{c0} &= .0293 \pm .0002, \\ \nu_0 &= 1.00 \pm .05. \end{aligned} \tag{52}$$

4.4. The failure probability at finite temperature

Our numerical studies of the RBIM and the RPGM were restricted to the $T = 0$ axis. We calculated the failure probability to estimate the critical disorder strength p_{c0} and the critical exponent ν_0. Here we will describe how the calculation of the failure probability could be extended to nonzero temperature.

To calculate the failure probability in the zero-temperature RBIM, we generate a sample by specifying a one-chain E of antiferromagnetic links, and then we construct the one-chain E' of minimal energy with the same boundary as E. Failure occurs if the cycle $D = E + E'$ is homologically nontrivial.

At nonzero temperature we should construct E' to belong to the homology class that minimizes free energy rather than energy. For a given sample with antiferromagnetic one-chain E, the free energy $F(E, h)$ of homology class h is found by summing over domain wall one-chains $\{E'\}$ such that $E + E' \in h$:

$$\exp[-\beta F(E,h)] = Z(E,h) = \sum_{E':E+E'\in h} \mathrm{e}^{-\beta H_E}, \tag{53}$$

where H_E denotes the Hamiltonian Eq. (1) with antiferromagnetic chain E. If the trivial homology class $h = e$ has the lowest free energy, then the sample is a "success"; otherwise it is a "failure." We can estimate the failure probability $P_{\mathrm{fail}}(p, T)$ by randomly generating many samples, and determining for each whether it is a success or a failure.

For the random bond Ising model on a torus, the sum Eq. (3) includes only the chains E' such that $E + E'$ is in the trivial homology class. To sum over the class h, we can augment E by adding to it a representative of h. For each h, we can compute

$$\frac{Z(E,h)}{Z(E,e)} = \exp[-\beta(F(E,h) - F(E,e))]; \tag{54}$$

the sample E is a success if this ratio of partition functions is less than one for each $h \neq e$.

The ratio is the thermal expectation value $\langle \mathcal{O}_h \rangle_K$ of an observable $\mathcal{O}_h$ that "inserts a domain wall" wrapping around a cycle C representing h. That is, the effect of $\mathcal{O}_h$ is to flip the sign of the bond variable τ_{ij} for each bond $\langle ij \rangle$ in C:

$$\mathcal{O}_h = \exp\left[-2K \sum_{\langle ij \rangle \in C} \tau_{ij} S_i S_j \right]. \tag{55}$$

In principle, we could measure $\langle \mathcal{O}_h \rangle_K$ by the Monte-Carlo method, generating typical configurations in the thermal ensemble of H_E, and evaluating $\mathcal{O}_h$ in these configurations. Unfortunately, this method might not produce an accurate measurement, because the configurations that dominate $\langle \mathcal{O}_h \rangle_K$ may be exponentially rare in the thermal ensemble—a configuration with excited bonds on C can have an exponentially large value of $\mathcal{O}_h$ that overcomes exponential Boltzmann suppression.

One solution to this problem is to express $Z(E,h)/Z(E,e)$ as a product of quantities, each of which *can* be evaluated accurately by Monte Carlo. Let $\{e = P_0, P_1, P_2, \ldots, P_{k-1}, P_k = C\}$ be a sequence of open chains interpolating between the empty chain and the cycle C, where $P_{j+1} - P_j$ contains just a single bond. We may write

$$\frac{Z(E,h)}{Z(E,e)} = \frac{Z(E,P_1)}{Z(E,P_0)} \cdot \frac{Z(E,P_2)}{Z(E,P_1)} \cdots \frac{Z(E,P_k)}{Z(E,P_{k-1})}. \tag{56}$$

Each ratio $Z(E,P_{j+1})/Z(E,P_j)$ is the expectation value of an operator that acts on a single bond, evaluated in the thermal ensemble of the Hamiltonian with antiferromagnetic bonds on the chain $E + P_j$; this expectation value can be evaluated by Monte-Carlo with reasonable computational resources. (For an application of this trick in a related setting, see [25].)

Using this method, we can determine whether $Z(E,h)/Z(E,e)$ exceeds one for any $h \neq e$ and hence whether the sample E is a success or a failure. Generating many samples, we can estimate $P_{\mathrm{fail}}(p,T)$. In principle, then we can calculate the failure probability for the optimal recovery scheme, in which p and T obey Nishimori's relation. By a similar method, we can calculate the failure probability for the RPGM. However, we have not attempted this calculation.

5. Conclusions

The three-dimensional random-plaquette gauge model, and the analogous antisymmetric tensor models in higher dimensions, provide new examples of multicritical points with strong disorder. These models have phase diagrams that qualitatively resemble the phase diagram of the two-dimensional random-bond Ising model.

Our results indicate that the boundary between the ferromagnetic and paramagnetic phases of the RBIM is reentrant rather than vertical below the Nishimori line. If the disorder strength p satisfies $p_{c0} < p < p_c$, then the ground state of the spin system does not have long-range order. As the temperature T increases with p fixed, long-range order is first restored, and then lost again as the temperature increases further. At $T = 0$ the spins are frozen in a disordered state driven by quenched randomness. But apparently this ground state is entropically unfavorable—at low but nonzero temperature typical states in the thermal ensemble have long-range ferromagnetic order.

This behavior seems less remarkable when considered from the viewpoint of our error recovery protocol. For given p and a specified error syndrome, the recovery method with optimal success probability proceeds by inferring the most likely homology class of errors consistent with the syndrome. There is no a priori reason for the most likely single error pattern (the ground state) to belong to the most likely error homology class (the class with minimal free energy) even in the limit of a large sample. Our numerical results indicate that for error probability p such that $p_{c0} < p < p_c$, the probability that the ground state does not lie in the most likely homology class remains bounded away from zero as $L \to \infty$.

In our numerical studies of the RBIM and RPGM at zero temperature, we have computed a homological observable, the failure probability. This observable has advantages over, say, the domain wall energy, because it obeys a particularly simple finite-size-scaling ansatz. Therefore, we have been able to determine the critical disorder strength p_{c0} and the critical exponent ν_0 to good accuracy with relatively modest computational resources.

Not surprisingly, our numerical values for p_{c0} are notably larger than rigorous lower bounds derived using crude combinatoric arguments in [9]: $p_{c0} \approx .1031$ compared with the bound $p_{c0} \geqslant .0373$ in the RBIM, and $p_{c0} \approx .0293$ compared with $p_{c0} \geqslant .0114$ in the RPGM.

The zero-temperature critical disorder strength p_{c0} is a lower bound on the value of the critical disorder strength p_c along the Nishimori line, and of special interest because of its connection with the accuracy threshold for robust storage of quantum information. Our result means that stored quantum data can be preserved with arbitrarily good fidelity if, in each round of syndrome measurement, qubit errors and syndrome measurement errors are independently and identically distributed, with error probability per qubit and per syndrome bit both below 2.9%. For qubit errors and measurement errors occurring at differing rates, an accuracy threshold could be inferred by analyzing an anisotropic random-plaquette gauge model, with differing disorder strength for horizontal and vertical plaquettes. Relating these threshold error rates to fidelity requirements for quantum gates requires further analysis of the sort discussed in [9].

We have also measured the critical exponent ν_0 that controls the divergence of the correlation length as p approaches p_{c0}, finding $\nu_0 \approx 1.46$ in the RBIM and $\nu_0 \approx 1.0$ in the RPGM. The value of ν_0 is also relevant to the efficacy of quantum error correction — through its connection with finite-size scaling, ν_0 determines how large the code block should be to achieve a specified storage fidelity, for p less than but close to p_{c0}.

Quantum computers are believed to be more powerful than classical computers—classical computers are unable to simulate quantum computers efficiently. The accuracy threshold for quantum memory is a fascinating phase transition, separating a low-noise quantum phase from a high-noise classical phase. In this paper, we have described one way to analyze this phase transition using methods from traditional statistical physics. Furthermore, the connection with quantum memory provides an enlightening new perspective on local spin and gauge systems with strong quenched disorder.

Acknowledgments

We gratefully acknowledge helpful discussions and correspondence with John Chalker, Tom Gottschalk, Alexei Kitaev, Hidetsugu Kitatani, Andreas Ludwig, Paul McFadden, Hidetoshi Nishimori, and Frank Porter. We particularly thank Andrew Landahl, Nathan Wozny, and Zhaosheng Bao for valuable advice and assistance. This work has been supported in part by the Department of Energy under Grant No. DE-FG03-92-ER40701, by the National Science Foundation under Grant No. EIA-0086038, by the Caltech MURI Center for Quantum Networks under ARO Grant No. DAAD19-00-1-0374, and by Caltech's Summer Undergraduate Research Fellowship (SURF) program.

References

[1] M. Mézard, G. Parisi, M.A. Virasoro, Spin Glass Theory and Beyond, World Scientific, Singapore, 1987.
[2] A.P. Young, Spin Glasses and Random Fields, World Scientific, Singapore, 1997.
[3] H. Nishimori, Statistical Physics of Spin Glasses and Information Processing, Oxford University Press, Oxford, 2001.
[4] A.Yu. Kitaev, Quantum error correction with imperfect gates, in: O. Hirota, A.S. Holevo, C.M. Caves (Eds.), Proceedings of the Third International Conference on Quantum Communication and Measurement, Plenum, New York, 1997.
[5] A.Yu. Kitaev, Fault-tolerant quantum computation by anyons, quant-ph/9707021, 1997.
[6] P.W. Shor, Scheme for reducing decoherence in quantum computer memory, Phys. Rev. A 52 (1995) 2493.
[7] A. Steane, Error-correcting codes in quantum theory, Phys. Rev. Lett. 77 (1996) 793.
[8] P.W. Shor, Fault-tolerant quantum computation, in: Proceedings, 37th Annual Symposium on Foundations of Computer Science, IEEE Press, Los Alamitos, CA, 1996, pp. 56–65, quant-ph/9605011.
[9] E. Dennis, A. Kitaev, A. Landahl, J. Preskill, Topological quantum memory, J. Math. Phys. 43 (2002) 4452–4505, quant-ph/0110143.
[10] H. Nishimori, Prog. Theor. Phys. 66 (1981) 1169–1181.
[11] A. Honecker, M. Picco, P. Pujol, Phys. Rev. Lett. 87 (2001) 047201, cond-mat/00010143.
[12] F. Merz, J.T. Chalker, Phys. Rev. B 65 (2002) 054425, cond-mat/0106023.
[13] H. Nishimori, J. Phys. Soc. Jpn. 55 (1986) 3305–3307.
[14] H. Kitatani, J. Phys. Soc. Jpn. 61 (1992) 4049–4055.
[15] P. Le Doussal, A.B. Harris, Phys. Rev. Lett. 61 (1988) 625–628.
[16] H. Nishimori, Derivatives of order parameters in the Ising spin glass, cond-mat/0206438, 2002.
[17] H. Nishimori, K. Nemoto, J. Phys. Soc. Jpn. 71 (2002) 1198, cond-mat/0111354.
[18] M.G. Alford, K.-M. Lee, J. March-Russell, J. Preskill, Nucl. Phys. B 384 (1992) 251–317, hep-th/9112038.
[19] J. Edmonds, Can. J. Math. 17 (1965) 449–467.
[20] F. Barahona, R. Maynard, R. Rammal, J.P. Uhry, J. Phys. A 15 (1982) 673–699.
[21] T. Horiguchi, T. Morita, J. Phys. A 15 (1982) L75–L80.
[22] F. Barahona, J. Phys. A 15 (1982) 3241–3253.
[23] N. Kawashima, H. Rieger, Europhys. Lett. 39 (1997) 85, cond-mat/9612116.
[24] F.D. Nobre, Phys. Rev. E 64 (2001) 046108.
[25] Ph. de Forcrand, M. D'Elia, M. Pepe, Phys. Rev. Lett. 86 (2001) 1438, hep-lat/0007034.

Secure Quantum Key Distribution with an Uncharacterized Source

Masato Koashi[1] and John Preskill[2]
[1]*CREST Research Team for Interacting Carrier Electronics, School of Advanced Sciences, The Graduate University for Advanced Studies (SOKENDAI), Hayama, Kanagawa, 240-0193, Japan*
[2]*Institute for Quantum Information, California Institute of Technology, Pasadena, California 91125*

(Received 27 August 2002; published 6 February 2003)

We prove the security of the Bennett-Brassard (BB84) quantum key distribution protocol for an arbitrary source whose averaged states are basis independent, a condition that is automatically satisfied if the source is suitably designed. The proof is based on the observation that, to an adversary, the key extraction process is equivalent to a measurement in the $\hat{\sigma}_x$ basis performed on a pure $\hat{\sigma}_z$-basis eigenstate. The dependence of the achievable key length on the bit error rate is the same as that established by Shor and Preskill [Phys. Rev. Lett. **85**, 441 (2000)] for a perfect source, indicating that the defects in the source are efficiently detected by the protocol.

DOI: 10.1103/PhysRevLett.90.057902 PACS numbers: 03.67.Dd

Quantum key distribution is an ingenious application of quantum mechanics, in which two remote parties (Alice and Bob) establish a shared secret key through the transmission of quantum signals. In the Bennett-Brassard (BB84) protocol [1], Alice sends a key bit to Bob by preparing a qubit in one of two conjugate bases and Bob measures the qubit in one of the two bases; the eavesdropper Eve, who does not know the basis chosen by Alice or by Bob, cannot collect information about the key without producing a detectable disturbance. This protocol, when suitably augmented by classical error correction and privacy amplification, is provably secure against any attack by Eve [2–5].

Though security can be proven without imposing any restriction on Eve's attack (other than the requirement that she has no *a priori* information about the basis used), it is necessary to place conditions on the performance of the source and detector employed in the protocol. In the Shor-Preskill proof [5], it is assumed that any flaws in the source and detector can be absorbed into Eve's basis-independent attack. The proof by Mayers [2], however, applies to a more general setting: although the source is perfect, the detector has never been tested and is completely *uncharacterized.* Indeed, the detector could be under the control of Eve's collaborator Fred. Fred is unable to send messages to Eve, but he knows Bob's basis and can adjust the measurement performed by the detector accordingly. Still, as Mayers showed, Fred cannot fool Alice and Bob into accepting a key that Eve knows, as long as the efficiency of the detector is basis independent. Since a real device could have an indefinite number of degrees of freedom, no test can fully characterize it; therefore, proving security in the case of an uncharacterized apparatus provides comfort to a highly suspicious user of the key distribution scheme.

In this Letter, we present a simple proof of the security of the BB84 protocol that applies to a setting opposite to that considered by Mayers: the detector is perfect and Fred controls the *source.* We, however, place one important restriction on Fred's attack—the source must not leak any information to Eve about the basis chosen by Alice. That is, the state emitted by the source, averaged over the values of Alice's key bit, is required to be independent of Alice's basis. Our proof applies to faulty sources that are notably more general than those encompassed by the Shor-Preskill proof; to give just one example, it applies to a source that performs perfectly when Alice chooses the $\hat{\sigma}_x$ basis but that rotates the qubit when Alice chooses the $\hat{\sigma}_z$ basis. Nevertheless, our proof shows that a secure key can be extracted from a sifted key at the same rate established by Shor and Preskill.

Our proof combines insights gleaned from both the Mayers proof and the Shor-Preskill proof. Following Mayers, we analyze the information about (Bob's) key collected by Eve in the case where Alice and Bob are using *different* bases. Following Shor and Preskill, we bound Eve's information by observing that Bob *could have* performed an error correction to remove any entanglement with Eve's probe before executing the measurement that extracts his final key. The core of our proof is the observation that a single quantum circuit computes Bob's final key in the $\hat{\sigma}_x$ basis and reverses the damage inflicted by Eve if the error rate is small in the $\hat{\sigma}_z$ basis. Using the same method, we can also prove security for the case of an uncharacterized detector.

Before proceeding to the proof, let us specify in more detail our models of the source and detector. Alice prepares a physical system with Hilbert space $\mathcal{H}_{\rm A}$, which has an arbitrary size, in one of four states $\hat{\rho}(a, g)$ with probability $p_{a,g}$; $a = 0, 1$ labels Alice's basis choice and $g = 0, 1$ is the value of her key bit. The choice of a is assumed to be completely random: $p_{a,0} + p_{a,1} = 1/2$. We assume that the states satisfy

$$p_{0,0}\hat{\rho}(0, 0) + p_{0,1}\hat{\rho}(0, 1) = p_{1,0}\hat{\rho}(1, 0) + p_{1,1}\hat{\rho}(1, 1), \tag{1}$$

© 2003 The American Physical Society

which is vital in the security proof. A convenient way to prepare such an ensemble is to introduce an auxiliary system A$'$ with Hilbert space $\mathcal{H}_{\mathrm{A}'}$. Alice first prepares $\mathcal{H}_{\mathrm{A}} \otimes \mathcal{H}_{\mathrm{A}'}$ in an entangled state $\hat{\rho}_{\mathrm{AA}'}$ and then performs a measurement M_a on system A$'$ alone. The measurement M_a gives a binary outcome, determining g. Equation (1) is then satisfied because the choice of the measurement, M_0 or M_1, does not affect the marginal state of $\mathcal{H}_{\mathrm{A}}$. Hence, if the source is realized in this way, there is no need to test its performance.

As noted in [6], if A$'$ is a qubit, M_0 is a measurement of $\hat{\sigma}_z$, and M_1 is a measurement of $\hat{\sigma}_x$, then security can be established by the method of Shor and Preskill. But our security proof invokes only the condition (1); no further properties of $\hat{\rho}_{\mathrm{AA}'}$, M_0, or M_1 need be specified.

At the end of the transmission channel $\mathcal{H}_{\mathrm{A}} \rightarrow \mathcal{H}_{\mathrm{B}}$, Bob switches between two measurements on $\mathcal{H}_{\mathrm{B}}$. We assume that the two measurements are modeled by a common quantum channel $\mathcal{H}_{\mathrm{B}} \rightarrow \mathcal{H}_2$, where $\dim \mathcal{H}_2 = 2$, followed by the measurement of the Pauli operator $\hat{\sigma}_z$ or $\hat{\sigma}_x$. In the security proof, we include the common quantum channel in the transmission channel between Alice and Bob, so that Bob receives a qubit at the end of the channel.

The protocol that we shall prove to be secure is the following: Let $\Omega \equiv \{1, \ldots, 4N(1+\epsilon)\}$. The variable denoted by $\bar{a}$ takes the value opposite to a.

Protocol 1 (BB84).—(1) Alice creates random bit sequences $\{a_i\}$ and $\{g_i\}$ for $i \in \Omega$. Alice randomly chooses a subset $R \subset \Omega$ with size $|R| = 2N(1+\epsilon)$. (2) Bob creates a random bit sequence $\{b_i\}$. (3) When $i \in R$, Alice sends $\hat{\rho}(a_i, g_i)$. When $i \in \bar{R}(\equiv \Omega - R)$, Alice sends $\hat{\rho}(\bar{a}_i, g_i)$. (4) Bob measures $\hat{\sigma}_z$ when $b_i = 0$ and measures $\hat{\sigma}_x$ when $b_i = 1$. For either case, he sets bit h_i according to the outcome ($h_i = 0$ for outcome 1 and $h_i = 1$ for outcome -1). (5) Bob announces $\{b_i\}$. Alice announces $\{a_i\}$ and R. If the size of $T \equiv \{i \in R | a_i = b_i\}$ is less than N, the protocol aborts. Bob decides randomly on a subset $S \subset \{i \in \bar{R} | \bar{a}_i = b_i\}$ with $|S| = N$ and announces (if he cannot do this, the protocol aborts). (6) Alice and Bob compare g_i and h_i for $i \in T$ and determine the error rate δ. If δ is too large, the protocol aborts. (7) Bob randomizes the positions of the N qubits in S by a permutation π and announces π. Bob announces a linear code C with $|C| = 2^r$ that corrects $N(\delta+\epsilon)$ errors occurring in random positions with probability exponentially close to unity. (8) The sifted key κ_{sif} of length N is defined as the sequence $\{h_i\}_{i \in S}$. The final key is the coset $\kappa_{\mathrm{sif}} + C^{\perp}$. (9) Alice obtains κ_{sif} by applying an error correction scheme to $\{g_i\}_{i \in S}$ via encrypted communication with Bob, consuming τ bits of the previously shared secret key. Then Alice obtains the final key.

Protocol 1 is the standard BB84 protocol, except for the use of $\bar{a}_i$ in place of a_i in steps (3) and (5), which we have adopted for later convenience in the proof. The random permutation π in step (7) is redundant, since it suffices to choose the code C randomly instead of doing the permutation. In the limit of large N, the achievable r/N reaches $1 - h(\delta)$ [where $h(\delta) = -\delta \log_2 \delta - (1-\delta)\log_2(1-\delta)$], and τ/N in step (9) approaches $h(\delta)$, resulting in the rate of key generation $1 - 2h(\delta)$.

Our proof uses some basic properties of (classical) error-correcting codes. The linear code C appearing in step (7) is an r-dimensional subspace of the binary vector space $\mathbf{F}_2^N$. The code $C^{\perp}$ appearing in step (8) is the orthogonal complement of C, called the dual of C. We can specify a linear coding function $G : \mathbf{F}_2^r \rightarrow \mathbf{F}_2^N$, which assigns a distinct codeword of C to each binary sequence of length r. We have assumed in the protocol that C corrects $N(\delta+\epsilon)$ errors occurring in random positions with probability exponentially close to unity. More specifically, there exists a set of correctable errors $\mathcal{E} \subset \mathbf{F}_2^N$ and a decoding function $f : \mathbf{F}_2^N \rightarrow \mathbf{F}_2^r$, satisfying

$$f(G(y) + x) = y \tag{2}$$

for any $y \in \mathbf{F}_2^r$ and any $x \in \mathcal{E}$. A random error with weight at most $N(\delta+\epsilon)$ belongs to $\mathcal{E}$ with probability exponentially close to unity. The function f is not necessarily linear and may be hard to compute, but we will need only its existence for the proof of security—Bob does not compute f in the actual protocol.

What Bob actually calculates is the coset $\kappa_{\mathrm{sif}} + C^{\perp}$ in step (8). One way to do this is to use the function $G^T : \mathbf{F}_2^N \rightarrow \mathbf{F}_2^r$, which is the adjoint (matrix transpose) of G satisfying $G^T(x) \cdot y = x \cdot G(y) \pmod 2$ for any $x \in \mathbf{F}_2^N$ and $y \in \mathbf{F}_2^r$. Since the kernel of $G^T(x)$ is $C^{\perp}$, the final key is the r-bit sequence $G^T(\kappa_{\mathrm{sif}})$. The duality between G and G^T will play an important role in the proof below.

In order to prove that protocol 1 is secure, we need to show that Eve's maximum knowledge I_1 about the final key is negligible. Note that Bob's final key is determined at step (8); step (9), which assures that Alice's key agrees with Bob's and leaks no information to Eve, is not relevant to I_1. Let us compare protocol 1 with a modified one.

Protocol 2.—(3)$'$ When $i \in R$, Alice sends $\hat{\rho}(a_i, g_i)$. When $i \in \bar{R}$, Alice also sends $\hat{\rho}(a_i, g_i)$. The other steps are the same as in protocol 1.

This modification follows Mayers's argument [2] except for the exchanged roles of the sender and the receiver. The only difference between protocols 1 and 2 is a flip in Alice's basis for $i \in \bar{R}$. But the bits $\{g_i\}$ for $i \in \bar{R}$ are kept secret by Alice. Hence, for Eve and Bob only the state averaged over $\{g_i\}$ is relevant, and this state is identical for the two protocols by the condition Eq. (1). Therefore, Eve's maximum knowledge I_2 about Bob's final key in protocol 2 is the same as I_1.

Next, let us further modify protocol 2 in favor of Eve, by allowing Eve to control Alice's source. Now Eve knows $\{a_i\}$ and $\{g_i\}$ and is free to prepare the states measured by Bob however she pleases. Since the states $\hat{\rho}(a_i, g_i)$ have been removed from the protocol and Bob's measurements are symmetric in b_i, the protocol is completely symmetric in $\{a_i\}$ and $\{g_i\}$. Therefore we may assume $a_i = g_i = 0$ without loss of generality. The resulting protocol is as follows.

Protocol 3.—(1) Alice randomly chooses a subset $R \subset \Omega$ with size $|R| = 2N(1+\epsilon)$. (2) Bob creates a random bit sequence $\{b_i\}$. (3) Eve prepares Bob's qubits and her ancilla system in a state. (4) Bob measures $\hat{\sigma}_z$ when $b_i = 0$ and measures $\hat{\sigma}_x$ when $b_i = 1$. For either case, he sets the bit h_i according to the outcome. (5) Bob announces $\{b_i\}$. Alice announces R. If the size of $T \equiv \{i \in R | b_i = 0\}$ is less than N, the protocol aborts. Bob decides randomly on a subset $S \subset \{i \in \bar{R} | b_i = 1\}$ with $|S| = N$ and announces (if he cannot do this, the protocol aborts). (6) Bob counts the number n of bits with $h_i = 1$ for $i \in T$ and determines the error rate $\delta = n/|T|$. If δ is too large, the protocol aborts. (7) Bob randomizes the positions of the N qubits in S by a permutation π and announces π. Bob announces a linear code C. (8) The sifted key $\kappa_{\rm sif}$ of length N is defined as $\{h_i\}_{i \in S}$. The final key is the coset $\kappa_{\rm sif} + C^{\perp}$.

Since the modifications in the protocol favor Eve, Eve's maximum knowledge I_3 about the final key in protocol 3 is no less than I_2: thus $I_1 = I_2 \leq I_3$. To complete the proof, we will show that I_3 is small—Eve cannot predict Bob's key accurately because Bob is measuring in the "wrong" basis.

Let us denote the Hilbert space of Eve's system as $\mathcal{H}_{\rm E}$ and that of the N qubits belonging to S as $\mathcal{H}_S$. We may imagine that Bob's measurement on set S is delayed until step (8) and denote by $\hat{\rho}$ the state over $\mathcal{H}_S \otimes \mathcal{H}_{\rm E}$ after the verification test on the set T is done, but before the qubits in S are measured. The test on T finds that the rate of error ($\hat{\sigma}_z = -1$) over N (or more) randomly chosen qubits is δ. If the qubits in the set S were also measured in the σ_z basis, then the joint probability of finding an error rate less than δ in T and finding more than $N(\delta + \epsilon)$ errors in S would be asymptotically less than $\exp[-\epsilon^2 N/4(\delta - \delta^2)]$ for any strategy by Eve. Ignoring any inefficient strategy that has only an exponentially small probability of giving an error rate less than δ in T, we conclude that for the state $\hat{\rho}$, the probability of finding more than $N(\delta+\epsilon)$ errors in S is exponentially small.

Let $\{|v\rangle_Z, v \in \mathbf{F}_2^N\}$ denote the "Z basis" of $\mathcal{H}_S$, where the value of the jth bit of v corresponds to the eigenvalue of $\hat{\sigma}_z$ on the jth qubit, and let $\{|v\rangle_X = \hat{H}^N |v\rangle_Z\}$ denote the "X basis," where $\hat{H}^N$ is the Hadamard transformation acting on the N qubits. The announcement of π in step (7) can be described as the transmission from Bob to Eve of a particle J in one of $N!$ orthogonal states $\{|\pi\rangle_{\rm J}\}$. The symmetrized state held by Bob and Eve after transmission of the particle is

$$\hat{\rho}_{\rm s} = (N!)^{-1} \sum_{\pi} |\pi\rangle_{\rm J}\langle\pi| \otimes (\hat{U}_\pi \otimes \hat{1}_{\rm E}) \hat{\rho} (\hat{U}_\pi^\dagger \otimes \hat{1}_{\rm E}). \quad (3)$$

Let $\hat{P}_{\mathcal{E}}$ be the projection of $\mathcal{H}_S$ onto the subspace spanned by the states $|e\rangle_Z$ such that $e \in \mathcal{E}$. The successful verification test ensures that the probability of finding an error pattern that is not in $\mathcal{E}$ is exponentially small: ${\rm Tr}[(\hat{P}_{\mathcal{E}} \otimes \hat{1}_{\rm E})\hat{\rho}_{\rm s}] \geq 1 - \eta$, where η is an exponentially small number. (We are now regarding the particle J as part of Eve's system E.) If we define $\hat{\rho}'$ as

$$\hat{\rho}' \equiv \frac{(\hat{P}_{\mathcal{E}} \otimes \hat{1}_{\rm E})\hat{\rho}_{\rm s}(\hat{P}_{\mathcal{E}} \otimes \hat{1}_{\rm E})}{{\rm Tr}[(\hat{P}_{\mathcal{E}} \otimes \hat{1}_{\rm E})\hat{\rho}_{\rm s}]}, \quad (4)$$

its fidelity [7] to $\hat{\rho}_{\rm s}$, $F(\hat{\rho}', \hat{\rho}_{\rm s}) \equiv [{\rm Tr}(\sqrt{\hat{\rho}'}\hat{\rho}_{\rm s}\sqrt{\hat{\rho}'})^{1/2}]^2$, is given by

$$F(\hat{\rho}', \hat{\rho}_{\rm s}) = {\rm Tr}[(\hat{P}_{\mathcal{E}} \otimes \hat{1}_{\rm E})\hat{\rho}_{\rm s}] \geq 1 - \eta. \quad (5)$$

In what follows, we will show that if the state $\hat{\rho}'$ instead of $\hat{\rho}_{\rm s}$ were used, Eve would have no information about the final key ($I_3 = 0$). Then we will infer that any actual strategy by Eve (that passes the verification test with a probability that is not exponentially small) gives her exponentially small information.

In protocol 3, Bob measures in the Z basis for the verification test, and in the X basis to generate the key—we need to show that if the error rate is low in the Z basis, then the key is random and private. Our proof invokes a quantum circuit that outputs the same r-bit final key as Bob finds in protocol 3, and that also expunges Eve's entanglement with the key bits. Though Bob might not have actually executed this circuit, it would be all the same to Eve if he had, which is sufficient to ensure privacy.

The circuit, shown in Fig. 1, uses an auxiliary system Q of r qubits initially prepared in the state $|0\rangle_X$ and is a composition $\hat{U} \equiv \hat{U}_2\hat{U}_1$ of two unitary operators $\hat{U}_1$ and $\hat{U}_2$. The operator $\hat{U}_1$, which calculates the final key, acts in the X basis as

$$\hat{U}_1 : |x\rangle_X \otimes |y\rangle_X \longrightarrow |x\rangle_X \otimes |y + G^T(x)\rangle_X. \quad (6)$$

Using the duality between G and G^T, we easily see that U_1 acts in the Z basis as

$$\hat{U}_1 : |x\rangle_Z \otimes |y\rangle_Z \longrightarrow |x + G(y)\rangle_Z \otimes |y\rangle_Z. \quad (7)$$

The operator $\hat{U}_2$ is defined in the Z basis as

$$\hat{U}_2 : |x\rangle_Z \otimes |y\rangle_Z \longrightarrow |x\rangle_Z \otimes |y + f(x)\rangle_Z, \quad (8)$$

and in the X basis acts as

$$\hat{U}_2 : |x\rangle_X \otimes |y\rangle_X \longrightarrow |\Psi_{x,y}\rangle_X \otimes |y\rangle_X. \quad (9)$$

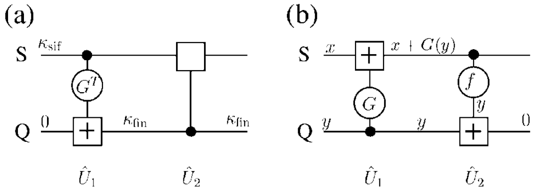

FIG. 1. (a) A quantum circuit calculating $\kappa_{\rm fin} = G^T(\kappa_{\rm sif})$ in the X basis. (b) The same circuit in the Z basis. When $x \in \mathcal{E}$, the final state of system Q is $|0\rangle_Z$.

Here $|\Psi_{x,y}\rangle$ is a rather complicated state of $\mathcal{H}_S$, but its exact form is not relevant here.

If the initial state of the ancilla Q is $|0\rangle_X$, then from Eqs. (6) and (9) we have

$$\hat{U}(|\kappa_{\mathrm{sif}}\rangle_X \otimes |0\rangle_X) = |\Psi_{x,\kappa_{\mathrm{fin}}}\rangle_X \otimes |G^T(\kappa_{\mathrm{sif}})\rangle_X; \qquad (10)$$

the final key $\kappa_{\mathrm{fin}} = G^T(\kappa_{\mathrm{sif}})$ is obtained by measuring the system Q in the X basis after execution of the circuit. Meanwhile, Eqs. (7) and (8) with $|0\rangle_X \propto \sum_y |y\rangle_Z$ lead to

$$\hat{U}(|x\rangle_Z \otimes |0\rangle_X) \propto \sum_y |x + G(y)\rangle_Z \otimes |y + f(x + G(y))\rangle_Z; \qquad (11)$$

if $x \in \mathcal{E}$, the final state of Q is $|0\rangle_Z$, due to Eq. (2). Then, Eq. (4) ensures that if the initial state of $\mathcal{H}_S \otimes \mathcal{H}_E$ is $\hat{\rho}'$, the final marginal state of Q is still $|0\rangle_Z$. Therefore, the final state $\hat{\rho}_Q$ of Q obtained when we start from the actual state $\hat{\rho}_s$ is exponentially close to $|0\rangle_Z$:

$$_Z\langle 0|\hat{\rho}_Q|0\rangle_Z \geq F(\hat{\rho}', \hat{\rho}_s) \geq 1 - \eta. \qquad (12)$$

Equation (12) establishes that the final key can be obtained from a complete X-basis measurement on the state $\hat{\rho}_Q$, whose fidelity to the Z-basis eigenstate $|0\rangle_Z$ is exponentially close to unity. From this, we conclude the following: (a) The mutual information I_3 between the final key and Eve, who may conduct any measurement on her system, is upper bounded by the von Neumann entropy $S(\hat{\rho}_Q)$ [8]. Since $\hat{\rho}_Q$ has an eigenvalue greater than or equal to $1 - \eta$, we have $I_1 \leq I_3 \leq S(\hat{\rho}_Q) \leq h(\eta) + \eta \log_2(2^r - 1) < h(\eta) + r\eta$. (b) The probability distribution p_y over the 2^r final keys is very close to uniform. In fact, the fidelity to the uniform distribution cannot be lower than the fidelity in Eq. (12). Thus we have $2^{-r}(\sum_y \sqrt{p_y})^2 \geq 1 - \eta$. Using the inequality $-2\log_2 x \leq r(1-x)^2 + (1-x^2)/(\ln 2)$ which holds for $x \geq 2^{-r/2}$ when r is large, the Shannon entropy of $\{p_y\}$ is bounded as $H(\{p_y\}) = r + 2\sum_y p_y \log_2(2^r p_y)^{-1/2} \geq r(2\sqrt{1-\eta} - 1) \geq r(1 - 2\eta)$.

The two imperfections of the final key derived in (a) and (b) can be combined into a single parameter by the following argument. Let us assume that Bob randomly chooses and announces a bit sequence $w \in \mathbf{F}_2^r$ and produces a new key $w + y$ which is truly uniformly distributed. If Eve's information about y is I_1, then her information about $w + y$ is

$$I = r - H(\{p_y\}) + I_1 < 3r\eta + h(\eta), \qquad (13)$$

which is also exponentially small, concluding the proof.

Finally, suppose that Bob uses a detector with imperfect efficiency, which has a "null" outcome (signifying a detection failure) in addition to the valid binary outcome. Our proof remains valid, provided that the efficiency (probability of obtaining a valid outcome) is the same for the two bases, and the size of Ω is increased.

Our proof of security applies to an uncharacterized source with basis-independent averaged states. By interchanging the roles of sender and receiver, the same proof can be applied to the case of an uncharacterized detector, considered by Mayers [2]. Indeed, in that case our proof allows a more general source (one triggered by a perfect measurement on half of an entangled state, as opposed to a perfect source) and a higher rate of key generation $[1 - 2h(\delta)$ rather than $1 - h(\delta) - h(2\delta)]$ than established by Mayers. In either case, by exploiting the duality between the operation that encodes a message using C and the operation that computes a $C^{\perp}$ coset, our proof illuminates the connection between a low error rate and successful privacy amplification.

It is also interesting to consider *characterized* imperfect sources and detectors that have limited basis-dependent flaws. One important case of a characterized defective source, recently analyzed in [9], is a source that occasionally emits two identical copies of a qubit, one of which can be intercepted by Eve. In this case, our proof does not apply because Eq. (1) is not satisfied. Security criteria for characterized sources and detectors are further discussed in [10].

We thank David DiVincenzo, Peter Shor, Andy Yao, and especially Daniel Gottesman and Hoi-Kwong Lo for helpful discussions. This work has been supported in part by the Department of Energy under Grant No. DE-FG03-92-ER40701, by the National Science Foundation under Grant No. EIA-0086038, and by the Caltech MURI Center for Quantum Networks under ARO Grant No. DAAD19-00-1-0374.

[1] C. H. Bennett and G. Brassard, in *Proceedings of IEEE International Conference on Computers, Systems and Signal Processing, Bangalore, India* (IEEE, New York, 1984), pp. 175–179.

[2] D. Mayers, in *Advances in Cryptography—Proceedings of Crypto '96* (Springer-Verlag, New York, 1996), pp. 343–357; J. Assoc. Comput. Mach. **48**, 351 (2001).

[3] H.-K. Lo and H. F. Chau, Science **283**, 2050 (1999).

[4] E. Biham, M. Boyer, P. O. Boykin, T. Mor, and V. Roychowdhury, in *Proceedings of the 32nd Annual ACM Symposium on Theory of Computing* (ACM Press, New York, 2000), pp. 715–724.

[5] P. W. Shor and J. Preskill, Phys. Rev. Lett. **85**, 441 (2000).

[6] D. Gottesman and J. Preskill, Phys. Rev. A **63**, 022309 (2001).

[7] A. Uhlmann, Rep. Math. Phys. **9**, 273 (1976); R. Jozsa, J. Mod. Opt. **41**, 2315 (1994).

[8] A. S. Holevo, Probl. Inf. Transm. (Engl. Transl.) **9**, 117 (1973).

[9] H. Inamori, N. Lütkenhaus, and D. Mayers, quant-ph/0107017.

[10] D. Gottesman, H.-K. Lo, N. Lütkenhaus, and J. Preskill, quant-pn/0212066.

PHYSICAL REVIEW A **67**, 033806 (2003)

Optimal sizes of dielectric microspheres for cavity QED with strong coupling

J. R. Buck and H. J. Kimble
Norman Bridge Laboratory of Physics 12-33, California Institute of Technology, Pasadena, California 91125

(Received 18 October 2002; published 21 March 2003)

The whispering gallery modes (WGMs) of quartz microspheres are investigated for the purpose of strong coupling between single photons and atoms in cavity quantum electrodynamics (cavity QED). Within our current understanding of the loss mechanisms of the WGMs, the saturation photon number n_0 and critical atom number N_0 cannot be minimized simultaneously, so that an "optimal" sphere size is taken to be the radius for which the geometric mean $\sqrt{n_0 N_0}$, is minimized. While a general treatment is given for the dimensionless parameters used to characterize the atom-cavity system, detailed consideration is given to the D_2 transition in atomic cesium at $\lambda_0 = 852$ nm using fused-silica microspheres, for which the maximum coupling coefficient $g_a/(2\pi) \approx 750$ MHz occurs for a sphere radius $a = 3.63\ \mu$m corresponding to the minimum for $n_0 \approx 6.06 \times 10^{-6}$. By contrast, the minimum for $N_0 \approx 9.00 \times 10^{-6}$ occurs for a sphere radius of $a = 8.12\ \mu$m, while the optimal sphere size for which $\sqrt{n_0 N_0}$ is minimized occurs at $a = 7.83\ \mu$m. On an experimental front, we have fabricated fused-silica microspheres with radii $a \sim 10\ \mu$m and consistently observed quality factors $Q \geqslant 0.8 \times 10^7$. These results for the WGMs are compared with corresponding parameters achieved in Fabry-Perot cavities to demonstrate the significant potential of microspheres as a tool for cavity QED with strong coupling.

DOI: 10.1103/PhysRevA.67.033806 PACS number(s): 42.50.Ct, 42.55.Sa, 32.80.−t

I. INTRODUCTION

Motivated by the pioneering work of Braginsky and Ilchenko [1], some of the highest-quality optical resonators to date have been achieved with the whispering gallery modes (WGMs) of quartz microspheres [2,3]. Over the wavelength range 630–850 nm, quality factors $Q \approx 8 \times 10^9$ have been realized, and cavity finesse $\mathcal{F} = 2.3 \times 10^6$ demonstrated [2,3]. Such high-quality factors make the WGMs of small dielectric spheres a natural candidate for use in cavity QED [1,4–20].

While much of the work regarding quartz microspheres has centered around achieving the ultimate quality factors [2,3], the quality factor of the resonator is one of the factors that determines the suitability of the WGMs for investigations of cavity quantum electrodynamics in a regime of strong coupling. In this case, the coherent coupling coefficient g for a single atom interacting with the cavity mode must be much larger than all other dissipative rates, including the cavity decay rate κ and the rate of atomic spontaneous emission γ; namely, $g \gg (\kappa, \gamma)$. Note that $2g = \Omega$ gives the Rabi frequency associated with a single quantum of excitation shared by the atom-cavity system [21,22]. The atom-field interaction can be characterized by two important dimensionless parameters: the saturation photon number $n_0 \propto \gamma^2/g^2$ and the critical atom number $N_0 \propto \kappa\gamma/g^2$. Since these parameters correspond respectively, to the number of photons required to saturate an intracavity atom and the number of atoms required to have an appreciable effect on the intracavity field, strong coupling requires that $(n_0, N_0) \ll 1$. Ideally one would hope to minimize both of these parameters in any particular resonator. Unfortunately, within the context of our current understanding of the loss mechanisms of the WGMs [3], the critical parameters (n_0, N_0) cannot be minimized simultaneously in a microsphere.

Motivated by these considerations, in this paper we explore possible limits for the critical parameters (n_0, N_0) for the WGMs of quartz microspheres. Following the analysis of Refs. [4,5,18], we study the particular case of a single atom coupled to the *external* field of a WGM near the sphere's surface. We show that there are radii that minimize (n_0, N_0) individually, and that there is an "optimal" sphere size that minimizes the geometric mean, $\sqrt{n_0 \times N_0}$, of these two cavity-QED parameters and allows both parameters to be near their respective minima. We also report our progress in the fabrication of small microspheres with radii $a \sim 10\ \mu$m, and compare our experimental results for Q with those from our theoretical analysis. Finally, we present a detailed comparison for the state of the art and future prospects for achieving strong coupling in cavity QED for both microsphere and Fabry-Perot cavities. Throughout the presentation, we attempt to develop a general formalism that can be applied to diverse systems. However, for definiteness we also present results for a particular system of some interest, namely, an individual cesium atom coupled to the WGMs of quartz microspheres.

II. MODES OF A MICROSPHERE

Solving for the mode structure of the resonances of a dielectric sphere in vacuum is a classic problem in electricity and magnetism, and the resulting field distributions have been known for some time [23]. The electric field of the TM, *electric type*, modes inside and outside a sphere of refractive index n at free-space wavelength λ_0 are respectively,

$$\begin{aligned}\vec{E}_{\mathrm{in}}(r,\theta,\phi) \propto\ & l(l+1)\frac{j_l(kr)}{kr}P_l^m(\cos\theta)e^{im\phi}\hat{r}\\ &+\frac{[krj_l(kr)]'}{kr}\frac{\partial P_l^m(\cos\theta)}{\partial\theta}e^{im\phi}\hat{\theta}\\ &+\frac{im}{\sin\theta}\frac{[krj_l(kr)]'}{kr}P_l^m(\cos\theta)e^{im\phi}\hat{\phi} \qquad (1)\end{aligned}$$

©2003 The American Physical Society

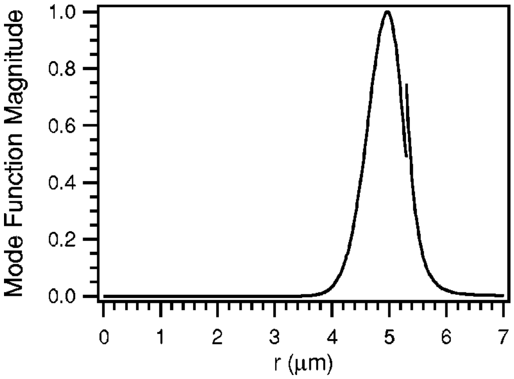

FIG. 1. The magnitude of the normalized mode function as a function of radius for the TM mode of a 5.305 μm radius sphere ($p=1, l=m=50$) with $\theta=\pi/2$ and $\phi=0$ for a wavelength of $\lambda_0=852.359$ nm and index of refraction $n=1.452\,46$. In our case, the function is normalized to have a maximum value of unity. Note that there is a discontinuity at the surface.

and

$$\vec{E}_{\rm out}(r,\theta,\phi)\propto l(l+1)\frac{h_l^{(1)}\left(\frac{kr}{n}\right)}{\frac{kr}{n}}P_l^m(\cos\theta)e^{im\phi}\hat{r}+\frac{\left[\frac{kr}{n}h_l^{(1)}\left(\frac{kr}{n}\right)\right]'}{\frac{kr}{n}}\frac{\partial P_l^m(\cos\theta)}{\partial\theta}e^{im\phi}\hat{\theta}+\frac{im}{\sin\theta}\frac{\left[\frac{kr}{n}h_l^{(1)}\left(\frac{kr}{n}\right)\right]'}{\frac{kr}{n}}P_l^m(\cos\theta)e^{im\phi}\hat{\phi}, \tag{2}$$

where a is the radius of the sphere, $k=2\pi n/\lambda_0$ is the wave vector inside the sphere, $j_l(x)$ is the spherical Bessel function, $h_l^{(1)}(x)$ is the spherical Hankel function, $(\hat{r},\hat{\theta},\hat{\phi})$ are unit vectors, and the $'$ refers to differentiation with respect to the argument. Note that the TM modes have a predominantly radial electric-field vector.

In order to satisfy the boundary conditions at the surface of the microsphere, the tangential components of the mode function immediately inside and outside the sphere must be equal. However, there is a discontinuity in the radial component of the electric field at the dielectric boundary (as can be seen from Fig. 1.) The eigenmodes are determined by solving for the roots of a characteristic equation [23], which can be reduced to

$$\frac{j_{l-1}(ka)}{j_l(ka)}-\frac{nh_{l-1}^{(1)}\left(\frac{ka}{n}\right)}{h_l^{(1)}\left(\frac{ka}{n}\right)}+\frac{n^2l}{ka}-\frac{l}{ka}=0. \tag{3}$$

Throughout this paper, we normalize the mode functions such that their maximum value is unity. This condition then yields for the $l=m$ modes of the sphere

$$\vec{\Psi}_{\rm in}(r,\theta,\phi)=N(l+1)\frac{j_l(kr)}{kr}\sin^l(\theta)e^{il\phi}\hat{r}+NF(r)\cos\theta\sin^{l-1}\theta e^{il\phi}\hat{\theta}+iNF(r)\sin^{l-1}\theta e^{il\phi}\hat{\phi} \tag{4}$$

and

$$\vec{\Psi}_{\rm out}(r,\theta,\phi)=NB(l+1)\frac{h_l^{(1)}\left(\frac{kr}{n}\right)}{\frac{kr}{n}}\sin^l\theta e^{il\phi}\hat{r}+NBH(r)\cos\theta\sin^{l-1}\theta e^{il\phi}\hat{\theta}+iNBH(r)\sin^{l-1}\theta e^{il\phi}\hat{\phi}, \tag{5}$$

where

$$F(r)=\frac{j_l(kr)}{kr}+\frac{l}{2l+1}j_l(kr)-\frac{l+1}{2l+1}j_{l+1}(kr), \tag{6}$$

$$H(r)=\frac{h_l^{(1)}\left(\frac{kr}{n}\right)}{\frac{kr}{n}}+\frac{l}{2l+1}h_{l-1}^{(1)}\left(\frac{kr}{n}\right)-\frac{l+1}{2l+1}h_{l+1}^{(1)}\left(\frac{kr}{n}\right), \tag{7}$$

$$B=\frac{\frac{j_l(ka)}{ka}+\frac{l}{2l+1}j_l(ka)-\frac{l+1}{2l+1}j_{l+1}(ka)}{\frac{h_l^{(1)}\left(\frac{ka}{n}\right)}{\frac{ka}{n}}+\frac{l}{2l+1}h_{l-1}^{(1)}\left(\frac{ka}{n}\right)-\frac{l+1}{2l+1}h_{l+1}^{(1)}\left(\frac{ka}{n}\right)}, \tag{8}$$

and N is the normalization factor. Because we will require the field outside the sphere to be as large as possible, we will choose the $p=1$ modes. Also, because the coherent coupling constant $g\propto 1/\sqrt{V_{\vec{P}}}$, where $V_{\vec{P}}$ is the cavity mode volume, we choose the $l=m$ modes, since they yield the smallest electromagnetic mode volume, as will be explained in the following section.

III. ELECTROMAGNETIC MODE VOLUME

The effective mode volume $V_{\vec{P}}$ associated with the electromagnetic field distribution $\vec{\Psi}(r,\theta,\phi)$ [4] is given by

$$V_{\vec{P}}=\int_{V_Q}\varepsilon(\vec{r})|\vec{\Psi}_{\vec{P}}(\vec{r})|^2{\rm d}V, \tag{9}$$

where

$$\varepsilon(\vec{r})=\begin{cases} n^2 & \text{if } r<a \\ 1 & \text{if } r>a \end{cases} \tag{10}$$

and $\vec{P}$ corresponds to the (p,l,m) mode. V_Q is the quantization volume discussed in Ref. [4]. As long as a radius r_Q is chosen large enough to include the effects of the evanescent field, the mode volume is relatively insensitive to the particular choice of quantization radius [24]. As discussed more extensively in Refs. [21,22] the interaction between the internal atomic degrees of freedom and the intracavity field is characterized by the coherent coupling constant $g(r,\theta,\phi)$, where

$$g(r,\theta,\phi)\equiv g_0\vec{\Psi}^{(p,l,m)}(r,\theta,\phi) \tag{11}$$

and

$$g_0\propto\frac{1}{\sqrt{V_{\vec{P}}}}. \tag{12}$$

Note that in the absence of damping, $2g(\vec{r})$ gives the frequency for Rabi nutation associated with a single photon in the cavity for an atom initially in the ground-state located at position $\vec{r}$ within the mode. Therefore, in order to maximize the coupling strength, one must endeavor to minimize the cavity mode volume.

In order to derive an answer that can be applied to different wavelengths, one can define a dimensionless mode volume parameter $\tilde{V}$ and plot as a function of a dimensionless sphere size parameter $\tilde{x}$ defined as

$$\tilde{V}=\frac{V_{\vec{P}}}{\left(\dfrac{\lambda_0}{2\pi n}\right)^3} \tag{13}$$

and

$$\tilde{x}=\frac{2\pi n a}{\lambda_0}, \tag{14}$$

where $V_{\vec{P}}$ is the cavity mode volume, n is the index of refraction at the free-space wavelength λ_0, and a is the sphere radius. The plots then only depend on the index of refraction (see Fig. 2).

Naively, one might assume that the sphere should be made as small as possible in order to minimize the electromagnetic mode volume, and hence to provide a maximum for g_0 and hence globally for $g(\vec{r})$. However, as shown in Figs. 2 and 3, the mode volume for the TM modes of a quartz microsphere actually passes through a minimum at some particular radius a_0. This behavior can be understood by noting that for $a<a_0$, the intrinsic, radiative losses are increasing rapidly and ultimately cause the mode to no longer be well confined by the sphere, with a concomitant increase of the mode volume. Note that in Fig. 2 and subsequent figures, we give results for $n\sim1.45$ corresponding to fused silica, as well as for $n=2.00$ and $n=3.00$. These latter cases serve to illuminate the role of n as well as being applicable to other materials (i.e., the index of refraction for GaAs is $n=3.4$ for $\lambda=1550$ nm [25]). For a very low-OH fused silica microsphere at $\lambda_0=852$ nm (the wavelength of the D_2 transition in atomic cesium) with index of refraction $n=1.452\,46$, the minimum mode volume $V_{\vec{P}}^{\min}\approx28.4\ \mu\mathrm{m}^3$ occurs for radius $a\approx3.73\ \mu$m corresponding to mode numbers $p=1, l=m=34$ (see Fig. 3). One might at first believe that this value for the radius represents the optimal sphere size for use as a cavity with single atoms. However, while the mode volume $V_{\vec{P}}$ plays an important role in determining the coupling constant [Eq. (12)], it is not the only parameter relevant

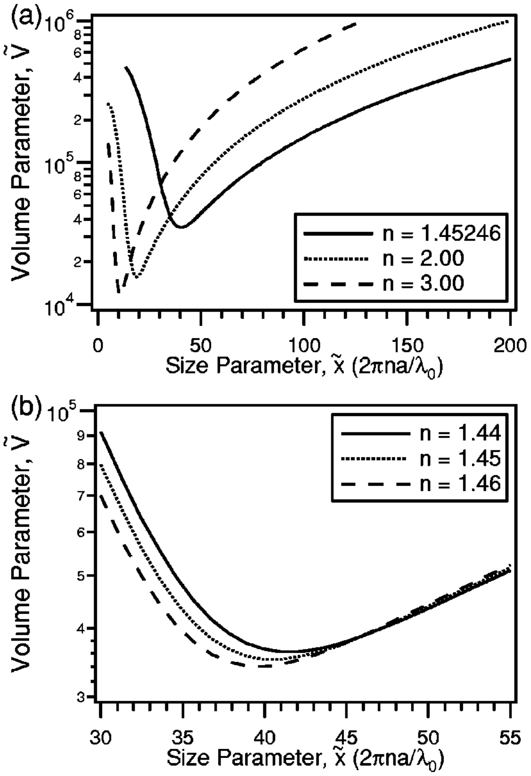

FIG. 2. (a) The dimensionless volume parameter $\tilde{V}$ [defined by Eq. (13)], as a function of the dimensionless size parameter $\tilde{x}$ [defined by Eq. (14)]. The solid line is for an index of refraction $n=1.452\,46$, the index of refraction for fused silica at $\lambda_0=852$ nm, with a minimum of $\tilde{V}=34\,883.4$ for $\tilde{x}=39.946\,9$ $(l=m=34)$. The dotted line is for an index of refraction $n=2.00$, with a minimum of $\tilde{V}=15\,596.2$ for $\tilde{x}=18.986\,4$ $(l=m=14)$. The dashed line is for an index of refraction $n=3.00$, with a minimum of $\tilde{V}=11\,546.4$ for $\tilde{x}=10.274\,8$ $(l=m=6)$. (b) Because the index of refraction for fused silica varies from $n=1.444$ at $\lambda_0=1550$ nm to $n=1.458$ for $\lambda_0=600$ nm (see Fig. 4), this plot of the dimensionless volume parameter $\tilde{V}$ as a function of the dimensionless size parameter $\tilde{x}$ is made for that range of values. The solid line is for an index of refraction $n=1.44$, with a minimum of $\tilde{V}=36\,247.5$ for $\tilde{x}=40.981\,2$, $(l=m=35)$. The dotted line is for an index of refraction $n=1.45$, with a minimum of $\tilde{V}=35\,161.1$ for $\tilde{x}=41.003\,6$, $(l=m=35)$. The dashed line is for an index of refraction $n=1.46$, with a minimum of $\tilde{V}=34\,129.1$ for $\tilde{x}=39.963\,1$, $(l=m=34)$.

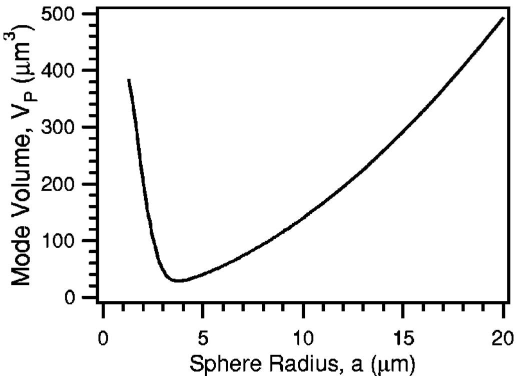

FIG. 3. The electromagnetic mode volume $V_{\tilde{p}}$ for the TM modes of a very low-OH fused silica microsphere as a function of sphere radius at the wavelength $\lambda_0 = 852$ nm for the D_2 line of atomic cesium. The minimum, 28.4 μm^3, occurs for radius $a_0 \approx 3.73$ μm corresponding to mode numbers $p = 1$ and $l = m = 34$.

to cavity QED with single atoms in a regime of strong coupling. As discussed in the following sections, the quality factor Q of a WGM has a strong dependence on the sphere radius, and must also be considered in an attempt to optimize the critical atom and saturation photon numbers.

IV. LOSSES IN DIELECTRIC SPHERES

For fused silica spheres with radius $a \gtrsim 15$ μm, the effect of intrinsic radiative losses can be safely neglected, since they allow quality factor $Q \gtrsim 10^{21}$, as illustrated in Fig. 5. Such large values of Q greatly exceed those imposed by technical constraints of material properties, such as bulk absorption and surface scattering.

However, as one moves to very small spheres with radius $a \lesssim 10$ μm, the intrinsic radiative Q falls steeply enough to become the dominant loss mechanism even in the face of other technical imperfections. When assessing the usefulness of microspheres for cavity QED, one must account for the entire set of loss mechanisms to determine the optimal size for the microsphere, which is the subject to which we now turn our attention.

The quality factors of the WGMs of fused silica microspheres are determined by several different loss mechanisms.

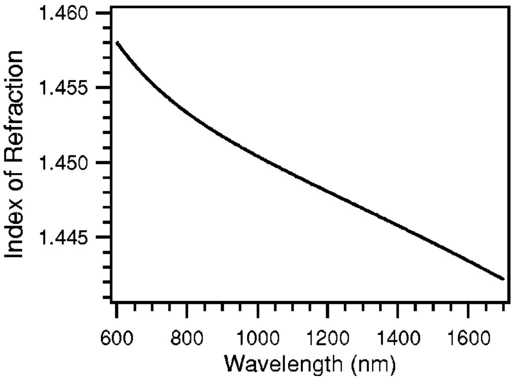

FIG. 4. The index of refraction of very low-OH fused silica as a function of wavelength.

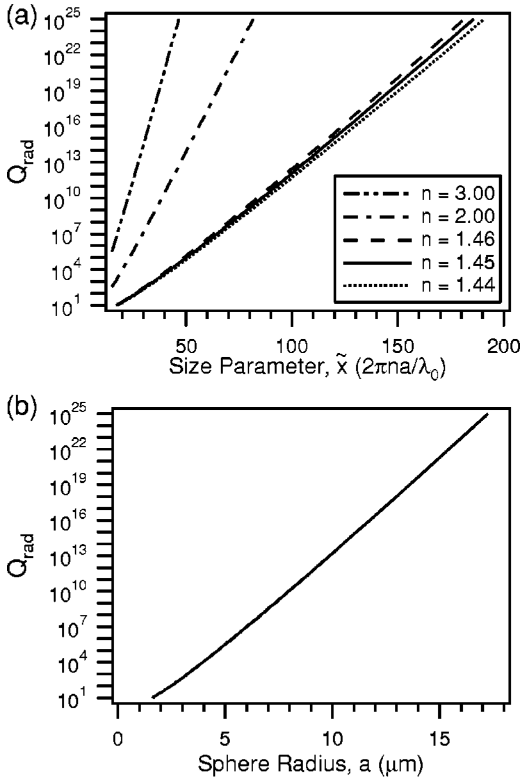

FIG. 5. (a) Semi-log plot of the radiative quality factor Q_{rad} for various indices of refraction as a function of the dimensionless size parameter $\tilde{x} = 2\pi na/\lambda_0$. (b) Semi-log plot of the radiative quality factor Q_{rad} as a function of sphere radius for a wavelength of $\lambda_0 = 852.359$ nm (index of refraction is $n = 1.452\,46$).

The overall quality factor can then be calculated by adding the different contributions in the following way [2]:

$$Q^{-1} = Q_{rad}^{-1} + Q_{mat}^{-1}, \tag{15}$$

$$Q_{mat}^{-1} = Q_{s.s.}^{-1} + Q_{w}^{-1} + Q_{bulk}^{-1}, \tag{16}$$

where Q_{rad} is due to purely radiative losses for an ideal dielectric sphere and Q_{mat} results from nonideal material properties. The principal mechanisms contributing to Q_{mat} are scattering losses from residual surface inhomogeneities ($Q_{s.s.}$), absorption losses due to water on the surface of the sphere (Q_w), and bulk absorption in the fused silica (Q_{bulk}). The intrinsic material losses are known very accurately, since they arise from absorption in the material at the wavelength of concern [26]. Considerably greater uncertainty is associated with the losses due to surface scattering and absorption due to adsorbed material on the surface of the sphere, of which water is likely the principal component. We will adopt the models for these losses presented in Refs. [2,3], extrapolated to the regime of small spheres of interest here.

A. Intrinsic radiative losses

The contribution to the quality factor for purely radiative effects Q_{rad} can be derived by following the arguments presented in Ref. [27]. These losses are due to the leakage of light from the resonator due to its finite dielectric constant and radius of curvature. The results can then be compared to numerical results obtained by Lorenz-Mie theory [28]. We find from Ref. [27] that

$$Q_{\mathrm{rad}}=\frac{1}{2}\left(l+\frac{1}{2}\right)n^{1-2b}(n^2-1)^{1/2}e^{2T_l}, \tag{17}$$

where

$$T_l=\left(l+\frac{1}{2}\right)(\eta_l-\tanh\eta_l), \tag{18}$$

$$\eta_l=\operatorname{arccosh}\left\{n\left[1-\frac{1}{l+\frac{1}{2}}\left(t_p^0\xi+\frac{l^{1-2b}}{\sqrt{l^2-1}}\right)\right]^{-1}\right\}, \tag{19}$$

$$\xi=\left[\frac{1}{2}\left(l+\frac{1}{2}\right)\right]^{1/3}, \tag{20}$$

and

$$b=\begin{cases}0 & \text{TE modes}\\ 1 & \text{TM modes.}\end{cases} \tag{21}$$

Also, n is the index of refraction and t_p^0 is the pth zero of the Airy function Ai. This p corresponds to the mode number (p,l,m). In our case, we are only interested in the $p=1$ modes of the sphere to maximize the electromagnetic field outside the sphere while maintaining a small mode volume. Note that these expressions for Q_{rad} become invalid in the limit of small l mode numbers. The error in the mode functions used to derive these results reaches 1% for $l=18$. However, the error is less than 0.2% for $l=76$ (This is the optimal sphere size discussed in Sec. VI). Fortunately, the expressions are valid in the regimes for which we are concerned. This has been confirmed by making comparisons with numerical values obtained using Lorenz-Mie scattering theory.

From Fig. 5, we see that the radiative Q falls approximately exponentially as the radius a is decreased, and can become quite important as the sphere size is decreased below 10 μm. For example, for a 15 μm radius sphere and a wavelength $\lambda_0=852.359$ nm, $Q_{\mathrm{rad}}\approx 2\times 10^{21}$. Therefore, the net quality factor would most certainly be dominated by other loss mechanisms in Eq. (15). However, for a 7 μm radius sphere, $Q_{\mathrm{rad}}\approx 4\times 10^{8}$, and the radiative losses can play a crucial role in the characteristics of the spheres that are optimal for use in cavity QED.

B. Material loss mechanisms

The quality factor due to bulk absorption Q_{bulk} in fused silica is actually known very well, since this depends only on the absorption of the material at the wavelength of concern [2]:

$$Q_{\mathrm{bulk}}=\frac{2\pi n}{\alpha\lambda_0}, \tag{22}$$

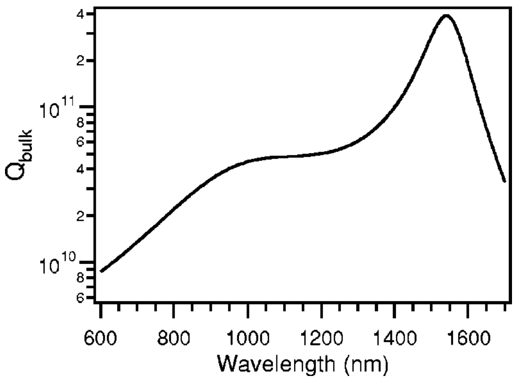

FIG. 6. The quality factor, Q_{bulk}, from Eq. (22) for a very low-OH fused silica microsphere as a function of wavelength. Because fused silica has a minimum in absorption at 1550 nm, there is a maximum for the quality factor due to bulk absorption of $Q_{\mathrm{bulk}}\sim 3.8\times 10^{11}$. At 852 nm, the quality factor due to bulk absorption is $Q_{\mathrm{bulk}}\sim 2.4\times 10^{10}$.

where n is the index of refraction, and α is the absorption coefficient of the material. From Fig. 6 we see that for very low-OH fused silica, the absorption coefficient at 852 nm is $\alpha\approx 4.5\times 10^{-4}\ \mathrm{m}^{-1}$ [26]. This would correspond to a quality factor of $Q_{\mathrm{bulk}}\sim 2.4\times 10^{10}$. Fused silica has a minimum in its absorption coefficient of $\alpha\approx 1.5\times 10^{-5}\ \mathrm{m}^{-1}$ at 1550 nm, which yields a quality factor of $Q_{\mathrm{bulk}}\sim 3.8\times 10^{11}$.

The quality factor due to surface scattering $Q_{\mathrm{s.s.}}$ and absorption by adsorbed water Q_{w} has also been studied and modeled, Albeit for larger spheres with $a\gtrsim 600\ \mu$m. For losses due to surface scattering, we follow the work of Refs. [2,3] and take

$$Q_{\mathrm{s.s.}}\sim\frac{3\varepsilon(\varepsilon+2)^2}{(4\pi)^3(\varepsilon-1)^{5/2}}\frac{\lambda_0^{7/2}(2a)^{1/2}}{(\sigma B)^2}, \tag{23}$$

where $\varepsilon=n^2$ is the dielectric constant and $\sigma B\sim 5\ \mathrm{nm}^2$ is an empirical parameter determined by the size and correlation length of the distribution of residual surface inhomogeneities. This quantity was reported in Ref. [3] based upon atomic force microscopy measurements of a microsphere.

The quality factor due to water adsorbed on the surface, Q_{w}, is given by [3]

$$Q_{\mathrm{w}}\sim\sqrt{\frac{\pi}{8n^3}}\frac{(2a)^{1/2}}{\delta\lambda_0^{1/2}\beta_w}, \tag{24}$$

where $\delta\sim 0.2$ nm is an estimated thickness for the water layer, and $\beta_w\sim 4.33\ \mathrm{m}^{-1}$ is the absorption coefficient of water at 852 nm.

Combining these various results, we display in Fig. 7 a curve for the quantity Q_{mat} as a function of sphere radius a for a wavelength $\lambda_0=852$ nm. This same figure shows the quality factor Q_{rad}, set by intrinsic radiative losses [Eq. (17)], as well as the overall quality factor $Q=Q_{\mathrm{rad}}Q_{\mathrm{mat}}/(Q_{\mathrm{rad}}+Q_{\mathrm{mat}})$. From this plot, we see that the radiative losses dominate the overall quality factor below a radius of $a\lesssim 8\ \mu$m, while the losses due to material proper-

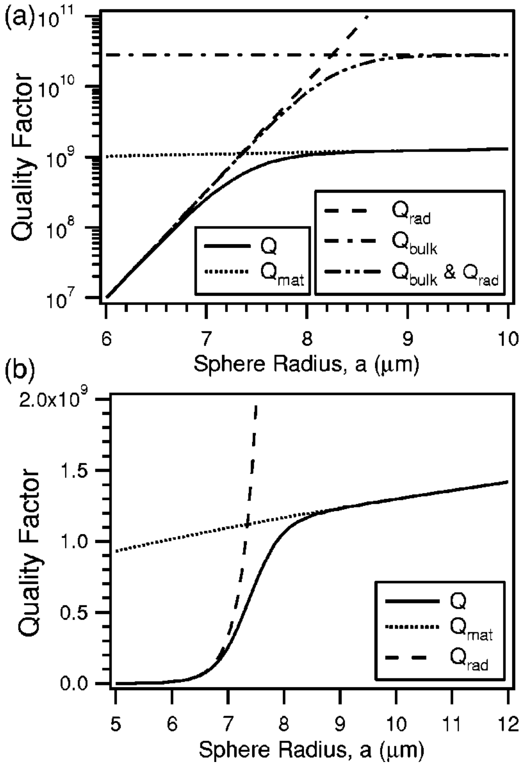

FIG. 7. (a) Semilog plot of the quality factors due to the various loss mechanisms discussed in Sec. IV for a very low-OH fused silica microsphere as a function of sphere radius for the $l=m$, TM modes at a wavelength of $\lambda_0=852$ nm. In particular, traces are shown for the quality factor due to purely radiative losses (Q_{rad}), the bulk absorption of fused silica (Q_{bulk}), both radiative losses and bulk absorption, the three loss mechanisms comprising Q_{mat}: ($Q_{\mathrm{bulk}}, Q_{\mathrm{s.s.}}, Q_{\mathrm{w}}$), and the predicted Q due to all four loss mechanisms. (b) This linear plot zooms in on the region of interest at the transition where the radiative losses become the dominant loss mechanism. The plot contains the quality factor due to purely radiative losses (Q_{rad}), the three loss mechanisms comprising Q_{mat}: ($Q_{\mathrm{bulk}}, Q_{\mathrm{s.s.}}, Q_{\mathrm{w}}$), and the predicted Q due to all four loss mechanisms.

ties are most significant for $a \gtrsim 8$ μm. Because of the extremely steep dependence of Q_{rad} on sphere size, the point of transition from material to radiative dominated loss should be reasonably insensitive to details of the models employed to describe the material losses. Although we focus our attention here on the wavelength appropriate to the particular case of the D_2 transition in atomic cesium, a similar analysis could be carried out for other wavelengths of interest using the above formalism, as for example the $2S \rightarrow 2P$ transition at 1.083 μm in metastable helium.

V. THE STRONG COUPLING REGIME

The ultimate goal that we consider here is to employ the WGMs of quartz microspheres as cavity modes for achieving strong coupling to atoms within the setting of cavity QED. The atom of choice in this paper is cesium, and in particular, the D_2 $(F=4 \mapsto F'=5)$ transition in cesium at $\lambda_0 = 852.359$ nm as an illustrative example. Such an analysis allows a direct comparison with the state of the art in Fabry-Perot cavities [29].

The coupling coefficient $g(\vec{r})$ is the coupling frequency of a single atom to a particular cavity mode and corresponds to one-half the single-photon Rabi frequency [21,22]. For an atom located just at the outer surface of the microsphere (i.e., in vacuum) and interacting with a whispering gallery mode $\vec{P}=(p,l,m)$, the coupling coefficient is given by [4]

$$g(a) \equiv g_a = \gamma_\perp |\vec{\Psi}_{\mathrm{out}}(a)| \sqrt{\frac{V_0}{V_{\vec{P}}}}, \tag{25}$$

where a is the sphere radius, $\gamma_\perp/2\pi = 2.61$ MHz is the transverse spontaneous decay rate for our transition in cesium, $V_0 = 3c\lambda_0^2/4\pi\gamma_\perp$ is the effective volume of the atom for purely radiative interactions, and $V_{\vec{P}}$ is the electromagnetic mode volume of the whispering gallery mode designated by $\vec{P}=(p,l,m)$.

Armed with a knowledge of g, we are now able to determine certain dimensionless parameters relevant to the strong coupling regime of cavity QED. In particular, we consider an atom-cavity system to be in the strong coupling regime when the single-photon Rabi frequency $2g$ for a single intracavity atom dominates the cavity field decay rate κ the atomic dipole decay rate $\gamma_\perp$ and the inverse atomic transit time T^{-1} [21,22]. We will defer further discussion of T^{-1}, however, this requirement relates to the need for atomic localization [4,5]. In the strong coupling regime, important parameters for characterizing the atom-cavity system are the two dimensionless parameters: the saturation photon number n_0, and the critical atom number N_0. The saturation photon number, given by

$$n_0 \equiv \frac{\gamma_\perp^2}{2g^2}, \tag{26}$$

corresponds to the number of photons required to saturate an intracavity atom [21,22]. The critical atom number, defined by

$$N_0 \equiv \frac{2\gamma_\perp \kappa}{g^2}, \tag{27}$$

corresponds to the number of atoms required to have an appreciable effect on the intracavity field [21,22]. Ideally, one hopes to minimize simultaneously both the critical atom number N_0 and the saturation photon number n_0 which corresponds to simultaneous maxima for both $g^2/\kappa\gamma_\perp$ and $g^2/\gamma_\perp^2$.

The saturation photon number and critical atom number are useful because of their physical meaning. However, one can define a new dimensionless parameter

$$\beta = \frac{8\pi^2 V_{\vec{P}}}{3\lambda_0^3} \frac{1}{|\vec{\Psi}_{\mathrm{out}}(a)|^2}, \tag{28}$$

that corresponds to the cavity mode volume in units of λ^3 weighted by the inverse of the strength of the mode function at the atomic position. This enables the equations for the saturation photon number and critical atom number to be expressed as

$$n_0 = \frac{\beta}{4Q_{\mathrm{atom}}} \tag{29}$$

and

$$N_0 = \frac{\beta}{Q_{\mathrm{cavity}}}, \tag{30}$$

where

$$Q_{\mathrm{atom}} = \frac{\pi c}{\lambda_0 \gamma_\perp} \tag{31}$$

and

$$Q_{\mathrm{cavity}} = \frac{\pi c}{\lambda_0 \kappa}. \tag{32}$$

This parameter β then also determines the coupling coefficient in the following manner:

$$g(a) = \sqrt{\frac{2\pi c \gamma_\perp}{\beta \lambda_0}}. \tag{33}$$

Therefore, we see that one can use a single parameter β combined with the properties of the atom to be used (λ_0 and $\gamma_\perp$) and the quality factor of the resonator, Q_{cavity}, to determine the three parameters (n_0, N_0, g_0) of importance in determining the quality of an atom-cavity system.

Figures 8 and 9 are plots of this dimensionless parameter β and of $1/\sqrt{\beta}$ as functions of the dimensionless size parameter $\tilde{x} = 2\pi n a/\lambda_0$ for a few values of index of refraction. Because the index of refraction for fused silica varies from $n = 1.444$ at $\lambda_0 = 1550$ nm to $n = 1.458$ for $\lambda_0 = 600$ nm (see Fig. 4), Figs. 8(b) and 9(b) are made for that range of values. From Figs. 8 and 9 one sees that there is a minimum for β and a maximum for $1/\sqrt{\beta}$ that depends on the index of refraction.

VI. STRONG COUPLING WITH CESIUM

The results of the previous section can now be used to determine the saturation photon number n_0 the critical atom number N_0 and the coupling coefficient $g(a)$ for any atomic transition. In our case, we are concerned with the D_2 transition in cesium ($\lambda_0 = 852.359$ nm). For this transition, the spontaneous transverse decay rate is $\gamma/2\pi = 2.61$ MHz. Also, at this wavelength the index of refraction for fused silica is $n = 1.452\,46$. This allows one to compute the coupling coefficient, $g(a) = \sqrt{2\pi c \gamma_\perp / \beta \lambda_0}$. Figure 10 shows that there is a maximum of $g/2\pi = 749.986$ MHz for a radius $a = 3.63$ μm, $(l = m = 33)$. Interestingly, because we are restricted to having the atom couple to the *external* field of the microsphere, the maximum in the coupling coefficient $g(a)$ does not coincide with the minimum for the mode volume, $V_{\vec{P}}$ (see Figs. 3 and 10.)

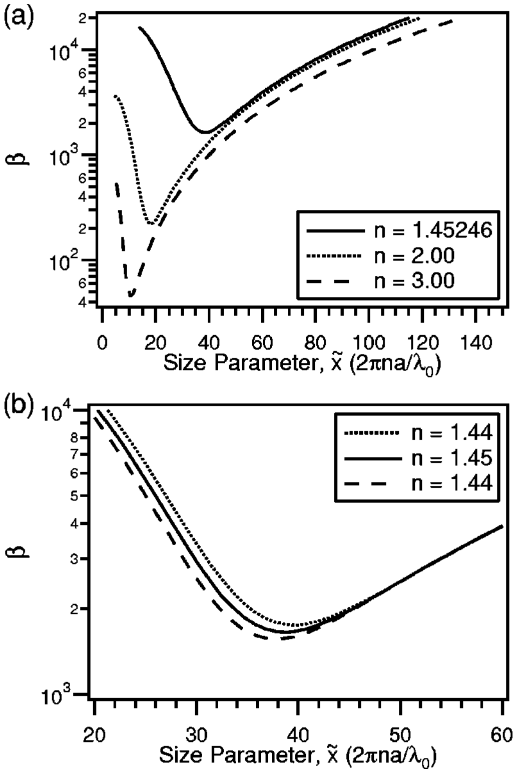

FIG. 8. (a) The dimensionless parameter β as a function of the dimensionless size parameter $\tilde{x} = 2\pi n a/\lambda_0$. For an index of refraction $n = 1.452\,46$ (i.e., the index of refraction for fused silica at $\lambda_0 = 852$ nm), there is a minimum of $\beta = 1\,632.01$ for $\tilde{x} = 38.883\,3$, $(l = m = 33)$. For an index of refraction $n = 2.00$, there is a minimum of $\beta = 221.124$ for $\tilde{x} = 17.876\,3$, $(l = m = 13)$. For an index of refraction $n = 3.00$, there is a minimum of $\beta = 45.374\,4$ for $\tilde{x} = 10.274\,8$, $(l = m = 6)$. (b) Because the index of refraction for fused silica varies from $n = 1.444$ at $\lambda_0 = 1550$ nm to $n = 1.458$ for $\lambda_0 = 600$ nm (see Fig. 4), this plot is made for that range of values. For an index of refraction $n = 1.44$, there is a minimum of $\beta = 1\,753.92$ for $\tilde{x} = 39.918\,8$, $(l = m = 34)$. For an index of refraction $n = 1.45$, there is a minimum of $\beta = 1\,653.7$ for $\tilde{x} = 38.877\,8$, $(l = m = 33)$. For an index of refraction $n = 1.46$, there is a minimum of $\beta = 1\,561.45$ for $\tilde{x} = 37.834\,8$, $(l = m = 32)$.

The saturation photon number n_0 is proportional to the dimensionless parameter β as shown in Eq. (29). Since the factor of proportionality is a constant that depends only on the properties of the particular atom of concern, the curve is determined by that of β along with the quality factor of the atomic resonance (in our case cesium), which is given by Eq. (31) to be $Q_{atom} = 6.738 \times 10^7$. Figure 11 is a plot of the saturation photon number for the D_2 transition in cesium as a function of sphere size. Figure 11 shows that there is a minimum for the saturation photon number of $n_0 = 6.055\,27 \times 10^{-6}$ for a sphere radius of $a = 3.631\,63$ μm $(l = m = 33)$.

The critical atom number N_0 is also proportional to the dimensionless parameter β as shown in Eq. (30). However,

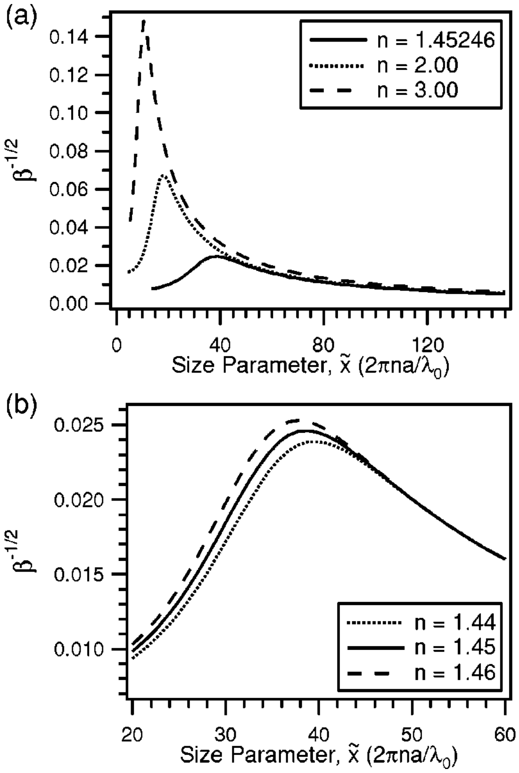

FIG. 9. (a) The dimensionless parameter $1/\sqrt{\beta}$ as a function of the dimensionless size parameter $\tilde{x}=2\pi na/\lambda_0$. For an index of refraction $n=1.452\,46$ (i.e., the index of refraction for fused silica at $\lambda_0=852$ nm), there is a maximum of $1/\sqrt{\beta}=0.024\,753\,6$ for $\tilde{x}=38.883\,3$, ($l=m=33$). For an index of refraction $n=2.00$, there is a maximum of $1/\sqrt{\beta}=0.067\,248\,4$ for $\tilde{x}=17.876\,3$, ($l=m=13$). For an index of refraction $n=3.00$, there is a maximum of $1/\sqrt{\beta}=0.148\,455$ for $\tilde{x}=10.274\,8$, ($l=m=6$). (b) Because the index of refraction for fused silica varies from $n=1.444$ at $\lambda_0=1550$ nm to $n=1.458$ for $\lambda_0=600$ nm (see Fig. 4), this plot is made for that range of values. For an index of refraction $n=1.44$, there is a maximum of $1/\sqrt{\beta}=0.023\,877\,9$ for $\tilde{x}=39.918\,8$, ($l=m=34$). For an index of refraction $n=1.45$, there is a minimum of $1/\sqrt{\beta}=0.024\,590\,8$ for $\tilde{x}=38.877\,8$, ($l=m=33$). For an index of refraction $n=1.46$, there is a minimum of $1/\sqrt{\beta}=0.025\,306\,8$ for $\tilde{x}=37.834\,8$, ($l=m=32$).

its factor of proportionality is the quality factor of the resonator, Q_{cavity}, which has a very strong dependence on the sphere radius a in the region below 10 μm (see Fig. 7). Therefore, the minimum for the critical atom number does not occur for the same sphere size as for the saturation photon number. Figure 12 is a plot of the critical atom number as a function of sphere size. Using for Q_{cavity} the model that incorporates all of the loss mechanisms discussed in Sec. IV (radiative losses, bulk absorption, surface scattering, and absorption due to water on the surface), we find that the minimum for the critical atom number $N_0=8.999\,35\times10^{-6}$ occurs for a sphere radius of $a=8.12015$ μm ($l=m=79$). At this radius, the coupling coefficient is $g/(2\pi)=304.16$ MHz.

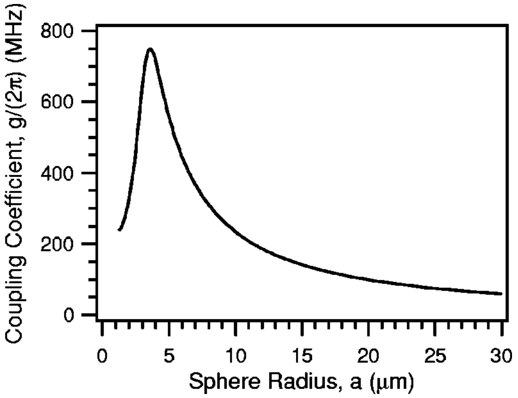

FIG. 10. The coupling coefficient, $g/2\pi$, as a function of sphere size for the D_2 transition in cesium ($\lambda_0=852.359$ nm). There is a maximum of $g/2\pi=749.986$ MHz for a sphere radius of $a=3.631\,63$ μm, ($l=m=33$). Note that the maximum for $g/2\pi$ does not coincide with the minimum for the cavity mode volume, $V_{\vec{p}}$ (see Fig. 3).

Unfortunately, as illustrated in Fig. 13, the minima for the two parameters, n_0 and N_0, do not occur for the same sphere radius. However, if one uses the minimum of the geometric mean of the two parameters, each can have a value near its respective minimum. The minimum of the geometric mean occurs for a sphere radius $a=7.830\,38$ μm ($l=m=76$). For this sphere size, the coupling coefficient is $g/2\pi=318.333$ MHz, the saturation photon number is $n_0=3.361\,07\times10^{-5}$, and the critical atom number is $N_0=9.278\,34\times10^{-6}$. Therefore, each cavity QED parameter can be made to achieve simultaneously a value near its respective minimum.

VII. PROGRESS IN SMALL SPHERE MANUFACTURE

A large portion of the work being done on microspheres has been to push the quality factors of the spheres to record levels [2,3]. This effort has produced some of the highest finesse ($\mathcal{F}=2.3\times10^6$) optical cavities to date with quality factors $Q\sim10^{10}$ [2,3]. However, we have seen that Q is not the only relevant factor in determining the suitability of the WGMs for cavity QED in a regime of strong coupling. In

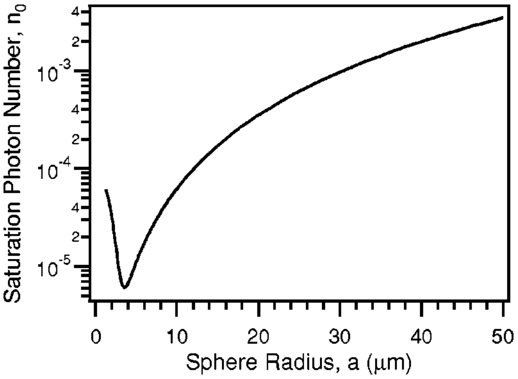

FIG. 11. The saturation photon number n_0 as a function of sphere size for the D_2 transition in cesium ($\lambda_0=852.359$ MHz). There is a minimum $n_0=6.055\,27\times10^{-6}$ for a sphere radius of $a=3.631\,63$ μm ($l=m=33$). At this radius, the coupling coefficient is $g/2\pi=749.986$ MHz.

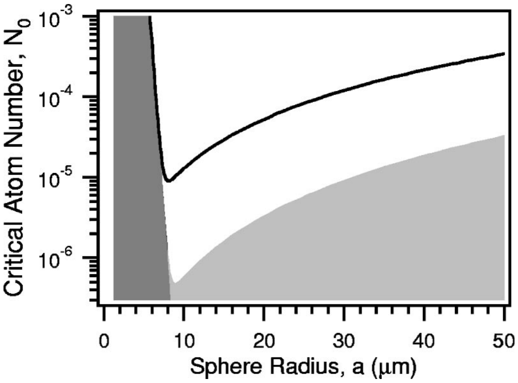

FIG. 12. The critical atom number N_0 as a function of sphere size for the D_2 transition in cesium ($\lambda_0=852.359$ MHz). There is a minimum $N_0=8.999\,35\times10^{-6}$ for a sphere radius of $a=8.1201\,5$ μm ($l=m=79$). At this radius, the coupling coefficient is $g/2\pi=304.16$ MHz. This plot of the critical atom number incorporates the model for the quality factor of the resonator, Q_{cavity}, outlined in Sec. IV, for the four loss mechanisms: bulk absorption, surface scattering, absorption due to water on the surface, and radiative losses. The dark gray region is bounded by the effects of purely radiative losses. The light gray region is bounded by the effects of both radiative losses and bulk absorption.

general, the preceding analysis demonstrates the requirement to push to microspheres of small radius, $a\lesssim10$ μm. Unfortunately, the experiments that have achieved the highest quality factors and which have investigated certain material loss mechanisms are of rather larger size, and hence not optimal for cavity QED in a regime of strong coupling. For example, the experiment of Ref. [3] achieved a quality factor of $Q=7.2\times10^9$ at 850 nm in a sphere of radius $a=340$ μm.

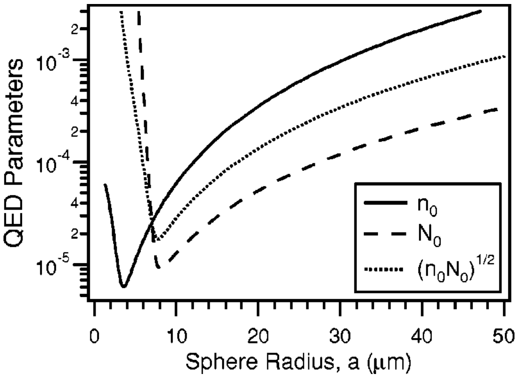

FIG. 13. This plot shows the two parameters, (n_0, N_0), of importance to cavity QED as a function of sphere radius. The geometric mean of these two parameters is also plotted. The solid line represents the saturation photon number n_0, the dashed line gives the critical atom number N_0, and the dotted line shows the geometric mean of the two parameters, $\sqrt{n_0N_0}$. The minimum of each plot corresponds to the following dimensionless parameters: $n_0=6.05527\times10^{-6}$ for $a=3.631\,63$ μm ($l=m=33$), and $N_0=8.999\,35\times10^{-6}$ at $a=8.120\,15$ μm ($l=m=79$). The two curves cross at $a=7.03$ μm with $n_0=N_0=2.56\times10^{-5}$. The geometric mean of these two parameters, $\sqrt{n_0\times N_0}$, is minimized for $a=7.830\,38$ μm ($l=m=76$). For this radius, the parameters are: $n_0=3.361\,07\times10^{-5}$ and $N_0=9.278\,34\times10^{-6}$. Note that the curve for N_0 assumes the model for the Q discussed in this paper, and that the coupling coefficient $g(\vec{r})$ is evaluated at the maximum of the mode function for $r=a$.

To explore the possibilities of cavity QED with strong coupling in substantially smaller spheres, we have undertaken a program to study fabrication techniques for quartz microspheres with $a\lesssim30$ μm, while still maintaining high-quality factors. We have been able to fabricate 10 μm radius spheres using an oxygen-hydrogen microtorch to melt the ends of very low-OH fused silica rods to form a sphere on the end of a stem. Light is then coupled to the sphere using frustrated total internal reflection of a prism, as in Refs. [3,4,31]. Our observations demonstrate that spheres of this size can be made consistently to have quality factors $Q\gtrsim0.8\times10^7$. While this is encouraging progress, the resulting Q is two orders of magnitude smaller than the theoretical maximum of $\approx1.3\times10^9$ for this size based upon the model discussed in Sec. IV.

One possible reason for this discrepancy could be the importance of minimizing the ellipticity of the small spheres. Because the small resonators fabricated by our technique have a stem protruding out of them, they are far from spherical. When coupling to an $l=m$ mode in spheres with $a\gtrsim100$ μm and hence large l, the mode is tightly confined to the equator; therefore, the poles do not have an appreciable impact on the mode structure or quality factor. In this case, it is not of critical importance to have the best sphere possible, but rather the best great circle possible to achieve large quality factors. However, this is not the case in small spheres with $a\lesssim10$ μm. As a decreases, the $l=m$ modes occupy an increasingly larger proportion of the sphere in polar angle, and the ellipticity of the sphere becomes increasingly important in determining the mode structure as well as the Q. However, while there is certainly room for improvement in our fabrication technique and in the resulting mode structures and quality factors, we shall see in the following section that the current results have promising implications.

VIII. COMPARING MICROSPHERES AND FABRY-PEROT CAVITIES

Figure 14 offers a comparison of the state of the art for Fabry-Perot and microsphere cavities for cavity QED, as well as projections of likely limits for each. It is interesting to note that in our projections for the limiting cases of each, microspheres allow for a significant improvement in the critical atom number N_0 relative to Fabry-Perot cavities. On the other hand, a principal advantage of Fabry-Perot cavities relative to microspheres would seem to be significant improvements in the saturation photon number n_0. The specific specific task at hand would then dictate which technology to apply.

As shown in Fig. 14, there has already been some progress in coupling atoms to the external fields of a microsphere [31]. The sphere employed for the work of Ref. [31] had a radius of $a\approx60$ μm, and quality factor $Q\lesssim5\times10^7$, corresponding to a mode volume of $V_{\vec{P}}\approx3.7\times10^3$ μm^3, coupling coefficient $g_a/(2\pi)\approx24$ MHz, saturation photon

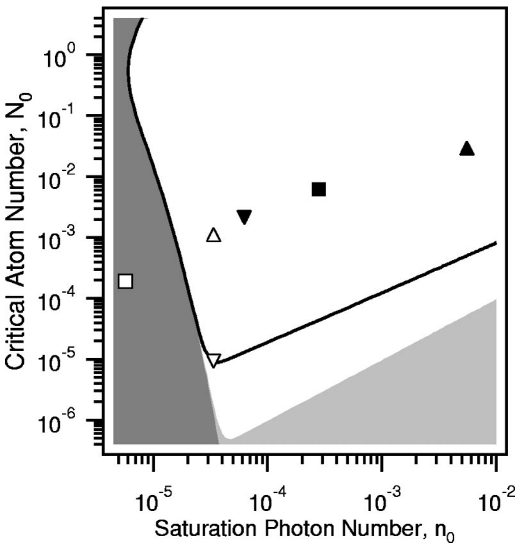

FIG. 14. The solid line gives a parametric plot of the critical atom number N_0 and the saturation photon number n_0, for fused-silica microspheres and the D_2 transition of atomic cesium, incorporating the loss mechanisms outlined in Sec. IV. The dark gray region is bounded by the effects of radiative losses. The light gray region is bounded by the effects of bulk absorption and radiative losses. This plot also offers a comparison of experimental and theoretical cavity QED parameters for microsphere and Fabry-Perot cavities. ■ represents the current state of the art for cavity QED in Fabry-Perot cavities as in Ref. [30]. □ is a projection of the practical limit for Fabry-Perot cavities based upon Ref. [29]. ▲ represents the 60 μm radius sphere implemented for cavity QED in Ref. [31]. ▼ is the current state of the art in 10 μm microspheres based upon the results presented in Sec. VI. △ is the currently achievable Q with the optimal sphere size of 7.83 μm based upon the analysis of Secs. IV and V. ▽ is the theoretically achievable $Q \sim 9.76 \times 10^8$ at the optimal sphere size, $a \approx 7.83$ μm.

number $n_0 = 5.54 \times 10^{-3}$, and critical atom number $N_0 = 2.99 \times 10^{-2}$. If instead this experiment were to be implemented with a smaller sphere with 10 μm radius and with quality factor $Q \sim 0.8 \times 10^7$ such as we have manufactured and described in Sec. VI, the following parameters would be achieved: a mode volume of $V_{\vec{p}} \approx 1.4 \times 10^2$ $\mu\mathrm{m}^3$, coupling coefficient $g_a/(2\pi) \approx 233$ MHz, saturation photon number $n_0 \approx 6.27 \times 10^{-5}$, and critical atom number $N_0 \approx 2.11 \times 10^{-3}$. Therefore, we see that currently achievable quality factors in spheres of radius 10 μm already would allow for impressive results in cavity QED with single atoms.

By comparison, the state of the art for Fabry-Perot cavities has already achieved the following results for the TEM_{00} modes [30]: a cavity finesse of $\mathcal{F} = 4.8 \times 10^5$, a mode volume of $V_\mathrm{m} \approx 1.69 \times 10^3$ $\mu\mathrm{m}^3$, coupling coefficient $g_0/(2\pi) \approx 110$ MHz, saturation photon number $n_0 \approx 2.82 \times 10^{-4}$, and critical atom number $N_0 \approx 6.13 \times 10^{-3}$. If one then looks at possible limits of Fabry-Perot technology for cavity QED as analyzed in Ref. [29], the following may be possible; a cavity of length $\lambda_0/2$ with a cavity finesse of $\mathcal{F} = 7.8 \times 10^6$ yields coupling coefficient $g_0/(2\pi) \approx 770$ MHz, saturation photon number $n_0 \approx 5.7 \times 10^{-6}$, and critical atom number $N_0 \approx 1.9 \times 10^{-4}$.

It is encouraging that the currently achievable results for small sphere manufacture would already allow the WGMs to compete favorably with the current state of the art in Fabry-Perot cavity QED. However, if one were able to manufacture and couple to spheres at the optimal size $a \approx 7.83$ μm with a $Q \sim 9.76 \times 10^8$ (the theoretical maximum predicted from the analysis of Sec. IV), the following results could be achieved: a mode volume of $V_{\vec{p}} \approx 90$ $\mu\mathrm{m}^3$, coupling coefficient $g_a/(2\pi) \approx 318$ MHz, saturation photon number $n_0 \approx 3.36 \times 10^{-5}$, and critical atom number $N_0 \approx 9.28 \times 10^{-6}$. This would represent a significant improvement over the current Fabry-Perot technology and be competitive with the likely limits of Fabry-Perot technology. However, even short of achieving this stated maximum Q for the WGMs, impressive results can already be attained. With a quality factor $Q \sim 0.8 \times 10^7$ at the optimal sphere radius $a \approx 7.83$ μm, one would obtain these same results [i.e., $g_a/(2\pi) \approx 318$ MHz and saturation photon number $n_0 \approx 3.36 \times 10^{-5}$), except that the critical atom number N_0, would increase to $N_0 \approx 1.13 \times 10^{-3}$. This is still an impressive gain over the current capabilities of Fabry-Perot cavities for the saturation photon number, with room for improvement in the critical atom number.

Overall, we thus find that the technologies of microspheres and Fabry-Perot resonators each have their advantages and disadvantages. However, there is one notable advantage of microspheres; they can be made cheaply and relatively simply given sufficient training and skill. By contrast, the Fabry-Perot cavities considered here require specialized coating runs with expensive equipment and considerable expertise, which is to be found at only a few locations worldwide. This alone makes microspheres an attractive alternative to Fabry-Perot cavities for cavity QED. Another unique advantage of the WGMs is the ability to control the cavity decay rate κ by controlling the coupling efficiency into and out of the microsphere (e.g., by adjusting the distance between a coupling prism and the microsphere [32]). Furthermore, as one moves to the limit of small cavities, the open geometry of microspheres offers a considerable advantage when compared to the geometry of Fabry-Perot cavities. Such possibilities combined with our projected values of the critical parameters, (n_0, N_0), shown in Fig. 14 point to the competitiveness of microspheres with current and future Fabry-Perot technology and demonstrate their potential as a powerful tool for cavity QED in the regime of strong coupling.

ACKNOWLEDGMENTS

We thank K. Birnbaum, S. J. van Enk, C. Hood, V. Ilchenko, A. Kuzmich, R. Legere, P. Lodahl, T. Lynn, H. Mabuchi, J. McKeever, T. Northup, D. Vernooy, and J. Ye for helpful discussions. This work was supported by the National Science Foundation, by the Office of Naval Research, and by the Caltech MURI on Quantum Networks administered by the Office of Army Research.

[1] V.B. Braginsky and V.S. Ilchenko, [Sov. Phys. Dokl. **32**, 307 (1987)].

[2] M.L. Gorodetsky, A.A. Savchenkov, and V.S. Ilchenko, Opt. Lett. **21**, 453 (1995).

[3] D.W. Vernooy, V.S. Ilchenko, H. Mabuchi, E.W. Streed, and H.J. Kimble, Opt. Lett. **23**, 247 (1998).

[4] D.W. Vernooy and H.J. Kimble, Phys. Rev. A **55**, 1239 (1997).

[5] H. Mabuchi and H.J. Kimble, Opt. Lett. **19**, 749 (1994).

[6] M.L. Gorodetsky and V.S. Ilchenko, Opt. Commun. **113**, 133 (1994).

[7] F. Treussart, J. Hare, L. Collot, V. Lefèvre-Seguin, D.S. Weiss, V. Sandoghdar, J.M. Raimond, and S. Haroche, Opt. Lett. **19**, 1651 (1994).

[8] J.C. Knight, N. Dubreuil, V. Sandoghar, J. Hare, V. Lefèvre-Seguin, J.M. Raimond, and S. Haroche, Opt. Lett. **20**, 1515 (1995).

[9] J.C. Knight, N. Dubreuil, V. Sandoghar, J. Hare, V. Lefèvre-Seguin, J.M. Raimond, and S. Haroche, Opt. Lett. **21**, 698 (1996).

[10] W. Jhe and J.W. Kim, Phys. Rev. A **51**, 1150 (1995).

[11] H. Chew, J. Chem. Phys. **87**, 135 (1987).

[12] V.V. Klimov and V.S. Letokhov, Opt. Commun. **122**, 155 (1996).

[13] V.V. Klimov, M. Ducloy, and V.S. Letokhov, J. Mod. Opt. **43**, 549 (1996).

[14] W. Klitzing, R. Long, V.S. Ilchenko, J. Hare, and V. Lefèvre-Seguin, New J. Phys. **3**, 14 (2001).

[15] M.M. Mazumder, D.Q. Chowdhury, S.C. Hill, and R.K. Chang, *Optical Processes in Microcavities* (World Scientific, Singapore, 1996), Vol. 3.

[16] A.J. Campillo, J.D. Eversole, and H.-B. Lin, *Optical Processes in Microcavities*, Ref. [15].

[17] R.E. Slusher and U. Mohideen, *Optical Processes in Microcavities* (Ref. [15]).

[18] A.B. Matsko, S.P. Vyatchanin, H.J. Kimble, and H. Mabuchi, Phys. Lett. A **192**, 175 (1994).

[19] D.J. Norris, M. Kuwata-Gonokami, and W.E. Moerner, Appl. Phys. Lett. **71**, 297 (1997).

[20] X. Fan, A. Doran, and H. Wang, Appl. Phys. Lett. **73**, 3190 (1998).

[21] H.J. Kimble, *Cavity Quantum Electrodynamics* (Academic Press, San Diego, 1994).

[22] H.J. Kimble, Phys. Scr., T **T76**, 127 (1998).

[23] J.A. Stratton, *Electromagnetic Theory* (McGraw Hill, New York, 1997).

[24] Because the WGMs are the modes of an open resonator, the mode volume, $V_{\vec{P}}$, diverges as $r_Q \rightarrow \infty$. However, this divergence is logarithmic, and $V_{\vec{P}}$ is quite insensitive to the choice of r_Q for a large range of values. For example, at the optimal sphere size discussed in Sec. VI where $l=76$, $V_{\vec{P}}$ varies by less than 1% for $10 < 2\pi n/\lambda_0 (r_Q - a) < 10^3$. In this case, we take $(r_Q - a) \approx 100\ \mu$m.

[25] *Handbook of Optics*, 2nd ed., edited by M. Bass (McGraw Hill, New York, 1995), Vol. II, Chap. 33, p. 63.

[26] C. Lin, *Handbook of Microwave and Optical Components* (Wiley, New York, 1991).

[27] V.V. Datsyuk, Appl. Phys. B: Photophys. Laser Chem. **54**, 184 (1992).

[28] H.-B. Lin, J.D. Eversole, and A.J. Campillo, Opt. Commun. **77**, 407 (1990).

[29] C.J. Hood, J. Ye, and H.J. Kimble, Phys. Rev. A **64**, 033804 (2001).

[30] C.J. Hood, T.W. Lynn, A.C. Doherty, A.S. Parkins, and H.J. Kimble, Science **287**, 1457 (2000).

[31] D.W. Vernooy, A. Furusawa, N.P. Georgiades, V.S. Ilchenko, and H.J. Kimble, Phys. Rev. A **57**, R2293 (1998).

[32] M.L. Gorodetsky and V.S. Ilchenko, J. Opt. Soc. Am. B **16**, 147 (1999).

15. Itoh, S., Kojima, H., Yurimoto, H.. *Lunar Planet. Sci.* **XXXI,** 1323 (2000) [CD-ROM].
16. Stolper, E. & Paque, J. M. Crystallization sequences of Ca-Al-rich inclusions from Allende: The effects of cooling rate and maximum temperature. *Geochim. Cosmochim. Acta* **50,** 1785–1806 (1986).
17. Yurimoto, H., Morioka, M. & Nagasawa, H. Diffusion in single-crystals of melilite: I. Oxygen. *Geochim. Cosmochim. Acta* **53,** 2387–2394 (1989).
18. Lasaga, A. C. in *Kinetics and Equilibrium in Mineral Reactions* (ed. Saxena, S. K.)) 81–114 (Springer, New York, 1983).
19. Wasson, J. T., Yurimoto, H. & Russell, S. S. ^{16}O-rich melilite in CO3.0 chondrites; possible formation of common, ^{16}O-poor melilite by aqueous alteration. *Geochim. Cosmochim. Acta* **65,** 4539–4549 (2001).
20. Kojima, T., Yada, S. & Tomeoka, K. Ca-Al-rich inclusions in three Antarctic CO3 chondrites, Yamato-81020, Yamato-82050 and Yamato-790992: Record of low-temperature alteration. *Proc. NIPR Symp. Antarct. Meteorites* **8,** 79–96 (1995).
21. Itoh, S., Kojima, H. & Yurimoto, H. Petrography and oxygen isotopic compositions in refractory inclusions from CO chondrites. *Geochim. Cosmochim. Acta* (in the press).
22. Shu, F. H., Shang, H., Glassgold, A. E. & Lee, T X-rays and fluctuating X-winds from protostars. *Science* **277,** 1475–1749 (1997).
23. Shu, F. H., Shang, H., Gounelle, M., Glassgold, A. E. & Lee, T. The origin of chondrules and refractory inclusions in chondritic meteorites. *Astrophys. J.* **548,** 1029–1050 (2001).
24. Gounelle, M. *et al.* Extinct radioactivities and protosolar cosmic rays: Self-shielding and light elements. *Astrophys. J.* **548,** 1051–1070 (2001).
25. Yurimoto, H., Asada, Y. & Hirai, K. Oxygen isotopic composition of fine-grained CAIs and genetic relation to coarse-grained CAIs. *Meteorit. Planet. Sci.* **36,** A230 (2001).
26. Clayton, R. N. Oxygen isotopes in meteorites. *Annu. Rev. Earth Planet Sci.* **21,** 115–149 (1993).
27. Krot, A. N., McKeegan, K. D., Leshin, L. A., MacPherson, G. J. & Scott, E. R. D. Existence of an ^{16}O-rich gaseous reservoir in the solar nebula. *Science* **295,** 1051–1054 (2002).
28. Krot, A. N. *et al.* Refractory calcium-aluminum-rich inclusions and aluminum-diopside-rich chondrules in the metal-rich chondrites Hammadah al Hamra 237 and Queen Alexandra Range 94411. *Meteorit. Planet. Sci.* **36,** 1189–1216 (2001).
29. Cameron, A. G. W. The first ten million years in the solar nebula. *Meteoritics* **30,** 133–161 (1995).
30. Yurimoto, H., Ito, M. & Nagasawa, H. Oxygen isotope exchange between refractory inclusion in Allende and solar nebula gas. *Science* **282,** 1874–1877 (1998).

Supplementary Information accompanies the paper on **www.nature.com/nature**.

Acknowledgements We thank J. T. Wasson and A. E. Rubin for loaning us the thin section and for discussions. We also thank A. Meibom, A. N. Krot and T. J. Fagan for discussions and for improving the English of this Letter. This work was supported by Monbu-Kagaku-sho grants.

Competing interests statement The authors declare that they have no competing financial interests.

Correspondence and requests for materials should be addressed to H.Y. (yuri@geo.titech.ac.jp).

Generation of nonclassical photon pairs for scalable quantum communication with atomic ensembles

A. Kuzmich, W. P. Bowen, A. D. Boozer, A. Boca, C. W. Chou, L.-M. Duan & H. J. Kimble

Norman Bridge Laboratory of Physics 12-33, California Institute of Technology, Pasadena, California 91125, USA

Quantum information science attempts to exploit capabilities from the quantum realm to accomplish tasks that are otherwise impossible in the classical domain[1]. Although sufficient conditions have been formulated for the physical resources required to achieve quantum computation and communication[2], there is a growing understanding of the power of quantum measurement combined with the conditional evolution of quantum states for accomplishing diverse tasks in quantum information science[3–5]. For example, a protocol has recently been developed[6] for the realization of scalable long-distance quantum communication and the distribution of entanglement over quantum networks. Here we report the first enabling step in the realization of this protocol, namely the observation of quantum correlations for photon pairs generated in the collective emission from an atomic ensemble. The nonclassical character of the fields is demonstrated by the violation of an inequality involving their normalized correlation functions. Compared to previous investigations of non-classical correlations for photon pairs produced in atomic cascades[7] and in parametric down-conversion[8], our experiment is distinct in that the correlated photons are separated by a programmable time interval (of about 400 nanoseconds in our initial experiments).

The theoretical proposal of ref. 6 (hereafter 'DLCZ') is a probabilistic scheme based upon the entanglement of atomic ensembles via detection events of single photons in which the sources are intrinsically indistinguishable, and generates entanglement over long distances via a quantum repeater architecture[9]. The DLCZ scheme, with built-in quantum memory and entanglement purification, is well within the reach of current experiments and accomplishes the same objectives as previous more complex protocols that require as yet unattainable capabilities[9,10].

In our experiment, we demonstrate a basic primitive integral to the DLCZ scheme. Specifically, an initial 'write' pulse of (classical) light is employed to create a state of collective atomic excitation as heralded by photoelectric detection of a first photon 1. After a programmable delay δt, a subsequent 'read' pulse interrogates the atomic sample, leading to the emission of a second (delayed) photon 2. The manifestly quantum (or nonclassical) character of the correlations between the initial 'write' photon 1 and the subsequent 'read' photon 2 is verified by way of the observed violation of a Cauchy–Schwarz inequality for coincidence detection of the (1, 2) fields[7]. Explicitly, we find $[\tilde{g}^2_{1,2}(\delta t) = (5.45 \pm 0.11)] \nleq [\tilde{g}_{1,1}\tilde{g}_{2,2} = (2.97 \pm 0.08)]$, where $\tilde{g}_{i,j}$ are normalized correlation functions for the fields (i, j) and $\delta t = 405$ ns is the time separation between the (1, 2) emissions. The capabilities realized in our experiment provide an important initial step towards the implementation of the full DLCZ protocol, which would enable the distribution and storage of entanglement among atomic ensembles distributed over a quantum network. Extensions of these capabilities could facilitate scalable long-distance quantum communication[6] and quantum state engineering[11]. For example, by employing spin-polarized samples in optical-dipole or magnetic traps[12], it should be possible to extend the interval δt to times of several seconds.

Our experiment arises within the context of prior work on spin squeezing[13,14], and in particular on atomic ensembles where significant progress has been made in the development of methods to exploit collective enhancement of atom–photon interactions provided by optically thick atomic samples[15–20]. Instead of homodyne or heterodyne detection of light as used in spin-squeezing experiments[18–20], the DLCZ scheme involves photon-counting techniques, which present stringent requirements for broad bandwidth detection and for the suppression of stray light from the atomic ensemble.

As illustrated in Fig. 1, an optically thick sample of three-level atoms in a lambda-configuration is exploited to produce correlated photons via the following sequence. With atoms initially prepared in state $|a\rangle$ by optical pumping, a laser pulse from the 'write' beam tuned near the $|a\rangle \rightarrow |e\rangle$ transition illuminates the sample and induces spontaneous Raman scattering to the initially empty level $|b\rangle$ via the $|e\rangle \rightarrow |b\rangle$ transition at time $t^{(1)}$. The 'write' pulse is made sufficiently weak so that the probability to scatter one Raman photon into the preferred forward-propagating mode $\psi^{(1)}(\mathbf{r}, t)$ is much less than unity for each pulse. Detection of a photon in the mode $\psi^{(1)}(\mathbf{r}, t)$ produced by the $|e\rangle \rightarrow |b\rangle$ transition results in a single excitation in the atomic level $|b\rangle$ distributed across the

© 2003 Nature Publishing Group

sample. In the ideal case, this coherently symmetrized state is[6]:

$$|\Phi_{1A}\rangle \approx \sum_{j=1}^{N} |a\rangle_1 \ldots |b\rangle_j \ldots |a\rangle_N \tag{1}$$

Although the initial detection of photon 1 generated by the 'write' beam is probabilistic, the detection of photon 1 results in the conditional state $|\Phi_{1A}\rangle$ with one collective atomic 'excitation'. This excitation can subsequently be converted into an excitation of the light field with high probability 'on demand' with a specified emission and a programmable pulse shape[6,10,21,22]. To achieve the conversion from atoms to field, a laser pulse from the 'read' beam tuned near the $|b\rangle \rightarrow |e\rangle$ transition illuminates the atomic sample, thereby affecting the transfer $|b\rangle \rightarrow |a\rangle$ for the sample with the accompanying emission of a second Raman photon 2 on the $|e\rangle \rightarrow |a\rangle$ transition. For an optically thick atomic sample, photon 2 is emitted with high probability into a specified mode $\psi^{(2)}(\mathbf{r}, t)$ offset in time by $t^{(2)} = t^{(1)} + \delta t$. The spatial and temporal structure of the modes $\psi^{(1,2)}(\mathbf{r}, t)$ are set by the geometry of the atomic sample and by the shape and timing of the 'write' and 'read' beams[21]. In our experiment, the modes of the (write, read) beams are spatially mode-matched, with measured visibility greater than 95% for the case of equal frequency and polarization. The time delay δt is limited in principle only by the coherence time between the levels $|a\rangle$ and $|b\rangle$, which can be long in practice.

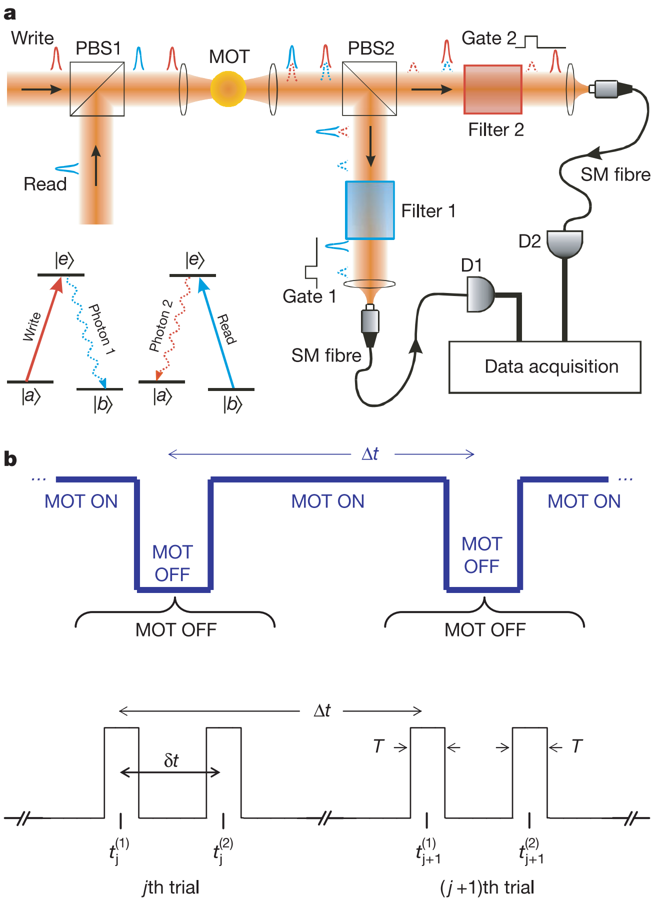

Figure 1 A simplified schematic of the experiment is presented. **a**, Diagram of the apparatus; **b**, the timing sequence for data acquisition. Further details are as follows. **a**, 'write' and 'read' pulses propagate sequentially into a cloud of cold Cs atoms (MOT), generating pairs of correlated output photons (1,2), with controlled separation δt. Fields with frequency near that of the $|a\rangle \leftrightarrow |e\rangle$ (or $|b\rangle \leftrightarrow |e\rangle$) transition are coloured red (or blue) here and in Figs 2 and 3. The 'write' and 'read' pulses have orthogonal polarizations, are combined into a single input at polarizing beam splitter PBS1, and are then focused into the Cs MOT with a waist of approximately 30 μm. The output fields are split by PBS2, which also serves as the first stage of filtering the ('write', 'read') beams from the (1,2) fields. For example, field 2 is transmitted by PBS2 to be subsequently registered by detector D2 while the 'read' pulse itself is reflected by 90° at PBS2 and then blocked by an acousto-optical modulator that serves as Gate 1. Further filtering is achieved by passing each of the outputs from PBS2 through separate frequency filters, each of which consists of a glass of Cs vapour optically pumped to place atoms into either $6S_{1/2}$, $F = 3$ or $F = 4$ (ref. 28). The small residual reflected (transmitted) light of the 'write' or 'read' pulse from PBS2 at frequency $\omega_{4,4}$ (or $\omega_{3,4}$) passes through a filter cell with atoms in the $F = 4(3)$ level. It is thereby strongly attenuated ($>10^6$), while the accompanying Raman-scattered light as photons 1(or 2) at frequency $\omega_{3,4}$(or $\omega_{4,4}$) is transmitted with high efficiency ($\simeq$80%). Transmission efficiencies from the MOT to detectors (D1, D2) are both about 30% for light with the spatial shape of the 'write' and 'read' beams and of the correct polarization. (D1, D2) have overall quantum efficiencies of approximately 50% (photon in to TTL pulse 'out'). **b**, Gating windows for the joint detection of photons (1,2) are centred at times $(t_j^{(1)}, t_j^{(2)})$ for the jth trial of the experiment during intervals when the MOT is 'OFF'.

The atomic sample for our experiment is provided by caesium atoms in a magneto-optical trap (MOT)[12], where the Cs hyperfine manifolds $\{|6S_{1/2}, F = 4\rangle, |6S_{1/2}, F = 3\rangle, |6P_{3/2}, F' = 4\rangle\}$ correspond to the levels $\{|a\rangle, |b\rangle, |e\rangle\}$, respectively. As illustrated by the timing diagram in Fig. 1, the MOT is chopped from ON to OFF with $\Delta t = 4\,\mu$s. In each cycle there is a 'dark' period of duration 1 μs when all light responsible for trapping and cooling is gated OFF, with less than 0.1% of atoms measured to remain in the $F = 3$ level at this stage. The jth trial of the protocol for single photon generation is initiated by a 'write' pulse which is resonant with the $6S_{1/2}, F = 4 \rightarrow 6P_{3/2}, F' = 4$ transition at frequency $\omega_{4,4}$ and that has duration $\simeq$51 ns (full-width at half-maximum, FWHM). A critical parameter for the experiment is the resonant optical thickness $\gamma_{4,4}$ of the atomic sample[21]. We measure $\gamma_{4,4} \simeq 4$–5 for cw excitation, corresponding to an attenuation of intensity $\exp(-\gamma_{4,4})$ in propagation through the MOT.

The 'write' pulse generates forward-scattered (anti-Stokes) Raman light around frequency $\omega_{3,4}$ from the $F' = 4$ excited level to the $F = 3$ ground level ($|e\rangle \rightarrow |b\rangle$) that is directed onto a single-photon detector D1. After a variable delay δt, the 'read' pulse illuminates the sample, with this pulse tuned to the $6S_{1/2}$, $F = 3 \rightarrow 6P_{3/2}$, $F' = 4$ transition at frequency $\omega_{3,4}$ with duration $\simeq$34 ns (FWHM). Raman (Stokes) light generated by the 'read' pulse around frequency $\omega_{4,4}$ from $F' = 4$ to $F = 4$ ($|e\rangle \rightarrow |a\rangle$) is directed onto a second single-photon detector D2.

By interchanging the frequencies for optical pumping of the filter cells described in Fig. 1, the (write, read) beams can be detected at (D1, D2) instead of the (1, 2) fields. An example of the resulting pulse profiles accumulated over many trials $\{j\}$ is presented in Fig. 2, where the origin in time is set to coincide with the approximate centre of the 'write' pulse, with the 'read' pulse following after a delay of $\simeq$415 ns determined by external control logic.

With the filter cells set to transmit the (1, 2) photons to the (D1, D2) detectors, respectively, we record histograms of the numbers $(n_1(t), n_2(t))$ of photoelectric events versus time, which are also displayed in Fig. 2. For the data presented here, the intensity of the 'write' pulse is kept low ($\sim 10^3$ photons per pulse), resulting in a time lag for the onset of the $n_1(t)$ counts in Fig. 2. As discussed in the Supplementary Information, the probability $p^{(1)}_{\text{write}}$ to generate an anti-Stokes photon 1 within the solid angle of our imaging system is $p^{(1)}_{\text{write}} \simeq 10^{-2}$ per pulse.

The 'read' pulse is about 100 times more intense than the 'write' pulse, leading to high efficiency $\zeta_{3\rightarrow 4} \simeq 0.6$ for the transfer of population $|b\rangle \rightarrow |a\rangle$, with $p^{(2)}_{\text{read}} \simeq \zeta_{3\rightarrow 4} p^{(1)}_{\text{write}}$ for the Stokes photon 2. Examples of the resulting detection events $n_2(t)$ are shown in Fig. 2. In contrast to the behaviour of $n_1(t)$, the intense 'read' beam generates $n_2(2)$ counts promptly. More extensive investigations of the timing characteristics of the emitted fields (1, 2) will be part of our subsequent investigations, including the relationship to electromagnetically induced transparency (EIT)[23,24].

A virtue of the DLCZ protocol is its insensitivity to a variety of

© 2003 Nature Publishing Group

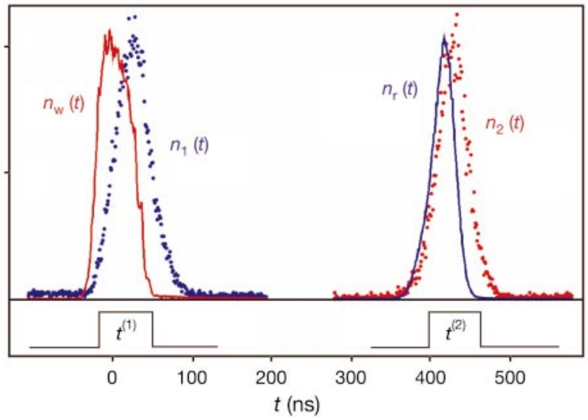

Figure 2 Normalized singles counts $n_i(t)$ are shown for the 'write', 'read' and (1,2) fields. The pulses around $t = 0$ are from detector D1 for the 'write' beam $n_w(t)$ (solid trace) and for photon 1, $n_1(t)$ (data points). The pulses around $t = 410$ ns are from detector D2 for the 'read' beam $n_r(t)$ (solid trace) and for photon 2, $n_2(t)$ (points). Note that in addition to the symmetrized excitation, each 'write' pulse also transfers several hundred atoms into the $F = 3$ level owing to spontaneous emission from its near-resonant character. However, atoms transferred into $F = 3$ via spontaneous decay are spatially uncorrelated, so that their contribution to the signal from the 'read' channel is strongly suppressed (by roughly the fractional solid angle collected, $\delta\Omega/4\pi \simeq 4\times10^{-5}$) as compared to the signal from single-atom excitations of the form $|\Phi_{1,A}\rangle$ (ref. 6).

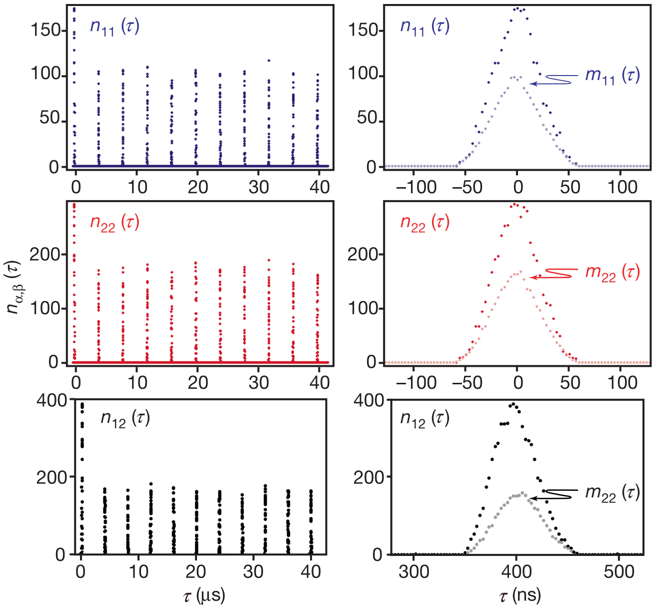

Figure 3 Time-resolved coincidences $n_{\alpha,\beta}(\tau)$ between the (1,1), (2,2) and (1,2) fields are displayed versus time delay τ. Left, $n_{\alpha,\beta}(\tau)$ is shown over 11 successive repetitions of the experiment. Right, the time axis is expanded to a total duration of 250 ns with $\tau = 0$ set to the centre of the gating window ($t^{(1)}$, $t^{(2)}$, $t^{(1)}$) for (n_{11}, n_{22}, n_{12}), respectively. The larger peak $n_{\alpha,\beta}(\tau)$ corresponds to detection pairs from the same trial j, while the smaller peak $m_{\alpha,\beta}(\tau)$ is for pairs from different trials as defined in the text. Typical acquisition parameters are as follows. Detectors (D1, D2) have average count rates of about (400 s^{-1}, 250 s^{-1}), respectively, while background counts with no MOT present are about 100 s^{-1}. Counts due to the MOT itself (with 'write' and 'read' beams blocked) are less than (10 s^{-1}, 20 s^{-1}) for (D1, D2). Dark counts with the inputs to the fibres blocked are less than 5 s^{-1}. All these numbers are for the gated-output mode of data acquisition as in Fig. 1 with $T = 60$ ns.

loss mechanisms, including inefficiencies in transport and detection of the (1, 2) photons. However, in an actual experiment, various non-ideal characteristics of the atom-field interaction (as in our MOT) do lead to deterioration of correlation for the (1, 2) photons (for example, imperfect filtering and/or background fluorescence as described in the caption of Fig. 2 and in the Supplementary Information). Fortunately there exists a well-defined border between the classical and quantum domains for the (1, 2) fields that can be operationally accessed via coincidence detection, as was first demonstrated in the pioneering work of Clauser[7].

As illustrated in Fig. 1b, electronic pulses from detectors (D1, D2) are separately gated with windows of duration $T = 60$ ns centred on times ($t^{(1)}$, $t^{(2)}$) corresponding to the approximate peaks of the ($n_1(t)$, $n_2(t)$) pulses shown in Fig. 2. Photoelectric events that fall within the gate windows are directed to a time-interval analyser (TIA) configured in a standard fashion for measurement of photoelectric correlations[25]. For a 'start' event from D1 within the interval $t_j^{(1)} \pm T/2$ for the jth trial of the experiment, the TIA records the times of 'stop' events from D2 within successive intervals $t_k^{(2)} \pm T/2$. Over many repetitions of the experiment, we thereby acquire time-resolved coincidences $n_{1,2}(\tau)$ between the (1, 2) fields, both within the same trial $k = j$ and for subsequent trials $k = j+1, j+2\ldots$ (that is, a 'start' event from trial j around time t_j and a 'stop' event from trial k around time t_k, where $t_k = t_j + (k - j)\Delta t$ for $k = j, j+1,\ldots$). By a 50%–50% beam splitter, the field 1 can be directed to detectors (D1, D2), and then in turn the field 2 to (D1, D2). We thus also acquire the time-resolved coincidences $n_{1,1}(\tau)$ and $n_{2,2}(\tau)$.

Figure 3 displays an example of data accumulated in this manner for coincidences $n_{\alpha,\beta}(\tau)$ between the (1,2), (1,1), and (2,2) beams, with successive peaks separated by the time between trials $\Delta t = 4$ μs. Note that there is an excess of coincidence counts in each of the initial peaks for joint detections from the same trial ($\tau < \Delta t$) as compared to $n_{\alpha,\beta}(\tau)$ from different trials ($\tau > \Delta t$). This excess is shown more clearly in the plots in the right column, which expand the time axis from the left column in Fig. 3. Here, data from successive trials $k = j+1,\ldots j+10$ have been offset to $\tau < \Delta t$ and then averaged for comparison with $n_{\alpha,\beta}(\tau)$ from the same trial j by introducing the quantity $m_{\alpha,\beta}(\tau) = (1/10)\sum_{k=j+1}^{j+10} n_{\alpha,\beta}(\tau + (k - j)\Delta t)$. As discussed in the Supplementary Information, statistical independence for trials with $k \neq j$ is enforced by the experimental protocol of reapplying the MOT and repumping beams after each trial.

From the data in Fig. 3, we determine the total number of coincidences $N_{\alpha,\beta} = \sum_{\{\tau_i\}} n_{\alpha,\beta}(\tau_i)$ with $(\alpha,\beta) = (1,2)$ obtained by summing over time bins $\{\tau_i\}$ for detection within the same trial j, and $M_{\alpha,\beta} = \sum_{\{\tau_k\}} m_{\alpha,\beta}(\tau_k)$ obtained from 'start' and 'stop' events from different trials ($j \neq k$). Fields for which the Glauber–Sudarshan phase-space function is well-behaved (that is, classical fields) are constrained by a Cauchy–Schwarz inequality for the various coincidence counts (Supplementary Information and ref. 25), namely:

$$[\tilde{g}_{1,2}(\delta t)]^2 \leq \tilde{g}_{1,1}\tilde{g}_{2,2} \qquad (2)$$

where $\tilde{g}_{1,1} \equiv N_{1,1}/M_{1,1}, \tilde{g}_{2,2} \equiv N_{2,2}/M_{2,2}, \tilde{g}_{1,2}(\delta t) \equiv N_{1,2}/M_{1,2}$.

For the data displayed in Fig. 3, we find $\tilde{g}_{1,1} = (1.739 \pm 0.020)$ and $\tilde{g}_{2,2} = (1.710 \pm 0.015)$, in correspondence to the expectation that the (1,2) fields should each exhibit gaussian statistics with $\tilde{g}_{1,1} = \tilde{g}_{2,2} = 2$ for the protocol of DLCZ in the ideal case, but here degraded by diverse sources of background counts (see Supplementary Information). By contrast, for the cross-correlations of the (1,2) fields, we record $\tilde{g}_{1,2}(\delta t) = (2.335 \pm 0.014)$, with $\delta t = 405$ ns. Hence the inequality of equation (2) for classical fields is strongly violated, namely $[\tilde{g}_{1,2}^2(\delta t) = 5.45 \pm 0.11] \nleq [\tilde{g}_{1,1}\tilde{g}_{2,2} = 2.97 \pm 0.08]$, where all errors indicate the statistical uncertainties. This violation of the Cauchy–Schwarz inequality clearly demonstrates the nonclassical character of the correlations between photons (1,2) generated by the (write, read) beams. Moreover, as discussed in more detail in the Supplementary Information, the measured coincidence rates in Fig. 3 explicitly document the cooperative nature of the

© 2003 Nature Publishing Group

emission process. Overall, we estimate that the probability $p_c^{(q)}$ for coincidence of the (1,2) photons due to collective atomic excitation as described by the state $|\Phi_{1A}\rangle$ is roughly $p_c^{(q)} \simeq 10^{-4}$ for each trial j, referenced to the output of the MOT.

The temporal extent of the photon wave packet $\psi(\mathbf{r}, t)$ for the (1,2) photons is also of some interest. To investigate this issue, we have carried out the experiment with expanded gate windows of duration $T = 140$ ns that then encompass the entire domains over which counts $n_1(t)$ and $n_2(t)$ are observed in Fig. 2. In this case, we record $\tilde{g}_{1,1} = (1.72 \pm 0.04)$, $\tilde{g}_{2,2} = (1.52 \pm 0.05)$, and $\tilde{g}_{1,2}(\delta t) = (2.45 \pm 0.10)$, now with δt set to be 320 ns. The classical inequality of equation (2) is once again not satisfied; $[\tilde{g}_{1,2}^2(\delta t) = 6.00 \pm 0.50] \nleq [\tilde{g}_{1,1}\tilde{g}_{2,2} = 2.61 \pm 0.11]$. These results with $T = 140$ ns also confirm that dead-time effects do not play a significant role in the current experiment.

As described in the Supplementary Information, the violation of the Cauchy–Schwarz inequality of equation (2) in the ideal case can be much larger than we have observed, namely $[\tilde{g}_{1,2}(\delta t)]^2/[\tilde{g}_{1,1}\tilde{g}_{2,2}] \simeq [(1+p)/(2p)]^2 \gg 1$, where $p \ll 1$ is the excitation probability. In our experiment, the size of the violation of the inequality was limited mostly by uncorrelated fluorescence from individual atoms in the atomic sample. This contribution will be made smaller in future experiments by moving to off-resonant excitation, which necessitates higher optical density. There is also a significant limitation due to the presence of the leakage light from the 'read' pulse. This classical pulse is only 9 GHz away from the single-photon field 2 of interest, and is filtered by a factor exceeding 10^{-9}. To achieve even stronger violation of the inequality, we must further improve the filtering capability.

Our observations of nonclassical correlations between the (1,2) photons represent the first important step in the realization of the protocol of DLCZ[6] for scalable quantum communication with atomic ensembles, although it is not yet sufficient for realization of the full protocol. Beyond the nonclassical correlations, our experiment also demonstrates successful filtering of the various fields and collective enhancement by the atomic ensemble, all of which are critical for realization of the full quantum repeater protocol. More generally, the capabilities that we have demonstrated should help to enable other advances in the field of quantum information, including implementation of quantum memory[22,26] and fully controllable single-photon sources[27], which, when combined, help to pave the avenue for realization of universal quantum computation[4].

Note added in proof: We have been made aware of a recently published related paper by van der Wal et al.[29]. □

Received 3 March; accepted 8 May 2003; doi:10.1038/nature01714.

1. Preskill, J. P. *Quantum Computation* Lecture Notes for Physics 219/Computer Science 219 ⟨http://www.theory.caltech.edu/people/preskill/ph229/⟩.
2. DiVincenzo, D. P. The physical implementation of quantum computation. *Fortsch. Phys.* **48,** 771–783 (2000).
3. Bose, S., Knight, P. L., Plenio, M. B. & Vedral, V. Proposal for teleportation of an atomic state via cavity decay. *Phys. Rev. Lett.* **83,** 5158–5161 (1999).
4. Knill, E., Laflamme, R. & Milburn, G. J. A scheme for efficient quantum computation with linear optics. *Nature* **409,** 46–52 (2001).
5. Raussendorf, R. & Briegel, H. J. A one-way quantum computer. *Phys. Rev. Lett.* **86,** 5188–5191 (2001).
6. Duan, L.-M., Lukin, M., Cirac, J. I. & Zoller, P. Long-distance quantum communication with atomic ensembles and linear optics. *Nature* **414,** 413–418 (2001).
7. Clauser, J. F. Experimental distinction between the quantum and classical field-theoretic predictions for the photoelectric effect. *Phys. Rev. D* **9,** 853–860 (1974).
8. Mandel, L. Quantum effects in one-photon and two-photon interference. *Rev. Mod. Phys.* **71**(2), S274–S282 (1999).
9. Briegel, H.-J., Duer, W., Cirac, J. I. & Zoller, P. Quantum repeaters: The role of imperfect local operations in quantum communication. *Phys. Rev. Lett.* **81,** 5932–5935 (1999).
10. Enk, S. J., Cirac, J. I. & Zoller, P. Photonic channels for quantum communication. *Science* **279,** 205–208 (1998).
11. Duan, L.-M. Entangling many atomic ensembles with laser manipulation. *Phys. Rev. Lett.* **88,** 170402–170405 (2002).
12. Metcalf, H. J. & van der Straten, P. *Laser Cooling and Trapping* (Springer, 1999).
13. Kitagawa, M. & Ueda, M. Nonlinear-interferometric generation of number-phase correlated fermion states. *Phys. Rev. Lett.* **67,** 1852–1854 (1991).
14. Wineland, D. J., Bollinger, J. J., Itano, W. M. & Moore, F. L. Spin squeezing and reduced quantum noise in spectroscopy. *Phys. Rev. A* **46,** R6797–R6800 (1992).
15. Kuzmich, A., Mølmer, K. & Polzik, E. S. Spin squeezing in an ensemble of atoms illuminated with squeezed light. *Phys. Rev. Lett.* **79,** 4782–4785 (1997).
16. Kuzmich, A., Bigelow, N. P. & Mandel, L. Atomic quantum non-demolition measurements and squeezing. *Europhys. Lett. A* **42,** 481–486 (1998).
17. Mølmer, K. Twin-correlations in atoms. *Eur. Phys. J. D* **5,** 301–305 (1999).
18. Hald, J., Sørensen, J. L., Schori, C. & Polzik, E. S. Spin squeezed atoms: A macroscopic entangled ensemble created by light. *Phys. Rev. Lett.* **83,** 1319–1320 (1999).
19. Kuzmich, A., Mandel, L. & Bigelow, N. P. Generation of spin squeezing via continuous quantum non-demolition measurements. *Phys. Rev. Lett.* **85,** 1594–1597 (2000).
20. Julsgaard, B., Kozhekin, A. & Polzik, E. S. Experimental long-lived entanglement of two macroscopic objects. *Nature* **413,** 400–403 (2001).
21. Duan, L.-M., Cirac, J. I. & Zoller, P. Three-dimensional theory for interaction between atomic ensembles and free-space light. *Phys. Rev. A.* **66,** 023818 (2002).
22. Fleischhauer, M. & Lukin, M. D. Dark-state polaritons in electromagnetically induced transparency. *Phys. Rev. Lett.* **84,** 5094–5097 (2000).
23. Harris, S. E. & Hau, L. V. Nonlinear optics at low light levels. *Phys. Rev. Lett.* **82,** 4611–4614 (1999).
24. Zibrov, A. S. *et al.* Transporting and time reversing light via atomic coherence. *Phys. Rev. Lett.* **88,** 103601 (2002).
25. Mandel, L. & Wolf, E. *Optical Coherence and Quantum Optics* (Cambridge Univ. Press, Cambridge, UK, 1995).
26. Schori, C., Julsgaard, B., Sørensen, J. L. & Polzik, E. S. Recording quantum properties of light in a long-lived atomic spin state: Towards quantum memory. *Phys. Rev. Lett.* **89,** 057903 (2002).
27. Pelton, M. *et al.* Efficient source of single photons: A single dot in a micropost microcavity. *Phys. Rev. Lett.* **89,** 233602 (2002).
28. Alexandrov, E. B., Balabas, M. V., Pasgalev, A. S., Verkhovskii, A. K. & Yakobson, N. N. Double-resonance atomic magnetometers: from gas discharge to laser pumping. *Laser Phys.* **6,** 244–251 (1996).
29. van der Wal, C. H. *et al.* Atomic memory for correlated photon states. *Science*, published online 22 May 2003 (doi:10.1126/science.1085946).

Supplementary Information accompanies the paper on **www.nature.com/nature**.

Acknowledgements H.J.K. gratefully acknowledges interactions with M. D. Lukin about various aspects of the experiment. This work was supported by the National Science Foundation, by the Caltech MURI Center for Quantum Networks, and by the Office of Naval Research.

Competing interests statement The authors declare that they have no competing financial interests.

Correspondence and requests for materials should be addressed to H.J.K. (hjkimble@caltech.edu).

Ultrafast terahertz probes of transient conducting and insulating phases in an electron–hole gas

R. A. Kaindl*, M. A. Carnahan*, D. Hägele*†, R. Lövenich* & D. S. Chemla*

* *Department of Physics, University of California at Berkeley, and Materials Sciences Division, E. O. Lawrence Berkeley National Laboratory, Berkeley, California 94720, USA*
† *Institut für Festkörperphysik, Universität Hannover, Appelstraße 2, 30167 Hannover, Germany*

Many-body systems in nature exhibit complexity and self-organization arising from seemingly simple laws. For example, the long-range Coulomb interaction between electrical charges has a simple form, yet is responsible for a plethora of bound states in matter, ranging from the hydrogen atom to complex biochemical structures. Semiconductors form an ideal laboratory for studying many-body interactions of electronic quasiparticles among themselves and with lattice vibrations and light[1–4]. Oppositely charged electron and hole quasiparticles can coexist in an ionized but correlated plasma, or form bound hydrogen-like pairs called excitons[5,6]. The pathways between such states, however, remain elusive in near-visible optical experiments that detect a subset of excitons with vanishing centre-of-mass momenta. In contrast, transitions between internal exciton levels, which occur in the

Efficient Engineering of Multiatom Entanglement through Single-Photon Detections

L.-M. Duan[1,2] and H. J. Kimble[3]

[1]*Institute for Quantum Information, MC 107-81, California Institute of Technology, Pasadena, California 91125-8100, USA*
[2]*Laboratory of Quantum Information, USTC, Hefei 230026, China*
[3]*Norman Bridge Laboratory of Physics 12-33, California Institute of Technology, Pasadena, California 91125, USA*

(Received 29 January 2003; published 23 June 2003)

We propose an efficient scheme to engineer multiatom entanglement by detecting cavity decay through single-photon detectors. In the special case of two atoms, this scheme is much more efficient than previous probabilistic schemes, and insensitive to randomness in the atom's position. More generally, the scheme can be used to prepare arbitrary superpositions of multiatom Dicke states without the requirements of high-efficiency detection and separate addressing of different atoms.

DOI: 10.1103/PhysRevLett.90.253601 PACS numbers: 42.50.Gy, 03.67.Mn

There is a large current interest in generation and engineering of quantum entanglement, with applications for fundamental tests of quantum mechanics [1], for high-precision measurements [2], and, in particular, for implementation of quantum communication and computation [3]. Although quantum entanglement is typically fragile to practical noise and technical imperfections, there exist elegant ways to overcome this sensitivity by designing schemes with inherent robustness to diverse sources of noise. Some schemes with this property have been known for entangling two single atoms [4–9] as well as for entangling macroscopic atomic ensembles [10,11]. In these schemes, feedback is typically applied to the system of interest based upon the outcome of certain measurements. The protocols are thereby probabilistic, succeeding only conditionally for particular measurement results. Imperfections and noise in these schemes decrease the success probability, but have no influence on the fidelity of the intended state generation for the "successful" subset of trials. In this way, a high-fidelity entangled state can be obtained simply by repeating the scheme successively.

Here, we propose a robust scheme to produce and engineer entanglement between multiple atoms in optical cavities. Compared with the previous robust schemes [4–11], our protocol has the following favorable features. (i) It is much more efficient in the sense that the success probability can be close to unity, whereas in the previous schemes [4,5,8–11], the success probability is required to be much smaller than 1 to have the property of inherent robustness. (ii) It is more insensitive to certain practical sources of noise, such as randomness in the atom's position, atomic spontaneous emission, or detector inefficiency. (iii) Individual addressing of atoms is not required [6], nor are single-photon states as initial resources [7]. (iv) Most importantly, our scheme is not limited to generation of two-atom entanglement. Indeed, we show that based on current experimental technology, it should be possible to generate any superposition of the Dicke states [12] between multiple atoms in an optical cavity. These Dicke states and their superpositions, including the multiparty GHZ states as special cases, are typically highly entangled, with many applications in quantum information science [2,13–15]. Their entanglement can be directly detected without separate addressing [2].

As the scheme here is inherently robust to noise, it works in principle for entangling atoms (or ions) both in free-space configurations and in high-Q cavities, albeit in the free-space case one has a much smaller efficiency to collect the emitted photons. In this Letter, for a close relation with the current experimental efforts [16–18], we assume that there is a standing-wave high-Q cavity around the atoms [19,20] to improve the collection efficiency.

To explain the scheme, let us start from the simplest case with two atoms trapped in two different cavities. The schematic setup is shown in Fig. 1(a), with the relevant atomic levels depicted in Fig. 1(b). The states $|g\rangle$, $|0\rangle$, $|1\rangle$ correspond to the hyperfine and the Zeeman sublevels of alkali atoms in the ground-state manifold, and $|e\rangle$ corresponds to an excited state. The atom is initially prepared in the state $|g\rangle$, but the basis vectors of a qubit are represented by the states $|0\rangle$ and $|1\rangle$. The transition $|g\rangle \rightarrow |e\rangle$ is driven adiabatically through a classical laser pulse with the corresponding Rabi frequency denoted by $\Omega(t)$ [21]. With the driving pulse, the atom is transferred with probability $p_c \simeq 1$ to the $|0\rangle$ and $|1\rangle$ states by emitting a photon from the transitions $|e\rangle \rightarrow |0\rangle$ or $|e\rangle \rightarrow |1\rangle$.

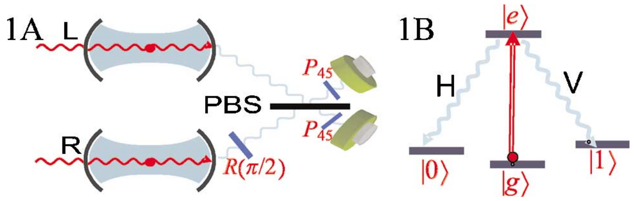

FIG. 1 (color online). (a) The schematic setup to generate entanglement between two atoms in different cavities **L** and **R**. (b) The relevant atomic level structure and the laser configuration.

© 2003 The American Physical Society

Without loss of generality, we assume that the transitions $|e\rangle \to |0\rangle$ and $|e\rangle \to |1\rangle$ are coupled to two degenerate cavity modes a^h and a^v with different polarizations h and v. The decay pulses from the two cavities are interfered at a polarization beam splitter (PBS), with the outputs detected by two single-photon detectors after a 45° polarizer [denoted as P_{45} in Fig. 1(a)]. The small fraction of the transmitted classical pulse can be easily filtered based on the frequency selection as detailed in Ref. [21]. For the decay pulse from the **R** cavity, a polarization rotator $R(\pi/2)$ is inserted before the PBS which exchanges h and v polarizations of the incoming photon. Conditioned upon registering one photon from *each* of the detectors, the two atoms in the cavities **L** and **R** will be prepared into the maximally entangled state

$$|\Psi_{LR}\rangle = (|01\rangle_{LR} + |10\rangle_{LR})/\sqrt{2}. \tag{1}$$

To see this, we write down the interaction Hamiltonian in the rotating frame, which, for each of the cavities, has the form (setting $\hbar = 1$)

$$H = \Omega(t)|e\rangle\langle g| + g_0|e\rangle\langle 0|a^h + g_1|e\rangle\langle 1|a^v + \text{H.c.}, \tag{2}$$

where g_0 and g_1 are the corresponding coupling rates. The cavity outputs a^{μ}_{out} ($\mu = h, v$) are connected with the cavity modes a^{μ} through the standard input-output relations $\dot{a}^{\mu} = -i[a^{\mu}, H] - \kappa a^{\mu}/2 - \sqrt{\kappa}a^{\mu}_{\text{in}}(t)$ and $a^{\mu}_{\text{out}}(t) = a^{\mu}_{\text{in}}(t) + \sqrt{\kappa}a^{\mu}$ [22], where κ is the cavity decay rate, and $a^{\mu}_{\text{in}}(t)$, with the commutation relation $[a^{\mu}_{\text{in}}(t), a^{\mu\dagger}_{\text{in}}(t')] = \delta(t - t')$, denotes the vacuum cavity input. We are interested in the limit for which the variation rate of $\Omega(t)$ is significantly smaller than the cavity decay rate κ. In this limit, we can define an effective single-mode bosonic operator a^{μ}_{eff} from the cavity output operator $a^{\mu}_{\text{out}}(t)$ as $a^{\mu}_{\text{eff}} = \int_0^T f(t)a^{\mu}_{\text{out}}(t)dt$ (see Refs. [21,23]), where T is the pulse duration and $f(t)$ is the output pulse shape, which is determined by the shape of $\Omega(t)$ as $f(t) = \sqrt{\kappa}\sin\theta(t)\exp[-(\kappa/2)\int_0^t \sin^2\theta(\tau)d\tau]$ with $\sin\theta(t) = \Omega(t)/\sqrt{|g_0|^2 + |g_1|^2 + |\Omega(t)|^2}$. After the driving pulse, for each of the cavities λ ($\lambda = \mathbf{L}, \mathbf{R}$), the final state between the atom and the corresponding cavity output has the form

$$|\Psi\rangle_{\lambda} = (g_0|0\rangle_{\lambda}|h\rangle_{\lambda} + g_1|1\rangle_{\lambda}|v\rangle_{\lambda})/\sqrt{|g_0|^2 + |g_1|^2}, \tag{3}$$

where $|\mu\rangle = a^{\mu\dagger}_{\text{eff}}|\text{vac}\rangle$, ($\mu = h, v$), and $|\text{vac}\rangle$ denotes the vacuum state of the optical modes.

If the driving pulses have the same shape $\Omega(t)$ for the **L** and **R** cavities, the output single-photon pulses from the two cavities will also have the same shape $f(t)$, and they will interfere with high visibility at the polarization beam splitter (PBS). If one gets a "click" from each of the detectors at the outputs of the PBS, the two incoming photons can be either both in h polarizations or both in v polarizations, and these two possibility amplitudes are coherently superposed when the incoming photon pulses overlap with each other with the same shape. Therefore, the measurement in Fig. 1(a), together with the polarization rotator $R(\pi/2)$, corresponds to projecting the whole state $|\Psi\rangle_L \otimes |\Psi\rangle_R$ between the atoms and the photons onto a subspace with the projection operator given by $P_s = |hv\rangle_{LR}\langle hv| + |vh\rangle_{LR}\langle vh|$. Within this measurement scheme, the state $|\Psi\rangle_L \otimes |\Psi\rangle_R$ is effectively equivalent to the four-particle GHZ state

$$|\Psi_{\text{eff}}\rangle \propto P_s|\Psi\rangle_L \otimes |\Psi\rangle_R \propto (|01\rangle_{LR} \otimes |hv\rangle_{LR} + |10\rangle_{LR} \otimes |vh\rangle_{LR})/\sqrt{2}. \tag{4}$$

The 45° polarizers in Fig. 1(a) project the photon polarizations to the $(|h\rangle + |v\rangle)/\sqrt{2}$ state. It immediately follows from Eq. (4) that after this measurement the two atoms will be prepared in the maximally entangled state (1). If one rotates the angles of the polarizers in Fig. 1(a), corresponding a measurement of the incoming photon polarizations either in the $\{|h\rangle, |v\rangle\}$ basis or in the $\{(|h\rangle + |v\rangle)/\sqrt{2}, (|h\rangle - |v\rangle)/\sqrt{2}\}$ bases, one can further demonstrate four-particle GHZ-type of entanglement between the atoms and the photons as indicated by the effective state (4) [24]. The 45° polarizer can also be replaced by a PBS with both of its outputs detected by single-photon detectors. The measurement success probability is then increased by a factor of 2 for each side, and the overall success probability of this scheme becomes $p_s = 2|g_0g_1|^2/(|g_0|^2 + |g_1|^2)^2$.

Before introducing the multiatom entangling scheme, we offer a few remarks about this two-cavity scheme. First, it is evident that the scheme is inherently robust to atomic spontaneous emission, output coupling inefficiency, and detector inefficiency, all of which contribute to loss of photons. Since a click from each of the detectors is never recorded if one photon is lost, these processes simply decrease the success probability p_s by a factor of η^2 (where $1 - \eta$ denotes the loss for each of the photons), but have no influence on the fidelity of the final state $|\Psi_{LR}\rangle$. Second, our scheme does not require localization of the atom in the cavity to the Lamb-Dick limit. For the standing-wave cavity shown in Fig. 1(a) and with the collinear pumping configuration proposed in Ref. [21], $\Omega(t)$, g_0, and g_1 depend on the atom's position through approximately the same cavity mode function. The pulse shape $f(t)$, which is determined by the ratios $\Omega(t)/g_0$ and $\Omega(t)/g_1$, thus becomes basically independent of the random variation in the atom's position. For a traveling-wave cavity or for a free-space configuration, the atom's position affects only the common phase of the coupling rates g_0 and g_1, and in this case, a transverse pumping configuration also suffices since the randomness in the common phase of g_0 and g_1 has no influence on the final entangled state $|\Psi_{LR}\rangle$. Finally, the success probability of our scheme is $p_s \sim 1/2$ in the ideal case with $g_0 \sim g_1$ and $\eta \sim 1$, which shows that the present scheme is significantly more efficient than the previous schemes

[4,5,8–11], where the success probability is required to be much smaller than 1 even if $\eta \rightarrow 1$.

We next extend our basic scheme to entangle multiple atoms in the same optical cavity. The schematic setup is shown by Fig. 2, with each of the N_a atoms taken to have the same level structure as depicted in Fig. 1(b) and with the atoms not separately addressable [16–18]. The initial state of the system has the form $|G\rangle = \bigotimes_{i=1}^{N_a} |g\rangle_i$ with all the atoms prepared to the ancillary state $|g\rangle$. The driving laser, incident from one side mirror, is now divided into M sequential pulses, with $M \geq N_a/2$. We assume that the intensity of the pulse is controlled so that for each of the M pulses, an approximate fraction $1/M$ of the atomic population is transferred adiabatically from the $|g\rangle$ state to the $|0\rangle$ or $|1\rangle$ states, by emitting on average N_a/M photons with h or v polarizations. The output photons from the cavity decay are split by a PBS according to their polarizations, and then registered through two single-photon detectors (called h and v detectors, respectively). For each driving pulse, we may or may not get a click from the h or v detectors, which are assumed *not* to distinguish one or more photons. For the whole M pulses, we can count the total number of "clicks" (n_h, n_v) registered from the (h, v) detectors, respectively. Of course, $n_h + n_v \leq N_a$ since there are only N_a atoms. If it turns out that $n_h + n_v = N_a$, the following Dicke state results for the N_a atoms:

$$|N_a, n_h\rangle = c(n_h)(s_0^\dagger)^{n_h}(s_1^\dagger)^{N_a - n_h}|G\rangle. \qquad (5)$$

Here, the collective operators $s_\mu^\dagger$ $(\mu = 0, 1)$ are defined as $s_\mu^\dagger = \sum_{i=1}^{N_a} |\mu\rangle_i\langle g|$, and the normalization coefficient $c(n_h) = [N_a! n_h!(N_a - n_h)!]^{-1/2}$. Except the trivial cases with $n_h = 0, N_a$, clearly the Dicke state $|N_a, n_h\rangle$ is entangled. The multiatom Dicke states and the GHZ states in general belong to different classes of entangled states, and the Dicke states are relatively more robust to the influence of noise [13]. The Dicke states have some interesting applications in quantum information processing and in high-precision measurements [14,15].

To understand why a Dicke state results conditioned upon the above type of measurement, we note that each atom has an equal probability to emit a photon with the same pulse shape for each driving pulse for the assumed sequence of adiabatic passages. Hence, each driving pulse involves a collective excitation of the atoms to the $|0\rangle$ or $|1\rangle$ levels with homogeneous superposition coefficients. For the subset of measurements for which we register N_a photoelectric events in total from the h and v detectors for the whole M pulses, each click of the detectors should correspond exactly to the emission of one and only one photon by the atoms. This is the case even if there are photon loss and detector inefficiencies, because we post select only the trials with exactly N_a photoelectric events. Therefore, for each click registered from the h or v detectors for these trials, we should apply correspondingly the collective operators $s_0^\dagger$ or $s_1^\dagger$ to the atomic state. After registering n_h h-polarized photons and $(N_a - n_h)$ v-polarized photons, we get exactly the state of Eq. (5). Similar to the two-cavity scheme, this multiatom entangling scheme is also robust to practical imperfections, such as a moderate randomness in the atoms' positions and various sources of photon loss. Again, photon loss reduces the success probability instead of the state fidelity.

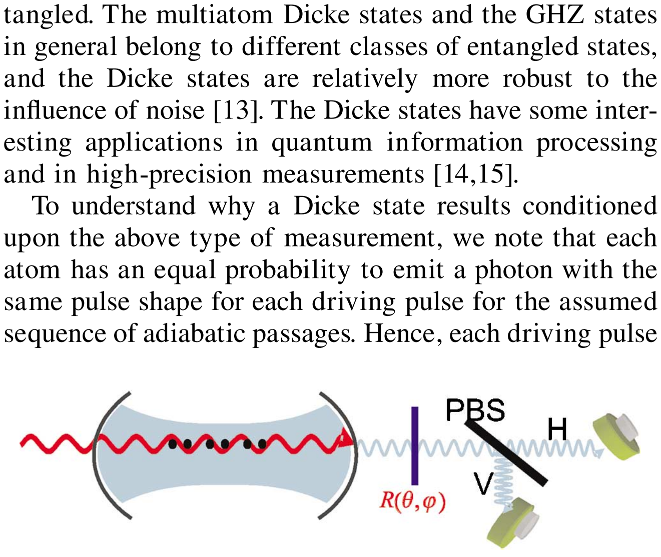

FIG. 2 (color online). The schematic setup to generate entanglement between multiple atoms in the same cavity. The polarization rotator $R(\theta, \varphi)$ is only required for generation of superpositions of the Dicke states.

To calculate the success probability of the multiatom entangling scheme, we note that the stepwise driving method described above is actually equivalent to the following one-step driving method: we transfer all the atomic population to the $|0\rangle$ and $|1\rangle$ levels with a single driving pulse, but both of the h and v polarized photons after the PBS need to be further split equally into M paths through a series of beam splitters, with separate photoelectric detection for each path. The state in Eq. (5) corresponds to the case when n_h h detectors and $(N_a - n_h)$ v detectors register a photoelectric event. When two or more photons go to the same path, the number of detector events is certainly less than N_a. So, for overall success with N_a events, we require that each photon follow a distinct path, for which the success probability is given by $p_{si} = (2M)!/[(2M - N_a)!(2M)^{N_a}]$ (in total there are $2M$ paths. For simplicity, we have assumed $g_0 \approx g_1$ so that one has equal probability to get h or v photons.) All photon loss processes simply contribute to an undercount probability $1 - \eta$ for each photon. Hence, the success probability to generate one of the Dicke states of Eq. (5) is $p_{\mathrm{succ}} = \eta^{N_a} p_{si}$, while the probability to obtain a specific Dicke state $|N_a, n_h\rangle$ is $p_{n_h} = p_{\mathrm{succ}} 2^{-N_a} N_a!/[n_h!(N_a - n_h)!]$. Excluding the trivial cases with $n_h = 0, N_a$, we then find that the success probability to obtain an entangled state from this scheme is $p_{en} = p_{\mathrm{succ}}(1 - 2^{-N_a+1})$, which tends to unity in the case $2M \gg N_a$ if we neglect contributions from photon loss (i.e., $\eta \rightarrow 1$). This scheme could thus be quite efficient. For instance, with $\eta = 0.70$ (0.20) and $M = 50$ (10) pulses, $p_{en} = 0.018$ (1.9×10^{-4}) for $N_a = 10$ (5) atoms, so that repeating this scheme on average $1/p_{en} \approx 56$ (5.4×10^3) times leads to a high-fidelity entangled state between 10 (5) atoms. In current experimental setups [16,17], the typical duration Δt of the adiabatic pulse is a few hundred nanoseconds, so that the total duration

$(M/p_{en})\Delta t \simeq 1$ (20) ms for entangling 10 (5) atoms with $\eta = 0.70$ (0.20). The currently available trapping time of atoms in high-Q cavities is about 1 sec [16].

Finally, we would like to extend further the above scheme to generate any superposition of the Dicke states $|N_a, n_h\rangle$. For this purpose, we simply insert a polarization rotator $R(\theta, \varphi)$ before the PBS as shown in Fig. 2, which transforms the photon polarizations according to $|h\rangle \rightarrow \cos\theta|h\rangle + \sin\theta e^{i\varphi}|v\rangle$ and $|v\rangle \rightarrow -\sin\theta e^{-i\varphi}|h\rangle + \cos\theta|v\rangle$. We assume that the parameters θ, φ can be separately controlled for each driving pulse, and are denoted by θ_m, φ_m for the mth pulse. As before, we consider only the subset of cases for which exactly N_a photoelectric events are registered from the whole M-pulse sequence. If the h (or v) detector clicks for the mth pulse with the control parameters θ_m, φ_m, the corresponding atomic excitation operator P_{m0} (or P_{m1}) is expressed by the collective operators $s_\mu^\dagger$ as $P_{m\mu} = \cos\theta_m s_\mu^\dagger - (-1)^\mu \sin\theta_m e^{i\varphi_m(-1)^\mu} s_{1-\mu}^\dagger$ ($\mu = 0, 1$). So, after N_a registered events, the final atomic state has the form $|\Psi_F\rangle = \prod_{i=1}^{N_a} P_{m_i\mu}|G\rangle$, where m_i ($i = 1, 2, \ldots, N_a$) denote the set of driving pulses for which we register a photon. Each operator $P_{m_i\mu}$ introduces two real parameters $\theta_{m_i}, \varphi_{m_i}$, so there are $2N_a$ independently controllable real parameters in the state $|\Psi_F\rangle$. The state $|\Psi_F\rangle$ can be written in general in the form

$$|\Psi_F\rangle = \sum_{n_h=0}^{N_a} b(n_h)|N_a, n_h\rangle, \tag{6}$$

where the Dicke states $|N_a, n_h\rangle$ are defined by Eq. (5), and the complex superposition coefficients $b(n_h)$ are functions of $\theta_{m_i}, \varphi_{m_i}$. Superpositions of the Dicke states have $2N_a$ degrees of freedom, which exactly equals to the number of control parameters $\theta_{m_i}, \varphi_{m_i}$.

Actually, we can prove that an *arbitrary superposition* of the Dicke states $|N_a, n_h\rangle$ [i.e., the state $|\Psi_F\rangle$ with any coefficients $b(n_h)$] is obtainable by choosing an appropriate set of control parameters $\theta_{m_i}, \varphi_{m_i}$. For the proof, we write the state (6) in the form $|\Psi_F\rangle = b(N_a)c(N_a) \times \sum_{n_h=0}^{N_a} b'(n_h)(s_0^\dagger)^{n_h}(s_1^\dagger)^{N_a-n_h}|G\rangle$, where $b'(n_h) = c(n_h)b(n_h)/[b(N_a)c(N_a)]$, and without loss of generality we have assumed $b(N_a) \neq 0$. Each of the atomic excitation operators $P_{m_i\mu}$ can be expressed as $P_{m_i\mu} \propto (s_0^\dagger - r_{m_i\mu}s_1^\dagger)$, where the complex coefficient $r_{m_i\mu}$, determined by the real parameters $\theta_{m_i}, \varphi_{m_i}$, is the relevant control parameter. To prepare a desired state $|\Psi_F\rangle$ with the superposition coefficients $b'(n_h)$, we need to choose the parameters $r_{m_i\mu}$ to satisfy the algebraic equation $\prod_{i=1}^{N_a}(s_0^\dagger - r_{m_i\mu}s_1^\dagger) = \sum_{n_h=0}^{N_a} b'(n_h)(s_0^\dagger)^{n_h}(s_1^\dagger)^{N_a-n_h}$. It immediately follows from this equation that the parameters $r_{m_i\mu}$ should be the N_a solutions of the N_ath-order algebraic equation $\sum_{n_h=0}^{N_a} b'(n_h)x^{n_h} = 0$, where x denotes the variable. In the complex domain, there always exist N_a solutions to the N_ath-order algebraic equation, and the parameters $r_{m_i\mu}$ are uniquely determined from these solutions if we do not care about the order of the excitation operators $P_{m_i\mu}$ (note that they commute with each other). This finishes the proof.

This work was supported by the Caltech MURI Center DAAD19-00-1-0374, by NSF Grants No. EIA-0086038 and No. PHY-0140355, and by the Office of Naval Research. L. M. D. was also supported by the CSF, the CAS, and the "97.3" project 2001CB309300.

[1] N. D. Mermin, Phys. Rev. Lett. **65**, 1838 (1990).
[2] J. J. Bollinger, W. M. Itano, D. Wineland, and D. Heinzen, Phys. Rev. A **54**, 4649 (1996); C. A. Sacket *et al.*, Nature (London) **404**, 256 (2000).
[3] M. A. Nielsen and I. L. Chuang, *Quantum Computation and Quantum Information* (Cambridge University Press, Cambridge, United Kingdom, 2000).
[4] C. Cabrillo, J. I. Cirac, P. G-Fernandez, and P. Zoller, Phys. Rev. A **59**, 1025 (1999).
[5] S. Bose, P. L. Knight, M. B. Plenio, and V. Vedral, Phys. Rev. Lett. **83**, 5158 (1999).
[6] M. B. Plenio, S. F. Huelga, A. Beige, and P. L. Knight, Phys. Rev. A **59**, 2468 (1999).
[7] J. Hong and H.-W. Lee, Phys. Rev. Lett. **89**, 237901 (2002).
[8] A. S. Sorensen and K. Molmer, quant-ph/0206142.
[9] I. E. Protsenko, G. Reymond, N. Schlosser, and P. Grangier, quant-ph/0206007.
[10] L. M. Duan, M. D. Lukin, J. I. Cirac, and P. Zoller, Nature (London) **414**, 413 (2001).
[11] L. M. Duan, Phys. Rev. Lett. **88**, 170402 (2002).
[12] L. Mandel and E. Wolf, *Optical Coherence and Quantum Optics* (Cambridge University Press, Cambridge, United Kingdom, 1995).
[13] W. Dür, G. Vidal, and J. I. Cirac, Phys. Rev. A **62**, 062314 (2000).
[14] P. Bouyer and M. A. Kasevich, Phys. Rev. A **56**, R1083 (1997).
[15] A. Cabello, Phys. Rev. A **65**, 032108 (2002).
[16] J. McKeever *et al.*, quant-ph/0211013 [Phys. Rev. Lett. (to be published)].
[17] A. Kuhn, M. Hennrich, and G. Rempe, Phys. Rev. Lett. **89**, 067901 (2002).
[18] Y. Shimizu *et al.*, Phys. Rev. Lett. **89**, 233001 (2002).
[19] T. Pellizzari *et al.*, Phys. Rev. Lett. **75**, 3788 (1995).
[20] J. I. Cirac *et al.*, Phys. Rev. Lett. **78**, 3221 (1997).
[21] L.-M. Duan, A. Kuzmich, and H. J. Kimble, Phys. Rev. A **67**, 032305 (2003).
[22] D. F. Walls and G. J. Milburn, *Quantum Optics* (Springer-Verlag, Berlin, Heidelberg, 1994).
[23] M. D. Lukin, S. F. Yelin, and M. Fleischhauer, Phys. Rev. Lett. **84**, 4232 (2000).
[24] J.-W. Pan *et al.*, Phys. Rev. Lett. **86**, 4435 (2001).

arXiv:quant-ph/0207076 v1 12 Jul 2002

Quantum teleportation of light beams

T. C. Zhang, K. W. Goh, C. W. Chou, P. Lodahl, and H. J. Kimble
Norman Bridge Laboratory of Physics 12-33, California Institute of Technology, Pasadena, CA 91125

(Dated: July 11, 2002)

We experimentally demonstrate quantum teleportation for continuous variables using squeezed-state entanglement. The teleportation fidelity for a real experimental system is calculated explicitly, including relevant imperfection factors such as propagation losses, detection inefficiencies and phase fluctuations. The inferred fidelity for input coherent states is $F = 0.61 \pm 0.02$, which when corrected for the efficiency of detection by the output observer, gives a fidelity of 0.62. By contrast, the projected result based on the independently measured entanglement and efficiencies is 0.69. The teleportation protocol is explained in detail, including a discussion of discrepancy between experiment and theory, as well as of the limitations of the current apparatus.

I. INTRODUCTION

The *No Cloning Theorem* prohibits making an exact copy of an unknown quantum state [1]. Yet, it is nevertheless possible to transport an unknown quantum state from one place to another without having the associated physical object propagate through the intervening space by way of a process termed *quantum teleportation* in the landmark work by Bennett et al. [2] in 1993. This “disembodied” transport of quantum states is made possible by utilizing shared quantum entanglement and classical communication between the sending and receiving locations. In recent years, quantum teleportation has played a central role in quantum information science and has become an essential tool in diverse quantum algorithms and protocols [3, 4].

By contrast, progress on an experimental front has been rather more modest in the actual attainment of quantum teleportation [5, 6, 7, 8]. An overview of these various experiments as well as operational criteria for gauging laboratory success can be found in Refs. [9, 10]. Significantly, to date only the experiment of Furusawa et al. [7] on continuous variables has achieved unconditional quantum teleportation [11].

The purpose of this paper is to present a report of our progress in the continuation of the experiment as reported by Furusawa et al. [7] and as described in Ref. [12]. We give a detailed description of our quantum teleportation apparatus and procedures, and include recent experimental results [13]. Some notable distinctions between our current experiment and the previous one by Furusawa et al. are improved EPR entanglement, better detection efficiencies, and ultimately, a higher fidelity between the input and teleported output states. We also investigate in some detail the various factors that limit the quality of the teleportation procedure under realistic conditions and as are applicable to the experimental setup. We provide a detailed model of the entire experiment that includes essentially all of the dominant loss mechanisms and utilize this model to gain insight into the limitations of the current apparatus and protocols, and thereby to discover methods of circumventing these limitations.

Our experiment is based on the continuous variable teleportation protocol first proposed in [14], which in turn was motivated by the work of Vaidman [15]. In our realization of this protocol, an entangled EPR state [16] is created from two independent squeezed fields. One half of this entangled state (called EPR1) is sent to Alice, who in turn combines it at a 50/50 beamsplitter with an unknown input state that is intended for teleportation. Note that the input quantum state is unknown to both Alice and Bob. Alice subsequently measures the x and p quadratures of the two output fields from the beamsplitter, the x quadrature for one beam and the p quadrature for the other. This measurement of (x, p) provides the continuous variable analogy to a Bell-state measurement for the discrete variable case [17]. In the limit of perfect EPR correlations, Alice gains no information about the input state. The output photocurrents from Alice’s two quadrature measurements are transmitted to Bob via classical information channels. Bob then uses them to perform a continuous phase space displacement on the second EPR beam (EPR2), thereby generating the teleported output state. For perfect EPR correlations, the teleported state has unit fidelity with the original unknown input state, as can be verified by “Victor” who both generates the original input and measures the teleported output. Of course, the limit of this ideal case is unattainable in any laboratory setting. This necessitates the introduction of operational criteria to gauge the success of the protocol, as discussed in Refs. [9, 10], and as will be applied in relation to our experiment.

The paper is organized as follows. In Sec. II we discuss the fidelity for quantum teleportation in the presence of losses and phase fluctuations, including importantly for the EPR beams. In Sec. III this model is connected to the laboratory via a detailed discussion of the generation of our EPR resource, including specifications of the optical parametric oscillator (OPO) parameters, the obtainable squeezing, and the characterization of the EPR state. The technical details of the actual implementation of the quantum teleportation protocol are discussed in depth in Sec. IV with emphasis on the phase-lock servo systems and the calibration of the classical information channels. Here, we also present new data on the teleportation of coherent states of light. These experimental data are compared to theoretical calculations based on the relevant parameters for the experiment, with each parameter measured in absolute terms without adjustment. Finally, we collect our conclusions in Sec. V, together with an outlook for future progress.

II. THEORY

In this section a theoretical description of the quantum teleportation protocol for continuous variables is given. This is a generalization of previous work in order to include all relevant detector inefficiencies and phase offsets for the experiment. The discussion is divided into two parts: in Sec. II A the effect of nonideal homodyne detectors is investigated while Sec. II B concerns phase fluctuations due to imperfect phase-lock servos. Both effects turn out to be of substantial importance in trying to accurately model experimental data.

A. Detection inefficiencies

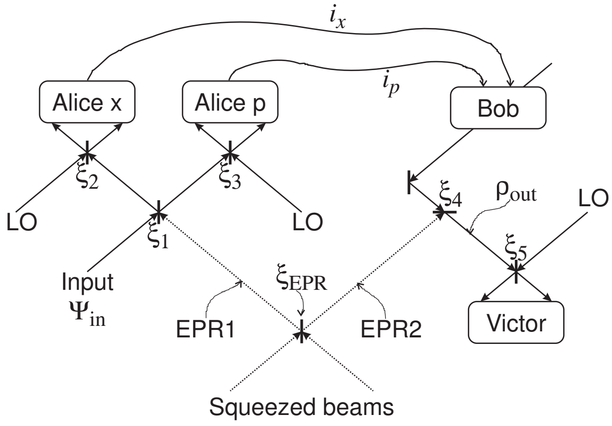

FIG. 1: Main parts in the teleportation protocol for continuous variables. Indicated are the relevant efficiencies ($\xi_{1\to5}, \xi_{EPR}$) that limit the teleportation fidelity.

Fig. 1 shows a simplified schematic of the experiment for teleportation of an unknown quantum state provided by the verifier Victor and characterized by a pure input state $|\psi_{in}\rangle$. The process is as follows: Alice performs measurements of the two quadratures x and p of the fields obtained by combining the unknown input state with EPR1. This is done by implementing two balanced homodyne detectors where the signal fields are each combined with a strong coherent local oscillator (LO) and the resulting output intensities are measured. Subtracting the two photocurrents from a given set of detectors results in a signal proportional to the quadrature amplitude, with the relevant quadrature selected by the phase of the LO. The efficiency of the homodyne detectors can be characterized by the visibilities (ξ_2, ξ_3) of the overlap between the LOs and the output beams from Alice's beamsplitter, as well as the detectors' quantum efficiency (α). Furthermore, the visibility (ξ_1) of the overlap between the input state and EPR1 is relevant.

Because of the nature of the EPR correlations, the effect of Alice's quadrature measurements is to project EPR2 onto a state that differs from the unknown input state only by a phase space displacement. The necessary displacement, however, depends on the outcome of Alice's measurements. Hence the task for Bob is to perform this phase space displacement with the classical information received from Alice by way of the photocurrents (i_x, i_p) shown in Fig. 1. In practice this is accomplished by overlapping EPR2 with a phase and amplitude modulated coherent state on a 99/1 beamsplitter. This modulation is directly driven (with suitable gain and phase compensation) by the photocurrents (i_x, i_p) from Alice's detectors. The relevant efficiency is the visibility (ξ_4) between EPR2 and the modulated coherent state. Finally, the quality of the teleportation can be checked by a third party (Victor) that performs homodyne detection on the output state. The visibility of Victor's homodyne detector is denoted ξ_5.

As discussed in more detail in Refs. [9, 10], the performance of the teleportation protocol can be quantified by the fidelity F, which is defined by

$$F = \langle \psi_{in} | \rho_{out} | \psi_{in} \rangle \,, \tag{1}$$

which is simply the overlap between the input state $|\psi_{in}\rangle$ (which is assumed to be a pure state) and the output state characterized by a density matrix ρ_{out}. In the limit of perfect detectors (unity efficiencies) but with a finite degree of EPR correlation, the fidelity for quantum teleportation of coherent states can be shown to be [7, 9]

$$F = \frac{2}{\sigma_Q} \exp\left[-\frac{2}{\sigma_Q} |\beta_{out} - \beta_{in}|^2 \right], \tag{2}$$

where

$$\sigma_Q = \sqrt{(1+\sigma_W^x)(1+\sigma_W^p)}, \tag{3a}$$

$$\sigma_W^x = \sigma_W^p = g^2 + \frac{1}{2} e^{2r_+}(1-g)^2 + \frac{1}{2} e^{-2r_-}(1+g)^2. \tag{3b}$$

Here σ_W^x and σ_W^p are the variances (in the Wigner representation) of the teleported x and p quadratures that emerge from Bob's beamsplitter (as shown in Fig. 1 at ρ_{out}). g is gain of the classical channels, where we have assumed that the two classical channels have the same gain and that any phase offsets have been appropriately compensated. Furthermore, β_{in}, β_{out} are the amplitudes of the unknown input field and teleported output field respectively. Finally, r_+, r_- are the anti-squeezing and squeezing parameters, respectively, for the two equally squeezed beams used to produce the EPR correlations, as will be discussed in detail in Sec. III C.

Any real experiment of course suffers from finite losses in propagation and detection, with the individual efficiencies being critical due to the fragility of quantum states of light. It turns out that the general expression (2) for the fidelity still applies to the case with losses, but the variances of the quadratures of the teleported field generalized. In addition, we take into account the fact that we do not observe the output state directly, but instead measure the output photocurrent from Victor's balanced homodyne detector. If we assume as before that the input states to Alice are coherent states, then the quadrature variance σ_V^x recorded by Victor for the teleported output state can be written as

$$\sigma_V^x = 1 - r_B^2 \xi_4^2 \xi_5^2 \eta_V^2 - g_x^2 \xi_1^2 + \frac{2 g_x^2}{\xi_2^2 \eta_{Ax}^2} + \frac{e^{-2r_-}}{2}\left(g_x \xi_1 + r_B \xi_4 \xi_5 \eta_V\right)^2 + \frac{e^{2r_+}}{2}\left(g_x \xi_1 - r_B \xi_4 \xi_5 \eta_V\right)^2 , \tag{4}$$

and the variance for the p quadrature is given by $\sigma_V^p = \sigma_V^x\,(g_x \to g_p, \eta_{Ax} \to \eta_{Ap}, \xi_2 \to \xi_3)$. The fidelity is then obtained by replacing $\sigma_W^{x,p}$ with $\sigma_V^{x,p}$ in Eqs. (3). The nonunit reflectivity of Bob's beamsplitter appears as a loss factor r_B, where in our experiment, $|r_B|^2 = 0.99$. η_i are detector efficiency factors directly related to the quantum efficiencies α_i by $\alpha_i = \eta_i^2$, where the subscripts denote Alice x, Alice p or Victor. $g_{x,p}$ are the suitably normalized gains for the x and p classical channels through which Alice sends information to Bob.

In terms of the model given in Fig. 1, the gains $g_{x,p}$ are given explicitly by

$$g_x = \frac{g_{x,(0)}}{\sqrt{2}} t_B \xi_2 \xi_5 \eta_{Ax} \eta_V , \tag{5a}$$

$$g_p = \frac{g_{p,(0)}}{\sqrt{2}} t_B \xi_3 \xi_5 \eta_{Ap} \eta_V . \tag{5b}$$

Here, $g_{x,(0)}$ and $g_{p,(0)}$ are dimensionless gains that account for the translation of the photocurrents $i_{x,p}$ into fields by Bob's amplitude and phase modulation, where the point of reference is immediately before his beamsplitter, which is taken to have amplitude reflection and transmission coefficients (r_B, t_B). Note that the formal limit of a phase-space displacement by Bob is achieved only for the case $(t_B \to 0, g_{x,(0)} \to \infty)$, with the product $t_B g_{x,(0)}$ held constant.

The convention that we adopt for the normalization of the gains $g_{x,p}$ in Eqs. (4) and (5) is such that $g_x = g_p = 1$ results in $\beta_V = \beta_{in}$, and hence reflects an optimal reconstruction of the input state for any sensible values of the squeezing parameters $r_\pm$. The caveat here is that since we measure Victor's photocurrent and not the field emerging from Bob, we effectively set $|\beta_V|^2 = |\beta_{in}|^2$ and not $|\beta_{out}|^2 = |\beta_{in}|^2$ as required by the protocol, where it can be easily shown that

$$|\beta_V|^2 = \xi_5^2 \eta_V^2 \, |\beta_{out}|^2 . \tag{6}$$

This defect in our measurement will be discussed quantitatively when we present our experimental data in Sec. IV D. Note that if Victor has perfect detection efficiency ($\xi_5 = \eta_V = 1$), the problem vanishes, and the result given in Eq. (4) is exact for the teleported output field emerging from Bob's beamsplitter.

The corresponding variances obtained by Alice's homodyne detectors are given by

$$\sigma_A^x = 1 + \frac{1}{4}\left(e^{-2r_-} + e^{2r_+} - 2\right) \xi_1^2 \xi_2^2 \eta_{Ax}^2 , \tag{7a}$$

$$\sigma_A^p = 1 + \frac{1}{4}\left(e^{-2r_-} + e^{2r_+} - 2\right) \xi_1^2 \xi_3^2 \eta_{Ap}^2 . \tag{7b}$$

Several limiting cases associated with these expressions are worth noting. In the classical case where there is no EPR entanglement ($r_+ = r_- = 0$), and with perfect homodyne detectors ($\xi_{1\to5} = \eta_i = 1$), we obtain $\sigma_V^x = \sigma_V^p = 3$, corresponding to three units of vacuum noise in Victor's homodyne detector. One unit stems from the vacuum noise intrinsic to the input coherent state, while the two extra units can be traced back as the quantum duties added in each crossing of the border between quantum and classical domains corresponding to Alice's quadrature measurements and Bob's phase space displacement [14]. This means that for classical teleportation of coherent states, the best achievement possible is reconstructing the input state with two extra units of vacuum noise added [9, 10]. The three vacuum units correspond to excess noise recorded in Victor's homodyne detector of 4.77 dB above the vacuum-state limit for his detector. With quantum entanglement it is possible to beat this limit and observe noise reduction below the 4.77 dB level in Victor's detector. The measured noise reduction can then be transferred into a fidelity through Eq. (2). As analyzed in Refs. [9, 10], the classical boundary for teleportation of coherent states is $F = 0.5$.

In the case of nonideal detectors, $g_x = g_p = 1$ still preserves optimal teleportation for the normalized gains, in the sense that $\beta_V = \beta_{in}$. However, the normalization is performed by effectively tuning the unnormalized gains $g_{(0)}$ by

$$g_{x,(0)}^{nonideal} \longrightarrow \left(\xi_2 \xi_5 \eta_{Ax} \eta_V\right)^{-1} g_{x,(0)}^{ideal} , \tag{8}$$

and similarly for p. Thus in the nonideal case, the actual gain is larger than in the ideal case, reflecting the fact that the gain must now compensate for Alice's and Victor's detection losses in order to ensure $\beta_V = \beta_{in}$. As a consequence, the fidelity drops below $F = 0.50$ with no entanglement ($r_\pm = 0$). In our experiment, the detection efficiencies are characterized by the measured visibilities and quantum efficiencies, which in the best case are given by $\xi_1 = 0.986$, $\xi_2 = \xi_3 = 0.995$, $\xi_4 = 0.988$, $\xi_5 = 0.985$, and $\alpha_V = \alpha_{Ax} = \alpha_{Ap} = 0.988$. With these experimentally achievable efficiency factors, we find that $\sigma_V^{x,p} = 4.84\,\mathrm{dB}$ and $F = 0.494$ when $r_\pm = 0$.

Fig. 2 shows the excess noise recorded by Victor and Alice x (or equivalently Alice p) as a function of the amount of squeezing, both for the ideal case with perfect detection efficiencies, and for the nonideal case with detector efficiencies given above. With no squeezing in the ideal case, we see from the solid curves that Victor obtains exactly 4.77 dB of excess noise as expected and as discussed above while Alice is shot-noise-limited. With imperfect detection efficiencies as shown by the dashed curves, Alice remains shot-noise-limited, while Victor records excess noise higher than 4.77 dB. In fact, the only relevant efficiencies that drive Victor's recorded noise above 4.77 dB involve Alice's homodyne detectors, namely (ξ_2, η_{Ax}) for the x quadrature, and (ξ_3, η_{Ap}) for the p quadrature. All other detection losses can be compensated by the gains $g_{x,p}$ when $r_\pm = 0$.

As the squeezing is increased so that now $r_\pm > 0$, Victor records noise reduction below the $r_\pm = 0$ level. By contrast, Alice's noise increases above the vacuum level at her detectors, and in the limit of infinite squeezing, Alice's noise diverges while Victor's excess noise is suppressed to the vacuum level. Notice that with perfect detection efficiencies, $\sigma_V^{x,p} < 4.77$ dB for any $r_\pm > 0$. With imperfect efficiencies, this is not true. In effect, some of the squeezing is "wasted" to compensate for the nonideal efficiencies. Since our experimental visibilities are close to unity, this loss can be neglected as it is below the level of other experimental uncertainties for small values of $r_\pm$. However, with large degrees of squeezing, the disparity between the ideal and nonideal cases increases and cannot be ignored, as can be seen from Fig. 2. The reason for this trend is that now the visibilities ξ_1 and ξ_4 that characterize the overlap of the EPR beams with Alice's and Bob's relevant beams, as well as the non-unit reflectivity r_B of Bob's beamsplitter, become important. The losses from non-unit ξ_1 and ξ_4 obviously cannot be compensated by the gains of the classical channels.

The noise reduction at Victor can be transferred into a teleportation fidelity, with the result plotted in Fig. 3. The solid and dashed curves for the ideal and nonideal cases mimic the conclusions discussed above for the variances $\sigma_V^{x,p}$ measured by Victor.

Of course, the teleportation fidelity is very dependent on the detector efficiencies. We investigate this point in more detail in Fig. 4, where the fidelity is plotted as a function of a single global visibility ξ (assuming $\xi_{1\to5} = \xi$) and where the quantum efficiencies of all the photodetectors are $\alpha = 0.988$. This figure clearly illustrates the need for a high amount of squeezing as well as very efficient spatial mode-matching of our optical beams to achieve high fidelity quantum teleportation.

B. Phase fluctuations

Not only losses associated with the detection efficiencies limit the achieved fidelity for quantum teleportation. Also the quality of the servo-control systems that lock various phases (e.g., the local oscillator phases at Alice's detectors) appear to be of significant importance, since phase deviations due to nonideal locking turn out to deteriorate the noise reduction measured by Victor. We will see that this mathematically corresponds to mixing in terms proportional to the anti-squeezed quadratures of the squeezed beams constituting the EPR state.

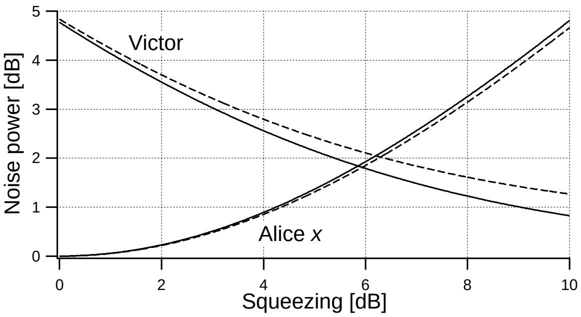

FIG. 2: Noise powers in dB above the vacuum-state limit for Alice's x detector and for Victor's detector as a function of the degree of squeezing of each squeezed vacuum state constituting the EPR state. The solid traces are for an ideal case where both Alice and Victor have perfect detection efficiency and all relevant beams are perfectly overlapped, that is, $\xi_{1\to5} = \alpha_i = 1$. The dashed traces show the noise levels for a real (nonideal) case where the visibilities correspond to the experiment described below and are $\xi_1 = 0.986$, $\xi_2 = \xi_3 = 0.995$, $\xi_4 = 0.988$, $\xi_5 = 0.985$, and the quantum efficiencies of photodetectors are $\alpha_i = 0.988$. The squeezing given in the figure is the squeezing just before the EPR beamsplitter.

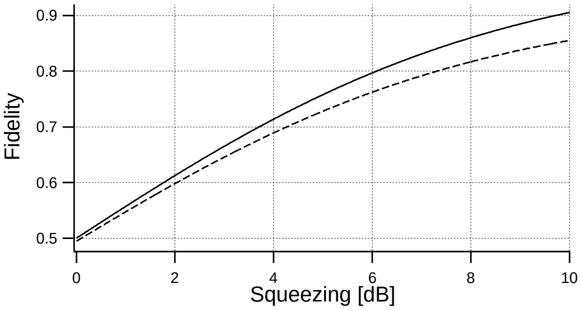

FIG. 3: The fidelity for Victor's teleported output as a function of the degree of squeezing with same parameters as in Fig. 2. Again, the solid trace describes a perfect case with ideal detectors, while the dashed trace describes the imperfect case as relevant to our experiment.

In a realistic model of the experiment we include phase offsets of four servo locks: the EPR lock, Alice's two homodyne detectors, as well as Bob's lock of the phase between the second EPR field and the classical field. The analysis presented here will be a straightforward generalization of the derivation in [18] based on the Heisenberg picture. The quadratures of the two EPR fields (1 and 2) are obtained by combining two squeezed fields with the angle between the squeezing ellipses equal to $\pi/2$. Although we have investigated a more complete model, here we account for the phase deviation away from $\pi/2$ by introducing an angle offset θ_E for field 2. In this sim-

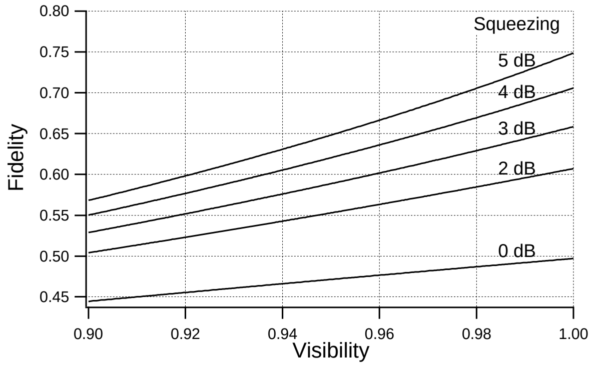

FIG. 4: Fidelity as a function of visibility for different values of the degree of squeezing. We have assumed $\xi_{1\to5} = \xi$ and $\alpha = 0.988$.

ple nonideal case, we obtain for the fields emerging from the EPR beamsplitter

$$\hat{x}_{1,2} = \frac{1}{\sqrt{2}} \left(e^{r_+} \hat{x}_1^{(0)} \mp \cos\theta_E e^{-r_-} \hat{x}_2^{(0)} \mp \sin\theta_E e^{r_+} \hat{p}_2^{(0)} \right), \tag{9a}$$

$$\hat{p}_{1,2} = \frac{1}{\sqrt{2}} \left(e^{-r_-} \hat{p}_1^{(0)} \mp \cos\theta_E e^{r_+} \hat{p}_2^{(0)} \pm \sin\theta_E e^{-r_-} \hat{x}_2^{(0)} \right), \tag{9b}$$

where $\hat{x}_{1,2}^{(0)}$ and $\hat{p}_{1,2}^{(0)}$ are vacuum state operators for (x, p) for the input beams 1 and 2 to the beamsplitter, respectively. Further downstream, EPR beam 1 is mixed with the unknown input state on a 50/50 beamsplitter creating the modes $\hat{u} = (\hat{a}_{in} - \hat{a}_1)/\sqrt{2}$ and $\hat{v} = (\hat{a}_{in} + \hat{a}_1)/\sqrt{2}$, and Alice measures the two quadrature amplitudes of the corresponding state in her homodyne detectors. Allowing for small phase deviations θ_{Ax} and θ_{Ap} in the detection process, we find that the quadratures measured by Alice now become

$$\hat{x}_u(\theta_{Ax}) = \hat{x}_u \cos\theta_{Ax} + \hat{p}_u \sin\theta_{Ax}, \tag{10a}$$

$$\hat{p}_v(\theta_{Ap}) = \hat{p}_v \cos\theta_{Ap} - \hat{x}_v \sin\theta_{Ap}. \tag{10b}$$

Finally, Bob performs a phase space displacement of the second EPR beam by overlapping with the coherent beam containing the classical information received from Alice. Allowing again for a phase offset θ_B in Bob's phase-space displacement, we calculate that the quadrature operators for the teleported state exiting the apparatus for investigation by Victor is given by

$$\hat{x}_V = \hat{x}_2 \cos\theta_B + \hat{p}_2 \sin\theta_B + \sqrt{2}\hat{x}_u(\theta_{Ax}), \tag{11a}$$

$$\hat{p}_V = \hat{p}_2 \cos\theta_B - \hat{x}_2 \sin\theta_B + \sqrt{2}\hat{p}_v(\theta_{Ap}), \tag{11b}$$

where the normalized gains of the classical channels have been taken to be unity. Using Eqs. (9) and (10), we arrive at expressions for the Heisenberg operators for the teleported field received by Victor, namely

$$\begin{aligned} \sqrt{2}\hat{x}_V =& \left(\cos\theta_B - \cos\theta_{Ax}\right) e^{r_+} \hat{x}_1^{(0)} + \left(\sin\theta_B - \sin\theta_{Ax}\right) e^{-r_-} \hat{p}_1^{(0)} \\ &+ \left[\cos\theta_E(\cos\theta_B + \cos\theta_{Ax}) - \sin\theta_E(\sin\theta_B + \sin\theta_{Ax})\right] e^{-r_-} \hat{x}_2^{(0)} \\ &+ \left[\sin\theta_E(\cos\theta_B + \cos\theta_{Ax}) + \cos\theta_E(\sin\theta_B + \sin\theta_{Ax})\right] e^{r_+} \hat{p}_2^{(0)} + \sqrt{2}\cos\theta_{Ax}\hat{x}_{in} + \sqrt{2}\sin\theta_{Ax}\hat{p}_{in}, \end{aligned} \tag{12a}$$

$$\begin{aligned} \sqrt{2}\hat{p}_V =& -\left(\sin\theta_B + \sin\theta_{Ap}\right) e^{r_+} \hat{x}_1^{(0)} + \left(\cos\theta_B + \cos\theta_{Ap}\right) e^{-r_-} \hat{p}_1^{(0)} \\ &+ \left[\sin\theta_E(\cos\theta_{Ap} - \cos\theta_B) + \cos\theta_E(\sin\theta_{Ap} - \sin\theta_B)\right] e^{-r_-} \hat{x}_2^{(0)} \\ &+ \left[\sin\theta_E(\sin\theta_{Ap} - \sin\theta_B) + \cos\theta_E(\cos\theta_B - \cos\theta_{Ap})\right] e^{r_+} \hat{p}_2^{(0)} + \sqrt{2}\cos\theta_{Ap}\hat{p}_{in} - \sqrt{2}\sin\theta_{Ap}\hat{x}_{in}. \end{aligned} \tag{12b}$$

By utilizing these expressions, the variances of the two quadratures measured by Victor can be calculated. Assuming the phase excursions are small, we expand to lowest order. We recall that the aim of this calculation is to describe the impact of phase fluctuations in the various servo-controls. Hence we assume that there are no static offsets (which we believe our current procedures adequately null), so that all the phase excursions vanish on average, $\overline{\theta} = 0$, and only deviations expressed by the second order moments contribute. Furthermore, it is assumed that all the phase fluctuations are independent, so that products of phases vanish on average.

After some algebra, we finally arrive at

$$\sigma_V(x) = \left\langle \Delta\hat{x}_V^2 \right\rangle = 1 + \left[2 - \frac{1}{2}\overline{\theta_{Ax}^2} - \frac{1}{2}\overline{\theta_B^2} - 2\overline{\theta_E^2}\right] e^{-2r_-} + \left[\frac{1}{2}\overline{\theta_{Ax}^2} + \frac{1}{2}\overline{\theta_B^2} + 2\overline{\theta_E^2}\right] e^{2r_+}, \tag{13a}$$

$$\sigma_V(p) = \left\langle \Delta\hat{p}_V^2 \right\rangle = 1 + \left[2 - \frac{1}{2}\overline{\theta_{Ap}^2} - \frac{1}{2}\overline{\theta_B^2}\right] e^{-2r_-} + \left[\frac{1}{2}\overline{\theta_{Ap}^2} + \frac{1}{2}\overline{\theta_B^2}\right] e^{2r_+}, \tag{13b}$$

where the various $\overline{\theta_i^2}$ are meant to be associated with the residual RMS fluctuations arising from the nonideal performance of our locking servos. Explicit dependence on the phase θ_V of Victor's LO is given by

$$\sigma_V[x(\theta_V)] = \sigma_V(x)\cos^2\theta_V + \sigma_V(p)\sin^2\theta_V. \tag{14}$$

These equations make quantitative the obvious intuition that the effect of the phase fluctuations is to add extra noise in the quadratures measured by Victor through components proportional to the anti-squeezed quadrature. In fact, relatively small phase fluctuations (∼ 1° RMS) can degrade the noise reduction that would otherwise have been recorded by Victor, and consequently also the achieved fidelity.

From these equations, we see that particular phase fluctuations contribute in quite different ways. Phase fluctuations at Bob contribute equally to excess noise in the x and p quadratures and will consequently be seen as a constant shift in the noise measured in Victor's homodyne detector while scanning the local oscillator. The same effect is found from fluctuations in the locking of the local oscillator phases at Alice x and Alice p provided $\overline{\theta_{Ax}^2} = \overline{\theta_{Ap}^2}$. However, phase fluctuations in the EPR lock are seen to modify Victor's x and p quadratures differently and therefore imply modulation of the noise measured by Victor. The relevant second order moments $\overline{\theta_i^2}$ for the various locks can be obtained experimentally by measuring the RMS noise of the error signals in locked operation. Typically measurements give $\sqrt{\overline{\theta_i^2}} \simeq 2$ to 6 degrees. From Eqs. (13) it is seen that fluctuations in the phase with which the squeezed beams are combined to form the EPR beams are most critical since $\overline{\theta_E^2}$ contributes with a coefficient four times higher than the other phase terms to the mixing with the anti-squeezing term.

Fig. 5 shows the calculated noise in Victor's homodyne detector for different levels of phase fluctuations in the EPR lock employing realistic values of squeezing and anti-squeezing for the experiment discussed in the following sections. The modulation of Victor's signal is seen to be up to about 0.2 dB peak to peak which turns out to imply a significant reduction of the achieved fidelity.

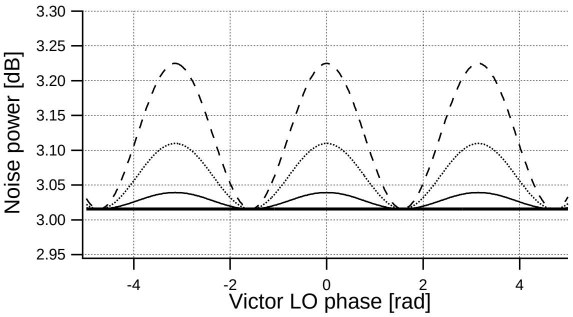

FIG. 5: Noise power recorded by Victor's balanced detector when scanning his local oscillator for $\sqrt{\overline{\theta_E^2}} = 0, 2, 4, 6$ degrees (corresponding to the bold, thin, dotted, and dashed curves, respectively), and for $\overline{\theta_{Ax}^2} = \overline{\theta_{Ap}^2} = \overline{\theta_B^2} = 0$. Realistic values of the degrees of squeezing (−3 dB) and of anti-squeezing (7 dB) have been used.

III. GENERATION OF THE QUANTUM RESOURCE

A more complete figure of the experimental setup is given in Fig. 6. A 10 W Verdi was used to pump a single frequency Ti:Sapphire laser operating at 866 nm. This laser system provided about 1.6 W of IR. About 80% to 85% of this light was sent to an external frequency doubler to generate an efficient 433 nm pump source for the optical parametric oscillator (OPO). Typically about 300 mW of blue light was produced that could be mode-matched to the OPO using a triangular ring cavity. Furthermore, the pump was divided into two beams, which allowed pumping the OPO from two directions to produce two independent squeezed beams. A detailed description of this setup for generation of highly squeezed light can be found in Ref. [19]. About 10% of the IR light from the Ti:Sapphire laser was spatially filtered in a mode cleaning cavity and used down stream in the experiment for locking the OPO, as local oscillators in the homodyne detectors, for Bob's displacement beam, and as the input coherent state for the actual teleportation. Combining the two squeezed beams on a 50/50 beamsplitter with the phases locked so that the squeezing ellipses are perpendicular to each other, the EPR state was generated which is the quantum resource necessary for the actual quantum teleportation protocol described previously in relation to Fig. 1. In the current section a detailed description of the generation of the EPR state is given with a careful characterization of both classical and quantum properties of the OPO. The actual implementation of the full teleportation protocol follows in Sec. IV.

A. Loss and gain in the OPO

The OPO cavity was a bow-tie ring configuration consisting of two curved mirrors (radius of curvature 5 cm)

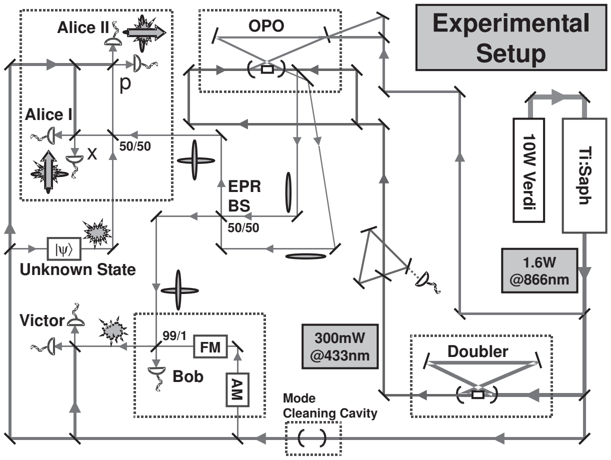

FIG. 6: Sketch illustrating the basic optical parts in the quantum teleportation experiment. See the main text for a careful discussion.

and two plane mirrors. The total cavity length was 48cm. The focus positioned between the two curved mirrors had a waist size of 21μm where the 1cm long nonlinear potassium niobate (KNbO$_3$) crystal was positioned. The use of a-cut potassium niobate allowed noncritical temperature phase-matching of a degenerate parametric process. To generate a pump for the OPO, the output from the Ti:Sapphire laser was frequency doubled in another external cavity also using potassium niobate as the nonlinear medium [20]. In this way 300 mW of pump light at 433 nm was generated.

In the OPO nonlinear down-conversion transformed energy from the pump field at 433 nm into the parametric field at 866 nm. In the current application the OPO was only driven below oscillation threshold, where spontaneous parametric emission can produce a squeezed vacuum state. The parametric field was resonant in the OPO while the pump light from the frequency doubler was divided into two beams, each of which was used in single pass of the OPO crystal from a counter propagating direction.

The OPO performance can be characterized once specifying the output coupler intensity transmission T, the effective nonlinearity E_{NL}, and the intracavity round-trip loss $\mathcal{L}$. In the current experiment the output coupler transmission was fixed at $T = 10\%$ which was chosen to optimize squeezing. The total information about the nonlinear interaction can be captured in the single parameter E_{NL} that depends on the focusing, length of the crystal, phase-matching and crystal properties. It can operationally be defined as $E_{NL} = P_2/P_1^2$, where P_2 is the second harmonic power generated in single pass frequency doubling of a fundamental pump P_1. In the current setup we measured $E_{NL} = 0.021W^{-1}$.

Contributing to the intracavity loss are nonideal antireflection coatings of the potassium niobate as well as leakage from the three high-reflection coated cavity mirrors. This passive loss was measured to be $\mathcal{L}_p = 0.3\%$. Unfortunately potassium niobate also suffers from an inherent loss mechanism that adds to the passive losses [21, 22]. This nonlinear loss arises in the OPO in the presence of the blue pump beam and has been termed blue-light-induced infrared absorption (BLIIRA). It is believed to originate from impurities in the crystal and is found to vary substantially from crystal sample to sample. At a high pump level of the OPO, BLIIRA turns out to be the dominating loss mechanism and eventually becomes the limiting factor for the amount of squeezing obtained. The losses $\mathcal{L}_b$ due to BLIIRA could be monitored in the OPO by measuring the reflection dip of the injected pump beam while scanning the cavity around resonance. Typical measurements of the total intracavity loss ($\mathcal{L} = \mathcal{L}_p + \mathcal{L}_b$) are shown in Fig. 7 as a function of the blue pump power. In this case the OPO was only pumped along one direction. We observe that the total loss increases up to about 2% at the highest pump level of $P_2 = 155$ mW.

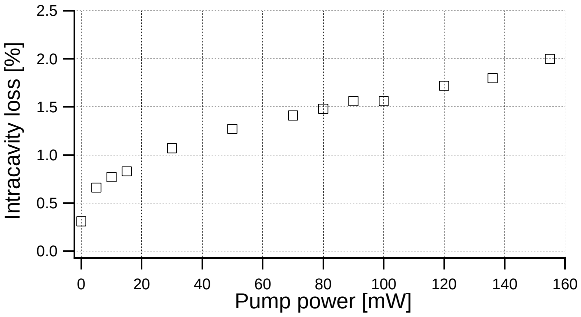

FIG. 7: Measured total intracavity round-trip cavity loss $\mathcal{L}$ as a function of the blue pump P_2. Note that the transmission T of the output coupler is not included.

The OPO could also be operated as a phase sensitive amplifier as a way to test the classical performance of the device. For that purpose an 866 nm beam was seeded into the OPO and by scanning the injection phase slowly, the amplification factor G was measured. When injecting the seed beam through the small transmission of a high reflection mirror and measuring the amplification of the light through the output coupler mirror, the gain is given by

$$G = \frac{1}{\left(1 - \sqrt{P_2/P_{2,t}}\right)^2}, \tag{15}$$

where $P_{2,t}$ is the oscillation threshold of the OPO given by

$$P_{2,t} = \frac{(T + \mathcal{L})^2}{4E_{NL}}. \tag{16}$$

Fig. 8 shows measured values of the gain as a function of pump power for single-sided pump of the OPO as well as the theoretical curve based on the measured loss and nonlinearity. The gain diverges as approaching threshold and from these data we estimate $P_t \simeq 190$ mW. The agreement between experiment and theory is apparently quite good, here with no adjustable parameters.

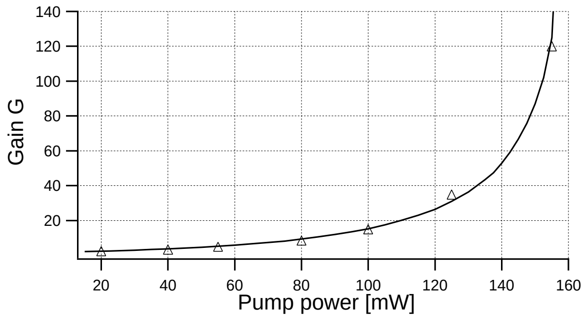

FIG. 8: Measured gain (points) and corresponding theoretical curve based on the measured loss and nonlinearity.

B. Squeezing

The phase-sensitive amplification in the OPO can be exploited for generating squeezed states of light. In this case the two input vacuum noise quadratures are amplified and deamplified, respectively, creating a squeezed vacuum state. Balanced homodyne detection allows phase sensitive detection of the quantum noise of the squeezed state. With this method the signal field is overlapped with a strong coherent local oscillator (LO) on a 50/50 beamsplitter. The two output beams from the beamsplitter are measured and the corresponding photocurrents subtracted. In this way the weak quantum noise of the signal is amplified to achieve a signal substantially above the thermal noise floor of the photodiodes. The photodiodes used were a special part made by Hamamatsu with a measured quantum efficiency $\alpha = 98.8 \pm 1.0\%$.

Two typical squeezing traces at different pump levels are presented in Fig. 9. They were obtained by recording Victor's noise power with the spectrum analyzer when scanning the phase of the LO. We observe the phase sensitive noise with the maximum and minimum corresponding to measuring the anti-squeezed and squeezed quadratures, respectively. With the signal beam blocked, the vacuum state level $\Phi_0^{(1)}$ was recorded, and squeezing corresponds to noise reduction below this level. By locking the LO phase to the squeezed quadrature, we obtained the flat traces below $\Phi_0^{(1)}$, as shown in Fig. 9. We infer squeezing of 3.73 dB below the vacuum level and anti-squeezing of 6.9 dB with pump power of 42 mW. At the higher pump level shown (107 mW), the degree of squeezing remained at 3.73 dB below the vacuum level while the degree of anti-squeezing increased to 10.8 dB.

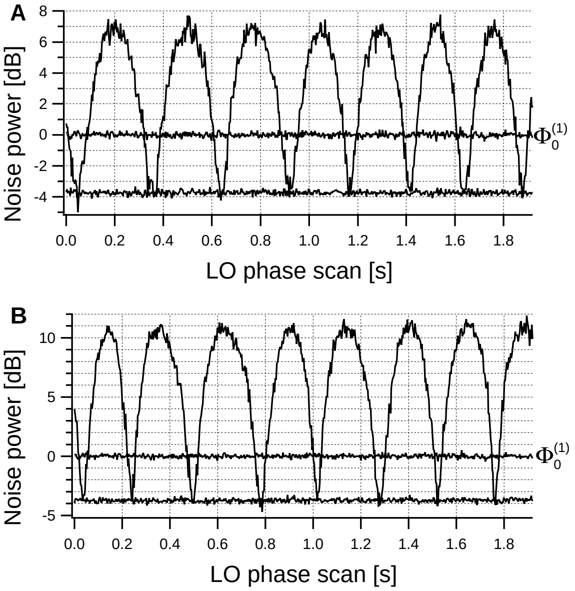

FIG. 9: Typical squeezing traces recorded by homodyne detection while scanning the phase of the LO. The measurement frequency was 1.475 MHz within a resolution bandwidth of 30 kHz and with a video bandwidth of 300 Hz. The flat traces at 0 dB are the respective vacuum levels $\Phi_0^{(1)}$, taken with a 5 trace average. Also displayed are the flat traces that correspond to the minimum noise level attained, again with a 5 trace average. These traces were obtained by locking the LO phase to the squeezed quadrature and lead to estimates of the squeezing and anti-squeezing of: (A) -3.73 dB and 6.9 dB with 42 mW pump power; and (B) -3.73 dB and 10.8 dB with 107 mW pump power. In both cases, the OPO was pumped from a single direction. Victor's detection efficiency was characterized by a homodyne visibility $\xi = 0.972$ and photodiode quantum efficiency $\alpha = 0.988$.

In the actual teleportation experiment the fidelity is ultimately limited by the amount of squeezing available. However, as discussed in Section II B, in a non-perfect experiment the amount of anti-squeezing is also important. In that section, we concluded that fluctuations in the servo locks will degrade the fidelity with contributions from the anti-squeezed quadratures. For that reason it is important to find the optimum operation point of the OPO where the degree of squeezing is large, while at the same point, the anti-squeezing has not grown too large. Such a compromise is made necessary by the BLIIRA, which limits the degree of quantum noise reduction in a power-dependent fashion, while the noise from the anti-squeezed quadrature continues to grow.

Fig. 10 shows the variation of the measured squeezing and anti-squeezing with the OPO pump power as well as the corresponding theoretical curves based on the measured experimental parameters (loss and nonlinearity) discussed in the previous section. The data have been corrected for the thermal noise level of the detectors, which was 17 dB below the vacuum noise level for an LO of 2 mW. The squeezing is seen to level off at about -3.5 dB already at a pump of 45 mW while the anti-squeezing increases with the pump. This indicates that in the teleportation experiment it would be most favorable to operate at this relatively weak pump level of the OPO and that decreased teleportation fidelity might be expected when increasing the pump further (e.g., due to mixing in of noise from the anti-squeezed quadrature from the imperfections in servo control discussed in Sec. II B).

We note that the measured squeezing is lower than predicted from the OPO parameters discussed above; indeed we predict about 4.7 dB squeezing at high pump level. This discrepancy might be due to offset fluctuations in the OPO lock as well as phase fluctuations between the local oscillator and the squeezed beam in the homodyne detector. In favor of such an explanation is the fact that the theory predicts the anti-squeezed quadrature better than the squeezing quadrature, and the broad maximum from the anti-squeezing (see Fig. 9) is expected to be much less sensitive to phase fluctuations than the narrow squeezing minimum.

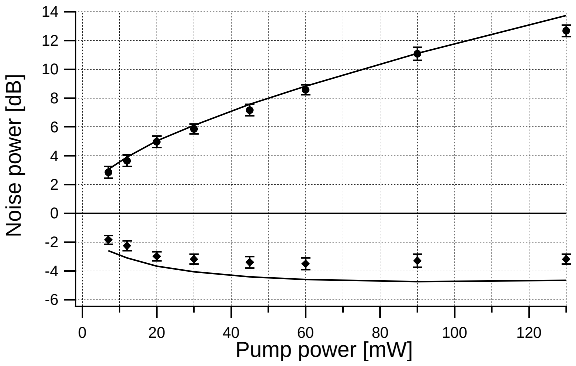

FIG. 10: Measured squeezing (diamonds) and anti-squeezing (dots) at a frequency offset of 1.475 MHz as a function of the OPO pump power when pumping from only one direction. The curves are the corresponding theoretical results for non-linearity $E_{NL} = 0.019W^{-1}$ and measured cavity loss similar to that given in Fig. 7. The measured quantum efficiency was $\alpha = 0.988$, the homodyne visibility $\xi = 0.990$, and the propagation loss of the squeezed beam was 5.7%.

The above data were taken when the OPO was only pumped from a single direction. In order to obtain two squeezed beams necessary to generate the EPR correlations, the OPO was pumped in two counter-propagating directions. In this case we expect lower squeezing than from a single pumped OPO due to increased BLIIRA. This reduction in squeezing was measured to range from less than 0.3 dB at total pump powers below around 80 mW, to 0.5 dB at higher pump powers. To estimate the degree of squeezing in the double-pumped case, we take the degree of squeezing obtained in Fig. 9 and correct for Victor's homodyne visibility and finite detector thermal noise, to find that in the single-pumped case, we have -4.1 dB of available squeezing. Thus we estimate that we have about -3.6 to -3.8 dB squeezing in the double-pumped case.

C. EPR correlations

The EPR correlated beams were generated by combining two independently squeezed beams with the relative phase servo-locked to be $\pi/2$. These continuous variable EPR correlations are of the type originally discussed by Einstein, Podolsky, and Rosen [16]. The two output beams 1 and 2 from the EPR beamsplitter possess correlations as expressed by the variances $\sigma(x_1 \pm x_2) = 2\sigma_\pm$ and $\sigma(p_1 \pm p_2) = 2\sigma_\mp$, where σ_+ and σ_- are the variances of the anti-squeezed and squeezed quadratures of the two input beams, i.e. $\sigma_+ > 1$, $\sigma_- < 1$, and $\sigma_+\sigma_- \geq 1$. Without squeezing we obtain the vacuum noise level for two beams $(\Phi_0^{(2)})$ where $\sigma(x_1 \pm x_2) = \sigma(p_1 \pm p_2) = 2$. We observe that x_1 and x_2 are correlated while p_1 and p_2 are anti-correlated both to a level below the vacuum noise level. This is the same kind of quantum correlations first recorded for the light from a nondegenerate OPO [23, 24]. While noise reduction below the vacuum level is achieved when measuring correlations between the two EPR beams, the noise from only one of the EPR beams is phase independent and above the vacuum level. Indeed we find that $V(x_{1,2}) = V(p_{1,2}) = (\sigma_+ + \sigma_-)/2 \geq 1$, where unity is the vacuum level for a single beam $(\Phi_0^{(1)})$.

Experimentally the quality of the EPR state was investigated both by measuring one EPR beam as well as the correlations between the two beams. The noise in a single beam was measured while scanning the EPR phase θ_{EPR} between the two squeezed beams slowly compared to the scan rate of the local oscillator in the homodyne detector. An example is presented in Fig. 11. The rapid sweep of the local oscillator ensured that both quadratures were measured for each value of θ_{EPR} and gives rise to the fast variations in the trace. As explained above, the noise of a single EPR beam is expected to be phase independent and arises when overlapping the two squeezed beams with a mutual phase difference of $\theta_{EPR} = \pi/2$. Hence, this allows identification of this point in Fig. 11, and we observe excess noise in this case about 5 dB above the vacuum noise level. Furthermore, when the two squeezed beams are combined in phase ($\theta_{EPR} = 0$), two squeezed beams exit the beamsplitter giving noise reduction in this case roughly 3 dB below vacuum noise.

A direct measurement of the correlations between the two EPR beams was obtained via balanced homodyne detection of both EPR beams and subtracting the resulting photocurrents from the two sets of balanced detectors. In these measurements the EPR phase was locked at $\theta_{EPR} = \pi/2$ and one of the homodyne detectors was locked to measure a fixed quadrature. The trace in Fig. 12 was recorded by scanning the local oscillator θ_{LO} of the second homodyne detector, thus recording the variance $\sigma\left(x_1 - x_2(\theta_{LO})\right)$. Reduction below the vacuum

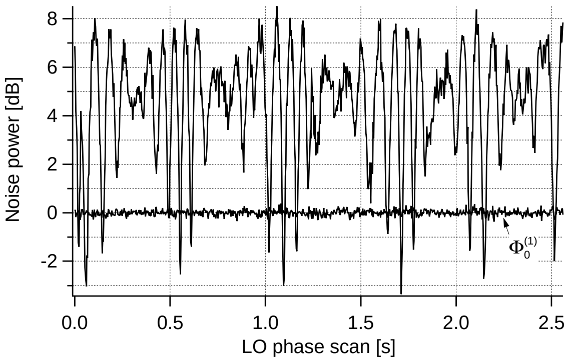

FIG. 11: Noise of one beam from the EPR beamsplitter as obtained by scanning the mutual phase difference between the two squeezed beams in addition to a rapid sweep (about 5 times faster) of the LO in the homodyne detector. The flat curve represents the vacuum state level for a single beam.

level for two beams ($\Phi_0^{(2)}$) was observed when the second homodyne detector measured the same quadrature as the first homodyne detector, i.e. for $\theta_{LO} = 0$. We observe correlations of the amplitude quadratures of about 2 dB with respect to the vacuum level. However, these data were taken in a non-optimized situation (e.g., inefficient OPO cavity alignment); the measured degree of squeezing at that time was under -3 dB. In the actual teleportation experiment inter-beam EPR correlations of more than 3 dB was obtained.

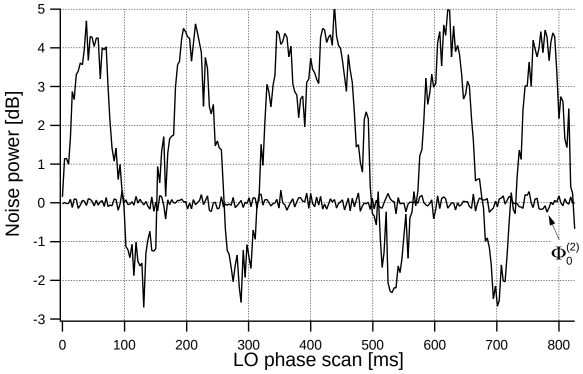

FIG. 12: Noise obtained by subtracting signals from two homodyne detectors measuring the two EPR beams while scanning one of the LO phases. The recorded quantity was $\sigma\left(x_1 - x_2(\theta_{LO})\right)$. The flat curve is the vacuum noise level for two beams.

IV. QUANTUM TELEPORTATION

Given the preceding description of how to generate the EPR state, we will now move on to discuss the complete quantum teleportation protocol. First the electronic servo locks implemented in the experiment are described, then the technique to calibrate the channels used by Alice to send classical information to Bob is presented. This establishes the basis for presenting the experimental results on quantum teleportation.

A. Phase locking

In the complete quantum teleportation experiment ten servo systems in total were implemented for locking optical phases and cavities. A summary of the locking techniques is given in Table I. Three of the servos (numbers $1-3$) are for locking cavities and use the standard Pound-Drever-Hall technique where reflection or transmission of RF modulation sidebands are used to derive an error signal. The frequency doubling cavity was locked by observing the cavity reflection dip off the input coupler, and generating an error signal using RF sidebands at 26 MHz. The OPO cavity was locked by observing a 1% pick-off from the transmitted light from a weak coherent beam injected through a high reflector. The injected signal carried 5 MHz sidebands for locking. Finally, the mode-cleaning cavity was locked in reflection using sidebands at 26 MHz.

The remaining seven servos were used to keep the optical phases properly aligned for successful teleportation [25]. Two weak injection beams were seeded into the two counterpropagating modes of the OPO and used for several purposes: to align the OPO cavity and the homodyne detectors, and to use for locking of optical phases. The two injected signals were phase modulated at 3 MHz (injection 1) and 5 MHz (injection 2) respectively, using an electro-optical modulator (EOM) in each signal path. The relative phase differences between the pump beams and the injected beams were locked using standard lock-in techniques where the error signal is derived from the phase sensitive amplification (due to the parametric gain in the OPO) of the injected signal. The phases are locked at maximum gain corresponding to the situation where the direction of the phasor of the coherent injected field is along the long axis of the squeezing ellipse of the squeezed vacuum beams.

The third phase-lock, the EPR phase lock, keeps the two independent squeezed beams incident on the EPR beamsplitter with a phase difference of $\pi/2$ to ensure the production of the EPR state. This was done by using 1% leakages from mirrors in the EPR beam paths. The DC interference signal between the two injected beams from the two distinct EPR paths was subtracted to produce an error signal centered around zero. This zero crossing corresponds to $\pi/2$ phase difference between the two squeezed beams.

To lock the local oscillators in Alice's two homodyne detectors, the RF beat notes between the LO and the 3 and 5 MHz sidebands on the injected beams were demodulated to produce the respective error signals for Alice I (3MHz) and II (5MHz). As the EPR phase lock described

NO.	BRIEF DESCRIPTION	LOCKING TECHNIQUE
1	Doubling cavity resonant to 866 nm	Pound-Drever-Hall via reflection, 26 MHz
2	OPO cavity resonant to 866 nm	Pound-Drever-Hall via transmission, 5 MHz
3	Mode cleaning cavity resonant to 866 nm	Pound-Drever-Hall via reflection, 26 MHz
4, 5	Relative phase between blue pump (433 nm) and injected beams 1 & 2 (866 nm) to zero (maximum gain)	Lock-in via 1% pick-off of cavity transmission
6	Relative phase between two squeezed beams to $\pi/2$ (to create EPR state)	DC interference fringe
7, 8	Alice's LOs to x and p quadratures	RF interference fringe, 3 MHz $\to x$, 5 MHz $\to p$
9	Bob's coherent beam to x quadrature	RF interference fringe, 3 MHz
10	Victor's LO to either x or p quadratures	RF interference fringe, 3 MHz $\to x$, 5 MHz $\to p$

TABLE I: Summary of the servo systems that were implemented. See main text for further discussion.

above already keeps the two injected beams at $\pi/2$ phase difference, the LOs in Alice I and II will also stay at $\pi/2$ relative phase difference. Bob's LO phase was locked using the RF interference fringe at 3 MHz between itself and the modulation sidebands transported with EPR2. This means that Alice I is locked to the same quadrature as Bob, which, by an arbitrary convention, sets Alice I as x and Alice II as p. Thus to complete the classical information channel, Alice I's measured output (photocurrent) was sent to Bob's amplitude modulator, and Alice II's output was sent to Bob's phase modulator. The teleported state then emerges from Bob's beamsplitter, and is sent to Victor for verification. Victor's LO phase can be either scanned, or locked to either 3 or 5 MHz to check x and p separately.

B. Classical information channels

A crucial part of the teleportation protocol is the transmission of classical information from Alice to Bob. In the present experiment the classical information is just the photocurrents from Alice's two homodyne detectors. These signals have to be faithfully transmitted to Bob without distortion and with proper phase and gain, and for that reason several RF amplifiers, filters and delay boxes were used in the classical channel paths. We typically measured Alice's and Victor's noise levels at 1.475 MHz, thus the electronics of the channels were optimized at that frequency. In the following we will present a method to perform the calibration of these classical channels.

To ensure that we are operating at a gain $g_x = g_p = 1$ such that $\beta_V = \beta_{in}$, we compared the photocurrents measured by Alice and Victor when there were no EPR beams present for the case of a coherent state of amplitude β_{in} sent to Alice as the input state. In practice, this was easily achieved by blocking the optical beam paths of the EPR state. In this case, it can be shown that when an amplitude or phase modulated beam is sent to Alice as the input state, the ratio between the spectral densities measured at Victor and Alice is given by

$$\frac{\Phi_V}{\Phi_A} = \frac{2}{\xi_2^2 \eta_A^2}, \tag{17}$$

where we have assumed Alice and Victor are measuring the same quadrature (either x or p), that $|\beta_{in}|^2 \gg 1$ and that the efficiencies are close to unity. We observe that Victor records a spectral density (i.e., noise power of the RMS photocurrent) two times (corresponding to 3 dB) higher than Alice x (or p). This factor of two can easily be understood since the input beam is split into two equal halves at Alice's 50/50 beamsplitter. Hence, this identifies a signature for the optimum condition of the classical gain.

On the other hand, for vacuum input, the ratio between Victor's and Alice's spectral densities, or equivalently, their variances since now $|\beta_{in}|^2 = 0$, is found to be

$$\frac{\sigma_V}{\sigma_A} = 1 + \frac{2}{\xi_2^2 \eta_A^2}, \tag{18}$$

when the classical gain is optimum. This means Victor's output is ≈ 3 times higher than Alice x (or p) again in the limit where all detector efficiencies are close to unity.

Fig. 13 shows the spectral density $\Phi_{Ax}(\Omega)$ of photocurrent fluctuations recorded at Alice x from input beams with modulation amplitudes corresponding to 24.9 dB and 0 dB (vacuum), respectively. The signal recorded at Alice p mirrors this trace, except that the coherent amplitude is shifted in phase by $\pi/2$, demonstrating that Alice x and p are $\pi/2$ apart in phase, as required. The corresponding traces for the spectral density $\Phi_V(\Omega)$ for Victor's detector are shown in Fig. 14. Here we show explicitly the $\pi/2$ phase shift when Victor's LO is phase-locked to the x and p quadratures, respectively. We see that Victor records 3 dB higher spectral density for the amplitude modulated input and 4.8 dB greater for the vacuum input, which indicates that the gain of the classical channels has been properly calibrated relative to the criteria of Eqs. (2) and (4).

We now turn our attention to the phases of the RF signals, keeping in mind the distinction between the phase

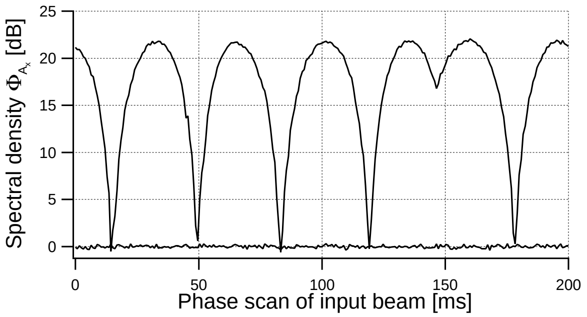

FIG. 13: Spectral density $\Phi_{Ax}(\Omega)$ relative to the vacuum level recorded by Alice x while scanning the phase of the input beam both for vacuum (flat trace), and an input beam with amplitude modulation at 24.9 dB above the vacuum noise level. The measured amplitude of this beam is 21.9 dB or 3 dB lower than the actual input, as explained in the text. The measurement frequency was 1.475 MHz, RBW 30 kHz, and VBW 1 kHz.

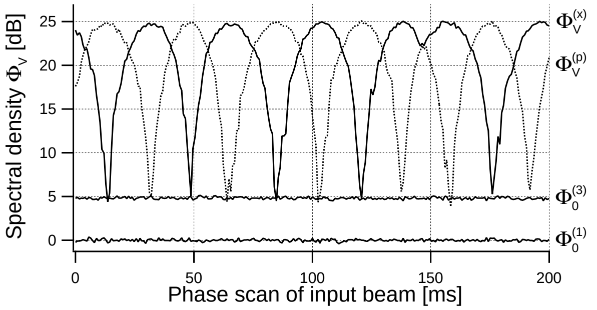

FIG. 14: Spectral density $\Phi_V(\Omega)$ relative to the vacuum level recorded by Victor while scanning the phase of the input beam. $\Phi_0^{(1)}$ is Victor's noise level for one unit of vacuum, while $\Phi_0^{(3)}$ shows the 2 extra units making 3 total units of vacuum noise measured in an attempt to recreate Alice's vacuum state input without any entanglement. $\Phi_V^{(x)}$ and $\Phi_V^{(p)}$ show the recreation of Alice's input coherent modulation amplitude of 24.9 dB, demonstrating that the peak input and output amplitudes are equal, and the x and p quadratures are indeed $\pi/2$ apart in phase. Victor's LO was phase-locked to the x and p quadratures respectively for these measurements.

of the optical carrier, and the phase of the RF signal at our measurement frequency, 1.475 MHz. We have already discussed optical phases in detail in Sec. IV A above, and indeed implicitly assumed correct optical phases in the discussion on finding optimal gain. In discussing RF phase, we will continue to assume that our optical phase-lock servos are working correctly.

Our goal is quantum noise subtraction at our analysis frequency, between the correlated beams EPR1 (measured at Alice and sent to Bob via the classical channels) and EPR2 at Bob's beamsplitter. Obviously, the best way to achieve this goal is for the relative RF phases of EPR1 and EPR2 to be zero for perfect subtraction. However, this is quite impractical in the current laboratory setup since EPR2 arrives at Bob's beamsplitter directly from the EPR beamsplitter, while EPR1 takes a very indirect route involving electrical photocurrents that travel much slower than light. It is sufficient, therefore, to ensure that the relative phase difference is a factor of 2π by implementing delays in the classical channels between Alice and Bob. In practice, we can also keep the phase difference any multiple of π and compensate for this by flipping the sign of Bob's optical phase-lock error signal. In this way, Bob *adds* EPR1 and EPR2 instead of subtracting them, thereby optically creating a π RF phase shift that compensates for the π phase delay in the classical channels.

Finally, Bob's two modulators must provide pure phase and amplitude modulation, respectively. This condition is satisfied by carefully controlling the input beam polarizations for the two temperature compensated EOMs.

Some care must be given to the maximum time delay allowed in our classical channels. This is set by the OPO linewidth (HWHM) of 5.4 MHz, corresponding to a correlation time between EPR1 and EPR2 of about 30 ns if the full bandwidth of the OPO were employed for teleportation. For a more detailed discussion see Ref. [18].

However, in our experiment, a much smaller effective bandwidth is employed corresponding to the detection bandwidth for Alice, the bandwidth of the classical channel from Alice to Bob, and the frequency range of Bob's modulators. Finally, there is the bandwidth employed by Victor in his verification of the protocol. For simplicity, here we assume that the effective detection bandwidth of our protocol is equal to the RF bandwidth, ν, of the spectrum analyzer employed by Victor in his analysis, typically around $\nu = 30$ kHz (see figures in Sec. IV C). The relevant issue is the ratio between our analysis frequency, $\Omega/(2\pi) = 1.475$ MHz, and ν. We see that this ratio is about 50 cycles. Thus 2π of RF phase delay in our classical channels contributes to a roughly 2% effect on the noise subtraction quality, which is small but not negligible.

When the gain and RF phase of the classical channels as well as the optical phases at Alice's and Bob's detectors were suitably optimized, Victor recorded a stable output while the phase of the unknown input state was being scanned, independent of the input state amplitude and phase over a wide range, as discussed below. In the case of vacuum input we obtain the flat trace at 4.8 dB (trace $\Phi_0^{(3)}$) in Fig. 14. The trace remained stable for tens of minutes, with fluctuations on the order of ±0.1 dB.

It was not a trivial task to realize the balance of the two classical channels due to above-mentioned reasons. One practical way that we employed to optimize the system and to judge the effectiveness of the two classical channels was to send RF modulated optical fields at 1.475MHz through the two injection ports of the OPO cavity. These modulated optical signals were allowed to propagate to Alice and Bob, just as the EPR beams would in the presence of blue pump. We could then easily optimize the subtraction of the two classical fields at Bob's 99/1 beamsplitter. In terms of the conditions stated above, this *classical noise* subtraction directly mimics the *quantum noise* subtraction that we perform using the entangled EPR state during quantum teleportation, which means that if we obtain good classical subtraction, we should in fact be operating at the optimal conditions for quantum teleportation. Typically the subtraction was about 25 dB for each channel.

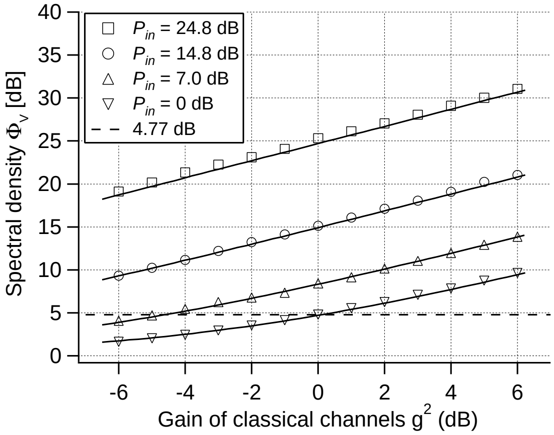

FIG. 15: Measured spectral density $\Phi_V(\Omega)$ from Victor's balanced homodyne detector as a function of gain for different amplitude-modulated coherent state and comparison with theory. The parameters for the theoretical curves were the measured visibilities: $\xi_1 = 0.985$, $\xi_2 = \xi_3 = 0.994$, $\xi_4 = 0.985$, $\xi_5 = 0.985$ and the detector quantum efficiency was $\alpha = 0.988$. The measurement frequency was 1.475 MHz. P_{in} corresponds to the actual power of the input state presented to Alice, in dB above the vacuum state.

In order to check the linearity and dynamical range for the classical channels, we measured Victor's output noise levels as a function of gain for input modulation sidebands of various amplitudes when the two classical channels were balanced. Fig. 15 shows the results for input beams with the following modulation amplitudes: 0 dB (vacuum), 7.0 dB, 14.8 dB and 24.8 dB, where in each case the full 2π of phase variation was explored. It shows that the linearity is very good from 0 dB to 25 dB input modulation amplitudes, which means we can teleport any coherent state amplitude within that range. The theoretical traces on the figure are based on our measured efficiencies without any adjustable parameters.

C. Teleportation results

Fig. 16 shows quantum teleportation results for a coherent input state. All traces are Victor's measured variances at 1.475 MHz and at pump power of 33/35 mW in the OPO paths 1 and 2, respectively. The amplitude of the input state was about 25.5dB higher than the vacuum level. Trace (a) is one unit of the vacuum noise, that is, the vacuum-state level or shot-noise level (SNL) of Victor, which is obtained by blocking Bob's beam. Trace (b) marks the 3 units of vacuum noise in the case of absent EPR beams but with Alice and Bob engaged nonetheless in the teleportation protocol, which is 4.8 dB above the SNL with our efficiencies close to 1 and is obtained by blocking the blue pumps in the experiment. Trace (c) shows the phase sensitive noise when the EPR beams and the AM sidebands on the input state are present, while Victor's LO is phase-locked to the x quadrature. Locking Victor's LO to the p quadrature produces an analogous trace with the peaks offset by $\pi/2$ in phase. Closer inspection of traces such as (c) in Fig. 16 shows that the minimum noise level is approximately 1.1 dB below the level of three units of the vacuum, although it is rather difficult to get an accurate reading because of the mismatch of scan rate and detection bandwidths. This noise level corresponds to 2.3 vacuum units. The peak of the trace should have the same amount of noise reduction, that is, from 354.8 to 354.1 vacuum units (from 25.50 dB to 25.49 dB), but this reduction is too small to observe in the graph. Trace (d) corresponds to the vacuum input state, which is obtained by blocking the modulated input beam. Acquisition parameters are: resolution bandwidth 30 kHz, video bandwidth 1 kHz and sweep time 200 ms.

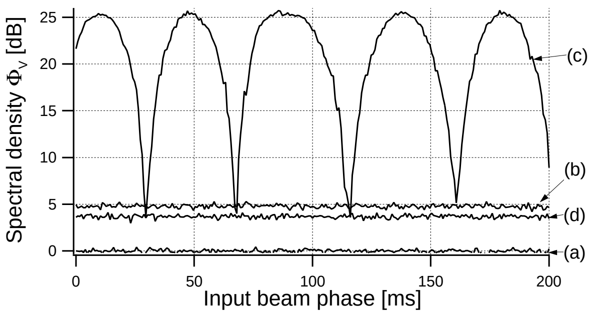

FIG. 16: Spectral density $\Phi_V(\Omega)$ recorded by Victor with the phase of the input beam scanning. Trace (a) is Victor's shot-noise level, trace (b) marks the 3 units of vacuum noise measured without entanglement, trace (c) is one quadrature of the teleported output coherent state, and trace (d) is the teleported output vacuum state (see text for details). For trace (c) Victor's LO was phase-locked to the x quadrature, while for traces (a), (b) and (d) Victor's LO was freely scanned, and a ten trace average was used. The average OPO pump power was 34 mW per beam, measurement frequency 1.475 MHz, RBW 30 kHz, and VBW 1 kHz.

The best noise reduction that we have obtained to date is shown in detail in Fig. 17. With the EPR beams present, the variances recorded by Victor are $\sigma_V^x = \sigma_V^p = 3.54 \pm 0.19$ dB, while with the EPR beams absent, $\sigma_V^x = \sigma_V^p = 4.86 \pm 0.12$ dB. The entanglement of the EPR beams thus leads to a quantum noise reduction of 1.32 ± 0.16 dB. This result was obtained with

40 mW pump power in each OPO path. The measurement parameters are the same as that in Fig. 16 except that the sweep time was 640 ms and we use a ten trace average for all traces. For this particular trace, the measured detection efficiencies were characterized by $\xi_1 = 0.986, \xi_2 = \xi_3 = 0.990, \xi_4 = 0.980, \xi_5 = 0.975$, and $\alpha_{Ax} = \alpha_{Ap} = \alpha_V = 0.988$.

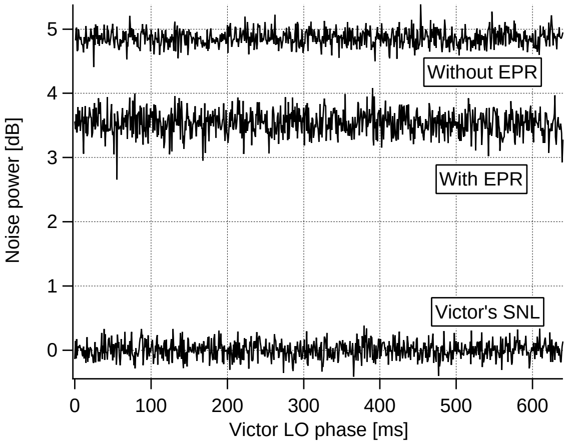

FIG. 17: Noise recorded by Victor showing in detail the reduction in the noise level with EPR beams (entanglement) present. With EPR beams, the measured variance at Victor was $\sigma_V^x = \sigma_V^p = 3.54 \pm 0.19$ dB. The average OPO pump power was 40 mW per beam, and acquisition parameters are the same as in Fig. 16. All traces use a ten trace average. SNL stands for shot-noise level.

A study of the dependence of the output variance on OPO pump power yields further insight into the experiment. Fig. 18 shows the variances of Alice and Victor as functions of pump power. From the squeezing results in Fig. 10, we can see that as the pump increases, both the squeezing and anti-squeezing increase, even though the squeezing increases very slowly. Therefore, the entanglement becomes stronger with increasing pump power. This phenomenon is reflected in the data shown in Fig. 18 at pump powers below 30 mW, where Alice's variance increases with pump power, whereas Victor's variance drops below 4.8 dB, as predicted. The best noise reduction for Victor was around 30 mW of blue pump for this particular set of data. Higher pump power did not help to reduce the noise; it instead increased both Alice's and Victor's variances even though we expect Victor's variance to continue to decrease, or at least remain stable. The likely culprits responsible for this degradation in performance will be discussed in the next sections. Chief among them is the performance of the various locking servos. As discussed in Sec. II B, fluctuations around the nominal ideal settings (e.g., $\pi/2$ for the squeezed beams that form the EPR beams) allows excess noise to contaminate the "quiet" quadratures, an effect that becomes more important as the degree of squeezing is increased.

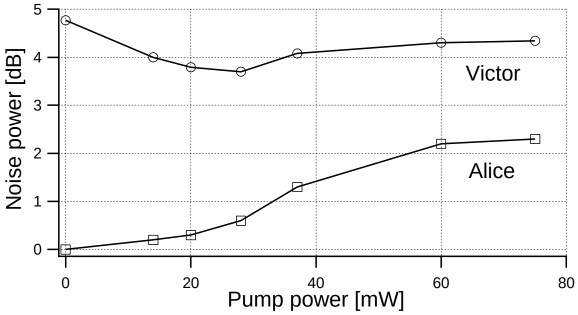

FIG. 18: Noise measured by Alice and Victor as functions of the pump of the OPO. The data points have been connected to ease viewing.

D. Teleportation fidelity

From the measured variances reported in Sec. IV C above, we can gauge the quality of the protocol by inferring the fidelity F via Eqs. (2) and (4). We first assume that the noise in the teleported output state ρ_{out} obeys Gaussian statistics [7, 9]. From the data in Fig. 17, where $\sigma_V^x = \sigma_V^p = 3.54 \pm 0.19$ dB, and where the gain g has already been set to unity by the techniques described in Sec. IV B, direct application of Eq. (2) gives $F = 0.61 \pm 0.02$.

Note that no correction whatsoever has been applied to this result; it corresponds to the fidelity obtained directly from Victor's photocurrent. We can certainly attempt to infer the fidelity associated with the field emerging from Bob's beamsplitter, rather than the photocurrent detected by Victor. To do so, we return to the issue pointed out earlier that we calibrate $g_{x,p}$ by ensuring $\beta_V = \beta_{in}$ as opposed to $\beta_{out} = \beta_{in}$. From the discussion in Sec. II A, we see that if Victor had unit detection efficiency ($\xi_5 = \eta_V = 1$), this issue would not arise at all. In our experiment where ($\xi_5 < 1, \eta_V < 1$), the actual unnormalized gains $g_{(0)}$ were set to be too large by a factor $(\xi_5 \eta_V)^{-1}$ than that neccessary for optimal reconstruction of Bob's field, instead of Victor's photocurrent. We can use Eq. (4) to compare Victor's variances when ($\xi_5 = \eta_V = 1$) and when ($\xi_5 < 1, \eta_V < 1$) with the same degree of squeezing as in Fig. 17. We thus infer that if Victor had perfect detectors, the variance of Bob's teleported output field (or equivalently now, Victor's variance as measured by his photocurrent) is given by $\sigma_W^{(x,p)} = \sigma_V^{(x,p)} = 3.47$ dB above the shot-noise level, which corresponds to an inferred fidelity of $F_B = 0.62$.

Returning to fidelity referenced to Victor's photocurrent, we estimate that with 42 mW pump power in each OPO path, where we have measured -3.73 dB squeezing and 6.9 dB anti-squeezing at Victor (see Fig. 9), the EPR entanglement at the EPR beamsplitter is characterized by the factors: $\sigma^- = -3.97$ dB and $\sigma^+ = 7.0$ dB. These numbers were obtained by back-propagating the squeezed beams to the EPR beamsplitter from Victor's homodyne detectors, considering the effects of Victor's homodyne efficiency $\xi_5 = 0.972$, photodiode quantum efficiency $\alpha_V = 0.988$ and the EPR homodyne efficiency $\xi_{EPR} = 0.985$. With measured efficiencies $\xi_1 = 0.985$, $\xi_2 = \xi_3 = 0.990$, $\xi_4 = 0.980$, $\xi_5 = 0.975$, the predicted variance of the teleported output state emerging from Bob's beamsplitter is $\sigma_W^{(x)} = \sigma_W^{(p)} = 2.82$ dB. The inferred fidelity would then be $F_P = 0.69$.

By contrast, our best entanglement-assisted noise reduction measured by Victor's balanced detector is 1.32dB below the level with no EPR beams, which corresponds to $\sigma_V^{(x)} = \sigma_V^{(p)} = 3.54$ dB and an inferred fidelity $F = 0.61$, as has been discussed.

To gain more insight into this discrepancy, we performed an analogous study to that shown in Fig. 18, where we plot the inferred fidelities from the measured variances versus pump power in Fig. 19. The inferred experimental fidelities peak at around 30mW corresponding to the minimum in Victor's measured variance. Here we also show the values of F that we might be able to reach with the current apparatus. First of all, the square symbols in Fig. 19 derive from the inferred degrees of squeezing at the EPR beamsplitter that are deduced from the data in Fig. 10. This was done from the measurement results by back-propagating the squeezed beams from Victor's homodyne detector to the EPR beamsplitter as previously described. In addition, the triangles in Fig. 19 correspond to the inferred fidelities from the theoretically predicted degrees of squeezing given by the solid line in Fig. 10. It can be seen that the disagreement between the predicted and measured fidelities is already apparent at low pump powers. However, the mismatch becomes more pronounced at higher pump powers where the measured fidelities start to decrease rather than increase with the pump level.

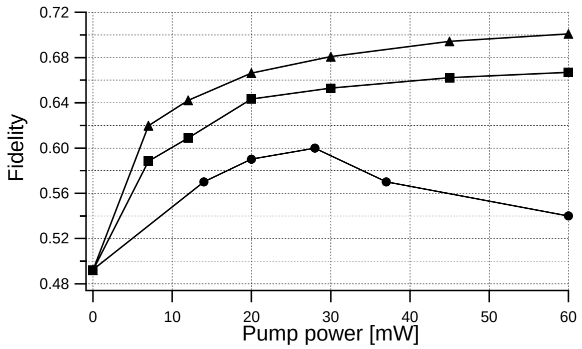

FIG. 19: Fidelity as a function of the OPO pump. Dots are the experimentally measured fidelities, squares are the expected fidelities given the measured degrees of squeezing shown in Fig. 10, and triangles are the expected fidelities based on our theoretically predicted degrees of squeezing in Fig. 10. Again, the lines connecting the data points are to ease viewing.

There are several factors contributing to the discrepancy between the measured and predicted variances and fidelities. The first is phase fluctuations from different locking systems, especially the EPR phase-lock. As discussed in Sec. II B, phase fluctuations add extra noise to the quadratures, and this effect is more pronounced at higher pump powers where the anti-squeezed quadrature is large. Another factor is the bandwidth of our two classical channels, which by bad design on our part, has been found to have excessive phase variation over the relevant RF bandwidth for the undistorted transmission of classical information. In fact, by an aforementioned technique, we measured the actual subtraction of the RF signal at 1.475 MHz through the classical channels and EPR2. It was found that frequency offsets of about 5 kHz led to drops in the cancellation from −25 dB to −20 dB. When the offset was 20 kHz, the cancellation is only −9 dB. Increasing the bandwidth while keeping relatively high isolation for the filter for various control signals (e.g., modulations at 3 and 5 MHz) in the classical channels will be helpful. A third reason for the discrepancy in Victor's variances is the imperfect character of Bob's EOMs, which cause coupling between the x and p quadratures, again resulting in contamination between squeezing and anti-squeezing. In order to reach higher fidelity, we are working to improve these aspects of the experiment.

V. CONCLUSION

We have described the details of recent experimental work to perform quantum teleportation for continuous variables. We have discussed a real experimental system where we considered many of the prevalent loss sources in our experiment, thus providing a detailed analysis of how the variances measured at Alice and Victor during teleportation vary with squeezing and ultimately OPO pump power. Phase fluctuations due to imperfect locking systems were also discussed, and it has been shown that nonideal detection schemes as well as phase fluctuations eventually degrade the noise reduction recorded by Victor and consequently reduce the teleportation fidelity.

We have discussed how to prepare experimentally the entangled EPR beams. Our entangled EPR fields at the EPR beamsplitter were typically characterized by $\sigma^- \simeq -4$ dB and $\sigma^+ \simeq 7$ dB according to our measured squeezing and efficiencies, which implies that our measured prospective fidelity would be 0.69.

The experimental setup and procedure was described in detail, including the OPO, the source of the entangled EPR fields. We have discussed optical phase-lock servo systems that ensure Alice is able to correctly measure the two orthogonal quadratures, x and p. Lastly, we have also described our classical channels through which classical information in the form of photocurrents obtained by Alice can be sent to Bob with the goals of minimal distortion and proper phase and gain in order to be sure that Bob can use that information to recover the original input state. The teleportation procedure was investigated for arbitrary unknown coherent states with any phase and a wide range of amplitudes.

The experiment clearly revealed the quduties that limit the classical performance of such a teleportation system. Victor unavoidably measures two extra units of vacuum noise if there is no entanglement. By employing the entangled fields of the EPR state, we demonstrated that the quduties were suppressed by $-1.32 \pm 0.16\,\mathrm{dB}$, which corresponds to an inferred fidelity of $F = 0.61 \pm 0.02$ for coherent states, which when corrected for the efficiency of detection by Victor, gives a fidelity of 0.62. The apparatus was shown to succeed for arbitrary coherent states with amplitudes up to 25dB above the vacuum level. This demonstrates that with entanglement, the procedure exhibits better performance than the classical bound of fidelity $F = 0.50$ [9, 10], and hence is genuinely a quantum protocol for unconditional teleportation.

We discussed Alice's and Victor's measured variances as functions of OPO pump power. The data in Fig. 18 showed that at low pump powers, Alice's measured variance σ_A increased and Victor's measured variance σ_V decreased with pump power, as expected. However, at higher pump powers (above ≈ 30 mW), while σ_A continued to increase with pump as expected, σ_V did not continue to decrease, but began increasing instead. This implied that the anti-squeezing quadrature contaminates the squeezed quadrature at high pump powers. Possible reasons for this contamination include fluctuations in the phase-lock servos, limited classical channel bandwidth and impure amplitude and phase modulators at Bob's station.

It is encouraging to note that our high detection efficiencies together with the relatively high degree of entanglement that we have achieved shows that our apparatus is capable of producing higher fidelity between the input and output states. In addition, a new scheme with the OPO pumped only by a single unidirectional blue beam to form the EPR state is being planned. We could then hope to obtain over $-5\,\mathrm{dB}$ of entanglement by mitigating high BLIIRA, and thus reducing the intracavity losses in the OPO. Such capabilities would be of interest to quantum information processing with continuous quantum variables [26].

Acknowledgments

The contributions of J. Buck and A. Furusawa are gratefully acknowledged. This research was funded by the National Science Foundation, by the Office of Naval Research, by the Caltech MURI on Quantum Networks administered by the Office of Army Research, and by the NSF sponsored Institute for Quantum Information. TCZ was partially supported by the EYTP of MOE, P. R. C.

---

[1] W. K. Wootters and W. H. Zurek, Nature **299**, 802 (1982).

[2] C. H. Bennett, G. Brassard, C. Crepeau, R. Jozsa, A. Peres, and W. K. Wootters, Phys. Rev. Lett. **70**, 1895 (1993).

[3] J. Preskill, *Lecture notes for Physics/Computer Science 219: Quantum Computation*, http://www.theory.caltech.edu/people/preskill/ph229 (1998).

[4] M. A. Nielsen and I. L. Chuang, *Quantum Computation and Quantum Information*, (Cambridge Univ. Press, Cambridge, 2000).

[5] D. Bouwmeester, J.-W. Pan, K. Mattle, M. Eibl, H. Weinfurter, and A. Zeilinger, Nature **390**, 575 (1997).

[6] D. Boschi, S. Branca, F. De Martini, L. Hardy, and S. Popescu, Phys. Rev. Lett. **80**, 1121 (1998).

[7] A. Furusawa, J. L. Sørensen, S. L. Braunstein, C. A. Fuchs, H. J. Kimble, and E. S. Polzik, Science **282**, 706 (1998).

[8] M. A. Nielsen, E. Knill, and R. Laflamme, Nature **396**, 52 (1998).

[9] S. L. Braunstein, C. A. Fuchs, and H. J. Kimble, J. Mod. Opt. **47**, 267 (2000).

[10] S. L. Braunstein, C. A. Fuchs, H. J. Kimble, and P. van Loock, Phys. Rev. A **64**, 022321 (2001).

[11] Recent press reports have described continuous variable teleportation from the group of H. Bachor and P. K. Lam at the Australian National University. Unfortunately, there is no scientific manuscript on which to base an assessment of these claims.

[12] J. L. Sørensen, "Nonclassical light for atomic physics and quantum teleportation", Ph.D. thesis, University of Aarhus (1998).

[13] The measurements described here were first reported at the 2001 Annual Meeting of the Optical Society of America, paper WG5 entitled "Quantum teleportation of quadrature phase amplitudes".

[14] S. L. Braunstein and H. J. Kimble, Phys. Rev. Lett. **80**, 869 (1998).

[15] L. Vaidman, Phys. Rev. A **49**, 1473 (1994).

[16] A. Einstein, B. Podolsky and N. Rosen, Phys. Rev. **47**, 777 (1935).

[17] S. J. van Enk, Phys. Rev. A **60**, 5095 (1999).

[18] P. van Loock, S. L. Braunstein, and H. J. Kimble, Phys. Rev. A **62**, 022309 (2000).

[19] E. S. Polzik, J. Carri, and H. J. Kimble, Phys. Rev. Lett. **68**, 3020 (1992); Appl. Phys. B **55**, 279 (1992).

[20] E. S. Polzik and H. J. Kimble, Opt. Lett. **16**, 1400 (1991).

[21] H. Mabuchi, E. S. Polzik, and H. J. Kimble, J. Opt. Soc. Am. B **11**, 2023 (1994).

[22] L. Shiv, J. L. Sørensen, E. S. Polzik, and G. Mizell, Opt. Lett. **20**, 2270 (1995).

[23] Z. Y. Ou, S. F. Pereira, and H. J. Kimble, Appl. Phys. B **55**, 265 (1992).

[24] Z. Y. Ou, S. F. Pereira, H. J. Kimble, and K. C. Peng, Phys. Rev. Lett. **68**, 3663 (1992).

[25] S. J. van Enk, J. of Mod. Opt. **48**, 2049 (2001).

[26] S. L. Braunstein and A. K. Pati (eds.), *Quantum Information Theory with Continuous Variables*, (Kluwer Aca-

demic Publishers, Dodrecht, 2000, in press).

PHYSICAL REVIEW A **67**, 032305 (2003)

Cavity QED and quantum-information processing with "hot" trapped atoms

L.-M. Duan,[1,*] A. Kuzmich,[2] and H. J. Kimble[2]
[1]*Institute for Quantum Information, MC 107-81, California Institute of Technology, Pasadena, California 91125-8100*
[2]*Norman Bridge Laboratory of Physics 12-33, California Institute of Technology, Pasadena, California 91125*

(Received 12 September 2002; published 17 March 2003)

We propose a method to implement cavity QED and quantum-information processing in high-Q cavities with a single trapped but nonlocalized atom. The system is beyond the Lamb-Dicke limit due to the atomic thermal motion. Our method is based on adiabatic passages, which make the relevant dynamics insensitive to the randomness of the atom position with an appropriate interaction configuration. The validity of this method is demonstrated from both approximate analytical calculations and exact numerical simulations. We also discuss various applications of this method based on the current experimental technology.

DOI: 10.1103/PhysRevA.67.032305 PACS number(s): 03.67.−a, 42.50.Gy

I. INTRODUCTION

Trapping of single atoms in high-Q cavities opens up exciting possibilities for the observation and manipulation of the dynamics of single particles and for control of their interactions with single-mode photons [1,2,4,5]. Such possibilities could have wide applications, such as for the generation of nonclassical or entangled optical pulses [6,7], for observing strong cavity-QED effects [4,5,8] and, more remarkably, for implementation of quantum communication and computation [9–13]. The trapping potential for confining single atoms can be created by diverse avenues, including by the cavity-QED light itself [4,5], by additional far-off-resonant trapping (FORT) beams [2], and by combining single trapped ions with high-finesse optical cavities [14,15]. In this paper, we will direct our attention principally to trapping in cavity QED by way of an additional FORT beam, although our results are applicable to broader settings.

The first experiment to achieve *strong coupling* in cavity QED with trapped atoms was that of Ref. [2], which employed an intracavity FORT beam and reported trapping lifetimes of 28 ms. By now, this experiment has attained much longer trapping times, with recent work demonstrating lifetimes in excess of 1 s [3,16]. By contrast, atomic localization by way of the cavity-QED field itself has led to trapping within a single axial well with mean trapping time $\tau \approx 340\ \mu\text{s}$ [4] and to localization across many axial wells with mean time $\tau \approx 280\ \mu\text{s}$ [5].

The long trapping times achieved with an intracavity FORT beam set the stage for diverse applications in quantum-information science, which motivates the current analysis. However, one of the main obstacles to the experimental demonstration of these applications is that the position of the trapped atom is not well fixed within the cavity. The coupling rate g between the atomic internal levels and the cavity mode depends on the atom's position $\mathbf{r}$ through the relation

$$g(\mathbf{r}) = g_0 \chi(\mathbf{r}) \tag{1}$$

with the mode function

$$\chi(\mathbf{r}) = \sin(k_0 z)\exp[-(x^2+y^2)/w_0^2], \tag{2}$$

where g_0 is the peak coupling rate, w_0 and $k_0 = 2\pi/\lambda_0$ are, respectively, the width and the wave vector of the Gaussian cavity mode, and z is assumed to be along the axis of the cavity. Due to the randomness of the atom's position $\mathbf{r}$, we have an unknown randomly changing coupling rate $g(\mathbf{r})$. Most of the applications of this setup assumed a fixed known coupling rate g. Therefore, before the experimental demonstration of these schemes, first one needs to solve the problem associated with the random coupling.

Intense experimental efforts have been taken to localize the atom inside the cavity so as to fix the coupling rate $g(\mathbf{r})$, with notable recent success attained via ion traps [14,15]. In the cavity-QED experiments employing cold atoms and without FORT beams [1,17,18], atoms were dropped through the cavity and followed random trajectories with large axial heating. As a result, the magnitude and the sign of $g(\mathbf{r})$ were not well controlled. With a FORT beam and with current experimental capabilities [2,3,16], an atom can be trapped inside one potential well along the cavity axis with a fixed sign of $g(\mathbf{r})$. But the atom still has appreciable kinetic energy and is not fully localized, leading to significant variations in the magnitude of the coupling rate $g(\mathbf{r})$.

The randomness of the coupling rate $g(\mathbf{r})$ comes from several contributions: first, the trapped atom is still quite hot in the current experimental setup. Its kinetic energy from the thermal motion is typically lower but not much lower than the depth of the trapping potential. The atom's oscillation amplitude d in the trap is comparable to the optical wavelength λ_0, so it does not satisfy the usually assumed Lamb-Dicke condition $d \ll \lambda_0$. Due to the thermal motion of the atom, the coupling rate $g(\mathbf{r})$ typically has a variation within a factor of 2 with the current experimental technique. Certainly, the atom will become better localized as cooling techniques are adapted to cavity QED and its energy is reduced [19,20]. However, due to the presence of the cavity and the trapping potential, it is still experimentally hard to achieve efficient cooling inside the cavity [19–21]. Furthermore, even if we assume that the atom has been precooled and localized initially to the Lamb-Dicke limit, the implemented

---

[*] Email address: lmduan@caltech.edu

1050-2947/2003/67(3)/032305(13)/$20.00

©2003 The American Physical Society

application protocols will still tend to heat the atom due to photon recoils from the spontaneous emissions [22,23]. As a result of the heating, the atom may go out of the Lamb-Dicke limit after a short time. Finally, even if we neglect all the motional and the heating effects of the trapped atom, there is still some uncertainty of the coupling rate. The intracavity field of the FORT beam forms many potential wells inside the cavity, and in current experiments, one cannot control and does not know precisely in which well the atom is trapped. The FORT beam has a wavelength λ_F different from the cavity-QED wavelength λ_0, so, even if the atom is kept very cold and well localized at the bottom of the trapping potential well, we still might not know exactly the coupling rate, since the bottoms of different potential wells have different coupling rates [24].

Here, to overcome these difficulties, we propose a method to do cavity-QED and quantum-information processing directly with hot atoms with an inhomogeneous distribution in position and/or a time-varying location. The method is based on adiabatic passages with a new interaction configuration. Adiabatic passages have been studied in the context of cavity QED [6,13,26,27], and have been adopted in some recent experiments [17,18]. Normally, schemes based on adiabatic passages are more insensitive to certain parameter changes compared with the corresponding Raman schemes. Some initial indication of insensitivity of the adiabatic passage scheme to certain parameter changes was already illustrated in Ref. [27] for a certain cavity-QED scheme. However, to make the whole system dynamics insensitive to variations of the coupling rate $g(\mathbf{r})$, the direct use of the usual adiabatic passage schemes is not enough to achieve this goal, and we also need to design a different and appropriate interaction configuration. The relevant dynamics of adiabatic passages are determined by the relative ratio between different coupling rates, and are almost independent of their absolute values. Thanks to this property, with an appropriate design of the interaction configuration, we can make different coupling rates have the same dependence on the atom's position $\mathbf{r}$, and, therefore, the system dynamics, determined by their relative ratios, will become independent of $\mathbf{r}$. As a result, though the atom's position may be unknown and time dependent, the output signal from the cavity is still controllable and has definitely known properties. This is the difference between the scheme here and the usual adiabatic passage schemes [13,17,18,27]. Note that the method described here is also different from some previous quantum computation schemes with hot trapped ions [28,29], where the Lamb-Dicke condition is still required.

The paper is arranged as follows: In Sec. II, we explain the basic idea of the method, and then describe and solve the model Hamiltonian analytically following some well-known approach based on the adiabatic approximation. This approximate analytical approach is still not enough to fully understand the experiments, so in Sec. III, we give an exact numerical simulation of the model, with the emphasis on checking the validity of the introduced approximations and calculating various kinds of noise magnitudes relevant for the on-going experimental efforts. The calculations show that we can get reasonably good signal-to-noise ratios with typical experimental values for the parameters. In Sec. IV, we briefly review some known cavity-QED and quantum-information processing schemes, and then discuss how to incorporate the present method into these schemes to improve their performance against the randomness in the atom's position. After this incorporation, with hot nonlocalized atoms, one can still realize many kinds of cavity-QED and quantum-information processing schemes, including, for instance, the controllable single-photon or entangled-photon source, quantum communication between cavities, atomic entanglement generation, teleportation, and Bell inequality detection. Section V gives a synopsis of parameters relevant to our current experiment for a single-atom trapping with a FORT beam at Caltech [2,3,16]. We summarize the results in the final section.

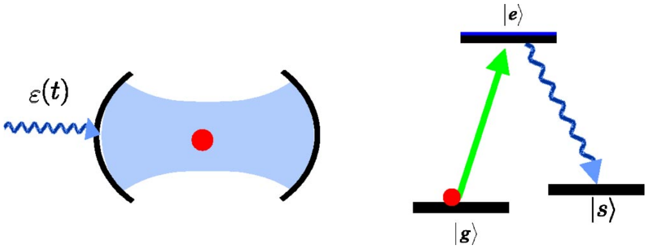

FIG. 1. Schematic setup. Left side: a single atom trapped in a high-Q cavity, which is driven by a classical laser pulse $\varepsilon(t)$. Right side: the relevant atomic level structure.

II. CAVITY QED WITH A NONLOCALIZED TRAPPED ATOM: THE SCHEME

A. Basic idea

First, we explain the basic idea of this method by considering a single trapped atom, which has three effective levels $|g\rangle$, $|e\rangle$, $|s\rangle$, as shown in Fig. 1. The two ground states $|g\rangle$ and $|s\rangle$ can correspond, for instance, to sub-Zeeman levels in the $F=3$ and $F=4$ manifolds, respectively, for the cesium atom. The transition $|e\rangle\rightarrow|s\rangle$ is coupled resonantly to the cavity-QED mode a with a coupling rate $g(\mathbf{r})$ in the form of Eq. (1). A classical laser field $\varepsilon(t)$ incident from one mirror of the cavity (see Fig. 1) drives the transition $|g\rangle\rightarrow|e\rangle$ through another cavity mode a'. We assume for simplicity that a and a' have the same spatial mode structure with the same frequency (for example, they can be of different polarizations) [25]. The driving laser $\varepsilon(t)$ is resonant to the transition $|g\rangle\rightarrow|e\rangle$, so it is far-off-resonant to the cavity mode a' with a large detuning ω_{gs}, where ω_{gs} denotes the splitting between the levels $|g\rangle$ and $|s\rangle$. Due to the off-resonant driving by $\varepsilon(t)$, a' can be described classically by its mean value $\langle a'\rangle=\alpha(t)e^{-i\omega_{ge}t}$ (ω_{ge} is the frequency splitting between the levels $|g\rangle$ and $|e\rangle$), which couples resonantly to the transition $|g\rangle\rightarrow|e\rangle$ with a Rabi oscillation frequency $\Omega(\mathbf{r},t)$. Since a and a' have the same spatial mode structure, the Rabi frequency $\Omega(\mathbf{r},t)$ will depend on the atom's position $\mathbf{r}$ by the same mode function $\chi(\mathbf{r})$, i.e., $\Omega(\mathbf{r},t)$ can be factorized as

$$\Omega(\mathbf{r},t)=\Omega_0(t)\chi(\mathbf{r})=r_o g_0\alpha(t)\chi(\mathbf{r}), \tag{3}$$

where r_o represents the fixed ratio of the Clebsch-Gordan coefficients for the transitions $|g\rangle \rightarrow |e\rangle$ and $|s\rangle \rightarrow |e\rangle$.

To understand the basic idea of this method, let us first look at a very simplified picture by neglecting the coupling of the mode a to the cavity output. The system is then described by the following simple Hamiltonian in the rotating frame (setting $\hbar = 1$):

$$H_{\text{sim}} = \Omega(\mathbf{r},t)\sigma_{eg} + g(\mathbf{r})a\sigma_{es} + \text{H.c.}, \tag{4}$$

where $\sigma_{\mu\nu} = |\mu\rangle\langle\nu|$ $(\mu,\nu = g,e,s)$ are the atomic transition operators, and H.c. stands for the Hermitian conjugate. The Hamiltonian H_{sim} has the well-known dark state $|D\rangle$ (the instantaneous eigenstate with a zero eigenvalue) with the form [27]

$$\begin{aligned}|D\rangle &= \frac{1}{\sqrt{|g(\mathbf{r})|^2 + |\Omega(\mathbf{r},t)|^2}}[g(\mathbf{r})|g\rangle|0\rangle - \Omega(\mathbf{r},t)|s\rangle|1\rangle] \\ &= \frac{1}{\sqrt{1 + |r_o\alpha(t)|^2}}[|g\rangle|0\rangle - r_o\alpha(t)|s\rangle|1\rangle],\end{aligned} \tag{5}$$

where $|0\rangle$ and $|1\rangle$ represent the zero- and the one-photon state of the cavity mode a. Note that the dark state $|D\rangle$ actually only depends on the ratio between the parameters $g(\mathbf{r})$ and $\Omega(\mathbf{r},t)$, so it becomes independent of the random atom position $\mathbf{r}$ with the interaction configuration specified above. If we start with the atom in the ground state $|g\rangle$, and gradually increase the Rabi frequency $\Omega(\mathbf{r},t)$, under the adiabatic approximation, the system will remain in the dark state $|D\rangle$, which gradually evolves into the final state $|s\rangle|1\rangle$. Due to the independence of the state $|D\rangle$ on the variable $\mathbf{r}$, the relevant dynamics of this adiabatic evolution also becomes independent of the random atom site $\mathbf{r}$. This is the basic idea of the method to eliminate the influence of the randomness on the coupling coefficient $g(\mathbf{r})$.

Note that to make the dark state and the relevant dynamics independent of the random atom position $\mathbf{r}$, the driving pulse and the cavity mode need to have the same spatial mode structure. This is why the classical driving pulse is matched to the spatial mode of the cavity field, both along the cavity axis and transversely, which is routinely accomplished by way of illumination from one side mirror of the cavity. This configuration is different from the original proposals for adiabatic dynamics in cavity QED [27] in which the propagation direction of the driving pulse is perpendicular to the cavity axis with uniform illumination intensity. It is also distinct from the configuration employed in some recent interesting experiments directed toward achieving a single-photon source [17,18], which likewise employed uniform illumination transverse to the cavity axis and for which the atom is not localized axially. As a result, in these experiments some of the dynamics, such as the output pulse shape and phase, still depend on the unknown position of the atom, and are thus not fully controllable, as has been seen from the experiments.

We also would like to mention that in this configuration, the driving field and the quantized cavity output are collinear, and they need to be separated afterwards. The separation can be done through either polarization or frequency selection. This separation is actually pretty easy in the present case. In typical experimental configurations, the classical field drives one cavity mode from one cavity mirror (say 1) with a large detuning, and the single-photon quantum field together with some transmitted driving field are output from the other cavity mirror (say 2, with the transmission rate $t_2 > t_1$). Most of the driving field has been filtered already by the high-finesse cavity itself. The ratio between the intensities of the classical driving field and the quantum field output from side 2 is the same as their ratio inside the cavity, which does not need to be very large, since both of the atomic transitions are enhanced by the cavity and thus have comparable strength. As will be seen in the numerical simulations in Sec. III, inside the cavity, the driving field is typically assumed to be about five times stronger than the single-photon field, and it is pretty easy to separate such a weak field with a polarization beam splitter at output side 2.

To guarantee an adiabatic evolution, we need to fulfill the adiabatic condition, which means that the evolution time T should be significantly longer than the frequency gap δ between the dark state and some other eigenstates of the Hamiltonian H_{sim}. The error probability due to the nonadiabaticity is estimated by $p_{ad} = 1/(\delta T)^2$. For the Hamiltonian H_{sim}, the frequency gap δ is given by $\delta = \sqrt{|g(\mathbf{r})|^2 + |\Omega(\mathbf{r},t)|^2}$. Thus, the adiabatic condition $[|g(\mathbf{r})|^2 + |\Omega(\mathbf{r},t)|^2]T^2 \gg 1$ depends on the atom position $\mathbf{r}$. If the coupling coefficient $g(\mathbf{r})$ changes by a factor of 2, the error probability p_{ad} will change by a factor of 4 for the same evolution time T. However, if T is sufficiently long, the error probability p_{ad} remains small, and the relevant system dynamics will be still very insensitive to the randomness of the atom's position. To estimate p_{ad}, we can use the average value of the coupling rate $g(\mathbf{r})$.

In the above simple picture, we neglect the coupling of the mode a to the cavity output. This is only a valid picture in the good-cavity limit with the evolution time $T \ll 1/\kappa$, where κ is the cavity decay rate. However, in practice, it is better to operate the system in the limit with $T \gg 1/\kappa$. There are several advantages of operating the system in this limit: first, without the requirement $T \ll 1/\kappa$, it is easier to satisfy the adiabatic condition for which T should be sufficiently long; second, in this limit it is easier to modulate the Rabi frequency $\Omega(\mathbf{r},t)$ by changing the intensity of the driving laser $\varepsilon(t)$ incident from one side mirror of the cavity. In this way, one can efficiently control the pulse shape of the cavity output by modulating the shape $\varepsilon(t)$ of the driving laser, which is useful for many applications. In the limit $T \gg 1/\kappa$, we need to take into account, from the beginning, the coupling of the mode a to the continuum cavity output, and the whole system will then have infinite levels. We will describe in the section this more involved interaction configuration. The above simple three-level picture, though it does not describe the real experimental configuration, does help in understanding the basic idea of the adiabatic method.

B. Theoretical model and its approximate analytical solution

Now we look at the more complicated theoretical model, which includes the coupling of the mode a to the continuum cavity output. If we adiabatically apply a classical driving pulse $\varepsilon(t)$ as shown in Fig. 1, one photon will be emitted from the transition $|e\rangle\rightarrow|s\rangle$, and the cavity will output a single-photon pulse. We want to show below that this single-photon pulse has a definite pulse shape which is independent of the randomness in the atom's position $\mathbf{r}$ and in the coupling rate $g(\mathbf{r})$. In this way, although the atom's position and the absolute value of the light-atom coupling rate are not fully controlled, we can nevertheless fully control the properties of the output single-photon pulse by modulating the driving laser pulse $\varepsilon(t)$. This is an important feature for many applications of this setup, which we will discuss in Sec. IV. There are several equivalent ways to describe the coupling of the mode a to the continuum cavity output [9,30,31]. Since we want to calculate the output pulse shape within the adiabatic approximation, it is convenient to use the Hamiltonian approach [30,31]. The derivation here is similar to the calculation in Ref. [30] for the pulse shape from an ensemble of atoms. The whole Hamiltonian, including the coupling to the cavity output, has the following form in the rotating frame [31]:

$$\begin{aligned}H={}&(\Delta-i\gamma_s/2)\sigma_{ee}+[\Omega(\mathbf{r},t)\sigma_{eg}+g(\mathbf{r})a\sigma_{es}+\text{H.c.}]\\&+i\sqrt{\kappa/2\pi}\int_{-\omega_b}^{+\omega_b}d\omega[a^{\dagger}b(\omega)-ab^{\dagger}(\omega)]\\&+\int_{-\omega_b}^{+\omega_b}d\omega[\omega b^{\dagger}(\omega)b(\omega)],\end{aligned}\tag{6}$$

where $b(\omega)$, with the standard commutation relation $[b(\omega),b^{\dagger}(\omega')]=\delta(\omega-\omega')$, denote the one-dimensional free-space modes that couple to the cavity mode a. We only need to consider the free-space modes within a finite bandwidth $[\omega_{se}-\omega_b,\omega_{se}+\omega_b]$ with the carrier frequency ω_{se} (ω_{se} is the frequency splitting between the levels $|s\rangle$ and $|e\rangle$), since all the modes outside of this bandwidth have negligible contributions to the dynamics due to the large detuning (larger than ω_b). Within this bandwidth, the coupling between $b(\omega)$ and the cavity mode a is approximately a constant, and we denote it by $\sqrt{\kappa/2\pi}$ for convenience, where κ is the effective cavity decay rate, as we will see. The bandwidth ω_b should be chosen to be much larger than κ, but still much smaller than ω_{se}.

We have assumed that the driving laser and the cavity mode a couple resonantly to the corresponding free-space atomic transitions. However, we emphasize that our scheme still works for the case of off-resonant coupling. By considering the off-resonant scheme, there is no win with respect to losses due to the atomic decay, since in this case the time scale also slows down. So it suffices here to consider the resonant coupling case. However, in the Hamiltonian (6), it is still helpful to include a single-photon-transition detuning Δ to account for the trapping potential difference for the levels $|g\rangle$ and $|e\rangle$ induced by the FORT beam (this potential is basically the same for the levels $|s\rangle$ and $|g\rangle$ for a FORT beam with linear polarization as in our current experiments). The potential difference between the level $|g\rangle$ and $|e\rangle$, in general, depends as well on the random atom position $\mathbf{r}$.

The imaginary part of the Hamiltonian (6) accounts for the spontaneous emission loss, where γ_s denotes the total spontaneous emission rate of the upper level $|e\rangle$. In writing this form, we have assumed that the spontaneous emission photon escapes and that the atom after a spontaneous emission will not be repumped. This is a good assumption for the interesting region where the spontaneous emission loss is not big, and the atom thus has a very small probability to be repumped after emitting a spontaneous emission photon. As a result of this assumption, the spontaneous emission only contributes to the leakage error which is properly represented by Eq. (6) [32].

We treat the atom's position $\mathbf{r}$ in the Hamiltonian (6) as a classical stochastic variable, and neglect its quantum nature. This is a good approximation for the current experimental situation where the atom is still quite hot. There have been some analyses of the noise from quantum motion effects in high-Q cavities with very cold atoms [33].

We start with the atom in the ground state $|g\rangle$, and then apply a classical driving pulse $\varepsilon(t)$. This pulse can efficiently control the time evolution of the Rabi frequency $\Omega(\mathbf{r},t)$ in the Hamiltonian (6). To see this, we write the input-output equation for the cavity mode a' [31]

$$\dot{a}'=-i\omega_{se}a'-\frac{\kappa}{2}a'-\sqrt{\kappa}a'_{\text{in}}(t),\tag{7}$$

where $a'_{\text{in}}(t)$ is the field operator for the input driving pulse coupling to the mode a', with $\langle a'_{\text{in}}(t)\rangle=\varepsilon(t)$ and $[a'_{\text{in}}(t),a'^{\dagger}_{\text{in}}(t')]=\delta(t-t')$. By assumption, the mode a' has the same frequency as the mode a, which is resonant to the free-space atomic transition $|s\rangle\rightarrow|e\rangle$, so the eigenfrequency of a' is ω_{se}. Such a situation corresponds, for example, to the case of the (a,a') modes of orthogonal polarization, but degenerate in frequency, although this is not an essential requirement. In Eq. (7), we have neglected the small depletion of a' caused by the coupling to the atomic transition σ_{eg}, since a' is driven by a strong classical pulse $\varepsilon(t)$ which dominates its time evolution. We write the mean values of a' and $a'_{in}(t)$ as $\langle a'\rangle=\alpha(t)e^{-i\omega_{ge}t}$ and $\langle a'_{\text{in}}(t)\rangle=\varepsilon(t)=\tilde{\varepsilon}(t)e^{-i\omega_{ge}t}$, where $\tilde{\varepsilon}(t)$ is the slowly varying amplitude of the driving laser. From Eq. (7), we get a time evolution equation for the mean value $\alpha(t)$, which has the following immediate solution:

$$\alpha(t)=\int_0^t\tilde{\varepsilon}(\tau)e^{(i\omega_{gs}-\kappa/2)(t-\tau)}d\tau.\tag{8}$$

The variation rate of $\tilde{\varepsilon}(\tau)$ is characterized by the inverse of the operation time T (the pulse duration), which is typically much smaller than the hyperfine frequency splitting ω_{gs} (about 9 GHz for cesium atoms). Hence, a partial integration of Eq. (8) yields

$$\alpha(t)\simeq\frac{\tilde{\varepsilon}(t)-e^{(i\omega_{gs}-\kappa/2)t}\tilde{\varepsilon}(0)}{-i\omega_{gs}+\kappa/2}\left[1+o\left(\frac{1}{\omega_{gs}T}\right)\right].\tag{9}$$

We assume that $\tilde{\varepsilon}(t)$ gradually increases from zero with $\tilde{\varepsilon}(0)\simeq 0$. Then, within a good approximation, we have $\alpha(t)\propto\tilde{\varepsilon}(t)$ from Eq. (9). In the following, without loss of generality, we assume $\alpha(t)$ to be real by choosing an appropriate constant phase of $\tilde{\varepsilon}(t)$. The time behavior of the Rabi frequency $\Omega(\mathbf{r},t)$ is completely determined by $\alpha(t)$ [note that $\Omega(\mathbf{r},t)=r_o g_0 \alpha(t)\chi(\mathbf{r})$ from Eq. (3)], that is, by the amplitude $\tilde{\varepsilon}(t)$ of the driving laser.

The dark state (5) can be rewritten as $|D\rangle=\cos\theta|g\rangle|0\rangle-\sin\theta|s\rangle|1\rangle$, with $\cos\theta=1/\sqrt{1+|r_o\alpha(t)|^2}$ independent of the atom's position $\mathbf{r}$. The state $|B\rangle$ complementary to the dark state is usually called the bright state with $|B\rangle=\sin\theta|g\rangle|0\rangle+\cos\theta|s\rangle|1\rangle$. To solve the dynamics governed by the Hamiltonian (6), we can expand the state $|\Psi\rangle$ of the whole system into the following superposition:

$$|\Psi\rangle=(c_d|D\rangle+c_b|B\rangle+c_e|e\rangle|0\rangle)\otimes|\mathrm{vac}\rangle+|s\rangle|0\rangle\otimes|\varphi_1\rangle, \tag{10}$$

where $|\mathrm{vac}\rangle$ denotes the vacuum state of the free-space modes $b(\omega)$, and

$$|\varphi_1\rangle=\int_{-\omega_b}^{+\omega_b} d\omega c_\omega b^\dagger(\omega)|\mathrm{vac}\rangle \tag{11}$$

represents the state (not normalized) of the single-photon output pulse. The coefficients c_d, c_b, c_e, and c_ω in Eq. (10) are time dependent. At the time $t=0$, we have $c_d=1$, $c_b=c_e=c_\omega=0$, and $\cos\theta=1$. After applying a classical driving pulse $\varepsilon(t)$, $\cos\theta$ slowly changes with $\alpha(t)$, and we need to compute the time evolution of all the coefficients c_d, c_b, c_e, c_ω in Eq. (10) by substituting $|\Psi\rangle$ into the Schrödinger equation $i\partial_t|\Psi\rangle=H|\Psi\rangle$.

To go on with this task, let us first take the adiabatic approximation, which assumes the time derivative $\partial_t\cos\theta\approx 0$. As a result, $\partial_t|D\rangle$ and $\partial_t|B\rangle$ become negligible. We will check the validity of the adiabatic approximation and calculate various nonadiabatic corrections in the following section through numerical methods. In the adiabatic limit, the populations in the bright state $|B\rangle$ and in the excited state $|e\rangle$ are negligible, so we assume $c_b\approx c_e\approx 0$. The coefficients c_d and c_ω satisfy the following evolution equations:

$$\dot{c}_d=-\sqrt{\kappa/2\pi}\sin\theta\int_{-\omega_b}^{+\omega_b} c_\omega d\omega, \tag{12}$$

$$\dot{c}_\omega=-i\omega c_\omega+\sqrt{\kappa/2\pi}c_d\sin\theta. \tag{13}$$

Equation (13) has the solution

$$c_\omega(t)=\sqrt{\kappa/2\pi}\int_0^t e^{-i\omega(t-\tau)}c_d(\tau)\sin\theta(\tau)d\tau, \tag{14}$$

which, substituted into Eq. (12), leads to

$$\begin{aligned}\dot{c}_d&=-\frac{\kappa}{2\pi}\sin\theta\int_0^t\frac{\sin[\omega_b(t-\tau)]}{t-\tau}c_d(\tau)\sin\theta(\tau)d\tau\\&\simeq-(\kappa/2)c_d\sin^2\theta.\end{aligned} \tag{15}$$

The approximation in Eq. (15) is valid since the bandwidth ω_b satisfies $\omega_b T\gg 1$, where the operation time T characterizes the time scale for a significant change of c_d and $\sin\theta$. Therefore, the dark-state coefficient c_d satisfies the cavity free-decay equation, with the decay rate κ replaced by the effective rate $\kappa\sin^2\theta$. This can be easily understood since $\sin^2\theta$ is the probability of the component $|s\rangle|1\rangle$ in the dark state $|D\rangle$, and it is exactly this component that couples to the cavity output. Equation (15) has the straightforward solution

$$c_d=\exp\left(-\frac{\kappa}{2}\int_0^t\sin^2\theta(\tau)d\tau\right). \tag{16}$$

We want to know the single-photon pulse shape $f(t)$ of the cavity output state $|\varphi_1\rangle$. Suppose now that T is the final time of the interaction (i.e., the operation time determined by the driving laser pulse is from 0 to T). The pulse shape $f(t)$ is connected with the coefficients $c_\omega(t)$ before the frequency components in $|\varphi_1\rangle$ by the Fourier transformation [31]

$$f(t)=\frac{1}{\sqrt{2\pi}}\int_{-\omega_b}^{+\omega_b} d\omega c_\omega(T)e^{-i\omega(t-T)}. \tag{17}$$

From Eqs. (14), (16), and (17), we finally obtain

$$f(t)=\sqrt{\kappa}\sin\theta(t)\exp\left(-\frac{\kappa}{2}\int_0^t\sin^2\theta(\tau)d\tau\right). \tag{18}$$

Note that the single-photon pulse shape $f(t)$ is completely determined by $\theta(t)$, i.e., by the driving pulse shape $\tilde{\varepsilon}(t)$, and is independent of the random atom's position $\mathbf{r}$ and the absolute value of the coupling coefficient $g(\mathbf{r})$. As we have mentioned before, this is the main advantage of this adiabatic method compared with either the Raman scheme or prior proposals based upon adiabatic passages with uniform illumination [17,18,27], and this feature is essential for many applications of this setup.

The above result is obtained within the adiabatic approximation, and in the adiabatic limit, the solution is independent of the atomic spontaneous emission rate γ_s and the detuning Δ. This is only a rough picture. In the following, we will solve exactly the dynamics governed by the Hamiltonian (6) without the use of the adiabatic approximation. The exact solution is necessary in the following two senses: first, we need to verify the above ideal picture and to find out under what condition this picture is approximately valid. Though in the three-level case, we have some simple estimation of the condition for the adiabatic following, it is not easy to figure out the exact adiabatic following condition for the more realistic situation of a continuum of external modes. In this case, the argument based on the level spacing is not valid. We need to know how long the operation time T should be to satisfy the adiabatic following condition. We also expect that the atomic spontaneous emission cannot be made negligible simply by increasing the operation time T. Its rate γ_s should be small enough to satisfy the strong-coupling condition $\kappa\gamma_s\ll\overline{g}^2$, where $\overline{g}$ denotes the average of the coupling rate $g(\mathbf{r})$ [34]. Second, in real experiments, the operation time T

is not infinitely long, and the coupling rate $\overline{g}$ cannot be arbitrarily larger than the decay rates κ and γ_s due to limitation of the technology (for instance, in Caltech experiments, typically, $\overline{g}/2\pi$ is around 20 MHz, and $\kappa/2\pi \sim \gamma_s/2\pi \sim 6$ MHz). In this case, there would be various nonadiabatic corrections to the above ideal picture, for instance, the atom may go down from the level $|e\rangle$ to $|s\rangle$ through a spontaneous emission, and then we lose the emitted photon and thus have no output from the cavity; or we have a single-photon output, but it is in a wrong and unknown pulse shape due to its sensitivity to the random atom position induced by the nonadiabatic contributions. It is desirous and important to calculate quantitatively the magnitudes of these noises to predict the real experiments. The exact solution of the system dynamics is only available with the numerical methods, which is the main task of the following section.

III. EXACT NUMERICAL SIMULATIONS

A. The numerical calculation method

In this section, we solve exactly the system dynamics governed by the Hamiltonian (6) through numerical simulations, and calculate various nonadiabatic corrections and noise magnitudes. For numerical simulations of the Hamiltonian (6), we need to discretize the free-space field $b(\omega)$ by introducing a finite but small frequency interval $\delta\omega$ between two adjacent modes. Then, in total we have about $N \approx 2\omega_b/\delta\omega$ free-space modes, with the j mode denoted by b_j. The frequency detuning ω_j of the j mode is given by $\omega_j = (j - N/2)\delta\omega$. To assure that there is no change of the physical result after the discretization, we should choose the frequency interval $\delta\omega$ much smaller than the inverse of the operation time T, and the bandwidth ω_b much larger than the cavity decay rate κ.

For the numerical simulation, we can similarly expand the state $|\Psi\rangle$ of the whole system in the form of Eq. (9), with the single-photon pulse state replaced by

$$|\varphi_1\rangle = \sum_{j=1}^{N} c_j b_j^\dagger |\text{vac}\rangle. \tag{19}$$

From the Hamiltonian (6), we get the following complete set of equations for the coefficients c_d, c_b, c_e, and c_j:

$$\dot{c}_d = -\dot{\theta} c_b - \kappa' \sin\theta \sum_{j=1}^{N} c_j, \tag{20}$$

$$\dot{c}_b = \dot{\theta} c_d - i\sqrt{\Omega^2(\mathbf{r},t) + g^2(\mathbf{r})}\, c_e + \kappa' \cos\theta \sum_{j=1}^{N} c_j, \tag{21}$$

$$\dot{c}_e = (-i\Delta - \gamma_s/2) c_e - i\sqrt{\Omega^2(\mathbf{r},t) + g^2(\mathbf{r})}\, c_b, \tag{22}$$

$$\dot{c}_j = -i(j - N/2)\delta\omega c_j + \kappa' \sin\theta c_d - \kappa' \cos\theta c_b, \tag{23}$$

where the effective decay rate $\kappa' \equiv \sqrt{\kappa\delta\omega/2\pi}$. We obtain the solutions of these coefficients by numerically integrating Eqs. (20)–(23) from the time $t=0$ to $t=T$, where T is the duration of the driving pulse $\tilde{\varepsilon}(t)$. We assume that $\tilde{\varepsilon}(t)$ is a Gaussian pulse so that $\alpha(t)$ is a Gaussian function of the time t, with its peak value at $T/2$, and a width t_w significantly smaller than $T/2$. All the functions of θ in Eqs. (20)–(23) are decided from $\cos\theta = 1/\sqrt{1 + |r_o \alpha(t)|^2}$ and $\sqrt{\Omega^2(\mathbf{r},t) + g^2(\mathbf{r})} = g(\mathbf{r})/\cos\theta$. To simulate the randomness of the atom position $\mathbf{r}$, we vary the value of $g(\mathbf{r})$ in the simulation to look at whether the final result changes with this variation.

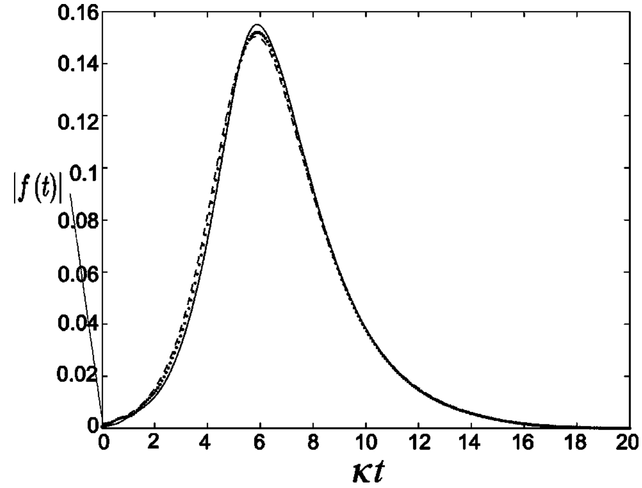

FIG. 2. The shape of the output single-photon pulse described by the amplitude $|f(t)|$ vs the time t for the coupling rates $g(\mathbf{r}) = 3\kappa$ (solid curve) and $g(\mathbf{r}) = 6\kappa$ (dotted curve). The dashed curve represents the pulse shape in the ideal adiabatic limit calculated from Eq. (16). In this figure, we have taken $\gamma_s = \kappa$, $\Delta = 0$, and $T = 20/\kappa$. The driving pulse $\tilde{\varepsilon}(t)$ is in a Gaussian shape with the peak at $t = T/2$ and a width $t_w = T/5$.

B. Shape of the output single-photon pulse

The output single-photon pulse shape $f(t)$ can be easily constructed from the solution of the coefficients c_j through a discrete version of Eq. (17). The result is shown in Fig. 2 for $g(\mathbf{r}) = 3\kappa$ and $g(\mathbf{r}) = 6\kappa$. Although we have not made definitive measurements, we estimate that $g(\mathbf{r})$ varies within a factor of roughly 2 in the current Caltech experiment [2,3,16]. Here and in the following, the pulse-shape function $f(t)$ is always renormalized according to $\int |f(t)|^2 dt = 1$ for convenience of comparison. We see that the two curves overlap very well, which confirms the prediction that the output pulse shape is very insensitive to the randomness of the coupling coefficient $g(\mathbf{r})$ when the adiabatic condition is satisfied (we take $T = 20/\kappa$ for this figure). We also draw in this figure the pulse shape $f(t)$ given by Eq. (18) derived in the ideal adiabatic limit, which agrees well with the exact numerical results. Therefore, within the adiabatic condition, we can use the analytical result (18) to design the shape of the output single-photon pulse by modulating the driving pulse shape $\tilde{\varepsilon}(t)$.

C. Noise magnitudes and the adiabatic condition

To quantify the noise magnitudes in this setup, we can define several error probabilities. First, we have the leakage error due to the atomic spontaneous emission. A photon may be emitted to modes other than the principal cavity mode through the spontaneous emission with the rate γ_s. As a result, the norm $|c_d|^2+|c_b|^2+|c_e|^2+\Sigma_{j=1}^{N}|c_j|^2$ of the state (10) decays with the time t, and we can use

$$P_{\mathrm{spon}}=1-|c_d(T)|^2-|c_b(T)|^2-|c_e(T)|^2-\sum_{j=1}^{N}|c_j(T)|^2 \tag{24}$$

at the final time T to quantify the total possibility of the spontaneous emission loss. Second, due to the finiteness of the operation time T and the pumping field amplitude $\tilde{\varepsilon}(t)$, the initial excitation in the dark state is not necessarily fully transferred to the output quantum signal at the final time, and we can use

$$P_{\mathrm{tran}}=|c_d(T)|^2+|c_b(T)|^2+|c_e(T)|^2 \tag{25}$$

at the time T to quantify the transmission inefficiency. In principle, we can arbitrarily decrease the transmission inefficiency by increasing the duration T or the amplitude $\tilde{\varepsilon}(t)$ of the pumping field. Finally, even if a photon is emitted into the cavity output field, it is not necessarily in the right pulse shape as given by Eq. (18) due to the nonadiabatic correction. This nonadiabatic correction depends on the random atom position and is unknown, so it is also a source of noise. To quantify this noise, we denote the ideal pulse shape given in Eq. (18) as $f_{\mathrm{id}}(t)$, and the real pulse shape calculated from the numerical simulation as $f_{\mathrm{real}}(t)$, then the shape mismatching error can be described by

$$P_{\mathrm{mis}}=\left|1-\frac{\int_0^T f_{\mathrm{real}}^*(t)f_{\mathrm{id}}(t)dt}{\left[\int_0^T|f_{\mathrm{real}}(t)|^2dt\int_0^T|f_{\mathrm{id}}(t)|^2dt\right]^{1/2}}\right|. \tag{26}$$

This quantity is directly related to the visibility of the fringes if we interfere two single-photon pulses from two such setups.

For the example shown in Fig. 2, with $g(\mathbf{r})=3\kappa=3\gamma_s$ (the other parameters are given in the figure caption), we have $P_{\mathrm{spon}}\approx 4.0\%$, $P_{\mathrm{tran}}\approx 0.04\%$, $P_{\mathrm{mis}}\approx 0.18\%$. The dominant source of noise is the leakage error P_{spon} induced by the spontaneous emission. If we increase the operation time T so that the adiabatic condition is better satisfied, the above-defined noise magnitudes can be reduced a little bit, but not too much. For instance, with the above example but with $T=30/\kappa$, we have $P_{\mathrm{spon}}\approx 3.33\%$ and $P_{\mathrm{mis}}\approx 0.15\%$. On the other hand, if T is reduced so that the adiabatic condition is not well satisfied, the error probabilities can significantly increase. Figure 3 shows the output pulse shapes for $g(\mathbf{r})=3\kappa$ and $g(\mathbf{r})=6\kappa$ with $T=5/\kappa$. The two curves are obviously different from each other and are also different from the ideal shape as given by Eq. (18). For the example with $g(\mathbf{r})=3\kappa=3\gamma_s$ and $T=5/\kappa$, we have $P_{\mathrm{spon}}\approx 36\%$, $P_{\mathrm{tran}}\approx 3.2\%$, $P_{\mathrm{mis}}\approx 2.7\%$. All the noise magnitudes significantly increase. In particular, the spontaneous emission loss becomes very big. This can be easily understood since without the adiabatic condition, the excited state $|e\rangle$ will be populated during the operation, and thus we have a correspondingly larger spontaneous emission loss.

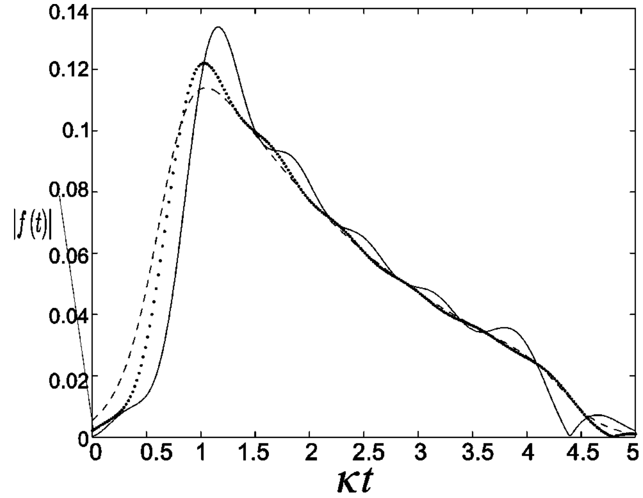

FIG. 3. The shape $|f(t)|$ of the output single-photon pulse for the coupling rates $g(\mathbf{r})=3\kappa$ (solid curve), $g(\mathbf{r})=6\kappa$ (dotted curve), and in the ideal adiabatic limit (dashed curve). We assumed the same condition as in Fig. 2, except that $T=5/\kappa$, which does not satisfy well the adiabatic condition.

D. The strong-coupling condition

Next we look at the requirement of the strong-coupling condition. Let $\overline{g}$ denote the average value of the coupling rate $g(\mathbf{r})$. Normally one requires $\overline{g^2}\gg\kappa\gamma_s$ to satisfy the strong-coupling condition. We can define the strong-coupling parameter d_{sc} as $d_{sc}=\overline{g^2}/\kappa\gamma_s$, and calculate the above-defined noise magnitudes P_{spon}, P_{tran}, P_{mis} under different values of the parameter d_{sc}. We assumed $T=30/\kappa$ and $\Delta=0$ in the calculation so that the adiabatic condition is well satisfied. It turns out that the spontaneous emission loss P_{spon} is always the dominant loss (about ten times larger than other sources of noise). Thus, in Fig. 4, we only show the calculation result for P_{spon} under different values of d_{sc}. The result can be approximately simulated by an empirical curve with $P_{\mathrm{spon}}\approx 1/(4d_{sc})$.

We can use this simple formula to estimate the spontaneous emission loss under different experimental conditions. Actually, in current experiments, the strong-coupling condition is only marginally satisfied. For instance, for the cesium atom in the Caltech group, $(\kappa,\gamma_s)/2\pi\approx(8,5.2)$ MHz (note that κ and γ_s here denote the energy decay rates, which are two times the corresponding amplitude decay rates) [2,3], and $\overline{g}/2\pi$ is expected to be ≈ 15 MHz for the transition $(6S_{1/2},F=4,m=+4)\rightarrow(6P_{3/2},F=4,m=+4)$ [Note that the transition $(6S_{1/2},F=4,m=+4)\rightarrow(6P_{3/2},F=5,m=+5)$ cannot be used as a Λ configuration though it has a slightly larger coupling rate $\overline{g}$]. These values lead to $d_{sc}=\overline{g^2}/\kappa\gamma_s\approx 5.4$ and a resulting spontaneous emission loss around 4.6%, which is quite accessible with the present tech-

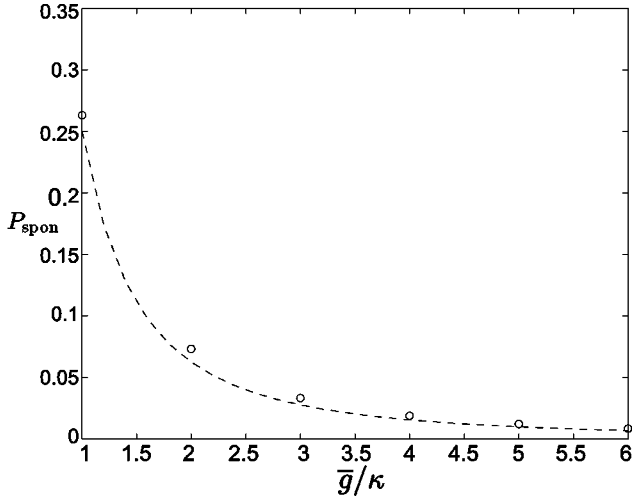

FIG. 4. The spontaneous emission loss P_{spon} vs the average coupling rate $\overline{g}$ (in the units of the cavity decay rate κ). We assumed $\Delta=0$ and $\gamma_s=\kappa$, so the strong-coupling parameter d_{sc} is simply $(\overline{g}/\kappa)^2$. The circles represent the results from the numerical calculation, and the dashed curve is from the empirical formula $P_{\mathrm{spon}}\approx 1/(4d_{sc})$ which simulates well the numerical results.

nology. As another example, in the recent experiment [18], one has $(\kappa,\gamma_s)/2\pi\approx(1.25{,}6.0)$MHz and $\overline{g}/2\pi\approx 2.5$ MHz according to the estimation there. With these parameters, $\overline{g}^2/\kappa\gamma_s\approx 0.83$ and we estimate that the spontaneous emission loss is about $P_{\mathrm{spon}}\approx 30\%$ if one uses the scheme here. If the usual adiabatic scheme is adopted with a uniform driving pulse perpendicular to the cavity axis, the spontaneous emission loss should be still significantly larger, as will be seen from the simulation in the last section.

E. The influence of the single-photon transition detuning

In the above calculations, we assumed $\Delta=0$. Finally, we discuss the influence of a nonzero single-photon detuning Δ. In Fig. 5, we show the calculation result of the exact pulse-shape function $f_{\mathrm{real}}(t)$ with a significant detuning $\Delta=\kappa$, and compare it with the ideal pulse shape function $f_{\mathrm{id}}(t)$ given by Eq. (18) for both the amplitude and the phase. The other parameters for this example are given in the figure caption. From the figure, we see that the two amplitudes $|f_{\mathrm{real}}(t)|$ and $|f_{\mathrm{id}}(t)|$ still overlap very well, but their phases become a bit different due to the detuning.

This phase difference is determined by the the detuning Δ, whereas the latter depends on the different level shift between ground and excited states, and hence varies with the atom position within the FORT beam. In the case of the simple level scheme depicted in Fig. 1, the states $|g\rangle$ and $|e\rangle$ would have spatially dependent level shifts of opposite sign, which would lead to variations in Δ comparable to the trap depth. Fortunately, there is a simple way to mitigate this difficulty by considering the multilevels involved for the FORT beam, as described in Ref. [35], so that the trapping potentials for the states $|g\rangle$ and $|e\rangle$ are very nearly the same. For example, for the experiment of Ref. [16], the difference in trap depth for $|g\rangle$ and $|e\rangle$ is roughly 10% of the trap depth. Relative to the current analysis, there is then a variation in Δ as the atom moves in the FORT potential, which is unknown when the adiabatic protocol is implemented. The curve in Fig. 5 is an attempt to estimate the impact of such random detunings by setting $\Delta=\kappa$, which exceeds the actual magnitude of any spatially dependent detunings for FORT depths up to about 50 MHz. The phase difference in the pulse-shape function caused by the unknown detunings is a source of noise, which contributes to the shape mismatching error defined in Eq. (26). For this example with $g(\mathbf{r})=3\kappa$, we have $P_{\mathrm{spon}}\approx 3.33\%$, $P_{\mathrm{tran}}\approx 10^{-4}$, which are basically the same as the corresponding case without detuning, but $P_{\mathrm{mis}}\approx 3.33\%$, which becomes significantly larger due to the contribution of the phase difference.

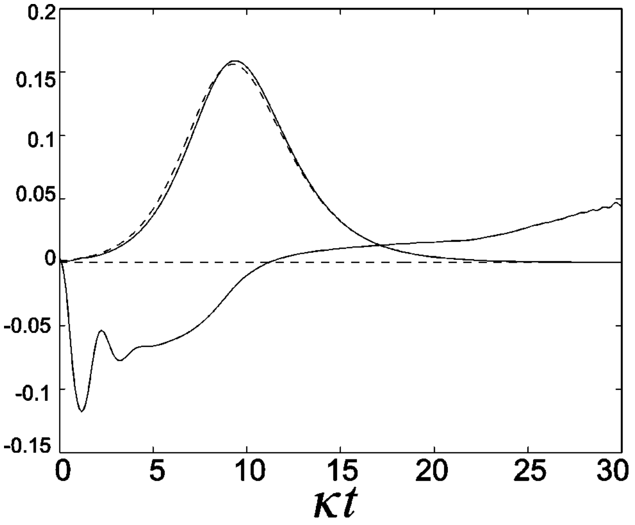

FIG. 5. The amplitude (the modulus) and the phase (divided by $\pi/2$) of the real pulse shape $f_{\mathrm{real}}(t)$ (two solid curves) and the ideal pulse shape $f_{\mathrm{id}}(t)$ (two dashed curves) vs the time t with the single-photon transition detuning $\Delta=\kappa$. We assumed $g(\mathbf{r})=3\kappa$, $\gamma_s=\kappa$, and $T=30/\kappa$. In this case, the main difference between $f_{\mathrm{real}}(t)$ and $f_{\mathrm{id}}(t)$ lies in the phase difference.

F. Comparison with the usual adiabatic scheme

In our scheme, the driving pulse is matched to a cavity mode which has basically the same spatial mode, structure as the cavity-QED light. In usual adiabatic schemes [18,27], the driving laser is assumed to be perpendicular to the cavity axis with uniform illumination intensity. We expect that with the present interaction configuration, our scheme is more insensitive to the randomness in the atom position. To compare the two configurations more quantitatively, we have calculated the output pulse shapes and noise magnitudes for both schemes.

First, let us assume that the atom has been trapped in one potential well, but the coupling rate $g(\mathbf{r})$ may vary within a factor of 2 due to the unknown atom's position. In Fig. 6, we show the calculation results of the output pulse shapes. The solid curve shows the pulse-shape function $|f(t)|$ when $g(\mathbf{r})=3\kappa$ and $\Omega_m(\mathbf{r})=15\kappa$, where $\Omega_m(\mathbf{r})$ is the maximum of $\Omega(\mathbf{r},t)$ with respect to time t [$\Omega(\mathbf{r},t)$ is assumed to be a Gaussian function of t as specified in the caption of Fig. 2].

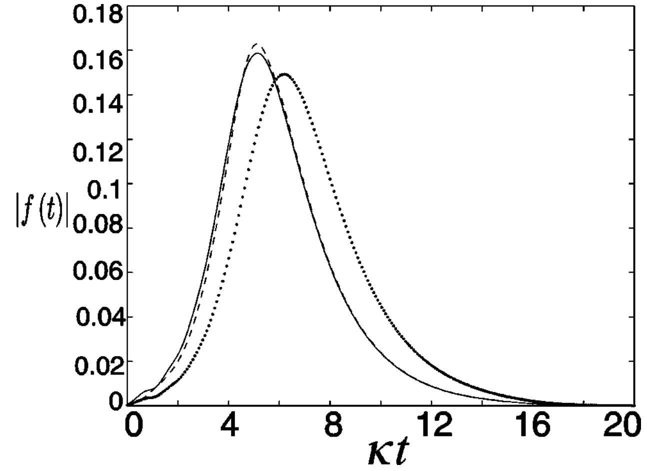

FIG. 6. The shape $|f(t)|$ of the output single-photon pulse for the following pairs of coupling rates and the driving Rabi frequencies: first, $g(\mathbf{r})=3\kappa$ and $\Omega_m(\mathbf{r})=15\kappa$ (solid curve); second, $g(\mathbf{r})=6\kappa$ and $\Omega_m(\mathbf{r})=30\kappa$ (dashed curve), and finally, $g(\mathbf{r})=6\kappa$ and $\Omega_m(\mathbf{r})=15\kappa$ (dotted curve). The other parameters are the same as in Fig. 2.

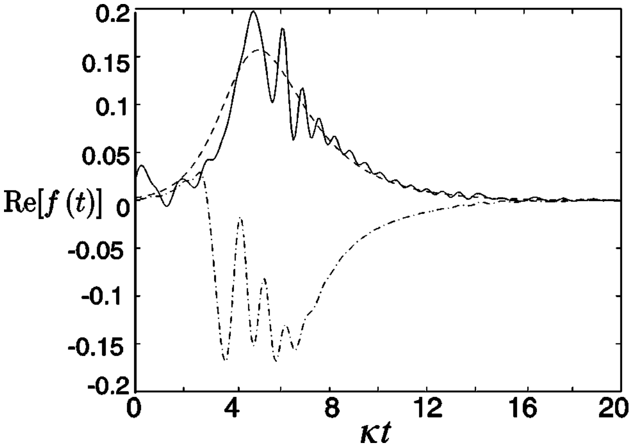

FIG. 7. The real part of the pulse-shape function $\mathrm{Re}[f(t)]$ as $g(\mathbf{r})$ varies with time in the form $g(\mathbf{r})=6\kappa\sin(4\pi t/T+\varphi_0)$ in the usual adiabatic scheme with $\varphi_0=0$ (solid curve) and $\varphi_0=\pi/2$ (dash-dotted curve), respectively. The dashed curve shows the ideal pulse shape calculated from Eq. (18). The other parameters in this figure are the same as those in Fig. 2.

Now, if $g(\mathbf{r})$ varies by a factor of 2 due to change of the atom's position, in our scheme the Rabi frequency will correspondingly change by the same ratio. The dashed curve shows the pulse shape for $g(\mathbf{r})=6\kappa$ and $\Omega_m(\mathbf{r})=30\kappa$. One can see that the two curves overlap very well with the mode mismatching noise smaller than 0.2%. In contrast, in usual adiabatic schemes with uniform illumination intensity, $\Omega_m(\mathbf{r})$ does not change as $g(\mathbf{r})$ varies with the atom position, so we have the same $\Omega_m(\mathbf{r})=15\kappa$. The dotted curve in Fig. 6 shows the pulse shape for $g(\mathbf{r})=6\kappa$ and $\Omega_m(\mathbf{r})=15\kappa$. It is significantly different from the above two curves with a notable mode mismatching noise $P_{\mathrm{mis}}\approx 6.9\%$. The improvement by this scheme would become more impressive if $g(\mathbf{r})$ has a larger variation, both in its magnitude and in its sign. If $g(\mathbf{r})$ gets a random sign as the atom goes through different axial positions of the cavity, in the usual adiabatic scheme, the pulse-shape function $f(t)$ will also pick up a random sign. However, in the present scheme, this random sign in $f(t)$ can be eliminated. Therefore, by this interaction configuration, the scheme is more robust to the random variation of the atom's position.

The improvement by this protocol is also very remarkable if we consider the case where the atom is not fixed in one potential well, and may move from well to well in the axial direction. The variation of the atom's position in the axial direction is typically fast compared with the operation time T, so we have a time-varying atom position $\mathbf{r}$ and coupling rate $g(\mathbf{r})$. Here, we consider an explicit form of the time variation of $g(\mathbf{r})$ by assuming $g(\mathbf{r}(t))=6\kappa\sin(4\pi t/T+\varphi_0)$, where the phase φ_0 is randomly chosen corresponding to the randomness in the initial atom's position. It is enough to illustrate the general result by considering this special example. First, let us calculate the output pulse shape $f(t)$ for the usual adiabatic scheme, where $\Omega_m(\mathbf{r})$ is fixed as a constant [17,18,27]. The solid and the dash-dotted curves in Fig. 7 show the real parts of $f(t)$ with initial phase $\varphi_0=0$ and $\varphi_0=\pi/2$, respectively [the imaginary parts of $f(t)$ are actually small and negligible]. The two curves do not overlap at all. Neither the magnitude nor the phase of the pulse shape $f(t)$ can be controlled with this scheme. We also calculate the spontaneous emission loss P_{spon} for this example. The average spontaneous emission loss is about $P_{\mathrm{spon}}\approx 25\%$.

Similarly, we can calculate the pulse shape for the same example with the present scheme. In this case, due to the atomic motion, $\Omega_m(\mathbf{r})$ varies with time in the same way as $g(\mathbf{r})$, but the ratio $\Omega_m(\mathbf{r})/g(\mathbf{r})$ is kept constant. Figure 8 shows the real part of the shape function $f(t)$ in this case, with the solid and the dash-dotted curves corresponding to the initial phase $\varphi_0=0$ and $\varphi_0=\pi/2$, respectively. Although the two curves do not overlap very well, they still look similar with the same phase. They also roughly agree with the ideal shape function given by Eq. (18), which is shown as the dashed curve in Fig. 8. The average mode mismatching noise

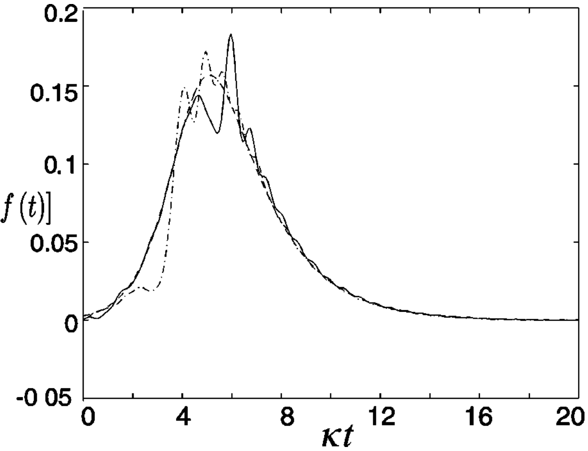

FIG. 8. The real part of the pulse-shape function $\mathrm{Re}[f(t)]$ calculated for the same example as in Fig. 7, but now for the present adiabatic scheme where the driving Rabi frequency varies in the same way as the the coupling rate when the atom moves.

for these two curves is given by $P_{\mathrm{mis}} \approx 1.1\%$, and the average spontaneous emission loss is $P_{\mathrm{spon}} \approx 9.4\%$. The spontaneous emission loss is also significantly reduced with the present scheme. This can be understood as follows: if one has a constant $\Omega_m(\mathbf{r})$ as the usual adiabatic scheme, when the atom moves to the place with $g(\mathbf{r})$ near to zero, the adiabatic condition is not well satisfied, and as a result, one has a considerably large spontaneous emission loss; however, in the present scheme, in the place where $g(\mathbf{r})$ is near zero, $\Omega_m(\mathbf{r})$ is also near zero. The excitation probability of the atom is then reduced, and the adiabatic condition is better satisfied. Consequently, one has a smaller spontaneous emission loss.

IV. APPLICATIONS

There have been many proposals to use the setup with single atoms in high-Q cavities for various applications, such as for the single-photon or entangled-photon source [6,7], for quantum communication between different cavities [9], for atomic quantum teleportation [11,12], and for quantum computation [13]. In these proposals, one always assumed that the atom is well localized so that the Lamb-Dicke condition is satisfied. However, one can apply the method here to all of the schemes mentioned above, to eliminate the challenging Lamb-Dicke condition. Basically, what one needs to do is to replace the Raman scheme with the adiabatic scheme, and to keep the pumping laser collinear with the cavity axis, so that the driving pulse and the cavity mode have the same spatial mode structure. All the calculation results (for the noise magnitudes, pulse shape, etc.) in this paper apply to these schemes. After the improvement, it becomes considerably easier to implement these schemes with the current technology. Here, we briefly review these schemes and discuss how to incorporate the present method into these schemes.

A. Controllable single-photon or entangled-photon source

It is desirable to have a single-photon source with all its properties fully controllable, including its emission direction, emission time, and pulse shape. This kind of source has important applications in some recent quantum-information processing schemes [36], which are normally based on the interference of different single-photon pulses. To get interference between different single-photon pulses, one requires all the pulses to be directional and have the same time shape. Recently, there have been significant experimental advances in the realization of the single-photon source [17,18,37–39]. In the experiments based on the solid-state material [37–39], the single-photon emitter has a fixed position, and one can, in principle, control the pulse shape well. However, the emitted pulse is typically not directional. On the other hand, in current experiments [17,18] with high-Q cavities, the emitted pulse is directional, but its shape is not well controlled since with uniform illumination of a perpendicular driving pulse, the waveform $f(t)$ depends on the time history of the coupling rate $g(\mathbf{r})$, which in turn depends on the atom's position. As the atom falls through the cavity, it has basically a random trajectory, leading to unknown variations in $g(\mathbf{r})$ both in magnitude and sign. It is a challenging experimental endeavor to demonstrate a single-photon source with all the properties mentioned above fully controllable.

The method in this paper shows that the single atom trapped in a high-Q cavity is a good candidate for the realization of the fully controllable single-photon source. Though the coupling rate $g(\mathbf{r})$ is not completely fixed in current setups due to the difficulty in fully localizing the atom, the emitted single-photon pulse has a definitely well-controllable time shape and emission direction with an appropriate design of the interaction configuration as has been shown before.

As shown in Ref. [7], with a more involved atomic level structure, it is possible to engineer entanglement between different single-photon pulses. It is straightforward to combine the method here with that scheme to eliminate the requirement of the Lamb-Dicke condition in Ref. [7] so that one can get an entangled single-photon source with the "hot" trapped atom as well.

B. Quantum communication between different cavities

The dynamics governed by the Hamiltonian (6) is reversible if we neglect the atomic spontaneous emission γ_s. Therefore, if one directs the emitted single-photon pulse back to the cavity, and at the same time reverses both of the time shapes of the single-photon pulse and the driving pulse, the single-photon pulse will be completely absorbed as long as the noise effects are negligible. It was first proposed in Ref. [9] that one can use this kind of a phenomenon to achieve quantum communication between different cavities, that is, to transfer quantum states of a trapped atom from one cavity to another cavity. For this purpose, one can require that the emitted single-photon pulse has a time-symmetric shape by modulating the driving pulse shape. For a time-symmetric pulse, its time reversal is itself, so we can directly input this pulse to another cavity with the same configuration but with a time-reversed driving pulse, then the single-photon pulse will be completely absorbed by this cavity, which transfers the atomic state from one cavity to the other one. The scheme in Ref. [9] is based on the Raman configuration, but it is straightforward to transfer it to the adiabatic configuration discussed in this paper so that it works with a hot trapped atom. Note that the same setup can also be used for storage of a single-photon pulse with a known shape [30,40,41].

To get a time-symmetric single-photon pulse for a complete absorption of the second cavity, Ref. [9] gives a numerical solution to the shape of the driving pulse. For the adiabatic configuration, one has an analytic expression (18) which connects the shape of the output single-photon pulse to the shape of the driving pulse, and this expression has been verified to be a good approximation under reasonable experimental parameters in Sec. III through the exact numerical calculations. With this analytical expression, it becomes easier to design the shape $\tilde{\varepsilon}(t)$ of the driving pulse. The form of $\sin\theta(t)$ can be easily solved from Eq. (18) (see also Ref. [40]) with the expression

$$\sqrt{\kappa}\sin\theta(t)=\frac{f(t)}{\sqrt{1-\int_0^t f^2(\tau)d\tau}}. \tag{27}$$

The form of sin $\theta(t)$ is immediately available from this equation for any desirable output pulse shape $f(t)$ (which has been assumed to be real and positive for simplicity). Then, the shape of the driving pulse can be easily decided from $\tilde{\varepsilon}(t)\propto\alpha(t)$ and $\sin\theta(t)=r_o\alpha(t)/\sqrt{1+|r_o\alpha(t)|^2}$, where r_o is the ratio of the Clebsch-Gordan coefficients. For instance, if we want to have a time-symmetric $f(t)$ in the period $0\leqslant t\leqslant T$ with the form $f(t)=\sqrt{\beta/2}\,\mathrm{sech}[\beta(t-T/2)]$, where we have assumed $\mathrm{sech}(-\beta T/2)\leqslant 1$, $\sin\theta(t)$ should be in the form $\sin\theta(t)=\sqrt{\beta/\kappa}\sqrt{1+\tanh[\beta(t-T/2)]}$. Note that we only have a solution of $\theta(t)$ when the rate $\beta<\kappa/2$, which is consistent with the observation that any pulse from the decay of a cavity cannot vary with time faster than the cavity decay rate. From $\sin\theta(t)$, we see that the shape $\tilde{\varepsilon}(t)$ of the driving pulse should be chosen according to

$$\tilde{\varepsilon}(t)\propto\sqrt{\frac{1+\tanh[\beta(t-T/2)]}{(\kappa/\beta-1)-\tanh[\beta(t-T/2)]}}. \tag{28}$$

As a special case, if $\kappa/\beta=2$, $\tilde{\varepsilon}(t)\propto e^{\beta(t-T/2)}$, which grows exponentially with the time t for the operation period $0\leqslant t\leqslant T$. Therefore, we have a simple solution to the driving pulse shape for quantum communication between two different cavities: for the first cavity, we apply an exponentially increasing pulse with $\tilde{\varepsilon}(t)=\tilde{\varepsilon}(0)e^{\kappa t/2}$, and for the second cavity we apply its time reversal, that is, an exponentially decreasing pulse with the decay rate $\kappa/2$. The pulse duration T should satisfy $\kappa T\gg 1$, and the initial value $\tilde{\varepsilon}(0)$ is determined by the requirement $r_o\alpha(T/2)=1$. The single-photon pulse connecting the two cavities then has a time-symmetric shape with $f(t)\propto\mathrm{sech}[\kappa(t-T/2)/2]$.

C. Entanglement generation and atomic quantum teleportation

If one has two cavities, each with an atom inside, one can maximally entangle these two atoms 1 and 2 by the following method: The two atoms are initially prepared in the state $|g\rangle$, and then we excite them to the state $|s\rangle$ with a small possibility $p_0\approx 1-\exp[-\kappa\int_0^T\sin^2\theta(\tau)d\tau]$ through an incomplete adiabatic passage. The output pulses from the two cavities, each with a mean photon number p_0, have a definite pulse shape as we have shown before, so that they can interfere with each other at a 50%-50% beam splitter. The outputs of the beam splitter are detected by two single-photon detectors, and if we register a photon from one of the detectors, due to the interference, we do not know from which cavity the registered photon comes. The two atoms 1 and 2 are thus projected to a quantum superposition state $(|g\rangle_1|s\rangle_2\pm|s\rangle_1|g\rangle_2)/\sqrt{2}$, which is maximally entangled. The method described here is just an adiabatic passage version of the scheme in Refs. [11,12]. By transformation from the Raman version to the adiabatic passage version, the output pulse shapes become insensitive to the random atom's position as is required for interference, which is important for the scheme to work with hot atoms.

After entanglement has been generated, one can use it for atomic Bell inequality detection, for quantum teleportation of atomic states [12], or even for realization of quantum repeaters [42]. To realize quantum repeaters, what one needs to do is to simply replace the atomic ensemble in the scheme in Ref. [42] by the setup of a single atom in a high-Q cavity.

For the above applications, in addition to the entanglement generation, we also need to do some single-bit operations. These single-bit operations should also be performed in a suitable way so that they are insensitive to the random atom position $\mathbf{r}$. One way is to still use adiabatic passages. It is possible to realize any single-bit operation with adiabatic passages [43,44], but for this purpose one needs to use a four-level scheme instead of the Λ configuration. There is actually a simpler way for getting robust single-bit operations based on the Raman transitions. Note that for single-bit operations, we do not need to use any cavity mode or cavity effect. We can shine two traveling-wave beams on the atom coupling to the transitions $|g\rangle\rightarrow|e\rangle$ and $|s\rangle\rightarrow|e\rangle$. They are assumed to be collinear and propagating along the x axis, which is perpendicular to the cavity axis z. The two traveling-wave beams are broad with the beam radius much larger than the typical variation length of the atom's position. With this condition, the two Rabi frequencies for the transitions $|g\rangle\rightarrow|e\rangle$ and $|s\rangle\rightarrow|e\rangle$ are given by $\Omega_1(\mathbf{r})=\Omega_{10}e^{i\omega_{ge}x/c}$ and $\Omega_2(\mathbf{r})=\Omega_{20}e^{i\omega_{se}x/c}$, respectively, where Ω_{10} and Ω_{20} are basically independent of the atom position $\mathbf{r}$. Under a large detuning Δ, the effective Raman coupling rate $\Omega_R\sim\Omega_1(\mathbf{r})\Omega_2^*(\mathbf{r})/\Delta\propto e^{i\omega_{gs}x/c}$ is very insensitive to the random atom's position $\mathbf{r}$, since c/ω_{gs} is typically much larger than the variation length of the position. Therefore, as long as we do not need to use the cavity effect, a Raman scheme with two broad collinearly propagating beams suffices to eliminate the sensitivity to the random atom's position.

D. Quantum computation

In principle, we can also use this setup for quantum computation [13], and eliminate the requirement of the Lamb-Dicke condition by performing all the quantum gates using adiabatic passages [43,45] with appropriate configurations. However, the requirements for a universal quantum computation are more challenging compared with the applications mentioned above, and this is somewhat a long-term goal, so we do not discuss here the details of this possibility.

V. DISCUSSION OF THE EXPERIMENTAL SITUATION

Finally, let us mention the current experimental situation related to this work at the Caltech group. In the Caltech experiment, a single cesium atom is trapped inside the high-finesse cavity with a FORT beam. The atomic states $|g\rangle$, $|s\rangle$, and $|e\rangle$ correspond to the hyperfine levels $(6S_{1/2},F=3,m=+3)$, $(6S_{1/2},F=4,m=+4)$, and $(6P_{3/2},F=4,m=+4)$, respectively. The FORT beam is incident on one of the cavity mirrors and resonant to a longitudinal mode of the cavity. Presently, the FORT wavelength λ_{FORT} is 936 nm. This wavelength was chosen because with such a beam, the trapping potentials for the ground $6S_{1/2}$ manifold and the excited $6P_{3/2}$ manifold are nearly identical. Considering only this reduced manifold of states, we find that the expression for the FORT potential of the ground states $|g\rangle$ and $|s\rangle$ is given [46] by

$$U_{FORT}(\mathbf{r})=\frac{\pi c^2\gamma_s}{2\omega_0^3}\left(\frac{2}{\Delta_2}+\frac{1}{\Delta_1}\right)I(\mathbf{r}). \tag{29}$$

Here, Δ_1 (Δ_2) is the detuning of the FORT light of frequency $\omega_{\mathrm{FORT}}=2\pi c/\lambda_{\mathrm{FORT}}$ from the $P_{1/2}$ ($P_{3/2}$) level, and $\gamma_s/2\pi\approx 5.2$ MHz is the spontaneous decay rate of the level $6P_{3/2}$. The intensity $I(\mathbf{r})$ of the standing-wave mode inside the cavity is given by

$$I(\mathbf{r})=\frac{8P}{\pi w_0^2}\sin^2\left(\frac{2\pi z}{\lambda_{\mathrm{FORT}}}\right)\exp\left(-\frac{x^2+y^2}{w_0^2}\right), \tag{30}$$

where $w_0\approx 25\ \mu$m is the waist of the Gaussian mode, and P is the power of the FORT beam inside the cavity. The trap frequencies ν_{axial}, ν_{radial} in the axial and radial directions follow from these expressions as

$$(\nu_{\mathrm{axial}},\nu_{\mathrm{radial}})=\frac{1}{2\pi\hbar}\left(\sqrt{2U_0\frac{\hbar^2\omega_{FORT}^2}{mc^2}},\sqrt{2U_0\frac{\hbar^2}{m(w_0)^2}}\right), \tag{31}$$

where $U_0=U_{FORT}(\mathbf{0})$ is the trap depth. The typical power of the FORT beam measured outside the cavity is about 1 mW, and the power P inside the cavity is enhanced by a factor of the cavity finesse, which is about 2200 at the wavelength of the FORT beam. With this number, the typical values for the trap depth and frequencies are given by $U_0\approx 38$ MHz, $\nu_{\mathrm{axial}}\approx 510$ kHz, and $\nu_{\mathrm{radial}}\approx 4.3$ kHz, respectively. The current achievable temperature T_{tem} of the trapped atom is a significant fraction of the trap depth U_0 (such as a half). With such a temperature, the spatial extent of the atomic motion in the axial and radial directions are estimated, respectively, by

$$\delta z/\lambda_{\mathrm{FORT}}\approx(1/2\pi)\arcsin\sqrt{k_B T_{\mathrm{tem}}/U_0}, \tag{32}$$

$$\delta r_{\perp}\approx w_0\sqrt{-\ln(1-k_B T_{\mathrm{tem}}/U_0)}, \tag{33}$$

which will induce significant variation of the coupling rate $g(\mathbf{r})$ given by Eq. (1). For example, for the temperature of half of the trap depth, the axial uncertainty is 120 nm, while the radial one is 15 μm. These uncertainties cause variations in g of 30% due to the radial motion, and 35% due to the axial one. Therefore, within the current experimental technique, it is important to use the method given in this paper to make the application schemes insensitive to the variation of $g(\mathbf{r})$. The time scale for the variation of $g(\mathbf{r})$ is estimated by the inverse of the trap frequencies ν_{axial} and ν_{radial} in the axial and radial directions, respectively. The operation time T is typically significantly shorter than $1/\nu_{\mathrm{radial}}$, but longer or comparable to $1/\nu_{\mathrm{axial}}$. So, we can take the static average of $g(\mathbf{r})$ in the radial direction, and the dynamical average of $g(\mathbf{r})$ in the axial direction as discussed in Ref. [34].

We also would like to note that although the method in this paper shows that many application schemes of the cavity-QED setup can be demonstrated before the achievement of efficient cooling of the trapped atom inside the cavity, the cooling is still an important and desirable technology yet to be achieved to significantly increase the trapping time of the atom. In addition, a combination of the cooling technology and the method here could further improve the performance of various application schemes.

VI. SUMMARY

In summary, we have shown that the setup with a single trapped atom in a high-Q cavity can be used to realize many cavity-QED and quantum-information processing schemes even if the atom is still hot and not fully localized in space (the Lamb-Dicke condition is not yet satisfied). This could significantly simplify the on-going experiments, since it means many interesting schemes can be demonstrated with the present technology before the achievement of efficient cooling inside the cavity. Even with further advances in atomic localization in cavity-QED, our scheme should lead to a greater robustness against certain experimental nonidealities. The basic idea of this method is to design an appropriate adiabatic passage so that the relevant dynamics only depend on the ratio of two coupling rates. Though each of the coupling rates is sensitive to the unknown or time-varying atom's position, their ratio is fixed and controllable, as the two rates depend on the random atom position in the same way with the appropriate interaction configuration that we have described. We confirm the validity of this method by solving the complete model, which describes the realistic setup. The approximate analytical solution and the exact numerical simulations agree with each other. From the numerical simulations, we also calculate quantitatively various noise magnitudes in this setup, and show that one can achieve reasonably good performance with the values of the parameters based on the present technology. Finally, we show that this method can be incorporated into many previous schemes, allowing the demonstration of these application schemes without the requirement of the full localization of the atom.

ACKNOWLEDGMENTS

L.-M.D. thanks Axel Kuhn for discussions. This work was supported by the Caltech MURI Center for Quantum Networks under ARO Grant No. DAAD19-00-1-0374, by the National Science Foundation under Grant No. EIA-0086038, and by the Office of Naval Research. L.-M.D. also acknowledge support from the Chinese Science Foundation, Chinese Academy of Sciences, and the national ''97.3'' project.

[1] For a review, see contributions in the special issue of Phys. Scr., T **76**, 127 (1998).

[2] J. Ye, D.W. Vernooy, and H.J. Kimble, Phys. Rev. Lett. **83**, 4987 (1999).

[3] J. McKeever and H.J. Kimble, in *Laser Spectroscopy: XIV International Conference*, edited by S. Chu and J. Kerman (World Scientific, Singapore, 2002).

[4] C.J. Hood *et al.*, Science **287**, 1447 (2000).

[5] P.W.H. Pinkse, T. Fischer, T.P. Maunz, and G. Rempe, Nature (London) **404**, 365 (2000).

[6] C.K. Law and H.J. Kimble, J. Mod. Opt. **44**, 2067 (1997).

[7] K.M. Gheri *et al.*, Phys. Rev. A **58**, R2627 (1998).

[8] A.C. Doherty, T.W. Lynn, C.J. Hood, and H.J. Kimble, Phys. Rev. A **63**, 013401 (2000).

[9] J.I. Cirac, P. Zoller, H.J. Kimble, and H. Mabuchi, Phys. Rev. Lett. **78**, 3221 (1997).

[10] S.J. Enk, J.I. Cirac, and P. Zoller, Science **279**, 205 (1998).

[11] C. Cabrillo, J.I. Cirac, P. G.-Fernandez, and P. Zoller, Phys. Rev. A **59**, 1025 (1999).

[12] S. Bose, P.L. Knight, M.B. Plenio, and V. Vedral, Phys. Rev. Lett. **83**, 5158 (1999).

[13] T. Pellizari, S.A. Gardiner, J.I. Cirac, and P. Zoller, Phys. Rev. Lett. **75**, 3788 (1995).

[14] G.R. Guthöhrlein, M. Keller, K. Hayasaka, W. Lange, and H. Walther, Nature (London) **414**, 49 (2001).

[15] J. Eschner, Ch. Raab, F. Schmidt-Kaler, and R. Blatt, Nature (London) **413**, 495 (2001).

[16] J. McKeever, J. Buck, A. Kuzmich, H.-C. Naegerl, D.M. Stamper-Kurn, and H.J. Kimble (unpublished).

[17] M. Hennrich, T. Legero, A. Kuhn, and G. Rempe, Phys. Rev. Lett. **85**, 4872 (2000).

[18] A. Kuhn, M. Hennrich, and G. Rempe, Phys. Rev. Lett. **89**, 067901 (2002).

[19] P. Horak, G. Hechenblaikner, K.M. Gheri, H. Stecher, and H. Ritsch, Phys. Rev. Lett. **79**, 4974 (1997).

[20] S.J. van Enk, J. McKeever, H.J. Kimble, and J. Ye, Phys. Rev. A **64**, 013407 (2001).

[21] H.W. Chan, A.T. Black, and V. Vuletic, e-print quant-ph/0208100.

[22] A.C. Doherty, A.S. Parkins, S.M. Tan, and D.F. Walls, Phys. Rev. A **56**, 833 (1997); T.A.B. Kennedy and P. Zhou *ibid.* **64**, 063805 (2001).

[23] H. Mabuchi, J. Ye, and H.J. Kimble, Appl. Phys. B: Lasers Opt. **68**, 1095 (1999).

[24] Reference [20] does offer some suggestions for operationally discriminating the atomic position (determined by the FORT potential minima) relative to the cavity-QED field.

[25] In principle, they can be also the same mode.

[26] K. Bergmann, H. Theuer, and B.W. Shore, Rev. Mod. Phys. **70**, 1003 (1998).

[27] A.S. Parkins *et al.*, Phys. Rev. A **51**, 1578 (1995).

[28] A. Sorensen and K. Molmer, Phys. Rev. Lett. **82**, 1971 (1999).

[29] J.F. Poyatos, J.I. Cirac, and P. Zoller, Phys. Rev. Lett. **81**, 1322 (1998).

[30] M. Fleischhauer, S.F. Yelin, and M.D. Lukin, Opt. Commun. **179**, 395 (2000).

[31] D.F. Walls and G.J. Milburn, *Quantum Optics* (Springer-Verlag, Berlin, 1994).

[32] A leakage error means that after a spontaneous emission, the system goes out of the Hilbert space spanned by the state (10) with all the possible coefficients, since in this case one has a photon in a spontaneous emission mode.

[33] A.C. Doherty, A.S. Parkins, S.M. Tan, and D.F. Walls, J. Opt. B: Quantum Semiclassical Opt. **1**, 475 (1999).

[34] More accurately, by the notation $\overline{g}$, we should specify the averaging method. For instance, in the Caltech experiment with an atom trapped by a FORT beam (see Sec. V for a discussion of the current experimental situation), the atom oscillates fast in the axial direction with an oscillation period typically smaller than the operation time T, so we should take the time average (the dynamical average) of $g(\mathbf{r})$ in the axial direction for each round of the driving pulse. The atom also oscillates in the radial direction, but the period is normally significantly longer than the operation time T. So, we can assume a fixed (unknown) radial position for each driving pulse, and this position changes for different rounds of the pulses. We then take an average (the static average) of the results over many rounds of the driving pulses. We have performed both kinds of averaging in the numerical simulation in Sec. III, and without surprise, they basically give the same result. If the temperature of the atomic motion is around half of the trapping potential as is the typical case in the Caltech experiment, the value of $\overline{g}$ from the accurate averaging is also close to the magnitude from some simple estimation, for instance, one can estimate it as the average of the minimum and the maximum $g(\mathbf{r})$. Hence, in the following, we will use the notation $\overline{g}$ without elaboration on the averaging methods, since the result is not sensitive to them.

[35] H.J. Kimble, C.J. Hood, T.W. Lynn, H. Mabuchi, D.W. Vernooy, and J. Ye, in *Laser Spectroscopy: XIV International Conference*, edited by Rainer Blatt *et al.* (World Scientific, Singapore, 1999), p. 80.

[36] E.g., E. Knill, R. Laflamme, and G.J. Milburn, Nature (London) **409**, 46 (2001).

[37] J. Kim, O. Benson, H. Kan, and Y. Yamamoto, Nature (London) **397**, 500 (1999).

[38] P. Michler *et al.*, Science **290**, 2282 (2000).

[39] Z. Yuan *et al.*, Science **295**, 102 (2002).

[40] M.D. Lukin, S.F. Yelin, and M. Fleischhauer, Phys. Rev. Lett. **84**, 4232 (2000).

[41] L.-M. Duan, J.I. Cirac, and P. Zoller (unpublished).

[42] L.-M. Duan, M. Lukin, J.I. Cirac, and P. Zoller, Nature (London) **414**, 413 (2001).

[43] L.M. Duan, J.I. Cirac, and P. Zoller, Science **292**, 1695 (2001).

[44] R.G. Unanyan, B.W. Shore, and K. Bergmann, Phys. Rev. A **59**, 2910 (1999).

[45] A. Recati, T. Calarco, P. Zanardi, J.I. Cirac, and P. Zoller, e-print quant-ph/0204030; B. Tregenna, A. Beige, and P.L. Knight, Phys. Rev. A **65**, 032305 (2002), and references therein; J. Pachos, and H. Walther, e-print quant-ph/0111088.

[46] S.J.M. Kuppens, K.L. Corwin, K.W. Miller, T.E. Chupp, and C.E. Wieman, Phys. Rev. A **62**, 013406 (2000).

Experimental realization of a one-atom laser in the regime of strong coupling

J. McKeever, A. Boca, A. D. Boozer, J. R. Buck & H. J. Kimble

Norman Bridge Laboratory of Physics 12-33, California Institute of Technology, Pasadena, California 91125, USA

Conventional lasers (from table-top systems to microscopic devices) typically operate in the so-called weak-coupling regime, involving large numbers of atoms and photons; individual quanta have a negligible impact on the system dynamics. However, this is no longer the case when the system approaches the regime of strong coupling for which the number of atoms and photons can become quite small. Indeed, the lasing properties of a single atom in a resonant cavity have been extensively investigated theoretically[1–11]. Here we report the experimental realization of a one-atom laser operated in the regime of strong coupling. We exploit recent advances[12] in cavity quantum electrodynamics that allow one atom to be isolated in an optical cavity in a regime for which one photon is sufficient to saturate the atomic transition. The observed characteristics of the atom–cavity system are qualitatively different from those of the familiar many-atom case. Specifically, our measurements of the intracavity photon number versus pump intensity indicate that there is no threshold for lasing, and we infer that the output flux from the cavity mode exceeds that from atomic fluorescence by more than tenfold. Observations of the second-order intensity correlation function demonstrate that our one-atom laser generates manifestly quantum (nonclassical) light, typified by photon antibunching and sub-poissonian photon statistics.

The usual laser theories rely on system-size expansions in inverse powers of critical atom and photon numbers $(N_0, n_0) \gg 1$, and arrive at a consistent form for the laser characteristics[13–17]. By contrast, over the past twenty years, technical advances on various fronts have pushed laser operation to regimes of ever smaller atom and photon number, pressing toward the limit of ‘strong coupling’ for which $(N_0, n_0) \ll 1$ (ref. 18). Significant milestones include the realization of one- and two-photon micromasers[19–21], as well as microlasers in atomic and condensed matter systems[22–24].

As illustrated in Fig. 1, our experiment consists of a single caesium atom trapped in a far-off-resonance trap (FORT) within a high-finesse optical cavity[12,25]. The lasing transition $6P_{3/2}$, $F' = 3' \rightarrow 6S_{1/2}, F = 4$ is nearly resonant with and strongly coupled to a single mode of this cavity. The coupling is parameterized by the Rabi frequency $2g_0$ for a single quantum of excitation, and the atom and field have amplitude decay rates γ and κ, respectively. The upper level $F' = 3'$ is pumped by the external drive Ω_3, while effective decay of the lower level $F = 4$ takes place via the combination of the drive Ω_4 and decay γ_{34}, $4 \rightarrow 4' \rightarrow 3$. In essential character this system is analogous to a Raman scheme with pumping $3 \rightarrow 3'$, lasing $3' \rightarrow 4$, and decay $4 \rightarrow 3$. Of particular relevance to our work are detailed treatments of the ion-trap laser[6–9].

We emphasize that a ‘one-and-the-same’ atom laser as illustrated in Fig. 1 is quite distinct from ‘single-atom’ micromasers[19–21] and lasers[22] for which steady state is reached through the incremental contributions of many atoms that transit the cavity, even if one by one[19,20] or few by few[22]. By contrast, in our experiment steady state is reached with one-and-the-same atom over a time interval $\delta t \approx 10^{-7}$ s that is much shorter than the trap lifetime $\Delta t \approx 0.05$ s. Our pumped atom–cavity system provides a continuous source of nonclassical light as a gaussian beam for the entire duration that an atom is trapped.

Because conventional lasers operate in the limit $(N_0, n_0) \gg 1$, there is a generic form associated with the laser threshold in the transition from nonlasing to lasing action that is independent of the model system[13,26]. However, as the system size is reduced, the sharpness of the laser ‘turn on’ is lost, with then no clear consensus about how to define the lasing threshold[26]. Well into the regime of strong coupling $(N_0, n_0) \ll 1$, even the familiar qualitative characteristics of a laser (for example, the statistical properties of the output light) are profoundly altered, leaving open the question of how to recognize a laser in this new regime.

To address this question, we have carried out extensive theoretical analyses for a four-state model based upon Fig. 1b for parameters relevant to our experiment. A synopsis of relevant results from this work is given in the Supplementary Information, with the full treatment presented in ref. 27. In brief, the steady-state solutions obtained from a semiclassical theory exhibit familiar characteristics of conventional lasers, including a clearly defined laser threshold and population inversion. The condition $C_1 \gg 1$ is required to observe threshold behaviour for one atom pumped inside the resonator, where for our experiment the cooperativity parameter $C_1 = 1/N_0 \simeq 12$. By contrast, the fully quantum analysis for the four-state model results in qualitatively different characteristics. In particular, the input–output relationship for the mean intracavity photon number $\bar{n}$ versus the pump intensity $I_3 = (\Omega_3/2\gamma)^2$ has several key features to be compared with experimental results presented below, namely the immediate onset of emission (‘thresholdless’ behaviour), and the saturation and eventual quenching of the output.

Our actual experiment is more complex than indicated by the simple drawing in Fig. 1, with many of the technical aspects described in more detail in refs 12 and 25. In brief, the principal cavity QED (cQED) parameters of our system are $g_0/2\pi = 16$ MHz, $\kappa/2\pi = 4.2$ MHz, and $\gamma/2\pi = 2.6$ MHz, where g_0 is based upon the reduced dipole moment for the $6S_{1/2}, F = 4 \leftrightarrow 6P_{3/2}, F' = 3'$ transition in atomic caesium. Strong coupling is thereby achieved $(g_0 \gg (\kappa, \gamma))$, resulting in critical photon and atom numbers $n_0 \equiv \gamma^2/(2g_0^2) \simeq 0.013$, $N_0 \equiv 2\kappa\gamma/g_0^2 \simeq 0.084$.

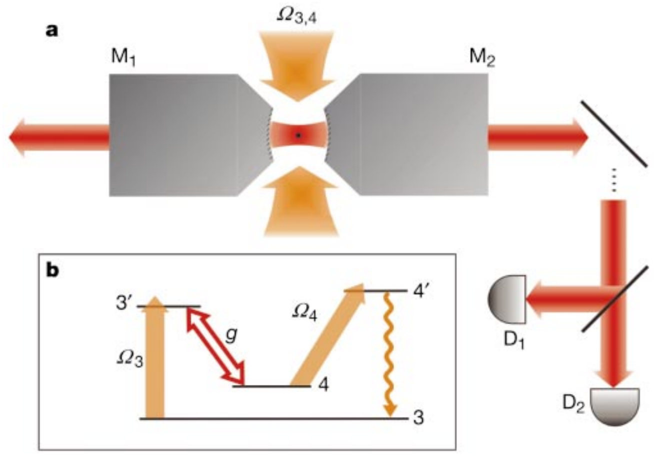

Figure 1 A simplified schematic of the experiment. **a**, A caesium atom (black dot) is trapped inside a high-finesse optical cavity formed by the curved, reflective surfaces of mirrors M_1 and M_2. Light generated by the atom's interaction with the resonant cavity mode propagates as a gaussian beam to single-photon detectors D_1 and D_2. **b**, The relevant transitions involve the $6S_{1/2}, F = 3,4 \leftrightarrow 6P_{3/2}, F' = 3', 4'$ levels of the D_2 line at 852.4 nm in atomic caesium. Strong coupling at rate g is achieved for the lasing transition $F' = 3' \rightarrow F = 4$ near a cavity resonance. Pumping of the upper level $F' = 3'$ is provided by the field Ω_3, while recycling of the lower level $F = 4$ is achieved by way of the field Ω_4 ($4 \rightarrow 4'$) and spontaneous decay back to $F = 3$. Decay $(3', 4') \rightarrow (3, 4)$ is also included in our model. Relevant cavity parameters are length $l_0 = 42.2\,\mu$m, waist $w_0 = 23.6\,\mu$m, and finesse $\mathscr{F} = 4.2 \times 10^5$ at $\lambda_{D_2} = 852$ nm.

© 2003 Nature Publishing Group

Atoms are trapped in the cavity by means of a FORT[28] with wavelength $\lambda_F = 935.6$ nm, which is matched to a TEM_{00} mode along the cavity axis. For all experiments herein, the trap depth is $U_0/k_B = 2.3$ mK (47 MHz) where k_B is the Boltzmann constant. The FORT has the important feature that the potential for the atomic centre-of-mass motion is only weakly dependent on the atom's internal state[12].

After the trap-loading stage (as described in the section on Methods), the transverse $\Omega_{3,4}$ fields are switched to pump and recycle the atomic population in the fashion depicted in Fig. 1b. Two examples of the resulting output counts versus time are shown in Fig. 2. By averaging traces such as these, we arrive at an average signal level versus time, as shown in the inset to Fig. 2a. Typical lifetimes for a trapped atom in the presence of the driving $\Omega_{3,4}$ fields are 50–100 ms, which should be compared to the lifetimes of 2–3 s recorded in the absence of these fields[12]. Significantly, the approximately exponential decay of the signal with time does not result from a time-dependent diminution of the flux from single trapped atoms, but rather from the average of many events each of a variable duration. That is, for a given set of external control parameters, each atom gives a reasonably well-defined output flux over the time that it is trapped.

For a fixed set of operating conditions, we collect a set of 60–300 traces as in Fig. 2, determine the average output flux for each trace, and find the mean and variance, as well as the trap lifetime for the set. Figure 3 displays a collection of such measurements for the mean intracavity photon number $\bar{n}$ as a function of the dimensionless pump intensity x, scaled in units of the fixed recycling intensity (see section on Methods). More precisely, the parameter x is the ratio of measured intensities, and can be written as $x \equiv (7/9)(I_3/I_4)$, where $I_{3,4} \equiv (\Omega_{3,4}/2\gamma)^2$. The factor of (7/9) is needed because the two transitions have different dipole moments. For these measurements, we estimate that the incoherent sum of intensities of the four Ω_4 beams is about 50 mW cm^{-2}, which corresponds to $I_4 \approx 13$. The output count rate at detectors $D_{1,2}$ is converted to intracavity photon number using the known propagation and detection efficiency $\xi = 0.05$.

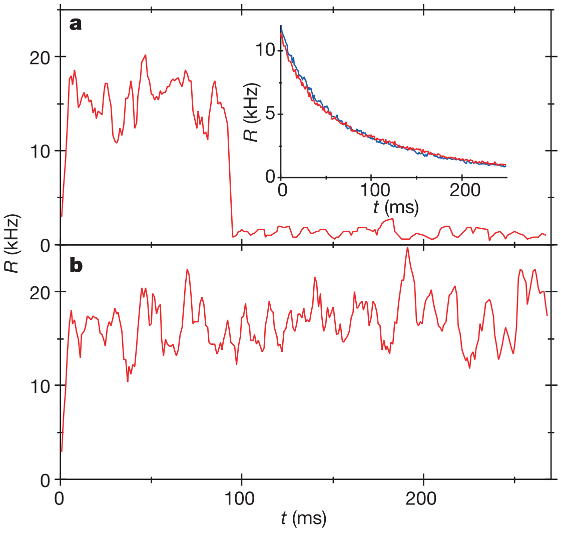

Figure 2 Total counting rate R recorded by detectors $D_{1,2}$ is displayed as a function of time for two separate trapped atoms, with the counts summed over 5-ms bins. At $t = 0$, the $\Omega_{3,4}$ fields are switched to predetermined values of intensity and detuning. In **a**, the atom is trapped for $t \simeq 90$ ms before escaping, with the background level due to scattered light from the $\Omega_{3,4}$ fields and detector dark counts evident as the residual output at later times. In **b**, the atom (atypically) remains trapped for the entire observation cycle $\simeq$270 ms and then is dumped. The inset in **a** displays R versus time obtained by averaging 400 such traces. Two cases are shown; in one, the number of atoms delivered to the cavity mode has been diminished by about two fold. The curves are nearly identical, so we conclude that cases with $N > 1$ atom play a negligible role. The overall detection efficiency $\xi = 0.05$ from intracavity photon to a detection event at D_1 or D_2 is made up of the following factors: $\eta = 0.60$ cavity escape efficiency, $T = 0.50$ for only mirror M_2 output, $\zeta = 0.33$ propagation efficiency from M_2 to $D_{1,2}$, and $\alpha = 0.5$ detection quantum efficiency at $D_{1,2}$.

Important features of the data shown in Fig. 3 include the prompt onset of output flux $\kappa\bar{n}$ emerging through the cavity mirrors $M_{1,2}$ as the pump intensity I_3 is increased from zero. In a regime of strong coupling, the atom–cavity system behaves as a 'thresholdless' device. With further increases in pump intensity I_3, the output flux saturates at a maximum value $\kappa\bar{n}_{max}$ around $x \simeq 0.1$. We attribute this behaviour to a bottleneck associated with the recycling of population $4 \rightarrow 4' \rightarrow 3$, with the rate-limiting step in the recycling process being spontaneous decay $4' \rightarrow 3$ at rate γ_{34} in the limit of large Rabi frequency $\Omega_4 \gg \gamma$. For a single intracavity atom, quanta can be deposited into the cavity mode no faster than the maximum recycling rate. As the pump level I_3 is increased beyond $x \approx 1$, the output flux $\kappa\bar{n}$ gradually drops, presumably owing to splitting of the pumped excited state $F' = 3'$ by the Autler–Townes effect, although this is still under investigation. Heating of the atomic motion at higher pump levels is certainly a concern as well; however, our simulations, which do not incorporate atomic motion, show the same trend as in Fig. 3 (ref. 27).

Beyond these considerations, we have also undertaken extensive theoretical analyses based both upon the four-state model shown in Fig. 1, as well as on the full set of Zeeman states for each of the levels $F = 3,4$ and $F' = 3',4'$ and two cavity modes, one for each of two orthogonal polarizations[27]. These analyses are in reasonable accord with the principal features of the data in Fig. 3. Moreover, our quantum simulations support the conclusion that the range of coupling values g that contribute to our results is restricted roughly to $0.5g_0 \lesssim g \lesssim g_0$. Furthermore, the simulations yield information about the atomic populations, from which we deduce that the rate of emission from the cavity $\kappa\bar{n}$ exceeds that by way of fluorescent decay $3' \rightarrow 4$, $\gamma_{43'}\langle\sigma_{3',3'}\rangle$, by roughly tenfold over the range of pump intensity I_3 shown in Fig. 3, where $\langle\sigma_{3',3'}\rangle$ is the steady-state population in level $3'$.

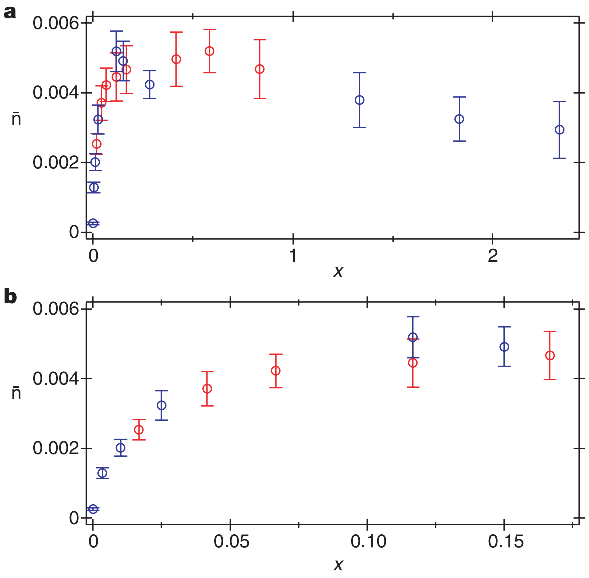

Figure 3 The intracavity photon number $\bar{n} \pm \sigma_n$, inferred from measurements as in Fig. 2, is plotted as a function of dimensionless pump intensity $x \equiv (7/9)\ (I_3/I_4)$ for fixed $I_4 = 13$ over two ranges of pump level x. **a**, $\bar{n}$ versus x is shown over the entire range $x = 0$ to 2.33 recorded in our measurements. **b**, An expanded scale displays $\bar{n}$ for small x. The immediate onset of emission supports the conclusion of 'thresholdless' lasing. The two independent sets of measurements (red and blue points) agree reasonably well.

© 2003 Nature Publishing Group

To investigate the quantum-statistical characteristics of the light emerging in the TEM_{00} mode of the cavity output, we probe the photon statistics of the light by way of the two single-photon detectors $D_{1,2}$ illustrated in Fig. 1. From the cross-correlation of the resulting binned photon arrival times and the mean counting rates of the signals and the background, we construct the normalized intensity correlation function (see the Supplementary Information)

$$g^{(2)}(\tau)=\frac{\langle:\hat{I}(t)\hat{I}(t+\tau):\rangle}{\langle:\hat{I}(t):\rangle^{2}} \qquad (1)$$

where the colons denote normal and time ordering for the intensity operators $\hat{I}$ (ref. 15). Over the duration of the trapping events, we find no evidence that $\langle:\hat{I}(t):\rangle$ is a function of t, although we do not have sufficient data to confirm quantitatively stationarity of the underlying processes.

Examples of two measurements for $g^{(2)}(\tau)$ are given in Fig. 4. In Fig. 4 a and b, we again have $I_4 \simeq 13$ and the pump intensity I_3 is set for operation with $x \simeq 0.83$ well beyond the 'knee' in $\bar{n}$ versus x, while in Fig. 4 c and d, the pump level is decreased to $x \simeq 0.17$ near the peak in $\bar{n}$. Significantly, in each case these measurements demonstrate that the light from the atom–cavity system is manifestly quantum (that is, nonclassical) and exhibits photon antibunching $g^{(2)}(0) < g^{(2)}(\tau)$ and sub-poissonian photon statistics $g^{(2)}(0) < 1$ (ref. 15). The actual coincidence data $n(\tau)$ used to obtain $g^{(2)}(\tau)$ are presented in the Supplementary Information. Significantly, these data directly provide evidence of the nonclassical character of the emitted light, with relatively minor corrections for background light required for the determination of $g^{(2)}(\tau)$.

Beyond the nonclassical features around $\tau \simeq 0$, $g^{(2)}(\tau)$ also exhibits excess fluctuations extending over $\tau \simeq \pm 1\,\mu\mathrm{s}$, with $g^{(2)}_{\max}(\tau) \simeq 1.7$. Fluctuations in the intensity of the intracavity light over these timescales are presumably related to the stochastic character of the pumping $3 \rightarrow 3'$ and recycling $4 \rightarrow 4' \rightarrow 3$ processes for a single, multi-state atom. Also of significance is the interplay of atomic motion and optical pumping into dark states by the $\Omega_{3,4}$ fields (which is responsible for cooling; ref. 29 and references therein), as well as Larmor precession that arises from residual ellipticity in polarization of the intracavity FORT[12,30]. Indeed, in Fig. 4a, c there is a hint of an oscillatory variation in $g^{(2)}_{\max}(\tau)$ with period $\tau \simeq \pm 2\,\mu\mathrm{s}$. Fourier transformation of the associated coincidence data leads to a small peak at about 500 kHz, which is near to the predicted frequency for axial motion of a trapped caesium atom at the bottom of the FORT potential, as well as to the Larmor frequency inferred from other measurements.

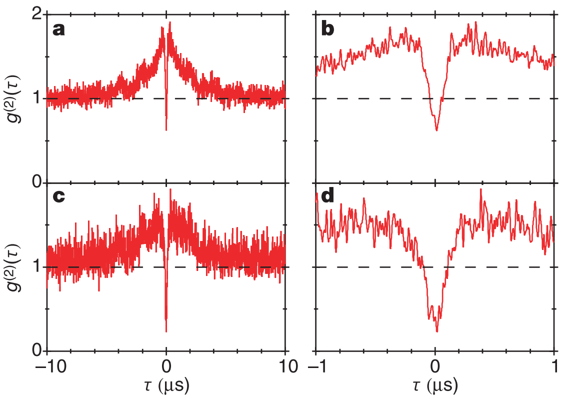

Figure 4 The intensity correlation function $g^{(2)}(\tau)$ is given for two values of the pump intensity in **a**–**d**, where **b** and **d** show the central features of **a** and **c** over a smaller range of τ. Panels **a** and **b** are for pump intensity parameter $x = 0.83$, whereas for **c** and **d**, $x = 0.17$. Note that the light exhibits sub-poissonian photon statistics and antibunching. All traces have been 'smoothed' by convolution with a gaussian function of width $\sigma = 5$ ns.

In agreement with the trend predicted by the four-state model discussed in the Supplementary Information, $g^{(2)}(0)$ increases with increasing pump intensity, with a concomitant decrease in these nonclassical effects. Moreover, our experimental observations of $g^{(2)}(\tau)$ are described reasonably well by the results obtained from more detailed quantum simulations based upon the entire manifold of Zeeman states for the caesium atom, two cavity modes with orthogonal polarizations, and a simple model to describe the polarization gradients of the $\Omega_{3,4}$ fields[27].

The realization of this strongly coupled one-atom laser is significant on several fronts. From the perspective of the dynamics of open quantum systems, our system demonstrates the radical departures from conventional laser operation wrought by strong coupling for the quantized light–matter interaction. On a more practical level, throughout the interval when an atom is trapped (which is determined in real time), our system provides an approximately stationary source of nonclassical light in a collimated, gaussian beam, as has been anticipated in the literature on one-atom lasers[1,3–6,8–11], and which has diverse applications. Some remaining technical issues in our work are to improve the modelling and measurements related to atomic motion, both within the FORT potential and through the polarization gradients of the $\Omega_{3,4}$ fields. We have employed our quantum simulations to calculate the optical spectrum of the light output, and have devised a scheme for its measurement. ☐

Methods

While the atom is trapped in a standing-wave FORT along the cavity axis, another set of fields (designated by $\Omega_{3,4}$ in Fig. 1) propagate in the plane transverse to the cavity axis and illuminate the region between the cavity mirrors. These fields are used not only for the pumping scheme described in association with the operation of the one-atom laser with strong coupling, but also for cooling in the trap-loading phase. Each $\Omega_{3,4}$ field consists of two orthogonal pairs of counter-propagating beams in a $\sigma^{+} - \sigma^{-}$ configuration.

Unfortunately, it is difficult to calibrate accurately the intensities $I_{3,4}$ for the $\Omega_{3,4}$ beams at the location of the atom in the region between the cavity mirrors. We estimate that our knowledge of either intensity is uncertain by an overall scale factor of about 2. However, we do know the ratio of intensities much more accurately than either intensity individually, and therefore plot the data in Fig. 3 as a function of this ratio.

In the pumping stage of the experiment, the fields are tuned 10 MHz blue of $F = 3 \rightarrow F' = 3'$ in the case of the Ω_3 beams and 17 MHz blue of $F = 4 \rightarrow F' = 4'$ in the case of the Ω_4 fields. The detuning between the $3' \rightarrow 4$ transition at $\omega_{4,3}$ and the cavity resonance ω_C is $\Delta_{CA} \equiv \omega_C - \omega_{4,3} = 2\pi \times 9$ MHz. These detunings are chosen operationally in a trade‘-off between achieving a large cavity output flux from the $3' \rightarrow 4$ transition while maintaining a reasonable lifetime for the trapped atom despite heating from the various fields[29]. The cavity length itself is actively stabilized with an auxiliary laser at wavelength $\lambda_C = 835.8$ nm that does not interfere with the trapping or the cQED interactions.

Our experimental protocol begins with the formation of a magneto-optical trap (MOT) above the cavity. After a stage of sub-Doppler cooling, the cloud of atoms is released. The $\Omega_{3,4}$ beams are then used as cooling beams (with independent settings of intensity and detuning) to load an atom into the FORT[12]. About ten atoms transit the cavity mode after each MOT drop, and the loading efficiency is set such that an atom is loaded into the FORT once every 3–10 drops. We then switch the intensities and detunings of the transverse fields $\Omega_{3,4}$ to the pumping configuration and record the cavity output by way of the single-photon detectors $D_{1,2}$ shown in Fig. 1. Each photoelectric pulse from $D_{1,2}$ is stamped with its time of detection (1-ns resolution) and then stored for later analysis, with examples of the record of output counts versus time displayed in Fig. 2.

Received 9 July; accepted 8 August 2003; doi:10.1038/nature01974.

---

1. Mu, Y. & Savage, C. M. One-atom lasers. *Phys. Rev. A* **46,** 5944–5954 (1992).
2. Ginzel, C., Briegel, H.-J., Martini, U., Englert, B.-G. & Schenzle, A. Quantum optical master equations: The one-atom laser. *Phys. Rev. A* **48,** 732–738 (1993).
3. Pellizzari, T. & Ritsch, H. Preparation of stationary Fock states in a one-atom Raman laser. *Phys. Rev. Lett.* **72,** 3973–3976 (1994).
4. Pellizzari, T. & Ritsch, H. Photon statistics of the three-level one-atom laser. *J. Mod. Opt.* **41,** 609–623 (1994).
5. Horak, P., Gheri, K. M. & Ritsch, H. Quantum dynamics of a single-atom cascade laser. *Phys. Rev. A.* **51,** 3257–3266 (1995).
6. Meyer, G. M., Briegel, H.-J. & Walther, H. Ion-trap laser. *Europhys. Lett.* **37,** 317–322 (1997).
7. Löffler, M., Meyer, G. M. & Walther, H. Spectral properties of the one-atom laser. *Phys. Rev. A* **55,** 3923–3930 (1997).
8. Meyer, G. M., Löffler, M. & Walther, H. Spectrum of the ion-trap laser. *Phys. Rev. A* **56,** R1099–R1102 (1997).
9. Meyer, G. M. & Briegel, H.-J. Pump-operator treatment of the ion-trap laser. *Phys. Rev. A* **58,** 3210–3220 (1998).

© 2003 Nature Publishing Group

10. Jones, B., Ghose, S., Clemens, J. P., Rice, P. R. & Pedrotti, L. M. Photon statistics of a single atom laser. *Phys. Rev. A* **60,** 3267–3275 (1999).
11. Kilin, S. Ya. & Karlovich, T. B. Single-atom laser: Coherent and nonclassical effects in the regime of a strong atom-field correlation. *JETP* **95,** 805–819 (2002).
12. McKeever, J. *et al.* State-insensitive cooling and trapping of single atoms in an optical cavity. *Phys. Rev. Lett.* **90,** 133602 (2003).
13. Sargent, M. III, Scully, M. O. & Lamb, W. E. Jr *Laser Physics* (Addison-Wesley, Reading, MA, 1974).
14. Haken, H. *Laser Theory* (Springer, Berlin, 1984).
15. Mandel, L. & Wolf, E. *Optical Coherence and Quantum Optics* (Cambridge Univ. Press, Cambridge, 1995).
16. Carmichael, H. J. *Statistical Methods in Quantum Optics 1* (Springer, Berlin, 1999).
17. Gardiner, C. W. & Zoller, P. *Quantum Noise* (Springer, Berlin, 2000).
18. Kimble, H. J. Strong interactions of single atoms and photons in cavity QED. *Phys. Scr.* **T76,** 127–137 (1998).
19. Raithel, G., Wagner, C., Walther, H., Narducci, L. M. & Scully, M. O. *Cavity Quantum Electrodynamics* (ed. Berman, P.) 57–121 (Academic, San Diego, 1994).
20. Haroche, S. & Raimond, J. M. *Cavity Quantum Electrodynamics* (ed. Berman, P.) 123–170 (Academic, San Diego, 1994).
21. Meystre, P. in *Progress in Optics* Vol. XXX (ed. Wolf, E.) 261–355 (Elsevier, Amsterdam, 1992).
22. An, K. & Feld, M. S. Semiclassical four-level single-atom laser. *Phys. Rev. A* **56,** 1662–1665 (1997).
23. Chang, R. K. & Campillo, A. J. (eds) *Optical Processes in Microcavities* (World Scientific, Singapore, 1996).
24. Vahala, K. J. Optical microcavities. *Nature* **424,** 839–846 (2003).
25. Ye, J., Vernooy, D. W. & Kimble, H. J. Trapping of single atoms in cavity QED. *Phys. Rev. Lett.* **83,** 4987–4990 (1999).
26. Rice, P. R. & Carmichael, H. J. Photon statistics of a cavity-QED laser: A comment on the laser-phase-transition analogy. *Phys. Rev. A* **50,** 4318–4329 (1994).
27. Boozer, A. D., Boca, A., Buck, J. R., McKeever, J. & Kimble, H. J. Comparison of theory and experiment for a one-atom laser in a regime of strong coupling. *Phys. Rev. A* (submitted); preprint available at ⟨http://lanl.arxiv.org/archive/quant-ph⟩.
28. Metcalf, H. J. & van der Straten, P. *Laser Cooling and Trapping* (Springer, New York, 1999).
29. Boiron, D. *et al.* Laser cooling of cesium atoms in gray optical molasses down to 1.1 μK. *Phys. Rev. A* **53,** R3734–R3737 (1996).
30. Corwin, K. L., Kuppens, S. J. M., Cho, D. & Wieman, C. E. Spin-polarized atoms in a circularly polarized optical dipole trap. *Phys. Rev. Lett.* **83,** 1311–1314 (1999).

Supplementary Information accompanies the paper on **www.nature.com/nature**.

Acknowledgements We gratefully acknowledge interactions with K. Birnbaum, C.-W. Chou, A. C. Doherty, L.-M. Duan, T. Lynn, T. Northup, S. Polyakov and D. M. Stamper-Kurn. This work was supported by the National Science Foundation, by the Caltech MURI Center for Quantum Networks, and by the Office of Naval Research.

Competing interests statement The authors declare that they have no competing financial interests.

Correspondence and requests for materials should be addressed to H.J.K (hjkimble@caltech.edu).

Quantum critical behaviour in a high-T_c superconductor

D. van der Marel[1]*, H. J. A. Molegraaf[1]*, J. Zaanen[2], Z. Nussinov[2]*, F. Carbone[1]*, A. Damascelli[3]*, H. Eisaki[3]*, M. Greven[3], P. H. Kes[2] & M. Li[2]

[1] *Materials Science Centre, University of Groningen, 9747 AG Groningen, The Netherlands*
[2] *Leiden Institute of Physics, Leiden University, 2300 RA Leiden, The Netherlands*
[3] *Department of Applied Physics and Stanford Synchrotron Radiation Laboratory, Stanford University, California 94305, USA*

* Present addresses: Département de Physique de la Matière Condensée, Université de Genève, CH-1211 Genève 4, Switzerland (D.v.d.M., H.J.A.M., F.C.); Los Alamos National Laboratories, Los Alamos, New Mexico 87545, USA (Z.N.); Department of Physics and Astronomy, University of British Columbia, Vancouver, British Columbia, V6T 1Z1, Canada (A.D.); Low-Temperature Physics Group, National Institute of Advanced Industrial Science and Technology, Umezono, Tsukuba, 305-8568, Japan (H.E.)

Quantum criticality is associated with a system composed of a nearly infinite number of interacting quantum degrees of freedom at zero temperature, and it implies that the system looks on average the same regardless of the time- and length scale on which it is observed. Electrons on the atomic scale do not exhibit such symmetry, which can only be generated as a collective phenomenon through the interactions between a large number of electrons. In materials with strong electron correlations a quantum phase transition at zero temperature can occur, and a quantum critical state has been predicted[1,2], which manifests itself through universal power-law behaviours of the response functions. Candidates have been found both in heavy-fermion systems[3] and in the high-transition temperature (high-T_c) copper oxide superconductors[4], but the reality and the physical nature of such a phase transition are still debated[5–7]. Here we report a universal behaviour that is characteristic of the quantum critical region. We demonstrate that the experimentally measured phase angle agrees precisely with the exponent of the optical conductivity. This points towards a quantum phase transition of an unconventional kind in the high-T_c superconductors.

In the quantum theory of collective fields one anticipates order at small coupling constant, and for increasing coupling one expects at some point a phase transition to a quantum-disordered state. Quantum criticality in the copper oxides, if it exists, occurs as a function of charge carrier doping x, at a particular doping level x_c close to where the superconducting phase transition temperature reaches its maximum value. When this phase transition is continuous, a critical state is realized right at the transition, which is characterized by scale invariance resulting in the above-mentioned power-law response up to some (non-universal) high-energy cut-off Ω.

The optical conductivity, $\sigma(\omega) = \sigma_1(\omega) + i\sigma_2(\omega)$, is the absorptive ($\sigma_1$) and reactive ($\sigma_2$) current response to a time-varying external electrical field of frequency ω, and is usually expressed as the correlation function of the currents $\mathbf{j}(\tau_1)$ and $\mathbf{j}(\tau_2)$ at times τ_1 and τ_2, which is $\chi_{jj}(\tau_1, \tau_2) = \langle \mathbf{j}(\tau_1), \mathbf{j}(\tau_2) \rangle$, by the Kubo formula. In Fig. 1 we present the experimental optical conductivity function $\sigma_1(\omega)$ of an optimally doped $Bi_2Sr_2Ca_{0.92}Y_{0.08}Cu_2O_{8+\delta}$ single crystal

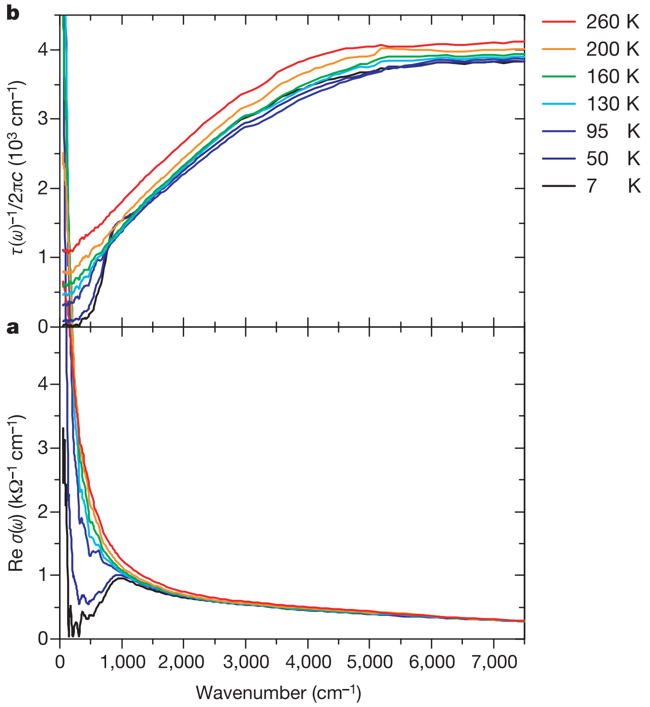

Figure 1 Optical properties along the copper-oxygen planes of $Bi_2Sr_2Ca_{0.92}Y_{0.08}Cu_2O_{8+\delta}$ for a selected number of temperatures. **a**, Optical conductivity and **b**, the frequency dependent scattering rate defined as $1/\tau(\omega) = \mathrm{Re}\{\omega_p^2/4\pi\sigma(\omega)\}$ (see Methods). The relatively high transition temperature ($T_c = 96$ K) of this crystal compared to previous reports on Bi-2212 is caused by the partial substitution of yttrium on the calcium sites.

© 2003 Nature Publishing Group

State-Insensitive Cooling and Trapping of Single Atoms in an Optical Cavity

J. McKeever, J. R. Buck, A. D. Boozer, A. Kuzmich, H.-C. Nägerl, D. M. Stamper-Kurn, and H. J. Kimble
Norman Bridge Laboratory of Physics 12-33, California Institute of Technology, Pasadena, California 91125

(Received 4 November 2002; published 3 April 2003)

Single cesium atoms are cooled and trapped inside a small optical cavity by way of a novel far-off-resonance dipole-force trap, with observed lifetimes of 2–3 s. Trapped atoms are observed continuously via transmission of a strongly coupled probe beam, with individual events lasting $\simeq 1$ s. The loss of successive atoms from the trap $N \geq 3 \rightarrow 2 \rightarrow 1 \rightarrow 0$ is thereby monitored in real time. Trapping, cooling, and interactions with strong coupling are enabled by the trap potential, for which the center-of-mass motion is only weakly dependent on the atom's internal state.

DOI: 10.1103/PhysRevLett.90.133602 PACS numbers: 42.50.Vk, 03.67.–a, 32.80.Pj

A long-standing ambition in the field of cavity quantum electrodynamics (QED) has been to trap single atoms inside high-Q cavities in a regime of strong coupling [1]. Diverse avenues have been pursued for creating the trapping potential for atom confinement, including additional far off-resonant trapping beams [2], near-resonant light with $\bar{n} \simeq 1$ intracavity photons [3,4], and single trapped ions in high-finesse optical cavities [5,6], although strong coupling has yet to be achieved for trapped ions. A critical aspect of this research is the development of techniques for atom localization that are compatible with strong coupling, as required for quantum computation and communication [7–12].

In this Letter we present experiments to enable quantum information processing in cavity QED by (1) achieving extended trapping times for single atoms in a cavity while still maintaining strong coupling, (2) realizing a trapping potential for the center-of-mass motion that is largely independent of the internal atomic state, and (3) demonstrating a scheme that allows continuous observation of trapped atoms by way of the atom-field coupling. More specifically, we have recorded trapping times up to 3 s for single Cs atoms stored in an intracavity far-off resonance trap (FORT) [13], which represents an improvement by a factor of 10^2 beyond the first realization of trapping in cavity QED [2], and by roughly 10^4 beyond prior results for atomic trapping [3] and localization [4] with $\bar{n} \simeq 1$ photon. We have also continuously monitored trapped atoms by way of strong coupling to a probe beam, including observations of trap loss atom by atom over intervals $\simeq 1$ s. These measurements incorporate auxiliary cooling beams, and provide the first realization of cooling for trapped atoms strongly coupled to a cavity. Our protocols are facilitated by the choice of a "magic" wavelength for the FORT [14–16], for which the relevant atomic levels are shifted almost equally, thereby providing significant advantages for coherent state manipulation of the atom-cavity system.

A major obstacle to the integration of a conventional red-detuned FORT within the setting of cavity QED is that excited electronic states generally experience a positive ac-Stark shift of comparable magnitude to the negative (trapping) shift of the ground state [13]. This effectively introduces a spatially dependent detuning between the atom and cavity resonances, an unfortunate additional complication [16]. However, due to the specific multilevel structure of cesium, the wavelength λ_F of the trapping laser can be tuned to a region where both of these problems are eliminated for the $6S_{1/2} \rightarrow 6P_{3/2}$ transition, as illustrated in Fig. 1 [14–16]. Around the magic wavelength $\lambda_F = 935$ nm, the sum of ac-Stark shifts coming from different allowed optical transitions results in the ground $6S_{1/2}$ and excited $6P_{3/2}$ states both being shifted downwards by comparable amounts, $\delta_{6S_{1/2}} \simeq \delta_{6P_{3/2}}$, albeit with small dependence on $(F', m_{F'})$ for the shifts $\delta_{6P_{3/2}}$.

The task then is to achieve state-independent trapping while still maintaining strong coupling for the $6S_{1/2} \rightarrow 6P_{3/2}$ transition. Our experimental setup to achieve this end is schematically depicted in Fig. 2 [2]. Significantly, the cavity has a TEM_{00} longitudinal mode located nine

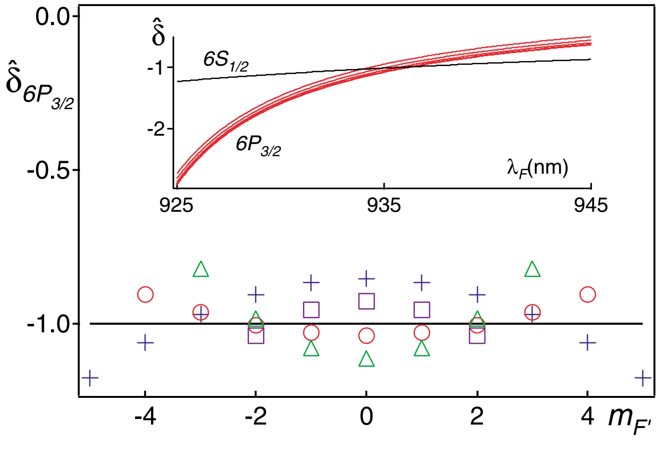

FIG. 1 (color online). ac-Stark shifts $(\hat{\delta}_{6S_{1/2}}, \hat{\delta}_{6P_{3/2}})$ for the $(6S_{1/2}, 6P_{3/2})$ levels in Cs for a linearly polarized FORT. The inset shows $(\hat{\delta}_{6S_{1/2}}, \hat{\delta}_{6P_{3/2},F'=4})$ as functions of wavelength λ_F. The full plot gives $\hat{\delta}_{6P_{3/2}}$ versus $m_{F'}$ for each of the levels $6P_{3/2}$, $F' = 2, 3, 4, 5$ for $\lambda_F = 935.6$ nm. In each case, the normalization is $\hat{\delta} = \delta/[\delta_{6S_{1/2}}(\lambda_F = 935.6 \text{ nm})]$.

© 2003 The American Physical Society

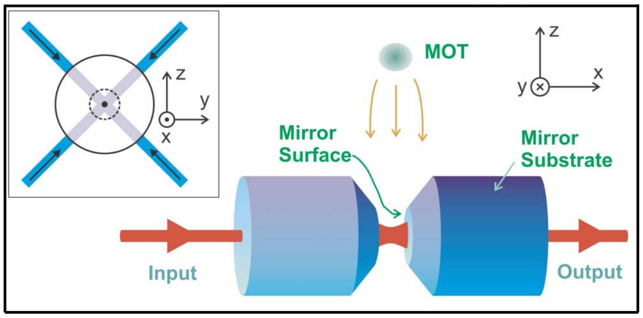

FIG. 2 (color online). Schematic of experiment for trapping single atoms in an optical cavity in a regime of strong coupling. Relevant cavity parameters are length $l = 43.0$ μm, waist $w_0 = 23.9$ μm, and finesse $\mathcal{F} = 4.2 \times 10^5$ at 852 nm. The inset illustrates transverse beams used for cooling and repumping.

mode orders below the mode employed for cavity QED at 852 nm, at the wavelength $\bar{\lambda}_F = 935.6$ nm, allowing the implementation of a FORT with $\delta_{6S_{1/2}} \simeq \delta_{6P_{3/2}}$. The field to excite this cavity mode is provided by a laser at $\bar{\lambda}_F$, which is independently locked to the cavity. The finesse of the cavity at $\bar{\lambda}_F$ is $\mathcal{F} \sim 2200$ [17], so that a mode-matched input power of 1.2 mW gives a peak ac-Stark shift $\delta_{6S_{1/2}}/2\pi = -47$ MHz for all states in the $6S_{1/2}$ ground manifold, corresponding to a trap depth $U_0/k_B = 2.3$ mK, which was used for all experiments.

Principal parameters relevant to cavity QED with the system in Fig. 2 are the Rabi frequency $2g_0$ for a single quantum of excitation and the amplitude decay rates (κ, γ) due to cavity losses and atomic spontaneous emission. For our system, $g_0/2\pi = 24$ MHz, $\kappa/2\pi = 4.2$ MHz, and $\gamma/2\pi = 2.6$ MHz, where g_0 is for the $(6S_{1/2}, F = 4, m_F = 4) \rightarrow (6P_{3/2}, F' = 5, m_F' = 4)$ transition in atomic Cs at $\lambda_0 = 852.4$ nm. Strong coupling is thereby achieved $[g_0 \gg (\kappa, \gamma)]$, resulting in critical photon and atom numbers $n_0 \equiv \gamma^2/(2g_0^2) \simeq 0.006$, $N_0 \equiv 2\kappa\gamma/g_0^2 \simeq 0.04$. The small transition shifts for our FORT mean that g_0 is considerably larger than the spatially dependent shift δ_0 of the bare atomic frequency employed for cavity QED, $g_0 \gg \delta_0 \equiv |\delta_{6P_{3/2}} - \delta_{6S_{1/2}}|$, whereas in a conventional FORT, $\delta_0 \sim 2|\delta_{6S_{1/2}}| \gg g_0$.

In addition to the FORT field, the input to the cavity consists of probe and locking beams, all of which are directed to separate detectors at the output. The transmitted probe beam is monitored using heterodyne detection, allowing real-time detection of individual cold atoms within the cavity mode [18]. The cavity length is actively controlled using a cavity resonance at $\lambda_C = 835.8$ nm, so the length is stabilized and tunable independently of all other intracavity fields [2]. The probe as well as the FORT beam are linearly polarized along a direction $\hat{l}_+$ orthogonal to the x axis of the cavity [17,19].

Cold atoms are collected in a magneto-optical trap (MOT) roughly 5 mm above the cavity mirrors and then released after a stage of sub-Doppler polarization-gradient cooling [13]. Freely falling atoms arrive at the cavity mode over an interval of about 10 ms, with kinetic energy $E_K/k_B \simeq 0.8$ mK, velocity $v \simeq 0.30$ m/s, and transit time $\Delta t = 2w_0/v \simeq 150$ μs. Two additional orthogonal pairs of counterpropagating beams in a $\sigma^+ - \sigma^-$ configuration illuminate the region between the cavity mirrors along directions at ±45° relative to $\hat{y}, \hat{z}$ (the "$y - z$ beams") and contain cooling light tuned red of $F = 4 \rightarrow F' = 5$ and repumping light near the $F = 3 \rightarrow F' = 3$ transition [20]. These beams eliminate the free-fall velocity to capture atoms in the FORT and provide for subsequent cooling of trapped atoms.

We employed two distinct protocols to study the lifetime for single trapped atoms in our FORT: (1) *Trapping in the dark* with the atom illuminated only by the FORT laser at $\bar{\lambda}_F$ and the cavity-locking laser at λ_C. For this protocol, strong coupling enables real-time monitoring of single atoms within the cavity for initial triggering of cooling light and for final detection. (2) *Trapping with continuous observation of single atoms* with cavity probe and cooling light during the trapping interval. In this case, atoms in the cavity mode are monitored by way of the cavity probe beam, with cooling provided by the auxiliary $y - z$ beams.

(1) In our first protocol, the $F = 4 \rightarrow F' = 5$ transition is strongly coupled to the cavity field, with zero detuning of the cavity from the bare atomic resonance, $\Delta_C \equiv \omega_C - \omega_{4\rightarrow 5} = 0$. In contrast to Ref. [2], here the FORT is *ON* continuously without switching, which makes a cooling mechanism necessary to load atoms into the trap. The initial detection of a single-atom falling into the cavity mode is performed with the probe beam tuned to the lower sideband of the vacuum-Rabi spectrum ($\Delta_p = \omega_p - \omega_{4\rightarrow 5} = -2\pi \times 20$ MHz). The resulting *increase* in transmitted probe power when an atom approaches a region of optimal coupling [21,22] triggers *ON* a pulse of transverse cooling light from the $y - z$ beams, detuned 41 MHz red of $\omega_{4\rightarrow 5}$. During the subsequent trapping interval, all near-resonant fields are turned *OFF* (including the transverse cooling light). After a variable delay t_T, the probe field is switched back *ON* to detect whether the atom is still trapped, now with $\Delta_p = 0$.

Data collected in this manner are shown in Fig. 3(a), which displays the conditional probability P to detect an atom given an initial single-atom triggering event versus the time delay t_T. The two data sets shown in Fig. 3(a) yield comparable lifetimes, the upper acquired with mean intracavity atom number $\bar{N} = 0.30$ atoms and the lower with $\bar{N} = 0.019$ [23]. The offset in P between these two curves arises primarily from a reduction in duration δt of the cooling pulses, from 100 to 5 μs, which results in a reduced capture probability. Measurements with constant δt but with $\bar{N}$ varied by adjusting the MOT parameters allow us to investigate the probability of trapping an atom other than the "trigger" atom and of capturing more than one atom. For example, with $\delta t = 5$ μs as in the lower set,

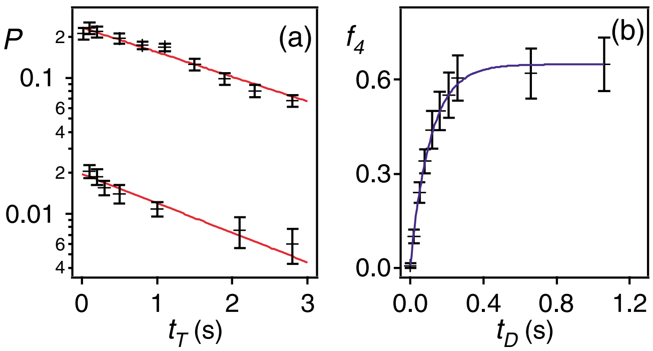

FIG. 3 (color online). (a) Detection probability P as a function of trapping time t_T. The upper data set is for mean intracavity atom number $\bar{N} \approx 0.30$, while the lower set is for $\bar{N} \approx 0.019$ atoms. Exponential fits (solid lines) yield lifetimes $\tau_{\mathrm{upper}} = (2.4 \pm 0.2)$ s and $\tau_{\mathrm{lower}} = (2.0 \pm 0.3)$ s. (b) The fractional population $f_4(t_D)$ in $F = 4$ following depletion of this level at $t_D = 0$. An exponential fit (solid line) gives $\tau_R = (0.11 \pm 0.02)$ s.

we have varied $0.011 \lesssim \bar{N} \lesssim 0.20$ with no observable change in either P_T or the trap lifetime τ. Since a conservative upper bound on the relative probability of trapping a second atom is just $\bar{N}/2$ (when $\bar{N} \ll 1$), these data strongly support the conclusion that our measurements are for single trapped atoms. We routinely observe lifetimes $2\ \mathrm{s} < \tau < 3\ \mathrm{s}$ depending upon the parameters chosen for trap loading and cooling.

Figure 3(b) explores scattering processes within the FORT that transfer population between the $6S_{1/2}, F = (3, 4)$ ground-state hyperfine levels. For these measurements, the $F = 4$ level is initially depleted, and then the population in $F = 4$ as well as the total $3 + 4$ population are monitored as functions of time t_D to yield the fractional population $f_4(t_D)$ in $F = 4$. The measured time $\tau_R = (0.11 \pm 0.02)$ s for reequilibration of populations between $F = (3, 4)$ agrees with a numerical simulation based upon scattering rates in our FORT, which predicts $\tau_R = 0.10$ s for atoms trapped at the peak FORT intensity in an initially unpolarized state in the $F = 3$ level.

Turning next to the question of the mechanisms that limit our FORT lifetime, we recall that parametric heating can be caused by intensity fluctuations of the trapping field [2,24]. From measurements of intensity fluctuations for our FORT around twice the relevant harmonic frequencies ($\nu_{\mathrm{axial}} = 570, \nu_{\mathrm{radial}} = 4.8$) kHz, we estimate a lower bound to the FORT lifetime of $\tau_p^{\mathrm{axial}} > 1.6$ s [25]. Although this estimate suggests that parametric heating could be a limiting factor in Fig. 3, we were later able to reduce the noise, giving a new lower bound $\tau_p^{\mathrm{axial}} > 9$ s. Unfortunately, the measured FORT lifetime increased only to $\tau = (3.1 \pm 0.4)$ s, indicating that other mechanisms are partially responsible for the observed decay.

A second suspect is a heating process described by Corwin *et al.* [26] associated with inelastic Raman scattering in an elliptically polarized FORT field [19]. We calculate rates Γ_s for spontaneous Raman scattering in our FORT to be 2.5 to 7 s^{-1} for transitions that change the hyperfine quantum number F, and between 0.8 and 2.5 s^{-1} when only m_F changes [27]. Based on Eq. 3 in Ref. [26] (a two-state model), we estimate an upper limit to the heating rate from this mechanism, $\Gamma_{IR} \lesssim 0.2\Gamma_s$, giving heating times as short as 0.7 s for the fastest calculated scattering rate. However, we have also undertaken a full multilevel simulation of the optical pumping processes, which indicates much slower heating, $\Gamma_{IR} \sim 0.02\ \mathrm{s}^{-1}$. We are working to resolve this discrepancy.

A third suspect that cannot be discounted is the presence of stray light, which we have endeavored to eliminate. For lifetimes as in Fig. 3, we require intracavity photon number $\bar{n} \ll 10^{-5}$, which is not trivial to diagnose. A final concern is the background pressure in the region of the FORT. Although the chamber pressure is 3×10^{-10} Torr (leading to $\tau \simeq 30$ s), we have no direct measurement of the residual gas density in the narrow cylinder between the mirror substrates (diameter 1 mm and length 43 μm), except for the trap lifetime itself.

(2) Toward the goals of continuous observation of single trapped atoms [3,4] and of implementing Λ schemes in cavity QED [7–9,28], we next present results from our second protocol. Here the $F = 4 \rightarrow F' = 4$ transition is strongly coupled to the cavity field, with $\Delta'_C \equiv \omega_C - \omega_{4\rightarrow 4} = 0$. In contrast to our protocol (1), the FORT and the transverse $y - z$ beams are left *ON* continuously, with the latter containing only light near the $F = 3 \rightarrow F' = 3$ resonance, with detuning Δ_3. Significantly, we observe trap loading with *no cooling light near the* $F = 4 \rightarrow F' = 5$ *transition.*

An example of the resulting probe transmission is shown in Fig. 4, which displays two separate records of the continuous observation of trapped atoms. Here the probe detuning $\Delta'_p = \omega_p - \omega_{4\rightarrow 4} = 0$ and the probe strength is given in terms of $\bar{m} = |\langle \hat{a} \rangle|^2$ deduced from the heterodyne current, with $\hat{a}$ as the annihilation operator for the intracavity field. We believe that the $y - z$ repumping beams (which excite $F = 3 \rightarrow F' = 3$) provide cooling, since without them the atoms would "roll" in and out of the near-conservative FORT potential (indeed no trapping occurs in their absence). In addition, this is a continuous cooling and loading scheme, so that we routinely load multiple atoms into the trap.

The most striking characteristic of the data collected in this manner is that $\bar{m}$ versus t always reaches its deepest level within the $\simeq 10$ ms window when the falling atoms arrive, subsequently increasing in a discontinuous "staircase" of steps. As indicated in Fig. 4, our interpretation is that there is a different level for $\bar{m}$ associated with each value N of the number of trapped atoms (with the level decreasing for higher N), and that each step is due to the loss of an atom from the cavity mode. In addition, we observe a strong dependence both of the initial trapping

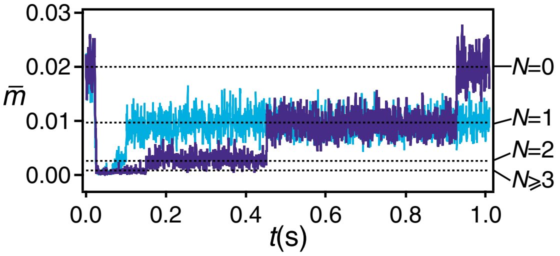

FIG. 4 (color online). Two traces of the continuous observation of trapped atoms inside a cavity in a regime of strong coupling. After an initial sharp reduction around $t = 0$ as atoms are cooled into the cavity mode, the intracavity field strength $\bar{m}$ increases in a discontinuous fashion as trapped atoms escape from the cavity mode one by one. rf detection bandwidth = 1 kHz, $\Delta'_C = 0 = \Delta'_p$, and $\Delta_3/2\pi = 25$ MHz.

probability and of the continuous observation time on the detuning of the transverse beams, with an optimal value $\Delta_3 \simeq 25$ MHz to the *blue* of the $3 \rightarrow 3$ transition, which strongly suggests blue Sisyphus cooling [29].

We stress that observations as in Fig. 4 are made possible by strong coupling in cavity QED, for which individual intracavity atoms cause the displayed changes in probe transmission. While $\bar{m}$ in Fig. 4 is only $\simeq 0.01$, it represents an output flux $\simeq 5 \times 10^5$ photons per second. The probe is also critical to the cooling, although it is not clear whether this beam is acting as a simple "repumper" [29] or is functioning in a more complex fashion due to strong coupling. We have not seen such striking phenomena under similar conditions for cavity QED with the $F = 4 \rightarrow F' = 5$ transition. Note that our ability to monitor the atom as well as to cool its motion are enabled by the state-insensitive character of the trap, since the net transition shifts are small, $(g_0, \Delta_3) \gg \delta_0$.

In summary, we have demonstrated a new set of ideas within the setting of cavity QED, including state-insensitive trapping suitable for strong coupling. Trapping of single atoms with $g_0 \gg (\delta_0, \kappa, \gamma)$ has been achieved with lifetimes $\tau \simeq 2$–3 s. Since intrinsic heating in the FORT is quite low (~ 11 μK/s due to photon recoil), we anticipate extensions to much longer lifetimes. Continuous observations of multiple atoms in a cavity have been reported, and involve an interplay of a strongly coupled probe field for monitoring and a set of $y - z$ cooling beams. Our measurements represent the first demonstration of cooling for trapped atoms strongly coupled to a cavity. Beyond its critical role here, state-insensitive trapping should allow the application of diverse laser cooling schemes, leading to further advances in quantum information science.

We gratefully acknowledge the contributions of K. Birnbaum, A. Boca, T.W. Lynn, S.J. van Enk, D.W. Vernooy, and J. Ye. This work was supported by the Caltech MURI Center for Quantum Networks under ARO Grant No. DAAD19-00-1-0374, by the National Science Foundation, and by the Office of Naval Research.

---

[1] For a review, see Phys. Scr. **T76**, 127 (1998).
[2] J. Ye *et al.*, Phys. Rev. Lett. **83**, 4987 (1999); D.W. Vernooy, Ph.D. thesis, California Institute of Technology, 2000.
[3] C. J. Hood *et al.*, Science **287**, 1447 (2000); Phys. Rev. A **63**, 013401 (2001).
[4] P.W. H. Pinkse *et al.*, Nature (London) **404**, 365 (2000).
[5] G. R. Guthöhrlein *et al.*, Nature (London) **414**, 49 (2001).
[6] J. Eschner *et al.*, Nature (London) **413**, 495 (2001).
[7] T. Pellizari *et al.*, Phys. Rev. Lett. **75**, 3788 (1995).
[8] J. I. Cirac *et al.*, Phys. Rev. Lett. **78**, 3221 (1997).
[9] S. van Enk *et al.*, Science **279**, 205 (1998).
[10] C. Cabrillo *et al.*, Phys. Rev. A **59**, 1025 (1999).
[11] S. Bose *et al.*, Phys. Rev. Lett. **83**, 5158 (1999).
[12] A. S. Parkins and H. J. Kimble, J. Opt. B Quantum Semiclassical Opt. **1**, 496 (1999).
[13] H. J. Metcalf and P. van der Straten, *Laser Cooling and Trapping*y (Springer-Verlag, Berlin, 1999).
[14] C. J. Hood and C. Wood, as described by H. J. Kimble *et al.*, in *Laser Spectroscopy XIV*, edited by (World Scientific, Singapore, 1999), p. 80.
[15] H. Katori *et al.*, J. Phys. Soc. Jpn. **68**, 2479 (1999); T. Ido *et al.*, Phys. Rev. A **61**, 061403 (2000).
[16] S. J. van Enk *et al.*, Phys. Rev. A **64**, 013407 (2001).
[17] C. J. Hood *et al.*, Phys. Rev. A **64**, 033804 (2001).
[18] H. Mabuchi *et al.*, Opt. Lett. **21**, 1393 (1996).
[19] Because of small stress-induced birefringence in the cavity mirrors, we align the directions of linear polarization along an axis that coincides with one of the cavity eigenpolarizations [17], denoted by $\hat{l}_\pm$. For initial polarization along $\hat{l}_+$, measurements of FORT [probe] polarization along $\hat{l}_-$ for the cavity output power P give $P_-/P_+ < 0.02$ [0.002] for the FORT [probe] beam.
[20] The (incoherent) sum of the four intensities is $I_{4-5} \sim 60$ mW/cm^2 for the cooling and $I_{3-3} \sim 40$ mW/cm^2 for the repumping light, with uncertainties of roughly 2 times.
[21] C. J. Hood *et al.*, Phys. Rev. Lett. **80**, 4157 (1998).
[22] Specific examples of single-atom detection events are omitted here. For $\Delta_p \simeq -g_0$, the increases in cavity transmission are quite similar to those in Refs. [3,21], while for $\Delta_p = 0$ the decreases are similar to those in Refs. [2,18], albeit now in the presence of the FORT.
[23] $\bar{N}$ is estimated from the mean number of atom transit events (of duration $\simeq 150$ μs) during the interval $\simeq 10$ ms from the falling MOT atoms, in the absence of trapping.
[24] T. A. Savard *et al.*, Phys. Rev. A **56**, R1095 (1997); C.W. Gardiner *et al.*, *ibid.* **61**, 045801 (2000).
[25] The predicted $\tau_p^{\text{radial}} > 10^4$ s.
[26] K. L. Corwin *et al.*, Phys. Rev. Lett. **83**, 1311 (1999).
[27] R. A. Cline *et al.*, Opt. Lett. **19**, 207 (1994).
[28] A. Kuhn *et al.*, Phys. Rev. Lett. **89**, 067901 (2002).
[29] D. Boiron *et al.*, Phys. Rev. A **53**, R3734 (1996), and references therein.

VOLUME 90, NUMBER 15 PHYSICAL REVIEW LETTERS week ending 18 APRIL 2003

Symmetric Extensions of Quantum States and Local Hidden Variable Theories

Barbara M. Terhal,[1,2] Andrew C. Doherty,[2] and David Schwab[3]
[1]*IBM Watson Research Center, P.O. Box 218, Yorktown Heights, New York 10598*
[2]*Institute for Quantum Information, Caltech 107-81, Pasadena, California 91125*
[3]*Department of Physics, Cornell University, 109 Clark Hall, Ithaca, New York 14853*

(Received 18 October 2002; published 16 April 2003)

While all bipartite pure entangled states violate some Bell inequality, the relationship between entanglement and nonlocality for mixed quantum states is not well understood. We introduce a simple and efficient algorithmic approach for the problem of constructing local hidden variable theories for quantum states. The method is based on constructing a so-called symmetric quasiextension of the quantum state that gives rise to a local hidden variable model with a certain number of settings for the observers Alice and Bob.

DOI: 10.1103/PhysRevLett.90.157903 PACS numbers: 03.65.Ud, 03.67.Mn

It was Bell [1] who quantified how measurements on entangled quantum mechanical systems can invalidate local classical models of reality. His original inequality has generated a field of research devoted to general Bell inequalities and experimentally observed violations of such inequalities.

Perhaps surprisingly, the nature of the set of states that violate local realism is poorly understood, although it is known from the seminal work of Werner [2] that not all entangled states violate a Bell inequality. Recent results in quantum information theory have revealed the complex structure of the set of entangled states but have as yet shed little light on the relation between this structure and violation of Bell inequalities. For example, it has been conjectured by Peres [3] that so-called bound entangled states which satisfy the Peres-Horodecki "partial transposition" criterion [4] (i.e., they have positive partial transpose), do not violate any Bell inequalities. There are various results that support this conjecture both in the bipartite and multipartite case, see Ref. [5], but none of the results is conclusive.

What has been lacking in the literature so far is a systematic way of deciding whether a quantum state does or does not violate some Bell inequality. The difficulty is that the possible types of local measurements and the number of measurements that observers can perform is in principle unbounded and the enumeration of Bell inequalities is computationally hard [6].

In this Letter we present the first systematic approach for constructing local hidden variable theories for quantum states, depending only on the number of local measurement settings for each observer. Our approach has yielded both numerically constructed local hidden variable theories for a variety of quantum states as well as analytical results for Werner states [2] and a class of bound entangled states based on real UPBs [7].

Before we can state our main result, we recapitulate the mathematics of local hidden variable (LHV) models and Bell inequalities for bipartite systems. We refer the reader to Refs. [3,6,8] for some literature on the theoretical formulation of general Bell inequalities. Each of the observers, Alice and Bob, has a set of local measurements. Let $i = 1, \ldots, s_a$ be the number of measurements for Alice and let each measurement have $o_a(i)$ outcomes. Let $k = 1, \ldots, s_b$ be the number of measurements for Bob and $o_b(k)$ be the number of outcomes per measurement. The probability $P_{ij,kl}$ denotes the probability that Alice's ith measurement has outcome j and Bob's kth measurement has outcome l. A local hidden variable model assumes the existence of a shared random variable between Alice and Bob that is used to locally generate a measurement outcome depending only on the choice of the local measurement (and not on the choice of the other, remote, measurement). The local hidden variable model generates the probability vector $\vec{P}$ with entries $P_{ij,kl}$ when it generates measurement outcomes in accordance with these probabilities. Mathematically one defines a convex set $S(s_a, s_b, o_a, o_b)$ which is the set of probability vectors $\vec{P}$ that can be generated by LHV models. It is known that S is a polytope and that the extremal vectors $\vec{B}$ of S are vectors with $0, 1$ entries [8]. These extremal vectors $\vec{B}$ correspond to the situation in which the outcomes of the measurements are determined with certainty and can be labeled by two sets of indices $\mathbf{m} = (m_1, \ldots, m_{s_a})$ where $m_i = 1, \ldots, o_a(i)$ and $\mathbf{n} = (n_1, \ldots, n_{s_b})$ where $n_k = 1, \ldots, o_b(k)$. A brief expression for these extremal vectors is

$$B_{ij,kl}^{\mathbf{m},\mathbf{n}} = \delta_{jm_i}\delta_{ln_k}. \tag{1}$$

In words, each extremal vector specifies a single outcome with probability one for each local measurement, independently of the measurement made by the other parties.

For a quantum mechanical system ρ in $\mathcal{H}_{d_A} \otimes \mathcal{H}_{d_B}$ the probability $P_{ij,kl}$ is given by $P_{ij,kl}(\rho) = \mathrm{Tr} E_{ij}^A \otimes E_{kl}^B \rho$. Here $\{E_{ij}^A \geq 0 : \sum_j E_{ij}^A = I_{d_A}\}$ are the POVM (positive operator-valued measure) elements for Alice's ith measurement and $\{E_{kl}^B\}$ are the POVM elements for Bob's kth

0031-9007/03/90(15)/157903(4)$20.00 © 2003 The American Physical Society

measurement. There is a violation of a Bell inequality if and only if $P_{ij,kl}$ cannot be generated by a LHV model, or $\vec{P} \notin S$.

In this Letter we prove the first necessary condition for a state to violate a Bell inequality depending only on the number of settings for Alice and Bob. We explicitly construct a LHV model in a $s_a = 2$ and arbitrary s_b setting (and vice versa) for any bound entangled state based on a *real* unextendible product basis (UPB) [4]. Then we discuss numerical work that shows that many of the known bipartite bound entangled states cannot violate a Bell inequality with two settings either for Alice or Bob. Finally, we partially reproduce and extend some of Werner's original results by showing that it is possible to use our procedure to analytically construct LHV theories for Werner states. It is noteworthy to mention that our methods (Theorem 1 and Theorem 2) straightforwardly generalize to multipartite states, even though we have not explored this direction.

We connect violations of Bell inequalities to the existence of a symmetric (quasi-) extension of a quantum state [9]. An extension of a quantum state ρ on, say, a system AB, is another quantum state defined on a system ABC such that when we trace over C we obtain the original quantum state ρ. We are interested in the situation where the system $C = A^{\otimes(s_a-1)} \otimes B^{\otimes(s_b-1)}$ and we demand that the extension be invariant under all permutations of the s_a copies of system A among each other and similarly invariant under any permutation of the B systems. It is clear that if the quantum state ρ is separable, i.e., $\rho = \sum_i p_i(|\psi_i\rangle\langle\psi_i|)_A \otimes (|\phi_i\rangle\langle\phi_i|)_B$, such an extension always exists: we just copy the individual product states onto the other spaces:

$$\rho_{\text{ext}} = \sum_i p_i(|\psi_i\rangle\langle\psi_i|)^{\otimes s_a} \otimes (|\phi_i\rangle\langle\phi_i|)^{\otimes s_b}. \tag{2}$$

If the state ρ is a pure entangled state, then it is also clear that such a symmetric extension cannot exist. The symmetry requirement implies that the pure entangled state ρ_{AB} must equal $\rho_{A'B}$, where A' is another A system, which is impossible. In popular terms we may say that pure entanglement is "monogamous": B cannot be entangled with A and A' at the same time. In some sense what we show in this Letter is that (i) a violation of a Bell inequality indicates that the entanglement in the quantum state is monogamous and (ii) there are many mixed entangled states whose entanglement is not monogamous.

Thus the existence of a symmetric extension can be viewed as a separability criterion (see Ref. [11] for a similar but stronger separability criterion where one demands that the symmetric extension has positive partial transposes). For considering Bell inequality violations we generalize our criterion slightly and ask whether a state has a symmetric *quasiextension* H_ρ which is not necessarily positive. In order to define this notion we need the definition of a multipartite entanglement witness, which is an entanglement witness which can detect any multipartite entanglement in a state. It has the property that for all states $\psi_1, \ldots, \psi_{s_a}, \phi_1, \ldots, \phi_{s_b}$, $\langle\psi_1, \ldots, \psi_{s_a}, \phi_1, \ldots, \phi_{s_b}|H_\rho|\psi_1, \ldots, \psi_{s_a}, \phi_1, \ldots, \phi_{s_b}\rangle \geq 0$.

Definition (symmetric quasiextension): Let $\pi: \mathcal{H}^{\otimes s} \rightarrow \mathcal{H}^{\otimes s}$ be a permutation of spaces $\mathcal{H}$ in $\mathcal{H}^{\otimes s}$. We define

$$\mathsf{Sym}(\rho) = \frac{1}{s!}\sum_\pi \pi\rho\pi^\dagger. \tag{3}$$

We, say, that ρ on $\mathcal{H}_A \otimes \mathcal{H}_B$ has a (s_a, s_b)-symmetric quasiextension when there exists a multipartite entanglement witness H_ρ on $\mathcal{H}_A^{\otimes s_a} \otimes \mathcal{H}_B^{\otimes s_b}$ such that $\mathrm{Tr}_{\mathcal{H}_A^{\otimes(s_a-1)}, \mathcal{H}_B^{\otimes(s_b-1)}} H_\rho = \rho$ and $H_\rho = \mathsf{Sym}_A \otimes \mathsf{Sym}_B(H_\rho)$.

The reason for considering such quasiextensions is clear from the following theorems which are the main results of this Letter.

Theorem 1: If ρ has a (s_a, s_b)-symmetric quasiextension, then ρ does not violate a Bell inequality with (s_a, s_b) settings.

Before proving this theorem, it is important to note the generality of the result; it holds for all possible choices of measurements which includes POVM measurements with an unbounded number of measurement outcomes. We show below that the quasiextension of ρ effectively creates a LHV model for ρ when Alice and Bob have s_a and s_b arbitrary measurements.

Proof: We prove our theorem by extracting a LHV model from the quasiextension. The LHV model for ρ for (s_a, s_b) settings should reproduce the vector $P_{ij,kl}(\rho) = \mathrm{Tr}E_{ij}^A \otimes E_{kl}^B\rho$ for all possible choices of POVM measurements $\{E_{ij}^A, E_{kl}^B\}$, as a convex combination of the extremal B vectors, i.e.,

$$P_{ij,kl}(\rho) = \sum_{\mathbf{m},\mathbf{n}} p_{\mathbf{m},\mathbf{n}}(\{E_{ij}^A, E_{kl}^B\}, \rho)B_{ij,kl}^{\mathbf{m},\mathbf{n}}, \tag{4}$$

where $p_{\mathbf{m},\mathbf{n}}(.) \geq 0$. If a symmetric quasiextension exists for ρ, then $\mathrm{Tr}E_{ij}^A \otimes E_{kl}^B\rho = \mathrm{Tr}(E_{ij}^A \otimes E_{kl}^B \otimes \mathbf{I})H_\rho$. Using the definition of the B vectors, the properties of the POVMs ($\sum_j E_{ij}^{A,B} = I_{d_{A,B}}$), and the symmetry properties of H_ρ it is not hard to verify that

$$P_{ij,kl}(\rho) = \mathrm{Tr}E_{ij}^A \otimes E_{kl}^B\rho = \sum_{\mathbf{m},\mathbf{n}}(\mathrm{Tr}\mathbf{E}_\mathbf{m}^A \otimes \mathbf{E}_\mathbf{n}^B H_\rho)B_{ij,kl}^{\mathbf{m},\mathbf{n}}. \tag{5}$$

Here $\mathbf{E}_\mathbf{m}^A = E_{1m_1}^A \otimes E_{2m_2}^A \otimes \ldots \otimes E_{s_a m_{s_a}}^A$ and similarly for $\mathbf{E}_\mathbf{n}^B$. Since H_ρ is a quasiextension $p_{\mathbf{m},\mathbf{n}}(\{E_{ij}^A, E_{kl}^B\}, \rho) \equiv \mathrm{Tr}\mathbf{E}_\mathbf{m}^A \otimes \mathbf{E}_\mathbf{n}^B H_\rho \geq 0$, and we have obtained a LHV model. □

One way of looking at this result is the following [12]. If ρ has a symmetric extension $\tilde{\rho}$, then instead of measurement on ρ, Alice and Bob can do measurements on $\tilde{\rho}$. Because of the symmetry Alice can do the first measurement on the first Alice space and the second measurement on the second Alice space, etc. But now these measurements are all commuting and can be considered as one big measurement. But we know that when Alice and Bob each have only a single measurement a LHV model for their measurements exists and thus we have a LHV model for the measurements on ρ. With this picture in mind, it is not hard to understand the following strengthening of our results (see also Ref. [10]):

Theorem 2: If ρ has a $(1, s_b)$-symmetric quasiextension, then ρ does not violate a Bell inequality with s_b settings for Bob and any number of settings for Alice.

Remark: The theorem also holds when Alice and Bob are interchanged.

Proof: The intuition behind this theorem relies on the fact that there are no violations of Bell inequalities when one party has only one measurement setting, thus suggesting that it is unnecessary to extend to copies of Alice's space as well as Bob's. Here is the local hidden variable model that we construct from a quasiextension H_ρ, on $\mathcal{H}_A \otimes \mathcal{H}_B^{\otimes s_b}$. We set

$$p_{\mathbf{m},\mathbf{n}}(\{E^A_{ij}, E^B_{kl}\}, \rho) = \frac{\Pi_{i'=1}^{s_a}(\mathrm{Tr}E^A_{i'm_{i'}} \otimes \mathbf{E}^B_{\mathbf{n}} H_\rho)}{(\mathrm{Tr}I_A \otimes E^B_{\mathbf{n}} H_\rho)^{s_a-1}}. \tag{6}$$

Each $p_{\mathbf{m},\mathbf{n}}$ is non-negative since H_ρ is an entanglement witness. We can substitute this expression in Eq. (4) and verify that we obtain the correct probabilities $P_{ij,kl}(\rho)$ by using the definition of the B vectors, the normalization of the POVMs, and the symmetry of H_ρ as before. □

This method for constructing LHV theories may be implemented both numerically and analytically. Let us first show a simple analytic construction of a $(2, 2)$-symmetric extension for *any* bound entangled state based on a *real* unextendible product basis [7]. Let $P_{BE} = I - \sum_i |a_i, b_i\rangle\langle a_i, b_i|$ be the projector onto such a bound entangled state, where $\{|a_i, b_i\rangle = |a_i^*, b_i^*\rangle\}$ is the real unextendable product basis. Our (unnormalized) extension will be $|\Psi\rangle_{A_2A_1} \otimes |\Psi\rangle_{B_1B_2} - \sum_i |a_i, a_i, b_i, b_i\rangle_{A_2A_1B_1B_2}$, where $|\Psi\rangle = \sum_i |ii\rangle$. It is evident that this extension has the desired symmetry property. It is not hard to verify that by tracing over the systems A_2 and B_2 we obtain $P_{BE}^2 = P_{BE}$. The existence of a symmetric $(2, 2)$ extension implies the existence of both $(2, 1)$ and $(1, 2)$ symmetric extensions for the state by tracing out copies of A or B, so any Bell inequality violation for this class of states must involve more than two measurement settings for both parties.

We have implemented numerical tests for the conditions of these two theorems. First, we look for the existence of a symmetric extension with $H_\rho \geq 0$. If such an extension does not exist, there is still the possibility that some other kind of quasiextension does exist. We have focused on the existence of a decomposable entanglement witness H_ρ because in both these cases the numerical problem corresponds to a semidefinite program [13]. We label the partitions of $\mathcal{H}_A^{\otimes s_a} \otimes \mathcal{H}_B^{\otimes s_b}$ into bipartite systems by p and we denote partial transposition with respect to one of the two subsystems as T_p. A decomposable entanglement witness may then be written as $H_\rho = P + \sum_p Q_p^{T_p}$, where $P \geq 0$, $Q_p \geq 0$ for all p.

Semidefinite programs correspond to optimizations of linear functions on positive matrices subject to trace constraints. They are convex optimizations and are particularly tractable both analytically and numerically. We show how to numerically construct symmetric extensions, the decomposable quasiextension case is very similar. The condition that the partial trace of H_ρ is ρ is equivalent to requiring that $\mathrm{Tr}(X \otimes \mathbf{I})H_\rho = \mathrm{Tr}X\rho$ for all operators X on $\mathcal{H}_A \otimes \mathcal{H}_B$. If we write X in terms of a basis $\{\sigma_i\}$ for the real vector space of Hermitian operators, then by linearity it is enough to check that this trace constraint holds for each element of the basis. We assume that the basis is orthogonal in the trace inner product $\mathrm{Tr}\sigma_i\sigma_j = \delta_{ij}$ and that $\sigma_0 = I_{d_A} \otimes I_{d_B}/\sqrt{d_A d_B}$. The index i ranges from zero to $(d_A d_B)^2 - 1$. Consider then this semidefinite program

$$\begin{array}{lcr} \text{minimize} & \mathrm{Tr}K, & \\ \text{subject to} & \mathrm{Tr}\mathsf{Sym}_A \otimes \mathsf{Sym}_B(\sigma_i \otimes \mathbf{I})K = r_i, & i > 0, \\ & K \geq 0, & \end{array}$$

where $r_i = \mathrm{Tr}\sigma_i\rho$. If the optimum is less than or equal to one, then, by adding a multiple of the identity to the optimal K, we obtain some K_ρ that satisfies $\mathrm{Tr}K_\rho = 1$ as well as the other constraints. If we define $H_\rho \equiv \mathsf{Sym}_A \otimes \mathsf{Sym}_B(K_\rho)$ it is clear that H_ρ is a (s_a, s_b)-symmetric extension of ρ. Duality properties of semidefinite programs imply that an optimum greater than one precludes the existence of a (s_a, s_b)-symmetric extension [13].

We have implemented this semidefinite program using SeDuMi [14] for several examples of bound entangled states with $d_A = d_B = 3$. The results are summarized in Table I. For example, the Choi-Horodecki (C-H) states considered in Ref. [15] depend on a parameter α and include separable ($\alpha \in [2, 3]$), bound entangled ($\alpha \in (3, 4]$), and nonpositive partial transpose (NPT) states for $\alpha > 4$. They turn out to have $(2, 1)$-symmetric extensions well into the range for which the states are entangled and even NPT. Over the range $\alpha \in [4.34, 4.84]$ they have decomposable symmetric quasiextensions but no symmetric extensions showing that the former property provides a strictly stronger sufficient condition for the existence of a LHV theory. The bound entangled states of [16] do not even have $(1, 2)$ extensions. These and many of the Bruß-Peres states [17] are therefore the strongest candidates for bound entangled states with Bell inequality violations. However, we have looked for but did not find Bell inequality violations for $(s_a = 2, s_b = 2)$ settings and three outcome projective measurements and for $(3, 3)$ settings and two outcome projective measurements.

Finally we considered Werner states [2] defined in dimensions $d = d_A = d_B \geq 2$ as $\rho_W = \frac{1}{d^3 - d}[I(d - \Phi) + (d\Phi - 1)V]$, where V is the flip operator. Werner [2]

TABLE I. Numerical results on the existence of symmetric extensions (ext) and decomposable quasiextensions (q-ext) for ($s_a = 1, s_b = 2$), ($s_a = 2, s_b = 1$), ($s_a = 1, s_b = 3$), and ($s_a = 3$, $s_b = 1$). For the one and two dimensional families of states [2,15,16] we performed a systematic search of the parameter space. For the high dimensional families [17,18] we make qualitative statements based on randomly chosen examples. Note that states may have an $(s, 1)$ extension and no $(1, s)$ extension. We have performed both tests in all cases, but the general results are unaffected although we do find examples of Bruß-Peres states with $(2, 1)$ extensions, say, but no $(1, 2)$ extensions.

	$(2, 1), (1, 2)$		$(3, 1), (1, 3)$
	ext	q-ext	ext
C-H [15]:$\alpha \in$	$[2, 4.33]$	$[2, 4.84]$	$[2, 4.00]$
Complex UPB [18]	Yes	Yes	Few
H-L [16]	No	No	No
Bruß-Peres [17]	Few	Few	No
Werner [2]	$d \geq 3$	$d \geq 3$	$d \geq 4$
Werner $d = 2$, $\Phi \geq$	$-1/2$	$-1/2$	$-1/3$

showed that for $\Phi \geq -1 + \frac{d+1}{d^2}$ these states do not violate any Bell inequality with an *arbitrary* number s_a, s_b of von Neumann measurements (in Ref. [19] the author constructs LHV models for arbitrary POVM settings for a more restricted range of Φ). We found that using symmetry techniques similar to those in Ref. [20] it is possible to *analytically* solve the dual optimization problem to the semidefinite program described above; see [21]. The value of the optimum establishes that *all* Werner states have symmetric extensions so long as $s_a + s_b \leq d$. Hence these states have LHV theories for all Bell experiments where the minimum number of settings $s = \min(s_a, s_b)$ satisfies $s + 1 \leq d$. This result is more general than Werner's in the sense that, as in Ref. [19], it holds for general POVM elements. It is weaker in the sense that the number of settings is bounded by the dimension of the space. Numerical and analytical results (see Table I and [21]) show that Werner states for $d = 2$ actually have symmetric (quasi-) extensions beyond this analytically derived bound.

Even though our method is the most powerful tool to date for constructing local hidden variable theories, we believe that it is unlikely that every LHV model can be constructed from a symmetric quasiextension. It has been proven that only separable states have ($s_a = 1, s_b \to \infty$) extensions; see Refs. [10,22]. This result can be extended to quasiextensions [23] even though LHV theories for entangled states with an arbitrary number of settings do exist [2,19]. Our work is only the starting point for a more thorough exploration of the existence of LHV models and (quasi-) extensions for entangled quantum states.

We thank Dave Bacon and Ben Toner for providing us with extremal Bell inequalities used in some of the numerical work. We are very grateful to Michael Wolf for his insightful comments on the original draft of this paper and for bringing Ref. [10] to our attention. B. M. T. and A. C. D. acknowledge support from the NSF under Grant No. EIA-0086038. A. C. D. acknowledges support from the Caltech MURI Center for Quantum Networks administered by the ARO under Grant DAAD19-00-1-0374 and B. M. T. from the NSA and the Advanced Research and Development Activity through ARO Contract No. DAAD19-01-C-0056. A. C. D. thanks Mark Kasevich and Steve Girvin for their hospitality at Yale University where part of this work was completed. D. S. thanks the IQI for support.

[1] J. Bell, Physics (Long Island City, N.Y.) **1**, 195 (1964).
[2] R. Werner, Phys. Rev. A **40**, 4277 (1989).
[3] A. Peres, Found. Phys. **29**, 589 (1999).
[4] M. Horodecki, P. Horodecki, and R. Horodecki, Phys. Rev. Lett. **80**, 5239 (1998).
[5] R. Werner and M. Wolf, Phys. Rev. A **61**, 062102 (2000); **64**, 032112 (2001); W. Dür, Phys. Rev. Lett. **87**, 230402 (2001); A. Acin, T. Durt, N. Gisin, and J. Latorre, Phys. Rev. A **65**, 052325 (2002); A. Acin, V. Scarani, and M. Wolf, quant-ph/0206084; D. Kaszilikowski, M. Zukowski, and P. Gnacinski, quant-ph/0107154.
[6] I. Pitowsky, Math. Progr. **50**, 395 (1991).
[7] C. Bennett *et al.*, Phys. Rev. Lett. **82**, 5385 (1999).
[8] R. F. Werner and M. M. Wolf, Quantum Inf. Comput. **1**, 1 (2001).
[9] A connection between Bell inequalities and extensions has been made previously by R. Werner [10].
[10] R. F. Werner, Lett. Math. Phys. **17**, 359 (1989).
[11] A. C. Doherty, P. A. Parrilo, and F. M. Spedalieri, Phys. Rev. Lett. **88**, 187904 (2002).
[12] M. M. Wolf (private communication).
[13] L. Vandenberghe and S. Boyd, SIAM Rev. **38**, 49 (1996).
[14] J. Sturm, SEDUMI VERSION 1.05,2001, http://fewcal.kub.nl/sturm/software/sedumi.html.
[15] P. Horodecki, M. Horodecki, and R. Horodecki, Phys. Rev. Lett. **82**, 1056 (1999).
[16] P. Horodecki and M. Lewenstein, Phys. Rev. Lett. **85**, 2657 (2000).
[17] D. Bruß and A. Peres, Phys. Rev. A **61**, 30 301(R) (2000).
[18] D. DiVincenzo *et al.*, quant-ph/9908070.
[19] J. Barrett, Phys. Rev. A **65**, 042302 (2002).
[20] T. Eggeling and R. F. Werner, Phys. Rev. A **63**, 042111 (2001).
[21] B. M. Terhal, A. C. Doherty, and D. Schwab, quant-ph/0210053.
[22] B. Schumacher and R. Werner (private communication); M. Fannes, J. Lewis, and A. Verbeure, Lett. Math. Phys. **15**, 255 (1988); G. Raggio and R. F. Werner, Helv. Phys. Acta **62**, 980 (1989).
[23] F. Spedalieri, A. C. Doherty, and P. Parrilo (to be published).

PHYSICS TODAY.org

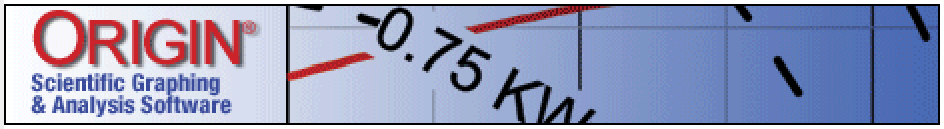
ORIGIN®
Scientific Graphing
& Analysis Software

Welcome!
John P Preskill

➡Access profile ➡Member logoff

Search

Table of contents
Past issues
Links to advertisers
Products advertised
Place an ad
Buyers' guide
About us
Contact us
Submit press release
American Institute of Physics
The Industrial Physicist
Computing in Science & Engineering
Journals
Virtual Journals

Article

Quantum Entanglement: A Modern Perspective

It's not your grandfather's quantum mechanics. Today, researchers treat entanglement as a physical resource: Quantum information can now be measured, mixed, distilled, concentrated, and diluted.

Barbara M. Terhal, Michael M. Wolf, and Andrew C. Doherty

> *"If two separated bodies, each by itself known maximally, enter a situation in which they influence each other, and separate again, then there occurs regularly that which I have [just] called entanglement of our knowledge of the two bodies."*
> --Erwin Schrödinger (translation by J. D. Trimmer)

Erwin Schrödinger coined the word *entanglement* in 1935 in a three-part paper[1] on the "present situation in quantum mechanics." His article was prompted by Albert Einstein, Boris Podolsky, and Nathan Rosen's now celebrated EPR paper that had raised fundamental questions about quantum mechanics earlier that year.

Einstein and his coauthors had recognized that quantum theory allows very particular correlations to exist between two physically distant parts of a quantum system; those correlations make it possible to predict the result of a measurement on one part of a system by looking at the distant part. On that basis, the EPR paper argued that the distant predicted quantity should have a definite value even *before* being measured if the theory were to claim completeness and respect locality. However, because quantum mechanics disallows such definite values prior to measuring, the EPR authors concluded that, from a classical perspective, quantum theory must be incomplete.

Schrödinger's 1935 perspective comes closer to the modern view: The wavefunction or state vector gives us

Also this month

Technical and Policy Issues of Counterterrorism--A Primer for Physicists

Quantum Entanglement: A Modern Perspective

Supernovae, Dark Energy, and the Accelerating Universe

Request product info

COMPANY SPOTLIGHT

Get your Troubleshooting CD
Click Here
KEITHLEY

The Video Encyclopedia of Physics Demonstrations – Online
Sign up for a FREE preview account to view all of the written material and a selection of videos.
Please visit us at www.physicsdemos.com

all the information that we can have about a quantum system. About entangled quantum states, he wrote, "The whole is in a definite state, the parts taken individually are not,"[1] which we now understand as the essence of pure-state entanglement. In that same 1935 article, Schrödinger also introduced his famous cat as an extreme illustration of entanglement: A cat physically isolated in a box with a decaying atom and vial of cyanide represents a quantum state having macroscopic degrees of freedom. If the atom were to decay and trigger the release of cyanide, the cat would die. The quantum-mechanical description of the system is a coherent superposition of one state in which the atom is still excited and the cat alive, and another state in which the atom has decayed and the cat is dead:

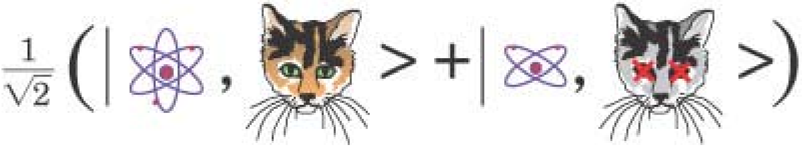

The isolated cat-trigger-atom-cyanide system as a whole is in a definite entangled state, even though the cat itself exists as a probabilistic mixture of being alive or dead.

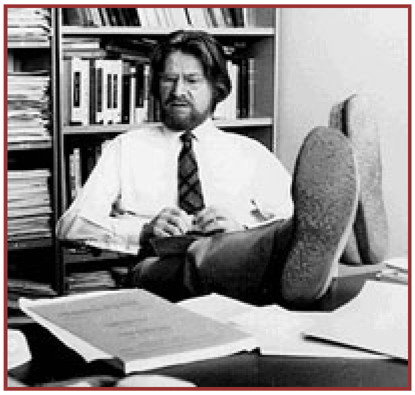

Figure 1

For the three decades following the 1935 articles, the debate about entanglement and the "EPR dilemma"--how to make sense of the presumably nonlocal effect one particle's measurement has on another--was philosophical in nature, and for many physicists it was nothing more than that. The 1964 publication[2] by John Bell (pictured in figure 1) changed that situation dramatically. Bell derived correlation inequalities that can be violated in quantum mechanics but have to be satisfied within every model that is local and complete--so-called local hidden-variable models. Bell's work made it possible to test whether local hidden-variable models can account for observed physical phenomena. Early and ongoing recent experiments[3] showing violations of such Bell inequalities have invalidated local hidden-variable models and lend support to the quantum-mechanical view of nature. In particular, an observed violation of a

Bell inequality demonstrates the presence of entanglement in a quantum system.

In 1995, Peter Shor at AT&T Research discovered that, for certain problems, computation with quantum states instead of classical bits can result in tremendous savings in computation time.[4] He found a polynomial-time quantum algorithm that solves the problem of finding prime factors of a large integer. To date, no classical polynomial-time algorithm for this problem exists.

Shor's breakthrough generated an avalanche of interest in quantum computation and quantum information theory. In this context, a modern theory of entanglement has begun to emerge: Researchers now treat entanglement not simply as a paradoxical feature of quantum mechanics, but as a physical resource for quantum-information processing and computation. A whole zoo of various kinds of pure and mixed entangled states may be prepared--well beyond the simple pure-state superpositions that Schrödinger envisioned. And those mixed entangled states may be measured, distilled, concentrated, diluted, and manipulated. A surprisingly rich picture of entanglement is now taking shape.

Entanglement for the 21st century

The discovery of quantum teleportation by IBM researcher Charles Bennett and five collaborators in 1993 marks the starting point of the modern view. In quantum teleportation (see the article by Charles Bennett in Physics Today, October 1995, page 24), an experimentalist, Alice, wishes to send an unknown state $|s\rangle = \alpha|0\rangle + \beta|1\rangle$ of a two-level quantum system to another experimentalist, Bob, in a distant laboratory. The two-level system could refer, for example, to the polarization of a single photon, the electronic excitation of an effective two-level atom, or the nuclear magnetic spin of a hydrogen atom. Alice and Bob do not have the means of directly transmitting the quantum system from one place to another (for photons, this could be the case when using a high-loss optical fiber), but let us imagine that they do share an entangled state. Consider the case in which Alice and Bob each have one spin of a shared singlet state of two spin-½ particles$|\Psi^-\rangle = 1/(2)^{0.5}(|,\downarrow\rangle - !\downarrow,\rangle)$, also called an EPR pair. Alice can transmit her spin $|s\rangle$ to Bob by performing a certain joint measurement on her spin state $|s\rangle$ and her half of the EPR pair. She tells

Bob the result of her measurement and, depending on her information, Bob rotates his half of the EPR pair to obtain the state $|s\rangle$. The teleportation protocol demonstrates that the resources of classical communication and the sharing of prior EPR entanglement are sufficient to transmit an unknown spin state $|s\rangle$. (For the experimental realization, see Physics Today, February 1998, page 18.)

The spin-singlet EPR state that Alice and Bob share in quantum teleportation is called a maximally entangled state. Even though the two spins together constitute a definite pure state, each spin state is maximally undetermined or mixed when considered separately. In mathematical terms, Alice's local density matrix--obtained by tracing over Bob's spin degrees of freedom, $\mathrm{Tr}_B(|\Psi^-\rangle\langle\Psi^-|)$--has equal probability for spin up and spin down. In keeping with Schrödinger's understanding of entanglement, one measures the amount of entanglement in a general pure state ϖ in terms of the lack of information about its local parts. The von Neumann entropy $S(\rho) = -\mathrm{Tr}(\rho \log \rho)$ is used as a measure of that information. In other words, the entropy of entanglement E of the pure state ϕ is equal to the von Neumann entropy of, say, Alice's density matrix $\rho = \mathrm{Tr}_B|\phi\rangle\langle\phi|$.

Mixed entanglement

In the quantum teleportation scenario, we imagined, unrealistically, that Alice and Bob shared an EPR pair free of noise or decoherence. More generally, Alice and Bob have quantum systems that interact directly or through another mediating quantum system--like Rydberg atoms in a laser cavity that interact via photons, or two ions in an ion trap that interact through phonon modes of the trap.[5] A related example of interest in quantum computation is an array of interconnected ion traps, each holding a small number of ions that are coupled by traveling photons or by ions that are moved between the traps.[6] The interaction, or "quantum link," between a pair of systems is subject to noise or decoherence through photon loss or heating of the phonons, for instance. For simplicity, assume that Alice and Bob's local operations on the quantum systems--operations on the ions in a single trap, say--are perfect, and their exchange of classical information is also perfectly noise free. That idealization enables one to measure the strength of the quantum link between the systems.

An essential question is, Given unavoidable noise levels, is it possible to establish a strong quantum link--a set of pure EPR pairs, in other words--between two systems? If it is, then the noise is weak enough to permit the error-free exchange of quantum information between the systems, since the teleportation through the generated EPR pairs will be error free. That capability may come at a certain cost, determined by the amount of noisy interaction required to generate an EPR pair. If it is not possible to generate EPR pairs, that decoherence in the system imposes a fundamental limitation on our ability to perform quantum information processing.

The possibility of generating shared EPR entanglement in noisy environments is not only of interest in entanglement theory, but is crucial for the realization of long-distance quantum communication[7] and possibly large-scale quantum computation. For example, it was recently shown[8] that fault-tolerant quantum computation can be achieved in the presence of very high noise levels in the interaction link--a link can have an error rate of two-thirds--between quantum systems that are "small" in a particular sense, if one assumes that local quantum processing on each end is (almost) error free.

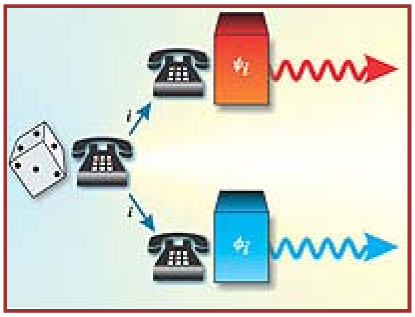

Figure 2

Pure quantum states have their entanglement quantified fairly intuitively by considering the degree of local "mixedness" or entropy. However, mixtures of entangled and unentangled states are murkier: Recognizing which mixtures are still entangled may be difficult. So, just what physical systems can we call "entangled"? An operational description--expressing entanglement in terms of its negation--is helpful. Suppose that Alice and Bob, working in their distant labs, each receive the same random number over the phone. Depending on the random number, each of them locally prepares a certain quantum state. The physical state of their whole system, expressed as a density matrix, typically exhibits correlations between the two systems. However, those correlations would be classical, since they arise from classical random numbers. A quantum state that can be prepared in this way *over the phone* is called "unentangled" or separable, and such a state can be mathematically expressed as a mixture of unentangled pure states (see figure 2). Conversely, a state is "entangled" if it cannot be prepared over the phone, but requires coherent interaction between the two systems or the transmission of superpositions of quantum states.

Measures of noisy entanglement

For mixed states, it is harder to establish a good measure of entanglement, since such a measure has to distinguish between entropy arising from classical correlations in the state--a state of thermal equilibrium, for example--and local entropy due to purely quantum correlations. Two measures of entanglement that have explicit physical meaning in the processing of quantum information have emerged from the quantum-link notion just described: the entanglement cost $E(\rho)$ of a quantum state and the distillable entanglement $D(\rho)$ of a quantum state, first defined in reference 9.

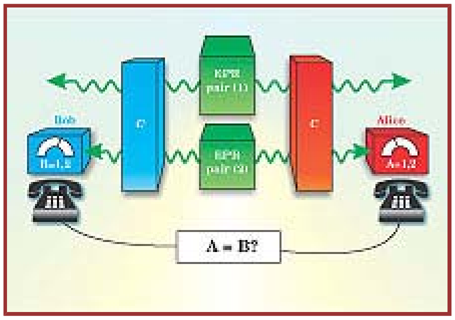

Figure 3

Assume that Alice and Bob have created, using their noisy link, many (n) shared copies of an entangled quantum state ρ; we denote such a collection as $\rho^{\otimes n}$. To distill some EPR pairs from those copies, Alice and Bob perform several rounds of local, error-free operations to their parts of the copies and communicate their measurements (or other classical data) to each other. Such a protocol is called entanglement distillation; figure 3 illustrates one round of such a scheme. The aim is to produce fewer states that are, however, more entangled than the initial ones. Ideally, the protocol produces nearly perfect maximally entangled EPR pairs in the limit of a large number of input states $\rho^{\otimes n}$ with $n \to \infty$. The distillable entanglement $D(\rho)$ is then the number of such EPR pairs that can be extracted per copy of ρ in this asymptotic limit.

The reverse process also has physical meaning. What is the smallest number k of EPR pairs that Alice and Bob initially need to create a set of n copies of ρ for $n \to \infty$ by local error-free operations? This asymptotic ratio k/n is the second measure of entanglement, the entanglement cost $E(\rho)$.

Reversible and irreversible manipulation

Attentive readers may have noticed a quirk in our notation: The formalism uses the same symbol E to denote both the entanglement cost for general states and the entropy of entanglement for pure states. The notation coincidence is harmless since the creation cost of a pure state equals the local entropy of entanglement E. Furthermore, for a pure state ϕ, it turns out that $E(\phi) = D(\phi)$ (see box 1 on page 50). Physically, this means that the process of entanglement dilution—converting EPR pairs into lesser entangled pure states ϕ—can be reversed without loss of entanglement. The reverse process is called entanglement concentration and it produces $D(\phi)n = E(\phi)n$ EPR pairs from an initial supply of n states ϕ.

For mixed states, D is believed to be generically less than E, which implies that the preparation of mixed states from EPR pairs is a process involving an irreversible loss of entanglement. Curiously, the $D < E$ conjecture has only been proven for some special classes of mixed states.[10]

In 1998, the Horodecki family of Gdansk, Poland (father Ryszard and sons Paweł and Michał), identified a class of entangled states that exhibit an extreme form of irreversibility. They proved that no entanglement can be distilled ($D = 0$) from these "bound entangled states."[11] And for a large set of states from that class, irreversibility was established by proving that entanglement is required to prepare the states $E > 0$.

Consider the metaphor illustrated in figure 4. If EPR pairs were nodes connected by lines or strands that represent quantum correlations

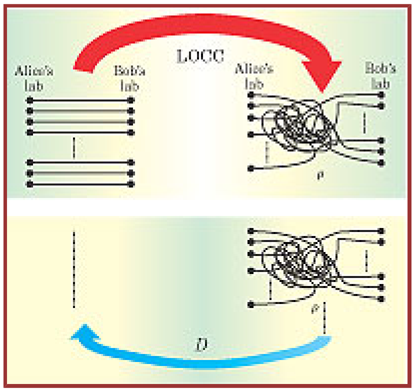

Figure 4

between particles, then one could think of mixed entanglement as entanglement in which the strands are simply mixed up. The mixing may make it hard to reconstruct which particle of Alice is entangled with which particle of Bob. Cutting a few strands reduces the clutter, but every line cut represents an EPR pair lost (compare this process with the distillation protocol in figure 3). Bound entangled states are those mixtures that are so thoroughly mixed up that every single line has to be cut to remove the noise or clutter from the system. But, when every line is cut, no entanglement remains to be distilled.

"Black holes" of quantum information

Because the modern theory of entanglement treats quantum states as physical resources for processing information, one might consider them hierarchically. A simple and ideal world would have only two classes of quantum states: unentangled, classically correlated states that are useless as a resource in quantum teleportation and don't violate any Bell inequalities, and entangled states whose distillation rate D measures their usefulness in quantum teleportation. If the distillation rate D is nonzero, one can distill from such states some EPR pairs, known to violate Bell inequalities.

Bound entanglement tells us that life is not so simple. Bound entangled states are costly ($E > 0$), but useless in various quantum-information-processing protocols like teleportation. Furthermore, there is evidence that bound entangled states do not violate any Bell inequalities.

In those two senses, bound entangled states are the "black holes" of quantum information theory. Entanglement goes in but is impossible to recover. And like black holes in the theory of gravitation, bound entangled states test the limits of our understanding and puzzle us by their intrinsic irreversibility.

Bound entanglement and partial transposition

In what sense are bound states so thoroughly mixed up that no entanglement at all can be extracted? Bound entangled states behave intrinsically differently from every other entangled state: They remain physical under the *unphysical* operation of partial transposition.

Researchers realized that they could characterize entanglement in terms of how states behave under certain unphysical operations.[12] In 1996, Asher Peres at the Technion-Israel Institute of Technology in Haifa, Israel, noted that matrix transposition is just such an unphysical operation when applied to entangled states. Taking the transpose of a system's density matrix produces another density matrix--a physically valid result. And taking the transpose of, say, Bob's part of an unentangled state $\psi_A \otimes \psi_B$ yields another physically valid quantum state, since each part of the quantum state can transform separately; ψ_A is not changed, and the density matrix of ψ_B is transposed. But when applied to part of a pure entangled state, matrix transposition produces an unphysical result. (For details, see box 2 on page 51.)

Peres conjectured that partial transposition was the defining criterion for entanglement. In other words, all entangled states--pure or mixed--should map onto unphysical states by partial matrix transposition, and all unentangled states will remain physical under the same operation.

Remarkably, the truth of that conjecture depends on the dimension of the underlying Hilbert spaces or phase spaces. If one considers the state of two spin-½ particles, the polarization degrees of freedom of two laser beams, or two modes of a light field having a Gaussian Wigner function, then, indeed, all entangled states map onto unphysical states by partial transposition. However, for two spin-one (or higher-dimensional system) particles or a Gaussian light field with at least two modes for both Alice and Bob, that is no longer true in general; there exist entangled mixed states that pass the "partial transpose" test and have therefore lost an essential property of entanglement.

The loss of that property is precisely what the Horodecki family showed would lead to a zero distillation rate *D*. Entangled states that pass the partial transpose test are the bound entangled states in which the entanglement is forever locked or "bound" inside.

Entanglement witnesses

Given that entanglement can be such a subtle property of quantum states, just how can one distinguish between entangled and unentangled states? A violation of a Bell inequality has been the traditional telltale sign of entanglement in a quantum system. Examples of such experiments[3] used pairs of entangled photons created from nonlinear optical processes, especially parametric down-conversion; the polarization degrees of freedom of the emitted photons carried entanglement. Alice and Bob checked for a Bell inequality violation by using local analyzers to measure the polarization of the photons along various angles.

Unfortunately, many quantum states, including the set of bound entangled states, are not known to violate any Bell inequality. And considering the existing limitations on experimental control of quantum systems, experimentalists prefer to check for entanglement using the fewest possible local measurements. The theoretical framework of an entanglement witness, of which a Bell inequality is a particular example,[13] addresses those two issues. The defining property of an entanglement witness W is that its expectation value with respect to any unentangled state ρ is always nonnegative, $\mathrm{Tr}(W\rho) \geq 0$. At the same time, there exist entangled states σ for which $\mathrm{Tr}(W\sigma) < 0$. Measuring W on a quantum state σ and finding a negative expectation value thus establishes the entanglement of σ. The good news is that there is an entanglement witness for every entangled state; given an experimental means, any entanglement, bound or otherwise, can be detected. The bad news is that entanglement witnesses are nonlocal observables. Nevertheless, one can measure the expectation value of W by measuring the expectation value of a number of local observables W_i, such that $W = \Sigma_i W_i$. Research is under way to determine the minimal number of local measurements for a given witness.[14]

Bell's communication advantages

Given the framework of entanglement witnesses, what is special about Bell inequalities? Although they can be considered a type of entanglement witness, Bell inequalities do not, strictly speaking, test for entanglement but for a departure from local hidden variable theories. Interpreted as such, Bell inequalities have taken on a whole new life in quantum-communication science. Researchers consider remote parties who have to carry out a certain task with minimal communication between them. One compares the amount of communication necessary if those parties are given shared random bits (that can be viewed as local hidden variables) or an entangled quantum state. Sharing entangled states leads to savings in communication precisely because the correlations in quantum states cannot always be adequately described by local hidden variable theories[15] (see the article by Andrew M. Steane and Wim van Dam, in Physics Today, February 2000, page 35).

What lies beyond

The efforts of the quantum information theorists over the past eight years would come to little if the theory were not supplemented by an ability to create and manipulate entanglement in the lab. There is a rapidly growing list of physical systems--optical and atomic systems especially--in which it is possible to prepare various kinds of entangled states. As discussed previously, the use of photonic degrees of freedom, such as polarization or momentum, has been a long-time favorite way to create entanglement.[3] Entangled states consisting of the quadrature observables of different modes of light have been prepared in optical parametric oscillators and optical fibers.[16] Entanglement in the states of motion of the valence electrons[5] of trapped ions or of Rydberg atoms in cavity quantum electrodynamics has involved up to four different atoms. Another promising avenue is the recently observed entanglement of large ensembles of atoms.[17]

This short review showcases just a few striking facets of the modern theory of entanglement. Most notably, entanglement shared between more than two subsystems is outside our scope here. The broader study of entanglement between many subsystems may lead the field to better understand the role of large-scale entanglement in quantum computation or quantum many-body systems.

We have focused on the role of entanglement in the transmission of quantum information. Entanglement also proves useful, however, when the goal is to transmit classical information as efficiently as possible.

Researchers are studying many measures of mixed entanglement beyond the two most prominent measures discussed in this review. As for bound entanglement, there is some evidence that it may have a role to play as "helper" entanglement, useless by itself, but useful when combined with other sources of entanglement. For entanglement-theory overview articles that highlight the field, see volume 1 of *Quantum Information and Computation* (July 2001).

Barbara Terhal *(terhal@watson.ibm.com) is a research staff member in the physical sciences department at the IBM Corp's T. J. Watson Research Center in Yorktown Heights, New York.* ***Michael Wolf*** *(mmwolf@tu-bs.de) is a physics PhD-student at the Technical University at Brunswick in Brunswick, Germany.* ***Andrew Doherty*** *(dohertya@its.caltech.edu) is a postdoctoral scholar in the quantum optics group at the California Institute of Technology.*

References

1. E. Schrödinger, *Die Naturwissenschaften*, **48,** 807 (1935); **49**, 823, 844 (1935). English trans. in *Proc. Am. Philos. Soc.* **124**, 323 (1980).
2. J. S. Bell, *Physics* **1**, 195 (1964).
3. A. Aspect, J. Dalibard, G. Roger, *Phys. Rev. Lett.* **49**, 1804 (1982); W. Tittel, G. Weihs, *Quantum Inf. Comput.* **1**, 3 (2001).
4. P. W. Shor, *SIAM J. Comput.* **26**, 1484 (1997). Available online at http://arxiv.org/abs/quant-ph/9508027. An earlier version is P. W. Shor, *Proc. 35th Annual Symposium on Foundations of Computer Science* (FOCS), IEEE Computer Society Press (1994) p. 124.
5. C. Sackett, *Quantum Inf. Comput.* **1**, 57 (2001); J. M. Raimond, M. Brune, S. Haroche, *Rev. Mod. Phys.* **73**, 565 (2001).
6. D. J. Wineland et al., *Proc. R. Soc. London* (in press). See draft online at http://arxiv.org/abs/quant-ph/0212079.
7. H.-J. Briegel, W. Dür, J. I. Cirac, P. Zoller, *Phys. Rev. Lett.* **81**, 5932 (1998); W. Dür, H.-J. Briegel, J. I. Cirac, P. Zoller, *Phys. Rev. A* **59**, 169 (1999).
8. W. Dür, H.-J. Briegel, http://arxiv.org/abs/quant-ph/0210069.

9. C. H. Bennett, D. P. DiVincenzo, J. A. Smolin, W. K. Wootters, *Phys. Rev. A* **54**, 3824 (1996). Available online at http://arxiv.org/abs/quant-ph/9604024.
10. G. Vidal, W. Dür, J. I. Cirac, *Phys. Rev. Lett.* **89**, 027901 (2002). Available online at http://arxiv.org/abs/quant-ph/0112131. K. G. H. Vollbrecht, R. F. Werner, M. M. Wolf, http://arxiv.org/abs/quant-ph/0301072.
11. M. Horodecki, P. Horodecki, R. Horodecki, *Phys. Rev. Lett.* **80**, 5239 (1998). Available online at http://arxiv.org/abs/quant-ph/9801069.
12. M. Horodecki, P. Horodecki, R. Horodecki, *Phys. Lett. A* **223**, 1 (1996).
13. B. M. Terhal, *Theor. Comput. Sci.* **287**, 313 (2002). Available online at http://arxiv.org/abs/quant-ph/0101032.
14. O. Guehne et al., http://arxiv.org/abs/quant-ph/0210134.
15. C. Brukner, M. Zukowski, J.-W. Pan, A. Zeilinger, http://arxiv.org/abs/quant-ph/0210114.
16. Z. Y. Ou, S. F. Pereira, H. J. Kimble, K. C. Peng, *Phys. Rev. Lett.* **68**, 3663 (1992); A. Furosawa, J. L. Sørensen, S. L. Braunstein, C. A. Fuchs, H. J. Kimble, E. S. Polzik, *Science* **282**,706 (1998); Ch. Silberhorn, P. K. Lam, O. Wiess, F. König, N. Korolkova, G. Leuchs, *Phys. Rev. Lett.* **86**, 4267 (2001).
17. B. Julsgaard, A. Zozhekin, E. S. Polzik, *Nature* **413**, 400 (2001).
18. C. H. Bennett, H. J. Bernstein, S. Popescu, B. Schumacher, *Phys. Rev. A* **53**, 2046 (1996).

Physics Today References

October 1995, page 24
February 1998, page 18
February 2000, page 35

© 2003 American Institute of Physics

APPLIED PHYSICS LETTERS VOLUME 83, NUMBER 2 14 JULY 2003

Atom mirror etched from a hard drive

Benjamin Lev,[a)] Yves Lassailly,[b)] Chungsok Lee, Axel Scherer, and Hideo Mabuchi
California Institute of Technology, Pasadena, California 91125

(Received 1 April 2003; accepted 16 May 2003)

We describe the fabrication of an atom mirror by etching of a common hard drive, and we report the observation of specular retroreflection of 11 μK cesium atoms using this mirror. The atoms were trapped and cooled above the hard drive using the mirror magneto-optical trap technique, and upon release, two full bounces were detected. The hard drive atom mirror will be a useful tool for both atom optics and quantum computation. © *2003 American Institute of Physics.*
[DOI: 10.1063/1.1592305]

Laser cooling and trapping techniques have made possible the preparation of extremely cold samples of atoms. Atom optics employs elements such as mirrors, lenses, gratings, and beam splitters to manipulate these cold atoms in a fashion similar to the familiar photon optics. The advent of the Bose–Einstein condensation of neutral atoms has enhanced the importance of developing atom optical elements. In particular, atom mirrors—surfaces that reflect atoms—play a crucial role in the field of atom optics, and it is of keen interest to develop mirrors that are simple to fabricate yet highly specular. In this letter we demonstrate a straightforward technique to produce large area, high resolution permanent-magnetic structures on flat, rigid, and inexpensive substrates.

Several types of atom mirrors have been fabricated using evanescent light fields,[1] dynamic magnetic fields,[2] and static magnetic fields.[3] Evanescent mirrors repulse atoms from a prism surface using a potential created by a blue-detuned light field. Although magnetic mirrors cannot generally be modulated as easily as evanescent mirrors, they do offer many advantages: passive operation, compactness (no laser access is needed), and much larger repulsive areas.

Magnetic mirrors employ a sheet of alternating current or magnetization to create an exponentially increasing potential near the mirror surface.[4] To lowest order, this potential is proportional to $B_0 e^{-ky}$. The surface field, B_0, sets the maximum atom energy that can be reflected, and the spatial period of the current or magnetization, $a=2\pi/k$, determines the amount of time the atoms interact with the mirror. The magnetic mirror approximates a perfectly flat mirror as B_0 increases and a decreases. For example, if $B_0=1$ kG and $a=1$ μm, a cesium atom in the $6^2S_{1/2}$ $F=4$, $m_F=4$ state will be reflected when dropped from a height of 0.4 m, and will only interact with the mirror for 5 μs if dropped from 2 cm.

Mirrors made from serpentine patterns of wires can produce time-dependent reflection potentials. However, they have not been fabricated with periods smaller than 10 μm, and the power dissipated by the small wires requires cooling by liquid nitrogen and pulsed operation.[5] Sinusoidal magnetization of audio-tape, floppy disks, and videotape can produce magnetic mirrors with magnetization periods down to 12 μm.[3] Mirrors made from millimeter-sized arrays of permanent magnets have been demonstrated, as have mirrors produced by 1–4 μm periodic structures fabricated by sputtering ferromagnetic material onto a grooved substrate patterned by electron-beam lithography.[6]

We recently fabricated a magnetic mirror by etching a common hard drive, and we have used this mirror to retroreflect a cold cloud of 10^6 cesium atoms. Hard drives offer several advantages for making and using atom mirrors. The common hard drive provides a large surface area of thin magnetic film whose surface is specifically designed to be very flat, smooth, and rigid. Furthermore, the film's remnant magnetic field and coercivity can be as large as 7 and 3 kG, respectively.[7] An atom mirror could in principle be fabricated with a 2 μm periodicity over the entire surface of the hard drive. Old or discarded hard drives may be used: an Apple hard drive from the mid-1990's was used for the experiment presented here.

We fabricate the mirror by etching 2 μm wide, $\sim$100 nm deep trenches into a 1 cm^2 section of the surface of the hard drive. These 100 nm trenches extend past the magnetic layer to form a periodic array of 1 μm wide, 30 nm thick, and 1 cm long stripes of cobalt alloy (see Fig. 1). The cobalt alloy is granular, which enhances the coercivity and allows us to magnetize the material in plane and parallel to the short axis of the magnetic strips. The typical grain size is 20–50 nm,[7] and we expect the magnetization to be uniform for our much larger features. We do not know the exact materials and thicknesses of the layers of the proprietary hard drive. However, etching $\sim$100 nm is sufficient to remove the magnetic layer.

Standard photolithography is used to create the etch

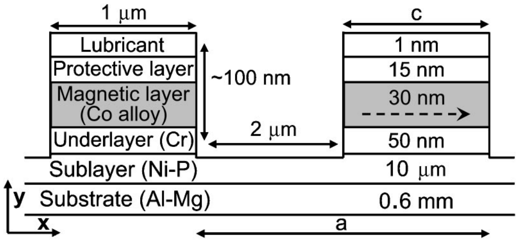

FIG. 1. A cross section of the etched hard drive. The magnetization is in-plane. See Ref. 7 for a description of the hard drive layers.

[a)] Electronic mail: benlev@caltech.edu

[b)] Present address: Laboratoire PHMC/Ecole Polytechnique, 91128 Palaiseau cedex, France.

0003-6951/2003/83(2)/395/3/$20.00

© 2003 American Institute of Physics
Downloaded 08 Jul 2003 to 131.215.107.152. Redistribution subject to AIP license or copyright, see http://ojps.aip.org/aplo/aplcr.jsp

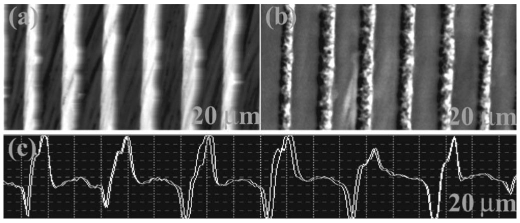

FIG. 2. 20 μm wide (a) AFM scan, (b) MFM scan, and (c) MFM cross-section of the etched hard drive surface.

mask. After cutting the hard drive into $2-3\,\mathrm{cm}^2$ sections, positive photoresist (TSMR-8900, Tokyo Ohka Kogyo Co.) is spun onto the cleaned hard drive surface for 40 s at 4200 rpm. A 15 s exposure followed by 65 s in the developer (NMD-W 2.38%) maps the photomask lines into the resist. The sample is ion milled with argon in a inductively coupled plasma (ICP) system. We etch for 8 minutes at a forward power of 100 W, ICP power of 400 W, and an argon flow of 40 sccm. The remaining photoresist is removed with acetone and, if necessary, a soft swab. To erase the hard drive's bits and magnetize it as a mirror, we insert the hard drive section into the field of an 8 kG electromagnet whose field is parallel to the surface and perpendicular to the magnetic stripes.

The magnetic field from the etched hard drive, with in-plane magnetization, M_0, parallel to the short axis of the magnetic stipes, is analogous to a periodic sheet of alternating in-plane magnetization $+M_0/2$ and $-M_0/2$. In the infinite array limit, the magnetic field above the surface is

$$B^2=B_1^2e^{-2ky}+2B_1B_3\cos(2kx)e^{-4ky}+B_3^2e^{-9ky}+\dots, \tag{1}$$

where $B_1=\mu_0M_0(1-e^{-kb})/\pi$, $B_3=\mu_0M_0(1-e^{-3kb})/3\pi$, and $b=30\,\mathrm{nm}$ is the thickness of the magnetic layer. The field has no components in the z direction, and rotates with a period equal to a in the $x-y$ plane. Cesium atoms in the $F=4$, $m_F=4$ state, which has the largest weak-field seeking magnetic moment, would have to be dropped from a height of 25 cm to penetrate to a height at which the second term in the expansion is equal the first, so to a good approximation the field may be written as

$$B\approx B_1e^{-ky}+B_3e^{-3ky}\cos(2kx). \tag{2}$$

For our hard drive mirror, B_1 is equal to 2–4 kG depending on the specific cobalt alloy. When $a=1\ \mu$m, the ratio of the first harmonic term to the purely exponential term for a cesium atom dropped from a height of 2 mm (20 mm) is 1×10^{-6} (1×10^{-3}) at the turning point $y=0.8\ \mu$m ($y=0.4\ \mu$m).

The etched hard drive used for the experiment has $a\approx3\ \mu$m and $c\approx1\ \mu$m resulting in a ratio of magnetic layer to gap that is approximately 1:2. Figures 2(a) and 2(b) show 20 μm wide atomic force microscopy (AFM) and MFM scans of the hard drive surface. The trenches in the AFM scan are dark, and the light to dark variation of magnetic strips shows the north and south poles of the magnetization. Figure 2(c) shows a 20 μm cross section of the MFM scan: peaks represent the north and south poles. To describe the field above our etched hard drive, Eq. (2) can be modified to account for the deviation from a 1:1 width ratio by multiplying B_1 by $\sin(\pi c/a)$ and B_3 by $\sin(3\pi c/a)$. In our device, the ratio of $c/a\approx1/3$ decreases the B_1 term by 0.9, but causes the corrugation term to nearly vanish.

The atom mirror is placed facing upwards in a vacuum chamber pumped to 5×10^{-9} Torr. In contrast to the experiments that use a standard magneto-optical trap (MOT) to trap and cool the atoms ~2 cm above the mirror, we use the mirror MOT technique to collect the atoms 1.5–4 mm above the surface.[8] A MOT requires the zero of a magnetic quadrupole field to be centered at the intersection of six circularly polarized laser beams coming from all cardinal directions. To satisfy this configuration near the hard drive surface, two 1 cm diameter beams of opposite circular polarization reflect at 45° from the $1\,\mathrm{cm}^2$ etched region. A retroreflected beam is positioned perpendicular to the 45° beams and grazes the surface of the hard drive. Aligning the axis of the quadrupole field with one of the 45° beams completes the mirror MOT configuration. The trapping lasers, each with an intensity of $4\,\mathrm{mW/cm}^2$ and 1 cm wide, are detuned by 10 MHz from cesium's $F=4$, $F'=5$ cycling transition. A repumping beam tuned to the $F=3$, $F'=4$ transition is superimposed onto both the grazing beam and a 45° beam. The atoms are loaded from a thermal vapor.

In previous experiments using a perfectly reflecting gold mirror, we have been able to trap 2×10^6 cesium atoms in a mirror MOT and cool them to 3 μK. One might expect trapping and cooling to be much less effective with the etched hard drive due to its poor qualities as an optical mirror: the reflectivity is only $\sim50\%$, it is a good optical grating, and the magneto-optical Kerr effect degrades the circularity of the reflected 45° beams. Nevertheless, we have been able to collect 1×10^6 atoms and subdoppler cool them to 11 μK. Achieving this low temperature is crucial because the atoms released directly from the mirror MOT, at a temperature of $\sim120\ \mu$K, expand too quickly and become too diffuse to detect by the time they reach the hard drive surface.

The poor optical reflectivity of the mirror does slightly complicate the subdoppler cooling procedure; however, with careful zeroing of the magnetic field it is still possible to achieve polarization-gradient cooling to 11 μK in a (downwards) moving reference frame. The atoms are optically pumped into the $F=4$, $m_F=4$ Zeeman substate just before being dropped, and we apply a 100 mG bias field parallel to the magnetic stripes in order to maintain alignment of the atomic spins while they are falling/bouncing.

We have been able to detect two full bounces of the atoms from the hard drive atom mirror. Figures 3(a) and 3(b) show data from five runs of the experiment. The top panel shows the mean position of the atoms above the hard drive surface as a function of time. Superimposed is a curve depicting the expected trajectory of a particle falling under gravity and bouncing from a hard wall. The slope of a line fit to the lateral expansion of the falling atom cloud provides a measure of the atoms' rms velocity. A nonspecular mirror would heat and diffusely scatter the reflected atoms as they bounce, resulting in a sharp increase of the cloud expansion rate. We made a linear fit to prereflection ($t<15$ ms) data in each of the data sets, and deviation from this line, postreflection, would be evidence of nonspecularly. The dashed segment demarcates the region of unfitted data, and we do not

Downloaded 08 Jul 2003 to 131.215.107.152. Redistribution subject to AIP license or copyright, see http://ojps.aip.org/aplo/aplcr.jsp

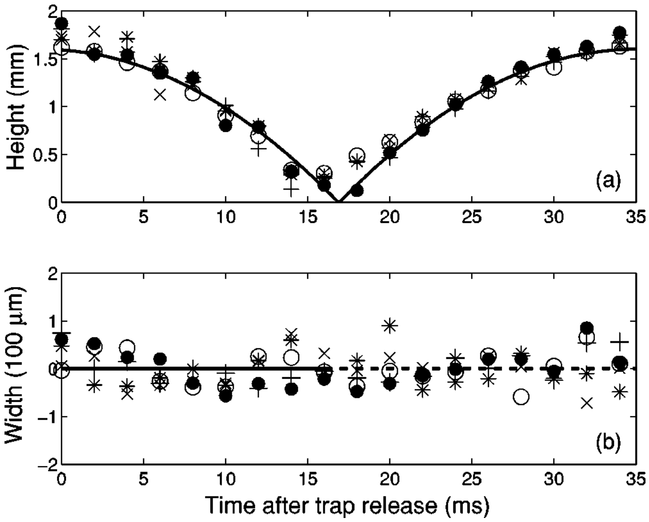

FIG. 3. Panel (a) shows the mean height of the atoms above the hard drive surface during the first bounce. Panel (b) shows the residuals from a linear fit to the width of the expanding atom cloud.

see any increase or offset of the residuals in this postreflection region: to within the experimental resolution, we do not detect any deviation from specular reflection.

We have realized a specular atom mirror built by etching a common hard drive. Magnetization periodicity of 3 μm has been achieved, and we believe it would be straightforward to reduce this to 2 μm with photolithography and to ~ 1 μm using a large area electron-beam writer. The hard drive atom mirror is compact, passive, relatively simple to fabricate, and possesses a large remanent magnetic field. Moreover, it has several desirable properties for applications beyond simple reflection of atoms. The hard drive's large coercivity should allow one to use wires fabricated directly on its surface to augment the mirror's ability to manipulate atoms. Likewise, electric pads could be printed on the surface. These pads would allow state-independent forces to act in concert with the state-dependent forces from the mirror's magnetic field to perform quantum logic gates necessary for quantum computation.[9] The mirror can trap cold atom gases in two dimensions, and can act as an adjustable grating when used in conjunction with a magnetic bias field.[10,11] Large area mirrors can be fabricated, and it seems possible that these mirrors could be useful for guiding or confining cold neutrons.[12] As hard drive platters are expected to have good surface flatness and substrate rigidity, it may be possible to create two-dimensional waveguides and other devices by holding an opposing pair of atom mirrors a few microns apart.

The authors thank the Roukes group and Marko Loncar. This work was supported by the Multidisciplinary University Research Initiative program under Grant No. DAAD19-00-1-0374.

[1] V. Savalli, D. Stevens, J. Estève, P. Featonby, V. Josse, N. Westbrook, C. Westbrook, and A. Aspect, Phys. Rev. Lett. **88**, 250404 (2002).
[2] A. Arnold, C. MacCormick, and M. Boshier, Phys. Rev. A **65**, 031601 (2002).
[3] E. Hinds and I. Hughes, J. Phys. D **32**, R119 (1999).
[4] G. Opat, S. Wark, and A. Cimmino, Appl. Phys. B: Photophys. Laser Chem. **54**, 396 (1992).
[5] K. Johnson, M. Drndic, J. Thywissen, G. Zabow, R. Westervelt, and M. Prentiss, Phys. Rev. Lett. **81**, 1137 (1998).
[6] A. Sidorov, R. McLean, F. Scharnberg, D. Gough, T. Davis, B. Sexton, G. Opat, and P. Hannaford, Acta Phys. Pol. B **33**, 2137 (2002).
[7] R. L. Comstock, *Introduction to Magnetism and Magnetic Recording* (Wiley, New York, 1999).
[8] J. Reichel, W. Hansel, and T. Hansch, Phys. Rev. Lett. **83**, 3398 (1999).
[9] J. Schmiedmayer, R. Folman, and T. Calarco, J. Mod. Opt. **49**, 1375 (2002).
[10] E. Hinds, M. Boshier, and I. Hughes, Phys. Rev. Lett. **80**, 645 (1998).
[11] P. Rosenbusch, B. Hall, I. Hughes, C. Saba, and E. Hinds, Phys. Rev. A **61**, 031404(R) (2000).
[12] V. Vladimirskiî, Sov. Phys. JETP **12**, 740 (1961).

Downloaded 08 Jul 2003 to 131.215.107.152. Redistribution subject to AIP license or copyright, see http://ojps.aip.org/aplo/aplcr.jsp

VOLUME 91, NUMBER 25 PHYSICAL REVIEW LETTERS week ending 19 DECEMBER 2003

Quantum Kalman Filtering and the Heisenberg Limit in Atomic Magnetometry

JM Geremia,* John K. Stockton, Andrew C. Doherty, and Hideo Mabuchi
Norman Bridge Laboratory of Physics, California Institute of Technology, Pasadena, California, 91125, USA

(Received 27 June 2003; published 19 December 2003)

The shot-noise detection limit in current high-precision magnetometry [I. Kominis, T. Kornack, J. Allred, and M. Romalis, Nature (London) **422**, 596 (2003)] is a manifestation of quantum fluctuations that scale as $1/\sqrt{N}$ in an ensemble of N atoms. Here, we develop a procedure that combines continuous measurement and quantum Kalman filtering [V. Belavkin, Rep. Math. Phys. **43**, 405 (1999)] to surpass this conventional limit by exploiting conditional spin squeezing to achieve $1/N$ field sensitivity. Our analysis demonstrates the importance of optimal estimation for high bandwidth precision magnetometry at the Heisenberg limit and also identifies an approximate estimator based on linear regression.

DOI: 10.1103/PhysRevLett.91.250801 PACS numbers: 07.55.Ge, 32.80.Pj, 33.55.Fi, 41.20.Gz

Magnetometry is fundamentally a *parameter estimation* process because, like all fields, magnetism cannot be directly observed. Rather, the strength of a magnetic field must be inferred from its influence on a probe such as an atomic spin ensemble [1]. In a canonical atomic magnetometer, such an ensemble would be prepared into a coherent spin state with its bulk magnetization polarized along the x axis, $\langle\hat{\mathbf{J}}(0)\rangle = (J, 0, 0)$(such as by optical pumping). Then, a magnetic field along the y axis with magnitude, B, would induce the atomic Bloch vector, $\langle\hat{\mathbf{J}}(t)\rangle$, to precess in the x-z plane with frequency, $\omega_{\mathrm{L}} = \gamma B$. Thus, the magnetic field could be estimated from the free induction decay of the atomic magnetization by monitoring the z component of the Bloch vector, $\langle\hat{J}_{\mathrm{z}}(t)\rangle = J\exp(-t/T_2)\sin(\omega_{\mathrm{L}}t)$, where T_2 is the transverse spin coherence time.

In practice, current atomic magnetometers operate by continuously pumping the atomic sample while a $\langle\hat{J}_{\mathrm{z}}\rangle$-dependent optical property of the ensemble is monitored [2–4]. Because of pumping, the atoms are constantly repolarized as they Larmor precess. For small fields (the relevant case when discussing detection limits), the ensemble rapidly achieves an equilibrium that is nearly polarized along the x axis, but with a steady-state offset, $\langle\hat{J}_{\mathrm{z}}\rangle_{\mathrm{ss}} \propto \gamma BJ$. The uncertainty in measuring $\hat{J}_{\mathrm{z}}$ is due to projection noise [5], $\langle\Delta\hat{J}_{\mathrm{z}}^2\rangle \equiv \langle\hat{J}_{\mathrm{z}}^2\rangle - \langle\hat{J}_{\mathrm{z}}\rangle^2$, which has a value of $J/2$ for a coherent spin state. Averaging a sequence of independent measurements of $\langle\hat{J}_{\mathrm{z}}\rangle_{\mathrm{ss}}$ with this variance leads to the conventional shot-noise detection limit for a total measurement time of t_{tot} [2,3],

$$\delta B \simeq \frac{1}{\gamma\sqrt{JT_2 t_{\mathrm{tot}}}}. \tag{1}$$

Since $\langle\Delta\hat{J}_{\mathrm{z}}^2\rangle$ sets an intrinsic limit on the field sensitivity, reducing the projection noise below its standard quantum limit would improve the precision. This naturally leads one to consider spin-squeezed states [6] where uncertainty in $\langle\hat{J}_{\mathrm{z}}\rangle$ is reduced by redistributing it into the orthogonal spin component so that $\langle\Delta\hat{J}_{\mathrm{y}}^2\rangle > J/2$. Since $\langle\hat{J}_{\mathrm{y}}\rangle$ does not directly affect the field estimation, spin squeezing should enable one to surpass the conventional shot-noise magnetometry limit.

An improved magnetometry protocol would ideally be implemented by utilizing the conditional spin squeezing that is automatically generated by continuous observation of an atomic sample [7–9]. This dynamically generated squeezing does not occur in steady-state (narrow-band) magnetometers because of the continuous optical pumping. However, it should be possible to enable sub-shot-noise magnetometry by turning off the optical pumping once a coherent spin state has been prepared followed by continuous observation of the atoms.

But the nature of conditional spin squeezing gives rise to potential complications that make it initially unclear how to exploit the reduced uncertainty for improved magnetometry. Figure 1 shows simulated data (generated according to a quantum trajectory model described below [10]) of a spin ensemble under continuous measurement with no external field, $B = 0$. As $\langle\Delta\hat{J}_{\mathrm{z}}^2\rangle$ decreases [shaded

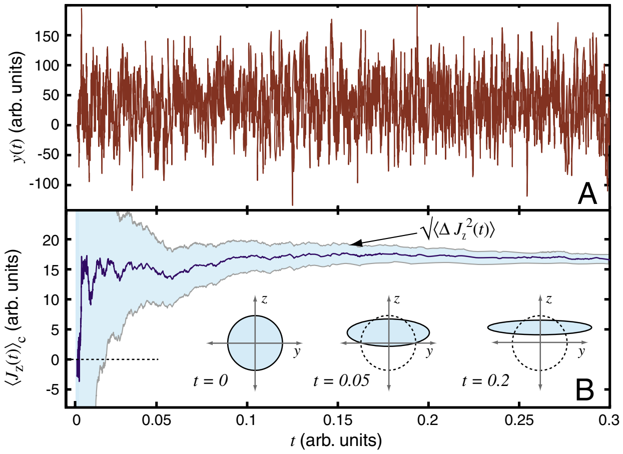

FIG. 1 (color online). (a) Simulated single-shot atomic magnetometry photocurrent low pass filtered at $F_{\mathrm{c}} = 2\pi\sqrt{J}/t_{\mathrm{tot}}$. (b) Corresponding diffusion of the atomic Bloch vector as conditional squeezing is produced by continuous quantum nondemolition observation.

© 2003 The American Physical Society

region in Fig. 1(b)] with the onset of spin squeezing, there is no apparent change in the noise of the associated $\langle \hat{J}_z(t)\rangle$ measurement, $y(t)$ [Fig. 1(a)], which is due to constant optical shot noise.

The dynamical generation of spin squeezing starting from an initial coherent state involves a stochastic transient at early times. As suggested by the error-ellipse diagrams of Fig. 1(b), conditional evolution gradually localizes the quantum spin state around a constant, but random, value of $\langle \hat{J}_z\rangle_c$. In an ensemble of continuous measurement trajectories, this constant value would be distributed with a variance of $J/2$ corresponding to $\langle \Delta \hat{J}_z^2\rangle$ of the initial coherent state. Therefore, the mean value of $\langle \hat{J}_z\rangle_c$ assumes a nonzero value *even in the absence of an applied magnetic field*, producing a stochastic offset in the photocurrent that must be distinguished from Larmor precession in a magnetometry experiment.

Fortunately, with appropriate filtering, Larmor precession of the spin state *can* be distinguished from the projection noise in such a way that the field estimation benefits from spin squeezing. In this Letter, we demonstrate that quantum trajectory theory [11,12] allows one to construct a Kalman filter [13–16] that optimally estimates the field magnitude from continuously observed conditional atomic dynamics. This filtering procedure enables Heisenberg limited magnetometry despite the optical shot noise and the transient effects of spin state estimation. Furthermore, we show that for time-invariant fields, our optimal strategy approximately reduces to the simple and intuitive data analysis procedure of linear regression which is a potentially simpler experimental approach to sub-shot-noise magnetometry.

We propose a magnetometer in which the atomic ensemble undergoes a continuous quantum nondemolition (QND) observation of $\hat{J}_z$. It has been shown that such a measurement can be implemented by detecting $\hat{J}_z$-dependent changes in the phase of an off-resonant cavity mode coupled to the atomic ensemble [9] or by the Faraday rotation of a far-detuned traveling mode [17,18] that passes through the ensemble. In both cases the magnetometer photocurrent is given by

$$y(t)dt = 2\eta\sqrt{M}\langle \hat{J}_z(t)\rangle_c dt + \sqrt{\eta}dW(t), \tag{2}$$

where $\langle \hat{J}_z(t)\rangle_c$ is the conditional expectation value of $\hat{J}_z$, η is the detector efficiency, and M (in units of frequency) is an implementation-dependent constant referred to as the *measurement strength.* The optical shot noise is reflected by stochastic increments, $dW(t)$, that obey Gaussian white-noise statistics, $E[dW] = 0$ and $dW^2 = dt$.

Conditional evolution of the atomic ensemble subjected to a magnetic field along the y axis and a QND measurement of $\hat{J}_z$ is described by the stochastic master equation,

$$d\hat{\rho}_c(t) = -i\gamma B[\hat{J}_y, \hat{\rho}_c]dt + M\mathcal{D}[\hat{J}_z]\hat{\rho}_c dt + \sqrt{M\eta}\mathcal{H}[\hat{J}_z]\hat{\rho}_c dW(t), \tag{3}$$

where $\hat{\rho}_c(t)$ is the reduced atomic density operator conditioned on the measurement record [12]. The superoperators, $\mathcal{D}$ and $\mathcal{H}$, are given by $\mathcal{D}[r]\hat{\rho} = r\hat{\rho}r^\dagger - (r^\dagger r\hat{\rho} + \hat{\rho}r^\dagger r)/2$ and $\mathcal{H}[r]\hat{\rho} = r\hat{\rho} + \hat{\rho}r^\dagger - \mathrm{tr}[(r + r^\dagger)\hat{\rho}]\hat{\rho}$, and the initial condition is an optically pumped coherent spin state along the x axis, $\hat{\rho}(0) = |J\rangle_x\langle J|$.

Each term in Eq. (3) has a physical implication for magnetometry. First, the Hamiltonian, $H(B) = \gamma B\hat{J}_y$, generates the desired Larmor precession signal used to detect the magnetic field. The second term reflects measurement-induced atomic decoherence that results from coupling the ensemble to the optical shot noise on the probe laser. As a result the length of the Bloch vector decays over time, $J(t) = J\exp(-Mt/2)$, and M can be related to a bound on the transverse spin relaxation, $T_2 \lesssim 2M^{-1}$. The significance of the third term in Eq. (3) is best seen by employing an approximation that holds for a large net magnetization and small field ($\omega_L t \ll 1$). For an ensemble polarized along the x axis, quantum fluctuations in $\langle \hat{J}_x\rangle$ are at least second order and the operator, $\hat{J}_x$, is well approximated by the length of the Bloch vector, $\hat{J}_x \rightarrow J$. Physically, this assumption capitalizes on the large value of J to treat the Bloch sphere as a locally flat phase space. This approximation is extremely good for both coherent and squeezed states with $J \gg 1$.

In a Gaussian approximation, the first and second moments of $\hat{J}_z$ are sufficient to completely characterize the atomic state. Therefore, equations of motion for the mean and variance,

$$d\langle \hat{J}_z\rangle_c = \gamma BJe^{-Mt/2}dt + 2\sqrt{M\eta}\langle \Delta \hat{J}_z^2\rangle dW(t), \tag{4}$$

$$d\langle \Delta \hat{J}_z^2\rangle = -4M\eta\langle \Delta \hat{J}_z^2\rangle^2 dt, \tag{5}$$

provide a closed representation of the magnetometer's conditional quantum dynamics (in the $\omega_L t \ll 1$ and $t \lesssim M^{-1}$ limits). The physical significance of Eq. (4) is that the atomic Bloch vector experiences two types of motion: deterministic Larmor precession and stochastic diffusion. Equation (5) reflects the deterministic reduction of $\langle \Delta \hat{J}_z^2\rangle$ as the atomic state is localized by the observation process, i.e., conditional spin squeezing.

Equations (4) and (5) can be used to implement an optimal estimation procedure that capitalizes on squeezing without mistaking measurement-induced Bloch vector rotations for true Larmor precession. Since the atomic dynamics are stochastic, the estimator must be described probabilistically—we desire a conditional probability distribution, $p(B|\Xi_{[0,t]})$, which measures the likelihood that the field has magnitude B given the measurement record, Ξ, defined in terms of the photocurrent, $d\Xi_t \equiv y(t)dt/(2\eta\sqrt{M})$. The estimated magnitude, $\tilde{B}$, and its uncertainty, $\Delta\tilde{B}^2$, are obtained from the moments

$$\tilde{B} = \int Bp(B|\Xi_{[0,t]})dB, \tag{6}$$

$$\Delta\tilde{B}^2 = \int (B - \tilde{B})^2 p(B|\Xi_{[0,t]}) dB \tag{7}$$

of the conditional distribution, $p(B|\Xi_{[0,t]})$.

Constructing a maximum-likelihood estimator is accomplished by defining an update rule that iteratively improves $p(B|\Xi_{[0,t]})$ as the measurement record is acquired. Prior knowledge of the distribution of magnetic field values is encoded in $p(B|\Xi_0)$, which may be assigned infinite variance in order to assure an unbiased estimate. Optimality requires that the conditional probability must be updated according to a Bayes's rule,

$$dp(B|d\Xi_t, \Xi_{[0,t)}) = dq(d\Xi_t|B, \Xi_{[0,t)})p(B|\Xi_{[0,t)}), \tag{8}$$

where $dq(d\Xi_t|B, \Xi_{[0,t)})$ is an infinitesimal conditional probability that describes the likelihood of the evolving measurement record, $d\Xi_t$, given a field with magnitude B and past history, $\Xi_{[0,t)}$. The utility of Bayes's rule is that $q(d\Xi_t|B, \Xi_{[0,t)})$ can be computed using quantum trajectory theory, Eqs. (4) and (5).

Implementing this parameter estimator is best accomplished by a (recursive) Kalman filter [13–15]. It can be shown that the filtering equations,

$$d\tilde{x} = \mathbf{A}\tilde{x}dt + D^{-2}(\mathbf{B} + \mathbf{V}\mathbf{C}^T)(d\Xi - \mathbf{C}\tilde{x}dt) \tag{9}$$

with $\tilde{x} \equiv (\tilde{J}_z \quad \tilde{B})^T$ ($\tilde{J}_z$ is the estimate of $\langle\hat{J}_z\rangle_c$),

$$\mathbf{A} = \gamma J e^{(-Mt)/2}\begin{pmatrix} 0 & 1 \\ 0 & 0 \end{pmatrix}, \qquad \mathbf{B} = \begin{pmatrix} \langle\Delta\hat{J}_z^2\rangle \\ 0 \end{pmatrix}, \qquad \mathbf{C} = (1 \quad 0),$$

$D = 1/(2\sqrt{M\eta})$, and $\tilde{x}(0) = 0$ implement Eq. (8). We note that it is possible to extend the Kalman filter to account for time-varying or stochastic fields [16] as well as to implement quantum feedback control [9,16].

The conditional quantum dynamics, particularly spin squeezing and the exponential decay of the Bloch vector, enter the estimation process via the covariance matrix,

$$\mathbf{V}(t) = \begin{pmatrix} \Delta\tilde{J}_z^2(t) & \Delta(\tilde{J}_z\tilde{B})(t) \\ \Delta(\tilde{B}\tilde{J}_z)(t) & \Delta\tilde{B}^2(t) \end{pmatrix}, \tag{10}$$

which describes the uncertainty in the parameter estimations of $\hat{J}_z$ and B. $\mathbf{V}(t)$ evolves deterministically according to the matrix Riccati equation,

$$\begin{aligned}\dot{\mathbf{V}} = {}& (\mathbf{A} - D^{-2}\mathbf{B}\mathbf{C})\mathbf{V} + \mathbf{V}(\mathbf{A} - D^{-2}\mathbf{B}\mathbf{C})^T \\ & + D^{-2}\mathbf{V}(\mathbf{C}^T\mathbf{C})\mathbf{V},\end{aligned} \tag{11}$$

subject to the initial conditions $\Delta\tilde{J}_z^2(0) = 0$ and $\Delta(\tilde{J}_z\tilde{B})(0) = 0$, with $\Delta\tilde{B}^2(0)$ chosen to reflect prior knowledge on the distribution of magnetic field values. Lacking any such knowledge, one can set $\Delta\tilde{B}^2(0) \to \infty$.

The smallest detectable magnetic field as a function of J and the measurement duration, t, is determined by the estimator variance, $\Delta\tilde{B}^2$. Solving the matrix Riccati equation [which is analytically soluble for the Kalman filter in Eq. (9)] provides the time-dependent magnetic field detection threshold, $\delta\tilde{B} \equiv \sqrt{\Delta\tilde{B}^2(t)}$,

$$\delta\tilde{B}(t) = \frac{M}{4\gamma J}\sqrt{\frac{(1 + 2\eta JMt)}{ae^{-Mt} + 4e^{-Mt/2}(4\eta J + 1) + b}} \tag{12}$$

with a and b given by

$$a = -[2\eta J(Mt + 4) + 1], \qquad b = Mt + 2\eta J(Mt - 4) - 3.$$

Expanding Eq. (12) to leading order in t provides an expression for the detection threshold,

$$\delta\tilde{B}(t) \approx \frac{1}{\gamma J}\sqrt{\frac{3}{M\eta t^3}}, \qquad t \gg (JM)^{-1}, \tag{13}$$

that is directly comparable to Eq. (1) when the measurement strength is chosen to be $M \sim T_2^{-1}$ such that maximal spin squeezing is achieved at time $t = M^{-1}$. Such a choice for M permits a superior $1/J$ (equivalently $1/N$) scaling that is characteristic of the Heisenberg squeezing limit [6,9]. The optical shot noise [of order unity in this model, see Eq. (2)] enters implicitly through the signal to noise ratio, $\mathrm{SNR} = J\sqrt{M}$, which highlights the utility of the Kalman filter as a whitening filter—it extracts the nonstationary spin squeezing and Larmor precession dynamics despite the presence of Gaussian noise.

Figure 2 shows numerical results that demonstrate the performance of our quantum Kalman filter (QKF). The simulations were performed for an atomic ensemble with $J = 4 \times 10^6$, $\gamma = 1$ kHz/mG, $\eta = 1$, and $M = 100$ kHz in a background magnetic field of $B = 1\ \mu$G. These values nearly correspond to a magnetometer constructed from $N = 10^6$ ground state Cs atoms coupled to a high-finesse optical cavity with single photon Rabi frequency $g_0 = 10$ MHz and decay rate, $\kappa = 1$ MHz. The QND measurement corresponds to a phase-quadrature homodyne detection of the transmitted cavity light with a cavity mode ($P = 100\ \mu$W) that is blue detuned by $\Delta = 1$ GHz from the Cs transition at $\lambda \sim 852$ nm. The initial

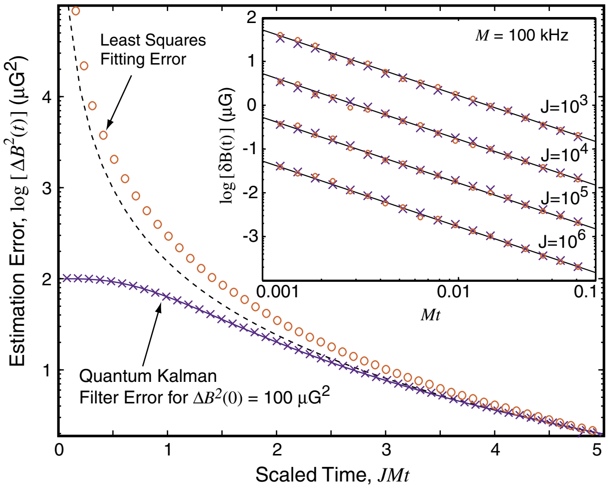

FIG. 2 (color online). Comparison of the estimation errors for a quantum Kalman filter and a linear least squares magnetic field determination. The inset plot highlights the $1/J$ (Heisenberg limited) scaling of both procedures for $t \gg (JM)^{-1}$.

estimator variance was chosen to be $\Delta\tilde{B}^2(0) = 100\ \mu\mathrm{G}^2$ which is the initial value that one would select given prior knowledge that the magnetic field could be treated as a Gaussian random variable with this variance. For the parameters we selected, Larmor precession and spin projection noise have comparable magnitudes on time scales of order $(JM)^{-1}$.

The Kalman estimation error (crosses in Fig. 2) was computed from the ensemble average, $E[(\tilde{B}_i - B)^2]$, for 10^5 trajectories, and the solid line shows the estimation uncertainty $\Delta\tilde{B}(t)$ obtained by integrating Eq. (11). Since our simulations were performed with $B = 1\ \mu\mathrm{G}$, the empirical performance of the QKF closely matches the solid line. The dotted line in Fig. 2 shows the analytic Riccati solution, given by Eq. (12), for $\Delta\tilde{B}^2(0) \to \infty$, which would be the expected QKF performance in a scenario with no prior knowledge of the magnetic field. Figure 2 also shows the estimation error for simple linear regression of the measurement record (open circles). Assuming that the Bloch vector has not decayed significantly, $\tilde{B}$ is proportional to the slope of a line fit to the (filtered) photocurrent, $y(t)$. The estimation error for linear regression was obtained by computing $E[(\tilde{B}_i - B)^2]$ for 10^5 trajectories. Although the QKF is clearly superior for short times, the two estimation procedures converge for $(JM)^{-1} \ll t < M^{-1}$ and provide a quantum parameter estimation with $\delta\tilde{B} \sim 0.01$ nG in $t \sim 1$ ms. The inset of Fig. 2 highlights the $\delta\tilde{B} \propto J^{-1}$ scaling that distinguishes both the QKF (crosses) and regression (open circles) estimators from the conventional shot-noise limit, Eq. (1). For sufficiently large times both estimators achieve the detection threshold in Eq. (13) (solid lines).

The QKF and linear regression differ mainly in how they treat the initial diffusive transient of $\hat{J}_z$ [Fig. 1(b)]. Since the QKF is derived from a quantum trajectory model, it is aware of the short-time diffusion and strategically underweights the photocurrent at early times [via the Kalman gain, $\mathbf{G} \equiv D^{-2}(\mathbf{B} + \mathbf{V}\mathbf{C}^T)$]. At late times the regression analysis manages to absorb the initial diffusive transient into the y intercept of the linear fit. Although $\langle\hat{J}_z(0)\rangle = 0$, the $\hat{J}_z$ localization process *gradually* determines an effective offset in the photocurrent during the interval $t \sim (JM)^{-1}$. Without explicit knowledge of the conditional dynamics the linear regression equally weights the photocurrent for $t < (JM)^{-1}$. This decreases the quality of the fit, but the resulting error becomes insignificant for $t \gg (JM)^{-1}$.

Our analysis suggests that estimation procedures based on conditional quantum dynamics can play a crucial role in optimizing both the sensitivity and the bandwidth in atomic magnetometry. While conventional steady-state magnetometers can only improve their detection capabilities by increasing the number of atoms or the averaging time, the quantum estimator can achieve greater precision for the same value of t and N by improving the measurement strength. The significance of the Kalman filter is the optimality that is guaranteed by its derivation from a Bayes's rule. Our finding that linear regression closely approximates the optimal procedure indicates a potentially simpler experimental procedure for sub-shot-noise magnetometry. Although Heisenberg limited spin squeezing should be possible using current techniques in cavity quantum electrodynamics (a discussion is provided in [9]), the experimental difficulty of achieving this limit makes it desirable to have an optimal estimator such as the QKF to fully exploit even a small amount of squeezing, to treat fluctuating fields, and to achieve estimator robustness [16]. In either case, estimation procedures that allow and account for conditional quantum dynamics — whether explicitly as in the QKF or implicitly as in linear regression — offer substantial improvement over steady-state procedures.

This work was supported by the NSF (PHY-9987541, EIA-0086038), by the ONR (N00014-00-1-0479), and by the Caltech MURI Center for Quantum Networks (DAAD19-00- 1-0374).

---

*Electronic address: jgeremia@Caltech.edu

[1] J. Dupont-Roc, S. Haroche, and C. Cohen-Tannoudji, Phys. Lett. A **28**, 638 (1969).

[2] I. Kominis, T. Kornack, J. Allred, and M. Romalis, Nature (London) **422**, 596 (2003).

[3] D. Budker, W. Gawlik, D. Kimball, S. Rochester, V. Yashchuk, and A. Weiss, Rev. Mod. Phys. **74**, 1153 (2002).

[4] C. Kim and H. Lee, Rev. Sci. Instrum. **69**, 4152 (1998).

[5] W. Itano, J. Berquist, J. Bollinger, J. Gilligan, D. Heinzen, F. Moore, M. Raizen, and D. J. Wineland, Phys. Rev. A **47**, 3554 (1993).

[6] M. Kitagawa and M. Ueda, Phys. Rev. A **47**, 5138 (1993).

[7] Y. Takahashi, K. Honda, N. Tanaka, K. Toyoda, K. Ishikawa, and T. Yabuzaki, Phys. Rev. A **60**, 4974 (1999).

[8] A. Kuzmich, L. Mandel, and N. P. Bigelow, Phys. Rev. Lett. **85**, 1594 (2000).

[9] L. Thomsen, H. Mancini, and H. Wiseman, Phys. Rev. A **65**, 061801 (2002).

[10] Please visit http://minty.caltech.edu/Ensemble for simulation source code and detailed notes on the Kalman filter derivation.

[11] H. Carmichael, *An Open Systems Approach to Quantum Optics* (Springer-Verlag, New York, 1993).

[12] H. Wiseman and G. Milburn, Phys. Rev. A **49**, 1350 (1994).

[13] V. Belavkin, Rep. Math. Phys. **43**, 405 (1999).

[14] H. Mabuchi, Quantum Semiclass. Opt. **8**, 1103 (1996).

[15] F. Verstraete, A. Doherty, and H. Mabuchi, Phys. Rev. A **64**, 032111 (2001).

[16] J. K. Stockton, J. Geremia, A. C. Doherty, and H. Mabuchi, quant-ph/0309101.

[17] A. Silberfarb and I. Deutsch, Phys. Rev. A **68**, 013817 (2003).

[18] G. A. Smith, S. Chaudhury, and P. S. Jessen, J. Opt. B: Quantum Semiclassical Opt. **5**, 323 (2003).

arXiv:quant-ph/0605228 v1 28 May 2006

Purification of large bi-colorable graph states

Kovid Goyal,[1, *] Alex McCauley,[1, †] and Robert Raussendorf[2, ‡]
[1] Institute for Quantum Information, California Institute of Technology, Pasadena, CA 91125
[2] Perimeter Institute, 31 Caroline St. N, Waterloo, N2L 2Y5, Canada

(Dated: May 26, 2006)

We describe novel purification protocols for bi-colorable graph states. The protocols scale efficiently for large graph states. We introduce a method of analysis that allows us to derive simple recursion relations characterizing their behavior as well as analytical expressions for their thresholds and fixed point behavior. We introduce two purification protocols with high threshold. They can, for graph degree four, tolerate 1% (3%) gate error or 20% (30%) local error.

I. INTRODUCTION

The known protocols in quantum information processing require a certain degree of quantum mechanical entanglement to achieve an advantage over their classical counterparts. Often, this quantum-mechanical 'essence' is provided in terms of in-advance prepared quantum states. For example, Bell states are used in a well-known protocol for quantum cryptography [1], and schemes for multi-party cryptographic tasks using Greenberger-Horne-Zeilinger (GHZ)-states and other Calderbank-Shor-Steane (CSS)-states have been devised [2]. Further, in quantum computation, multi-particle entangled states can be used to streamline the execution of gates and sub-circuits via gate teleportation [3], and cluster states represent a universal resource for quantum computation by local measurements [4].

In most realistic scenarios the quality of entangled resource states is degraded by the effects of decoherence, and methods of error detection or -correction are required to counteract this process. One such method is state purification where a (close to) perfect copy of a quantum state is distilled out of many imperfect ones. Purification has first been described for Bell states [5, 6, 7] and subsequently generalized to bi-colorable graph states/ CSS-states [8, 9, 10]. Recently, a protocol for the purification of W-states has been presented [11]. State purification is used, for example, to establish a perfect quantum channel between two parties [5], to efficiently create long-range entanglement via quantum repeaters [12] or to render certain schemes for topological fault-tolerant quantum computation universal [13].

Imperfect initial states are not the only sources of error for realistic state purification. With the exception of certain schemes of topological quantum computation such as [13], errors in the gates for purification also need to be taken into account.

What can we expect to gain from an imperfect purification procedure? In the process of purification the errors of the initial state are replaced by the errors of the purifying gates. Thus, the amount of error may be reduced if the quality of the initial states is low compared to the quality of the gates for purification (but above threshold). Further, purification can be used to *condition* the error of a quantum state. For example, imperfect Bell state purification can be used to establish a perfectly private if imperfect quantum channel [14]. In a multi-party scenario, for some protocols the purification gates act locally on each copy of the state to purify, resulting in a local or close to local error model for the final state. This feature attains relevance in the context of fault-tolerant quantum computation. Threshold theorems have been established for increasingly general types of error including coherent and long-range errors [15, 16] but there are realistic scenarios in which standard error-correction appears to fail [17]. In such a situation, state purification may be used to turn the error model into a more benign one.

The focus of this paper is purification of bi-colorable graph states by imperfect means, a subject that has previously been studied in [9, 18, 19]. We are interested in the interplay between threshold and overhead. Specifically, we seek protocols that (I) work with erroneous purification gates; (II) have a high threshold and good quality of the output state; (III) scale efficiently; and (IV) are analytically tractable.

Hashing protocols have a high threshold in the error of the initial state and require only a minimal resource overhead, but they break down as soon as the purification gates become slightly imperfect. Recursive protocols such as [8] also have a high threshold for error in the initial states and furthermore work with imperfect purification gates, but they are exponentially inefficient in the number of particles.

Our protocols are resistant to initial as well as purification errors and are computationally efficient. As a bonus, our protocols are analytically tractable for a wide class of errors. Specifically, our base protocol described in Section III can be analyzed for arbitrary input states and general probabilistic Pauli errors in the purification gates. This fact arises through a special locality property. So far, the exponential increase of parameters in the description of n-particle mixed states—even mixed stabilizer states—has been found an obstacle to analytic discussion, and only severely restricted error models have

---

[*] kovid@theory.caltech.edu
[†] mccaule@caltech.edu
[‡] rraussendorf@perimeterinstitute.ca

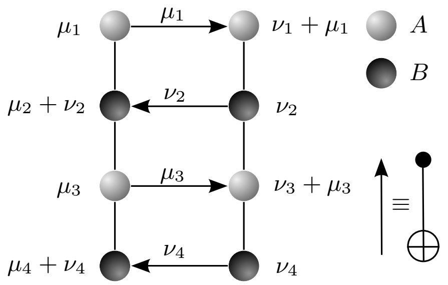

FIG. 1: Action of MCNOT in the graph basis. The arrows represent the direction of syndrome (or Z error) flow (i.e. the action of the MCNOT on the stabilizer)

been treated in the literature.

This paper is organized as follows: in Section II we briefly review the protocol [8] for purification of bi-colorable graph states. In Sections III - IV C we describe our purification protocols and characterize them in terms of purification threshold, output quality and overhead. We conclude with a discussion of our results in Section V.

II. A BRIEF REVIEW

Consider a graph $G(V,E)$ with vertex set V and edge set E. $G(V,E)$ is bi-colorable if V can be partitioned into two disjoint subsets A and B such that every edge in E connects a vertex in A with a vertex in B. E defines a *neighborhood* relation on elements of V; $\mathrm{neigh}(j) := \{i \in V : (i\ j) \in E\}$. Define the correlation operators

$$\mathrm{K}_j := \mathrm{X}_j \prod_{\mathrm{neigh}(j)} \mathrm{Z}_j \tag{1}$$

where $\mathrm{X}, \mathrm{Y}, \mathrm{Z}$ are the Pauli matrices. A graph state is a $|V|$-qubit state $|\boldsymbol{\mu}\rangle$ ($\boldsymbol{\mu} \in \{0,1\}^{|V|}$) that satisfies the eigenvalue equations

$$\mathrm{K}_j \,|\boldsymbol{\mu}\rangle = (-1)^{\mu_j}\,|\boldsymbol{\mu}\rangle\,, \forall j = 1 \ldots |V|. \tag{2}$$

The states $\{|\boldsymbol{\mu}\rangle\}$ form a basis of the Hilbert space of $|V|$ qubit states called the *graph basis*.

We now briefly discuss the post-selection protocol of [8]. The protocol works by taking two identical copies of a bi-colorable graph state and performing multiple CNOTs (MCNOT) between them, in a definite pattern as illustrated in Fig. 1. Relabeling states in the graph basis to reflect the partition into colors A and B (i.e. $|\boldsymbol{\mu}\rangle \equiv |\boldsymbol{\mu}_A, \boldsymbol{\mu}_B\rangle$), the effect of the MCNOT is [8]

$$|\boldsymbol{\mu}_A, \boldsymbol{\mu}_B\rangle\,|\boldsymbol{\nu}_A, \boldsymbol{\nu}_B\rangle \mapsto |\boldsymbol{\mu}_A, \boldsymbol{\mu}_B + \boldsymbol{\nu}_B\rangle\,|\boldsymbol{\nu}_A + \boldsymbol{\mu}_A, \boldsymbol{\nu}_B\rangle \tag{3}$$

where $+$ is element wise addition modulo 2. Notice that information about $\boldsymbol{\mu}_A$ has been copied into state two and information about $\boldsymbol{\nu}_B$ has been copied into state one. We then measure local observables X and Z on copy two, and reconstruct from the measurement outcomes the eigenvalues of all K_j with $j \in A$. Suppose we get -1 at the kth qubit. Then we know that either μ_k or ν_k was 1, but we don't have enough information to decide which one, so we throw away the states and start again. We keep doing this until all measurements are clear. By this procedure we correct, to lowest order, errors in the qubits of color A. In the next round we interchange the roles of colors A and B and so purify the B qubits. We can concatenate this procedure to achieve desired levels of purity. Because we are post-selecting states on the basis of a global measurement outcome, this protocol is inefficient for large states. This inefficiency can be addressed by using error correction instead of post-selection, to which we now turn.

III. THE 3-COPY PROTOCOL

The simplest way to get enough information to perform error correction is to do the MCNOT on three copies instead of two. The 3-copy protocol consists of two sub-protocols. We use three identical copies of the state in each sub-protocol. The output of the first sub-protocol is used as input for the next. Thus, we need nine copies to run a single round. Let the three identical copies be $\rho^{(0)}$, $\rho^{(1)}$, $\rho^{(2)}$. Sub-protocol 1 ($P1$):

i. Partition the graph into two colors A and B ($V = V_A \cup V_B$ and $V_A \cap V_B = \varnothing$).

ii. Perform the MCNOT between copies $\rho^{(0)}$ and $\rho^{(1)}$ and $\rho^{(0)}$ and $\rho^{(2)}$ such that information about qubits of color A flows from $\rho^{(0)} \rightarrow \rho^{(1)}$ and $\rho^{(0)} \rightarrow \rho^{(2)}$. As a side effect information about B will flow from $\rho^{(1)}, \rho^{(2)} \rightarrow \rho^{(0)}$. See Fig. 3a.

iii. Measure qubits of color A in the X basis and qubits of color B in the Z basis in states $\rho^{(1)}$ and $\rho^{(2)}$. This is a measurement of K_j for $j \in A$. If the measurement of K_j gives $+1(-1)$ we get a syndrome of $0(1)$. Thus, for each $j \in A$ we have two bits of syndrome $\sigma_j^{(1)}, \sigma_j^{(2)}$.

iv. Apply the correction $\prod_{j\in A} \mathrm{Z}_j^{\sigma_j^{(2)}\cdot\sigma_j^{(3)}}$ to $\rho^{(0)}$.

For sub-protocol P2 the roles colors A and B are interchanged.

First, we will analyze this protocol with ideal CNOT gates. This will allow us to derive simple closed form recursion relations characterizing the behavior of the protocol, as well as analytical estimates of the threshold and efficiency. In Section III B we generalize to noisy gates. The analysis is restricted to density matrices that are diagonal in the graph basis (i.e. probabilistic mixtures of graph states). At the end of Section III B, we will show that our results are valid for arbitrary density matrices.

A. Ideal gates

Eq. (3) implies that the effect of the MCNOT on $\rho^{(0)}$, $\rho^{(1)}$ and $\rho^{(2)}$ is

$$\begin{aligned} |\boldsymbol{\mu}_A^{(0)}, \boldsymbol{\mu}_B^{(0)}\rangle &\mapsto |\boldsymbol{\mu}_A^{(0)}, \boldsymbol{\mu}_B^{(0)} + \boldsymbol{\mu}_B^{(1)} + \boldsymbol{\mu}_B^{(2)}\rangle \qquad (4) \\ |\boldsymbol{\mu}_A^{(1)}, \boldsymbol{\mu}_B^{(1)}\rangle &\mapsto |\boldsymbol{\mu}_A^{(1)} + \boldsymbol{\mu}_A^{(0)}, \boldsymbol{\mu}_B^{(1)}\rangle \\ |\boldsymbol{\mu}_A^{(2)}, \boldsymbol{\mu}_B^{(2)}\rangle &\mapsto |\boldsymbol{\mu}_A^{(2)} + \boldsymbol{\mu}_A^{(0)}, \boldsymbol{\mu}_B^{(2)}\rangle \qquad (5) \end{aligned}$$

Eq. (2) implies that the effect of the correction is

$$|\boldsymbol{\mu}_A^{(0)}, \boldsymbol{\mu}_B^{(0)}\rangle \mapsto |\boldsymbol{\mu}_A^{(0)} + \boldsymbol{\sigma}, \boldsymbol{\mu}_B^{(0)}\rangle\,, \qquad (6)$$

where $\sigma_j := \sigma_j^{(1)} \cdot \sigma_j^{(2)}$. By measuring $\rho^{(1)}$ and $\rho^{(2)}$, we get two bits of syndrome for each qubit of color A in $\rho^{(0)}$. The syndrome is conclusive, it allows us to identify, to lowest order in error probability on which state the error occurred. We can thus do error correction instead of post-selection. This will make the protocol scale efficiently in the size of the states. The price is a reduction of the threshold value.

We now derive a recursion relation for the expectation values $\langle \mathrm{K}_j \rangle$, $j \in 1 \dots N$. They yield a necessary and sufficient condition for purification. For the moment we assume that the initial state ρ is diagonal in the cluster basis, i.e., ρ is a probabilistic mixture. It is then safe to consider error probabilities. This assumption is not necessary, however. It is removed in Section III B. Define $P_j(\rho)$ as the probability to find the eigenvalue -1 in the measurement of K_j on ρ as

$$P_j(\rho) := \mathrm{Tr}\left[\frac{1 - \mathrm{K}_j}{2}\rho\right] = \frac{1 - \langle \mathrm{K}_j \rangle}{2}. \qquad (7)$$

Consider sub-protocol $P1$. In order to analyze this protocol we make use of the fact that the error correction operation is local. It only uses information about $\langle \mathrm{K}_j \rangle$ in each copy to apply a correction to the jth qubit in $\rho^{(0)}$. Thus, $\langle \mathrm{K}_j \rangle$ should have nice decoupled recursion relations. We will later derive the recursion relations for the expectation value of arbitrary stabilizer elements, which in general are more complex.

First consider qubits of color B. From Eq. (4) $\mu_j^{(0)} \mapsto \mu_j^{(0)} + \mu_j^{(1)} + \mu_j^{(2)}$. Since our copies are identical we have $P_j(\rho^{(0)}) = P_j(\rho^{(1)}) = P_j(\rho^{(2)}) = P_j$. Then, $P_j \mapsto P_j^3 + 3P_j(1 - P_j)^2$. In terms of expectation values,

$$\langle \mathrm{K}_j \rangle' = \langle \mathrm{K}_j \rangle^3\,. \qquad (8)$$

Under concatenation of $P1$ with itself qubits of color B are *polluted* with $\langle \mathrm{K}_j \rangle_{\rho^{(0)}} \to \langle \mathrm{K}_j \rangle_{\mathrm{I}} = 0$.

Turning our attention to qubits of color A we note that error correction fails if $\mu_j = 1$ for more than one copy. Thus, $P_j \mapsto P_j^3 + 3P_j^2(1 - P_j)$. In terms of expectation values

$$\langle \mathrm{K}_j \rangle' = \frac{1}{2}\left(3 - \langle \mathrm{K}_j \rangle^2\right)\langle \mathrm{K}_j \rangle\,. \qquad (9)$$

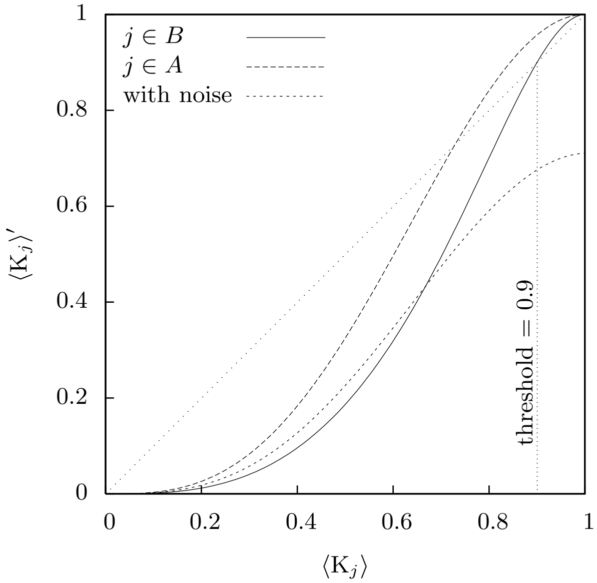

FIG. 2: Recurrence curves for the 3-copy protocol. These simple curves fully encapsulate the behavior of the protocol with ideal gates. The point of intersection with $\langle \mathrm{K}_j \rangle' = \langle \mathrm{K}_j \rangle$ gives the threshold. If the gates are too noisy the protocol breaks down, as indicated by the lowest curve.

Under concatenation of $P1$ with itself qubits of color A are *purified* with $\langle \mathrm{K}_j \rangle_{\rho^{(0)}} \to \langle \mathrm{K}_j \rangle_{|\mathbf{0}\rangle\langle\mathbf{0}|} = 1$.

Sub-protocol $P2$ is identical to $P1$ except that the roles of A and B are interchanged and the three copies are the output states from running $P1$ three times. The 3-copy protocol is the composition of $P2$ with $P1$. Let $P = P2 \circ P1$, then Eq. (8) and Eq. (9) imply that under the action of P

$$\langle \mathrm{K}_j \rangle' = \begin{cases} \frac{1}{8}\left(3 - \langle \mathrm{K}_j \rangle^2\right)^3 \langle \mathrm{K}_j \rangle^3 & \text{if } j \in A, \\ \frac{1}{2}\left(3 - \langle \mathrm{K}_j \rangle^6\right)\langle \mathrm{K}_j \rangle^3 & \text{if } j \in B. \end{cases} \qquad (10)$$

The recursion relations Eq. (10) have, for each color, a unique repulsive fixed point in the interval $(0, 1)$ which separates the basins of attraction for the trivial fixed point at 0 and the nontrivial fixed point at 1. The upper fixed point corresponds to the perfect cluster state. Thus, the stated protocol purifies a cluster state if and only if

$$\begin{aligned} \langle \mathrm{K}_j \rangle &> 0.7297 \text{ for all j in } A \\ \langle \mathrm{K}_j \rangle &> 0.9003 \text{ for all j in } B. \qquad (11) \end{aligned}$$

These thresholds should be compared with the corresponding numbers for the post-selection protocol [9]. A direct comparison in terms of $\langle \mathrm{K}_j \rangle$ is possible for the particular case where only independent local phase flip errors are assumed for the initial states in protocol [8]. Then, the P1 recursion relation for $\langle \mathrm{K}_j \rangle$ with $j \in B$ is $\langle \mathrm{K}_j \rangle' = \langle \mathrm{K}_j \rangle^2$ and for $j \in A$ is $\langle \mathrm{K}_j \rangle' = \frac{2\langle \mathrm{K}_j \rangle}{1 + \langle \mathrm{K}_j \rangle^2}$. The resulting threshold values are $\langle \mathrm{K}_j \rangle_{\mathrm{th}} = 0.2956$ for $j \in A$ and $\langle \mathrm{K}_j \rangle_{\mathrm{th}} = 0.5437$ for $j \in B$.

Returning to our protocol, it is possible to derive recursion relations for the expectation values of arbitrary stabilizer elements. They are not in general decoupled, but there is still a notion of locality. The generalized relation allows us to compute the recursion relations for stabilizers with small support efficiently. Define

$$\mathrm{K}_{\boldsymbol{a},\boldsymbol{b}} := \prod_{i=1}^{|V_A|} \mathrm{K}_i^{a_i} \prod_{j=1}^{|V_B|} \mathrm{K}_j^{b_j}, \tag{12}$$

where $\boldsymbol{a} \in \{0,1\}^{|V_A|}$ and $\boldsymbol{b} \in \{0,1\}^{|V_B|}$. The terms in the first product act on qubits of color A, while those in the second product act on qubits of color B. Then (see Appendix A) under the action of sub-protocol $P1$,

$$\langle \mathrm{K}_{\boldsymbol{a},\boldsymbol{b}} \rangle' = \frac{1}{2^{|\boldsymbol{a}|}} \sum_{\boldsymbol{a}_1,\boldsymbol{a}_2 \ll \boldsymbol{a}} (-1)^{\boldsymbol{a}_1 \cdot \boldsymbol{a}_2} \langle \mathrm{K}_{\boldsymbol{a}+\boldsymbol{a}_1+\boldsymbol{a}_2,\boldsymbol{b}} \rangle \langle \mathrm{K}_{\boldsymbol{a}_1,\boldsymbol{b}} \rangle \langle \mathrm{K}_{\boldsymbol{a}_2,\boldsymbol{b}} \rangle, \tag{13}$$

where $\boldsymbol{f} \ll \boldsymbol{g}$ iff $f_j = 0$ whenever $g_j = 0$. Equations (9),(8) are special cases for $\langle \mathrm{K}_{\boldsymbol{a},\boldsymbol{b}} \rangle = \langle \mathrm{K}_j \rangle$ with $j \in A, B$ respectively. An interesting feature of this equation is that it relates a correlator of weight $w = |\boldsymbol{a}| + |\boldsymbol{b}|$ to correlators of weight no more than w. This makes it feasible to calculate the correlators of small weight.

In order to discuss the behavior of this protocol under concatenation with itself, it is useful to switch back to probability variables. Then Eq. (10) implies that if the protocol is concatenated with itself k times,

$$P_j(\rho(k)) \leq \left(\frac{P_j(\rho(0))}{P_{\mathrm{th}}} \right)^{2^k} \tag{14}$$

where P_{th} is the threshold error probability. The k-concatenated protocol requires 3^{2k} identical copies, thus the protocol is exponentially efficient under concatenation and the efficiency is independent of the size of the graph. We conclude that under concatenation the protocol reaches the reference state $|\mathbf{0}\rangle$ with efficient use of resources.

B. Noisy gates

Now we investigate what happens to this protocol when the CNOT gates themselves are noisy. In the 3-copy protocol CNOT gates act on the same qubit in two states $\rho^{(m)}$ and $\rho^{(n)}$. We model a noisy two qubit gate as an ideal gate followed by the two qubit depolarizing channel (i.e. the $SU(4)$ invariant channel)

$$\mathrm{T}^{(k)} := (1-p_2)[\mathrm{I}] + \frac{p_2}{16} \sum_{i,j=1}^{4} \left[D_i^{(k,m)} \otimes D_j^{(k,n)} \right] \tag{15}$$

where $D_{i,j} \in \{\mathrm{I},\mathrm{X},\mathrm{Y},\mathrm{Z}\}$ and k is the qubit index. $D^{(k,m)}$ acts on the kth qubit of $\rho^{(m)}$. The Z gates applied in the error-correction steps and the measurement of the syndrome are assumed to be noiseless. This is natural since the Pauli phase flips Z may be omitted as physical operations and instead accounted for in the classical syndrome processing. We will include the effect of measurement errors in the analysis when we consider the more sophisticated protocols, that have higher thresholds than the 3-copy protocol. If we consider the effect of $\mathrm{T}^{(k)}$ only on $\langle \mathrm{K}_j \rangle$ in state $\rho^{(0)}$, then using Eq. (2) we can reduce the noise to an effective error. For every $k \in V : k \in \mathrm{neigh}(j) \cup \{j\}$

$$\mathrm{T}_{\mathrm{eff}}^{(k,j)}(\rho^{(0)}) = (1-\frac{p_2}{2})[I] + \frac{p_2}{2}[Z_j^{(0)}]. \tag{16}$$

If $k \notin \mathrm{neigh}(j) \cup \{j\}$ then $\mathrm{T}_{\mathrm{eff}}^{(k,j)}$ is just the identity map. Since every error channel commutes with every CNOT, we can model the noisy MCNOT as the ideal MCNOT followed by $|V|$ noise channels.

The error channel Eq. (15) is local (i.e. it acts only on qubit k in $\rho^{(m)}$ and $\rho^{(n)}$. Also the error operators are Pauli operators, which map graph states to graph states keeping ρ diagonal in the graph basis. Thus we can expect the noisy recursion relations to have the same form as Eq. (10). Considering only sub-protocol $P1$, the jth qubit in $\rho^{(0)}$ is affected by $2(d+1)$ error channels. The total probability that it is flipped by an error is $\frac{1-(1-p_2)^{2(d+1)}}{2}$. Thus, for qubits of color B

$$\langle \mathrm{K}_j \rangle' = \alpha^2 \langle \mathrm{K}_j \rangle^3, \tag{17}$$

where $\alpha = (1-p_2)^{(d+1)}$.

The situation is a little more complex for qubits of color A as the error in the MCNOT between $\rho^{(0)}$ and $\rho^{(1)}$ is propagated by the MCNOT between $\rho^{(0)}$ and $\rho^{(2)}$. However, the form of the recursion relation remains the same. We get

$$\langle \mathrm{K}_j \rangle' = \frac{\alpha^2}{2} \left(2 + \alpha^{-1} - \langle \mathrm{K}_j \rangle^2 \right) \langle \mathrm{K}_j \rangle. \tag{18}$$

For a derivation see Appendix A 2. Composing sub-protocols $P1$ and $P2$ we get the recursion relations for

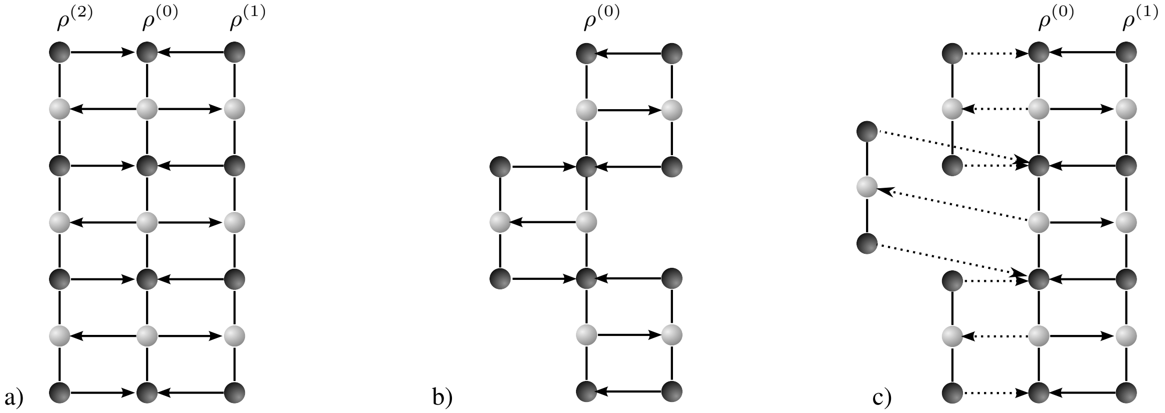

FIG. 3: The MCNOT for sub-protocol P_1 in a) The 3-copy protocol, b) The band-aid protocol and c) The conditional band-aid protocol. The dotted lines in c) indicate that the band-aids are applied only if there is an ambiguous syndrome at that location. Here we show graphs of degree 2, but these protocols can be applied to graphs of any degree.

the 3-copy protocol with noisy gates

$$\langle \mathrm{K}_j \rangle' = \begin{cases} \frac{\alpha^8}{8}\left(2+\alpha^{-1}-\langle \mathrm{K}_j\rangle^2\right)^3 \langle \mathrm{K}_j\rangle^3 & \text{if } j \in A, \\ \frac{\alpha^4}{2}\left(2+\alpha^{-1}-\alpha^4\langle \mathrm{K}_j\rangle^6\right) \langle \mathrm{K}_j\rangle^3 & \text{if } j \in B, \end{cases} \tag{19}$$

Here, qubits of color A behave worse. Solving the recursion relations for fixed points, we find that there are two non-trivial positive fixed points (see Appendix B) for $\alpha > 0.9902$. Consider the interval $[0,1]$. It has at most three fixed points $0 = f_0 < f_1 \leq f_2 \leq 1$. f_0 and f_2 are attractive while f_1 is repulsive. Thus f_2 will be a stable fixed point for $\alpha > 0.9902$ and $\langle \mathrm{K}_j\rangle_{\text{initial}} > f_1$. This gives a threshold for the noise affecting the gates that scales inversely proportional to the graph degree d,

$$p_{\text{th}} \approx \frac{9.8\times 10^{-3}}{d+1}. \tag{20}$$

Specifically for degrees 2 and 4 we obtain,

$$p_{\text{th}} = \begin{cases} 0.328\ \% \text{ for } d=2, \\ 0.197\ \% \text{ for } d=4. \end{cases} \tag{21}$$

This is a rather low value, but it will be substantially improved when we consider more sophisticated protocols.

We now show that the recursion relations Eq. (19) are valid regardless of whether or not the considered states are diagonal in the cluster basis. To see this, let us define a depolarization operator $\mathcal{D}$ which converts an arbitrary n-qubit mixed state ρ into an n-qubit mixed state $\rho_D = \mathcal{D}\rho$ that is diagonal in the cluster basis. $\mathcal{D}$ takes the form

$$\mathcal{D} = \left(\prod_{\boldsymbol{a}} \frac{[I]+[\mathrm{K}_{\boldsymbol{a},\boldsymbol{0}}]}{2}\right)\left(\prod_{\boldsymbol{b}} \frac{[I]+[\mathrm{K}_{\boldsymbol{0},\boldsymbol{b}}]}{2}\right), \tag{22}$$

where $\boldsymbol{a}$ and $\boldsymbol{b}$ are vectors in a basis of $\{0,1\}^{|V_A|}$ and $\{0,1\}^{|V_A|}$ respectively.

We only consider P1, the first round of the protocol. It is associated with a transformation $P1 : \rho \longrightarrow \rho' = \mathrm{R}\left(\rho^{\otimes 3}\right)$. R and $\mathcal{D}$ commute, i.e.,

$$\mathrm{R}\left((\mathcal{D}\rho)^{\otimes 3}\right) = \mathcal{D}\circ \mathrm{R}\left(\rho^{\otimes 3}\right), \tag{23}$$

for any ρ. For a proof see Appendix C.

Consider a recursion relation of the form

$$\langle \mathrm{K}_{\boldsymbol{a},\boldsymbol{b}}(\rho_D')\rangle = f_{\boldsymbol{a},\boldsymbol{b}}\left(\{\langle \mathrm{K}_{\boldsymbol{i},\boldsymbol{j}}(\rho_D)\rangle\}\right), \tag{24}$$

with $f_{\boldsymbol{a},\boldsymbol{b}}$ some function depending on $\boldsymbol{a},\boldsymbol{b}$ as in Eq. (13). Now,

$$\begin{aligned} \langle \mathrm{K}_{\boldsymbol{a},\boldsymbol{b}}(\rho_D')\rangle &= \mathrm{Tr}\left(\mathrm{K}_{\boldsymbol{a},\boldsymbol{b}}\,\mathrm{R}\left((\mathcal{D}\rho)^{\otimes 3}\right)\right) \\ &= \mathrm{Tr}\left(\mathrm{K}_{\boldsymbol{a},\boldsymbol{b}}\,\mathcal{D}\circ\mathrm{R}\left(\rho^{\otimes 3}\right)\right) && \text{(by Eq. (23))} \\ &= \mathrm{Tr}\left(\mathcal{D}^\dagger(\mathrm{K}_{\boldsymbol{a},\boldsymbol{b}})\rho'\right) && \text{(trace cyclicity)} \\ &= \langle \mathrm{K}_{\boldsymbol{a},\boldsymbol{b}}(\rho')\rangle. && (\mathcal{D}^\dagger \equiv \mathcal{D}) \end{aligned}$$

Similarly, $\langle \mathrm{K}_{\boldsymbol{i},\boldsymbol{j}}(\rho_D)\rangle = \langle \mathrm{K}_{\boldsymbol{i},\boldsymbol{j}}(\rho)\rangle$, such that

$$\langle \mathrm{K}_{\boldsymbol{a},\boldsymbol{b}}(\rho')\rangle = f_{\boldsymbol{a},\boldsymbol{b}}\left(\{\langle \mathrm{K}_{\boldsymbol{i},\boldsymbol{j}}(\rho)\rangle\}\right). \tag{25}$$

Thus, a recursion relation of the form of Eq. (24) such as Eq. (19) holds for all states ρ and not just for diagonal states $\rho_D = \mathcal{D}\rho$.

IV. IMPROVED PROTOCOLS

A. The error model

In the following, we consider a scenario where graph states are created locally from product states, then distributed to several parties and subsequently purified. Errors occur in each of these steps. Specifically,

- There is a two qubit error T Eq. (15) associated with each C-PHASE gate in the creation of the graph state, with probability p_2

- A local depolarizing error with probability p_1 occurs on each graph state qubit during transmission
- Every CNOT gate used in purification carries a 2-qubit error Eq. (15), with error probability p_2. Every measurement is modeled by a one qubit depolarizing channel with error probability p_2 followed by a perfect measurement.

B. The band-aid protocol

In order to raise the threshold of the 3-copy protocol, we will try to combine the strategies of error-correction and post-selection (which has a higher threshold). One way to do this is to use small highly purified GHZ states, i.e. band-aids, to purify the graph one vertex at a time. The usual MCNOT is performed between the band-aid and the large graph state as shown in Fig. 3b. This copies information about the central vertex into the band-aid which is then measured to give a syndrome. Since the band-aid is highly purified (for example by post-selection), it doesn't pollute the large state much. It is important to note that the error correction is still local, and we expect the recursion relations to be de-coupled as in the case of the 3-copy protocol.

The band-aid protocol also has two sub-protocols. The first one $P1$ is

i. Partition the graph into two colors A and B ($V = V_A \cup V_B$ and $V_A \cap V_B = \varnothing$).

ii. The band-aids are placed over the large state such that each central qubit of the band-aid is over a vertex of qubit A for all qubits of color A. Perform the MCNOT as shown in Fig. 3b

iii. Measure the central qubit of each band-aid in the X basis and the other qubits in the Z basis. For each band-aid multiply the measured eigenvalues. If the product is (-1)1 then the syndrome bit σ_j is (1)0.

iv. Apply the correction $\prod_{j\in A} Z_j^{\sigma_j}$ to the large state.

$P2$ is the same as $P1$, with the roles of colors A and B reversed.

Consider sub-protocol $P1$. For qubits of color B the argument is very similar to the 3-copy protocol, except that each qubit is affected by 2 gates from each of d band-aids. Thus,

$$\langle \mathrm{K}_j\rangle' = (1-p_2)^{2d}\,\langle \mathrm{K}_j\rangle\,\langle \mathrm{K}_j\rangle_b^{d}\,, \tag{26}$$

where $\langle \mathrm{K}_j\rangle_b$ is the constant initial purity of the band-aid.

For qubits of color A, first suppose that the CNOT gates are ideal. Then, a simple transfer of purity occurs.

$$\langle \mathrm{K}_j\rangle' = \langle \mathrm{K}_j\rangle_b\,. \tag{27}$$

If the gates are noisy, Eq. (27) is multiplied by a noise factor of the form $(1-p_2)^{f(d)}$ as in the case of the 3-copy protocol. There is a subtlety involving the temporal ordering of the band-aids. The band-aids do not all commute with each other. There are $1 + d(d-1)$ band-aids that affect qubit j. One of them is the band-aid that is used to purify the qubit. On average $k = \frac{d(d-1)}{2}$ of the rest will be applied before the purifying one. Any effect from the k prior band-aids will be erased by the purifying band-aid (See Eq. (27)). The purifying band-aid has $d+1$ noisy CNOTs affecting $\langle \mathrm{K}_j\rangle$, since the noisy MCNOT is modeled as an ideal MCNOT followed by noise, no information about the noise is propagated to the band-aid. Thus, the noise will commute with the error correction procedure. Since a measurement error that flips the central qubit of the band-aid will cause us to apply the wrong error correction operator, it can also be reduced to an effective error as given by Eq. (16). Thus, $f(d) = 2(d+1) + k$ and we have

$$\langle \mathrm{K}_j\rangle' = (1-p_2)^{\frac{d(d+3)+4}{2}}\,\langle \mathrm{K}_j\rangle_b\,. \tag{28}$$

Combining sub-protocols $P1$ and $P2$, we get the recursion relations for the band-aid protocol with noisy gates as well as noisy measurements

$$\langle \mathrm{K}_j\rangle' = \begin{cases} (1-p_2)^{\frac{d(d+7)+4}{2}}\,\langle \mathrm{K}_j\rangle_b^{d+1} & \text{for } j \in A, \\ (1-p_2)^{\frac{d(d+3)+4}{2}}\,\langle \mathrm{K}_j\rangle_b & \text{for } j \in B. \end{cases} \tag{29}$$

The behavior of qubits of color A is worse and we will use their purity as the final purity of the large state.

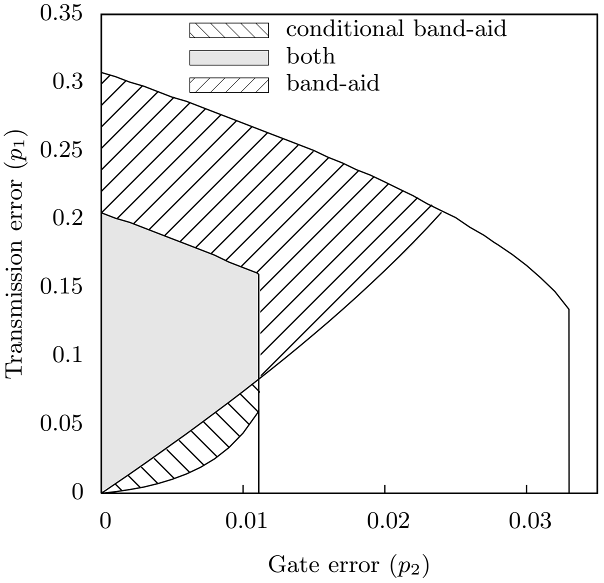

FIG. 4: Trade-off curves for the band-aid and conditional band-aid protocols ($d = 4$). The decreasing curves represent the breakdown of the post-selection protocol, when there is too much error. The increasing curves demarcate the region where the final purity of the purified states is higher than the purity of the unpurified states. It makes sense to purify in the shaded regions.

As per our error model in Section IV A, the noisy C-PHASE, C-NOT and measurement gates are parametrized by p_2. The noisy transmission channel is parametrized by p_1. For the final result, we need to know the quality of the band-aids. We assume that these are also created locally, then transmitted and purified. The band-aids however, are of fixed size and may thus be purified by the post-selection protocol [9] with the higher threshold. The output quality of the purified band-aids is, to leading order in p_2

$$\langle \mathrm{K}_j \rangle_b = 1 - (d+1)p_2, \tag{30}$$

such that

$$\langle \mathrm{K}_j \rangle = 1 - \frac{1 - d(3d+11) + 6}{2} p_2, \tag{31}$$

for small p_2. As Eq. (31) shows, with increasing graph degree the effect of errors in the purification process is strongly enhanced. One may therefore ask the question whether it is useful to purify at all or whether the transmitted state should be used right away. To decide this we compute $\langle \mathrm{K}_j \rangle$ after graph state creation and transmission,

$$\langle \mathrm{K}_j \rangle = (1 - p_2)^{\frac{d(d+1)}{2}} (1 - p_1)^{d+1}. \tag{32}$$

See Appendix D for a derivation. We compare this expression with Eq. (29) and find that there is indeed a parameter region where it makes sense to purify. This region is displayed for graphs of degree $d = 4$ in Fig. 4. It is bounded from above and right by the curve which indicates the breakdown of the band-aid purification according to the post-selection protocol [9]. In general, the threshold of the band-aid protocol for degree d graph states equals the threshold for purification of a $d+1$ qubit GHZ state with the post-selection protocol [8]. However, the output purity of the band-aid protocol is smaller. Only above the ascending curve is it advantageous to purify.

C. The conditional band-aid protocol

In order to correct the d^2 dependence of the fixed point in the band-aid protocol, we will combine it with the 3-copy protocol. The hybrid protocol, called the conditional band-aid protocol, sacrifices in threshold to improve the fixed point. The fixed point behavior, at least to linear order in gate noise, is almost as good as that of the post-selection protocol.

This protocol proceeds in the same fashion as the 3-copy protocol, except that two copies are used per round and wherever a measurement of K_j yields eigenvalue -1 (i.e. an error), a post-selected band-aid is applied to purify qubit j (See Fig. 3). For small gate noise, we expect to have to apply only a few band-aids per round, nonetheless, the threshold is set by the qubits to which we have to apply band-aids. Locations where a measurement of K_j yields 1 are error free to lowest order. Once again, we have two sub-protocols, P_1 and P_2 each purifying a different color.

The analysis is similar to that used in arriving at Eq. (19) for the 3-copy protocol. However, the situation is complicated by the fact that the band-aids are applied conditioned on the results of measuring $\rho^{(1)}$. As a result, the recursion relations for the one point correlators are no longer completely de-coupled. We can however find a simple lower bound on them.

Define $\langle \mathrm{K}_b \rangle$ to be the minimum purity of the post-selected band-aid. It is a constant. For simplicity we assume that all qubits in the band-aid have this purity. As before, we assume that the graph of the large state is translationally invariant, i.e. all vertices have the same degree. The definition $\beta \equiv (1 - p_2)^2 \langle \mathrm{K}_b \rangle$ will be useful. Consider qubits of color A in sub-protocol P_1, then by a derivation similar to Eq. (18)

$$\langle \mathrm{K}_j \rangle' = \frac{\alpha}{2} \left(2\alpha \langle \mathrm{K}_j \rangle + \langle \mathrm{K}_b \rangle - \alpha \langle \mathrm{K}_b \rangle \langle \mathrm{K}_j \rangle^2 \right), \tag{33}$$

where $\alpha = (1 - p_2)^{d+1}$ as before.

So far, we have been exact. Now consider sub-protocol P_2. Again focus on qubits of color A. Break P_2 down into two steps. In step one, we apply the MCNOT to $\rho^{(0)}$ and $\rho^{(1)}$. It can be readily verified that $\langle \mathrm{K}_j \rangle \mapsto \alpha \langle \mathrm{K}_j \rangle^2$. In step two, band-aids conditioned on the measurement outcome are applied to qubits of color B. Let $\boldsymbol{y} \in \{0,1\}^d$ be the measurement results for the neighbors of qubit j. A measurement result of one means a band-aid must be applied at that location. If a band-aid is applied to a neighbor of j, $\langle \mathrm{K}_j \rangle$ is affected by the errors on the band-aid, characterized by $\langle \mathrm{K}_b \rangle$ and by two noisy CNOTs. Thus $\langle \mathrm{K}_j \rangle \mapsto \beta^{|\boldsymbol{y}|} \langle \mathrm{K}_j \rangle$. Summing over measurement outcomes and including step one, we get

$$\langle \mathrm{K}_j \rangle' = \alpha \left(\sum_{k=0}^{d} \left(\sum_{|\boldsymbol{y}|=k} q_{\boldsymbol{y}} \beta^k \right) \right) \langle \mathrm{K}_j \rangle^2, \tag{34}$$

where $q_{\boldsymbol{y}}$ is the probability of measurement outcome $\boldsymbol{y}$. Unfortunately, $q_{\boldsymbol{y}}$ is a function of the general stabilizer expectation values $\langle \mathrm{K}_{\boldsymbol{a},\boldsymbol{b}} \rangle$, so we will resort to finding a lower bound. Since $q_0 = 1 - \sum_{\boldsymbol{y} \neq 0} q_{\boldsymbol{y}}$, we can rewrite the above equation as

$$\begin{aligned} \langle \mathrm{K}_j \rangle' &= \alpha_a \left((1 - \sum_{\boldsymbol{y} \neq 0} q_{\boldsymbol{y}}) + \sum_{k>0}^{d} \sum_{|\boldsymbol{y}|=k} q_{\boldsymbol{y}} \beta^k \right) \langle \mathrm{K}_j \rangle^2 \\ &\geq \alpha \left(1 - (1 - \beta^d) \sum_{\boldsymbol{y} \neq 0} q_{\boldsymbol{y}} \right) \langle \mathrm{K}_j \rangle^2, \end{aligned}$$

using $\beta \leq 1$ to arrive at the inequality.

Now, q_0 is just the probability that no error is detected on any of the neighbors of j. Let p_j be the probability of detecting an error on site j. Then by definition, $\langle \mathrm{K}_i \rangle = 1 - 2\sum_{y|y_i=1} q_y$. This implies that $\sum_{\boldsymbol{y}\neq 0} q_{\boldsymbol{y}} \leq \sum_{i\in \mathrm{neigh}(j)} \frac{1-\langle \mathrm{K}_i\rangle}{2}$. Putting this into the above inequality,

$$\langle \mathrm{K}_j \rangle' \geq \alpha \left(1 - \frac{d}{2}(1-\beta^d)\,(1-\langle \mathrm{K}_i\rangle)\right) \langle \mathrm{K}_j\rangle^2 , \qquad (35)$$

where $\langle \mathrm{K}_i \rangle$ is the purity of qubits of color B from the previous round.

Solving for the fixed point, we get, to leading order in gate noise p_2,

$$\langle \mathrm{K}_j \rangle = 1 - 2(d+1)p_2. \qquad (36)$$

Comparing this to Eq. (30), we see that the fixed point scaling with degree is almost as good as in the post-selection protocol. We now apply the conditional band-aid protocol to the same situation; of a graph state being shared amongst widely separated parties, as for the band-aid protocol. The results for a degree four state are plotted in Fig. 4. We see that the threshold (upper) curve is worse, whereas the fixed-point (lower) curve is better for this protocol, as compared to the band-aid protocol. The total purifiable area is smaller, indicating that it breaks down faster. In some sense, we have traded threshold for fixed point. These conclusions hold for arbitrary degree and the curves are independent of the size of the state, making this protocol eminently suitable for the purification of large bi-colorable graph states.

V. CONCLUSION AND OUTLOOK

We have described novel purification protocols for bi-colorable graph states and discussed their performance. The criteria for our protocols are that they do not break down in the presence of small amounts of noise in the purification process, that they have a high purification threshold and good output quality, scale efficiently and are analytically tractable.

Our final protocol can, for relevant graph states of degree 4, tolerate 1% gate or 20% local transmission error. These are about 1/3 and 2/3 of the respective values for the post-selection protocol [8, 9]. However, in contrast to this reference protocol, our protocol scales efficiently with the graph size.

All our protocols can be treated analytically. In particular, for the 3-copy protocol we derive closed, exact one-dimensional recursion relations in the appropriate observables, irrespective of the size of the state.

We would like to comment on the influence of the graph degree for the purification threshold. First note that for the three-copy protocol of Section III, in the case of perfect purification gates, the recursion relations Eq. (10) are completely independent of the graph structure, and so are the thresholds Eq. (11). This behavior changes if noise is included in the purification. The critical noise level per purification gate—at which the protocol breaks down—scales inversely proportional with the graph degree. The unfavorable dependence on the graph degree is present in all three protocols we discuss. Thus, the lesson we learn for the case of noisy purification is "Beware of large graph degrees". Large graph degrees occur, for example, in graphs states corresponding to codewords of concatenated CSS-codes.

We would also like to comment on the structure of the non-trivial fixpoint in our protocols. In the case of erroneous purification gates, the nontrivial fixed point is not completely specified by the lowest order expectation values $\langle \mathrm{K}_j \rangle$ and it remains to be discussed which error correlations are removed by the purification protocol. As a first result in this direction, for the 3-copy protocol discussed in Section III we have shown (in Appendix A 3) that correlations of stabilizer expectation values located on non-overlapping supports are not introduced by the purification procedure if they are absent initially. This implies that such correlations are absent in all purified states which end up at the same fixed point as the perfect state. We show in Appendix B that the fixed point for two-generator correlations with distinct support is unique, which is enough to establish the result that all states at the fixed point obey the relation $\langle \mathrm{K}_i\, \mathrm{K}_j \rangle = \langle \mathrm{K}_i \rangle \langle \mathrm{K}_j \rangle$ for such correlations.

A question of further interest is whether the non-trivial fixed point of the protocol is unique at all levels of correlations. This would imply $\langle \mathrm{K}_{\boldsymbol{i}+\boldsymbol{j}} \rangle = \langle \mathrm{K}_{\boldsymbol{i}} \rangle \langle \mathrm{K}_{\boldsymbol{j}} \rangle$ for all correlations with distinct supports.

Another question of further interest is whether the described or related protocols may be used to boost the threshold value for fault-tolerant quantum computation [20, 21, 22, 23, 24] based on graph states.

Acknowledgments

We would like to thank John Preskill, Frank Verstraete, Jiannis Pachos, Maarten van den Nest, Eric Hostens, Akimasa Miyake, Wolfgang Dür, Simon Anders, Hans Briegel, Panos Aliferis and Krittika Kanjilal for useful discussions. KG is supported by DOE Grant No. DE-FG03-92-ER40701. RR has been supported at Caltech by MURI under Grant No. DAAD19-00-1-0374 and by the National Science Foundation under contract number PHY-0456720, and is supported by NSERC of Canada and MRI of Ontario. Additional support was provided by the KITP Santa Barbara during the workshop "Topological Phases and Quantum Computation" and by the Austrian Academy of Sciences.

APPENDIX A: GENERALIZED RECURSION RELATIONS

We now derive the generalized recursion relations (Eq. (13)) for the 3-copy protocol. While the method used for this derivation is less intuitive, it yields recursion relations for arbitrary stabilizer elements and can handle noisy gates easily.

1. Noiseless Gates

In order to derive Eq. (13) we work in the *stabilizer basis*. Because $\rho^{(0)}$ is diagonal and the set $\{\langle \mathrm{K}_{\boldsymbol{a},\boldsymbol{b}}\rangle\}$ where $\boldsymbol{a} \in \{0,1\}^{|V_A|}, \boldsymbol{b} \in \{0,1\}^{|V_A|}$ forms a complete set of observables, we can write an expansion $\rho^{(0)} = \frac{1}{2^{|V_A|+|V_B|}} \sum_{\boldsymbol{a},\boldsymbol{b}} \langle \mathrm{K}_{\boldsymbol{a},\boldsymbol{b}}\rangle \mathrm{K}_{\boldsymbol{a},\boldsymbol{b}}$.

Consider sub-protocol P_1, that purifies the A sub-graph. The initial state is $\rho^{(0)} \otimes \rho^{(1)} \otimes \rho^{(2)}$, which can be re-written as a sum over $\boldsymbol{a}, \boldsymbol{b}$ of terms of the form

$$\langle \mathrm{K}_{\boldsymbol{a}^{(0)},\boldsymbol{b}^{(0)}}\rangle \langle \mathrm{K}_{\boldsymbol{a}^{(1)},\boldsymbol{b}^{(1)}}\rangle \langle \mathrm{K}_{\boldsymbol{a}^{(2)},\boldsymbol{b}^{(2)}}\rangle \times \mathrm{K}_{\boldsymbol{a}^{(0)},\boldsymbol{b}^{(0)}} \mathrm{K}_{\boldsymbol{a}^{(1)},\boldsymbol{b}^{(1)}} \mathrm{K}_{\boldsymbol{a}^{(2)},\boldsymbol{b}^{(2)}} . \tag{A1}$$

Performing step ii, this term becomes

$$\langle \mathrm{K}_{\boldsymbol{a}^{(0)},\boldsymbol{b}^{(0)}}\rangle \langle \mathrm{K}_{\boldsymbol{a}^{(1)},\boldsymbol{b}^{(1)}}\rangle \langle \mathrm{K}_{\boldsymbol{a}^{(2)},\boldsymbol{b}^{(2)}}\rangle \times \mathrm{K}_{\boldsymbol{a}^{(0)}+\boldsymbol{a}^{(1)}+\boldsymbol{a}^{(2)},\boldsymbol{b}^{(0)}} \mathrm{K}_{\boldsymbol{a}^{(1)},\boldsymbol{b}^{(0)}+\boldsymbol{b}^{(1)}} \mathrm{K}_{\boldsymbol{a}^{(2)},\boldsymbol{b}^{(0)}+\boldsymbol{b}^{(2)}} . \tag{A2}$$

Now consider step iii. Suppose we get measurement outcomes $\boldsymbol{\lambda}^{(1)}, \boldsymbol{\lambda}^{(2)}$ for the stabilizers in sub-graph A on copies $\rho^{(1)}, \rho^{(2)}$. Then the resultant state is given by applying the projector

$$\frac{1}{2^{2|V_A|}} \prod_{j=1}^{|V_A|} [\mathrm{I}] \otimes \left([\mathrm{I}] + (-1)^{\lambda_j^{(1)}} \mathrm{K}_j^{(1)} \right) \otimes \left([\mathrm{I}] + (-1)^{\lambda_j^{(2)}} \mathrm{K}_j^{(2)} \right) \tag{A3}$$

This projector acts trivially on $\rho^{(0)}$, so in the following we track only what happens to the kets in the Hilbert spaces of $\rho^{(1)}, \rho^{(2)}$. After applying the projector Eq. (A3) to the term Eq. (A2), we have a sum over all binary vectors $\boldsymbol{J}^{(1)}, \boldsymbol{J}^{(2)} \in \{0,1\}^{|V_A|}$ of terms of the form

$$\frac{(-1)^{\boldsymbol{\lambda}^{(1)}\cdot \boldsymbol{J}^{(1)} + \boldsymbol{\lambda}^{(2)}\cdot \boldsymbol{J}^{(2)}}}{2^{2|V_A|}} \mathrm{K}_{\boldsymbol{a}^{(1)}+\boldsymbol{J}^{(1)},\boldsymbol{b}^{(0)}+\boldsymbol{b}^{(1)}} \times \mathrm{K}_{\boldsymbol{a}^{(2)}+\boldsymbol{J}^{(2)},\boldsymbol{b}^{(0)}+\boldsymbol{b}^{(2)}} ,$$

where $\cdot$ denotes the bitwise inner product. Discarding $\rho^{(1)}, \rho^{(2)}$, we perform a partial trace over these systems (recalling that $\mathrm{K}_{\boldsymbol{a},\boldsymbol{b}}$ are all traceless except $\mathrm{K}_{\boldsymbol{0},\boldsymbol{0}} = \mathrm{I}$). Inserting the matrix element from system-0 back in, we get the term

$$\delta_{\boldsymbol{b}^{(0)},\boldsymbol{b}^{(1)}} \delta_{\boldsymbol{b}^{(1)},\boldsymbol{b}^{(2)}} \frac{(-1)^{\boldsymbol{\lambda}^{(1)}\cdot \boldsymbol{a}^{(1)} + \boldsymbol{\lambda}^{(2)}\cdot \boldsymbol{a}^{(2)}}}{2^{2|V_A|}} \times \mathrm{K}_{\boldsymbol{a}^{(0)}+\boldsymbol{a}^{(1)}+\boldsymbol{a}^{(2)},\boldsymbol{b}^{(1)}} , \tag{A4}$$

where $\delta_{\boldsymbol{p},\boldsymbol{q}}$ is the Kronecker delta on each component of $\boldsymbol{p}, \boldsymbol{q}$. Note that we must have $\boldsymbol{b}^{(0)} = \boldsymbol{b}^{(1)} = \boldsymbol{b}^{(2)}$ or the term goes to zero.

Now examine the action of the Pauli [Z] operator in this basis. $[\mathrm{Z}]\, \mathrm{K}_{\boldsymbol{a},\boldsymbol{b}} = \mathrm{Z}\, \mathrm{K}_{\boldsymbol{a},\boldsymbol{b}}\, \mathrm{Z} = -1^k\, \mathrm{K}_{\boldsymbol{a},\boldsymbol{b}}$, where $k = 0$ iff Z and $\mathrm{K}_{\boldsymbol{a},\boldsymbol{b}}$ commute. Effectively, Z is a diagonal matrix with entries ±1. Identical reasoning applies to X and Y. This will make it very easy to add gate noise into the analysis. It also allows us to say that the net effect of the error-correction step iv is to multiply Eq. (A4) by a factor of $(-1)^{(\boldsymbol{\lambda}^{(1)} \times \boldsymbol{\lambda}^{(2)})\cdot (a_0+a_1+a_2)}$, where $(\boldsymbol{p} \times \boldsymbol{q})_j \equiv p_j \cdot q_j$. Changing basis to $\boldsymbol{a} \equiv \boldsymbol{a}^{(\boldsymbol{0})} + \boldsymbol{a}^{(\boldsymbol{1})} + \boldsymbol{a}^{(\boldsymbol{2})}$, $\boldsymbol{b} \equiv \boldsymbol{b}^{(0)}$. Then the term becomes

$$\delta_{\boldsymbol{b},\boldsymbol{b}^{(\boldsymbol{1})}} \delta_{\boldsymbol{b},\boldsymbol{b}^{(\boldsymbol{2})}} \frac{(-1)^{\boldsymbol{\lambda}^{(1)}\cdot \boldsymbol{a}^{(1)} + \boldsymbol{\lambda}^{(2)}\cdot \boldsymbol{a}^{(2)} + (\boldsymbol{\lambda}^{(1)} \times \boldsymbol{\lambda}^{(2)})\cdot \boldsymbol{a}}}{2^{2|V_A|}} \mathrm{K}_{\boldsymbol{a},\boldsymbol{b}}$$

Note that in this notation, and ignoring the delta functions, the original coefficient in Eq. (A1) is $\langle \mathrm{K}_{\boldsymbol{a}+\boldsymbol{a}^{(1)}+\boldsymbol{a}^{(2)},\boldsymbol{b}}\rangle \langle \mathrm{K}_{\boldsymbol{a}^{(1)},\boldsymbol{b}}\rangle \langle \mathrm{K}_{\boldsymbol{a}^{(2)},\boldsymbol{b}}\rangle$.

Summing over measurement outcomes, the coefficient of $\mathrm{K}_{\boldsymbol{a},\boldsymbol{b}}$ is

$$\langle \mathrm{K}_{\boldsymbol{a}+\boldsymbol{a}^{(1)}+\boldsymbol{a}^{(2)},\boldsymbol{b}}\rangle \langle \mathrm{K}_{\boldsymbol{a}^{(1)},\boldsymbol{b}}\rangle \langle \mathrm{K}_{\boldsymbol{a}^{(2)},\boldsymbol{b}}\rangle \times \sum_{\boldsymbol{\lambda}^{(1)},\boldsymbol{\lambda}^{(2)}} \frac{1}{4} (-1)^{\boldsymbol{\lambda}^{(1)}\cdot \boldsymbol{a}^{(1)} + \boldsymbol{\lambda}^{(2)}\cdot \boldsymbol{a}^{(2)} + (\boldsymbol{\lambda}^{(1)} \times \boldsymbol{\lambda}^{(2)})\cdot \boldsymbol{a})}$$

The sum can be re-expressed as

$$\prod_{j=1}^{|V_A|} \frac{1}{4} (-1)^{\lambda_j^{(1)}\cdot a_j^{(1)} + \lambda_j^{(2)}\cdot a_j^{(2)} + \lambda_j^{(1)}\cdot \lambda_j^{(2)}\cdot a_j} .$$

If $a_j = 0$, then the jth term is zero unless $a_j^{(1)} = a_j^{(2)} = 0$, in which case it is 4. Hence for the term $\langle \mathrm{K}_{\boldsymbol{a}+\boldsymbol{a}^{(1)}+\boldsymbol{a}^{(2)},\boldsymbol{b}}\rangle \langle \mathrm{K}_{\boldsymbol{a}^{(1)},\boldsymbol{b}}\rangle \langle \mathrm{K}_{\boldsymbol{a}^{(2)},\boldsymbol{b}}\rangle$ to survive the procedure, we must have $\boldsymbol{a}^{(1)}, \boldsymbol{a}^{(2)} \ll \boldsymbol{a}$. If this holds, then an overall factor of $2^{|V_A|-|\boldsymbol{a}|}$ comes out. If $a_j = 1$, then a straightforward calculation shows that the jth term contributes a factor of $2(-1)^{a_j^{(1)}\cdot a_j^{(2)}}$. The overall numerical factor is thus $\frac{1}{2^{|\boldsymbol{a}|}}$. To get the new value of $\langle \mathrm{K}_{\boldsymbol{a},\boldsymbol{b}}\rangle$, we simply sum over $\boldsymbol{a}^{(1)}, \boldsymbol{a}^{(2)}$ since these and only these will contribute to the support of $\mathrm{K}_{\boldsymbol{a},\boldsymbol{b}}$ under P1. This gives Eq. (13)

2. Noisy Gates

Adding noise to the gates requires very little additional work. We can rewrite the depolarizing channel on qubit j of copy k as

$$D_j^{(k)}[\rho] = \frac{1}{2} \left([\mathrm{I}] + [\mathrm{Z}]_j^{(k)} \right) \frac{1}{2} \left([\mathrm{I}] + [\mathrm{X}]_j^{(k)} \right) [\rho] \equiv P_Z^{(j,k)} P_X^{(j,k)}$$

We have written the noise channel in this form to illustrate how the noise components act as projectors $P_{Z_j}^{(k)}$, $P_{X_j}^{(k)}$, since the effective Pauli operators have ±1 on the diagonal. If a specific ket is affected by noise on site j of copy k, it will be an eigenvector of $D_j^{(k)}$ with zero eigenvalue.

The noise from a CNOT at site j between copies i and k is

$$E_j^{(i),(k)} \equiv (1-p_2) + p_2(P_{Z_j}^{(i)} P_{X_j}^{(i)})(P_{Z_j}^{(k)} P_{X_j}^{(k)}) \qquad \text{(A5)}$$

If a ket $\mathrm{K}_{\boldsymbol{a},\boldsymbol{b}}$ is affected by any of these noise terms (that is, if the noise anti-commutes with $\mathrm{K}_{\boldsymbol{a},\boldsymbol{b}}$), it will be projected to zero and thus acquire a $(1-p_2)$ multiplier overall.

The noise from the first MCNOT is $E_{01} \equiv \prod_j E_j^{(0),(1)}$, and from the second MCNOT is $E_{02} \equiv \prod_j E_j^{(0),(2)}$. Clearly the overall multiplier is independent of the measurement outcomes, so the analysis for Eq. (A3) still holds. The recursion relations are then similar in structure to Eq. (13), except that coefficients dependent on $(1-p_2)$ are inserted before each term.

We illustrate this by calculating the recursion relations for $\langle \mathrm{K}_j \rangle$. Specializing to single point stabilizers, let d_j be the degree of j. If $j \in B$, there is no sum, and $\langle \mathrm{K}_j \rangle \to E_j \langle \mathrm{K}_j \rangle^3$. The only noise terms that anti-commute with $\mathrm{K}_{\boldsymbol{j}}$ (and hence give factors of $(1-p_2)$) are those in $j \cup N_j$. There are $2(d+1)$ of these (since there are two sets of noisy gates), so $\langle \mathrm{K}_j \rangle \to (1-p_2)^{2(d+1)} \langle \mathrm{K}_j \rangle^3$, which is Eq. (17).

Now suppose $j \in A$. Let $\boldsymbol{j} = (0, \ldots, 0, j, 0, \ldots, 0)$. Our sum is over $\boldsymbol{a}^{(1)}, \boldsymbol{a}^{(2)} \in \{\boldsymbol{0}, \boldsymbol{j}\}$, and $\boldsymbol{b} = \boldsymbol{0}$. Since we are interested only in $\langle \mathrm{K}_j \rangle$, our effective noise model is $[\mathrm{X}]_k \mapsto [\mathrm{Z}]_j \forall k \in N_j$ and $[\mathrm{X}]_j \mapsto [\mathrm{I}]$. All other noise terms do not affect the state. Then

$$E_{01} \mapsto \Big((1-p_2) + p_2 P_Z^{(j,0)} P_Z^{(j,1)}\Big)^{d+1}. \qquad \text{(A6)}$$

A similar replacement holds for E_{02}. E_{01} acts on terms $\mathrm{K}_{\boldsymbol{j}+\boldsymbol{a}^{(1)}+\boldsymbol{a}^{(2)},\boldsymbol{0}} \mathrm{K}_{\boldsymbol{a}^{(1)},\boldsymbol{0}}$, and gives a factor of 1 iff $\boldsymbol{j}+\boldsymbol{a}^{(1)}+\boldsymbol{a}^{(2)} = \boldsymbol{0}, \boldsymbol{a}^{(1)} = \boldsymbol{0} \Rightarrow \boldsymbol{j} = \boldsymbol{a}^{(2)}, \boldsymbol{a}^{(1)} = \boldsymbol{0}$, and a factor of $(1-p_2)^{d+1}$ otherwise.

Performing the MCNOT between $\rho^{(0)}$ and $\rho^{(2)}$, the noise channel E_{02} acts on the kets $\mathrm{K}_{\boldsymbol{j}+\boldsymbol{a}^{(1)},\boldsymbol{0}} \mathrm{K}_{\boldsymbol{a}^{(2)}}$, which gives a factor of 1 iff $\boldsymbol{j}+\boldsymbol{a}^{(1)} = \boldsymbol{0}, \boldsymbol{a}^{(2)} = \boldsymbol{0}$ and $(1-p)^{d+1}$ otherwise. Putting in each of the four cases $a_j^{(1)}, a_j^{(2)} \in \{0,1\}$ gives us Eq. (18).

3. Behavior of Correlations

If we take two qubits j, k such that $\mathrm{neigh}(j) \cap \mathrm{neigh}(k) = \oslash$, then the noise terms on sites in $\mathrm{neigh}(k) \cup k$ do not affect terms involving j and vice-versa. Hence the sum over terms in the recursion relation for $\langle \mathrm{K}_{jk} \rangle$ will factor into $\langle \mathrm{K}_j \rangle \langle \mathrm{K}_k \rangle$. If initially $\langle \mathrm{K}_j \, \mathrm{K}_k \rangle = \langle \mathrm{K}_j \rangle \langle \mathrm{K}_k \rangle$, then the 3-copy protocol will not generate any new correlations between these regions.

APPENDIX B: UNIQUENESS OF THE FIXED POINT

Here we show that the 3-copy protocol has a unique fixed point for stabilizer elements $\langle \mathrm{K}_{\boldsymbol{a},\boldsymbol{b}} \rangle$ with weight $w = |\boldsymbol{a}| + |\boldsymbol{b}| \leq 2$. The recursion relations for stabilizer elements of weight $w > 1$ (see Eq. (12)) depend only on stabilizer elements whose weight is at most w. Thus, we can use an inductive argument. If all the stabilizer elements of weight less than w have reached a fixed point, they become constants and then the recursion relation for elements of weight w will have the same form as those for weight one (i.e. they will depend only on stabilizer elements of weight w). First consider the case when $|\boldsymbol{a}|, |\boldsymbol{b}| \leq 1$. The recursion relations have the form

$$\begin{aligned} f(z) &= az + bz^3 \\ g(z) &= cz + dz^3, \end{aligned}$$

with $a, c > 0$ and $bd < 0$. The presence of noise doesn't change the form of the recursion relations, it only multiplies each term by a number between zero and one (see Section A 2). Let $y = z^2$ and $x = dy + c$. Define

$$p(x) := f(g(z))/z - 1 = bx^4 - bcx^3 + adx - d.$$

Without loss of generality, assume $b < 0$. The signature of $p(x)$ is

$$\begin{aligned} p(x) &: -++- \\ p(-x) &: ----. \end{aligned}$$

Then by Descartes' Rule of Signs [25], $p(x)$ has at least two complex roots. Thus the recursion relation $f(g(z)) = z$ has at most two positive fixed points. The recursion relation $g(f(z)) = z$ can be analyzed identically. It was already argued in Section III B that this means that there is a unique attractive fixed point.

Now consider the case $|\boldsymbol{a}| = 2$ and $|\boldsymbol{b}| = 0$. The recursion relations now have the form

$$\begin{aligned} f(z) &= az^3 + bz + c \\ g(z) &= dz^3. \end{aligned}$$

It is easily checked that a, c and d are positive. The sign of b is harder to fix, but we note that for there to be a fixed point at all, b must be negative. The case $f(g(z)) = z$ is easily analyzed as above, to show that there are at most two positive roots. Let $p(z) = g(f(z))$. To conclude the proof we need two technical results. 1) If the smallest support expectation value $\langle \mathrm{K}_a \rangle$ has reached its fixed point value $\langle \mathrm{K}_a \rangle_{\mathrm{fp}}$ then the physically allowed values for $\langle \mathrm{K}_{a+a'} \rangle$ form the interval $I = [2 \langle \mathrm{K}_a \rangle_{\mathrm{fp}} - 1, 1]$. 2) $f(z) \geq 0$ for all $z \in I$. Proof of 1. a) z allowed $\Rightarrow z \in I$: $P = \frac{1-\mathrm{K}_a}{2} \frac{1-\mathrm{K}_{a'}}{2}$, with $a \neq a'$, is a projector, hence $\langle P \rangle \geq 0$. Thus $z = \langle \mathrm{K}_{a+a'} \rangle \geq \langle \mathrm{K}_a \rangle + \langle \mathrm{K}_{a'} \rangle - 1$ (*). Evaluate (*) at fixed point $\langle \mathrm{K}_a \rangle_{\mathrm{fp}}$. $z \leq 1$ is obvious. b) $z \in I \Rightarrow z$ allowed: For an initial state of the protocol, interpolate between $\rho_1 = \langle \mathrm{K}_a \rangle_{\mathrm{fp}} \, \rho_{++} + (1 - \langle \mathrm{K}_a \rangle_{\mathrm{fp}})/2 \, (\rho_{+-} + \rho_{-+})$ and $\rho_2 = \langle \mathrm{K}_a \rangle_{\mathrm{fp}} \, \rho_{++} + (1 - \langle \mathrm{K}_a \rangle_{\mathrm{fp}}) \rho_{--}$. (The signs "±" refer to the eigenvalues of K_a and $\mathrm{K}_{a'}$, respectively.) Proof of 2. Be $\langle \mathrm{K}_a \rangle_{\mathrm{fp}}, \langle \mathrm{K}_b \rangle_{\mathrm{fp}} > 0$ and $z \in I$. Assume as an hypothesis $f(z) < 0$. Apply (*) to the state after application of P1, at the fixed point $\langle \mathrm{K}_a \rangle_{\mathrm{fp}}$, $\forall a \in A$. Hence $0 \geq f(z) \geq 2 \langle \mathrm{K}_b \rangle_{\mathrm{fp}} - 1$. (Under P1 the fixed point value $\langle \mathrm{K}_a \rangle_{\mathrm{fp}}$ for $a \in A$ is mapped to $\langle \mathrm{K}_b \rangle_{\mathrm{fp}}$ for $b \in B$, assuming all vertices have the same degree.) Thus, $\langle \mathrm{K}_b \rangle_{\mathrm{fp}} \leq 1/2$. But then $\langle \mathrm{K}_b \rangle_{\mathrm{fp}} = 0$. Contradiction. Hence $f(z) \geq 0$.

Now, $p''(z) = g''(f(z)) f'(z)^2 + g'(f(z)) f''(z)$ such that, with 2), $p'' \geq 0$ for all $z \in I$. Thus, $p(z)$ is convex on I. With 1), I is a single interval such that $p(z)$ and z intersect at most twice in I. At most one of these fixed points is attractive.

APPENDIX C: THE DEPOLARIZING OPERATOR

In order to prove that the depolarizing operator $\mathcal{D}$ defined in Eq. (22) commutes with the evolution operator $\mathrm{R} = \mathrm{Tr}_{(1,2)} \, M \circ \mathcal{E} \circ U$, we note that the protocol step P1 consists of a unitary part U, an error channel $\mathcal{E}$ comprising probabilistic Pauli errors and a measurement $\mathrm{Tr}_{(1,2)} \, M$, where M is a projector. U consists of a set of transversal CNOT-gates and acts on the stabilizer as

$$\begin{array}{rcl} \mathrm{K}^{(0)}_{\boldsymbol{a},\boldsymbol{b}} & \longrightarrow & \mathrm{K}^{(0)}_{\boldsymbol{a},\boldsymbol{b}} \, \mathrm{K}^{(1)}_{\boldsymbol{a},\boldsymbol{0}} \, \mathrm{K}^{(2)}_{\boldsymbol{a},\boldsymbol{0}}, \\ \mathrm{K}^{(1)}_{\boldsymbol{a},\boldsymbol{b}} & \longrightarrow & \mathrm{K}^{(1)}_{\boldsymbol{a},\boldsymbol{b}} \, \mathrm{K}^{(0)}_{\boldsymbol{0},\boldsymbol{b}}, \\ \mathrm{K}^{(2)}_{\boldsymbol{a},\boldsymbol{b}} & \longrightarrow & \mathrm{K}^{(2)}_{\boldsymbol{a},\boldsymbol{b}} \, \mathrm{K}^{(0)}_{\boldsymbol{0},\boldsymbol{b}} \,. \end{array} \tag{C1}$$

Now note that $\frac{[I]+[\mathrm{K}^{(1)}_{\boldsymbol{0},\boldsymbol{b}} \, \mathrm{K}^{(0)}_{\boldsymbol{0},\boldsymbol{b}}]}{2} \frac{[I]+[\mathrm{K}^{(0)}_{\boldsymbol{0},\boldsymbol{b}}]}{2} \frac{[I]+[\mathrm{K}^{(2)}_{\boldsymbol{0},\boldsymbol{b}} \, \mathrm{K}^{(0)}_{\boldsymbol{0},\boldsymbol{b}}]}{2} = \frac{[I]+[\mathrm{K}^{(0)}_{\boldsymbol{0},\boldsymbol{b}}]}{2} \frac{[I]+[\mathrm{K}^{(1)}_{\boldsymbol{0},\boldsymbol{b}}]}{2} \frac{[I]+[\mathrm{K}^{(2)}_{\boldsymbol{0},\boldsymbol{b}}]}{2}$ etc, such that

$$U \circ \mathcal{D}^{(0)} \mathcal{D}^{(1)} \mathcal{D}^{(2)} = \mathcal{D}^{(0)} \mathcal{D}^{(1)} \mathcal{D}^{(2)} \circ U. \tag{C2}$$

The operations $\mathcal{D}^{(0)} \mathcal{D}^{(1)} \mathcal{D}^{(2)}$ and $\mathcal{E}$ commute because both are linear combinations of Pauli super-operators,

$$\mathcal{E} \circ \mathcal{D}^{(0)} \mathcal{D}^{(1)} \mathcal{D}^{(2)} = \mathcal{D}^{(0)} \mathcal{D}^{(1)} \mathcal{D}^{(2)} \circ \mathcal{E}. \tag{C3}$$

The measurements comprising $\mathrm{Tr}_{(1,2)} \, M$ are of stabilizer operators $\mathrm{K}^{(1)}_{\boldsymbol{0},\boldsymbol{b}}$, $\mathrm{K}^{(2)}_{\boldsymbol{0},\boldsymbol{b}}$ on the states $\rho^{(1)}$, $\rho^{(2)}$, respectively. They are performed via one-qubit measurements and classical post-processing. $\mathrm{K}^{(1)}_{\boldsymbol{0},\boldsymbol{b}}$, $\mathrm{K}^{(2)}_{\boldsymbol{0},\boldsymbol{b}}$ commute with the Kraus operators in (22), such that

$$\begin{aligned} \underset{(1,2)}{\mathrm{Tr}} \, M \circ \mathcal{D}^{(0)} \mathcal{D}^{(1)} \mathcal{D}^{(2)} &= \underset{(1,2)}{\mathrm{Tr}} \, \mathcal{D}^{(0)} \mathcal{D}^{(1)} \mathcal{D}^{(2)} \circ M \\ &= \mathcal{D}^{(0)} \circ \underset{(1,2)}{\mathrm{Tr}} \, M. \end{aligned} \tag{C4}$$

Eqs. (C2), (C3) and (C4) yield Eq. (23)

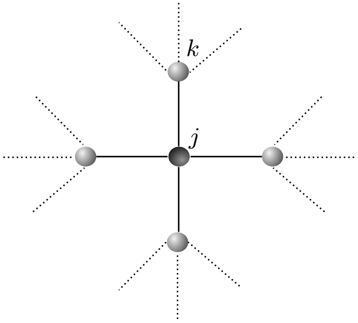

FIG. 5: Creation of a degree ($d = 4$) bi-colorable graph state, the figure will have the same local structure for other degrees/topologies as long as its edges are d-colorable and its vertices are bi-colorable

APPENDIX D: CREATION OF A BI-COLORABLE GRAPH STATE

Here we discuss the noise structure of a bi-colorable graph that is created using noisy C-PHASE gates. The noisy gates are modeled as the ideal gate followed by two qubit depolarizing noise as defined in Eq. (15). The graph state is created by performing C-PHASE gates between qubits in the $|+\rangle$ state. The noise structure of the final state depends on the temporal ordering of these gates. If we assume that the underlying graph has constant degree d and that its edges are d-colorable, then the N qubit graph state can be created in d timesteps with Nd C-PHASE gates. At each timestep all the gates corresponding to edges of a particular color are performed. Thus, at every timestep $t \in \{1, \ldots, d\}$, each qubit is affected by an error channel of the form of Eq. (15).

We are interested in the value of $\langle \mathrm{K}_j \rangle$, so we focus on the neighborhood of qubits j in the larger graph. Since the graph is bi-colorable, it contains no three cycles, and one can draw a diagram of the form of Fig. 5. The gates are represented by both solid as well as dashed lines. The noise channels corresponding to the solid lines each contribute an effective error $\mathrm{T}_{\mathrm{eff}}$ as defined in Eq. (16) to qubit j. Now consider the qubit k which is a neighbor of the central qubit j. Each dashed line also contributes an effective error $\mathrm{T}_{\mathrm{eff}}$ to qubit j, but only if the C-PHASE gate corresponding to the solid line between k and j was performed in a previous timestep. This is because Z_k errors commute with K_j and X_k errors would be propagated by the C-PHASE to $\mathrm{X}_k \, \mathrm{Z}_j$ errors, that also commute with K_j. Thus there are a total of $\frac{d(d-1)}{2} + d = \frac{d(d+1)}{2}$ noise channels affecting the qubit j. This gives,

$$\langle \mathrm{K}_j \rangle = (1 - p_2)^{\frac{d(d+1)}{2}}. \tag{D1}$$

---

[1] A. Ekert, Phys. Rev. Lett. **67**, 661 (1991).

[2] K. Chen and H.-K. Lo (2004), arXiv:quant-ph/0404133.

[3] D. Gottesman and I. L. Chuang, Nature (London) **402**, 390 (1999).

[4] R. Raussendorf and H. Briegel, Phys. Rev. Lett. **86**, 5188 (2001), eprint, arXiv:quant-ph/0010033.

[5] C. H. Bennett, G. Brassard, S. Popescu, B. Schumacher, J. A. Smolin, and W. K. Wootters, Phys. Rev. Lett. **76**, 722 (1996).

[6] C. Bennett, D. DiVincenzo, J. Smolin, and W. Wootters, Phys. Rev. A **54**, 3824 (1996).

[7] H.-K. Lo and H. F. Chau, Science **283**, 2050 (1999).

[8] W. Dür, H. Aschauer, and H.-J. Briegel, Physical Review Letters **91**, 107903 (2003).

[9] H. Aschauer, W. Dür, and H.-J. Briegel, Phys. Rev. A **71**, 012319 (2005).

[10] E. Hostens, J. Dehaene, and B. D. Moor (2005), arXiv:quant-ph/0510096.

[11] A. Miyake and H. J. Briegel, Phys. Rev. Lett. **95**, 220501 (2005).

[12] W. Dür, H.-J. Briegel, J. I. Cirac, and P. Zoller, Phys. Rev. A **59**, 169 (1999).

[13] S. Bravyi (2005), arxiv:quant-ph/0511178.

[14] H. Aschauer and H. J. Briegel, Phys. Rev. Lett. **88**, 047902 (2002).

[15] B. M. Terhal and G. Burkard, Phys. Rev. A **71**, 012336 (2005).

[16] P. Aliferis, D. Gottesman, and J. Preskill, Quant. Inf. Comput. **6**, 097 (2006).

[17] R. Klesse and S. Frank, Phys. Rev. Lett. **95**, 230503 (2005).

[18] W. Dür, M. Hein, J. I. Cirac, and H.-J. Briegel, Phys. Rev. A **72**, 052326 (2005).

[19] C. Kruszynska, S. Anders, W. Dür, and H. J. Briegel (2005), arXiv:quant-ph/0512218.

[20] M. A. Nielsen and C. M. Dawson, Phys. Rev. A **71**, 042323 (2005), arXiv:quant-ph/0405134.

[21] C. M. Dawson, H. L. Haselgrove, and M. A. Nielsen, Phys. Rev. Lett. **96**, 020501 (2006), arXiv:quant-ph/0509060.

[22] P. Aliferis and D. W. Leung, Phys. Rev. A **73**, 032308 (2006).

[23] M. Varnava, D. E. Browne, and T. Rudolph (2005).

[24] R. Raussendorf, J. Harrington, and K. Goyal (2005), arXiv:quant-ph/0510135.

[25] D. Smith and M. Latham, *The Geometry of Rene Descartes with a facsimile of the first edition* (Dover Publications, New York, 1954).